VOLUME I

Coastal Engineering

1974 PROCEEDINGS

PROCEEDINGS OF THE

Fourteenth
Coastal Engineering
Conference

June 24-28, 1974 • Copenhagen, Denmark

Volume I

AMERICAN
SOCIETY OF
CIVIL
ENGINEERS
FOUNDED
1852

ACKNOWLEDGMENTS

FOREWORD

These International Conferences on Coastal Engineering have grown over the years since 1950 in attendance, in the number of papers presented, and in scope of engineering and scientific content There has been an even greater increase in the work of arranging for a conference--a task which, if well done, gives the erroneous impression of requiring little effort The physical arrangements and the social events of this conference have been superbly done and the Coastal Engineering Research Council and the other sponsoring organizations are most grateful to Chairman Sørensen, Professor Lundgren and the Copenhagen Organizing Committee.

As these conferences have grown in international standing, the number of interesting papers by qualified authors submitted for consideration has increased so greatly as to preclude scheduling all of them in a full week of parallel sessions. The onerous task of selection from among papers of high quality was carried out by the Papers Committee and the Council as equitably as they knew how to do—but, under the circumstances, there may have been some inequities in the choices made—and to those authors so affected the Council is sincerely apologetic.

A topic of considerable professional importance to engineers engaged in coastal work is the scarcity of statistical data on wave action—and the incompleteness of much of the data available This situation becomes both surprising and disturbing, in view of the fact that the effect of ocean waves is a unique characteristic of coastal engineering and that the solution of almost every coastal problem involves consideration of the incident wave climate. There are many natural phenomena for which long-time records and extensive geographical coverage are readily available—rainfall, stream flow, solar radiation, wind velocity, cloud cover and many more, but—the climatology of ocean waves, a phenomenon of overriding importance to coastal engineers and scientists, is fragmentary and much of it is of questionable validity Space does not permit a full discussion of this serious deficiency in the basis for sound planning and design. Providing these data will require national or international programs of observation and analysis Where such programs are inadequate, or lacking entirely, coastal engineers should exert their influence to bring them about under the auspices of a permanent public agency and to put the data in form for engineering and scientific application

Morrough P O'Brien, Chairman
Coastal Engineering Research Council
American Society of Civil Engineers

CONTENTS

THEME SPEAKERS

PART I

THEORETICAL AND OBSERVED WAVE CHARACTERISTICS

CONTENTS

CONTENTS

CONTENTS

CONTENTS

CONTENTS

CONTENTS

CONTENTS

CONTENTS

CONTENTS

CONTENTS

CONTENTS

CONTENTS

CONTENTS

CONTENTS

CONTENTS

CONTENTS

STUDIES IN COASTAL GEOMORPHOLOGY

CONTRIBUTING TO COASTAL ENGINEERING

André Guilcher, University of Western Brittany

Brest, France

INTRODUCTION

The first point to examine in this lecture is why the coastal geomorphologist
thinks he is able to bring a contribution in civil engineering applied to
coastal problems.

One answer to this question is that the main purpose of the geomorphologist
is to explain the coastal landforms - spits, estuaries, tidal marshes,
deltas, coral reefs, and so on - and that the understanding of processes
in evolution is necessary when the engineer wants to act on natural features
in order to modify them artificially. As a matter of fact, the engineer him-
self tries often to explain these features, but in such a case he becomes
a geomorphologist. Instead of one man acting in both fields, research and
engineering, we may conceive a collaboration between two men acting simultan-
eously.

On the other hand, the geomorphologist does not restrict his scope to the
study of the landforms in themselves, but he extends his investigations to
the sediments. It is widely accepted that sedimentology is included in geo-
morphology, provided the sediments are not studied without other purpose
than their own properties and characteristics, but if these properties are
considered to be an element in explanation of landforms. The geomorphological
features, spits, deltas, and so on, are often completely made of sediments,
or it may happen also that the sediments, when contributing for a small part
to the bulk of the features, give essential data on the origin and develop-
ment of the landforms. So, this is another aspect which must be considered.

Thirdly, the geographer is convinced that his action consists essentially
in pointing to relations between phenomena instead of investigating them
separately, because this line in thought is the best way to discover
explanations. And, as a matter of fact, the geomorphologist is a geographer
in a number of countries, as, for example, in Germany, France, Poland, the
USSR, also very often in England, the Netherlands and Denmark, and even in
the United States sometimes, although more unfrequently. In the coastal
field of research, the consideration of different facts examined together
leads to pay attention to certain consequences of some civil engineering

1

works, whereas these consequences would not have been perceived otherwise.
The result is that the geographical treatment of coastal problems may be
fruitful in that it may avoid errors and thus save money.

Examples of these different points will be given in this lecture. They will
be taken often, although not exclusively, from the speaker's personal
experience.

SIGNIFICANCE OF OBLIQUE RUNNELS AND RIDGES

Runnels and ridges are frequently met with on the lower part of wide
sandy beaches. Generally they run parallel to the general direction of the
beach, but they may be sometimes oblique to the trend of the shoreline.
This is the case, for example, on the coast of the Landes of Gascony
(Guilcher, Godard and Visseaux, 1952), in South-West Lancashire, in Picardy
at the South of the mouth of the Somme River, and along the so-called Langue de
Barbarie (Guilcher and Nicolas, 1954), a long spit between the lowermost
course of the Senegal River and the Atlantic Ocean. As an average, these
features are some hundreds of metres long (from 100 metres to more than 1 km);
they occur in sets, the distal end of the ridges lying always in the same
direction: South in the Landes of Gascony and on Langue de Barbarie, North
in Picardy and in Lancashire. Observations made during several weeks have
shown that they correspond to long sequences of moderate surf, while they
tend to be levelled after periods of heavy surf lasting for several days.

Oblique runnels and ridges are associated with the predominance of an
oblique swell. This conclusion derives from investigations including the
consideration of swell, wind, coastal current and beach evolution. It
was especially supported by observations in the Landes and in Senegal.
In both cases the swell is generated in the storm belt of temperate
latitudes, and has little to do with the local winds, even on the Landes
coast in spite of its location in longitude. The waves travel from
WNW or NW, and, consequently, the coastal drift runs to the South. The
oblique ridges, which tend to face the dominant wave attack, and thus
illustrate Lewis' (1931, 1938) and Schou's (1945) principles in beach
evolution, may be interpreted as an adaptation en échelon of the beach to
the swell. In Picardy, the wave attack by the swell travelling in the
English Channel causes a coastal drift to the North East, resulting similarly
in oblique ridges and runnels.

The conclusion is that, when oblique ridges occur on a beach, they can be
used to predict the direction of wave attack and coastal drift, even if
direct observations on waves and currents are not available. This feature
may thus be used in terms of coastal engineering, not only on outer coasts
as those of Gascony and Senegal, but even on inner coasts facing lagoons,
where waves running on very short fetches are also able to create oblique
ridges of shorter wave length. Example may be found on the inner side
of Magilligan spit, Lough Foyle, Northern Ireland, and in Rustico Lagoon,

Carte morphologique

Figure 2^A

Figure 2^B

Nord

Legend:
- Sable
- Dunes 4
- Dunes 5
- Dunes 6
- Direction des dunes
- Schorres, mangroves, marais au colmatage avancé
- Terrains construits

0 1 2 3 4 5 Km.
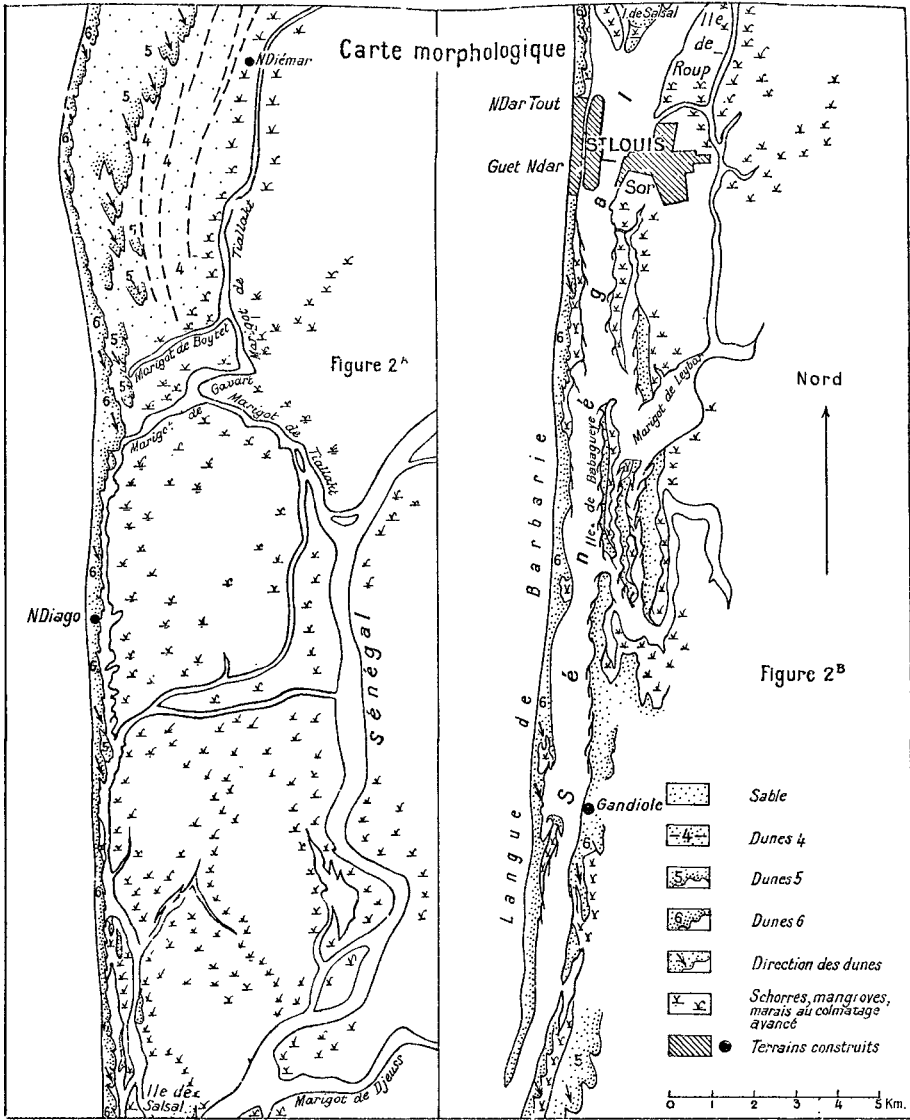
FIG. 1 – Langue de Barbarie along the lower course of Senegal River.

Figure 10
Ile de Babagueye

Sable

Crochets de sable

Direction des dunes

schorres mangroves

sable et vase

0   150   300   450m

SÉNÉGAL FL.

NDiago

Babagueye

Ile aux Bois

Ile de Safal

Langue de Barbarie

Salsal

Sénégal

Ile de Roup

StLouis

Figure 9
Répartition de la mangrove
sur le Sénégal
en amont de Saint-Louis

+   mangrove
terrains bâtis

0   1   2   3   4Km
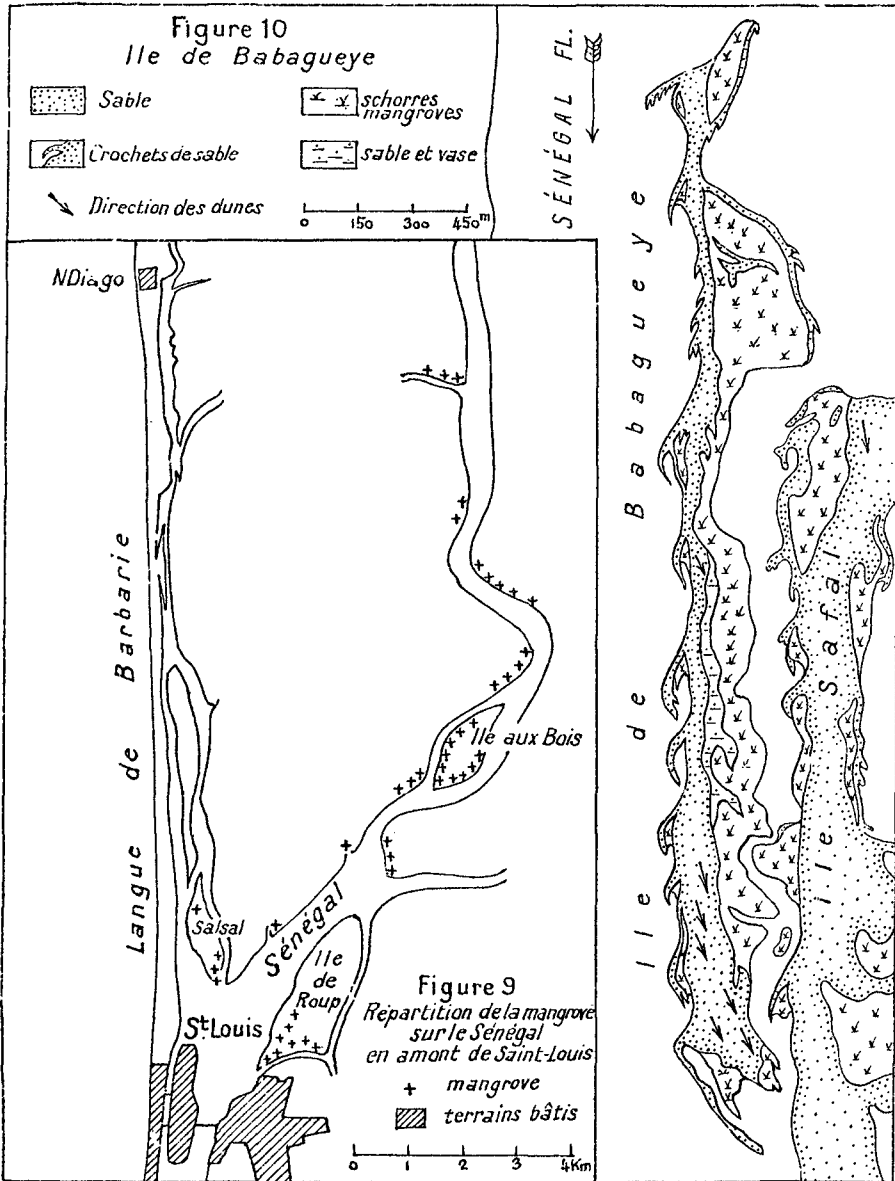
FIG. 2 - Spits of Azov type along Babagueye Island, lower course of Senegal River.
See location on figure 1.
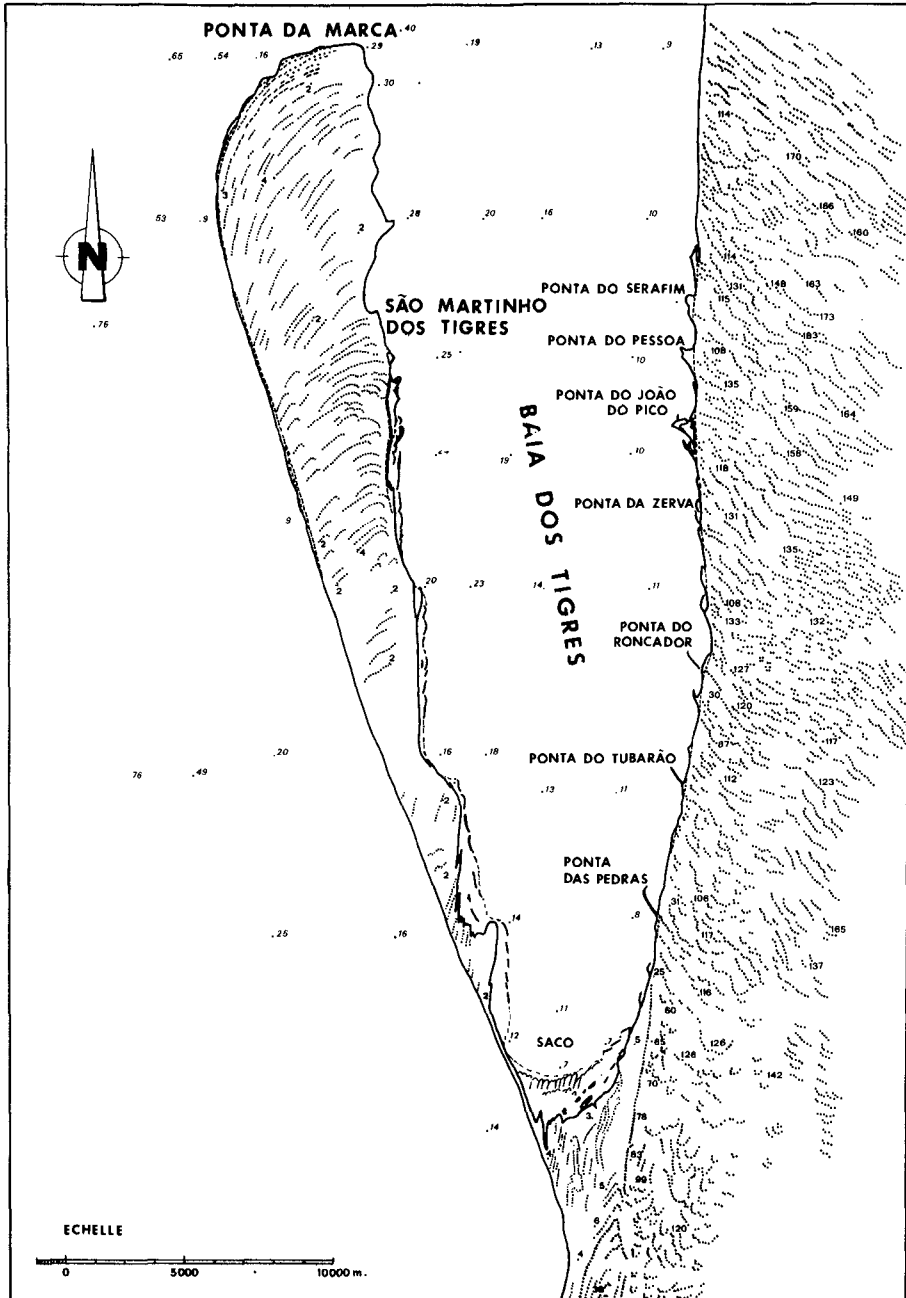
FIG. 3 - Tiger Bay and Spit, Angola. Smaller spits of Azov type on both sides of the bay.

North coast of Prince Edward Islsnd, Canada. In these cases, the waves are
obviously generated by the resultant of local winds.

SPITS OF AZOV TYPE IN LAGOONS

On the open sandy coasts of West Africa, from the Straits of Gibrsltar to
Capetown, the forces in action work in two opposite directions (Guilcher,
1954; Davies, 1972, p. 43, 141 and 144). In the northern section, as far
South as Southern Senegal, the dominant fsctor is the swell generated in the
storm belt of boreal temperate latitudes, as previously said, which results
in a coastal drift to the South. In the southern section, the symmetrical
dominant factor is the heavy swell generated in the Southern Ocean, which
travels from the Southwest or the South-South-West. It causes a coastal
drift to the North from Capetown to Gabon, and from Liberia to the Republic
of Guinea; and, on the North coast of the Gulf of Guinea, in Ivory Coast,
Ghana, Dahomey, Nigeria, the drift varies according to the angle of incidence
of the southern swell, in the different parts of the coast. The morphological
effect of the transport of sand by the coastal drift has been the creation
of large spits, especially in the southern section where the best ones are
Cape Lopez in Gabon, and the peninsulas of Luanda, Palmeirinhas, Lobito,
Porto Alexandre and Tigers in Angola (Guilcher, Medeiros, Esteves and
Oliveira, 1974). All grow, of course, from South to North. The largest
spit in the North is Langue de Barbarie, already mentioned.

On the lee, sheltered side of the spits, however, wide lagoons occur, where
waves generated by local winds replace the swell of foreign origin acting
on the outer coast. It happens that the resultant direction of wind action
is the same ss the coastal drift on the outer coast, namely, from North
to South in the North, and from South to North in the South.

The result of wind wave action on the lagoon shores has been the formation
of sets of spits, more or less evenly spaced, the best ones being found
behind Langue de Barbarie in Senegal (Guilcher and Nicolas, 1954), and in
Palmeirinhas and Tigers lagoons in Angola (Guilcher and others, 1974).
These spits, although much smaller than the outer spits which shelter them,
are distinctly larger than the oblique ridges snd runnels previously discussed;
in addition, these spits occur exclusively in lagoons while the oblique runnels
and ridges sre mostly found on outer coasts; so that it is necessary not
to confuse these two classes of spits.

Such sets of spits evoluting under the influence of wind waves in areas where
the dominant wind blows more or less parallel to the coast have been described
on coasts of the USSR by Zenkovich (1967, p. 141 and 515) and others, especially

on the northwestern coast of the Sea of Azov, as spits of Azov type. The
following explanation was put forward by Budanov (1956) to account for the
regular spacing of the spits which is a frequent feature in the type. The
regular spacing results from simplification by erosion of former intermediate
spits, as a consequence of transverse waves (i.e., running perpendicular to
the coast). The distance between the residual spits corresponds to the fetch
necessary to the waves formed in the main wind belt between spits to pre-
dominate over the transverse waves.

So far as the Azovian spits on West Africa are concerned, it seems that they
could be used for experiments in coastal engineering. Since the forces in
action are parallel on the outer and inner coasts, but weaker in the lagoon,
the Azovian spits may be considered as small scale features resembling those
used in artificial tanks, and coastal works planned for the outer beach
could be initially tested on these spits. One advantage of such tests re-
latively to those usually made in tanks is that the scale for experiments
would be considerably larger than in tanks, since the Azovian spits reach one
to several kilometres long, as for example in the Bay of Tigers, Angola
(Baia dos Tigres in Portuguese; Great Fish Bay on British charts). It
would be, of course, necessary to be cautious in extrapolation of results
to the outer coast; but the same remark may be made for results obtained
in tanks.

PROBLEMS IN DELTA GROWTH AND EROSION

Deltas are features which depend on a continuous excess of supply of
sediments by the river upon the redistribution far away of these sediments
by sea action. If, for some reason, the supply decreases, the equilibrium
can be broken and erosion can replace sedimentation on the delta front or
on spits depending directly on the delta. The decrease in supply may be
natural or artificial. Natural decreases may be caused, for example, by
changes in the river course and, consequently, affect only the part of the
delta which has been abandoned. Artificial decreases may result from dams
built upstream across the river and trapping the bedload and the sediments
in suspension.

Artificial decreases in supply by dams have appeared more and more fre-
quently in modern times, as a consequence of development in power production,
industrialization, and irrigation. Two examples will be quoted here: the
Nile delta in Egypt, and the Gatumbela delta in Angola.

The front of the Nile delta is presently suffering a severe erosion. The
shore retreat is especially large around the Damietta and Rosetta mouths,
but it occurs also in the centre, where another distributary ended at the
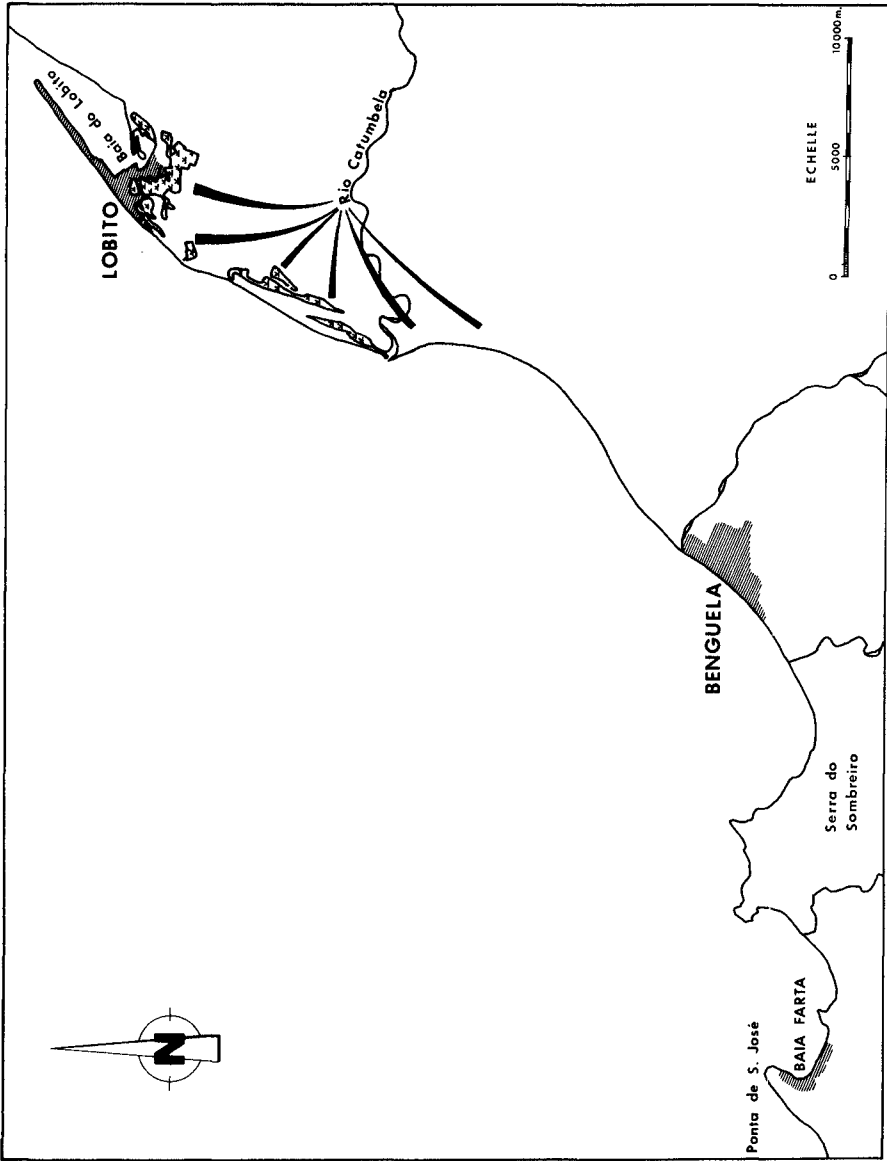
FIG. 4 - Lobito Spit, Angola, and its relation with Catumbela Delta.

time of the Pharaons. The retreat has begun after the building of the
first Aswan dam in 1902, and it increased afterwards. It has reached
several hundreds of metres in some places. It seems clear that the main,
if not unique, cause of the retreat is the building of the dam, which
has been much elevated and enlarged in recent times, and traps the sediments
coming previously from Ethiopia. These events have led the Egyptian
authorities to ask for scientific investigations, and an international
commission of geomorphologists was planned. Finally, the meeting of this
commission had to be postponed for several reasons. Anyhow, it appears
doubtful that the erosion could be stopped useless considerable protecting
works would be made, since the natural conditions have been completely
disturbed by the dam.

At Lobito, Angola (Guilcher and others, 1974), occurs one of the most
interesting spits of the coast of West Africa. The sediments included in
the spit derive from the delta of the Catumbela Rriver, which is partly
reworked by the southern swell (see above) and thus deflected to the
North. In present time, however, the Lobito spit suffers erosion as its
inner, southwestern end. This erosion is likely to be related to the building
of a dam on the lower course of the Catumbela River, although the relation
is not so certain than in the case of the Nile delta. Actually, the Lobito
harbour authorities are faced with two problems: erosion of the inner end
of the spit by lack of supply; and continuation of progradation of the
distal end by reworking of the material already included in the spit, which
tends to join the coast of the mainland and thus to close the harbour.

In cases such as the Nile delta and Lobito spit, the contribution of the
geomorphologist is to act as a geographer in showing relations between
phenomena, and, when dams are planned on a river which ends in a delta,
he has to give warning about the further evolution of the coast. He must
recall that a river is not isolated in Nature and that modifications on
one side can lead to other modifications on another side.

THE CASE OF LUANDA AND PALMEIRINHAS SPITS, ANGOLA

Luanda and Palmeirinhas spits are two major features in North Angola, 11 km
and 34 km long, not far apart, which are considered here because they
demonstrate how a spit cannot be studied in itself but must be replaced
in its environment, according to principles of graphical research (Guilcher
and others, 1974).

Palmeirinhas spit is presently vigorously fed with sand coming from the
South, as usually on this West African coast. Its growth continues to
go on at its distal end. A cut seems to have occurred temporarily in the

FIG. 5 - Luanda and Palmeirinhas Spits, Angola.

southwestern part of the spit, but this cut has been subsequently filled up and more active since a long time.

Luanda spit, on the contrary, which shelters the large commerical harbour of the city of Luanda, is presently a tiny and unstable feature, only 200 metres wide as an average; its main part has been recently an island (actually its name is La Ilha) and is presently connected with the mainland only by a bridge; its southwestern part is even more unstable and its shape is subject to frequent modifications. All these facts show that Luanda spit is a relict feature, which has been built in different conditions.

Geomorphological observations lead to the conclusion that the evolution of Luanda spit has been a function of the growth of Palmeirinhas spit. An examination of air photographs of the islands lying in Palmeirhinhas lagoon behind the spit, shows that one of these islands, Ilha São João do Cazanga, is probably the innermost, southwestern part of Luanda spit, since it is made of successive beach ridges which could not be shaped in the present situation. At that time, Ilha São João do Cazanga was not yet sheltered by Palmeirinhas spit; it was a living feature, under the influence of the oceanic swell. Subsequently, Palmeirinhas spit grew more and more, thus preventing any substantial sand supply to Luanda spit by coastal drift. Only small spits of Azov type are now formed in Palmeirinhas lagoon.

The knowledge of this evolution is obviously useful for the engineer who tries to prevent or to delay the decay of Luanda spit by the building of groynes or by other procedures.

THE CASE OF PITSUNDA DELTA, ABKHASIA, USSR

The Bzibi River, which flows to the Black Sea at Pitsunda, Abkhasia (Zenkovich, 1967, p. 364), has a large solid load as the other rivers of the south side of the Caucasus, as a result of the mountainous topography and the heavy rainfall under the Pontic climate. Consequently, it has built at present sea-level a delta, which is the successor of a Sarmatian (Miocene) delta now uplifted and truncated by cliffs. It is well known that the Black Sea coasts of the USSR, as well on the Caucasus side as in Crimea, have been chosen as sites for the setting of numerous holiday resorts, owing to their mild climate. Accordingly, the Soviet authorities have built a set of several big and high hotels on the delta front, just on the seashore, to allow the holiday-makers to enjoy the sandy beach immediately at their outdoors.

The trouble is that the Bzibi delta has been prograded on a submarine slope
cut by canyons or gullies and leading directly to depths exceeding 500 metres.
When the speaker visited Pitsunda in October, 1970, with other coastal geo-
morphologists, it was evident that the authorities had not taken into
account the submarine topography off the delta when the construction of
the group of hotels was decided: they considered only the charm of the
site. Afterwards, however, anxiety arose from warnings of Russian geo-
morphologists as V.P. Zenkovich. Studies were undertaken, which showed
that slumpings actually occur on the submarine slope in canyons and gullies
from time to time, at Pitsunda and in other places along the coasts of
Abkhasia and Georgia. In the speaker's opinion, the danger is extremely
serious, if the situation at Pitsunda is compared with what occurs from
time to time off Abidjan, Ivory Coast. In that area, a big submarine
canyon, the so-called Trou Sans Fond, occurs just in front of the the
coastline which consists of a sandy beach along which the material drifts
from West to East. The Trou Sans Fond engulfs periodically huge masses
of sand from the beach: perhaps 400 000 cubic metres per year, according
to Varlet (1958), (see also Martin, 1973). The most spectacular phenomenon
occurred in 1905. A sliding of the beach occurred and lasted for 35
minutes; the wharf,70 metres long, disappeared into the sea with its
warehouse; the coastline retreated for 60 to 80 metres, and the depth
just in front of the initial coastline increased from 5 to 25 metres.
Subsequently, the shore and foreshore were quickly reworked by the sea.

What has happend off Abidjan could well happen at Pitsunda. The difference
lies in the set of hotels built at Pitsunda. A slumping as quick as in Ivory
Coast would certainly result in an extremely heavy loss of lives, since
the people in the upper floors of the buildings could not escape owing to
the destruction of lifts and staircases by cracks and fissures preceding
the collapse. The Abkhasian authorities are now aware of this, and they
try to prevent a disaster by building groynes on the delta front to check
the lateral migration of sand. Such groynes, however, seem of little
efficiency relatively to the threat on the hotels, and it seems that the
best would have been not to build them just in front of the sea, but at
some hundreds of metres inside the delta. The preliminary consideration
of the geomorphology, the submarine processes in progress, and the com-
parison with Ivory Coast would have saved much trouble.

                    THE IMPACT OF TECTONICS

The geomorphologist does not consider only present-time features; he
tries to explain the present by the past, and his scope involves particu-
larly the tectonics, which can have acted in former times or are still in
progress. Of particular interest are the tectonics which have played a
role and are often still working in deltas, and in coastal plains such

as the Netherlands. The largest deltas in the world are usually old features, which include a huge pile of sediments, the deposition of which extended over tens of millions of years as a result of a long continued subsidence. Three examples will be quoted here among others,

The thickness of deposits in the Niger Delta amounted to 8,000 m since the Eocene, and their total volume is about 500,000 cubic kilometres (Hospers, 1970).

In the Mississippi Delta, the thickness of sediments has reached 19,000 metres since the end of the Oligocene (Crouch, 1959), and the quaternary terraces plunge beneath the recent sediments in the South, whereas they have been uplifted in the North, the contact between the uplift and the downthrow occurring along hinge line.

The Danube Delta is located at the contact between the southern end of the subsided Russian shield and the hercyno-cimmerian massif of Dobrogea; it is also a subsidence area, but possibilities of temporary upheavals alternating with downwarping persist and have lead to a complex mobilism during the Quaternary (Panin, 1972).

As to the coastal plain of the Netherlands, its downwarping is a part of the larger subsidence of the North Sea basin, which reached some 7500 to 9000 metres since the Carboniferous. The area of maximum depression has moved in the course of time: it seems to be located now in the northern-most parts of the Netherlands, whereas just before it was situated in the Velsen-Castricum region near Amsterdam, where the top of the Eemian marine deposits of the last Interglacial (more or less 100,000 years BP) lies at 27 m, or locally deeper, below the present datum at the Velsen excavation; whilst it is found at several metres above the same datum in presumably stable areas (Van Straaten, 1957).

Some of these subsidences have a real effect in modern times. In the Mississippi Delta, for example, where the active part of the structure shifts from place to place inside the general site which remains the same, the abandoned successive subdeltas are partly drowned although their age does not exceed a few thousand years: basins between distributaries are completely submerged, levees are hardly above water level while they initially supassed it for several metres. Compaction accounts for a part of this phenomenon, but subsidence is certainly associated (Russell, 1959; Guilcher, 1963). The Dutch coastal engineers are well aware of this for their country, where subsidence is largely taken into account in the huge works known as the Delta Plan, which were undertaken after the great storm surge of Jan. 31 and Feb. 1st, 1953, in Zeeland and in Holland. It is necessary that consideration of tectonics is made in civil engineering works in all other countries too.

MEASUREMENTS OF RATE OF SEDIMENTATION ON TIDAL MARSHES

Sedimentation by mud is a common process in estuaries and sheltered
bays around the world. In temperate countries where mangrove is absent,
two kinds of areas are distinguished in this environment: the lower one
is the mud flat, or slikke, which is devoid of vegetation; the upper one
is the tidal marsh, or schorre, which is covered by phanerogams accepting
a submerison in salt water during spring tides. At an intermediate level
a third zone often exists, the high slikke, which bears a vegetation of
Salicorniae growing in Spring and Summer and disappearing in Winter.

It may be interesting to engineers to know the rate and peculiarities of
sedimentation in this environment, because harbours are quite often situated
in estuaries. Consequently, they must know the contribution which has been
brought in this field by geomorphologists of Western Europe. The first
results were published by Richards (1934) for Denmark; they were followed
by Steers (1948, 1964) for England, and by Verger (1955), Guilcher and
Berthois (1957) and others for various marshes of Western France. A
fuller bibliography may be found in Guilcher and Berthois (1957).

The investigations bear mainly on tidal marshes or schorres, and accessorily
on high slikkes. They consist mainly in scattering by hand a thin layer
of sand by patches on the schorre under the vegetation cover. The patches
have 1 metre in diameter as an average and are located by a stake. The
sand is firstly protected by vegetation and subsequently buried under the
mud, so that it serves as a mark for further corings, which show the
thickness of sedimentation as a function time. The corings can be
repeated for many years. If sand patches are scattered in reasonable
number and in various sites across the marsh, the measurements carried
on regularly in all patches give an accurate idea of the rates of
sedimentation. Experiments on high slikkes are not so numerous than
on schorres; where they have been made, they show that the deposition of
mud is more rapid in these sites, which lie at a lower level and are more
frequently drowned, but also that deposition alternates with erosion, in
other words that the sedimentation is more irregular. On schorres or
tidal marshes, the rate of upward accretion depends on two main factors:
The altitude, from which derives the duration of submersion by sea water
at spring tides; and the distance from the main creeks acting as feeders
of muddy water.

In addition, other methods have been used by Guilcher and Berthois (1957).
They have measured the rate of horizontal retreat on micro-cliffs which
often separate the tidal marshes from the mud flats; they used for this
as land marks the stakes in the sand patches. They also took repeatedly
photographs from the same points in the same directions, in order to
visualize the general evolution of the marsh (especially the micro-cliffs)
during several years.

The results are diverse, because the natural conditions, and primarily
the mud supply, vary considerably from marsh to marsh and from estuary to
estuary. It is unnecessary to summarize here the figures which were ob-
tained from Denmark and Wales to Western France. What is of interest is
to know the existence of the method by sand scattering, and also its
limitation. As a matter of fact, it does not seem to be suitable for
tropical, or even subtropical, marshes, since in these areas many more
burrowing animals such as crabs and crocodiles dwell in the mud, and
would disturb the sand patches and prevent precise measurements.

ORIGIN OF ESTUARINE MUD; ITS PRACTICAL INTEREST

From numerous studies carried out in Europe and in America during the last
35 years and summarized by Guilcher (1967), it appears that the origin
of sediments in estuaries and sheltered bays is much more diverse than it
was thought just after the Second World War. Sometimes the sediments come
from the sea, as in the Dutch estuaries: this conclusion derives from
extremely accurate studies made in the Netherlands. It must be noticed,
however, that the material provided by the North Sea to the Dutch estuaries
was initially of continental origin, since it was carried by the icecaps
which covered that area during several periods of the Pleistocene. In
other cases, as in the small Breton estuaries and also in some places at
least in Kerry, Ireland, and in California, the mud is supplied from the
cliffs cutting the lower parts of the slopes of the estuaries themselves,
and providing periglacial material in Brittany and glacial material in
Kerry. But in several Breton estuaries, additional material comes from
dunes existing in front of the sea, the sand of which is pushed into the
estuary by wind or/and by tidal currents (examples found in Audierne,
in Le Conquet, in Aber Benoît, and in Laita River. See Cotton de Bennetot
and others, 1965, and Guilcher and Berthois, 1957). In still other
places, the sediments come from upstream by rivers, and such is the case
in most large estuaries, as the Loire estuary studied intensively by
L. Berthois (references in Guilcher, 1967). The main evidence in this
estuary is that the suspended-matter content is always higher at all
depths during the ebb than during the flood.

The origin of sediments is obviously of primary importance for engineers
when they try to prevent the sedimentation in harbour accesses. This is
why the civil engineering services of Nantes harbour asked for more than
ten years Prof. Berthois' collaboration, and gave him facilities to gather
a wealth of observations on currents, temperature, salinity, and suspended
matter content at many stations. Similar observations were made by the
same scientist with the help of local authorities in various countries such
as Guinea, French Guiana, Madagascar, etc., and this collaboration has
always proved fruitful.
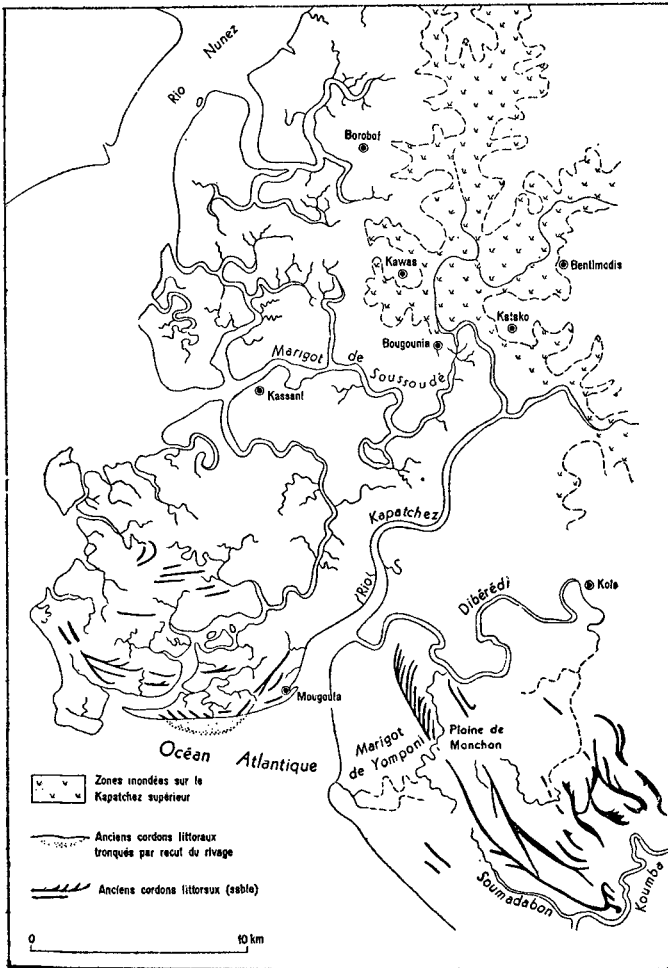
FIG. 6 - Kapatchez River, Republic of Guinea. The symbols
show in order: drowned areas around Upper
Kapatchez; old beach ridges truncated by shore
retreat; old beach ridges existing now.

A particularly typical case was observed in the Republic of Guinea
(formerly French Guinea: Guilcher, 1956-1959) where the Kapatchez River
was quickly filled in its inner reaches between 1930 and 1954 by a tre-
mendously muddy sedimentation at a time when other estuaries in the same
region were approximately in a state of equilbrium. A study was under-
taken by the speaker in 1954, in order to determine the origin of this
sudden deposition, which rendered the rice cultivation in the lowlands
almost impossible because it modified the circulation of fresh and salt
water. It was found, after elimination of other hypotheses, that the mass
of mud which settled in the inner part of the estuary came from old
mud flats in front of the open sea immediately west of the mouth of the
estuary. These mud flats were retreating rapidly in 1954, perhaps as a
consequence of recent changes in tidal currents, so that mud was put in
suspension, went into the estuary with the incoming tide, and settled
there at slack tide. These results were obtained by using typically
geomorphological methods: examination of vertical air photographs, which
showed an old system of coastal sandy ridges, which had developed from
East to West, and was truncated by coastal retreat as to leave intact
only their inner and outer ends. The critical point being thus located
on photographs, a visit of the shore allowed field observations which con-
firmed and precised the facts. To counteract the mud invasion it was
decided to connect the upper Kapatchez with another tidal river, the
Soussoude, and to cut the communication with the lower Kapatchez. The
case of Kapatchez River seems thus to be an excellent sample of coastal
geomorphology applied to estuarine management.

LAKE AHÉMÉ, DAHOMEY, AN EXAMPLE OF COASTAL
RESEARCH APPLIED TO FISHERIES MANAGEMENT

In 1957 the speaker was engaged in investigations in the coastal region
of Western Dahomey, where fishermen complained for a decrease in pro-
ductivity of fisheries in Lake Ahémé, which lies at some distance behind
the coast. The purpose of the research was to determine whether the
decrease was due to a quick silting up in the lake, and, if so, to
give advices about the works to undertake.

A general survey of the coastal region was made, including the lake of
course (Guilcher 1959 a, b and c). As usually on the North coast of the
Gulf of Guinea, the zonation includes present sandy ridges in front of
the ocean, and, behind them, a set of older ridges more or less preserved
and surrounded by swamps. Some of the old ridges may belong to the last
interglacial high sea level; the other ones are likely to be holocene.
Lake Ahémé is an old estuary which has been cut from the ocean by the
silting-up of the swamps and the progradation of the coastline. The
mechanism of fluviatile supply by the Mono River, the main river in the
country, and the Couffo River, which ends in Lake Ahémé, were analyzed,

and also the conditions in which these rivers flow to the sea (struggle between river current and surf, with seasonal variation in the former). Enquiries were also make in villages.

The conclusion was that the decrease in lake productivity was not due to natural causes. It is true that Lake Ahémé tends to become shallower by sedimentation, but the process of silting up in it must be very low. Actually, the diminution of the stock of fish has come from an over-fishing due to the increase of population. Consequently, it seemed ad-visable to develop fisheries in the sea, where they already existed, and cooperative organisms were actually organized with this purpose in 1959.

It must be pointed out that this investigation has saved much money in preventing useless and expensive works to dredge silt from Lake Ahémé. The research was not confined to pure physical geography: it has been a global enquiry, involving all aspects of the problem in physical, human, financial and political fields.

CONCLUSION

It thus seems that the contribution of the geomorphologist, or even better, of the geographer to coastal research is often fruitful. Along with the civil engineer, he is able to bring elements to solve coastal problems; he can suggest sometimes relations between phenomena of different orders which could have been forgotten without his intervention; he can save money in many instances. In present time, the progress in knowledge of coastal processes and evolution is so large that a recent geographical book by Davies (1972) includes excellent maps on a world wide scale on which diverse processes are indicated with their morphological conse-quences. This book, written by a geographer, should be widely used by all those who are in charge of coastal engineering.

REFERENCES

- Budanov, V. I., 1956. Observations on formation and development of spits of Azovian type. Trudy Okeanogr. Kom. Akad. Nauk SSSR, vol I: 90-97 (in Russian).

- Cotton de Bennetot, M., Guilcher, A., and Saint-Requier, A., 1965. Morphologie et sédimentologie de l'Aber Benoit, Finistére. Cah. Oceanogr., 17: 377-387

- Crouch, R. W., 1959. Inspissation of post-Oligocene sediments in southern Louisiana. Bull. Geol. Soc. Amer., 70: 1283-1292.

- Davies, J. L., 1972, Geographical variation in coastal development. Oliver and Boyd, Edinburg, 204 pp.

- Guilcher, A., 1954. Dynamique et morphologie des cotes sableuses de
  l'Afrique atlantique. Chhiers Inf. Géogr., 1: 57-68.

- Guilcher, A., 1956. L'envasement de l'estuaire du Rio Kapatchez (Guinéa
  Francaise) et ses causes. XVIIIe Congr. Int. Géorge., Rio de Janeiro,
  vol. 2 (published 1959) :241-247.

- Guilcher, A., 1959 a. La région cotière du Bas-Dahomey occidental. Bull.
  I.F.A.N., 21, B: 357-424.

- Guilcher, A., 1959 b. Coastal sand ridges and marshes and their continen-
  tal environment near Grand Popo an Ouidah, Dahomey. In: Second Coastal
  Geography Conference, Baton Rouge, Louisiana: 189-212.

- Guilcher, A., 1959 c. Travaux de géomorphologie appliquée dans le
  domaine littoral et estuarien. Rev. Geomorphol. Dyam., X: 145-147.

- Guilcher, A., 1963. Estuaries, deltas, shelf, slope. In: The Sea,
  ideas and observations, Hill Editor, New York and London, 3: 620-654.

- Guilcher, A., 1967. Origin of sediments in estuaries. In: Estuaries,
  Lauff editor, Am. Ass. Adv. Sci., Washington: 149-157.

- Guilcher, A., and Berthois, L., 1957. Cinq années d'observations sédimen-
  tologiques dans quatre estuaires-témoins de l'Ouest de la Bretagne.
  Rev. Géomorphol. Dynam., 8: 67-86.

- Guilcher, A., Godard, A., and Visseaux, E., 1952. Formes de plage et houle
  sur le littoral des Landes de Gascogne, particulièrement à Mimizan. Rev.
  Gèorg. Pyrénées et Sud-Ouest, 22:99-117

- Guilcher, A., Medeiros, C. A. Esteves de Matos, J., and Oliveira, J. T.
  1974. Les restingas (flèches littorales) d'Angola, spécialement celles
  du Sud et du Centre. Finisterra (Lisbon), in press.

- Guilcher, A., and Nicolas, J. P., 1954. Observations sur la Langue de
  Barbarie et les bras du Sénégal aux environs de Saint-Louis. Bull.
  Com. Océanogr. Et. Côtes, VI: 227-249.

- Hospers, J., 1970. The geology of the Niger delta area. Geol. East
  Atlantic Continental Margin, Symposium, Cambridge, 4:125-142.

- Lewis, W. V., 1931. The effect of wave incidence on the configuration of
  a shingle beach. Georg. Journ., 78:129-148.

- Lewis, W. V., 1938. The evolution of shoreline curves. Proc. Geol. Ass.,
  49:107-127.

- Martin, L., 1973. Morphologie, sédimentologie et paléogeégraphie au Quater-
  naire récent du plateau continental ivoirien. Thesis Paris 340 pp.

- Nielsen, N., 1935. Eine Methode zur exakten Sedimentationsmessung. Studien
  über die Marschbildung auf der Halbinsel Skalling. Kgl. Danske Vid.
  Selskub., Biol. Med., 12, 4, 98 pp.

- Panin, N., 1972. Histoire quaternaire du delta du Danube. Cercetari marine
  (Bucuresti), 4:5-15.

- Richards, F. J., 1934. The salt marshes of the Dovey estuary. IV; The
  rates of vertical accretion, horizontal extension, and scarp erosion.
  Ann. of Botany, 48:225-259.

- Russell, R. J., 1959. Background for field excursions in the Mississippi
  Delta. In: Second Coastal Geography Conference, Baton Rouge, Louisiana:
  363-422.

- Schou, A., 1945. Det Marine Forland. Copenhagen, 236 pp.

- Steers, J. A., 1948. Twelve years' measurement of accretion on Norfolk
  salt marshes. Geol. Mag., 85:163-166.

- Steers, J. A., 1964. The coastline of England and Wales. 2nd ed., Cambridge,
  750 pp. (see chapter XIV).

- Van Straaten, L.M.J.U., 1957. The Holocene deposits. In: Van Straaten
  and De Jong, Editors: the excavation at Velsen. Verhand. Kon. Ned. Geol.
  Mijnb. Gen., Geol. Ser., 17 (2): 158-183.

- Varlet, F., 1958. Le régime de l'Atlantique près d'Abidjan, Côte d'Ivoire.
  Etudes Eburnéennes, VII:97-257.

- Verger, F., 1955. Sur le processus de colmatage des rives de l'anse de
  l'Aiguillon. C.R.Ac.Sci., 241:1970-1971.

- Zenkovich, V. P., 1967. Processes of coastal development. Oliver and
  Boyd, Edinburgh and London, 738 pp.

HISTORY OF SOME ASPECTS

OF

MODERN COASTAL ENGINEERING
*
J. W. Johnson

INTRODUCTION

Upon first being invited to present a theme paper on the history of modern
coastal engineering, the task appeared relatively simple--especially since
the term "coastal engineer" in general usage dates back only to about 1950
when the first conference on coastal engineering was held in Long Beach,
California. I was immediately reminded, however, of the Preface to
the Proceedings of this first conference wherein Morrough P. O'Brien in
referring to the term "coastal engineering" stated that, "It is not
a new or separate branch of engineering, and there is no implication
intended that a new breed of engineer and a new society are in the
making. Coastal Engineering is primarily a branch of civil engineering
which leans heavily on the sciences of oceanography, meteorology, fluid
mechanics, electronics, structural mechanics, and others." In the almost
twenty-five years since this conference this statement remains true, but
it might be emphasized that the continued growth in this field, as
evidenced by the success of the conferences on coastal engineering, has
been in a large measure due to the interdisciplinary background and
cooperation of the participants--be they engineers, geologists, applied
mathematicians, oceanographers, etc.

Recognizing that Bruun (1972) at the Vancouver conference gave a review
of the history of coastal defense as it developed since the year 1000,
the decision was made that this discussion would be confined to a pre-
sentation of the origin of some of the theories, methods and techniques
as now practiced in the United States by present-day coastal engineers.
This restriction to the United States was due to the fact that historical
information on the origin of certain practices in Europe and elsewhere
was not readily available to me. What is reported herein may in reality
be a rediscovery of techniques and methods used by the Dutch and Danes
several hundred years ago! Some of the procedures discussed below date
back to early in the last century, but with an appreciable increase in
theoretical development occurring in the early part of this century.
In many instances, however, a considerable increase in both theory
and application resulted from research and development during and
following World War II. For brevity, only a few of the important
more or less standard procedures utilized by the coastal engineer are
discussed below. These are: (a) forecasting and hindcasting of sea
and swell; (b) transformation of waves in shoaling water; (c) littoral
processes; (d) wave forces on structures; and (e) tidal estuaries. The
intent has been to trace the development of these areas from what appears

---
*

University of California, Berkeley, California

to be their earliest practical use up through the postwar years and into
the early 1950's. I am sure that you can appreciate that to document in
detail the vast number of papers that have been presented on various
aspects of coastal engineering since 1950 would be a voluminous compilation
and therefore beyond the scope of this brief paper. For example, in the
proceedings of the fourteen conferences on coastal engineering held to
date, over 1,000 papers have been presented! If, however, a recent summary
paper is available which covers the developments in the above listed areas
of interest from about 1950 to the present, then reference to it is
presented.

FORECASTING AND HINDCASTING OF SEA AND SWELL

An empirical relationship for the highest wave that can be generated by
wind blowing over a given fetch was developed by Stevenson (1874) in
the middle of the last century. This formula has been used by engineers
over the years and still is presented in present-day engineering books
on the design of coastal structures exposed to wave action (Quinn, 1961;
Minikin, 1963). Stevenson's formula related wave height to fetch; that
is, the basic data were obtained where the wave height was controlled by
fetch rather than wind speed. The Stevenson formula in which the wave
height in feet is equal to 1.5 times the square root of the fetch in
nautical miles appears to be still valid for large storms in portions
of the North Sea.

Early in World War II it became evident that amphibious landings would be
necessary on various coastlines in the world, and reliable procedures
would be required to permit the forecast of wave and surf conditions at
selected landing sites (Bates, 1949; Revelle, 1969). In the fall of
1942 the Scripps Institution of Oceanography at La Jolla, California,
undertook the task of developing a basis for forecasting sea, swell,
and surf. The task, sponsored by the Army Air Force and the Navy Hydro-
graphic Office, was conducted by H. U. Sverdrup and W. H. Munk with
M. P. O'Brien serving in an advisory capacity. The initial effort on
the project was the development of a forecasting manual (U.S. Navy, 1944a)
and the training of Air Force officers to apply the forecasting techniques
to amphibious operations. This forecasting manual was based on all avail-
able observations of wave characteristics, wind velocity, and fetch. A
series of graphs was presented showing significant wave height and period
as functions of wind velocity and fetch. O'Brien (1944) suggested that,
since the assumptions made in developing the graphs in the manual were
for a frictionless fluid under the action of gravity, model laws could
be developed to discover dynamically similar conditions of fetch, duration,
wind velocity, wave height, and wave period which should simplify the
analysis and presentation of observations. O'Brien's concept of using
nondimensional parameters apparently was accepted by Sverdrup and Munk
(1947) in the revision and publication of the forecasting manual wherein
all variables were presented in only two dimensionless graphs--a fetch
graph and a duration graph.

In subsequent years additional and more accurate data than previously were available on wind waves were obtained from both the laboratory and the field by research workers throughout the world, and refinements to the forecasting procedures resulted (Bretschneider, 1952; Neumann, 1953). For the benefit of the practicing engineer, the Coastal Engineering Research Center (U.S. Army, 1966 and 1974) has summarized the various relationships between wind, waves, and fetch into simple graphs for the speedy solution of wave fore-casting (or hindcasting) problems.

The use of the forecasting procedure discussed briefly above has also been of great value to the coastal engineer in compiling for design purposes statistical information on wave climate at selected localities. Where adequate synoptic weather maps are available for the adjacent ocean area, the wind and fetch can be derived from the maps and the resulting wave heights and periods for each day computed. Wave conditions in tabular form or "wave roses" can be compiled for a sufficiently long period to be re-presentative of the locality under study. Information on the most severe wave conditions for the period for which weather maps are available also can be derived. The first known compilation of statistical wave data as an aid to the practicing engineer was that prepared for the U.S. Army, Corps of Engineers, for five open sea localities along the California coast by the Scripps Institution of Oceanography (1947). In this study the daily weather maps for the Pacific Ocean for the 3-year period, 1936-1938, inclusive, were used and considered to represent average conditions along the California coast. Over subsequent years the hindcasting technique has been used extensively to provide design wave data for many localities through-out the world. The acquisition of such data now appears to be a standard coastal engineering procedure, since it is faster and generally cheaper than operating a wave recorder to obtain similar information of equal reliability.

It is important to mention that early investigators of the generation and propagation of wind waves recognized that waves are not uniform; that is, a spectrum of wave heights and periods exists. In the development of the wave forecasting procedure (U.S. Navy, 1944a) it was believed that the wave characteristics would apply to the larger waves present, but no attempt was made to describe these waves more specifically. In the revision of this early procedure Sverdrup and Munk (1947) introduced a statistical term to define "the larger waves" as waves having "average height and period of the one-third highest waves." The waves described by these averages are called "significant waves." The currently used graphs relating the wave, wind and fetch characteristics thus refer to the significant waves. Considerable research on wave spectrum has been done, and is continuing, but to summarize the results of these studies would be beyond the scope of this paper; however, one can appreciate the effort being made in this important area of research, when it is noted that sixteen chapters of the Proceedings of the 1972 Coastal Engineering Conference held at Vancouver are devoted to this subject!

TRANSFORMATION OF WAVES IN SHOALING WATER

The transformation of waves in shallow water involves the change of wave
height, length, and velocity with depth. For the case of waves of small
amplitude advancing directly toward a gently sloping beach O'Brien* in the
mid-thirties used the theory presented by Lamb (1932) and summarized the
wave transformation relationships up to a point shortly before the waves
break. This summary was later published by the Beach Erosion Board (U.S.
Army, 1942). To compare this theoretical relationship with experiments
a series of field observations were conducted at the Scripps Institution
of Oceanography (1944a) by photographing waves as they moved shoreward
along the 1000 ft-long Scripps pier. These observations involved (a)
change in wave height along the pier with special emphasis on breaker
characteristics, (b) breaking of waves on gently sloping beaches, (c)
comparison between forecast and observed heights of breakers, and (d)
the velocity of waves in shallow water. Some of these data were later
published in manual form by the Hydrographic Office (U.S. Navy, 1944b)
for use in the wave and surf forecasting program described previously.

The above discussion is concerned with waves advancing directly toward
shore; however, when waves more shoreward from deep water and approach
the shoreline at an angle, the wave crests are bent because the inshore
portion of the wave travels at a lower velocity than the portion in deep
water; consequently, the crests tend to conform to the bottom contours.
One of the first engineers to recognize this phenomenen apparently was
Harrison (1848) who observed,

> "that the waves in deep water proceed forward,
> in the direction of the wind, till they arrive
> in shallower water, when the velocity of the
> part which reaches the shallow, being lessened,
> the whole wave wheels around, and breaks nearly
> at right angles on the beach."

Later this process was termed "wave refraction" by Davis (1912) who utilized
the drawing shown in Figure 1 to illustrate the general refraction of swell
on an irregular coastline. Orthogonals to the wave crests were used to
qualitatively illustrate the concentration of energy at the headlands and
the spreading of energy in the embayments. Later Johnson (1919) adopted
the concepts of Davis (1912) with the slightly modified refraction diagram
shown in Figure 2. In the summer of 1929 M. P. O'Brien was retained by the
Board on Sand Movement and Beach Erosion, U.S. Army, to investigate some
of the aspects of coastal processes. The presentation by Johnson (1919)
on refraction and the accompanying figure (shown here as Figure 2) suggested
to O'Brien* that a quantitative estimate of the relative distribution of

---

* Private communication, March 15, 1974.
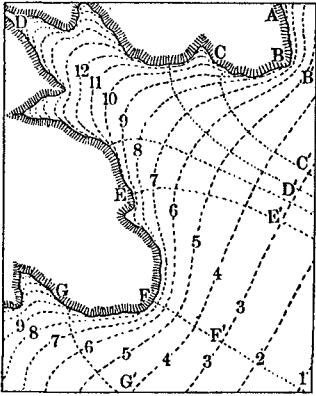
FIG. 1   Refraction diagram of
         Davis (1912)
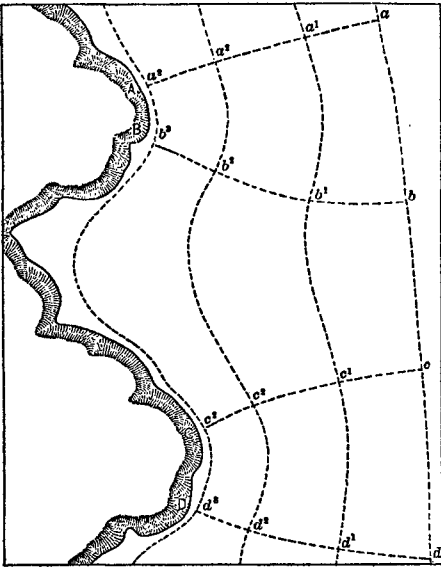
FIG. 2   Diagram by Johnson (1919) to
         illustrate the process of wave
         refraction, whereby wave attack
         is concentrated on headlands.
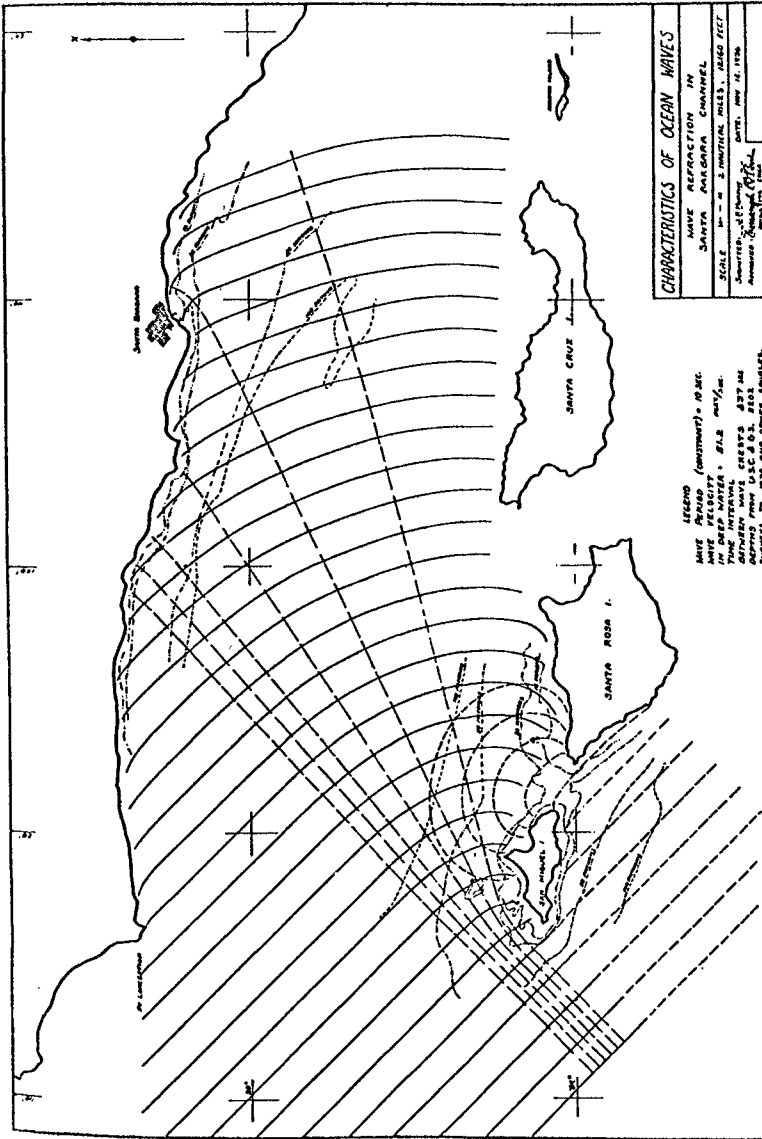
FIG. 3   Wave refraction diagram used by M. P. O'Brien in 1936 in appraising the littoral drift problem at Santa Barbara Harbor, California.

wave height along an irregular shoreline should be possible. Applying
Snell's Law, O'Brien developed a procedure for graphically plotting the
advance of a wave to a curving shoreline over a mildly irregular bottom.
The method employed was very nearly the same as for light and sound waves
in which each point on the wave front is considered as a radiating center.

One of O'Brien's earliest refraction diagrams is shown in Figure 3 and
was used in 1936 in appraising the problem of beach erosion at Santa
Barbara, California. Several early laboratory studies of wave refraction
were made under O'Brien's direction to confirm the refraction effects
derived from a graphically constructed wave refraction diagram. These
laboratory studies involved waves moving at an angle to a straight beach,
around an island, around a breakwater tip, and over a submarine canyon
(McCrone, 1940, Wilhoyt, 1940; and Milner, 1941).

O'Brien's general procedure of plotting wave crests was published by the
Beach Erosion Board (U.S. Army 1942) and the Hydrographic Office (U.S.
Navy, 1944b). Isaacs (1947) devised a system whereby the orthogonals
to refracted wave fronts could be constructed directly without first
drawing the wave fronts. This method has the advantage of eliminating an
entire graphical step and its attendant inaccuracies. It also results
in a considerable saving in plotting time, especially in cases where
many refraction diagrams are required. In 1948 the wave front method
was revised and printed, along with the Isaacs method of plotting orthogonals,
by the U.S. Navy Hydrographic Office in a general report on the graphical
construction of wave refraction diagrams (Johnson, O'Brien, and Isaacs,
1948).

Another important development in wave theory which arose during World War II
was concerned with the development of mobile breakwaters to afford shelter
during amphibious landing operations (Townson, 1973c). The principal problem
was the diffraction of waves around the ends of the breakwaters. The major
mathematical contribution to the studies was that of Penny and Price (1944)
who recognized that the mathematical theory on the diffraction of water
waves in some respects is similar to the theory of the diffraction of light
and sound waves by screens and diffraction gratings. In addition to the
diffraction of waves around the end of a breakwater Penny and Price (1944)
also considered the diffraction of waves into the lee of islands and through
single and multiple breakwater gaps. It was concluded also that the theory
was true for waves on water of any depth. Later Putnam and Arthur (1948)
introduced a simplified solution to the Penny and Price theory and conducted
laboratory experiments on the diffraction of waves around the end of a
semi-infinite impermeable breakwater with various incident wave directions
Laboratory data were compared with the complete and simplified solutions,
with the best agreement between theory and experiment occurring in the lee
of the breakwater. In other experiments the Penny and Price theory for
breakwater gaps was confirmed (Blue and Johnson, 1949; Carr and Stelzriede,
1952).

It is of interest to note that Iribarren (1953), in reviewing the Spanish
practice in harbor design, reports using the principles of refraction
and diffraction in 1932 and 1941, respectively. He referred to refraction
as the "wave-front pattern" and diffraction as "lateral wave expansion."
Most of Iribarren's published material appeared in the Spanish journal,
Revista de Obras Publicas, which perhaps had only limited distribution
outside the country--consequently, his methods apparently were little known
to coastal engineers outside of Spain. The details of Iribarren's procedure
in preparing refraction diagrams have been summarized in an English trans-
lation by Iribarren (1949).

In some localities, such as in the Gulf of Mexico, where waves may travel
many miles over a gently sloping, relatively shallow bottom, friction and
percolation may be of considerable importance in the transformation of waves.
Early theoretical work in this field was done by Putnam (Putnam and Johnson,
1949; Putnam, 1949) with laboratory studies conducted later to test the
theories (Savage, 1953). Bretschneider and Reid (1954) extended the work
of Putnam (1949) and developed formulas and graphs for facilitating the
computation of wave height changes resulting from the combined effect of
friction, percolation, and refraction together with the direct shoaling
effect. A field investigation of wave energy loss in shallow water ocean
waves off the coasts of Louisiana and Texas has been made by Bretschneider
(1954) and compared with the theoretical treatments mentioned above.

Breakers and Surf

As waves move shoreward from deep water they may refract and diffract, but
eventually they break on a beach or possibly reflect from a cliff. Perhaps
of most interest to the engineer is the transformation of the waves in the
nearshore area and then the character of the breaker and the wave uprush
on the beach. Theoretical considerations (Biesel, 1952; Wiegel, 1954;
Skjelbreia, 1958; Masch and Wiegel, 1961) and the use of refraction dia-
grams permit estimates of the change in wave height and direction up to
the breaker zone, but the characteristics of breaking waves (height, depth
of breaking, effect of beach slope, velocity field, etc.) have by necessity
been established empirically from field and laboratory experiments. Most
of these data were obtained during and shortly following World War II; al-
though refinements to the relationships have been and are still being
made by research workers, as is evidenced from an inspection of the numerous
papers in the proceedings of the past conferences on coastal engineering.
Much of the wartime field data were made at the Scripps Institution of
Oceanography (1944a and 1944b) and at the Woods Hole Oceanographic Institute
(Edmondson and Clarke, 1944). Laboratory work was conducted in wave tanks
at the University of California, Berkeley, and at the Beach Erosion Board,
Washington, D.C. Much of these data remain in unpublished reports at the
various institutions and laboratories; however, the data applicable to
engineering problems such as breaker characteristics, wave runup, etc.,
have been published, but they also are incorporated in the publication,
Shore Protection Planning and Design and its recently published revision
Shore Protection Manual. Thus such data are readily available to the design
engineer.

Littoral Processes

Since ancient times the problem of littoral drift has been an important
factor in determining the success or failure of many harbors throughout
the world. The basic principles of littoral processes were little understood,
or appreciated, in the early days with the result that many harbors became
useless in only a few years following construction. A few notable examples
of some early harbors have been described recently by Townson (1973a). Exper-
ience was the primary guide to the harbor engineer in the past, and numerous
papers on the state-of-the-art appeared in various engineering journals.
For example, Harrison (1848) discussed "The causes that are in constant
operation tending to alter the outline of the English coast to affect the
entrances of the rivers and harbors, and to form shoals and deeps in the
bed of the sea." By the turn of the last century a considerable background
of practical information had been assembled on sedimentation of harbors and
the results published in various technical journals. For a review of the
early studies on movement of coastal material in Great Britain the reader
is referred to the paper by Townson (1974). More or less paralleling the
activities of the coastal engineer was the work of the geologist who was
concerned with the scientific aspects of shoreline processes. One of the
early comprehensive discussions of these processes was that of Gilbert (1883)
who is perhaps best known for his classical research on the transportation
of debris by flowing water (Gilbert, 1914). Later Johnson (1919) formulated
the concepts and nomenclature that appears to be generally accepted today
by engineers and geologists working in this field of study.

To improve navigation channels at many harbors throughout the world break-
waters, jetties, and other shoreline structures have been constructed. The
immediate effect of such structures in many instances was to interrupt the
normal movement of sediment in the littoral zone. Dent (1916) in commenting
on beach erosion in the vicinity of New York City emphasized "the damage
that must inevitably result to beaches as a whole if the erection of structures
that interfere with littoral drift is allowed to continue." That is, deposition
of sand in the navigation channel may eventually occur, but the effect on
the adjacent shoreline may be serious for a considerable distance both upcoast
and downcoast from the structure.

The serious erosion problems which occurred at numerous inlets along the east
coast of the United States which had been stabilized by jetties led to a
Congressional Act* in 1935 which designated the Corps of Engineers, U.S. Army,
to be responsible for evaluating the effects of the construction of a littoral
barrier on the adjacent shoreline. Perhaps the first estimate of the rate of
sediment movement along a coast was made by O'Brien** in the summer of 1929

---

* Public Law 409, 74th Congress, 1935

** Private communication, May 15, 1974.

in his first assignment as an engineer in the coastal field for the Beach
Erosion Board in connection with investigations on the South Shore of Long
Island, 1933.   The growth of the sand spit at Fort Tilden threatened to
encroach on the Ambrose Channel, and a jetty was proposed to act as a sand
trap.   The particular problem was to predict the stable shoreline to be
expected with this jetty and the number of years during which it would
be an effective trap.   Fortunately, the shoreline at Fort Tilden, a military
reservation, had been surveyed at regular intervals during the preceding
century, and the available records showed the successive positions of the
high water line.   From these data, an average net rate of transport of about
300,000 cubic yards per year was computed.

Another contribution to a better understanding of the problem of littoral
drift and the development of a procedure for estimating the rate of drift
was that of Munch-Petersen who discussed the problem as early as 1914.
The Munch-Petersen formula which has given results which were consistent
with direct observations in Denmark has been described in detail by
Svendsen in 1938.

The experience with various shoreline structures, some of which are mentioned
above, suggested to M. P. O'Brien that a systematic series of laboratory
experiments might well provide a better understanding of the basic processes
involved and thereby lead to a more rational approach to the design of coastal
structures.   Borland (1930), working as a graduate student at the University
of California under the direction of O'Brien, conducted experiments on (a)
a model of the beach at Long Branch, N. J. to determine the extent of the
similarity between model and prototype where the transportation of sand by
longshore currents and wave motion was studied, (b) a flat ocean bottom of
sand with a cliff which was subject to erosive action of waves (groins were
placed similar to those in the prototype to evaluate their effect on the
beach); (c) the erosive action of waves on a beach located at the base of
a bulkhead (the beach slope was varied to determine the effect on filling an
scouring); and (d) the refraction of waves entering a bay with an opening about
one-fifth of the width of the bay (the equilibrium shape of the shoreline
was established).

One of the early efforts in the designing of a program for a detailed field
study of shoreline processes was that of Krumbein(1944a). This study was conducted
in 1942 at Half Moon Bay, California, wherein a "closed system" permitted
the discovery and specification of the principal fundamental relations
governing the behavior of matter in the system.   Later in the same year
Krumbein(1944b) conducted what is believed to be the first comprehensive laboratory
study of shore currents and sand movement.   Dimensionless relationship between
littoral current, rate of littoral drift and wave characteristics were pre-
sented.   Additional laboratory experiments on littoral currents and littoral
drift later were made by Saville in 1950 and the results compared with Krumbein(1944b).

For a summary of the developments in the mechanics of sand transport since these earlier studies, the reader is referred to the work of Komar and Inman (1970) and Komar (1971).

As discussed above littoral drift is generated by waves breaking at an angle with the shoreline. In order to determine a more general relationship between the velocity of the longshore current and such variables as the height and period of the breakers, breaker angle, and beach slope, a series of experiments were conducted at the University of California during World War II. These studies consisted of laboratory work at Berkeley (Putnam, 1944; O'Brien, 1945; and Putnam and O'Brien, 1945) and field work at Oceanside, California (Scripps Institution of Oceanography,1945). The results of these various studies were presented in postwar publications by Putnam, Munk, and Traylor (1949) and Inman and Quinn (1952). Subsequent to this early work on littoral currents considerable additional studies have been made in the surf zone on such problems as the variation of the longshore current across the surf zone, rip currents, surf beat, wave decay due to breaking, edge waves, etc. (Komar and Inman, 1970; Komar, 1971).

Another littoral process of considerable importance in some engineering pro-blems is the seasonal changes of beaches. Both the geological (Cornish, 1898; Johnson, 1919) and engineering (Dent, 1916) literature recognized that beach profiles changed throughout the year depending on the intensity of wave attack. One of the early attempts to determine the characteristics of a beach profile as related to the wave conditions were the laboratory experiments of Meyer (1936) and Waters (1939) wherein it was demonstrated that the characteristics of an equilibrium profile of a beach was related to wave steepness. Additional laboratory, as well as field, measurements confirmed the general findings of the early laboratory studies, but refined the relationship between the variables. (Bascom, 1951 and 1954; Shepard, 1950; Rector, 1954; Watts and Dearduff, 1954; and Watts, 1954).

WAVE FORCES ON STRUCTURES

Some common types of engineering structures that must be designed to withstand the forces resulting from wave action are breakwaters, jetties, bulkheads, revetments, groins, piers, and offshore drilling platforms. Of these structures, breakwaters appear to be the earliest conceived by man--many constructed several hundred years B.C. and consisted either of rubble mounds or vertical masonary walls. Some of the other structures mentioned above are of fairly recent origin with their use being primarily confined to controlling coastal erosion. Piers consisting of pile structures have long been in use, but the early pile structures generally were in protected areas where wave action was relatively light. More recently, with the advent of oil production in offshore areas where wave action may be extremely severe, the design problems involved in withstanding high wave forces have become complex. A brief review of the development of the present-day design procedures for breakwaters and offshore structures follows.

Breakwaters

As recently discussed by Townson (1937b), the practical experience with
construction methods in the early days was transferred from one area to
another with varying degrees of success. The pioneer effort to provide
a more rational method of breakwater design was that of Thomas Stevenson
(1874) who as early as 1842 conducted an extensive series of dynamometer
measurements on the forces of waves (Stevenson, 1849). Other dynamometer
measurements of wave forces were made around the turn of the last century
in the Great Lakes and in Florida by Gaillard (1904). A later improvement
in the design of breakwaters was the theory developed by Sainflou (1928)
for calculating the pressures on vertical walls. This theory was based
on certain approximations of standing waves in front of the wall. Later
Molitor (1935) developed an empirical method of computing wave pressures by
breaking waves on a vertical breakwater using the prototype test data
gathered by Gaillard (1904). The Sainflou relationship was for non-breaking
wave conditions. Bagnold (1939) using models conducted experiments on wave
pressures resulting from breaking waves.

Although rubble mounds have been used as breakwaters since earliest times,
it appears that Iribarren (1938) was the first to propose a formula for the
rational design of such structures. The experimental coefficient in the
Iribarren formula was determined from observations of actual breakwaters
exposed to wave action for several years. Hudson (1953), using a modified
Iribarren formula that was dimensionally homogeneous, conducted laboratory
tests on small-scale rubble breakwaters to evaluate the variables contained
in the coefficient of the Iribarren formula. Later Hudson (1959) extended
this work to develop a new armor unit stability formula. The Hudson formula
resulted from years of model testing for a large variety of shapes of natural
and artificial armor units. Values of the experimental coefficients of these
various shapes are available in published form (Hudson, 1974; U.S. Army,
1966 and 1974).

Pile Structures

Offshore drilling for oil was first practiced at Summerland, California,
by "whipstocking" from shore in 1894 (Amer. Pet. Inst., 1961). Later there
were other California wells located in this area on relatively lightweight
piers extending into the ocean. The first well in heavy seas was drilled
a short distance off the Louisiana coast in 1938. The first well ever
drilled out of sight of land was in 1946, also off the Louisiana coast.

With the advent of extensive drilling from platforms located many miles
offshore in the Gulf of Mexico, the problems of the design of pile structures
to resist heavy wave action began to receive considerable attention in the
late 1940's. The methods used in designing the early offshore platforms is
not known to the writer, but what appears to be the first published paper

on wave forces on a piling was that of Munk (1948). This method, however, only considered the drag force resulting from the oscillatory flow of water past the pile. In 1949 M. P. O'Brien reviewed the theory of wave forces on piling and suggested that an additional term should be included in the force equation to represent the acceleration force on the displaced volume of the fluid. In this equation the total force is obtained by adding linearly the drag and acceleration terms. The theoretical studies were followed by both laboratory (Morison, et al., 1950; Morison, O'Brien, and Johnson, 1954) and field studies (Wiegel, et al., 1957) to determine the experimental coefficients which appeared in the force equation. Considerable theoretical studies have subsequently been accomplished by several investigators, and many oil companies involved in offshore exploration and production have instrumented their platforms in the Gulf of Mexico to obtain wave force measurements under hurricane conditions (Reid, 1956; Skjelbreia, 1961). Most of these studies were concerned with circular piles in which the pile diameter is small compared with the wave length and the drag and acceleration forces are both important. The diffraction theory by MacCamy and Fuchs (1954), however, appears to be more suitable to the case where the pile diameter is large compared to the wave length; that is, the acceleration force is predominant.

TIDAL ESTUARIES

The engineering problems encountered in tidal lagoons and estuaries are numerous and complex and involve such phenomena as tidal currents, mixing, stratified flow, sedimentation at both the entrance and within the tidal basin, etc. Many of the early problems in estuaries were concerned with the diffi- culties of maintaining adequate depths at the entrances for navigational purposes. Townson (1974) briefly reviews the experiences of some harbors in Great Britain early in the last century. Stevenson (1874) on commenting on "The evils of loss of tidal water," observed that almost all maritime engineers, both then and earlier held:

> "that if the water that enters from the sea be
> reduced in quantity, the low-water sectional area
> at the mouth of the river will be reduced; so that if
> the amount of water displaced be sufficiently great,
> the channel will shut up altogether, and navigation
> be ruined."

Similarly Eads (1878) stated a number of general principles regarding tidal inlets which subsequent experience has shown to be valid; for example, one quotation is:

"Every inlet into the sounds or tidal basins
which border the eastern sea coast of the United
States is an evidence of the stability of the ebb
and flow of the tides to maintain a depth of channel
from the ocean into these basins, and to resist the
influence of the wave action which would otherwise
soon shut off these basins from all connection with
the sea.

These, in reality, are continually striving to
barricade the river current and prevent it from entering
the sea."

Reynolds (1887) pioneered the use of moveable-bed tidal models with
apparently valid results. For an excellent summary of some of the
important early model work on rivers and estuaries, the reader is referred
to the work of Freeman (1929). O'Brien (1935 and 1972) in the design
and testing of a model of the Columbia River estuary from 1932 to 1936
drew heavily on the 1887 experience of Reynolds (1887) on the Mersey model,
as well as later work by others on models of the Mersey, Severn, and
Seine.

As evidenced by the above quotes from Stevenson (1874) and Eads (1878) the
importance of the tidal flow (tidal prism) was long recognized as the primary
agent in maintaining the entrance channel into lagoons and estuaries. For
a tidal basin separated from the sea by an opening through which water may
freely flow in and out, a known periodic variation of level in the sea
will result in a periodic rise and fall of level in the basin. A. H. Gibson
in 1920 developed a graphical method for the rather complex equations for this
hydraulic phenomenon; and Chapman (1923) shortly thereafter developed a
theoretical solution which agreed within two or three percent of the involved
special graphical method of Gibson. Apparently the theory by Chapman (1923)
was the basis for the later analysis on flow in tidal inlets by Brown (1928)
and Keulegan and Hall (1950). The paper by Brown (1928) was the first
analytical treatment of the hydraulic regimen of inlets on sandy coasts;
it deals with the flow in an inlet channel of known geometry. Later Escoffier
(1940) utilized Brown's equations as the basis for an analysis of the stability
of an inlet. A critical review of the analyses of Brown (1928) and Escoffier
(1940) has been made recently by O'Brien (1971).

In 1930-31 O'Brien (1931a) made an exhaustive study of inlets and beaches
of the Pacific Coast of the United States; one result of this study was the
elucidation of the relationship between the inlet area below mean sea level
and the tidal prism (O'Brien 1931b). Later a study of the Sacramento-San Joaquin
River Delta (U.S. Congress, 1934) showed that the flow areas of the interior
channels depended upon the upstream tidal volume. The same study revealed
the fact that the minimum flow area of the inlet connecting the San Francisco
Bay with the ocean and the distance from the inlet throat to the crest of the
outer bar were approximately linear functions of the tidal prism. Later

O'Brien (1967) reanalyzed all available data on areas of tidal inlets and their corresponding tidal prisms, on the East, Gulf, and Pacific coasts of the United States. More recently, the characteristics of Pacific Coast tidal inlets have been investigated and some aspects of inlet behavior discussed (Johnson, 1973).

An important aspect of flow in many estuaries is that of the interaction between the fresh water flow from upland drainage and the salt water from the ocean. One of the earlier theoretical treatments of density flow was that of Taylor (1931) who showed that a form of Froude number governed the scaling of models involving this flow phenomenon. Perhaps the first engineering application in the United States to modeling a density flow was that of O'Brien and Cherno (1934) in connection with the investigations of a proposed salt-water barrier in San Francisco Bay. In many present-day estuarine model studies, the form of Froude number used by O'Brien and Cherno is referred to as the densimetric Froude number (Barr, 1963; Ippen, 1966).

SUMMARY

A brief history is presented on several techniques and methods which are now standard procedures of the engineer in arriving at the rational design of coastal engineering projects. This review is an attempt to establish the originator, as well as the later developers, of the various procedures. In general, development was gradual up to about World War II when research efforts accelerated rapidly and the increase in knowledge of the fundamental mechanics of processes in the nearshore zone increased many-fold. Postwar research in various coastal engineering areas has continued at a relatively high rate as evidenced by the many high caliber publications in the varous technical journals.

REFERENCES

American Petroleum Institute (1961). History of petroleum engineering, New York, p. 13.

Bagnold, R. A. (1939). Interim report on wave pressure research. Journal, Inst. of Civil Engineers, London, No. 7, June 1939, pp. 202-226.

Barr, D.I.H. (1963). Model simulation of vertical mixing in stratified flow. The Engineer, Vol. 215, No. 5587, Feb. 22, 1963, pp. 345-352.

Bascom, W. N. (1951). The relationship between sand size and beach-face slope Trans., American Geophysical Union, Vol. 42, No. 6, Dec. 1951, pp. 866-874.

Bascom, W. N. (1954). Characteristics of natural beaches. Proc., Fourth Conf. on Coastal Engin., Council on Wave Research, 1954, pp. 163-180.

---

* – Indicates unpublished or limited edition papers. Such papers are available in the Water Resources Center Archives, Univ. of Calif., Berkeley, Calif. 94720.

Bates, C. C. (1949). Utilization of wave forecasting in the invasions of
    Normandy, Burma, and Japan. Annals, New York Academy of Sciences,
    Vol. 51, Art. 3, May 1949, pp. 545-572.

Biesel, F. (1952). Study of wave propagation in water at gradually varying
    depth. Proc., U.S. National Bureau of Standards Symposium on Cravity
    Waves, U.S. Nat. Bur. of Standards Circular 521, Nov. 1952, pp. 243-253.

Blue, F. L., Jr. and Johnson, J. W. (1949). Diffraction of water waves passing
    through a breakwater gap. Trans., American Ceophysical Union, Vol. 30,
    No. 5, Oct. 1949, pp. 705-718.

Borland, W. M. (1930). Model studies of beach erosion. M.S. Thesis in Mechanical
    Engineering, Univ. of Calif., Berkeley, Calif., May 1930.

Bretschneider, C. L. (1952). Revised wave forecasting relationships. Proc.,
    Second Conf. on Coastal Engin., Council on Wave Research, 1952, pp. 1-5.

Bretschneider, C. L. (1954). Field investigation of wave energy loss in shallow
    water ocean waves. Beach Erosion Board, Tech. Memo No. 46, U.S. Army,
    Wash., D.C., Sept. 1954.

Bretschneider, C. L. and Reid, R. O. (1954). Modifications of wave height due
    to bottom friction percolation and refraction. Beach Erosion Board, Tech.
    Memo. No. 45, U.S. Army, Wash., D.C., Oct. 1954.

Brown, E. I. (1928). Inlets on sandy coasts. Proc., Amer. Soc. Civil Engineers,
    Vol 54, 1928, pp. 505-553.

Bruun, P. (1972). The history and philosophy of coastal protection. Proc.,
    Thirteenth Conf. on Coastal Engin., American Society of Civil Engineers,
    1972, pp. 33-74.

Caldwell, J. M. (1950). Sedimentation in harbors. Applied Sedimentation,
    John Wiley & Sons, 1950, pp. 291-299.

Carey, A. E. (1903-04). The sanding-up of tidal harbours. Minutes of Proceeding,
    Inst. of Civil Engineers, London, Vol. 156, 1903-04.

Carr, J. H. and Stelzriede, M. E. (1952). Diffraction of water waves by break-
    waters. Proc., U.S. National Bureau of Standards Symposium on Cravity
    Waves, U.S. Nat. Bur. of Standards Circular 521, Nov. 1952, pp. 109-125.

Chapman, M. A. (1923). A note on the fluctuation of water-level in a tidal-power
    reservoir. Philosophical Magazine, Sixth Series, Vol. 46, 1923, pp. 101-108, 1923.

Cornish, V. (1898). On sea-beaches and sand banks. Ceographical Journal, Vol. 11,
    1898, pp. 528-628.

Davis, W. M. (1912). Die erklarende beschreibung der landformen. Leipzig und
    Berlin, Druck und Verlag von B. G. Teubner.

Dent, E. J. (1916). The preservation of sandy beaches in the vicinity of
    New York City. Trans., Amer. Soc. of Civil Engineers, Vol. 80, 1916,
    pp. 1780-1805.

Eads, J. B. (1878). Improvement of the mouth of the St. Johns River. Sun and
    Press Book and Job Rooms. Jacksonville, Florida (copy of original report
    available in the Engineering Societies Library, United Engineering Center,
    New York).

*Edmondson, W. T. and Clarke, F. L. (1944). Measurement of waves, surf, and
    shore conditions on Martha's Vineyard and Cape Cod. Woods Hole Oceanographic
    Inst., Sept. 15, 1944 (unpublished).

Escoffier, F. F. (1940). The stability of tidal inlets. Shore and Beach, Vol. VIII,
    No. 4, Oct. 1940, pp. 114-115.

Freeman, J. R. (1929). Hydraulic laboratory practice. The American Society of
    Mechanical Engineers, New York, N. Y.

Gaillard, D. D. (1904). Wave action in relation to engineering structures.
    Prof. Papers of the Corps of Engineers, U.S. Army, No. 31, Wash., D.C.

Gilbert, G. K. (1883-84). The topographic features of lake shores. Fifth Annual
    Report, U.S. Geological Survey, Wash., D.D., 1883-84, pp. 69-123.

Gilbert, G. K. (1914). The transporation of debris by flowing water. U.S.
    Geological Survey, Prof. Paper 86.

Granthem, K. N. (1953). Wave run-up on sloping structures. Trans., American
    Geophysical Union, Vol. 34, No. 5, Oct. 1953, pp. 720-724.

Harrison, J. T. (1848). Observations on the causes that are in constant operation
    tending to alter the outline of the English coast, to affect the entrances
    of the rivers and harbours, and to form shoals and deeps in the bed of the
    sea. Minutes of Proceedings, Inst. of Civil Engineers, London, Vol. 7, p.343.

Hudson, R. Y. (1953). Wave forces on breakwaters. Trans., American Society of
    Civil Engineers, Vol. 118, pp. 653-674.

Hudson, R. Y. (1959). Laboratory investigation of rubble-mound breakwaters.
    Jour., Waterways and Harbors Division, American Society of Civil Engineers,
    Vol. 85, No. WW3, Sept. 1959, Part 1, pp. 93-121.

Hudson, R. Y. (1974). Concrete armor units for protection against wave attack.
    U.S. Army Engineer Waterways Exp. Station Misc. Paper H-74-2, Jan. 1974.

Inman, D. L. and Quinn, W. H. (1952). Currents in the surf zone. Proc., Second
    Conf. on Coastal Engin., Council on Wave Research, 1952, pp. 24-36.

Ippen, A. T. (1966). Estuary and coastline hydrodynamics. McGraw-Hill Book Co.,
    Inc., N.Y., 1966, Chap. 17 by G. H. Keulegan, pp. 546-574.

Iribarren, R. (1938). Una formula para el calculo de los digues de escollera.
    M. Bermejillo, Usabiago y H., July 1938, Pasajes, Spain. (See English
    Translation; The Bulletin of the Beach Erosion Board, Vol. 3, No. 1,
    January 1, 1949, pp. 1-16.

Iribarren, R. and Nogales y Olano, M. C. (1949). Penetration of waves and
    swells into harbours; means of predicting them and limiting their
    action; reference to model experiments, Section II, Comm. 4, XVII
    Int. Navigation Congress, Lisbon, 1949, pp. 31-80.

Iribarren, R. (1949). Currents and the sweeping of sand due to swell.
    Bulletin of the Permanent Int. Assoc. of Navigation Congresses, 1949,
    pp. 96-128.

Iribarren, R. (1953). Spanish practice in harbor design. Proc., Third
    Conf. on Coastal Engin., Council on Wave Research, 1953, pp. 177-184.

*Isaacs, J. D. (1947). Graphical construction of refraction diagrams
    directly by orthogonals. Univ. of Calif. Hyd. Engin. Lab. Rept.
    HE-116-273, Nov. 21, 1947 (unpublished).

Iversen, H. W. (1952). Laboratory study of breakers. Proc., U.S. National
    Bureau of Standards Symposium on Gravity Waves, U.S. Nat. Bur. of Standards
    Circular 521, Nov. 1952, pp. 9-32.

Iversen, H. W. (1953). Waves and breakers in shoaling water. Proc., Third
    Conf. on Coastal Engin., Council on Wave Research, 1953, pp. 1-12.

Johnson, D. W. (1919). Shore processes and shoreline development. John
    Wiley and Sons, N.Y., 1919.

Johnson, J. W., O'Brien, M. P. and Isaacs, J. D. (1948). Graphical con-
    struction of wave refraction diagrams. U.S. Navy, Hydrographic Office,
    H. O. Pub. No. 605, Jan. 1948.

Johnson, J. W. (1959). The littoral drift problem at shoreline harbors.
    Trans., Amer. Soc. of Civil Engineers, Vol. 124, 1959, pp. 525-546.

Johnson, J. W. (1973). Characteristics and behavior of Pacific Coast tidal
    inlets. Jour. Waterways, Harbors and Coastal Engineering Division, Amer.
    Soc. of Civil Engineers, August 1973, pp. 325-339.

Keulegan, G. H. and Hall, J. V., Jr. (1950). A formula for the calculation
    of the tidal discharge through an inlet. The Bulletin of the Beach
    Erosion Board, U.S. Army, Vol. 4, No. 1, Jan. 1, 1950, pp. 15-29.

Komar, P. D. and Inman, D. L. (1970). Longshore and transport on beaches.
    Journal of Geophysical Research, Vol. 75, No. 30, Oct. 30, 1970, pp.
    5914-5927.

Komar, P. D. (1971). The mechanics of sand transport on beaches. Journal
    of Geophysical Research, Vol. 76, No. 3, Jan. 20, 1971, pp. 713-721.

Krumbein, W. C. (1944a). Shore processes and beach characteristics. Beach Erosion Board, Tech. Memo No. 3, U.S. Army, Wash., D.C., May 1944.

Krumbein, W. C. (1944b). Sand currents and sand movement on a model beach. Beach Erosion Board, Tech. Memo No. 7, U.S. Army, Wash., D.C., Sept. 1944.

Lamb, H. (1932). Hydrodynamics, 6th ed., Cambridge University Press.

MacCamy, R. C. and Fuchs, R. A. (1954). Wave forces on piles: a diffraction theory. Beach Erosion Board, Tech. Memo No. 69, U.S. Army, Dec. 1954.

Masch, F. D. and Wiegel, R. L. (1961) Cnoidal waves, tables of functions. Council on Wave Research, Mar. 1961.

Mason, M. A. (1952). Some observations of breaking waves. Proc., U.S. National Bureau of Standards Symposium on Gravity Waves, U.S. Nat. Bu. of Standards, Circular 521, Nov. 1952, pp. 215-220.

*McCrone, W. P. (1940). Model study of wave refraction around a breakwater. M.S. thesis, Univ. of Calif., Berkeley, May 1940.

*Meyer, R. D. (1936). A model study of wave action on beaches. M.S. thesis, Univ. of Calif., Berkeley, 1936.

*Milner, F. (1941). Model study of wave refraction in a submarine valley. M.S. thesis, Univ. of Calif., Berkeley, May 1941.

Minikin, R. R. (1963). Wind, waves and marine structures. Charles Griffin & Co., Ltd., London, 1963, p. 33.

Molitor, D. A. (1935). Wave pressures on sea-walls and breakwaters. Trans. Amer. Soc. of Civil Engineers, Vol. 100, pp. 984-1002.

Morison, J. R., O'Brien, M. P., Johnson, J. W., and Schaaf, S. A. (1950). The force exerted by surface waves on piles. Jour. of Petroleum Technology, Pet. Branch, Amer. Inst. of Mining & Metal. Engineers, Vol. 2, No. 5, May 1950, pp. 149-150.

Morison, J. R., Johnson, J. W. and O'Brien, M. P. (1954). Experimental studies of forces on piles. Proc., Fourth Conf. on Coastal Engin., Council on Wave Research, 1954, pp. 340-370.

Munk, W. H. (1948). Wave action on structures. American Inst. of Mining and Metal. Engineers, Tech. Publ. No. 2322, Class G., Pet. Tech., Mar. 1948.

Neumann, G. (1953). On ocean wave spectra and a new method of forecasting wind-generated sea. Beach Erosion Board, Tech. Memo No. 43, U.S. Army, Wash., D.C., Dec. 1953.

O'Brien, M. P. (1931a). Report on sand movement and beach erosion along
the Pacific coast of the United States. (Seven volumes, consisting
of 3 parts and 18 appendices. Original in Coastal Engineering
Research Center Library, Fort Belvoir, Virginia).

O'Brien, M. P. (1931b). Estuary tidal prisms related to entrance area.
Civil Engineering, Vol. 1, No. 8, May 1931, pp. 738-739.

O'Brien, M. P. and Cherno, J. (1934). Model law for motion of salt water
through fresh. Trans., Amer. Soc. of Civil Engineers, Vol. 99, 1934,
pp. 576-594.

O'Brien, M. P. (1935). Models of estuaries. Trans., American Geophysical
Union, Part II, August 1935, pp. 485-492.

*O'Brien, M. P. (1939). Summary of theory of oscillatory waves (First
draft), Beach Erosion Board, U.S. Army, Wash., D.C., July 5, 1939
(unpublished).

*O'Brien, M. P. (1944). Memorandum concerning "Wind waves and swell,
principles in forecasting," Univ. of Calif. Hyd. Engin. Lab. Report.
HE-116-7, Berkeley, Sept. 5, 1944 (unpublished).

*O'Brien, M. P. (1945). Analysis of laboratory experiments on littoral
currents. Univ. of Calif. Hyd. Engin. Lab. Rpt. HE-116-64, Berkeley,
Mar. 8, 1945 (unpublished).

*O'Brien, M. P. (1946). The causes of plunging and spilling breakers.
Univ. of Calif. Hyd. Engin. Lab. Rept. HE-116-92, Jan. 23, 1946
(also see the Bulletin of the Beach Erosion Board, Vol. 3, No. 3,
July 1, 1949).

O'Brien, M. P. (1967). Equilibrium flow areas and tidal inlets on sandy
coasts. Proc., Tenth Conf. on Coastal Engin., Soc. of Civil Engineers,
1967, pp. 676-686.

*O'Brien, M. P. (1971). A critical review of the E.I. Brown analysis
of inlets on sandy coasts. Univ. of Calif. Hyd. Engin. Lab. Rpt.
HEL-24-10, Dec. 1971 (unpublished).

O'Brien, M. P. (1972). Field and laboratory studies; navigation channels
of the Columbia River Estuary. Proc. Thirteenth Conf. on Coastal Engin.,
Amer. Soc. of Civil Engineers, pp. 2475-2498.

*Penny, W. G. and Price, A. T. (1944). Diffraction of sea waves by break-
waters. Directorate of Miscellaneous Weapons Development, History
No. 26, Section III(D), 1944. (also see Phil. Trans. Royal Soc.
of London, Series A, Vol. 244, 1952, pp. 236-253).

*Putnam, J. A. (1944). Littoral currents, Univ. of Calif. Hyd. Engin.
    Lab. Rpt. HE-116-12, Berkeley, Oct. 18, 1944.

*Putnam, J. A. and O'Brien, M. P. (1945). Laboratory investigations of
    littoral currents-II. Univ. of Calif. Hyd. Engin. Lab. Rpt. HE-116-103,
    Berkeley, May 10, 1945 (unpublished).

 Putnam, J. A. and Arthur, R. S. (1948). Diffraction of water waves by break-
    waters. Trans., American Geophysical Union, Vol. 29, No. 4, Aug. 1948,
    pp. 481-490.

 Putnam, J. A. and Johnson, J. W. (1949). The dissipation of wave energy
    by bottom friction. Trans., American Geophysical Union, Vol. 30, No. 1,
    Feb. 1949, pp. 67-74.

 Putnam, J. A. (1949). Loss of wave energy due to percolation in a permeable
    sea bottom. Trans., American Geophysical Union, Vol. 30, No. 3, June 1949,
    pp. 349-356.

 Putnam, J. A., Munk, W. H. and Traylor, M. A. (1949). The prediction of
    longshore currents. Trans., American Geophysical Union, Vol. 30, No. 3,
    June 1949, pp. 337-345.

 Quinn, A. DeF. (1961). Design and construction of ports and marine structures.
    McGraw-Hill Book Co., New York, 1961, p. 38.

 Rector, R. L. (1954). Laboratory study of equilibrium profiles of beaches.
    Beach Erosion Board, Tech. Memo No. 41, U.S. Army, Aug. 1954.

*Reid, R. O. (1956). Analysis of wave force experiments at Caplen, Texas.
    Texas Agriculture and Mechanical University, Dept. of Ocean., Tech.
    Rept. No. 38-4, Jan. 1956 (unpublished).

 Revelle, R. (1969). The age of innocence and war in oceanography. Oceans,
    Vol. 1, No. 3, March 1969, pp. 5-16.

 Reynolds, O. (1887). On certain laws relating to the regime of rivers and
    estuaries, and on the possibility of experiments on a small scale.
    Report of the British Association for the Advancement of Science, 1887,
    pp. 555-562. Also see reports of 1889, pp. 327-343; 1890, pp. 512-534;
    and 1891, pp. 386-404.

 Sainflou, M. (1928). Essai sur les digues maritimes verticales. Annales
    des Ponts et Chaussées, Vol. 4, No. 5, Paris, 1928.

 Savage, R. P. (1953). Laboratory study of wave energy losses by bottom
    friction and percolation. Beach Erosion Board, Tech. Memo No. 31,
    U.S. Army, Wash., D.C., Feb. 1953.

 Saville, T., Jr. (1950). Model study of sand transport along an infinitely
    long, straight beach. Trans., American Geophysical Union, Vol. 31,
    No. 4, August 1940, pp. 555-565.

*Scripps Institution of Oceanography (1944a). The transformation of waves in shallow water; Part I, May 11, 1944; Part II, May 15, 1944; Part III, June 7, 1944; and Part IV, June 1, 1944 (unpublished).

*Scripps Institution of Oceanography (1944b). Effect of bottom slope on breaker characteristics as observed along the Scripps Institution pier. Scripps Inst. of Ocean. Wave Project Rept. No. 24, La Jolla, Calif., Oct. 23, 1944 (unpublished).

*Scripps Institution of Oceanography (1945). Longshore currents. Scripps Inst. of Ocean. Wave Project Rept. No. 40, La Jolla, Calif., April 23, 1945 (unpublished).

Scripps Institution of Oceanography (1947). A statistical study of wave conditions at five open sea localities along the California coast. Scripps Inst. of Ocean., Wave Project Rept. No. 68, La Jolla, Calif., July 1, 1947 (unpublished).

Shepard, F. P. (1950). Beach cycles in southern California. Beach Erosion Board Tech, Memo No. 15, U.S. Army, Jan. 1950.

Skjelbreia, L. (1959). Gravity waves, Stokes' third order approximation, tables of functions. Council on Wave Research, June 11, 1958.

Skjelbreia, L. (1961). The clamp-on force meter. Proc., Seventh Conf. on Coastal Engin., Council on Wave Research, 1961, pp. 701-702.

Spring, F. J. E. (1912-13). Coastal sand travel near Madras Harbor. Minutes of Proc., Inst. of Civil Engineers, London, Vol. 194, 1912-13, pp. 153-171.

Stevenson, T. (1849). Account of experiments upon the force of waves of the Atlantic and German Oceans. Trans., Royal Society of Edinburgh, Vol. 16, 1849, pp. 23-32.

Stevenson, T. (1874). Design and construction of harbours: a treatise on maritime engineering. Edition 2, Edinburgh.

*Svendsen, S. (1938). Munch-Petersen's formel for materialvandring. Stadsoog Havneigenioren, December 1938 (For an English translation of this article, see the Bulletin of the Beach Erosion Board, U.S. Army, Wash., D.C., Vol. 4, No. 4, Oct. 1, 1950, pp. 1-31).

Sverdrup, H. U. and Munk, W. H. (1947). Wind, sea, and swell: Theory of relations for forecasting. Hydrographic Office, U.S. Navy, H. O. Publ. No. 701, March 1947.

Taylor, G. I. (1931). Effect of variation in density on the stability of superposed streams of fluid. Proc., Royal Society of London, Series A, Vol. CXXXII, pp. 499-523.

Townson, J. M. (1973a). History of coastal engineering. The Dock and
    Harbour Authority, Vol. LIV, No. 631, May 1973, pp. 16-19.

Townson, J. M. (1973b). History of breakwaters. The Dock and Harbour
    Authority, Vol. LIV, No. 633, July 1973, pp. 98-101.

Townson, J. M. (1973c). History of wave and tide theory. The Dock and
    Harbour Authority, Vol. LIV, No. 637, Nov. 1973, pp. 247-249.

Townson, J. M. (1974). The history of the movement of coast material.
    The Dock and Harbour Authority, Vol. LIV, No. 639, Jan. 1974, pp. 324-327.

*U.S. Army (1933). Interim report of Beach Erosion Board, Office of the
    Chief of Engineers, Corps of Engineers, Wash., D.C., April 15, 1933.

U.S. Army (1942). A summary of the theory of oscillatory waves. Beach
    Erosion Board, Tech. Rept. No. 2, Corps of Engineers, Wash., D.C.

U.S. Army (1966). Shore protection planning and design. Coastal Engineering
    Research Center, Corps of Engineers, Wash., D.C., 1966.

U.S. Army (1974). Shore protection manual. Coastal Engineering Research
    Center, Corps of Engineers, Wash., D.C., 1974.

U.S. Congress (1934). Sacramento, San Joaquin, Kern Rivers, California.
    U.S. Congress, House Document No. 191, 73rd Congress, 2nd Session,
    1934, Wash., D.C.

U.S. Navy (1944a). Wind waves and swell, principles in forecasting, H.O.
    Misc. 11,275. Hydrographic Office, Wash., D.C.

U.S. Navy (1944b). Breakers and surf, principles in forecasting, H.O.
    No. 234, Hydrographic Office, Wash., D.C., Nov. 1944.

*Waters, C. H. (1939). Equilibrium slope of sea beaches. M.S. Thesis, Univ.
    of Calif., Berkeley, California.

Watts, G.M. (1954). Laboratory study of effect of varying wave periods on
    beach profiles. Beach Erosion Board, Tech. Memo No. 53, U.S. Army, Wash.,
    D.C., Sept. 1954.

Watts, G. M. and Dearduff, R. F. (1954). Laboratory study of effect of
    tidal action on wave-formed beach profiles. Beach Erosion Board, Tech.
    Memo No. 52, U.S. Army, Wash., Dec. 1954.

Wiegel, R. L. (1954). Gravity waves, tables of functions. Council on Wave
    Research, Feb. 1954.

Wiegel, R., Beebe, K. E., and Moon, J. (1957). Ocean-wave forces on circular
    cylindrical piles. Trans., Amer. Soc. of Civil Engineers, Vol. 124, 1959,
    pp. 89-113.

Wiegel, R. L. (1959). Sand by-passing at Santa Barbara, California. Jour.
    Waterways and Harbors Div., Proc., Amer. Soc. Civil Engineers, Vol. 85,
    June 1959, pp. 1-30.

*Wilhoyt, E. E. (1940). A model study of wave refraction around an island.
    M.S. Thesis, Univ. of Calif., Berkeley, May 1940.

COASTAL ENGINEERING AND OFFSHORE LOADING FACILITIES.

by Eco W. Bijker,
    Delft University of Technology,
    Department of Civil Engineering.

Coastal engineering proves to be a combination of technical, partly empirical
knowledge and basic research into the fundamentals which are decisive for
the design criteria of constructions along and in the sea.

It is indicated how this coastal engineering can contribute to the solution
of the problems around various types of offshore loading and unloading stations.

Sea at windforce 10-11

Photo by de Lange from Heavy weather sailing
by K. Adlard Coles by courtesy of Hollandia
N.V. Baarn (Neth.).

COASTAL ENGINEERING AND OFFSHORE LOADING FACILITIES.

by Eco W. Bijker
    Delft University of Technology,
    Department of Civil Engineering.

According to the title the coastal engineering aspects of offshore loading faci-
lities will be discussed. The economical evaluation and the navigational, indus-
trial and sociological aspects of these facilities will therefore not be consi-
dered in this paper. This does not imply that the author is of the opinion that
those developments which would require more transport and therefore more loading
facilities, should be accepted without discussion. This is, however, in our human
society a decision of the total community. We, as human beings - members of this
community - must take part in this decision. We must also certainly not forget
our responsibility in this respect, when we are working in our engineering pro-
fession. Yet, in order to be able to make good decisions the various possibilities
have to be evaluated without too much emotion. In this paper the contribution
coastal engineering can give to the issue of offshore loading and unloading facil-
ities will be discussed.

It seems worthwhile to start with a closer definition of the terminology used in
the title. Although Coastal Engineering does not need any further explanation at
this conference, its various aspects in relation to offshore loading facilities
will be discussed briefly.

Coastal Engineering is just as well the skill of the engineer to apply technical
knowledge to constructions to be made along the coast or offshore, as the research
into new developments of this science which may result even in completely new
techniques. It will not always be easy to distinguish between basic research in
order to deepen the insights in the fundamentals and in research to streamline
the application of earlier developed basic knowledge. It is more or less the old
distinction between research and development. Especially the Coastal Engineering
Conferences always contribute to the further deepening of the fundamental know-
ledge, while examples of applications also are given.

In principle, basic science means the knowledge of the physical phenomena and
backgrounds and the description thereof in models of some kind (mathematical,
electrical or hydraulic, to mention only three). Also these design procedures
and computational techniques can be as such, the result of, or be made possible
by other achievements of science. The availability of the modern, very fast elec-
tronic digital computers made an entirely new design procedure possible. In this
case, however, the base of the method is a part of the science achieved long ago.
This may hold even for rather unorthodox structures such as mooring towers or
oil rigs in deep water (100 m and more). The base of the computation of these
constructions is the force exerted by waves and current on the seperate units
(piles and bars). Up to this moment these forces are calculated with the proce-
dure developed by M.P. O'Brien and quoted as the formula of Morison. In this
procedure the normal drag forces resulting from the flowing water and the inertia
forces resulting from the accelerations are distinguished. Although this proce-
dure gives an excellent possibility for computation, it is still based on the
traditional knowledge of potential flow for the computation of the inertia forces
and empirical information about turbulent flow around submerged bodies for the
computation of the drag force. Consequently all computations require empirical
coefficients which should not be applied outside the region covered by the expe-
riments, from which they are determined.

Some research has started already in order to correlate, for instance, the shed-
ding of vortices with the coefficients to be applied in the computation of the
inertia forces. As soon as forces have to be determined on piles making an angle
with the current direction or the direction of propagation of the waves, basic
difficulties will arise. Also in this case, as a first and indeed reasonably
workable solution, the coefficients for such circumstances can be determined by
tests. However, if the constructions are becoming bigger and the design criteria
more severe, it will be compulsory to design more to the limit of the possibili-
ties. In that case the unavoidable scatter in results of the determination of
empirical coefficients may be too much. This scatter can be avoided only if the
fundamentals of the current pattern including the boundary layer around a sub-
merged body of any arbitrary form in an oscillating current are studied.

More or less the same problem shows up if the wave is considered, being the
first thing to be determined if a construction in the open sea has to be de-
signed. Starting from a first order sinusoidal solution based on an irrotational
flow, more sophisticated·wave theories have been developed. With the description
of the wave in a spectral form, an insight has been obtained into how the energy
is distributed over the wave, but still no distinct description of the real wave
is achieved. Yet, sometimes this description is required for the computation.

Especially the forces exerted by breaking waves - the so called impact forces -
which are of much higher magnitude (10 times or more) than the normal wave forces,
are of importance, even when their duration is very short. For big structures
such as breakwaters and bulky structures in the open sea these forces are studied
and measured in model and even in the prototype. One of the first examples - due
to the complicated form of the combined steel and reinforced concrete structure,
a rather difficult one - is the big discharge sluice in the Haringvliet in the
Netherlands.
Another example of a structure of which the design is influenced by these impact
forces is the Hanstholm breakwater in the host country of this 14th Coastal Engi-
neering Conference, while in the design of the Ekofisk storage tank measures have
been taken to decrease the impact forces. But also in this case, the physical
phenomenon of the impact forces is not completely understood. This understanding
is required in order to determine whether these forces also occur on units which
have a much smaller cross-section with respect to the waves, such as piles and
bars of, for instance, offshore mooring towers.

One of the unknown factors in this phenomenon is the role of entrapped air or
dissolved gas in the water. It will be clear that reproduction of these effects
on scale in models with normal atmospheric pressure will cause scaling diffi-
culties. At the occasion of the inauguration of the windwave flume of the Delft
Hydraulics Laboratory in 1968, Prof. Lundgren made the prediction that "within
10 years we would be again in Delft for the inauguration of a windwave flume
with a controlable pressure lower than the atmospheric pressure.

The beginning of the fullfilment of his prediction is there. In the laboratory
of Fluid Mechanics of the Department of Civil Engineering of the Delft Universi-
ty of Technology Kolkman executes tests on impact forces in a small wave flume
with less than atmospheric pressure. It is hoped that these tests, which are
executed in close cooperation with the Delft Hydraulics Laboratory, will give
us a better insight in the influence of the enclosed air on the impact forces.

Moreover, at the Neth. Ship Model Basin in Wageningen a 200 m long, 16 m wide
and 8 m deep flume is in operation for research on cavitation by ships propel-
lors. In this flume the pressure can be lowered to 35 cm water column. With
the installation of a wave generator in this flume Lundgren's prediction be-
comes reality.

The same situation with regard to the state of the art exists in the field of
the computation of sediment transport under the influence of waves and currents.
Most of the work done in this field up to today is based on the development of
turbulent boundary layers based on the work of Von Karman and Prandtle. For a
good understanding of the transport of material under waves it will be neces-
sary to study the boundary layers and the concentration distribution in this
layer for turbulent conditions in oscillatory flow.

The examples given above about the necessity of further fundamental research in
order to be able to solve problems which are met today, are only a few of much
longer list and only meant as examples. In the discussion later on in this paper
some of these points will be highlighted again. However, while this basic and
fundamental research is very necessary, at this very moment big structures
have to be designed and constructed. Therefore, also the knowledge of Coastal -
and Ocean - Engineering based on the rich experience of our predecessors is
invaluable. The term Coastal Engineering will be seen, therefore, as the total
of all knowledge in this field, including the study of the fundamentals; so a
more practical and a more fundamental part.

The second part of the title, Offshore Loading, and of course Unloading, Fa-
cilities is also self explanatory. Yet it might be worthwhile to summarize
what could be understood under this heading. Under Offshore Loading Facilities
all facilities are understood which make it possible to load or unload ships at
some distance from the coast; in principle an extension of the main tasks of
the ports to the more or less open sea.

In order to understand better why there is a tendency to move facilities off-
shore a short sketch of the developments of ports from places inland to the
coastline and even further will be given. Historically, harbors have been built
at places where sufficient connections with the hinterland were available and
where protection was obtained from all evils from the sea. These evils were as
well waves and currents as human ennemies. Thus harbors were in most cases si-
tuated well inland, at the boundary of the high or at any rate reasonable dry
land where fresh water was available.

Since the draft of the vessels was then still small, no great difficulties with
accessibility were encountered. This could not always be said of the accessibil-
ity from a nautical point of view. But in this case the disadvantage was some-
times also the strength of the harbor, as for instance for the place where many
of the men of war in Nelson's time were built and equipped, the small harbor
Bucklers Hard at the Beaulieu River.

With increasing draft of the ships, more difficulties were encountered. In case
a harbor was constructed at a river or tidal inlet, the depth of the approach
was in most cases restricted by a bar. First, men attempted to avoid these
shallow areas by finding other ways. Sometimes also by developing ingenious de-
vices for temporily decreasing the draft of the ships as, for instance, near
the island Pampus for Amsterdam with "ships camels". With increasing technical
possibilities also new channels were excavated. The two major ports of the

Netherlands, Rotterdam and Amsterdam, both have a long history in finding new
and deeper ways to the sea. Both have dredged in a certain time of their his-
story special deeper canals to the sea and both have abandoned these approaches
again. They have now both their, also artificially made definitive (?) fair-
ways to sea - for Amsterdam the North Sea Canal and for Rotterdam the Rot-
terdam Waterway. By these measures the two ports are connected by deep water
canals or rivers with the sea. But now, with the development of the V.L.C.C.'s
and U.L.C.C.'s and also of the third generation container ships these ports
have some disadvantages as result of the fairly long distance from sea. This
long sailing distance, leading in most cases through more or less densely popu-
lated areas, causes certain hazards to navigation and therefore to the popula-
tion living in that area. Moreover - and this is especially of importance for
the container traffic - it costs time. This has led to the tendency to shift
the harbors as much as possible toward the shoreline. This has been done already
in Rotterdam, with the construction of Europoort on the Maasvlakte, it is consi-
dered by London with the Foulness project, by Hamburg with the new deep sea har-
bor at the Elbe mouth, and by Amsterdam with the new oil and container harbor
south of the existing harbor mouth at IJmuiden. In all these cases the harbor
designs are protruding seaward through the existing coastline. One of the rea-
sons for these activities is certainly also the scarcity of land for harbor
facilities in the urban areas more land inward.

From these projects to a complete island harbor is only one step, might it be
with seven league wading boots. The idea is in other respects not so new. In 1957
five participants of the International Course in Hydraulic Engineering at Delft,
Campos, Muddappa, Shams, the late Shirdan and Vajda made a project for an is-
land harbor in front of IJmuiden.

When the Coastal Engineering group of the Department of Civil Engineering of the
Delft University of Technology started in 1969 with a more thorough review of
those projects, first of all an inquiry was made among the most important po-
tential users of such islands. At that moment only little enthusiasm was found
for moving so far from the mainland as long as reasonably priced land for port
and industrial purposes could be obtained ashore. Certainly the problems arising
from transporting a great number of workers daily to and from the island are
big and numerous. The other solution, viz.: lodging the workers on the island
during, for instance, one week involves sociological problems.

A less radical solution is to restrict the offshore facility for only loading
or unloading bulk goods, such as oil and ore. In that case the transport of
the oil and ore towards the mainland needs special consideration.

The third main group of industries to be located on offshore islands could
be those which include not completely avoidable risks. They may include un-
loading stations for dangerous goods such as, for instance, liquified gas.

As a last point, also airfields might be included under "offshore loading faci-
lities". This then more from the Coastal Engineering point of view than from
the transportation problems related to the loading and unloading of huge crowds
of passengers travelling with the modern and future air giants. An example of
such an offshore airfield is the project made by the I.P.H.C. for the second
national airport in Holland, south of Rotterdam. By this solution all approaches
by planes to the airfield are over sea.

Through the consideration of the title already a first appraisal of the problems
has been made. In the following the coastal engineering aspects of the various
possibilities will be discussed somewhat more in detail.

The most well known and most widely used offshore loading and unloading facili-
ty is the Single Buoy Mooring. It is developed for those places where the ap-
proach to the mainland causes great difficulties with respect to the mainte-
nance of an approach channel of sufficient depth. In these cases the buoy is
laying normally not too far from the shore and the load is pumped to or from the
buoy via a pipeline. Due to the typical features of the coasts where these buoys
were placed initially, that are the coast of delta's where oil was found, the
sea bed on which the pipeline would have to be placed was normally rather flat,
and sometimes even muddy. In this case no problems will arise with a partly un-
buried pipeline. In case a breaker region has to be crossed, it will be neverthe-
less wise to bury the pipeline. In the still relatively limited depth near the
shore, neither the laying of the pipeline, nor the burying will impose insur-
mountable problems. This, however, is mainly a compliment to be payed to the
practical coastal engineers.

In the case S.B.M.'s are used as loading points for offshore oilfields, the
depth in which they have to be placed and in which the pipelines will have to be
layed will be most likely much greater. It is, moreover, in those areas not un-
likely that the sea bed will be rather undulating, for instance, covered with
big ripples or sand dunes. Burying the pipeline in those cases will be much more
complicated. If the pipeline will be placed in a dredged trench one cannot ex-
pect with certainty that this trench will be filled in naturally. Recent soun-
dings of the trench for the sewage outfall for Scheveningen going about 7000 m
from the shore into sea, have shown that this trench has not been filled in
during the past ten years. Sinking of the pipeline by liquifying or jetting
will not always be possible due to the composition of the bottom and will,more-
over, in the case of jetting not solve the problem of the filling in of the
trench. If the pipeline can be kept unburied with regard to shiping (anchors),
in relatively deep water, no serious problems have to be expected with respect
to the forces exerted by waves and currents on the pipeline. However, if the
bottom is erodible a scour area under the pipeline may develop. If the erosion
is even, the pipeline will sink into the scouring hole. This erosion will stop
when the lowest point of the scouring hole is about $1\frac{1}{2}$ times the pipe diameter
below the surrounding sea bed. This value which is the result of tests, with and
without waves, executed in various laboratories, is still valid when the pipe-
line follows the erosion in such a way that an opening is still maintained be-
tween the pipeline and bottom. Ultimately, one can expect that the scouring will
stop.

Difficulties will arise now if at some places the pipeline is covered already
due to locally intensive scouring and sand movement at the top of a sand dune.
Just as when the pipeline is locally supported by clay layers or rock no sinking
can occur here. Now, scour occurs between two of those points leaving the pipe-
line to behave as a girder supported and clamped at two points, or even as a
string. It depends on the flexibility of the pipe and on the distance between
the two possible points of support whether this will cause unacceptable stresses
in the pipe.

Since the sinking of the pipeline due to scouring is limited with respect to the surrounding sea bed, the maximum curvature can be determined if the height of the dunes and the distance over which the pipe has scoured itself in the dune, are known. Procedures to calculate the behaviour of the pipe in such circumstances are under development at this moment at the Coastal Engineering Group of the Delft University of Technology.

Also the laying of pipelines from lay barges will cause problems at great depths. Since the stingers from the lay barges have only limited lengths the very long S curve by which the pipeline goes from the barge to the sea bed will cause great tensions and danger on unacceptable deformation of the pipeline cross section. This may be solved, at least partly, by applying pretension in the pipeline via the anchor system of the lay barges. The whole system has to be calculated as a rather complicated mass-spring system, for working in wave conditions in order to improve working time. For the crossing of very deep under sea canyons suspended pipelines may be considered.

A very special point of concern of all offshore Single Point Moorings is the execution of the mooring operation and the handling of the tanker during unloading. Up to this moment a limit is set for these operations by weather and wave conditions, especially with regard to the behaviour of the floating pipeline. An improvement can be certainly achieved by making the buoys so large that the hawsers and pipelines can be stored on reels. Since these buoys are manned, also a helicopter deck is provided. This much heavier spar buoy has also the advantage that the movement of the buoy is less, and therefore, the forces in the bow hawsers and the anchor chains will show fewer and lower peak values.

When these single buoy moorings are used as a loading station for an offshore oilfield it might also be useful to create some storage there. In that case a combination of a mooring point and storage tank can be developed. The buoy is then still heavier and will be much more quiet, which again can decrease the peak forces in anchor chains and mooring lines. Of course precautions must be taken that no spillage of oil can occur if a collision between buoy and tanker would take place. This can be achieved by placing the tanks deep in the buoy, at any rate below the keel of the fully loaded ships.

In order to decrease the difficulties with the mooring systems of the buoys, fixed mooring towers could be considered. These can be executed either as jacket constructions or as gravity structures. Also these mooring towers can be combined with storage tanks. In this case the designing engineer will be confronted wih a new set of problems, viz.: the placing and foundation problems. Especially during the last phase of the sinking operation, large horizontal forces may occur due to the sideways escape of the water between the sea bed and the bottom of the structure.

The foundation problems result largely from the earlier mentioned impact forces. Especially when the structure is placed on relatively fine sand there may occur liquefaction due to the fact that water cannot escape sufficiently quickly with short lasting forces executed by the structure on the subsoil. In order to determine this possibility the forces have to be calculated starting from the mass-spring system of structure, surrounding water and that part of the soil mass that is influenced by the movement of the structure. Up to now no reliable computational procedures are developed for this problem. One of the first things

to be done, therefore, is to decrease the magnitude of the impact forces as much
as possible. This can be done using the system of the Ekofisk tank, where the
wave forces - and especially the impact forces - are decreased by damping cham-
bers around the actual storage tank. Another possibility is to decrease the
cross section of the structure in the area most affected by the wave forces.
The storage part with large cross section is kept then deep under water and
the shaft which forms the connection between the actual storage tank and the
mooring and living platform is constructed as a slender column, or a number of
slender columns. With these forms of the tanks difficulties with stability may
be expected in the final phase of sinking when only the shaft with the small
cross section intersects the waterline.

Especially for the tanks which have a rather great cross section at the water-
line it may be difficult to execute the mooring system in such a way that the
ship can swing around it. Moreover, in all solutions discussed up to now the
tanker is laying in almost unprotected water. Because also in the case of the
combined mooring and storage tower which has a great cross section at the water
level and which will orovide for that reason some - may it be still limited -
wave protection, it is possible and likely that due to current the tanker will
not lay in that lee area. Practice up to this moment tends to indicate that the
mooring can be executed until waves are not higher than 2.5 m and the loading
can go on until the waves has reached a height of 5 m. When these restrictions
result from the behavior of floating pipelines, the limits can be probably
higher if the mooring hawsers and pipelines are stored on reels on the platform.
If the restrictions are the result of the working conditions on the ship an in-
crease in the workability can be only achieved by decreasing the wave height or
changing the ship design. The first item could be realized if the storage capac-
ity should be so much that more than one storage tank is required. By placing
these tanks in the proper position a sheltered area could be obtained. This
principle has been studied in Delft some years ago by Beck as part of his
master's thesis. From his study it became clear that the storage tanks should
be placed rather close together in order to obtain sufficient wave damping.
From the transmittance of the wave energy follows that the wave damping due to
tanks with a spacing equal to the diameter of the tanks will be only 30%.
In the case of tanks with a circular form the damping will be even less due to
the typical diffraction phenomena occurring around a cylinder. This solution
tends already to an offshore harbor installation if the storage function of
the harbor is considered. Beck worked this out for the Dutch coast as a possi-
ble alternative for the extension of the oil storage in Rotterdam and the un-
loading facilities for V.L.C.C.'s up to 500.000 DWT. He assumed tanks with a
diameter of 80 m placed in water of 30 m depth. The net storage capacity of
each tank will be then 120.000 m^3. Placing 35 tanks in a row, a total storage
capacity of 4,200,000 m^3 and mooring facilities for three to four carriers
can be obtained. The S.B.M.'s providing these mooring facilities are situated
so that a reasonable protection is obtained for winds from the western quadrant.
The attractiveness of this solution depends for a great part on the cost re-
quired for the maintenance of an approach channel to the mainland. For the con-
ditions along the Dutch coast these maintenance cost prove to be much lower than
was expected originally. It is therefore questionable if a solution as described
here will be feasible, taking also into account the costs for pumping the oil
ashore. If the processing industries would also be placed offshore the solution
would become much more attractive. Solutions of that kind will be discussed
later on.

Another example of an offshore loading station is a project for combined storage
and loading of bauxite ore, just off the mouth of the Corantijn River in Suriname.
This was designed by Fekkes (also as part of a master's thesis in Delft) as a
floating structure. Due to the limited available depths in the Corantijn, the
barges bringing the ore from the mines to sea cannot have a draft greater than
5 to 6 m. Fekkes decided on barges of 100 x 20 x 5 m^3 with a D.W. Tonnage of
4000. They unload the ore, moored in an artificial harbor made in the large
floating loading and storage platform. This platform has a length of 460 m, a
width of 135 m and draft varying between 15 and 11 m, depending on the stage of
loading of the storage platforms. The artificial barge harbor has a depth varying
with the draft of the total installation between 6 and 10 m. The storage area is
67 x 400 m^2 and can contain 100,000 tons of ore, being the loading capacity of two
bulk carriers. The seagoing ore carrier is moored alongside the platform. The ore
is loaded either direct from the barges into the carrier or via the storage area.
The main reason for the choice of this solution are the very poor foundation con-
ditions in this area. An additional advantage is now, however, that if the floa-
ting structure is allowed to adjust itself to the actual wind and current situa-
tion, also the approach and mooring of the carriers will be facilitated. The plat-
form will be moored, therefore, at the bow to an anchoring construction driven
sufficiently deep into the soft soil. The protection in the artificial harbors is
such that the barges stay there under the worst possible conditions, whereas the
carriers have to leave the platform in order to ride out the most severe storms
in open sea. These conditions occur not more than some days per year.

When the offshore storage of crude is considered, the next more or less logical
step is to situate the processing industry offshore as well. The least expensive
construction material for such an island is undoubtly sand. By building such an
island, again quite some fundamental Coastal Engineering problems show up. They
can be split generally into three main catagories:
a. What are the influences of the island on the near surroudings, especially the
   coast, if the island is located close to the coast?
b. How must the shores of the island be constructed and what should be the ele-
   vation of the island?
c. How should the island be actually built?
Especially when the island is constructed close to the shore it may have an im-
portant and even destructive influence on the coastal regime. In the case an im-
portant part of the longshore sandtransport is caused by, or at any rate stimu-
lated by wave motion, the decrease in wave motion by an island of sufficient size
(say 3 x 6 km.) will cause a local decrease in sandtransport capacity along the
coast of the mainland. This will result in an accretion of the coast near the is-
land and subsequently erosion of sand from the adjacent beaches. This will be even
more evident if there is a net drift in one direction. If the safety of the shore
depends on the beaches (for instance with sand dune coasts) this will cause
serious problems. This influence should be studied, therefore, beforehand.
When this harbor area is constructed so close to the shore that it can be con-
nected to it by dams this point is even more critical. Due to the unavoidable
increase of possible sea currents as result to the existence of the island also
some scouring of the surrounding seabed may be expected.

For the construction of the shores of the island the main choice will be between
a rigid construction and a soft one. It should be stated at once that both types
of protection should and can have the same safety and that they have to be both
designed starting from the same wave condtions. That is to say, that just in the
case with a rigid protection by sea wall, (comparable with a breakwater) for the
design of a soft protection by a sandy of gravel beach the wave condtions must be
known in detail in order to be able to make an optimalization.

It will not be necessary to go into detail into the construction of the seawall,
since this can be done along the lines of the more or less accepted and well
known procedures. It will be interesting, however, to see if it is indeed possible
to design an island only protected by sand beaches. As an example an island of a
length of some 6000 m laying with the long side perpendicular on the prevailing
wind and wave direction is considered. Due to the current and wave system a long-
shore sand drift may be generated along the exposed sides of the island. It will
be the task of the coastal engineering science to determine the longshore sand
drift, assuming the profile of the artificial beach. The material lost will have
to be supplied at any rate. This suppletion must be executed so that not only the
shore itself, but also the windward corners a and b of the island are kept stable.
It is possible to construct at these corners some sort of bulkheads which give
fixed limitations to the beaches. Here could be supplied just that quantity of
sand that is required to keep the beaches in an equilibrium condition. It is not
unlikely that in that case the form of the most exposed beach between the points
a and b will develop into a hollow line, as indicated on the sketch. It is obvi-
ous that the knowledge of the longshore sand drift is of the greatest importance
for the determination of the form of this beach. The sand can be brought to the
both points by supply lines from a borrow pit somewhere in the harbor basin.
The sand will be brought to this borrow pit by trailing suction dredgers. This
operation can be executed more or less continuously throughout the year. It is,
however, also possible to supply once per year or even once per several years a
quantity sufficient for that period. In that case, sorts of storage areas of. sand
will be made at the points a and b. This sand could be brought to those places
by seaworthy bottom dredgers, which pump their load to a loading buoy by floating
pipeline. From this buoy, a sunken pipeline will bring the sand ashore. At this
moment the design of such a seaworthy dredger which can operate in waves of 3 m
and which can ride out under own power all wave conditions, is ready for the con-
struction stage.

However, this longshore sand drift is not the only source of sand loss of such a
beach. Because of economical reasons the slopes of the artificial beaches will be
made as steep as possible, at any rate much steeper than the natural beaches.
Especially in rather deep water this difference will be important. Since this
slope will be steeper than the equilibrium slope a seaward transport can be ex-
pected. It will be clear that only a good evaluation of the possibilities of
sandy beaches as a protection can be made if this offshore transport is known.
This must be and is one of the topics of the research in coastal engineering.
The fundamental approach will be the detailed study of the water movement in the
area along the coast that is influenced by the waves. Also at this conference
various investigators publish the results of their works in this field. When this
water motion is known, the sand movement as a result of this motion has to be
evaluated. This motion has to be regarded as the result of the turbulence in the
boundary layer under the waves and the general circulation pattern studied in the
research projects mentioned just before. Although already promising results have
been obtained, it is not yet possible to give definite results.

Since, however, it is necessary to give information on this subject now already,
also another line of approach is used, viz.: the so called external approach. In
this approach some basic relationships between wave attack, grainsize of beach
material, beach slope and onshore- offshore movement are established. These re-
lationships can be calibrated with data from prototype and model. In one of the
publications of this conference a workable schematization of this onshore- off-
shore sand transport is given.

The supply of the sand to compensate for the offshore motion must, in principle, be supplied evenly over the whole length of the beach. This, again, however, can be done once per year or once per several years. From a detailed study it might prove also possible to chose such a curvature of the beach that the longshore drift generated by the waves is such that sufficient sand is available for the offshore motion.

An intermediate solution between the complete soft protection of a sandy beach and a rigid protection in the form of a seawall is the protection with coarser material, for instance gravel. Also this solution is applied at various places and studied by various investigators. Of these studies reports are given just as well at this conference.

A special point of concern for these island loading stations is the level of the terrain. This level could be much below the surrounding sea level in the case of offshore airfields or industrial areas, while it will be difficult to apply this solution in the case of a harbor. A great difference in level between the industrial area and actual quay level will be rather troublesome and uneconomical. With respect to the rather large area of the island, it will be important to determine the water level upon which the design has to be based as accurately as possible. A thorough knowledge of the motion of big bodies of water in seas or over ocean shelves is compulsory therefore.

In this paper the contribution of coastal engineering to this topic of offshore loading and unloading points is given. It is stimulating to notice that all points mentioned in this paper also are discussed at this 14th conference by contributors giving the results of current research.
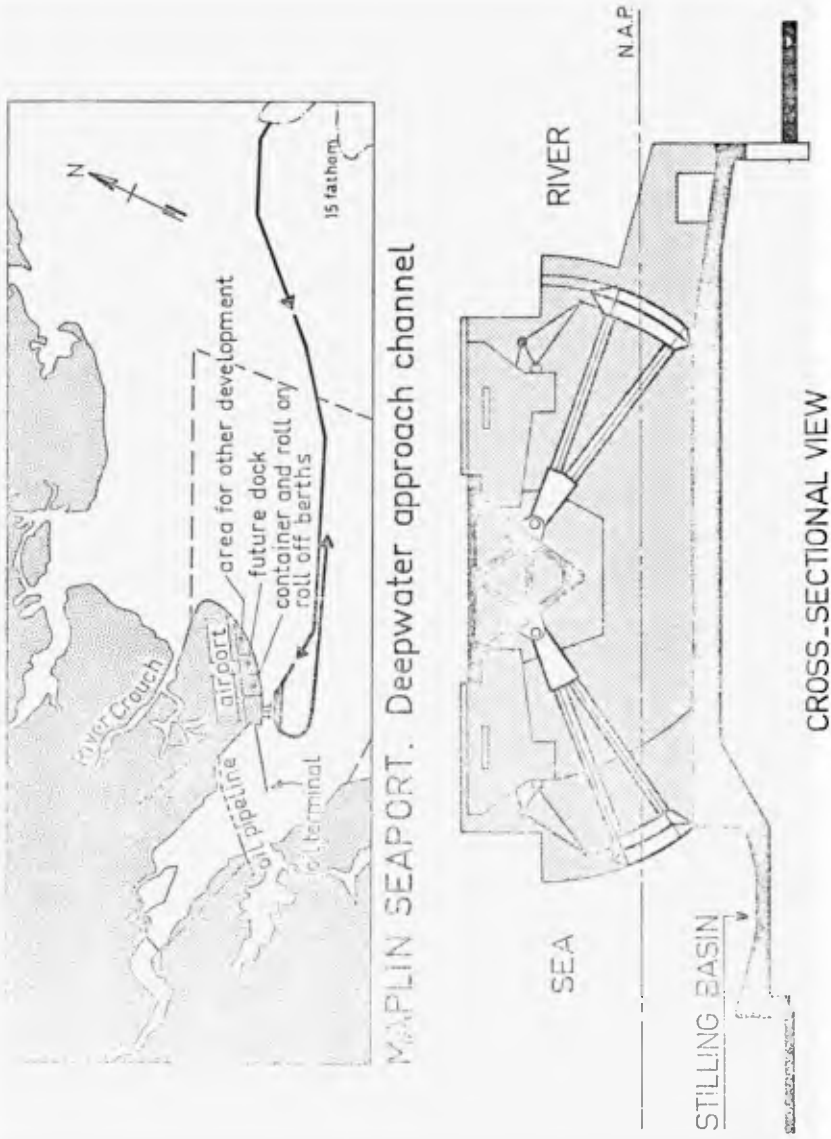
MAPLIN SEAPORT. Deepwater approach channel

CROSS-SECTIONAL VIEW

HARINGVLIET DISCHARGE SLUICE
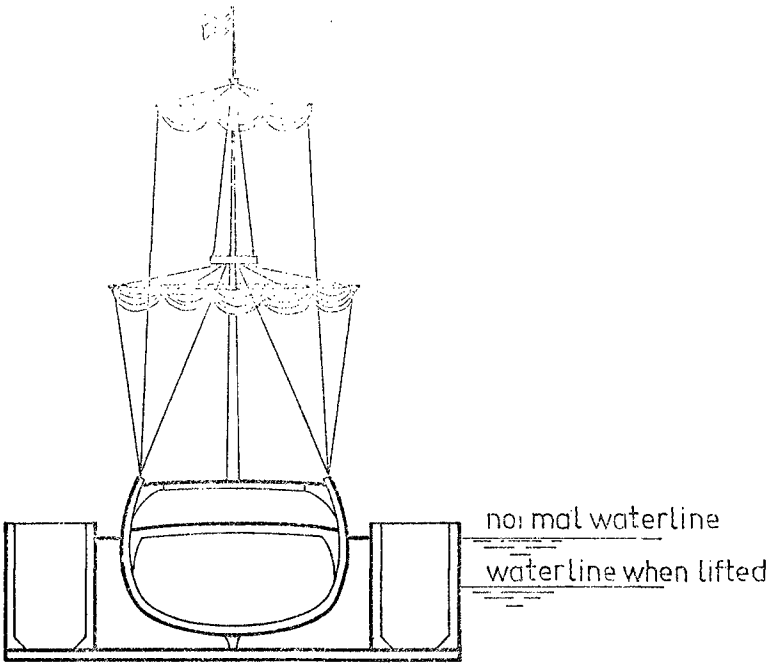
SHIPS CAMELS
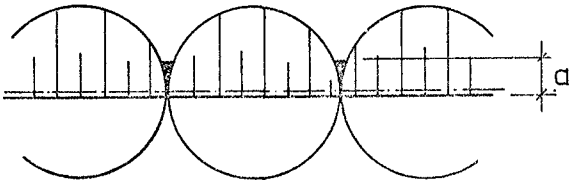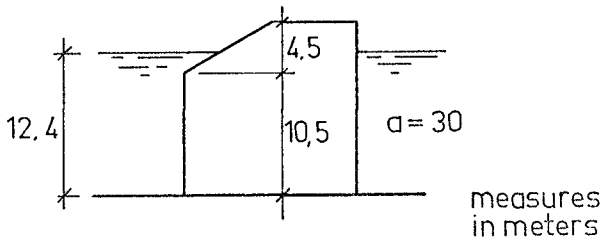
CROSSECTION AND PLAN OF
BREAKWATER OF HANSTHOLM
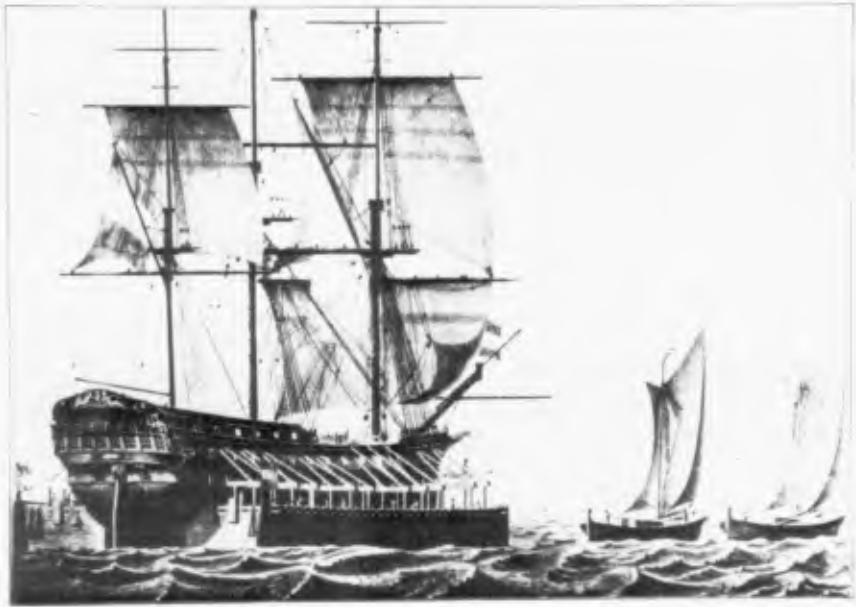
Oorlogsschip zeilende op een scheepskameel, getrokken door twee Marker waterschepen.

SPAR

MAIN TRUNK

ACCOMMODATION DECK

MACHINERY DECK

METERING DECK

EMERGENCY TANKDECK

ELEVATOR SHAFT

SLOPTANK DECK

DIVING DECK

DOUBLE BOTTOM FUEL & FRESHWATER TANKS

ANCHORING DECK

MAINPUMP DECK

WATER TREATMENT DECK

TURNTABLE
ACCOMMODATION
DIVING DECK
CONTROL POWER
FULL WATER
METERING DECK
ANCHORING DECK
SLOP TANK
PUMPS

WATER TREATMENT

BALLAST PUMPS

FIXED BALLAST

TANKER LOAD RATE 5 000 TON/HR
SPAR STORAGE CAP 300 000 BBL
SPAR RECEIVING RATE 100 000 BBL/D

SPAR TYPE STORAGE TERMINAL

HELIDECK

TANKER 50000 DWT

22 m

MOORING ROPE REEL
TURNTABLE

MOORING TRUNK

FENDER CONSTR.

22 m Ø

BUOYANCY COMPARTMENTS

12 m Ø

52 m

6.6 m Ø

BALLAST COMPARTMENT

33 m

2 HOSES 10"

SINGLE BUOY MOORING

by courtesy of S.I.P.M.

SKETCH OF POSSIBLE ISLAND-HARBOUR
OFFSHORE IJMUIDEN
(International Course Hydraulic Engineering,
1957-1958)
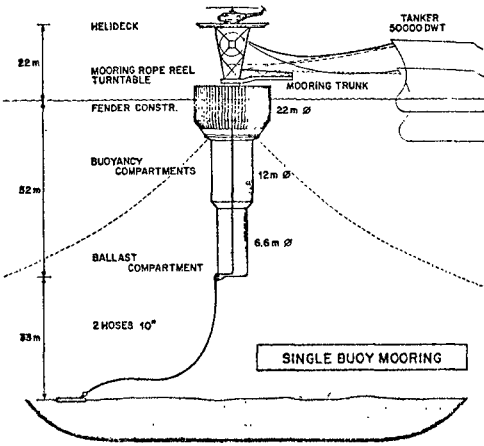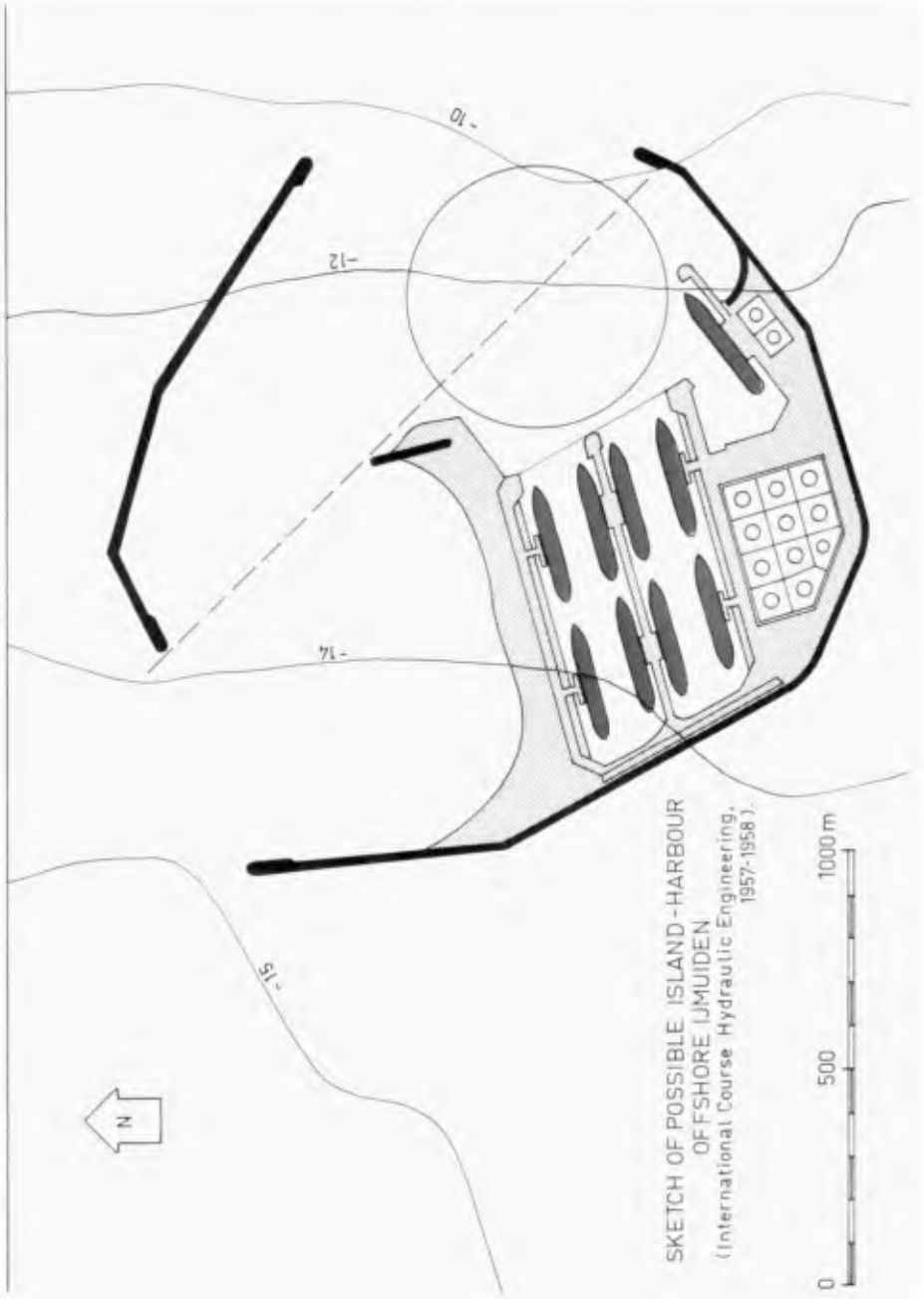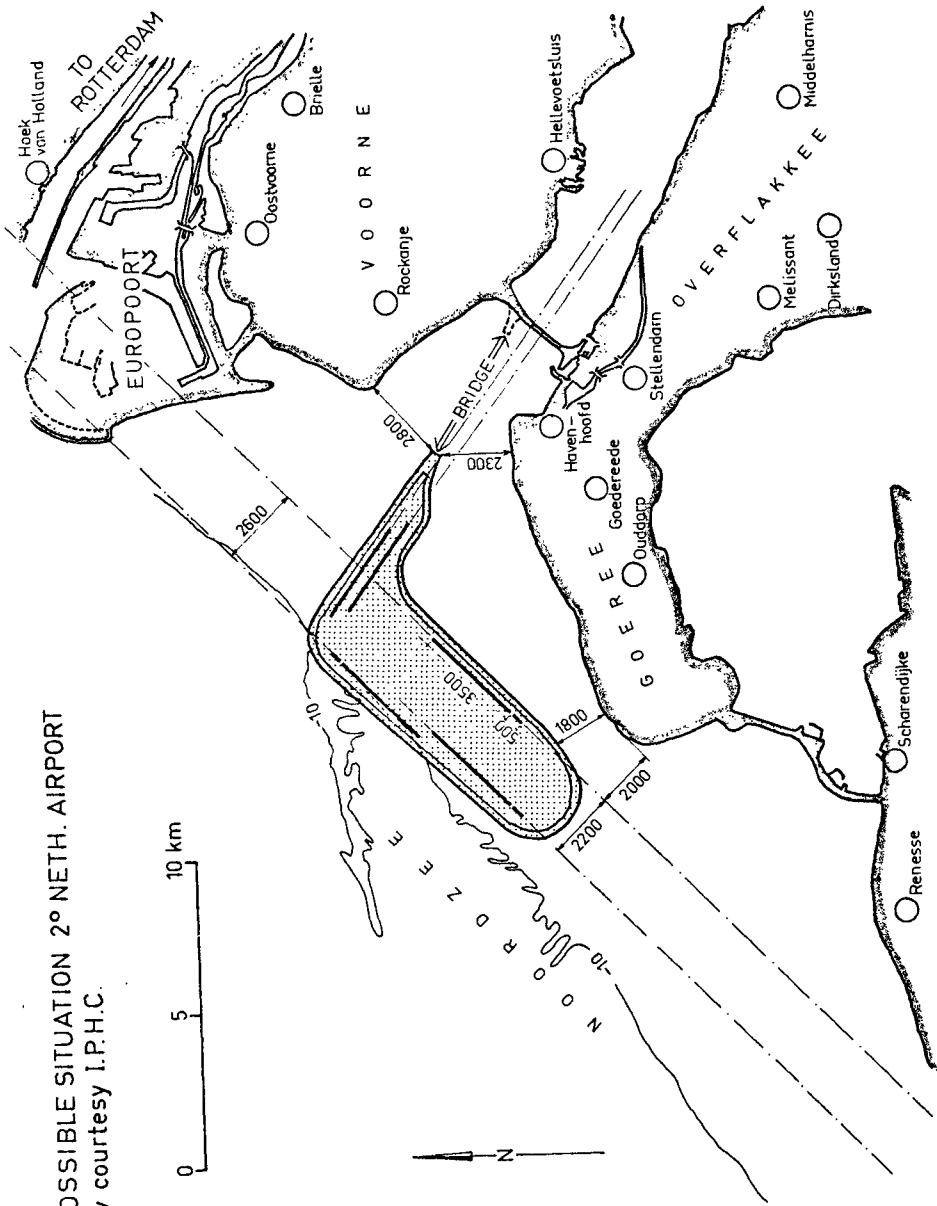
POSSIBLE SITUATION 2° NETH. AIRPORT
by courtesy I.P.H.C.

S.B.M.

pipeline to
storage tanks   single
                       buoy
                       mooring

380m
500.000 dwt tanker
length 380 m.
beam   66 m.
draught 27 m.

schaal 1:5000

turning circle for ships

N

W ——✳—— O

Z

0   500m   1000m
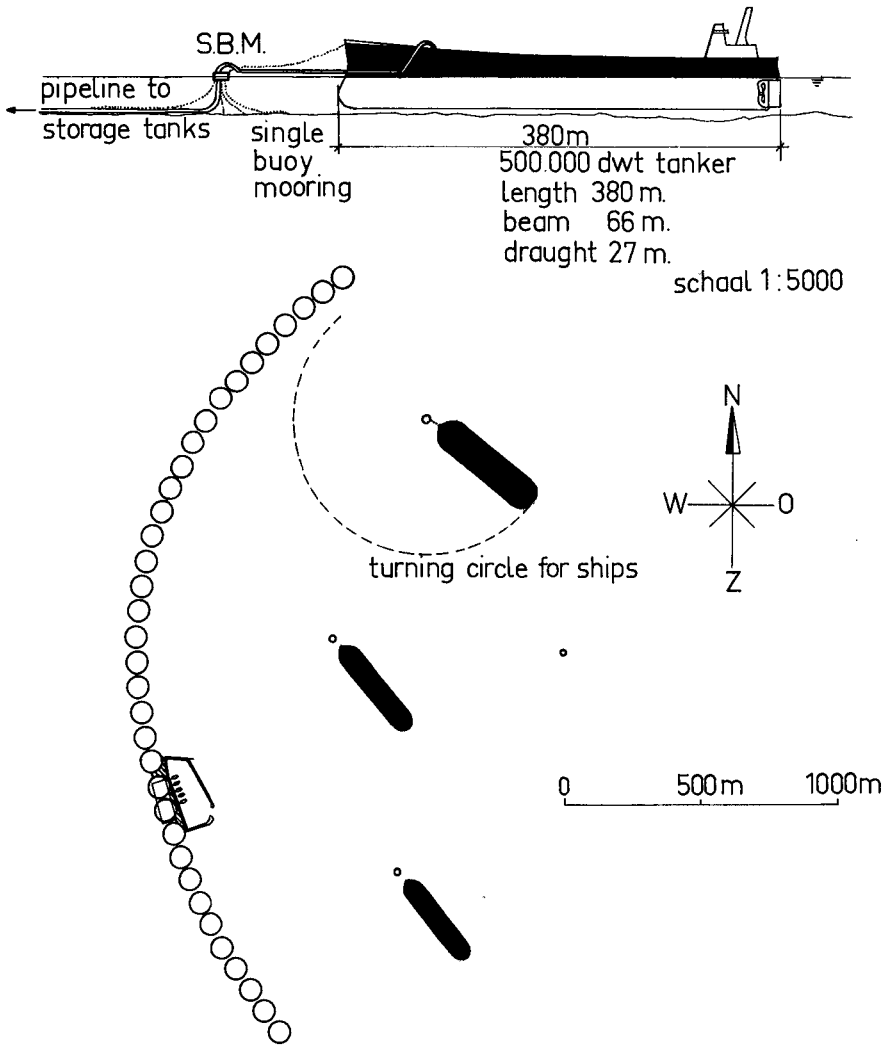
LAYOUT OF STORAGE TANKS AND S.B.M.'s

(acc. to BECK)

6°10'

57°10'

6°

5°50'

57°

0

0

10

10

20

20

30

30

Nickerie river

Bluffpunt

Nieuw Nickerie

Springlands

Skeldon

40

Papegaaien island

Robinson island

Yessah island

50

60
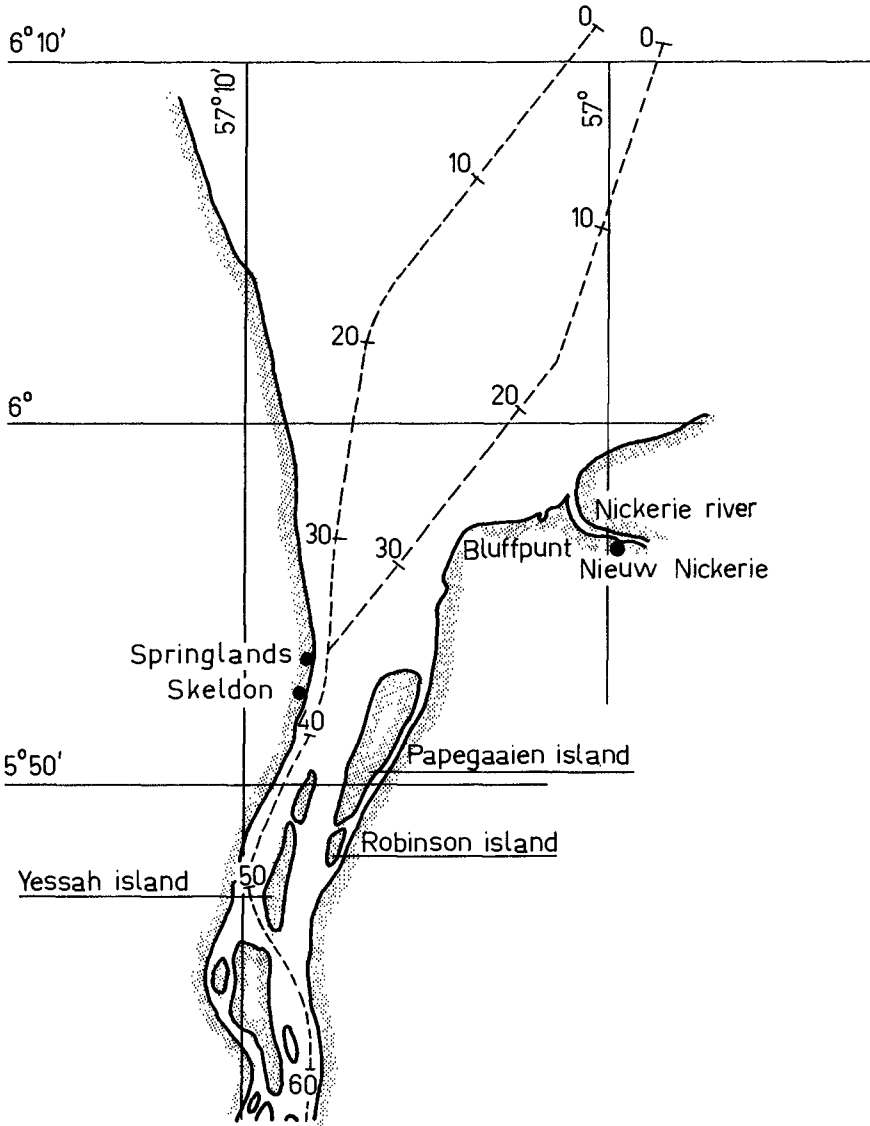
MOUTH OF CORANTIJN – RIVER (West – Suriname)
(from: NEDECO; Surinam Transportation Study)

anchoring cables

80

460

380

5

45

135

85

measurements in m.

barge

storage area

storage area

bulkcarrier

tugboats

PLAN OF PLATFORM

bulk carrier

storage area

+3

135

barges

0 -

— 11 to 15
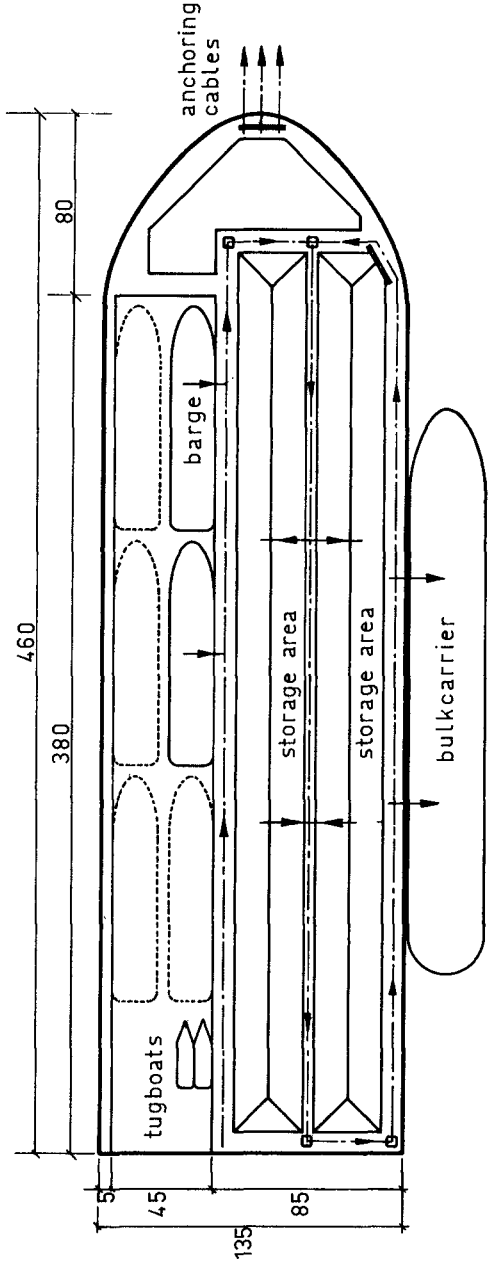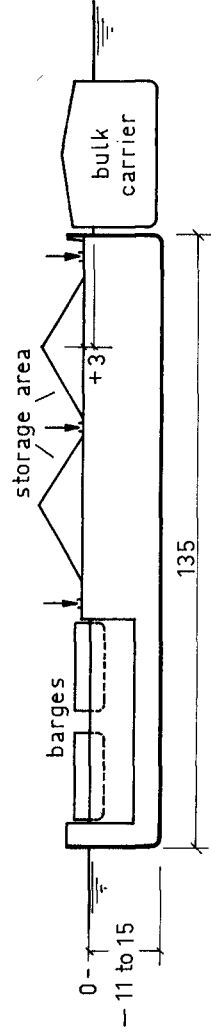
PLAN AND CROSSECTION OF FLOATING ORE TERMINAL (acc. to Fekkes)

Prevailing wave directions

supply point for artificial feeding

a

Possible borrow areas

b

supply point for
artificial feeding

—— original coastline
— — possible development of coastline ⎱
→ main tidal currents ⎰
⇒ sand drift
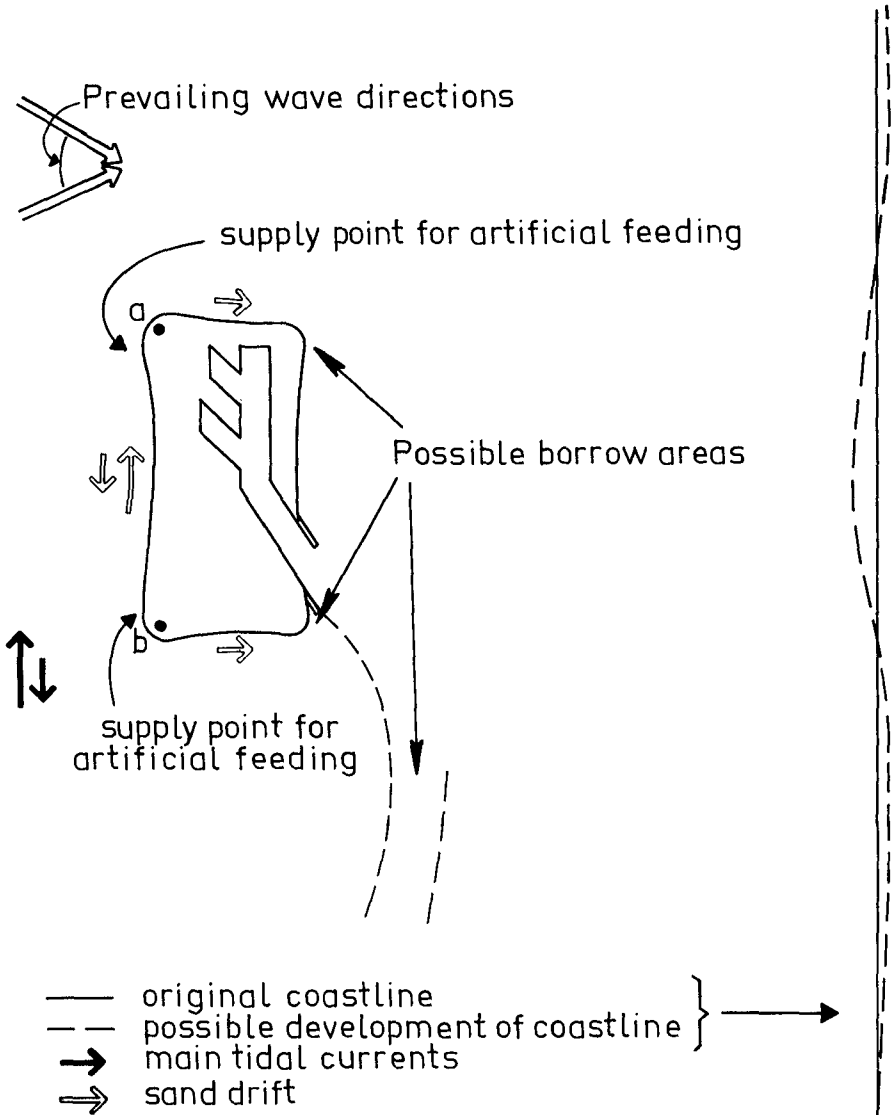
LAYOUT OF POSSIBLE ISLAND IN FRONT OF SANDY COAST.

Hirtshals Harbor, Denmark

PART I

THEORETICAL AND OBSERVED WAVE CHARACTERISTICS

Hanstholm Harbor, Denmark

CHAPTER 1

EXTREME LEVELS ARISING FROM METEOROLOGICAL SURGES

by

P Ackers and T D Ruxton

ABSTRACT

The design of coastal works depends on estimating the probabilities of extreme water levels, as well as of waves Previous studies of surge-affected levels have extrapolated observed annual maxima or the n highest levels in n years to predict rarer events In addition to using these well-established methods, in this study of tide levels on the Essex coast of Britain a long term record of extreme levels was synthesised by adding surge residuals at the time of predicted HW to predicted HW levels, treating them as statistically independent events Many more large surge residuals have been measured than extreme water levels as many surges are associated with small tides Events with return periods up to 1000 years may be estimated without extrapolating beyond the range of observed surge residuals and predicted tides This method is assessed in relation to previous methods and information relevant to the design of coastal works in the south western part of the North Sea was obtained In addition to forecasting the probabilities of high tide levels, the study included wave forecasts and the encounter probabilities of combinations of sea level and wave height for various aspects of coastal developments

Extreme levels arising from meteorological surges, by Peter Ackers, hydraulics consultant, and David Ruxton, chief engineer, Binnie and Partners, Artillery Row, London.

69

EXTREME LEVELS ARISING FROM METEOROLOGICAL SURGES

by

P. Ackers and T.D. Ruxton

INTRODUCTION

In connection with developments proposed on the Essex coastline
north of the Thames estuary (see Fig. 1a for location), the effects of
tide, surges, wind and waves had to be assessed, to determine the
probabilities of extremely high water levels, of large waves and of their
simultaneous occurrence. The importance of this aspect of design is amply
illustrated by the catastrophic effects of the 1953 North Sea surge tide
which breached the coastal defences of England and Holland. On that
occasion a surge of 6.8 ft was added to a predicted high tide level of 8.3 ft
above O.D.N. High spring tides here have a range of about 19 ft, rising
to 10.5 ft above O.D.N. (ordnance datum based on mean sea level at
Newlyn).

Previous studies of extreme levels around Britain's coasts have used
past observations of annual maximum levels at long established tide gauges,
or the number of highest levels observed in a similar number of years,
extrapolating these observations to predict rarer events (Lennon, 1963;
Suthons 1963). Similar methods have also been used elsewhere (Dronkers,
1960; Wemelsfelder, 1939). To design coastal works, for slope protection,
overtopping or drainage, requires a full assessment of the probabilities of
combinations of sea levels and wave heights. In order to combine wave
forecasts with associated water levels, the observations of extreme levels
had to be classified against wind data so that cross-probabilities could be
assessed. As winds and surges are both dependent on similar meteorological
influences, it was appropriate to separate surge residuals from observed
tidal elevations by subtracting predicted astronomical tides. This
separation led to the concept of also synthesising a longer record of
extreme water levels by adding the distribution of surge residuals at HW
to predicted tide levels at HW, as if they were independent events.

South-east England is undergoing a change of sea level relative to the
land. This secular trend has also to be taken into account. The level of
coastal works relative to the sea is dropping at the rate of about 0.34 m
per century, and this has a significant effect on the design of tide-excluding
works. No new work was undertaken on this aspect, previous studies
(Rossiter 1972) having established the current secular variation. Results
may thus be expressed in terms of the year 2000, by adding 0.34 mm per
year to levels related to the present, or to earlier years.

DATA AVAILABLE

Tide levels around south-east England have been observed for many years. There are reports of extraordinary tides in the 13th century, 1663, and on three occasions in both the 18th and 19th centuries. · Since the storm surge of 1928 a reliable gauge has been operated at Southend, and in 1956 the Storm Tide Warning Service (STWS) was set up as a result of the 31st January/1st February 1953 calamity.

Positive surges have been classified into three groups external, generated north of Scotland and propagated southwards through the North Sea; internal, generated within the area by northerly winds; easterly, arising from the set-up by strong local easterly winds in the southern north sea. The distribution of the storm surge additions to predicted water levels is thus associated with the distribution of winds.

Previous studies have shown that the record from the gauge at Southend Pier is the best available in the area. A near-continuous record exists since 1929, the gauge support is firm, and the site is close enough to deep water to avoid local shallow-water effects. These data had also been used in determining the secular variation.

The Institute of Oceanographic Sciences (IOS) had listed all levels above 11.0 ft ODN for the period 1929 to 1968. Values for the last five years were added to complete the list. None of these high levels occurred in the summer months and more occurred in October than in any other month. The analysis therefore used a July to June "storm-surge year" rather than the calendar year. 10 year running means show some grouping of levels above 11.0 ft O.D.N. into adjacent years, the average varying from 13 to 31 in a 10 year period. This bunching is apparent in the historic data as well, although the reason is unknown.

Predictions of astronomical tides are available in Admiralty Tide Tables (ATT) for yearly periods,based on tidal theory. The tidal coefficients have been adjusted from time to time on the basis of new observations. Until 1950 the Equation Method was used for Southend, from 1951 to 1968 the Harmonic Shallow Water Correction method, and from 1969 the Extended Harmonic method. In this study the distribution of astronomical tide levels have been taken from ATT for 1969-73, to avoid times when the methods, coefficients or datum have been adjusted. It was not practicable to average over the 19-year cycle of the nodal tide, but this 19 year variation is of very small amplitude.

IOS also provided lists of all days in the period 1929-1969 when surge residuals (observed water level minus predicted water level at HW) exceeding 2 ft and 3 ft occurred at Southend. Data was available on the distribution of surge residual either side of HW (actually at clock hour intervals, which could differ by $\pm \frac{1}{2}$ hr from hourly intervals relative to HW). Graphical records were obtained from the STWS for all surges over 2 ft from 1956, for the months between September and April when the service operates.

ANALYSES AND RESULTS

Annual maxima of tidal levels

The prediction of extreme values is affected by the extent to which the spread of the frequency distribution (defined by the standard deviation) varies as the duration of record is increased. If the standard deviation decreases there may be a theoretical upper limit to the level that may be obtained; if the standard deviation increases there is no such limit. The ratio of the standard deviations of the one-year maxima (δ_1), and of the two-year maxima (δ_2) indicates the curvature of the function. Gumbel (1934) assumed that the transformed frequency curve defined by $Y = \ln(-1nP)$ was a straight line and that $\delta_1 = \delta_2$. Barricelli (1943) allowed δ_1/δ_2 to vary between 1 and 1.21, the value associated with a normal distribution of annual maxima. Jenkinson (1955) fitted a curved function to the data, given by

$$Y = \frac{1}{k} \ln\left(1 - \frac{H - Ho}{a}\right) \qquad \ldots\ldots \text{equ 1}$$

where H is an observed height, k, a and H_o are empirical constants with k defined by

$$k = \frac{\log \delta_1 - \log \delta_2}{\log 2} \qquad \ldots\ldots \text{equ 2}$$

If k is positive, the curve is convex upwards approaching a theoretical limit. If k is negative, the reverse curvature indicates no such limit. When k = 0, the Gumbel result emerges.

Lennon (1963) showed that for west coast tidal data the Gumbel method was less suitable than the alternatives. Suthons (1963) preferred Jenkinson's non-linear theory for east and south-coast ports. As there is now a 30 percent longer record for Southend than when Suthons made his analysis, it was desirable to repeat the study, using all high tide levels greater than 11 ft ODN adjusted for secular variation to the base year 2000, and using a storm-surge year in defining annual maxima. The results are plotted in fig. 2, together with the Jenkinson curve for $\delta_1/\delta_2 = 0.894/0.992 = 0.900$.

The broken line includes the necessary adjustment if the secular variation continues beyond year 2000 at its present rate of 0.011 ft/yr. The results are also expressed as encounter probabilities in table 1. This probability is given by $(1 - P_n)$ where

$$P_n = e^{-N/T} \qquad \ldots\ldots \text{equ 3}$$

T is the calculated return period of a particular high tide-level and N is the encounter period.

Table 1.   Encounter probabilities of high water levels.

Level	Referred to 1973	13.7	14.2	14.7	15.2	15.7	16.2	16.7	17.2
(ft)	Referred to 2000	14.0	14.5	15.0	15.5	16.0	16.5	17.0	17.5
Encounter	10	0.46	0.23	0.18	0.12	0.08	0.05	0.03	0.02
period	25		0.57	0.42	0.27	0.18	0.12	0.08	0.06
(N) years	50			0.62	0.46	0.34	0.23	0.15	0.11

Combination of predicted tides and surge frequency distribution

     The high water levels in the ATT for the 5 year period 1969-1973 were enumerated into 0.5 ft intervals, and probabilities of occurrence were assigned to each range.   This distribution of astronomical tides is shown in fig 3.   The predictions by the EH method for this period were compared with the HSWC method predictions for 1964-1968, and there were noticeable differences especially for tides in the range 10.5 to 11.4 ft.   The more recent method of prediction is presumably the more accurate, and has the added advantage of providing hourly height predictions as well as high and low waters.   The two methods have been described by Doodson (1957) and Rossiter and Lennon (1968).

     The distribution of surge heights was based on the IOS listing of residuals exceeding 2 ft for 41 years of record.   This was extended to lower values graphically, assuming that half the 705 tides each year have a positive discrepancy from predicted levels because of meteorological influences.   Corrections were made for gaps in the record, giving the following frequency distribution

Table 2 Frequency distribution of surge residuals.

Range of HW surge residual (ft)	-1.0 to +1.0	1.1 to 2.0	2.1 to 3.0	3.1 to 4.0	4.1 to 5.0	5.1 to 6.0	6.1 to 7.0
Average number of occasions per year	637	30	3.71	0.53	0.122	0.025	0.049

The combined frequency of statistically independent events is obtained by the product of their separate frequency distributions.   This assumption may be questioned because both surges and high tides show seasonal effects so that they could have a different chance of occurring simultaneously than if they were randomly distributed in time.   Also there is likely to be some interaction between surges and tides, the linear super-position of meteorological surges on astronmical tides ignoring non-linear features of tidal propagation.

The interdependence due to seasonal variations was examined by a
more detailed analysis based on six two-monthly periods per year. In
most instances an equal or slightly greater probability is predicted from
the seasonal analysis. The small difference is attributed to the different
seasonal distributions of the two events, the times of equinoctial tides
being a period of average surge activity only. As the annual data are
easier to use and provide greater detail, the use of annual data was
considered justified.

The possible interaction of large surges with large tides is influenced
by the limited energy that can be introduced into the sea by combinations
of astronomical and meteorological forces. This is believed to be partly
the reason that the peak of the surge residual tends to avoid the time of HW.
It may also transpire that whereas a 6-7 ft surge residual at HW occurs
twice in 40 years when associated with HW levels of 9.5 ft ODN or less,
such a surge may not be physically possible with HW levels greater than
say 10 ft ODN when the sea will have less capacity for absorbing more
tidal energy. Although no quantitative assessment of these facets was
possible with the data available, the assumption of independence and
linear addition are likely to be conservative on the open coastline. This
would not be so in estuaries which cause tidal amplification.

The combined frequencies of predicted tides and surges are shown in
table 3.

Table 3. Number of occasions per year for combinations of predicted tide
and surge addition at HW.

PREDICTED TIDE ft	7.2	7.7	8.2	8.7	9.15	9.65	10.15	10.6	11.1
SURGE ADDITION	OCCASIONS PER YEAR								
0 ft	63.7	72.0	87.2	94.2	71.3	42.0	21.0	7.0	1.27
1.35 ft	3.00	3.39	4.11	4.44	3.36	1.98	0.99	0.33	0.06
2.35 ft	0.371	0.419	0.507	0.548	0.415	0.244	0.122	0.041	0.007
3.4 ft	0.053	0.060	0.073	0.078	0.059	0.039	0.018	0.006	0.001
4.4 ft	0.012	0.013	0.017	0.019	0.014	0.008	0.004	0.001	<0.001
5.4 ft	0.003	0.003	0.003	0.004	0.003	0.002	0.001	<0.001	<0.001
6.4 ft	0.005	0.006	0.007	0.007	0.005	0.003	0.002	0.001	<0.001

Heights of predicted tides are in ft above ODN as at 1971, and the medians
of the class intervals are given. Surge additions are in ft, and also are given
as the medians of the class intervals. From Table 3, the number of times
a given high water level was reached or exceeded was extracted, and adjusted
to year 2000. These data are presented in fig 4 in terms of return periods
for given levels, and in effect form a synthesised record of extreme water
levels extending to events with a return period of 1000 years. Also shown

on fig 4 are the actual observations of high levels over the 44 years of
record at Southend.

It will be appreciated that this method implicitly assumes that the
two distributions are in fact truncated, there being no predicted tides
above elevation 11.4 ft ODN (1971) to extend table 3 to the right to the
next interval and no surge residuals exceeding 7.0 ft to extend the table
downwards to another interval. The first of these implicit assumptions
is readily accepted: there is an upper limit to the predicted tides which
is very closely approached in any 5 year period. The second assumption
might be questioned. The distribution of surge residuals could be
extrapolated beyond the range of observations, for example on the basis
of extreme value theory, and incorporated as an additional row in Table 3.
The effect on the overall distribution would be small however.

Comparison of methods

Both the observed and synthesised data in fig 4 show a change in
slope at about elevation 13.3 ft ODN (2000). Levels above this value are
only reached by surges greater than 3 ft, and any attempt to predict the
probabilities of rarer events from lower values could have been misleading.
The agreement between observations and synthesised data for return
periods up to 44 years suggests that the assumptions made may be
reasonable, but clearly scope exists for detailed statistical research.

The results in terms of encounter probability are given in table 4.

Table 4. Probabilities that certain levels will be exceeded in a given
          period of years.

Level (ft ODN) (year 2000)	14.0	14.5	15.0	15.5	16.0	16.5
Return period, T, yrs	12.2	19.5	32	55.5	103	203
Encounter 10	0.56	0.40	0.27	0.16	0.09	0.05
period, 25	0.87	0.72	0.54	0.36	0.22	0.11
yrs 50	1.00	0.99	0.98	0.59	0.38	0.22

We may also compare the predicted return periods by extrapolation from
the annual maxima frequency analysis with those deduced from the
combination of predicted HW levels and the frequency distribution of
observed surges.

Table 5. Comparison of return periods of extreme water levels.

Level, (ft ODN, year 2000)	12.0	13.0	14.0	15.0	16.0	17.0
Annual maxima method	0.66	3.9	12.2	32	100	424 yrs
Combination method	0.86	5.0	19.2	52	150	305 yrs
Actual observation	0.86	4.0	11.0	44yrs		

Other results

It was clear when tabulating extreme water levels that surges tend
to affect groups of successive tides, so that they are not randomly
distributed in time. In 40 years, only 571 of 1388 surge residuals greater
than 2 ft, and 226 of 426 surge residuals greater than 3 ft, were on
isolated days. All other surge-affected tides occurred in association with
similar surges on one or more adjacent days. It follows that when large
surges and tides coincide very high levels are likely to be reached by a
number of successive tides, and the encounter probabilities deduced must
be viewed with this important fact in mind. In 1965/6 there was a
succession of 15 days when the surge residual > 3 ft (and 16 > 2 ft). In
the notable 1953 surge sequence, there were 3 days > 3 ft and 7 > 2 ft.

The design of coastal works is dependent on the durations for which
levels may exceed selected values. An analysis was based on the cumulative
durations for the decade 1951-1960 in excess of levels equivalent after
secular adjustment to 9, 10, 11 and 12 ft ODN (1973). When divided by the
number of events, average durations are obtained. These are compared with
the 1953 surge in table 6.

Table 6. Durations of level exceedances.

	> 9ft	> 10ft	> 11ft	> 12ft
Average (hrs)	1.35	1.02	1.00	1.16
1953 event (hrs)	5.6	5.1	4.5	3.8

This illustrates the prolongation of high water levels by meteorological
surges. This is also shown in fig. 5 which compares some recorded tide
curves of extreme events with the sinusoidal shape to which the predicted
curves of a mean spring tide closely approximate.

WAVE GENERATION

A detailed account of the study of waves is beyond the scope of this
paper. Forecasts were based on an analysis of Shoeburyness anemograph
records for the same period, 1929-68, as was covered by the IOS data on
surge residuals. The wind data were classified into three populations,
depending on whether there was a surge residual of > 3 ft, < 3 ft but >2 ft,
or under 2 ft at HW on the day in question, because of the correlation between

the incidence of surges and particular weather systems in the southern
North Sea. All maximum hourly wind speeds in the Meteorological Office's
(MO) daily listings in excess of 27 knots (force 7) were considered,
together with hourly maxima on every day for which a surge residual over
2 ft had been recorded. The resultant wind roses, are given in fig. 6,
and the distributions within the three populations are shown in table 7.

Table 7. Number of occasions in 40 years when winds coincided with surges.

Wind speed (Beaufort scale)	10	9	8	7	6	5	4	3	2
No surge	4	47	251	594	⊢———— 12,370 ————————⊣				
Surges 2 ft - 2.9 ft	1	6	33	95	203	297	259	53	5
Surges ⩾ 3 ft	2	7	19	60	103	112	80	10	3

The Essex coast is exposed to north east and easterly winds but the wind
records show that these are not directions from which gales often blow. The
most relevant sector is from 40 deg. to 120 deg. from true north, with an
average of 5 gales a year. Standard methods were used to estimate the waves
that would arise for given wind condition in the range 7 to 10 on the Beaufort
scale. (Bretschneider, 1970, Ippen, 1966). Allowance was made for
shallowing water as the coast is approached, and for the fetch. The longest
fetch is 650 km on 40 deg. bearing but the last 70 km are in shallow water
(see fig. 1). The highest waves are generated over a 280 km fetch on bearing
60 deg, which follows the general alignment of submerged channels in
approaching the coast, thus being less affected by shallow water and
refraction. The computational scheme used for wave forecasting is shown
in fig. 7.

The likelihood of winds, and hence of waves, occurring with high water
levels can be assessed by combining the chance of the two eventualities,
wind frequency having been separated (admittedly crudely) into three surge-
associated populations. Waves exceeding a significant height of 7.5 ft are
likely to occur on a day when the tide level exceeds 11.8 ft ODN (2000) about
once in 50 years, and waves over 10.5 ft height about once every 500 years.
The chances of high wave activity on a day when abnormally high water
levels occur are very remote. With a tide level of 14.8 ft ODN (2000) it
may be only once in 5000 years, so that the chance of waves with significant
height of 7.5 ft or larger occurring with the level reached by the 1953
storm surge is too remote for such a prediction to be justified by the data.

This infrequency arises because here the predominant winds are off-
shore ones, and strong winds from the north-east and east are few in number.
Table 8 shows the combined tide, surge and wave probabilities. Combinations
with a probability of 1 in 1000 in any year are·

a)   13 2 ft (4.0 m) ODN (2000) with waves > 7.5 ft (2.3 m)
b)   12.8 ft (3.9 m) ODN (2000) with waves > 9.1 ft (2.8 m)
c)   12.6 ft (3.85m) ODN (2000) with waves > 10.5 ft (3.2 m)

The combined distribution of water levels with waves exceeding 7.5 ft
(2.3 m) has also been added to fig. 4

CONCLUDING REMARKS

    In connection with the design of coastal works, the probabilities of
combinations of waves and tides have to be assessed so that slope protection,
crest elevations, drainage works etc. can be designed for events of
appropriate probabilities. The proposed developments on the Essex
coastline required a comprehensive study of both waves and tides. Surge
affected tides were considered by several methods, including a new approach
that treats surge residuals and predicted astronomical events as statistically
independent. Comparison with other results suggests that the method is
useful, but further research into the validity or limitations of the assump-
tions is necessary.

ACKNOWLEDGEMENTS

REFERENCES

Barricelli, N.A., (1943) 'Les plus grands et les plus petits maxima ou
minima annuels d'une variable climatique'. Arch. Math. Naturv. Oslo,
46, No. 6.

Bretschneider C.L., (1970) 'Forecasting relations for wave generation'.
Look Lab. Hawaii, 1, No. 3, July, 1970.

Doodson, A.T., (1957) 'The analysis and prediction of tides in shallow
waters'. Int. Hydrogr. Rev. 34, 1957.

Dronkers, J.J., (1960), 'Investigations of the tides and storm surges for
the Deltamark in the south western part of the Netherlands,' Chap. 32,
Proc. 7th, Coastal Engineering Conf., The Hague, 1960.

Gumbel, E.J., (1934) ' Les plus grands ages en suisse'. J statist.
Rev. Econ. suisse, Berne, 70, Fasc. 4, 1934.

Ippen, A. T., (1966) 'Estuary and coastline hydrodynamics'. Eng. Soc. Mon., McGraw Hill.

Jenkinson, A. F., (1955) 'Frequency distribution of the annual maximum (or minimum) values of meteorological elements'. Quart J Roy. Met. Soc., 81, pp. 158-171.

Lennon, G. W., (1963b) 'A frequency investigation of abnormally high tide levels at certain west coast ports'. Proc. Instn. Civ. Engrs., 25, pp 451-484.

Rossiter J. R., and Lennon, G. W., (1968) 'An intensive analysis of shallow water tides'. Geophys. Journ. Roy. Astr. Soc., 16, 1968.

Rossiter, J. R., (1972), 'Sea-level observations and their secular variations'. Phil. Trans. R. Soc. Lond. A. 272, pp 131-140.

Suthons, C. T. Cdr.,(1963) 'Frequency of occurrence of abnormally high sea levels on the east and south coasts of England'. Proc. Instn. Civ. Engrs., 25, pp 433-450.

Wemelsfelder P. J., (1960), On the use of frequency curves of stormfloods, Chap. 33, Prc. 7th Coastal Engineering Conf., The Hague, 1960.

TABLE 8

Combined tide, surge and wave probabilities

Level in ft ODN		Number of occasions level exceeded in 1000 years					Probability that wave occurs on a day of stated surge	WAVE HEIGHT (ft)			
year 1971*	year 2000*	TOTAL	with <2ft surges	with 2-3ft surges	with >3ft surges			7 5 – 9 0	9 1 – 10 4	10 5 – 12 0	>7 5
							a) >3ft surge	2,55 x 10⁻³	–	2 55 x 10⁻³	
							b) 2-3ft surge	12 6 x 10⁻³	2 1 x 10⁻³	1 05 x 10⁻³	
							c) <2ft surge	2 88 x 10⁻³	0 3 x 10⁻³	–	
17 0	17 3	1	–	–	1			2 55 x 10⁻³	–	2 55 x 10⁻³	0 005
16 5	16 8	3	–	–	3			7 65 x 10⁻³	–	7 65 x 10⁻³	0 015
16 0	16 3	6	–	–	6			15 3 x 10⁻³	–	15 3 x 10⁻³	0 031
15 5	15 8	12	–	–	12			30 6 x 10⁻³	–	30 6 x 10⁻³	0 061
15 0	15 3	22	–	–	22			56 x 10⁻³	–	56 x 10⁻³	0 112
14 5	14 8	37	–	–	37			94 x 10⁻³	–	94 x 10⁻³	0 184
14 0	14 3	61	–	–	61			0 155	–	0 155	0 31
13 5	13 8	101	–	–	101			0 258	–	0 258	0 52
13 0	13 3	164	–	7	157			0 40) 0 49 0 09)	0 014) 0,014	0 40) 0 407 0 007)	0 91
12 5	12 8	405	–	169	236			0 60) 2 73 2 13)	0 355) 0 355 -)	0 60) 0 777 0 177)	3 86
12 0	12 3	800	60	413	327			0 835) 5 2)6 208 0 173)	0 8670 885 0 018)	0 835) 0 434)1 269 -)	8 36
11 5	11 8	2620	1380	828	412			1 05) 10 45)15 48 3 98)	-) 1 74)2 15 0 41)	1 05) 0 87)1 92 -)	19 55
11 0	11 3	6478	4630	1376	472			1 20) 17 35)31 90 13 35)	-) 2 89)4 28 1 39)	1 20) 1 44)2 64 -)	38 82

*Rise in sea level of 0 011ft/year assumed up to these dates no rise subsequently
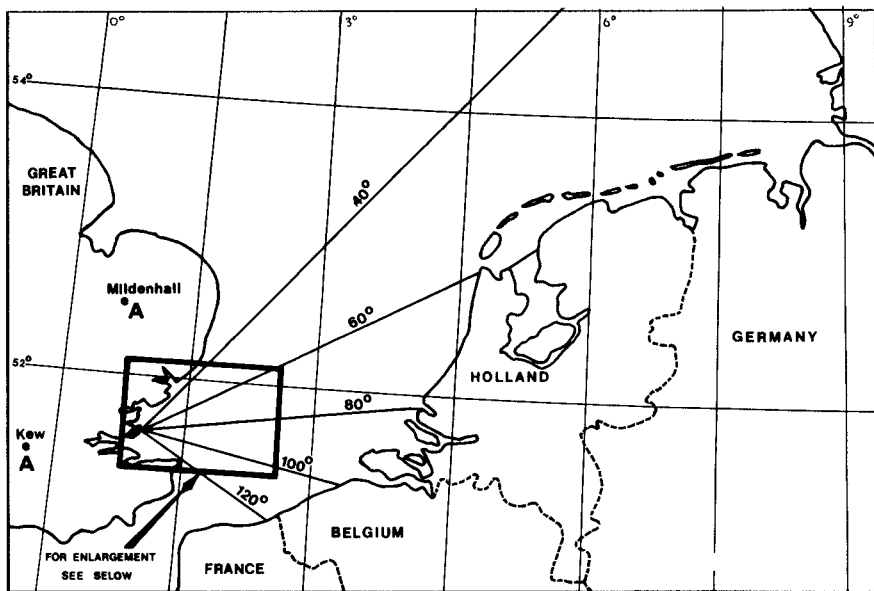
(a) **SOUTHERN NORTH SEA** Fetch Lines
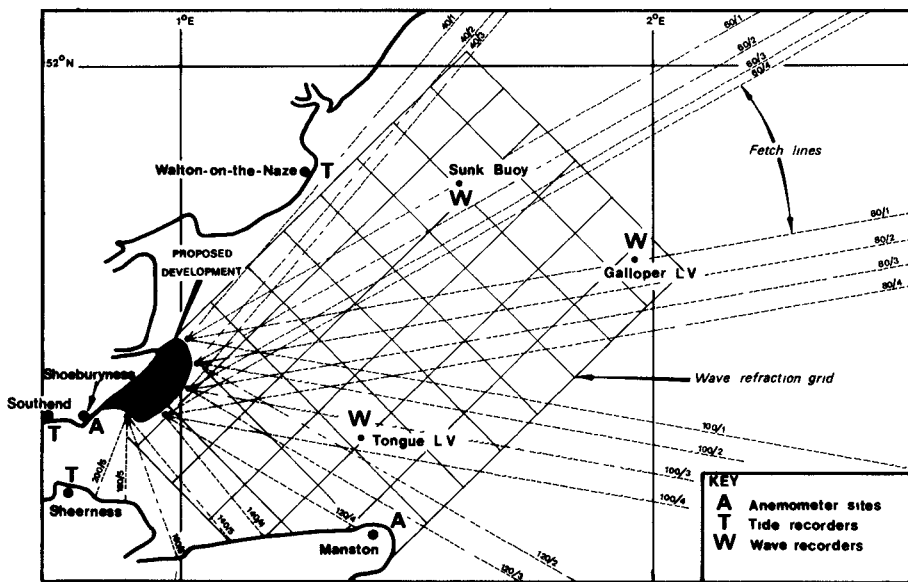
Fig 1

(b) **STUDY AREA** showing refraction grid and fetch lines used in wave generation analysis
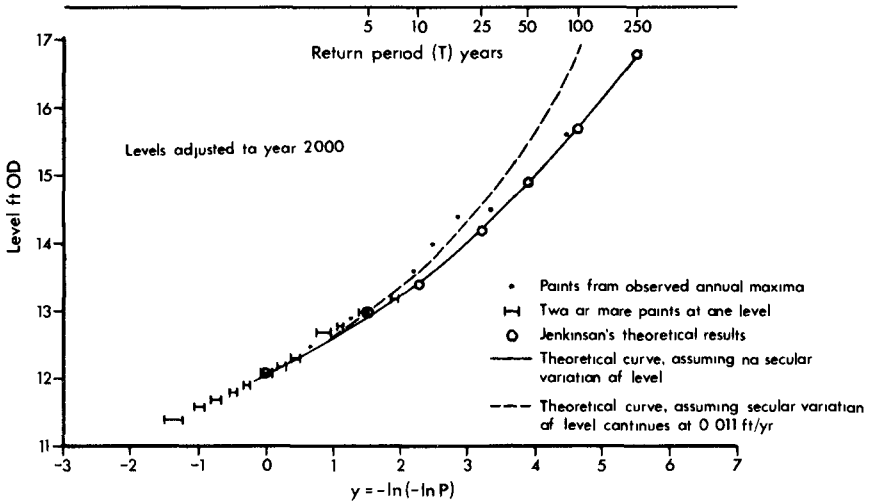
Fig 2   RETURN PERIODS OF EXTREME WATER LEVELS AT SOUTHEND
(Predicted by considering annual maximum high water levels)
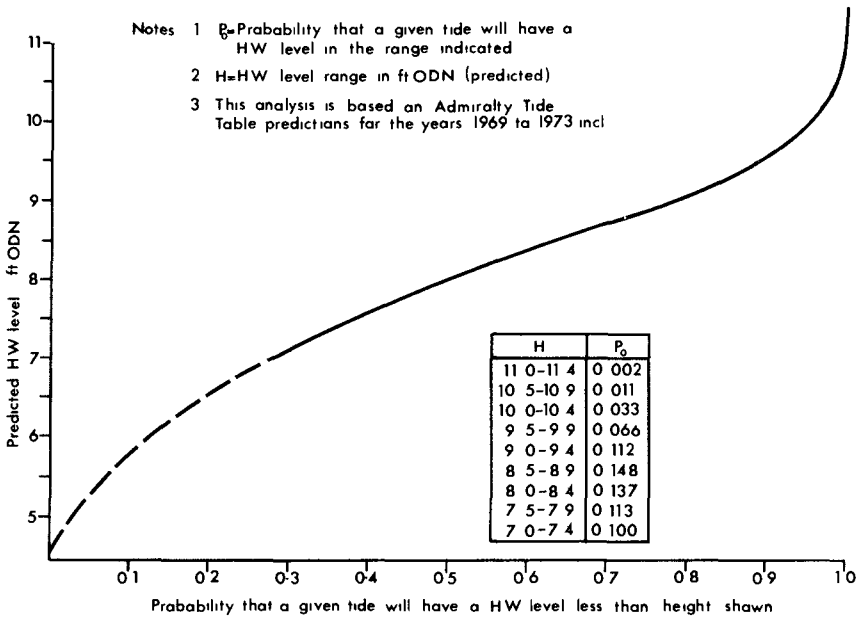
Fig. 3   PROBABILITIES OF PREDICTED HIGH WATER
LEVELS AT SOUTHEND

Level exceed ft(ODN)

KEY

O – Computed values from combination of
tide and surge distributions

+ – Observed values from 44 years record 1929–1973

□ – Computed values from combination of tide,
surge and wind distributions

A secular variation of 0 011 ft/year
has been used upto the alternative
base years of 1971 and 2000
but assumed to be zero after
these dates

Irrespective of
wave condition

With waves greater
than 7 5 ft

ln T

Return period T (years)

Fig 4

**RETURN PERIODS OF EXTREME WATERLEVELS
WITH STATED WAVES AT SOUTHEND**

(Predicted by combining tide, surge and wind probabilities)
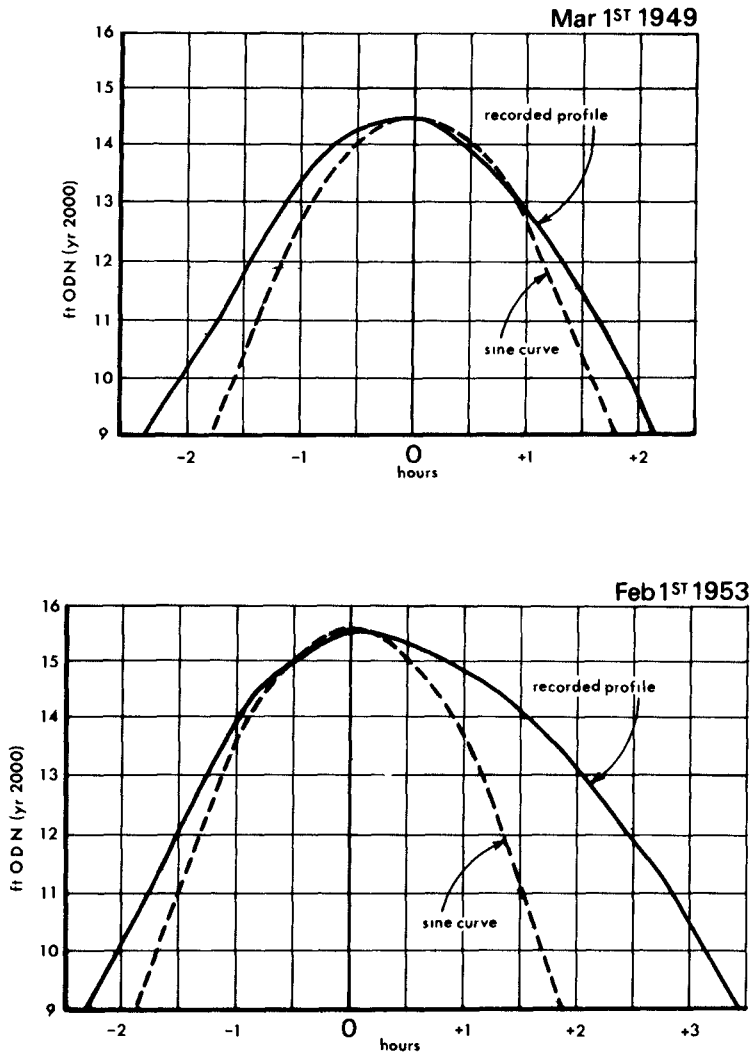
Fig 5   PROFILES OF EXTREME EVENTS
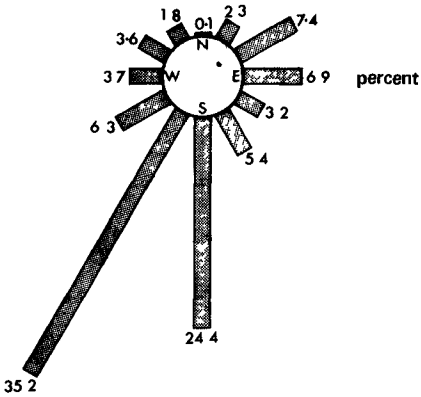
a) FREQUENCY DISTRIBUTION
OF WINDS GREATER
THAN FORCE 7

Wind speed Beaufort scale	No surge	Surges 2 0'-2 9'	Surges ≥ 3 0'
10	4	1	2
9	47	6	7
8	251	33	19
7	594	95	60
6		203	103
5		297	112
4		259	80
3	12,370	53	10
2		5	3
Less than 2		–	–

NUMBER OF OCCASIONS WHEN WINDS COINCIDED WITH

d) COINCIDENCE OF STORMS AND SURGES
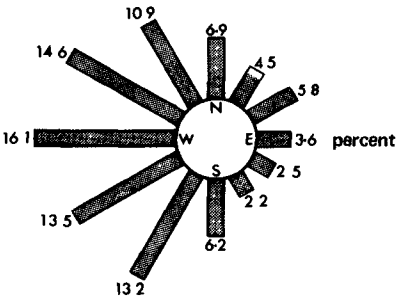
b) FREQUENCY DISTRIBUTION
OF WINDS WITH
2 0'–2 9' SURGES
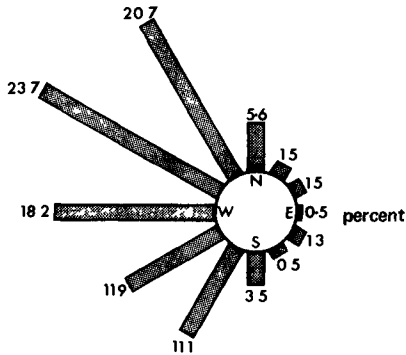
c) FREQUENCY DISTRIBUTION
OF WINDS WITH
SURGES ⩾ 3 0'

NOTES   1 Figures refer to the 40 years of wind record at Shoeburyness from
1929 to 1968, and surges at Southend for the same period

2 All winds are the maximum mean hourly winds for a given day

Fig 6   SHOEBURYNESS WIND ANALYSIS

```
┌───────────┐
│   START   │
└───────────┘
      │
      ▼
┌──────────────────────────────────────────────┐
│                DEEP ZONE                       │
│ From cross-section, identify limiting depth    │
│ and therefore effective deepwater, fetch       │
│ Enter chart 1 to obtain  ₙH′₀,  ₙT′₀           │
└──────────────────────────────────────────────┘
      │
      ▼ n=1
┌──────────────────────────────────────────────┐
│               SHALLOW ZONE                     │
│ Using  Δxₙ,  h̄ₙ & ĥₙ  calculate                │
│                                                │
│  0 01 ₙH′ₛ  Δxₙ       ₙT′₀²                     │
│  ──────────────   &   ────                     │
│     h̄ₙ²               h̄ₙ                       │
│                                                │
│ when n = 1, the approximation                  │
│   ₙH′ₛ = ₙH′₀  is used                          │
└──────────────────────────────────────────────┘
      │
      ▼
┌──────────────────────────────────────────────┐
│ Using chart 2 , obtain  ₙK_f  Equivalent       │
│ deepwater wave height, neglecting extra        │
│ fetch becomes                                  │
│        ₙH₀ = ₙK_f  ₙH′₀                         │
└──────────────────────────────────────────────┘
      │
      ▼
┌──────────────────────────────────────────────┐
│ Enter chart 1 with  ₙH₀ to give effective      │
│ fetch at beginning of increment, ₙF′_e         │
│ Effective fetch at end of increment becomes    │
│      ₙ₊₁F′_e = ₙF′_e + Δxₙ                      │
└──────────────────────────────────────────────┘
      │
      ▼
┌──────────────────────────────────────────────┐
│ Enter chart 1 with ₙ₊₁F′_e to give             │
│ equivalent deepwater wave height and           │
│ period                                         │
│        ₙ₊₁H′₀, ₙ₊₁T′₀                           │
└──────────────────────────────────────────────┘
      │
      ▼
┌──────────────────────────────────────────────┐
│ Calculate  ₙ₊₁T′₀²  and obtain                 │
│            ────                                 │
│             h̄ₙ                                  │
│ ₙK_s from chart 3, ₙK_r obtained from          │
│ refraction analysis                            │
└──────────────────────────────────────────────┘
      │
      ▼
┌──────────────────────────────────────────────┐
│   ₙ₊₁H′ₛ = ₙK_r ₙK_s ₙ₊₁H′₀                     │
└──────────────────────────────────────────────┘
      │
      ▼
┌──────────────────────────────────────────────┐
│ Wave breaks if                                 │
│       ₙ₊₁H′ₛ > 0 78 ĥₙ                          │
└──────────────────────────────────────────────┘
      │
      ▼
┌───────────┐
│   n = N   │
│  FINISH   │
└───────────┘
```

┌──────────────────────────────────┐
│ ₙ₊₁H′₀ ₙ₊₁T′₀ ₙ₊₁H′ₛ   │
│ carried forward to   │
│ next increment   if   │
│ wave breaks then   │
│   ₙ₊₁H′ₛ = 0 78 ĥₙ   │
└──────────────────────────────────┘

Notation -

Chart 1   Bretschneider (1970) deepwater chart
Chart 2   Ippen (1966) Fig 3 20
Chart 3   Ippen (1966) Fig 3 21

$_nH'_o$ deepwater wave significant height at start of increment 'n'

$_nT'_o$ deepwater wave significant period at start of increment 'n'

Δx_n length of fetch increment

$\bar{h}_n$ mean depth of fetch increment

$\hat{h}_n$ minimum depth occurring in increment

$_nH'_s$ significant wave height at start of increment

$_{n+1}H'_s$ significant wave height at end of increment (becomes $_nH'_s$ for next increment)

$_nK_f$ friction coefficient

$_nH_o$ equivalent deepwater wave height neglecting additional fetch

$_nF'_e$ effective fetch at start of increment

$_{n+1}F'_e$ effective fetch at end of increment (becomes $_nF'_e$ for next increment)

$_{n+1}H'_o$ equivalent deepwater wave significant height at end of increment including additional fetch (becomes $_nH'_o$ for next increment)

$_{n+1}T'_o$ equivalent deepwater wave significant period at end of increment including additional fetch (becomes $_nT'_o$ for next increment)

$_nK_s$ shoaling coefficient

$_nK_r$ refraction coefficient

N   number of shallow zone increments

Fig. 7

WAVE FORECASTING
COMPUTATION SCHEME

CHAPTER 2

CALIBRATION OF A HURRICANE STORM SURGE PROGRAM

by

Ronald M. Noble[1] and James A. Hendrickson[2]

Abstract

The "Bathystrophic Storm Tide Theory" is used to predict
open-coast storm surge due to major hurricanes. The model
described here is used to calculate storm-surge effects such
as flood elevations needed for designing nuclear power plant
safety related structures. In order to establish the model's
viability the numerical techniques have been verified and
the model calibrated using available field data.

Numerical verification was performed for special cases
where the governing equations of the model could be analyti-
cally solved. Inherent in the governing storm-tide equations
are certain undetermined coefficients that describe the
effects of wind drag and bottom friction. These coefficients
were determined by correlating computer predicted results to
hurricane storm surge hydrographs of record.

As a result of this study, we find excellent agreement
between computer predicted and analytical results.

Introduction

Storm surges caused by maximum intensity hurricanes or
"Probable Maximum Hurricanes" (PMH) constitute a major hazard
for nuclear power plants located at coastal sites. Failure
to design adequately for the effects of such a maximum hurri-
cane on the water level may result in catastrophic consequence
for the power plant. The Atomic Energy Commission has selected
the PMH storm as the parameter to be considered in designing
structures to ensure adequate safety.

The surge (rise in the water level) and the attendant
wave activity as functions of time and caused by a PMH storm
are used to determine the changing water level at the site of
a proposed plant. This information is then considered when

---

[1]Manager, Marine Services, Dames & Moore, Los Angeles, Cal.
[2]Manager, Advanced Technology, Dames & Moore, Los Angeles, Cal.

designing sea walls, protective barriers, bulkheads, cooling
water suction and discharge pipes, and other coastal struc-
tures associated with the plant.

Until recently, hurricane storm-surge calculations were
based on a simplified, one-dimensional, pseudo-static model,
considering only the effects of the onshore wind drag and
the variations in mean water depth.   More recent studies
(1,2) are based on the so-called "Bathystrophic Storm Tide
Theory" and include the Coriolis effects of the time-dependent,
alongshore, fluid motion on the water level.   These investi-
gations, however, have produced cumbersome computer programs
because the dynamic hurricane-wind-field data must be input
from graphically constructed isovel and wind vector figures.

The computer program described here solves the basic
mathematical equations for the surge problem by using highly
accurate numerical techniques.   In addition, the inputs
necessary to the program are simplified, so that only the
basic design hurricane parameters are needed.   The hurricane
wind field and the barometric pressure variation at any point
in the storm, which in previous programs had to be supplied,
can now be calculated using the computer program based on the
PMH hurricane model (3).   This program is being used in most
safety analysis reports for nuclear generating plants submit-
ted to the U. S. Atomic Energy Commission.

This paper presents verification of the numerical model
used to solve storm tide equations.   Also presented are
results of a calibration study, correlating computer pre-
dicted results to hurricane storm surge of record.

Storm Surge Model

The model is based on the general equations of horizontal
fluid flow simplified to eliminate certain second-order terms
and to be quasi-one-dimensional in nature.   The model is
designed to analyze open-coast storm surge resulting from
passage of an ideal PMH.

The basic equations on which the model is based may be
written as follows:

$$\frac{df}{dt} = kUU_y - \frac{Kf\,|f|}{(h+\eta)^2} \tag{1}$$

$$\frac{d\eta}{dx} = \frac{kUU_x + \Omega f}{g\,(h+\eta)} \tag{2}$$

The x-axis is taken generally perpendicular to the coastal
bathymetry contours (shown in Figure 1), with the origin
located in deep water (600 to 900 ft.).   The other parameters
in the above equations are:

f   = flow-flux in the direction of the y-axis
           (perpendicular to the x-axis and along
           constant depth bathymetry contours)
U   = wind velocity
U_x, U_y = wind velocity component along the x-axis
           and y-axis, respectively
k   = wind stress coefficient
K   = bottom friction coefficient
η   = surge elevation above stillwater level
h   = stillwater depth at a given instant of time
           (includes the effects of tides, barometric
           pressure effects, and any initial surge
           effects due to meteorological anomalies)
Ω   = Coriolis parameter = 0.5235 sinΦ, rad/hr
Φ   = degrees north latitude
g   = acceleration of gravity taken as
           32.2 ft/sec^2

    Equations 1 and 2 result from the basic horizontal flow
equations with the following assumptions:

    1. Wind gradients and water depth variations in a
        direction normal to the x-axis are assumed to be
        small; thus, the problem becomes essentially
        one-dimensional.

    2. No flow occurs in the x-direction, and the surge
        elevation occurs instantaneously in time; thus,
        a hypothetical vertical barrier to fluid motion
        normal to the coast is presumed.

FIGURE 1
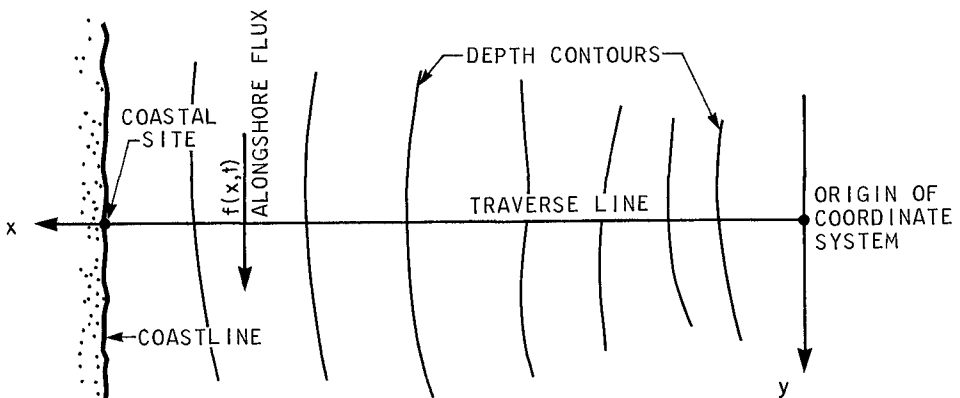
The relationship governing wind stress, T_o, is usually in the following form:

$$\frac{\vec{T_o}}{\rho_\omega} = \frac{\rho_a}{\rho_\omega} C_D U^2 \frac{\vec{U}}{|U|} = k |U| \vec{U} \qquad (3)$$

where
  C_D = drag coefficient
  ρ_ω = density of fluid
  ρ_a = density of air
  U = wind velocity (at the 10-meter level)

Several studies (4,5,6) indicate that the drag coefficient, C_D, has the form:

$$C_D = A + B (1-U_o/U)^2 \qquad (4)$$

where
  A = constant
  B = constant
  U_o = critical wind velocity, below which C_D = A

In comparing the four equations above, the wind stress coefficient obtains the form:

$$k = \rho_a/\rho_\omega \left[A+B (1-U_o/U)^2 \right] \qquad (5)$$

Wilson (4) correlates the work of numerous investigators in an attempt to determine the value of the coefficients A and B. From the above investigation, the following values for A and B are indicated:

$$A = 1.0 \text{ to } 1.1 \times 10^{-3}$$
$$\qquad (6)$$
$$B = 1.2 \text{ to } 1.8 \times 10^{-3}$$

The critical wind velocity, U_o, is between 13 and 16 miles per hour. The density ratio, ρ_a/ρ_ω, for standard conditions (20°C and 29.92 in. Mercury) and for sea water is taken to be:

$$(\rho_a/\rho_\omega)_{STP} = 1.17 \times 10^{-3} \qquad (7)$$

The density ratio is affected by changes in the barometric pressure, the dewpoint temperature, and the air temperature. In the case of a PMH hurricane acting on coastal waters, the greatest variation in this ratio is caused by local barometric pressure changes. Assuming a linear relationship between air density and barometric pressure, the density ratio becomes:

$$(\rho_a/\rho_\omega) \approx 1.17 \times 10^{-3} \times \frac{P}{29.92} \qquad (8)$$

where
  P = local barometric pressure in inches Mercury

The local pressure, P, in the presence of a hurricane (3) may be taken as:

$$P = P_\eta - (P_\eta - P_o) \left[1 - \exp(-R/\rho) \right] \tag{9}$$

where

P_η = asymptotic pressure of hurricane
P_o = central pressure of hurricane
R = radius of maximum winds
ρ = radial distance from hurricane center

Thus, the pressure is determined from Equation 9, and the wind-stress coefficient takes the form of:

$$k = \left[CSK1 + CSK2 \ (1 - U_o/U)^2 \right] \times 1.17 \times \frac{P}{29.92} \tag{10}$$

The coefficients CSK1 and CSK2 obtain values of 10^{-3} times those shown for A and B values, and the critical velocity, U_o, is taken as 15 miles per hour.

The bottom-friction factor, K, is largely dependent on the bottom condition. There is evidence (2) that K depends on the prevailing slope of the sea bottom and on the length of the traverse line (distance of the deep water origin from shore). Most evidence indicates that K has a value in the range of 0.002 to 0.005 for the form of the bottom-friction effect assumed in Equation 1.

The numerical scheme used to solve Equations 1 and 2 will not be described here. Details of the numerical program are described in another study (7). Also described in that study is the hurricane model used to define the input wind field.

<div align="center">Verification of Model</div>

The numerical scheme was verified by comparing computer predicted results to simplified, known analytical solutions. The first hypothetical case tested was for a rectangular basin of constant depth. The basin had vertical sides over which a wind, constant in time but variable in space, acts. The wind distribution was assumed to be Gaussian, with a maximum value occurring at the end of the basin. The geometry for this test case is shown in Figure 2 below.

FIGURE 2
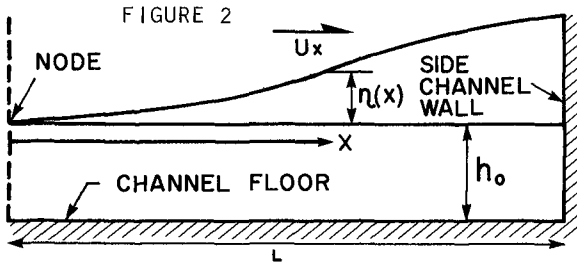
The value of the surge is assumed to be zero at the origin of coordinates (x = 0). It is further assumed that the wind acts along the x-axis. Thus, if the effects of bottom friction are ignored, Equation 2 may be used to determine the steady-state solution for the surge amplitude. The detailed analytical solution is shown in an earlier study (7).

Figure 3 shows the analytical solution for the surge amplitude as well as the results obtained from the computer program. Figure 3 indicates that the output of the program shows negligible deviation from the theoretical results. Additional analytical cases were studied, and they indicate comparable agreement with computer predicted results (7).

The computer program was correlated to historical hurricane data of record primarily to determine the two constants (CSK1 and CSK2) appearing in the wind-stress coefficient taken from Equation 10. Recorded hydrographs at known shoreline locations and recorded meteorological and oceanographical data were obtained for several severe historical hurricanes. Much of this data was obtained from the National Oceanic and Atmospheric Administration (NOAA). The following data of record were used:

1. Hurricane Carla (1961)--Galveston and Sabine Pass, Texas, hydrographs
2. Hurricane of 1949--Brazos Port, Texas, traverse
3. Hurricane Carol (1954)--Newport, Rhode Island, traverse
4. Hurricane Audrey (1957)--Eugene Island, Louisiana, traverse
5. Hurricane Camille (1969)--Peak surge at Biloxi, Mississippi

The hurricane data were digitized and used as input to the computer model in order to generate a surge hydrograph. The computer-generated hydrographs were then compared with the hydrographs of record to obtain appropriate wind-stress coefficients.

Three comparison methods were used to judge the accuracy of calculated hydrographs relative to recorded hydrographs. In the first method, a point-by-point comparison was made by looking at the percentage difference between the two hydrographs at each time-step. The time-steps were defined by the times given for the hurricane-wind-field data.

The second method takes an overview of the hydrograph while emphasizing the maximum surge. With this method, the sum of the squares of the differences between the two hydrographs were computed for the duration of the hydrograph. Also, a percentage difference at the point of maximum surge was calculated.

FIGURE 3
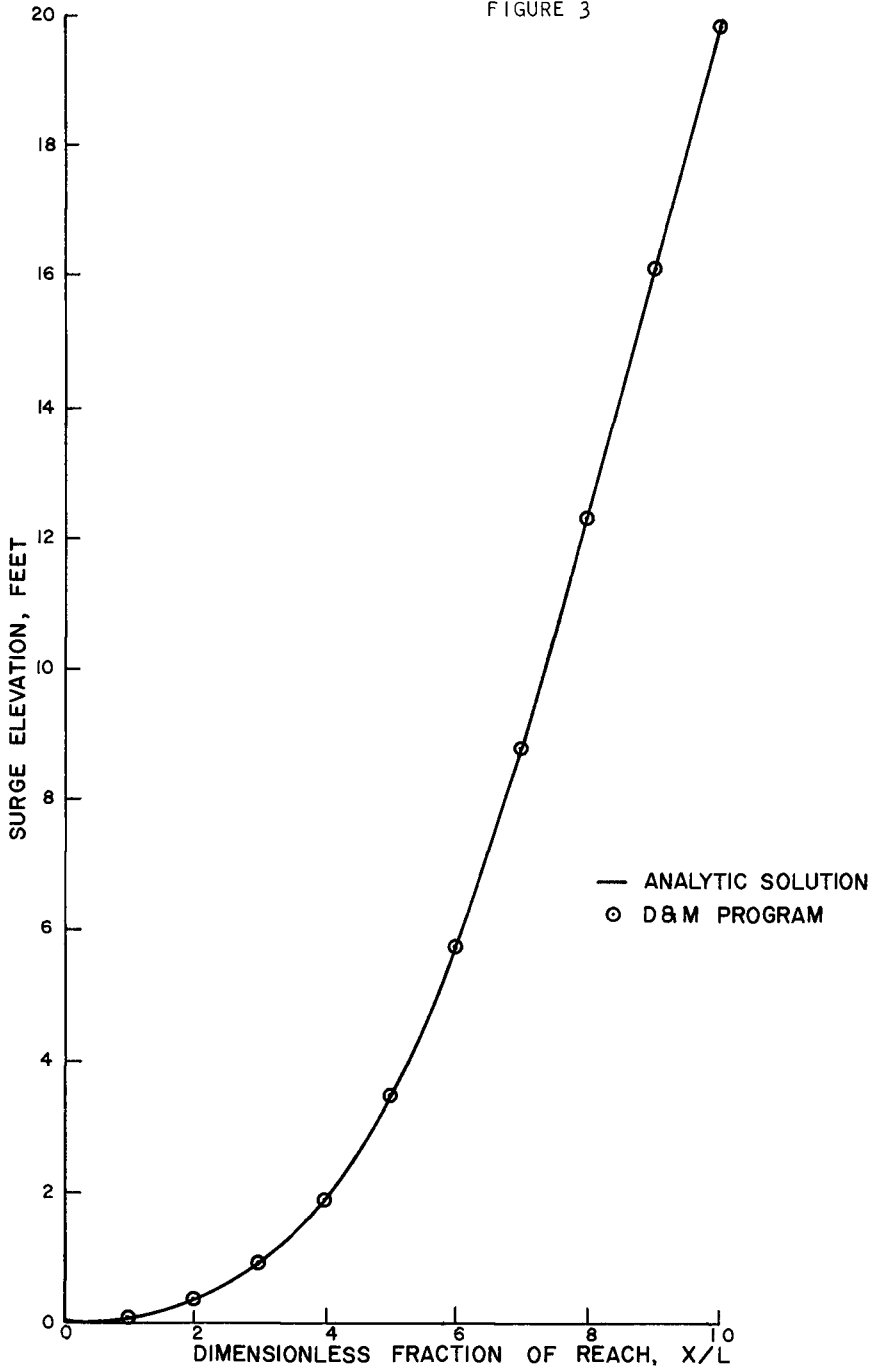
The final comparison method showed the average percentage difference, for each one-third portion, between the two hydrographs. The "fit" of the critical middle-third of the hydrograph was then analyzed. This section is considered critical because it exhibits a rapid rise in water elevation and shows the maximum water levels.

The above described methods of comparison resulted in a four "best fit" correlation criteria. These criteria, in order of importance, were taken to be:

1. The maximum calculated surge must be greater or equal to that observed.
2. The middle third of the calculated hydrograph must, on the average, be greater than the corresponding portion of the observed hydrograph.
3. The deviation between the calculated hydrograph and the observed hydrograph (exemplified by the sum of squares of differences) should be a minimum.
4. The beginning and end thirds of the calculated hydrograph relative to the observed hydrograph should exhibit a minimum skewness, with a minimum error being desirable.

The limits between which the calibrating input parameters (for wind and bottom friction) were allowed to vary have been discussed previously. Using these limits in conjunction with the criteria for "best fit," the input parameters were handled in the following manner:

1. A value of CSK1 was held constant while values of CSK2 were varied between the limits previously discussed. This procedure was followed for the full range of CSK1 values.
2. The bottom friction factor for each pair of CSK1 and CSK2 was varied until the "best fit" condition was reached.

Hurricane Carla hydrographs (Galveston and Sabine Pass stations) exhibited strong correlation with computer predicted results. The Eugene Island hydrograph exhibited fair correlation; while the Freeport and Narragansett Bay cases exhibited poor correlation. Based on an overall assessment of the study results, the following wind-stress coefficient values were selected:

$$CSK1 = 1.0 \times 10^{-6}$$
$$CSK2 = 1.4 \times 10^{-6}$$

(11)

A strong correlation between bottom friction coefficients and predicted hydrographs was not observed in this study. However, bottom friction coefficients appear to lie within the range of 0.002 to 0.005.

For example, a bottom-friction coefficient of about 0.003 was indicated for the Sabine Pass traverse, which is relatively long. The Galveston traverse, which is shorter, has a bottom-friction coefficient of about 0.002.

The detailed correlation analysis is contained in reference 7. An example of a correlation computer run for the case of Hurricane Carla (Galveston traverse) is shown in Figure 4.

A hydrograph of record was not available for Hurricane Camille. However, peak surge elevations could be estimated from debris lines indicating high water marks near Biloxi, Mississippi. This surge elevation, along with Hurricane Camille data, was used to cross-verify correlation results.

The wind-stress coefficient values used were obtained from the correlation study. A bottom-friction coefficient of 0.002 was chosen due to the comparable length of the Biloxi and Galveston traverses. The numerical model indicated a peak surge that closely matched the observed high-water debris marks.

Conclusions

It is extremely important when designing coastal structures, especially nuclear power plants, to properly assess the magnitude of hurricane storm surges. Simplified one-dimensional models are the currently accepted means of calculating hurricane storm surge. The model discussed here was verified and correlated with historical hurricane data. Although reasonable correlation was obtained, it is apparent that reliable hurricane data is severely limited.

As additional hurricane data is received, a more refined storm-surge model can be considered. Such a model should include the effects of convective transport, coastal flooding, and two-dimensional aspects.

References

1. Bretschneider, Charles L., "Storm Surges," Advances in Hydroscience, Vol. 4, 1967, pp. 341-417.

2. Marinos, G., and Woodward, Jerry W., "Estimation of Hurricane Surge Hydrographs," Journal of the Waterways and Harbors Division, Proceedings of ASCE, Vol. 94, May 1968, pp. 189-215.

3. U. S. Department of Commerce, "Meteorological Characteristics of the Probable Maximum Hurricane, Atlantic and Gulf Coasts of the United States," Memorandum HUR 7-97, Interim Report, May 1968.

FIGURE 4

HURRICANE DATA

RADIUS TO REGION OF MAXIMUM WIND SPEED (R) =   46.00 NAUTICAL MILES
TRANSLATIONAL VELOCITY (VT) =   3.00 KNOTS
ASYMPTOTIC PRESSURE (PN) =   29.92 INCHES-HG
CENTRAL PRESSURE (PO) =   27.84 INCHES-HG
LATITUDE (PHI) =   28.55 DEGREES
MAXIMUM WIND VELOCITY (UMAX) =   115.00 MPH
CONSTANT PART OF WIND STRESS COEFF. (ESK1) =   .1000-05
MULTIPLIER OF VELOCITY DEPENDANT PART OF WIND STRESS COEFF. (ESK2) =   .1400-05

OCEANOGRAPHIC DATA

INITIAL SURGE HEIGHT (HI) =   1.87 FEET
ASTRONOMICAL TIDE (HA) =   .00 FEET
BOTTOM FRICTION COEFFICIENT (BOTF) =   .00200
EXPONENT OF DEPTH FOR BOTTOM FRICTION EFFECT (CONSO) =   2.000000

PLOT OF SURGE HEIGHT IN FEET

TIME (HR)	SURGE(FT) ACTUAL (X)	CALCUL (*)	PERCENT (DIFF.)
6.0	16.38	16.10	-.4
12.0	18.78	18.89	-.6
18.0	18.48	18.71	-.2
24.0	18.16	17.18	5.6
30.0	19.38	18.44	4.9
33.0	19.64	18.56	5.7
36.0	20.28	20.05	1.1
39.0	20.60	20.36	1.4
42.0	20.98	21.98	-4.7
45.0	21.38	21.62	-.2
48.0	21.95	21.72	1.2
51.0	21.98	22.40	-1.9
54.0	22.18	21.42	3.4
57.0	21.08	21.54	-2.2
60.0	20.88	21.05	-.8
63.0	22.18	22.34	-.7
66.0	21.58	20.55	4.8
69.0	20.38	19.33	5.2
72.0	19.08	18.99	-.5
75.0	20.08	19.67	2.0
78.0	19.48	18.13	6.9
81.0	17.08	15.40	9.8

SUM OF SQUARES OF DIFFERENCES =   12.53
PERCENTAGE DIFFERENCE AT MAXIMUM SURGE =   -.7113

AVERAGE OF PERCENT ERRORS FOR EACH 1/3 PORTION OF CALCULATED CURVE
FRONT THIRD =   2.622
MIDDLE THIRD =   -.751
BACK THIRD =   4.069

"BEST FIT" CONDITION FOR GALVESTON TRAVERSE

4.   Wilson, B. W., "Note on Surface Wind Stresses Over Water
     at Low and High Speeds," Journal of Geophysical Records,
     Vol. 65, No. 10, October 1960, pp. 3377-3382.

5.   Keulegan, G., "Wind Tides in Small Closed Channels,"
     Research Paper 2207, National Bureau of Standards, 1951.

6.   Van Dorn, W. G., "Wind Stresses on an Artificial Pond,"
     Journal of Marine Research, Vol. 12, 1953, pp. 216-249.

7.   Dames & Moore, "Verification Study of Dames & Moore's
     Hurricane Storm Surge Model with Application to Crystal
     River Unit 3 Nuclear Plant, Crystal River, Florida,"
     FSAR, AEC Docket No. 50-302, for Florida Power Corpor-
     ation, July 13, 1973.

CHAPTER 3

STORM SURGE EFFECTS AT LEIXÕES

by C. Campos Morais, research officer

and F. Abecasis, head Hydraulics Dep.

Laboratório Nacional de Engenharia Civil, Lisboa, Portugal

ABSTRACT

In this paper, the effects of a storm surge that happened on the 16th-17th January 1973 in the harbour of Leixões are analysed and described. These effects were of two types:
- As the storm surge coincided with a spring tide and rough seas, severe damages occurred in the outer breakwater, mainly in its head.
- Associated to the storm surge range phenomena happened in the nº 2 dock; these movements, acting on a ship berthed in a nodal zone, caused several breakings in the ropes and damages in harbour structures.

The characteristics of the storm surge and of the waves are analysed. Their effects on the breakwater are described.

By comparing the periods of long waves observed in the tide records with the resonance periods of the inner docks it was possible to conclude that the intensity of the range phenomena observed was due to a half wave lenght resonance.

Having in mind the affinities with the phenomena referred to above, the effects of range action in an oil terminal and new damages in the outer breakwater, that occurred in January and February 1974 respectively, are also briefly examined.

1. GENERAL

The Leixões harbour lies in open coast in the northern part of Portugal facing the North Atlantic (fig.1). As this is a reach of the coast with the general alinement north-south, it is exposed to the severe wave conditions of this zone of the Atlantic Ocean, storms with waves of significant height up to 7 to 8 m and individual waves up to 12 to 13 m being relatively frequent (about once a year). The tidal range is about 3.80 m.

At present, the harbour is formed (fig. 2) by an outer basin approximately square shaped, with a side of about 1,000 m, protected by breakwaters, and two inner docks(nº 1 and nº 2),the first being rectangular and the second having an irregular shape. In order to improve the shelter conditions in the approach zone of the entrance of the harbour and in the harbour itself there is an outer break -

98

water, 900 m long.

The harbour construction started in 1884-1892 ;   it was formed
at that time only by the outer basin. In 1937-1941 the nº 1 inner dock
and the outer breakwater, as a submerged breakwater, with a top ele
vation of +1 m above datum were built (datum is arbitrary, a few cen
timeters below the minimum low water level, astronomical spring ti-
des). The cover layer of the breakwater was formed by concrete
cubic blocks of 90 metric tons. The construction of the nº 2 inner dock
started by the end of the fifties and is still in expansion. In 1971 the
outer breakwater was raised until +15 m, in order to create   behind
it a crude oil terminal for 100,000 tdw tankers.   This raising was
carried out by means of a sloping mound structure, the cover layer of
which, with an upper berm at elevation +11.50 m is formed by 40 metric
tons tetrapods (fig. 3); between +11.50 m and +15 m there is a con
crete superstructure with a curved face looking seawards.

In this paper the effects of a storm surge that happened on the
16th-17th January 1973 are analysed and described. These effects
were of two types:

- As the storm surge coincided with a spring tide and rough
seas, severe damages occurred in the outer breakwater, mainly in its
head.

- Associated to the storm surge range phenomena happened in
the nº 2 dock; these water movements, acting on a ship berthed in
a nodal zone, caused several breakings in the ropes and collision of
the ship against harbour structures, which were damaged.

Having in mind the affinities with these phenomena, the effects
of range action in the oil terminal and new damages in the break-
water, that occurred in January and February 1974 respectively, are
also briefly examined.

2. STORM ON THE 16th-17th JANUARY 1973

2.1 - Storm characteristics

Figs. 4 and 5 show synoptic charts of the meteorological si-
tuation corresponding to the 16th January 1973 at 00:00 and to the
17th January 1973. Barometric fall of 20 mm Hg started at 00:00
of Jan. 16, the minimum of 740 mm Hg lasted for 12 hours (from
20:00 of Jan. 16 to 08:00 of Jan. 17). Normal atmospheric pressu
re (760 mm) was reached at 22:00 of Jan. 17 and 770 mm pressure
was recorded at 12:00 of Jan. 18 (see fig. 6). As can be seen,
the centre of the low pressure associated with strong winds passed
just over Leixões, causing a "storm surge".

The following table is formed with predicted and occurred sea
levels as recorded by a normal tide gauge (fig. 8) placed   within the
outer harbour (fig. 2).

Residuals reached a maximum of +53 cm (at 20:00 of 16/1).
Regarding storm wind wave data it is stressed that:

- Unfortunately there are no local data recorded at Leixões.

- Although the storm which hit Leixões more intensely at down
of the 17th has not been a F.A.S., as it had mainly local characte

ACTUAL AND FORECAST TIDAL LEVELS																
HW	LW	HW	LW	HW	LW	HW	L.W	HW	LW	HW	LW	HW	LW	HW	LW
ACTUAL VALUES																
2 80	1 35	3 00	1 08	2 82	0 90	2 95	0 96	3 48	1 46	3 78	1 10	3 12	0 44	3 18	0 18
11 30	17 20	23 40	6 20	12 30	18 50	1 20	7 20	14 00	20 00	2 10	8 40	14 30	20 50	3 10	9 10
14th Jan		15th Jan		16th Jan			17th Jan			18th Jan					
FORECAST VALUES																
2 74	1 25	2 85	1 19	2 89	1 13	3 10	0 96	3 08	0 93	3 36	0 70	3 26	0 73	3.57	0 48
11 56	17 23	0 34	6 13	13 07	18 42	1 36	7 28	14 06	19 46	2 28	8 26	14 57	20 37	3 15	9 14
DIFERENCE BETWEEN ACTUAL AND FORECAST VALUES (cm)																
+6	+10	+15	-8	-7	-23	-15	0	+14	+53	+42	+40	-14	-29	-39	-30

Minim pressure

ristics, with strong winds which resulted from the low pressure cen
tre passing almost over Leixões, it is noted that on the 16th a 14 m
wave height was recorded at K meteorological ship.

     - The storm was of exceptional duration (24 hours).

     - In fig. 7 wave data referring to Baleeira (Algarve),   Sines
and Peniche (Portuguese west coast) can be seen. Data were record
ed with Datawell waverider buoys. Note that to an increase from
south to north in the wave heights there does not correspond an in
crease in periods, which is evidence of the local character to   the
north.

2.2 - Occurrence of long period waves

     If the tide record is searched (fig. 8) for long period waves and
the part of the record that corresponds to the occurrence of the
storm surge (fig. 9) is more carefully inspected, it is possible   to
observe that waves with periods of about 4, 8, 16, 20 and 40 minu
tes were present, with rather significant amplitude. The   more per
sistent wave is the 4 minutes one, more precisely 220 s.

2.3 - Damages in the outer breakwater

     During the storm the outer breakwater was severely overtopped.
As a consequence of this overtopping the structures of the oil ter
minal itself, mainly the steel ones, and the oil leading pipes   were
bent (fig. 10).

     The looking landwards steel doors of a transformer station lo
cated inside the concrete superstructure of the   breakwater were
carried away, apparently by suction action (fig. 11).Some tetrapods
of the cover layer of the breakwater were broken.   But the most
severe damages occurred in the head of the breakwater   that   was
practically destroyed: many tetrapods were broken or carried away;
the end concrete block of the superstructure supporting the light-
house and the neighbouring one fell down by undermining action of the
waves, that carried away the small rock blocks of the   underlayer
over which they were placed, and the following concrete block was
slightly displaced laterally (fig.s 12, 13, 14, 15).   To this effect
strongly contributed the presence of the cilindrical concrete monolith

that supported the lighthouse of the submerged breakwater before the raising operation, though the upper part of this cilindrical block was mechanically destroyed during the raising works, as this block originated a concentration of strong currents from the breaking wa ves on the damaged zone.

Model test were run after the accident in order to obtain a better knowledge of the destruction process and the best solution for the repairing works, to be carried out during the summer 1973.

2.4 - Disturbances caused by long period waves

2.4.1 - Damages on the bridge between nº 1 and nº 2 docks

A 160 m long freighter with general cargo berthed between bollards nº 26 and 36 of the north quay (nº 2 dock) broke the ropes at 23:00 on Jan. 16, 1973. Thrown adrift she then hit at 23:30 the abutment of the Leixões cantilever bridge and broke bollards nº 26 and 33. The bridge was damaged. At 10:30 of Jan. 17/1/1973 bad weather conditions persisted and the same ship, though secured by two tugs, was lurching so heavily that springs and a bollard (nº38). were broken (fig. 16).

2.4.2 - Interpretation of the resonant mechanism

If the two docks are considered as a sole rectangular dock 1220 m long it is seen that a half wave length resonance may occur with a nodal zone on the ship's position, with a fundamental resonant period of 212 to 225 s, embracing that of about 220 s whose presen ce was noted at the tide record.

Thus the disturbances caused by the ship which damaged the bridge and the bollards at about 23:00 of the 16th and 10:30 of the following day are explained. The nodal zone positioned in the berthing zone of the ship has horizontal movements which in turn are aggravat ed by the constriction between the two docks. Horizontal movements and corresponding velocities can be easily calculated, for selected va lues of d, T and H (d = 12 m. T = 225 s, and for instance, H=0.5 m) Excursion (horizontal movement):

$$\frac{\sqrt{g}\ HT}{\pi\sqrt{d}} = 32\ m$$

Maximum velocity:

$$\frac{\sqrt{g}\ H}{\sqrt{d}} = 0.45\ m/s$$

3. SIMILAR PHENOMENA IN 1974

3.1 - New damages in the outer breakwater (February 1974)

A storm occured in February 1974, after the head of the outer breakwater had been reconstructed. During this storm no major da mages happened. However several tetrapods of the zone near the head were broken or carried away (fig. 17, 18).

3.2 - Disturbances caused in berth n⁰ 1 of the oil terminal by long period waves

3.2.1 - General

Frequent problems have occurred after ships are berthed in n⁰ 1 berth of the oil terminal, caused by long period waves (fig.19 shows berth n⁰ 1 inside view).

A possible hypothesis for predicting the resonance period consists in considering the water mass limited by the outerbreakwater, the north breakwater of the outer basin and the end of its south breakwater as a triangular wedge (fig. 20). For $d = 16.5$ m and $l = 650$ m

$$T_1 = 1.308 \times \frac{2 l}{\sqrt{gd_1}} = 133 \text{ s}$$

is the fundamental resonant period of the wedge water mass[*],which is compatible with the existence of a nodal zone in the region of berth n⁰ 1. However, pure reflection non-resonant situations caused by the corner between the two breakwaters may occur for a wider range of periods. In the generated stationary system for some periods a node line can appear near berth n⁰ 1.

3.2.2 - Disturbances caused in January 1974 in a tanker moored at berth n⁰ 1

A brief report will be made of a typical accident which happened with a 137,000 dwt tanker ("Ortins de Bettencourt") on the 21st and 22nd January, 1974.

An analysis of the rapid rotation tide records of those days shows that there were waves with periods of 2 to 4 minutes with amplitudes up to 50 cm, probably amplified (fig. 21).

It is expected that the situation will be worse for periods near 2 min (for instance the 133 s period above mentioned) as it was admitted that this could be a resonant situation. As the triangular wedge is quite wide it is expected that the response curve will be smooth, corresponds to a poorly selective situation.

The accident which happened with the "Ortins de Bettencourt" was as follows:

"At about 23:30 hours of the 21st this ship, which was unloading, started moving, going as far as 10 to 15 m ahead and astern 3 to 4 m from the berth. Two tugs assisted the ship, which reduced those distances to respectively about 8 and 2 m. At 3:30 our tugs were assisting the ship and the two kinds of movement were reduced to 5 m and 1 m respectively. Meanwhile five ropes has been broken".

---

[*] - Wilson, B. Hendrickson, J.A. and Kilmer, R.E."Feasibility study for a surge-action model of Monterey Harbour,California", Cont. Report n⁰ 2-136 U.S.Army Corps of Engineers, Waterways Experiment Station, Vicksburg, U.S.A.

4. PREVIOUS STUDIES ON RANGE PHENOMENA AT LEI-XÕES

Previous studies on range phenomena at Leixões have been pre
sented by C.K.Abecasis (XVII th International Navigation Congress,
Lisbon, 1949, Section II. Subjet 4) and F. Abecasis et al. (XIX th
International Navigation Congress, London,1957. Section II. Subjet 1).
In these papers two strips of long periods of waves are referred
to as existing frequently at Leixões and in other zones of the Por-
tuguese coast: the first one between 2 and 5 minutes (120 to 300 sec)
with predominance of 3 to 4 minutes; the second one between 15 and
20 minutes, mainly in the zone of the upper limmit   (20 minutes) .
The occurrence of long period waves of both strips is often asso-
ciated with atmospheric depressions and rough seas. This is in accor
dance with the long period waves recently observed and described in
this paper.
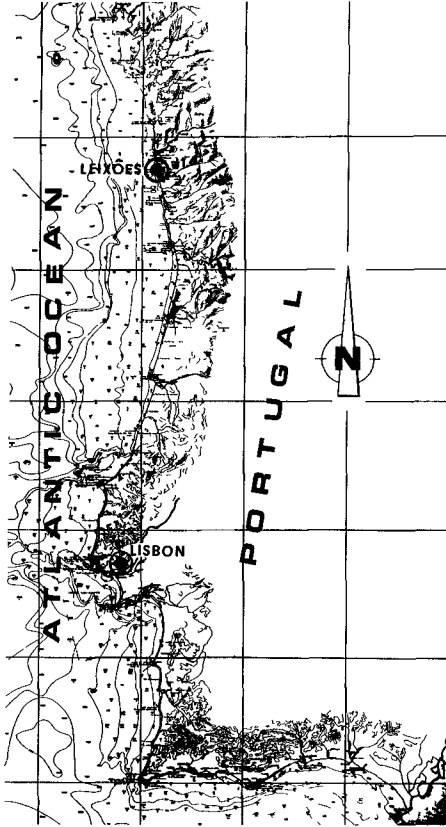
Fig. 1 - Location of Leixões
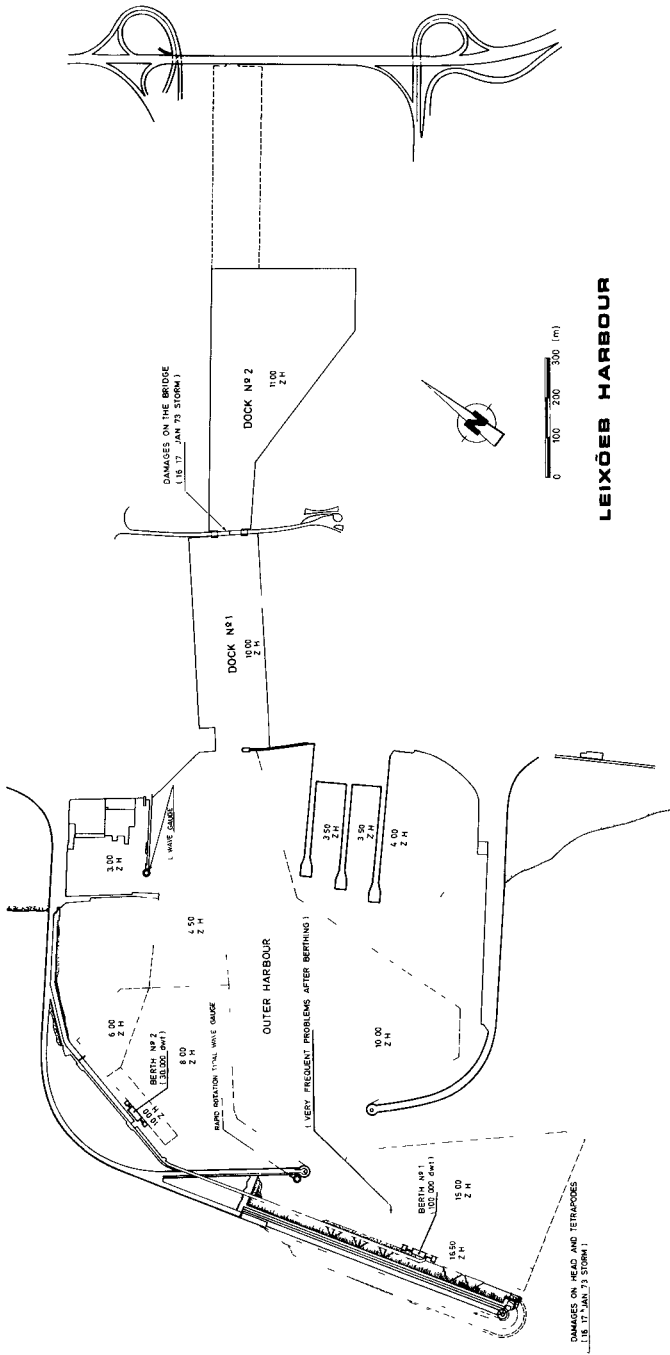
Fig. 2 – Lay-out of Leixões Harbour

PLANT   VIEW

SEA

+15 00

+11 50   +7 25

+7 25

+7 20

+4 00

OLD LIGHT HOUSE BASIS

-5 00

A — — —   Á

CROSS SECTION   A-Á

+15 00

+10 50

9 50

+7 25

+4 00

+1 00

I = 4/3

TETRAPODS 40 ton

R M >0 3 ton

R M >15 ton

R M >3 ton

R M >0 5 ton

I = 3/2

(0 00)

TOT
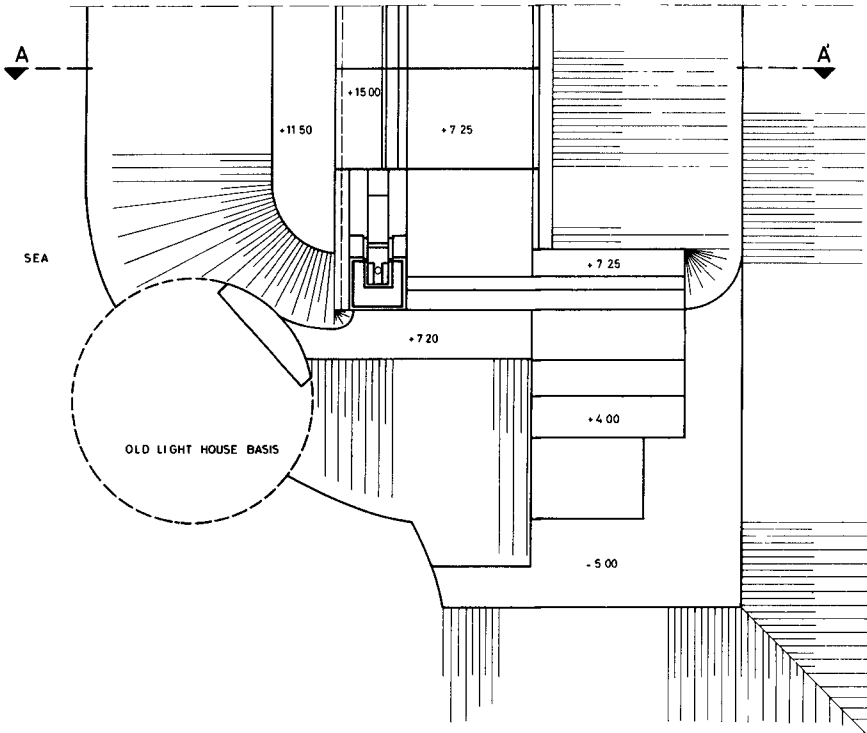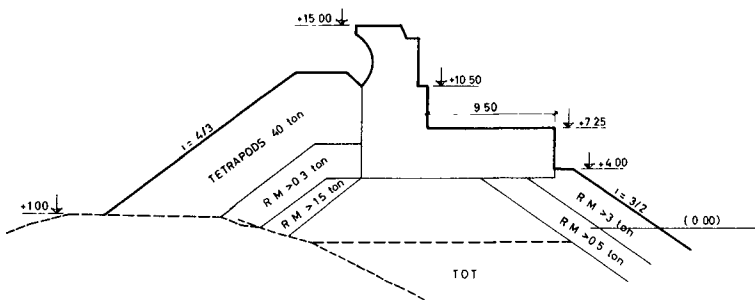
Fig. 3 - Head and cross-section of North breakwater
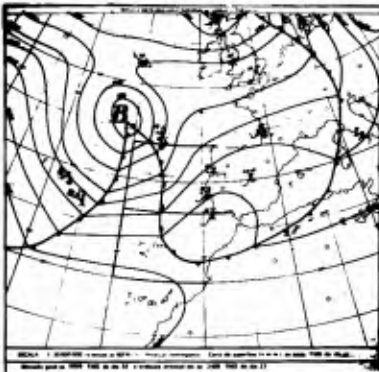
Fig. 4 - Synoptic chart
(16/1/73, 00:00)
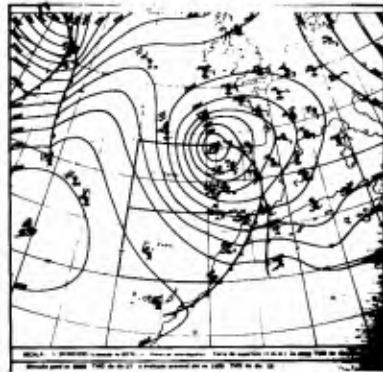
Fig. 5 - Synoptic chart
(17/1/73, 00:00)
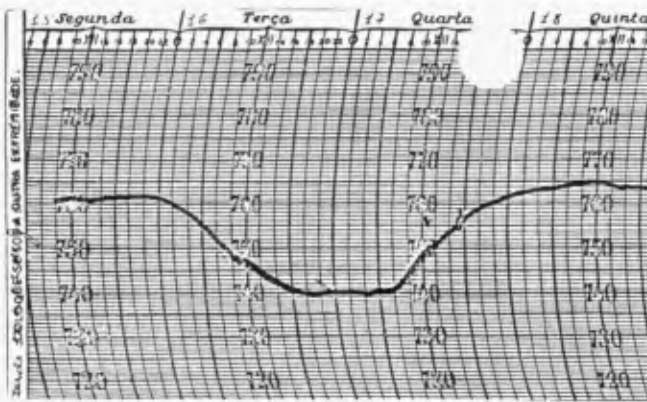
Fig. 6 - Barometric record
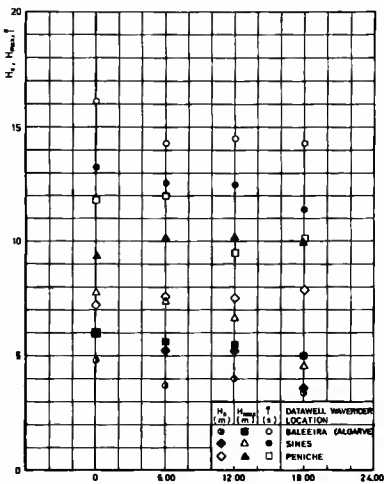
Fig. 7 - Wave data
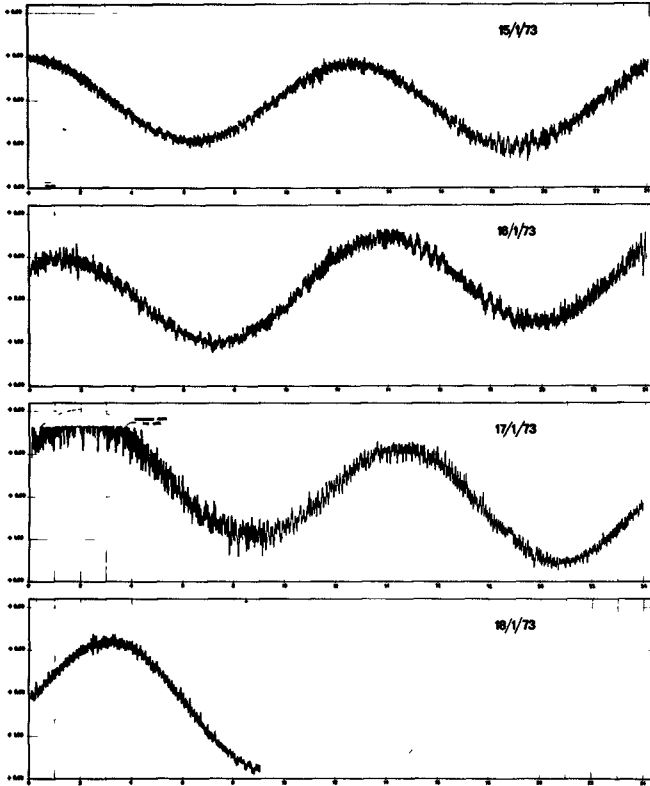
Fig. 8 - Tide record
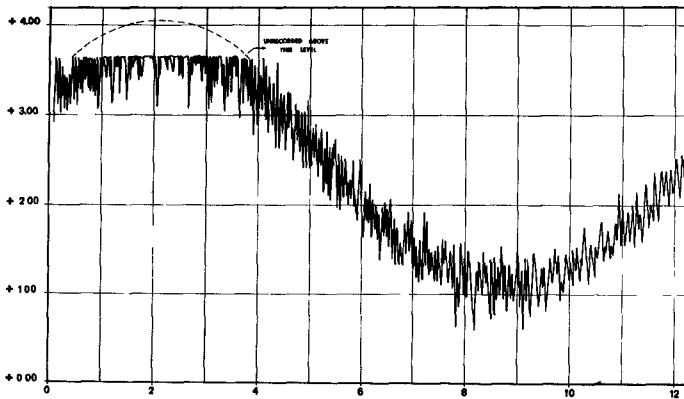
Fig. 9 - Tide record (close-up)

Fig. 10

Fig. 11

Fig. 12

Fig. 10 – Damages caused
by overtopping

Fig. 11 – Damages caused
by overtopping (cont.)

Fig. 12 – Damages at the head

Fig. 13 – Damages at the head
(cont.)

Fig. 14 – Damages at the head
(cont.)

Fig. 13

Fig. 14
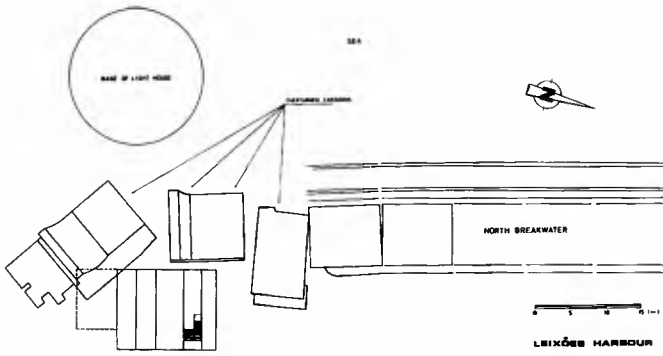
Fig. 15 - Damages at the head (cont.)

Fig. 16 - Damages on the bridge

Fig. 17 - New damages at
          North breakwater

Fig. 18 - New damages at
          North breakwater

Fig. 19 - Berth nº 1 (view)
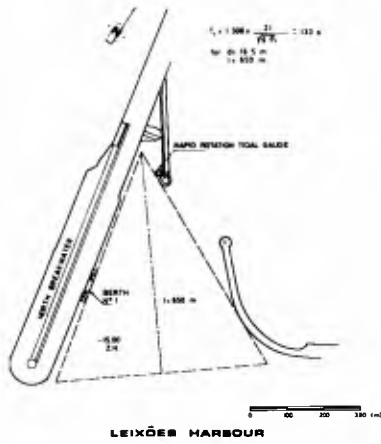
Fig. 20 - Hypothetical
           ressonant area
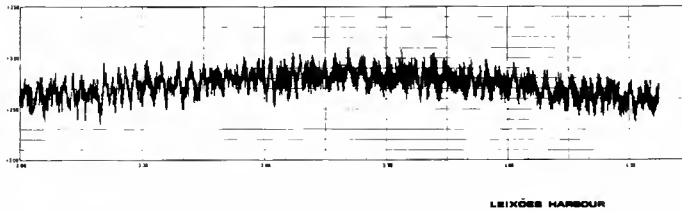
Fig. 21 - Rapid rotation tidal gauge record (22/1/74)

CHAPTER 4

ON THE PORTUGUESE WAVE REGIMEN

Júlio Patriarca Barceló

Research Officer. Department of Hydraulics

Laboratório Nacional de Engenharia Civil. Lisboa. Portugal

SYNOPSIS

Some general characteristics of the wave regimen along the Portuguese coast and the zones next to it are presented. The paper is of a chiefly informative nature and results from the analysis of values obtained during an initial stage of swell observation, applied to studies carried out at the Laboratório Nacional de Engenharia Civil(LNEC),Lisbon. Presently, a network of observation posts is being installed on the Portuguese coast. These posts will be duly equipped and will make it possible to gather systematic observation as regards swell as well as to make a much more accurate analysis of the wave regimen and of the wave trains.

1 - BASIC CONSIDERATIONS ABOUT WAVE OBSERVATION IN PORTUGAL

Proper knowledge of the waves along a coast will only be achieved through a network of posts for carrying out systematic observation, constantly updated information making it possible to study any changes in regimen. In an indirect way, the expense of installing these posts will no doubt prove compensating because of the economy they will originate in the works and in their use (not to mention problems connected with sea traffic and fishing safety, whose importance and seriousness cannot be estimated in numbers). Under the circumstances an undertaking of this type is an official charge to be borne by state organizations, and data regarding the wave regimen should be made public and immediatly available to the individuals in charge of the studies and projects (such as meteorology information).

Presently, the best model study techniques make use of the simulation of irregular waves and therefore a more accurate knowledge of the real wave train structures is necessary. Besides, this knowledge has many advantages for practical applications in general. Thus the present tendency is towards using highly accurate, automatic and autonomous recording instruments and to treat the recorded values so as to give special importance to spectral analysis and to the definition of the statistic parameters characteristic of the wave trains. There is also a tendency to use observation means that will give immediate information (accelerometer buoys), which is of great practical importance.

The absence of the abovementioned network of posts along the Portuguese coast made it necessary to make the best possible use, with the degree of approximation considered sufficient, of the data available on waves, and to analyse this data according to the practical needs met with, extrapolating whenever necessary.

The results of the study of Figueira da Foz wave regimen, on the west coast, were thus made known and first applied at the LNEC between 1964 and 1966, based on the observations made since 1954 by Figueira da Foz Harbour Authority with a tachymeter and signal buoy for determining wave heights, periods and directions, completed by the observation of the directions with the SIMATHA (a set of horizontal rods connec

Fig. 1 - SIMATHA (Sines) Equipment for wave observation (directions and periods).

ted to a vertical rotating axle, which allows to read angles and distances by adjusting the horizontal rods to the wave crests and also determine the values of the period by cronometer during the sightings — see figure 1).

A study of the wave regimen in the Portimão harbour zone was subsequently made based on the observations made since 1958 by the Maritime Services comprising only the observation of directions and periods by SIMATHA, in view of the model study of this harbour. Additional information on the south coast was supplied by the observations carried out since 1970 by the Portuguese Hydrographic Institute in the Huelva harbour zone (Spain), in view of the model study of this harbour's bar (using a pressure wave recorder and radar).

In 1965 an observation post equipped with a pressure wave recorder and radar was installed in Leixões harbour by Douro and Leixões Harbour Authority in order to collect data for the extensive work that was going to be carried out in this port, which is one of the most important harbours in the country (owing to deficient exploitation it has not yet supplied complete information). A pressure wave recorder and SIMATHA were also installed that year in Lagoa de Albufeira, south of the Tagus, by the Lisbon Harbour Authority, to gather data for the model study of Lisbon harbour.

In May 1971 a Symposium on wave data, SIDAM 71, was carried out in Lisbon, for promoting wave observation and studies on the Portuguese wave regimen under cooperation and coordination of the different official organizations (Harbour Department, Hydrographic Institute, National Meteorologic Department and LNEC).

In 1971 the Harbour Department installed posts in the north of Peniche (fishing harbour in the west coast, north zone) and Sines (future large sea harbour on the southern zone of the west coast). These posts were equipped with accelerometer buoys connected to reading stations with radio transmission and with SIMATHAS for observing the directions. In 1972 the Harbour Department installed a similar post in Baleeira (Sagres, western end of the Algarve coast) where a small fishing harbour
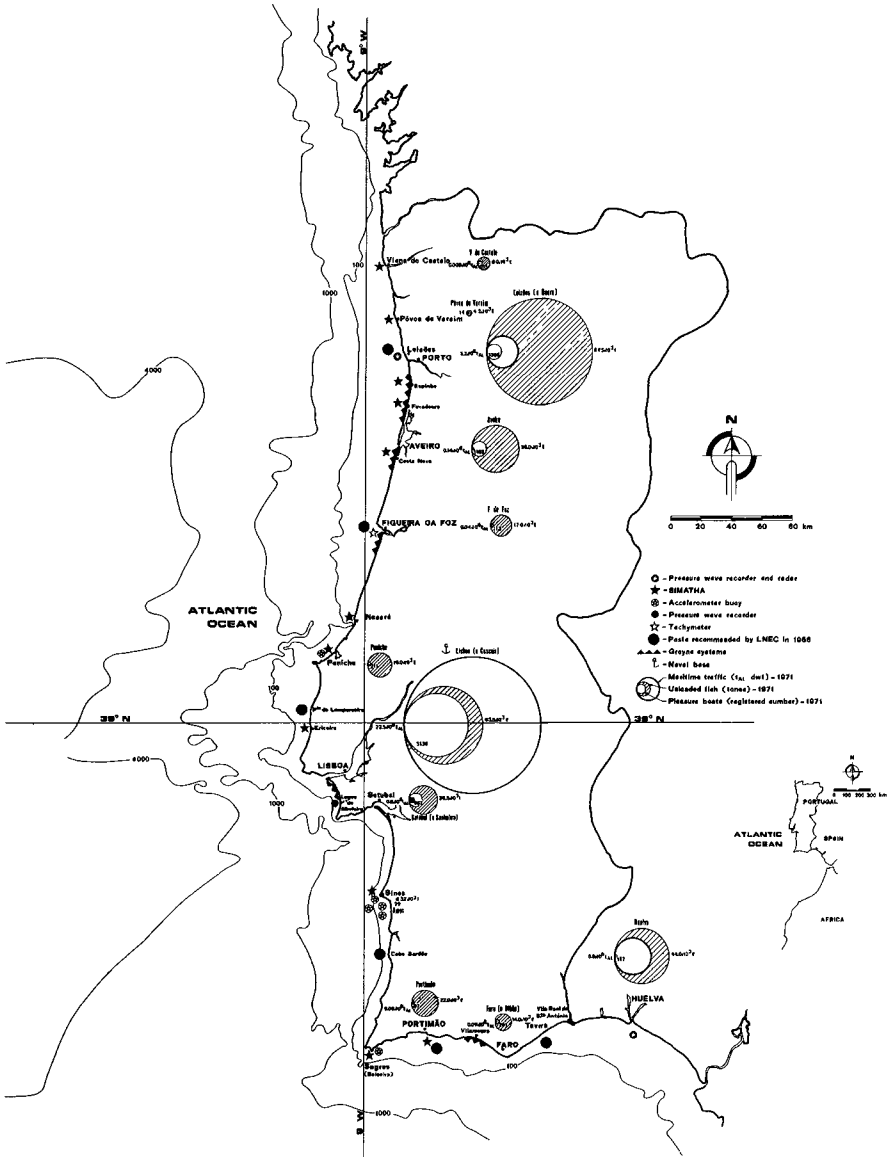
Fig.2 - Map of the Portuguese coast.

(and refuge for pleasure boats) is to be built. In 1973 three accelerome ter buoys were installed in Sines by the official organization in charge of the construction of this port (Department of Sines Area).

In 1957 there had been an attempt to install in Portimão an Amer ican WH1 pressure cell with land transmission by cable but after some damages the connecting cable was cut off by a wrecked ship and the method abandoned A similar cell was available at Leixões in 1962, at- tempts to install it having failed ; further attempts of installation during that year also proved unsuccessful.

Besides the posts referred to, there are also visual observations carried out at the lighthouses along the coast and some additional SIMATHA posts in the north coast. Other types of information that may be referred to are the American charts on the sea and swell conditions studies of the North Atlantic (based on the observation carried out at meteorologic ships) and the previsions of the National Meteorologic De- partment transmitted by television.

Figure 2 shows a map of the Iberian peninsula with the sites re- ferred to. Besides, it also gives a general idea of the importance of the different harbours and coastal zones as far as sea traffic, fishing and pleasure sailing are concerned (based on 1971 official statistics). The groyne systems constructed or under construction, as for instance at Figueira da Foz, are also indicated. Note also that ships with up to 1 million dwt are envisaged in Sines. In Cascais (near Lisbon) a harbour with moorings for 800 pleasure boats, in the first stage, has been des- igned and in Vilamoura (south coast) another harbour with moorings for 500 pleasure boats, in the first stage, will be inaugurated.

2 - PRACTICAL CONSIDERATIONS ABOUT WAVE OBSERVATION EQUIPMENT

Some practical aspects have to be borne in mind with regard to the main types of automatic equipment (pressure wave recorders, acceler- ometer buoys and radar).

In addition to supplying immediate information, accelerometer buoys also present the advantage that routine operations are easier and do not require such elaborate means as pressure wave recorders. This is due to the fact that their weight is about 90 kg and their autonomy of 9 months. It cannot however be forgotten that these buoys must have a pe riodical inspection (which could be every fortnight) because of the danger of maritime deposits in the links of the chain and cable that connect a massive in the bottom, and which may cause, among other accidents, rup- ture and disappearance of the buoy (these considerations are based on recent facts at Baleeira – see figures 3, 4, 5, 6 and 7), adequate painting of the buoys is therefore indispensable.

The risk of disappearance of the buoys owing to other causes must also be taken into account (there have also been instances). A sim- ple inspection routine has therefore to be followed, which will not be too difficult as the buoys transmit a radio signal which can be referenced . The accelorometer buoy of Baleeira was only operative from November

Fig.3 - DATAWELL type acceler-
ometer buoy (Sines, 19th Sept.
1971).
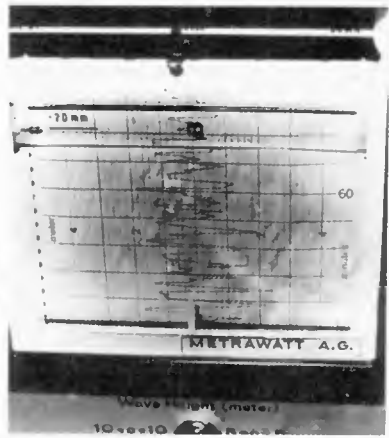
Fig.5 - Mainland recorder
of an accelerometer buoy
(Sines).

Fig.6 - Aerial view of Baleeira
(12th April 1973).

Fig.4 - An aspect of the instal-
lation operations of an acceler_
ometer buoy. Cables and links
(Sines, 19th September 1971).

Fig.7 - Hydrographic survey of
Baleeira (1959).

1972 to December 1973. The accelerometer buoy of Sines was operative from September 1971 to September 1973. The accelerometer buoy of Peniche was operative from September 1971 to February 1973. All the buoys of the Harbour Department have disappeared and that of Sines was not found. It must be said that the Harbour Department does not possess the necessary means to keep this equipment in good conditions of assistance. The three buoys of Department of Sines Area, which have their own maintenance team, have been operating very efficiently.

Regarding pressure wave recorders placed on the bottom, although they may be dragged away in fishing areas (or even during the working of the assisting ship), the risk of disappearance is smaller. However, if they are damaged, a month of information may be lost (this is generally the time of their autonomy) without the possibility of intervening. Pressure wave recorders need more powerful means as well as larger and more higly qualified teams for the routine operations, not only because of their location at the bottom but also because of their weight which is about 600 kg. Besides, divers will be needed to carry out the monthly routine operations, whereas accelerometer buoys will only need this type of assistance during the initial location operation. Also, assistance operations in pressure wave recorders are difficult in sea zones where the sea is often rough, as for instance in the northwestern coast.

The operation of pressure wave recorders may also be affected by the obstruction of its membrane through sea deposits or sanding up, or there may even be excavations during storms that bury the equipment, with subsquent sanding up (as occurred in Leixões)

Accelerometer buoys, besides supplying immediate information, can also be connected to special reading units with immediate automatic treatment of the recorded information, thus simplifying reading operations, which are always necessary in the case of pressure wave recorders.

Taking into account the criterion adopted chiefly by the Dutch and Americans and now also by Portugal (in connexion with Sines and the posts of the Harbour Department) and bearing in mind what has just been said about pressure wave recorders and accelerometer buoys, it can be concluded that it is the buoys that offer the best conditions, from the practical point of view and with regard to treatment of information. Nevertheless considering the characteristics described, it is indispensable to the suitable exploitation of a network of posts to dispose of well equipped and qualified teams.

On the other hand a network of posts will only be complete if wave direction observation means are added to the accelerometer buoys, or else pressure wave recorders Radar will be the best method. It is pointed out however that powerful radar should be used, offering better possibilities of echo captation, in order not to limit its use. Also in this case the need arises for qualified personnel to operate the radar

The radar used in Huelva, with a peak power output of 5 kilowatts, a frequency band of about 9 375 MHz, and a range of 3 to 30 miles, showed deficiencies in the information concerning wave directions, as opposed to the radar of Leixões, with 20 kilowatts, 9 375 MHz and 0.75 to

Fig.8 – CHATOU type pressure wave
recorder (experimental stage in
January 1965 at the Tagus estu-
ary).

Fig.9 – Adjustment of pressure
wave recorder (Huelva).

Fig.10 – Typical record of pressure wave recorder (Lagoa de
Albufeira, 5th October 1965 at 22.09h. T_C = 10.28s; H_S = 1.79m).

Fig.11 – Waves at Huelva in front
of Prácticos observation post
(25th June 1970).

Fig.12 – Aerial view of Huelva
observation zone (13th October
1973 at 9.30h).

Fig.13 - Huelva radar (block and sighter).

Fig.14 - Huelva radar (block with camera).

Fig.15 - Hydrographic survey of Huelva bar (June 1970).

Fig.16 - Huelva radar (aerial).
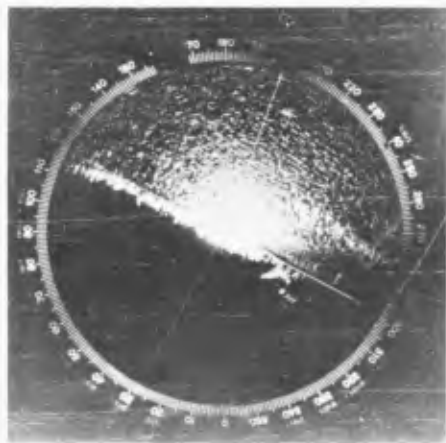
Fig.17 - Typical image supplied by Huelva radar(26th Jan.1971 at 21.00h. $T_C = 8.0s$; $H_S = 0.70m$).

Fig.18 - Aerial view of Leixões
harbour (5th April 1973 at
13.00h).

Fig.19 - Typical image of Lei-
xões radar (non identified
photograph).

Fig.20 - Hydrographic survey
of Leixões harbour (1950,
updated).
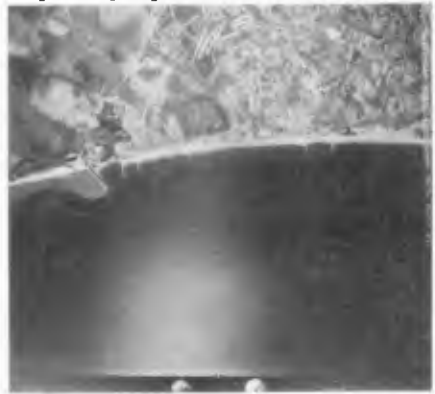
Fig.21 - Vilamoura groyne sys
tem.SW wave action(12th April
1973 at 13.00h).Construction
phase of the marina.

Fig.22 - Aerial view of Peniche
(2nd March 1973 at 13.00h).

Fig.23 - Hydrographic survey
of Peniche harbour(1915, updated).

Fig.24 - Aerial view of Lagoa de Albufeira(9th March 1973, 13.00h).

Fig.25 - Hydrographic survey of Lagoa de Albufeira(1961).

Fig.26 - Aerial view of Sines (16th March 1973,at 13.00h).
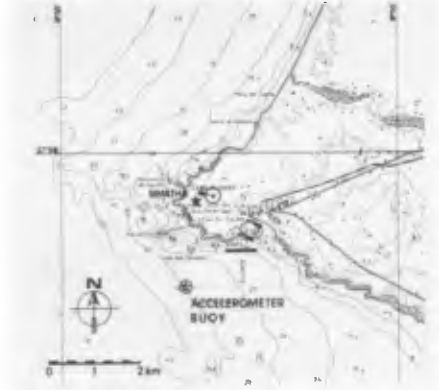
Fig.27 - Hydrographic survey of Sines (1972).

Fig.28 - Aerial view of Portimão(12th April 1973 at 13.00h).
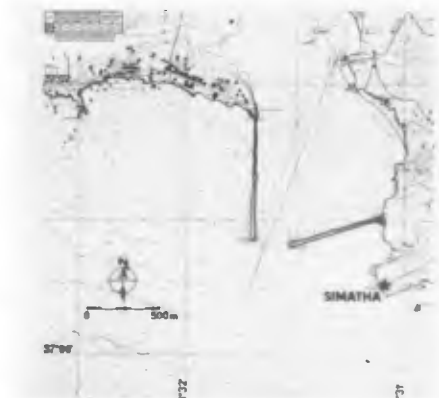
Fig.29 - Hydrographic survey of Portimão (1961).

18 miles, which supplied images with greater contrast of the waves and is therefore considered to be more suitable.

The Tucker Draper method has been used by the Hydrographic Institute to analyse the recordings of the wave recorders in the cases of Huelva and Lagoa de Albufeira.

The cost of the accelerometer buoys is about 15 000 US dollars (DATAWELL, Dutch make, including land station equipment). The cost of the pressure wave recorder is about 12 000 US dollars (CHATOU, French origin). The cost of the radar used in Huelva was 3 200 US dollars (AR 305 B - ANRITSU ELECTRONIC WORKS, LTD).

Figures 8 to 29 illustrate some aspects regarding pressure wave recorders and the use of radar in the observation of wave directions, and show some air photographs and hydrographic surveys of the places referred to.

3 - GENERAL CHARACTERISTICS OF THE WAVE REGIMEN IN THE ZONES OF PORTIMÃO (Algarve coast) AND HUELVA (southeast coast of Spain)

3.1 - Portimão

The only information available are wave direction and period observations (mean values of the period of the individual waves of the trains with 21 waves), using SIMATHA and references to wave heights based on visual observation from the lighthouses, which are considered with great reservation (in this case it is considered that the said observations are not sufficiently accurate owing to the high values estimated for the wave height, however other studies make reference to the results of observations carried out at lighthouses on the western coast, which agree closely with those obtained by the wave recorders).

The observations carried out in 1964/1966 by the Maritime Services, for a zone with depths between 10 and 15 m are presented. The general characteristics of the regimen can be analysed in figure 30. The periods of calm amounted to about 70%, 37% of the waves coming from the SE quadrant and 63% from SW quadrant, there being two different regimens, one for each quadrant. In the SE quadrant the periods are limited to maximums of about 11 to 12 s whereas in the SW quadrant there are periods greater than 16 s rising to maxima of about 20 s. The period distribution is asymmetric with a maximum of between 6 and 7 s. The calculations carried out for the maximum fetch, which can be defined for the SE quadrant owing to the limitation imposed by the neighbouring coast, have made it possible to determine the maximum period, which amounts roughly to 11 s and the maximum heights, about 4 m.

3.2 - Huelva

The observations made with a pressure wave recorder and radar between October 1970 and September 1971 will be considered. The wave
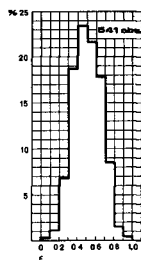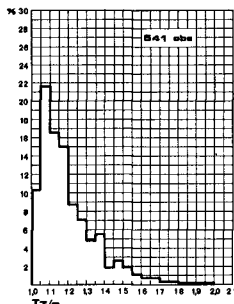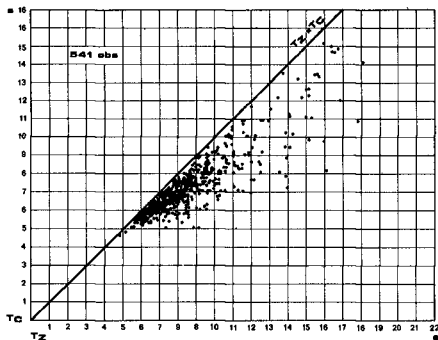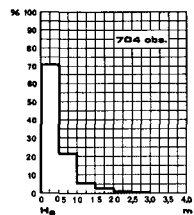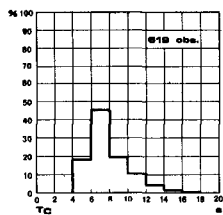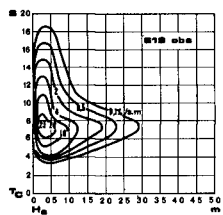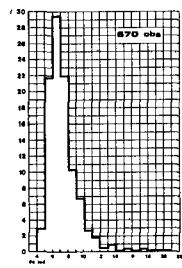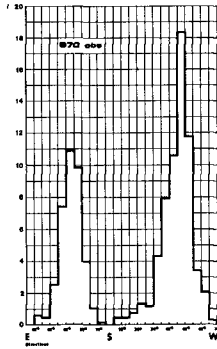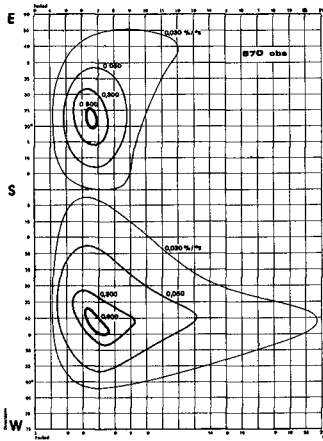
Figs.30 and 31 — Portimão's wave regimen (10 to 15m depth) and Huelva's wave regimen (10m depth).

recorder was located at a depth of 10 m. The values of the significant heights of the wave trains on the surface (H_s), the values of the crest period (T_c) and up zero crossing period (T_z) as well as the spectral width (ϵ) were considered.

The general characteristics of the regimen can be analysed in figures 31 and 32. A range of periods T_c comprised between 4 and 18 s have been observed with a maximum at step 6-8 s. The values of height distribution presented include the states of calm. 70% of the states of the sea show heights between 0 and 0.5 m corresponding to maximum occurrence. Maximum heights which occur very seldom lie between 2.5 and 3.0 m (significant height values). The binary T_c, H_s has a very different distribution from those presented for the Portuguese west coast. It has a maximum at 6-8 s and 0-0.5 m, maximum values of wave heights associated with the most frequent periods and the heights associated with the larger periods are rather unimportant (these waves come from the North Atlantic with a great decrease in the energy of the wave trains owing to the refraction and diffraction). The relation T_z/T_c shows values between 1.00 and 2.00, there being about 64% between 1.00 and 1.20. It is for the lowest values of the period that the values nearest to 1.00 are obtained (which is due to the filter effect). Hence the fact that these periods are similar to those of Portimão zone (which will better correspond to the values of T_z).

As regards the distribution of the wave directions it must be said that this radar showed some deficiencies in so far as it was difficult to detect waves less than 60 cm high. This brought gaps of the order of 90% and the observations of wave directions were subsequently completed by a method similar to SIMATHA. The values of the binary direction-significant height have a maximum corresponding to the greatest density of occurence for the pair of values $210^o/220^o$, 0/0.50 m, and another for values $180^o/190^o$, 0/0.50 m (see figure 32).
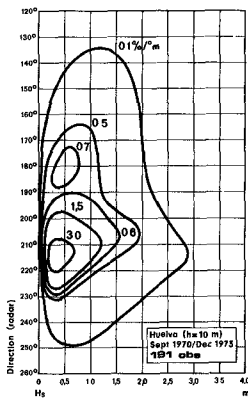
Fig.32 – Huelva. Correlation curves between wave directions and wave heights (10m depth).

Daily routine observations (two a day) were considered in the groupings made, storm recordings (extra routine) having been left out. The gaps observed in the wave recorder were less than 1%.

4 - GENERAL CHARACTERISTICS OF THE WAVE REGIMEN IN THE LAGOA DE ALBUFEIRA ZONE (center-south zone of the west coast)

The paper gives the values for the year of 1967, included in the experimental period of 1965-1968, with values obtained by a pressure wave recorder and worked out by the Lisbon Hydrographic Institute for the model study of the Tagus estuary (Lisbon harbour). There is no thrust-worthy information of wave direction observation, although a SIMATHA had been placed in this zone. The wave recorder had been placed at a depth of 20 m.

The general characteristics of the regimen can be analysed in figure 33. A range of periods T_C (crest periods) lying within 6 and 16 s, with a maximum of occurrence in step 8 to 10 s, has been observed. Height distribution is asymmetric, a percentage of 26% of waves below 0.5 m having been observed, with a maximum situated between 0.5 and 1.0 m and heights up to 6.0 m. These are significant height values in the zone where the observation was carried out. Extrapolation towards deep water, based on wave diagrams, gives heights of about 9.0 m for the NNW storms. T_C, H_S presents the distribution shown in figure 33, greater heights being connected with greater periods. As can be seen in this figure, the con-centration of points regarding the low values of the period happens near the straight line $T_C = T_Z$ (as in the case of Huelva) and then spreads, the widest differences being found for the highest values of the period.

The parameters described for Huelva were considered and the same criterion was adopted in the statistic groupings. The gaps observed in the exploitation of this pressure wave recorder (in 1967) amounted to 34%. It therefore became necessary to take into account the month of November 1965 instead of November 1967 which was missing (this was possible because of the characteristics of regularity of the wave regimen during these years).

5 - GENERAL CHARACTERISTICS OF THE WAVE REGIMEN OF FIGUEIRA DA FOZ ZONE (north zone of the west coast)

The first elements of the wave regimen study, that were revealed between 1964 and 1966, were based on the observations made by the Fi-gueira da Foz Harbour Authority using tachymeter and a signal buoy, placed at the depth of 12 m, from 1954 to 1960. With this system were made observations of heights, periods and directions (see figures 34 to 40).

The general characteristics of the wave regimen can be analysed in figure 34. In the method adopted observed heights were limited to 20 cm. One set of periods ranged from 6 to 20 s, (obtained by chronome-try of 21 consecutive waves and calculation of the mean values of the individual periods) which are closer to the values of T_Z because the waves of smaller individual period are overlapped by the dominant waves and are not observed (which diminishes the relation between the maximum individual height and the significant height). Height distribution (signifi-cant heights, calculated according to the mean of one third of the waves with greater train height) is asymmetric, there being a percentage of 20% of waves below 1.0 m, with 6% of calm sea (heights below the measuring
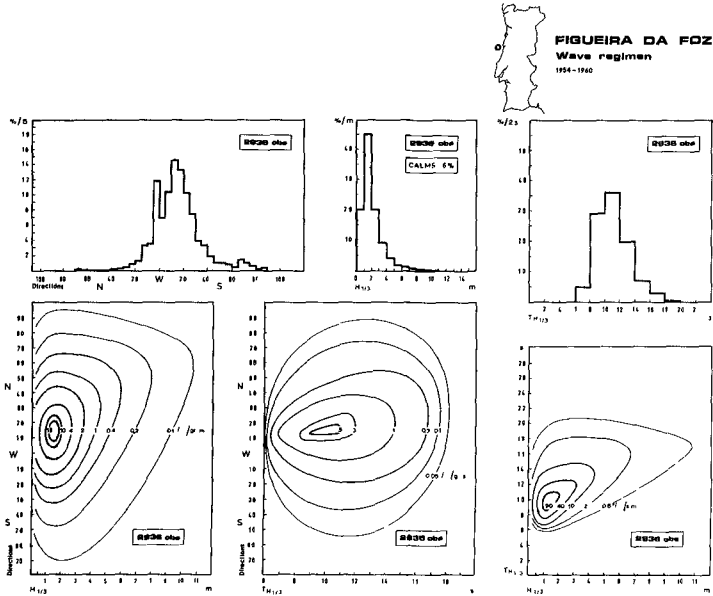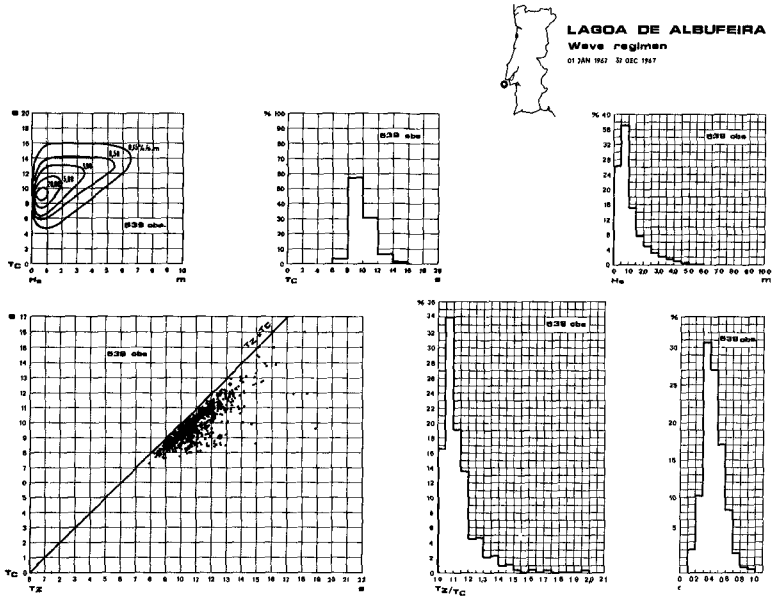
Figs.33 and 34 - Lagoa de Albufeira's wave regimen (20m depth) and Figueira da Foz's wave regimen (deep water).
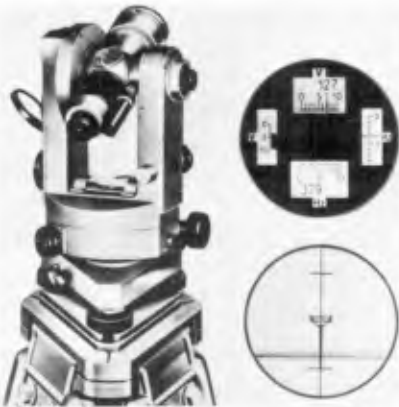
Fig.35 - Tachymeter, reading scales, signal buoy(Figueira da Foz).

Fig.36 - Observation tower(Figueira da Foz - May 1962).

Fig.37 - Breaking waves at Figueira da Foz (May 1962).

Fig.38 - Record of the observation and calculation of the values (Figueira da Foz).
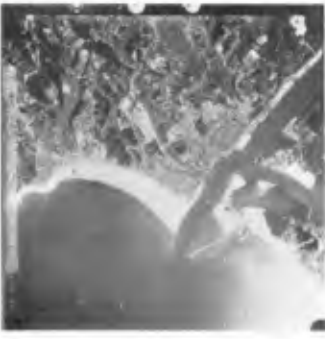
Fig.39 - Aerial view of Figueira da Foz(2nd March 1973 at 13.00h).
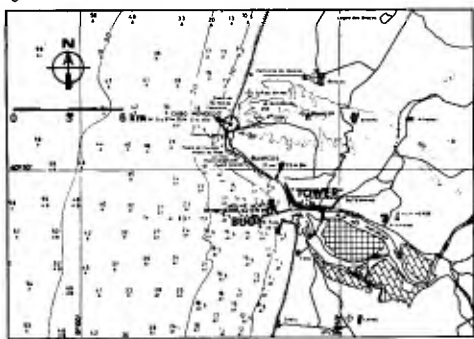
Fig.40 - Hydrographic survey of Figueira da Foz (1914, updated).

range of the tachymeter included), a maximum at step 1 to 2 m and heights up to 11 m. These values concern the height of waves off shore (deep water), by extrapolation of the values of the zone under observation. The distribution of the off shore wave direction is regular, almost symmetric around step W- 10° to 20°- N, very different from that in the south coast.

With this method of observation and during the time considered 18% of gaps due to various reasons were observed (among them the disappearance of the signal buoy during storms, lack of visibility, sundays and holidays during which the observation team was not active, etc.).

6 - CHARACTERISTICS OF OCEAN WAVE TRAINS

Further to the considerations made at the IX Coastal Engineering Conference (1964), the correlation graph between the mean values of the wave periods and the significant height values are presented, taking as a basis the graph presented in 1960 by Prof. Wiegel, which comprises all sorts of different observations, from experimental flumes, lakes, and gulfs to ocean zones, and including in this graph besides the observations of Figueira da Foz (deep water) also those of Lagoa de Albufeira and Huelva (both in the observation zone).
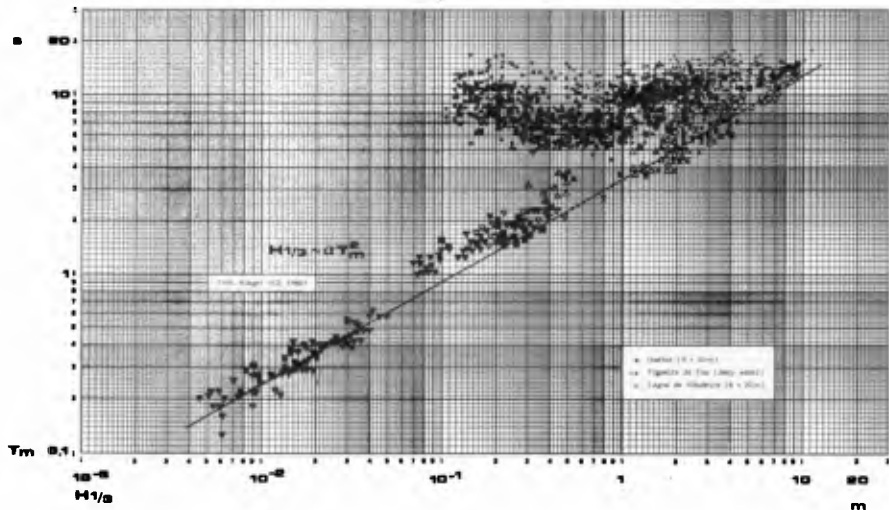
Fig.41 - Graph of correlation between $H_{1/3}$ and T_m.

The values concerning these observations differ from the law defined by Sibul, the same as the values of the other observations carried out in the North Atlantic, but they tend towards the straight line defined from the experimental values in the zone of greater heights and periods. Figure 41 shows the points concentration concerning Figueira da Foz (1954 and an extreme value of 1956 with $H_S = 11$ m), Huelva (1971) and Lagoa de Albufeira (Jannuary 1967, which is a representative month); the points concentrations tend to the theoric limit straight line in Prof. Wiegel's graph.

Three spectral curves are defined hereafter regarding the cases of Huelva, Lagoa de Albufeira and Figueira da Foz and corresponding to typical cases. It can be said that, on the whole, the spectra of Huelva
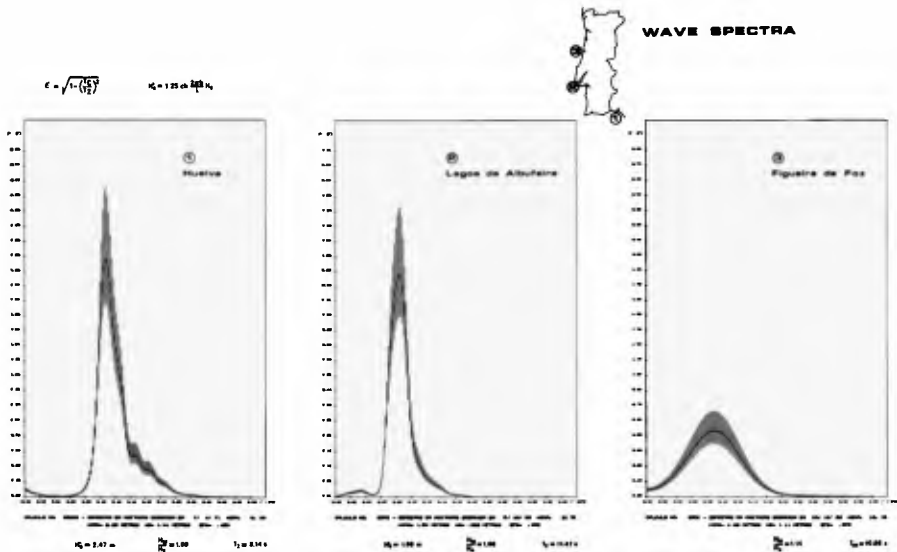
Fig. 42 - Wave spectra.

and Lagoa de Albufeira (obtained from the records of the pressure wave recorders and regarding the orbital movement near the bottom) are of the same type, with spectral width values near 0.45, which corresponds to maximum occurrences. There is however greater concentration of energy in the higher frequencies in the case of Huelva, the opposite being true in connexion with Lagoa de Albufeira. In the case of Figueira da Foz, the spectrum was obtained schematically from the tachymeter observations, which is less accurate, and a different type of spectral curve was obtained. As regards the relations between maximum and significant wave heights, the value for the two first cases is approximately 1.60, which is closer to Prof. Wiegel's values than to the value obtained for Figueira da Foz, 1.15. This shows the influence of the observation method (in which secondary waves overtopping dominant waves were not observed by tachymeter). In figure 42 values H_S concern the amplitude of the bottom orbital movement and the values H'_S the surface heights. It should be noted that accelerometer buoys supply direct information on the surface sea conditions, which has indubitable advantages.

In accordance with the data on figure 43 it can be said that: off Figueira da Foz, significant waves with heights between 12.0 and 12.5 m have a probability of occurrence of 1 every 10 years; in Lagoa de Albufeira the 8.0 m wave has a probability of 1 every 10 years (in the observation zone), and in the Huelva observation zone the probability of occurrence for 2.5 m waves is 1 a year. In the straight line regarding Figueira da Foz there is a point, at maximum heights, which deviates from the straight line; this is due to lack of observation during storms because
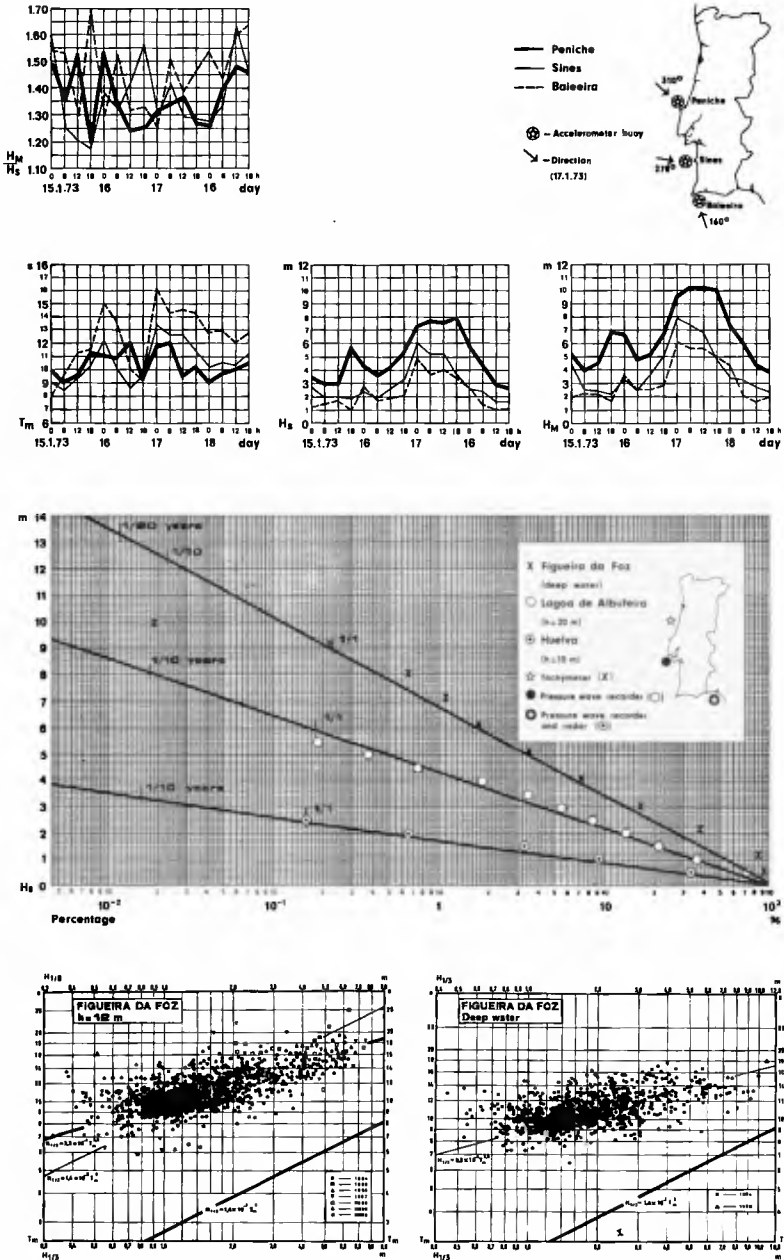
Fig.43 - Characteristic elements of the western and southern coast wave regimen.

there is frequent rupture and disappearance of the signal buoy on these occasions.

From the 3 accelerometer-buoys of the Harbour Department used in Peniche, Sines and Baleeira can be obtained typical data on the variation of the wave characteristics by analysing the data regarding the north storm that occurred in January 1973, which associated with a depression, caused damages in some works as well as erosions and overtopping in different places. The maximum H_S values recorded were 7.9 m (Peniche, 25 m
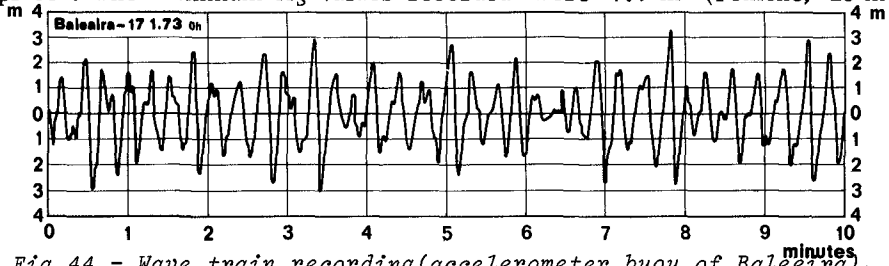
Fig.44 - Wave train recording (accelerometer buoy of Baleeira).

depth), 6.0 m (Sines, 43 m depth) and 4.8 m (Baleeira, 32 m depth). The mean periods were respectively 10.1 s, 13.3 s and 16.1 s. The periods at Baleeira were on the whole higher than on the other two places, which might be due to the attenuation of the smaller period wave components due to the refraction and diffraction to which swell is subject as far as Baleeira. Figure 43 shows the data regarding these observations, including the relationships between significant heights H_S and maximum individual heights H_M, and the wave directions in the zones under observation.

7 - CONCLUSIONS

The nature of the Portuguese coast, with rather high tides, particularly strong sea (on the west coast) and all sorts of coastal formations, fully justifies the existence of a well equipped and efficient network of posts to carry out a thorough observation of the waves.

A network of posts installed according to the schemes envisaged could supply useful information regarding any point of the coast by drawing wave diagrams to make it possible to know the regimen off shore and from it also that on the different parts of the coast (by drawing in computer the wave diagrams).

The ideal solution for wave observation seems to be to combine accelerometer buoys with radar controlled automatically by the radio-signal of the buoy. Radar would thus operate during the routine established for the accelerometer buoy and during the storm recordings, without the assistance of an operator.

The relations between T_m and $H_{1/3}$ are difficult to define for the observations considered in this work due to the scattering of the points. There is however a tendency of the extreme values towards the limit straight line defined in Prof. Wiegel's graph. In the case of Figueira da Foz approximate relations were defined as can be seen in figure 43.

CHAPTER 5

WAVE STATISTICS ALONG THE NORTHERN COAST OF EGYPT

By

M. Manohar (1), I.E. Mobarek (2), A. Morcos (3) & H. Rahal (4)

ABSTRACT : As a forerunner of a comprehensive study of wave and energy
climate of the Nile Delta coast covering a period of more than 50 years,
wave measurements taken in 3 locations along the coast in the year 1972
were statistically analysed. Shortcut methods based on statistical
approach were used to analyse the wave records enabling quicker analysis.
Spectral analysis of the wave records indicates narrow spectral band
similar to Raleigh distribution. The histograms and frequency distribu-
tion curves of significant wave heights, and the relationships between
various statistical parameters such as H_{max}, $H_{1/10}$, $H_{1/3}$ and H_{rms} also
agree closely with Raleigh distribution curves and parameters enabling
the use of Raleigh distribution function in subsequent studies. Finally
since the wave characteristics and wave energy climates are most important
in the analysis of coastline changes, they are drawn from the data obtained
from the analysis.

INTRODUCTION : Statistical characteristics of the ocean surface are of
interest when the dynamics of coastal accretion and erosion is considered.
When the coast and beaches are composed of loose sediment such as along
the Nile Delta coast, this assumes more importance since energy even of
smaller magnitude affects the coast.

THEORY : Waves are the primary force operative on the beach and the most
common ones are generated by winds. Ocean waves are complex in character
due to variations in wind pressure which generate them. The period, celerity
and wave length of the waves are exceedingly irregular and therefore, statis-
tical methods must be used to describe their properties. Though wave heights
are nearly as irregular, it is easier to define the wave height since it
rises from ready reference level. Thus if a satisfactory statistical dis-
tribution of wave height is possible, the expected wave height can be
reasonably predicted.

The statistical characteristics of ocean surface are related to the wave
spectra which in turn may be used to describe the processes of wave
generation and wave decay.

---

(1) Hydrodynamics Engineer (UNESCO), Unesco Project ARE 81, Coastal Erosion
    Study, Alexandria, ARE.
(2) Assoc. Prof. of Civil Engineering, Cairo University, Cairo, ARE.
(3) Senior Engineer, Coastal Erosion Study, Academy of Science and Techno-
    logy, Cairo, ARE.
(4) Engineer, Coastal Erosion Study, Academy of Science and Technology,
    Cairo, ARE.

132

The theoretical distribution function for wave height variability based
on the assumption of random phase and a narrow spectrum is the Raleigh
distribution function (3). According to Longuet Higgins, if the statistics
of wave amplitude can be approximated by the statistics of wave envelope
function, and if the wave heights are considered proportional to the wave
amplitude, wave heights can be expected to follow Raleigh distribution.
Subsequently, Cartwright and Longuet Higgins (1) reviewed Rice's (5)
derivation of a frequency function for a sum of a number of functions of
a random phase with a wide frequency band. Rice's frequency function
includes a parameter ε which is a measure of width of the energy spectrum.
Raleigh's distribution is a special case of Rice's more general frequency
function.

Raleigh's frequency function is of the form $\quad p(H) = \dfrac{\pi}{2} \dfrac{H}{\mu} \, e^{(-\frac{\pi}{4}) \frac{H^2}{\mu^2}}$ $\quad$ (1)

where H= wave height and $\mu=$ mean wave height. The nth moment about the
origin is given by

$$M_n = \int_0^\infty H^n \, p(H) \, dH \qquad (2)$$

or by certain transformations

$$M_n = \left(\frac{2\mu}{\sqrt{\pi}}\right)^n \Gamma \left(\frac{n+2}{2}\right) \qquad (3)$$

For n=0 to 3, equations (1) and (2) give

$$M_o = 1$$
$$M_1 = \mu$$
$$M_2 = \frac{4}{\pi} \mu^2 \qquad (4)$$
$$M_3 = \frac{6}{\pi} \mu^2$$

Generally μ $\quad$ estimated from $\overline{H} = H_{mean}$ = average wave height and $\sqrt{M_2}$ = μ =

maximum probable estimates of both H_{avg} and H_{rms} may be found from $\sqrt{\overline{H^2}} = H_{rms}$.

The probability distribution function of H may be written as

$$p(H) = \int_0^H p(H) \, dH = 1 - e^{-H^2/M_2} = 1 - e^{(-\frac{\pi H^2}{4\mu^2})} \qquad (5)$$

According to Longuet Higgins, $H_{1/n}$, the average of the highest 1/n waves
in a group of N waves can be expressed as

$$H_{1/n} = M_2 \left| \sqrt{\ln n} + \frac{n\sqrt{\pi}}{2} \, \text{erf} \, \sqrt{\ln n} \, \right| \qquad (6)$$

From (6), ratio of $\dfrac{H_{1/3}}{H_{rms}}$ = 1.416 and $\dfrac{H_{1/3}}{\mu}$ = 1.598.

Similar calculations may be made for all values of n from 1 to infinity.

Other relationships obtained by Longuet Higgins (3) and Putz (4) (from statistical analyses of 20 minute records) and spectrum analysis are given below.

	Longuet Higgins	Putz	Spectrum Analysis
H_{avg}	0.625 $H_{1/3}$	0.624 $H_{1/3}$	1.772 $\sqrt{E}$
$H_{1/10}$	1.27 $H_{1/3}$	1.29 $H_{1/3}$	3.600 $\sqrt{E}$
H_{max}	1.77 $H_{1/3}$ (from record of 300 waves)	1.87 $H_{1/3}$ (average of 25 twenty minute records)	$H_{1/3}$ = 3.60 $\sqrt{E}$ where E= wave energy

Longuet Higgins (3) also showed that the most probable value of the maximum wave height depends upon the length of records or number of waves N. The table below gives values of H_{max} / $H_{1/3}$

N	H_{max} / $H_{1/3}$
10	1.11
20	1.25
50	1.42
100	1.53
200	1.64
500	1.77
1000	1.86

Whereas the wave spectra describes the characteristics of ocean surface, and the processes of wave generation and decay, the significant wave height, distribution of wave heights, distribution of wave periods, and marginal and joint distribution of wave heights and periods will describe the wave variability. Similarly, just how the significant wave height is related to the probability distribution and also the wave spectrum, can best be described by a histogram (that is, percent occurrence of waves in each wave height range), period spectrum diagram (sum of energy or square of wave heights for each range of period or frequency) and cumulative frequency distribution curve (that is, percent less or equal to occurrences for each significant wave height range).

The ultimate objective of these statistical studies along the Nile Delta coast is the determination of the wave height and wave energy (or energy flux or power H^2T) climate along the entire coast. These can be drawn in the form of their respective roses in relation to their directions.

<u>FIELD DATA</u> : Field data were obtained by means of OSPOS (offshore pressure operated-suspended) wave recorders anchored near the bottom in 3 different locations in Abuquir, Burullus and Ras el Bar in 6-8 m depths in the sea facing the 245 km long coastline (fig. 1). These recorders are essentially pressure meters which when placed in certain depths under water, measure and record the variations in pressure caused by the waves. In the instrument, the pressure variations are converted into straight horizontal displacements by a recording pen. Since the recording periods of the instruments used in the field were 20 minutes once every four hours, 6 wave records were obtained for each day.

<u>DATA ANALYSIS</u> : In the analysis of wave records, initially the crest to trough heights of all waves in the 20 minute record were scaled manually and the number of waves (equal to the zero up-crossings) was counted. Since the above procedure was found to be time consuming and laborious, some shortcuts were made as follows: (a) from the 20 minute record, a representative 10 minute length of record was chosen, (b) a mean water line (zero line was drawn by the eye),(c) number of crests was then counted. A crest is defined as a point where the water level is momentarily constant, falling to either side. Some crests may be below the mean water level, (d) number of times, the record crosses the zero line moving in an upward direction was then counted. These also represent the zero up-crossings and the number of waves in the interval, (e) the maximum one-third of the highest waves was then measured,&(f) from such data, $H_{1/3}$, $H_{1/10}$, H_{max}, period T (also equal to T_z = period of zero crossings), period T_c = period of crests and the spectral width parameter calculated from the relationship

$$\varepsilon^2 = 1 - \left(\frac{T_c}{T_z}\right)^2$$

Even this method was found to be time consuming and therefore another shortcut method namely the one proposed by Draper (2) in 1966 was used. In that method $H_{1/3}$ was calculated from the most probable value of the height H_1 of the highest wave in the specific interval of time (4 hours in these cases). H_1 was obtained from the records by adding the height 'A' of the highest crest and depth C of the lowest trough both measured as positive from the mean water line. Then the calculation of $H_{1/3}$ and H_1 was a simple process and depended only on the number of waves and ratio of $H_{1/3}$ / H_1.

The above simpler and fast procedure was possible because relationships between $H_{1/3}$ and H_1, number of zero up-crossings and H_{max}, $H_{1/3}$ and $H_{1/10}$, $H_{1/3}$ and H_{avg}, etc. could be obtained from the two previously described procedures.
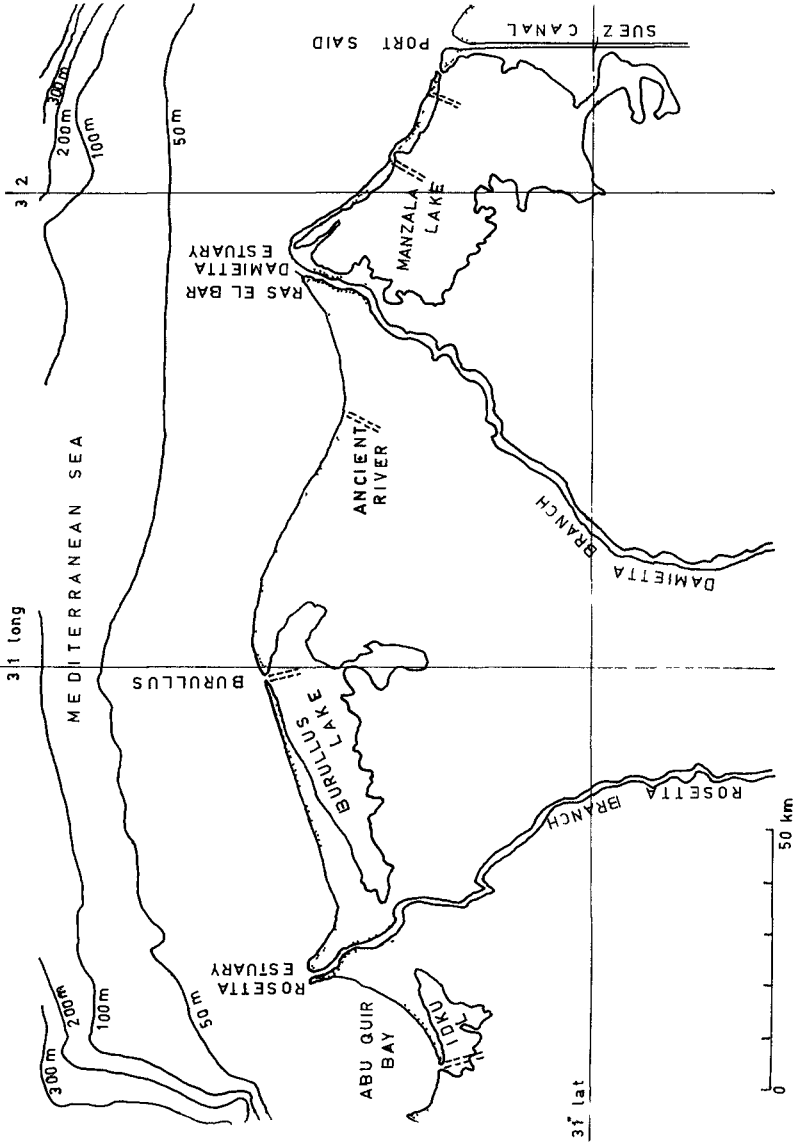
Fig 1. Nile Delta Coast

RESULTS FROM ANALYSIS : Figs. 2 and 3 are typical wave period spectra diagrams in which all waves were grouped around an average frequency of 0.050 sec^{-1}. Whereas in fig. 2, the frequency f and $\frac{H^2}{f}$ represent the axes, fig. 3 gives ΣH^2 on the ordinate and T on the abscissa. Both show narrow spectral width and insignificant contribution of energy at the two lower ends of the curves. Fig. 4 is a typical histogram of the frequency of occurrence of significant wave heights for Burullus area for August-December 1972. Figs. 5 and 6 represent significant wave height cumulative frequency distribution curves partially and collectively for the Burullus area. Figs. 7 and 8 show the relationship of the statistical parameters $H_{1/3}$, $H_{1/10}$ and H_{max} again for the Burullus area. The theoretical curves from the Raleigh distribution analysis are also indicated in the figures. Similar analysis was made for the two other areas also and they also show good agreement between theory and field data.

It is evident that a distribution similar to Raleigh distribution could describe the wave spectra, frequency distribution, and relationships between various statistical parameters (such as $H_{1/3}$, $H_{1/10}$, H_{max}, etc.).

With the knowledge of the wave heights from the above analysis and their directions from the synoptic weather maps wave height roses and wave energy flux/roses were calculated for the coast. Figs. 9 and 10 indicate the wave height and energy flux roses respectively for the Burullus area. Fig. 11 was drawn to determine the most predominant wave period for various classes of waves and it is interesting to find that a small range of periods namely 7-9 sec predominates over other periods.

Similar curves were drawn for other areas also so as to get wave height and wave energy climate along the entire coast. Since the period under study was only 8 months, conclusions regarding the climates could not be given in this paper. A more detailed study using hindcasting procedures to get the wave heights of previous years to discern any cyclic behaviour in the climates is under way. The present study is only a forerunner of such study and has given promising analysis for further use.

SUMMARY AND CONCLUSIONS : In order to study the wave climate along the Nile Delta coast, waves were measured in 3 places by offshore pressure operated recorders placed in 6-8 m depths. Since analysis of the records was time consuming, some short-cut methods were employed.

Period spectrum and energy spectrum of waves show narrow spectral band similar to Raleigh distribution. Relationships between various statistical parameters such as H_{max}, $H_{1/10}$, $H_{1/3}$ and H_{rms}, the histograms and frequency distribution curves drawn by using the wave data also indicate very close agreement with Raleigh distribution parameters and curves. With the use of synoptic charts for wave directions, wave height roses and wave energy roses were drawn for the coast to determine the wave height and wave energy climate along the coast.
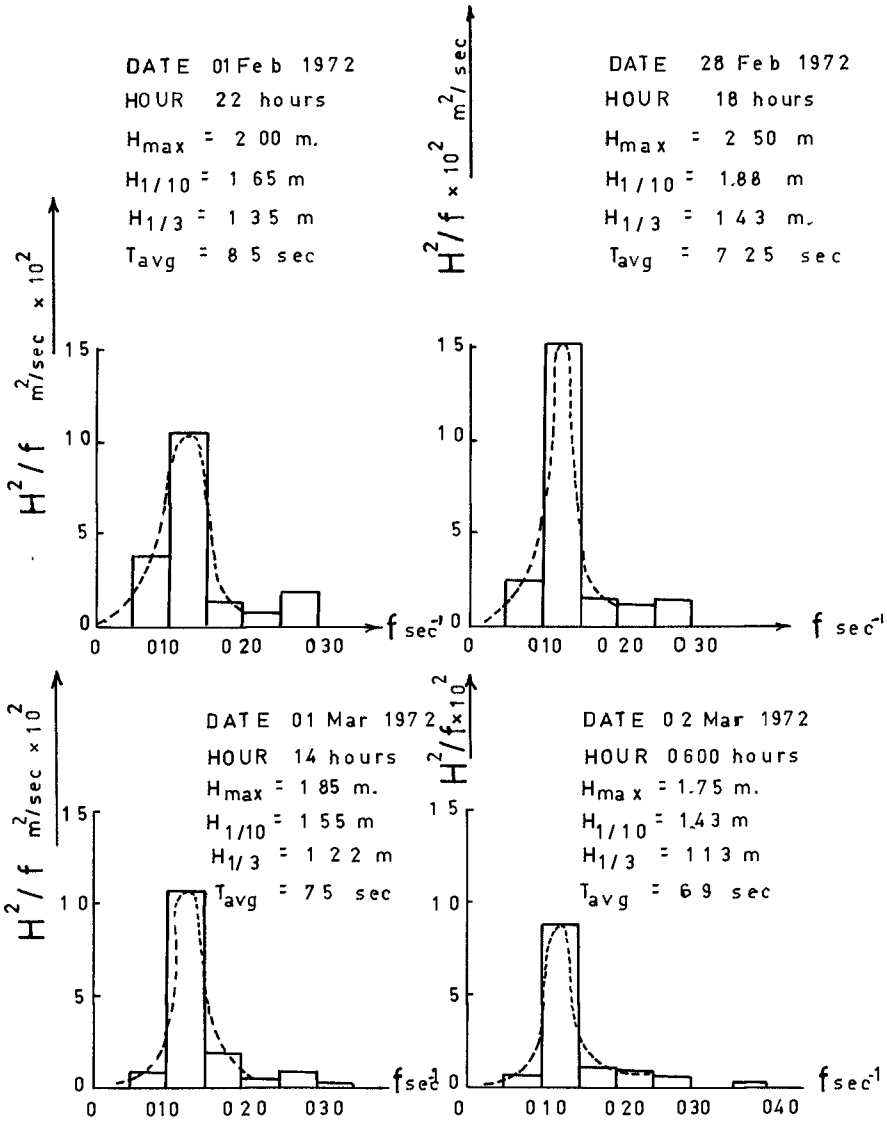
Fig. 2: Wave Period Spectrum   (ABU QUIR)
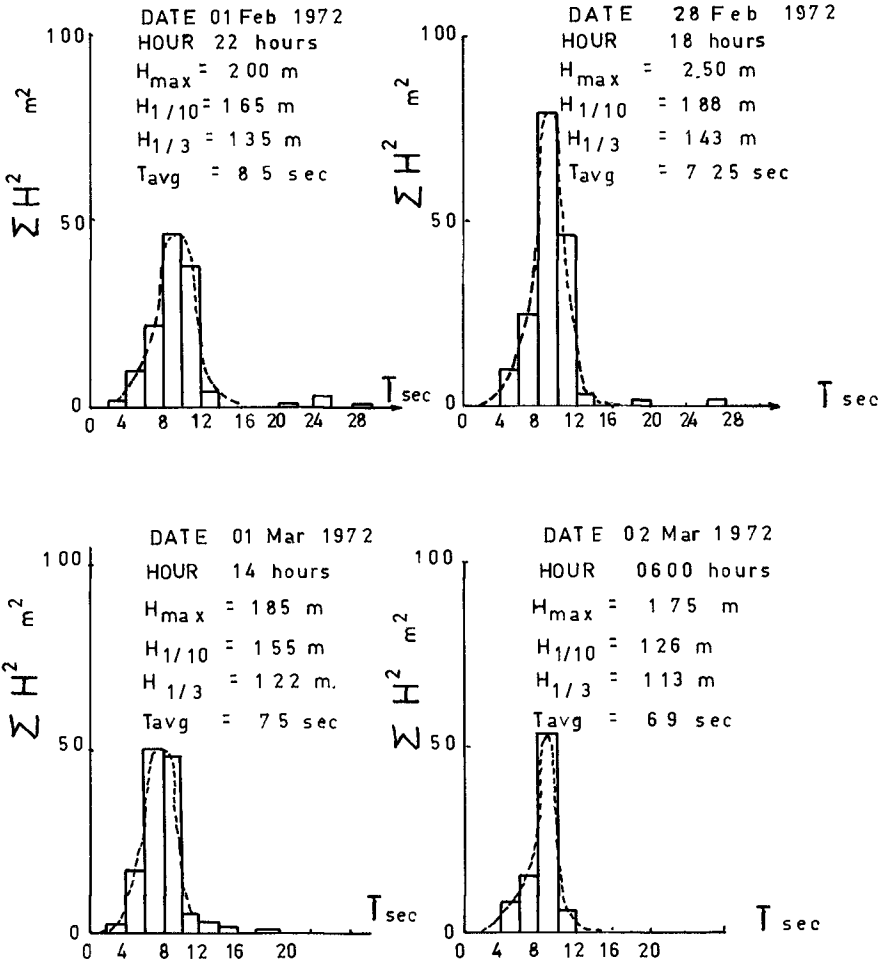
Fig. 3: Wave Spectrum - ABU-QUIR
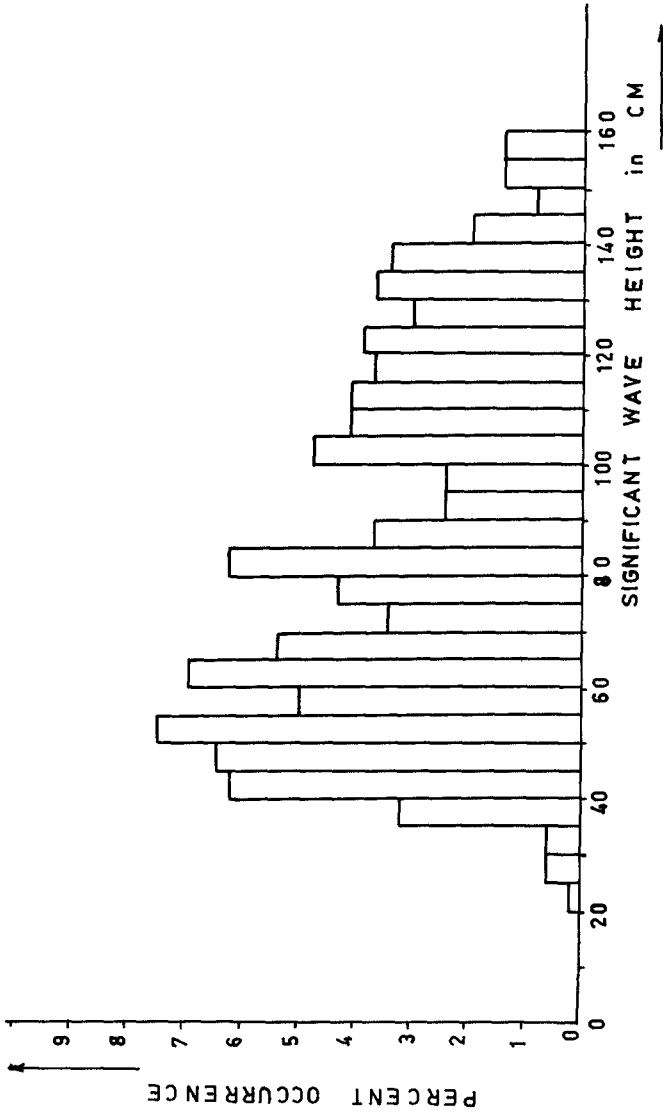
Fig. 4   Frequency of Occurrence - Burullus

(AUG TO DEC 1972)
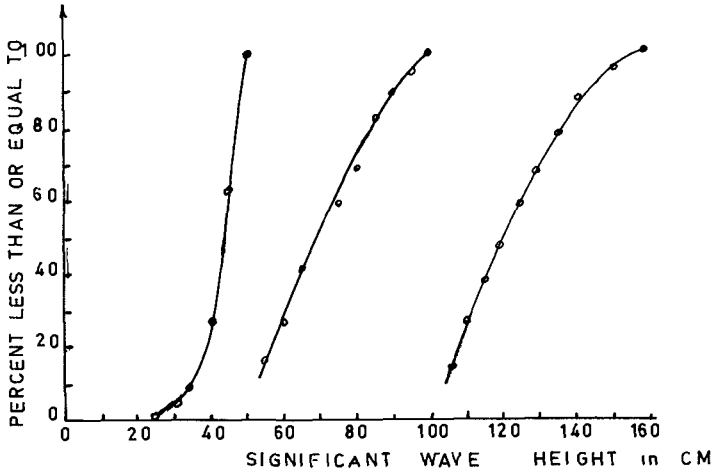
Fig. 5. Partial Cumulative Distribution of $H_{1/3}$

(BURULLUS)
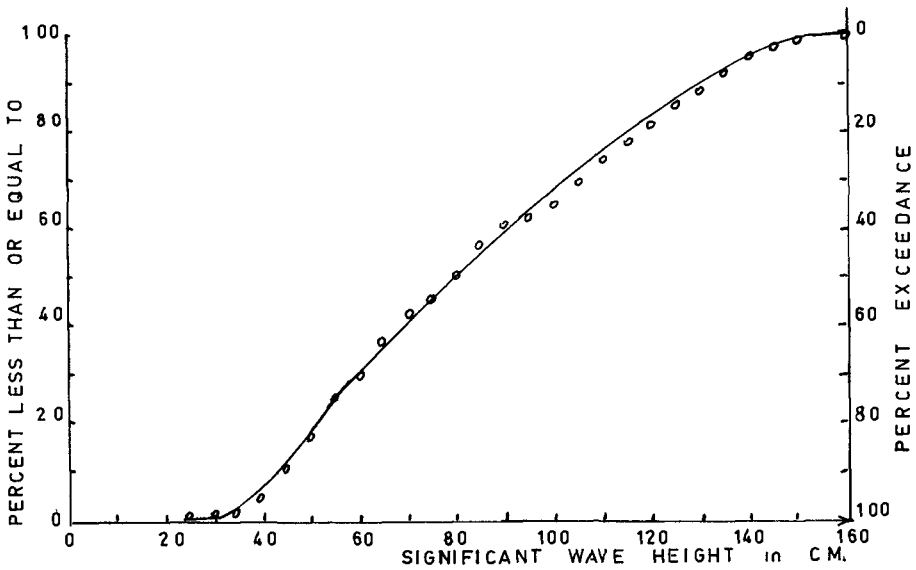
Fig. 6: Cumulative Frequency Distribution of $H_{1/3}$

ABU QUIR (APRIL TO AUGUST 1972)
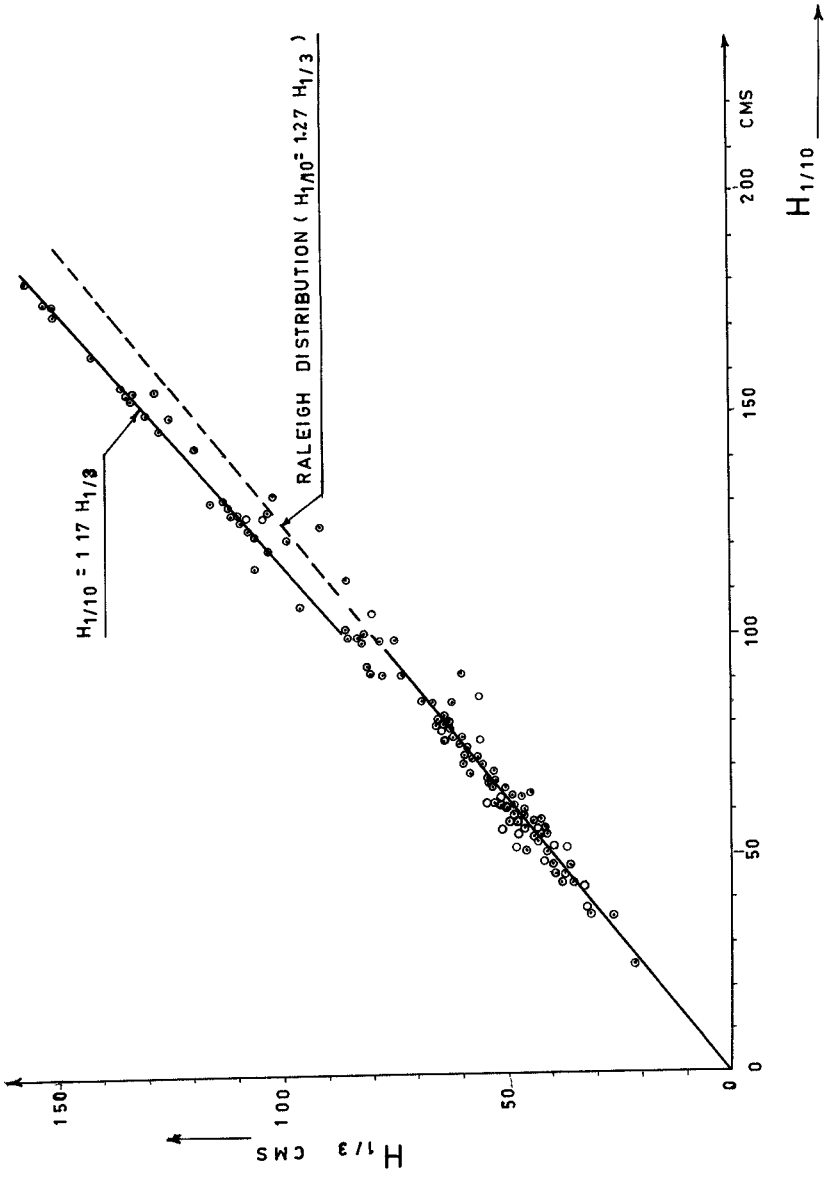
Fig. 7: $H_{1/10}$ Versus $H_{1/3}$ — Burullus
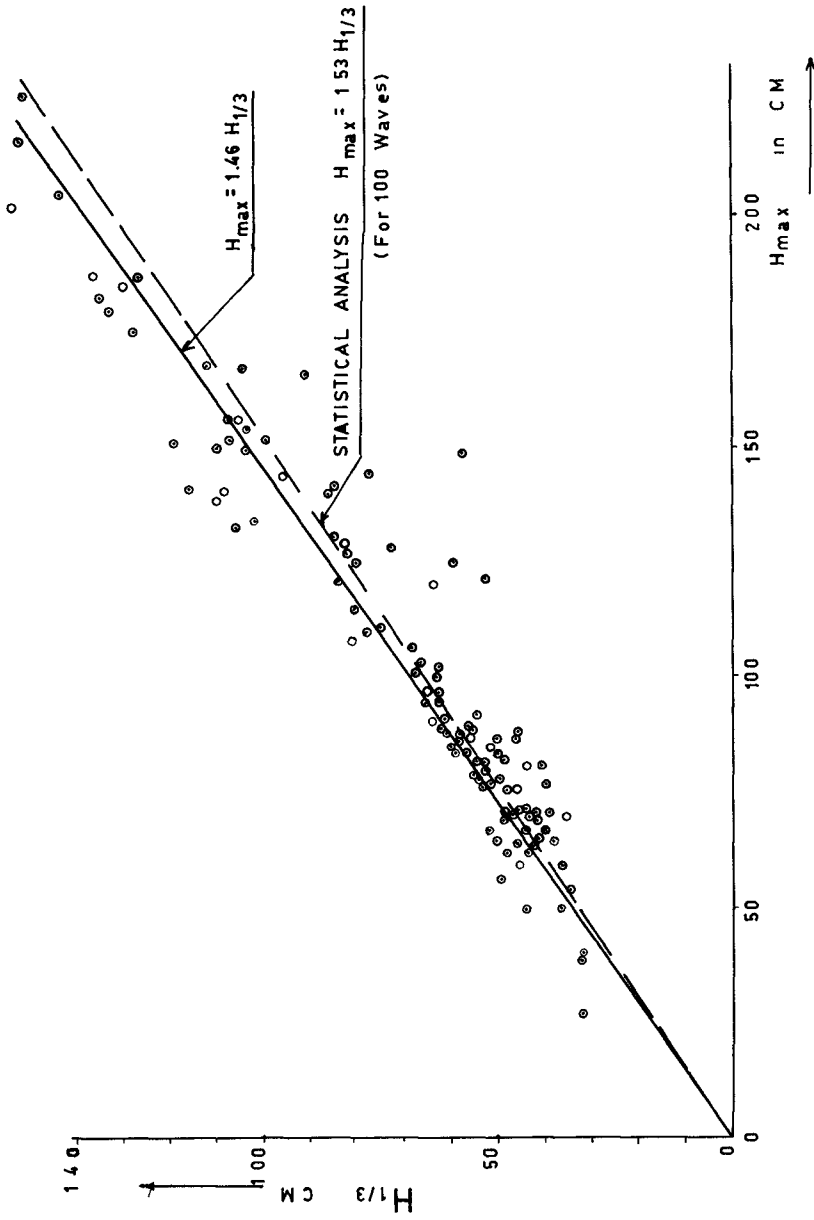
Fig.8: H_{max} Versus $H_{1/3}$ — Burullus.

$H_{max} = 1.46\ H_{1/3}$

STATISTICAL ANALYSIS $H_{max} = 1.53\ H_{1/3}$

(For 100 Waves)

H_{max} in CM

$H_{1/3}$ CM

AUGUST 1972

SEPTEMBER 1972

OCTOBER 1972

NOVEMBER 1972

DECEMBER 1972

> 0 cm
> 50 cm
> 75 cm
> 100 cm
> 125 cm

ALL WAVES T > 9 SEC.

SCALE   1 CM = 5%

NOTE PERCENTAGES ARE BASED
ON EACH MONTH SEPARETLY
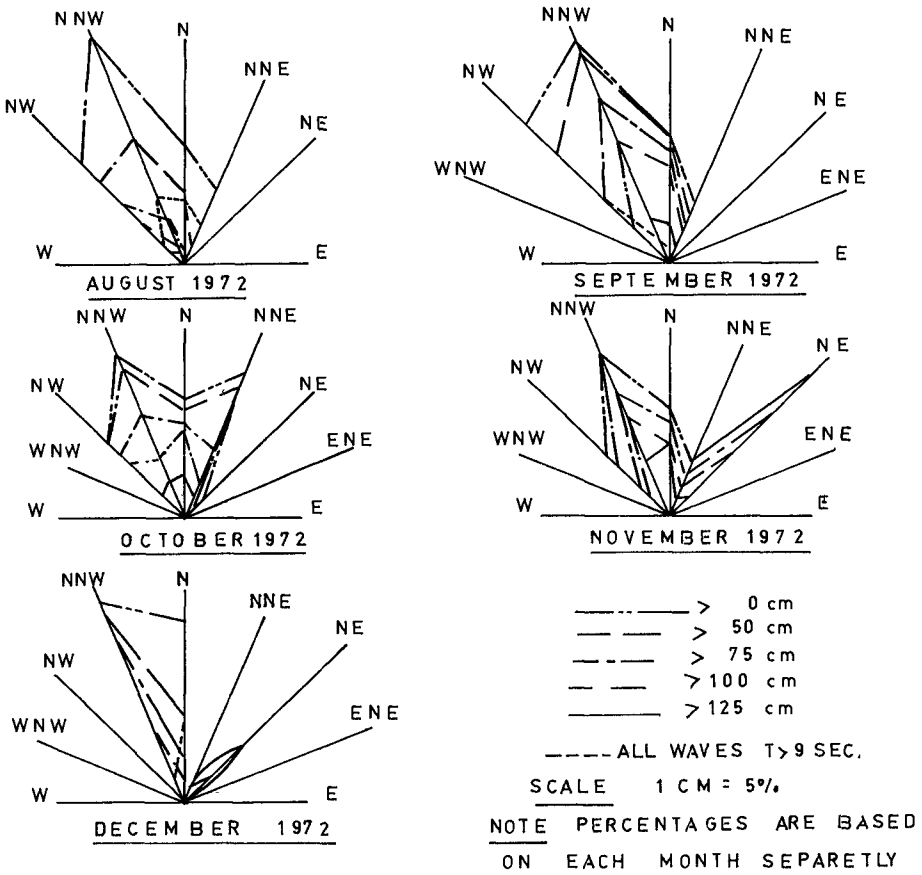
Fig. 9: Monthly Wave Rose Burullus
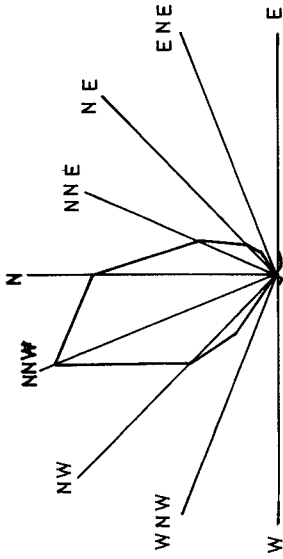
TOTAL ENERGY FLUX ROSE — BURULLUS

(AUG to DEC 1972)

MONTHLY ENERGY FLUX ROSE
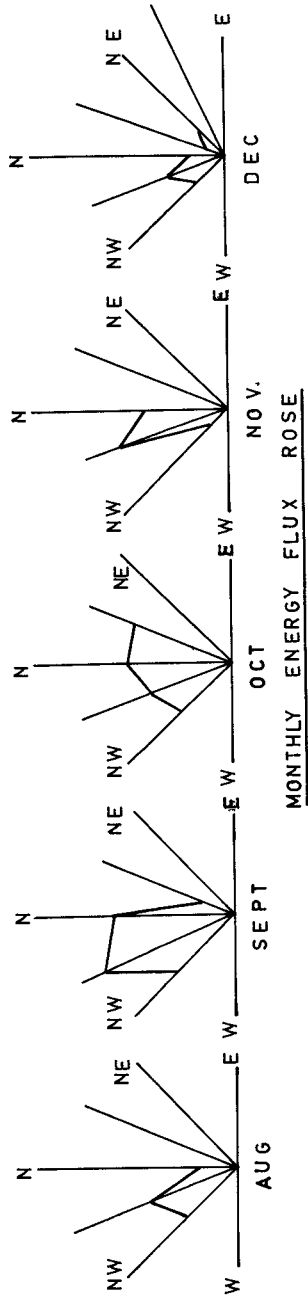
Fig.10 Monthly & Total Energy Flux Roses Burullus

SCALE 1 C M = 200 m^2 sec.
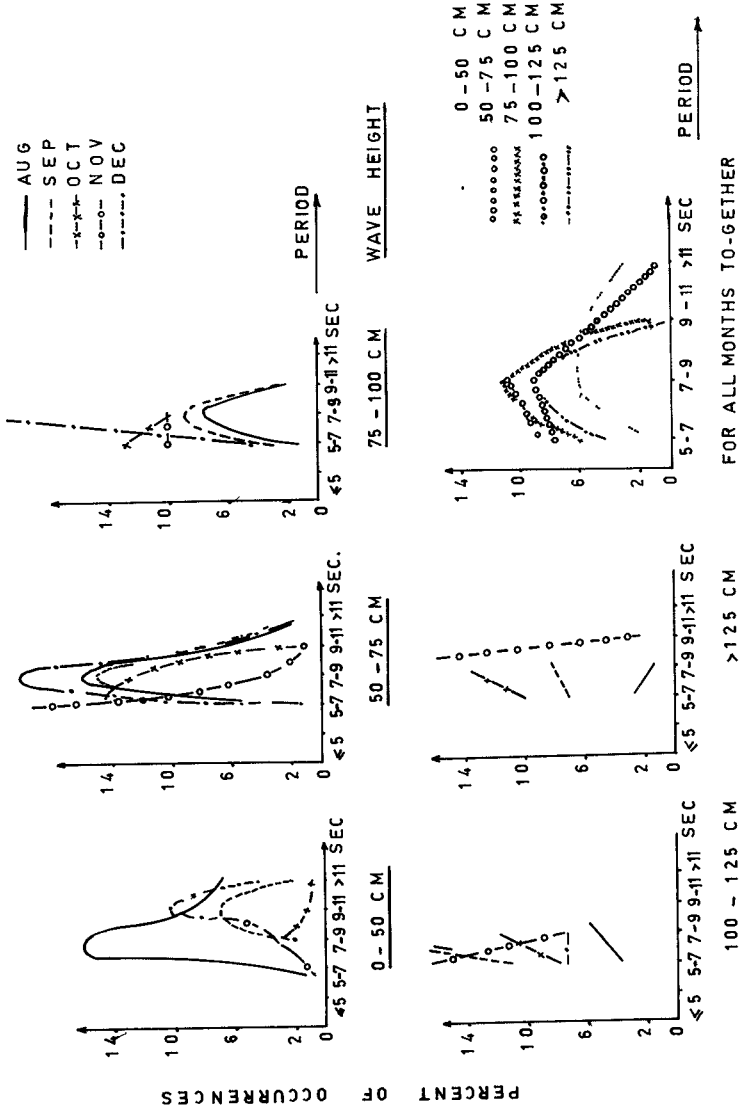
Fig 11. Percentage of Occurrences of Periods   Burullus

(AUG to DEC 1972)

The above study is a forerunner of a comprehensive study using hindcasting procedures to determine the wave climate for a large period of years (about 60 years).

REFERENCES :

(1) CARTWRIGHT, D.E. & LONGUET HIGGINS, M.S. (1956) - The Statistical Distribution of the Maxima of a Random Function. Proc. Roy. Soc. London; series A, vol. 237.

(2) DRAPER, L. (1966) - The Analysis and Presentation of Wave Data. A Plea for Uniformity. Proc. 10th Conf. on Coastal Engineering, A.S.C.E., New York, N.Y.

(3) LONGUET HIGGINS, M.S. (1952) - On the Statistical Distribution of Heights of Sea Waves. Journal of Marine Research, vol. XI, No. 3, New Haven, Conn. USA.

(4) PUTZ, R.R. (1952) - Statistical Distribution for Ocean Waves. Trans. Amer. Geophy. Union, vol. 33, No. 5, Washington DC.

(5) RICE, S.C. (1945) - The Mathematical Analysis of Random Noise. Bell System Technical Journal, No. 23 (1944) and No. 24 (1945), New York.

CHAPTER 6

WIND AND WAVE RELATIONSHIPS IN A SHALLOW WATER AREA

by J.S.Driver* and J.D.Pitt**

1. ABSTRACT

An instrumentation system to record direct measures of both wind and wave conditions has been installed at the Wash. Data from these instruments are used in conjunction with long term wind records from another station to predict the frequency and duration of extreme conditions.

2. INTRODUCTION

A proposed freshwater storage scheme on the foreshore of the Wash[4] (a 25 km square bay on the East coast of England) involves the construction of sand fill embankments up to 14 m high in an intertidal area.

An assessment of wave characteristics is required for the design of surface protection on the seaward facing slopes, and in planning construction.

Methods of wave prediction such as those set out by Ippen[1] have limited application in shallow water areas. Although some allowance can be made for the effects of shoaling, friction and refraction, such calculations are a poor substitute for field data. The situation in the Wash is particularly difficult as a tidal range of over 8 m acts over an area of complex topography with extensive drying banks.

An instrumentation system comprising three wave recorders and three anemometers was installed in the locations shown in Figure 1 and tide levels were recorded nearby at West Stones.

The paper describes the type of instruments used, the data obtained and the method of analysis.

3. DEFINITIONS

Wave analysis:

T_z — Mean zero-crossing period (for upward zero-crossings)

H_1^1 — Total of the highest crest above mean water level and lowest trough below mean water level, after depth attenuation correction.

H_2^1 — Total of the second highest crest above mean water level and the second lowest trough below mean water level, after depth attenuation correction.

H_s(3 hours) — Significant wave height (average height of the highest one third waves).

H.W. — High Water

H.W.period — The period at and around H.W. for which the water depth is sufficient to support waves.

*   John S.Driver, Institute of Oceanographic Sciences, Crossway, Taunton, Somerset, TA1 2DW.
** John D.Pitt, Binnie and Partners, Artillery House, Artillery Row, London SW1P 1RX.
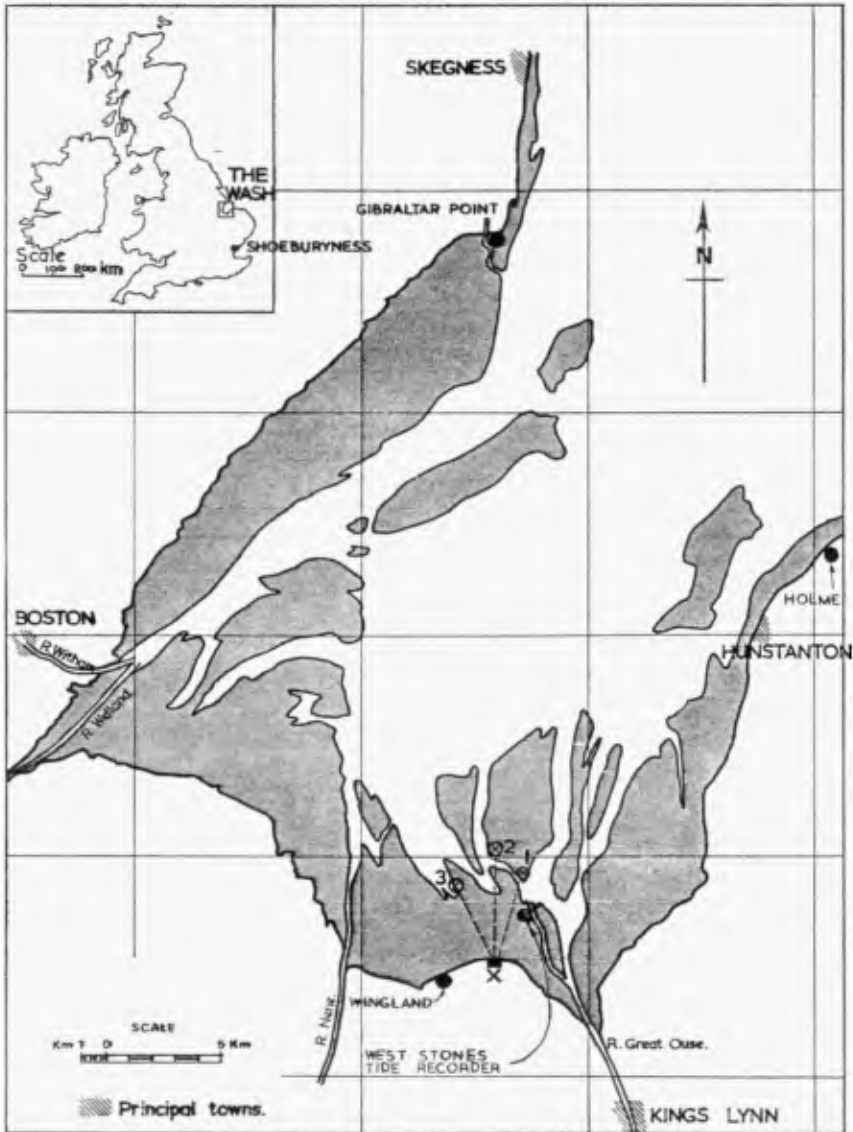
LOCATION OF INSTRUMENTS

Figure I.

Wave event   - A H.W. period accompanied by measured waves of
                      1.0 m or greater.

Storm event   - The occurrence of a storm in which the maximum wind
                      speed is force 7 or greater (Beaufort scale - U.K.).

4. OBJECTIVES

In the design of rip rap or other surface protection against wave attack,
it is necessary to determine not only the magnitude of the waves to be
expected but also the duration of attack and the probability of occurrence
of any event.   It may prove more economical to design for waves with a
return period of 10 years (say) on the basis that occasional damage
can be repaired at a lower cost than the additional sum involved in
providing longer term protection.

A study of the frequencies of events is therefore necessary so a method of
analysis has been adopted which enables an estimate of the return periods
of wave events to be made.   However, it is equally important to determine
which parameters relating winds and waves are dominant in this situation.
The maximum wave height may be governed either by the severity of the worst
storms expected or by physical restraints such as water depth and fetch
length.

5. INSTRUMENTATION

5.1 Wave Recorders (Figure 2)
5.1.1 Choice of instrument
Three types of instrument were considered as possibilities for this
situation:

    1. Surface piercing (wave staff)
    2. Accelerometer buoy
    3. Sub-surface transducer

The first system was not chosen because of its vulnerability to damage and
fouling which is unfortunate since the inherent wide frequency response of
such a system would enable both short period waves and tides to be measured.

The buoy measuring systems, perhaps best exemplified by the Waverider,
would also have adequately measured the short period waves (but not the tides).
However, the difficulties of mooring wave buoys in narrow channels precluded
their use.

Two types of pressure transducer were considered possibilities on grounds of
their rugged and proven designs and also their availability bearing in mind
that the installation was programmed to take place within six months of
defining the requirement.   The two systems chosen were:-

    (1) The Van Reijsen-Boersma Seawave Meter
    (2) The Institute of Oceanographic Sciences (previously National
        Institute of Oceanography) F.M. wave recorder.   Both systems
        could be connected to shore by cable link.

All wave measurement systems represent a compromise and in this instance
the errors introduced by depth attenuation correction and the difficulties
of laying long cables were the disadvantages to be set against operational
reliability.   Identical instruments had been used on the Dee Estuary Study[4]
in Cheshire during 1969/70 with acceptable results.

Figure 2.   Wave Recorder

Figure 3.   Cable Laying

The use of radio transmission for relaying the signals to shore would have
been ideal but no suitable equipment was available, neither was the use of
a transmitting aerial at the sea end considered a reliable proposition.

The operating principles for both systems are indicated in Figure 4.
Both pressure transducers modulate a carrier frequency with the pressure
information.   These signals are relayed to the shore along the armoured
cables and amplified before being demodulated.   Further amplification is
then necessary to drive the chart recorder pen movements.   Some obvious
differences between the Boersma and IOS instruments lie in the transducer
operating principles: in the Boersma a metal bar is maintained in low
frequency operation and this carrier frequency is then modulated by the
force applied to the end of the bar, but with the IOS transducer a deflecting
diaphragm causes the gap between the plates of a capacitor to vary and this
modulates the frequency of a 100 kHz oscillator.   Additionally the IOS
instrument filters out tidal information so as to record wave data only.

5.1.2 Choice of Sites
Having thus chosen the instruments it became necessary to site both sea
units and shore recording stations in such a way that the maximum cable
lengths for each site should not exceed about 7 km.   Figure 1 indicates
the sites chosen.   All transducers were mounted in protective housings of
a common type designed for the Dee Estuary Study but modified to suit the
Wash sites.   In each case the housings were installed on sandbanks but near
deepwater channels.   The supporting columns for the housings were jetted
into the sand to a depth of 6 metres.   At a high water spring tide the
depths of water above each pressure transducer were typically:

                    Site 1 - 3.5 m
                    Site 2 - 3.5 m
                    Site 3 - 4.7 m

The cable routes across the sea bed to the shore station site are also
indicated on Figure 1.   Again a compromise was involved since road access
in this area of reclaimed land is very limited.

5.1.3 Power supplies and wave recorder sampling clock
The nearest source of mains power was 5 km from the shore station so an
inverter system was designed to provide a 240 volt 50 Hz sypply from a
12 volt Nickel Cadmium battery pack.   The batteries were replaced about
once every two weeks with a freshly charged set.   A separately powered
Keinzle impulse clock movement was modified as follows: the escapement
oscillation rate was slowed by adding a little additional mass to either
side of the balance wheel.   In this way the 12 hours rotation of the hour
hand was increased to a nominal 12 hours 26 minutes.   A pair of cams were
then fitted to the hour hand shaft and these operated a low torque switch,
the result being a 15 minute 'on' period once every high tide.   The switch
in turn controlled a relay which energised the inverter and hence
simultaneously switched on the three wave recorders.

5.1.4 Cable laying (figure 3)
The laying of long cables in an intertidal area was a major achievement and
the work was undertaken by a specialist contractor who had successfully
carried out a similar operation in the Dee estuary.   Cable lengths in the
Wash were 5,600 m,   6,600 m and 6,400 m for sites 1, 2 and 3 respectively,
and had to be routed across areas where conditions varied from firm sand
to soft silt.
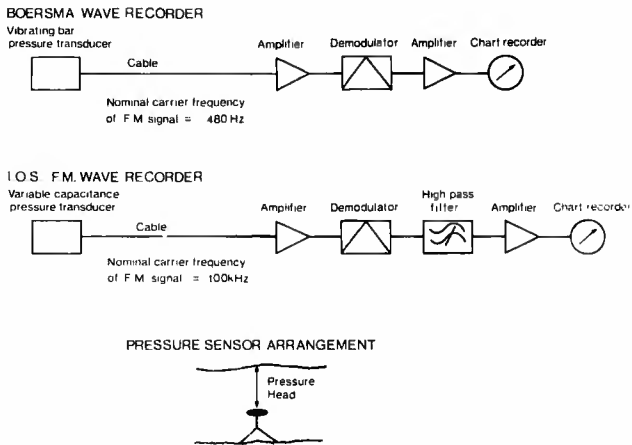
Figure 4. Block Schematic for Wave Recorders
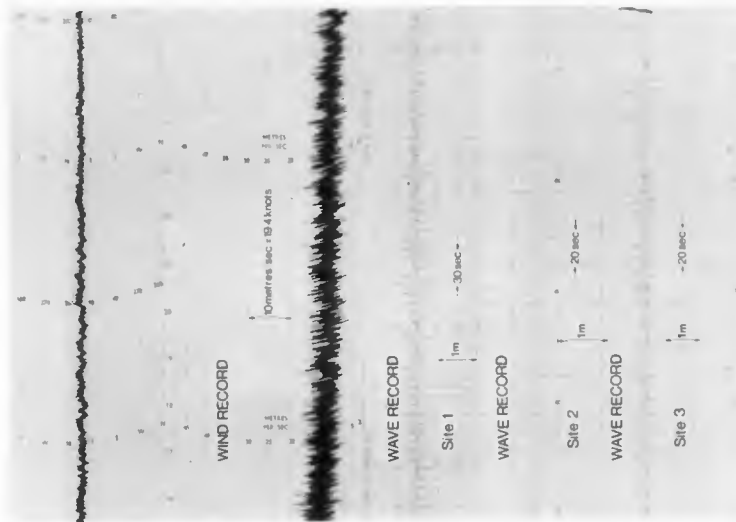
Figure 5. Typical Data in original form

Cables were buried to a depth of 0.5 m using a mole plough which was towed across the sand banks by modified agricultural plant.   The equipment was loaded on to an ex-army landing craft and work was carried out at low water after the craft had grounded.   Each cable run took several low water periods to complete, the equipment being re-loaded on to the landing craft at high water.   Towing the plough when submerged under water enabled cable routes to cross the many shallow channels.

5.1.5 <u>Operational problems</u>
When the cables were first laid a crosstalk problem manifested itself between the Boersmas and the IOS recorder.   This was traced to the land link where an unscreened cable had been used on one section.   Replacement of this cable and re-arrangement of the earthing within the shore hut did much to reduce the effect.

From time to time some impulsive interference was observed on the signals being received from the transducers.   This appeared as random 'spikes' on the wave records.   It has not been possible to trace the origin of this interference but neither has it been difficult to carry out a 'smoothing' operation by eye when analysing the wave records.   One of the problems inherent to measuring waves with pressure transducers in a sheltered area is that many recordings show no wave activity and in this situation any electrical interference present will predominate.   Clearly the effects of such interference should only be assessed at a time when reasonable wave activity is present.

The IOS instrument incorporated a galvonometer pen recorder of 100 mm chart width which has proved reliable under conditions of greatly varying temperature and humidity.   The Boersma shore unit was, however, interfaced with a two channel potentiometer recorder the feedback loop of   which   demonstrated instability in these conditions.   This recorder was replaced by a new type with a 240 mm chart width.   Considerable trouble was then experienced with changes in paper width under varying humidity and at the time of writing a third type of two channel recorder is in use, this time with a 100 mm chart.

The duration of the tidal cycle deviates from the mean by up to an hour and furthermore the difference between the time of high water and its predicted value may be as much as 30 minutes.   The time lag between high water and time of recording may therefore be considerable and careful adjustment of the tidal clock is required to minimise the effect so that records are not taken except at or near to high water.

5.1.6 <u>Calibration of instruments</u>
All three transducers were tested over the range 0 - 276 KN/m^2 in a pressure vessel at the IOS Wormley laboratory using a Budenburg deadweight pressure gauge as a reference.   With the sensitivities thus obtained it was then possible to calibrate the recording electronics with the following full scale deflections:

    Boersma : $\pm$ 4.0 m initially but changed to $\pm$ 4.5 m and $\pm$ 6.5 m
                when the replacement potentiometer recorders were fitted.

    IOS : F.M.: $\pm$ 2.5 m.

A larger full scale deflection was necessary with the Boersma recorder since the tidal information was also being displayed.

DATE	SITE	WAVE PARAMETERS				WIND VELOCITY		WATER DEPTH
		H_1'	H_2'	H_s (3hrs)	Period T_z	KNOTS	DIR.°	(metres)
2-4-73	1.	3·32	3·10	2·53	5·28			4·5
	2	1·15	1·09	0·99	5·46	44	330	4·9
	3	1 63	1·58	1·40	5·64			5·5
19-9-73	1	1·95	1·76	1·15	4·04			4·0
	2	0·98	0·96	0·64	3 72	33	330	4·4
	3	1·09	1 04	0·79	4·36			5·0
21-10-73	1							
	2					34	290	
	3	1·70	1·48	1·17	3·86			4·3
26-11-73	1	1·33	1·19	0·94	4·44			3·8
	2					24	315	
	3							
8-12-73	1	1·37	1·34	0·97	5·70			
	2					20	350	4·3
	3							
13-12-73	1	1·45	1·03	0·95	5·00			4·0
	2	1·81	1·71	1·26	4·80	40	310	4·4
	3	1·84	1·57	1·31	4·92			5·0
14-12-73	1	1·45	1·31	1·08	4·92			4·1
	2	1·58	1·46	1·20	4·88	31	320	4·5
	3	1·63	1 45	1·19	5·14			5·1
8-1-74	1	0·74	0·66	0·46	3·90			3·9
	2					46	140	
	3	1·21	1·04	0·74	4·12			4·9
17-1-74	1	1·54	1·34	0·97	5·04			3·8
	2					40	310	
	3	2·02	1·66	1·24	4·52			4·8
16-4-74	1							
	2					18	050	
	3	1·76	1·52	1·20	4·22			3·2
24-5-74	1							
	2	1·02	1·00	0·81	5·18	25	060	4·8
	3	3·33	2·48	2·17	4·68			5·4

TABLE I. WAVE EVENTS DECEMBER 1972 – MAY 1974

5.1.7 Measurement accuracy of instruments

In a system using pressure measurement to derive wave height the
corrections for the depth attenuation effect introduce the largest single
source of error.   This is particularly so with the Wash installation where
relatively short period waves have been recorded and correction factors of
the order of 0.5 are typical.   The errors are considered to be at least
± 10%.

An estimated total error of 3% can be attributed to the following effects:

1. Dynamic pressures on the measuring head caused by the wave
   particle velocity.
2. A non-linearity of the transducer calibration curves.

A further ± 5% is allowed for instrumental error where this constitutes
the effects of component tolerance, discriminator non-linearity and chart
recorder inaccuracies.   The Boersma system has exhibited a zero drift
problem which appears also to have affected the overall gain to the extent
of possibly 10%.   However, further work is to be carried out in order to
assess both the reasons for this drift and to quantify the error.

5.2 Wind Recorders

Three continuously recording Munro "rotating cup" anemometers were
installed in the Autumn of 1972 to obtain data on the local winds over the
Wash.   The distribution of wind recorders around the coast enables the
variation in wind velocity over the area to be detected.   The specification
of instrumentation and the method of analysis are in accordance with
standards laid down by the British Meteorological Office so that data is
compatible with that from other recording stations.

Data return was 93% overall from Gibraltar Point - an extremely high value
resulting from diligent inspection by a local warden who took on the job
of maintaining the instrument.

6. DATA

The available data comprises wind records and wave records from the
instruments described in section 5 together with 40 years of wind data from
Shoeburyness (Figure 1).   Other wave data in the form of visual observations
by the Kings Lynn pilots have been obtained and these will be of use in
correlating wave conditions at the recorder sites and those in the channels.

The total population of events being considered includes storm events in
addition to wave events.   (Not all storms generate waves).   Problems in
commissioning and maintaining the instruments have resulted in some events
passing when not all the wave recorders were operating.   It is, however,
encouraging to note that some data have been recorded for all events since
November 1972.

The 11 wave events recorded up to May 1974 are listed in Table 1.   Water
depths given in column 9 were obtained using tide recorders installed in
the Wash.   The measurement of sea level in the Wash is discussed in detail
by Pugh and Waller[5].

7. ANALYSIS

Two distinct approaches are possible in assessing the frequency of events.
The first is along the lines proposed by Gumbel in which the magnitude of
the waves would be plotted against the frequency of occurrence.   Extrapolation
of the best fit line gives an indication of the frequency of extreme events.
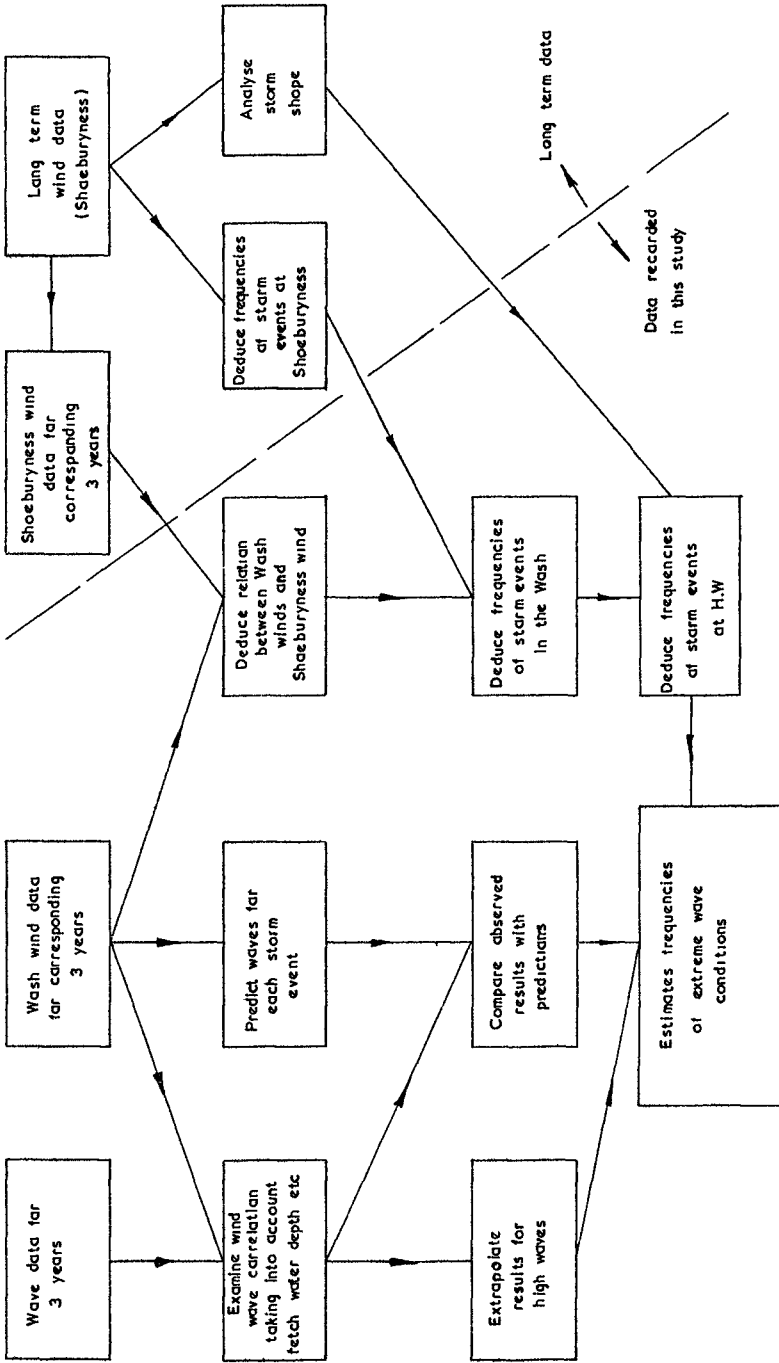
Figure 6   FLOW DIAGRAM FOR DATA ANALYSIS
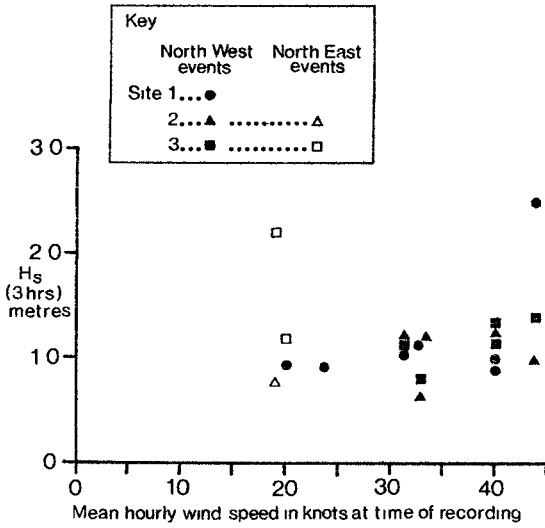
Figure 7 WAVE HEIGHT / WIND SPEED
SCATTER DIAGRAM

Class	High water level (metres) O D (Newlyn)	Approximate water depth at sites (metres)	Probability of occurrence on any tide
1	0·75 - 1 25	2·0	0·0007
Mean Neaps 2	1 25 - 1·75	2·5	0·0034
3	1·75 - 2·25	3·0	0·168
4	2 25 - 2·75	3·5	0·250
Mean Springs 5	2·75 - 3·25	4·0	0·291
6	3·25 - 3·75	4·5	0 208
7	3·75 - 4·25	5·0	0·460
8	4·25 - 4 75	5·5	0·0003

TABLE 2   TIDE LEVEL ANALYSIS

This method however relies on there being complete data available over a long period and data from 2 or 3 years records are not sufficient.

The second approach, adopted here, has been to study case histories and use existing theories on wave generation to correlate wave height and period with the prevailing wind conditions and water depth.   The frequency of occurrence of wind conditions is then assessed using available long term wind data.   Figure 6 illustrates the flow diagram for data analysis.

In the analysis of the wave data, the method used was that proposed by Draper[2].

8.   WIND WAVE CORRELATION

8.1   Wind direction
For the purpose of this analysis, wind direction has been divided up into four 90° sectors, namely 45° either side of SE, SW, NW and NE.   Selection of these sectors is based on inspection of the orientation of the Wash (Figure 1).

8.2   South East sector
Storm events from the south east sector occur several times each year but since the winds blow offshore over a short shallow fetch, large waves are not generated in the area of interest.   Only one storm event has been accompanied by a wave event and on this occasion the maximum wave height was 1.2 m with a wind speed of 46 kts.

8.3   South West sector
Storm events from the south west are the most frequent but again the winds are offshore and over a short shallow fetch.   Although these storm conditions need to be assessed in considering construction, the generation of large waves does not occur.   The maximum wind recorded during a high water period was 50 kts and the wave height was only 0.6 m.

8.4   North West sector
Waves generated by winds from the NW sector have been dominant amongst the data collected so far, and account for eight of the eleven wave events listed in Table 1.

An important observation is that the wave period even of the largest waves is only about 5 seconds.   The implication is that waves are generated over a short fetch (less than 30 km) and during a period of only one or two hours.   It is therefore evident that waves are generated locally within the Wash rather than further out in the North Sea.

The wave events for the NW sector are represented on a scatter diagram (Figure 7) showing the mean hourly wind speed and wave height.   With the rather limited data it is not considered valid to put in a best fit line yet, but it can be seen that with the exception of one extreme event, the data are reasonably consistent.   It is tempting to dismiss this one point as "experimental error", but visual observations by the Kings Lynn pilots have confirmed that waves of this size do occur, and some explanation must be sought.   To some extent, it can be accounted for by the fact that water depth on this occasion was greater than on others and that the wind direction was more in line with the deep shipping channel nearby.

The waves so far recorded do not appear to be depth limited but in extreme wind conditions, the maximum wave size expected in a three hour period would be so limited on a mean tide.
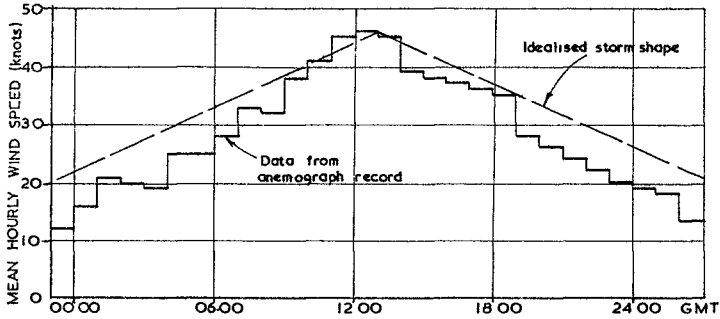
Storm of 20th January 1965 showing how a typical storm is idealised as a triangular distribution of wind speed with time

Figure 8   STORM SHAPE

IDEALISED STORM (Force 10 peak)

IDEALISED TIDAL CYCLES
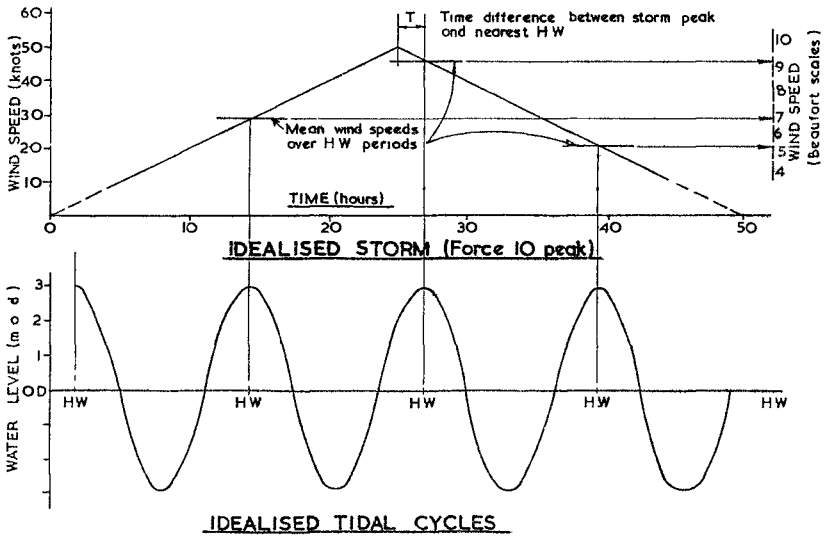
Figure 9   Example of wind speeds at consecutive HW for force 10 storm event

SECTOR.	N_F : N$^{\text{o}}$ OF STORM EVENTS WHEN MAX WIND IS FORCE F			
	N_{10}	N_9	N_8	N_7
S . E.	0·04	0·31	2·15	3·85
S . W.	0·14	1·00	4·32	9·61
N . W.	0·01	0·09	0·56	1·34
N . E.	0·01	0·08	0·61	2·91

TABLE 3. AVERAGE N$^{\text{o}}$ OF STORM EVENTS PER YEAR.

F MAX FORCE OF STORM EVENT	CORRESPONDING N$^{\text{o}}$ OF H W. PERIODS WITH MEAN WIND SPEED F.			
	F = 10	F = 9	F = 8	F = 7
10	0·20	0·56	0·48	0·48
9	–	0·28	0·64	0·56
8	–	–	0·36	0·72
7	–	–	–	0·36

TABLE 4. N$^{\text{o}}$ OF HIGH WATER PERIODS AFFECTED BY STORMS

SECTOR.	N$^{\text{o}}$ OF HIGH WATER PERIODS WITH STORMS			
	F = 10	F = 9	F = 8	F = 7
S . E	0·008	0·11	1·00	3·08
S . W	0·028	0·36	2·26	7·20
N . W.	0·002	0·031	0·26	0·94
N . E	0·002	0·028	0·28	1·53

TABLE 5. AVERAGE N$^{\text{o}}$ OF H.W. PERIODS WITH STORM EXPECTED EACH YEAR.

8.5   North East sector

Only two events from the NE have been recorded during the period of study though the wind analysis (section 9) shows that their frequency of occurrence is as great as for storms from the NW.   It is particularly important to assess the wave conditions accompanying storms from the NE since this is the direction in line with fetch lengths up to 800 km extending across the North Sea from Denmark.   Large waves can   therefore be expected at the mouth of the Wash but an extensive sand bar limits the progression of such waves into the bay so maximum wave heights are likely to be depth limited.   It becomes important to know what water depths are to be expected and Table 2 gives the results of an analysis of predicted tide levels.

9.   PROBABILITY OF OCCURRENCE OF STORM EVENTS AT H.W.

9.1   Correlation of data.

In a recent report by Binnie and Partners[4] on "Waves and Tides at Maplin" an extensive analysis of wind data from Shoeburyness (Figure 1) was made. In that study, Shoeburyness was selected not only because of its proximity to the area of interest but because the data available covered a 40 year continuous period.   In predicting event frequencies the length of available data is of great importance.   It was felt that if an overall correlation between Shoeburyness winds and the winds over the Wash could be found then the results of the earlier analysis would be most valuable.   Direct correlation for every storm could not be expected because of the considerable distance between the two areas (approx. 150 km) but results were sufficiently good to be used.

9.2   Frequency of storm events

Having established the correlation between the Wash winds and those at Shoeburyness, we can now extract from the results of the Maplin analysis, the frequencies of storm events.   Table 4 shows these data in a modified form.

To assume that all storm events are such that the peak coincides with H.W. is unnecessarily conservative and the following sections describe a method in which the frequencies of storm events are converted into frequencies of "H.W. events", i.e. occasions when strong winds occur at H.W.

9.3   Storm shape

Shellard[3] demonstrated that there was a relationship between the maximum hourly mean and the maximum mean over 3, 6, 12, and 24 hours for a particular storm.   This theory was corroborated by analysis of 20 storms at Shoeburyness and the Wash and leads to the idealisation of storms as a standard shape.   It was further shown that a triangular distribution of wind speed with time was most consistent with the data - as shown in Figure 8.

9.4   Effect of time difference between storm peak and H.W.

For any event when the storm peak occurs at a known time from the nearest H.W. then, using the storm shape obtained in section 9.3, we can deduce the average wind speed both at that high water and at adjacent high waters. Each storm event in fact affects up to 3 H.W.'s by varying degrees (Figure 9). This analysis leads to the results given in Table 4 and when combined with the storm frequency data, the number of H.W. events accompanied by winds of various forces is derived (Table 5).

10. FREQUENCY OF EXTREME CONDITIONS

The return periods of large waves can be estimated from the figures in Table 5, which gives the average number of storm events occurring at H.W., together with a knowledge of the wind-wave relationship. Figure 7 shows the available data on this but until a further year's data are available, it is not proposed that any firm results are abstracted.

11. CONCLUSIONS AND FURTHER WORK

1. The complex topography, shallow water and high tidal range of the Wash largely invalidate the use of conventional methods in assessing the wave characteristics at the proposed construction sites.

2. The chosen approach of measuring waves at the sites and relating these to the observed winds and long term wind records has so far given encouraging results.

3. The installation of suitable instrumentation presented difficult engineering problems but these have now been successfully overcome.

4. Results to date indicate that waves in the Wash are locally generated and that fetch length is normally the limiting parameter. Only 2 storms from the N.E. have been recorded but in extreme conditions it is expected that waves would be depth limited.

5. A method of analysis has been developed which enables long term wind data to be used to estimate the probability of occurrence of extreme wave events. The probability of storm events occurring at high water was assessed and taken into account.

6. A further year's data are being obtained.

7. Future work proposed includes the use of a wave refraction programme to plot back tracks of wave fronts from the wave recorder sites. It is intended that this will help in understanding the progression of wave trains across the Wash.

12. ACKNOWLEDGMENTS

This paper is published with the permission of The Water Resources Board, Reading, who commissioned the Wash Feasibility Study. The program of Wave recording which forms part of this study is being carried out by Binnie and Partners in conjunction with IOS Taunton. However the opinions expressed are those of the authors.

13. REFERENCES

1. Ippen, A.T. (1966)   Estuary and Coastline Hydrodynamics

2. Draper, L. (1966)   "The analysis and presentation of wave data - a plea for uniformity." (Proc. 10th Int. Cong. on Coastal Eng.).

3. Shellard, H.C. (1973)   Private communication from the Meteorological Office.

4. Binnie & Partners report: Maplin Waves at Tides (1973)
                             Dee Estuary Study (1971)
                             Wash Feasibility Study (1973)

5. Pugh, D.T. and Waller, W.R. (1974). "Sea Level Measurements in the Wash". (14th Int. Conf. on Coastal Engineering).

CHAPTER 7

WAVE GROUP FORMATION AMONG

STORM WAVES

H. RYE [*]

ABSTRACT

Wave data obtained in the North Sea for stormy weather con-
ditions are analyzed to determine the extent of wave group
formation among large waves; i.e. the number of large waves
succeeding each other in one single run. Three periods
associated with the passage of high sea states are examined.
The average correlation between succeeding wave heights is
found to be +0.24, which indicates that wave heights do
have a "memory". Wave group formations are found to be
more pronounced when the sea is growing than decaying. The
average lengths of wave runs are calculated.

---

[*] Dept. of Port and Ocean Engineering, Norwegian Institute
of Technology, Trondheim, Norway.

At present affiliated to the River and Harbour Lab. (VHL)
at the Norwegian Institute of Technology, 7000 Trondheim,
Norway.

INTRODUCTION

Offshore activity in the North Sea has intensified the study
of storm wave properties in this area. Such studies are
important because a better understanding and description of
the storm waves may improve engineering practice in this
hostile environment.

The larger waves in a sea state occur more or less in a
random fashion due to the statistical behaviour of the sea
surface. However, it is sometimes experienced that large
waves tend to stick together, as illustrated in Fig. 1
which shows waves recorded in the North Sea during a storm
($H_{1/3} \simeq 10$ m). The recording shows three large waves
succeeding each other in one single run. This paper con-
siders the extent of such wave group formation among large
waves recorded during storm conditions in the North Sea.

There is an old Icelandic saying which says: "Sjaldan er
ein baran stök", which means: "A large wave comes rarely
alone". The offshore engineer should pay attention to the
experience gained by the Icelandic fishermen, because wave
group formation among large waves may be important in many
engineering aspects. For example, the fact that large
waves tend to stick together, may justify use of regular
waves when fixed structures are tested in a wave flume.
Also, for the evaluation of mooring forces, wave group for-
mation among large waves is of interest because moored
structures sometimes tend to respond to the wave height
envelope rather than to the actual wave. (HSU and BLENKARN
1970, KAPLAN 1970).

Previous studies on wave group formation are relatively few.
Nolte and Hsu studied the wave group formation by considering
the statistical properties of the wave height envelope (NOLTE
and HSU 1972), and the results were compared to actual wave
measurements obtained from the Gulf of Mexico. Goda has
studied the wave group formation among large waves by means
of numerical experiments on wave statistics with spectral
simulation (GODA 1970). Also, Wilson and Baird have presen-
ted some field results on wave group formation by considering
the extent of runs of waves larger than the significant wave
height (WILSON AND BAIRD 1972). The method of analysis
applied by Goda has partly been adapted in this study.
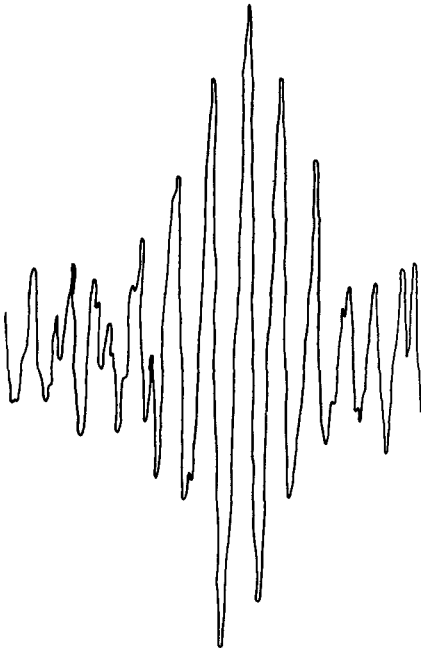
Figure 1.   Part of a wave record obtained under stormy
              conditions in the North Sea

DATA RECORDING AND REDUCTION

A "Waverider" accelerometer buoy transmitted wave data from
outside Utsira, Norway (Fig. 2). The water depth was about
100 m (Fig. 3). Waves were recorded every third hour with a
duration varying between 8 and 20 minutes for each recording.
The data were recorded on a strip chart and the wave heights
were read off according to the zero-up-cross method.

The data applied for the analysis were collected from three
storms, occuring in October, November and December 1970.   60
recordings were read off, and all of the records were selec-
ted so that some waves larger than 4 m were present in each
recording. This was done to ensure that the wave records
analyzed were describing relatively heavy sea states.

Figure 2

The location of the wave recording site
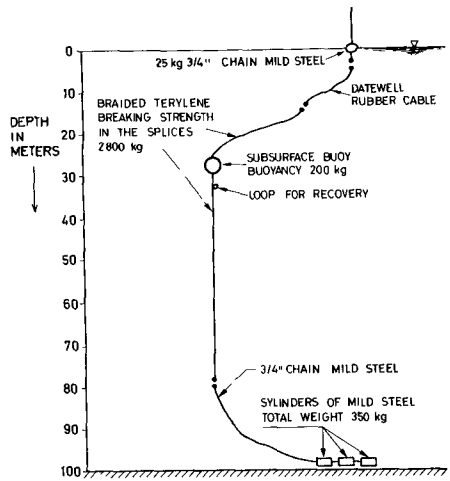
Figure 3

The wave recorder and the mooring system

Wave periods were not considered in this study because the
wave heights were regarded more important. Wave heigths
lower than 0.5 m were excluded because sometimes it was
experienced that runs of large waves were divided by the
presence of small waves which were regarded to be of secon-
dary interest for engineering activity (Fig. 4). (The ex-
tent of small waves present in the wave record may also
depend on the resolution of the wave recorder (HARRIS 1970)).

Fig. 5 shows the average wave height $\bar{H}$ for all the recordings.
The 60 recordings were divided into two groups, according
to whether $\bar{H}$ was recorded during growing wave height condi-
tions (denoted by "G") or decaying wave height conditions
(denoted by "D"). This was done because the statistical
properties of the sea surface were different for the two
cases, as will be shown later.

SHOULD THIS ONE BE
INCLUDED ?
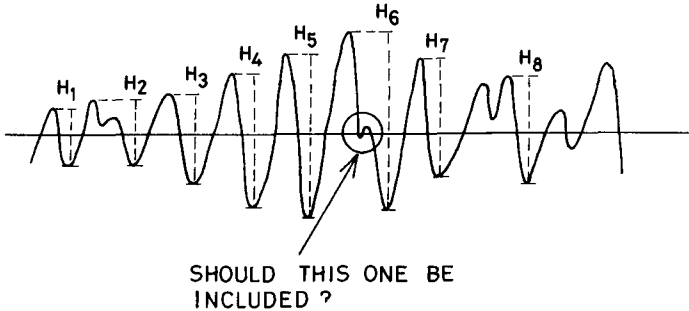
Figure 4.   Illustration of the presence of relatively
             small waves, splitting one run of large
             waves into two separate runs.

WAVE HEIGHT CORRELATIONS

The first question was whether waves have a "memory"
or not. A correlation coefficient   between succeeding wave
heights was computed according to the formula

$$\phi(k) = \frac{1}{\phi(0)} \cdot \frac{1}{N-k} \sum_{i=1}^{N-k} (H_i - \bar{H})(H_{i+k} - \bar{H}) \tag{1}$$

where
$$\phi(0) = \frac{1}{N} \sum_{i=1}^{N} (H_i - \bar{H})^2$$

N   = Number og waves in the actual recording

$\bar{H}$ = Average wave height

k   = Number of lags between the waves in sequence

All the waves H_i are "sequentially" spaced because the wave
periods are not considered. If succeeding waves are un-
correlated, all the $\phi(k)$ for $k \geq 1$ would approach zero when
N goes to infinity. However, $\phi(1)$ was found to be different
from zero, as shown on Fig. 5. An average value of +0.24
was found. The value of 0.24 indicates that waves do have
a memory, and the positive sign indicates that large waves
tend to be succeeded by large waves, while small waves tend
to be succeeded by other small waves.

The next question is to what extent wave characteristics
during growth may be distinguished from wave characteristics
during decay. From Fig. 5, it is apparent that $\phi(1)$ tends
to be larger during wave growth (denoted by G) than during
wave decay (denoted by D). $\phi(1)$ tends to be close to 0.30
during wave growth, while during decay, $\phi(1)$ is closer to,
or lower than 0.20. The wave group formation seems therefore
to be more pronounced during wave growth conditions than
during decay conditions. The reason for this finding will
be considered later in this paper.
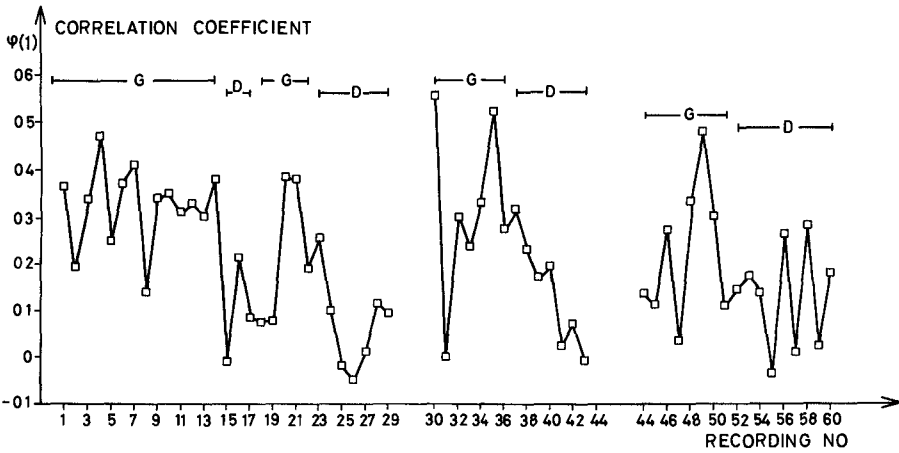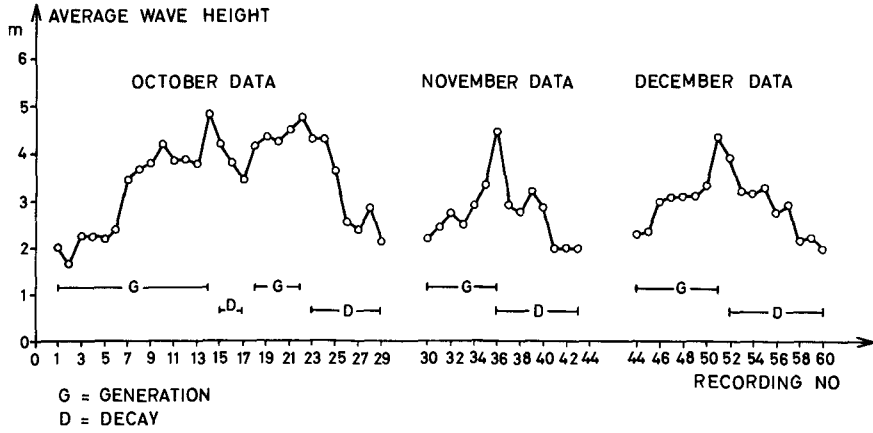
Figure 5   The average wave height H̄ and the correlation
coefficient φ(1) for 60 recordings

The correlation coefficients $\phi(2)$ and $\phi(3)$ were also computed, but they were not found to vary significantly from zero, on the average.

STATISTICS OF RUNS OF HIGH WAVES

Fig. 6 shows the wave heights to follow the Rayleigh distribution comparatively well. In order to include all of the 60 recordings on the same diagram, the average wave height was used as unity for each of the recordings.

Provided that the wave heights follow the Rayleigh distribution, the number of waves that exceed some fixed level (say the level of $H_{1/3}$) may be evaluated from the formula

$$\text{Prob} \quad (H > H_{1/3}) = \exp(- \frac{H_{1/3}^2}{8m_o}) = \exp(-2) \approx 0.134 \quad (2)$$

where m_o is the variance of the wave record and $H_{1/3}$ is equal to four times this variance.
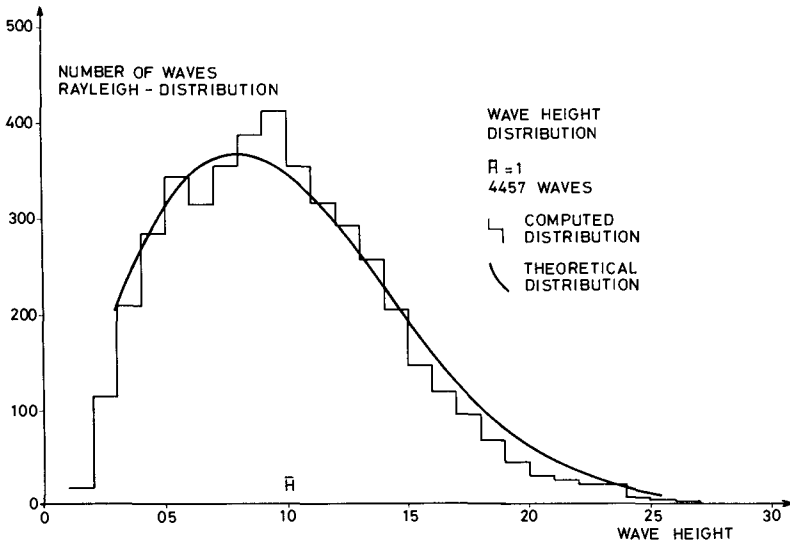
Figure 6.   The average distribution of the wave heights.
             Waves lower than 0.5 m are excluded. The
             average wave height H is unity for each re-
             cording.

The probability of the occurrence of waves larger than $H_{1/3}$ may be treated as illustrated in Fig. 7, which shows two waves (H_3 and H_4) larger than $H_{1/3}$ occurring in one run and another single wave (H_8) larger than $H_{1/3}$ which occurs in another run. The probability that j waves larger than $H_{1/3}$ succeed each other in one single run is denoted $P(j)$. Provided that only waves larger than the significant wave height are considered, the relation

$$\sum_{j=1}^{\infty} P(j) = 1 \qquad\qquad (3)$$

holds. The results from a calculation of $P(j)$, averaged for all the 60 recordings, are shown in Fig. 8.

PROBABILITY OF WAVE
GROUP FORMATION
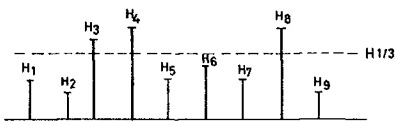
Figure 7

Illustration of two runs of waves larger than the significant wave height
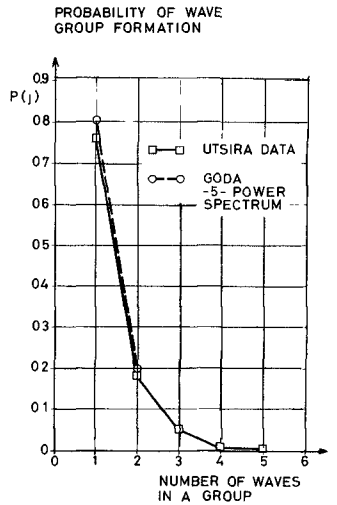
Figure 8

The average probability of occurrence $P(j)$ of runs of waves larger than $H_{1/3}$ for the field data and from the numerical simulation by Goda applying a Pierson - Moskowitz type spectrum

P(j) may be determined analytically provided that the
wave heights are assumed to succeed independent of the
preceding wave height; i.e. the waves are assumed to have
no "memory". This case would correspond to $\phi(1)$ equal to
zero on Fig. 5. For this case P(j) is given by

$$P(2) = P(1) \cdot Q$$
$$P(3) = P(1) \cdot Q^2$$
$$\cdot$$
$$\cdot$$
$$\cdot$$
$$P(j) = P(1) \cdot Q^{j-1} \qquad \text{for } j \geq 1 \qquad (4)$$

and the relations (3) and (4) lead to

$$P(1) = 1 - Q \qquad (5)$$

where Q is the probability of occurrence of the event.
(For the event (2), Q is equal to 0.134). From (5), all
the P(j) will be given by (4).

A somewhat similar computation was carried out by GODA (1970)
by means of a spectral simulation on a computer applying a
Pierson - Moskowitz type spectrum as the spectral input.
The runs of high waves computed by Goda have been replotted
in Fig. 8 and appear to be relatively similar to the results
obtained from the field data. However, the data material
applied by Goda is relatively sparse and only two points are
shown.

It is noted that the power dependency of j in (4) indicates
that on a semi-logarithmic plot, the P(j)'s will follow
straight lines, as shown in Fig. 9.

The P(j) values computed from the field data are also shown
in Fig. 9. They show that the wave group formation is more
pronounced than would be expected from a completely random
distribution of the wave height successions. This result
is in accordance with Goda's results (which are shown in
Fig. 8 and replotted on a semi-logarithmic plot in Fig. 10),
and also in accordance with Wilson and Baird's conclusions
from their study of the wave climate outside Nova Scotia
(WILSON and BAIRD 1972). Also, the results shown in Fig. 9
are consistent with the positive correlation found for
$\phi(1)$ shown in Fig. 5.

PROBABILITY OF
WAVE GROUP FORMATION

PROBABILITY OF
WAVE GROUP FORMATION
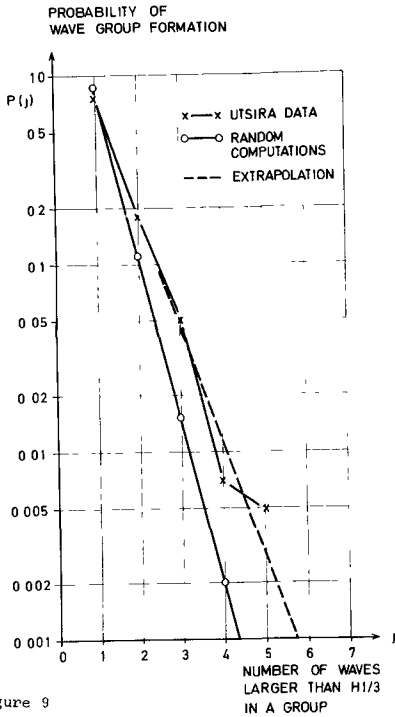
Figure 9

Figure 10

The average occurrence P(j) of runs of waves
larger than $H_{1/3}$ for the field data plotted on
semi-logarithmic paper as compared to P(j)
computed from equation (4)   (Q = 0 134)
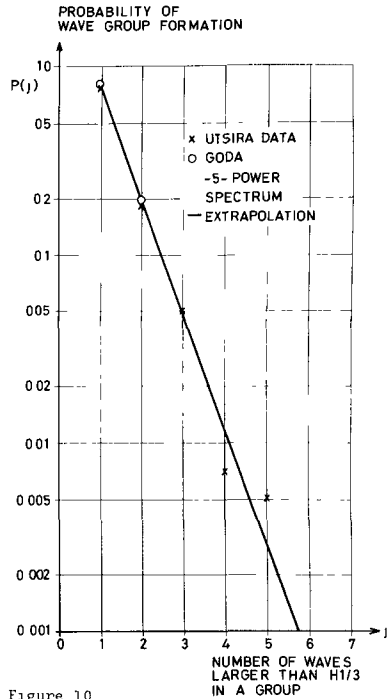
The results from Figure 8 replotted on a
semi-logarithmic plot

If the field data are separated into the cases for wave
growth (G) and wave decay (D) conditions, the average values
of P(j) differ, as shown in Fig. 11. The wave group formation
appears to be more pronounced during wave growth conditions
than during wave decay. It is recalled that the same tendency
was noted for the φ(1)-values; φ(1) tends to be larger during
wave growth conditions than during wave decay.
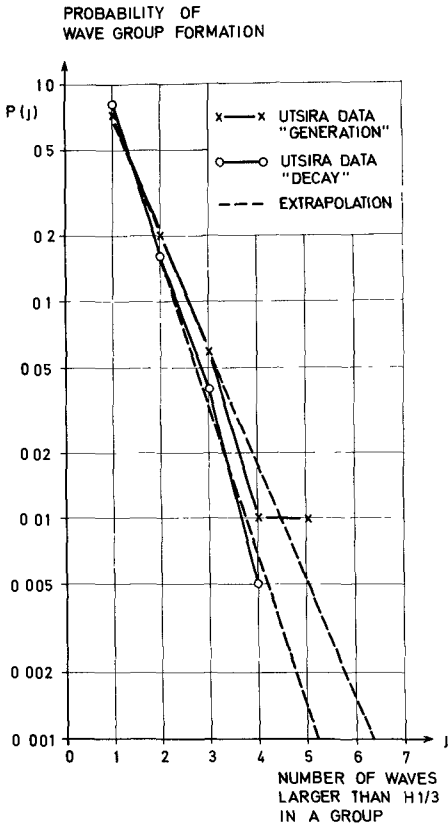
Figure 11.   The average probability of occurrence P(j) of
              runs of waves larger than $H_{1/3}$ for the field
              data when they are divided into the case for
              wave growth and wave decay

The explanation for this finding may not be obvious.
Longuet-Higgins has shown theoretically that wave group for-
mation tends to be more pronounced for a narrow-band spec-
trum (LONGUET-HIGGINS 1957). Because swell is described by
a narrow-band spectrum, one might expect that the wave group
formation would be more pronounced during wave decay than
during wave growth. However, the result shown in Fig. 11
is contrary to this expectation.

On the other hand, the beginning of the wave decay is usu-
ally due to changes in the wind field, both in strength and
direction. This changing is likely to lead to a rela-
tively "confused" sea state; the state of "regular swell" is
likely to occur at a later stage of the decay (say, when
the maximum waves of the sea state have passed below 4 m).

In addition, recent research results have shown the wave
energy spectrum to be much more sharply peaked than would
be expected from a Pierson - Moskowitz type spectrum (The
JONSWAP Project, HASSELMANN et. al. 1973). Fig. 12 shows
the average JONSWAP spectrum and Fig. 13 shows an example
of a spectrum recorded during wave growth at Utsira. They
look very similar. Goda concluded that the controlling
factor for the length of the wave runs appears to be the
spectral peakedness (GODA 1970). Thus the sharply peaked-
ness of the wave spectra during the wave growth stage may
be another reason why the group formation tends to be more
pronounced during wave growth than during decay.
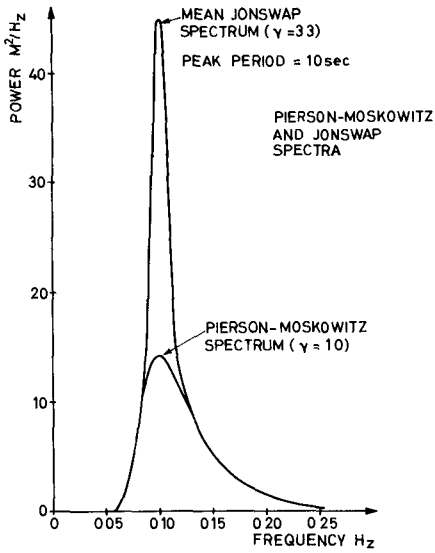
Figure 12

The average JONSWAP spectrum recorded outside
the island of Sylt under fetch-limited, wave-
growth conditions as compared to the Pierson-
Moskowitz spectrum
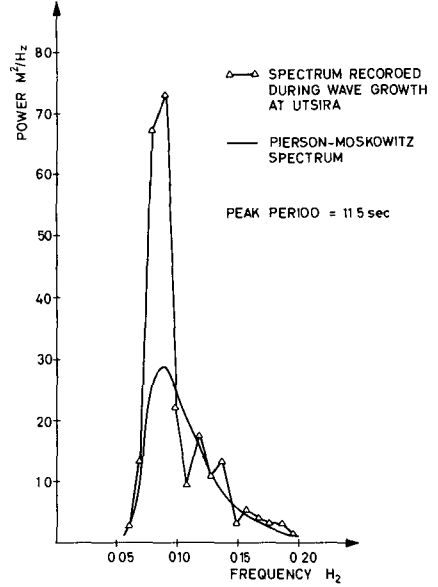
Figure 13

Wave spectrum recorded during wave-growth
conditions at Utsira

At the presentation of this paper it was suggested that the
extent of wave group formation might correlate to the spec-
tral width parameter ε.   However, the ε parameter for a
Pierson - Moskowitz type spectrum appears to be highly sensi-
tive to the choice of high-frequency cut-off to the spectrum:
ε varies between 0.4 and 0.8, depending on the cut-off fre-
quency applied (GODA 1970).   This is so because ε is depen-
dent on the fourth moment of the spectrum while the Pier-
son - Moskowitz spectrum varies with the minus fifth power
of the frequency at the high-frequency range.   No correla-
tion between the φ(1) (given by (1)) and ε was found.

Fig. 14 compares the wave group formation recorded during
wave growth to the wave group formation from a very narrow-
banded spectrum simulated on the computer by Goda. The simu-
lated waves described by the narrow-band spectrum (which
has a high-frequency tail falling off as frequency to the
minus tenth power) shows a much larger extent of wave group
formation than the field data.

Fig. 15 is an extrapolation based on the straight line drawn
for the field data (wave growth data) shown in Fig. 11. The
line denoted A represents the probabilities P(j) based on
the computations given by (4), while the line denoted B re-
presents the field data extrapolated for the wave-growth
case. Note that P(6), for instance, is about 40 times
larger for the field data than for the evaluation based on
the theory. This leads to the conclusion that the probabili-
ties P(j) for wave group formation among large waves are
much more pronounced than would be expected from a completely
random distribution of the wave heights for large j.

Similar computations were also carried out for the event
of H_i lower than $H_{1/3}$. For this case Q in (4) equals to
1 - 0.134 = 0.866.

Based on the random theory, the average length E_M of wave
runs was computed according to the formula

$$E_M = \sum_{j=1}^{\infty} jP(j) = \frac{1}{1-Q} \qquad (6)$$

where (4) and (5) have been used. The second moment of P(j)
is

$$E = \sum_{j=1}^{\infty} j^2 P(j) \qquad (7)$$
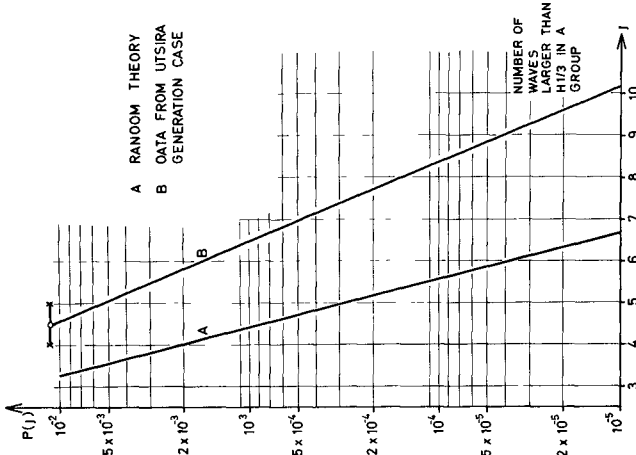
Figure 15

The average probability of occurrence P(j) for the wave growth data extrapolated as compared to the determination of P(j) according to equation (4).
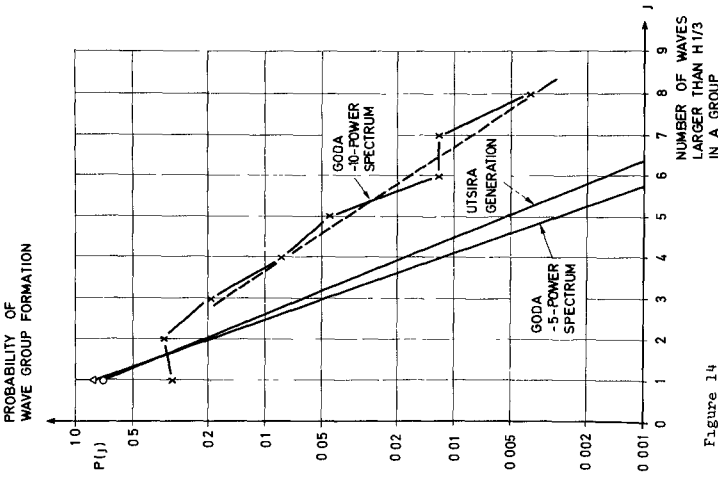
Figure 14

The average probability of occurrence P(j) of runs of waves for the wave growth data as compared to the wave runs obtained with spectral simulation applying a spectrum with a high-frequency tail falling off as frequency to the minus tenth power

The standard deviation σ is therefore

$$\sigma^2 = E - E_M^2 \qquad\qquad (8)$$

where E and E_M are evaluated from (7) and (6).

The results from the computations based on (4) as compared to the field results are shown in Table I.

CASE	AVERAGE	STANDARD DEVIATION
1. UTSIRA - DATA	1,35	0,61
2. WAVE - GENERATION	1,41	0,69
3. WAVE - DECAY	1,26	0,51
4. RANDOM - COMPUTATIONS	1,15	0,42

Table I.   The average duration E_M and the standard deviation σ for runs of waves larger than $H_{1/3}$.

A similar computation was also carried out for the event that H_i is lower than $H_{1/3}$. The results are shown in Table II.

CASE	AVERAGE	STANDARD DEVIATION
1. UTSIRA - DATA	7,71	6,23
2. WAVE - GENERATION	8,05	6,63
3. WAVE - DECAY	7,26	5,70
4. RANDOM - COMPUTATIONS	7,46	6,95

Table II.   The average duration E_M and the standard deviation σ for runs of waves smaller than $H_{1/3}$.

The tables show that the standard deviations of the runs of
high (or low) waves are relatively large, especially for
the runs of low waves.

Table III shows the mean number of waves between two runs of
waves larger than $H_{1/3}$.

	E_M $H > H_{1/3}$	E_M $H < H_{1/3}$	MEAN LENGTH OF TOTAL RUN FOR H1/3 TO H1/3
RANDOM COMPUTATIONS	1 15	+ 7 46 =	8 61
UTSIRA AVERAGE	1 35	+ 7 71 =	9 06
UTSIRA GENERATION	1 41	+ 8 05 =	9 46
UTSIRA DECAY	1 26	+ 7 26 =	8 52

Table III.   The mean number of waves between two runs of
               waves larger than $H_{1/3}$.

This number was simply evaluated by adding the E_M for
$H_i < H_{1/3}$ and for $H_i > H_{1/3}$ together. The table shows the
average number of waves between two runs of waves larger
than $H_{1/3}$ to be 9, on the average, for all the cases con-
sidered. This result is also in accordance with Goda's com-
puter simulations, applying a Pierson - Moskowitz type of
spectral input.

It should, however, be stressed that this result is depen-
dent on the specific wave height level chosen. Say, if a
level above the significant wave height level had been
chosen, the mean length between two runs of large waves would
have been larger.

CONCLUSIONS

The results derived in this paper may be summarized as
follows:

1.   The wave group formations among large waves are found
      to be larger than would be expected from an estimate
      based on a completely random successions of the wave
      heights.

2.   The field results compare well to the results obtained
      numerically by Y. Goda.

3.   Wave group formations tend to be more pronounced for
      a growing sea than for a decaying sea.

For offshore practice, conclusion No. 1 will be of particular
importance because a large probability of a single run with
many large waves might justify the use of regular waves when
fixed structures are tested in a wave flume.

ACKNOWLEDGEMENTS

The author would like to thank Prof. P. Bruun for his
suggestions and the Royal Norwegian Council for Scientific
and Industrial Research (NTNFK) for permission to use
their data.

REFERENCES

1. Y. GODA: Numerical Experiments on Wave
                          Statistics with Spectral Simulation.
                          Report of the Port and Harbour
                          Research Institute, Vol. 9, No. 3,
                          1970, Japan.

2. L. HARRIS: The Analysis of Wave Records.
                          Proc. from the Coast. Eng. Conf. 1970.

3. K. HASSELMANN et.al.: Measurements of Wind-Wave Growth and
                          Swell Decay during the Joint North
                          Sea Wave Project (JONSWAP).
                          Ergänzungsheft no. 12, Reihe A,
                          Deutschen Hydrographischen Zeit-
                          schrift, 1973.

4. F.H. HSU &   Analysis of Peak Mooring Force Caused
    K.A. BLENKARN: by Slow Vessel Drift Oscillation in
                          Random Seas. Proc. from the Off-
                          shore Tecn. Conf. 1970. OTC paper
                          No. 1159.

5. P. KAPLAN: Hydrodynamic Analysis applied to a
                          Mooring and Positioning of Vehicles
                          and Systems in a Seaway. Eigth Sym-
                          posium on Naval Hydrodynamics ARC -
                          179. 1970.

6. M.S. LONGUET-HIGGINS: The Statistical Analysis of a Random,
                          Moving surface. Phil. Trans. Roy.
                          Soc. Vol. 249. A. 966, 1957.

7. K.G. NOLTE &   Statistics of Ocean Wave Groups.
    F.H. HSU: Proc. from Offshore Tecn. Conf. 1972.
                          OTC paper No. 1688.

8. J.R. WILSON &   A Discussion of Some Measured Wave
    W.F. BAIRD: Data. Proc. from the Coast.Eng.
                          Conf. Vancouver 1972.

CHAPTER 8

THE LARGE-HEIGHT RESPONSE OF TWO WAVE RECORDERS

by

L. Draper*, J.D. Humphery[+] and E.G. Pitt[+]

ABSTRACT

Two commonly used deep-water wave recorders which depend on
acceleration measurement were calibrated on a 14 metre diameter
vertical wheel, and also on much smaller laboratory test rigs,
over a range of wave periods likely to be encountered at sea.
The results showed that the instruments behaved according to
expectations. In addition, spectra from two instruments of the
same types which were deployed within one mile of each other
were compared and shown to be similar.

INTRODUCTION

Instrumental·wave recordings have been made all over the world
for many years, and these recordings have been used to produce
design criteria for coastal and offshore structures and for many
other purposes. An accuracy of +10% has usually been sufficient
for these purposes. However, with the advent of the North Sea
oil industry, it has become necessary to reduce the errors, since
overbuilding is prohibitively expensive, and underbuilding
potentially dangerous. Wave heights to an accuracy of +2% are
often specified in the formulation of oil-rig design criteria,
even though the sea's surface may be difficult to define in
severe conditions.

It appeared that no accelerometer wave recorder had been
calibrated over a simulated wave height of greater than 3 metres,
even though waves of seven times this height are sometimes
recorded, and these recordings are used to predict waves of
10 times this height and more.

It was felt that this discrepancy between calibration con-
ditions and wave heights experienced in real life was unacceptable,
and so two representative accelerometer wave recorders were tested
on the Big Wheel (Ferris Wheel) at Southsea Fun-Fair. To check
the instrument responses over a range of periods down to about
5 seconds, low-amplitude laboratory tests were also made. This
was because the maximum speed of the big wheel gave a rotational
period of 13.6 seconds. The laboratory tests also enabled a
check to be made on the linearity of the recording systems.

*Institute of Oceanographic Sciences, Wormley, Godalming,
  Surrey, England.

[+]Institute of Oceanographic Sciences, Taunton, Somerset, England.

It appears that little work has been done to compare the
spectral responses of wave recorders working under similar con-
ditions. A comparison of the responses of the same two types
of recorder has also been made.

Scope of the Experiment

Instruments used

1. I.O.S. Shipborne Wave Recorder (S.B.W.R.) (see
Tucker, M.J., "A Shipborne Wave Recorder", Transactions
of the Institution of Naval Architects, Vol. 98, 1956).
This type of recorder has been used to obtain virtually
all the I.O.S. deep-water wave records. It is one of
the recorders being used by the North Sea Oceanographic
Study Group, and Governmental design criteria for off-
shore structures are based partly on its records. The
recorder consists of two sensor units (one on each side
of the ship) and electronic processing circuitry. Each
sensor unit consists of a pressure sensor and an accelero-
meter.

The position of the sea surface with respect to each
unit is detected by its pressure sensor, and the position
of each unit with respect to an arbitrary reference level
is determined from a double integration of the accelerometer
signal. A simple addition of these two outputs from each
pair of sensors gives a signal proportional to wave height,
from which ship motion has automatically been eliminated.
The placing of identical units on each side of the vessel
doubles the sensitivity and has other advantages.

A minute or so after switching on, the instrument
settles down, and the output consists of fluctuations, due
to the sea waves, about a mean line on the recorder. Because
the pressure sensors were not subject to any hydrostatic
pressure during this experiment, the chart deflexions pro-
duced were caused only by the changes in acceleration
experienced by the accelerometers.

Two S.B.W.R.s were tested. Both had been used at sea,
but they were completely refurbished before the experiment.

2. Waverider. The Waverider wave measurement system
is also in use by the North Sea Oceanographic Study Group
and is manufactured by Datawell of Haarlem, Netherlands.
An accelerometer is enclosed within a surface-following,
moored buoy. The accelerometer signal is integrated twice,
and the resultant signal modulates a radio transmitter.
Batteries, giving a working life of approximately ten
months, and a voltage stabiliser, are also enclosed within
the buoy shell.

        The wave-modulated radio signals are received at a
shore station which may be up to 50 kilometres from the
buoy. The receiver demodulates the signals with a phase-
locked loop circuit, and the analogue output is presented
on a strip-chart.

        To ensure that the experiment was carried out to the
satisfaction of the manufacturers, Mr P.L. Gerritzen of
Datawell attended as an observer. The instrument used was
new when tested, it had not been put into the sea.

    The Big Wheel and laboratory experiments gave no indication
of how the two types of recorder would respond to real sea con-
ditions; they merely measured the instrument's abilities to
record their own vertical movement. An attempt has now been made
to compare the performance of the two types of instrument working
under similar conditions at sea.

    A Waverider and a S.B.W.R. have been operated simultaneously
in at least two positions: (1) at the Sevenstones Light Vessel off
Land's End, and (2) the M.V. 'Edelstein', operating at 61°20'N on
the Greenwich meridian. The Waverider was usually operated within
a kilometre of the ship in each case. Although each pair of
recorders obviously does not measure exactly the same waves, spectra
can be computed from records taken at the same time.

Details of the Big Wheel (Ferris Wheel) Experiment

        The wheel was made in Italy; its diameter was measured care-
fully and was found to be 14.0 metres. The Waverider and two
S B.W.R.s were placed approximately at the apices of an equilateral
triangle on the wheel. Each instrument was carefully lashed down
so that it did not experience any spurious vibration which could
have interfered with correct operation. When all the instruments
and necessary power supplies had been fitted into the cars, the
wheel was carefully balanced so that its rotational speed was
constant throughout a revolution.

        It was necessary to provide a 240 volts 50 Hz supply for each
S.B.W.R. Although each car carried a mains supply derived from a
fairground generator, it was felt that it would be unwise to use
this to energise the recorders. The required supply was therefore
derived from a 12 volt accumulator and an inverter.

        The response of the S.B.W R. is closely linked to the stability
of the 80 volt, 1000 Hz oscillator. Thus if the oscillator voltage
falls by 1%, then the recorder response is reduced by 1%. To allow
for voltage variations, the oscillator voltage was measured after
each run. Corresponding corrections would then be made to the
responses where necessary. Each S.B.W.R.'s performance was recorded
in situ by its own chart recorder.

        The transmitter aerial provided by Datawell for the Waverider
buoy was too long for the experiment, it caught in the bracing as
the wheel turned. A stub-aerial with a loading-coil was therefore
used

    The Waverider receiver was set up in a vehicle close to the
base of the wheel. It was run from a portable generator providing
240 volts, 50 Hz. A reserve receiver was provided by the
Interservice Hovercraft Unit, and was set up at I.H.U. some
thirteen kilometres from the test site. Although this system
worked satisfactorily, the record showed some evidence of unlocking;
this was probably due to the use of a temporary aerial and the
presence of interference-sources in the area.

    The wheel could be rotated at constant speeds giving
rotational periods between 13.6 to 30 seconds. Each experimental
run was for 10 revolutions after the wheel had attained a steady
speed. The period was determined as the average period for the
10 revolutions. Individual revolutions were also timed; these
showed some variation, but resultant errors were insignificant

RESULTS OF THE EXPERIMENTS

Big Wheel

    The results of the 14-metre height experiments are shown
graphically in figure 1. The reason why part of the Shipborne
Wave Recorder response is greater than unity is that, when the
pressure units are in circuit, attenuation of wave motion with
depth reduces the combined response of the units and a nominal
sensitivity of 0.835 times the maximum is used. A full description
of the rotational experiments can be found in NIO Internal Report
A 63.

Shipborne Wave Recorder - Big Wheel

    It can be seen that, relative to the theoretical response,
the instrumental sensitivity increases slightly with increasing
period. This is a phenomenon which has been known for a long
time but which is not understood. Departures from the theoretical
values are

        Recorder No. 1   0% at 14 seconds
                            4% high at 25 seconds

        Recorder No. 2   2% low at 17 seconds
                            0% at 24.5 seconds

        Chart reading errors are of the order of ±0.5%.

Waverider - Big Wheel

    The response of the instrument was very close to the
theoretical values. This instrument gave only slightly less
response than was expected; at 13.5 seconds it was 0.8% low and
at 30 seconds 2.4% low.

Laboratory

    The Shipborne wave recorder was tested on a 1 metre diameter
arm in the Institute's laboratory at Wormley and the Waverider on
the 3 metre diameter calibration rig at NPL Hythe. The Shipborne
recorder was tested at periods from 6 to 36 seconds and the

Waverider from 2 to 10.8 seconds. The results are shown in figure 2.

S.B.W.R. - laboratory

     The agreement here between theoretical and experimental curves
is similar to that in the Big Wheel experiment. The discrepancies
between experimental and theoretical curves are:

               At 6 seconds   0.2% high
               at 15 seconds   1% low
               at 25 seconds   3.3% high

          Chart reading errors are of the order of ±0.5%.

Waverider - laboratory

     The instrument did not appear to change sensitivity over the
period range of from 2 to 10.8 seconds, and the absolute response
was correct to within chart reading errors.

               Spectral Comparisons between a Waverider and
               the S.B.W.R. at the Sevenstones Light Vessel

     A Waverider buoy was deployed near the Sevenstones Light
Vessel for several periods between 1971 and 1972 in connection
with trials being carried out in the area. The Waverider chart
records were subsequently made available to us.

     A total of twelve pairs of simultaneous S.B.W.R. and Waverider
records were digitized and the spectra computed. An example of
these spectral comparisons are shown in figure 3, as well as the
equilibrium spectra proposed by Phillips.

     It will be seen that at longer periods the spectra from the
two instruments agree well, and lie within the 95% confidence
limits for the calculation.

     However, on several of the spectra the S.B.W R. gives more
energy than does the Waverider at periods of around 10 seconds. Also,
at short periods, the S.B.W.R spectra contain more energy than
do the Waverider spectra. This is due to errors in the S.B.W.R.
response correction at higher frequencies and can be overcome for
many purposes by substituting a theoretical spectrum at periods
of less than about 5 seconds.

                         CONCLUSIONS

     The outcome of the project is a highly satisfactory one in
that the instruments perform well within the limits of error
normally ascribed to wave recording in general. As the bulk of
wave information from British and adjacent waters has come from
these two types of instrument it is encouraging that their
responses differ so little from the theoretical values. The major
questions still remaining to be resolved are how well the devices

sense the true position of the sea surface, and also the unresolvable
problem of what is meant by the position of the sea surface when, in
a storm, the vertical distance between 100% water and 99% air could
be of the order of 1 metre.

ACKNOWLEDGEMENTS

FIGURE 1

COMPARISON OF THEORETICAL AND EXPERIMENTAL RESPONSES FOR THE SHIPBORNE WAVE RECORDERS AND WAVERIDER BUOY

BIG WHEEL EXPERIMENT

① THEORETICAL RESPONSE OF S B W R

② RESPONSE OF S B W R Nº I (CROSSES)

③ RESPONSE OF S B W R Nº 2 (LARGE CIRCLES)

④ THEORETICAL RESPONSE OF WAVERIDER

⑤ RESPONSE OF WAVERIDER (BLACK DOTS)

FIGURE 2

COMPARISON OF THEORETICAL AND
EXPERIMENTAL RESPONSES FOR THE
SHIPBORNE WAVE RECORDERS AND
WAVERIDER BUOY

LABORATORY EXPERIMENT

① THEORETICAL RESPONSE OF S B W R

② RESPONSE OF S B W R (CROSSES)

③ THEORETICAL RESPONSE OF WAVERIDER

④ RESPONSE OF WAVERIDER (CIRCLES)
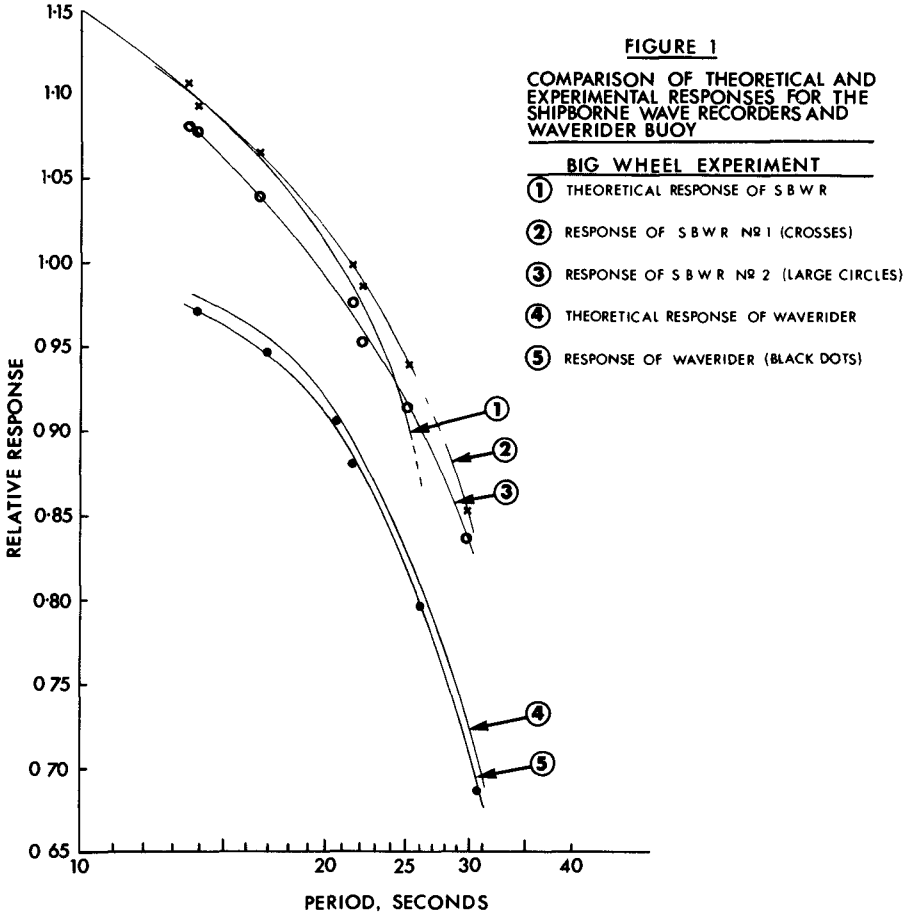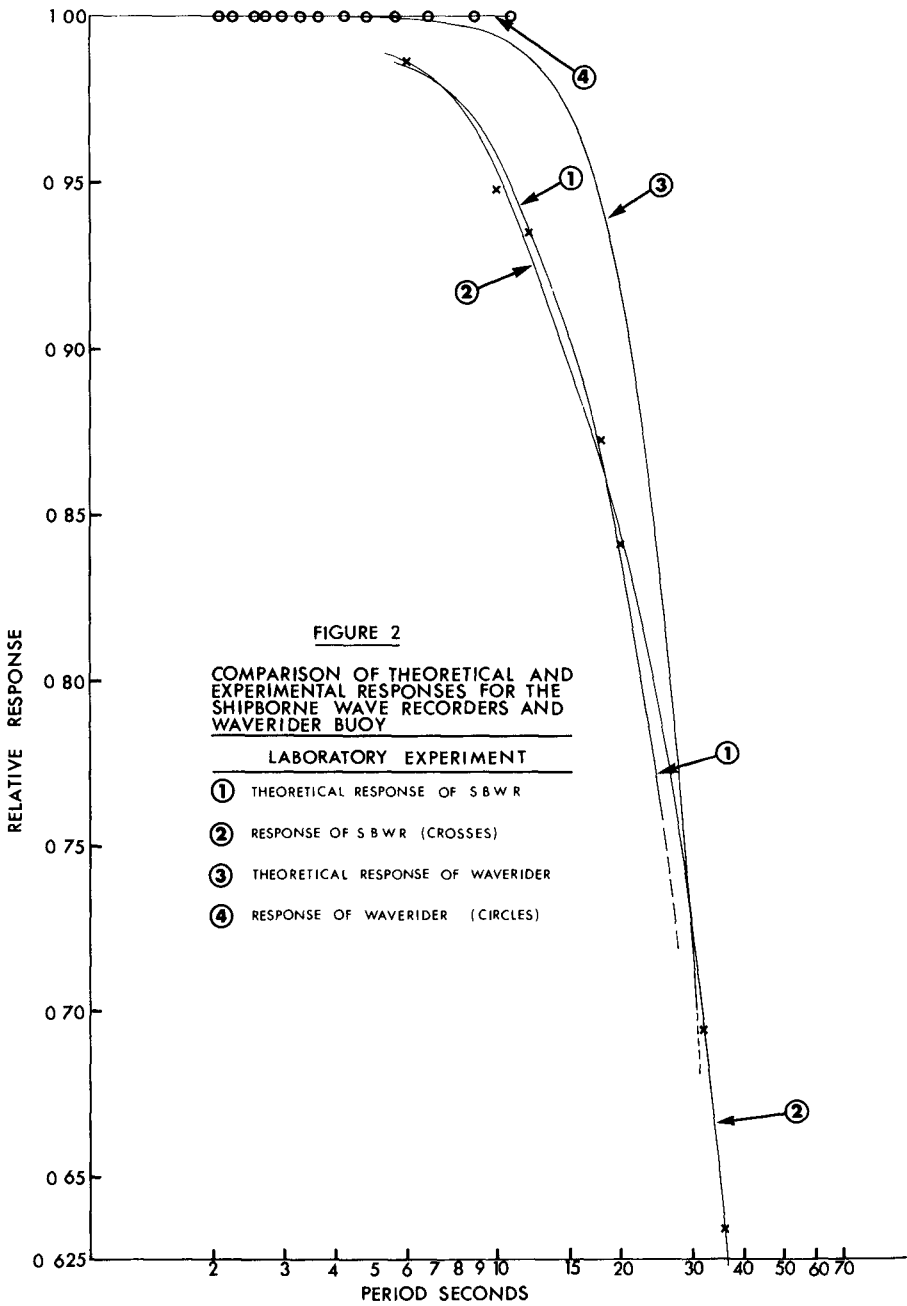
FIGURE 3.

TIME 0900 7th MARCH 1972.
SEVEN STONES.

x--x SBWR
•——• W/R

95%
CONFIDENCE
INTERVAL

PHILLIPS
EQUILIBRIUM
SPECTRUM

VARIANCE PER UNIT — BANDWIDTH — m²/Hz

FREQUENCY (Hz)
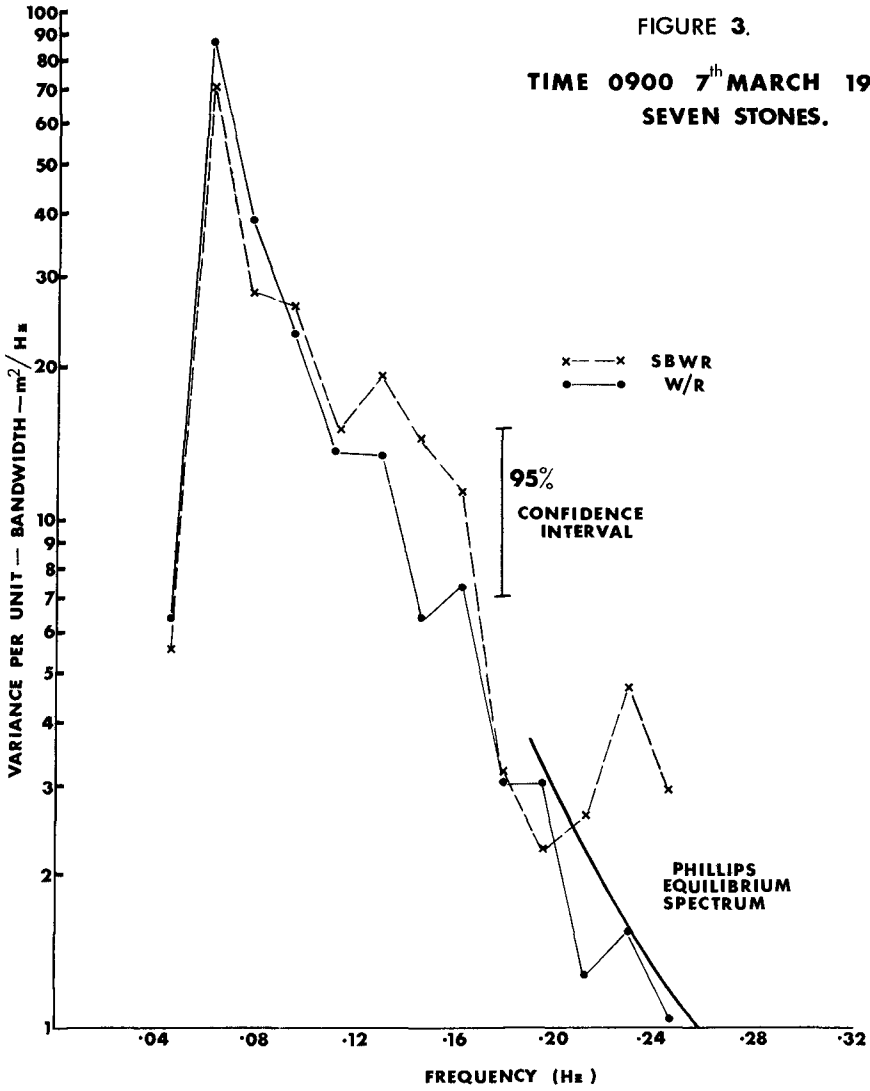
CHAPTER 9

A TRANSMISSION LINE WAVE HEIGHT TRANSDUCER

* C.M.G. Zwarts

Summary

A simple but accurate wave transducer has been developed for the measurement of waves and tidal levels on inland and coastal waters. It consists of a tunnel diode oscillator, using a transmission line to sense the water-level. The output voltage consists of a square wave, with a period linearly proportional to the water-level. In addition an analog output signal is provided. The quasi-static accuracy of the instrument is equal to or less than 0.2%.

Figure 1

Prototypes undergoing field tests in Lake Ontario.

*   Instruments Section, National Research Council of Canada, Montreal Road Laboratories, Ottawa, Ontario, Canada.

Introduction

Waves have been measured, on inland and coastal waters, with various types of transducers of which the more common are:

Pressure cell, anchored to the bottom, measuring the pressure variation due to waves at the surface.

Accelerometer, mounted in a floating buoy, giving the surface-acceleration of the wave.

Wave-staff, using to sense the water-level: ohmic contacts at small regular intervals; parallel resistance wires; insulated wire as capacitance.

In this paper a wave transducer which needs a mounting frame, like the resistive and capacitive type wave-staff, is described. The instrument exploits the large change in dielectric constant from air to water (1:80)[1], as in the capacitive wire wave-staff, but in a different manner. It is the variation in electromagnetic impedance at the air-water interface, caused by the difference in dielectric constant, which is used to obtain the wave height information. An electromagnetic wave, directed towards the water surface with a transmission line eliminating focussing problems, will reflect very efficiently from the water surface. The time it takes for the wave to travel from the source to the water-level and back to the source is a direct measure for the water-level relative to the source. The method developed to extract the wave information from the time delay is however essentially different from the conventional time domain reflectrometry or echo-range finding methods, in principle and embodiment. Instead of directing a voltage step or pulse down the line and measuring the time delay, an oscillation is set up in the line, with the length of line directly determining the frequency. The oscillation is maintained with a simple tunnel diode circuit[2][3][4] over the input terminals of the transmission line. The tunnel diode is operated as a bistable device, being changed states by the reflected wave from the water surface. Since the voltage reflects with phase reversal on the water surface, the tunnel diode is triggered alternatively into both dynamicly stable states; to produce over the input terminals of the transmission line a square wave oscillation with its period being linearly related to the position of the water surface. (See Figure 2.)

The ideal transducer design, in which there is an immediate conversion from the measurand into a frequency, is closely approached by the "Transmission Line Wave Height Transducer" described in this paper. This near optimum design gives two distinct advantages, namely:

1)   calibration is permanent, being nearly independent of environmental
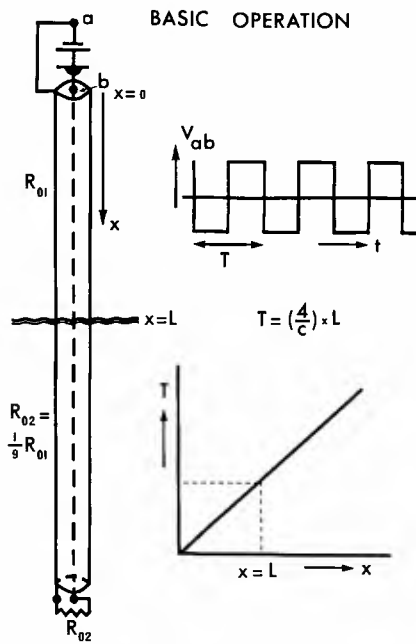
Figure 2

Top and Bottom Assembly   Tubular Transmission Line

Figure 3

and other factors.

2)   the period modulated output signal is ideal for digital processing,
recording, telemetry methods or transmission by cable without
loss of accuracy.

The transmission line consists of two concentric aluminum
tubes, approximately 1 and 2 inches in diameter, assembled in sections
of ten-foot lengths. The outer tube is perforated with a regular
distribution of holes, Figure 3. The rigid coaxial tubular transmission line
is extended at the top with a twenth-foot length of coaxial cable to prevent
the frequency of oscillation becoming too high with near complete immersion.
The frequency of oscillation, in the MHz-range, is scaled down considerably
with logic circuitry to make period measurement and recording more
convenient and accurate. The prototypes had a down count factor of
$N = 5 \times 2^{14}$, whereas the commercial instrument has $N = 2^{13}$.

The output signal consists of a square wave oscillation of
which the period gives the water-level or wave profile. In some cases
however an analog output signal will be required. An accurate period-
to-voltage converter was designed and added to the instrument to make the
wave gauge useful for both digital and analog data processing and
recording. The block diagram of the complete transducer is shown in
Figure 4.

BLOCK DIAGRAM
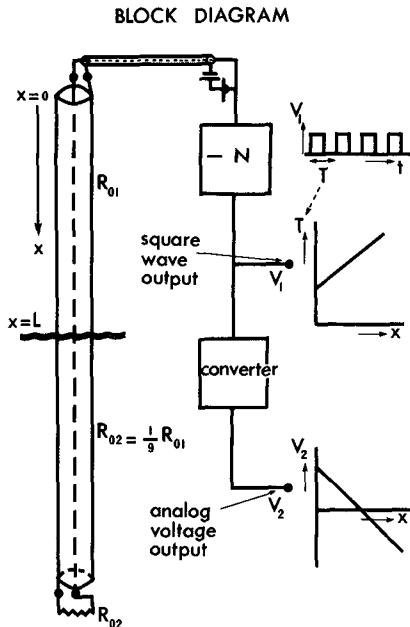
Figure 4

Analysis of Circuit Operation Using a Graphic Method

The simplified transducer circuit is shown in Figure 5. The tunnel diode circuit is connected at x = 0 to the transmission line, which is terminated with R_{O2}. The resistance R_{O2} represents the characteristic impedance of the transmission line in water for $x \geqslant L$.

The v - i characteristic curve for a tunnel diode is shown in Figure 6. The tunnel diode has a negative resistance region for $V_p < V < V_v$. The operating point will be unstable, if the load-line intersects this region, and with suitable conditions steady oscillation occurs.
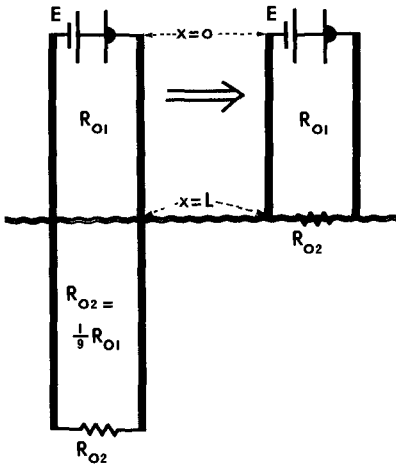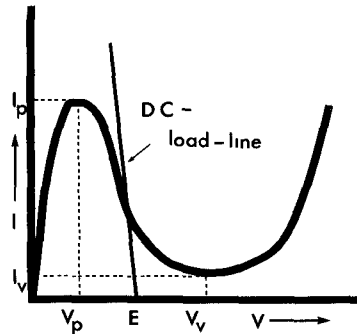
Figure 5   Figure 6

The problem essentially consists of finding the periodic solution

$$V = f_1 \left(t - \frac{x}{u} \right) + f_2 \left(t + \frac{x}{u} \right) , \qquad \text{at } x = 0$$

of the linear wave equation

$$\frac{\partial^2 V}{\partial x^2} - \frac{1}{u^2} \cdot \frac{\partial^2 V}{\partial t^2} = 0$$

f_1 is an arbitrary function of the argument $(t - \frac{x}{u})$ and represents a wave
travelling with velocity u to the right. Similarly f_2 represents a wave
travelling to the left. To solve this problem analytically is not easy since
the tunnel diode introduces a non-linear boundary condition at $x = 0$. There
is however a very elegant graphic method to solve this kind of problem,
its major feature being the ease with which it handles non-linear boundary
conditions.[5] This method allows the wave form at $x = 0$ for $t \geqslant 0$ to be
determined in a simple manner.
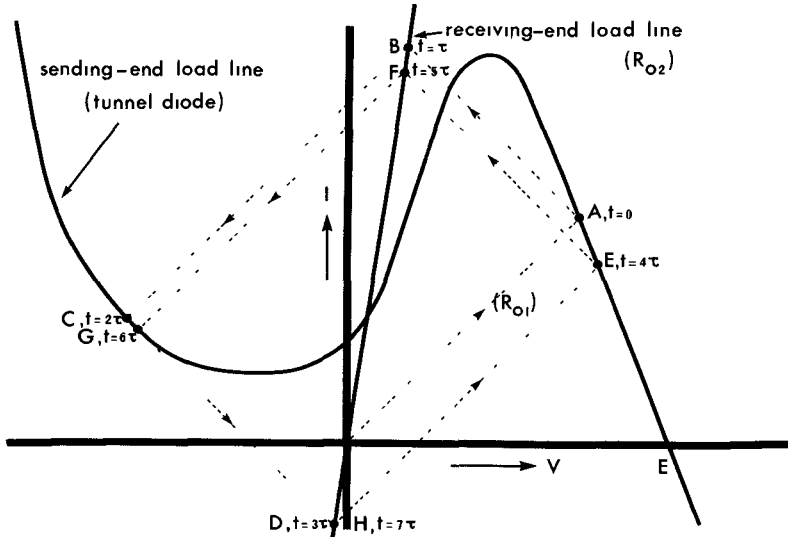
Figure 7

The graphic method, in our case, consists of drawing the load lines,
presented by the sending- and receiving-end impedances, as they are seen by
the transmission line, in the i-v-plane, as shown in Figure 7. The intersection
of the sending-end load line with the conductance line of the transmission line,
point A, gives the initial voltage and current at $t = 0$, travelling down the line.
Projecting, starting from this point, alternatively on the receiving- and sending-
end load lines give the current and voltage at intervals τ for $x = 0$ and $x = L$
alternatively. Continuing this process of projections will eventually give the
steady state solution. One notices that, for this particular example, the
approximate steady state values are reached after only two rounds of projections,
since continued projection will give the same points E, F, G, and H. The
steady state values for the voltage for $x = 0$ and $t \geqslant 0$ can now be simply read
from Figure 7, and are presented by the points E and G. The resulting voltage

wave-form at the sending-end, x = 0, is therefore a square wave, with a 50% duty cycle, having a slightly different positive and negative amplitude, Figure 8.
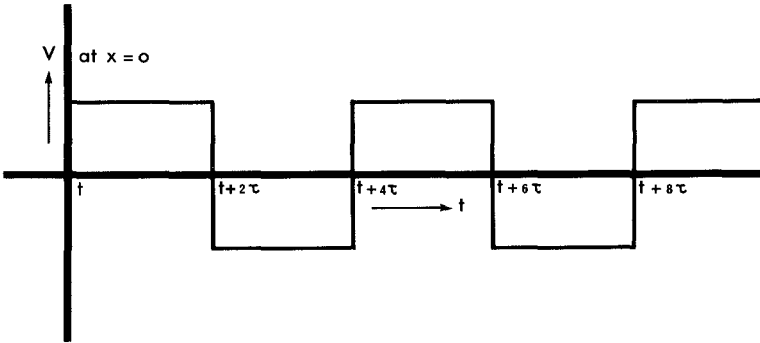
Figure 8

Since $T = 4\tau$ and $\tau = \frac{L}{c}$, c being the propagation speed and L being the length of transmission line above the water surface, it follows that

$$L = (\frac{c}{4})\, T.$$

The period T of the square wave oscillation is hence linearly related to the position of the water surface.

Derivation of Output Period T_O and Sensitivity S

In the actual transducer circuit a twenty-foot length of flexible coaxial cable is inserted between the rigid transmission line (used as the sensor) and the tunnel diode to prevent the frequency of the oscillation becoming too high, Figure 9. This could occur with the rigid transmission line nearly fully immersed. The flexible coaxial cable does not alter the operation, it only shifts the operating frequency to a more convenient lower level.
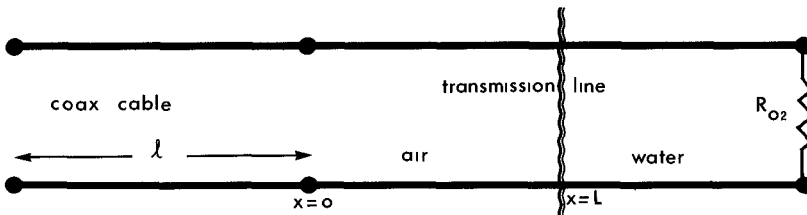
Figure 9

The one way propagation delay time is:

$$\tau = \frac{\sqrt{\varepsilon_r}\, \ell}{c} + \frac{L}{u} \simeq \frac{1}{c} \cdot (\sqrt{\varepsilon_r}\, \ell + L)$$

ε_r = relative dielectric factor of coaxial cable ($= 2.25$)
u = propagation speed in transmission line ($u \simeq c$)
ℓ = length of coaxial cable ($\simeq 20$ ft.)
L = length of tubing above water surface.

The period of oscillation T is four times τ, hence:

$$T = \frac{4}{c} \cdot (\sqrt{\varepsilon_r} \cdot \ell + L)$$

This period T is very short (typically less than 0.2μ sec) and considerable frequency scaling is used to increase the period to a value larger than 10 msec. This frequency scaling makes period recording and measurement much more convenient and accurate. With a frequency scaling factor N the output period of the transducer becomes:

$$T_o = N \cdot T = \frac{4N}{c} \cdot (\sqrt{\varepsilon_r}\, \ell + L)$$

$$N = \text{count down factor } (= 5 \times 2^{14}).$$

The output frequency f_o is.

$$f_o = \frac{1}{T_o} = \frac{c}{4N} \cdot \frac{1}{(\sqrt{\varepsilon_r} \cdot \ell + L)}$$

The sensitivity S is

$$S = \frac{\triangle T_o}{\triangle L} = \frac{4N}{c}$$

Substituting the approximate numerical values given yields:

$$T_o \simeq (10 + \frac{L}{3}) \text{ msec.}$$

$$f_o \simeq \frac{100}{1 + \frac{L}{30}} \text{ Hz}$$

$$S \simeq \frac{1}{3} \text{ msec/ft.}$$

Dynamic Measurements

As derived, the sensitivity S is only dependent on N and c, both constants. One could state in general that S is largely independent of factors such as the temperature, pressure, humidity, dielectric constant, conductivity, cleanness of tube surfaces, etc.

Static Measurements

The stability of the device becomes an important factor when measuring slowly varying levels. The main factor in the expression for T_o accounting for possible temperature effects is the relative dielectric factor of the coaxial cable. Another factor (which however does not appear in the expression for T_o since we have assumed negligible switching times for the tunnel diode) to be considered is the capacitance of the tunnel diode and the effect of variations in it, due to temperature changes, on the output period. Both effects remain small resulting in a very stable device relative to temperature variations.

Design of Transmission Line

A transmission line can be made up of two parallel conductors, irrespective of the particular shape as long as their cross section remains constant; there is thus in principle a very large choice[6]. The prototype was made up of standard aluminum conduit, with the inner tube centered inside the outer tube. The inner tube is held concentric with sets of 1/4 inch diameter nylon screws (3 scews, 120°) at intervals of about three feet. This method allows sturdy positioning of the inner tube with negligible interference with the operation of the transducer. A small disadvantage of tubing is that openings have to be made in the outer tube to allow the water to freely flow in and out the space between the two tubes to assure equalizing of outside and inside water-level. The tubular construction still seems to be a rather optimum structure·

    1.   It presents a very strong mechanical structure, needing a limited amount of supports and spacers.
    2.   Eliminates electrical interference from external sources, due to its enclosed structure.
    3.   The circular form has little interference with waves and is moreover equal for waves from any direction.
    4.   The space between the two tubes remains dark enough to eliminate biological growth.

5. The tubular construction with holes in the outer tube will reduce erroneous readings due to splashing and wave build up.

6. Any length of transmission line can be readily made up joining additional sections with screw couplings.

The connection between the transmission line and the electronic circuitry is made via a coaxial cable of 50 ohms. It is therefore required that the characteristic impedance of the transmission line is approximately 50 ohms. Using for the outer tube an ID of 2 inches and an inner tube with an OD of 1 inch gives a characteristic impedance:

$$R_o \,=\, 60 \, \ln \, (\frac{r_2}{r_1}) \simeq 42 \, \Omega$$

It was experimentally determined that this small mismatch can be tolerated since it did not interfere with the operation of the transducer.

Parameters Affecting Dynamic Accuracy

An interesting feature of the tubular structure chosen for the transmission line is that it allows the outer tube to act as a filter by the appropriate choice of the number and the diameter of the holes in the outer tube. One could, in general, distinguish three different time constants for the filter.

    level recording and tidal waves: time constant in fraction
        of hours.
    tsunamis and harbour seiches· time constant in fraction
        of minutes.
    wind generated wave   time constant in fraction of
        seconds.

For level recording, measuring tidal waves, tsunamis or harbour seiches one hole in the bottom part of the outer tube suffices.

The appropriate number, size and distribution of the holes for wind generated waves has been determined experimentally, simulating wave conditions by moving the tube sinusoidally up and down in still water.

The rate of change of the water surface, for steep waves with an amplitude of several feet and higher, is considerable. With falling water-level, a film of water is left behind on the "inner" tube surfaces, which falls at a slower rate than the water surface. This causes the effective dielectric constant in the transmission line, above the water surface, to be somewhat larger, resulting in a slight decrease of the propagation speed in the transmission line

over the wetted length of line. The measured wave height is now somewhat
larger than the actual wave height.

The dynamic simulation (vertical sinusoidal movement of transmission
line) shows therefore the net result of the restriction in equalizing flow through
the holes and the wetting of the "inside" surfaces of the transmission line.
Figure 10 shows an increase in response, due to wetting, before the response
rolls off, indicating that the restriction in flow through the holes becomes the
dominant factor at the higher rates of vertical water movements. The dynamic
tests were conducted with a length of twenty feet of transmission line, of which
half was immersed in the water. The hole distribution, on the outer tube over
the twenty-foot length, consisted of two 3/4 inch holes, directly opposite,
spaced vertically at intervals of 6 inches, with every successive pair being
rotated over 90°.
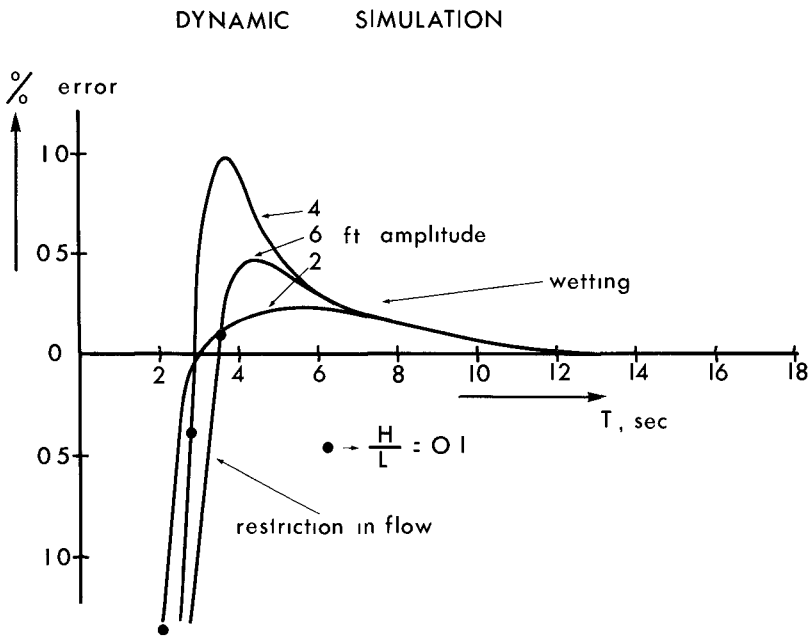
Figure 10

The down counting of the oscillator frequency (several MHz) by a large factor N, to produce a low output frequency, has a certain effect on the dynamic response of the transducer, especially if N is taken too large. The transducer has a dynamic limit resolution since one has to wait one output cycle before information is available of the water-level over that period of time. Each output cycle measured constitutes an average of the wave input signal over that period of time. This filtering action, with N normally chosen such that the output frequency varies between 50 to 100 Hz, can be considered negligible. However if the output period is made to be of the same order of magnitude as the wave period a considerable filtering action results. This effect can be analysed analytically if we assume the waves to be sinusoidal, evaluating the integral,

$$\int_{t_n}^{t_{n+1}} f(t) \, dt = N = \text{constant} \qquad \text{in which,}$$

$f(t)$　=　frequency before scaling down

N　=　count down factor

$t_{n+1} - t_n$　=　instantaneous period of scaled down frequency.

Working out the integral to obtain an expression $t_{n+1} = F(t_n)$ gives

$$t_{n+1} = \frac{1}{\pi f} \text{arctg} \left[(1-\alpha^2)^{\frac{1}{2}} \, \text{tg} \left\{ \frac{\pi f \beta}{\alpha} (1-\alpha^2)^{\frac{1}{2}} + \text{arctg} \left(\frac{\text{tg}(\pi f t_n) + \alpha}{(1-\alpha^2)^{\frac{1}{2}}} \right) \right\} - \alpha \right]$$

in which:

$$\alpha = \frac{\frac{1}{2}H}{(\sqrt{\epsilon_r} \cdot \ell + L)} \, , \qquad \beta = \frac{2NH}{c}$$

$\sqrt{\epsilon_r} \cdot \ell$ =　electrical length of coaxial cable

L　=　half the total length of transmission line

N　=　frequency scaling factor

c　=　propagation speed of light

H　=　total amplitude

For a transmission line 20 ft. long, with 20 ft. of coaxial cable and $N = 5 \times 2^{14}$,

$$\alpha = \frac{H}{80} \qquad \text{and} \qquad \beta = \frac{H}{6000}$$

The relation $t_{n+1} = F(t_n)$ is illustrated in Figure 11 for the worst case,

i.e.: waves with a steepness factor $\delta = 0.14$.

EFFECT of FREQUENCY SCALING on WAVE HEIGHT RESPONSE

for Scaling Factor $N = 5 \times 2^{14}$

Error vs Period for Breaking Waves, $\dfrac{H}{L} = 0\ 14$
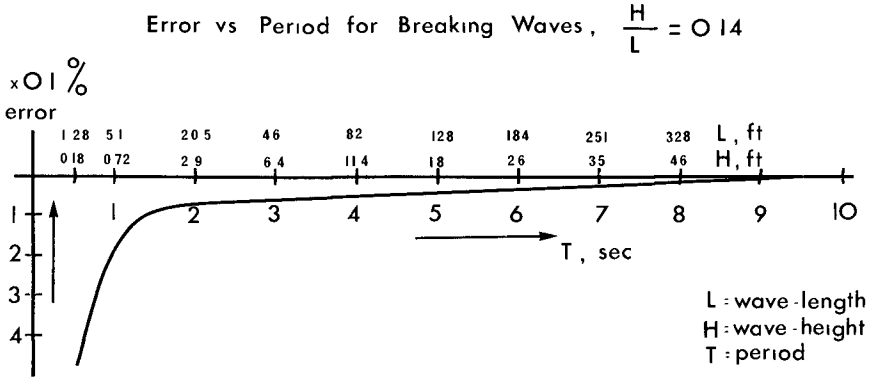
Figure 11

Period to Analog Voltage Converter

Since in some cases an analog output voltage might be required for recording the wave data, a circuit has been designed to convert accurately the output period into an analog voltage. The essential feature of the designed circuit is that it converts the wave height information from period into voltage in the same format, i.e.. for each output cycle a proportional constant voltage level is produced.

The operation of the converter consists basically of a precision ramp signal which is swtiched back to its reference level for every completed output cycle. The ramp voltage level is sampled just prior to switching by a sample-and-hold-circuit to produce a constant output voltage, updated at every successive completed output cycle. Since the output frequency is about two orders of magnitude higher than the wave frequencies, the output voltage of the converter appears as a continuous signal when measuring waves. Except for a slight smoothing, no filtering is required.

Discussion of Accuracy and Experimental Results

The wetting of the "inner" surfaces of the transmission line is the major source of error. There is a static and dynamic wetting error. For a slowly falling water-level a very thin stable film of water clinges to the "inner" surfaces, but with fast rates of change (several ft./sec) a film of water runs off the tube surfaces. Both of these errors increase the response   the water-level measured is lower than the actual level and the wave height measured is larger than the actual wave height (wetting increases slightly the effective dielectric constant in the line above the water surface, decreasing the propagation speed).

The restriction in equalizing flow through the holes, for the pattern chosen, has to be taken into account for wave surfaces having a rate of vertical change beyond several ft./sec.

The transmission line is made up of two concentric aluminum tubes. Aluminum can be used very successfully in sea water[7,8]. If aluminum is corroded by water, the attack takes the form of pitting and there is no general corrosion or gradual thinning as occurs with steel. The rate of pitting decreases rapidly with time and follows a relation: $d = Kt^{1/3}$, d = max. pit depth, K = constant, t = time. Pitting should have little effect on the accuracy since the tubes are only used to guide the electromagnetic waves. Galvanic corrosion has been greatly reduced by DC-isolation of the tubes from the electronic circuitry and the use of non-conducting mounting brackets.

The first prototype built has been field tested, summer of 1971, in Lake Ontario, Figure 1, and the results obtained compared with a resistive step type wave-staff, closely mounted together. Figure 12 shows the good agreement obtained for the power spectra of these two completely dissimilar wave measuring instruments.

Four other units were field tested in Lake Ontario. during the summer of 1973. The instruments worked reliably throughout the season but the wave data gathered have not been processed and are as yet not available. There was considerable algae growth on the outer tube, the

holes remained open however and there was no sign of growth inside, between the tubes. No field data available as yet on fouling in sea water.

DISPLACEMENT   SPECTRA
of

Transmission Line and Step Type Wave-Staffs

solid line step type

broken line transmission line

ft^2/rad per sec

sampling rate 2200/0 48 sec

length of record 176 min

filter bandwidth O OI Hz

smoothing periodogram method

rad/sec
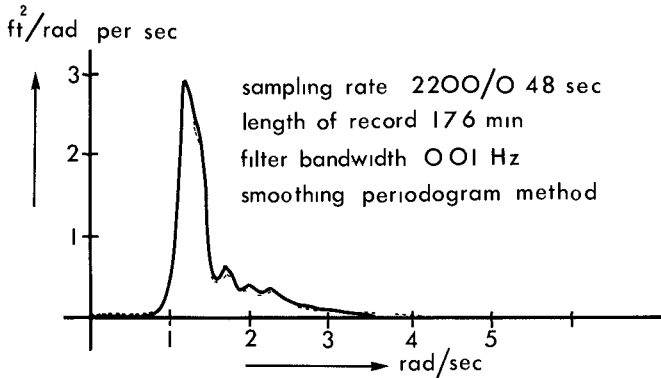
Figure 12

Quasi-static conditions, in fresh and salt water (sp.gr.1.025), were simulated in the laboratory using a transmission line, 20 ft. long. Figure 13 shows the laboratory set-up used for these tests. The accuracies attained are demonstrated by plotting the differences between measured and theoretical values for the period, Figure 14 and Figure 15 (the measurements were obtained with a commercial version of the transducer, Model P116).

The small error developing, with the transmission line moving out of the water, is due to the wetting of the tube surfaces. This error represents the maximum possible quasi-static error for each level of immersion, since it implies wetting over the total length of the transmission line above the water surface at each measured level. From the results obtained one can define the accuracy to be better than 0.2% for quasi-static measurements. (Use of a non-wetting coating on the tube surfaces will substantially improve the accuracy; the maximum wetting error, 0.2%, being the dominant error.)

Transducer in Laboratory Set–up

Figure 13

It might be noted that under typical laboratory conditions it takes about 4 to 5 hours for the wetting effect to completely disappear. Under field conditions it can be expected to disappear much more quickly due to air circulating between the tubes, stimulating evaporation, resulting in a negligible error and improved accuracy.

The results of the dynamic tests are shown in Figure 10 (the period-to-voltage converter was used for the dynamic tests and its error is therefore included in the total dynamic measuring error). Waves were simulated moving the transmission line vertically, in a sinusoidal fashion. The restriction in equalizing flow starts to dominate the wetting effect, for the amplitudes 2, 4 and 6 ft. chosen, for very steep (close to breaking) deep water waves of equal amplitudes. This would indicate that for normal wave activities the error in the wave height measurement is not appreciable.

The transducer has a temperature coefficient of 510^{-3} inch/°F, which applies only when measuring still water-levels, since temperature variations only produce a parallel shift and hence keeping the dynamic sensitivity S constant. The maximum length for the transmission line is 90 ft.; "dry" tests with metal bar electrical shorting showed no deterioration of accuracy over that length. The period-to-voltage converter is very accurate and its output voltage signal has essentially the same accuracy as given by the period information of the square wave output signal. The transducer operates from a 12 volt battery and has a total current consumption of 32 mA.

Conclusions

In this paper a very simple, rugged, but accurate wave measuring device has been described, which forms a very attractive alternative for existing wave gauges. The output signal format, a low frequency, period modulated signal-derived directly without intermediate conversion steps from the psotion of the water surface - is very convenient for recording, transmitting and digital processing. The sensitivity S of the transducer as derived earlier, is only a function of the propagation speed u of the electromagnetic signal and the frequency division factor N of the electronic circuitry. The calibration is hence permanent and largely independent of changes in environmental and circuit parameters. Patent applications have been filed and a license granted to a Canadian firm for the manufacturing of the instrument.

STATIC   SIMULATION in FRESH   WATER

Error vs Un–immersed Length I
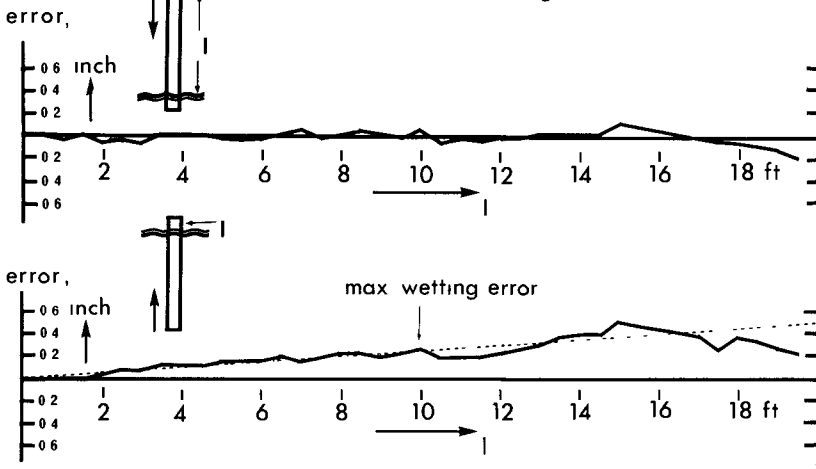
Figure 14

STATIC   SIMULATION in SALT   WATER

Error vs Un–immersed Length I
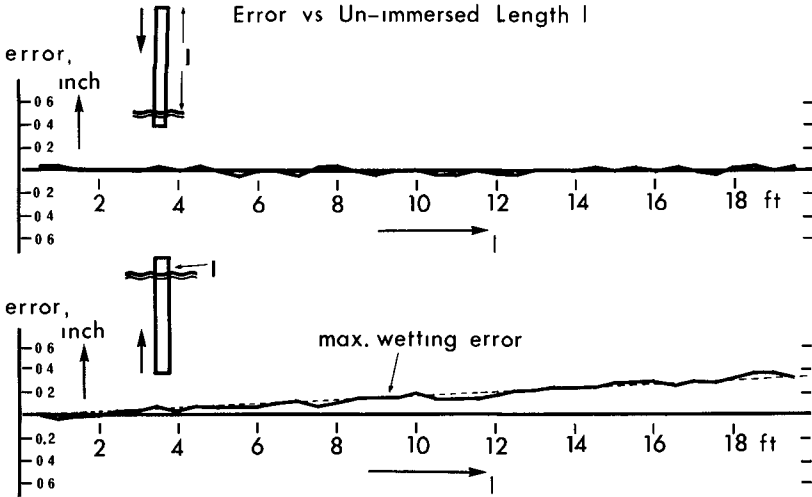
Figure 15

References

1.   Handbook of Chemistry and Physics,
           Chemical Rubber Publishing Co., 1953.

2.   Transistor Manual, General Electric,
           New York, 1964.

3.   Tunnel Diodes, M.A. Lee et al, Chapman and Hall Ltd.,
           London, 1967.

4.   Transmission Lines with Pulse Excitation,
           G. Metzger, J.D. Vebre, Academic Press Inc.,
           New York, 1969.

5.   R.S. Singleton, Finding Transmission Reflections,
           Electronics, October 28, 1968.

6.   The Physics of Transmission Lines,
           P. Grivet, Academic Press Inc.,
           New York, 1970.

7.   H.P. Godard, The Corrosion Behaviour of Aluminum in Natural Waters,
           The Canadian Journal of Chemical Engineering,
           October, 1960.

8.   E.D. Verink and P.F. George, Aluminum Alloys for Desalination
           Service, Materials Protection and Performance,
           May, 1973.

CHAPTER 10

A LOW-COST INSHORE WAVE DIRECTION
INDICATOR

G. de F. Retief and A.P.M. Vonk
Research Engineers
Fisheries Development Corporation of South Africa Ltd.,
Cape Town, R.S.A.

ABSTRACT

Although many attempts have been made in the past to measure the direction of propagation of ocean waves, a need for a simple, reliable solution to the problem has remained. The technique described here, intended for near-shore usage, makes use of a simple bottom-mounted flow direction indicator. The influence of rip and longshore currents on wave direction recordings is identi"ied and a means of reducing these steady state current effects by a reduction in gauge sensitivity is presented, along with various possible recording and analysis techniques. Useful-ness of the gauge is established as a simple engineering tool with certain limitations and examples are given of wave direction recordings related to meteorological data. A possible usage of the gauge as an approximate sediment transport indicator is also proposed.

INTRODUCTION

Situations very often arise in Coastal Engineering where a theoretical prediction of swell direction is not feasible for various reasons and the direct measurement of the directional properties of swell approaching a coastline is required. This need for measured directional spectra is well illustrated by the many ingenious ways proposed in the past (refs. (1) to (4)) to solve the problem and to solve it especially for storm conditions when optical techniques become ineffective.

Wave direction can be measured either remotely by optical or radar techniques, by the measurement of phase difference in signals from surface or submerged wave gauge arrays, or by an analysis of internal orbital wave motion or surface geometry.

The primary function of the instrument described here was the measurement of dominant swell directions in harbour development studies, where boat traffic excluded the use of surface measure-ment techniques. A simple, robust system was required which would lend itself to automatic analysis and which was not depen dent on specific weather conditions such as a choppy sea surface, required for radar techniques.

The underwater approach was therefore chosen, but because of

212

the fundamental problem that underwater monitoring must automatically include longshore and rip current effects which cannot be readily removed from the flow recordings, the more sophisticated methods of cross-spectral analysis of components of orbital motion did not seem warranted. Instead a completely non-spectral approach was adopted where the mean direction of the horizontal component of the forwards and backwards motion of each wave is recorded directly in a method based on Nagata's approach (ref. (5)) of identifying individual waves displaying longcrestedness. It has since been found that the backwards or return component of oscillatory wave motion appears either to tend towards the direction of bed slope at a site or to be more influenced by rip and longshore currents than the forwards or incident component. The fundamental difference then between this instrument and previous simple monitoring techniques is that these incident and return components of oscillatory motion of each wave have been separated and rip current and topographical effects have to some extent been isolated. By reducing the sensitivity of the gauge, as explained later, the bias due to longshore currents has been further reduced. Significant wave periods have been extracted from the records by Thompson's group period method (ref. (8)).

This individual-wave type of analysis does not give the more academic and complete energy-frequency-direction solutions of the spectral techniques (refs. (6) and (7)). It is also only suited to swell and not locally-generated wind-wave conditions, and is obviously limited to water depths at which the sensor can still "feel" the orbital motion of waves. However, the instrument is simple and easy to use and has produced results which should be useful for engineering purposes.

GAUGE - PRINCIPLE OF OPERATION

Fig. 1(a) shows one of the first prototype models of the sensor, which is known as the DOSO - Direction of Swell Orthogonals - Gauge. Basic components of the sensing head are shown schematically in fig. 1(c).

The forwards and backwards components of orbital motion or, as referred to above, the incident and return motions of each wave passing the sensor cause the brush to tilt the pendulum, which is freely mounted in the neoprene diaphragm, until contact is made with the annular resistance coil. The coil has linear characteristics and the voltages recorded at pendulum contact are proportional to flow direction. The container is filled with oil to balance pressure on the diaphragm and to insulate the circuitry and lubricate the contact point. A brush is used as resistance head to eliminate vortex oscillation effects which were encountered during flume testing.

The sensor thus registers direction of flow but not velocity and can be used separately from the recorder (fig. 1(a)) or mounted directly on the recorder container (fig. 1(b)) which in

a)   Remote Mounting   b)   Recorder Mounting

NYLON BRUSH

NEOPRENE DIAPHRAGM

PENDULUM

PLEXY-GLASS CONTAINER

RESISTANCE COIL

OIL FILLING

RECORDER

FILLER PLUG

SECURING BOLT   DIRECTION INDICATOR
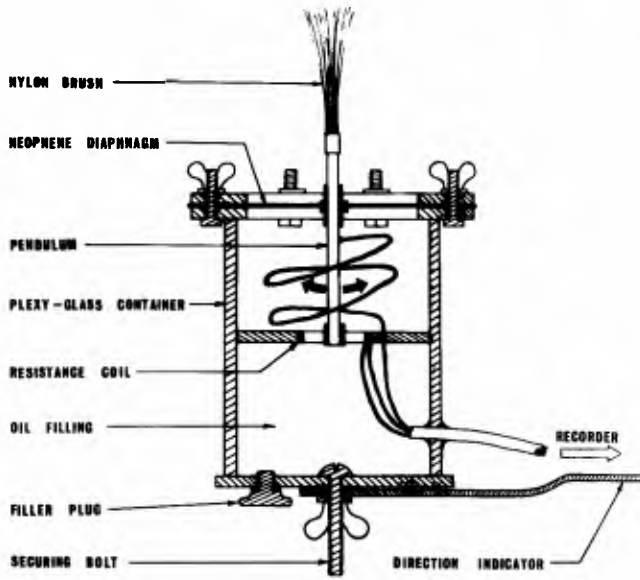
c)   Construction Details

Fig. 1   DOSO Sensing Head

turn is clamped in a tripod on the seabed.   Separate shore-
based recording was used during the development of the sensor
when its action was also monitored remotely by U.W.T.V.   Later
models have been incorporated with a self-contained recorder
operating for one month unattended.

Four types of recording have been attempted.   Firstly,
direct analogue recording of signals shown on the left of
fig. 2.   Due to slow recorder response and clutter of vertical
lines on the record, this technique was replaced with a pulse-
actuated hammer recorder, activated by half-second integrals
of direction record.   The two charts show extracts of records
from a simple unidirectional wave system on the right and a
double system on the middle.   Each dot represents a half-second
of record and in this case the incident motion of each wave is
on the upper side of the record and the return flow on the lower
side, approximately 180° apart.   To the right of each chart
extract is a summation of half-second integrals over half-an-
hour in histogram form.   It can be seen that the mean swell
direction in the righthand recording could have been estimated
merely by inspection of the chart record, whereas in the double
system the histogram is needed to define the two swells clearly.
The slightly narrower return spectrum is the typically subdued
image of the more sensitive and more accurate incident spectrum.
To handle the data automatically, the half-second integrals of
record were also digitised and recorded on magnetic tape.   A
fourth technique, which promises to be the most economical in
cost and power consumption, is the conversion of voltage records
to low-frequency audio tones which can then be recorded on a
slow-playing audio tape recorder.   This produces a complete,
self-contained sensor/recorder system at a cost of under a few
hundred dollars.

The system used at present is shown diagrammatically in
fig. 3.   The signal from the recorder is amplified, split up
into half-second increments (less than half-second records are
ignored) and then transmitted to the pulse-actuated chart
recorder, in addition to being converted to a digital format
for recording on magnetic tape cassettes.   The chart record is
then used for inspection purposes and the cassettes are used
for computer processing.

TEST RESULTS

Tests on the DCSO have thus far been carried out at two
sites near Cape Town shown in fig. 4.   Station 1 near Gordon's
Bay was chosen because of the double refraction of swell enter-
ing the larger bay and then finally the smaller Gordon's Bay,
causing the waves to be well filtered, with a very narrow band
width and displaying longcrestedness.   Station 2, on the other
hand, is directly exposed to the South Atlantic Ocean and is
also prone to rip and longshore currents.   The latter site is
under investigation for a proposed nuclear power station
coolant outfall and back-up data were thus readily available.
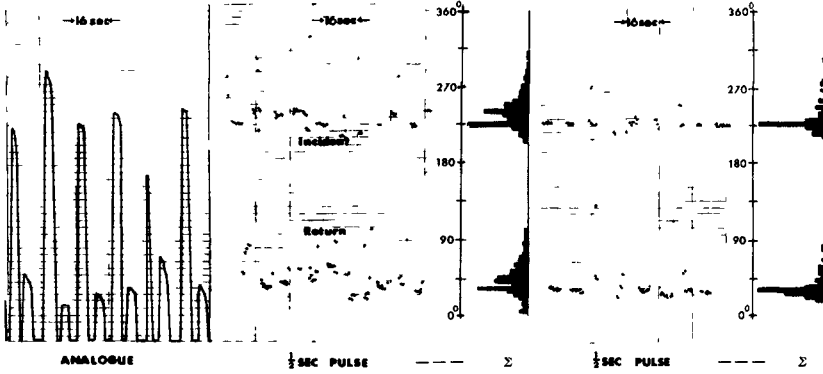
Fig. 2   Data Presentation
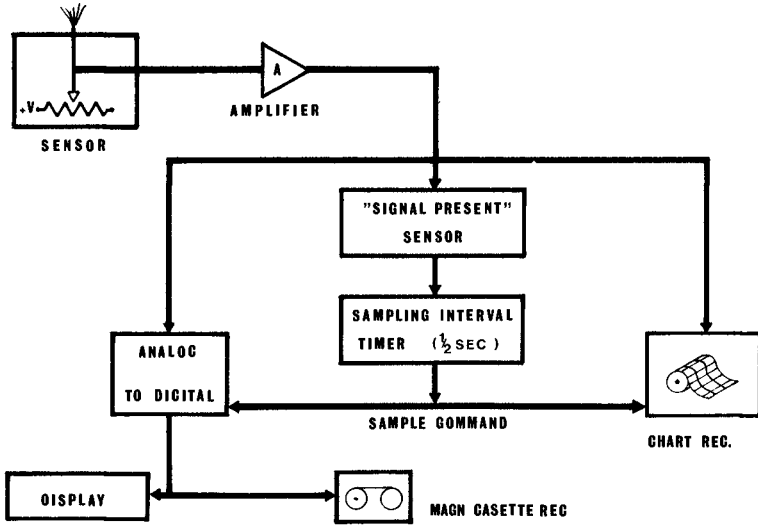
Fig. 3   Recording Technique
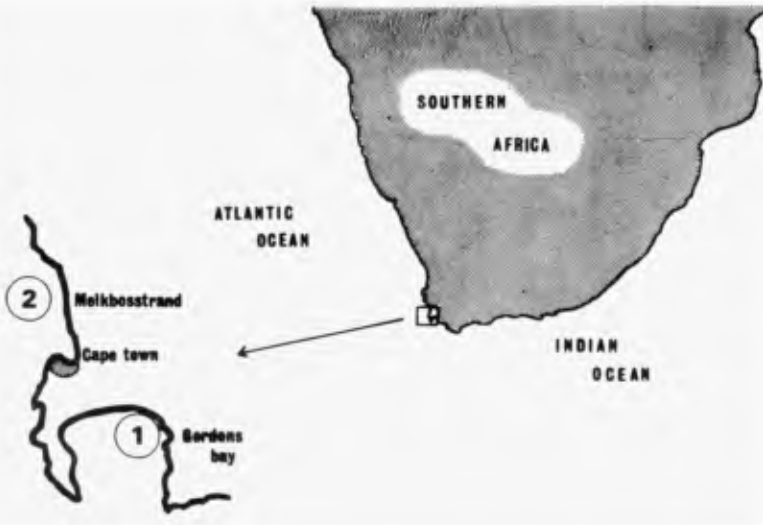
Fig. 4   DOSO Test Sites

After laboratory flume testing the sensor was installed
at Station 1, orientated by a diver using a sighting compass
held at the end of a string attached to the resistance brush.
This technique was used for calibration checks before and
after each recording and was checked later against a geo-
detically fixed base line on the seabed at Station 2.
Results of the two orientation techniques were identical
within sighting accuracy of 1° azimuth.

After a series of repeatability tests at Station 1
which produced very satisfactory results, a directional check
was made in 6,5m water for a significant wave of 0,7m ampli-
tude and 14 sec period.   By varying the lever arm length of
the resistance brush the sensitivity of the sensor can be
varied.   For this test contact velocity was set at 0,1 m/sec.
Wave fronts traced from an aerial photograph are shown as
dotted lines in fig. 5.   The incident spectrum is on the
righthand side of the degree circle and the orthogonal to
the wave front passing through the recording position is shown
as an arrow.   Because of the absence of any noteworthy steady
state currents during the test and because the wave orthogonals
approximately parallel the direction of bed slope at the site,
the incident and return spectra can be seen to be within about
1° of 180° apart.

Further tests were carried out in the Gordon's Bay area
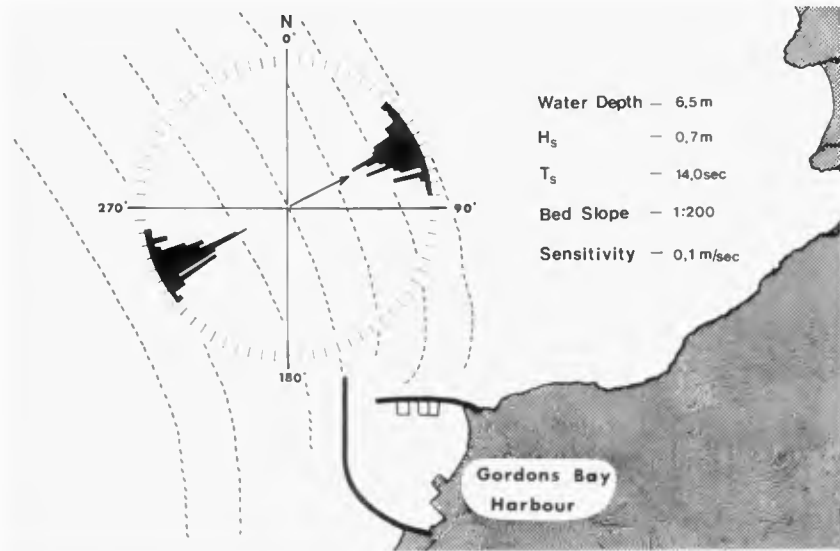
Fig. 5   DOSO Calibration - Station 1
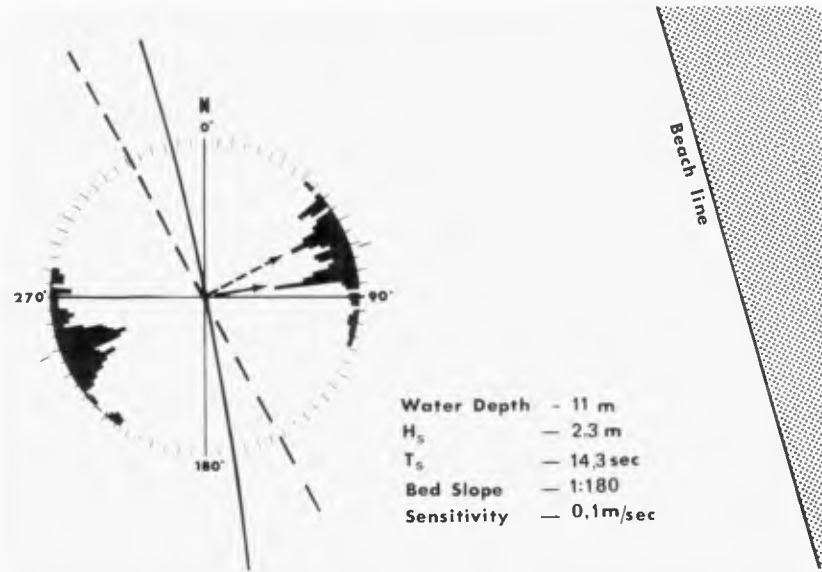
Fig. 6   DOSO Calibration - Station 2

at different water depths and a set of tables was then drawn
up indicating approximate minimum wave heights and periods
which will be recorded for various gauge sensitivity values,
and the unit has been tested down to 30m water depth where
all waves greater than 0,65m amplitude with a 12 sec average
period registered on the recorder.   The width of the spectrum
in this case was a mere 6°.

        Attention was then turned to Station 2, which is, as
mentioned above, exposed to wider deepsea spectra and current
effects.   Sensitivity of the gauge was changed to 0,3 m/sec
contact velocity which is the order of the maximum longshore
current velocities measured at the site.   In this way back-
ground clutter would hopefully be removed from the recording
and as only the higher velocity component of oscillatory
motion would be recorded, the resultant vector of wave and
current velocities combined would be less influenced by the
longshore current component.   The gauge was installed in 11m
of water about 1km offshore and fig. 6 shows a double wave
front traced from aerial photographs superimposed on the
incident and return histograms.   Orthogonals to the wave
fronts are again shown and coincide with the incident peaks.
The return spectrum can again be seen to be a subdued version
of the incident spectrum.   This same record is shown on the
lower half of fig. 7 with a Station 1 record above for com-
parison purposes.
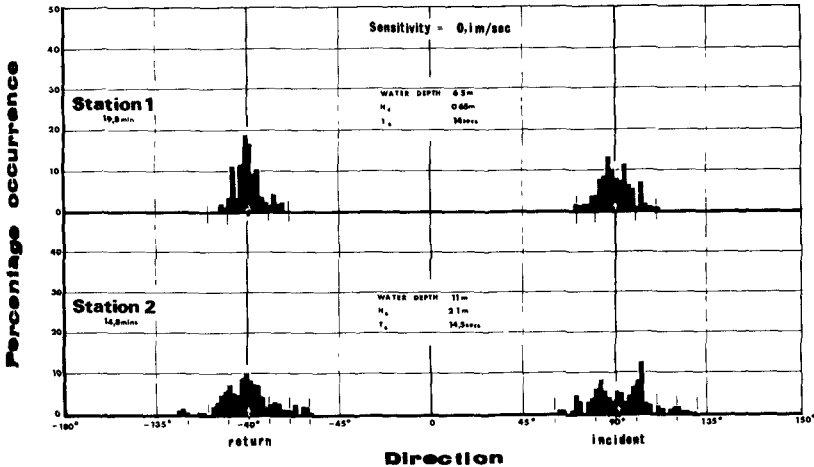
Fig. 7   Comparison of Direction Spectra from the two test sites
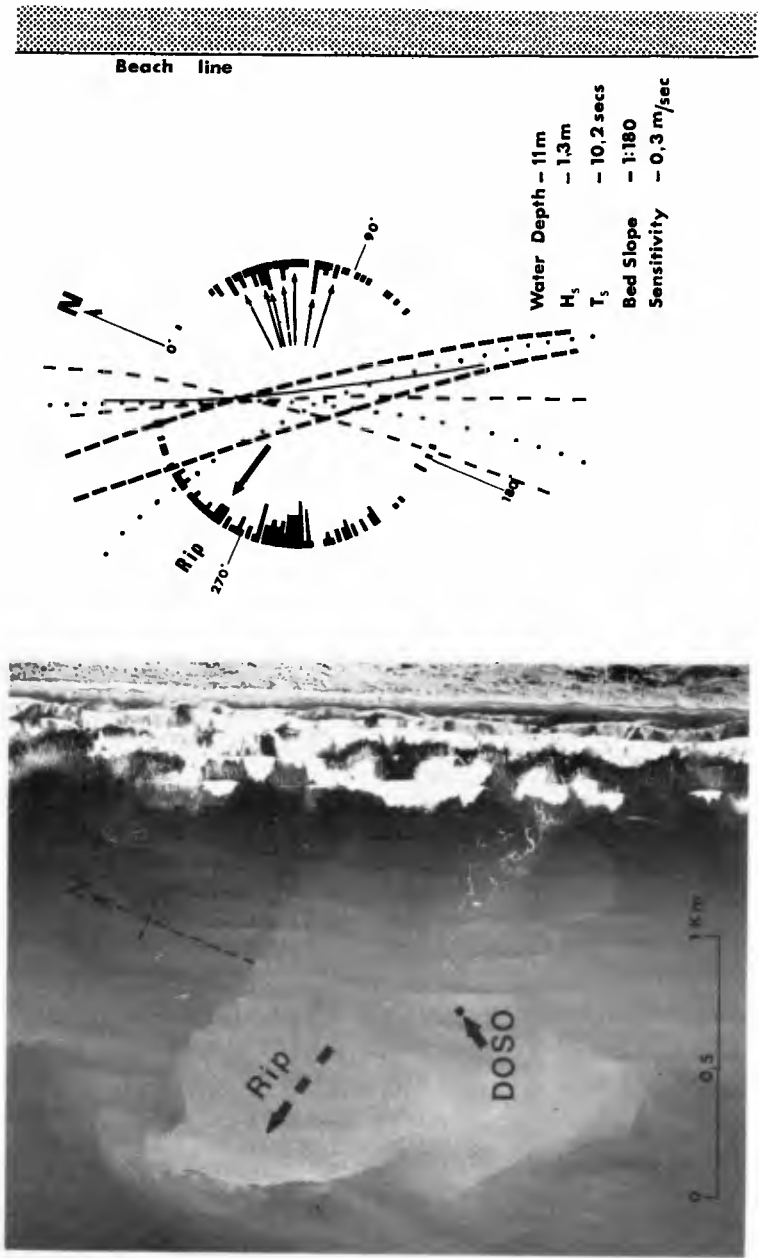
a) Aerial Photo Test Site   b) Wave Traces and Direction Histograms

Fig. 8   Calibration during Complex Wave and Current Conditions

To investigate the effects of rip currents on records, a survey was made during very mixed sea conditions following a storm. Fig. 8(a) is an aerial photograph of Station 2 showing the DOSO position 1km offshore, and a large rip current with an estimated average velocity of about 0,3 m/sec passing through the DOSO position. A series of 18 aerial photographs taken over a ten-minute period were used to try to reproduce the full width of the directional spectrum and traces from the photographs, along with attendant orthogonal arrows, are shown superimposed on the DOSO histograms in fig. 8(b). It can be seen that the return histogram on the left does not reflect the directional spectrum at all and the effect of the rip current is clearly noticeable.

To carry the study one step further, several weather systems were analysed in conjunction with DOSO records. Fig. 9(a) shows in the top lefthand square a double low-pressure system developing to the south-west on the 16th of the month. On the 17th the southerly low had migrated eastwards until it disappeared to the east on the 18th. The northerly low-pressure system remained stationary on the 17th and approached Station 2 from the west on the 18th. The direction spectra plotted at 6-hourly intervals are shown not as percentage occurrence here but as total time recorded over a 30 min period. Incident spectra are again on the right. Recording resolution was 1,5°. Degrees of direction on the horizontal axis reflect the actual recorded direction of water motion; the capital letters below show these directions in terms of source direction of the swell. Spectral analysis of wave height records measured separately produced component frequencies which could be related to the group periods read off the DOSO records. Reading the histograms from the bottom upwards, the large south-westerly peak at 18.00 on the 18th generated by the southerly low-pressure system can be seen to decay at 00.00 on the 19th and disappear altogether shortly afterwards at 06.00. The west/south-westerly peak, i.e., the one on the right, remained longer till 06.00 on the 19th and then degenerated into a mixed westerly sea as the front approached the coast. Rip currents can be seen at 06.00 on the 19th. Significant height ranged from 2,7m to 1,9m during this period and wave periods were from 10 to 13 seconds.

Fig. 9(b) shows the development and decay of a single south-westerly low-pressure system passing eastwards, reflected once again by a two-day delay in records. The histograms at 12-hour intervals indicate a slight drift of about 5° to south as the front passes, with once again a degeneration into a wide band at 12.00 on the 25th. A shore-based radar sighting of wave direction on the morning of the 25th is shown arrowed. Note the variations in direction of the return spectra as opposed to the relative constancy of the incident spectra. Significant wave heights varied from 1,9m to 2,3m, periods from 12 to 15 sec.

As an indicator of sediment transport patterns in the
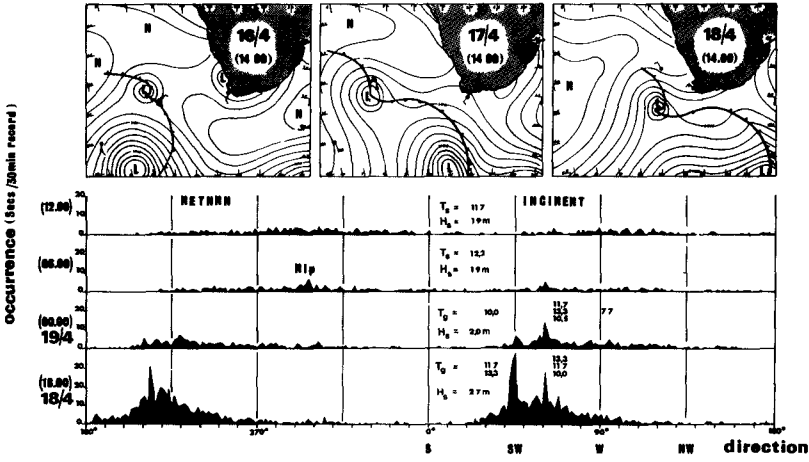
a) Double System
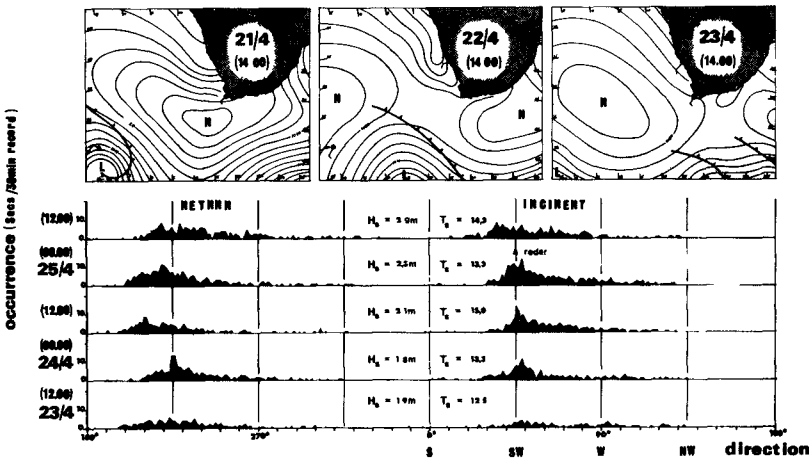
b) Single System

Fig. 9   Wave Direction Spectra at Station 2 related to
Weather Systems

near-shore zone, the sensitivity of the gauge can be set at
the predicted entrainment velocity of the average sediment
particle size at a site.   In this case, for illustration
purposes the gauge was already set at 0,3 m/sec contact
velocity. This could correspond to the linear flow entrain-
ment velocity of say a particle of about 0,8mm diameter.
By plotting directly the actual direction occurrence data
from the DOSO in arbitrary time units, one can draw an
approximate vector history at a point of sediment transport
patterns - fig. 10.   The beach is shown here merely for
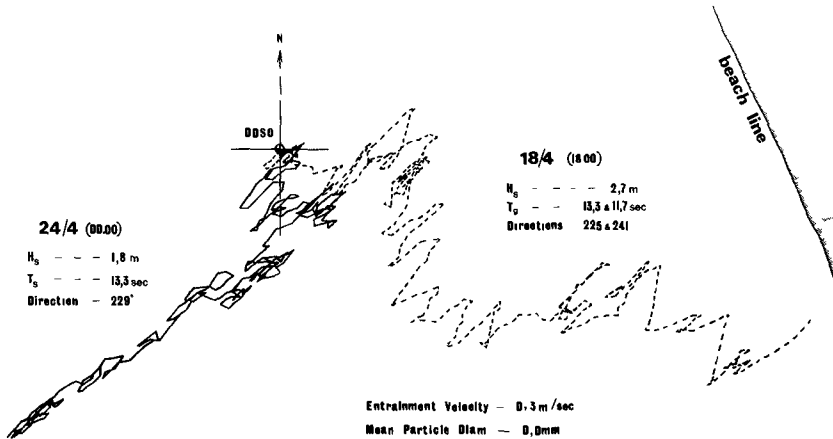
Fig. 10   Representation of littoral transport from DOSO recordings

reference purposes, the scale is meaningless.   One has in-
correctly assumed that the velocities acting on the sediment
are constant above the threshold velocity, thus the picture
indicates merely a trend, but is nevertheless an easily
obtainable control for, say, sediment tracking operations.
The examples here, originating at the DOSO point, are extracts
from the spectra in the two previous diagrams - the double-
peaked system is on the right and the single system on the
left.

CONCLUSION

There is a need for a simple and reliable means of measur-
ing the direction of waves approaching a coastline.   Within
the limitations described above, the technique proposed
appears to fulfil this need by providing the engineer with
an instrument which is simple and easy to use and which has
produced results which can be directly understood and

interpreted in terms of the dominant swell affecting coastal
engineering works.

REFERENCES

1.   Bowden, K.F., and White, R.A.   Measurements of the
     Orbital Velocities of Sea Waves and their Use in Deter-
     mining the Directional Spectrum.   Geophys. J.R. Astr.
     Soc. (1966) 12, 33-54.

2.   Draper, L.   Instruments for Measurement of Wave Height
     and Direction in and around Harbours.   Proc. Instn. Civ.
     Engrs., Vol. 37 (May 1967).

3.   Grace, R.A.   How to Measure Waves.   Ocean Industry (Feb.
     1970).

4.   Cartwright, D.E.   A Brief Survey of Methods for Finding
     the Directions of Sea Waves.   D. & H.A. (Oct. 1961),
     pp. 199 - 201.

5.   Nagata, Y.   The Statistical Properties of Orbital Wave
     Motions and their Application for the Measurement of
     Directional Wave Spectra.   J. Oceanogr. Soc. Japan, 19,
     4 (1964).

6.   Panicker, N.N., and Borgman, L.E.   Directional Spectra
     from Wave Gauge Arrays.   Proc. 12th Conf. on Coastal
     Engr. (1970).

7.   Chakrabarti, S.K.   Wave Train Direction Analysis.   J.
     Waterways and Harbours Div. A.S.C.E. Vol. 97, No. WW4
     (Nov. 1971).

8.   Thompson, W.C.   Period by the Wave-Group Method.   Proc.
     13th Conf. on Coastal Engr. (1972).

CHAPTER 11

CURRENT MEASUREMENTS USING A TILTING SPAR

by

R. L. Lowe, D. L. Inman and C. D. Winant

Scripps Institution of Oceanography, University of California

La Jolla, California 92037

ABSTRACT

The dynamic response of the spar to oscillatory flow has been examined by modeling as well as computer analysis of the non-linear differential equation. Field measurements using the tilting spar have been made. These measurements are compared with theory and with other more direct measurements of the wave field.

The tilting spar has been used to estimate wave direction. These estimates generally agree well with directional estimates made using a pressure sensor array and a two-component current meter.

INTRODUCTION

The tilting spar used in the Shelf and Shore (SAS) System (Lowe, Inman and Brush, 1972) is being used to measure horizontal currents. The SAS System is a general purpose data acquisition system for use in coastal waters. Instrumentation in the upper portion of the spar is used to measure low and high frequency oscillation. Thus, the shelf station (Figure 1) itself acts as a basic sensor.

The tilting spar section of the shelf station consists of a rigid,air filled, filament wound pipe, with a 8.9 cm outside diameter. The spar is coupled through a universal joint to the bottom anchor assembly so that it is free to tilt in any direction in response to horizontal currents. Motion is detected by accelerometers orthogonally mounted in the top section of the station. The signals from the accelerometers are digitized and telemetered to the shore station where they are analyzed.

MODEL STUDY

The shelf station is a forced, damped oscillator and as such will have a resonant frequency. A model study was conducted to determine if this resonant frequency could be observed.

A 1/7th scale model of the station was constructed and tested in the wind and wave channel at Scripps Institution of Oceanography. Displacements of the station were measured photographically and wave height and period were measured using digital wave staffs. The model was driven by waves of periods from 2.0 to 9.0 seconds.
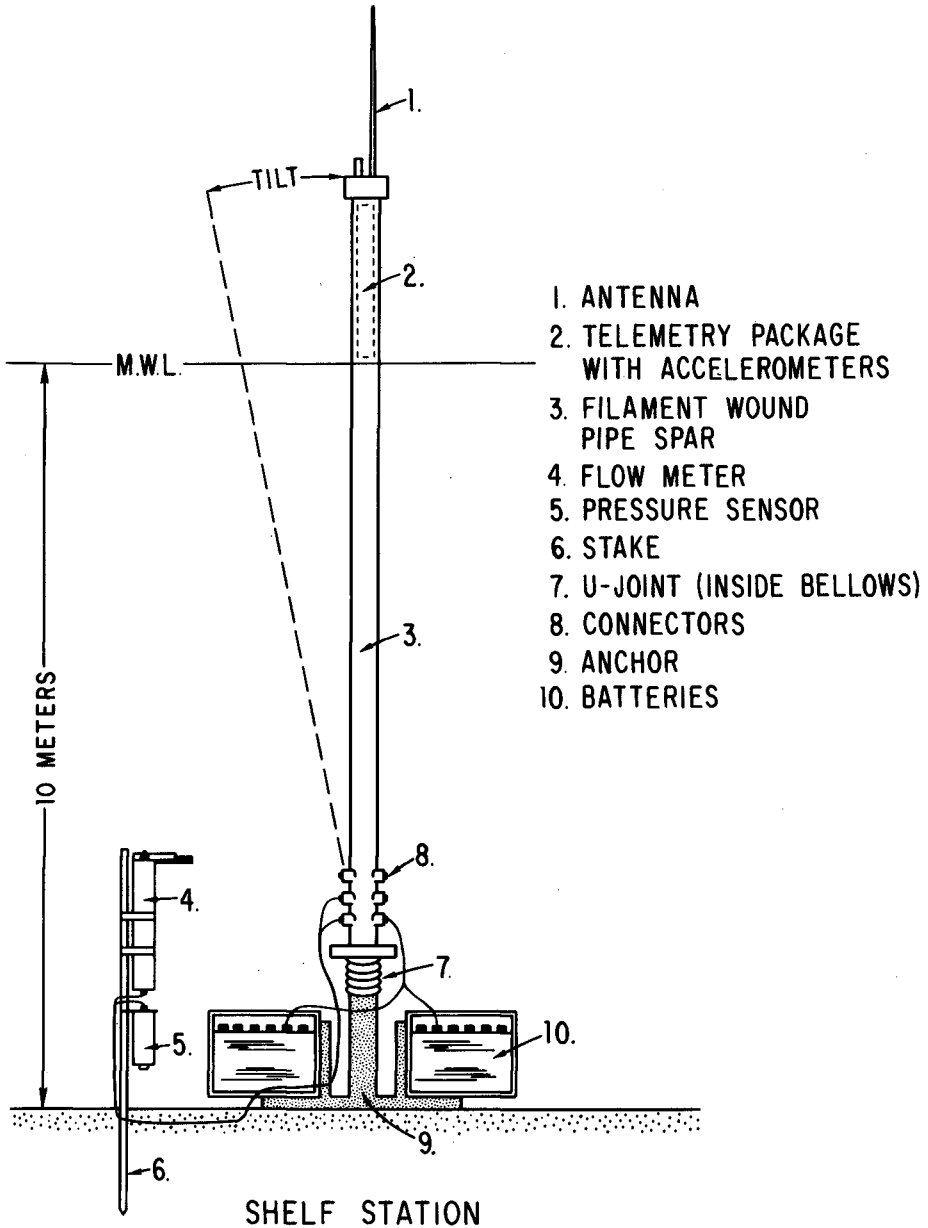
Figure 1. Schematic illustration of the shelf station installation.
   Tilt angle is measured by accelerometers in top portion of the spar.

To obtain a meaningful resonance curve by sweeping wave frequency, requires that the maximum forcing torque, the restoring moment, the drag coefficient, and the coefficient of inertia remain the same for each driving frequency. These are accomplished by adjusting wave height with frequency to maintain a constant Strouhal number*, and by normalizing the displacements to equivalent maximum acceleration and displaced volume.

Figure 2 gives the resonance curve for angular displacement normalized to the resonant frequency (f_1 = 0.16 Hz) for equivalent maximum acceleration and displaced volume. The curve is of the proper shape and should reflect with some accurancy the resonant frequency of the full size spar. However, the model does not accurately reflect the magnitude of the resonance while constant Strouhal conditions preserve the drag coefficient, the smaller orbital velocities under scaled conditions generate drag torques that are only 2% of what is necessary to compare in scale to those of the full scale spar.

ANALYSIS OF EQUATION OF MOTION

The tilting spar's motion can be described by considering the various forces acting on it. Because the spar is firmly anchored, only forces that produce torques about the universal joints are considered. Four moment producing forces are acting on the spar. A buoyant force acting with a moment arm equal to the distance from the U-joint to the center of buoyancy times the sine of the tilt angle (θ). This moment is represented by the first term on the left hand side of equation (1).

Two forces caused by the waves are represented by the second and third terms of equation (1). The first of these forces is the force that would exist on the water particles within the enclosed volume of the submerged spar in the absence of the spar. This force is distributed along the vertical axis of the spar. The second of the wave generated forces is the virtual mass force, caused by a moving body in an accelerating fluid.

A drag force must also be included which is chosen to be proportional to the square of the relative velocity of the water and the spar. This force is also distributed along the vertical axis of the spar and is represented by the fourth term on the left of equation (1).

These moment producing forces must be balanced by inertial forces which accelerate the spar. The term of the right hand side of equation (1) is the moment of the spar itself.

---

* The Strouhal number is defined as $u_m T/D$ where u_m is the maximum orbital velocity, T is the wave period and D is the spar diameter.
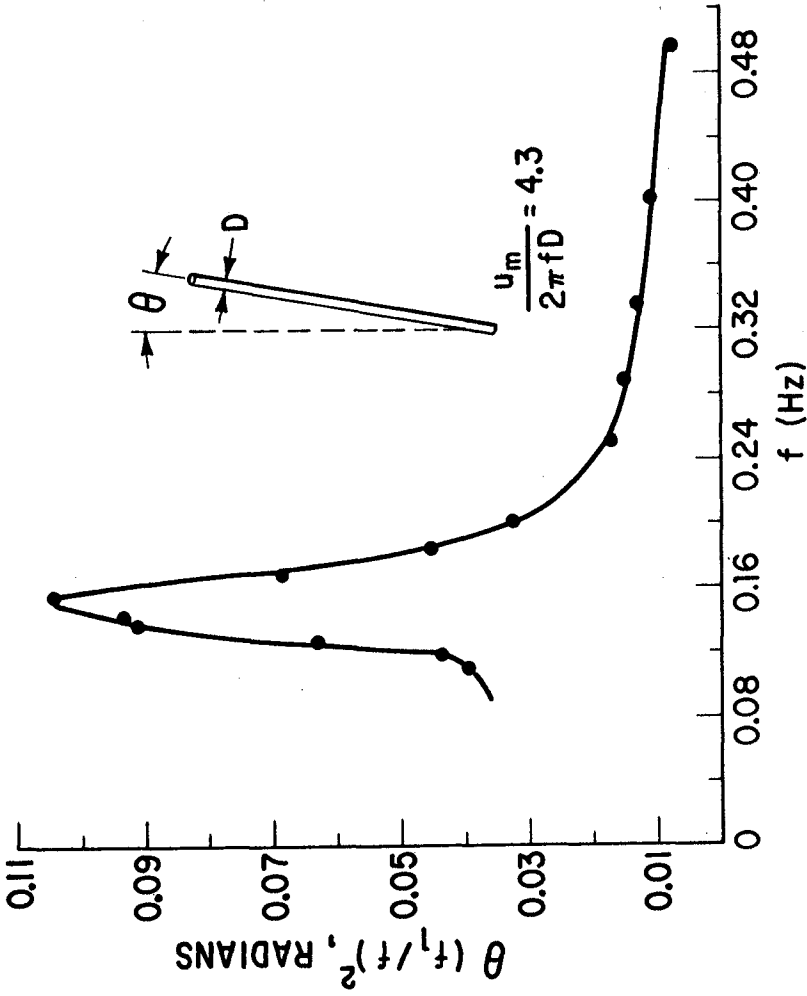
Figure 2. Response curve obtained from 1/7th scale model of spar. Resonance is observed at 0.16 Hz. The magnitude of the resonant peak does not reflect the full scale spar.

$$\sin(\theta)g \, Z_B \, M_B - \rho a \int_{-h}^{0} \pi r^2 \, z \, dz - \rho c_a \int_{-h}^{0} (a - \theta z) \, \pi r^2 \, z \, da$$

$$-1/2 \, c_f \, \rho \int_{-h}^{0} |u - \theta z| \, (u - \theta z) \, 2rz \, dz \;=\; -\ddot{\theta} \, I_s \qquad (1)$$

where: θ is the angle of tilt of the spar measured from the vertical,
g is the acceleration of gravity, Z_B is the distance from the U-joint
to the center of buoyancy, M_B is the net buoyancy, ρ is the density of
sea water, u is the horizontal water particle velocity, a is the hori-
zontal water particle acceleration, r is the radius of the spar, z is
the distance from the U-joint to any point on the vertical axis, h is
the water depth, c_f is the drag coefficient, $\dot{\theta}$ is the angular velocity
of the spar, $\ddot{\theta}$ is the angular acceleration of the spar, I_s is the
moment of inertia of the spar, and c_m is the virtual mass coefficient.

The equation of motion (1) is a non-linear ordinary differential
equation which has been numerically integrated. It was assumed that the
spar did not flex and that the velocity profile under the wave was
independent of depth (i.e., shallow water wave theory applies). θ was
assumed small such that $\sin\theta \approx \theta$. Response of tilt angle versus wave
frequency for various maximum orbital velocities were computed. Figure 3
is a plot of these response curves. It is clear from these curves that
at high velocities (large waves) resonance is not apparent. At low
orbital velocities however, there is a marked resonance occurring at
about 0.1 Hz.

MEASUREMENT OF TILT ANGLE

Two accelerometers orthogonally mounted in the top of the spar
detect the motion caused by the water movement. For waves with periods
ranging from 16 sec to 5 sec, both the acceleration due to gravity and
the horizontal motion must be taken into account. Equation (2) describes
the acceleration along one axis.

$$a(t) \;=\; -g \sin\theta(t) + L \frac{d^2 \left[\sin\theta(t)\right]}{dt^2} \qquad (2)$$

where: a is the measured acceleration, g is the acceleration of gravity,
L is the length of the spar, θ is the angle of tilt from the vertical
in the x, z plane. a(t) can be expressed as:

$$a(t) \;=\; \sum_{n=0}^{k} A_n \, e^{in\Delta\sigma} \qquad (3)$$
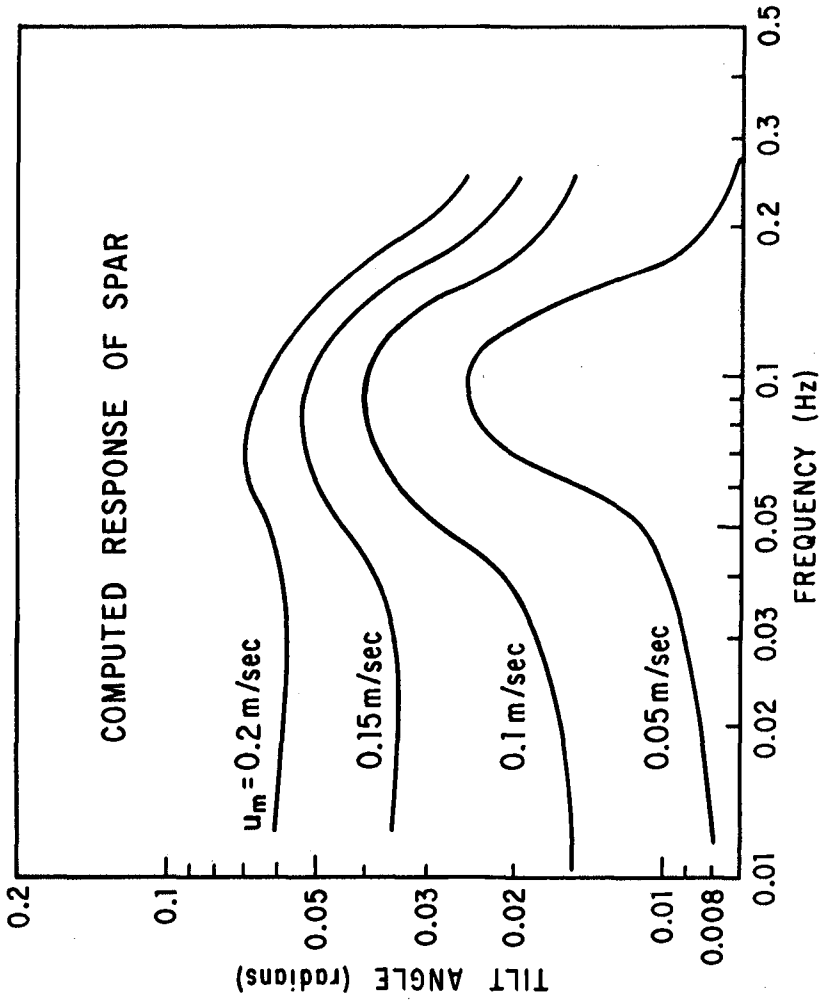
Figure 3. Computed response of the spar for various maximum orbital velocities (U_w). These curves were obtained by integrating equation (1).

where the A_n are the Fourier components, i is $\sqrt{-1}$, k is the number of incremental frequencies, $\Delta\sigma$ is the angular frequency resolution.

Solving equation (2) for each of the coefficients defined in equation (3) gives

$$a(t) = -g\sin\theta_n(t) + L\frac{d^2\left[\sin\theta_n(t)\right]}{dt^2}A_n e^{in\Delta\sigma}$$

let $X_n = \sin\theta_n(t)$

$$\frac{d^2X_n}{dt^2} - \frac{g}{L}X_n = \frac{A_n}{L}e^{i\Delta\sigma t}$$

The general solution of this differential equation is

$$X_n = B_n e^{i(n\Delta\sigma t + \phi)}$$

where ϕ is an arbitrary phase angle

$$\frac{d^2X}{dt^2} = -B_n(n\Delta\sigma)e^{i(n\Delta\sigma t + \phi)}$$

substituting for X and $\frac{d^2X}{dt^2}$ gives

$$-B_n(n\Delta\sigma)e^{i(n\Delta\sigma t + \phi)} - \frac{g}{L}B_n e^{i(n\Delta\sigma t + \phi)} = \frac{A_n}{L}e^{in\Delta\sigma t}$$

dividing them by $e^{in\Delta\sigma t}$ and replacing $e^{-i\phi}$ with $(\cos\phi - i\sin\phi)$.

$$-B_n(n\Delta\sigma)^2 - \frac{g}{L}B_n = \frac{A_n}{L}(\cos\phi - i\sin\phi)$$

ϕ can be eliminated by noting $i \sin\phi = 0$; $\phi = 0$. Solving for B_n gives

$$B_n = - \frac{A_n}{g + L(n\Delta\omega)^2}$$

We can now write $\sin\theta_n (t)$ in terms of the Fourier coefficient of $a(t)$:

$$\sin\theta (t) = \sum_{n=0}^{k} - \frac{A_n}{g + L(n\Delta\sigma)^2} e^{in\Delta\sigma t}$$

With the above procedure the spectra and the time series of the angle of tilt can be obtained from the accelerometer data.

Figure 4 is a plot of the position (in the x-y plane) of the shelf station as a function of time. The predominant motion is on-offshore which is caused by the swell and wind driven wave. However, a longshore motion is also present and has a period on the order of 60 seconds as illustrated in Figure 5.

FIELD MEASUREMENTS

Field data was collected in order to evaluate the computer model outlined above and to determine if the tilt of the spar can be used to determine the direction of wave propagation. The field installation consisted of a line array of four bottom mounted pressure sensors, orthogonally mounted accelerometers in the top of the spar, and a two-component electromagnetic current meter mounted at the base of the station. The axis of the accelerometers were aligned to be 45° with respect to the line array. The current meter was mounted to measure horizontal currents in the on-offshore longshore direction. Data from the sensors was digitized and transmitted to the shore station where it was recorded digitally. A data run consists of 4096 samples from each of the sensors at a rate of 4 samples per second. The site of the installation was off Torrey Pines Beach approximately 3 kilometers north of Scripps Pier in 10 meters of water. These digital data were analyzed using Fast Fourier Transform techniques. Tilt angles were computed as outlines above. Surface wave velocities were computed from the pressure records using linear wave theory. The pressure sensor was located at the base of the spar.

Results from 16 data runs are summarized in Figure 6. Of the four wave periods examined reasonably good agreement was found for wave periods of less than 10 seconds. Poor agreement was found for long period waves. The model predicted tilt angles that are too low by about
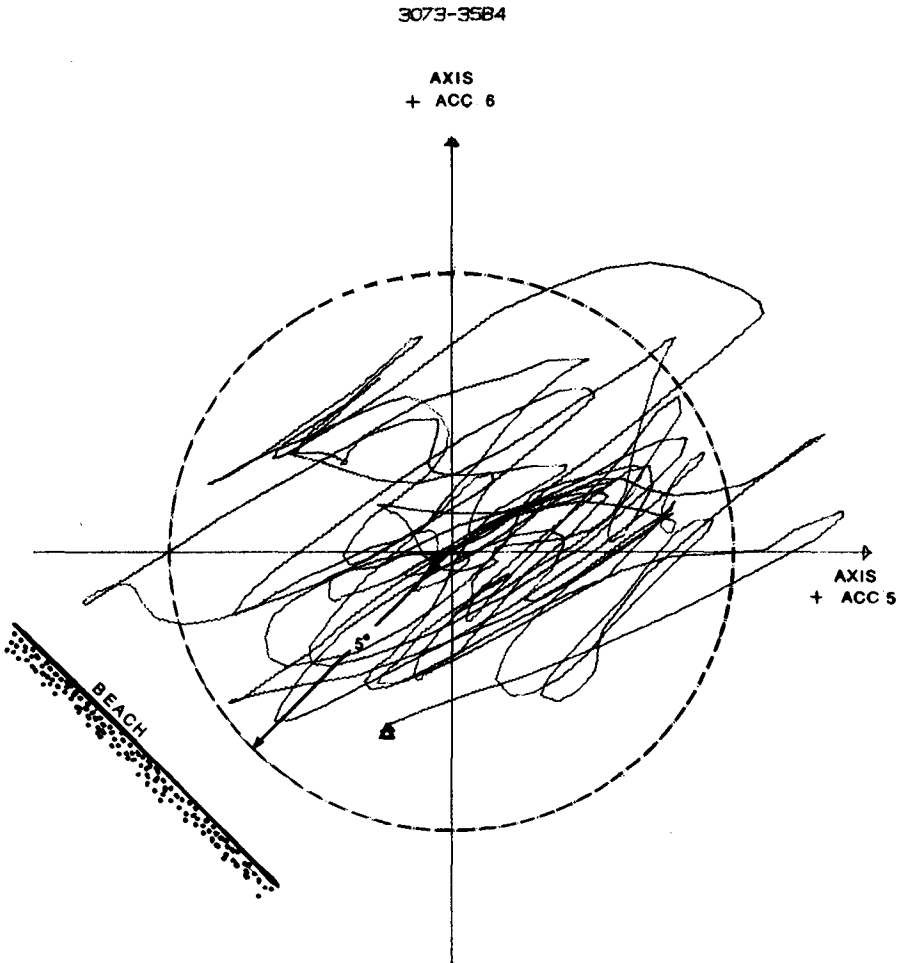
Figure 4. Angle of tilt of the shelf station as derived from the accelerometer data. The predominant on-offshore motion is caused by wind waves and swell. The 5⁰ tilt grid represents a displacement of 0.9 meters from the vertical. Unfiltered loci of motion for 256 seconds of data is represented in this plot. Shelf station was in 10 meters of water on B Range of SIO.
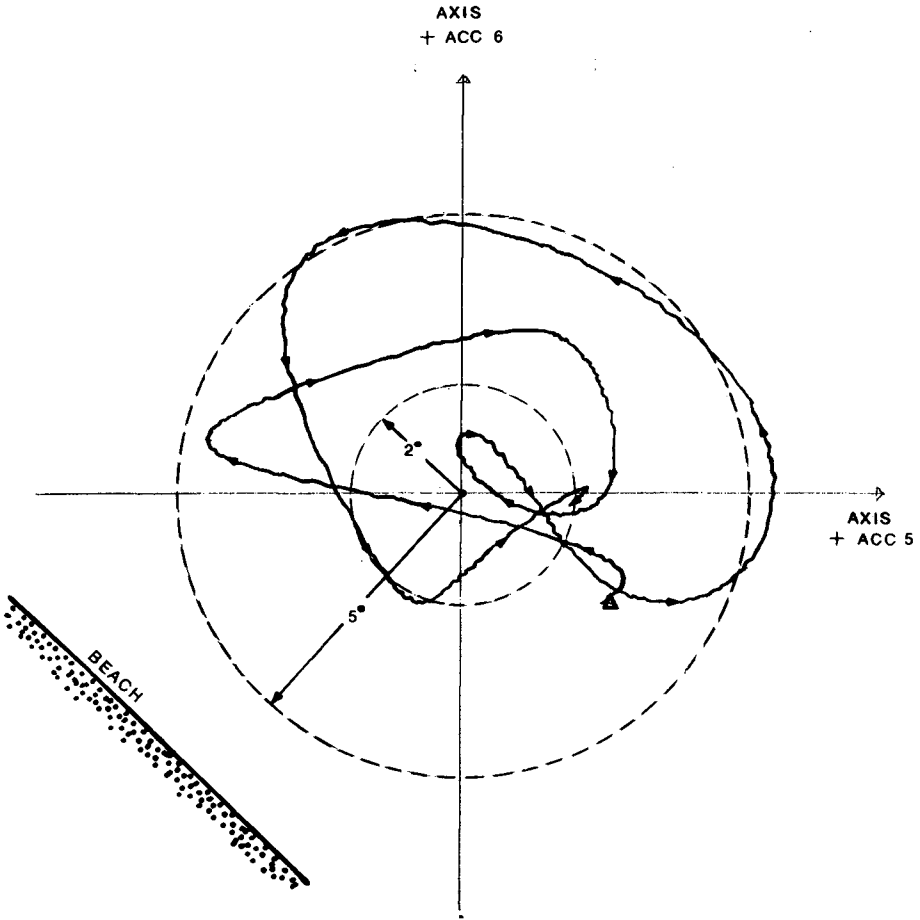
Figure 5. Angle of tilt of the shelf station with the wind waves and
swell removed using inverse FFT filter. Only oscillations with periods
greater than 40 seconds are shown. This motion is in general agreement
with edge wave theory.
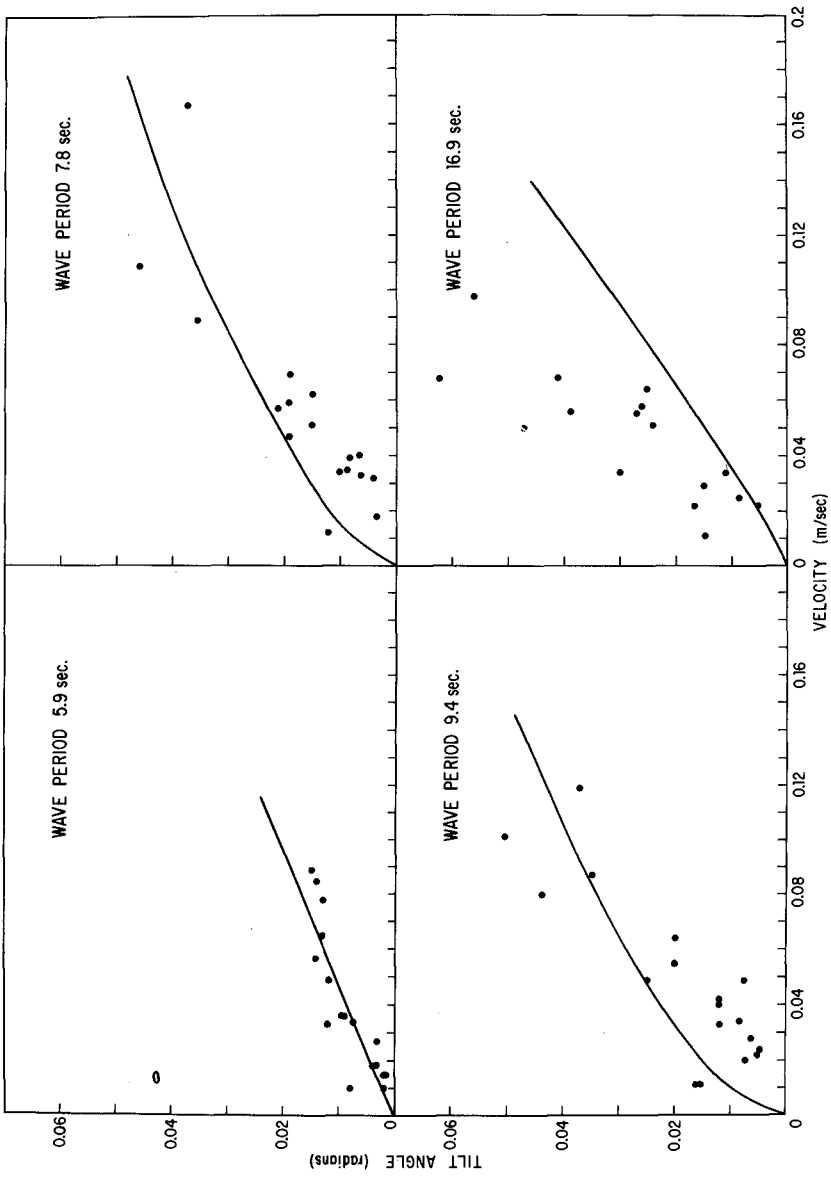
Figure 6. Comparison between predicted tilt angle and measured tilt angle versus velocity for four wave periods. Tilt angle measured using accelerometers. Velocity computed from pressure spectra using linear wave theory.

a factor of two for 17 second waves. The discrepancy is probably caused
by the fact that the model treats the drag and inertia coefficients as
constants independent of the velocities and wave period. The work of
Keulegan and Carpenter (1956) has shown that both the drag coefficient
(c_f) and inertia coefficient (c_m) depend on the Strouhal number. At
values of the Strouhal number less than 4, the drag coefficient is
approximately one and the inertia coefficient approximately two, which
are the values used in the computer model. For period parameter values
close to 15, c_f increases to approximately two and c_m decreases to less
than one

For the long period waves the period parameter does fall into the
range where both c_f and c_m can no longer be treated as constants.
It would seem therefore, that to predict the current from tilt angle for
these long period waves, the computer model must be changed to include
variations in these coefficients.

Data from the pressure sensor array was used to determine the
direction spectra of the wind waves and swell. The techniques used are
described by Pawka (1974). Direction was also obtained using the electro-
magnetic current meter and a pressure sensor using the techniques devel-
oped by Bowden and White (1966). Finally, the direction is estimated
using the orthogonal accelerometers.

The analysis techniques for the accelerometer is simply to FFT
each accelerometer channel to obtain the spectra values. The estimate
of the direction for each frequency band of interest is the vector defined
by this orthogonal set of data spectral values.

The comparison of these three methods for obtaining wave direction
is contained in Table 1. In general, the three methods agree to within
$\pm 5^\circ$. When large differences in directional estimates occur it is most
likely caused by bimodal direction spectra as indicated by the parameter
$P(a_0)$. $P(a_0)$ is a measure of the fit to a unimodal spectra for the array.
The smaller $P(a_0)$, the more closely the measure spectral can be repre-
sented by a single direction.

RESULTS AND CONCLUSIONS

The main incentive to study the motions of the tilting spar was
to ascertain the spectra of the currents driving the system. The ana-
lytical expression describing the dynamics of the spar show reasonably
good agreement with field measurements for wave periods of less than 10
seconds. It is believed that if the variations in the drag and inertial
coefficients are included in the equation, agreement over a wider range
of frequency can be obtained.

The generally good agreement obtained between the directional
estimates obtained from the spar and the pressure sensor array suggests
it can be used in obtaining wave climate. This is based not on the
accurancy of the results, but on the reliability of the instrumentation
system. In the more than three years the SAS system has been operating,

Table 1.   Comparisons of directional information for some November runs.
The periods and E_p were obtained from pressure sensor data. Also shown
are the angles obtained from current meter data and accelerometer data.

DIRECTION COMPARISONS

RUN	PEAK	PERIOD	$E_p(cm^2)$	ARRAY α_0	$P(\alpha_0)$	CURRENT METER α	ACCELEROMETER α_a
SAS 1-30 Nov 73-01	1	8.8	344	0^0	0.7	2^0S	2^0N
	2	7.4	146	2^0N	5.1	1^0N	3^0N
SAS 1-30 Nov 73-02	1	12.3	118	8^0S	13.0	13^0S	11^0S
	2	7.4	49.8	1^0N	6.8	2^0N	7^0S
SAS 1-04 Nov 73-02	2	14.2	62.3	18^0S	4.3	23^0A	16^0S
	1	6.0	149	1^0S	24.9	11^0S	4^0S
SAS 1-05 Nov 73-02	1	16.8	183	17^0S	3.2	18^0S	15^0S
	2	6.0	156	4^0N	43.1	14^0N	6^0N
SAS 1-08 Nov 73-01	2	14.2	99.2	24^0S	0.6	26^0S	23^0S
	1	9.8	104	2^0N	1.5	4^0S	4^0S
SAS 1-08 Nov 73-03	2	14.2	39.2	25^0S	0.7	27^0S	27^0S
	1	9.8	202	4^0S	15.5	10^0S	9^0S
SAS 1-09 Nov 73-01	1	14.2	85.5	18^0S	2.9	20^0S	21^0S
	2	8.1	60.4	8^0S	53.2	6^0S	9^0S
SAS 1-09 Nov 73-03	2	16.8	42.5	24^0S	0.6	25^0S	21^0S
	1	8.1	60.4	8^0S	53.2	6^0S	9^0S
SAS 1-10 Nov 73-01	2	14.2	67.5	24^0S	0.8	25^0S	16^0S
	1	9.8	284	4^0S	14.0	4^0S	5^0S
SAS 1-10 Nov 73-02	1	10.9	310	8^0S	7.5	16^0S	16^0S
SAS 1-10 Nov 73-04	2	14.2	53.9	24^0S	1.3	27^0S	21^0S
	1	9.8	238	16^0S	18.8	17^0S	15^0S
SAS 1-11 Nov 73-03	2	14.2	26.3	27^0S	0.9	28^0S	21^0S
	1	9.8	370	11^0S	28.2	17^0S	14^0S
SAS 1-11 Nov 73-04	1	8.8	225	26^0S	59.7	17^0S	16^0S
SAS 1-12 Nov 73-01	2	14.2	22.3	25^0S	0.7	28^0S	23^0S
	1	9.8	288	11^0S	32.5	11^0S	10^0S

Definition of Terms:

Peak: In a multi-modal energy spectra the peaks are ordered with
            respect to their energies.

Period: The modal period for the defined peak of the data of all 4
            sensors.

E_p: The energy contained in a spectra peak at 10 m depth, average
            of the data of all 4 sensors.

α_o: The direction of the best fit to a single wave train for the
            4 sensor array measured from the vertical to the array. The
            fitting technique is based on the minimum value of $P(\alpha_o)$.

α: The angle where the directional spectrum obtained from orbital
            velocity records reaches a maximum, measure from the normal
            to the beach, but corrected to the alignment of the array.

α_a: The angle obtained from accelerometer data.

the accelerometer has proven to be the most reliable sensor. The station
has proven its integrity by surviving extreme storm conditions. It has
proven its ability to remain on station while retaining a size and weight
compatible with small boat deployment.

ACKNOWLEDGEMENTS

REFERENCES

Bowden, K. F. and R. A. White, 1966, "Measurement of the orbital velocities
        of sea waves and their use in determining the directional spectrum",
        Geophysical Jour. Roy. Astronomical Soc., vol 12, p. 33-54.

Keulegan, G. H. and L. H. Carpenter, 1956, "Forces on cylinders and plates
        in an oscillating fluid", National Bureau of Standards, Report 4821,
        31 pp., 28 figs.

Lowe, R. L., D. L. Inman and B. M. Brush, 1973, "Simultaneous data system
        for instrumenting the shelf", 13th International Conf. Coastal
        Eng., Amer. Soc. Civil Eng., p. 95-112.

Pawka, S. S., 1974, "Study of wave climate in nearshore waters", Proc.
        in the International Symposium on Ocean Wave Management and
        Eng., vol 1, p. 745-760.

CHAPTER 12

BASIC SYSTEMS OF WIND WAVE FIELD

By Yu.M.Krylov[1], S.S.Strekalov[2], V.Ph.Tsyploukhin[3]

The study of wind waves is usually carried out in the following manner. At the first moment a homogenous wind field with the constant speed directed from the shore to the basin is occured over the water surface restricted by a straight shore line. It is required to calculate statistic wave characteristics as functions of time and distance from the shore. When solving the problem in such a way the explorers [1-6] usually came to a conclusion of the system development of gravitational waves with a main energy maximum the amplitude and period of which rise in process developing from small magnitudes to limiting values.

Some explorers noted that the two-or three-wave systems under the conditions of constant wind are available. The first results of this theory were obtained by L.Ph. Tytov. In studies of stereophotographs of sea waves he noted and discribed quantitatively two types of waves: "prevailing" and "large". [7]. It is possible to show that the first type of waves has a phase speed that is less than wind speed, and the second one is equal to wind speed. At a later time G.Neumann [6] generalizing results of ocean observations has come to the conclusion that under the action of constant wind three "specific" wave systems which have phase speeds less, equal and 1.2 more than the speed of wind are developed. However, Tytov's and Neumann's results didn't receive a progress, and later on they were substituted by the conception of continuous wave spectrum with one energy maximum [3-6]. Nevertheless, the opinions of availability of two-or three-wave systems as a typical feature of wind rough sea [8,9] were published in the press. Spectra with two or three maxima were obtained by some explorers, but whether particular emphasis was not placed upon this phenomenon by them, or they didn't explain this correctly considering that the second maximum is condi-

[1] Prof., Dr.Phys.-Math.Sc., State Research Project Inst.of Sea Transport, USSR, Moscow.

[2,3] Scientific worker, M.Sc.Tech., State Research Project Inst.of Sea Transport, USSR, Moscow.

tioned by non-linear effects [12,13].

In practice in deep-water basin under the action of constant wind two main, but not one gravitational wave systems having substantial distinctive features are developed regularly. Under natural conditions this phenomenon appears particularly in water-basin at small distance from the shore with gentle off-shore wind when wave lengths of two main systems difference several times, and the interferences came from the neighbour basin areas are practically absent. In Fig.1 examples of frequency spectra and oscillogram models of waves providing visual proof of the availability of two vibratory processes are shown. On the spectra two maxima with phase speeds equal and less than wind speed are clearly defined. A system with phase speed equal to wind speed is called as a resonance one, and a system with phase speed less than wind speed is called as a pre-resonance one. In Fig.2 the relationships of main parameters of two systems where C_i/v and $g\sigma'_i/v^2$ are independent on gx/v^2 are shown, and where

C_i – system phase speed

σ'_i – root-mean-square deviation of rough sea elevation

V – wind speed on upper boundary of water layer

g – gravity acceleration

x – distance to leeward shore

Value $i=1$ complies with the resonance system, and $i=2$ with the pre-resonance one. Observation data and laboratory measurements were obtained by means of statistic analysis of wave recordings. Phase speed was determined from the position of the energy maximum on the frequency scale, and the root-mean-square deviation σ'_i from the area under the spectral density curve of each system. Maximum relative errors of measurements of dimensionless parameters are not more than $\pm 25\%$.

Data from Fig.2 points out to the following regularities of observed systems. The phase speed of resonance system is equal to wind speed, and the pre-resonance speed rises rapidly when moving away from the shore and reaches the 0.8-0.9 limit of wind speed approximately. The pre-resonance system reaches an energy saturation rather rapidly, and the resonance one continues to develop. At an early stage of process development the energy of pre-resonance system is more than the energy of resonance one, and vice versa at the later stages. A resonance system appears at some distance from the shore (the more distance, the more speed of wind), and reaches energy saturation at a rather great distances from the shore (under condition of neces-

sary duration of wind action). At the main stage the
energies of both systems are increased in direct propor-
tion to the distance from the shore. It is rather note-
worthy that pre-resonance system doesn't occur with the
equation $gx/v^2=0$, as it was known earlier, but with the
value $gx_0/v^2>0$ where x_0 - critical distance from lee-
ward shore independing on physical characteristics of
turbulent viscous underlayer of air flow when transiting
from the land to the sea. This new regularity is shown
in Fig.2 with dashed lines for various parameter values
of gx_0/v^2.

Physical cause of resonance system development con-
sists in such phenomenon that among the whirlwinds occu -
ring in turbulent frontier layer and carried by the wind
there are always such ones the horizontal dimensions of
which are close to the length of gravitational waves
spreading at a speed of wind. These whirlwinds are exact-
ly responsible for the initiation and development of a
resonance system. Physics of a pre-resonance system de-
velopment was studied by many explorers [1-3, 10]. The
pre-resonance system occurrence is due to the whirlwind
movements in turbulent viscous under-layer of wind flow.
This system is developed in such a manner that the indu-
ced field of pressure in the air flow gives the growth of
waves on the reverse communication scheme until the sup-
plied energy to be balanced by a dissipation.

Apart from two main systems the third, a super-reso-
nance one with the phase speed more than wind speed is de-
veloped. Physical cause of initiation and development of
this system consists in non-linear interaction of two
main systems. According to Phyllips' a frequency of wave
interaction (the amplitude of which is linearly increa-
sing with time) is equal to doubled lesser frequency mi-
nus another one [10]. When taking as $C_2=0.8$ v in accor-
dance with Fig.2 $C_3=1.3$ v may be obtained for super-re-
sonance system which is in agreement with the Neumann's
results [6]. An energy of the third system is commensu-
rable with the energy of both another systems at the la-
ter stages of their process development. In consequence
of three systems availability long-period waves with dif-
ferential frequencies are developed as it is confirmed by
the spectral analysis data [5].

The given facts and considerations may explain the
rough sea process of the wind waves in a new fashion from
the united point of view. At a laboratory, lakes and ponds
one system is dominant   (pre-resonance); in the seas
two systems (resonance and pre-resonance), in the oceans-
-three systems (super-resonance, resonance and pre-reso-
nance) [20].

Besides, the studies of wave pressures and loads of
irregular standing waves upon sea breakwater of vertical

type in full-scale conditions were conducted.

In the Soviet Union as it was reported earlier [22] a hydraulic research station constructed at the head of sea breakwater of vertical type is in operation.

Synchronous recording of sea level and wave pressure on various levels at a breakwater and also wave parameters in approaches to the structure are provided by measuring procedures.

Oscillogram models of waves and wave loads fixed on a wave recording buoy (I) and at a breakwater (II) are presented in Fig.3. On the oscillograms there are the following recordings: (1 and 3) fluctuations of sea level recorded by electrocontact wave-recorder on a buoy and at a breakwater respectively; (2.4-10) wave pressure fluctuations measured by pressure transmitter on a buoy at 2.8 m depth and at a breakwater of +1.3; +0.4; -0.6; -2.9; -7.3; -9.5 and-11.2 elevations respectively; time marks were equal 1 sec.

In Fig.3 the data was initial for computer calculations of the total wave load at a breakwater (Fig.4).

In Fig.4 the values R_i^+ and R_i^- are of positive and negative loads in wave crest and trough phases respectively, and R_i is a"range" of wave load.

Materials of observed measurements allowed for obtaining of new data on probability structure of wave field pressure and wave loads at a breakwater [21].

On the basis of observed wave analysis and wave pressure recordings at a vertical type breakwater it is shown that the rough surface of sea at a breakwater may be represented in form of the limited number totality of the frequency spectrum components (no more than 3-5). On the frequency scale these components comply with energy maxima in wind wave spectrum. Squares of amplitude's components are proportional to their dispersions, and in this case the sum of dispersions is equal to dispersion of the total process.

Changing continious frequency spectrum of sea level at a breakwater from e (μ) to discrete spectrum with frequencies μ_i of main energy-carrier maxima in the spectrum, and appropriate dispersions σ_i^2, where

$$\sigma_3^2 = \sum_i \sigma_i^2 \qquad (1)$$

is a dispersion of a total dispersion process of water level at a breakwater, and an energy-carrier interval of the i-component is characterized by (μ_i', μ_i'').

Such scheme for three components as illustration is showed in Fig.5.

Dispersion of wave load for i - component in linear approximation will be given as [23]

$$(\sigma_R^2)_i = 2 g \rho \int_{\mu_i'}^{\mu_i''} e(\mu) \frac{th^2 K_i H}{K_i^2} d\mu \qquad (2)$$

where K_i - wave number related to the frequency of energy maximum of i-component by equation

$$\mu_i^2 = g K_i \, th \, K_i H \qquad (3)$$

(H-depth at a breakwater, g - water density).

The total load on a breakwater is formed as a result of effect upon it by i-components (i=3-5) of wave field.

So, the dispersion of load to be

$$\sigma_R^2 = \frac{4(g\rho)^2}{x^2} \sum_i \frac{(\sigma_3^2)_i}{K_i^2} th^2 K_i H \qquad (4)$$

where σ_3^2 - dispersion of sea level for i-component connected with its frequency spectrum by equation

$$(\sigma_3^2)_i = \frac{1}{g\rho} \int_{\mu_i'}^{\mu_i''} e(\mu) d\mu \qquad (5)$$

(x^2 - wave reflection coefficient from breakwater).

The given method of wave load determination was used for calculation of maximum wave load upon, the breakwater in the port of Sheskharis on given measured parameters of wave frequency spectrum at a breakwater.

The calculations were carried out for 11 instances at heights of $h_{1\%}$=0.9-2.2 m, $\overline{\tau}$=4.4-7.8 sec and relative depths of H/λ =0.17-0.45.

For given wave parameters and relative depths the rated values of positive and negative loads of one per cent security accounts for 4.6-15.8 t/m.

A correlation between rated loads and measured ones shows that for mentioned wave parameters and relative depths the rated loads exceed the measured ones both in case of wave crests coming to a breakwater, and troughs. In some instances the exceeding reaches 15-18 per cent.

Adequate agreement between the rated and measured wave load values indicates that the probability sampling of theoretical model which may be used in engineering practice was made correctly.
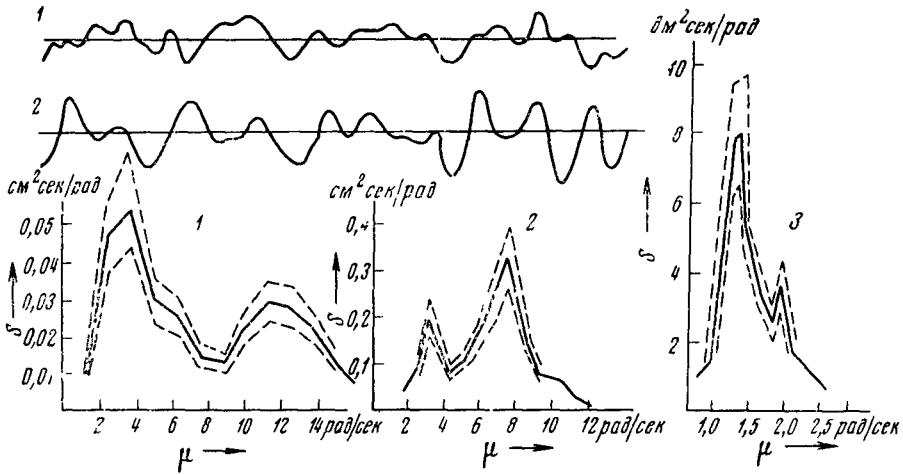
Fig.1.   Oscillogram models of waves and
         frequency spectra $e(\mu)$ for the
         following stages of wind wave deve-
         lopment:

1 - in an initial stage [20] ; 2 - in an
early stage [20] ; 3 - in the later stage
[18].
Confidence limit of 90% probability are
showed by dashed line
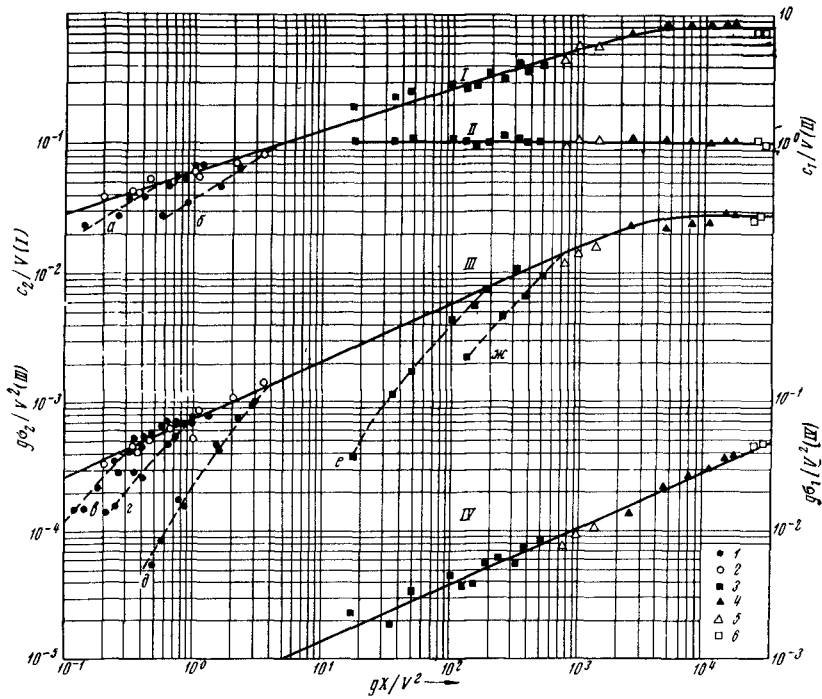
Fig. 2.   Relationships C_2/V(I), C_1/V(II),
$g\delta_2^2/V^2$(III), $g\delta_1/V^2$(IV) on gx/V^2 obtai-
ned from laboratory data:
          1- [15]; 2- [14];
from observation data:
          3- [16,17]; 4- [10]; 5,6- [18,19].
The initial stages of wave growth in
gx_o/V^2 parameters of pre-resonance sys-
tem are showed by dashed line;

a — gx_o/V^2=6.9x10^{-3}, V=9 m/sec.;

б — 7.6x10^{-2}, 6 m/sec.;

в — 6.5x10^{-4}, 15 m/sec.;

г — 6.9x10^{-5}, 9 m/sec.;

д — 7.6x10^{-2}, 6 m/sec.;

е — 7.7,   3.2 m/sec.;

ж — 3.7x10, 2 m/sec.
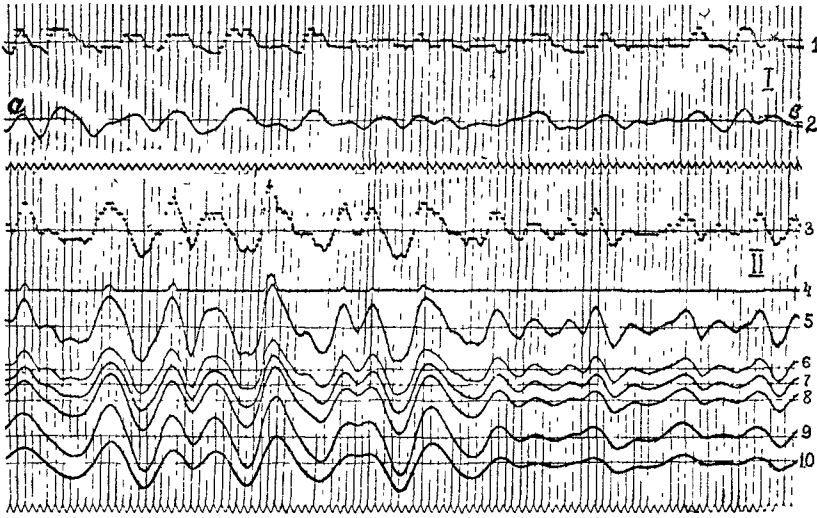
Fig. 3. Oscillogram models of waves and wave loads
at breakwater (II) and in approaches to it (I)
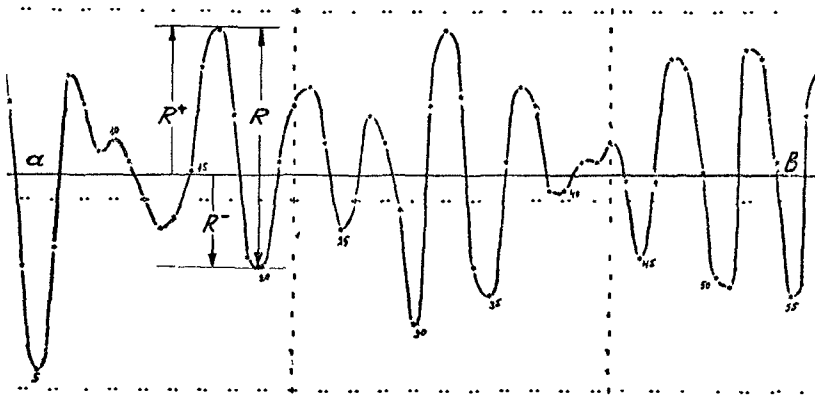
Fig. 4. Scheme of changes of measured total wave
loads at breakwater
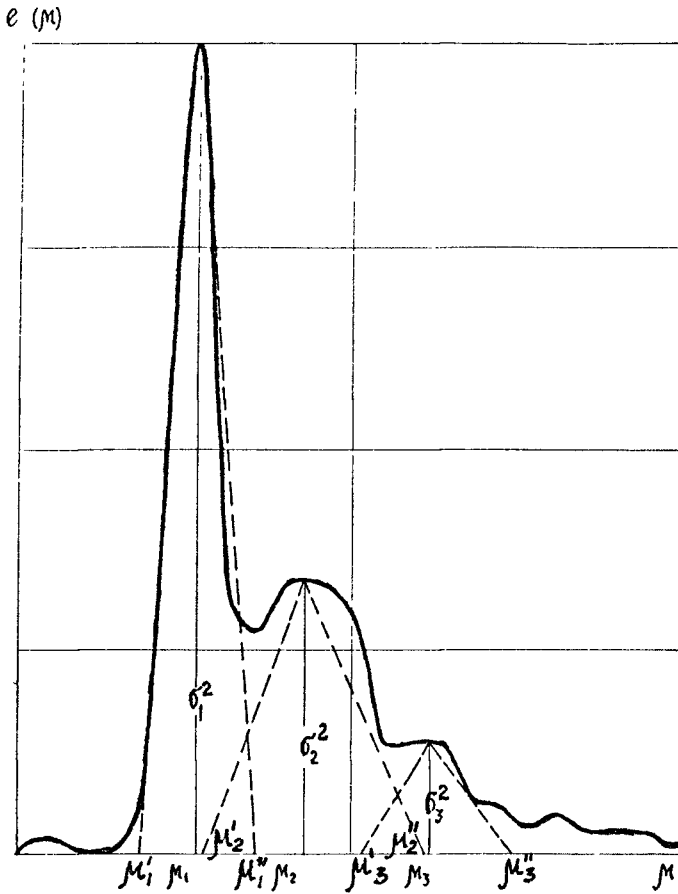
Fig.5. Approximation diagram of sea-level frequency spectrum (solid line) with three components of wave field (dashed line)

References

1. Шулейкин В.В. Физика моря, изд.3, М., 1969.

2. Титов Л.Ф. Ветровые волны. Л., 1969.

3. Китайгородский С.А. Физика взаимодействия атмосферы и океана. Л., 1970.

4. Крылов Ю.М. Спектральные методы исследования и расчета ветровых волн. Л., 1966.

5. Бычков В.С., Стрекалов С.С. Морские нерегулярные волны. М., 1971.

6. Kinsman B. Wind waves, New-Jersey, 1965.

7. Зубов И.Н. Динамическая океанология. М.-Л., 1947.

8. Лонгинов В.В. Динамика береговой зоны бесприливных морей. М., 1963.

9. Ржеплинский Г.В. Тр.Гос.океаногр.ин-та, 48, 1959.

10. Phillips O.M. The dynamics of the upper ocean. Cambridge, 1966.

11. Garrett J. Mar.Res., 1969, 27, N 3.

12. Pierson W.J. J.Geophys.Res., 1959, 64, N 8.

13. Давидан И.Н. Тр.координационных совещаний по гидротехнике. 50, 1969.

14. Mitsuyasu H. Rep.Res.Inst.Appl.Mech., 1968, 16, N55.

15. Hidy G.M., Plate E.J. J.Fluid Mech., 1966, 26, N 4.

16. Кононкова Г.Е., Кузнецов В.В. Вестник Моск.унив.1970, № 4.

17. Kononkova G.E., Kuznetsov V.V. Abstr.Pap.12, Coast. Eng.Conf.Washington, 1970.

18. Ржеплинский Г.В. и др. Тр.Гос.океаногр.ин-та, 93,1968.

19. Strekalov S.S., Massel S.T. Arch.hydrotechn., 1971, 18, N 4 (Gdansk).

20. Крылов Ю.М., Цыплухин В.Ф. Исследование вероятностной структуры поля волн и волновых давлений у глубоководной сплошной преграды. Океанология, 1973, № 2.

21. Крылов Ю.М., Кузнецов В.В., Стрекалов С.С. Системы поля ветровых волн. Докл. АН СССР, т.208, № 4, 1973.

22. Krylov Yu.M., Kuznetsov A.I., Sakharov S.M., Tsyploukhin V.Ph. Effects of irregular wave loads upon sea breakwater of vertical type. Abstr.of papers to be presented at the 13th International Conference on coastal engineering. July 10-14, 1942. Vancouver, B.C., Canada.

23. Крылов Ю.М. Линейная теория взаимодействия нерегулярных трехмерных волн с жесткой вертикальной стенкой. Тр.Союзморниипроекта, вып.27(33), М., "Транспорт",1969.

CHAPTER 13

THE LOSSES OF INNER ENERGY IN SEA WAVES

By Prof. Dr. Eng. Sci. V.K. SHTENCEL.[*]

As it is known Lamb in his time suggested that ener-
gy losses in waves stipulated by liquid viscosity should
be calculated by a formular:

$$W_{\nu} = 2\pi^2 \rho g \frac{h^2}{\lambda^2} \nu \tag{1}$$

where ν is kinematic viscosity coefficient

The following prototype observations and laboratory
experimental data showed that actual losses tens and
hundreds times exceed those calculated by this formular.
This can be explained by the turbulent character of ac-
cording to Lamb, suggested to substitute the turbulent
viscosity coefficient determined depending on wave para-
meters (instead of the kinematic viscosity one). The best
known are the suggestions of Dobroklonsky who puts for-
ward the following dependence for turbulent viscosity
coefficient:

$$\nu_t = 2,51 \cdot 10^{-2} \frac{h^2}{\tau} \quad (cm^2 sec^{-1})$$

and Bouden: $\nu_t = 2,8 \cdot 10^{-5} \frac{h \cdot \lambda}{\tau} \quad (cm^2 sec^{-1})$

Even these dependences give nearly 100 times divergence

[*]Head of the Chair of Ports of Leningrad Water
Transport Institute
Dvinskaja 5/7 Leningrad, 198035. USSR.

in calculation.

Considering suggestions of other investigators one can find out more than 300 times discrepancy. Such variability testifies that recommended functional connections betwee wave parameters and turbulent viscosity coefficient are not correct.

Modern knowledge on liquid structure can explain these discrepancies.

A number of latest works in this field bring to conclusion that the main kinematic elements of water are particles consisting of several hundreds of molecules. If we cease to consider water particles as some part of continuous medium without definite dimensions, and begin to consider it as the transfer and deformation of real particles, we can notice that the conventional division of motion to laminar and turbulent is not complete.

As we know, any fluid motion which can be described as periodical or which is to some extent a regular vortex model is not a turbulent flow is that the turbulent pulsations by their nature are of chaotical character. At present, when considering waves, the majority of experts find turbulent and laminar regimes in them by analogy with water flows. In fact, looking at real waves during storms, when it is even difficult to determine their characteristic owing to chaotical combination of crests and troughs, one can suppose turbulent nature of motion. If we consider two-dimentional waves in laboratory chute, however, strict regularity of surface periodical fluctuations becomes evident; pressures and velocities at a point vary strictly periodically as well. Not a single experimenter could find high-frequency pulsations characteristic for turbulent regime in swell waves and standing ones.

Therefore, it should be admitted that regular wave motion itself is not turbulent. On the other hand, due to

periodical velocity and pressure variations at a point,
it could not be considered as laminar.

Fluid pressure is the motion of material particles
having definite geometrical dimentions at each moment. It
can be supposed that with laminar motion there are either
no particle deformations or they result from outer acti-
ons (the change of distance between boundary surfaces,
for instance). With turbulent motion the particle defor-
mations undoubtedly take place which can be seen from va-
riations of all parameters measured. These deformations
have accidental character which is characteristic for
turbulent motion. With wave motion particle deformations
occur strictly periodically and that causes particular
properties of wave flow. Therefore, it seems expedient to
consider the wave motion as the third main type of fluid
motion. Comparing various types of fluid motion we can
see clear indications of difference between them.

Laminar motion.

1. There are no particle deformations or they are
connected with external local actions (broadening or nar-
rowing boundary surfaces).

2. Motion has laminated character, separate jets move
parallel each other without mixing.

3. Velocity value and direction at each point of area
occupied by moving fluid with set motion are constant.

4. Inner energy losses are stipulated by fluid mole-
cular viscisity.

5. Energy losses due to friction are proportional to
the first degree of velocity.

Turbulent motion.

1. Particle deformations are of accidental character
with high frequencies.

2. Particle motion has chaotical character; fluid
continuously mixed.

3. Value and direction of velocity at any point are

continuously varying. It has frequencies of hundreds of hertz. Variations are of accidental character.

4. Inner energy losses are stipulated by mixing in the thickness of final fluid masses (by turbulent viscosity).

5. Energy losses due to friction are proportional to the velocity in degree 1,75 - 2.

Wave motion.

1. Particle deformations are strictly periodical with low frequencies.

2. Particle perform oscillatory motions along definite trajectories. This motion is accompanied by laminated "orbital" motion reducing when the depth increases. Particles are not mixed.

3. Value and direction of velocity at any point periodically vary. Frequency is equal to wave period. The fluctuations of velocities are strictly regular.

4. Inner energy losses are stipulated by molecular v viscosity and particle deformation losses.

5. Though some authors suppose that the losses due to friction are proportional to the square velocity, this problem should be specially studied.

One should distinguish real waves and that we call wave motion. Wave motion itself, as any other, is an abstraction. Under wave motion we understand one of the components of real fluid motion namely: oscillatory particle motion along definite trajectories and connected with them periodical deformations of particles, without breaking the nearest order between particles. Real waves are the result of summing up turbulent motion to the system of wave motions. Cutting to minimum the effect of external turbulizing factors, it is possible to get more or less pure wave motion in laboratory. The effect of turbulency becomes quite essential for storm waves in open weakens for ocean swells' waves the relation bet-

ween wave motion and turbulent one will vary in behalf of
the first one. To estimate this phenomenon properly it is
rather useful to divide motion to its compounds: wave and
turbulent ones.

With wave motion the fluid particles are subjected to
the periodical deformations. Analysing these deformations
one can obtain[1]equations for swell waves in Lagrange
variables:

$$x = x_o + r \sin \varphi + k\, r^2 \left(-\frac{\sigma t}{2} + \frac{1}{4} \sin 2 \varphi \right)$$

(2)

$$y = y_o + r \cos \varphi + k\, r^2 \left(\frac{1}{2} + \frac{1}{4} \cos 2 \varphi \right)$$

where: $\varphi = \sigma t - k\, x_o$,

　　　x and y varying particle coordinates,

　　　x_o and y_o - coordinates of particles at rest,

　　　$\sigma = \dfrac{2\pi}{\tau}$, k $= \dfrac{2\pi}{\lambda}$, r $= \dfrac{h}{2}\, e^{-\frac{2\pi\, y_o}{\lambda}}$,

　　　h, λ and τ - height, length and wave period cor-
　　　respondingly.

Now let's define deformation energy losses. If we take
two moments t_1 = 0 and t_2 = t and consider the position
of two closely situated particles, the distance change
between them during t will be:

$$dx - dx_o = -\, kr \cos \varphi \; dx_o - \frac{k^2 r^2}{2} \cos 2 \varphi \; dx_o$$

(3)

Relative deformation of each centimeter of infinitely
small fluid layer is:

$$\mathcal{E} = \frac{dx - dx_o}{dx_o} = -\, k\, r \cos \varphi - \frac{k^2 r^2}{2} \cos 2 \varphi$$

(4)

Then the rate of deformation will be:

$$\frac{d\mathcal{E}}{dt} = k\, \sigma\, r \sin \varphi + \sigma\, k^2 r^2 \sin 2 \varphi$$

(5)

R.N.Ivanov in his works [2] on film extension based on a great number of experiments showed that the force of resistance to film extension is proportional to velocity. If these conclusions be spread to the case of infinitely small fluid layer deformations considered, the energy absorbed by 1 cm^2 of this layer may be obtained in the form of:

$$dW_d' = a\,\rho\,\frac{\partial \mathcal{E}}{\partial t}\,d\mathcal{E} \, , \qquad (6)$$

where a - proportionality constant factor, which can be called deformation dissipation coefficient.

Substituting all the values in formular (6) we obtain the following expression:

$$dW_d' = a\,\rho\,(\,k\,\sigma\,r\,\sin\varphi + k^2\,\sigma\,r^2\,\sin 2\varphi\,)\,dt \qquad (7)$$

As the particle deformation sign changes in a half of a period (half a period goes compression and the other half - extension), integrating expression (7) when $x_o = 0$ for a half a period and doubling it we obtain energy losses by an infinitely small fluid layer, whose area is 1 cm^2 for the whole period:

$$W_d' = \pi\,a\,\rho\,\sigma\,(k^2\,r^2 + k^4\,r^4) \qquad (8)$$

To obtain energy loss values over all water thickness, we integrate expression (8) over the depth:

$$W_d = \int_0^{-\infty} W_d'\,dy_o = \frac{1}{2}\,\pi\,a\,\rho\,k\,\sigma\,r_o^2\,(\,1 + \frac{k^2\,r_o^2}{2}\,)$$

Or substituting values k , σ and r_o we get:

$$W_d = \frac{a\,\rho\,\pi^3\,h^2}{2\,\lambda\,\tau}\left[\,1 + \frac{1}{2}\,(\,\frac{\pi\,h}{\lambda}\,)^2\,\right]$$

i.e. , energy loss value of disturbed fluid related to 1 cm^2 of surface during the period. Obviously, energy

losses during a second will be equal to:

$$W_d = \frac{a \, \rho \, \pi^3 h^2}{2 \, \lambda \, \tau^2} \left[1 + \frac{1}{2} \left(\frac{\pi h}{\lambda} \right)^2 \right] \qquad (9)$$

Coefficient dimension a from formular (9) $cm^2 \, sec^{-1}$ - coincides with the dimension of kinematic viscosity coefficient and hence from the dimention condition we may assume the following dependence:

$$a = m \, \frac{h \lambda}{\tau} \qquad (10)$$

Generally, it seems possible to consider that inner energy losses in waves can be represented as:

$$W = W_\nu + W_d + W_t \qquad (11)$$

where: W_ν – kinematic viscosity losses

W_d – particle deformation losses

W_t – turbulency losses.

Taking into account Lamb dependence (1) we can write down:

$$W = 2 \pi^2 \rho \, g \, \frac{h^2}{\lambda} \left(\nu + \nu_d + \nu_t \right) \qquad (12)$$

where ν, ν_d and ν_t the coefficients of kinematic viscosity, deformation energy dissipation and turbulent viscosity, correspondingly.

Comparing (12) and (9) we get:

$$\nu_d = m, \, \frac{h \lambda}{\tau} \left[1 + \frac{1}{2} \left(\frac{\pi h}{\lambda} \right)^2 \right] \qquad (13)$$

where m, is an empirical coefficient.

If determining coefficient ν_d experimentally it turns out that it varies with depth as the turbulent viscosity coefficient does, this may be taken into account by exponential dependence for m, . In the latter case we

have to integrate equation (8) to make the numerical co-
efficient more exact.

As the wave turbulency depends on external turbulizing
factors, when looking for functional dependence for ν_t ,
the wind parameters (velocity and action duration) should
be taken into account first of all. The existing depen-
dencies for ν_t accounting only wave parameters do not
meet this condition and therefore they give results dif-
fering 300 times and more from each other.

REFERENCES

I. Штенцель В.К. Особый характер волнового движения
жидкости и его учет в теории морских волн. "Океаноло-
гия". т. УI. вып. 5. 1966.
2. Иванов Р.Н. Гашение энергии в пленках поверхностно-
активных веществ. Изв. АН СССР, серия географ.-геофиз.,
№ I, 1938.

CHAPTER 14

ENHANCEMENT OF DIRECTIONAL WAVE SPECTRUM ESTIMATES[a]

by

Narayana N. Panicker,[1] M. ASCE

and

Leon E. Borgman[2]

ABSTRACT

Determination of the directional distribution of ocean surface waves is of practical importance and analytical schemes for it are developed and discussed here. Based on a generalized representation of wave properties such as surface elevation, subsurface pressure or horizontal components of water particle velocity, acceleration or wave force, two general schemes of analysis are developed. In one scheme the predictive equations for the directional distribution of both the amplitude and phase of waves are derived. Distribution of energy as a function of direction for random waves is obtained in the other scheme. Fourier series parameterization is used to represent directional spectrum. The truncation of the series dictated by data limitations introduce directional spread and negative side lobes for the estimated directional spectrum. A procedure to remove these undesirable side lobes by a non-negative smoothing function is described. The smoothing causes further directional spread. Methods for obtaining better directional resolution are discussed. Data adaptive spectral analysis techniques such as Maximum Likelihood Method and Maximum Entropy Method are suggested.

1. INTRODUCTION

The directional spectrum of ocean waves is a distribution of wave energy with both frequency and direction. This information is useful and necessary for understanding and predicting coastal processes like littoral sediment transport and diffraction and refraction of waves as well as for the prediction of motions and stresses in floating and fixed structures. Several different techniques of measurement and analysis are used for obtaining directional wave spectra. Panicker (17) gave a review of these techniques. A common method is the use of an array of wave gages to record wave properties at several different points in the wave field and analyze the data to obtain the directional spectral density distribution for each frequency of interest. Two analytical schemes were developed by the authors for the determination of directional spectra. The schemes are generalized by use of transfer functions between measured wave properties and surface wave amplitudes. These, an extension of the work reported in 1970 by Panicker and Borgman (14), are reported here. Fourier series parameterization is used to estimate directional spectrum but the limited number of gages in an array necessitates truncation of the Fourier series resulting in negative side lobes for the spectrum. A scheme for removing the negative side lobes by a non-negative smoothing function is developed and

---

258

described. Truncated Fourier series and smoothing may reduce the directional
resolution. Possible methods for obtaining higher directional resolution are
also discussed.

2. ANALYTICAL SCHEMES

Two schemes of analysis are developed: the amplitude and phase detection
scheme (Locked-Phase Analysis) and the spectrum approach (Random-Phase Analysis).
A general representation of wave properties is used so that the resulting
Fourier-Bessel expressions equally apply to array measurements of any wave
property such as surface elevation, subsurface pressure, water particle velocity,
water particle acceleration and linearized wave force.

2.1 General representation of a measurable wave parameter

The analytical schemes developed here are good for a general array in which
the different sensors may be placed arbitrarily and measure not necessarily the
same properties. Such a property, q, may be represented in terms of the wave
amplitude, r, as

$$q = rh\left[U \cos(kx \cos\theta + ky \sin\theta - 2\pi ft + \phi)\right.$$

$$\left. + V \sin(kx \cos\theta + ky \sin\theta - 2\pi ft + \phi)\right] . \tag{1}$$

Here the angular function, h, specifies the directional property of the measured
parameter and

$$h = \begin{cases} 1, & \text{if the property measured is non-directional such as pressure} \\ \cos\theta, & \text{if the x-component of a property is measured} \\ \sin\theta, & \text{if the y-component is measured.} \end{cases}$$

(x,y,z) are the sensor coordinates with z measured positively downward from still-
water level, k is the wave number (2π/wave length), θ the vector wave direction,
and f the frequency, t is time elapsed and ϕ the corresponding phase angle.
$U(f,z)$ and $V(f,z)$ are transfer functions for the various wave properties and are
tabulated in Table 1. For facility for use in a general scheme of computation
the wave properties in Table 1 are written in code in the first column of the
table. The code is in the form of a 3-digit number of the form $w_1 w_2 w_3$ where w_1
is the property studied such as water level, pressure, etc., w_2 is information
on relative water depth such as deep or shallow, and w_3 is the directionality
information of the property. The following cases are studied:

w_1: 1 = water level, 2 = subsurface pressure, 3 = water particle velocity,
       4 = water particle acceleration, 5 = force;

w_2: 0 = unaffected by depth, 1 = intermediate water depth, 2 = deep water;

w_3: 0 = non-directional property, 1 = x-component, 2 = y component.

The following additional notations are used in Table 1: ρ = water density,
g = acceleration due to gravity, Z_2 = stillwater depth, C_D = coefficient of

Table 1.   Transfer Functions for Wave Properties in Equation (1)

CODE $w_1w_2w_3$	U	V
100	1.0	0
210	$\rho g \dfrac{\cosh k(Z_2-z)}{\cosh kZ_2}$	0
220	$\rho g \exp(-kz)$	0
311	$2\pi f \dfrac{\cosh k(Z_2-z)}{\sinh kZ_2}$	0
312	0	$2\pi f \dfrac{\sinh k(Z_2-z)}{\sinh kZ_2}$
321	$2\pi f \exp(-kz)$	0
322	0	$2\pi f \exp(-kz)$
411	0	$(2\pi f)^2 \dfrac{\cosh k(Z_2-z)}{\sinh kZ_2}$
412	$-(2\pi f)^2 \dfrac{\sinh k(Z_2-z)}{\sinh kZ_2}$	0
421	0	$(2\pi f)^2 \exp(-kz)$
422	$-(2\pi f)^2 \exp(-kz)$	0
511	$C_D \dfrac{\rho}{2} D_P \sqrt{8/\pi}\ \sigma \dfrac{2\pi f \cosh k(Z_2-z)}{\sinh kZ_2}$	$C_M \rho \dfrac{\pi D_P^2}{4} (2\pi f)^2 \dfrac{\cosh k(Z_2-z)}{\sinh kZ_2}$
512	$-C_M \rho \dfrac{\pi D_P^2}{4} (2\pi f)^2 \dfrac{\sinh k(Z_2-z)}{\sinh kZ_2}$	$C_D \dfrac{\rho}{2} D_P \sqrt{8/\pi}\ \sigma \dfrac{2\pi f \sinh k(Z_2-z)}{\sinh kZ_2}$
521	$C_D \dfrac{\rho}{2} D_P \sqrt{8/\pi}\ \sigma\, 2\pi f \exp(-kz)$	$C_M \dfrac{\rho\pi D_P^2}{4} (2\pi f)^2 \exp(-kz)$
522	$-C_M \rho \dfrac{\pi D_P^2}{4} (2\pi f)^2 \exp(-kz)$	$C_D \dfrac{\rho}{2} D_P \sqrt{8/\pi}\ \sigma\, 2\pi f \exp(-kz)$

drag in force calculation, C_M = coefficient of mass in force calculation, D_p = diameter of object on which wave force is measured and σ = root-mean-square horizontal velocity of water particles in wave. Linear wave theory is used to obtain the quantities in Table 1 and in addition, linearization of drag force in the wave force expression is used for the transfer functions for force measurements (Borgman (4)).

2.2 Locked-Phase Analysis

2.2.2 General Development

Very often in the directional analysis of ocean waves the waves are assumed random and the computed directional spectrum does not retain any phase information. But for a phase-locked wave field as in some laboratory tanks or in some coastal regimes dominated by distant swells, an analysis procedure that would yield distribution of phase as well as amplitude as a function of wave direction may be appropriate. A deterministic scheme of analysis for it using the Fast Fourier Transform (FFT) technique is described below.

Let q_n be a wave parameter measured at time t_n on a sensor located at (x,y,z). Then q_n is the sum of the contributions from all the frequencies, $f_o...f_M$, and directions θ_m. Let the component amplitudes for each frequency $m\Delta f$ be $r_m(\theta)$. Directions here are vector wave directions measured positive anti-clockwise from the X-axis. Using notations of Eq. 1 but substituting $\gamma = kx \cos\theta_m + ky \sin\theta_m$, one may write

$$q_n = \sum_{m=o}^{M} \int_{-\pi}^{\pi} r_m h \left[U \cos\{\gamma - 2\pi f_m t_n + \phi_m\} + V \sin\{\gamma - 2\pi f_m t_n + \phi_m\} \right] d\theta_m . \tag{2}$$

Let the duration of the record be T with a total of N data points. The FFT relationships involving data sampling interval Δt and frequency interval Δf are as follows:

$$\Delta t \cdot \Delta f = 1/N, \quad \Delta f = 1/T, \quad f_m = m\Delta f \quad \text{and} \quad t_n = n\Delta t. \tag{3}$$

Using these one can write down Eq. 2 as

$$q_n = \Delta f \sum_{m=o}^{M} B_m \cos\frac{2\pi mn}{N} + \Delta f \sum_{m=o}^{M} C_m \sin\frac{2\pi mn}{N} \tag{4}$$

where

$$B_m = T \int_{-\pi}^{\pi} r_m h\{U \cos(\gamma+\phi_m) + V \sin(\gamma+\phi_m)\} d\theta_m \tag{5}$$

and

$$C_m = T \int_{-\pi}^{\pi} r_m h\{U \sin(\gamma+\phi_m) - V \cos(\gamma+\phi_m)\} d\theta_m . \tag{6}$$

If we let $M = \frac{N}{2} - 1$ and let A_m as

$$
A_m = \begin{cases} 0, & \text{if } m = M+1 = N/2 \\[2mm] \dfrac{1}{2} (B_m - \imath\, C_m), & \text{if } 1 \leq m \leq M = \dfrac{N}{2} + 1 \\[2mm] \dfrac{1}{2} (B_{N-m} + \imath\, C_{N-m}), & \text{if } \dfrac{N}{2} + 1 \leq m \leq N-1 \end{cases} \tag{7}
$$

it can then be shown from Eqs. 4 and 7 that

$$
q_n = \Delta f \sum_{m=o}^{N-1} A_m\, e^{\imath 2\pi m n/N}. \tag{8}
$$

A_m is thus the finite Fourier transform of q_n. They form a Fourier transform pair and A_m is given as

$$
A_m = \Delta t \sum_{n=o}^{N-1} q_n\, e^{-\imath 2\pi m n/N}. \tag{9}
$$

$\overline{A}_m$, the complex conjugate of the FFT coefficient A_m of the time series at a gage for frequency $m\Delta f$, for $0 < m < N/2$, can now be written from Eqs. 5, 6, and 7 as

$$
\overline{A}_m = \frac{T}{2} (U-\imath V) \int_{-\pi}^{\pi} r_m\, e^{\imath\phi_m}\, e^{\imath(kx\, \cos\theta_m + ky\, \sin\theta_m)} d\theta_m \tag{10}
$$

or

$$
\frac{2\,\overline{A}_m}{T(U-\imath V)} = \int_{-\pi}^{\pi} r_m\, e^{\imath\phi_m}\, e^{\imath kD\, \cos(\theta_m - \beta)} d\theta_m \tag{11}
$$

where D is the radius vector from the origin to the gage, inclined at an angle β to the x-axis (see Fig. 1). The objective is to determine amplitude r_m and phase ϕ_m for each frequency $m\Delta f$ as a function of wave direction θ_m. Amplitude and phase may be either continuous or discrete functions of direction. Expressions for these two cases are derived below.

2.2.2 Continuous functions for amplitude and phase

Let the amplitude and phase function, $F(\theta)$, be expressed as a complex Fourier series:

$$
F(\theta) = \frac{a_1 + \imath a'_o}{2} + \sum_{n=1}^{N} (a_n \cos n\theta + b_n \sin n\theta) + \imath \sum_{n=1}^{N} (a'_n \cos n\theta + b'_n \sin n\theta). \tag{12}
$$

This can be written as an exponential Fourier series as

$$
F(\theta) = \sum_{n=-N}^{N} \alpha_n\, e^{\imath n\theta} \tag{13}
$$

where

$$
\alpha_n = \begin{cases} \dfrac{1}{2} \ (a_n + b_n') + i(a_n' - b_n) \ , & \text{if } n > 0 \\[2mm] \dfrac{1}{2} \ (a_o + ia_o') \ , & \text{if } n = 0 \\[2mm] \dfrac{1}{2} \ (a_{-n} - b_{-n}') + i(a_{-n}' + b_{-n}) \ , & \text{if } n < 0 \end{cases} \tag{14}
$$

Substituting Eq. 14 in Eq. 11 and dropping subscript m from θ, one gets

$$
\frac{2 \ \overline{A}_m}{T(U-iV)} = \int_{-\pi}^{\pi} \sum_{n=-N}^{N} \alpha_n \ e^{in\theta} h \ e^{ikD \ \cos(\theta-\beta)} \, d\theta. \tag{15}
$$

In the Locked-Phase analysis the function h is 1.0, $\cos\theta$ or $\sin\theta$ depending on the wave parameter measured being non-directional, x-component or y-component. In the Random-Phase analysis described in the next section, pairs of measurements are used and therefore, in general, instead of three there could be six angular functions $H(\theta)$ as defined in the exponential form below.

$$
H = \sum_{r=-2}^{2} d_r \ e^{ir\theta} \tag{16}
$$

where d_r is defined for the six different cases in Table 2 as follows:

Table 2. Values of d_r in Eq. 16

Case	$H(\theta)$	d_{-2}	d_{-1}	d_0	d_1	d_2
1	1.0	0	0	1	0	0
2	$\cos\theta$	0	$\frac{1}{2}$	0	$\frac{1}{2}$	0
3	$\sin\theta$	0	$\frac{1}{2}$	0	$-\frac{1}{2}$	0
4	$\cos^2\theta$	$\frac{1}{4}$	0	$\frac{1}{2}$	0	$\frac{1}{4}$
5	$\cos\theta \ \sin\theta$	$\frac{1}{4}$	0	0	0	$-\frac{1}{4}$
6	$\sin^2\theta$	$-\frac{1}{4}$	0	$\frac{1}{2}$	0	$-\frac{1}{4}$

Substituting Eq. 16 in Eq. 15 and $\psi = \theta-\beta$, one gets

$$
\begin{aligned}
\frac{2 \ \overline{A}_m}{T(U-iV)} &= \sum_{n=-N}^{N} \alpha_n \sum_{r=-2}^{2} d_r \int_{-\pi}^{\pi} e^{i(n+r)(\psi+\beta)} \ e^{ikD \ \cos\psi} d\psi \\[2mm]
&= \sum_{n=-N}^{N} \alpha_n \sum_{r=-2}^{2} d_r \ e^{i(n+r)\beta} \Bigg[\int_{-\pi}^{\pi} \cos(n+r)\psi \ e^{ikD \ \cos\psi} d\psi \\[2mm]
&\quad + i \int_{-\pi}^{\pi} \sin(n+r)\psi \ e^{ikD \ \cos\psi} d\psi \Bigg]
\end{aligned} \tag{17}
$$

263

Abramowitz and Stegun (1) gives the value of the first integral as

$$\int_{-\pi}^{\pi} \cos(n+r)\psi \ e^{ikD \cos\psi} d\psi = 2\pi i^{n+r} J_{n+r}(kD) \tag{18}$$

where $J_{n+r}(kD)$ is the Bessel function of the first kind and order $(n+r)$ with the argument kD. The value of the second integral is zero as the integrand is odd. Substituting this and α_n from Eq. 14 one gets

$$\frac{2 \bar{A}_m}{T(U-iV)2\pi} = \frac{a_o + ia_o'}{2} \sum_{r=-2}^{2} d_r \ e^{ir\beta} \ i^r J_i(kD)$$

$$+ \sum_{n=1}^{N} \frac{1}{2}\left[(a_n + b_n') + i(a_n' - b_n)\right] \sum_{r=-2}^{2} d_r \ e^{i(n+r)\beta} \ i^{n+r} J_{n+r}(kD) \tag{19}$$

$$+ \sum_{n=1}^{N} \frac{1}{2}\left[(a_n - b_n') + i(a_n' + b_n)\right] \sum_{r=-2}^{2} d_r e^{-i(n-r)\beta} \ i^{-n+r} J_{-n+r}(kD)$$

Equation 19 can be simplified by noting that

$$J_{-r}(kD = (-1)^r J_r(kD) \ \text{and} \ i^{-r}J_{-r}(kD) = i^r J_r(kD)$$

and assigning for various cases in Table 2 a dummy parameter ε as follows·

$$\varepsilon = \begin{cases} 1.0, \ \text{for cases 1, 4, 5, 6} \\ i \ , \ \text{for cases 2, 3} \end{cases}$$

Let

$$A_o^* = \frac{d_o J_o(kD)}{\varepsilon} + \sum_{r=1}^{2} \frac{d_r e^{ir\beta} + d_{-r} e^{-ir\beta}}{\varepsilon} \ i^r J_{n+r}(kD) \tag{20}$$

$$A_n^* = \sum_{r=-2}^{2} \frac{d_r e^{i(n+r)\beta} + d_{-r} e^{-i(n+r)\beta}}{\varepsilon} \ i^r J_{n+r}(kD) \tag{21}$$

$$B_n^* = \sum_{r=-2}^{2} \frac{-id_r e^{i(n+r)\beta} + id_{-r} e^{-i(n+r)\beta}}{\varepsilon} \ i^r J_{n+r}(kD) \tag{22}$$

Then Eq. 19 can be expressed as

$$\frac{2 \bar{A}_m}{T(U-iV)\pi\varepsilon} = (a_o + ia_o')A_o^* + \sum_{n=1}^{N} i^n (a_n A_n^* + b_n B_n^*)$$

$$+ \sum_{n=1}^{N} i^{n+1} (a_n'A_n^* + b_n'B_n^*). \tag{23}$$

It may be noted that A_o^*, A_n^*, and B_n^* are all real-valued functions. They are evaluated and tabulated in Table 3. Equation 23 is the desired relationship for evaluating the directional function $F(\theta)$ for frequency $m\Delta f$ in terms of its Fourier series coefficients a_o, a_o', a_1, a_1', etc. and expressions similar to it exist for other frequencies. Equation 23 may be written in matrix form as follows:

$$Re \ \frac{2 \ \overline{A}_m}{T(U-iV)\pi} = \left[A_o^*, \ - A_1^*, \ -B_1^*, \ -A_2^*, \ - B_2^*, \ldots \right] \left[a_o, \ a_1', \ b_1', \ a_2, \ b_2, \ldots \right]^T \quad (24)$$

$$Im \ \frac{2 \ \overline{A}_m}{T(U-iV)\pi} = \left[A_o^*, \ A_1^*, \ B_1^*, \ -A_2^*, \ -B_2^*, \ldots \right] \left[a_o', \ a_1, \ b_1, \ a_2', \ b_2', \ldots \right]^T \quad (25)$$

Here superscript T denotes a transpose of the matrix indicated. By inverting the matrices the coefficients for the complex Fourier series can be obtained and the directional distribution functions for amplitude a_m and phase ϕ_m for each frequency $m\Delta f$ can be evaluated as follows:

$$r_m(\theta) = \left[\left\{ \frac{a_o}{2} + \sum_{n=1}^{N} (a_n \cos n\theta + b_n \sin n\theta) \right\}^2 \right.$$
$$\left. + \left\{ \frac{a_o'}{2} + \sum_{n=1}^{N} (a_n' \cos n\theta + b_n' \sin n\theta) \right\}^2 \right]^{\frac{1}{2}} \quad (26)$$

$$\phi_m(\theta) = \arctan \left\{ \frac{\frac{a_o'}{2} + \sum_{n=1}^{N} (a_n' \cos n\theta + b_n' \sin n\theta)}{\frac{a_o}{2} \sum_{n=1}^{N} (a_n \cos n\theta + b_n \sin n\theta)} \right\} \quad (27)$$

2.2.3 Amplitudes and Phases of Discrete Wave Trains

In the discrete case the complex phase-amplitude function $F(\theta)$ is assumed to have non-zero values only at a finite number of discrete directions. $F(\theta)$ may be written as

$$F(\theta) = \sum_{m=1}^{M} (r_m + ir_m') \delta(\theta-\theta_m) \quad (28)$$

where $\delta(\theta-\theta_m)$ is a Dirac delta function representing a spike at $\theta = \theta_m$ and zero elsewhere. A relationship analogous to Eq. 11 can be used to evaluate $F(\theta)$.

Table 3. Values of A_o^*, A_n^*, and B_n^* for Different Cases

(All Bessel functions, J_n, here have argument kD)

Case	$H(\theta)$	ε	A_o^*	A_n^*	B_n^*
1	1.0	1.0	J_o	$2 J_n \cos n\beta$	$2 J_n \sin n\beta$
2	$\cos\theta$	i	$J_1 \cos\beta$	$-J_{n-1} \cos(n-1)\beta$ $+J_{n+1} \cos(n+1)\beta$	$-J_{n-1} \sin(n-1)\beta$ $+J_{n+1} \sin(n+1)\beta$
3	$\sin\theta$	i	$J_1 \sin\beta$	$J_{n-1} \sin(n-1)\beta$ $+J_{n+1} \sin(n+1)\beta$	$-J_{n-1} \cos(n-1)\beta$ $-J_{n+1} \cos(n+1)\beta$
4	$\cos^2\theta$	1.0	$\frac{1}{2}(J_o - J_2 \cos^2\beta)$	$J_n \cos n\beta - \frac{1}{2} J_{n-2} \cos(n-2)\beta$ $- \frac{1}{2} J_{n+2} \cos(n+2)\beta$	$J_n \sin n\beta - \frac{1}{2} J_{n-2} \sin(n-2)\beta$ $- \frac{1}{2} J_{n+2} \sin(n+2)\beta$
5	$\cos\theta \sin\theta$	1.0	$-\frac{1}{2}(J_2 \sin^2\beta)$	$\frac{1}{2} J_{n-2} \sin(n-2)\beta$ $- \frac{1}{2} J_{n+2} \sin(n+2)\beta$	$-\frac{1}{2} J_{n-2} \cos(n-2)\beta$ $+ \frac{1}{2} J_{n+2} \cos(n+2)\beta$
6	$\sin^2\theta$	1.0	$\frac{1}{2}(J_o + J_2 \cos^2\beta)$	$J_n \cos n\beta + \frac{1}{2} J_{n-2} \cos(n-2)\beta$ $+ \frac{1}{2} J_{n+2} \cos(n+2)\beta$	$J_n \sin n\beta + \frac{1}{2} J_{n-2} \sin(n-2)\beta$ $+ \frac{1}{2} J_{n+2} \sin(n+2)\beta$

$$\frac{2 \overline{A}_m}{T(U-iV)} = \int_{-\pi}^{\pi} Fh \ e^{ikD \ \cos(\theta_m-\beta)} \ d\theta \tag{29}$$

Substituting for F from Eq. 28 and for h with appropriate values of $H(\theta_m)$ from Table 2 and evaluating the integral involving Dirac delta function, one gets

$$\frac{2 \overline{A}_m}{T(U-iV)} = \sum_{m=1}^{M} (r_m + r'_m) H(\theta_m) e^{ikD \ \cos(\theta_m-\beta)} \tag{30}$$

Separating the real and imaginary parts of Eq. 30 one can obtain as many pairs of equations as there are gages, for r_m and r'_m.

$$Re \ \frac{2 \overline{A}_m}{T(U-iV)} = \sum_{m=1}^{M} \left[r_m H(\theta_m) \ \cos kD \ \cos(\theta_m-\beta) \right]$$
$$- \sum_{m=1}^{M} \left[r'_m H(\theta_m) \ \sin kD \ \cos(\theta_m-\beta) \right] \tag{31}$$

$$Im \ \frac{2 \overline{A}_m}{T(U-iV)} = \sum_{m=1}^{M} \left[r_m H(\theta_m) \ \sin kD \ \cos(\theta_m-\beta) \right]$$
$$+ \sum_{m=1}^{M} \left[r'_m H(\theta_m) \ \cos kD \ \cos(\theta_m-\beta) \right] \tag{32}$$

A least-square analysis is appropriate for obtaining r_m and r'_m from Eq. 31 and Eq. 32. By computing the modulus and argument from r_m and r'_m one obtains the wave amplitude and phase respectively.

2.3 Random-Phase Analysis

2.3.1 General Development

     Randomness in an ocean wave field may be introduced by assuming phase angles to be random variables. Let the phase angle be an independent random variable uniformly distributed over the interval $-\pi$ to π. Let the directional spectral density function $S(f,\theta)$ for $f > 0$ and $-\pi \le \theta \le \pi$ be such that the total energy E contained in the waves traveling in the direction between $\theta - \frac{\Delta\theta}{2}$ and $\theta + \frac{\Delta\theta}{2}$ and having frequencies between $f - \frac{\Delta f}{2}$ and $f + \frac{\Delta f}{2}$ is

$$E = \int_{\theta - \frac{\Delta\theta}{2}}^{\theta + \frac{\Delta\theta}{2}} \int_{f - \frac{\Delta f}{2}}^{f + \frac{\Delta f}{2}} 2\rho g S(f,\theta) df \ d\theta \tag{33}$$

where ρ is water density and g the acceleration of gravity. However, the total energy per unit crest width and unit wavelength of a wavelet of amplitude, r is $\rho g r^2/2$. When Δf and $\Delta\theta$ are sufficiently small one can therefore write an equivalent surface wave amplitude in terms of the directional spectral density

$$r \simeq \sqrt{4S(f,\theta)\Delta f\ \Delta\theta} \tag{34}$$

After Pierson and Marks (18) one may therefore represent the random sea surface as the following pseudo-integral

$$q(x,y,t) = 2 \int_{o}^{\infty} \int_{-\pi}^{\pi} \sqrt{S(f,\theta)\,df\ d\theta}\ \cos(kx\ \cos\theta + ky\ \sin\theta - 2\pi ft + \phi) \tag{35}$$

The above pseudo-integral should be considered only as a concise and descriptive symbolization of the limiting process indicated and not as an actual integral. $q(x,y,t)$ is a Gaussian stochastic process in the three parameters x, y, and t; see Takano (19, p. 86).

Let q' be any wave parameter at time t and measured at a gage located at (x,y,z') and let q" be a wave parameter measured at time $t + \tau$ and another gage located at $(x+X, y+Y, z")$. Analogous to Eq. 2 with corresponding primes for circular functions h and transfer functions U and V, and using Eq. 35, one may write down q' and q" as follows

$$q' = 2 \int_{o}^{\infty} \int_{o}^{2\pi} \sqrt{S\ df\ d\theta}\ h'\Big[U'\ \cos\{kx\ \cos\theta + ky\ \sin\theta - 2\pi ft + \phi\}$$
$$+ V'\sin\{kx\ \cos\theta + ky\ \sin\theta - 2\pi ft + \phi\}\Big] \tag{36}$$

$$q" = 2 \int_{o}^{\infty} \int_{o}^{2\pi} \sqrt{S\ df\ d\theta}\ h"\Big[U"\cos\{k(x+X)\cos\theta + k(y+Y)\sin\theta - 2\pi f(t+\tau) + \phi\}$$
$$+ V"\sin\{k(x+X)\cos\theta + k(y+Y)\sin\theta - 2\pi f(t+\tau) + \phi\}\Big] \tag{37}$$

The cross-covariance $C_{q'q"}$ between q' and q" is the expectation of the product q'q". Evaluating the expectations of the various terms in the product and substituting $\gamma = kX\ \cos\theta + kY\ \sin\theta$, the cross-covariance between measurements at the two gages can be written in terms of the co-spectrum c(f) and quadrature spectrum q(f) as follows.

$$C_{q'q"} = 2 \int_{o}^{\infty} c(f)\cos\ 2\pi f\tau df + 2 \int_{o}^{\infty} q(f)\sin\ 2\pi f\tau df \tag{38}$$

where

$$c(f) = \int_{o}^{2\pi} Sh'h"\Big[(U'U" + V'V")\cos\gamma + (U'V" - V'U")\sin\gamma\Big]d\theta \tag{39}$$

$$q(f) = \int_{o}^{2\pi} Sh'h"\Big[(U'U" + V'V")\sin\gamma - (U'V" - V'U")\cos\gamma\Big]d\theta\ . \tag{40}$$

The cross-spectrum is defined as c - iq. It may be obtained as the product the complex conjugate of FFT coefficient of one gage record with the FFT

coefficient of the other and divided by the duration of the record.   The
complex conjugate of the cross-spectrum may be written as

$$c + iq = \left[(U'U'' + V'V'') + i(V'U'' - U'V'') \right] \int_0^{2\pi} S_{h'h''} e^{i\gamma} d\theta \, . \qquad (41)$$

If we let D and β be the spacing and orientation between two gages of a pair
(see Fig. 1) and $h'h'' = H(\theta)$ be one of the circular functions noted in Table 2,
Eq. 41 can be written as

$$\frac{c + iq}{(U' + iV')(U'' - iV'')} = \int_0^{2\pi} SH \; e^{ikD \, \cos(\theta - \beta)} \, d\theta. \qquad (42)$$

     This expression can be used to evaluate the directional spectral density
function $S(f, \theta)$. Two cases may be considered $S(\theta)$ for each frequency as a
continuous function of direction and $S(\theta)$ discrete in directions.

2.3.2 Continuous Function for Directional Spectrum

     When wave energy is distributed continuously around the circle, $S(\theta)$ may
be represented as a Fourier series.

$$S(\theta) = \frac{a_o}{2} + \sum_{n=1}^{N} (a_n \cos n\theta + b_n \sin n\theta). \qquad (43)$$

This is equivalent to the series obtained by setting the imaginary part zero
in the complex Fourier series representation in Eq. 12 of the Locked-Phase
Analysis.   The results derived there may be used here with suitable modifica-
tion and the following equations analogous to Eq. 24 and Eq. 25 are obtained.

$$Re \; \frac{c + iq}{(U' + iV')(U'' - iV'')\pi\varepsilon} = \left[A_o^*, -A_2^*, -B_2^*, A_4^*, B_4^*, \ldots \right] \left[a_o, a_2, b_2, a_4, b_4, \ldots \right]^T \qquad (44)$$

$$Im \; \frac{c + iq}{(U' + iV')(U'' - iV'')\pi\varepsilon} = \left[A_1^*, B_1^*, -A_3^*, -B_3^*, \ldots \right] \left[a_1, b_1, a_3, b_3, \ldots \right]^T \, . \qquad (45)$$

Here A_o^*, A_1^*, B_1^*, etc. are as tabulated in Table 3.   The Fourier series coef-
ficients a_o, a_1, b_1, etc. of the directional spectral density function $s(\theta)$ may
be obtained by matrix inversion. As there are as many cross-spectra between
gages as there are pairs of gages, the number of equations available is equal
to the number of pairs of gages. That is, the greatest number of harmonics up
to which $S(\theta)$ can be represented is at the most the number of gage pairs.

2.3.3 Discrete Energy Analysis

     If $S(\theta)$ has non-zero values only at a finite number of directions, an
analysis analogous to the one in Section 2.2.3 may be made by representing

S(θ) in terms of a Dirac delta function·

$$S(\theta) = \sum_{m=1}^{M} r_m \, \delta(\theta-\theta_m) \tag{46}$$

The following results similar to Eq. 31 and Eq. 32 may be obtained.

$$Re \; \frac{c + iq}{(U'+iV')(U''-iV'')} = \sum_{m=1}^{M} r_m \, H(\theta_m) \cos \, kD \, \cos(\theta_m-\beta) \tag{47}$$

$$Im \; \frac{c + iq}{(U'+iV')(U''-iV'')} = \sum_{m=1}^{M} r_m \, H(\theta_m) \sin \, kD \, \cos(\theta_m-\beta) \tag{48}$$

The discrete energy values r_m for each direction θ_m may be obtained from Eq. 47 and Eq. 48 by a least-square analysis.

3.   SMOOTHING OF DIRECTIONAL SPECTRUM

When a Fourier series parameterization is used to represent directional spectrum as in Eq. 43, the quality of the result will depend greatly with the total number of harmonics of the Fourier series representation. The number of Fourier series coefficients that can be evaluated from the data, however, is limited by the number of gages and their placement in an array. The maximum number of harmonics that can be evaluated by the Random-Phase Analysis is at the most equal to the number of pairs of gages in an array and half the number of gages by the Locked-Phase Analysis. All but the first terms of a Fourier series take negative values and therefore negative side lobes show up when directional spectrum is represented by a truncated Fourier series. The negative side lobes in an energy spectrum is objectionable because energy spectral density is non-negative. It is undesirable also because negative side lobes may mask the real signals at the corresponding directions and therefore deteriorate directional resolution. Longuet-Higgins (11) proposed methods to use the available Fourier coefficients to fit the data best to a limited number of principal directions by making use of the fact that the real spectrum is non-negative. But when the directional spectrum is a unimodal continuous distribution for each frequency its estimation may be enhanced by convoluting it with a non-negative smoothing function to remove the negative side lobes. Smoothing functions for directional spectra were proposed and used by Longuet-Higgins, Cartwright and Smith (12). A procedure for using one such smoothing function $W_2(\theta)$, suggested by Borgman (5) is described below.

$$W_2(\theta) = R_N \cos^{2N}(\theta/2) \tag{49}$$

where N is the total number of harmonics. R_N is such that the area under $W_2(\theta)$ is unity and the value of the effective width (width of a rectangle of the same height and equal area) is the reciprocal of R_N. Let the unsmoothed directional

spectrum be represented as a Fourier series:

$$S(\theta) = \frac{a_o}{2} + \sum_{k=1}^{N} (a_k \cos k\theta + b_k \sin k\theta) \tag{50}$$

Let $W_2(\theta)$ be expressed as a Fourier series as follows:

$$W_2(\theta) = \frac{1}{2\pi} + \frac{1}{\pi} \sum_{k=1}^{N} C_{kN} \cos(k\theta) \tag{51}$$

where C_{kN} have to be evaluated consistent with Eq. 49. Convoluting $S(\theta)$ with $W_2(\theta)$ of Eq. 51, one gets the smoothed spectrum $S_2(\theta)$ as follows:

$$
\begin{aligned}
S_2(\theta) &= \int_{-\pi}^{\pi} S(\theta')W_2(\theta-\theta')d\theta' \\
&= \frac{a_o}{2} + \sum_{k=1}^{N} C_{kN}(a_k \cos k\theta + b_k \sin k\theta)
\end{aligned} \tag{52}
$$

Thus to obtain the smoothed spectrum one only has to evaluate the coefficients C_{kN}. This can be done by expanding Eq. 49 in the form of the Fourier series in Eq. 51. Details of a numerical procedure for this is given by Panicker (16). The coefficients are computed for each of the Fourier series representations up to the one with a maximum of 8 harmonics and tabulated in Table 4.

4. DIRECTIONAL RESOLUTION

The analytical procedures developed in the previous sections were applied to actual data to obtain directional spectra. The necessary computer programs were developed and described along with the details of the analysis by Panicker (16). Some results obtained are shown here in the context of a discussion on directional resolution.

Smoothing of the directional spectrum causes a broadening of the directional spread. This can be seen in Fig. 2 where the results obtained for a simulated single sinusoid with a 4-gage star array are shown. One notices that the effective width of the directional spectrum represented to 4 harmonics and obtained with W_2 smoothing is about 98° and without smoothing the effective width is 40°, but the ideal result for the single sinusoid would be a single spike at the input direction with no directional spread. This indicates an inherent directional spread on account of the truncated Fourier series representation of directional spectrum and an additional spread owing to W_2 smoothing which is necessary to remove the negative side lobes of the truncated series. However, when real data from the ocean is used to obtain directional spectrum, as done by Panicker and Borgman (14), it is not obvious how much of the directional spread is real and how much is due to the truncation and smoothing of the Fourier series. Figures 3 and 4 are directional

Table 4.   Values of R_N and C_{kN} for $W_2(\theta)$

No. of Harmonics N	Reciprocal of Effective Width R_N	Fourier Coefficients, C_{kN}							
		k=1	2	3	4	5	6	7	8
1	$\dfrac{1}{\pi}$	$\dfrac{1}{2}$							
2	$\dfrac{4}{3\pi}$	$\dfrac{2}{3}$	$\dfrac{1}{6}$						
3	$\dfrac{8}{5\pi}$	$\dfrac{3}{4}$	$\dfrac{3}{10}$	$\dfrac{1}{20}$					
4	$\dfrac{64}{35\pi}$	$\dfrac{4}{5}$	$\dfrac{2}{5}$	$\dfrac{4}{35}$	$\dfrac{1}{70}$				
5	$\dfrac{128}{63\pi}$	$\dfrac{5}{6}$	$\dfrac{10}{21}$	$\dfrac{5}{28}$	$\dfrac{5}{126}$	$\dfrac{1}{252}$			
6	$\dfrac{512}{231\pi}$	$\dfrac{6}{7}$	$\dfrac{15}{28}$	$\dfrac{5}{21}$	$\dfrac{1}{14}$	$\dfrac{1}{77}$	$\dfrac{1}{924}$		
7	$\dfrac{1024}{429\pi}$	$\dfrac{7}{8}$	$\dfrac{7}{12}$	$\dfrac{7}{24}$	$\dfrac{7}{66}$	$\dfrac{7}{264}$	$\dfrac{7}{1716}$	$\dfrac{7}{3432}$	
8	$\dfrac{16384}{6435\pi}$	$\dfrac{8}{9}$	$\dfrac{28}{45}$	$\dfrac{56}{165}$	$\dfrac{14}{99}$	$\dfrac{56}{1287}$	$\dfrac{4}{429}$	$\dfrac{8}{6435}$	$\dfrac{1}{12870}$

spectra obtained for two different frequencies from the CERC 5-gage array de-
signed by Borgman and Panicker (6) and installed off Pt. Mugu, California by
the U. S. Army Corps of Engineers. It may be seen that W_2 smoothing removes
the spurious side lobes resulting from the truncation of Fourier series. One,
however, suspects that W_2 smoothing has caused broadening of the directional
band width and reduction of directional resolution.

It might be emphasized that higher directional resolution does not neces-
sarily associate itself with a narrow directional spectrum. The highest di-
rectional resolution ($\pm 3°$) achieved so far for ocean wave measurements is for
the directional spectra of 7 sec waves obtained by a radio back-scatter technique
off Wake Island, Pacific Ocean and reported by Teague, et al. (20). The most
interesting feature of these high-resolution directional spectra is their broad
directional band width with as much as 1% of the peak energy density showing up
at directions opposite to the wind. Longuet-Higgins, Cartwright and Smith (12)
also reported broad directional spectra, but the results obtained by them
using a pitch-roll buoy and Fourier series parameterization with smoothing
were not considered to have sufficient resolution to support the conclusion.
However, the results of Teague, et al. (20) warn against restrictive assump-
tions on directional spread about the mean wind direction, such as $\pm 45°$ of

Arthur (2) and ±90° of Cote, et al. (9). Arbitrary parameterizations such as the tent functions of Oakley (13) to fit the data to narrow directional spectra also may not be the appropriate methods for ocean waves.

As Teague, et al. (20) has shown, high resolution directional spectra can be obtained by good measurement techniques. On the analysis side, data adaptive techniques of analysis [Lacoss (10)] for array data hold promise for high resolution. Maximum Likelihood Method [Capon (8)] and Maximum Entropy Method [Burg (7)] are two such nonlinear techniques. A review of these are given by Panicker (17). The advantage of these methods is that arbitrary parameterizations such as Fourier series representation are not used but the data content is used to determine the window shape. The analytical development described in Section 2.31 of this paper would be applicable for the Maximum Likelihood Method also. O. H. Oakley (personal communication) computed directional spectra using the Maximum Likelihood Method and obtained good directional resolution with a 4-gage star array. In this method only an additional Hermitian matrix inversion is required and therefore the computer time requirements are comparable to those for the direct Fourier transform method of Barber (3). Lacoss (10) and Burg (7) reported that Maximum Entropy Method gave still higher resolution; but Burg (7) noted that with arrays having unequal spacings the determination of the Maximum Entropy Spectrum became very difficult. This is still subject to active research.

5. SUMMARY AND CONCLUSIONS

Two general schemes for the directional analysis of surface waves have been developed and described. A generalized representation of wave properties was used so that the equations derived are applicable to the analysis of different kinds of measurements such as surface elevation, subsurface pressure or either of the horizontal components of water particle velocity, acceleration or wave force. The necessary transfer functions were tabulated. The amplitude and phase detection scheme (Locked-Phase Analysis) is a deterministic, Fast Fourier Transform method to determine the distribution of amplitude and phase as a function of direction and is applicable to phase-locked systems such as wave fields in some laboratory tanks and some coastal regimes dominated by distant swells. Cases of amplitudes and phases both as continuous functions of directions and discrete were considered. The Random-Phase Analysis is a spectrum approach to obtain the distribution of wave energy density as a function of direction for each frequency and both continuous and discrete distributions were considered. Fourier series parameterization was used for the directional distribution functions and explicit equations were derived for calculating the Fourier series coefficients. There are two such equations for each gage in the Locked-Phase Analysis and for each gage-pair in the Random-Phase Analysis. The evaluation of the Fourier series coefficients is done by inverting a matrix of quantities describing the array geometry relative to wave length and multiplying it with a matrix of quantities derived from the FFT coefficients of sensor outputs as stated in Eq. (24) and Eq. (25) for Locked-Phase Analysis and Eq. (44) and Eq. (45) for Random Phase Analysis. It was noted that representation of directional spectrum by truncated Fourier series resulted in negative side lobes for the spectrum. Negative side lobes for spectrum are unrealistic and undesirable and they have to be removed. Computational procedure for this by use of the non-negative W_2 smoothing function was described.

Results obtained using data from simulation and from the CERC 5-gage array off Point Mugu, California were discussed. It was found that representation by a truncated Fourier series introduced considerable directional spread to a simulated sinusoid and W_2 smoothing caused further directional spread. Better directional resolution than that obtained by Fourier series parameterization would be desirable.

High directional resolution does not necessarily go with narrow directional spectrum. A directional sprectrum obtained by radio backscatter technique was found to have the highest directional resolution so far reported, yet the spectrum itself was broad showing considerable energy values in all directions. Therefore arbitrary parameterizations such as tent functions for narrow spectra may not yield high directional resolution for ocean waves.

For analysis to obtain high resolution directional spectra from wave gage arrays, data adaptive techniques of analysis such as Maximum Likelihood Method and Maximum Entropy Method hold promise. The general scheme of analysis reported here may also be used for a Maximum Likelihood estimation in lieu of the Fourier series parameterization described.

APPENDIX 1. REFERENCES

1. Abramowitz, M. and Stegun, I. A., "Handbook of Mathematical Functions," Dover Publications, New York, 1965.

2. Arthur, R. S., "Variability in Direction of Wave Travel," Ocean Surface Waves, Annals of New York Academy of Science, Vol. 51, pp. 511-521, 1949.

3. Barber, N. F., "The Directional Resolving Power of an Array of Wave Detectors," Ocean Wave Spectra, Prentice-Hall, Inc., Englewood Cliffs, N. J., pp. 137-150, 1961.

4. Borgman, L. E., "Ocean Wave Simulation for Engineering Design," Proceedings, ASCE Conference on Civil Engineering in the Oceans, San Francisco, pp. 31-74, September 1967.

5. Borgman, L. E., "Directional Spectra Models for Design Use for Surface Waves," Technical Report HEL 1-12, Hydraulic Engineering Laboratory, University of California, Berkeley, June 1969.

6. Borgman, L. E. and N. N. Panicker, "Design Study for a Suggested Wave Gage Array off Point Mugu, California," Technical Report HEL 1-14, Hydraulic Engineering Laboratory, University of California, Berkeley, January 1970.

7. Burg, J. P., "The Relationship Between Maximum Entropy Spectra and Maximum Likelihood Spectra," *Geophysics*, Vol. 37, No. 2, pp. 375-376, April 1972.

8. Capon, J., "High-Resolution Frequency-Wave Number Spectrum Analysis," *Proceedings of the IEEE*, Vol. 57, No. 8, pp. 1408-1418, August 1969.

9. Cote, L. J., J. O. Davis, W. Marks, R. J. McGough, E. Mehr, W. J. Pierson, J. F. Ropek, G. Stephenson, and R. C. Vetter, "The Directional Spectrum of a Wind Generated Sea as Determined from Data Obtained by the Stereo Wave Observation Project," *Meteorological Papers*, Vol. 2, No. 6, New York University, June 1960.

10. Lacoss, R. T., "Data Adaptive Spectral Analysis Methods," *Geophysics*, Vol. 36, No. 4, pp. 661-675, August 1971.

11. Longuet-Higgins, M. S., "Bounds for the Integral of a Non-negative Function in Terms of its Fourier Coefficients," *Proceedings*, Cambridge Philosophical Society, Vol. 51, part 4, pp. 590-603, October 1955.

12. Longuet-Higgins, M. S., D. E. Cartwright, and N. D. Smith, "Observations of the Directional Spectrum of Sea Waves Using the Motions of a Floating Buoy," *Ocean Wave Spectra*, Prentice-Hall, Inc., Englewood Cliffs, N. J., pp. 111-136, 1963.

13. Oakley, O. H., "Directional Wave Spectra Measurement and Analysis Systems," presented at the SNAME Seakeeping Symposium, '20th Anniversary of St. Denis-Pierson paper,' Webb Institute of Naval Architecture, October 1973.

14. Panicker, N. N. and L. E. Borgman, "Directional Spectra from Wave Gage Arrays," *Proceedings*, 12th International Conference on Coastal Engineering, Washington, D. C., pp. 117-136, September 13-18, 1970.

15. Panicker, N. N. and L. E. Borgman, "Computer Simulation for the Design of Wave-Gage Arrays," *Proceedings*, 1971 Summer Computer Simulation Conference, Boston, Massachusetts, pp. 861-867, July 1971.

16. Panicker, N. N., "Determination of Directional Spectra of Ocean Waves from Gage Arrays," *Technical Report* HEL 1-18, University of California, Berkeley, p. 315, August 1971.

17. Panicker, N. N. "Review of Techniques for Directional Wave spectra," *Proceedings*, International Symposium on Ocean Wave Measurement and Analysis (WAVES 74), New Orleans, September 1974.

18. Pierson, W. J. and W. Marks., "The Power Spectrum Analysis of Ocean Wave Records," *Transactions*, American Geophysical Union, Vol. 33, 1952.

19. Takano, K., "On Some Limit Theorems of Probability-Distributions," Annals of the Institute of Statistical Mathematics, Tokyo, Vol. 6, pp. 37-113, 1954.

20. Teague, C. C., G. L. Tyler, J. W. Joy, and R. H. Stewart, "Synthetic Aperture Observations of Directional Height Spectra for 7s Ocean Waves," *Nature Physical Science*, Vol. 244, No. 137, pp. 98-100, August 13, 1973.
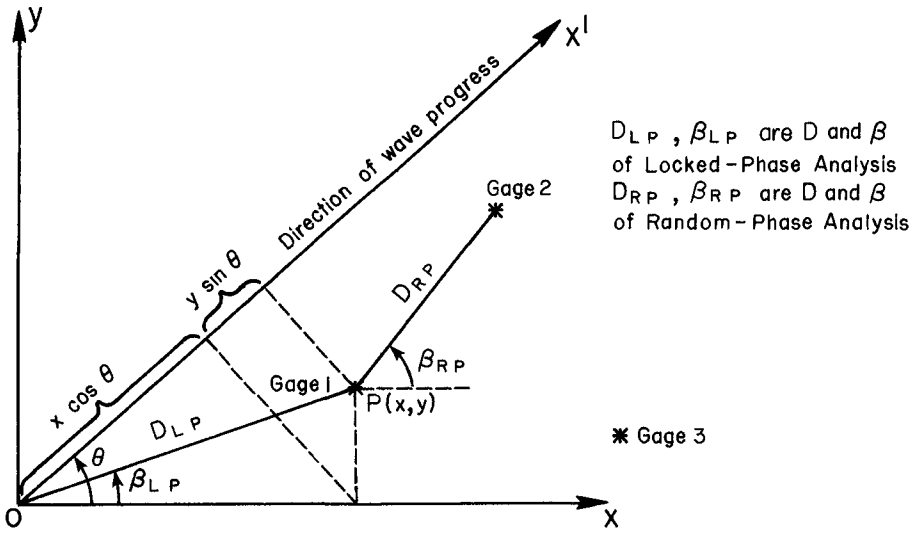
FIG. I DEFINITION SKETCH FOR WAVE DIRECTION ANALYSIS
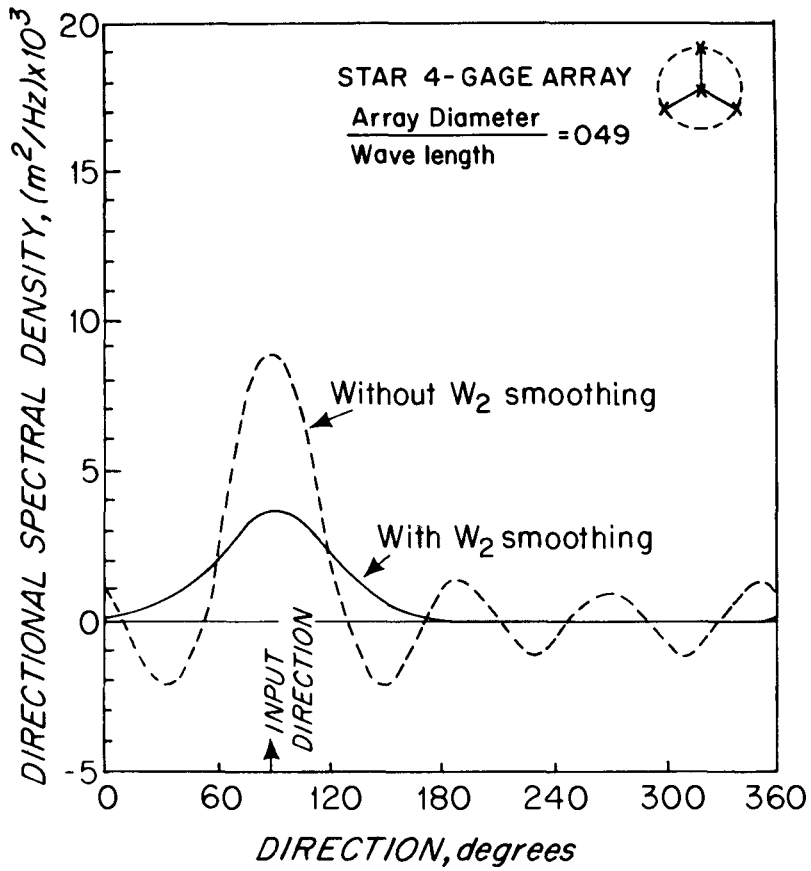
FIG. 2. FOURIER SERIES REPRESENTATION OF DIRECTION OF A SINGLE WAVE TRAIN USING FOUR HARMONICS
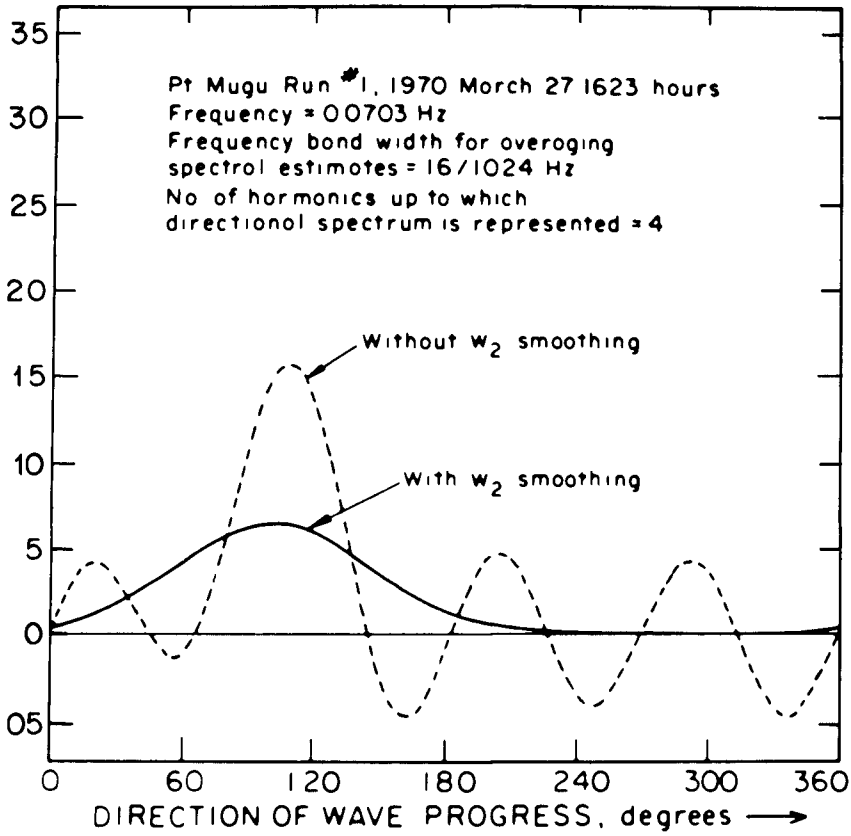
FIG. 3. DIRECTIONAL SPECTRUM OBTAINED FOR FREQUENCY
0.0703 Hz WITH AND WITHOUT W$_2$ SMOOTHING
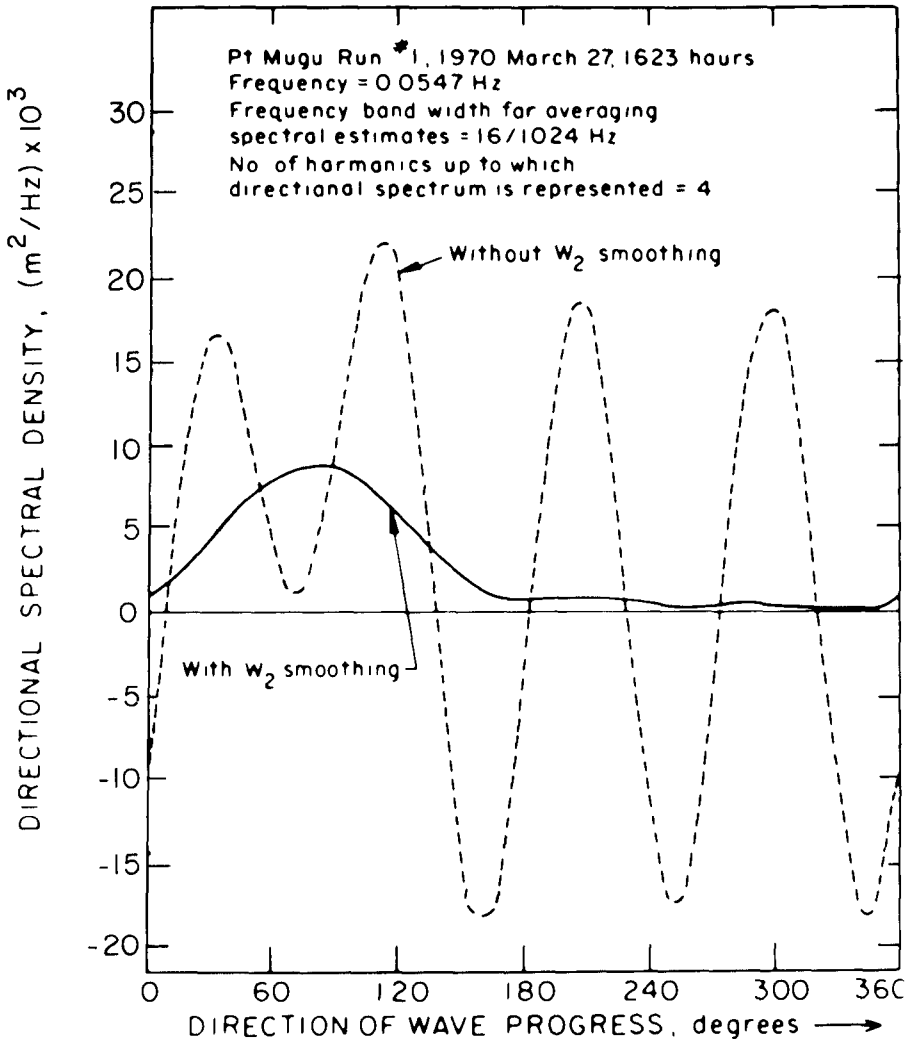
FIG. 4 DIRECTIONAL SPECTRUM OBTAINED FOR FREQUENCY
0 0547 Hz WITH AND WITHOUT W₂ SMOOTHING

CHAPTER 15

OPTIMAL DESIGN FOR WAVE SPECTRUM ESTIMATES

M. A. Tayfun,[1] C. Y. Yang,[2] and G. C. Hsiao[3]

ABSTRACT

Non-stationarity in an actual wave field restricts the application of the existing methods of estimating spectra. Despite the enormous amount of research work in the past, an analyst today is still faced with the lack of a unique procedure capable of providing a spectrum estimate which can be considered as the most accurate for the wave data collected under conditions where the stationarity assumption is in doubt. In this paper a generalized method is presented for estimating one dimensional frequency spectrum considering the non-stationarity. The generalized method and the associated design relations provide an effective measure for assessing the statistical quality of spectrum estimates, and a natural criterion as to how to select an optimal sample size. Concepts are illustrated by actual wave data analysis, and the validity of the procedure is demonstrated by simulation. In a simple manner, all concepts and methods developed for the non-stationary frequency spectrum apply to the wave number spectrum with spatial inhomogeneity. For simplicity, the presentation here will be primarily directed to the frequency spectrum.

INTRODUCTION

The computation of one dimensional frequency or wave number spectra is of fund-amental importance in a statistical description of the ocean surface. However, the applicability of the existing methods [Blackman and Tukey, 1959; Hinich and Clay, 1968; Jenkins and Watts, 1969; Otnes and Enochson, 1972] is restricted by the basic assumption of stationarity or homogeneity. This constraint is violated in many cases of considerable interest such as the storm-generated waves, and the shallow water waves undergoing spatial modifications due to bottom friction, refraction and shoaling. The results given by Ploeg [1972] clearly indicate that, during the history of a storm generated wave field, major spectral components change in magnitude as much as 200% within twelve minutes. In the absence of a physically meaningful spectral theory for non-stationary processes, the selection of a sample size consistent with stationarity or spatial homogeneity becomes a major concern. In the time domain this selection is limited to 15-20 minutes [Harris, 1972; Borgman, 1972], based on the general experience in wave analysis but without a formal criterion. Tayfun et al. [1972] have shown that, even in a seemingly stationary wave field, significant differences in magnitude and shape exist between the stationary and non-stationary spectral estimates computed from the same set of data at various times. Realistic wave fields have a general time-dependent character, and a sweeping assumption of stationarity cannot be justified for a wave field on a visual or, an intuitive basis. The selection of a sample size in space is even more subjective and ambiguous due to the lack of experience [Schule et al., 1971; Collins, 1972].

---

[1] Assistant Professor of Civil Engineering
[2] Professor of Civil Engineering and Marine Studies
[3] Associate Professor of Mathematics, University of Delaware, Newark, Delaware 19711

Having limitations on the available sample size for spectral analysis presents serious difficulties in the description of the statistical quality of spectrum estimates, and, therefore, in establishing a uniquely determined design rationale for estimating a spectrum which can be considered as the most accurate available from the data. The basic criteria for the statistical quality of a spectral estimate are its bias (or resolution) and variability (or stability). Bias is a measure of how well an estimate approximates the true spectrum Variability is a consistency description for spectral estimates. The former arises as a direct consequence of the imperfections of various lag windows or spectral filters, and the latter essentially as a result of employing a single sample record A good quality estimate is therefore characterized by negligible bias (or high resolution) and low variability (or high stability). In the present state of the art variability of estimates is described in terms of probability confidence intervals in analogy with the properties of a chi-square variate. This analogy has proven satisfactory under fairly general conditions [Borgman, 1972]. However, since chi-square confidence intervals are constructed with reference to the spectral estimates themselves, the requirement that an estimate have negligible bias is clearly of paramount importance in this approach. With no limitation on the sample size and in the absence of periodic components, it is in principle possible to construct spectrum estimates with negligible bias by taking larger sample sizes. In this case a variability criterion based on the chi-square confidence intervals alone constitutes an adequately simple design criterion for spectrum estimations. On the other hand, with limitations placed on the sample size on account of either computational practicality or non-stationary conditions, spectrum estimates should realistically be expected to have bias as well as variability errors. In such cases a spectral design in terms of the chi-square confidence intervals alone cannot be justified, and a more effective design criterion based on the optimal balance between bias and variability errors is required.

The purpose of this study is, therefore, to present a generalized method and an optimal design rationale for wave spectrum estimations under realistic conditions in an objective manner. The approach is based on the non-stationary spectral theory developed by Priestley [1965, 1966, 1967] from a smooth extension of the classical stationary concepts. Previous work in this area [Brown, 1967, Tayfun et al., 1972] indicated the applicability of this concept to ocean waves. Further investigations of the non-stationary spectral theory reveals that a generalized approach and a uniquely determined design rationale for estimating spectra are possible based on an optimization of the statistical errors concisely contained in a relative mean-square error criterion. This criterion consists of bias of estimates in both time and frequency domains (or, space and wave number domains) as well as variability, and, therefore, provides an effective measure to describe the overall statistical quality of spectrum estimates. A minimization of the relative mean-square error expressed as a function of a general filter or, lag window characteristics and various wave field parameters yields a unique set of design relations in terms of shapes and parameters of filters and the sample size. The general concept and the associated design relations are presented primarily in physical terms and emphasis is placed on the application to ocean waves.

GENERALIZED SPECTRAL REPRESENTATION OF NON-STATIONARY PROCESSES

In a random wave field the surface oscillations from the mean water level observed at a fixed position is a one-dimensional zero-mean random process. If the wave field is stationary, this process admits a stochastic Fourier representation of the form

$$\eta(t) = \int_{-\infty}^{\infty} e^{i\omega t} \, dZ(\omega) \tag{1}$$

where $i = \sqrt{-1}$, $Z(\omega)$ is a zero-mean random process continuously indexed with respect to a frequency parameter ω and with orthogonal increments such that, for a non-negative even function $S(\omega)$,

$$<dZ(\omega) \, d\overline{Z}(\omega')> = \begin{cases} 0, & \omega \neq \omega' \\ S(\omega) \, d\omega, & \omega = \omega' \end{cases} \tag{2}$$

where the overbar denotes the complex conjugate.

The mean energy per unit horizontal area of wave motion is proportional to the mean-square of the surface oscillations given, using (1) and (2), by

$$<|\eta(t)|^2> = \int_{-\infty}^{\infty} S(\omega) \, d\omega$$

The function $S(\omega)$ is recognized as the two-sided energy spectral density of the wave process. Replacing the time t with a spatial variable x and the frequency ω with the wave number k in the preceding equations yields the representation of a homogeneous wave field with the wave number spectral density $S(k)$.

The general representation (1) is in an abstract form in which neither an explicit probability structure nor any specific physical considerations are taken into account. It simply states that the process $\eta(t)$ may be regarded as a superposition of many harmonic components with different frequencies and time-independent random amplitudes $dZ(\omega)$. Realizing that $\eta(t)$ is real and negative frequencies have no physical meaning, the representation (1) can be rewritten as

$$\eta(t) = \int_{0}^{\infty} \{\cos\omega t \, dV_1(\omega) + \sin\omega t \, dV_2(\omega)\} \tag{3}$$

where

$$dV_1(\omega) = dZ(\omega) - dZ(-\omega)$$
$$dV_2(\omega) = i\{dZ(\omega) + dZ(-\omega)\} \tag{4}$$

are mutually orthogonal processes both real and such that

$$<|dV_1(\omega)|^2> = <|dV_2(\omega)|^2> = 2 <|dZ(\omega)|^2> = 2S(\omega) \, d\omega$$

Furthermore, if the processes V_1 and V_2 are chosen so that

$$dV_1(\omega) = 2\{S(\omega) \, d\omega\}^{1/2} \cos\phi_\omega$$
$$dV_2(\omega) = -2\{S(\omega) \, d\omega\}^{1/2} \sin\phi_\omega \tag{5}$$

in which ϕ_ω are independent random variables identically and uniformly distributed in the interval $[0,2\pi]$, it is seen that (1) reduces to

$$\eta(t) = \sqrt{2} \int_0^\infty \cos(\omega t + \phi_\omega) \ \sqrt{2S(\omega)d\omega} \tag{6}$$

The above form of (1) corresponds to Pierson's [Pierson and Marks, 1952] well-known stationary Gaussian model where the quantity $2S(\omega)$ is the one-sided energy spectral density.

When the wave field is non-stationary the process $\eta(t)$ can be represented in the generalized form [Priestley 1965, 1966, 1967, 1973],

$$\eta(t) = \int_{-\infty}^\infty A(t,\omega) \ e^{i\omega t} \ dZ(\omega) \tag{7}$$

where the new quantity $A(t,\omega)$ is a deterministic modulating function of time and frequency. Equation (7) states that $\eta(t)$ is the superposition of many harmonic components, with different frequencies and time-dependent random amplitudes $\{A(t,\omega)dZ(\omega)\}$. In the limiting case when $A(t,\omega) \rightarrow 1$, equation (7) reduces to (1) for the stationary wave process.

The mean-square of the process $\eta(t)$ is readily obtained, using (2) and (7), as

$$<|\eta(t)|^2> = \int_{-\infty}^\infty |A(t,\omega)|^2 \ S(\omega)d\omega \tag{8}$$

Hence, the non-stationary spectral density of the wave process is given by

$$S(t,\omega) = |A(t,\omega)|^2 \ S(\omega) \tag{9}$$

As in the stationary case, equation (7) for the non-stationary wave process $\eta(t)$ may be rewritten in the form [Brown, 1967],

$$\eta(t) = \sqrt{2} \int_0^\infty \cos(\omega t + \phi_\omega) \ \sqrt{2S(t,\omega)d\omega} \tag{10}$$

ESTIMATION OF NON-STATIONARY SPECTRA

Having developed the above theoretical basis, the attention may now be focused on the main problem which is to estimate, for a given wave record $\eta(t)$, the non-stationary spectral density $S(t,\omega)$. This estimation is based on a filtering technique with two fundamental concepts [Priestley 1965, 1966, 1967]. One is the concept of resonance. It is well-known in system response theory that when a disturbance is applied to a linear system whose natural frequency is ω, the output response will be primarily in the neighborhood of that frequency ω. In this manner, when the sample record $\eta(t)$ (disturbance) is passed through a linear filter (system) with a central frequency ω, the output is a record with Fourier components primarily around ω. The second concept concerns the time lag between the input and output records. The response of a system to an impulsive disturbance usually lasts for a short time. Quantitatively, this system

behavior is described by the width of its system impulse response function. For a
system or filter with a narrow impulse response function, the output record at any
instant t for a general input sample record depends only on that part of the input
sample in the immediate neighborhood of t. In applying the above two concepts in the
filtering technique, one may conclude that when η(t) is passed through a filter with a
narrow frequency response centered around ω, the output will be a record whose frequency
composition is primarily around ω, and whose magnitude at each instant relates only to
those of the input sample η(t) in the neighborhood of the same time. To put these ideas
in a mathematical form, let g(t) be the narrow impulse response function of a filter
with a natural frequency centered around ω = 0. Assume further that g(t) is a con-
tinuous function identically zero for values $|t| \geq h$, where h is a positive constant
(width parameter), and that it is normalized so that

$$2\pi \int_{-h}^{h} |g(u)|^2 \, du = 1$$

Then, the function g(t)exp(-iωt) corresponds to the impulse response function of a filter
which has the same form as that of g(t) but whose natural frequency is shifted to the
central frequency ω. The output record

$$U(t,\omega) = \int_{-h}^{h} g(u)\eta(t-u) \, e^{-iu\omega} \, du \tag{11}$$

represents at each time t that part of the sample η(t) in the neighborhood of frequency
ω. Now, if one further processes the output record U(t,ω) by a squaring and an
averaging (or weighting) operations over the neighboring values in time, the end result
is the mean-square in the vicinity of frequency ω and time t. This is identical with
the definition of power spectrum density with the addition of a time trend. To
formalize the squaring and averaging operations in a mathematical form, let w(t) be a
non-negative weighting function identically zero for values $|t| \geq T'$, where T' is a
positive width parameter, and properly normalized so that

$$\int_{-T'}^{T'} w(u) \, du = 1$$

The estimated non-stationary spectral density at frequency ω and time t is

$$\hat{S}(t,\omega) = \int_{-T'}^{T'} w(u) \, |U(t-u,\omega)|^2 \, du \tag{12}$$

It is evident from (11) and (12) that the minimum sample length that is required in
this procedure is

$$T_{min} = 2(h + T') \tag{13}$$

In the filtering process (11), it is required that the impulse response function
g(t)exp(-iωt) be narrow (small h) so that the output retains the instantaneous behavior
of the input sample η(t). In the mean time it is required that the output record
U(t,ω) consist of primarily components with frequencies in the neighborhood of ω. Since
the frequency composition of the output record through the filtering process is directly
related to the frequency response function of the filter in the sense that a narrow

frequency response function provides an output with high frequency concentration around ω, it is evident that a filter which has both a narrow frequency response function and a narrow impulse response function is required. In other words, the function g(t) is required to have high "resolving" powers over both frequency and time domains. Unfortunately, the two requirements are conflicting because the impulse and frequency response functions are a Fourier transform pair, and, therefore, if one is narrow, the other must be wide. This leads to the problem of an optimal choice for g and its width h so that both criteria are satisfied to a certain degree. These characteristics are quite unlike those of a filter in the stationary analysis where there is no inherent requirement on the local time, and the filter is required to be narrow in the frequency domain only.

In the selection of the weighting function w(t) it is required that its effective width T' be much wider than the width h of g(t) so that whereas g(t) operates on the input sample record locally in time, w(t) will do so over a substantially larger time interval to provide a sufficient averaging or smoothing effect. On the other hand smoothing over a very large interval in time introduces a smudging error and, therefore, decreases the resolution of the estimates Ŝ over time. Consequently, the selection of the weighting function w(t) and its width T' should be made on the basis of a trade off between the two conflicting requirements, a satisfactory resolution in time and an adequate stability for the estimates Ŝ(tΔt,ω).

OPTIMAL DESIGN RELATIONS

In general, the estimate Ŝ will have errors on account of the imperfections of the filter and weighting functions g(t) and w(t), the non-stationarity in the wave process, and the analysis of only one sample or one realization. The imperfections of g and w, and the non-stationarity of a wave process introduce bias or resolution errors to the estimate Ŝ over both time and frequency. The consequence of using only one sample is reflected in the variability or stability errors. The overall statistical quality of the spectral estimates of the form (12) is characterized by the relative mean-square error function defined, at a prescribed time t and frequency ω, by

$$M = \frac{<\{\hat{S}-S\}^2>}{S^2} = \frac{\text{bias}^2\{\hat{S}\}}{S^2} + \frac{\text{var}\{\hat{S}\}}{S^2} , \qquad (14)$$

where bias $\{\hat{S}\} = <\hat{S}> - S$, and var$\{\hat{S}\} = <\hat{S}^2> - <S>^2$. The function M depends on the functional forms of g(t) and w(t), the parameters h and T', and spectral bandwidth characteristics in time and frequency associated with the wave process [see, e.g., Priestley, 1966]. In an implicit manner, the functional form of M can be written concisely in the form

$$M = M\{\tilde{C},h,T',B_o(t,\omega), B_f(t,\omega)\}, \qquad (15)$$

where $\tilde{C} = (C_{g1},C_{g2},C_{w1},C_{w2})$ denotes a set of coefficients which determine the characteristic shapes of g(t) and w(t), and $B_o(t,\omega)$ and $B_f(t,\omega)$ are defined as bandwidth parameters of the theoretical spectral density S(t,ω) regarded as a distribution over time and frequency, respectively. These parameters are given by

$$B_o(t,\omega) = \left|\frac{S}{\partial^2 S/\partial t^2}\right|^{1/2} \quad \text{and} \quad B_f(t,\omega) = \left|\frac{S}{\partial^2 S/\partial \omega^2}\right|^{1/2} \qquad (16)$$

The spectral bandwidth over frequency $B_f(t,\omega)$ with the dimension $(time)^{-1}$ is a well-known concept (with an exclusion of time dependency) in the stationary analysis. It is a measure of the shape of $S(t,\omega)$ as a function of frequency. A small value $B_f(t,\omega)$ indicates a highly peaked spectral density over frequency. The spectral bandwidth $B_0(t,\omega)$ with the dimension (time) is similarly defined, and it provides the measure for the temporal variation of the spectral density $S(t,\omega)$. Therefore, this parameter reflects the non-stationarity in a wave process. The smaller $B_0(t,\omega)$ is, the stronger is the non-stationarity. In the limiting case, when $S(t,\omega) \to S(\omega)$, corresponding to a stationary process, $B_0(t,\omega) \to \infty$.

Insomuch as the mean-square error M reflects the overall errors associated with the imperfections of $g(t)$ and $w(t)$, and the parameters h and T', the optimal procedure must be based on those parameters that minimize the error M for a given wave process characterized by the bandwidth parameters $B_0(t,\omega)$ and $B_f(t,\omega)$. This approach yields a set of unique optimal design relations in terms of the minimum estimation error for a given wave situation, the optimal shapes $g(t)$ and $w(t)$, the parameters h and T', and the optimal sample size [see Appendix 1 for derivations]. These design relations in general have a time and frequency dependent nature. However, of the various possible choices of the optimal design criterion, that which minimizes the maximum possible error over the ranges of both the frequency and the time of interest provides the simplest one amenable to practical computations. Specifically denoting the optimal values by the subscript zero, these relations are summarized as follows.

$$M_o = 3 \left\{ \frac{C_{g1} C_{g2} C_{w1} C_{w2}}{2 \, B_0 B_f} \right\}^{2/3} \tag{17}$$

is the minimal estimation error, where B_0 and B_f denote respectively the values $B_0(t,\omega)$ and $B_f(t,\omega)$ which minimize the product $\{B_0(t,\omega) B_f(t,\omega)\}$, i.e.,

$$B_0 B_f = \min_{T_1 \le t \le T_2 \atop \omega} \{B_0(t,\omega) B_f(t,\omega)\} \tag{18}$$

where the selected wave record covers the interval (T_1, T_2). The optimal values of the parameters h and T' are given respectively by

$$h_o = \left\{\frac{3}{M_o}\right\}^{1/4} \frac{C_{g1}}{B_f} \quad \text{and} \quad T_o' = \left\{\frac{M_o}{3}\right\}^{1/4} \frac{B_0}{C_{w1}} \tag{19}$$

with the ratio

$$\left[\frac{h_o}{T_o'}\right] = \left[\frac{C_{w1}^2 \, C_{g1}^2}{B_0^2 \, B_f^2 \, C_{w2} C_{g2}}\right]^{1/3} \tag{20}$$

The optimal sample size $(T_{min})_o$ is obtained from (13) using the above values of h and T'. In the preceding results, the constants $C_{w1} = \sqrt{0.2}$, $C_{w2} = 6\pi/5$, $C_{g1} = \pi/\sqrt{3}$, and $C_{g2} \approx .1528$ relate to the optimal weighting and filter functions given by

$$w(t) = (3/4T_o') \{1-(t/T_o')^2\} \; ; \quad |t| \le T_o' \tag{21}$$

and

$$g(t) = (6\pi h_o)^{-1/2} \{1 + \cos(\pi t/h_o)\} \; ; \quad |t| \le h_o \tag{22}$$

corresponding, respectively, to the Parzen and Hanning windows in the stationary spectral theory [Jenkins and Watts, 1969].

The salient features of the optimal design relations can be pointed out as follows:

(1) The minimal error M_o consists of bias and variability errors in a one to two ratio. This is a consequence of the fact that bias errors are more sensitive to changes in the design parameters h and T' as compared to variability errors. Hence, the proper balance between bias and variability should be maintained in this estimation procedure in contrast with the general tendency in the routinely used procedures such as the autocorrelation and the Fast Fourier Transform techniques to disregard bias errors completely and to base the spectral design purely on a variability criterion.

(2) In the limiting case of a homogeneous process; i.e., as $B_o \to \infty$, it is readily seen that $M_o \to 0$, h_o and $T_o' \to \infty$, as the ratio $(h_o/T_o') \to 0$. The spectral estimates with the asymptotic property $(M_o \to 0)$ are referred to as consistent estimates in the classical spectral theory. The results in this particular limiting case are very much in accord with the general character of the conventional analysis. Therefore, there is, in principle, no bounded optimal spectral design relations in the homogeneous case. However, from a practical point of view, the limiting form of the design relations implies that in such cases one should take longer sample sizes, while decreasing the ratio (h_o/T_o'), until the spectral estimates attain a consistent, or simply convergent behavior.

(3) One particularly interesting feature about the time and frequency independent design relations is that, given a record length T, they provide the functions g(t) and w(t) with constant width parameters h_o and T_o', and therefore require a fixed minimum record length $(T_{min})_o$ to construct spectral estimates which are, in statistical quality, at least equal to or better than the estimate characterized by the maximum M_o.

(4) It is recalled from the definitions (16) that $B_o(t,\omega)$ and $B_f(t,\omega)$ relate inversely to the second partial derivatives of a spectral density over time and frequency, respectively. Hence, being derived from the minimal product $B_o(t,\omega) B_f(t,\omega)$, the parameters B_o and B_f are associated with the narrowest peaks and valleys in a spectrum in time and frequency. Moreover, it is the simultaneous occurence of these peaks and/or valleys over both time and frequency, as evidenced by the product $B_o B_f$ in (18), which characterizes the maximum error M_o. Therefore, the dimensionless product $B_o B_f$ serves as an overall measure of significant spectral characteristics of a wave process in the sense that the larger this product is, the more accurate the estimation procedure becomes. On the other hand, it is realized that a background knowledge on the parameters B_o and B_f is required before one can proceed to compute the spectral density in a given realistic situation. These parameters must be estimated approximately either on a valid theoretical basis, or from "pilot" estimates of a spectral density

DIGITAL COMPUTATIONS

In digital computations of the non-stationary spectrum of a wave process $\eta(t)$, the optimal design relations remain invariant provided that a few simple modifications are made in the estimation procedure as follows. Consider a wave record $\eta(t)$ digitally sampled at intervals of Δt so that one has a sequence $\eta_1, \eta_2, \quad$, where $\eta_n \simeq \eta(n\Delta t)$. To make sure that no errors will be introduced in the digital computation due to aliasing errors, assume that the interval Δt is at most equal to the Nyquist interval. Under this assumption it is convenient to regard the sequence $\{\eta_n\}$ as if it consisted of points at unit time intervals. This is equivalent to transforming the original frequency scale into a standarized dimensionless frequency $\omega^* = \omega\Delta t$ defined in the interval $(-\pi, \pi)$.

Consequently, the estimated spectral density, say $S_d(n,\omega^*)$, of the discrete sequence $\{\eta_n\}$ and that of the actual wave process $\eta(n\Delta t)$ are related to one another in the form

$$\hat{S}(n\Delta t, \omega^*/\Delta t) = \Delta t \; \hat{S}_d(n,\omega^*), \quad |\omega^*| < \pi \tag{23}$$

where

$$\hat{S}_d(n,\omega^*) = \sum_{j=-M}^{M} w_j \; |U_{n-j}(\omega^*)|^2 \tag{24}$$

and

$$U_n(\omega^*) = \sum_{j=-N}^{N} g_j \; \eta_{n-j} \; e^{-ij\omega^*} \tag{25}$$

are the discrete time analogues of (11) and (12), with $g_j = g(j\Delta t)$ and $w_j = w(j\Delta t)$ derived from the continuous time versions $g(t)$ and $w(t)$. The integer width parameters N and M are now interpreted as the largest integers smaller than $(h_o/\Delta t)$ and $(T_o'/\Delta t)$, respectively, where h_o and T_o' are as previously defined as in (19). Hence, it follows from (21) and (22) that

$$g_j = (6\pi N)^{-1/2} \; \{1 + \cos(j\pi/N)\} \; ; \; j = -N,\ldots,-1,0,1,\ldots,N \tag{26}$$

and for $M \gg 1$

$$w_j = (3/4M) \; \{1 - (j/M)^2\} \; ; \; j = -M,\ldots,-1,0,1,\ldots,M \tag{27}$$

It is evident that the optimal length of the sequence $\{\eta_n\}$ is now given by $2(N + M)$.

ILLUSTRATIVE APPLICATIONS

EXAMPLE 1: A Storm Generated Non-stationary Wave Field. A significant application of the proposed spectral estimation procedure and the associated optimal design relations is in the analysis of storm generated extreme waves. A particularly interesting analysis of such a non-stationary wave field has been illustrated by J. Ploeg [1972] in terms of the time history of one dimensional frequency spectra collected on Lake Ontario during a storm on October 24-25, 1971. The reference covers about 13 hours of the storm with approximately 200 sequential spectral analyses performed through the Fast Fourier Transform technique using 16 minute overlapping segments, with the starting points approximately 4 minutes apart. With a proper caution to the non-stationary effect, Ploeg presents the results of Lake Ontario study in three figures [Figures 7 through 9 – J. Ploeg, 1972], and draws various conclusions as follows. The spectral history of the storm-generated wave field [Figure 7 – Ploeg] shows the familiar build-up with the peak of the spectrum density continuously shifting to the lower frequencies, while [Figure 8 – Ploeg] the higher frequency spectral components reach saturation and remain essentially stationary. The non-stationarity of the wave process at lower frequency spectral components, in particular at the peak spectral component is clearly observed. The time history of the spectral peak frequency [Figure 9 – Ploeg] shows a tendency to jump between discrete frequencies, while shifting towards lower values in a manner consistent with the shifting of the entire spectral density function to lower frequencies as the wave field builds up, with the higher frequency components remaining saturated. There is no physical explanation offered for the jumps of the spectral peak frequency. It is quite plausible that this effect is due to the "overshoot" effect observed in the typical growth of a spectral component [Barnett and Sutherland, 1968; Plate, 1971].

It is of interest to apply the optimal design relations to such non-stationary wave records. However, before one can proceed to do so, it is necessary to know the spectral bandwidth parameters B_o and B_f of the wave field. Hence, the first step is to estimate these parameters on a theoretical basis and/or from pilot estimates of the spectral density. In the particular case of a storm generated wave field, a theoretical basis is provided by the concept of equilibrium range [Phillips, 1965] which asserts that the spectral growth of a wave component is limited by breaking. Neglecting the overshoot effect, and for the general case of finite fetch, and variable wind conditions, the concept requires that the spectral density function $S(t,\omega)$ have the form

$$S(t,\omega) = \beta \; g^2\omega^{-5} \; ; \quad \omega \geq \omega^*(t) \tag{28}$$

where β is a dimensionless constant dependent in general on wind speed and fetch [Strekalov, et al., 1972], g is the gravitational acceleration, and $\omega^*(t)$ denote the time-dependent spectral peak frequency. In other words, $\omega^*(t)$ provides the required time-dependency, and, therefore, $(d\omega^*/dt)$ relates in a fairly simple manner to the rate at which the front face of the spectrum builds up as a result of the net rate of energy input between the generative wind and the dissipative breaking and friction effects. Hence, from (16), and (28), it follows that

$$B_f(t,\omega) \simeq \omega/\sqrt{30} \; ; \quad \omega \geq \omega^*(t) \tag{29}$$

and

$$B_o(t,\omega) \simeq \begin{cases} \dfrac{\omega}{\sqrt{51}} \; \left| \; 6 \left[\dfrac{d\omega}{dt}\right]^2 - \omega \dfrac{d^2\omega}{dt^2} \; \right|^{-1/2} \; , & \omega \simeq \omega^*(t) \\ \\ \infty & ; \text{ otherwise} \end{cases} \tag{30}$$

The minimum of the product of the above two parameters as defined by equation (18) is then

$$B_o B_f = \begin{cases} \min_{T_1 \leq t \leq T_2} \{B_o(t,\omega) B_f(t,\omega)\} \; ; & \omega \simeq \omega^*(t) \\ \\ \infty & ; \text{ otherwise} \end{cases} \tag{31}$$

The spectral bandwidths B_o and B_f must be estimated numerically on the basis of the preceding guideline (31) and from pilot estimates of the time history of the spectral peak frequency ω^*. Such pilot estimates can be obtained in a heuristic fashion either through conventional techniques by using overlapping segments of a sample or, through the generalized filter method described in this paper in an iterative manner [see, e.g., Tayfun et al., 1972]. The time history of the spectral peak frequency $\omega^*(t)$ obtained by Ploeg has been reproduced in part in the lower part of Figure 1 here. This data is associated with the extreme wind-wave conditions and, for the purpose of illustrating the optimal design considerations, is used here as the pilot estimates. The spectral bandwidth characteristics computed numerically on the basis of these pilot estimates and the relation (31) are likewise presented in Figure 1. Table 1 summarizes the optimal design considerations and the expected quality of spectral estimates in various intervals $(T_1,T_2) = (1800, 1900)$, $(1900, 2000)$, and $(2000, 2100)$. The design relations in each of the preceding intervals are based on the peak spectral component in the neighborhood of an instant where non-stationarity is the most stringent, indicated by the vertical dashed lines A, B, and C, respectively (Figure 1).

EXAMPLE 2:   A Spatially Inhomogeneous Wave Field. As an example of a spatially inhomogeneous wave process, consider a unidirectional wave field where waves in a fully developed state at deep water propagate towards the shore into intermediate and shallow water regions over a variable depth topography with a mean slope s. Assuming no dissipative effects and no wind-generation, the wave field is stationary in time, but

Time Interval (hrs)	B_o (sec)	B_f (sec-1)	$B_o B_f$	Quality, M_o (%)	h_o (sec)	T_o' (sec)	Sample Size, $(T_{min})_o$ (sec)
1800 - 1900	500	.20	100	≤ 3.12	29	358	774
1900 - 2000	170	.22	37	≤ 6.4	22	145	334
2000 - 2100	280	.20	56	≤ 4.9	25	223	496

TABLE 1. Optimal spectral design considerations in a storm-generated wave field.

inhomogeneous in space due to wave shoaling. Using a reference frame with a positive x-axis extending from the deepwater surface toward the shore, the rate of change of energy spectral density along a way ray (the x-axis) is [Collins, 1972]

$$d\{cS(x,k)\}/dx = 0, \tag{32}$$

where $S(x,k)$ and $c = \omega/k$ are respectively the inhomogeneous spectral density and the phase speed. It is noted that the frequency of a wave component is conserved whereas the corresponding wave number is depth-dependent. Based on this result and from an integration of (32) between two points, one at deep water denoted by the subscript zero ($x_o = 0$), and the other towards the shore at a location x where the water depth is $D = D(x)$, it follows that

$$S(x,k) \approx k \, k_o^{-1} \, S_o(k_o). \tag{33}$$

Using the relation between the shallow water wave number k and deep water k_o,

$$k_o = k \tanh kD \tag{34}$$

equation (33) can be written in the form

$$S(x,k) = \coth kD \, S_o(k_o). \tag{35}$$

A comparison of (35) with (9) indicates that the function $\coth kD$ corresponds to the squared modulating function $|A|^2$ in the general definition of an inhomogeneous spectrum density.

The spatial and wave number bandwidth parameters $B_o(x,k)$ and $B_f(x,k)$, respectively, are derived from (16) and (33) (see Appendix 2). The dimensionless forms of these parameters and the spectral product $\{B_o(x,k)B_f(x,k)\}$ are presented in Figure 2 as functions of the dimensionless depth kD. For a given mean slope s, for all wave numbers $k \geq k*$ (the spectral peak wave number), and in the region of interest $\infty > D(x) \geq D$, it is seen from Figure 2 that

$$B_o = \lim_{kD(x) \to k*D} \left[B_o(x,k) \right] \quad \text{and} \quad B_f = \lim_{kD(x) \to k*D} \left[B_f(x,k) \right] \tag{36}$$

In deep water, $D \to \infty$, and $B_o \to \infty$, as the wave field becomes spatially homogeneous. For shallow water with small k*D values

$$B_o \approx \frac{2D}{\sqrt{3}^{-1} s} \tag{37}$$

Hence, in this region the spatial inhomogeneity of the wave process is proportional directly to the local slope s, and inversely to the depth D as intuitively expected. A similar argument for the wave number spectral bandwidth B_f indicates that, as $D \to \infty$,

$B_f \to (k_o^* /2\sqrt{3})$, the spectral bandwidth at deep water. Moreover this limiting value is an upper bound, and B_f monotonically decreases as the water depth becomes shallower In other words, the spectral density $S(x,k)$ becomes increasingly peaked. In general then, since the product $B_o B_f$ decreases as the slope s becomes larger and/or the depth D becomes shallower, the estimation procedure is expected to be increasingly less accurate. To illustrate the effect of variations in the bottom slope s, consider the density $S(x,k)$ at a location with depth D = 10 ft , deep water spectral peak wave number k_o^* = 0.076 (ft^{-1}). Hence, it follows from (34) that $k^*D = 1.0$. The dimensionless values B_o, B_f, and therefore the product $B_o B_f$ are obtained from Figure 2 by using $kD(x) = k^* D = 1.0$. For mean bottom slope s (1/120, 1/90, 1/60, 1/30), the optimal design parameters are summarized in Table 2. It is seen that as the slope increases, the wave process becomes more inhomogeneous, the available sample size is increasingly limited, and the expected quality of estimates rapidly diminishes. It should be emphasized that this is true for the spectral estimates in the vicinity of the peak wave number k_o^* = 0.1 (ft^{-1}) at depth D = 10 ft where the spatial inhomogeneity is the most stringent. The accuracy of estimates corresponding to other wave numbers at the same depth, and of all estimates at depths larger than D = 10 ft will be equal to or better than M_o.

Slope,s	B_o (ft)	B_f (ft^{-1})	$B_o B_f$	Quality,M_o (%)	h_o (ft)	T_o' (ft)	Sample Size, $(T_{min})_o$ (ft)
1/120	1400	0.0154	21.6	$\leq$ 14	250	1450	3400
1/90	1050	0.0154	16.2	$\leq$ 18	240	1280	3020
1/60	700	0.0154	10.8	$\leq$ 24	220	830	2100
1/30	350	0.0154	5.4	$\leq$ 37	200	460	1320

TABLE 2   Optimal spectral design considerations in a shoaling wave field.

The preceding discussion provides a simple theoretical basis to investigate the validity of the proposed estimation procedure and the associated design relations. With this purpose in mind, consider the case with variable depth profile illustrated in Figure 3, and assume that the fully developed deep water conditions can be characterized in terms of a Pierson-Moskowitz spectrum [Pierson and Moskowitz, 1964] given in the wave number domain by

$$S_o(k_o) = 0.5 \, \alpha \, k_o^{-3} \exp\{-\gamma g^2 (v \, k_o)^{-4}\}, \tag{38}$$

where $\alpha(= 8.1 \times 10^{-3})$ and $\gamma(= 0.74)$ are dimensionless constants, v is the wind speed, with the spectral peak wave number k_o^* given by

$$k_o^* = (0.52\gamma)^{1/2} (g/v^2) \tag{39}$$

The inhomogeneous wave number spectral density $S(x,k)$ at a given depth $D(x) = D$ is readily obtained from (33) and (38). For the profile shown in Figure 3 with k_o^* = 0.076 (ft^{-1}) (i.e., v $\simeq$ 18 ft. sec^{-1}), the theoretical forms of the inhomogeneous density $S(x,k)$ at locations (1,2,3) corresponding to the values D = 50, 20, and 10 (ft) are plotted in Figure 3. The spectral density $S(x,k)$ at D = 50(ft) is not influenced by shoaling effects, and, therefore, is the same as the deep water density $S_o(k_o)$. As the depth gets shallower at locations 2 and 3, the deep water spectral components are modified from lower wave numbers to the higher in a non-uniform manner as the form of the spectral density $S(x,k)$ becomes increasingly more peaked.

With the foregoing theoretical results on inhomogeneous spectra, it is then possible to generate realization of inhomogeneous wave series by a Gaussian wave surface model and a simulation technique (see Appendix 3). Finally the optimal estimation procedure

is applied to the simulated wave series to obtain wave spectra. The estimated spectra obtained through (23), (24), and (25), and based on the required design relations in Table 2 corresponding to s = 1/90 and D = 10 (ft), are presented in Figure 3 for comparison with the theoretical forms. It is seen that, although the accuracy in the vicinity of a spectral peak, in particular at D = 10 (ft), is relatively poor as expected, the estimates in general agree very favorably with the theoretical forms. Thus the validity of the spectral design considerations is demonstrated.

SUMMARY AND CONCLUSIONS

A generalized procedure was described for estimating one dimensional non-stationary frequency spectra or inhomogeneous wave number spectra. In constrast to the autocorrelation approach, the procedure is based on a direct filter method which carries a simple physical interpretation and is therefore convenient to apply to actual wave fields.

The optimal design relations for the estimation procedure are constructed on the basis of a simple objective design criterion to minimize the overall statistical estimation errors which arise as a result of the imperfections of the filter and the weighting functions. Prior to the application of the estimation procedure, various spectral characteristics of the sampled wave field in time-frequency or space-wave number have to be estimated on the basis of a valid theoretical guideline and/or from pilot estimates of spectra. One of these characteristics, B_f, the spectral bandwidth in frequency is a familiar concept in the stationary analysis. The spectral bandwidth, B_o, in time or space is defined similarly and provides a measure for the inherent non-stationarity in a wave record. The spectral product $B_o B_f$ is the most significant quantity for assessing the feasibility of the proposed estimation procedure in a given situation in the sense that the larger this product is, the more feasible it is to achieve accurate spectrum estimates. In the limiting case as $B_o B_f \to \infty$ (i.e., as $B_o \to \infty$) corresponding to a dominantly stationary wave process, the procedure reduces to the stationary analysis accordingly.

Two illustrative examples are given. The first example is for the non-stationary storm wave records from Lake Ontario, October 24-25, 1971, by which the use of the estimation procedure is demonstrated. The second example is for the analysis of inhomogeneous wave number spectra of digitally simulated wave records in a shoaling wave field. By the second example, the validity of the design criterion and the estimation procedure is demonstrated through a comparison between theoretical and estimated spectra.

APPENDIX 1: DERIVATION OF OPTIMAL DESIGN RELATIONS

The relative mean-square error (14) is approximately given by [Priestley, 1969]

$$M \simeq (1/4) \{B_w^2/B_o^2(t,\omega) + B_\Gamma^2/B_f^2(t,\omega)\}^2 + C(T')^{-1} \int_{-\infty}^{\infty} |\Gamma(\omega)|^4 \, \omega \qquad (A40)$$

where $\Gamma(\omega)$ is the Fourier transform of the filter g(t), and

$$B_\Gamma = \left\{ \int_{-\infty}^{\infty} \omega^2 |\Gamma(\omega)|^2 \, d\omega \right\}^{1/2} \qquad (A41)$$

$$B_w = \left\{ \int_{-T'}^{T'} t^2 \, w(t) \, dt \right\}^{1/2} \qquad (A42)$$

$$C = \lim_{T' \to \infty} \left\{ 2\pi T' \int_{-T'}^{T'} w^2(t) \, dt \right\} \tag{A43}$$

The error M is the sum of the squared bias of an estimate $\hat{S}(t,\omega)$ over both the time and frequency, and its variance, corresponding respectively to the first and second group of terms in (A40). Utilizing the normality properties of the functions $g(t)$ and $w(t)$, two characteristic functions, $G(u)$ and $W(u)$, may be defined such that

$$G(u) = h^{1/2} g(uh) \quad ; \quad |u| < 1 \tag{A44}$$

$$W(u) = T' w(uT') \quad ; \quad |u| < 1 \tag{A45}$$

By virtue of the above definitions, it is easily shown that

$$B_\Gamma = h^{-1} \left\{ 2\pi \int_{-1}^{1} |dG/du|^2 \, du \right\}^{1/2} \overset{\text{def}}{=} h^{-1} C_{g1} \tag{A46}$$

$$\int_{-\infty}^{\infty} |\Gamma|^4 d\omega = h \left\{ 4\pi \int_{0}^{2} \left| \int_{-1}^{1-y} G(u+y)\overline{G}(u) \, du \right|^2 dy \right\} \overset{\text{def}}{=} h \, C_{g2} \tag{A47}$$

$$B_w = T' \left\{ \int_{-1}^{1} u^2 W(u) \, du \right\}^{1/2} \overset{\text{def}}{=} T' C_{w1} \tag{A48}$$

$$C = 2\pi \int_{-1}^{1} W^2(u) \, du \overset{\text{def}}{=} C_{w2} \tag{A49}$$

The error M given by (A40) can now be rewritten in terms of the parameters h, T', and the set of coefficients $\tilde{C} \equiv (C_{g1}, C_{g2}, C_{w1}, C_{w2})$, which depend only on the characteristic functions, in the form

$$M \approx (1/4) \left\{ C_{w1}^2 (T')^2 B_0^{-2}(t,\omega) + C_{g1}^2 h^{-2} B_f^{-2}(t,\omega) \right\}^2 + C_{g2}C_{w2} \, h(T')^{-1} \tag{A50}$$

An optimization of the preceding expression with respect to h and T' yields the following

$$M_0 = 3 \left[\{C_{w1}C_{w2}C_{g1}C_{g2}\}/\{2B_0(t,\omega)B_f(t,\omega)\} \right]^{2/3} \tag{A51}$$

denotes the minimal estimation error M consisting of the bias and variability errors in a one to two ratio, and corresponding to the optimal values of h and T' given by

$$h_0 = (3/M_0)^{1/4} \{C_{g1}/B_f(t,\omega)\} \tag{A52}$$

$$T_0' = (M_0/3)^{1/4} \{B_0(t,\omega)/C_{w1}\} \tag{A53}$$

Moreover, an examination of M_0 indicates that the conditions

$$\min_{W(u)} \{C_{w1}C_{w2}\} \quad \text{and} \quad \min_{G(u)} \{C_{g1}C_{g2}\} \tag{A54}$$

constitute two formal optimality criteria for choosing and possibly constructing the characteristic functions, $W(u)$ and $G(u)$, respectively. One such possibility is to

expand W(u) and G(u) in series (e.g. Fourier series or Legendre functions) with unknown coefficients, and to determine these coefficients through (A54). In particular, by letting $W(u) = \Sigma A_i P_i(u)$, in which A_i snd P_i denote, respectively, the unknown coefficients and Legendre functions of the first kind, it is easily verified that a unique solution to the first functional in (A54) is obtained, with $A_0 = 1/2$, $A_2 = 1/2$, and $A_i = 0$ for $i \neq 0,2$, as

$$W(u) = (3/4) (1 - u^2) \quad ; \quad |u| < 1 \tag{A55}$$

Therefore, $C_{w1} = \sqrt{0.2}$, $C_{w2} = 6\pi/5$, and the minimal product $\{C_{w1}C_{w2}\} = 1.686$. Interestingly, (A55) corresponds to the well-known Parzen window in the ststionary analysis [Jenkins and Watts, 1969].

The problem of finding a unique optimal G(u) in a similar manner becomes cumbersome due to the more complicate nature of the second functional in (A54). Nonetheless, the criterion in (A54) serves as a figure of merit for choosing an optimal form G(u) from the collection of spectral windows in the stationary analysis. Table 3 compares the relevant properties of most of the well-known window shapes consistent with the class of functions $\{G(u)\}$. Among the four different functions examined, the optimal one is the Hanning window given by

$$G(u) = (6\pi)^{-1/2} (1 + \cos u\pi) \quad ; \quad |u| < 1 \tag{A56}$$

Filter G(u)	C_{g1}	C_{g2}	$C_{g1}C_{g2}$
$(6\pi)^{-1/2} (1 + \cos\pi u)$	$\pi/\sqrt{3}$	.1528	.2778
$(2\pi)^{-\frac{1}{2}} \cos \frac{1}{2} (\pi u)$	$\pi/2$	.1875	.2946
$(3\pi/4)^{\frac{1}{2}} (1 - |u|)$	$\sqrt{3}$	.1725	.2988
$\{15/(32\pi)\}^{\frac{1}{2}} (1 - u^2)$	$\sqrt{(5/2)}$	.1926	.3045

TABLE 3. Properties of spectral windows.

The optimal weighting function w(t) and the filter g(t) sre now readily obtained from (A55) and (A56), and by using the definitions (A45) and (A44), respectively.

It is noted that the optimal design relations developed above depend on time t and frequency ω through the bandwidth parameters $B_0(t,\omega)$ and $B_f(t,\omega)$. However, considering a slightly different design criterion to minimize the maximum possible mean-square error over both the time and frequency, i.e.,

$$\min_{h,T', \tilde{C}} \left[\max_{t,\omega} M\{\tilde{C},h,T',B_0(t,\omega)B_f(t,\omega)\} \right] \tag{A57}$$

provides the time- and frequency-independent design relations which are the simplest for practicsl estimations of ocean wave spectra. These are readily included in the above optimal design relations, and they correspond to replacing the product $\{B_0(t,\omega)B_f(t,\omega)\}$ in (A51) with

$$B_0B_f = \min_{\substack{T_1 \leq t \leq T_2 \\ \omega}} \{B_0(t,\omega)B_f(t,\omega)\} \tag{A58}$$

where the selected record covers the interval (T_1,T_2), and interchanging $B_f(t,\omega)$ and $B_0(t,\omega)$ in (A52) and (A53), respectively, with their corresponding vslues $\tilde{B}_f$ and B_0 which realize (A58).

APPENDIX 2: SPECTRAL BANDWIDTHS IN SHOALING WAVES

From (16) and (33), the spatial bandwidth parameter is

$$B_o(x,k) = (D/\sqrt{2}\,s)\{1 +(\sinh 2kD/2kD)\}^{3/2} \{1 +(3 + \cosh 2kD)(\sinh 2kD)(4kD)^{-1}\}^{-\frac{1}{2}} \quad (A59)$$

Similarly, from (16) and (33), the spectral bandwidth $B_f(x,k)$ is given by

$$B_f(x,k)=| 2D^2\mathrm{csch}^2kD[1-k\ S_o^{-1}(dS_o/dk_o)\tanh kD] + S_o^{-1}(d^2S_o/dk_o^2)$$

$$(\tanh kD + kD\ \mathrm{sech}^2kD)^2|^{-\frac{1}{2}} \quad (A60)$$

Assuming that the deep water wave field is in a fully developed state, the wave number spectral density $S_o(k_o)$ can be expressed by using again the concept of equilibrium range, this time, in the form

$$S_o(k_o) = (\beta/2)\ k_o^{-3} \quad , \quad k_o \ge k_o^* \quad (A61)$$

where k_o^* is the spectral peak wave number. Hence, using (A61) in (A60), $B_f(x,k)$ is rewritten in an approximate but more tractable form as

$$B_f(x,k)\simeq (k/2\sqrt{3})\{(1/3)(kD/\sinh kD)^2 + [1 +(2kD/\sinh 2kD)]^2\}^{-\frac{1}{2}} \quad (A62)$$

The dimensionless forms of $B_o(x,k)$ and $B_f(x,k)$ given by (A59) and (A62), and the product $\{B_o(x,k)B_f(x,k)\}$ are illustrated in Figure 2 as functions of the dimensionless depth kD. By definition and from Figure 2, it follows that

$$B_oB_f = \min_{k,D(x)} \{B_o(x,k)B_f(x,k)\} = \lim_{kD(x)\to k^*D} \{B_o(x,k)B_f(x,k)\} \quad (A63)$$

APPENDIX 3: SIMULATION OF AN INHOMOGENEOUS WAVE SERIES

If the deep water wave field characterized by the spectral density $S_o(k_o)$ is assumed to be Gaussian, within the constraints of the linear wave theory and outside of the breaker zone, the surface oscillations $\eta(x,t)$ admit the pseudo-integral representation

$$\eta(x,t) = \sqrt{2} \int_0^\infty \cos(kx - \omega t + \phi_k) \sqrt{S(x,k)dk} \quad (A64)$$

as an inhomogeneous Gaussian process. In the above representation ϕ_k are independent random phases uniformly distributed in the interval $[0,2\pi]$ as in (6), $\omega^2=$ gk tanh kD(x), with D(x) and S(x,k) denoting, respectively, the variable depth profile and the associated one-sided inhomogeneous spectral density whose theoretical forms at various depths are illustrated in Figure 3. The representation (A64) characterizes the wave process completely as a bivariate random process stationary in time t, and inhomogeneous in space x. Moreover, it provides a convenient basis to digitally simulate samples of the surface as a bivariate (time-space) series $\eta(n\Delta x,m\Delta t)$ (n = 1,2,...; m = 1,2...), where Δx and Δt denote respectively suitably chosen spatial and temporal sampling intervals, or, as a stationary univariate time series $\eta(x, m\Delta t)$ (m = 1,2,...) at a specified location x, or, as an inhomogeneous space series $\eta(n\Delta x, t)$ (n = 1,2,...) at a prescribed time t [see, e.g., Shinozuka and Jan; 1971]. The space series $\eta(n\Delta x, t)$

corresponds to a digitized stereophotographic or laser profile of the surface. In this instance, the reference time value t is immaterial as the process $\eta(x,t)$ is stationary. In particular, choosing t = 0 for convenience, and denoting the wave number interval outside of which S(x,k) is of insignificant magnitude by $[k_L, k_R]$, such a space series is readily obtained from a digital analogue of (A64) by

$$\eta(n\Delta x) = \sqrt{2} \sum_{j=1}^{J} \cos(\tilde{k}_j n\Delta x + \phi_{k_j}) \{S(n\Delta x, k_j)\Delta k\}^{\frac{1}{2}} \qquad (A65)$$

in which $k_j = (k_L + j\Delta k)$ (j = 1,2,...,J) with J = $(k_R - k_L)/\Delta k$ corresponds to a proper discretization of the wave number k, ϕ_{k_j} (j = 1,2,..,J) the associated random phases, and $\tilde{k}_j = (k_j + \delta k_j)$, where δk_j is a small random wave number introduced to avoid the periodicity of the simulated series, and is uniformly distributed in the interval $[-(\Delta k'/2), (\Delta k'/2)]$ with $\Delta k'$ chosen such that $\Delta k >> \Delta k'$. A sample space series $\eta(n\Delta x)$ of the wave process investigated here was simulated in the described manner implementing (A65) with $\Delta x = 4$ (ft), $k_L = 0.01$, $k_R = 0.41$, $\Delta k = 0.01$, $\Delta k' = 0.002$, and J = 40, with the sample extending from the deep water reference ($x_0 = 0$, corresponding to n = 1) towards the shore up to x = 5400 (ft) (corresponding to n = 1350), satisfactorily covering and well over the region of interest where 50 > D(x) $\geq$ 10 (ft).

REFERENCES

Barnett, T. P., and A. J. Sutherland, A note on an overshoot effect in wind-generated waves, J. Geophys. Res., 73, p. 6879, 1968.

Blackman, R. B., and J. W. Tukey, The Measurement of Power Spectra, Dover Publications, 1959.

Borgman, L. E., Confidence intervals for ocean wave spectra, Proc. 13th Coastal Eng. Conf., 1 (10), 237-250, 1972.

Brown, L. J., Methods for the Analysis of Non-Stationary Time Series with Applications to Oceanography, Lab. Rep. HEL 16-3, 135 pp., Hydraulic Eng., University of California, Berkeley, California, 1967.

Collins, J. I., Prediction of shallow-water spectra, J. Geophys. Res., 77, (15), 2693 - 2707, 1972.

Harris, D. L., Characteristics of wave records in the coastal zone, Waves on Beaches, Academic Press, 1972.

Hinich, M. J., and C. S. Clay, The application of the discrete Fourier transform in the estimation of power spectra, coherence, and bispectra of geophysical data, Reviews of Geophysics, 6, 347 - 363, 1968.

Jenkins, G. M., and G. G. Watts, Spectral Analysis and Its Applications, Holden Day, 1969.

Otnes, R K., and L. Enochson, <u>Digital Time Series Analysis,</u> John Wiley and Sons, 1972.

Phillips, O. M., <u>The Dynamics of the Upper Ocean</u>, Cambridge University Press, London, 1966.

Pierson, W. J., and W. Marks, The power spectrum analysis of ocean wave records, <u>Trans. Amer. Geophys. Union</u>, <u>33</u> (6), 835 – 844, 1952.

Pierson, W. J., and L. Moskowitz, A proposed spectral form for fully developed wind seas based on the similarity theory of S. A. Kitaigorodskii, <u>J. Geophys. Res.</u>, <u>69</u> (24), 5181 – 5190, 1964.

Plate, E. J., Limitations of spectral analysis in the study of wind-generated water surface waves, <u>Proc. 1st Inter. Symp. on Stochastic Hydraulics</u>, 522 – 539, 1971.

Ploeg, J., Some results of a directional wave recording station, <u>Proc. 13th Coastal Eng. Conf.</u>, <u>1</u> (4), 131 – 144, 1972.

Priestley, M B., Evolutionary spectra and non-stationary processes, <u>J. Roy. Statist. Soc.</u>, <u>27B</u> (2), 204 – 237, 1965.

Priestley, M. B., Design relations for non-stationary processes, <u>J. Roy. Statist. Soc.</u>, <u>28B</u> (1), 228 – 240, 1966.

Priestley, M. B., Power spectral analysis of non-stationary processes, <u>J. Sound Vibration</u>, <u>6</u> (1), 86 – 97, 1967.

Priestley, M. B., and H. Tong, On the analysis of bivariate non-stationary processes, <u>J. Roy. Statist Soc.</u>, <u>35B</u> (2), 153 – 166, 1973.

Schule, J J., L. S. Simpson, and P. S. DeLeonibus, A study of fetch-limited wave spectra with an airborne laser, <u>J. Geophys. Res.</u>, <u>76</u>, 4160 – 4171, 1971.

Shinozuka, M., and C -M. Jan, <u>Simulation of Multi-variate and Multi-dimensional Processes II, Civil Eng. -Eng. Mech Rep. 12</u>, 41 pp., Columbia University, New York, N.Y., 1971.

Strekalov, S. S., V. Ph. Tsyploukhin, and S. T. Massel, Structure of sea wave spectrum, <u>Proc. 13th Coastal Eng. Conf.</u>, <u>1</u> (14), 307 – 314, 1972.

Tayfun, M. A., C. Y. Yang, and G. C. Hsiao, Non-stationary spectrum analysis of ocean waves, <u>Proc. 13th Coastal Eng. Conf.</u>, <u>1</u> (11), 251 – 269, 1972.
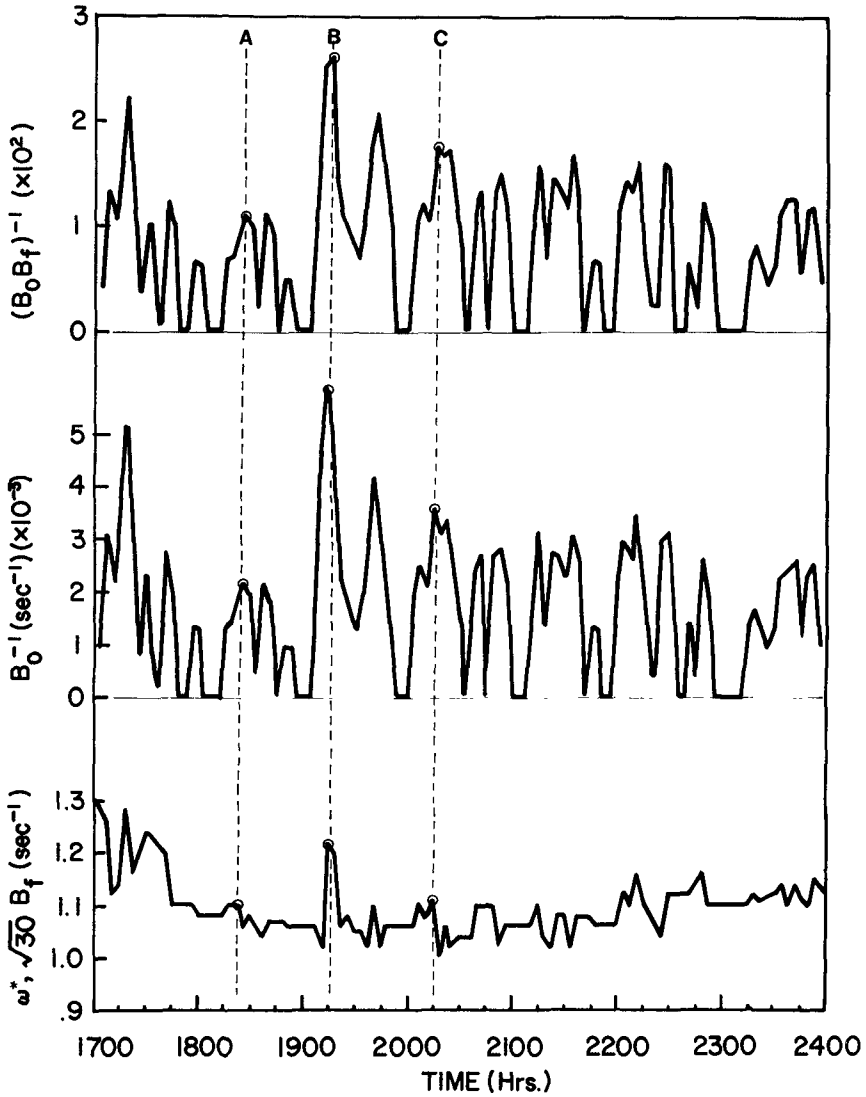
FIG. 1. Time Histories of Spectral Bandwidths and Spectral Peak Frequency
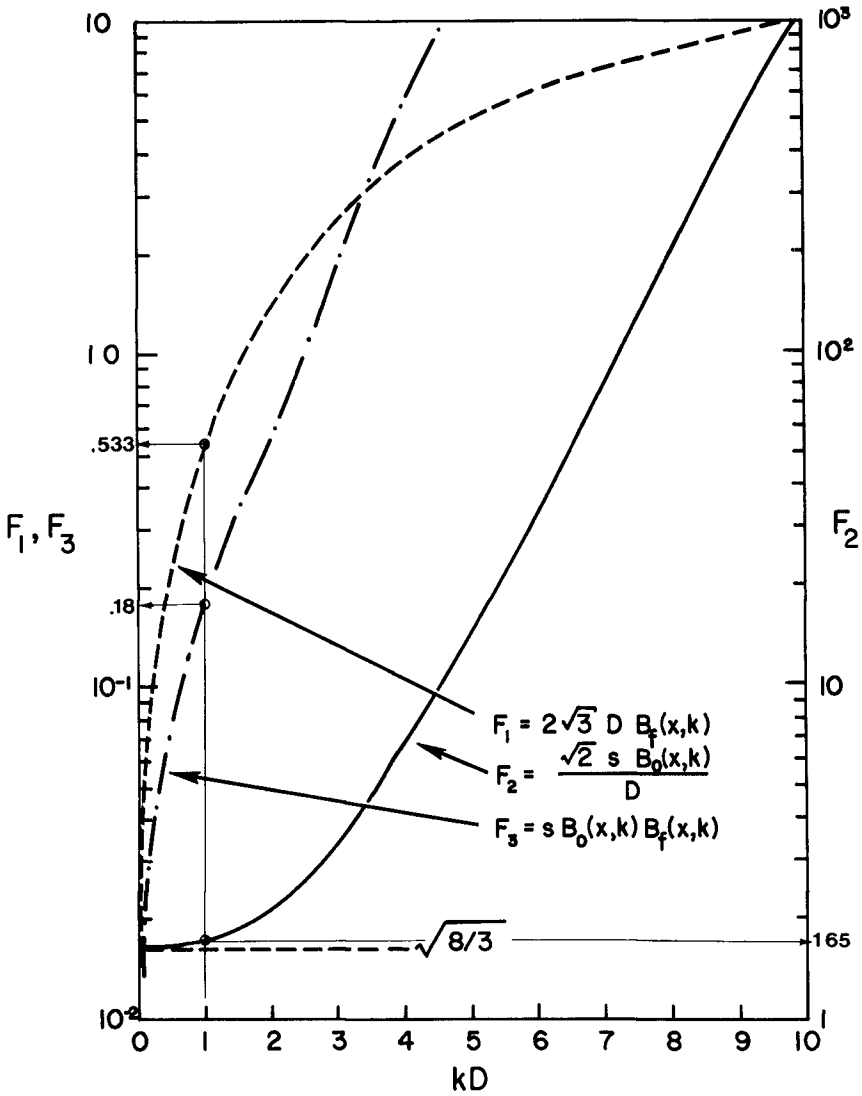
FIG. 2. Spectral Bandwidths in a Unidirectional Shoaling Wave Field
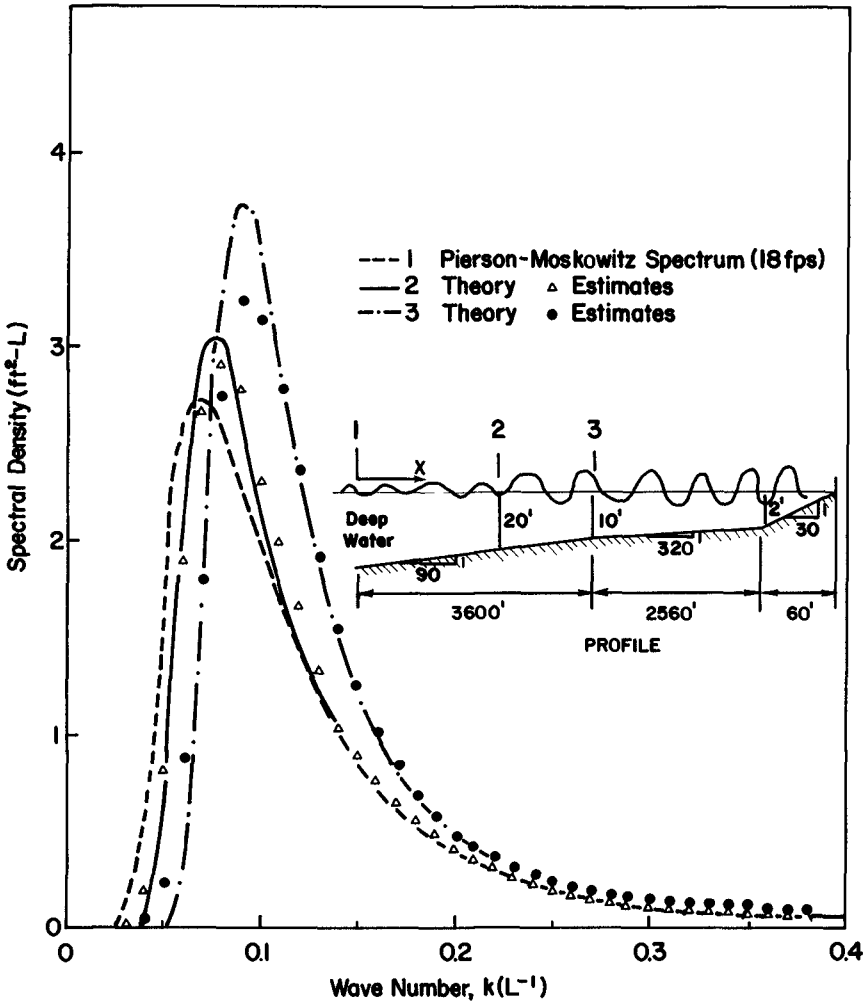
FIG. 3. Theoretical Spectra and Spectral Estimates in a Unidirectional Shoaling Wave Field

CHAPTER 16

SPECTRA AND BISPECTRA OF OCEAN WAVES

by

OLE GUNNAR HOUMB

Division of Port and Ocean Engineering
The University of Trondheim
The Norwegian Institute of Technology

INTRODUCTION

The two dimensional (directional) power spectrum gives an
adequate description of water waves that may be regarded as
a linear superposition of statistically independent waves.
In such cases the sea surface is linear to the first order
and the surface displacement is represented by

$$\eta(t) = \sum_{n=1}^{\infty} a_n \sin(\omega_n t + \phi_n)$$

where a_n are the amplitudes of individual waves and ϕ_n is a
radomly distributed phase angle, and the process is stationary.

Under such circumstances the wave surface is Gaussian, which
means that ordinates measured from MWL are normally distributed
if they are sampled at constant intervals of time. It is equally
important that the wave heights are Rayleigh distributed.

This formulation of the wave surface is widely used e.g. in
wave forcasting.

There are, however, phenomena such as wave breaking, energy
transfer between wave components and surf beat which can only
be described by higher order effects of wave motion (1, 2, 3,
4). In this case the two dimensional power spectrum fails to
give an accurate description of the wave surface. This means
that the first and second order moments (mean and covariance)
no longer give all the probability information, and we have to
consider higher order moments (5, 6, 7).

Third order moments of non-zero value indicate positive values of the bispectrum.

This paper gives an introduction to the bispectrum and some examples of bispectra calculated from wave records obtained during storm situations.

THE BISPECTRUM

The bispectrum, $B(f_1, f_2)$, of a random stationary wave record is defined as the Fourier transform of the mean third order products

$$B(f_1, f_2) = \frac{1}{(2\pi)^2} \int\int_{-\infty}^{+\infty} S(\tau_1, \tau_2) e^{-if_1\tau_1 - if_2\tau_2} d\tau_1 d\tau_2 \qquad (2.1)$$

where

$$S(\tau_1, \tau_2) = \overline{\eta(t)\ \eta(t+\tau_1)\ \eta(t+\tau_2)} \qquad (2.2)$$

and the overbar denotes ensemble means.

If $\eta(t)$ is real and stationary we have the following relations

$$B(f_1, f_2) = B(-f_1, -f_2)^* \qquad (2.3)$$

and

$$B(f_1, f_2) = B(f_2, f_1) = B(-f_1, -f_1-f_2) = B(-f_1-f_2, f_1)$$
$$= B(f_2, -f_1-f_2) = B(-f_1-f_2, f_2) \qquad (2.4)$$

where * denotes complex conjugate. As a consequense of equations 2.3 and 2.4 the bispectral values fall within an octant.

For a purely stationary Gaussian process the bispectrum has the value of zero.

It is of interest also to note that information on the relative directional spread of waves is derivable from the bispectrum which is calculated from one single wave record.

If, however, the wave surface has a non-Gaussian distribution the

bispectrum has a non-zero value, which is also the case for the
third order moments. It then follows that the third order
products $\eta(t)^3$ are also non-zero. This can physically be
interpreted as the peaking of waves with harmonics that are
in phase with the fundamental. In other words, significant
non-zero values in the bispectrum suggest that the wave sur-
face can be approximated with an expression like

$$\eta(t) = a_1 \sin 2\pi ft + a_2 \sin 4\pi ft + \text{------} \qquad (2.5)$$

which is a surface as given by the Stokes wave theory. The
bispectrum thus indicates whether harmonic couplings between
wave components are significant.

The possibility of triple interactions could be evaluated by
a trispectral analysis. Trispectral interactions contribute
nothing to $\eta(t)^3$ but somewhat to $\eta(t)^4$ which means, physically,
that the waves tend to be assymetric about the crest. Such
waves can be said to be close to breaking, and they are therefore
in an irreversible state. There is much evidence for assuming
that assymetric waves are liable to formation of shock pressures.

Trispectral calculations may therefore have practical consequences
in that the probability of obtaining shock pressures on marine
structures may be evaluated. To the author's knowledge, such
calculations based on ocean wave data have not yet been made.
For confidence to be placed in the trispectral estimates the
calculations would require such long wave records that problems
pertaining to stationarity might occur.

From elementary statistics the skewness g is known as third
order moment that is used to estimate to which degree data
have a Gaussian distribution.

Fisher (8) has developed a test for normality that is widely used
in statistics. The test can be summarized in terms of the inquality

$$\frac{g}{\sqrt{\text{var } g}} > g_{1-\alpha/2} \qquad (2.6)$$

where

$$g \quad = \frac{\overline{\eta(t)^3}}{\overline{\eta(t)^2}^{3/2}}$$ (2.7)

$$\text{var } g = \frac{6N(N-1)}{(N-2)(N+1)(N+3)}$$

N = number of values where $\eta(t)$ is known

If the inequality 2.6 holds, the hypothesis of a Gaussian distribution is rejected at the level α. In other words, α is the probability that the hypothesis is rejected even if the distribution is Gaussian.

BISPECTRA OF HARMONIC WAVES

Bispectra were calculated for the following artifical waves

$\eta_1(t) = 10 \cos 0.08t$

$\eta_2(t) = 10 \cos 0.08t + 1.25 \cos 0.16t$

$\eta_3(t) = 10 \cos 0.08t + 2.5 \cos 0.16t$

$\eta_4(t) = 10 \cos 0.08t + 5 \cos 0.16t$

$\eta_5(t) = 10 \cos 0.04t + 5 \cos 0.08t$

$\eta_6(t) = 10 \cos 0.04t + 5 \cos 0.08t + 2.5 \cos 0.12t$

$\eta_7(t) = 10 \cos 0.04t + 5 \cos 0.08t + 2.5 \cos 0.12t$
        $+ 1.25 \cos 0.16t$

$\eta_8(t) = 10 \cos 0.04t + 5 \cos 0.08t + 2.5 \cos 0.12t$
        $+ 1.25 \cos 0.16t + 0.625 \cos 0.20t$

These are all harmonic waves with a fundamental frequency of 0.04 Hz. $\eta_2(t)$ to $\eta_7(t)$ are all of the Stokes type with peaked wave crests and we should expect significant skewness as well as bispectral values.

.

Figs. 1 to 7 show bispectra calculated for $\eta_1(t)$ to $\eta_7(t)$
respectively. The upper part in these Figs. shows the bispec-
trum, whereas the central part indicates the spectrum and the
lower parts show one wavelength of the wave surface. The
bispectral value of 1.9 in Fig. 1 means $10^{1.9}$ m^3 Hz^{-2}.
$B(0.08, 0.08) = 10^{1.9}$ indicates a weak interaction of the
frequency 0.08 Hz with itself. In fig. 2 we find
$B(0.08, 0.08) = 10^{5.4}$ m^3 Hz^{-2} and a lower value at $B(0.08, 0.16)$,
from which we can conclude that the dominant component of $\eta_2(t)$
is that of f = 0.08 Hz. Proceeding to Fig. 4 we can see that
the dominant component is still f = 0.08 Hz, but the inter-
acting frequencies are now (0.08, 0,08), (0.08, 0.16) and
(0.16, 0.16) Hz. From the lower part of Fig. 4 we can also
see that the deviation from cosine surface is very significant.

The surface represented by $\eta_8(t)$ is the result of 5 harmonic
components. It is clearly seen from Fig. 8 that the inter-
acting frequences are (0.04, 0.04), (0.08, 0.04), (0.08, 0.08),
(0.12, 0.04), (0.12, 0.08), (0.16, 0.04). The skewness is
also computed for the 8 surfaces and the results are summarized
below.

Surface	$\eta_1(t)$	$\eta_2(t)$	$\eta_3(t)$	$\eta_4(t)$	$\eta_5(t)$	$\eta_6(t)$	$\eta_7(t)$	$\eta_8(t)$
Skewness	$0.92 \cdot 10^{-4}$	0.259	0.485	0.760	0.860	1.06	1.17	1.26

The skewness increases with the number of harmonic components,
that is with the peakedness of the surface.

Kinsman (9) concludes from studies of the skewness of waves that
values between 0.090 and 0.336 give rise to significant
corrections of the Gaussian distribution.

BISPECTRA OF WAVE RECORDS

The data were recorded off the coast of Northern Norway at a
depth of 80 meters, using a Waverider. The sampling interval
was 0.5 sec corresponding to a Nyquist frequency of 1 Hz.

Aliasing should therefore appear at frequencies higher than
1 Hz, a situation whichis satisfactory because shorter waves
are not measured properly by a Waverider and they are also
without interest in this case.

Three typical examples of storm wave situations were selected
for bispectrum analysis. The results are shown in Figs. 9, 10
and 11, along with the spectra of the same wave records.

In Fig. 9 there are four ridges of positive bispectral values,
which indicate interactions of the spectral peak with itself
and higher frequencies. In the same way the negative bi-
spectral value is interpreted as interactions between the
spectral peak and lower frequencies.

Peaks of the energy spectrum are associated with ridges in
the bispectrum.

As expected, there is a positive bispectral ridge at the spectral
peak which indicates interactions within the peak in Fig. 9.
$B(0.125, 0.125) = 10^{11}$ m^3 Hz^{-2} indicates that the secondary peak
of the spectrum at ~ 0.125 Hz is real, whereas $B(0.094, 0.031) =$
$- 10$ m^3 Hz^2 can be interpreted as an interaction which produces
parts of the secondary peak.

Fig. 10 reveals three main ridges in the bispectrum and a
singly peaked spectrum. The strongest interactions appear at
$f_1 = 0.188$ Hz where 0.188 and 0.094 Hz contribute to the peak
in producing the difference frequency 0.09 Hz. As a result of
the bispectral ridges in Fig. 11 one may raise the question as
to whether real peaks in the spectrum have been smoothed out.

In Fig. 11 the three peaks in the spectrum are beautifully
accompanied by three distinct bispectral ridges, indicating
that all three peaks are real. The peak interacts strongly
with itself which gives the sum frequency of ~ 0.156 Hz i.e.
the second spectral peak. The third peak is believed to be
caused by interaction between 0.125 and 0.094 Hz, as indicated
by the middle bispectral ridge.

The test on normality, as described in the text, was applied
to estimate the deviations from normality of the three re-
cords, and the results are summarised in the table below.

Situation	α	G	$g_1 - \alpha/2$	g
Fig. 10	0.20	1.4734	1.2816	0.075
	0.10		1.6449	
Fig. 11	0.20	1.9245	1.2816	0.102
	0.10		1.6449	
Fig. 12	0.20	1.1132	1.2816	0.059
	0.10		1.6419	

From these results it is clear that wave records represented
by Fig. 9 and 11 are closely normally distributed, but there
are sizeable deviations from normality in the record of which
Fig. 10 shows the spectrum.

CONCLUSION

The bispectrum can be used to estimate the extent of harmonic
couplings between wave components in an irregular wave surface.
Significant bispectral values thus indicate some evidence for
using the Stokes wave theory in describing waves on inter-
mediate and deep water.

Secondary spectral peaks are found to be real, and not intro-
duced by the analysis methods, when they are associated with
significant bispectral values at the same frequency. In cases
where bispectral ridges are not accompanied with spectral peaks,
it may be questioned whether such peaks are smoothed out in the
analysis. Finally, it is shown that both the bispectrum and
skewness are good measures of the wave surface deviation from
the Gaussion distribution.

The wave records from which significant nonzero bispectra
were calculated, were all obtained during relatively extreme
wave conditions.

REFERENCES

1. Munk, W.H.: Surf beats. Trans. Amer. Geophys. Union,
              30, 6, pp 849-854, 1949.

2. Longuet-Higgins, M.S. and R.W. Stewart: Radiation stress
              and mass transport in gravity waves, with
              application to surf beats. J. Fluid Mech.
              1962.

3. Hasselmann, K.: On the non linear energy transfer in a
              gravity-wave spectrum, Part I. General
              theory.

4. Phillips, O.M.: On the dynamics of unsteady gravity waves
              of finite amplitude, Part I. The elementary
              interactions. J. Fluid Mech., 9. 2, pp 192-217.
              1960

5. Hasselmann, K. et al.: Measurements of Wind-Wave Growth
              and Swell Decay during the Joint North Sea
              Wave Project (JONSWAP). Deutsches
              Hydrographisches Institut, Hamburg. Reihe A,
              Nr. 12, 1973.

6. Barnett, T.: Observations of Wind Wave Generation and
              Dissipation in the North Sea: Implications
              for the Offshore Industry. Offshore
              Technology Conference, 1972.

7. Garrett, J.: Field Observations of Frequency Domain Statistics
              and Nonlinear Effects in Wind-Generated Ocean
              Waves. The University of British Columbia,
              Phd. thesis 1970.

8. Fisher, R.A.: Statistical methods for research workers.
              Oliver & Boyd, 1950.

9. Kinsman, B.: Surface waves at short fetches and low wind
              speeds - a field study. Chesapeake Bay
              Institute technical report XIX. 1960.

Fig.1. Bispectrum of η_1 (t) = 10 cos 0.08 t
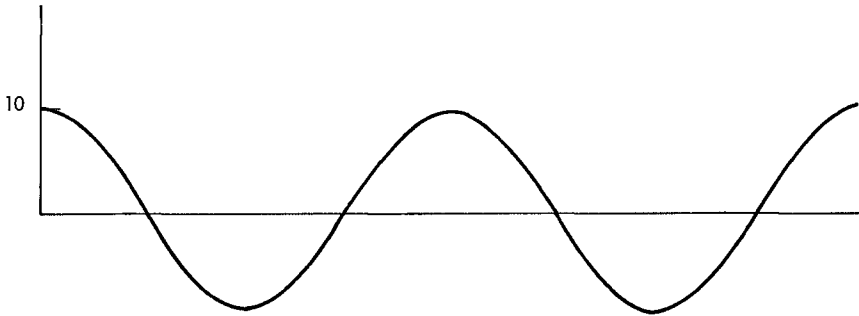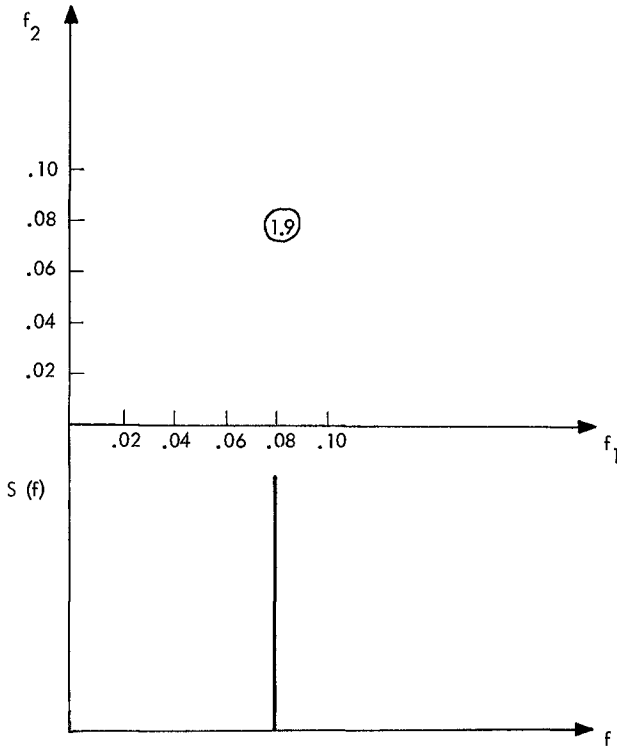
Fig.2.   Bispectrum of $\eta_2 (t) = 10 \cos 0.08 t + 1.25 \cos 0.16 t$
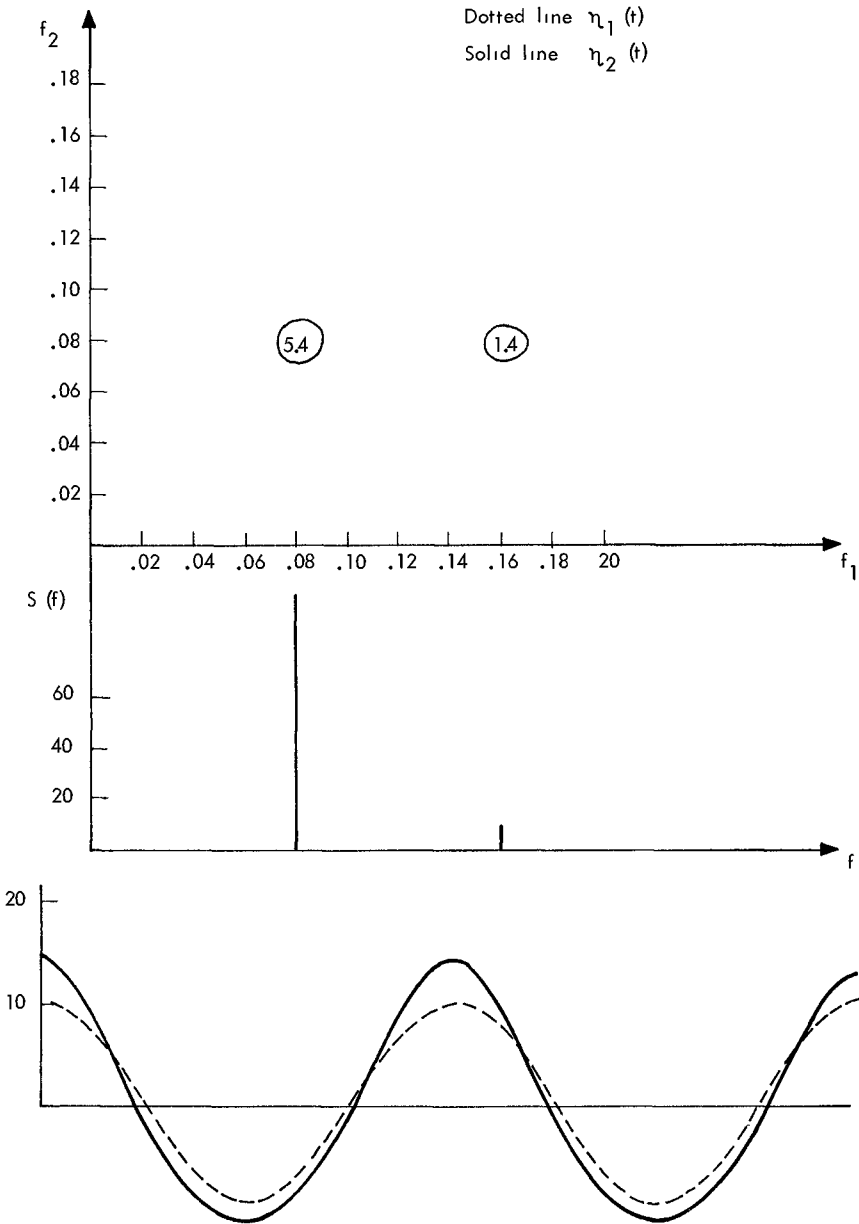
Fig. 3   Bispectrum $\eta_3(t) = 10 \cos 0.08\, t + 2.5 \cos 0.16\, t$

Dotted line $\eta_1(t)$
Solid   line $\eta_3(t)$
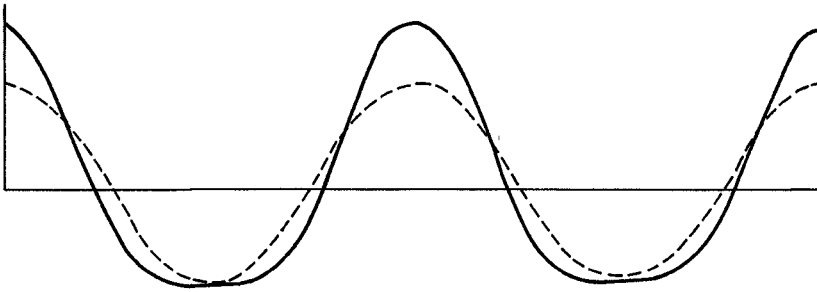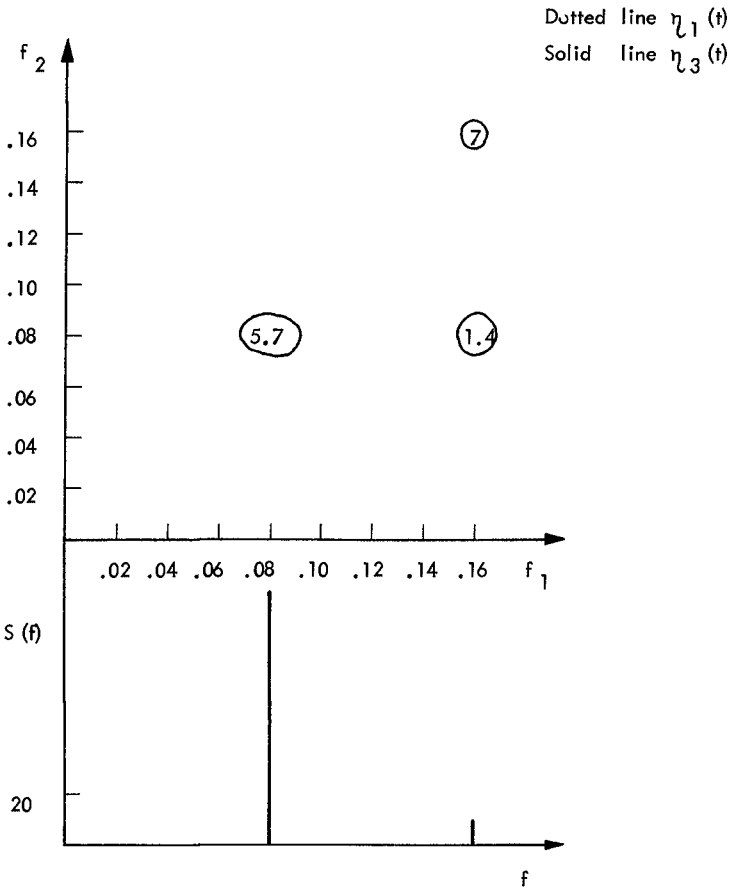
Fig.4. Bispectrum of η_4 (t) = 10 cos 0.08t + 5 cos 0.16 t

Dotted line η_1 (t)

Solid line η_4 (t)
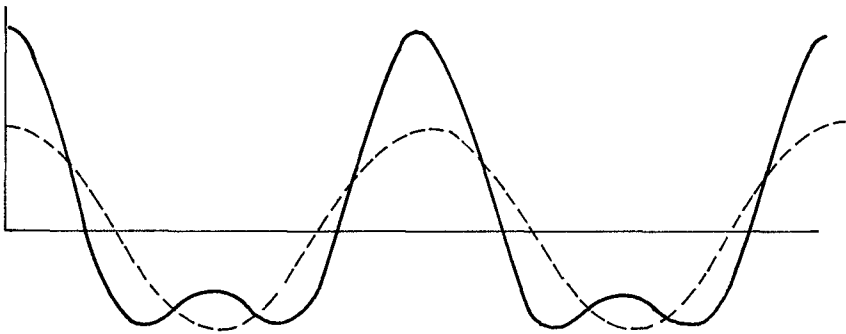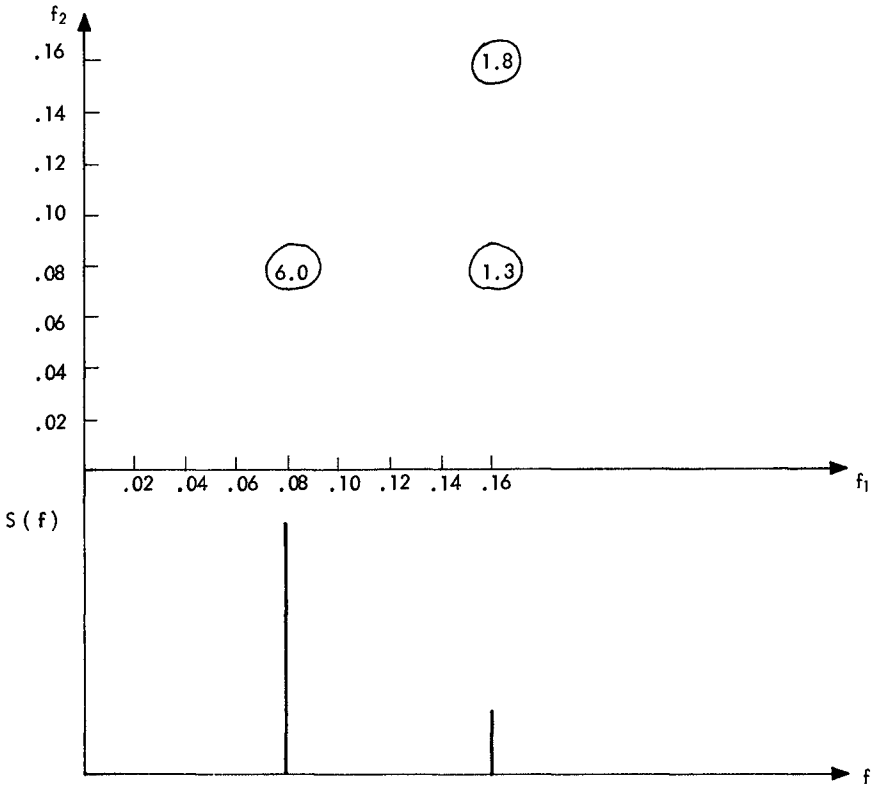
Fig. 5   Bispectrum of $\eta_5(t) = 10 \cos 0.04 t + 5 \cos 0.08 t$

Dotted line $\eta_1(t)$
Solid   line $\eta_5(t)$

f_2

.16

.14

.12

.10

.08   (1.7)   (1.5)

.06

.04   (6.0)

.02

.02 .04 .06 .08 .10 .12 .14 .16 f_1

S (f)

f

Fig. 6   Bispectrum of η_6 (t) = 10 cos 0.04 t + 5 cos 0.08 t + 2.5 cos 0.12 t
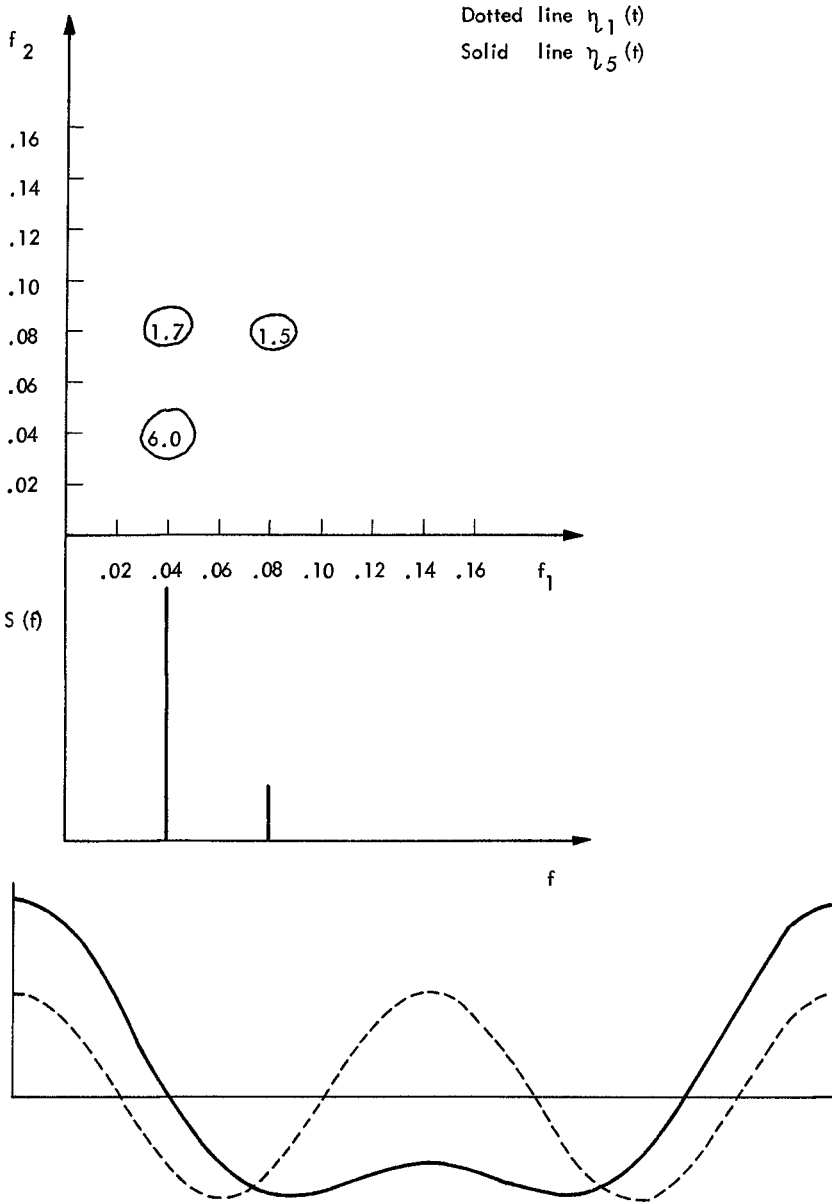
Dotted line η_1 (t)
Solid line η_6 (t)
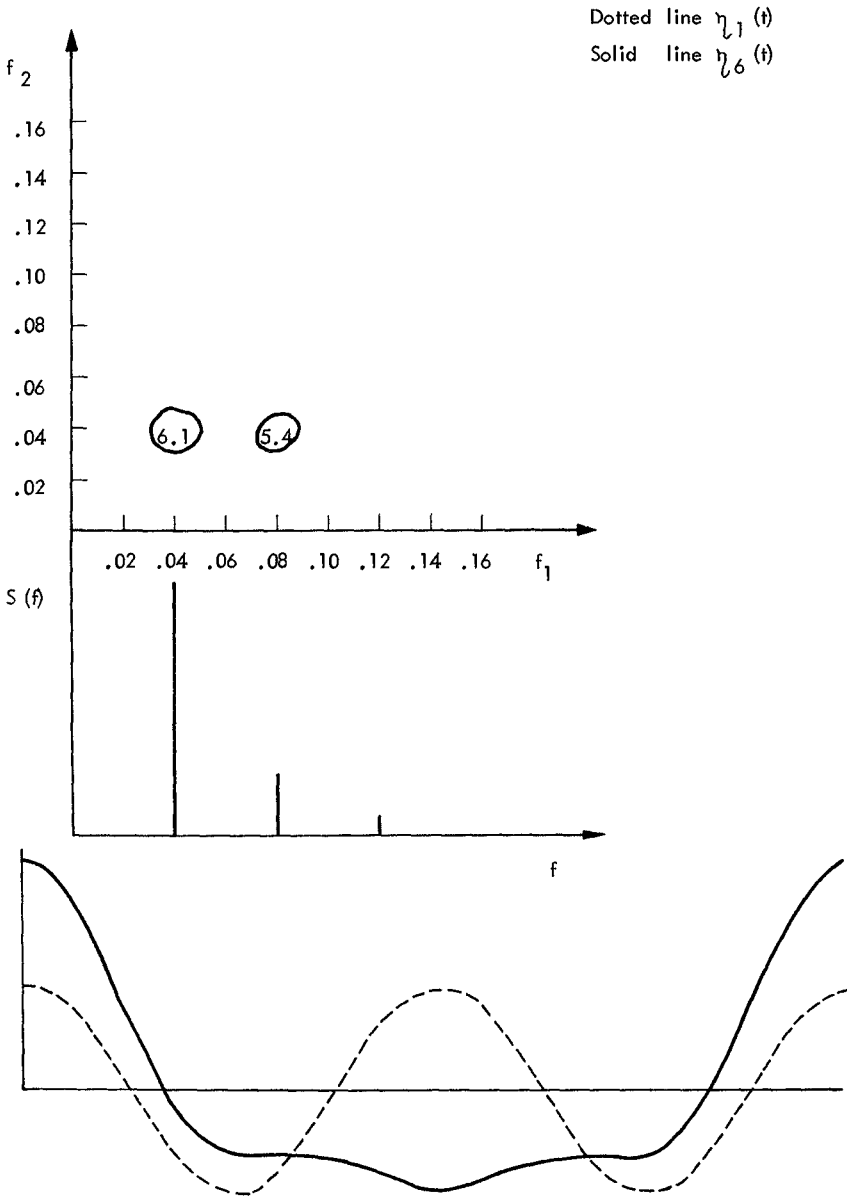
Fig. 7   Bispectrum of $\eta_7(t)$ = 10 cos 0.04t + 5 cos 0.08t + 2.5 cos 0.12t + 1.25 cos 0.16t

Fig.8. Bispectrum of η_8 (t) = 10cos 0.04 t + 5 cos 0.08 t + 2.5 cos 0.12 t
+ 1.25 cos 0.16 t + 0.625 cos 0.20 t

Dotted line η_1 (t)
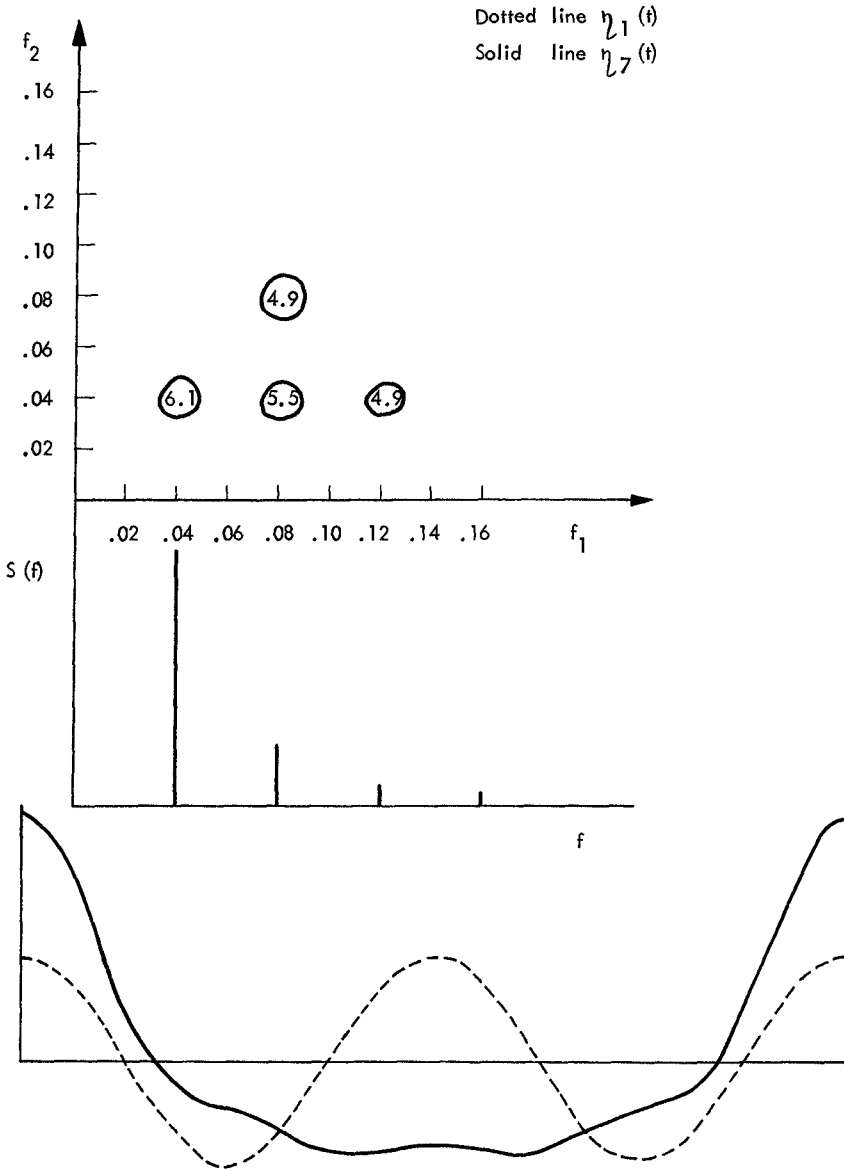
Solid line η_8 (t)
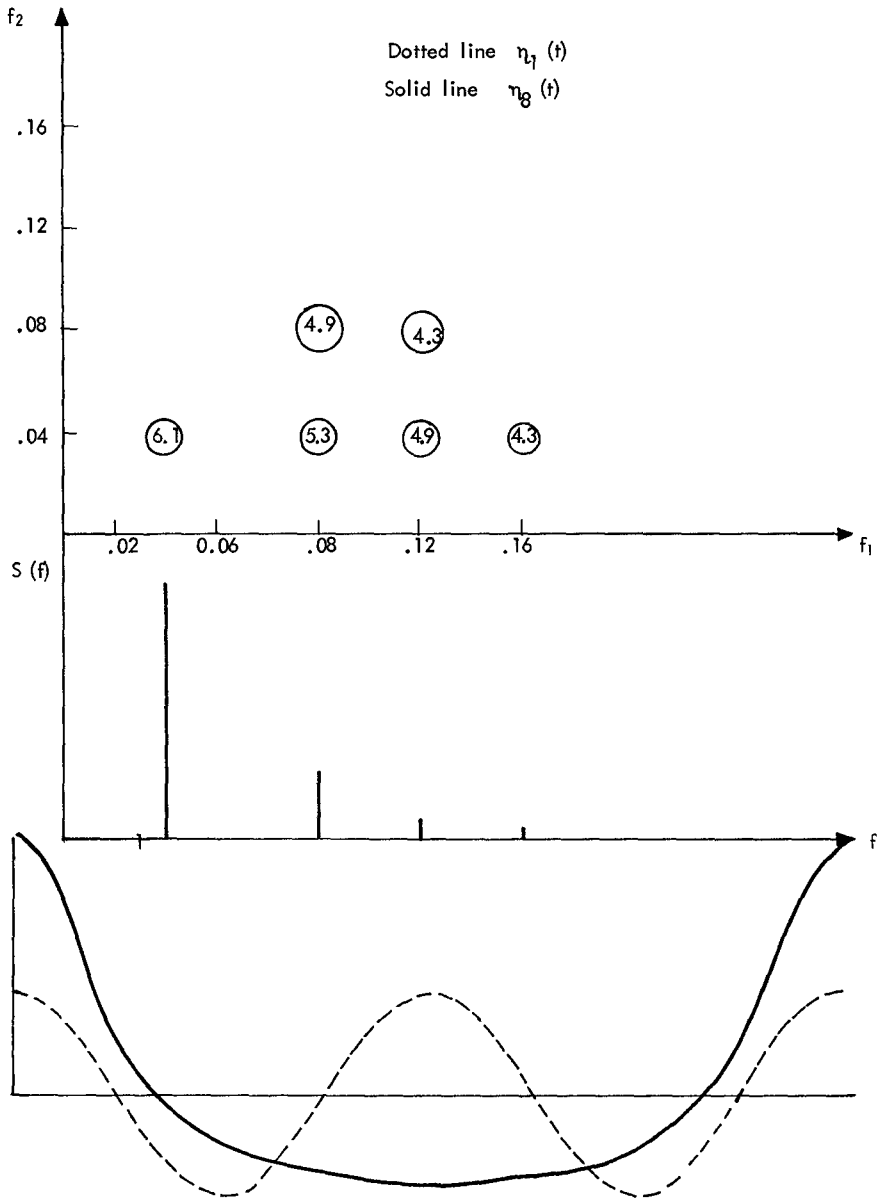
Fig. 9   Bispectrum of wave record 711219.03.
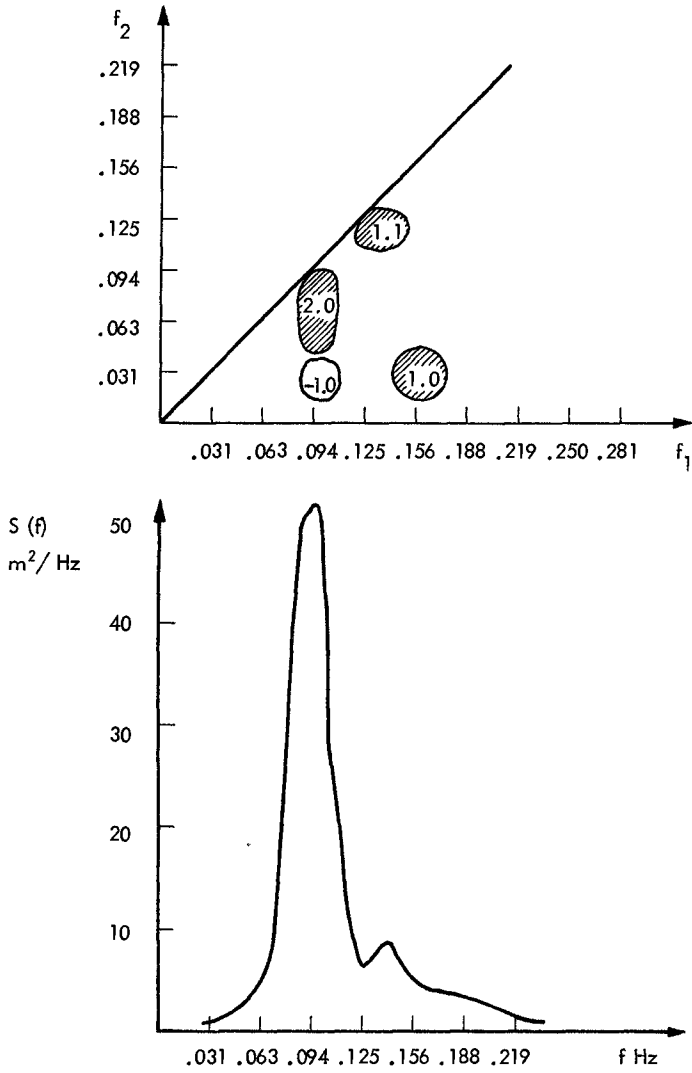
Fig.10.   Bispectrum of wave record   711218.21
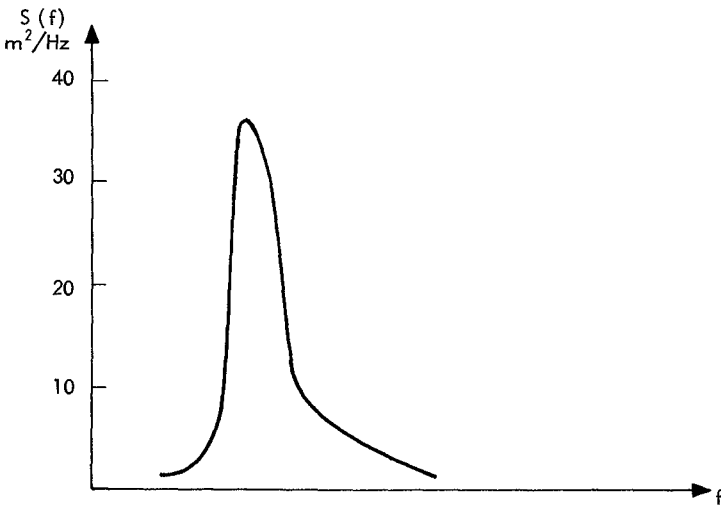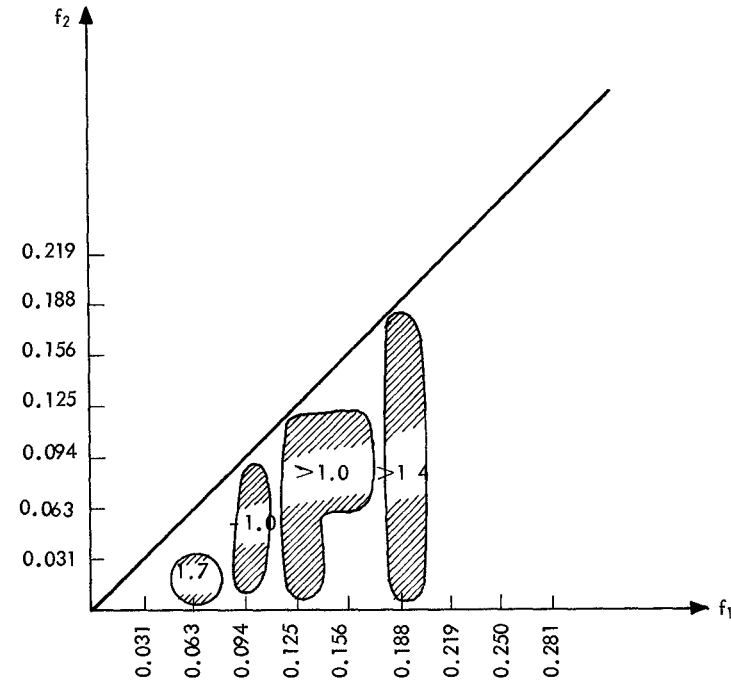
Fig 11.   Bispectrum of wave record   711208.21.

$B (f_1 , f_2) = 3.0$

means $B (f_1, f_2) = 10^3 \, m^3 / Hz^2$
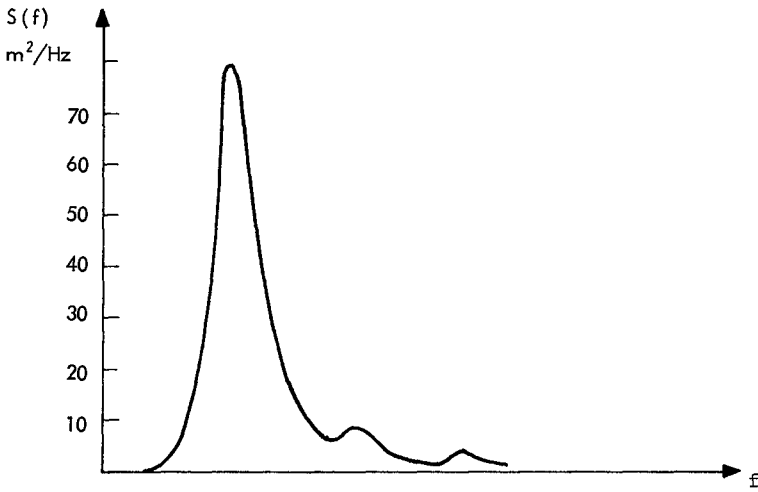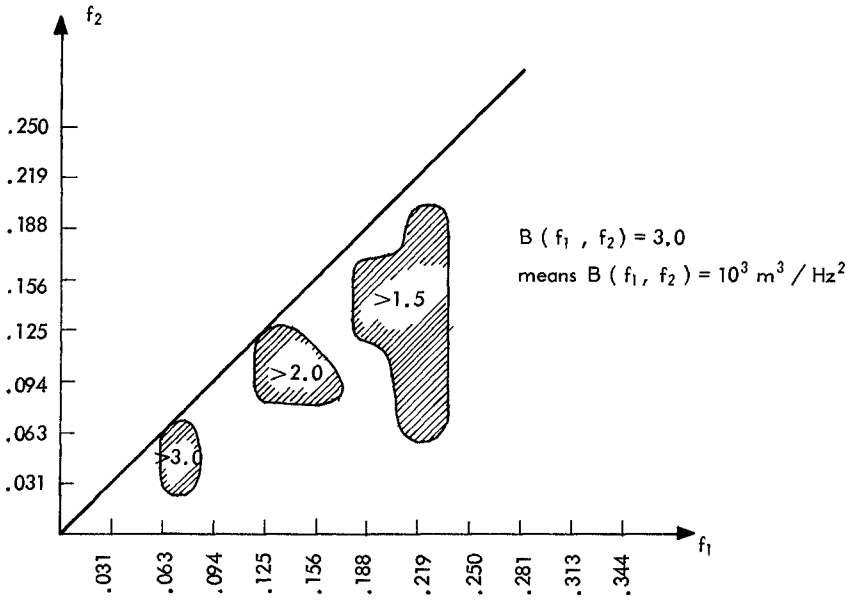
CHAPTER 17

LABORATORY GENERATION OF WAVES OF CONSTANT FORM

J. Buhr Hansen* and Ib A. Svendsen*

ABSTRACT

The paper reports measurements of waves generated by a piston type
wave generator. The experiments show that for 0.10 < h/L < 0.65 the
waves produced by a sinusoidal piston motion can be described as a
second order Stokes wave superimposed by a free second harmonic wave.
Results are presented for the height and phase velocity of the free
second harmonic wave and compared with theories by Fontanet (1961)
and others. Finally, the height of the free second harmonic wave is
successfully reduced by a non-sinusoidal time variation of the piston
motion, whereas addition of a rotation to the flap motion appears to
yield only minor improvements.

1. INTRODUCTION

The waves produced by a sinusoidal motion of a flap type wave genera-
tor do not have the ideal constant form which should be expected from
the regularity of the flap motion. As the waves propagate they slowly
change form in a periodic way, which depends on both the wave steepness
H/L and the relative water depth h/L (H being the wave height, L the
wave length, and h the undisturbed water depth, Fig. 1).
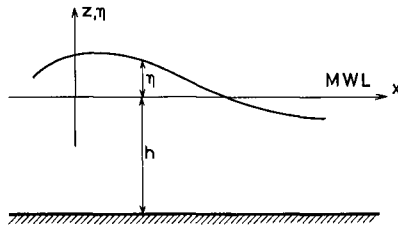
Fig. 1 Definition sketch

*Assoc. Prof., Institute of Hydrodynamics and Hydraulic Engineering
(ISVA), Technical University of Denmark, DK-2800 Lyngby

Fig. 2 shows (in one of the more extreme cases) the time variation of the surface elevation at different points along a wave flume. This pattern will be familiar to most laboratory people. The reason for the irregularities is, of course, that a rigid flap cannot exactly produce the variation of the particle motion which corresponds to a progressive wave of constant form.

The first reference to this phenomenon seems to be in Biésel and Suquet (1951), whose description clearly accounted for the basic principle described above. Since then many others have given more or less conscious experimental reports of the phenomenon (see e.g. Morison and Crooke (1953), Le Méhauté et al. (1968), Iwagaki and Sakai (1970)) and several contributions have directly treated the problem analytically, numerically and in experiments (see e.g. Fontanet (1961), Goda (1967), Madsen et al. (1970), Madsen (1970), Madsen (1971), Hulsbergen (1972), Daugaard (1972), Mei and Ünlüata (1972)).
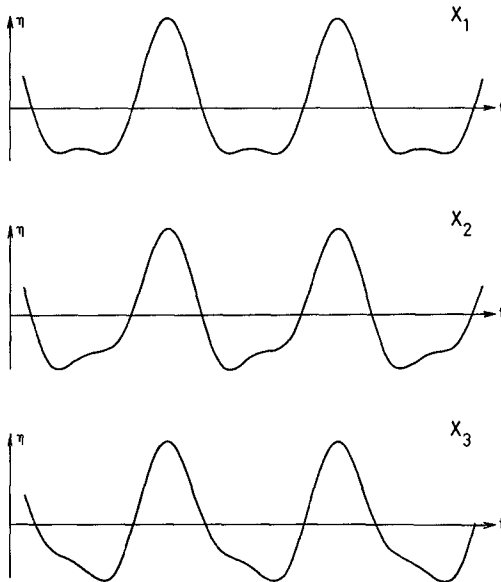
Fig. 2   Wave profile at different stations
         in a wave flume

An analysis of Fig. 2 suggests as a crude explanation of the motion that a smaller wave is travelling down the flume superimposed on the main wave, but with a somewhat smaller speed. Theoretical considerations show (Fontanet (1961)) that to the lowest approximation the period of this wave is $T/2$ (where T is the period of the main wave), and its height is $O(H^2)$. Accordingly this wave is denoted the 'free second harmonic wave'. [The phenomenon should not be confused with the second-

ary wave crest, which for sufficiently large wave steepness is predicted
in the wave trough by the second order Stokes' theory. That is a purely
theoretical effect caused by the truncation of the Stokes' theory to sec-
ond order at or beyond its limit of validity.]

   Hence, if we include all terms to second order the surface elevation
η can be written as the superposition of a second order Stokes' wave and
a free second harmonic wave, i.e.

$$\eta = a_1 \cos(\omega t - kx) + a_2 \cos 2(\omega t - kx) + a_{22} \cos(2\omega t - k_{22}x + \alpha_{22}) \quad (1-1)$$

where $\omega = 2\pi/T$ is the wave frequency and $(k, k_{22}) = 2\pi(L, L_{22})^{-1}$ the wave
numbers which satisfy the dispersion relations

$$\omega^2 - g\,k\,\tanh kh = 0 \qquad\qquad\qquad (1-2)$$

$$(2\omega)^2 - g\,k_{22}\,\tanh k_{22}h = 0 \qquad\qquad (1-3)$$

   It is important to notice that the wave pattern (1-1) apart from re-
presenting the disturbed wave profile of Fig. 2 also exhibits an appar-
ent variation in mean water level from place to place. This can be
seen if we for a moment follow a wave crest by assuming $\omega t - kx = 0$, i.e.
$\omega t = kx$. Then (1-1) reads

$$\eta_{crest} = a_1 + a_2 + a_{22} \cos[(2k - k_{22})x + \alpha_{22}] \qquad (1-4)$$

and a similar expression for the wave trough. Hence, except for small
terms the upper and lower envelope of the wave motion will be constant
in time but meander with x as shown in Fig. 3.
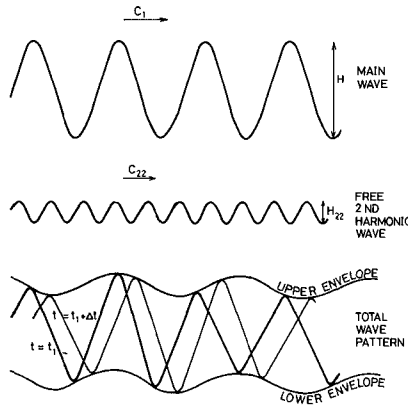
Fig. 3 Superposition of second order
        Stokes main wave
        and free second harmonic wave

   As (1-4) shows the amplitude of the meander will equal the amplitude
of the free second harmonic wave. Also the maxima and minima for the
envelopes appear at fixed points down the wave flume, the position of
which depends only on the main wave data and the phase angle α_{22} between
the main wave and the free second harmonic wave at the wave generator.

It is the purpose of this paper to present some measurements of the phenomenon described above to check the model (1-1) and to report results obtained by giving the flap of the wave generator a non-sinusoidal motion, scaled to reduce the (unwanted) free second harmonic wave motion to a minimum.

During the experiments several other unwanted effects have appeared. Some of them are obviously third or higher order phenomena, others have not been understood at all. The more important af these will be discussed in Section 5, the primary concern being to ensure that they have no or only negligible influence on the measurements in question.

2. EXPERIMENTAL SET-UP

The experiments were made in a wave flume, 60 cm wide and 25 m long (Fig. 4). Waves were generated by a hydraulic flap type wave generator. The wave generator was controlled by a mini-computer (Type PDP8E) which produced an electrical signal for the instantaneous position of the flap. The computer was also used for collecting data from the measurements. Three series of experiments have been made, distinguished by the type of the wave generator flap:

   (a) Pure sinusoidal translation (piston motion), ($e \sin \omega t$)
   (b) Pure sinusoidal motion with combined translation and rotation ($e_b(1 + e_s z/(e_b h)) \sin \omega t$, e_b and e_s being flap amplitudes at the bottom and the surface)
   (c) Piston motion composed of two sines
       ($e \sin \omega t + e_{22} \sin(2\omega t + \varphi)$)

In all experiments a wave height meter was mounted on a small carriage travelling slowly along the flume (about 1 cm per wave period). Information from the wave height meter was collected, by the computer 100 times per wave period and through a determination of each maximum and minimum for the instantaneous surface elevation the series of wave heights were computed and stored in digital form.

The data were analysed simultaneously by a digital filter* which passed only the total second harmonic component of the wave motion corresponding to the second and third terms in (1-1). Here again the series of heights of the total second harmonic component were computed and stored in digital form.

During one travel of the carriage down the flume the total wave height and the height of the total second harmonic component were stored in the computer for about 500 consecutive waves, constituting one run or test.

---

*The authors have been informed that the digital filter used is a fourth order band-pass filter of the Chebyshev type with 2 dB ripple. The first harmonic component is damped 48 dB ($\sim$ 250 times) by the filter. Due to the design criteria for this type of filter only 20 sampled values per wave period are passed through the filter (private communication with Mr. Peter Schiolten).
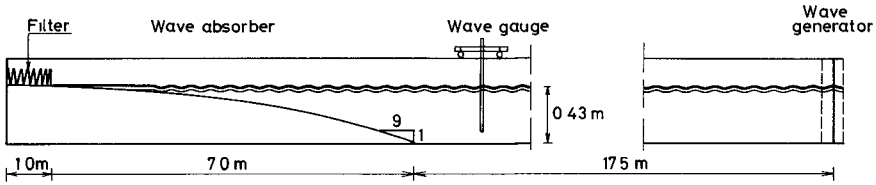
Fig. 4 Wave flume

3. EXPERIMENTAL RESULTS FOR SINUSOIDAL FLAP MOTION

These experiments comprise points (a) and (b) in the list above.
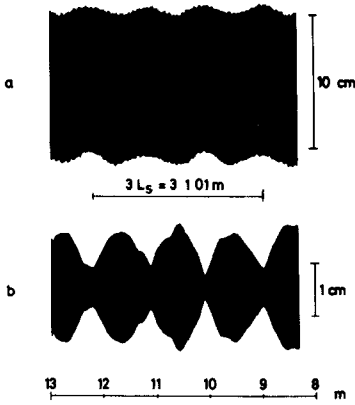
Fig. 5
Record of total wave motion
and total second harmonic motion

Fig. 5 shows an example of a record compressed to show the variation of the wave motion envelopes. Part a represents the total wave motion, part b the total second harmonic motion.

First of all the meander pattern predicted by the simple model described in the introduction is easily recognized. It is also found in each experiment to be fixed in time relative to the wave generator as (1-4) shows, the position and meander length depending only on the main wave data.

This effect is repeated in the total second harmonic component as a beat (or wave group) pattern emerging from addition of the two second order terms in (1-1). Apparently the total second harmonic component of (1-1) can also be written (neglecting the phase angle α_{22})

$$\eta^{(2)} = (a_2 - a_{22}) \cos 2(\omega t - kx) + 2a_{22} \cos\left(2\omega t - \frac{2k + k_{22}}{2}\, x\right) \cos\left(\frac{1}{2}(k_{22} - 2k)x\right)$$

$$(3-1)$$

where the last term represents the group effect. Notice, that since

this emerges from two waves of different wave lengths but the <u>same fre-</u>
<u>quency</u>, the group pattern is stationary in the flume.

From (3-1) (or (1-4)) we see that the theoretical distance between
two maxima or two minima will be $L_{s,1}$ where

$$\frac{1}{2} (k_{22} - 2k) L_{s,1} = \pi \qquad (\text{or} \quad (2k - k_{22}) L_{s,1} = -2\pi) \qquad (3-2)$$

so that

$$L_{s,1} = \frac{L \ L_{22}}{L - 2L_{22}} \qquad (3-3)$$

where L corresponds to k and L_{22} to k_{22}. Hence $L_{s,1}$ is also the meander
wave length.

The height $H_{22} = 2 a_{22}$ of the free second harmonic wave can be found
as half the difference between $H_{max}^{(2)}$ and $H_{min}^{(2)}$ which again can be deter-
mined with fair accuracy from part b of the figure. Thus

$$H_{22} = \frac{1}{2} (H_{max}^{(2)} - H_{min}^{(2)}) \qquad (3-4)$$

3.1 RESULTS FOR H_{22}

The values of H_{22} measured in this way are shown in the four figures,
6 a through 6 d, representing four different wave steepnesses. The ab-
scissa is h/L and the ordinate H_{22}/H_2.

H_2 in the figures has been determined as

$$H_2 = \frac{1}{2} (H_{max}^{(2)} + H_{min}^{(2)}) \qquad (3-5)$$

and these values are in Table 3-1 compared with the theoretical values
determined from Stokes' theory. Some typical cases have been chosen
and the agreement is not exciting, though in some cases it is remark-
ably good. We shall return to this point later on.

Table 3-1 Comparison of theoretical and measured values of H_2

Test No.	h	$\frac{h}{L}$	H	$\frac{H}{L}$	H_2 theor.	H_2 meas.	$\left(\frac{H_{22}}{H_2}\right)_{meas}$	$\frac{H_{22,meas}}{H_2,theor}$
	cm		mm		mm	mm		
2-10B	43	0.171	119.6	0.048	21.5	20.3	0.20	0.19
4-10B	30		82.5	0.047	14.6	15.5	0.27	0.29
2-10D	43		27.7	0.011	1.15	1.25	0.21	0.23
4-10D	30		19.3	0.011	0.80	0.72	0.42	0.38
2-6A	43	0.290	100.4	0.068	13.1	12.9	0.50	0.49
4-6A	30		67.1	0.065	8.37	8.32	0.35	0.35
2-6C	43		35.0	0.024	1.59	1.40	0.45	0.40
4-6C	30		24.7	0.024	1.13	0.97	0.67	0.57
2-3A	43	0.463	63.3	0.068	7.00	9.61	0.28	0.38
4-3A	30		44.4	0.069	4.90	5.16	0.27	0.28
2-3C	43		20.5	0.022	0.73	0.60	0.51	0.42
4-3C	30		14.3	0.022	0.51	0.41	0.51	0.41
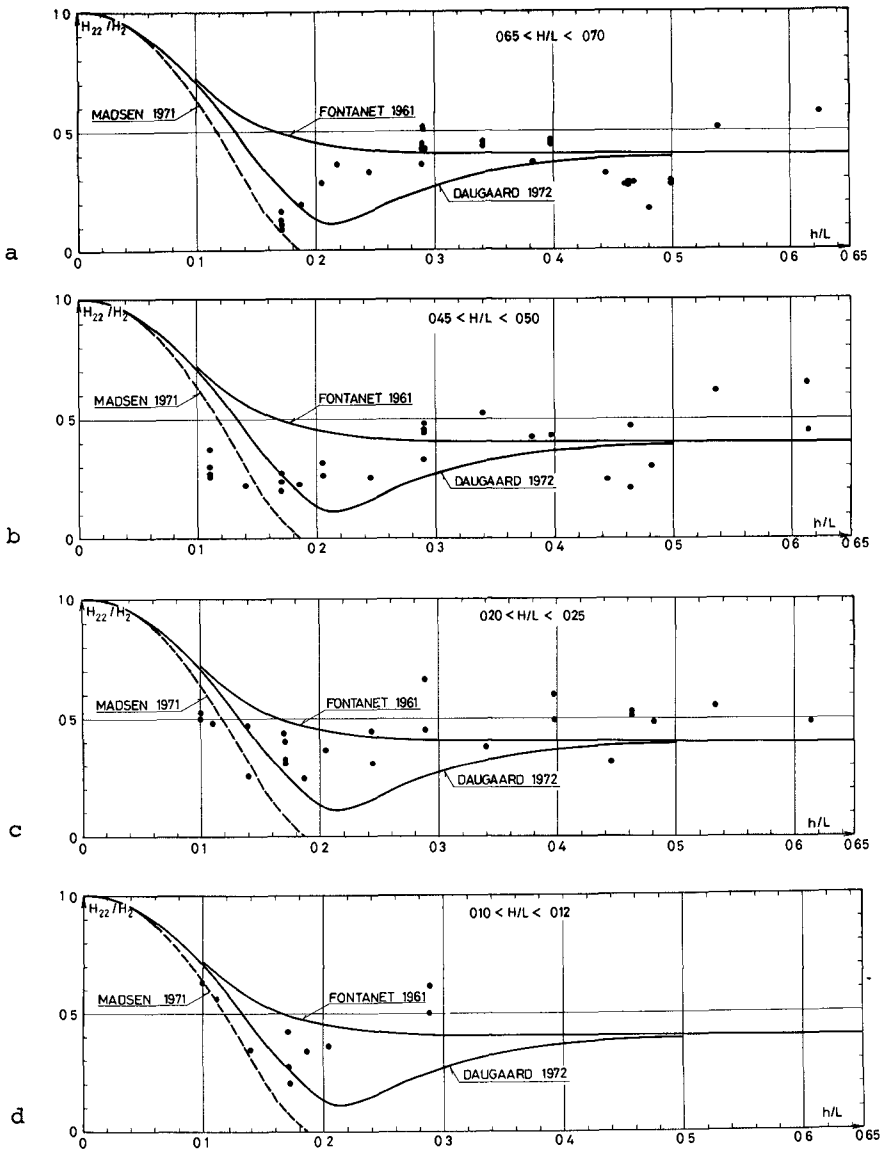
Fig. 6   Theoretical and experimental results for H_{22}

H_{22} has been determined theoretically by Fontanet (1961), his results being shown in the figures too. Also the shallow water approximation by Madsen (1971) is plotted. This theory, however, will only yield reasonable approximations for h/L < 0.05 (or 0.1 at most), and in that region other effects mentioned later will influence the results. Finally, the results obtained by Daugaard (1972) is shown in the Figs. 6 a through 6 d.

The experimental results in the region $0.1 < h/L < 0.65$ show two important deviations from the theoretical prediction by Fontanet.

One is a certain dependence of the results on the main wave steepness. The theory shows no such variation because it is only a second order theory. As the free second harmonic wave is of the second order, non-resonant interaction between the main wave and the free second harmonic wave will be of the third order.

The other deviation is represented by the actual variation of H_{22}/H_2, which shows two minima, one for h/L about 0.15, the other close to $h/L = 0.45$.

The minimum at $h/L = 0.15$ is consistently found for all wave steepnesses, — even for the small waves of $1-1.25\%$. It is in this connection interesting to notice that although Madsen's theory is too inaccurate for $h/L > 0.1$, it does frame the experimental results around this minimum. Daugaard's theory even shows a minimum but shifted to $h/L \sim 0.22$. It should be mentioned here, that Daugaard's theory is an approximate second order theory, where some of the smallest second order terms have been omitted. It is not satisfactory but is included to emphasize, what is also indicated by the experimental results, that the failure of Fontanet's theory to predict the details of the variation of H_{22}/H_2 does not seem to be a fundamental shortcoming of a consistent second order approximation.

The other minimum has a somewhat more doubtful character. It is only recorded for the steeper waves (those of 5% and 7%), and when the records of the second harmonic component at this minimum is analysed more closely it appears that the beat effect shown in Fig. 5 b oscillates down the wave flume. The resulting range in H_{22}/H_2 corresponds to a factor of $2-2.5$, of which H_2 is responsible for at least a part, as Table 3-1 shows. This probably affects the reproducibility of the experiments even for the largest waves.

Actually Table 3-1 shows results for three different values of h/L. The first group of data is for $h/L = 0.171$, corresponding to the first minimum in results for H_{22}/H_2. The good agreement between theory and measurements of H_2 for this group of tests reflects the general impression that the model represented by (1-1) for h/L in this region gives a realistic description of the wave pattern in the flume. All the wave groups of the second harmonic signal have the same form (only the amplitude being slightly modified with increasing x due to energy dissipation).

This also applies to the second group, where $h/L = 0.29$. An exception is the last test which, however, also shows a poor agreement in Fig. 6 c with the rest of the data obtained for that wave period.

The last group of points refer to the second minimum and here the agreement is unsatisfactory. It may be worth-while to notice that the value of measured H_{22} over theoretical H_2 tends to bring the points to the value predicted theoretically by Fontanet. As mentioned above the amplitude of the group pattern oscillates with x around this value of h/L, distance between two maxima being $10-15$ times L_s. No corresponding oscillation can be detected in the first harmonic component. The values in Table 3-1 are mean values and the maximum values for H_{22}/H_2 are also about 0.40.

In spite of all these uncertainties evidence presented in Section 4 seems to show that the value of H_{22}/H_2 is about 0.30 for $h/L \sim 0.45$, which means that there is a (weak) minimum there.

3.2 RESULTS FOR THE MEANDER LENGTH L_s AND PHASE VELOCITY c_{22}

The theoretical value $L_{s,1}$ of L_s determined by (3-3) is shown in Fig. 7. Since (3-3) involves only linear considerations, $L_{s,1}$ is independent of the wave steepness.
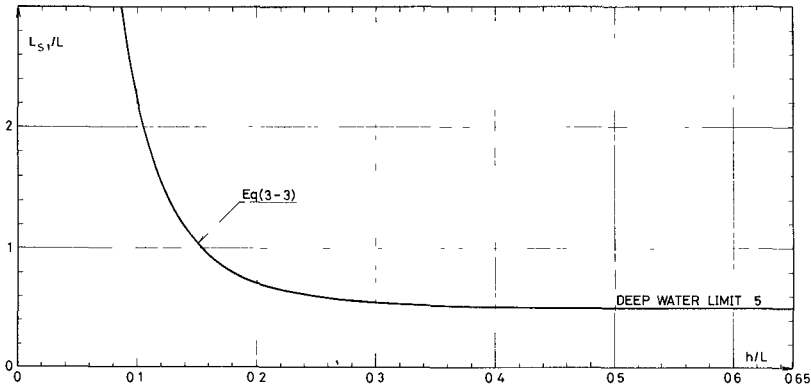
Fig. 7   Theoretical values of $L_{s,1}/L$ for the meander length

The experimental results for L_s, however, shows a quite marked variation with H/L. This is shown in Fig. 8 where the ratio $L_s/L_{s,1}$ between the experimental and the theoretical meander length has been plotted versus H/L (or kH) for 5 values of h/L. For sufficiently small values of h/L (less than about 0.11) L_s will decrease with increasing wave steepness. For $h/L \sim 0.11$, L_s is independent of H/L, and then for $h/L >$ 0.11, L_s increases with H/L.

The reason for this is, of course, partly connected with the fact, that for waves of finite amplitude the phase velocity depends on the wave steepness. In Stokes wave theory this dependence is represented from the third order approximation, for cnoidal waves already in the first approximation. Since the amplitude of the main wave is always more than ten times that of the second harmonic component, it is consistent to infer that it is primarily the value of the main wave length L in (3-3) which depends on H/L.

If we introduce the third order Stokes' approximation L_3 for L by writing $c_3 = L_3/T$ but stick to the linear values for L_{22}, then (3-3) can be written

$$\frac{L_{s,3}}{L_{s,1}} = \frac{c_3}{c_1} \frac{c_1 - c_{22}}{c_3 - c_{22}} \tag{3-6}$$

where $c_1 \equiv L/T$. (Actually in the experiments where $h/L < 0.14$ a cnoidal approximation for L would be justified.) This has been utilized in
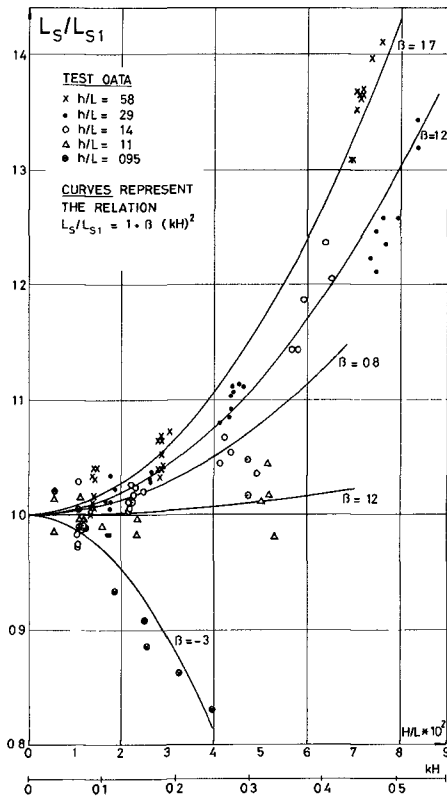
Fig. 8 Experimental results for L_s versus H/L

Fig. 9 which shows theoretical curves for the ratio c_3/c_1. Here c_3 given by Brink-Kjær (1974) as

$$c_3 = c_1 \left(1 + A - \frac{(kH)^2}{4\ kh\ \tanh kh}\right)^{1/2}$$

$$A = \frac{(kH)^2\ (9 + 8\ \cosh^4 kh - 8\ \cosh^2 kh)}{32\ \sinh^4 kh} \tag{3-7}$$

corresponds to zero net mass transport (as it must be expected in a closed wave flume). The abscissa is again h/L. From the measured values of L_s has been calculated the value of c_{22} under the assumption that in (3-6) $L_{s,3} = L_s$, and that c_3 is given by (3.7). We then get

$$\frac{c_{22}}{c_3} = \frac{1}{1 + c_3 T/(2\ L_s)} \tag{3-8}$$

The empirical values of c_{22} thus obtained have also been plotted in Fig. 9, and for comparison the theoretical linear curve for c_{22} is shown too.

We see that there still is a variation of the empirically determined c_{22} values which generally increase with H/L. Also the absolute values are somewhat in contradiction with Goda (1967) who reported measurements of c_{22} about 15% below the linear theoretical values. Although his measurements were all in fairly shallow water ($0.05 < h/L < 0.10$) it seems unlikely from Fig. 9 that c_{22} should be so small even in that interval.

Comparing Figs. 8 and 9 it should be noticed that the value of L_s is much more sensitive to small changes in the phase velocity of the main wave than is c_{22} calculated from L_s. Hence, provided c_3 is a fair approximation to the phase velocity of the main wave, the relatively accurate measurements of L_s yield good results for c_{22}.

However, even with the third order effects included the value of c_{22} is larger than predicted by linear theory.

It turns out that there is another effect which at least in principle draws in that direction. That is caused by the net particle motion in the main wave, which represents a mean velocity U given by

$$\frac{U}{c_1 (kH)^2} = \frac{1}{8\ \sinh^2 kh} \left(\cosh 2k(z + h) - \frac{\sinh 2kh}{2kh}\right) \tag{3-9}$$

(In (3-9) has been assumed that the return flow added to yield zero mass transport is constant over the water depth. In a real wave flume this may not be true, because the downrush from the beach can cause a stronger return flow along the bottom. This has not been checked.)
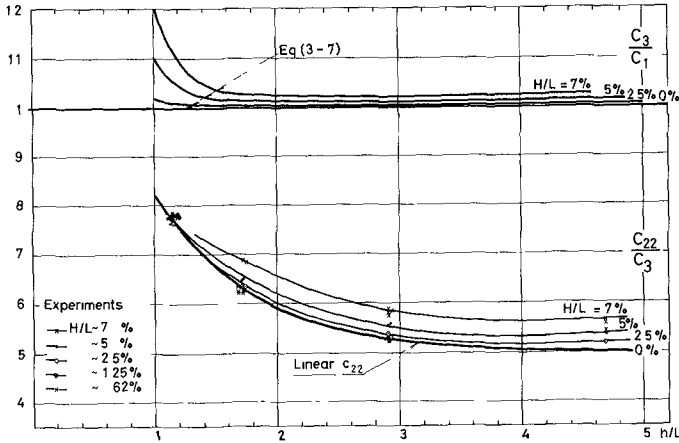
Fig. 9   Phase velocities for main wave and
         free second harmonic wave

In the case of deep water waves, which at least applies to the results for $h/L = 0.58$ in Fig. 8, the wave length L_{22} of the free second harmonic wave is $L/4$. Therefore, in the free second harmonic wave, the water motion is largely restricted to the upper part of the water body where the mean (or net) particle motion of the main wave will be in the direction of wave propagation as Fig. 10 shows. Retaining the assumption that the two waves, the main wave and the free second harmonic wave, do not interact, then yields a physical model, where the net particle motion of the main wave near the surface merely acts as a current carrying the free second harmonic wave with it, and thus virtually adding to the phase velocity of that wave, a contribution which is also $O(H^2)$.
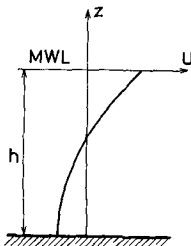
Fig. 10
Net particle velocity in
second order Stokes wave
with zero mass transport

The order of magnitude of this effect can be obtained from (3-9) as U
at the surface (it must actually be somewhat less, say 70%). From (3-9)
we get at z = 0 (and thus neglecting higher order effects)

$$\frac{U_s}{c(kH)^2} = \frac{1}{8 \sinh^2 kh} + \frac{1}{4} - \frac{\coth kh}{8 kh} \qquad (3-10)$$

which has been confirmed to within 10 - 15% by actual measurements.

It appears (as an example) that for
h/L = 0.62 and H/L = 7% the full effect
of U_s on c_{22} will change c_{22}/c_{13} in
Fig. 9 from 0.565 to 0.52 against the
theoretical value of 0.50. Thus the
effect of the net particle velocity
seems at least to be of the right or-
der of magnitude.

3.3 THE EFFECT OF INCLUDING ROTATION
IN THE MOTION OF THE WAVE GENERATOR

As mentioned in the introduction, the
free second harmonic wave appears be-
cause the water motion induced by the
rigid flap does not correspond exactly
to motion in a progressive wave of con-
stant form.

In particular for increasing h/L the
piston motion becomes a poor approxima-
tion. Hence it is natural to investi-
gate, to which extend the height of the
free second harmonic wave can be reduced
by letting the motion of the wave gener-
ator be a combination of a translation
and a rotation, the time variation re-
maining sinusoidal.

In Fig. 11 are shown results for
H_{22}/H_2 when the motion of the wave gen-
erator varied from zero motion at the
bottom ($e_b/e_s = 0$) to pure translation
($e_b/e_s = 1$), e_b and e_s being flap ampli-
tudes at the bottom and the surface,
respectively.

The general impression is that the
free second harmonic motion can be re-
duced by this measure but not to a
level, which makes the results accept-
able. In particular in the third case,
corresponding to deep water, one would
have expected a much more pronounced
effect from a rotation of the flap.

The two first parts of the figure
shows a minimum for H_{22}/H_2 for all wave
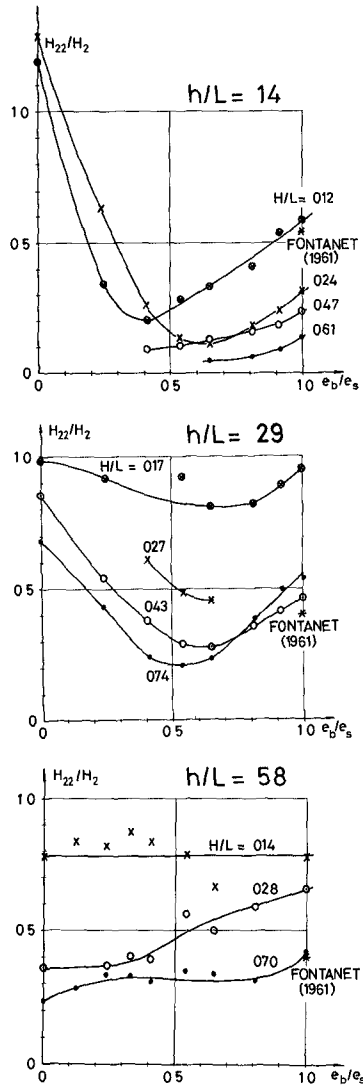
Fig. 11 Variation of H_{22}/H_2
with rotation of flap

steepnesses. The corresponding optimum value of e_b/e_s, however, is much smaller than would be expected from an estimate based on linear wave theory.

Since the effect of rotation is so relatively small we shall not go further into the various curiosities of the results.

4. GENERATION OF WAVES OF CONSTANT FORM
BY A NON-SINUSOIDAL FLAP MOTION

The third series of tests (type (c) mentioned above) aimed at reducing the free second harmonic motion by introducing a compensation for this motion of the same frequency 2ω but in antiphase.

Thus the flap motion ξ in question is a pure translation with the time variation

$$\xi = e_1 \sin \omega t + e_{22} \sin(2\omega t + \beta_{22}) \tag{4-1}$$

where β_{22} is the phase angle between the two components of the flap motion.

These experiments could have been based on the results reported in Section 3.2 for H_{22}, together with information on the phase angles α_{22} for the free second harmonic waves produced there. However, having not been able to measure α_{22} with sufficient accuracy the experiments were instead of optimized to yield minimum H_{22}/H_2. In this way values are obtained for e_{22} and α_{22} which can be converted — by means of the linear wave generator theory (Biésel and Suquet (1951)) — to a total secondary wave height, from which a $H_{22}^!$ is determined.

Hence the value of H_{22} emerging from this series of tests serve not only as a check on the idea of reducing the unwanted secondary wave motion by a more complicated time variation of the flap motion. It can also be used as a control on the measurements of H_{22} reported in Section 3.

Figs. 12 and 13 show results for $H_{22}^!$ and $\alpha_{22}^!$ the imaginary free second harmonic motion generated by the last term in (4-1) in antiphase to the anticipated free second harmonic motion in order to quench the latter.
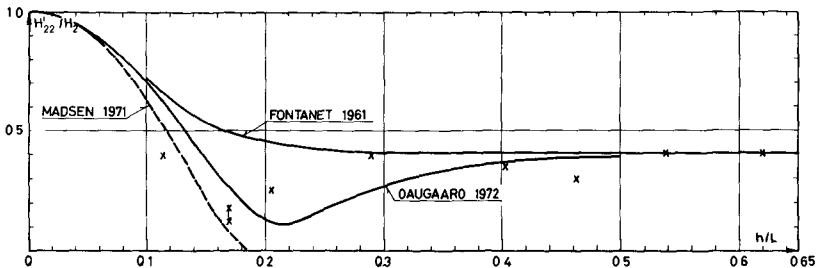
Fig. 12 Values of $H_{22}^!/H_2$ corresponding to optimal choice of e_{22} in (4-1)
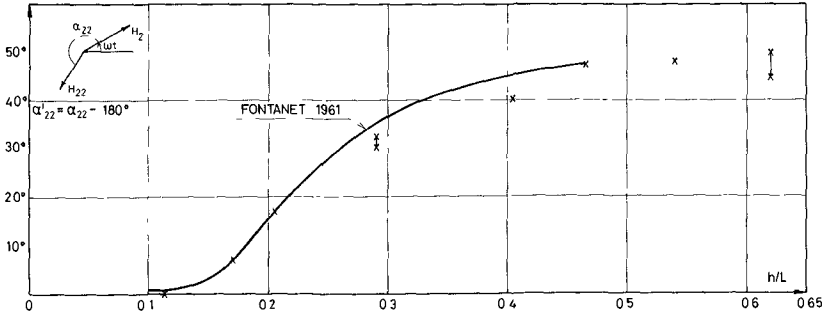
Fig. 13   Values of α'_{22} corresponding to optimal choice of β_{22} in (4-1)

Of particular interest is the confirmation of the two minima at h/L = 0.15 and 0.45.

Also the different nature of the minima are confirmed. Around h/L = 0.15 an e_{22} value determined according to the Fontanet theory will yield a free second harmonic motion as large as or larger than that of pure sine flap motion. At h/L = 0.45 the value of H_{22} can be reduced to 8% of H_2 by the optimal flap motion (H'_{22}/H_2 = 0.30), but an H'_{22}/H_2 = 0.40 as suggested by Fontanet's theory will yield an actual H_{22} which is only 16% of H_2.

In Fig. 14 is shown the values achieved for the free second harmonic motion by the optimal choice of e_{22} and β_{22} in (4-1). Since the flap still does not follow the ideal particle motion of a purely progressive wave, there must still be some free second harmonic motion left. On the other hand, even for the steepest waves H_2 is only a fraction of H and hence the disturbance is in most cases reduced to 1 or 2% of the main wave height.
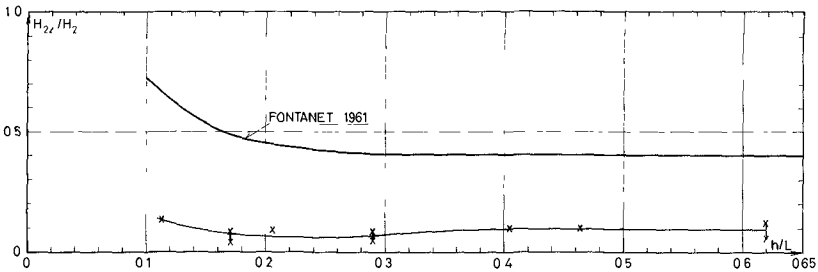
Fig. 14   Values of H_{22} with flap motion according to (4-1)

This conclusion does not apply to the region h/L < 0.1, i.e. long waves. For such waves Stokes' theory yields poor results as soon as the waves have any appreciable height, and really good results cannot be expected for a flap motion like (4-1). Instead a ·cnoidal time variation of the flap should be used, and no attempts have been made in that direction so far.

In Fig. 15 is shown a record of the wave motion in the flume with
T = 1.0 s, H = 11 cm, h = 43 cm, i.e. the same wave as in Fig. 5. H_{22}/H_2
is in Fig. 15 reduced to 0.10 by the
non-sinusoidal flap motion, resulting
in an almost constant second harmonic
component. (Instead a second order
reflection becomes clearly visible.
This problem is discussed in more de-
tail in Section 5.) The overall im-
pression, however, gives support for
the conclusion that for experimental
purposes the flap motion used yields
a considerable improvement of the wave
motion.
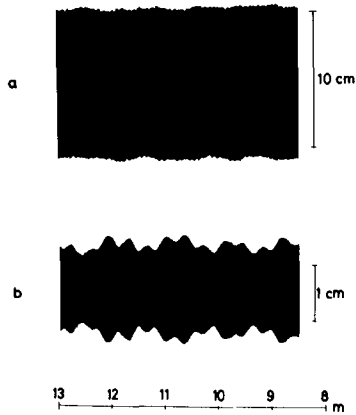
Fig. 15
Record of total wave motion and
total second harmonic motion for
non-sinusoidal flap motion

5. DISCUSSION OF OTHER PHENOMENA OBSERVED

In the experiments were observed or recorded some phenomena, other
than the main object of the study.

The most obvious is the attenuation of the waves down the flume. In
terms of wave heights the measured values for $\Delta H/H$ ranged between 0.002
per m for the longest waves and 0.006 - 0.013 per m for h/L about 0.5.
Hence the total reduction in wave height over the 17 m test section was
in some cases 20% corresponding to 36% of the energy at the wave genera-
tor being dissipated.

As all boundary layers are laminar the relative attenuation should
be linear and independent of the wave steepness, which is confirmed by
the measurements. Assuming boundary layers at the bottom and side walls
yield $\Delta H/H$ values up to 0.0035. If in addition a boundary layer at the
free surface is included, corresponding to a flexible film there (Van
Dorn (1966)) the theoretical attenuation will exceed all measured values
of $\Delta H/H$, being 0.022 for h/L ~ 0.5.

Another phenomenon is caused by resonant interaction between the
waves present in the flume. This occurs when $\Delta k = k_{22} - 2k$ is small,
i.e. for h/L small. The phenomenon was reported by Goda (1967) who
found a variation with x of not only the amplitudes of the second and
higher harmonic wave components. Also the first harmonic component
showed a periodic amplitude variation with x, indicating slow-rate ex-
change of energy between the wave components. Mei and Ünlüata (1972)
studied the problem analytically on the basis of the non-linear long
wave equations and found good agreement with Goda's results.

Fig. 16 shows a record for h/L = 0.095 which clearly exhibits the
same effects. Part a is the total wave motion, part b the first har-
monic component, and part c the total second harmonic motion. (There

is a certain amount of first order reflection, which was later removed
by introduction of the beach shown in Fig. 4.)
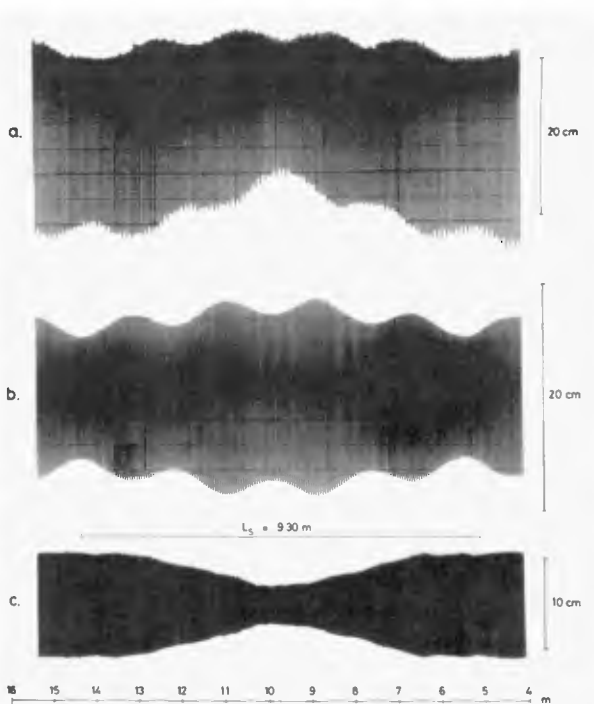
Fig. 16   Wave record with resonant interaction
          (T = 2.3 s, h = 43 cm, $\overline{H}$ = 21 cm)

The phenomenon has not been studied explicitly in the experiments
reported herein. However, it may be worth-while to mention that the
resonant interaction in Fig. 16 at h/L = 0.095 (kh = 0.60) could not
have been predicted by Mei and Ünlüata's analysis. Actually their the-
ory is not valid at all for so large h/L, which is obvious, considering
the fact that included in the phenomenon is a free second harmonic wave
with frequency 2ω which corresponds to h/L = 0.19 (linear shallow water
theory) or h/L ~ 0.22 (Stokes). The non-linear dispersion relation

$$\frac{\omega}{\sqrt{g/h}} = kh\ (1 - \frac{1}{6}(kh)^2) \tag{5-1}$$

used by Mei and Ünlüata yields no solution at all for k_{22} in the present
case. This is illustrated in Fig. 17. The criterion for the occurrence
of resonant interaction is Δk/k << 1. Therefore as Fig. 17 shows the
resonant interaction must vanish when h/L becomes more than 0.12 - 0.14
(provided (1-2) is the proper dispersion relation). This is confirmed
by the experimental results.
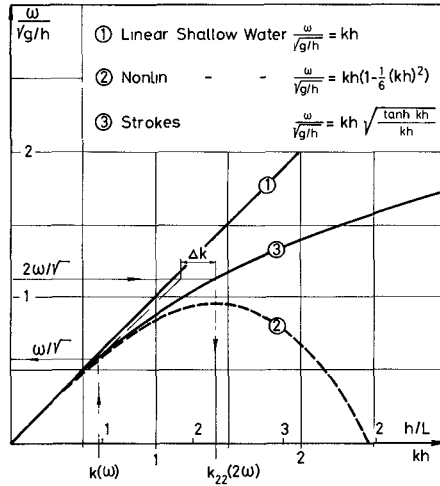
Fig. 17 Dispersion relations

A third irregularity which is observed for the shorter waves with
5 - 7% steepness, is shown in Fig. 18. The record represents the time
variation at a fixed point after the start of the wave generator. Ob-
viously, after some time the waves separate into groups with a beat
amplitude which appears to depend strongly on the wave steepness. The
pattern resembles the instability analysed by Benjamin and Feir (1967)
although the beat length does not agree very well with their disturb-
ance of maximum amplification. The phenomenon did not influence the
measurements of L_s and H_{22} as it only occurred at the end of the flume
for the wave heights and periods in question.
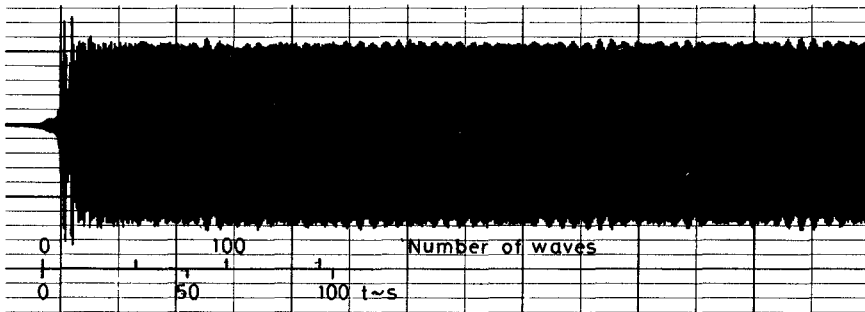
Fig. 18 Instability of waves at the end of the flume
         (H = 3.8 cm, T = 0.65 s, h = 30 cm)

Finally should be mentioned the second harmonic reflection which has
already been shown in Fig. 15, part b. The frequency of the wave re-
flected is 2ω and the reflection was largest for waves of 2 - 2.5% steep-
ness (more than 10% of H_2) and independent of the water depth. It is

likely that it is generated by the breaking process — the characteris-
tics of which depends on the wave steepness.

6. SUMMARY AND CONCLUSION

   The results from measurements on waves produced by sinusoidal piston
motion of a flap type wave generator show that in the region tested,
i.e. 0.10 < h/L < 0.65, the wave motion in the flume is well described
by (1-1). That is by a second order Stokes wave superimposed by a small
free second harmonic wave with half the period of the main wave. This
model ignores all higher order effects.

   In the experiments were measured the total wave motion, and the first
and second harmonic components. In Section 2 are described details of
the experiments and the technique used for analysing data.

   Results for the height of the free second harmonic wave component
are shown in Fig. 6, and for its phase velocity in Fig. 9. All these
results were obtained by sinusoidal piston motion of the flap.

   In Fig. 11 some results are presented for the influence of an addi-
tional rotation of the flap.

   Finally, in Section 4 are given results for a non-sinusoidal piston
motion of the wave generator. The phase angle and amplitude of the
second harmonic component of the flap motion were designed to minimize
the free second harmonic wave.

   In general it is found that the reproducibility of the measurements
improves with increasing wave steepness, and apart from a series of
unwanted side-effects (Section 5) which do not affect the measurements
the results seem to be consistent.

   This is also confirmed by the conclusion that the non-sinusoidal
flap motion of Section 4 yields a wave motion in the flume which for
almost all practical purposes may be said to represent a wave of con-
stant form.

7. REFERENCES

1. Benjamin, T.B., and Feir, J.E., 'The Disintegration of Wave Trains
   on Deep Water,' Part 1, Jour. Fluid Mech., Vol. 27, 3, 1967, pp.
   417-430.
2. Biésel, F., and Suquet, F., 'Les Appareils Générateurs de Houle en
   Laboratoire,' La Houille Blanche, Vol. 6, Nos. 2, 4 and 5, 1951.
3. Brink-Kjær, O., 'Amplitude Dispersive Waves. A Comparison Between
   Phase Velocities,' Prog. Rep. 33, Inst. Hydrodyn. and Hydraulic
   Engrg., Tech. Univ. Denmark, 1974, pp. 27-33.
4. Daugaard, E., 'Generation of Regular Waves in the Laboratory,'
   Unpubl. thesis (in Danish), Inst. Hydrodyn. and Hydraulic Engrg.,
   Tech. Univ. Denmark, 1972.
5. Fontanet, P., 'Theorie de la Génération de la Houle Cylindrique
   par un Batteur Plan,' La Houille Blanche, Vol. 16, Nos. 1-2, 1961.

6. Goda, Y., 'Travelling Secondary Wave Crests in Wave Channels,' Appendix to Rep. No. 13, Port and Harbour Res. Inst., Ministry Transp., Japan, 1967.
7. Hulsbergen, C.H., 'Golfopwekking in Relatief Ondiep Water,' Waterloopkundig Laboratorium, Delft, 1972.
8. Iwagaki, Y., and Sakai, T., 'Horizontal Water Particle Velocity of Finite Amplitude Waves,' Proc. 12th Conf. Coastal Engrg., Vol. 1, 1970, pp. 309-325.
9. Le Méhauté, B., Divoky, D., and Lin, A., 'Shallow Water Waves: A Comparison of Theories and Experiments,' Proc. 11th Conf. Coastal Engrg., 1968, pp. 86-106.
10. Madsen, O.S., 'Waves Generated by a Piston-Type Wavemaker,' Proc. 12th Conf. Coastal Engrg., 1970, pp. 589-607.
11. Madsen, O.S., 'On the Generation of Long Waves,' Jour. Geophys. Res., Vol. 36, 1971, pp. 8672-8683.
12. Madsen, O.S., Mei, C.C., and Savage, R.P., 'The Evolution of Time-Periodic Long Waves of Finite Amplitude,' Jour. Fluid Mech., Vol. 44, 1, 1970, pp. 195-208.
13. Mei, C.C., and Ünlüata, Ü., 'Harmonic Generation in Shallow Water Waves,' in 'Waves on Beaches,' R.E. Meyer, ed., 1972, pp. 181-202.
14. Morison, J.R., and Crooke, R.C., 'The Mechanics of Deep Water, Shallow Water and Breaking Waves,' Tech. Memo No. 40, Beach Erosion Board, 1953.
15. Sørensen, P.S., and Schiolten, P., 'Digital Control of Hydraulic Generators,' Unpubl. thesis (in Danish), Inst. Circuit Theory and Telecommunication, and Inst. Hydrodyn. and Hydraulic Engrg., Tech. Univ. Denmark, 1973.
16. Van Dorn, W.G., 'Boundary Dissipation of Oscillatory Waves,' Jour. Fluid Mech., Vol. 24, 4, 1966, pp. 769-780, (Corrigendum, Jour. Fluid Mech., Vol. 32, 4, 1968, pp. 828-829).

CHAPTER 18

A PROGRAMMABLE IRREGULAR WAVE GENERATOR

by

Norman B. Webber[1] and Colin D. Christian[2]

ABSTRACT

An account is given of the various design considerations in the development of a low-cost programmable wave generator for a laboratory channel. The ability of this equipment to reproduce prototype spectra is critically discussed.

1. INTRODUCTION

With advances in wave recording equipment, reliable data are now becoming available on the spectra of waves likely to be encountered during storm conditions at particular sites where there are coastal engineering problems. There is therefore a need to reproduce these wave mechanically in the laboratory by methods that are sufficiently versatile to cover a wide range of conditions whilst being reasonably economical in cost.

The paper describes the development and testing of such a generator. All of the equipment, with the exception of those standard components which were obtainable commercially, was designed, fabricated, and assembled in the laboratory.

2. THE WAVE CHANNEL

The channel is of rectangular section 14m long, 0.45m wide and 0.45m deep, and has glass panels on both sides throughout its length. It is provided with an end beach of slope 1:6, consisting of non-ferrous shavings and a mattress-like material (hairlok), which is almost fully absorbent.

3. MECHANICAL SYSTEM

3.1 Choice of system. A servo-controlled electro-hydraulic system was the obvious and conventional choice for the type of programmed operation envisaged. Such a system, shown in diagrammatic form in Fig. 1 is capable of providing fast response and close control whilst satisfying the requirements of reliability and reasonable economy.

The principal components are the wave paddle, actuator (or ram), servo-valve, positional feed-back transducer and oil hydraulics motor.

---

1. Senior Lecturer, Department of Civil Engineering, University of Southampton, United Kingdom.

2. Assistant Engineer, Livesey and Henderson, Consulting Engineers, London, United Kingdom.

A piston-type paddle was selected because of its simplicity and because the facility would be used mainly in connection with shallow-water waves. Neoprene rubber was fitted to the periphery and this was found to be very effective in minimising leakage.

3.2 Criteria for Design.   The criteria for design were the velocity and force to be applied. It was desired to produce a range of frequencies between 0.2 Hz and 3 Hz, and wave heights of up to 0.15m. For velocity, the minimum water depth (say 0.12m) was the criterion,whilst for force, the maximum water depth (say 0.35m) was the criterion. From these consider-ations, and utilising the curves of Gilbert, Thompson and Brewer[1] for regular waves, the maximum velocity was estimated at 0.3m/s and the maximum force at 450N. For the irregular waves the final design criteria selected were:

$$\text{maximum velocity} - 0.45\text{m/s}$$

$$\text{maximum force} \quad - 450\text{N}$$

$$\text{maximum stroke} \quad - 0.45\text{m}$$

3.3 Design of Components.   In order to meet the dynamic requirements, a 1.1kW power unit capable of circulating 4.5 1/min (1 imp. gal/min) at a pressure of 13.8N/mm^2 (2000 lbf/in^2) was purchased. The flow demand was such that the supply pressure needed to be only 6.9 to 10.3N/mm^2 (1000-1500 lbf/in^2), but the wastage of power was not an important consideration in the case of equipment that would only operate intermittently.

The actuator was of the balanced, double-ended type, with the advantage of symmetry in both directions. The dimensions of the rod were 0.46m long, 19.1mm diameter, operating in a cylinder of diameter 25mm.

To be compatible with these dimensions of actuator and system dynamics a servo-valve delivering 4.54 1/min at 6.89N/mm^2 was required. A Moog servo-valve type 76 was selected.

A closed-loop control system was required in which the output is represented by a mechanical or electrical quantity, and this is compared with the reference input. The comparison between output and reference input results in an actuating signal which is the difference between these quantities and acts in a manner to maintain the output at the desired value. For a well-designed system, control is almost independent of the load dynamics. The feed-back element selected was a Sangamo Controls linear variable differential transducer with built-in oscillator and detector, and requiring only a DC voltage for operation. The output depends upon the load impedance and is linear to an accuracy of 1%. The transducer in effect acts as a reference for the position of the paddle since, by applying a particular voltage to the control system the paddle tends to move to the point correspond-ing to the given voltage.

A Moog servo-controller provides the electronic control element. Essentially, this consists of two operational amplifiers and a power supply. Overall gain may be varied over a 100.1 range.

The assemblage of the actuator, servo-valve and linear variable differential transducer is shown in Fig. 3.

3.4 Stability of Control System.   Having selected the components of
the control system it remained to check the stability of the system.   The
lowest natural frequency of the system controls the stability and in
practice this is the frequency of the valve-piston-load combination which
was estimated to be 20 Hz.   The gain setting should be the maximum available
compatible with stability.

Stability was considered using a sine wave generator with frequencies
of 0.1 to 3 Hz and a system gain varying between 14 and $60s^{-1}$.   For a gain
of $20s^{-1}$ the motion of the paddle was smooth to the eye for frequencies down
to 0.3 Hz but below this judder was evident at the ends of the stroke.

4.   GENERATION OF COMMAND SIGNAL

Controlling the mechanical system is a command signal which must produce
the required spectrum of waves, whilst taking into account the transfer
function (paddle-to-wave motion) and the response of the generator, both of
which may vary due to parameters such as water depth and system gain.

The use of an analogue white noise generator and a set of filters to
produce the desired effect was rejected on the grounds that the frequency
of conventional white noise generators does not usually extend down as low
as that required and there are problems due to drift and output variability.

Therefore it was decided to employ digital means, taking advantage of
the medium-sized computer available at the University.   Punched paper tape
rather than magnetic tape was chosen because of the relative cheapness of
the hardware required to handle it.

The tape code is ISO8 and the format depends to some extent on the
programming language.   ISO8 employs 7 data bits and one parity bit.

After considering the various alternatives it was finally decided to
use a tape speed of 100 characters/s with a 2-digit converter, the 1%
accuracy attainable being compatible with paddle accuracy for a 0.1m stroke.
The punched paper tape reader is a Computer Terminals OR 10 unit and the
digital-to-analog converter a Varadyne Systems DAC-29 series.

It was necessary to design additional circuitry to provide the following
functions:

(1) Operation of tape reader at a pre-determined rate.

(2) Storage of information read by tape reader.

(3) Sequencing of tape reader, storage register, and up-dating of
    digital to analogue converter.

(4) Smoothing and scaling of analogue signal.

These operations were performed by digital and analogue circuits built
on a module basis making use of plug-in circuit cards and dual-in-line
packaging of integrated circuits.

A mean value control was provided because it is convenient if the
paddle is kept in a central position during the time that no signal is

received from the tape recorder. The system block diagram is shown in Fig. 4.
Two modes are incorporated: (1) a loop mode in which a continuous tape loop
may be used to generate a periodic motion or a short length of tape to produce
a solitary wave or step function (2) a trigger mode for normal program tapes,
heralded by £S and terminated by £F.

Two inverting amplifiers were introduced. Three ranges of scale were
provided to suit the paddle motion travel - 0.1m, 0.15m and a potentiometer
control to provide any desired value.

The performance of the complete punched-tape interface unit in response
to various numbers on the punched tape was investigated. For high gains of
the order of $60s^{-1}$, the system was unstable, any error signal causing
oscillations of 10 Hz with an amplitude of 3mm. For gains of 14 or less the
response was slow and large errors in position of the order of 8% were evident.
Finally, a compromise setting for the gain of approximately $30s^{-1}$ was used
which resulted in positional accuracy of approximately 1% whilst maintaining
a smooth motion and reasonable frequency response.

5. PRODUCTION OF COMMAND TAPES

The specification for the command tape is that the waves produced shall
have the required spectral density function.

Two methods may be used for the digital simulation of sea waves:

(1) Superposition of sine waves, with random values appropriately
    assigned.

(2) Digital filtering of random numbers.

Goda[2] has used the first method with 50 components, with some success.
It is anticipated that the non-linear transformation of waves would have a
smoothing effect.

The second method does not recognise any discrete frequencies and
therefore should result in a continuous distribution of energy which is more
realistic of an actual sea state. The procedure generally adopted is to
filter a sequence of random numbers, generated such that they possess a
normal probability distribution and that the magnitude may be predicted.

The filter used may be considered as a constant parameter linear system
whereby

$$a_1 x_1(t) + a_1 x_2(t) = a_1 \left[y_1(t) + y_2(t) \right] \qquad (1)$$

the LHS representing input and the RHS representing output and

$$y(t) = \int_0^\infty h(\tau)x(t-\tau)d\tau \qquad (2)$$

or the output is given by the convolution integral of a weighting function
$h(\tau)$ times the input at some time τ earlier.

A time series with specific power spectral density and probability
density function may be produced by exciting a specially designed filter
with white noise. The characteristic of white noise is a constant spectral

density function and a specific probability distribution; for physical
purposes it is band-limited otherwise it would have an infinite variance.

Borgman[3], Shvetsov and Shorin[4] use the digital version of Eq.(2):

$$\eta(t_k) = \Sigma \, {}^{n \, = \, K}_{n \, = \, -K} \, h(\tau_n)x(t_k - \tau_n)d\tau_n \qquad (3)$$

where $x(t_k)$ are the series of random numbers constituting the white noise.

The Fourier transform of $h(\tau)$ is known as the frequency response function
$H(f)$ given by

$$H(f) = \int_0^\infty h(\tau)\exp(-j2\pi f\tau)d\tau \qquad (4)$$

It may be shown that if the spectrum of random numbers $S_x(f)$ is equal
to unity for the range of frequencies envisaged then $H(f) = \sqrt{S(f)}$, the required
spectrum.

In the present case the filter has to take account of the response
function of the signal-paddle movement - wave motion system as well as the
desired spectrum. By making use of the convolution theorem it is possible
to perform the filtering in the frequency domain instead of the time domain
and by using FFT methods considerable computing time was saved.

The 'white noise' may be regarded as a sampled time series and is
generated as a series of pseudo-random numbers on a computer by a standard
routine such that the probability density distribution is Gaussian and the
series only repeats after 2^{43} numbers.

It may thus be arranged that the time series produced will be the
sampled time series representing the water surface elevation. The length
of the transforms used to simulate the filter may be the same as the number
of data points it is desired to be produced. However, a more efficient
method is to filter segments of the record and then to add them.

As stated earlier, it was necessary to incorporate in the command signal
a transfer function from paddle motion to wave motion (wave amplitude/stroke)
and this was based on small amplitude theory[5] given by:

$$\frac{a}{e} = \frac{2\sinh^2 2\pi d/L}{\sinh(2\pi d/L)\cosh(2\pi d/L) + 2\pi d/L} \qquad (5)$$

Fig. 5 shows that the agreement with theory for regular waves is quite
good for frequencies between 0.5 Hz and 1 Hz, and probably acceptable to
beyond these limits, dictated by secondary harmonics at the low frequency
end and wave breaking at the higher.

The command signal to paddle motion in terms of amplitude and phase
were incorporated. The two functions were combined to form the frequency
response $T(f)$ as

$$T(f) = \frac{a}{e}(f) \times \frac{e}{R}(f) \qquad (6)$$

where R represents the command signal.

6. INVESTIGATION OF PERFORMANCE

A number of records of actual sea states at sites in the English Channel were available. These were analysed for their spectral and statistical properties.

Command tapes were then prepared using the method previously described. In all, 8 prototype records were simulated, together with 2 arbitrary spectra and 2 Moskowitz spectra. Water depth in the channel was maintained at 0.35m throughout and scales were chosen to correspond with water depths where applicable.

All the tapes used in the tests consisted of 8000 numbers giving a running time of 5min 20s.

The waves in the channel were recorded by means of a capacitance probe and tape recorder, subsequently being analysed for their spectral and statistical properties. The power spectral density function was computed by FFT directly, using Hanning smoothing for the spectral window. Over several runs, repeatability was found to be within 3 per cent.

The variation of spectral form along the channel was also examined and it was found that there was very little variation, although there was a tendency for the higher frequency energy to diminish with distance from the paddle, presumably due to turbulent dissipation.

Some typical comparative spectra are shown in Fig. 6. Also, the probability distribution of water surface elevation, $p(\eta)$, and normalised wave heights, $p(H/\sigma)$, were computed in each case and compared with Gaussian and Rayleigh distributions, respectively (Fig. 7).

Spectra from the Nab Tower were, on the whole, successfully simulated, errors in variance being less than 3%. A greater resolution would probably have revealed a shape similar to the prototype.

The Eastbourne spectrum was simulated with a variance having an accuracy within 6%, and it will be noted that the peak energy has been increased by about 15% and shifted to a slightly higher frequency. Difficulties were encountered with the production of the command tapes and this probably affected the performance.

The prototype spectra for Jersey are of interest because they exhibit double peaks, indicating chop superimposed on swell – a very difficult sea state to represent by the zero crossing method of analysis. Reproduction is not particularly good especially in respect of a lack of energy in the high frequency portion. This may be due to shortcomings of the digital filter program.

The spectral shape for the Moskowitz spectrum was reasonable but variance of the command tape was too low.

The graphical representation of the probability distribution of water surface elevation showed, in general, a positive skewness which was also exhibited by the computed values of skewness and these were greater than prototype values.

The graph of frequency response and coherence function showed that there was very little non-linearity since the coherence function differed little from unity. The frequency response showed good agreement with that predicted by sinusoidal tests.

7. CONCLUSIONS

A wave machine has been developed which is operated directly by a computer generated time series representing paddle positions. The total cost of the machine, excluding labour, was less than £1000 ($2300).

The command signal is generated by digitally filtering random numbers, the filter being designed so that the waves produced represent the desired energy spectrum. The FFT method was very efficient, but errors in the resulting time series could not be predicted with confidence. Some improvement of the filtering system is needed.

A variety of spectra, including prototype and theoretical, were used to demonstrate the feasibility of simulating sea state in this way. Generally, the performance was reasonable, but the accuracy of modelling was found to depend upon the magnitude and shape of the spectrum to be reproduced. Double-peaked spectra were the least satisfactory. In all cases, running time should be considerably increased.

The linear transfer function for the paddle to wave process was found to be reasonably valid. But wind, or other means, would need to be introduced if the higher frequencies are to be simulated correctly.

The system at present suffers from some measure of over-damping. The gain should be increased, with the introduction of dither and compensatory circuitry to minimise judder. The aim should be a flat frequency response to approximately 3 Hz.

It is hoped to produce a Mk2 model which will incorporate the improvements outlined above and to replace the punched tape input by direct on-line from a mini-computer.

ACKNOWLEDGEMENTS

REFERENCES

1. GILBERT, G., THOMPSON, D.M. and BREWER, A.J. (1971), 'Design Curves for Regular and Random Wave Generators', J. Hyd. Res., vol. 9, pp. 163-196.

2. GODA, Y. (1970), 'Numerical Experiments on Wave Statistics with Spectral Simulation', Rpt. Port and Harbour Res. Inst. of Japan, vol. 9, pp. 7-57.

3. BORGMAN, L.E. (1967), 'Ocean Wave Simulation for Engineering Design', Tech. Rpt. HEL-9-13, Hyd. Eng. Lab., University of California (Berkeley).

4. SHVETSOV, K.Y. and SHORIN, A.N. (1969), 'The Modelling of Sea Waves by Digital Computer', Oceanology, vol. 9, pp. 578-584.

5. BIESEL, F. and SUQUET, F. (1953), 'Laboratory Wave Generating Apparatus', Proj. Rpt. 39, St. Anthony Falls Hydraulic Laboratory, University of Minnesota.

NOTATION

$H(f)$ -- Frequency response function

L -- Wave length

S_f -- Power spectral density function

S_x -- Spectrum of random numbers

a -- Wave amplitude

d -- Water depth

e -- Stroke

$h(\tau)$ -- Weighting function

$x(t_k)$ -- Series of random numbers

$x(t)$ -- Time dependent variable

$y(t)$ -- Time dependent variable

η -- Water surface elevation

σ -- Standard deviation

τ -- Time lag
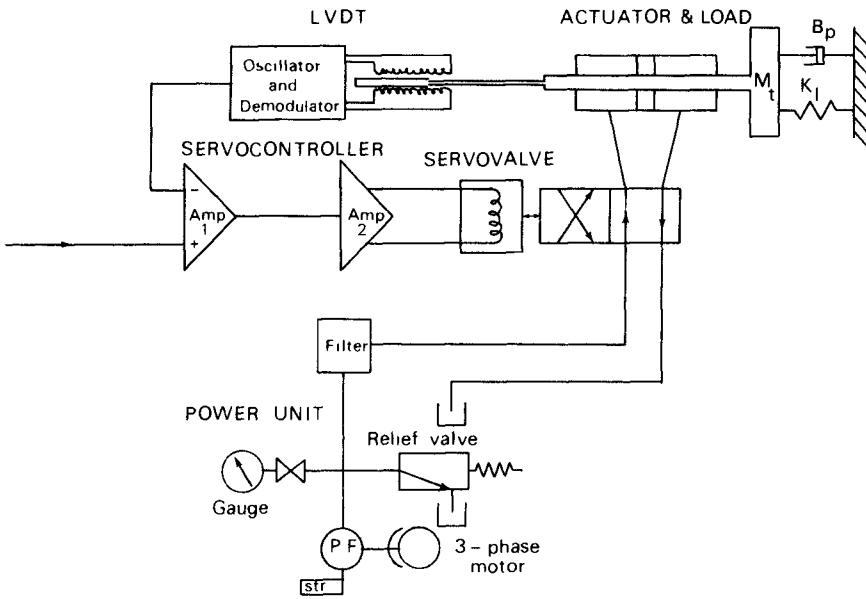
Fig 1   Hydraulic circuit
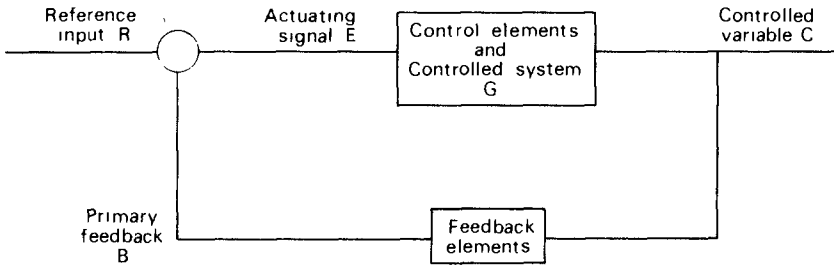
Fig 2   Closed-loop control system
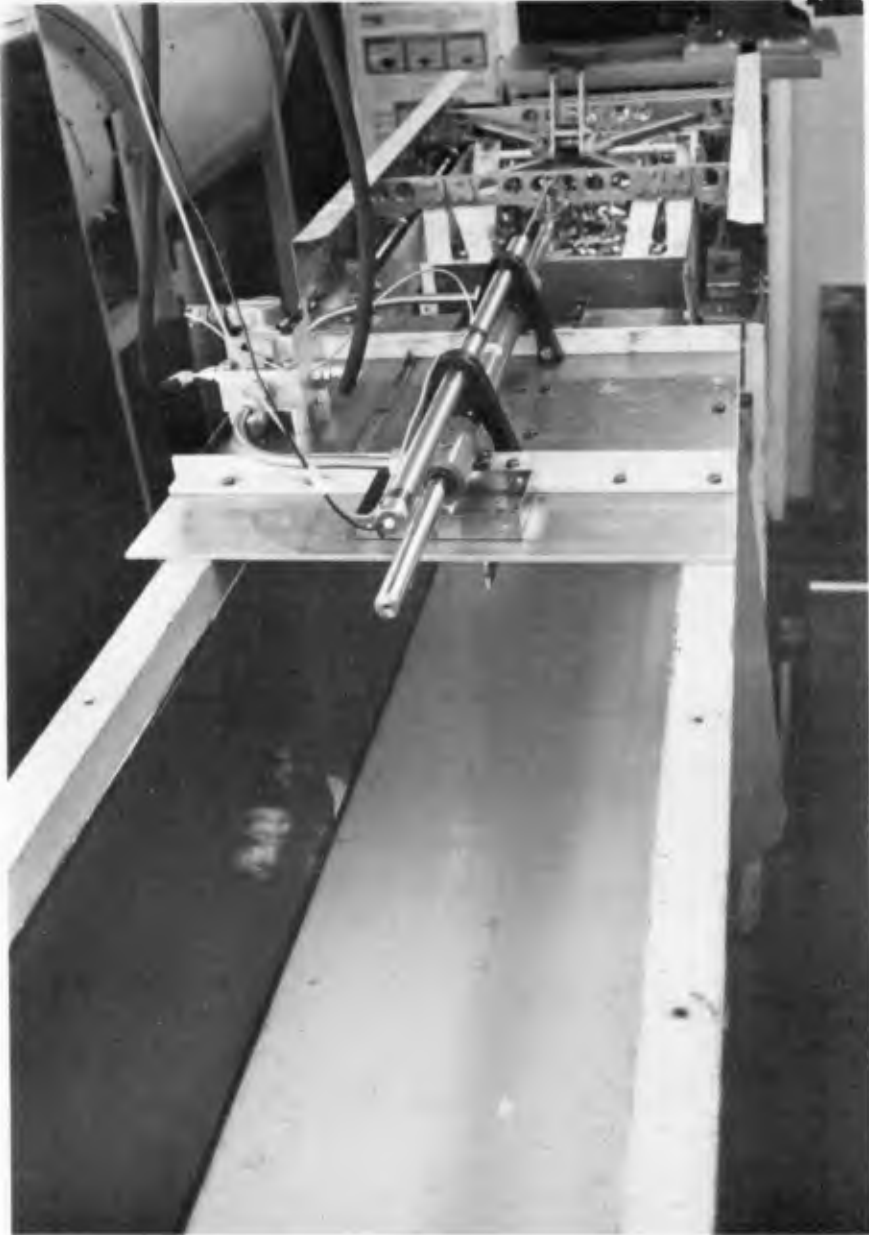
FIGURE 3   Servo-mechanism assemblage, showing actuator
servo-valve and feed-back transducer
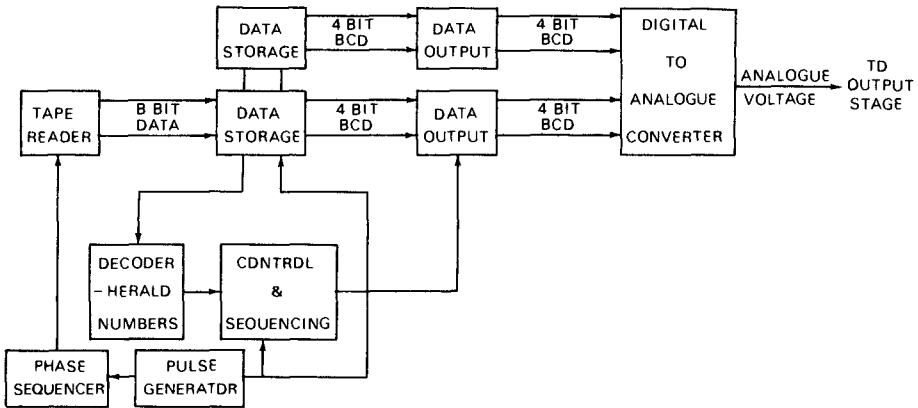
Fig 4   Block diagram of punched tape interface
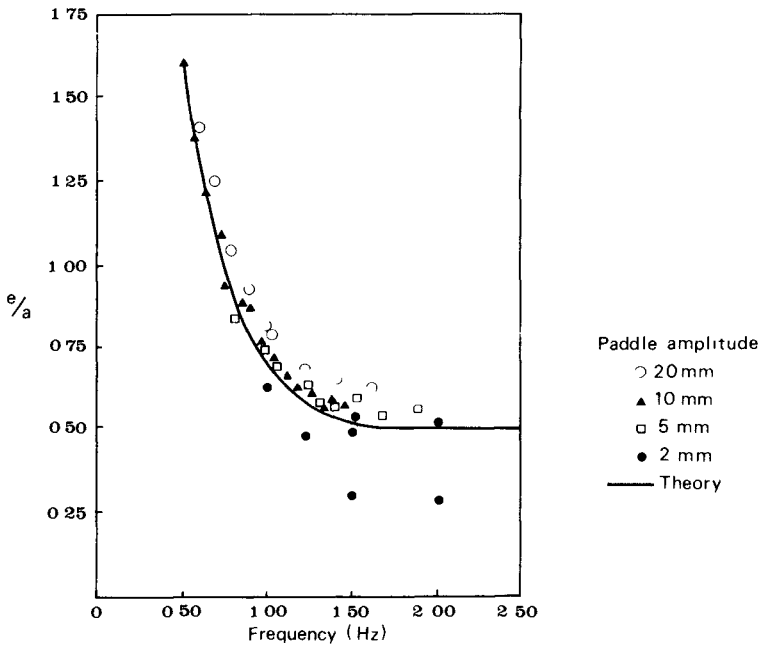
Fig 5   Comparison of experimental and theoretical values of ratio paddle amplitude / wave amplitude

(a) Nab Tower, English Channel

(b) Eastbourne, English Channel

(c) Jersey, English Channel

(d) Moskowitz (wind speed 25 m/s)
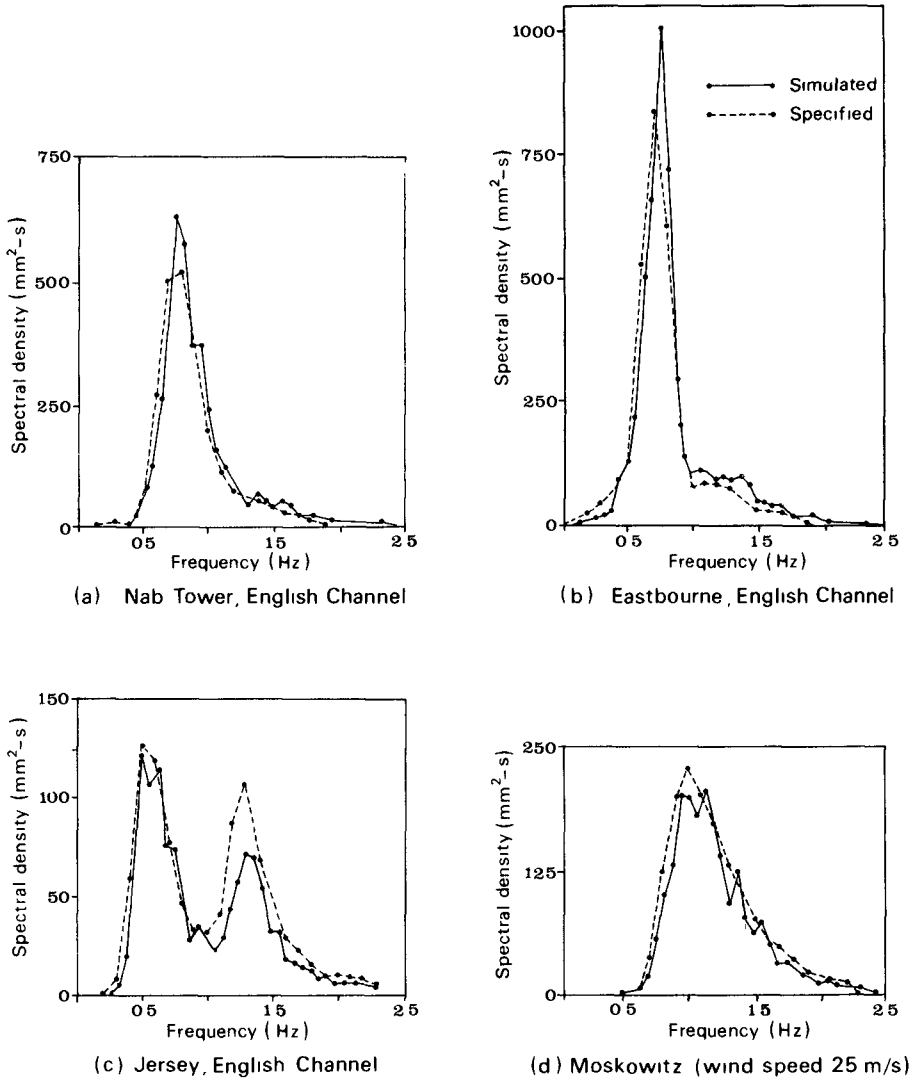
Figure 6   Simulated spectra

CHAPTER 19

RANDOM WAVE SIGNAL GENERATION BY MINICOMPUTER

by

Ed. R. Funke*

ABSTRACT

The computer programmed implementation of a pseudo-random noise generator based on the use of a binary feed-back shift register and an associated digital filter is described. Descriptive details are given for the compensation of the filter for the various dynamic transfer functions in the system. The random signal generator has been programmed both for a dedicated computer (NOVA 1200 with 4K core) which can carry up to 50 different spectra in core at any one time and for the EAI 640 with 16K core and disc storage which was used to investigate the spectral and statistical properties of the generated wave. JONSWAP spectra with 0.6 and 1.0 Herz centre frequencies were generated and observed at locations from 5 to 40 meters from the wave maker using a hydraulically operated machine in a partial piston and partial hinged flap mode in 0.9 meter of water. Measurements indicate that JONSWAP spectra can be closely matched in the flume. The 1.0 Herz spectrum is less stable as a function of distance, all spectra indicate a significant decrease of the spectral peak as a function of distance from the wave maker and the ratio of H_{max}/H_{av} is in general larger than that observed by Wiegel and Kukk.

1.0   INTRODUCTION

The term 'random wave' is used in this paper to describe a water wave which is generated to simulate a natural sea state. Strictly speaking the method used for the purpose of this study produces a 'pseudo-random' time series and as such the series is deterministic and repetitive and can be re-started from the same initial conditions. The method is logically quite similar to the hard wired devices described by Ref. 1, 2 and 3. Because of the flexibility and power of a general purpose digital computer, it was possible to compensate for several dynamic transfer functions of the wave making machinery, to monitor the generated wave at the test site and to adjust the input spectrum in order to match the spectrum of the generated wave as closely as possible to the desired reference spectrum.

It is, however, not clear how accurately one needs to reproduce the specified spectrum during the synthesis of the

*Senior Research Officer, National Research Council of
 Canada, Ottawa, Ontario, K1A 0R6, Canada.

natural sea state. The reference spectrum which is to be
synthesized, whether it is an observed or a theoretical
spectrum, is an approximation in itself. Nevertheless,
it is thought to be important to know how accurately one
can match the reference spectrum by the simulation especially
by using simple wave making machinery and in the absence of
costly wind generating equipment.

The wave flume and the wave maker that were used in this
study are described in Fig. 1. The wave maker is powered by
a single hydraulic piston which is attached to the rigid board
through two separate linkages on top and bottom. Individual
settings on the linkages permit the board to operate either
in a purely piston or a purely hinged-flap mode. Alternatively
a combination of piston and flap motion is possible. For the
experimental work described here, the settings were such that
a 0.3 meter displacement of the top linkage corresponded to
0.173 meter displacement on the bottom. All tests were
carried out with 0.9 meter of water depth in the flume. The
partial flap mode of the wave board was found helpful in en-
hancing the generation of the higher frequencies.

The beach of the wave flume is adjustable and the top of
the beach is set to be at the still water level. Reflections
were measured along the flume and were found to be 12% at
1.0 Herz, from there going down to 3% at 0.6 Herz and then
increasing again to 13% at 0.28 Herz.

The wave probe is a capacitive proximity gauge (Ref. 4).
Its linear range of operation is restricted to 1/4 of the dia-
meter of the outside guard ring. For the reason that this
instrument has no physical contact with the water surface, it
is ideally suited for wave measurements in the laboratory.
However, the range over which this instrument was used ex-
ceeded the recommended linear portion and therefore it was
necessary to linearize the data. This was executed by a
computer program using a table look-up procedure.

Figure 2 describes the digital computer equipment which
was harnessed to the project. The intent was primarily to
use a small minicomputer like the NOVA 1200 as a dedicated
signal generator which may then be used for all coastal
studies requiring the simulation of random waves. This
machine with 4000 words of core, a slow paper tape reader, a
typewriter and one channel of digital to analog conversion
cost approximately $8000. It was programmed in Assembly
language and can store 50 different spectral generating
functions which could be selected by switch settings.

However, for the purpose of the study described in this
paper a more sophisticated program was required which not
only generated a random wave but also monitored the waves at
the selected location in the flume and carried out the data

conversion and analysis that was required. The digital pro-
cessor used for this purpose was the EAI 640 minicomputer with
16000 words of core. Figure 2 shows only those peripheral
devices that were actually used in this project. Programming
on the EAI 640 for this job was executed in Fortran under an
in-house developed operating system which permitted the crea-
tion of separately compiled job functions which were data
compatible with any other job program through a common disc
storage medium. Through the use of this system a highly
modular approach to programming and computer use was possible
which allowed the execution of large jobs inspite of limited
core memory availability. The EAI 640 program was equipped
also to compute and punch on paper tape the digital filter
function which may then be loaded into the NOVA 1200. This
tape is only 0.4 meter long.

2.0   THE TRANSFER FUNCTIONS BETWEEN THE POINT OF SIGNAL
      GENERATION AND WAVE MEASUREMENT

     Figure 3 summarizes the various factors that affect the
wave generation signal and which must be accounted for if a
wave is to be produced at some distance from the wave maker
with a specified variance spectral density. This considera-
tion applies whether the signal source is an digital or an
analog random noise or is derived from an analog or digital
tape of a prototype wave recording. In either case, the
signal will first be affected by the analog low-pass filter
which is inevitably used to smoothen out or band limit the
,raw noise. The low-pass filter used for this system is a
third order Butterworth and is described by Ref. 5. It has
a cut-off frequency set to 2 Herz.

     The dynamics of the electro-hydraulic servo system of the
wave maker depends on the servo valve and the design of the
other electronic and hydraulic components and will have to be
measured for each individual wave maker. In addition it is
possible that the depth of water, the particular settings of
the electronic servo loop-gain and the mechanical gains of the
linkages can influence the dynamic behaviour of the system.
The particular machine used for this study exhibited a first
order low-pass characteristic with a cut-off at 1.5 Herz
which did not change measurably when the water level was
dropped from .9 to .6 meters.

     The next transfer function of importance describes the
relationship between the displacement of the wave board and
the corresponding wave amplitude. This function is described
by Ref. 6 and depends on the depth of water, the wave period and
the mode of the wave board operation, i.e. piston or flap mode,
or a combination mode. If the board is used in the piston mode,
then for deep water and short period conditions the wave height
is typically twice the stroke length of the board. For longer
periods of the wave, that is lower frequencies, the stroke
amplitude must be significantly amplified. The theoretical

relationship describing this transfer function, as given by
Ref. 6, is based on a first order wave theory. Experimental
verification agrees with this function to within 5%.

As the wave propagates down the flume, its spectrum changes.
The higher frequencies appear to be dissipated and the peak of
the spectrum tends to shift to a lower frequency. This phenom-
enon is probably due to a nonlinear transfer of energy between
adjacent bands of frequencies. It is not possible to describe
this transformation in terms of a simple multiplying function.
Experimental measurement and adaptation of the input spectrum
was used successfully to compensate for this deficiency.

3.0 THE CHOICE OF THE THEORETICAL SPECTRUM

During the initial experimental work in connection with
this project, it was first decided to use the Pierson-Moskovitz
spectrum for a fully developed sea (Ref. 7). Visual assessment
of the waves failed to convince the observers that the result
looked realistic. As a consequence, it was decided to use the
more recent JONSWAP spectrum (Ref. 8, 9) with parameters $\gamma = 7$,
$\sigma_a = .07$ and $\sigma_b = .09$. It was then felt that the waves gener-
ated by these specifications did resemble a natural sea state
more closely. Occasional breaking waves were observed along
the entire length of the flume.

4.0 THE COMPUTER PROGRAMS

Figure 4 summarizes the various computer programs that
were used for the experimental work. Initially, the program
SPECTH was called to generate a frequency discrete representa-
tion of the JONSWAP spectrum with the specified parameters.

The program *RWGEN1* has the 'real time' capability to
generate the required analog signal for the wave maker and to
provide data acquisition as well. However, on first enter-
ing this program, various initializations are being executed
by it, including the derivation of a generating function which
is then used for the purpose of digitally filtering the pseudo-
random noise according to the specified reference spectrum. This
digital filter function is also compensated at this stage for
the various transfer functions described in Section 2.

While *RWGEN1* is in the 'on-line mode', analog data
from the wave probe are read into core and recycled so that
only the last 2048 samples of the water surface variation
are being recorded. On depressing a switch, the program
exits and subsequent programs are now called to linearize
the data, to remove the mean value and to perform a variance
spectral density analysis with 0.03 Herz resolution. The re-
sults are displayed for visual inspection and comparison, as
a result of which the user may decide to modify the input
spectrum to *RWGEN1*. This modification has been done either

by recalling *SPECTH* and specifying new and different
spectral parameters or by using a differencing algorithm
which compares the reference spectrum with the measured
spectrum and creates from this a new input spectrum. This
latter method worked quite well for spectra with peaks at
0.6 Herz but failed completely when the peak was at 1 Herz.

4.0   THE ALGORITHM FOR THE GENERATION OF THE RANDOM WAVE

     In general terms, the method used to generate a 'random'
signal with a specified variance spectral density consists of
a random number generator algorithm which is followed by a
digital filter. The digital filter is represented by its
'impulse response' function which is numerically convolved
with the output of the random number generator. This method
has been described by Ref. 1, 2 and 3 although the former
uses analog methods to solve the convolution integral.

     The random noise source for this system is a programmed
implementation of the 'linear feedback shift register' which
is a well known pseudo random noise generator (Ref. 3, 10,
11, 12). This register is shown symbolically in Fig. 5.
Its output consists of a string of 'ones' and 'zeros' which
are generated by a feedback arrangement from at least two
cells of the register and which are summed by a 'modulo 2'
adder (exclusive OR). Following this, all cells of the
register are shifted to the right by one position with the
first bit in the sequence being discarded. The order of the
'ones' and the 'zeros' is random in the sense that the out-
come of each cell value is uncorrelated with the outcome of
the adjacent cells at least up to the cycle length T_n of the
sequence. This implies that the variance spectral density of
the sequence is essentially flat over the range from $1/T_n$ to
$1/(2\Delta T)$ where ΔT is the stepping interval of the shift register.

     The binary number sequence of the generator is repetitive
and the period of repetition depends on the particular choice
of the feedback cells. Only for a few combinations of these
cells will the register generate the maximum cycle length,
that is to say that it will produce all possible patterns of
'ones' and 'zeros' including the 'all ones' pattern for the
first n cells. The 'all zeros' pattern is not possible. It
is important to realize that the flat spectral density of the
binary sequence is guaranteed only if the sample length over
which the spectral analysis is carried out consists of an
integer multiple of the maximum cycle length. This means
also that the output of the digital filter, which is driven
by the binary sequence, only meets its spectral requirements
over the same interval. Consequently, experiments using these
random waves should be restricted to intervals corresponding
to integer multiples of the maximum cycle length of the shift
register. Figure 5 lists the cycle lengths of different

feedback arrangements and the corresponding periods. It may
be seen that the choice is not quite as large as one might
wish. This deficiency can be overcome by using a 4-point
rather than a 2-point feedback (Ref. 10).

The register length of 65 cells is matched to the length
of the digital filter function with which the binary random
number sequence is convolved. However, the effective length
of the shift register that participates in the regeneration
procedure is only n cells. The remaining (65-n) cells serve as
a delay line memory.

The digital filtering operation consists now of multiply-
ing the value of each cell of the shift register with a
corresponding weight in the filter function. Since the cell
values are but one or zero, this operation requires only
selected addition, an operation suitable for computers without
a hardware multiply feature such as the NOVA 1200. The weights
are scaled so that the summation will, at no time, result in
an overflow condition.

The output of the digital filter is fed into a digital to
analog converter which is then followed by the low-pass analog
filter with a 2 Herz cut-off frequency (Ref. 5).

The initial condition of the binary shift register is of
significance in the formation of subsequent sequences. In
order to insure that the entire register of 65 cells starts
off with a bit pattern that belongs to the set of all patterns
in the maximum cycle length, it is best to run the generator
for at least   65 steps, where the first n cells may have
any starting condition except all zeros.

5.0   THE COMPUTATION OF THE DIGITAL FILTER

The digital filter consists of a string of 65 integer
numbers which are the time discrete representation of the
impulse response function of the equivalent analog filter.
The digital filter function is obtained by the Inverse
Fourier Transform of the required amplitude spectrum and an
associated phase spectrum.

The amplitude spectrum is obtained directly from the
reference variance spectral density which is first compensated
for the various transfer functions described in Section 2.
Subsequently, the square root may be applied to the variance
and finally the function must be discretized by interpolation
over the range from 0 to some upper frequency limit. This
latter operation was found to be more important than initially
expected for the following reason.

Since the Inverse Fourier Transform produces nearly twice

as many points as are contained in the input spectrum, and
since the digital filter function must finally be made up of
65 points, it is necessary to represent the input function
by 33 equally spaced points including one at 0 and one at
the maximum frequency f_m. However wave spectra, especially
the JONSWAP spectra, are very peaked. It was found that one
of the 33 points of the discrete representations <u>must</u> fall
on the peak of the input spectrum or else the output from
the digital filter will not possess a spectrum with a peak
frequency at the same location as the input spectrum, but
rather at the frequency with the largest discrete representa-
tion.

The upper frequency limit of the discrete representation
determines the stepping rate of the signal generation which
is $\Delta T = 1/(2 \cdot f_m)$. The dilemma is this: If f_m is chosen
too large, then the stepping interval is agreeably small but
the discrete representation of the spectrum by the 33 points
is too coarse to preserve some of the finer details. If the
f_m is made smaller to improve the discrete representation of
the spectrum, then the stepping interval is too coarse and
inspite of heavy analog filtering the output signal will not
be smooth. A compromise is required and it was found quite
satisfactory to use the following algorithm: Find the peak
frequency f_p and divide this by 14. This gives the fre-
quency increment. Multiply this by 32 to get the upper
frequency limit, f_m. With this, $f_m = 2.286 \cdot f_p$.

A phase spectrum must be assumed and there are an in-
finite variety of choices. The simplest phase spectra are
either 90° or 0° for all frequencies. The former results in
an anti-symmetric and the latter in a symmetric impulse
response function. The anti-symmetric function is preferable
since it is less likely to contain a bias for truncated func-
tions and for this reason the 90° phase is used in this
program. Other phase spectra, such as the random phase
spectra, produce a variety of different random wave sequences.
However, the impulse response functions which result from the
use of random phases do not in general converge to zero at
either end and this can result in excessive start-up trans-
ients.

Since the Inverse Fourier Transform is obtained from the
co and quadrature spectrum, rather than the amplitude and
phase spectrum, the equivalent operation to selecting the
90° phase spectrum is the clearing of the co spectrum and
the equivalencing of the quadrature spectrum with the am-
plitude spectrum.

6.0   DESCRIPTION OF EXPERIMENTAL RESULTS

Figure 6 illustrates the generation of a JONSWAP

spectrum with 0.6 Herz centre frequency. For this sequence
of tests a difference algorithm was used to improve the
generation of the spectrum. All measurements were made 36
meters from the wave maker.

To start with, the reference spectrum was compensated
and used to generate the random wave. After 15 minutes of
operation it was assumed that steady state prevailed in the
flume and 2048 samples were taken. The measured and the
reference spectra were compared in the right hand column of
Fig. 6. The measured spectrum was found broader than the
reference spectrum and a new input spectrum was computed by
the formula: New Input Spectrum = Old Input Spectrum + α ·
(Reference Spectrum - Measured Spectrum) where α = 0.5 is a
convergence factor. The new input spectrum was compared to
the reference spectrum on the left hand column of Fig. 6.
It was clearly established that the digital filter function
for a JONSWAP spectrum with a 0.6 and 0.8 Herz peak fre-
quency could be improved by a feedback arrangement based on
a difference algorithm.

As a further test, a signal for a fully developed JONSWAP
spectrum at 0.6 Herz was generated and the water surface varia-
tion was observed and analysed at intervals along the flume
from 5 to 40 meters from the wave board at 5 meter intervals.
This is illustrated in Fig. 7. The spectra exhibited varia-
tion in the peak frequency and the magnitude of the spectral
peak.

Figure 8 illustrates the attempt to shape the input
spectrum for a 1 Herz JONSWAP spectrum. On the left hand
column of this figure, the solid line shows the shape of the
desired JOHSWAP spectrum. The top figure gives also the
shape of the input spectrum which had to be made considerably
more narrow. The middle figure shows the same input spectrum
after its discrete representation by 33 points prior to the
Inverse Fourier Transform. Because of the previously
explained limitation in discretizing the input spectrum over
the interval from zero to f_m the input spectrum cannot be
described internally by greater definition than is shown in
Fig. 8.

The result of the signal generation was measured again
at 36 meters from the wave board and is shown in the bottom
left illustration in Fig. 8. The measured spectrum exhibited
a marked shift to the left. On the right hand side of Fig. 8
it is shown that one may compensate for this shift at the
36 meter flume location by creating a new input spectrum
which has been artificially shifted to the right.

The same 1 Herz JONSWAP spectrum had been studied at
different locations along the flume as shown in Fig. 9. In

this illustration it is quite apparent that the process of a shift in the spectral peak is more likely a matter of a transfer of energy from the original to adjacent frequency bands but predominantly in the direction of lower frequencies. In this manner the spectrum appeared to spread out and shift.

Table I summarizes various statistical properties of the random waves as observed at the test locations in the flume. The input spectrum for the 0.6 Herz wave had a $\gamma = 8.0$ (i.e. the ratio of the peak value in the JONSWAP spectrum to the corresponding peak in the Pierson-Moskovitz spectrum). It will be noticed that the γ-value decreased with increasing distance from the wave board. There also appeared to be a decreasing trend in the peak frequency. There was no significant change in the RMS-value. Other statistical wave parameters showed no significant trend but indicated inconsistency over the length of the flume by as much as $\pm 14\%$. The ratios H_{max}/H_{av}, $H_{max}/H_{1/3}$, and $H_{1/3}/H_{av}$ were observed by Ref. 13 to cover the following ranges 1.9-2.6, 1.29-1.91 and 1.37-1.85 respectively. It will be noticed that the comparable parameters for the simulated wave were generally higher.

Similar observations were made for the 1.0 Herz JONSWAP spectrum which are shown in Table II. It also appeared that the RMS-value decreased significantly with distance from the wave board while the H_{max} value tended to increase.

The input spectrum for this example had a $\gamma = 20$ and it may be seen that this extreme peak had dropped to $\gamma = 10$ within 5 meters from the board.

7.0   CONCLUSIONS

To insure consistent spectral distributions, it is considered important that experimentation with pseudo-random noise sources are carried out over a period which corresponds to an integer multiple of the maximum cycle length of the generator. Improved choice of cycle lengths could be obtained if a 4-point rather than a 2-point feedback shift register is used. Improved definition in the calculation of the digital filter is recommended and could be obtained if the shift register and the digital filter would be expanded from 65 to 129 elements.

Further details of the study including computer programs will be included in a future report.

REFERENCES

1.   Thompson and Shuttler, Signal Generation for Random Wave Simulation. Hydraulic Research Station, Wallingford. Int. Report No. 103, April 1972.

2. Fryer, Gilbert and Wilkie, A Wave Spectrum Synthesizer. Journal of Hydraulic Research, Vol. 11-1973-No. 3.

3. Anderson, Finnie and Roberts, New Noise Generator Synthesizes Pseudo-Random Gaussian Noise. Hewlett-Packard Journal, Sept. 1967.

4. C.M.G. Zwarts, Non-Contacting Capacitive Transducers. National Research Council of Canada, M.E. Report MI-836, Sept. 1972.

5. T.D. Reed, A Simplified Approach to the Design of Low-Pass Active Filters. Royal Aircraft Establishment Tech. Rep. 67224, Sept. 1967.

6. Gilbert, Thompson and Brewer, Design Curves for Regular and Random Wave Generators. Hydraulic Research Station, Wallingford. Int. Report No. 81, June 1970.

7. J. Ploeg, Wave Climate Study Great Lakes and Gulf of St. Lawrence, Vol. I, National Research Council of Canada, M.E. Report No. MH-107A.

8. Rye, Byrd and Tørum, Sharply Peaked Wave Energy Spectra in the North Sea. Offshore Technology Conference 1974, Paper No. OTC 2107.

9. K. Hasselmann et all., Measurement of Wind-Wave Growth and Swell Decay during the JOINT NORTH SEA WAVE PROJECT (JONSWAP), Deutsche Hydrographische Zeitschrift Ergaenzungsheft, Reihe A(8°), Nr. 12, 1973.

10. W.D.T. Davies, System Identification for Self-Adaptive Control. Book, Wiley-Interscience 1970, Chapter 3.

11. Smith and Hamilton, Logical Design of a Digital Pseudo-random Noise Generator, IEEE Trans, Nuclear Science 1966, p.371 to 381.

12. S.W. Golomb, Shift Register Sequences, Book, Holden-Day Inc.

13. R.L. Wiegel, Oceanographic Engineering, Book, Prentice-Hall Inc., p.201.
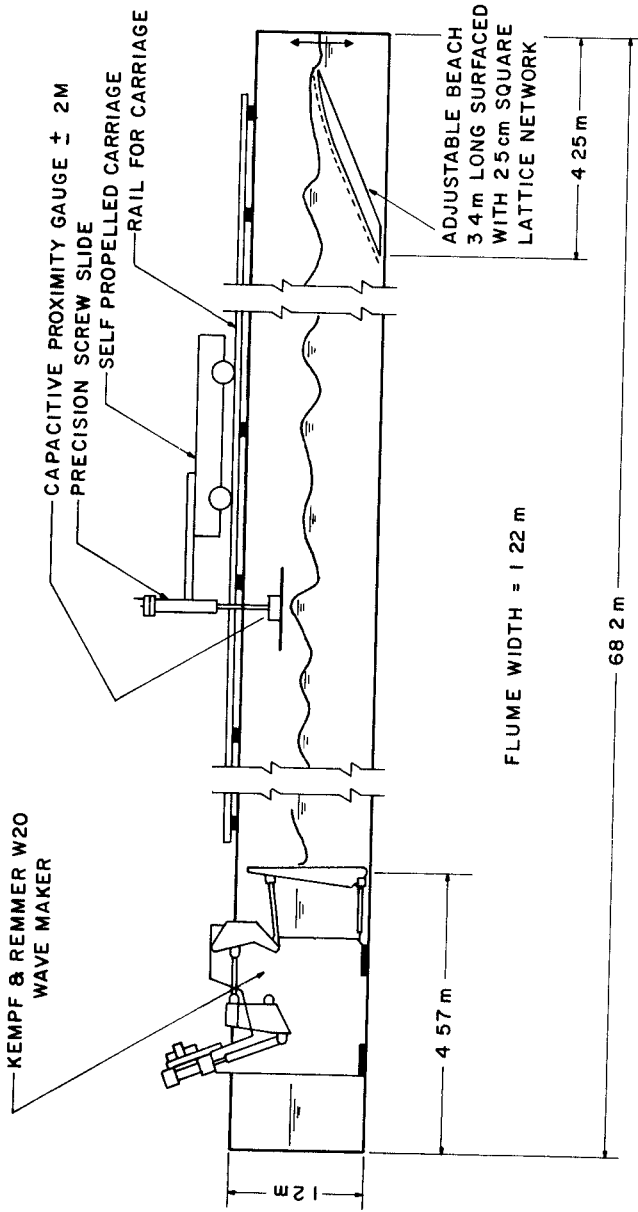
FIG 1
STEEL WAVE FLUME
AT HYDRAULICS LABORATORY
N·R C – OTTAWA

SYSTEM CONFIGURATION OF THE EAI 640 COMPUTER
AND NOVA 1200 FOR THE
GENERATION OF RANDOM WAVES
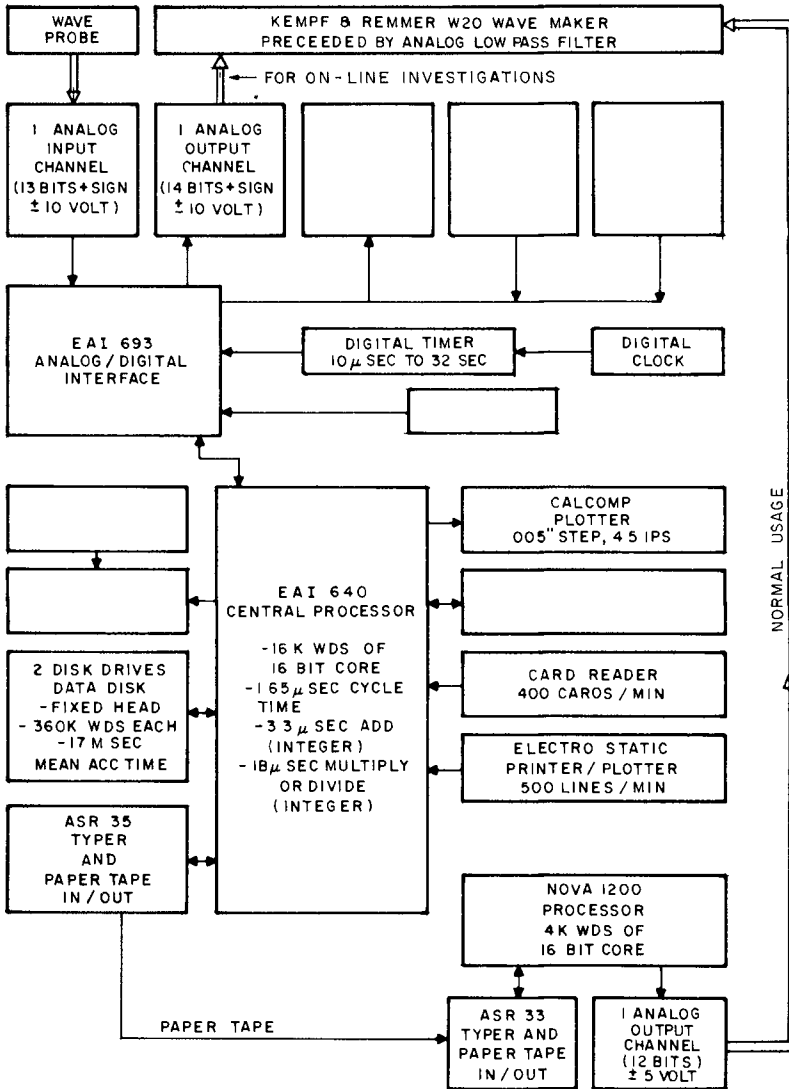
FIG 2

TRANSFER FUNCTIONS FROM SIGNAL SOURCE TO TEST SITE

```
┌─────────────────────┐
│    SIGNAL SOURCE     │
└─────────────────────┘
           │
           ▼
┌─────────────────────────────────┐
│       ANALOG LOW-PASS           │
│           FILTER                │
│        ( IF APPLICABLE )        │
│  2·0 Hz 3RD ORDER LOW PASS      │
└─────────────────────────────────┘
           │
           ▼
┌─────────────────────────────────┐
│       SERVO DYNAMICS            │
│       OF WAVE MAKER             │
│  ( 1·5 Hz IST ORDER LOW PASS )  │
└─────────────────────────────────┘
           │
           ▼
┌─────────────────────────────────┐
│  WAVE BOARD TO WAVE HEIGHT      │
│     TRANSFER FUNCTION,          │
│       I ST ORDER THEORY,        │
│   THIS IS A FUNCTION OF:        │
│      DEPTH OF WATER,            │
│   LINKAGE SETTING AND           │
│      WAVE PERIOD                │
└─────────────────────────────────┘
           │
           ▼
┌─────────────────────────────────┐
│       NON - LINEAR              │
│     ENERGY TRANSFER             │
│  BETWEEN FREQUENCIES,           │
│  A FUNCTION OF DISTANCE         │
└─────────────────────────────────┘
           │
           ▼
┌─────────────────────┐
│   FINAL SPECTRUM     │
└─────────────────────┘
```
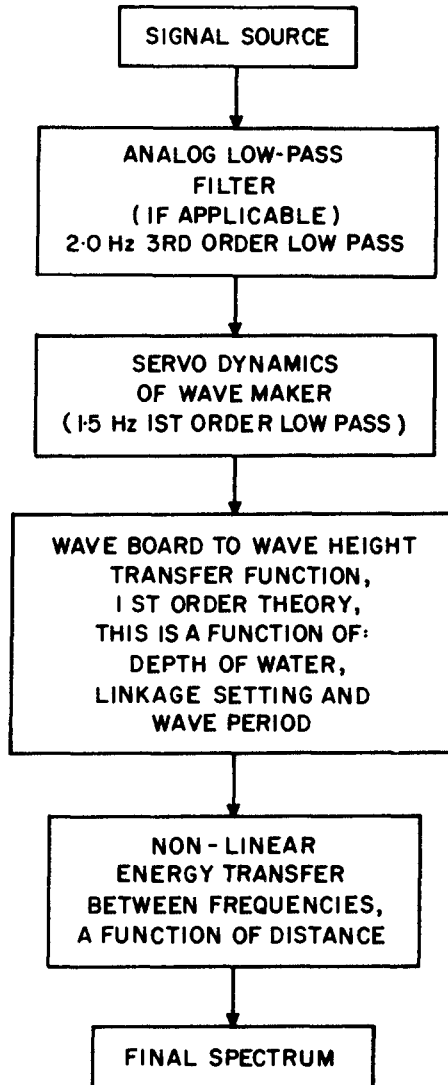
FIG 3

FLOW CHART OF
COMPUTER OPERATIONS FOR
RANDOM WAVE GENERATION

✳ SPECTH ✳
COMPUTES A THEORETICAL
WAVE SPECTRUM, E G JONSWAP
INPUT f_0 , γ , σ_0 & σ_b

PAPER TAPE
TO NOVA 1200

✳ RWGEN I ✳
— COMPENSATES FOR TRANSFER FUNCTIONS
— GENERATES 'GENERATING FUNCTION'
— OPTIONAL OUTPUT OF PAPER TAPE FOR NOVA 1200
— OPTIONALLY GENERATES PSEUDO RANDOM NOISE,
    COMPUTES FILTER OUTPUT AND D/A CONVERTS
— ANALOG / DIGITAL CONVERTS 2048 SAMPLES
    OF WAVE RECORD
— ON SETTING OF SENSE SWITCH,
    TERMINATES PROGRAM EXECUTION
— OPTIONAL CALIBRATION RAMP OUTPUT

LOW - PASS
FILTER

ANALOG OUT
TO WAVE MAKER

ANALOG IN
FROM WAVE GAUGE

✳ LINRZE ✳
APPLIES LINEARIZATION FUNCTION
TO ALL DATA BY TABLE LOOK-UP

✳ DTREND ✳
REMOVES MEAN VALUE FROM DATA

✳ PSD2 ✳
COMPUTES VARIANCE SPECTRAL DENSITY
VIA FAST FOURIER TRANSFORM

✳ PLOT 2 ✳
PLOT THEORETICAL & MEASURED SPECTRA

✳ SPECTH ✳
MODIFY DRIVING SPECTRUM

FIG 4

PSEUDO RANDOM NOISE GENERATOR

Shift register diagram labelled: p 1 2 r … n … 64 (with modulo-2 adder ⊕ feeding back)

FEED BACK REQUIREMENT FOR MAXIMUM CYCLE LENGTH
OF LINEAR FEED BACK SHIFT REGISTERS

n	r	CYCLE LENGTH 2^N-1	REPETITION PERIODS AT ΔT = 0.250 sec	AT ΔT = 0.300 sec	AT ΔT = 0.350 sec
5	2	31	7.75 sec	9.3 sec	10.85 sec
6	1	63	15.75	18.9	22.05
7	1	127	31.75	38.1	44.45
9	4	511	2 min 7.75 sec	2 min 33.3 sec	2 min 58.05 sec
10	3	1,023	4 min 15.75 sec	5 min 6.9 sec	5 min 58.05 sec
15	11	32,767	2 HR 16 min 31.75 sec	2 HR 43 min 50.1 sec	3 HR 11 min 8.45 sec
17	11	131,071	9 HR 6 min 7.75 sec	10 HR 55 min 21.3 sec	12 HR 44 min 34.85 sec
20	3	1,048,575	72 HR 49 min 3.75 sec	87 HR 22 min 52.5 sec	101 HR 56 min 41.25 sec

NOTE   ⊕ MODULO 2 ADDER
i.e. p IS TRUE IF r OR n IS TRUE
BUT NOT IF r AND n ARE TRUE

FIG 5

REFERENCE SPECTRUM JONSWAP WITH
Y = 7 0 , σ_a = 0 07 , σ_b = 0 09 AT 36 METERS FROM WAVE BOARD

--- INPUT SPECTRUM

---- MEASURED SPECTRUM

METERS²/ Hz

FREQUENCY IN Hz
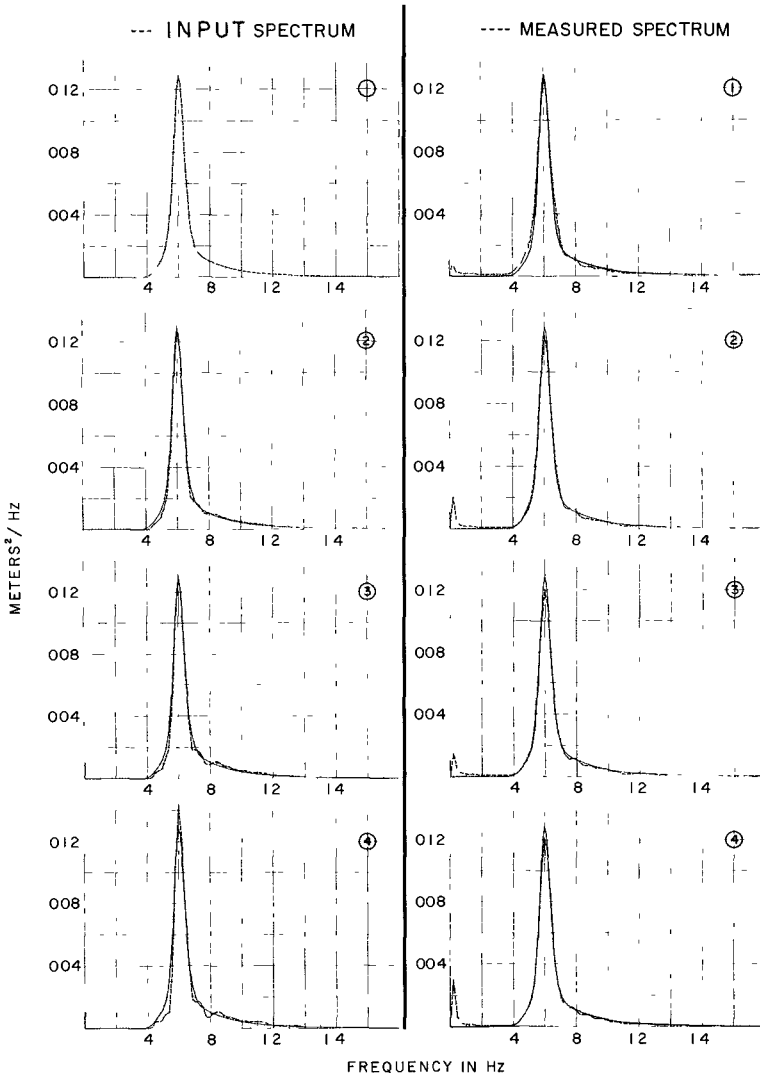
IMPROVING THE SPECTRUM BY
FEED BACK

FIG 6
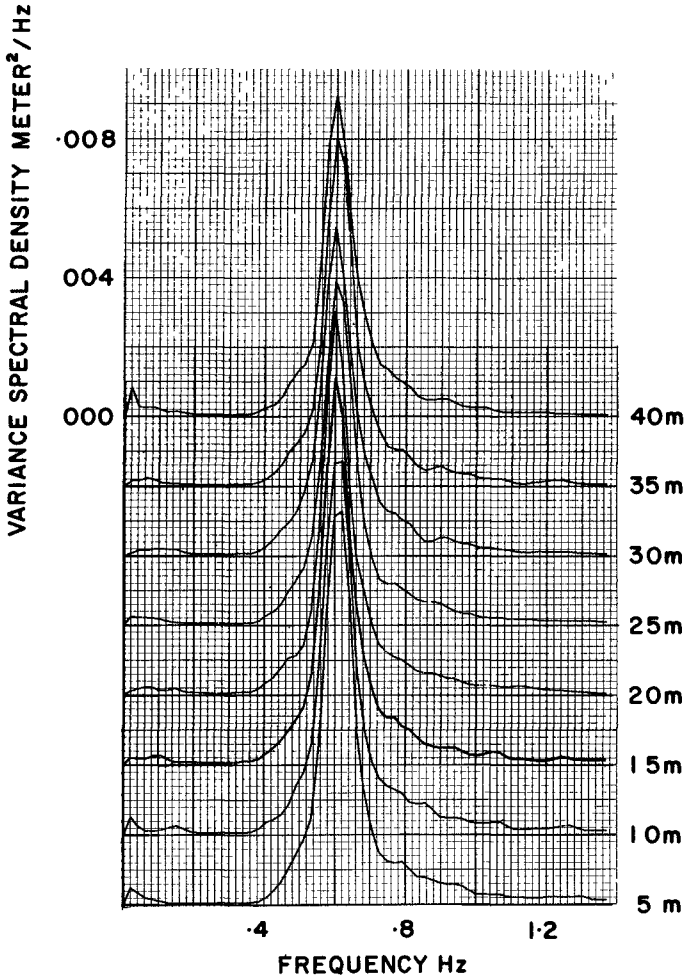
THE PROPAGATION OF THE SPECTRUM

AS MEASURED FROM 5 TO 40 METERS FROM THE WAVE BOARD,

INPUT SPECTRUM : JONSWAP WITH

$\gamma = 8 \cdot 0$, $\sigma_a = 0 \cdot 04$, $\sigma_b = 0 \cdot 08$

FIG 7
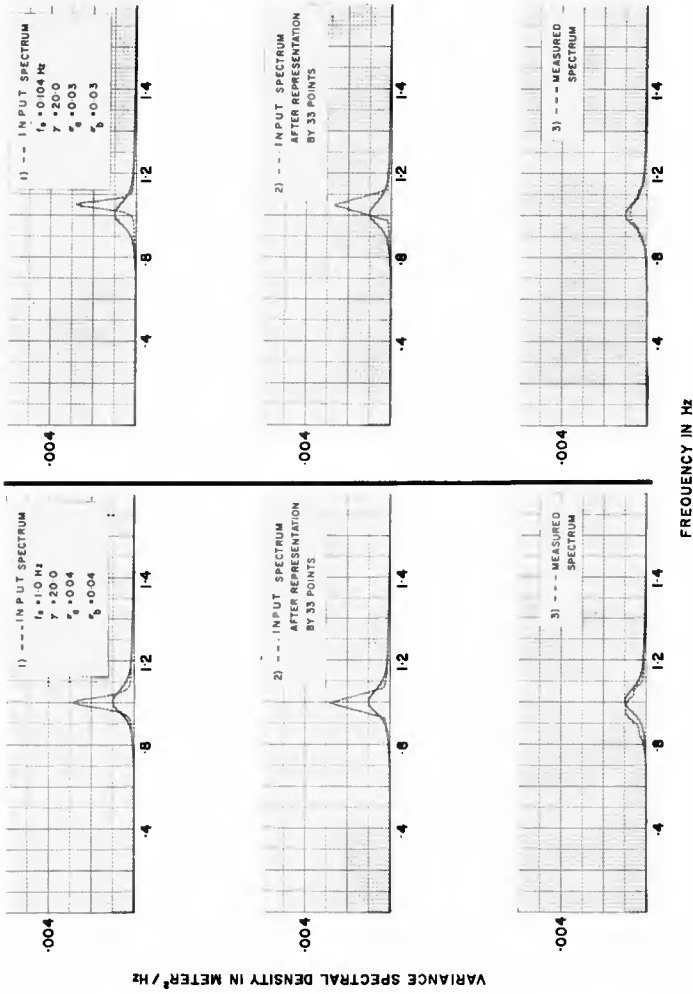
GENERATION OF A JONSWAP SPECTRUM WITH

$f = 1.0$ Hz AT 36 METERS FROM WAVE BOARD AND

$\gamma = 7.0$, $\sigma_a = 0.07$, $\sigma_b = 0.09$

FIG. 8
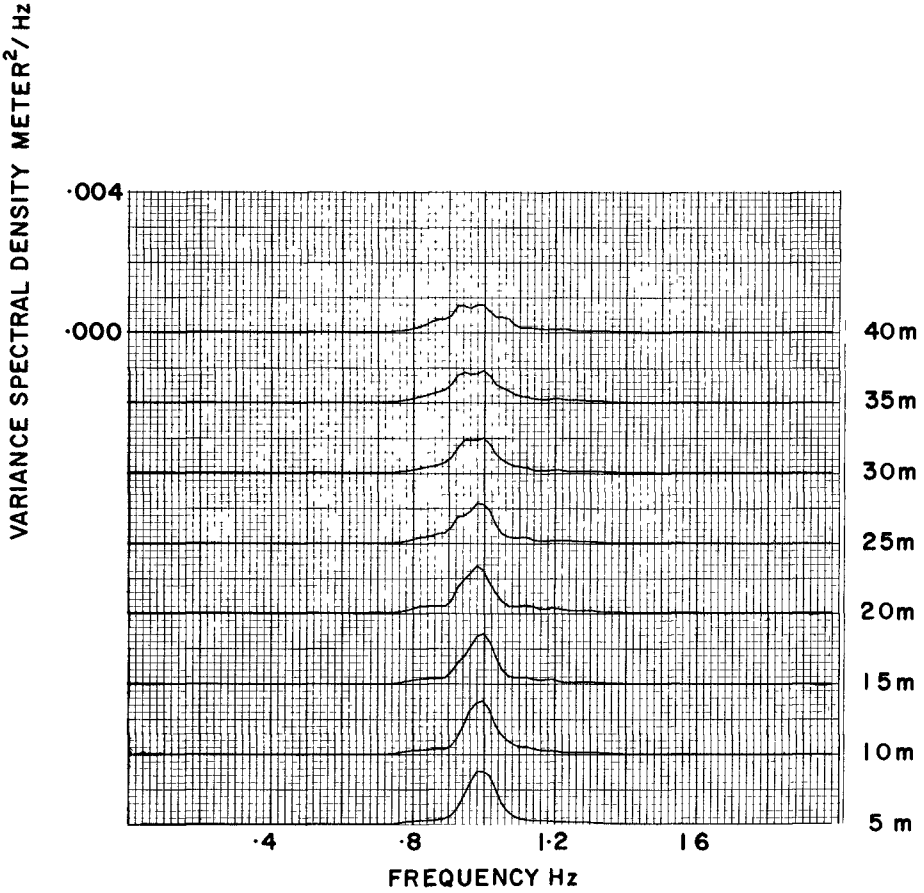
THE PROPAGATION OF THE SPECTRUM

AS MEASURED FROM 5 TO 40 METERS FROM THE WAVE BOARD,

INPUT   SPECTRUM · JONSWAP WITH

$\gamma = 20\cdot0$, $\sigma_a = 0\cdot04$, $\sigma_b = 0\cdot04$

FIG 9

TABLE I

WAVE PROPERTIES AS A FUNCTION OF DISTANCE FROM WAVE BOARD FOR AN
INPUT JONSWAP SPECTRUM WITH

F_{peak} = 0.6 Hz, γ = 8.0, σ_a = 0.04, σ_b = 0.08

Y	f_o	γ	RMS	$H_{1/3}$	$H_{1/10}$	H_{max}	H_{av}	H_{rms}	T_{av}	T_{max}	$\dfrac{H_{max}}{H_{av}}$	$\dfrac{H_{max}}{H_{1/3}}$	$\dfrac{H_{1/3}}{H_{av}}$
5	.611	6.75	.039	.14	.18	.25	.09	.10	1.55	1.52	2.79	1.8	1.6
10	.610	6.35	.039	.14	.18	.26	.09	.10	1.54	1.59	2.89	1.85	1.6
15	.603	6.23	.040	.14	.18	.25	.09	.10	1.57	1.62	2.50	1.8	1.6
20	.601	6.08	.039	.14	.18	.28	.09	.10	1.61	1.63	3.11	2.0	1.6
25	.605	5.65	.039	.13	.18	.24	.08	.09	1.56	1.57	3.00	1.84	1.63
30	.600	5.17	.038	.13	.18	.22	.08	.09	1.58	1.59	2.85	1.80	1.63
35	.604	5.68	.039	.13	.18	.27	.08	.09	1.54	1.61	3.37	2.07	1.63
40	.599	4.99	.037	.13	.16	.21	.08	.09	1.57	1.62	2.60	1.60	1.63

TABLE II

WAVE PROPERTIES AS A FUNCTION OF DISTANCE FROM WAVE BOARD FOR AN
INPUT JONSWAP SPECTRUM WITH

F_{peak} = 1.0 Hz, γ = 20.0, σ_a = 0.04, σ_b = 0.04

Y	f_o	γ	RMS	$H_{1/3}$	$H_{1/10}$	H_{max}	H_{av}	H_{rms}	T_{av}	T_{max}	$\dfrac{H_{max}}{H_{av}}$	$\dfrac{H_{max}}{H_{1/3}}$	$\dfrac{H_{1/3}}{H_{av}}$
5	.989	10.08	.016	.051	.073	.086	.035	.039	1.00	.98	2.45	1.68	1.46
10	.993	10.33	.015	.056	.070	.092	.034	.039	1.00	.98	2.70	1.64	1.65
15	.993	9.81	.015	.055	.070	.089	.032	.037	1.01	1.01	2.78	1.62	1.72
20	.983	8.69	.015	.055	.072	.105	.031	.037	1.00	.95	3.39	1.91	1.77
25	.987	7 56	014	.053	.072	.098	.030	.036	1.01	.95	3.27	1.85	1.77
30	.995	6.83	.014	.052	.072	.109	.029	.035	1.01	.96	3.76	2.10	1.79
35	.995	6.37	.014	.054	.075	.106	.030	.036	1.03	.99	3.53	1.96	1.80
40	.990	5.20	.013	.051	.073	.104	.028	.034	1.00	1.03	3.71	2.03	1.82

Y = Distance from Flap in Meters.
T_{max} is the period of H_{max} in seconds.

CHAPTER 20

MODEL TESTS WITH DIRECTLY REPRODUCED NATURE WAVE TRAINS

Helge Gravesen[*], Ebbe Frederiksen[**], Jens Kirkegaard[*]

INTRODUCTION

Hydraulic model tests are still recognized as the best and in many cases the only tool, indeed, for investigations of design criteria for harbours concerning

   a) the effect of wave disturbance on moored ships in harbour basins and at offshore terminals,

   b) stability of structures and wave forces on structures.

Model tests with waves have until recently usually been made with regular waves varying the wave height, wave period, wave direction for each test run. An important improvement in the model technique has been the development of irregular wave generators, capable of generating waves directly from nature wave records.

The following aspects are presented below

   1) A discussion on the methodology of wave model tests.

   2) A method for direct reproduction of nature wave records.

   3) A method for determining the incoming wave heights in a short wave flume with a reflecting structure and reflection from the wave generator paddle.

---

[*]   Danish Hydraulic Institute (DHI)
    Oster Voldgade 10, DK-1350 Copenhagen K, Denmark.

[**] Institute of Hydrodynamics and Hydraulic Engineering (ISVA),
    Technical University of Denmark, DK-2800 Lyngby.

I. DISCUSSION ON THE METHODOLOGY OF WAVE MODEL TESTS

I.I Introduction

In wave model tests the following types of waves may be used as input to the models:

1) Regular Waves with constant heights and periods.

2) Irregular Waves

    2.I) Artificial irregular waves generated on basis of wave spectra.

    2.2) Wave trains reproduced directly from nature wave records. (See Section 2 in this paper).

    2.3) Wind flume waves. The waves are generated either by wind alone, or by wind superimposed upon paddle generated waves.

The first section of this paper presents a discussion of which of the above methods should be employed to produce the most reliable results for different types of wave model tests. To illustrate this, the fundamental physics of three common problems from harbour engineering practice are considered. It is demonstrated that the requirements to wave reproduction depend upon the type of problem considered.

I.2 Moored Ship

One of the motions of a moored ship exposed to an external force is supposed to correspond approximately to the following equation:

$$m\ddot{x} + b\dot{x} + kx = F(t) \tag{1}$$

In the general case where

    $F(t) = 0$ for $t<0$ the approximate solution to equation (1) for $\delta<0.6$ is the following:

$$x(t) = -\frac{2\pi}{T_o}\int_0^t \frac{F(s)}{m}\left[e^{\frac{\delta}{T_o}(s-t)} \sin\frac{2\pi}{T_o}(t-s)\right]ds \tag{2}$$

where $\omega_o = \sqrt{\frac{k}{m}}$, $T_o = \frac{2\pi}{\omega_o}$

and the logarithmic decrement

$$\delta = \frac{bT_o}{2m} \tag{3}$$

For the free damped oscillator
δ may be found through

$$e^{\delta} = \frac{x_n}{x_{n+1}} \tag{4}$$

where x_n and x_{n+1} are two consecutive maximum amplitudes.

The equation (2) shows that because of the damping, a time scale T exists for the problem

$$T = \frac{T_0}{\delta} = pT_0 \qquad\qquad (5)$$

$$p = \frac{1}{\delta} \qquad\text{(Fig. 1)} \qquad\qquad (6)$$
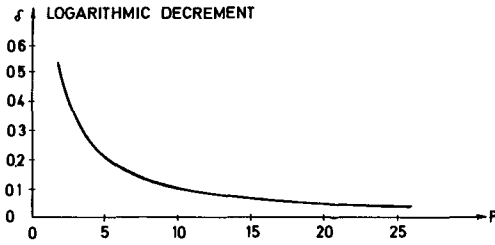
Fig. 1

This means that when the periods of the exiting force are not too different from the natural period T_0, which may be the case for moored vessels, it is roughly the maximum of the mean values over this time scale T of the exiting force weighted together with the response function shown below, which determine the maximum oscillation and the critical mooring and fender forces of the vessel. In other words, if, for instance, T is equal to two times the natural period of the ship oscillation the maximum oscillation and forces will be reached after only two consecutive waves of that particular period.

For this type of problems it therefore seems essential to reproduce the waves with a correct succession of waves as is believed done most effectively by directly reproduced wave trains.
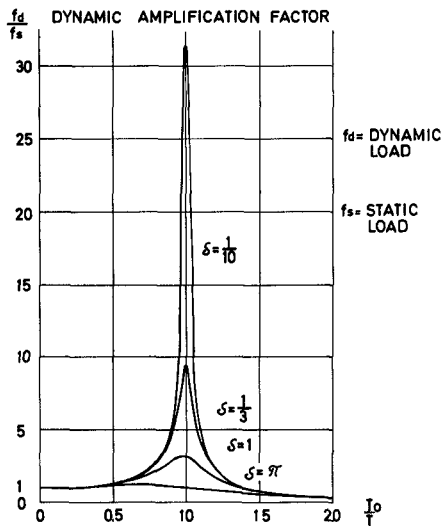
Fig. 2. Amplitude response curve
for the damped oscillating system.

1.3 Vertical Face Breakwater

As another example a vertical face breakwater may be considered.

The natural period of such a structure as a whole including the "elastic" element of the soil is usually an order of magnitude smaller than the mean wave period.

This case may be illustrated by the simple system

$$mx + kx = F(t) \tag{7}$$

$$T_o = 2\pi \sqrt{\frac{m}{k}} \tag{8}$$

where the impulse F(t) may have characteristics as shown below in Fig. 3.

In this case, it is the characteristics of the individual wave such as the height, steepness, skewness, connections with the preceding wave, etc., which are the determining factors.

In this case the wave height distribution should be reproduced correctly, but also the shape of the waves is so important that waves generated in a wind-wave flume are required.
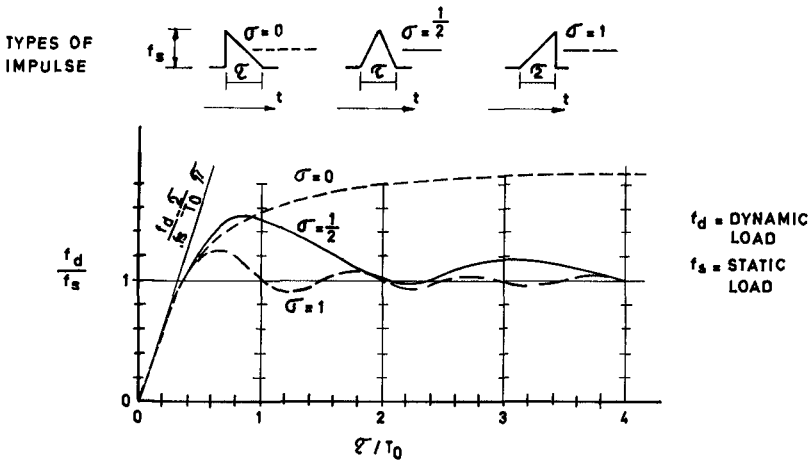
Fig. 3.   Amplitude response curve for an elastic system exposed to an impulse.

1.4 Rubble Mound Breakwater

A third example is the rubble mound breakwater where model tests have shown the same general stability of the armour layer on the seaward side when tested in irregular waves and in regular waves with the height equal to the significant height of the irregular waves, but different results for the requirements to the lower limit of the armour layer on the seaward side. Also the stability of the harbour side armour layer as function of crest elevation will be different for the two types of model waves.

In this case it seems likely that the wave height distribution is the determining characteristic , and either of the irregular wave generation techniques may be applied to this problem.

1.5 Conclusion

From the three cases considered it may be concluded that the directly reproduced nature wave trains (with superimposed wind for vertical face breakwater) apply in all cases, and that this method of wave generation is therefore superior to other known methods.

It should be emphasized that although a number of problems may be solved by this method, the important problem of obtaining and selecting representative wave data still remains to be solved.

A discussion of this problem, however, is beyond the scope of the present paper, and it does not give any limitations of the validity of the conclusion above.

2. REPRODUCTION OF NATURE WAVE TRAINS

2.1 General Principle

The wave generators at DHI and ISVA consist of a hydraulic servosystem, which gives a vertical wave paddle a horizontal translational movement. The position of the paddle is controlled by an electric signal from the "Wave Function Generator" (WFG). The control signal is generated on the basis of a punched tape record of nature waves. This digital record is converted to an analog electric signal, which after integration over time is fed into the servo system of the wave generator. The mean period of the model wave train is controlled by the reading speed of the punched tape, and the amplification in the WFG determines the wave heights.

2.2 Theory

In monochromatic shallow water waves (surface elevation $\eta = \frac{H}{2} \cos (\omega t)$) the horizontal particle velocity at a fixed point may be approximated with

$$u = \frac{C}{D} \cdot \frac{H}{2} \cos (\omega t) = \frac{C}{D} \cdot \eta(t) \tag{9}$$

C is the velocity of wave propagation, D is the water depth.

Assuming that a similar proportionality between the surface elevation and the horizontal particle velocity is valid for irregular shallow water waves, also, a given wave train may be generated by moving the wave generator paddle with the velocity, u, and the paddle position, x, may therefore be written:

$$x(t) = \int_0^t \frac{dx}{dt} \, dt = \int_0^t u \, dt = \frac{C}{D} \int_0^t \eta(t) \, dt \tag{10}$$

The general theory of generating monochromatic waves by means of oscillating vertical plate was described by Biésel, ref. [1]. He found that the transfer function from paddle amplitude, x_0, to wave amplitude is

$$\frac{a}{x_0} = \frac{2 \sinh^2 (kD)}{\sinh(kD) \cdot \cosh(kD) + kD} = K \tag{11}$$

In order to see how the described method for wave generation agrees with Biésel's formula we shall apply the method to a monochromatic wave train $\eta = a \cos \omega t$. The paddle position will be

$$x = \frac{C}{D} \int_0^t a \cos (\omega t) = \frac{C}{D} \cdot \frac{a}{\omega} \sin \omega t \tag{12}$$

so that

$$\frac{a}{x_0} = \frac{D \cdot \omega}{C} = \frac{D \frac{2\pi}{T}}{\frac{L}{T}} = \frac{2\pi D}{L} = k \cdot D = K_1 \tag{13}$$

where L is the wave length, T is the wave period, and k is the wave number.

In Fig. 4 Biésel's transfer function K and the simple transferfunction K_I are plotted against $\frac{L}{D}$. We see that K_I is identical to K for $\frac{L}{D} \geq 6$ i.e. in the shallow water region.

As a nature wave train most often has its energy distributed over a wide range of periods (frequencies), this method of reproducing waves will sometimes lead to a distortion of the wave train, because not all of the component waves are shallow water waves. Fig. 4 indicates that the heights of these short period components will be reproduced with too small wave heights in the model.
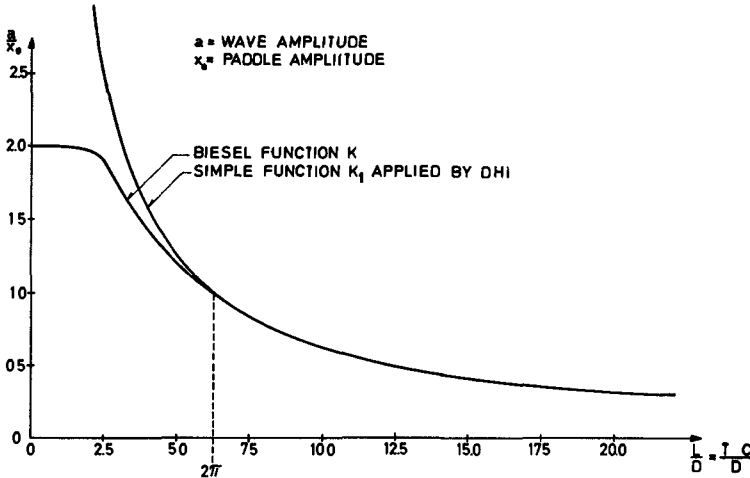
Fig. 4.   Transferfunctions from paddle movement to wave profile.

2.3 Testing of the Method of Reproduction

Tests have been run in the 0.6 m wide wave flume at ISVA. To reduce reflection from the end of the flume opposite the wave generator a wooden slope with an inclination of 1.17 was placed in the flume.

A total of 36 tests have been run varying wave height and period and the water depth. The prototype wave record was the same for all tests namely a record from the Danish North Sea Coast, recorded near Hanstholm during a storm in February 1973 by a waverider accelerometer buoy.

The two wave trains, model and prototype respectively were recorded simultaneously on an analog tape recorder, and later analyzed on a digital computer. The prototype record was taken from the WFG and the model record from a conductivity wave gauge in the flume, 10.16 m from the mean position of the paddle.

The recorded wave trains have been compared by means of cumulative wave
height distribution, H-T-distributions ($\overline{H}$ versus T) and wave energy
spectra with corresponding coherence function. A sample of each of
these graphs is shown in Fig.s 5, 6 and 7.
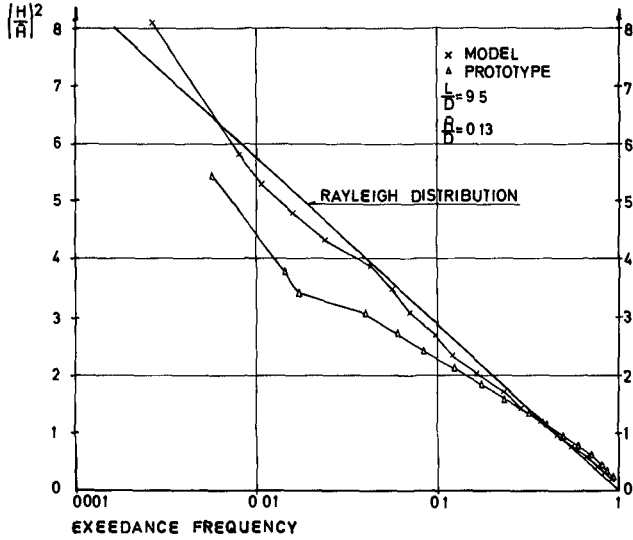
Fig. 5.   Cumulative wave height distribution.
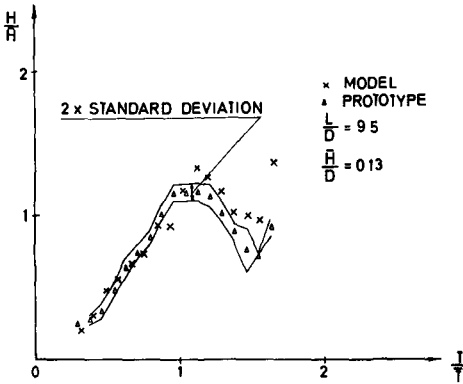
Fig. 6.   H-T-distribution
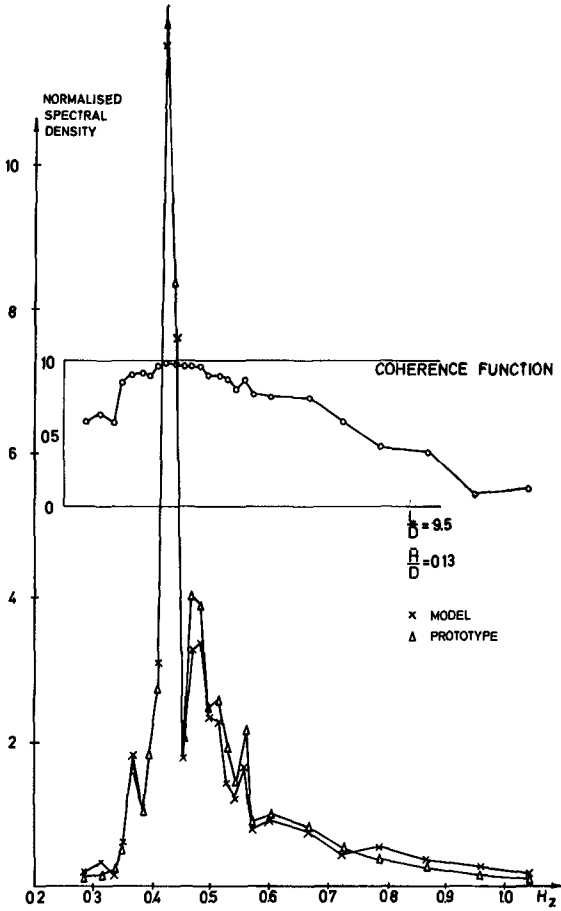
Fig. 7.   Wave energy spectra.

2.4 Results of Tests

In order to summarize all the results it was decided to calculate the percentage of the total prototype wave energy being reproduced with a coherence greater than 0.8.   This quantity, which is of course an arbitrary measure for the goodness of the reproduction, has been plotted against $\frac{L}{D}$ in Fig. 8 and against $\frac{H}{D}$ in Fig. 9.
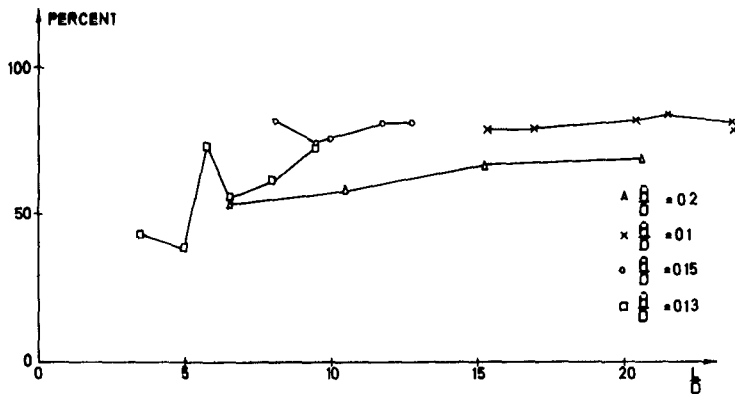
Fig. 8.   Percentage of total prototype wave energy reproduced
with coherence greater than 0.8.
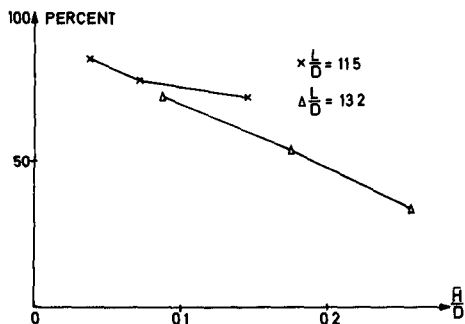
Fig. 9.   Percentage of total wave energy
reproduced with coherence greater than 0.8.

It is obvious that the best reproduction is obtained with long and low
waves.   General limits for the validity of the applied method of re-
production cannot be given because the range of $\frac{L}{D}$ and $\frac{H}{D}$, for which the
method produces reliable results, depends very much upon the accuracy
that is needed for a particular problem.

Maximum accuracy (app. 80% of the total energy reproduced with a
coherence greater than 0.8) is obtained with $\frac{L}{D} \geqslant 10$ and $\frac{H}{D} < 0.05$.

A visual correlation between the input prototype wave train and the
generated model wave train may be obtained from Fig. 10. It is possible
to identify each of the longer waves, whereas details are blurred. This
is probably because short period waves are not reproduced correctly and
that they move with another celerity than the longer period waves.

PROTOTYPE

$\frac{R}{D}$ = 0 22 $\frac{L}{D}$ = 65

0 1 2 3 4 5 SEC
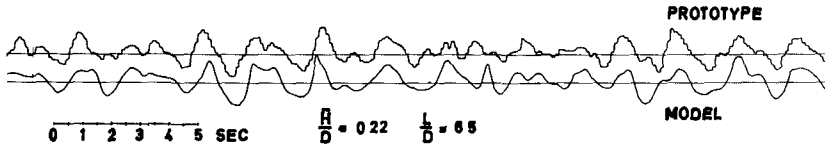
MODEL

Fig. 10. Prototype and model wave trains.

3. IRREGULAR WAVES IN SHORT FLUME WITH A REFLECTING STRUCTURE

3.1 Introduction

Model tests with reflecting structures have always given rise to a lot
of problems. In tests with regular waves one has had to use only the
results from the first few waves before the re-reflection from the wave
generator or other boundaries begin.

The problem with irregular waves may be solved in long wind wave flumes,
in which the reflected wave energy is more or less suppressed by the
wind stress. This is, however, a very expensive solution, and a method
of controlling the waves in a short flume was therefore developed at
DHI.

Irregular waves in short flumes require a reproduction method for irre-
gular waves of a quality such as presented in Section 2, because even
with the application of wind, the length of the flume is not great
enough to allow the wind to change the waves generated by a wave paddle
to "nature waves". The waves must in other words be born as nature
waves.

When the waves hit a reflecting structure they are more or less re-
flected and the reflected waves travel backwards in the flume and are
partially re-reflected from the wave generator. This re-reflection of

energy implies that the resultant incident wave energy is larger than
the energy generated initially. Hence it is essential to determine the
reflection characteristics at both ends of the flume. The method
developped for this is described in the following section.

3.2 Controlling Principle

As mentioned in Section 2 the reproduced wave heights may be controlled
by changing the amplification factor in the wave function generator and
the mean period may be changed by varying the reading speed of the
punched tape. With fixed amplification factor and reading speed, tests
were run for the following three situations (Fig. 11):

   1. Sloping beach providing almost complete absorption.

   2. Completely reflecting structure (vertical plate).

   3. Partly reflecting structure (object to be tested).

IRREGULAR WAVES IN SHORT FLUMES
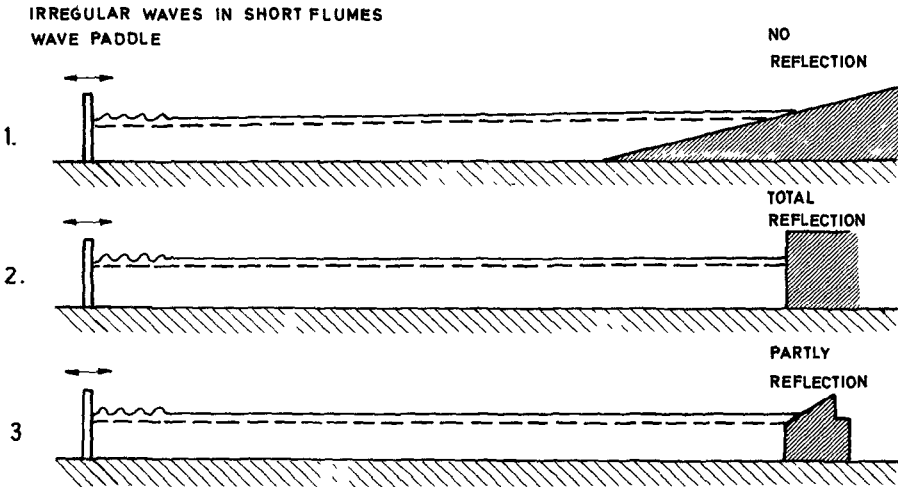
Fig. 11. Test program with the same wave input.

In all these tests the zero crossing period T_z, the mean wave height $\overline{H}$
and the root mean square value of the water surface elevation h are
recorded at a number of positions along the flume.

The total potential energy of a wave motion is represented by the
quantity $h^2_{rms} = \overline{h^2}$. The kinetic energy may be assumed to be equal to
the potential energy.

In the second test (with the fully reflecting plate) the function

$h^2_{rms}(x)$ is determined at a number of points at various distances x from the plate (x = 0) where each "wave component" is reflected creating "standing waves". The function slopes off fairly rapidly with increasing values of x, because the various "components" have different wave lengths. At some distance from the plate the function $h^2_{rms}(x)$ reaches a stationary value (with little scatter) due to the continuous (non-discrete) nature of the spectrum.

If there were no re-reflection from the paddle the fully reflecting plate would give a stationary value of h^2_{rms} equal to twice the value of h^2_{rms} for the purely progressive waves advancing towards the flume beach in the first series. The actual stationary value is somewhat larger because of the re-reflection.

In the tests with the sloping face structure the reflection is less than 100% because of overspill and energy loss.

The influence of re-reflection may be estimated by the following calculations.

Calculation of reflection and re-reflection

$\overline{h^2_g}$ = initially generated energy

$\overline{h^2_i}$ = incoming energy (total)

$\overline{h^2_r}$ = reflected energy

β_r = reflection coefficient for energy

β_{rr} = re-reflection coefficient for energy

$$\overline{h^2} = \overline{h^2_i} + \overline{h^2_r} \qquad \overline{h^2_r} = \beta_r \ \overline{h^2_i} \tag{14}$$

$$\overline{h^2_i} = \overline{h^2_g} + \beta_{rr}\overline{h^2_r} = \overline{h^2_g} + \beta_{rr}(\beta_r\overline{h^2_i}) \tag{15}$$

$$\overline{h^2_i} = \frac{\overline{h^2_g}}{1 - \beta_{rr}\beta_r} \tag{16}$$

$$\overline{h^2} = (1 + \beta_r)\overline{h^2_i} = \overline{h^2_g} \frac{1 + \beta_r}{1 - \beta_{rr}\beta_r} \tag{17}$$

$$h_{rms,i} = \frac{1}{\sqrt{1 - \beta_{rr}\beta_r}} \ h_{rms,g} \tag{18}$$

	No reflection	Total reflection	Breakwater section
$\overline{h^2}$	E_1	E_2	E_3
$\overline{h^2_g}$	E_1	E_1	E_1
β_r	0	1	β_r
β_{rr}	-	β_{rr}	β_{rr}

By measuring E_1, E_2, and E_3 the coefficients β_r and β_{rr} and hence the correction coefficient may be calculated.

$$\alpha = \frac{1}{\sqrt{1 - \beta_{rr}\beta_r}}$$

In tests with a partly sloping face breakwater performed in a 20 m long wave flume $\alpha = 10\%$ is a typical value.

Under the basic assumption that the re-reflection does not change the characteristics of the wave essentially, the other linear parameters for the wave height are also increased with the correction coefficient α.

In order to check the reliability of this method extensive tests have been performed in a 70 m long and in a 20 m long programmed paddle wind-wave flume with wind at natural scale and the same generated wave trains. The test program contained detailed measurements of shock pressures on circular caissons and the results obtained were in good agreement in the two types of tests.

ACKNOWLEDGEMENT

REFERENCE

[1] Biésel, F.: Theoretical study of a certain type of wave machine. La Houille Blanche, Vol 6, No. 2, 1951.

CHAPTER 21

MEASUREMENT OF INCIDENT WAVE
HEIGHT IN COMPOSITE WAVE TRAINS

by

Åke Sandstrom[1]

ABSTRACT

A method is proposed for measurement of the incident wave height in a
composite wave train. The composite wave train is assumed to consist of
a superposition of regular incident and reflected waves with the same
wave period. An approximate value of the incident wave height is ob-
tained as the arithmetic mean of the wave heights measured by two
gauges separated a quarter of a wave length. The accuracy of the method
in relation to the location of the gauges and the wave parameters is
investigated using linear and second order wave theory. Results of
the calculations are presented in diagrams.

INTRODUCTION

At model tests with regular waves in a wave flume it is often difficult
to determine the height of the incident waves which attack a model in
the flume. The model causes reflected waves which move backwards
towards the wave generator and by superposition give rise to a com-
posite wave train. In many cases, the distance from the wave generator
to the model is too short to allow the incident wave height to be
measured without disturbing influence by reflected waves. Within a
distance of some wave lengths from the wave generator, disturbances
from the wave generation make accurate recording impossible. In the re-
maining part of the flume up to the model, the situation in flumes of
limited length often is that there is no point where the waves have
grown to the full height before reflected waves of considerable height

---

[1]Research Engineer, Hydraulics Laboratory,
Royal Institute of Technology, Stockholm, Sweden

arrive.

In many cases, it is therefore necessary to record the composite waves
and in some way separate the incident wave from the recordings. A
method, which has often been used, involves location of the nodes and
anti-nodes. This is achieved by slowly moving a wave gauge horizontally
along the wave train. The distance between nodes and anti-nodes is a
quarter of a wave length. The wave heights at a node and anti-node are
measured and the incident wave height is calculated as the arithmetic
mean of the two values. The drawback of this method is that it may be
difficult to locate the nodes if the reflected wave is small.

PROPOSED METHOD OF MEASUREMENT

A couple of two wave gauges assembled at a fixed distance of a quarter
of a wave length is used. The couple is placed in an arbitrary position
along the wave train. An approximate value of the incident wave height
is obtained as the arithmetic mean of the two recorded heights. If one
of the gauges happens to be located at a node, according to linear
wave theory, the correct incident wave height is received. If the loc-
ation of the gauges deviates from this ideal location, the obtained
wave height will differ slightly from the correct value.

ACCURACY OF THE METHOD

To be able to calculate the occurring errors, the envelopes of the
composite wave train are studied. Using linear wave theory an ex-
pression for the envelopes can be deduced as

$$y = \frac{+}{-} \frac{H}{2} \sqrt{(1 - K_r)^2 \cos^2 kx + (1 + K_r)^2 \sin^2 kx} \tag{1}$$

where H is the incident wave height and $K_r \cdot H$ is the height of the re-
flected waves (Fig. 1).

The values of the wave heights H_1 and H_2, which are registered by the
two gauges, can be calculated from equation (1). The approximation for
for the incident wave height is
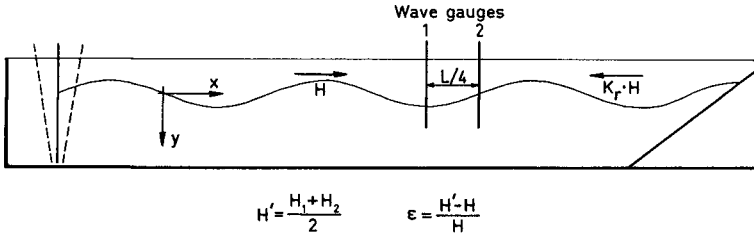
Fig. 1. Notation.

$$H' = \frac{1}{2}(H_1 + H_2)$$
(2)

and the relative error is

$$\varepsilon = \frac{H' - H}{H}$$
(3)
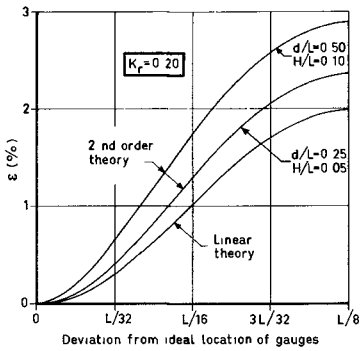
Fig. 2. Error vs. location of the gauges.
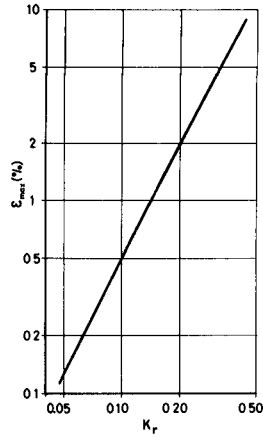
Fig. 3. Maximum error vs. reflection coefficient according to linear theory.

The error is shown in Fig. 2 (linear theory) for $K_r = 0.20$ vs. the deviation from the ideal location for the couple of gauges. The maximum error ε_{max} occurs when the gauges are situated half way between nodes and anti-nodes. The error grows with the height of the reflected waves - approximately as the square of K_r (Fig. 3).

The linear wave theory implies small steepness of the waves and gives a sinusoidal water surface. Waves of finite amplitude have narrow crests and broad shallow troughs. In order to study the influence on the accuracy of the method of the unsymmetrical wave profile of steep waves a second order wave theory is used. According to Rundgren (1) the wave profile of a composite wave train, correct to the second order of H, is given by the following equation

$$
y = \frac{H}{2} \left\{ (1 + K_r) \sin kx \cos \sigma t - (1 - K_r) \cos kx \sin \sigma t - \right.
$$
$$
- \frac{kH}{4} \coth kd \left[(1 + K_r)^2 \left(\cos^2 \sigma t + \frac{3 \cos 2\sigma t - \tanh^2 kd}{4 \sinh^2 kd} \right) \cdot \right.
$$
$$
\cdot \cos 2kx - (1 - K_r)^2 \left(\sin^2 \sigma t - \frac{3 \cos 2\sigma t + \tanh^2 kd}{4 \sinh^2 kd} \right) \cos 2kx +
$$
$$
\left. \left. + (1 - K_r)^2 \left(1 + \frac{3}{2 \sinh^2 kd} \right) \sin 2\sigma t \sin 2kx \right] \right\} \tag{4}
$$

where H = incident wave height

      $K_r \cdot H$ = reflected wave height

      $k = 2\pi/L$

      $\sigma = 2\pi/T$

Fig. 4 shows examples of wave profiles for successive times (time step T/16) during one wave period calculated with equation (4). Because of interaction between incident and reflected waves of finite amplitude the amplitude at the nodes is not equal to zero for $K_r = 1.00$, as can be seen in Fig. 4 c. This means that the error ε is not zero even with the gauges placed at the ideal location with one gauge at a node and the other at an anti-node. Goda and Abe (2) have calculated corrections which should be applied to reflection coefficients and incident wave
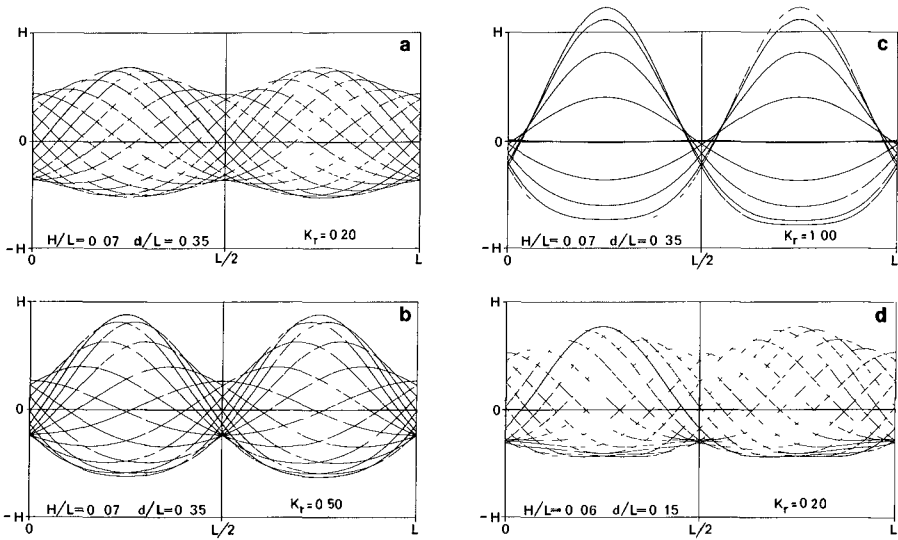
Fig. 4. Calculated wave profiles.

heights calculated from measured amplitudes at nodes and anti-nodes.
For small ratios of depth to wave height the second order theory gives
profiles with humps on the troughs, Fig. 4 d, which is an indication
that the theory is not satisfactory for those waves.

The envelopes of some wave trains and the corresponding values of ε
were calculated with equation (4). In Fig. 2 examples of results are
shown for a steep deepwater wave and a wave with ordinary steepness and
intermediate depth of water. The error ε is somewhat greater than
according to the linear theory. In Fig. 5, the maximum error ε_{max} is
shown for $K_r = 0.10$ and 0.20 vs. the steepness of the incident wave
(H/L) and the relative depth of water (d/L). Above the dashed lines
humps occur on the wave troughs, cf. Fig. 4 d.

The method described is very useful for the measurement of incident
wave height when the superposed reflected waves are not too high (K_r
less than about 0.20). When K_r is greater it is, however, easy to
locate the nodes approximately, so that the couple of gauges can be
placed near enough the ideal location to give acceptable accuracy.
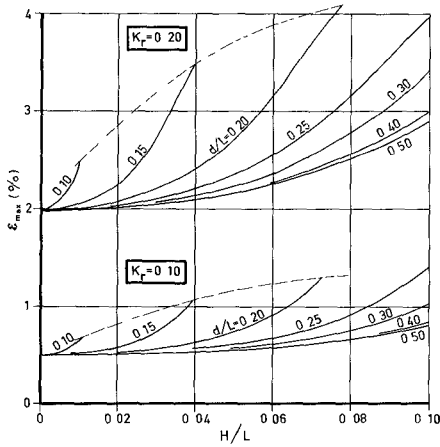
Fig. 5. Maximum error according to second order wave theory.

REFERENCES

1. Rundgren, L. 1958. Water Wave Forces. A Theoretical and Laboratory
   Study. Bull. No. 54 of the Div. of Hydraulics, Royal Inst. of Tech.,
   Stockholm.

2. Goda, Y. and Abe, Y. 1968. Apparent Coefficient of Partial Re-
   flection of Finite Amplitude Waves. Report of the Port and Harbour
   Research Institute, Vol. 7, No. 3, 1968.

CHAPTER 22

ORIGIN, EFFECT AND SUPPRESSION OF SECONDARY WAVES

by C.H. Hulsbergen [*]

1 Abstract

Beoch profile formation moy be severely affected by secondary waves which, together
with the bosic wave, alwoys originote from a sinusoidally-moving wave board The
ascertoinment af this experimental fact is fallowed by an investigation of the behaviour
of the generated waves ond their interactions It appears thot the many choracteristic
features, omong which the spatial beat phenomenon and the secondary crest formotion,
ore generally in good accordonce with the theories of Fontanet [14], ond Kravtchenko
and Santon [20] It is concluded thot on "outer" onolysis, e g by plotting the x-t-
lines of visible peoks, is only of limited use to describe the "inner" character of the
complex phenamenan. The subsequent study of the effect of secandary woves on o
horizontol sond bed reveols thot not only the wave form, but alsa the sand transport
varies spotially, resulting in the farmation of bars and troughs This typical behoviour of
the onshare-affshore transport is provisionally investigated in a small pulsating water black.
Finally, a methad is described which suppresses the secondary waves, by using a low
rectangular sill an the atherwise harizantal battom

2 Introduction

Secandory woves, solitons, ar disturbing waves are three different nomes for a peculior
kind of wove phenamenon which hos been reparted under various conditions All des-
criptions mention that a regular progressive wave ar swell is accampanied by one ar
more extra wave crests of o smaller height and with a lower prapagotion speed Secon-
dary waves have been reparted in loboratary experiments with nan-breoking waves over
o horizontol bed [4,5,11,15,16,18,24,25,31], an o slope or neor an obrupt variation in
depth, with or without breaking [13,16,19,24,26,27,30], under notural conditions [6,10],
[21], ond in onolyticol or numericol computotions [7,8,12,14,20,23,24,32,35]. The exis-
tence of the phenamenan is na longer o matter of dispute, olthough in its outer oppearance
it hos sometimes been confused with the - real - wove reflection or with the - non real -
"crête secondaire" af Miche [18] With respect ta the arigin ond the nature of secondary
waves, however, na comman apinian or complete theory exists os yet, in which situotion
voriaus deviating interpretotions hove been put forward This paper is mainly confined ta
the cose of progressive waves over a horizontol bottom, generated by o sinusoidally-moving
piston-type wave board It combines some experimentol results with existing - but portly

[*] Project engineer, Delft Hydroulics Laboratory, The Netherlonds

forgotten – theories, trying to describe and understand the observed phenomena.
In 1969 the starting point for this study was the experimentally-observed fact that beach
profile formation may severely be affected by secondary waves Fig 1 shows three beach
profiles which all had developed to entirely different equilibrium positions in identical
wave channels under the same wave conditions The profiles appeared to be strongly in-
fluenced by the sand bars and troughs, which had developed from the originally horizon-
tal section of the bed This bar system, although being outside the breaker zone, con-
trolled to a great extent the position and the type of breaking, and thus the water move-
ment and sand transport in the surf zone The formation and the geometry of the bar system,
which was not caused by wave reflection, seemed to correspond with and to intensify the
secondary surface waves which had been present from the beginning, although they were
hardly visible then Apparently, these small secondary waves originated at the wave board,
and a set of experiments were conducted in order to establish the exact nature of the
produced waves

3 Origin and behaviour of secondary waves

3 1 Experimental conditions and measuring procedure

The tests were conducted in two different wave channels, 1 24 m and 0.91 m wide, with
smoothly finished sides and bottoms The lengths of the horizontal sections were 9 m and
13 m respectively, and both channels ended with a 1 in 20 sloping beach as a wave
absorber No other wave absorbers or filters were used A vertical board, sinusoidally
oscillating in a horizontal plane, was used as a wave generator Wave periods T varied
from 1 15 s to 1 92 s, the water depth h varied from 0 10 m to 0.55 m, and the wave
height H varied between 0 02 m and 0 15 m The water depth to wave length ratio h/L
thus varied from 0.05 to 0 20, and the Ursell parameter $Ur = HL^2/h^3$ varied between 2
and 104 In general four different wave board strokes were chosen for each h/L-value
The wave form was measured in the centre line of the channel in points 0 2 m apart
over a distance of at least 6 m, starting near the wave board A harmonic analysis
yielded the local amplitudes of the first, second, third and fourth harmonic components
a_1, a_2, a_3 and a_4, averaged over three wave periods The resulting regular spatial vari-
ation of a_n, an example of which is presented in fig. 2, forms the essential basis for a
further analysis

3 2   Two different interpretations

The typical wave forms did not differ from those reported earlier, e g $\begin{bmatrix}5,15,16\end{bmatrix}$. An almost sinusoidal wave form near the wave generator deforms, while propagating, gradually into a non-symmetric one, with a small hump behind the main crest. This hump may develop, depending on the value of Ur, into a definite secondary crest, located in the trough of the main wave. On that location, the wave form is symmetric again with respect to the crests   Further downwave this process is repeated in reverse, until the appr sine form is reached again, etc. (see fig 3)   At any fixed place   the wave form is constant in time   At a first glance, one could take the hump or secondary crest as an extra wave, having the same period as the main wave, and propagating with a lower speed because of the difference in wave heights   According to this viewpoint, e.g. $\begin{bmatrix}15,16,24\end{bmatrix}$, both waves should be just in phase at the locations where a sine wave results, which has a smaller height than at all other locations   The incorrectness of this viewpoint may be demonstrated by the following argument: if the difference in height would be the only reason for the difference in celerity, there would be no reason at all for the sine wave to change its form, because at that location both waves would have the same height, period, and water depth, and thus the same celerity   According to a different point of view $\begin{bmatrix}18,23\end{bmatrix}$, the symmetrical wave form with the secondary crest should be regarded as a superposition of the main wave with period T and a smaller wave with period T/2, the so-called second harmonic free wave   One crest of this smaller wave contributes to the visible secondary crest, while its other crest coincides with the main wave crest and makes it higher than normal   Thus, the second harmonic free wave is here exactly in phase with the second harmonic component of the basic wave   The resulting sine wave, on the other hand, is caused by the fact that the free and the coupled second harmonic waves are exactly out of phase and are almost cancelled out   Care must be taken, however, not to be misled by the outer appearance of the waves   In general, the visible peaks do not correspond to the crests of real waves, simply because a recorded wave form has no own identity as soon as it must be regarded as the summation of more than one participating wave   This second point of view agrees well with what may be expected on the basis of literature

3 3 Theoretical considerations

Fantanet [14] predicts the amplitude and the phase of the second harmonic free wave, which is always the by-product of a sinusoidally-moving piston-type wave board (fig 4) For low h/L-values the free and the coupled second harmonic waves are virtually 180° out of phase Kravtchenko and Santon [20] predict the generation and the interesting behaviour of a set of two waves, generated by two interacting free waves, with T_1, C_1, L_1, A_1 and T_2, C_2, L_2 and A_2 as period, celerity, length and amplitude, respectively. The new interaction waves have periods defined by the sum and difference frequencies of the interacting waves:

$$1/T_* = \left| 1/T_1 - 1/T_2 \right| \text{ and } 1/T_*' = 1/T_1 + 1/T_2 \qquad (3\text{-}1)$$

The corresponding celerities are

$$C_* = L_1 L_2 (T_1 - T_2)/T_1 T_2 (L_1 - L_2) \text{ and } C_*' = L_1 L_2 (T_1 + T_2)/T_1 T_2 (L_1 + L_2) \qquad . (3\text{-}2)$$

The corresponding amplitudes are given by

$$A_* = A_1 A_2 \; \gamma_{1,2} \text{ and } A_*' = A_1 A_2 \; \eta_{1,2} \qquad (3\text{-}3)$$

where $\gamma_{1,2}$ and $\eta_{1,2}$, non-dimensionless coefficients of interaction, are very lengthy functions of L_1, L_2 and h [20]

So the interacting basic wave (period T) and Fantanet wave (period $T/2$) produce two extra waves with periods $T_* = T$ and $T_*' = T/3$ according to (3-1), whereas their celerities C_*, C_*' and amplitudes A_*, A_*' are given by (3-2) and (3-3) As an example, fig 5 presents the values of $\gamma_{1,2}, \eta_{1,2}$ and $\eta_{1,2}/\gamma_{1,2}$ as a function of h/L_1 for $T_1 = 1\,56s$ and $T_2 = 0\,78s$ The basic wave is regarded as a third-order Stokes wave, i e composed of three harmonic components, with amplitudes A_1, A_2' and A_3', all propagating with the same celerity C_1 of the basic wave

We have, then, six different "waves", viz three pairs of waves with periods $T, T/2$ and $T/3$ respectively In each pair both waves thus have equal periods T/n ($n = 1,2,3$), but different celerities (fig 6) Each pair can of course give only a single value of a_n in the harmonic analysis at a specific location, obtained by adding the constituent amplitudes as vectors Each resulting amplitude a_n must then theoretically display a rhythmic spatial behaviour Its maximum and minimum values are the sum and the difference, respectively, of the amplitudes of the participating "waves" Because of the difference in celerities, the faster wave of the pair will overtake the slower one within a certain distance, the overtake length L_{ov} It follows immediately that

$$L_{av} = L_{slow} \; C_{fast}/(C_{fast} - C_{slow}) \qquad (3\text{-}4)$$

where the subscripts fast and slow refer to the faster and slower wave, respectively As an example, fig 7 shows the expected behaviour of a_1 as a function of the phase angle $\varphi(x)$ between the constituent amplitudes A_1 and A_* It should be noticed that the celerities of a_1 and A_1 are in general not equal.

3 4 Comparison of theory with experiments
The second harmonic amplitude a_2

Supposing that a_2 is the vector summation of the second harmonic Stokes amplitude A_2' and the Fontanet amplitude A_2, both amplitudes follow from the maximum and minimum a_2 values (see figs 2,7):

$$\text{Stokes 2nd order: } A_2' = (a_{2max} + a_{2min})/2 \qquad \qquad .\quad .(3\text{-}5)$$

$$\text{Fontanet } : A_2 = (a_{2max} - a_{2min})/2 \qquad \qquad .(3\text{-}6)$$

provided that $A_2' \geqslant A_2$, which is true according to Fontanet [14]. In fig. 8 the experimentally determined value of A_2', A_2 and A_2/A_2' have been plotted, together with the respective theoretical curves of Miche [28] and Fontanet [14] The fact that a_{2min} is always found near the wave board (fig 2) is in support of Fontanet's phase relationship (fig 4) From (3-4) it follows for the overtake length of a_2:

$$L_{ov2} = L_2 C_1/(C_1 - C_2) \qquad \qquad .\ (3\text{-}7)$$

or in dimensionless form:

$$L_{ov2}/L_1 = C_2/2(C_1 - C_2) \text{ or } L_{ov2}/L_1 = L_2/(L_1 - 2L_2) \qquad \qquad .\ .\ (3\text{-}8)$$

The measured and theoretical values of L_{ov2}/L_1 have been plotted in fig 9, which show a reasonable agreement For relatively deep water, $L_1 = 4L_2$ and $C_1 = 2C_2$, so that from (3-8):

$$L_{ov2} = L_1/2 \qquad \qquad .\ .\ (3\text{-}9)$$

In this case, the overtake length is apt to be mixed up with the reflection phenomenon For shallow water conditions, $(C_1 - C_2)$ diminishes to very small values (see fig 6) which would give very long overtake lengths according to (3-8) However, in shallow water the celerity increases with the wave height, which affects C_1 more than C_2 Therefore, the denominator in (3-8) is increased remarkably, causing the overtake length to decrease, if C_1 increases only slightly So in order to find the correct value of L_{ov}, one must insert the correct (wave height adapted) values of C and L in (3-8). In fig. 9 the 3rd order Stokes theory [34] was used to find L_{ov2}/L_1 for $H/h = 0.4$, but a cnoidal theory may perhaps work out better In view of the difficulty to measure the exact celerity of a wave, especially when secondary waves are present, the argument may be reversed in that from (3-7) and from the exactly-measurable overtake length the proper wave celerity can be determined:

$$C_1 = L_{ov2} C_2/(L_{ov2} - L_2) \qquad \qquad .\ .(3\text{-}10)$$

The first harmonic amplitude a_1

From fig 2 it appears that L_{ov1} is equal to L_{ov2} When the theoretical expressions for C_1, C_*, L_1 and L_* are substituted in (3-4), it follows that $L_{ov1}/L_1 = L_2/(L_1-2L_2)$, so that indeed $L_{ov1} = L_{ov2}$ The experiments (fig 2) show that $a_{1\ max}$ is always found near the wave board; the theory [20] is not clear on this point In order to determine A_1 and A_* from the experimental values of a_{1max} and a_{1min}, the wave reflection must be taken into account, because reflection alone also causes a certain variation in a_1 With respect to A_1, reflection does not interfere and the normal formula holds:

$$A_1 = (a_{1max} + a_{1min})/2 \qquad\qquad . \ (3\text{-}11)$$

According to [17] the reflection coefficient is about 5 %, and especially for Ur < 28 the reflection appeared to be the dominating feature, causing much scatter. So only for Ur > 28 the values of A_* have been determined as

$$A_* = (a_{1max} - a_{1min})/2 \qquad - 0\ 05\ A_1 \qquad\qquad .. \ (3\text{-}12)$$

Fig 10 shows for the larger values of h/L_1 a remarkable discrepancy between $A_{*experim.}$ according to (3-12) and A_{*theor} according to (3-3) The reason may be that the magnitude of A_*, which is only a few mm, is small compared to the disturbing influence of reflection

The third harmonic amplitude a_3

From the experimental results (fig 2) it appears that a_3 has a similar spatial behaviour as a_2 Indeed, when the theoretical values for C_1, C_*', L_1 and L_*' are substituted in (3-4), the result is again that $L_{ov3} = L_{ov2}$, so

$$L_{ov1} = L_{ov2} = L_{ov3} \qquad\qquad . \ (3\text{-}13)$$

One complication appears in the behaviour of a_3 For the higher Ur-values (fig 2, run 30), there seems to be an extra, smaller overtake length, apparently caused by yet another wave with period $T/3$ This might be a third order free wave, generated by the wave board in analogy with Fontanet's wave, but no information exists with respect to such a wave So a certain error must be accepted in determining the amplitudes A_3' and A_*' according to

$$A_3' = (a_{3max} + a_{3min})/2 \qquad\qquad . \ (3\text{-}14)$$

and $$A_*' = (a_{3max} - a_{3min})/2 \qquad\qquad . \ (3\text{-}15)$$

For the lower Ur-values, a_3 is so small (order 1 mm) that a further analysis is useless
in view of the scatter. Therefore, only those results were used in (3-15) for which
$A_3' \geqslant 2$ mm. A reasonable agreement is shown to be present in fig. 11 between
A_*' experim. and A_*' theor., although there is considerable scatter. The ratio A_*'/A_3'
has been plotted in fig. 12; it displays a similar trend as A_2/A_2' in fig. 8.

The fourth harmonic amplitude a_4

The harmonic analysis was done for four harmonics, but a_4 was so small that it has not
been plotted. As an average value, it may be stated that the magnitude of a_4 was
about 50 $^o/o$ of a_3.

3.5 The wave form

The presence of a number of waves with different celerities, predicted by the combined
theories and confirmed by the experiments, has as a consequence that the wave form
varies from place to place The wave form at any place is predictable if the amplitudes,
the celerities and the initial phase-angles of all participating waves are known. From
section 3 4 it follows that this is indeed the case to a certain degree of accuracy,
especially for the celerity and the initial phase angles An example of a resulting x-t
diagram for the participating wave crests is given in fig   13 for $h/L_1 = 0$ 10, with
the following relative celerities (compare fig 6):
$C_2/C_1 = 0$ 821, $C_*/C_1 = 0$ 695 and $C_*'/C_1 = 0$ 868
Near the wave board, indicated as place no   1, the six waves are phased as follows:

A_1 and A_* are in phase
A_2' and A_2 are 180° out of phase $\left.\right\}$ place no 1, $x = 0$ . ... (3-16)
A_3' and A_*' are 180° out of phase

With increasing x the initially symmetric wave form loses its symmetry, because the
phase-relation (3-16) changes But as soon as the crest of A_2 and A_*' has just been
overtaken by the corresponding harmonic components of the basic wave, another
symmetric wave results, quite different from (3-16).

A_1 and A_* are 180° out of phase
A_2' and A_2 are in phase $\left.\right\}$ place no 2, $x = L_o/2$ ....(3-17)
A_3' and A_*' are in phase

Because the basic wave is faster than any other wave, firstly some undisturbed basic waves will pass along a certain point far enough from the wave board Then, as the slower waves reach this point one by one, the wave form will be unstationary for same time. Only after the arrival of the slowest wave, a new stationary wave develops, now containing all disturbing waves together with the basic wave $\begin{bmatrix} 3 \end{bmatrix}$ So the basic wave of permanent form is always present, but generally not in an explicitly visible form. Starting for example from the conditions $h/L_1 = 0.10$, $H/h = 0.36$ and $T_1 = 1.56s$, the following amplitudes result from section 3.4:

$$
\begin{array}{ll}
A_1 \ \ = 3.82 \ cm \ \left.\right\} \\
A_2' \ = 1.72 \ cm \ \left.\right\} & \text{3rd order Stakes wave, basic wave} \\
A_3' \ = 0.79 \ cm \ \left.\right\} \\
A_2 \ \ = 1.24 \ cm \ - & \text{2nd harmonic free wave (Fantanet)} \\
A_* \ \ = 1 \ 44 \ cm \ \left.\right\} & \text{interaction waves (Kravtchenka and Santan)} \\
A_*' \ = 0.73 \ cm \ \left.\right\}
\end{array}
$$

Based an the experimental results in figs 10 and 11, A_* and A_*' have been reduced to 0,965 cm and 0,635 cm, respectively With these amplitudes, and their phase relationships fram fig 13, various wave farms were reconstructed in fig. 14 far place no. 1, place na. 2 and 9 intermediate lacations; far camparisan alsa the undisturbed basic wave has been platted Obviously, the crest af the campased wave farm does in general nat caincide with the crest af the basic wave, nar is a secondary crest identical with the crest af ane af the participating smaller waves Twa mare camments may be made an figs. 13 and 14 Firstly, the tatal wave height varies and has a minimum at place no. 1 and a maximum near place na 2 Secandly, a horizontal section thraugh the x–t diagram results in an instantaneaus wave surface which shaws in general na regular spatial recurrence system, because the avertake length is in general nat a multiple of the variaus wave lengths invalved

Of all lacatians, places na 1 and 2 display the mast characteristic wave farms, which will be analyzed in same detail

At place na 1, $x = k \ L_{av}$, where $k = 0,1,2,3,.$ .. . Here practically a sine wave results, cansisting mainly of A_1 and A_*, a_1 being maximum; a_2 and a_3 reach their minimum values. Of all measured values, the fallowing averages result:
$a_{2min}/a_{1max} = 0.10$ and $a_{3min}/a_{1max} = 0 \ 027$.

At place no. 2, $x = (k + 1/2).L_{ov}$ where $k = 0,1,2,3,\ldots$. Here the resulting wave
is far from sinusoidal, a_1 being minimum and both a_2 and a_3 being maximum. Of all
measured values in this place, the ratios a_{2max}/a_{1min} and a_{3max}/a_{1min} have been
plotted in fig. 15 as a function of Ur Two lines have been drawn to represent these
points and an additional line in agreement with section 3.4 represents the fourth har-
monic. On the basis of these lines, and taking into account the relevant phase rela-
tianship (3-17), wave forms were constructed for various values of Ur (fig. 16) For
Ur $\geqslant$ 13 a secondary crest exists in the trough centre, which is in accordance with
Madsen's value of $4\pi^2/3$ [23]. These "reconstructed" wave forms may be compared with
experimental wave forms recorded in place no. 2, presented in fig. 17. For both figures
16 and 17 the relative height of the secondary crest increases with Ur as shown in fig. 18,
where also some of Galvin's results [15] have been plotted. The discrepancy between the
reconstructed and the direct experimental values of H'/H_{tot} may partly be due to the fact
that, especially for higher Ur-values, 5th and higher harmonic components do participate
in fig. 17, but not in fig 16

4 Influence of secondary waves on a harizontal sand bed

Considering sand transport, the behaviour of the orbital motion near the bed is of more
direct relevance than the fluid surface [1] Simultaneous measurements of the wave profile
and the orbital velocity near the bed carried out in a long wave channel with a fixed
harizontal bottom, revealed that their behaviour is virtually the same (fig. 19). This is
substantiated by a harmonic analysis of the orbital velocity, plotted as a function af the
distance from the wave baard (fig. 20) The regular spatial behaviour of the orbital
velocity field must have as a consequence that the onshore-offshore sand transport varies
spatially, too. In order to check this, tests were run in a 1.20 m wide wave channel,
with a smooth horizontal concrete bottom over the first section af 2 m from the wave
board. A horizantal flat sand bed extended over the next 9 m, terminating in a 1 on 20
sloping spending beach Fig 21 shows the experimental conditions and the resulting bed
farms. Ur varied from 40 ta 57 The wave lengths produced in the sand bed are very
clearly equal to the respective overtake lengths. In test T73-1, a bar-trough system with
a smaller reference length, caused by wave reflection, is superimposed on the large scale
bar system. Looking back from these results to fig. 1, the cause of the undulating bed
profile is clear now, realising that L_{ov} is appr. 3.20 m for the given conditions. These
bars, once formed fram on initially flat bed, may on their turn provoke new secondary

waves, which oll interfere with the breoker type ond breoker locotion, the woter circulo-
tian, and the morphological development in the surf zone and on the beoch. On certain
occosions, the undulations hove even been seen to develop into lorge breaker bors.
Although the drostic influence of the disturbing woves, vio the formation of bors and
traughs, on the beach profile development wos quite cleor in the case under considero-
tian, it is also cleor thot such an influence moy be present without recognizing it os
such, so that a general worning seems useful here For instance, from Bognold's clear
description [2, p461 etc] it con sofely be concluded that he was confronted with similar
phenomeno in his tests On the other hond, the interrelotion between secondory woves,
bar systems ond beoch behaviour seems not to be restricted to model experiments [22],
so that the present study moy be of o more generol opplicotion. Therefore, the bed pro-
files in fig. 21 hove been converted into o rote of tronsverse sond transport by using the
sond balance Fig 22 shows the result for T73-2, where also the wave form is presented
far vorious locations For $x = 5$ m, one overtoke length from the wove boord, the
sinusoidol motion has no preference for o certoin directian, ond consequently the sand
transport rate is zero In generol, the magnitude ond the direction of the sand tronsport
oppeors ta be remarkobly dependent an slight differences in the wave form.

5 Experiments in o pulsoting woter block

5 1 Apporatus ond procedure

In order to study the effect of higher harmonic components in the orbitol motion on the
transverse sand tronspart, some preliminary tests were run in a very simple and small
pulsating woter block. This apparatus, originolly on ideo of Silvester [29, 33] consists
of o bottomless perspex box, forced by a programmable wove generotor to oscillate over
o bed (fig. 23). In this bed, o sond bed and two sand traps are installed. The block
moves under woter in o perspex tonk. Before each test, the sondbed is smoothed
ond mode flush with the fixed bed. The tests are divided into periods of 5 minutes, after
which the trapped sond is collected in order to define the net sediment tronsport rote ond
direction. Ripples are formed in the first 1 ar 2 minutes, sometimes stoying in fixed posi-
tions, sometimes moving, but not necessarily in the some direction os the net sediment
transport

5 2   Test results

Throughaut the tests, a basic period of 1 40s was used, with an amplitude A_1 = 0.05 m.
In the first series of tests, of 15 min. each, the influence of the 2nd harmonic companent
A_2 was investigated   With a sinusaidal movement, an almost zero net transport is found,
as expected (fig. 24)   By adding the second harmonic component with A_2/A_1 = 5 ^{o}/o and
10 ^{o}/o, respectively, and with the same phase relationship (φ_2 = 0) as occurs in a 2nd
order Stokes wave, a marked influence appears on the transport pattern. By visual obser-
vation, this was caused by the circumstance that vortex formation and behaviour is very
sensitive to the form of the orbital velocity. The correspondig velocity is also shown in
fig   24
In a second series of tests of 25 mın. each, a second harmonic component with A_2/A_1
= 20 ^{o}/a was added, but naw with a phase relatian varying fram φ_2 = 0^a (like in
a 2nd order Stokes wave) to φ_2 = 90° (fıg   25)   The resulting sand transports for twa
sand diameters are presented in fig. 26   Clearly, these are all only quite preliminary
results, both qualitatively and ouantitatively speakıng, and further tests with better
equipment are planned   Nevertheless, it seems that this very close dependence of the
dırection and the rate of transverse sand transport on slight varıations in the wave form
and the arbital velocıty field, is important for any basic study of beach profile develap-
ment

6   Suppression of secondary waves

In order to suppress the parasitic waves, Biésel and Suquet [4] suggested already in 1951
to use a more realistic motion of the wave board than a simple harmonic oscillation.
Work along this line has recently led   to encouraging results [9,23] . Also a different
method may be thaught of, which has provisianally been tested   In this method, the
experimental fact is used that a bar or sıll, placed on the horizantal bottom of a wave
channel, generates free higher harmonic waves when regular waves proceed aver it.
[16,19,27] . Na theory being available on this subject, a trial and error method was
used in order to find a sıll of such dimensıons and on such a location, that it would
produce a second harmonic free wave of the same height and exactly 180° out of phase
with respect to the Fontanet wave. One af the results is presented in figs. 27 and 28,
giving the characteristıcs of the sill, the wove forms and the hormonic analysis for two
runs with the same rectongular sıll on two different locatıons. Without o sill, a secondary

wave was clearly visible In both cases the influence of the sill - with a thickness of only 0 1 h - was surprisingly great In run D, a virtually permanent wave form resulted downwave from the sill, while a distinct secondary wave was still visible between the wave flap and the sill. This optimum result was obtained with the far end of the sill at a distance of 3 m from the wave flap, corresponding to L_{av}. When the sill was moved to different locations, the resulting wave form immediately deteriorated. The worst result was obtained for run B, where the sill was shifted over a distance of $L_{av}/2$. This suggests that the overtake length is an important parameter in determining the optimum sill location, although the physical process is not well understood. By looking at it, a certain analogy seems to exist with the effect of a bulb on the waves generated near a ship's bow.

7 Conclusions

a. Secondary waves may be generated by the wave board, or may be provoked by a
    sill, bar, slope, or by breaking waves
b   Secondary waves, generated by the wave board, may adequately be described by
    combining the theories of Fontanet [14], and Kravtchenka and Santon [20].
c. Secondary waves may have a very pronounced influence on beach profile formation,
    although this influence may be quite difficult to recognize as such.
d   The rate and the direction of the transverse sand transport under waves is very
    delicately dependent of the wave form, i.e the form of the orbital velocity field.
e   An adequately designed sill of rectangular cross-section may be used to suppress
    the Fontanet wave

References

1   Adeyema, M D., 12th C E C., chapter 27, 1970
2   Bagnold, R.A , J Inst Engrs , 27, 1947, pp 447 - 469
3. Bendykawska, G., Rozprawy Hydratechniczne, 1971, no. 28, pp 27 - 39
4. Biésel, F and Suquet, F., La Houille Blanche, 1951, no. 2,4,5 and 1952 no. 6
5   Baczar-Karakiewicz, B., Archiwum Hydratechniki, 19, 1972, no. 2, pp 197 - 210
6   Baczar-Karakiewicz, B , Archiwum Hydratechniki, 20, 1973, no. 1, pp 47 - 58
7. Baczar-Karakiewicz, B , Razprawy Hydratechniczne, 1973, no. 32, pp 51 - 67

8.   Bryant, P. J , J Fl. Mech., <u>59</u>, 1970, part 4, pp 625 - 644

9.   Buhr Hansen, J., and Svendsen, I.A , T.U. Denmark, Inst af Hydr. Eng. progr. rep. 32, 1974, pp 3 - 8

10   Byrne, R. J., J af Geaph. Res , <u>74</u>, 1969, na. 10, pp 2590 - 2596

11   Caldwell, J M , Pracs 1st Conf an Ships and Waves, 1954

12   Dingemans, M. W., Delft Hydr Lab Repart no. R 729 - II, 1973

13   Flinterman, J , and Stein, T., Delft Hydr Lab , Repart na 08114, 1953

14   Fantanet, P., La Hauille Blanche, 1961, no. 1,2

15   Galvin, C J , CERC-nate an secandary waves, Sept. 1970

16. Gada, Y., et al Part and Harbaur Res Inst Rept na.13, with appendix, 1967

17   Greslou, L , and Mahé, Y , 5th C E C. chapter 7, 1954

18. Hulsbergen, C.H., Delft Hydr. Lab , Res rep. na. S 55 - III, 1972

19. Jalas, P., La Hauille Blanche 1962 na. 6, pp 758 - 769

20. Kravtchenka, J , et Santan, L , 7th Gen. Meeting I.A.H.R. <u>2</u>, 1957, chapter D2

21. Larras, J , I A H.R , 1963, pp 351 - 352

22   Lau, J., and Barcilan, A , J af Phys Oceanagraphy, <u>2</u>, 1972, na 4, pp 405 - 410

23   Madsen, O S , J af Geaph. Res <u>76</u>, 1971, na. 36, pp 8672 - 8683

24   Madsen, O.S , Mei, C.C , and Savage, R P , J Fl.M <u>44</u>, 1970, part I, pp 195 - 208

25   Marcau, C , Thesis, Univ. af Grenable 1969

26. Masan, M.A., and Keulegan, C.H , B E.B. Eng. notes, na. 19, Tech. Mem. 5, 1944

27. McNair, E C., and Sarensen, R M , 12th C. E C. chapter 26, 1970

28   Miche, M , Annales des Pants et Chaussées 1944

29   Magridge, G R., ASCE, J. Hydr Div., HY7, 1970, pp 1587 - 1604

30. Onaszka, J , Razprawy Hydratechniczne, 1973, na. 32, pp 69 - 84

31   Santan, L., IVes Jaurnées de l'Hydr , Questian III, Rappart 6, 1956

32   Schweigman, C , Delft Hydr. Lab , Res. rep. na S 13, 1965

33   Silvester, R., J af the Inst af Engrs., Austr <u>37</u>, Oct-Nav 1965, pp 311 - 321

34. Skjelbreia, L., 3rd order Stakes wave tables, Council an wave res 1958

35   Takana, K , La Hauille Blanche, 1960, na. 3, pp 247 - 259
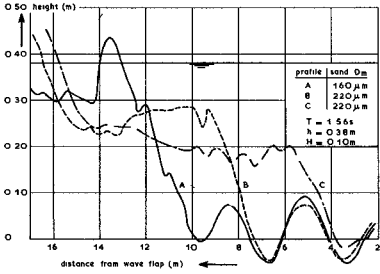
Figure 1: Beach profiles affected by secondary waves
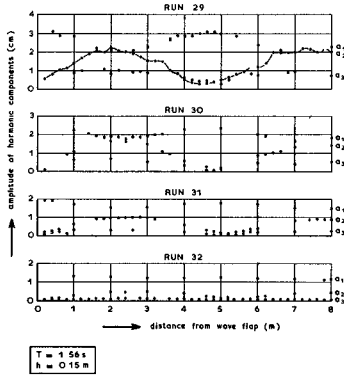
Figure 2: Typical variation af harmonic amplitudes
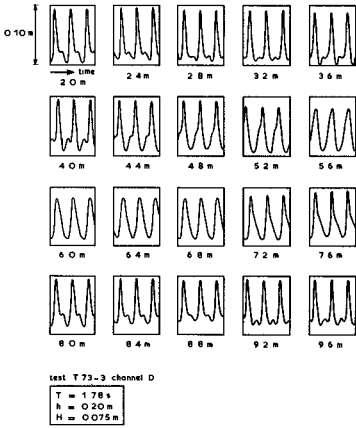
Figure 3: Typical variatian af wave farms
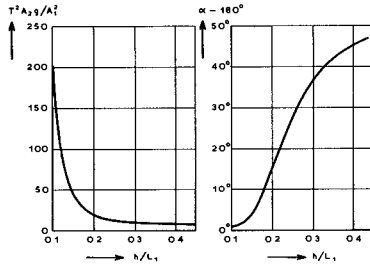
Figure 4. Characteristics af Fantanet wave
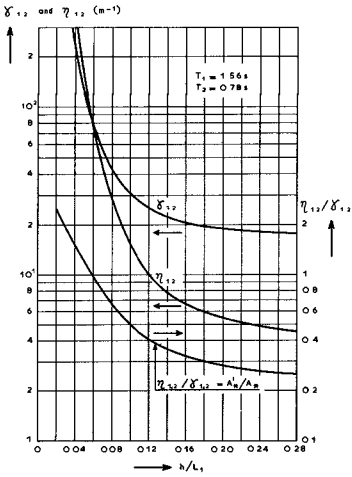
Figure 5:   Coefficients of interoction occording
            to Krovtchenko ond Sonton
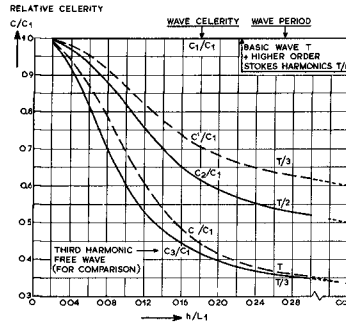
Figure 6:   Relative wove celerities; influence
            of wove height neglected
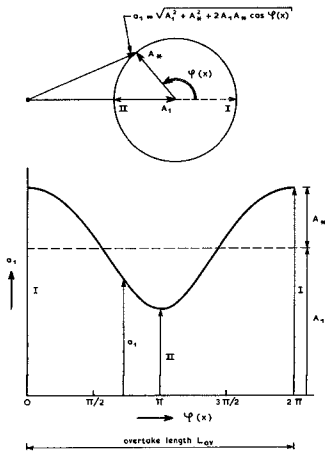
Figure 7:   Vector summotion of
            A_1 ond A_* ond resulting
            spotiol behaviour of a_1
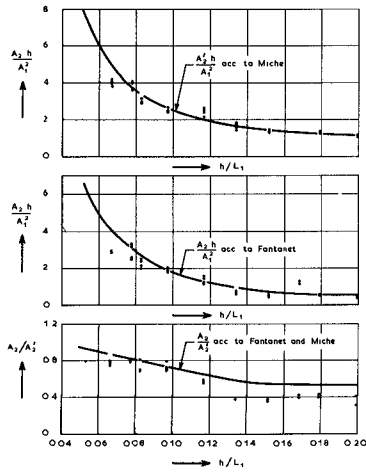
Figure 8:   Comporison of theory ond
            experiments for 2nd harmonic
            components A_2 and A_2'
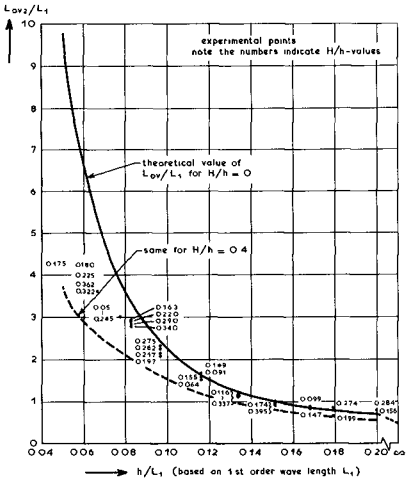
Figure 9: Dimensionless overtake
length L_{ov2}/L_1
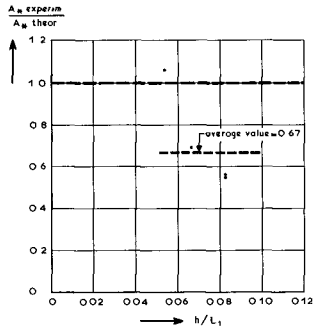
Figure 10· Comparison of theory and
experiments for 1st harmonic
component A_*
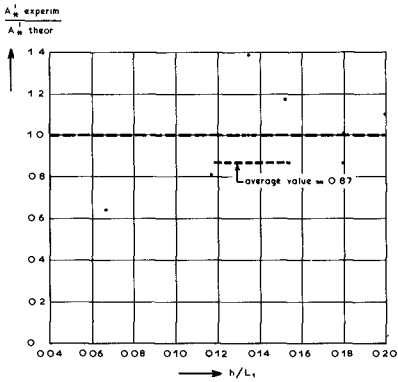
Figure 11: Comparison of theory and
experiments for 3rd harmonic
component A_*'
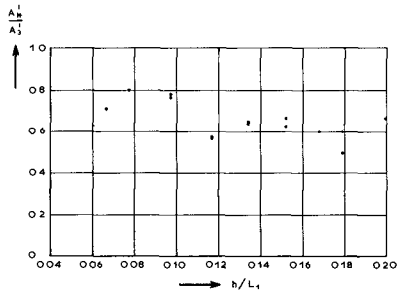
Figure 12: Experimental ratio A_*'/A_3'
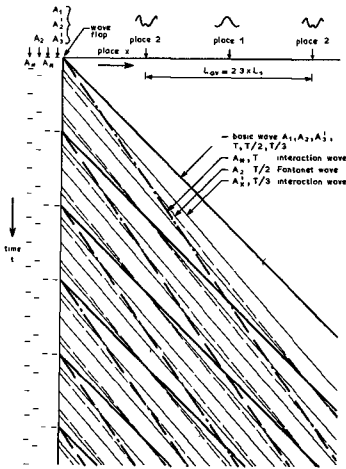
Figure 13: x-t diagram af participating wave crests far $h/L_1 = 0.10$
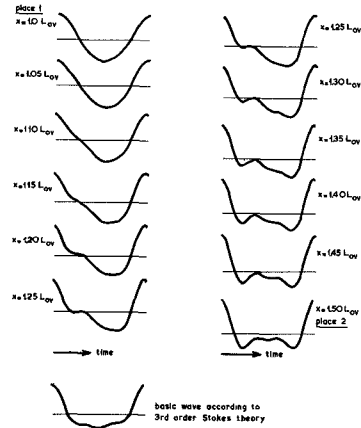
Figure 14: Theoretical wave farms far $h/L_1 = 0.10$ and $A_1/h = 0.18$
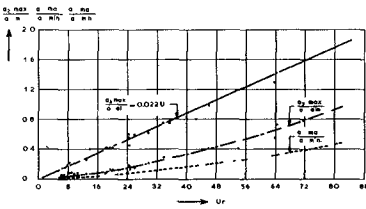
Figure 15: Relative amplitudes at $x = (1/2 + k) L_{av}$
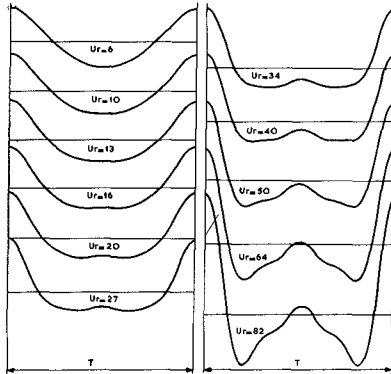
Figure 16: Wave forms at $x = (1/2 + k) L_{av}$, recanstructed fram figure 15
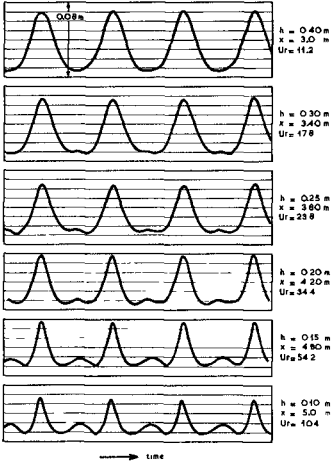
Figure 17: Experimental wave forms for T = 1 92 s at x = 1/2 L_ov
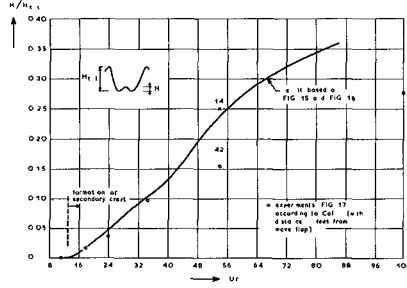
Figure 18: Relotive height of secondory crest at x = (1/2 + k)L_ov
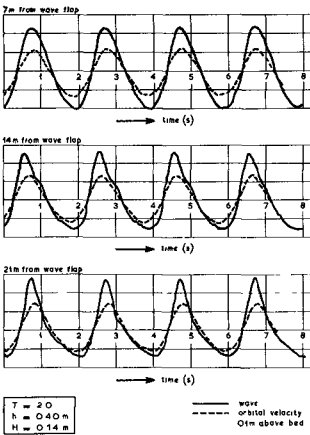
Figure 19: Simultaneous wove and orbitol velocity
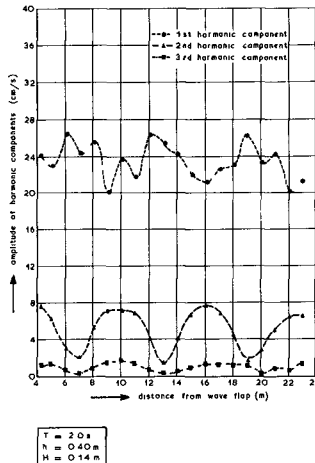
Figure 20· Spatiol behaviour of hormonic omplitudes in orbital velacity
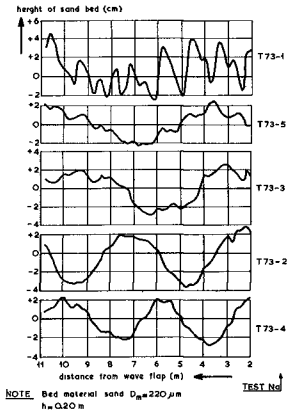
Figure 21: Influence of secondary waves on an initially flat horizontal bed

Figure 22: Typical wave forms and resulting sand transport

Figure 23: Pulsating water block
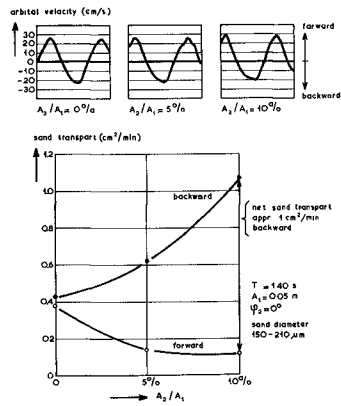
Figure 24: Influence of 2nd harmonic component on orbital velocity and sand transport
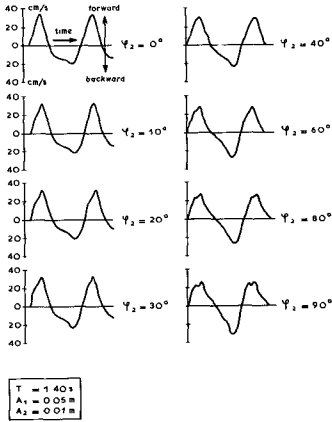
Figure 25. Velocity of pulsating block
            with variable φ_2
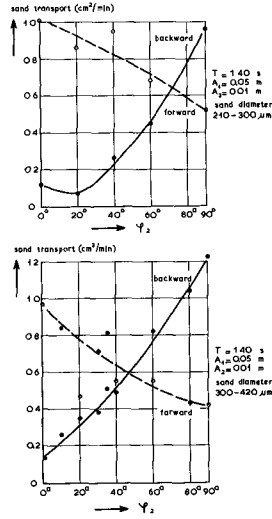
Figure 26· Influence of phase of
            2nd harmonic component
            on sand transport
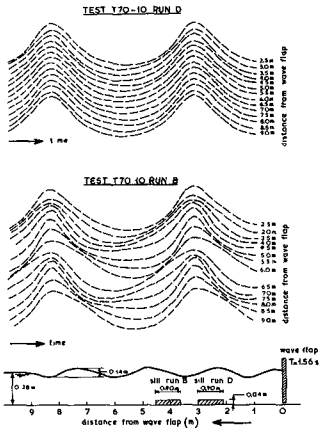
Figure 27: Typical wave form variation
            as influenced by location
            of low sill
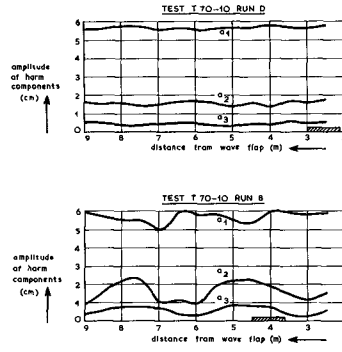
Figure 28: Harmonic amplitude variation as
            influenced by location of sill

CHAPTER 23

TRANSFORMATION OF IRREGULAR WAVES IN SHOALING WATER

Tetsuo Sakai
Assistant Professor
and
Yuichi Iwagaki
Professor
Department of Civil Engineering
Kyoto University
Kyoto, Japan

ABSTRACT

In the numerical method of prediction of wind waves in deep water, Hasselmann's nonlinear interaction theory is applied. This method assumes the energy balance of individual component waves. However, the total energy balance must exist in the transformation of irregular waves in shoaling water. In this investigation, experiments were carried out on the transformations in shoaling water of composite waves having two components and random waves having one or two main peaks.

It was found that the elementary component wave height of the composite waves and the elementary peak power of the random waves decrease with decrease in the water depth. This reason can be explained qualitatively by the theory of the elementary component wave height change of finite amplitude waves in shoaling water. The secondary component wave height of the composite waves and the secondary peak power of the random waves increase with decrease in the water depth. This can be explained qualitatively by Hamada's theory of nonlinear interaction in uniform depth.

INTRODUCTION

The mechanism of transformation in shoaling water of wind waves, swell, tsunami and so on is one of the elementary problems in coastal engineering. In fact, the action of waves on coastal and offshore structures is the most important factor in design of the structures in coastal and offshore zones. In this case, the accurate estimation of the transformation of waves predicted in deep water is required. In the traditional design, irregularity of waves in actual coasts has not been taken into account directly, and irregular waves have been represented by regular waves having a significant wave height and period. However, it is expected that phenomena inherent in irregular waves occur in some cases. Recently, irregularity of waves is taken into account directly in design.

On the transformation of irregular waves in shoaling water, there are some investigations which irregularity of waves is taken into account directly by the power spectral density representation. Bretschneider[1] and Tang-Ou[2] discussed the transformation of irregular waves by assuming the independency of individual components. However, it is expected that the nonlinearity of waves becomes predominant near the breaking point and the assumption of independency of the components becomes unsuitable.

In general, Hasselmann's nonlinear interaction model[3] is used in the transformation of irregular waves in deep water. The validity of this model has been confirmed on the transformation of irregular waves in uniform depth[4].

However, in the case of the transformation of waves in decreasing depth, the total energy balance including the energy dissipations due to boundary friction and wave breaking must exist.

In this investigation, the transformations of composite waves and random waves having predominant peaks are discussed experimentally. It is tried to explain the transformations by the theory of shoaling of finite amplitude waves. In addition to the power spectral density, the frequency distributions of water level, crest height and wave height are also important to represent irregular waves. However, they are not discussed here. It should be noticed that the word "composite waves" means the waves consisting of finite number of sinusoidal waves and the word "random waves" means the waves consisting of infinite number of sinusoidal waves and determined only stochastically.

EXPERIMENTS ON TRANSFORMATION OF IRREGULAR WAVES IN SHOALING WATER

COMPOSITE WAVES

a) Experimental apparatus
A wave tank at the Department of Civil Engineering, Kyoto University was used. The length of the tank is 28m, the height 75cm and the width 50cm. A hydraulic composite wave generator of piston type is installed at one end of the tank(see Photo.1). This generator consists of 8 pistons[5]. The period ratio of one piston to the next piston is $1/\sqrt{2}$. The generator generates the composite waves by imposing these motions upon the wave board simultaneously.

As seen in Fig.1, a wave absorber was installed at the opposite end of the tank snd a uniform sloping beach was set in the middle part of the tank. This beach was made of alminium plates. The slope of the beach was 1/20. Its length was 7.2m and the height of the slope tail was 36cm. In the experiments, the water depth in the uniform depth region was kept constant(36cm). Therefore, waves after breaking flew over the beach tail. In this wsy, the wave reflection from the beach and wsve setup and down were made to be negligible as much as possible.

One wave gauge was set in the uniform depth region and three on the beach. The water level variations at four measuring points were recorded simultaneously with a magnetic tape recorder. The positions of two wave gauges in the uniform depth region and at the deepest measuring point on the beach were fixed during the experiments(see Fig.1). The wave gauge in the shallowest measuring point on the beach was set at the breaking point of the composite waves. The breaking point of the composite waves was determined as the deepest one among the breaking points varying with time. Four measuring points were numbered as 1, 2, 3 and 4 in order from offshore.

b) Procedure of experiment and analysis
The composite waves were generated by using two pistons of the generator. Before the experiments of composite waves, the experiments of monochromatic waves using each one of these pistons were carried out. The period ratio of two pistons used was $1/\sqrt{2}$. The analog data in the magnetic tape recorder were converted into the digital data(the time increment was 0.08sec) with a A-D convertor. The experimental conditions are shown in Table 1.

The monochromatic waves consist of one elementary component and the harmonic components. In so far as the nonlinear interaction of 2nd order, the harmonic component is only the component of two times the elementary component frequency.
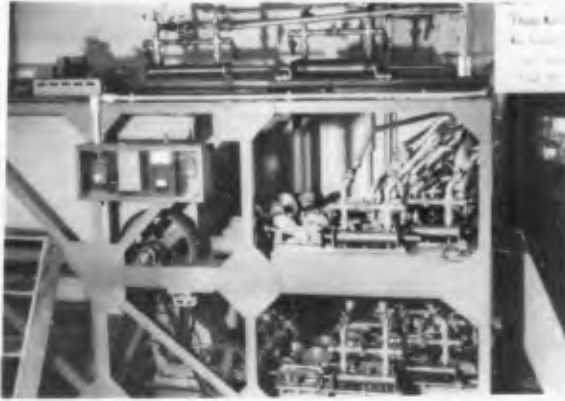
Photo.1   Composite wave generator
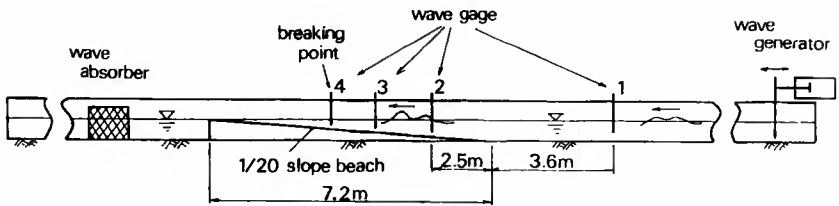
Fig.1   Experimental apparatus(composite waves)

Table 1 Experimental conditions(composite waves)

Run No.	Wave period	Water depth				Wave height at h_1
		Gauge No.1 uniform depth	No.2	No.3	No.4	
	T(sec)	h_1(cm)	h_2(cm)	h_3(cm)	h_4(cm)	H_1(cm)
1	1.00	36.0	23.5	14.3	6.0	1.2
2	0.71	36.0	23.5	14.3	6.0	1.8
3		36.0	23.5	14.3	6.0	
4	1.20	36.0	23.5	14.7	8.8	2.0
5	0.85	36.0	23.5	14.7	8.8	3.0
6		36.0	23.5	14.7	8.8	
7	1.40	36.0	23.5	14.2	7.2	0.7
8	0.91	36.0	23.5	14.2	7.2	1.9
9		36.0	23.5	14.2	7.2	
10	1.60	36.0	23.5	15.5	8.3	1.3
11	1.13	36.0	23.5	15.5	8.3	2.9
12		36.0	23.5	15.5	8.3	
13	1.80	36.0	23.5	15.5	9.1	2.5
14	1.27	36.0	23.5	15.5	9.1	1.8
15		36.0	23.5	15.5	9.1	
16	2.00	36.0	23.5	15.0	8.6	2.2
17	1.41	36.0	23.5	15.0	8.6	1.5
18		36.0	23.5	15.0	8.6	
19	2.20	36.0	23.5	15.2	8.1	2.1
20	1.56	36.0	23.5	15.2	8.1	1.3
21		36.0	23.5	15.2	8.1	
22	2.40	36.0	23.5	15.5	8.6	1.8
23	1.70	36.0	23.5	15.5	8.6	1.3
24		36.0	23.5	15.5	8.6	
25	2.60	36.0	23.5	16.1	9.9	2.8
26	1.84	36.0	23.5	16.1	9.9	2.4
27		36.0	23.5	16.1	9.9	

Let the lower frequency of two monochromatic waves used be $f^{(1)}$, the higher $f^{(2)}$, and two times these elementary frequencies $f^{(11)}$ and $f^{(22)}$ respectively. Then, because of the nonlinear interaction of 2nd order, it is expected that further two components frequencies of which are the summation and difference of $f^{(1)}$ and $f^{(2)}$, that is, $f^{(1+2)}$ and $f^{(2-1)}$ exist in addition to above mentioned four components. Let two elementary wave periods be $T^{(1)}$ and $T^{(2)}$. Then the following relationships are given[6].

$$
\left.
\begin{array}{ll}
f^{(1)}=1/T^{(1)}=5/(5\,T^{(1)}), & f^{(22)}=2f^{(2)}\doteqdot14/(5\,T^{(1)}), \\
f^{(2)}=1/T^{(2)}=1/(T^{(1)}/\sqrt{2})\doteqdot7/(5\,T^{(1)}), & f^{(1+2)}=f^{(1)}+f^{(2)}\doteqdot12/(5\,T^{(1)}), \\
f^{(11)}=2\,f^{(1)}=10/(5\,T^{(1)}), & f^{(2-1)}=f^{(2)}-f^{(1)}\doteqdot2/(5\,T^{(1)}).
\end{array}
\right\}
\quad \cdots\cdots\cdots\cdots (1)
$$

c) Examples of experimental results
     Fourier analyses were carried out and the spectra of the component wave height were obtained for all measuring points of all experimental cases in Table 1. A computer KDC-II of Kyoto University Computation Center was used for the Fourier analysis. Fig.2 shows the component wave height spectra of run No.6(composite waves) $H^{(\ )}$ in the uniform depth region and at the breaking point(Gauge No.4). The unit of abscissa is $1/(5T^{(1)})$. As seen in Eq.(1), 2, 5, 7, 10, 12 and 14 of the abscissa correspond to $f^{(2-1)}$, $f^{(1)}$, $f^{(2)}$, $f^{(11)}$, $f^{(1+2)}$ and $f^{(22)}$ respectively. In the uniform depth region, as shown in the figure (1), all of four secondary components $H^{(11)}$, $H^{(22)}$, $H^{(1+2)}$ and $H^{(2-1)}$ are considerably smaller than two elementary components $H^{(1)}$ and $H^{(2)}$. On the other hand, at the breaking point, as seen in the figure (2), all of four secondary components grow up and are not negligible.

RANDOM WAVES

a) Experimental apparatus
     The same wave tank as in the experiments of composite waves was used. In this case, an electro-hydraulic random wave generator(see Photo.2) was used. This random wave generator is installed at the opposite tank end of the composite wave generator. Several kinds of input signal are available in this generator. In this experiment, the modified random noises passing through 15 bandpass filters having the center frequencies ranged from 0.2Hz to 5.0Hz were utilized.

     As seen in Fig.3, a uniform sloping beach was installed in the middle part of the tank as in the experiments of composite waves. This beach was made of alminium plates, and the slope of the beach was 1/20. Its length was 9.4m and the height of the beach tail was 47cm. The water depth in the uniform depth region was kept constant(47cm) to make negligible the effect of wave reflection as in the case of composite waves.

     In the experiments, four wave gauges and the magnetic tape recorder were also used. The breaking point of random waves varies with time and could not be determined. So the depths of three measuring points on the beach were fixed as 31cm, 20cm and 10.5cm respectively during the experiments independently of the breaking point.

b) Procedure of experiment and analysis
     At first, the experiments of random waves having power spectral density distribution of narrow band were carried out. Such random waves were considered to correspond to the monochromatic waves and generated by using one of the bandpass filters. Secondly, the experiments of random waves having two main peaks in power
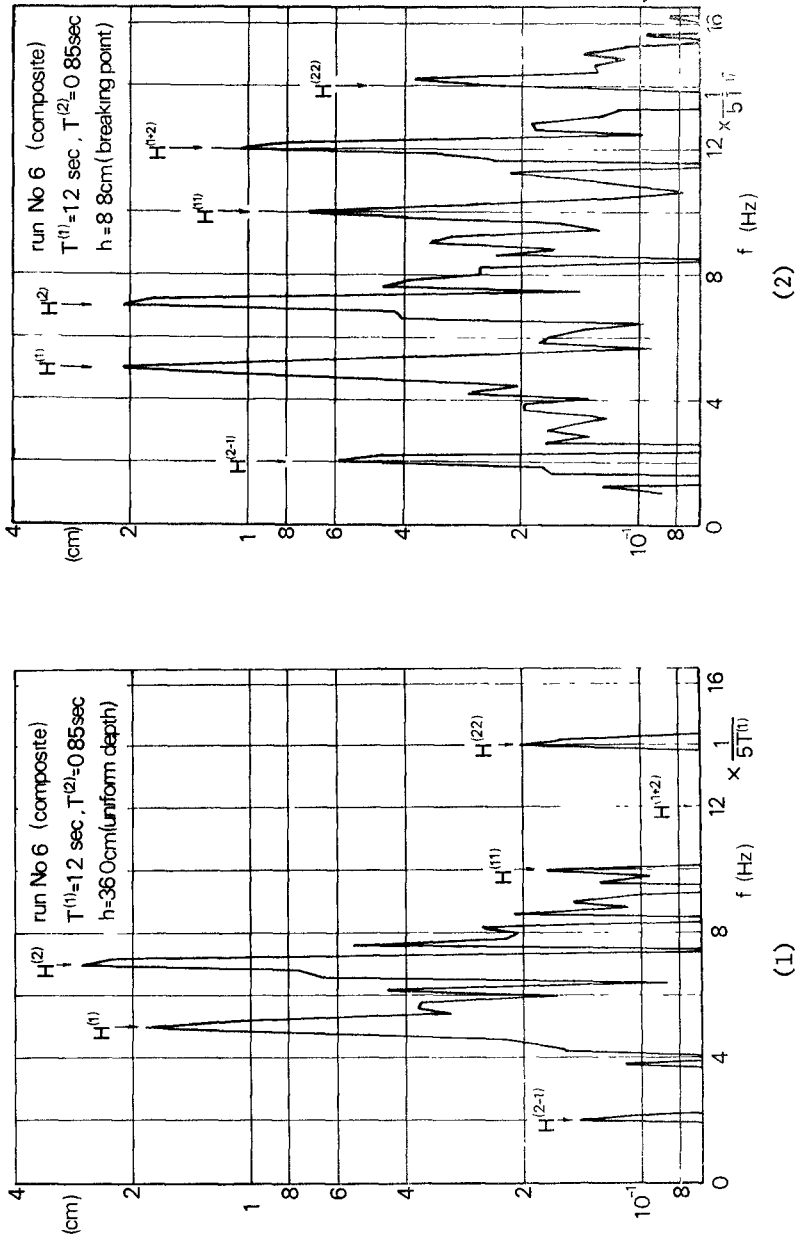
Fig.2 Example of component wave height spectra of composite waves

Photo. 2   Random wave generator
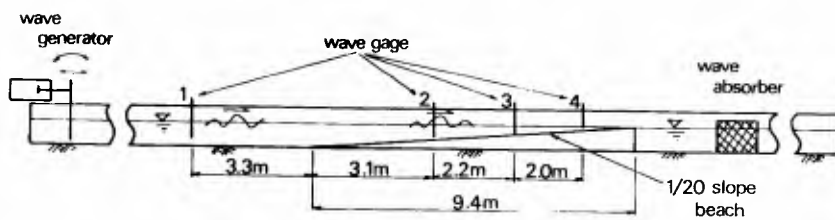
Fig. 3   Experimental apparatus (random waves)

spectral density distribution were carried out. These random waves were considered to correspond to the composite waves having two elementary components and generated by using two of the bandpass filters. As in the case of composite waves, the analog data in the magnetic tape recorder were converted into the digital data with the time increment of 0.08sec by the A-D convertor for the numerical computations. The experimental conditions are shown in Table 2.

Power spectral densities were calculated for all records of water level variation by Blackman-Tukey's method, in which the number of data was 2000, the number of maximum lag 200, and the degree of freedom about 20. Also KDC-II of Kyoto University Computation Center was used for the numerical computations.

c) Examples of experimental results
Fig.4 shows the power spectral density distributions at four measuring points in Run No.4. In the uniform depth region(full line), the main peak of power spectrum exists at about 0.8Hz and the subpeak at about two times the main peak frequency(1.6Hz). As the water depth decreases, the power of main peak decreases after the initial increase and the power of subpeak increases after the intial decrease. At the shallowest measuring point(chain line), the power of subpeak grows up to more than 30% of that of main peak.

CHANGES OF ELEMENTARY AND SECONDARY COMPONENT WAVE HEIGHTS OF COMPOSITE WAVES

a) Change of elementary component wave height of finite amplitude waves in
   shoaling water
In Fig.5, the solid and chain curves are the shoaling curves of finite and small amplitude waves respectively. As indicated in the figure, solid curves of the right hand side group are calculated by using the energy flux of the third order approximation of Stokes waves and those of the left hand side group calculated by using the second approximation of hyperbolic waves[7]. It is assumed that the wave height change of waves of a given deep-water wave steepness obeys the rule shown by these shoaling curves and the wave profile is represented by the summation of the elementary component, the component of two times the elementary frequency(the second harmonics) and the component of three times the elementary frequency(the third harmonics) as the third order approximation of Stokes waves[8].

The wave profile of 3rd order approximation of Stokes waves is given by Eq. (2) where L is the wave length, $\theta=2\pi x/L-2\pi t/T$, x the coordinate in the direction

$$\eta/L=A_1 \cdot \cos\theta + A_2 \cdot \cos 2\theta + A_3 \cdot \cos 3\theta \qquad\qquad (2)$$

of wave propagation and T the wave period. Let the elementary component wave height be $H^{(1)}$ and the deep-water wave height H_0. Then the ratio $H^{(1)}/H_0$ is written as

$$H^{(1)}/H_0 = 2A_1 \cdot (H_0/L_0)^{-1} \cdot (h/L)^{-1} \cdot h/L_0 , \qquad\qquad (3)$$

where L_0 is the deep-water wave length and h the water depth. A_1 is given by

$$A_1 = a/L, \quad H/L = 2 \cdot a/L + 2\pi^2(a/L)^3 \cdot f_3 , \qquad\qquad (4)$$

$$f_3(h/L) = \frac{3}{16} \cdot \left\{ 8\left(\cosh\frac{2\pi h}{L}\right)^6 + 1 \right\} \Big/ \left(\sinh\frac{2\pi h}{L}\right)^6 . \qquad (5)$$

Since the value of h/L is determined by giving the values of H_0/L_0, $H^{(1)}/H_0$ can

Table 2   Experimental conditions(random waves)

Run No.	Filter frequency	Water depth			
		Gauge No.1 uniform depth	No.2	No.3	No.4
	f(Hz)	h_1(cm)	h_2(cm)	h_3(cm)	h_4(cm)
1	1.28	46.7	31.0	19.9	10.3
2	1.25	46.8	31.1	20.0	10.4
3	1.00	46.8	31.1	20.0	10.4
4	0.80	46.7	31.0	19.9	10.3
5	0.50	46.7	31.0	19.9	10.3
6	1.60,1.00	46.7	31.0	19.9	10.3
7	1.00,0.63	46.7	31.0	19.9	10.3
8	0.80,0.50	46.7	31.0	19.9	10.3
9	0.63,0.40	46.7	31.0	19.9	10.3
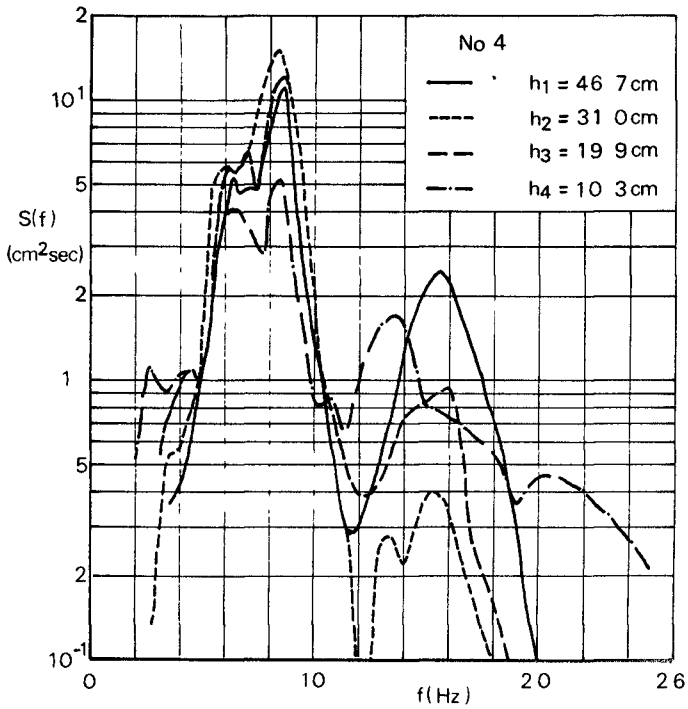
Fig.4   Example of power spectral densities of random waves
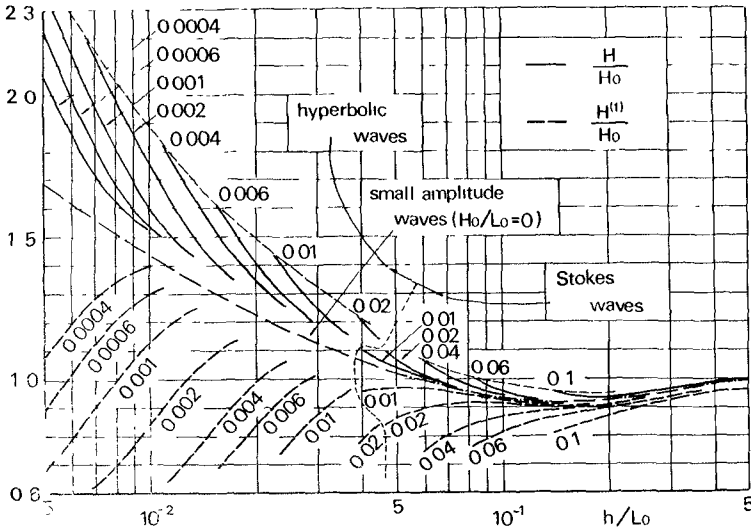
Fig.5   Change of elementary component wave height based on shoaling theory of finite amplitude waves
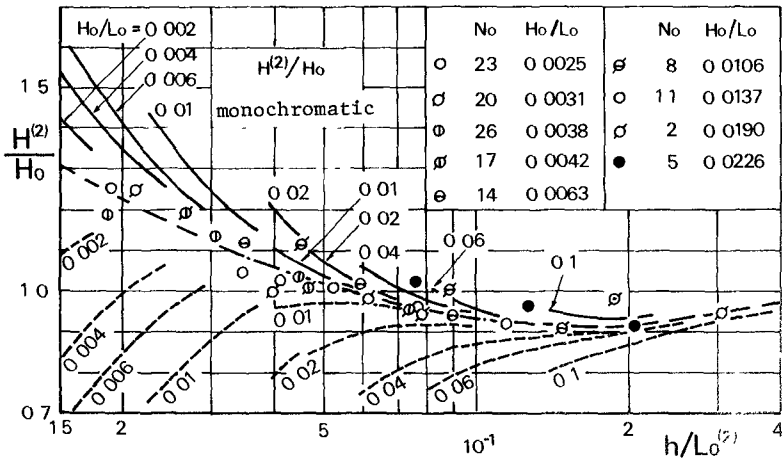
(1)

Fig.6   Changes of elementary component wave heights of monochromatic and composite waves

be obtained by using Eq.s (4), (5) and (3). The broken curves in Fig.5 show the changes of $H^{(1)}/H_0$ calculated in this manner. It should be noticed that while the wave height increases in shoaling water the elementary component wave height decreases.

b) Effects of internal viscosity and boundary friction
    Before the change of elementary component wave height is discussed, the effects of internal viscosity and boundary friction were examined. In order to estimate the effect of bottom friction, the theoretical result for wave height change on a uniform sloping beach derived by Tsuchiya and Inoue[9] was utilized, which takes into account the effect of bottom friction. It was found that the effect of bottom friction on the wave height reduction is about 1%. Considering that the effects of internal viscosity and sidewall friction are the same order of magnitude as that of bottom friction, the effects of internal viscosity and boundary friction are expected to be the same order of magnitude as the experimental errors and therefore negligible.

c) Changes of elementary component wave heights of monochromatic and composite
    waves
    Changes of two elementary component wave heights $H^{(1)}$ and $H^{(2)}$ are compared with the theoretical curves in Fig.5. The value of deep-water wave length is calculated by using the relationship of small amplitude waves $L_0 = gT^2/(2\pi)$ from two elementary wave periods $T^{(1)}$ and $T^{(2)}$. Unfortunately, the water leakage through the gap between the beach plate and the tank bottom near the toe of beach was inevitable. Therefore, it was expected that the some wave energy loss existed between two measurement points in the uniform depth region and on the beach. After all, the data in the uniform depth region were abandoned and the deep-water wave height H_0 was determined by assuming that both values of $H^{(1)}/H_0$ and $H^{(2)}/H_0$ at the water depth h_2 agree with the theoretical values of shoaling curve of small amplitude waves(the chain line in Fig.5).

    Fig.6 (1)∿(3) show the experimental results and the theoretical curves in Fig.5. Fig.6 (1) shows the results of the elementary component $H^{(2)}$ of the monochromatic waves of shorter period, Fig.6 (2) the elementary component of longer period $H^{(1)}$ of the composite waves, and Fig.6 (3) the elementary component of shorter period $H^{(2)}$ of the composite waves. As seen in the figure (1), the elementary component wave height $H^{(2)}$ of the monochromatic waves of the shorter period does not show such decrease that the theory predicts. The experimental values scatter around the shoaling curve of small amplitude waves. The experimental results of the elementary component wave height $H^{(1)}$ of the monochromatic waves of longer period are not presented here, but those show the same behaviour.

    On the other hand, in Fig.6 (2), the elementary component wave heights $H^{(1)}$ of longer period of the composite waves, except for Runs No.6 and No.9, depart from the curve by the small amplitude wave theory and decrease. However, as seen from the experimental values of deep-water wave steepness, the rates of decrease in experimental values are smaller than those in theoretical values. In Fig.6 (3), the elementary component wave heights $H^{(2)}$ of shorter period of composite waves decrease more rapidly than the theoretical curves. In any way, it is interesting that the decrease in elementary component wave height of composite waves in shoaling water is explained qualitatively by the theory of elementary component wave height change of finite amplitude waves in shoaling water.

d) Changes of secondary component wave heights of monochromatic and composite
    waves
    The linear composite waves having two elementary components are represented

(2)

(3)
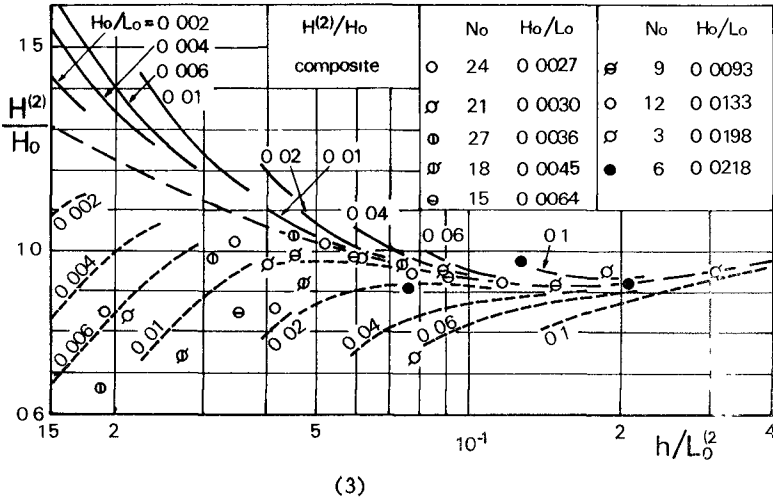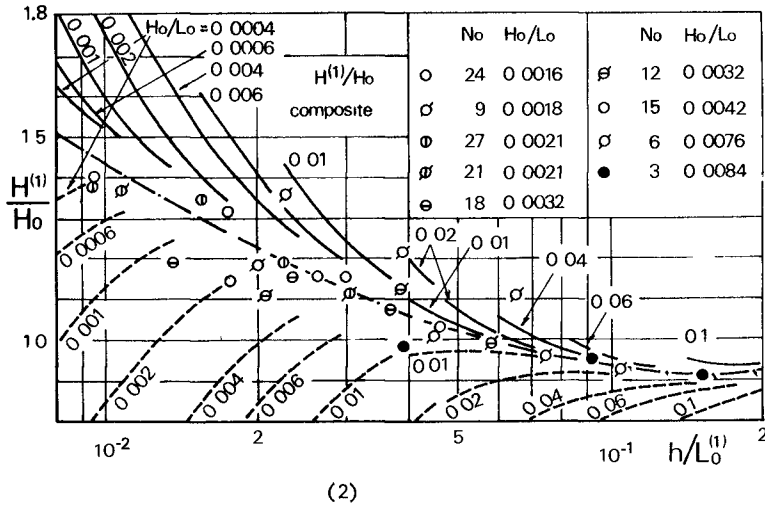
Fig.6   Changes of elementary component wave heights of monochromatic
        and composite waves

as follows:

$$\eta = a_1 \cdot \cos k_1 (x - c_1 t) + a_2 \cdot \cos k_2 (x - c_2 t) , \qquad - \quad - \quad - \tag{6}$$

where the suffix means the elementary component, k is the wave number and c the wave celerity. c_1 and c_2 are related to k_1 and k_2 respectively with the small amplitude wave theory. Let two elementary component wave heights be H_1 and H_2. Then $H_1 = 2a_1$ and $H_2 = 2a_2$. Four secondary components are produced due to the nonlinear interaction of the second order. Hamada[6) derived the following relations of these four secondary component wave heights H_{11}, H_{22}, H_{1+2} and H_{2-1} theoretically:

$$H_{11} = \frac{2}{g}\left\{ 2 k_1 c_1 B_{11} \coth 2 k_1 h + \frac{1}{2} b_1^2 k_1^2 - \frac{1}{4} b_1^2 k_1^2 (\coth^2 k_1 h - 1) \right\}, \quad - \quad - \quad - \quad - \quad - \tag{7}$$

$$H_{22} = \frac{2}{g}\left\{ 2 k_2 c_2 B_{22} \coth 2 k_2 h + \frac{1}{2} b_2^2 k_2^2 - \frac{1}{4} b_2^2 k_2^2 (\coth^2 k_2 h - 1) \right\}, \quad - \quad - \quad - \quad - \tag{8}$$

$$H_{1+2} = \frac{2}{g}\left\{ (c_1 k_1 + c_2 k_2) B_{1+2} \coth (k_1 + k_2) h + \frac{1}{2} (k_1^2 c_1 b_1 a_2 + k_2^2 c_2 b_2 a_1) - \frac{1}{2} b_1 b_2 k_1 k_2 (\coth k_1 h \coth k_2 h - 1) \right\}, \tag{9}$$

$$H_{2-1} = \frac{2}{g}\left\{ (c_2 k_2 - c_1 k_1) B_{2-1} \coth (k_2 - k_1) h + \frac{1}{2} (k_1^2 c_1 b_1 a_2 + k_2^2 c_2 b_2 a_1) - \frac{1}{2} b_1 b_2 k_1 k_2 (\coth k_1 h \coth k_2 h + 1) \right\}, \tag{10}$$

where $b_1 = a_1 \times c_1$, $b_2 = a_2 \times c_2$,

$$B_{11} = \frac{-\frac{3}{2} b_1^2 k_1^3 c_1 (\coth^2 k_1 h - 1)}{-4 k_1^2 c_1^2 \coth 2 k_1 h + 2 k_1 g}, \quad ----- \quad -- \quad ---------- \quad ----- \tag{11}$$

$$B_{22} = \frac{-\frac{3}{2} b_2^2 k_2^3 c_2 (\coth^2 k_2 h - 1)}{-4 k_2^2 c_2^2 \coth 2 k_2 h + 2 k_2 g}, \quad ----- \quad ----- \quad -- \quad -------- \tag{12}$$

$$B_{1+2} = \frac{b_1 b_2 k_1 k_2 (c_1 k_1 + c_2 k_2)(1 - \coth k_1 h \coth k_2 h) - \frac{1}{2} b_1 k_1^3 a_2 c_1^2 (\coth^2 k_1 h - 1) - \frac{1}{2} b_2 k_2^3 a_1 c_2^2 (\coth^2 k_2 h - 1)}{-(c_1 k_1 + c_2 k_2)^2 \coth (k_1 + k_2) h + (k_1 + k_2) g}, \tag{13}$$

$$B_{2-1} = \frac{b_1 b_2 k_1 k_2 (c_2 k_2 - c_1 k_1)(1 + \coth k_1 h \coth k_2 h) - \frac{1}{2} b_1 k_1^3 a_2 c_1^2 (\coth^2 k_1 h - 1) + \frac{1}{2} b_2 k_2^3 a_1 c_2^2 (\coth^2 k_2 h - 1)}{-(c_1 k_1 - c_2 k_2)^2 \coth (k_1 - k_2) h + (k_1 - k_2) g} \tag{14}$$

In order to compare the experimental values of secondary component wave heights with Hamada's theoretical values, the composite waves at uniform depths h_i (i=1∿4), which correspond to the water depths at measuring points, are considered. In this case, the experimental values $H^{(1)}$, $H^{(2)}$, $T^{(1)}$ and $T^{(2)}$ are adopted as H_1, H_2 and two wave periods. Fig.7 (1)∿(4) show the comparisons of experimental values of four secondary component wave heights with theoretical ones calculated in such a manner. Fig.7 (1) and (2) show the results of Run No.s 1∿3 which form one group. Fig.7 (3) and (4) show the results of Run No.s 16∿18 which form the other group. The values of L_0 were calculated by using the relationship of small amplitude waves and the frequencies of secondary components. As seen in the figures, the behaviours of increase in the experimental values of four secondary component wave heights shown with thick lines are explained qualitatively by the theoretical lines shown with thin lines.

(1)

(2)

(3)

(4)
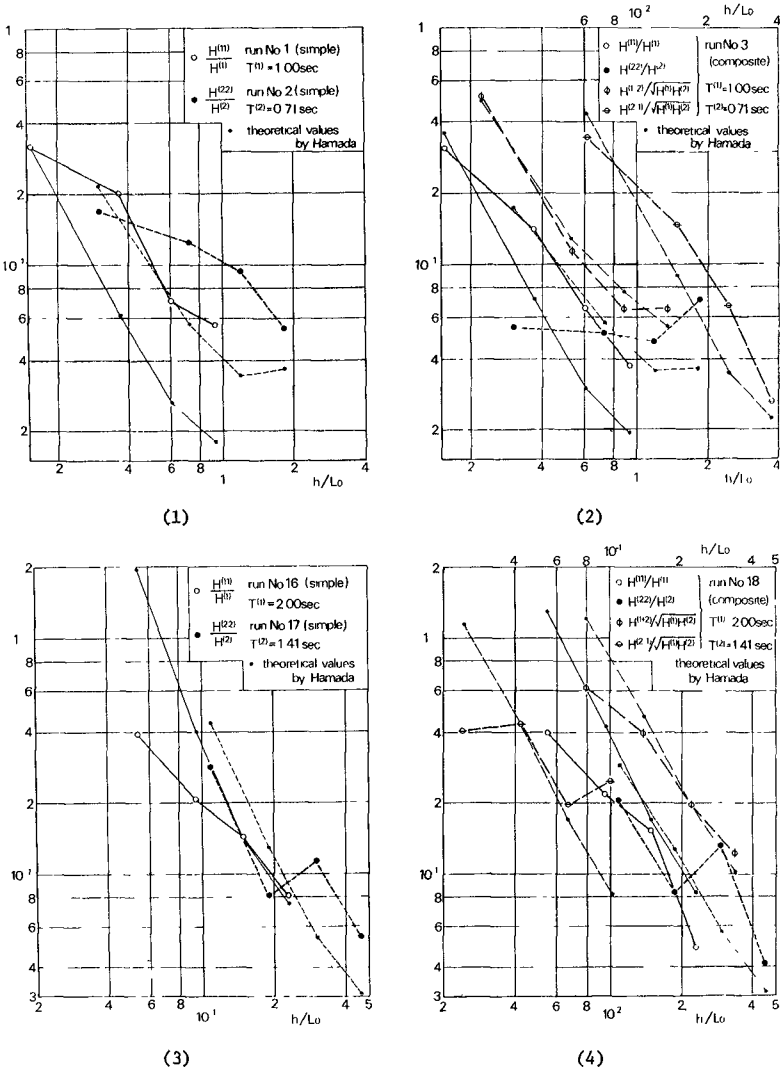
Fig.7 Changes of secondary component wave heights of monochromatic and composite waves

CHANGES OF ELEMENTARY AND SECONDARY PEAK POWERS OF RANDOM WAVES

a) Changes of elementary peak power of random waves having one main peak

Fig.4 shows the change of power spectra of Run No 4 in the case of random waves having one predominant frequency in power spectra. Although the predominant frequency changes slightly at four measuring points, it is denoted as $f^{(1)}$ to correspond to the elementary component frequency of the composite waves. The subpeak appears at about two times the value of $f^{(1)}$ which is denoted as $f^{(11)}$. The power spectral densities $S(f^{(1)})$ and $S(f^{(11)})$ at these two frequencies $f^{(1)}$ and $f^{(11)}$ are called the elementary and secondary powers respectively. The changes of values of $\sqrt{S(f^{(1)})}$ in shoaling water are discussed in comparison with the theoretical curves of elementary component wave height change of finite amplitude waves shown with the broken line in Fig.5

The values of L_0 were calculated by using the relationship of small amplitude waves and the values of $f^{(1)}$. The power spectral density $S_0(f^{(1)})$ at the frequency $f^{(1)}$ in deep water was assumed as the quantity corresponding to the deep-water wave height H_0. This quantity was calculated by assuming that the value of $\sqrt{S(f^{(1)})/S_0(f^{(1)})}$ agrees with that of the shoaling curve of small amplitude waves(chain line) in the uniform depth region.

Fig.8 (1) shows the experimental results of $\sqrt{S(f^{(1)})/S_0(f^{(1)})}$ of random waves having one main peak in comparison with the theoretical curves of elementary component wave height change of finite amplitude waves. As seen in the figure, the experimental values scatter considerably. The experimental values of Run No.s 4 and 3 are much larger than the values of theoretical curves(broken line). However, the experimental values of Run No.s 5, 2 and 1 show the behaviour of decrease as well as the theoretical curves. The parameter of theoretical curves is the deep-water wave steepness H_0/L_0. For the purpose of comparison, a dimensional quantity $f^{(1)2}S_0(f^{(1)})^{1/2}$ is calculated as the quantity corresponding to H_0/L_0 of monochromatic waves. However, in the case of random waves having one main peak, it is difficult to find the relationship between this dimensional parameter and the change of elementary peak power.

In Fig.8 (1), the experimental values by Sawaragi and Tabata[10] are also shown. The decrease of elementary peak power is explained qualitatively by the theoretical curves.

b) Changes of elementary peak power of random waves having two main peaks

Fig 8 (2) shows the experimental values of two elementary peak powers in the case of random waves of Run No s 6∿9. In the figure, $S(f^{(1)})$ and $S(f^{(2)})$ mean the peak powers of the lower and higher frequencies respectively. In this case, the experimental values of all runs decrease in the same manner as the theoretical curves Further, the larger the value of the parameter $f^{(1)2}S_0(f^{(1)}))^{1/2}$ corresponding to the deep-water wave steepness, the more rapidly the experimental value of power decreases. As in the case of composite waves, it is interesting that the decrease of two elementary peak powers of random waves is explained qualitatively by the theoretical curves of elementary component wave height change of finite amplitude waves.

c) Changes of secondary peak powers of random waves

The case shown in Fig.4 is of random waves having one main peak, and it is easy to detect the secondary peak in the power spectral density distribution. However, in the random waves having two main peaks Run No.s 6∿9, four secondary peaks must exist and it is difficult to detect them in the distribution. Therefore, only the secondary peak powers of random waves having one main peak are discussed
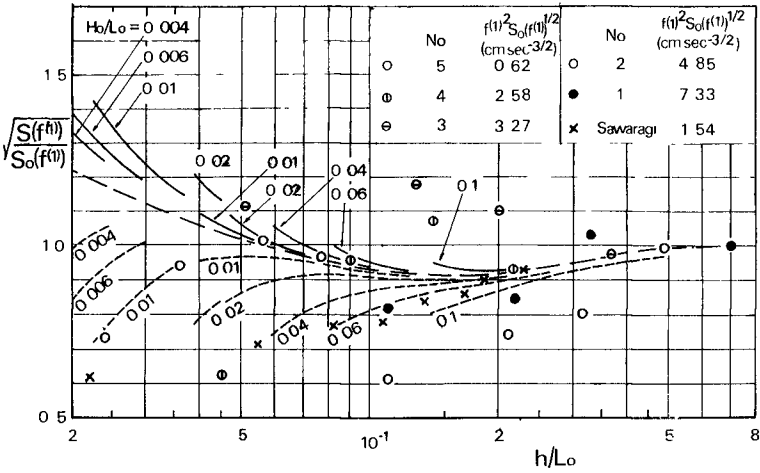
Fig. 8 (1)   Changes of elementary component powers of random waves
(one main peak)
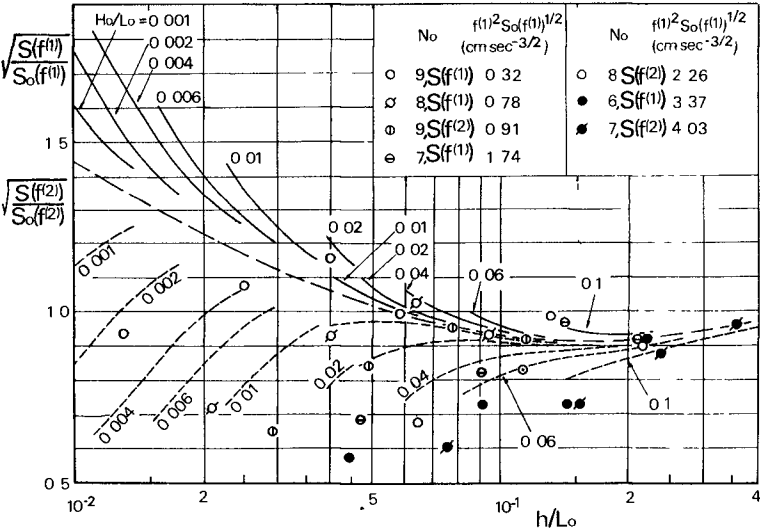
Fig. 8 (2)   Changes of elementary component powers of random waves
(two main peaks)

here.

Let the power spectral density of linear random waves in uniform depth be $S_1(\omega)$, in which the spectrum is two-sided and ω is the angular frequency $2\pi f$. Hamada[6] derived the secondary power spectral density $S_2(\lambda)$ due to nonlinear interaction of 2nd order in uniform depth as follows:

$$S_2(\lambda) = \int_{-\infty}^{\infty} K(\omega, \lambda) \cdot S_1(\lambda - \omega) \cdot S_1(\omega) d\omega , \quad \cdots \cdots \cdots \cdots \cdots \cdots \cdots \cdots \cdots (15)$$

where $K(\omega, \lambda)$ is given as

$$K(\omega, \lambda) = \frac{1}{4}\left[\frac{gkk(\lambda-\omega)}{\omega(\lambda-\omega)} + \frac{\omega(\lambda-\omega)}{g} - \frac{\lambda^2}{g} + \lambda^2\left\{ \frac{g(\lambda-\omega)k^2 + g\omega k^2(\lambda-\omega)}{\omega(\lambda-\omega)\lambda} \right. \right.$$

$$\left. \left. + \frac{2gkk(\lambda-\omega)}{\omega(\lambda-\omega)} + \frac{\omega(\lambda-\omega)}{g} - \frac{\lambda^2}{g} \right\} \middle/ \{g|k + k(\lambda-\omega)| \cdot \tanh|k + k(\lambda-\omega)|h - \lambda^2\} \right] , \quad \cdots \cdots (16)$$

and k and $k(\lambda-\omega)$ are wave numbers which are functions of ω and $\lambda-\omega$ respectively.

In order to compare experimental values with the theoretical ones above mentioned, the random waves in the same uniform depth as the water depth at each measuring point were assumed. As the linear power spectral density $S_1(\omega)$, the distribution consisting of an elementary peak and the base shown by a chain line in Fig.9 is adopted. The peak expressed by a broken line is the theoretical secondary peak power spectral density calculated by Eq.(15). Fig.10 shows the changes of secondary peak powers $S(f^{(11)})$ of Run No.s 2∿5 in comparison with the theoretical secondary peak powers calculated in such a manner. L_0 in the abscissa was the calculated deep-water wave length of small amplitude waves by using the frequency $f^{(11)}$. As seen in the figure, the experimental values of secondary peak powers $S(f^{(11)})$ increase, in some cases after the initial decrease with decrease in the water depth, and are not negligible compared with the elementary peak powers. This experimental behaviour is explained qualitatively by Hamada's theory.

CONCLUSIONS

In this investigation, the mechanism of transformation of irregular waves (composite and random waves) in shoaling water was discussed experimentally. The damping due to internal viscosity and boundary friction was found to be negligible because it is of the same order of magnitude as the experimental error.

The elementary component wave heights of composite waves consisting of two elementary components and the elementary peak powers of random waves having one or two main peaks decrease, in some cases after the initial increase, with decrease in the water depth. This was explained by the theory of elementary component wave height change of finite amplitude waves in shoaling water derived from the shoaling curves of finite amplitude waves.

The four secondary component wave heights of composite waves consisting of two elementary components and the secondary peak powers of random waves having one main peak increase, in some cases after the initial decrease with decrease in the water depth, and become to be not negligible compared with the elementary component wave heights and powers. This was explained by the theory of nonlinear interaction of 2nd order of composite and random waves in uniform depth.
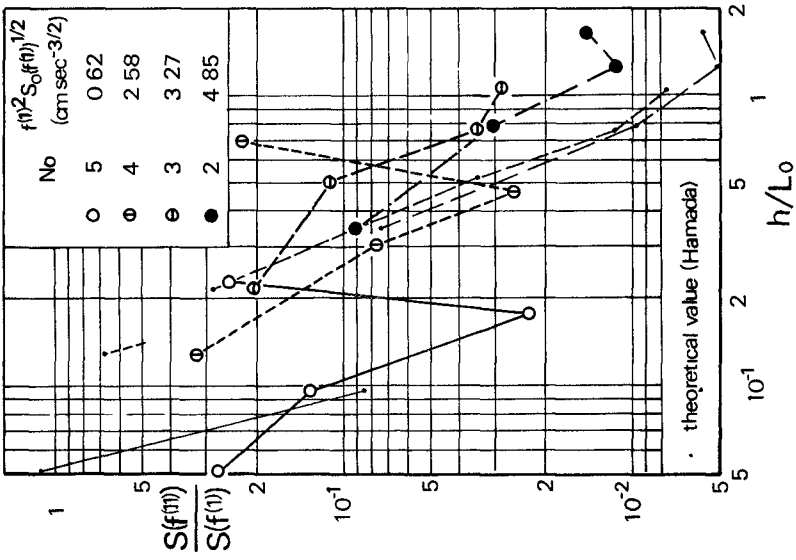
Fig.10 Changes of secondary component powers of random waves
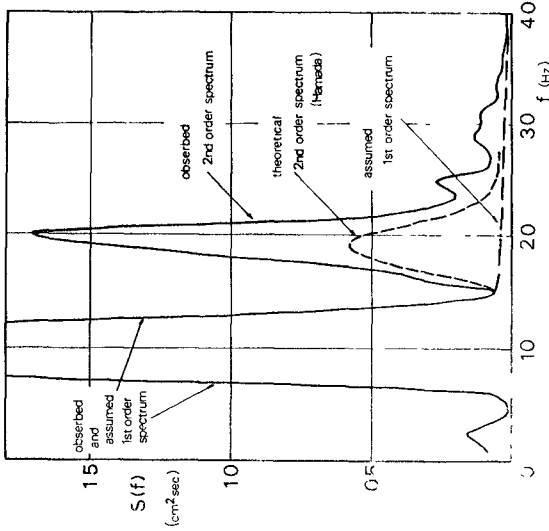
Fig.9 Theoretical distribution of secondary component power of random waves

REFERENCES

1) Bretschneider, C. L. : Modification of wave spectra on the continental shelf
    and in the surf zone, Proc. 8th Conf. Coastal Engineering, pp.17-33, 1963.
2) Tang, F. L. W. and S. H. Ou : Researches on the deformation of wave spectra
    in intermediate water area by calculation, Proc. 13th Conf. Coastal
    Engineering, pp.271-288, 1973.
3) Hasselmann, K.   Weak Interaction Theory of Ocean Waves, Basic Developments
    in Fluid Dynamics, Vol.2, pp.117-182, Academic Press, 1968.
4) Mitsuyasu, H. : A note on the nonlinear energy trasfer in the spectrum of
    wind-generated waves, Rep. Res. Inst. Appl. Mech., Kyushu Univ., Vol.XVI,
    No.54, pp.251-264, 1968
5) Iwagaki, Y., Y. Tsuchiya and A. Ishida : A generator of irregular waves
    and analysis of generated waves, Proc. 13th Cong. International Association
    for Hydraulic Research, Vol.5-1, pp.289-292, 1969
6) Hamada, T. : The secondary interactions of surface waves, Rep. Port and
    Harbour Res. Inst. No.10, 1965
7) Iwagaki, Y. : Hyperbolic waves and their shoaling, Proc. 11th Conf. Coastal
    Engineering, pp.124-144, 1969.
8) Skjelbreia, L. : Gravity Waves, Stokes' Third Order Approximation, Table
    of Functions, Council on Wave Research, The Engineering Foundation, 1959.
9) Tsuchiya, Y. and M. Inoue   Basic study on wave damping due to bottom friction
    (1), Proc. 8th Conf. Coastal Engineering in Japan, pp.19-24, 1961(in
    Japanese).
10) Sawaragi, T. and T. Tabata : Transformation of irregular waves in decay area,
    Proc. 19th Conf. Coastal Engineering in Japan,pp 143-148,1972(in Japanese).

CHAPTER 24

CRITICAL TRAVEL DISTANCE OF WAVES IN SHALLOW WATER

by

Winfried Siefert[*]

Abstract

A new criterion for shallow water wave analysis is evalua-
ted from prototype data off the German coast on the reef
and wadden sea areas south of the outer Elbe river.

Correlations of mean wave heights $\bar{H}$ with mean wave peri-
ods $\bar{T}$, and wave height distribution factors $C_{1/3} = \dfrac{H_{1/3}}{\bar{H}}$
respectively show that the mean periods and both complete
height and period distributions of waves in shallow water
can be expressed as functions of mean height and topo-
graphy. So the mean wave height $\bar{H}$ proves to be the cha-
racteristic parameter for the description of the complete
shallow water wave climate. The upper envelop of the va-
lues $\bar{H}$ = f (meteorology, topography) is defined as the
case of fully developed sea, which leads to the function
of the highest mean wave heights $\bar{H}_{max}$. This parameter is
plotted with 3 topographical parameters:

    depth of water d,

    distance s from deep water area, and

    mean wave steepness δ .

The curves $\dfrac{\bar{H}_{max}}{d}$ versus s for different d show distinct
maxima for varying distances $s_{crit.}$ from the deep water

[*] Dr.-Ing., Strom- und Hafenbau Hamburg, Coastal Engineer-
ing Research Group "Neuwerk", 219 Cuxhaven, West Germany

area. This critical travel distance of waves in shallow
water is dependent on the depth of water only. It re-
presents the length, on which the waves grow before the
beginning decay due to shoaling effects:

$$s_{crit.} = 0,264 \cdot (d + 1)$$

with s in kilometres and d in metres. It points out that
the distance from deep water, where the shallow water
wave spectrum reaches its critical maximum, grows with
the depth of water. Storm tides with extreme water
levels transfer the line of critical travel distances
coastward, and the probability of destruction rises, as
this effect brings a larger increase in wave height
than usually recognized.

Introduction

The Port of Hamburg Authority is planning a deep sea
harbor at the outer entrance of the Elbe river. Much
preliminary work has been done concerning tides,
currents, wind conditions etc. and also waves. Investi-
gations in the estuary, off the German North Sea coast,
in water depths between 0.3 m and 10 m for more than
10 years at 29 wave stations (fig. 1) provided the basic
material for the evaluation of a new criterion for
shallow water wave analysis. Before this can be treated
in detail, some general remarks are necessary:

Analyses of about 15,000 wave records in terms of S-M-B-
method showed that mean periods and both complete height
and period distributions of waves in shallow water can
be expressed as functions of mean height $\bar{H}$ and topography.

The dependence upon the meteorological situation is not
analyzed here because of the following aspects:
From the engineer's point of view often the highest
possible waves are of special interest, i.e. the upper
envelop of the strongly scattering values

$$\bar{H} = f \text{ (meteorology, topography)}.$$
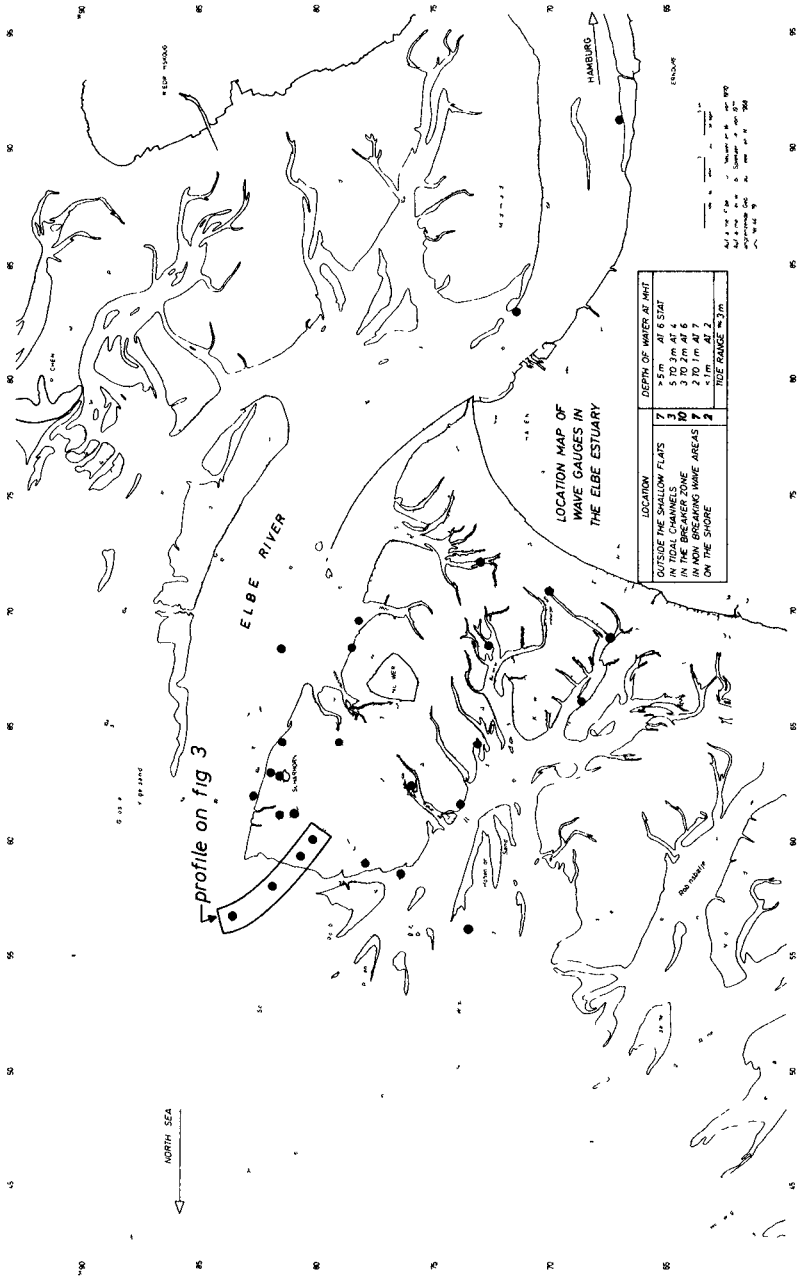
Fig. 1

Wave Investigations in the Elbe Estuary

This leads to functions for the highest possible mean wave heights $\overline{H}_{max}$ for fully arisen sea, which become almost horizontal in shallow water (i.e. independent of the wind conditions) at high wind forces from 6 to 7 Bft onwards.

As structural design is nearly always concerned with wave conditions at higher wind speeds, the simplification of neglecting special meteorological characteristics proves to be admissable.

Topographical Parameters

Under this supposition the knowledge of $\overline{H}_{max}$ as the representative wave parameter is decisive. As its value can be calculated as a function of topography, the latter has to be expressed by parameters. The most common topographical parameter is the depth of water d, but it is surely not the only important one. This may be stressed by fig. 2, showing the highest single wave H_{max} in a natural spectrum as a function of d. There is a wide range of offers with a scattering up to 100%, indicating that important connections were neglected. Fig. 3 with a typical profile of decreasing water depth in the breaker zone of the Scharhornriff (see fig. 1) leads to the conclusion that there is of course a strong influence of d, but not all of the shown parameters do change continuously with d, especially the steepness factor and the wave height distribution factor $C_{1/3} = H_{1/3}/\overline{H}$. Wave steepness decreases from 0.005 to 0.0025 and then remains constant. It turns out that the mean steepness is only a weak function of d and much more an indicator for the dominating wave character, i.e. whether waves are breaking or not, for instance.

The wave height distribution factor also decreases, from 1.52 to 1.40, but then increases to 1.45, i.e. the wave height distribution at first narrows and then widens again (SIEFERT, 1973).

Data from different regions indicate that there are influences of other topographical parameters that have
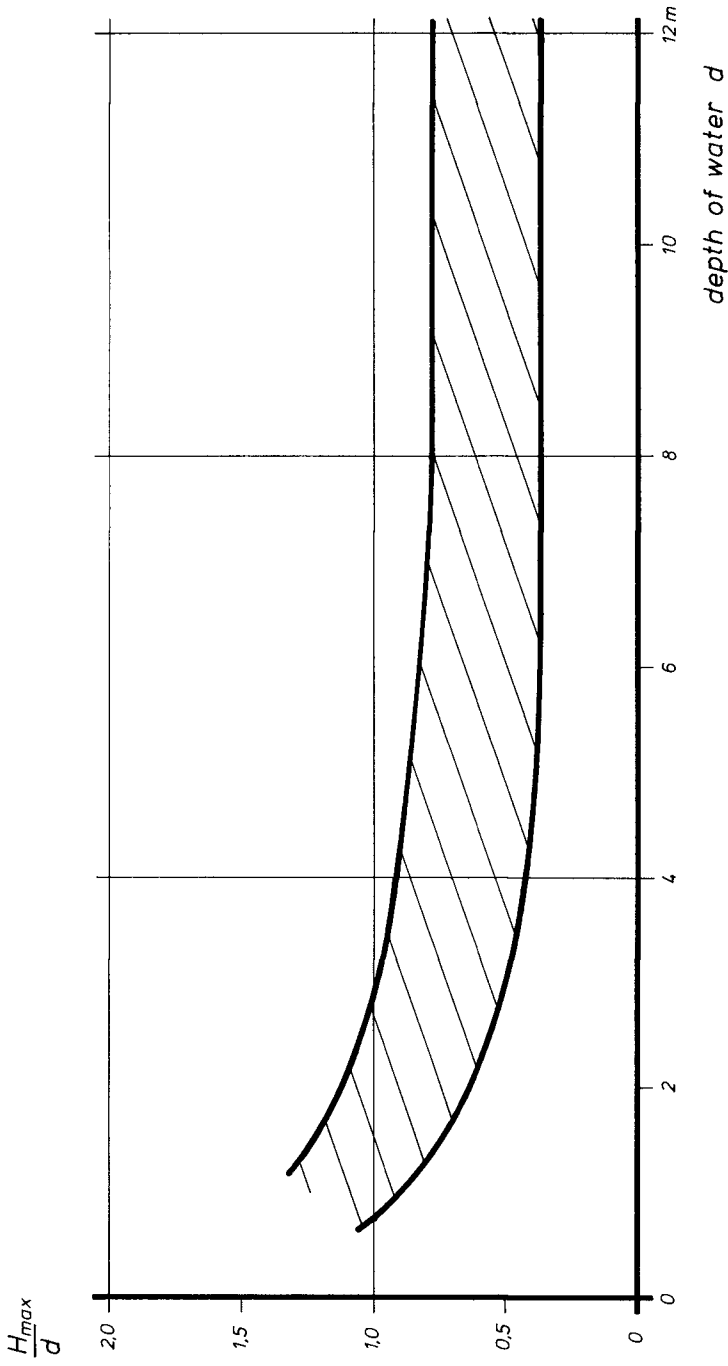
Fig. 2

$\dfrac{H_{max}}{d}$ vs. d,

Range of Functions from Various Authors

$$\frac{\bar{H}}{g\,T^2}$$

CALCULATION

0,006

0,004 0.0042 0.0041

REGISTRATION

0.0029 (SB)
0.0026 (1)
0,002 0.0023 0.0021 (SW)
0.0021 (2)

$$\frac{\bar{H}}{d}$$

0.237 (1) 0.250 (2)
0,25 0.232 (SB)
0.213 (SW)
0,20
0.179
0,15 0.149
0,10
0.099
0,05

$$\frac{H_{1/3}}{\bar{H}}$$

.153 REGISTRATION
1,50
.146
146 (SW) 1.46 (2)
CALCULATION 1.41 (1)
1,40 1.40
1,30

m BELOW MHW

MHW
0
-1,0 SB
SW
-2,0 (1)
-3,0
-4,0
-5,0
-6,0
SR SL SA SB (cf fig 1)
SW
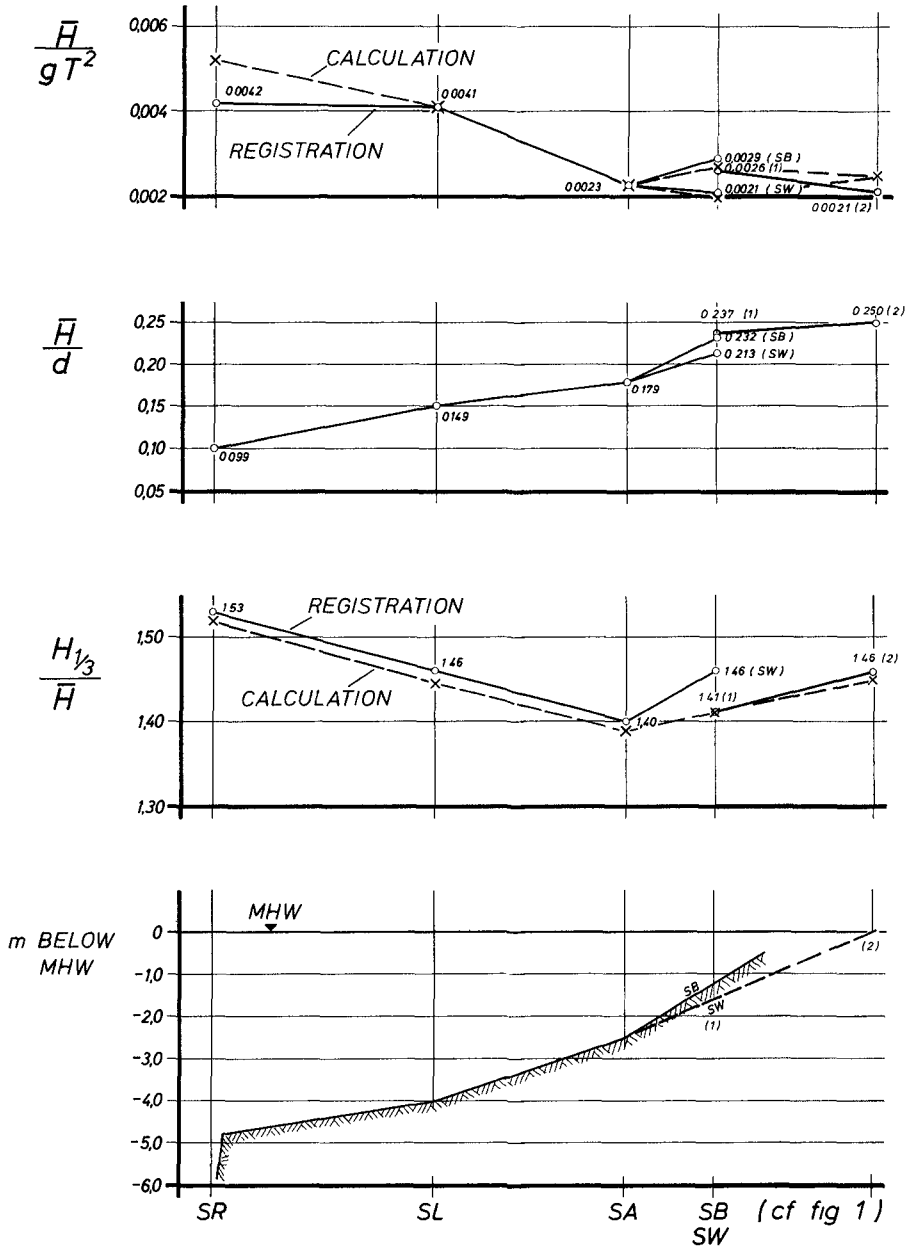
Fig. 3
Variation of Wave Parameters
with Decreasing Depth

to be regarded. They lead to the calculated best-fit li-
nes on fig. 3. The additional parameters are the mean
wave steppness $\delta = \bar{H}/\bar{L}$ and the distance s from deep wa-
ter areas. So we get some sort of "2nd order parame-
ters", and topography can be expressed by

    the depth of water d,
    the distance s from deep water areas, and
    the mean wave steepness.

The table shows the mean steepnesses of deep water and
typical shallow water areas as used in the following
derivations:

<div align="center">

Mean Steepnesses

of Waves in Shallow Water

</div>

AREA	$\delta = \dfrac{\bar{H}}{\bar{L}} \approx 10 \cdot \dfrac{\bar{H}}{g\bar{T}^2}$
WATER DEPTH >10 m	0.055
TIDAL CHANNELS	0.060
NON-BREAKING WAVE AREA	0.050
EDGE OF TIDAL FLATS	0.040
BREAKER ZONE	0.025

The influence of this parameter on the value of $\bar{H}_{max}$ was
evaluated as

$$\frac{H(\delta)}{H(\delta_o)} = \frac{1}{1 - \dfrac{\delta_o - \delta}{3\delta_o}} = \frac{3\delta_o}{2\delta_o + \delta}$$

It is obviously not very strong, but leads for example
to breaking waves being 20% higher than non-breaking wa-
ves in the same depth of water (fig. 4).

$$\frac{1}{1-\dfrac{\delta_0-\delta}{3\,\delta_0}}$$
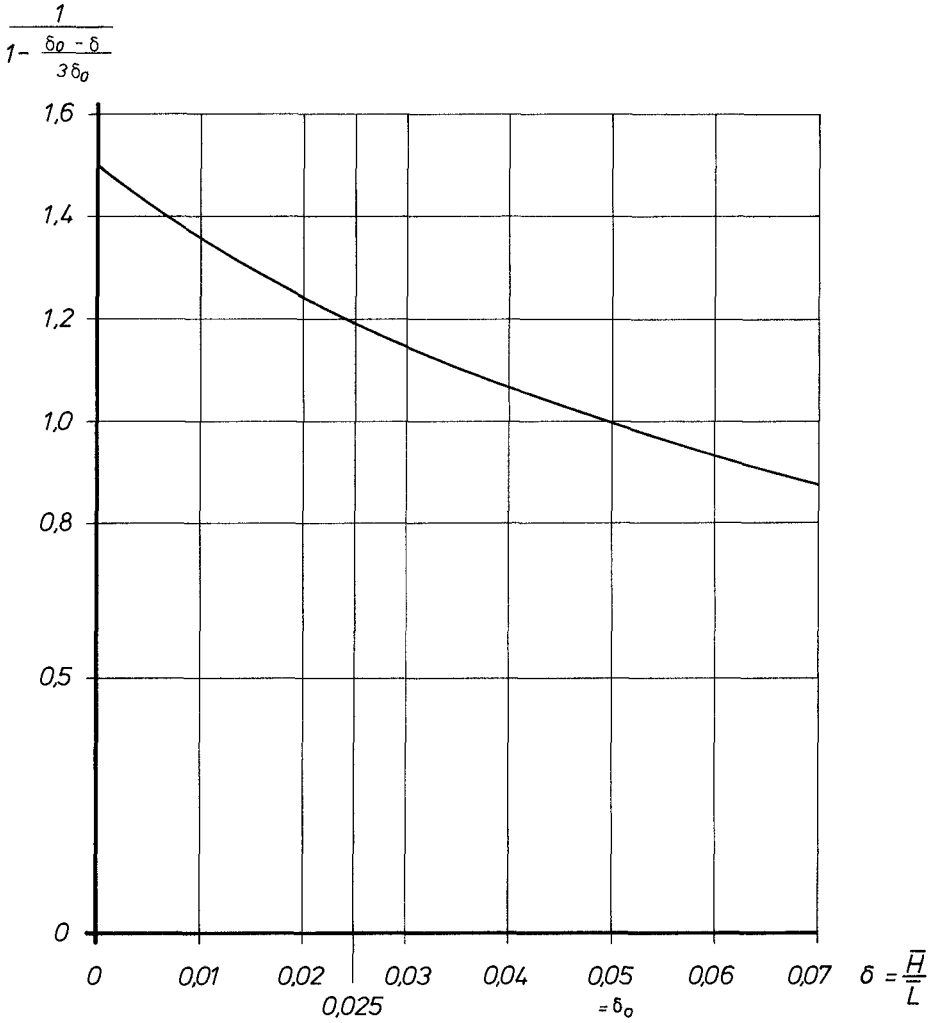
Fig. 4
Influence of Mean Wave Steepness
on Wave Height

Wave Height as Function of Travel Distance

The influence of the distance s from deep water areas on
the wave height at a shallow water location can be much
greater, and the investigation of this led to an inter-
esting conclusion. To consider the importance of this
parameter, the ratio $\overline{H}_{max}/s$, corrected by δ , was plott-
ed against d/s in log-log-paper (fig. 5). The values
summarize at an upper envelop that can be expressed by
the equation

$$\frac{\overline{H}_{max}}{s} \cdot (1- \frac{\delta_o - \delta}{3\,\delta_o}) = 0.2 \cdot (\frac{d+1}{s})^{1.16-0.06\cdot \ln (\frac{d+1}{s})}$$

This function leads to special curves for different d
and δ . Fig. 6 contains the curves for a water depth of
2 m as an example. They rise to a maximum at a certain
distance s and then - with increasing distance from deep
water - decrease asymptotically to the height of pure
wind waves originated in the shallow water area.
Doubtlessly the most interesting point is the maximum.
It indicates that waves, running from deep onto shallow
water, relatively quickly increase in height and there-
after, under the influence of bottom friction and energy
dissipation, slowly decrease. So at first there is no
wave height decay to be expected when waves have reached
shallow water. This zone of decay begins behind a zone
of wave height increase at the edge of the shallow wa-
ter area.

For constant wave characteristic the locality of the
peak is a function of d. In prototype however waves are
changing their character, expressed by different δ .
Fig. 7 demonstrates that in these cases there are peaks
as well, though it is a little bit more complicated to
fix them exactly.
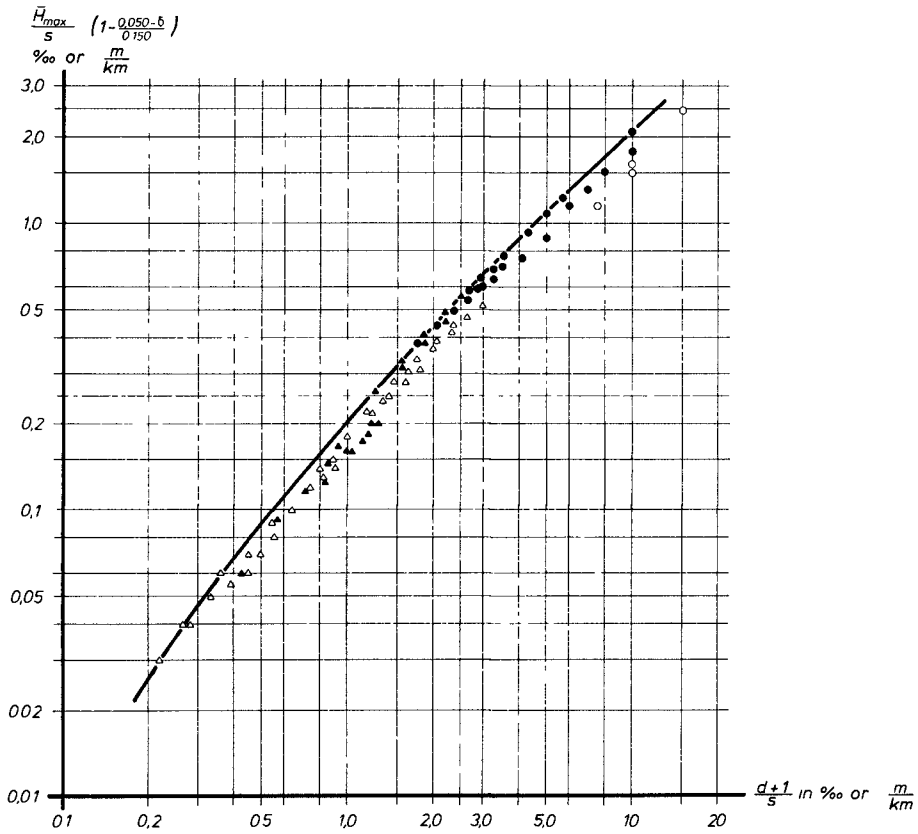
Fig. 5

$\bar{H}_{max} = f(d,s,\delta)$ with depth of water d(in m), distance from deep water area s(in km), mean wave steepness $\delta = \dfrac{\bar{H}}{L}$
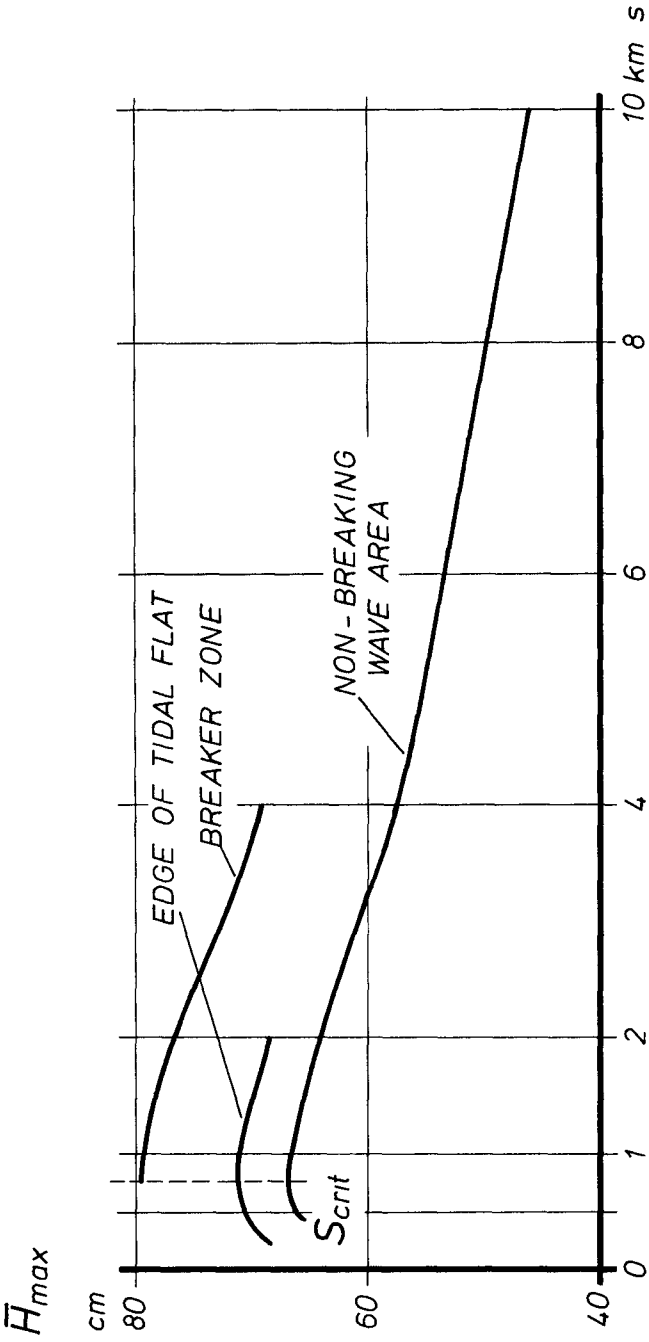
Fig. 6

Example for Evaluation of Critical Travel Distance
in Shallow Water of Constant Depth (d = 2,0 m)

WAVE
HEIGHT
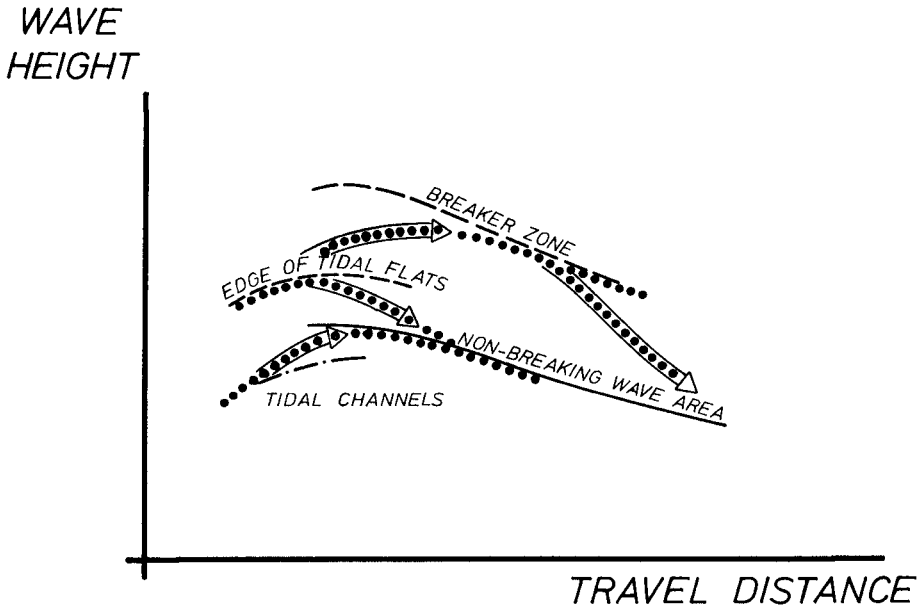
TRAVEL DISTANCE

Fig. 7
Example for Evaluation of
Critical Travel Distance
in Transitional Waters

Discussion

For the idealized case of waves running from deep water
over a relatively steep slope into an area of constant
water depth, the location of the peaks can be expressed
as a function of d (fig. 8). As at these points the wa-
ves reach their highest values, this location is defined
as

"critical travel distance s_{crit}."

$$\frac{\bar{H}_{max}}{d} \quad for \quad \delta = \delta_0 = 0{,}050$$

CRITICAL TRAVEL DISTANCES
$s_{crit} = 0{,}264 \, (d+1)$

$d = 0{,}5 \, m$

$d = 1{,}0 \, m$

$d = 1{,}5 \, m$
$d = 2{,}0 \, m$
$d = 4{,}0 \, m$
$d = 10 \, m$
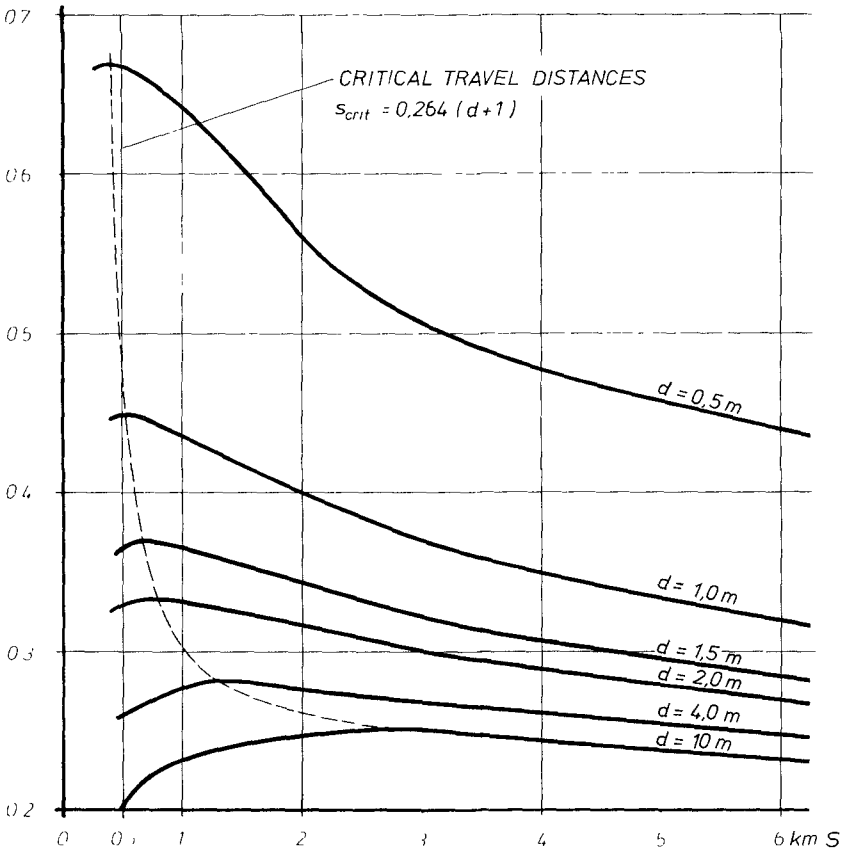
Fig. 8
Critical Travel Distances

With

$$s_{crit.} = 0.264 \, (d+1)$$

$s_{crit.}$ increases linearly with d, i.e. relatively higher

waves can proceed the further landward the deeper the wa-
ter is. Besides this the influence of s on the ratio
$\bar{H}_{max}/d$ decreases with increasing d as a result of weaker
influence of bottom friction etc. So this graph enables
us to demonstrate, in what amount storm tides with extreme
water levels transfer the line of critical travel dist-
ances coastward, and the probability of destruction rises,
as this effect brings a larger increase in wave height
than usually recognized. So during rise and fall of the
water level the critical travel distance varies and leads
to a range that should be avoided by coastal structures.

$s_{crit.}$ is a function of d only, but the height of the
highest mean wave height $\bar{H}_{max}$ at the critical travel
distance is a function of d and δ :

$$\bar{H}_{max} (s_{crit.}) = 0.223 \cdot \frac{3\delta_o}{2 \delta_o + \delta} \cdot (d+1)$$

with $\delta_o = 0.050$.

The results as a whole may be surprising, but they are
for instance in agreement with and similar to the ana-
lysis of GALVIN (1969) for breaker travel on slopes:
There waves do not immediately acquire the height theo-
retically due to d, but only after travelling a certain
distance. The energy transfer from wave to bottom and
the shoaling effect need a certain time to develop the
wave character that may be theoretically derived.

Some other investigations, undertaken in the US some
years ago, may be mentioned in this connection: Theo-
retical approaches and laboratory tests with waves
running from deep water over a steep slope into shallow
water of constant depth (MADSEN and MEI, 1969; ZABUSKY
and GALVIN, 1968). They indicate that single waves are
devided into 2 or 3 secondary waves with the first wa-
ve being the highest one, slowly decreasing on its way
in shallow water. Moreover the ratio H over deep water
wave height H_o increases more quickly the smaller the
depth is. This is a verification of the statement that

the critical travel distance is reached earlier with decreasing water depth.

Summary

As the critical travel distance of waves in shallow water can obviously be fixed or be at least estimated, its knowledge may lead to a certain revision of today's dimensioning criteria: The location of buildings should not be $s_{crit.}$, possibly landward of $s_{crit.}$, but maybe planning demands a location near a deep water area. In this case a point seaward of $s_{crit.}$ can be more suitable avoiding steepening of waves in front of it and perhaps even shoaling.

References

FÜHRBÖTER, A.,   Field Investigations in Surf Zones
BÜSCHING, F. and   Proc. 14th Conf. on Coastal Eng.,
DETTE, H.H.:   Copenhagen 1974

GALVIN, C.J. jr.:   Breaker Travel and Choice of Design
                        Wave Height. Journal of the Water-
                        ways and Harbors Div., ASCE,
                        Vol. 95, No. WW 2, 1969

MADSEN, O.S. and   Dispersive Long Waves of Finite
MEI, C.C.:   Amplitude over an Uneven Bottom.
                        MIT, Rep. No. 117, Cambridge 1969

SIEFERT, W.:   Shallow Water Wave Characteristics.
                        Proc. 13th Conf. on Coastal Eng.,
                        Vancouver 1972, ASCE, Vol. 1, New
                        York 1973

SIEFERT, W.:   Uber den Seegang in Flachwasserge-
                        bieten. Mitt. des Leichtweiß-Inst.
                        der Techn. Univ. Braunschweig,
                        Vol. 40, 1974

ZABUSKY, N.J. and   Secondary Waves as Solitons. Trans-
GALVIN, C.J.:   actions AGU 49, No. 1, Washington
                        1968

CHAPTER 25

MASS TRANSPORT IN GRAVITY WAVES ON A SLOPING BOTTOM

by E.W.Bijker 1), J.P.Th.Kalkwijk 2) and T.Pieters 3).

Summary
    In the present investigation the influence of bottom slope on mass
transport by progressive waves was investigated, both theoretically
and experimentally. Theoretical considerations based on linear wave
theory show the greatest influence of the slope on the bottom drift
velocities for relatively long waves and steep slopes. The numerical
values, however, remain rather small (influence less than 20%). In
addition, the experiments show that the bottom drift velocities are
more determined by the local parameters than by the magnitude of the
bottom slope in the cases examined. Considering the net bottom velo-
cities, the discrepancy between the horizontal bottom theory (Longuet-
Higgins) and experimental results is considerable. Taking into account
the first harmonic of the local wave form and the small slope effect
for relatively small depths in horizontal bottom theory does show,
however, the same tendency as the experimental results.

1.   Introduction
    The complexity of the mechanism of sediment movement under wave
action makes the choice of the proper model bed material in coastal
movable bed models often difficult.Therefore, a better knowledge of
one of the details of this mechanism, namely the net mass transport in
waves, would assist in determining the correct sediment scale or at
least to recognize scale effects, if they are inevitable. Though the
role of the mass transport velocity is not fully understood, experi-
ments from past investigations suggest that it influences the near
bottom and suspended sediment transport. Especially the influence of
the beach slope on behaviour of this phenomenon in the model is then
important, because of the frequently observed distortion in these
models.
    This paper reports results of experiments to determine mass trans-
port velocities on three sloping bottoms. In particular attention was
paid to the resultant bottom velocities, since those are most impor-
tant for sediment studies. The considerations are limited to the off-
shore region. Section 2 gives a brief survey of previous work. Section
3 aims at predicting the net bottom velocities as they occur on a gent-
ly sloping bottom; section 4 describes the various experiments carried
out; sections 5 and 6 compare the experimental and theoretical results
and give the conclusions.

2.   Review of previous work
    Theoretical or experimental results for mass transport velocities
over gently sloping bottoms are very scare. Most investigations have

---

1) Prof.of Coastal Engineering, Delft University of Technology, Depart-
   ment of Civil Engineering.
2) Assoc.Prof.of Hydraulic Engineering, Delft University of Technology,
   Department of Civil Engineering.
3) Student of Civil Engineering, Delft University of Technology.

447

been carried out with horizontal bottoms. In this connection Longuet-Higgins (1) has made a most important theoretical contribution. In his paper he gives solutions for very low waves (laminar boundary layer conduction solution). In these cases good agreement between theory and experiment was obtained for values of kh (k = wave number, h = water depth) between 0.9 and 1.5. Experiments for higher values of kh generally yielded a mass transport velocity profile ressembling better the Stokes profile. This is reported in (2).

Despite of the fact that Russell and Osorio (3) carried out their experiments with higher waves, the tendencies predicted by Longuet-Higgins were confirmed. Though in most of their cases the boundary layer was turbulent, Longuet-Higgins showed in the appendix of their paper that, in particular, the velocity just outside the boundary layer at the bottom does not depend on the value of the (eddy) viscosity, provided it is constant. In general, it may be concluded, however, that the results for the high waves are less good than for the low waves.

Brebner, Askew and Law (4) examined the influence of roughness on the mass transport. In general, they found at the bottom a smaller velocity than predicted by Longuet-Higgins theory. They suggest that this is caused by the turbulent boundary layer. Noda (5) - using in his computations an eddy viscosity, being a function of distance from the wall {see also (6)} - attempted to explain this phenomenon, but he only found a significant effect for the case of standing waves. Sleath (7) attempted to explain the phenomenon by taking into account convective acceleration terms. His corrections (both positive and negative) amount to an order of 10% for the cases considered.

Another attempt of Sleath (8) to determine differences between Longuet-Higgins theory and experiments is based upon the introduction of damping waves in the longitudinal direction. His mathematical formulation yields three possible solutions for the Longuet-Higgins case (low waves). Unfortunately, it is not clear under which circumstances the various solutions hold. Moreover the experimental support is weak.

For a gently sloping bottom Russell and Osorio (2) observed for a single case considered, no significant differences from the results on a flat bottom. Lau and Travis (9) also considered a sloping bottom, but they were primarily interested in the consequences of partial reflection on mass transport velocity profiles.

Concluding, one may remark that net velocity profiles in physical models, although already very schematized, are not satisfactorily predicted by existing theories for cases with relatively high waves. In order to indicate tendencies at best, Longuet-Higgins theory can be used.

3.   Theoretical considerations

In this section it is attempted to predict the behaviour of the net bottom velocities in progressive waves propagating on a gently sloping bottom. As a consequence of the latter limitation, partial reflection of the progressive waves will be disregarded.

A conventional x,z coordinate system is used as shown in figure 1 (page 4).

The following two-dimensional equation of motion holds for the boundary layer at the bottom (vertical velocity negligible):

$$\frac{\partial u}{\partial t} + u \frac{\partial u}{\partial x} + \frac{1}{\rho} \frac{\partial p}{\partial x} = \nu \frac{\partial^2 u}{\partial z^2} \qquad \{1\}$$

In the following it will be also assumed that the velocity remains small, so that the convective acceleration terms in the equation $\{1\}$ can be neglected. Furthermore, since in first order of approximation the fluid motion in the interior is not influenced by viscosity, the pressure gradient in the thin boundary layer at the bottom (assumed to be equal to the pressure gradient just outside the boundary layer) is also equal to the corresponding local acceleration, so:

$$\frac{1}{\rho} \frac{\partial p}{\partial x} = - \frac{\partial u_\infty}{\partial t} \qquad \{2\}$$

and eqn.$\{1\}$ changes into:

$$\frac{\partial u}{\partial t} - \frac{\partial u_\infty}{\partial t} = \nu \frac{\partial^2 u}{\partial z^2} \qquad \{3\}$$

In the case under consideration (progressive waves) the horizontal fluid motion is given by $\{$see (10) and (11)$\}$:

$$u = A(x) \left[\cos\left(\omega t - \phi(x)\right) - e^{-\frac{h+z}{\delta}} \cos\left(\omega t - \phi(x) - \frac{h+z}{\delta}\right) \right] \qquad \{4\}$$

in which

$$\delta = \left(\frac{2\nu}{\omega} \right)^{\frac{1}{2}}$$

$$A(x) \cos\left(\omega t - \phi(x)\right) = u_\infty$$

$$\frac{\partial}{\partial x} \phi(x) = k(x)$$

The result for u can be conceived of as the first order result for the Eulerian velocity in the boundary layer. The time average of this result yields a zero net velocity. To determine the mean second order Eulerian velocity, the equations of motion have to be applied again. From the equation of continuity:

$$\frac{\partial u}{\partial x} + \frac{\partial w}{\partial z} = 0 \qquad \{5\}$$

the small second order vertical velocities can be derived.
This yields:

$$\eta(x) = a(x)\cos\left[\omega t - \pi(x)\right]$$

$$tg\alpha = -\frac{dh}{dx}$$
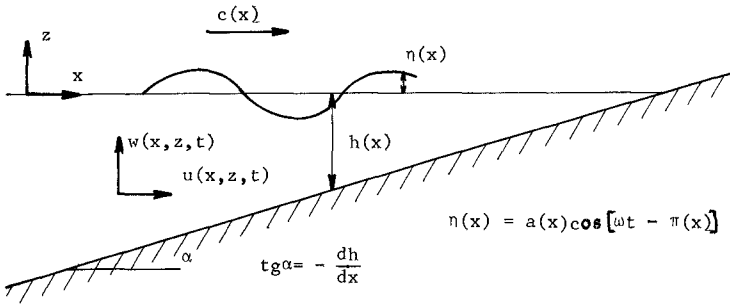
fig.1. Definition sketch
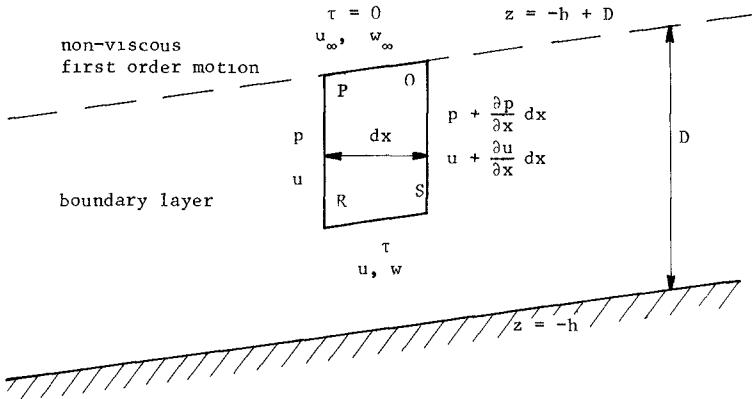
fig.2. Spatial fixed volume in boundary layer

$$w= +A \; \delta \; k \; \left[\left\{ \frac{1}{2} \, e^{-\mu} \, \{\sin\mu \, +\cos\mu\} - \frac{1}{2} \right\} \cos\psi + \left\{ -\mu \, + \frac{1}{2} \, e^{-\mu} \{\sin\mu - \cos\mu\} + \frac{1}{2} \right\} \sin\psi \right]$$

$$-\delta \, \frac{dA}{dx} \left[\left\{ \mu \, - \frac{1}{2} \, e^{-\mu} \{\sin\mu \, -\cos\mu\} \, - \frac{1}{2} \right\} \cos\psi \, + \left\{ \frac{1}{2} \, e^{-\mu} \, \{\sin\mu + \cos\mu\} - \frac{1}{2} \right\} \sin\psi \right]$$

$$-A \, \frac{dh}{dx} \; \left[\{-e^{-\mu} \cos\mu \, +1\} \, \cos\psi \, +\{e^{-\mu}\sin\mu\} \, \sin\psi \right] \qquad\qquad \{6\}$$

This complicated result is due to the fact that derivatives of A(x) and h(x) must be taken into account.

Application of the law of conservation of momentum to a spatial fixed element (P Q R S in figure 2, page 4) yields:

$$\frac{\partial}{\partial t} \iiint_V \rho u \; dV = \{\rho uw\}dx \; -\{\rho uw\}_\infty dx \; +\tau \; dx \; - \int_z^{-h+D} \frac{\partial}{\partial x}\left(\frac{p}{\rho} + u^2 \right) dx \; dz \qquad \{7\}$$

Taking the time average yields:

$$\nu \, \frac{\partial \hat{u}}{\partial z} \; =\overline{\{uw\}} \; -\overline{\{uw\}}_\infty \; - \int_z^{-h+D} \frac{\partial}{\partial x}\overline{\left(\frac{p}{\rho} + u^2 \right)} \; dz \qquad\qquad \{8\}$$

so that:

$$\overline{u} = \; \frac{1}{\nu} \int_{-h}^{z} \left(\overline{\{uw\}} \; -\overline{\{uw\}}_\infty \right) \, dz \; - \; \frac{1}{\nu} \int_{-h}^{z} \int_z^{-h+D} \frac{\partial}{\partial x}\left(\overline{\frac{p}{\rho}} + \overline{u^2} \right) dz \; dz \qquad \{9\}$$

since the left member of eqn.{7} is then equal to zero.
The pressure term in eqn. {9} will again be derived from the interior of the fluid. Taking the time average of the governing equation of motion (neglecting viscous terms) yields:

$$\frac{1}{\rho} \, \frac{\partial}{\partial x} \, \overline{p} = - \, \frac{1}{2} \, \frac{\partial}{\partial x} \, \overline{u^2} \; - \overline{w \, \frac{\partial}{\partial z} \, u} \qquad\qquad \{10\}$$

and at the bottom   (w = 0):

$$\frac{1}{\rho} \frac{\partial}{\partial x} \overline{P} = - \frac{1}{2} \frac{\partial}{\partial x} \left(\overline{u_\infty^2} \right) \qquad \{11\}$$

Physically the gradient of the time mean pressure arises from the
variation of the mean water level.
After substituting $\{4\}$, $\{6\}$ and $\{11\}$ in $\{9\}$ the mean value $\overline{u}$ can
be calculated:

$$\overline{u} = \frac{A^2 k}{\omega} \left[- \frac{1}{2}\mu \ e^{-\mu} \{\sin\mu + \cos\mu\} + \frac{1}{2} e^{-\mu} \sin\mu - e^{-\mu} \cos\mu + \frac{1}{4} e^{-2\mu} + \frac{3}{4} \right]$$

$$+ \frac{A}{\omega} \frac{dA}{dx} \left[\frac{1}{2}\mu \ e^{-\mu}\{\sin\mu - \cos\mu\} + 2e^{-\mu} \sin\mu + \frac{1}{2} e^{-\mu} \cos\mu + \frac{1}{4} e^{-2\mu} - \frac{3}{4} \right]$$

$$\{12\}$$

The result obtained is the Eulerian mean velocity. The mean particle
velocity (Langrangian velocity) can be derived using the relation:

$$\overline{U} = \overline{u} + \overline{\frac{\partial u}{\partial x} \int^t u \ dt} + \overline{\frac{\partial u}{\partial z} \int^t w \ dt} \qquad \{13\}$$

Using the results obtained from u and w, the remaining unknown terms
in the right member of eqn.$\{10\}$ yield:

$$\overline{\frac{\partial u}{\partial x} \int^t u \ dt} + \overline{\frac{\partial u}{\partial z} \int^t w \ dt} =$$

$$= \frac{A^2 k}{\omega} \left[\frac{1}{2}\mu \ e^{-\mu}\{\sin\mu + \cos\mu\} - \frac{1}{2} e^{-\mu} \sin\mu - e^{-\mu} \cos\mu + \frac{1}{2} e^{-2\mu} + \frac{1}{2} \right] +$$

$$+ \frac{A}{\omega} \frac{dA}{dx} \left[- \frac{1}{2}\mu \ e^{-\mu} \{\sin\mu - \cos\mu\} - \frac{1}{2} e^{-\mu} \cos\mu + \frac{1}{2} e^{-2\mu} \right] \qquad \{14\}$$

Eqs. $\{12\}$ and $\{14\}$ substituted in eqn.$\{13\}$ gives the result desired:

$$\overline{U} = \frac{A^2 k}{\omega} \left[-2e^{-\mu} \cos\mu + \frac{3}{4} e^{-2\mu} + \frac{5}{4} \right] + \frac{A}{\omega} \frac{dA}{dx} \left[2e^{-\mu} \sin\mu + \frac{3}{4} e^{-2\mu} - \frac{3}{4} \right]$$

and at the edge of the boundary layer: $\qquad \{15\}$

$$\overline{U}_\infty = \frac{5}{4} \frac{A^2 k}{\omega} - \frac{3}{4} \frac{A}{\omega} \frac{dA}{dx} \qquad \{16\}$$

The first term in expression $\{15\}$ is the same as derived by Longuet-
Higgins for progressive waves on a horizontal bottom. The dimensionless
expression between brackets in the second term, giving the distribution
in the boundary layer, is the same as derived for a standing wave. It
should be stressed however, that this result holds for progressive
waves with varying amplitude, caused for example by a gently sloping bot-
tom.

Both dimensionless functions between brackets are also given in
(1), (5) and (6), where in the two latter publications both laminar
and turbulent boundary layers are considered.

Since A is the amplitude of the velocity at the bottom of the in-
terior of the fluid (at the edge of the boundary layer) it can be ex-
pected to increase continuously in a progressive wave, propagating on
the slope before breaking. Therefore, the first term of the right mem-
ber of eqn.{16} (the Longuet-Higgins term) indicates a continuous in-
crease of the net bottom velocity in a progressive wave, propagating
over a constant slope. Subsequently, the derivative of A with respect
to x, is positive in that case, so that the second term of the right
member of eqn. {16} indicates a diminishing influence on the net bot-
tom velocity as predicted by the Longuet-Higgins theory. An assessment
of the influence of the latter term is possible by considering the
transformation of a progressive wave propagating on a beach using the
energy concept (linear theory). Then the expression for the amplitude
of the oscillating bottom velocity is:

$$A = \hat{u}_\infty = \frac{a_0 \omega}{\sinh kh} \left[\frac{2 \cosh^2 kh}{2kh + \sinh 2kh} \right]^{\frac{1}{2}} \qquad \{17\}$$

This expression represents the influence of a varying water depth,
but it does not contain derivatives with respect to x. Therefore, the
influence of the correction term in eqn.{16} is proportional to the
slope of the bottom. Normalizing the correction term with the Longuet-
Higgins term yields for U_∞ :

$$\overline{U}_\infty = \frac{5}{4} \frac{A^2 k}{\omega} \left[1 - \frac{3}{5} \frac{1}{Ak} \frac{dA}{dh} \frac{dh}{dx} \right] \qquad \{18\}$$

For a constant slope the dimensionless correction term is a function
of $k_0 h$ (or kh), only, and is graphically represented in fig.3, page 8.
The figure shows that in general the influence of the correction term
is small. Its influence is greatest for the relatively long waves; or,
in other words, near the breaker zone. Under practically all conditions
its value will remain below 0.2, for slopes up to 1:10. It is also very
doubtful whether the linear wave theory can be applied to the breaker
zone. The shallower the water, the more important the non-linear effects.
Due to shoaling, for instance, the waves obtain a very pronounced crest
and flat trough. The corresponding velocity at the bottom will behave
the same, and in fact higher harmonics must be taken into account then.
If these harmonics have the same celerity, ref.(3) indicates how to take
them into account:

$$\overline{U}_\infty = \frac{5k}{4\omega} \left[A_1^2 + A_2^2 + \ldots\ldots\ldots \right] \qquad \{19\}$$

in which A_1, A_2 ..... are the amplitudes of the bottom velocities due
to the various harmonics.
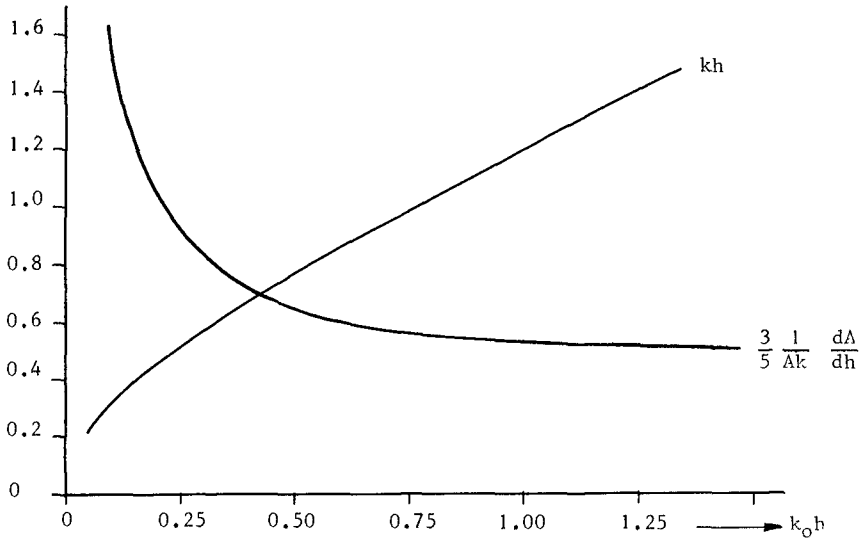
fig.3. Slope effect according to eqn.18

4.   Experiments
4.1.   General remarks
        Experiments were carried out in a wave flume, 30 m long, 0.80 m
wide and 0.60 m deep. Waves were generated by a wave-paddle, oscil-
lating with different amplitudes - if necessary - at the bottom and
still water levels (see fig.4, page 10).
        Three different beach slopes were used, viz. 1:10, 1:25 and 1:40.
The slope surface was rigid, whereas its roughness was varied, viz.
painted smooth concrete, glued sand grains and artificial ripples.
The diameter of the sand grains was between 1.6 and 2.0 mm; length
and heigth of the symmetrical ripples were 80 mm and 18 mm, respect-
ively. The water depth in front of the beaches (h_h) was constant
(0.45 m). During all experiments wave profiles over the full length
of the flume were recorded and the data were analyzed by means of
Fourier-analysis. In this way the character of the waves and their
behaviour on the beaches (higher harmonics, position and nature of
breaking, etc.) were determined. Furthermore, disturbances to the
mass transport, such as caused by reflection, seiches and free higher
harmonics, could be distinguished.
Table I gives a survey of the data of the waves, used in the experi-
ments:

number of the wave	T in sec.	H_o in m	H_o/L_o	H_h/L_h	$k_h h_h$
1	1.0	0.094	0.058	0.060	1.88
3	1.5	0.043	0.010	0.015	1.04
4	1.5	0.095	0.026	0.033	1.04
5	1.5	0.181	0.046	0.059	1.04
7	2.0	0.095	0.014	0.023	0.72

TABLE   I   Initial wave properties

The waves, before reaching the beach, agreed very well with the second
order Stokes wave form (see table II).
All waves applied broke on the beaches. The reflection was always less
than 6%. In all experiments the amplitude of the free second harmonic
component did not exceed 12% of the value of the first harmonic.

number of the wave	a_1 in m	$\dfrac{a_1}{a_{1\,refl.}}$ in %	$\dfrac{a_1}{a_2}$	theor.$\dfrac{a_1}{a_2}$ (Stokes)	$\dfrac{a_{2free}}{a_1}$ in %
1	0.043	3.6	8.3	8.8	1.2
3	0.021	4.0	16.3	17.0	2.0
4	0.043	5.2	8.0	7.5	2.3
5	0.078	4.6	3.9	4.2	5.9
7	0.045	6.0	5.1	5.1	11.8

TABLE II   Measured wave properties above the horizontal bottom
in the front of the beaches.
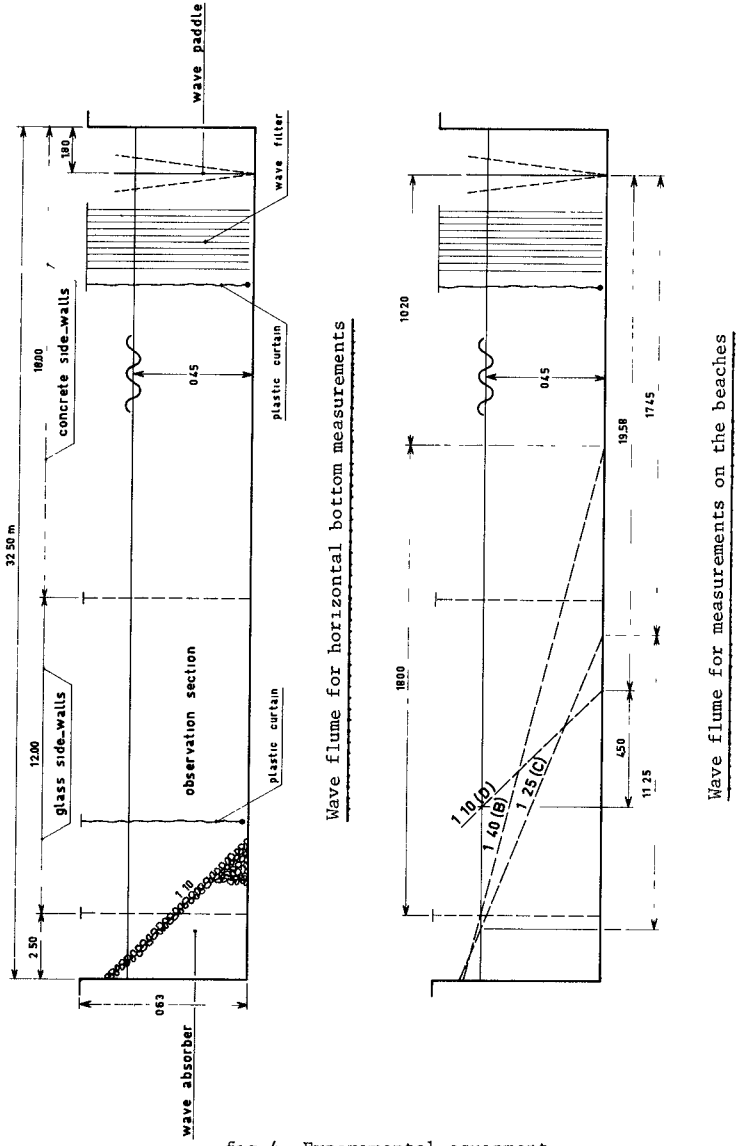
fig.4. Experimental equipment

The breaking behaviour of the waves was usual; with increasing
beach slope the form of breaking changed from spilling to plunging
and the breaker depth decreased.

Preliminary experiments with a horizontal bottom showed the neces-
sity for taking special measures against disturbing influences; a
plastic curtain was hung in front of the wave generator, to prevent
drift currents induced by the machine, to enter the measuring section.
The surface was kept clean by addition of a small amount of surface
tension reducing agent.

To ensure that in all cases a steady state was reached, the wave
generator was started 15 hours before making definite measurements.
Some mass transport velocity profiles, recorded after only half an
hour, did not show, however, significant differences with the final
results.

4.2. Measurements

The mass transport velocities were determined by filming small
rigid particles, with about the same density (995-1005 kg/m^3) as
water, measuring the displacement during an integer number of wave
periods and dividing by time. In this way mean particle velocity
profiles were constructed for corresponding places (depths) on the
various beaches (fig.5, page 12). This method of measurement is very
time consuming. Direct measurement, using for instance, a current
meter on a fixed location, however, is not possible, since this would
yield the mean Eulerian velocity, whereas the resultant Lagrangian
velocity is required. Because of the dimensions of the rigid particles
(5 mm dia.), the measured velocities represent averaged values over at
least the dimension of the grains. This averaging effect is greatest
near the bottom, where the vertical gradient of the mass transport
velocity is usually largest.

5.   Discussion of results
5.1. Preliminary experiments

These results with a horizontal bottom and those of Russell and
Osorio (3) show similar agreement with the theory developed by Longuet-
Higgins (1):
-   the distribution over the depth was rather well predicted for the
    waves 3, 4 and 5 ($k_h h_h$ = 1.04), whereas the agreement became less
    for the waves 1 and 7 ($k_h h_h$ = 1.88 and 0.72, respectively);

-   the bottom velocities disagreed less than those at the surface;
-   the predicted values, however, are mainly too large as compared
    with the measurements. This deviation becomes stronger with in-
    creasing wave amplitude.
On the basis of the rather good agreement with other experiments, it
was decided to continue with the sloping bottoms.

5.2. Sloping bottoms
5.2.1. Smooth bottom

It is not possible to give all experimental results in this limited
paper. Therefore, only a typical example of transport velocities
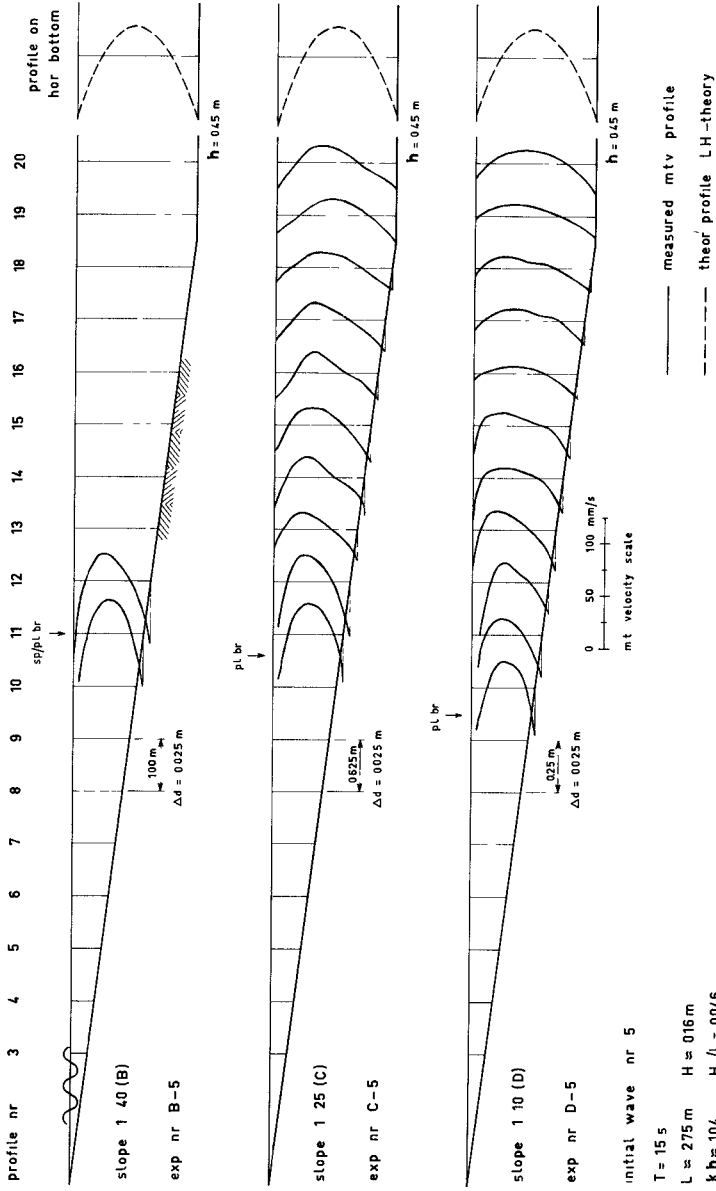
fig.5. Same initial wave on beaches with different slopes

for a smooth bottom is given in fig.5, page 12. Generally speaking, the
tendencies shown by the experiments are confirmed by Longuet-Higgins
theory. The latter predicts initially, for the case shown in fig.5, a
forward flow at the bottom and at the surface, and a back flow in the
center of the body of water. Approaching the beach the value of kh
gradually decreases. As a consequence, the basic profile of the mass
transport gradually changes into a shape where a back flow occurs at
the surface. The latter, however, only occurs when steepness of the
wave and relative water depth are small. The same phenomenon was also
observed by Russell and Osorio (3). When the water depth becomes very
small the surface velocities increase considerably. This was also in
agreement with the results of Mei, et al.(2). The flume side walls may
have an influence on the surface velocities, however. Therefore, the re-
sults for the deeper regions must be treated with some caution {see also
(2)}.
    The behaviour of the mass transport profile close to the breaker
region is different. In that region the flow profile has the same shape
for all waves, namely rather strong forward velocities at bottom and sur-
face, with a back flow in between. There, the velocities could obtain
values greater than predicted by Longuet-Higgins theory. In the breaker
zone, the net bottom velocities were always directed toward deeper water.
Differences in these velocities could not be distinguished, despite the
fact that the waves on the various slopes could break in different ways
(spilling or plunging).
    Outside the breaker zone, the theoretical Longuet-Higgins values
(based on local wave height) considerably exceeded the experimental
values. This is shown in figures 6 and 7 (pages 14 and 15) in more detail.
Both figs.6 and 7 give bottom velocities; in fig.6 the results are given
for 3 waves with equal wave heights, but different periods over 3 differ-
ent slopes. Fig.7 contains the results for a wave with constant period,
but different heights, also propagating over 3 different slopes. The ex-
perimental bottom velocities in these figures are normalized by the
theoretical Longuet-Higgins value determined using the local wave height.
This might be an inconsistent way of normalizing, but the wave heights at
the various slopes did not show great differences, provided the initial
wave was the same. As a consequence, the values obtained are well compar-
able.
    The scatter of the experimental data shown in the parts a and b of
figures 6 and 7 is smaller than the reported values might indicate. This
is caused by the method of normalizing applied to small velocities.
    The solid curves in the figures, valid for the various slopes, were
calculated by means of an averaging procedure applied to the non-dimen-
sional measured values.
In these figures, the correction according to eqn. {18} (see also fig.3)
for the 1:10-slope, is plotted using dotted curves. The correction based
on eqn. {19}, in which only the experimental first harmonic is considered
(practically the same for the various slopes with the same initial waves),
is plotted in the same way. For a better comparison, in fact, the higher
harmonics should be taken into account as well. Since these terms in
eqn.{19} occur in quadratic terms, they are neglected here. In fact both
influences have to be superimposed.
    In can be concluded from the figures that the correction to the
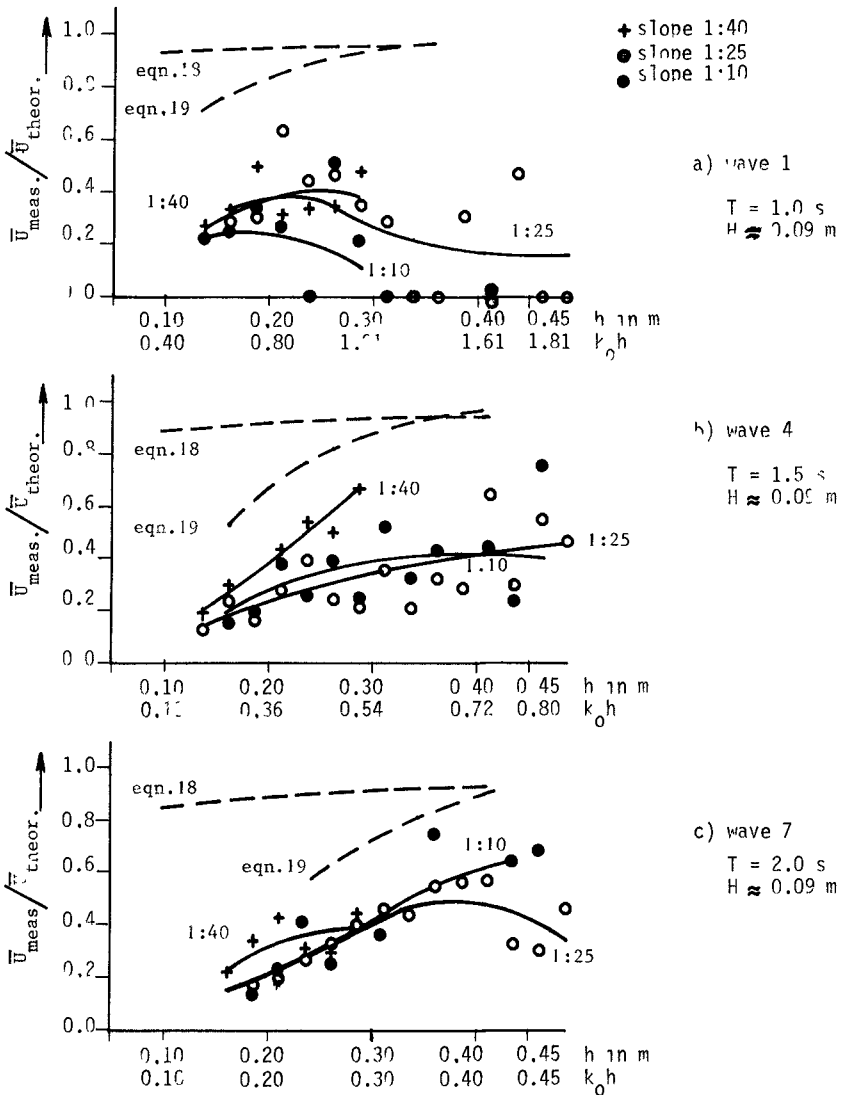
fig.6. Bottom drift velocities in waves with different periods
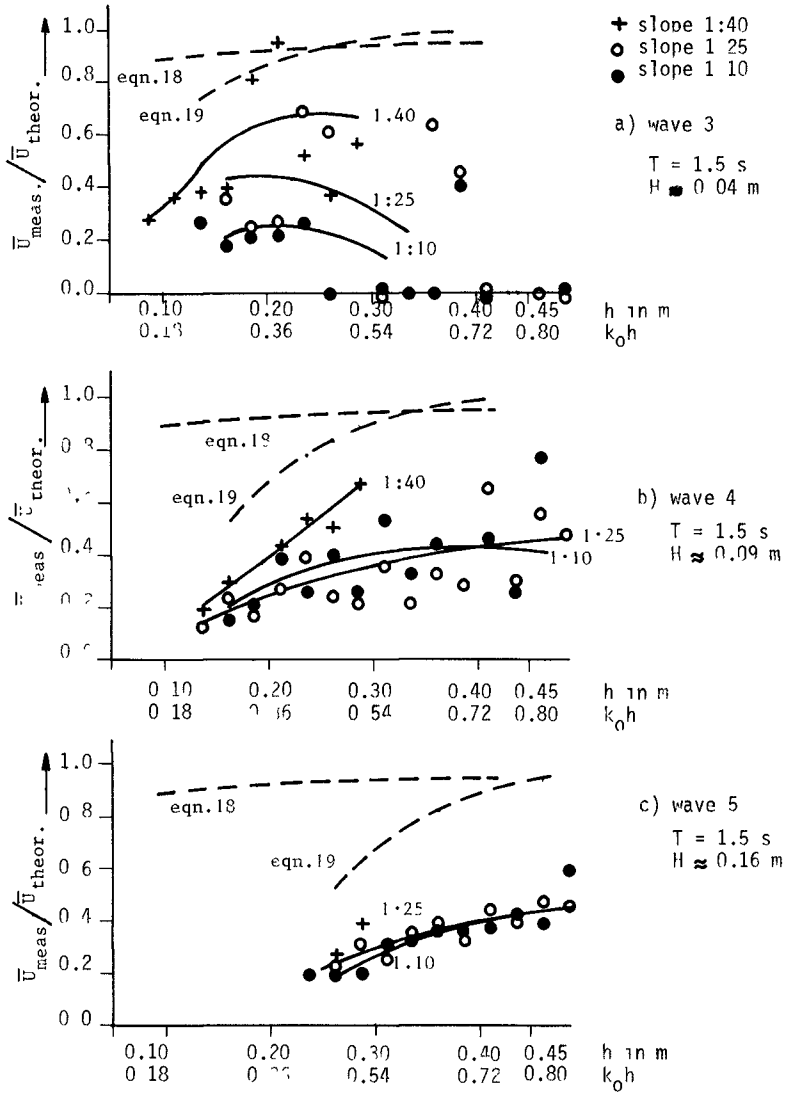
fig.7. Bottom drift velocities in waves with different heights

Longuet-Higgins values using the first harmonic is generally greater
than the correction for slope. In the region where the corrections
are most significant (small kh values), the former can be 3 times
greater than the latter. Though both corrections diminish the theoret-
ical values, they are always still greater than the experimental
values. Nevertheless, the tendencies predicted by the corrections are
confirmed by the experiments. Considering, for instance, fig.6, the
corrections for the longest wave are greatest and this is rather well
confirmed by the experiment. In fig.7 a similar behaviour of predicted
and measured values can be observed.
     The steepness of the slope does not seem to have a very signifi-
cant influence on the bottom velocities. The 1:40 slope may show some-
what higher values; in general, the differences with the results for
the other slopes are small.
     Concluding, one can say that the bottom velocities are primarily
determined by the local wave parameters, such as depth, height and
shape of the wave. The gradient of the bottom has no significant in-
fluence. In the cases examined, distortion of the model has only minor
consequences for these velocities. Although the distortions used in
this model were not perfect (the initial water depth remained constant
while the slope varied), there is enough experimental support for this
conclusion {see also (3)}. It is also suggested that distortion of pro-
totype situations with less steep slopes is permitted as far as bottom
velocities are concerned. The explicit proof, however, has not been de-
livered.

5.2.2. Rough bottom
     The experiments with the slope surface with sand roughness show the
same tendencies as mentioned before (see fig.8, page 17).The only dif-
ference compared to the smooth slope is that all velocities at compara-
ble places are somewhat smaller, especially those at the bottom. The
thickness of the layer, where the latter velocities occur, decreases
slightly at corresponding places.

5.2.3. Artificial ripples
     The artificial ripples prove to have an important influence on the
drift profile. The initially forward velocity at the bottom is reduced
to about zero, whereas close to the bottom a consistent flow is in-
duced. The direction of this current seems to depend on the wave steep-
ness. Wave 3 (H_h/L_h = 0.015) shows a forward velocity, whereas waves
4 and 5 (H_h/L_h= 0.033, resp. 0.059) show a strong backward current at
the same level (fig.8, page 17). The consistency of the forward current
(small wave steepness) seems to depend on the bottom slope. This
phenomenon indicates the existence of a critical wave steepness for the
reversal of this current between 0.033 and 0.015.
     At this moment the amount of experimental data on rough bottoms like
these, is not sufficient to draw general conclusions. The profiles ob-
served, however, are so different from the smooth cases, that further
investigations in this field are justified.

6.   Conclusions
     As fas as it is permitted to draw general conclusions for the area
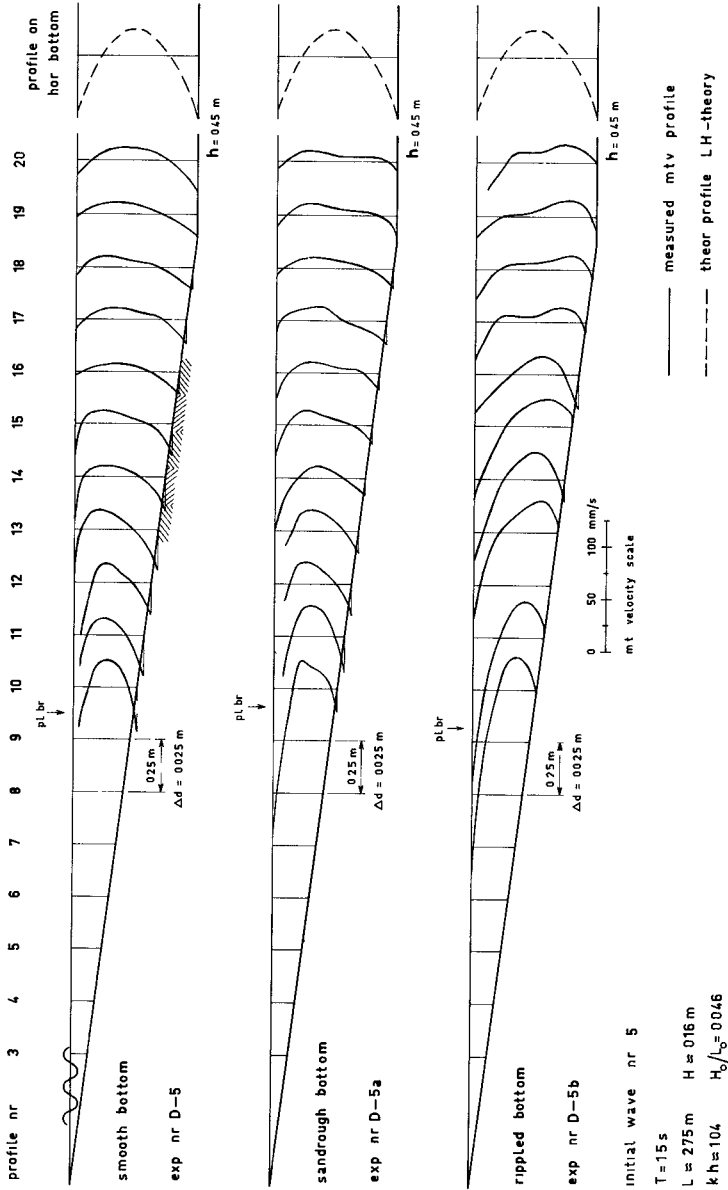
fig.8. Same wave on beaches with different bottom roughness (slope 1:10)

outside the breaker zone from this restricted number of experiments, it can be noted that:
- the bottom transport velocities on the slopes seem to be determined by the local depth rather than by the slope-angle;
- the bottom velocities predicted by the horizontal bottom theory are too large for the sloping bottom;
- the discrepancy between theory and experiment increases with decreasing depth and increasing relative wave length and wave height;
- the inclusion of the change in wave form and slope effect appears to explain the behaviour of the bottom velocities qualitatively;
- the drift velocities change slightly for increasing bottom roughness and considerably when a ripple-like roughness is present.

List of symbols

a = amplitude of surface elevation
A = maximum orbital velocity at the bottom outside the boundary layer
c = wave phase celerity
D = boundary layer thickness
$\delta = \left(\dfrac{2\nu}{\omega} \right)^{\frac{1}{2}}$
h = local still water depth
H = wave height
$k = \dfrac{\partial}{\partial x}\phi(x)$ = local wave number
L = wave length
p = normal pressure
t = time
T = the wave period
τ = shear stress
u = horizontal Eulerian velocity component
U = horizontal particle (Lagrangian) velocity component
w = vertical Eulerian velocity component
$\omega = \dfrac{2\pi}{T}$
x = horizontal coordinate
z = vertical coordinate
$\mu = (h+z)/\delta$
ν = kinematic viscosity of water
ρ = specific density of water
ϕ = phase, depending on horizontal coordinate x
$\psi = \omega t - \phi(x)$

subscript "o" refers to deep water value.
subscript "1" or "2" refers to first or second harmonic component, respectively.
subscript "h" refers to value on horizontal bottom.
subscript "∞" refers to value just outside the boundary layer.

References

(1) - Longuet-Higgins, M.S., "Mass transport in water waves", Phil.Trans. Roy.Soc.London, A., No.903, Vol.245, pp.535-581, 1953.
(2) - Mei, C.C., Liu, P.L.F. and Carter, T.G., "Mass transport in water waves; Theory and Experiments", M.I.T. Dept.Civil Eng.,Ralph M. Parsons Lab.Report No.146, 1972.
(3) - Russell, R.C.H. and Osorio, J.D.C., "An experimental investigation of drift profiles in a closed channel", Longuet-Higgins, M.S., "The mechanics of the boundary layer near the bottom in a progressive wave", Proc.6th Conf.on Coastal Eng., Chap.10, pp.171-193, 1958.
(4) - Brebner, A., Askew, J.A. and Law, S.W., "The effect of roughness on the mass transport of progressive gravity waves", Proc.10th Conf.on Coastal Eng., Chap.12, pp.175-184, 1966.
(5) - Noda, H., "On the oscillatory flow in turbulent boundary layers in- duced by water waves", Bull.Disas.Prev.Res.Inst., Kyoto Univ., Vol. 20.Part 3, No.176, pp.127-144, 1971.
(6) - Johns, B., "On the mass transport induced by oscillatory flow in a turbulent boundary layer", Journ.of Fluid Mech., Vol.43, Part 1, pp.177-185, 1970.
(7) - Sleath, J.F.A., "A second approximation to mass transport by water waves", Journ.of Mar.Res., 30 (3), pp.295-304, 1972.
(8) - Sleath, J.F.A., "Mass transport in water waves for very small ampli- tude", Journ.of Hydr.Res.11, No.4, pp.369-383, 1973.
(9) - Lau, J. and Travis, B., "Slowly varying Stokes waves and submarine longshore bars", Journ.of Geophys.Res., Vol.78, No.21, pp.4489- 4497, 1973.
(10) - Schlichting, H., "Boundary layer theory", Sixth Edition, 1966.
(11) - Batchelor, G.K., "An introduction to fluid dynamics", Cambridge University Press, 1967.

==========

CHAPTER 26

SURF SIMILARITY

J.A. Battjes
Civil Engineering Department
Delft University of Technology
Netherlands

ABSTRACT

This paper deals with the following aspects of periodic water waves breaking
on a plane slope breaking criterion, breaker type, phase difference across
the surfzone, breaker height-to-depth ratio, run-up and set-up, and reflection.
It is shown that these are approximately governed by a single similarity para-
meter only, embodying both the effects of slope angle and incident wave steep-
ness. Various physical interpretations of this similarity parameter are given,
while its role is discussed in general terms from the viewpoint of model-
prototype similarity.

FLOW PARAMETERS

Consider a rigid, plane, impermeable slope extending to deep water or to
water of constant depth from which periodic, long-crested waves are approaching.
The wave crests are assumed to be parallel to the depth contours.

The motion will be assumed to be determined wholly by the slope angle α,
the still water depth d and the incident wave height H at the toe of the slope,
the wave period T, the acceleration of gravity g, the viscosity μ and the mass
density ρ of the water, g, μ and ρ are assumed to be constants. Effects of surface
tension and compressibility are ignored.

Let X be any dimensionless dependent variable, then

$$X = f(\alpha, \frac{H}{L_0}, \frac{d}{L_0}, Re)$$ (1)

in which Re is a typical Reynolds number, and

$$L_0 = \frac{gT^2}{2\pi},$$ (2)

466

i.e. the deep-water wavelength of small-amplitude sinusoidal, longcrested
gravity surface waves with period T. The ratio H/L_0 is a wave steepness,
if we define this parameter in a generalized sense as the ratio of a wave
height to a wave length.

Variations in the flow regime are brought about mainly by variations of
α and H/L_0, for the Reynolds number is usually larger than some minimum value
above which variations in its actual value do not significantly affect the
resultant motion, while for waves breaking on the slope, the value of the
relative depth in front of the slope is not important either, this is well
established for the relative run-up [7] and the reflection coefficient [14],
for instance. So, in summary one can say that for waves breaking on the slope
(1) reduces to

$$X \underset{\sim}{\sim} f(\alpha, \frac{H}{L_0}) \quad , \tag{3}$$

while it will be shown in the following that for many overall-properties
of the breaking waves (3) reduces further to

$$X \underset{\sim}{\sim} f(\xi) \quad , \tag{4}$$

in which ξ is a similarity parameter, defined by

$$\xi = \frac{\tan \alpha}{(H/L_0)^{\frac{1}{2}}} \quad . \tag{5}$$

To the author's knowledge, this parameter was first used by Iribarren and
Nogales [8], for determining whether wave breaking would occur. Its more
general usefulness in the context of surf problems was suggested by Bowen
et al [3].

FLOW CHARACTERISTICS DETERMINED BY THE SIMILARITY PARAMETER ξ

Breaking criterion

Iribarren and Nogales [8] have given an expression for the condition at which
the transition occurs between non-breaking and breaking of waves approaching
a slope which is plane in the neighbourhood of the still-water line. They use
the shallow-water trochoidal theory for uniform, progressive waves. According

to this theory, progressive waves are at the limit of stability if their amplitude ($\frac{1}{2}H$) equals the mean depth (d). Thus, denoting the condition of incipient breaking by the index "c",

$$\frac{1}{2}H_c = d_c \tag{6}$$

The depth d_c at which this would occur is equated by Iribarren and Nogales to the mean undisturbed depth in the one-quarter wavelength adjacent to the still-water line, or

$$d_c = \frac{1}{2} (\frac{1}{4} L_c \tan \alpha_c) = \frac{1}{8} L_c \tan \alpha_c \quad . \tag{7}$$

The wavelength L_c is calculated as $T_c \sqrt{gd_c}$, so that

$$d_c = \frac{1}{8} T_c \sqrt{gd_c} \tan {}_c \quad . \tag{8}$$

Elimination of d_c between (6) and (8) gives

$$(T\sqrt{g/H} \tan \alpha)_c = 4\sqrt{2} \tag{9}$$

or, substituting (2) and rearranging,

$$\xi_c = (\frac{\tan \alpha}{\sqrt{H/L_0}})_c = \frac{4}{\sqrt{\pi}} \approx 2.3 \quad . \tag{10}$$

Laboratory experiments by Iribarren and Nogales and others [8, 13] have confirmed the validity of (10), with the proviso that $\xi \approx 2.3$ corresponds to a regime about halfway between complete reflection and complete breaking. This quantitative agreement is considered to be fortuitous because one can raise valid objections against the derivations on several scores. These pertain to the numerical estimates used by Iribarren and Nogales, rather than to the approach as such. For instance, the limiting height for waves in shallow water is given by (6) as twice the depth, which is unrealistic. A height-to-depth ratio of order one seems more reasonable. The author has elsewhere [1] suggested more realistic values for the various numerical factors in (6), (7) and (8), which however happened to yield exactly the criterion (9) again. Even so, the fact that (9) is correct not only qualitatively but also quantitatively is still

considered to be somewhat fortuitous, because derivations such as these can be useful for indicating the form in which the respective variables are to be combined, but they cannot in general be expected to give correct quantitative predictions.

The derivation given by Iribarren and Nogales suggests a physical interpretation of the parameter ξ, at least if wave breaking occurs ($\xi < \xi_c$). Consider the local steepness of the breaking waves. Their celerity is proportional to $(gd)^{\frac{1}{2}}$, their wavelength to $T(gd)^{\frac{1}{2}}$, and their steepness to $H/(T(gd)^{\frac{1}{2}})$, or to $(H/gT^2)^{\frac{1}{2}}$, since H/d is of order one for waves breaking in shallow water. Thus, the parameter ξ, given by

$$\xi \equiv \frac{\tan \alpha}{\sqrt{H/L_0}} = \frac{1}{\sqrt{2\pi}} \frac{\tan \alpha}{\sqrt{H/gT^2}} \quad , \tag{11}$$

is roughly proportional to the ratio of the tangent of the slope angle (the slope "steepness") to the local steepness of the breaking wave. The criterion for breaking given by Iribarren and Nogales can therefore be said to imply that incipient breaking corresponds to a critical value of this ratio.

Breaker types

So far the parameter ξ has been considered only in the context of a breaking criterion, that is, as an aid in answering the question whether wave breaking will occur. However, it also gives an indication of how the waves break. The main types are surging, collapsing, plunging and spilling breakers [9, 15, 4]. These occur in the order of increasing wave steepness and/or decreasing slope angle. The transition from one breaker type to another is of course gradual. The values of α and H/L_0 mentioned in what follows should be considered as indicating the order of magnitude only of the values in the transition ranges.

Galvin [4] has presented criteria regarding breaker types in terms of an "offshore parameter" $H_0/(L_0 \tan^2 \alpha)$, in which H_0 is a deep-water wave height calculated from the motion of the generator bulkhead and the water depth, and an "inshore parameter" $H_b/(gT^2 \tan \alpha)$. The index "b" refers to values at the break point, which is taken to be the most seaward location where some point of the wave front is vertical, or, if this does not occur, the location where foam first appears at the crest.

Galvin's offshore parameter can be written as ξ_0^{-2}, in which the index "0"

refers to deep water (wave height). Converting the critical values of the offshore parameter given by Galvin to values of ξ_0 gives

surging or collapsing   if $\xi_0 > 3.3$

            plunging   if $0.5 < \xi_0 < 3.3$

            spilling   if $\xi_0 < 0.5$

These results are based on experiments on slopes of 1 5, 1 10 and 1 20.

The inshore parameter used by Galvin, $H_b/(gT^2 \tan \alpha)$, is not equivalent to the parameter ξ_b used here. However, a re-analysis of Galvin's data in terms of $\xi_b = (H_b/L_0)^{-\frac{1}{2}} \tan \alpha$ showed that the classification of breakers as plunging or spilling could be performed equally well with ξ_b as with Galvin's inshore parameter [1]. The following approximate transition values were found

surging or collapsing if $\xi_b > 2.0$

            plunging   if $0.4 < \xi_b < 2.0$

            spilling   if $\xi_b < 0.4$

The possibility of using a parameter equivalent to ξ_b as a breaker type discriminator has also been noted by Galvin in a more recent review of breaker characteristics [5].

Phase difference across the surfzone

Not only the form of a breaking wave varies with ξ, but the distance of the break point from the mean water line as well. This distance, expressed in wave-lengths, is estimated at roughly $(d_b \cot \alpha)/(\frac{1}{2}T \sqrt{gd_b}) \approx 0.8 \xi_b^{-1}$, where we have put $H_b \approx d_b$. Observations by the author on slopes between 1 3 and 1·25, with ξ-values from 0.15 to 1.9, have indicated that his estimate is qualitatively correct, but that it is roughly 20% too high. With spilling breakers there are at least two breaking or broken waves in the surf zone simultaneously. This number ranges from zero to two for plunging breakers. Collapsing breakers occur almost at the instantaneous water's edge, so that there is at most one of these present at any one time. Reference should be made in this connection to Kemp [10], who points out that the total phase difference across the surf zone is indicative of the type of wave motion, and of the corresponding equilibrium profile

of sand or shingle beaches.

Breaker height-to-depth ratio

The ratio of wave height to water depth at breaking is an important parameter of the surf zone, it is here denoted by the symbol γ_b.

$$\gamma_b = \frac{H_b}{d_b} \qquad (12)$$

The depth d_b is here defined as the still-water depth at the break point.

Values of γ_b generally range between 0.7 and 1.2. Bowen et al [3] suggest that γ_b may be a function of ξ_0 only. The data presented by them are given in fig. 1. In addition, data have been plotted from Iversen [9], from Goda [6], and from unpublished results obtained by the present author.

It can be observed that the results from Bowen et al [3] form a separate group, outside the range of the others. The reason for this is not known. The other points in fig. 1 show a weak trend with ξ_0. For values of ξ_0 less than about 0.2, in the range of spilling breakers, they are scattered about a value of $\gamma_b \approx 0.8$, while there is a slow increase with ξ_0 for higher values.

The scatter in the results may partly be due to the fact that for this purpose the independent variables H/L_0 and α cannot adequately be combined in the single parameter ξ. However, even the values of γ_b presented by various authors for the same values of α and H/L_0 show considerable scatter. This is undoubtedly to some extent due to the difficulties and ambiguities inherent in defining (experimentally) and measuring breaker characteristics. Another factor contributing to the scatter may be the occurrence of parasitic higher-harmonic free waves which are often inadvertently generated along with the intended wave train. The secondary waves affect the breaking process in a manner depending on the phase difference with the primary wave, which in turn depends (among others) on the distance from the wave generator. This distance is not commonly introduced as an independent variable, so that any effects which it may have on the results can appear as unexplained scatter.

Set-up, run-up and run-down

The set-up is defined as the wave-induced height of the mean level of the water surface above the undisturbed water level. Theoretical and experimental

results [11, 3] indicate that the gradient of the set-up in the surf zone on
gently sloping beaches is proportional to the beach slope, the coefficient of
proportionality is a function of γ, the average height-depth ratio of the waves
in the surf zone. The maximum set-up is roughly equal to $0.3 \gamma H_b$.

The run-up height R_u is defined as the maximum elevation of the waterline
above the undisturbed water level. A simple and reliable empirical formula for
the run-up height of waves breaking on a smooth slope has been given by Hunt
[7]. It can be written as

$$\frac{R_u}{H} = \xi \qquad \text{for } 0.1 < \xi < 2.3 \quad . \tag{13}$$

An investigation by Battjes and Roos [2] of some details of the run-up of
breaking waves on dike slopes (1·3, 1·5, 1 7), such as the mean velocity of
advance, particle velocities, layer thickness and so on, has shown that many
of these parameters are functions of ξ only if normalized in terms of the
incident wave characteristics.

Measurements of the run-down height R_d (minimum elevation of the waterline
above the undisturbed water level) are very scarce, and, if available, not very
accurate since run-down is rather ill-defined experimentally. An analysis of
the measurements by Battjes and Roos [2], supplemented with unpublished data
gathered for this study, has indicated that in the experimental range
(cot α = 3,5,7,10; 0.02 < H/L_0 < 0.09, 0.3 < ξ < 1.9) the run-down height R_d
is roughly equal to $(1 - 0.4 \xi)R_u$. In other words, the ratio of the variable
part of the vertical motion of the waterline $(R_u - R_d)$ to the maximum elevation
above S.W.L. is approximately 0.4ξ. It has a maximum value of about 1 for waves
in the transition from non-breaking to breaking, and decreases with decreasing
ξ. For very small ξ the set-up constitutes the greater part of the run-up height.

Reflection and absorption

The relative amount of wave energy that can be reflected off a slope is
intimately dependent on the breaking processes and the attendant energy dissi-
pation. Because of this, and in view of the fact that these processes appear
to be governed to such a large extent by the parameter ξ, it is natural to try
to relate the reflection coefficient to ξ.

The reflection coefficient r is defined as the ratio of the amplitude of
the reflected wave to the amplitude of the incident wave. The estimation of r

on a slope generally takes place according to a procedure given by Miche [13]
who assumes that the reflected wave height equals the maximum height possible
for a non-breaking wave of the given period on the given slope, in other words,
only the energy corresponding to the height in excess of the critical height
is assumed to be dissipated. This gives

$$r_{th} = \frac{(H_0/L_0)_c}{H_0/L_0} \qquad \text{if this is less than 1}$$

$$= 1 \qquad \text{otherwise,}$$

(14)

in which $(H_0/L_0)_c$ is the critical steepness for the onset of breaking, for
which Miche uses an expression derived previously by him [12]. The index "th"
refers to "theoretical". The actual reflection coefficient will be smaller than
r_{th} due to effects of viscosity, roughness, and permeability. Miche recommends
a multiplication factor of 0.8 for smooth slopes.

Miche's assumption regarding the reflection coefficient can be expressed
in terms of ξ and Iribarren and Nogales' breaking criterion. Substitution of
(5) into (14) gives

$$r_{th} = (\xi/\xi'_c)^2 \qquad \text{if this is less than 1}$$

$$= 1 \qquad \text{otherwise,}$$

(15)

in which ξ'_c is the critical value of ξ for the onset of breaking, as
distinguished from ξ_c, the value given by Iribarren and Nogales for the con-
dition halfway between the onset of breaking and complete breaking ($\xi_c \sim 2.3$),
for which the reflection coefficient is about 0.5 [7, 8]. So (15) becomes

$$r \sim 0.1 \, \xi^2 \qquad \text{if this is less than 1}$$

$$= 1 \qquad \text{otherwise}$$

(16)

An extensive series of measurements of the reflection coefficient of plane
slopes has recently been presented by Moraes [14]. His results for slopes with
$\tan \alpha = 0.10$, 0.15, 0.20 and 0.30 have been replotted in terms of r vs ξ in fig. 2.
The experimental points for the four slopes more or less coincide with each other
and with the curve representing eq. (16) for $\xi < 2.5$, i.e. as long as the waves
break. For $\xi < 2.5$ they diverge, gentler slopes giving less reflection than
steeper slopes (at the same value of ξ).

GENERAL COMMENTS REGARDING THE PARAMETER ξ

In the preceding paragraphs examples have been given of a number of characteristic surf parameters for the determination of which it is not necessary to specify both α and H/L_0, but only the combination $\tan \alpha/(H/L_0)^{\frac{1}{2}}$. It may be useful to summarize them here a breaking criterion, the breaker type, the breaker height-to-depth ratio, the number of waves in the surf zone, the reflection coefficient (therefore also the discrimination between progressive waves and standing waves), and the relative importance of set-up and run-up. They have been collected in Table 1. Characteristic values of ξ are given in the upper row of the table. Each of the following rows indicates how one of the parameters just mentioned varies with ξ.

The recognition of the possibility that several properties can roughly be expressed as functions of ξ alone contributes to a more unified understanding of the phenomena involved. Such understanding would be deepened by further insight in the nature of the parameter ξ itself. One interpretation has already been mentioned in the preceding, when it was observed that ξ is approximately become proportional to the ratio of the tangent of the slope angle to the shallow-water wave steepness. Also, ξ^{-1} had been seen to be approximately proportional to the number of wavelengths within the surf zone. This is in essence equivalent to saying that ξ is approximately proportional to the relative depth change across one wavelength in the surf zone. This interpretation is obviously relevant to the dynamics of the breaking waves, particularly with regard to their rate of deformation. It makes it plausible that ξ is of importance, but it does not prove that ξ serves as the sole determining factor for the (suitably normalized) parameters of the surf. Indeed, there are valid arguments which throw doubt on this possibility of full similarity. In this regard it is useful to consider two situations of different slope angle and wave steepness as a prototype and a distorted scale model thereof. It is well known that Froudian model-prototype similarity can be obtained even in distorted models, provided the assumption of hydrostatic pressure distribution is valid both in the prototype and in the model. Pertinent scale ratios (λ) are given in Table 2, expressed in terms of the horizontal and vertical geometrical scales and the scale of the gravitational acceleration (unity).

ξ	~ 0.1	0.5	1.0	2.0	3.0	4.0	5.0
	spilling	breaking	plunging	collapsing/surging		no breaking	
H_b/d_b	0.8	1.0	1.1	1.2			
$N^{*)}$	6-7	2-3	1-2	0-1	0-1		
r	10^{-3}	10^{-2}	10^{-1}	4×10^{-1}	8×10^{-1}		
	absorption			reflection			
	progressive wave			standing wave			
	set-up predominant		run-up predominant				

$^{*)}$ number of waves in surf zone

Table 1

Variable	Symbol	Scale ratio
horizontal length	ℓ	λ_ℓ
depth	d	λ_d
gravity acceleration	g	$\lambda_g = 1$
bottom slope	$\tan \alpha$	$\lambda_{\tan \alpha} = \lambda_d \lambda_\ell^{-1}$
wave height	H	$\lambda_H = \lambda_d$
wave length	L	$\lambda_L = \lambda_\ell$
wave celerity	$c \sim (gd)^{\frac{1}{2}}$	$\lambda_c = \lambda_d^{\frac{1}{2}}$
wave period	$T = L/c$	$\lambda_T = \lambda_\ell \lambda_d^{-\frac{1}{2}}$

Table 2 - Scale ratios for a distorted long-wave model.

Since ξ is defined as

$$\xi = (\frac{gT^2}{2\pi H})^{\frac{1}{2}} \tan \alpha \quad , \tag{17}$$

its scale ratio is

$$\lambda_\xi = \lambda_T \, \lambda_H^{-\frac{1}{2}} \, \lambda_{\tan \alpha} \, , \tag{18}$$

which becomes, using the values given in Tabel 2,

$$\lambda_\xi = (\lambda_\ell \lambda_d^{-\frac{1}{2}})(\lambda_d^{-\frac{1}{2}})(\lambda_d \lambda_\ell^{-1}) = 1 \quad . \tag{19}$$

In other words, a distorted long-wave model which is dynamically similar
to its prototype necessarily has the same ξ as this prototype. Conversely,
a distorted wave-model with the same value of ξ as its prototype is similar
to this prototype if the pressure distribution in both is hydrostatic. This
is not the case in breaking waves in shallow water, where some effects of the
vertical accelerations must be taken into account due to the fact that the
surface curvature is locally strong. Thus, the existence of similarity of the

surf in distorted models is not proved, and must be doubted to the extent
that deviations from the long-wave approximations have a significant effect.
Such effects are certain to be of importance for the details of the local
flow patterns, but this is not necessarily the case for overall properties of
the surf. The final check on this must of course be obtained empirically.
In this regard it appears justified to draw the conclusion from the data
presented above that the factor ξ is a good indicator of many overall proper-
ties of the surf zone, and may indeed be called a similarity parameter. The
importance of this parameter for so many aspects of waves breaking on slopes
appears to justify that it be given a special name. In the author's opinion
it is appropriate to call it the "Iribarren number" (denoted by "Ir"), in
honor of the man who introduced it and who has made many other valuable
contributions to our knowledge of water waves.

REFERENCES

1. Battjes, J.A., Computation of set-up, longshore currents, run-up
    and overtopping due to wind-generated waves, Communications on
    Hydraulics, Delft University of Technology, Rep. 74-2, 1974.

2. Battjes, J.A. and Roos, A., Characteristics of flow in periodic wave
    run-up, in press, 1974.

3. Bowen, A.J., Inman, D.L. and Simmons, V.P., Wave "set-down" and set-up,
    J. Geoph. Res., 73, 8, 1968, p. 2569-2577.

4. Galvin, C.J. Jr., Breaker Type Classification on Three Laboratory
    Beaches, J. Geoph. Res., 73, 12, June 1968, p. 3651-3659.

5. Galvin, C.J. Jr., Wave breaking in Shallow Water, in Waves on Beaches,
    Ed. R.E. Meyer, Academic Press, New York, 1972, p. 413-456.

6. Goda, Y., A synthesis of breaker indices, Trans. Jap. Soc. Civ. Eng.,
    2, 2, 1970, p. 227-230.

7. Hunt, I.A., Design of seawalls and breakwaters, Proc. ASCE, 85, WW3,
    Sept. 1959, p. 123-152.

8. Iribarren, C.R. and Nogales, C., Protection des Ports, Section II,
    Comm. 4, XVIIth Int. Nav. Congress, Lisbon, 1949, p. 31-80.

9. Iversen, H.W., Laboratory Study of Breakers, Nat. Bur. of Standards,
    Circular 521, Washington, D.C., 1952, p. 9-32.

10. Kemp, P.H., The relationship between wave action and beach profile
    characteristics, Proc. 7th Conf. Coastal Eng., The Hague, 1960.

11. Longuet-Higgins, M.S. and Stewart, R.W., A note on wave set-up, J.
    Mar. Res., 21, 1963, p. 4-10.

12. Miche, R., Mouvements ondulatoires de la mer en profondeur constante
    ou décroissante, Ann. des Ponts et Chaussées, 114è Année, 1944.

13. Miche, R., Le pouvoir réfléchissant des ouvrages maritimes exposés
     à l'action de la houle, Ann. des Ponts et Chaussées, 121è Année, 1951,
     p. 285-319.

14. Moraes, Carlos de Campos, Experiments of Wave Reflexion on Impermeable
     slopes, Proc. 12th Conf. Coastal Eng., Washington, D.C., 1970, Vol. I,
     p. 509-521.

15. Patrick, D.A. and Wiegel, R.L., Amphibian tractors in the surf, Conf.
     Ships and Waves, 1, 1954, p. 397.
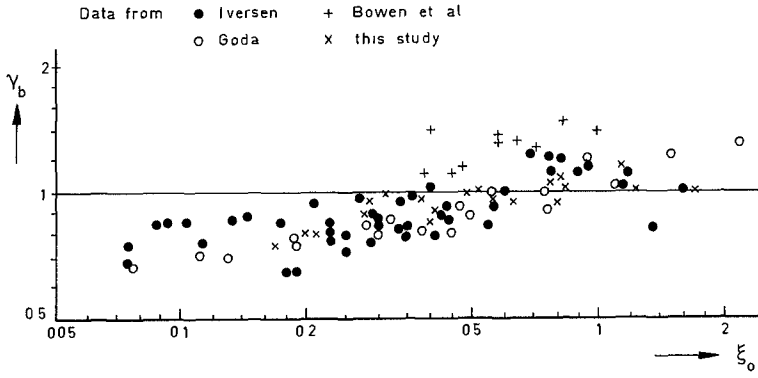
Figure 1 - Height-depth ratio at breakpoint vs. the similarity parameter.
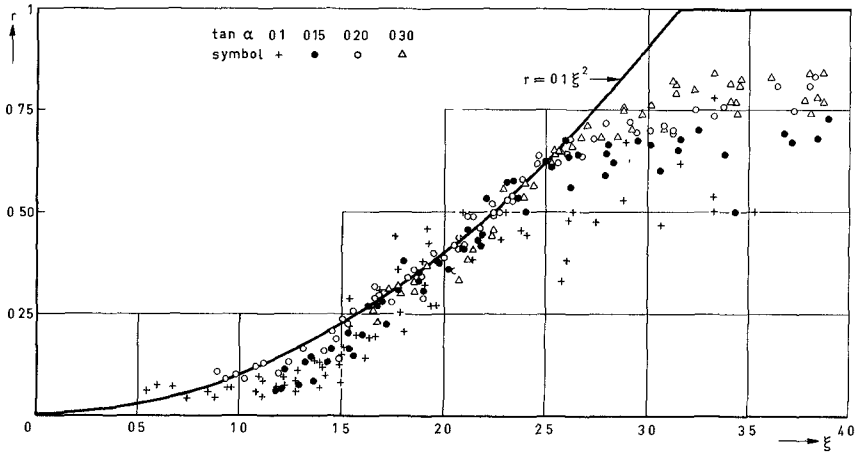
Figure 2 - Reflection coefficient vs. the similarity parameter.

CHAPTER 27

On Wave Deformation After Breaking

Toru Sawaragi
Professor of Civil Engineering
Osaka University, Osaka,Japan

and

Koichiro Iwata
Lecturer of Civil Engineering
Osaka University, Osaka,Japan

ABSTRACT

Waves will dissipate their energy rapidly after breaking. In this paper, the three factors , (i) formation of a horizontal roller,(ii) bottom friction,and (iii) turbulence with air entrainment, which will contribute to the energy dissipation, are dealt with experimentally and theoretically

The horizontal roller formed by a plunging breaker is approximated as a Rankine-type vortex by experiments,and it is calculated that 15%-30%of wave energy is dissipated due to the formation of horizontal roller alone from a breaking point to a point of the roller disappearance.

A bottom shear stress due to a breaker is measured by the shear meter deviced by the authors and it is clarified that the energy dissipation due to bottom friction is a little

Main part of the energy dissipation is taken to be caused by the turbulence with air entrainment. It is indicated that an incident monocromatic wave is transformed into a higher frequency wave due to the turbulence. Furthermore, a new basic equation for breaking waves with a turbulence term expressed by a Reynolds stress is presented The theoretical curves computed numerically have a consistent agreement with the experimental results

1 INTRODUCTION

Phenomenon of wave breaking and wave deformation after breaking has been a matter of great interest to coastal engineers as well as investigations in the hydrodynamic field. Therefore, so far, in the experimental and theoretical approaches,numerous investigations have been done to clarify the mechanism of wave deformation in a surf zone

In the theoretical treatments, many investigations have assumed model waves such as solitary wave and bore with some appropriate assumptions that waves have their critical heights as progressive waves,etc However, these theoretical works could not explain sufficiently the mechanism of wave deformation after breaking. In the experimental investigations various studies have been carried out mainly on a sloping beach model.There necessarily exist,in the sloping beach model,return flow,wave set-up and set-down,wave shoaling and wave reflection Since these factors interact very complicatedly,the important characteristics of turbulence caused by wave breaking,can not be clarified in details.Mason(1951)already pointed out the necessity of experimental investigations on a horizontal bottom Galvin (1969) carried out some experiments on a composite slope consisted of an approach ramp with a 1/15 slope leading up to a horizontal surface and showed facts about the characteristics at the breaking point. But the mechanism of wave deformation after breaking was not discussed

As above mentioned, these foregoing investigations seem to be unable to clarify the mechanism of wave deformation or wave energy dissipation in a surf zone Thus, the application of a more special experimental method to reveal the characteristics of turbulence itself or a more reasonable theoretical treatment will be required

The present paper is to clarify the mechanism of wave deformation and energy dissipation in experimental and theoretical treatments

2 BEHAVIOR OF WAVES AFTER BREAKING

2-1 Equipment and Procedure

Experiments were conducted to clarify such hydrodynamic behaviors of waves at a breaking point and after breaking as breaker types,scale of splash and horizontal roller,wave height attenuation, etc.,by using an indoor wave tank in 0.7m width,0 95m height and 30m length At one end of the tank was installed a flap-type wave generator which was controlled by an electric dynamic shaker and could generate waves

in different periods and amplitudes. At the other end of the tank, a horizontal bottom was installed and connected to the channel bottom with a slope of 1/18 as shown in Fig.-1. In this horizontal bottom, there are no return flow and shoaling effect as observed in a sloping beach. Therefore, turbulence itself caused by breaking can be deduced. Wave heights were measured by resistance-type wave gauges. A wave height in deep water, H_o, is calculated by the small-amplitude wave theory (Wiegel,1964)from a measured wave height in front of the wave generator. For each experimental run, by using a high speed cine-camera(100-200 frames/sec), the breaking region was filmed through a grid on glass walls of the channel with the camera axis kept at the still water level. From these films, the scale of the horizontal roller, the domain of the roller existence, the scale of splash and the region of air entrainment in the breaker were decided. To obtain the movement of water particles in the breaker, particles of a mixture of xylen and carbontetrachloride with zinc oxide for coloring,with a specific gravity corresponding to that of the water, were introduced in the surf zone. Point to point movement of the particles was then recorded on films, from which each particle velocity was obtained by superposition of projected film frames to give a distance and a time interval of movement. Wave heights in the breaking zone was estimated as ten-wave averages from wave gauge recorders compareing with film analyses. The incident waves were forced to break themselves on a horizontal bottom or just at the corner between the elevated horizontal bed and the sloping bed. The test program is shown in Table-1.

h	H_0	T_0	H_0/L_0
7 cm	3.5 ~ 11.5 cm	0.8, 1.0, 1.2 sec	0.016 ~ 0.115
11 cm	6.0 ~ 12.0 cm	0.8, 1.0, 1.2 sec	0.031 ~ 0.105
14 cm	7.5 ~ 13.5 cm	0.8, 1.0, 1.2 sec	0.033 ~ 0.105

Table - 1. Test program

2-2 Experimental Results

Breaker type and breaker height
A breaker is classified into a plunging breaker and a spilling breaker as shown in Fig.-2. But a surging breaker (or a collapsing breaker) occurring in a sloping beach is not observed in this case. Therefore, the surging breaker is a particular breaking pattern in a sloping beach. The transient region between the two breaker types is given as follows

$$H_o / h_b = 0.72 \quad\text{---------------------------------- (1)}$$

Fig.-3 shows the relation between wave steepness,H_o/L_o, and the ratio,H_b/h_b, of breaker height H_b and water depth h_b. It is recognized that H_b/h_b becomes larger as H_o/L_o is larger and that H_b/h_b for a plunging breaker is larger than that for a spilling breaker.

Characteristics of turbulence after breaking
The pattern of wave deformation after breaking is clearly different between a plunging breaker and a spilling breaker. In case of the plunging breaker, as shown in Fig.-4(a), there exist a horizontal roller and a splash. The horizontal roller draws air bubble deep into the water body and the air bubble rises rapidly upwards as the roller disappears. On the other hand, in case of the spilling breaker, as shown in Fig.-4(b), keeping the symmetry of wave forms at the crest, a white cap is observed at the cusped-crest and the air entrainment is limitted on the wave front face. In Fig.-4, the origin of X is just a breaking point and X_B,X_V,X_C and X_A indicate a point where a wave crest touches down the water, a roller disappears, a splash touches down the water and air bubble disappears from the water body, respectively. Fig.-5 shows the relation of $X_B/L,X_V/L,X_C/L,X_A/L$ and H_o/L_o, where L is the wave length at the depth of h calculated by the small-amplitude wave theory(Wiegel,1964). It is recognized that the relation of $X_B/L \lessgtr X_V/L \lessgtr X_C/L \lessgtr X_A/L$ is established and that X_A/L is largely affected by h/L_o and H_o/L_o. Judging from Fig.-3, X_A/L for a

Fig.- 1   Laboratory installation

Fig.-2. Breaking pattern and breaking criteria.

Fig.- 3. Breaker height.

Fig.-4 Sketch of charateristics of wave breaking pattern.

Fig -5 Relation among X_B/L, X_V/L, X_S/L, X_A/L and H_o/L_o
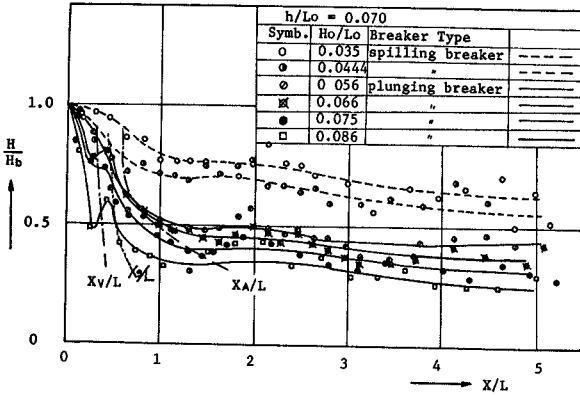
Fig.-6. Wave height attenuations after breaking (h/L_o=0 070)

plunging breaker is recognized to be larger than that for a spilling breaker Fig -6 shows a wave height attenuation after breaking. It is made clear that the degree of wave height attenuation becomes larger as H_0/L_0 is larger and that it is closely connected to the turbulence of breaking waves That is, the wave height attenuation for $X/L \leq X_A/L$ is larger than that for $X/L \geq X_A/L$ In case of a plunging breaker, the wave height attenuation is the largest for $X/L \leq X_V/L$, which indicates that some of the energy is transmitted into the kinematic energy of the horizontal roller

3 EFFECT OF HORIZONTAL ROLLER ON WAVE ENERGY DISSIPATION

The hydrodynamic characteristics of the roller were made clear by the above-mentioned experiments in Section 2 As shown in Fig -7, the distribution of the angular velocity of the roller is approximated as a Rankine type vortex so that the angular velocity can take a maximum value at $r = r_0$ In the experiments, r_0 is nearly equal to 0 44H_b as shown in Fig -8

Now, consider the effect of the horizontal roller on wave energy dissipation The kinematic energy, E_r, of this roller is defined as follows (Hino,1971)

$$E_r = \frac{1}{4} \mathcal{S} \pi (q_0 r_0)^2 (1 + 4 \ell_n(a/r_0)) , \text{---------(2)}$$

where q_0=angular velocity at $a=r_0$, $\mathcal{S}$= water density
If the breaking wave energy is assumed to be expressed as the same expression as before breaking, the energy dissipation from the breaking point to the point of the roller disappearance, E_L, is given as follows

$$E_L = \frac{1}{8} \mathcal{S} g(H_b^2 - H_V^2)L , \text{-- (3)}$$

where H_V=wave height at a point of the roller disappearance Therefore, the rate of energy transmitted to this roller, $\mathcal{E}_r$, is given in Eq (4)

$$\mathcal{E}_r = \frac{E_r}{E_L} = \frac{2 \pi (q_0 r_0)^2 (1 + 4 \ell_n(a/r_0))}{gL (H_b^2 - H_V^2)} \text{---------------------------- (4)}$$

Now, putting the relation of r_0=0 44H_b into Eq (4), the following expression is obtained

$$\mathcal{E}_r = \frac{1 216 q_0^2(1 + 4 \ell_n(a/r_0))}{gL (1 - (H_V/H_b)^2)} \text{------- (5)}$$

Fig -9 shows the theoretical values of Eq (5) and the experimental results The theoretical values show that $\mathcal{E}_r$ takes a larger value as q_0^2/qL becomes larger and a/r_0 becomes larger The experimental results indicate that 15%-30% of the energy dissipation of wave is transmitted to the kinematic energy of the roller. Therefore, it is concluded that the most of the energy will be dissiapted by the other factors such as bottom friction, splash and turbulence with air entrainment, etc

sym	r cm	q sec
●	2 5	12 0
◗	3 2	16 9
✖	3 7	11 1
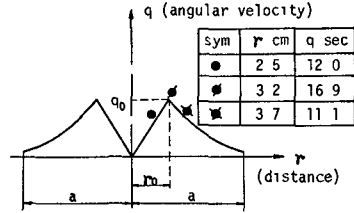
Fig -7   Distribution of an angular velocity of horizontal roller

SYM	hb/Lo	SYM	hb/Lo
○	0 0697	◐	0.0489
●	0 0700	⋈	0 0449
◑	0 0622	◓	0 0311
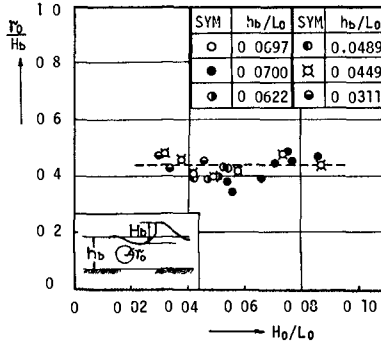
Fig -8   Relation between r_0/H_b and H_0/L_0.
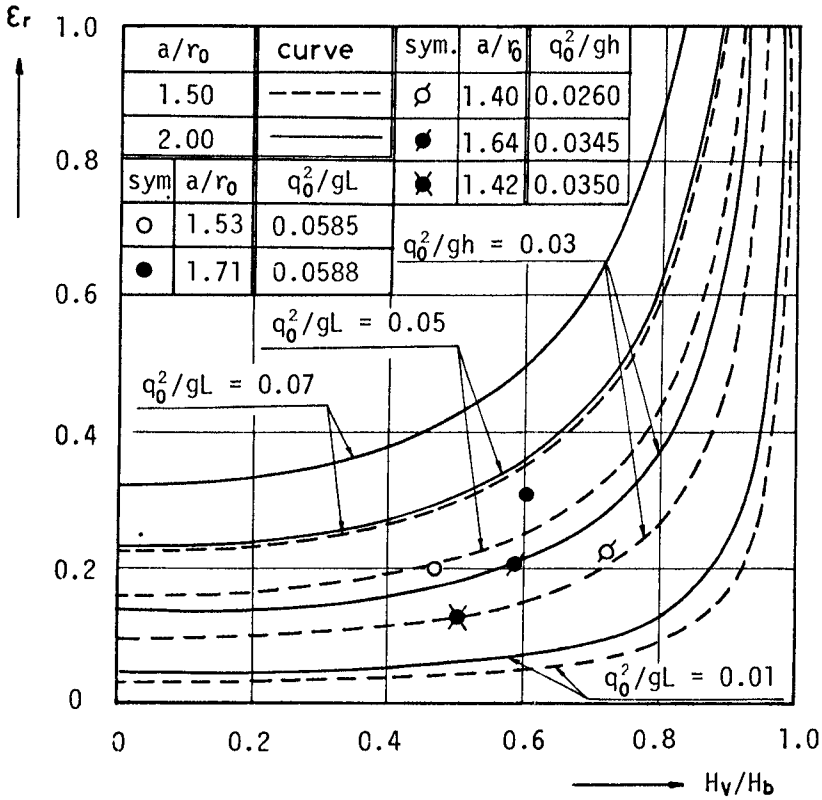
Fig.-9.   Relation between $\mathcal{E}_r$ and H_v/H_b.

4 EFFECT OF BOTTOM FRICTION ON WAVE ENERGY DISSIPATION

4-1 Equipment and Procedure

A bottom shear stress due to wave motion was measured by the shear meter deviced by the authors A schematic view of the shear meter is shown in Fig -10 A small raised channel was set transversely from wall to wall of the frame below the shear plate To prevent flow through gaps under the plate, the channel was filled with mercurry until its meniscus touched the underside of the shear plate as Eagleson (1962) already deviced If the flow under the shear plate is not stopped, the pressure gradient is different between above and below the shear plate, which causes a force acting in the opposite direction to the original wave force

A shear force acting on the shear plate is measured by converting the force into a moment of the supporting shaft The shear plate is subjected to a force due to wave pressure gradient in addition to the shear force Therefore, the force due to the pressure gradient is calculated from the pressure difference measuered by pressure measuring tubes Before measuring bottom friction force due to breaking waves, the shear meter was checked under various laminar conditions, and it is recognized that the results coincide well with the theoretical values as shown in Table-2, in which theoretical values are calculated by using the theory of Iwagaki-Tuchiya-Chin (1965)

4-2 Experimental Results

Fig -11 shows time profiles of a bottom shear stress and a wave , and it indicates that the time prifiles of the shear stress due to a plunging breaker is very asymmetric as compared with those in the case of a spilling breaker Fig.-12 shows change of non-dimensional maximum bottom shear stresses which act in the wave propagation direction and its opposite direction for the two type of breakers In Fig - 12, X is a distance from a breaking point and the dotted lines express the shear stress estimaeted by the smooth laminar boundary layer theory(Iwagaki- Tuchiya-Chin,1965)given as follows

$$\frac{\zeta_{b\ max}}{\varsigma g H} = \frac{\sqrt{2\nu}}{g\ \sinh(\ kh\ )} (\ \frac{\pi}{T})^{3/2} \quad , \quad \text{------------------------------------ (5)}$$

where,ν = kinematic fluid viscosity, $\zeta_{b\ max}$= maximum bottom shear stress, k=2π/L, ς = fluid density and H=wave height at the depth of h

From this figure, it will be pointed out that the maximum bottom shear stresses in the region for $X \lessgtr X_A$ are considerably larger than those in the region for $X > X_A$ Therefore,it is made clear that the bottom shear stresses become larger due to the turbulence with air entrainment As shown in Fi -11, the time profiles of the bottom shear stresses are very asymmetric, and then the coefficient of the bottom friction used earlier can not be applied Then, the newly defined bottom friction coefficient, $\hat{C}_f$, is used in this study, which is defined as follows

$$\hat{C}_f = \frac{1}{2\pi}(\ \theta_c \hat{C}_{fc} + \theta_t \hat{C}_{ft}\ ) \quad , \quad \text{------------------------------ (6)}$$

$$\hat{C}_{fc} = 2|\overline{\zeta}_{bc}| / |\overline{u}^{-2}_{bc}| \quad , \quad \hat{C}_{ft} = 2|\overline{\zeta}_{bt}|/|\overline{u}^{-2}_{bt}| \Bigg\} \quad \text{-------------------- (7)}$$

$$\theta_c + \theta_t = 2\pi \Bigg\}$$

where θ = phase, U_{bc}= horizontal bottom particle velocity moving toward wave propagation direction, U_{bt}= horizontal bottom particle velocity moving toward anti-wave propagation direction, ζ_{bc}= bottom shear stress acting toward wave propagation direction, ζ_{bt}= bottom shear stress acting anti-wave propagation direction, and the sign, — indicates mean value about the time

Fig -13 indicates the change of $\hat{C}_f$ as waves propagate, from which $\hat{C}_f$ is recognized to have no clear characteristics as waves propagate Fig -14 shows the relation among $\hat{C}_f$, $\hat{C}_{ft}$, $\hat{C}_{fc}$ and Reynolds number Re (= $\overline{U}_b^2 \cdot T/\nu$) It is shown that $\hat{C}_f$, $\hat{C}_{ft}$, $\hat{C}_{fc}$ become larger as Re is smaller But, the experimental values are generally larger than the theoretical value, $\hat{C}_f$= 4 5 $R_\theta^{\frac{1}{2}}$ based on the smooth laminar boundary layer theory(Iwagaki-Tuchiya-Chin,1965)

The coefficient of bottom friction, f , already used in the fields observations is defined as follows(Putnam-Johnson,1949).

$$f = \zeta_{b\ max} / \varsigma u^2_{b\ max} \quad , \quad \text{--------------------------------} \quad (8)$$

where $\zeta_{b\ max}$ = maximum bottom shear stress, $U_{b\ max}$ = maximum horizontal particle velocity at the bottom
Fig -15 shows the relation between f and Reynolds number R_{eT} (= $U^2_{b\ max}$ · T/ν), in which the straight
line indicates the theoretical values based on the smooth laminat boundary layer theory The experi-
mental values after breaking indicate 2 - 4 times larger than the theoretical value, $f = 2\ 08R^{-\frac{1}{2}}_{eT}$ (Iwa-
gaki-kakinuma-miyai,1965)
    Now, the energy dissipation due to bottom friction is discussed The mean energy loss, $\overline{E}_{fb}$,due to
the bottom friction per unit area is calculated by the following equation

$$\overline{E}_{fb} = \frac{1}{T} \int_0^T \overline{U}_b \overline{\zeta}_b \ dt \quad , \quad \text{--------------------------------} \quad (9)$$

where $\overline{U}_b$ and $\overline{\zeta}_b$ are a mean value of horizontal particle velocity and a shear stress at the bottom in
the region of the same sign under wave motion, respectively On the other hand, the following relation
is derived by the energy balance for a wave

$$\frac{d}{dx}(C_g E) = \overline{E}_{fb} + \overline{E}_{ft} \quad , \quad \text{--------------------------------} \quad (10)$$

where C_g= group velocity of wave, E = wave energy , and $\overline{E}_{ft}$ mean energy loss due to some other causes
than the bottom friction
    If E and C_g satisfy Eq (11),the ratio, $\mathcal{E}$, of energy loss due to the bottom friction to the total
energy loss for dx is represented by Eq.(12) as follows·

$$\left.\begin{array}{l} E = \frac{1}{8}\varsigma g\ H^2 \\[2mm] C_g= C \end{array}\right\} \quad \text{--------------------------------} \quad (11)$$

$$\mathcal{E} = \frac{\overline{E}_{fb}}{\frac{d}{dx}(C_g E)} = \frac{4\int_0^T \overline{\zeta}_b \cdot \overline{U}_b \ dt}{gH\cdot T\ C\ (\ dH/dx)} \quad \text{--------------------------------} \quad (12)$$

    Using the experimental values for wave height attenuation and shear stresses , $\mathcal{E}$ is calculated by
Eq (12) as shown in Table-3 From this calculation, it is clear that the energy loss due to the bottom
friction is quite small, that is , while a wave propagate to the distance about the twice wave length,
the rate of the energy loss due to the bottom friction takes 9% of the total energy at most
    After all, it is concluded that the energy dissipation due to a horizontal roller and bottom fric-
tion is a little. Therefore, the authors have to admit that the turbulence with air entrainment is the
most important factor for a wave decay after breaking

h (cm)	28		(water temperature = 8°c)					
T (sec)	0 8		1 0			1 2		
h/Lo	0 28		0 179			0 124		
H (cm)	0 4	1 25	1 0	1 16	1 56	0 66	1 19	1 57
$(F_b\ max)ex$ (gr)	0 260	0 920	0 690	0 868	1 130	0 521	1 137	1 389
$(\zeta_b\ max)ex$ (gr/cm²)	0 164	0 572	0 454	0 570	0 743	0 354	0 723	0 944
$(\zeta_b\ max)theo.$(gr/cm²)	0 176	0 500	0 500	0 520	0 780	0 376	0 678	0 895
$\dfrac{(\zeta_b\ max)ex}{(\zeta_b\ max)theo.}$	0.942	1 140	0.910	0.982	0 953	0 942	1 070	1 050

Table -2. Comparison of measured shear stresss with theoretical values under
laminar boundary condition (ex =experiment,and theo =theory)
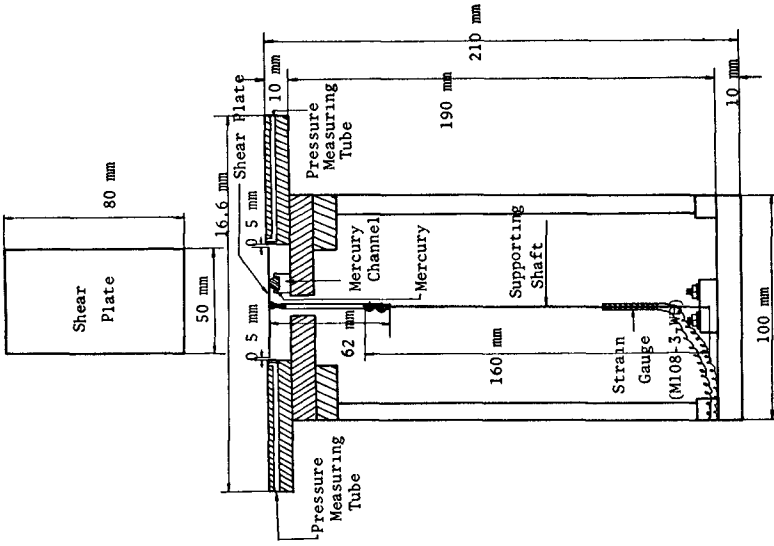
Fig.-10. Schematic view of the shear meter.
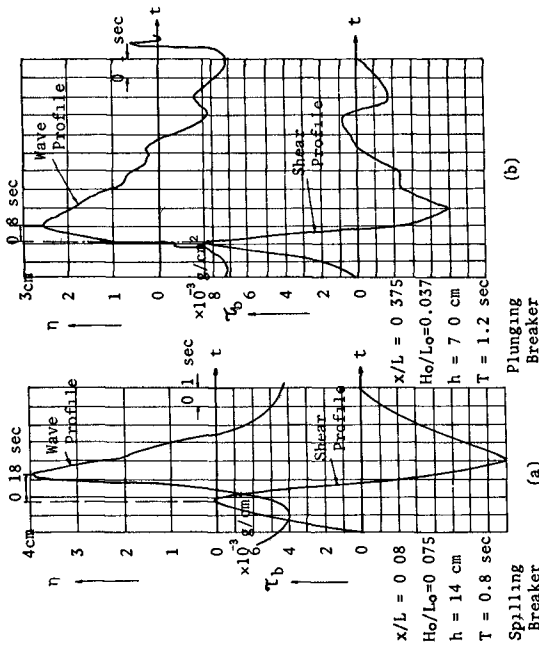
Fig.-11. Time-histories of shear stresses and waves.

Type	H_0/L_0	crest	trough
spilling b.	0 048	▲	●
plunging b.	0 057	△	⌀
h/L = 0 071			

$$\frac{\tau_{b\ max}}{\mathcal{g}\ gH} = \frac{\sqrt{2\ \nu}}{g\ \sinh\ kh}\left(\frac{\pi}{T}\right)^{3/2}$$
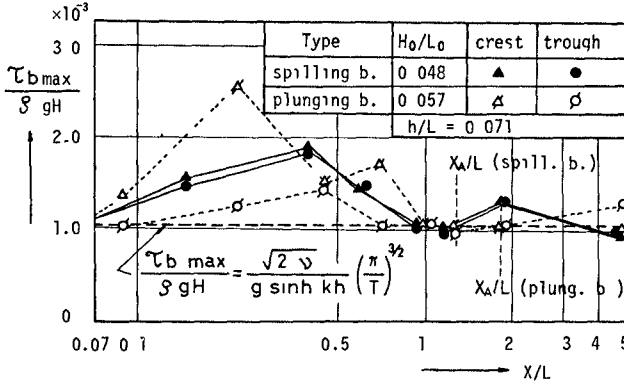
Fig.-12.   An example of relations between $\tau_{b\ max}/\mathcal{g}gH$ and X/L

SYM	h/Lo	Ho/ Lo	8reaker
◆	0 031	0 018	spilling
◆	0 031	0 037	plunging
◆	0 140	0 075	spilling
◇	0 140	0 095	plunging
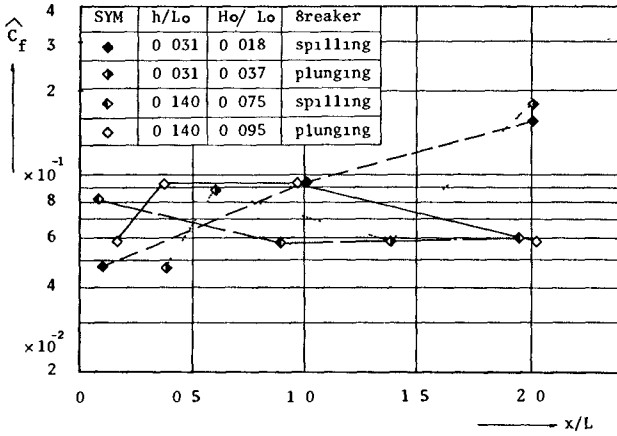
Fig.-13.   Change of the coefficient, $\hat{C}_f$ as wave propagates
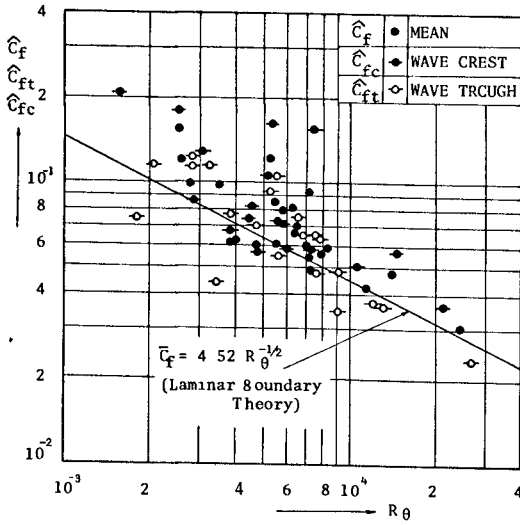
Fig -14. Relation among $\widehat{C}_f, \widehat{C}_{ft}, \widehat{C}_{fc}$ and R_Θ .
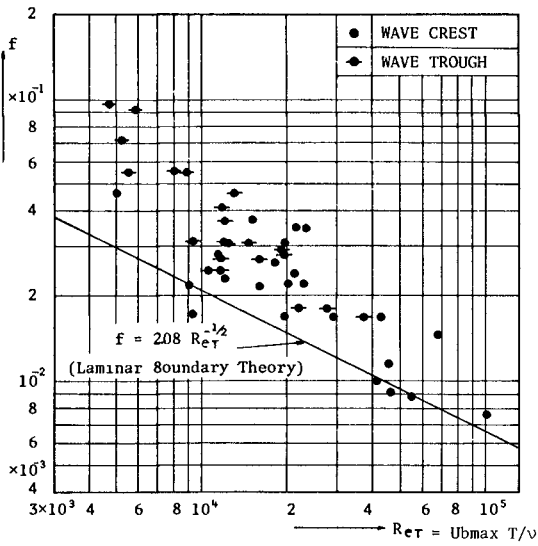
Fig.-15. Relation between f and R_{eT}.

RUN	h cm	T sec	Hʙ cm	H cm	x/L	C/√gh	ε×10²	Breaker
5	7	1 2	5 0	4 4	0 25	1 07	0 8	spilling
"	"	"	"	2 7	1 40	0 97	4 0	"
"	"	"	"	2 6	2 10	0 94	8 9	"
6	7	1 2	8 0	5 0	0 30	1 07	0 6	plunging
"	"	"	"	3 2	1 50	1 14	4.2	"
"	"	"	"	2 7	2 20	1 03	5 5	"
13	14	0 8	6 3	5 4	0 85	0 87	1 7	spilling
"	"	"	"	4.9	1 30	0 99	2 2	"
"	"	"	"	4 6	2 00	0 94	7 7	"
14	14	0 8	9 5	5 4	0 95	0 94	1 0	plunging
"	"	"	"	5.0	1 30	0 99	1.9	"
"	"	"	"	4 7	2.05	0.94	2 6	"

Table -3   Calculated results of ε

5. EFFECT OF TURBULENCE ON WAVE ENERGY DISSIPATION

5-1 Fourier Analysis of Wave Profile

It is necessary to measure an accurate time-history of water particle velocity in order to clarify the characteristics of turbulence. It will be impossible on account of a lack of precise measuring instruments Since a wave profile is thought to be as an expression of turbulence after breaking, it will be expected that some features of turbulence can be deduced by analysing wave profiles The authors adopt Fourier analysis as one method, which can deduce characteristcs of frequencies of a wave.

Wave profiles were recorded by a magnetic-tape with sample time was 16 sec , and data were cut discretely at each 1/30 sec interval. The Fourier analysis was carried out by FFT method (Cooley-Tukey, 1965)

Figs.-16 - 18 show changes of wave height spectra as waves propagate At the breaking point, the wave is composed of harmonic frequencies against the monocromatic frequency of incident waves and immediately after breaking wave heights of the harmonic frequency waves become larger than those of the monocromatic incident waves As shown in Fig -19, however, the higher frequency waves disappear in a short time as the wave propagate after breaking. In the case of h/L=0.0311, as shown in Fig -17 and-18, the incident waves are transformed into higher frequency waves, such as twice or three times frequency waves of the incident waves, regardless of breaker types in the distance of three times the wave length from the breaking point. But, in the case of h/L=0 140(see Fig -16), the above-mentioned fact can not be observed. This means that the relative water depth, h/L$_o$ plays an important role to transform a wave into a higer frequency wave rather than the breaking pattern , although this mechanism is not yet clear

5-2. Basic Equation for Breaking Wave

The mechanism of transformation of the monocromatic incident waves into higher frequency waves is very complicatedly Therefore, the authors avoid a direct discussion of this mechanism and only discuss a wave height attenuation by using the following turbulence model,

Two-dimensional Navier-Stokes equation with terbulence terms is given as follows(Ishihara-Homma, 1957)

$$\left. \begin{array}{l} \varsigma\dfrac{DU}{Dt} = -\dfrac{\partial P}{\partial x} + \mu\nabla^2 U + \left(\dfrac{\partial P_{xx}}{\partial x} + \dfrac{\partial P_{zx}}{\partial z} \right) \\[2em] \varsigma\dfrac{DV}{Dt} = -g - \dfrac{\partial P}{\partial z} + \mu\nabla^2 V + \left(\dfrac{\partial P_{zx}}{\partial x} + \dfrac{\partial P_{zz}}{\partial z} \right) \end{array} \right\} \quad\text{----------------(13)} $$
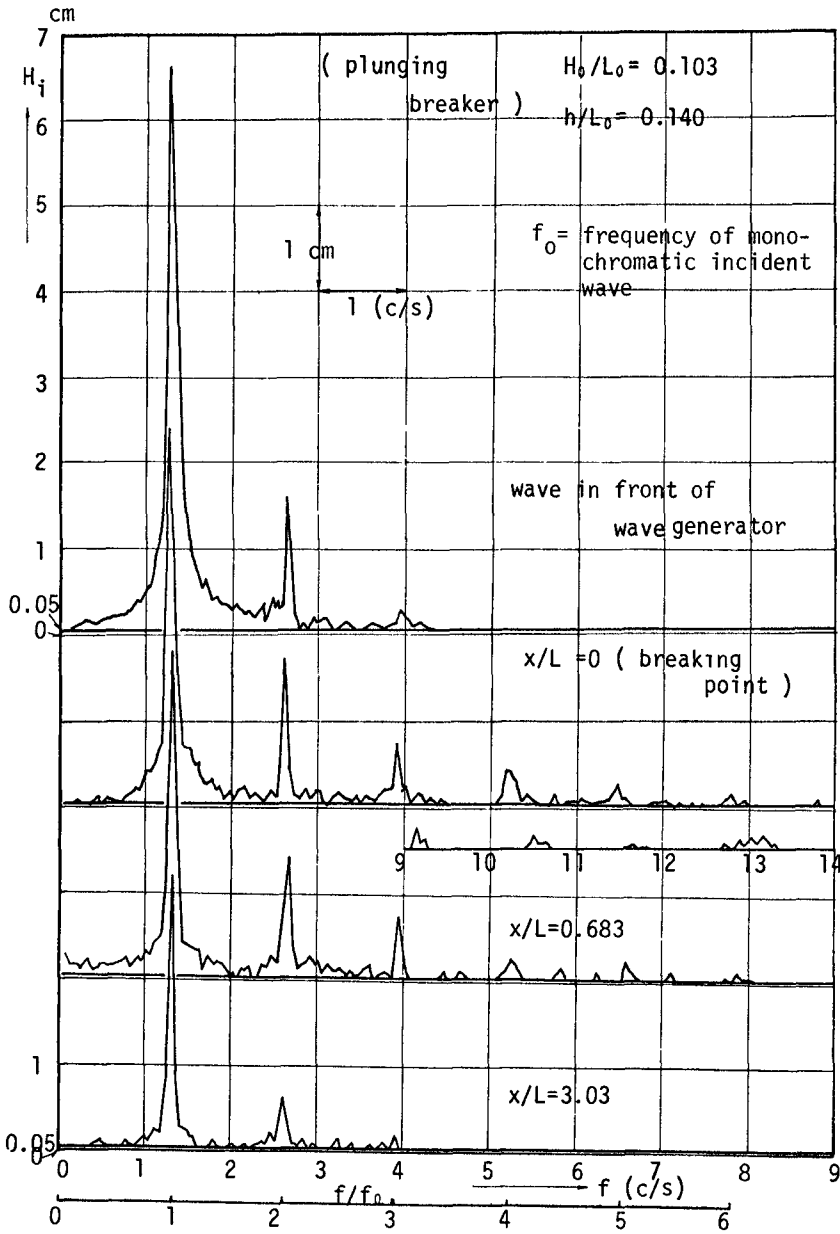
Fig.-16. Change of wave height spectrum. $(h/L_0=0.140)$
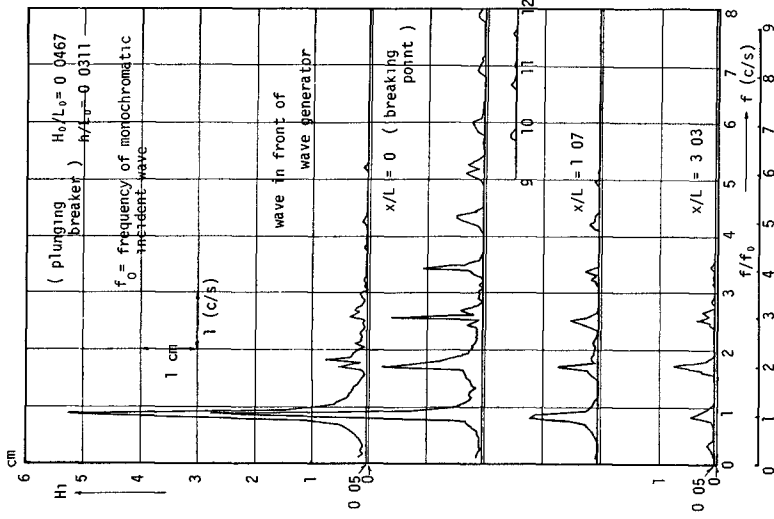
Fig -17   Change of wave height spectrum (h/L$_0$=0 0311)
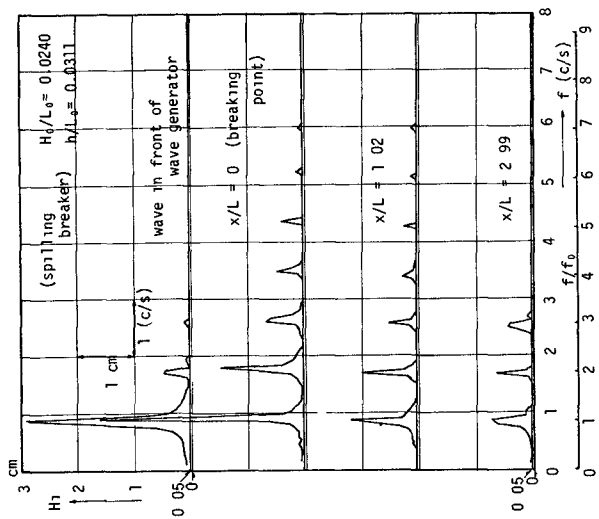
Fig -18   Change of wave height spectrum (h/L$_0$=0 0531)
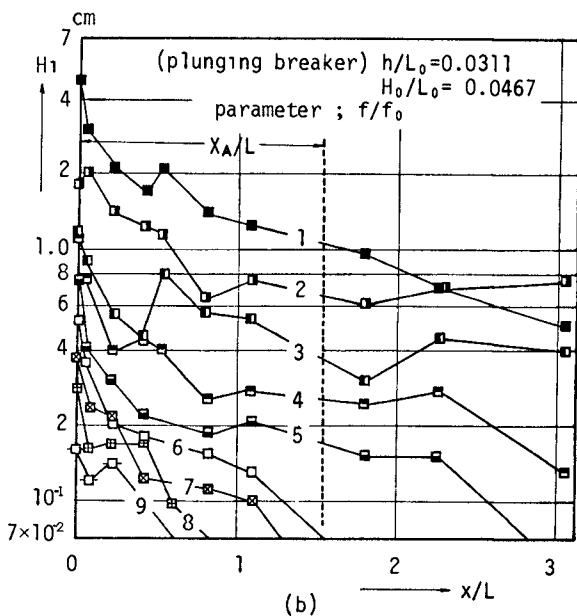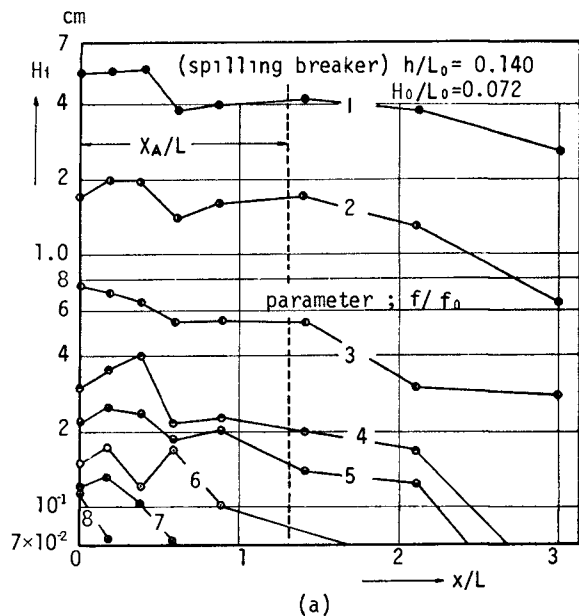
Fig.-19.   Attenuation of wave heights of harmonic
frequency waves as waves propagate.

where, P_{xx}, P_{zx} and P_{zz} = Reynolds stresses, $\nabla^2 = \frac{\partial^2}{\partial x^2} + \frac{\partial^2}{\partial z^2}$, μ = coefficient of fluid viscosity, g= gravity acceleration, t=time coordinate, p=pressure, V=vertical velocity of a water particle, U= horizontal velocity of a water particle, x = horizontal coordinate and z= vertical coordinate with the origin at the bottom

On the assumptions that (1) $DV/Dt=0$, (11) terms due to molecular viscosity are considerably small as compared with terms due to Reynolds stress, (111) ($O(\partial P_{xx}/\partial x)$ and $O(\partial P_{zx}/\partial x)$) $\gg$ ($O(\partial P_{zz}/\partial z)$ and $O(\partial P_{zx}/\partial z)$), Eq (13) is transformed into the following equation

$$\frac{\partial U}{\partial t} + U\frac{\partial U}{\partial x} + g\frac{\partial \eta}{\partial x} - \frac{\partial}{\partial x}(P_{xx} + P_{zx}) = 0 , \quad\text{-----------------------} \quad (14)$$

where η = wave profile

Assuming that P_{xx} and P_{zx} are able to be represented by the equation(15), the equation(14) is transformed into Eq.(16) as follows

$$P_{xx}' = L_1^2\left(\frac{\partial U}{\partial x}\right)\left|\frac{\partial U}{\partial x}\right| \propto -L_x^2\left(\frac{U}{h}\right)^2 \Big\}$$
$$P_{zx} = L_2^2\left(\frac{\partial U}{\partial z}\right)\left|\frac{\partial U}{\partial z}\right| \propto -L_z^2\left(\frac{U}{h}\right)^2 \Big\}\quad\text{---------------------} \quad (15)$$

and

$$\frac{\partial U}{\partial t} + U\frac{\partial U}{\partial x} + g\frac{\partial \eta}{\partial x} + \frac{\partial}{\partial x}\left(K(\eta + h)\left(\frac{U}{h}\right)^2 \right) = 0 \quad\text{--------------} \quad (16)$$

in which L_x and L_z = mixing length and $L_x^2 + L_z^2 = K (h + \eta)^2$ is assumed, where K is defined as the coefficient of turbulence intensity.

Therefore, the basic equations for a breaking wave are given as follows

$$\frac{\partial U}{\partial t} + U\frac{\partial U}{\partial x} + g\frac{\partial \eta}{\partial x} + \frac{\partial}{\partial x}\left(K (h + \eta)^2\left(\frac{U}{h}\right)^2 \right) = 0 \Big\}$$

and from the law of mass conservation $\qquad\qquad\qquad\qquad\qquad\qquad\qquad$ ----------- (17)

$$\frac{\partial \eta}{\partial t} + \frac{\partial}{\partial x}(U (h + \eta)) = 0 \Big\} .$$

Now, change the variables as follows

$$X^* = x/h , \quad T^* = (t/h)\sqrt{gh} , \quad U^* = U/\sqrt{gh} \quad\text{and}\quad H^* = (h + \eta)/ h \quad\text{--------} \quad (18)$$

then, Eq.(19) is obtained from Eq (17) by means of the finite difference method(Keller-Levine-Whitham, 1960) as follows

$$H^*(P) = \tfrac{1}{2}(H^*(R_1) + H^*(Q_1)) - \frac{\Delta T^*}{2\Delta X^*}(U^*(R_1)H^*(R_1) - U^*(Q_1)H^*(Q_1))$$

$$U^*(P) = \tfrac{1}{2}(U^*(R_1) + U^*(Q_1)) - \frac{\Delta T^*}{2\Delta X^*}(\tfrac{1}{2}(U^{*2}(R_1) - U^{*2}(Q_1)) + (H^*(R_1) - H^*(Q_1)))$$

$$\qquad\qquad\qquad\qquad\qquad\qquad - \frac{K\Delta T^*}{2\Delta X^*}(H^{*2}(R_1)U^{*2}(R_1) - H^{*2}(Q_1)U^{*2}(Q_1))$$

$$\text{----------- (19)}$$

The numerical procedure is, in outline, to compute a wave height and velocity on a set of net points (X^*, T^*). In the calculation, the spatial net and time net are chosen to be uniform, $X^*=i\Delta X^*$ and $T^*=k\Delta T^*$, where, ΔT^* and ΔX^* are chosen to satisfy a stability condition, the so-called Courant condition, stated as follows

$$\Delta T^* \leq \min_{P_1}\left(\frac{\Delta X^*}{U^*(P_1) + \sqrt{H^*(P_1)}} \right) \quad\text{--------------------------------} \quad (20)$$

The calculation is carried out by using the mesh width of $\Delta X=0.02$ and $\Delta T=0.004$, for which it was confirmed that the solutions were convergent and stable Unknown values, H(P) and U(P) at a point P, are calculated from the known values at point Q_1 and R_1 as shown in Fig.-20 by using Eq (19)
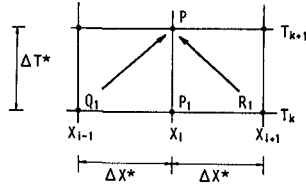
Fig.-21 shows the calculated values for wave height attenuation, in which the theoretical value of Horikawa-Kuo(1966) based on the energy method is also shown In this calculation, a solitary wave (Boussinesq,1872) is used as an initial wave condition From this figure, it is recognized that the degree of wave height attenuation becomes larger as K becomes larger and that the theoretical value for K=0.5 fairy agrees with the value of Horikawa-Kuo for $\beta=5$ Furthermore, Fig -22 shows that the theoretical values calculated by using experimental data as initial wave conditions considerably coincides with experimental results and that K for a plunging breaker is very large as compared with that for a spilling breaker

This fact indicates that the stronger the intensity of the turbulence, the greater the wave height attenuation, and therefore, it will be pointed out that the intensity of turbulence of the plunging breaker is larger than that for a spilling breaker

Fig -20   Mesh points

6 CONCLUSION

In this paper, wave deformation after breaking is discussed The energy dissipation after breaking is dominated by turbulence with air entrainment in the case of a spilling breaker In the case of a plunging breaker, some of the wave energy are dissipated by the formation of horizontal roller in addition to the turbulence with air entrainment Due to this turbulence, a monocromatic incident wave is transformed into a higher frequency wave in some condition This mechanism is unknown and it is required to clarify the characteristics of turbulence after breaking by a future investigation

REFERENCES

Mason,M A   Some Observations of Breaking Wave, Gravity Waves,N B S Circular,521,1951.

Galvin, C J   Breaker Travel and Choice of Design Wave Height, Proc. of ASCE, WW2,May, 1969

Wiegel, R L   Oceanographical Engineering, Prentice-Hall, Englewood,Cliff,N J.,pp 11-21,1964

Hino,M and T Yamazaki, Formation of Roller and Energy Dissipation at Vertical Plate due to Wave, Proc of 18th Conf on Coastal Eng. in Japan, 1971 (in Japanese)

Eagleson,P S   Laminar Damping of Oscillatory Waves, Proc of ASCE, Vol 88, No HY3 , 1962

Iwagaki,Y ,Y Tuchiya and K Chin Experimantal Study on Wave Attenuation due to Bottom Friction (3), Proc of 12 th Conf on Coastal Eng in Japan, 1965 (in Japanese)

Putnam,J A and J W Johnson The Dissipation of Wave Energy by Bottom Friction, Tran A G U , Vol.30, No 1,Feb ,1949.

Iwagaki,Y ,T. Kakinuma and H Miyai· On Bottom Friction Coefficient in Coastal Beaches, Proc. of 12th Conf on Coastal Eng in Japan, 1965 (in Japanese)

Cooley,J W. and J W Tukey An algorithm for the machine calculation of complex Fourier series, Math , Compt.,19, pp 297-301,1965

Ishihara,T and H.Homma Applied Hydraulics, Vol.1, Maruzen-Press, Tokyo, pp 35-40, 1957 (in Japanese)

Keller,H B ,D A Levine and G B Whitham Motion of a Bore over a Sloping Beach,Jour. of Fluid Mech , Vol.7, 1960

Boussinesq,J   Théorie des ondes et des remous qui se propagent le long d'un canal rectangulaire
horizontal,en communiquant au liquide contenu dans ce canal de vitesses sensiblement pareilles de la
surface au fond, Liouville's J Math Vol.17, 1872
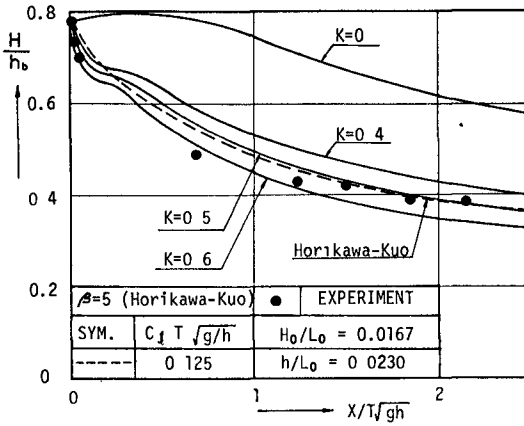
Fig -21. Theoretical values of wave height attenuations.(By using solitary wave as an initial wave condition)
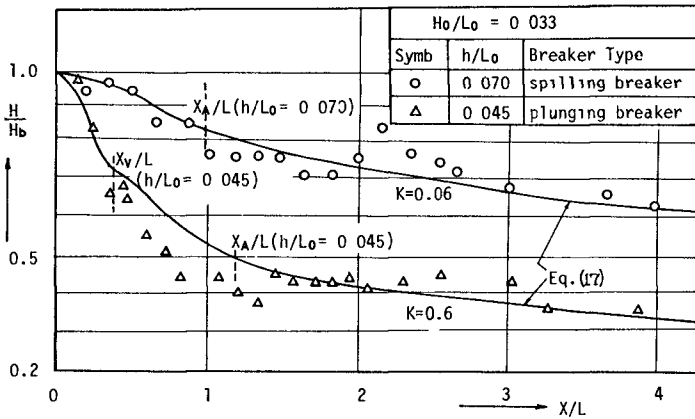
Fig.-22. Comparison of calculated theoretical values with experimental results. (By using experimental data as an initial wave condition)

CHAPTER 28

WATER-WAVE INTERACTION IN THE SURF ZONE

D. Howell Peregrine

Lecturer in Mathematics
University of Bristol
England.

Abstract

In the surf zone on beaches, there are strong effects which cannot be described by linear equations. This paper describes a number of wave interactions that can take place, using the simplest set of equations that give an adequate qualitative description. The results are of value for comparison with detailed experimental measurements and for gaining understanding of surf zone processes.

Introduction

The region of breaking and broken waves on a beach is important for the study of waves on beaches, from whatever point of view it is approached. From a theoretical viewpoint the turbulent, unsteady, flow presents many difficulties. The wave motions do not satisfy linear equations, so that the superposition of solutions, which gives such power to linear analysis and makes Fourier techniques so revealing, is not available. Indeed, the high level of turbulence means that accurate equations for describing the flow are not known. In this paper particular solutions of approximate non-linear equations are considered with a view to gaining some understanding of the processes involved.

The equations are the finite-amplitude shallow-water wave equations, which may be written:

$$\frac{\partial u}{\partial t} + \frac{u \partial u}{\partial x} + g\frac{\partial h}{\partial x} = g\frac{\partial h}{\partial x}0, \tag{1}$$

$$\frac{\partial h}{\partial t} + \frac{\partial}{\partial t}(hu) = 0, \tag{2}$$

in which, h is the total depth of water, h_0 is the depth below the still water level of the sea bed, which is assumed to be rigid and impermeable, and u is the mean horizontal water velocity. Multiple values arise in solutions of these equations and these are excluded by introducing discontinuities representing bores and satisfying the bore relations:

$$h_1(u_1 - V) = h_2(u_2 - V), \tag{3}$$

$$h_1 u_1 (u_1 - V) + \tfrac{1}{2}gh_1^2 = h_2 u_2 (u_2 - V) + \tfrac{1}{2}gh_2^2, \tag{4}$$

These equations of motion are usually derived, e.g. in Peregrine (1972), for the laminar flow of an inviscid fluid, however, similar equations are found for long waves on shear flows (Blythe et al, 1972).

500

For river flows it is found that turbulent dissipation is adequately
represented by the addition of a term $- f u |u|$ to the right-hand side
of equation (1). It is likely that adding such a friction term may give quite
a good representation of real wave motions. Friction is discussed by
Longuet-Higgins (1972) and briefly by Meyer and Taylor (1972). It is not
included here since it impedes analysis of the equations and it is expected
to have only a quantitative, damping, effect on solutions.

The bore relations are found to be in agreement with experiment
for stationary bores (hydraulic jumps), e.g. see Rajaratnam (1967) for a
discussion. For travelling bores there are difficulties in measuring the
velocity V of the bore because of the strong turbulence at its front.
However, Miller's (1968) measurements, despite their wide scatter, are consistent
with the theoretical values.

It is important to realise the limitations of the shallow-water theory.
These are well illustrated by bores, which are represented mathematically
by abrupt discontinuities, but in reality the changes in level and velocity
are spread over several times the depth. Similarly the equations of motion
are only applicable to variations in velocity and amplitude that are also
spread over many times the depth. Close to the shoreline where the mean
depth of water is small these are quite acceptable limitations, but where
waves have just broken, or are moving shorewards as spilling breakers, the
shallow-water theory is inappropriate. Thus this theoretical treatment is
most pertinent to what may be called the "inner surf zone".

It is worth noting that the equations do not predict wave breaking.
When a solution reaches a point where the slope of the water surface becomes
large, and multiple values of the solution are avoided by inserting a
discontinuity, the correct interpretation is that the approximation of
long gentle waves, which is essential for the equations, is no longer valid.
In practice, it is observed that waves often break, and it is reasonable
to fit a bore discontinuity. However, if the assumed discontinuity has a
depth ratio of less than 1.6 any bore formed will be at least partly undular,
and it will be best described by the Boussinesq equations if no breaking
occurs.

A number of authors have used this analytical approach to waves
on beaches, usually of uniform slope. A bore advancing toward a beach
through still water is treated numerically in Keller et al (1960) and
by Freeman and Le Mehaute (1964), whilst an asymptotic analysis of its
approach to the shore line is in Ho and Meyer (1962). A standing wave
solution, without any bore is given by Carrier and Greenspan (1958).
Jeffrey (1964,1967) determines the time, if any, at which a sinusoidal
wave propagating into still water over a uniform slope would "break".
Carrier (1966) gives results for waves approaching a shore when they
are sufficiently gentle that they do not break. By limiting attention to
very slowly varying depth Varley et al (1971) and Cumberbatch and Wen (1973)
deduce a number of results for waves entering still water. Run-up may be
discussed in the same theoretical context, results are reviewed by Meyer
and Taylor (1972).

The philosophy behind the present work is the accumulation of relevant
solutions of the non-linear equations that may assist the interpretation

and collection of data so that empirical rules for wave properties may
be refined. Some relatively simple examples are discussed in this
paper, taking a horizontal bottom for simplicity, though the results
are directly transferable to situations with variable depth. In particular
the analysis of bore interactions suggests a way of plotting field
measurements to learn more about actual surf zones.

Introductory Analysis

    Analysis is simplified by introducing the "local long-wave velocity"
c, defined by

$$c^2 = gh. \tag{5}$$

Then equations (1) and (2), after some simple algebra may be written

$$\left[\frac{\partial}{\partial t} + (u+c)\frac{\partial}{\partial x} \right] (2c+u) = g\frac{dh_0}{dx} , \tag{6}$$

$$\left[\frac{\partial}{\partial t} + (u-c)\frac{\partial}{\partial x} \right] (2c-u) = -g\frac{dh_0}{dx}. \tag{7}$$

Alternatively, these equations take the form

$$\frac{\partial(2c+u)}{\partial S} = g\frac{dh_0}{dx}, \tag{8}$$

$$\frac{\partial(2c-u)}{\partial R} = g\frac{dh_0}{dx}, \tag{9}$$

if characteristic variables R,S defined by

$$2cdR = dx - (u+c)dt, \tag{10}$$

$$2cdS = dx - (u-c)dt, \tag{11}$$

are used. These define two families of characteristic lines:

$$C_+, \quad R = \text{constant}, \quad \frac{dx}{dt} = u+c; \tag{12}$$

$$C_-, \quad S = \text{constant}, \quad \frac{dx}{dt} = u-c. \tag{13}$$

(e.g. see Stoker, 1957, or Abbot, 1969). It is the existence of the relatively
simple equations (8) and (9) that permits solutions, or some properties of
solutions, to be found in particular cases.

    For a horizontal bottom these equations simplify and can be integrated
to give·

$$P = 2c+u = \text{constant on } C_+ \text{ lines}, \tag{14}$$

$$Q = 2c-u = \text{constant on } C_- \text{ lines} \tag{15}$$

The variables P and Q are called "Riemann invariants". If one family

of characteristics, e.g. C_- , come from a region of uniform flow the
appropriate invariant, Q, is equal to the same constant everywhere; such
solutions are called "simple waves" Characteristics may be thought of as
"elementary" waves of the system of equations - indeed they are the paths
in (x,t) space of small amplitude long waves.

If c is used in the bore relations (3), V is given by

$$V = \frac{c_2^2 u_2 - c_1^2 u_1}{c_2^2 - c_1^2},$$

(16)

and then, after substitution for V, equation (4) becomes

$$2c_1^2 c_2^2 (u_1 - u_2)^2 = (c_2^2 - c_1^2)^2 (c_1^2 + c_2^2).$$

(17)

"Reflection" from a bore

In a solution of the shallow-water equations with a bore fitted at
a discontinuity travelling in the +x direction, the bore and its path are
determined by·

(i) the conditions in front of it (i.e. u_1, c_1 or P_1, Q_1), since
$V > u_1 + c_1$ it meets two characteristics on that side.

(ii) the value P_2 of P on the C_+ characteristic behind the bore
which catches it up since $u_2 + c_2$ > V.

This is shown in the (x,t) plane in figure 1.
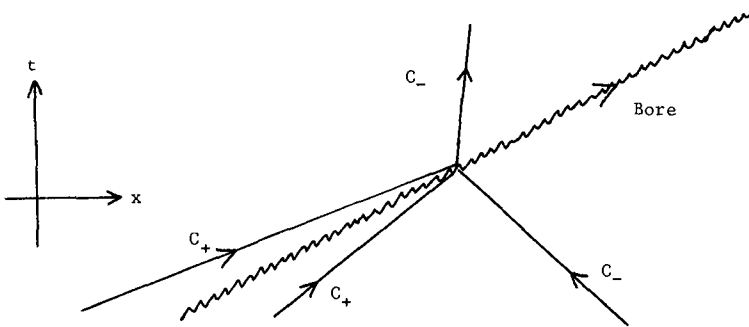
Figure 1.   The four characteristics passing through one point on a bore's path.

In particular the velocity V and the value Q_2 of Q on the C_- characteristic behind the bore are determined. Q_2 is always less than Q_1, the difference can easily be evaluated in terms of the strength of the bore,

$$B = c_2/c_1, \quad \text{i.e.} \quad B^2 = h_2/h_1,$$

by using equation (17), and is

$$Q_1 - Q_2 = c_1 \left[2(1-B) + \frac{B^2-1}{B} \left(\frac{B^2+1}{2} \right)^{\frac{1}{2}} \right] \tag{18}$$

$$= c_1 q,$$

say. Values of $q = q(B)$ are displayed in figure 2.
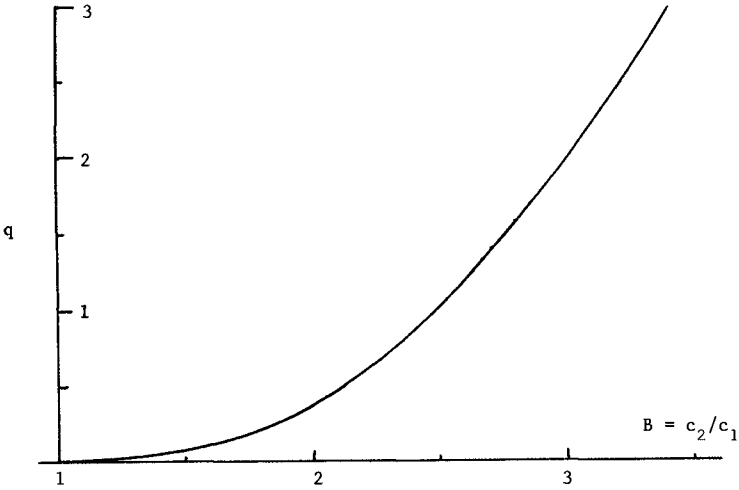
Figure 2. The change in Q at a bore, divided by c_1.

One way to interpret this result is to consider a bore travelling over a flat bottom into uniform conditions P_1, Q_1, with the wave behind the bore being of only limited extent before the same uniform conditions are recovered. Then as the C_- characteristic from the bore propagates into these uniform conditions they are disturbed because Q is less than Q_1. In fact, for such a wave

$$u = u_1 + \tfrac{1}{2} c_1 q \quad \text{and} \quad c = c_1 (1 - \tfrac{1}{4} q).$$

and thus since $q > 0$ and $c^2 = gh$, the wave coming back from a bore is
a wave of depression. However, the C_- characteristic only travels backwards
if $u - c < 0$, but $u - c = u_1 - c_1 + \frac{3}{2} c_1 q$ and is less than zero when

$$q < \frac{4}{3}(1 - \frac{u_1}{c_1}).$$

(e.g. for the case $u_1 = 0$, $q < 4/3$ implies $B < 2.695$ or $h_2/h_1 < 7.263$)

This wave of depression can be thought of as a form of "reflection" from
a bore.

On a beach, such a reflected wave would start when a wave breaks, at
least, if it breaks in sufficiently shallow water. However, it would be
propagating in the direction of increasing depth and from equation (19) one
may deduce that this causes Q to increase. Thus for waves incident on a
beach the amplitude of the wave would be due to both these opposing influences.

Small amplitude waves and bores

A small amplitude wave is most naturally described in the context of
the finite-amplitude shallow-water equations as a small change in P,(or Q)
travelling along the C_+ (or C_-) characteristics. There are three ways
in which a small amplitude wave can meet a bore travelling in the +x
direction, corresponding to the three characteristics; C_+ and C_- in front
and C_+ from behind the bore. In all three cases the resulting wave
propagates along the C_- characteristic behind the bore. Thus for a wave
which originally travelled along a C_+ characteristic, interaction with a
bore reverses its direction of travel.

The magnitude of changes in the waves may be found by evaluating
$dQ_2/dP_1, dQ_2/dQ_1, dQ_2/dP_2$ at the bore, where suffices 1 and 2 refer to values
in front of and behind the bore respectively, and in each derivative the
other pair of Riemann invariants are kept constant. A straightforward
algebraic manipulation of the differential of the bore relation (17) together
with the definitions of P and Q gives

$$\frac{dQ_2}{dQ_1} = \frac{B[U(B^4+B^2+2) + 2(B^4-1)]}{U(2B^4+B^2+1) + 2B(B^4-1)}, \tag{19a}$$

$$\frac{dQ_2}{dP_1} = \frac{B[U(B^4+B^2+2) - 2(B^4-1)]}{U(2B^4+B^2+1) + 2B(B^4-1)}, \tag{19b}$$

$$\frac{dQ_2}{dP_2} = \frac{-U(2B^4+B^2+1) + 2B(B^4-1)}{U(2B^4+B^2+1) + 2B(B^4-1)}, \tag{19c}$$

where $U = (u_2 - u_1)/c$. Note, that in terms of U and B the bore relation
(17) is

$$2B^2U^2 = (B^2-1)^2(B^2+1). \tag{20}$$

From these results all changes in the wave's properties may be found.

For example, consider a wave dQ_1 meeting the bore on a C_- characteristic. The relative change in amplitude is

$$\frac{dh_2}{dh_1} = \frac{c_2 dc_2}{c_1 dc_1} ,$$

but $dc_1 = \frac{1}{4} dQ_1$ and $dc_2 = \frac{1}{4} dQ_2$ since $dP_1 = dP_2 = 0$ and thus

$$\frac{dh_2}{dh_1} = B\frac{dQ_2}{dQ_1}$$

Since both $B > 1$ and $dQ_2/dQ_1 > 1$, this wave is always increased in amplitude.

From the geometry of the characteristics in the (x,t) plane, shown in figure 3, the change in length of a small amplitude wave may be calculated;
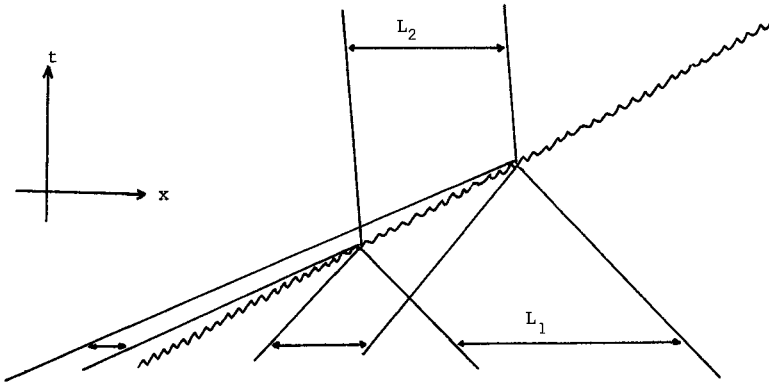
Figure 4. Arrangement of characteristics when a long small amplitude wave meets a bore.

$$\frac{L_2}{L_1} = \frac{B(B^2-1)+U}{B^2-1+B^2U} \quad \text{in this case,} \tag{21a}$$

$$= \frac{B(B^2-1)+U}{B^2U-(B^2-1)} \quad \text{for an incident wave } dP_1, \tag{21b}$$

$$\text{and} \quad = \frac{B(B^2-1)+U}{B(B^2-1)-U} \quad \text{for an incident wave } dP \tag{21c}$$

A better measure of the change in a wave is the change in its volume (area for a two-dimensional wave), i.e.

$$dA = Ldh.$$
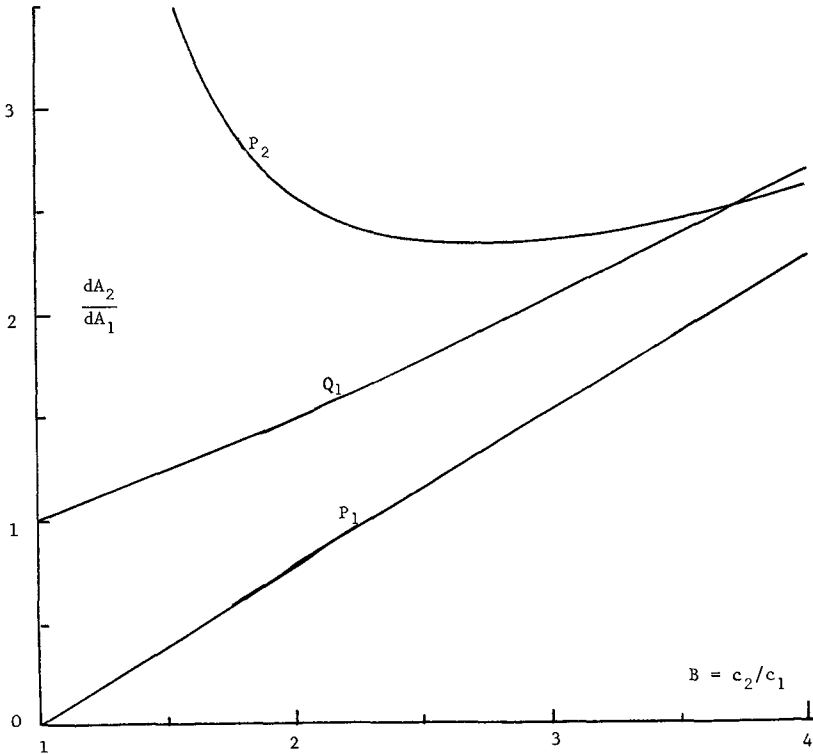
Figure 4. The relative change in volume when a small amplitude wave meets a bore. The curves are labelled with the corresponding Riemann invariants of the incident wave.

Values of dA_2/dA_1 for the three different types of incident wave are shown in figure 4. The change in volume can be explained ny noting that there is a small change dV in the velocity of the bore while it is interacting with the incident wave. A number of cases lead to an amplification of the wave. These results only apply to waves long enough to be described by the shallow-water equations.

The energy density at a point is

$$E = \tfrac{1}{2}\rho u^2 h + \rho gh(\tfrac{1}{2}h-h_0) = \rho(u^2+c^2-2c_0^2)c^2/2g, \tag{22}$$
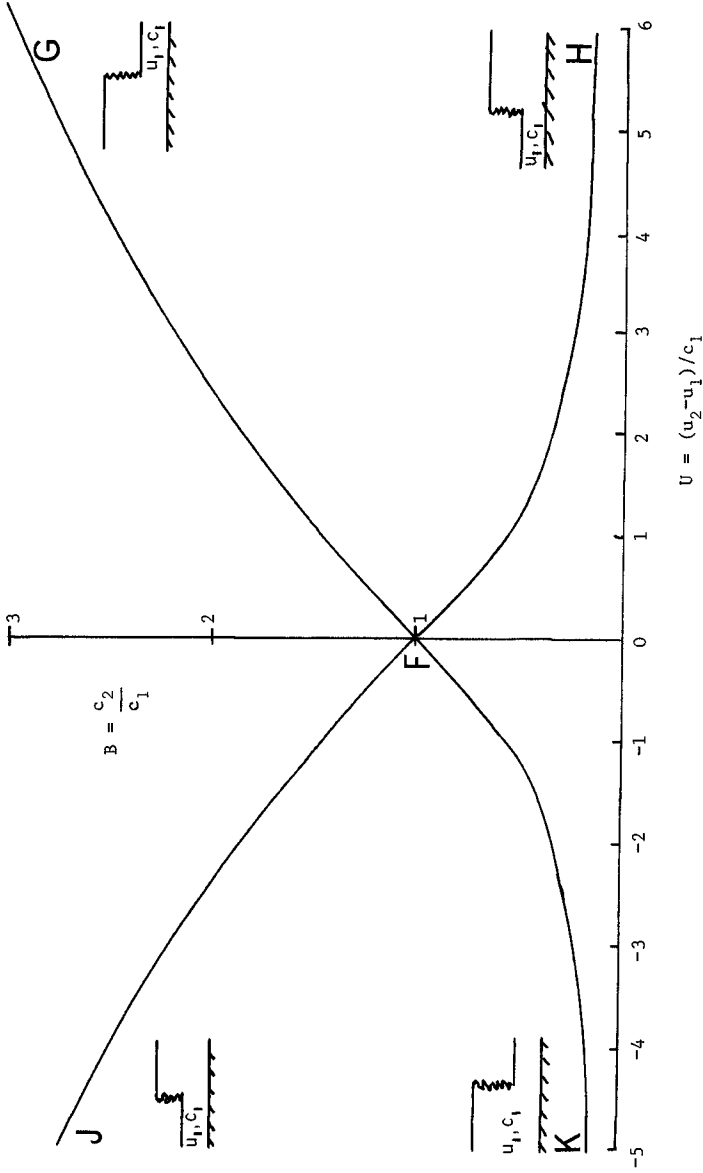
Figure 5. The bore relation, equation (17), in the (u,c) plane. The coordinates are given in terms of non-dimensional variables. The branch KFG represents a bore facing the +x direction, and the branch JFH represents a bore facing the −x direction, as indicated in the small sketches.

so that the energy of an infinitesimal wave is given by

$$gdE/\rho = c^2 u du + 2(c^2-c_0^2)cdc$$

$$= \tfrac{1}{2}(c^2-c_0^2 + cu)cdP + \tfrac{1}{2}(c^2-c_0^2-cu)cdQ. \qquad (23)$$

When an infinitesimal wave traverses any finite amplitude flow   dE varies,
on the other hand for any flow over a flat bottom at least   dP   or   dQ
will be constant, e.g. see Peregrine (1967) for a treatment of reflection of
an   infinitesimal wave by a sloping beach.   Thus the energy of an infinitesimal
wave is not very useful in this context.

Interaction of bores

     When one bore meets, or catches up with, another the result of their
interaction may include one or two bores.   The interaction is most easily solved
by considering the (u,c) plane.   The bore relation (17) defines a pair of lines
in the (u,c) plane for each point (u_1, c_1).   The points on these lines are
possible values of (u_2,c_2).   This pair of lines is plotted in figure 5 for
the point $(0,1)$ (effectively the relation (20) between B   and   U), for other
values of u_1 the lines are simply translated and for other values of c_1
the scale is changed appropriately

     When one bore catches another the initial configuration is as shown in
figure 6 where bore B_2 is necessarily travelling faster than B_1.   This can
be displayed in the (u,c) plane by representing the states (u_i,c_i) for $i = 1,2,3$
by points labelled F_i, $i = 1,2,3$ with lines representing the relevant bore
relations joining each state, as in figure 7.   This makes it clear that after
the bores meet a single bore from F_1 to F_3 is not possible.

     The alternative form of transition between two levels of water is a simple
wave of depression.   That is a long wave propagating in the $+x$(or $-x$) direction
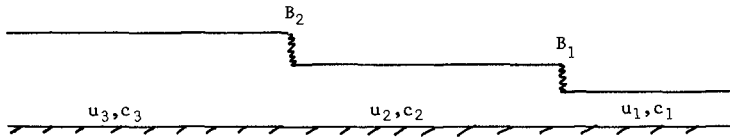
Figure 6.   One bore catching another.
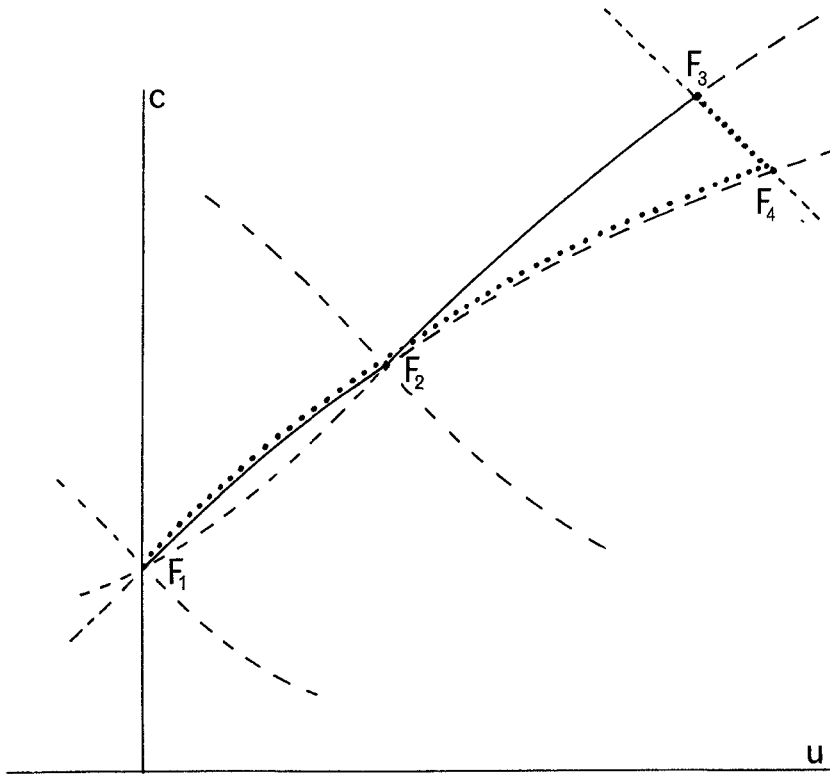
Figure 7.   One bore catching another· the (u,c) plane. Bore B_1 connects
states F_1 and F_2 , bore B_2 connects states F_2 and F_3 , the corresponding
bore relations are shown by a continuous line. After the interaction the
single bore B_3 connects states F_1 and F_4 and a simple wave connects states
F_4 and F_3 as indicated by the dotted line.
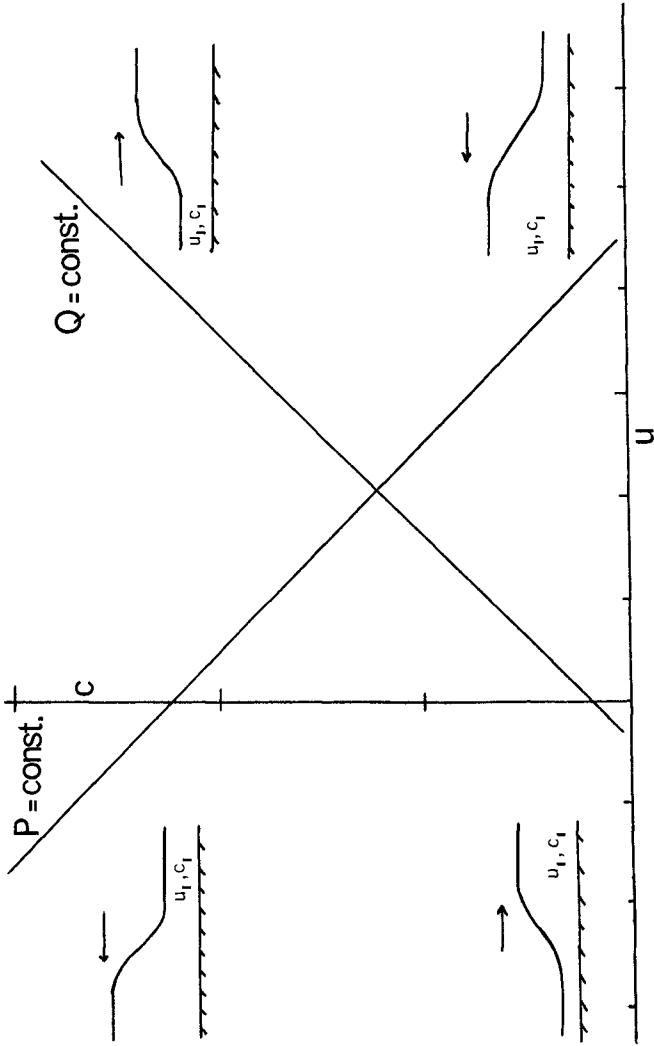
Figure 8. Simple waves of depression in the (u,c) plane, Units arbitrary, but in ratio indicated. Waves Q = constant propagate in the +x direction, and P = constant in the -x direction, as indicated in the small sketches.
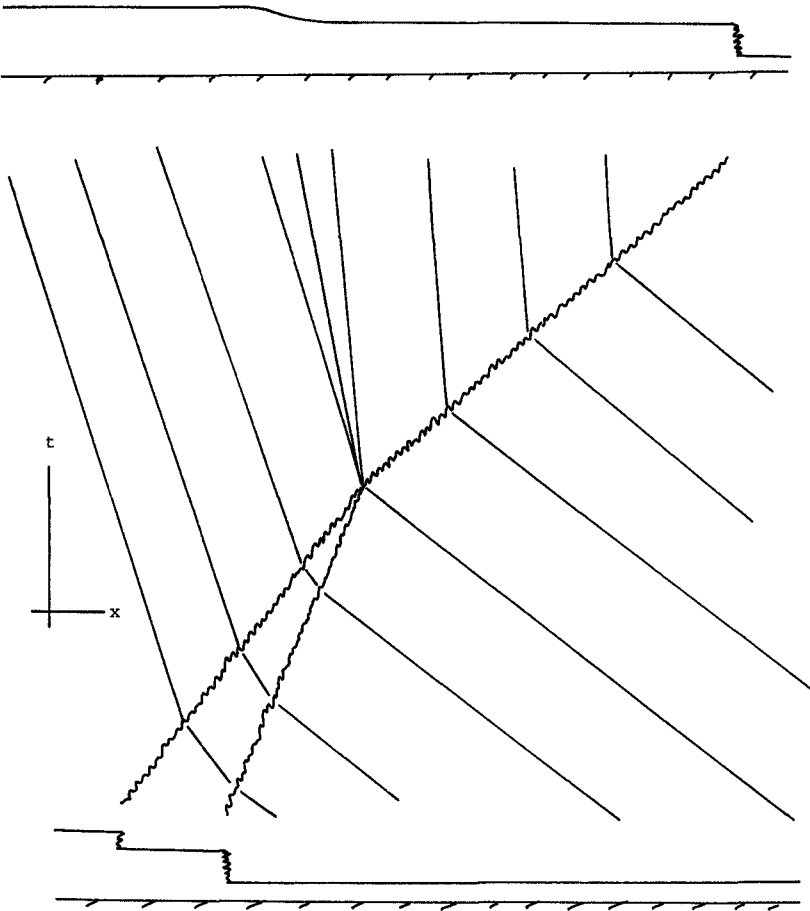
Figure 9   Diagram of (x,t) plane showing one bore catching another, with the
C- characteristics and the bore paths shown.   Below and above the diagram are
representations of the initial and final states.
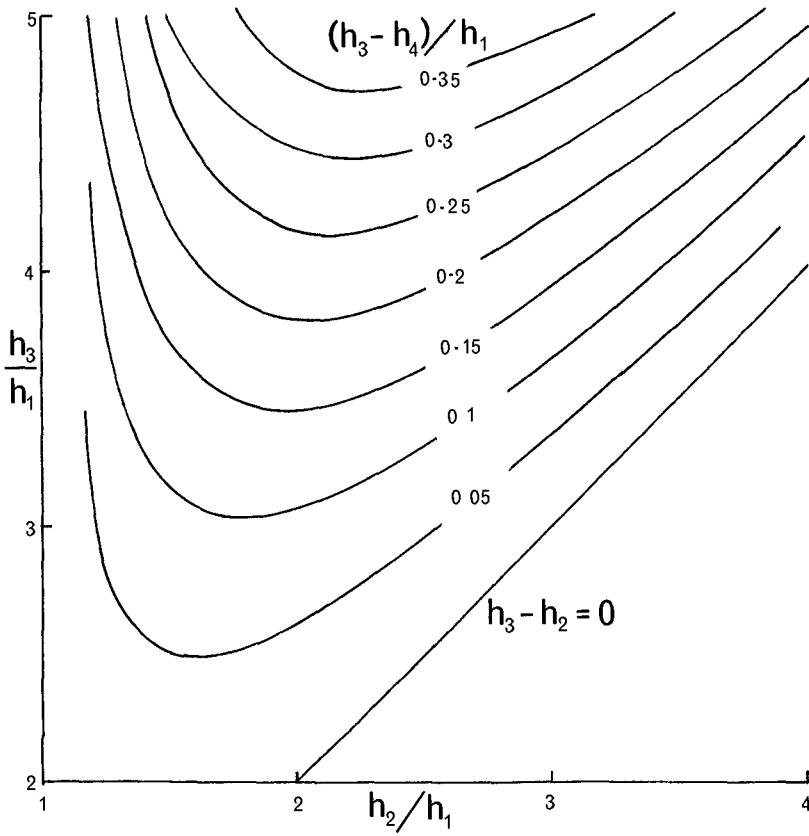
Figure 10. The amplitude of the simple wave resulting from a bore of depth h_3 catching one of depth h_2 propagating into water of depth h_1. The resulting bore has depth h_4 behind it.

with Q (or P) constant. The possible (u,c) states are thus connected by
the straight lines Q = 2c-u = constant, (or P = 2c+u = constant) as shown
in figure 8. (In the figures of the (u,c) plane the unit for c is chosen
to be twice that for u, thus the lines P,Q constant are ate 45° to the u and
c axes.) Referring again to figure 7, the only simple wave which can propagate
back into the conditions (u_3,c_3) is one with P = constant. Thus after the
bores have met the (u,c) diagram is as indicated by the dotted line in figure
7, and the result is a bore plus a simple wave. Figure 9 is a diagram showing
characteristics in the (x,t) plane for such an interaction.

   The difference of levels may be calculated, using equation (17) and
equation (14) applied to the states F_3 and F_4. Numerical results for
$(h_3-h_4)/h_1$, shown in figure 10, indicate that the simple wave has a
relatively small amplitude e.g. when $h_3 = 5h_1$ the maximum value of (h_3-h_4)
is $0.4h_1$ thus $(h_3-h_4) = 0.08h_3$.

   Other interactions between bores and simple waves may be analysed in
a similar manner. The result of each interaction is given in the table. In
the cases marked * the end result depends on the relative sizes of the bore
and the wave and the interaction takes a very long time to reach its final
state.

l.h.s \ r.h.s.	B_+	B_-	W_+	W_-
B_+	W_- B_+	B_- B_+	*	W_- B_+
B_-	do not meet	B_- W_+	do not meet	*
W_+	*	*	do not meet	W_- W_+
W_-	do not meet	*	do not meet	do not meet

B = bore, W = simple wave of depression, suffix $\pm$ represents travel in
$\pm$ x direction.

A similar approach is used to study shock wave interaction in gas dynamics (e.g. Courant and Friedrichs, 1948, section IIID).   Other solutions of gas-dynamic problems may be transferred to the water-wave context.   For example, this paper is confined to two-dimensional examples but the intersection of bores at an angle to each other may be solved by methods used for intersecting shock waves.

Analysis of observations

In the previous section the (u,c) plane is used to analyse bore interactions.   It can also be of value in interpreting actual wave motion.   If measurements of velocity, u, and of total depth, giving c, are available as functions of time for a point in the surf zone, then a corresponding trajectory can be plotted in the (u,c) plane.   If the shore line is in the +x direction the variation of Q will indicate the amount of reflection whereas the variation of P will correspond to the incident waves.

Conclusions

The examples give an indication of some of the non-linear processes acting in the surf zone.   An appropriate next step is to use numerical modelling in conjunction with further analytical work to synthesize a qualitative picture of all wave action in the surf zone.   There is no intrinsic difficulty in finding numerical solutions and there is plenty of scope for further analysis.

Comparison with experiment and with prototype observations is desirable.   Firstly to obtain a good representation of turbulent dissipation, and then to assess the importance of other factors such as a mobile, porous bed and effects at the instantaneous shoreline.

The most intractable problem is probably that of providing an adequate description of wave breaking in order to give a good representation of the input to the surf zone.

References

Abbot, M.B. 1966.   An introduction to the method of characteristics.
                    Thames and Hudson, London

Blythe, P.A., Kazakia Y. and Varley E. 1972. The interaction of large
                amplitude shallow-water waves with an ambient shear flow.
                        Jour. Fluid Mech. $\underline{56}$, pp241-255.

Carrier, G.F. 1966. Gravity waves on water of variable depth.
                        Jour. Fluid Mech. $\underline{24}$, pp641-659.

Carrier, G.F. and Greenspan, H.P. 1958. Water waves of finite amplitude on
                a sloping beach. Jour. Fluid Mech. $\underline{4}$, pp97-109.

Courant, R. and Friedrichs, K.O. 1948.   Supersonic flow and shock waves.
                        Interscience, New York.

Cumberbatch, E. and Wen, S. 1973. Some results on the approach of a slowly-
                varying gravity wave to a beach.
                        Geophys. Fluid Dynamics $\underline{5}$ pp313-328.

Freeman, J.C. and LeMehaute, B. 1964. Wave breakers on a beach and surges
                on a dry bed. Proc.Amer.Soc.Civil Eng.Jour.Hyd.Div. $\underline{94}$,
                        March, pp187-216.

Ho, D.V. and Meyer, R.E. 1962. Climb of a bore on a beach. Part 1. Uniform
                beach slope. Jour.Fluid Mech. $\underline{14}$, pp305-318.

Jeffrey, A. 1964.   The breaking of waves on a sloping beach, Zeit.angew.Math.
                        und Phys.$\underline{15}$, pp97-106, Addendum 1965, $\underline{16}$, p712.

Jeffrey, A. 1967.   On a class of non-breaking finite amplitude water waves.
                        Zeit.angew.Math.und Phys. $\underline{18}$, pp57-65,
                        Addendum p918.

Keller, H.B., Levine, D.A. and Whitham, G.B. 1960. Motion of a bore over a
                sloping beach. Jour.Fluid Mech. $\underline{7}$, pp302-316.

Longuet-Higgins, M.S. 1972. Recent progress in the study of longshore
                currents. in "Waves on Beaches" editor R. Meyer, Academic
                        Press, New York, pp203-248.

Meyer, R.E. and Taylor, A.D. 1972. Run-up on beaches. in "Waves on Beaches",
                ed. R. Meyer, Academic Press, New York, pp357-411.

Miller, R.L. 1968. Experimental determination of run-up of undular and fully
                developed bores. Jour.Geophys.Res. $\underline{73}$, pp4497-4510.

Peregrine, D.H. 1967. Long waves on a beach. Jour.Fluid Mech.$\underline{27}$, pp815-827.

Peregrine, D H. 1972. Equations for water waves and the approximation
                       behind them. in "Waves on Beaches" ed. R Meyer,
                              Academic Press, New York, pp95-121.

Rajaratnam, N 1967.   Hydraulic jumps. Adv. in Hydroscience $\underline{4}$, pp197-280.

Stoker, J.J. 1957   Water Waves. Interscience, New York.

Varley, E., Venkataram, R and Cumberbatch.E. 1971. The propagation of large
                       amplitude tsunamis across a basin of changing depth.
                       Part I. Off-shore behaviour.
                              Jour.Fluid Mech. $\underline{49}$, pp775-801

CHAPTER 29

FIELD INVESTIGATIONS IN SURF ZONES

by Hans Henning DETTE [1] and Alfred FÜHRBÖTER [2]

ABSTRACT

During storm surges considerable wave energies are dissipated in surf zones; the energy transfer rates are in the order of one up to two powers of ten higher than outside the surf zone. A breaker parameter β introduced by FÜHRBÖTER (1974) with regard to a quantitative breaker classification, especially of the intermediate types between surging and spilling, was found to be convenient for practical application. The breaker parameter β is in close relation with the horizontal asymmetry parameter α of the breaking wave. With decreasing breaker parameter the asymmetry is increased and reverse.

Within the longshore currents macro-turbulences were discovered. The periodical fluctuation parameter γ was found to increase nearly linearily with decreasing breaker parameter; the narrower the area is, where the main energy is dissipated the smaller becomes the mean periodical fluctuation which seems to be independent of the wave period but reaches up to 7 and more fluctuations within the wave period.

The mean longshore currents velocities reached up to 1.5 m/s above the seabottom; the coefficient of variation was scattering considerably between 400 per cent at low velocities ($\overline{v}_L$ = 0.1 m/s) and 20 per cent at the highest velocities ($\overline{v}_L$ = 1.5 m/s). The instantaneous longshore current velocities were nearly symmetrically distributed around the mean velocity, the mean amplitudes were nearly constant and reached approx 0.35 m/s whereas the periodical fluctuation decreased from 2.6 s at low mean velocities up to 1.7 s at high velocities.

---

[1] Dr.-Ing., [2] Prof. Dr.-Ing., Leichtweiß-Institut für Wasserbau of the Technical University Braunschweig, Germany, Hydrodynamics and Coastal Engineering Division

1. INTRODUCTION

Surf zones are known as areas of strong interactions where the wave
energy originating from hundreds of miles is dissipated within a narrow
zone. In prototype the wave energy is mainly transformed by air entrain-
ment during wave breaking and turbulent mixing processes.

So far mostly qualitative-morphological investigations in surf zones
are known. The comprehensive field measurements carried out at the west
coast of the North Sea Island of Sylt were aimed at quantitative-physi-
cal data with regard to the energy dissipation rates and the bottom
wave induced longshore currents which mainly affect the longshore trans-
port of sediments in surf zones.

By chance valuable data obtained during the unusual series of 5 heavy
storm surges in November and December 1973, a sequence which had
not been observed since 100 years (LAUCHT,1974) could be included into
the study.

2. WHY INVESTIGATIONS IN PROTOTYPE?

Before results are presented the necessity of expensive prototype in-
vestigations instead of surf investigations carried out at low expendi-
ture in laboratories has to be discussed. In the field of wave research
hydrodynamic conformities can be transferred from small scale models to
prototype in most cases by means of FROUDE's and REYNOLDS's law of simi-
larity; but this procedure is doubtful with regard to surf studies,
even in theoretical approaches surf processes cannot be described com-
pletely.

Surf investigations at small scales must lead to wrong results due to
the influence of surface tension because the air entrainment during
breaking and thus a main dissipation factor cannot be taken into consi-
deration (FÜHRBÖTER, 1970). According to SKLADNEV and POPOV (1969) waves
should have at least heights of about 0.5 m in order to avoid scale
effects. Due to the fact that such wave heights cannot yet be rebuilt

in three-dimensional models surf research consequently has to be carried
out in prototype at higher risks.

3. LOCATION OF THE SURF INVESTIGATIONS AND MEASURING EQUIPMENT

At the German North Sea coast the west coast of the Island of Sylt
(Figure 1) is most favourable for surf investigations, because it is
exposed to wave attack from southwest to northwest and waves higher
than 1 m can be expected all over the year.
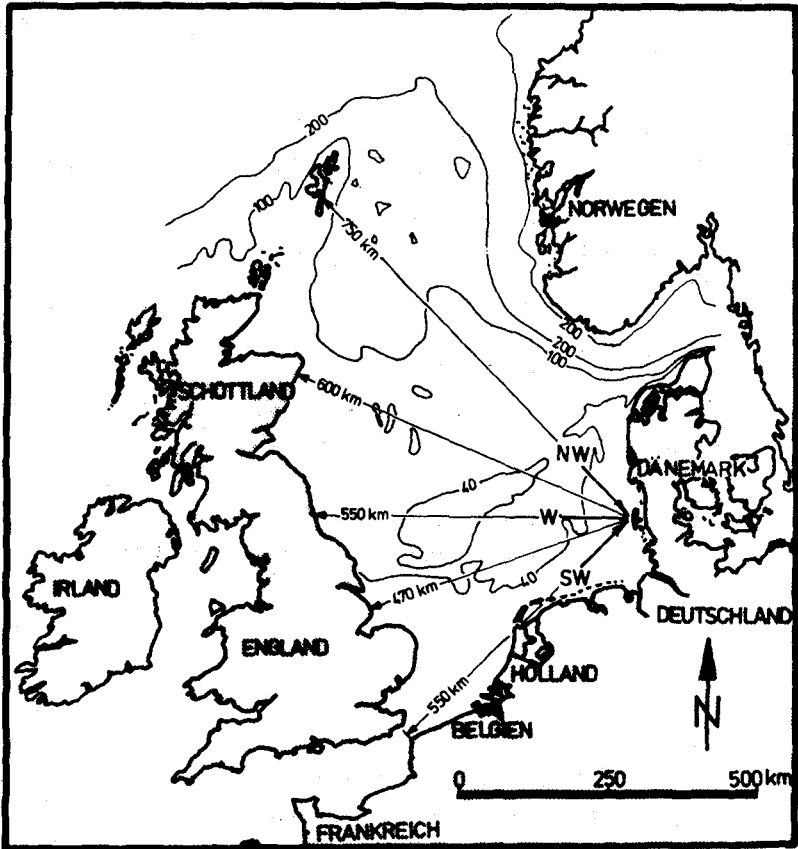
Figure 1:   Exposed location of the Island of Sylt/North Sea

The offshore area of Sylt (Figure 2) is characterized by a longshore
bar extending at a distance of approx. 300 m parallel to the shoreline.

Outside the surf zone wave recordings are carried out continuously by
the AMT FÜR LAND- UND WASSERWIRTSCHAFT HUSUM at the stations W_1 up to
W_4 (1280 m distant from the shoreline). The wave recorders are placed
on the seabottom and work an the principle of ultrasonic. Additionally
two electromagnetic two-component current meters (type: COMEX) working
on FARADAY's principle were installed at the stations W_1 and W_3.
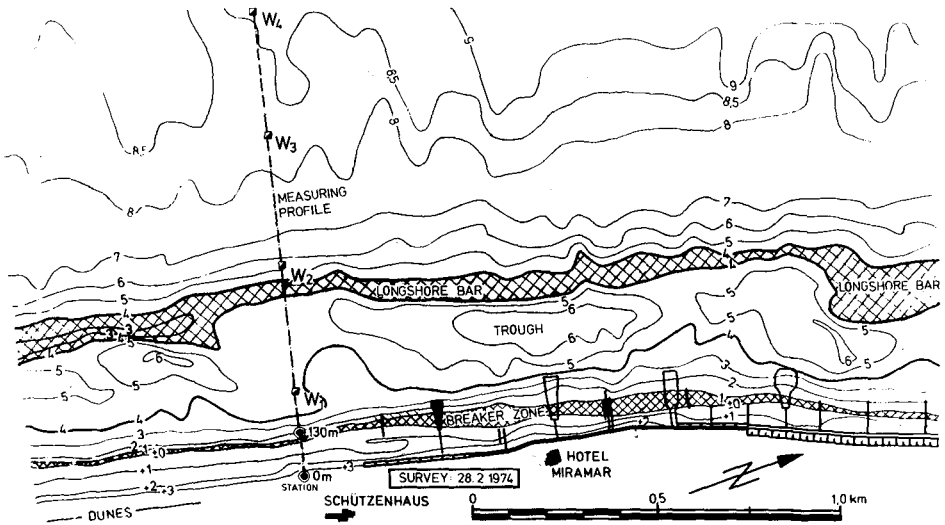
Figure 2: Offshore area of the west coast of Sylt

The data obtained from the above mentioned stations (further details
see DETTE (1974 a)) were used as input for the evaluations of field
measurements carried out in the surf zone. The measuring equipment there
consisted out of pressure cells and two electromagnetic two-component
current meters (type: COLNBROOK, Ltd.). Figure 3 shows the installation
of the current meter and a pressure cell protected against seawater;
fixed at a steel pipe.

Figure 3: Installation of a two-component electromagnetic current
           meter and a pressure cell protected against seawater

4. ENERGIES IN THE SURF ZONE

In order to illustrate the strong interactions occurring in surf zones
Figure 4 shows the evaluation of the mean power delivery rate $\Delta \bar{N}$ in the
offshore area of Sylt obtained from a sequence of 100 waves by applica-
tion of the linear wave theory and expression in the electrical unit of
power kW (see FOHRBÜTER (1974)).

From these results it is obvious that the energy transfer rate is by
one up to two powers of ten lower outside the surf zone than inside
where in the breaking zone a maximum of .6 kW per m^2 and unit width was
obtained during a measurement in April 1973 (Figure 4).

Regular visual observations of the waves breaking in the surf zone re-
vealed the difficulty if not impossibility of defining the position and
extension of the main breaker zone. By means of measuring sequences of
waves at short distances in- and outside of the breaker zone and evalu-
ating the characteristic wave height parameters for each station it
seems possible to find the breaker zone; this is shown for one example

on Figure 5.
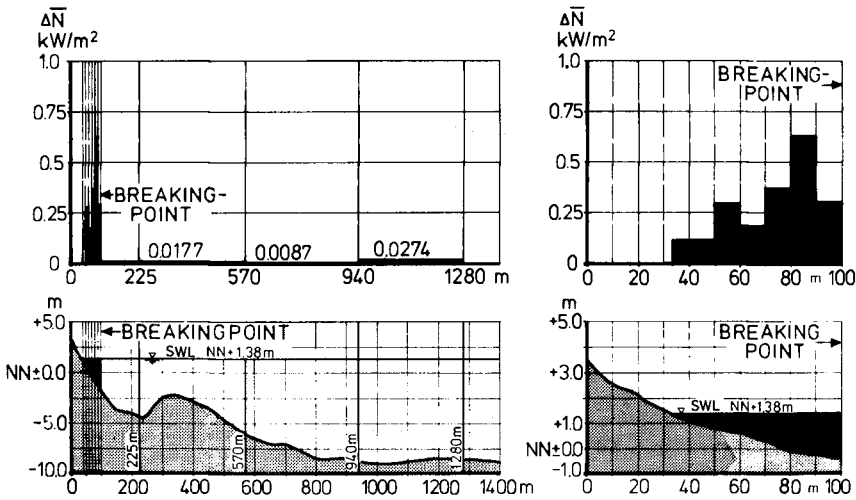
Figure 4: Energy transfer rates outside and inside the surf zone by evaluation of a sequence of 100 waves and application of linear wave theory
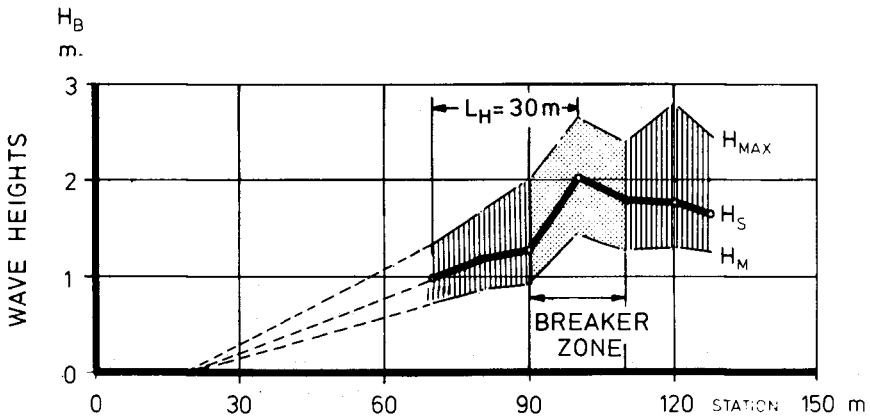
Figure 5: Characteristic wave height parameters evaluated from a sequence of 100 waves inside and outside the surf zone during the storm surge of November 6th, 1973

Instead of using the maximum wave heights the significant values are
preferred because they represent approximately the mean wave energy.
For the example on Figure 5 the breaker zone lies between station 90 m
and 110 m.

By means of the wave measurements at short distances in the surf zone a
theoretical quantitative breaker classification suggested by FÜHRBÖTER
(1974) could be checked with regard to a practical application.

The breaker parameter β is defined, as follows:

$$\beta \ = \ \frac{L_H}{L_B}$$

L_H = Half-decay length = horizontal distance from the
breaking point of the wave up to that point where the
maximum wave height   (breaker height) has been reduced
to 50 per cent (in analogy to the half-decay time in
nuclear physics)

L_B = Wave length in the surf zone.

Low breaker parameters mean plunging breakers ($\beta < 1$) and high ($\beta > 3$)
spilling breakers. The qualitative difference between these breaker
types and their intermediate types prevailing in most cases is replaced
with breaker parameter β by a quantitative classification which repre-
sents from the physical point of view that width of the surf zone where
75 per cent of the approaching wave energy is dissipated.

The half-decay length L_H on Figure 5 is for the significant values
L_H = 30 m, the appropriate significant wave length reached L_B = 70 m so
that a breaker parameter β = 0.43 was calculated. From 19 measurements
during the first storm surge between November 5th and 7th, 1973 the β
parameters were evaluated (DETTE (1974 b)); they varied in between
β = 0.2 and β = 1.0. These results are in agreement with visual classi-
fications in which an intermediate breaker type ranging in the neigh-
bourhood of plunging breakers was observed.

The breaker parameter β was found to be in close relation to the hori-
zontal asymmetry-parameter α

$$\alpha = \frac{\Delta L}{L}$$

ΔL = Length of the leeside part of the wave

L = Total wave length

of the breaking wave. With decreasing breaker parameter the asymmetry is
increased and reverse. This is of high importance with regard to the
orbital velocities of the surf waves (BÖSCHING (1974)) which are deci-
sive with regard to the on- and offshore transport of sediments.

5. CHARACTERISTICS OF THE LONGSHORE CURRENTS

5.1 GENERAL RESULTS

The orbital velocities are acting in the direction of wave propagation;
they can be ragarded as alternating currents according to the movement
of the waves. Contrary to this the longshore currents are generally
treated as a continuous current generated by the longshore component of
the wave movement and maintained as compensating current due to the
balance of wave energy and friction losses. In prototype however the
longshore currents are not only affected by the orbital currents they
are additionally superimposed by complex two- (e.g. bottom return flows,
mass transport) and three-dimensional currents (rip currents as local
return flows into the open sea). Being aware of these facts nevertheless
field studies on the longshore currents and relations to the wave heights
in the surf zone were started. With regard to the longshore currents it
was found that their structure mainly depends upon a phenomenon that
steep waves in shallow water decompose in two or more waves (solitons)
with different heights and periods during the process of breaking
(Figure 6). GALVIN (1972) recently pointed out that this occurrence
influences the mechanism of breaking waves. HOM-MA (1962) and later on
KENNEDY and LOCHER (1972) indicated that the above decomposition might
be of importance for the longshore transport of sediments but denied
that this phenomenon would stand in any relation to the longshore currents.
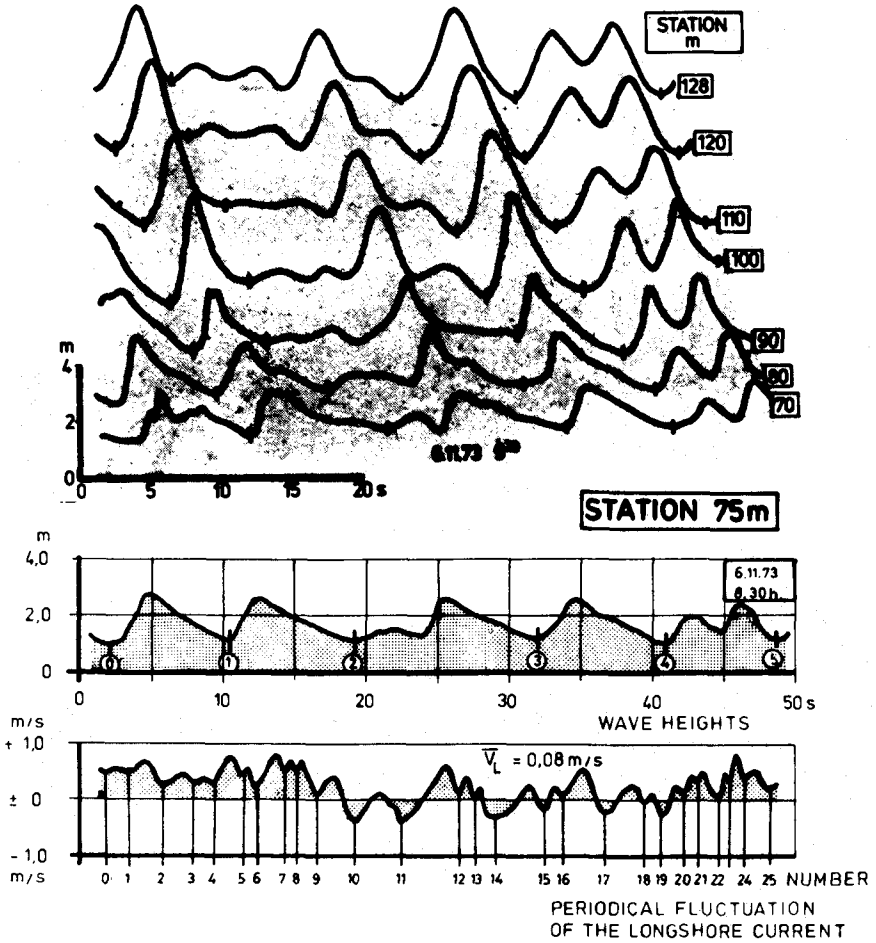
Figure 6: Decomposition of steep waves (solitons) within the surf zone
and relationships to the structure of longshore currents

By means of a high time-limit release (approx. 0.1 sec) of the used
electromagnetic two-component current meters it was possible in compa-
rison to earlier field measurements with floating buoys, dye, balloons
etc. which only allowed to obtain mean velocities, to discover macro-
turbulent processes within the longshore currents. It could be proved
that the longshore currents cannot be regarded any longer as steady or
quasi-steady flows, they showed fluctuations in the range of $\pm$ 100 per
cent and occurred with periods up to 9-fold of the wave periods. It was
not unusual that a mean longshore current velocity of $\overline{v}_L$ = 1.0 m/s
fluctuated within fractions of time from $\pm$ 0 m/s up to 2 m/s as it can
be seen e.g. on Figure 7.
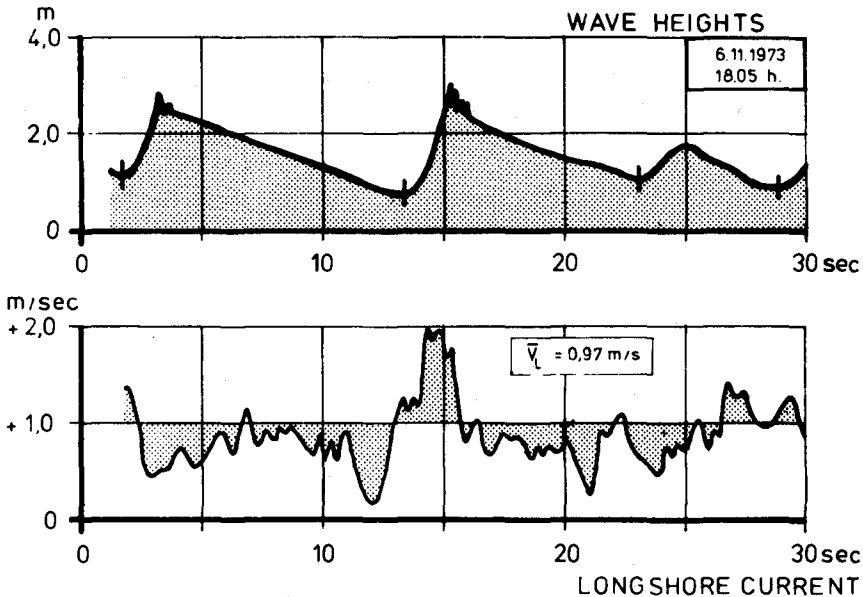
Figure 7: Fluctuations of the longshore current velocity

Based on this fact the high transport capacities of such currents can
be explained, besides the orbital and surf turbulences within the long-

shore current, additionally accelerations and retardations were observed
so that comparisons with steady flows having the same mean velocity
seem to be impossible. By definition of a periodical fluctuation para-
meter γ

$$\gamma \quad = \quad \frac{T_B}{T_v}$$

T_B =   Mean wave period in the surf zone

T_v =   Mean periodical fluctuation of the longshore
               current

finally a nearly linear relationship was discovered (Figure 8); the
periodical fluctuation parameter increases with decreasing breaker
parameter β (see Chapter 4). This means that the smaller becomes the
area where the main energy is dissipated (75 per cent) the smaller
also becomes the periodical fluctuation of the longshore current.
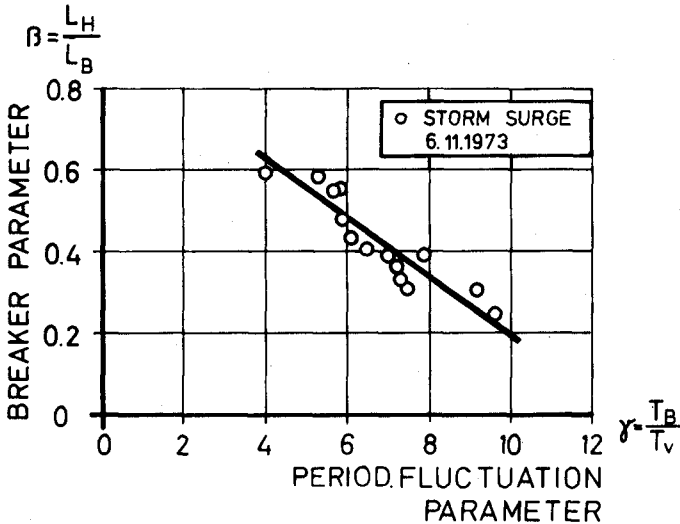
Figure 8:   Relationships between the breaker parameter β and the
               periodical fluctuation parameter γ of the longshore currents

5.2   DETAILS OF THE LONGSHORE CURRENT ANALYSIS

5.2.1 METHOD OF DATA EVALUATION

With regard to an evaluation of the longshore currents occurring in the
surf zone of Sylt more than 150 analogous registrations of 15 minutes
duration each were collected, most of them during the unusual sequence
of 5 heavy storm surges in November and December 1973. Intervals of
10 minutes duration were deemed to be sufficient in order to receive
representative data for each measurement. The analogous registrations
were digitized at intervals of one fifth of a second so that a total
of 3000 instantaneous velocities was available for the analysis of
longshore current characteristics by means of electronical data pro-
cessing (ICL 1906 S of the Technical University of Braunschweig).

5.2.2 MEAN LONGSHORE CURRENTS, THEIR STANDARD DEVIATIONS AND COEFFICIENTS OF VARIATION

By the measurements of the longshore currents it could be confirmed
that the highest longshore current velocities have to be expected du-
ring two different weather conditions:

1. Heavy storm surges with the waves approaching at small
    breaking wave angles ($\Theta_B < 25^0$) and high breakers of
    more than 3 m (Figure 10).

2. Winds blowing nearly parallel to the shoreline causing
    great breaking wave angles ($\Theta_B > 25^0$) and low breakers
    with heights less than usually 1 m (Figure 11).

In both cases mean bottom longshore current velocities up to 1.5 m/s
were evaluated. Figure 9 shows for example the time history of the
heaviest storm surge in the sequence of storm surges which occurred at
the 19th and 20th of November 1973 when wave heights up to 7.2 m were
recorded at station W_4 (1280 m distant of the shoreline) and wave heights
up to 3.3 m in the surf zone. The drawing gives an idea of relation-
ships between tide, wind velocity and direction as the causing factors
and the longshore currents and wave heights as the generated parameters.
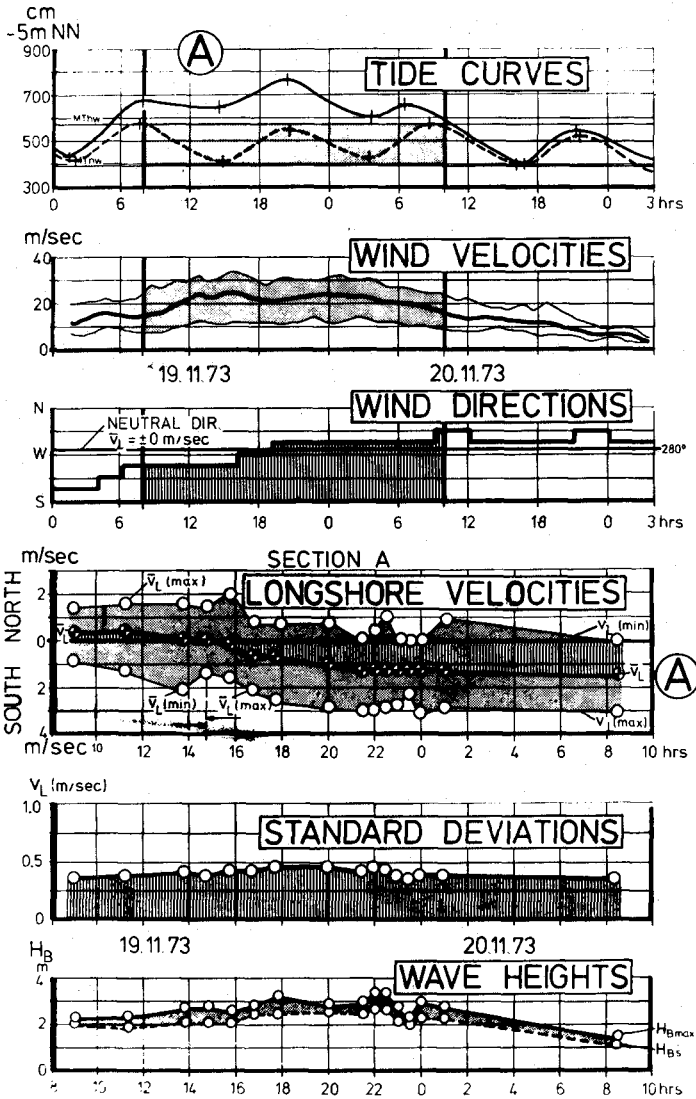
Figure 9: Time history of a heavy storm surge

With the shifting of the wind directions the mean longshore flow direction changed nearly at the same time; besides it is remarkable that instantaneous velocities in opposite flow direction at mean values of more than 1.0 m/s occurred.

Figure 10 gives an idea of the mean longshore velocities when the wind was blowing nearly parallel to the shoreline from south (section A) and north (section C); besides measurements are shown when the wind was blowing from land to sea (section B) and small waves were diffracted around the island of Sylt.

For all measurements carried out at Sylt the maximum and minimum longshore current velocities within the 10-minute registrations are plotted against the appropriate mean velocities in classes of 0.1 m/s (Figure 11). The regression lines indicate that there seems to exist a nearly linear relationship between the extreme (maximum and minimum) and the mean velocities.

With regard to the temporal variability the standard deviations were investigated; Figure 12 shows by the linear regression that the standard deviations increase slightly from 0.33 m/s up to 0.42 m/s over the range of mean velocities from $\overline{v}_L$ = 0 m/s up to 1.5 m/s.

By means of evaluating the statistical coefficient of variation it is illustrated more clearly that the longshore current velocities are scattering in a high range between 400 per cent at small velocities ($\overline{v}_L$ = 0.1 m/s) and 20 per cent at the highest velocities ($\overline{v}_L$ = 1.5 m/s).

5.2.3 HISTOGRAMS OF THE DISTRIBUTION OF THE LONGSHORE CURRENT VELOCITIES, PERIODICAL FLUCTUATIONS AND AMPLITUDES

Figure 14 shows histograms of the distributions of the longshore current velocities, periodical fluctuations and amplitudes during the storm surge of 19th/20th November 1973. The mean values are inserted, as well as the wave periods and the periodical fluctuation parameter γ.
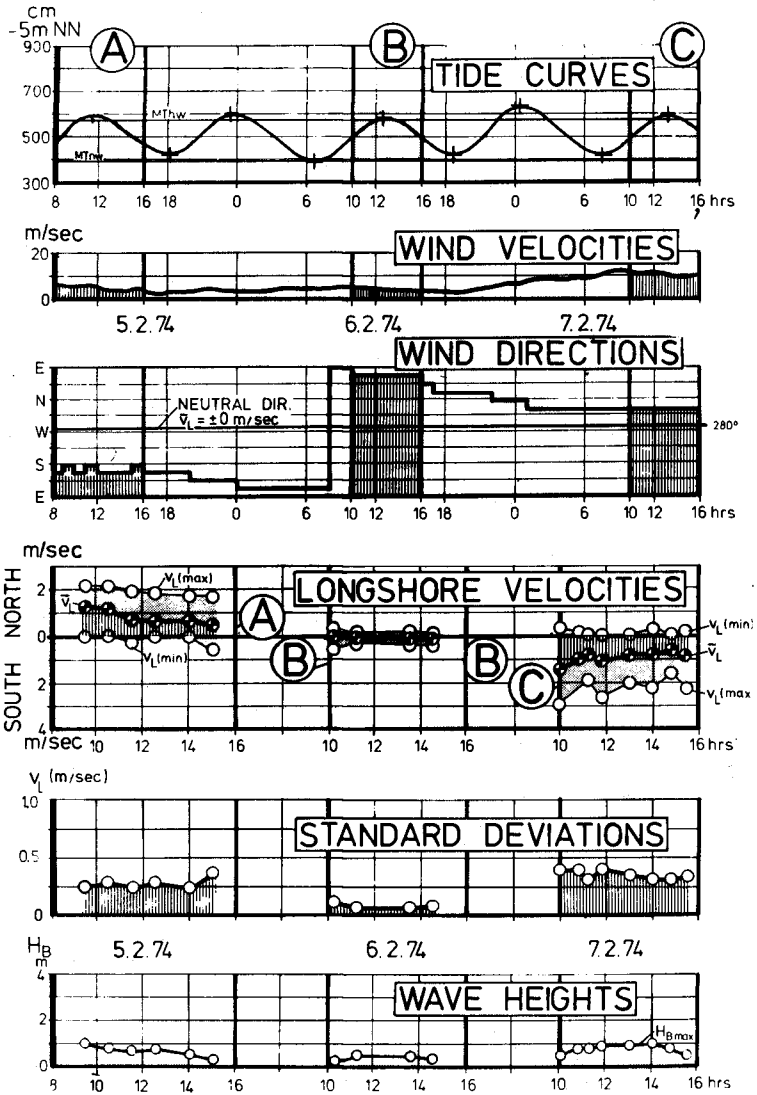
Figure 10: High longshore current velocities caused by winds blowing parallel to the shoreline
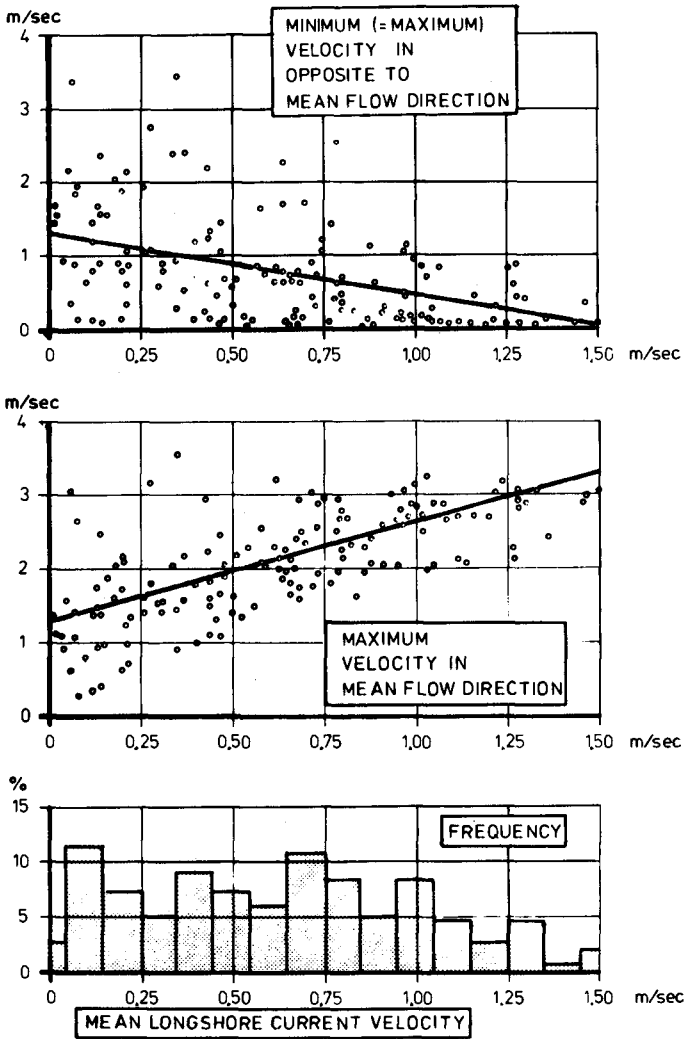
Figure 11: Maximum and minimum longshore current velocities in relation to the mean velocities and frequency
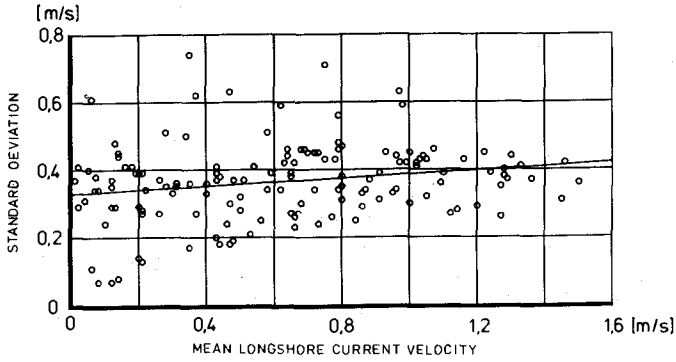
Figure 12: Temporal variability of the longshore current velocities illustrated by their standard deviations

$$C_V = \frac{S_V}{\overline{V}_L}$$

$$S_V = \sqrt{\frac{1}{n}\sum_{n=1}^{n=3000}(V_L - \overline{V}_L)^2}$$
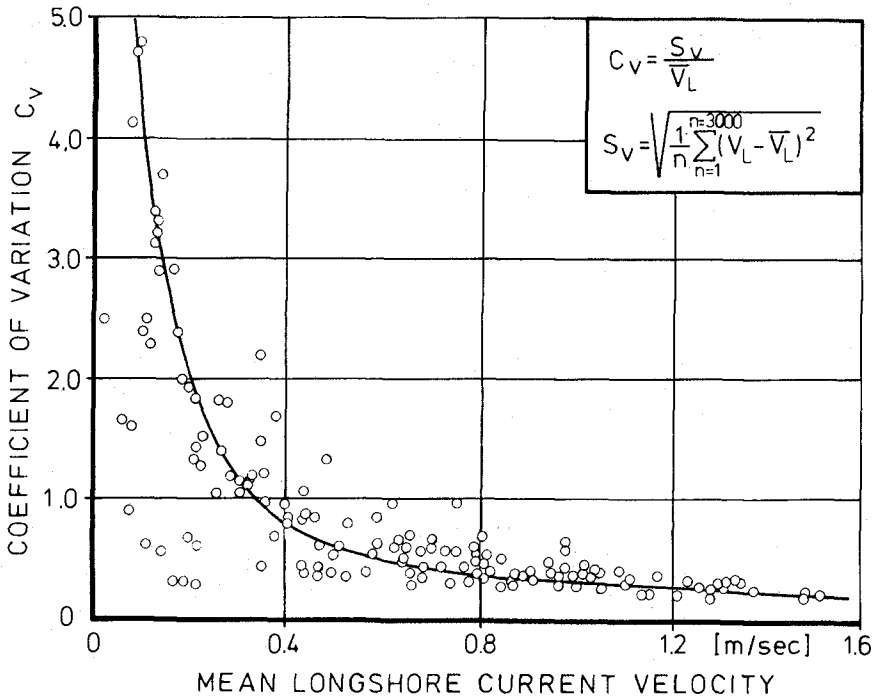
Figure 13: Coefficient of variation of the longshore current velocities
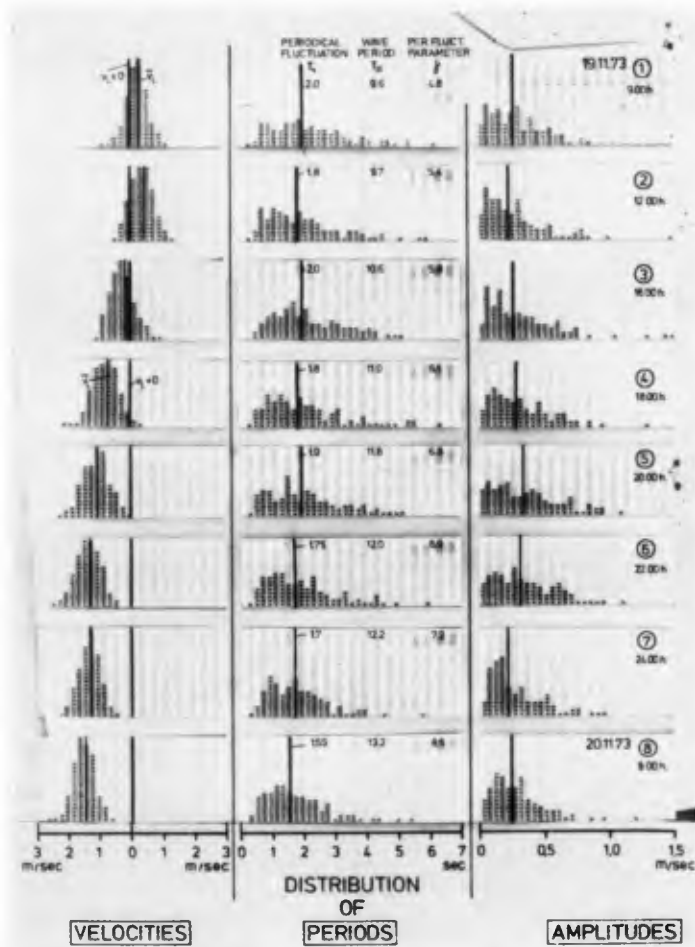
Figure 14: Histograms of the distributions of the longshore currents, periodical fluctuations and amplitudes during storm surge of 19th/20th November 1973

5.2.4 MEAN LONGSHORE CURRENT AMPLITUDES AND PERIODICAL FLUCTUATIONS

Analogous to the considerations of the maximum and minimum longshore current velocities in relation to the mean velocities the mean amplitudes and periodical fluctuations of all measurements were plotted against the mean velocities (Figure 15 and 16). The regression line shows that the amplitudes are nearly constant and reach 0,35 m/s.

whereas the periodical fluctuations decrease from T_v = 2.6 s at small
mean velocities $\overline{v}_L$ = ± 0 m/s) up to T_v= 1.7 s at the highest mean velo-
cities ($\overline{v}_L$= 1.5 m/s).
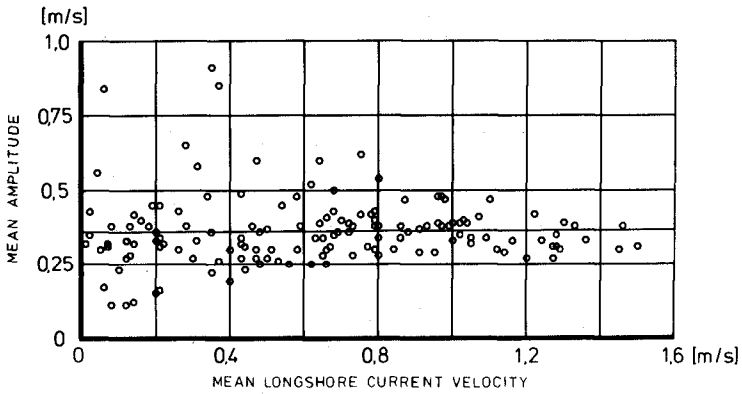
Figure 15: Mean amplitudes of the longshore currents in relation to
           the mean velocities
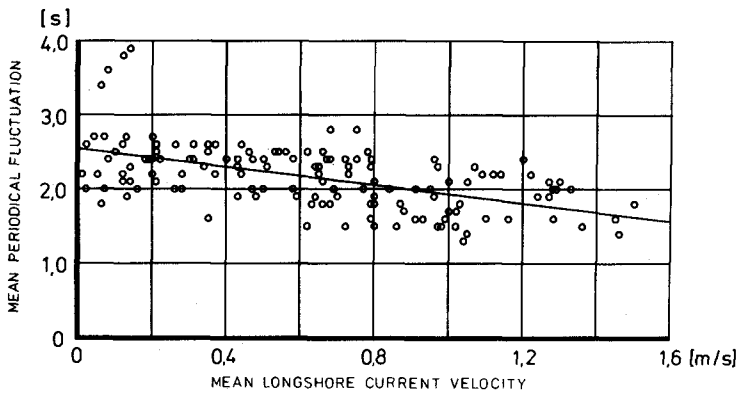
Figure 16: Mean periodical fluctuations of the longshore currents in
           relation to the mean velocities

6. CONCLUSIONS

With the above given results of surf measurements in prototype even
during severe storm surges which are part of a thesis completed in 1974
(DETTE, 1974 b) a contribution is presented with regard to a quantita-

tive knowledge.Though the data are scattering inevitably due to the complex nature of waves it is possible to find relationship between the governing parameters in the surf zone.

7. ACKNOWLEDGEMENTS

8. REFERENCES

BÜSCHING, F.   Über Orbitalgeschwindigkeiten irregulärer Brandungswellen
     1974   Mitt. d. Leichtweiß-Institits der Techn.Univ.Braunschweig
                 Heft 42, 1974

DETTE, H.H.   Wellenmessungen und Brandungsuntersuchungen vor Wester-
     1974 a   land/Sylt, Mitt. d. Leichtweiß-Instituts d.Techn.Univ.
                 Braunschweig, Heft 40, 1974

DETTE, H.H.   Über Brandungssströmungen im Bereich hoher REYNOLDS-
     1974 b   Zahlen, Mitt. d. Leichtweiß-Instituts der Techn.Univ.
                 Braunschweig, Heft 41, 1974

FOHRBÜTER, A.   Air Entrainment and Energy Dissipation in Breakers
     1970   Proceedings 12th Coastal Engineering Conf., Washington USA

FOHRBÜTER, A.   Einige Ergebnisse aus Naturuntersuchungen in Brandungs-
     1974   zonen, Mitt. d. Leichtweiß-Instituts d. Techn.Univ.
                 Braunschweig, Heft 40, 1974

GALVIN, C.J.   Wave Breaking in Shallow Water in "Waves on Beaches"
     1972   edited by R.E. Meyer, Academic Press, Inc. New York and
                 London, 1972

HOM-MA, M.   Suspended sediment due to Wave Action; Proceedings
HORIKAWA, K.   8th Coastal Engineering Conference 1962

     1962

KENNEDY, J.F.   Sediment Suspension by Water Waves in "Waves on Beaches"
LOCHER, F.A.   edited by R.E. Meyer, Academic Press, Inc. New York and
     1972   London, 1972

LAUCHT, H.   Die Sturmfluten 1973 und ihre Wirkungen im Hamburger
     1974   Hafen, HANSA-Schiffahrt-Schiffbau-Hafen
                 111. Jahrg., No. 11, 1974

SKLADNEV, M.F.   Studies of Wave Loads on Concrete Slope Protection of
POPOV, J.Ja.   Earth Dams, Symposium: Research on Wave Action,
     1969   Paper No. 7, Delft, Niederlande, 1969

CHAPTER 30

FIELD MEASUREMENTS OF NEARSHORE VELOCITIES

David A. Huntley[1] and Anthony J. Bowen[2]

Abstract

      Two component electromagnetic flowmeters are being used as the basis of an apparatus to measure nearshore velocities on natural beaches. The flowmeters are mounted on free standing tripods, 1 m. base side and 0.3 m. high, to measure the two components of horizontal flow, and have been used in depths of up to 4 m. and up to 150 m. from the shoreline. The apparatus has proved both flexible and reliable on beaches ranging from steep shingle (slope ∿ 0.13) to very shallow sand (slope∿ 0.01) and under a wide variety of wave conditions, including full storm waves on a beach of intermediate slope (∿ 0.04).

      Results show that a single flowmeter can be used on a tidal beach to measure the variation of the flow field along a line perpendicular to the shoreline. In this way edge waves and steady nearshore circulation patterns have been detected. If several flowmeters are placed on a line perpendicular to the shoreline, the progress of individual waves can be followed as they pass over each flowmeter in turn, and hence propagation speeds, changes of wave form and the development of lower frequency wave motion close to the shoreline can be studied.

[1] Institute of Oceanographic Sciences,
Bidston, Cheshire, England.

[2] Department of Oceanography, Dalhousie University,
Halifax, N. S., Canada.

Introduction

In recent years there has been a considerable increase in the theoretical understanding of modes of water motion trapped or generated in the narrow region bordering the coastline. Steady longshore currents, rip currents and wave set-up and set-down have all been explained in terms of the transfer of momentum from the incoming, breaking waves. Edge waves have been shown to be a possible cause of rip currents and of various sedimentary features which exhibit a regular, longshore rhythmical pattern. A number of recent theories have been concerned with the process of wave breaking, and the importance of the resulting turbulent velocity field and intensive vertical and horizontal mixing to many nearshore processes has also been highlighted.

Despite the fundamental importance of these phenomena to coastal engineering, reliable field observations of the velocity field close to the shore are at present relatively rare, particularly in the surf zone. However such measurements are needed urgently to evaluate the validity of the new theoretical ideas, and to suggest where these ideas are inadequate and need further improvement.

This paper describes a research programme to measure nearshore velocity fields, based on electromagnetic flowmeters. Some preliminary results using a single flowmeter and a line of three flowmeters perpendicular to the shoreline are discussed.

Electromagnetic Current Meters.

The two-component electromagnetic flowmeters originally developed by Tucker and co-workers (1970) at the National Institute

of Oceanography, and now marketed by Colnbrook Instrument Development
Limited, Poyle Road, Colnbrook, Buckinghamshire, England, were
chosen for the present research programme since they are well suited
to the violent nearshore environment, being rugged and compact, with
no moving parts and a relatively fast response time. The measuring
head itself, discus shaped, 11.4 cms. in diameter and 3.8 cms. deep,
contains a circular solenoid developing an alternating magnetic field
of about $\pm$ 60 guass perpendicular to the circular plane of the discus.
Dissipation is about 8 watts. Water flowing through this field in the
plane of the discus produces, by electromagnetic induction, a potential
gradient perpendicular to the flow. Two pairs of electrodes mounted on
the discus detect the two components of the electric field and hence
measure the two components of the flow. The electrode sensitivity is
about 200 $\mu V/ms^{-1}$, and calibration experiments have confirmed that
this remains constant to about 1% for currents up to at least 3 ms^{-1}.

        The directional properties of the flowmeter have been des-
cribed by Tucker (1972). In the plane of the discus, the measured
current amplitude is accurate to better than 5% for any direction of
flow, though there is a small systematic variation in the error as the
flow direction changes relative to the electrode alignment. The res-
ponse to flow out of the plane is more complex, but is approximately
correct for tilt in the range $\pm$ 30° out of the discus plane. The time
constant and noise level of the flowmeters depend on the waveform and
frequency of the alternating current driving the magnetic field. In
the present instrument an alternating square wave drive of 40Hz.
results in a time constant of about 0.1 sec. (3 dB point $\approx$10 Hz.), and
a noise level equivalent to a rms current of 5 mm s^{-1} was achieved in
the field experiments; these characteristics have been considerably
improved in more recent instruments (Tucker- private communication).
The long-term stability of these flowmeters has allowed them to be
used as ships' logs, and our experiments confirm that they can be used

to measure the mean flow patterns in the nearshore zone at least over
a period of several hours.

Figure 1 shows the mounts which were used to hold the heads,
aligned to measure the horizontal flow field, on beaches in water of
depth varying from 10 cms. to more than 4 m.. Non-magnetic materials
were used throughout to prevent distortion of the flowmeter field. The
spars holding the heads were of stainless steel, and supported the
heads from below so that turbulence generated by the mounts would not
pass over the heads themselves; calibration of the instruments in
steady flows confirmed that the turbulence from the spars did not
contribute significantly to the overall noise level. At the opposite
end of the spars demountable underwater plugs were used, so that
different lengths of electrical cable could be used, depending upon
the distance of the instruments from the shore-based electronics units.
The tripods themselves were constructed of aluminium alloy angle, with
a base triangle of 1 m. sides and standing about 0.3 m. high. Lead
weights at the corners of the base could be added to counteract the
torque due to violent flow around the head. For very shallow water,
simple triangular bases of aluminium angle were used to hold the flow-
meter heads as little as 10 cms. from the sea-bed.

The larger tripods could also hold capacitance pressure sensors
below the flowmeters; measurements of the two horizontal components of
flow and the vertical displacement of the water surface at a point
allow an approximate directional spectrum of the surface waves to be
calculated.

This apparatus was designed for use on tidal beaches. The
tripods were placed in situ above the low water mark at low water, and
were then covered for several hours spanning high water as the tide
rose and fell. The instruments were placed at known positions relative
to a fixed origin above the high water mark, with the flowmeter elec-
trodes aligned by eye to within 2° of the offshore and longshore
directions.

This simple method of mounting the flowmeters has proved both

flexible and reliable on beaches ranging from a steep shingle beach
(slope ∿ 0.13) to a very shallow sandy beach (slope ∿ 0.01), and under
a variety of wave conditions, including full storm waves on a beach
of intermediate slope (∿ 0.04); experiments have not yet been con-
ducted under storm conditions on the steepest beaches. Position and
orientation changes of the tripods could be checked at each low water.
When the triangular tripod bases were dug into the beach to a depth
of about 10 cms., and the electric cable to the flowmeter similarly
dug in, no lateral movement was detected on any of the beaches and
tilt of the heads out of the horizontal plane was at most a few
degrees.

The chief problems in the field experiments occurred in
making a satisfactory connection between the flowmeter spar and the
electric cable connecting it to the shore-based instruments. The low
voltage signal from the electrodes is very susceptible to being
swamped by spurious voltages due to leakage from the current leads
driving the magnetic field solenoid; impedances less than 1000 MΩ
between the drive and the electrode leads cause appreciable
deterioration in the signal to noise ratio. Although co-axial leads
were used throughout in order to minimize the pick-up between the
electrode and solenoid drive circuits, connections to the spars were
particularly prone to damage when the tripods were dug up and moved
to other locations, and the instruments could become unworkably
noisy unless care was taken in making the demountable connections.

The shore-based instruments driving the flowmeters were
housed in a Land Rover vehicle parked as close to the shoreline as
possible, to obtain maximum offshore distance to the flowmeters with
the minimum length of cable. Experiments have now been conducted with
up to 150 m. of cable to the spars and, with suitable calibration
adjustments, this length could probably be considerably increased with-
out significant decrease in the signal to noise ratio. The Land Rover
contained the flowmeter electronics and both analogue and digital
logging apparatus. The digital logger was a battery driven magnetic

tape machine able to record up to 10 analogue and 1 digital channels
every 1/3 second; signals from five flowmeters could be recorded
every 1/3 second continuously for a period of up to 2 hours.

A single flowmeter on tidal beaches

On tidal beaches, a single fixed flowmeter can be used to
measure the variation of the velocity field along a line perpendicular
to the shore, by making use of the change of shoreline position during
a tidal cycle. We have used this technique to measure nearshore drift
currents, incident gravity waves, edge waves and high frequency motion
close to the shore.

An implicit assumption is that the velocity field is quasi-
stationary as the shoreline moves. The validity of this assumption can
be checked by comparing measurements made at the same distance from the
shore on the rising and falling tide. As an example, figure 2 shows
measurements of steady longshore currents in a wide surf zone on a
shallow beach, where the point at 93m. and the lower point at 115m.
were measured on the rising tide and the remaining points on the
falling tide. The consistency of these results confirms that, at least
for the steady longshore currents, the velocity field remained reason-
ably stationary over a 4 hour period. Also plotted in figure 2 are
drift velocities obtained by measuring the longshore displacements of
floats over periods of order 2 minutes at different distances from the
shoreline; the results are seen to be in good agreement with the flow-
meter data.

Since the flowmeters measure both onshore and longshore compon-
ents of the mean flow as functions of offshore distance, they can also
be used to detect nearshore circulation cells. For example measurements
on a steep beach gave onshore and longshore drift currents which varied
with offshore distance as shown in figure 3b. These currents have been
interpreted as measurements along a line A in a nearshore circulation
cell system shown schemmatically in figure 3a.

In addition to the mean flow, average properties of the fluctuating
motion can also be measured at different distances from the shoreline using a
single flowmeter. The measured velocity fluctuations in any chosen frequency
band may be due to gravity waves or edge waves, and both may be either stan-
ding or progressive waves. Edge waves are modes of wave motion trapped to a
shoaling coastline by refraction; their amplitude varies sinusoidally along
the shore and decays rapidly seaward from the shoreline. By measuring the
r.m.s. amplitudes of both onshore and longshore flow at different distances
from the shoreline with a single flowmeter, it is possible to distinguish
between gravity and edge waves, and standing and progressive wave motion.

The relative phase of the onshore and longshore components of
velocity measured simultaneously by a single flowmeter assists in distin-
guishing these wave components. If we define the offshore and longshore
co-ordinates as the x and y directions respectively, then it is readily
shown that the velocity potentials ϕ for a gravity wave of frequency σ
can be written

$$\phi \sim \sin k_1 x \cos (k_2 y - \sigma t) \qquad \text{for a standing wave formed by reflection at the shoreline}$$

and $\phi \sim \cos (k_1 x + k_2 y - \sigma t)$ for a progressive wave,

where k_1, k_2 are the onshore and longshore wave numbers. The onshore and

longshore velocities are $u = \dfrac{\partial \phi}{\partial x}$ and $v = \dfrac{\partial \phi}{\partial y}$ respectively, and hence
these velocity components are in quadrature for standing gravity waves and
in phase or antiphase for progressive gravity waves. Similarly the velocity
potentials for edge waves of frequency σ and longshore wave number λ can be
written

$$\phi \sim f(x) \cos \lambda y \cos \sigma t \qquad \text{for standing waves}$$

and $\phi \sim f(x) \cos (\lambda y - \sigma t)$ for progressive waves, where
$f(x)$ is a function which decays rapidly offshore (Eckart 1951; see also
Bowen and Inman, 1969). Once again $u = \dfrac{\partial \phi}{\partial x}$ and $v = \dfrac{\partial \phi}{\partial y}$; in this case
therefore the onshore and longshore velocities are in phase or antiphase

for standing edge waves and in quadrature for progressive edge waves.

These considerations have enabled us to distinguish short
period standing edge waves in the velocity field on a steep beach
(Huntley and Bowen, 1973).

An array of 3 flowmeters at different distances from the shoreline.

Although useful data can be obtained using a single flow-
meter, arrays of flowmeters, measuring simultaneously at different
positions in the nearshore zone, provide considerably more information.
The condition of a statistically stationary velocity field can be
relaxed or even dropped, relative phases at different positions can be
measured, and progressive movement of individual waves can be followed.

A closely spaced array of flowmeters on a line at right-angles
to the shoreline can be used to study the horizontal turbulence in the
nearshore zone and, in principle, could provide a measurement of the
horizontal eddy viscosity as a function of distance across and seawards
of the surf zone. Simultaneous measurements of turbulence and incident
wave orbital velocities provide an estimate of the total "radiation
stress" at different distances from the shoreline. Since the flow-
meters measure not only the fluctuating components but also the steady
flow at a point, this technique could provide a direct test of the
theories of longshore current generation based on radiation stress and
horizontal eddy viscosity (Bowen, 1969, Longuet-Higgins, 1970a,b).

With an array perpendicular to shore it is also possible to
follow the progress of individual waves as they pass over each flow-
meter in turn, and hence wave propagation speeds, changes of wave form
and the development of lower frequency wave motion close to the shore-
line can be studied. Figure 4 shows some preliminary results from
simultaneous measurements of onshore-offshore horizontal velocities at
three different distances from the shoreline. The right hand side of
the diagram shows the beach profile, with offshore distance from the
shoreline plotted upwards and the offshore distance axis itself
representing approximately the mean sea level; the positions of the
three flowmeters relative to this profile are shown as dots A,B and C.

The left hand side of the diagram shows a short example of the onshore velocity time series measured with these flowmeters. In each case negative velocities represent flow towards the shoreline; flowmeter C was uncalibrated during this experiment. Oblique lines have been drawn to join the peak onshore velocities of chosen waves at each of the flowmeters.

The breaking regime for the incident waves during the time of these measurements was complex, though typical of many beaches when an offshore bar is present. The incident swell waves, with a period of about 8 seconds and average height of about 0.5 m., broke on the offshore bar on the shoreward side of flowmeter C, but reformed and ceased to break as they passed over the crest of the bar and approached flowmeter B. The waves then broke a second time shorewards of flowmeter A, with a surf zone about 10m. wide. The time series of onshore-offshore velocities reveal details of this wave behaviour. At flowmeter C the time series of velocities under the unbroken swell waves has the form of an amplitude modulated sine wave, but the re-formed waves in much shallower water at flowmeters B and A show the rapid acceleration and deceleration about the peak onshore velocities characteristic of peaked solitary-wave motion. The increase in onshore currents as the waves steepen between B and A is also clear.

The average phase velocities of individual wavecrests can be found from the time lag between the passage of the waves over successive flow-meters, and in figure 4 these phase velocities are represented by the slopes of the straight lines joining crests in each of the flowmeter records. As expected, the phase velocity between flowmeters B and A is less than between C and B as the waves travel more slowly in the shallower water. There is also a marked dependence of the phase velocity of a wave on the amplitude of onshore velocity under its crest. Thus in figure 5 an enlarge-ment of a portion of the onshore velocity time series from the three flow-meters shows, in the top record, a low wave followed by a much higher wave. As the waves progress over flowmeters B and A, the higher wave travels more quickly than the low wave, causing the two waves to merge together in

record A. A similar effect can be seen at the beginning of the record
in figure 4 and, towards the end of this figure the opposite effect
can also be seen where a high wave begins to leave a smaller wave be-
hind. Such merging and splitting of wave crests must be very
significant in forming the frequency spectrum of wave energy in the
nearshore region.

When the reciprocal of the time lags, for example between A
and B, are plotted against water particle velocities under crests, as
in figure 6, the dependence of the phase velocity, c, on the particle
velocities, u, is clearly seen. The approximate straight-line fit to
these data is in good agreement with the characteristic equation for
finite amplitude shallow water waves. Investigation of the propagation
of these waves is continuing.

As the shoreline receded on this tidal beach, the effect of
the outer bar became more pronounced and the onshore array of flowmeters
was able to detect further changes in the waveforms of the incident
waves (figure 7). In particular, the inner flowmeters show that the
re-formed waves on the shoreward side of the bar became bore-like, with
rapid acceleration to peak onshore velocities, and were frequently split,
with a train of waves following the forward face of the bore. Splitting
of the wave crests in this way is characteristic of the formation of
undular bores and has been observed on other beaches (Gallagher, 1972,
Huntley and Bowen (in press)). In this case the undulations were formed
as a result of a weakening of the breakers as they passed over the crest
of the bar and into the deeper water beyond (cf. Gallagher, 1972).

Figures 8 and 9 show examples of the complete range of para-
meters measured with the array in this field experiment; the long-
shore component of the middle flowmeter was not operating. As expected
for refracted incident waves, the longshore flow components are small
in figure 8, but closer to the shoreline, in figure 9, the longshore
flow is comparable to the onshore flow, and a low frequency component
is very marked. The period of this low frequency motion is approximately

24 seconds, and is thus in good agreement with the measurements made by Emery and Gale (1951) of swash period on beaches of comparable slope.

There are indications that the onshore and longshore components of this low frequency motion are in antiphase, which would be consistent with standing edge wave motion. An edge wave of this period would have wavelengths of about 15 m. and 45 m. for a zero and first order mode respectively, and either of these values could account for the fact that the motion is observed only with the nearshore flowmeter, since the amplitude of edge wave motion decays rapidly offshore and becomes negligible at a distance from the shoreline comparable with the edge wave wavelength. Possible non-linear mechanisms for generating low frequency edge waves include interaction between two incident wave trains (Gallagher 1971), or growth of edge waves from standing waves formed by reflection at the shoreline (Guza and Davis 1974). Huntley and Bowen (in press) have also suggested that edge waves may be formed on steep beaches, by strong interaction between incident waves and a natural low frequency swash motion characteristic of the beach slope and surf zone width. It is possible that a similar interaction occurred on this beach.

References:

Bowen, A. J. (1969). The generation of longshore currents on a
        plane beach. J. Mar. Res. 27 206-215.

Bowen, A. J. and Inman, D. L. (1969). Rip currents, 2. Laboratory
        and field observations. J. Geophys. Res. 74 5479-5490.

Eckart, C. (1951). Surface waves in water of variable depth,
        Wave report Scripps Instn. Oceanogr., SIO-ref. 51-12.
        100. 99 pp.

Emery, K. O. and Gale, J. F. (1951). Swash and swash marks.
        Trans. Am. Geophys. Un., 32 31-36.

Gallagher, B. (1971). Generation of surf beat by non-linear wave
        interactions, J. Fluid Mech., 49 1-20.

Gallagher, B. (1972). Some qualitative aspects of non-linear wave
        radiation in a surf zone. Geophys. Fl. Dyn. 3 347-354.

Guza, R. T. and Davis, R. E. (1974). Exitation of edge waves by
        waves incident on a beach. J. Geophys. Res. 79 1285-1291.

Huntley, D. A. and Bowen, A. J. (1973). Field observations of
        edge waves. Nature, 243 160-162.

Huntley, D. A. and Bowen, A. J. (in Press). Comparison of the
        hydrodynamics of steep and shallow beaches, Proceedings,
        Symposium on nearshore sediment dynamics and sedimentation.
        Southampton 1973 (ed. J. R. Hails and A. Carr) Wiley: London.

Longuet-Higgins, M. S. (1970a) Longshore currents generated by
        obliquely incident sea waves 1. J. Geophys. Res. 75
        6778-6789.

Longuet-Higgins, M. S. (1970b). Longshore currents generated by
        obliquely incident sea waves 2. J. Geophys. Res. 75 6790-6801.

Tucker, M. J. (1972). Electromagnetic current meters; an assessment
        of their problems and potentialities. Proc. Soc. Underwat.
        Tech., 2 53-58.

Tucker, M. J., Smith, N. D., Pierce, F. E. and Collins, E. P. (1970).
        A two-component electromagnetic ship's log, J. Inst. Navig.
        23 302-316.
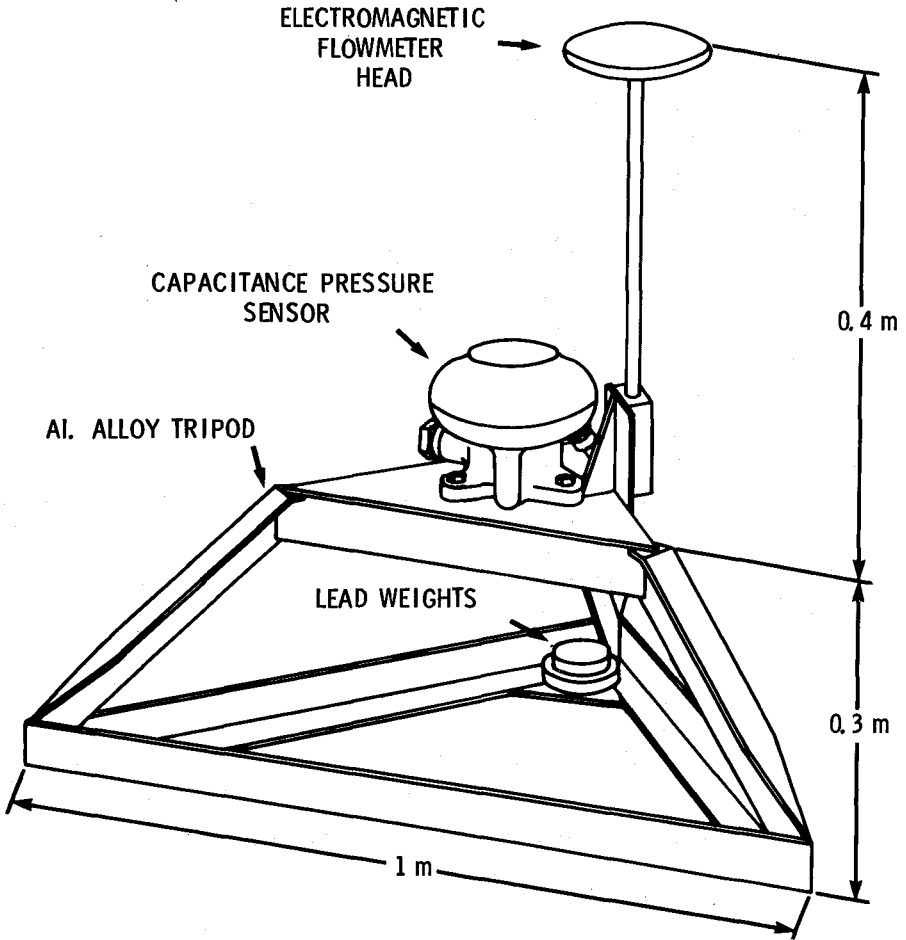
Figure 1.   Schemmatic diagram of the flowmeter mount.
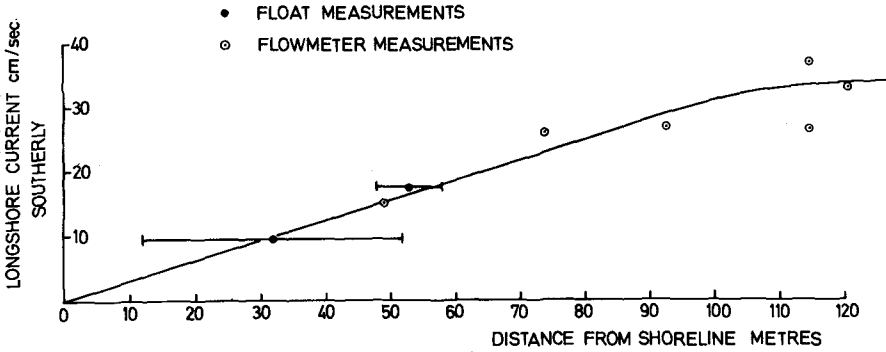
Figure 2. Longshore drift currents on a shallow (slope 0.01) beach.
The surf zone was about 250 m wide. (From a forthcoming book
to be published by John Wiley and Sons Ltd. - HAILS/CARR:
Nearshore Sediment Dynamics and Sedimentation).
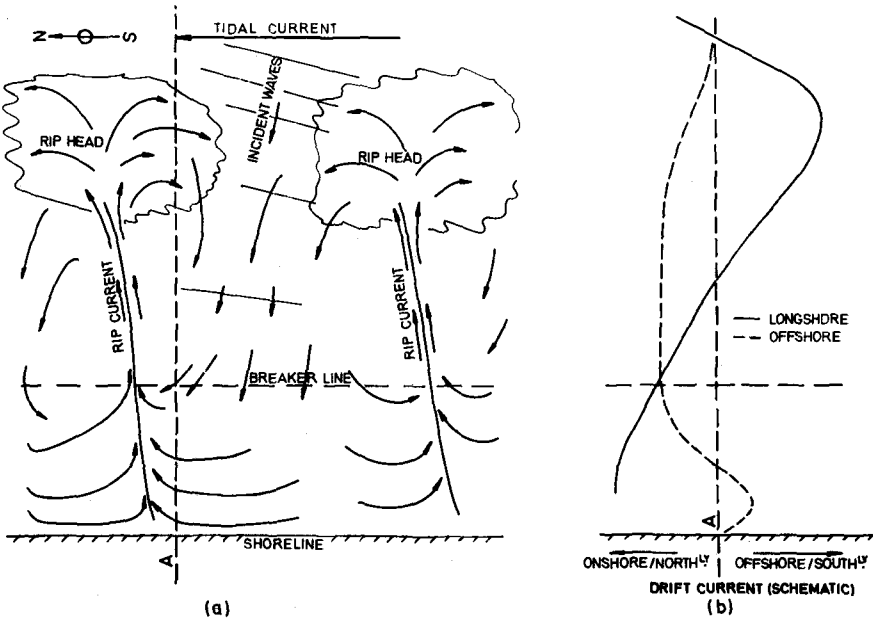
Figure 3. (a) Schematic diagram of a nearshore circulation system
detected on a steep beach.

(b) The measured variation of longshore and on/offshore
current amplitude with distance from the shoreline. These
measurements are consistent with measurements along a
line A in figure 3a.

(From a forthcoming book to be published by John Wiley
and Sons Ltd. - HAILS/CARR: Nearshore Sediment Dynamics
and Sedimentation).
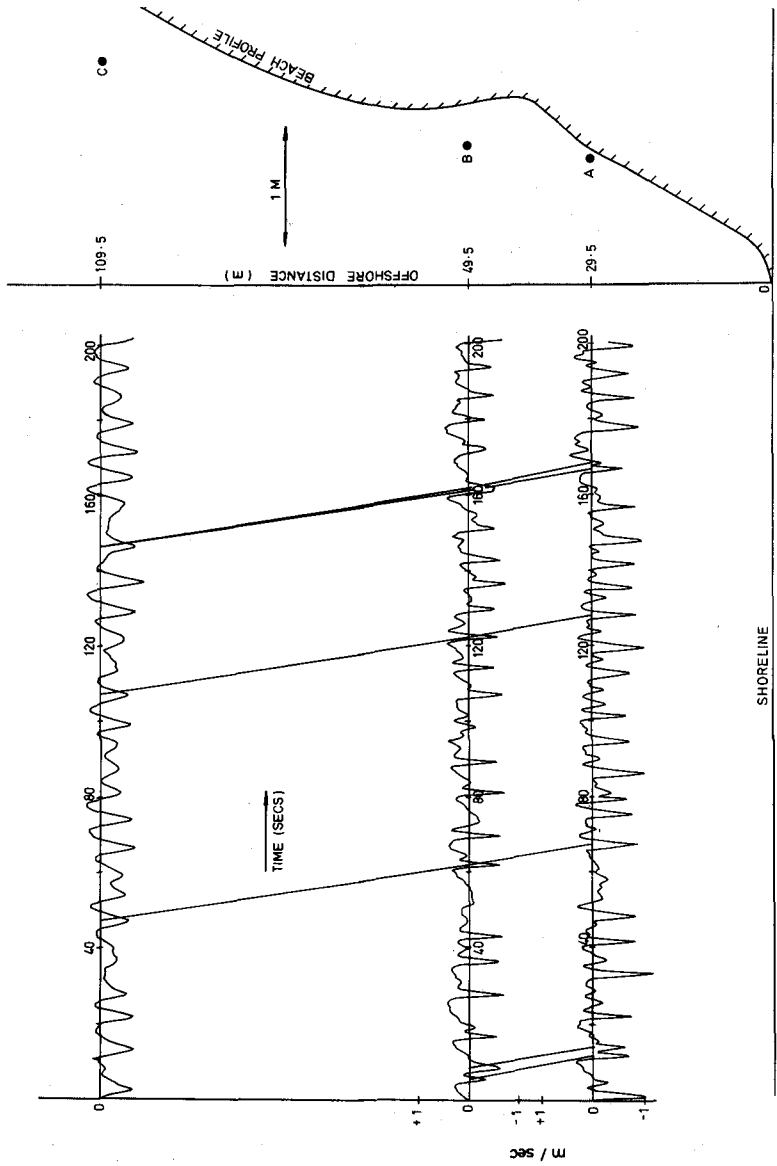
Figure 4. Simultaneous records of on/offshore velocities at three different points along a line perpendicular to the shoreline. The beach profile and positions of the flowmeters are shown on the right-hand side of the diagram.
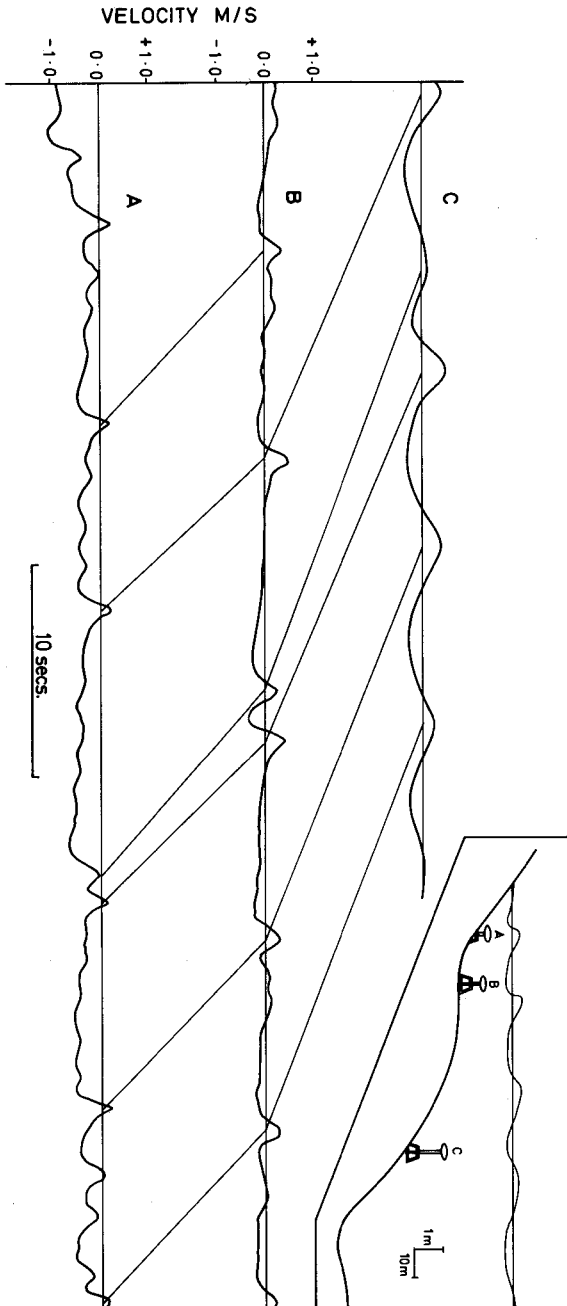
Figure 5. Onshore currents at different distances from the shore-
line. The inset shows the positions of the flowmeters.
The sketched flowmeters and their mounts are not to scale.
The record for flowmeter C is uncalibrated.
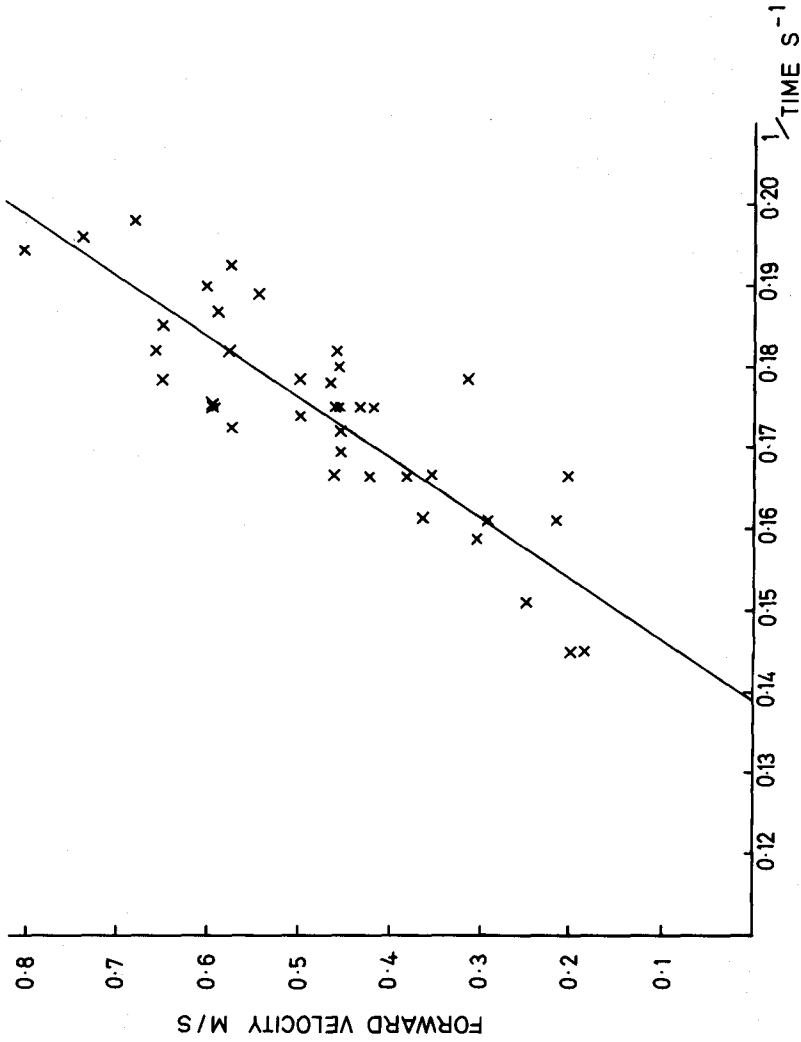
Figure 6. The reciprocal of the time for a wave to travel between flowmeters B and A, plotted against the forward velocity under the wave. The solid line through the data points is the theoretical variation based on the characteristic equation.
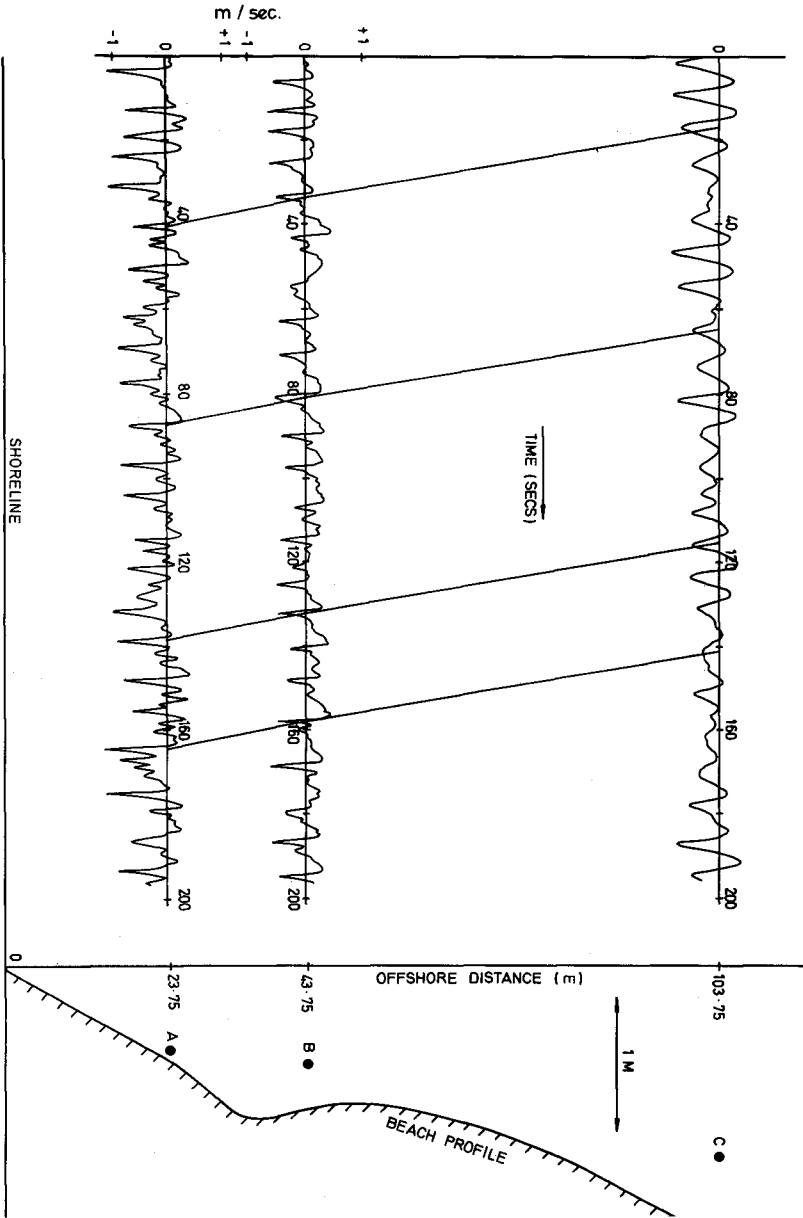
Figure 7. As figure 4, but with each flowmeter closer to the shoreline.
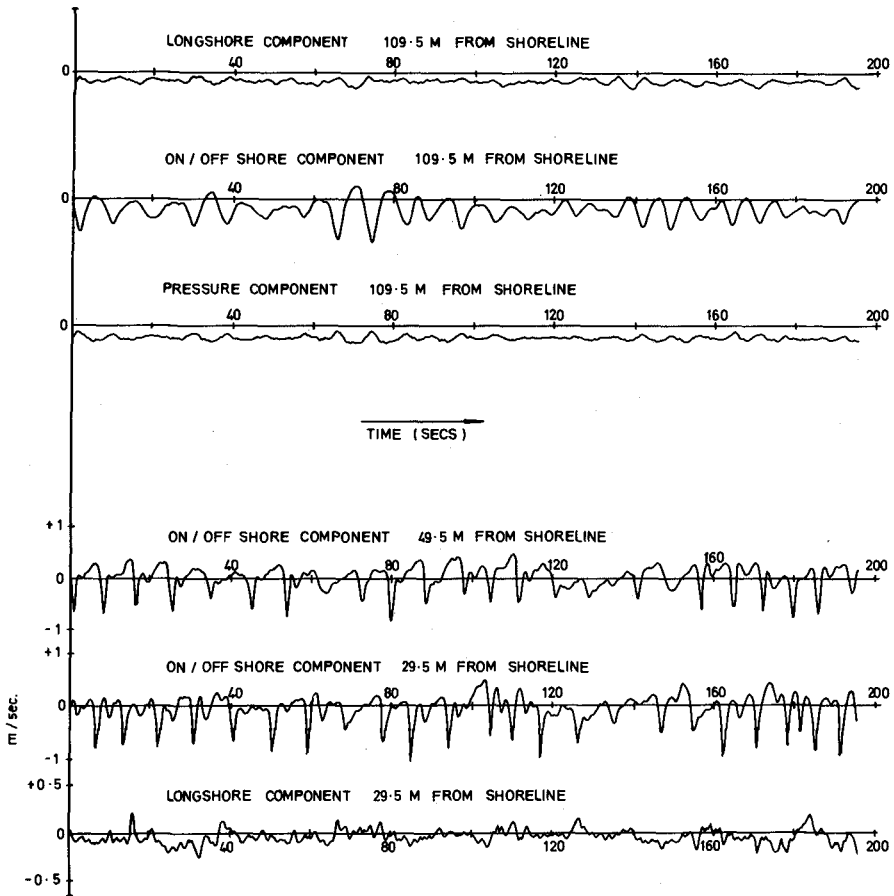
Figure 8. Simultaneous measurements made using three flowmeters and a pressure sensor along a line perpendicular to the shoreline. The longshore component of the flowmeter at 49.5 m. from the shoreline was not operating.
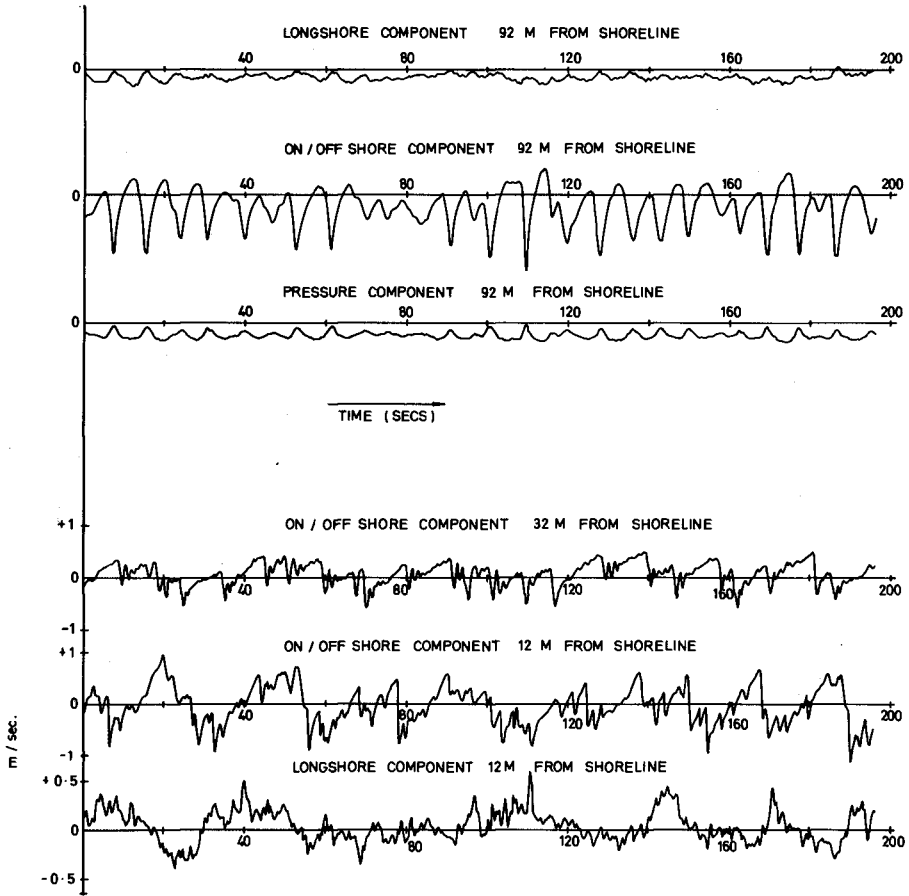
Figure 9. As figure 8, but with each instrument closer to the
           shoreline.

CHAPTER 31

VELOCITIES UNDER PERIODIC AND RANDOM WAVES

by

Allen Lee

Research Student, Fluid Dynamics Unit , Edinburgh University

Clive A. Greated

Director, Fluid Dynamics Unit, Edinburgh University

and

Tariq S. Durrani

Research Fellow, Electronics Dept., Southampton University

ABSTRACT

Using the linear approximation for predicting velocities under periodic water waves, relationships are established between the velocity spectrum and the surface elevation spectrum for three-dimensional waves. The two dimensional forms of these relationships are used for comparison with velocity and elevation spectra measured in a laboratory wave tank. The predicted distortion of the spectrum shape can be observed in the experimental results. Velocity measurements were recorded using a laser velocimeter employing a rotating diffraction grating for shifting the optical frequencies. This allows measurement without sign ambiguity. The random waves were generated using a servo-driven paddle with a filtered white noise input.

558

INTRODUCTION

One of the main problems in coastal engineering is to determine the velocity distribution beneath ocean waves; for the purpose of predicting wave forces on structures and sediment transport behaviour etc. Direct measurements in the ocean are difficult because of the violent action in the waves of most interest. Data interpretation is also difficult, due to the distortion in the results given by conventional velocity meters. There is, however, a range of methods in wide use, for measuring surface elevation spectra and surface probability distributions. Hence if a generally valid relationship between surface statistics and under-surface velocity statistics for waves can be established, the problem of accurately predicting wave force distributions reduces to that of applying a trans-formation to measured surface statistics.

The search for such a relationship is well suited as a laboratory research problem, particularly with the increasing availability of random wave generating machines. Reliable wave height gauges are also in common use. Until recently the velocities under the waves were still measured with ultrasonic meters or rotating vane meters, with the consequent interference to the flow. In this paper we show that the velocities can be measured without disturbing the flow, if the laser doppler velocimeter technique (referred to as L.D.V.) is used. The method is explained and our laboratory apparatus, with the L.D.V., is described. We are using this system to examine the link between water surface position and the velocities beneath the surface for random waves. The results given here are drawn from the experiments we did to see the limitations of the linear wave theory. Comparisons are made between measured velocity spectra and those obtained by 'linearly' transforming surface elevation spectra.

THE LINEAR WAVE EQUATIONS

Using the linearized potential flow equations, i.e. neglecting second order terms in the equations of motion, the potential under a periodic wave of surface profile

$$\eta (x,t) = a \cos (\mu x - \omega t)$$

is

$$\Phi (x,z,t) = \frac{ga}{\omega} \frac{\cosh \mu (z + h)}{\cosh \mu h} \sin (\mu x - \omega t) \quad (1)$$

where μ is the wave number, ω the frequency, z the position above still water level and h the water depth. The wave number and frequency are related by the equation

$$\omega^2 = g\mu \tanh (\mu h) \quad (2)$$

The concept of a velocity potential can be extended to three-dimensional seas.

Consider the random surface defined at any point (x,y) to be

$$\eta (x,y,t) = \sum_i C_i \cos (\mu_i x + \nu_i y - \omega_i t - \epsilon_i) \quad (3)$$

where $\{C_i\}$ are Gaussian distributed variables representing the random amplitudes of the stochastic surface; $\{\mu_i, \nu_i\}$ are now wave numbers in the x and y directions respectively; $\{\omega_i\}$ are the component frequencies and $\{\epsilon_i\}$ the random phases. According to the linear approximation the stochastic potential is now given by

$$\Phi(x,y,z,t) = g\sum_i \frac{C_i}{\omega_i} \frac{\cosh\left[\sqrt{\mu_i^2 + \nu_i^2} \cdot (z+h)\right]}{\cosh\left[\sqrt{\mu_i^2 + \nu_i^2} \cdot h\right]} \sin\left[\mu_i x + \nu_i y - \omega_i t - \epsilon_i\right]$$

(4)

Defining $\mu_i = k_i \cos\theta_i$ and $\nu_i = k_i \sin\theta_i$ the frequency spectrum of the surface elevation is related to the three-dimensional spectrum by

$$\Phi(\omega) = \int_0^\infty \int_0^{2\pi} k \ \Phi(k,\theta,\omega) dk d\theta$$

(5)

The instanteous frequencies and wave numbers are related by

$$\omega_i^2 = g k_i \tanh k_i h$$

(6)

From equation (4) the instantaneous velocities at vertical position z in the x and y directions respectively are

$$U_x = \frac{\partial\Phi}{\partial x} = g \sum_i \frac{C_i \mu_i}{\omega_i} \frac{\cosh k_i (z+h)}{\cosh k_i h} \cos(\mu_i x + \nu_i y - \omega_i t - \epsilon_i) (7)$$

and

$$U_y = \frac{\partial\Phi}{\partial y} = g \sum_i \frac{C_i \nu_i}{\omega_i} \frac{\cosh k_i (z+h)}{\cosh k_i h} \cos(\mu_i x + \nu_i y - \omega_i t - \epsilon_i)$$

(8)

In a laboratory channel with no motion in the y direction then equation (7) holds with $\nu_i = 0$ so the relationship between the surface elevation spectrum $\Phi(\omega)$ and the horizontal velocity spectrum $\psi(\omega)$ is

$$\psi(\omega) = \omega^2 \frac{\cosh^2 k (z+h)}{\sinh^2(kh)} \Phi(\omega)$$

(9)

In writing equation (9) the dispersion relationship of equation (6) has been introduced. Equation (9) is the formula that gives the transformation from the elevation to velocity spectrum in the two-dimensional laboratory situation. This theoretical transformation is to be compared with experiment.

Starting from equations (7) and (8) one can also compute statistics which are applicable to the three-dimensional situation. For example, we find that the expected value of the instantaneous horizontal velocity in deep water is

$$E[U_x^2 + U_y^2] = \tfrac{1}{2} \sum_i E[\omega_i^2 C_i^2 e^{2 \cdot \frac{\omega_i^2 z}{g}}]$$

i.e. an exponential decay with depth. As yet though,we have no means of comparing theory with experiment in a three-dimensional sea.

THE LASER DOPPLER VELOCIMETER

The laser doppler system for measuring particle velocities is not well known to experimenters interested in waves. We intend to show that the instrument is both simple to set up and convenient to use. Its accuracy is well documented in the journals (Durrani and Greated, 1973 and 1974).

Essentially the method depends on   Doppler's principle that relative motion between a source of radiation and an observer produces a change in the frequency of the observed radiation. Although there are many optical arrangements, the twin beam system is the most common. In this a laser beam is wavefront or amplitude divided into two separated and coherent parallel beams. A lens is used to focus these into the flow, where the resulting optical fringe pattern is produced. Micro-scopic particles, which exist in and characterise most flows, will scatter light from this fringe pattern in a predominantly forward direction. If the scattered light is collected over a large solid angle and directed onto a photomultiplier or photo-diode, an electrical signal is produced by the intensity fluctuations on the detector surface. These fluctuations are directly due to particles crossing the fringes at a frequency f_D which is related to their velocity V by the formula

$$f_D = \frac{V}{d}, \text{ where } d = \frac{\lambda}{2 \sin \Phi/2} = \text{Fringe spacing}$$

(Φ is the beam crossing angle as the light enters the flow). If the light is collected over a small solid angle the scattered components of the two beams will heterodyne on the detector surface, again to produce a signal at frequency f_D (component frequencies $\{f_L + (f_D/2)\}$, $\{f_L - (f_D/2)\}$). The velocity v is the component at   right-angles to the laser beams bisector. If it had the value -v, the detector would still only register the fringe crossing or shifted frequency as f_D positive. This means that in all reversing flows such as waves, the velocity sign information is normally lost. The usual solution is to give a steady offset frequency f_S to the laser frequency f_L of one of the beams. The scattered light is then

$$\left(f_L + \frac{f_D}{2} + f_S \right) \quad \text{and} \quad \left(f_L - \frac{f_D}{2} \right)$$

with a resulting detected signal of $\left(f_S + f_D \right)$. The effect is merely that of adding a D.C. offset to an electrical A.C. signal. Three methods of producing this offset will be discussed.

(a) The Circular Diffraction Grating.

The grating is rotated in the plane perpendicular to the laser output, at a constant frequency of N Hz. Then for K line pairs on the grating there will be a frequency difference between the +1 and -1 diffraction orders of N x K. The grating line pairs act as moving sources and give a conventional Doppler shift. The other grating method is to image the line pairs into

the flow instead of forming a two beam fringe pattern. The
image spacing is then given by the law of optical imaging and
the grating movement is given to the image to produce the
required offset.

(b) Acoustic Bragg Cell

     This is a well known device whereby an ultrasonic wave
train is directed across the laser beam path. When the two
are inclined at precisely the Bragg angle for the medium,
(in the plane of the ultrasonic wave direction and the beam)
then the cell will act as a blazed phase grating and shift
most of the laser energy into one of the first diffraction
orders, with a frequency shift equal to the ultrasonic
frequency, i.e. of the order ten or a hundred mega-Hertz.
A second cell operated at a slightly different ultrasonic
frequency is used on the second beam so the resulting difference
remains in the 100 kHz range.

(c) Phase Modulators

     These devices use crystals which will, upon applying
a sawtooth voltage across them, give an effect such as Pockels
phase modulation to a beam of light passing through the crystal.
When combined with the second beam a phase modulation in the
fringe pattern, and hence in the scattered light, is produced,
giving the required offset at a frequency related to that of the
sawtooth voltage used. Its chief advantage is that it only
needs a few hundred volts D.C. to operate whereas most electro-
optic devices need several thousand volts A.C. for efficient
use.

     Once the electrical signal (with its frequency fluctuations
proportional to the particle velocities) is obtained from the
detector it is most conveniently converted to an amplitude
fluctuation by a frequency tracking device with phase locked
feedback and fast response. The output is then directly pro-
portional to the wave particle velocity and may be recorded for
later analysis.

                    EXPERIMENTAL APPARATUS

     Our work has been carried out on an open channel 5 m. long
     30 cm. deep and 30 cm. wide. It is connected to large
storage tanks and the water level can be raised or lowered by the
use of a pump, as required. In our initial work we used a simple
flap paddle to generate periodic waves with a synchronous electric
motor providing the drive. For our work with random waves a
mechanical wave generator, as indicated on figure 2, was used.
It is not   hydraulic in its operation and is extremely light
compared to such devices. Its motion comes from an oscillating
electric motor which is capable of responding to a random signal.
There is almost no mechanical inertia so this is provided
electronically by varying the mean position of the oscillating
motor armature to give whatever trim is required. The paddle
is cylindrical at the back and thus produces no backwave. The
signal imput is obtained at present by bandpass filtering of
white noise produced by an analogue device.

     The wave heights are followed using a resistance type
gauge with platinum wire elements. It is driven by a low
frequency oscillator (200 Hz) and the resulting output signal
is rectified and smoothed before recording. Both a flat beach
and a curved beach with wire mesh covering have been used.

They have reflection co-efficientsof about 6% and 3% respectively.

The L.D.V. was set up on two parallel vertical optical benches, on a rig shown in figure 3. This configuration enabled the velocities to be scanned in depth by merely sliding the prism and lens to a different position on the bench, and moving the detector correspondingly. We took special care to ensure that no part of the rig was in contact with the channel, and any floor vibration was damped by the rubber supporting pads under the steel rig.

Early on in the project we decided to use a rotating diffraction grating to eliminate the sign ambiguity of the L.D.V. The device is an 8 cm. glass disc with 3600 radial lines of chromium, driven by a 50 cycle synchronous electric motor via a 2 : 1 step-down brass gearing. This acts as a fly-wheel and gives excellent stability. For use with a 5 mW He-Ne laser we chose the method of imaging the grating into the flow. The arrangement gave adequate intensities of signal which we detected with a photo-diode device.

The signal processing for the periodic waves consisted only of a storage oscilloscope and a manual wave analyser. For the random waves the signals from the frequency tracker and the wave-height gauge we recorded simultaneously on two channels of an F.M. tape recorder. These signals were later processed by analogue methods. A spectrum analyser with automatic graph plotter was used over the range 0.3 Hz to 5 Hz and gave the energy spectra directly, with suitable scaling factors for the axes. A digital correlator was used to obtain probability density curves, autocorrelation curves and cross correlation curves, with the displays being outputted to an X-Y plotter.

RESULTS FROM PERIODIC WAVES

For the case of periodic waves, if the experimenter is satisfied that the waves are stable, there is no need for a complex analysing system. Once the waveheight, wavelength and frequency have been measured using, for instance, only an oscilloscope and a pair of battery powered bare-wire probes, then the L.D.V. signal may be scanned manually with a wave analyser. When the L.D.V. frequency signal is at that of the analyser a pulse will be produced. For periodic waves there will be a train of pulses which can be displayed on the oscilloscope and their separation in time noted. Thus a chart can be built up giving frequency change against time, i.e. particle velocity against time, as in figure 4(a). We have used this method on several occasions and have found it extremely good at recording small variations in the velocity-time trace (figure 4b). Also we have used the method to build up the velocity depth profiles in figure 5, measuring from the channel bed up to the inside of the wave crests. The variation of velocity with time in figure 4b is for a sinusoidal wave of period 0.41 s. and crest to trough height 1.73 cm. Since the water depth was 24 cm. and the wavelength 31.6 cm. we considered this to be a deep water wave. The velocity trace shown is believed to consist of the main wave plus a harmonic at 5 times the basic frequency and about one tenth the main wave amplitude. This could be due to either a reflection interacting with the paddle, or some underflow from the beach. The most interesting parts of the trace are the incomplete parts which were recorded above the trough level. The highest velocity was recorded well above the mean surface at 24.5 cm. i.e. only

a few mm. under the crest maximum. The velocity value at the
crest is several times that recorded at 15 cm. depth (lowest
trace).

　　　For a set wave the velocity was usually measured at depth
intervals of 2 cm. and a wave cycle in figure 4b is typically
constructed from about 50 points.

　　　The depth profiles for the above wave and a similar wave
in a depth of 15 cm. are shown in figure 5.　　The dashed
profiles were calculated from the linearized wave equation,
and the agreement is good for the deep water wave.

RESULTS FOR RANDOM WAVES

　　　For three different input spectra,we have measured, from
the wave gauge, the surface elevation spectra and, from the
L.D.V., the velocity spectra. For a water depth of 21.75 cm.
the signals were recorded for positions above the channel bed
of 0.8 cm., 8.4 cm. and 16.6 cm. The amplitude probability
densities of these signals are shown in Figure 6. Those for the
3 surface elevation signals are almost identical whereas the
velocity density narrows considerably with depth. This amplitude
fall-off is expected and we intend to study in detail the R.M.S.
velocity amplitude profile with depth,at a later date. It is well
known that water surface elevations for random waves are assumed
to have an approximately Gaussian probability density. The
elevation densities and the velocity densities all show some
deviation from Gaussianity but they serve to confirm the
assumption.

　　　The measurements were made in a water depth of only 21.75 cm.
with the water bed frequently disturbed during the passage of wave
trains. So it was decided that the dispersion curve should be
calculated in full for the determination of wave number. The
curve is shown in fig. 7, with the usual deep water and shallow water
approximations as dashed lines. The wave numbers were then used
to compute the transformation function in equation 9.

　　　The measured spectra are shown in figs. 8, 9 and 10, part A
being the surface elevation and part B the velocity spectrum in
each case. Part A also shows the transfer function over the
relevant frequency range. The velocity spectra predicted by
equation 9 are shown superimposed on the measured spectra, for
simple comparison. The predicted effect is to shift the energy
to lower frequencies with enhancement of low frequency peaks.
This is clearly confirmed experimentally and in several cases
the peaks in the surface spectra may be identified in the velocity
spectra, with considerable change in their energy content.

　　　Autocorrelation and cross-correlation functions have been
obtained from the random wave data, however, they are of quite
a complicated form and are consequently difficult to interpret.
We are hoping to achieve success with the correlation analysis,
in the near future.

CONCLUSIONS

　　　The laser doppler velocimeter has been shown to be highly
suitable for the laboratory study of periodic and random water

waves. The initial results of a project studying the
relationship between wave elevations and particle velocity
fluctuations show that the system described is practical
and versatile. The results for periodic waves, with the
data from inside the wave crests, indicate the shortcomings
of the linearized wave equation near the water surface.
Further study in this upper region promises to be of great
interest. The spectral results, while confirming the general
value of linear wave theory, show that the inclusion of non-
linear terms in the theory will be necessary if accurate wave
particle velocity spectra are to be predicted.

REFERENCES

T.S. Durrani and C. Greated, 1973 'Statistical analysis and
computer simulation of laser Doppler velocimeter systems',
Trans. IEEE, Vol. IM 22, No. 1, pp.23-34.

T.S. Durrani and C. Greated, 1974 'Theory of L.D.V. Tracking
systems', Trans. IEEE, Vol. AES. 10, No. 4, pp. 418-428.

Fig. 1 L.D.V. SYSTEMS
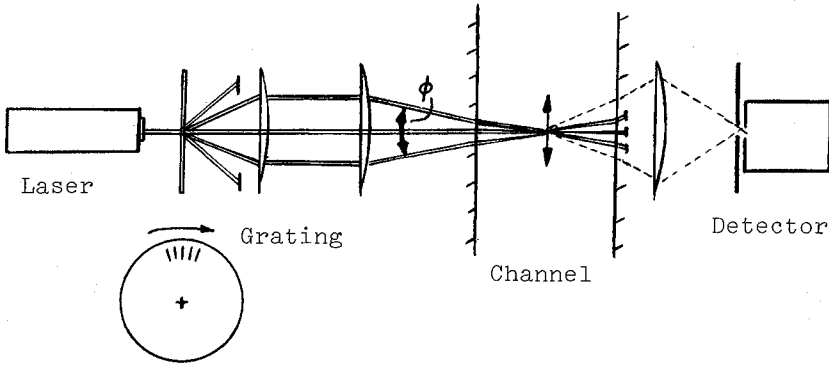
(a)   With diffraction grating imaged in the flow
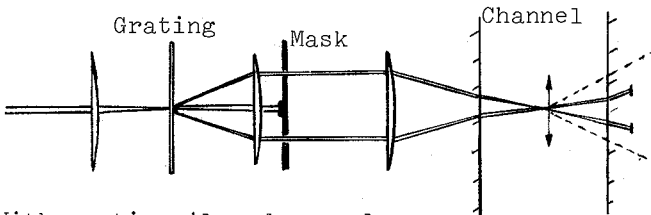
(b)   With grating ±1 orders only
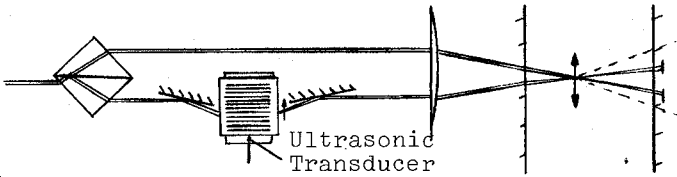
(c) With Bragg Cell
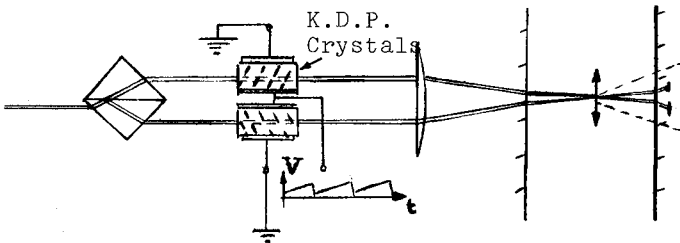
(d) With Phase modulators

Fig. 2

RANDOM WAVE GENERATOR

WAVE HEIGHT GAUGE

TO RECTIFIER
&
SMOOTHER

STEPDOWN GEARS

DRIVE COG TO
ELECTRIC
MOTOR

INPUT
SIGNAL

FEEDBACK FROM
STRAIN GAUGES

FEEDBACK FROM
TACHOMETER

NOISE
GENERATOR

SHAPING
FILTER

AMPLIFIER
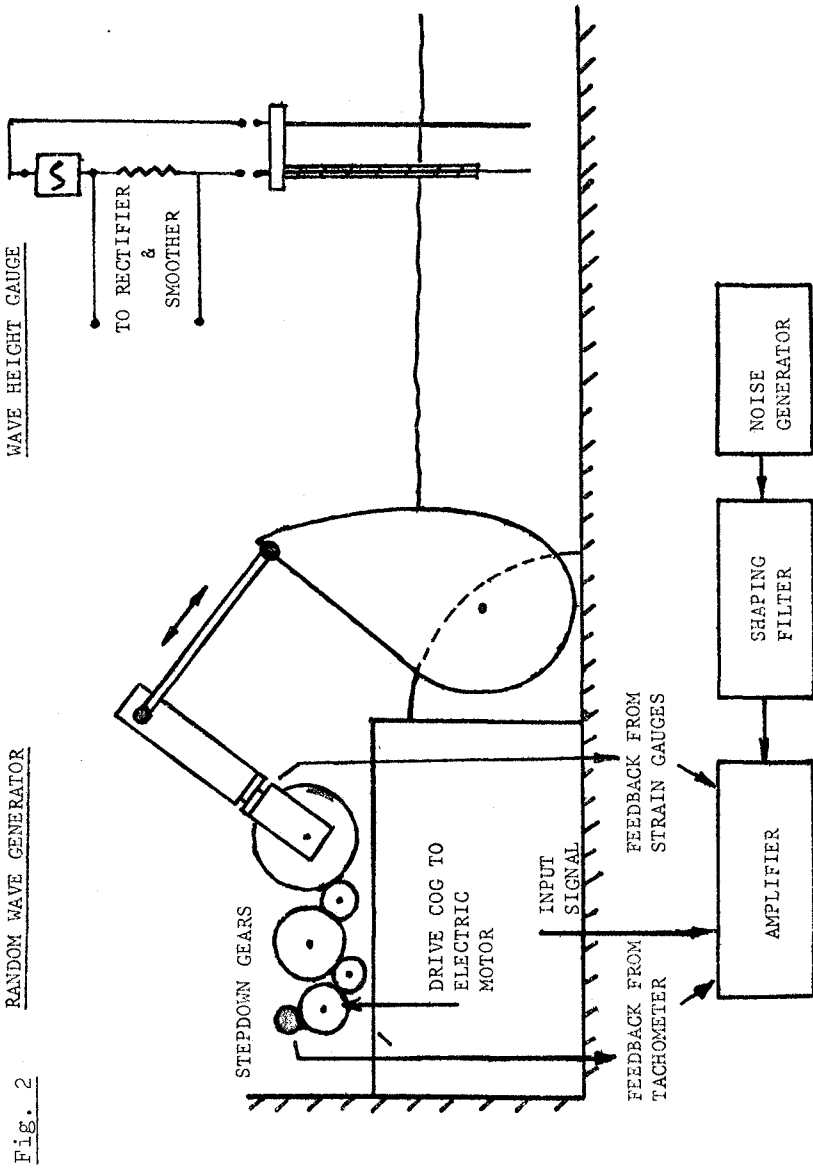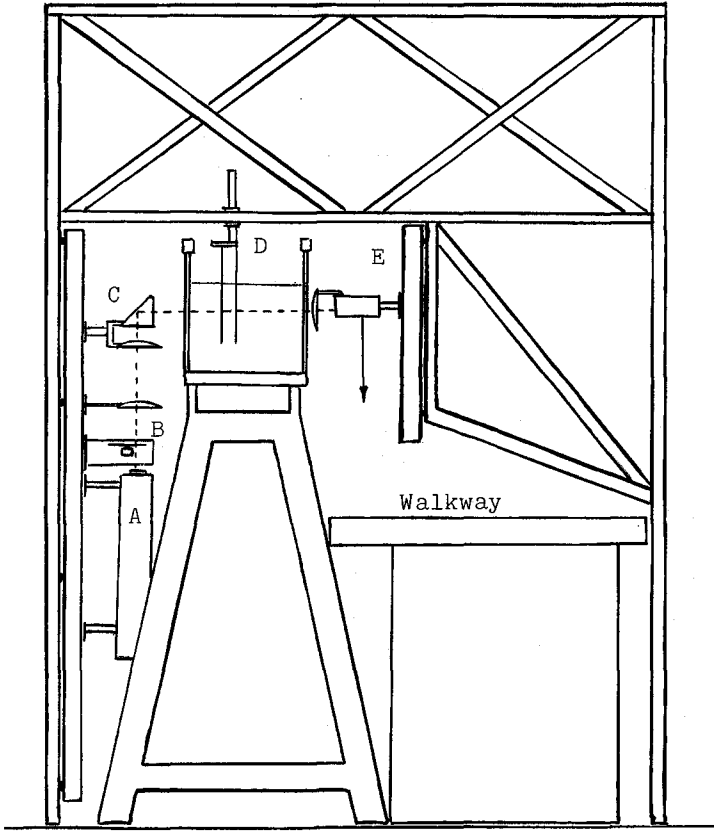
Fig. 3   L.D.V. and support Rig

A - Laser   D - wave height gauge
B - Rotating Grating   E - detector (photo-diode)
C - Right angle prism

Wave Tank Beach
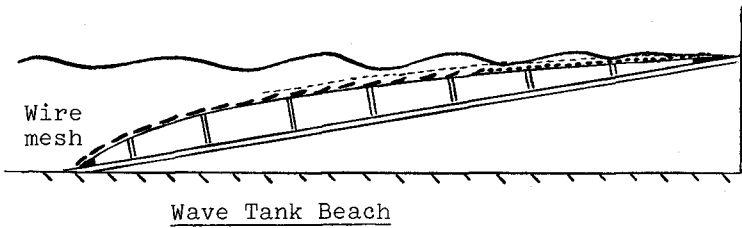
$$f_D = k|U_x|$$

Particle Orbit
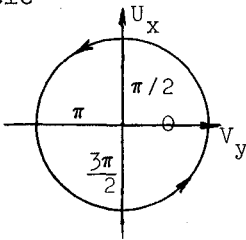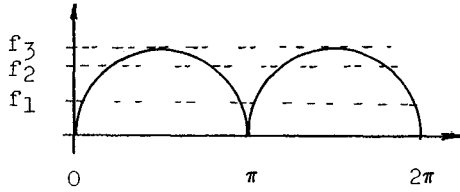
Fig. 4a

For each setting of frequency f_D the wave analyser gives a pulse train.
The occurrence of a velocity component is thus verified. Its sign is fixed by observation of crest passing the L.D.V.
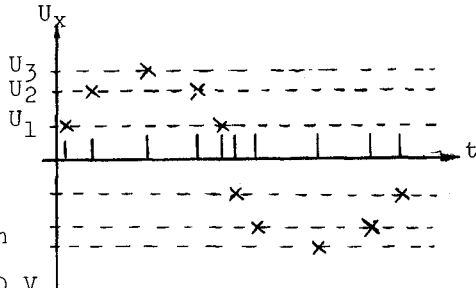
Fig. 4b   Velocity trace-deep water wave
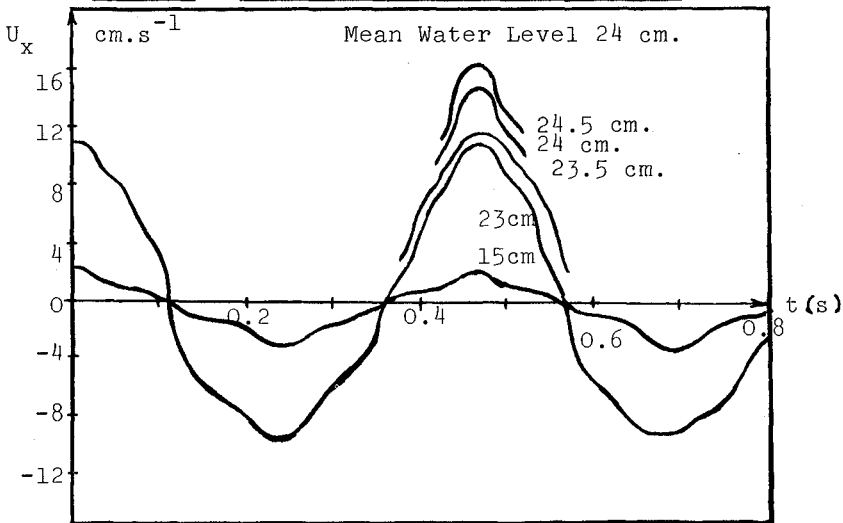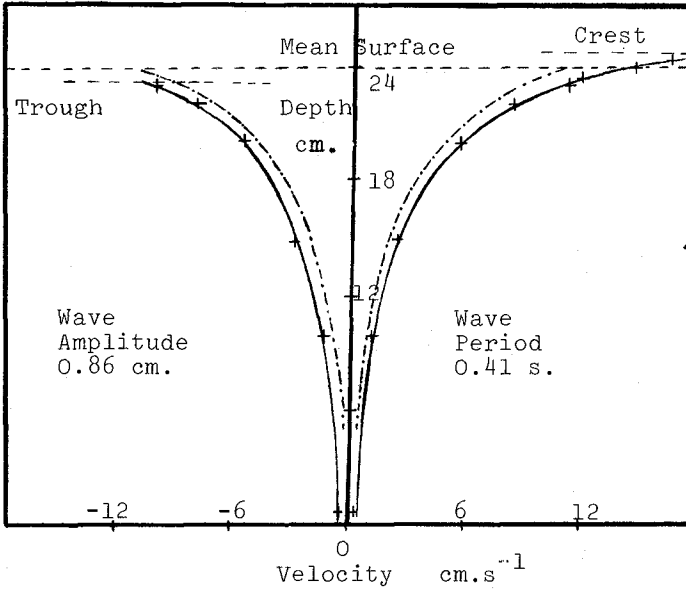
Fig. 5   Velocity-depth Profiles

Fig. 6.

Fig. 7 Dispersion Relationship

Horizontal velocity spectrum 1
16.6 cm. above bed

Measured ———
predicted — —

Surface elevation spectrum 1
water depth 21.75 cm

Transfer T
function

Frequency Hz.

Energy Density (cm.s⁻¹)²s.

Energy Density cm²s.

Horizontal velocity spectrum 2
8.4 cm. above bed

Measured ———
Predicted – – –

Surface elevation spectrum 2
water depth 21.75 cm.

Transfer function T_2

Horizontal velocity spectrum 3
0.8 cm. above bed

Measured ————
predicted – – –

Energy Density (cm.s.$^{-1}$)^{2}s.

Frequency Hz.

Surface elevation spectrum 3
water depth 21.75 cm.

Transfer
function T$_3$

T$_3$

Energy Density cm.^{2}s.

Frequency Hz.

CHAPTER 32

INTERNAL VELOCITIES IN THE UPRUSH AND BACKWASH ZONE.

Patrick H. Kemp
Reader, University College, London.

David T. Plinston.
Senior Research Engineer, Institute of Hydrology, U.K.

ABSTRACT.

In an earlier paper the authors reported the results of both field and hydraulic model investigations into the reaction of beaches to the action of waves of low phase difference. These waves are those whose time of uprush on the beach is equal to or less than 0.7 T, where T is the wave period. The present paper summarises the study of the internal velocity field under similar conditions. By making certain simplifying assumptions based on observations of the profile of the wave during uprush and backwash, the surging wave is open to quantitative description. For very low phase differences the uprush is approximately the reverse of the backwash, but to a different time scale. However, as the phase difference approaches the limit for the surging condition, the uprush starts and may remain in the form of a bore

INTRODUCTION.

The essentially oscillatory nature of the uprush and backwash of waves under surging conditions bears a close resemblance to the phenomena of standing wave systems on rigid impermeable slopes. This problem has been studied by Miche (1944) and it was thus possible to compare the results of the investigation with Miche's solution for low waves on steep slopes. The theory assumed the water movement on the beach to be sinusoidal, and also that the uprush and backwash were identical in nature but of opposite sign. The phase difference according to Miche would thus always be 0.5. This is not true in the case of beaches, and in the study of water velocities on the beach outlined below, this was taken into account.

It is essential to separate uprush and backwash, since the initial boundary conditions are so different. The backwash starts from zero velocity everywhere on the beach and a 'wedge' of water then moves down the beach, the water surface remaining essentially plane from the instantaneous position of the waterline on the beach to the break-point, throughout the backwash duration. In the case of the uprush the kinematics of the breaking wave are involved. For very low phase differences (say $t/_T < 0.3$) the uprush is approximately the reverse of the backwash but to a different scale. However, as the phase difference approaches the limit for the surging condition, the uprush starts and may remain in the form of a bore. Thus, there are two possible methods of solution.

The general characteristics of the flow on a beach under surging and plunging conditions are such that the retardation of the uprush and subsequent acceleration of the backwash are equal and continuous over the point of zero velocity, and are progressively greater at points further from the break-point. Most significantly, the velocity is zero at all points simultaneously and the backwash is completed before the following wave breaks, as described by Kemp and Plinston (1968).

For plunging conditions the uprush velocity is not zero at all points simultaneously. The water nearer the breakers begins to move seaward before the water further up the beach comes to rest, and the backwash is not complete before the following wave breaks.

FLOW DESCRIPTION.

Figure 1. illustrates the basis of the present formulation of flow velocities, where l_b ia the total runup distance from the break-point to the limit of uprush.

Miche's theory described a symmetrical cycle of uprush and backwash, and on the basis of his analysis the component of velocity along the beach slope at a time θ measured from the instantaneous stillwater level is given by

$$V = \frac{1}{\sin \alpha} \frac{\pi H}{2} \left(\frac{g}{\alpha L}\right)^{\frac{1}{2}} \cos \left(\left[\frac{2\pi g}{L}\right]^{\frac{1}{2}} \theta\right)$$

The movement of the water's edge on the beach is also sinusoidal, and the distance s' from the breaker position to the edge can be expressed as

$$s' = \frac{l_b}{2}\left[1 - \cos\left(\frac{2\pi\theta}{T}\right)\right]$$

In fact, the movement of the water on the beach for the low long waves postulated by Miche is asymmetrical. However, a sinusoidal motion can be maintained by treating the uprush and backwash as two independent cycles of period t for the uprush, and $T - t$ for the backwash. For the uprush the time θ is measured from the breaking point, and for the backwash from the limit of uprush. Thus for the uprush

$$\frac{s'}{l_b} = \frac{1}{2}\left(1 - \cos\frac{\pi\theta}{t}\right) \tag{1}$$

and for the backwash

$$\frac{a'}{l_b} = \frac{1}{2}\left(1 + \cos\frac{\pi\theta}{T-t}\right) \tag{2}$$

By comparing curves based on these equations with the data from model experiments, it was found that the sine curve appears to be satisfactory for the backwash, but that a better description of the uprush can be developed by introducing the characteristics of a bore into the uprush equation.

Backwash velocities. The derivation of the instantaneous velocities from the changing geometry of the water level on the beach is made possible by making assumptions based on observations of surging waves. They are:

1.   The beach is plane, of slope $\tan \alpha$.
2.   The velocity of water on the beach is everywhere zero at the temporal limit of uprush.
3.   There is no loss or gain of water into or out of the beach.
4.   The water surface remains plane from the limit of uprush to the break-point throughout the backwash period, though the slope can vary.
5.   The velocity is uniform from bed to water surface, for a given position 'a' from the breakers.
6.   The position of the edge of the backwash, s' from the break-point

cen be described by e function of l_b, θ, end $T - t$

7.   The backwesh is complete in the time $T - t$, i.e. eurging
conditions only ere considered.

The eymbols used ere defined in the glossery end in
Figure 1.

The expreeeions for the internal velocities aseociated
with both uprush and beckwash ere besed on the normel equation of continuity,
on the geometry of the eystem, end on the obeerved varietions in weter level
et the breekere during the weve cycle.

The continuity equation ie given by

$$\frac{\partial(z'v')}{\partial e} = \frac{\partial z'}{\partial \theta} \qquad (3)$$

end if it is eseumed that the beach and water surfece are plane, then
$z' = y' (1 - \frac{s}{e'})$. The distence from the breakers to the edge position
is given by equetion (2) in the form

$$s' = \frac{l_b}{2} \left(1 + \cos \pi \frac{\theta}{T - t} \right) \qquad (2)$$

An experimental study of the verietion in water level et
the breek-point cen be closely deecribed by

$$y' = y_0 \cos \frac{\pi}{2(T - t)} \theta \qquad (4)$$

where y' ie the water depth et eny time θ from the commencement of
breaking.

From the assumption thet the weter eurface end beech are
plene it follows that

$$z' = y' \left(1 - \frac{s}{s'} \right) \qquad (5)$$

Differentieting equetion (3) with respect to θ

$$\frac{\partial z'}{\partial \theta} = \frac{\partial y'}{\partial \theta}(1 - \frac{s}{e'}) + y'\frac{\partial}{\partial \theta}(1 - \frac{e}{e'}) \qquad (6)$$

Differentiating equetion (2) end writing

$$\frac{\partial}{\partial \theta} (1 - \frac{e}{e'}) = \frac{e}{(s')^2}\frac{\partial e'}{\partial \theta}$$

enables equation (6) to become

$$\frac{\partial}{\partial e}(z'v') = \frac{\partial z'}{\partial \theta} = \frac{\partial y'}{\partial \theta}(1 - \frac{s}{e'}) - y'\frac{e}{(s')^2}\left(\frac{l_b}{2} . \frac{\pi}{T-t} \ \text{ein} \ \frac{\pi \theta}{T-t}\right) \qquad (7)$$

Integrating with respect to s gives

$$z'v' + f(\theta) = \frac{\partial y'}{\partial \theta}\left(s - \frac{s^2}{2s'}\right) - y'\cdot\frac{s^2}{2(s')^2}\left(\frac{1_b}{2}\cdot\frac{\pi}{T-t}\sin\frac{\pi\,\theta}{T-t}\right) \quad (8)$$

where $f(\theta)$ can be defined from the boundary conditions by putting
$s = 0$ or $s = s'$. Using s = s' i.e. z' = 0,

$$0 + f(\theta) = \frac{\partial y'}{\partial \theta}\frac{s'}{2} - \frac{y'}{2}\left(\frac{1_b}{2}\frac{\pi}{T-t}\cdot\sin\frac{\pi\,\theta}{T-t}\right) \quad (9)$$

Substituting into (8) and putting $z' = y'(1 - \frac{s}{s'})$ and reerranging
and dividing by $y'(1 - \frac{s}{s'})$ gives

$$v' = -\frac{1}{y'}\frac{\partial y'}{\partial \theta}\frac{(s'-s)}{2} + \frac{1_b}{4}\frac{\pi}{T-t}\frac{(s'+s)}{s'}\sin\frac{\pi\,\theta}{T-t} \quad (10)$$

Using the water level equation (4)

$$\frac{\partial y'}{\partial \theta} = -\frac{\pi}{2}\frac{1}{T-t}\,y_0\sin\frac{\pi}{2}\frac{\theta}{T-t} \quad (11)$$

Substituting (4) and (11) into (10), gives

$$v' = \frac{\pi}{2(T-t)}\frac{(s'-s)}{2}\tan\frac{\pi\theta}{2(T-t)} + \frac{1_b}{4}\frac{\pi}{T-t}\frac{(s'+s)}{s'}\sin\frac{\pi\,\theta}{T-t} \quad (12)$$

This is the horizontal component of the velocity parallel to the beech,
so the velocity v parallel to the beach is $\frac{v'}{\cos\alpha}$.
Equations (12) and (2) can be combined to give

$$v = \frac{1}{\cos\alpha}\frac{\pi\,1_b}{.4(T-t)}\left[\frac{3}{2}\sin\frac{\pi\,\theta}{T-t} + \frac{s}{1_b}\tan\frac{\pi\,\theta}{2(T-t)}\right] \quad (13)$$

Clearly a velocity only exists when there is water on
the beach at the particular value of $a/1_b$ choaen. This means that $s/1_b$
must be leas than or equal to $s'/1_b$.   When $a/1_b = s'/1_b$ then
the edge of the backwash has reached the position chosen. Immediately
the velocity falls to zero as the beach becomes dry.   If in equation
(13) $s/1_b$ is put equal to $s'/1_b$ and the substitution from equation
(2) used in the form

$$\frac{s'}{1_b} = \cos^2\frac{\pi\,\theta}{2(T-t)} \quad (14)$$

$$v = \frac{1}{\cos\alpha}\frac{1_b}{.2(T-t)}\sin\frac{\pi\,\theta}{T-t} \quad (15)$$

and the time of occurrence ia found from equation (14)

$$\frac{s}{l_b} = \frac{s'}{l_b} = \cos^2 \frac{\pi \theta}{2(T-t)} \tag{16}$$

Thus using equation (16) for the chosen s/l_b , θ can be computed for the condition $s = s'$, hence using (15) the velocity at this value of s and θ can be found. This is the backwssh velocity immediately before the beach becomes dry st this s/l_b.

To find the maximum backwash velocity for a particular position s/l_b and the absolute maximum backwash velocity occurring on the beach at any s/l_b and any θ :

abbreviating equation (13) for convenience, the velocity just before the beach becomes dry is

$$v_1 = \frac{3}{2} \sin R \theta + \frac{s}{l_b} \tan R \theta \tag{17}$$

where $R = \frac{\pi}{2} \left(\frac{1}{T-t} \right)$ and $v_1 = v \cos \alpha . \frac{4(T-t)}{\pi l_b}$

For a particular value of s/l_b in equation (17) $\frac{\partial v}{\partial \theta} = 0$ will give the value of $R\theta$ for the maximum velocity.

$$\frac{\partial v}{\partial \theta} = 3R \cos 2R\theta + R \frac{s}{l_b} \sec^2 R\theta. \tag{18}$$

This has been plotted as line ABC in Figure (2), s/l_b plotted against $\frac{\theta}{T-t}$. The condition that there is water on the beach i. e. the limiting s/l_b , $\frac{0}{T-t}$ relation, equation (16) is also plotted as line DBE on the graph. For values of s/l_b from 0 up to the value corresponding to B on the graph, the backwash velocity reaches a maximum before the beach becomes dry. For larger values of s/l_b up to 1 the maximum velocity is not reached before the beach becomes dry at that point.

Hence the line ABD gives the time $\frac{\theta}{T-t}$ for the maximum velocity at any chosen s/l_b.

Uprush velocities.

The uprush can be in the form of either

(a)   a simple surge similar to the backwash in reverse,
                or
(b)   a bore   or
(c)   a combination of (a) and (b), the bore form giving way to the simple wedge-type surge.

Considering the uprush to be in the form of a wedge, the result can be shown to be,

$$v = -\frac{1}{\cos\alpha}\cdot\frac{l_b}{4\,T}\left(\frac{3}{2}\sin\frac{\pi\theta}{t} + \frac{s}{l_b}\tan\frac{\pi\theta}{2t}\right) \tag{19}$$

This is the expression for backwash velocity (equation 13) with $T-t$ replaced by t.

If it is assumed that the height of the bore front z' decreases linearly with distance up the beach, then

$$z' = y_0\left(1 - \frac{s'}{l_b}\right) \tag{20}$$

if the bore height is zero at the limit of uprush.
If it is assumed that the velocity of the bore front is given by

$$v' = k(gz')^{\frac{1}{2}} \qquad\text{where } k \text{ is a constant,}$$

and since

$$\frac{\partial s'}{\partial \theta} = v' \tag{21}$$

substitution gives

$$\frac{\partial s'}{\partial \theta} = k\left(gy_0(1-\frac{s'}{l_b})^{\frac{1}{2}}\right)$$

Integrating with respect to θ and noting the bound $s' = 0$ when $\theta = 0$, gives

$$s' = k(gy_0)^{\frac{1}{2}}\cdot\theta - k^2 gy_0\frac{1}{4l_b}\theta^2 \tag{22}$$

Substituting $s' = l_b$ when $\theta = t$, gives

$$l_b = k(gy_0)^{\frac{1}{2}}t - k^2 gy_0\frac{1}{4l_b}\cdot t^2 , \qquad\text{a solution of}$$

which is

$$k(gy_0)^{\frac{1}{2}} = \frac{2l_b}{t} \tag{23}$$

Substituting this in equation (22) gives

$$\frac{s'}{l_b} = \frac{2\theta}{t} - \left(\frac{\theta}{t}\right)^2 \tag{24}$$

From equations (21) and (24) $\quad v' = \frac{2\,l_b}{t}\left(\frac{1-\theta}{t}\right) \tag{25}$

On comparing equation (24) with experimental values it was found that the experimental points lay between this curve and the sine curve from the linear theory of Miche, indicating that the uprush is a combination of the two conditions.

In order to find the internal velocity v' at any other

position in the uprush , it is neceesery to look at t ha behaviour of
the water surfaoe. The experimentsl results showad that the depth of
water st the breek-point rapidly echievee e level corresponding to
the height of the bore et breaking, and that this depth remains constant
throughout the uprush.   It follove from the assumption that the bore front
diminishes in height linesrly with distence up the beach, that if the
water surface is assumed plsne et any time, ssy at the temporal limit
of uprush, then it csn be said that the watar surface lies on the same
plane in epace throughout the uprush.

It follows from continuity of volume and from the essumption
of the plane water surfsce that

$$v' = \frac{2\ l_b}{\cos \alpha t} \cdot \frac{(1 - \frac{\theta}{t})^3}{1 - s/l_b} \tag{26}$$

This ie the horizontal component of velocity, and the velocity parallel
to the beach will be,

$$v' = \frac{2\ l_b}{\cos \alpha t} \frac{(1 - \frac{\theta}{t})^3}{1 - s/l_b} \tag{27}$$

Figure 3 illustrates the form taken by typical resulte
from model teets, compared with the theoretical curves for a bore type
and wedge type uprush.

Field obeervations mede with emall propellor ourrent
meters fixed to stakes set into the beech ehowed that t he flow broadly
followed the same pattern.

The limitations of the predicted velocitiee both for
uprush and beckweeh sre those imposed by the assumptions. The backwesh
seems to be edequately described by the eine function expression. So
far as the uprush is concarned, long low wavee seam to be described
by the wedge form. Tha complete bore form ie echieved towards the
limit of eurge conditions. Between the two there is e wide range
when both forms are combined. Obeervations on the coast showed that
the uprush was of the bore form during the observational periods.

Beckwash measuremente on the coast gave good qualitstive
agreement with theory, but generally the maximum predicted velocitiee
were higher than those observed. For practical purposed, the significant
weve period and mean uprush time were used in the theory, and individual
wave velocity measurements could be expected to show considerable
varistions from the mean predicted valuee. Tha variations from weve
to wave were of the eame order es the differences between measured and
predicted valuee.

Referencea.

Kemp P.H. & Plinston D.T.   1968   Beaches produced by waves of low
          phaae difference.   Proc.Amer. Soc. Civ. Engrs. Jour.
          Hydr. Div.   HY5. pp 1183-1195.

Miche, M. 1944.   Mouvements ondulatoires de la mer.   Annales des
          Ponts et Chausses.

Glossary.

l_b =   breaker length.

s   =   distance from the break-point.

a'   =   variable diatance from the break-point.

T   =   wave period.

v   =   velocity, as defined in the text.

t   =   time of uprush, or time.

x   =   horizontal coordinate,

y   =   water depth at break-point.

y_0 =   water depth at break-point at temporal limit of uprush.

z   =   vertical coordinate

     =   beach slope measured at mean water level.

0   =   time

'   =   (suffix) denoting variable quantity.

FIG 1.

FIG.2.

$H_b = 2.44$ cm
$T = 1.16$ s

$S/l_b = 0$

bore 0.4

$S/l_b = 0$

actual velocity

wedge

$S/l_b = 0$

$0.4 \, \theta$ sec.
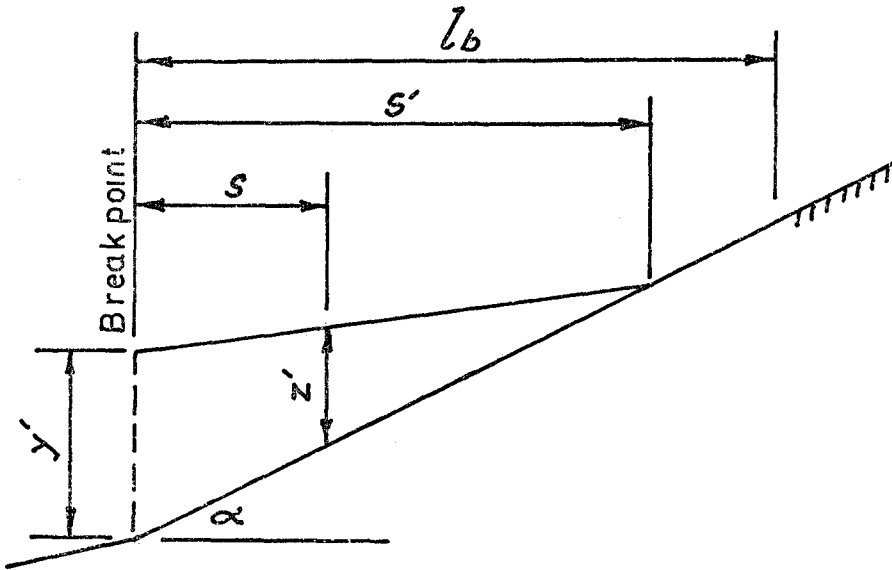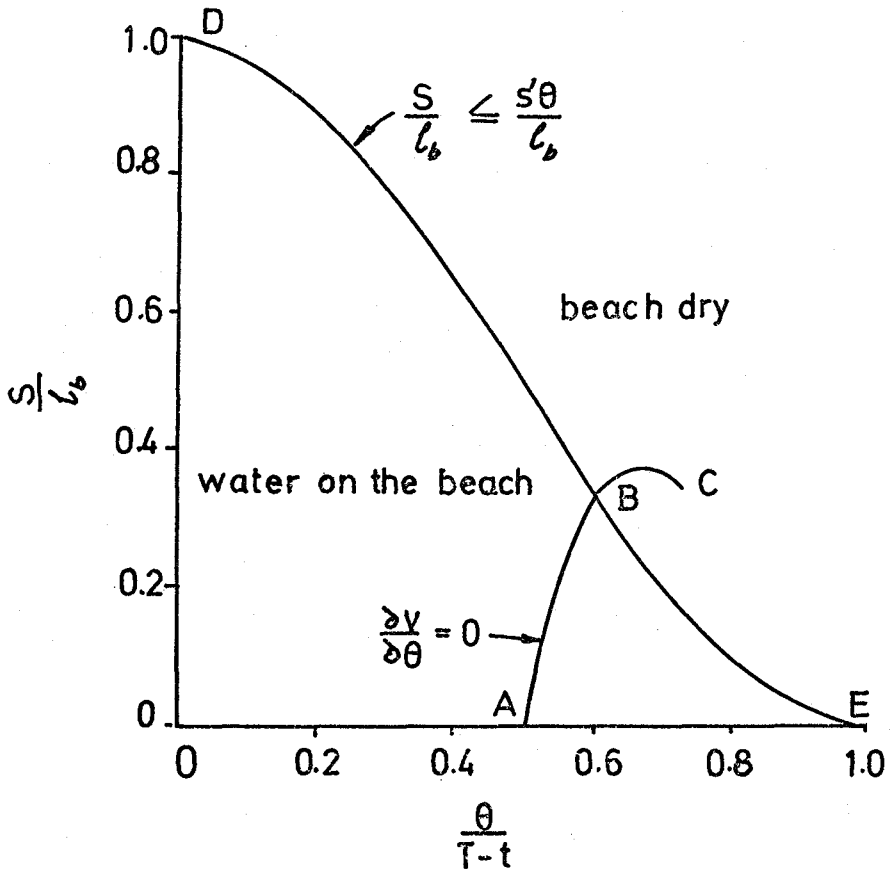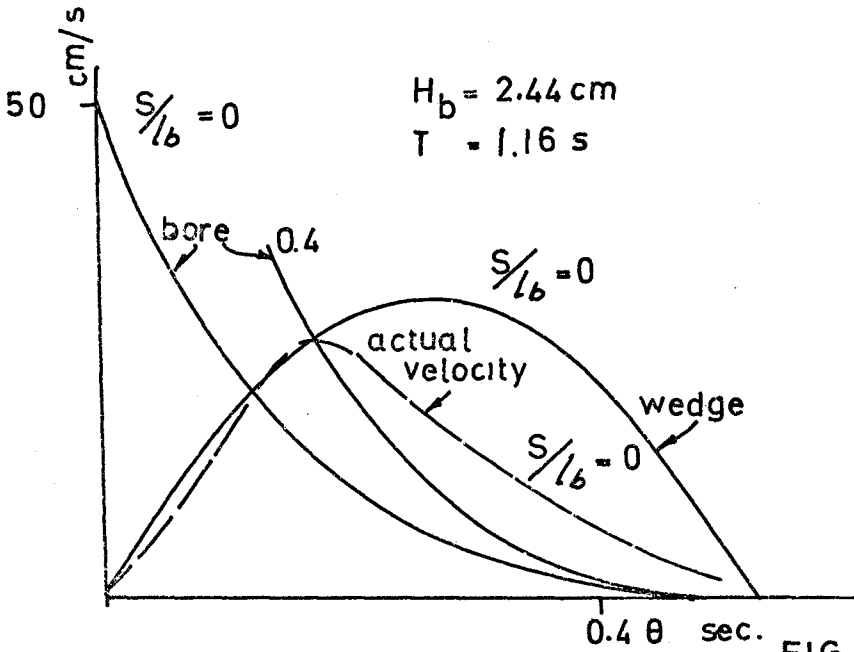
FIG.3.

CHAPTER 33

RESULTS OF OCEAN WAVE-CONTINENTAL SHELF INTERACTION[1]

by

Victor Goldsmith[2]
and
Joseph M. Colonell[3]

Abstract

Extensive wave refraction computations and analyses have been made utilizing eleven depth grids on the inner continental shelf along the east coast of the United States. The most important process determining shelf and shoreline wave energy distribution is the interaction of the ocean surface waves with the numerous shelf relief elements. This ocean wave-continental shelf interaction results in a non-uniform wave energy distribution that varies widely with different wave input conditions such as wave approach direction, wave length, and tide level. Techniques are being developed to manipulate and analyze these extensive wave data (encompassing over 500 wave refraction diagrams and associated computations), in order to increase understanding of the complex wave behavior resulting from the ocean wave-continental shelf interaction.

INTRODUCTION

Along the east coast of the United States where the wide, shallow and high relief continental shelf (5) interacts with ocean waves as far as 60 nautical miles from shore, the shoreline wave energy distribution becomes highly irregular and complex. Eleven regional and localized wave refraction computational studies have been made on this shelf and along the shoreline encompassing depth grids with a total of a quarter-million depths and 50,000 wave orthogonals (Figure 1 and Table 1). Along each of these orthogonals 17 different wave parameters were calculated and the values printed out at intervals of approximately 0.5 to 1.0 miles as the waves progress landward from deep water. Computational procedures for these studies have been previously described (3).

Examples of four of the 124 wave refraction diagrams computed for the First Order Virginian Sea Wave Climate Model (7) are presented in Figures 2 through 5, which typify the results obtained for widely varied deep water wave conditions. Attention is focussed upon the variation between low and high tide conditions (Figures 2 and 3) of wave ray

convergences and divergences (i.e. wave energy concentration and diminution, respectively) along the shoreline, especially at the major resort city of Virginia Beach (located approximately at $x = 120$). Also of considerable significance are the variations that occur with different wave approach directions (AZ) and wave periods (T) as shown in Figures 3 through 5.

In order to gain a greater understanding of this complex wave behavior, shoreline histograms were constructed of wave energy, wave height (Figure 6), power gradient and shelf contour maps of wave energy, wave height (Figure 7), and maximum values of wave-induced bottom velocities.

Finally, the shoreline wave ray histograms are being subjected to spectral analysis (Figure 8) in an attempt to determine whether the apparent periodicity of wave energy concentrations has a firm statistical basis.

RESULTS AND DISCUSSION

Effects of Shelf Geomorphology

The regional studies of the shelf wave refraction and shoaling effects from Saco Bay, Maine to Cape Hatteras, North Carolina (3,4) indicate a spatial periodicity in shoreline wave energy distribution. This shoreline periodicity results from the interaction of the ocean waves with the numerous relief elements of the continental shelf. These shelf relief elements include the shelf-edge canyons (for 12-second or longer waves) such as Baltimore, Washington and Norfolk Canyons; shelf valleys such as the shelf extension of Hudson, Delaware and Chesapeake Bays; ridge and swale bathymetry, most notably adjacent to southeastern Cape Cod, south shore of Long Island, Barnegat Bay, New Jersey, Delmarva Peninsula and Virginia Beach, Virginia; and shore-connected northeast-oriented ridge systems such as Monomoy Island, Cape Cod; Bethany Beach, Delaware; False Cape, Virginia; and Rodanthe, Cape Hatteras.

Shoreline Wave Energy Distribution

The resultant shoreline wave energy distribution varies with wave approach direction, wave period, stage of the tide and changes in sea level from the inverse barometric effect associated with moderate to severe storms. This spatial variation in shoreline wave energy distribution (i.e. alternate zones of wave energy concentration and diminution) also varies directly with the wave length of the incoming waves. For waves of 6-8 seconds these periodic zones are most prominent at spacings of 1-5 miles in length along the shoreline (Figures 2 through 4) while for waves of 12-14 seconds these zones may be 10-25 miles in length (Figure 5). The variations in the widths of these zones appear related to the distance from shore that the waves begin to interact with the

shelf relief elements. This spatial wave energy distribution along the shoreline will affect the morphology and the long-term erosional history of the shoreline (6). Clearly, these trends should be considered in any shoreline planning or management endeavor.

Continental Shelf Wave Energy Distribution

In addition to the shoreline effects, this ocean wave-shelf inter-action results in offshore areas of "confused seas" which should be identified and noted in the planning for offshore port siting proposed for this region. Note the strong "straight caustic" along the seaward rim of the Delaware canyon (top of Figure 5). Though most apparent for AZ = 157.5° and T = 12 sec, because of the canyon orientation and the abrupt change in depth, such an area of presumed surface disturbance will also occur under other conditions in which the waves travel into abruptly deeper water (2). Two of the computed wave parameters, the maximum horizontal components of the wave-induced bottom velocity and acceleration, can also be applied to shelf sediment transport studies. These two parameters are needed in wave force calculations for proposed offshore structures. The effects of these wave parameters will also vary with different wave approach conditions. As a result of these refraction computations, a library of wave information is available for analyses of regional studies of ocean wave-continental shelf interaction, resulting shoreline and shelf effects, and for delineation of areas favorable to the placement of coastal structures.

Historical Shoreline Changes

Wave refraction computations were made offshore from Wachapreague, Virginia (Figure 1) using both 1852 and 1934 bathymetry (6). Comparison of the bathymetric surveys of 1852 and 1934 indicates that, during this 82-year time interval, these barrier islands have become substantially offset (up to 1 km) seaward on the downdrift side of the inlets. The inlets have migrated southward while the ebb-tidal deltas remained sta-tionary. The offshore bathymetry has undergone concomitant changes within the same 82-year interval, most notably in the ridge and swale bathymetry, which has deepened in the troughs and built upward on the crests.

Using standard computational wave refraction techniques (3) and the older bathymetry it was determined that in 1852 the shorter wave-length northeast waves (T = 4-6 secs) tended to concentrate wave energy at the south ends of these islands, whereas longer northeast waves (T = 12 secs) tended to concentrate wave energy at the north ends of the islands (Figure 9). Moreover, the longer waves approached the shore with their wave orthogonals more perpendicularly to the shoreline than the shorter waves. Thus the more accretional waves built up the shore-line on the downdrift sides of the inlets; while the shorter erosional waves eroded the shoreline on the updrift sides. This effect was

amplified by a feed-back mechanism--the more the inlet offset the greater
the refraction of the longer waves, which resulted in more buildup and a
decrease in littoral drift, especially to the north. However, a tendency
since 1852 for the shoreline wave energy distribution to become more uni-
form along any one of these barrier islands suggests that when the wave
energy distribution reaches equilibrium the growth of the inlet offsets
will cease, and the inlets will become more stable.

Spectral Analysis of Shoreline Energy Distributions

The spatial periodicity of wave energy concentrations suggested by
histograms such as Figure 6 prompts further inquiry. Using standard
spectral analysis procedures (1), the initial results of such inquiry
are typified by Figure 8. Some support is provided for an assumption
of spatial periodicity with spectral peaks being indicated for shore-
line intervals of 5.3 and 12.0 nautical miles for the wave conditions
AZ = 45° and T = 14 sec. However, limitations of the "data" preclude
the formation of any firm conclusions at this point.

CONCLUSIONS

The intimate relationship of inner continental shelf relief and
shoreline wave conditions has been demonstrated by wave refraction
computations for several locations on the U.S. east coast. The results
serve as a guide to interpretation of coastal processes for engineering
purposes as well as scientific inquiry.

REFERENCES

1. Blackman, R.B., and Tukey, J.W., 1958. Measurement of Power Spectra:
       Dover Publications, Inc., 190 p.

2. Chao, Y.Y., and Pierson, W.J., 1972. Experimental studies of the
       refraction of uniform wave groups near a straight caustic: J.G.R.
       v. 77, p. 4545-4554.

3. Colonell, J.M., Farrell, S., and Goldsmith, V., 1973. Wave refraction
       analysis: Aid to interpretation of coastal hydraulics: A.S.C.E.
       Hydraulics Div. Conf.: Hydraulic Engineering and the Environment,
       Montana State Univ., Bozeman, Aug. 15-17, 1973.

4. Goldsmith, V. and Colonell, J., 1970. Effects of nonuniform wave
       energy in the littoral zone. Proc. 12th Coastal Engr. Conf.,
       Sept. 13-18, 1970, Washington, D.C., p. 767-785.

5. Goldsmith, V., Sutton, C.H., and Davis, J.S., 1973. Bathymetry of
       the Virginian Sea - Continental Shelf and Upper Slope, Cape
       Henlopen to Cape Hatteras: Bathymetric Map, VIMS SRAMSOE No. 39.

6. Goldsmith, V., Byrne, R.J., Sallenger, A.H.,Jr. and Drucker, D.M.,
       1974. The influence of waves on the origin and development of
       the offset coastal inlets of the Delmarva Peninsula: 2nd Inter-
       national Estuarine Conference: Geology Section - Coarse-grained
       sediment transport and accumulation in estuaries: Myrtle Beach,
       S.C., 15-18 Oct. 1973. VIMS Contrib. No. 579 (in press).

7. Goldsmith, V., Morris, W.D., Byrne, R.J. and Whitlock, C.H., 1974.
       Wave Climate Model of the Mid-Atlantic Continental Shelf and
       Shoreline: I - Model description, shelf geomorphology, and
       preliminary data analysis: VIMS SRAMSOE No. 38 (in press).

WAVE REFRACTION COMPUTATION DEPTH GRIDS

Northern and Middle Atlantic Coastal Shelf of the United States

Name	Corner Coordinates (North latitude/West longitude)				Grid Density (nm)
	NE	SE	SW	NW	
1. Saco Bay, Maine	43°32'/70°16'	43°25'/70°16'	43°25'/73°23.5'	43°32'/70°23.5'	0.1
2. Wells Beach, Maine	43°21'/70°23'	43°12'/70°23'	43°12'/70°35'	43°21'/70°35'	0.1
3. Monomoy-Nauset, Cape Cod First Order	41°45'/69°40'	41°25'/69°40'	41°25'/70°00'	41°45'/70°00'	0.2
4. Monomoy-Nauset, Cape Cod (Nauset Beach, Cape Cod) Second Order	41°44'/69°53'	41°38'/69°53'	41°38'/69°58'	41°44'/69°58'	0.1
5. Cedar-Gilgo, Long Island First Order	40°40'/72°45'	39°55'/72°45'	39°55'/73°44'	40°40'/73°44'	0.2
6. Cedar-Gilgo Beach, Long Island; Second Order	40°38.5'/73°15'	40°30'/73°15'	40°30'/73°28'	40°38.5'/73°28'	0.1
7. Virginian Sea; First Order	38°50'/74°00'	35°15'/74°00'	35°15'/76°00'	38°50'/76°00'	0.5
8,9. Virginian Sea; Second Order Wachapreague (1852 & 1934)	37°45'/75°10'	37°20'/75°10'	37°20'/75°43'	37°45'/75°43'	0.25
10. Virginian Sea; Second Order (southeast Virginia)	37°00'/75°30'	36°30'/75°30'	36°30'/76°00'	37°00'/76°00'	0.25
11. Virginian Sea; Third Order	37°00'/75°50'	36°45'/75°50'	36°45'/76°00'	37°00'/76°00'	0.1
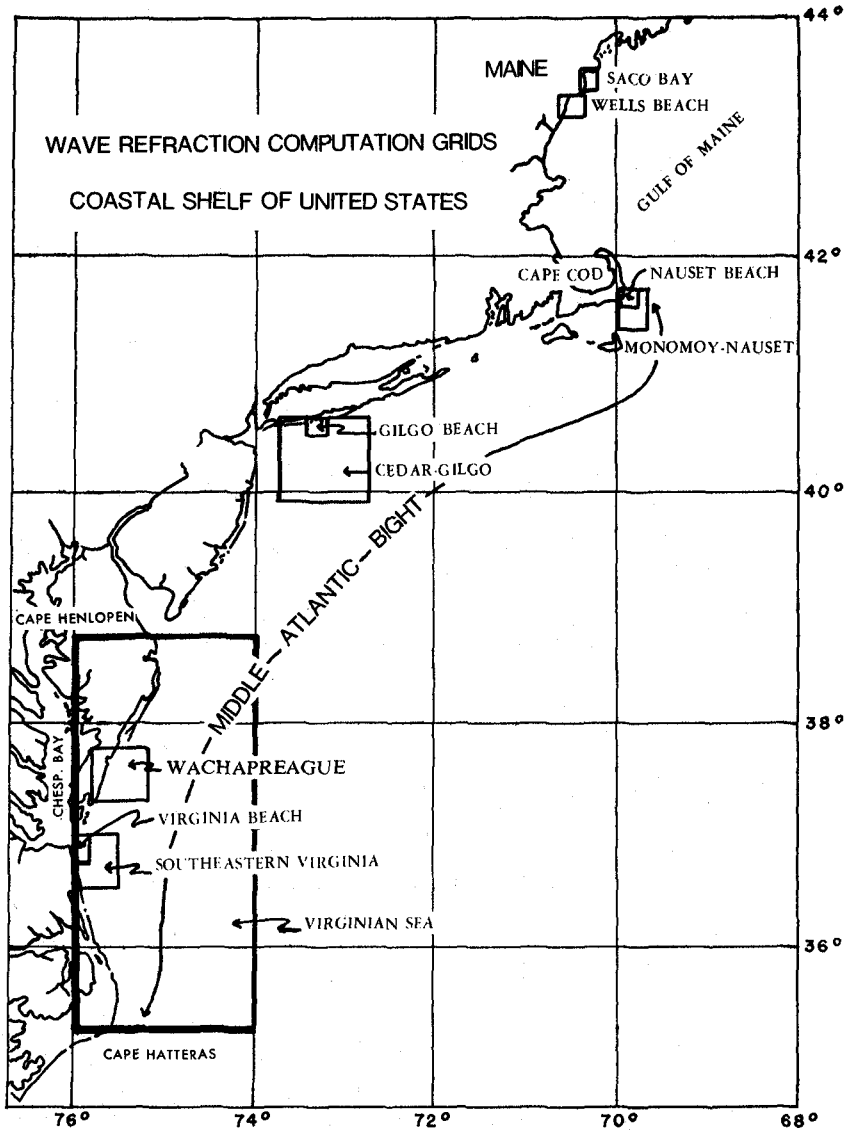
Figure 1.   Wave refraction computation grids on the northeast
            and middle Atlantic continental shelf of the United
            States.

VIRGINIA SEA...T = 8 SEC...AZ =-45.0 DEG...HT = 2 FT
TIDE=0.0
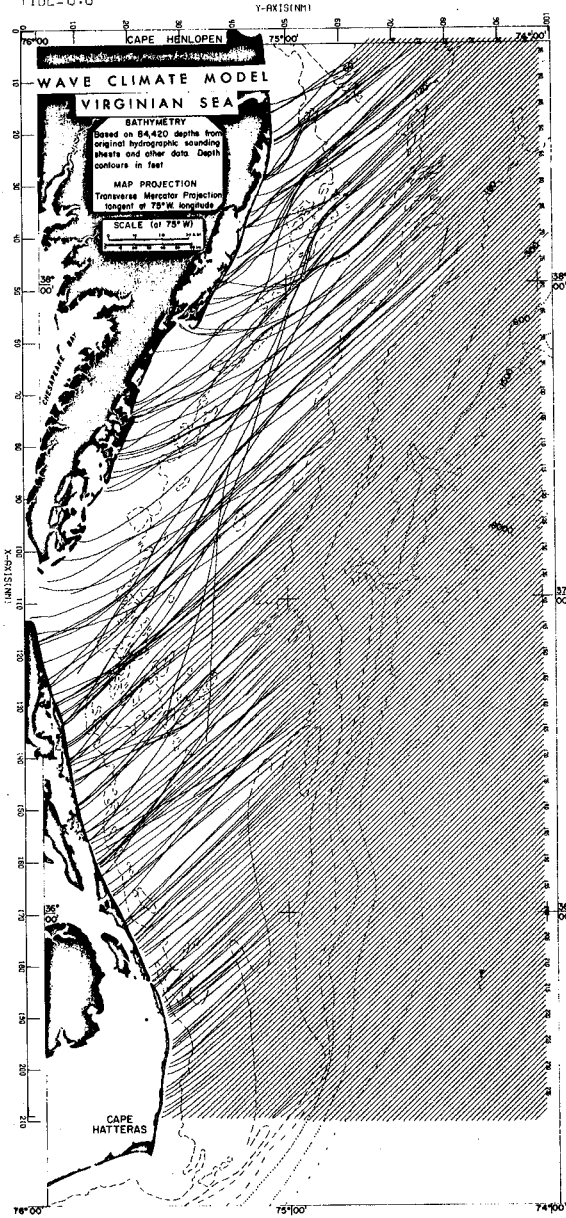
Figure 2. Wave refraction diagram of the wide, shallow and high relief U.S. continental shelf from Cape Henlopen, Delaware, to Cape Hatteras, North Carolina, with waves from the northeast with a period of 8 seconds, deep water height of 2 feet, and low tide conditions. Note the alternate shoreline zones of wave energy concentration and diminution as indicated by convergence and divergence of the wave orthogonals. Also computed were values of 17 different wave parameters at approximately one-mile intervals along each orthogonal.

VIRGINIA SEA...T = 8 SEC...AZ =-45.0 DEG...HT = 2 FT
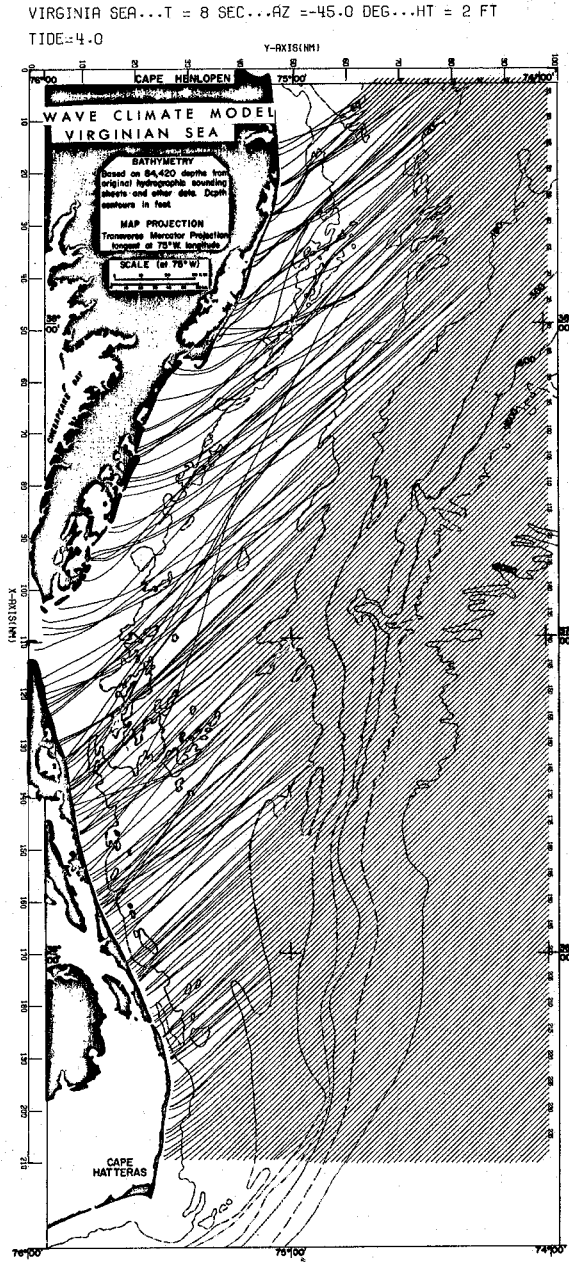
TIDE=4.0

Figure 3. First order computation grid of the Virginian Sea Wave Climate Model for AZ=45.°, T=8 sec., Ht=2 ft., and Tide=+4 ft.
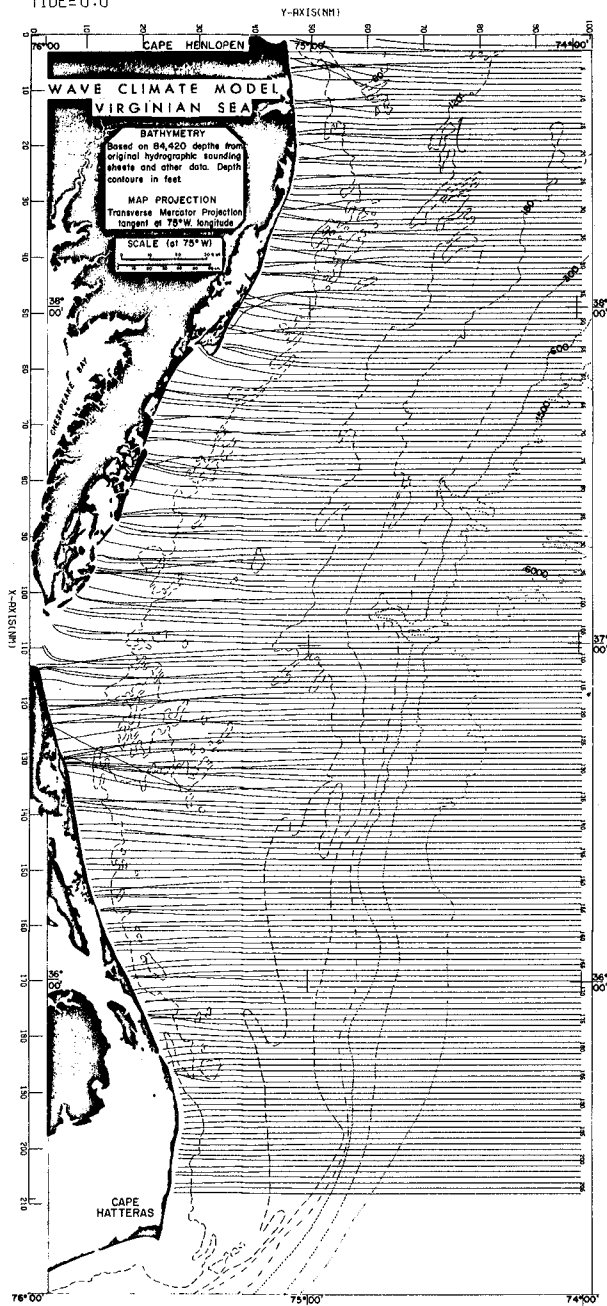
Figure 4. First order computation grid of the Virginian Sea Wave Climate Model for Az=90°, T=8 sec., Ht=2 ft., and Tide=0.

VIRGINIA SEA...T = 12 SEC...AZ =-157.5 DEG...HT = 2 FT
TIDE=0.0
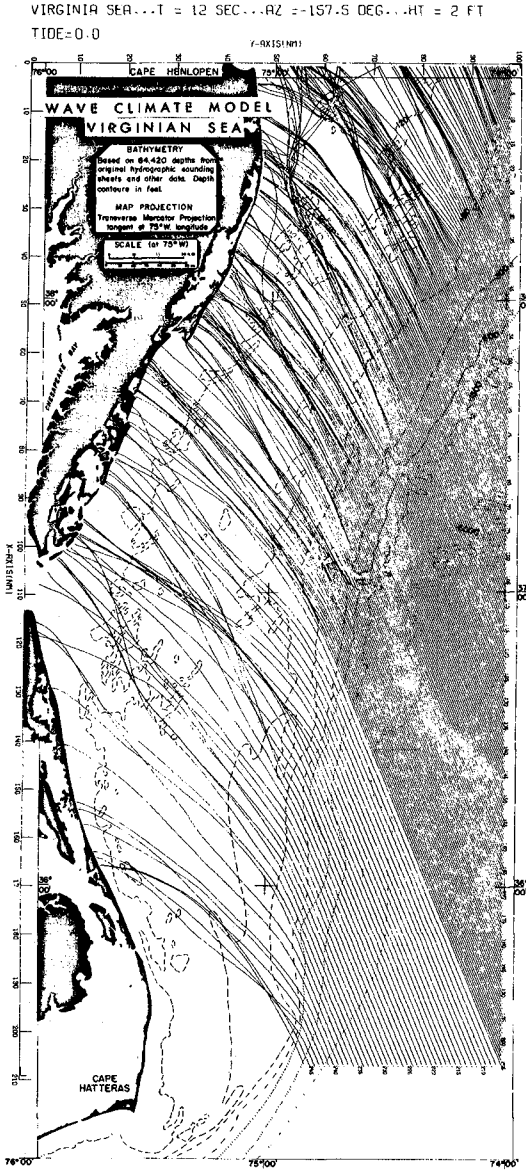
Figure 5. First order computation grid of the Virginian Sea Wave Climate Model for AZ=157.5°, T=12 sec., Ht=2 ft., and Tide=0.
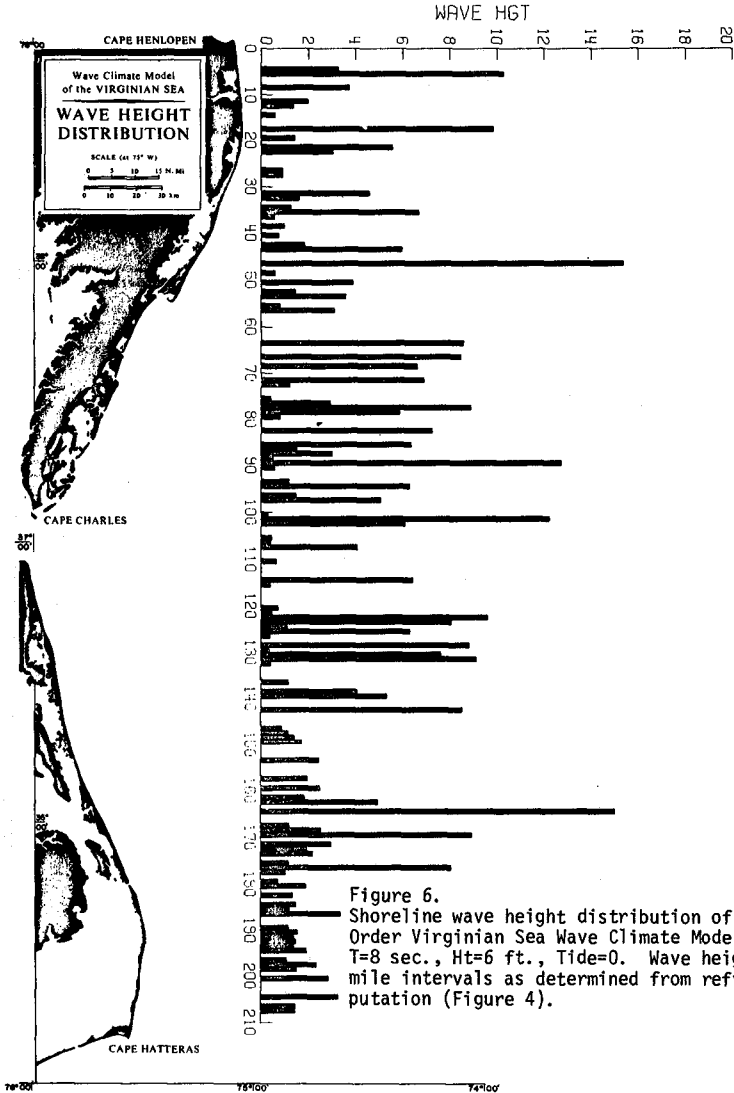
Figure 6.
Shoreline wave height distribution of the First Order Virginian Sea Wave Climate Model for AZ=90°, T=8 sec., Ht=6 ft., Tide=0. Wave heights for one-mile intervals as determined from refraction computation (Figure 4).

Figure 7.
Shelf wave height distribution of the first order Virginian Sea Wave Climate Model for Az=90°, T=8 sec., Ht=6 ft., Tide=0. Wave heights, calculated at less than one mile intervals along each wave orthogonal (Fig.4), are contoured at one meter intervals (i.e., approximately 3, 6, & 9 feet). Note the large wave heights at Chesapeake Bay Entrance.
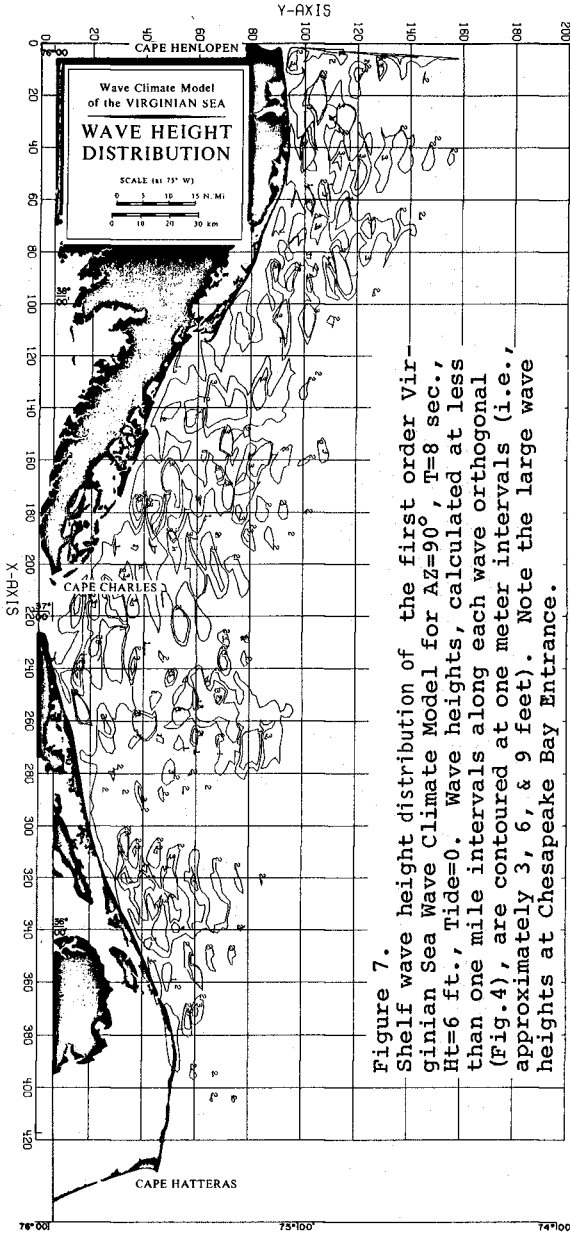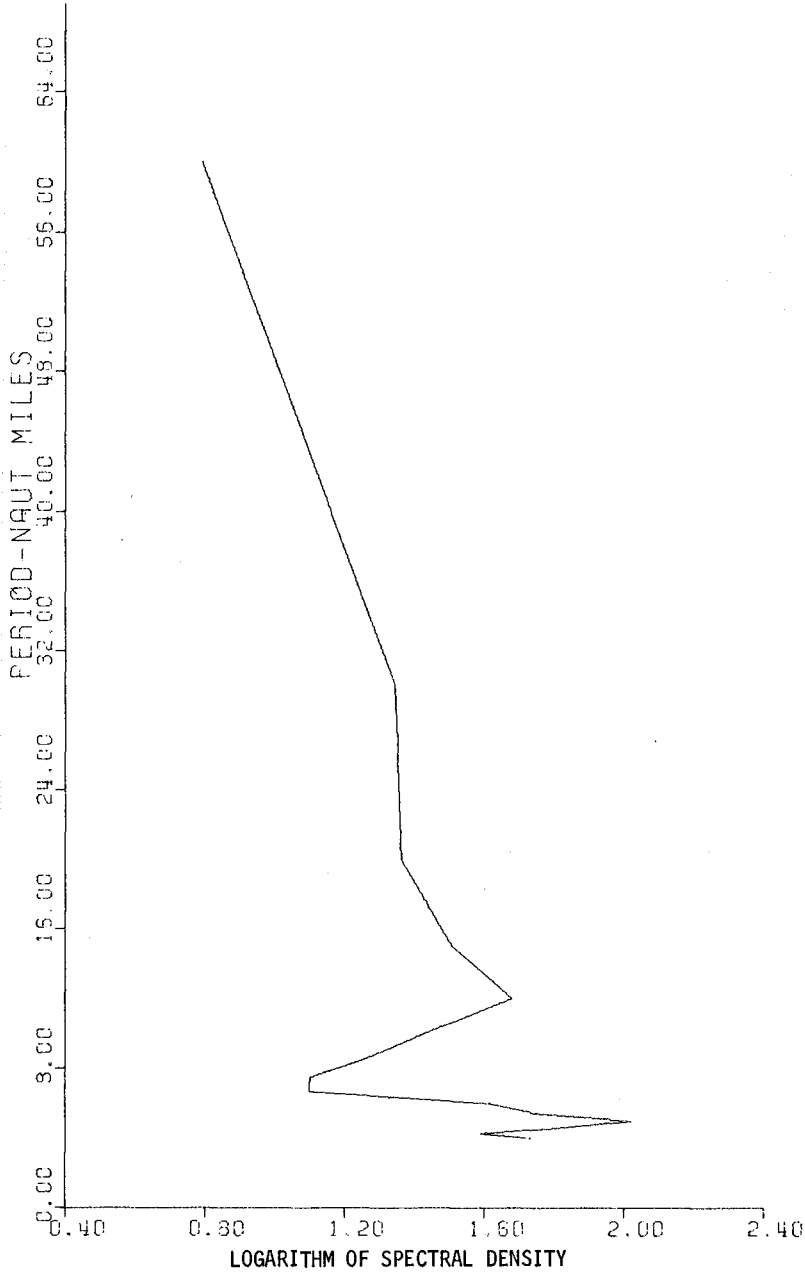
Figure 8. Spectral analysis of shoreline wave height distribution for AZ=45°, T=14 sec., Ht=6 ft., and Tide=0 (Figure 6). From the First Order Virginian Sea computation grid. Note the strong peaks at shoreline intervals of 5.3 and 12. nautical miles.
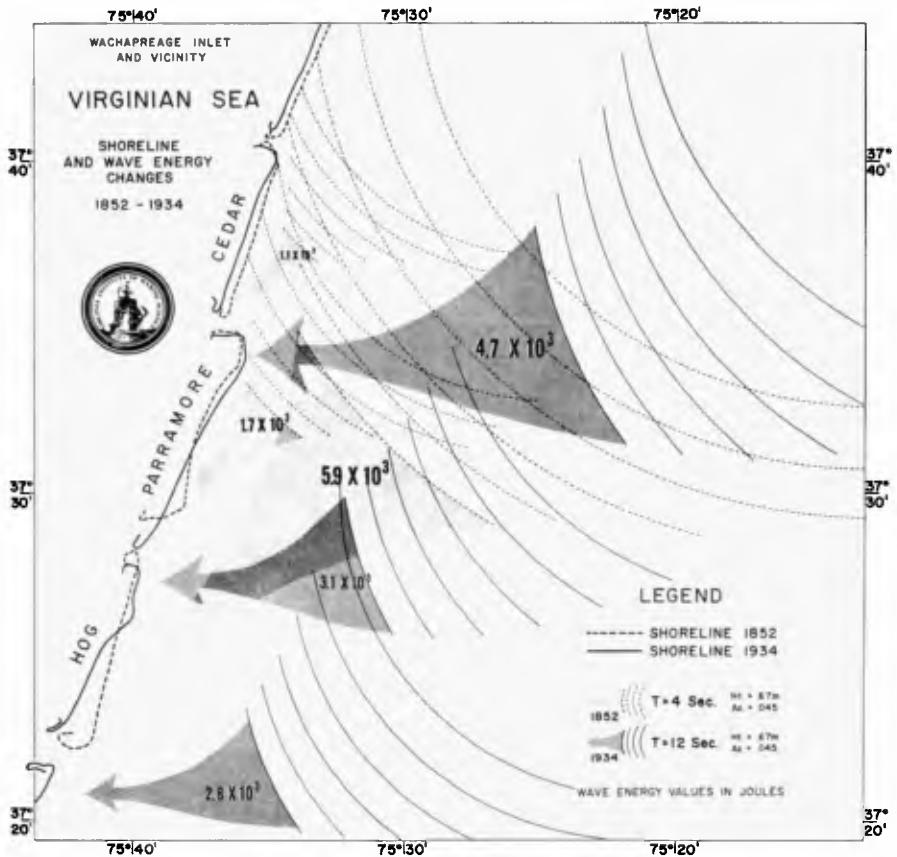
Figure 9. Schematic illustrating the close relationships between historical shoreline changes along the eastern shore of Virginia between 1852 and 1934 and the wave refraction computations using 1852 and 1934 bathymetry (Wachapreague computation grids in Fig. 1 and Table 1).

CHAPTER 34

DIFFRACTION OF GRAVITY WAVES BY LARGE ISLANDS

Peter L. Christiansen [*]

Abstract. The combined refraction and diffraction of long gravity
water waves for certain depth variations around large islands is
investigated analytically in a circular-symmetric geometry. Creep-
ing waves are shown to exist for bottom profiles less convex than
required by the trapping criterion due to Longuet-Higgins and Shen
et al. From an asymptotic representation of the solution to the
scattering problem the decay exponent and the diffraction coeffi-
cient is extracted. These "canonical" quantities may then be used
for the construction of diffracted fields around smooth islands of
more complex shape in accordance with J.B. Keller's Geometrical
Theory of Diffraction.

INTRODUCTION

Analytical investigations of refraction and diffraction effects
for gravity water waves are not too frequent in the literature. Sager
[1-4] has studied the pure refraction phenomenon for various bottom
profiles while the pure diffraction problem for constant depth is
identical with well-known scattering problems in acoustics and elec-
tromagnetic theory. Combinations of the two phenomena have been
treated by Homma [5], Vastano and Reid [6], and Lautenbacher [7].
In the present paper another example is added to this collection of
solutions.

[*] Laboratory of Applied Mathematical Physics
Technical University of Denmark
DK-2800 Lyngby, Denmark.

GRAVITY WAVES ON FREE WATER SURFACE

Small waves on shallow water. Waves on free water surfaces can propagate under the influence of gravity. Such gravity waves satisfy the equations

$$(1) \quad \nabla\eta + \frac{1}{g}\,\bar{v}_t = 0$$

and

$$(2) \quad \nabla\cdot(h\bar{v}) + \eta_t = 0$$

where $\eta = \eta(\bar{r};t)$ is the elevation of the water surface above the undisturbed level, $\bar{v} = \bar{v}(\bar{r};t)$ is the horizontal velocity field, $h = h(\bar{r})$ is the water depth, and g is the constant acceleration due to gravity. The position vector of the field point is $\bar{r}$ and t is the time. The equations are valid for small amplitudes ($\eta \ll h$) and shallow water ($h \ll L$) where L is the wave length. Combination of (1) and (2) yields the modified two-dimensional wave equation for η

$$(3) \quad \nabla\cdot(h\nabla\eta) = \frac{1}{g}\,\eta_{tt}\,.$$

We shall consider time-harmonic solutions with angular frequency ω

$$(4) \quad \eta(\bar{r};t) = \eta(\bar{r})e^{-i\omega t}\,.$$

Here $\eta(\bar{r})$ must satisfy the modified two-dimensional Helmholtz's equation

$$(5) \quad \nabla\cdot(h\nabla\eta) + \frac{\omega^2}{g} = 0\,.$$

A special depth profile. In the present paper we consider a special circular-symmetric depth profile (see Fig. 1)

$$(6) \quad h(\bar{r}) = h_o\left(\frac{r}{r_o}\right)^{2\alpha} \qquad 0 \leqslant \alpha < 1$$

where r is one of the polar coordinates (r,θ) for $\bar{r}$. The power of r

has been denoted 2α for convenience. On the circle $r = r_o$ $h = h_o$, the reference depth. Insertion of (6) into (5) yields

(7) $\nabla \cdot ((\dfrac{r}{r_o})^{2\alpha} \nabla \eta) + k_o^2 \eta = 0$

where we have introduced the reference propagation constant

(8) $k_o = \dfrac{\omega}{\sqrt{h_o g}}$.

The advantage of our choice (6) for $h(\bar{r})$ is that the solutions to (7) can be expressed in terms of well-known functions of the polar coordinates.

Concave bottom   Conical bottom   Convex bottom
$(0 < \alpha < \tfrac{1}{2})$ $(\alpha = \tfrac{1}{2})$ $(\tfrac{1}{2} < \alpha < 1)$
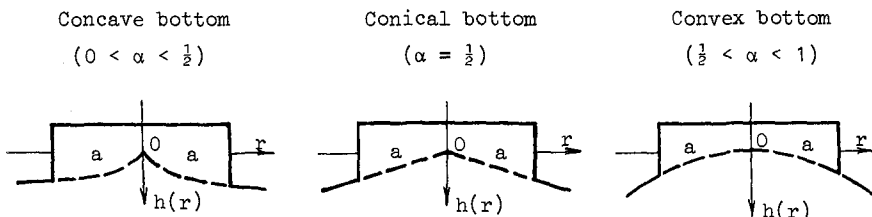
Fig. 1. Circular island (radius a and water depth $h(\bar{r}) = (\dfrac{r}{r_o})^{2\alpha}$).

<u>Short waves.</u> In the short-wavelength limit ($k_o r \gg 1$) the elevation can be represented by

(9) $\eta(\bar{r}) \sim A(\bar{r}) e^{ik_o S(\bar{r})}$

where the phase S and the amplitude A are reel functions of $\bar{r}$ that remains bounded for $k_o r \to \infty$. The assumption (9) which is used in geometrical optics (see [8], e.g.) is sometimes called Debye's assumption. Insertion of (9) in (7) yields the eiconal equation

(10) $(\nabla S)^2 = (\dfrac{r_o}{r})^{2\alpha}$

and the transport equation

(11) $\dfrac{2\alpha}{r}\dfrac{\partial S}{\partial r} + 2\nabla A \cdot \nabla S + A \Delta S = 0$.

<u>The ray tracing and the phase variation.</u> The wave fronts are the
curves $S(\bar{r}) = $ const. where $S = S(\bar{r})$ are solutions to (10). Is is,
however, easier to determine the wave orthogonals or rays as extremal
curves to the Fermat's principle

(12) $\delta\displaystyle\int_{P_1}^{P_2} \left(\dfrac{r_o}{r}\right)^{\alpha} ds = 0$.

According to (10) the water surface can be viewed as an inhomogeneous
two-dimensional medium with refractive index $(r_o/r)^{\alpha}$. The distance
element measured along the curves $r = r(\theta)$ is denoted ds. The varia-
tional principle (12) therefore states that the rays from a point P_1
to a point P_2 proceed in such a manner that the passage time becomes
stationary. The obvious wave orthogonals, $\theta = $ const., through the
top of the profile at the origin of the coordinate system, 0, are not
included in (12).

By solving of the Euler equation corresponding to (12) we find
that rays are sine spirals. Thus the family of rays through P_s
(r_s, θ_s) away from 0 becomes

(13) $\left(\dfrac{r_s}{r}\right)^{1-\alpha} = \dfrac{\sin(\phi_s - (1-\alpha)(\theta - \theta_s))}{\sin\phi_s}$ for $\theta > \theta_s$

where the parameter ϕ_s is the angle between the unit vectors $\hat{r}_s$ and
$\hat{t}_s$ at P_s (see Fig. 2). The angle ϕ between the unit vectors $\hat{r}$ and $\hat{t}$
at P can be shown to be

(14) $\phi = \phi_s - (1-\alpha)(\theta - \theta_s)$.

Integration of (10) along the rays through P_s given by (13)
yields
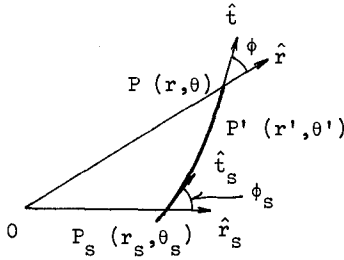
Fig. 2. Sine spirals through P_s (r_s, θ_s).

$$(15) \quad S(P) = S(P') + \frac{r_o^\alpha \, r_s^{1-\alpha}}{1-\alpha} \, \sin\phi_s (\mathrm{ctn}(\phi_s - (1-\alpha)(\theta - \theta_s))$$

$$- \mathrm{ctn}(\phi_s - (1-\alpha)(\theta' - \theta_s))) \,.$$

Here $S(P)$ $(S(P'))$ is the phase at a point P (r, θ) $(P'$ $(r', \theta'))$. The points P and P' lie on the same ray through P_s. (See Fig. 2.)

<u>Energy conservation.</u> By means of (10) the transport equation can be converted into

$$(16) \quad \frac{dA}{A} = -\tfrac{1}{2}(\frac{\alpha}{r} \, \hat{r} \cdot \hat{t} + \nabla \cdot \hat{t}) ds \,,$$

where $\hat{r}$ and $\hat{t}$ are the unit vectors shown in Fig. 2. Integration of (16) along the rays (13) yields after some calculation

$$(17) \quad A(P) = A(P') \, (\frac{\sin(\phi_s - (1-\alpha)(\theta - \theta_s))}{\sin(\phi_s - (1-\alpha)(\theta' - \theta_s))})^{\frac{\alpha}{1-\alpha} + \frac{1}{2}}$$

$$\times \, (\frac{\sin((1-\alpha)(\theta' - \theta_s))}{\sin((1-\alpha)(\theta - \theta_s))})^{\frac{1}{2}} \,.$$

Here P and P' must lie on the same side of P_s. Like (11) equation (17) expresses the fact that the energy is conserved along a pencil of rays.

EXCITATION OF GRAVITY WAVES

Green's function. Gravity waves are usually excited by an incident plane wave. However, for $r \to \infty$ our model is not valid because $h \to \infty$ according to (6). Thus the shallow water condition ($h << L$) is violated. We shall therefore consider a point source placed at a finite point P_s (r_s, θ_s). The source has the somewhat artificial property that it adds the volume of water pr. length and time unit, $q(t)$, in a vertical thin column from the bottom of the sea to the water surface. Furthermore, the source oscillates harmonically with time such that

$$(18) \quad q(t) = q_s e^{-i\omega t},$$

where q_s is a constant. Mathematically, we have played for safety since the wave field excited by the source simply is a Green's function. This is determined as the solution to the inhomogeneous Helmholtz's equation

$$(19) \quad \nabla \cdot \left(\left(\frac{r}{r_o} \right)^{2\alpha} \nabla \eta \right) + k_o^2 \eta = - \ell_s \frac{\delta(r-r_s)\delta(\theta-\theta_s)}{r}$$

which is obtained by addition of the source term, $h(r_s)q(t)\delta(\bar{r}-\bar{r}_s)$, on the right hand side of (2). The position vector for P_s is $\bar{r}_s$ and δ is Dirac's delta function. The source strength (a complex length) has been denoted

$$(20) \quad \ell_s = - i\omega \left(\frac{r_s}{r_o} \right)^{2\alpha} \frac{q_s}{g} .$$

Furthermore, the Green's function must satisfy the radiation condition

$$(21) \qquad \lim_{r \to \infty} r^{\frac{3\alpha+1}{2}} \left(\frac{\partial \eta}{\partial r} - ik_0 (\frac{r_0}{r})^\alpha \eta \right) = 0 .$$

$\underline{\text{Separation of variables}}$ yields the Green's function

$$(22) \quad \eta(r,\theta;r_s,\theta_s) = \frac{i\ell_s}{4} \frac{1}{1-\alpha} (\frac{r_0^2}{r_s r})^\alpha$$

$$\times \sum_{n=-\infty}^{\infty} H^{(1)}_{\frac{\sqrt{\alpha^2+n^2}}{1-\alpha}} \left(\frac{1}{1-\alpha}(k_0 r_0)^\alpha (k_0 r_s)^{1-\alpha} \right)$$

$$\times J_{\frac{\sqrt{\alpha^2+n^2}}{1-\alpha}} \left(\frac{1}{1-\alpha}(k_0 r_0)^\alpha (k_0 r)^{1-\alpha} \right) e^{in(\theta-\theta_s)}$$

$$\text{for } r < r_s ,$$

where $H^{(1)}_\nu(z)$ $(J_\nu(z))$ is the Hankel function of first kind (Bessel function) of argument z and order ν. For the derivation of (22) a standard result from [9] has been used. The excitation for $r > r_s$ is obtained by interchange of r and r_s in (22) due to reciprocity.
$\underline{\text{Asymptotic representation.}}$ By transforming (22) into a contour integral we obtain the representation

$$(23) \quad \eta(r,\theta;r_s,\theta_s) \sim \ell_s D_s(\phi_s) e^{ik_0(S(P)-S(P_s))} \frac{A(P)}{A(P'_{s,1})}$$

in the short-wavelength limit $(k_0 r_0)^\alpha (k_0 r_s)^{1-\alpha}/(1-\alpha) \gg 1$ by means of the Debye representations of the cylinder functions, the method of steepest descent and (13) after a lengthy calculation. We have written (23) in a form which shows that the field, η, can be viewed as being produced by a ray through P_s and the observation point P (r,θ) (see Fig. 2). The angle ϕ_s is then determined from (13) by insertion of the value of (r,θ) at P. In the phase factor, $\exp\{ik_0(S(P)-S(P_s))\}$, the difference between the phases $S(P)$ and

$S(P_s)$ at P and P_s, respectively, is given by (15) with $\theta' = \theta_s$. The point $P'_{s,1}$ (r',θ') on the ray $P_s P$ is a reference point with the property

$$(24) \quad r_s^{\frac{1}{2}}[\sin(1-\alpha)(\theta'-\theta_s)]^{\frac{1}{2}}[\sin(\phi_s-(1-\alpha)(\theta'-\theta_s)]^{-\frac{\alpha}{1-\alpha}-\frac{1}{2}} = 1 .$$

As a consequence of (17) the divergence factor for the pencil of rays emanating from P_s becomes

$$(25) \quad \frac{A(P)}{A(P'_{s,1})} = \frac{(\sin(\phi_s-(1-\alpha)(\theta-\theta_s)))^{\frac{1}{2}+\frac{\alpha}{1-\alpha}}}{r_s^{\frac{1}{2}}(\sin((1-\alpha)(\theta-\theta_s)))^{\frac{1}{2}}} .$$

For $\alpha = 0$ this expression reduces to $r_{P_s P}^{-\frac{1}{2}}$ where $r_{P_s P}$ is the distance from P_s to P. Finally, the source factor

$$(26) \quad D_s(\phi_s) = \frac{e^{i\frac{\pi}{4}}}{\sqrt{8\pi k_o}} (\frac{r_o}{r_s})^{\frac{3\alpha}{2}} (1-\alpha)^{\frac{1}{2}}(\sin\phi_s)^{-\frac{\alpha}{1-\alpha}}$$

describes the emission of rays from a unit source at P_s. For $\alpha \neq 0$ the radiation is anisotropic due to the sloping bottom at the source. The asymptotic representation of the Green's function (22) thus confirms the ray interpretation of the field and yields a determination of the source factor $D_s(\phi_s)$ (26).

SCATTERING OF GRAVITY WAVES

A circular island. As an example of a scattering problem we consider diffraction by a circular island with center at 0 and radius a (see Fig. 3). The mathematical formulation of the problem then consists of (19) for $r \geqslant a$ and $r_s \geqslant a$, (21), and the boundary condition
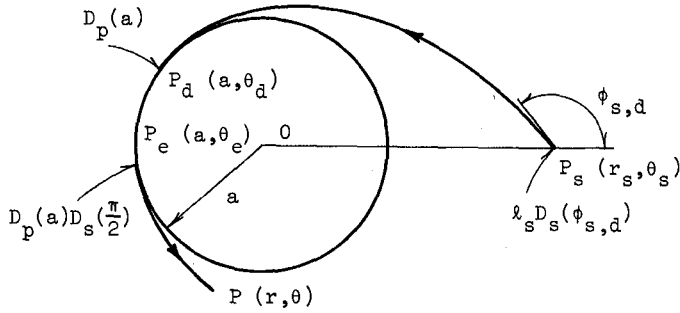
Fig. 3. Diffraction by a circular island.
Propagation in negative direction and
multiple circulations are not shown.

(27) $\dfrac{\partial \eta}{\partial r} = 0$ for $r = a$

which expresses full reflection at the island.

<u>Sommerfeld's method.</u> The solution can be written in the following
form

(28) $\eta(r,\theta;r_s,\theta_s) = \dfrac{\ell_s}{k_o a}\left(\dfrac{r_o}{a}\right)^{2\alpha}\displaystyle\sum_{p=1}^{\infty}\dfrac{\cos\nu_p(\theta-\theta_s\mp\pi)}{\sin\nu_p\pi}$

$$\dfrac{R_{\nu_p}(k_o r_s)R_{\nu_p}(k_o r)}{R_{\nu_p}(k_o a)\dfrac{\partial^2}{\partial k_o r\,\partial\nu}R_{\nu_p}(k_o r)\bigg|_{\substack{r=a\\ \nu=\nu_p}}} \quad \text{for} \quad \left.\begin{array}{c}0\\-\pi\end{array}\right\} \le \theta-\theta_s \le \left\{\begin{array}{c}\pi\\0\end{array}\right.$$

by means of Sommerfeld's method [10]. Here

(29) $R_\nu(k_o r) = \dfrac{1}{(k_o r)^\alpha} H^{(1)}_{\frac{\sqrt{\alpha^2+\nu^2}}{1-\alpha}} \left(\dfrac{1}{1-\alpha} (k_o r_o)^\alpha (k_o r)^{1-\alpha}\right)$

and ν_p is the p'th root in the equation

(30) $\dfrac{\partial}{\partial k_o r} R_\nu(k_o r)\Big|_{r=a} = 0$

in the first quadrant of the complex ν-plane. The advantage of an expression like (28) is that it gives a rapidly convergent representation of the diffracted field in the short-wave length limit $(k_o r_o)^\alpha (k_o r_s)^{1-\alpha}/(1-\alpha) \gg 1$. The diffracted field is present everywhere outside the island. It is, however, only a dominant part of the total field in the geometric-optics shadow region, i.e. the region where no incident or reflected field is present (see [11], e.g.). Such a region can be shown to exist behind the island with respect to the source point when $0 \leqslant \alpha < \frac{1}{2}$. For larger values of α the rays become so curved that every point behind the island is reached by a direct ray from the source. The rest of this paper is devoted to an investigation of the diffracted field.

Asymptotic representation. By insertion of the Debye representations and the transition region representations (see [12], e.g.) of the cylinder functions in (28) we have obtained the following result

(31) $\eta(r,\theta;r_s,\theta_s) \sim \ell_s D_s(\phi_{s,d}) e^{ik_o(S(P_d)-S(P_s))} \dfrac{A(P_d)}{A(P'_{s,1})}$

$\times \sum\limits_{p=1}^{\infty} D_p(a)\Big[e^{(ik_o(\frac{r_o}{a})^\alpha - \beta_p(a))a(\theta_e - \theta_d)}$

$+ e^{(ik_o(\frac{r_o}{a})^\alpha - \beta_p(a))a(2\pi-\theta_e+\theta_d)}\Big] \times \sum\limits_{q=0}^{\infty} e^{(ik_o(\frac{r_o}{a})^\alpha - \beta_p(a))a2\pi q}$

$\times D_p(a) D_s(\frac{\pi}{2}) e^{ik_o(S(Q)-S(P_e))} \dfrac{A(Q)}{A(P'_{e,1})} \ .$

Below we shall discuss the symbols used in this formula. It turns
out that the diffracted field at P (r,θ) can be viewed as being pro-
duced by the ray system partly illustrated in Fig. 3.

The creeping wave. The essential feature of the ray tracing is the
existence of a creeping wave travelling around the island in positive
and negative direction (from P_d (a,θ_d) to P_e (a,θ_e) in Fig. 3). The
creeping wave which is excited by a tangentially incident ray, P_sP_d,
continuously launches tangentially diffracted rays, P_eP e.g., into
the surrounding sea. In this sense the creeping wave is a "semi-
trapped" wave which only exists for $0 \leqslant \alpha < 1$. According to a crite-
rion due to Longuet-Higgins [13] and Shen et al. [14] trapped waves
around circular islands are found when $O(h(r)) > r^2$, i.e. for $\alpha > 1$.
The creeping wave travels with the free space propagation constant at
the boundary of the island $(= k_o(r_o/a)^\alpha)$ and is strongly damped due to
the energy loss to the diffracted rays. This phenomenon is described
by the decay exponent, $\beta_p(a)$. As a consequence, the phase factor for
the creeping wave, P_dP_e, becomes $\exp\{(ik_o(r_o/a)^\alpha - \beta_p(a))a(\theta_e-\theta_d)\}$ as
seen in (31). From the asymptotic representation of (28) follows

$$(32) \qquad \beta_p(a) \sim 2^{-\frac{1}{3}} e^{-i\frac{\pi}{6}} x_p'(1-\alpha)^{\frac{2}{3}} (k_o(\frac{r_o}{a})^\alpha a)^{\frac{1}{3}} a^{-1}$$

where $-x_p'$ is the p'th zero of the derivative of the Airy function of
first kind

$$(33) \qquad Ai(x) = \frac{1}{\pi} \int_o^\infty \cos(\frac{1}{3} t^3 + xt)dt .$$

Finally, (31) shows that the creeping wave possesses a modal structure
which is expressed in the summation with index p.

The incident ray and the diffracted ray. For the incident ray, P_sP_d,
$\phi_{s,d}$ is given by ϕ_s in (13 and 14) with $(r,\theta) = (a,\theta_d)$ and $\phi = \frac{\pi}{2}$.
The emission of rays from the source is described by ℓ_s (20) and
$D_s(\phi_{s,d})$ given by (26) with $\phi_s = \phi_{s,d}$. The phase factor and the

divergence factor becomes $\exp\{ik_o(S(P_d) - S(P_s))\}$ and $A(P_d)/A(P'_{s,1})$ given by (15) and (25), respectively, with $\theta' = \theta_s$, $\theta = \theta_d$ and $\phi_s = \phi_{s,d}$.

We obtain the coordinate θ_e for P_e by letting $r_o = a$, $\phi_s = \frac{\pi}{2}$, and (r,θ) equal to the coordinates of P in (13). The emission of a pencil of diffracted rays from P_e is described by $D_s(\frac{\pi}{2})$ given by (26) with $\phi_s = \frac{\pi}{2}$. The phase factor and the divergence factor for the ray, P_eP, are $\exp\{ik_o(S(P) - S(P_e))\}$ and $A(P)/A(P'_{e,1})$, respectively, where $P'_{e,1}$ is a reference point on P_eP corresponding to $P'_{s,1}$ on P_sP_d. These factors are still given by (15) and (25), respectively, but now $\theta' = \theta_s = \theta_e$, $r_s = a$, and $\phi_s = \frac{\pi}{2}$.

The diffraction processes. The remaining factor in the asymptotic representation of (28) is viewed as describing the diffraction processes at P_d and P_e where the creeping wave starts and ends. Due to reciprocity the description of these two events must be the same function of the radius of curvature of the island (and of the depth at the coast line), $D_p(a)$. As a consequence $D_p^2(a)$ occurs in (31) and we find

$$(34) \quad D_p(a) \sim \frac{2^{\frac{1}{3}} e^{-i\frac{\pi}{12}}}{\sqrt{x'_p} \, Ai(-x_p)} (1-\alpha)^{-\frac{1}{6}} (\frac{a}{r_o})^{\frac{\alpha}{2}} (k_o(\frac{r_o}{a})^\alpha a)^{\frac{1}{6}} .$$

The asymptotic representation of (28) thus confirms the ray interpretation of the field in terms of creeping waves and ordinary rays. Furthermore, a determination of the decay exponent $\beta_p(a)$ (32) and the diffraction coefficient $D_p(a)$ (34) is provided.

APPLICATION OF THE RESULTS

According to J.B. Keller's Geometrical Theory of Diffraction (see [15] e.g.) the decay exponent and the diffraction coefficient are "canonical" quantities which apply for the construction of the
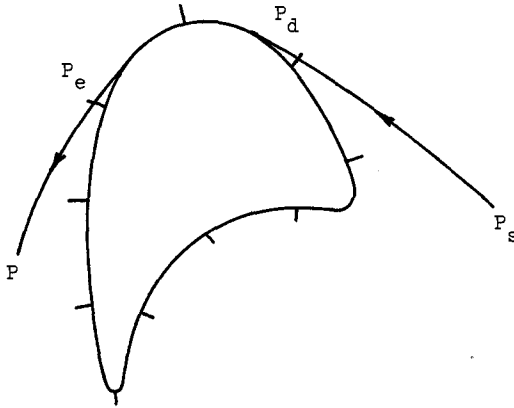
Fig. 4. Diffraction around an island of complex shape.

diffracted fields around scatterers of generalized shape. In the case
of gravity water waves β_p (32) and D_p (34) are conjectured to be
applicable at islands of more complex shape (see Fig. 4) at least when
the gradient of the bottom profile is perpendicular to the coast line.
The local variations in radius of curvature, depth, and profile shape
must then be taken into account in the proper manner in (31).

ACKNOWLEDGEMENT

REFERENCES

[1] Sager, G., Gerlands Beitr. Geophysik, 82 (1973) 210.

[2] Sager, G., ibid., 82 (1973) 309.

[3] Sager, G., ibid., 82 (1973) 361.

[4] Sager, G., ibid., 82 (1973) 505.

[5] Homma, S., Geophys. Mag., 21 (1950) 199.

[6] Vastano, A.C. and R.O. Reid, J. Marine Res., 25 (1967) 129.

[7] Lautenbacher, C.C., J. Fluid Mech., 41 (1970) 655.

[8] Kline, M. and I.W. Kay, Electromagnetic Theory and Geometrical Optics, Interscience (1965) 11.

[9] Kamke, E., Differentialgleichungen I, Akademische Verlagsgesell-schaft (1967) 440.

[10] Sommerfeld, A., Lectures on Theoretical Physics, Vol. 6, Academic Press (1964) 214.

[11] Lewis, R.M. and J.B. Keller, Asymptotic Methods for Partial Differential Equations, Courant Institute of Mathematical Sciences, New York University, EM-194 (1964) 70.

[12] Christiansen, P.L., Comparative Studies of Diffraction Processes, (to be published) 184.

[13] Longuet-Higgins, M.S., J. Fluid Mech., 29 (1967) 781.

[14] Shen, M.C., R.E. Meyer, and J.B. Keller, Phys. Fluids, 11 (1968) 2289.

[15] Keller, J.B., J. Opt. Soc. Amer., 52 (1962) 116.

CHAPTER 35

THE EFFECT OF WAVE REFRACTION OVER DREDGED HOLES

by

J M Motyka
Higher Scientific Officer
Hydraulics Research Station
Wallingford, Great Britain

and

D H Willis
Assistant Research Officer
National Research Council of Canada
Ottawa, Canada

ABSTRACT

Preliminary results are presented of a study of the beach erosion caused by wave refraction over offshore dredged holes.   A mathematical model is used of an idealised sand beach, typical of those on the English Channel and North Sea coasts of Great Britain.   Depth and side slopes of dredged area and original water depth before dredging were varied.   Beach erosion increased with increasing hole depth and with decreasing original water depth.   The effects of side slope and hole depth will be separated in future work, as will the effects of hole shape.   Beach erosion due to holes in water depths greater than half the length of "normal" waves, or a fifth of the length of extreme waves, was negligible.

INTRODUCTION

Large deposits of sand and shingle exist off the coasts of Great Britain, and the commercial exploitation of these resources for aggregate and reclamation material has become a major industry.   At present approximately 11% of the national requirement for aggregate is supplied from offshore;   this is some 15 million cubic metres per year. An additional 5 million cubic metres was won from the offshore seabed for reclamation in 1973.

There is pressure to increase this exploitation.   In Ref 1
  the Advisory Committee on Aggregates have said:

  "We think it is important that the marine sand and
  gravel industry should be encouraged to make the
  maximum possible contribution, especially as increases
  in the price of land, particularly in the South East,
  are likely to make land won sand and gravel more
  expensive, and so diminish the economic disadvantages
  of marine won aggregates."

We at the Hydraulics Research Station are involved in
offshore dredging as expert advisors to the Crown Estate
Commissioners, the public body responsible for letting
licences for dredging.   We examine dredging proposals
submitted to us by the Crown Estate Commissioners, and
advise whether or not the proposal is likely to have an
adverse effect on the adjacent coastline.   In forming our
opinion we ask ourselves four questions:

  1.   Is the dredging area far enough offshore so that
       beach drawdown into the hole will not occur?   For
       this we rely on the work of Watts in Ref 2.
  2.   Is the dredging in deep enough water that it will
       not interrupt the onshore movement of shingle?   The
       work of Crickmore, Waters and Price, Ref 3, seems to
       indicate that this must be in water of depth 18 m or
       greater for the wave climates experienced on the
       English Channel and North Sea coasts of Britain.
  3.   Does the dredging area exclude bars and banks which
       might provide some natural wave protection to the
       coast?
  4.   Is the dredged hole sufficiently far offshore and in
       deep enough water that refraction of waves over it
       will not cause significant changes in the pattern of
       alongshore transport of beach material?   This is
       the subject of the present paper.

A study of this refraction effect is under way, using a
mathematical model of an idealised beach.   This paper
presents the results of the early work on the model, and
describes the future programme of testing.

MATHEMATICAL MODEL
The mathematical model is described in Ref 4.   It
consists of two parts:

1.   The beach plan shape model, also presented in Ref 5,
     which calculates temporal changes in beach shape
     caused by alongshore sediment transport.   This
     transport is calculated from the breaking wave con-
     ditions using the Scripps Formula, as modified by
     Komar in Ref 6.

$$Q = \frac{0.045}{\gamma_s} \rho g \, H_b^2 \, Cg \, \text{Sin} \, 2\alpha_b$$

where Q = the volume rate of alongshore sediment
             transport
       γ_s = the submerged unit weight of beach
             material in place
        ρ = the mass density of water
        g = the acceleration due to gravity
        H_b = the breaking wave height
        Cg = the group velocity of the waves at breaking
        α_b = the angle between the breaking wave front
             and the beach

2.   A simplified version of the Abernethy and Gilbert
     wave refraction model is used, see Ref 7.   By
     calculating the paths of wave orthogonals over the
     nearshore seabed, this determines the non-uniform
     breaking wave conditions from the assumed uniform
     waves in deep water.

The model performs the following operations:

1. Calculates breaking wave conditions from deep water
    wave conditions by refraction over the inshore
    seabed.
2. Calculates rates of alongshore sediment transport on
    the beach from the breaking wave conditions.
3. Calculates changes in beach plan shape.
4. Distributes accretion and erosion over the inshore
    seabed.
5. Recalculates refraction and returns to 2.

TESTING PROGRAMME

In order to complete an exhaustive study of the effects on
beach plan shape of refraction over dredged holes, it
would be necessary to investigate the following 12
parameters.

1. Properties of the beach: plan shape, grain size,
    profile shape.
2. Properties of the deepwater wave climate: height,
    period, direction.
3. Properties of the dredged hole: distance offshore,
    original water depth, depth of dredging, width,
    length, and side slopes.

Several of these can be eliminated with thought.   For
example, once the beach profile is specified, so is a
relationship between the distance of the hole offshore and
the original water depth in which it is dredged.   We
therefore chose a profile composed from a number of surveyed
profiles of the sand beaches at Great Yarmouth, on the East
Coast of Britain.   The area offshore of Great Yarmouth is
one of the most heavily dredged in the country.

This decision also permitted a deepwater wave climate to be
specified, typical of that on the North Sea and English
Channel coasts of Britain.   This is summarised in Table 1

where the datum of direction is normal to the beach.

TABLE 1

DURATION (DAYS)	HEIGHT (M)	PERIOD (S)	DIRECTION (DEGREES)
$1\frac{1}{2}$	2.00	8	10
$88\frac{1}{2}$	0.41	5	20
90	0.36	5	10
90	0.35	5	- 10
$1\frac{1}{2}$	1.79	8	10
$88\frac{1}{2}$	0.47	5	10

For most of the year, wave periods are 5 sec and mean heights are less than half a metre. Initial tests indicated a need for storms in the climate and two have been specified, each of $1\frac{1}{4}$ days duration with heights of approximately 2 m and period 8 sec. Deep water wave directions were selected by trial and error to produce a net alongshore transport of beach material of 30,000 m³/yr, typical of these coasts. An infinitely long, straight beach was assumed.

Grain size of beach material is not a parameter in the alongshore transport calculation. Komar, Ref 6, believes that the effects of beach slope and grain size compensate for each other. However, in an earlier mathematical model study of the beach at Bournemouth, attempting to reproduce beach build-up against a long groyne, we found transport rates of shingle of approximately 1/10 of those predicted by the Scripps equation. Nevertheless, our idealised beach is sand and we feel justified in using the equation unmodified for grain size.

Dimensions of the dredged hole were examined in a series of preliminary tests. Varying hole length, the dimension parallel to the beach, had little or no effect on the pattern of accretion and erosion on the beach. Hole

width simply determined the location of beach erosion or
accretion, not the amount.   A rectangular hole of 880 m
length and 305 m width was therefore chosen arbitrarily.

The important hole dimensions are clearly depth and side
slopes.   In our mathematical model approach these two are
linked by the size of our refraction grid, 176 m.   Thus
for a 1 m deep hole, the steepest slope we can test is only
a quarter of the steepness of the steepest for one 4 m deep.

We are left, then, with only two parameters to test, hole
depth and original water depth, if the effect of side
slopes is not taken into account.   The effect of side
slope and hole depth will be separated in future work.

RESULTS

In Fig 1, starting from an original beach on the zero line,
the effects on beach plan shape of each element in the wave
climate are shown.   The positive ordinate indicates sea-
ward accretion and the negative ordinate landward erosion.
Clearly the storms, despite their relatively short duration,
have a much more serious effect than the long periods of
"normal" wave activity.   In fact the "normal" waves serve
to reduce the damage caused by storms.

The first tests were run for a period equivalent to 10
years, and in each case stability had been almost reached
after two years.   All subsequent results, Figs 2 and 3,
show beach plan shapes after 2 years.

As might be expected, these results show an increase in
beach erosion with increasing depth of hole, see Fig 2,
and with decreasing original water depth and distance
offshore, see Fig 3.   On the seaward boundary of the
refraction grid, in 18 m of water which represents half a
5 sec wavelength and a fifth of an 8 sec wavelengh, even
the deepest hole tested causes only 4 m of beach erosion,
see Fig 2.

PRELIMINARY CONCLUSIONS

We believe our results to be conservative, that is predict-
ing larger amounts of erosion than would occur in nature.
This is due to the fact that erosion is caused by
differences in sediment transport along the beach, and the
assumption in the refraction calculation that wave energy
cannot propagate along the wave front tends to exaggerate
these differences.

At present, dredging is not allowed shoreward of the 18 m
depth contour on sediment supply considerations.   Our
results suggest that for the North Sea and English Channel
coasts of Britain, the effects of wave refraction also
point to an 18 m minimum depth.   This is approximately
half the wavelength of the most common wave period, and a
fifth of the length of the extreme wave period;   hence it
may be possible to extrapolate our results to other
areas on a wavelength basis.

It has not been possible to separate the effects of hole
depth from those of side slopes to date.   We wish to
examine this problem in the future, to determine which is
the most important;   this will probably involve the
introduction of a much finer refraction grid in the
vicinity of the hole.   Such a fine grid will also allow
the study of holes with shapes other than rectangular.

REFERENCES

1.   "Preliminary report of the Advisory Committee on
     Aggregates", Department of the Environment, Great
     Britain, September 1973.

2.   WATTS, G M "Behaviour of offshore borrow zones in
     beach fill operations" Proceedings of the 10th
     Congress of the International Association for Hydraulic
     Research, London 1963, Vol 1 pp 17-24

3.   CRICKMORE, M J, WATERS, C B and PRICE, W A   "The
     measurement of offshore shingle movement" Proceedings
     of the 13th Conference on Coastal Engineering 1972,
     Vol II, pp 1005-1025

4.   WILLIS, D H and PRICE, W A "Trends in the application
     of research to solve coastal engineering problems" in
     "Nearshore sediment dynamics and sedimentation" edited
     by Hails and Carr, John Wiley & Son Ltd, in preparation

5.   PRICE, W A, TOMLINSON, K W and WILLIS, D H "Predicting
     changes in the plan shape of beaches" Proceedings of
     the 13th Conference on Coastal Engineering, 1972,
     Vol II, pp 1321-1330

6.   KOMAR, PAUL D "The longshore transport of sand on
     beaches" PhD thesis, University of California, San
     Diego, 1969

7.   ABERNETHY, C L and GILBERT, G "Refraction of a wave
     spectrum", Hydraulics Research Station, Report
     No INT 117, in preparation.
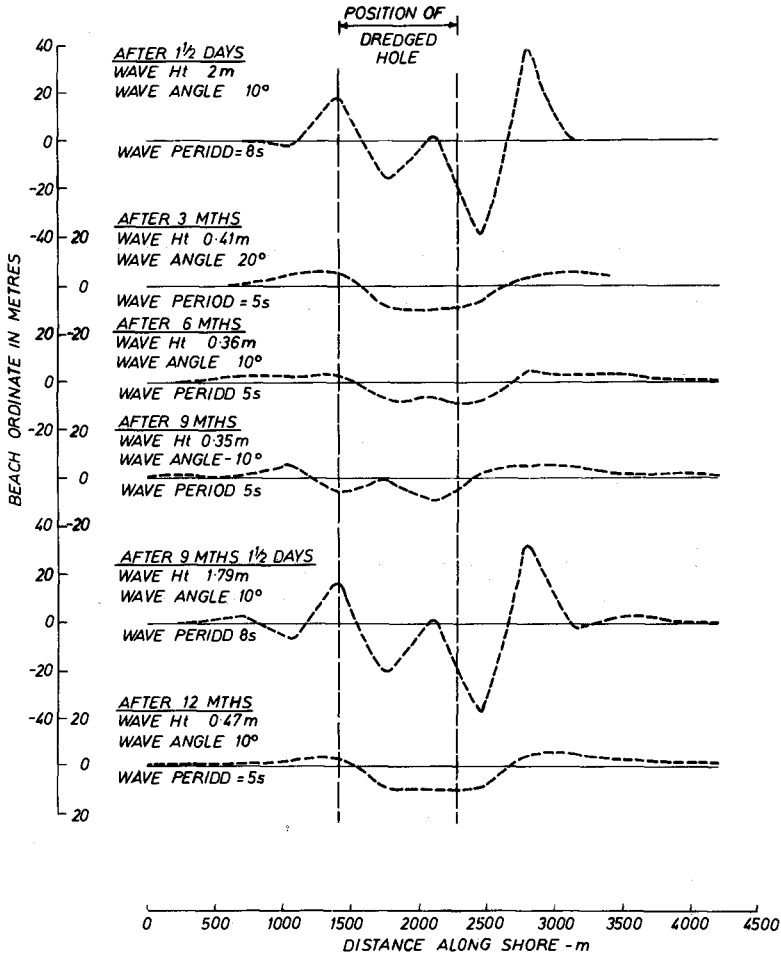
BEACH PLANSHAPE
DUE TO REFRACTION OVER 2m DEEP HOLE, 1220m OFFSHORE

FIG 1
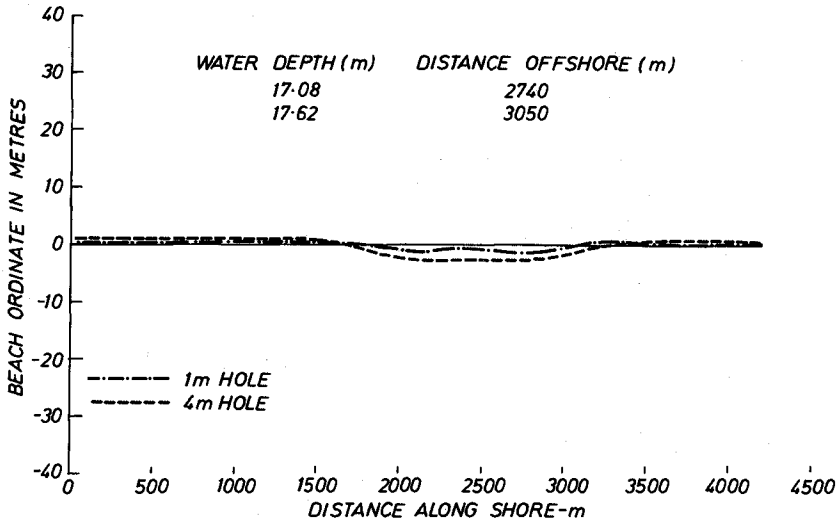
PLANSHAPE OF BEACH

DUE TO REFRACTION OVER DREDGED HOLE, 2740 m OFFSHORE

FIG 2

PLANSHAPE OF BEACH

DUE TO REFRACTION OVER 3m DREDGED HOLE
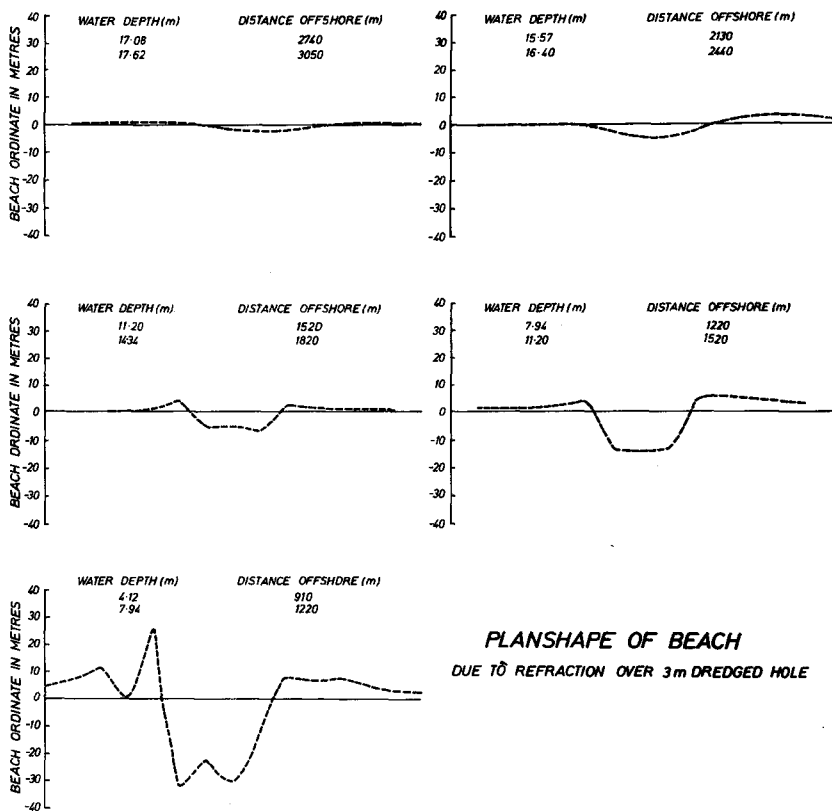
FIG 3

CHAPTER 36

WATER WAVES ON A BILINEAR SHEAR CURRENT

by

Robert A. Dalrymple[1]

Abstract

A water wave theory is presented to describe waves propagating on a
bilinear shear current flowing in the direction of the waves. The theory
is derived assuming an ideal fluid in which a current exists, having a
vertical velocity profile which varies linearly from a mean water level
velocity of U_S, an interfacial velocity U_I at depth, d, and a bottom
velocity U_B. The theory is developed first for small amplitude waves
and then extended to any arbitrary order by a numerical perturbation
technique for symmetric waves. For measured waves, an irregular form
of the theory is presented to provide a representation of these waves
for analysis.

Introduction

In the design of offshore structures, it is necessary to use water
wave theories that incorporate into their formulation a mean current, as
currents are always present under design conditions. In the past, several
techniques have been tried to incorporate the current. First, a constant
current, having the same velocity over the depth and flowing in the direc-
tion of the wave, was assumed as, for instance, in the Stream Function
wave theory (Dean, 1965). Recently, Dalrymple (1974) developed the linear
shear current theory, which extended the Stream Function wave theory by
allowing the inclusion of a current which varied linearly over the depth.
This model could be carried to any order, thus extending the analyses
of Biesel (1950) and Tsao (1959). (See also Dalrymple, 1973.)

In this paper, a better model is proposed, which fits an ambient current
with a velocity profile which varies linearly over the depth from a mean
water level velocity of U_S to an interfacial velocity, U_I at some depth,d.
From U_I, the velocity again varies linearly to the bottom velocity, U_B. By
including the interfacial velocity, the designer is allowed more flexibility
in modeling the design current. This model, the bilinear shear current theory,
is developed first for small amplitude symmetric waves and then for finite

---

[1]Assistant Professor, Department of Civil Engineering, University of
Delaware, Newark, Delaware   19711.

amplitude waves; in either case, the waves are characterized by the wave height, H, the wave period, T, the water depth, h, and the current parameters (U_S, U_I, d, U_B). A final form of the theory is presented for the representation of measured wave data, which is characterized by the measured, digitized, free surface elevations and the current parameters.

Mathematical Formulation of the Boundary Value Problem

Several assumptions must be made a priori to enable the formulation of a boundary value problem. First, the waves are assumed to be long crested, which makes the problem two-dimensional and, secondly, the waves propagate without change in form. With this last assumption, the coordinate system may be translated with the wave celerity, C, thus rendering the wave motion steady in time. Next the fluid is assumed incompressible, or mathematically,

$$\frac{\partial(U + u - C)}{\partial x} + \frac{\partial v}{\partial y} = 0 \qquad (1)$$

where U is the ambient current and (u,v) are the horizontal and vertical wave-induced water particle motions in the (x,y) directions. A stream function, $\psi(x,y)$ may now be defined by

$$\left. \begin{aligned} -\frac{\partial \psi}{\partial y} &= U + u - C \\[2ex] \frac{\partial \psi}{\partial x} &= v \end{aligned} \right\} \qquad (2)$$

Lastly, the current is assumed to be well-established and the effect of viscosity is neglected. The applicable equations of motion then are the Euler equations, Lamb (1945).

$$(U + u - C)\frac{\partial(U + u - C)}{\partial x} + v\frac{\partial(U + u - C)}{\partial y} = -\frac{1}{\rho}\frac{\partial p}{\partial x} \qquad (3)$$

$$(U + u - C)\frac{\partial v}{\partial x} + v\frac{\partial v}{\partial y} = -\frac{1}{\rho}\frac{\partial p}{\partial y} - g \qquad (4)$$

Cross-differentiating to eliminate the pressure, p, and the acceleration due to gravity, g, and substituting the stream function yields

$$-\frac{\partial \psi}{\partial y}(\nabla^2\psi) + \frac{\partial \psi}{\partial x}(\nabla^2\psi) = 0 \qquad (5)$$

where ∇^2 is the two-dimensional Laplacian operator. This equation requires that the fluid vorticity, $\nabla^2\psi$, be constant along a streamline, therefore, the equation may be integrated to yield

$$\nabla^2\psi = f(\psi) \tag{6}$$

where $f(\psi)$ is the vorticity distribution function. The classical theories of Airy (1845) and Stokes (1847) correspond to the irrotational case, $f(\psi) = 0$ everywhere. In this paper, $f(\psi)$ is assumed to be a constant in each of the two fluid regions depicted in Figure 1.

The theoretical form of the ambient shear current is expressed as

$$U(y) = \begin{cases} U_B + (U_I - U_B)(\frac{h+y}{h-d}), & \text{for } -h \le y < -d + \zeta(x) \\ U_S + (U_S - U_I)(-\frac{y}{d}), & \text{for } -d + \zeta(x) \le y \le \eta(x) \end{cases} \tag{7}$$

Here, $\zeta(x)$ and $\eta(x)$ are the displacements of the interface and the free surface due to the passage of the wave.

Substituting $U(y)$ into Equation 6 results in two differential equations:

$$\nabla^2\psi_1 = -\left[\frac{U_I - U_B}{h-d}\right] \text{ for} \begin{cases} -h \le y < -d + \zeta(x) \\ 0 \le x < L \end{cases}$$
$$\nabla^2\psi_2 = -\left[\frac{U_S - U_I}{d}\right] \text{ for} \begin{cases} -d + \zeta(x) \le y \le \eta(x) \\ 0 \le x < L \end{cases} \tag{8}$$

where L is the wave length. The subscripts on the stream functions denote the fluid regions for which they are applicable; ψ_1, the lower region and ψ_2, the surface region.

To fully prescribe the boundary value problems for ψ_1, ψ_2, boundary conditions must be specified. At the horizontal bottom, no vertical flow is allowed,

$$\frac{\partial\psi}{\partial x} = 0 \text{ on } y = -h \tag{9}$$

For periodic waves, the stream function must be periodic over a wave length.

$$\psi_i(x,y) = \psi_i(x+L,y) , i = 1, 2. \tag{10}$$

At the free surface, the pressure must be a constant. To mathematically express this condition, the Bernoulli equation, which is valid along a stream-line, is used:
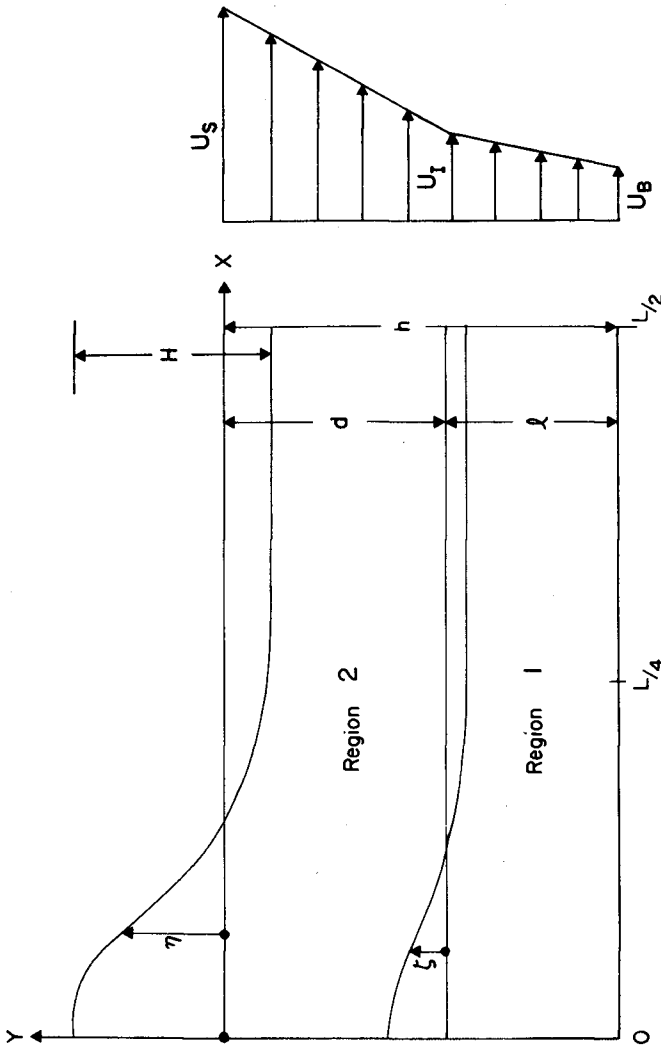
FIGURE 1   DEFINITION SKETCH FOR A WAVE ON A
BILINEAR CURRENT, AS SEEN BY OBSERVER
MOVING WITH THE WAVE

$$y + \frac{(U + u - c)^2 + v^2}{2g} + \frac{p}{\rho g} = Q(\psi), \text{ a constant.} \tag{11}$$

The boundary condition, called the Dynamic Free Surface Boundary Condition (DFSBC), then is expressed on the free surface streamline as

$$\eta + \frac{\left[\left(\frac{\partial \psi_2}{\partial x}\right)^2 + \left(\frac{\partial \psi_2}{\partial y}\right)^2\right]}{2g} = \bar{Q}, \text{ a constant on } y = \eta(x) \tag{12}$$

Also on the free surface, it is specified that the presence of the wave does not change the mean water level; that is, $\eta(x)$ must have a zero mean.

$$\frac{1}{L} \int_0^L \eta(x) \, dx = 0 \tag{13}$$

For small amplitude waves, it is convenient to use an alternative form of the condition, called the Kinematic Free Surface Boundary Condition (KFSBC), which requires the free surface to be a streamline,

$$-\frac{\partial \psi}{\partial y} \frac{\partial \eta}{\partial x} = \frac{\partial \psi}{\partial x} \text{ on } y = \eta(x) \tag{14}$$

Note that this requirement is true by definition when using a stream function representation of the fluid flow.

Across the interface between the two fluid regions, the velocities and pressures must be continuous. From the Bernoulli equation applied to the uppermost streamline in Region 1 and the lowermost streamline in Region 2, the pressures across the interface will be continuous if the horizontal and vertical velocities are continuous. Therefore, the interfacial boundary conditions may be specified as

$$\left.\begin{array}{c} -\dfrac{\partial \psi_1}{\partial y} = -\dfrac{\partial \psi_2}{\partial y} \\[2ex] \dfrac{\partial \psi_1}{\partial x} = \dfrac{\partial \psi_2}{\partial x} \end{array}\right\} \text{ on } y = -d + \zeta(x) \text{ for all } x \tag{15}$$

Finally, it is required that the interfacial displacement have a zero mean

$$\frac{1}{L} \int_0^L \zeta(x) \, dx = 0 \tag{16}$$

For a small amplitude wave, it is again convenient to use the alternative condition

$$-\frac{\partial\psi}{\partial y}\frac{\partial\zeta}{\partial x} = \frac{\partial\psi}{\partial x} \quad \text{on } y = -d + \zeta(x) \tag{17}$$

Small Amplitude Bilinear Shear Current Theory

For small waves, all nonlinear terms in the boundary conditions are linearized using the rationale that terms of $O(H/L)$ are small, therefore, terms of $O((H/L)^2)$ are negligible.

The free surface and interfacial displacements are assumed to be sinusoidal in x and given by

$$\eta(x) = \frac{H}{2} \sin kx$$

$$\tag{18}$$

$$\zeta(x) = \frac{b}{2} \sin kx$$

where k is the wave number ($k = 2\pi/L$).

The stream functions are assumed to be of the following form

$$\psi_1(x,y) = -(U_B - C)y - (U_I - U_B)\frac{(hy + \frac{y^2}{2})}{(h-d)} + D \sinh k(h+y) \sin kx \tag{19}$$

$$\psi_2(x,y) = -(U_S - C)y - (U_S - U_I)\frac{y^2}{2d} + (A \sinh ky + B \cosh ky) \sin kx \tag{20}$$

These stream functions satisfy the periodicity requirements and the bottom boundary condition. The coefficients, A, B, and D must now be found to satisfy the remaining boundary conditions.

Using the KFSBC, Equation 14, and retaining only the linear terms.

$$B = (U_S - C)\frac{H}{2} \tag{21}$$

The DFSBC must be satisfied at the free surface. In a linear analysis, the DFSBC is expanded in a Taylor Series about $y = 0$ and analytically

continued up to $y = \eta$. Keeping only the first term,

$$\overline{Q} = \left\{ \frac{\left[\left(\dfrac{\partial \psi_2}{\partial y}\right)^2 + \left(\dfrac{\partial \psi_2}{\partial x}\right)^2\right]}{2g} \right\} + \eta \frac{\partial}{\partial y} \left\{ y + \left[\frac{\left(\dfrac{\partial \psi_2}{\partial x}\right)^2 + \left(\dfrac{\partial \psi_2}{\partial y}\right)^2}{2g}\right] \right\} \text{on } y = 0 \qquad (2\ )$$

Substituting for ψ_2 and retaining only the linear terms,

$$A = \frac{H}{2} \frac{(g + (U_S - C)(U_S - U_I)/d)}{(U_S - C)k} \qquad (23)$$

in order that $\overline{Q}$ be a constant.

At the interface, the linear kinematic condition can be written as

$$\frac{\partial \psi_1}{\partial x} = (U_I - C)\frac{\partial \zeta}{\partial x} \quad \text{on } y = -d \qquad (24)$$

or

$$D = \frac{(U_I - C)b}{2\sinh k\ell} \qquad (25)$$

The requirement that the vertical velocities be continuous across the interface yields

$$D = \frac{-A \sinh kd + B \cosh kd}{\sinh k\ell} \qquad (26)$$

The last boundary condition to be satisfied is the equality of the horizontal velocities across the interface,

$$\frac{(U_I - U_B)}{\ell} \frac{b}{2} - Dk \cosh k\ell = \frac{(U_S - U_I)}{d} \frac{b}{2} - (Ak \cosh kd - Bk \sinh kd) \qquad (27)$$

Substituting for $\frac{b}{2}$, D, and B in terms of A yields, after some algebra,

$$\left[\left[\frac{(U_S-U_I)}{d} - \frac{(U_I-U_B)}{\ell}\right]\frac{1}{(U_I-C)} + k \coth k\ell\right]\left[(U_S-C)^2 - \left[g + (U_S-C)\frac{(U_S-U_I)}{d}\right]\frac{\tanh kd}{k}\right]$$

$$= g + (U_S-C)(U_S-U_I)/d - (U_S-C)^2 k \tanh kd. \tag{28}$$

This is the dispersion relationship which relates the wave number, k, to the given characteristics of the wave and current.

The final forms of the stream functions are

$$\psi_1(x,y) = -(U_B-C)y - (U_I-U_B)(hy + \frac{y^2}{2})/\ell + \frac{H}{2}\left[(U_S-C)\cosh kd - \frac{(g + (U_S-C)(U_S-U_I)/d)}{(U_S-C)k}\right.$$

$$\left.\sinh kd\right]\frac{\sinh k(h+y)}{\sinh k\ell}\sin kx \tag{29}$$

$$\psi_2(x,y) = -(U_S-C)y - \frac{(U_S-U_I)}{2d}y^2 + \frac{H}{2}\left[(U_S-C)\cosh ky + \frac{(g + (U_S-C)(U_S-U_I)/d)}{(U_S-C)k}\sinh ky\right]$$

$$\cdot \sin kx \tag{30}$$

The small amplitude form of the bilinear shear current theory, Equations (27), (28), and (29), generalized the work of a number of previous investigators. For example, Sir G. I. Taylor (1955), investigating wave breaking by bubble breakwaters in infinitely deep water, treated the case for $U_B = U_I = 0$ and $h \to -\infty$. Thompson (1949), earlier treated the case of a shear current in the lower layer. Binnie and Cloughley (1971) investigated the problem of stationary waves (C=0) on the same current profile, i.e., $U_S = U_I$. All of the results of these earlier investigators are a special case of the bilinear shear current theory, as, in fact, is the wave propagating in still water.

Finite Amplitude Bilinear Shear Current Theory

To extend the bilinear shear current theory to large waves, that is, when (H/L) is not necessarily small, all the nonlinear terms in the boundary conditions must be retained and, further, the free surface conditions must be applied directly on the free surface. To do this efficiently, some of the boundary conditions are specified in a least squares form. The boundary conditions are thus rewritten as:

$$E_1 = \frac{2}{L}\int_0^{L/2}(Q(x) - \bar{Q})^2 dx \tag{31}$$

$$\text{where } \bar{Q} = \frac{2}{L}\int_0^{L/2}Q(x) dx \text{ on } y = \eta(x)$$

$$E_2 = \frac{2}{L} \int_0^{L/2} \eta(x) \; dx \tag{32}$$

$$E_3 = \eta(0) - \eta(\tfrac{L}{2}) - H \tag{33}$$

$$E_4 = \frac{2}{L} \int_0^{L/2} \left(-\frac{\partial \psi_2}{\partial y} + \frac{\partial \psi_1}{\partial y} \right)^2 dx \tag{34}$$

$$E_5 = \frac{2}{L} \int_0^{L/2} \left(\frac{\partial \psi_2}{\partial x} - \frac{\partial \psi_2}{\partial x} \right)^2 dx \tag{35}$$

and
$$E_6 = \frac{2}{L} \int_0^{L/2} \zeta(x) \; dx \tag{36}$$

The error terms E_1, E_4, and E_5 are the mean square error to the DFSBC and the interfacial conditions. The E_2, E_3 and E_6 terms are the constraint terms on the solution, stating that the mean water level remain unchanged, the wave height be specified as H, and the interface not be displaced by the wave. For an exact solution to the boundary value problem then, all the E_i (i=1,6) would be zero. Note also that the symmetry of the wave has been used to reduce the range of the integration to only L/2.

It is convenient to define an objective function, OF, which must be minimized towards zero, using a Lagrange multiplier approach. (See, for example, Hildebrand, 1965).

$$OF = E_1 + \lambda_1 E_2 + \lambda_2 E_3 + E_4 + E_5 + \lambda_3 E_6 \tag{37}$$

where the λ_i (i=1,3) are the Lagrange multipliers. Again, if OF is zero, or very small, the problem is solved.

The stream function for each region is assumed to be given by a series expansion of the following form

$$\psi_1 (x,y) = - (U_B - C)y - (U_I - U_B)(hy + y^2/2)/(h-d) + \sum_{n = NN + 2}^{NN + \left(\frac{NN-2}{2}\right) + 1} X(n)$$

$$\cdot \; \sinh k_n \, (h+y) \cos k_n x \tag{38}$$

where $k_n = 2(n - (NN+1)) \; \pi/L$

$$\psi_2 (x,y) = -(U_S - C)y - (U_S - U_I)\frac{y^2}{2d} + \sum_{n = 3,5}^{NN-1} (X(n) \; \sinh \frac{(n-1)\pi y}{L} + X(n+1) \cos h \frac{(n-1)\pi y}{L})$$

$$\cdot \cos \frac{(n-1)\pi x}{L} \tag{39}$$

The parameter, NN, is related to the order of the wave theory; NN=2·order +2. These stream functions satisfy the governing differential equations, (8), and the periodicity and bottom boundary conditions exactly. The X(n) are unknown constant coefficients, which then must be chosen to reduce OF towards zero. The other unknowns are the wave length, L, and the value of the free surface and interface streamlines, $\psi_2(x,\eta)$ and $\psi_2(x, -d+\zeta)$.

The free surface and interface displacements are obtained by solving (39) by substituting the appropriate value of the streamline.

To solve for the unknowns, a trial set of X(n) are necessary. These can be obtained by neglecting the shear current in the upper layer, keeping only the U_S term, assuming a first order wave, setting $\psi_2(x,\eta) = 0$ and using the wave length obtained from (28). The trial values of X(3) and X(4) are then obtained from (39), by examining the wave crest, (y = H/2, X = 0) and the wave trough, (y = -H/2, x = L/2). The remaining X(n) are set to zero.

With these trial X(n), the value of OF is quite large. An iterative numerical perturbation technique is thus used to minimize OF with respect to the X(n). To facilitate this, the objective function is quasi-linearized by expanding all terms of OF at iteration (j + 1) in a first order Taylor series in X´(n) at iteration (j) where X´(n) are small changes in the X(n).

$$OF^{j+1} = OF^{j} + \sum_{n=1}^{NN + \left(\frac{NN-2}{2}\right) + 1} \frac{\partial (OF^{j})}{\partial X(n)} \; X´(n) \tag{40}$$

Next, OF^{j+1} is minimized with respect to the X(n) and the Lagrange multipliers. This results in (3NN+6)/2 equations for the same number of unknowns. By solving these equations by matrix techniques for the X´(n), new values of the X(n) are obtained.

$$X(n)^{j+1} = X(n)^{j} + \alpha \, X´(n)^{j} \tag{41}$$

Substituting these new values into OF results in a smaller error. This procedure is then iterated until OF is acceptably small. Typically this requires about twenty iterations. Note that α in (41) is, in general, near one; however, for near breaking waves, an instability results if α is not less than one-half.

Analysis of a Measured Wave Propagating on a Bilinear Shear Current

The bilinear current wave theory may also be modified for use in the analysis of measured wave data where the free surface displacement and the current is known and can be approximated by a bilinear shear current. The governing equations and the boundary conditions at the interface are the same as before. The kinematic free surface condition is modified so as to ensure the predicted free surface displacement, η_{p_i}, at each digitized

time point, i, corresponds to the measured free surface displacement, η_{m_i}. There are assumed to be I data points corresponding to the total free surface profile.

The stream functions for the two regions are

$$\psi_1(x,y) = -(U_B-C)y - (U_B-U_I)\frac{(hy+y^2/2)}{(h-d)} + \sum_{n=3NN+5}^{4NN+5} X(n) \sinh\frac{2\pi m_n(h+Y)}{L}$$

$$\cdot \cos\left(\frac{2\pi m_n t}{T} + X(3m_n + 3)\right) \tag{42}$$

$$\psi_2(x,y) = -(U_S-C)y - (U_S-U_I)y^2/2d + \sum_{n=1,2..}^{NN}\left[X(3n+1)\sinh\frac{2n\pi y}{L} + X(3n+2)\cosh\frac{2n\pi y}{L}\right]$$

$$\cdot \cos\left[\frac{2n\pi t}{T} + X(3n+3)\right] \tag{43}$$

where $m_n=n - (3NN+4)$ and NN is now the order of the wave theory. The unknowns again are the X(n), and L, T, $\psi_2(x,\eta)$, $\psi_2(x, -d+\zeta)$, which are defined as X(1), X(2), X(3) and X(3NN+4) for convenience.

The stream functions are periodic in L, ψ_1 satisfies the bottom boundary condition, and a phase angle, X(3n+3), necessary to fit an irregular water surface, is introduced.

To determine the X(n) which best satisfies the remaining boundary conditions, an objective function is defined:

$$OF^j = \frac{1}{I}\sum_{i=1}^{I}(Q_i-\bar{Q})^2 + \frac{1}{I}\sum_{i=1}^{I}\left(-\frac{\partial\psi_2}{\partial y} + \frac{\partial\psi_1}{\partial y}\right)_i^2 + \frac{1}{I}\sum_{i=1}^{I}\left(\frac{\partial\psi_2}{\partial x} - \frac{\partial\psi_1}{\partial x}\right)_i^2 + \frac{1}{I}\sum_{i=1}^{I}(\eta_m-\eta_p)_i^2$$

$$+ \frac{1}{L}\int_0^L \zeta(x)\, dx \tag{44}$$

Here the integral form for least squares is replaced by a summation over the I data points. Again, if OF is equal to zero, the boundary value problem would be solved exactly. The numerical perturbation procedure is exactly the same as in the previous case, given a trial set of X(n) , obtained as before, a better set of coefficients is found by minimizing OF^{j+1} in its quasi-linearized form with respect to all the X(n) , and solving for the $X'(n)$ which are added to the $X(n)^j$ to obtain the $X(n)^{j+1}$. This procedure is repeated until O^j is acceptably small.

In this application it is assumed that only wave length and the coefficients are affected by the region below the interface; therefore, in the least squares procedure, the wave period, T, and the NN phase angles are determined solely by the fit to the free surface conditions.

Results and Comparisons with Previous Theories

    Due to the lack of laboratory or field data for the empirical verification
of either form of the bilinear shear current theory, analytic validity
must be used to verify the theories. As an example, a shallow water wave
was generated propagating on a bilinear shear current flowing against the
wave direction. In Table 1, the errors to the boundary condition at the free
surface and the interface are given as well as the characteristic values of
the wave and current. The maximum error occurs in the mean displacement of
the interface, with an error, in this case, of 0.0689 ft. (0.021m), which is
acceptably small. More iterations or terms in the series solution reduces
the error further, thus substantiating the validity of the solution.

    Table 1. Dimensionless Errors to Boundary Conditions of a Shallow Water
              Wave Propagating Against a Bilinear Shear Current

    Given Data: H = 6.29 ft. (1.92m), T = 10 sec., h = 10.0 ft. (3.05m),

                 U_S = -1.0fps (-0.305m/sec.), U_I = -0.2fps (-0.06m/sec.)

                 at d = 5.0 ft. (1.52m), U_B = 0.0fps.

                 Twelfth order wave theory with 12 iterations, with resulting
                 wave length of 201.59 ft. (61.44m).

E_1/h	E_2/h	E_3/h	E_4/c^2	E_5/c^2	E_6/h
(Eq.31)	(Eq.32)	(Eq.33)	(Eq.34)	(Eq.35)	(Eq.36)
2.44×10^{-6}	2.37×10^{-3}	1.62×10^{-3}	5.30×10^{-6}	1.57×10^{-6}	6.89×10^{-3}

    To illustrate the necessity of an adequate representation of both the wave
and the current, a comparison was made between the bilinear shear current,
the linear shear current and the Stream Function wave theories. For
each theory, a 50-foot (15.2m) high wave was generated in 100 feet (30.48m)
of water with a 3.0fps (1.9m/sec.) mean water level current. The difference
between a constant current (Stream Function) velocity profile and the bilinear
velocity profile (U_I=U_B=0 and d=25 feet (7.62m)) under the wave crest is quite
large and would obviously result in a vast disparity in wave forces. The linear
shear current theory is shown in both its linear and finite amplitude form.
The finite amplitude theory compares more favorably with the bilinear theory
than does the Stream Function as it is a better model to the bilinear current.
The linear theory results in quite large errors as it is unable to represent
the wave profile correctly. These data are shown in Figure 2.

    Finally, the irregular form of the bilinear theory was compared with the
irregular forms of the linear shear current theory (Dalrymple, 1974) and
the Stream Function theory (Dean, 1965). The measured wave was taken from
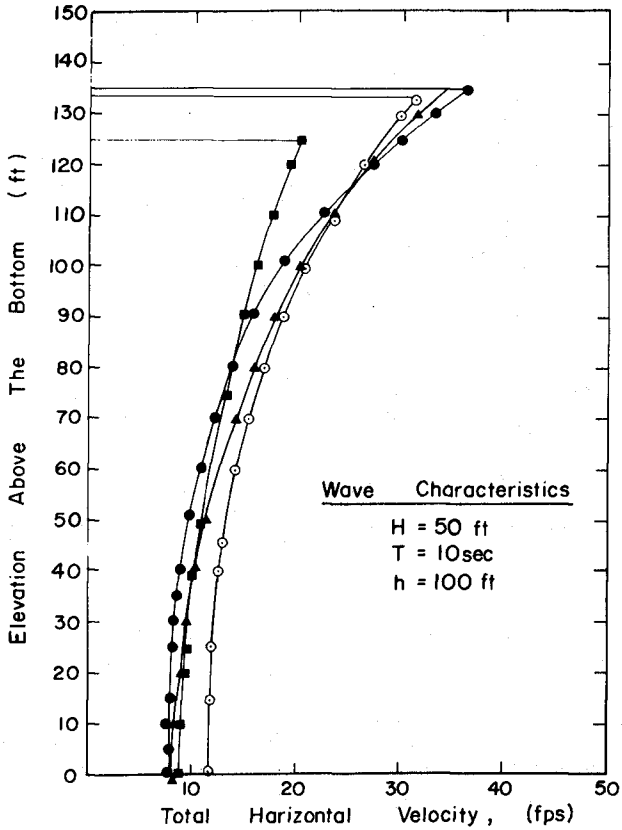
FIGURE   2   COMPARISON   OF   LINEAR   AND   BILINEAR
             HORIZONTAL   VELOCITY   PROFILES   UNDER
             THE   CREST   OF   THE   CASE   A   WAVE
             FOR   3   FPS   CURRENT   AT   STILL   WATER
             LEVEL   (y = 0)

Dean (1965), his Figure 5, and represents a wave 39 feet (11.89m) in height with a 14-second period propagating in 98 feet (29.9m) of water. For the Stream Function theory, no current was assumed, for the linear shear current theory, $U_S=2.0$fps (.61m/sec.), $U_I \neq U_B=0$, and d=25 feet (7.62m). The representation of the free surface and the fits to the boundary conditions were approximately the same in magnitude for all of the wave models; however, the differences in the predicted currents under the wave crest are quite significant. Also, the wave lengths of the predicted waves varies with the velocity profile as is shown at the top of Figure 3. With the exception of the small amplitude wave theory, the bilinear shear current has the shortest wave length; it also has the less current over the water depth. The more current over the water depth, the longer the wave (or the more the influence of the current on the wave).

Conclusions

Three representations of water waves propagating on a bilinear shear current flowing in the direction of the wave have been presented. As has been shown the models are analytically valid. The empirical validity awaits adequate field or laboratory studies.

The importance of including the correct form of the ambient current is to be emphasized. There are large disparities in maximum velocities and wave length for the same waves propagating on different currents, which would be greatly enhanced in wave force calculations (as the drag force is proportional to $(U + u)/U + u/)$.

Acknowledgments

FIGURE 3   MEASURED   WAVE   FIT   BY   STREAM   FUNCTION   WAVE
            THEORY   AND   LINEAR   AND   BILINEAR   SHEAR   CURRENT
            MODELS,   WITH   TOTAL   HORIZONTAL   VELOCITY   PROFILES
            PREDICTED   UNDER   WAVE   CREST.

References

Airy, G. B., "Tides and Waves," Enclyclopedia Metropolitan, Vol. 5, p. 241-396,
    1845.

Biesel, F., "Etude Théorique de la Houle en Eau Courante," La Houille Blanche,
    No. 5A, p. 279-285, 1950.

Binnie, A. M. and T. M. G. Cloughley, "The Lengths of Stationary Waves on
    Flowing Water," J. Hydraulic Research, Vol. (9), No. 1, p. 35-41, 1971.

Dalrymple, R. A., "Water Wave Models and Wave Forces with Shear Currents,"
    Tech. Report No. 20, Coastal and Ocean Engineering Lab, University of
    Florida, Gainesville, 163 pp., 1973.

Dalrymple, R. A., "A Finite Amplitude Wave on a Linear Shear Current," J. Geo-
    physical Research, Vol. 79, No. 27, Sept. 20, 1974.

Dean, R. G., "Stream Function Representation of Nonlinear Ocean Waves," J. Geo-
    physical Research, Vol. 70, No. 18, Sept. 15, 1965, p. 4561-4572.

Hildebrand, F. B., "Methods of Applied Mathematics," 2nd Ed., Englewood Cliffs:
    Prentice-Hall, Inc., 362 pp., 1965.

Stokes, G. G., "On the Theory of Oscillatory Waves," Trans. Camb. Phil. Soc.,
    Vol. 8, p. 441-455, 1847.

Taylor, G. I., "The Action of a Surface Current Used as a Breakwater," Proc.
    Royal Soc., A.231, p. 466-478, 1955.

Thompson, P. D., "The Propagation of Small Surface Disturbances Through Rotational
    Flow," Annals, N.Y. Academy of Science, Vol. 51, Art. 3, p. 463-474, 1949.

Tsao, S., "Behavior of Surface Waves on a Linearly Varying Current," Moskov.
    Fiz.- Techn. Inst. Issled. Mekhi Pril. Mat., Vol. 3, p. 66-84, 1959.

CHAPTER 37

COMPUTER AID FOR OPTIMUM DESIGN OF TSUNAMI WAVES

Toshio Iwasaki
Professor of Tohoku University

Abstract

The tsunami process of their generation and propagation to the
near-coast offshore region is discussed. Purpose is to give optimum
configurations of tsunami waves of large magnitude, which can be used
as boundary conditions for the analysis of the dynamic process near
the shore or around structures in coastal zone.
   They are obtained by numerical computations along the southern
coast of the Hokkaido and the Sanriku Coast for various tsunami sources
set on the continental shelf facing to the Japan Submarine Trench.
Dispersive nature of the tsunamis seems to make the problem very compli-
cated.   However statistical results thus obtained can be accepted for
the base of design of structures.

INTRODUCTION

In 1933 a large tsunami had attacked the Sanriku Coast.   Since
then construction of counter measures against tsunami has been continued
there, which was accelerated by the experience of the Chilean Earthquake
Tsunami in 1960.   Now in 1974, almost all lowland areas are protected by
sea walls, revetments and dikes.   Design method used for such structures
was conventional such that their height was determined by maximum traces
of the inundation of some peculiar tsunami selected from past records
with or without some margin.   This method seems to follow the technique
of the river engineering for the design of river embankments.   However
flow direction against their horizontal alignment are completely dif-
ferent.   So their functions against tsunamis are doubtful if many dynamic
phenomena such as harbour resonance, shoaling, runnp and overtopping are
not examined.
   Basically, tsunami waves are generated by the sea bottom dislocation
in consequence of underwater earthquake and are considered as transient
waves.   Especially the source regions of tsunamis which attacked the
Japan lslands were ordinally at the western slope of the Japan Submarine
Trench and the distance to the coast was nearly the same order of the
breadth of the source.   Consequently tsunamis are still in the dispersive
process even at the coastline.   Moreover these waves are transformed by
reflection and refraction superposed by the shelf resonance and the edge
waves.   So that it is extremely difficult to estimate the tsunami wave
configurations for analysis of dynamic nature when intruding the coastal
area.
   Thus the tsunami process can be divided into two, one is the process
of generation and propagation to the region such as harbour entrance or
just off the coastal beach, where the depth is about 100 or 200 meters,
say.   We call this region near-coast offshore region.   The other is the
process nearer than this region.
   This paper concerns to the former.   Purpose is to give optimum

configurations of tsunami waves in the near-coast offshore region which will make possible the analysis of the second process for the design of structures against tsunamis. Firstly the idea of designed tsunami was proposed. Then the dimensions of the sourse areas were calculated, which enabled to construct the mathematical models for several kinds of tsunami magnitude and source locations.

DESIGNED TSUNAMI

K. Iida had published historical records of tsunamigetic earthquakes during 1868 and 1962 as shown in Table 1.[1] Up to date, selected tsunamis for the design of protection works on the Sanriku Coast were the Sanriku Large Tsunami in 1933 and the Chilean Earthquake Tsunami in 1960 which

Table 1

Maximum Run-up	Japan			Sanriku Coast			Magnitude m
	Numbers of generation	Summation	Average return period	Numbers of generation	Summation matio	Average return period	
$0.0 - 0.63^m$	37	84	1.1	21	44	2.1	-1
0.63- 1.25	24	47	2.0	11	23	4.4	
1.25- 2.50	10	23	4.1	5	12	7.8	0
2.5 - 5.00	6	13	7.2	3	7	13.4	1
5.0 -10.0	4	7	13.4	2	4	23.1	2
10.0 -20.0	1	3	31.3	0	2	47.6	3
20.0-40.0	2	2	47.6	2	2	47.6	4

magnitudes proposed by Imamura were both 3. This recurrence interval is 31.3 years in Japan and 47.6 years in the Sanriku Coast as shown in Table 1. As such recurrence interval is considered as proper by river engineers, it may be chosen also for the standard design of tsunami structures. Then budget balance of the amount of investments against the benefit may become possible.

THE SOURCE AREAS OF THE TSUNAMIS

The wave sources are usually assumed as elliptic which dimensions can be estimated by the following equations.

$$m=2.61 M - 18.44 \tag{1}$$
$$M=6.27 + 0.76 \log_{10} \ell \tag{2}$$
$$\varepsilon=\tanh \left[1.5 \tanh \left((\frac{\pi}{2012})^{1/2} \cdot \ell^{2/3}\right)\right) \tag{3}$$
$$2a=\ell/\varepsilon \tag{4}$$
$$2b=\ell \cdot (1 - \varepsilon^2)^{1/2} /\varepsilon \tag{5}$$
$$S=\pi \, ab \tag{6}$$
$$\log_{10} E_t=0.6m + 11.4 - \log_{10} 9.8 \tag{7}$$

m and M are the magnitudes of the tsunami and the earthquake respectively.

ε, ℓ, a, b, S are the eccentricity, the distance between foci in km, the half length of the major axis in km, that of the minor axis in km and the area of the source in square km respectively. And E_t is the tsunami energy in ton-meter units.

Such ellipse has been proposed by Iida as the aftershock area of earthquake. However Dr. T. Hatori analysed all tsunami records around Japan during 1959 and 1968 using the adverse refraction diagrams and concluded that aftershock area was roughly equal to tsunami source area.[2] This is checked here in fig.1 where the relationship between ℓ and M is shown. Full circles were obtained from the wave source ellipses obtained by Hatori including other materials since 1929. Iida (1959)[3] and Wilson (1962)[4] proposed empirical equations for aftershock areas. It can be said that wave sources are usually larger than aftershock areas. However the discrepancy of these equations from the data gives overestimate around M of 8.0 which is the most important magnitude for the design purpose. So the relationship is adjusted as given in Eq. (2).

Fig. 2 shows the relationship between the eccentricity ε and ℓ in which full circles are plotted again from Hatori's data. Data are scattered. However Eq.(3) which was presented by Wilson may be used successfully to represent this relationship.

Eq.(1) represents the relationship between tsunami and earthquake magnitudes m and M proposed by Iida and is used in general. And also the relations between tsunami magnitude m and tsunami energy E_t (erg) are shown in fig.3 where full circles are obtained from various literatures given by Japanese scientists. The straight line shows Eq.(7) given by Dr. R. Takahashi (1950) which expresses average values although data are remarkably scattered.[5]

Regional pattern of the sea bottom movement is most difficult to estimate as depth is over two thousand meters and there are many hypothesis about it. For example, one model is given such that the longer axis as a fault line and the linear distribution of the bed displacement from zero at the edges to some extent at the fault line which are upheaval on one side and downthrust on the other side. Other models are given by optimum estimation to realize the most favourable wave hight distribution along coasts for actual records by numerical tests. However a simple uniform distribution of upheaval is used here tentatively, which is given by the following equation.

$$\eta_{max} = \sqrt{\frac{2E_t}{w_o S}} \qquad (8)$$

η_{max} is the maximum dislocation and w_o is the unit weight of the sea water. The time history is assumed as linear.

Using equations of (1) to (8), dimensions of tsunami sources and the amount of upheaval are calculated for various magnitudes of earthquake or tsunami. Table 2 shows three examples which are used for mathematical models in the following.
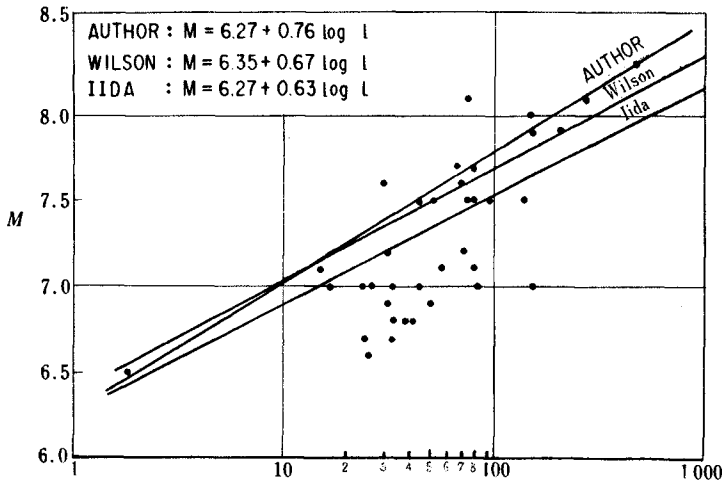
Fig.1. Relationship of Earthquake Magnitude M to the Distance between Foci.
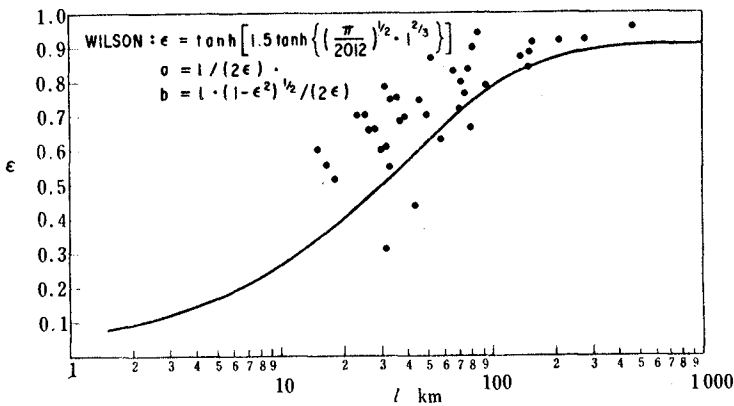
Fig.2 Relationship of Eccentricity of Source Region to the Distance between Foci.
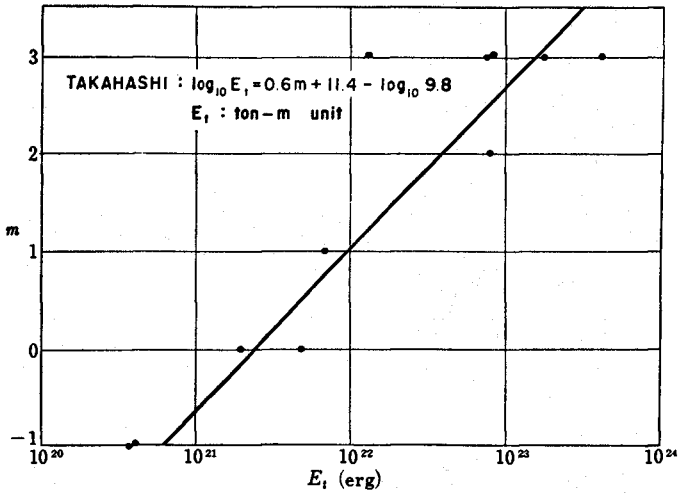
Fig.3   Relationship of Earthquake Energy E_t (erg)
        to Tsunami Magnitude m.
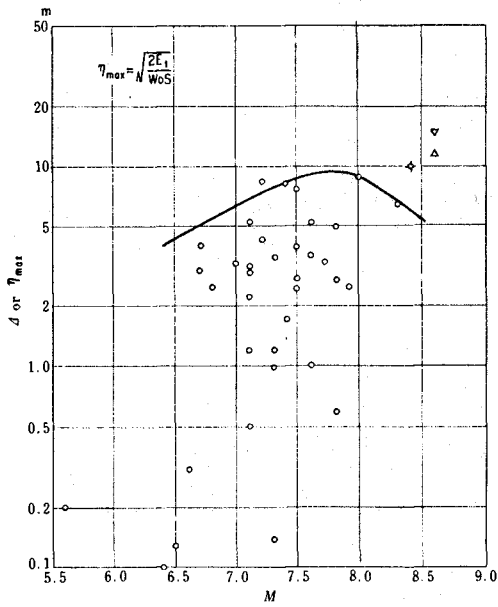
Fig.4   Relationship of Maximum Dislocation
        η_{max} to Earthquake Magnitude M.

Table 2

m	M	E_t (ton-m)	a(km)	b(km)	η_{max} (m)
1	7.45	1.000×10^{11}	32.61	27.35	8.534
2	7.85	3.985×10^{11}	70.72	42.28	9.301
3	8.23	1.585×10^{12}	202.00	89.77	7.535

In fig. 4 the relationship between the maximum dislocations η_{max} and the earthquake magnitudes M thus computed is shown by a curve with plotted data of white circles given by Wilson for the resultants of maximum horizontal and vertical ground displacements Δ. Although they are not the same definition, our estimation is certified to give reasonable results for the design purpose. The maximum three points of M of 8.5 were obtained in the Mino-Owari earthquake in Japan (1891), Assam earthquake in India (1897) and the Alaskan earthquake in USA (1899). It seems curious that our estimation has the maximum dislocation of about 10 meters at the magnitude of 7.8, however the resulted maximum water elevation increases monotonously with the magnitude as shown afterwards.

NUMERICAL COMPUTATION SCHEME AND THE BOUNDARY CONDITIONS

Basic equations are;

$$\frac{\partial M}{\partial t} + \frac{M}{h+\zeta-\eta} \cdot \frac{\partial M}{\partial x} + \frac{N}{h+\zeta-\eta} \cdot \frac{\partial M}{\partial y} = -g(h + \zeta - \eta)\frac{\partial \zeta}{\partial x} - \frac{\tau_{bx}^*}{\rho_w} \tag{9}$$

$$\frac{\partial N}{\partial t} + \frac{M}{h+\zeta-\eta} \cdot \frac{\partial N}{\partial x} + \frac{N}{h+\zeta-\eta} \cdot \frac{\partial N}{\partial y} = -g(h + \zeta - \eta)\frac{\partial \zeta}{\partial y} - \frac{\tau_{by}^*}{\rho_w} \tag{10}$$

$$\frac{\partial \zeta}{\partial t} - \frac{\partial \eta}{\partial t} = -(\frac{\partial M}{\partial x} + \frac{\partial N}{\partial y}) \tag{11}$$

in which x, y are the horizontal orthogonal axis. The total depth H is the undisturbed water depth h plus the surface deviation ζ minus the vertical upheaval of the sea bottom η, then

$$H = h + \zeta - \eta \tag{12}$$

In the long-period waves the velocity distributions along the vertical to the still water surface can be assumed uniform and are expressed by U and V for x and y directions. Then the volume flux per unit width are expressed by M=UH and N=vH respectively.

τ_{bx}^* and τ_{by}^* are (x, y) components of the bottom friction and are expressed by

$$\vec{\tau}_b = \rho_w \gamma_b^2 \mathbf{V} |\mathbf{V}| \tag{13}$$

where $\mathbf{V}$ is the velocity vectors, ρ_w is the density of water and γ_b^2 is

the friction facter and is taken as 2.6 x 10^{-3} c.g.s. tentatively.

Procedures to make up the finite-difference schemes are basically the same proposed by Dr. Hino and not described here (1972)[6]. Discharge flux M and N and water levels ζ are computed at different grid points shown in fig. 5 in a staggered scheme, which computations are alternative in the time step Δt.

Fig. 6 shows the schematic domain to be calculated. ABOCD is the boundary in the sea and DEA is the coastal boundary. In deep sea linear long waves of negligible amplitude can be assumed, then characteristics are derived for progressive and retrogressive waves following to Dr. Kajiura[7],

$$z^{\pm} = \frac{Q}{bc} \pm \zeta = const \qquad (14)$$

in which c is the wave celerity and b is the breadth. Eq.(14) can be transformed as

$$\text{for the positive x direction} \qquad \frac{M}{c} + \zeta = z_{M+}$$

$$\text{for the negative x direction} \qquad \frac{M}{c} - \zeta = z_{M-}$$

$$\text{for the positive y direction} \qquad \frac{N}{c} + \zeta = z_{N+} \qquad (15)$$

$$\text{for the negative y direction} \qquad \frac{N}{c} - \zeta = z_{N-}$$

If their is no wave invading from outside,

on the boundary AB, $N=0$ and $z_{M-} = 0$ then, $M=c\,\zeta$

on the boundary OC, $N=0$ and $z_{M+} = 0$ then, $M=-c\,\zeta$

on the boundary OB, $M=0$ and $z_{N+} = 0$,   then $N=-c\,\zeta$

on the boundary CD, $M=0$ and $z_N^- = 0$, then then $N=c\,\zeta$

The values of ζ or M and N at points just one step outside of the boundary are assumed to propagate from points on the boundary with the celerity of long waves.

On the coastal boundary, only normal component of discharge flux is assumed zero but parallel component is not.   Then there are 12 kinds of coastal boundary conditions.

Fig. 7 shows the computed domain in which the south coast of Hokkaido, the Sanriku Coast and the Japan Submarine Trench are included. The coastal boundary was simulated by the zigzag grid line and depth in front of it was assumed as that of just one step inside grid points. The space difference DS was 24 kilometers and time difference DT was 30 seconds.   Instability was not experienced and amoothing technique was not employed.

EFFECTS OF THE UPHEAVE VELOCITY OF THE SEA BED

Numerical tests were performed to investigate effects of upheave velocity of the sea bed upon the configurations in near coast offshore

O   DISCHARGE FLUX M,N
●   WATER LEVEL ζ
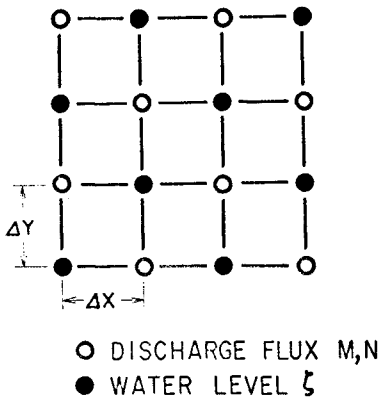
Fig.5   Schematic Grid Points
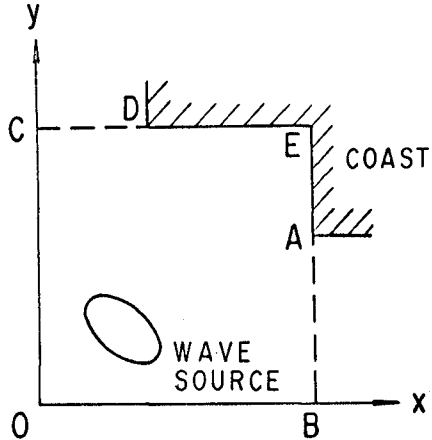
Fig.6   Schematic Domain
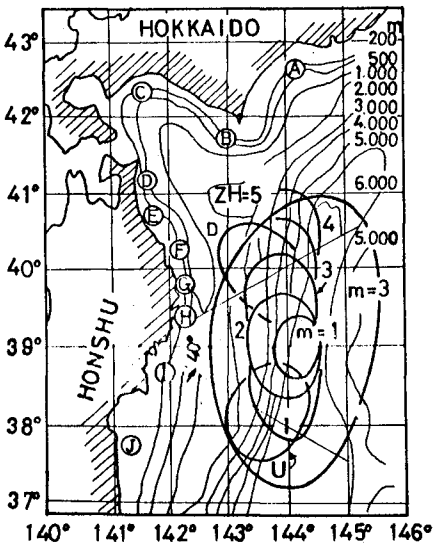
Fig.7   The Computed domain
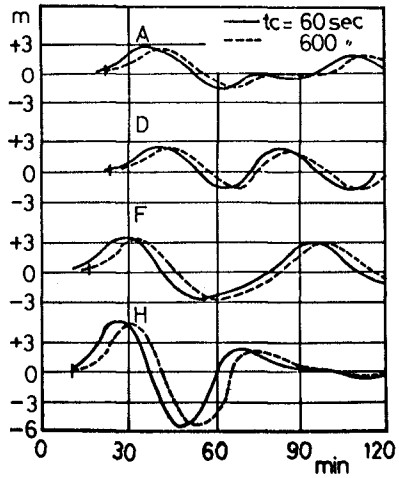
Fig.8   Effects of the upheave
        velocity of the Sea Bed.

region. For this purpose the source area for the tsunami magnitude m of
3 which dimension is given in table 2 is set as shown in fig.7. The
maximum upheaval η_{max} was constant as 5.19 meters because of the feasi-
bility of the time spacing. The duration times to this maximum upthrust
t_c were changed as five kinds such as 60, 90, 210, 300 and 600 secs in
which the velocity of the bed movement was constant.
    Fig.8 shows computed wave profiles at the grid points just one step
inside from the coastal boundary where the depths were about 200 meters
as shown by points of A, D, F and H in fig.7. Only two extreme cases are
shown here such that t_c are 60 and 600 secs.
    Hammack and Raichlen defined the disturbance time-size ratio by
$t_c \cdot \sqrt{gh}/b$ in which b was the half-length of the breadth of the disturbance
in the direction of the wave propagation, which was assumed in this
case as that of the minor axis, that was 90 kilometers.[7] h was given by
the mean depth of the source which was 4925 meters along the minor axis.
Then values of this no-dimensional ratio are between 0.147 and 1.471.
Due to Hammack and Raichlen, such movements are classified as impulsive
bed deformation and the ratio of the maximum wave heights thus generated
ζmax and the maximum upheaval η_{max} is constant. As shown in fig.8,
two configurations are almost same at each point except the difference
of the arrival time which support the theory of Hammack and Raichlen
and make our attempt somewhat easier.

        COMPARISON OF WAVE CONFIGURATIONS AT PERIPHERAL POINTS
        AND THOSE IN NEAR-COAST OFFSHORE REGION

    Fig.9 shows the tsunami waves at the peripheral point on the major
axis P_{6-11} and at the nearest offshore point A calculated for the wave
source of m of 3. Also in fig.10, those at the peripheral point on the
minor axis P_{10-21} and at the point 1 are compared.
    At the peripheral points, abrupt water rises are shown followed by
oscillations which periods are about 10 minutes on the major axis and
15 minutes on the minor axis each. However at the near-coast offshore
points, very slow undulations with the periods of about 70 minutes are
computed. However such period was not observed at the Sanriku Large
Tsunami of 1933 when the periods were reported as 10 to 20 minutes.
    The Ursell numbers are computed following the proposal by Hammack
and Raichlen such as,

$$U = \zeta_o^{\ 3} / h^3 \ || \ \zeta_x \ ||^{\ 2} \tag{17}$$

, in which U is the Ursell number, ζ_o is the maximum water rise and
ζ_x is the space derivative on the first wave and is computed by the
maximum time derivative divided by the long wave celerity c $(=\sqrt{gh})$.
Then at P_{6-11}, U= 8.7 x 10^{-4} and at A, U=860. This means the waves are
linear under frequency dispersion process at the peripheral points, but
are finite and non-linear under amplitude dispersion process at the near-
coast offshore points. Hammack and Raichlen had pointed that soliton
formation might be expected for the Ursell number of the order 1.
However Galvin had reported three solitons for the Ursell number of 100
to 500 (1972), which had been supported by the numerical experiments by
Tsuchiya-Yamada (1973).[8][9] So such soliton formation is expected on the
tsunami propagation from the peripheral to the coast. The space grids
were too coarse to make realize such dispersion. If the wave could be
dispersed into three solitons as pointed by Galvin and Tsuchiya-Yasuda,
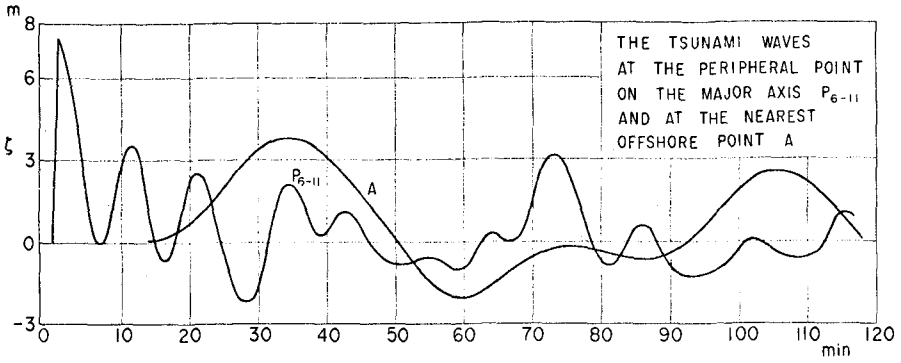
Fig.9   Comparison of Wave Configurations at Peripheral Points
        and those in Near-coast Offshore Region
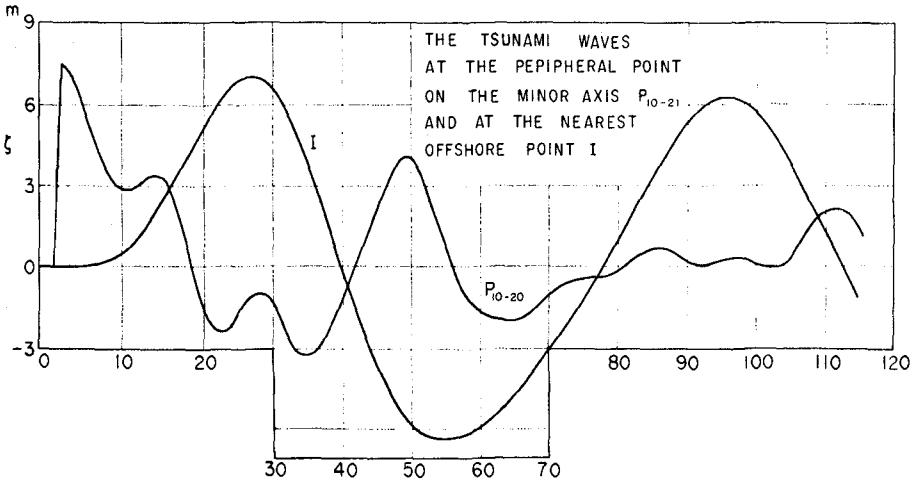
Fig.10   Comparison of Wave Configurations at Peripheral Points and
         those in Near-coast Offshore Region

the period might be about 20 minutes which should support observations.

EFFECTS OF THE TSUNAMI MAGNITUDES

To investigate effects of the tsunami magnitudes upon the wave heights in near-coast offshore region, numerical tests were carried out for the wave sources with different magnitude. Their centers and two axis are coincided with each other. As mentioned above, the bed deformation is impulsive. So the duration time of the bed upheaval was taken as constant of 60 seconds.

Fig. 11 is an example. In fig.12, the white circles are plotted by the first maxima in fig. 11. As these waves are stopped by the vertical wall with perfect reflection, the heights of the stationary waves will be double to them which were plotted in triangles. The straight line is given by the following equation of Wilson,

$$\log_{10} \zeta \max = 0.75 \ M - 5.07 \tag{18}$$

The curve was presented by Iwasaki (1973).[00] Then the doubled maxima are rather closely forcasted by Wilson's formula.

The arrival time of the long wave to the point which distance from the peripheral point is X' may be approximated by $X'/\sqrt{g\bar{h}'}$, where $\bar{h}'$ is the mean depth along the path. The toe of the rising limb appeared rather earlier than this time.

In fig. 13, no-dimensional time difference between $X'/\sqrt{g\bar{h}'}$ and the arrival time of the first maximum t_{max} as computed by

$$T\max = t_{max} \cdot \sqrt{\frac{g}{h}} - \frac{X'}{\bar{h}} \tag{19}$$

is taken as the ordinate and $X'/\bar{h}$ is taken as the abscissa. It is found that in the case of the magnitude of 3 the first maxima get retarded from the front more and more as the travel distance increases. This is contrary to the prediction by the finite amplitude long wave theory, which shows clearly the effects of dispersion. However in cases of the magnitudes of 2 and 1, such retardation gets restored for the increase of the travel distance.

In fig. 14, the ratios of the maximum wave amplitudes and the maximum ground upheavals ζ_{max}/η_{max} are plotted against the no-dimensional travel distances $X'/\bar{h}$. Clearly these ratios decrease with the travel distance and approach to constant values when $X'/\bar{h}$ is larger than 200. Points F, G, H and I are off the Sanriku Coast with nearly the same distance to the source. However values of ζ_{max}/η_{max} at these points are remarkably scattered with each other which may be attributed to the effects of the local bottom topography.

EFFECTS OF THE SOURCE LOCATIONS

As shown in fig.7, five source areas of the magnitude of 2 were set so that their major axes are coincided to the same meridian line but their centers are shifted along it. Such models are called as ZH 1, ZH 2,···, ZH 5. Results are shown in fig. 15-18 in which waves are drawn so as the times when the first waves get back to the undisturbed level to coincide with each other. As shown in them, the first wave configurations at each point are not so sensitive with the variation of the
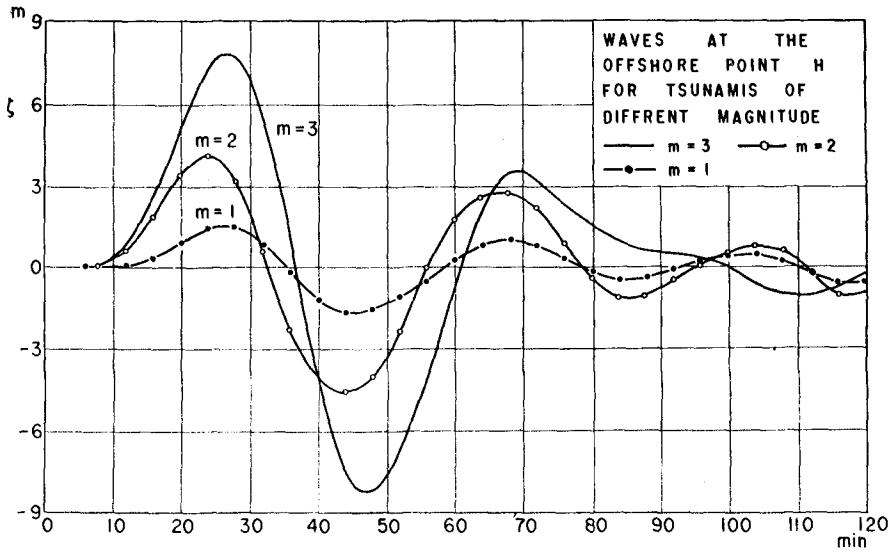
Fig.11 Effects of the Tsunami Magnitudes
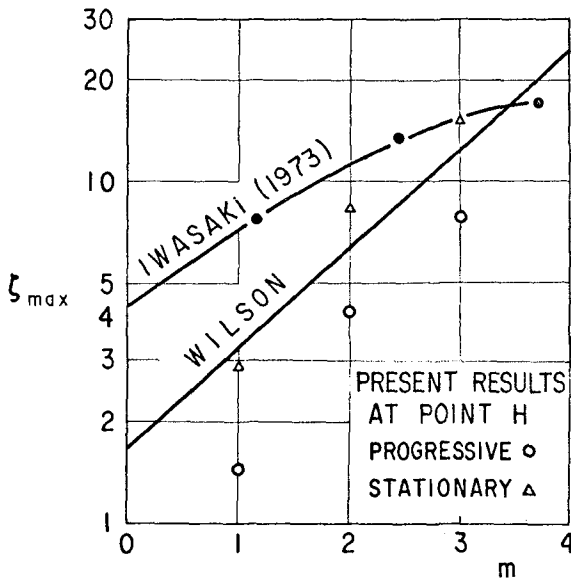
Fig.12 Relationship of the Maximum Amplitudes to the Tsunami Magnitudes
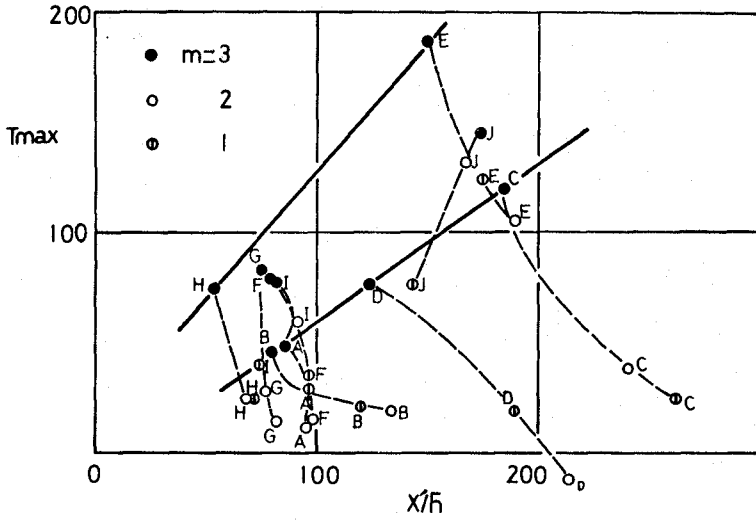
Fig.13 Relationship of T_{max} to $X'/\bar{h}$
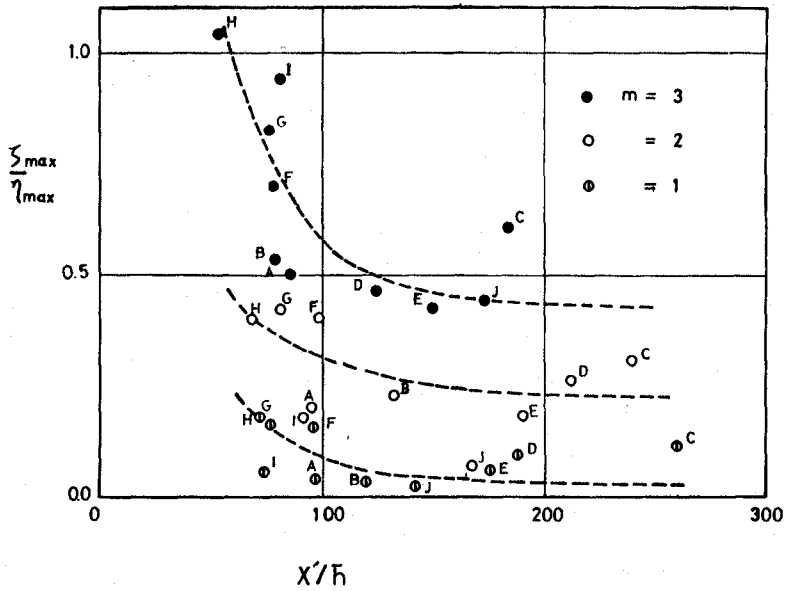
Fig.14 Relationship of ζ_{max}/η_{max} to $X'/\bar{h}$
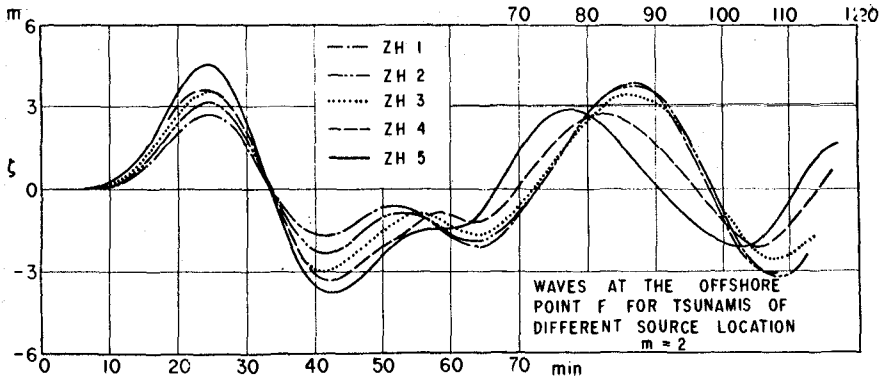
Fig.15 Effects of the Source Location at Point F
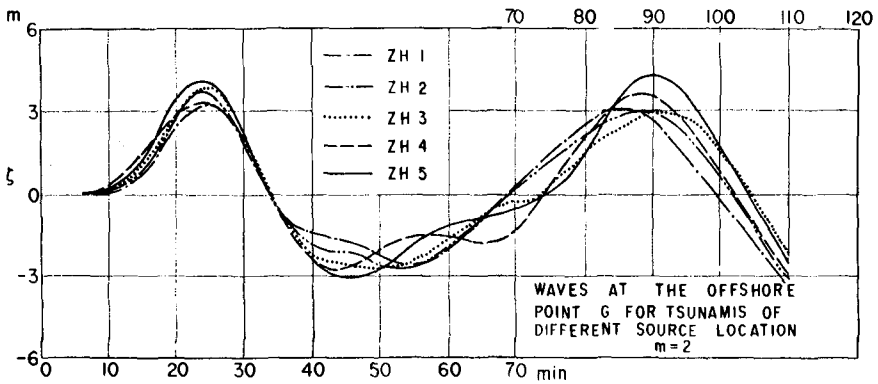
Fig.16 Effects of the Source Location at Point G
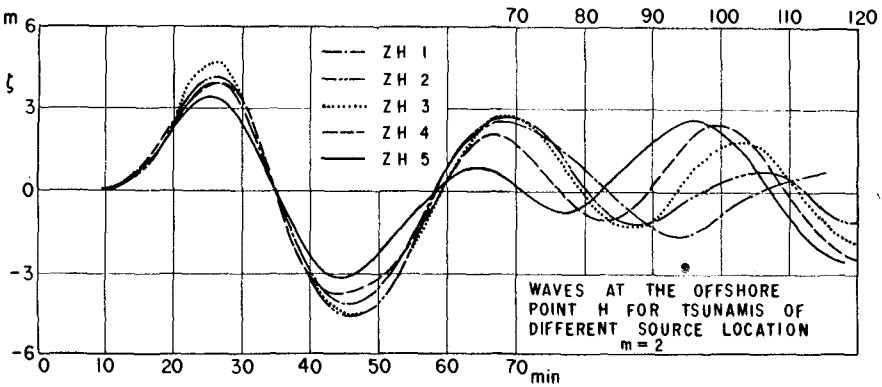
Fig.17 Effects of the Source Location at Point H

center location, but are very much unique at each points. This result is
important for the design purpose and stresses the inevitable necessity
of the numerical model tests.

EFFECTS OF DIRECT1ON OF THE INCIDENT WAVES

Lastly three models were tested to investigate effects of direction
of the incident waves. As shown in fig. 7, the wave source of which the
direction of the minor axis is normal to the coast is called as PZC and
that of which the axis direction is 20 degrees northward to PZC is called
as PZU. Also the wave source of which the minor axis is rotated 20
degrees southward to PZC is called as PZD.
    Results are shown in fig.19-22. In every case, the tsunami magnitude
is 2. At the point F, PZU gives the highest wave as this source approaches
to F most closely. Same result is obtained at the point 1 where PZD gives
the heighest. At G and H, the wave source PZC gives the maximum, which is
in accord to the common sense.

CONCLUSIONS

Near-coast offshore wave forms along the Sanriku and the southern
coast of Hokkaido are obtained by the numerical computations with the
tsunami source models of three kinds of magnitude set on the western
slope to the Japan Submarine Trench. Conclusions thus obtained are as
follows;
1. The dimensions of the source areas are reasonably estimated by eqs.
(1) to (7).
2. Computation scheme and the boundary conditions discussed here make
possible the computation of tsunami waves.
3. If the tsunami magnitudes are between 1 and 3 and the wave sources
are located such that shown in this paper, sea bed movement can be
classified as impulsive bed deformation. So the deformation velocity
can be assumed tentatively. Computed configurations in near-coast
offshore region are not sensitive to this and are decided by the maximum
upheaval.
4. At the peripheral points of the wave source, abrupt water rises are
shown followed by oscillations with periods of 10 to 15 minutes for the
tsunami magnitude of 3. However very slow undulations with period of
about 70 minutes are computed in the near-coast offshore region. This
should be checked by the investigation of the soliton formation in the
future.
5. The first maxima at the vertical cliff nearest to the source can be
approximated by Wilson's empirical equation. When m=3, the first maxima
get retarded from the front more and more as the travel distance increases.
However when m=2 and 1, such retardation gets restored with the travel
distance.
    Variation of the first maxima due to locality is remarkable in the
range of $X'/\bar{h}$ smaller than 100.
6. The first wave configurations are not so sensible to the variation
of the center location of the wave source, if their major axes are on
the same meridian line and the variation is confined to the extent
treated in this paper.
7. The highest wave is obtained when the minor axis of the wave source
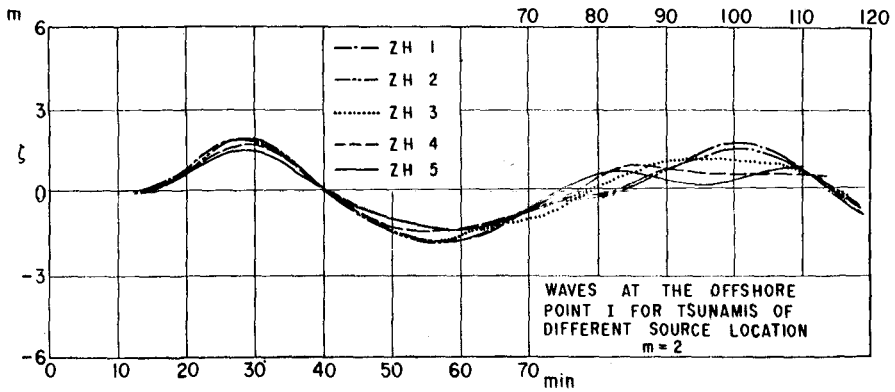
Fig.18 Effects of the Source Locations at Point I
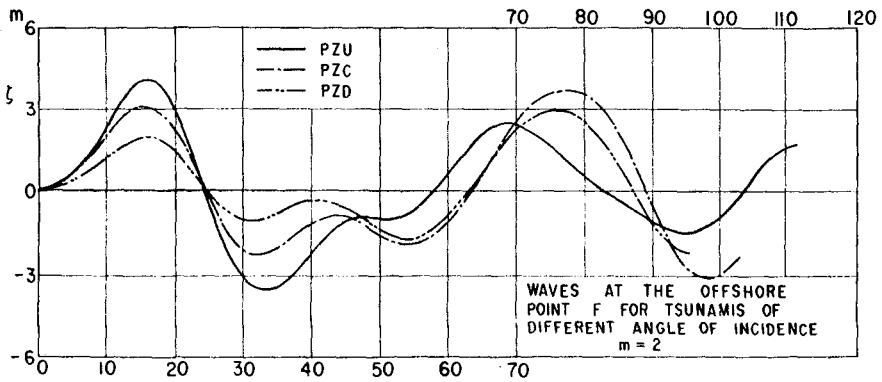
Fig.19 Effects of the Direction of the Incident Waves at Point F
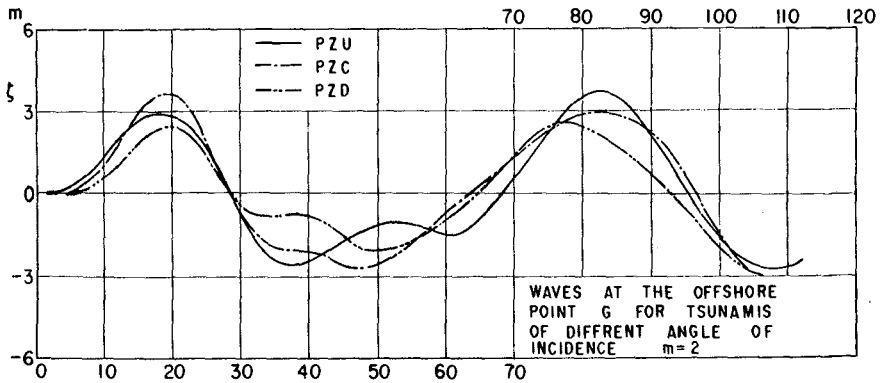
Fig.20 Effects of the Direction of the Incident Waves at Point G
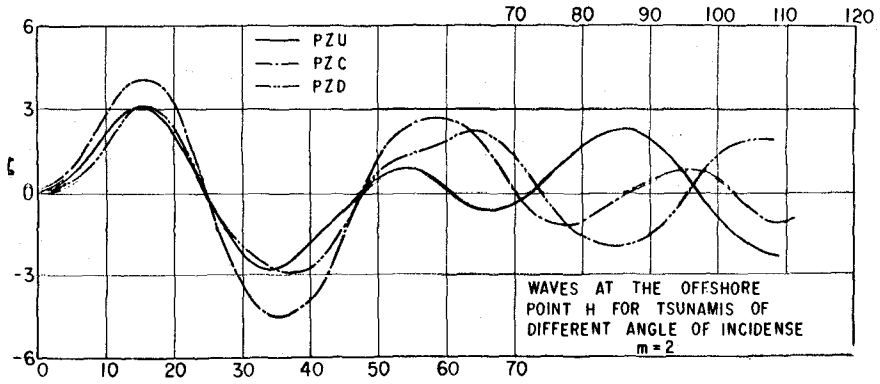
Fig.21 Effects of the Direction of the Incident Waves at Point H
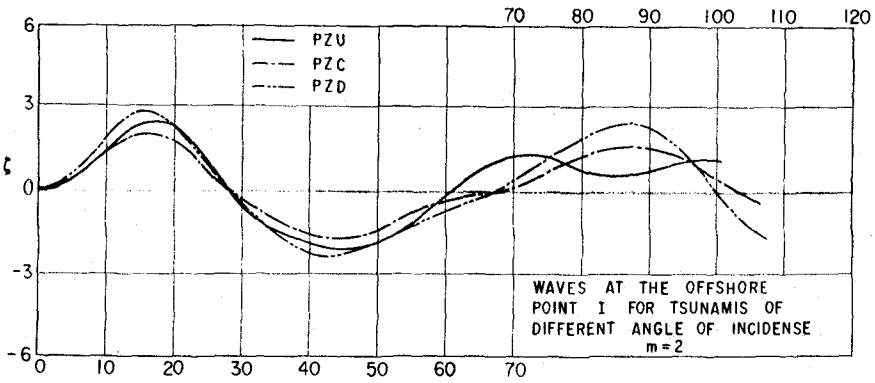
Fig.22 Effects of the Direction of the Incident Waves at Point I

is normal to the coast line, or when the source area gets closest to the coast.

REFERENCE

1) K. Iida, "Magnitude of Tsunamigenic Earthquake, Aftershock Area, And Area of Tsunami Origin." Geophysical Papers dedicated to Professor Kenzo Sassa. (1963)
2) T. Hatori, "Dimensions and Geographic Distribution of Tsunami Sources near Japan." B.E.R.I. vol.47 (1969)
3) K. Iida, "Earthquake Energy and Earthquake Fault" J. Earth Sci., Nagoya Univ. vol.7(2) (1959)
4) B. Wilson, "The Nature of Tsunamis, their Generation and Dispersion in Water of Finite Depth." NESCO Tech. Report No. SN 57-2 (1962)
5) R. Takahashi, "Potential Tsunami Inundation Along Japan Sea Coast. B.E.R.I. vol.28 (1950)
6) M. Hino, "Fluid Analysis (I)" Proc. ASCE vol.57 (1972)
7) J.L. Hammack, F. Raichlen, "Tsunamis-A Model of their Generation and Propagation." C.1.T. Report No. KH-R-28 (1972)
8) C.J. Galvin, "Wave breaking in Shallow Water. Waves on Beaches and Resulting Sediment Transport. edited by R.E. Meyer, Academic Press (1972)
9) Y. Tsuchiya, T. Yasuda, "Wave Transformation in Shallow Water – On the Generation of Solitons" Proc. 20th Interine Coastal Engineering (1973) (in Japanese)
10) T. Iwasaki, "The Wave Sources of the Designed Tsunamis" Prof. 20th Interine Coastal Engineering (1973) (in Japanese)

Trans, Denmark

PART II

COASTAL SEDIMENT PROBLEMS

Danish West Coast
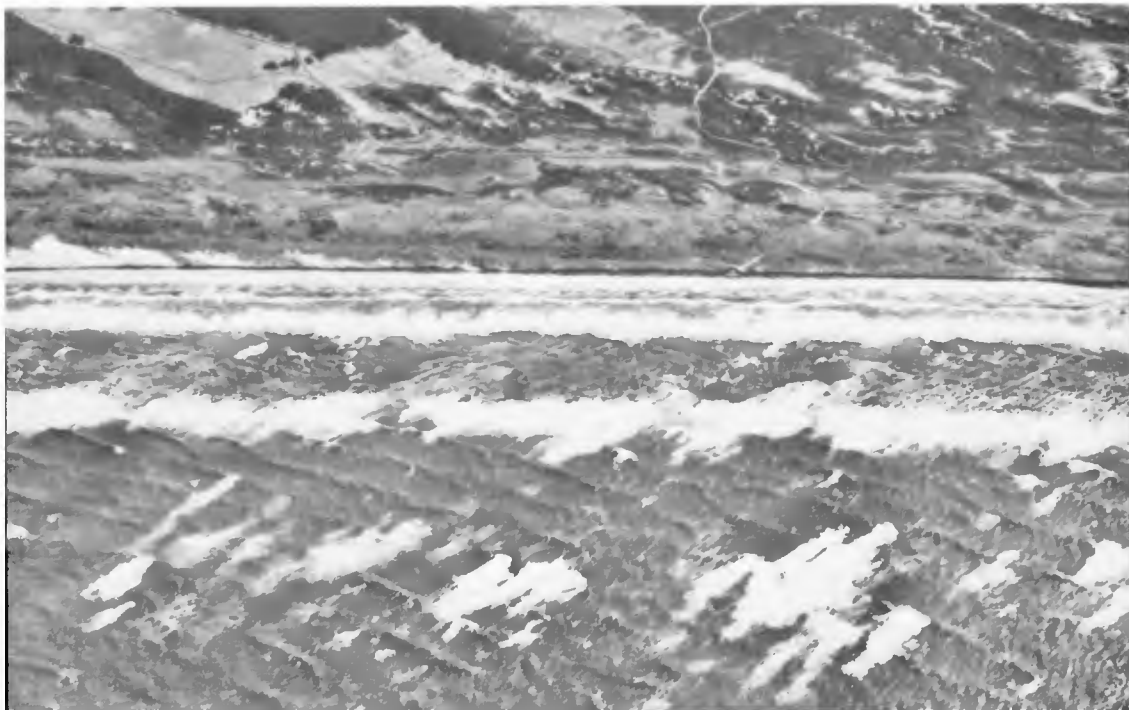
CHAPTER 38

FEASIBILITY OF COASTAL MORPHOLOGICAL MODELS

By

Evald Nielsen, Dr.Sc.,
Project Manager, Unesco,
Nile Delta Studies

ABSTRACT

The paper deals with the initial ideas and concepts for development of
a morphological model for a Delta coast, having particularly the Nile
Delta in mind. The paper concentrates on the offshore zone, in which
sediment is assumed primarily to be transported in suspension and during
periods of sufficient agitation by the combined action of waves and
ocean currents. In the Nile Delta great offshore changes take place
due to the deprivation of the shelf area of Nile sediments by the
closure of the Aswan High Dam, and serious nearshore long-range changes
are expected to result from the changes to the offshore morphology.
The modelling aids in establishing the mechanisms of the Delta shore,
but the primary goal of the model is reliable prediction of future
coastal changes. Fundamentally, the modelling is based on verification
of the model - by trial and error - against known states of the model
domain.

Part A of the paper deals with the general concepts, while especially the
entrainment of sediments is treated in Part B of the paper, yielding
practical formulas for determining the treshold values for sediment
entrainment by unidirectional flow and by wave action.

PART A - THE GENERAL CONCEPTS

1. Introduction

        The paper is the prelude to the work of developing a workable
mathematical model for the prediction of future morphological changes
to the Nile Delta continental shelf area, and although the subject is
treated in a general manner, the Nile Delta area shown in sketch map
fig. 1 is constantly being kept in mind and being referred to.

The motivations of a Nile Delta model have been discussed briefly by
the author in (1). A model seems to provide the only rational manner
for systematic recording and analysis of the large number of space and
time data collected for the Nile Delta, and for predicting future changes
if such predictions are to be not mere guess-work. No research worker
on coastal processes underestimates the complexities of the actual
processes in nature and the limitations of laboratory experiments, and
it is realized that no exact modelling shall ever be possible.

663

A few words on terminology are called for. Geomorphology deals with the 'sleeping', i.e. static surface of the Earth, and the generally used term 'dynamic geomorphology' applying to changes to the surface forms is really a misphrasing. Geomorphology is a descriptive discipline dealing only with space and materials, while 'dynamic geomorphology' dealing also with time and changes and the physical processes causing the changes is quantitative and interdisciplinary. Scheidegger (2) uses the term 'geodynamics' in connection with endogenetic surface features due to processes occurring inside the solid Earth and reserves the term 'geomorphology' for exogenetic surface features due to processes occurring outside the solid Earth. However, as mentioned for instance by Strakhov (3), the endogenetic features are of sufficient magnitudes to influence strongly the exogenetic processes and their effects upon the surface morphology and evolution. Consolidation settlement of clayey sediments are for instance on the border between endogenetic and exogenetic features, and even within historical time intervals tectonic changes including seismic effects can affect the coastal morphology and thus the past geomorphological states used for verification of models of evolution and prediction. While the Nile Delta model will be designed primarily for prediction of geomorphological changes within the next 50 years or less, the model will none the less be tested against evidence of past changes, in historical and recent geological time. It must be an essential condition for a model that it is stable over past time intervals, during which the physical processes were not significantly affected by sea level variations or endogenetic processes.

The contemplated model is most easily perceived by imagining the continental shelf area - in the case of the Nile Delta some 250x50 km^2 - during a storm. The prior storm has left the sea bottom in a state involving sorting of sediments according to water depths, but with the sorting being influenced by the ocean current pattern, and over the sea bottom area the in-situ density of the sediments varies with sediment characteristics. This varying sea bottom with its geographical shape formed through thousands of years of delta build-up is now agitated by the combined action of waves and currents. The intensity of agitation varies not alone with depth, but also with geographical location in the Eastern Mediterranean. Driven by the ocean currents, clouds with varying concentrations of fine suspended sediments move continuously across the shelf area and into areas, in which the entrainment and transport capacity does not correspond to the actual concentrations of suspended materials, and deposition or elevation of materials takes place. The resulting accretion and erosion over the shelf area determines the new morphology of the sea bottom after the storm, and the process repeats itself with each storm, every time creating a new sea bottom topography. The modelling aims primarily at reproducing the described processes and extending them into the future. The emphasis is upon the long-range mechanisms and changes, rather than on the detailed short-range changes.

2. The model

A morphological state of the domain to be modelled must be defined to include not alone the surface topography, but also the sediment characteristics that influence the subsequent morphological states.

As a first approximation the definition may be limited to include the sediment characteristics influencing the subsequent states within a specified time interval, but this limitation has to be used with caution, for instance for finegrained sediments consolidating gradually or for non-cohesive sediments being slowly compacted under wave action. The important sediment characteristics are composition and density, grain shape, and inner structure of the sediment deposits to the depth at which appreciable interactions between water motions and sediments cease.

A set of subsequent morphological states determined at specified time intervals constitute in themselves an 'inactive' model and may be presented graphically as for instance by the so-called T-X diagrams. In case the changes between subsequent states can be related to the forces acting during the respective time intervals by a common 'law' applying to all space and time intervals, the 'inactive' model becomes an active model representing the total time interval of the set of determined morphological states. Provided a reasonably accurate statistical record can be established of forces acting prior to the time interval of the determined states, the model may be operated back in time and may be checked against features known from maps of the past or from historical and geological records. Once properly verified, the model may be applied to prediction of future morphological changes, using the expected forces as inputs.

Thus, the sediments of the sea bottom constitute the medium of the model, the hydrodynamic forces are the inputs of the model, and the morphological changes are the outputs. The response factor of the model is the above mentioned 'law' representing the relationship between forces and changes. The changes are initially expressed by quantities of sediments shifted by the forces and are transformed into morphological changes by volumetric considerations. The model must be verified against two or more known past morphological states.

The model is discrete in space and time. The force inputs are statistical quantities, and the verification of the model against known states determined at considerable time intervals implies that resulting changes over the time interval will be related to resulting forces. Predicted future states based on expected values of force inputs will represent cumulative changes and will be expressed in terms of probabilities of occurrence.

The response factor is deterministic, relating the model outputs to statistically described inputs. The true response factor, or 'law', is a general sediment transport formula and cannot be determined exactly, due to the complexities of the processes involved, which in themselves contain elements of probability, in turbulence, grain interactions and sediment structure. The verification of the model against known states aims at determining suitable approximations to the true 'law' and is based upon the fact, that the 'law' is a unique physical relationship (with statistical values for probability elements) between the sediment characteristics and the forces acting directly upon the sediments and is invariant in space and time.

3. The model domain and its boundaries

        The model domain must be delineated so that the boundary conditions
are determinable. The 'law' itself is invariant with respect to the
boundary conditions, but the forces - and hence the sediment movements
within the model domain - may depend upon conditions outside the domain,
and it would then become necessary to know the 'feed-back' functions.
In case the true 'law' were known, it would suffice to determine the
forces and the 'feed-backs' across the boundaries in order to operate
a model with known sediment characteristics and use it for morphological
predictions. In the present case, the 'law' itself must be determined
from differences between known morphological states, assuming the force
fields for the corresponding time interval to be known and also the
characteristics of the sediment involved in the transition from one
state to another. Sediment budget calculations, including sediment
fluxes across boundaries and also sediment discharges through estuaries
and outlets, are then absolutely necessary for an overall control of the
adequacy of the determined approximation to the true 'law' and for safe-
guarding the stability of the model.

The nearshore and offshore zones are here defined respectively as the
zones within which and beyond which wave breaking significantly affects
the sediment transport. The empirical, two dimensional relationship
between wave energy and sediment transport capacity, or a modified form
of it, must for the time being suffice as the 'law' for the nearshore
zone, but sediment fluxes across the internal boundary between the near-
shore and offshore zones cannot be ignored, and the condition of geo-
morphological continuity across the common boundary gives rise to inter-
actions ('feed-backs') between the two zones. In the model the two zones
are treated as separate subdivisions, with a common active boundary.
The 'law' for the offshore zone will, by a procedure of trial and error,
be determined from verification against two (or more) known morphological
states. The present detailed knowledge of the mechanisms of sediment
entrainment and sediment transport will guide the trial and error procedure.

Determination of boundary conditions, including 'feed-backs' across the
boundaries dominates the modelling treatment of any shore area and rather
limits the extent to which the subject matter can be treated in a general
manner. In the case of the Nile Delta the boundary conditions can be
dealt with without introducing unreasonable simplifying assumptions. The
model domain will cover the continental shelf from Abuquir to Port Said
(see sketch map fig. 1). The western boundary at Abuquir is in relation
to Nile sediment quantities practically neutral in respect of sediment
fluxes, as the shore formations to the west are indurated with calcareous
materials. Along the offshore boundary at the shelf edge Corioli effects
and shallow water refraction tend to turn the west to east ocean currents
shoreward. At Port Said the nearshore zone is bounded by the breakwater
protecting the entrance to the Suez Canal and to a certain extent also
by the entrance channel to the canal. The offshore conditions east of
Port Said do not materially affect the sediment transport processes inside
the model domain, and the eastern offshore boundary conditions (sediment
fluxes) can, therefore, be determined from the processes inside the model
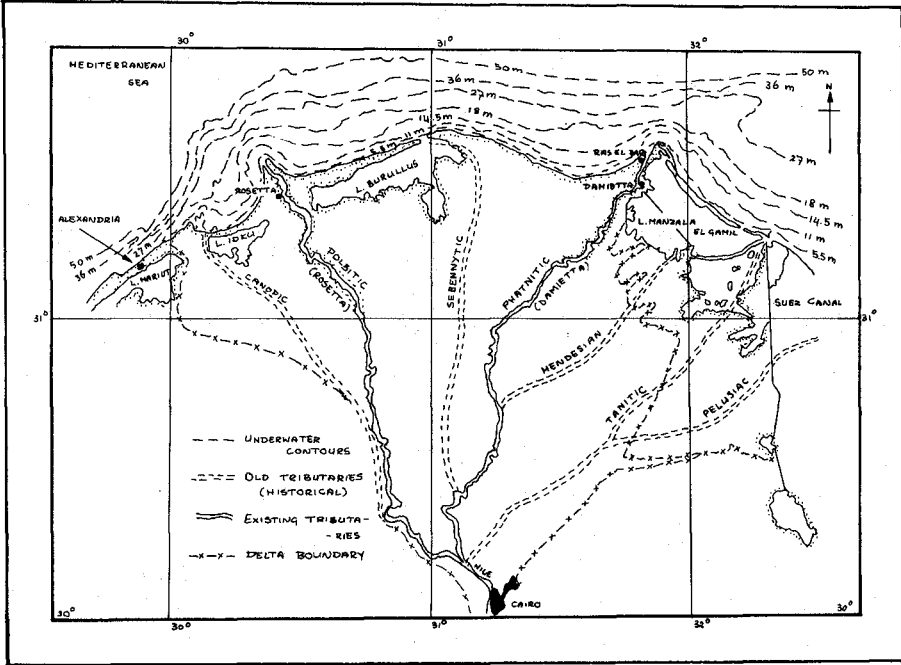
FIG. 1. - NILE DELTA.

domain.   Quantitatively, the morphological changes in the offshore zone
by far exceeded the nearshore sediment movements during the time interval
between the verification states of the Nile Delta model, and the offshore
sediment movements are expected still to be dominant.   The offshore
processes will, therefore, significantly affect the processes in the
nearshore domain, whereas the nearshore processes cannot significantly
affect the processes in the offshore zone except maybe close to the
common boundary.   Hence, the sediment fluxes across the internal boundary
between the two zones can with reasonable accuracy be determined solely
from the offshore processes and thereafter be introduced as known quantities
in the nearshore model.   Aeolian sediment fluxes across the shore boundary
are rather insignificant for the offshore zone, but an estimated quantity
may be introduced in the sediment budget.   The Nile sediment discharges
prior to the closing of the Aswan High Dam in 1964 are reasonably well
known, and by far the greater quantities were deposited on the offshore
shelf and reworked.   Sediment discharges from lake outlets are insignificant
except locally, but can be judged from flow studies in the outlets.

The offshore model domain of the Nile Delta can thus be treated independently
of the nearshore zone and overall sediment budget calculations can be made.
And with neutral west and east boundaries of the nearshore zone and known
sediment fluxes across the seaward boundary, the nearshore zone can be
dealt with, in respect of budget calculations, without necessarily knowing
a priori the significant aeolian fluxes across the shore boundary.

4. Verification of the model

4.1   The offshore domain

        The offshore model involves vast quantities of shifting sediments
and continuously varying sea bottom morphology, both due to the vast
pre-1964 yearly sediment deposits and the subsequent post-1964 inequili-
brium of the offshore areas.   The Nile Delta project shall not be able
to carry out repeated detailed and exact surveys of the sea bottom
configurations on the continental shelf, and in large parts of the
shelf the changes over few years are likely to be of some magnitude or
smaller than the accuracy of the surveys, but may none the less involve
large quantities of sediments due to the vast area of the shelf.   The
model is, therefore, to be verified against the cumulative changes of
some 50 years, this being the period between the last accurate hydro-
graphic survey in 1920-1924 and the present survey being carried out by
the project.   The hydrodynamic forces will be hindcast for the verifi-
cation interval.

The response factor of the model, the 'law', essentially involves quantities
of sediments entrained and the vectorial transport distance of the entrained
sediments, both corresponding to prevailing specified hydrodynamic condi-
tions.   Morphological changes in terms of erosion or accretion - possibly
accompanied by changes to sediment characteristics - would at any one
location of the model domain be determined as the resulting, or cumulative,
difference between the sediments entrained at that particular location
and the sediments originating from other locations of entrainment, being
deposited at the location considered.   Entrainment and deposition are not

necessarily mutually exclusive. The entrainment mechanisms are different from transport mechanisms, but both are functions of grain size, and coarser grains entrained elsewhere could under some circumstances possibly settle down, while finer sediments are being entrained at the same location.

In case the true 'law' for the model were known, the quantities of sediments entrained and deposited at each location of the model domain could be determined uniquely, and assuming known hydrodynamic conditions throughout the verification period and known or calculable sediment fluxes across the external boundaries of the model domain, successive applications of the 'law' would automatically transform one known state of the model domain into another known state. When the true 'law' is not known, but has to be replaced with an adequate approximation to be determined from two known morphological states, the question arises whether the two known states alone yield a unique, although approximate, solution, or whether different expressions for the 'law' could yield the same cumulative changes in space over the verification interval. As the physical relationship for sediment transport, and both relationships are invariant in space and time, only one unique 'law' can satisfy the cumulative changes <u>throughout</u> the space domain, and an approximation to the 'law' can only satisfy the cumulative changes throughout the space domain with corresponding approximation. If a sufficiently accurate approximation to the law can at all be found, it can be considered as a unique solution, and theoretically two known states suffice for the determination of the 'law'. The proposed procedure for verification of the model is feasible in theory. The practical difficulties arise partly from the trial and error procedures needed and partly from the inaccuracies ('noise') in the model and the stability of the model with time.

4.2 The nearshore domain

When the generally accepted empirical formula for alongshore transport in the nearshore zone is applied as the 'law', the verification of the nearshore model against known states consists of determining the coefficients entering into the two-dimensional formula. The coefficients depend on sediment characteristics and would vary along the shore. The rather important, but not well known aeolian sediment fluxes across the shore boundary would enter into the verification procedures. The model is sensitive to geographical changes caused by the shifting sediments, and during the successive applications of the 'law', adjustments must be made for changing wave refraction and shore alignment. The empirical two-dimensional formula used as the 'law' yields no information about the geographical changes caused by the calculated quantities of erosion and accretion in the nearshore zone. This subject matter needs further general research developments. The governing factor for determination of the actual geographical changes is the dynamical equilibrium profile, but the variable phase shift between hydrodynamic forces and corresponding profile changes caused by the limited onshore-offshore transport capacity of the wave depends upon the <u>sequence of events</u> causing the changes, and the actual sequence of events (determined from hindcastings) would have

to be considered when verifying the model against known cumulative changes
over the period of verification. The resulting geographical changes would
also depend upon the nearshore and downshore boundary conditions. In the
case of the Nile Delta the Rosetta estuary cone must have been a source
area since 1964.

It would be characteristic for a true three-dimensional model, that it
should be able to reproduce oscillatory changes caused primarily by
variations to the input forces, and it should also be able to reproduce
a sawtoothed coastline when operated with unidirectional, oblique waves
as input. Both conditions are fulfilled in nature, the latter even on
rocky coasts (i.e. SW-coast of India, Eastern part of Turkey's Black Sea
coast). On soft sediment coasts the reproduction of sawtoothed coastlines
involves the relationship between maximum alongshore transport capacity
and the capacity of the sea to shape equilibrium profiles, which again
depends upon the capacity of the sea to change the offshore zone. The
offshore changes, involving shifting of large quantities of sediments
under less active forces than those affecting the narrow nearshore zone,
take place at a slower rate than that applying to nearshore changes.
Consequently, erosion of the nearshore zone will initially leave a bench
in the profile, while places of accretion in the nearshore zone will act
as drains towards the offshore zone, because offshore 'supports' for the
nearshore accretions can only be built up very slowly.

Letting the nearshore model operate with a unidirectional wave input on
a preliminary straight and infinitely long coast should result in (1)
beginning bench erosion at some place of the coast, (2) increasing
amount of sediment transport downshore and correspondingly decreased
bench erosion, (3) saturation and deposition of sediments and offshore
draining of sediment, and (4) renewed bench erosion. The offshore
draining of sediments, due to lack of offshore 'support', would presumably
take place in the same manner as rip currents, and in a model with uni-
directional and uniform wave action the offshore sediment drainage and
rip currents would be likely to coincide. The bench erosion would
decrease with widening bench as the shore direction would assymptotically
approach the wave crest direction, and at the same time the offshore
'support' for accretion would gradually increase, permitting a shore
advance. For this imaginary uniform operation of the nearshore model,
any point of beginning bench operation could initially be taken as a
nodal point with zero alongshore transport, and any downshore point of
sediment drain could be taken as the downshore boundary of the model.
The results of the model operation would then be the transformation of
a straight shore into a sawtoothed shore. The average position of the
sawtoothed shore would be parallel to the original shore, but shifted
inland a distance corresponding to the quantities of sediments drained
to the offshore, and the original shoreline will divide the side of the
'sawtooth' parallel to the wave crests into two unequal sections, with
the shorter one closest to the point of the tooth. However, in soft
shore sediments the short side of the 'sawtooths', perpendicular to the
wave crests, is unstable, and the whole sawtooth pattern would continuously
move upshore, involving an overall downshore sediment transport fed at

the upshore boundary. In the Nile Delta the sawtoothed coast can, some-
what imperfectly, be observed for instance, at Baltim Sea Resort during
periods of dominating north-westerly storms, and the Rosetta estuary
cone is an upshore source area.

It is to be noted that bar formations are natural parts of the nearshore
zone, and that the sawtoothed pattern is more pronounced on steeper shores
with coarser sediments than on flatter shores with finer sediments, along
which rip currents are also not very marked. It is logical to believe,
that on flatter shores with finer sediments alongshore moving water masses
and their sediments gradually return to the offshore zone and not as bursts
of saturated flows. It is also to be noted that interactions between
after-storm landwards shifts of storm bar formations and alongshore sedi-
ment transport in the nearshore zone may create temporary spit formations
and land build-up that would interfere with the more regular shore changes
patterns described above.

In case the nearshore model were operated in the above described imaginary
uniform manner in conjunction with the offshore model, the tendency by the
sea to create equilibrium profiles would cause corresponding offshore
erosion off the eroded bench sections and alongshore offshore sediment
transport (by ocean currents and/or the alongshore component of wave
mass transport) until halted by the sediment drains from the nearshore,
but the offshore processes would initially take place at a much slower
rate than the nearshore changes. However, ultimately the nearshore bench
erosion would decrease assymptotically, but the upshore shift of the saw-
tooth pattern of the shoreline would continue at a rate, that would be
much greater than the corresponding shifts in the pattern of the offshore
zone. Therefore, the nearshore and offshore models will, due to the
different hydrodynamic processes, always remain out of phase, even in
the imaginary uniform model, and both as regards rates of changes in
plan as rates of changes in profile. These phase shifts will cause
considerable difficulties for determining the boundary conditions along
the active boundary between the nearshore and offshore zones, unless the
rates of changes are so widely different that the two zones may be treated
practically independently, adjusting the model only at long time intervals.

The above described behaviours of a three-dimensional nearshore model and
its relations to the offshore model are fundamental for three-dimensional
modelling of the nearshore zone. However, within the limits of this
paper the 'law' for a three-dimensional nearshore model cannot be discussed
further.

5. Details of the offshore model

5.1 The domain

        The model is discrete in space and time. The space intervals are
chosen as large as possible governed by the condition that with adequate
approximation a subdivision may be considered uniform in respect to mor-
phology and hydrodynamic forces. The time intervals are chosen as minimum
one year so as to eliminate seasonal changes to the sea bottom configuration,

particularly 'summer' and 'winter' beaches. For a two-dimensional near-
shore model the space divisions become stretches of uniform shore in
respect of sediments and wave direction. The offshore space divisions
may be increased in size with increasing water depths and decreasing
rates of change.

With large offshore space subdivisions the resulting sediment flow for
the whole subdivisions is calculated and thereafter referred to one
single point representing the subdivisions. The contour lines and
gradient lines of the sea bottom may conveniently be used as division
lines for the space divisions. Changes in profiles for each time interval
would be represented by quantities of erosion or accretion referred to
single points along the profile and representing the width of sea bottom
between adjacent profiles. The point 'loads' must be converted into a
continuous line distribution along the profile either by linear sections
or by drawing a smoothed-out equilibrium profile through the points.
For each time interval adjustments can subsequently be made to the
contour lines by linear or smoothing-out procedures. After successive
applications for a number of time intervals, profile and contour changes
may be large enough to warrant corrections to wave refraction patterns.

Although some idea of changes to sediment characteristics may be gained
from successive time interval operations of the model, core drillings
in the sea bottom give the best indication of possible layerings and
changes to sediment characteristics during the model verification period.

5.2 The sediments on the Nile Delta shelf

        The source of the Nile Delta sediments is primarily the rocks of
Ethiopia and Eritrea, the red soil weathering products of the Tertiary
outpourings particularly yielding montmorillonitic clays, but some
contribution could come from the upper Nile valley and the deserts.
International atlases show the general sediment types on the continental
shelf area of the Nile Delta. The sediments are fine sands, silts and
clays, deposited by the Nile branches and reworked by the sea. The
nearshore zone and estuary cone consist of fine sands and some silts,
while silts and soft clays (muds) dominate the offshore zone. Beyond
the breaker zone, in 5-6 m water depth, the medium grain sizes are
generally less than 0,15 mm. Judging from processes of deposition and
from experience with silts elsewhere, there is reason to believe that
the sediment structure in the offshore zone is very loose with close to
maximum water content and that clayey sediments are soft and muddy.
Biogenic materials may be present, but hardly dominating except on the
outer part of the shelf. Terrestrial organic materials are likely only
to be found in places where ancient lagoonal deposits or one-time emergent
sea bottom may be eroded. It is to be expected that silt and clay deposits
tend to be cohesive in their natural state.

5.3 The water motions on the Nile Delta shelf

So far little is known about the actual currents near the sea
bottom of the Nile Delta continental shelf. The ocean surface currents
are not expected to exceed 0,5-1 knot (0,25-0,50 m/sec), except maybe
under special wind conditions; prior to 1964 the velocities would also
have been greater near the Nile branch estuaries during the flood seasons.
The maximum tidal currents - according to atlas information (4) moving
in a NW-SE direction over the shelf - can only be in the order of 0,2
m/sec in 10 m water depth, 0,1 m/sec in 40 m depth and about 0,08 m/sec
in 80 m depth. The maximum particle velocity near sea bottom for a 5 m
wave with 10 sec period would be about 2,2 m/sec in 10 m water depth,
1,3 m/sec in 20 m depth, 0,60 m/sec in 40 m depth and about 0,13 m/sec
in 80 m depth, and the corresponding figures for say a 3 m wave with 8
sec period would be respectively 1,2 m/sec; 0,8 m/sec; 0,07 m/sec and
0,02 m/sec. Long period seiches (1-2 min or more) with appreciable
nearshore amplitudes (0,5 m) are said to occur, but rarely as compared
to the frequency of occurrence of regular storms, and standing waves could
no doubt also be generated in the Eastern Mediterranean basin by particular
meteorological surface pressure distributions, but standing waves would
probably be infrequent and imperfect due to the relatively rapid moving
cyclonic pressure distributions characteristic for the Eastern Mediterranean.

Consequently, the combined wave and ocean current action is dominating,
with wave action playing the major role up to 20-40 m depths and ocean
currents becoming increasingly important at larger depths, provided the
ocean bottom currents are of the same magnitude and with approximately
the same directions as the surface currents, a condition which may not
necessarily be fulfilled on the Nile Delta shelf. The tidal motions
alone, decreasing strongly with water depth, are not likely to play any
major role for sediment entrainment and transport. The ocean currents
on the shelf are presumably generated partly by the circulation off the
shelf and partly by wind and pressure over the shelf area. Density
currents generated on the shelf itself are not likely to be of importance.

PART B - THE DETAILED PROCESSES

1. Sediment entrainment

1.1 General remarks

The scarcity of definite quantitative knowledge about entrainment
and transport distances of in-situ sediments by combined oscillatory and
unidirectional fluid motions is evident from scanning the literature.
For verification of the model against known states and with known total
sediment budgets it suffices to know the relative values of entrainment
and transport over the model domain. Initially and until more definite
knowledge is made available by the Nile Delta project itself or from
outside research, the project must be guided by the available relevant
literature. Presently it is a matter of examining the fundamental factors
involved in determining the response factor, or 'law', of the model, i.e.
the factors governing entrainment of the sediments and transport of the
entrained sediments.

The existence of the delta built-up by Nile sediments testifies to the
fact, that large quantities of sediments from the two Nile branches did
settle on the shelf itself, and approximate budget calculations show that
the major part of the Nile sediments stayed on the shelf off the delta.
The distribution pattern of the sediments on the shelf and the present
shelf area topography further indicate that the major part of the Rosetta
branch sediments remained west of Burullus while the major part of the
Damietta branch sediments settle down primarily off the shore between the
Damietta estuary and Port Said and Lake Bardawil area. However, at both
river branches sizeable quantities of Nile sediments were deposited west
of the respective estuaries. It may further be remarked that even ocean
currents with relatively small velocities acting continuously over the
shelf area would have a very great sediment transport capacity, so that
in case this transport took place continuously, all the Nile sediments
would have been transported away from the Nile Delta shelf area and not
deposited in the above described pattern.

Therefore, it stands to reason that the current velocities most of the
time were below the minimum entrainment values, and that the currents
during deposition also were below the values needed to keep the entrain-
ment sediments in constant suspension. From the present knowledge of the
shelf sediment characteristic it may also be surmized that no large scale
migratory sediment movements take place along the offshore sea bottom
areas, whereas bed transport may well take place in the estuary cone
areas with somewhat coarser sediments.

1.2   Entrainment of sediments by unidirectional flow

        Considering the limited accuracy of modelling procedures and the
present state of basic knowledge of sediment transport processes, it is
useless to delve into great detail of the transport mechanisms in order
to determine the relative sediment transport over the model domain.
Comparison of Hjulstrøm's diagrams (reproduced in (2) and (5)) with the
results of Boneville, Pernecker, Vollmers and Dou Go-zen (6) yields a
fair presentation of sediment entrainment relationships. All the diagrams
are in log-log representation and visual similarities conceal great
differences in actual values. Hjulstrøm's emirically determined dia-
grams refer to average flow velocities in rivers and streams and to
sediments of uniform texture. There are significant differences between
the actual values of the original paper of 1935 (2) and the later paper
of 1939 (5). Dou Go-zen's diagrams is based on theoretical considerations
involving the submerged weight of the grains, the water depth and the
adhesion between the thin water films surrounding the single grains. In
the quoted reference it is not stated clearly whether the mean velocity
refers to mean over cross section of flow or mean of near-bottom currents.
Boneville's diagram introduces the non-dimensional parameters

$$D* = (\frac{\rho' \cdot g}{\nu^2})^{1/3} \cdot D \quad \text{and} \quad R* = \frac{u* \cdot D}{\nu} \text{, with } \rho' = \frac{\rho_s - \rho}{\rho} \text{,}$$

ρ_s and ρ specific mass of respectively grains and fluid, ν= kinematic
viscosity, D = grain diameter, $u*$= shear velocity representing equally

well tangential stress $\tau = \rho \cdot u_*$. Bonneville also introduces mean flow velocity v by writing the Strickler formula as $v = 21 \cdot (\frac{h}{D})^{1/6} \cdot \sqrt{h \cdot I}$ and $u_* = 0,15 \cdot (\frac{D}{h})^{1/6} \cdot v$. The coefficient 0,15 is $\sqrt{g}/21$, and g would thus be 9,81 m/sec^2 and the subsequent diagram is in meter units. $21 \cdot (\frac{h}{D})^{1/6}$ would be Chezy's coefficient of dimension $m^{\frac{1}{2}} \cdot sec^{-1}$.

Bonneville's diagrams represent $v = 22 \cdot h^{1/6} \cdot D^{1/12}$ (h and D in m) for 0,01 cm$< D \le$ 0,1 cm and $v = 55 \cdot h^{1/6} \cdot D^{13/30}$ for D>0,1 cm, in non-dimensionless formulation respectively $D* = 2,5 \cdot R*^{4/5}$ for R*<12 and $D* = 3,8 \cdot R*^{5/8}$ for R*>12. The diagrams are valid only for R*>1. With $\rho' = 1,65$; g=981 cm.sec^{-1}; $v = 0,01$ cm^2.sec; $D* = 253 \cdot D$ (D in cm) and R*=1 corresponds to D*=2,5 or D=0,01 cm. This is below D-values for minimum entrainment velocities in Hjulstrøm's and Dou Go-zen's diagram, and $v = D^{1/12}$ certainly cannot remain valid for very fine sediments. Hjulstrøm's diagram (5) has minimum value of v for D$\sim$0,4-0,5 mm, whereas the 1935 diagram and Dou Go-zen's diagrams have minimum value for D=0,2 mm. Introducing the constant factors in Dou Go-zen's formula yields

$$v^2 = 11200 \, D + \frac{3,4}{D} (1 + 0,0082 \cdot h), \text{ v in cm.sec}^{-1}, \text{ h and D in cm.}$$

For h=0 minimum value of v occurs for $D^2 = 3,4/11200$, D=0,0175 cm and is v=20 cm.sec^{-1} and not about 14 m.sec^{-1} as shown in the diagram. The strong dependence of v on h for fine materials is not easily explainable physically and is much more pronounced than for Hjulstrøm's or Dou Go-zen's diagrams.

Many formulas introduce critical drag in the form $\tau_{cr} = const \cdot g \cdot (\rho_s - \rho) \cdot D$, with $\rho_s - \rho$ being <u>mass</u> per unit volumen. Leliavsky (7) plotted different tests results and arrived at the simple expression $\tau_{cr} = const \cdot D$, which is identical to the above formula if the tests were made on materials with same ρ_s. It is obvious from Leliavsky's diagram that application is doubtful for d<1,0 mm. Introducing $\tau_{cr} = \rho \cdot u_*^2$, $R* = \frac{u_* \cdot D}{v}$ and $D* = (\frac{\rho' \cdot g}{v^2})^{1/3} \cdot D$ in the critical drag formula yields $R*^2 = const \cdot D*^3$, where the constant is the same as in the drag formula. The constant may be determined from Leliavsky's diagram with $\tau_{cr} = 500$ grams per sq.m for D=3 mm, or 0,5 kg.m^{-2} = const.1650 kg.m^{-3} 0,003 m, or const=0,1, and $D* = 2,15 \cdot R*^{2/3}$ as against $D* = 3,8 \cdot R*^{5/8}$ by Bonneville.

Hjulstrøm's and Dou Go-zen's diagrams depict entrainment under flow
conditions varying from flow over a smooth surface of fine materials
bordering on clays via flow over coarser materials able to form ripples
to flow over a rough bottom with ration between drag force and gravita-
tional force determining initial entrainment. A minimum value of the
curve v versus D is recognized by both authors. For D<0,004 cm (refer
(6), p.38) the surface 'breaks' suddenly and the sediments go into
suspension, but for increasing value of v with decreasing grain size.
With u_* proportional to v and only slightly dependent on D (refer (6),
p.39), v^2 would approximately be proportional to the tangential shear
stress, and in case the shear strength of the sediments increases approxi-
mately proportionally to $D^{-\frac{1}{2}}$, ε_K in Dou Go-zen's formula would be nearly

constant with dimension force/length. For fine sand and silt fractions
the'cohesion' between the grains is probably not cohesion in exactly the
same sense as used for clay minerals (D<0,0002 cm), but the shearing
behaviour of loosely deposited fine sands and silts does approach that
of 'quick' clays (8). The undrained shear strength would, however, vary
strongly with the porosity, and for same grain size the porosity can vary
very much according to conditions of deposition and consolidation. If,
however, bottom materials with D<0,004 cm go directly into suspension
when broken loose by the flow, such a bottom would have been formed by
slow settlement of the same materials during small flow velocities and
would in so case be near the loosest state of deposit. Its shear strength

then conceivably vary approximately linearly with D^{-1}, so that $\rho.v^2 \simeq const/D$,
where the constant would in some intricate manner represent the forces
binding together the particles of any size D and involving the water films
around the grains, but not in the manner expressed in the last part of
Dou Go-zen's formula.

Hjulstrøm's and Dou Go-zen's diagrams represent clearly a superposition
of an approximately linear relationship in D expressing drag force $\rho.v^2$
on coarse materials and an approximately hyperbolic relationship expressing
shear stress $\rho.u_*^2$ on a fine material bottom surface, and through the
superposition the diagrams are made applicable to the whole range of
materials above clay size. Mixed materials as found in nature will no
doubt present special problems, as such soils according to the grain size
distribution and consolidation may vary in character from being sandy to
being clayey. The project will study these problems in the laboratory on
actual Delta materials with in-situ composition and properties.

The above quoted entrainment formulas are based on flume tests or flows
in rivers and streams and corresponding mean velocities across the flow
section and boundary layer conditions and are not necessarily directly
applicable to velocities of unidirectional flow measured in-situ near the
sea bottom. Especially the strong dependence on depth h may be questionable
for the open shelf area beyond the breaker zone and up to 100 m depth and
more. In view of the many uncertainties involved as shown in the above
deliberations, Hjulstrøm's diagram may serve as well as any other formula
as basis for initial model verification. Within the ranges of grain size
found on the Delta shelf the diagram may for practical (computerized) use

be expressed by the algebraic formula $v^k = a_1 \cdot D^m + a_2 \cdot D^{-n}$, (k,m and n positive), in which m/k and n/k represent the extreme slopes in the log-log representation of the combined curve. k,m,n, a_1 and a_2 are determined from the following values read from Hjulstrøm's diagram:

> Slope m/k : D=1 cm, v=100 cm.sec^{-1}, D=0,01 cm, v=4 cm/sec
> Slope n/k : D=0,0002 cm, v=150 cm.sec^{-1}, D=1 cm, v=0,8 cm/sec
> Min. velocity 12 cm.sec^{-1} (for 0,02 cm<D<0,03 cm).

The resulting <u>dimensional</u> equation is

$$v^{1,56} = 1320 \cdot D^{1,09} + 0,71 \cdot D^{-0,96}$$

For coarse materials the equation reduces to $v^2 = 10,000 \cdot D^{1,40}$, and for fine materials to $v^2 = 0,65 \, D^{-1,23}$. These powers to D are somewhat different from those in Dou Go-zen's formula, but there is really no reason to expect any simple algebraic expression with rounded exponents when the complexities of the entrainment processes are borne in mind.

If Hjulstrøm's diagram is substantially correct, dimensional analysis of the above formula would show that $v^2 \approx g \cdot D$ for coarse materials and $v^2 \approx c / \rho \cdot D$ (c=cohesion) for fine materials are too simplified relationships, although dimensionally correct. This is no wonder, as Hjulstrøm's curve really represents physical entrainment processes varying continuously in character from fine to the coarse materials, involving over half the range varying cohesive type forces obeying non-mechanical physical laws and also smooth bottom boundary flow, and over the other half of the range rough, ripple forming bottom conditions with correspondingly varying turbulence and drag forces on single sediment grains.

When the formula $v^{1,56} = 1320 \cdot D^{1,09} + 0,71 \cdot D^{-0,96}$ (v in cm.sec^{-1}, D in cm) is not non-dimensional, it is to be interpreted that materials of a certain diameter D will be entrained at a correspondingly defined velocity v given by the formula, whichever the entrainment mechanism may be.

1.3 Entrainment of sediments by wave motion

Plotting the laboratory results of different investigations in a D*/R* diagram, Bonneville and Pernecker (refer (6)) conclude that relations D*=f(R*) for unidirectional flows are also applicable for initiation of sediment transport by wave motion if

$$R* = 2,2 \cdot \frac{D}{\nu} \left| \frac{\nu \cdot H^2}{T^3 \cdot \sin^2 h \frac{2\pi d}{L}} \right|^{1/4}$$

where H,T,L are the wave characteristics and d is water depth. Introducing maximum particle velocity near the sea bottom (first order)

$$U = \frac{\pi \cdot H}{T \cdot \sinh \frac{2\pi d}{L}} \quad \text{and} \quad D* = \frac{(\rho' \cdot g)^{1/3}}{\nu^2} D \quad \text{into formula } D* = 2,5 \, R*^{4/5} \text{ yields}$$

$$R* = 2,2 \cdot \frac{D}{\nu} \cdot \left| \frac{\nu \cdot U^2}{\pi^2 \cdot T} \right|^{1/4} \quad \text{and} \quad U^2 = D \cdot T \cdot \frac{(\rho' \cdot g)^{5/3}}{\nu^{1/3}} \cdot \frac{\pi^2}{2,5^5 \cdot 2,2^4}$$

or with $\nu=0,01$ cm^2.sec^{-1}, g=981 cm.sec^{-2}, $\rho'=1,65$ $\underline{U^2/T = 4470 \cdot D}$
(U in cm.sec^{-1}, T in sec, D in cm).

U/T is an acceleration and in case the maximum acceleration near the sea
bottom, with phase angle $\pi/2$ with U, is denoted by U', the relation between

U and U' is $U' = \frac{2\pi}{T} \cdot U$, yielding from above equation $|U \cdot U'| = 28000 \cdot D$,

indicating that U and U' might play equal roles for the entrainment of
coarse sediments. The relationship D*=2,5 R*$^{4/5}$ is probably not valid
for D*<5, or D<0,02 cm, and certainly not down to D=100μ as shown in the
nomograph. Grains of diameter D will be entrained at any water depth if
$U^2/T \geq 4470 \cdot D$, where U is maximum orbital velocity. Reverting to H,T,L and d,

$$U^2/T = \frac{H^2}{T^3} \cdot \frac{\pi^2}{\sin^2 h \frac{2\pi d}{L}}$$, L being a function of T and d. In a(d,T) diagram

the lines $U^2/\pi^2 H^2 \cdot T$ = const. can be drawn, showing equal entrainment
capacity in terms of d and T (fig.2), but of course varying with H^2.

With $U = \frac{\pi \cdot H}{T \cdot \sinh \frac{2\pi d}{L}}$, lines for $\frac{U}{\pi \cdot H}$ = const. are shown in fig. 3 in terms

of T and d. The diagrams figs. 2 and 3 can be superimposed on each
other, yielding (H,D) lines shown in fig. 3 (for maximum and minimum
values of D only).

It is seen from the superimposed H-lines in fig. 3, that sediment entrain-
ment takes place at nearly constant orbital velocity over the (T,d) range,
depending practically only upon H. From figs. 2 and 3 can also be calculated
that entrainment of sediments with D=0,02 cm takes place at the following
values of U

H cm	100	200	300	400	500	600
U cm.sec^{-1}	29	30	32	33	32	32

or av. U$\sim$32 cm.sec^{-1}, and entrainment for D=1 cm at the following values of U

H cm	100	200	300	400	500	600
U cm.sec^{-1}			190	210	225	205

or av. U$\sim$210 cm/sec. Introducing these values in the equation

$(k.U)^{1,56}= 1320 \cdot D^{1,09} + 0,71 \cdot D^{-0,96}$, in which k is a constant, yields k=0,38
for D=0,02 cm and k=0,48 for D=1 cm. Tentatively a factor $\underline{k=0,40}$ is proposed
for the Nile Delta model. As the velocity is governing, it $\underline{\text{is}}$ reasonable to
assume initially for the verification of the model that the $\underline{\text{same}}$ formula
applies both for sediment entrainment by unidirectional flow $\underline{\text{and}}$ by wave
motion, provided v in unidirectional flow is replaced with $\underline{0,40 \cdot U}$ in wave
motion. Here again the dimensional aspects are ignored, attributing the
lack of non-dimensionality to the complexities of the true mechanisms,
involving boundary layer turbulence influenced by D and also cohesional
forces for finer sediments.

1.4 Entrainment of sediments by combined wave and current action

If the entrainment criterium for the formula D*=2,5·R*$^{4/5}$ is initial
movement of sediments, the reduction factor k found for the orbital velocity
originates presumably from lesser turbulence in the boundary layer of
oscillating motion than for unidirectional flow. The combined wave and

$$C = T^3 \propto SINH^2 \frac{2\pi d}{L} \qquad \frac{U^2}{T} = \frac{\pi^2 H^2}{C}$$

Sediments will be entrained for $U^2/T^2 \geqslant 4470 D$

U = max. orbital velocity (cm/sec)
H = wave height (cm)
D = grain size (cm)
T = wave period (sec)

For same wave height, lines C = constant represent
sets of (T, d) with equal entrainment capacity
D > 0.02 cm.   H < 0.78 D

FIG. 2. - ENTRAINMENT OF SEDIMENTS BY WAVE MOTION.

FIG.3. - DIAGRAMS FOR $U/_{\pi H}$ = CONSTANT AND $U^2/_{\pi^2 H^2 T}$ = CONSTANT.

$$U = \frac{\pi H}{T * SINH \frac{2\pi d}{L}} \qquad C = T * SINH \frac{2\pi d}{L} \qquad \frac{U}{\pi H} = \frac{1}{C}$$

U = max. orbital velocity   (cm/sec)
H = wave height   (cm)   H < 0.78
T = wave period   (sec)

For same wave height, lines $1/C$ = constant represent sets of (T, d) with equal max. orbital velocity

current motion is likely to increase the turbulence, depending upon
relative magnitudes and directions. However, for the relative effects
of different combined wave and current motions, such increased turbulence
may be of lesser importance.

The question arises, however, whether current velocities and reduced orbital
velocities (numerical values) shall be added vectorially, or numerically,
independently of directions. There is for the author an intuitional
motivation for the latter, maybe coupled with a weighting function
reflecting dominance of one or the other motion. Knowledge on this problem
is very scarce, and the project shall have to study this matter further.

2. Quantities of sediments entrained and transported

2.1 Sediments in suspension

        The difficulties to be overcome in order to determine the quantities
of sediment entrained during wave motion can be judged for instance from
(9), in which Einstein takes recourse to a strictly empirical approach in
order to deal with fine sediments in suspension, and from the more theore-
tical approaches of (10) and (11). Field measurements and laboratory tests
show a considerable upwards diffusion of fine sediments during wave motion,
and assuming turbulent flow and equilibrium between settlements due to
gravity and upwards movements due to diffusion towards lower concentrations
as for uniform flow, the concentrations at specified levels above the sea
bottom can be expressed in terms of fall velocity of suspended particles,
shear velocity of flow and von Karman's constant, provided the concentration
at a reference level near the sea bottom can be determined by measurements.

Jensen and Sørensen (12) found by field measurements in the open sea, that
the transport by ocean currents of fine materials brought into suspension
by wave action could be calculated from the concentrations for unidirectional
flow, when the concentration near the bed is determined solely from wave
conditions and the concentrations at higher levels solely from the ocean
current flow profile with shear velocity $u_* = 0,05$ times average velocity
over depth. These authors also believe that there is an (unproven) propor-
tionality between the concentration near the bed and the third power (U^3)
of maximum orbital velocity near the sea bottom. From observations of
agitated seas it appears that the equilibrium distribution of suspended
materials is reached quickly once the initial entrainment velocities are
reached, and that the sediments settle relatively fast after cessation of
wave action. In the quoted reference (12) with silt of 0,08 mm median diam.
90% of the actual materials in the sea have settling velocities less than
7.10^{-3} m/sec, and the materials are practically all within 7 m from the sea
bottom, requiring thus max. 20 min. for settling on the bottom if no currents
are present. The period of effective entrainment can thus be determined from
B/1.2-1.4 above, while relative quantities of entrainment could possibly be
determined from U^3 and the equilibrium concentrations, and the transport
directions and distances are determined by the actual ocean currents. The
wave mass transport is of secondary order, but may play a role in shallower
water with largest concentrations of suspended materials. The influence of
the elliptic tidal flows along the Delta coast is presumably negligible.

In the case of the transport of suspended materials in the sea, an average
current velocity over the depth can most likely be applied, thus facilitating
the numerical integration of the sediment concentrations over the profile.

The work and suggestions cited from reference (12) will be studied closer
by the project, probably in collaboration with the Suez Canal Authority,
faced with a similar problem at the entrance of the Suez Canal. The
results will have to be generalized to be applicable to all conditions
in the shelf area.

2.2 Bed load sediments

In the Nile Delta shelf area considerable quantities of sediment
are being eroded from the estuary cones, and a considerable part of the
eroded sediments is most likely being transported as bed load, mainly by
ocean currents after agitation by wave action. In order to verify a model
comprising all sediment movements not affected by wave breaking, it will
most probably be necessary to take the estuary cone materials into consideration.
The proposals by Sternberg (13), modified to consider the combined wave
and current motions, may perhaps be applicable for this part of the trans-
port; being based on a logarithmic velocity profile in the boundary layer,
the method is akin to and can be compared with the classical bed load
calculations (refer for instance (6), p.41). This problem is, however,
outside the scope of this paper, but it is worth to note, that after
Bagnold (14) the bed load transport (flux per unit area per time unit)
for unidirectional flow is proportional to u_*^3, and in Sternberg method
u_* is calculated as $u_*=5,47.10^{-2}.U_{100}$, where U_{100} is mean velocity measured
100 cm above the sea bed. In (12) u_* is taken as 0,05 times the average
ocean current velocity over the depth of the flow profile. According to
Bagnold and Sternberg the average mass per unit area of bed load sediments
moved by combined wave and current action would be proportional to U^2.

3. Geomorphological changes

To specific hydrodynamic conditions correspond specific 'saturation'
profiles of suspended sediments, and in case a profile is undernourished,
it will soon pick up additional materials from the sea bottom, while sedi-
ment will be deposited in profiles overnourished due to greater influxes
than discharges from a specific area. This is a three-dimensional model
akin to the two-dimensional model for nearshore changes, in which erosions
or accretions are determined from the variations in wave power and trans-
port capacity.

In practical application the model will have to operate with fields of
varying wave and current intensities and corresponding concentrations and
rates of movement of suspended sediments. In principle the model will be
Eulerian, dealing with discrete differential variations with time, in each
point representing a subdivision of the model area. Theoretically, the
deposition of erosion per unit time in each unit area of the model is
determined (i) from the variation in entrainment capacity as determined
from the force fields, water depths and sediment characteristics and (ii)

from the variation in concentration along the ocean current flow lines through the unit area. In practice, the calculations will be made for large discrete space and time intervals, but this presents no principal problems. The wave motion contributes only to the sediment entrainment, while only the ocean currents contribute to the shifting of the sediments. If the entrainment force field can be considered constant over a time unit and over distance v along the flow line, where v is the ocean current flow velocity, a surface $z=f(x,y)$ can represent the momentaneous total sediment concentrations above the model area, and a new surface $z=g(x,y)$ created by shifting all the ordinates z a distance $v=h(x,y)$ along the flow lines would represent the sediment distribution over the model area one time unit later. If the agitating motion suddenly stopped and the suspended sediments settled rapidly, the difference between $z=f(x,y)$ and $z=g(x,y)$ would represent the morphological changes (in volumen) over the model area during the time unit considered. The entrainment force field need, however, not be constant for any length of time, and neither the ocean current velocity field, and the sediment concentration variations and the morphological changes must be calculated by taking the force and velocity variations with time into consideration.

CONCLUDING REMARKS

This paper outlines the initial thoughts on how to establish and operate a geomorphological model covering the Nile Delta continental shelf area. Years of trial and error and further development work may lie ahead and only the future can show whether the task is possible in the sense, that fairly reliable predictions of future coastal changes can be made by operating the model. Theoretical and practical studies by the project or elsewhere may well change the concepts or introduce new ideas and approaches, but a start has to be made and it is believed that the chances for success are greatly improved, if during all project studies the ultimate goal of creating a model for prediction is kept in mind.

The many deterministic and statistic inaccuracies involved in the model framework are only too obvious for the coastal engineer, but it is fundamental for the proposed modelling, that satisfactory verification against known states of the model area is the decisive element governing the stability and usefulness of the model. In dealing with nature's processes the author advocates the principle of determining first the approximate framework through some assessible upper and lower limit values of the unknown factors and thereafter gradually increasing the accuracy by narrowing the margin between the upper and lower limit values. Once the stage is reached, where a model can reproduce the resemblance of a known state from another known state, the processes of refinement can be tackled rationally.

ACKNOWLEDGEMENTS

REFERENCES

(1) NIELSEN, EV. (1973) - Coastal Erosion in the Nile Delta. Nature
    and Resources, Unesco.

(2) SCHEIDEGGER, A.E. (1970) - Theoretical Geomorphology.

(3) STRAKHOV, N.M. (1967) - Principles of Lithogenesis.

(4) Oceanographic Atlas of the North Atlantic Ocean (1968) - Section 1,
    Tides and Currents; U.S. Naval Oceanographic Office.

(5) KUENEN, Ph.H. (1960) - Marine Geology.

(6) PIANC (1969) - Section II, Subject 4.

(7) LELIAVSKY, S. (1959) - An introduction to Fluvial Hydraulics (p.45).

(8) Norwegian Geotechnical Institute (1961) - Publication No. 45.

(9) EINSTEIN, H.A. (1972) - Sediment Transport by Wave Action; 13th Coastal
    Engineering Conference 1972,(p. 933).

(10) KENNEDY, J.F. & LOCHER, F.A. (1972) - Sediment Suspension by Water
     Waves. Waves and Beaches (ed. R.E.Meyer), (p.249).

(11) TELEKI, P.G. (1972) - Wave Boundary Layers and their Relation to
     Sediment Transport. Shelf Sediment Transport (ed. Swift et al.),
     (p.21).

(12) JENSEN, J.K. & SØRENSEN, T. (1972) - Measurement of Sediment Suspension
     in Combination of Waves and Currents. 13th Coastal Engineering
     Conference 1972 (p.1097).

(13) STERNBERG, R.W. (1972) - Predicting Initial Motion and Bed Load Trans-
     port of Sediment Particles in the Shallow Marine Environment. Shelf
     Sediment Transport (ed. Swift et al.) (p.61).

(14) BAGNOLD, R.A. (1963) - Beaches and Nearshore Processes. The Sea
     (ed. M.N.Hill), vol. III, (p.507).

(15) PROJECT EGY/70/581 (1973) - Technical Report No.1 (to be published
     shortly), Academy for Scientific Report and Technology, Egypt,
     United Nations Development Programme (UNDP) and United Nations
     Educational, Scientific and Cultural Organization (UNESCO).

CHAPTER 39

LONGSHORE CURRENTS AND WAVES AT BURULLUS COAST

By

M. Manohar (1), I.E. Mobarek (2) and A. Morcos (3)

ABSTRACT : Littoral currents within the breaker zone and currents other
than those induced by waves beyond the breaker zone exist with considerable
magnitude along the Nile Delta coast. Analysis of the littoral currents
within the breaker zone by four semi-empirical formulae involving energy,
momentum and radiation stress principles indicates good correlation bet-
ween predicted and observed velocities. Galvin-Eagleson approach gives
the best fit. Current data are statistically analysed enabling the
determination of the magnitude, direction and percentage of occurrence
of any particular littoral current for any particular period.

More comprehensive studies of the currents climate within the breaker
zone and beyond the breaker zone for the entire Nile Delta coast covering
a large number of years are under way.

INTRODUCTION : The complex offshore and nearshore processes which change
continually are mainly due to two sources of energy, namely due to waves
and due to currents other than those induced by waves. In the very shallow
water zone and especially the breaker zone when waves break at an angle
with the beach, the momentum of the breaking waves generates a longshore
current along the beach and thus inside the breaker zone, such wave-induced
currents predominate over other currents, though the situation may be re-
versed beyond the breaker zone and other currents such as tidal or wind
driven currents may predominate.

Though there has been many attempts for a theoretical solution of the
longshore currents, they have not been highly successful. The main defects
are in the assumptions made in regard to the variables which simplify the
complexity too drastically. Moreover, rip currents, types of breakers,
underwater topography and interdependence of some of the variables further
complicate the analysis. Similarly empirical analysis can be only as good
as the data on which it is based and data even with sophisticated instru-
mentation are very difficult to get especially in the breaker zone.

THEORY : There are at least three different methods of analysis of longshore
currents namely (i) use of semi-empirical formulae based on theory and field
data which require obtaining the best fit between actual field data and
predicted velocities for each particular location; (ii) combining the

---

(1) Hydrodynamics Engineer (UNESCO), Unesco Project ARE 81, Coastal Erosion
Study, Alexandria, ARE.
(2) Assoc. Prof. of Civil Engineering, Cairo University, Cairo, ARE.
(3) Senior Engineer, Coastal Erosion Study, Academy of Science and
Technology, Cairo, ARE.

individual variables linearly through a method known as multiple linear regression (6), and (iii) attempting a non-linear approximation using a product form of optimum powers of individual variables. However, only the first approach was attempted in this paper due to the type of available field data.

There are at least 15 different equations proposed by different investigators (1,2,3,5,7,8,9,10,11,12,13,14,15) but they can be divided into four classes namely: the momentum balance, energy balance, conservation of mass and empirical correlation of data. All of them are based on simplified bottom topography, and a steady state of equilibrium either in terms of momentum exchange, energy and conservation of mass, or continuity. Some are based on rip currents also though they have not been used in this study due to the absence of rip currents in the area of field study.

The following four formulae were used.

1. Brebner and Kamphuis (2), 1963.

   (a) Energy Balance

$$V_{\ell Be} = \frac{8H_o}{T^{1/3}} \left| \sin 1.65\theta_o + 0.1 \sin 3.30\theta_o \right| \sin\alpha^{1/3} \quad \text{in ft/sec} \quad (1)$$

   (b) Momentum Balance

$$V_{\ell Bm} = \frac{14H_o^{\frac{5}{4}}}{T^{\frac{1}{2}}} \left| \sin 1.65\theta_o + 0.1 \sin 3.30\theta_o \right| \sin\alpha^{1/3} \quad \text{in ft/sec} \quad (2)$$

In these V_ℓ = longshore component of current in the breaker zone, H_o = deep water wave height, T = period, θ = angle between the wave crest and the bottom contours, and $\tan\alpha$ = beach slope.

They have the advantage that they contain deep water equivalents of wave characteristics which are the fundamental variables available from wave forecasting techniques. In the energy balance principle, the total energy of an incoming wave is assumed to be dissipated in the breaking wave, in the frictional resistance of the bottom and in generating the longshore current. The momentum approach considers the momentum given to a volume of water put into motion in the direction of wave propagation when the wave breaks. The alongshore component of this momentum provides energy of the longshore component.

2. Galvin-Eagleson (5), 1965. The Galvin-Eagleson formula, namely:

$$V_{\ell G} = KgT \tan\alpha \sin 2\theta_b \quad \text{(m/sec)} \tag{3}$$

is based on both field and laboratory data and on the momentum balance principle. K, a coefficient, has been assumed to be unity though it varies from 0.6 to 1.1 .

3. Komar-Inman (1,10,11), 1970. The Komar-Inman formula, namely:

$$V_{\ell K} = 2.45 U_m \sin\theta_b \quad \text{(m/sec)} \tag{4}$$

is based on both field and laboratory data and assumes that the long-
shore currents are generated from the longshore component of the radiation
stress. U_m = maximum horizontal component of the orbital velocity of the

breaking wave = $\frac{1}{2}$ γ_b C_b where $\gamma_b = \frac{H_b}{d_b}$ and $C_b = \sqrt{gd_b} = g(\frac{H_b}{\gamma_b})^{\frac{1}{2}}$ (5)

FIELD MEASUREMENTS AND ANALYSIS : Measurements of currents were made at
Burullus and Ras el Bar, of the Nile Delta coast (figs.1,2) both inside
and outside the breaker zone by means of simple floats whose movements
were observed with time between two stations marked by poles. However,
only Burullus data have been reported in this paper. Within the breaker
zone, only surface currents were measured whereas beyond the breaker zone,
measurements were made in three depths, namely, the bottom, mid depth, and
surface at each station.

Simultaneously with the current measurements, wave measurements were also
made in 6-8 m depths by means of OSPOS wave recorders. With the wave
characteristics known in 6-8 m depths, values of $\frac{d}{L_o}$, shoaling coefficient,
refraction coefficient (assuming parallel contours) and subsequently deep
water wave height, breaker depth, breaker height and breaker angle were
obtained by standard procedures (4). The bottom slopes up to 6 m depths
were obtained from the monthly hydrographic surveys of the coast. Thus
with all the necessary data, longshore current velocities were calculated.
Fig. 3 shows comparison between predicted and measured velocities at
Burullus. Though the predicted velocities differ from the observed
velocities, the deviations are systematic and can be approximated by a
constant factor in each case. Galvin-Eagleson formula gives the best
fit, a conclusion previously reached by others (9) also.

Typical statistical analysis of the currents is indicated in figs. 4,5,
and 6. Fig. 4 shows the percentage of occurrence of currents for each
month whereas fig. 5 is another schematic representation of percentage
distribution. Fig. 6 represents a form of cumulative frequency distribu-
tion curve with percentage of occurrence (percent equal to or less than)
against the velocity range. From these, it is possible to determine the
directional changes in velocities, percentage of occurrences of any
magnitude of velocity and its direction. Since the direction of wind
generating the waves and wave energy govern the magnitude and direction
of littoral currents, percentages of wave energy and of wind causing the
currents are shown in figs. 7 and 8. Fig. 8 shows the existence of a
linear relationship between percentages of wave energy and current.
Fig. 9 represents some typical data of currents beyond the breaker zone.
Preliminary studies indicate that currents beyond the breaker zone generated
by forces other than those due to waves play a predominant role in the
movement of sediment along the Nile Delta coast. Since the study is
incomplete, it is not described here.
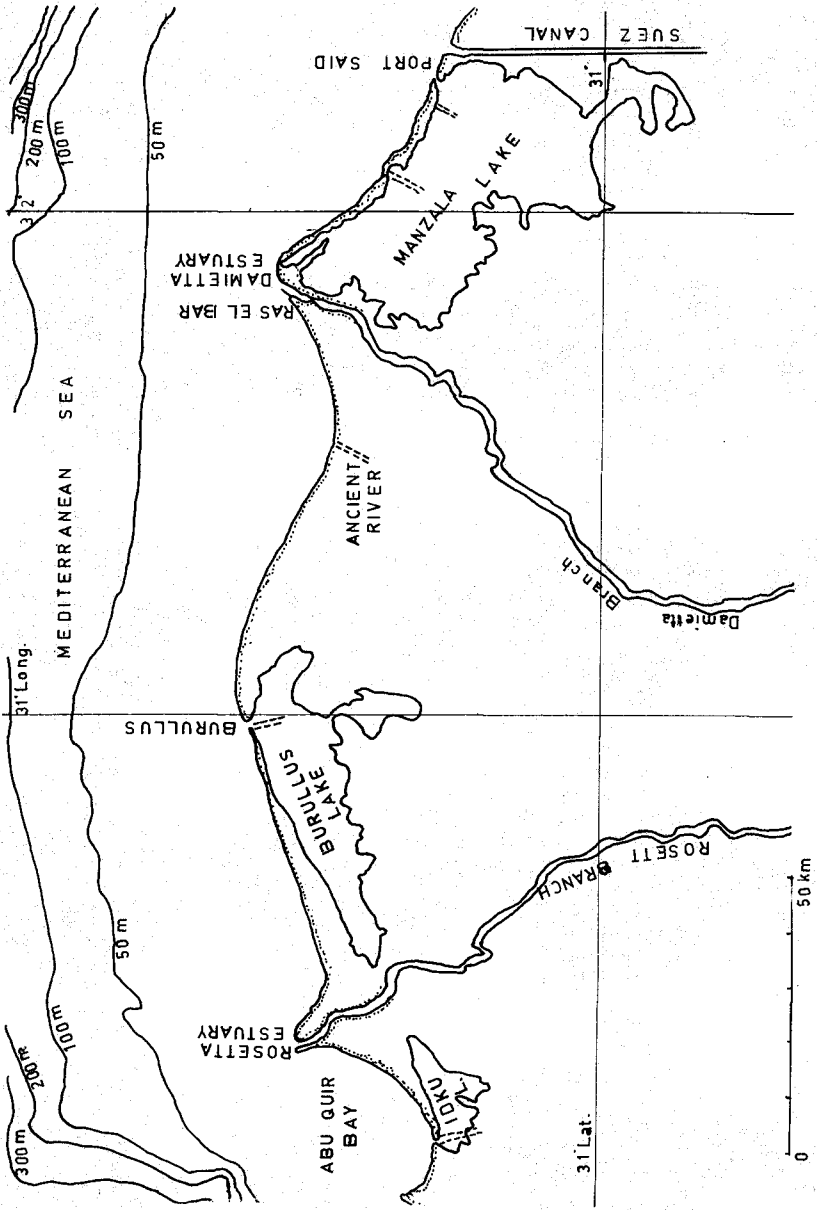
Fig. 1: Nile Delta Coast
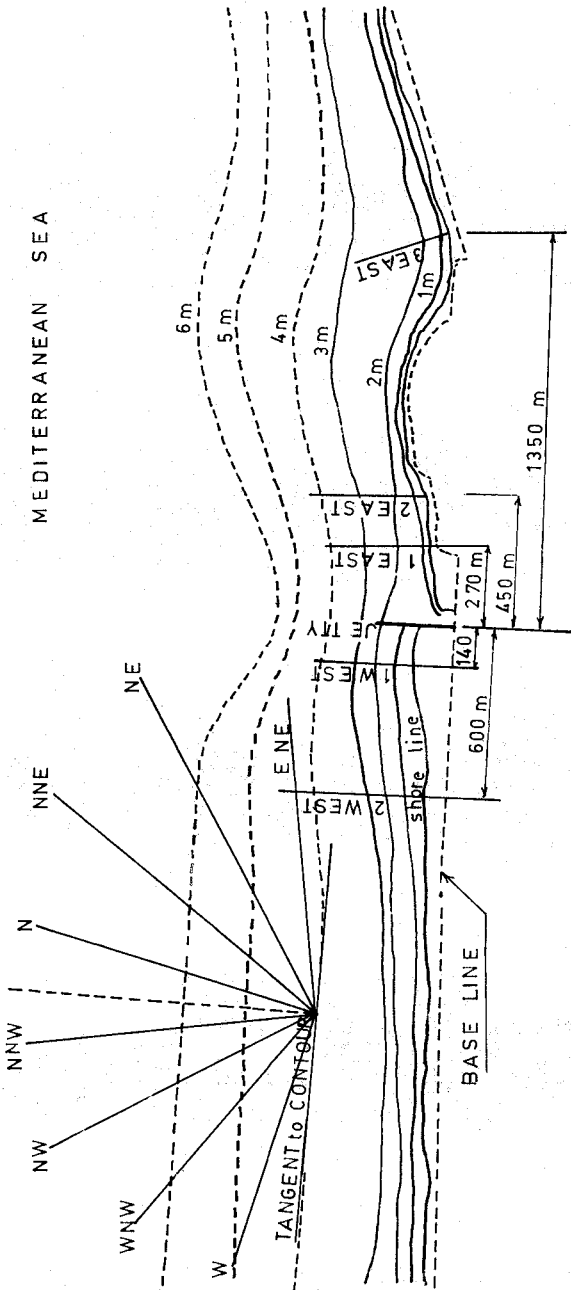
Fig. 2: Map Showing Burullus and Measuring Stations
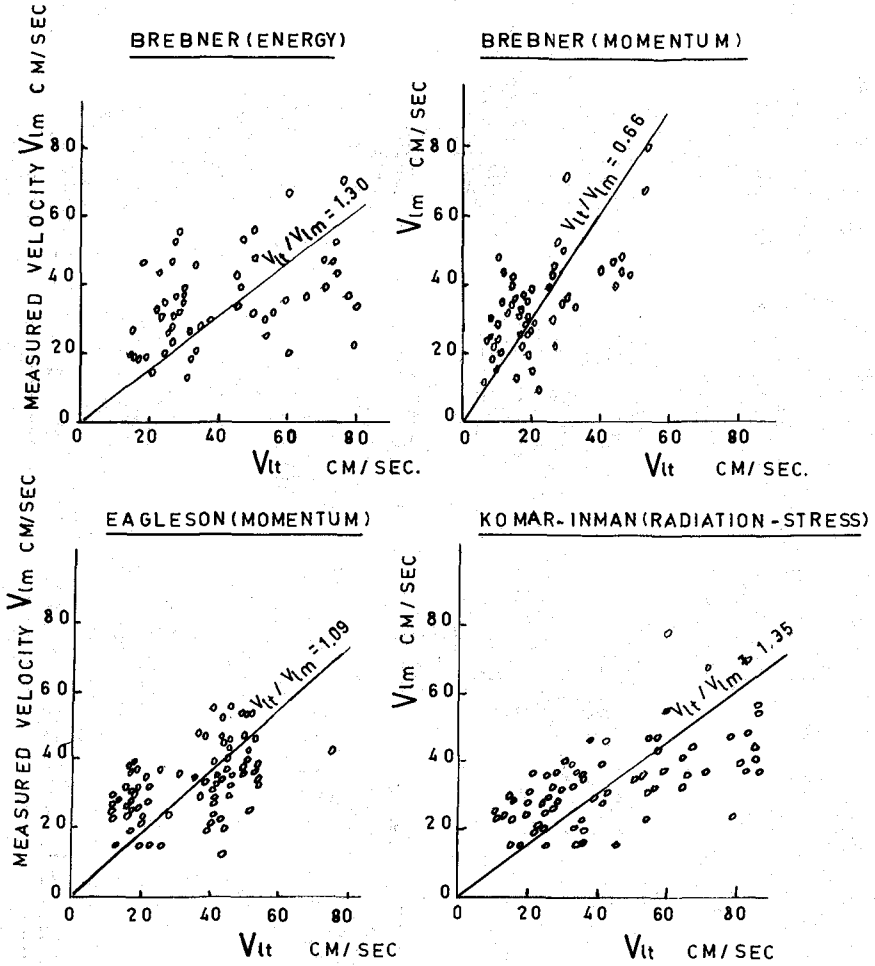
Fig 3: Correlation Curves Between Predicted and Observed Currents in the Breaker Zone at Burullus Area
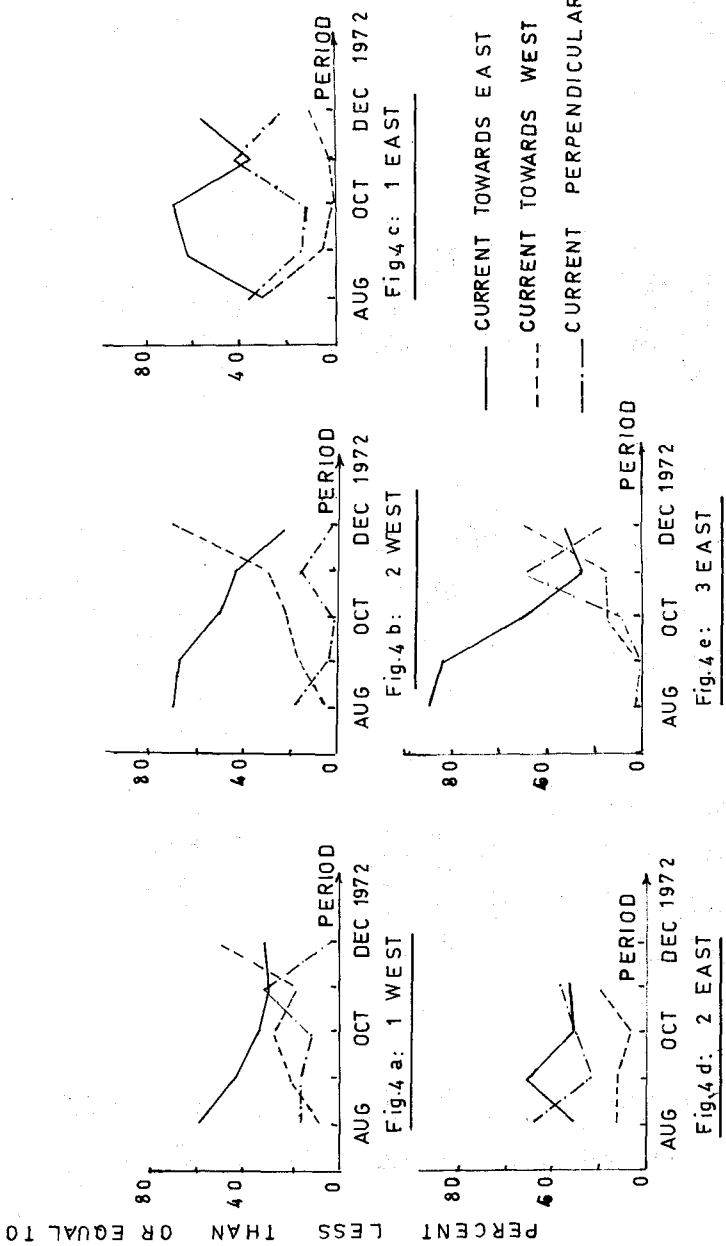
Fig. 4: Percentage of Occurrence of Currents for Each Month

(BURULLUS AREA)
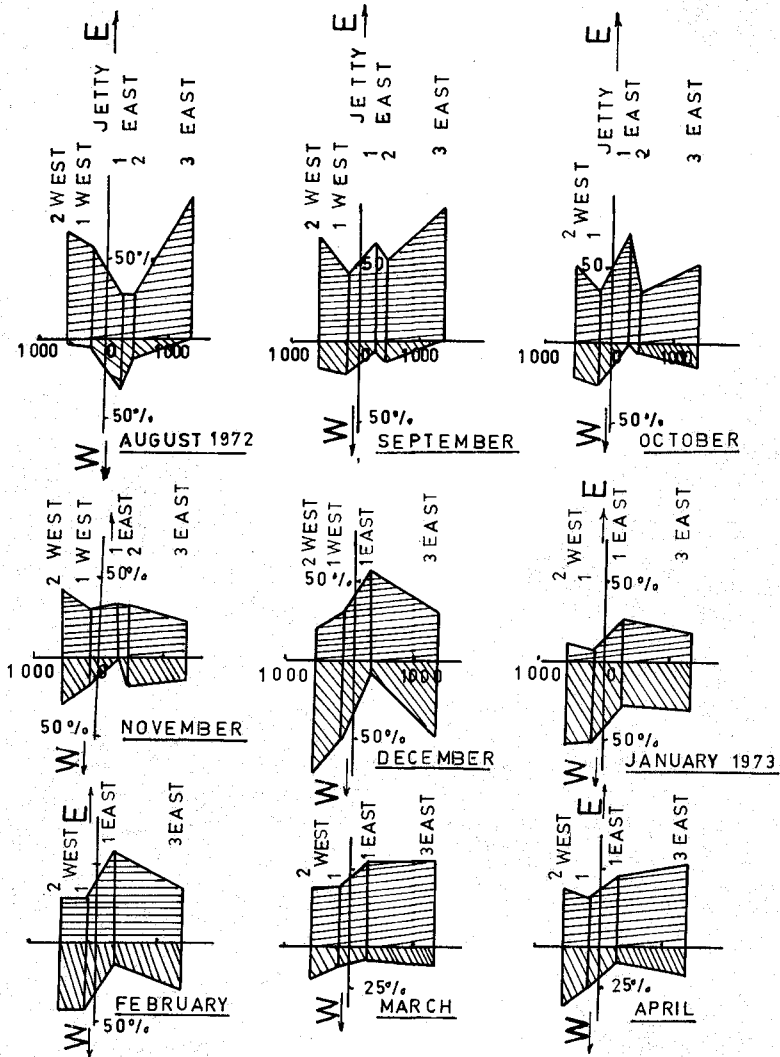
Fig.5: Percentages of Current Directions Against

Measuring Stations at Burullus
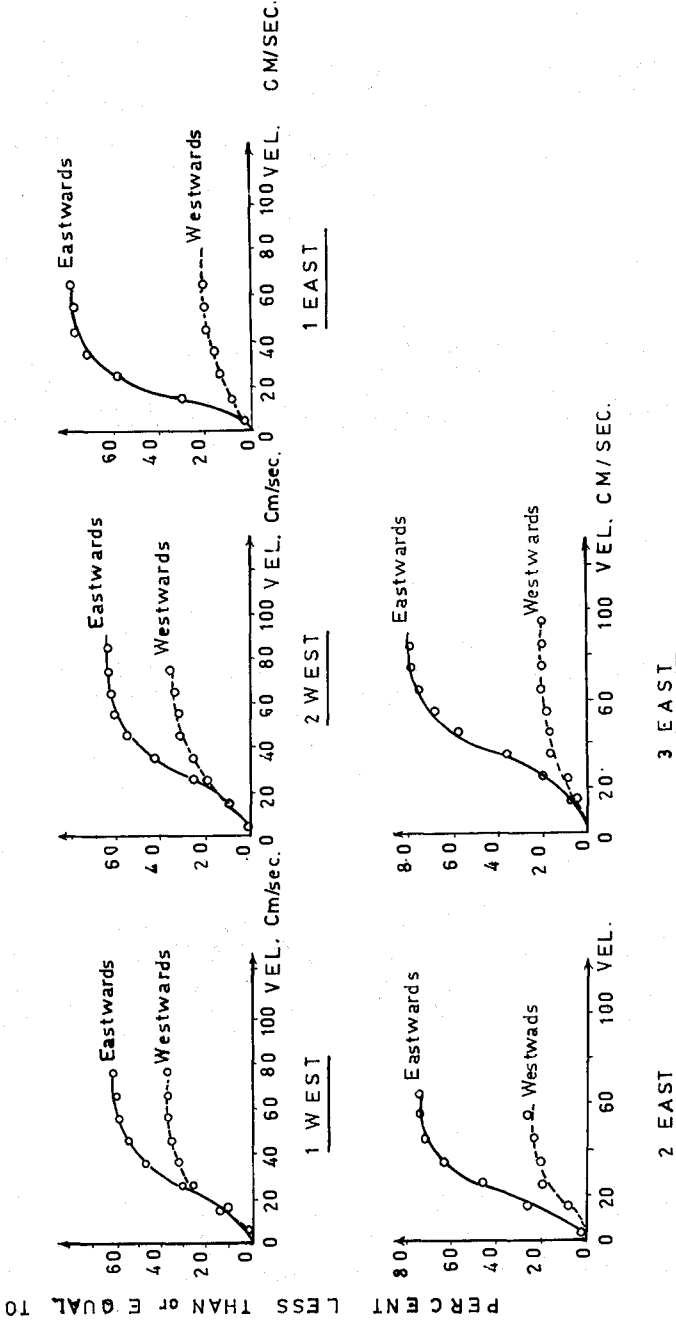
Fig. 6: Cumulative Frequecy Distribution Curves

(BURULLUS)
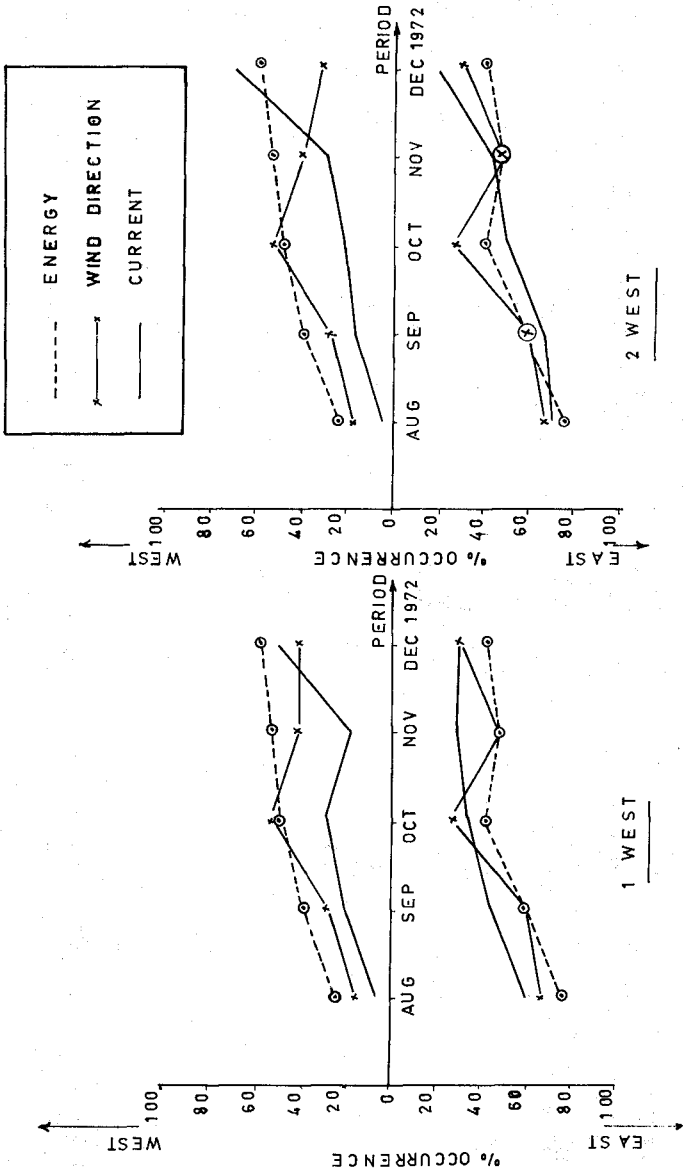
Fig. 7: Percentage Of Occurrence Of Currents , Wave
Energy and Wind Directions Against Months
at Burullus
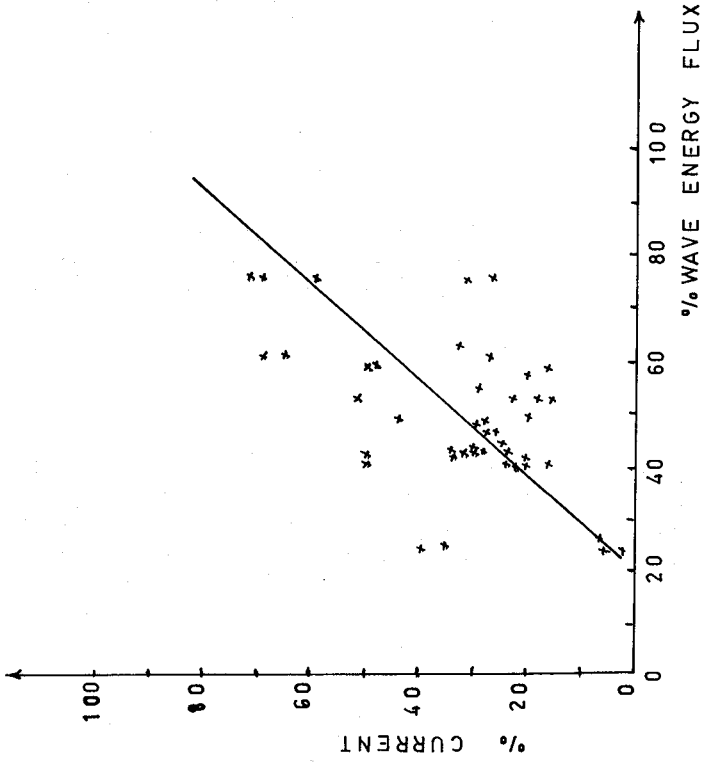
Fig.8: Percentage of Currents vs Percentage of Wave Energy Flux

STATION   5 W
Date :   5 / 4 / 1973   Time: 12.30 : 13.45
Weather calm   negligible wave action
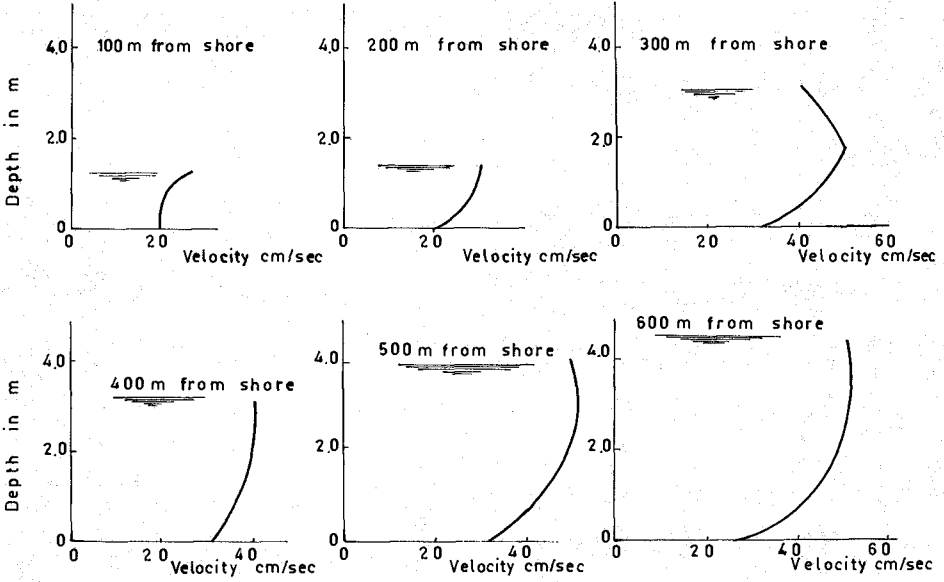
STATION   5 W
Date :   5 / 4 / 1973   Time : 10.30 - 11.30
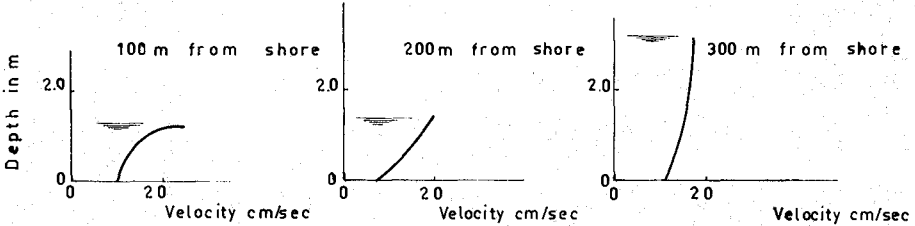
Fig. 9 : Typical   Current   Distribution
          Beyond   Breaker   Zone

SUMMARY AND CONCLUSIONS : Analysis of littoral currents within the breaker
zone measured during October-December 1972 at Burullus were checked with
four semi-empirical methods involving energy and momentum balance and
assuming steady state of equilibrium, constant underwater slopes and
straight and parallel depth contours. The constant factor between the
predicted and observed velocities in a particular direction is as follows:-
Galvin-Eagleson : 1.09; Brebner-Kamphuis (energy) : 1.30; Brebner-Kamphuis
(momentum) : 0.66 and Komar-Inman : 1.35 . Statistical analysis of the
current data namely determination of percentage of occurrence of currents
with respect to months, and cumulative frequency distribution curves for
different velocity ranges enable the determination of magnitude, direction
and percentage of occurrence of any particular littoral current for any
particular period.

Currents other than those induced by waves exist beyond the breaker zone
indicating their importance in the analysis of sediment movement along
the coast.

The above analysis of littoral currents is only a forerunner of a comprehen-
sive study of current climate (within the breaker zone and beyond the
breaker zone) along the Nile Delta coast covering a large number of years.

REFERENCES :

(1) BOWEN, A.J. (1969) - The Generation of Longshore Currents on a Plane
     Beach, Journ. of Marine Research, vol. 37, New Haven, Conn. USA.

(2) BREBNER, A. & KAMPHUIS, J.N. (1963) - Model Tests on the Relationships
     Between Deep Water Wave Characteristics and Longshore Currents, Civil
     Engineering Research, Report No.31, C.E. Dept., Queens University,
     Kingston, Ontario, Canada.

(3) BRUUN, P.M. (1963) - Longshore Currents and Longshore Troughs. Journ.
     of Geophysical Research, Washington D.C., vol. 68, No.4 .

(4) COASTAL ENGINEERING RESEARCH CENTER (1965) - Shore Protection-Planning
     and Design. Tech. Report No.4, 3rd ed. Dept. of the Army, US Corps
     of Engineers, Washington, DC.

(5) GALVIN, J.C. & EAGLESON, P.S. (1965) - Experimental Study on Longshore
     Currents on a Plane Beach. Tech. Memo No. 10, US Army Coastal Engineering
     Research Center, Washington DC.

(6) HARRISON, W. & KRUMBEIN, W.C. (1964) - Interaction of the Beach-Ocean-
     Atmospheric System at the Virginia Beach, Virginia. Tech. Memo. 7, US
     Army Coastal Engineering Research Center, Washington DC.

(7) INMAN, D.L. & QUINN, W.H. (1951) - Currents on the Surf Zone. Proc.
     IInd Conf. on Coastal Engineering. Council of Wave Research, Univ.
     of California, Berkeley, California, USA.

(8) INMAN, D.L.; KOMAR, P.D. & BOWEN, A.J. (1969) - Longshore Transport
     of Sand. Proc. 11th Conf. on Coastal Engineering A.S.C.E., vol. 1,
     New York.

(9) KING, C.A.M. (1972) - Beaches and Coasts. 2nd ed., Edward Arnold Ltd,
     London, UK.

(10) KOMAR, P.D. & INMAN, D.L. (1970) - Longshore Sand Transport of Sand,
     vol. 75, No. 50, Journ. of Geophysical Research, Washington DC.

(11) LONGUET HIGGINS, M.S. & STEWARD, R.W. (1964) - Radiation Stress in
     Water Waves: A Physical Discussion with Applications. Deep Sea Research.
     vol. 11, Washington DC.

(12) LONGUET HIGGINS, M.S. (1970) - Longshore Currents Generated By Obliquely
     Incident Sea Waves. Journ. of Geophys. Research, vol. 75, Washington.

(13) NAGAI, S. (1954) - On Coastal Groins. Proc. 1st Conf. on Coastal
     Engineering, Tokyo, Japan.

(14) PUTNAM, J.A.; MUNK, W.H. & TRAYLOR, M.R. (1949) - Prediction of Long-
     shore Currents. Trans. Amer. Geophys. Union, Washington DC, vol. 30.

(15) SONU, C.J.; Mc CLOY, J.M. & Mc ARTHUR, D.S. (1966) - Longshore Currents
     and Nearshore Topography. Proc. 10th Conf. on Coastal Engineering,
     A.S.C.E., New York, vol. 1, Chapt. 32.

CHAPTER 40

COMPUTATION OF LONGSHORE CURRENTS

Ivar G. Jonsson[1], Ove Skovgaard[2] and Torben S. Jacobsen[3]

ABSTRACT

The steady state profile of the longshore current induced by regular, obliquely incident, breaking waves, over a bottom with arbitrary parallel bottom contours, is predicted. A momentum approach is adopted. The wave parameters must be given at a depth outside the surf zone, where the current velocity is very small. The variation of the bottom roughness along the given bottom profile must be prescribed in advance. Depth refraction is included also in the calculation of wave set-down and set-up. Current refraction and rip-currents are excluded. The model includes two new expressions, one for the calculation of the turbulent lateral mixing, and one for the turbulent bottom friction. The term for the bottom friction is non-linear. Rapid convergent numerical algorithms are described for the solution of the governing equations. The predicted current profiles are compared with laboratory experiments and field measurements. For a plane sloping bottom, the influence of different eddy viscosities and constant values of bottom roughness is examined.

1. INTRODUCTION

When breaking waves approach a straight coastline at an oblique angle, a mean current tends to be set up parallel to the coastline. The prediction of such longshore currents and the associated sediment transport is of prime importance for the coastal engineer.

It has been general practice to predict the alongshore sediment transport based on simple refraction calculations. When this method is used, all wave orthogonals stop at the breaker line, and the bathymetry in the surf zone is excluded in the prediction. To calculate the profile of the longshore current would be a better starting point, and then calculate the sediment transport. Such a prediction is not yet possible, but the present paper is a step in the above-mentioned direction. A recent survey of the subject has been given by Longuet-Higgins (1972).

---

[1]Assoc. Prof., Inst. Hydrodyn. and Hydraulic Engrg. (ISVA), Tech. Univ. Denmark, DK-2800 Lyngby
[2]Sen. Res. Fellow, ISVA
[3]Ass. Oceanographer, Ministry of Environment, Denmark
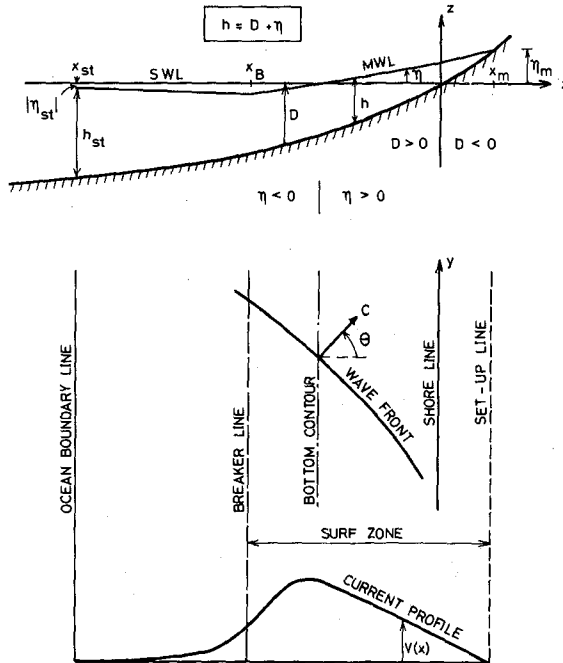
Fig. 1-A Cross section and plan

A steady state theoretical model is presented here, which for a given arbitrary variation of parallel depth contours and bottom roughness predicts the profile (mean over depth) of the longshore current (see Fig. 1-A) from given values of regular wave parameters. Continuous breaking in the surf zone is assumed. Depth refraction is included, also in the calculation of wave set-down and set-up. Current refraction and rip-currents are excluded. The model does not assume infinite water depth, where the ocean boundary condition (see Fig. 1-A) is formulated.

In contrast to most other models, the present study uses a non-linear bottom shear stress term. The model has the same two independent parameters (breaker height to depth ratio and bottom roughness) as Thornton (1971). The approach is different in this respect from Longuet-Higgins (1970), which has three parameters (breaker height to depth ratio, a constant C (in the friction term), and a constant N (in the mixing term)).

The applied numerical method is easy to use for arbitrary variations of bottom profile and roughness. The examples presented in the paper have a constant bottom slope and roughness, however.

2. ASSUMPTIONS AND SHORTCOMINGS

As regards the sea bed, we assume straight and parallel bottom con-
tours (but allow for an arbitrary bottom profile), so Snell's law can
be applied. Furthermore the depth in the surf zone must be monotonously
decreasing. The waves are regular Stokes waves of the lowest order, i.e.
the phase velocity is $O(H^0)$, particle velocities are $O(H^1)$, momentum,
pressure and energy are $O(H^2)$, et cetera, where H is the wave height,
and 'O' denotes 'order of magnitude'. In the surf zone, furthermore,
the usual shallow water approximations are made. The breaking criterion
used is

$$H_B = \beta \, h_B \qquad\qquad\qquad (2.1)$$

in which h_B is the water depth at the breaker line (Fig. 1-A). β is a
dimensionless figure (of the order 1), which is assumed constant through
the surf zone, thus implying spilling breakers. So in the surf zone,
the wave height is determined by Eq. 2.1, without indices.

Outside the surf zone, energy losses are neglected, although a bed
shear stress is included also in this zone, see Eq. 3.4 a. The effect
of this inconsistency is considered small. The ocean boundary line
(see Fig. 1-A) is so chosen, that the actual current velocity is very
small here. Along this line we also assume parallel wave orthogonals
and constant wave height. So we end up with a one-dimensional model,
since rip-currents are neglected. Thus the variations in the mean water
level (η) and in the current velocity (V) are dependent only on the dis-
tance from the shore line. Current refraction (see Jonsson et al. (1971),
and Jonsson (1971 b)) is neglected. This can to some extent be justified,
using the argument that the angles of incidence are normally small where
the current velocities are high (i.e. in the surf zone) and vice versa.
For the detailed assumptions leading to expressions for the turbulent
bed shear and the lateral turbulent mixing, reference is made to Chap-
ter 4.

The current velocity is assumed parallel to the coast and constant
over depth in any vertical. Wind effects are excluded.

It would be fair to mention also, what are considered to be the major
shortcomings of our model: These are the use of linear wave theory and
of regular waves, and the neglect of current refraction and rip-currents.
(In a recent study, James (1972) introduced finite amplitude waves.
Battjes (1974) used irregular waves, but on the other hand neglected
lateral mixing.) Also the mixing length hypothesis introduced in Chap-
ter 4 may be doubtful, especially outside the breaker line.

3. THE MOMENTUM EQUATIONS

In this study a momentum approach is adopted for a steady state situ-
ation. So the equilibrium equations perpendicular to and parallel to
the shore line must be formulated. It should be noticed that all forces
and stresses in these equations are mean values over the wave period T.
All forces in vertical sections are first integrated over depth, and are
given per unit horizontal length.

EQUILIBRIUM PERPENDICULAR TO THE SHORE LINE

Assuming no net shear stress at the bottom, only pressure and (normal) momentum forces have resulting components at right angles to the coast. (Shear forces at the ends of the element in Fig. 3-A cancel out.)
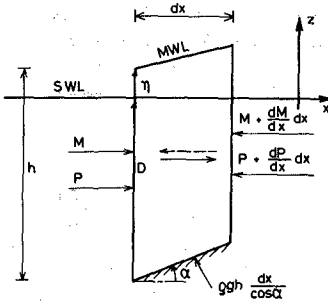
Fig. 3-A
Forces having components
perpendicular to the
shore line

M and P being momentum and total pressure forces over depth h $(= D + \eta$, see Fig. 1-A) per unit length in the y-direction, horizontal equilibrium yields

$$d(M+P)/dx + \rho g h \tan \alpha = 0 \qquad (3.1)$$

ρ and g are density and acceleration due to gravity. Note the difference between D and h, being undisturbed and actual depth, respectively. The 'excess normal stress' σ_{xx} is defined by

$$\sigma_{xx} \equiv M + P - \frac{1}{2} \rho g h^2 \qquad (3.2)$$

For normal incidence, σ_{xx} is simply the radiation stress. If Eq. 3.2 is inserted into Eq. 3.1, we find, using also $h = D + \eta$ and $\tan \alpha = - dD/dx$

$$d\sigma_{xx}/dx = - \rho g h \, d\eta/dx \qquad (3.3)$$

Eq. 3.3 constitutes in fact two ordinary differential equations, one inside and one outside the breaker line. If σ_{xx} is known (Chapter 4), Eq. 3.3 can be integrated to yield the mean water level η (wave set-down and set-up, Chapter 5).

EQUILIBRIUM PARALLEL TO THE SHORE LINE

Neglecting the wind, we have three types of forces having resultant components parallel to the shore line. Firstly there is the 'driving force' T_w, which is the flux of y-momentum across a plane parallel to the shore line, created by the oblique water particle velocities. The gradient of T_w is balanced by the bed shear stress τ_b and by the gradient of the horizontal shear force T_v due to turbulent mixing.

As we neglect dissipation outside the surf zone, the gradient of T_w vanishes here. So, again, we deal with a system of two equations. With the sign conventions in Fig. 3-B we get:

Outside the surf zone	$- \tau_b + dT_v/dx = 0$	(3.4 a)
In the surf zone	$dT_w/dx - \tau_b + dT_v/dx = 0$	(3.4 b)
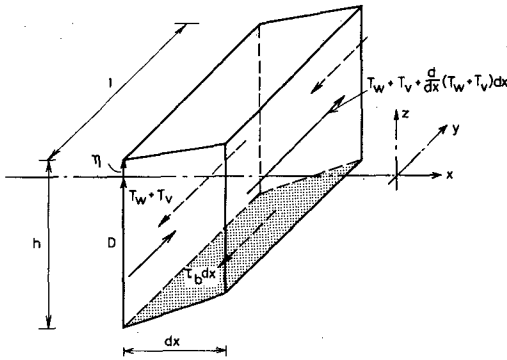
Fig. 3-B
Forces parallel to the
shore line

The equilibrium conditions, Eqs. 3.3 and 3.4, are in fact formally correct for a one-dimensional situation, as considered here. The problem is that neither of the four quantities σ_{xx}, T_w, τ_b, and T_v can be determined with any great accuracy.

4. CALCULATION OF FORCES AND STRESSES

In this chapter we shall derive expressions for σ_{xx} (to be used in Eq. 3.3), as well as for T_w, τ_b, and T_v (to be used in Eq. 3.4).

PRESSURE AND MOMENTUM FORCES

The 'wave normal stress' σ_{xx} can be calculated from the momentum flux tensor (see for instance Longuet-Higgins (1970) p. 6780, Eq. 12), or taken directly from Jonsson (1971a) Eq. 2.9, by putting $\varepsilon = 0$, $\delta = \pi/2$, and substituting α by θ, or from Jonsson and Jacobsen (1973) Eq. 2

$$\sigma_{xx} = \frac{1}{16} \rho \, g \, H^2 \, G + \frac{1}{16} \rho \, g \, H^2 (1 + G) \, \cos^2\theta \qquad (4.1)$$

in which

$$G \equiv 2kh/\sinh 2kh \qquad (4.2)$$

k is the wave number $\equiv 2\pi/L$, where L is the wave length. θ is the angle of incidence, Fig. 1-A.

The wave shear force T_w is also easily calculated from the momentum flux tensor, or taken directly from Jonsson (1971a) Eq. 2.10, by putting $\varepsilon = 0$, $\delta = \pi/2$, and substituting α by θ. With the sign convention in Fig. 3-B we find

$$T_w = -\frac{1}{16} \rho \, g \, H^2 (1 + G) \, \sin\theta \, \cos\theta \qquad (4.3)$$

BOTTOM FRICTION

The essence of the calculation of the bottom shear stress presented below is the introduction of a simple interpolation formula, based on expressions for a pure current and a pure wave motion, assuming rough

turbulent flow. (A similar consideration, for waves and currents going in the _same_ direction, was proposed with some success by Jonsson (1966).)

   Consider first waves at right angles to the current direction. The particle velocities just above the wave boundary layer are shown in Fig. 4-A. It is now assumed that the instantaneous bottom shear stress $\vec{\tau}_b'$ is
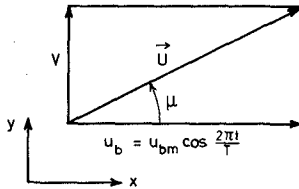
Fig. 4-A
Instantaneous particle velocity $\vec{U}$
near the sea bed. u_{bm} is the
maximum wave particle velocity

in the direction of the vector sum $\vec{U}$ of the longshore current velocity V and the instantaneous wave particle velocity u_b

$$\vec{\tau}_b' = f' \ \frac{1}{2} \ \rho \ |\vec{U}|\vec{U} \tag{4.4}$$

   The problem is hereafter to determine a reasonable expression for the friction factor f'. For $\mu = 0^{\circ}$ (no current, see Fig. 4-A), f' equals the wave friction factor f_w, as defined by Jonsson (1967). Similarly, for $\mu = 90^{\circ}$ (no waves), f' equals the current friction factor f_c. So, in the absence of measurements and theory, the following simple interpolation formula is suggested

$$f' = f_w + (f_c - f_w) \ \sin \mu \tag{4.5}$$

Through μ, f' becomes a function of time t. Introducing Eq. 4.5 in Eq. 4.4 we find the following expression for the mean value of the bottom shear stress parallel to the coast

$$\tau_b = f_s \ \frac{1}{2} \ \rho \ V^2 \tag{4.6}$$

with

$$f_s = f_c + \left(\frac{2}{\pi} \ \sqrt{1+(u_{bm}/V)^2} \ E(m) - 1 \right) f_w \tag{4.7}$$

In Eq. 4.7, u_{bm} appears from Fig. 4-A, and E is a complete elliptic integral of the second kind, with parameter m given by

$$m = \frac{u_{bm}^2}{u_{bm}^2 + V^2} \tag{4.8}$$

(In the actual calculations it proved necessary to deal with the complementary parameter.) For a weak current, Eqs. 4.6 and 4.7 reduce to $\tau_b = (1/\pi) \ f_w \ \rho \ u_{bm} \ V$, which equals the expression used by Thornton (1971), see also Lundgren and Jonsson (1961).

   The wave friction factor f_w is a function of the ratio between wave particle amplitude at the bottom, a_{bm}, and the Nikuradse sand roughness, k_N. In this study the expression proposed by Jonsson (1963,1967) is used, as modified by Skovgaard et al. (1975). The modification is simply that a constant value, $f_w = 0.24$, is used for $a_{bm}/k_N < 2$. (Recently Riedel et al. (1973) have made comprehensive measurements of f_w in an

oscillating water tunnel. For $a_{bm}/k_N > 1$, their values are apparently
only about 60% of those used here, and so will result in a stronger
longshore current, all other things being equal.)

The current friction factor f_c is a function of the ratio between
the water depth and the roughness. The usual expression for f_c:
$f_c = 0.32/\log_e^2(11h/k_N)$ was used in a slightly modified form to avoid
the singularity at $h = k_N/11$. For details, see Olsen and Vium (1974).

Up to this point, bottom friction has been calculated for wave inci-
dence perpendicular to the current. Considering the uncertainty in the
determination of τ_b, however, Eqs. 4.6 and 4.7 will be used without cor-
rection for θ being different from zero. An example of the calculated
variation of f_s is shown in Fig. 4-B. The bottom is a plane slope. The
amplification of the current friction factor due to the wave is quite
clear, as expected most noticeable where the current is weak.
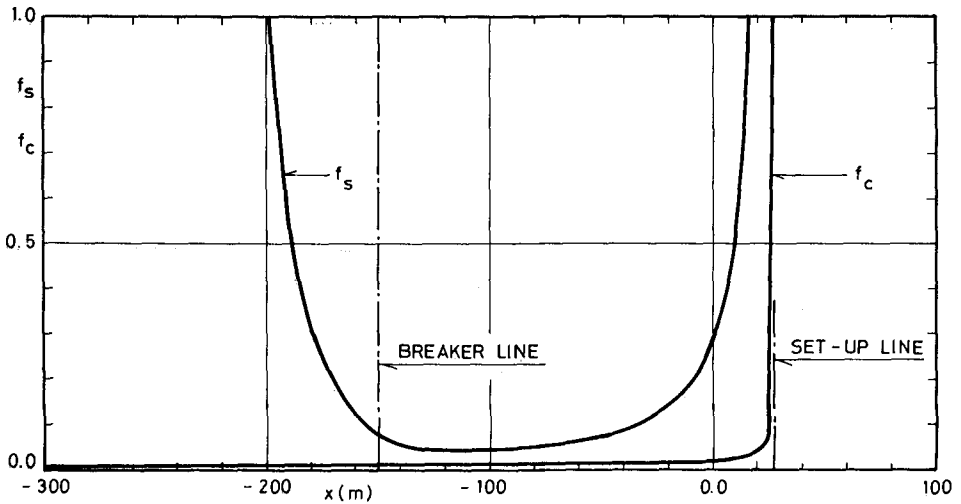
Fig. 4-B   Friction factors f_s (current + wave) and
f_c (pure current) for a plane slope 1:50.
$T = 8$ s, $H_{st} = 2$ m, $\theta_{st} = 30°$ ($\Rightarrow \theta_o \approx 45°$),
$h_{st} = 10$ m ($\Rightarrow x_{st} \approx 500$ m), $\beta = 0.8$, $k_N = 0.10$ m

TURBULENT MIXING

Finally we shall evaluate the lateral shear force T_v over total depth,
due to turbulent mixing. In our model we have adopted a mixing length
consideration, relating the mixing length to the wave particle amplitude.
Using the classical Prandtl approach, we write the correlation expression
for the shear stress as the product of the mean values of the absolute
values of the turbulent velocity fluctuations u' and v', i.e.

$$\tau/\rho = - \overline{u'v'} \approx \overline{|u'|}\ \overline{|v'|} \tag{4.9}$$

In the x-direction we then assume

$$\overline{|u'|} \approx \frac{2}{\pi} u_m \cos \theta = \frac{4}{T} a_m \cos \theta \qquad (4.10)$$

$a_m = u_m T/(2\pi)$ being the amplitude of the wave particle motion. In the y-direction we find, with $a_m \cos \theta$ as a mixing length

$$\overline{|v'|} \approx \ell \, dV/dx \approx a_m \cos \theta \, dV/dx \qquad (4.11)$$

Since the eddy viscosity ν_T is defined from $\tau/\rho \equiv \nu_T \, dV/dx$, we find from Eqs. 4.9, 4.10, and 4.11

$$\nu_T = \frac{4}{T} a_m^2 \cos^2\theta \qquad (4.12) \qquad\qquad T_v = \rho \, h \, \nu_T \frac{dV}{dx} \qquad (4.13)$$

In the surf zone, shallow water approximations are introduced in Eq. 4.12. Outside the breaker line, Eq. 4.12 is also used (with a mean-over-depth value of a_m^2), although a quite different mixing mechanism exists here. It is expected that Eq. 4.12 overestimates the eddy viscosity in this region.

An analogous approach was originally proposed by Thornton (1971). He uses shallow water approximations also outside the surf zone, and his value of ν_T is half that given by Eq. 4.12. (It is difficult to have any strong opinion of which of the two expressions for ν_T is the best. Nor is the effect on the velocity profile large, see Fig. 7-B. It should be mentioned, however, that an analytical error has crept into Thornton's expression for dT_v/dx, which is the first term on the right hand side of his Eq. 37. The water depth ought to be moved in between the brackets, since it is a function of x and thus also should be differentiated. The error stems from his Eqs. 8 and 36, where differentiation and integration seem to be performed in the wrong order.)

5. NUMERICAL SOLUTION

Having found expressions for σ_{xx}, T_w, τ_b, and T_v in Chapter 4, it is now possible to solve the momentum equations 3.3 and 3.4. Since we neglect the 'feed-back' of the current on the wave motion, it is possible to solve the momentum equation perpendicular to the shore independently of the one parallel to the shore. (So V is in fact neglected in the calculation of η.) Using the water depths thus obtained (i.e. including set-down and set-up), the longshore current emerges as a solution to the momentum equation parallel to the shore.

WAVE HEIGHT AND BREAKING DEPTH

Outside the breaker line, the <u>wave height</u> is determined from the assumption of constant transmission of wave power between orthogonals. From Eqs. 23 - 25 and 39 in Skovgaard et al. (1975) we get with $K_f' \equiv 1$

$$\left[\frac{H}{L_o}\right]^2 = \left[\frac{H_{st}}{L_o}\right]^2 \frac{1 + G_{st}}{1 + G} \frac{c_{st}}{c} \frac{\cos \theta_{st}}{\cos \theta} \qquad (5.1)$$

where G is defined by Eq. 4.2. Here the phase velocity is $c = c_o \tanh kh$, with $c_o = L_o/T = gT/(2\pi)$; the suffix o refers to the reference value for deep water. In the surf zone, the wave height is determined by $H = \beta \, h$.

The angle θ in Eq. 5.1 is determined from Snell's law $c/\sin \theta =$ $c_{st}/\sin \theta_{st}$, i.e. (suffix st referring to the ocean boundary line)

$$\cos \theta = \sqrt{1 - (c/c_{st})^2 \sin^2\theta_{st}} \tag{5.2}$$

Remark that only for $(c_o/c_{st}) \sin \theta_{st} < 1$, we can define a reference value θ_o for deep water. This is the reason, why our model is formulated with an arbitrary bottom depth at the ocean boundary line. In a laboratory experiment, one can choose wave period and wave maker angle independently of each other. So one can easily find a situation, where
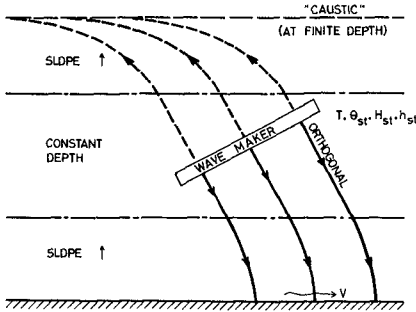
Fig. 5-A
Experiment where θ_o
is not defined

θ_o simply is not defined. Such a case corresponds to an imaginary caustic behind the wave maker as sketched in Fig. 5-A. If the present model had demanded deep water data as input, we could not compare calculations with an experiment like that shown in Fig. 5-A.

The water depth h_B at the breaker line is determined by the condition, that the wave height must be continuous at this line, using Eqs. 2.1 and 5.1. This results in a transcendental equation with one root h_B, which is determined by a Newton-Raphson iteration.

WAVE SET-DOWN AND SET-UP

The variation in the MWL outside the breaker line is determined by Eq. 3.3, with H determined by Eq. 5.1. The solution to this first-order initial value problem is (Jonsson (1973)) $\eta = - H^2 G/(16 h)$ for $x_{st} \le x <$ x_B, see Fig. 1-A. This corresponds in fact to $\eta = 0$ at infinite water depth. From the above solution we find at the ocean boundary line: $\eta_{st} = - H_{st}^2 G_{st}/(16 h_{st})$. For a given x, $D = h - \eta$ is given, and not h. Therefore the equation for η is transcendental.

The variation in the MWL in the surf zone is determined by Eq. 3.3, with $H = \beta h$. The initial condition for this first-order problem is $\eta = - \beta^2 h_B/16$ for $x = x_B$. This corresponds to $G = 1$ (i.e. shallow water approximation) in the above expression for η at x_B, and so gives a slight discontinuity here. The solution is, using Jonsson and Jacobsen (1973)

$$[1 + 8/(3 \beta^2) - 2 D c^*] \eta = - D + 5 h_B/6 + c^*(D^2 + \eta^2 - h_B^2) \tag{5.3}$$

for $x_B \le x \le x_m$. In Eq. 5.3, $c^* \equiv g \sin^2\theta_{st}/(2 c_{st}^2)$. For the determination of x_m, see below. For a given x, i.e. D known, Eq. 5.3 is a quadratic equation in η.

The maximum set-up, η_m, is determined from Eq. 5.3 with $D = -\eta_m$

$$\eta_m = \frac{5}{16} \beta^2 h_B (1 - \frac{6}{5} c^* h_B) \qquad (5.4)$$

It is perhaps surprising to observe that in this model, the maximum set-up is independent of the bottom profile in the surf zone, for the same value of the water depth at the breaker line. η_m then determines x_m for a given beach profile.

Thornton (1971) p. 299, neglects the effect of waves approaching at an angle $\neq 0$ in his calculations of η. An evaluation of the effect of refraction on η_m is given by Jonsson and Jacobsen, Fig. 2.

THE LONGSHORE CURRENT

The current velocity distribution $V(x)$ is determined by Eq. 3.4. The differential equations turn out to be of the form

$$g_1(x) \ d^2V/dx^2 + g_2(x) \ dV/dx + f(x,V) = g_3(x) \qquad (5.5)$$

where $g_3(x)$ vanishes outside the surf zone (Eq. 3.4 a). $g_1(x)$, $g_2(x)$, $g_3(x)$, and $f(x,V)$ are known functions of x and V. So V is the solution to two second-order, non-linear, ordinary differential equations. The boundary conditions are: Vanishing current for $h = h_{st}$ and $h = 0$, and matching of the current and its gradient at the breaker line. Note that x_{st} must be so chosen that the actual velocity (in an experiment or in a field case) is very small here.

The matched (at $x = x_B$) boundary value problem is solved as a sequence of pairs of linear boundary value problems, using Newton's method (i.e. Taylor expansion of the non-linear term), see e.g. Bailey et al. (1968) pp. 153-156. As initial value in the Newton iteration was used $V(x) \equiv 0$ for $x_{st} \leq x \leq x_m$. The linear boundary value problems are solved by piecewise interior orthogonal collocation (or global spline-collocation), see Skovgaard (1973) Secs. 4 and 5. A basic idea of orthogonal collocation is that the solution of the differential equation is represented by a finite series of orthogonal polynomials. The unknown coefficients in this representation are found by satisfying the associated conditions and the differential equations at an appropriate number of selected points. In this project shifted Jacobi polynomials were used. Most of the calculations were performed with the simplest form of Jacobi polynomials, namely Legendre polynomials, and with about 20 terms in the series for each differential equation. The described numerical model was programmed in PL/I, using version 5.4 of the IBM OS PL/I (F) compiler. All floating point calculations were done with approximately 16 decimal digits.

6. COMPARISON WITH MEASUREMENTS

In this chapter some comparisons will be made between calculated longshore currents and observations. These are few, however, if only for the reason that many problems arise in the selection of suitable data. For laboratory measurements a closer inspection of the data will sometimes reveal that a fully developed rough turbulent flow was not present – as assumed in the mathematical model. Field measurements,

on the other hand, are difficult to perform, so necessary information as input to our model is often lacking. A special problem is a reasonable choice of bottom roughness. In both cases the prediction of β (= H/h in the surf zone) is also difficult.

LABORATORY EXPERIMENTS

Fig. 6-A shows the calculated current profile, corresponding to data from laboratory Exp. No. 29 by Putnam et al. (1949).
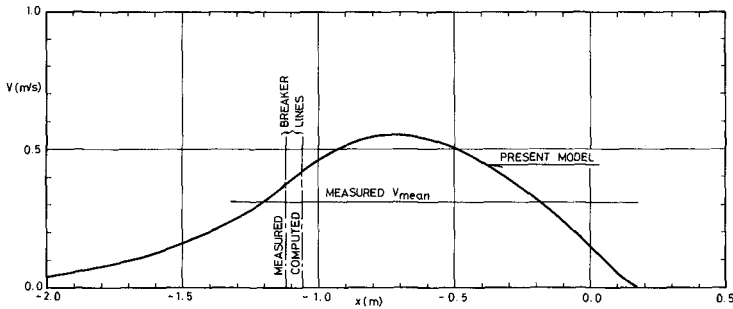
Fig. 6-A Putnam et al. (1949). Plane slope 0.098.
T = 0.95 s, H_{st} = 0.093 m, θ_{st} = 49°8, h_{st} = 0.50 m,
β = 0.8 (estimated), k_N = 0.006 m

The present test has a well defined bottom (1/4" pea gravel, bonded with a thin grout) so the applied value of the Nikuradse roughness parameter of 0.006 m is rather reliable. With a chosen value of β = 0.8 (measured value of H_B/h_B is 0.72) a reasonable agreement with the rather vaguely defined mean longshore current is observed. It is noted that the values H_{st} and θ_{st} were calculated from h_{st} (arbitrarily chosen) and from measured quantities at the breaker line, using linear theory.

Galvin and Eagleson (1965) gave more detail, presenting current velocity profiles at several stations along a plane, smooth, concrete laboratory beach. In Fig. 6-B, calculated velocity profiles corresponding to β-values of 0.8 and 1.42 are shown together with measurements from Test No. 3 in Ser. III. The reason for trying also a value as high as 1.42 are the findings of Komar and Gaughan (1973). This value turned out to give a very good prediction of breaker heights, when one uses linear wave theory. Although this is no real justification for using the value uncritically in this study, the prediction of the maximum current velocity and of the breaker point is seen to be good. Another reason for using a higher value of β here than for Putnam's experiment, is the difference in wave steepness in the two cases (bed slope were almost equal): It seems that breaking was of the plunging type in the latter case, while it in Putnam's Exp. No. 29 probably was a transition phenomenon between spilling and plunging. (At the breaker line, Galvin and Eagleson measured β = 1.13.) The high calculated velocities near and outside the breaker line could be caused by the choice of a too high eddy viscosity in this region, as mentioned in Chapter 4, see also Fig. 7-B.
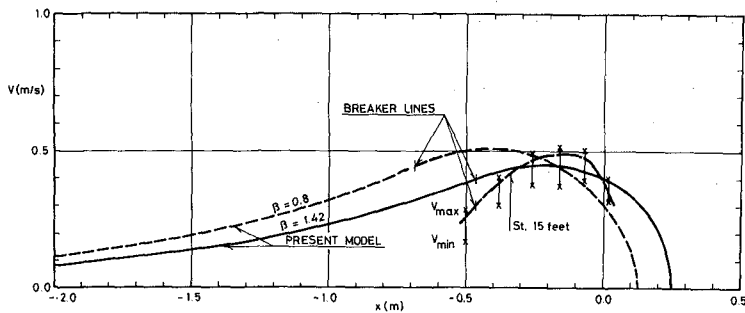
Fig. 6-B   Galvin and Eagleson (1965) Ser. III, Test No. 3.
           Plane slope 0.109 (nearshore average).
           $T = 1.125$ s, $H_{st} = 0.051$ m, $\theta_{st} = 27^{\circ}$, $h_{st} = 0.351$ m,
           $k_N = 0.0003$ m (estimated)

FIELD MEASUREMENTS

    An attempt has been made also to predict the longshore current for
an actual beach. To this end an observation from Trancas Beach (Jan. 19,
1962), as reported by Ingle (1966), has been used. The result is shown
in Fig. 6-C. A rather good agreement between theory and measurement is
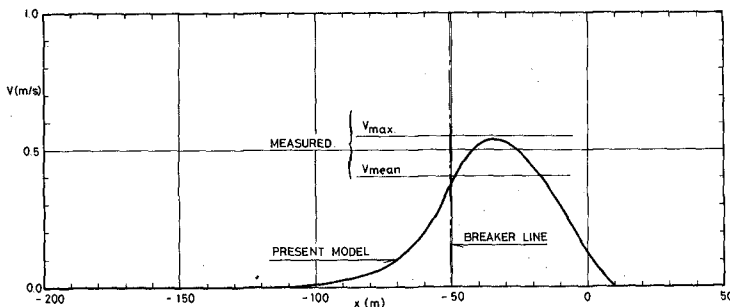
Fig. 6-C   Ingle (1966). Trancas Beach, Jan. 19, 1962.
           Slope 0.0244 (estimated).
           $T = 8.5$ s, $H_{st} = 0.74$ m, $\theta_{st} = 18^{\circ}.1$, $h_{st} = 4.00$ m,
           $\beta = 0.8$ (estimated), $k_N = 0.02$ m (estimated)

observed for $\beta = 0.8$. This is perhaps a little surprising, since break-
ers were probably plunging. On the other hand, Fig. 6-B already demon-
strated that V_{max} is not very sensitive to which value is chosen for β.
Furthermore, Ingle's data were incomplete, so the water depth at the
breaker line had to be calculated as H_B/β, and β was chosen equal to
0.8. This value was then used to calculate H_{st} and θ_{st} (from H_B and θ_B)
at the arbitrary start depth 4.00 m. Due to incomplete information for
the bottom profile, a plane slope was assumed.

7. SOME EFFECTS OF β, k_N AND ν_T

It has already been inferred from Fig. 6-B that the calculated maximum current velocity is not too much affected by the chosen ratio between breaker height and water depth, β, within certain reasonable limits, naturally. Nor is the calculated width of the surf zone very sensitive to reasonable changes in β. On the other hand the position of the surf zone changes very much, as can be seen: Both the breaker line and the set-up line move drastically.

As regards the bottom roughness, k_N, we have tried in the examples of Chapter 6 not to make manipulations with the numerical input values chosen. In each case, a bottom roughness is estimated after careful inspection. (For a natural sand beach, see for instance Skovgaard et al.(1975).) This is important to observe, since it turns out that such an estimate is indeed crucial in our model. This can be seen from Fig. 7-A, showing
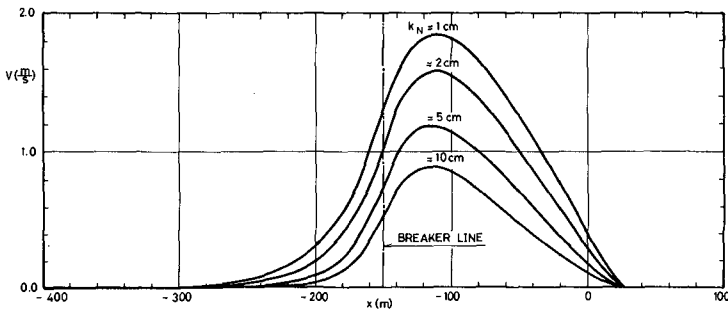
Fig. 7-A   Influence of bottom roughness on
calculated velocity profiles
(Otherwise data as in Fig. 4-B)

calculated velocity profiles for four different roughnesses. It shows that, in this region of roughness parameters, a reduction of the roughness by a factor of ten will increase the maximum velocity in the present model by a factor of two. (It can be inferred from the figure that had we chosen a value of k_N = 5 cm in Fig. 6-C, the agreement with Ingle's measurement would become poorer.) Generally, it should be emphasized that very little is known about the bottom roughness of natural beaches under the combined effects of (breaking) waves and currents. The k_N-values chosen in Fig. 7-A do not necessarily represent what can be expected to be found in nature.

Finally, it has been investigated how sensitive the results are to a change in the eddy viscosity ν_T, Eq. 4.12, since this expression is based on some rather daring assumptions. The results are presented in Fig. 7-B. It appears that reducing ν_T by a factor of two (which is about the same as using Thornton's expression, see Chapter 4) does not have any large effect on the longshore current. The calculated maximum velocity is only increased by some 10%. Velocities outside the breaker line are as a whole reduced, naturally. Since it is felt that the present model probably exaggerates mixing outside the surf zone, the effect

of a drastic reduction of ν_T in this region was investigated also. Reducing it by a factor of 100 changes the total mass flux significantly, as would be expected. The reduction in V_{max} is only about 10%, however.
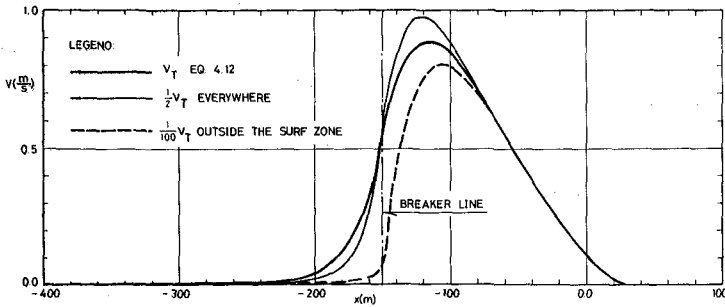
Fig. 7-B   Influence of eddy viscosity on
           calculated velocity profiles
           (Data as in Fig. 4-B)

8. CONCLUSIONS

The proposed method makes it possible to predict (in a steady state) the profile of the longshore current, induced by regular waves, over a bottom with arbitrary parallel bottom contours, when the wave parameters are known at some arbitrary depth, where the actual velocity is very small. Also the breaker height to depth ratio (assumed constant through the surf zone), and the bottom roughness variation must be prescribed. The variations in the mean water level (set-down and set-up) are included in the mathematical model, with proper regard taken to the effect of refraction.

The method includes two new expressions, one for the calculation of the turbulent lateral mixing, and one for the bottom friction. In contrast to most other works, the friction term is non-linear in this study.

The governing differential equations for the current are of the second order, ordinary and non-linear. The matched, two-point boundary value problem is solved as a sequence of pairs of linear, matched boundary value problems, using Newton's method. This linear differential equations are solved by piecewise orthogonal collocation.

The maximum current velocity depends heavily on the bottom roughness, but rather little on the chosen breaker height to depth ratio. On the other hand, the predicted position of the surf zone is very much affected by the latter quantity. Therefore both the roughness and the breaker height to depth ratio should be chosen with great care in each case.

9. ACKNOWLEDGEMENTS

10. REFERENCES

1. Bailey, P.B., Shampine, L.F., and Waltman, P.E., 'Nonlinear Two Point Boundary Value Problems,' Academic Press, New York, 1968.
2. Battjes, J.A., 'Computation of Set-Up, Longshore Currents, Run-Up and Overtopping Due to Wind-Generated Waves,' Report No. 74-2, Communications on Hydraulics, Dept. of Civil Engrg., Delft Univ. of Technology.
3. Galvin, C.J., and Eagleson, P.S., 'Experimental Study of Longshore Currents on a Plane Beach,' U.S. Army Coastal Engrg. Res. Center, Tech. Memo 10, Washington, D.C., 1965.
4. Ingle, J.O., Jr., 'The Movement of Beach Sand,' Elsevier Publ., Amsterdam, 1966.
5. James, I.D., 'Some Nearshore Effects of Ocean Waves,' Ph.D. thesis No. 8258, Univ. Cambridge, Nov. 1972.
6. Jonsson, I.G., 'Measurements in the Turbulent Wave Boundary Layer,' Int. Ass. Hydr. Res., Proc. 10th Congr., Vol. 1, 85-92, London, 1963.
7. Jonsson, I.G., 'The Friction Factor for a Current Superimposed by Waves,' Basic Res. - Prog. Rep. 11, 2-12, Coastal Engrg. Lab and Hydraulic Lab., Tech. Univ. Denmark, 1966.
8. Jonsson, I.G., 'Wave Boundary Layers and Friction Factors,' Proc. 10th Conf. Coastal Engrg., Tokyo 1966, Vol. I, Chap. 10, 127-148, Am. Soc. Civ. Engrs., New York, 1967.
9. Jonsson, I.G., 'A New Proof of an Energy Equation for Surface Gravity Waves Propagating on a Current,' Basic Res. - Prog. Rep. 23, 11-19, Coastal Engrg. Lab. and Hydraulic Lab., Tech. Univ. Denmark, 1971(a).
10. Jonsson, I.G., 'The Basic Equations for Current-Depth Refraction of Surface Gravity Waves. Irrotational Flow,' Prog. Rep. 24, 39-49, Inst. Hydrodyn. and Hydraulic Engrg. (ISVA), Tech. Univ. Denmark, 1971(b).
11. Jonsson, I.G., 'Simplified Calculation of the Set-Down for Obliquely Incident Water Waves,' Prog. Rep. 31, 9-11, Inst. Hydrodyn. and Hydraulic Engrg. (ISVA), Tech. Univ. Denmark, 1973.
12. Jonsson, I.G., and Jacobsen, T.S., 'Set-Down and Set-Up in a Refraction Zone,' Prog. Rep. 29, 13-22, Inst. Hydrodyn. and Hydraulic Engrg. (ISVA), Tech. Univ. Denmark, 1973.
13. Jonsson, I.G., Skougaard, C., and Wang, J.D., 'Interaction Between Waves and Currents,' Proc. 12th Conf. Coastal Engrg., Washington, D.C.1970, Vol. I, Chap. 30, 489-507, Am. Soc. Civ. Engrs., New York, 1971.
14. Komar, P.D., and Gaughan, M.K., 'Airy Wave Theory and Breaker Height Prediction,' Proc. 13th Conf. Coastal Engrg., Vancouver 1972, Vol. I, Chap. 20, 405-418, Am. Soc. Civ. Engrs., New York, 1973.
15. Longuet-Higgins, M.S., 'Longshore Currents Generated by Obliquely Incident Sea Waves,' Parts 1 and 2, J. Geophys. Res., Vol. 75, No. 33, 6778-6789 and 6790-6801, 1970.

16. Longuet-Higgins, M.S., 'Recent Progress in the Study of Longshore
    Currents,' 203-248 in 'Waves on Beaches and Resulting Sediment
    Transport,' ed. R.E. Meyer, Academic Press, New York, 1972.
17. Lundgren, H., and Jonsson, I.G., 'Bed Shear Stresses Induced by
    Waves and a Current,' Basic Res. - Prog. Rep. 1, 6-7, Coastal
    Engrg. Lab., Tech. Univ. Denmark, 1961.
18. Olsen, T.G., and Vium, M.P., 'Coastal Currents Generated by Breaking
    Waves,' (In Danish), unpublished M.Sc. thesis, Inst. Hydrodyn. and
    Hydraulic Engrg. (ISVA), Tech. Univ. Denmark, 1974.
19. Putnam, J.A., Munk, W.H., and Traylor, M.A., 'The Prediction of
    Longshore Currents,' Trans. Am. Geophys. Union, Vol. 30, No. 3,
    337-345, 1949.
20. Riedel, H.P., Kamphuis, J.W., and Brebner, A., 'Measurement of Bed
    Shear Stress Under Waves,' Proc. 13th Conf. Coastal Engrg.,
    Vancouver 1972, Vol. I, Chap. 31, 587-603, Am. Soc. Civ. Engrs.,
    New York, 1973.
21. Skovgaard, O., 'Selected Numerical Approximation Methods,'
    Dan. Center Appl. Math. and Mech. (DCAMM), Tech. Univ. Denmark,
    Report No. 62, 71 pp., 1973.
22. Skovgaard, O., Jonsson, I.G., and Bertelsen, J.A., 'Computation
    of Wave Heights Due to Refraction and Friction,' to appear in Proc.
    Am. Soc. Civ. Engrs., J. Waterways, Harbors and Coastal Engrg. Div.,
    Vol. 101, No. WW 1, 1975.
23. Thornton, E.B., 'Variation of Longshore Current Across the Surf
    Zone,' Proc. 12th Conf. Coastal Engrg., Washington, D.C. 1970,
    Vol. I, Chap. 18, 291-308, Am. Soc. Civ. Engrs., New York, 1971.

CHAPTER 41

COMPUTER EVALUATION OF LITTORAL TRANSPORT

Theodor R. Mogel[1]
Robert L. Street[2]

ABSTRACT

Hindcast deepwater wave statistics and bottom hydrographic data are combined with a water-wave refraction analysis to estimate the littoral transport in a beach zone. The effects of hindcast data station location, of wave ray density in the breaker zone, of changes in the bottom-fitting surface in the depth calculation of the refraction analysis, and of methods of smoothing the contribution of individual rays to the littoral transport computation are explored.

INTRODUCTION

Dobson (1967) at Stanford developed and verified a simple and theoretically sound computer program for water wave refraction. This paper summarizes the evolution of the Stanford refraction program into the area of littoral transport.

There is now a body of rational theory and systematic experiments that show a definite and causal relationship between alongshore power and littoral transport. Most recently these relationships have been documented by Galvin (1972), Komar and Inman (1970) and Longuet-Higgins (1972). In addition, offshore wave energy can be evaluated in terms of hindcast data over the region that covers the source of the waves. When the hindcast data and the relationship between alongshore power and sand transport are brought together with computer programs for wave refraction and a systematic evaluation of alongshore power, the engineer has the tools necessary for the development of design data and rational decision making. Mogel, Street and Perry (1970) provided the first computer based analysis utilizing the above concepts. In the intervening years the empirical relationship between alongshore power and sand transport has been given a rational theoretical basis and the Stanford programs have been refined and improved.

THE COMPUTATION

Figure 1 is a flow chart of the computation process. First a refraction analysis (Mogel et al. 1970) is made of all applicable periods and directions. The refraction is done over two grids of hydrographic data. The OUTER GRID is used to bring waves from deep water where they are not refracting. It is represented by still water depths specified at

---

1. Research Engineer, Dept. of Civil Engineering, Stanford University, U.S.A.

2. Professor, Dept. of Civil Engineering, Stanford University, U.S.A.

the intersections of two sets of mutually perpendicular, equally spaced
lines. The grid spacing is made large to speed computation. The INNER
GRID is used to give the detail necessary to accurately represent the
coastal zone. The inputs to the OUTER analysis are a grid of hydro-
graphic data, wave ray starting cards and program control parameters.
The refraction program uses a least square surface fit on the depth data
to compute the depth and derivatives necessary for the computations.
The spacing of the wave rays is chosen to give adequate coverage of the
beach zone. The OUTER analysis produces a set of wave ray starting cards
for the INNER analysis. The INNER GRID computation, like the OUTER has
as inputs a grid of hydrographic data, the above mentioned wave ray start-
ing cards and program control parameters. The output of the INNER compu-
tation is a set of wave breaking statistics giving the parameters of each
of the deep water waves when they break. The criteria used for breaking
is when $H/d > 0.78$.

    The wave breaking data are used as an input to the alongshore power --
littoral transport computation step. Also used are hindcast data giving
month by month deep water statistics on height, direction, period, and
average frequency. The hindcast data used were compiled by National
Marine Consultants Inc. (1960) using meteorological records and charts
along the California coast for the years 1956, 1957, and 1958.

    The other inputs needed are the coordinates of the locations in the
beach zone where sand transport data are needed. The output is a set of
month by month and yearly tables of alongshore energy and littoral trans-
port.

    Figure 2 shows a section of the Northern California coast where com-
putations were made. The boxed areas around Trinidad Head show the INNER
and OUTER computation grids. The Southeast corner of each grid is used
as the origin. All results are presented in terms of grid units. The
computations were part of a study to determine the effect of damming the
Mad River, located between Trinidad Head and Cape Mendocino, and remov-
ing a source of beach material. Station 1 and Station 2 are two of the
National Marine Consultants' hindcast stations. The directional histo-
grams show the annual deep water wave energy. As can be seen, Station 1
has considerably more energy from the North and West than Station 2. The
interpolated station is derived from Stations 1 and 2 by assuming the
waves originate at the intersection of a line connecting the two stations
and a line from the computation zone at the heading of the particular wave
direction. The energy value used is then computed by interpolation based
on the two lengths. For example, point A is considered the origin of
waves traveling Northeast.

    Figure 3 shows the effect of the three hindcast stations on the an-
nual net littoral transport. The horizontal axis shows the North-South
location and the vertical axis the potential sand transport with positive
Northern transport. As expected from the energy diagram, Station 1 pro-
duces more Northerly transport than Station 2 and the interpolated station
produces transport between the two. The interpolated station is used
henceforth. These computations were done with a least squares quadratic
surface fit over 12 grid points in the refraction program and by fitting
a parabola through the contribution of each wave in the four rays nearest

the transport computation point. The curves are rather rough with large influences from individual wave rays.

Figure 4 shows transport calculations made using a 24 point least squares, cubic-surface fit in the depth computation and the six nearest rays for the transport calculations. The cubic surface in the depth calculation allows the second derivatives to vary over a computation grid. These are used to compute refraction coefficients. The variable second derivatives lead to a smoother variation of the refraction coefficient with changes in wave ray location.

In Figure 4 the upper curve is the gross transport obtained by summing the absolute value of the individual ray contributions. The solid lower curve is the net transport. The dashed curve is the result of doubling the ray density. The wide variation indicates more refinement may be necessary.

Figure 5 shows a ray by ray computation of the energy factor for West - 11 sec waves with deep water height of 20 ft. The circular points are the rays added when the ray density was doubled. The dashed line shows the energy factor calculated by fitting a parabola to the nearest six rays considering all rays; the dotted line shows the energy factor calculated by fitting a parabola through the nearest six rays considering half of the rays. The large variations of the energy factor here show the reason for the large variations of littoral transport seen in Figure 4. The solid curve is based on the average of the six nearest rays. The fit using the six ray average seems to be more representative. The large variations in the individual rays are a result of the roughness of the depth data used in the refraction analysis. Fitting a parabola through these energy factor values only accentuates the roughness.

Figure 6 shows the gross and net transport using the six ray average. It may be interesting to note that the average transport is about 10% of the gross transport and that the variations are about 5% of the gross.

Figure 7 shows, as an example, the distribution of wave rays along the coast for SW - 11 sec waves. Such a set of rays is required for each period and direction for which significant energy exists in the hindcast data.

CONCLUSIONS

We have developed a tool to help the engineer make decisions on the effects on coastal areas caused by large scale engineering projects. The major weakness in the method is the relationship between alongshore power and littoral transport. However, qualitatively when the alongshore power is Northerly, the sand will move North also. The actual littoral transport could be calibrated for a given area by comparing a sample of measured transports against calculated and adjusting the computations accordingly. We feel that the quality of the hindcast data can have large effects on the quality of the results as well (Mogel and Street, 1974).

REFERENCES

R. S. Dobson (1967), "Some Applications of a Digital Computer to Hydraulic
    Engineering Problems," Tech. Rep. No. 80, Dept. of Civil Engineering,
    Stanford University, Stanford, California, DDC AD No. 659309.

C. J. Galvin, Jr. (1972), "A Gross Longshore Transport Rate Formula," Proc.
    13th Coastal Engineering Conference, Vancouver, ASCE, Chap. 50, pp.
    953-970.

P. D. Komar and D. L. Inman (1970), "Longshore Sand Transport on Beaches,"
    J. Geophysical Res., V. 75, No. 30, Oct. 20, pp. 5914-5927.

M. S. Longuet-Higgins (1972), "Recent Progress in the Study of Longshore
    Currents," Waves on Beaches (R. E. Meyer, Ed.), Academic Press, pp.
    203-248.

T. R. Mogel, R. L. Street and B. Perry (1970), "Computation of Alongshore
    Energy and Littoral Transport," Proc. 12th Coastal Engineering Con-
    ference, Washington, Chap. 57, pp. 899-918.

T. R. Mogel and R. L. Street (1974), "Wave Refraction and Littoral Trans-
    port Computation," Int. Symp. on Ocean Wave Measurement and Analysis,
    New Orleans, ASCE, V. 1, pp. 790-798.

National Marine Consultants, Inc. (1960), "Wave Statistics for Seven Deep
    Water Stations Along the California Coast," Santa Barbara, California.

OUTER GRID
RAY STARTING CARDS

STEP SIZE	STEP I	OUTER GRID
INNER GRID LOCATION	OUTER GRID	HYDRO GRAPHIC
PRINTOUT INTERVAL	REFRACTION ANALYSIS	DATA

INNER GRID
RAY STARTING CARDS

STEP SIZE	STEP 2	INNER GRID
PRINOUT INTERVAL	INNER GRID	HYDROGRAPHIC
	REFRACTION ANALYSIS	DATA

BREAKING WAVE
DATA

COORDINATES OF	STEP 3	DEEP WATER
COMPUTATION POINTS	LITTORAL TRANSPORT	WAVE HINDCAST
	COMPUTATION	DATA

MONTHLY AND ANNUAL
TABLES OF
ALONGSHORE ENERGY
AND LITTORAL TRANSPORT

COMPUTATION FLOW CHART
FIGURE 1

LONGITUDE - DEGREES WEST

POLAR HISTOGRAMS OF ANNUAL DEEP WATER WAVE ENERGY IN
10⁷ FT-LBS PER YEAR
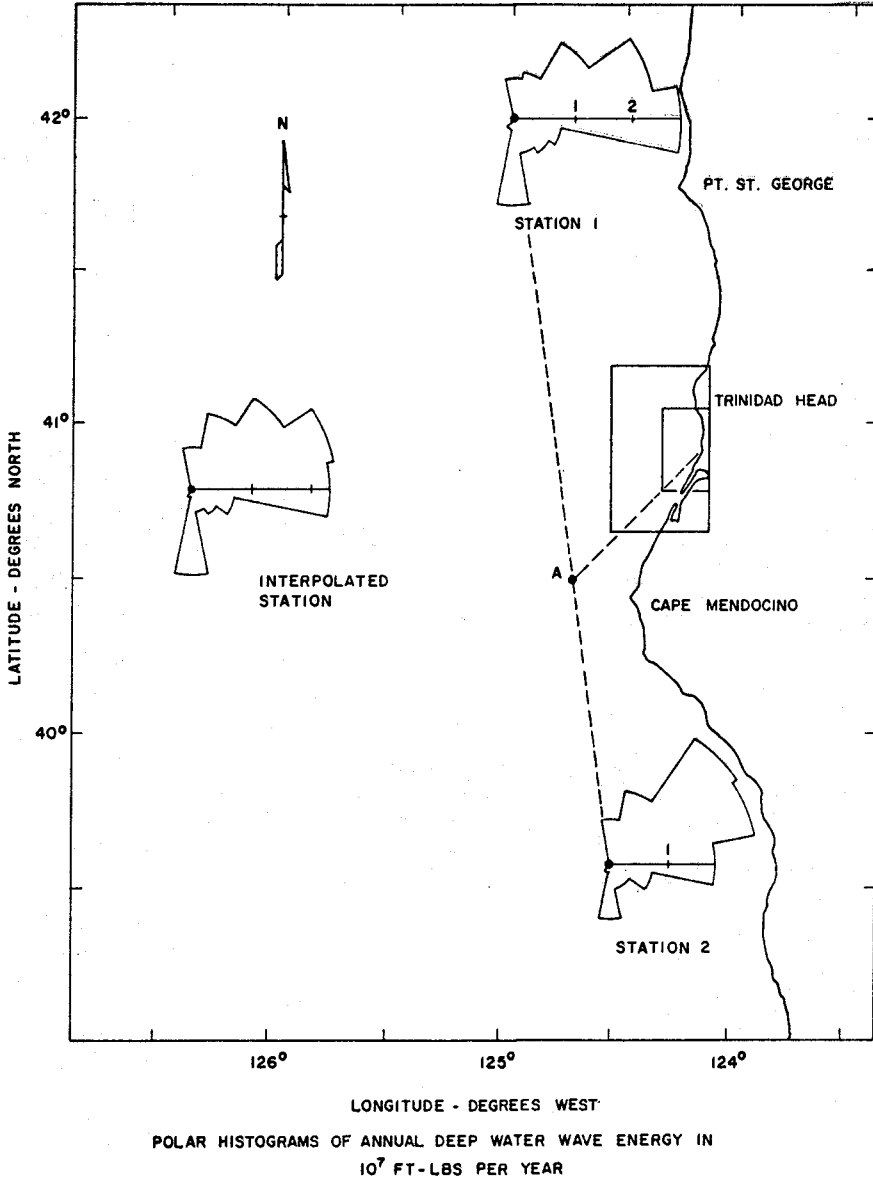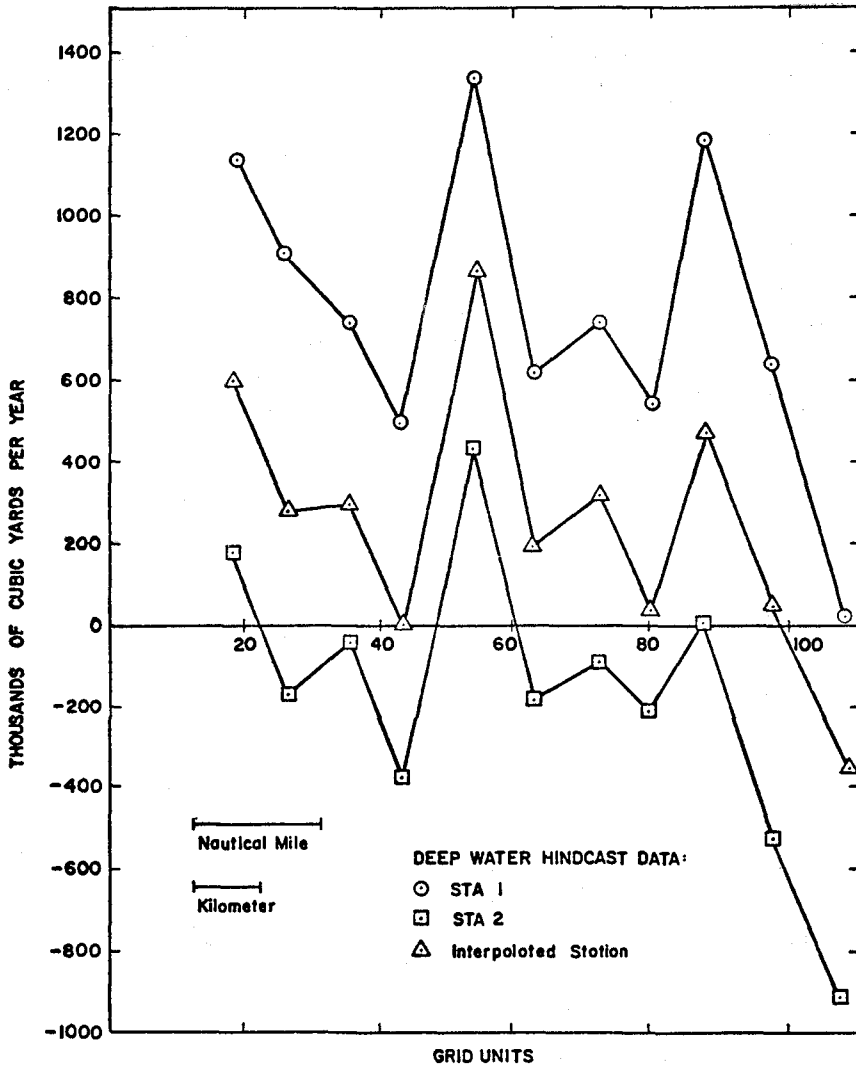
FIGURE 2

Littoral Transport Using 12 Point Quadratic Surface in
Refraction Program, Parabola through 4 Nearest Rays.

FIGURE 3
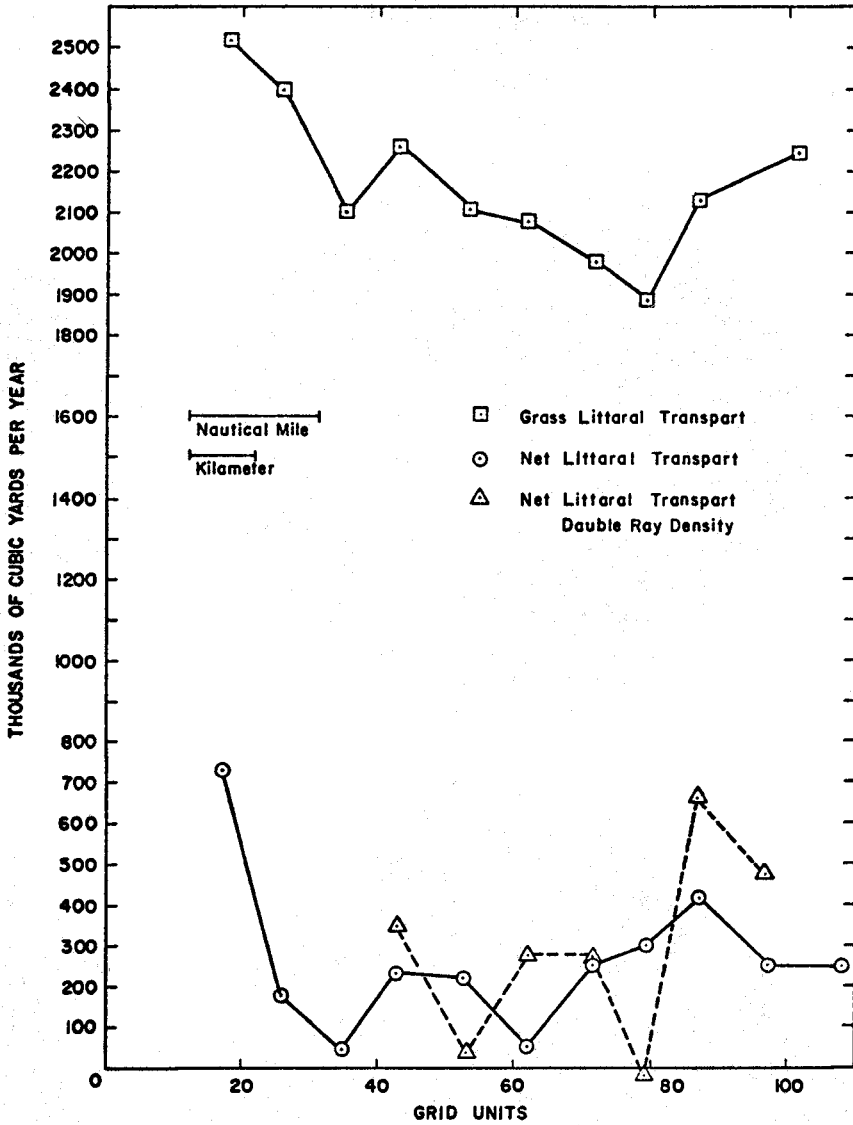
Littoral Transport Using 24 Point Cubic Surface in
Refraction Program, Parabola through 6 Nearest Rays.

FIGURE 4
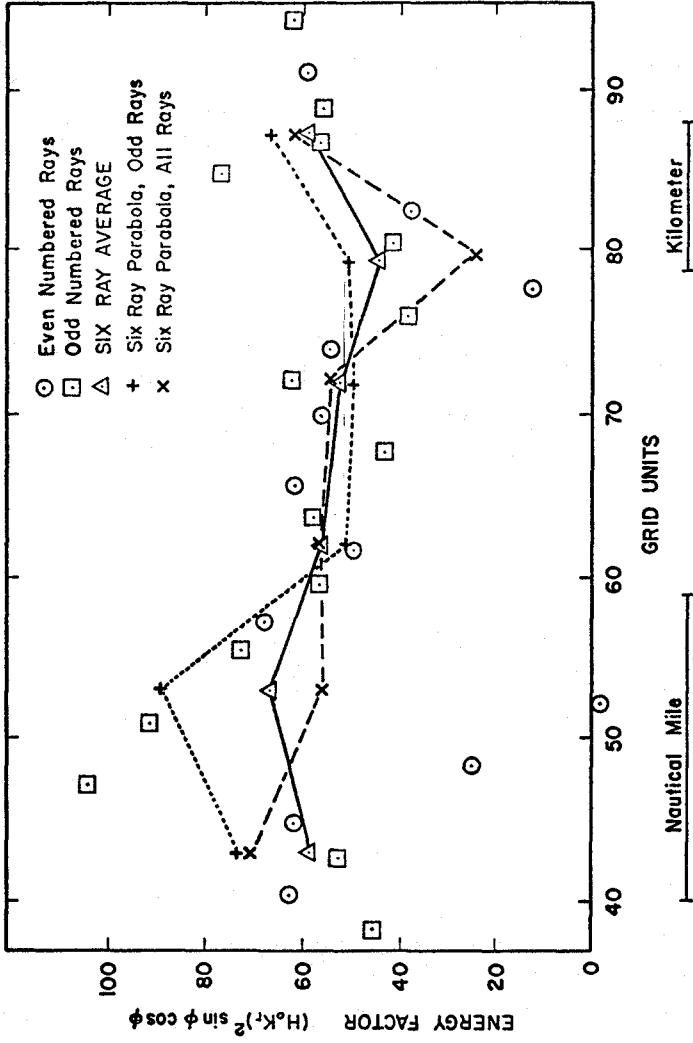
ENERGY FACTOR FOR WEST - 11 SEC
Breaking Waves with H_o = 20 feet.

FIGURE 5
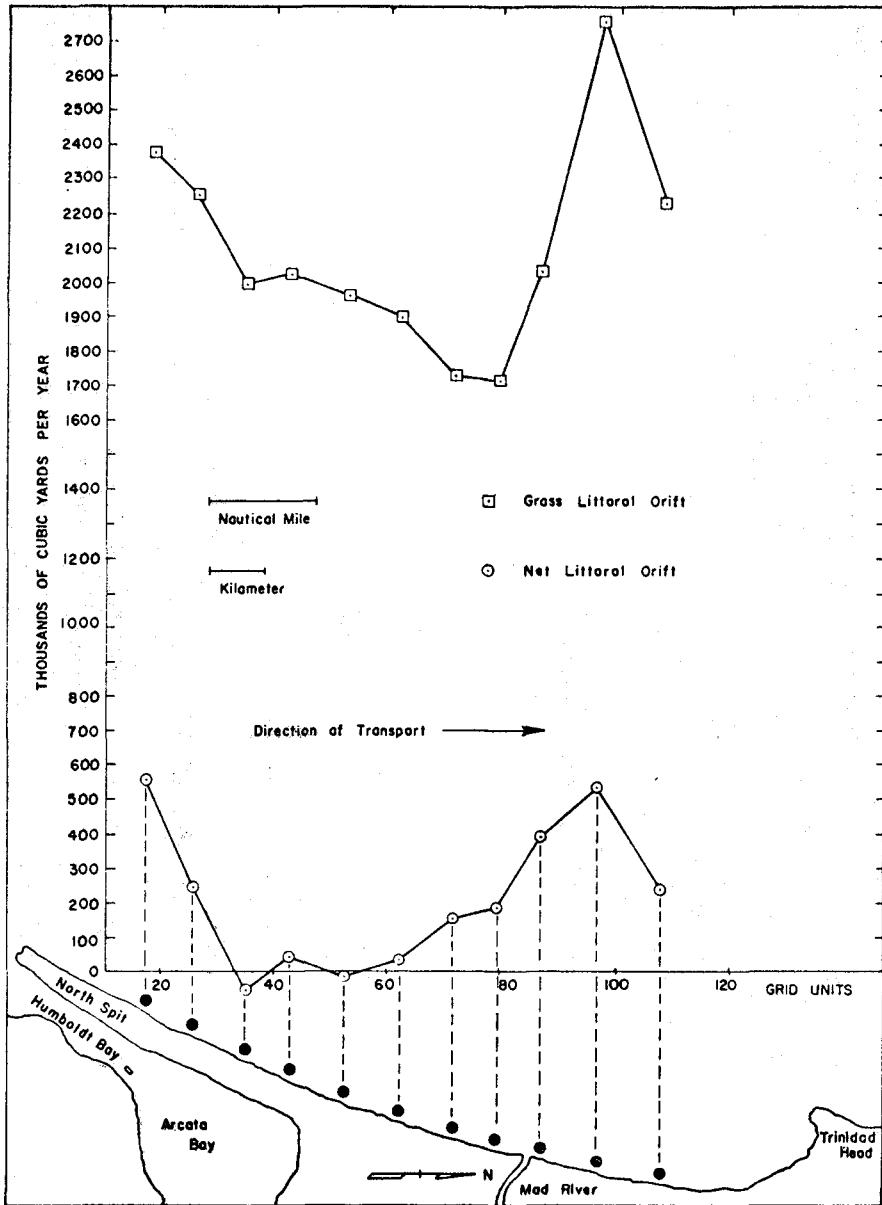
Littoral Transport Using 24 Point Cubic Surface in
Refraction Program, Average of 6 Nearest Rays.

FIGURE 6
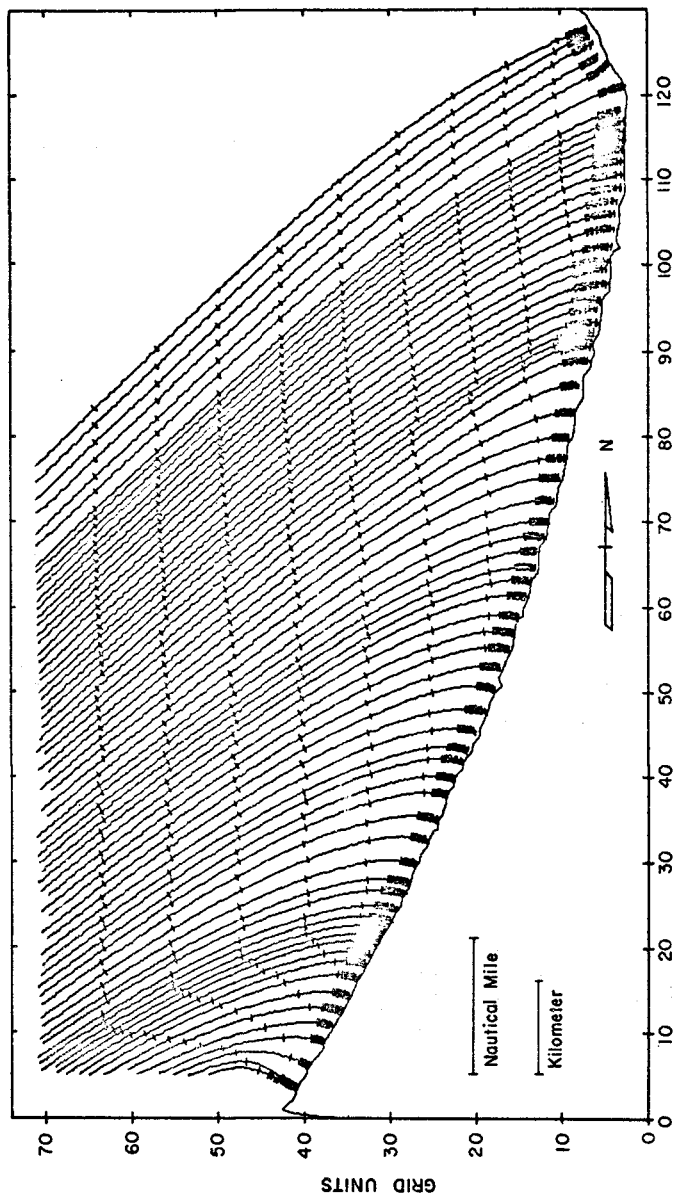
GRID UNITS

INNER GRID REFRACTION DIAGRAM, SW - II SEC

FIGURE 7

CHAPTER 42

COMPARISON BETWEEN THE RESULTS OF LITTORAL-DRIFT COMPUTATIONS
AND CUBATURE OF DEPOSITS IN A DREDGED CHANNEL

V.F.MOTTA
Professor of Coastal Engineering
Applied-Hydrology Centre, Porto Alegre,
Brazil

J.V.BANDEIRA
Radioactive Research Institute, Belo Ho
rizonte, Brazil

ABSTRACT

The total annual volume of littoral drift on either side of
the mouth of Sergipe estuary, in the Northeast of Brazil, has been de
termined by applying Caldwell's, Castanho's and Bijker's methods to
the wave characteristics that had been recorded at a twenty-metre
depth of water, over a whole year, for the design of an offshore oil
terminal.

The three computation methods yielded the same order of mag
nitude which was found to amount to about 800000m³/year. The dominant
drift is southwestward, ánd its predicted amount is 660000m³/year.
It was also found that although the three methods lead to total re
sults of the same order of magnitude, they do not agree as to the vari
ation of littoral drift over the year for the same waves.

An eight-metre deep shipping channel has been dredged accross
the bar. The channel was surveyed in December 1971, August and Decem
ber 1972, and a cubature of the deposits was made after the littoral-
drift computations had been carried out. As the latter had been per
formed on a monthly basis, a comparison became possible between pre
dicted and actual volumes of deposits for the same lengths of time.

The predicted volumes for the whole year were found to be
from 34 to 46% greater than the actual results. However, for the time
interval August-December 1972 a remarkable agreement was found be
tween predicted and actual results.

I) STATEMENT OF THE PROBLEM

Aracaju harbour, sited at the capital of the State of Sergi
pe, in the Northeast of Brazil, lies inside an estuary with small up
land flow. Although the estuary offers stable depths of 8 to 10m and
widths from 600 to 1000m, its entrance is restricted by a bar over
which the control depth has remained at a value of 3.5 ± 0.5m over the
last fifty years. Fig. 1 is a key map of the area under consideration.

Long, fairly straight, flat sand beaches stretch out to both
sides of the estuary entrance, on a Southwest to Northeast alignement.
The mean beach slope is 1/276 from the 0m to the -5m contour. Littoral
drift occurs on both shoreline directions. The littoral-drift materi

KEY MAP (ARACAJU BAR, STATE OF SERGIPE, BRAZIL)

FIG. 1
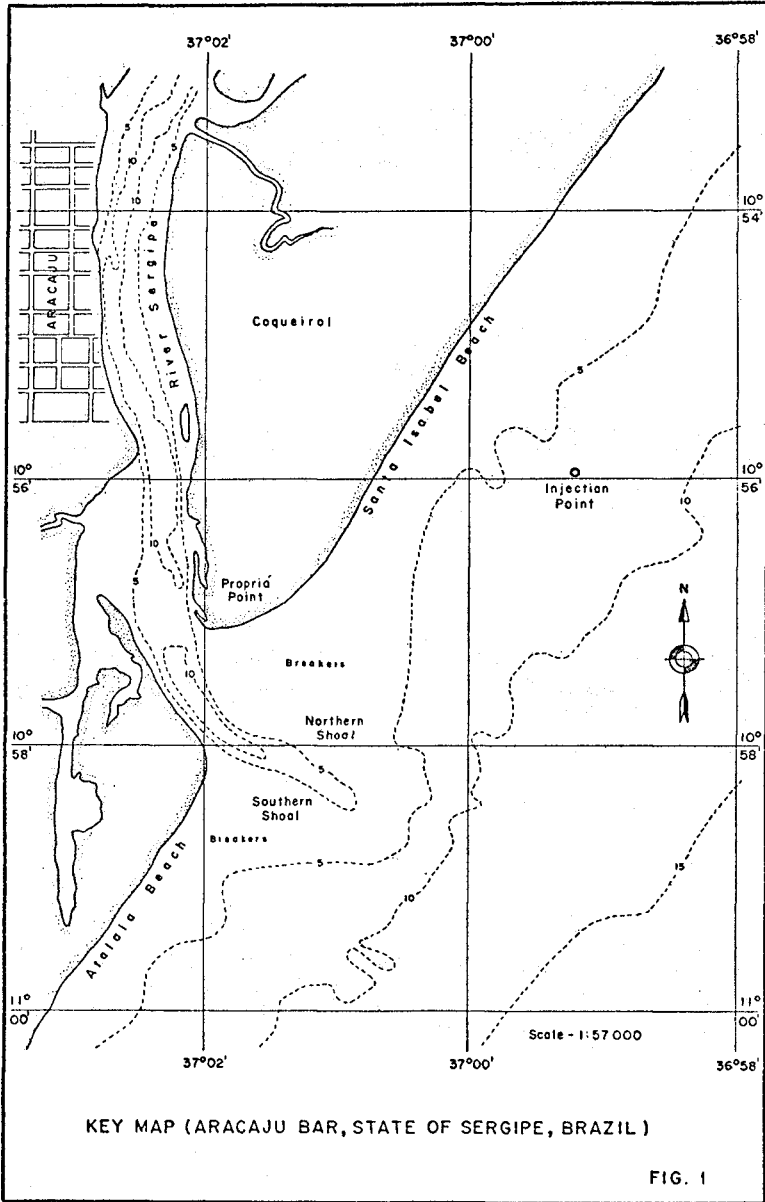
al is fine sand with a mean diameter of 0.11mm. The bed material in
the outer stretches of the estuary is the same fine sand from the con
tinental shelf. The mean spring tidal range at the estuary entrance
is about 2m.

        A radioactive-tracer experiment carried out from January to
June 1971 by INSTITUTO DE PESQUISAS RADIOATIVAS (IPR-Nuclear Research
Institute, Belo Horizonte) with the assistance of INSTITUTO DE PESQUI
SAS HIDRÁULICAS DA UNIVERSIDADE FEDERAL DO RIO GRANDE DO SUL (Hydrau
lics Research Institute of the Federal University of Rio Grande do Sul)
on behalf of DEPARTAMENTO NACIONAL DE PORTOS E VIAS NAVECÁVEIS (DNPVN
- the Brazilian Federal Dock and Harbour Authority) showed the along
shore drift of sand to be negligible seawards of the breaker zone.
Since the sediment transport brought down by the upland flow to the es
tuary mouth is also negligible, littoral drift was shown to be the na
tural mechanism that brings about bar formation off the estuary entran
ce.

        A few years earlier wave characteristics had been recorded
over a whole year at a 20m depth of water, a few kilometres to the
south of the estuary entrance, for the design of an offshore oil termi
nal. The waves were recorded by an inverted echosounder ("Houlographe
Neyrpic") from September 1965 to September 1966. Two 12 minute long
wave records were taken daily, at 09.00 and 17.00 hours. At the time
of each record the wave directions were visually observed at a known
depth of water from a tower on the shore.

        When the results of the radioactive-tracer experiment were
analysed the senior author suggested that the junior author - then a
graduate student of Coastal Engineering at the Applied-Hydrology Cen
tre in Porto Alegre but already a member of the IPR staff - should
undertake an academic exercise computing the annual volume of littoral
drift on either side of the Sergipe estuary entrance. The computations
would be made by applying Caldwell's, Castanho's and Bikjer's methods
to the wave characteristics that had been recorded for the design of
the oil terminal. The aim of the exercise [1] was to compare the
figures provided by the three methods.

        However, DNPVN decided to dredge an eight-metre deep approach
channel accross the bar shortly after the radioactive-tracer experiment
reached completion. This channel was surveyed in December 1971, August
and December 1972. When the littoral-drift computations had already
been carried out, a cubature of the deposits in the dredged channel was
made. As the littoral-drift computations had been carried out on a
monthly basis, a comparison became possible between the computed results
and the volumes of deposits in the dredged channel for corresponding
lengths of time.

        II)   AN OUTLINE OF THE WAVE CLIMATE OFF ARACAJU

        The wave records have been analysed according to the Tucker-
Draper method. The mean periods (upward zero crossings) vary from 5
to 10 seconds. Fig. 2 shows the statistical distribution of the mean
periods for the whole year. The most frequent (58.2%) mean period is
6 seconds.

        The statistical distribution of significant wave heights for
the whole year can be seen in Fig. 3. Significant wave heights at a
20m depth of water range from 0.6 to 2.5m, 1.1m being the most frequent

value (16.6%). The significant and maximum wave height exceedance
curves are shown in Fig. 4. Fig. 5 is the exceedance curve of deep-wa
ter significant wave steepness (significant wave height   associated
with the mean period in the same record).

        Fig. 6 shows the distribution of wave directions at a 5m
depth of water regardless of periods and wave heights. The most fre
quent (23.6%) angle of wave attack is 5° to the north of the normal
to the shoreline. Most of the waves at the 5m depth (70.8%) come
from the north of the latter.

        The above information refers to the year as a whole. How
ever, the wave climate off Sergipe undergoes some interesting sea
sonal changes. As far as periods are concerned the changes are small
but it was ascertained that from September to March over 70% of the
waves have periods of 5-6s. From April to August slightly longer
waves occur with mean periods of 7-10s.

        The seasonal variation in wave heights is more marked.
Higher waves occur from April to October than from November to March.
The most frequent (8.7%) maximum wave height throughout the year is
1.8m, at a 20m depth. The sum of the monthly percentages of wave
heights above 1.8m varies between 25.6% and 38.6% from November to
March and between 38.6% and 90.0% from April to October.

        The most marked seasonal variation is the one associated
with angles of wave attack at a given depth. From November to March
the waves come from the north of the normal to the shoreline during
practically all the time. From April to October the waves come from
both quadrants, predominantly from the south in September.

        In short, the summer waves are not so high as the winter
waves the mean periods are about the same but in the summer the
angles of wave attack are greater than in the winter and more stead
ily to the other side of the normal to the shoreline. In the summer
they range from 15° to 20°. In the winter they amount to about 7°.

            III)   MAIN FEATURES OF THE COMPUTATIONS

        This paper will not delve into the details of the three
methods used to compute the annual volumes of littoral drift. The
reader is referred to the publications in which they were proposed.
Only some relevant features will be pointed out here.

        The littoral-drift computations were carried out on a month
ly basis. For each month the total number of seconds in the month
was divided by the number of wave records that had actually been taken
in the particular month under consideration. Each record was repre-
sented by a monochromatic wave of which the period was the mean
period of the record, and the direction was the wave direction that
had been visually observed when the record was made. The transport
capacity of this monochromatic wave in cubic metres per second was
calculated for each record, by each of the three methods in hand. The
same wave was supposed to act during the length of time corresponding
to the quotient of the number of seconds in the month by the number of
records actually taken. So far, evaluations of littoral-drift annual
volumes have usually been made by assuming that one monochromatic wave
acts all the time during the whole year.

        When using Castanho's method all the waves were supposed to
break as solitary waves and spilling breakers. The beach roughness

T_{med}	5	6	7	8	9	10
%	9.87	58.22	23.98	5.03	2.13	0.77
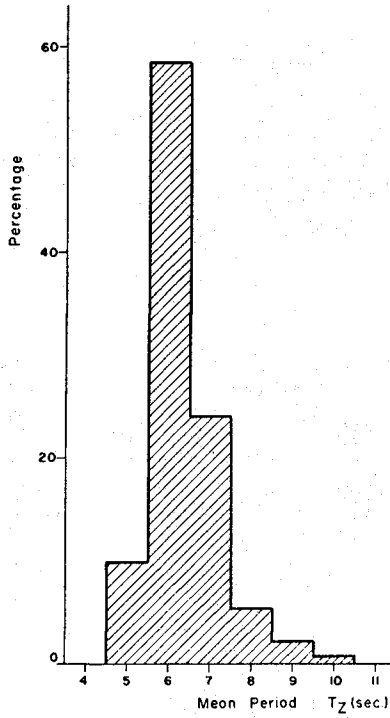
ANNUAL DISTRIBUTION OF THE MEAN PERIODS

FIG. 2

Hs	0.6	0.7	0.8	0.9	1.0	1.1	1.2	1.3	1.4	1.5	1.6	1.7	1.8	1.9	2.0	2.1	2.2	2.3	2.4	2.5
%	1.16	1.35	6.00	13.73	6.12	16.63	11.99	8.51	7.93	5.42	5.03	2.13	5.03	2.71	1.55	1.55	0.39	0.19	0.39	0.19
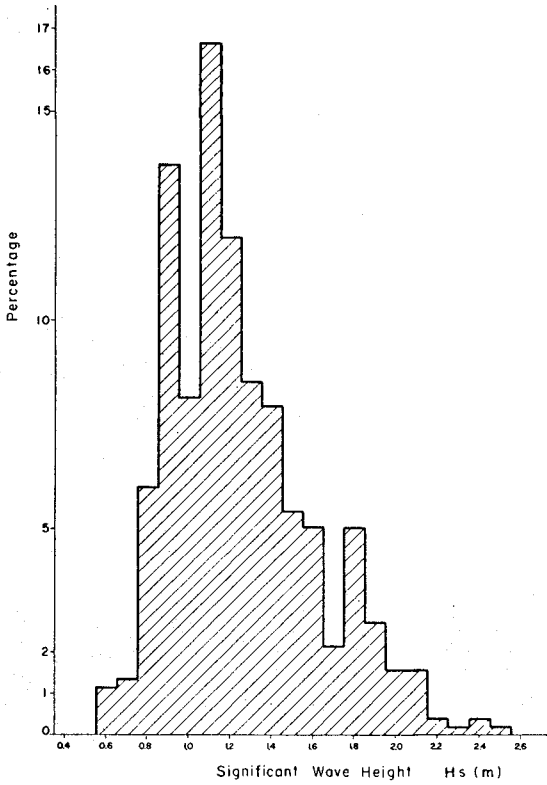
ANNUAL DISTRIBUTION OF THE SIGNIFICANT WAVE
HEIGHTS AT A 20 m DEPTH OF WATER

FIG. 3

Significant (Hs) and Maximum (Hmax) Wave Height (m)

SIGNIFICANT AND MAXIMUM WAVE HEIGHT
EXCEEDANCE CURVES

FIG. 4

EXCEEDANCE CURVE OF DEEP-WATER SIGNIFICANT
WAVE STEEPNESS

FIG. 5

ANNUAL DISTRIBUTION OF WAVE
DIRECTIONS AT A 5m DEPTH OF
WATER, REGARDLESS OF PERIODS
AND HEIGHTS

FIG. 6
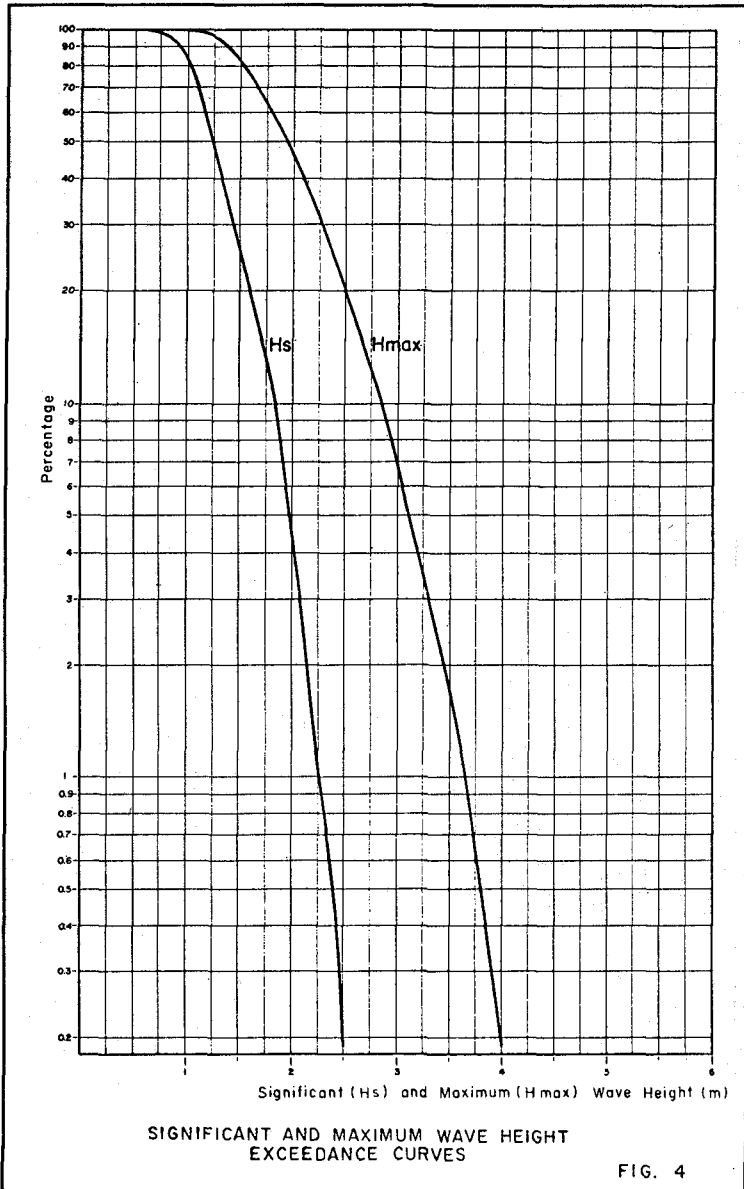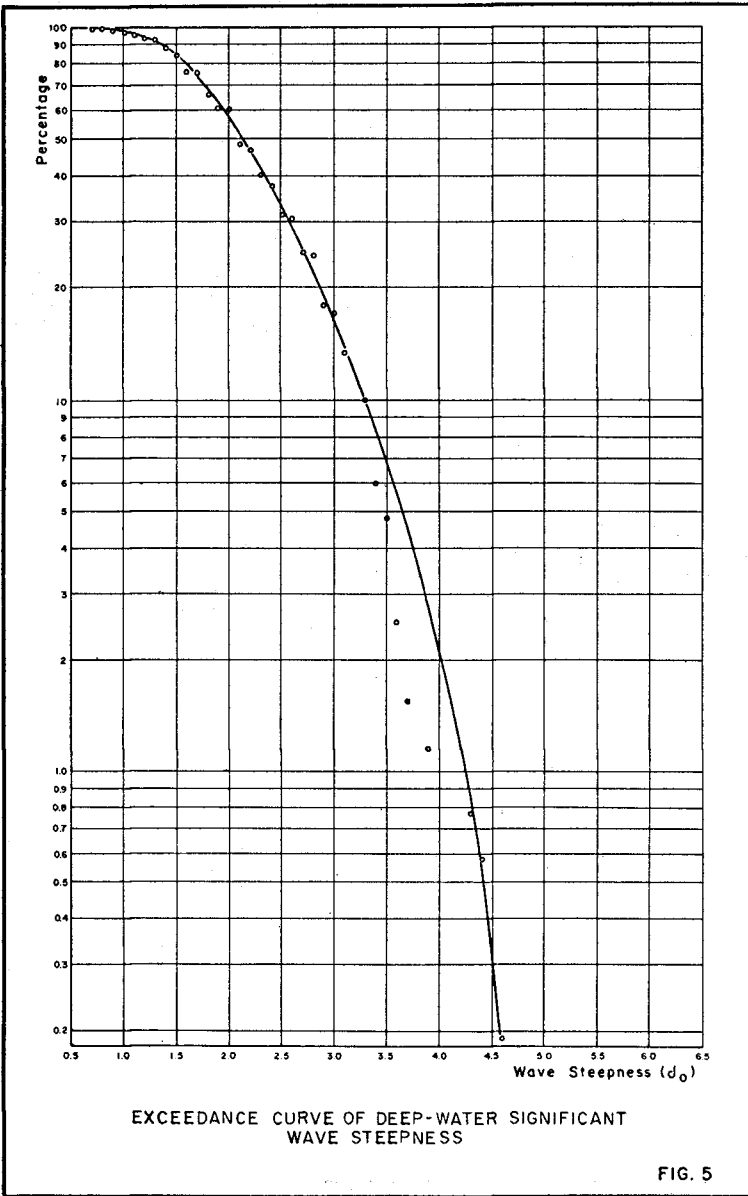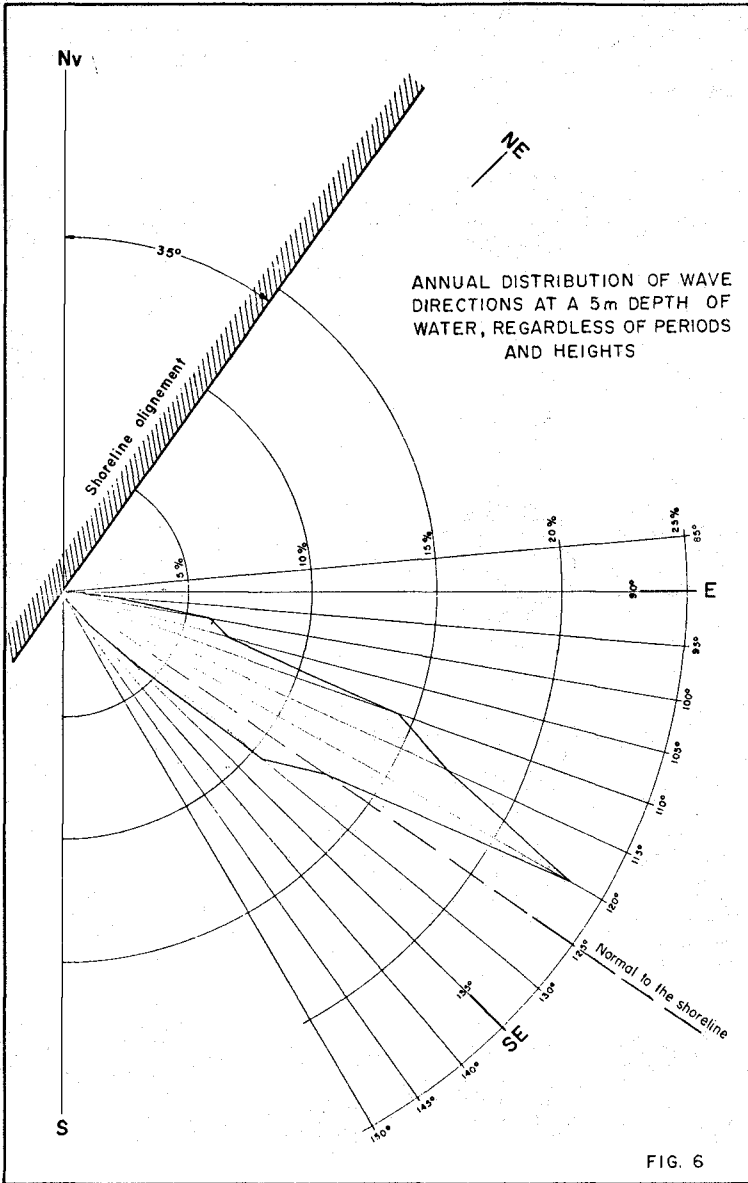
coefficient was taken as 0.004 (smooth beach). Incidentally, it was
noticed that the transport capacities as calculated by Castanho's method
are very little sensitive to the values adopted for the beach roughness coefficient.

        Bijker's method essentially consists of assessing the increase due to the presence of waves in the transport capacity of a
littoral current. As the only littoral current along the Sergipe
coast is the longshore current brought about by the incoming oblique
waves themselves, the "reference" current used in the application of
Bijker's method was the longshore current as given by the Eagleson
formula for idealized conditions [8] . Such ideal conditions are a
reasonable approximation of the Sergipe shore.

        The seaward boundary for applying Bijker's method was the
-6m contour as it had been established by the radioactive-tracer experiment and done by Bijker himself in his calculations for the Queensland
coast in Australia [6] , [7] .

        Unlike Castanho's, Bijker's method is rather sensitive to
the value adopted for the apparent bed roughness (half the ripple
height) in the logarithmic formula for the Chezy coefficient. The
value adopted for the apparent bed roughness was r = 0.17m which is
the same value as used by Bijker himself in his calculations for
Queensland [6] , [7] . The geometry and exposure of the Sergipe coast
can be taken as fairly similar to that case.

        Caldwell's formula was used in metric units, and the total
energy of the breakers was determined by solitary-wave theory.

        IV)   THE RESULTS OF THE COMPUTATIONS

        The following table summarizes the results of the littoral-
drift computations for the whole year.

                         TABLE I

Method	Total annual volumes of littoral drift in both shoreline directions (in $10^3 m^3$)	Percentages of total volumes in each shoreline direction %	
		NE-SW	SW-NE
Caldwell	826.8	80.8	19.2
Castanho	785.8	86.0	14.0
Bijker	757.1	83.3	16.7

Bearing in mind all the approximations contained in the computations, the three methods are seen to agree in this particular case to all practical purposes. They predict a total annual volume of littoral drift in both shoreline directions of the order of $800000m^3$ per year. There is also a fair agreement as to the distribution of the annual volume in each shoreline direction. The dominant drift would be southwestward and amount to about $660000m^3$ per year.

However, the three methods do not agree as to the variation of littoral drift over the year for the same waves. This fact is brought out by Fig. 7 which pictures the variation of the total monthly values of littoral drift in both shoreline directions throughout the year for each method. It becomes apparent that Castanho's method predicts a heavier littoral drift during the summer months. Caldwell's formula shows a more even distribution of littoral-drift volumes throughout the year. Bijker's method also predicts a heavier littoral drift during the summer months, although the dominance over the winter months is not so marked as according to Castanho.

Bijker's and Castanho's methods agree in that the month with the heaviest littoral drift is January (a summer month in the Southern Hemisphere). According to the Caldwell formula July (a winter month) would have the heaviest littoral drift.

On the order hand, Bijker's and Caldwell's formulae agree in that April, September and October would be the months during which the direction of the net littoral drift would be the reverse of the dominant direction over the year (NE to SW). According to Castanho's method only in May the net littoral drift would be directed from SW to NE.

The agreement between the three different methods for the total annual results should be regarded as fortuitous, due to peculiar features of each method and of the wave climate off Sergipe. The same agreement may not be expected for a different wave climate.

The wave periods off Sergipe are short, and their range of variation throughout the year is small. As a result, the values of deep-water wave steepness are high most of the time. This causes the angle of wave attack at breaking depth (α_b) to be the main factor in determining the changes in the transport capacity of the waves over the year.

It was noticed that for α_b values below a certain limit, the transport capacity as predicted by Castanho's method is consistently smaller than the ones predicted by the other two methods. The reverse is true for α_b values above another limit. In the Castanho -Bijker comparison the critical values are 6° and 14° for the Sergipe coast. In the Castanho-Caldwell comparison the two critical values coincide at about 12°.

It so happens off Sergipe that the summer waves are lower than the winter waves but in the summer the angles of wave attack are greater than in winter. As a result, a compensation effect makes the three different methods predict about the same value for the total annual volume of littoral drift, although they also predict different variations of littoral-drift intensities throughout the year.

METHOD	ANNUAL VOL. OF LITTORAL DRIFT (m³)
BIJKER	757100
CALDWELL	826800
CASTANHO	785800

BIJKER'S METHOD ——
CALDWELL'S METHOD ·······
CASTANHO'S METHOD -----

(m³/month)
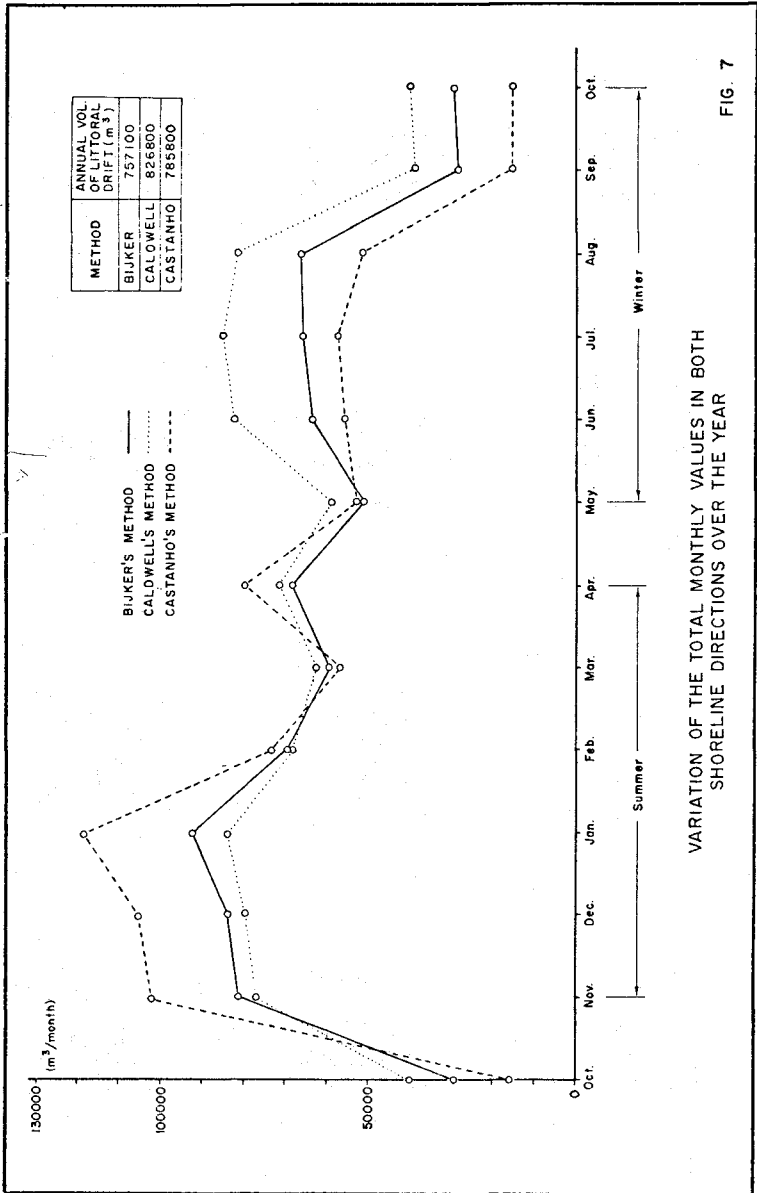
FIG. 7

VARIATION OF THE TOTAL MONTHLY VALUES IN BOTH
SHORELINE DIRECTIONS OVER THE YEAR

V)   THE CUBATURE OF DEPOSITS IN THE DREDGED CHANNEL

          The channel accross the Aracaju bar has been dredged to a
depth of 8m with a bottom width of 80m. After the dredging reached
completion the channel was surveyed in December 1971, August and December
ber 1972. The cubature of the deposits has been made by the junior
author, and particular care has been taken to check on that the side
slopes had already reached equilibrium in the earliest survey
available.
          The following table displays the results of the cubature
and the littoral-drift computations for the same lengths of time.

TABLE II

Time Interval / Method	Dec 71 - Aug 72 (in $10^3 m^3$)	Aug 72 - Dec 72 (in $10^3 m^3$)	Total for the year (in $10^3 m^3$)
Caldwell	594.4	232.4	826.8
Castanho	582.4	203.4	785.8
Bijker	548.3	208.8	757.1
Cubature	336.0	228.0	564.0

          The predicted results were expected to exceed the cubature
results for two reasons:

     a)   the computations had been carried out with the signifi
          cant wave heights;

     b)   some of the littoral-drift material may not stay in the
          channel as deposits since it may be flushed out offshore
          or brought back to the downdrift coast by the tidal flow
          from the estuary.

          The relative errors for the whole year were respectively
+ 46.6% for Caldwell's formula, + 39.3% for Castanho's method and
+ 34.2% for Bijker's method. However, for the August 72 - December 72
time interval the agreement between predicted and actual results was
remarkably good.
          The time intervals between successive surveys were not short
enough to enable an assessment of which computation method had best
predicted the history of the deposits. In particular, the actual time
intervals (December 71 - August 72 and August - December 72) between
the successive surveys include both summer and winter months.
          Obviously the agreement of the three methods for the August
- December 72 time interval is due to the peculiar features predicted
by each method for the variation of littoral-drift intensities over
the year as shown in Fig. 7.
          It is not possible to give a definite explanantion of the
agreement between predicted and actual results for the particular
time interval August - December 1972. However, the most likely expla
nation is that the actual wave action during that time was more severe

than in the corresponding time interval of the standard year used for
the computations.

        VI) CONCLUSIONS

        1)   For the particular wave climate off the coast of Sergi
pe, in the Northeast of Brazil, Caldwell's, Castanho's and Bijker's
methods lead to practically the same total annual volumes of littoral
drift in both shoreline directions: about 800000 cubic metres per
year.

        2)   The three methods also practically agree for the annual
volumes in each shoreline direction.

        3)   However, the three methods do not agree as to the varia
tion of littoral-drift intensities over the year for the same waves.

        4)   The agreement for the total annual volume of littoral
drift must be considered as fortuitous, due to the particular features
of each method and of the wave climate off Sergipe.   It may not be
expected for a different wave climate.

        5)   A comparison has been made between computed volumes of
littoral drift and deposits in a dredged channel accross the Aracaju
bar for the same lengths of time.   The relative errors for the whole
year were respectively + 46.6% for Caldwell's method, + 39.3% for
Castanho's method and + 34.2% for Bijker's method.   However, for the
August 72 - December 72 time interval the agreement between predicted
and actual results was remarkably good.

        6)   Even when only monochromatic waves are taken into
account, the state of the art of littoral-drift evaluation remains
open to research and further improvement.

        VII)   BIBLIOGRAPHICAL REFERENCES

1)   Bandeira, J.V. "An Evaluation of the Annual Volume of Littoral
     Drift around the Sergipe Estuary Entrance" (in Portuguese).
     Instituto de Pesquisas Radioativas (IPR/CBTN), Belo Horizonte,
     Brazil, November 1972.

2)   Caldwell, J.M. "Wave Action and Sand Movement near Anaheim Bay"
     Beach Erosion Board, Technical Memorandum NÇ 68, 1956.

3)   Castanho, J.P. "Wave Breaking and Littoral Drift" (in Portuguese).
     Paper NÇ 275.   Laboratório Nacional de Engenharia Civil, Lisbon,1966.

4)   Bijker, E.W. "Some Considerations about Scales for Coastal Models
     with Movable Bed", Publication NÇ 50, Delft Hydraulics Laboratory,
     1967.

5)   Bijer, E.W. "Littoral Drift as a Function of Waves and Currents"
     Proceedings of the 11th Conference on Coastal Engineering, Lon
     don, 1968, Vol. I, pag. 415-435.

6)   Bijker, E.W. "Longshore Transport Computations". Vol. 97, NÇ WW4,
     Journal of the Waterways, Harbors and Coastal Engineering Division,
     November 1971.

7) Bijker, E.W. "Littoral-Drift Computations on Mutual Wave and
    Current Influence". Report N⁰ 71-2, Delft Hydraulics Laboratory,
    June 1971.

8) Eagleson, P.S. "Theoretical Study of Longshore Currents on a
    Plane Beach". M.I.T. Department of Civil Engineering, Hydrodyna
    mics Laboratory, Report N⁰ 82, 1965.

9) U.S. Army Coastal Engineering Research Center. "Shore Protection,
    Planning and Design". Technical Report N⁰ 4, 1966.

10) U.S. Navy Hydrographic Office. "Sea and Swell Charts".
    Washington, 1st edition, 1948.

CHAPTER 43

MEASURING SAND DISCHARGE NEAR THE SEA-BOTTOM

Dieter WENZEL

Dipl.-Ing., Amt für Land- und Wasserwirtschaft

D-2250 Husum, Fed. Rep. of Germany

Abstract

The direct and continuous measurement of the littoral drift is an essential problem with investigations on erosion of sandy coasts, as for instance at the island of Sylt. The measuring conditions require equipment of very particular features.

Recent measurements have supplied informations about the conditions of sound propagation in sediment loaded water, leading to the conception of a sand discharge measuring device. It will consist in a combination of a current meter and a sand concentration meter.

A convenient equipment is actually being developed. It is to supply an idea about the magnitude of the instantaneous sand discharge, the approximate remaining sediment transport vector, the phases of maximum and minimum sediment load, and so on. Consequently it will help to obtain a reliable statement about erosion processes, indispensable information for successful coastal engineering work.

1. Introduction

The island of Sylt (Northern Germany) continuously loses material of its western coast by erosion. The beach consisting of sand is exposed to the surf of the open North Sea. The coast of the central part yields in the mean by 1 m a year. At the northern and southern ends the mean loss runs up even to 4 m a year.

Coastal engineering work in this area has to maintain the shore line in order to protect considerable material values (fig. 2). But so far no efficient shore protection method has been found. The most recent action, a beach nourishment at Westerland in 1972, is still being under study (ref. 3).

As in other places, the actual relationships between wind data, wave characteristics, surf currents, tidal currents, and coast erosion are not yet well known. The links between hydrological forces and results of morphological processes are to be detected. This aim requires to make up the energy balance on the one hand, and to measure the morphological process itself, i.e. the sand transport, on the other.

An idea about the intensity of sediment transport on the west coast of Sylt is given by the effects of storms: Dunes and cliffs may lose 6 m
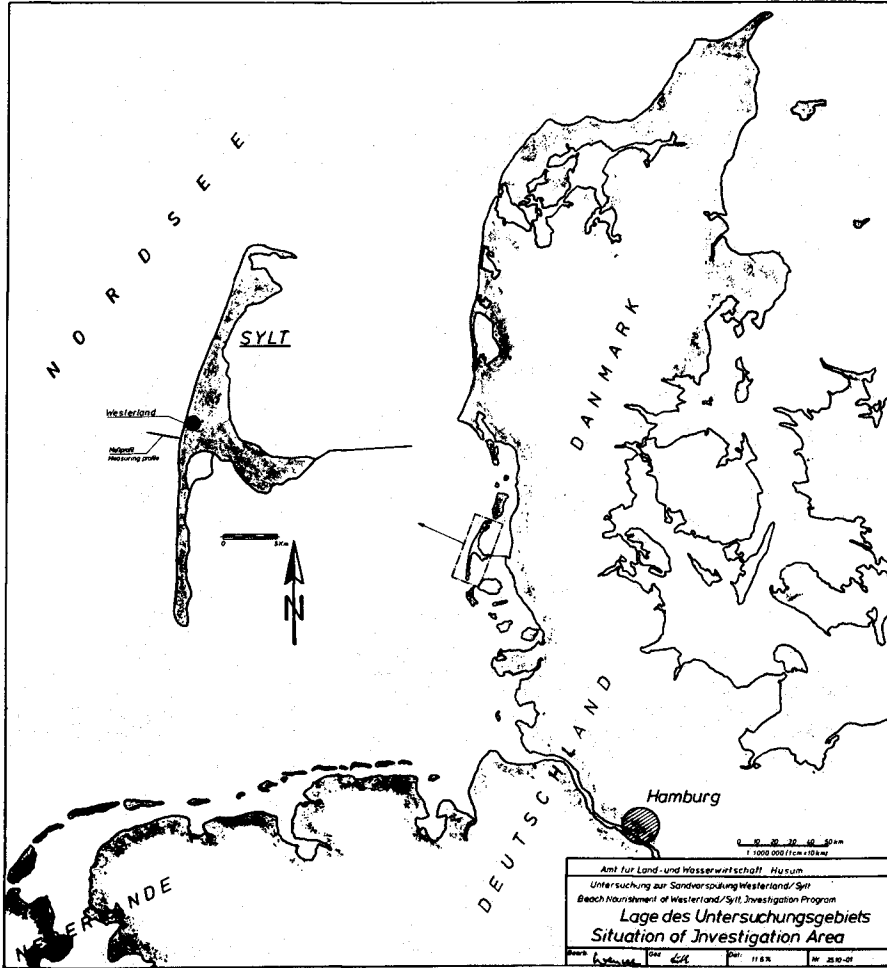
Fig. 1. The situation of the investigation area

Fig. 2. Aerial view of the town of Westerland (to the east)

Fig. 3. COMEX electromagnetic current-meter, mounted on its support

of depth during 3 hours, and the beach level may change by 2 m in 6 hours.

2. Requirements

As weather and waves may change frequently and rapidly, continuous mea-suring facility is necessary, and that with high resolution in time during periods of hours and with low resolution in time during periods of months. The measuring equipment has to be independent of water colour and turbidity which are variable. Moreover, it is the scope of this study to measure not only the suspended sediment, but above all the sediment coarser than that normally in suspension within the Stokes ranges, i.e. up to about 2 mm Ø. For the above reasons, no sand trap or turbidity (light absorp-tion) device can be used.

The measuring conditions in this area are difficult because of the shallow water (max. depth 10 m), mobile sea-bottom (sand) and considerable wave heights (maximum measured during storm in November 1973: 6,8 m). Installa-tion and inspection of submarine units is possible only during about six weeks a year (June and September) due to the atmospheric conditions.

An equipment adapted to these conditions must present particular features such as:

- permanent installation on the sea-bottom, but possibility of being moved to another measuring place

- strong mechanical resistance to high orbital movement by a construction without moving parts

- continuous operation and reliability for at least eight months

- a marine cable link for power and data transmission

- data transmission unaffected by variable electrical resistances in the cable and transitions

- indicating and recording data ashore.

3. Present Measuring Devices and Results

In accordance with the above-mentioned features, some measuring devices have been installed and operated (fig. 4).

3.1. Current-Meters (S1, S2)

Data about current velocities in the Sylt site have been gathered so far by means of electromagnetic current-meters: An electric tension is induced by the water passing through an alternating electromagnetic field. These current-meters allow the measurement of orbital movement with a resolution of 0,1 s as well as the measurement of tidal currents, projected onto two horizontal axes. The distance sensor - sea-bottom varies from 0 to 1 m, depending on the level of the sea-bottom (fig. 3).

The results show that the mean longshore component changes its direction in the tidal rhythm and reaches about 0,6 m/s (fig. 5). The mean compo-nent perpendicular to the shore varies very little and runs up to 0,3 m/s.

Fig. 4. The measuring profile near Westerland, looking to the north.

MThw = mean tide high water level

MTnw = mean tide low water level
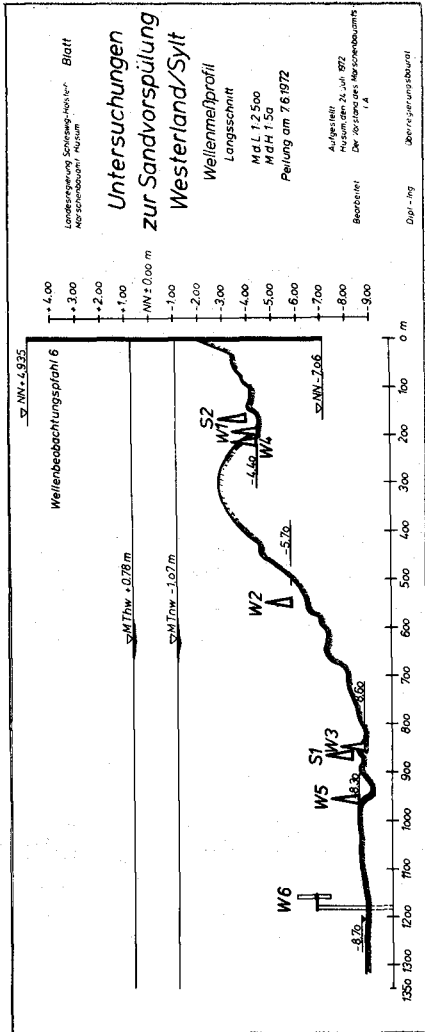
Fig. 5. Current recordings.

calm weather, low waves

p = component perpendicular to shore

l = longshore component

p passage of a wind field with increasing and decreasing waves
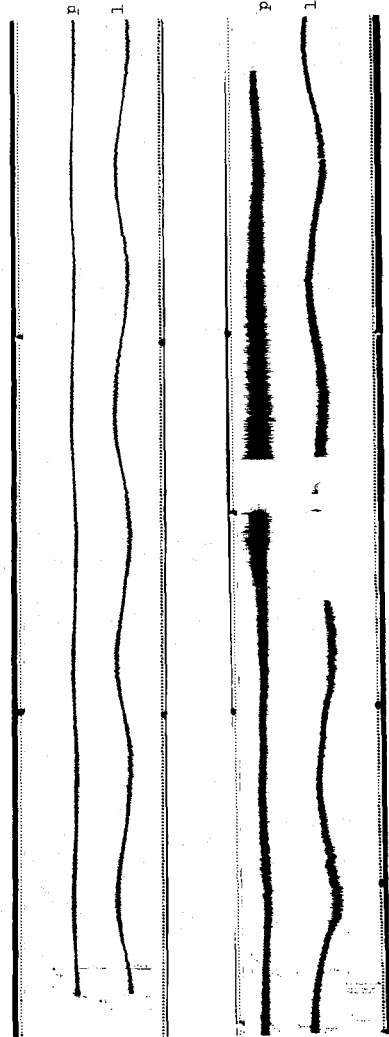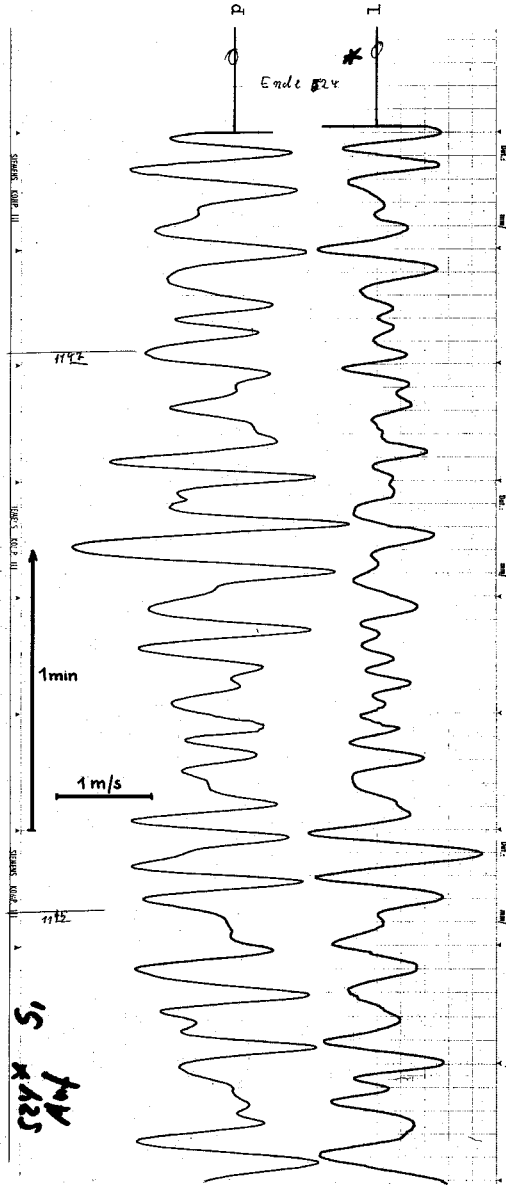
Fig. 6. Orbital currents during storm. Max. wave height
about 6 m

p = component perpendicular to shore
l = longshore component

They are superimposed by the orbital movements caused by waves. The ampli-
tude of the orbital velocities comes up to 2,9 m/s in one axis, depending
on wave height and direction (fig. 6). Hence the considerable sediment
transport in the site can be explained: the orbital movement causes the
sand to be whirled up. Consequently the tidal and surf currents are enabled
to transport sediment grains of a far greater diameter than corresponding
to their mean velocity (ref. 6).

3.2. Wave Gauges (W1 - W3, W6)

Recent measurements with ultrasonic wave gauges have demonstrated the inten-
sity of sound absorption in sediment loaded water. These wave gauges work
exactly like reversed echo-sounders, installed on the sea-bottom (fig. 7).
They are emitting pulse-trains at a rate of 8 pulses p.s. and a sound
frequency of about 100 kHz. The emitted sound energy is in the order of
60 W. The distance sensor - sea-bottom varies from 0 to 1 m, depending on
the level of the sea-bottom. It can be evaluated ashore by the appearance
of multiple echos on the oscilloscope (fig. 8).

It turned out that no echo was received from the sea-surface during periods
of high waves. On the oscilloscope, variable layers of concentrated
intermediate reflectors (sand grains) could be observed. They passed the
sound beam like clouds, their passage taking generally some minutes (fig.
9). With very high waves, absence of surface echos was recorded even for
hours. This effect is more marked on the measuring stations near the
beach, where the surf energy is liberated and takes action on erosion.

The station W6 is equipped with a sound velocity measuring device. The
output is a frequency proportional to the sound velocity. This device
has run so far for one day only, but proves able to give useful data.
The short term variation is only $0,25 \ldots 0,35$ m/s $\hat{=} 1,8 \ldots 2,5 \times 10^{-4}$,
which seems to be due to the inherent limits of the device.

4. Intended Realization

4.1. Object to Be Measured

Sand discharge, Q_{sed}, is defined as the volume of sand transported per
time unit through a definite area, A. L (load or sand concentration)
be the ratio between a certain volume of sediment and the total volume
of water-sediment-mixture, in which it is contained:

$$L = \frac{V_{sed}}{V_{tot}} , \qquad 0 \leqq L \leqq 1$$

L is one variable magnitude to be measured continuously as an average
value in the measuring area: $L = f(t)$.

The discharge of water-sediment-mixture can be obtained by measuring the
current velocity in a definite area: $Q_{tot} = v \cdot A$. v is another
variable magnitude to be measured continuously: $v = f(t)$.

Consequently, sand discharge is obtained as

$$Q_{sed} = L \cdot Q_{tot} = L \cdot v \cdot A,$$

i.e. by continuous multiplying the current velocity by the sand concen-
tration.
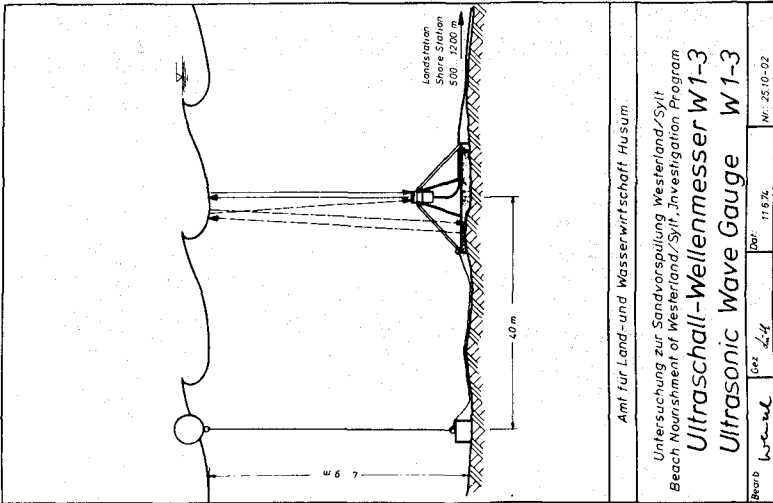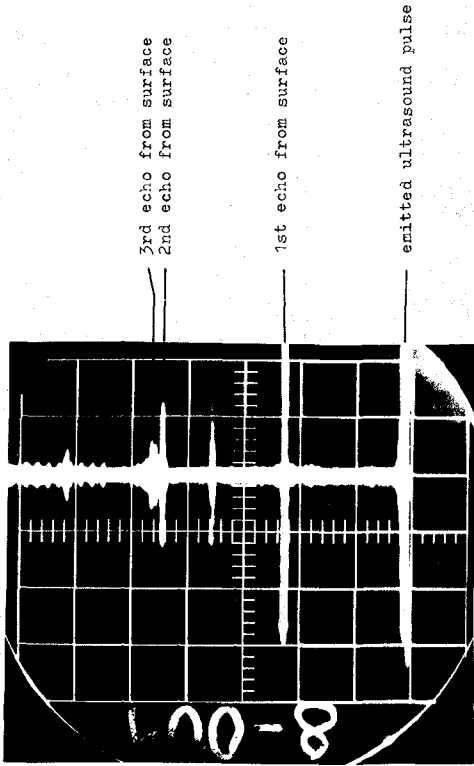
Fig. 8. Oscillogramme of wave gauge, low waves

3rd echo from surface
2nd echo from surface
1st echo from surface
emitted ultrasound pulse

Amt für Land- und Wasserwirtschaft Husum

Untersuchung zur Sandvorspülung Westerland/Sylt
Beach Nourishment of Westerland/Sylt, Investigation Program

Ultraschall-Wellenmesser W 1-3
Ultrasonic Wave Gauge W 1-3

Landstation
Shore Station
500 1200 m

40 m

Fig. 7. Ultrasonic wave gauges W1 - W3

Fig. 9. Comparison of wave record and consecutive oscillogrammes (rate 1 photo/s).
Max. wave height about 1,5 m. From photo no 0 to no 24, a "sand cloud" is passing (visible in the lower part of the wave record).

The area A is a constant, defined by the construction of the sensor.
It has to be constant for any direction of v.

As the main quantity of sediment is moved near the bottom, this area
is to be placed here in a way giving the average of a certain layer
(ref. 4).

The parameter L can be measured by three acoustic phenomena: sound re-
flection, sound absorption, and variation of sound velocity in sediment
loaded water. The sound reflection method seems to be more difficult in
gauging than using sound absorption. As to sound absorption, refer to
3.2., where it is shown empirically that there is a distinct correlation
between load and absorption. It is to be noted, that the effect appear-
ing here as absorption is due mainly to a scattered reflection by fine
particles.

Sound velocity in sea water is given by the classical LAPLACE-formula

$$c = \sqrt{\frac{\pi}{\rho \cdot \varkappa}},$$

signifying that it depends on temperature, salinity, and pressure:

$$c = f(T, S, P) \qquad (ref. 1, 5)$$

Among these parameters temperature has the greatest influence.

Approximate calculation is possible for instance by (ref. 1):

$$c = 1445,5 + 4,62T - 0,0452T^2 + (1,32 - 0,007T) \times (S - 35)$$

with c $[m/s]$
T = temperature $[°C]$
S = salinity $[°/oo]$

These formulas do not take into account the presence of sediment in
the water. This is done by a formula by URICK/BERGMANN (ref. 1):

$$c_o^2 = \frac{1}{[\rho_2 \alpha + \rho_1(1-\alpha)] \cdot [\beta_2 \alpha + \beta_1(1-\alpha)]}$$

with c_o = sound velocity in a suspension
ρ_1 = density of pure liquid
ρ_2 = density of suspended material
β_1 = compressibility of pure liquid
β_2 = compressibility of suspended material
α = part of volume of suspended material in the suspension
c_1 = sound velocity of pure liquid

Analysis proves that $\dfrac{c_1}{c_o} = f(\alpha)$ is a parabolic curve (ref. 1). That means

that sound velocity depends well on sediment load, but in a certain range
any value of measured sound velocity may belong to two values of sediment
load. The function is ambiguous in a certain range. A combination of
sound velocity measurement with sound absorption measurement will be
useful.

4.2. Measuring Device

An equipment for the measurement of both parameters, the current velocity
v and the sand concentration L, is actually being developed. The physical
principle applied for both is ultrasound (fig. 10, 11).

The current-meter measures the velocity vector projected on two orthogonal
horizontal axes by comparing the relative sound speeds upstream and down-
stream. An optional feature, computing and taking into account the true

Fig. 10.
Sand discharge measuring
device, planned con-
struction
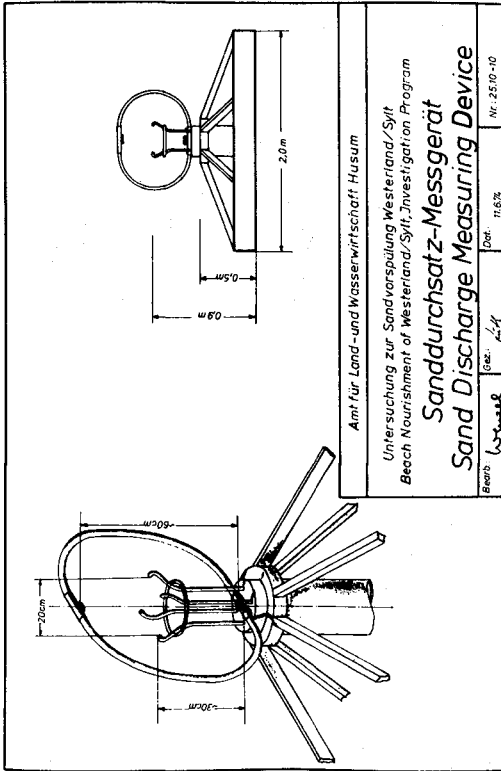
Fig. 11.
Sand discharge measuring
device, block diagram
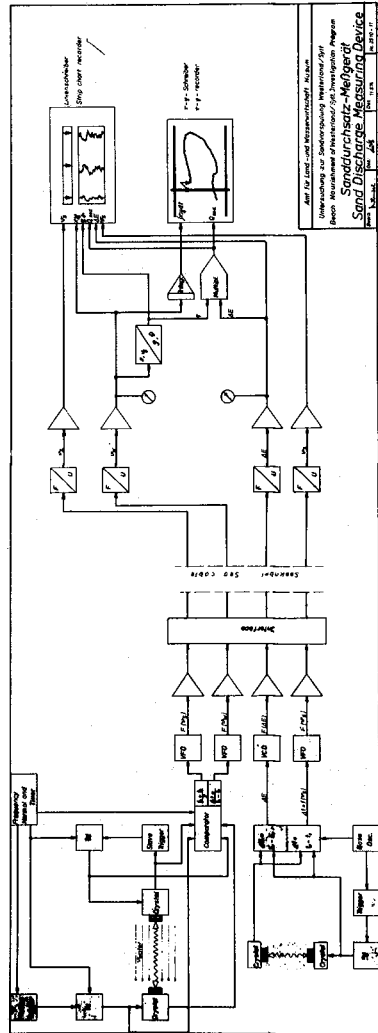
sound velocity, allows to increase the accuracy of computed current velocity. Moreover, output and recording of the sound velocity will be very useful for getting data about sand concentration. A convenient equipment is designed and manufactured by an industrial company.

It will be combined with a sand concentration measuring device. The sand concentration in the water is obtained by measuring the sound absorption in a vertical axis. It is arranged in this sense in order to minimize the disturbance of the horizontal currents and to get the average of a certain layer (0,6 m). At the same time, this device, too, will compute and output the sound velocity.

It is essential that the sand concentration is measured in exactly the same point as the current velocity: the three measuring axes form a cross of axes each of which being perpendicular to the others.

The shore station of the equipment has to compute magnitude and direction of current velocities, sand concentration, sand discharge, and to record data, including continuous recording of the sound velocity in order to increase the redundance.

5. Problems to Be Resolved

The accurate calibration of the sand concentration meter presents certain difficulties as it is to be done full-scale. The influence of granulometry is to be examined during gauging work. The respective effects of sand grains and enclosed air bubbles are to be discerned. This can be done by means of the existing ultrasound wave gauges.

Some more experience is needed to find the best mechanical construction for the submarine unit, as to good hydrodynamic shape, sufficient resistance against damage, minimum affection by fouling etc.

6. Future Investigations

The sand discharge measuring device actually under development is expected to supply continuous data any time and at any weather condition (as to storm and wave heights), particularly in autumn and winter, the seasons of heaviest attacks to the shore. The actual object is to obtain one operational equipment, giving information about direction and magnitude of sediment transport during all tidal phases.

Integration of the x,y-components of the current vectors over the time (e.g. entire tides) and recording by a x-y-recorder will produce approximately the course of a fictive water particle (fig. 12), supposing that a uniform velocity field surrounds the measuring point. The vector from the beginning to the end of such a recording over an entire tide is considered as the remaining current vector. In the same way the sand discharge vectors may be recorded. The recording will supply an idea about the approximate remaining sediment transport vector, a very important information for shore protection work.

Another useful presentation of measured data will be the immediate display of the current velocity vector integrated over the time as before, directly correlated point by point to the correspondent sand concentration (fig. 13). This plotting allows to recognize at which tidal phases the maxima and minima of sediment load arise. It seems to be able to facilitate the comprehension of the mechanism of sediment transport.
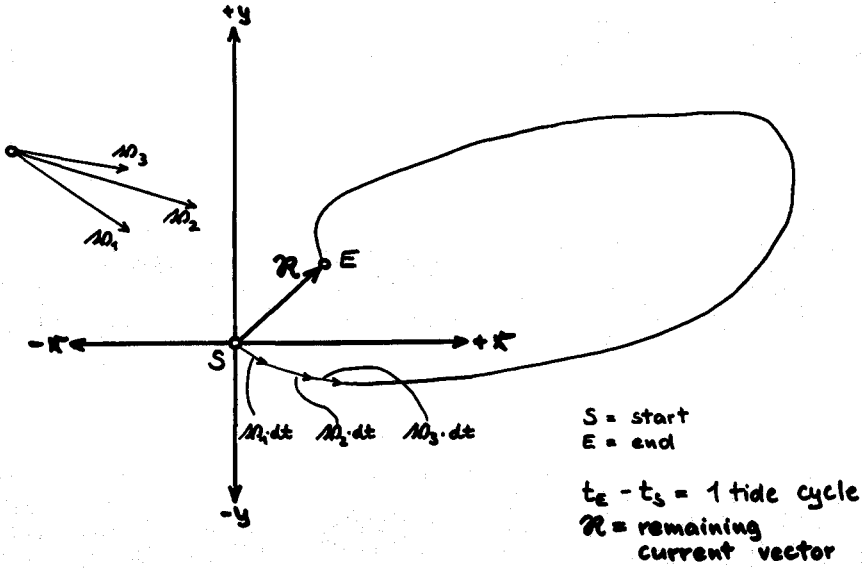
Fig. 12. Display of the remaining current vector.
v_1, v_2, v_3= instantaneous current vectors
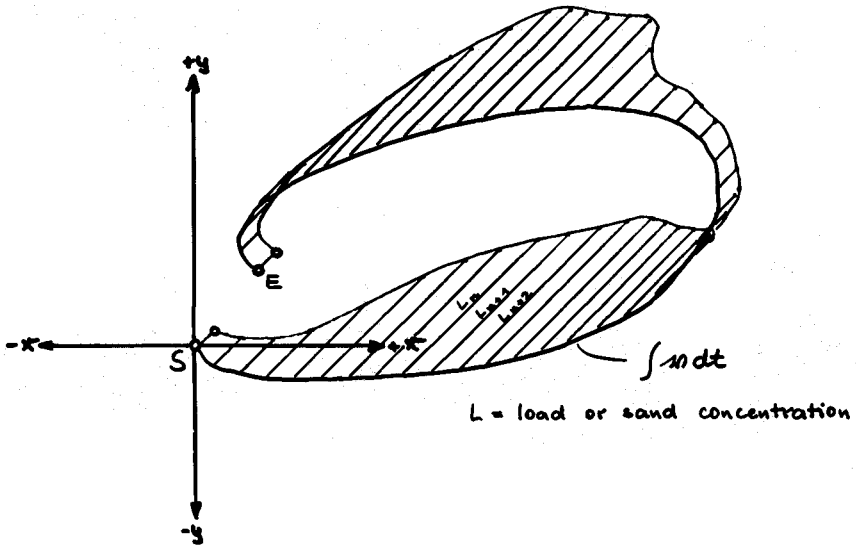
Fig. 13. Simultaneous display of current vectors and sand concentration

Formerly tracer measurements have been executed using radioactive and fluorescent tracers to study the sediment transport. They permit "static" measuring only of the sediment transport, as the tracer distribution is recorded at determined moments with rather long intervals. The processes between measuring moments are not stated. In order to obtain current information about sediment transport, "dynamic" measuring as by sand discharge measuring is necessary. For this purpose the aim is to install a series of equal stations supplying a reliable statement about erosion processes, when combined with energy balance considerations and tracer measurements.

7. Conclusions

Successful coastal engineering work at sand coasts subject to an important surf requires the knowledge of the erosion process. One way of investigational approach to this problem is the measurement of sand discharge in situ, at any time, particularly at heavy storm surges. An equipment for this purpose must be fit for severe environmental conditions. Using ultrasonic devices will allow to combine continuous current metering and continuous metering of sand concentration in the water. The arithmetical product of both will give the sand discharge through a definite area presented as a vector.

The feasibility of applying this method is demonstrated by the use of ultrasonic wave gauges, operated during periods of high waves. The sediment load in the water caused variable sound absorption. A first sand discharge measuring device is actually being developed. The principal problem to be resolved is to gauge accurately the sand concentration meter. The device is to be installed at the west coast of the island of Sylt (Germany).

8. Acknowledgements

REFERENCES

1. Bergmann, L.: Der Ultraschall. 6th ed., Stuttgart, S. Hirzel Verlag, 1954

2. Dietrich, G. and Kalle, K.: Allgemeine Meereskunde. 2nd ed., Berlin, Gebr. Borntraeger, 1965

3. Führböter, A., Köster, R., Kramer, J., Schwitters, J., and Sindern, J.: Sandbuhne vor Sylt zur Stranderhaltung. Die Küste, Heide, no 23, 1972, p. 1-62

4. Glover, J.R., Bhattacharya, P.K., and Kennedy, J.F.: An electrooptical system for measurement of mean and statistical properties of sediment suspensions. IIHR Report no 120, Iowa City, 1969

5. Kroebel, W. and Mahrt, K.-H.: Direct Precision Measurements of Sound Velocity and Discussion of Resulting Differences to Values Calculated from Salinity, Temperature and Pressure, Using the Wilson-Formula. Proceedings of Interocean '73, Düsseldorf, Vol. 2, Paper IO 73 - 655, 1973

6. Yalin, S.: Die theoretische Analyse der Mechanik der Geschiebebewegung. Mitteilungsblatt der Bundesanstalt für Wasserbau, Karlsruhe, no 8, 1957

CHAPTER 44

SEDIMENT THRESHOLD UNDER OSCILLATORY WAVES

Paul D. Komar and Martin C. Miller

School of Oceanography, Oregon State University
Corvallis, Oregon, U.S.A. 97331

ABSTRACT

As the velocity of the water motion near the bottom under oscillatory waves is increased, there comes a stage when the water exerts a stress on the particles sufficient to cause them to move. This study reviews data on threshold of sediment motion under wave action and compares the results with the established curves for threshold under a unidirectional current.

For grain diameters less than about 0.05 cm (medium sands and finer) the threshold is best related by the equation

$$\frac{\rho\, u_m^2}{(\rho_s - \rho)\, g\, D} = 0.21\, (\, d_0 \, / \, D\,)^{1/2}$$

where u_m and d_0 are the near-bottom velocity and orbital diameter of the wave motion, ρ is the density of water, and ρ_s and D are respectively the density and diameter of the sediment grains. For grain diameters greater than 0.05 cm (coarse sands and coarser) the equation

$$\frac{\rho\, u_m^2}{(\rho_s - \rho)\, g\, D} = 0.46\pi\, (\, d_0 \, / \, D\,)^{1/4}$$

gives the best prediction of threshold.

Evaluating the drag coefficient with the graph of Jonsson for wave motions, the data on threshold under waves is found to show good agreement with the curves of Shields and Bagnold for the threshold under a unidirectional current.

INTRODUCTION

As the velocity of a fluid flow over a bed of sediments is increased, there comes a stage when the fluid exerts a stress on the particles sufficient to cause them to move from the bed into the flow and be transported. This stage is generally known as the threshold of sediment movement, or as the critical stage for erosion or entrainment. The purpose of this paper is to examine the threshold of sediment motion under oscillatory water-wave motion. This report is an extension of a previous paper [Komar and Miller (1973)], our intent being to first review the findings of that paper and then to compare the results on the threshold under waves with the curves that have been proposed for the threshold under unidirectional currents [Shields (1936); Bagnold (1963)].

Five sets of previously published data will be utilized in the analysis of the threshold. Bagnold (1946) and Manohar (1955) oscillated a bed of sediment through still water within a tank. Besides investigating the threshold, both studies generated ripple marks and vortex water motions which agree with comparable wave channel and prototype observations, indicating the reliability of observations obtained in this manner. Rance and Warren (1969) conducted threshold studies in an oscillating flow water tunnel using material as coarse as 4.8 cm diameter. The advantage of oscillating the bed as in the studies of Bagnold and Manohar, or utilizing the water tunnel as by Rance and Warren is that prototype periods, orbital diameters, and velocities can be obtained. In ordinary wave tanks the periods are generally limited to less than 2 to 3 seconds. However, the threshold data of two such studies is included in this review; Horikawa and Watanabe (1967) and Eagleson, Dean and Peralta (1958). Horikawa and Watanabe utilized a 25 meter long wave tank with wave heights ranging up to 7 cm and periods up to 2.19 sec [maximum bottom orbital velocities up to 8.5 cm/sec]. The Eagleson, Dean and Peralta data is of interest because it consists of the threshold of single isolated grains resting on an otherwise fixed granular bed. Due to page limitations their data will not be presented in the paper; it was found that it did agree with the other sets of

TABLE 1. - Granular Materials Used in Studies
of Threshold of Motion

A. Bagnold (1946)

Symbol	material	density, (gm/cm³)	diameter, D (cm)
+	steel grains	7.90	0.060
●	quartz sand	2.65	0.330
○	quartz sand	2.65	0.080
⊗	quartz sand	2.65	0.036
⊘	quartz sand	2.65	0.016
⊙	quartz sand	2.65	0.009
■	coal	1.30	0.800
◨	coal	1.30	0.250
□	coal	1.30	0.036

B. Manohar (1955)

symbol	material	density, (gm/cm³)	diameter, D (cm)
⏀	Del Monte sand No. 2	2.65	0.0280
◕	B.E.B. sand No. 1	2.63	0.0786
⊘	coarse sand No. 1	2.60	0.1006
⊖	coarse sand No. 2	2.60	0.1829
∅	B.E.B. sand No. 2	2.63	0.1981
▽	glass beads No. 1	2.49	0.0235
▼	glass beads No. 2	2.54	0.0610
△	polyvinyl chloride pellets	1.28	0.317
▲	polystyrene pellets	1.052	0.317

data and supported the conclusions arrived at within this paper.

    The available data represents a wide spectrum of sediment types: grain diameters range from 0.009 to 4.8 cm, and densities from 1.052 gm/cm^3 (polystyrene plastic) to 7.90 gm/cm^3 (steel grains). This is summarized in Tables 1 and 2 along with the graphic symbols utilized throughout the paper. A scheme of symbols has been employed to clarify the comparisons; all the varieties of circles signify grains composed of ordinary quartz, the plus symbol (+) is that for steel grains (density greater than quartz), while the triangles, squares, and other miscellaneous shapes represent grains of density lower than quartz (limestones, coal, glass beads, and plastics).

    Many equations have been proposed for the threshold of sediment motion under waves; Silvester and Mogridge (1971) present thirteen different equations gathered from the literature. This review will center on the equation presented by Bagnold (1946) and the empirical graph of Rance and Warren (1969), these giving the best results.

TABLE 2. — Granular Materials Used in Study of
Threshold by Rance and Warren (1969)

symbol	material	density (gm/cm^3)	diameter, D (cm)
◬	limestone chips	2.72 - 2.55	0.409, 0.777, 1.072, 1.321, 1.387, 1.742, 2.042, 2.515
◇	glass spheres	2.54 - 2.44	0.592, 0.884, 1.186
◈	concrete cubes	2.39	4.775
◧	coal	1.37 - 1.29	0.706, 1.372, 2.042, 3.251, 4.521
◈	perspex cubes	1.19	3.200

ANALYSIS

        Utilizing the data collected in his experiments, Bagnold (1946)
deduced an empirical relationship for the threshold which may be written
as

$$\frac{2\pi}{T} = a \left[\frac{\rho_s - \rho}{\rho} g \right]^{1/2} \frac{D^{0.325}}{d_0^{0.75}} \tag{1}$$

where T and d_0 are the wave period and near-bottom orbital diameter,
D and ρ_s are the grain diameter and density, and g is the acceleration
of gravity. This empirical relationship is not dimensionally correct so
that the coefficient a is not dimensionless. Utilizing

$$u_m = \frac{\pi d_0}{T} \tag{2}$$

for the maximum horizontal velocity u_m associated with the orbital
bottom motion, equation (1) can be algebraically manipulated to

$$\frac{\rho u_m^2}{(\rho_s - \rho) g D} = a' (d_0 / D)^{1/2} D^{0.15} \tag{3}$$

which is dimensionless except for the residual $D^{0.15}$ factor. Dropping
this factor leaves the dimensionally correct relationship

$$\theta_t' = \frac{\rho u_m^2}{(\rho_s - \rho) g D} = a'' (d_0 / D)^{1/2} \tag{4}$$

which is shown in Figure 1 along with the data of Bagnold (1946). The
straight-line fit yields $a'' = 0.21$ in equation (4). Inclusion of the
$D^{0.15}$ factor decreases the data scatter but the straight-line fit does
not quite pass through the origin.
        Figure 2 utilizes the data obtained by Manohar (1955) to test the
relationship of equation (4). Manohar collected data for both laminar
and turbulent boundary layers whereas Bagnold indicated that his boundary
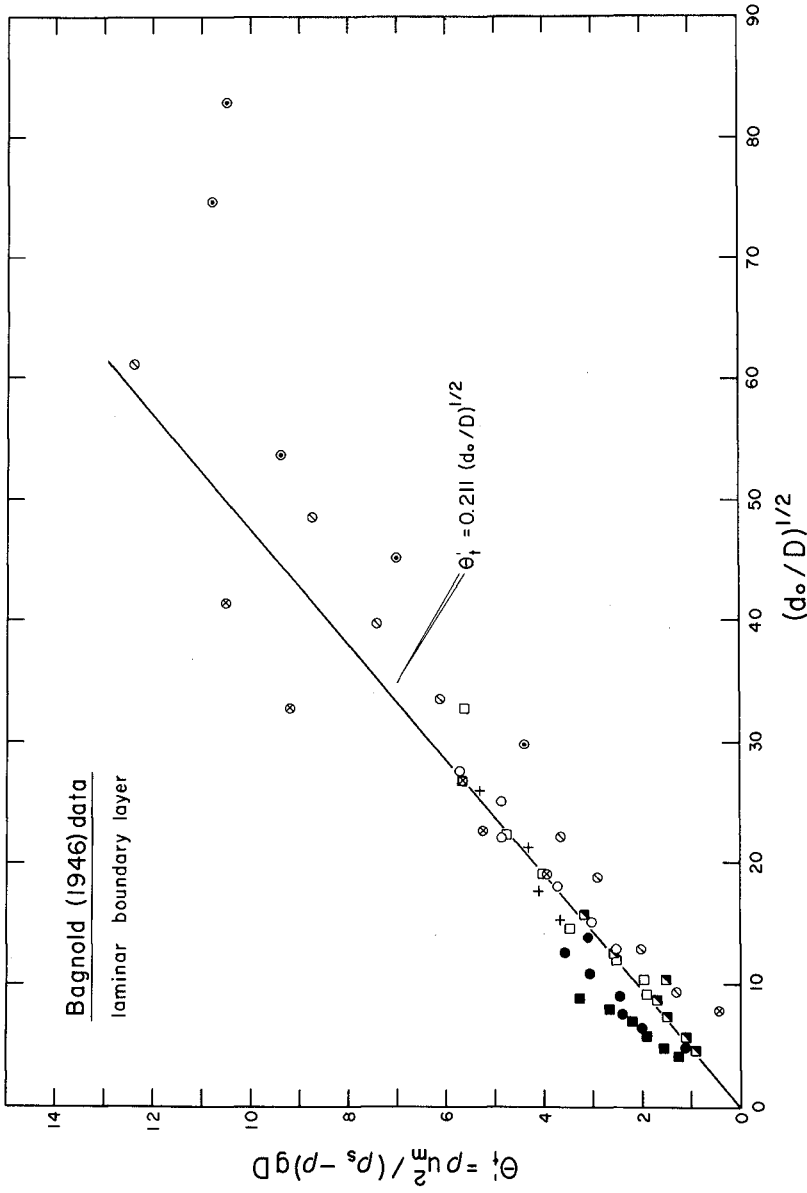
Figure 1: An examination of equation (4) using the data of Bagnold (1946). Symbols are defined in Table 1.
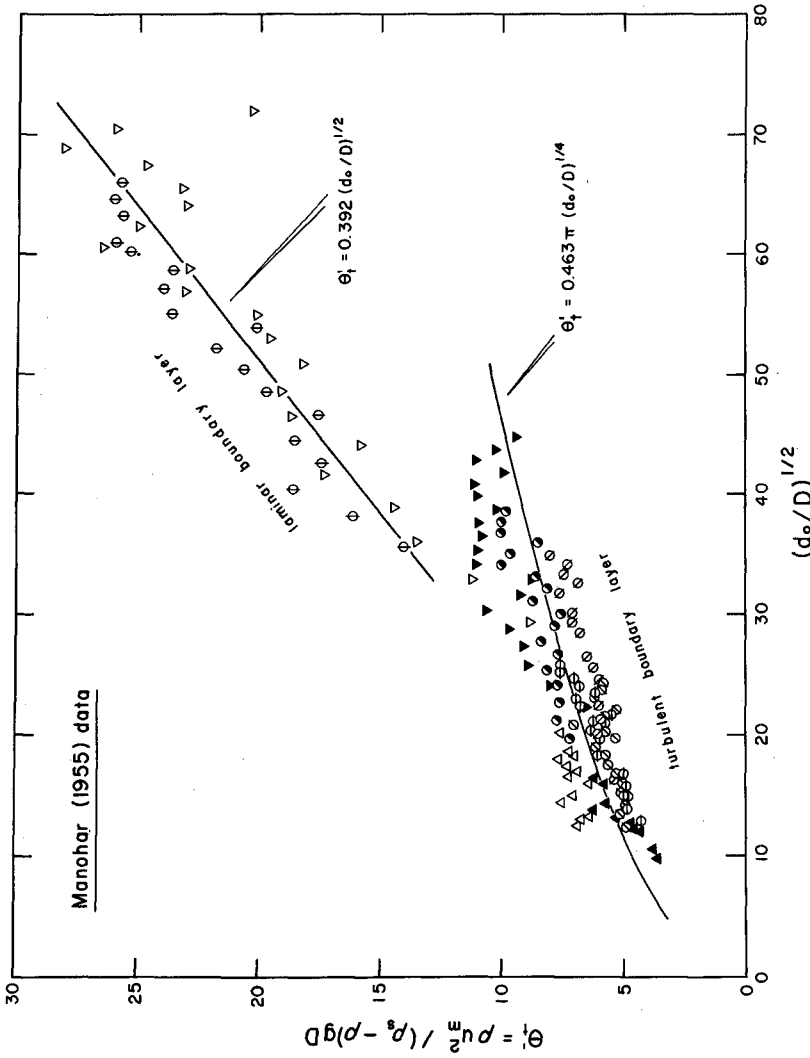
Figure 2: An examination of equation (4) using the data of Manohar (1955). Symbols are defined in Table 1.

layer was laminar in all cases. It is seen in Figure 2 that Manohar's data with a laminar boundary layer yields a good straight-line relationship which gives $a'' = 0.39$ in equation (4). This value for a'' is higher than the value obtained with the data of Bagnold (1946). Determining when the threshold of sediment movement has been achieved and sufficient grain movement occurs is rather subjective and in all probability this difference in a'' values between the two sets of data results from this personal difference between the observers' judgements.

The wave tank data of Horikawa and Watanabe (1967) yields $a'' = 0.3$ in equation (4), just about the average of the values from the Bagnold and Manohar data. However, the Horikawa and Watanabe data shows a better trend if d_0/D is to the 1st power in equation (4) rather than to the 1/2 power. The choice for the value of a'' in equation (4) will be discussed again later in this paper.

Also apparent in Figure 2 is that when the boundary layer is turbulent the data follows no systematic trend according to equation (4). Another relationship for the threshold under a turbulent boundary layer is required. Rance and Warren (1969) found good empirical trends between the ratio d_0/D and the dimensionless number $\rho u_m/(\rho_s - \rho)gT$ which represents the ratio of the acceleration forces to the effective gravity force acting on a grain. Their experiments were for coarse grains in which the boundary layer would be turbulent. Figure 3 plots the data of Manohar (1955) obtained in a turbulent boundary layer against these dimensionless ratios. It is seen that there is a very smooth trend, grains of widely differing diameters and densities agreeing. Also shown is a curve which is based on the data trends as given in Rance and Warren (1969, Fig. 1); it is clear that there is a remarkable agreement between the data of Manohar and that of Rance and Warren. The data of Eagleson, Dean and Peralta (1958) is also in agreement. The graph of Figure 3 can therefore be used to evaluate the threshold conditions of sediment movement when the boundary layer is turbulent.

The essentially straight line of Figure 3 yields the equation
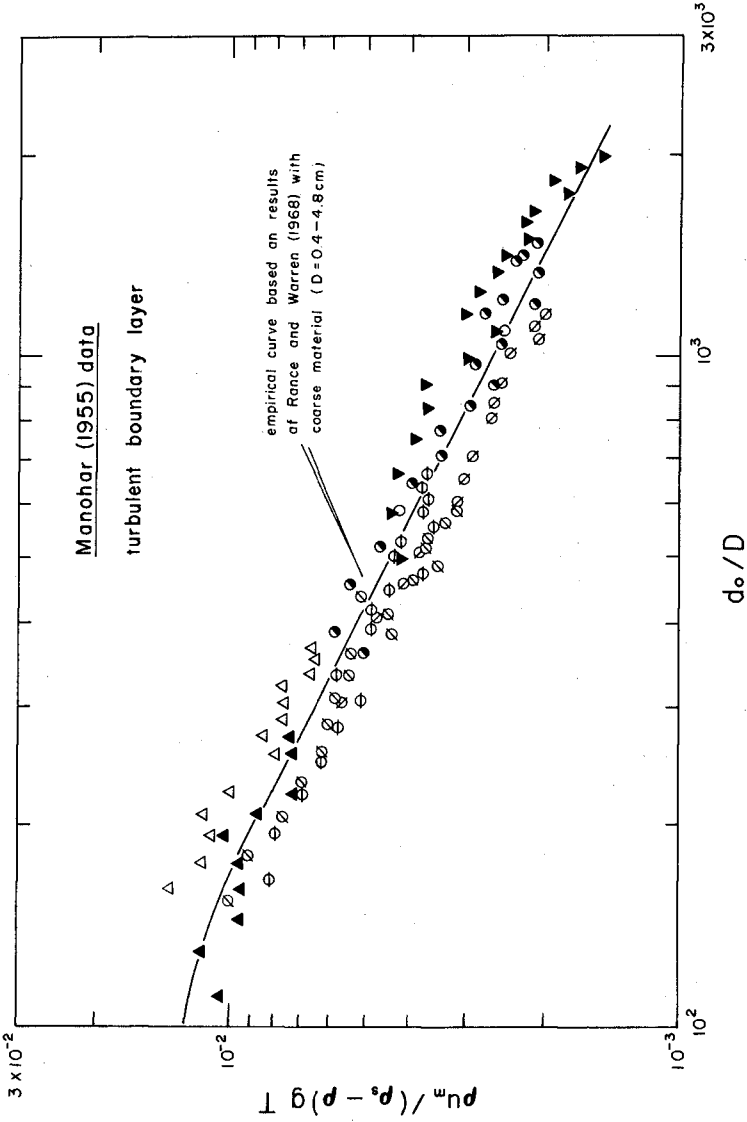
Figure 3: A comparison of the threshold data of Manohar (1955) for a turbulent boundary layer with the empirical curve of Rance and Warren (1969). Symbols defined in Table 1.

$$\frac{\rho \, u_m}{(\rho_s - \rho) \, g \, T} = 0.463 \Big/ (d_o/D)^{0.75} \tag{5}$$

Again utilizing equation (2), equation (5) becomes

$$\frac{\rho \, u_m^2}{(\rho_s - \rho) \, g \, D} = 0.463\pi \, (d_o/D)^{1/4} \tag{6}$$

which is very similar to equation (4) except that d_o/D is to the
1/4 power. This equation is shown in Figure 2 compared to the coarse
grain data of Manohar, plotting as a parabola.

In summary, we found that when the grain size is small and the
boundary layer is apparently laminar equation (4) can be used to evaluate
the threshold condition under waves, and when the grain size is coarse
and the boundary layer turbulent the empirical curve of Figure 3 or
equations (5) or (6) can be used. In our preceeding paper [Komar and
Miller (1973)] we further analyzed the data with respect to the nature
of the boundary layer. We concluded that for grain diameters less than
about 0.05 cm (medium sands and finer) the sediment threshold is reached
before individual grains shed eddies and therefore the boundary layer is
laminar. Under these conditions equation (4) applies. For grain diameters
greater than 0.05 cm (coarse sands and coarser) the individual exposed
grains shed eddies prior to reaching threshold so that the boundary layer
is essentially turbulent when the threshold is finally achieved. This
would agree with the observations of Bagnold and Manohar on the nature
of their boundary layers. However, comparisons with the Reynolds numbers
and so on that have been proposed for determining the conditions of the
boundary layer were inconclusive. The value of δ/D where δ is the
thickness of the boundary layer, is uncertain due to the uncertainty in
the evaluation of δ. The transition appears to occur at approximately
$\delta/D = 0.1$ to 0.3, depending on whose equation for δ you use. The
critical grain size of 0.05 cm is the same as that found in the threshold
of sediment motion under unidirectional steady currents; it is the

position of the minimum in the threshold curve such as that presented
by Bagnold (1963) [see Figure 5 of this paper]. The causes for the
division at this critical 0.05 cm diameter are therefore probably the
same. When graphed in the proper format, equations (4) and (6) give a
similar appearance to curves derived theoretically by Carstens, et. al
(1969) although the magnitudes of the values differ. This is taken to
indicate basic agreement with their theoretical developments on the
threshold under waves.

COMPARISONS WITH UNIDIRECTIONAL FLOW THRESHOLD

In this section we shall compare the results for the threshold
under oscillatory motions with the established curves for threshold
under a unidirectional steady current. The left sides of equations
(3), (4) and (6), denoted by θ_t' , are seen to be very similar to the
relative stress

$$\theta = \frac{\tau}{(\rho_s - \rho) g D} = \frac{0.5 f \rho u_m^2}{(\rho_s - \rho) g D} \qquad (7)$$

employed by Shields (1936), Bagnold (1963), and others in the
unidirectional threshold. All that is required is that θ_t' or ρu_m^2
be multiplied by $0.5f$, where f is a drag coefficient such that
we obtain the stress $\tau = 0.5 f \rho u_m^2$. Jonsson (1967, Figure 6) provides
the necessary graph for the evaluation of the friction factor f for
wave motions. He demonstrates that f is a function of the Reynolds
number $u_m(0.5d_o)/\nu$, ν being the viscosity, and the parameter $(0.5d_o)/D$.
For each of the many data sets we have evaluated these parameters, utilizing
the graph of Jonsson to obtain f , finally giving the θ_t value of
equation (7). This then can be compared to the results for unidirectional
flow.

Shields (1936) related θ_t to $u_* D/\nu$, where $u_* = \sqrt{\tau/\rho}$,
for the unidirectional flow data. Figure 4 presents just such a graph
with the Shields curve and the data on oscillatory flow threshold.
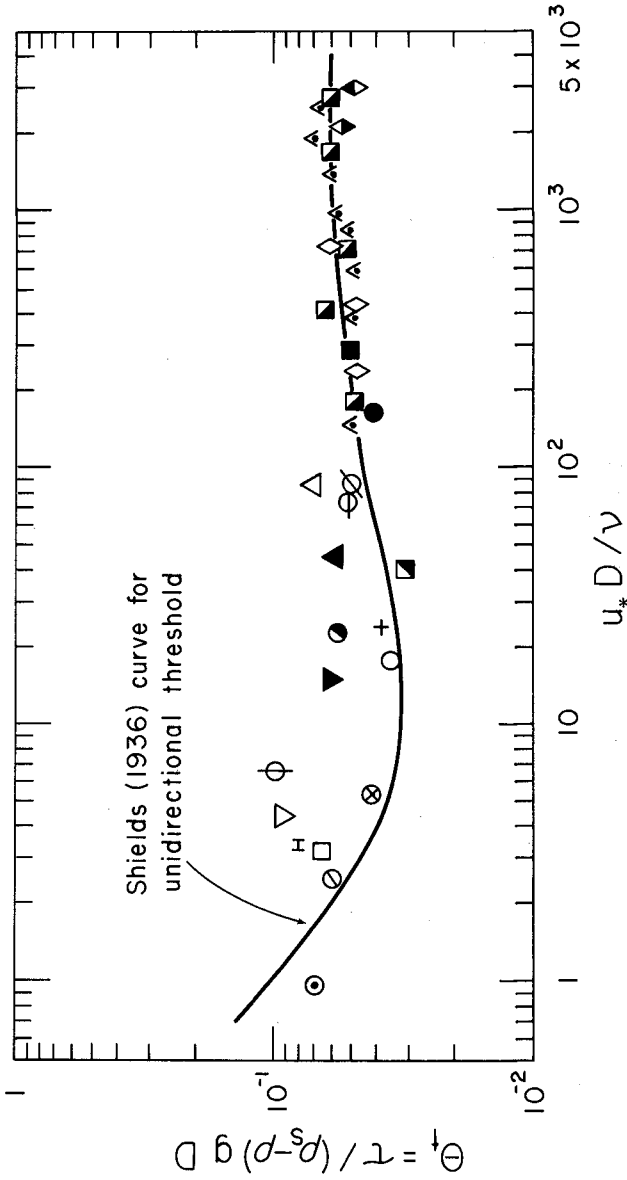
Figure 4: Comparison between the Shields curve for threshold under unidirectional currents and the threshold data for oscillatory wave motions. Symbols are defined in Tables 1 and 2. The H symbol is for the data of Horikawa and Watanabe (1967).

The first fact of interest is that individual sets of data for a given
grain size and density plot as essentially a single point. Figures 1,
2 and 3 spread the data out according to wave period and orbital diameter
(or velocity), whereas in Figure 4 the data for a given grain D and ρ_s
plots in a single position. This indicates that the drag coefficient f
adequately accounts for the effects of the wave periodicity on the drag
stress. The agreement between the data and the right limb of the curve
is particularly good. The data is mainly that of Rance and Warren (1969).
The data on the left half of the graph is more scattered but this is due
principally to the systematic differences between the results of Bagnold
(1946) and Manohar (1955). The Bagnold data is seen to agree better with
the Shields unidirectional curve while the Manohar data is displaced
above the curve. It should be pointed out that the degree of scatter is
comparable to the scatter in the original data from unidirectional flow
upon which the curve was originally based. Utilizing the Bagnold data
alone, Madsen and Grant (in press) have similarly demonstrated agreement
with the Shields curve.

From a practical standpoint, the Shields graph is particularly
difficult to employ since it relates the threshold to u_*D/ν . For
this reason, Bagnold (1963) represented it as θ_t versus the grain
diameter D directly. Such a graph is presented in Figure 5 along
with the oscillatory flow threshold data. Again there is good agreement
on the right limb of the curve and more scatter on the left, the Bagnold
data showing best agreement on the left. Strictly speaking, only the
quartz data should have been plotted in the graph. In order to go from
the Shields curve of Figure 4 to the curve of Figure 5, Bagnold (1963)
had to assume the grains had the density of quartz. In spite of this
it is seen that the other density grains show fair agreement with the
curve.

For the laminar boundary layer Jonsson (1967, p. 134) gives

$$ f = 2 \left[\frac{u_m \, (0.5 \, d_o)}{\nu} \right]^{-1/2} \tag{8} $$
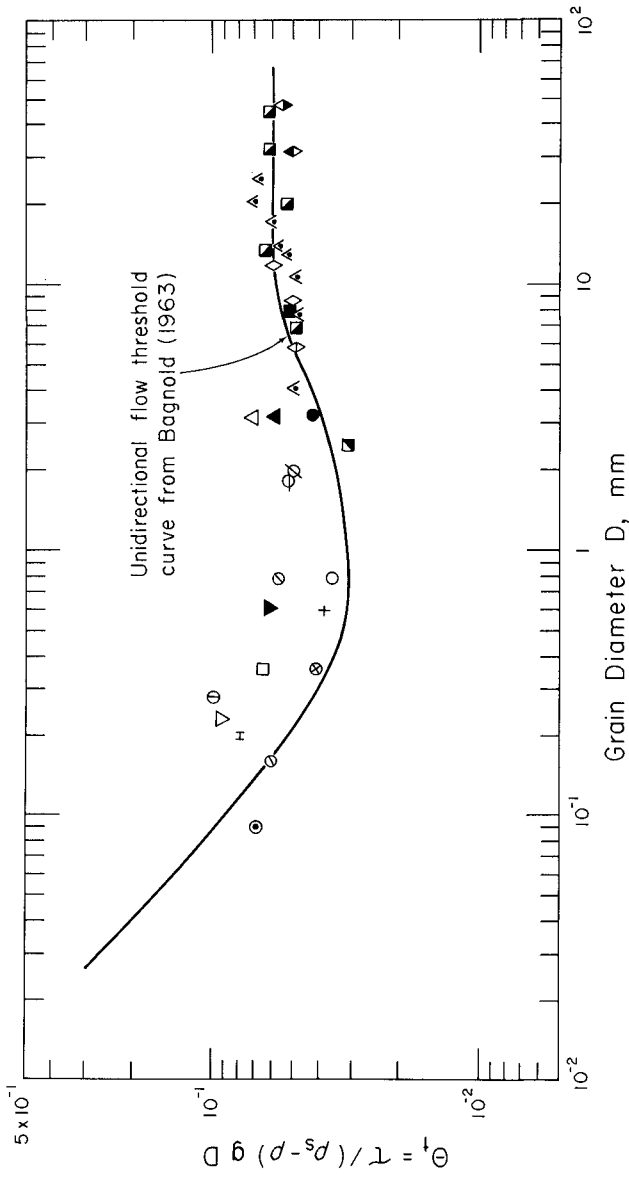
Figure 5: Comparison between the Bagnold (1963) curve for threshold under unidirectional flow and the threshold data for oscillatory wave motions. Symbols defined in Tables 1 and 2 except for H which signifies data of Horikawa and Watanabe (1967).

for the drag coefficient. Multiplying equation (4) by this gives

$$\theta_t = \frac{\tau_t}{(\rho_s - \rho) g D} = \frac{a'' \sqrt{2}}{\left(\frac{u_m D}{\nu}\right)^{1/2}} \qquad (9)$$

suggesting that a plot of θ_t versus the Reynolds number $u_m D/\nu$
might be most logical for the case of the oscillatory threshold. Such
a plot is shown in Figure 6. The heavy curve shown is our own
interpretation as to the best fit to the data as such a graph has not
been previously presented. Also shown are the straight lines according
to equation (9) with $a'' = 0.21$ (from the Bagnold data alone), and with
$a'' = 0.30$ (the average of the Bagnold and Manohar results). The heavy
curve is made to approach the straight line where $a'' = 0.21$ since
the Bagnold data gave the best comparisons to the Shields and Bagnold
(1963) curves for unidirectional threshold.
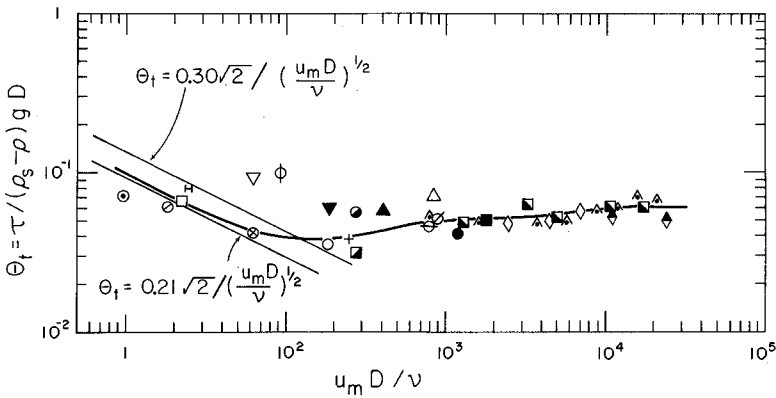
Figure 6: Threshold θ_t versus the Reynolds number
$u_m D/\nu$. Symbols defined in Tables 1 and 2.

PRACTICAL EVALUATION OF THRESHOLD UNDER WAVES

Given a grain diameter D and density ρ_s , it is difficult to
employ Figures 4 and 6 to estimate the threshold under waves. This is
because $u_* D/\nu$ and $u_m D/\nu$ contain the fluid flow characteristics as
well as the sediment diameter. Figure 5 is somewhat better in that the
threshold is related directly to D alone. Application of this figure
yields the stress τ_t for threshold which can in turn give the bottom
orbital velocity u_m for sediment movement. This requires evaluation
of the drag coefficient f from the graph of Jonsson (1967) which is
also not a straight-forward procedure. It is apparent that a simpler
approach would be to go directly to equations (4) and (6), the equation
depending on whether the grain size is larger or smaller than 0.05 cm.
Doing this avoids any evaluation of the drag coefficient. The approach
can be simplified even further when it is recognized that for oscillatory
wave motions the threshold for a given grain D and ρ_s can be specified
by a wave period T and orbital velocity at the bottom u_m . This is
shown graphically in Figure 7, based on the two equations. The graph
does assume ρ_s = 2.65 gm/cm³ and so applies only to normal quartz
sands. For D > 0.05 cm, equation (6) is employed and it is seen that
there is a set of curves, one for each wave period. The higher the
period the greater the orbital velocity u_m required for threshold.
For D < 0.05 cm, equation (4) is utilized with a" = 0.21 , obtained
from the Bagnold data alone. More study is required on the best value
for this a" coefficient; this value was selected in part on the basis
of the agreement between the Bagnold data and the curves of Shields (1936)
and Bagnold (1963) shown above. It is seen in Figure 7 that there is
some difficulty in joining the curves in the region of D = 0.05 cm.
At high periods (T ⩾ 10 sec) they do join smoothly, but at lower
periods they are offset and we have had to join them by dashed curves
indicating a compromise in the results. For periods T ⩽ 5 seconds
there will be some uncertainty as to the u_m for the threshold of grain
sizes on the order of D = 0.05 cm obtained with Figure 7 or the basic
equations. Under these circumstances it may be best to utilize Figure 5,
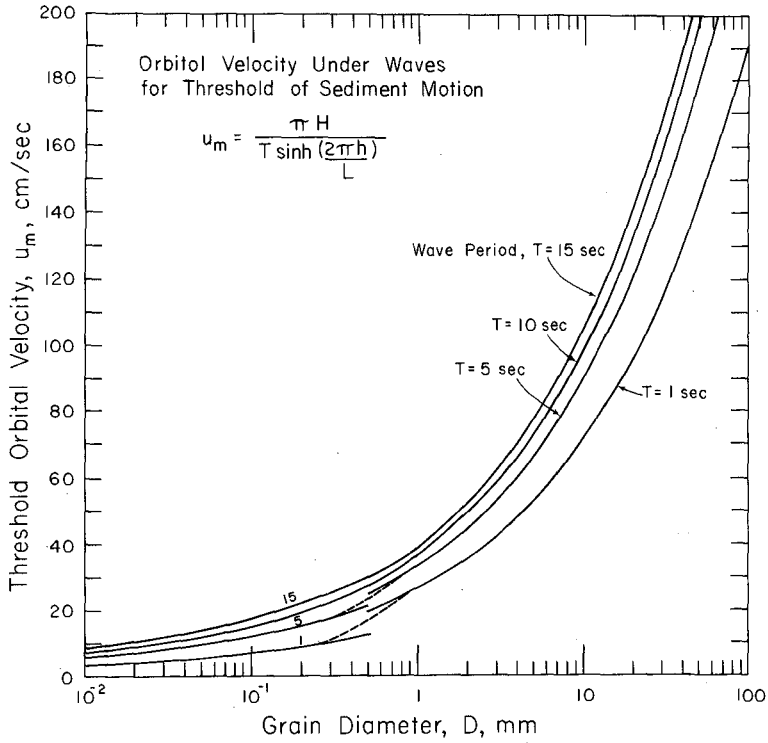
Figure 7: The near-bottom orbital velocity u_m for sediment threshold under waves.

but even there it is apparent that there must be considerable uncertainty as to the exact position of the curve.

The graph of Figure 7 has the obvious advantage that it is very straight-forward to employ, yielding the wave period T and bottom orbital velocity u_m necessary for sediment threshold. There are of course many combinations of water depth h, wave period T, and wave height H, that could yield the required velocity u_m.

Probably the most severe short-coming to the results presented here is the total lack of field data as to the threshold under waves.
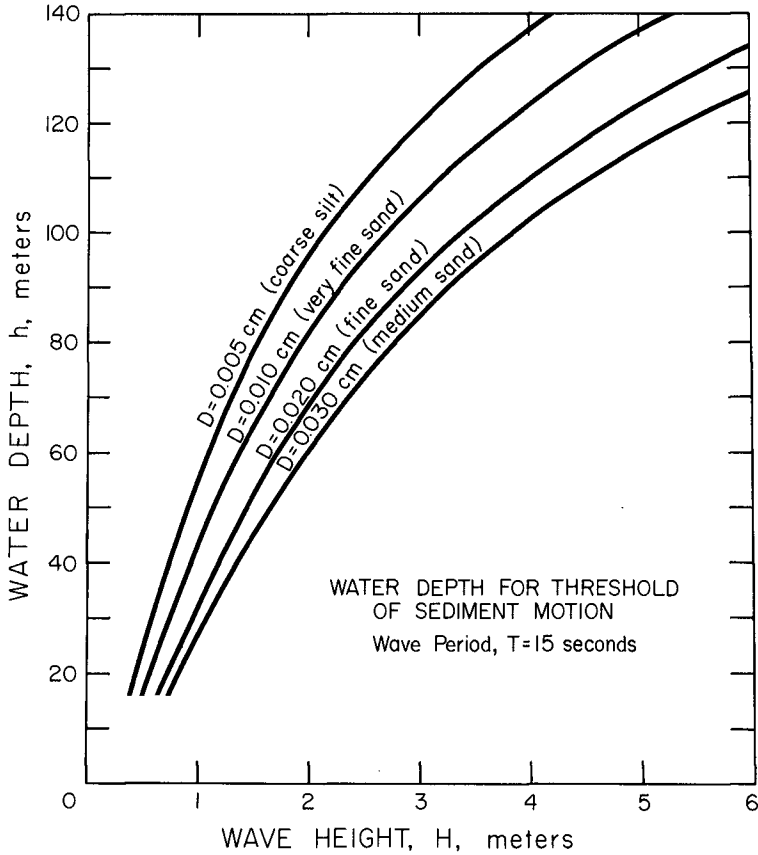
Figure 8: The water depth to which the sediment grain
         sizes shown can be placed in motion by waves of
         period 15 seconds.

The difficulties involved in obtaining such observations are apparent.
We do have some indications of threshold under waves from the observations
of symmetrical oscillatory ripple marks on continental shelves. For
example, we (Komar, Neudeck and Kulm, 1972) have found such ripples in
bottom photographs on the Oregon continental shelf in water depths as
great as 125 meters, sometimes deeper. Figure 8 gives the expected water

depth of sediment motion for a wave period T = 15 seconds and a range
of grain diameters and wave heights. These curves are based on the
above threshold equations. It is seen that expected wave heights would
be capable of moving the bottom sediments and producing the observed
ripple marks at 125 meters water depth on the Oregon shelf. As
discussed by Silverster and Mogridge (1971), equations of the sort
presented in this paper can be expected to give conservative results
as to the depth of sediment motion in the oceans. The most important
effects might be that interactions of wave trains of slightly differing
period would generate higher instantaneous velocities, and small
protruberances on the bed could cause sediment motion at lower velocities
than implied by the analysis. The conservative nature of the equations
was another reason for our selection of $a'' = 0.21$ in equation (4)
rather than 0.30 obtained from an average of all the data. Before we
can make proper estimates of the threshold of sediment motion under
real ocean wave conditions, some of these effects must be more
thoroughly investigated.

ACKNOWLEDGMENTS

REFERENCES

Bagnold, R. A. (1946) Motion of waves in shallow water, Interaction
     between waves and sand bottom: Proc., Royal Society London,
     series A, v. 187, p. 1-15.

Bagnold, R. A. (1963) Mechanics of marine sedimentation: in *The Sea*,
     edited by M. N. Hill, Interscience Publ., p. 507-582.

Carstens, M. R., F. M. Neilson, and H. D. Altinbilek (1969) Bed forms
     generated in the laboratory under an oscillatory flow: Analytical
     and experimental study: U.S. Corps of Engineers, Coastal Engineering
     Research Center, Tech. Memo. No. 28, 39 p.

Eagleson, P. S., R. G. Dean, and L. A. Peralta (1958) The mechanics of
     the motion of discrete spherical bottom sediment particles due to
     shoaling waves: U.S. Army Corps of Engineers, Beach Erosion Board,
     Tech. Memo. No. 104, 55 p.

Horikawa, K., and A. Watanabe (1967) A study of sand movement due to wave action: Coastal Engineering in Japan, v. 10, p. 39-57.

Jonsson, I. G. (1967) Wave boundary layers and friction factors: Proc. 10th Conf. on Coastal Engr., p. 127-148.

Komar, P. D., R. H. Neudeck, and L. D. Kulm (1972) Observations and significance of oscillatory ripple marks on the Oregon continental shelf: in *Shelf Sediment Transport*, edited by Swift, Duane and Pilkey, Dowden, Hutchinson & Ross, Inc., Stroundsburg, Pa., p. 601-619.

Komar, P. D., and M. C. Miller (1973) The threshold of sediment movement under oscillatory water waves: Jour. Sedimentary Petrology, v. 43, p. 1101-1110.

Komar, P. D., and M. C. Miller (in press) On the comparison between the threshold of sediment motion under waves and unidirectional currents with a discussion of the practical evaluation of the threshold: Journal Sedimentary Petrology.

Madsen, O. S., and W. D. Grant (in press) The threshold of sediment movement under oscillatory waves: A discussion: Jour. Sedimentary Petrology.

Manohar, Madhav (1955) Mechanics of bottom sediment movement due to wave action: U.S. Army Corps of Engineers, Beach Erosion Board, Tech. Memo. No. 75, 121 p.

Rance, P. J., and N. F. Warren (1969) The threshold movement of coarse material in oscillatory flow: Proc. 11th Conf. on Coastal Engr., p. 487-491.

Shields, A. (1936) Anwendung der Ahnlichkeits Mechanik und der Turbulenzforschung auf die Geschiebe Bewegung: Preuss. Versuchanstalt fur Wasserbau und Schiffbau, Berlin, 20 p.

Silvester, R., and G. R. Mogridge (1971) Reach of waves to the bed of the continental shelf: Proc. 12th Conf. on Coastal Engr., p. 651-667.

CHAPTER 45

STABILITY OF A SAND BED UNDER BREAKING WAVES

by

Ole Secher Madsen
Assistant Professor of Civil Engineering
Ralph M. Parsons Laboratory
Massachusetts Institute of Technology
Cambridge, Massachusetts 02139

ABSTRACT

The possible effect on the stability of a porous sand bed of the flow induced within the bed during the passage of near-breaking or breaking waves is considered. It is found that the horizontal flow rather than the vertical flow within the bed may affect its stability. An approximate analysis, used in geotechnical computations of slope stability, indicates that a momentary bed failure is likely to occur during the passage of the steep front slope of a near-breaking wave. Experimental results for the pressure gradient along the bottom under near-breaking waves are presented. These results indicate that the pressure gradient is indeed of sufficient magnitude to cause the momentary failure suggested by the theoretical analysis. The loss of stability of the bed material due to the flow induced within the bed itself may affect the amount of material set in motion during the passage of a near-breaking or breaking wave, in particular, in model tests employing light weight bed material. The failure mechanism considered here is also used as the basis for a hypothesis for the depth of disturbance of the bed in the surf zone. The flow induced in a porous bed is concluded to be an important mechanism which should be considered when dealing with the wave-sediment interaction in the surf zone.

INTRODUCTION

One of the most challenging and important problems facing the coastal engineer is that of sediment transport caused by wave action. The difficulties involved in this problem, in particular if one considers the wave-sediment interaction in the surf zone, are quite obvious when one realizes our extremely limited understanding of the fluid motion associated with near-breaking or breaking waves.

In view of the enormous difficulties associated with an accurate description of the processes involved in the wave-sediment interaction in the surf zone, it is quite surprising that simple empirical relationships for the rate of alongshore sediment transport have been obtained. Thus, the empirical relationship obtained by Komar and Inman (1970) suggests the immersed weight transport rate to be proportional to the alongshore component of wave energy flux. Longuet-Higgins (1972) interpreted the transporting force in terms of the radiation stress concept

776

and presented a semi-theoretical argument for the applicability of a
relationship of the type suggested by Komar and Inman (1970). Although
existing empirical relationships for the alongshore rate at sand trans-
port are extremely useful for engineering purposes they do represent a
considerable simplification of the actual processes involved in the wave-
sediment interaction. If we are ever to rise above the level of pure
empiricism when dealing with the wave-sediment interaction taking place
in the surf zone it is obvious that we need a better understanding of
the fundamental mechanisms involved in the process.

   The purpose of this paper is to present evidence of the possibly
very important role played in the wave-sediment interaction in the surf
zone by the flow induced in the porous bed. The recognition of the pos-
sible importance of this mechanism was arrived at through discussions
with Dr. William R. James at the U.S. Army, Coastal Engineering Research
Center. While diving in the surf zone his observation that "just prior
to the passage of the crest of a near-breaking wave the bottom seemed to
explode" gave the impetus to consider the flow induced in the porous bed
as a possible explanation of this "explosion". The initial idea was that
the pressure distribution on the bottom associated with a near-breaking
wave would induce a vertical flow out of the porous bed of sufficient
magnitude to produce bed failure, piping. The effects of a vertical flow
into and out of a porous bed on the initiation of sediment movement have
previously been considered by Martin (1970) in the case of steady flow.
Considering wave motion as a special application, Martin (1970) concluded
that this would not induce a vertical flow of sufficient magnitude to
affect the bed stability significantly. When dealing with waves approach-
ing breaking this conclusion still holds, however, when recognizing the
large horizontal pressure gradient associated with the steep forward
slope of a near-breaking wave, it is intuitively clear that a signifi-
cant horizontal, rather than vertical, flow may be induced in the porous
bed. This horizontal flow within the bed will exert a force on the bed
material and may produce a horizontal shear failure of the bed.

   An analysis of stability of a plane horizontal bed, consisting of a
cohesionless sediment, subject ot the flow induced within the bed by a
pressure distribution on the bed surface is outlined. For a detailed
presentation of this development the reader is refered to Madsen (1974).
The result of this analysis shows that a momentary failure of the bed
may occur due to the flow induced within the porous bed provided the
magnitude of the horizontal pressure gradient exceeds a critical value.
The order of magnitude of this critical horizontal pressure gradient
does not seem to be beyond the range one would expect to be associated
with near-breaking waves. However, no information on the actual value
of this quantity is available, so to assess the order of magnitude of
the pressure gradient along the bottom associated with near-breaking
waves an experimental investigation was undertaken in a laboratory wave
flume.

   The results of the experiments clearly indicate that the critical

pressure gradient is exceeded for the wave conditions tested, thus rendering active the mechanism of momentary failure of the bed caused solely by the flow induced within the porous bed. From a discussion of the implications of this mechanism, it appears that it may affect the rate of sediment transport in the surf zone, in particular it may play an important role in movable bed model tests using light weight granular material. The momentary bed failure is also used to hypothe-size a possible mechanism responsible for burial of tracer particles in the surf zone. Although this discussion is of a rather qualitative nature it does indicate that the effect of the flow induced in the por-ous bed may be an important factor, which should be considered when investigating the wave-sediment interaction in the surf zone.

THEORETICAL MODEL OF BED INSTABILITY

When a surface wave travels over a impermeable bottom it exerts a pressure on the bottom. For waves of permanent form this pressure may be predicted from existing wave theories which indicate that the wave associated bottom pressure under the crest exceeds that under the trough. Considering now the bed to consist of a slightly porous material, such as sand, the pressure variation along the bed surface would induce a flow in the porous bed. Reid and Kajiura (1957) considered the flow induced in a porous bed in the context of evaluating the wave attenua-tion due to percolation. From their results it may be inferred that it is reasonable for an only slightly permeable bed material to neglect the unsteadiness when evaluating the pore pressure distribution within the bed. The accuracy of this approach was recently substantiated experi-mentally by Sleath (1970).

In contrast to these previous investigations the present study focusses its attention on waves approaching breaking. It is a well-known fact that the surface profile of near-breaking waves becomes increasingly asymmetric with a forward leaning crest having a steep front slope and a flat back. In a qualitative sense this asymmetry of the surface profile will also be present in the pressure distribution on the bottom. In the following analysis we retain formally this asymmetry by assuming an in-stantaneous pressure distribution on the horizontal bed surface given by

$$p_o = \bar{p}_o + p_o^+(x) \tag{1}$$

as illustrated in Fig. 1. The average pressure, $\bar{p}_o$, in Eq. 1 corresponds to the average weight of the water above the bed, i.e., $\bar{p}_o = \rho g h$ where h is the depth of undisturbed water of density ρ. Unsteadiness has been neglected in accordance with Reid and Kajiura (1957) and $p_o^+(x)$ is the instantaneous bottom pressure associated with the wave motion. As a first approximation the pressure distribution may be assumed periodic with a wave length L as indicated in Fig. 1.

With the coordinate system shown in Fig. 1 and introducing the pore
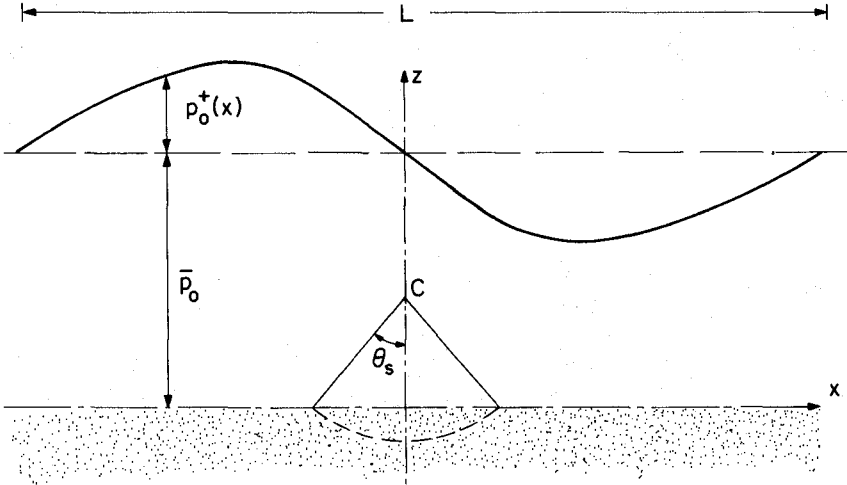
Figure 1: Definition of Coordinate System. Bottom pressure dis-
tribution and limiting slip circle indicated.

pressure in excess of hydrostatic pressure

$$p^+ = p - \bar{P}_o + \rho gz \qquad (2)$$

where p is the actual pore pressure, the governing equation for p^+ be-
comes, Darcian flow in the bed being assumed

$$\nabla^2 p^+ = \frac{\partial^2 p^+}{\partial x^2} + \frac{\partial^2 p^+}{\partial z^2} = 0 \qquad (3)$$

with the boundary condition

$$p^+ = p_o^+(x) \quad ; \quad z = 0 \qquad (4)$$

$$p^+ \to 0 \quad ; \quad z \to -\infty \qquad (5)$$

With the assumed periodicity of the pressure distribution, $p_o^+(x)$,
it is an easy task to find the solution for $p^+(x,z)$ by using the Fourier
series representation of $p_o^+(x)$.
    Corresponding to the predicted pore pressure distribution within

the bed the flow induced in the bed may be found from Darcy's law.
Through the action of viscous forces this flow of pore fluid will act
on the grains of the bed material giving rise to a force on the solids
in the direction of flow. This force, the seepage force F_s, is per
unit volume equal to the pressure gradient (Terzaghi and Peck, 1967).

$$F_s = (F_{s,x}, F_{s,z}) = -\nabla p^+ = -(\frac{\partial p^+}{\partial x}, \frac{\partial p^+}{\partial z}) \tag{6}$$

Disregarding, for the moment, the unsteadiness of the problem,
failure of the bed due to a purely vertical flow out of the bed is
generally believed to take place when the vertical seepage force,
$F_{s,z}$, exceeds the effective gravity force acting on the solids
(Terzaghi and Peck, 1967). If the density of the saturated bed mater-
ial is denoted by ρ_t, the effective density of the bed material will
be $\rho_t' = \rho_t - \rho$, and the critical vertical gradient can be expressed as

$$(F_{s,z})_{crit} = -(\frac{\partial p^+}{\partial z})_{crit} = (\rho_t - \rho)g \tag{7}$$

The action of this force is often considered in geotechnical pro-
blems where it may produce failure of the soil, piping. The interaction
of the vertical flow into and out of the bed with the turbulent flow
above the bed was considered by Martin (1970) and Martin and Aral (1971)
who studied its influence on incipient motion of particles on the bed
water interface.
    To evaluate the effect of a horizontal flow induced in a porous
bed, consider a thin horizontal slice of thickness δ at the bedwater
interface. The force resisting the horizontal seepage force would be
the mobilized internal friction between the grains at a depth δ. For
a cohesionless material this intergranular friction may be expressed
in terms of the effective (intergranular) normal stress and the angle
of internal friction, ϕ, of the material. The balance of these forces
leads to an expression for the critical horizontal pressure gradient

$$(F_{s,x})_{crit} = -(\frac{\partial p^+}{\partial x})_{crit} = -(\frac{\partial p_o^+}{\partial x})_{crit} = (\rho_t - \rho)g \tan \phi \tag{8}$$

where the horizontal gradient of the pressure associated with the wave
motion is introduced since a thin slice close to the surface of the
bed is being considered.
    For steady open channel flow the magnitude of the horizontal pres-
sure gradient is insignificant and it is not surprising that its effect
was neglected by Martin (1970). However, for a wave motion, in parti-
cular as the waves approach breaking, the horizontal pressure gradient
associated with the steep forward slope of the crest may be consider-
able. In fact, it may be shown by solving Eqs. 3, 4, and 5 for an as-
sumed asymmetric pressure distribution such as the one indicated in

Fig. 1, that the maximum horizontal pressure gradient exceeds the max-
imum vertical gradient by a considerable amount. This observation,
in conjunction with the indication of Eqs. 7 and 8 that the critical
pressure gradient in the vertical direction exceeds that in the hori-
zontal direction, since ϕ generally is less than 45°, suggests that
the horizontal rather than the vertical flow induced in the porous bed
is likely to affect the stability of the bed.

    To investigate further the likelyhood of the horizontal pressure
gradient exceeding the critical value given by Eq. 8 let us for simpli-
city assume that the vertical pressure distribution associated with the
wave motion is hydrostatic. Then,

$$p_o^+ = \rho g \eta \tag{9}$$

where η is the free surface elevation relative to the stillwater level
and Eq. 8 becomes

$$-\frac{1}{\rho g} \left(\frac{\partial p_o^+}{\partial x}\right)_{crit} = -\left(\frac{\partial \eta}{\partial x}\right)_{crit} = \frac{\rho_t - \rho}{\rho} \tan \phi \tag{10}$$

    Choosing values representative of a relatively loose sand in sea-
water (Terzaghi and Peck, 1967, Tables 6.3 and 17.1), the value of the
right hand side of Eq. 10 is found to be of the order 0.5. One can
readily imagine that the steep forward slope of a near-breaking wave
exceeds this value of 0.5, thus indicating that the horizontal flow
induced in the bed indeed is likely to be of sufficient magnitude to
affect the stability of the bed.

    At this point it should be emphasized that, whereas the neglect of
unsteadiness was justified when obtaining the pore pressure distribution
within the bed, the neglect of unsteadiness in the analysis of the bed
stability makes the prediction of bed failure a formal one. The time
interval during which an elemantary bed volume is affected by a suffi-
ciently large horizontal pressure gradient to induce failure, i.e., the
time it takes the steep forward slope of a near-breaking wave to pass
overhead, is relatively short and inertia terms should be considered
where analyzing the details of the bed stability. Thus, the predicted
failure is not to be interpreted in the geotechnical sense of the word,
i.e., the failure will not cause a soil packet to be forced out of the
bed. Rather, the predicted failure should be interpreted as a "momen-
tary failure" taking place for the short period of time during which
the horizontal pressure gradient exceeds the critical gradient given
by Eq. 10.

    Keeping this interpretation of the predicted failure in mind a
more realistic, yet simple, analysis of the stability of the bed may
be performed once the pore pressure distribution within the bed is
determined from Eqs. 3, 4, and 5. A comparatively simple analysis
due to Bishop (Terzaghi and Peck, 1967), which is used in geotechnical
evaluations of slope stability, is used in the present context, and
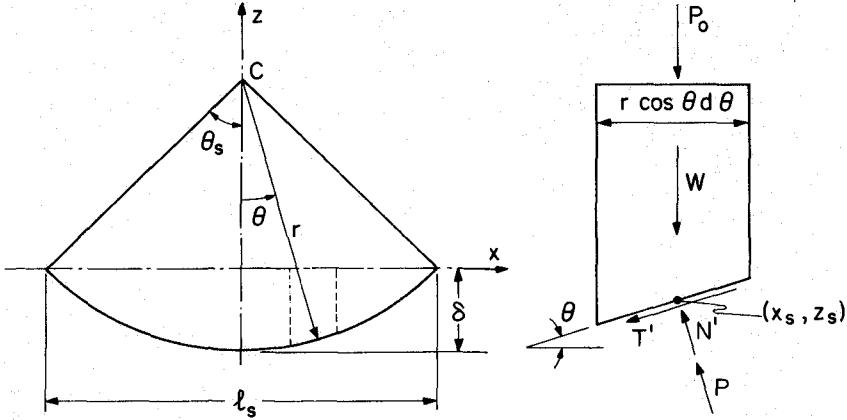
Figure 2: Limiting slip circle, Notation and the forces acting on an
elementary segment of the material above the slip circle

leads to further insight into the extent of the bed failure than did the
preceding simple analysis. The formal application of slope stability
analyses to unsteady problems involving water waves has previously been
performed by Henkel (1970) and as presented at this conference by Dr.
Mitchell.

For this analysis the bed failure is assumed to take place along a
circular arc, the slip circle indicated in Fig. 1. For the purpose of
briefly outlining the analysis, the details may be found in Madsen (1974),
the limiting slip circle is shown in Fig. 2 along with the forces acting
on a small bed element above the slip circle. Bishop's simplified method
assumes that the forces acting on the sides of the small element have no
vertical component. Thus, with the notation indicated in Fig. 2, vertical
equilibrium of the forces acting on a small element gives

$$P_o + W + T' \sin \theta - (N' + P) \cos \theta = 0 \tag{11}$$

in which

$\quad P_o$ = external pressure force; Eq. 1 = $(\bar{p}_o + p_o^+(x_s))r \cos \theta \, d\theta$

$\quad W$ = total weight of slice = $\rho_t g \, z_s r \cos \theta \, d\theta$

$\quad T'$ = frictional force = $\tau_f \, r \, d\theta = \sigma_n' \tan \phi \, r \, d\theta \tag{12}$

$\quad N'$ = intergranular, effective normal force = $\sigma_n' \, r \, d\theta$

P = pore pressure force; Eq. 2 = $(\bar{p}_o + p^+ + \rho g z_s)$ r dθ (12)

where the shear stress, τ_f, mobilized at failure is related to the effective normal stress, σ_n', through

$$\tau_f = \sigma_n' \tan\phi \qquad\qquad (13)$$

Introducing Eq. 12 in Eq. 11 leads to an equation for the effective normal stress along the slip circle which may be used in conjunction with Eq. 13 to evaluate the mobilized shear stress along the slip circle. This mobilized shear stress will resist the driving forces associated with the external pressure force. A measure of this resistance is the moment of the shear forces around the center of the slip circle and when this moment is equated to the moment of the driving forces, the external pressure, an equation for the angle θ_s (see Fig. 2) defining the limiting slip circle is obtained. It is emphasized that this determination of the angle θ_s may be carried out numerically in the general case, provided the pore pressure distribution within the bed is known. In view of the formal application of this type of analysis to the present problem some simplifying assumptions are introduced which allow an analytical expression for θ_s to be obtained. The assumptions made are that the external pressure distribution, $p_o^+(x)$ shown in Fig. 1, is antisymmetric around $x = 0$, and that the pressure varies linearly over the horizontal extent of the slip circle, l_s in Fig. 2, and has a magnitude of

$$-\frac{1}{\rho g}\left\langle\frac{\partial p_o^+}{\partial x}\right\rangle l_s = \alpha \qquad\qquad (14)$$

The implications of these assumptions are discussed by Madsen (1974); here we just state the resulting approximate equation which, in spite of the many assumptions, captures the essense of the analysis,

$$\frac{1}{3}\frac{\sin^2\theta_s}{1 - \theta_s\cot\theta_s} = \frac{\rho_t -\rho}{\rho}\frac{\tan\phi}{\alpha} \qquad\qquad (15)$$

from which the angle θ_s, defining the limiting slip circle, may be obtained if the value of the right hand side is known.

Whether or not the material above the limiting slip circle is in a state of momentary failure depends on whether or not Eq. 15 has a solution for θ_s. Defining the right hand side of Eq. 15 as a stability number

$$C_s = \frac{\rho_t -\rho}{\rho}\frac{\tan\phi}{\alpha} \qquad\qquad (16)$$

with the dimensionless pressure gradient, α, given by Eq. 14, it is
found that for $C_s > 1$ no solution for θ_s can be found from Eq. 15.
For a given material and fluid a large value of C_s is associated with
a small value of the pressure gradient, α. That no solution for θ_s
can be found in this case is simply expressing the fact that the
pressure gradient is of insufficient magnitude to cause a bed failure.
The left hand side of Eq. 15 approaches the limit of unity as $\theta_s \to 0$,
which is indicative of a very shallow failure. Thus, $\theta_s \to 0$
expresses the limiting condition for which failure of the bed occurs
and corresponds to a value of the stability number $C_s = 1$. In terms
of the corresponding pressure gradient, the critical gradient, this
corresponds to

$$\alpha_{crit} = \frac{\rho_t - \rho}{\rho} \tan \phi \tag{17}$$

which is seen to be the same result as previously obtained, Eq. 8.
Finally, for large values of the pressure gradient, $C_s < 1$, Eq. 15
has solutions for θ_s, thus indicating that failure does occur and that
the bed material above the limiting slip circle is in a state of momen-
tary failure during the short time of passage of the large pressure
gradient. The extent of this failure below the bed surface, δ in Fig. 2,
may be obtained if for example the horizontal extent of the slip circle,
1_s, is known. From geometrical considerations one then obtains

$$\frac{\delta}{1_s} = \frac{1 - \cos\theta_s}{2 \sin\theta_s} \tag{18}$$

Fig. 3 presents a graphical solution of Eqs. 15 and 18 as a function
of the stability number C_s, and is, Madsen (1974), valid only so long
as $\theta_s < \frac{\pi}{2} - \phi$.

The somewhat more involved analysis of the bed stability has pro-
vided some insight into the extent of the bed failure, although the
predicted value of the critical horizontal pressure gradient was the
same as that obtained from the simplified analysis. It is again empha-
sized that the neglect of unsteadiness in the stability analysis makes
the predicted failure a formal one, which is to be interpreted as a
"momentary failure". The theoretical results have, however, indicated
that such a momentary failure is highly likely to occur since the crit-
ical horizontal pressure gradient α_{crit} is of the order 0.5, which is
a value certainly expected to be exceeded under the steep forward slope
of a near-breaking wave.
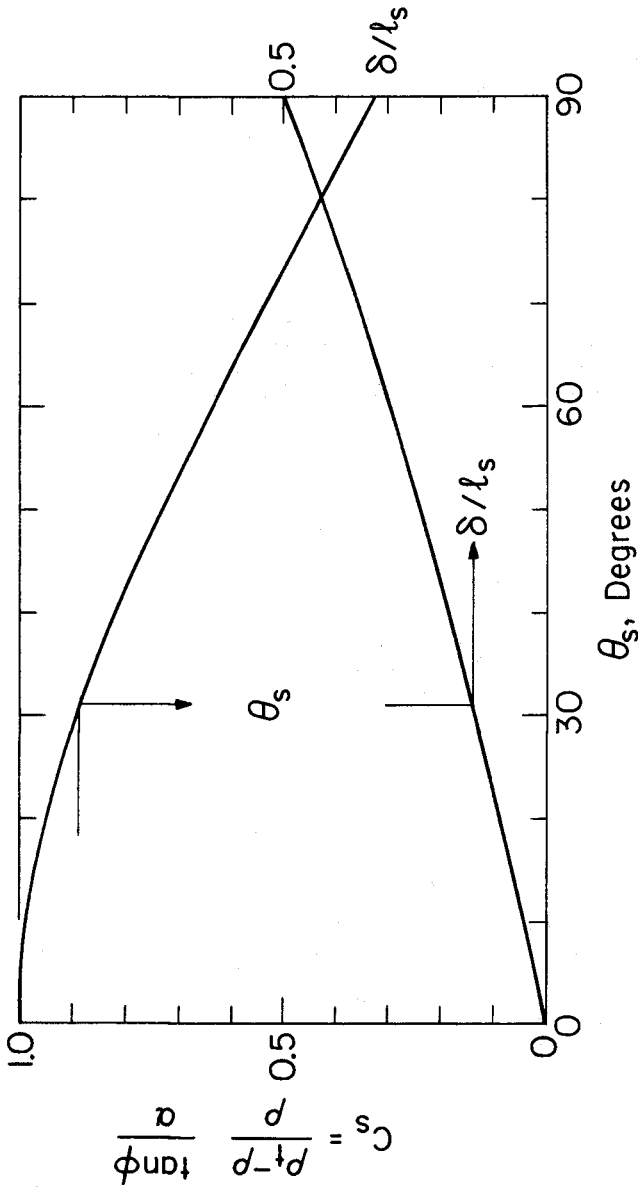
Figure 3: Graphical solution of Eqs. 15 and 18 as a function of the stability number C_s. $C_s > 1$ no solution. Valid only for $\theta_s < \pi/2 - \phi$.

EXPERIMENTAL DETERMINATION OF THE PRESSURE GRADIENT

The theoretical considerations presented in the preceding Section showed the all important role played by the horizontal gradient of the pressure on the bottom associated with waves in the surf zone in determining the possible influence of the flow induced in the porous bed on the bed stability. In order to establish the magnitude of this pressure gradient some laboratory experiments were performed in a 30 m long, 75 cm wide and 90 cm deep wave flume in the Ralph M. Parsons Laboratory at M.I.T. This flume is equipped with a variable speed drive flap-type generator capable of producing sinusoidal waves. Approximately 18 m from the generator the flume terminates in a 1 on 10 sloping impermeable beach consisting of a steel frame with plywood boards.

The wave motion taking place in the flume is measured by parallel wire resistance-type wave gages, which measure the surface fluctuations at one point as a function of time. The wave measurements are recorded on Permapaper using one of the two channels of a Sandborn, Model 296, recorder.

To measure the pressure variation on the bottom under breaking waves, a 30 by 30 cm square of the plywood beach was cut out a distance of 2.5 m up the slope. This square was replaced by two aluminum plates mounted flush with the plywood surface. One of these plates contained the pressure taps which were placed approximately along the centerline of the flume a distance of 1.7 cm apart. This distance was dictated by the space requirements necessary to connect the pressure taps to the system of pipes and copper tubing, which in turn connected the pressure taps to the pressure chambers on the two sides of the diaphragm of a differential pressure transducer, Pace Engineering Co., Model KP15, series 20442. The other aluminum plate provided the necessary access to the region below the beach. The measured pressures were recorded on the second channel of the Sandborn recorder. Thus, when the two pressure taps in the beach were connected to the pressure transducer the pressure difference, Δp, between these two positions, 1.7 cm apart, was recorded. If only one tap was hooked up the other side of the diaphragm being connected to the constant hydrostatic pressure in the fluid under the beach, the recorded pressure would correspond to the pressure at one point on the bottom associated with the wave motion.

In principle the analysis is simple keeping our main goal in mind. According to the theory presented in the previous Section, we would expect the mechanism discussed there to be active when the bottom pressure gradient exceeds the value of $0.5 \rho g$. Thus, if the pressure difference between the two pressure taps in the bottom of the wave tank exceeds $\Delta p / \rho g = 0.5 \cdot 1.7$ cm ≈ 0.85 cm, the intended mission is completed. However, this pressure difference is indeed small and since it is associated with the passage of the steeply sloping front of a near-breaking wave, it may have only a very short duration which raises questions about the response characteristics of the pressure measurement system.

Characteristics of the Pressure Measuring System

Expecting to measure pressure differences of the order 1 cm of water, i.e. 1 gm/cm^2, the diaphragm to be used in the pressure transducer should be very sensitive. Since the natural frequency decreases with increasing sensitivity of the diaphragm the choice of diaphragm involves a compromise. A reasonable compromise turned out to be a diaphragm having a maximum pressure range of 350 gm/cm^2 for which it was still possible to electronically amplify the signal such that pressure differences of the order 1 cm of water could be recorded on the Sandborn recorder. The drawback of using this heavy diaphragm is its susceptibility to mechanical vibrations. This difficulty was partially overcome by performing the experiments during periods of low traffic intensity on the adjacent street.

The response characteristics of the system were obtained from "balloon tests" the details of which are presented by Madsen (1974). These tests showed the pressure measuring system to have a natural frequency of the order $f_o = 27$ sec^{-1} and a damping coefficient $\mu = 0.7$, i.e. close to critical damping. This damping was achieved by filling one of the copper tubes connecting the pressure taps to the transducer with steel wool shavings.

Based on these response characteristics it is concluded that signals of periods longer than 0.2 sec would be accurately recorded by the system with recorded pressure differences corresponding to those obtained from a static calibration of the system. Static calibration of the pressure transducer set-up showed this to have a linear response and the electronic amplification of the signal was chosen such that a 10mm deflection of the pen on the Sandborn recorder corresponded to a pressure difference of 10mm of water.

Characteristics of the Generated Waves

Due to the shortage of funds for experimental equipment only one pressure transducer was available and this quite clearly necessitates that the position of the pressure taps be close to the point of breaking of the incident waves. Invoking the approximate analogy between the pressure gradient along the bottom and the slope of the free surface it is evident that the breaking wave to be measured must be significantly larger than 1.7 cm, the distance between the pressure taps, in order for the measured pressure difference to express accurately the pressure gradient along the bottom.

Galvin (1968) obtained criteria for the occurrence of various breaker types, spilling or plunging, on laboratory beaches. From his Fig. 1 it is clear that the more gently breaking wave, the spilling breaker, is associated with the smaller slope of the front of the wave crest as breaking is approached. This indicates that the pressure gradient along the bottom would be smaller for a spilling breaker than for a plunging breaker, hence breaking waves of the spilling type seem crucial in the present context. Guided by the result of Galvin (1968) that spilling breakers occur when

$$\frac{H_o}{L_o} \geq 4.8 \ tan^2\beta \tag{19}$$

where H_o and L_o are the deep water wave height and wave length respectively,
and tan β is the beach slope, one obtains for the present experimental
set-up (tan β = 0.1) that the incident wave steepness should exceed the
value 0.05 to ensure breakers of the spilling type. To generate a wave of
this considerable steepness it was necessary to choose a relatively short
wave period, T = 0.95 sec, for a water depth of h_o = 38 cm in the constant
depth portion of the flume.

Immediately following the start of the wave generator a uniform wave
train of height H = 9 cm existed in the flume. This corresponds to a deep
water wave steepness of the order 0.07 which according to Galvin's criterion
should be sufficient to produce spilling breakers. Initially the breakers
were indeed of the spilling type, although showing some plunging character-
istics, and they all broke in approximately 10 cm water depth. After some
time, however, the initially uniform wave train developed some strong beat
features with some waves breaking before some after reaching the initial
break-point. Eventually, after 15 to 30 minutes, a quasi-steady condition
was reached where some waves broke even before reaching the slope, some
broke approximately 2 m up the slope, others 3 m up the slope. Although
the beat effect exhibited a strong periodicity, with approximately every
fifth wave breaking at a certain location, this variation in breaker position
seemed to be a rather undesirable situation.

The details of the observed wave anomaly are presented by Madsen (1974),
where a possible explanation of its appearence may also be found. Here it
suffices to say that the wave instability seems to be associated with the
development of a long period standing wave in the flume. Rather than avoid-
ing the problems associated with the observed variability in breaker position
by for example running the experiments in bursts, i.e., starting the wave
maker from rest and only use the first waves for the measurements, it was
decided to live with this anomaly since it to some extent could be used to
our advantage.

The reason for this choice of wave conditions, H ≈ 9.0 cm, T = 0.95 sec
in 38 cm of water, was the observation stated previously that approximately
one out of five waves broke 2 m up the slope whereas one of five waves broke
approximately 3 m up the slope. Thus, positioning the pressure taps, re-
cording the pressure difference between two points on the bottom, 2.5 m up
the slope, i.e., in 13 cm of water, would serve the purpose of measuring
the pressure difference associated with a wave of broken form as well as
that associated with a wave approaching breaking. This was particularly
found desirable since the wave breaking 2 m up the slope was a definite
spilling breaker which, as previously mentioned, is the crucial breaker-
type to investigate in the present context.

Experimental Results

With the account given in the preceding sections of the characteristics
of the pressure transducer set-up and the incident waves the experimental
results obtained may be presented.

As previously mentioned the basic purpose of the experiments was to demonstrate that the pressure gradient along the bottom associated with near-breaking or breaking waves was of sufficient magnitude to cause a momemtary failure of a porous bed as predicted by theory. With the pressure transducer set-up as described we may measure and record the pressure difference, Δp, between the two pressure taps, $\Delta x = 1.7$ cm apart. This pressure difference may in turn be used to evaluate the approximate magnitude of the pressure gradient along the bottom

$$\frac{\partial p_o^+}{\partial x} \approx \frac{\Delta p}{\Delta x} \tag{20}$$

The choice of wave conditions and position of the pressure taps, in 13 cm of water, allow the measurement of the pressure difference associated with spilling breakers, breaking just prior to passing the pressure taps, as well as the pressure difference associated with waves approaching plunging. The surface profile, η, obtained at the location of the pressure taps is presented in Fig. 4 and demonstrates clearly the arrival of an already broken wave, indicated by S, followed by a wave approaching breaking, indicated by P. In addition to the surface profile, Fig. 4 also shows the measured pressure difference between the two pressure taps. The somewhat ragged appearance of the recorded pressure difference is due to mechanical vibrations as previously mentioned. With the calibration of the pressure transducer set-up being 10 mm pen deflection corresponding to 10 mm water column it is readily seen from Eq. 20 that the critical pressure difference, Δp_{crit}, indicating that the momentary failure will occur, is given by $\Delta p_{crit}/\rho g = 0.5 \cdot \Delta x = 8.5$ mm. As is evident from the results presented in Fig. 4 this critical pressure difference is indeed exceeded in the experiments by the spilling breaker as well as by the wave approaching plunging. In view of the different appearance of the surface profiles of the two different breaker types it is interesting to note that their associated pressure differences are highly similar.

By analyzing several records similar to that presented in Fig. 4 it was found that the maximum pressure difference for the already broken spilling breaker was between 10 and 15 mm water column with a pronounced mean value of 12 mm. The corresponding values for the wave approaching plunging were 10 to 13 mm with a mean value of 11 mm. This corresponds to a mean value of the maximum pressure gradient along the bottom

$$\frac{1}{\rho g} \left| \frac{\partial p_o^+}{\partial x} \right|_{max} \approx \begin{array}{ll} 0.71 & \text{(spilling breaker)} \\ 0.65 & \text{(plunging breaker)} \end{array} \tag{21}$$

which clearly demonstrates that the pressure gradient found from these experiments is of sufficient magnitude to render active the mechanism of momentary failure of the bed discussed in the preceeding Section.

The above information is in essense all we set out to obtain. However,
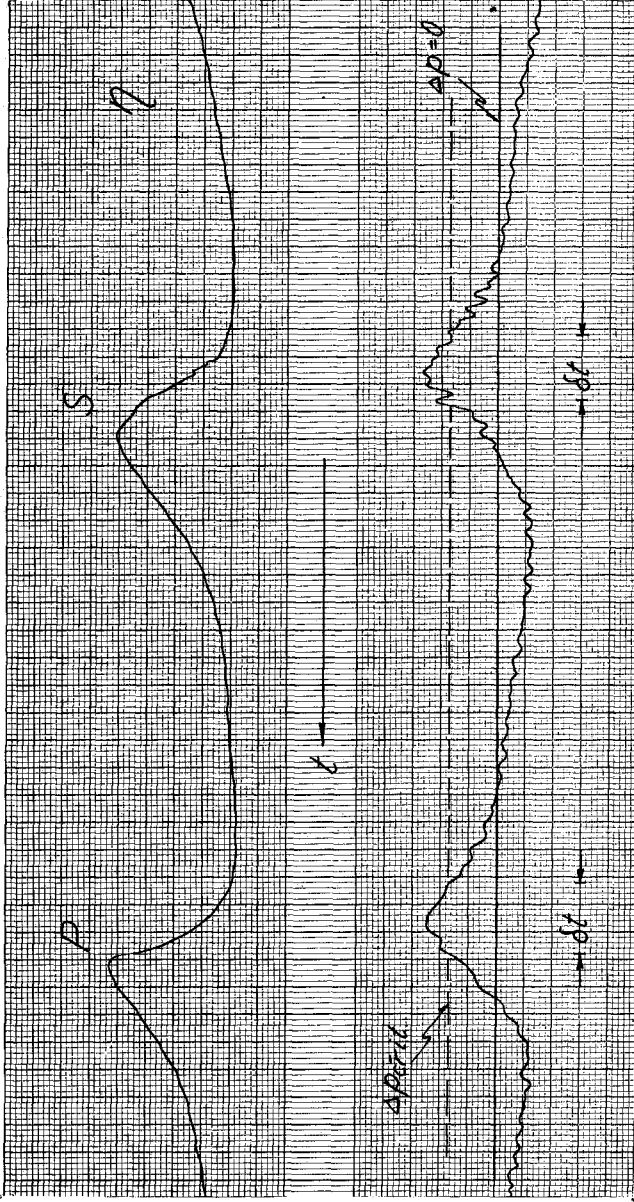
Figure 4: Typical surface profile, η, and pressure difference, Δp, corresponding
to an already broken spilling breaker, S, and a wave approaching plunging,
P. Critical value $\Delta p_{crit} = 8.5$ mm water column indicated along with time
interval δt during which $\Delta p > \Delta p_{crit}$.

in order to estimate the order of magnitude of the spatial extent of the momentary failure additional information on for example the horizontal extent of the failure, l_s in Fig. 2, is necessary. This extent is clearly related to the distance, δx, over which the average pressure gradient, defined by Eq. 14, exceeds its critical value. Considering the parameters involved, it seems obvious that the distance $\delta x \sim l_s$ is proportional to the height of the wave breaking overhead, H_B, with the constant of proportionality being primarily a function of breaker type. From the present experiments it is possible to estimate the average value of the pressure gradient during the time interval, δt, see Fig. 4, when the critical pressure gradient is exceeded. For the spilling breakers it is found that

$$\frac{1}{\rho g} \left\langle \frac{\partial p_o^+}{\partial x} \right\rangle_{\delta t} = 0.64 \tag{22}$$

which may be taken as a representative value of α in Eq. 14. The time interval δt is found from the experiments to be $\delta t = 0.11$ sec (± 0.01 sec) and the problem is that of transforming this time interval, δt, into an equivalent horizontal distance $\delta x \sim l_s$ over which the average horizontal pressure gradient is given by Eq. 22.

The simplest possible relationship among space and time would be of the form $\delta x = c\ \delta t$. An approximate value of c may be obtained by measuring the pressure variation with time at a point and compare the magnitudes of the quantities $\partial p/\partial t$ and $\partial p/\partial x$. From such an analysis (see Madsen, 1974) it is found that a value of $c \simeq 44$ cm/sec seems appropriate during the time interval δt and leads to an estimate of $l_s/H_B = O(0.5)$ for the present experiments. It should be noted that the experimentally determined value of c is quite different from the value obtained from say linear wave theory ($c \simeq 100$ cm/sec). In view of the strong nonlinearities and rapid changes in wave form as breaking is approached this can hardly be considered surprising.

DISCUSSION OF THE RESULTS

An analysis considering only the forces associated with the flow induced within the porous bed itself by the pressure exerted on the bed surface by a passing near-breaking or broken wave showed that a failure of the bed would take place if the horizontal gradient of the wave induced bottom pressure exceeded the value

$$\frac{1}{\rho g} \left| \frac{\partial p_o^+}{\partial x} \right|_{max} = \frac{\rho_t - \rho}{\rho} \tan \phi \tag{23}$$

Corresponding to a relatively loose sand the value of the right hand

side of Eq. 23 is approximately 0.5 and a laboratory investigation showed
that this critical value of the pressure gradient along the bottom was
indeed exceeded by breaking waves of the spilling as well as of the plung-
ing type, thus implying that a failure of the type considered here is likely
to occur under natural conditions.

The analysis of the bed instability due to the flow within the bed
did not account for the inertia of the material in failure. Thus, the
prediction of failure during the short time interval as the steep forward
slope of a near-breaking wave passes, cannot be interpreted in the geotech-
nical sense, i.e., the failure does not result in the removal of the material
above the limiting slip circle. Rather, the predicted failure should be
interpreted as a "momentary failure" causing the bed material above the slip
circle to lose its stability.

The implication of this momentary failure caused solely by the flow
within the bed itself is that the bed material in failure is unable to re-
sist any additional force. In particular, sand grains on or near the bed-
water interface would be unable to resist any force due to the turbulent
flow of water above the bed. The instability of the bed due to the flow
induced in the bed may consequently significantly influence the amount of
bed material set in motion during the passage of a near-breaking wave and
hence play an important role in the wave-sediment interaction taking place
in the surf zone. Qualitatively the above discussion agrees with the bot-
tom "explosion" described in the Introduction.

When realizing that movable bed model tests often are performed employ-
ing very light weight bed material, such as plastic, it is quite clear from
Eq. 23 that, due to the low value of $(\rho_t - \rho)/\rho$, the effects of the flow in-
duced in the bed may be pronounced and possibly even extend beyond the surf
zone. Some evidence of this was brought out in the discussions following
the presentations by Dr. Kamphuis and Dr. Ince at the Fourteenth Coastal
Engineering Conference. Although they reported to have had considerable
success in using light weight materials in reproducing topographical changes
outside the region of breaking waves they had experienced considerable dif-
ficulties in reproducing features influenced by breaking waves. The effect
is readily observed in a demonstration wave flume using a beach consisting
of light weight granular material. Subject to incident waves one can ob-
serve the beach material oscillate with the incident waves to a considerable
depth below the bed surface.

Although not causing material to be removed from the bed, the momentary
failure due to the flow induced in the bed may cause a slight motion of the
material above the limiting slip circle. This slight motion may cause in-
dividual grains to slide past each other and exchange position. This "mix-
ing" process may be demonstrated by the simple experiments just outlined,
and may cause a particle initially on the surface of the bed to slowly work
its way into the bed to a depth given by the maximum depth of the failure,
δ in Fig. 2.

The above hypothesis would lead to an estimate of the maximum burial
depth of a tracer particle or as it is sometimes referred to: the depth of
distrubance, in the surf zone. A rough estimate of the order of magnitude

of this quantity may be obtained from the present investigation if we take the value of $[(\rho_t -\rho)/\rho]$ $\tan\phi = 0.5$ and the value of α corresponding to Eq. 22. In this case the stability number, Eq. 16, has a value of $C_s = 0.5/0.64 = 0.78$ and Fig. 3 yields

$$\delta = 0.22 \, l_s \tag{24}$$

From the estimate of $l_s \simeq 0(\frac{1}{2} H_B)$ obtained in this investigation, Eq. 24 indicates a burial depth, or depth of disturbance, of the order $\delta \simeq (0.11 \, H_B)$ where H_B is the wave height of the breaking wave. Although the above result is limited to the particular experimental conditions for which the estimates of C_s and l_s were obtained it does agree in form as well as in the order of magnitude with the results for the depth of disturbance reported by King (1951) who found depths of disturbances of the order $0.04 \, H_B$. Recent results by Williams (1971) indicate disturbance depths far greater than those reported by King (by a factor of up to 10), in addition Williams found grain size to have a negligible effect contrary to the results of King (1951) who found the depth of disturbance to increase with increasing grain size. The present hypothesis suggests that the depth of disturbance may vary from one location to another being affected primarily by local wave conditions (breaker type) and to a lesser degree by sediment characteristics. Thus, in a qualitative sense the predicted depth of disturbance based on the hypothesis presented here seem quite reasonable.

Some evidence to the effect that mechanisms other than bed form migration are responsible for the burial of tracer particles in the surf zone may be found in Clifton et al. (1971) who found bed forms to be absent in the high energy breaker zone. Also, James (1974) mention results of field investigations in the nearshore zone which show tracer dispersion depths within the bed exceeding 14 cm whereas a nearby bottom elevation monitor showed maximum changes in bottom elevation to be less than 3 cm. These observations along with the hypothesis for the depth of disturbance presented here, which clearly needs further confirmation to be considered more than a hypothesis, suggest that one should be cautious in interpreting measured burial depths of tracer particles in the surf zone as being indicative of the thickness of the layer of bed material being transported along the shore by the combined action of waves and wave induced currents.

It is hoped that the present investigation, although in many aspects of a preliminary nature, has served its purpose of pointing out that the effect of the flow induced in the porous bed is a mechanism which should be considered in many problems, in particular where dealing with the wave-sediment interaction in the surf zone. To quantitatively take the effect into consideration when evaluating say the longshore rate of sediment transport awaits further progress in our understanding of the mechanisms involved in this process.

REFERENCES

Clifton, H.E., Hunter, R.E., and Phillips, R.L., 1971, "Depositional Struc-
     tures and Processes in the Non-barred High-energy Nearshore", J. Sed.
     Petrology, Vol. 41, No. 3, 651-70.
Galvin, C.J., 1968, "Breaker Type Classification on Three Laboratory Beaches",
     J. Geophys. Res., 73, 3651-3659.
Henkel, D.J., 1970, "The Role of Waves In Causing Submarine Landslides", Geo-
     technique, Vol. 20, No. 1, 75-80.
James, W.R., 1974, "Multilayer Markov Mixing Models for Studies of Coastal
     Contamination", W.C. Krumbein Memoir, Geological Soc. of America.
King, C.A.M., 1951, "Depth of Disturbance of Sand on Sea Beaches by Waves",
     J. Sediment Petrol., 21, 131-140.
Komar, P.D., and D.L. Inman, 1970, "Longshore Sand Transport on Beaches", J.
     Geophys. Res., 75, 5914-5927.
Longuet-Higgins, M.S., 1972, "Recent Progress in the Study of Longshore Cur-
     rents" in Waves on Beaches, Meyer, R.E. (Editor), Academic Press.
Madsen, O.S., 1974, "The Stability of a Sand Bed under the Action of Break-
     ing Waves", R.M. Parsons Lab., M.I.T., Tech. Rep. No. 182.
Martin, C.S., 1970, "Effects of a Porous Sand Bed on Incipient Sediment Mo-
     tion" J. Water Resources Res., Vol. 6, No. 4, 1162-1174.
Martin, C.S., and Aral. M.M., 1971, "Seepage Force on Interfacial Bed Par-
     ticles", A.S.C.E., J. Hydr. Div., HY 7, 1081-1100.
Reid, R.O., and Kajiura, K., 1957, "On the Damping of Gravity Waves over a
     Permeable Sea Bed", Transactions, Am. Geoph. Union, Vol. 38, No.5, 662-
     666.
Sleath, J.F.A., 1970, "Wave-induced Pressures in Beds of Sand", Proc. A.S.C.E.,
     J. Hydraulics Div., 96, 367-379.
Terzaghi, K., and R.B. Peck, 1967, Soil Mechanics in Engineering Practice,
     2. Edition, John Wiley & Sons.
Williams, A.T., 1971, "An Analysis of Some Factors Involved in the Depth of
     Disturbance of Beach Sand by Waves", J. Marine Geology, Vol. 11, 145-158.

CHAPTER 46

SEDIMENT TRANSPORT IN RANDOM WAVES AT CONSTANT WATER DEPTH

by

Hsiang Wang and S. S. Liang*
University of Delaware, Newark, Delaware, U.S.A.

Abstract

Sediment transport in random waves at constant water depth is analyzed by dividing the flow field into two regions--the internal region and the boundary layer region. The suspension and transport of sediment in these two regions are treated separately. The total transport is then obtained as the total of these regions through matching boundary.

In the bed layer, the load concentration is assumed to be proportional to the specific weight of the sediment and to the probability that the fluctuating lifting force exceeds the weight of the sediment. The bed load is then transported by the secondary flow (which is unidirectional) in the boundary.

In the internal flow region, the sediment suspension is treated as a diffusion problem with the intensity of diffusion to be proportional to the amplitude of fluid particle motion. The transport velocity is assumed to be the same as the mass transport velocity of the wave.

The predominant mode of transport is found to be suspended load. The total transport in a wind-generated wave field can be expressed as a power law of wind speed. For the case tested, the power should be of the order of 4.

1. INTRODUCTION

The analysis presented in this paper applies only to regions well beyond the surf zone where the flow field, though irregular in appearance, can be described in reasonable detail without going into micro-structures. In other words, the water surface variations, the internal flow characteristics, and the pressure field can still be expressed in manageable mathematical expressions in gross terms.

To facilitate calculations of sediment motion, the flow field is divided into two zones. The upper zone, where viscosity plays a negligible role except

---

*Now at Stone and Webster, Boston, Massachusetts.

on water mass transport, is termed zone of suspended load. In this zone, sediment is in a state of suspension due to the combined effects of turbulence and orbital motion of fluid mass. The lower zone, which is a thin turbulent boundary layer near the sea bed created by wave motion overhead, is termed bed load layer following Einstein's terminology. In this zone, sediment particles roll, slide, and sometimes jump. As stated by Einstein (1972), the measureable thickness of this turbulent boundary layer is usually rather small; 5 - 10 m.m. are very common values. However, since it is directly adjacent to the sea bed, it could be very effective in sediment transport. The suspended load can be considered to occupy the full water depth. There-fore, although the sediment concentration may be relatively small, the trans-port rate may still be appreciable. From these observation, sediment trans-port in both zones need proper attention.

Therefore, the analysis naturally breaks down into investigating the following four parts systematically: 1) Bed Load Concentration, 2) Bed Load Transport, 3) Suspended Load Concentration, and 4) Suspended Load Transport.

The problems are first formulated for monocromatic wave train and the results are then generalized for random waves. The total sediment transport rate is obtained through matching boundary conditions of the two zones. Because of the complicated mathematical formulations, computer programs are developed to facilitate numerical computations.

2. BED LOAD

Concentration--Let the bed-load concentration be expressed as $\overline{C}_0 = N_s W$ where N_s is the number of particles per unit volume inside the bed layer and $W = A_1 D^3 \gamma_s$ is the dry weight of sediment particle. Since in a unit volume N_s is inversely proportional to the size of the sediment particle and is proportional to the probability, p, of a sediment particle to be set in motion, we have

$$C_o = A_o \; p \; \gamma_s \qquad\qquad (1)$$

where A_0 is an empirically determined constant. The probability, p, is equal to the probability that the instantaneous lift exceeds the weight of the particle (Einstein, 1950), i.e.,

$$p = p \; (\overline{L} + L' > W)$$

where $\overline{L}$ is the mean lift force and L' is the fluctuating component of the lift force.

On the further assumption that in a turbulent boundary layer L' is a random process following a normal distribution of zero mean and standard deviation proportional to the mean lift ($\sigma = \eta_o L$, where η_o is a constant of proportionality), Einstein arrived at the following expression for the probability distribution function

$$p = \frac{1}{\sqrt{2\pi}} \int_{B_* \psi - \frac{1}{\eta_o}}^{\infty} e^{-\frac{z^2}{2}} dz \qquad (2)$$

where $B_* = \dfrac{2A_3}{C_L \eta_o}$; D is equivalent diameter of the sediment particle; C_L is the lift coefficient of sediment particle; A_3 is a constant and $\psi = \dfrac{(\rho_s - \rho) gD}{\rho u^{-2}}$

is known as the flow intensity function in which u is the amplitude of the oscillatory flow velocity in the direction of wave propagation. Therefore, the problem of determining the bed-load concentration, aside from a number of constants of proportionality, becomes a problem of determining the horizontal velocity in the boundary layer.

Analogous to the laminar case (Schlichting, 1960), Kalkanis (1964) proposed the following expression for the horizontal velocity component in a fluctuating turbulent boundary layer.

$$u = u_o \{1 + f_1^2 - 2f \cos f_2\}^{1/2} \cos(wt + \theta) \qquad (3)$$

in which $f_1 = 0.5\, e^{-\frac{133}{a\beta D} y}$, $f_2 = 0.5\,(\beta y)^{2/3} \approx 0.3\beta y$, $\theta = \tan^{-1} \dfrac{f_1 \sin f_2}{1 - f_1 \cos f_2}$, and

$\beta = \sqrt{\dfrac{\omega}{2\gamma}}$. Therefore, the bed-load concentration in a monocromatic wave train

can be determined through Eqs. (1), (2), and (3). For, random waves, the velocity is expressed by

$$u = \sum_i u_{oi} [\cos (k_i x - \omega_i t + \varepsilon_i) - f_{1i} \cos (k_i x - \omega_i t + f_{2i} + \varepsilon_i)] \qquad (4)$$

where $\sum_i U_{oi} = \int_o^\infty S(\omega) d\omega$ and $S(\omega)$ the spectral density function of wave energy.

Transport

Within the boundary layer of a wave field, the first order effect is to relieve the sediment particles of all or part of their weight so as to bring them into a state of incipeint equilibrium. At this state, if there is no other incidental current, the net transport will result only from higher order effect.

Now treat the mass transport velocity as the second order effect such that, to the second order, the velocity field inside the boundary can be expressed as:

$$(u + U_e) \; \hat{e}_x + (v + V_e) \; \hat{e}_y$$

where U_e and V_e are the second order velocity components and are of the order of εu and εv, respectively. The ε is a perturbation parameter of the order of ak for deep water wave and hk for shallow water wave. Substituting the above expression into the boundary layer equation in the horizontal direction yields,

$$\frac{\partial(u + U_e)}{\partial t} + \frac{\partial(u + U_e)^2}{\partial x} + \frac{\partial(u + U_e)(v + V_e)}{\partial y} = -\frac{1}{\rho}\frac{\partial p}{\partial x} + \nu\frac{\partial^2}{\partial y^2}(u + U_e) \qquad (5)$$

To the second order, the pressure inside the boundary layer is equal to that at the outer edge of the boundary layer, the mean momentum equation inside the boundary layer reduces to a balance between shear stress and Reynolds stress:

$$\frac{\partial(\overline{uv})}{\partial y} = \nu\frac{\partial^2 \overline{U}_e}{\partial y^2} \qquad (6)$$

From Eq. (3) or (4) the vertical velocity component inside the boundary layer can be obtained through continuity relation. The shear stress $\overline{uv}$ can then be solved through the fact that u and v are orthogonal functions. The second order horizontal velocity $\overline{U}_e$ is then solved from Eq. (6) when the following boundary conditions are specified:

(1) At the outer edge of the boundary layer, the mean shear stress is negligible.

$$\frac{\partial U_e}{\partial y} = 0 \qquad at \qquad y = \infty$$

(2) At the bottom, the velocity is zero

$$\overline{U}_e = 0 \qquad \text{at} \qquad y = 0$$

The solution obtained is in the Eulerian reference frame. The true mass transport velocity, which is a Lagrangian property, is obtained through transformation of coordinate (Longuet-Higgins, 1953) by

$$\overline{U} = \overline{U}_e + (\int u\,dt)\frac{\partial u}{\partial x} + (\int v\,dt)\frac{\partial u}{\partial y} \qquad (7)$$

The solution is (Liang and Wang, 1973)

$$\overline{U} = \sum_i \frac{0.5\ k_i\ u_{oi}^2}{2\nu(E_i^2 + 0.09\beta_i^2)} \{-e^{-E_i y}\ \sin 0.3\beta_i y[E_i y + \frac{1.5\ E_i^2 - 0.225\beta_i^2}{E_i^2 + 0.09\beta_i^2}]$$

$$-e^{-E_i y}\ \cos 0.3\beta_i y[0.3\beta_i y + \frac{1.2\ \beta_i\ E_i}{E_i^2 + 0.09\beta_i^2}]$$

$$+\frac{0.15\ \beta_i}{2\ E_i}\ (e^{-2E_i y} - 1) + \frac{1.2\ \beta_i\ E_i}{E_i^2 + 0.09\beta_i^2} \}$$

$$+\sum_i \frac{k_i\ u_{oi}^2}{2\ \omega_i}\ \{1 - e^{-E_i y}\ \cos 0.3\beta_i y + 0.25\ e^{-2E_i y}$$

$$+ 0.5\ e^{-E_i y}\ y[E_i\cos 0.3\beta_i y + 0.3\beta_i \sin 0.3\beta_i y]\}$$

$$+\sum_i \frac{0.5\ k_i\ u_{oi}^2}{2\omega_i(E_i^2 + 0.09\beta_i^2)}\ \{0.5(E_i\ e^{-E_i y})^2 - 0.5(0.3\beta_i e^{-E_i y})^2$$

$$+ 0.5\ e^{-E_i y}\ \cos 0.3\beta_i y[-E_i^2 + (0.3\beta_i)^2]$$

$$- 2(0.5)E_i 0.3\beta_i\ e^{-E_i y}\ \sin 0.3\beta_i y\} \qquad (8)$$

where $E_i = \dfrac{133\ \sinh(k_i h)}{a_i \beta_i D}$

3. SUSPENDED LOAD

Concentration

Generally, sediment suspension in a fluid media is treated as a diffusion-dispersion process. This line of approach is followed here. The diffusion equation takes the following form:

$$\frac{\partial C}{\partial t} + \nabla \cdot (C\underset{\sim}{V}_s) = \nabla \cdot (e_m \nabla C) \tag{9}$$

where C is sediment concentration (Mass/volume); V_s is the particle velocity vector and e_m is the diffusion coefficient. For suspended sediment in a wave field, the concentration and velocity can both be divided into three components:

$$C = \overline{C}(x,y) + C_w(x,y,t) + C^{'}(x,y,t)$$

$$\underset{\sim}{V}_s = \overline{\underset{\sim}{V}} + \underset{\sim}{V}_w + \underset{\sim}{V}^{'}$$

Here, $\overline{C}$ and $\overline{V}$ are the mean values, C_w and $\underset{\sim}{V}_w$ are the wave induced components,

and $C^{'}$, $\underset{\sim}{V}^{'}$ are the turbulent fluctuations. Substituting C and V into the

diffusion equation and taking the time average yields

$$\nabla \cdot (\overline{C}\ \overline{\underset{\sim}{V}} + \overline{C_w \underset{\sim}{V}_w} + \overline{C^{'}\underset{\sim}{V}^{'}}) = \nabla \cdot (e_m \nabla \overline{C}) \tag{10}$$

Integrating and assuming $C = 0$, $\nabla C = 0$ at free surface the following equation is arrived at:

$$\overline{C\underset{\sim}{V}} = e_m \nabla \overline{C} - \overline{C_w \underset{\sim}{V}_w} - \overline{C^{'}\underset{\sim}{V}^{'}} \tag{11}$$

The right hand side of the above equation represents the effects of molecular diffusion, wave agitation and turbulent diffusion. In the usual context of the diffusion process (Hinze, 1962) it is further assumed that

$$\overline{C_w \underset{\sim}{V}_w} = -e_w \nabla \overline{C} \ ; \quad \overline{C^{'}\underset{\sim}{V}^{'}} = e^{'} \nabla \overline{C}$$

where e_w and $e^{'}$ are, respectively, the diffusion coefficients of wave motion and turbulence. Since molecular diffusion is usually negligible, the task of solving Eq. (11) rests on the estimation of e_w and $e^{'}$. Following Prandtl's mixing theory, these coefficients are assumed to be proportional to certain

characteristic velocities and mixing lengths. For sediment suspension in a wave field, it is reasonable to assume that the characteristic velocities for both e_w and $e^{\bullet}$· are proportional to the amplitude of the vertical velocity component of the wave field. Furthermore, if mixing lengths are treated as constant in the flow field, a commonly adopted assumption, the diffusion equation becomes

$$\overline{CV} = \sigma V_m \frac{d\overline{c}}{dy}$$

(12)

where σ is a constant of proportionality and V_m is the amplitude of the vertical velocity component. For small amplitude waves it is expressed as

$$V_m = \frac{a\omega}{\sinh ky} \sinh ky$$

where a is the wave amplitude; w is the angular frequency; k is the wave number, h is the water depth and y is the vertical coordinate measured from sea bottom, as shown below:
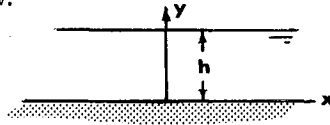
Figure 1. Definition Sketch

For regular waves, the solution of Equation (12) is:

$$\frac{\overline{C}}{\overline{C}_r} = [\frac{\tanh (\frac{ky}{2})}{\tanh (\frac{ky_r}{2})}]^R$$

(13)

in which y_r is a reference level where $\overline{C} = \overline{C}_r$ and $R = \frac{G \sinh kh}{\sigma \, k \, a \, \omega}$ where G is the mean particle settling velocity.

For random wave systems, the suspended sediment distribution function can be shown as equal to

$$\frac{\overline{C}}{C_r} = \sum_i [\frac{\tanh \frac{k_i y}{2}}{\tanh \frac{k_i y_r}{2}}]^{R_i}$$

(14)

where $R_i = \dfrac{G \sinh k_i h}{\sigma\, k_i a_i \omega_i}$ and $\sum\limits_i a_i^2 = \int\limits_0^\infty S(\omega)\,d\omega$. For shallow water, both

Equations (13) and (14) reduce to power law.

Transport--In a wave field, it has been shown by Longuet-Higgins (1953) that the field equation for mass transport, correct to the second order, takes the following form:

$$\nabla^4 \Psi \quad (u\,\frac{\partial}{\partial x} + v\,\frac{\partial}{\partial y}) \int \nabla^4 \psi_s \, dt + \nabla^4 \int \frac{\partial \psi_s}{\partial y}\,dt\,\frac{\partial \psi_s}{\partial x} \tag{15}$$

where Ψ is the mass-transport velocity stream function, u and v are the first order velocity components, and ψ_s is first order stream function. In the present case of random wave field, the first order velocity components and stream functions are, respectively:

$$\begin{matrix} u \\ v \end{matrix} = \sum_i U_{oi} \begin{matrix} \cosh_i k_i y \\ \sinh \ k_i y \end{matrix} \cos(k_i x - \omega_i t + \Sigma_i)$$

$$\psi_s = -\sum_i \frac{a_i i}{k_i} \frac{\sinh k_i y}{\sinh k_i h} \cos(k_i x - \omega_i t + \Sigma_i)$$

where Σ is the random phase angle. Substituting the above equations into Equation (15), we have

$$\nabla^4 \Psi = \nabla^4 \ (\sum_i \frac{u_{oi}^2}{4\omega_i} \ \sinh 2\,k_i y) \tag{16}$$

Let
$$\psi(0) = 0 \tag{17}$$

then the requirement of zero net mass transport in the whole field yields

$$\psi(h) = 0 \tag{18}$$

at the outer edge of the interior region. Furthermore, at the bottom of the interior region (y = 0), the horizontal velocity must be matched with the outer edge velocity of the boundary layer; i.e.,

$$\frac{\partial \psi}{\partial x}\bigg|_{y=0} \quad U_\infty$$

where $\overline{U}_\infty$ can be deduced from Equation (18). With the boundary conditions so defined, solution of ψ can be obtained from Equation (16). The mass transport velocity can then be obtained through differentiation. The solution is

$$\overline{U} = \sum_i \frac{a_i^2 \omega_i k_i}{4 \sinh^2 k_i h} \left\{ 2 \cosh 2k_i y + \frac{3 \sinh2 \, k_i h}{2k_i h} \left(\frac{y^2}{h^2} - 2\frac{y}{h}\right) \right\}$$

$$+ \sum_i \frac{U_{oi}^2 k_i}{4\nu(E_i^2 + 0.09\beta_i^2)} \left[\frac{1.2\beta_i E_i}{E_i^2 + 0.09\beta_i^2} - \frac{0.3}{4}\frac{\beta_i}{E_i} \right]$$

$$\left[\frac{3}{2}(\frac{y^2}{h^2} - 2\frac{y}{h}) + 1 \right] \tag{20}$$

4. RESULTS

Before examining the case of sediment transport in random waves, it is instructional to compare our results with some of the existing information which, unfortunately, is limited to monocromatic wave trains.

Behattacharya (1971) studied the sediment suspension in shoaling waves experimentally. Those data obtained near horizontal bed were compared with Equation (13) and the value of σ was found to be 5.15 m. $(\rho_s/\rho = 2.83)$(Fig. 2). The mass transport velocity for a regular wave train in a constant water depth is illustrated in Fig. (3) with a roughness of D = 0.0005 to .00015. The theoretical results of Longuet-Higgins (1953) and Hwang (1970), and the experimental results of Russell(1957), are also shown in the same figure to offer some comparisons.

For random waves, the case illustrated here assumes the following input condition: water depth (h) = 7.5 m., density ratio (γ_s/γ) = 2.83, viscosity (ν) = 0.976 x 10^{-6} m^2/sec., mean sand grain size (D) = 0.65 m.m. The random wave is generated in accordance with the deepwater wave spectrum of Pierson and Moskowitz (1964).

For the bed load, Table 1 shows the concentration for various wind speed: Figure 4 illustrates the mass transport velocity distribution inside the boundary layer. For the suspended load, Figure 5 plots the concentration for various wind speeds; the mass transport velocities are shown in Figure 6.

The total transport of sediment (the summation of bed load and suspended load) is shown in Figure 7.

Bed-Load Concentration

TABLE 1

$h = 7.5^{m}$, $\rho s/\rho = 2.83$, $\nu = 0.976 \times 10^{-6}$ m^{2}/sec , $D = 0.65^{mm}$

$s(\omega) = (0.0081$ $g^{2}/\omega^{3})$ EXP $[-0.74$ $(g/v\omega)^{4}]$

v (knots)	ψ	p	C_o (PPM)
20	0.227	0.723	1201.324
25	0.079	0.882	1465.064
30	0.035	0.913	1516.925
35	0.018	0.923	1533.957
40	0.010	0.928	1541.190

Although the wave spectrum chosen here may not be compatible with the finite depth case, the results illustrated above revealed a number of interesting facts:

1) The bed load is of minor importance in sediment transport if the wave is the only factor under consideration.

2) The suspended load concentration increases rapidly with increasing wind velocity. However, the gradient of the suspended load in the water column decreases as wind speed increases.

3) For small wind velocity (or small waves) the shape of the mass transport velocity distribution in the vertical direction is similar to that obtained in the laboratory; the velocity possesses forward components at the surface and bottom layers with return flow in the middle. As the wind speed increases,the forward velocity component at the surface layer diminishes and eventually becomes return flow, thus, the wave mass transport advances with the wave celerity at the lower half of the water column and returns from the upper half.

4) The direction of the sediment transport is with the direction of wave propagation; the reate of transport can be approximated by a power law of wind speed; i.e.,

$$Q_S = A(V)^n$$

where A is a constant. For the case studied, the value of n is approximately equal to 4.

Acknowledgment

References

1. Bhattacharya, P. K. (1971), Sediment Suspension in Shoaling Waves, Ph.D. Thesis, University of Iowa.

2. Einstein, H. A. (1950), The Bed-Load Function for Sediment Transportation in Open Channel Flows, U. S. Dept. Agric., Soil Conserv. Serv., Tech. Bull. No. 1026.

3. Einstein, H. A. (1972), Sediment Transport by Wave Action, Proc. 13th Conf. on Coastal Engineering.

4. Hinze, J. O. (1959), Turbulence, McGraw-Hill, New York.

5. Huang, N. W. (1970), Mass Transport Induced by Wave Motion, J. Mar. Res., Vol. 28.

6. Kalkanis, G. (1964), Transportation of Bed Material Due to Wave Action, Tech. Memo. No. 2, U. S. Army Coastal Engineering Res. Center.

7. Liang, S. S., and Wang, H. (1973), Sediment Transport in Random Waves, TR26, College of Marine Studies, University of Delaware.

8. Longuet-Higgins, M. S. (1953), Mass Transport in Water Waves, Phil. Trans. Royal Soc. of London, (A) 245.

9. Pierson, W. J., and Moskowitz, L. (1964), A Proposal Spectral Form for Fully Developed Wind Seas Based on the Similarity Theory of S. A. Kitaigorodskii, J. Geophys. Res., Vol. 69, No. 24.

10. Russell, R. C. H., and Osorio, J. D. C. (1957), An Experimental Investigation of Drift Profile in a Closed Channel, Proc. 6th Conf. Coastal Engineering.

11. Schlichting, H. (1960), Boundary Layer Theory, McGraw-Hill, New York.
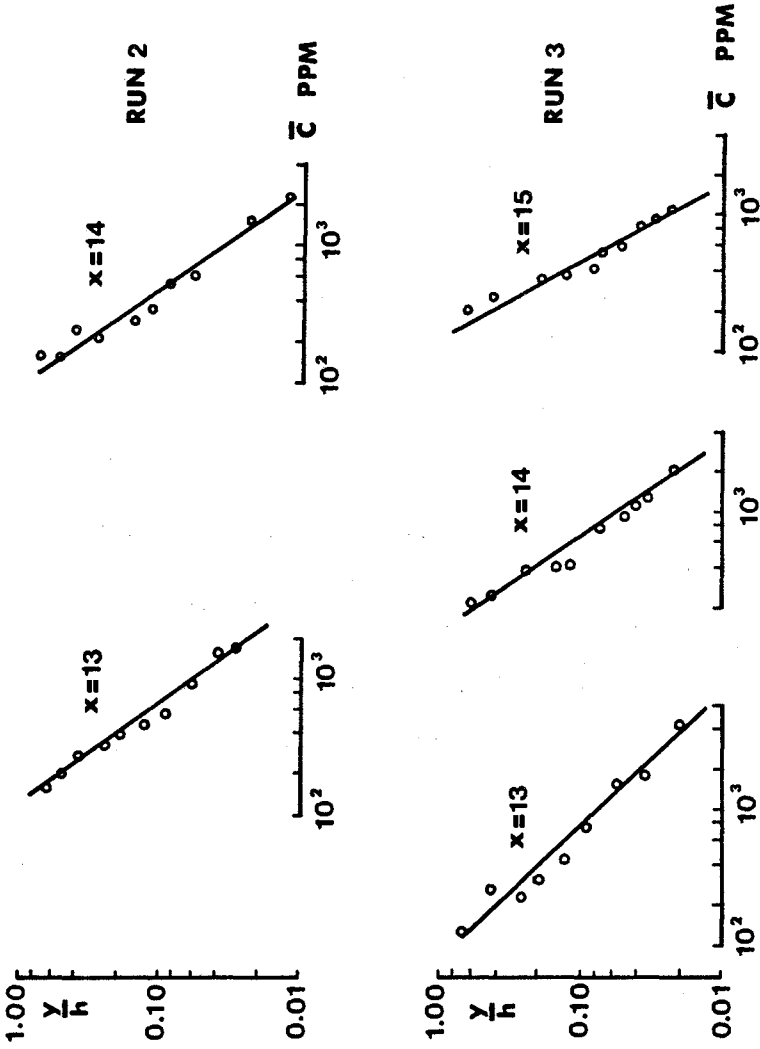
Figure 2   Comparison between experimental data and theoretical prediction for σ = 5.15 m.
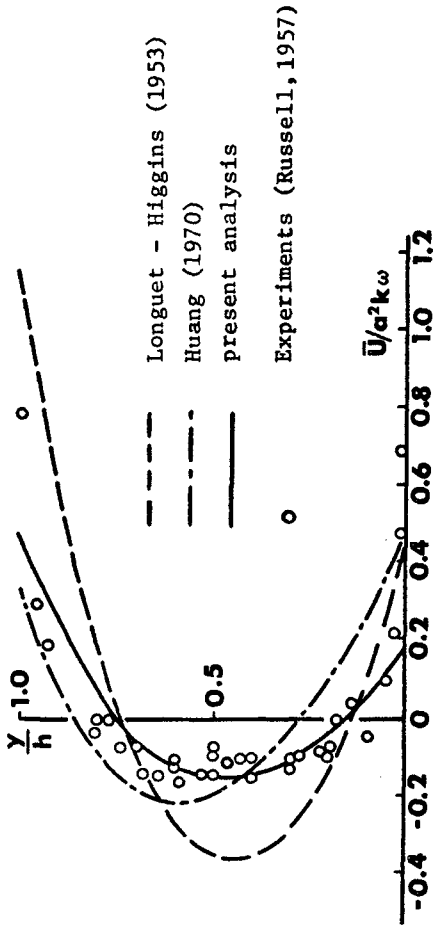
Figure 3 Comparison of mass transport velocities between theories and experiments.
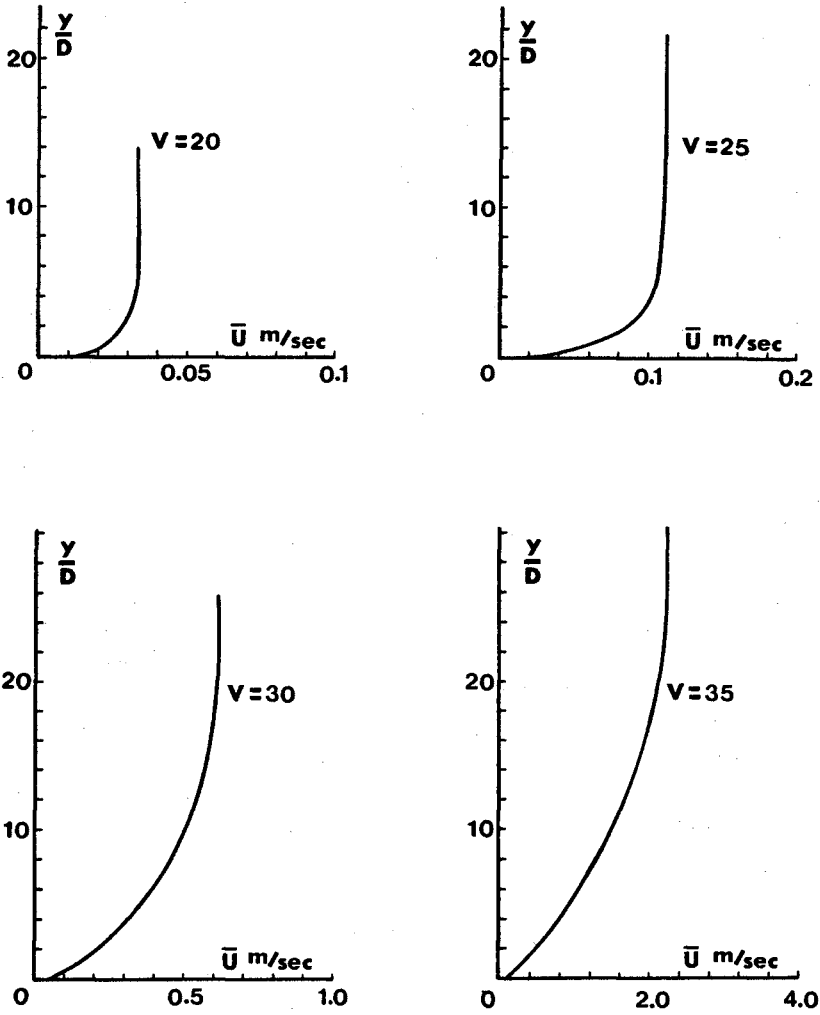
Figure 4

Mass transport velocity distribution inside the boundary layer under a random wave train.
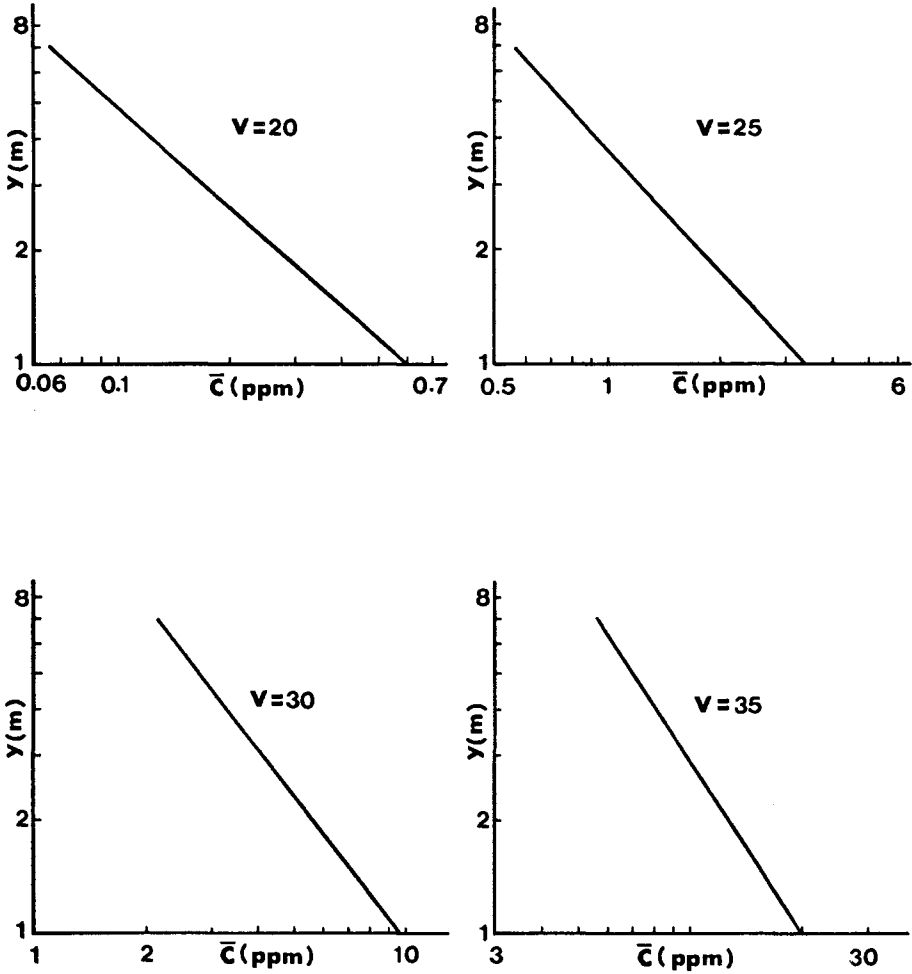
Figure 5   Suspended Sediment Concentration vs. Wind Velocity
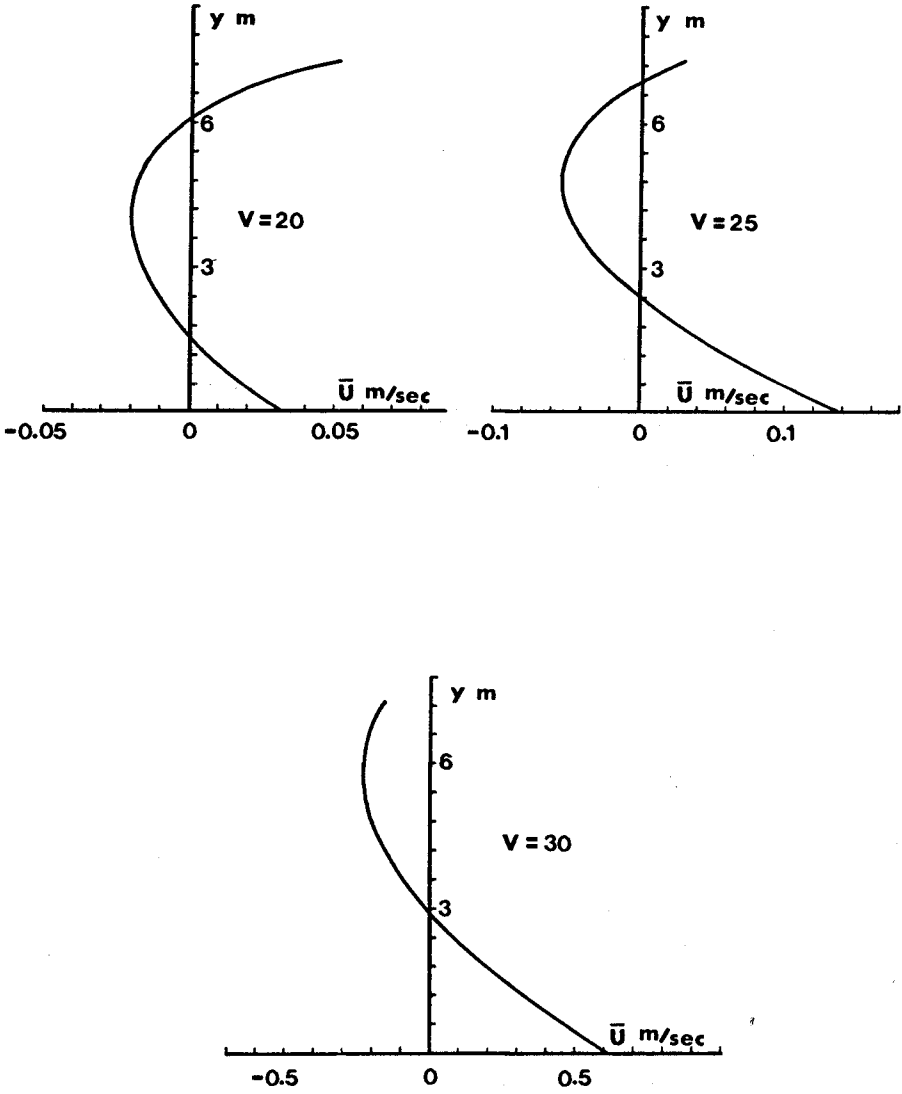
Figure 6

Mass transport velocities under random waves

h = 7.5m

ρ_s/ρ = 2.83

ν = 0.976 x $10^{-6}m^2$/sec

D = 0.65 m.m.
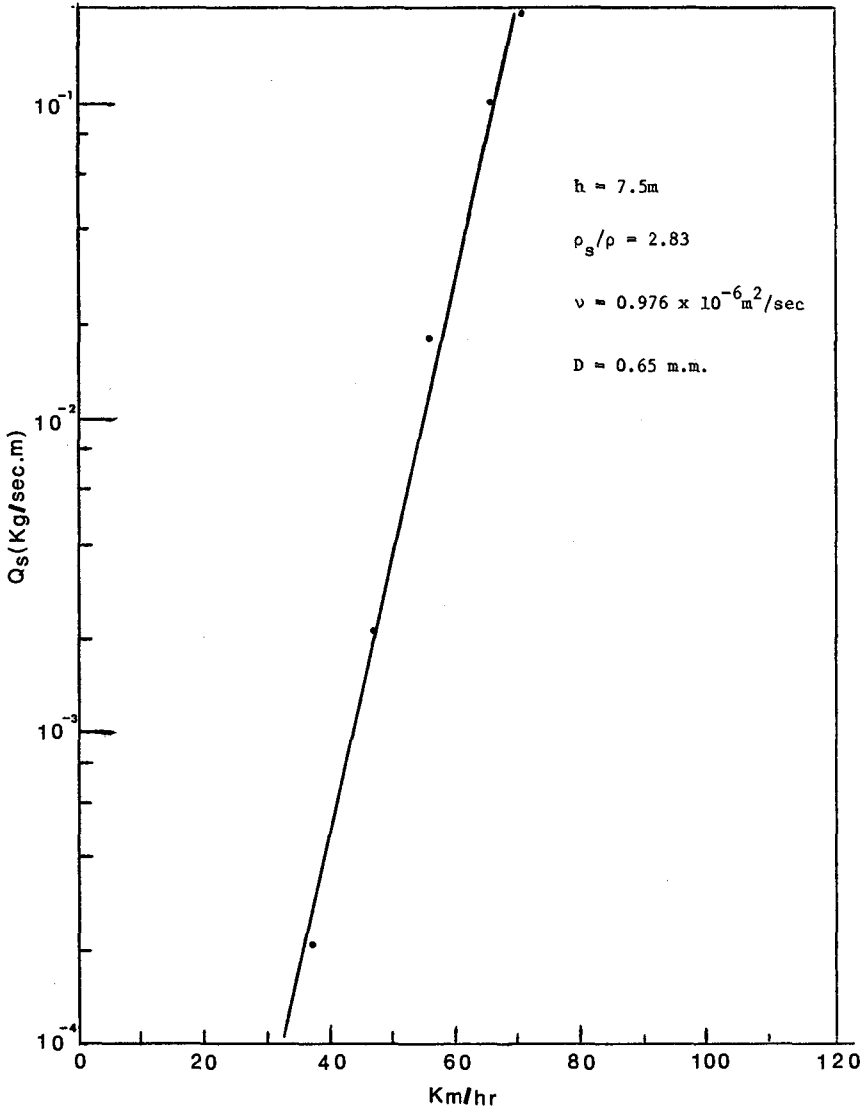
Figure 7   Rate of Sediment Transport vs. Wind Speed

CHAPTER 47

MODE AND PERIOD OF SAND TRANSPORT IN THE SURF ZONE

Benno M. Brenninkmeyer, S.J.

ABSTRACT

   Three almometers-water opacity measuring devices-emplaced
perpendicular to the beach,measure instantaneously and continu-
ously the sediment concentration across the surf zone. Most of the
variance of the sand movement is centered in frequencies of less
than 0.25 Hz and between 1.15 and 1.25 Hz. Modes and frequency
of sand transport differ within each of the dynamic zones of the
surf. The motion of sediment in the inner and outer surf zones
is small and virtually independent of the deep water wave periods.
Outside the breaker zone, bed load movement is somewhat coincident
with the prevailing swell period. Lighter concentrations move pre-
dominantly with a 0.8-0.9 second periodicity. In the breaker zone,
sand moves along the bottom with frequencies equal to that of both
the swell and sea, but most of the power is in lower frequencies.
In the breaker zone sand is rarely thrown into suspension. In the
transition zone, sediment motion is largely by suspension with a
period a little longer than the swell.

INTRODUCTION

   Measurement of water opacity and therefore particulate concen-
tration have been made for quite some time. Shelford and Gail (1922)
seem to have been the first to use various light emitting sources
opposite a photo-cell in the field. Since then, many others, among
them, Jakuschoff (1932), Petterson (1934), U.S. Interagency on
Water Resources (1963), Homma and others (1965) and those mentioned
by Das (1972) have used this principle. Longinov (1968) was the
first to use photocells to measure suspended sediment concentra-
tion in the nearshore zone. Most of the instruments, used by these
researchers, measure sediment concentration at a given point per
unit time. The almometer (Brenninkmeyer, 1973, in press) can
measure, at 1cm intervals, from 10 to 500 grams of sediment per
liter of water in the bottom 1.2 meters of water simultaneously
and continuously. This is achieved by placing a vertical series
of 64 photo-electric cells opposite a high intensity flourescent
lamp (Figure 1). The two parts are encased in separate water
tight acrylic cylinders and attached to metal poles which are
anchored in the substrate up to a meter apart. This separation
allows an unimpeded sediment and water flow between the cylinders.
The voltage change of each of the photo cells, as more or less
sediment passes in front of them, is sampled up to every one
fifth of a second, multiplexed and recorded on magnetic tape.

   Three almometers were partially buried in a line perpendicu-
lar to shore on the beach at Point Mugu, California₃ This area,
located 95 km northwest of Los Angeles, trends N 50 W and is

Department of Geology and Geophysics, Boston College, Chestnut
Hill, Massachusetts   02167

Figure 1. The almometer emplaced on the beach. The device con-
sists of two acrylic cylinders; in one is a flourescent lamp
in the other, 64 photo-electric cells.

influenced by a western swell which, during the two week test,
was 75 to 90 cm in height with a 13-16 second period. Almost
half the time the local wind waves were less than 30 cm high
with a 4-8 second period. They also came from the west. The
tides are mixed, with a predominant semidiurnal component.
The tides have a mean range of 1 m and an extreme range of
2.8 m. The sand on the foreshore has a mean diameter of 0.16mm.

SAND MOVEMENT IN THE SURF ZONE

The three almometers were emplaced, one on the shoreface
(15 cm below MLLW), the second in the lower beachface (30 cm

above MLLW) and the third on the upper beachface (90 cm above
MLLW) so that as the tide, rose and fell, each of the dynamic
zones of the surf regime could be sampled. Only infrequently
can the sediment movement caused by a single wave be detected
with certainty across all three stations. Figure 2 is a typical
example. Since the tide at the time depicted, was 1 m high, the
shoreface (1) is under the breaker zone, the lower beachface
(2) is in the middle surf zone and the upper beachface (3) is
in the transition zone (Schiffman, 1965), the area where the
leading edge of the surf plows into the backwash. Noteworthy
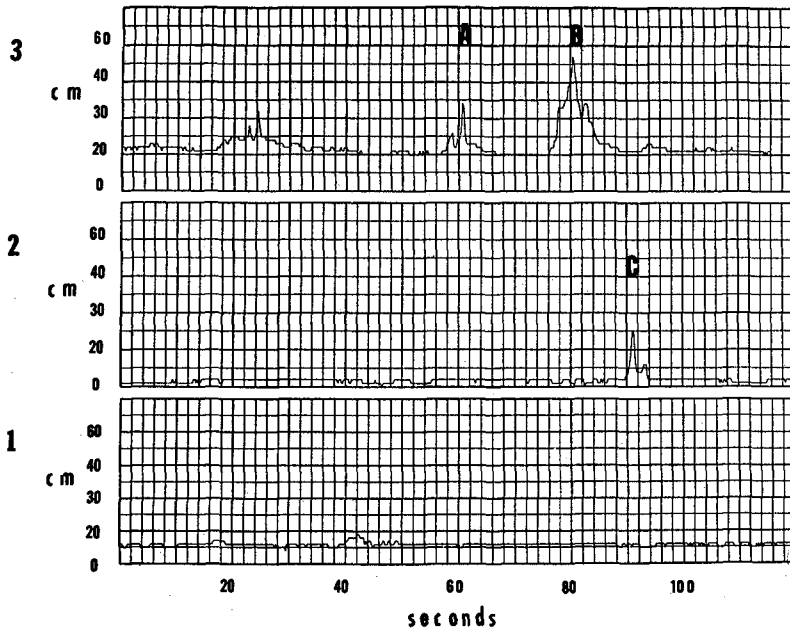
Figure 2 Time rate of change across the surf zone in the
elevation of the sediment concentration of 135 grams per
liter. 1) Breaker zone 2) Middle surf zone 3) Transition
zone.

is the relatively little movement of sand in the breaker zone and the great agitation in the transition zone. A and B probably represent an incoming bore and its backwash. As Emery and Gale (1951) have pointed out, the swash period is considerably longer than the wave period, which at this time was 13 seconds. After the incoming swash passed, no deposition had taken place. Whereas, after the backwash 1 cm had been deposited. During or after more than half the backwashes deposition takes place.

The only real movement in the middle surf zone (2) was due to the backwash from B to C. The spacing of the two stations was 32 m so that the backwash velocity responsible for these sand uplifts was 2.3 m per second. Either this velocity was not sufficient to keep the sand in suspension or, more likely, another surge coming in overtopped the backwash and entrained the top of the backwash back towards the beach. In either case the suspension cloud diminished in elevation from 26 to 21 cm above the bottom.

TIME SERIES ANALYSIS

In order to determine the frequency of sediment movement a spectral analysis was performed on sets of 6000 data points covering a 20 minute period. The spectra manifest four diverse forms. In the most common, the great majority of the power is in the low frequencies,less than 0.1 Hz (Figure 3A). Sometimes, these peaks are coincident with the swell period but more usually they are longer than half a minute. Much less common are the spectra where the preponderance of the power is in the higher frequencies (Figure 3B) with periods of less than a second. Often the variance is split between these ranges Figure 3C. When this occurs there is a peak in the 0.15-0.25 Hz band. Here the peak is centered on 4.5 seconds. In between from 0.25 to 1.15 and especially beyond 1.25 Hz there is little power in any frequency. Only rarely does the spectra display a Dirac delta or impulse function (Figure 3D) if the station is under water. This form is to be expected only when a station is above the swash line. Yet a comparison of parts A and D in Figure 3, taken from the same station and the same time, but depicting different concentrations, shows that right inside the breaker zone there is little movement of the bottom while considerable quantities of sand, in a 70 gram per liter slurry, are moved with a periodicity greater than 13 seconds.

The frequencies in the 1.1-1.3 Hz band may or may not be present depending on the concentration under consideration. Figure 3C, 3E and 3F show three different concentrations for the same station located in the inner surf zone. The 0.81 and 0.86 second periods are absent from the 70 gram per liter concentration while they are present in the 40 and 375 gram per liter densities. The only time that these periods are of paramount
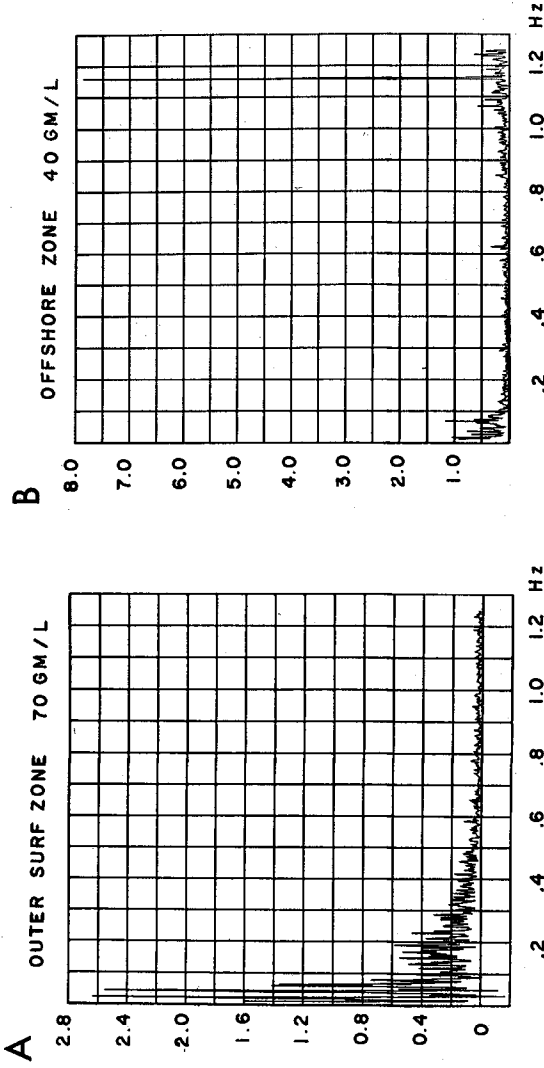
Figure 3   Diverse forms of the power spectra of sediment movement in the surf zone. Part A, all the power is in the lower frequencies. Part B most of the power is in the high frequencies.
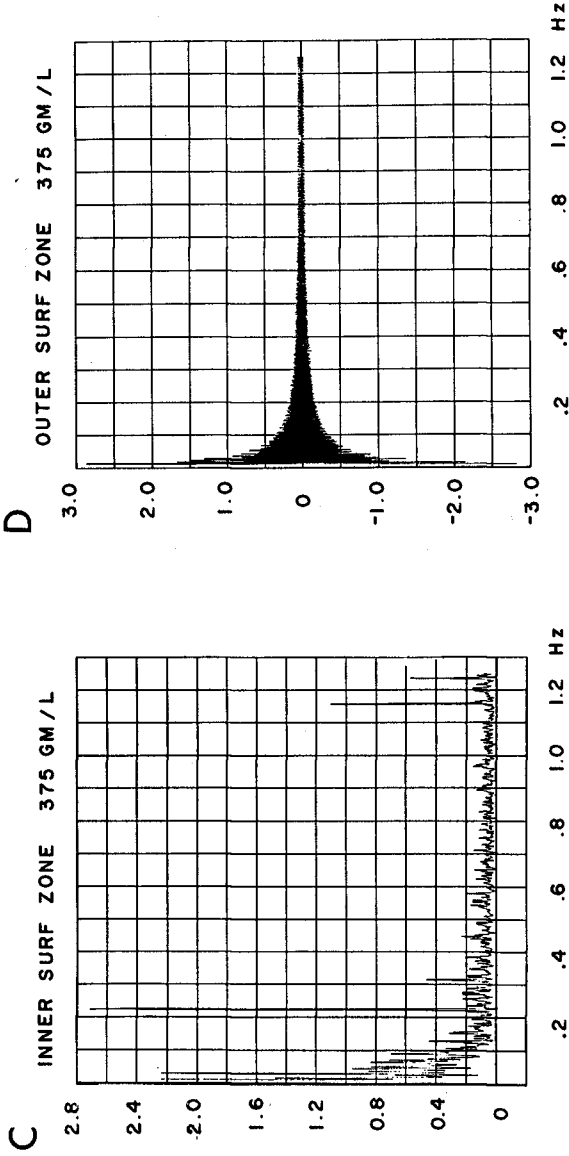
Figure 3 Part C most of the power of the spectrum is in .22 Hz band.
Part D only infrequently does an impulse function or no movement of
sand occur while the area is under water.
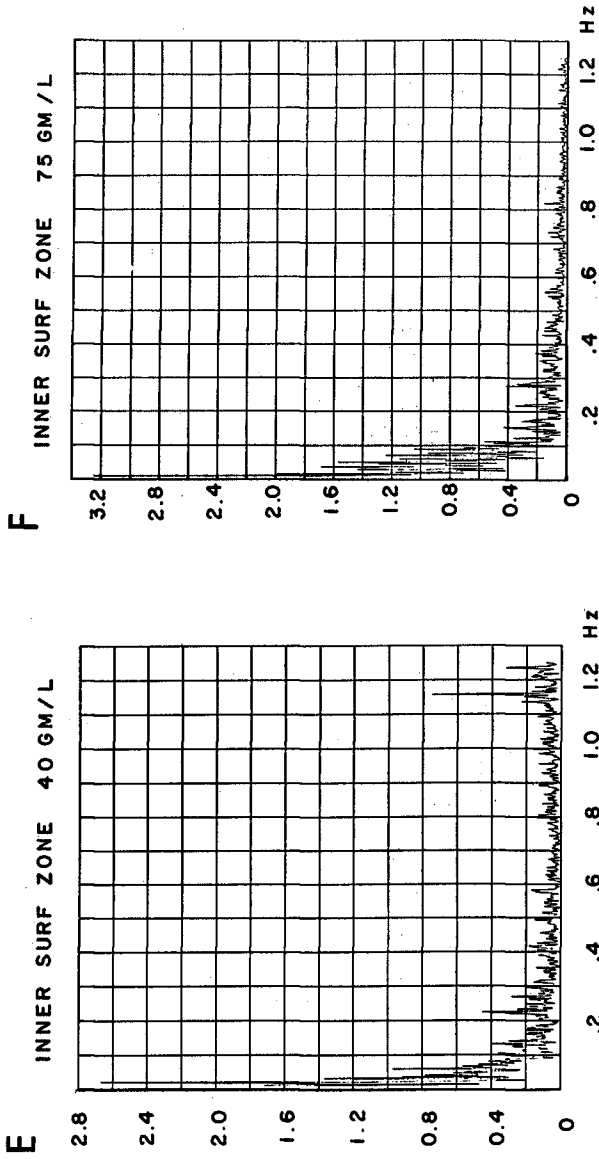
Figure 3 Part E. In the inner surf zone the 40 gm/l concentration
changes elevation with a periodicity of greater than 16 seconds and
0.81 and 0.86 seconds. Part F. The latter periods are absent in the
70 gm/l concentration.

importance is in the lighter concentrations outside the breaker
zone (as in Figure 3(B) where they may be the only frequencies
present. Their significance is somewhat mystifying. They probably
represent smaller movements superimposed on longer period steady
drift. Yet everytime that a short periodicity occurs anywhere in
the nearshore zone it is in this 0.8-0.9 second band. For short
period movements one would expect a range of frequencies. But this
is not the case. They may well be the fundamental mode of short
term sand movement in response to the local turbulent component
of the water which exist up to 1.5 Hz (Huntley and Bowen, 1974).

An enlargement of the lower frequencies, representative of
the response of sediment to deep water waves in the different
areas of the nearshore environment, is shown in Figure 4. Note
that the power of sediment movement in cm^2 has been multiplied
by 10. The power of the waves is in ft^2. Even with this tenfold
increase in the power of the sediment movement, it seldom attains
that of the deep water waves. In each set, the coherency between
the waves and sediment is extremely low (0-0.2) in the middle and
higher frequencies. It improves somewhat (0.2-0.4) for the lower
frequencies, shown here, for the 375 gm/l concentration in the
breaker zone and outside the breaker zone, and for all the con-
centrations in the transition and swash zones.

Outside the breaker zone only the heaviest concentrations,
moving near the bottom, are somewhat influenced by the swell
waves, whereas the lighter concentrations are caught up in the
turbulence and have little response to the longer period sea or
swell. Inside the breaker zone the sediment have a periodicity
of movement that equals that of the swell and also the local sea.
The lighter concentrations lag somewhat behind the predominant
swell period and are less effected by the sea. Yet their main
period of movement is much longer than either the sea or swell.
So that in one area within the breaker zone, not every wave
causes sand motion. This is perhaps, not valid for the entire
breaker zone. The position of the plunge point is not constant,
especially over a 20 minute time span and some of the breakers
may have dissipated their energy before reaching the station
or after passing it.

In the surf zone sediment movement is either non existant,
spread out over many intermediate frequencies, each of which
has relatively low amplitude, or moves only infrequently, less
than once every 30 seconds. It appears, therefore, that sediment
movement, in this zone, is virtually independent of the deep
water wave periods. Dependency has to be sought in reflection,
or other sources of energy such as edge waves, or the inter-
action between successive bores. Also the backwash may still be
effective in this zone. There is a progressive increase sea-
wards in the period of the bed load movement. This lengthening
of the period seems to die out in the outer surf zone.
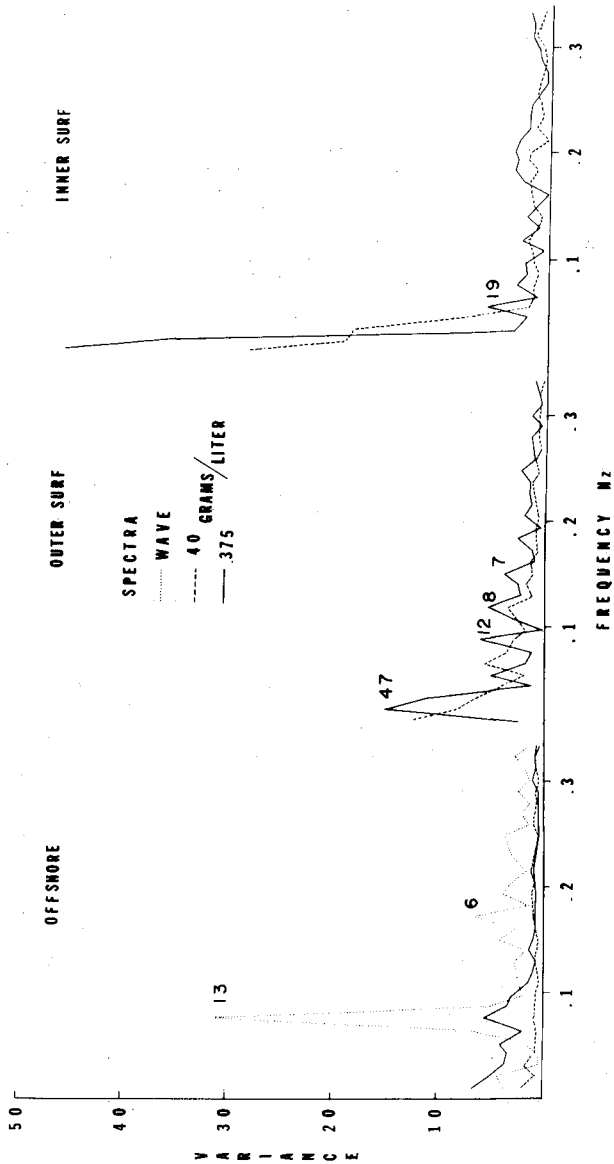
Figure 4 Wave and 40 and 375 gram per liter spectra power for the offshore and outer and inner surf zones. The sand spectra has been multiplied by a factor of ten. High tide. Wave height 90 cm approaching land at a 20° angle. Wave spectrum courtesy of the U.S. Army Corps of Engineers, Coastal Engineering Research Center.
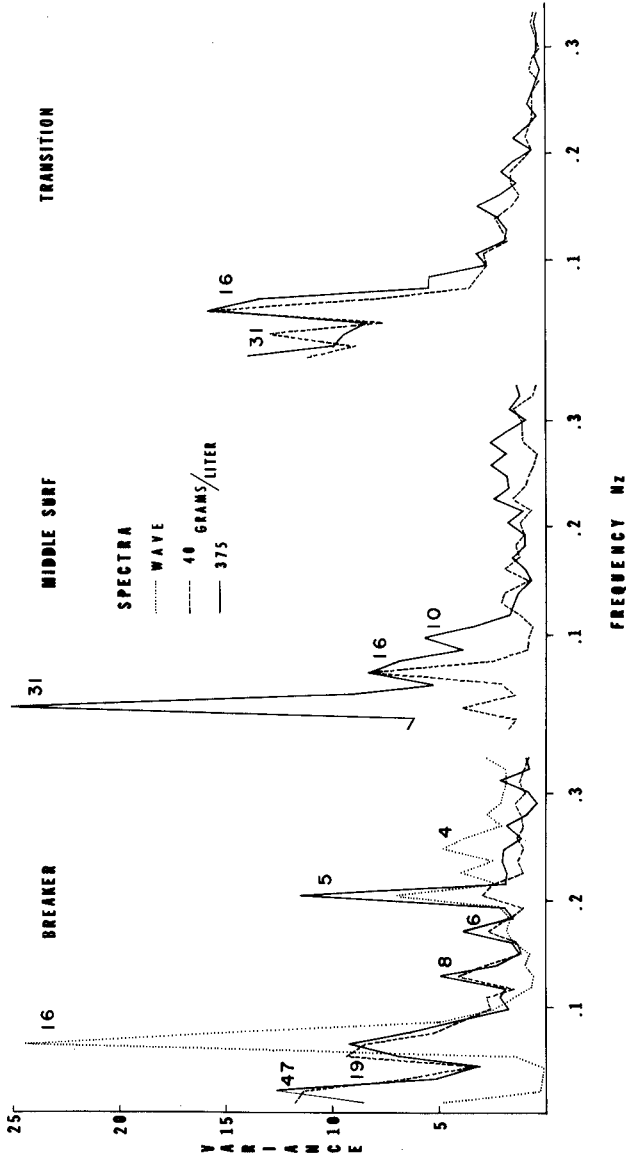
Figure 4B Wave and 40 and 375 gram per liter spectra for the breaker, middle surf and transition zones. The sand spectra power has been multiplied by a factor of ten. Flood tide. Wave height 75 cm, approaching land at a 20° angle. Wave spectrum courtesy of the U.S. Army Corps of Engineers, Coastal Engineering Research Center.
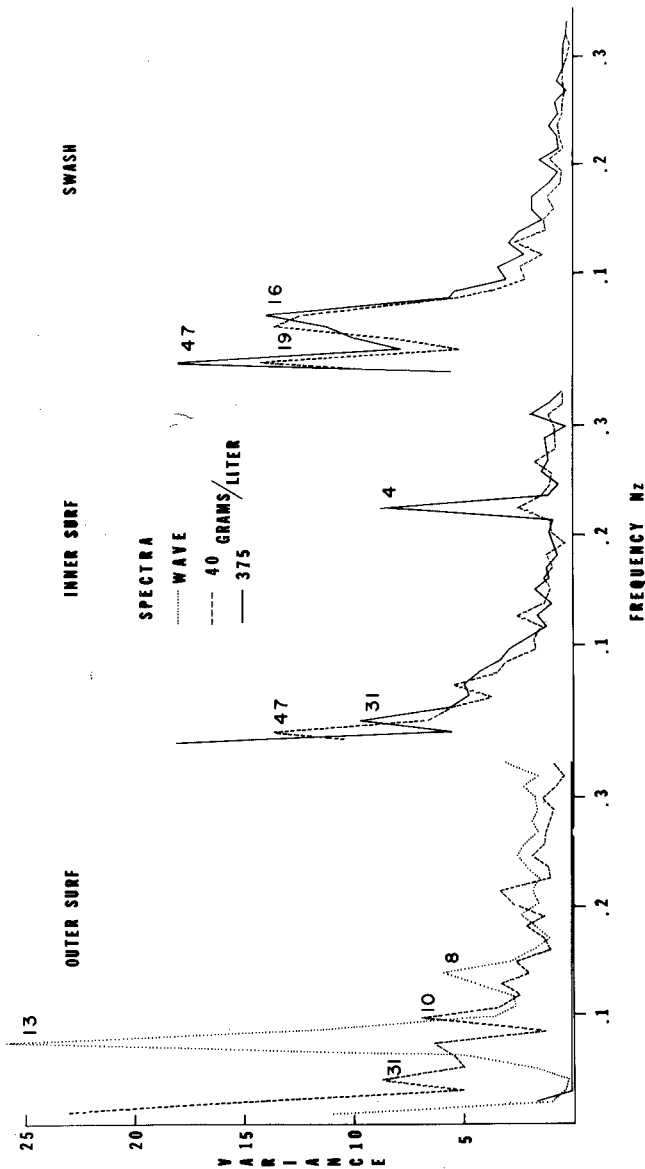
Figure 4C Wave and 40 and 375 gram per liter spectra for the outer and inner surf and swash zones. The sand spectra power has been multiplied by a factor of ten. Beginning of flood tide. Wave height 75 cm approaching land at 5°. Wave spectrum courtesy of U.S. Army of Engineers, Coastal Engineering Research Center.

In the transition and swash zones, the main swell period re-
appears in both concentrations with a lag of up to 3 seconds.
This undoubtedly, represents the retardation of the incoming
bore and coincident with that, the backwash period. The presence
of the local waves is barely detectible since these have diss-
ipated their relatively low energy prior to reaching the station
in interference with the backwash from the swell.

SEDIMENT DENSITY DISTRIBUTIONS

The density distribution of the sediment in the water column
of the surf zone also varies with the dynamic zone. Suspension
of sediment occurs in clouds of short duration. Suspension of
sediment is defined, herein, as any sediment concentration reach-
ing an elevation greater than 15 cm above the bottom. This limit
is the demarcation line between frequent and occasional occurences.
In the 9 tidal cycles studies, 1213 times did the 150 gm/1 con-
centration reach this elevation. Only once did sand of 500 gm/1
density reach 1 m above the bottom. The lighter concentrations
usually mimic each other in space and time rather closely. The
heavier concentrations follow a much more subdued path and show
reversals in elevation not experienced by the lighter concen-
trations,(Figure 5). Nor, in every instance, are the heavy con-
centrations effected when the lighter concentrations are raised
above the bottom. Over 87% of these sand fountains (Zenkovich,
 1967) occur when the still water level is within 30 cm above
or below the bottom elevation at the station, ie. in the trans-
ition zone. More than twice as many of the fountains occur on
the flood tide at the beachface station as compared to the ebb.
Part of an explanation may be that the upper beachface is above
the ground water level on the flood tide, whereas on the ebb tide
it is below the ground water table (Emery and Foster, 1948, Fausak,
1970). Below the ground water table there is a surface tension
combined with a probable decrease in the sand roughness coeff-
icient making it more difficult for the sand to be suspended.

The sand uplifts range in duration from only half a second to
53 seconds, averaging 10.2 seconds. Their duration is dependent
on water velocity. In the breaker zone, the sand fountains last
an average of 5 seconds before they are carried out of the measure-
ment field of the almometer. In the transition zone, when that is
located on the lower beachface where it is relatively flat (1:50),
the sand fountains remain for 15 seconds; on the upper beachface,
where it is steeper (1:25), their duration is 11 seconds. On the
ebb tide the fountains last somewhat longer than on the flood
tide.

The water level is insignificant in effecting the heights
attained by the suspension clouds. They average 24 cm in height
even if the still water level is over a meter and a half above
the bottom.
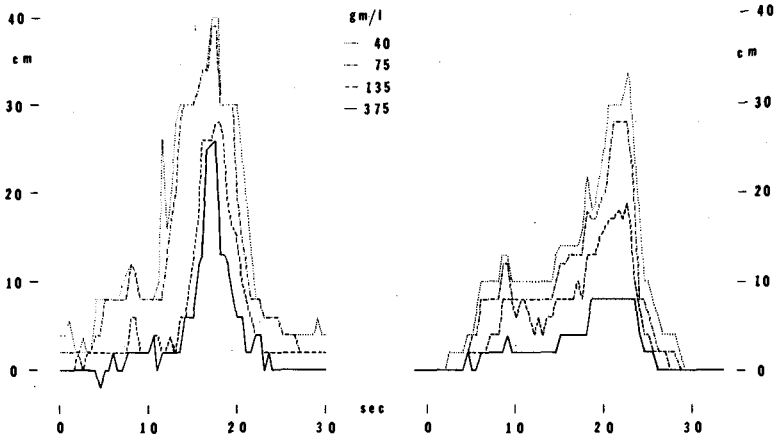
Figure 5 Fluctuations in elevation of various concentrations of sand within suspension clouds at the still water level
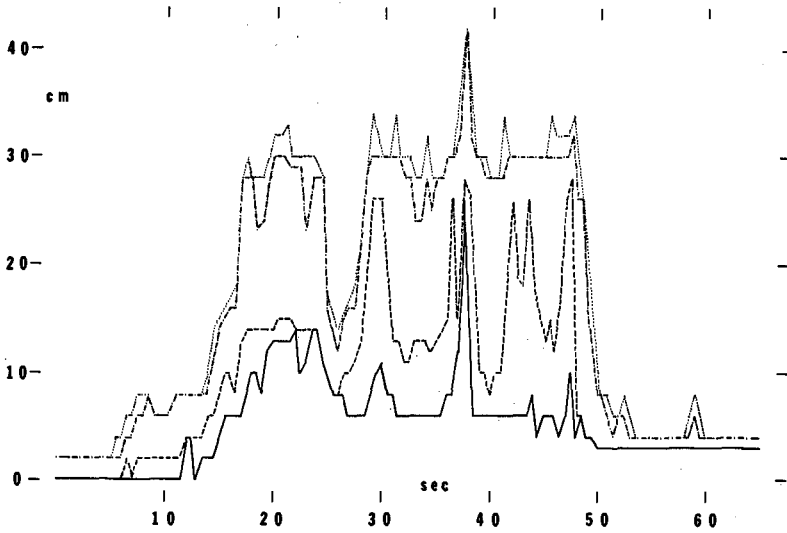
The average time between the sand fountains on the flood tide
at the upper beachface is 1.7 minutes when the still water level
is 0-30 cm below the station and 2.6 minutes when it is 0-30 cm
above it. During the same tidal stages on the ebb tide,the average
is 3.3 and 5.0 minutes respectively. Plotting the actual times
between occurences (Figure 6) show that only two small peaks stand
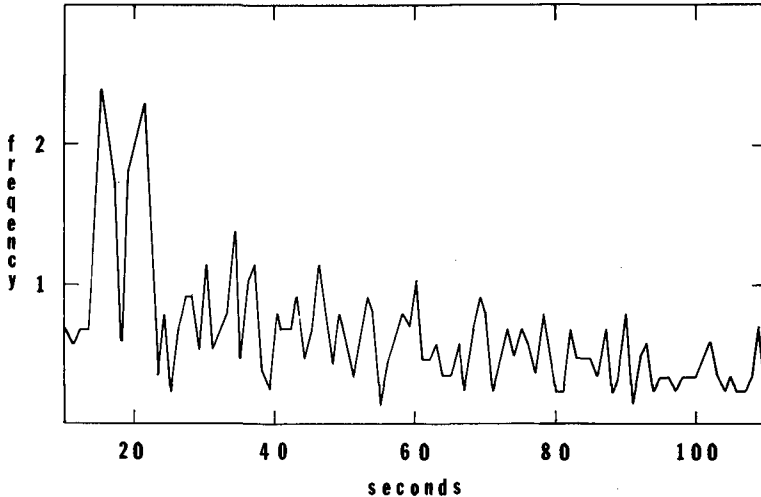
Figure 6   Frequency of occurence of sand fountains on the upper
beachface.

out amidst all the scatter. The 15 second peak represent a 2 second
retardation of the average swell period during the test, the
second peak should be the corresponding backwash period.

There are various causes for the suspension of the sand in this
zone. Measurements of the water velocities inside the surf zone
(Longinov, 1961) show that the maximum vertical components occur
right after the horizontal maximum or when the horizontal compo-
nent is zero;when the water is changing from shoreward movement
to seaward. Suspension in the latter case can occur when the
backwash has a velocity greater than $(gh)1/2$ so that the incoming
bore cannot progress against it, resulting in a hydraulic jump
or roll wave. At an average backwash velocity of 180 cm/sec
(Dolan, Ferm and McArthur, 1969) the water depth at which the
Froude number becomes critical is just under 30 cm. In the breaking
of this roll wave there is a brief suspension of much sediment.

Then the water movement eally stops and most of the suspendeds
fall back to the bottom. The deposits of these suspendeds may
well form the steep sided symmetrical ripples so common in the
transition zone on steep beaches (Clifton and others, 1971).
These ripples, on their own, may cause more suspension by creating
a barrier to the backwash flow and again setting up a hydraulic
jump.

Also, at the inner breaker line, the wave front is saturated
with air bubbles which penetrate the bottom. The ascent of these
bubbles have a suctional effect sufficient to draw up sand
(Aibulatov, 1966).

Only four percent of the suspension clouds occur in the breaker
zone. The sand surface changes often, with differences in elevation
of the bottom of more than 6 cm per wave not uncommon. But great
quantities of sand are rarely thrown into suspension. This dearth
of sand fountains near the primary breaker suggests that the water
and the air entrapped in the breaker does not reach the bottom but
is absorbed in the water layers above it.

CONCLUSIONS

Measurements of changes in elevation of different sand concen-
trations within the surf zone have shown that diverse responses
to the incoming waves are operative in each of the dynamic zones.
Most of the sediment movement within each of these zones occurs
with a periodicity two to three times longer than that of the
incoming waves. Just outside the breaker zone, when sediment does
move, the bed load is transported in pulses coincident with the
prevailing swell period. A much shorter periodicity prevails
in the lighter concentrations. Inside the breaker zone, sand moves
with frequencies equal to both the swell and sea periods. The sand
surface changes rapidly with differences in elevation of more
than six centimeters per wave not uncommon. Here sand is rarely
thrown into suspension. After the transformation of the wave into
a bore in the outer surf zone, sediment movement is absent or
small and therefore almost independent of the deep water wave
periods. In the inner surf zone, suspended sediment transport
increases in frequency, elevation and duration. In the transition
zone sand movement by suspension becomes predominant. Upheavals
of the sand are common and show a variety of different shapes
in response to secondary breakers penetrating the bottom or hy-
draulic jumps. The frequency of movement reflects the predominant
swell and backwash period with a lag of up to three seconds.

REFERENCES

Aibulatov, N.A., 1966, Investigations of longshore migration
      of sand in the sea: Moscow Nauka Publ., 159p. (In Russian)
Brenninkmeyer, B.M., 1973, Synoptic surf zone sedimentation
      patterns: Unpl. dissertation, Univ. of Southern California,
      274 p.
-----,in press, In situ measurement of rapidly changing high
      sediment concentrations: Marine Geology.
Clifton, H.E., Hunter, R.E., and Phillips, R.L., 1971, Depositional
      structures and processes in the non-barred high-energy near-
      shore: Jour. Sed. Petrology, v.41, p. 651-670.
Das, M.M., 1972, Suspended sediment and longshore transport data
      review: Thirteenth Conf. on Coastal Engineering, p. 1027-1048.
Dolan, R., Ferm, J.C. and McArthur, D., 1969, Measurements of
      beach process variables, Outer Banks, North Carolina:
      Louisiana State Univ., Coastal Studies Inst., Tech. Rept.,
      64, 79p.
Emery, K.O. and Foster, J.F., 1948, Water table in marine beaches:
      Jour. Marine Research, v.3, p.644-654.
-----,and Gale, J.F.,Swash and swash marks: Am. Geophys. Trans.,
      v. 32, p.31-36.
Fausak, L.E., 1970, The beach water table as a response variable
      of the beach-ocean-atmosphere system: Unpl. thesis Virginia
      Inst. Marine Science, 52p.
Homma, M., Horikawa, K. and Kajima, R., 1965, A study of suspended
      sediment due to wave action: Coastal Engineering in Japan,
      v.3, p.101-122.
Huntley,D.A. and Bowen, A.J., 1974, Field measurements of nearshore
      velocities: fourteenth conf. on Coastal Engineering.
Jakuschoff, P., 1932, Schwebestoffbewegung in Flussen in Theorie
      und Praxis: Inst. fur Wasserbau der Technischen Hochschule
      Berlin, Mitteil., 10, 24p.
Longinov, V.V., 1961, The determination of maximum wave velocities
      in the shore zone of the sea: Akad. Nauk SSSR Inst. Okeanol.
      Trudy, v48, p.287-308 (in Russian)
-----,1968, Determination by a photoelectric method of sand suspen-
      sion concentration in the littoral zone during waves:
      Gosudarstvennyi proektno-konstruktorskii i Naucho-issledovatel'
      skii Institut Morskogo Transporta (Leningrad) v.20/26, p.
      89-92 (in Russian).
Schiffman, A., 1965, Energy measurements of the swash-surf system:
      Limnology and Oceanography, v.10, p.255-260.
Shelford, V.E. and Gail, F.W., 1922, A study of light penetration
      into sea water made with the Kunz photoelectric cell with
      particular reference to the distribution of plants: Puget
      Sound Biol. Station Pub. v.3, p.141-176.
U.S. Interagency Committee on Water Resources, 1963, Measurements
      and analysis of sediment loads in streams:Rept 14, 151p.
Zenkovich, V.P., 1967, Processes of coastal development: New York,
      Interscience, 738p.

CHAPTER 48

Sand Transport and Coastal Stability, Lancashire, U.K.

by

Dr. William Reginald Parker

Senior Scientific Officer, Institute of Oceanographic Sciences

Taunton U.K.

Abstract

The stability of an alluvial coast depends upon the local sediment budget. Along the shore, changes from erosion to accretion may reflect changing sediment fluxes, sediment residence times and patterns of sediment movement. Processes influencing these parameters, such as mud sedimentation or migration of intertidal channels will, through their influence on beach gradients and sediment transport patterns, affect the processes and rates of coastal dune erosion and the safety of the dune protected hinterland.

A qualitative description of some of the various processes and phenomena linking foreshore and dune stability with sediment circulation and coastal evolution is presented.

Introduction

Formby Point lies on the eastern side of the Irish Sea, 17 km north of Liverpool, between the estuaries of the Mersey and Ribble, Fig. 1. To the south west is the complex of sandbanks and channels of Liverpool Bay. The floor of the eastern Irish sea slopes gently west from the long sandy foreshore and sand dune systems leading north to the Ribble estuary.

The area has a high tidal range (Mean Spring Range 8.2m) and is subject to large meteorological surge contributions to high waters (Lennon 1963 [a,b]). Maximum local wave conditions occur with strong winds from the south west, west or north west (Darbyshire 1958, Murthy and Cooke 1962). Waves are fully developed except from the

828
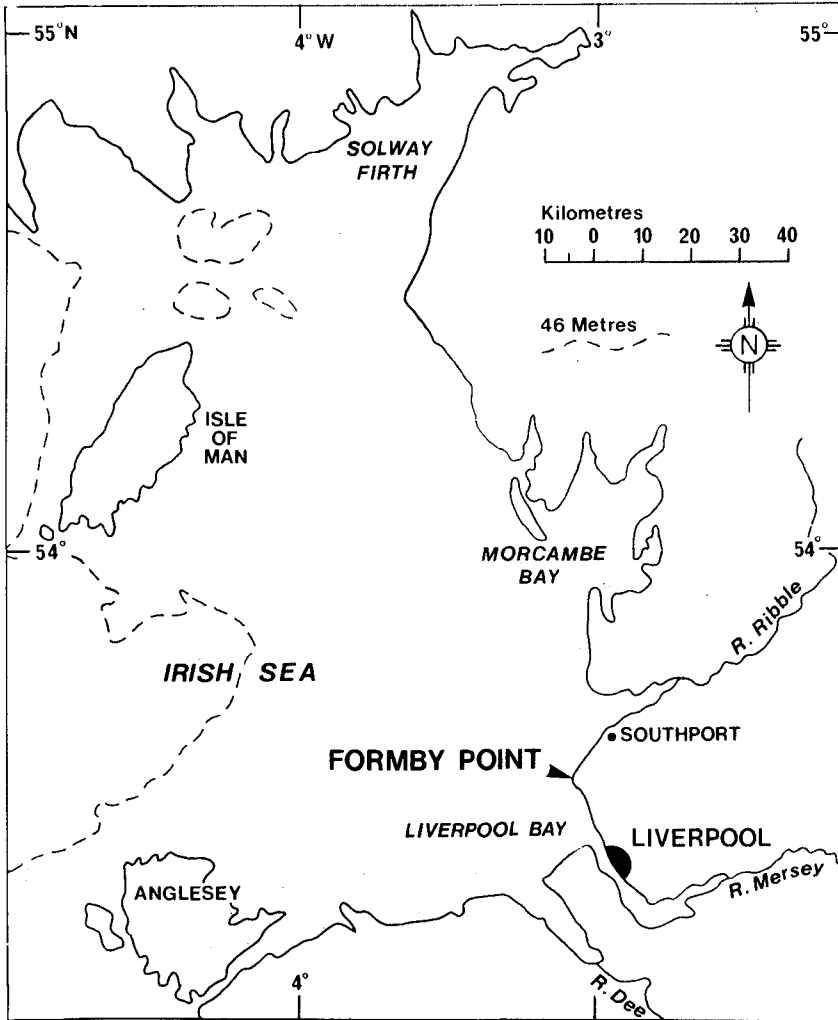
Fig. 1 LOCATION OF FORMBY POINT

Fig 2

CHANGES IN AREA ABOVE BAY DATUM 1833 1912

1833

AREA ABOVE L.B.D.

1912

(from M.0.h.3 charts)
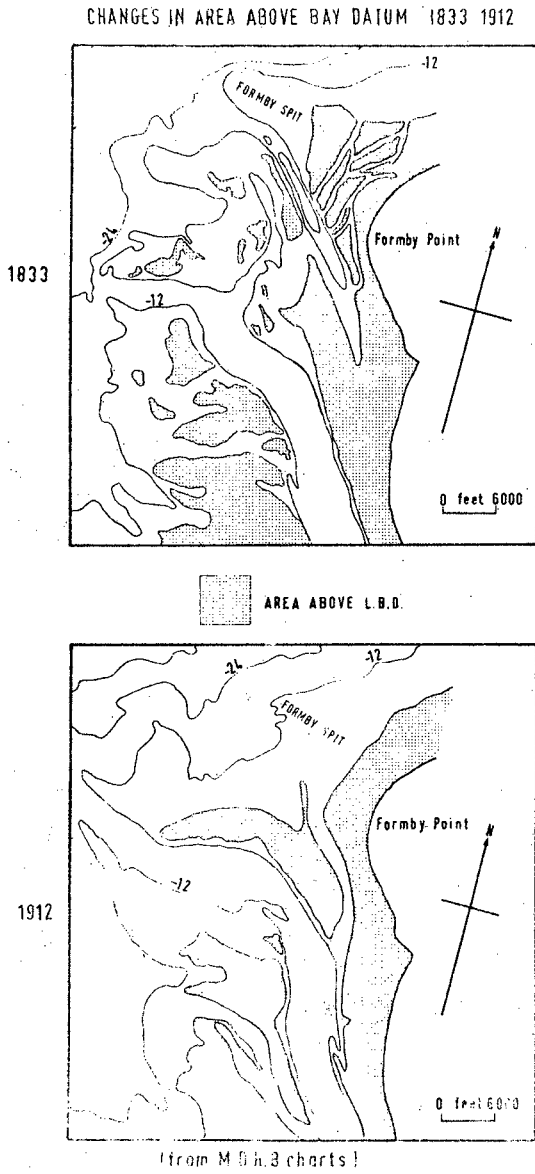
southerly or easterly quadrants and show little seasonal variation in
either period or spectral characteristics although waves are generally
higher in the autumn and winter months. The most common wave conditions
are those with a significant wave height of between 0.5 and 1.0 m and
a zero-crossing period of between 4.0 and 4.5 seconds (6.1% of the time)
(Draper and Blakey 1969).

The local estuary waters have a mean salinity of 32.00% (Bowden
1955, 1960) but inshore, large tidal variations in salinity may occur
in some channels with freshwater input. Outside the main channel of
the estuary flows are only weakly stratified especially in the near-
shore areas. Studies of residual regional water movements (Bowden 1960,
Best 1973, Halliwell 1973, Sharaf El Din 1970) show that near bed
residual water flow is, over a wide area, south or south east into
Liverpool Bay.

The floor of the eastern Irish Sea is covered with fine or medium
sand with varying amounts of mud and some areas of gravel (Wright et.
al. 1971, Cronan 1969). The regional pattern of residual sand move-
ment is virtually unknown. Evidence from sandwaves and hydrological
measurements (Belderson and Stride 1969, Sly 1966) suggest sediment
transport towards the south east.

Coastal Evolution and Morphology

The nearshore regions of south west Lancashire have been subject
to considerably bathymetric changes during the recent past (Fig. 2).
The sand dune system on this coastline (Fig. 3) have a history of
cyclical development related to periods of coast erosion and accretion
(Blanchard 1953, Greswell 1953, Parker 1971, 1975). The most recent
dune sequence has grown north westwards and the angle of 16° between
it and the present eroding coast indicates the extent of reorientation
of the coast as does the exposure and erosion of Holocene sediments
underlying the foreshire.

Plate 1

From 450' south just north of Dale Slack Gutter (Fig. 4)
Note beach ridges, wet (white) patches on upper foreshore
in middle centre of plate. Photograph by John Mills Ltd.,
Liverpool.

Plate 2

Beach in eroding sector of coast. North west mark (Fig. 4)
and Victoria Road (caravan site) in left middle ground.
Holocene sediments in runnels near left.. Photograph by
John Mills Ltd., Liverpool

Fig 3

COASTAL MORPHOLOGY
AND AREAS OF EROSION
AND ACCRETION

N

Kilometres
0   1   2   3

ACCRETING

LWM HWM HWS

ERODING COAST

ACCRETING

PROTECTED

Dunes complex

pre 1920

post 1920

Dune and Beach
ridge crests
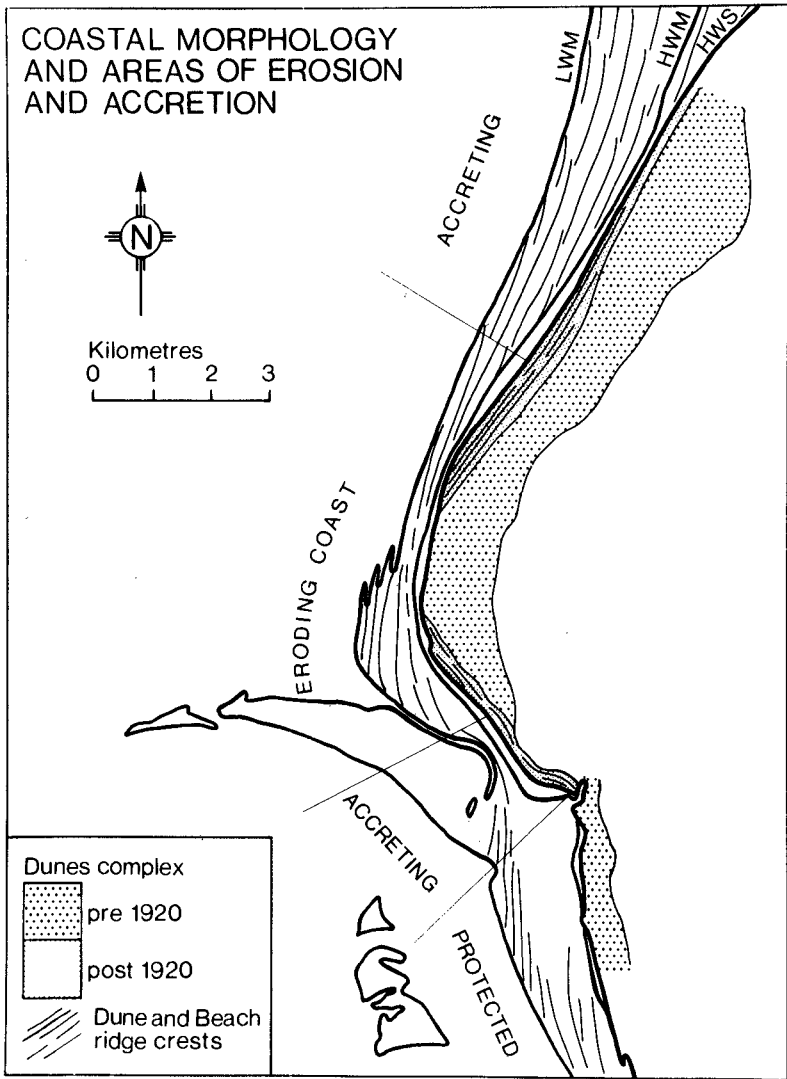
Fig 4
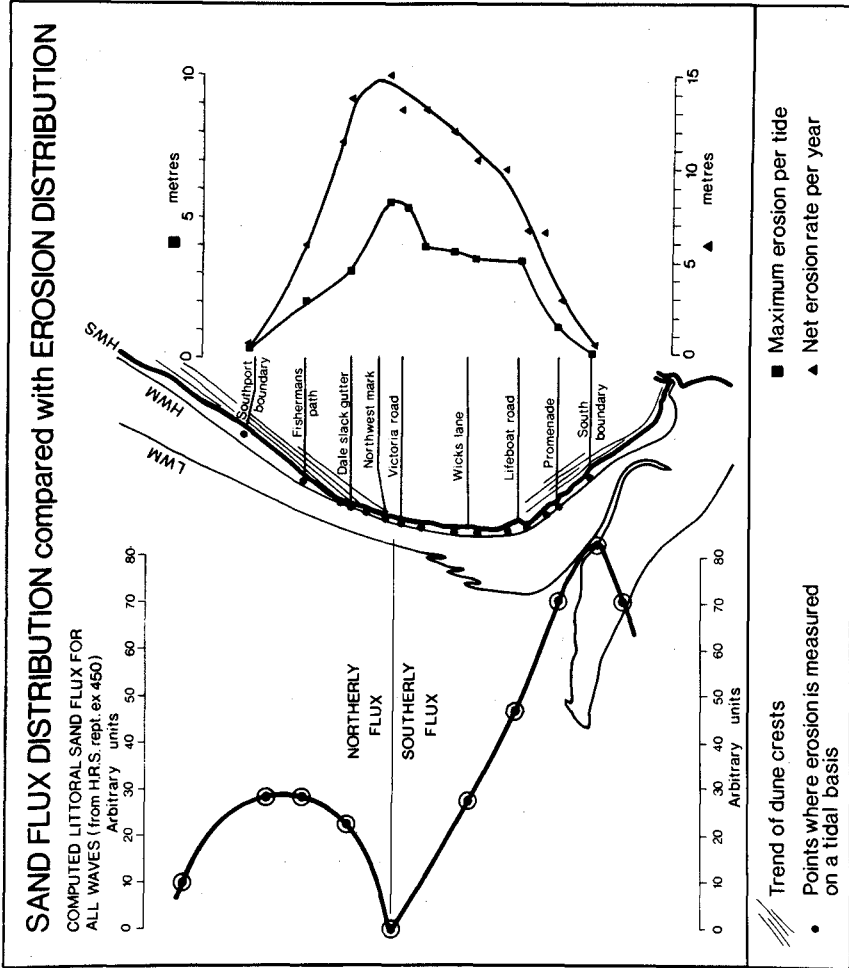
Data on Sand Flux from Hydraulics Research Station, Wallingford.
Report No. EX.450. Crown Copyright. Published by permission
Controller, H.M.S.O. Courtesy Hydraulics Research Station.
Wallingford, England.

Along this coastline a range of conditions of stability exist (Fig. 3). In the north of the area rapid accretion of the coast allows intertidal and high water mark sand extraction to the extent of over 200,000 tons per year. This typical ridge and runnel foreshore shows long continuous runnels with regularly spaced rip channels. Southwards from this area of accretion a change takes place through a retreating, though uncliffed coast, to a retreating sand cliff coastline.

The transition, illustrated in Plate 1, looking south towards the eroding coast, is accompanied by a reorientation of HWM, the exposure on the foreshore of the underlying Holocene sediments, and erosion of the sub-beach Holocene surface (Plate 2). On the eroding sector of coast the beach ridges are less continuous with more closely spaced rip channels (Plate 2).

On the eroding sector of the coast long and short term erosion varies from north to south (Fig. 4). Comparisons between these measured rates and distributions of erosion and theoretical calculations of sand flux (HRS 1969) show interesting correlation. The agreement between the erosion predicted from the sand flux distribution and the distribution of erosion 'on site' is good.

Studies of the processes of cliff erosion (Parker 1971, 1975) and their comparison with model work of Edelman (1968, 1973) and Meulen and Gourlay (1968), indicate that meteorological surge contributions to high water of spring tides are primarily responsible for producing tide levels sufficient for a wide range of rates of erosion (Parker 1971, 1975). A still water level of +9.6m above local chart datum (Liverpool Bay Datum) has been identified beyond which rates of erosion rise dramatically (Fig. 5). The accelerated rates of erosion may lead to serious local threats of flooding (Plates 3 and 4).

Southwards the rate of erosion decreases and inshore of a wider intertidal area the change to accretion takes place (Plate 5).

Fig 5

Tide level is S.W.L.
above L.B.D. in metres

S.W.L.... Still water level
L.B.D....Liverpool Bay
datum

undercutting ——►|+ soaking

Tide height in metres

CLIFF EROSION PER TIDE PLOTTED
AGAINST TIDE HEIGHT
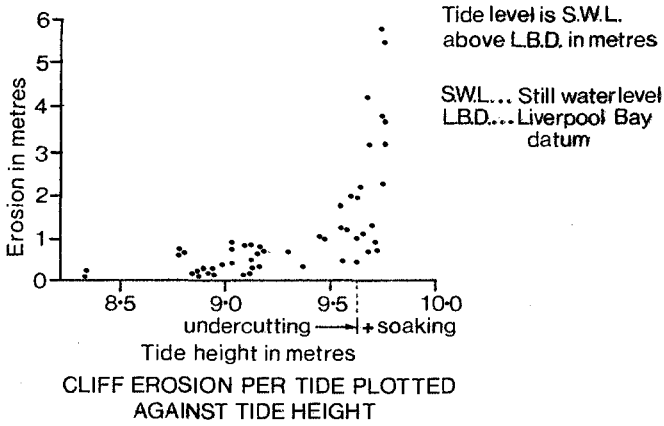
TABLE 1

Sequence of sand transport on a Ridge

L.W.   Currents draining runnel move sand along shore.

          (Sand swept landward by swash over ridge crest into
          (runnel filling with water
          (
Flood   (Breaker zone over ridge crest.. Sand moved landwards
Tide   (into runnel which is site of long shore current.
          (Development of dune bedforms in runnel.
          (
          (Breaker zone decays. Long shore currents decline.
          (Low sand movement.

High   Low currents, little sediment movement
Water

          (Breaker zone develops over ridge. Long shore currents
          (generated. Sand moved along runnel. Sand swept
          (landward over ridge into longshore current.
          (
Ebb   (Sand swept landward by swash into runnel draining
Tide   (alongshore. Breaker zone develops over next ridge
          (to seaward. Ridge exposed.
          (
          (Runnel drains. Currents move sand alongshore.

L.W.

Plate 3

Wave Erosion exploits deflated hollow in frontal dunes protecting
nature reserve at Dale Slack Gutter (Fig. 4).

Plate 4

Waves breach deflated remnants of frontal dune protecting
large blow-out at Lifeboat Road (Fig.4).

Sediment Transport Patterns and Stability

The aim of this study was to examine the modes and patterns of sand movement on the foreshore as an aid to establishing the mechanisms of balance along this sector of coastline and to guide consideration of remedial action.

If, for a sandy alluvial coastline, a dynamic balance between onshore sand transport and littoral drift is a valid model of the mechanism of coastal stability, then the erosion of the sand dune cliffs is but a sympton of the budgetary relationship of the foreshore and adjacent offshore areas. The model must also include an evaluation of the sand supply across the foreshore to the dunes. That the dunes are being eroded indicates that there is a deficit in supply across the foreshore.

The mechanisms and sequence of sand transport on beaches have been widely studied. Field observations on this multibarred foreshore (reported in Parker 1971 and 1975) suggest that:

1.   Most of the sediment moves as 'bed load', as dunes and ripples;

2.   Transport is concentrated into zones. The runnels, and the plane area of the upper foreshore between the most landward runnel and the cliff, are zones dominated by longshore transport. This is particularly true of the runnels. The beach ridges are zones where transport vectors are normal to the shoreline.

3.   Beaches of the timing of sand movement on the beach ridges the landward vectors of sand movement are short.

On both the flood and ebb tides the times of most intensive sand transport on the ridges is associated with those times when longshore currents (Bruun 1962, 1963, Chiu and Bruun 1964) are most active. The sand swept landward over the ridge crests into the runnel is thence moved alongshore by the runnel currents. The sequence of events is outlined in Table 1.

It is apparent therefore that the runnels and their associated longshore and rip current systems play an important role in the sand circulation pattern of this foreshore. The sand circulation pattern

Fig 6

FORESHORE SEDIMENT TRANSPORT
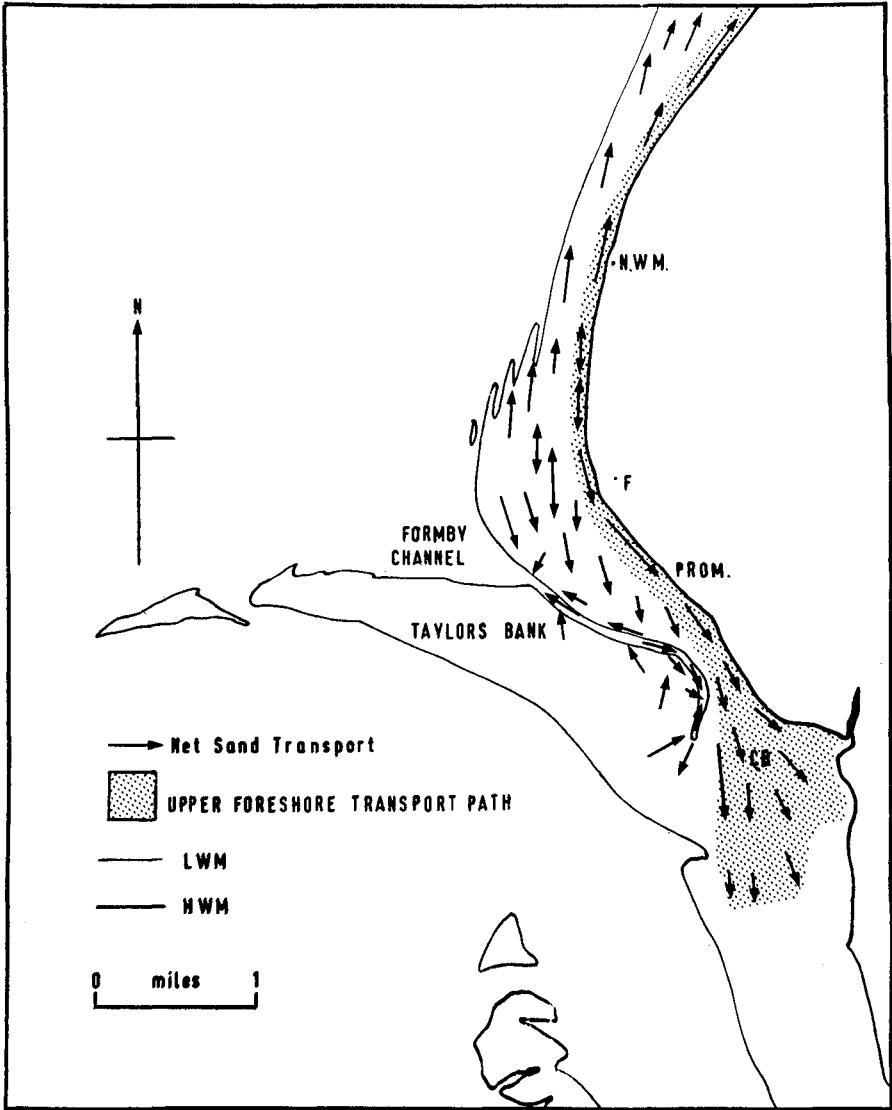
shown in Fig. 6 is based on field observations of water flow and
observation of bed form patterns (Parker 1975).

It is suggested that the exchange of sediment between the runnel
system and the dunes is low. This is supported by the correspondence
between erosion and sand flux computed for high water conditions only.
The computations relate to transport in the upper foreshore transport
path only and that they reflect field conditions suggests that they
describe the principal component of the mechanism.

Because of the orientation of the coast and beach ridges both
north and south of the centre of Formby Point, the sand in the runnels
moves offshore. Thus within much of the intertidal zone of this
multibarred foreshore the topography controlled sand transport pattern
moves sand away from high water mark.

Aeolean sand transport is ineffective despite the dominance of
onshore westerly winds (Reynolds 1956). The runnels, remaining wet at
low water, and the wet areas of the upper foreshore, produced by the
water table perched on the underlying Holocene sediments, are effective
barriers to the aeolean nourishment of the dunes trapping what little
sand is blown onshore. Heavy pedestrian usage of the dunes and an
absence of any management policy ensures the destruction of vegetation
and severe deflation of the dunes.

The waters of Liverpool Bay are on the whole turbid (Halliwell and
O'Connor 1966). Intertidal mud sedimentation is widespread on this
foreshore (Parker 1973, 1975) but the survival of the deposited mud is
restricted to those areas protected topographically from ebb breakers,
e.g. runnels (Parker 1975). The mud layers which develop in the runnels
act as a brake on the sediment mobility. The erosion and transfer of
the mud into an intertidal channel during low water appears to be
significant in the mechanisms of coastal evolution, affecting the

Fig 7

POSITION OF FORMBY CHANNEL
IN 1956 & 1964 RELATED TO
SAND TRANSPORT PATTERN

Formby Channel in: Dunes: Kilometre

1956   pre 1920   0   ½   1

1964   post 1920   1_1 Profile lines

Runnel sand transport   • Hydrological stations

Upper foreshore, longshore
transport zone
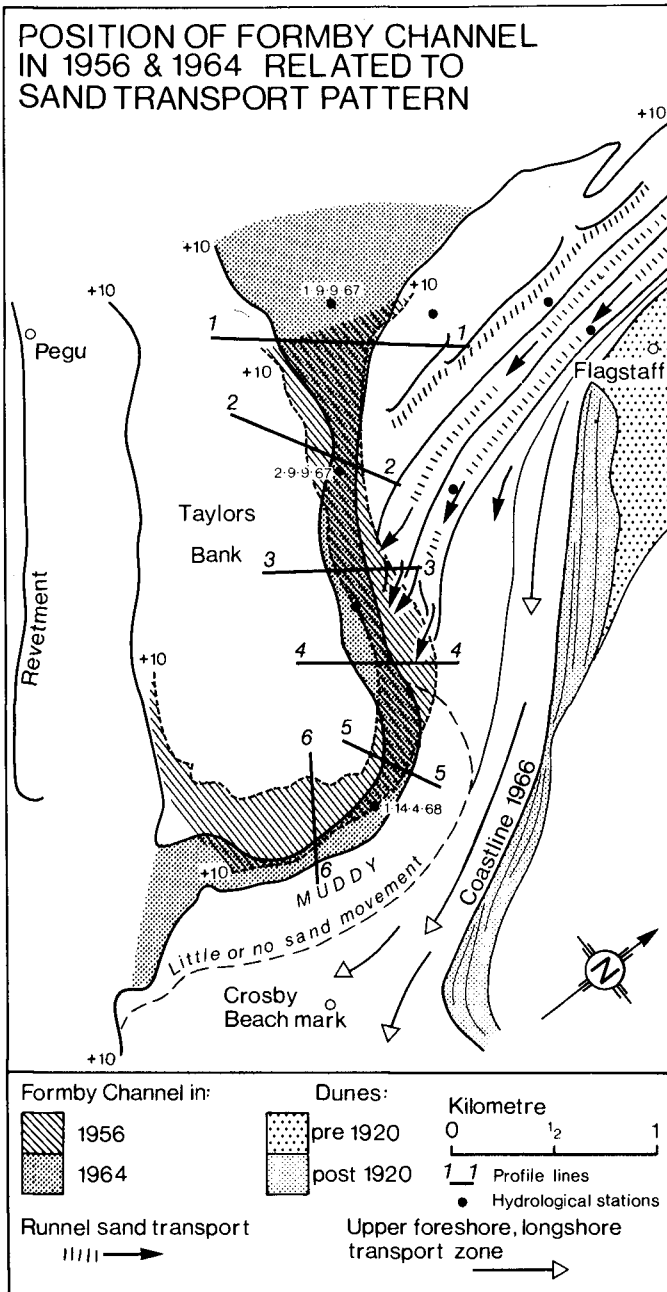
stability of the southerly section of presently accreting coast. Thus

within the central section of this stretch of coast all the natural

processes appear to act in concert to achieve a high rate of coastal

recession.

In the south of the area, the operation of the natural processes

in this direction is somewhat more subtle. The change from erosion to

accretion in the south of the area (Figs. 3 and 4) takes place inshore

of a wide intertidal area bounded to the south by an intertidal channel

(Plate 5), Formby Channel. This channel has a history of instability,

becomming narrow, shallow, more sinuous and migrating inshore. Previous

reports on this area e.g. Price and Kendrick 1963, have suggested the

possible importance of this channel as a sand feed route. The shoreward

migration of the channel is threatening the stability of the southern

sector of coast because the inshore bank of the channel, topped by the

frontal dunes (Plate 5) is sliding into the channel.

However, the more far-reaching effects on local coastal stability

stem from the interaction of the southerly sand flux (Fig. 4) and the

sedimentation processes within the channel. The southerly component

of the local littoral sand flux (Fig. 6) may be considered in two parts;

that occurring in the intertidal runnels and that occurring on the plane

area between the most landward runnel and the cliffs (the'Upper

Foreshore' route).

The juxtaposition of these fluxes and Formby Channel is shown in

Fig. 7.

The runnels discharge sand, during the ebb tide and over low water,

into Formby Channel. The affected sector of channel bank has prograded

rapidly. Reference to Figs. 7 and 8 reveals that the sector of the

channel where the banks are prograding rapidly (Sector 2-4) is not

where the channel is filling. The rapid filling of the channel is on

either side (Sectors 1-2 and 4-6).

Plate 5

From 450 feet oblique view south over Formby Channel showing
beach ridges (nearground) approaching the Channel and frontal dunes
protecting housing and farmland (left). Compare with channel
sectors on Fig. 7.

Fig 8

Longitudinal profiles of Formby Channel : Levels of channel thalweg at profile lines and mud content
along thalweg
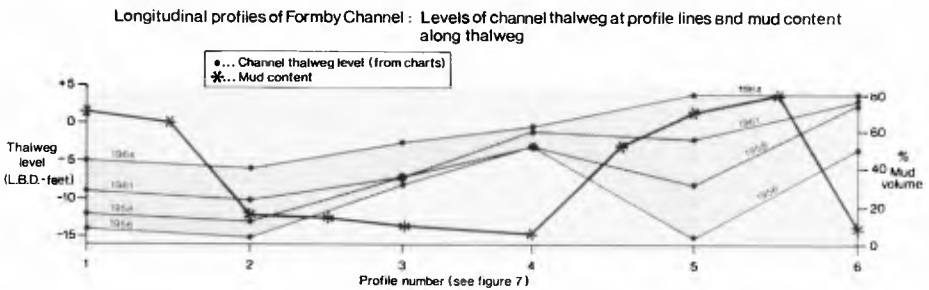
Sedimentation within the Channel

In view of the apparent importance of this channel in past studies, and because no previous examination of conditions within the channel had been made, two lines of investigation were followed.

A series of hydrological experiments were carried out to examine the flow patterns within the channel, calculate water and solids discharge and residual transport, try to measure peak boundary stress values and sediment movement, whence, using information on the distribution of mud and sand in the channel sediments, some approach could be made to rationalising the more recent channel history. A number of interesting relationships emerge.

The rate of thalweg accretion is most rapid in the areas of high mud content in the sediment (Fig. 8).

Residual water flow suggests ebb dominance between sections 1 and 4 but no distinct drift around section 5 (Fig. 9). Examination of temporal variation of U_* (as a measure of boundary shear stress) suggests a separation of sediment movement, ebbwise in Sections 1-3 floodwise at Section 5. Combination of these hydrological data with visual observations of the processes operating during the ebbtide and over low water leads to a closer understanding of the mechanisms operating within the channel, particularly the influence of mud sedimention.

Sedimentation Sequence within the Channel

During low water sand and soft mud, eroded from the floors of the runnels, is discharged into the channel between sections 2 and 4 by the runnel currents (see Fig. 7). Currents draining from the channel carry the sediment to feed the muddy area at the northwest (outer) end of the channel between sections 1 and 3.

During the flood tide some mud and sand is swept into the channel from the northwest, but much of the mud deposited between sections 2 and

Fig 9

COMPUTED MEAN VELOCITIES AND C.R.W.D. FOR STATIONS

1.9.9. 67   2.9.9.67.   1.14.4.68.
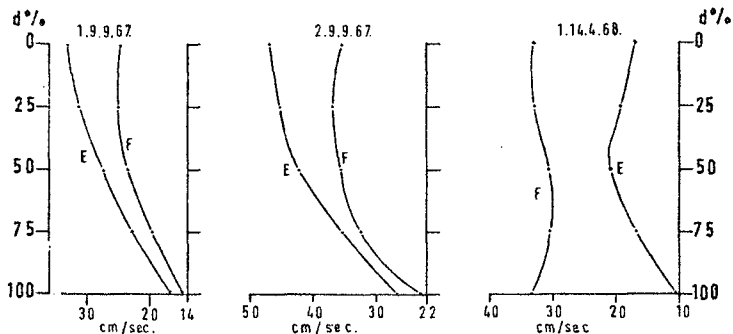
Computed Mean Flood(F) and Ebb(E) Velocity Profiles
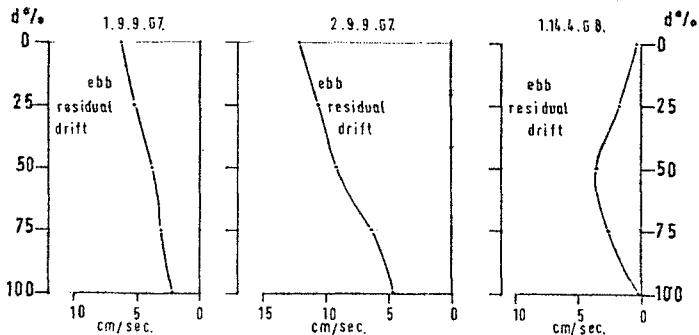
C.R.W.D. - Computed Residual Water Drift, computed by Liverpool
University, Department of Civil Eningeering Hydrological Research
Group programme.   Courtesy A. R. Halliwell and B.A. O'Connor.
d% = depth as % of total flow depth

Fig 10

SUMMARY OF DATA FOR STATION 1·14·4·68
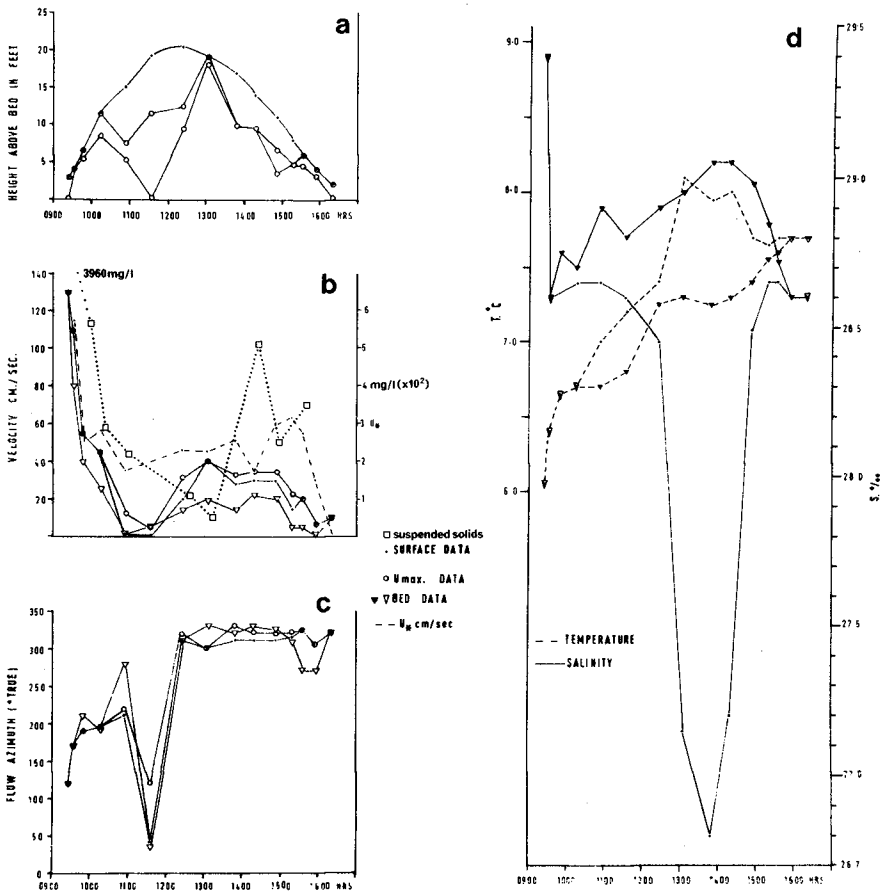
Surface data refers to data on water surface elevation (a), velocity (b), direction of flow (c) and temperature and salinity (d).

Umax data refers to elevation of the velocity maximum in the flow profiles (a).

Suspended solids refers to mean concentration in profiles (b).

4 at slack of low water is re-eroded and swept into the inner part of
the channel, sections 4 to 6. The long stand of high water in this
section of the channel (Fig. 10) allows mud to settle over the inter-
tidal area between the channel and the frontal dunes (Fig. 7) as well
as in the floor of the channel and the slow drainage on the ebb,
coupled with protection from breakers, ensures its survival to be
exposed and dessicate over low water. The ebb accelerates out of the
channel, scouring the mud and sand from the central section of the
channel (profile 3 and 4) sweeping this sand and mud northwest towards
sections 1 and 2. During this time, as the intertidal area drains, more
sand and mud is fed from the foreshore via the runnels into the channel
which continues to drain northwest over low water.

     These studies indicate a number of effects operating within and
aound the channel:

   a) The divergence of residual sediment transport from the"central"
       feeder from the foreshore.

   b) The supply of sediment to the channel and the location of the
       areas of rapid filling, influenced by the hydrological control
       on mud sedimentation, lead to the changes in shape and
       migration of the channel.

   c) The hydrological conditions in the inshore bend of the channel
       is allowing mud to spread over the foreshore thus influencing
       the mobility of the sand there and its availability for
       contributing to the local longshore and onshore flux.

   d) The migration of the channel and its associated sedimentation
       pattern is restricting the width of the upper foreshore
       longshore transport route (Fig. 7) and this is resulting in the
       starvation of a bank to the south which protects an area of
       large housing development.

Conclusion

This research was an attempt to relate qualitatively the structure of interaction of some of the various sedimentary processes operating in an area of variable coastal stability. In the complex situation which exists in the real sea it is the essential first step towards identifying those components which might appropriately be quantified.

It is apparent that sediment transport on the foreshore is one part of an interacting system whereby, in this particular case, the processes in one area affect coastal stability in another area through their interaction with an inbetween component, the tidal channel. The individual mechanisms are relatively simple but their grouping into interacting groups produces the complexity of the natural sedimentary situation which provide the practising engineer with his decisive problems.

References

Belderson, R.H. and Stride, A.H. 1969. Tidal Currents and Sand Wave Profiles in the North-Eastern Irish Sea. Nature 222 pp 74-75.

Best, R., Ainsworth G., Wood, P.C, and James, J.G. 1973. Effects of Sewage sludge on the Marine Environment: a case study of

Liverpool Bay. Proc.Instn. Civ.Engrs. 55 (2) pp 43-66
paper 7605. Discussion 55 (2) pp 755-765.

Blanchard, B.A. 1953. The Ecology of the Sand Dune Systems of
South West Lancashire. Ph.D. Thesis, Liverpool
University.

Bowden, K.F. 195 5. Physical Oceanography of the Irish Sea, Min.of
Agric. Fish and Food Fishery Investigation. Series II.
Vol. 18 No. 8 H.M.S.O.London.

Bowden, K.F. 1960. Circulation and Mixing in the Mersey Estuary.
I.A.S.H. Comm. of Surface Waters, Publ. 51 pp 352-360.

Bruun, P. 1962. Longshore Currents in One and Multi-Bar Profiles
Relation to Littoral Drift. Proc. 8th Conference
Coastal Engineering. Council on Wave Research, Ch.15
pp 211-247.

Bruun, P. 1963 Longshore Currents and Longshore Troughs. Journal
Geoph. Res. 68 (4) pp 1065-1078.

Chiu, Tsao-Yi and Bruun, P. 1964. Computation of Longshore Currents
by Breaking Waves. Engineering Progress at University
Florida. 18 (3) Tech. Paper 279, March 1964.

Cronan, D.S. 1969. Recent Sedimentation in the Central North Eastern
Irish Sea. Report No. 69/8. Institute of Geological
Sciences, H.M.S.O. London.

Darbyshire, M..1958. Waves in the Irish Sea. The Dock and Harbour
Authority, December 1958 pp 245-248.

Draper, L. and Blakey, A. 1969. Waves at the Mersey Bar Light Vessel.
N.I.O. (now I.O.S. Wormley). Internal Report A.37 pp1-4,
Figs. 11.

Edelman, T. 1968. Dune Erosion during Storm Conditions. Proc.
11th Conference on Coastal Engineering pp 719-722.

Edelman, T. 1973. Dune Erosion during Storm Conditions. Proc.
12th Conference on Coastal Engineering pp 1305-1312.

Greswell, R..K. 1953. Sandy Shores in South Lancashire. Liverpool
University Press.   181 p..

Halliwell, A.R. 1973. Residual Drift near the Sea Bed in Liverpool Bay.
an Observational Study. Geophys. J.R. astro Soc. 32.
439-458.

Halliwell, A.R. and O'Connor,B.A..1966. Suspended Sediment in a
          Tidal Estuary (Mersey). Proc. 10th Conference on Coastal
          Engineering. pp 687-706.

Lennon, G.W.. 1963[a]. The Identification of Weather Condition associated
          with the Generation of Major Storm Surges along the West
          Coast of the British Isles. Q.J.R.Met.Soc. 89 (381).

Lennon, G.W. 1963[b]. A Frequency Investigation of Abnormally High Tide
          Levels at certain West Coast Parts. Proc. Inst. Civil
          Engrs. 25. pp 451-484.

Meulen, T. van der, and Gourlay, M.R. 1968. Beach and Dune Erosion
          Tests. Proc. 11th Conference Coastal Engineering.
          pp 701.707.

Murthy, T.K.S. and Cook, J., 1962. Maximum Wave Heights in Liverpool
          Bay. Vickers Armstrong Department of Design. Report No.
          V3031/Hydro./04.

Parker, W.R., 1971. Aspects of the Marine Environment at Formby Point
          Lancashire. Ph.D.Thesis, Liverpool University, 2 vols.
          Unpublished.

Parker, W.R. 1973. Folding in Intertidal Sediments on theWest
          Lancashire Coast, England. Sedimentology 20. pp 615-623.

Parker, W.R. 1975. Sediment Mobility and Erosion on a Multi-barred
          Foreshore in 'Nearshore Sediment Dynamics and Sedimentation'
          J.R.Hails and A.P.Carr (Editors). John Wiley & Sons.
          In Press.

Price, W.A., and Kendrick, M.P. 1963. Field and Model Investigations
          into the Reasons for Siltation in the Mersey Estuary. Proc.
          Instn. Civil Engrs. 24. pp 473-518.

Reynolds, G. 1956. A Wind Analysis for the Northern Irish Sea. Q.J.
          R.Met, Soc. 82 (354) pp 469-480.

Sharaf.El Din, S.H. 1970. Some Oceanographic Studies on the West
          Coast of England. Deap Sea Res. 17 pp 647-654.

Sly, P.G. 1966. Marine Geological Studies in Liverpool Bay and
          Adjacent Areas. Ph.D.Thesis, Liverpool University.
          Unpublished.

Wright, J..E., Hull, J.H., McQuillin, R. and Arnold, S.E. 1971. Irish
          Sea Investigations 1969-70. Institute of Geological
          Sciences Report 71/19. 55p. H.M.S.O. 1971.

CHAPTER 49

DIFFERENTIAL MOVEMENT OF COARSE SEDIMENT PARTICLES

by

Alan Paul Carr[1]

ABSTRACT

This paper mainly describes experiments that have been carried out on two
shingle beaches on the south coast of England.

The results for the higher energy environment of Chesil Beach showed that
largest tracer material travelled farthest, and best correlations tended to
be with the short axis.   At Slapton, however, different sediment parameters
appeared significant at various times.   Where linear parameters were
relevant correlations were again best with the short axis, but smaller material
travelled farthest.   This may reflect different wave regime, a less efficient
sediment rejection mechanism, finer grades of sediment or better adjustment of
tracer to indigenous background material at Slapton.

There was a marked degree of selectivity at both sites between material recovered
along a particular zone of the beach as compared with the overall recovery on
the same day, and between the overall recovery for a particular day as compared
with the originally injected tracer.   Attempts have been made to correlate
wave data from f.m.pressure recorders with longshore transport of the coarse
grades of sediment in the inter-tidal zone.   While at Chesil wave direction,
frequency and height were all important there were no obvious relationships
at Slapton.   The results have relevance in respect of beach stability and
in the conclusions drawn from tracer studies using coarse grades of sediment.

INTRODUCTION

The differential transport and sorting of varying sediment sizes has been widely
observed in aeolian, fluvial and marine environments.   The phenomenon has
economic importance particularly in the realms of natural and induced stability
of the sea bed and the foreshore.   For example, artificial beach replenishment
is accepted as being more effective if particular grades of sediment are chosen
in relation to specific beach conditions (e.g. Krumhein and James, 1965).

As Wood (1970) has observed: 'The extensive literature on the engineering
properties of a natural beach is principally concerned with fine to medium sand
foreshores.   In consequence, a number of generalisations have been made
concerning the properties of a beach that do not apply .... to a shingle
or even a coarse sand beach'.   It is with such grades of sediment that this
paper is concerned.

To some extent investigations using these coarse particles are simplified
by the diminishing importance of tidal currents relative to waves, and
suspension and saltation relative to bedload.   The actual samples are also
more readily physically measurable.   However, considerable problems remain.
For example, there are the differing effects of waves offshore, in the breaker
zone, and onshore where permeability adds yet a further complication to wave
height, period, and steepness.   Similarly, for the sediment, there are
questions of relevance of shape, roundness and specific gravity;   the manner
of the vertical distribution of tracer through the disturbed part of the
beach, and the further complication of the inter-relationship of different
ranges of sizes of particles within samples having the same mean.

[1]Principal Scientific Officer, Institute of Oceanographic Sciences, Taunton,England.

Even in the apparently simpler situation of uni-directional flow
Kellerhals and Bray (1971) have written: 'Describing the (gravel) bed material
------- in quantitative terms is a difficult task which presently involves
a series of largely subjective decisions about sampling locations, time of
sampling, and sampling procedure. Different investigators can therefore
arrive at widely different results ----'.

Castenho (1970) has demonstrated a similar diversity of opinion relating to
differential longshore transport within the sand fraction.

There is also argument as to the importance of biological processes, such as
kelp-rafting (e.g. Emery and Tschudy, 1941), within the coarse sediment grades.

On a more detailed scale there are problems of terminology, in particular
that of the use of the words 'shingle' and 'gravel' and some of the disagreements
in the literature may stem from this cause. Emery (1955) preferred 'gravel
beach' ------- 'to avoid the term "shingle" which' (he thought connoted)
'imbrication and flat shape'. Wood (1970) wrote: 'By definition, a shingle
beach is one in which the mean particle size D_{50} is larger than 10 mm.
The mean size is most often in the range 10 - 40 mm'. Carr (1971) used
'shingle' to refer to material at least partly rounded and sorted by marine
processes, and falling within the range 4 mm to 256 mm long diameter or
equivalent. It thus included the pebble and cobble categories of the
Wentworth Scale. It is in this sense that the term is used here.

This paper describes work carried out by two component bodies within the UK
government's Natural Environment Research Council, initially by the (then)
Nature Conservancy and latterly by the Institute of Oceanographic Sciences.
The study is primarily concerned with the results obtained from two contrasting
English shingle beaches, Chesil and Slapton, although reference is also made
to a third beach at Budleigh Salterton (Fig 1). The data from Chesil Beach
tend to emphasise the relationship between gross wave characteristics and
sediment sorting; those from Slapton demonstrate the apparent variability
of sediment parameters.

FIELD EXPERIMENTAL STUDIES

(a) Chesil Beach, Dorset

Chesil Beach is one of the three major shingle structures on the coast of
Great Britain, and the only one primarily of barrier form, being backed by
the shallow Fleet lagoon for much of its length. The beach extends more
than 18 km from Chesilton in the east, where it terminates against the cliffs
of the so-called Isle of Portland, to an essentially arbitrary limit in the
west. Opposite the Fleet, Chesil Beach is between 150 and 200 m wide, but
is narrower at both ends. For much of its distance there is a picture of a
progressively increasing crest height, the maximum of +14.7 m O.D. (Ordnance
Datum, which is approx. mean sea level) being found near Chesilton. Pebble
size above low water mark also increases in the same direction (Fig 2).
During the studies described mean pebble size for long diameter (a) in the
experimental area fell between 6.4×10^{-3} and 6.3×10^{-2} m. Taking the whole
beach nearly 98.5% of the pebbles and cobbles are of flint and chert (Carr
and Blackley, 1969) and 1.2 per cent of quartzite. Both types have a specific
gravity of about 2.6.

Offshore, the beach drops at a gradient broadly similar to that of the seaward
face above low water mark - 1 in 10 overall but exceeding 1 in 3 - for a
horizontal distance of approximately 70 m (Neate, 1967). Thereafter, it
shelves gently to about -18 m O.D. some 270 m offshore opposite Wyke Regis.
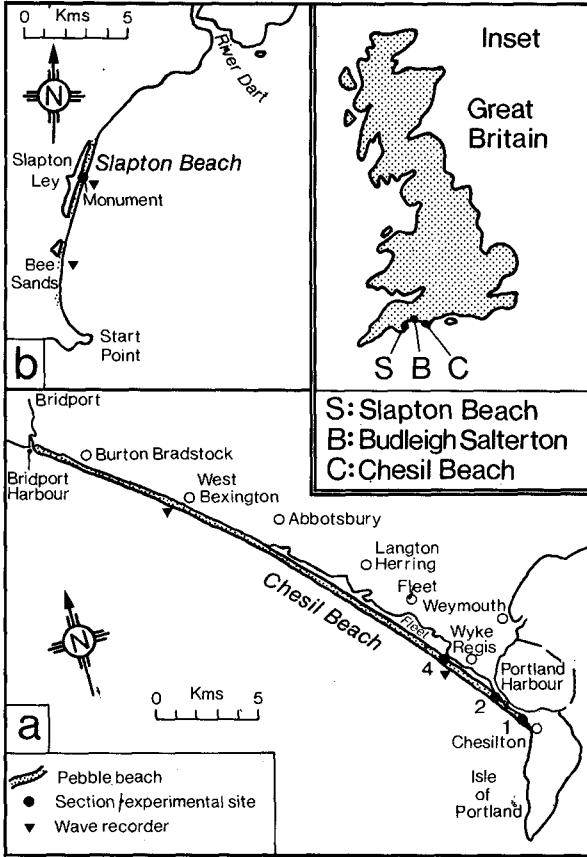
Only minor coast protection works exist, none of which are within the experimental area.

The tidal range varies from about 1.3 m at neaps to 3.5 m at springs. Tidal velocities do not exceed 1.0 ms^{-1}. Wave data were obtained from two f.m. pressure units located offshore and linked to analogue recorders on land. The wave recorder at Wyke was 100 m and that at West Bexington 250 m offshore

(Fig 1). Hardcastle and King (1972) showed that for both sites the most frequent wave period (T_z) is between 10.0 and 10.5 seconds while 50% of the significant waves (H_s) (Tucker, 1963) exceed 0.26 m at Wyke and 0.23 m at West Bexington.

Earlier studies (Carr, 1969) had examined the grading of indigenous pebbles above low water mark (Fig 2). They had also shown that, when comparing the spherical and oblong flints and cherts with the discoid quartzites for any given position on the beach, the only identical dimension, ratio or shape index was the short axis $(\underline{c})$. Thus a linear regression line drawn between the short axis of the two geological types had a slope of $45°$ (Carr, Gleason and King, 1970).

Three experiments at Chesil are summarised in this paper. Two, using introduced geological tracers, previously subject to marine processes elsewhere, are reported more fully in Carr (1971). The other study, based on the local material, is described by Gleason and Hardcastle (1973).

For both geological tracer experiments wave heights were slightly above average, but did not exceed 1.2 m. In the first of these experiments wave periods were somewhat longer and for the second somewhat shorter, than normal. During the February 1971 indigenous pebble study wave heights were representative of the yearly pattern although wave periods were rather longer, the mode falling at 13.0 seconds.

The first tracer experiment, begun in October 1969, used quartz granulites taken from the beach at Rosemarkie, Scotland. This material, like the indigenous sediment, has a specific gravity of about 2.6. Long diameter $(\underline{a})$ ranged from approximately that of the local material at the site (2.5 x 10^{-2} m) to a maximum of 1.1 x 10^{-1} m. Some 17,200 pebbles and cobbles were placed at mid-tide level on the surface of the beach at Wyke (Fig 1) since the purpose of the experiment was primarily to relate transport of the introduced tracer to the wave parameters, rather than to sum the overall movement of that part of the beach subject to wave action.

The results showed:

i) That tracer of a comparable size to the background material was incorporated within it. Somewhat larger material tended to remain on the surface possibly by 'rejection' (Moss, 1962, 1963) upwards or inability to he drawn downwards. This effect was most pronounced under periods of long, low swell where turbulence was at a minimum and where percentage recoveries were higher. Gross discrepancies in size were accommodated by very large material being combed down below low water mark, there to remain.

ii) There was a clear relationship between greater longshore transport and increasing size of particle (Table 1 and Fig 3a). Taking the whole recovered sample for any day, best correlations were marginally given with the short axis, $(\underline{c})$. While in the short term this relationship appeared linear, over the longer term it took a logarithmic form similar to the exponential grading of the local material, and the long axis $(\underline{a})$ became best correlated. On one occasion (24 November 1969) given consistent wave approach from an easterly direction and low wave height $(< 0.3$ m$)$ (so that only the top few layers of pebbles were moved), the grading of the surface tracer was reversed with the coarsest recovered tracer particles towards the northwest. Table 1 shows that this sorting mechanism is even more evident where recoveries at high, mid, and low water mark are analysed separately. All the tables in this paper utilise standard statistical procedures and assume (correctly) an essentially normally distributed
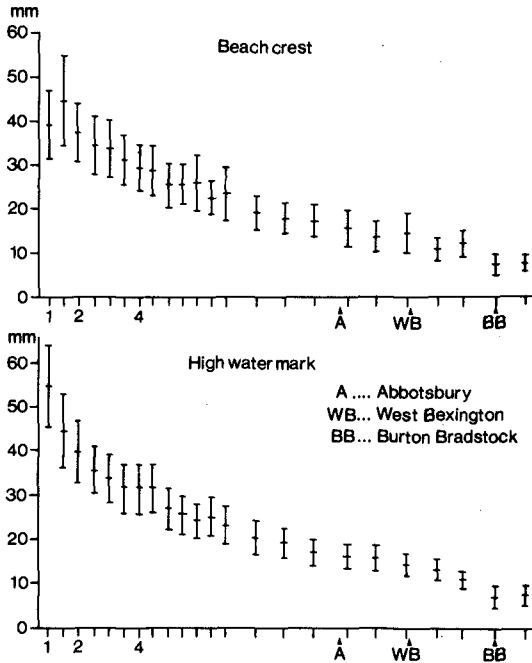
population for both tracer (at the time of introduction) and indigenous
material.

iii) Rates of movement at Wyke reached 343 m after the first day but after
165 days, often with much more severe conditions, the farthest recorded
material was only 3952 m southeast of its origin. This reflects the
proportion of time that material is out of circulation by being ahove or below
the zone of wave action; hy burial; and by intermittent transport opposite
to the prevailing direction. Data show that lateral movement of individual
pebbles is not necessarily greater under storm conditions even with the
same angle of wind-wave or swell approach because of the effect of depth
of mixing.

Only one aspect of the second tracer study, in late 1970, will be discussed
here.

The experiment used 12,350 quartzitic conglomerates with a specific gravity
of about 2.7 and 5,350 basalts with a S.G. of 2.83 - 2.90. As before,
the particles had been rounded by beach processes elsewhere. The basalts,
and approximately half the conglomerates, were injected at the Wyke site.
The proportions recovered of the former geological type to the latter
varied from 15 to over 50%. This is what would be expected if the heavier
specific gravity pehbles worked their way into the heach (low recovery)
and the beach was combed down afterwards resulting in their re-exposure
(high recovery). Longshore travel was less for the basalts probably hecause
of the compounded effect of greater burial time and smaller movement even
when on the surface because of the relatively greater specific gravity.

Date (Oct.1969)	Duration (tides)	Position	n=	Particle dimensions			Ratios			Indexes			Notes
				a	b	c	b/a	c/b	c/a	$\sqrt[3]{\frac{c^2}{ab}}$	$\sqrt[3]{\frac{bc}{a^2}}$	$\frac{a+b}{2c}$	
24	2	HW	72	●	●	●							
		MW	45	●	●	●							
25	4	HW	70	●	●	●							
28	6	HW	50			●		●	●	●		●	Significant correlations on some ratios & indexes but negligible gradient (i.e. <1% per 100m)
		MW	34	●			●				●		
		LW	27	●									
27	8	HW	144	●	●	●							
		MW	124	●	●	●							
		LW	253	●	●	●							
28	10	HW	70	●	●	●							
		MW	40	●	●	●							
		LW	32	●	●	●							
29	12	HW	30	●	●			●	●	●	●	-●	Significant correlations on some ratios and all indexes but negligible gradient (i.e. <1% per 100m)
		MW	38	●	●								
		LW	28	●		●							
24 Nov.	44	MW	100			-●							For whole sample (n=255) a=.05, b=-, c=.05
		LW	28	-●	-●	-●							

Key
● p=.001
● p=.01
● p=.02
● p=.05
● p=.1

Table 1

Chesil Beach: tracer experiment 1969. Probability levels for correlation coefficients (where p ⩽ 0.1) between pebble axis/index (y) against distance travelled alongshore in metres (x). Coarsest material always travelled furthest. Direction of grading is reversed for 24 November. n = Number of individuals. For all tables; a, b, c = long, intermediate, short axis in mm; HW, MW, LW = high, mid, low water; p = probability level. p ⩽ .001 means that there is 1 possibility in 1000 or less of such a result occurring by chance. As n increases the same significance level may be obtained by a lower correlation coefficient (r) but the level of explanation (r^2) will also be lower.
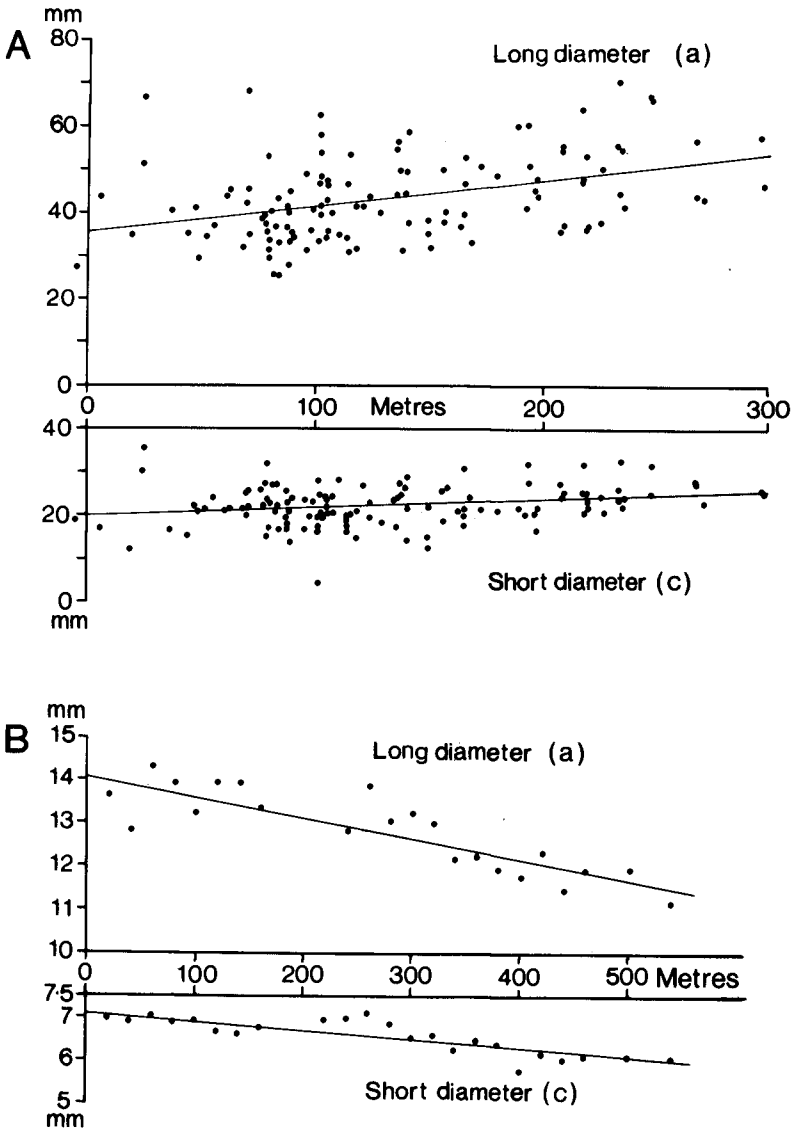
Figure 3
Relation of particle size (y) to distance travelled alongshore (x)
in tracer experiments.
(a) Chesil Beach. Data for 27 October 1969, mid-tide zone.
    n = 124 individuals.
(b) Slapton Beach. Data for 8 October 1973, high tide zone.
    n = 23 group mean samples.

Section No.	Mean dimension	Frequency = 1/Tz	Signif. wave height (Hs)	Hs^½	Sine 2θ (where θ is angle normal to beach)	Wave direction at site (degrees)	Key	
	a						● p = ·001	Table 2
1	b						● p = ·01	
	c				●	●	● p = ·02	
	a	●	●	●			● p = ·05	
2.	b	●	●	●				
	c	●	●	●	●	●		
	a	●	●	●				
4	b	●	●	●	●	●		
	c							

Chesil Beach: daily sampling of indigenous material over a one month period (February 1971). Probability levels for correlation coefficients between pebble axes and wave parameters.   n = 28 (days). (After Gleason and Hardcastle, 1973).

The month-long experiment in February 1971 which employed the local material, was designed to show the change in particle size with varying wave conditions at each of three sampling sites (Fig 1) (Gleason and Hardcastle, 1973). Since the beach is graded alongshore, with the smallest material towards the western end, (Fig 2) it follows that waves from the prevailing direction of fetch (southwest) should cause a decrease in pebble size at the sampling sites. The best correlation would be expected at Wyke where the angle of wave approach would be most oblique to the beach.

Table 2, modified slightly from Gleason and Hardcastle (1973), gives the probability levels for the correlations between linear parameters against wave direction ($\emptyset°$); frequency ($^1/T_z$); significant wave height (H_s); ($H_s^{\frac{1}{2}}$); and Sine 2θ, where θ is the angle of swell approach relative to a

line normal to the beach (Longuet-Higgins, 1970a, b).   It shows, firstly, that as in the case of the earlier studies, the short diameter ($\underline{c}$) gives the best correlations and, secondly, that the modified wave parameters ($\frac{1}{T_z}$ and H_s^2) appear to be the most significantly correlated factors.   Wave frequency ($1/T_z$) was important in vertical sorting of material; wave direction (φ°) and Sine 2θ in longshore transport, H_s^2 in both processes.

b) Slapton Beach, Devon

Start Bay extends from Start Point in the south to the mouth of the River Dart in the north, a distance of some 13 km (Fig 1).   The largest unit within the bay is Slapton barrier beach which is nearly 5 km long and between 100 and 140 m in width at high tide.   Its crest generally falls within the range 6.0 m $\pm$ 0.5 m O.D.   As in the case of Chesil this is affected by waves only rarely.

There is an overall trend throughout the coastline of Start Bay for the natural beach material to become coarser from north to south but this is liable to be obscured both by variations within the four component units and from month to month.   About 85% of beach particle analyses taken in 1971 - 72 fell within the granules (-1 to -2$\emptyset$) and small pebbles (-2 to -4$\emptyset$) categories (where phi ($\emptyset$) = $-\log_2$ diameter in mm), although a considerable number of the samples contained some coarser material generally of a siliceous, quartzitic or schistose nature.   Within the -1 to -4$\emptyset$ range about 85% of the shingle is flint, chert or quartz.   Sediment size falls abruptly away from the coastline.

In the centre of the Bay the exposed beach has an overall slope of 1 in 15 reaching as much as 1 in 7.   The gradient of the beach below low tide level continues at the same order of slope until approximately -7.5 m; thereafter it shelves gently to reach -14.5 m O.D. about 600 m offshore.   Still further offshore the topography is influenced by the coarse sand and shell of the Skerries Bank which extends from near Start Point some 6.5 km towards the northeast.   The minimum depth of the Bank below sea level is -4.7 m O.D., although most of the crest is between -7.5 m and -9.0 m O.D.

Again, as in the case of Chesil, only minor coast protection works exist; none of these affect the Slapton experimental area of the Bay.

The tidal range varies from about 1.8 m at neaps to 4.4 m on springs.   For the Slapton wave recorder site, some 200 m offshore, the most frequent wave period (T_z) is between 6.0 and 6.5 seconds with 50% of the significant waves (H_s) exceeding 0.16 m.   (June 1972 - 73 data).   The Skerries Bank has the effect of causing marked variations in the height, period, and direction of waves reaching the shore at high, as compared with low water.

Following work on the size and geological distribution of the local sediment (Gleason, Blackley and Carr, 1975) and a rather inconclusive experiment along the lines of the work by Gleason and Hardcastle at Chesil, it was decided to carry out short-term tracer experiments on Slapton Beach.   These used shingle from the western end of Chesil Beach which meant that, although the specific gravity remained the same as at Slapton, shape varied somewhat, primarily because of the different proportions of geological types.   This introduced material was coated with a commercially available polyurethane finish which proved resistant enough for the short-term beach studies and which did not appear to affect the hydraulic properties of the sediment.

A short trial in October, 1972, using 800 kg of labelled material, was intended solely for developing the sampling technique.   Two full experiments were undertaken subsequently, one in February and the other in October, 1973. In both experiments surface sampling was carried out along the beach at pre-determined intervals and over a specified areal extent.   Samples were collected

at high-tide and low-tide levels with an additional series at mid-tide
level as the tidal range increased from neaps to springs.   The techniques
are described in greater detail by Gleason, Blackley and Carr (1975) but
rely on group mean values, not, as in the case of Chesil, on individual
pebbles. Sampling took place alongshore for at least two sites beyond the
farthest at which statistically valid data were obtained, to minimise the
possibility of 'pulsed' distributions, of which there had been some suggestion
at Chesil, escaping notice (Carr, 1971).   In the trial and February experiment
the tracer had a mean size of -2.40 $\emptyset$.   Slightly larger pebbles, having a
mean of -2.98 $\emptyset$, were used in the October experiment.   Three tonnes of tracer
were employed for each phase in February; five tonnes in October.   This
represents two batches of approximately 1.5×10^7 and one of 6.0×10^6
pebbles, respectively.   All tracer was deposited on the surface at mid-tide
level.

Wave data were obtained from recorders similar to those used at Chesil
but with data output on magnetic tape.   For the first experiment wave
direction was observed by compass from Torcross headland; for the second
experiment direction was also abstracted from photographs of the display of
a 3.2 cm X-band radar located at the same site.

Wave conditions during the experiments were highly atypical.   Thus in the
relevant period in February 1973 nearly 50% of the wave periods were between
7.5 and 8.5 seconds with a further 40% longer than this (up to 15.5 seconds).
Waves above 0.3 m were almost totally lacking.   In October about 75% of
wave periods were between 5.0 and 6.5 seconds and none exceeded 8.0 seconds.
Waves below 0.3 m were grossly under-represented.

Those occasions where statistically significant longshore grading occurred
are shown in Tables 3 and 4, for February and October, respectively.   For
February the probability levels are given for the calculated linear
correlations between negative mean phi values as derived from frequency and
weight v. net distance travelled, and for linear, log and distance squared
(d^2) correlations between the particle dimensions and net distance travelled.
For October the probability levels are for the calculated linear and log
correlations between particle dimensions, ratios and shape indexes v. net
distance travelled.   In all cases the sediment parameter was y and the distance
travelled x.   The representative shape indexes are those of Sneed and Folk
(1958), Krumbein (1941), and Wentworth (1922) - Cailleux (1945).

Furthest travelled material reached 1138 m north of the injection site
in the five days of the October 1973 experiment but statistically valid
samples were only contained within a distance of -150 m and + 560 m
of the origin.   The comparable distances for the longer February experiment
are -50 m and +230 m.

In all instances maximum longshore transport coincided with smallest
particle size (e.g. Fig 3b) hence there was a predominance of negative
correlations for the linear parameters.   Even where positive correlations
occur, as after the first tide following injection of the second tracer in
February 1973, this only reflects longshore transport of tracer in the
opposite direction because of a reversal in the angle of wave approach relative
to a line normal to the beach.   The differing signs for the ratio and indexes
vis-a-vis linear parameters (for October 1973) is, in part, a response to the
relative significance of a, b and c in the various functions and to a link
between pebble shape and size, for the introduced tracer material.   The
change in sign for ratios and shape indexes in October after 5 and 9 tides,
respectively, may possibly be explained by the limited travel at low water
by tide 5 and the legacy of a different direction of wave approach from the
beginning of the experiment.

Table 3

Key

p = ·001	p = ·001
p = ·01	p = ·01
p = ·02	p = ·02
p = ·05	p = ·05

Notes:
- *origin at +10m
- All original tracer d² calc. from false origin @ +30m from tide 9 onwards
- All / From origin
- All / From origin
- Ø from origin
- Ø from origin
- Ø from origin
- All / Origin ⟶ N / Origin ⟶ S

Date (February 1973)	Duration (tides)	Position	–Ø Frequency (linear)	–Ø Weight (linear)	a Linear	a Log	a d²	b Linear	b Log	b d²	c Linear	c Log	c d²	Notes
13am	1	HW												
13pm	2	HW												
15	5	HW / MW / LW												
16	7	LW												
17	7 + 9	HW / LW												*origin at +10m
18	3 + 11	MW / LW												All; From origin
19	5 + 13	HW / MW / LW												All; From origin; Ø from origin
20	7 + 15	MW / LW												Ø from origin
21	9 + 17	MW / LW												Ø from origin; All; Origin ⟶ N; Origin ⟶ S

Slapton Beach: tracer experiment, February 1973. Probability levels where p ≤ 0.05 for correlations between –Ø (Ø = –log₂ diameter in mm) and linear parameters (y) v. distance travelled alongshore in metres (x). Calculated from injection point (= origin) unless otherwise stated. Upright figures represent first, italics second, phase of experiment. n (no. of group samples) averages 6 but varies between 3 and 8. Note the varying significance of different parameters. Finest material always travelled furthest.

Table 4

Slapton Beach: tracer experiment, October 1973. Probability levels (n ≤ 0.1) for correlations between size/ratio/index (y) v. distance travelled alongshore in metres (x). n = no. of group samples. From injection point (= origin) unless otherwise stated. Note the variability of types of sorting and reversal of trends (e.g. between ratios and shapes at 7 and 9 October LW). Finest material always travelled furthest (see text).

Unlike at Chesil and at Budleigh (see below) gradients of linear regression lines for ratios and indexes are of the order of 1% or more for each 100 m alongshore.   In all three sites linear regression lines for axes exceed this   gradient.

Equally important is the way in which different factors assume importance on varying occasions.   Thus, during the February tracer experiment, there is grading at high water after one tide and at mid-water after five tides, both only on the $\underline{c}$ axis.   At high water, after five tides, significant grading is restricted to the $\emptyset$ scale (which in so far as it reflects anything, should have closest affinities with the intermediate axis, $\underline{b}$).   Phi scale and d^{2} are closely linked.   Similarly, in the October experiment there are occasions where there is clear preference for grading on linear parameters (e.g. at high water after four and seven tides, and high and mid water after nine tides). At other times, notably at low water, selection by shape appears more important.

Overall, correlations are rather better with the $\underline{c}$ axis than other linear dimensions.

There was a marginally significant correlation (at the 0.1 probability level) for wave period (T_z) v. $\underline{c}$ axis for the February experiment.   Apart from this there was no instance of any correlation between wave period, height, direction, spectral width or modified wave parameter (e.g. H_s^{2}) and any sediment parameter for either experiment even although the study of the indigenous material in May 1972 had shown limited correlations on Slapton Beach for wave height ($H_s^{\frac{1}{2}}$) and angle of wave approach ($\emptyset$). (1 occasion at .001, 3 occasions at .01, 1 occasion at .02 for H_s^{2}; 3 occasions at .02 for $\emptyset^{o}$). These results may reflect better adjustment of the local material to wave parameters.

c) Budleigh Salterton, Devon
Budleigh beach is located some 35 km west of Chesil Beach and has a wave regime somewhat intermediate between that of Chesil and Start Bay. However, the principal interest is the way in which the largely discoid quartzites, which form the source of the beach pebbles and cobbles (mean long axis ($\underline{a}$) falls between 1.9×10^{-2} and 1.0×10^{-1} m), are supplied by landslips of the Triassic Pebble Beds in the cliffs behind the centre of the beach.   The material is ill-sorted, but comparatively well-rounded, prior to becoming available to shoreline processes.

Sampling was carried out on four occasions between October 1971 and October 1972, using 16 section lines spaced at either 200 or 300 m intervals.   Initially up to six samples containing 200 individuals were taken on each line to include the cliffs, beach/cliff junction, storm crest, and high, mid, and low water marks. The three linear axes were measured as before and these, plus the ratios and indexes, were correlated against distance alongshore (as linear, log or d^{2} regression equations).   Distances were computed both from the eastern end of the beach and from the centre, which is coincident with the source of supply. There were no significant correlations for any of the sites to the rear of high water mark at the time of sampling.

Table 5 lists those occasions where probability levels $\leqslant 0.05$ for dimensions, ratios, and indexes v. linear and d^{2} relationships for distance alongshore.   The most important points are:
i) when significant grading occurs it is generally along the whole beach length with smallest material at the eastern end.   However, slips have the effect of both interrupting longshore transport and supplying new material so that in June 1972 grading ran in each direction with mean size increasing from the centre of the beach;
ii) it is possible to have size grading from the centre and shape grading from the end co-existing although, while index v. distance correlations are highly significant, the actual range of shapes available is somewhat limited for this beach and lithology.

Table 5

Budleigh Salterton, Devon: grading of indigenous beach pebbles and cobbles. Probability levels for correlation coefficients (where p ≤ 0.05) for dimension/ratio/index (y) v. linear and squared distance alongshore in metres (x). Log equations were also calculated but significance levels were almost invariably lower and are omitted from the Table. All regression equations are from (east) end of beach except June 1972 linear parameters (open circles) which were calculated from centre outwards (see text).

Table column structure (rotated in original):

Date	Position	Particle dimensions — a (Linear, d²), b (Linear, d²), c (Linear, d²)	Ratios — b/a (Linear, d²), c/b (Linear, d²), c/a (Linear, d²)	Shape indexes — $\sqrt[3]{\frac{c^2}{ab}}$ (Linear, d²), $\sqrt[3]{\frac{bc}{a^2}}$ (Linear, d²), $\frac{a+b}{2c}$ (Linear, d²)	Notes
Oct '71	HW				n=15
	MW				n=16
	LW				{ n=15 linear dimensions / n=16 ratios & indexes
Feb '72	HW				n=15 } No mid-tide samples taken
	LW				n=15
June '72	HW				n=16
	MW				{ n=15 linear dimensions / n=13 ratios & indexes
	LW				n=16
Oct '72	HW				n=16
	MW				{ n=16 linear dimensions / n=15 ratios & indexes
					Low water sampling incomplete

Key:
- ● p = ·001
- ● p = ·01
- ● p = ·02
- ● p = ·05
- ○ p = ·001
- ○ p = ·01
- ○ p = ·02
- ○ p = ·05

DISCUSSION

It was concluded from the Chesil results that when the wave energy flux was high enough, and waves approached obliquely to the shore, the largest material located in the inter-tidal zone travelled farthest. This view has been held by a number of earlier workers in the field (e.g. Richardson (1902) for Chesil; Kidson and Carr (1961) for Bridgwater Bay, and Jolliffe (1964) for Sussex, England).   It is not clear, from the Chesil data, however, to what extent the results are influenced by the size of the background sediment ('traction carpet') nor whether the greater movement of larger material is a function of relative or absolute size.

The reduced movement of the higher specific gravity basalts, compared with the other pebble types, suggests that where sources are readily available they might be of significance in beach replenishment schemes although, again, the results may be the effect of the ratio of the quantities of pebbles of different specific gravities rather than the specific gravity as such.   There is also the possibility that denser pebbles might be combed down below the area to be protected in a fashion comparable to the 'oversize' granulites.

The best correlations between different geological types, and to some extent for longshore transport, were with thickness (short axis, c) in spite of the greater potential percentage error in measurement of this parameter.

This reflects the prevalent position of rest for the entire beach pebble population, and that the short axis is the most susceptible parameter to swash-backwash movement.   As such, pebble thickness should be relevant in beach stability.

At Chesil, shape appeared relatively unimportant as had been shown to be the case in laboratory studies with oscillatory flow (Rance and Warren, 1968; Hydraulics Research Station, 1969).   Even when statistically significant correlations occurred in the field the slope of the linear regression line between the shape index and distance travelled was low.

At Slapton sorting appears to be based on different criteria ($\emptyset$ frequency and weight; linear parameters; ratios and shape indexes) from time to time.   Even where there is an intimate mix of the background population, as was the case during the tracer experiments, it is not easy to isolate the relevant factors which are so highly inter-related.   Where linear parameters are relevant, the short axis (c) correlations were again better than for a and b. With greater wave energy, grading only occurred at high water sampling sites and with c. The restriction to high water may be explained by the more consistent wave data then (see below), or by the complicating effect of turbulence and swash-backwash interaction at mid and low-tide levels, particularly with the shorter wave periods characteristic at Slapton.   The short axis dominance would correspond to the higher wave energy environment at Chesil.   It is interesting that where one parameter has been used in previous work it has almost invariably been the weight, through sieving ($\emptyset$), or the long (a) or intermediate (b)axis (e.g. Kellerhals and Bray, 1971).

Shape-sorting such as that at Slapton, has been widely reported elsewhere, e.g. by Cailleux (1948) for the beaches between the River Var and Antibes and Dobkins and Folk (1970)at Tahiti-Nui.   Krumbein (1941) suggested that '--- shape may play its most important role in the selective transportation of the particles'. While it is tempting to argue that shape-sorting may be a response to the generally lower wave energy at Slapton as compared with Chesil there was no valid correlation between shape and wave parameters at Slapton during the 1973 experiments. The overall lack of correlation between sediment parameters and Slapton wave data is almost certainly a result of the east-facing aspect of the site and the increased influence of the Skerries Bank at certain periods in the tidal cycle.   This has the effect of preventing equilibrium between sediment and hydraulic processes being obtained before wave parameters are again modified.

However, the basic difference between Chesil and Slapton is the way in which
smaller material travelled furthest in both Slapton beach tracer experiments.
Any effect of tidal currents is marginal, the gross longshore sediment transport
being related to prevailing wave direction.   Similar results (where a_{max} varied
between approx 1.1 and 7.6 x 10^{-2} m) were attributed to 'strong--- longshore
currents' operating on indigenous sediment at Duktoth Spit, Alaska (Hayes, 1973).
Incidentally, Jolliffe (1972) noted that on the sea bed, in depths of 9-18 m,
smallest pebbles also travelled farther than larger.   Further research needs
to be undertaken in this field.

At both Chesil and Slapton there are many occasions where the t-statistic
(Table 6) demonstrates the degree of selection of tracer between the overall
and zonal daily recoveries, and between them and the injected population,
frequently at a 0.001 probability level.   At Chesil it was suggested that
such differentiation reached its maximum with the coarsest sediment grades under
low, long period, swell but the same order of selectivity has since been shown
to occur at Slapton with shorter, wind-driven waves.

While this paper has not been concerned with the detailed processes affecting
a coarse sediment beach, it is pertinent to ask to what extent sorting normal
to the beach, through the beach (as laminae), and alongshore, are associated.
The Chesil experiment by Gleason and Hardcastle (1973) suggested that wave
height (as $H_s^{\frac{1}{2}}$) is relevant in sorting, both alongshore and at right angles to
the beach.   An oblique angle of wave approach is clearly necessary for longshore
selection.   Gleason and Hardcastle found that sorting downbeach was also
correlated with wave frequency ($\frac{1}{T^2}$).   This conclusion is very much in line with
earlier work by Miller (1958) on turbulence, and by Kemp (1960, 1963) on 'phase
difference'.   It is not clear where 'rejection' of inappropriate grades of
particle from the traction carpet fits in (Moss, 1962, 1963).   That is, whether,
at Chesil, the largest material travels furthest as a function of greater
surface area or because it is 'rejected' more frequently either by working
its way upwards or being stranded on the surface as smaller pebbles work their
way down through the beach.

CONCLUSIONS

Much has been written about the problems of scale in hydraulic model studies.
These problems relate to size and form of waves, size and shape of sediment, and
the means of representation of geographical areas.   However, it is possible
to study particular parameters under a controlled, but restricted, range of
conditions.

With field experiments on the beach there is a far wider range of potential
difficulties stemming, in part, from the inter-action of hydraulic and
sedimentary parameters.   Studies often do not provide representative environmental
conditions.   Particularly with shingle there are the complications of cusps and
strandlines on the surface and laminae with depth; the legacy of residual
grading; a lack of equilibrium with wave data because of the variability of the
latter; the effect of the traction carpet; increasing angularity of sediment
with diminishing size, and of relation between tracer and background particle
size.

Instrumentation of sediment movement, wave data and longshore currents (e.g. by
electromagnetic flowmeters) also presents a problem, especially in severe
conditions.

Analysis of the results is complicated by selective recoveries and by the inter-
relation of sedimentary parameters which precludes the use of multivariate
techniques.   More important, selective recoveries also cast doubt on the
validity of many tracer experiments which have used   coarse grades of material.

Table 6

Key: p = ·001 (●), p = ·01 (●), p = ·05 (•)

(a)

Date (Oct. 1969)	n =	a t	a p	b t	b p	c t	c p	Notes
24	194	2·652	●	3·918	●	5·114	●	
25	105	2·824	●	2·806	●	4·213	●	
26	193	1·071		1·063		2·177	•	
27	711	5·403	●	5·481	●	3·221	●	c = nearly ·001
28	276	0·729		1·365		2·907	●	
29	137	2·069	•	2·129	•	4·102	●	
24	255	4·252	●	3·584	●	2·077	•	November

(b)

	Injected Material n=699	5am n=1572 (1)	7 MW n=723 (5)	n=2040 (7)	n=2224 (6)	n=1636 (11) 10
a	13·002	10·657	1·370 (-)	2·210	4·085	-0·705 (-)
b	18·899	17·283	6·349	7·987	13·269	10·431
c	-0·547 (-)	4·744	-11·502	-13·513	-8·600	-10·785

7 (5) n=1666 (All)
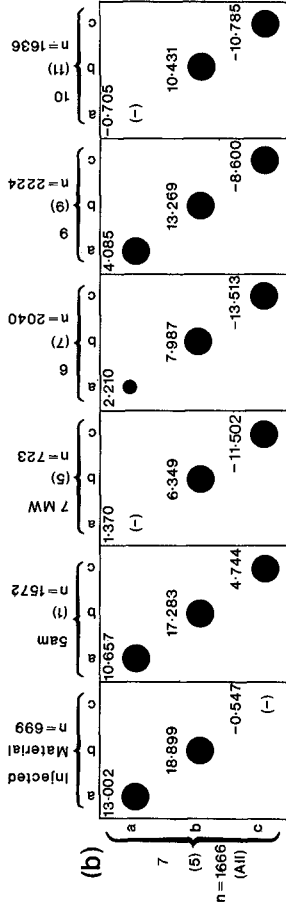
t-statistic: to test whether two samples come from the same population. The greater the value of t the more different the recovered sample. Probability (p) shown when < 0.05. n = number of individuals. Examples are taken from: (a) Chesil Beach tracer experiment, 1969. Comparison of material recovered to original population injected (After Carr, 1971). (b) Slapton Beach tracer experiment, October 1973. Probability that injected population, sub-population for 7 October MW, and whole recovered populations for other days are the same as the whole recovered population on 7 October. No. of tides shown in brackets. (Negative values result when the sample mean in the column is smaller than the corresponding value in the row). Note the variability from day to day; the selection within a population (7 October all v. 7 October MW) and the change in proportions between the linear parameters (e.g. the positive value of c for 5 October (after 1 tide)).

Wood (1970) wrote: 'With the variation of weather, tide and mobility of a
shingle beach profile it is unlikely that any direct general relationship
will be found between longshore energy flux and littoral drift even for the
same beach, and no reliable quantitative solution of general applicability
is foreseeable, without separation of the many parameters'.   There is a need
to carry out intensive short-term studies to see the precise relation of
hydraulic parameters to sediment in the inter-tidal and nearshore zones.
Such results could well be of real economic value.

REFERENCES

Cailleux, A. 1945. Distinction des galets marins et fluviatiles, Bull. Soc.
              Geol. France, 5, 375-404.

Cailleux, A. 1948. Lithologie des dépôts émergés actuels de l'embouchere du
              Var au Cap d'Antibes, Bull. de l'Institut Oceanographique,
              Monaco, No. 940, 1-11.

Carr, A.P. 1969. Size grading along a pebble beach: Chesil Beach, England.
              J. Sedim. Petrol., 39, 297-311.

Carr, A.P. 1971. Experiments on longshore transport and sorting of pebbles:
              Chesil Beach, England. J. Sedim. Petrol., 41, 1084-1104.

Carr, A.P. and M.W.L.Blackley. 1969. Geological composition of the pebbles
              of Chesil Beach, Dorset. Proc. Dorset Nat. Hist. Archaeol.Soc.,
              90, 133-140. (Volume for 1968).

Carr, A.P., Gleason, R. and A.C.King. 1970. Significance of pebble size and
              shape in sorting by waves. Sediment. Geol., 4, 89-101.

Castanho, J. 1970. Influence of grain size on littoral drift, 12th Inter.
              Coastal Engineering Conf., Washington, Proceedings,
              2, 891-898.

Dobkins, J.A. and R. L. Folk. 1970. Shape development on Tahiti-Nui, J.Sedim.
              Petrol., 40, 1167-1203.

Emery, K.O. 1955. Grain size of marine beach gravels, J.Geol., 63,39-49.

Emery, K.O. and R.H. Tschudy. 1941. Transportation of rock by kelp,
              Geol. Soc. Am.Bull., 52, 855-862.

Gleason, R., Blackley, M.W.L. and A.P.Carr. 1975. Beach stability and
              particle size distribution, Start Bay. J.Geol.Soc.Lond., 131.

Gleason, R. and P.J.Hardcastle. 1973. The significance of wave parameters
              in the sorting of beach pebbles, Estuar. & Coast. Mar.Sci.,
              1, 11-18.

Hardcastle, P.J. and A.C.King. 1972. Sea wave records from Chesil Beach,
              Dorset. Civil Engineering, 67, 299-300.

Hayes, M.O. 1973. The investigation of form and processes in the coastal zone,
              pp. 11-41 in Coastal Geomorphology, ed. D.R.Coates. Proc.
              3rd Annual Geomorph. Symposia, Binghampton, N.Y., Sept.1972.

Hydraulics Research Station. 1969. Threshold movement of shingle subject to
              wave action. H.R.S., Wallingford, U.K. Notes 15,December.

Jolliffe, I.P. 1964. An experiment designed to compare the relative rates of
              movement of different sizes of beach pebbles. Proc.Geol.Ass.,
              75, 67-86.

Jolliffe, I.P. 1972. Offshore gravel extraction and coastal regime.
              International Geography 1972, Vol.1, 643-644. 22nd Inter.
              Geog. Congress, Montreal.

Kellerhals, R. and D.I.Bray. 1971. Sampling procedures for coarse fluvial
sediments, J.Hydraul. Div.Am.Soc.Civ.Engrs., 97,
1165-1180.

Kemp, P.H. 1960. The relation between wave action and beach profile
characteristics, 7th Inter. Coastal Engineering Conf.,
The Hague. Proceedings, 262-277.

Kemp, P.H. 1963. A field study of wave action on natural beaches, Inter.
Assoc. of Hydraulic Research, London. 1, 131-138.

Kidson, C. and A.P.Carr. 1961. Beach drift experiments at Bridgwater Bay,
Somerset, Proc. Bristol Nat.Soc., 30, 163-180.

Krumbein, W.C. 1941. Measurement and geological significance of shape and
roundness of sedimentary particles, J.Sedim.Petrol.,
11, 64-72.

Krumbein, W.C. and W.R.James. 1965. A lognormal size distribution model for
estimating stability of beach fill material, Tech.Mem.16,
U.S. Army Coastal Engineering Research Center.

Longuet-Higgins, M.S. 1970a and b. Longshore currents generated by
obliquely incident sea waves, 1 and 2. J.Geophys.Res.,
75, 6778-6789; 6790-6801.

Miller, R.L. 1958. A study of the relation between dynamics and sediment
pattern in the zone of shoaling wave, breaker and foreshore.
Ecologae. Geol. Helv., 51, 542-551.

Moss, A.J. 1962. 1963. The physical nature of common sandy and pebbly
deposits, 1 and 2. Am.J.Sci., 260, 337-373; 261, 297-343.

Neate, D.J.M. 1967. Underwater pebble grading of Chesil Bank, Proc. Geol.Ass.,
78, 419-426.

Rance, P.J. and N.F.Warren. 1968. The threshold of movement of coarse
materials in oscillatory flow, 11th Inter. Coastal Engineering
Conf., London. Proceedings, 1, 487-491.

Richardson, N.M. 1902. An experiment on the movement of a load of brickbats
deposited on the Chesil Beach, Proc.Dorset Nat.Hist.
Antiq. Fld.Club, 23, 123-133.

Sneed, E.D. and R.L.Folk. 1958. Pebbles in the Lower Colorado River, Texas,
a study in particle morphogenesis, J.Geol., 66, 114-150.

Tucker, M.J. 1963. Analysis of records of sea waves, Minut.Proc. Inst. Civ.
Engrs., 26, 305-316.

Wentworth, C.K., 1922. The shape of beach pebbles, U.S.Geol.Surv.Prof.Papers,
131-C, 75-83.

Wood, A.M.M. 1970. Characteristics of shingle beaches: the solution to some
practical problems, 12th Inter.Coastal Engineering Conf.,
Washington. Proceedings, 2, 1059-1075.

CHAPTER 50

Dynamics and Morphology of Sand Banks
in the Surf Zone of Outer Tidal Flats

by

Harald Göhren[*]

1. Abstract

Extended sand banks ranging up to some hundred acres
with a crest height in the MHW-level are typical struc-
tures of the outer tidal flats of the south-eastern
North Sea coast (Fig. 1).

Primary forms grow up in the surf zone at the sea-side
tidal flat border. They are formed like bars and migra-
te towards the coast with a surprisingly high velocity,
up to 150 m/year.

The movement is caused by strong erosion on the sea-side
slope - which is shaped beach-like - and deposition at
the steeper land-side (lee-side) slope.

It was found that surf action at the bar is linked with
strong unidirectional currents across the crest, up to
100 cm/s. The currents are most likely generated by wa-
ve set-up in front of the bank and by wind-drift water
motion.

The migration velocity of the sand banks decreases with
increasing distance from the tidal flat border. This

[*]Dr.-Ing., Strom- und Hafenbau Hamburg, Coastal Engineer-
   ing Research Group "Neuwerk", 219 Cuxhaven, West Germany

871
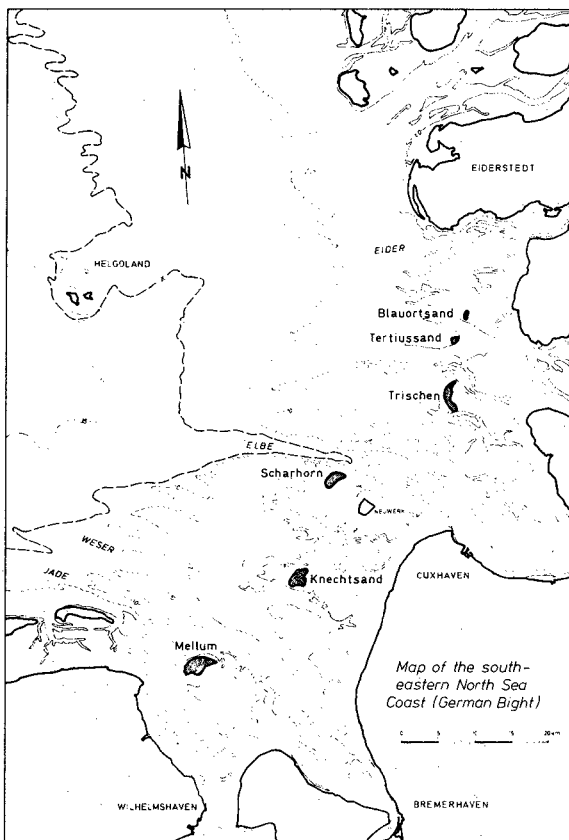
Fig. 1

effect seems to be most important when generation of new
banks continues. It leads to "overtaking" and "interaction"
of the single structures, thiswise growing together and
building up the large sand banks as described above and
gives an explanation of the development of large offsho-
re sand banks and dune islands on tidal flats.

2. Sand Banks on the Outer Tidal Flats of the South-Eastern North-Sea Coast

Extended tidal flats cover the south-eastern North Sea coast from DEN HELDER, Netherlands to ESBJERG, Denmark. A chain of dune islands and large sand banks streches along the sea-side rim of this tidal flat region, the latter ones concentrating in the German Bight (Fig. 1).

Fig. 2

Aerial view of "Scharhörn", a sand bank in the tidal flats of the Elbe Estuary (German Bight, North-Sea)

Fig. 2 gives a look from a birds eye on the sand bank of Scharhörn in the Elbe Estuary, a typical structure of that kind. The bank or plate has an extension of more then 4 km^2, this area lying just a few cm above mean high water. Because of this height the plate cannot be generated by tidal currents. The sand on the top is coarser than the sand in the surrounding flats. That is the reason for the bright surface compared with the darker shining flats around, which are wet and partly muddy. The tidal range is about 3 m in this coastal

region; the extended flats around the islands submerge
during high tide and are then covered by a water layer
of about 1.5 m.

We discover a tiny dune island at the north-western edge
of the plate on the aerial photo indicating that sand
transport by wind occurs. But there is no opportunity
for growing up large dunes, and Scharhörn like the other
plates in the vicinity (Mellum, Knechtsand, Trischen)
cannot be compared with the well known large dune is-
lands along the Dutch and German North Sea coast, to
the west of the area plotted in Fig. 1.

3. Morphology of the Sand Bank of Scharhörn

The morphology of the sand banks in the German Bight has
been studied by several authors (Ref. 4 to 10). The
morphologic behaviour of Scharhörn, which is typical,
shall be described in this paper, using the results of
recent investigations.

Scharhörn as well as the other big sand banks are exposed
to erosion at their sea-side shores. Due to surf action
at their western flanks and deposition on the opposite
sides the banks migrate slowly towards the east. Never-
theless we find high plates in most of these areas in
the oldest charts, indicating that they are more or less
stable though they are migrating, a fact which will be
explained later.

The migration of Scharhörn is demonstrated in Fig. 3.
Here the MHW-contour of the west and north-west shore
is plotted in 4 different periods, beginning more then
100 years ago. The origin of the oldest survey is
dubious and between 1868 and 1930 no surveys are
available, so that we don't know what actually happened
in that time. The average velocity of displacement is
about 15 m/year, but it is decreasing in the last years,
and it will be demonstrated that the migration will

stop and even reverse
temporaryly in the
very near future.

On the aerial foto
(Fig. 2) a smaller bank
in front of the large
plate is to be seen,
having obviously a
similar crest height
and the same coarse
sand on top (Fig. 4).
This bank looks like
a bar or a sand wave.
It is several km long
and several 100 m
broad. A more or less sharp crest seperates the sea-side
and the lee-side slope of the bar, the crest height being
only a few cm below MHW. The sea-side slope is flatter
than the lee-side one and is beach-shaped. The surface of
the sea-side slope is
doubtlessly formed by
breaking waves.

Fig. 3
Displacement of the MHW-
contour of Scharhörn

The generation of this
particular bar has been
investigated by a
series of consecutive
levellings (Fig. 5)
and aerial fotos
(Fig. 6). Primary
small accumulations
of sand were obser-
ved in 1948 at the
tidal flat border.
They grew up to two
sand waves, which began to migrate coastwards with a con-
siderable speed. The plots in Fig. 5 and 6 give an
impression of this displacement. It seems evident

Fig. 4
Grain size distribution in
a profile across the
bar in front of Scharhörn
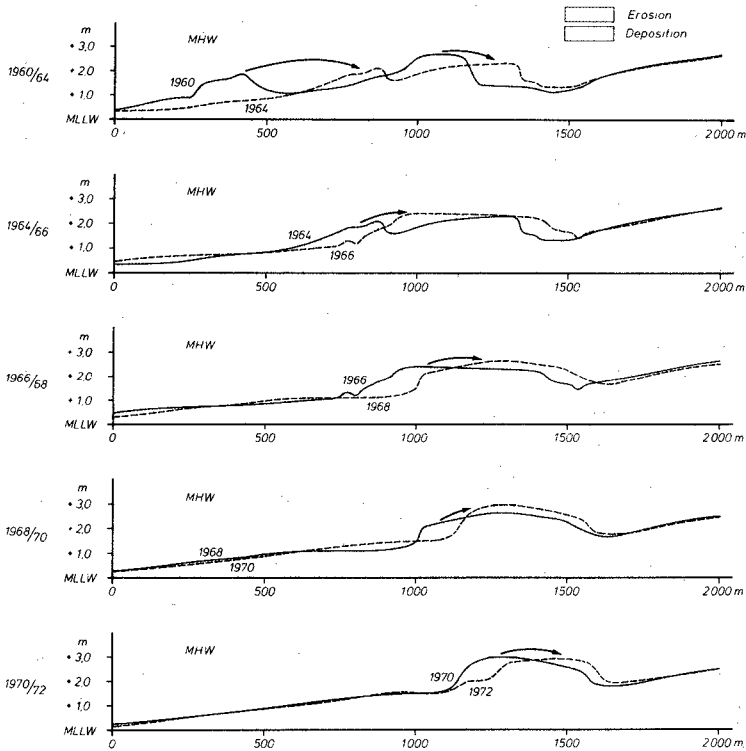
Fig. 5

Displacement of the bars in front of Scharhörn,
indicated by a comparison of consecutive profiles

(especially from a comparison of the consecutive profi-
les) that sand is eroded on the sea-side slope, pushed
across the crest and deposited on the lee-side.

The two bars – observed in 1957 – traveled with different
velocities, the more exposed one (bank I) faster than the
second (bank II). This led to an "overtaking" of the
single structures, thiswise growing together and obvious-
ly diminishing the movement after that event. The maximum
displacement exceeded about 150 m/year, a surprisingly
high value for a surf influenced coastal structure.

It can be expected that
the migration conti-
nues and the bar
"touches" the large
plate of Scharhörn.
Then this one will
get a supply of new
sand and a rough
comparison of con-
secutive charts
indeed will give
an impression of
"returning a step"
in the eastward
displacement.
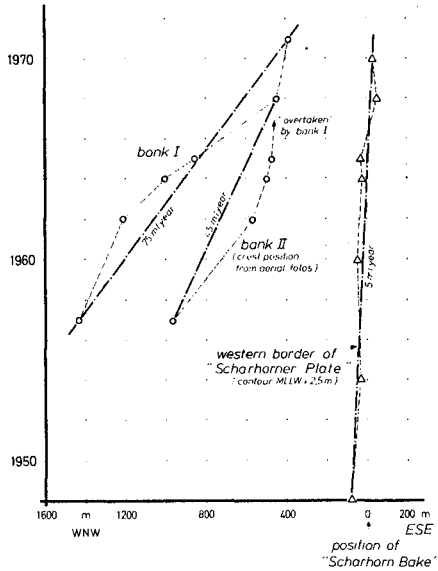
Fig. 6

Displacement of the sand bank of
Scharhörn and of the small banks
(migrating bars) in front of it

4. Current Observations

It can be concluded from the morphologic study that
neither normal tidal currents nor the common longshore
currents of the breaker zone can be predominant forces
for the sand movement in the region of the tidal flat
sand banks. In order to investigate the acting forces
and to confirm the presumed principle of sand movement
across the bar (Fig. 7), an array of 4 current meters
was set up in summer 1973. The positions are plotted
in Fig. 8. Fig. 9 shows a station with the recording
current meter as it was used (a type which has been
developed in Germany especially for research in
shallow waters and tidal flats). The measuring level
is about 40 cm above bottom.

The records of the
4 meters which were
taken over several
months' contain a
couple of wind-
influenced tides
and - fortunately -
3 storm surges which
occured at the German
North-Sea coast
during the fall of
that year.
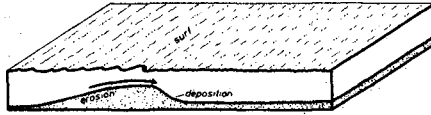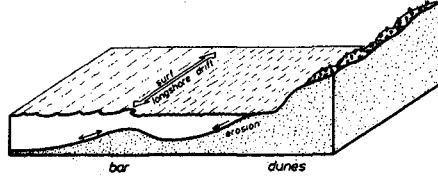
Fig. 7

Main sediment transport at a
common surf beach and a
migrating bar in a tidal flat

The measurements
confirm in prin-
ciple what is
known from former
investigations (Ref. 2), that high velocities, up to
100 cm/s, prevail in the tidal flats during storm tides,
whereas at normal (calm wind) tides current velocities
seldom exceed 40 cm/s.

In Fig. 8 the maximum velocities at mean tide and during
the 4 storm tides are plotted. The latter exceed 80 to
100 cm/s and are obviously directed perpendicular to the
bar and also to the big bank of Scharhörn. The currents
in front of the bar and in the trough behing it are of
similar magnitude but they are directed towards north-
east in a more longshore pattern

Fig. 10 enables a comparison of a 12 days' record of
station 12 (top of the bar) and 13 (in front of the
bar). It is a period of continuous strong winds blowing
coastwards. Due to the prevailing winds currents are
almost unidirectional - perpendicular to the shoreline.
During the storm tides maximum velocities at both po-
sitions are almost equal, averaged over the whole period
howerer they are higher on the bar than in front of it
(and also behind it).
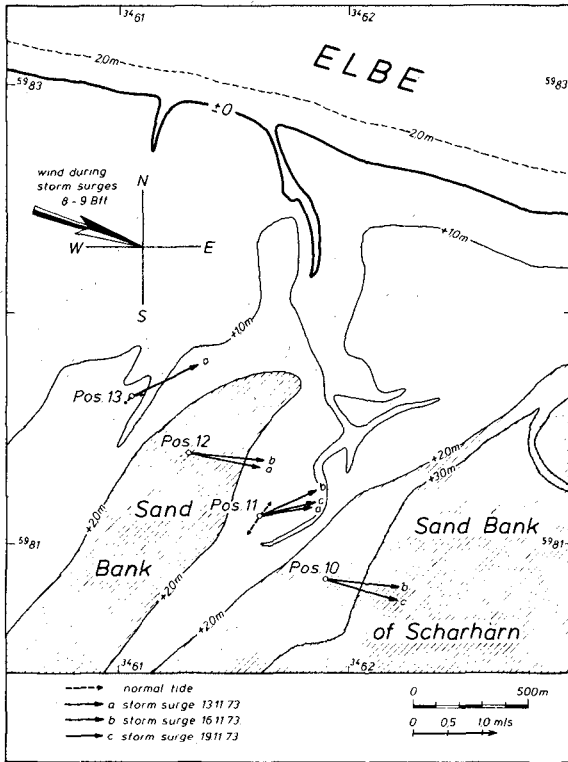
Fig. 8
Maximum current velocities (0.4 m above
bottom) at Scharhörn during storm surges
     in Nov. 1973 and at normal tides

There is no theory available to satisfyingly describe
this current pattern which must be generated by wind
sheer stress, wave set-up and inclinations of the water
level due to the displacement of the tidal wave and to
the coastal topography.

5. Conclusions

Putting all these
observations to-
gether, which could
be proved and com-
pleted by investi-
gations on other
sites, a satisfac-
tory hypothesis on
the generation and
stability of the
extended sand banks
along the sea-side
rim of the tidal
flats in the Ger-

Fig. 9

Recording current meter on a
tidal flat station at low water

man Bight can be established. Generation can be explained
by the effect of single small sand bars formed in the surf
zone of the tidal flat border, migrating and growing to-
gether due to their decreasing travelling velocity when
they get shelter by approaching new ones. The sand move-
ment in this system is mainly generated by strong uni-
directional currents perpendicular to the bar axis. Sand
on the sea-side slope of the bar is stirred up by breaker
action and pushed across the crest to be deposited behind
it in a zone of relative calmness. Fig. 11 gives a
schematic sketch of this morphologic principle. (It must
be noted in this context that in the south-eastern North
Sea winds from south-west to north-west are prevailing
and only these directions generate wind set-up in the
German Bight which is necessary to permit that "overflow"
of the banks and bars).

Stability of the thiswise produced "large banks" despite
of continuous erosion at their sea-side shores can be
explained by the sand supply from approaching new migrat-
ing bars. This process is of cause not continuous and
periodic, so that the large sand banks are suffering
long-range variations of position and magnitude. There
are indeed not enough long-term surveys available to
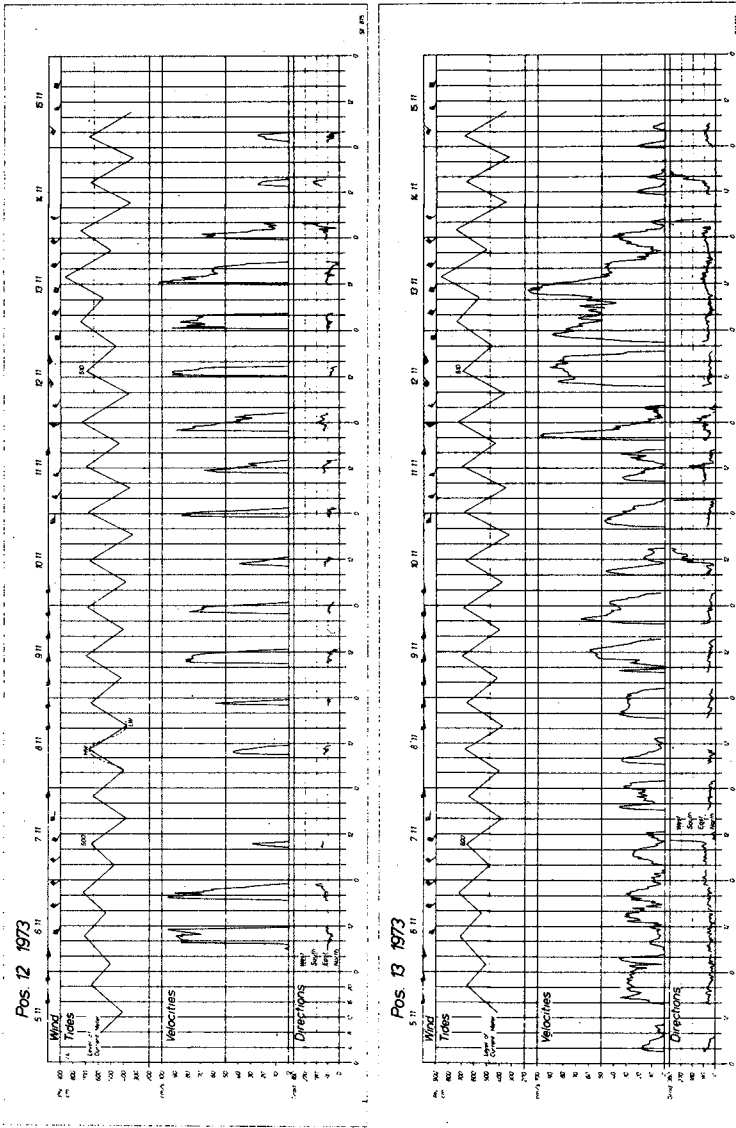
Fig. 10

Records of current meters on top (Pos. 12) and
in front (Pos. 13) of the bar of Scharhörn

satisfyingly in-
vestigate these
morphologic
processes. But the
fact that we find
descriptions or
drawings of large
banks already in
navigational
manuals and sea
charts of the
middle age at
almost the same
sites proves that
a long-term sand
supply from sea
must exist coun-
ter-balancing the
losses of material
which all sand banks in this region are suffering on
their sea-side shores.
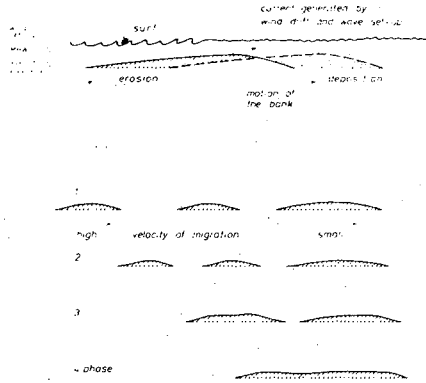
Fig. 11

Principle of generation of a
large sand bank from small
migrating bars in a tidal flat

References

1. GIERLOFF-   Luftbild und Küstengeographie am Bei-
   EMDEN, H.G.:   spiel der deutschen Nordseeküste.
                   Schriftenreihe des Instituts für Lan-
                   deskunde in der Bundesanstalt für
                   Landeskunde und Raumforschung,
                   H. 4, 1961

2. GÖHREN, H.:   Triftströmungen im Wattenmeer. Mit-
                   teilungen des Franzius-Instituts für
                   Grund- und Wasserbau der Technischen
                   Universität Hannover, H. 30, 1968

3. GÖHREN, H.:   Studien zur morphologischen Entwick-
                   lung des Elbmündungsgebietes. Ham-
                   burger Küstenforschung, H. 14, 1970

4. HOMEIER, H.:   Das Wurster Watt - Eine historisch-
                       morphologische Untersuchung des Kü-
                       sten- und Wattgebietes von der We-
                       ser- bis zur Elbmündung. Forschungs-
                       stelle Norderney, Jahresbericht 1967

5. KRAMER, J.:   Natürliche Entwicklung des Großen
                       Knechtsandes und seine Bedeutung
                       für den Küstenschutz. Forschungs-
                       stelle Norderney, Jahresbericht 1960

6. LANG, A.W.:   Untersuchungen zur morphologischen
                       Entwicklung des südlichen Elbe-
                       Ästuars von 1560 bis 1960. Hambur-
                       ger Küstenforschung, H. 12, 1970

7. LINKE, G.:   Die Entstehung der Insel Scharhörn
                       und ihre Bedeutung für die Überle-
                       gungen zur Sandbewegung in der
                       Deutschen Bucht. Hamburger Küsten-
                       forschung, H. 11, 1969

8. SCHÄFER, W.:   Mellum, eine Düneninsel der deut-
                       schen Nordseeküste. Abh. Sencken-
                       berg. Naturforsch. Ges., 457, 1941

9. WIELAND, P.:   Untersuchung zur geomorphologischen
                       Entwicklungstendenz des Außensandes
                       Blauort. Die Küste, H. 23, 1972

10. WOHLENBERG, E.:   Entstehung und Untergang der Insel
                       Trischen. Mitt. Geogr. Ges. Hamburg,
                       Bd. XLIX, 1950

CHAPTER 51

A SCHEMATIZATION OF ONSHORE-OFFSHORE TRANSPORT

by D. H. Swart[*]

Abstract

The investigation reported herein covers two aspects of the schematization of coastal processes on sandy beaches in a direction perpendicular to the coastline, viz.: (1) the prediction of equilibrium beach profiles and (2) the corresponding offshore sediment transport due to wave action. A physically-based schematic model of the onshore-offshore profile development was tested on available small-scale and full-scale model tests and physically-based empirical relationships were derived to enable the application of the model to both small-scale and prototype conditions.

1 Analysis

Onshore-offshore transport at any section in a non-equilibrium profile can be characterized as being a combination of bed load transport and suspended load transport. The division between these two modes of transport is not well-defined, due to the complicated water and sediment movement close to the bed. It will, however, be assumed that the total sediment transport in any section can be divided into: (1) bed load, which can be represented as being a sediment concentration multiplied by a layer thickness and a characteristic sediment particle velocity, and (2) suspended load in the form of convection transport in the rest of the section. These assumptions place no restrictions on the further application of the theory.

At the moment the state of the art regarding the prediction of concentration and velocity distribution in the vertical is not so advanced that a uniform theory exists which can predict these two quantities with suitable accuracy both inside the breaker zone and seawards of the breaker point. As it is, however, both in prototype situations and in the design of three-dimensional small-scale models of quite some importance to be able to predict quantitatively the onshore-offshore transport, it was decided to make a schematization of the external properties of the profile development. This external schematization will be used to predict offshore transport until the research regarding the internal mechanism (sediment entrainment, concentration and velocity distribution in the vertical) is so far advanced that onshore-offshore transport can be predicted via the internal mechanisms.

This schematization was aided by all two-dimensional model experiments regarding profile development, available in the Delft Hydraulics Laboratory, as well as by full-scale tests performed by the Coastal Engineering Research Center and supplied to the Delft Hydraulics Laboratory by T. Saville (jr).

[*] Project engineer, Delft Hydraulics Laboratory, The Netherlands

Consequently the wave conditions of the tests covered o wide ronge, viz.:

$$0,07 \text{ m} \leqslant H_o \leqslant 1.71 \text{ m}$$
$$1.04 \text{ s} \leqslant T \leqslant 11.3 \text{ s}$$

The particle diameter showed a smoller voriation, D_{50} voried between 0.1 mm and 0.23 mm, while the bed material in all tests was sand. The waves in all tests were regular waves. As in all Delft Hydroulics Laborotory tests a net seaward movement of sediment occurred, the present paper deals only with the prediction of offshore transport. From the results of the available tests it become apparent that the profile development can be characterized into three definite zones (see Figure 1), each with its own transport mechonism, viz.: (1) the bockshore, which is mostly eroded to above the wave run-up limit, (2) a transition areo at the seaward extremity of the developing profile, which is formed due to the fact thot the point of beginning of movement, londwards of which ripples ond bars ore formed on the bed, does normolly not coincide with the horizontal bed of the flume, and (3) the real developing profile where transport under wave oction takes place (called the D-profile). The some zones also occur in prototype. In order to enable the development of o usoble theory for the predicition of offshore tronsport in the D-profile, it is essential thot the limits between the above-mentioned three areas (zones) can be found uniquely in terms of the wove conditions and bed material characteristics.

2 Limits of the D-profile

From the definition of the bockshore it is opparent that the boundary between the bockshore ond the D-profile, i.e. the upper limit of the D-profile, is o function of the maximum wave run-up.

Using the formula of Hunt [5] for wave run-up, it can be stated in general that the maximum wave run-up η is given by:

$$\eta = a_1 H \tan a \left(\frac{H}{\lambda_o} \right)^{b_1} \qquad \qquad \ldots\ldots(1)$$

where H = wove height

$\tan o$ = wetted beach slope

λ_o = deep water wove length

a_1 and b_1 = constants

Wiegel [10] determined the relationship between the beach slope and the median particle diameter D_{50}. For all types of beaches he found a general relationship of the form:

$$\tan a = a_2 \, D_{50}^{c_2} \qquad\qquad\qquad \ldots\ldots(2)$$

where a_2 and c_2 = constants, depending on the type of beach under consideration; $c_2 > 0$.

Combination of equations (1) and (2) and regrouping of the terms yielded a general equation for the dimensionless upper limit of the D-profile of the following form:

$$\frac{h_o}{D_{50}} = f(H_o^e \, D_{50}^c \, T^b) \qquad\qquad\qquad \ldots\ldots(3)$$

where h_o = upper limit of D-profile relative to the still-water level. When all the available small-scale and full-scale data were correlated to equation (3), the following relationship was found (see Figure 2):

$$\frac{h_o}{D_{50}} = 7644 - 7706 \exp\left(- 0.000143 \; \frac{H_o^{0.488} \, T^{0.93}}{D_{50}^{0.786}}\right) \qquad \ldots\ldots(4)$$

The lower limit of the D-profile does not coincide with the point of beginning of movement, as predicted by for instance Goddet [4] and Bonnefille and Pernecker [1], but is assumed to be some function of it. Physically it can be seen as a transition between the area of combined bed load and suspended load (the D-profile) and only bed load (transition area). Analogous to the above-mentioned studies [1], [4] regarding beginning of movement of sediment under wave action, it will thus be assumed that:

$$\frac{h_m}{\lambda_o} = f \left(\frac{H_o^a}{T^b D_{50}^c} \right) \qquad\qquad\qquad \ldots\ldots(5)$$

where h_m = lower limit of the D-profile, relative to the still-water level
a, b and c = constants as long as $D_{50} \leqslant 0.5$ mm (see [1]).

Correlation of equation (5) to the available small- and full-scale data led to a relationship for the lower limit of the D-profile of the following form (see Figure 3):

$$\frac{h_m}{\lambda_o} = 0.0063 \exp\left(4.347 \; \frac{H_o^{0.473}}{T^{0.894} D_{50}^{0.093}}\right) \qquad \ldots\ldots(6)$$

3 Transport schemotizotion in the D-profile

In order to be oble to formulote o simplified form for the transport formulo, it is essentiol to make one ossumption, viz. that the developing beach will eventuolly reach o stoble situotion under persistent wove action. This stable situation implies two aspects, viz. (1) an equilibrium position ond (2) an equilibrium farm of the profile. As can be seen from Figure 4, in which a measure of the valume of sediment in the D-profile relative to the point of maximum wave run-up, $(L_2 - L_e)$, has been plotted ogainst time far o small-scale test which lasted in tatal 3878 haurs, the concept of equilibrium is a reasonable one. Using this assumption it is passible ta write up an equation far the determination of the time-dependent offshore sediment transport S_y in the D-profile af the form:

$$S_y = r(R_\infty - R_t) \qquad\qquad\qquad \ldots\ldots(7)$$

where S_y = time-dependent offshore sediment transport in the D-profile
  R_t = a time-dependent D-prafile characteristic, which will be defined later
  R_∞ = the equilibrium value of R_t, i.e. $R_t \xrightarrow{t}{}_\infty R_\infty$
  r   = o constant far o specific set of boundary conditions.

A study af various passible farms of the function R_t reveoled that if R_t is chasen as a schematic length $(L_2 - L_1)$ (see Figure 1 far an explanation of $(L_2 - L_1)$), a reasonobly gaod correspondence is abtained with the availoble test results. Thus on equatian af the fallawing farm results:

$$S_y = s_y (W - (L_2 - L_1)_t) \qquad\qquad\qquad \ldots\ldots(8)$$

where $(L_2 - L_1)_t$ = volue af $(L_2 - L_1)$ at time t.
    W = equilibrium value af $(L_2 - L_1)$
    s_y = a canstant for a specific set of baundary canditions.

If s_y and W are known, the affshare transport S_y con be calculated far any location in the D-profile by moking an oppropriate choice of the onshore- and offshore profile thicknesses δ_1 and δ_2 respectively (see Figure 1).

4 Evaluation of the data

In order to enable the prediction of s_y and W in terms of the wave conditions and bed material characteristics, all available appropriate small- and full-scale tests were elaborated. The criteria handled for the choice of the tests ta be used for the evaluation of the schematization, are the following: (1) frequent soundings af the bed must be available, to allow a good extrapolation of the time-dependent data to the equilibrium situation, and (2) no secandary effects must have accurred. Secondary effects can either originate fram an imperfect motion of the wave board, or from the shoaling and breaking of waves over bars in the nearshore D-profile. Secondary effects of the first type are clearly restricted to model fests, the second type 'of secondary effect can occur both in the model and the prototype. Consequently tests in which secondary effects of the first type occurred were not evaluated, while the tests with secondary effects of the second kind were evaluated. From the remaining tests results of the form shawn in Figure 5 were abtained. The curve of the equilibrium length W against the dimensionless position in the D-profile (δ_1/δ) determines fully the equilibrium D-profile, while a combination of the two curves enables the calculation of the offshare transport at any time in a non-equilibrium profile.

5 The equilibrium length W

The W-curve can be fully determined if the value of W at for instance the water line (W_r) is known, as well as thei ratio W/W_r in the rest of the profile.

In order to enable the calculatian of the value of W_r as a function of the boundary conditions, a representative slope m_r was defined:

$$m_r = \frac{\delta}{2W_r} \qquad \qquad \dots\dots(9)$$

where m_r = schematized equilibrium slope af the D-profile at the water line.

Earlier studies regarding the criteria which will determine the transition between step and bar profiles, (see Nayak[7]), revealed that the deepwater wave steepness H_o/λ_o, the absolute value of the wave weight H_o and the sediment particle diameter D_{50} are of importance. In a study to determine the transitian between erasion and accretion in the area above the water line [8], it was found that the average slope m_a at the water line was also of influence. In the present study the schematic equilibrium slope m_r was used instead af the average actual slope. When this approach was applied to the available model and prototype data in the same manner as described in [8], good results were

obtained, as can be seen in Figure 6, which yields o relationship of the form:

$$m_r \frac{H_o}{\lambda_o} = 1.51 * 10^3 \left[H_o^{0.132} \ D_{50}^{-0.447} \left(\frac{H_o}{\lambda_o} \right)^{-0.717} \right]^{-2.38}$$

$$+ 0.11 * 10^{-3} \quad \ldots \ldots (10)$$

Equation (10) defines the volue of W_r for a specific set of boundary conditions.

The variation in the ratio W/W_r over the D-profile determines the dimensionless form of the D-profile. Wiegel [10] classified beaches into three groups, viz. protected, moderately protected and exposed beoches. For each of these three types of beaches he gives a relationship between the beoch slope in the oreo between the limit of wave run-up ond the low-water line and the medion particle diameter D_{50}. An increose in particle diameter leads to on increose in beoch slope. Eagleson et ol [2] studied the forces on a discrete spherical bed lood porticle outside the breoker zone. They predicted the slope of the bed in this area os o function of the boundary conditions. For bigger particle diameters the slope decreoses. The above-mentioned two results indicote that the curvature of profiles with coarser bed material is bigger thon with finer bed materiol. This conclusion is confirmed by the elaborated results (see [9]). An equation for W/W_r of the following form (see Figure 7) was found:

$$\frac{W}{W_r} = 0.7 \ \Delta_r + 1 + 3.97 * 10^7 \ b \ D_{50}^2 \ \Delta_r^{1.36 * 10^4 \ D_{50}} \quad \ldots \ldots (11)$$

where $\Delta_r = \dfrac{h_m - \delta_2}{\delta}$ = dimensionless position in the D-profile, measured positively
                                    downwards from the still-water level.

$b = \begin{cases} 1 & \text{for } \Delta_r > 0, \text{ i.e. below the still-woter level} \\ 0 & \text{for } \Delta_r \leqslant 0, \text{ i.e. above the still-water level.} \end{cases}$

A correlation of equation (11) to all available smoll-scale three-dimensional model tests and prototype cases reveoled that this equation con also be applied to these conditions, without making a significant error.

6 The caastal canstant s_y (two-dimensional case)

The s_y-curve can be fully determined if, (1) the maximum value s_{ym} of s_y, (2) the location af s_{ym} and (3) the distribution of s_y/s_{ym} across the D-profile is known.

A study af the available literature an the formation of step and bar profiles, as summarized by Nayak [7], led to the conclusion that s_{ym} will be determined by the following relationship:

$$s_{ym} = f (H_o/\lambda_o,\ H_o\ T,\ D_{50},\ H_o/h_m) \qquad\qquad \ldots\ldots(12)$$

where H_o/h_m = a measure of the type of breaking wave.

A correlation of this formula ta the available small- and full-scale data led to the following equatian (see Figure 8):

$$\ln \left(\frac{s_{ym}T}{D_{50}}\right) = 10.7 - 28.9 \left[H_a^{1.68} \left(\frac{H_o}{\lambda_a}\right)^{-0.9} D_{50}^{-1.29} \left(\frac{H_a}{h_m}\right)^{2.66}\right]^{-0.079}\ldots(13)$$

A study of the available data led to the conclusion that the position of the maximum value of s_y will be a function of the ratio H_o/h_m and the absolute value of the wave height, (see Figure 9), viz.:

$$\Delta_{2m} = 0.8 - 1.1\ H_a^{-0.55} \left(\frac{H_a}{h_m}\right)^{2.69} \qquad\qquad \ldots\ldots(14)$$

When the characteristics of the backshore erasian, transition slope growth, the distribution across the D-profile of W, the lacation and magnitude of s_{ym} are all known, it can be shown (see [9]) that it is possible ta calculate mathematically the distribution of s_y across the D-profile. As this is, however, a tedious procedure invalving the solutian of seven nan-linear equations, an appraximate distribution of s_y/s_{ym} was determined from the available test results (see Figure 10), viz.:

In the area landwards af the lacatian of s_{ym}:

$$s_y/s_{ym} = \frac{0.93}{1 + 1.01\ X^{2.11}} + 0.07 \qquad\qquad \ldots\ldots(15)$$

In the area seawards of the lacation of s_{ym} :

$$s_y / s_{y_m} = \frac{0.99}{1 + 1.14 \, X^{2.11}} + 0.01 \qquad \qquad \dots \dots (16)$$

In both coses

$$X = \Delta_m \left(\frac{H_o}{\lambda_o} \right)^{-1} \left(\frac{H_o}{h_m} \right)^2 \qquad \qquad \dots \dots (17)$$

where Δ_m = obsolute value of the dimensionless position in the D-profile, meosured
relative to the locotion of s_{y_m}

$$= \left| \frac{\delta_2 - \delta_{2m}}{\delta} \right|$$

δ_{2m} = volue of δ_2 where $s_y = s_{ym}$.

As both s_y ond W are now known, it is possible to determine both the equilibrium profile
ond the offshore sediment transport in the two-dimensionol cose.

7 The coostol constant s_y (three-dimensional cose)

Due to the superposition of a longshore current to the wave field, the momentary resultant
current velocities at the bed, as well as the resultant bed sheor in the three-dimensional
case, will be higher than in the two-dimensional case. As has been stated eorlier, the
values of W for the two- and three-dimensional cases do not differ significantly from each
other. As the sediment transport is a function of the bed shear, it seems reolistic to
assume that the offshore transport rate of sediment in the three-dimensional cose will be
higher than in the two-dimensional case. This implies that s_y will also be higher than
for the two-dimensional case. The mean increase in the bed sheor due to a combined
current and wave action can be found by numerical integration, viz.:

$$\frac{\overline{\tau_{wc}}}{\tau_w} = 1 + (1.91 - 1.32 \sin \phi_b) \left(\frac{v}{\xi_J u_o} \right)^{(1.24 - 0.08 \sin \phi_b)} \qquad \dots \dots (18)$$

where $\xi_J = C_h \sqrt{\frac{f_w}{2g}}$

C_h = Chézy-coefficient
f_w = wave friction factor, according to Jonsson [6].
v = average longshore current velocity at a certoin water depth
u_o = orbital velocity at the bed
ϕ_b = angle of wave incidence at breaking
τ_{wc} = bed shear due to combined current ond wove action
τ_w = bed shear due to current action only.

The increase in the coastal constant s_{ym} can be correlated to the increase in bed shear, viz.:

$$\frac{s_{ym3D}}{s_{ym2D}} = (\frac{\overline{\tau_{wc}}}{\tau_w})^{4.5} \qquad \qquad \dots\dots(19)$$

where s_{ym2D} and s_{ym3D} are the two- and three-dimensional values respectively of s_{ym}.

A combination of equations (13), (18) and (19) will yield the value of s_{ym} in the three-dimensional case. The location of this value is still given by equation (14). The distribution of s_y/s_{ym} should be calculated with the aid of the mathematical procedure involving 7 non-linear equations, which has already been mentioned in section 6, and which is derived elaborately in [9].

8   Application of the theory

The method described in this paper can be used to compute time-dependent and equilibrium profiles, as well as the corresponding offshore sediment losses. In Figure 11 a comparison is shown between a final profile, given by Eagleson et al [3], and a theoretical equilibrium profile, calculated with the aid of equations (10) and (11). The correspondence is rather good. In Figure 12 a comparison is given between measured and theoretically computed offshore sediment losses, for a storm period in the Netherlands in February, 1953. The exact longshore current velocities are not known, however, as can be seen, the order of magnitude of the computed losses corresponds well with the measured losses. The method can also be used to compute offshore sediment losses after beach replenishment.

9   Restrictions and recommendations

When applying the theory, it should be kept in mind that the lower limit of the D-profile has been determined by using the assumption that $D_{50} \leqslant 0.5$ mm. This places a restriction on the maximum particle size for which the method can still be applied. All tests used for the elaboration in the present study were performed with regular wave attack. Under prototype conditions, where the waves are random, the wave spectrum will determine which representative wave height should be used in the application. This aspect of the problem should be studied in more detail. A test programme should be designed to assist in the extension of the theory to include onshore sediment movement.

10   Conclusions

The principal conclusions of the investigation described in this paper may be summarized as follows:

(1) The upper limit of the actual developing profile (called D-profile in this paper) is related to the maximum wave run-up and is of the form given in equation (4).

(2) The lower limit of the D-profile is related to the beginning of movement of bed material under wave action and is of the form given in equation (6).

(3) The offshore transport at any location in the D-profile at any time t is proportional to the difference between the equilibrium profile form and the profile form at time t, according to equation (8).

(4) The sediment transport at the upper and lower limits of the D-profile are not necessarily negligible; these transport follow the same time-dependent variation as given by equation (8).

(5) The form of the dimensionless equilibrium D-profile is determined by the particle diameter according to equation (11).

(6) The horizontal scale of the equilibrium D-profile is determined by the absolute value of the deepwater wave height, the deepwater wave steepness and the particle diameter, according to equation (10).

(7) The equilibrium beach slope at the upper limit of the D-profile increases with increasing particle diameter, while the equilibrium slope at the lower limit of the D-profile decreases with increasing particle diameter.

(8) The equilibrium D-profile under three-dimensional conditions is as a first approximation equal to that under corresponding two-dimensional conditions.

(9) The rate of offshore transport under three-dimensional conditions is higher than under corresponding two-dimensional conditions, due to the increase in the average bed shear (equation 19)).

REFERENCES

1   BONNEFILLE, R. and PERNECKER, L.
    "Le début d'entrainement des sédiments sous l'action de la houle";
    Bulletin du Centre de Recherches et d'Essais de Chatou, No. 15, Mars, 1966.

2   EAGLESON, P.S., DEAN, R.G., and PERALTA, L.A.
    The mechanics of the motion of discrete spherical and bottom sediment particles due to shoaling waves;
    Beach Erosion Board, Technical Memorandum No. 104, Washington, 1958.

3   EAGLESON, P.S., GLENNE, B. and DRACUP, J.A.
     Equilibrium characteristics of sand beaches;
     Proceedings ASCE, J. Hydraulics Division, Paper No. 3387, pp. 35-57, Volume 89,
     January, 1963.

4   GODDET, J.
     "Etude du début d'entrainement des matérieux mobiles sous l'action de la houle";
     La Houille Blanche, No. 2, pp 122-135, Mars-Avril,   1960.

5   HUNT, I.A.
     Design of seawalls and breakwaters;
     Proceedings, ASCE, Journal of the Waterways and Harbours Division, 85, No. WW3,
     paper 2172, pp. 123-152, September, 1959.

6   JONSSON, I.G.
     Measurements in the turbulent wave boundary layer;
     Proceedings, 10th I.A.H.R. Congress, London, Volume I, Paper 1-12, pp. 85-92, 1963.

7   NAYAK, I.V.
     Equilibrium profiles of model beaches;
     Ph.D. thesis, University of California, California, 1970.

8   SWART, D.H.
     The effect of distortion on coastal profiles (in Afrikaans);
     M.Eng. thesis, University of Stellenbosch, South Africa, 176 pp., March, 1971.

9   SWART, D.H.
     Offshore transport and equilibrium profiles;
     Publication no. 131, Delft Hydraulics Laboratory, 244 pp., 1974.

10   WIEGEL, R.L.
     Oceanographical Engineering;
     Englewood Cliffs, New Jersey, Prentice Hall, 532 pp., 1964.
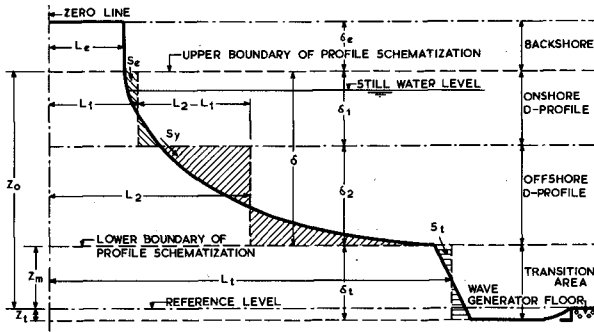
Figure 1:   Schematization of beach profile
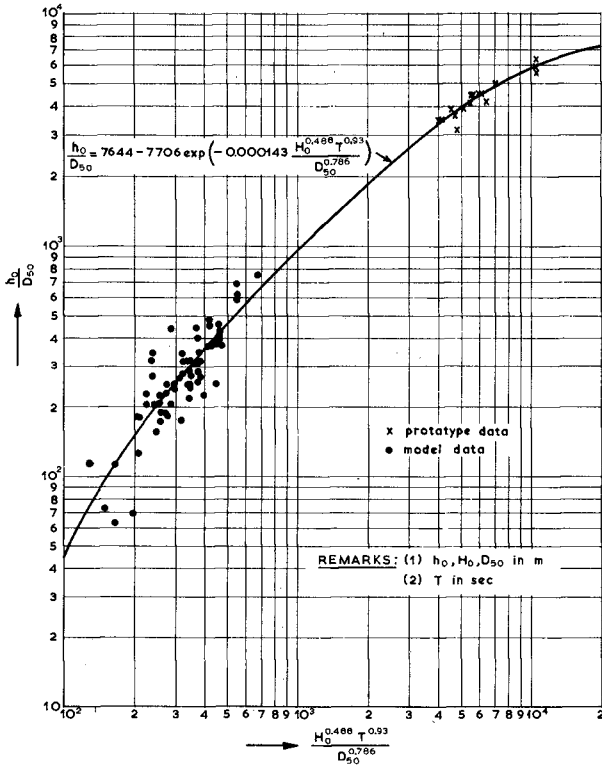
Figure 2:   Upper limit of D-profile

$$\frac{h_m}{\lambda_o} = 0.0063 \exp\left(4.347 \ \frac{H_o^{0.473}}{T^{0.894} D_{50}^{0.093}}\right)$$

REMARKS: (1) $h_m, \lambda_o, H_o, D_{50}$ in m
         (2) T in sec
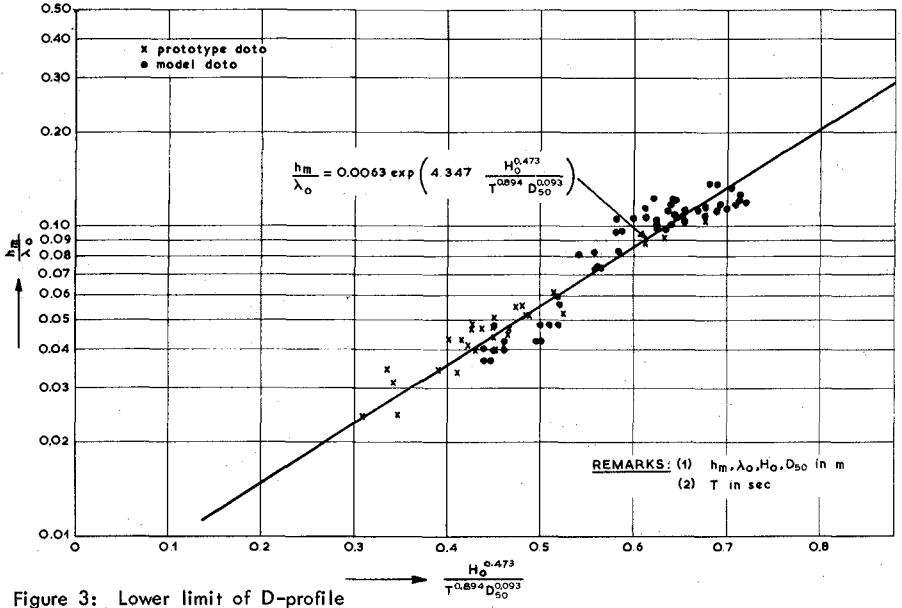
Figure 3: Lower limit of D-profile

$$L_2 - L_e = 4.524 - 2.686 \bar{e}^{0.00664t} - 0.568 \bar{e}^{0.0008t}$$

REMARKS: W = 4.524 m
          $s_y = 0.777 \times 10^{-3}$ m/hr
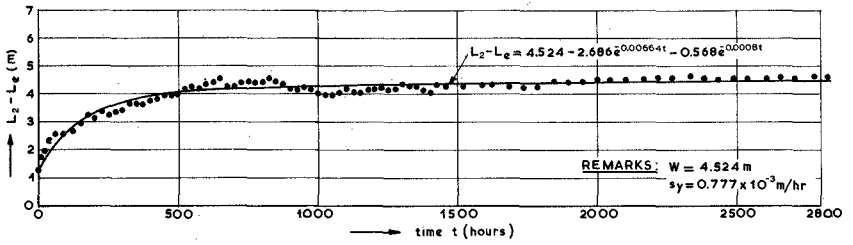
Figure 4: Time-variation of $(L_2 - L_e)$
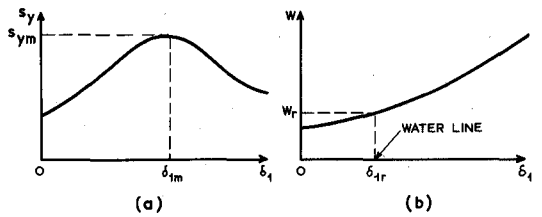
Figure 5: Form of results

(a)   (b)
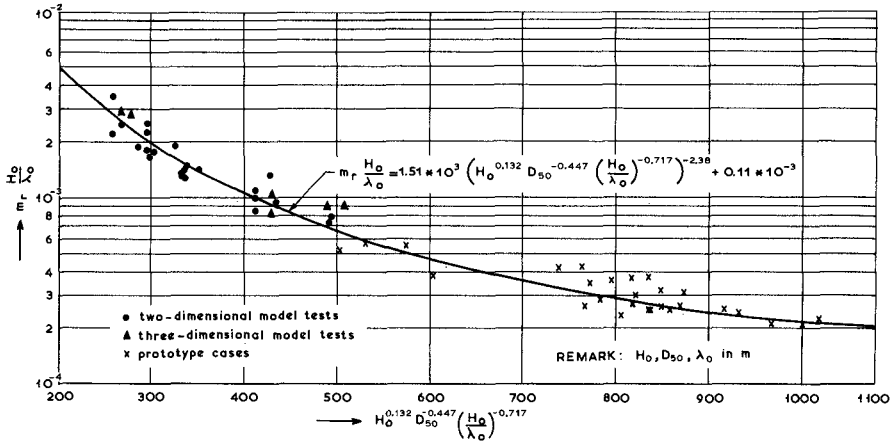
Figure 6: Horizontal scale of the equilibrium D-profile

$$m_r \frac{H_0}{\lambda_0} = 1.51 * 10^3 \left(H_0^{0.132} D_{50}^{-0.447} \left(\frac{H_0}{\lambda_0} \right)^{-0.717} \right)^{-2.38} + 0.11 * 10^{-3}$$
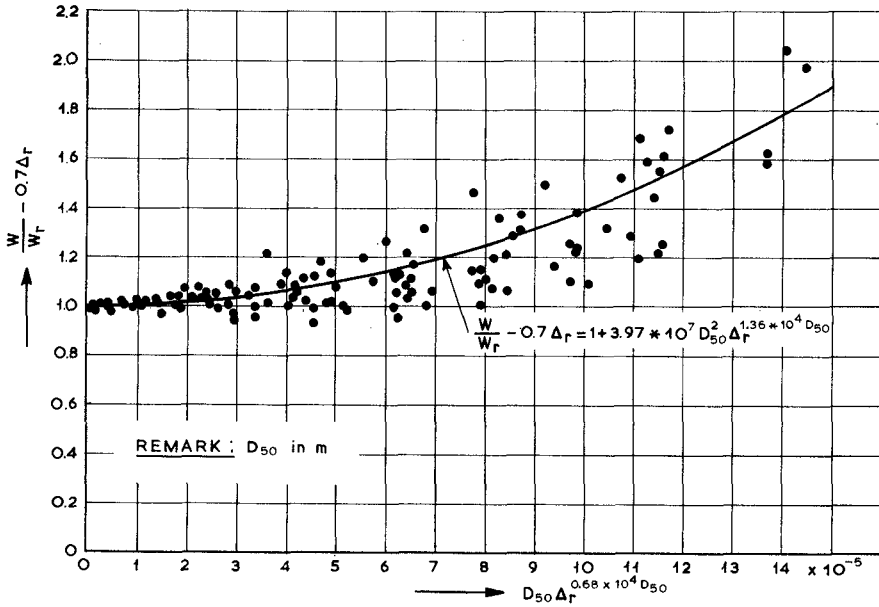
Figure 7: General relationship for W/W_r (two-dimensional cases)

$$\frac{W}{W_r} - 0.7 \Delta_r = 1 + 3.97 * 10^7 D_{50}^2 \Delta_r^{1.36 * 10^4 D_{50}}$$
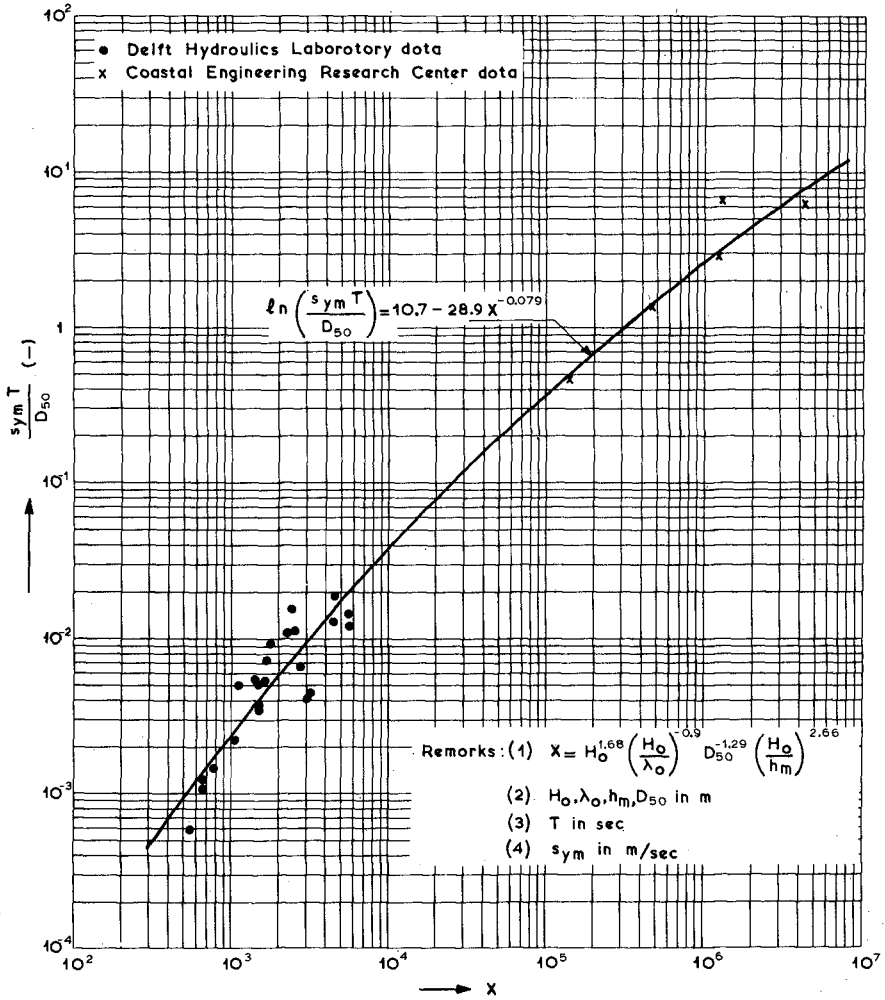
Figure 8: Magnitude of s_{ym}

Figure 9: Position of s_{ym}

● Delft Hydraulics Laboratary data
x Coastal Engineering Research Center data
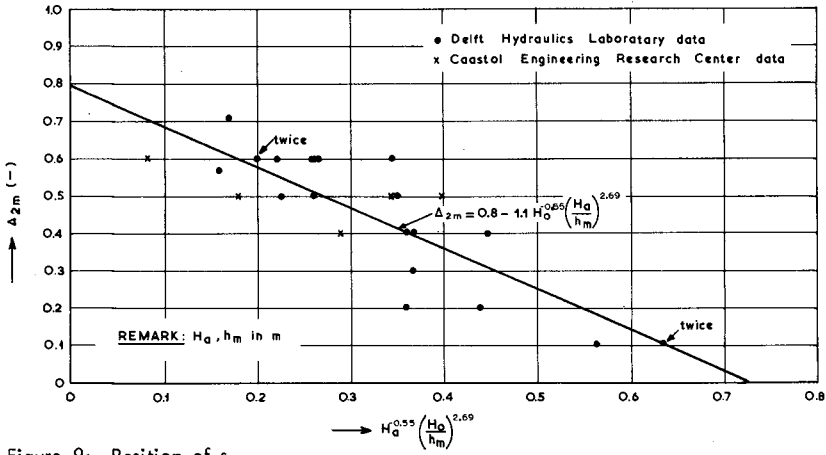
REMARK: H_o, λ_o, h_m in m
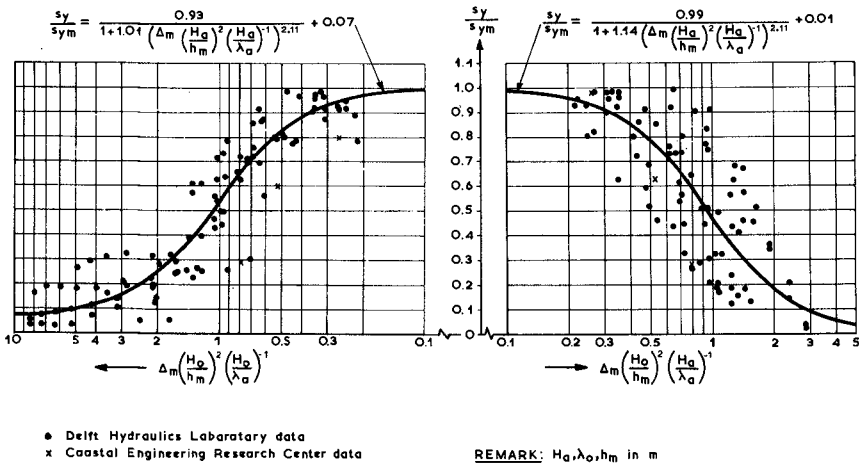
Figure 10: Distribution of s_y/s_{ym}
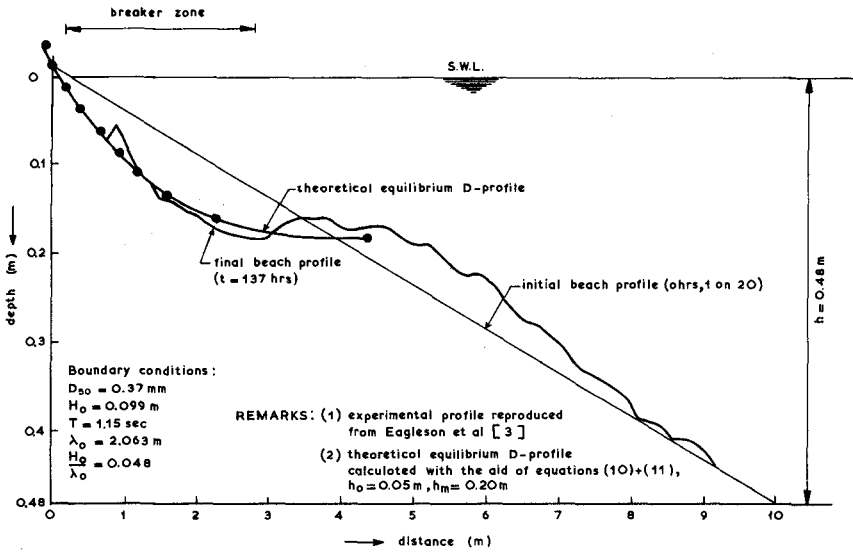
Figure 11: Comparison of theoretical and experimental equilibrium profiles
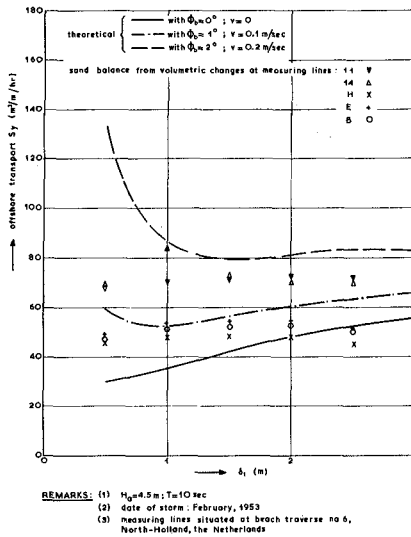
Figure 12:

Comparison of theoretical
and measured transport
rates in prototype

CHAPTER 52

THEORY ON FORMATION OF RIP-CURRENT
AND CUSPIDAL COAST

By Mikio Hino

Professor, Department of Civil Engineering
Tokyo Institute of Technology
O-okayama, Meguro-ku, Tokyo

SYNOPSIS : The hydrodynamic instability theory is developed on the for-
mation of rip-current and cuspidal coast. The most prefered wave length
is shown to be about four times the distance from the shore to the breaker
zone. Typical patterns of flow field and bottom configurations are re-
presented. Finally, the theory is compared with field observations.

I INTRODUCTION

Recently two theories have been proposed on the mechanism of for-
mation of rip-currents. Bowen's theory which has been presented in
Journal of Geophysical Research in 1969 is based on the forced mechanism
caused by standing edge waves which induce the spatially periodic distri-
bution of radiation stress.

On the other hand, in 1972 the author proposed a hydrodynamic in-
stability mechanism. A series of papers on this problem has been published
in the Proceedings of Japanese Conference on Coastal Engineering and the
Technical Report of Department of Civil Engineering, Tokyo Institute of
Technology.

The author's basic idea is as follows; If waves are incident on a
straight coastal line and if the water depth is uniform along it, the uniform
wave-setup along the shoreline should be formed caused by the radiation
stress of incident waves. Such a uniformly long wave-step would be un-
stable to an infinitesimal disturbance, as if a slender rod compressed
axially buckles when a critical compressive stress is exceeded. Moreover,
if waves are obliquely incident, the same mechanism as that for sand-wave
formation in open channels will operate to form sand-bars caused by long-
shore currents.

901

II BASIC EQUATIONS

The motion of water is described by eqs. (1), (2) and (3) in terms of the mean surface elevation η , the vertically averaged horizental velocity components U and V in offshore and longshore directions and water depth below the still water surface h(x),

$$\rho \partial \left[u \left(h + \eta \right) \right] / \partial t + \partial \left[\rho \left(h + \eta \right) u^2 \right] / \partial x$$

$$+ \partial \left[\rho \left(h + \eta \right) uv \right] / \partial y + \partial s_{xx} / \partial x + \partial s_{xy} / \partial y$$

$$= - \rho g \left(h + \eta \right) \partial \eta / \partial x - \rho \tilde{C} u \qquad \cdots \quad (1)$$

$$\rho \partial \left[v \left(h + \eta \right) \right] / \partial t + \partial \left[\rho \left(h + \eta \right) uv \right] / \partial x$$

$$+ \partial \left[\rho \left(h + \eta \right) v^2 \right] / \partial y + \partial s_{xy} / \partial x + \partial s_{yy} / \partial y$$

$$= - \rho g \left(h + \eta \right) \partial \eta / \partial y - \rho \tilde{C} v \qquad \cdots \quad (2)$$

$$\partial \left(h + \eta \right) / \partial t + \partial \left[u \left(h + \eta \right) \right] / \partial x$$

$$+ \partial \left[v \left(h + \eta \right) \right] / \partial y = 0 \qquad \cdots \quad (3)$$

where $\tilde{C}$ means the frictional coefficient having dimension of velocity, and s_{xx}, s_{yy} and s_{xy} represent the radiation stress tensor introduced by Longuet-Higgins and Stewart (1964),

$$\left.\begin{array}{l} s_{xx} = 3E / 2 - Ec^2 \left(\sin \theta / c \right)^2 , \quad s_{xy} = Ec \cos \theta \left(\sin \theta / c \right) \\[6pt] s_{yy} = E / 2 + Ec^2 \left(\sin \theta / c \right)^2 \\[6pt] E = \frac{1}{8} \rho g (2a)^2 \\[6pt] (2a) = r \left(h + \eta \right) \qquad (0 \leq x \leq L_B) \\[6pt] \tilde{C} = \frac{2}{\pi} C' U_{max} = \frac{2}{\pi} C' (\frac{r}{2} \sqrt{gh}) = C_d \sqrt{gh}, \quad C_d = r C' / \pi, \quad C' = O(0.01) \end{array}\right\} \quad (4)$$

where E expresses energy of wave, c is wave celerity and L_B is the distance from shore to a breaker zone. By Snell's reflection law, $(\sin \theta / c)$ remains constant in course of the propagation of wave.

The last equation to solve the problem is the conservation equation of bottom material transport;

$$\partial h / \partial t = \partial \left(C_s u \right) / \partial x + \partial \left(C_s v \right) / \partial y \qquad \cdots \quad (5)$$

where C_s is the transport coefficient of bottom material and is considered to be dependent not only on the material but also on the wave characteristics and water depth. However, for the time being it is assumed to be a constant.

Small perturbations are imposed on the steady state. Hence, the variables are expressed as

$$U = u'(x, y, t)$$
$$V = V_0(x) + v'(x, y, t)$$
$$\eta = \eta_0(x) + \eta'(x, y, t)$$
$$h = d(x) + h'(x, y, t)$$

(6)

where $V_0(x)$ represents the longshore current, $\eta_0(x)$ is the wave setup in an equilibrium state, and $d(x)$ means the initial water depth.

Equation (6) is substituted into equations (1), (2), (3) and (5). The 0-th order terms yield the wave setup equations,

$$\partial \eta_0 / \partial x = -(3\gamma^2 / 8) \cos^2 \theta / [1 + (3\gamma^2 / 8) \cos^2 \theta] \cdot \partial h_0 / \partial x \cdots (7)$$

and the velocity distribution of longshore current,

$$V_0(x) = -(5\gamma^2 / 16 C_d)(\cos \theta \cdot \sin \theta_B \cdot \sqrt{h_{0B} + \eta_{0B}})[(h_0 + \eta_0) / (h_{0B} + \eta_{0B})]$$

$$\cdot [d(h_0 + \eta_0) / dx] \quad \cdots\cdots\cdots\cdots\cdots\cdots\cdots\cdots\cdots\cdots\cdots\cdots\cdots\cdots \quad (8)$$

On the other hand, the first-order perturbation terms give the linearized equation for perturbation variables. Henceforward, variables will be nondimensionalized by the gravitational acceleration g and the distance from shoreline to the breaking zone L_B. For instance $u / \sqrt{gL_B} \rightarrow u$, $x/L_B \rightarrow x$ and $t \sqrt{g/L_B} \rightarrow t$. Moreover, primes to express perturbed quantities will be omitted henceforth,

$$\frac{\partial w_i}{\partial t} + A_{i1} \frac{\partial u}{\partial x} + A_{i2} \frac{\partial u}{\partial y} + a_i u + B_{i1} \frac{\partial v}{\partial x} + B_{i2} \frac{\partial v}{\partial y} + b_i v$$

$$+ C_{i1} \frac{\partial \eta}{\partial x} + C_{i2} \frac{\partial \eta}{\partial y} + c_i \eta + D_{i1} \frac{\partial h}{\partial x} + D_{i2} \frac{\partial h}{\partial y} + d_i h = 0 \quad (9)-(12)$$

$$(i = 1, 2, 3, 4)$$

where $w_1 = u$, $w_2 = v$, $w_3 = \eta$ and $w_4 = h$ and A_{i1}, A_{i2}, a_i etc. are functions of x which are complicated and lengthy; for instance,

$$A_{12} = V_0(x)$$
$$a_1 = C_d / \sqrt{h_0 + \eta_0}$$
$$C_{11} = (3\gamma^2 / 8)[1 - (h_0 + \eta_0)(\sin^2 \theta / c^2)] + 1$$
$$C_{12} = (5\gamma^2 / 16) \cos \theta (\sin \theta / c) \sqrt{(h_0 + \eta_0)}$$
$$c_1 = -(3\gamma^2 / 8) \cdot (\sin^2 \theta / c^2)[d(h_0 + \eta_0) / dx]$$
$$D_{11} = (3\gamma^2 / 8)[1 - (h_0 + \eta_0)(\sin^2 \theta / c^2)]$$
$$D_{12} = C_{12}$$
$$d_1 = c_1$$

(13)

$$
\left.\begin{aligned}
a_2 &= V_0'(x) \\
B_{22} &= V_0(x) \\
b_2 &= C_d / \sqrt{h_0 + \eta_0} \\
C_{21} &= (5\gamma^2/16)[\cos\theta(\sin\theta/c)]\sqrt{h_0 + \eta_0} \\
C_{22} &= 1 + \gamma^2/8 + (3\gamma^2/8)(\sin\theta/c)^2 (h_0 + \eta_0) \\
c_2 &= -(C_d/\pi)[V_0(h_0 + \eta_0)^{3/2}] + (5\gamma^2/32) \cdot \\
&\quad [\cos\theta(\sin\theta/c)](h_0 + \eta_0)^{-1/2}(h_0' + \eta_0') \\
D_{21} &= C_{21} \\
D_{22} &= C_{22} - 1 \\
d_2 &= c_2
\end{aligned}\right\} \quad (14)
$$

III   SOLUTION OF FULL EQUATIONS

In this section, a method is presented which solves straightforwards the full equations (linear simultaneous partial differential equations) for the four dependent variables, eqs. (9) through (12).

a) Linear ordinary differential equations

The temporal and spatial changes of the perturbation variables are expressed as eq. (15),

$$
\left.\begin{aligned}
u(x,y,t) &= U(x)\exp[iky+pt] \\
v(x,y,t) &= V(x)\exp[iky+pt] \\
\eta(x,y,t) &= Z(x)\exp[iky+pt] \\
h(x,y,t) &= H(x)\exp[iky+pt]
\end{aligned}\right\} \quad (15)
$$

The perturbations are assumed to be periodic with wave number k in the longshore direction, and to grow exponentially with time. If the real part of p which is to be determined later as an eigen-value problem is positive, the small perturbation is unstable to develop fully into large bottom configuration and strong longshore current system.

Substitution of the above Fourier component decomposition expression into eqs. (9) – (12) gives a system of linear simultaneous ordinary differential equations,

$$F_1 U(x) \qquad\qquad + r_1 Z'(x) + R_1 Z(x) + s_1 H'(x) + S_1 H(x) = - pU(x)$$

$$F_2 U(x) + G_2 V(x) + r_2 Z'(x) + R_2 Z(x) + s_2 H'(x) + S H(x) = - pV(x)$$

$$f_3 U'(x) + F_3 U(x) + G_3 V(x) \qquad\qquad + R_3 Z(x) \qquad\qquad + S_3 H(x) = - pZ(x)$$

$$f_4 U'(x) \qquad\qquad + G_4 V(x) \qquad\qquad\qquad\qquad\qquad\qquad = - pH(x)$$

$$(16)$$

where F_i, f_i, G_i, . . . (i = 1, 2, 3, 4) are functions of x and given as follows,

$$F_1(x) = C_d / [h_0(x) + \eta_0(x)]^{1/2} - ik V_0(x)$$

$$f_1 = G_1 = g_1 = 0$$

$$R_1 = -(3r^2/8)(\sin\theta/c)^2 (h_0'(x) + \eta_0'(x))$$
$$\qquad + ik(5r^2/16)[\cos\theta(\sin\theta/c)](h_0(x) + \eta_0(x))^{1/2}$$

$$r_1 = (3r^2/8)[1 - (\sin\theta/c)^2 (h_0(x) + \eta_0(x))] + 1$$

$$S_1 = R_1$$

$$s_1 = r_1 - 1$$

$$(17)$$

$$F_2(x) = dv_0(x)/dx$$

$$G_2(x) = C_d / \sqrt{h_0(x) + \eta_0(x)} + ik V_0(x)$$

$$R_2(x) = (5r^2/32)[\cos\theta(\sin\theta/c)](h_0(x) + \eta_0(x))^{-1/2} \cdot (h_0'(x)$$
$$\qquad + \eta_0'(x)) - C_d V_0(x) / [2(h_0(x) + \eta_0(x))^{3/2}] + ik [(r^2/8)$$
$$\qquad + (3r^2/8)(\sin\theta/c)^2 (h_0(x) + \eta_0(x)) + 1]$$

$$r_2(x) = (5r^2/16)\cos\theta(\sin\theta/c)\sqrt{(h_0(x) + \eta_0(x))}$$

$$S_2(x) = R_2(x) - ik$$

$$s_2(x) = r_2(x)$$

$$f_2(x) = g_2 = 0$$

$$(18)$$

$$f_3 = h_0(x) + \eta_0(x) + C_s$$

$$F_3 = h_0'(x) + \eta_0'(x)$$

$$G_3 = ik [h_0(x) + \eta_0(x) + C_s]$$

$$R_3 = ik V_0(x)$$

$$S_3 = ik V_0(x)$$

$$g_3 = r_3 = s_3 = 0$$

$$(19)$$
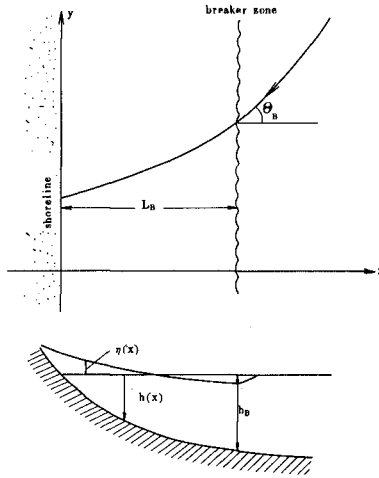
Fig. 1 : Coordinate system and symbols
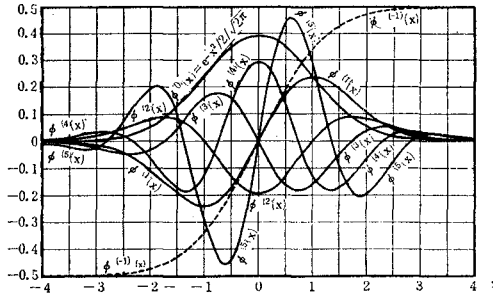
Fig. 2 : Graph of Hermitian polynomial functions
          mutiplied by $\exp\left(-x^2/2\right)/n!$

$$f_4 = -C_s$$

$$G_4 = -ikC_s$$

$$F_4 = g_4 = R_4 = r_4 = S_4 = s_4 = 0$$

$$\left.\begin{array}{c} \\ \\ \\ \end{array}\right\} \quad (20)$$

b) Boundary conditions

   The boundary conditions imposed on the above system of differential equations are written as

$$U(x) = 0 \qquad\qquad (x = 0)$$

$$U(x) \to 0 \qquad\qquad (x \to \infty)$$

$$Z(x) \to 0 \qquad\qquad (x \to \infty)$$

$$H(x) \to 0 \qquad\qquad (x \to \infty)$$

$$\left.\begin{array}{c} \\ \\ \\ \\ \end{array}\right\} \quad (21)$$

c) Eigenvalue problem, Determination of p

   Equations (16) together with the imposed boundary conditions at s at the coast and the infinity (21) constitute the eigenvalue problem. Two methods of solution may be applied; that is, (a) the finite diference approximation of equations (16) reduces them into a set of simultaneous linear equations which requires the determinant of coefficient matrix to be zero. (b) The dependent variables are expressed by series of Hermitian polynomials which are substituted into equations (16). By applying the minimum weighted residual method, a set of linear equations for the expansion coefficients is obtained which also defines the eignevalue problem.

   The unknown functions U, V, H and Z of x, are expanded as the series of Hermitian polynomial functions. Figure 2 shows the Hermitian polynomial functions of the lower order multiplied by $e^{-x^2/2}$. As may be imagined, these curves seem to represent the real bottom topography. As a consequence, it is expected that the Hermitian polynomial series expansion will converge rapidly,

$$U(x) = \sum_{n=1}^{\infty} \alpha_n e^{-x^2/2} H_{2n-1}(x)$$

$$V(x) = \sum_{n=1}^{\infty} \beta_n e^{-x^2/2} H_{2(n-1)}(x)$$

$$Z(x) = \sum_{n=1}^{\infty} \gamma_n e^{-x^2/2} H_{2(n-1)}(x)$$

$$H(x) = \sum_{n=1}^{\infty} \delta_n e^{-x^2/2} H_{2(n-1)}(x)$$

$$\left.\begin{array}{c} \\ \\ \\ \\ \\ \\ \end{array}\right\} \quad (22)$$

where H_n's are the Hermite polynomial functions. In order to satisfy not only the boundary condition of $U(x)$ defined at $x = \infty$ but also one at $x = 0$, only the odd order Hermite polynomials are considered in the first expression of eq. (22). While other variables ($V(x)$, $Z(x)$ and $H(x)$) are expressed as sum of the even order Hermite functions.

The Hermitian series expression eq. (22) is substituted into eq. (16). These equations are multiplied by the n-th order Hermite function and integrated with respect to x from 0 to infinity. This procedure is the so-called moment method (one of minimum weighted residual methods). If we truncate the Hermite expansion at the n-th term, we obtain the $4n \times 4n$ dimensional linear simultaneous equations for the unknown expansion coefficients. These equations are represented in the matrix form as given by eq. (23). This matrix system defines the typical eigenvalue problem of p.

$$
\begin{pmatrix}
I^{(1)} & O & K^{(1)} & L^{(1)} \\
\\
I^{(2)} & J^{(2)} & K^{(2)} & L^{(2)} \\
\\
I^{(3)} & J^{(3)} & K^{(3)} & L^{(3)} \\
\\
I^{(4)} & J^{(4)} & O & O
\end{pmatrix}
\begin{pmatrix}
\alpha_1 \\ \alpha_2 \\ \vdots \\ \alpha_n \\ \beta_1 \\ \beta_2 \\ \vdots \\ \beta_n \\ \gamma_1 \\ \gamma_2 \\ \vdots \\ \gamma_n \\ \delta_1 \\ \delta_2 \\ \vdots \\ \delta_n
\end{pmatrix}
= -p
\begin{pmatrix}
\alpha_1 \\ \alpha_2 \\ \vdots \\ \alpha_n \\ \beta_1 \\ \beta_2 \\ \vdots \\ \beta_n \\ \gamma_1 \\ \gamma_2 \\ \vdots \\ \gamma_n \\ \delta_1 \\ \delta_2 \\ \vdots \\ \delta_n
\end{pmatrix}
\qquad (23)
$$

$$\mathbf{A} \cdot \mathbf{Y} = (-p) \mathbf{Y} \qquad \cdots (23\,a)$$

where

$$\mathbf{Y} = [\, \alpha_1, \alpha_2, \cdots \alpha_n, \beta_1, \cdots \beta_n, \gamma_1, \cdots \gamma_n, \delta_1, \cdots \delta_n \,]^T$$

In this matrix representation, the elements $\mathbf{I}$, $\mathbf{J}$, $\mathbf{K}$ and $\mathbf{L}$ further constitute the submatrix system which are to be determined by the equations given

$$I_{m,n}^{(1)} = \frac{\sqrt{2}}{(2m-1)!\sqrt{\pi}} \cdot \int_0^\infty e^{-x^2/2} H_{2m-1}(x) H_{2n-1}(x) F_1(x) dx \quad \cdots (24)$$

$$K_{m,n}^{(1)} = \frac{\sqrt{2}}{(2m-1)!\sqrt{\pi}} \cdot \int_0^\infty e^{-x^2/2} H_{2m-1}(x) [\, \{ H'_{2(n-1)}(x) - x H_{2(n-1)}(x) \}$$

$$r_1(x) + R_1(x) H_{2(n-1)}(x)]dx \qquad \cdots (25)$$

$$L_{m,n}^{(1)} = \frac{\sqrt{2}}{(2m-1)!\sqrt{\pi}} \cdot \int_0^\infty e^{-x^2/2} H_{2m-1}(x) [\, \{ H'_{2(n-1)}(x) - x H_{2(n-1)}$$

$$(x) \} s_1(x) + S_1(x) H_{2(n-1)}(x)]dx \qquad \cdots (26)$$

and for $i = 2, 3$ and 4

$$I_{m,n}^{(i)} = \frac{\sqrt{2}}{(2(m-1))!\sqrt{\pi}} \cdot \int_0^\infty e^{-x^2/2} \cdot H_{2(m-1)}(x) \cdot$$

$$[-f_i(x) H_{2n}(x) + H_{2n-1}(x) F_i(x)] dx \qquad \cdots \quad (27)$$

$$J_{m,n}^{(i)} = \frac{\sqrt{2}}{(2(m-1))!\sqrt{\pi}} \cdot \int_0^\infty e^{-x^2/2} \cdot H_{2(m-1)}(x) H_{2(n-1)}(x) G_i(x) dx$$

$$\cdots \quad (28)$$

$$K_{m,n}^{(i)} = \frac{\sqrt{2}}{(2(m-1))!\sqrt{\pi}} \cdot \int_0^\infty e^{-x^2/2} \cdot H_{2(m-1)}(x) \cdot$$

$$[-r_i(x) H_{2n-1}(x) + H_{2(m-1)}(x) R_i(x)] dx \qquad \cdots \quad (29)$$

$$L_{m,n}^{(i)} = \frac{\sqrt{2}}{(2(m-1))!\sqrt{\pi}} \cdot \int_0^\infty e^{-x^2/2} H_{2(m-1)}(x) \cdot$$

$$[-H_{2n-1}(x) s_i(x) + H_{2(n-1)}(x) S_i(x)] dx \qquad \cdots \quad (30)$$

The eigenvalue problem posed by eq. (23) is solved numerically applying the Library subroutine supplied for the system HITAC 8800. The results will be presented in the subsequent section.

After inspection of the components of eigenvector coresponding to a maximum eigenvalue, it was found that the maximum of the eigenvector components (that is the coefficients α_n, β_n, γ_n and δ_n) corresponds not necessarily to δ_n's, the coefficients in the series expansion of bottom deformation. That is to say, the instability mechanism may sometimes dominate in the fluid system rather than in the bottom topography. In such a case, it was also found that the longshore celerity of instability propagation which is given by $\text{Im}(p)/k$ where Im means the imaginary part is too much higher than that observed in real phenomena. This may be spurious instability caused by the temporally averaged fundamental equation, which necessitated us to proceed to the improved analysis to be described in the next section. In consequence of these discussions, the bottom mode maximum eigenvalue is defined for which the maximal value of 32 components of the eigenvector corresponds to anyone of the coefficients of δ_n. The surface or fluid mode maximum eigenvalue is defined for which the maximum conponent of the corresponding eigenvector is either one of α_n, β_n or γ_n.

Several parameters are grouped into the following two parameters,

$$\Phi = (3\gamma^2/8 C_d)(d h/d x)_B$$

$$\Lambda = C_s / C_d \, h_{0B}$$

$$(31)$$

IV. METHOD OF SOLUTION BASED ON RESPONSE TIME CONCEPT

a)   Concept of response time

To solve analytically a system of Eqs. (9) to (12) seems to be formidably difficult. Methods of analysis of the modern fluid dynamics are to attack complicated problems not purely mathematically but to solve them after simplification of original equations through the physical interpretation of the basic equations. This attitude has been established by L. Prandtl when he proposed the concept of boundary layer in 1904.

Turning to our problem, the fact is soon appreciable that the response of fluids is quick to the deformation of bottom boundary, while the bottom materials respond very much slowly to the changes in the fluid system. Therefore, the state of fluid system may be considered to be quasi-stationary; that is u, v and η are weakly time-dependent only through a gradual change in the bottom topography $h(x, y; t)$. The concept of response time has already been proposed and applied in the first paper of a series of author's reports on this problem in which the Fourier series expansion is used to express the unknown variables as a preliminary attack.

b)   Quasi-stationary solution for fluid system

In the linearized partial differential equations except the last one, i.e. eqs. (9) – (11), the terms of partial differentiation with respect to time are omitted to be solved for a given stationary bottom configuration. The unknown variables u, v and η and the given bottom depth h are expressed in terms of the Hermite polynomials as follows,

$$
\left.
\begin{aligned}
u(x,y) &= \sum_{n=1}^{\infty} \alpha_n H_{2n-1}(x) e^{-x^2/2} e^{iky} \\
v(x,y) &= \sum_{n=1}^{\infty} \beta_n H_{2(n-1)}(x) e^{-x^2/2} e^{iky} \\
\eta(x,y) &= \sum_{n=1}^{\infty} \gamma_n H_{2(n-1)}(x) e^{-x^2/2} e^{iky} \\
h(x,y) &= \sum_{n=1}^{\infty} \delta_n H_m(x) e^{-x^2/2} e^{iky} \\
&\quad (m = 2(n-1) \text{ or } m = 2n-1)
\end{aligned}
\right\} \quad (32)
$$

In the above equations, the function $h(x, y)$ and thus δ_n's are assumed to be given, for the time being; while u, v and η, that is α_n's, β_n's and γ_n's are considered unknown. In order to elucidate clearly the way of thinking, the general expressions of eqs. (32) are simplified, taking only one term of the series but instead multiplying them by $\exp(ik_1 x)$ to compensate for the elimination of other terms, into eq. (33)

$$
\left.
\begin{aligned}
u(x,y) &= \alpha H_1(x) e^{-x^2/2} e^{i(k_1 x + k_2 y)} \\
v(x,y) &= \beta H_1(x) e^{-x^2/2} e^{i(k_1 x + k_2 y)} \\
\eta(x,y) &= \gamma H_m(x) e^{-x^2/2} e^{i(k_1 x + k_2 y)} \\
h(x,y) &= \delta H_m(x) e^{-x^2/2} e^{i(k_1 x + k_2 y)}
\end{aligned}
\right\} \quad (33)
$$

Substituting eqs. (33) into eqs. (9) – (11) and applying the moment method (i.e. integrating both sides between $(0, \infty)$ after multiplication by $H_m(x)$, one obtains the linear simultaneous equations for the unknown coefficients, α, β and γ ;

$$
\begin{pmatrix} I_1 & J_1 & K_1 \\ I_2 & J_2 & K_2 \\ I_3 & J_3 & K_3 \end{pmatrix} \begin{pmatrix} \alpha \\ \beta \\ \gamma \end{pmatrix} = -\delta \begin{pmatrix} L_1 \\ L_2 \\ L_3 \end{pmatrix} \qquad (34)
$$

where

$$
\begin{aligned}
I_i &= \int_0^\infty [\{ik_1 A_{i1}(x) + ik_2 A_{i2}(x) + a_i(x)\} H_1(x) - A_{i1}(x) H_2(x)] H_m(x) e^{-x^2/2} \, dx \\
J_i &= \int_0^\infty [\{ik_1 B_{i1}(x) + ik_2 B_{i2}(x) + b_i(x)\} H_2(x) - B_{i1}(x) H_3(x)] H_m(x) e^{-x^2/2} \, dx \\
K_i &= \int_0^\infty [\{ik_1 C_{i1}(x) + ik_2 C_{i2}(x) + c_i(x)\} H_m(x) - C_{i1}(x) H_{m+1}(x)] H_m(x) e^{-x^2/2} \, dx \\
L_i &= \int_0^\infty [\{ik_1 D_{i1}(x) + ik_2 D_{i2}(x) + d_i(x)\} H_m(x) - D_{i1}(x) H_{m+1}(x)] H_m(x) e^{-x^2/2} \, dx
\end{aligned} \qquad (35)
$$

Therefore, the unknown coefficients α, β and γ are obtained

$$
\begin{pmatrix} \alpha \\ \beta \\ \gamma \end{pmatrix} = -\delta \begin{pmatrix} I_1 & J_1 & K_1 \\ I_2 & J_2 & K_2 \\ I_3 & J_3 & K_3 \end{pmatrix}^{-1} \begin{pmatrix} L_1 \\ L_2 \\ L_2 \end{pmatrix} \qquad (36)
$$

c) Instability of bottom boundary

If the coefficient δ is considered to be a slowly varing function of time as suggested by the response time concept, the velocity field u and v are also weak functions of time.

Equations (33) together with eq. (36) are substituted into the conservation equation of bottom material transport, eq. (12), to obtain

$$
H_m(x) \frac{\dot{\delta}(x)}{\delta(x)} = C_s [\alpha_*(ik_1 H_1(x) - H_2(x)) + \beta_*(ik_2) H_2(x)] + \varepsilon \qquad (37)
$$

where ε is a residual term and $\alpha_* = \alpha/\delta$, $\beta_* = \beta/\delta$. Applying the moment method, (that is multiplying $H_m(x)$ on both side of the above equation and integrating in the range $(0, \infty)$, one obtains the solution,

$$
\delta(t) = A e^{pt} \qquad (38)
$$

where A is an integration constant and p is given by

$$p = \frac{\sqrt{2}}{\sqrt{\pi}} \frac{C_s}{m!} \left[\alpha * \int_0^\infty \left\{ ik_1 \, H_1(x) H_m(x) - H_2(x) H_m(x) \right\} e^{-x^2/2} \, dx \right.$$
$$\left. + \beta * \int_0^\infty \left\{ ik_2 \, H_2(x) H_m(x) e^{-x^2/2} \, dx \right\} \right] \tag{39}$$

The initial perturbations may be stable or unstable depending on the sign of the real part of p,

$$R(p) > 0 \; : \; \text{unstable}$$

$$R(p) = 0 \; : \; \text{neutral}$$

$$R(p) < 0 \; : \; \text{stable}$$

The maximum value of $R(p)$ has been sought for a family of parameters k_1 and m for the fixed values of the langshore wave number of rip current and cusp k_2, the incidence angle of waves θ, and the bottom slope dh/dx.

V. THEORETICAL RESULTS AND COMPARISON
WITH FIELD OBSERVATIONS

a) Stability diagram
   Figures 3 a) and b) show examples from results of this eigenvalue problem obtained by the methods described in III and IV, respectively, (Hino (1973 a and b)). In these figures, the abscissa is the wave number k in the direction of shoreline, and the ordinate is the real part of the maximum eigen values. It is evident that the most unstable mode appears at k = 1.6, that is the wave length in longshore direction of rip current and cusp is

$$L = 2\pi / k \cong 4 \tag{40}$$

Since unit of length is chosen as a distance from shoreline to breaker zone, the most prefered wavelength L_r of rip and cusp is about four times the distance from the shore to the breaker zone L_B,

$$L_r \cong 4 \, L_B \tag{40a}$$

b) Theoretical prediction of flow fields and bottom topography
   Simultaneously with the determination of eigenvalue p, the eigen vectors which are coefficients of the Hermite series are determined. Therefore, the rip current and cuspidal bottom system are reconstructed from eq. (22), and shown in figures 4, 5 and 6. Figure 4 illustrates the results of theoretically determined flow field, bottom topography for the case of normal wave incidence. The cellular flow field develops and the so-called rip channel is to be formed. Figures 5 and 6 are also the theoretical results for an oblique wave incidence. It is noted that the longshore current becomes to meander and the sand bars to develop.

c) Comparison with field observation
   Figure 7 cited from the report on field experiments (Public Works
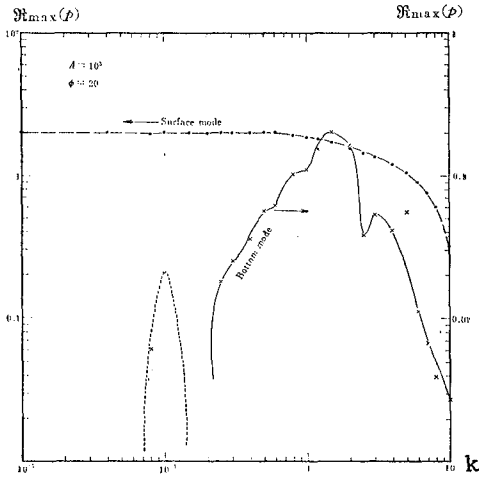
Fig. 3 a) : An example of the instability-curve determined by the method described in III.
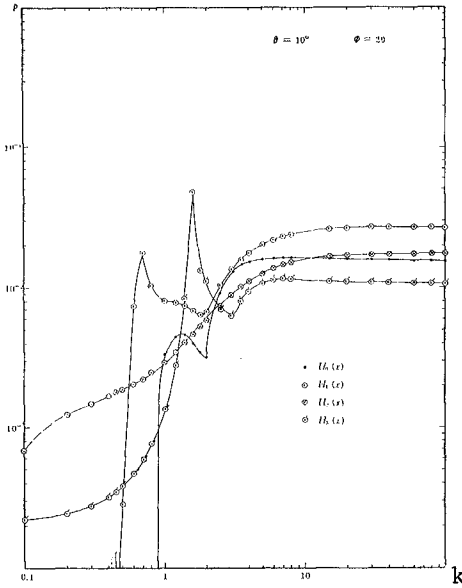
Fig. 3 b) : An example of the instability-curve determined by the method described in IV.
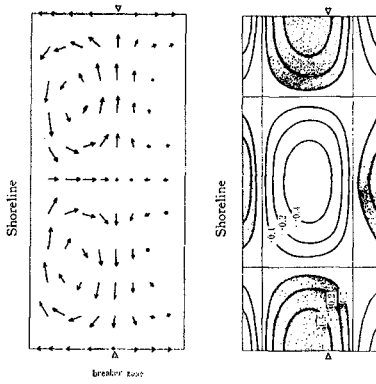
Fig. 4 : The cellular pattern of
secondary current (left) and
perturbation in bottom topo-
graphy – the shaded areas are
scoured – (right), for normal
wave incidence, $k=1.6$, $\Phi=2$,
$\Lambda=10^3$.
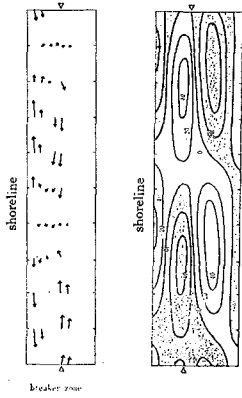
Fig. 5 : The cellular partern of
secondary current (left) and
the accompanied perturbation
in bottom topography – the
shaded regions are scoured
(right); $\Theta=10^\circ$, $k=0.6$, $\Phi=2$,
$\Lambda=10^3$.
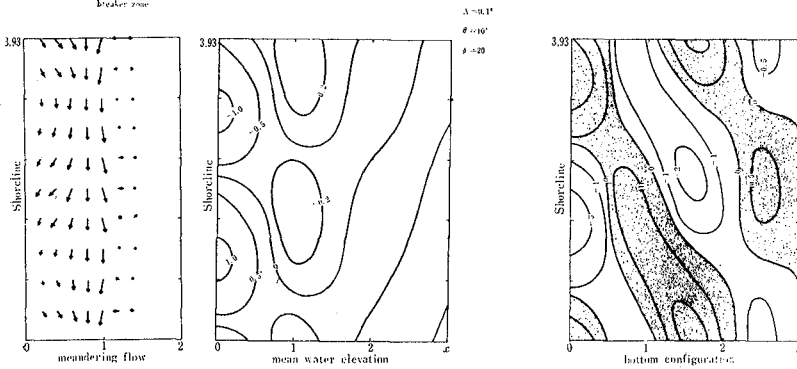
Fig. 6 : The meandering flow pattern composed of the basic
longshore current and secondary perturbation flow (left),
the perturbation in mean water elevation (middle) and the
perturbation in bottom topography – the shaded areas are
scoured (right) ; $\Theta=10^\circ$, $k=1.6$, $\Phi=20$, $\Lambda=10^3$.
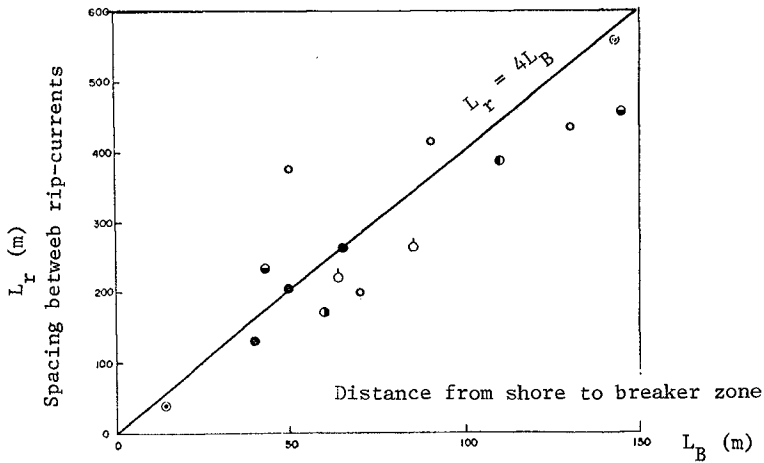
Fig. 7 : Comparison between the theoretical prediction and
the field observation (cited from the report of Public
Works Research Institute, Ministry of Construction)
on the relation of Lr $\cong$ 4.0 L_B, eq. (40 a).
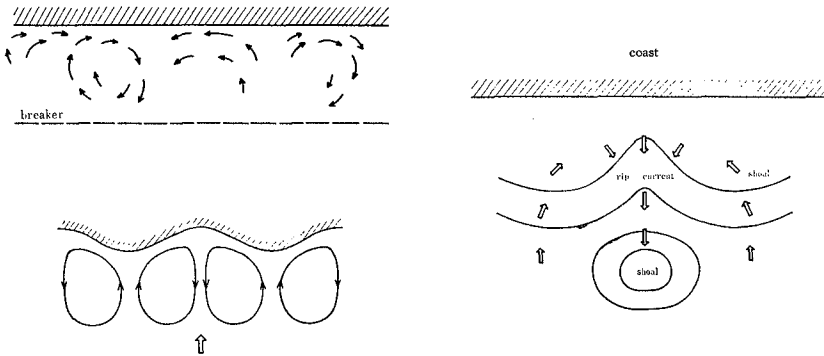
Fig. 8 : Schematic representation of cellular flow patterns
(above left) from the papers by Horikawa et al. (1971)
and Sonu (1972), and of rip current and rip-channel
(right) drawn schematically by the present author
based on the field observation by Sonu (1972).

(a)

(b)
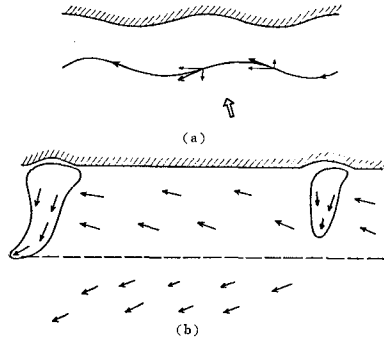
Fig. 9 : Field observation of
         meandering shore currents
         for oblique wave incidence

breaker zone

(a) Perturbation in bottom depth

breaker zone

(b) Change in bottom depth contour

original coastal line

(c) Cuspidal coast and crescent bar
    (fully developed stage)
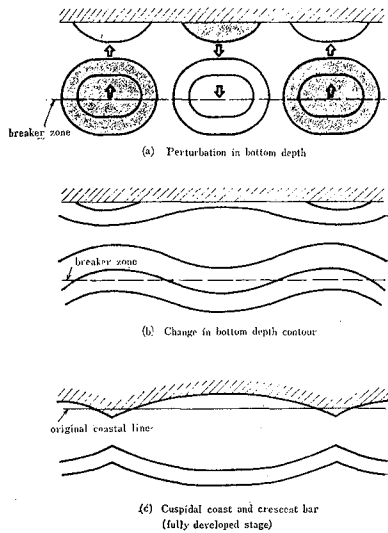
Fig. 10 : Theoretically estimated change in bottom depth
           contour and formation of cuspidal coast and
           crescent bar.
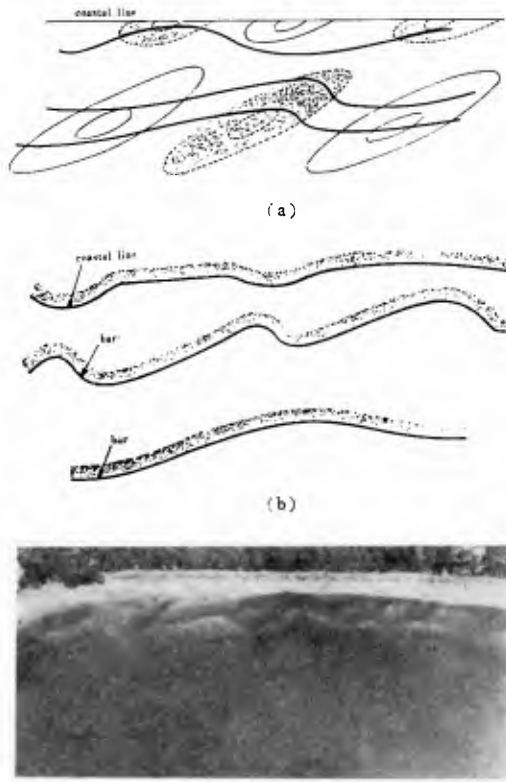
Fig. 11 : Theoretically estimated
bottom contour (a) and longshore
meandering bars by aerial photography (b)

Research Institute, Ministry of Construction) represents the relationship between the wave length of rip current generation L_r and the distance from shore to breaker zone L_B , showing a good agreement with the theoretical prediction, eq. (40a).

Figure 8 is the schematic representation of results of field observation by Horikawa et al (1971) and Sonu (1972) of longshore current system when waves are incident normally. These figures agree qualitatively with figure 4. In comparing the theory with expriments, it should be remarked that the theory predicts the initial stage of developments which may be treated by linearization, while field data are obtained in general for the fully developed stage where the nonlinear effects predominate.

Figure 9 illustrates schematically the results of field observation performed by Horikawa et al (1971) and Sonu (1972) which are to be compared with the theoretical results, figures 5 and 6.

The process of development of cuspidal coast and crescent bar may be explained by the author's theory. The cyclic perturbation in bottom depth accompanied by periodic shore current system (figure 10a)), if it is superposed on the original bottom configuration, composes undulating contour lines (fig. 10 b)). If the instability mechanism develops further into the nonlinear region, the offshore currents are intensified, the onshore currents becoming weak. At the same time, shorelines will be cyclically excavated and deposited (fig. 10 c)).

Formation of longshore meandering bars (fig. 11 b)) may also be explained by the superposition of perturbed bottom and the original contour line (fig. 11 a)).

VI. CONCLUSION

Formation of the systematic feature of shore current and shore bottom topography is shown to be results of the hydrodynamic instability caused by the radiation stresses. The linearized perturbation equations for the vertically averaged velocity components u and v, the water surface elevation η and the scouring depth of bottom h are derived. The dependent variables are assumed to have functional forms such as u (x, y, t) = $U(x)$exp (iky + pt) and so on. Consequently, the fundamental partial differential equations are reduced to the simultaneous ordinary differential equations for variations in the offshore direction. These constitute an eigenvalue problem for the temporal exponential growth rate p under the given boundary conditions.

Two methods of solving the problem are presented. One is the moment method (a procedure of the minimum weighted residual methods) based on the Hermite polynomial expansions of the dependent variables. The other is the quasi-stationary analysis based on the response time concept. Both methods reduce the simultaneous ordinary differential equations to the matrix form of eigenvalue problem.

Results of computation show that the system of shore current and bottom topography is hydrodynamically unstable for a small perturbation.

For a given bottom movability, the temporal exponential growth rate has a peak value at a certain longshore spacing about four times a distance from shoreline to breaken zone.

The cellular flow patterns of perturbed secondary currents as well as the contour maps of bottom scouring and water surface elevation are shown. The several results obtained in this investigation conform with results of qualitative field observations reported by oceanographical geologists and coastal engineers.

REFERENCES

Bowen, A. J. (1969) : Rip currents, 1. Theoretical investigations, J. Geophy. Res., Vol. 74, No. 23, pp. 5467-5478.

Hino, M. and Hayashi, N. (1972) : Theory on generation of rip currents, Proc. 19th Conference on Coastal Eng., Japan Soc. of Civil Engrs., pp. 93-96. (in Japanese); Coastal Engineering in Japan Vol. 16, 55-60, (in English)

Hino, M. (1972) : Shore-current system and deformation of shore bottom, Preprint of 1972 Fall Conference of Oceanographical Soc. of Japan, pp. 151-152. (in Japanese) ; Also Technical Report No. 13, pp. 99-113, Department of Civil Eng., Tokyo Inst. of Tech., Dec. (in English)

Hino, M. (1973 a) : Hydrodynamic instability theory on the formation of systematic shore current and coastal topography, Part II Solution by Galerkin's procedure based on Hermitian polynomial expansion, Technical Report No. 14, pp. 27-41, Department of Civil Eng., Tokyo Inst. of Tech., June. (in English)

Hino, M. (1973 b) : Theory on generation of rip currents, Part III A simplified theory, Proc. 20th Conference on Coastal Eng., J.S.C.E., pp. 339-344.

Horikawa, K., Sasaki, T., Fukui, W., Igarashi, H. and Kito, H. (1971) : Field observation of shore currents (Part I), Proc. 18th Conference on Coastal Eng. (Japan), Japan Soc. of Civil Engrs., pp. 395-400.

Longuet-Higgins, M. S. (1970) : Longshore currents generated by obliquely incident sea waves, 1., J. Geophy. Res., Vol. 75, No. 33, pp. 6778-6789.

Longuet-Higgins, M. S. and Stewart, R. W. (1964) : Radiation stresses in water waves ; a physical discussion, with applications, Deep-Sea Res., Vol. 11, pp. 529-562.

Public Works Research Institute, Ministry of Construction (1974) : Field observation on wave and coastal currents, Tech. Memo. No. 916.

Sonu, C. J. (1972) : Field observation of nearshore circulation and meandering currents, J. Geophy. Res., Vol. 77, No. 18, pp. 3232-3247, June.

Sonu, C. J. (1972) : Comment on paper by A. J. Bowen and D. L. Inman, 'Edge wave and crescentic bars' J. Geophy. Res.

CHAPTER 53

TWO-DIMENSIONAL BEACH TRANSFORMATION DUE TO WAVES

by

Tsuguo Sunamura and Kiyoshi Horikawa

Coastal Engineering Laboratory
Department of Civil Engineering
University of Tokyo
Bunkyo-ku, Tokyo
Japan

ABSTRACT

Important physical parameters controlling sandy beach
transformation were clarified on the basis of the result
obtained by a laboratory test. They were not only wave
steepness but also beach gradient and a ratio of sand size to
wave length. These parameters enabled the previously obtained
laboratory beach profiles to be classified into newly-
proposed three beach types. These parameters were also found
to be effective in grouping the data of shoreline changes
both in laboratories and in fields.

INTRODUCTION

Sandy beach transformation by waves is one of the most
interesting problems for coastal engineers and also for
coastal geomorphologists. Intensive and multiple studies
have been conducted since the beginning of 1950's, both in
laboratories and in fields. However, the physical processes
have not yet been fully understood.

Table 1   Test cases and condition.

Case No.	deep water wave height (H_O)	wave period (T)	grain size of sand (d)	initial beach slope (tan β)	duration wave action (t)
1	3.4 cm	1 sec	0.7 mm	1/10	160 hr
2	3.4	1	0.2	1/10	160
3	7.6	1	0.7	1/10	160
4	7.6	1	0.2	1/10	160
5	7.6	2	0.7	1/10	160
6	7.6	2	0.2	1/10	160
7	3.4	1	0.7	1/20	160
8	3.4	1	0.2	1/20	160
9	7.6	1	0.7	1/20	160
10	7.6	1	0.2	1/20	160
11	7.6	2	0.7	1/20	160
12	7.6	2	0.2	1/20	160
13	3.4	1	0.7	1/30	160
14	3.4	1	0.2	1/30	160
15	7.6	1	0.7	1/30	160
16	7.6	1	0.2	1/30	160
17	7.6	2	0.7	1/30	160
18*	7.6	2	0.2	1/30	160

* Result of this case is not used in this paper.
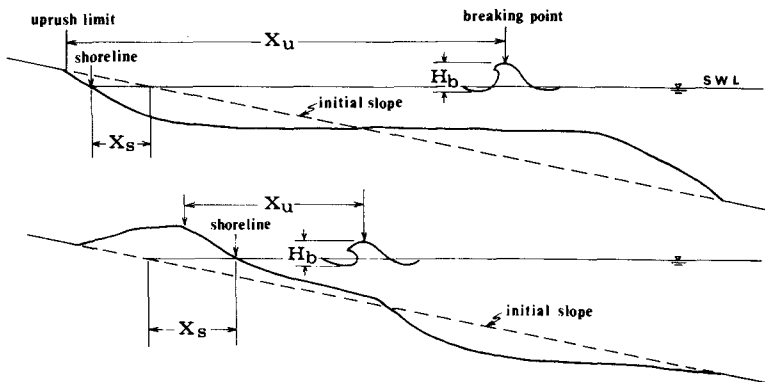
Fig. 1   Definition sketch.

    Based on the result of a wave flume experiment, the
present study attempted to find out important physical param-
eters governing shore transformation. Using the parameters,
(1) laboratory beach profiles were classified according to
a newly proposed criterion, and (2) shoreline changes both in
laboratories and in fields were discussed.

                        LABORATORY EXPERIMENT

    A wave flume equipped with a flap-type wave maker was
used; its dimension was 25 m long, 1.5 m deep, and 0.8 m
wide. The flume was divided into two equivallent parts by a
splitter wall which was placed in the center of the flume.
Two beaches having the same initial slope and the different
mean diameters of quartz sands were set up respectively in the
two parts of the flume; one was a 0.2 mm-sand beach and the
other a 0.7 mm-sand beach. The specific gravity was 2.65 and
Trask's sorting coefficient was 1.1, for both sands. The
initial slope was uniform and three kinds of the gradient
were selected: 1/10, 1/20, and 1/30. The same waves were
allowed to act simultaneously on both beaches. Two kinds of
wave height, i.e. 3.4 cm and 7.6 cm, and two kinds of wave
period, i.e. 1 sec and 2 sec were adopted here. The total
duration of wave action was 160 hours for each experimental
run. Table 1 is a list of experimental cases.

    In order to examine the relationship between beach pro-
file change and wave behavior inside surf zone, the following
physical quantities were measured at certain intervals of
time: beach configuration, shoreline displacement, X_S, breaker
height, H_b, the distance from breaking point to limit of up-
rush, X_u (see Fig. 1), and the time for a wave to travel
from its breaking point to the uprush limit, τ. Since the
beach profile was not always exactly two-dimensional, the
profile measurement was done in the center of the beach.

    Figure 2 shows temporal change of beach profiles; each
group indicates the results obtained under the same experi-
mental condition except for initial slope.
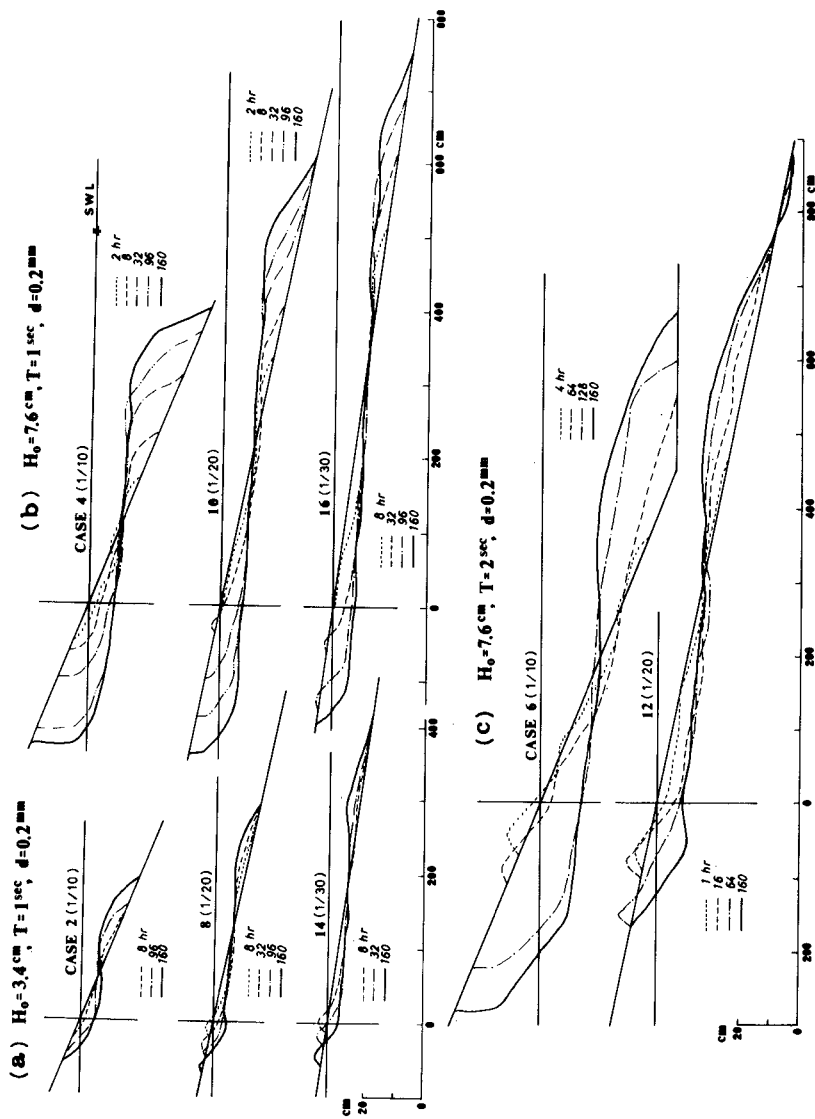
Fig. 2 Beach profile changes (1).
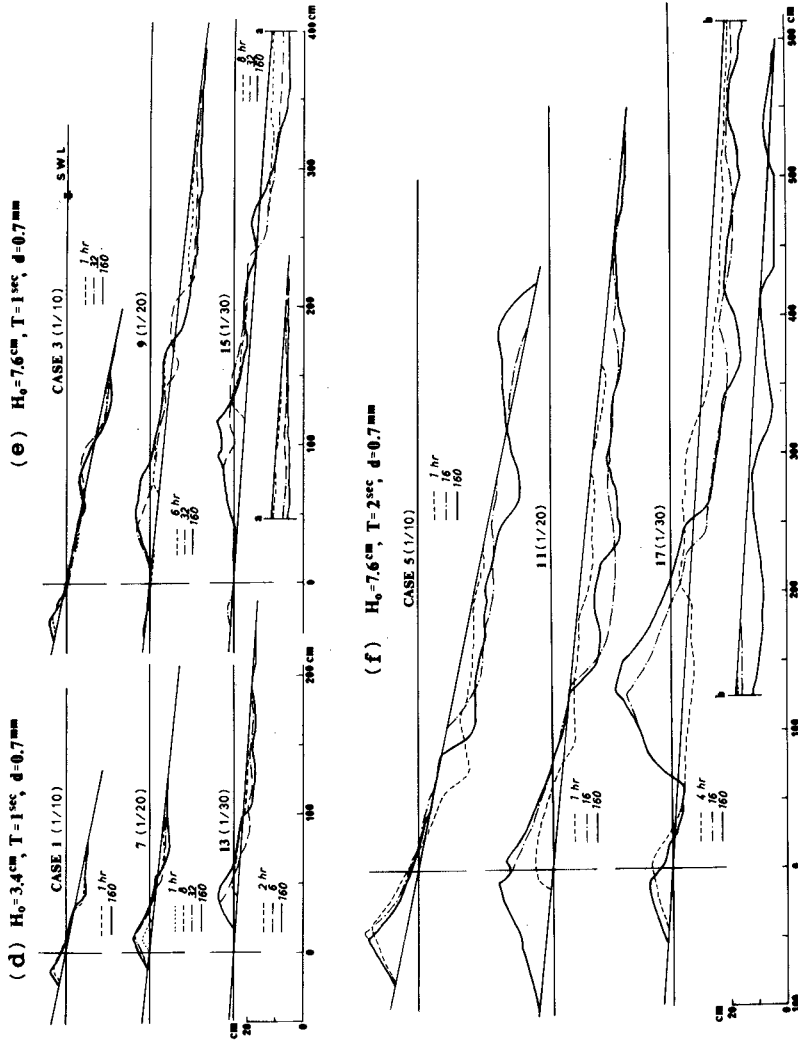
Fig. 2 Beach profile changes (2).

BEACH PROFILE CHANGE

A New Beach Profile Classification

Johnson (1949), Iwagaki and Noda (1962), and Nayak (1970) have proposed the parameters by which beach profiles could be classified into bar or step types and have provided the criteria (Fig. 3). In this figure, H_O = deep water wave height, L_O = deep water wave length, and d = grain size of beach sand. These previous studies do not take beach gradient into consideration. The present experimental cases are also plotted in Fig. 3.

According to these criteria, Cases 2, 8, and 14 must become step type. However, the final profiles of these cases show bar type (Fig. 2(a)). On the other hand, the criteria except for Nayak's one tell that Cases 3, 9, and 15 should be bar type. It is very difficult to recognize the final profile of Case 9 as a bar (Fig. 2(e)); this is typical of step type.

There are two reasons for that these criteria do not suffice: (1) the judgement of " bar " or " step " is sometimes very hard due to complexity of beach configuration, and (2) the parameters are inadequate.

The comparison among Cases 3, 9, and 15 in particular (Fig. 2(e)) shows that the initial beach slope has a great effect on the final configuration. It is clear that the initial slope is an essential factor in considering beach profile pattern. Then, this study proposes a new beach classification which is based on the displacement of topography from the initial beach slope (Fig. 4):

        Type I: a shoreline retrogresses and sand
              accumurates in offshore zone,
        Type II: a shoreline advances and sand piles
             up offshore, and
        Type III: a shoreline prograges and no sand
             deposition takes place offshore.

Any beach profile can be classified into these three
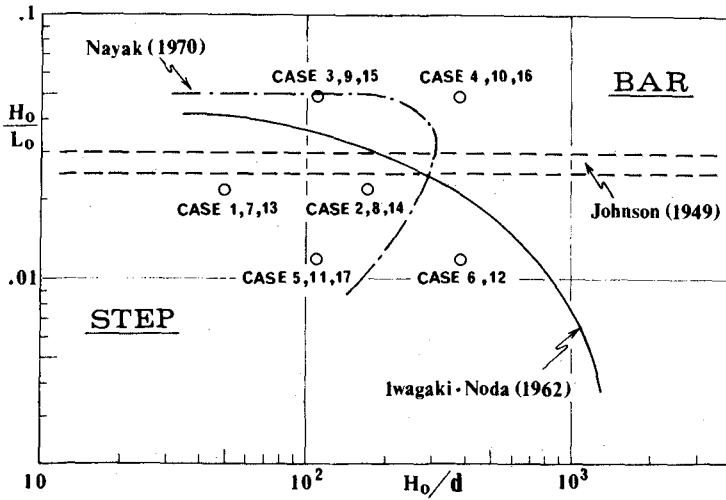
Fig. 3   Previous criteria for generation of bar and step.
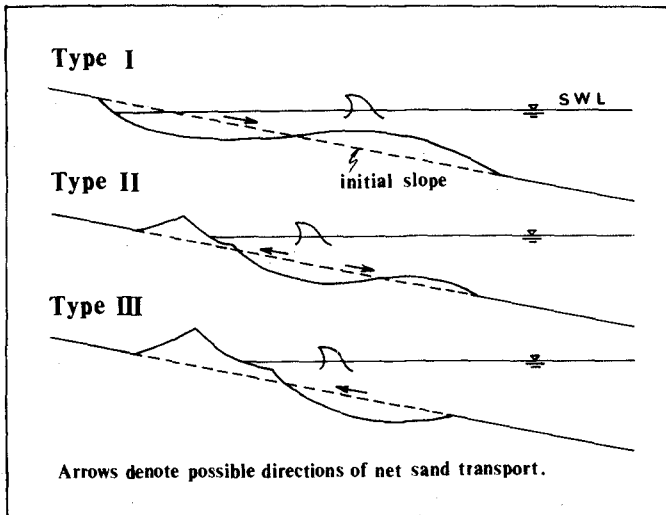
Fig. 4   New beach profile classification.

types without much difficulty. Before applying this grouping, we must clearly state major parameters dominant in shore deformation process.

Dominant Parameters in Beach Transformation

Figure 5 shows the relationship between $X_u^* L_O / H_{b*}^2$ and H_{b*}/d, where $X_u^* = X_u$ at the final stage, and $H_{b*} = H_b$ at the initial stage. In this paper, the " final stage " means the state after a 160-hour wave action, while the " initial stage " denotes the state immediately after wave action, i.e. at the time when the beach slope was scarecely changed.

Although the data points in Fig. 5 are widely scattered, there is a tendency as shown by the straight line, which is expressed by

$$X_u^* L_O / H_{b*}^2 = 0.018 \ (\ H_{b*}/d \ )^2 \ . \tag{1}$$

This equation indicates that X_u at the final stage can be inferable from H_b at the initial stage, L_O, and d.

In Fig. 6, open circles show the data at the final stage, while solid circles present the data at a measuring time less than 160 hours. The following relation can be established independent of time:

$$X_u/L_O = 0.39 \ (\ \tau/T \ )^{1.2} \ , \tag{2}$$

where T = wave period. The final stage is given by

$$X_u^*/L_O = 0.39 \ (\ \tau^*/T \ )^{1.2} \ . \tag{3}$$

Figure 7 shows the relationship between H_b/H_O and H_O/L_O, for various bottom slope. All the data plotted here were the results which Goda (1970) synthesized giving correction to the previous data of laboratory tests conducted on a uniform and fixed bottom slope (Bowen et al., 1968; Goda, 1964; Iversen, 1951; Mitsuyasu, 1962; Toyoshima et al., 1968).
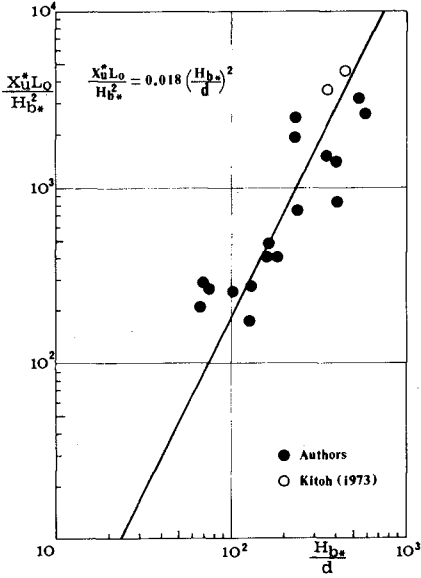
Fig. 5   Relation of $X_u^* L_O / H_b^2$
         and H_{b*}/d.
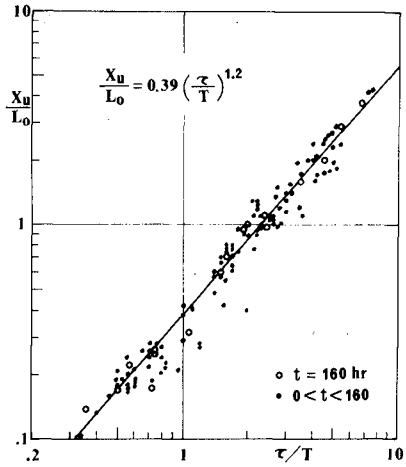
Fig. 6   Relation of X_u/L_O
         and τ/T.

These straight lines are shown by

$$H_b/H_O = (\tan \alpha)^{0.2} (H_O/L_O)^{-0.25}, \qquad (4)$$

where $\tan \alpha$ = bottom slope.

Equation (4) can be applied to a uniformly sloped sandy beach at the initial stage, on the assumption that the influences of friction and percolation by sandy bottom on the breaker height could possibly be neglected. Consequently, the following equation is written:

$$H_{b*}/H_O = (\tan \beta)^{0.2} (H_O/L_O)^{-0.25}, \qquad (5)$$

where $\tan \beta$ = initial sandy beach slope.

From Eqs. (1), (3), and (5), we can get

$$H_O/L_O = 2.76 (\tau^*/T)^{0.4} (\tan \beta)^{-0.27} (d/L_O)^{0.67}, (6)$$

where τ^*/T = phase-difference at the final stage. The " phase-difference ", which was defined as τ/T by Kemp (1960), is an important quantity that can explain differences in beach profile.

According to the observation, the final profile showed Type I when the following condition was satisfied:

$$\tau^*/T \gtrsim 2, \qquad (7)$$

while Type III was formed under conditions of

$$\tau^*/T \lesssim 2. \qquad (8)$$

Hence, the boundary between Types I and III is

$$H_O/L_O = 4 (\tan \beta)^{-0.27} (d/L_O)^{0.67}. \qquad (9)$$

This equation indicates that H_O/L_O, $\tan \beta$, and d/L_O are dominant parameters in grouping beach profiles created under fully long duration of wave action. The validity of these

parameters will be investigated below using the previous wave flume data. Before doing this, the check of temporal shore-line changes is needed, because shoreline position is one of essential criteria of the newly proposed classification.

Figure 8 is a schematic diagram of temporal shoreline changes. There are two typical changes: (1) a shoreline does not return to its original position (Fig. 8(1)&(2)), i.e. an irreversible change can be seen, and (2) once advanced or retreated shoreline returns to its original at a time of t_1 and then retrogrades or prograces (Fig. 8(3)& (4)), i.e. a reversible change can be appreciated.

Figure 9 illustrates actual shoreline changes; Cases 6, 8, 9, and 14 present reversible changes. These cases show that $t_1 \leqq 40$ hours. After t_1, an irreversible state attains. When applying the new classification, it is necessary to use the data in which a shoreline change is in an irreversible state.

The time of t_1 would depend on experimental conditions, but the quantitative relation has not yet been obtained. The estimation of t_1 is possible if the data of temporal shore-line change is available. The previous beach profile studies do not usually provide such a data. Hence, the authors assumed here that a shoreline change was in an irreversible state if the wave duration was more than 40 hours, irrespective of test conditions.

The final beach profiles of the previous tests which satisfied the following three conditions were used: (1) a wave flume was used, (2) sand or gravel was used as bed mate-rial, and (3) wave duration was more than 40 hours (Eagleson et al., 1961; Horikawa et al., 1973; Monroe, 1969; Raman and Earattupuzha, 1972; Rector, 1954; Saville, 1957; Tsuchiya and Yoshioka, 1970; Watts, 1954).

Result of Classification
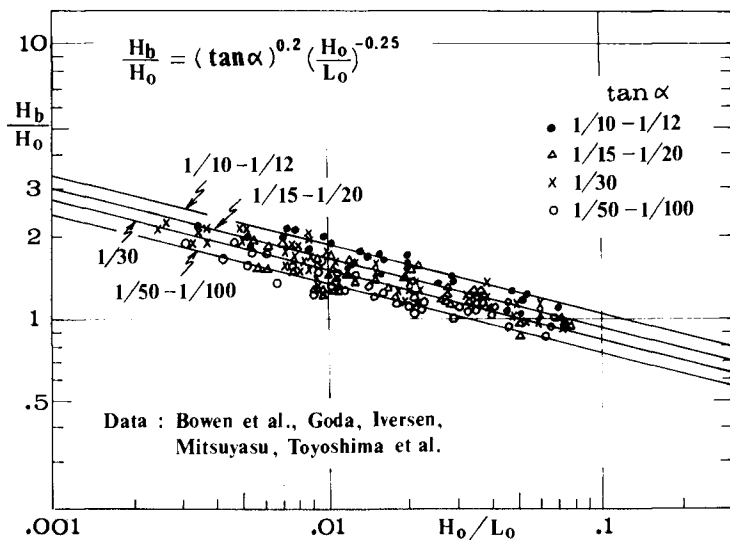
Fig. 7   Relative breaker height and deep water
         wave steepness for various bottom slope.
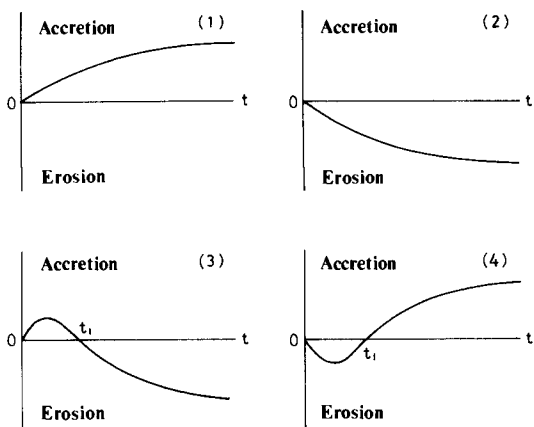
Fig. 8   Schematic diagram showing temporal
         shoreline changes.
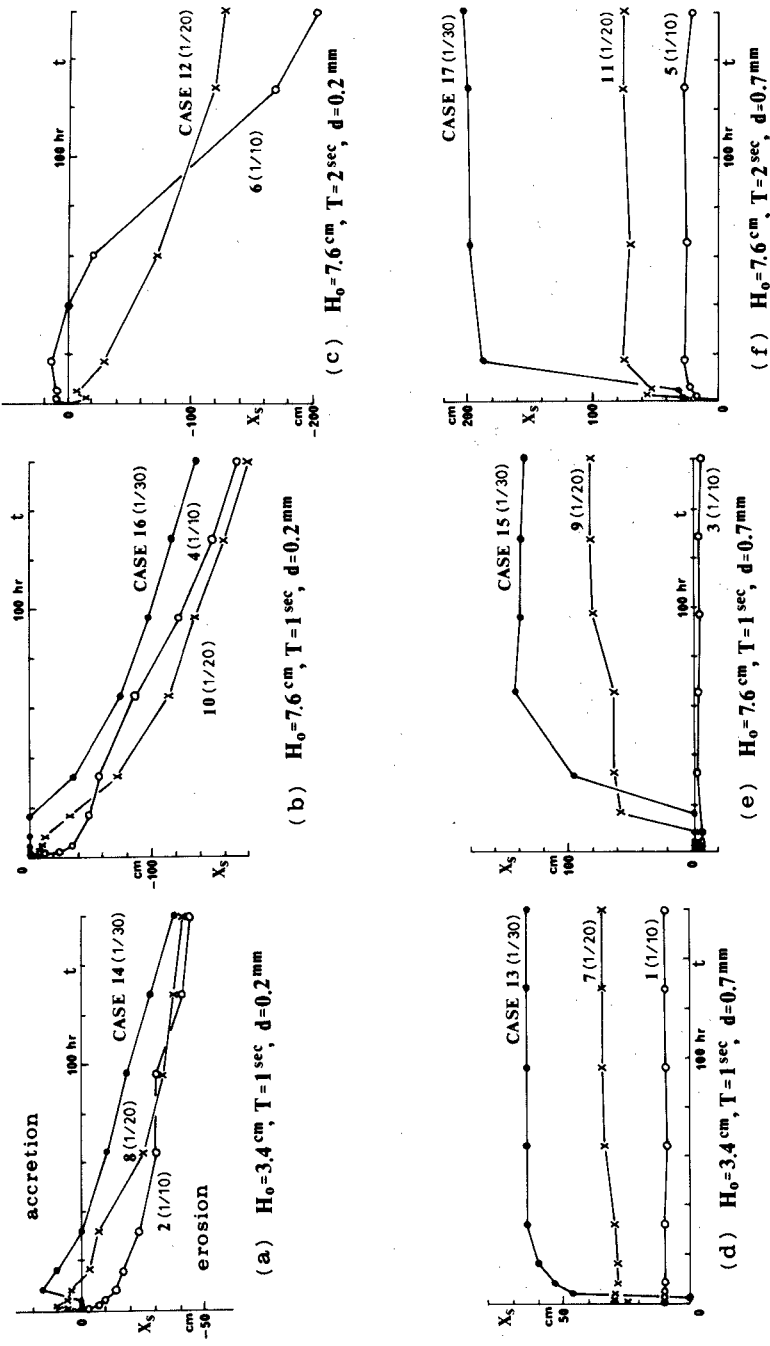
Fig. 9 Temporal shoreline changes.

　　　As shown in Fig. 10, almost all the data points of Type III are in the following region:

$$H_O/L_O \leqq 4 \ (\ \tan \beta \ )^{-0.27} (\ d/L_O \ )^{0.67}, \qquad (10)$$

while Type I is in

$$H_O/L_O \geqq 4 \ (\ \tan \beta \ )^{-0.27} (\ d/L_O \ )^{0.67}. \qquad (11)$$

The region for Type II is given by

$$4 \ (\ \tan \beta \ )^{-0.27} (\ d/L_O \ )^{0.67} \leqq H_O/L_O$$

$$\leqq 8 \ (\ \tan \beta \ )^{-0.27} (\ d/L_O \ )^{0.67}. \quad (12)$$

　　　It is interesting that fully-developed shore topography is distinguishable by these dimensionless three parameters.

SHORELINE CHANGE

Laboratory Shoreline Change

　　　A review of Fig. 4, with special attention to shoreline change, presents that Type I shows an eroded shoreline, while Types II and III denote advanced ones. Figure 10 indicates that these parameters would be effective in grouping the data of shoreline change. To confirm this, additional data of Saville (1957), whose experiment fulfilled the above-mentioned three requirements, were also plotted in Fig. 11.

　　　All the data points are distinctly grouped into two areas, i.e. erosion and accretion, although there is an intricate region between them.

Field Shoreline Change

　　　Using the same parameters and assuming the existence of
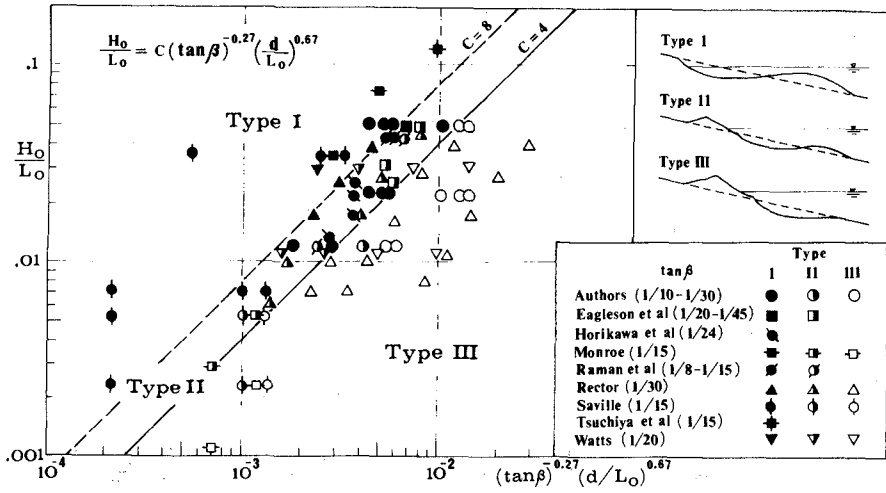
Fig. 10 Classified laboratory beach profiles.
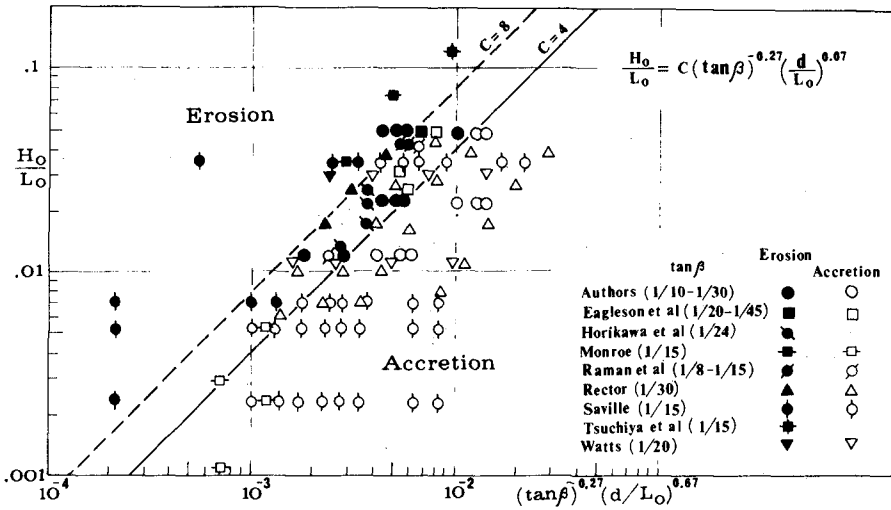
Fig. 11 Shoreline change in the laboratory.

two-dimensionality in nature, the authors attempted to analyze
the previous field data (Agemori, 1967; Chang and Tang, 1970;
Darling, 1960; Japan Atomic Power Co., 1960; Ministry of
Transport, 1962; Ozaki, 1972; 1973; Rao and Kassim, 1970;
Saville, 1957; Sonu, 1968; Wiegel et al., 1953). Figure 12
shows the result. The judgement of " erosion " and
" accretion " was based on the shoreline deviation from its
position at the beginning of an investigation term. Maximum
wave height during that term was adopted for H_O (or H); wave
period corresponding to this height was used for calculation
of L_O. Mean grain size of subaerial beach sand was taken as a
representative value of d. In Fig. 12, $\tan \overline{\beta}$ stands for the
averaged submarine slope from shoreline up to a water depth of
about 20 m; this value was tentatively taken here.

The data points in parentheses are the results of proto-
type experiment conducted by Saville (1957). It is interesting
that these results and the field data showing erosion are in
the same region.
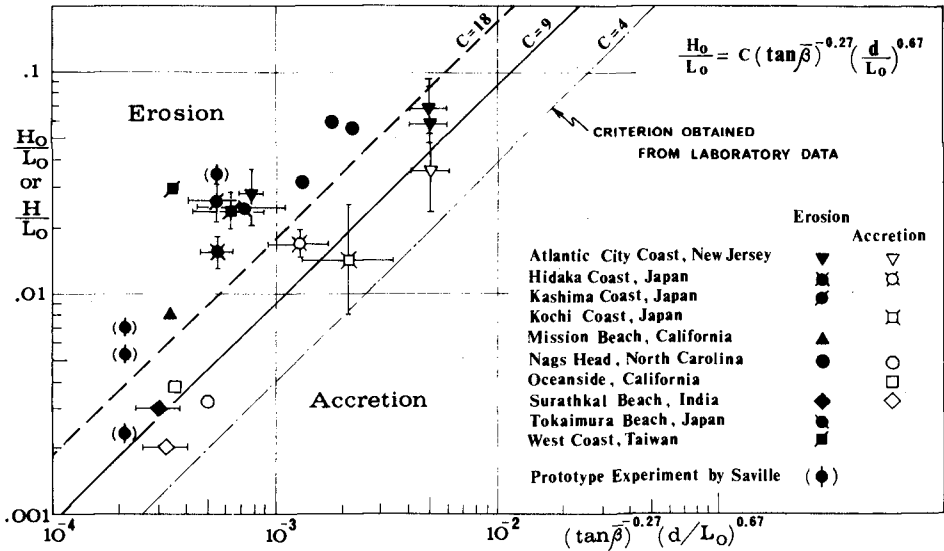
Fig. 12 Shoreline change in the field.

Figure 12 indicates that there is a similar trend to
the laboratory result in Fig. 11, although the boundary
between erosion and accretion shifts leftwards as a whole.
One reason for this shift would probably be scale effect.

There are several problems in such a treatment of field
data: (1) the check of two-dimensionality in nature, (2) the
investigation of time effect on actual beach transformation
under varying wave field, (3) the treatment of sand grain
size which is generally a function of time and space, (4) the
definition of " initial " beach slope, and (5) the examination
of tidal effect on shoreline change. The clarification of
these points is necessary for the future development of this
study.

CONCLUSION

Major parameters governing sandy beach transformation
were found to be not only wave steepness but also beach slope
and a ratio of sand grain size to wave length. These param-
eters were effective in classifying fully-developed beach
topography, and also helpful to grouping the data of shore-
line changes both in laboratories and in fields.

ACKNOWLEDGEMENT

REFERENCES

Agemori, C. (1967): On littoral transport along the Kochi coast. Proc. 14th Jap. Conf. Coastal Eng., pp.280-285. (in Japanese).

Bowen, A. L., D. L. Inman and V. P. Simmons (1968): Wave set-down and set-up. Jour. Geophys. Res., 78, pp. 2569-2577.

Chang, K. S. T. and F. L. W. Tang (1970): Studies on the shore process and wave features of the Western coast of Taiwan. Proc. 12th Conf. Coastal Eng., pp.729-737.

Darling, J. M. (1960): Seasonal changes in beaches of the North Atlantic coast of the United States. Proc. 7th Conf. Coastal Eng., pp.236-248.

Eagleson, P. S., B. Glenne and J. A. Dracup (1961): Equilibrium characteristics of sand beaches in the offshore zone. B.E.B. Tech. Memo., 126, 66p.

Goda, Y. (1964): Wave forces on a vertical circular cylinder: experiments and a proposed method of wave force computation. Rep. Port and Harbour Res. Inst., Ministry of Trans., 8, 74p.

Goda, Y. (1970): A synthesis of breaker indices. Proc. Jap. Soc. Civ. Eng., 180, pp. 39-49. (in Japanese).

Horikawa, K., T. Sunamura and H. Kitoh (1973): A study of beach transformation by wave action. Proc. 20th Jap. Conf. Coastal Eng., pp.357-363. (in Japanese).

Iversen, H. W. (1951): Laboratory study of breakers. Proc. Symposium Gravity Waves, U.S. Bur. Stds., Cir. 521, pp. 9-32.

Iwagaki, Y. and H. Noda (1962): Laboratory study of scale effects in two-dimensional beach processes. Proc. 12th Conf. Coastal Eng., pp.194-210.

Japan Atomic Power Co. (1960): Report of field investigation on the Tokaimura beach. Rep. 2, 77p. (in Japanese).

Johnson, J. W. (1949): Scale effect in hydraulic model involving wave motion. Trans. A.G.U., 30, pp. 517-525.

Kemp, P. H. (1960): The relationship between wave action and beach profile characteristics. Proc. 7th Conf. Coastal Eng., pp. 262-277.

Kitoh, H. (1973): A basic study of beach processes. Unpub.
    M.Sc. Thesis, Univ. of Tokyo, 119p. (in Japanese).
Ministry of Transport (1962): On the physical condition
    of Kashima Industrial Port. 294p. (in Japanese).
Mitsuyasu, H. (1962): Experimental study on wave force
    against a wall. Rep. Trans. Tech. Res. Inst., 47, 39p.
    (in Japanese).
Monroe, F. F. (1969): Oolitic aragonite and quartz sand:
    laboratory comparison under wave action. C.E.R.C. Misc.
    Paper 1-69, 22p.
Nayak, I. V. (1970): Equilibrium profiles of model beaches.
    Proc. 12th Conf. Coastal Eng., pp.1321-1340.
Ozaki, A. (1972): A study of countermeasure for sand deposi-
    tion in small harbor. Proc. 19th Jap. Conf. Coastal Eng.,
    pp.47-51. (in Japanese).
Ozaki, A. (1973): On the effect of initial beach slope on
    equilibrium shore profiles. Memoir 28th Annual Conv.
    Jap. Soc. Civ. Eng., pp.88-89. (in Japanese).
Raman, H. and J. J. Earattupuzha (1972): Equilibrium condi-
    tions in beach wave interaction. Proc. 13th Conf.
    Coastal Eng., pp.1237-1256.
Rao, P. S. and P. Kassim (1970): Field study of Surathkal
    beach. Proc. 12th Conf. Coastal Eng., pp.1365-1381.
Rector, R. L. (1954): Laboratory study of equilibrium
    profiles of beaches. B.E.B. Tech. Memo., 41, 38p.
Saville, T., Jr. (1957): Scale effects in two dimensional
    beach studies. Proc. 7th Meeting I.A.H.R., pp.(A3)1-8.
Sonu, C. J. (1968): Collective movement of sediment in lit-
    toral environment. Proc. 11th Conf. Coastal Eng., pp.
    373-400.
Toyoshima, O, M. Tominaga and H. Hashimoto (1968): Experi-
    mental study of wave deformation after breaking. Rep.
    Inst. Pub. Works, 133, pp.121-129. (in Japanese).
Tsuchiya, Y. and S. Yoshioka (1970): Experimental study of
    beach deformation by wind waves (1). Memoir 25th Annual
    Conv. Jap. Soc. Civ. Eng., pp.97-98. (in Japanese).
Watts, G. M. (1954): Laboratory study of effect of varying
    wave period on beach profiles. B.E.B. Tech. Memo., 53,
    19p.
Wiegel, R. L., D. A. Patrick and H. L. Kimberley (1953):
    Wave, longshore current and beach profile records for
    Santa Margarita River Beach. IER, Univ. of Calif., Ser.
    3, Issue 357, 6p.

CHAPTER 54

EQUILIBRIUM PROFILES OF COARSE MATERIAL UNDER WAVE ATTACK

by E. van Hijum [*)]

Abstract. In order to obtain design criteria for artificial gravel beaches, a research
programme was drawn up to study the behaviour of gravel beaches under wave attack.
The present paper gives the main results of the first step in this programme, viz. the
determination of the dimensions, form and way of formation of an equilibrium profile
under regular, perpendicular wave attack. One of the conclusions is that gravel with
a $D_{90} < 6 * 10^{-3}$ m is sensitive to scale effects.

1   Introduction. Coarse material, such as gravel and light rubble, has recently been
applied in the Netherlands as a bank protection in areas exposed to wave attack. An
example is the gravel beach at the Zuidwal, the southern bank of the harbour entrance
to Rotterdam (Figure 1). In order to reduce the waves inside the new harbour mouth and
the connected basins, a wave-damping beach is planned. In order to achieve the desired
energy absorption, such a beach can consist of granular material under a small angle
of inclination. For nautical and hydraulical reasons it is not possible to make the beach
slope flatter than about 1:10. Such a slope can only be achieved by using gravel.
Contrary to conventional types of bank protection, the profile of a gravel layer will be
deformed when exposed to wave attack. Data on the fluctuation of the profile under
design wave conditions are required to ensure an adequate design. For this reason
the Public Works Department of the Dutch Government charged the Delft Hydraulics
Laboratory to perform investigations into the behaviour of gravel beaches under wave
attack. The tests were performed in the De Voorst Laboratory of the Delft Hydraulics
Laboratory.

2   Problem schematization. In solving the present problem one may follow a line as
demonstrated in Figure 2. For correct profile development and longshore transport the
sediment motion in the model has to fulfil the following conditions:
-   the mechanism has to be the same as in the prototype
-   in this mechanism scale effects have to be of such an order that they can be
    neglected.
Firstly the transport mechanism itself will be studied. Roughly speaking sediment transport
under progressive waves will be caused by one of the types of mechanism shown in

*)   Project engineer, Delft Hydraulics Laboratory, The Netherlands

939

Figure 3. In this figure the groin diameter D is kept constant and the bed shear stress
τ is increasing. Starting at a shear stress of zero and increasing τ the bed initially
stays in o situation of rest or eventually an armoured bed. After τ has reached a
critical value τ_{cr} bed load transport starts occurring. The larger grains of the grain
distribution will be moved onshore and the smaller grains offshore. At increasing τ
the phase of ripple formation is reached. Now the mechanism of sediment transport
changes completely. Under a wave crest at the lee side of a ripple an eddy is formed
which picks up material from the ripple trough and from the flatter slope of the ripple.
When the horizontal component of the orbital velocity decreases to zero, the eddy,
still containing the material, lifts and explodes. With the following negative horizontal
orbital component under the wave trough the material coming from the eddy is moved
in a direction opposite to the wave direction. During this phase material is dropped
on the flatter slope of the ripple and on the preceeding ripple, or it stoys in suspension,
dependant of the absolute time of the wave trough and the fall velocity of the grains.
The material, that stays in suspension, will be transported in positive direction under
the next wave crest and will be dropped somewhere onshore. Thus, the grains with a
larger diameter will move offshore and the grains with a smaller diameter onshore.
This is just opposite to what happens when transport takes place as bed load only.
At increasing τ a stage is reached when the ripples disappear and transport takes place
as a combination of bed load and real suspended load. Next the problem of simulating
these mechanisms in a model must be studied. As far as known at this moment, it is
only possible to scale down the mechanism of the bed load transport, for the boundary
conditions $\tau_r \tau_{ch}^{-1}$ and $\tau_v \tau_{ch}^{-1}$ (Figure 3) will not be the same in model and pro-
totype, just as is the case with the relative ripple dimensions and the relative fall
velocity of the grains. In the present model it is thus necessary to stay below the
lowest value of $\tau_r \tau_{ch}^{-1}$. This seems to be a reasonable assumption for gravel. The
mechanism is now known, but in this mechanism scale effects will be possible. In order
to deduce these scale effects and besides to determine the profile fluctuation and the
transport of gravel perpendicular to the coast, o series of tests was performed with regular
perpendicular wave attack (Figure 2, step 1). Knowing which conditions are necessary
to prevent these scale effects, the series of tests can be extended with three-dimensional
tests, for the longshore component of the gravel transport will be on scale if the
component perpendicular to the coast is on scale and the water movement is on Froude-
scale. In order to get a better insight into gravel movement under wave action in the
prototype the present tests will have to be extended with steps 3 and 4. This paper will
be restricted to the first step.

3 First step: regular woves, perpendicular wave attack

3.1 Problem analysis.
In describing the phenomenon of profile formation, two groups of parameters can be composed:

a The external parameters characterizing the wave attack and the initial beach geometry, viz. wave height and wave length on deep water (H_o, L_o), wove period (T), depth of foreshore (h), height of beach top (k), initial slope (tg a) and grain diameter (D). Becouse of the fact that the larger grains of a grain distribution seem to be deciding for the bed load transport, for characterizing this grain distribution the D_{90} was chosen. D_{90} means that 90 % of the weight of a sample has a smaller diameter than D_{90}.

b The internal parameters, chorocterizing the resulting equilibrium profile and the sediment transport during the formation of the profile. These parameters are shown in Figure 4:

h_A = height of wave run-up above the still-water level on the initial (straight) slope

h_F = height of the beach crest = height of wave run-up above the still-water level on the equilibrium profile

h_B = depth below the still-water level of the point of initial movement on the initial slope

l_S and l_K = defining the position of the step

$tg \gamma$ = gradient of the equilibrium profile at the still-water level

β = angle of repose under water

$S(y)$ = mean resulting sediment transport in y-direction between two points in time. The time between these points has to be much longer than the wave period.

For a correct reproduction of the external parameters in a model Froude's law of similarity has to be fulfilled, so $n_{H_o} = n_{L_o} = n_h = n_D = n_v^2 = n_c^2 = n_T^2 = n_y = n_z = n_l$, where n_l = (length in prototype)/(length in model), v = orbital velocity, c = phase velocity. For transmission of movement the following conditions have to be fulfilled: $n_{v2/\Delta gD} = n_{C_L} = n_{C_M} = n_{C_D} = 1$, where $\Delta = (p_s - p_w)/(p_w)$, p_s = density of the sediment, p_w = density of the water, C_L = lift coefficient, C_M = added-mass coefficient, C_D = drag coefficient. From the condition $n_{v^2/\Delta gD} = 1$ and Froude's law of similarity it follows that $n_\Delta = 1$. To achieve $n_{C_L} = n_{C_M} = n_{C_D} = 1$ the conditions given by the numbers of Reynolds, Strouhald, Keulegan- Carpenter etc. will have to be fulfilled. This is impossible. In unidirectional flow this stage will approximately be reached if the Reynolds number varies between about 10^3 and 10^5 (subcritical flow). Less is known about this subject for the case of waves, so, in order to determine possible scale effects, the way to be followed now will be to do tests with several diameters ond regard one diameter as a prototype for a smaller one.

3.2   Tests. A survey of the performed tests is shown in Table 1. The choise of the
external parameters was limited by three conditions:
1   The dimensions of the available wave flumes
2   The H-L diagram of Galvin [2], in order to stay out of the area of secondary waves
3   The condition to remain below the ripple criterion, as is shown in chapter 2
The combinations H-T were formed in such a way, that, concerning wave steepness,
a series with constant T partly overlapped the next series with higher T. The tests with
the coarsest particle diameter have been carried out in a flume with the following
dimensions: length 35 m, width 5 m, depth 1.5 m. The remaining tests were done in
a flume with o length of 100 m, a width of 4 m ond a depth of 1 m. Starting with o
straight slope the profile was sounded after 0, 3, 9, 27,... minutes of wave attack.
These increasing time intervals were chosen because the profile changes in the beginning
of a test were the greatest. A test was stopped when profile fluctuations becam negligible.
This state of equilibrium was in the present test series reached after 0.5 - 4 hours. The
soundings were made by an automatic profile follower, recorded on punched tape and
processed by a computer. The mean resulting transport of gravel in y-drection in a time
interval, S(y), was calculated by application of the continuity equation for the gravel
between two successive soundings. Wave height and form, measured with a movable
gauge of the resistance type, and orbital velocities, measured with a velocity meter of
the propeller type, were recorded on paper and on tape. Sediment sorting along the
equilibrium profile was determined by taking a large number of surface samples. In order
to make it possible to study the water movement and grain movement in slow motion,
a part of the second flume was provided with side windows and films were made of
about twenty tests.
3.3   Test results. This chapter contains only the main results. More detailed information
can be found in [1].
3.3.1   Profile formation. The process of profile formation is fully described by Zenkovich,
Kemp and many others and can be found in [1], [3] and [7]. A gravel beach, attacked
by waves, will partly be deformed. The lower limit is fixed by the point of initial
movement, the upper limit by the wave run-up on the initial profile or in the equilibrium
profile. Deformation will occur until every point of the profile is in static or dynamic
equilibrium. From literature it is known that two possible basic forms of the equilibrium
profile exist. These two forms are indicated with several names:

1 summer, normal, accretion, step profile

2 winter, storm, erosion, bar profile

The first two sets of names do not say very much. The distinction that is made by the third set is dependent of the initial slope of the beach, because of the fact that the same equilibrium profile at a steep initial slope leads to erosion while at a flatter slope it might lead to accretion. Only the fourth set of names gives a clear distinction in the form of the equilibrium profile (see Figure 4). The bar-type form has a more pronounced bar in the vicinity of the breaker point. The criterion for the appearance of a bar will be given in chapter 3.3.3. The influence of the grain diameter on the profile form and profile formation is shown in Figure 5. At decreasing diameter the offshore transport of material increases at constant wave height and wave period. The same happens at constant diameter and wave period and increasing wave height. In Figure 6 the influence of the wave period is shown, and Figure 7 gives the influence of the initial slope. The initial slope does not influence the equilibrium profile, except at the connection points with the initial profile of course. In all these figures the transport lines give the mean resulting transport of gravel in y-direction in the mentioned time interval. Onshore transport is called positive.

3.3.2 Scale effects. If the material responds on scale the following conditions have to be fulfilled: $n_{h_A} = n_{h_F} = n_{l_S} = n_{l_K} = n_{h_B} = n_l$; $n_\gamma = n_\beta = 1$; $n_{S(y)} = n_l^2 \, n_t^{-1}$; $n_t = n_l^{\frac{1}{2}}$, where n_t = time scale profile formation. From the measurements of the internal parameters it appears that even for high Reynolds number the Froude law of similarity is not applicable for the two finest materials with a D_{90} of $1.8 * 10^{-3}$ m and $4.4 * 10^{-3}$ m. These two materials respond to the wave attack as if they were smaller materials. This scale effect is demonstrated in Figure 8, where the material with $D_{90} = 7.1 * 10^{-3}$ m is regarded as prototype. The horizontal axis shows the D_{90} and the vertical axis n_p/n_l, where n_p = the calculated scale of the internal parameters and n_l = the length scale of the external parameters. From this figure it can be concluded that material with $D_{90} > \sim 6.0 * 10^{-3}$ m responds on scale. Popov [4] found an analogous tendency. Only h_A is not influenced by scale effects. Thus it can be concluded that scale effects are restricted to the transport mechanism and do not play a role in porosity and roughness of the material in the present tests. The time scale during profile formation is deduced from the S(y) lines, and is demonstrated in Table 2. This table confirms the conclusion made above. From Figure 8 scale coefficients can be derived:

for h_B, l_K, l_S : $\delta_1 = \left[\dfrac{D_{90}}{D(\delta_1)}\right]^{\frac{1}{2}}$, where $D(\delta_1) = 6 * 10^{-3}$ m; if $D_{90} \geqslant D(\delta_1)$, then $\delta_1 = 1$

for h_F : $\delta_2 = \left[\dfrac{D_{90}}{D(\delta_2)}\right]^{\frac{1}{2}}$, where $D(\delta_2) = 4 * 10^{-3}$ m; if $D_{90} \geqslant D(\delta_2)$, then $\delta_2 = 1$

3.3.3 Profile type. As stated in chapter 3.3.1 two profile types are possible, viz. step profiles and bar profiles. The criterion for appearance of a bar will, at a constant material- and water density, be a function of H_o, T and D_{90} and perhaps also of the initial slope. Scale effects can also play a role. The relation with H_o, T and the initial slope is studied at a constant D_{90} (= $4.4 * 10^{-3}$ m). The wave periods were 1.2, 1.6 and 2.0 seconds, the initial slopes 1:5 and 1:10. It seems reasonable to assume that the generation of a bar takes place at a certain pattern of water movement on the beach. Four characteristic moments can be distinguished in this water movement, viz. the moment of breaking (t_o), the moment when the breaking wave crest reaches the mean-water level (t_1), the moment of eliminating of the backrush velocity of the preceeding wave by the uprush velocity of the directly following wave (t_2) and the moment of maximum wave run-up (t_3). These points were fixed by studying the films made during the tests in slow motion (factor 24). The result is shown in Figure 9. In this figure the vertical axis shows the phase difference $(t_i - t_o)/T$, with i = 0, 1, 2, 3, and the horizontal axis shows $H_o^2 L_o^{-1}$ that appears to be the governing parameter group at constant D_{90}. Of the tests with tg a = 0.2 t_o, t_1, t_2 and t_3 are shown, of the tests with tg a = 0.1 only t_o and t_3. From this figure it can be concluded that, in contrast with what is found by Kemp [3] , the phase difference between wave breaking and maximum wave run-up alone cannot be used as criterion for the change from a step to a bar profile, for, depending on $h_{breaking}/h_B$, the phase difference t_3/T increases with decreasing initial slope, while changing from step to bar profile occurs at the same value of $H_o^2 L_o^{-1}$. The influence of D_{90} and the scale effects in the bar-step criterion are deduced by considering all tests. This leads to the criterion $H_o^2 L_o^{-1} D_{90}^{-1} \delta_1^{-3} = 2.5$ (see Figure 10). Because of the different transport mechanisms there is no point in trying to find any agreement between this criterion and analogous criterions for sand beaches (e.g. Larras, Iwagaki, Nayak).

3.3.4 Relations between internal and external parameters. In an analogous way as done for the bar-step criterion governing groups of external parameters were composed for the internal parameters. These groups are shown in Table 3. Initial slope, height of beach

top and depth of forshore (if $h_B < h$) do not influence the profile form (l_S, h_F, h_B, γ, β, bar/step), but only the position of the profile in horizontal direction (l_K), the time necessary until equilibrium is reached and, of course, $S(y)$. Figure 7 shows this for the influence of the initial slope. The form of the part of the profile between beach crest and bar or step can be approached by a parabola with horizontal axis. This parabola is, just as the height of the bar, a function of $H_o D_{90}^{-1}$. With all these relations it will now be possible to calculate and sketch the equilibrium profile for given a grain diameter and design wave conditions. This is described in detail in $\begin{bmatrix} 1 \end{bmatrix}$. In the present paper only the graphs of h_A, h_F, h_B, l_S, l_K and tg γ are given. Figure 11 shows $h_A D_{90}^{-1}$ as a function of $c_o H_o g^{-\frac{1}{2}} D_{90}^{-3/2}$. The transport mechanism does not influence $h_A D_{90}^{-1}$ and there are no scale effects. Thus some values taken from profiles of sandy beaches given by Saville jr. $\begin{bmatrix} 5 \end{bmatrix}$ and Watts and Dearduff $\begin{bmatrix} 6 \end{bmatrix}$ are also shown in this figure. In the figures 12, 13 and 14 the relations of h_F, l_S and l_K with the governing external parameters are given. It appears that the profile type does not influence the location of the step. Figure 15 shows $h_B D_{90}^{-1}$ as a function of $H_o D_{90}^{-1} \delta_1^{-1}$. For low waves with a low period there appears to be a dependency on the wave period too. In the insertion $h_B D_{90}^{-1}$ is given as a function of $c_o H_o g^{-\frac{1}{2}} D_{90}^{-3/2} \delta_1^{-3/2}$ for values of this parameter group of less than about 200. Figure 16 shows that it is possible that material is deposited below the point of initial movement. In Figure 17 the relation between tg γ and $H_o D_{90}^{-1}$ is given. No scale effects are found in this parameter, perhaps due to the fact that the scale effects work in the same sense on the vertical (h_B) and horizontal (l_S) parameters. A maximum value for tg γ is reached for $H_o D_{90}^{-1} \approx 10$. For very small waves with no profile formation it is obvious that tg γ must equal the initial slope.

3.3.5 Optimal initial slope. For optimal design of artificial beaches it is important to known at which initial slope for given a grain diameter and design wave conditions minimum erosion and accretion will occur. Figure 7 shows that this will happen when the beach crest tends to disappear. The beach crest disappears when l_S equals l_K. With the method of least squares best fitting lines were calculated for l_S and l_K. l_S appears to equal l_K when:

$$H_o D_{90}^{-1} \delta_1^{-1} \left\{ 1.98 - (tg\ a)^{-1/3} \right\} = 12.48$$

Figure 18 shows tg a as a function of $H_o D_{90}^{-1} \delta_1^{-1}$. The optimal initial slope for a given $H_o D_{90}^{-1} \delta_1^{-1}$ is found on or just to the right of the graph.

3.3.6 Critical velocity. The water movement under a progressive short wave can roughly be devided into two zones, viz. an upper zone, where the water movement is hardly influenced by the bed, and a lower zone ("boundary layer") of a much smaller thickness. Figure 19 gives an idea about possible velocity profiles (component parallel to the bed) in these two layers. The maximum value in time of this component, measured just above the lower zone at the point of initial movement on the initial slope is defined here as the critical velocity. Movement of material at this point was generated when this component had its maximum value and was in all tests in positive direction. From the tests it appeared that the critical velocity at a constant grain diameter increased with the water depth. The results of one series are shown in Figure 19. Detail A gives a possible explanation: at increasing water depth and wave height the thickness of the lower zone increases too, and just outside this lower zone a higher velocity is needed to provide a grain with the same surrounding flow pattern. The critical velocity appears to reach a constant value for $h_B D_{90}^{-1} \delta_1 \approx 80$, while $v_{crit} (g D_{90})^{-\frac{1}{2}} \approx 2.0$. This phenomenon has to be kept in mind when simulating sediment movement in a pulsating water apparatus.

3.4 Limitations in use and recommendations for further research. It is clear that it is only permissible to use the obtained results within the tested range of the parameter groups. It will be interesting to know what happens at higher values of $H_o D_{90}^{-1}$ and $c_o H_o g^{-\frac{1}{2}} D_{90}^{-3/2}$. Due to the appearance of scale effects at smaller diameters and due to the restriction to remain below the ripple criterion, wave flumes of much bigger proportions than used for the present tests will be needed.

References

1 Delft Hydraulics Laboratory. Reports M 1216 part I, M 1216 part II, M 1063 part III, 1974

2 Galvin, C.J. Finite amplitude shallow water waves of periodically recurring form. CERC – note, sept. 1970

3 Kemp, P.H. The relationship between wave action and beach profile characteristics. Proc. 7th Conf. on Coast. Eng. 1960

4 Popov, I.J. Experimental research in formation by waves of stable profiles of upstream faces of earth dams and reservoir shores. Proc. 7th Conf. on Coast. Eng. 1960

5 Saville, J.T. Scale effects in two-dimenional beach studies. Trans. I.A.H.R., 7th Gen. Meeting, 1957

6 Watts, G.M. and Dearduff, R.F. Laboratory study of effect of tidal action on wave-formed beach profiles. Beach Erosion Board, Techn. Mem. no. 52, 1954

7 Zenkovich, V.P. Processes of coastal development. Oliver and Boyd, Edinburgh and London, 1967

grain diameter	$D_{90} = 1.8 \quad 4.4 \quad 7.1 \quad 16.5 \quad (10^{-3} \text{ m})$
$(\rho_s = 2650 \text{ kg m}^{-3})$	$D_{50} = 1.3 \quad 3.4 \quad 6.1 \quad 13.0 \quad (10^{-3} \text{ m})$
wave height	$0.037 - 0.468 \quad$ (m)
wave period	$1.2 \quad 1.6 \quad 1.83 \quad 2.0 \quad 2.44 \quad$ (s)
initial slope	$1 : 5 \qquad 1 : 10$
depth of foreshore	$0.25 \quad 0.40 \quad 0.50 \quad 0.80 \quad 1.00 \quad$ (m)
height of beachtop	$\backsim$ and still-water level

Table 1   Survey of external parameters

"prototype" D_{90}	"model" D_{90}	length scale n_l	time scale n_t
$4.4 * 10^{-3} \text{ m}$	$1.8 * 10^{-3} \text{ m}$	2.44	< 1
$7.1 * 10^{-3} \text{ m}$	$4.4 * 10^{-3} \text{ m}$	1.61	≈ 1
$16.5 * 10^{-3} \text{ m}$	$7.1 * 10^{-3} \text{ m}$	2.32	$> 1 \; (\sim n_l^{\frac{1}{2}})$

Table 2   Time scale during profile formation

internal parameters	external parameters
$h_B \, \delta_1 \, D_{90}^{-1}$	$H_o \, D_{90}^{-1}$
$l_S \, \delta_1 \, D_{90}^{-1}$	$H_a \, D_{90}^{-1}$
$l_K \, \delta_1 \, D_{90}^{-1}$	$H_a \, D_{90}^{-1} \, (\text{tg}\alpha)^{-1/3}$
$h_F \, \delta_2^{-1} \, D_{90}^{-1}$	$c_a \, H_o \, g^{-\frac{1}{2}} \, D_{90}^{-3/2}$
$h_A \, D_{90}^{-1}$	$c_a \, H_o \, g^{-\frac{1}{2}} \, D_{90}^{-3/2} \, \text{tg}\alpha$
γ	$H_o \, D_{90}^{-1}$
β	angle of repose under water $(\sim 30^{\alpha})$

Table 3 Relations between internal and external parameters
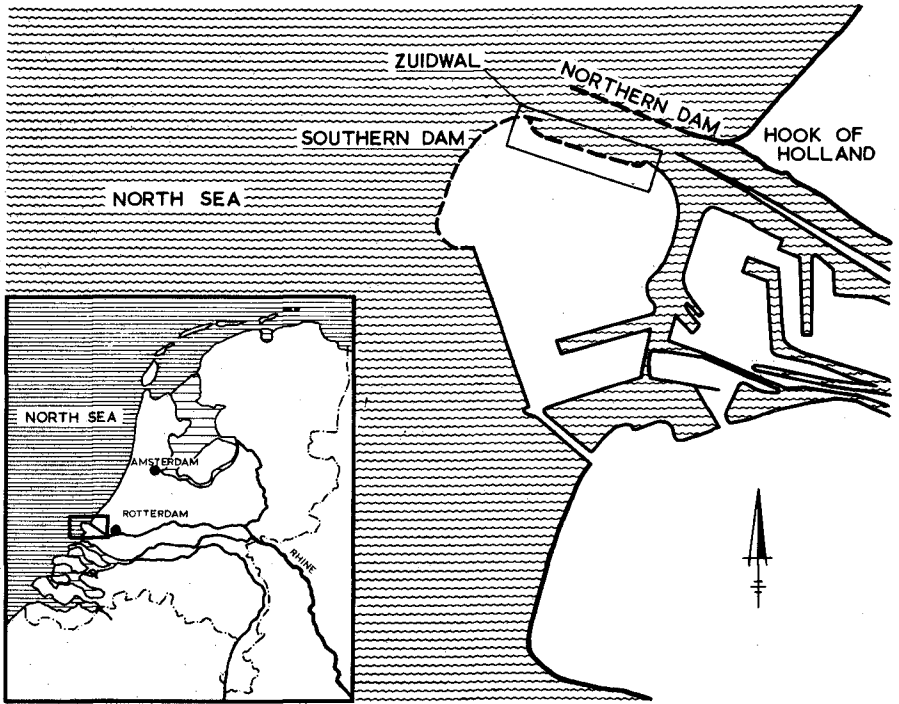
Figure 1:   Situation Zuidwal
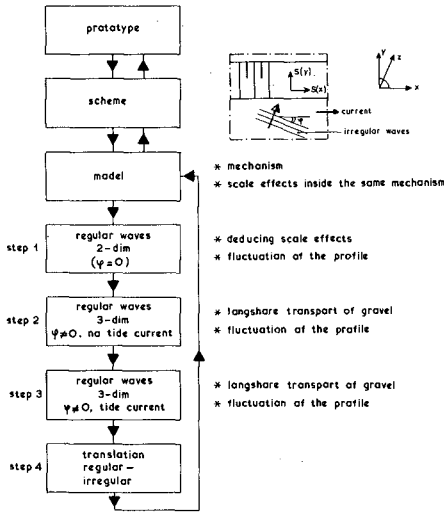
Figure 2:   Problem schematization

Figure 4:   Definition sketch

Figure 3:   Transport mechanisms
            under waves
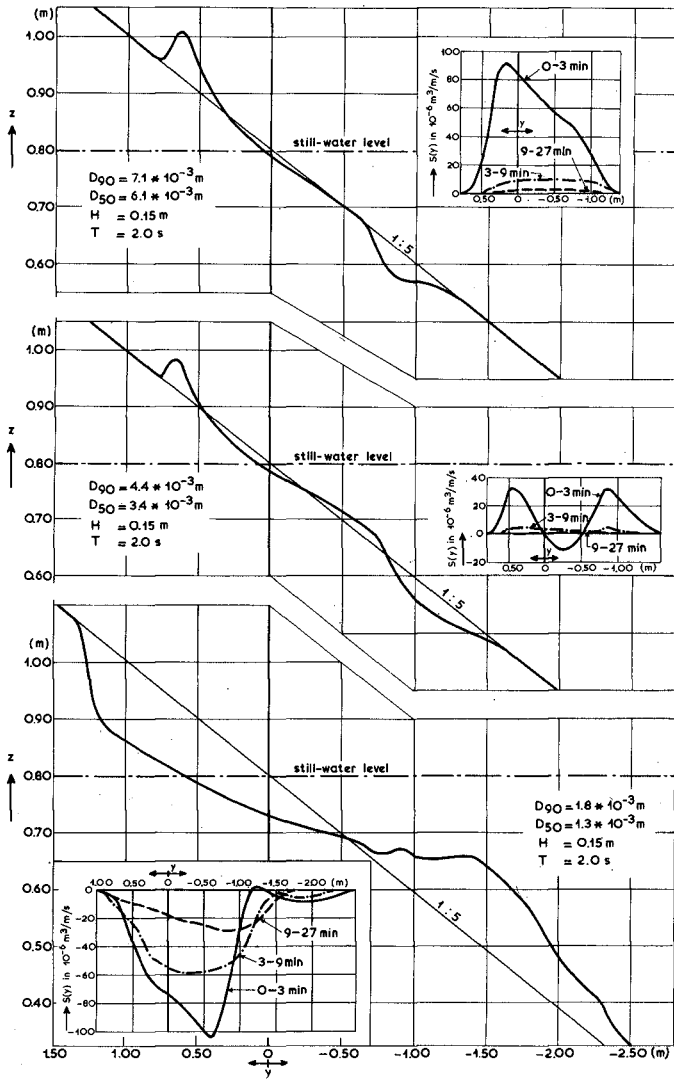
Figure 5: Influence of groin diameter
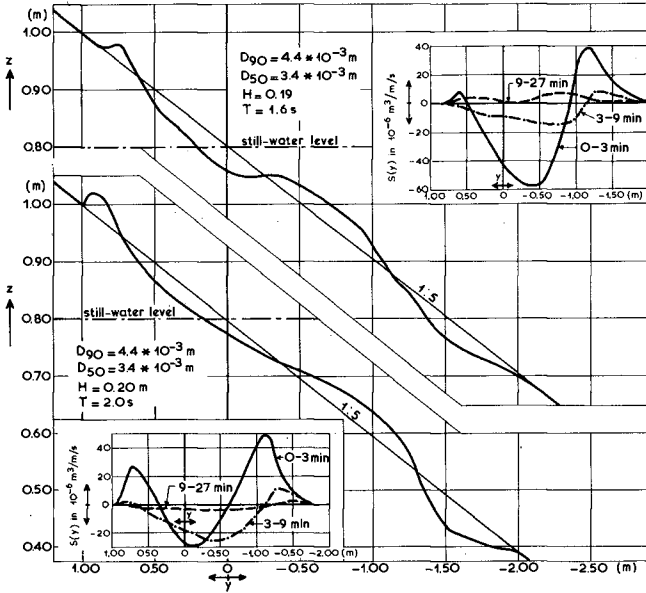
Figure 6:   Influence of wove period
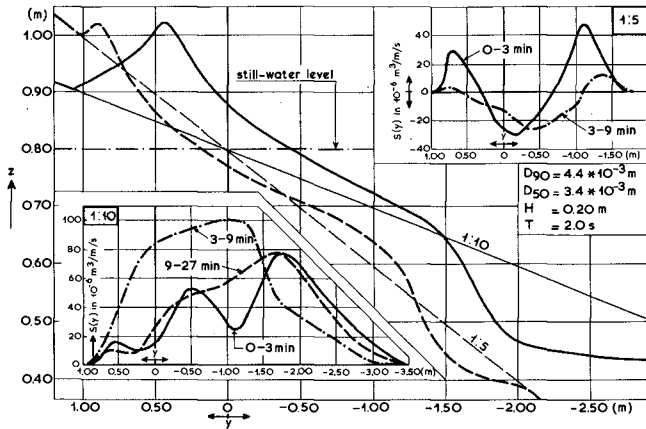
Figure 7:   Influence of initiol slope
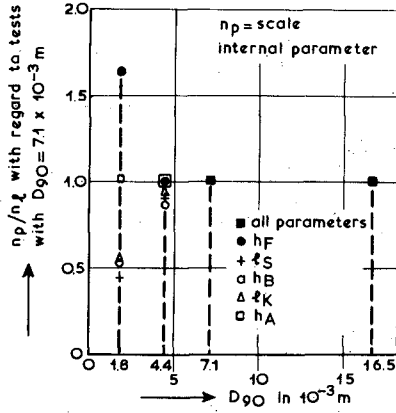
Figure 8:   Scale effect
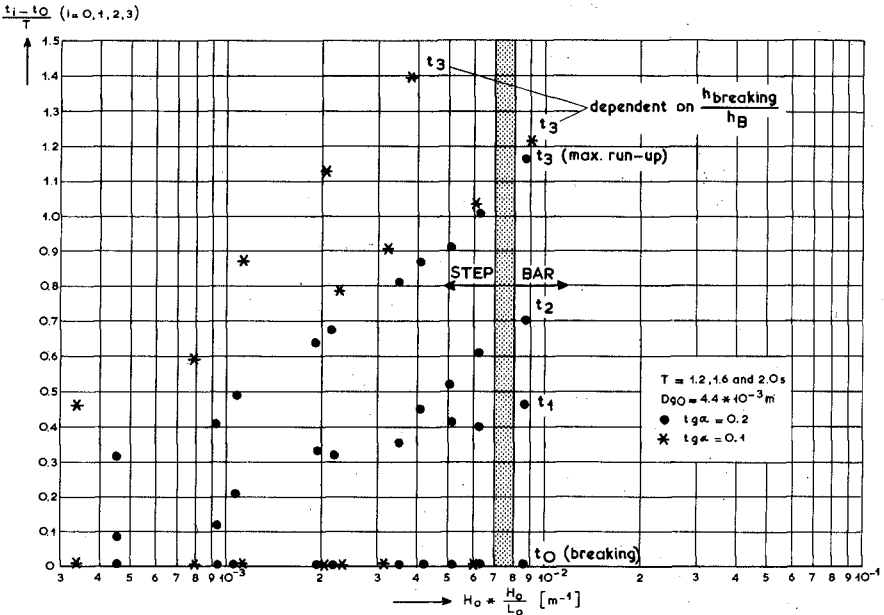
Figure 9:   Water movement in the equilibrium profile
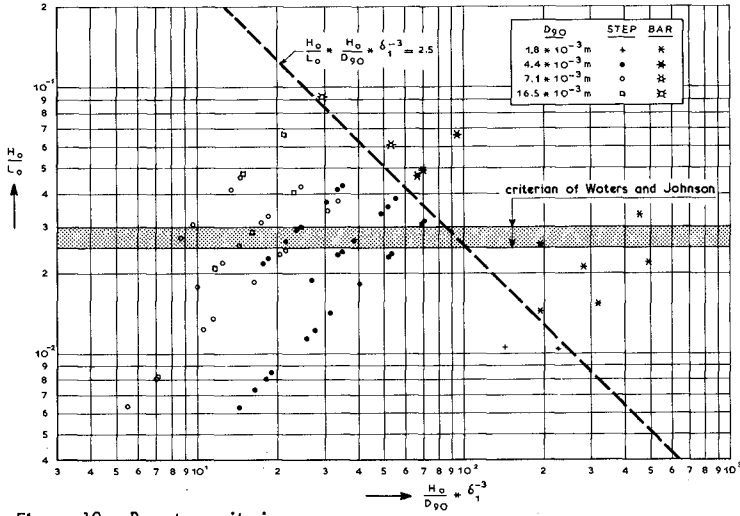
Figure 10: Bar-step criterion

$$\frac{h_A}{D_{90}} = \left(\frac{1.1 c_0 H_0}{g^{1/2} D_{90}^{3/2}}\right)^{0.83} tg\,\alpha$$
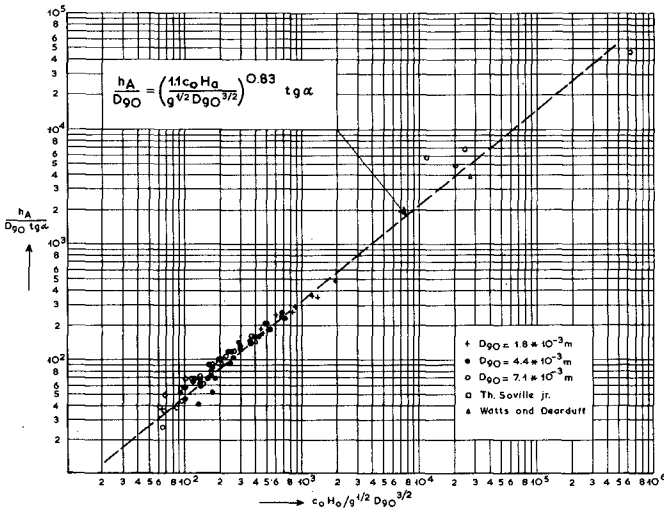
Figure 11: Wave run-up on the initial slope
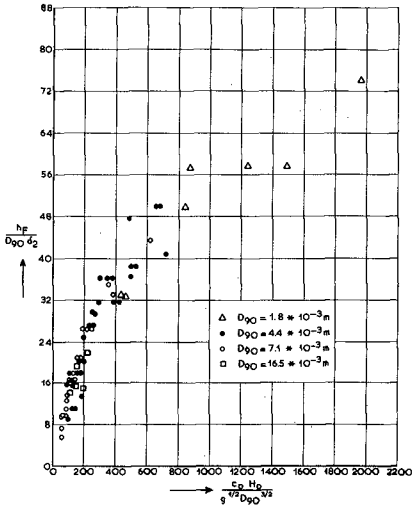
Figure 12: Wave run-up in the equilibrium profile
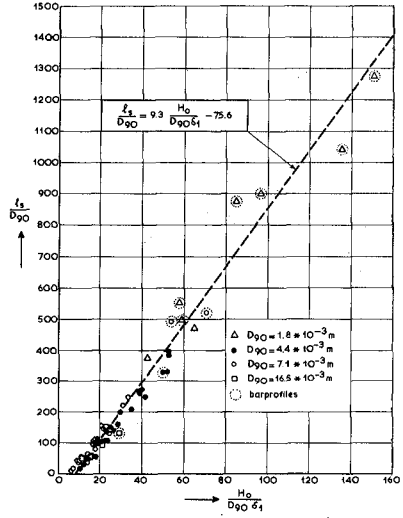
Figure 13: Location of the step
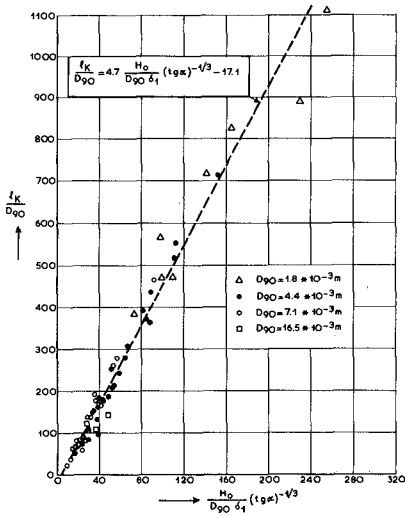
Figure 14: Location of the step
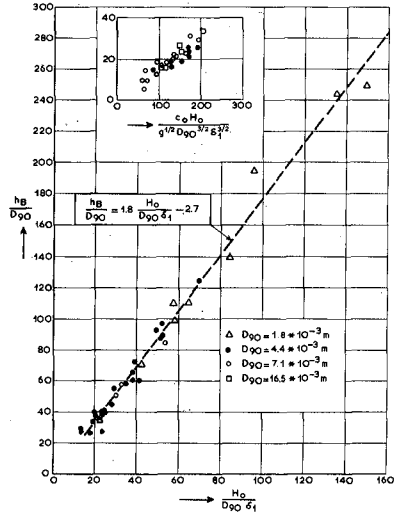
Figure 15: Depth of initial movement on the initial slope
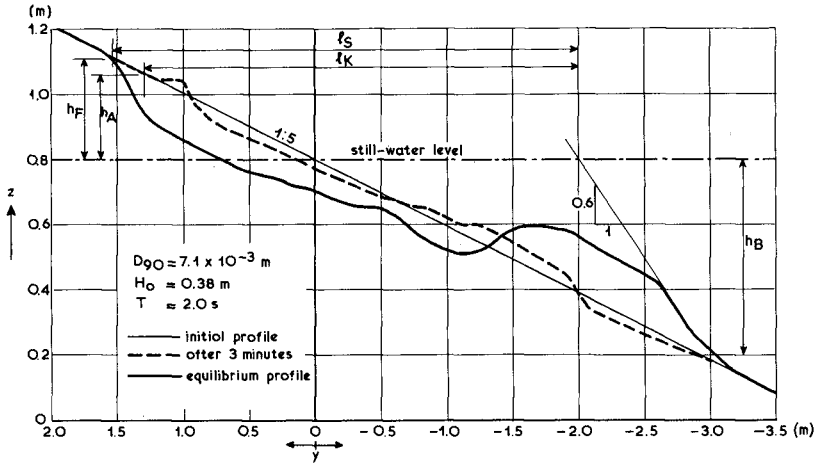
Figure 16:   Deposit of material below the point of initial movement
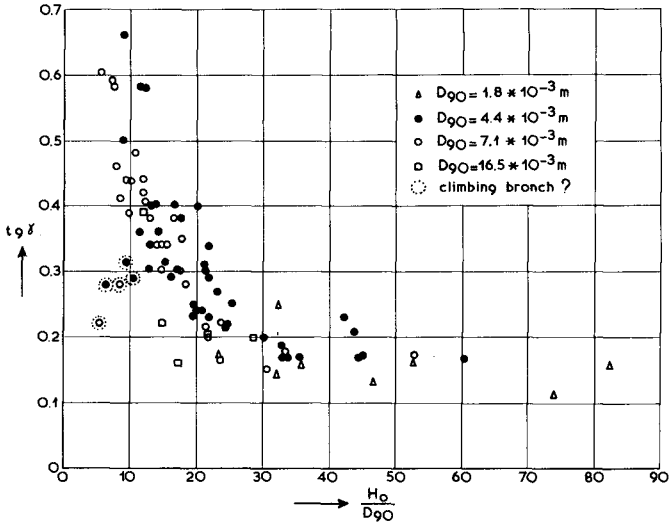
Figure 17:   Slope of equilibrium profile at still-water level
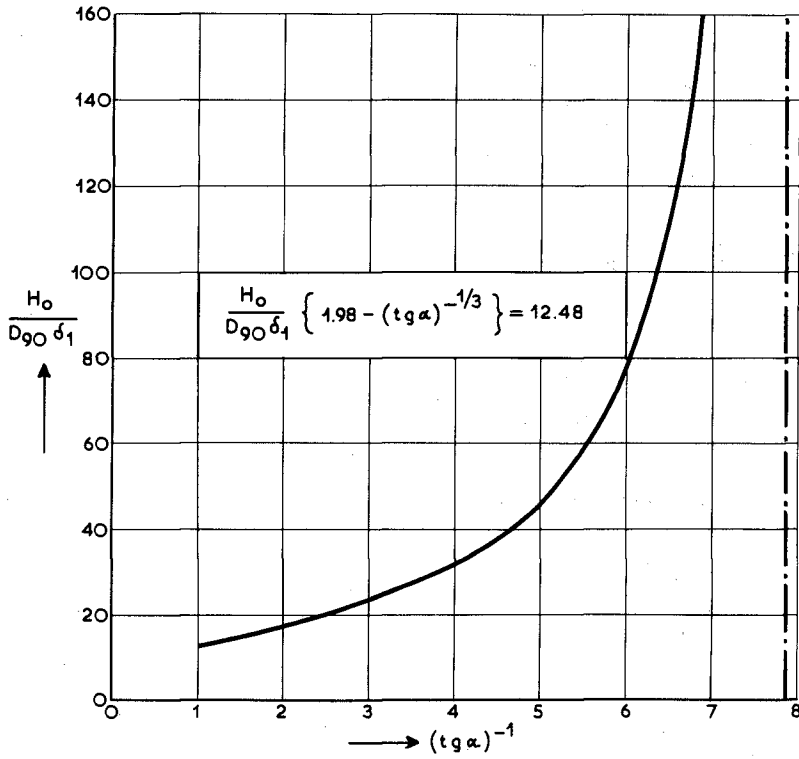
Figure 18:   Disappearance of the beach crest
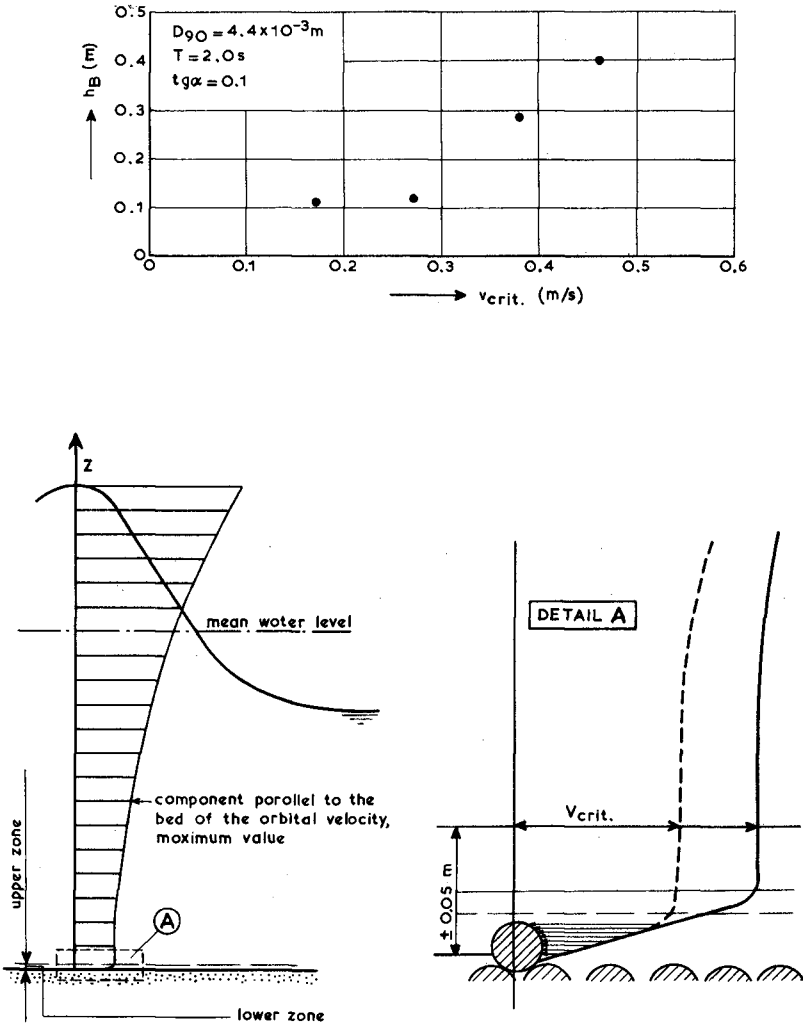
Figure 19: Critical velocity as function of
water depth

CHAPTER 55

LAB PROFILE AND REFLECTION CHANGES FOR $H_o/L_o=0.02$

by

Charles B. Chesnutt[1] and Cyril J. Galvin, Jr.[2]

ABSTRACT

Reflection coefficients and profile changes were measured during four lengthy experiments in two relatively long, narrow wave tanks. Each tank had a periodic wave generator at one end and a 0.2 mm movable sand bed at the other end. Generator period (1.90 sec), water depth (2.33 ft), nominal wave height before reflection (0.36 ft), and initial sand slope (1:10) were constant in the four experiments. Measured reflection coefficients ($K_r = H_r/H_i$) ranged from 0.05 to 0.30, with the typical time variation of K_r related to profile changes as follows: K_r increased by a factor of 3 to 4 within the first minutes while a steep foreshore was built on the undeformed profile; K_r fluctuated and dropped to a lower value as the inshore widened; K_r increased as the offshore steepened. Large variations in K_r near the end of the experiments appeared to result from minor profile changes. The apparently similar experiments showed very different rates of profile development, implying control by other variables such as water temperature or tank geometry. "Equilibrium" in these experiments was never reached, even after as many as 375 hours of wave action.

I. INTRODUCTION

Wave heights in movable bed, coastal engineering laboratory experiments vary both in space and in time in a manner illustrated by Figure 1. Such variability is common over the constant depth section of wave tanks with movable beds (Savage, 1962; Fairchild, 1970a, 1970b; Galvin and Stafford, 1970).

The preliminary study (Galvin and Stafford, 1970) from which Figure 1 is taken has shown that wave height variability in simple wave tanks is caused largely by wave reflection from the tank boundaries, especially from the movable boundary. Spatial wave height variability results from the envelope of superposed incident, reflected, and re-reflected waves. Temporal wave height variability, indicated by the range of wave heights

---

[1] Hydraulic Engineer, Coastal Processes Branch, U.S. Army Coastal Engineering Research Center, Ft. Belvoir, Virginia

[2] Chief, Coastal Processes Branch, U.S. Army Coastal Engineering Research Center, Ft. Belvoir, Virginia
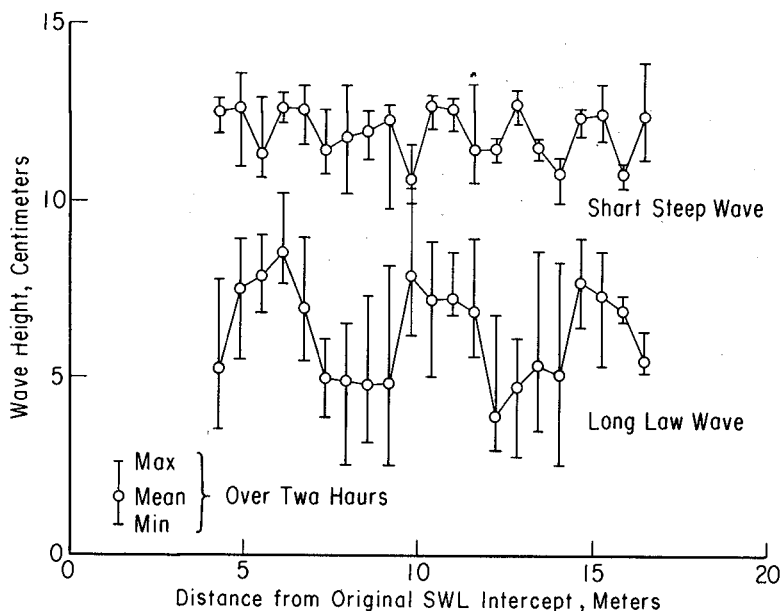
Figure 1.   Examples of Wave Height Variability in Long Narrow Tank
            (Wave Heights are Averages of Ten Consecutive Waves)

at each distance on Figure 1, results from the changing reflectivity and
position of the developing movable bed profile.

     In order to study the interaction between wave height variability
and profile development, ten experiments were conducted at the U.S.
Army Coastal Engineering Research Center. This paper reports major
results from four of the ten experiments, all four of which were run
under the same wave conditions. The results affect the planning and
interpretation of coastal engineering movable bed experiments, in-
cluding both research and model experiments.

II. DATA COLLECTION AND REDUCTION

Experimental Conditions. Two wave tanks were constructed of aluminum
panels within a large, 3-ft (0.9-m) deep, outdoor, fresh water, con-
crete test basin. Piston-type wave generators produced the waves.

Wave generator stroke (0.39 ft, 0.12 m), wave period (1.90 sec), and
water depth (2.33 ft, 0.71 m) were held constant. In the constant-
depth section these conditions produced a nominal wave height of 0.36
ft (0.11 m), wave length (computed from linear theory) of 14.3 ft
(4.4 m) and relative depth of 0.163. The equivalent deepwater wave
steepness was 0.021. Water temperature in the outdoor test basin
varied from 30°C to 7°C during the testing seasons, which lasted
from late spring through late autumn. The movable beds (consisting
of 0.2 mm sand smoothed to an initial slope of 1:10) were graded in
the same manner for each experiment to insure that initial conditions
were the same. Each of the two tanks had a control tank next to it,
situated so that the same generator simultaneously produced the waves
in both the test tank and the control tank. The control tank had
a 1:10 smooth concrete slab instead of a movable bed.

Because wave conditions were held constant, the four experiments
in this paper are identified in Table 1 by a combination of tank width
and initial test length. Each experiment had a different initial test
length (the distance from the wave generator to the still water line
on the initial sand slope).

TABLE I. Defining Variables of the Four Experiments

Experiment No.	Tank Width		Initial Test Length	
	ft	m	ft	m
0-06	6	1.8	100	30.5
1-06	6	1.8	93	28.4
0-10	10	3.0	61.7	18.8
1-10	10	3.0	54.7	16.7

Data Collection. Each experiment was performed in a series of runs. During
each run, data on water temperature, wave breaking, and wave reflection were
collected. After each run, profile surveys were made according to the schedule
shown on Figure 2. The special surveys marked in Figure 2 were more detailed
and included surface sand sampling.

The experimental procedure for the four experiments varied only in the
timing of some special surveys, the duration of the experiments, and a beach
replenishment procedure used in Experiment Nos. 0-06 and 0-10. In these two
experiments, the beach face had eroded to the back of the tank after 54 hours
and 62 hours, respectively. After this happened, the dimensions of the back-
shore zone (from limit of uprush to the back of the tank) were artificially
stabilized by periodically rebuilding a scarp whose crest was approximately
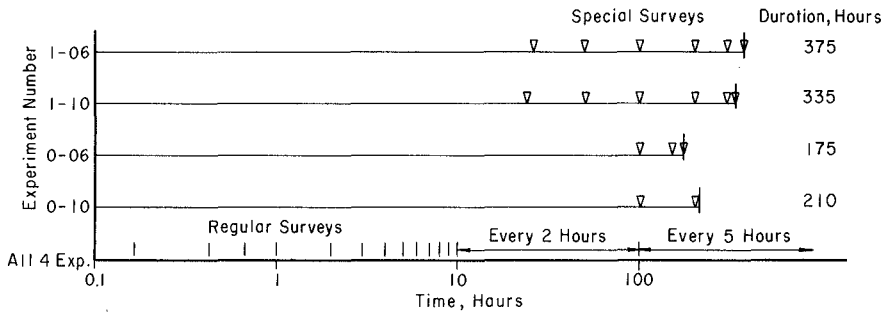
Figure 2.   Frequency of Data Collection

0.5 ft from the back of the tank and 0.7 ft above the upper limit of the beach face.

The principal measurements were the wave envelopes and the profile surveys, both measured by instruments mounted on a carriage which traveled along the tank walls. Wave heights were measured using the FWK Model-1 CERC Laboratory Wave Gage (Stafford, 1972) and a paper chart recorder. The envelopes of wave heights were recorded along the centerline of each tank from near the toe of the movable bed to near the wave generator, and except for runs during the first ten hours, they were recorded starting one hour before the end of the run. A typical wave envelope is shown in Figure 3.

Profile surveys were made with point gages modified by replacing the point with a gimballed foot which provided a flat, 1-in. diameter surface to rest on the sand. The gages were read to the nearest 0.01 ft. Regular surveys were made along ranges 2 ft (0.61 m) apart starting 1 ft (0.30 m) from the walls (Figure 4). Along a given range, elevations were surveyed at distance intervals of 0.5 ft (0.15 m) from the station at the back of the tank to station +10; at intervals of 1 ft (.30 m) from +10 to +23; and at intervals of 0.5 ft from +23 to the toe of the slope. The origin (Station 0.0) of the coordinate system is the intersection of the still water level and the initial sand surface, which is called "original SWL intercept" on figure axes. The distance and elevation pairs were re- corded on sets of computer scanning sheets for each tank, range and survey number.

Photographs of the breaking wave were taken at the start and end of each run, as well as at the time of the wave envelope recording. In Experi- ment Nos. 1-06 and 1-10, the position and type of breaker were determined and recorded at the time of the envelope measurement. Water temperature was measured in °C at the bottom of the tank and at the water surface at the beginning and end of each day. This procedure gave an approximate average temperature for each run.

Experiment No. 1-06 at 8 Hours

Range 3

Chart Speed = 1mm/sec , Carriage Speed ≈ 50 mm/sec

Sta. 50   Sta. 55   Sta. 60   Sta. 65   Sta. 70   Sta. 75

Distance from Original SWL Intercept, Feet
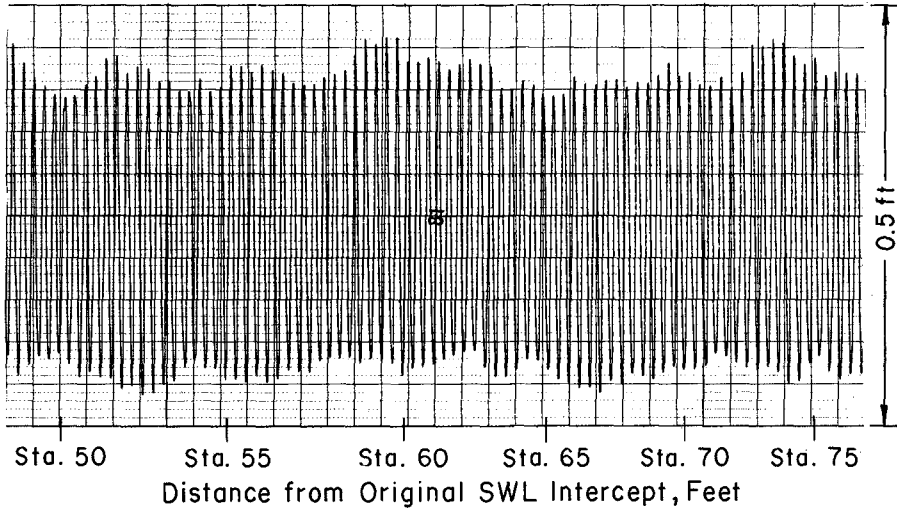
Figure 3.   Example Wave Envelope

Data Reduction.   The reflection coefficient was determined from the wave
records by measuring the wave height at the nodes and antinodes of the wave
envelope (Figure 3) and using the formula

$$K_r = \frac{H_r}{H_i} = \frac{H_a - H_n}{H_a + H_n}$$

where K_r = reflection coefficient, H_r = reflected wave height, H_i = incident
wave height, H_a = wave height at the antinode, and H_n = wave height at the
node.   As illustrated by the envelope on Figure 3, locations of nodes and
antinodes are not always clear.   Independent checks of the reflection co-
efficients indicate that the values obtained are reproducible and correctly
indicate at least relative magnitudes of K_r.

The point gage survey after each run produces a three-dimensional
picture of the sand surface at that time.   Since as many as 125 such surveys
were made in a given experiment, the analysis and presentation of these data

Ronges are 2 ft. apart
Range 1 is 1 ft. from wall

Toe of
Initial Slope
Sta. + 23.5

Original SWL
Intercept
Sta. 0

SIX-FOOT WIDE TANK

Toe of
Initial Slope
Sta. + 23.5

Original SWL
Intercept
Sta. 0

TEN-FOOT WIDE TANK
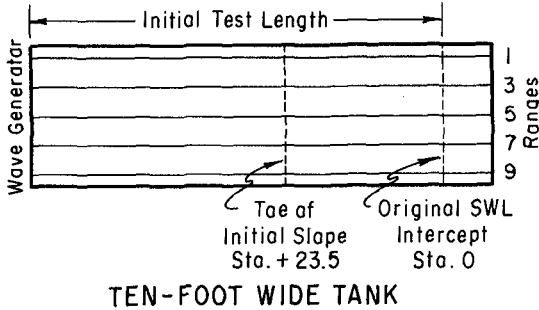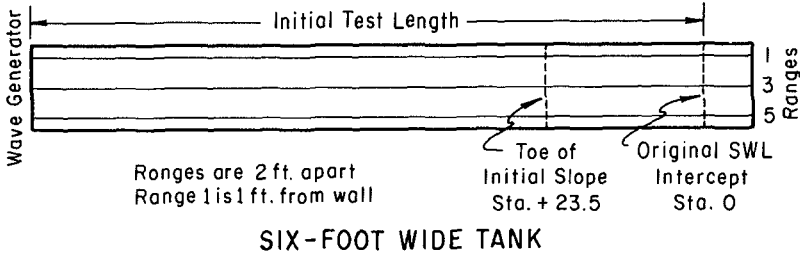
Figure 4. Survey Ranges in the Two Test Tanks

require special procedures. These surveys measured the three space vari-
ables (onshore-offshore distance, alongshore distance or range, and depth)
at each time during the experiment. The method selected for presenting the
data involves fixing the alongshore distance by selecting data from a given
range and analyzing the surveys along that range. The surveyed distance/
elevation pairs along that range are used to obtain the interpolated position
of equally spaced depths, for example, -0.1, -0.2, -0.3, etc. on the hypo-
thetical profile in Figure 5a. These contour positions from each survey are
then plotted against time as shown in Figure 5b.

On Figure 5b, a horizontal line represents no change in contour
position. An upward-sloping line indicates landward movement of contour
position, that is, erosion; likewise, a downward sloping line indicates
deposition. The slope of a line indicates the rate of erosion or de-
position (horizontally) at that elevation. The x's at time t_2 on Figure
5b indicate multiple contour positions at elevation -0.2 which is shown
by the dashed line on Figure 5a. Only the most seaward contour position
is used in this paper.

a. Profile Line

b. Movement of Contour Position
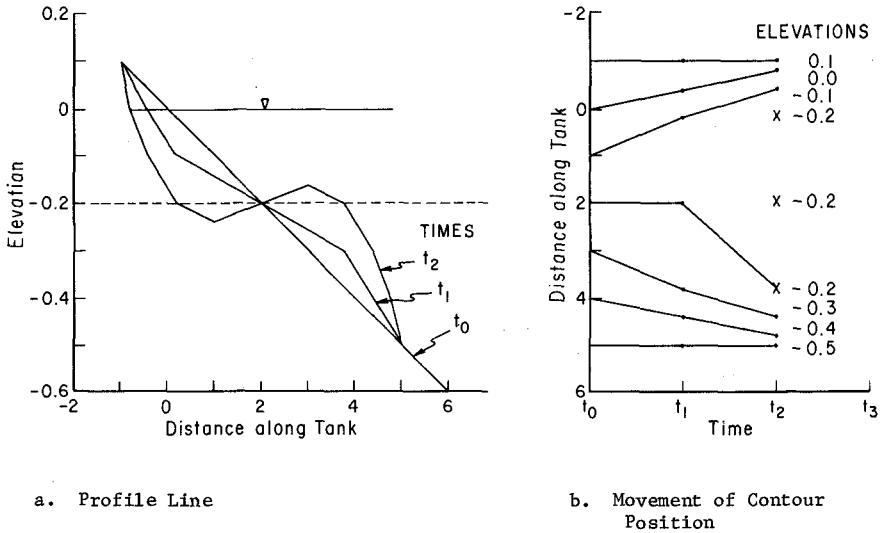
Figure 5. Interpretation of Contour Position Plots
(Figures 8, 11, 13, and 14)

To supplement the profile changes, breaker type and breaker position were determined from the slides and by visual observations, and the breaker depth was then determined from the profile surveys.

III. GENERAL RESULTS

Reflection Coefficients. Figure 6 presents the values of the reflection coefficient versus time for the four experiments. All tests show the same general pattern of variation, although the inferred initial condition was too transient to show on the time axis of Figure 6.

  a. In the first few minutes of all experiments, it is inferred that the reflection coefficient rose sharply because of the following facts. Waves breaking on the concrete slab gave measured K_r ranging from 0.03 to 0.07. Since the permanent slope of the concrete slab was identical to the initial slope of the movable bed, there is no reason to doubt that these low K_r values also occurred during the first moment of testing on the movable bed. However, the first K_r measurements from the movable bed, which occurred after 12 to 20 minutes of wave action, gave measured K_r ranging from 0.14 to 0.19 in the four experiments.

  b. After the initial high values of reflection and for the next few hours the reflection coefficient varied from 0.08 to 0.17. The
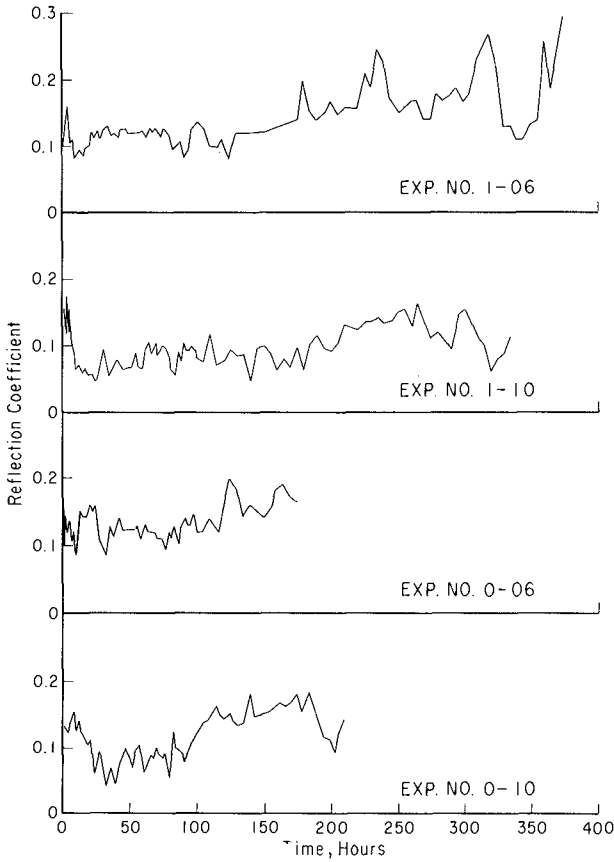
Figure 6. Time Variation of Reflection Coefficient for Four Experiments with Identical Generated Wave Conditions

period of high values and high variability was followed by a drop in the reflection coefficient. The time at which the drop occurred varied from 4 to 20 hours. Experiment No. 0-06 varied slightly from this pattern (Figure 6).

    c. For an extended period of time (duration varying from 60 to 160 hrs), the reflection coefficient was relatively small ($K_r \leq 0.13$ in the six-ft tank and ≤ 0.11 in the ten-ft tank).

d. For the remainder of each experiment, the reflection coefficient
increased in mean value and in variability (for example, varying from 0.10
to 0.30 in Experiment No. 1-06).

The reflection coefficient varied from 0.05 to 0.30 in the four
experiments, which is a large variation considering the generated wave
conditions were held constant. The time at which the reflection coeffi-
cient began to increase (paragraph d, above) varied in each experiment.

Profile Development. The profile in each experiment developed in a similar
sequence as the sediment adjusted to the imposed wave conditions (Figure 7).
Early profiles (solid line on Figure 7) had a steep foreshore zone (from the
limit of uprush to the seaward limit of backwash), a short inshore zone (from
the toe of the foreshore to just seaward of the breaker) with a longshore
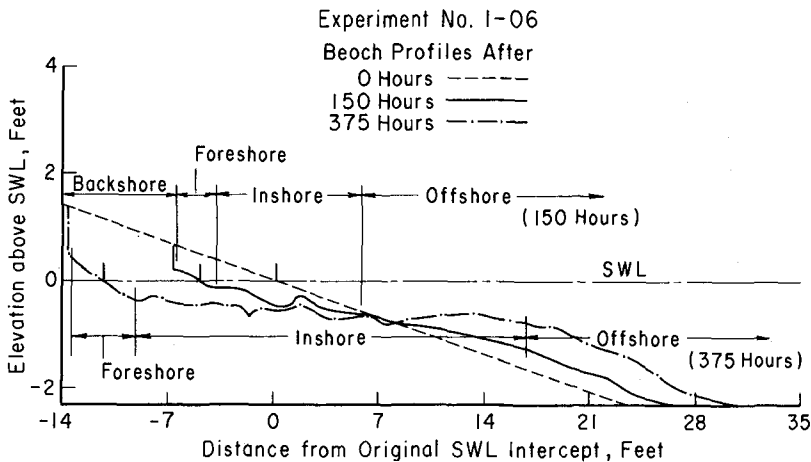
Figure 7. Typical Features of Profile Development

bar formed at the breaker position, and a gently-sloping offshore zone (from
the seaward edge of the inshore zone to the seaward edge of sand). Later
profiles (broken line in Figure 7) also had a steep foreshore zone, but the
inshore zone widened to a long flat shelf which terminated in a relatively
steep offshore zone. It is evident that the eroding foreshore and accreting
offshore were complementary processes because the depth over the inshore re-
mained relatively constant.

Breaker Evolution. The wave broke as a plunging breaker on the early pro-
files and, as the inshore zone slope became flatter, the breaker type changed
to spilling, and the depth at breaking increased.

IV. SUMMARY OF THE FOUR EXPERIMENTS

The results of Experiment No. 1-06 are representative of the four experiments and are described in detail below. Highlights of the other experiments, especially where they deviate from Experiment No. 1-06, are then presented in following sections.

Experiment No. 1-06. Figure 8 is a plot of the movement of the contour positions at 0.1 ft contour intervals for Experiment No. 1-06. Superimposed on the plot is the movement of the breaker position. During part
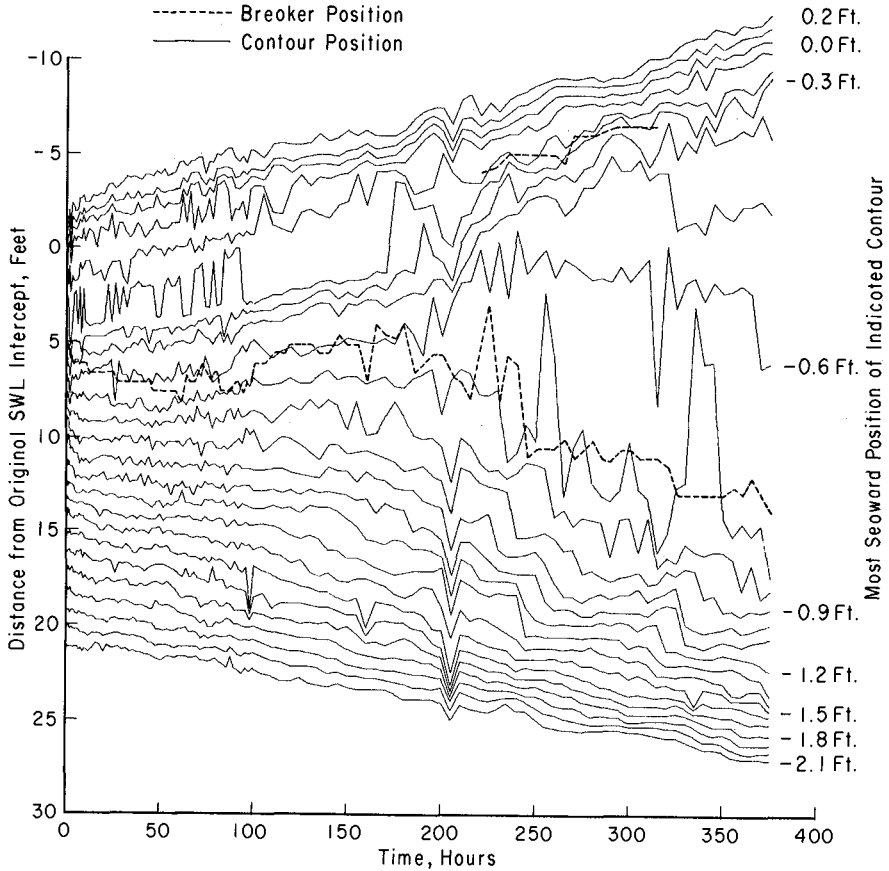
Figure 8. Movement of Contour Positions at Range 3 During Experiment No. 1-06

of the experiment each wave broke twice.

Within the first hour, the foreshore evolved to an equilibrium
slope that did not change significantly throughout the 375 hours of the
test.   The constancy of the foreshore slope is indicated by the approxi-
mately equal spacing between the +0.2, +0.1, 0.0, and -0.1 ft contour
positions in Figure 8.   The slope of the 0.0 ft contour position line
indicates that the average rate of shoreline retreat was 0.03 ft/hr.

Within the first hour the plunging breaker formed a longshore bar,
and for the first 180 hours the wave broke mostly at a depth of 0.6 ft.
As more material was eroded from the foreshore and deposited offshore,
the length of the inshore zone increased and its slope decreased.   As a
result of the flatter slope, the breaker type after 105 hours began
fluctuating between plunging and spilling.   After 180 hours, the breaker
position coincided with the general seaward movement of the -0.7 ft
contour and the breaker type was primarily spilling.   As the breaker
moved in the seaward direction, the longshore bar eroded (the shoreward
movement of the -0.3, -0.4, and -0.5 ft contours after 210 hours in
Figure 8).   The material deposited seaward of the breaker eventually
reached an elevation of -0.8 ft and formed the long, flat shelf in the
inshore zone and the relatively steep slope in the offshore zone.   Between
220 and 315 hours the wave broke twice: by spilling at a depth of 0.7 ft,
and by plunging at the toe of the foreshore.

The largest fluctuations in contour position in Figure 8 are two
temporary shifts of about 10 and 12 feet in the position of the -0.7 ft
contour.   The same shifts occurred simultaneously at all three surveyed
ranges (Figure 9), showing that the movable bed had a largely two-di-
mensional profile, and suggesting that significant net sand transport
occurred across the inshore zone.   Only the most seaward contour is
plotted on Figure 8, but the large shifts in the -0.7 ft contour represent
the removal of a bar projecting slightly above the -0.7 ft contour on
the seaward portion of the inshore (Figure 7).   The removal of this
bar shifted the most seaward contour across the relatively flat inshore,
as would occur on Figure 5a for the most seaward contour position at
the elevation of the dashed line, if the bar on profile t_2 were re-
moved.

The temporal variation of the reflection coefficient in Experi-
ment No. 1-06 is shown in the top curve in Figure 6.   Between 4 and 175
hours, the reflection coefficient was 0.12 or less.   After 125 hours, the
reflection coefficient showed a general upward trend, but with two
large fluctuations.   The overall upward trend in K_r occurred at a time
when the width of the offshore zone decreased, that is, the average
slope of the offshore steepened.   For example, in Figure 8 the dis-
tance between the prograding -1.0 and -2.0 ft contours at 175 hours was
about 10 ft (the same slope as the initial 1:10), but between 180 and
300 hours, this distance decreased to 7 feet.   Therefore, a nominal
average slope of the offshore zone steepened by about 43% at the same
time that the reflection coefficient (exclusive of fluctuations) in-
creased by approximately 33% (Figure 6).
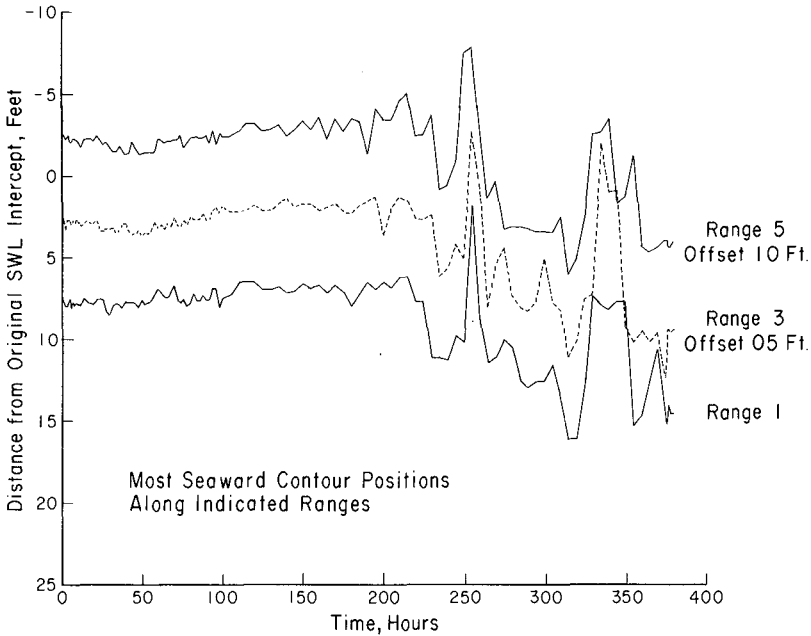
Figure 9.   Movement of −0.7 ft Contour Position Indicating Two-Dimensionality
            During Experiment No. 1-06

The large fluctuations in K_r after 175 hours coincided with fluctuations in the position of the −0.7 ft contour (Figure 10). Peak values of K_r occurred when the −0.7 ft contour was in its more seaward position. Since a more seaward position of a fluctuating contour on an otherwise stable slope necessarily steepens the average slope seaward of that contour, the K_r peaks also correlate with a steepening of the seaward portion of the profile. However, the magnitude of the K_r fluctuations appears to be out of proportion to the magnitude of the changes of the whole profile. If the correlation shown on Figure 10 is substantiated by other data, then there appears to be a very sensitive adjustment of total profile reflectivity to minor profile changes.

Experiment No. 1-10. Figure 11 presents profile development along the center range during Experiment No. 1-10. In this experiment the tank was 4 ft wider and the initial test length was 38.3 ft shorter than in Experiment No. 1-06. The same sequence of profile development occurred, but at a slower rate. In Experiment No. 1-10 (Figure 11), the shoreline retreated an average of 0.01 ft/hr, or approximately one-third the rate of Experiment No. 1-06 (Figure 8).
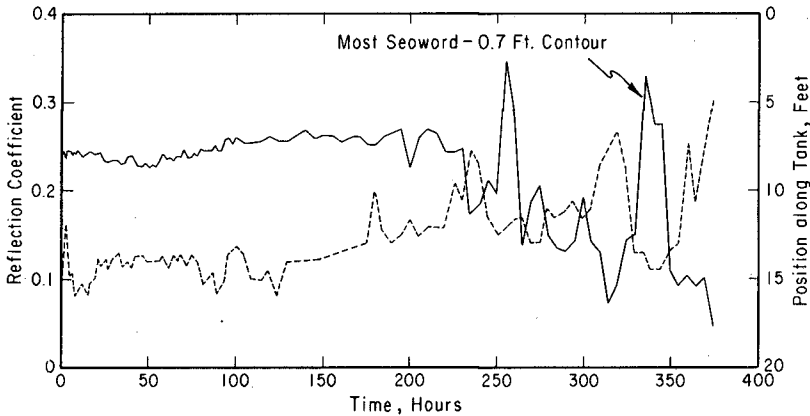
Figure 10.   Fluctuations in Reflection Coefficient and -0.7 ft Contour
             Position During Experiment No. 1-06

     Profile shape in Experiment No. 1-10 exhibited significantly greater
lateral variations than in Experiment No. 1-06, as illustrated by the com-
parison of the movement of the -0.6 ft contour position along five ranges
in Experiment No. 1-10 (Figure 12). The flat shelf in the inshore zone
developed (over a 100-hour period) first along range 9 and last along
range 1, although the shoreline retreat rates along all profiles were
equal. Although there was greater variation in the shape and position
of the offshore zone in Experiment No. 1-10, there was less variation in
the value of the measured reflection coefficient (Figure 6), perhaps
because lateral variation in profile development smoothed out the sharp
K_r fluctuations found in the narrow tank of Experiment No. 1-06.

Experiment No. 0-06. The only difference in initial conditions between
Experiment No. 0-06 and Experiment No. 1-06 was the initial test length
which was 7 ft greater in No. 0-06. The contour positions at the center
range are shown in Figure 13. The approximately horizontal lines marking the
foreshore contour positions after 54 hours indicate the stabilized shore-
line position produced by the repeated backshore replenishment. During
the first 50 hours, the shoreline retreated at a rate which varied from
0.06 ft/hr to 0.14 ft/hr, or an average rate of 0.10 ft/hr.

Experiment No. 0-10. Figure 14 presents profile development along the
center range of Experiment No. 0-10. The inshore in this experiment
developed over a 45-hour period first along range 1 and last along range 9,
that is, opposite to results from Experiment No. 1-10 shown in Figure
12 (data available at CERC). The shoreline retreat rate averaged 0.08
ft/hr during the first 50 hours.
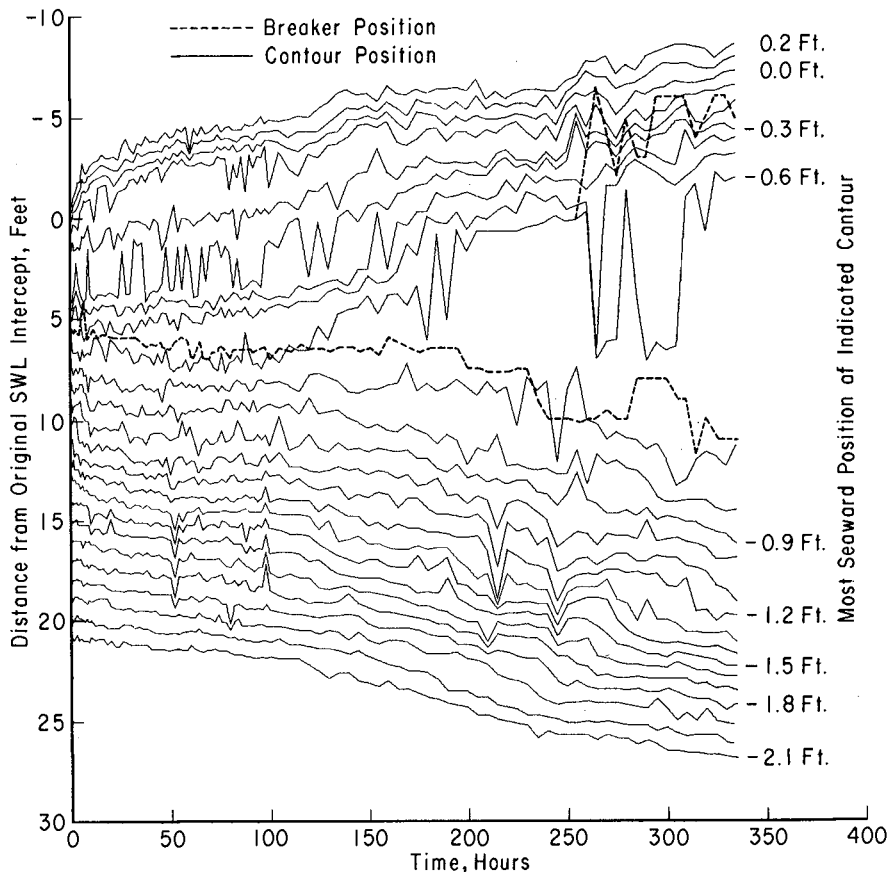
Figure 11.   Movement of Contour Positions at Range 5 During Experiment
             No. 1-10

V.   PROFILE REFLECTIVITY

     At least three processes reflect wave energy from the movable bed
in typical coastal engineering laboratory experiments. These include
the conversion of potential energy stored in runup on the foreshore into
a seaward traveling wave, the seaward radiation of energy from a plunging
breaker, and reflection of the incident wave from the movable bed, parti-
cularly where the depth over the movable bed changes significantly. Depth
changes are significant if the depth difference is an appreciable fraction
of the average depth over a horizontal distance less than a wavelength.
For conditions of these experiments, the wavelength is 14.3 ft seaward
of the movable bed and approximately 9 ft in the inshore zone.
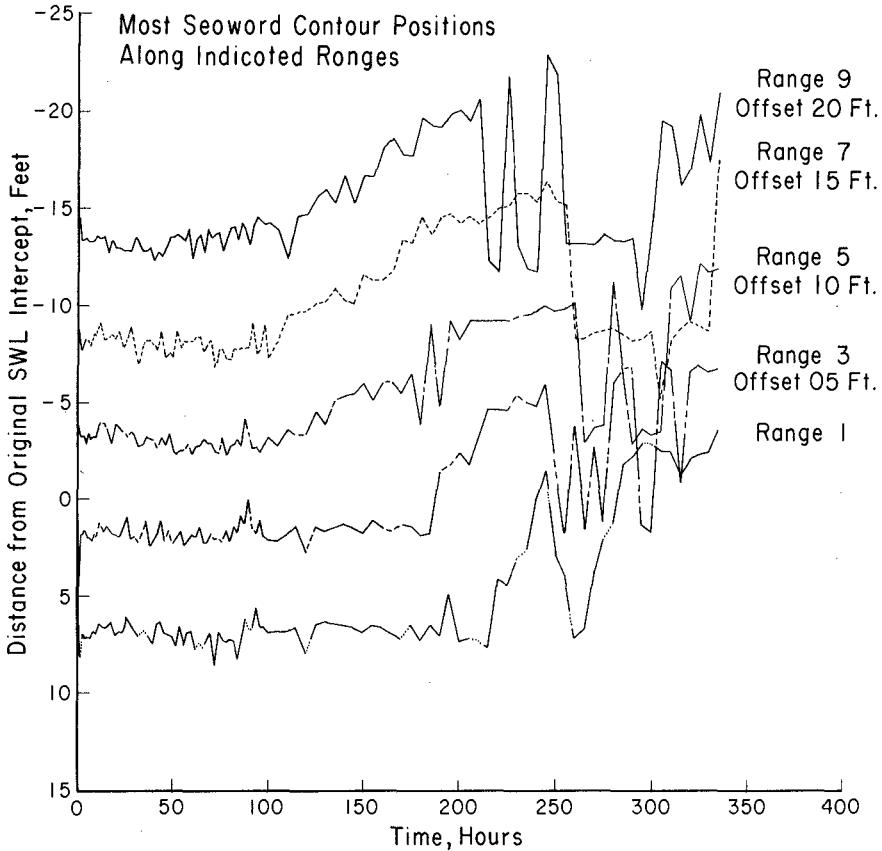
Figure 12. Movement of -0.6 ft Contour Position Indicating Lack of Two-
             Dimensionality During Experiment No. 1-10

Reflection from the Foreshore. The foreshore zone developed a relatively
stable slope within the first hour of testing, well before the other ele-
ments of the movable bed profile had become prominent. The developed
foreshore had a slope of about 1:6.5, which is considerably steeper than
the initial 1:10 slope of the movable bed. The initial high values of K_r
are probably the result of reflection from the foreshore of waves which
dissipated relatively little energy until almost at the foreshore. Re-
flection from the foreshore is a function of the height of the wave reaching
the foreshore, and this height would diminish as the inshore and offshore
segments of the profile (Figure 7) became prominent.
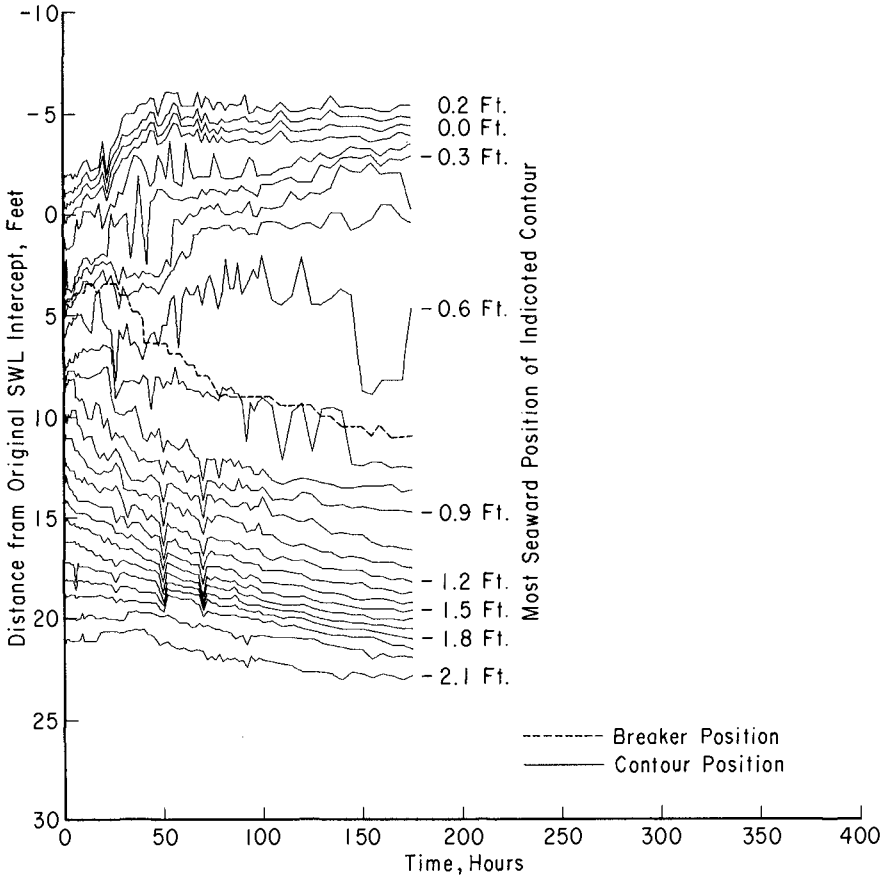
Figure 13.   Movement of Contour Position at Range 3 During Experiment
              No. 0-06

Reflection as Result of Wave Breaking.   On the concrete slab the wave broke as
a plunging breaker and on the movable bed profile the breaker was initially a
less well-developed plunger and evolved to a spilling breaker.   The concrete
slab had the same slope (1:10) as the initial slope of the movable bed.
Because the total reflection was significantly less on the concrete slab
($K_r \approx 0.05$), where the plunger is assumed to contribute relatively more to
the total reflection, it is likely that reflection from the movable bed
by breaking was never very important, and became less important as the
breaker type changed to spilling.
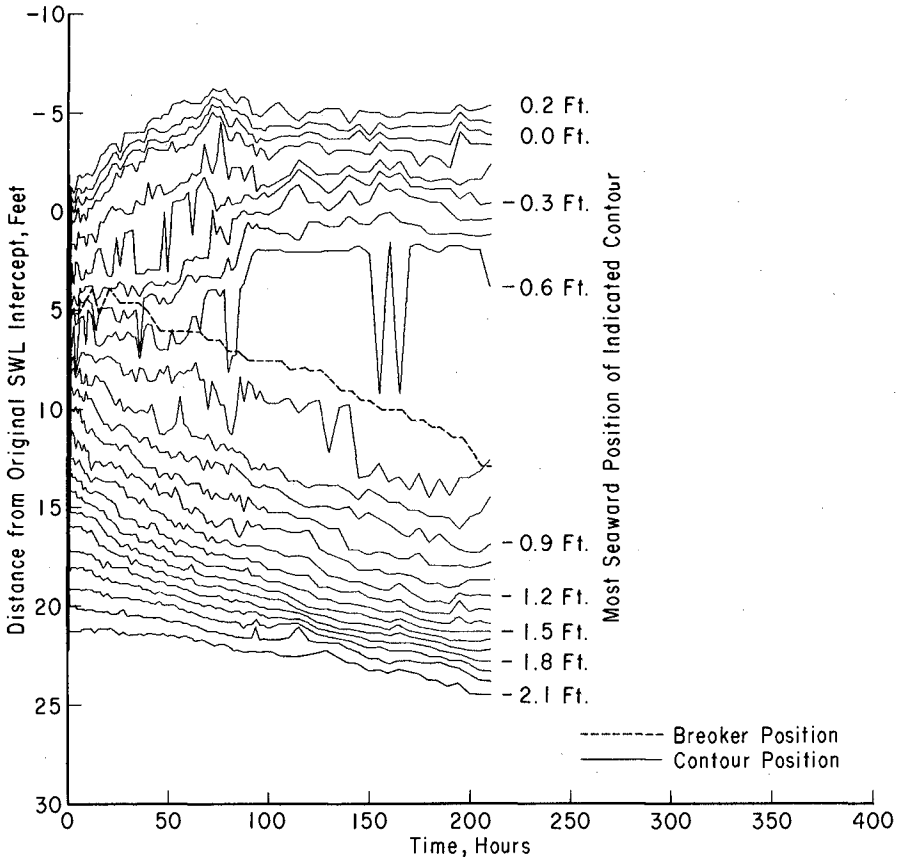
Figure 14. Movement of Contour Positions at Range 5 During Experiment
            No. 0-10

Effect of Inshore and Offshore. As the experiment proceeded, the inshore
widened and the offshore steepened. At first the widening of the inshore
dominated and the lowering of the reflection after the high initial values
(Figure 6) is attributed to the greater energy dissipation in the inshore.
The later steepening of the offshore correlates well with the trend toward
higher K_r later in all the experiments, as can be seen by comparing the
offshore contour positions on Figures 8, 11, 13, and 14 with the appropriate
reflection curve on Figure 6. The earlier onset of higher reflection in
Experiment Nos. 0-06 and 0-10 (Figure 6) is explained by the quicker devel-
opment of the offshore reflector in those experiments (Figure 13 and 14).

With the development of the two reflecting zones (foreshore and off-shore) separated by a relatively flat inshore zone, the measured reflected wave was composed of two reflected waves. A change in phase or amplitude of either reflected wave would change the phase and amplitude of the measured wave. Part of the long-term K_r variability can be attributed to the change in phase difference between these two reflected waves as the foreshore retreated landward and the offshore built seaward.

The apparent correlation between the movement of the -0.7 ft contour in Experiment No. 1-06 and the variability of the reflection coefficient (Figure 10) suggests that the reflection is very sensitive to small changes in the depth near the seaward edge of the inshore zone. (In a less pronounced way, the -0.6 ft contour position also varies with the changing values of K_r in Experiment No. 1-10 (Figure 6 and 11).) This variability in the depth would cause variability in the reflection of the incident wave from the offshore slope and variability in the amount of energy trapped on the inshore shelf.

VI. CONCLUSIONS

Reflection Results

a. For constant incident wave conditions in four experiments with a movable sand bed, the reflection coefficient (K_r) varied from 0.05 to 0.30. This indicates a possible range of measured wave heights from 0.25 to 0.47 ft for the nominally constant 0.36-ft height used in these four experiments. Under the same wave conditions, K_r from a 1:10 concrete slab varied only from 0.03 to 0.07.

b. K_r correlates with profile changes. K_r more than doubled in the first few minutes of wave action on the movable bed due to development of the steeper foreshore. The reflection decreased as the inshore widened. Later increases in K_r occurred when the offshore began to steepen. Large fluctuations in K_r occurred at times of large shifts in contour position on the relatively flat inshore zone.

c. Because of the variable profile reflectivity, incident wave measurements to characterize a coastal engineering experiment should be based on calibration of the wave generator rather than spot wave measurements during the experiment.

d. Further work needs to be done in quantifying the different processes causing reflection from a profile and in determining the importance of phase difference on profile reflectivity.

Profile Results.

a. Profiles in all four experiments developed in the same sequence.

b. The foreshore attained its equilibrium slope within the first hour of testing and maintained this slope throughout the experiments. The position

of the foreshore retreated at average rates which varied from 0.04 to 0.10 ft/hr, averaged over the first 50 hours of each experiment.

c. "Equilibrium" profiles were not attained after as many as 375 testing hours (as many as 470,000 waves).

d. Initial slopes for two-dimensional coastal engineering experiments with a movable bed should be chosen according to the purpose of the experiments. For experiments which presume an "equilibrium" profile, an approximation of that "equilibrium" profile should be used to start the test, as done by Savage (1959) and Fairchild (1970a). However, data in this paper suggest caution in the determination of "equilbrium" conditions.

e. Further work needs to be done on the effect of water temperature, tank width, and initial test length on profile development.

REFERENCES

Fairchild, J.C., "Laboratory Tests of Longshore Transport" in Proceedings
    of the 12th Conference on Coastal Engineering, Chapter 55, pages 867-
    889, 1970a.

Fairchild, J.C., "Wave Diffraction in a Laboratory Movable-Bed Setup,"
    Bulletin and Summary of Research Progress Fiscal Years 1967-69,
    Vol. III, U.S. Army, Corps of Engineers, Coastal Engineering
    Research Center, Washington, DC, pp. 29-40, 1970b.

Galvin, C.J. and R.P. Stafford, "Wave Height Variability on Laboratory
    Beaches," Transactions of the American Geophysical Union, April 1970,
    p. 322.

Savage, R.P., "Laboratory Study of the Effect of Groins on the Rate of
    Littoral Transport: Equipment Development and Initial Tests,"
    U.S. Army Beach Erosion Board Technical Memorandum No. 114, 56 pp.,
    June 1959.

Savage, R.P., "Laboratory Determination of Littoral-Transport Rates,"
    Journal of the Waterways and Harbors Division, ASCE, No. WW2,
    May 1962, pp. 69-92.

Stafford, R.P., "Investigation and Procedure for Calibration of CERC
    Laboratory Wave Gage, FWK Model-1," CERC Laboratory Report
    (Memorandum for Record), 27 July 1972.

CHAPTER 56

TRACER TESTS IN THE MIDDLE NORTH SEA

E. Bratteland and P. Bruun
Division of Port and Ocean Engineering
The Norwegian Institute of Technology

INTRODUCTION

Tracing of sediment transport has so far mostly been concen-
trated in rivers and particularly in estuaries and in shallow
coastal waters with main interest on navigational, erosional
and some pollutionary aspects. With the ever increasing oil
activites in the North Sea, knowledge on bottom sediment
movements at large water depths is becoming more and more
important. Little tracing has been undertaken on the offshore
sea bottom at depths exceeding 20 - 30 meters.
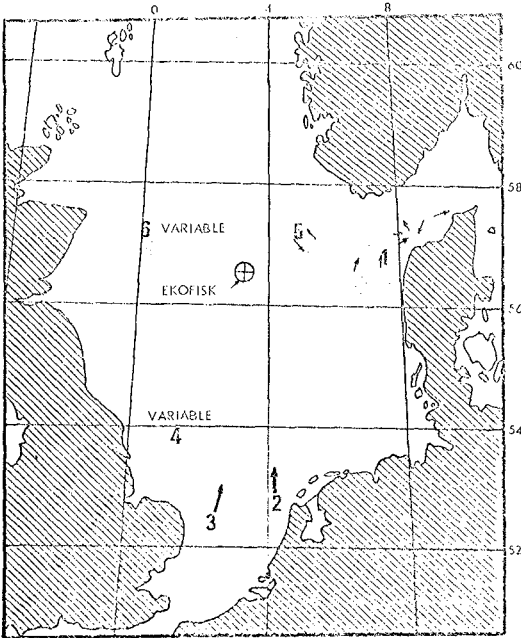
FIG. 1   NORTH SEA
1-6 sand wave areas,
arrows indicate
direction of sand
wave propagation.

This paper describes tests using fluorescent tracers carried out at the Phillips Petroleum Company's production platform, "GULF TIDE", located at the Ekofisk site in the middle of the North Sea.

56° 31'   34,5 "   N
 3° 13'   00.5 "   E

The water depth in the area is 70 meters.
See Figs. 1 and 2.

FIG. 2   GULF TIDE

EXPERIMENTAL PROCEDURES.
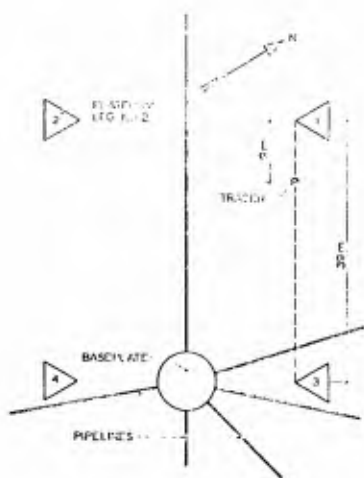
200 lbs of blue fluorescent tracer were placed 9 m from one of the platform legs on March 15. 1973. The tracer reproduced the actual grain size distribution at the site with a D_{50} of about 0.12 mm and was placed in a half circle around 50 cm in radius and in a 5 cm layer. An idealized layout of the bottom installations and the positioning of the tracer is shown in Fig. 3.

FIG. 3   IDEALIZED BOTTOM
            INSTALLATIONS AND
            TRACER POSITIONING

Table 1:   DATA ON SAMPLING

DATE OF SAMPLING	SAMPLING AT DISTANCES (m)							SAMPLING PROCEDURE
	1.5	3.0	4.5	7.5	15	30	60	
MAY 3.1973	X	X						PLATES
JUNE 10. "		X	X					"
JULY 12. "	X	X	X	X				"
AUG. 20. "			X	X				"
OCT. 10. "				X	X			"
JUNE 20.1974					X	X	X	GRAB

The samples taken are shown in Table 1.

Introductory all samples were taken by divers forcing a 30 by
30 cm plastic plate covered with grease down into the sea bottom.
Except from this sampling the divers were only swimming over the
sampling area at approximately ten feet above the sea bed every
fourteen days to inspect the bases of the platform legs.
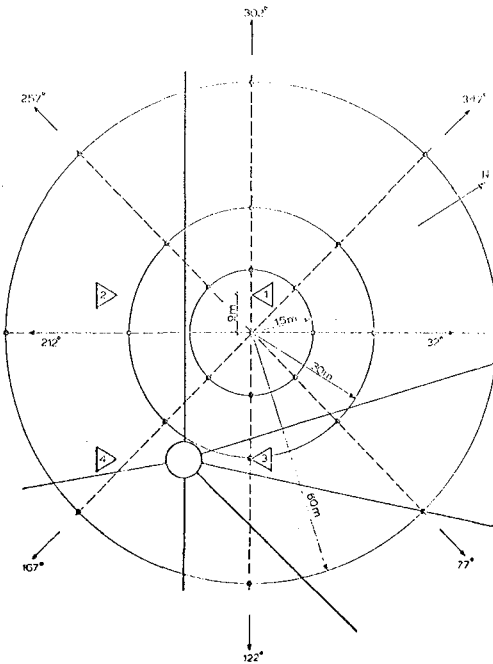
FIG.4   SAMPLING SCHEME

The latest set of samples on June 20. 1974 were taken by a
simple self-releasing grab-type sampler lowered from a boat.
Samples were taken in 8 different directions as shown in Fig. 4,
for distances 15, 30 and 60 m. Samples nearer the tracer source
were taken in the same directions.

WIND, WAVES AND CURRENTS.

Long-term distributions of wind and wave observations from
weather ship "Famita" positioned about 100 km north of the
Ekofisk area are shown in Figs. 5 and 6. The wind velocity is
the 10 min. average. Wave heights were observed visually and
corresponds reasonably well to the significant wave height.
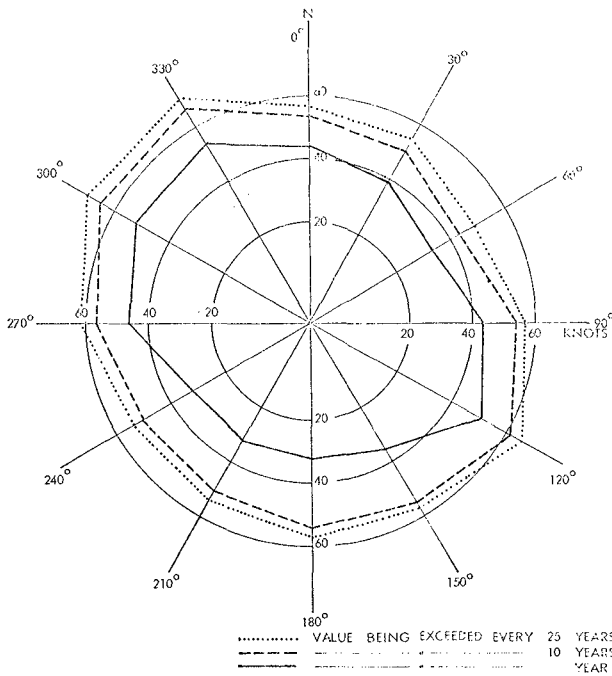
FIG. 5   WIND FREQUENCY AS A FUNCTION
         OF DIRECTION. (1959-69). REF. (1).
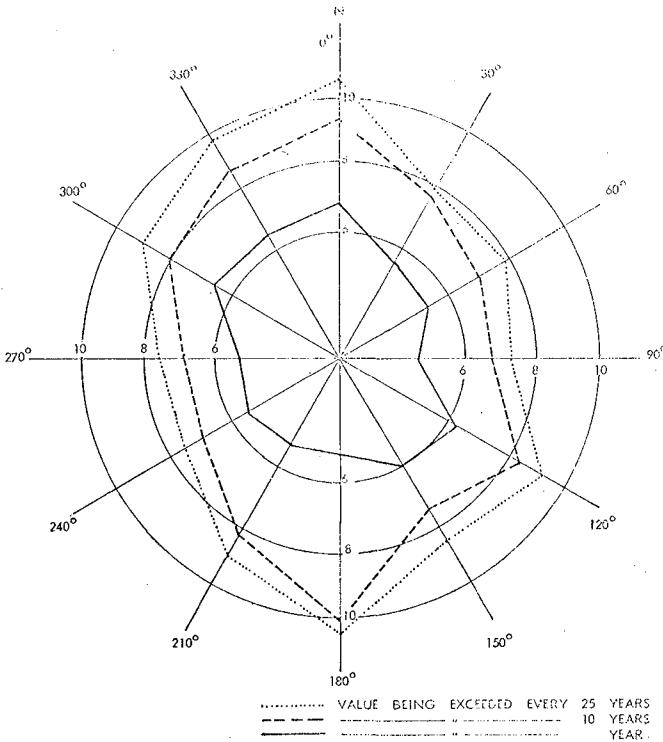
FIG. 6   WAVE HEIGHT FREQUENCY AS A FUNCTION OF
         DIRECTION, VISUALLY OBSERVED WAVES
         (1959-69).   REF. (1).

For a one year period the wind observations were distributed
as shown in Fig. 7. Wind was calm with undeterminable
direction in 2.9% of the time.
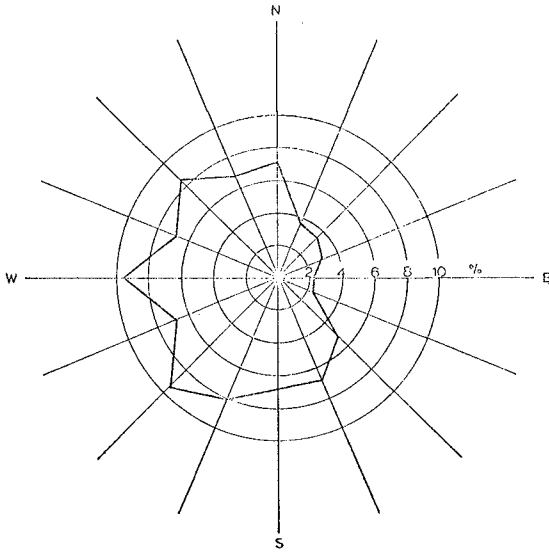
FIG. 7   WIND DISTRIBUTION ON DIRECTIONS
         MARCH 1973 - MARCH 1974

The predominant wind directions are NW, W to SW. Comparing
to Fig. 5 it is noted that the highest value of wind velocity
could be expected from NW or SE. Comparison of wind and wave
directions indicates that they are quite close and Fig. 7
should therefore give a fairly correct impression of wave
directions in the area during the one year period.

Figs. 8 and 9 give the distribution of wave heights and wave
periods observed at the Gulf Tide over a one year period.
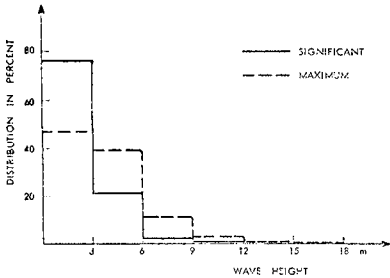
FIG. 8   DISTRIBUTION OF WAVE HEIGHTS   FIG. 9   DISTRIBUTION OF
         FEBR. 1973 - FEBR. 1974   WAVE PERIODS
                                                        FEBR. 1973 -
                                                        FEBR. 1974
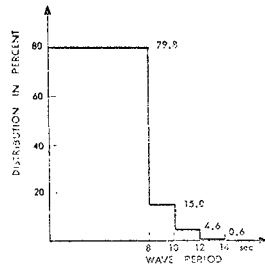
Three current meters were installed on the Gulf Tide at
9, 27 and 58 m water depth. Unfortunately the meters have
been out of order part of the time. For the 27 and 58 m
depth the results of 137 days of recordings from February -
August 1973 are shown in Table 2.

Table 2:   CURRENT OBSERVATIONS.
           137 DAYS RECORDINGS FEBR.-AUG. 1973.

CURRENT DIRECTION	27 m WATER DEPTH				58 m WATER DEPTH			
	PERCENT OF TIME WITH CURRENT SPEED (KNOTS)				PERCENT OF TIME WITH CURRENT SPEED (KNOTS)			
	0-1/4	1/4-½	½-3/4	Σ=	0-1/4	1/4-½	½-3/4	Σ=
N					0.1	0.1		0.2
NE	4.0	4.4	1.3	9.7	0.9	1.7		2.6
E	36.5	43.4	0.4	80.3	8.0	9.7	0.1	17.8
SE	2.5	7.1	0.4	10.0	11.5	20.7	29.4	61.6
S					4.2	4.1	8.6	16.9
SW					0.5	0.1	0.1	0.7
W						0.1		0.1
NW						0.1		0.1
Σ=	43.0	54.9	2.1		25.2	36.6	38.2	

This table show a clockwise turning of the predominant current
direction with increasing depth, perhaps indicating the effect
of the earth's rotation. Unfortunately no current recordings
closer to the bottom were obtained.

The observation of currents at 9 m depth unfortunately were
inadequate. Surface currents needless to say shift continually
with the wind. The effect in deeper water may be seen as an
integrated result combined with tidal currents running mainly
E-W and possibly density current phenomena by which slightly
higher salinity and temperature water flowing north is balanced
by slightly higher density water flowing south.

TRACER RESULTS

The result of the samplings in TABLE 1 are shown in Figs. 10 -
14 where concentrations are given in tracers per cm^2, while
Fig. 15 gives the concentration in tracer grains per cm^3.

The concentrations found by the plastic plate sampling
procedure could be influenced by arbitrary conditions at the
sampling point.   Still most of the samles seem to give reason-
able results.   The results e.g. show an expected tendency to
decreasing concentration with increased distance and time.

FIG. 11 SAMPLING JUNE 10, 1973

FIG. 10   SAMPLING MAY 3, 1973
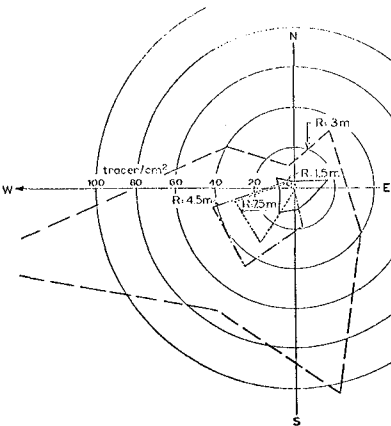
FIG. 12   SAMPLING JULY 12, 1973
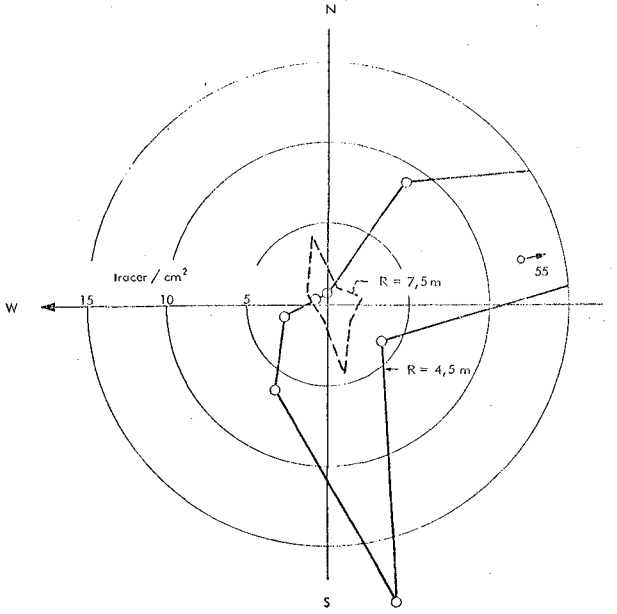
FIG. 13   SAMPLING AUG. 20. 1973
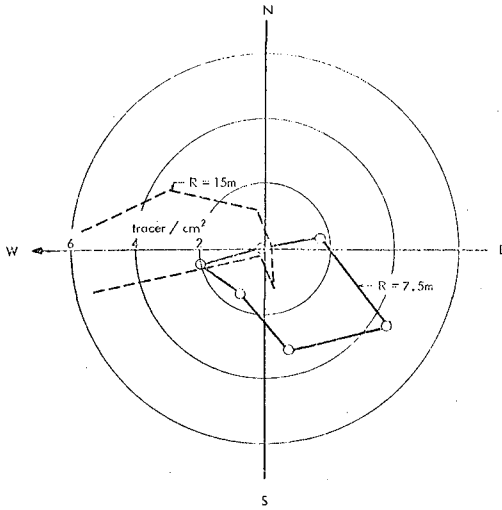
FIG. 14   SAMPLING OCT. 10. 1973
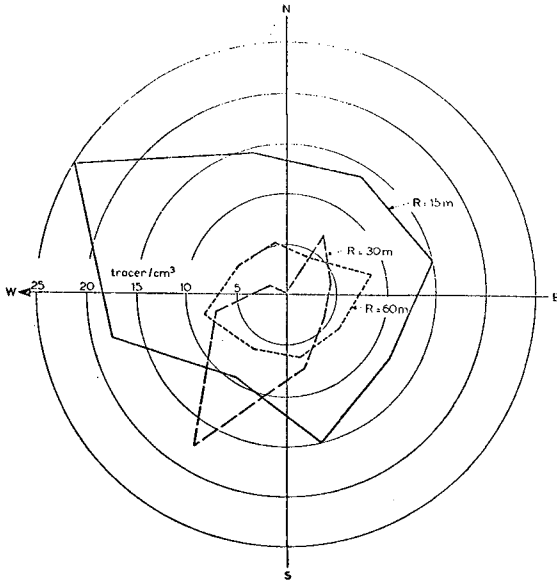
FIG. 15   SAMPLING JUNE 20. 1974
          (GRAB-SAMPLING)

DISCUSSION.

The results of the tracing on the Ekofisk site clearly showed
that the bottom sediments are moving. The fine sand has a
critical velocity for incipient motion well below the actual
water particle velocities at the bottom during a moderate to
heavy storm. A wave of 10 sec. period and 6 m height would
according to first order theory give water particle velocities
at 70 m water depth of about 0.22 m/s, while the critical
velocity for incipient motion of the fine sand probably is
around 0.15 m/s. The effect of waves in the transportation of
sediment is negligible. Fluid displacement due to wave action
can, however, be important when coupled with a stronger or
weaker current at the sea bed. At the 58 m water depth the
current exceeded ½ knot (0.25 m/sec) during 38 percent of the
time. (Table 2).

Indications are that the current and wave actions at the
Ekofisk site should be able to move the fine bottom sediments
at the site. This has been verified by the tracer tests.

Fig. 15 shows the result of the sampling carried out in June
1974, demonstrating the movement which took place over an
extended period of time. This included some extraordinarily
severe winter storms in November and January. The latter storms
caused several shipwrecks including one platform, The TRANSOCEAN
61, which broke up and sank. These storms were typical SW to NW
storms but of an intensity which caused waves of up to about
20 meters at the Ekofisk site.

The distribution of tracers may be interpreted as follows:

The 15 m and 60 m distributions are not far from being symme-
trical N-S as well as E-W the latter being more predominant then
the former. This may be seen as a result of the scattering by
waves coming from SW to NW causing the coarsest particles to tend
to move towards the E, perhaps with a southward tendency due to
current action (as also revealed by the earlier samplings). It
will be a tendency for relatively finer particles to move in the
opposite direction i.e. W. This tendency will predominate when
ripple marks have been found and the relatively rapid forward
movement of water particles over the rippled bottom causes the
development of small eddies downstream of the steep slope of the
ripple marks. These eddies contain some particles which, by the
relatively slower backward movement of water particles, wash up
as independent elements above the ripple marks where the total
water movement may easily be in the direction opposite to the
direction of wave propagation.

The distribution for 30 m distance shows a definite NE-SW
trend, mainly due to one particular strong concentration towards
SW (to S). This could be accidental, resulting from the limitations
of the sampling technique by which a coverup of tracer particles
below sampling level is still possible.

The possibility of movement in any one of the eight directions
where samples were taken is given by the concentration (number of
tracer grains) found in sampling points in this direction. If
one grain moved in all directions in a relative magnitude given
by the ratio between the concentrations in these directions, the
integrated resulting movement is obtained by adding concentrations
times travel distances in length and direction as vectors.

The resulting mass movements are obtained by multiplication of
the resulting concentration and the length of migration. This
is done in Fig. 16. Assuming that the concentrations at e.g.
30 m distance represent conditions between 23 m and 45 m and
similarly for the 15 m and 60 m distance, one would then know
the development within an area limited by an inner circle of
7.5 m and an outer circle of 75 m., covering an area of about
17.500 m^2 . According to Fig. 16 the resultant direction of
drift within the said area is towards SSW. The magnitude of drift
of tracer grains was 800 grains/cm$^3 \cdot$ m.
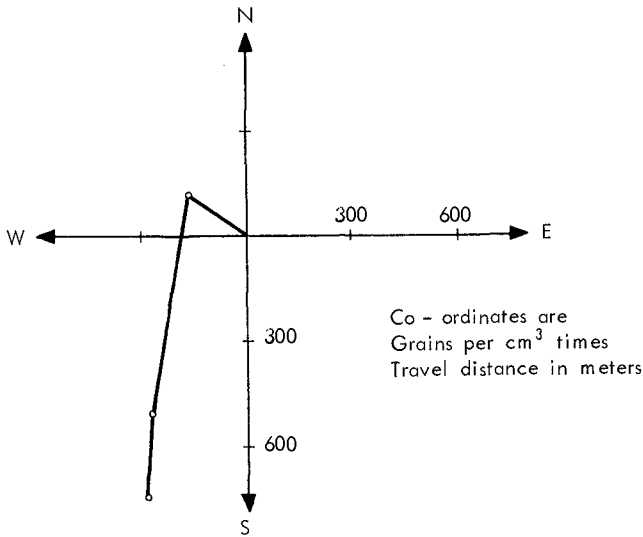
FIG. 16   RESULTING MASS MOVEMENT

In order to quantify this number one has to know the depth of
movement. The sampling penetrated about 4 cm down in the
bottom and the concentration refers to that depth. It is not
very likely that movement penetrated deeper in an unobstructed
bottom. One therefore arrives at the fact that the resultant
movement

$$= \frac{0.04 \cdot 800 \cdot 1 \cdot 1 \cdot 1}{30.000} \text{ m}^4 = \frac{4 \cdot 800 \cdot 10^6}{30.000} \text{ cm}^4 = 10^5 \text{ cm}^3 \cdot \text{cm} = 0.001 \text{ m}^3 \cdot \text{m}$$

which in practical terms may be visualised as 1 mm layer of the
bottom i.e. a layer of about 8 grains, moving   averagely 1 m
during the period of record of about 15 months $\approx$ 450 days.

This is a very small quantity. In this respect it should,
however, be borne in mind that seen on the geological time
scale this quantity would be detrimental to existing bottom
topography and depth if it were a continous trend extending
over larger bottom areas. The result would be deep erosion
in some areas and considerable accumulation in others. The
fact that the sea exists and in its present shape has existed
for some thousand of years proves that the resultant bottom
movements must be very small.

SUMMARY AND CONCLUSION.

(1) It is apparent that at about 70 m depth forces by waves and/or
currents are strong enough at any time of the year to move the
fine bottom sand at the EKOFISK site.

(2)   The movements recorded must be a result of combined current
and wave action.   The importance of wave action under moderate
wave conditions apparently is that the oscillating water move-
ment breaks the sand particles loose from the bottom after
which currents carry the material with them.   During periods of
heavier wave action, i.e. waves from SW to NW during fall and
winter storms, the asymmetrical water motion (waves in heavy storms
are shallow water waves!) moves the material in the direction of
wave propagation - and probably also in the opposite direction as
the bottom is horizontal and bottom-creep material and suspended
materials behave differently.   The bottom current apparently were
predominant towards S still makes its influence felt mainly on
the suspended particles.   The combined result of current and
wave motion would, in this case, be a resulting movement towards
SSW-SW-as actually found by averaging the movements found.   The
direction of propagation of sand waves indicated in Fig. 1 shows
for area five a direction of travel which does not deviate too
much from the resulting direction found by the tracer experiments.

(3)   An attempt was made to quantify the results based on
assumptions which may be open to discussion - but a resulting
movement of 1 mm times 1 meter in 450 days seems - at least -
to have the right dimension.   The movement during single storms
is not known, but the maximum surface concentration recorded
has been of the order of 100 grains/cm^2.   If it is assumed that
this layer extends 10 mm down this would correspond to a concen-
tration of about 1 in 60 or to an average movement of ab. 0.2
millimeter or two grains' thickness.   This still assumes that
the bottom is entirely unobstructed.

REFERENCES.

(1)   L. Håland, O.G. Houmb and B. Pedersen:
      "Long Term Distributions of North Sea Waves".

CHAPTER 57

FORMATION OF DUNES BY TIDAL FLOWS

by

M.S. Yalin[1]   and   W.A. Price[2]

ABSTRACT

Schematical relations for the size of dunes and for the duration of
their development are derived assuming that the large scale formations on
the surface of a movable bed are due to the largest eddies of turbulence.
The considerations are confined to the simplest case of a two-dimensional
flow and to the cohesionless granular material. The relations for tidal   ·
dunes are obtained by generalising the relations for unidirectional flow
dunes. Special cases and the validity regions of the forms presented are
discussed; suggestions for future measurements and model tests are included.

INTRODUCTION

The study of large scale sand waves, or shortly dunes, is becoming
increasingly important in the marine engineering field. For example, there
is considerable activity taking place with oil exploration in the North Sea
and there is a need to bring the oil ashore by pipelines. Sometimes these
will cross dune fields and there is the risk that previously buried lines
will become exposed as sand waves move on. Considerable loads could then be
set up on the pipes due to wave and current action with the high risk of
breakages. An estimate of the UK expenditure on pipelines during the next
5 years is £ 1000M. Clearly research on the formation of sand waves is
therefore justified on these grounds alone.

The second example concerns the circulation of material in relatively
small oceans like the North Sea (Fig. 1). Until quite recently civil
engineering works were built in estuaries without too much regard being paid
to their effect on ocean circulations but we are approaching the time in
the North Sea, because estuarial works are being constructed on a massive
scale, when this is no longer the case. The Dutch have already completed
their Delta plan, and in the long term the permanent solution to the tidal
flooding problems in London might come with the construction of a causeway
at the mouth of the Thames estuary. Collectively these schemes are bound
to affect circulations of water and sediment in the sea. It will be out of
the question to build physical models of such large areas so undoubtedly

---

[1] Professor of Hydraulics, Queen's University, Kingston, Ontario,
     Canada.

[2] Senior Principal Scientific Officer, Head of Coastal Engineering
     Division, Hydraulics Research Station, Wallingford, Berkshire,
     England.
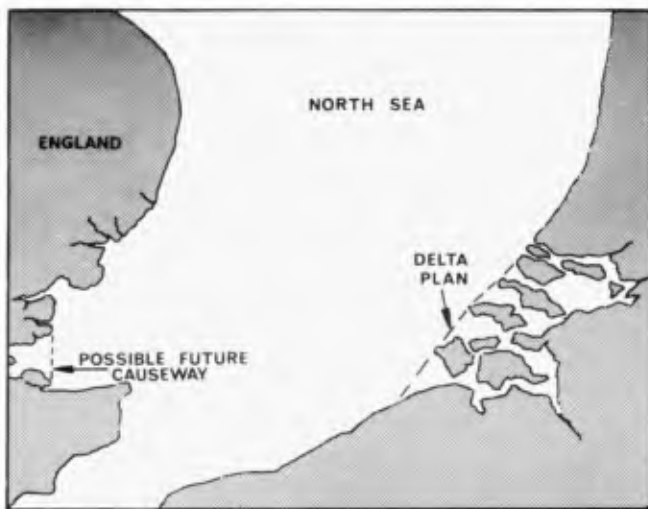
Fig. 1.   Southern North Sea
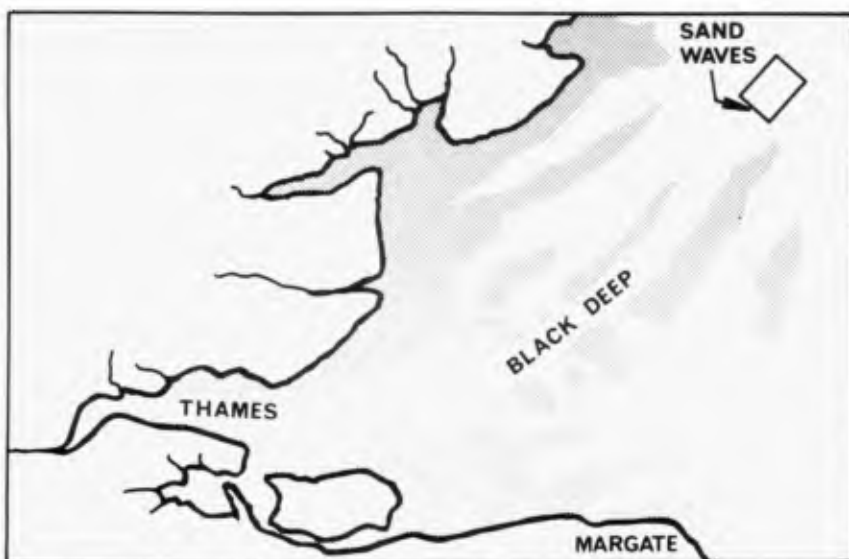
Fig. 2.   Outer Thames Estuary

mathematical models will be used. The laws of sediment transport in general and the factors that affect the formation of dunes in particular will require to be better understood if reliable predictions on the behaviour of future projects are to be made.

The third example, and the one that provided the impetus for the work described in this note, concerns the problems associated with dredging and maintaining large navigation channels. Figure 2 shows the Outer Thames Estuary with its complexity of banks and channels. One of these channels, the Black Deep, is the main navigation channel to the Port of London and it is interesting that at its downstream end it crosses a large sand wave field. There are proposals to deepen this channel so that engineers are interested to know the size of the features that will eventually form in the deepened area and the rate at which they will reform.

An idea of the shape and size of dunes forming in the North Sea can be conveyed with the aid of the data in Ref. [1], where it is reported that on the floor of the North Sea, south of a line from Norfolk to Den Helder in Holland, echo sounding has revealed the presence of ridges about 5 m. high and about 30 m. apart, normally orientated at right angles to the tidal streams. The example of sand waves forming in the Outer Thames Estuary can be found, e.g. in Ref. [2]. This work contains a number of informative diagrams provided by the Institute of Oceanographic Sciences (Taunton) and obtained with the aid of the side scan sonar. IOS (Taunton) have shown that although the dunes forming in the Black Deep field are not all the same, there are fairly distinct areas exhibiting sand waves of the same general characteristics. From the diagrams of Ref. [2] one can also observe that on the backs of the larger features there are sometimes smaller ones and their orientation is often different from that of larger main features.

The present paper concerns the formation of dunes by tidal flows. Attention is focussed on the following two aspects which in the authors' view are the most pertinent to the maintenance of deep navigation channels:

1.   The size of dunes

2.   The duration of their development

It is hoped that the relations derived may prove to be useful in the planning of future measurements aiming to reveal the correlation between the dunes forming on a sea bed and the currents generating them.

In agreement with the prevailing contemporary view, it is assumed that the large scale formations on the surface of a movable bed are due to turbulence or to be more exact to the largest eddies of turbulence.

If the flow is not uniform and the intensity in the variation of flow boundaries is appreciable, then in addition to the eddies of turbulence the flow may contain the eddies of separation. The authors think that the latter eddies also contribute to the formation of the bed surface. However, since the contribution of these eddies depends on their number, size and distribution (in the body of the flow), and since these factors are determined by the topography of the sea bed (which varies from one location of the sea

bed to another in an arbitrary manner and which can thus not be described in general terms) the present study is confined to the consideration of turbulent eddies only.

EDDY STRUCTURE OF TURBULENCE

Turbulence is pictured nowadays as a multitude of eddies (or disturbances) superimposed on the time average fluid motion. These eddies have random instantaneous sizes ℓ_1 and they travel in all possible directions random distances ℓ_2 forming thereby what is called the "turbulent mixing process". It has been established that the lengths ℓ_1 and ℓ_2 are of the same order. Considering this, and also the fact that any clear distinction between ℓ_1 and ℓ_2 is impossible, it has become a custom to consider both lengths (ℓ_1 and ℓ_2) by a single length-order ℓ called the scale of turbulence. The order ℓ corresponding to a location of the space occupied by a turbulent flow is the average value of all ℓ_1 and ℓ_2 encountered at that location.

The eddies are not permanent: some eddies present at an instant t_1, are no longer present at an instant t_2. On the other hand, during the time interval $t_2 - t_1$ a set of "new" eddies is generated instead. First the largest of all eddies occur. The size L of these largest (initial) eddies is comparable with the size h of the flow (flow depth in the case of an open channel)

$$L \approx h .\qquad\qquad(1)$$

With the passage of time the initial eddies lose their stability and disintegrate into a number of smaller eddies. These smaller eddies in turn give birth to even smaller eddies and this "cascade of disintegration" continues to take place until such a small value A, say, of the eddy Reynolds number $\ell_1 . U_1/\nu$ is achieved (where U_1 is the velocity of eddy motion and ν kinematic viscosity) that the eddy becomes stable, i.e. no longer divisible. Clearly the average length ℓ_{min} of the smallest disturbances must thus be determined by the form

$$\ell_{min} = A \frac{\nu}{U} .\qquad\qquad(2)$$

It follows that the linear scale ℓ of turbulence is the average size of the disturbances varying between the upper and lower limits L and ℓ_{min} which are given by (1) and (2) and which are referred to as the linear scales of macroturbulence and microturbulence respectively:

$$\ell_{min} < \ell < L .\qquad\qquad(3)$$

Usually the scale ℓ is "measured" in terms of the size h of the flow, and therefore its distribution along the depth of a stationary and uniform two dimensional flow is expressed in the following manner

$$\ell = h \cdot f \left(\frac{y}{h} \right) \quad ^{*)}$$ (4)

DUNE LENGTH

Two-dimensional unidirectional flow in an open channel

As is explained in Ref. [6] the length Λ of dunes must be proportional to the size L of the largest macroturbulent eddies generating them:

$$\Lambda = \alpha \cdot L \quad .$$ (5)

Since in the case of a unidirectional flow in an open channel the size of the largest eddies approximates the flow depth h (eqn (1)) the relation (5) yields

$$\Lambda \approx \alpha \cdot h \quad ,$$ (6)

The dimensionless proportionality factor α in general is not a constant. The field and laboratory data show (Ref. [6]) that α can only be treated as a constant if the grain size Reynolds number $X = v_* D / \nu$ is sufficiently large (larger than ≈ 45 , say). In this case $\alpha \approx 2\pi = $ const and the relation (6) becomes

$$\Lambda \approx 2\pi \cdot h \quad .$$ (7)

If, on the other hand, X is smaller than ~ 45 (i.e. if the turbulent flow is not fully developed but is in a transitional or hydraulically smooth regime) then α appears to vary as a function of the Reynolds number X and the ratio h/D .

The conditions described follow from the family of curves shown in Fig. 3. This family of curves, which represents the functional relation

$$\frac{\Lambda}{D} = \psi_\Lambda \left(X, \frac{h}{D} \right) \quad \text{and consequently} \quad \alpha = \frac{\Lambda}{h} = \phi_\Lambda \left(X, \frac{h}{D} \right)$$

was determined from a very large number of field and laboratory data supplied by more than a dozen different authors. (See each of the individual curves together with the data determining it in Chapter 7 of Ref. [6].) Note from Fig. 3 that the "curve" corresponding to $X \geq 42.66$ (mentioned earlier as ≈ 45) is a straight line C implying (7). Note also that the relation (7) can already be adopted, with an accuracy sufficient for all

---

*) A general description of the contemporary approach to turbulence can be found, e.g. in Refs. [3], [4], [5].
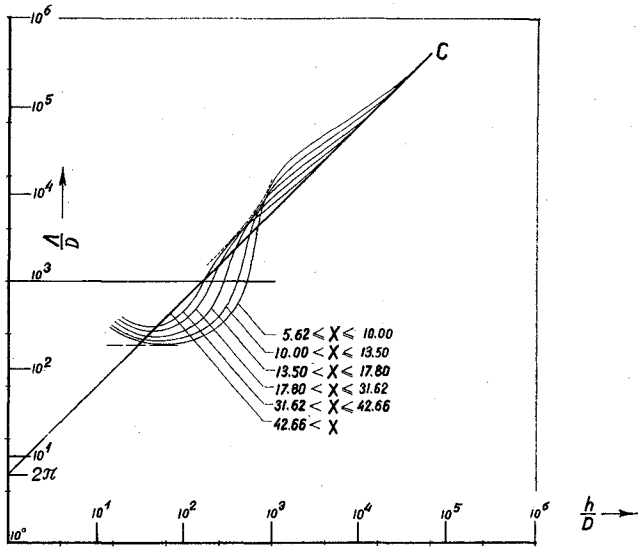
Fig. 3
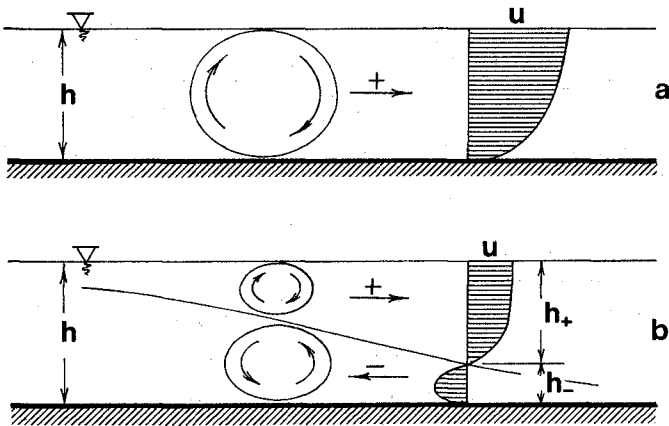
Fig. 4

practical purposes, when X is larger than ≈ 20, say.

Tidal Flow

In the case of a tidal flow it is often observed that the length Λ of dunes is about six times the flow depth (i.e. as implied by the relation (7)). However, it would be wrong to assume that the dune length formula for unidirectional flow should be regarded as applicable to all cases of tidal flow. The authors prefer to believe that the basic mechanism of the formation of dunes is the same, i.e. that they are also formed by the largest macroturbulent eddies as in the unidirectional case and consequently their length should still be given by a relation such as eqn (5). On the other hand, one has no reason to think that the values of the dimensionless proportionality factor α should necessarily be the same as those for unidirectional flow, nor has one any reason to believe that the time average size $\bar{L}$ of the largest eddies (averaged over one periodic cycle) should necessarily approximate to the time average flow depth $\bar{h}$. In fact one would expect that $\bar{L}$ should be _smaller_ than h . Indeed in the case of a tidal flow, the largest eddies of the size comparable with h (Fig. 4a) can only form if the whole thickness (h) of the fluid is moving in only one direction (i.e. when the tidal flow is virtually a unidirectional flow). When the flow is reversing, then one flow takes place on top of the other moving in the opposite direction (Fig. 4b) and the size of the largest eddies forming at such times must be smaller than h . But if in some parts of the periodic cycle the size L approximates h , while in others it is smaller than h , then the time average value $\bar{L}$ should be smaller than the time average flow depth $\bar{h}$.

The size of the largest eddies can always be "measured" in terms of the flow thickness:

$$\bar{L} = \beta \cdot \bar{h} \quad , \tag{8}$$

In the case of a unidirectional flow $\beta \approx 1$ (and the bars signifying the time average over the period T become redundant); in the case of a tidal flow $\beta < 1$. In the latter case the value of β varies depending on the nature of tidal flow. The conditions reflected by Fig. 4b suggest that the value of β should increase with the decrement of the ratio $T_\pm/T$ where $T_\pm$ stands for that part of the period T in which the fluid is moving in both directions (where both h_+ and h_- (in Fig. 4b) are different from zero). According to Ref. [7] for a given geometry of the flow boundaries and a specified fluid the ratio $T_\pm/T$ must decrease with the increasing values of the dimensionless parameters

[(tidal wave length)/$\bar{h}$]   and   [(effective bed roughness)/$\bar{h}$]. (9)

DURATION OF DEVELOPMENT OF DUNES

General (Unidirectional flows)

In the case of a bed covered by (two-dimensional) sand waves (Fig. 5) the elevation z of the bed surface and the transport rate p (per unit width) vary as functions of position x and time t :

$$z = f_z (x , t)$$

$$p = f_p (x , t) \quad .$$

(10)

As is well known these functions are interrelated by the Exner-Polya eqn

$$\frac{\partial z}{\partial t} + \frac{1}{\gamma_s} \frac{\partial p}{\partial x} = 0$$

(11)

i.e.

$$- \frac{(\partial z/\partial t)}{(\partial p_v/\partial x)} = 1$$

(12)

$(p_v = p/\gamma_s$ volumetric transport rate).

It would be only reasonable to express x, z and t as some fractions of the wave length Λ , of the wave height Δ and of the development duration T respectively. Similarly it would be only natural if the local transport rate p is expressed in terms of the space average transport rate p_m which for the two dimensional case under consideration implies

$$p_m = \frac{1}{\Lambda} \int_x^{x + \Lambda} p \, dx \quad .$$

(13)

Introducing the dimensionless variables

$$\xi = \frac{x}{\Lambda} \quad , \quad \Theta = \frac{t}{T}$$

and functions

(14)

$$\zeta = \frac{z}{\Delta} \quad , \quad \Pi = \frac{p}{p_m} = \frac{p_v}{(p_v)_m}$$

the relation (12) can be expressed as follows

$$- \left[\frac{\Delta \Lambda}{T \, p_m} \right] \cdot \frac{(\partial \zeta/\partial \Theta)}{(\partial \Pi/\partial \xi)} = 1 \quad .$$

(15)

If the ratio of - $(\partial z/\partial t)$ to $(\partial p_v/\partial z)$ is a constant, namely unity (eqn (12)) then the ratio of the dimensionless versions of these quantities
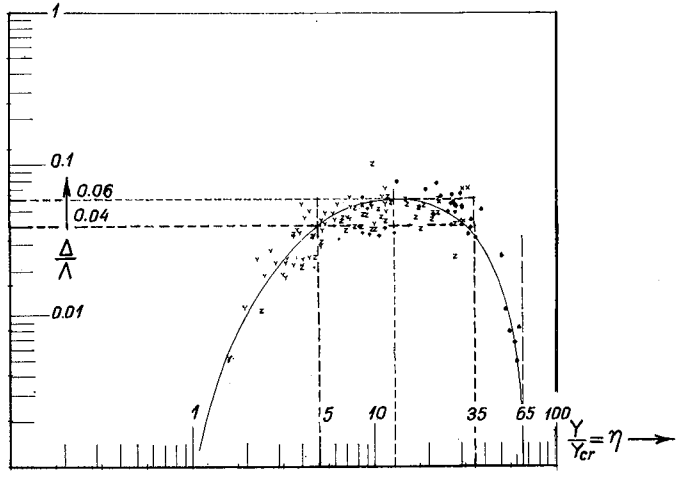
Fig. 5
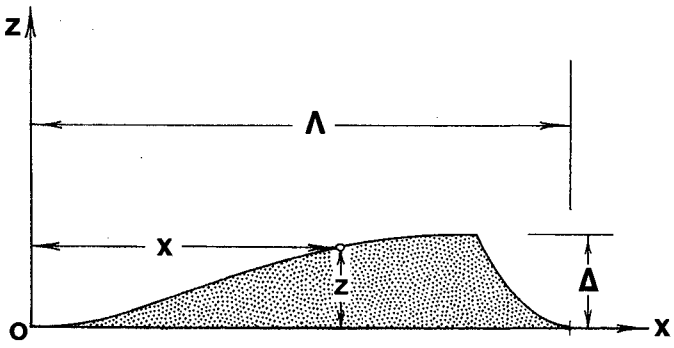
Fig. 6

(i.e. of $- (\partial \zeta / \partial \theta)$ to $(\partial \Pi / \partial \xi)$) must also be a constant (even if not unity):

$$- \frac{(\partial \zeta / \partial \theta)}{(\partial \Pi / \partial \xi)} = \text{const} \quad . \tag{16}$$

Substituting (16) in (15) one arrives at the relation

$$T = \text{const} \cdot \frac{\Delta \Lambda}{p_m} \tag{17}$$

which indicates that the duration T of the development of a sand wave is directly proportional to its volume per unit width $\approx (1/2) \cdot \Delta \Lambda$ and inversely proportional to the transport rate p_m (per unit width).

Since in the present derivations the quantity p_m is treated as a constant the space averaging procedure (13) must be associated with a specified instant. Accordingly p_m must be interpreted, for example, as the overall rate of sediment transport which takes place at $t = 0$ (i.e. over the flat initial bed just before the growth of sand waves) or as that taking place at $t \gtrsim T$ (i.e. over the bed covered with developed sand waves) and so on. The difference in the decision on this score can affect only the numerical value of the constant in the expression (17). The exact value of this constant (corresponding to an adopted definition of p_m) can be revealed only by experiment. For the present, however, one can simply take const $\approx 1/2$.*

The values of Λ, Δ and p_m, which appear in (17), must either be revealed by measuring these quantities in the area of interest or they must be estimated with the aid of appropriate graphs and/or relations. For example, knowing the values of the characteristic parameters h, D, S and ν and thus of the dimensionless variables h/D and $X = v_* D/\nu$ (where $v_* = \sqrt{gSh}$) the value of Λ/D and thus the length of dunes Λ can be predicted from the graph in Fig. 3. Similarly, knowing the values of $Y = (\gamma/\gamma_s) hS/D$ and Y_{cr} (from the Shields' curve) and consequently of the relative transport intensity $\eta = Y/Y_{cr} = \tau_o/(\tau_o)_{cr}$ one can predict the steepness Δ/Λ and thus the dune height Δ from the graph in Fig. 6.

---

*   The value of the constant would then be exactly 1/2 if the two dimensional sand waves were strictly triangular, and if the transport rate which figurates in (17) were the time-space average rate

$$\frac{1}{T} \int_o^T p_m \, dt = \frac{1}{T\Lambda} \cdot \int_o^T \int_x^{x + \Lambda} p \, dx \, dt \quad .$$

The transport rate p_m can be predicted by means of a bed load formula. The least complicated (and yet not the least reliable) would be a bed load formula of the following (Meyer-Peter/Bagnold) form

$$p = C \rho v_*^3 (1 - \frac{1}{\eta})^m \qquad (18)$$

where $C = 8$ and $m = 1.5$ (Meyer-Peter) [*]

or $C = 0.4$ and $m = 1.0$ (Bagnold)   .

Substituting in (17) the values

$$\text{const} \approx \frac{1}{2} \quad , \quad \Lambda = h \, \phi_\Lambda \, (X, \frac{h}{d}) \quad , \quad \Delta = \Lambda \, \phi_\Delta \, (\eta) \quad \text{and} \quad (18)$$

one determines the expression of the duration of development in terms of the characteristic parameters

$$T \approx \frac{1}{2C} \cdot \frac{\left[h \cdot \phi_\Lambda \, (X, \frac{h}{D}) \right]^2 \cdot \phi_\Delta \, (\eta)}{\rho \, v_*^3 \, (1 - \frac{1}{\eta})^m} \qquad (19)$$

(where the functions ϕ_Λ and ϕ_Δ are given by the graphs in Fig. 3 and Fig. 6 respectively).

Special cases (unidirectional flows)

(i) Observe from Fig. 6 that dunes can be present only if

$$1 < \eta < \approx 65 \quad . \qquad (20)$$

In the great majority of practical cases, dunes are likely to occur in the following "inner part" of the "existence region" (20):

$$\approx 5 < \eta < \approx 35 \quad . \qquad (21)$$

But, as can be seen again from Fig. 8, in this "inner part" the value of Δ/Λ varies within the relatively narrow interval

$$\approx 0.04 < \frac{\Delta}{\Lambda} < \approx 0.06 \quad . \qquad (22)$$

---

[*]   The fact that the (apparently different) bed load formulae of Meyer-Peter and Bagnold can be written in the unified manner (18) is demonstrated in Ref. [6].

Hence, for any η larger than ≈ 5 and smaller than ≈ 35 one can take simply.

$$\frac{\Delta}{\Lambda} = \phi_\Delta (\eta) \approx 0.05 . \tag{23}$$

(ii) As has been pointed out earlier, when $X > \approx 20$, then the dune length, i.e. the expression in the square brackets in (19), can be simplified as follows

$$\Lambda = h \cdot \phi_\lambda (X, \frac{h}{D}) \approx 2\pi \cdot h . \tag{24}$$

Substituting (23) and (24) into (19) one arrives at the reduced version

$$T \approx \left[\frac{\pi^2}{10\ C} \right] \frac{h^2}{\rho\ v_*^3\ (1 - \frac{1}{\eta})^m} \tag{25}$$

(which is valid for $\approx 5 < \eta < \approx 35$ and $X > \approx 20$).

(iii) If η is sufficiently large (larger than ≈ 10, say) then $1/\eta$ becomes negligible in comparison to unity and the expression for T reduces even further. It becomes

$$T \approx \left[\frac{\pi^2}{10\ C} \right] \frac{h^2}{\rho\ v_*^3} \tag{26}$$

(which is valid for $\approx 10 < \eta < \approx 35$ and $X > \approx 20$). It follows that for sufficiently large values of the Reynolds number X, and the relative transport intensity η the duration of development of dunes tends to become proportional to the square of the flow depth and inversely proportional to the cube of the flow velocities (as any u is proportional to v_*).

Tidal flows

The eqn (19), and thus (25) and (26), were derived by evaluating (17) with the aid of the unidirectional flow relations. Hence (19), (25) and (26) should be generalised to tidal flows with some reservation and only if the factor β in eqn (8) is near unity (i.e. if the numerical values of the parameters (9) are rather large). If $\beta \ll 1$ then the relation (17) can still be regarded as valid, but Λ, Δ and p_m should be evaluated differently:

$$\left. \begin{aligned} \Lambda &= \alpha_1 \bar{L} = \alpha_1\ \beta\ \bar{h} \\[2mm] \Delta &= \psi_\Delta (\eta) \cdot \Lambda \\[2mm] \bar{p}_m &= C_1\ \rho\ \bar{v}_*^3\ (1 - \frac{1}{\eta})^n \end{aligned} \right\} \tag{27}$$

Here the to date unknown values of α_1 , ψ_Δ , C_1 and n may not be the same as those of α , ϕ_Δ , C and m respectively. *

Substituting (27) in (17) (and assuming again that const $\approx 1/2$) one obtains

$$T \approx \frac{1}{2} \frac{[\alpha_1 \overline{L}]^2 \cdot \psi_\Delta (n)}{C_1 \rho \overline{v}_*^3 (1 - \frac{1}{n})^n} \tag{28}$$

i.e.

$$T \approx \frac{1}{2} \frac{[\alpha_1 \beta] \cdot (\overline{h})^2 \cdot \psi_\Delta (n)}{C_1 \rho \overline{v}_*^3 (1 - \frac{1}{n})^n} \quad . \tag{29}$$

This relation will also yield special cases analogous to (25) and (26). However, the numerical values of the validity regions must be expected to differ from those of (25) and (26) (the more so, the smaller is the factor β).

In closing this section it should be mentioned that even the values of C given for unidirectional flows are far from reliable. Indeed the values of C given above, (eqn (18)), strictly speaking, correspond to a "flat bed". If the bed is covered with sand waves, then C varies, and in fact decreases, with the increasing value of the sand wave steepness Δ/Λ (and perhaps with some other factors). In other words, the factor C is not a constant but a certain function:

$$C = \phi_C (\Delta/\Lambda , \ldots) \quad . \tag{30}$$

The values of C given by (18) correspond merely to a special value of this function

$$C = \phi_C (0 , \ldots) \approx \text{const} \quad . \tag{31}$$

The variation of C due to Δ/Λ is not "negligible" as it has often been observed that the discrepancy between the actual (measured) values of the transport rate over an undulated bed and those predicted by a transport formula can reach an order of magnitude. No transport formula has been produced to date (even for unidirectional flows) that contains a factor (analogous to C) given as a function of (at least) Δ/Λ in a clear and numerically usable manner.

---

* In the relations (27) v_* and n signify some typical values over a periodic cycle.

SUGGESTIONS FOR FUTURE MEASUREMENTS, MODEL TESTS

The relations presented in the preceding section are rather schematical in their nature and the regions of their existence are either based on some estimated orders or they are not known at all. However, in spite of these shortcomings these relations can at least give some "hints" as to how future measurements aiming to correlate dunes and currents should be orientated.

The most fundamental point that follows from Section 3 is that the length Λ of dunes is determined by the size of the largest eddies, i.e. by some "lengths" inherent in the internal structure of the flow rather than by those characterising its external geometry (like flow depth, width and so on); the fact that the size of the largest eddies is determined by (and thus is proportional to) the external dimensions of the flow is beside the point for (as can be inferred e.g. from Fig. 4) the proportionality factors can vary from one case to another considerably.

The best way of determining the size $\bar{L}$ of the largest eddies would be with the aid of oscillograms of velocity fluctuations in space (by means of samples of the stochastic process $u = f(x)$ corresponding to various instants). However, the realisation of such a method would require the simultaneous operation of a number of current meters placed along the flow direction x near the bed, which is certainly very costly and difficult. Hence, it would perhaps be more reasonable to make an attempt to determine $\bar{L}$ with the aid of the velocity fluctuations in time (from the samples of the process $u = \phi(t)$ corresponding to various fixed points in space). In this case, the following procedure (which can be applied to both model and prototype) can be suggested:

1.   Specify a location M in the plane of the flow area,* and record in a continuous manner (for a few periodic cycles) the behaviour of the velocity u along the flow direction x (in that location) at a level y near the bed. The recorder should have a sufficiently good response as to register at least those fluctuations of u which are due to macroturbulence. The recorded oscillograms will appear (for one periodic cycle) as the random function (curve) $u = \phi(t)$.

2.   Divide the period T into n intervals and determine for each interval i the average duration $(t_L)_i$ corresponding to the longest, i.e. slowest, fluctuations (caused by the passage of the largest macroturbulent eddies). Multiply these values of $(t_L)_i$ with the corresponding average value of the flow velocity $\bar{u}_i$ of the same interval i . The product $(t_L)_i \cdot \bar{u}_i$ can be regarded as a sufficiently accurate approximation of the maximum eddy size L_i

---

*   Of course, the "location M" in the plane of the prototype may itself be an area of a considerable size.

corresponding to phase i of the periodic cycle

$$L_i = (t_L)_i \cdot \bar{u}_i \quad .$$ (32)

3.   Determine the average value of L_i over the periodic cycle

$$\bar{L} = \frac{1}{n} \sum_{i=1}^{n} (t_L)_i \cdot \bar{u}_i \quad .$$ (33)

This is the value with which the length of dunes is expected to be correlated.

As is well known the large scale sand waves are often accompanied by smaller waves superimposed on them. Is this because the spectral density function of the process $u = f(x)$ has perhaps two, or more, peaks? (at least at some parts of the periodic cycle and/or for certain values of the flow Reynolds number and the relative roughness). It should be worthwhile to carry out the spectral analysis of the process $u = f(x)$ (via $u = \phi(t)$) to clarify this point.

Once the values of $\bar{L}$ for various locations of the prototype sea area are determined and the corresponding values of Λ are measured, one should be able to see how $\bar{L}$ and Λ are correlated: i.e. whether the ratio $\Lambda/\bar{L} = \alpha$ remains constant over the area subjected to measurements, and if not how it varies ... and so on. The same applies to $\bar{L}$ and $\bar{h}$, i.e. to the ratio $\bar{L}/\bar{h} = \beta$. If the distribution of the values of α and β over the sea area under investigation are revealed, then the dune length Λ can be correlated (in that area) with the aid of the flow depth (h) only:

$$\Lambda = (\alpha\beta) \cdot \bar{h} \quad .$$ (34)

If from the prototype measurements a satisfactory correlation between, say, Λ and $\bar{L}$ is achieved, then it may be helpful for model tests. Indeed, in this case some predictions can be made even with the model having rigid flow boundaries (provided, of course, that the model is sufficiently large and that its roughness is adequate). Since in a Froudian model the Reynolds numbers are smaller than their prototype counterparts, only the macroturbulent eddies will be reproduced in the vertical model scale λ_h , i.e. correctly; the microturbulent eddies will be distorted. Indeed, as can be seen from eqn (2) which can be written as

$$1_{min} \sim \frac{\nu}{U} \sim \frac{\bar{h}}{\left(\dfrac{v_*\bar{h}}{\nu}\right)} = \frac{\bar{h}}{Re_*}$$ (35)

it is clear that if $\lambda_{Re_*} < 1$ then $\lambda_{\ell_{min}} > \lambda_h$. The fact that the relative size of microturbulent eddies (i.e. $\ell_{min}/\bar{h}$) in the model will thus be larger means that the model oscillogram u" will not possess as fine a structure as its prototype counterpart u' . However, this should hardly be

relevant with regard to the reproduction of dunes (which are caused by the largest eddies). The following tests can be carried out:

(i)   Construct the model as to be geometrically similar to the existing prototype, i.e. without introducing any of the planned modifications. Run the flow, measure the oscillograms u" (in the locations M''_j corresponding to the prototype locations M'_j) and determine the distribution of the model values $(\overline{L})''_j$ in plane. If the model roughness and the flow are adequate the field of $(\overline{L})''_j$ will be similar to the prototype field $(\overline{L})'_j$. If it is not, then the model roughness must be adjusted until $(\overline{L})''_j / (\overline{L})'_j \approx \lambda_h$ is achieved (theoretically for all j).

(ii)   Modify the model according to the planned development (introduce the planned navigation channels, etc.) and determine again the values of $(\overline{L})''_j$. This time they will be different (at least in some locations), for the alteration of the flow boundaries will inevitably alter the flow and its macroturbulent structure (varying with the external dimensions of the flow). The ratio of the "new" and "old" values of $(L)_j$ will signify how many times the size of dunes will become larger or smaller as the result of the modification.

(iii) Similarly, determine the "new" time average velocities $\overline{u}''$ at the bed of the model navigation channel, and compare them with the "old" values of $\overline{u}''$ in the same location. The introduction of a larger depth (navigation channel) will almost certainly yield $u''_{new}/u''_{old} = N < 1$. Knowing N one can predict that the dunes on the bed of the proposed navigation channel will grow $\approx N^3$ times more slowly (see eqns (27) to (29)) than they grow on the plane bed at the same area, ... and so on.

    In the case of a movable bed model the most important dimensionless variable is the relative flow intensity $\eta = \tau_o/(\tau_o)_{cr}$. The model bed material and the distortion must be selected so that the ratio η is identical in model and prototype, i.e. so that

$$\lambda_\eta = 1 \qquad\qquad (36)$$

is valid. Note that the dune steepness Δ/Λ , the dimensionless transport rate $p_m / \rho\, v_*^3$ and the duration T of the dune development are those aspects (functions) of the two-phase motion which vary most intensively with η ; no similarity of the aspects mentioned can be achieved if $\lambda_\eta = 1$ is not provided. On the other hand if $\lambda_\eta = 1$ is provided, then the error in similarity of these aspects can only be due to the non-equality of the remaining variables determining them. Since the role of the remaining variables in determining Δ/Λ , $p_m / \rho\, v_*^3$ and T can be regarded as "small" (in comparison to that of η) the error due to the omission of their identity should also be "small". This, however, does not mean that one should not even try to achieve the identity (of at least some) of the remaining variables wherever possible.

REFERENCES

[1]   Stride, A.H. and Cartwright, D.H., "Sand transport at the southern
        end of the North Sea". Dock and Harbour Auth., 39, 1958.

[2]   Langhorne, D.N., "A Sandwave Field in the outer Thames Estuary,
        Great Britain". Marine Geology, 14, 1973.

[3]   Monin, A.S. and Yaglom., "Statistical Fluid Mechanics: Mechanics of
        Turbulence", Vol. 1. The MIT press, 1971.

[4]   Landau, L.D. and Lifshitz, E.M., "Fluid Mechanics", Ch III.
        Pergamon Press, Oxford, 1959.

[5]   Panchev, S., "Random Functions and Turbulence". Pergamon Press,
        Oxford, 1971.

[6]   Yalin, M.S., "Mechanics of Sediment Transport", Ch VII.
        Pergamon Press, Oxford, 1972.

[7]   Yalin, M.S. and Russell, R.C.H., "Shear Stresses due to Long Waves".
        Journal of Hydraulic Research, Vol. 4, No 2, 1966.

LIST OF RELEVANT SYMBOLS

x	direction of flow	τ_o	bed shear stress (at $y = 0$)
y	direction perpendicular to x	$v_* = \sqrt{\tau_o/\rho}$	shear velocity
t	time	u	flow velocity at a level y
g	acceleration due to gravity	γ	specific weight of fluid
ℓ	scale of turbulence	γ_s	specific weight of grains
L	size of the largest eddies	D	representative grain size
ρ	fluid density	Λ	dune length
ν	kinematic viscosity	Δ	dune height
h	flow depth	T	duration of dune development
S	slope of the free surface	p	sediment transport rate

If A is a quantity then:

A_{cr} is the critical value of A (at the beginning of sediment transport)

$\overline{A}$ is the time average value of A (averaged over a periodic cycle)

A' and A'' prototype and model values of A respectively

$\lambda_A = A''/A'$ the scale of A .

CHAPTER 58

NEW METHOD FOR THE REDUCTION OF SOUNDINGS IN THE
TIDAL AREA OF THE GERMAN BIGHT AND IN TIDAL FLATS,
WITH THE OUTER ELBE SERVING AS EXAMPLE

Bernhard Gerken

1. Introduction

The topographic survey by sounding the water bottom is becoming
an ever increasing part of the work of engineers and scientists
on the German North Sea coast.

In order to fulfil the various tasks in the estuariers of tidal
rivers in the foreshore areas, charts are needed with depth data
of the greatest possible accuracy. The problem now is this:
There exists a big accuracy gap between, on the one hand, the
values obtained by the levelling method or by means of the water
line method, often applied in the tidelands, yielding accuracies
from 1/4 to 1 dm and, on the other hand, the soundings carried
out from vessels in the adjacent sea area.

According to the investigations into the accuracy of nearshore
hydrographic surveying, a tenfold of inaccuracy - compared with
the above given values - must be assumed. Scientific studies of
the natural processes in the foreshore area (the major programme
of the German Research Society (DFG) "Sandbewegung im Deutschen
Küstenraum" / The shift of sand in the German coastal area / may
be cited here as an example) do not yield a reliable picture so
long as the accuracy standard of tideland surveys is not approxi-
mately reached.

Moreover, the Offices of the Federal Republic of Germany and of
her coastal provinces that have been entrusted with sea surveying,
each use their own methods which have often evolved differently
in the course of history. So, additional difficulties by frequent
overlappings of surveyed areas are inevitable.

Comparative studies, e.g. calculating balances of sandy material
from maps showing variations in depth will inevitably entail cri-
ticism so long as no standard methods are used.

The problem of hydrographic surveying is to precisely determine
the water level at the moment of sounding. Due to the tides with
constantly changing water levels, the reduction of each measured
water level to a standard reference level is of special importance.

2. General Aspects

2.1. Reduction methods in the Outer Elbe Estuary

For the calculation of water levels which are needed for
the charting of depths, different methods are used that
have been dealt with several times in the literature.
GÖHREN, 1968, has given a summary of the methods that
are especially used in the Outer Elbe. He has studied and
inter-compared the following four reduction methods:

a) Reduction according to the propagation velocity of the
   tidal wave;

b) Reduction according to the propagation velocity as
   under a) and height reduction according to the high
   water gradient between two stations;

c) Reduction according to mean tidal curves;

d) Reduction according to the propagation velocity of the
   tidal wave as under a) and height reduction according
   to changes in tidal range.

In the area of the Outer Elbe, the method b) is used by
FORSCHUNGSGRUPPE NEUWERK, the method c) by WASSER- UND
SCHIFFFAHRTSAMT CUXHAVEN and the method d) by DEUTSCHES
HYDROGRAPHISCHES INSTITUT.

The result of GÖHREN's investigation shows that the method b)
yields the best values just about the time of high water, and
that with the method c) the best correlation is obtained between
the reduced and observed water levels during the remaining times
of the tides. The method d) is mainly used with good results in
sea areas for the compilation of charts that are to serve for the
calculation of water levels; however, in the estuaries it is in-
ferior to the methods b) and c).

On account of the special tasks of the WASSER- SCHIFFAHRTSAMT
CUXHAVEN, the sounding of shipping routes cannot be limited to
the times of high water, but has to be carried out during the
whole working day with different tide phases.

Furthermore, the WASSER- UND SCHIFFAHRTSAMT CUXHAVEN, in contrast
to the FORSCHUNGSGRUPPE NEUWERK which uses several subsidiary gauges
for the reduction, uses only the tide gauge of 1st order at Cux-
haven-Steubenhöft.

For about 50 years, the method c) - though improved in the course
of time - has been used quite successfully in the Elbe Estuary.
Owing to the network of subsidiary gauges in the Elbe Estuary that
has been densified in the meantime, there was now the opportunity
for a more critical examination of the method.

Comprehensive preliminary examinations of many details have shown
that reduction errors in the order of 3-4 dm occurred with the
method c) applied so far by WASSER- UND SCHIFFAHRTSAMT CUXHAVEN;
in exceptional cases they amounted to between 5 und 6 dm and on
average they lay between 1 and 2 dm. These errors were found
by reducing tides (that had actually occurred and had been ob-
served at the reference gauge) to the subsidiary gauges established
in the Outer Elbe and by comparing them with the water levels re-
gistered there.

2.2 Description of the method c) that has been applied so far.

The reduction method which is still being used by the
WASSER- UND SCHIFFAHRTSAMT CUXHAVEN refers the sounded water
depths to the mean tidal conditions in the area of obser-
vation. The Outer Elbe area has been subdivided into indi-
vidual zones for which, according to the tidal phase, water
level correction values against the reference gauge at Cux-
haven-Steubenhöft can be taken from Tables. Thus the water
level at the place of sounding is obtained from the simul-
taneously observed water level at the reference gauge, cor-
rected by the above mentioned value.

For soundings in the Outer Elbe, Tables have been established
showing the necessary reduction values for certain zones of
the area to be sounded. These Tables are based on recordings
of subsidiary gauges or other gauges of 3rd order, from which
mean tidal curves have been constructed.

If during sounding operations mean conditions occur, a good
correlation is obtained between reduced and measured water lev-
els. With increasing deviations from the mean conditions the
reduction error will also increase.

The reduction results given under paragr. 2.1 do no longer
meet the requirements concerning the accuracy of depth charts
as given in the Introduction. This induced us to develop a
method the maximum errors of which were not to exceed 2 dm
and with mean errors not greater than 0.5 - 1 dm. The fol-
lowing results have been obtained when studying the new meth-
od which differs fundamentally from all methods known so far.

3. Reduction method according to the variation in travel time
   of the tidal wave and height reduction according to the
   M.H.W./M.L.W. gradient.

   3.1 Theoretical principles
       M.H.W./M.L.W. gradient

       If the tidal curve of an outer gauge is compared with
       the pertaining tidal curve of a reference gauge, differ-
       ing vertex values of H.W./L.W. are obtained as a rule.
       From the distance of the outer gauge to the reference
       gauge and from the above mentioned vertex values the
       H.W./L.W. gradient is determined.

       The difference of the pertaining vertex values will in
       the following be denoted as *h-value.

       When inter-comparing many tides, a good correlation of
         *h-values is in general found, both in themselves and
       between each other.

       From the statistical mean value the M.H.W. resp. the
       M.L.W. gradient can be determineds for each outer gauge
       according to the conditions that will be laid down be-
       low, under paragr. 3.2

       Variation in travel time

       Travel time means the temporal motion of the tidal ver-
       tices between the outer gauge and the reference gauge.
       The travel times of the H.W. vertices of several tides
       are approximately equal, and so are the travel times of the
       L.W. vertices.

       When intercomparing the travel times of both vertices,
       greater differences dependent on distances, are obtained.
       The variation in travel times between the vertices that is
       not directly measurable is an essential part of this paper.

In order to make the variation in travel times measurable, the
Δh-value had to be assumed as constant. This was possible be-
cause for a number of studied tides the Δh-values showed only minor
fluctuations (the deviations of the Δh-values from the statistical
mean values amounted to a maximum of only 5 cm).

When using the averaged Δh-value the travel time can be deter-
mined in the required intervals (according to fig.1 as an example
for every hour, for the establishment of Reduction Tables in inter-
vals of 10 minutes).

Apart from the natural astronomical influences, stronger meteoro-
logical influences may essentially affect both the travel time and
the Δh-values. Therefore, as far as possible, only undisturbed
tides, the so-called "fair weather tides" have been used for the
investigations. As soundings of the Outer Elbe that are carried out
from vessels are only possible up to wind forces of 5 Bft., only
tides up to this limit were evaluated.

It must be noted that, for the determination of the mean Δh-
values, the statistical mean tidal curves of the respective outer
gauge could not be used; mean tidal curves in temporal relation
to the reference gauge had to be calculated (cf. fig. 2). Moreover,
as an additional limitation of the sources of errors, the tide was
divided (as with the method used so far) into L.W. and H.W. areas
(fig. 2).

Through the introduction of the variation in travel time, a re-
duction according to equal times its inherent errors became
unnecessary.

From fig. 8 it can be seen that the characteristic form of the
tidal curve obtained through reduction is maintained in spite of
changes due to morphological and meteorological conditions. This
has, to the authors' knowledge, so far not been the case with the
known methods throughout the entire tide.

For the better understanding of the different effects of both
reduction methods, two tides that have actually occurred have
been reduced according to both methods (fig.7). The resulting
differences in water levels have been compared with the values
read from the outer gauge. It can be seen that with the reduction
according to the old method, only a constant line of water level
differences, in dependence of the respective tide of the reference
gauge can bei obtained. Here, the new method has advantages, as
the water level differences remain _variable_ and adapt to a great
extent to the measured water level differences.

According to the afore described general knowledge, the following
principles can be set up for the establishment of a reduction
method by means of Tables:

a) From statistical data the rise of the M.H.W. and M.L.W. lines
   referred to the reference gauge can be determinded and calcu-
   lated as a constant mean value, dependent on the reduction
   place. This is the Δh-value.

   If the Δh-value is not equal to the difference value that
   has actually occurred at the time of sounding, this value is
   entered directly into the reduction as an error. According to
   an examination it will amount to just a few cm (cf. fig. 6).

b) By introducing the constant difference value Δh, the vari-
   ation in travel time can bei determined throughout a tide in
   any phase.

If the variation in travel time that has thus been determineds
does not agree with the values that have actually occurred during
the time of sounding, cm-differences will be obtained resulting
from the minute-deviation (fig. 6). Depending on the rise of the
tidal curve von the day of measurements, these differences are
additionally entered as errors in the reduction. They may, how-
ever, reduce the error in the final result or eliminate it, as
well.

From the above given theoretical considerations the reduction
according to fig. 3 can be formulated as follows:

> The water level at the place of soundings at the time t'
> is equal to the water level at the reference gauge in
> the time interval T' (theoretical time interval between
> H.W. resp. L.W. vertices of the reference gauge and the
> sounding time) $\pm$ ΔT (travel time in the time interval T)
> $\pm$ Δh.

The reduction method developed from the described criteria
can be named:

> "Beschickung nach der Laufzeitveränderung der
> Tidewelle und Höhenreduzierung nach dem MThw/
> MTnw-Gefälle"
> (Reduction according to the variation in travel
> time of the tidal wave and height reduction
> according to the M.H.W./M.L.W. gradient).

3.2 Compilation of Reduction Tables

From these reduction formulae, tables can bei compiled for
practical use that will enable reductions in the area of
investigation which - in comparison to the old method-
require only little additional time.

For this purpose the work listed below was necessary;

a) From the outer gauges that were needed for the investi-
gations, as well as from the reference gauge at Cuxhaven-
Steubenhöft, 20 tidal curves correctly registered with re-
gard to height and time were selected. Tides influenced
by wind forces of more than 5 Bft. were not used for the
further investigation.

b) For each of the 10 gauges that are available in the area
of investigations the T.H.W. and T.L.W. gradients to the
reference gauge were determined in cm as Δh-value.
There it was found that the T.H.W. gradient nearly equals
the T.N.W. gradient. Only in the "Neuwerker Fahrwasser"

that is separated from the main channel by the jetty
"Kugelbake" did greater deviations from both these gradients
occurr.   While in the main channel maximum differences of
up to 5 cm were observed, differences of 15 cm could be   stated
in the "Neuwerker Fahrwasser". In order to avoid considerable
reduction errors, a linear interpolation had to be carried out
in the Tables for the "Neuwerker Fahrwasser".

c) For each gauge (outer gauge and reference gauge) <u>the mean
   tidal curves (fig. 4) have been calculated</u>, referred to the
   arrival time of T.L.W. resp. T.H.W. at the reference gauge.
   From the mean tidal curve thus obtained of each gauge the
   time intervals (in hours and minutes) referred to the mean
   arrival times of the T.L.W. resp. T.H.W. of the reference
   gauge have been calculated and compiled in Tables, under
   consideration of the previously determined height difference
   values   h in 10 minutes intervals (referred to the reference
   gauge).

d) As in the area of studies only 10 subsidiary gauges were
   available, a division into a greater number of reduction
   squares had to be made in order to diminish the reduction
   errors. The side lengths of the squares should not be greater
   than 2-3 km.

   As limitation of the individual spuares the main hyperbolic
   lines according to the Hi-Fix method had been selected. This
   was necessary with regard to the treatment of sounding data and
   the manual and electronic data processing, especially in order
   to simplify the conversion into the GAUSS-KRÜGER coordinate
   system.

   If the squares thus determined are not directly fitted with
   a subsidiary gauge - and this ist the case with most of the
   squares - the Table values have to be determineds by interpo-
   lation.

   In contrast to the method used so far, with a division trans-
   verse to the river axis, the new division into squares takes
   into account the noticeable differential transverse gradient.

3.3 Instruction for the use of the Tables

By means of the Tables, the reduction can be made in the
following steps:

a) To determine the gauge data of the reference gauge.
   For this purpose the arrival time of the vertex at the
   reference gauge prior to the sounding time has to be noted.

b) To determine the sounding place for the selection of the
   Reduction Table.

c) To determine, from the selected Table and the pertaining
   square number, the respective height difference Δh.

d) To calculate the time interval T' by means of the sounding
   time t'.

e) To determine the theoretical time interval T from the Table,
   by means of the time interval T' and the pertaining square
   number.

f) To calculate the theoretical sounding time t for the re-
   ference gauge and to read the water level above zero from
   the tidal graph.

g) To reduce the height of the water level at the reference
   gauge to the Δh-value.

Thus, the height of the water level above gauge zero at the
sounding place is determined.

3.4 Reduction errors

The reduction errors keep within the limits required under para-
graph 2.2.

4. Further improvements of the reduction

When thinking of a further limitation of the reduction errors,
a much denser gauge network will have to be required. This re-
quirement seems justified, as from gauges established in short

distances the water level at the sounding time can be obtained
directly without conversion or through simple interpolation with
decimetre accuracy.

This, however, requires an absolutely reliable operation of all
gauges with regard to height and time; at least control readings
at the respective gauges would have to be made before and after
the sounding. Apart from the fact that thus uneconomical loss of
time would have to be put up with, it cannot be hoped to realize
this method, neither today nor in the foreseeable future. When
taking into account maximum distaces of 4-5 km between the gauges
in the Outer Elbe area, about 25 gauges would have to be available.

As with the new reduction method errors exceeding 1.5-2 dm are
not to be expected (on the average less than 1 dm) and as, on the
other hand, with a view to future coastal research and coastal en-
gineering, an accuracy of $\pm$ 1 dm will have to be required, a re-
liable permanent gauge of 1st order at the lower end of the soun-
ding area, i.e. approximately off the position of the lightvessel
ELBE I at the "Grossvogelsand-West" would have to be required.

This new gauge as a radio linked tide gauge which could permanently
be interrogated would be of valuable help for further diminishing
the error that remains even with the application of the new re-
duction method.

Improvements of the present method seem to be possible as here
the travel time of the tide vertices from the "outer gauge"
(required above) to the reference gauge, as well as the height
difference value   h become known. From the data of both gauges,
the distance of which could approximately be 45 km, more im-
portant deviations from the   h- and travel time values incor-
porated in Tables could be found and eliminated. Besides, it
would be imaginable to use the outer gauge as reference gauge.
Thus, waiting periods would not arise in the reduction, and a
reduction on board with the appropriate additional electronic
equipment would be possible. The effect of the location of the
reference gauge is represented in fig. 5.

5. Final remarks

The ever increasing requirements concerning the accuracy of
depth charts of the ELBE Estuary are the motive for these in-
vestigations. The tidal area of the Outer Elbe with its tran-
sition into the open sea and the adjacent tidal flats with their
various hydraulic and morphologic problems provide the oppor-
tunity to deal thoroughly with the problem of reduction.
This study aims at diminishing the gap between the tideland
survey by levelling which can be done with high precision and
the hydrographic survey so far often carried out unsatisfacto-
rily. By further refinement of the technical position fixing
and sounding devices better results are possible and desirable.

In the authors' opinion, the new method could also be applied
in other tidal coastal areas with due consideration of the
respective local conditions. This will no doubt require criti-
cal examination with regard to such tidal areas. The first
examinations according to the new method have been carried out
by RICHTER in the area of the WASSER- SCHIFFAHRTSAMT TÖNNING
and has found as a result high reduction accuracies.

Map of the Outer Elbe
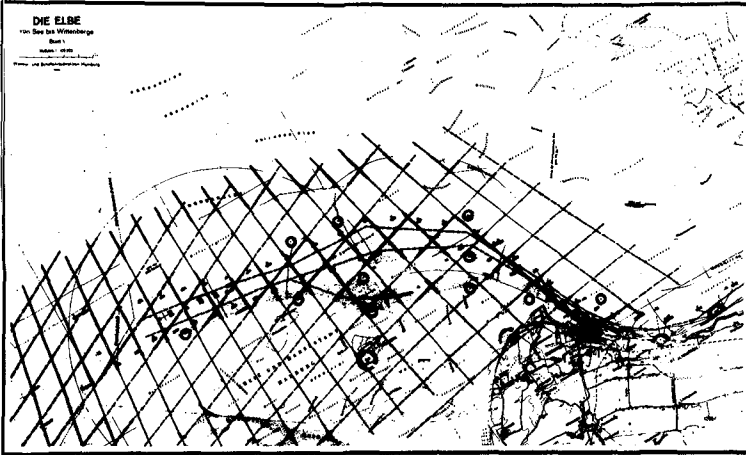
fig. 1

Reduction according to the variation in Travel Time
and Height Reduction according to the M.H.W./M.L.W. gradient
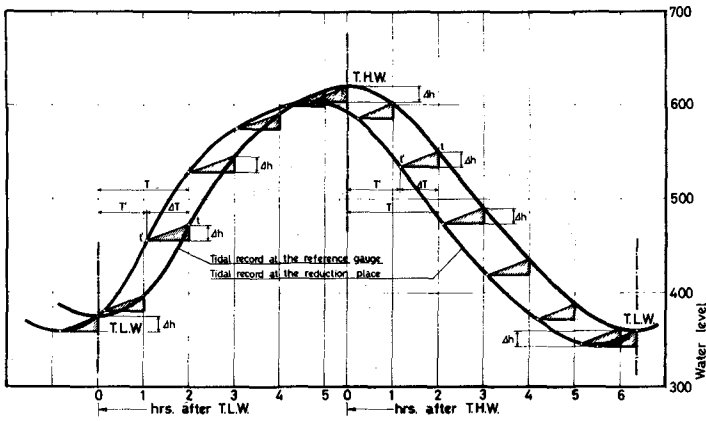
fig. 2

Determination of the water level at the sounding place

H = water level at the sounding place
H = water level at the reference gauge
Δh = height difference according to the mean H.W./L.W. gradient
t = hour at the sounding place

T = actual temporal distance between T.L.W / T.H.W. reference gauge and hour of sounding at the sounding place

T = Theoretical temporal distance (const.) between T.L.W / T.H.W. reference gauge and hour of sounding at the sounding place
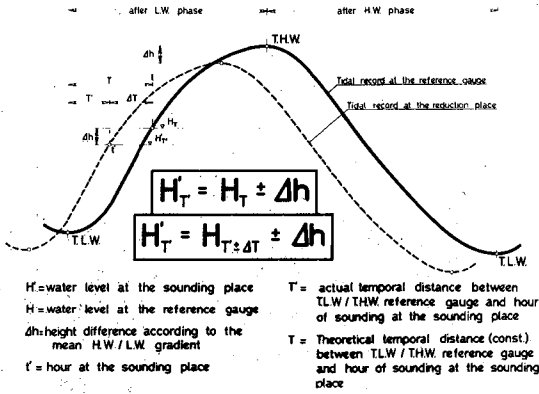
fig. 3

Determination of the „mean tidal curve"
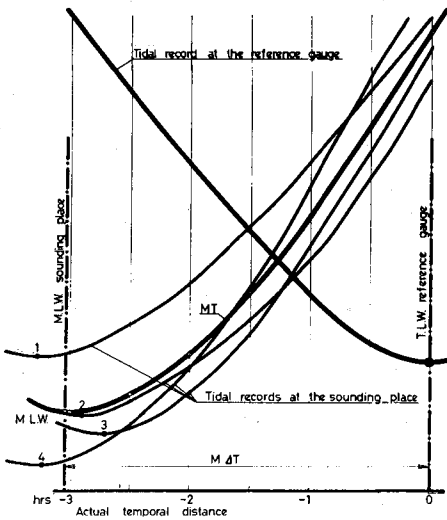
fig. 4

Effects of the location
of the reference gauge
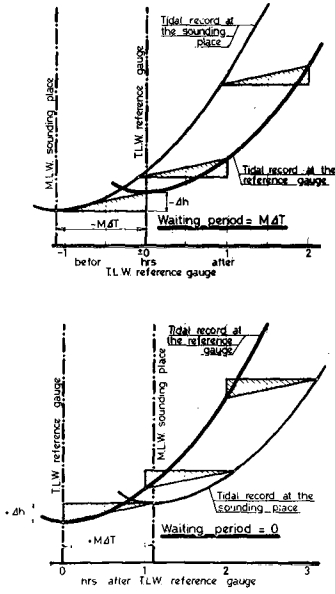
fig. 5

Maximum reduction errors
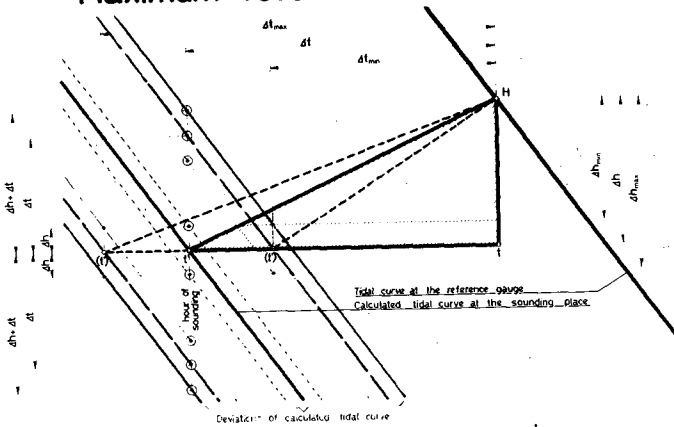
fig. 6

Effects of the reduction

Gauge Cuxhaven

Gauge Gr. Vogelsand

former reduction method

new reduction method

measured differences in water level

hrs after T.H.W. at the reference gauge - Cuxhaven
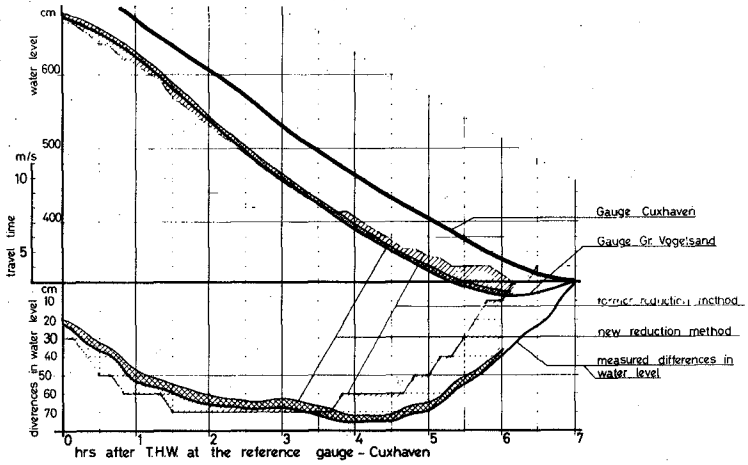
fig. 7

Deviations of reduced and observed water levels

Reduction to the gauge Cuxhaven

Gauge Kugelbake

Tidal record at the gauge Cuxhaven

Tidal record at the gauge Kugelbake

former reduction method

new reduction method
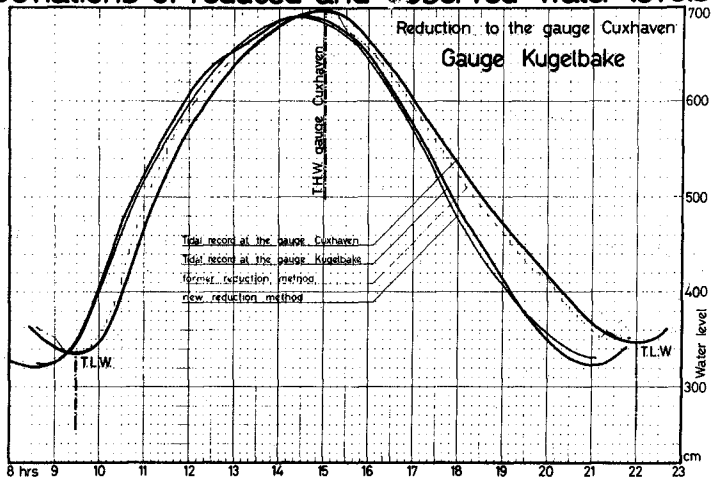
CHAPTER 59

Giant and Mega Ripples in the German Bight and Studies of
their Migration in a Testing Area (Lister Tief)

Horst Pasenau
Johannes Ulrich

Institut für Meereskunde an der Universität Kiel

Abstract

In a lot of regions the bottom of the North Sea is covered
with large ripple fields, especially in the estuaries and
in the tidal channels. A great number of echo sounding pro-
files (29.500 n.m.) were evaluated to determine the bounda-
ries of these areas and to describe the dimension of patterns.
Special investigations of the hydrographic situation, the
distribution of deposits and the migration of ripples under
the influence of tidal currents only, were carried out in a
testing area in the Lister Tief on 11 cruises since 1971.

General Distribution of Ripples

There are several comprehensive descriptions of the distri-
bution of deposits of the German Bight. But these maps don't
show the processes of permanent transposing of movable mate-
rial. Transversal current ripples can be considered especially

suitable as qualitative indicators of sediment transport
processes on the sea floor. Thus an attempt has been made
to schedule all areas of the south-eastern North Sea where
the bottom shows such ripples. It is impossible to carry
out a synoptical survey of the bottom of this large region
of the North Sea. Therefore 29.500 n.m. of echo soundings
obtained by numerous institutions of coastal research from
1964 to 1971 have been evaluated for characteristic patterns.
The results have been presented on 22 sheets on the scale
1:100 000 (J. ULRICH, 1973). A comprehensive map of all
sheets is shown in Fig. 1. From comparative investigations
of several years it is shown that most of the ripple fields
changed their boundaries only a little. The sounding tracks
do not always run normal to the ripple crests because the
surveys were predominantly carried out for nautical purposes
and, therefore, the mapping can give only qualitative infor-
mation. The largest ripple fields can be found in estuaries
of the rivers Ems, Weser and Elbe as well as in the tidal
channels between the islands and the large tidal flats which
are characteristic of the coasts of the German Bight. Regions
of larger patterns with heights of 2.0 to 10 m. can be found
between 6 and 20 m. depth in the areas with sand of coarse
and partly medium grain size, whereas the medium and fine
sand areas of the tidal channels, the edges of the estuaries
and, frequently, even the slopes of sandbanks, reefs and bars
are characterized by smaller patterns less than 2 m. height.
The areas of the tidal flats shallower than mean low spring
tide are not investigated by this mapping. It must be con-
sidered that in this region, which partly falls dry at low
tide, large fields of small ripples could be found.

Testing Area

Patterns of remarkable variety in shape and dimension are in
the zone of the German-Danish frontier - in the Lister Deep
(location see Fig. 1). During every tide through this tidal
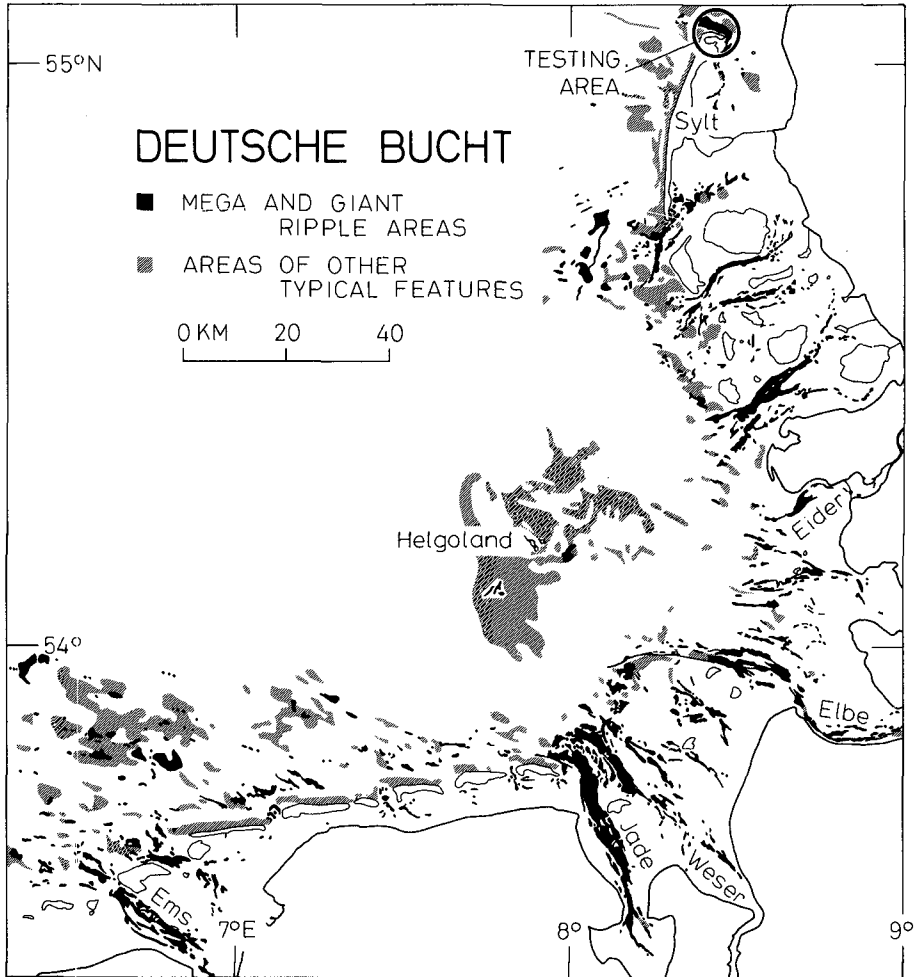
Fig. 1 Ripple areas in the German Bight

channel about 520 Mio m^3 of water streams into the Bight
closed by two dams which connect the island Rømø and the
island Sylt with the mainland. There is no remarkable fresh

water flow - so the bottom of the channel is formed by tidal
streams only. During 11 cruises in a testing area on fixed
tracks narrow echo soundings were made since 1971. The employed
navigation system Hydrodist NRB 201 with a deviation of $\pm$ 1 m.
gives a sufficient accuracy of bearings even for detailed ana-
lysis. Fig. 2 shows the boundaries of the testing area, the
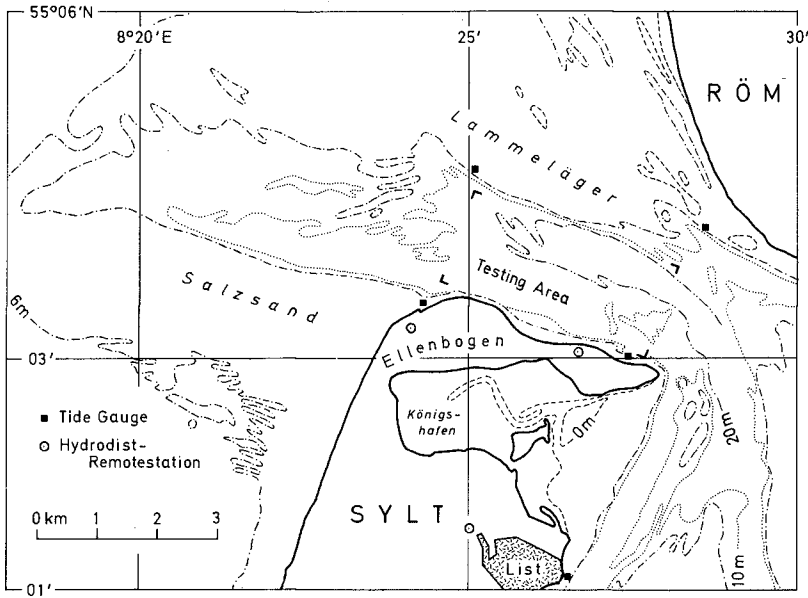
Fig. 2   Testing area in the Lister Tief

positions of the remote-stations of the Hydrodist-System and
apart from that, the positions of the tidal gauges additionally
established for this investigation for the correction of echo
soundings. The testing area extends from 1.6 km to 3.6 km, the
water depths range from 10 m. to 40 m. The tidal range deter-
mined by the mean of ten years is 1.71 m. Numerous current
measurements from anchored ships yielded that even 15 minutes

past low water the current reaches the opposing direction
and 25 minutes later velocities of more than 1.00 m/sec
have occurred in general. Such measurements will be comple-
ted by the application of floats. Fig. 3 shows the great
spatial and temporal variability of currents during ebb and
flood.
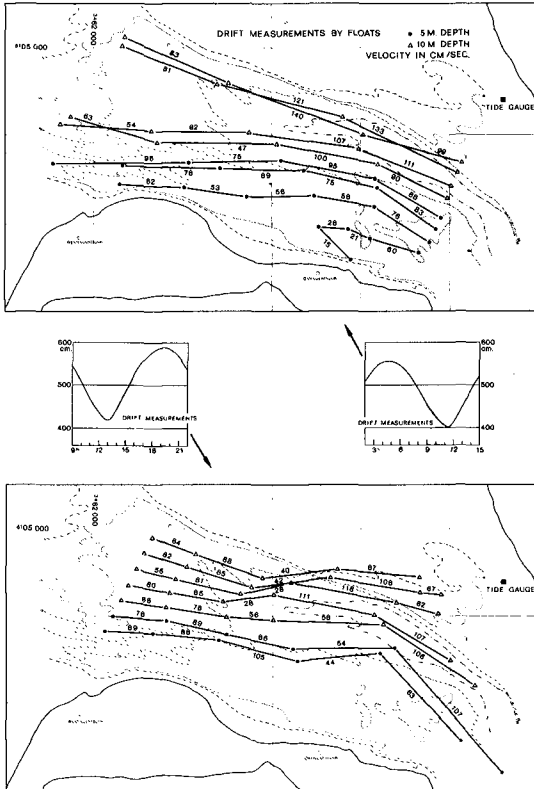
Fig. 3   Drift measurements by floats. The values at the tra-
         jectories are calculated means in cm/sec between the
         positions taken by means of Hydrodist.

Bathymetry

As mentioned above soundings were taken on fixed tracks.
They run parallel to the axis of the channel in a lateral
distance of 50 m, if possible in the given time for our ex-
plorations, in addition to that in a distance of 25 m.
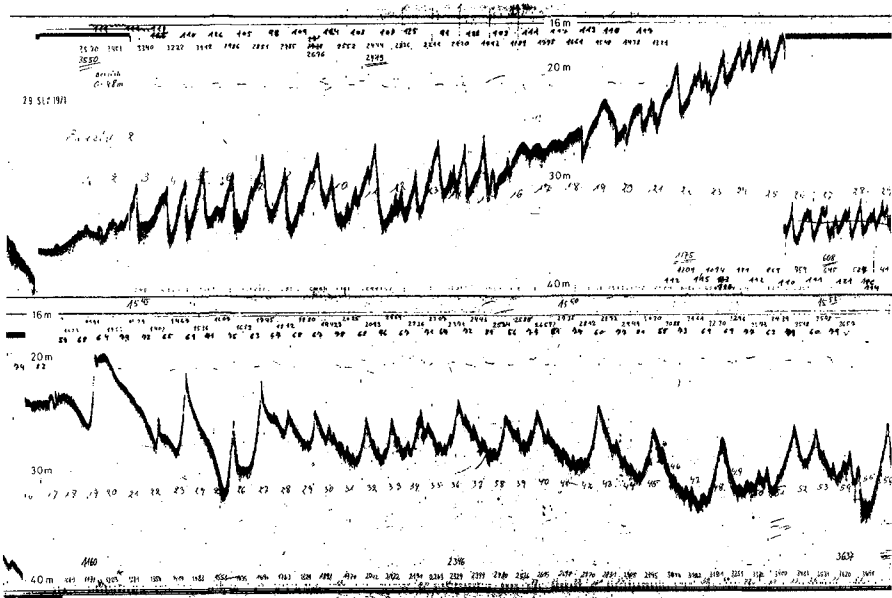
Fig. 4   Echo soundings of giant and mega ripples in the
         Lister Tief area

Fig. 4 shows two sections of the original copies of echo
soundings. After the correction referring to the tide gauge
level the whole system of tracks is drawn enlarged five-times
and gives a quasi-spatial impression (Fig. 5). A system of
giant ripples with heights up to 11 m. and wave lengths of
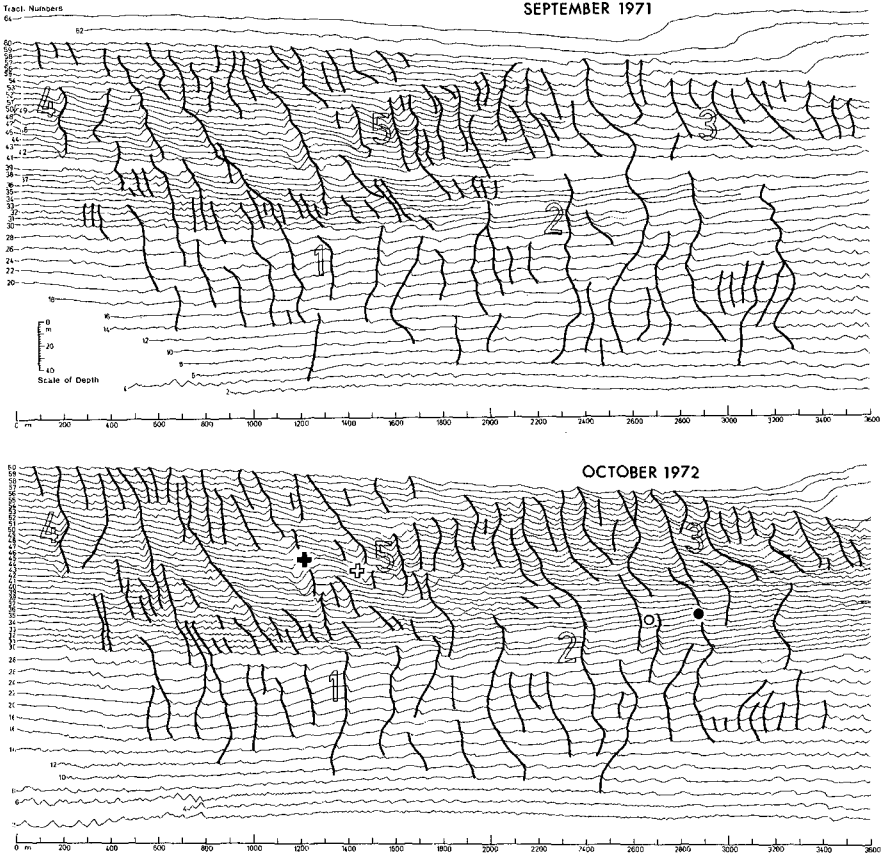
Fig. 5   Series of corrected sounding
         numbers: see text
         cross and dots: positions of bottom samples
         described in Fig. 7

more than 300 m is overshaped in a lot of regions by mega
ripples which can have heights of 2 m. On the other hand,
Side-Scan-Sonar recordings have shown these two systems

but especially on so called luff slopes, is covered with
extensive regions of small ripples in the max. dimension
of some ten of centimeters which can not be detected by
vertical echo sounding because of physical and technical
reasons.

Migration of Ripples

As to the asymetrical shape and the observed migration of
ripples the Lister Tief can be devided into two areas: In
the northern part, we find westward moving ebb-orientated
patterns, in the southern part, on the contrary, eastward
moving flood-orientated ones. The highest ripples can be
found in the northwestern part of the area. From additional
analysis of the geometrical parameters of the giant ripples
as height, wave length and depth of water no significant
relations to the rate of migration could be deduced.
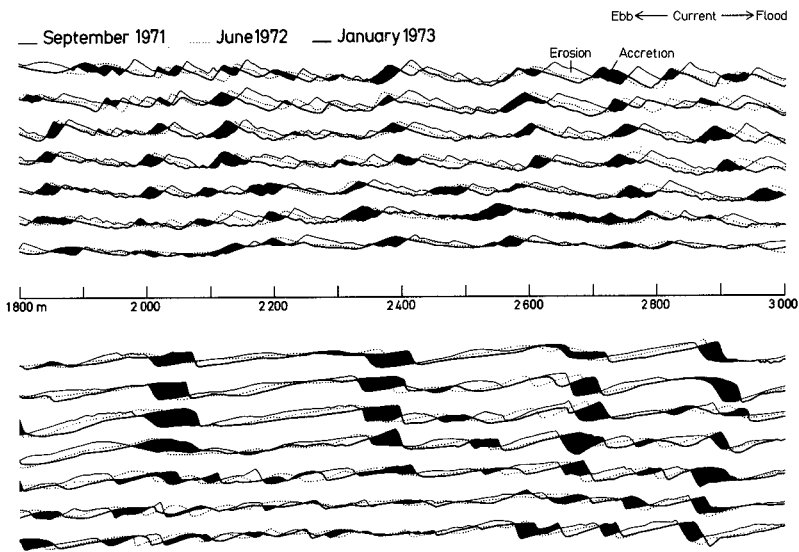
Fig. 6   Flood- and ebb-orientated ripples

The amount of migration is shown in Fig. 6 which represents
a section of the northern part the ripples of which are
shifting westward mainly and in a distance of five 50 m.-
tracks of the southern part that is ripples which are
shifting eastward on the whole. Even reverse motion of ripp-
les in contrast to the general direction of migration can
be observed. From a calculation of transport of sediments
with the help of transposition of shape results - for the
northern part - a transport amount of about 5 t. p 10 m.
cross-section of the channel, and for the southern part some-
times even more than double of the amount. But this need not
be the real amount of transported material, for the main
transport of sediment even seems to occur in suspension be-
cause of the high velocity of the currents - that is more
than 1.0 m/sec in the mean. The highest value measured on
the surface was about 1.0 m/sec.

Sediments

By comparison of a great number of bottom samples a sorting
by the influence of currents can be seen. In general, finer
sediments occur in the eastern flood-orientated part and
more coarse sediments in the western ebb-orientated part of
the Lister Tief. Finer deposits can be found in the ripple
troughs, which we already know from many investigations in
several other regions. The Md-value of fractions varies be-
tween 200 m. and 1000 m. For example on the crest of the ebb-
orientated ripple marked in Fig. 5 we found out an Md-value
of 850 μm. and for the luffward trough of 640 μm. On the other
hand in the region of flood-orientated ripples we find values
of about 570 μm. on the crest and 290 μm. in the adjacent
trough respectively. These values are means of several samples
(Fig. 7).[*]

----

[*]The numerous samples are analyzed thoroughly for interpreta-
tion by Dr. Lüneburg, Institut für Meeresforschung, Bremer-
haven.
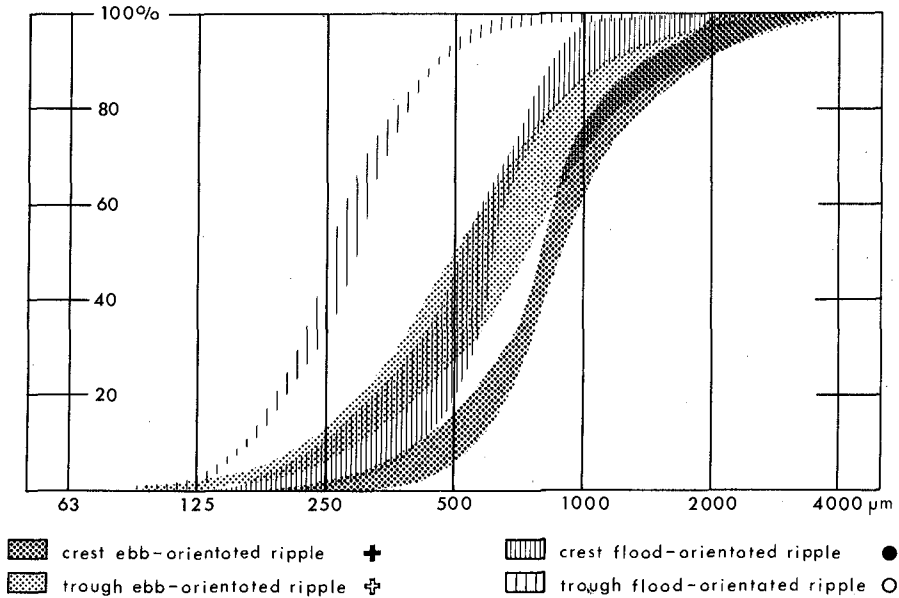
Fig. 7   Cumulative curves of fractions found at the positions
          marked in Fig. 5

Looked at more closely some remarkable phenomena are to
discern in Fig. 5. As a help we have marked the courses of
ripple crests whereever the profiles were to be correlated
clearly. Considerable shift velocities appear in several areas.
As examples for this fact we have the patterns signified with
number 1 (about 60 m/year) or with number 2 (of the same va-
lue) in the flood-orientated part, and the same with number 3
in the ebb-orientated part. There may be relationships be-
tween the speed of ripple migration (in this case patterns
> 2 m) and the current velocities. Obviously the difference
of in- and outflow is of great importance. In several places
we found values of more than 20 m/sec difference. The travel-

ling direction is determined by the direction of higher
flow (A. H. STRIDE, 1963). On the other hand some ripples
remain in their position for a long time only with small
oscillations from a position of rest like the patterns with
number 4 and 5. Remarkable are the depressions adjacent to
the lee slopes with a maximum depth of 2 m. and a width about
50 m., they may be moulded by strong eroding eddies. The ana-
lyses have not been finished yet, but the preliminary results
give hope for the assumption that from this model in full
scale some new facts about the kind of sediment transport
under the influence of tides can be deduced.

References

STRIDE, A. H., 1963: Current-swept sea floors near the
            southern half of Great Britain.
            Quart. J. Geol. Soc. London, 119.

ULRICH, J., 1973: Die Verbreitung submariner Riesen- und
            Großrippeln in der Deutschen Bucht.
            Ergänzungsheft zur Deutsch. Hydrogr. Zeitschr.
            Reihe B, 14.

ULRICH, J. und H. PASENAU, 1973: Morphologische Untersuchungen
            zum Problem der tidebedingten Sandbewegung im Lister
            Tief. Die Küste, 22.

CHAPTER 60

PREDICTION OF THE HEIGHT OF TIDAL DUNES IN ESTUARIES

by

Horst Nasner[1]

ABSTRACT

In this paper prototype data of echo soundings of tidal dunes
are analysed. A good relation between the fresh water dis-
charge and the sand wave migration velocity in the upper
part of a tidal river could be determined. The limitation
of the dune heights as a function of the mean current velo-
cities over the crests and the bed material characteristics
is presented. States of equilibrium are described by dimen-
sionless parameters and the latter compared with model tests.

INTRODUCTION

In estuaries with beds of sand-sized material significant
sand waves or tidal dunes can occur. These sand waves are
very important for navigation, because the draft of vessels
is limited by the crests of the bed forms.

A program of bottom soundings has been conducted on the Weser
River (West Germany), downstream from km 18 to km 59 (Fig.1).
Recently, a study was initiated at the Franzius Institut to
analyse the resulting data of the soundings from 1966 to
1972 with the goal of gaining a better understanding of ti-
dal dunes and the factors which influence their behaviour.
The test reaches chosen for the investigation are presen-
ted in Fig. 1.

---

[1]Dr.-Ing., Scientific Assistant, Franzius-Institut
Technical University of Hannover, Germany
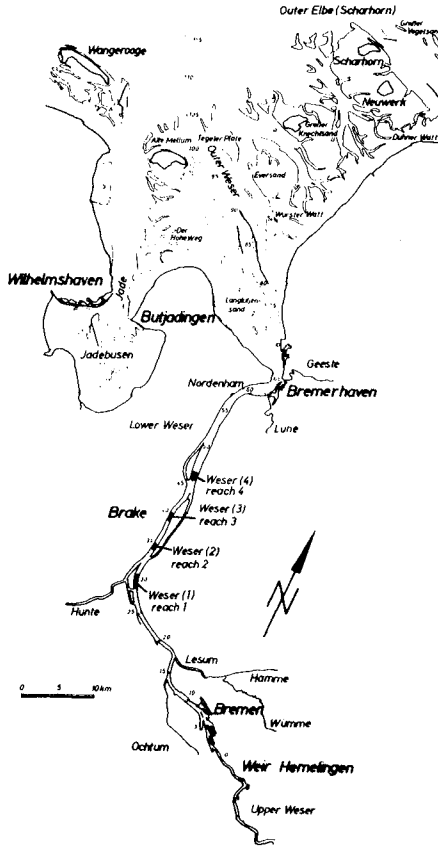
Fig. 1   Weser River with Test Fields
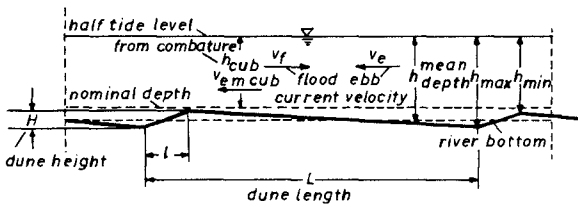
Fig. 2   Definition Sketch

RESULTS OF THE MEASUREMENTS

In the upper part of a tidal region the mean current velo-
cities are influenced by the fresh water discharge Q_o. The
mean tidal range in the Weser varies from 3.35 m in reach 1
to 3.47 m in reach 4. The semi-diurnal tides in the Weser
River are quite regular in range and duration of the flood
and ebb currents. The four study reaches in the Weser are
ebb predominant. The height and migration of the sand waves
are influenced significantly by the long term change of the
mean ebb current velocities v_{em} as a consequence of the long
term change of the fresh water discharge Q_o. As the mean
tidal range does not vary much for a wide range of Q_o, the
half tide level is nearly constant. By means of a cubature
for a mean tide and different fresh water discharges Q_o, the
current data in the navigation channel were calculated. They
are presented as follows:

Q_o	Reach 1 $v_{em\ cub}$	Reach 2 $v_{em\ cub}$	Reach 3 $v_{em\ cub}$	Reach 4 $v_{em\ cub}$
m^3/s	cm/s	cm/s	cm/s	cm/s
100	82	92	81	83
282	88	97	86	87
600	94	100	89	92

In the cubature the calculated mean ebb current velocity
$v_{em\ cub}$ is referred to a constant bottom level (nominal
depth h_{cub}, Fig.2). In fact however, the level of the
dune crests varies as a function of the mean ebb current
velocities over the dune crests $v_{em\ max}$ ($h_{min}=f(v_{em\ max})$;
$v_{em\ max} = f(Q_o)$). Only the mean values $\bar{H}$ of the dune
heights and the mean level of the dune crests are treated.

From the diagrams in Fig. 3 it can be seen, that the domi-
nant parameter for the change of the bottom pattern in the
Weser River is the fresh water discharge, which influences
directly the current data and indirectly the sand wave
height $\bar{H}$ and the sand wave velocity $\bar{u}$. The variation of the
wave height $\bar{H}$ with time is more significant than the vari-
ation of the wave length (dashed line in the upper diagram
of Fig. 3).

There is no correlation between the sand wave characteristics
and the temperature of the Weser River (Fig. 4). During the
winters of 1970/1971 and 1971/1972 the dunes were as high
as they were during the summer months of the previous years
and the velocities showed a similar tendency, in spite of
the low water temperature (Fig. 3). The reason must be
seen in the low fresh water discharge, and as a consequence,
in the low ebb-current velocities during the winter periods
of 1970/1971 and 1971/1972. Consequently it can be stated,
that water-temperature does not effect substantially the
dune-height.

A strong correlation(r) and a nearly linear relation be-
tween sand wave velocity $\bar{u}$ and $\bar{Q}_o$ (mean fresh water dis-
charge between the soundings) is apparent from the plotting
in Fig. 5. The scattering of the points for reach 1 is
similar to that for the other study reaches.

With increasing fresh water discharge the mean ebb-current
velocity increases. The prototype data showed that - start-
ing with equilibrium conditions - with increasing abb-
current velocities $v_{em\ cub}$ the dune crests are eroded un-
til a new state of equilibrium with flatter dunes is
established. With decreasing Q_o and $v_{em\ cub}$ the dune crests
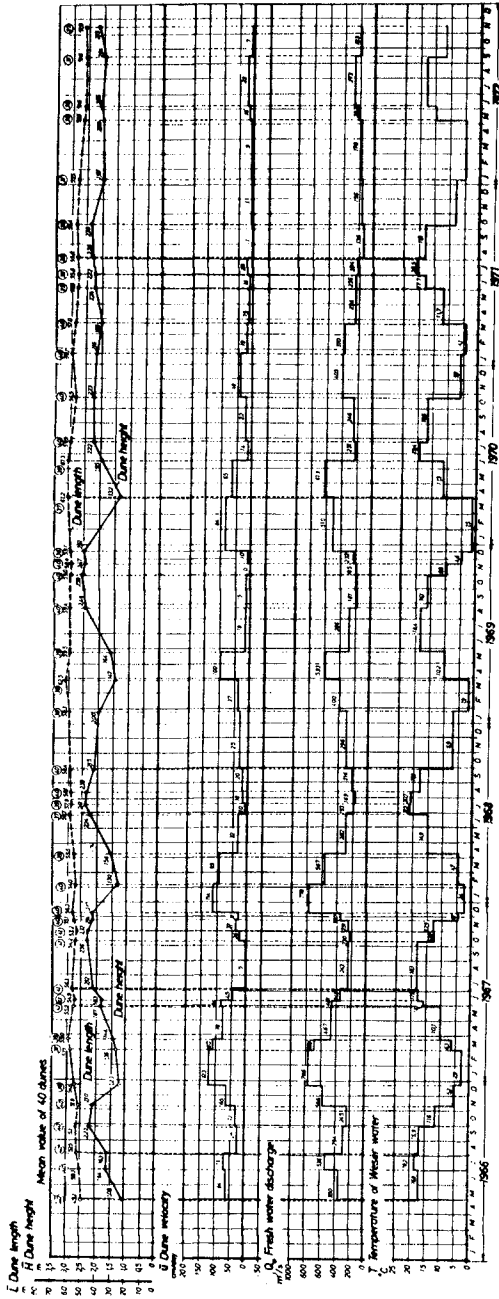
Fig. 3   Dune Characteristics of Test Field 1
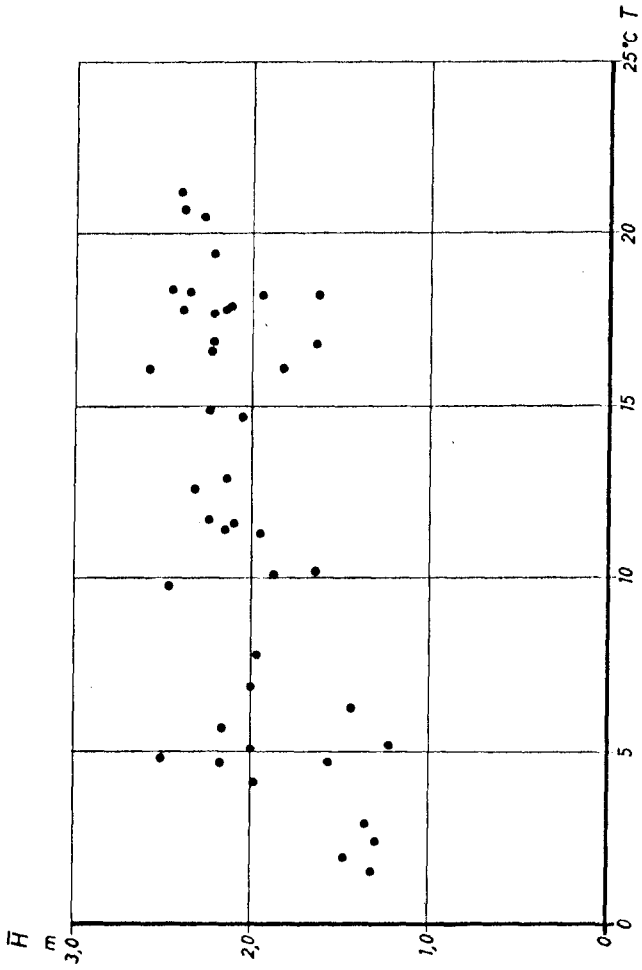
Fig. 4   Dune Height $\bar{H}$ and Temperature T of Weser Water (Reach 1)
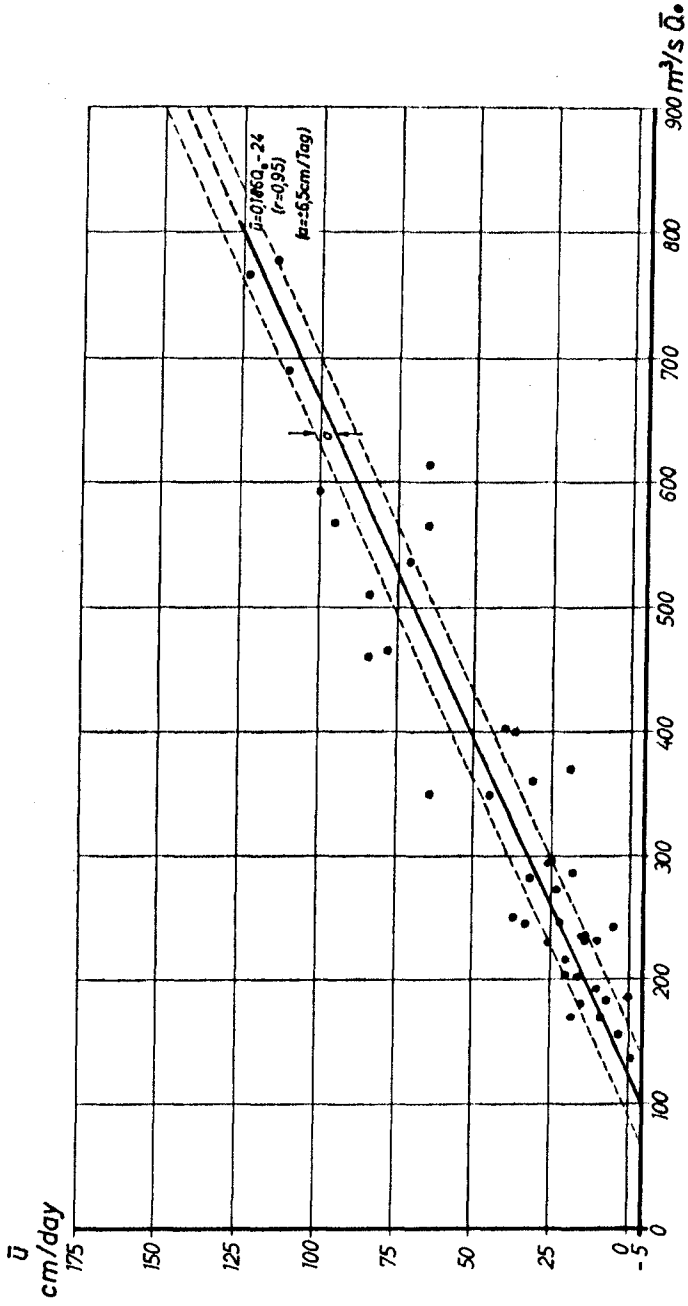
Fig. 5   Relation between Dune Velocity $\bar{u}$ (cm/day) and Fresh
Water Discharge Q_o (Reach 1)

rise due to sedimentation until another new state of equi-
librium is reached (Fig. 6).

There is a certain phase-lag between the change of Q_o and
the change of the sand wave height $\bar{H}$. In a first approach,
a state of equilibrium is reached when there is a quasi-
steady freshwater discharge for about 30 days, $Q_{o\ 30}$.
Each state of equilibrium is characterised by a certain
limiting mean ebb current velocity over the dune crests
$v_{em\ max} = v_g$, which is a function of the sediment charac-
teristics. The results for $v_g = f(\bar{D}_m, \frac{D90}{D_{10}})$ are as follows:

Reach	$\bar{D}_m$ mm	$\dfrac{D_{90}}{D_{10}}$	v_g cm/s
1	0,54	3,40	100
2	0,55	3,48	104
3	0,36	2,08	93
4	0,47	3,04	96

$$\text{with} \quad \bar{D}_m = \sum_{D_{10}}^{D_{90}} \frac{D}{9}$$

$\bar{D}_m$ is the mean value of some samples taken in September
1972 in the different dune fields of the Weser River.
Samples taken in 1969 show the same general tendency of
grain sizes in the different study reaches. It is there-
fore assumed that the grain diameter $\bar{D}_m$ does not change
much with time.

By means of the diagram of Fig. 6 a prediction of the average
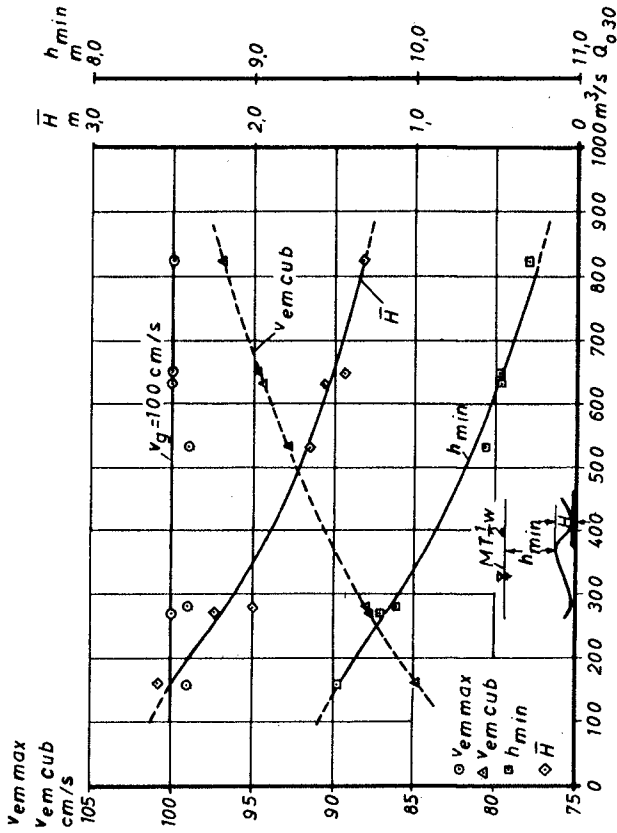
Fig. 6　Equilibrium values for different fresh water discharges (Reach 1)

crest height, h_{min}, below the mean tide level is possible
for a wide range of fresh water discharges Q_o. If the
current velocity $V_{em\ cub}$, the nominal depth h_{cub} and
$v_g = f(\bar{D}_m, \frac{D_{90}}{D_{10}})$ is known, the average crest height can be
determined by means of the following equation

$$h_{min} = \frac{V_{em\ cub}}{v_g} \cdot h_{cub}.$$

For every reach, all states of equilibrium are charac-
terised by two constant dimensionless parameters which
are defined as follows

$$\alpha_{MIN} = \frac{\bar{w}}{v_g} \qquad (1)$$

where $\bar{w}$ is the fall velocity of the sediment particles
(after WIEDENROTH, 1967, (5))

$$\bar{w} = \frac{11,15}{d} \left(\sqrt{1 + 9,7\ (\gamma_s - 1) \cdot g \cdot d^3} - 1\right)$$

and $v_g = v_{em\ max}$.

The second dimensionless parameter is given by:

$$f_{MAX} = \frac{v_g}{g \cdot \bar{D}m} \qquad (2)$$

with g = acceleration due to gravity.

The results obtained for the 4 test reaches in the
Weser River are as follows:

Reach	α_{MIN}	f_{MAX}	$\bar{D}_m$ mm	v_g cm/s	$\bar{w}_m$ cm/s
1	0,080	189	0,54	100	8,0
2	0,079	200	0,55	104	8,2
3	0,061	245	0,36	93	5,7
4	0,075	200	0,47	96	7,2

COMPARISON WITH RESULTS OF MODEL TESTS

In a first step, the results of the prototype measure-
ments are compared with model tests where the water
depths in the flume was between 0,25 m and 1,0 m.
(DILLO, 1960; FRANZIUS-INSTITUT, 1960,(1),(2)).

The bottom pattern in the model tests changed at cer-
tain mean current velocities v_m from ripples to sand
waves with ratios H/L similar to those observed in
prototype with water depths of about 10 m. The mean
diameter D_m of the sands used in the model tests were:

$$D_m = 0,3 \text{ mm } (\text{"Syltsand"})$$
$$D_m = 0,2 \text{ mm } (\text{"Norderneysand"})$$
$$D_m = 0,36 \text{ mm} (\text{"Huntesand"})$$

The mean flow velocities at which sand waves in the
model started forming were:

$$v_m = 90 \text{ cm/s } (\text{"Syltsand"})$$
$$v_m = 82 \text{ cm/s } (\text{"Norderneysand"})$$
and $$v_m > 85 \text{ cm/s } (\text{"Huntesand"})$$

The dimensionless values α and f were calculated in
the same way as α_{MIN} and f_{MAX} for the prototype data
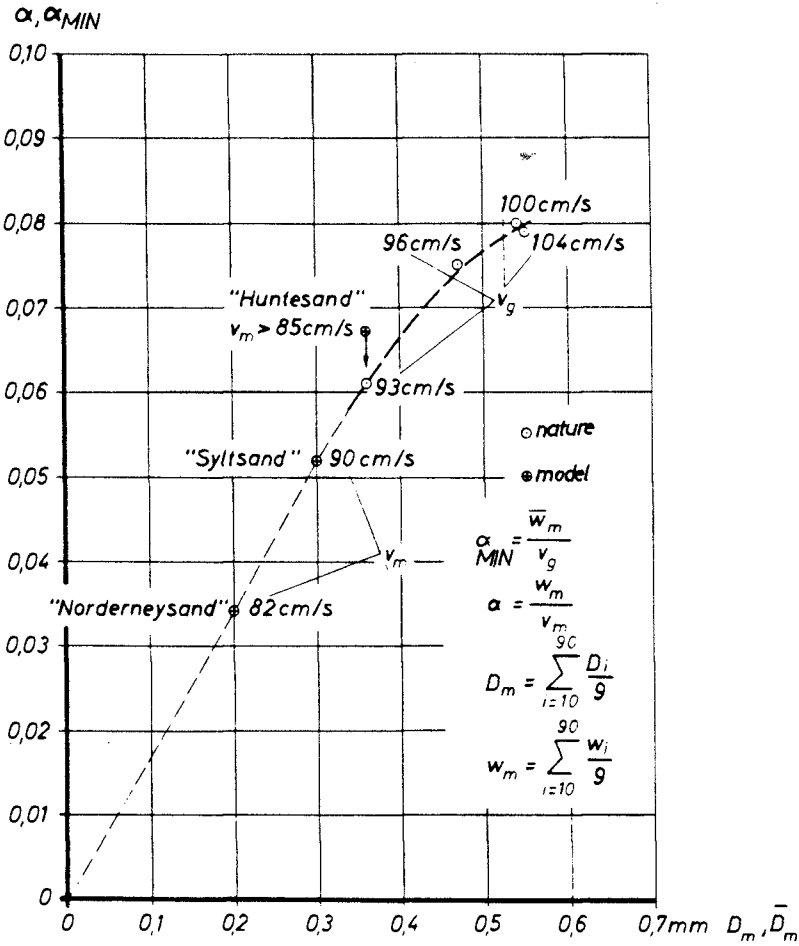
Fig. 7   Relation between α and D_m in prototype and model
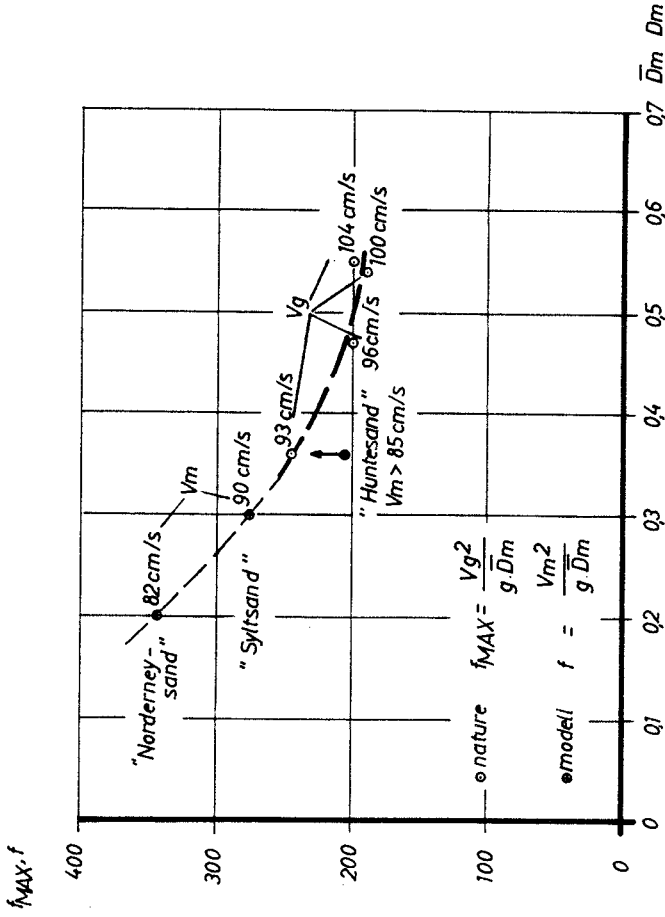
Fig. 8   Relation between f and D_m in prototype
and model

and are plotted in Fig. 7 and 8. It can clearly be seen
that model and prototype data show the same tendency.

CONCLUDING REMARK

It should be the goal of further investigations in the
prototype and in the model to gain a functional relation-
ship between the sediment data and both α and f.

ACKNOWLEDGEMENT

REFERENCES

1. DILLO, II.G.:   Sandwanderung in Tideflüssen
                         Mitteilungen des Franzius-Instituts
                         für Grund- und Wasserbau der Techni-
                         schen Hochschule Hannover, Heft 17,
                         1960

2. FRANZIUS-INSTITUT: Berechnungen des Feststofftranspor-
                         tes in der mittleren Hunte, un-
                         published report, 1960

3. NASNER, H.:   Über das Verhalten von Transport-
                         körpern im Tidegebiet, Mitteilungen
                         des Franzius-Instituts, Heft 40,1974

4. NASNER, H.:   Dynamisches Verhalten von Trans-
portkörpern, Vergleiche von Messun-
gen in der Natur und im Modell
Mitteilungen des Franzius-Instituts
Heft 40, 1974

5. WIEDENROTH, W.:   Untersuchungen über die Förderung
von Sand-Wasser-Gemischen durch
Rohrleitungen und Kreiselpumpen.
Diss, Technische Hochschule Hannover,
1967.

CHAPTER 61

EXPERIENCE WITH MOVABLE BED TIDAL MODELS

E.Giese[1], H.Harten[2], H.Vollmers[3]

INTRODUCTION

A particular problem, of those arising in the economic deve-
lopment of estuary regions, concerns the maintenance and en-
largement of navigation channels. The sediment transport
plays an important role in connection with this problem.
Though the hydrodynamical processes are today, with the help
of mathematical procedures, fairly exactly grasped, there is
still insufficient knowledge about the related transport
processes, the formation of ripples and dunes and of long-
term periodical morphological changes.

Nevertheless, the engineer wants information about sediment
transport for his planning. A well-known aid is the movable
bed hydraulic model, which has been technically developed to
simulate the natural fluid-sediment interaction. Such models
are not yet standard in hydraulic research institutes and
furthermore, they are not easy to handle. This is probably
due to a lack of suitable similarity criteria for insuring
valid experimental results. However, there exist recently
developed somewhat compromised similarity relationships,
which can be used for distorted movable bed tidal models.

The experience gained with the movable bed model Elbe I at
the Bundesanstalt für Wasserbau (BAW) in Hamburg provides
an incentive for investigating special cases in other large
tidal models of the German North-Sea coast. These models
are presented in Fig. 1. From west to east:

1) Ing.(grad))   Bundesanstalt für Wasserbau (BAW)
2) Dipl.-Ing.)   Hamburg, Germany
3) Dr.-Ing.   )

1051

a) Ems-model   Scales 1:500/100
b) Jade-Weser-model   "   1:800/100
c) Elbe-model I   "   1:800/100
d) Elbe-model II   "   1:500/100
e) Eider-model   "   1:250/50

The investigations involved morphological changes in areas
with navigation channels, training structures, dumping pla-
ces for dredged material, changes of water levels in connec-
tion with deepened channels, new high water dikes and in-
fluence of storm tides for models a) through d) and a dam-
ming up for model e) with regard to scour protection up-and
downstream of the weir reach.

EQUATIONS AND ASPECTS

The following dimensionless parameters describe the sediment
transport:

$$R_* = \frac{u*. D}{\nu} \quad \text{(Reynolds-Number)} \tag{1}$$

$$F_* = \frac{u*^2}{\varrho' g D} \quad \text{(Froude-Number)} \tag{2}$$

$$D_* = \left(\frac{\varrho'. g}{\nu^2}\right)^{1/3} . D = \left(\frac{R*^2}{F_*}\right)^{1/3} \quad \text{(Sedimentological Diameter)} \tag{3}$$

$$G_* = \frac{q_s'}{\varrho \cdot u_*^3} \quad ; \quad g_* = \frac{q_s'}{\varrho_s \cdot g \cdot D \cdot u_*} \quad \text{(Transport Numbers)} \tag{4}$$

u_* = shear velocity $[L . T^{-1}]$
D = characteristic grain diameter $[L]$
ν = kinematic viscosity $[L^2 T^{-1}]$
ϱ, ϱ_s = specific density of the fluid $[M . L^{-3}]$
      and bed material
ϱ' = relative specific density $= \frac{\varrho_s - \varrho}{\varrho}$ $[1]$
g = gravitational acceleration $[L . T^{-2}]$
q_s' = specific sediment transport $[dyn L^{-1} T^{-1}]$

$(\wedge) = (L, h, D, \varrho')$ (Comparison of prototype and   (5)
model parameters)

These relationships are suitable for the description of va-
rious phenomena. One obtains a similarity function from the
comparison of prototype-model parameters in equation 5,
where the quantities L = length, h = depth, D = grain dia-
meter and ϱ' = relative specific density provide the basis of
the model. Since the estuaries of our coastline are conside-
red to be of the "well-mixed" type, in which the salinity
decreases uniformly from the sea mouth to the river, but
where the fresh water and salt water are fairly well-mixed
throughout the vertical, density effects are neglected in
flows described by the similarity criteria.

The scale relations for movable bed models are extensively
discussed in our paper submitted to the 13th Conference [5].
The scale relations are based on roughness conditions of the
bed material considering different light weight materials.
Gehrig's calculations in Fig. 2 [1] show good agreement with
the empirically developed expression of Lacey and Inglis.
This may serve for an initial assignment of model scales.

Due to the premise that model dunes should be geometrically
similar to their counterparts in prototype, an extension of
the time scale must be considered, mostly for distortions
larger than 5. For the Elbe model I with a distortion of 8,
the multiplier α , first estimated empirically and later on
calculated, reflects the deviation from a "Froudian Model".
Yalin also derived this in his paper presented at the 13th
Conference [6]. He labeled his multiplier ξ .

The calculations for time extensions are based on the inter-
action between average stream velocity and sediment trans-
port in preference to shear stress. Water level slope, water
depth, grain diameter and grain density as well as kinematic
viscosity of the fluid and roughness coefficients of the
whole system are the main variables.

The idea to work with "Non-Froudian models" is not new. At
the former "Preussische Versuchsanstalt"in Berlin where

Casey and Shields carried out their basic research, Krey developed a model technique for rivers with stationary uniform discharge. With the use of natural sand, from which the finest particles had been removed to avoid cohesive influence, an agreement with nature-like sediment transport was achieved with the aid of steeper slopes for model and water level ($\sim$ 1:600). In these cases the discharge steps must be calibrated in relation to different water-depths.

Prototype and model values of our estuaries are listed in Fig. 3, a graph after Krey: the dimensioned roughness coefficient K against a variation of the Reynolds-number. For u . R we set u_* . h (shear velocity times water depth). Following the ordinates to the parameter for channels with bed material of fine sands, the total roughness coefficients of the considered river sections can be estimated. From this the average flow velocity $u = \dfrac{u_* \cdot K}{g}$ is available both for the prototype and model. The comparison of these results show finally the deviation from the Froude law, as similarly shown in Yalin's interpretation. The too intensive mobility of the bed material in the model can be reduced with the time extension $\alpha = \dfrac{\lambda u}{\sqrt{\lambda_y}}$.

The verification of prototype and model values with Yalin's criteria are presented in Fig. 4 [6]. On the left side in the Y/Ycr - X plane the presence of ripples on dunes would not be expected, when polystyrene is selected with a diameter larger or equal 2 mm. In the model, X or R_* according to Yalin must always be larger than 25. To achieve the similarity of dunes, prototype and model points should be both outside the shaded region in the X - Y plane on the right side. These assumptions are given for all models with distortions between 5 and 8. However, the necessary deviation from a "Froudian model" has an upper limit. Test results in the Elbe model I, with a distortion of 8, showed only practical α or ξ values of up to 1.5 for this relative long estuary with one tide generator. Beyond this limit the water level slope flattened during the last part of the ebb phase. Only short estuaries or sections with two-sided tide generation

allow smaller extensions of more than 1.5. Therefore rough-
ness coefficients given by the similarly reproduced bed de-
formations limit the scale of distortion. In Fig. 5, left
graph A, the correlation between α and distortion n with dif-
ferent length scales λ_y is presented. Because the unshaded
region is only available, the upper limit with α = 1.5 com-
bined with a length scale 1:800 allows a distortion of n=8.
This was selected for the Elbe model I with a resulting
suitable vertical scale of 1:100.

However, it must be mentioned that the first empirically
estimated time extension for this model with α = 1.4 was
used throughout all tests. Adequate to lower distortions the
necessary time extensions decreased. This leads to an appro-
ximation of the Froude law for distortions < 5. From this it
is obvious that we sometimes have much trouble finding the
effective artificial roughness which reproduces similar wa-
ter level slopes in highly distorted models with fixed beds.

A further correlation of polystyrene grain diameter with
Yalin's limitation of X $\geq$ 25 in Fig. 5, right graph B, shows
the small range outside of the shaded area. Fortunately we
found polystyrene grains with a diameter of about 2 mm which
satisfy these requirements.

Of special significance is the morphological time scale,
i.e. the time necessary for equal changes of the morphology
in prototype and model. The relationship of significant
transport depends on the F_* values above the critical va-
lues, given in the Shields-diagram (Fig. 6).

Prototype and model values of our estuaries are noted and
reveal the influence of grain diameter and density. A rela-
tive high mobility can be found in nature and a diminished
one in the model, both caused by maximum velocities during
the steepest rising or falling water in the flood or ebb
phases.

Fig. 7 presents a variation of the Shields diagram with a
correlation of the grain diameter versus grain Reynolds-
number. Parameters are the grain Froude-number and grain

density. The natural sand, D = 0.4 mm, shows an F_* of 0.5.
The available polystyrene with 2 mm diameter gives $F_* \sim 0.3$
(after calculations for the Elbe-model given in the appen-
dix) and consequently a lower mobility.
In the model $F_* = 0.5$ requires a grain diameter of 1.0 mm
but this would be outside of the limitation of $X = R_* > 25$
(right of the dashed vertical).

The morphological similarity can be expressed as a time re-
lation, in which natural changes are reproducible in the mo-
del. Historical tests showed that model changes occur more
rapidly than according to the time scale specified by Froude.
Finally the morphological scale was found empirically to be
1:705, (2 minutes in the model to about one day in nature).

INDICATIONS TO THE MODEL CONSTRUCTION

Movable bed models should be set up in closed heatable halls
to avoid large deviations in water-temperatures. It is re-
commended that the tidal region be built to include the to-
tal area of tidal influence, for only in this way can the
effect of artificial structures be precisely eliminated. In
considering a combination of a "fixed and movable model
section", technical model simplifications are allowed in the
fixed bed area, which then only has a secondary function.
Fig. 8 depicts the Elbe model I, situated in a 40 x 112 m
test hall. Various deviations from the natural course were
necessary to optimally fit the model into the hall.

In addition to the usual equipment, test halls should have
movable service bridges with which the entire surface area
of the hall can be covered, so that all work and measure-
ments can be carried out without having to step inside of
the model (Fig. 9).

In addition to special constructions for tide generation,
such as a steerable sector gate, exact quantitative water
dispersion adequate to discharge cross-section and electro-
nic optical tide curves reader, the areally acting irriga-
tion and drainage system is especially important (Fig. 10).

This last installation is an essential tool for the whole
success of the work. Other measuring installations shall not
be described; they are generally well-known.

RESULTS

Historical morphological development investigations in the
Elbe-model I showed good agreement between nature and model.
The relation between alternating flow processes during a
tide and the thereby established sediment transport can be,
through proof of hydrodynamic similarity, better comprehen-
ded for the total estuary region in the model than in natu-
re. Detailed descriptions of the first practical tests which
have been carried out to prove the stabilization effect of
a new main navigation channel north-west of Cuxhaven are
given in the Proceedings of the 13th Conference.

According to Fig. 11, the minimum local silting distribution
was found for test II with a tangential extension of the
existing training wall. Prototype sounding control measure-
ments verified the occurrence of advantageous developments
for the stabilization.

A new method must be found for models to measure the spread
of first dredged and later on dumped material. This is sig-
nificant for the maintenance and deepening of main naviga-
tion channels.

Dumping fields in the outer Elbe with examples of several
measuring points in Fig. 12 show that the dumped material
was not brought back to the widened Center Channel. To
measure the spreading, the artificial model sediment (poly-
styrene) serves itself as tracer. But single grains with
2 mm diameter can only bear radioactivity when a suitable
element can be bound onto their surfaces. Therefore the
element bromine was used, which could be bound chemically
with polystyrene. The duration of the presented tests was
150 tides or about 33 hours in the model. This nearly cor-
responds to the 36 hour half-life of bromine. More details
are described in our paper for the IAHR Congress in Istan-
bul 1973.

A large area bottom training was investigated in the Elbe
model II. For this purpose a segment of the model was fitted
with a movable bed. The similarity to nature was also very
evident. The situation map in Fig. 13 shows the Elbe area
between Brunsbüttel and Scheelenkuhlen (km 684-km 696).
8.5 million m³ were to be dredged out of the river bed to
build up the foreshore for industrial areas. The dredging
fields, marked with I through IV, are outside of the main
navigation channel, and the widening of the cross-section
favours the hydraulic requirements. The discharge became
more balanced, velocities showed more parallel directions
and the bottom deformations flattened.

The results in Fig. 14 show for test 0 with the existing
condition in the longitudinal profile a relatively unsteady
formation of dunes with different elevations. Test 6 indi-
cates the same length after the dredging with a more flat-
tened bottom. These developments explain the interaction of
the fluid-sediment movement and the effectiveness of train-
ing actions.

CONCLUSIONS

Movable bed tidal model techniques have developed substan-
tially in the past few years. However, experimental results
have been only sparsely published. Experience has shown
that such models are very useful and that even with small
construction changes a definite morphological development
resulting from outside forces and bottom topography is de-
monstrated.

O'Brien's relations [2] between minimum flow area and tidal
prism could be proved both by calculation and model tests.
Fig. 15 presents a simplified calculation method in a me-
tric system. Definite cross-sections of the German North
Sea coast show similar proportions to estuaries of the Pa-
cific coast. These relations have a special bearing on the
enlargement of navigation channels.

Finally it should be stated that movable bed models have

definite advantages over fixed bed models because there is
a direct interaction between fluid motion and sediment trans-
port processes.

REFERENCES

[1] GEHRIG, 1967, Über die Frage der naturähnlichen Nachbil-
        dung der Feststoffbewegung in Modellen. Mitteilungen
        des Franzius-Instituts für Grund-und Wasserbau der
        Technischen Hochschule Hannover, Heft 29.

[2] M.P.O'BRIEN, 1969, Equilibrium Flow Areas of Inlets on
        Sandy Coasts. Journal of the Waterways and Harbors
        Division, Proceedings of the American Society of
        Civil Engineers, February.

[3] GIESE, 1971, Fahrwasserumbildungen in der Unter-und
        Außenelbe. Die Wasserwirtschaft H. 3.

[4] GIESE, TEICHERT, VOLLMERS, 1972, Das Tideregime der Elbe,
        Hydraulisches Modell mit beweglicher Sohle.
        Mitteilungsblatt der BAW, Nr. 31.

[5] VOLLMERS, GIESE, 1972, Elbe Tidal Model with Movable Bed.
        13th International Conference on Coastal Engineer-
        ing, Vancouver B.C., Canada.

[6] YALIN, 1972, On the Geometrically Similar Reproduction
        of Dunes in a Tidal Model with Movable Bed.
        13th International Conference on Coastal Engineer-
        ing, Vancouver B.C., Canada.

[7] GIESE, TEICHERT, VOLLMERS, 1973, The Tidal Regime of the
        Elbe-River, Hydraulic Model with Movable Bed.
        International Symposium on River Mechanics, Bangkok,
        Thailand.

[8] VOLLMERS, GIESE, 1973, Measurement of Sediment Transport
        by Radioactive Tracers in a Tidal Model with Mova-
        ble Bed. 15th Congress of the IAHR, Istanbul,Turkey.
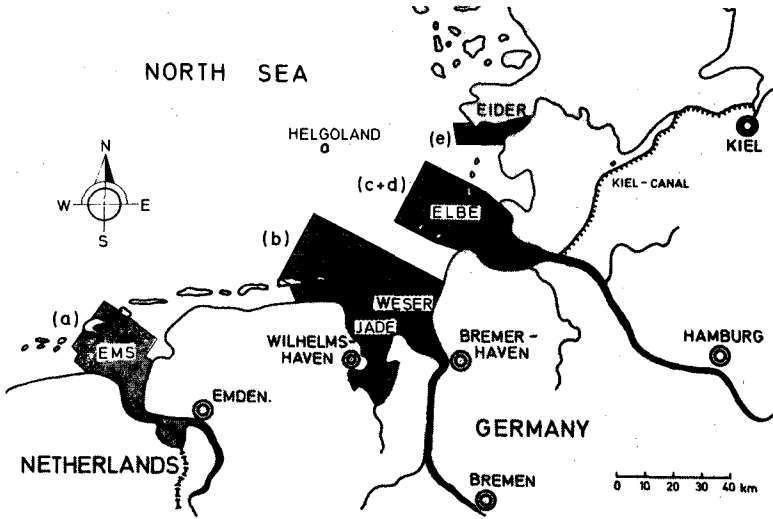
FIG.1. - ESTUARY MODELS OF THE GERMAN NORTH-SEA COAST
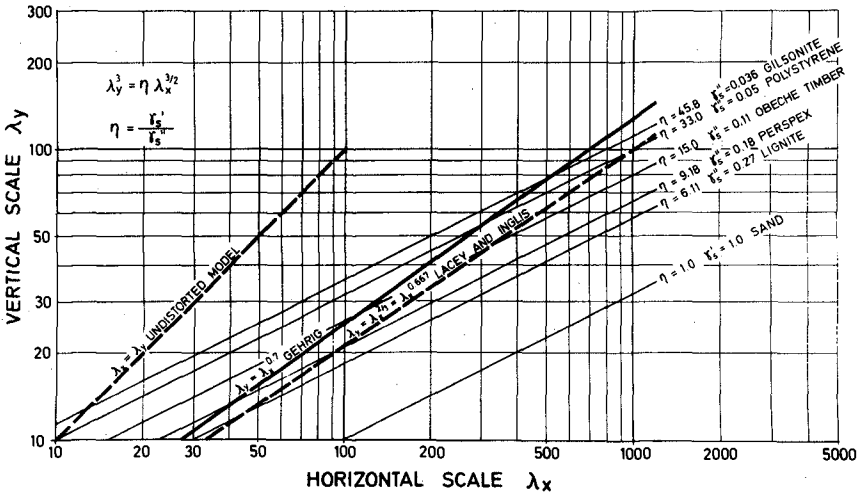
FIG.2. - SCALE RELATIONS FOR MOVABLE BED MODELS (CONSIDE-
RING ROUGHNESS) AFTER GEHRIG [1]

	PROTOTYPE	MOOEL
ELBE – MOOEL I	O	o
WESER – JAOE – MOOEL	⊖ ⊖	⊖ ⊖
ELBE – MOOEL II	X	x
EMS – MODEL	+	+

WATER TEMPERATURE °C	5	10	13.2	15	20	25	30
COEFFICIENT ς s/m²	0.79	0.92	1.0	1.05	1.19	1.32	1.46

R = HYDRAULIC RAOIUS; J = WATER LEVEL SLOPE

FIG.3. – ROUGHNESS COEFFICIENT K VERSUS KREY'S NUMBER
u.R.ς OR NUMBER u.R. WHEN ς ~1 (WATER TEMPERA-
TURE 13,2°C)

$$X = R_* = \frac{u_* \cdot D}{\nu}$$

$$Y = F_* = \frac{\varsigma \cdot u_*^2}{\varsigma_s \cdot D}$$

$$Z = \frac{h}{D}$$

	PROTOTYPE	MODEL
ELBE – MODEL I	O	o
WESER – JAOE – MOOEL	⊖ ⊖	⊖ ⊖
ELBE – MODEL II	X	x
EMS – MODEL	+	+
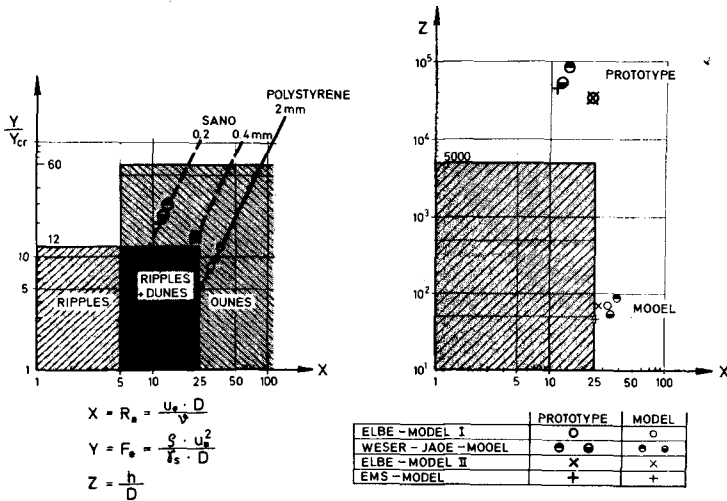
FIG.4. – YALIN'S CRITERIA ON THE GEOMETRICALLY SIMILAR
REPRODUCTION OF DUNES IN A TIDAL MODEL WITH
MOVABLE BED [6]

A: OISTORTION ANO LENGTH SCALE

DEVIATION FROM A FROUDIAN MOOEL = α

AVAILABLE FOR SHORT ESTUARIES (TWO-SIOED TIDE GENERATION)

UPPER LIMIT FOR LONG ESTUARIES (ONE TIDE GENERATOR)

$\lambda_x = \frac{1}{400}$
$\lambda_x = \frac{1}{600}$
$\lambda_x = \frac{1}{800}$
$\lambda_x = \frac{1}{1000}$

OISTORTION $n = \lambda_y / \lambda_x$
$\alpha = f(n, \lambda_x)$

B: LENGTH SCALE, GRAIN DIAMETER ANO GRAIN REYNOLOS NUMBER, RESPECTIVELY

POLYSTYRENE $D'(mm) = 0.5$ 1.0   1.5   2.0   2.5

ELBE-MODEL I

GRAIN REYNOLOS NUMBER $X''_{\bullet} = R''_{\bullet} = \frac{u''_{\bullet} \cdot D}{\nu}$
$\alpha = f(\lambda_x, D, X'')$
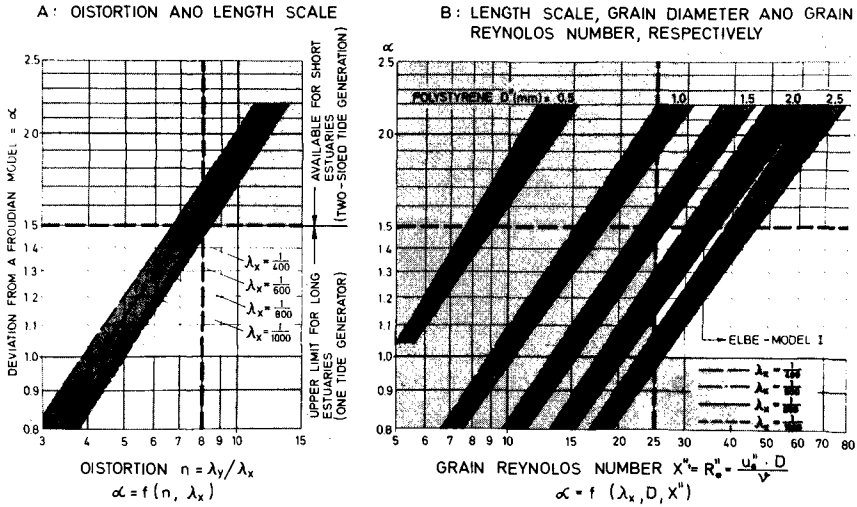
FIG.5. – CORRELATION OF THE DEVIATION FROM A FROUDIAN
MODEL (EXAMPLE ELBE-ESTUARY, $u''_{\ast} = 0.0575$ m/s)

SAND   PDLYSTYRENE
0.2mm 0.4mm 2mm

$F_{\bullet} = \frac{\tau_o}{(\gamma_s - \gamma) \cdot D}$

MOTION

NO MOTION

$R_{\bullet} = \frac{u_{\bullet} \cdot D}{\nu}$

	PROTOTYPE	MODEL
ELBE – MODEL I	O	O
WESER – JADE – MODEL	◐ ◑	◕ ◔
ELBE – MODEL II	×	×
EMS – MODEL	+	+
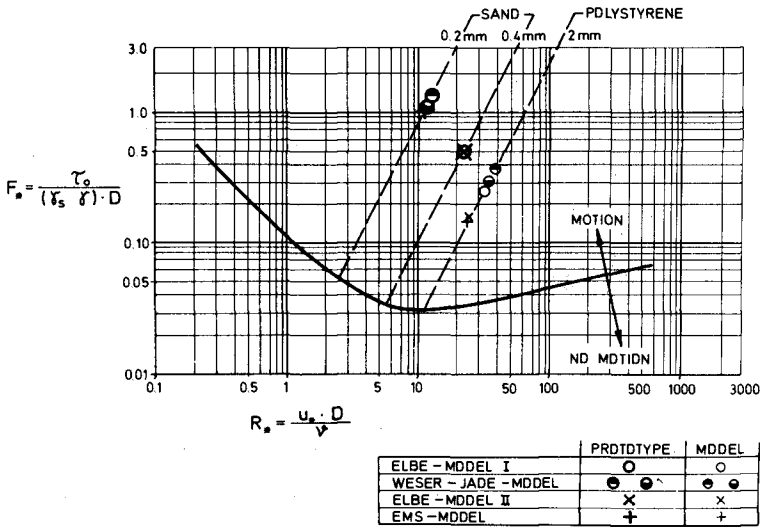
FIG.6. – SHIELDS-DIAGRAM, DIMENSIONLESS CRITICAL SHEAR
STRESS VERSUS SHEAR REYNOLDS NUMBER
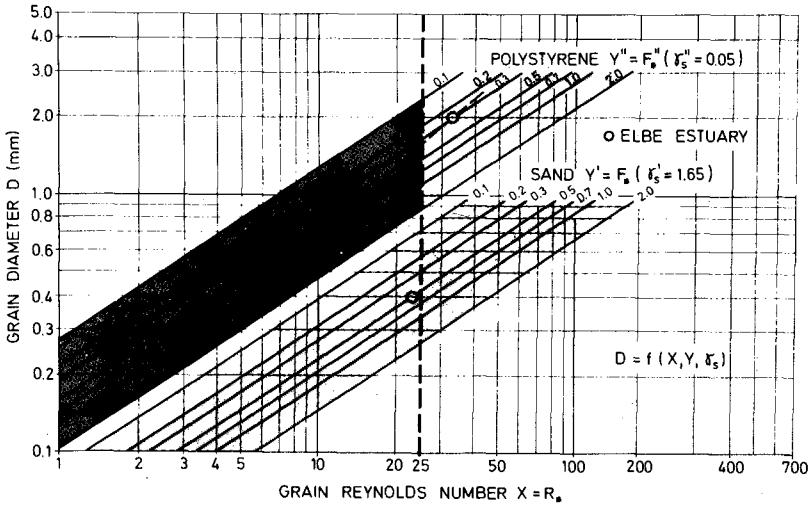
FIG.7. — CORRELATION OF THE GRAIN DIAMETER, GRAIN
         REYNOLDS NUMBER, GRAIN FROUDE NUMBER AND
         GRAIN DENSITY, RESPECTIVELY
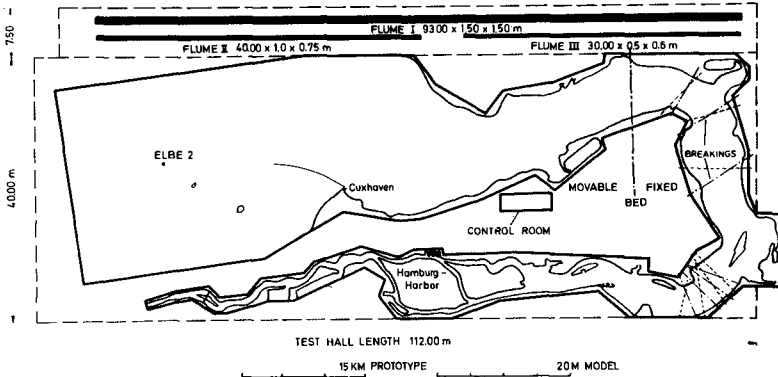
FIG.8. — SITUATION MAP OF THE HALL WITH THE ELBE-MODEL I

FIG.9. - SERVICE BRIDGES
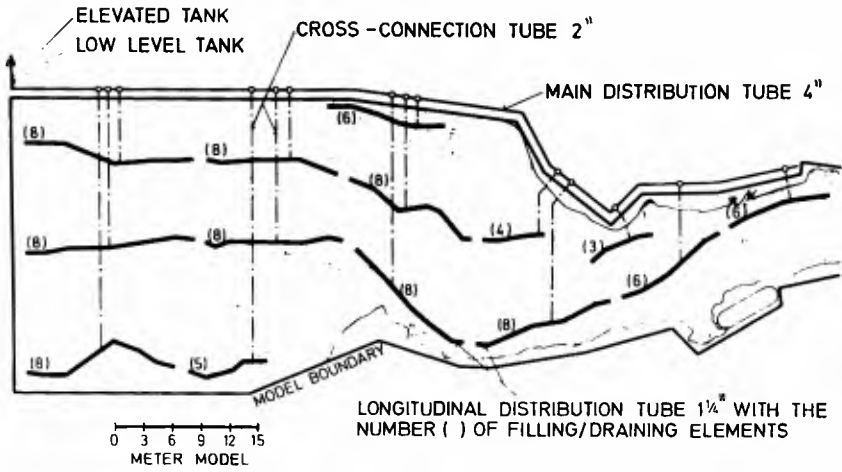
FIG.10. - IRRIGATION AND DRAINAGE SYSTEM
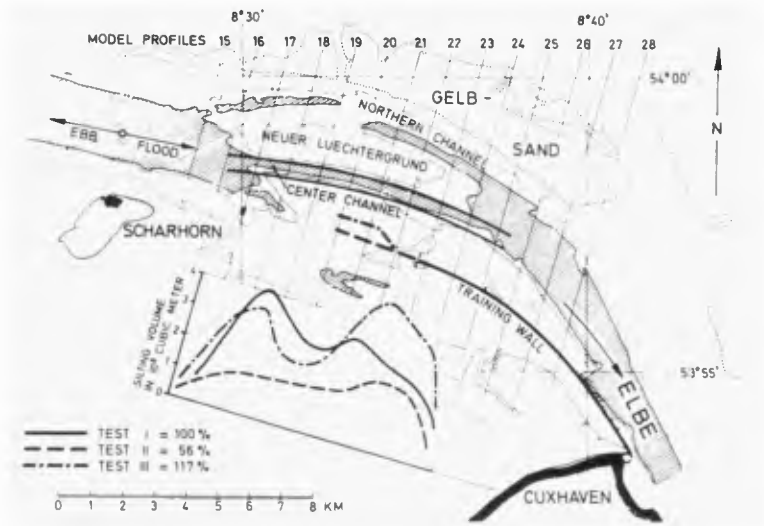
FIG. 11. - SCHEMES FOR THE TRAINING WALL EXTENSION, MEA-
SURED SILTING RATES IN THE NEW "CENTER CHANNEL"
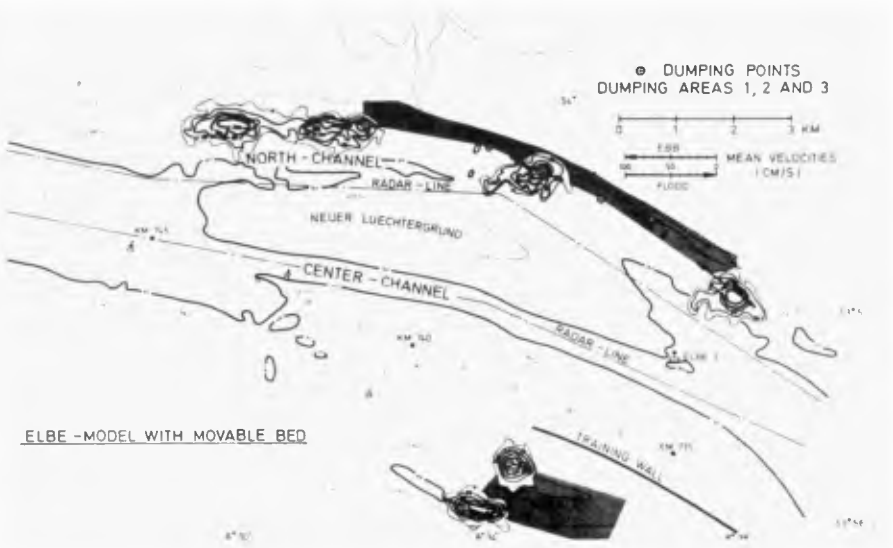
FIG. 12. - SPREADING OF DUMPED MATERIAL IN THE OUTER ELBE
(MODEL TESTS WITH RADIOACTIVE TRACERS)
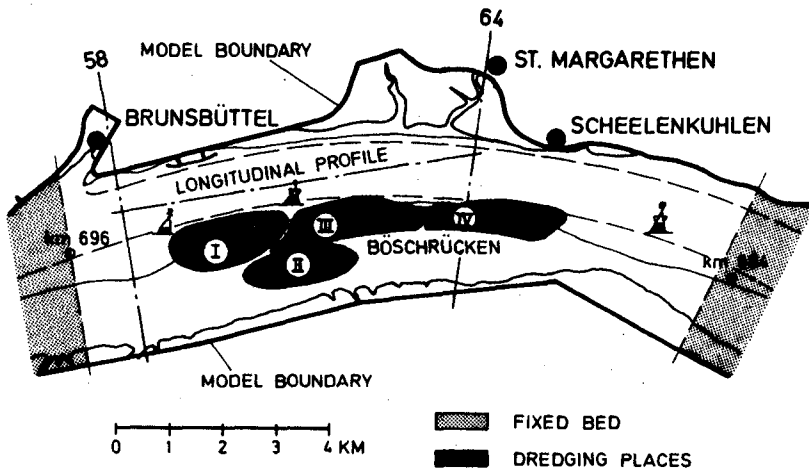
FIG.13. – SITUATION MAP OF THE ELBE RIVER BETWEEN
          BRUNSBÜTTEL AND SCHEELENKUHLEN (km 684-km 696)
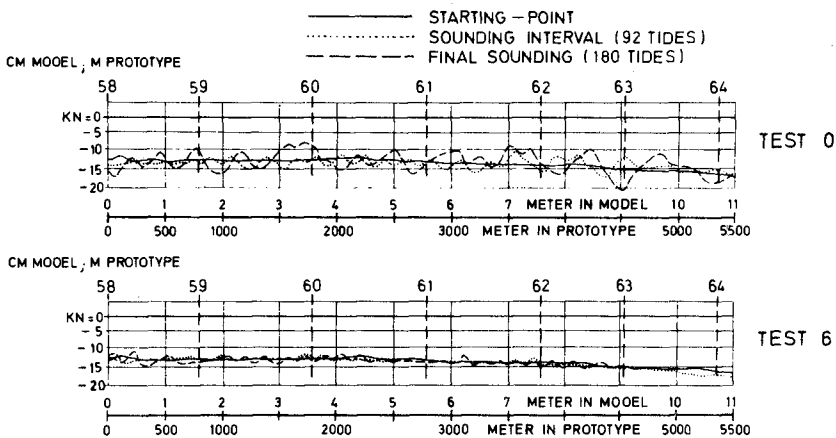
FIG.14. – ELBE MODEL II, LONGITUDINAL PROFILE BETWEEN THE
          CROSS SECTIONS 58 – 64 (TESTS 0 AND 6)
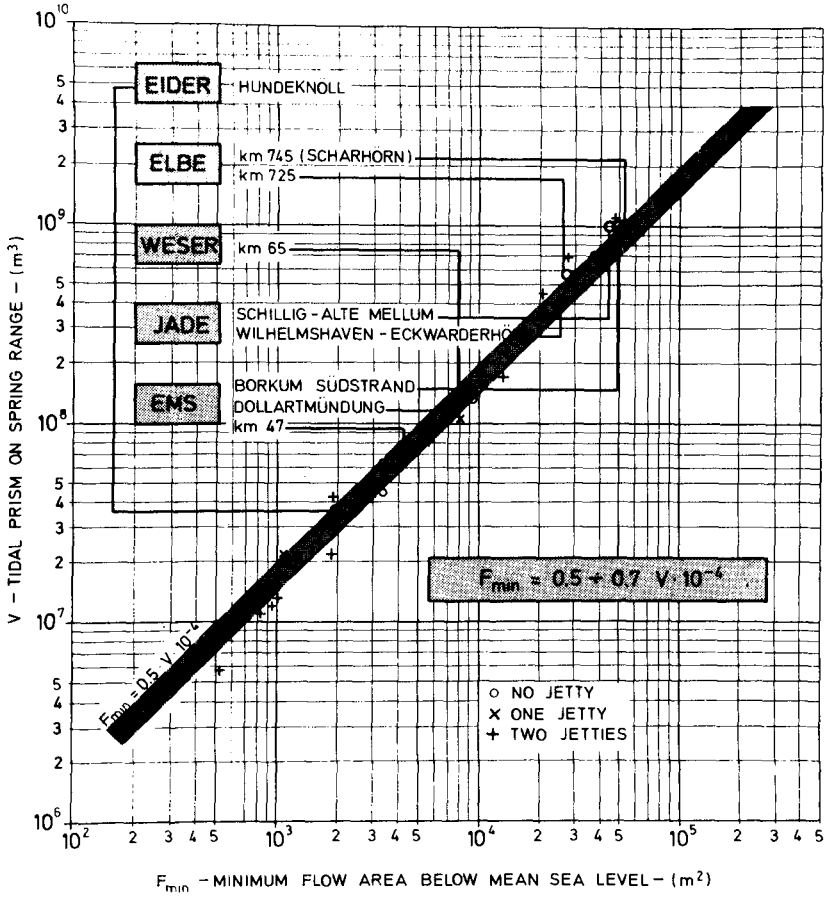
FIG.15. — MINIMUM FLOW AREA AND TIDAL PRISM (AFTER O'BRIEN
        [2])

APPENDIX

CALCULATIONS FOR THE ELBE MODEL I WITH MOVABLE BED

$h' = 13.5\ m$
$D' = 0.4\ mm$
$L' = 28.3\ km$
$H = 0.7\ m$ $\Big\}\ J' = 2.5 \cdot 10^{-5}$ between Brunsbüttel and Cuxhaven
$\gamma_s'/\gamma = 1.65$
$\nu = 10^{-6}\ m^2/s$; $g = 9.81\ m/s^2$; $\mathcal{S} = \gamma/g = 101.94\ kp\,s^2/m^4$

Bed material in the model : Polystyrene $\gamma_s'' = 0.05$, $D'' = 2\ mm$

$\lambda_{\gamma_s} = \dfrac{0.05}{1.65} = \dfrac{1}{33}$; $\lambda_D = \dfrac{0.002}{0.0004} = 5$

$\lambda_Y = \dfrac{1}{100}$ vertical scale relation

$\lambda_x = \dfrac{1}{800}$ length scale relation $\qquad n = \dfrac{\lambda_Y}{\lambda_x} = 8$ distortion

$z' = \dfrac{h'}{D'} = \dfrac{13.5}{0.0004} = 33750$

$z'' = \dfrac{h''}{D''} = \dfrac{0.135}{0.002} = 67.5$ $\qquad \lambda_z = \dfrac{67.5}{33750} = \dfrac{1}{500}$

$x' = \dfrac{u_*' \cdot D'}{\nu}$; $u_*' = \sqrt{\dfrac{\tau'}{\mathcal{S}}}$; $\tau' = \gamma \cdot h' \cdot J' = 1000 \cdot 13.5 \cdot 2.5 \cdot 10^{-5}$
$\qquad\qquad = 0.3375$

$\qquad\qquad u_*' = \sqrt{\dfrac{0.3375}{101.94}} = \underline{0.0575\ m/s}$

$x' = \dfrac{0.0575 \cdot 0.0004}{10^{-6}} = \underline{23}$ $\qquad Y_{cr}' = 0.035$ (Shields)

$Y' = \dfrac{101.94 \cdot 0.0575^2}{1650 \cdot 0.0004} = \underline{0.51}$ $\qquad Y'/Y_{cr}' = \dfrac{0.51}{0.035} = \underline{14.57}$

$x'' = \dfrac{u_*'' \cdot D''}{\nu}$; $u_*'' = \sqrt{\dfrac{\tau''}{\mathcal{S}}}$; $\tau'' = \gamma \cdot h'' \cdot J'' = 1000 \cdot 0.135 \cdot 2 \cdot 10^{-4}$
$\qquad\qquad = 0.027$

$\qquad\qquad u_*'' = \sqrt{\dfrac{0.027}{101.94}} = \underline{0.0163\ m/s}$

$x'' = \dfrac{0.0163 \cdot 0.002}{10^{-6}} = \underline{32.6}$ $\qquad Y_{cr}'' = 0.032$ (Shields)

$Y'' = \dfrac{101.94 \cdot 0.0163^2}{50 \cdot 0.002} = \underline{0.271}$ $\qquad Y''/Y_{cr}'' = \dfrac{0.271}{0.032} = \underline{8.47}$

$\lambda_x = \dfrac{32.6}{23.0} = 1.42$; $\lambda_Y = \dfrac{0.271}{0.51} = \dfrac{1}{1.88}$

$u_*' \cdot h' = 0.0575 \cdot 13.5 = 0.776$ $\quad\Big($ Krey's number $u \cdot R \cdot \mathcal{S}$ with $\mathcal{S} = 1$
$u_*'' \cdot h'' = 0.0163 \cdot 0.135 = 0.0022$ $\quad$ water temperature $13.2°C$; $R = h \Big)$

Choose the roughness coefficient K from Krey's graph for channels with bed material of fine sand :

$$K' = 47 \quad ; \quad K'' = 25$$

$\dfrac{u}{u_*} = \dfrac{K \cdot \sqrt{h \cdot J}}{\sqrt{\mathcal{S}}} = \dfrac{K \cdot \sqrt{h} \cdot \sqrt{J} \cdot \sqrt{\gamma}}{\sqrt{\gamma \cdot h \cdot J} \cdot \sqrt{g}} = \dfrac{K}{\sqrt{g}}$

Prototype : $u' = \dfrac{u_*' \cdot K'}{\sqrt{g}} = \dfrac{0.0575 \cdot 47}{3.14} = \underline{0.86\ m/s}$

Model : $u'' = \dfrac{u_*'' \cdot K''}{\sqrt{g}} = \dfrac{0.0163 \cdot 25}{3.14} = \underline{0.13\ m/s}$

$\qquad\qquad \lambda_u = \dfrac{u''}{u'} = \dfrac{0.13}{0.86} = 0.15$

Necessary time extension for the tide period after Froude

$$\alpha = \dfrac{\lambda_u}{\sqrt{\lambda_Y}} = \dfrac{0.15}{\sqrt{\frac{1}{100}}} = \underline{1.5}$$

[Calculations with the "Technical System" : kp , m , s]

CHAPTER 62

SCALE LAWS FOR BED FORMS IN LABORATORY WAVE MODELS

by

G.R. Mogridge*

ABSTRACT

An experimental study of the variables governing the
development of bed forms under wave action has been con-
ducted. A wide range of conditions was covered by the use
of a wave flume and an oscillating water tunnel. Scale laws
for modelling bed forms are developed using the results of
these experiments. It is recommended that the model sedi-
ment used should be the same density as in the prototype and
its size should be scaled geometrically. If this is not
practical, it is shown how the scale laws can be used to
minimise the distortion of the bed forms produced in the
model.

INTRODUCTION

The roughness of a sediment bed is dependent on the

sediment grain size and the bed forms which occur as a result

of the oscillatory fluid motion generated by waves. Thus,

the scales for a movable bed wave model should be chosen to

reproduce bed forms so that energy losses and wave attenua-

tion in the model are dynamically similar to those in the

prototype. In addition, sediment transport rates depend not

only on the shear stresses caused by the bottom roughness,

but also to a great extent on the shape and size of the bed

forms as described by Mogridge (3) and Inman (1). In an

attempt to significantly improve the design of movable bed

*Assist. Research Officer, Hydraulics Laboratory, National

 Research Council, Ottawa, K1A 0R6, Canada.

wave models, scale laws are developed which govern the re-
production of bed forms.

SCALE LAWS GOVERNING SEDIMENT TRANSPORT IN MOVABLE BED WAVE MODELS

Yalin (5) has shown that for a movable bed wave model,
any quantitative property may be expressed as a function of
the following dimensionless variables,

$$\pi_Q = f_a \left\{ \frac{v_* D}{\nu}, \frac{\rho v_*^2}{\gamma_s D}, \frac{\rho_s}{\rho}, \frac{a}{D} \right\} \tag{1}$$

where ρ is the density of the fluid,

ρ_s is the density of the sediment,

γ_s is the submerged specific weight of the sediment,

i.e. $(\rho_s - \rho)g$,

ν is the kinematic viscosity of the fluid,

D is the sediment grain size,

a is the amplitude of the fluid orbital motion

immediately outside the boundary layer,

v_* is the shear velocity, i.e. $\sqrt{\tau/\rho}$,

τ is the bottom shear stress.

The boundary layer is fully developed rough turbulent, when
the magnitude of the first variable in Eq. 1, i.e. Reynolds
Number, is very large. Under these conditions which normally
occur when bed forms are present, the Reynolds Number has no
effect and may be neglected. Therefore, from Eq. 1, the
scales for the movable bed model may be obtained from,

$$\frac{n_\rho n_{v_*}^2}{n_{\gamma_s} n_D} = 1, \quad \frac{n_a}{n_D} = 1, \quad \frac{n_{\rho_s}}{n_\rho} = 1 \tag{2}$$

where the scale n is defined as the prototype value on the model value of the parameter. Then,

$$n_{\rho_s} = n_\rho = 1,$$

$$n_{\gamma_s} = 1,$$

$$n_a = n_D = n,$$

$$n_{v_*}^2 = n_{\gamma_s} n_D = n,$$

or
$$n_{v_*} = n^{1/2} \tag{3}$$

However, according to Yalin (5), for the mass movement of sediment it is not necessary that $n_{\rho_s} = n_\rho$. Thus, a model may be designed such that $n_{\gamma_s} \neq 1$, and,

$$n_{v_*}^2 = n_{\gamma_s} n_D \tag{4}$$

If the model has bed forms, then the roughness of the bottom may be considered to be some combination of the roughness due to the bed forms and the sand roughness k_s. This effective roughness will be called k. If the model is distorted, or if either or both the sand roughness and bed forms are distorted, then N_k is the distortion of the roughness. The scaling laws for bed forms are developed in order

to reduce this roughness distortion, and to reduce the distortion of the bottom shear stress and wave attenuation. Careful modelling of the shape and size of the bed forms also ensures that sediment transport rates will be similar to those in the prototype.

For a fully developed rough turbulent boundary layer such as would normally occur when bed forms are present, the logarithmic velocity distribution is assumed.

$$U_\delta = 2.5 \ v_* \ \ln \left(\frac{30\delta}{k}\right), \tag{5}$$

where k is used for the total roughness instead of k_s for the sand roughness alone, and δ is the boundary layer thickness. Kamphuis (2), used Eq. 5 to derive the relationship,

$$\frac{a}{\delta} = \text{constant} \cdot \ln \left(\frac{30\delta}{k}\right), \tag{6}$$

and shows that these equations may be approximated by,

$$\frac{U_\delta}{v_*} = \text{constant} \cdot \left(\frac{30\delta}{k}\right)^{1/6}, \tag{7}$$

and

$$\frac{a}{\delta} = \text{constant} \cdot \left(\frac{30\delta}{k}\right)^{1/6}. \tag{8}$$

Since $n_a = n$, Eq. 8 results in,

$$n_\delta = n^{6/7} \ n_k^{1/7} = n \ N_k^{1/7}, \tag{9}$$

where N_k is the roughness distortion,

$$N_k = \frac{n_k}{n}.$$

From Eq. 7,

$$n_{U_\delta} = n_{v_*} \cdot \frac{n_\delta^{1/6}}{n_k^{1/6}}. \tag{10}$$

Therefore, since the scale of U_δ is the same as the velocity scale outside the boundary layer, i.e.,

$$n_{U_\delta} = n^{1/2}, \tag{11}$$

then substituting for n_δ in Eq. 10 gives,

$$n_{v_*} = n^{1/2} N_k^{1/7}, \tag{12}$$

and since $n_{v_*}^2 = n_\tau$ if $n_\rho = 1$, then,

$$n_\tau = n N_k^{2/7}. \tag{13}$$

Equation 12 shows that a distortion of the bottom roughness has only a small effect on the scale of the shear velocity. If the bottom roughness is undistorted then,

$$n_{v_*} = n^{1/2}, \tag{14}$$

and $$n_\tau = n. \tag{15}$$

Equation 4 then is,

$$n = n_{\gamma_s} n_D.$$ (16)

SCALE LAWS GOVERNING THE REPRODUCTION OF BED FORMS

Quantitative properties of bed forms resulting from wave action may be expressed as a function of the following dimensionless variables

$$X_1 = \frac{\gamma_s D^3}{\rho \nu^2}, \; X_2 = \frac{\rho D}{\gamma_s T^2}, \; X_3 = \frac{\rho_s}{\rho}, \; X_4 = \frac{A}{D},$$ (17)

where A is the orbit length of the flow oscillation immediately outside the boundary layer.

Experiments on bed forms have been conducted by the author (4) at the Coastal Engineering Laboratory, Queen's University at Kingston.   These experiments were conducted in a laboratory wave flume and an oscillating water tunnel, in order to cover the range from model to prototype conditions. Natural sand as well as low density materials were used as sediments.   The results showed that bed form length Λ and bed form height Δ are independent of the viscosity variable X_1, and as an approximation may also be considered independent of X_3.   Therefore, the bed form length and height may be expressed by the following equations,

$$\frac{\Lambda}{D} = f_\Lambda (X_2, X_4)$$ (18)

$$\frac{\Lambda}{D} = f_\Lambda (X_2, X_4) \qquad\qquad (19)$$

The functions f_Λ and f_Λ are given by the curves in Figs. 1 and 2, which are the result of the experiments described in reference (4). From Eqs. 18 and 19, exact similarity of the bed forms is achieved if,

$$n_{X_2} = 1 \text{ and } n_{X_4} = 1. \qquad\qquad (20)$$

Thus
$$n_D = n_{\gamma_s} n, \qquad\qquad (21)$$

and
$$n_A = n_a = n. \qquad\qquad (22)$$

In addition, it must be ensured that similarity laws for sediment movement over the bed forms are satisfied. However, Eqs. 16 and 21 cannot be satisfied simultaneously unless $n_{\gamma_s} = 1$. The scale laws obtained from Eqs. 21 and 22 become then,

$$n_D = n_A = n. \qquad\qquad (23)$$

Because there is no distortion of the bottom roughness,

$$n_{v_*}^2 = n, \qquad\qquad (24)$$

and
$$n_\tau = n. \qquad\qquad (25)$$

Thus, if the model sediment has a specific weight identical to that of the prototype sediment, and a grain size scaled
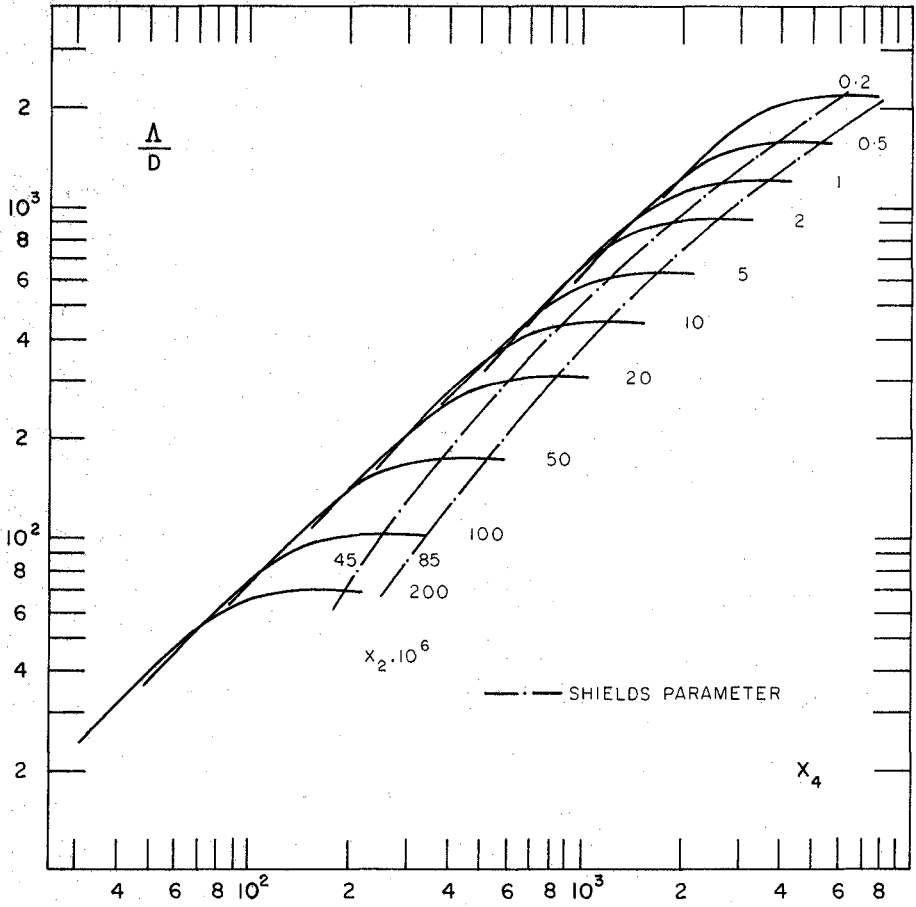
FIG·I   DESIGN CURVES FOR BED FORM LENGTH
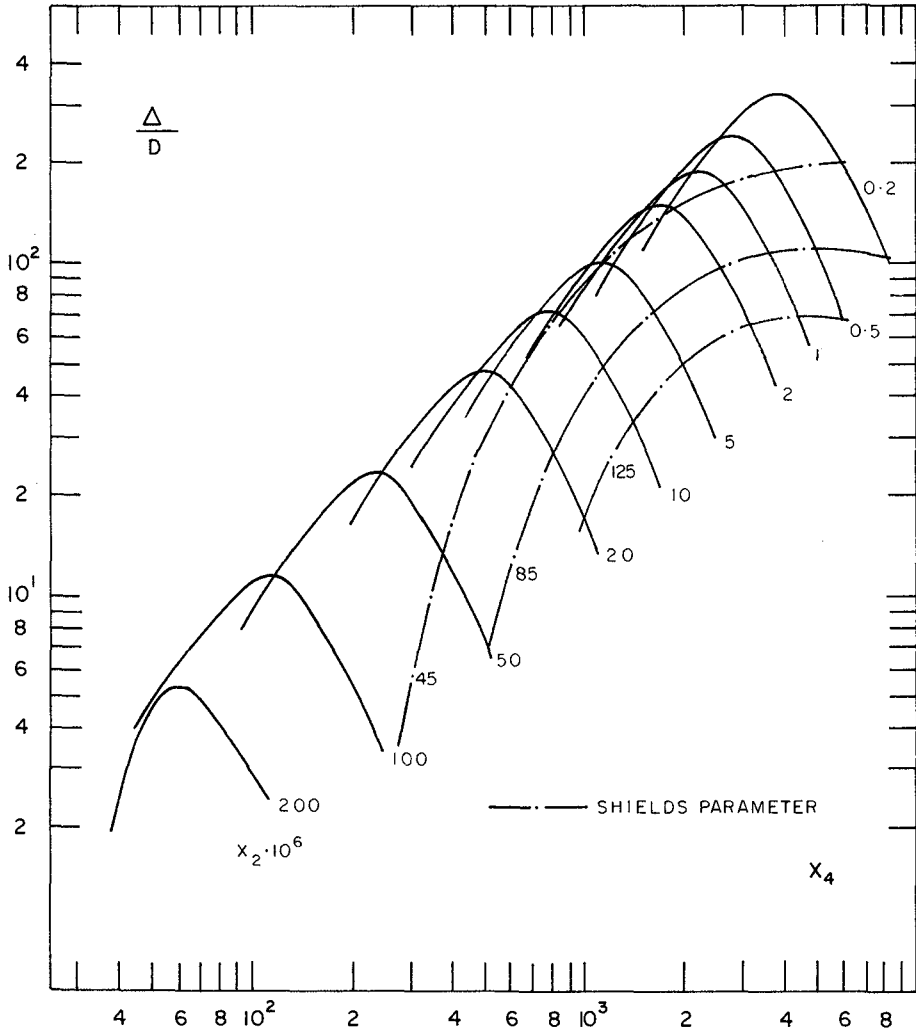
FIG·2 DESIGN CURVES FOR BED FORM HEIGHT

geometrically to the general model scale n, the bed forms and
the sediment transport over them will be modelled exactly.
In many cases such a model is not practical because the model
sediment would need to be too fine. The model must therefore
be designed with n_D < n and from Eq. 21, n_{γ_s} > 1. Then, if
it can be assumed that the effective roughness is mainly
dependent on the bed form roughness, similarity of the shear
stress will occur as long as similarity of the bed forms is
obtained. This similarity will occur when the bed form
length and height ratios are approximately independent of X_2
and directly proportional to X_4. Then it is not necessary
for either n_{X_2} = 1, or n_{X_4} = 1. In Figs. 1 and 2, for the
sections of the curves which are at a slope of 1:1,

$$\frac{\Lambda}{D} \propto \frac{A}{D}, \text{ and } \frac{\Delta}{D} \propto \frac{A}{D} \tag{26}$$

Therefore, $$n_\Lambda = n_\Delta = n_A = n \tag{27}$$

Equation 27 is satisfied approximately in the range defined
by,

$$6.5 < \frac{\rho U_\delta^2}{\gamma_s D} < 40. \tag{28}$$

For the Shields parameter in Eq. 28 less than 6.5, there
is no sediment movement. When it is greater than 40, the bed
forms have lengths and heights which are not directly propor-
tional to the fluid orbit length A, and are dependent on the

sediment grain size. Here, a distortion of the grain size
will usually cause a distortion of the bed form length and
height, so that,

$$n_D \neq n, \quad n_\Lambda \neq n \text{ and } n_\Delta \neq n.$$

From Eq. 17,

$$n_{X_2} = \frac{n_\rho n_D}{n_{\gamma_s} n_T^2} = \frac{n_D}{n_{\gamma_s} n}, \tag{29}$$

and

$$n_{X_4} = \frac{n_A}{n_D} = \frac{n}{n_D}. \tag{30}$$

And for similarity of sediment movement Eq. 4 must be
satisfied, i.e.

$$n_{V_*}^2 = n_{\gamma_s} n_D, \tag{4}$$

where

$$n_{V_*} = n^{1/2} N_k^{1/7} \tag{12}$$

However, until n_{X_2} is determined, the distortion of the bed
roughness N_k cannot be known, so as an initial approximation
N_k is taken as unity, so that,

$$n = n_{\gamma_s} n_D. \tag{31}$$

To model bed forms and the sediment movement occurring
over them, the model should be designed as follows. A value

of γ_s is chosen for the model sediment material, which gives n_{γ_s}. From Eq. 31, the sediment size scale is obtained, i.e.,

$$n_D = \frac{n}{n_{\gamma_s}}.$$

From Eq. 29, n_{X_2} is obtained and thus X_2 for the model. Equation 30 gives n_{X_4} and X_4 may be determined for the model. The distortion of the bed form length may be obtained by first determining the constant m_1 from Fig. 1.

$$m_1 = \frac{(\Lambda/D) \text{ for } X_2, \; X_4 \text{ in prototype}}{(\Lambda/D) \text{ for } X_2, \; X_4 \text{ in model}} = \frac{n_\Lambda}{n_D} \qquad (32)$$

Substituting n_D from Eq. 30 into Eq. 32,

$$m_1 = \frac{n_\Lambda}{n} \cdot n_{X_4},$$

from which,

$$n_\Lambda = \left[\frac{m_1}{n_{X_4}}\right] \cdot n. \qquad (33)$$

Therefore, the distortion of the bed form length is

$$N_\Lambda = \left[\frac{m_1}{n_{X_4}}\right]. \qquad (34)$$

If the slope of the line joining X_2, X_4 for the prototype and the model is exactly 1:1, then,

$$m_1 = n_{x_4} \, ,$$

and there is no distortion, i.e.,

$$n_\Lambda = n.$$

As can be seen in Fig. 1, curves for constant values of the Shields parameter defined in Eq. 28 are approximately at a slope of 1:1. And because the Shields parameter is held constant in the model design, then the distortion of the bed form length will never be very large. However, the curves for constant Shields parameter in Fig. 2 display considerable curvature so that severe distortions of bed form height are possible, particularly if a very low density sediment is used in the model.

If, as a result of the first choice for the model sediment γ_s, the distortion of the bed form length is too large, then an improved design may be obtained by choosing a different sediment density. An exactly similar calculation can be made using Fig. 2 to obtain,

$$m_2 = \frac{n_\Delta}{n_D} , \tag{35}$$

and to determine the distortion of the bed form height,

$$N_\Delta = \left[\frac{m_2}{n_{x_4}} \right] \tag{36}$$

Now knowing the sediment size and bed form size in the model from the initial calculation using Eq. 31, the bottom roughness k and thus N_k should be determined. Then Eq. 4 becomes,

$$n \; N_k^{2/7} = n_{\gamma_s} n_D$$

from which a more accurate calculation of n_D can be made. However, this calculation is dependent on the use of a reliable method for determining bottom roughness. Different methods have been proposed, for example by Yalin (6) and Mogridge (3), but confirmation with experimental data is necessary. Until such data is available it must be assumed that bottom roughness distortion is minimised by reducing the bed form distortion.

Now as an example of the model design method outlined above, assume prototype conditions as a wave period equal to 10 seconds, a wave height of 2 metres in a water depth of 9 metres. Assume the sediment diameter to be 1 mm and a sediment of coal with specific gravity of 1.2. Therefore,

$$n_{\gamma_s} = \frac{1.65}{0.2} = 8.25$$

Substituting n_D from Eq. 31 into Eq. 29,

$$n_{x_2} = \frac{1}{n_{\gamma_s}^2} = 1/68.$$

Therefore,

$$X_{2_m} = 42.1 \times 10^{-6}.$$

Substituting n_D from Eq. 31 into Eq. 30,

$$n_{X_4} = n_{\gamma_s} = 8.25.$$

Therefore,

$$X_{4_m} = 2910/8.25 = 353.$$

Assuming a general model scale of $n = 50$,

$$n_T = n^{1/2} = 7.16.$$

Therefore, $T_m = 1.4$ seconds, $d_m = 18$ cm, $H_m = 4$ cm. From
Eq. 30,

$$n_D = \frac{n}{n_{X_4}} = \frac{n}{n_{\gamma_s}} = \frac{50}{8.25} = 6.06.$$

Therefore, the sediment diameter in the model D_m, is 0.165 mm.
Now m_1 is obtained from Fig. 1.

$$m_1 = \frac{1400}{230} = 6.09.$$

Therefore, the distortion of the bed form length is,

$$N_\Lambda = \left[\frac{m_1}{n_{X_4}}\right] = \frac{6.09}{8.25} = 0.737,$$

i.e. $n_\Lambda = 0.737 \, n$.

If such a distortion is not considered satisfactory,
then the calculation should be repeated for a different model
sediment density. A similar procedure should also be followed
to design the model according to the bed form height criterion.

The design procedure has been carried out for a single
water depth. If the depth varies, as is normally the case in
a mobile bed wave model, then although n_{x_2} and n_{x_4} remain
constant, m_1 and m_2 vary. Therefore, the distortion can
vary with the water depth. This difficulty does not occur
however, if, $m_1 = m_2 = n_{x_4}$.

CONCLUSIONS

In movable bed wave models, bed forms should be produced
to scale to ensure similarity of wave attenuation and sediment
transport rates. To model bed forms it is recommended that
the sediment used should be the same density as in the proto-
type and its size should be scaled geometrically. On a
smooth bottom resulting from using a fine sediment, it may
be necessary to initiate the generation of bed forms by an
artificial roughness, after which the bed forms will spread
rapidly. If, by scaling geometrically, the sediment size
becomes too fine to be practical, an alternative scaling
procedure can be used. The method which has been described
uses a low density sediment, larger in diameter than that
resulting from scaling geometrically. When the Shields

parameter is held constant in model and prototype, distortion
of the bed form length will usually be small, but a large
distortion of the bed form height is possible if care is not
exercised in the model design.

ACKNOWLEDGEMENTS

REFERENCES

1.   Inman, D.L. and Tunstall, E.B., "Phase Dependent Rough-
     ness Control of Sand Movement", Proc. 13th Conf. on
     Coastal Eng., Vancouver, 1972, pp.1155-1171.

2.   Kamphuis, J.W., "Short Wave Models with Fixed Bed
     Boundary Layer", Proc. ASCE, Vol. 99, No. WW4, Nov.
     1973, pp.471-483.

3.   Mogridge, G.R., "Wave Generated Bed Forms", Ph.D.
     Thesis, Dept. of Civil Eng., Queen's University at
     Kingston, 1972.

4.   Mogridge, G.R. and Kamphuis, J.W., "Experiments on Bed
     Form Generation by Wave Action", Proc. 13th Conf. on
     Coastal Eng., Vancouver, 1972, pp.1123-1142.

5.   Yalin, M.S., "The Theory of Hydraulic Models",
     MacMillan, 1971.

6.   Yalin, M.S., "On the Average Velocity of Flow over a
     Movable Bed", La Houille Blanche, No. 1, 1964, pp.45-51.

CHAPTER 63

DELAY DISTANCE IN SUSPENDED SEDIMENT TRANSPORT

by

Masataro HATTORI

Professor, Department of Civil Engineering
Chuo University, Tokyo

Abstract

In the previous paper (Hattori, 1969), a theory for the distribution of suspended sediment concentration due to standing waves was obtained on the basis of the concept of "delay distance" which accounted for the fluid-particle interaction and the inertia effect of sediment particles.

The purpose of this paper is to make clear the physical dependence of delay distance to wave and sediment characteristics.

The evaluation of delay distance from experimental results of distribution profiles of suspended sediment concentration is made by the assumption that the horizontal diffusion coefficient of suspended sediment is nearly equal to the vertical one. An empirical expression of delay distance is obtained as follows;

$$|\delta_x|/\widehat{\xi} = 1.35(w_0/\widehat{u})^{3/2}.$$

The following theoretical expression for delay distance is obtained from the equation of motion for a discrete particle suspended in one-dimensional unsteady fluid flow.

$$\frac{|\delta_x|}{\widehat{\xi}} = A\left(\frac{w_0}{\widehat{u}}\right)^{3/2}\left(\frac{h}{w_0 T}\right)^{1/2}.$$

INTRODUCTION

It has been noticed from experimental evidences that the horizontal distribution of suspended sediment concentration due to standing waves became a periodic pattern. As seen in Fig. 1, an example of experimental results obtained by the writer, the sediment concentration at a level from the bottom attaines a maximum value at the antinode and a minimum one at the node of standing waves. ")

The vertical distribution of suspended sediment concentration represents a linear relationship with respect to the height from the

1086

bottom on semi-logarithmic scale.

Although the vertical distribution profile of sediment concentration suspended by wave actions has been investigated by many researchers(1), only few investigations have been made on the horizontal distribution profile.

As well known, the linear wave theory gives no convective transport of suspended sediment, because of the orbits of fluid particles caused by wave motions are closed.   The diffusive transport by the turbulence induced by wave motions is of the gradient type and has a tendency to uniformalize the concentration of suspended sediment in the horizontal direction.   Thus, the formation of periodic distribution profile of suspended sediment concentration can not be explained either by the convective transport or by the diffusive transport.

The writer(2) previously presented a theory by the analytical model based on the concept of a "delay distance" in order to give a physical explanation in the formation of periodic distribution profile of sus-pended sediment concentration.   The delay distance introduced in the theory accounts for the fluid-particle interaction and the inertia effect of sediment particles.

In the previous theory, the velocity difference between the sediment and the fluid particles was assumed to be equal to the production of the delay distance and the local gradient of fluid particle velocity. Kennedy and Locher(3) also presented a theory for suspended sediment concentration due to progressive waves.   In their theory, they intro-duced the concept of a "delay time", which based on the same idea as the writer's.

The theory by the writer was substantiated by comparisons with experiments performed in a two-dimensional wave flume, 30 m long, 0.80 m wide, and 0.70 m deep.   However, the physical properties of delay dis-tance, such as the dependence of wave characteristics, has not fully examined.

The purpose of this paper is to clarify the relation between the delay distance and wave characterictics together with sediment properties on the basis of experimental results and the theoretical consideration.

                    OUTLINE OF THE PREVIOUS THEORY

As mentioned in the introduction of this paper, the concept of delay distance was introduced into the theory for the horizontal and vertical distribution of suspended sediment concentration.   The relative motion between the sediment and the fluid particles gives rise to the delay distance in suspended sediment transport.   The assumption was made that the sediment particle moves at the same velocity as that of the fluid some distance behind it.

Assume that the delay distance and the diffusion coefficient of

suspended sediment are independent of the space and time variables. The conservation equation for suspended sediment concentration in a two-dimensional case can be written as

$$\frac{\partial C}{\partial t} = -\frac{\partial}{\partial x}\left[C\left(u + \delta_x\left|\frac{\partial u}{\partial x}\right|\right)\right] - \frac{\partial}{\partial z}\left[C\left(w + \delta_z\left|\frac{\partial w}{\partial z}\right|\right)\right] + \epsilon_{sx}\frac{\partial^2 C}{\partial x^2} + \epsilon_{sz}\frac{\partial^2 C}{\partial z^2} + w_0\frac{\partial C}{\partial z} , \tag{1}$$

in which C is the concentration of suspended sediment, w_0 is the settling velocity of sediment particles, δ is the delay distance, ϵ_s is the diffusion coefficient of suspended sediment, u and w are the horizontal and vertical velocities of fluid particles, x and z are the horizontal and vertical coordinates, and t is the time. Subscripts x and z represent the values in the x- and z- directions respectively. The coordinate system and notations are shown in Fig. 2.

The three following assumptions were used to obtain the analytical solution of Eq. (1); 1. The horizontal distribution profile for suspended sediment concentration is given by the same relation as obtained from the one-dimensional equation for sediment concentration by neglecting terms with respect to the vertical motion in Eq. (1). 2. The vertical distribution profile at various sections is geometrically similar. 3. The fluid motion due to standing waves is given by the long wave theory. Then, the horizontal and vertical velocity components of fluid particles are expressed as

$$u = H\sqrt{\frac{g}{h}}\cos kx \sin \omega t , \tag{2}$$

and

$$w = H\omega\frac{z}{h}\sin kx \sin \omega t , \tag{3}$$

in which H is the amplitude of standing waves, h is the water depth, k is the wave number, ω is the angular frequency, and g is the gravitational acceleration.

With the preceding assumptions stated, the time averaged concentration of suspended sediment due to standing waves was obtained as

$$\overline{C}(x,z) = \overline{C}(0,a)\exp\left[\alpha(1 - \cos kx) - \frac{\beta}{h}(z - a)\right], \tag{4}$$

in which

$$\alpha = \widehat{u}|\delta_x|/\epsilon_{sx} , \tag{5}$$

$$\beta = w_0 h/\epsilon_{sz} , \tag{6}$$

and a is the reference level with respect to the vertical distribution of suspended sediment concentration. The bar represents the time averaged value over one wave period. The mean horizontal velocity of fluid particles averaged over the horizontal distance between the nodal and antinodal sections of standing waves is obtained from Eq. (2) as

$$U = \frac{4}{L}\int_0^{L/4} u \, dx = \frac{2HL}{\pi h T}\sin \omega t . \tag{7}$$

In Eq. (5), $\hat{u}$ denotes the amplitude of mean horizontal velocity of fluid particles and is written by Eq. (7) as follows;

$$\hat{u} = 2HL/\pi hT \, , \tag{8}$$

where T is the wave period and L is the wave length.

EVALUATION OF THE DELAY DISTANCE FROM EXPERIMENTAL RESULTS

Since the delay distance can not directly be measued in model experiments, the evaluation of delay distance has to be made with experimental results of suspended sediment concentration profiles.

According to the theory, the distribution profile of the time averaged concentration of suspended sediment in the horizontal direction is determined by the parameter α which is given in terms of the delay distance, the diffusion coefficient and the wave characteristics. As seen in Eq. (5), the diffusion coefficient of suspended sediment in the horizontal direction is also an unknown quantity to be determined from experimental results.

Figures 3 through 5 illustrate comparisons with the theory and the experiments for the horizontal and vertical distributions of suspended sediment concentration.   In those figures, α and β are assumed so as to best fit to the experimental values.

It is noticed from Figs. 4 and 5 that there is a high concentration layer near the bottom.   Since suspended sediment in this layer behaves as if it were a viscous fluid, the theory can not apply to the motion of suspended sediment near the bottom.

As seen in Figs. 4 and 5, the vertical distribution of suspended sediment concentration in the upper region, $z/h > 0.2$, is expressed by a linear relationship on semi-logarithmic scale.   This fact means that the vertical diffusion coefficient, ε_{sz}, is constant with respect to the height from the bottom.   Therefore, the diffusion coefficients for each test run are calculated from Eq. (6) with aids of experimental results of the vertical distribution of sediment concentration at the nodal section ($x=0$).

It needs to estimate the horizontal diffusion coefficient in advance of the evaluation of delay distance.   The wave motion is unsteady and has the two velocity components both in the horizontal and vertical directions.

As a first approximation, the evaluation of delay distance is made by the assumption that the horizontal diffusion coefficient is almost equal to the vertical one.   Under this assumption the delay distance is computed from Eq. (5) by putting $\varepsilon_{sx} \doteqdot \varepsilon_{sz}$.

Two quantities related to the standing wave motion are defined to obtain a non-dimensional expression for the delay distance.   The

amplitude of mean horizontal velocity of fluid particles, $\widehat{u}$ given by Eq. (8), is used as a velocity scale.   As a length scale we define the following quantity being propotional to the amplitude of the mean horizontal displacement of fluid particles due to standing waves.

$$\widehat{\xi} = H/(h/L) . \tag{9}$$

Figure 6 illustrates the relation between $|\delta_x|$ and $\widehat{u}$.   Although the evaluated values of delay distance are rather scattered, it may be considered that the delay distance of suspended sediment has a decreasing tendency with the increase in the mean horizontal velocity of fluid particles.

The ratio of the delay distance to the mean horizontal displacement of fluid particles, $|\delta_x|/\widehat{\xi}$, is plotted in Fig. 7 as a function of $w_0/\widehat{u}$ which represents the inertia effect of suspended sediment particles. Within the limit of this study, the relation between $|\delta_x|/\widehat{\xi}$ and $w_0/\widehat{u}$ is shown by the full line in Fig. 7, from which the following expression is obtained.

$$|\delta_x|/\widehat{\xi} = 1.35(w_0/\widehat{u})^{3/2} . \tag{10}$$

THEORETICAL CONSIDERATION ON THE DELAY DISTANCE

Let us consider a discrete sediment particle suspended in one-dimensional unsteady flows.   The equation of motion for the particle is obtained by the equilibrium condition between the inertia and the drag forces of the particle and is written as follows;

$$\frac{du_s}{dt} = \frac{3}{4} \frac{KC_{D_1}w_f}{d\ w_s} |u_f - u_s|(u_f - u_s) , \tag{11}$$

in which u_f and u_s are the velocities of the fluid and the sediment particles, d is the diameter of sediment particle, w_f and w_s are the specific weights of the fluid and sediment, C_{D_1} is the drag coefficient, and K is a propotional constant.

The terminal settling velocity of the sediment particle, w_0 , is given by Eq. (12).

$$w_0^2 = \frac{4}{3} \frac{gd}{C_{D_2}} \frac{w_s}{w_f} . \tag{12}$$

In Eq. (12), C_{D_2} is the drag coefficient.   From Eqs. (11) and (12), we obtain Eq. (13) under the assumption of $C_{D_1} \fallingdotseq C_{D_2} \approx C_D$.

$$\frac{du_s}{dt} = \frac{Kg}{w_0^2} |u_f - u_s|(u_f - u_s) . \tag{13}$$

By the definition of delay distance, the velocity difference between the fluid and the sediment particles can be written as

$$u_f - u_s = |\delta_x| \frac{\partial u_f}{\partial x} \,. \tag{14}$$

Substituting Eq. (14) into Eq. (13), we obtain Eq. (15).

$$\frac{du_s}{dt} = K \delta_x^2 \frac{g}{w_0^2} \left| \frac{\partial u_f}{\partial x} \right| \frac{\partial u_f}{\partial x} \,. \tag{15}$$

It may be supposed from the experimental results that the rate of velocity change of sediment particles is almost equal to that of fluid particles. By putting $du_s/dt \approx du_f/dt$, Eq. (15) is rewritten by Eq. (16).

$$\frac{du_f}{dt} = K \delta_x^2 \frac{g}{w_0^2} \left| \frac{\partial u_f}{\partial x} \right| \frac{\partial u_f}{\partial x} \,. \tag{16}$$

In the previous theory, we assumed that the delay distance is constant with respect to the space and time variables. Therefore, with use of the relations, $u_f \approx \widehat{u}$, $x \approx L$, and $t \approx T$, Eq. (16) is replaced by Eq. (17).

$$\frac{\widehat{u}}{T} = A' \delta_x^2 \frac{g}{w_0^2} \left(\frac{\widehat{u}}{L} \right)^2 \,. \tag{17}$$

In Eq. (17) A' is a constant. From Eqs. (8) and (9), the relation of $\widehat{u}$ to $\widehat{\xi}$ is given as

$$\widehat{u} = 2\widehat{\xi}/\pi T \,. \tag{18}$$

Substituting Eq. (18) into Eq. (17), the relative delay distance of suspended sediment is expressed in the form

$$\frac{|\delta_x|}{\widehat{\xi}} = A \left(\frac{w_0}{\widehat{u}} \right)^{3/2} \left(\frac{h}{w_0 T} \right)^{1/2}, \tag{19}$$

where A is a constant.

The theoretical expression for delay distance by Eq. (19) confirms the experimental evidence that the relative delay distance is propotional to $(w_0/\widehat{u})^{3/2}$. However, the experimental results on Fig. 7 do not indicate the dependence of the term $(h/w_0 T)^{1/2}$ in Eq. (19) to the relative delay distance. It may be considered that the difference between the theoretical and the empirical expressions results from the assumptions used in the evaluation of delay distance.

CONCLUSIONS

The dependence of delay distance to wave and sediment characteristics was discussed on the basis of experimental results and theoretical con-

sideration.

The evaluation of delay distance from experimental results of distribution of suspended sediment concentration was made by the assumption that the horizontal diffusion coefficient of suspended sediment is almost equal to the vertical one.　　The relation between $|\delta_x|/\hat{\xi}$ and $w_0/\hat{u}$ was shown in Fig. 7, and was obtained as follows;

$$|\delta_x|/\hat{\xi} = 1.35(w_0/\hat{u})^{3/2}.$$

On the other hand, the following expression for delay distance was obtained theoretically from the equation of motion for a discrete particle suspended in one-dimensional unsteady flow.

$$\frac{|\delta_x|}{\hat{\xi}} = A\left(\frac{w_0}{\hat{u}}\right)^{3/2}\left(\frac{h}{w_0 T}\right)^{1/2}.$$

It was considered that the difference between the theoretical and empirical expressions resulted from the assumptions underlying the evaluation of delay distance.　　Further detailed investigations are desirable to make more accurate evaluation of delay distance.

REFERENCES

1) Das, M.M.: Suspended sediment and longshore sediment transport data review, Proc. of 13th Conference on Coastal Engineering, Chapter 54, 1972, pp. 1027-1048.
2) Hattori, M.: The mechanics of suspended sediment due to standing waves, Coastal Engineering in Japan, Vol. 12, 1969, pp. 69-81.
3) Kennedy, J.F. and F.A. Locher: Sediment suspension by water waves, Waves on Beaches and Resulting Sediment Transport, Academic Press, 1972, pp.249-295.
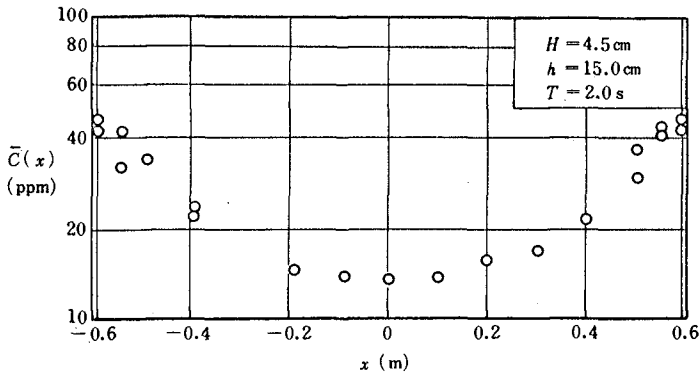
Fig. 1　Example of experimental result of the horizontal distribution profile of suspended sediment concentration.
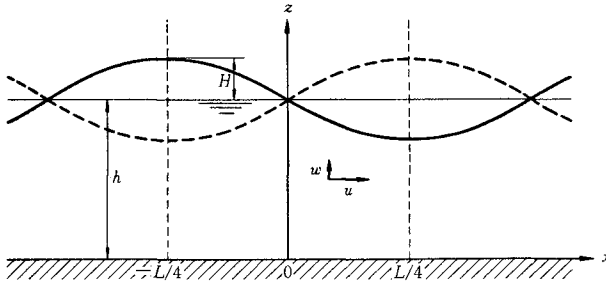
Fig. 2   Definition sketch.
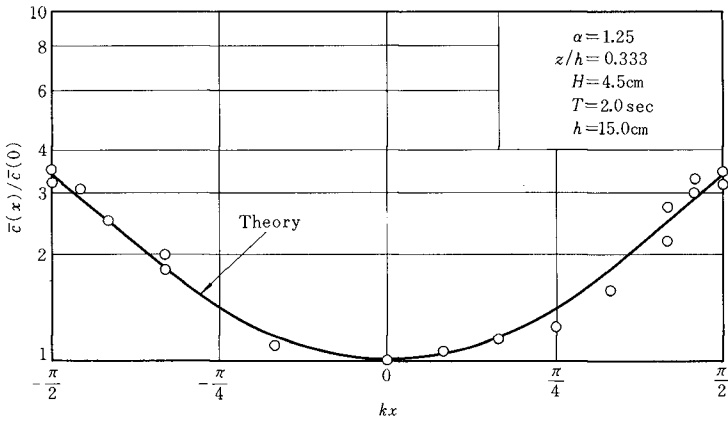
Fig. 3   The horizontal distribution of suspended sediment
          concentration.
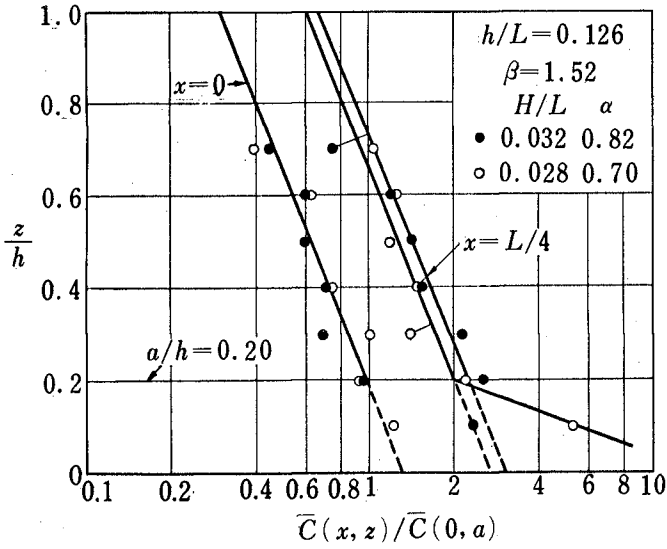
Fig. 4　The vertical distribution of suspended sediment concentration.
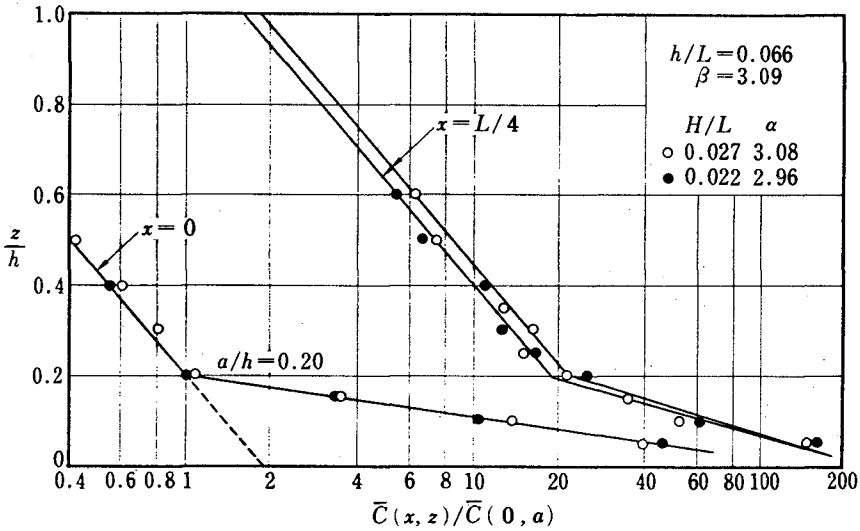
Fig. 5　The vertical distribution of suspended sediment concentration.
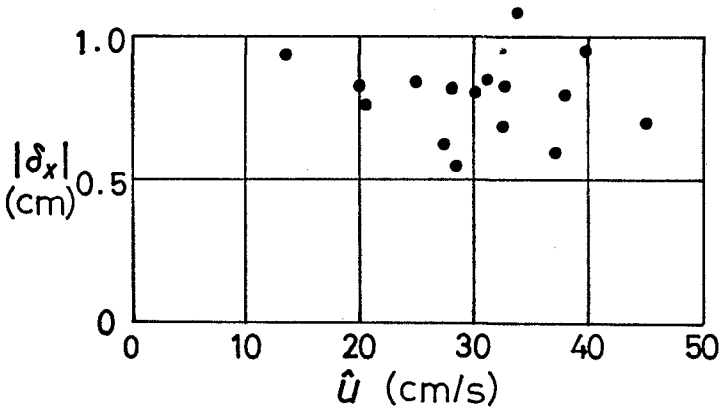
Fig. 6   Relation between the delay distance and the mean
          horizontal velocity of fluid particles.
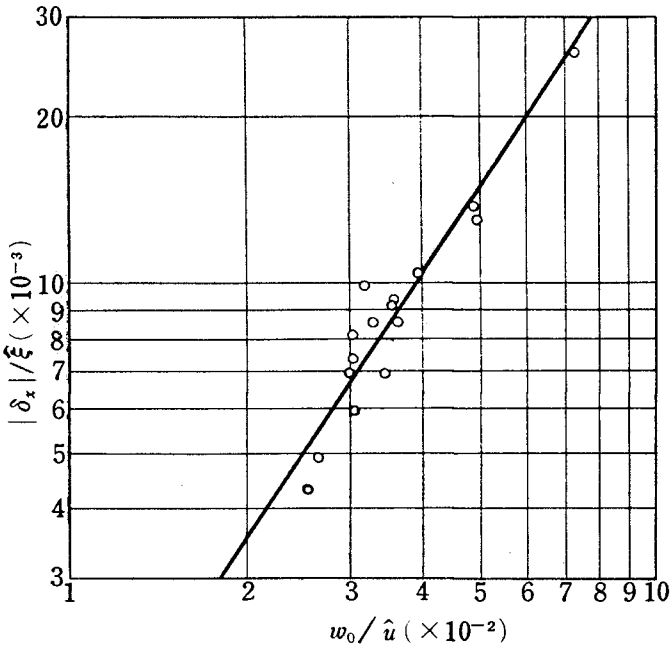
Fig. 7   Relation between $|\delta_x|/\hat{\xi}$ and $w_0/\hat{u}$.

CHAPTER 64

FIELD INVESTIGATIONS OF SUSPENDED SEDIMENT

by

Tadeusz BASIŃSKI

Sen. Res. Scientist, Institute of
Hydroengineering, Polish Academy
of Sciences, Gdańsk

Andrzej LEWANDOWSKI

Res. Engineer, Institute of Hydroengineering,
Polish Academy of Sciences, Gdańsk

ABSTRACT

A radiometric probe and sand traps have been applied
to measure a distribution of the suspended sediment in a
vertical profile.
The first stage of investigations, comprising the laboratory
tests and first experiments in the Baltic Sea, were carried
out in 1973.
As results of the above experiments calibration curve for
radiometric probe has been obtained and some weak points of
the method have been overcome.
Six sand traps of bamboo type were situated in different
distance from a shoreline and by turns perpendicular or pa-
rallel to the shoreline. It enables the determination of
percentage distribution of suspended sand in vertical profile
and along a bottom profile during a wave cycle.

1. Introduction

The paper presents the results of field investigations
concerning the vertical distribution of suspended sediment
in the surf zone. The investigations were carried out in 1973
in Coastal Research Station at Lubiatowo in Poland.
The shore profile there has a mean slope about 1:95 with three
bars and average grain diameter D_{50} =0,15 mm.
Two methods have been applied during investigations – the
radiometric method with the use of radiometric probe and the
method with the use of sand traps.

The experiments concerning the radiometric method are to be carried out in two stages.
The purposes of first stage were as follows:

- to come to know the measurement technique

- to determine the weak points of the probe

- to determine the magnitude of expected errors.

The experiments concerning the first stage have been completed.
In the second stage we intend

- to determine the vertical distribution of suspended sediment concentration

- to determine the thickness of sand layer which moves close to the bottom

- to determine the changes of bottom compactness caused by wave action.

All above experiments are to be carried out in early autumn 1974 together with the simultaneous measurements of the wave height, wave amplitude, wave period, angle of incidence and position of breaking line and measurements of bottom profile perpendicular to the shoreline.

2. Radiometric method

2.1. Principle of measurement.

Concentration of suspended sediments in water may be determined by absorption of gamma radiation. Intensity of gamma radiation passing through the absorber of the thickness l is described by the well know formula:

$$I = I_o \, e^{-\bar{\mu}l} = I_o \, e^{-\rho\mu l} \qquad\qquad /1/$$

where: I_o – incident radiation intensity,

I – intensity of radiation passed by the absorber,

$\bar{\mu}$ – linear absorption coefficient,

μ – mass absorption coefficient,

ρ – absorber density,

l   – absorber thickness

The above formula describes the absorption of the narrow beam of monoenergetic gamma radiation. Both the source and the detector should be collimated but if discrimination level of the detector is choosen for registrating the photons of primary energy only, the beam collimation is unnecessary, and the same results as for collimated beam would be obtained.

Mass absorption coefficient μ does not depend on the absorber density, it depends only on its chemical composition. If the chemical composition of absorber does not change and absorber thickness is constant, then the formula /1/ may be expressed as follows:

$$I = I_o e^{-C\rho} \qquad\qquad /2/$$

where: $C = \mu l.$

Solving equation /2/ for density one obtains:

$$\rho = \frac{1}{C} \ln \frac{I_o}{I} \qquad\qquad /2a/$$

Density of the mixture of water and sand depends on the concentration of sand. Knowing the mixture density one can calculate the concentration of the sand in the mixture.

2.2. Probe construction.

The probe have been designed and carried out by the Institute of Physics and Nuclear Techniques in Krakow, Poland, according to our requirements. The probe consists of radioactive source which is Co^{60} with activity 5 mCi and a counter with the scintillation crystal, photomultiplier and electronic part where there is input amplifier, discriminator and output amplifier.
Impulses occurs at the discriminator output only when the amplitude of input impulse is higher than the choosen discrimination level.
The probe is supplied with high voltage and low voltage but the impulses are transmitted by the individual cables.
Probe dimensions are as follows: length - 880 mm, diameter - - 36 mm, weight - 15 kG.
The impulses from the probe are transmitted to the laboratory building and counted by the scaler.
The radioactive source and the counter are placed inside two vertical aluminium tubes of 40 mm in internal diameter and 50 cm in external diameter [fig.1].
The tubes are attached to the platform construction that way to ensure constant distance of 46 mm between them [fig.2].
The tubes are driven into the sea bottom and are filled up by sea water though they are closed at the bottom.
The source and counter may be lifted up or lowered down by the help of electric lift directed from the laboratory. The movement is simultaneous and the line connecting the sensitive area of the counter and source is always horizontal. The velocity of the movement is 2.2 cm/s in both directions and the probe position is always known owing to two selsyn motors and counters.

2.3. Probe calibration

     The readings of radiometric probe doesn't depend only
upon the suspended sand concentration but also on:
     - natural gamma radiation
     - variable chemical composition of sea water
     - variable chemical composition of sediment.

The influence of the above factors should be taken into con-
sideration but some of them may be neglected.
     For instance in Lubiatowo region changes of chemical
composition of sea water and sediment are slight. According to
carried out investigations the changes of water density caused
by temperature have almost no influence on probe readings [1] .
The probe calibration may be carried out in laboratory in
tanks where instead of suspended sediment there is a chemical
solution of known density or when there is controlled volume
of suspended sediment.
It is also possible to perfom calibration in the field by
simultaneous measurements of sand concentration and sampling.
     The calibration of our probe was made in the tank full
of water where the distance between source and counter was
the same as for field measurement [fig.3] .
The perspex sheets were placed between tubes in order to in-
troduce sand into the space between the sheets.
By changing the distance   L it was possible to obtain diffe-
rent thickness of sand layer which was to simulate the sedi-
ment concentration.
As a result of such procedure a calibration curve has been
obtained [fig.4] . In order to check the extreme points of
the curve which is a straight line in semilogarithmic system
the measurements of the saturated sand density and sea water
density have been performed at Lubiatowo.
The results of those measurements coincieded with the calibra-
tion curve.
Right now we have also results of measurements taken in trans-
lucent water during calm sea which may be treated as a basis
for relative measurements.
Using the same tank as for calibration purposes the tests
concerning the resolution power of the probe have been also
carried out.
The vertical resolution for water-sand contact is about 3.5 cm
and for water-air coutact about 3.0 cm [fig.5] .

2.4. Experiments in the Baltic Sea.

During the first experiments which were performed in the sea
in 1973, we met some difficulties. At first the difference of
4 mm between tube diameter and probe diameter was to small
causing the probe wedging.

Moreover the electrochemical corrosion of internal surface
of aluminium tubes caused a deposit which also diminished
the tube diameter.
Under the waves action the platform together with the attached
tubes was strained what brought about the leakages at the
tubes joints. The small perticles of sand got into the tube
and setteled down making the probe movement difficult.
Then fouling occurred at the tubes surface.
All those difficulties have been overcome but it had taken
much time and doesn't allow to obtain results as quick as it
was planned.

3.   Sand traps method.

    The second method which have been applied to investigate
the vertical distribution of suspended sediment consisted in
using sand traps.
Such sand traps have been already used in Japan [2]   and
because they were made of bamboo and had articulated joint at
the bottom, they were subjected to oscillatory currents and
were unable to assume vertical position.
The hydraulic model investigations of those sand traps have
been also carried out in Japan and some empirical formulae
have been determined.
    The applied sand trap was designed and made according
to the bamboo samplers.
It has a length of 3 to 4 m and consists of elements made of
perspex tube with internal diameter 40 mm and external dia-
meter 50 mm. Every element has a length of 20 cm and two
openings with the dimensions 1 cm x 5 cm   [fig.6] .
In 1973 several experiments were carried out with the use of
such sand traps. The purpose of experiments in Lubiatowo was
the determination of percentage distribution of suspended
sand in vertical profile and along a bottom profile during a
wave cycle. The wave cycle is deemed as whole wave field
during a passage of an atmospheric pressure system.
The experiment No.1 have been performed during the period of
5 days. The wind velocity was up to 14 m per sec and the
maximum wave height measured at the depth of 3.4 m was 1 m
[fig.7] .
The openings of all six sand traps were situated by turns
perpindicular or parallel to the shoreline.
The experiments results were as follows.
The sediment movement in suspended form begins between the
second and third bar.
At the third bar the suspended sediment appears only near
the bottom in the layer of several centimetres.
Between second and third bar the volume of suspended sediment
transported in perpendicular or parallel direction is the
same and 60 percent of total volume is transported in the
layer of 40 cm from the bottom.
The total suspended sediment transport rate between first
bar and second one is much higher than between second and
third bar and longshore direction of sediment prevails.

In the vicinity of first bar suspended sediment transport is
most intense and takes place in whole cross-section.
        The experiment No.4 have been carried out during the
period of 7 days, but the waves were much higher than during
the experiment No.1 [fig.8] . The investigations with the
use of sand traps have also been performed in Libya to deter-
mine a vertical distribution of suspended sediment at site of
designed sea water intake [fig.9] .
On the basis of carried out experiments it may be concluded
that sand traps present a cheap and quick way to determine
a distribution of the suspended sand transported in a vertical
profile and through the profile perpendicular to a shoreline.

References

1. Florkowski T., Cameron I.F. - A simple radioisotope X-ray
   transmission gauge for measuring suspended sediment con-
   centrations in rivers. Radioisotope instruments in industry
   and geophysics, IAAE, Vienna, 1966.

2. Fukushima H., Kashiwamura M. - Some experiments on bamboo
   samplers. Coastal Engineering in Japon, vol.1, 1958.
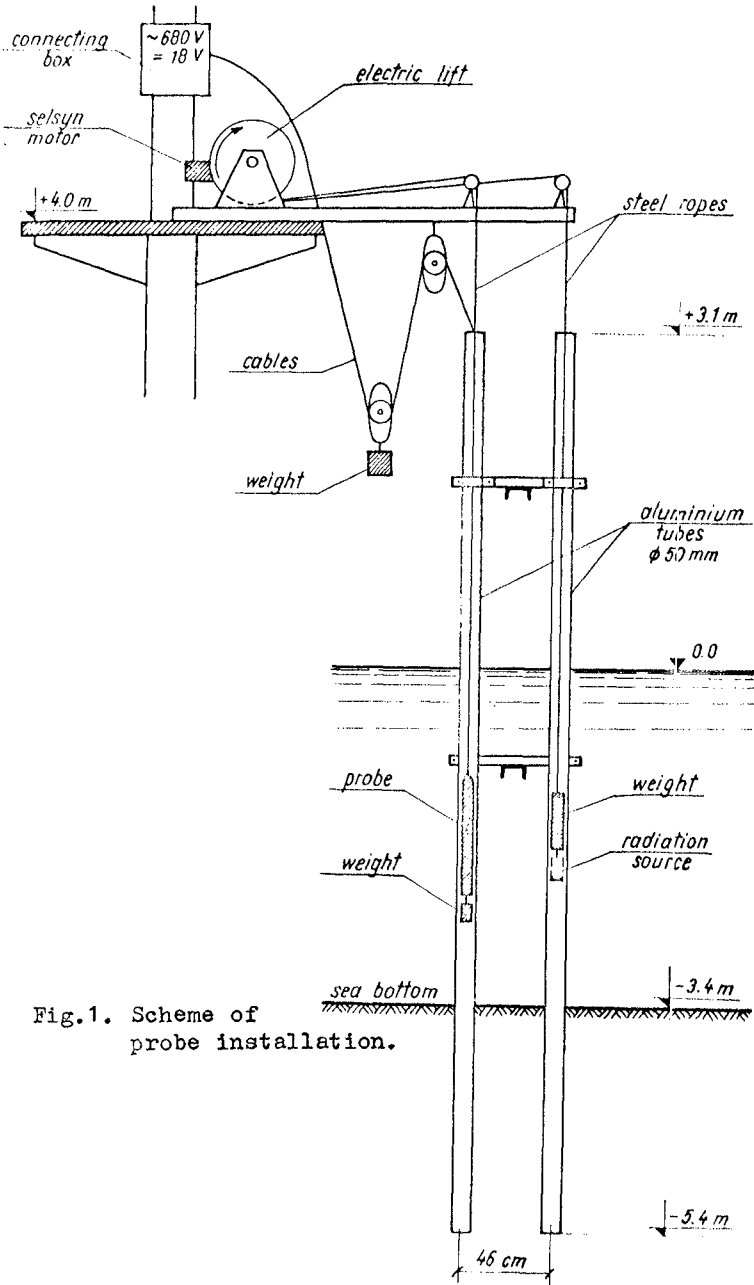
Fig.1. Scheme of
        probe installation.

Fig.2. Measuring island with probe installation.
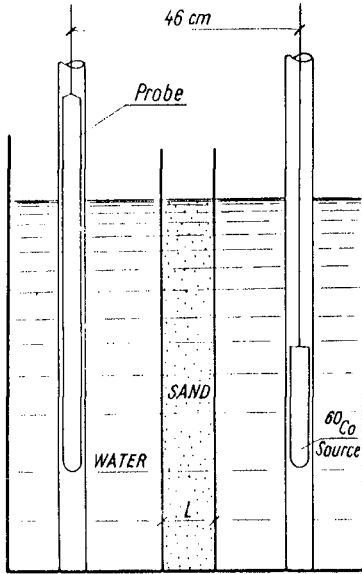
Fig.3. Tank for probe calibration.
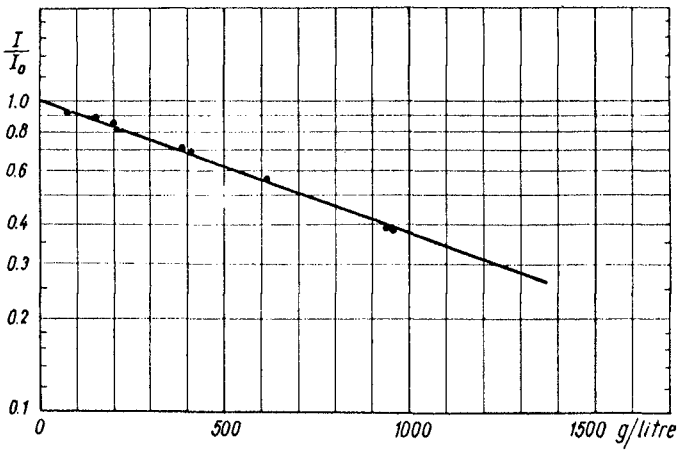
Fig.4. Calibration curve.
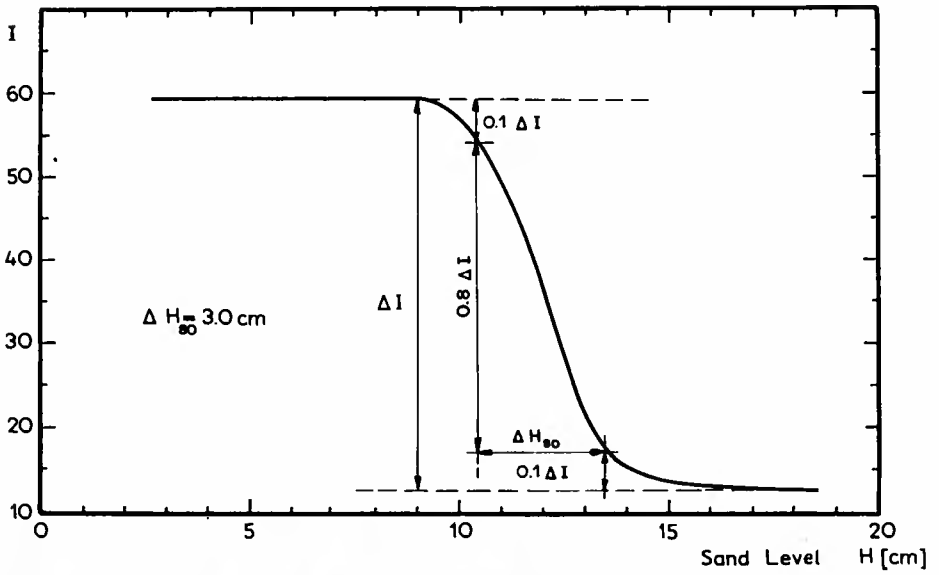
Fig.5. Resolution for water-sand contact.
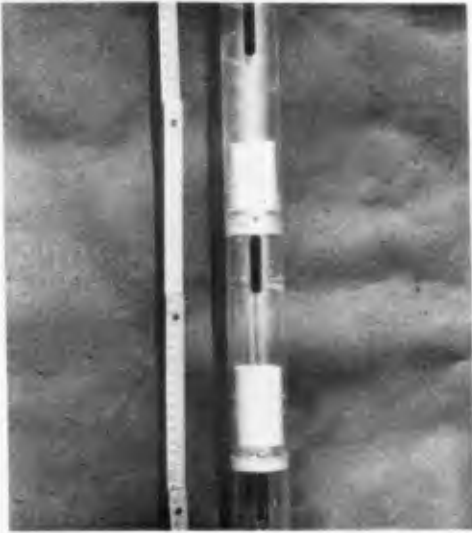
Fig.6. Sand trap.

Fig.7. Results of experiment No.1.
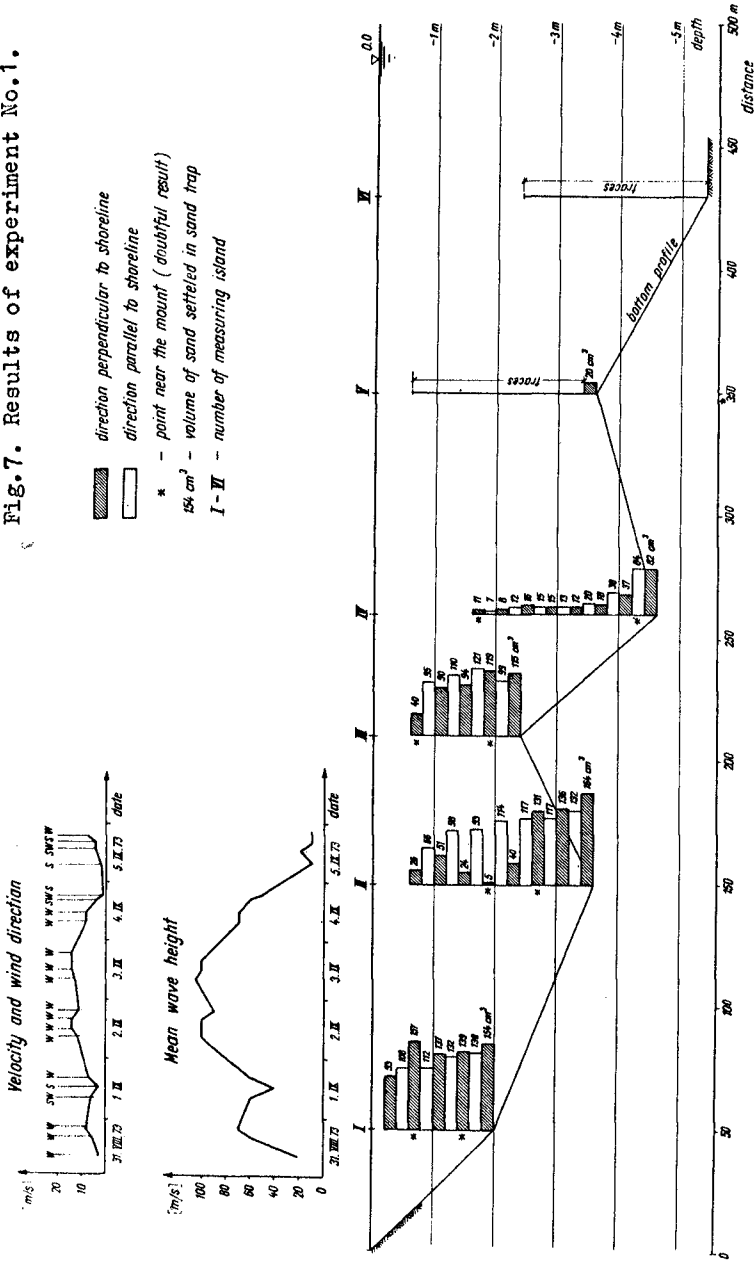
Fig. 8: Results of experiment No. 4.
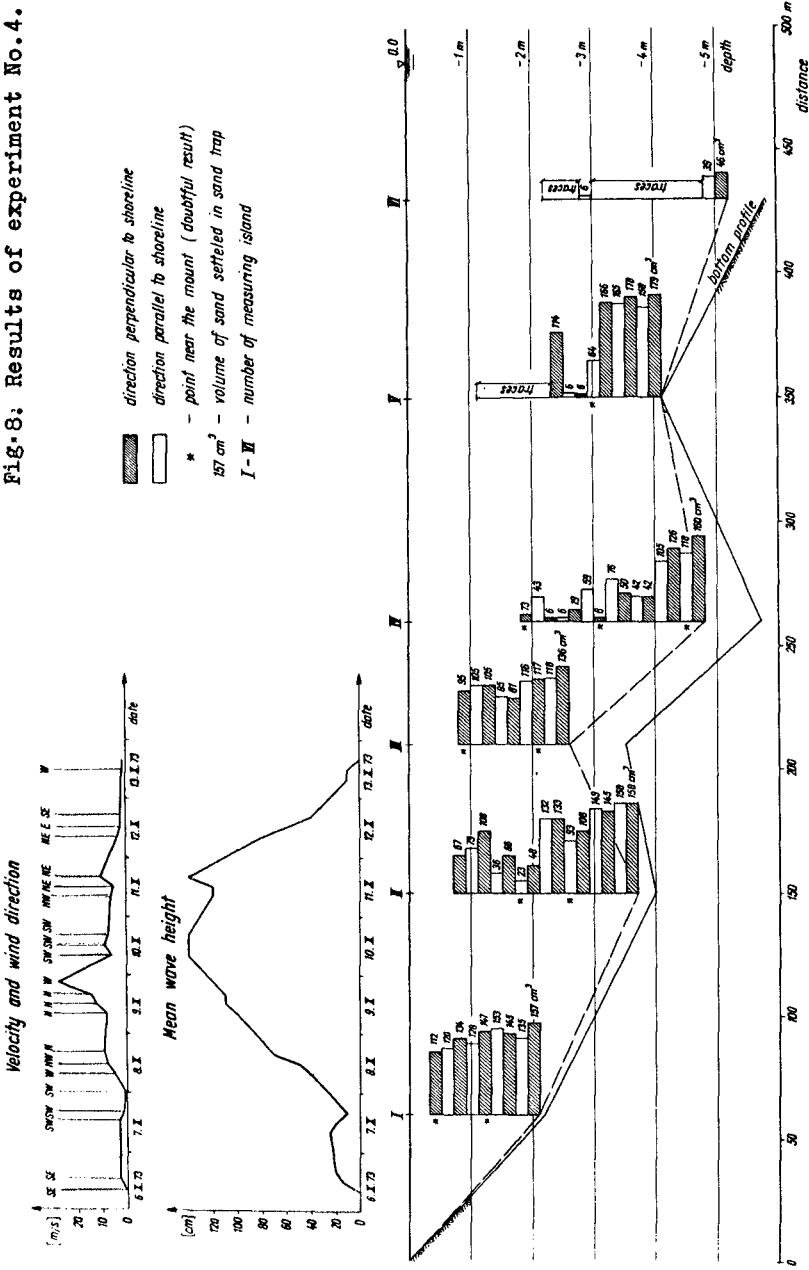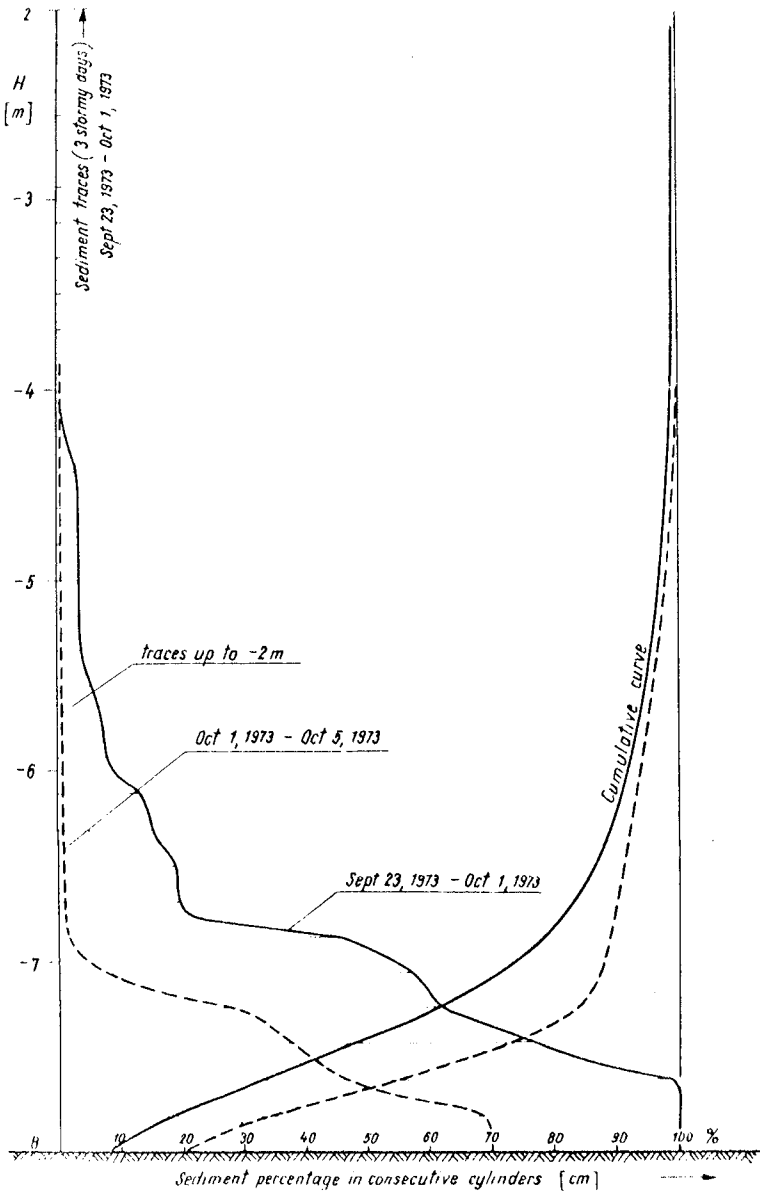
Fig. 9. Results of experiment in Libya.

CHAPTER 65

NUMERICAL MODELLING OF SUSPENDED SEDIMENT

by

BRIAN A. O'CONNOR* AND SAMIR ZEIN[+]

ABSTRACT

The present paper describes the application of a two-dimensional numerical suspended sediment model to problems having analytical solutions, as well as to laboratory and field situations.

The model is based upon an implicit finite-difference solution to a two-dimensional (longitudinal and vertical) diffusion-advection equation for suspended sediment transport. Horizontal eddy diffusion is neglected in comparison with vertical diffusion and vertical water motion is assumed negligible in comparison with the sediment fall velocity.

The various applications indicate that the greatest errors in the model are due to large spatial concentration gradients and that errors can be controlled by a suitable choice of space and time step. In addition, it is considered that the model has great flexibility and seems to have an acceptable level of accuracy, at least in the field situations tested, provided the physical parameters of the model can also be determined accurately.

INTRODUCTION

The production of larger and larger ships has resulted in the development of new ports and harbours as well as in the re-development of existing ones. The deep draughts of modern vessels requires the provision and maintenance of safe, deep, port approach channels. Dredging and/or training works may be necessary in some situations and can so interfere with the free movement of sediment on the sea bed as to produce a chain reaction of events culminating in the appearance of dangerous shoals in unwanted positions.

The consequence of engineering works can be studied with the help of in-situ field observations and/or small scale hydraulic model tests. However, the advent of the high speed computer has led, in recent years, to the development of mathematical models i.e. the analytical or numerical solution of equations which directly or indirectly describe the physical processes at work in a particular situation. The size and complexity of present-day engineering problems often requires that a digital or analogue computer is used to solve the equations.

The present paper describes a simple mathematical model which endeavours to describe the settling and dispersal of suspended sediment in two-dimensional flow situations. The authors are concerned, in particular with the accuracy and usefulness

---

* Senior Lecturer in Civil Engineering: Simon Engineering Laboratories, University of Manchester, Manchester, U.K.

+ Postgraduate student in Civil Engineering: University of Salford, Salford, U.K.

of the model in describing real engineering situations. Attention has been confined
to quasi-steady flow situations and thus the effects of vertical flows and accelerations
are not included in the model.

THE MODEL

The mathematical model is based upon an implicit finite-difference solution
to the two-dimensional sediment diffusion-advection equation:

$$\frac{\partial C}{\partial t} = \frac{\partial}{\partial y} \left(\varepsilon_y \frac{\partial C}{\partial y} + w_f C \right) - \frac{u \partial C}{\partial x} \quad \dots \quad \dots \quad \dots \quad \dots \quad (1)$$

where C is the sediment concentration.

x, y are horizontal and vertical co-ordinates respectively
w_f is the sediment fall velocity in still water

ε_y is a vertical sediment diffusion coefficient
u is the horizontal sediment velocity and is taken equal to the velocity
of the surrounding fluid

Horizontal eddy diffusion is neglected in comparison with vertical diffusion,
and vertical flows are assumed negligible in comparison with w_f.

The formulation of the model has been described elsewhere [1,2,3] and
consequently only a brief outline is considered here. The three-dimensional space-
time plane (x,y,t) is divided into blocks of size $\Delta x/2$, Δy, $\Delta t/2$ as indicated in
Fig. 1. The differential terms in eq. 1 are then written in difference form
either at the centre of each vertical block (e.g. $i\Delta x$, $(j+\frac{1}{2})\Delta y$, $(n+\frac{1}{2})\Delta t$) or at
mesh points ($i\Delta x$, $j\Delta y$, $(n+\frac{1}{2})\Delta t$). For example, the following difference forms may
be used at mesh points.

$$\frac{\partial C}{\partial t} = 2(C_{i,j}^{n+\frac{1}{2}} - C_{i,j}^n) / \Delta t + 0(\Delta t) \quad \dots \quad \dots \quad \dots \quad \dots \quad \dots \quad \dots \quad \dots \quad (2a)$$

$$w_f \frac{\partial C}{\partial y} = (C_{i,j+1}^{n+\frac{1}{2}} - C_{i,j-1}^{n+\frac{1}{2}}) / 2\Delta y + 0(\Delta y^2) \quad \dots \quad \dots \quad \dots \quad \dots \quad \dots \quad \dots \quad (2b)$$

$$\varepsilon_y \frac{\partial^2 C}{\partial y^2} = \varepsilon_{i,j}^{n+\frac{1}{2}}(C_{i,j+1}^{n+\frac{1}{2}} - 2C_{i,j}^{n+\frac{1}{2}} + C_{i,j-1}^{n+\frac{1}{2}}) / \Delta y^2 + 0(\Delta y^2) \quad \dots \quad \dots \quad \dots \quad \dots \quad (2c)$$

$$u \frac{\partial C}{\partial x} = 2u_{i,j}^{n+\frac{1}{2}} (C_{i,j}^n - C_{i-\frac{1}{2},j}^n) / \Delta x + 0(\Delta x) \quad \dots \quad \dots \quad \dots \quad \dots \quad \dots \quad \dots \quad (2d)$$

where indicies $(n+\frac{1}{2})$, i, j indicate values of the parameters at time $(n+\frac{1}{2})\Delta t$,
and position $i\Delta x$, $j\Delta y$. $0(\ )$ indicates that the difference equations contain small
order terms which result from a Taylor Series expansion of C about the point being
considered in the space-time plane. The small order terms are assumed to be negligibly
small.

More accurate difference equations can be used by including some of the higher
order terms. For example,

$$\frac{\partial C}{\partial y} = (C_{i,j-2}^{n+\frac{1}{2}} - 8C_{i,j-1}^{n+\frac{1}{2}} + 8C_{i,j+1}^{n+\frac{1}{2}} - C_{i,j+2}^{n+\frac{1}{2}}) / 12\Delta y + 0(\Delta y^4) \quad \dots \quad \dots \quad \dots \quad \dots \quad (3a)$$

$$\frac{\partial^2 C}{\partial y^2} = (-C_{i,j+2}^{n+\frac{1}{2}} + 16C_{i,j+1}^{n+\frac{1}{2}} - 30C_{i,j}^{n+\frac{1}{2}} + 16C_{i,j-1}^{n+\frac{1}{2}} - C_{i,j-2}^{n+\frac{1}{2}}) / 12\Delta y^2 + 0(\Delta y^4) \quad \dots \quad \dots \quad (3b)$$

2

These are particularly useful for the vertical direction where large concentration gradients may exist.

Repeated application of eq. 1 and 2 or 3 to points between the sea bed and surface produces a set of linear simultaneous equations relating the concentration at time $(n +\frac{1}{2})\Delta t$ to those occuring at time $n\Delta t$. The use of known boundary conditions at the sea bed and surface and at upstream and downstream boundaries enables any unknown concentrations outside the boundaries to be eliminated. Once initial $(n\Delta t)$ concentrations are specified the simultaneous equations can be solved by matrix methods in order to find the unknown concentrations over the vertical at position $i\Delta x$ and time $(n +\frac{1}{2})\Delta t$. This solution process may be repeated at $(i +\frac{1}{2})\Delta x$, $(i +1)\Delta x$ etc. until the downstream boundary is reached. The time step is then advanced $(\Delta t/2)$ and the process repeated.

The replacement of differential terms by difference equations is an approximation and introduces errors into the model. Other errors are introduced by computer round-off and in the present scheme by writing the convective transport term $(u\partial C/\partial x)$ at time level $(n\Delta t)$ instead of at $(n + \frac{1}{2})\Delta t$. The magnitude of the total error present in the model can be established only if analytical solutions to a problem are known. Unfortunately this is impossible and the best that can be done is to test the model against simplified analytical solutions or the results of controlled laboratory tests. This is the approach adopted by the present authors. The model is then applied to existing field data on a variety of problems in order to examine the usefulness of the model in real situations.

NUMERICAL TESTS

One-dimensional situations

Initially the one-dimensional form of eq. 1 was used for numerical tests. This eliminates errors due to the convective transport term and enables comparisons to be made with known analytical solutions (Dobbins[4], O'Connor[15]). The model was operated with various space and time steps and for various values of the model parameters (Zein[2]). A particular sediment problem was considered in which sediment was assumed to be suddenly eroded from the sediment bed at a constant rate. The flow depth and vertical diffusion coefficient were kept constant w.r.t. space and time and the initial concentration was taken equal to zero. In addition, various difference schemes were examined (e.g. Crank Nicolson, Stone and Brian, Fully Implicit). The results may be summarised as follows:

(1) The computational scheme was stable and there were no exponential growths of errors. This is to be expected for implicit schemes. It is suggested that the best results are obtained for the particular problem studied above if $\alpha = (w_f\Delta y/ \varepsilon_y) << 1$

(2) Losses or grains of mass were acceptable for reasonable space and time steps.

(3) Numerical diffusion (dissipation error) was present in one-sided schemes (e.g. Fully Implicit) but the effect was probably negligible for reasonable space and time steps. This generally means dividing the depth into perhaps forty intervals, with the model time step determined from the equation

$$\Delta t = \Delta y/(2 \gamma w_f) \qquad \text{...} \quad \text{...} \quad \text{...} \quad \text{...} \quad (4)$$

with $\gamma \geqslant 1$.

(4) The largest errors in the model were dispersion errors and arose from the nature of the bed boundary condition. This required the model to distribute a block of sediment over the flow depth at each time interval and consequently errors are propagated from the area of large concentration gradient at the bed boundary. Errors from this source could be reduced by the use of appropriate space and time intervals and are negligible as the numerical solution approaches the one-dimensional steady state solution i.e. the analytical solution to eq. 1 with $(\partial C/\partial t = u\partial C/\partial x = 0)$.

(5) Difficulty is experienced in modelling the near-bed zone when $\varepsilon_y \rightarrow 0$ since $\partial C/\partial y \rightarrow \infty$. The problem can be overcome by introducing a "false bed" boundary condition or reducing the near-bed zone. (O'Connor[1], Cardona[3]).

Two-dimensional situations

The effect of errors from the longitudinal transport term are less easy to check since two-dimensional analytical solutions only exist for very simple problems. However, a series of model tests was carried out for a particular sediment problem for which an analytical solution existed (Mei[5]). The problem was one of describing the steady state (eq. 1 with $\partial C/\partial t = 0$) sediment distribution for the case of steady uniform flow down a two-dimensional channel in which one section of the bed was non-erodable (Fig. 2). The flow depth, velocity of flow and vertical diffusion coefficient were all kept constant over space and time. The sediment concentration at the bed boundary was maintained at a constant value of unity at all times. The computer solution was operated from an initial concentration of zero until a steady state solution was reached. The results for various flow and sediment parameters were considered to be good (see for example Fig. 3). Maximum errors were confined to surface levels and are associated with small absolute concentration values as well as areas with steep concentration gradients. For reasonable space and time steps errors were generally less than 10% and improved accuracy could always be obtained by a suitable reduction in space and/or time step.

A further series of numerical tests was performed with the computer model in order to check on longitudinal sediment dispersal. If eq. 1 is averaged over the flow depth, a one-dimensional diffusion-advection equation can be produced which incorporates an effective longitudinal dispersion coefficient. The magnitude of the dispersion coefficient can be calculated from a knowledge of the sediment and flow parameters (Elder[6], Sümmer[7]). It may also be calculated by operating the two-dimensional model for long enough to achieve an effective one-dimensional situation. The rate of change of the standard deviation (σ_x) of the depth averaged longitudinal distribution curves is then proportional to the effective longitudinal dispersion coefficient ($D_x = \partial \sigma_x^2/2\partial t$).

Model results are shown in Fig. 4 for a particular sediment suspension exponent ($Z = w_f/(\beta Ku_*)$; β is the ratio of the vertical sediment diffusion coefficient to the vertical momentum transfer coefficient; K is Von Karman's Constant; u_* is the shear velocity equal to $\sqrt{\tau_b/\rho}$; τ_b is the applied bed shear stress; ρ is the fluid density) and for two particular velocity profiles with flow depth. The dispersion of sediment is seen to be greater than that for fluid particles alone and agrees reasonably well with theory. It should be noted, however, that the theories assumed a totally reflecting bed boundary condition while the computer solutions were operated for an absorbing bed boundary condition (Zein[2]).

The numerical tests indicated above suggest that the numerical accuracy of the model is reasonable at large diffusion times for the particular problems studied. They provide no means of testing the usefulness of the model at small diffusion

times. Consequently, laboratory tests were used for this purpose.

LABORATORY TESTS

Because the computer model is applicable to two-dimensional flows, it was decided to build a special flume with flexible walls which could be moved at different flow speeds. The reduction of wall shear stress and the partial suppression of secondary motions means that a narrow flume behaves effectively as a much wider one. It was also constructed much more cheaply than a wide glass or perspex channel. The outer part of the flume was constructed of marine plywood so that an externally braced channel some 50 ft. long and 21" wide was formed. The moving walls were made of butyl rubber and were supported by a system of vertical rollers spaced at intervals of 4ft. along the flume. A 5/16" diameter rubber cord was fixed to the top of the belt to prevent it riding down the rollers. Both belts were driven simultaneously through a bevel gear and belt drive system from a variable speed electric motor located at the downstream end of the flume. A false floor was also fitted between the rollers, and roughness elements, consisting of 3/16" high, $\frac{1}{4}$" wide wooden batterns, were fixed to it at 2" centres. Thin vertical brass strips (3/8" wide) were also fixed to the sides of the false floor at 4ft. centres to prevent lateral deflection of the walls towards the centre of the flume. Water was supplied from a constant head tank in the laboratory roof and flowed into the channel through a vaned entry section. The water level was controlled by an overflow weir fitted inside an existing rectangular flume; the water being guided towards the weir by fixed vertical walls (Fig. 5).

Considerable experimental work was undertaken so as to improve entry conditions to the flume as well as to produce the best configuration of bed roughness and speed of movement of the walls. Only the downstream half of the flume was used for the sediment tests and lateral flow uniformity was achieved over some 70% of the flume width with the walls moving at some 70% of the mean flow speed. Longitudinal dispersion due to lateral inhomogeneity was further reduced by injecting sediment over the full width of the flume.

Slug injection tests were performed in the flume with polystyrene particles (s.g. 1.04) with a size range between 250-300 μ and with a measured fall velocity of 7.45 x 10^{-3} ft./sec. Sediment concentrations were measured by a battery of syphons with an estimated accuracy of 5-10 ppm. Water velocity profiles were measured by a miniature (1 cm diameter) current meter and water surface slopes were measured with differential manometer. Sediment concentrations were measured at three elevations and at 20, 26 and 32 seconds after sediment injection for various positions down-stream of the injection point. The experimental results indicated that maximum concentrations changed by 100% between 20 and 32 seconds. Sampling times were, of course, limited by the length of the flume.

The computer model was then operated with measured values for w_f, u and h, and with the measured sediment distribution at 20 seconds as initial values. The vertical diffusion coefficient was kept constant over space and time and was determined from the equation

$$\varepsilon_y = (w_f h)/(6Z) \quad \ldots \quad \ldots \quad \ldots \quad \ldots \quad \ldots \quad \ldots \quad (5)$$

while Z was determined using $\beta = 1$ and K = 0.4. Two values of u_* were used (viz. Table 1) based on estimates of u_* made by considering the gradient of the velocity-depth curve as well as the longitudinal slope of the water surface.

The boundary conditions used in the model were

(1) At the bed : $y = 0$: $t \geqslant 0$

$$\varepsilon_y \frac{\partial C}{\partial y} = 0 \quad \cdots \quad \cdots \quad \cdots \quad \cdots \quad \cdots \quad \cdots \quad \cdots \quad (6)$$

(2) At the surface : $y = h$: $t \geqslant 0$

$$\varepsilon_y \frac{\partial C}{\partial y} = - w_f C \quad \cdots \quad \cdots \quad \cdots \quad \cdots \quad \cdots \quad \cdots \quad \cdots \quad (7)$$

(3) Upstream boundary : $x = 0$: $t \geqslant 0$: $0 \leqslant y \leqslant h$

$$C = 0 \quad \cdots \quad \cdots \quad \cdots \quad \cdots \quad \cdots \quad \cdots \quad \cdots \quad (8)$$

(4) Downstream boundary.

Determined by upstream concentrations, initially set to zero.

The results for a typical set of observations are shown in Fig. 6, while the test parameters are shown in Table 1. Agreement between observations and model is considered to be good. Numerical errors, based on the one-dimensional work are considered to be negligible and may be less than $\frac{1}{2}\%$. Convective transport errors were minimised by using very small Δx steps. Uncertainties in the determination of w_f and u_x were tested by operating the model with these quantities changed by 20%. The effect was found to be small (Fig. 6). The largest source of error is, in fact, considered to be due to the sampling method. The syphon samplers could not determine simultaneous concentrations within the expanding sediment cloud.

TABLE 1. Model parameters used for laboratory tests

w_f ft/sec.$\times 10^3$	h ft.$\times 10$	u_{mean} ft/sec.$\times 10$	u_{wall} ft/sec.$\times 10$	u_x ft/sec.$\times 10^2$		ft^2/sec.$\times 10^3$	Δy ft.$\times 10^2$	Δx ft.$\times 10^2$	Δt secs.
7.45	8.94	9.1	3.71	2.69	4.0	4.8	2.4	4	9.1	3.35	6.1

w_f (measured) : 7.45×10^{-3} ft/sec. ; u_x (slopes) : $3-5 \times 10^{-2}$ ft/sec.; $\gamma = 1$;

The technique adopted was to sample three sections in the leading part of the concentration cloud at a fixed time and then to repeat the test for the centre and trailing part of the cloud keeping one sampling station as a common control. The concentration at a point is thus the average of at least five separate tests. The scatter on experimental results is thus large since nearly instantaneous concentrations are being recorded : the computer produces the turbulent average concentration.

It should also be noted that good results were obtained in the present test with a spatially constant value of ε_y. This is due to the nature of the present problem which eliminates large concentration gradients at the lower boundary (eq.6). If entrainment was allowed from the bed boundary, ε_y would probably have to vary with elevation above the bed.

FIELD RESULTS

Comprehensive field observations are extremely scarce and those available are generally incomplete in one or more details. Unfortunately the authors were not

able, due to limitations of finance, to perform field tests themselves. Three
existing sets of results have, therefore, been used.

1.   Sewage sludge dumping in the Irish Sea (U.K.)(Ref. 8)

     The model was applied to results collected as part of a sewage sludge disposal
study in the Irish Sea (Fig. 7). The vertical distribution of sludge was measured
with photo-electric monitoring probes, at 6, 43 and 53 minutes after the release of
a ship load of sludge containing 10.9% dry solids. The vessel's discharge speed was
about 6 kts. and the initial length of sludge patch was about 1 mile. The width of
the patch was observed to increase over the monitoring period from some 66 - 164 to
246 ft. The weather on the test day (5th May 1970) was good with a calm sea and
light north-westerly winds (force 1-2). The water was some 100 ft. deep and the
release was about mid-ebb tide with surface velocities of 3 ft/sec. Vertical
stratification was small with surface and bed salinities differing by some 0.2% .
Water velocity and salinity/temperature profiles were measured over the flow depth
from an anchored vessel during the course of the experiment. The test area is
subject to semi-diurnal tides with a range on the test day of some 19 ft.

     The model was operated with observed average values of flow depth and water
flow. It was assumed that the sludge settled with an effective fall velocity equal
to the median value which was obtained from laboratory settling tests at the
appropriate field concentration. If the particles did not flocculate, and were
unaffected by turbulence etc., the model could be applied to a series of grain sizes
(or fall velocities). The vertical diffusion coefficient was estimated from eq. 5
with β = 1.0, K = 0.40 and u_* estimated from the water velocity profile. The same
boundary conditions employed in the laboratory tests were used (eq. 6 - 8) while
the concentration distribution at 6 minutes was used as initial values. A good
estimate of initial values can also be obtained from the initial dimensions of the
sludge patch and the solid's content of the sludge cargo.

     Initial calculations with the model soon demonstrated that lateral spreading
was important. Model values computed without lateral spreading were in error by
some 100%. The model was then modified so that at the end of each time step the
sediment concentrations were spread over the estimated plume width which was also a
function of depth. The results are shown in Figs. 8a and 8b and the model parameters
used are shown in Table 2. Agreement between model and field results is considered
good. Numerical errors are difficult to estimate but the one-dimensional work
suggests they will be less than 5%. Convective transport errors are negligible since
the results are for the maximum concentration area in the centre of the sludge patch.
This was confirmed by reducing Δx by a factor of two. Again, the largest difference
between model and observation could well be attributed to observational inaccuracy
since the photo-electric probes have a reading accuracy of some 10-20 ppm.

TABLE 2. Model parameters for the Irish Sea Tests

w_f ft/sec. x 10^3	h ft.	u_* ft/sec. x 10^2	ε_y ft^2/sec. x 10	Δy ft.	Δx ft.	Δt mins.
1.39	100	8.1	5.4	1	360	6

2.   Sediment spoil disposal on the Potomac Estuary (USA)(Van Der Kreeke[9])

     The results from a field and mathematical model investigation into the
longitudinal and vertical distribution of sediment in a dredging plant outfall plume

was used to test the model. The discharged sediment had a mean size of 45   and was discharged at a rate of approximately 10 lb/sec. through a pipe-line on to a shallow plateau in the homogeneous tidal zone (Fig. 9). The discharge point was located near the estuary bed and was some 10 ft. below the water surface. Tides in the Potomac are semi-diurnal with a mean range of 2.1 ft. Field observations indicated that the maximum length of outfall plume was 3 miles and that its width remained constant except possibly at times of slack water.

The computer model was used to determine the vertical and longitudinal sediment distribution throughout a flood or ebb tide. Many of the parameters used in the model were those adopted by Van Der Kreeke who proposed a simple one-dimensional analytical model for the sediment distribution in the plume. He considered the change in vertical sediment concentration within a column of water equal to the flow depth as it drifted downstream with the depth-mean tidal velocity. Sediment entrainment and particle settling were allowed at the bottom of the block. This simple model thus neglects the longitudinal spreading action due to velocity gradients over the flow depth.

The model was operated initially with a constant spatial and temporal diffusion coefficient and with a constant water depth (10 ft.). A further test was conducted with a depth constant diffusion coefficient which varied sinusoidally with time according to the equation.

$$\varepsilon_y = \varepsilon_{y\,min} + (\varepsilon_{y\,max} - \varepsilon_{y\,min}) \sin wt$$

where $w = 2\pi/T$ and T is the tidal period.

The velocity field was synthesized by applying a sinusoidal time variation, similar to eq. 9, to the measured depth distribution of velocity at maximum flow rates.

The model boundary conditions were:

(1) At the surface : $-_{\mid}$eq. 7 was used.
(2) At the bed :

$$\varepsilon_y \frac{\partial C}{\partial y} = - w_f C^{\infty} \qquad \cdots \quad \cdots \quad \cdots \quad \cdots \quad \cdots \quad \cdots \quad (10)$$

where C^{∞} is the steady-state one-dimensional bed concentration.
The value used for C^{∞} was estimated by an examination of field
sediment profiles remote from the outfall plume.

(3) Upstream boundary : eq. 8 was used.
(4) Downstream boundary : one-dimensional conditions were used.
(5) Injection point : This was located five mesh intervals downstream of x = 0
     and the concentration was held constant over the depth at 1250 ppm (Van
     Der Kreeke[9]). However, any space or time varying quantity could have been
     used).

The initial (t = 0) concentration was taken as zero.

The longitudinal mesh spacing (Δx) used in the present model was varied to allow for the very small velocities occuring at the start of the tide. Interpolation errors arising from the convective term were thus kept to a minimum. The mesh spacing was increased five fold once the bed velocities exceeded 0.1 ft/sec.

The model results are shown in Figs. 10 and 11, while the model test parameters are given in Table 3. Comparison with field results and with Van Der Kreeke's model is also shown.

TABLE 3. Model parameters for Potomac Tests

w_f ft/sec. x 10^3	h ft.	u_* ft/sec. x 10^2		ε_y ft/sec. x 10^2		C ppm	Δy ft.	Δx ft.	Δt min.
8.0	10	7.5	15* / 7.5	5	10* / 5	272	272* / 0	1	1.25 / 6.25	1.04

Half tidal period : 6 hours : $\beta = 1.0$: K = 0.40 : $\gamma = 1$:
* indicates max./min. values for sinusoidal variations

The computer results show how the sediment is stretched out along the estuary by the tidal currents as well as the dominating effect of the sediment fall velocity once maximum velocities have been exceeded (after + 3 hours). The effect of allowing a sinusoidal time variation in sediment entrainment (C^∞) and vertical diffusion coefficient is also seen. Much smaller concentrations are achieved towards slack-water since C^∞ is zero at slack water (+ 6 hours). Comparison of Van Der Kreeke's results with the slack water results shows that the neglect of longitudinal dispersion produces higher concentrations in the middle reaches of the sediment field (100 - 1000 ft.) . Both models will show the same final values at the outfall and at distant downstream points. Figs. 10 and 11 show some differences at down-stream points since a slightly different C^∞ value was used in the two models (c.f. 197 and 272 ppm.).

The numerical model has great flexibility and problem parameters can be changed as desired with each space and time interval. For example, sediment settling on to the bed can be re-entrained at will. The simpler analytical models cannot do this and changing problem parameters is a lengthy process. However, the Potomac tests do demonstrate one difficulty of modelling shallow water systems. It is desirable, on accuracy grounds, to use a reasonable number of vertical intervals. This then means that the model time step will be small unless the sediment has an extremely small fall velocity (eq. 4). Small time steps imply, in turn, that small horizontal space steps (Δx) will be required, particularly if flow velocities are relatively small. Consequently a large amount of computer store and run-time may be required to model shallow systems with a high degree of accuracy.

The numerical accuracy of the Potomac results is difficult to establish but seems, from Figs. 10 and 11, to be adequate for engineering purposes since the two-dimensional results are at least as good as the simpler one-dimensional model which was considered adequate by Van Der Kreeke.

3. Sediment intrusion into a tidal lock - Mersey Estuary (U.K.)(O'Dell[10])

Gladstone Lock is situated at the entrance to the Mersey Estuary (U.K.) and connects part of the impounded dock system of Liverpool with the tidal Mersey Estuary (Fig. 7). The impounded water level in the dock system falls slowly over a period of time due to locking operations, gate leakage etc. The level is restored by allowing spring tides to flow freely into the lock and docks once the flood tidal level exceeds the dock water level. The difference in density of the dock and estuary water generates a combined tidal and density exchange flow (Halliwell and O'Dell[11]). The levelling process thus allows sediment to enter the dock system.

Various sediment measurements had been made in the lock as part of a general siltation study (Halliwell and O'Dell[11]). In particular, the variation of sediment concentration with time was measured continuously over a five year period at a

fixed position near the estuary bed at the lock entrance. Also, vertical profiles of sediment concentration and horizontal water velocity were available throughout a level period at a station in the middle of the lock and inside the dock itself (Fig. 7). The model was, therefore, used to predict the longitudinal and vertical distribution of sediment within the lock and, in particular, illustrate the variation in vertical sediment profiles with time at the central position during a levelling period of some 110 minutes.

The model parameters are particularly difficult to define in this complex non-homogeneous flow situation. The sediment is a mixture of flocculated silt/clay and organic matter with a dispersed mean size between $5 - 10\mu$. Its effective size during the levelling process is, however, much higher due to the effects of flocculation, turbulence and differential particle settlements. An effective particle fall velocity was estimated by fitting analytical one-dimensional steady-state sediment profiles to other field observations in the tidal part of the estuary. In addition, field observations of similar sediment settling in the Thames Estuary (U.K.)(Owen[12]) were also used to help in deciding a value for w_f (Zein[2]).

The magnitude of the vertical diffusion coefficient was originally (Zein[2]) determined from eq. 5 but some difficulty was experienced in obtaining a good model fit, particularly in the lower half of the flow profile. Further tests were then made with ε_y determined by the equation:

$$\varepsilon_y = \frac{w_f}{Z} y(1 - y/h) \quad \ldots \quad \ldots \quad \ldots \quad \ldots \quad \ldots \quad \ldots \quad (11)$$

The model then gave good results (Cardona[3]) over the measured part of the flow depth (90%) but predicted near-bed concentrations were considered to be unreasonably high ($> 400,000$ ppm). Finally, eq. 11 was used over the major part of the flow depth with constant values of ε_y for four vertical mesh spacing near the bed and surface.

The suspension exponent (Z) was modified to include the reduction of vertical mixing by vertical density gradients i.e.

$$Z = w_f/(\beta' Ku_*) \quad \ldots \quad \ldots \quad \ldots \quad \ldots \quad \ldots \quad \ldots \quad (12a)$$

$$\beta' = (\beta K')/K \quad \ldots \quad \ldots \quad \ldots \quad \ldots \quad \ldots \quad \ldots \quad (12b)$$

where K' is a reduced Von Karman constant and is probably a function of flow Richardson number (Ri). For example, K' might be given by the equation

$$K' = K(1 + a Ri)^b$$

where the constants a, b depend on whether momentum ($a = 10$; $b = \frac{1}{2}$) or salt ($a = 3.33$; $b = -3/2$) transfer is considered (Bowden and Gilligan[13]). The coefficients appropriate to sediment transfer in non-homogeneous flow may well be equal to those for salt transfer.

The value of β' used in the present tests was 0.61 and is the value found from calculations on vertical sediment profiles in the tidal estuary almost opposite to Gladstone Lock (O'Connor[14]). Also, this value of β' corresponds to a Ri value of 0.114 which is the right order of magnitude for the vertical density stratification in the Mersey Narrows/Gladstone Lock area.

The water depth changed by some 10% over the levelling period and consequently the average value was used in the model. The measured flow field at the central observation point was used for all longitudinal positions. Continuity principles

suggest that errors due to both approximations are probably less than 10%.

u_* is an exceedingly difficult parameter to estimate in this complex flow situation. Estimates of a mean value have been made by matching analytical velocity profiles with field observations (O'Connor[15]). A temporal variation in u_* was obtained initially by considering the temporal change in near bed velocity i.e.

$$u_* = K_1 u_{\eta} \qquad \ldots \quad \ldots \quad \ldots \quad \ldots \quad \ldots \quad (14)$$

where K_1 is a constant with a possible value of $0.5 - 0.6$ and u_{η} is the velocity at level $\eta = y/h$ below the surface: a value of η appropriate to 1m above the bed is usually used.

The model boundary conditions were:

(1) At the surface : equation 7 was used.

(2) At the bed :

$$\varepsilon_y \frac{\partial C}{\partial y} = -M\left[\left(\frac{u_*}{u_{*c}}\right)^2 - 1\right] - w_f \delta_o C$$

where $0 \leq \delta_o \leq 1$ and is dependent upon the value of u_* compared with u_{*c}. For example, $\delta_o = 1$ if $u_* \geq u_{*c}$ and $\delta_o = 0$ if $u_* < u_{*c}$. M is an erosion constant with a possible value of $1.7 - 2.0$ gm/m²/sec based on laboratory tests for silt/clay sediment (Cormault[16]).

(3) Lock entrance ($x = 0$) :

Concentration specified from field observations with an assumed depth variation based on various measurements in the area over a period of years.

(4) Lock exit ($x = 1000$ ft.):

The dock concentration was maintained at the same value as the final channel exit section.

Initial sediment values were obtained by interpolation from the measured field observations at the lock entrance, mid-point and exit.

The model was operated with fixed values of w_f and h and with various values of u_*, u_{*c} and M until a reasonable fit was obtained with the field observations (Fig.13). The values of the final model parameters are shown in Table 4, while the time variation of u_* is shown in Fig. 14. The effect of suppressing sediment re-entrainment (δ_o now equals zero) when $t \geq 90$ mins is also shown in Fig. 13.

TABLE 4. Model parameters for Gladstone Lock Tests

w_f ft/sec. x 10³	h ft.	$u_{*\ max}$ ft/sec. x 10²	u_{*c} ft/sec. x 10²	M gm/m²/sec.	Δy ft. x 10	Δx ft.	Δt mins.
3.67	43	3.62	1.75	1.875	7.2	9.8	1.63
Level period : 110 mins ; $\beta = 1$; $\beta' = 0.61$; $K' = 0.274$; $\gamma = 1$;							

Agreement between field and model results is considered reasonable. An improved fit could be obtained by allowing M to vary spatially, w_ρ to vary with time and by making small adjustments to the magnitude and temporal distribution of u_*. However, the field programme was not extensive enough to allow such refinements to be made. It is also interesting to note that the values of the final parameters are those to be expected from the physical situation. Even u_*, which at first sight seems low, is probably correct since a note with the field observations indicated that a layer of fluid mud existed on the lock bed during the test period.

Various response tests were also tried with the model and the most sensitive parameters were found to be u_* or u_{*_C}. A 20% change in u_{*_C} produced a 14% change in the maximum concentration value at 90% depth. The response for M was about a half of that for u_{*_C}. By contrast, numerical errors, based on the one-dimensional tests, were thought to be less than 2% at the maximum concentration point. Consequently, it is considered that larger errors can arise by an incorrect choice of physical parameter than from schematization errors.

CONCLUSIONS

The simple computer model is applicable to both laboratory and field situations and seems to produce acceptable results provided the physical parameters can be defined to a sufficient level of accuracy.

Numerical errors within the model are produced mainly from large spatial gradients but the errors can be controlled by a suitable choice of space and time interval.

The model is considered to be extremely flexible since model parameters can be readily varied over space and time. However, it is less useful in shallow water situations involving small flow velocities due to possible computer storage and run-time limitations.

REFERENCES

1. B.A. O'CONNOR. A Mathematical Model for Sediment Distribution. Proc., 14th
    Congress IAHR, Vol. 4, France 1971.

2. S. ZEIN. Sediment Diffusion in Open-Channels, M.Sc. Thesis, Manchester
    University 1973.

3. L.R. CARDONA. Numerical Models for Suspended Sediment Distribution. M.Sc.
    Thesis, Manchester University 1974.

4. W.E. DOBBINS. Effect of Turbulence on Sedimentation. Trans. ASCE, Vol. 109,
    1943.

5. C.C. MEI. Non-uniform Diffusion of Suspended Sediment. Proc. ASCE, Hyd. Div.
    Vol. 95, HY1, Jan. 1969.

6. J.W. ELDER. The Dispersion of Marked Fluid in Turbulent Shear Flow. J. Fluid
    Mec. Vol. 5, No. 4, 1959.

7. M. SÜMMER. Turbulent Dispersion of Suspended Matters in a Broad Open-Channel.
    Proc. 14th Congress IAHR, Vol. 1, France 1971.

8. DEPARTMENT OF THE ENVIRONMENT. Out of Sight Out of Mind. Report of a Working
    Party on the Disposal of Sludge in Liverpool Bay. Vol. 2, HMSO, London 1972.

9. J. VAN DER KREEKE. Sediment Pollution in Coastal Waters. Proc. 12th Coastal
    Eng. Conf., Ch. 9, Vol II, Washington D.C. 1970.

10. M. O'DELL. Silt Distributions and Siltation Processes. Ph.D. Thesis, Liverpool
    University, 1969.

11. A.R. HALLIWELL AND M. O'DELL. Density Currents and Turbulent Diffusion in
    Locks. Proc. 12th Coastal Eng. Conf. Ch. 119, Vol. II, Washington, D.C. 1970.

12. M.W. OWEN. The Effect of Turbulence on the Settling Velocities of Silt Flow.
    Proc. 14th Congress of IAHR, Vol. 4, France 1971.

13. K.F. BOWDEN AND R.M. GILLIGAN. Features of Estuarine Circulation as represented
    in the Mersey Estuary. Lim. and Ocean. Vol. 16, No. 3, 1971.

14. B.A. O'CONNOR. Suspended Load Calculations in a Tidal Estuary. Proc. 12th
    Coastal Eng. Conf. Ch. 117, Vol. II, Washington D.C. 1970.

15. B.A. O'CONNOR. Sediment Movement in a Tidal Estuary. Ph.D. Thesis, Liverpool
    University 1969.

16. P. CORMAULT. Determination Experimental due Debin Solide D'erosion de Sediments
    Fins Cohesifs. Proc. 14th Congress of IAHR, Vol. 4, France 1971.
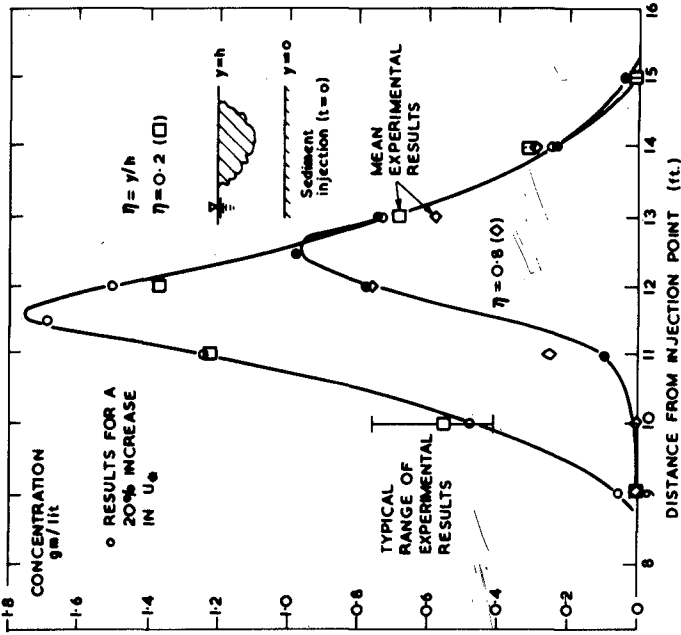
FIG. 6.   CONCENTRATION DISTRIBUTION AFTER 32 SECONDS
           FROM INJECTION
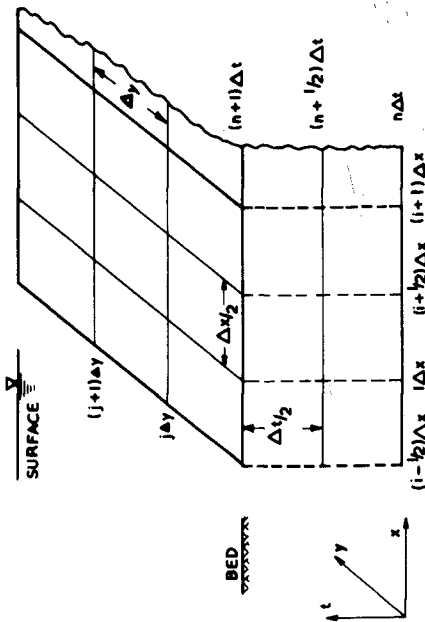
FIG. I.   SPACE-TIME PLANE DISCRETIZATION

DEPTH ($\eta = Y/h$)
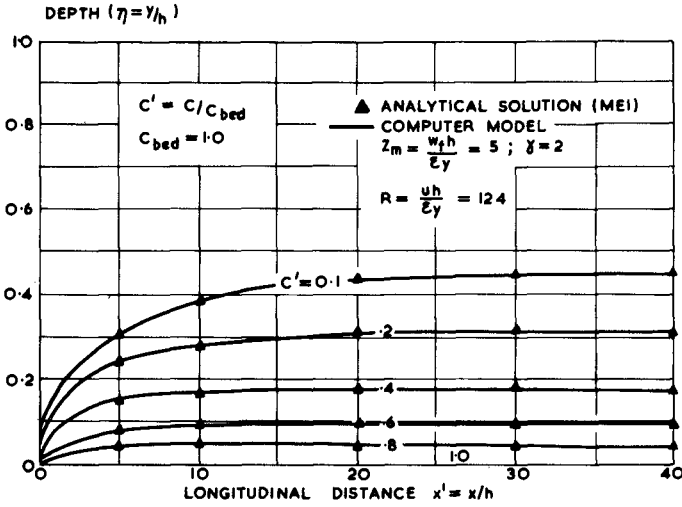
FIG. 3.   DIMENSIONLESS STEADY-STATE SEDIMENT CONCENTRATIONS
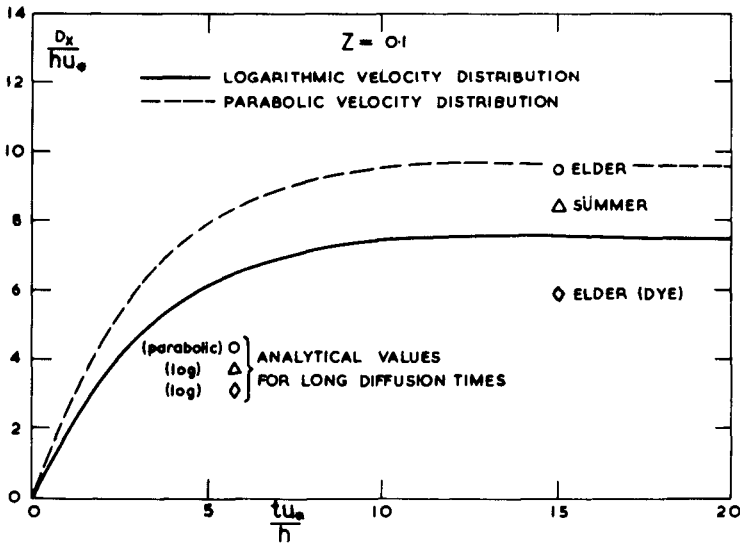
FIG. 4.   COMPARISON OF ANALYTICAL AND NUMERICAL LONGITUDINAL
          DISPERSION COEFFICIENTS

(b)

CROSS-SECTION OF FLUME

WOODEN EXTENSION WALLS

END GATE
2' WIDE x 10" DEEP

DRIVING MOTOR

ROLLERS

WOODEN SUPPORT

WOODEN BRACKET

PULLEY

RUBBER BELT

FALSE BOTTOM

OUTER FRAME

FLOW STRAIGHTENERS

OUTSIDE FRAME

RUBBER BELTS

INLET

HAIR LOCK

SCREEN

8·5'

34"

12·5'

2'

11·5'

21"

50'

12·5"

18"

21"

21"

12"
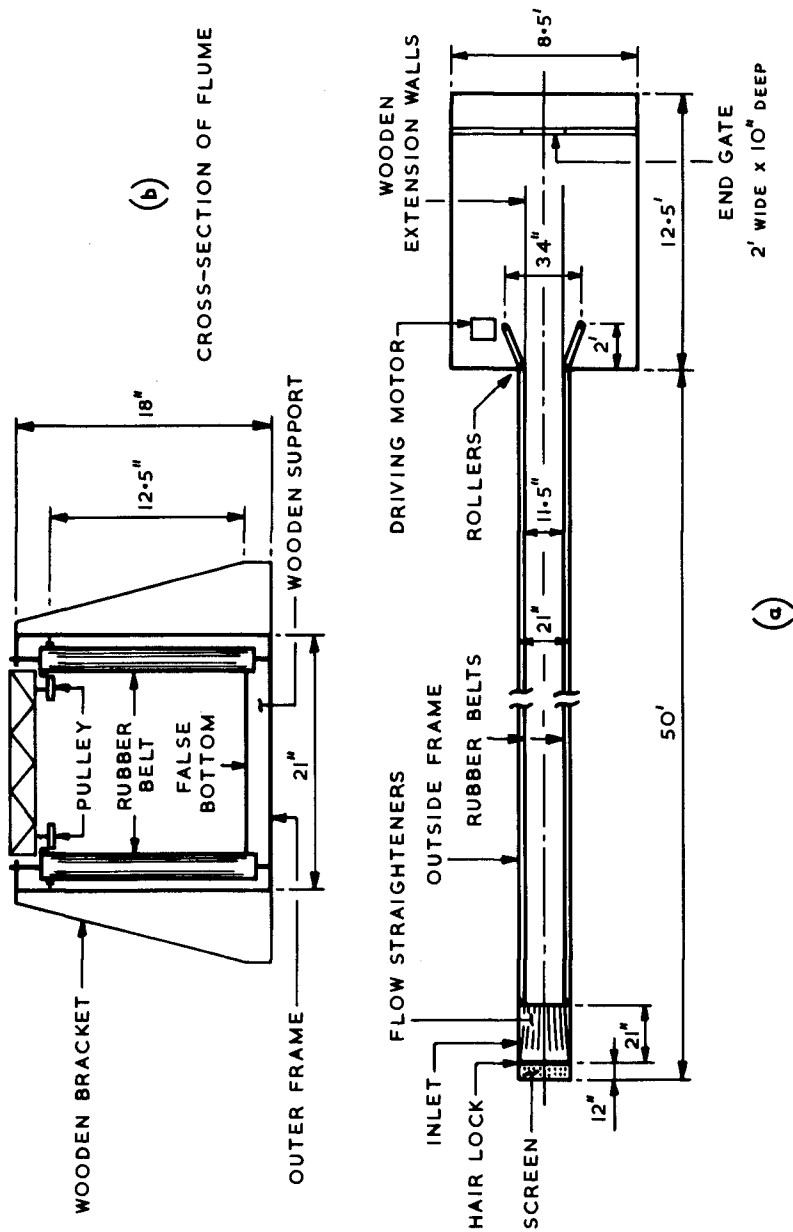
FIG. 5   SCHEMATIC SKETCH OF THE APPARATUS

(a)
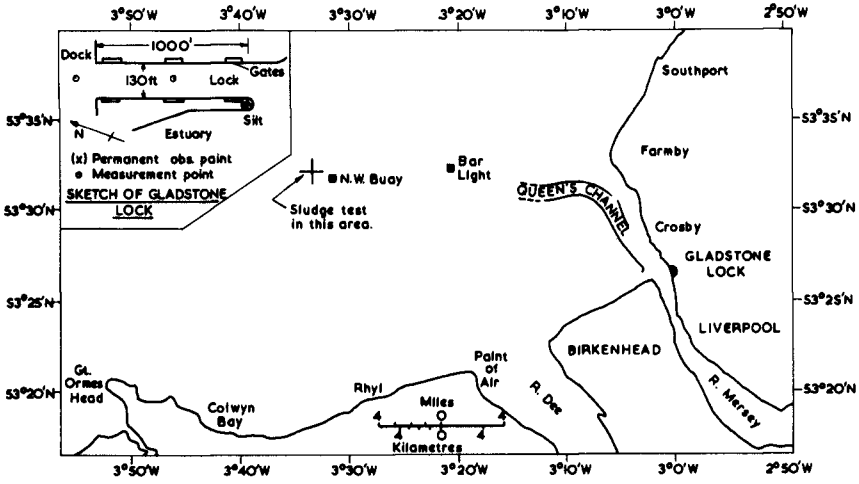
FIG. 7   IRISH SEA AND MERSEY ESTUARY LOCATION PLAN.
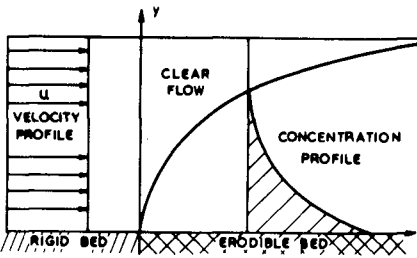
FIG. 2.   TWO-DIMENSIONAL STEADY FLOW CASE
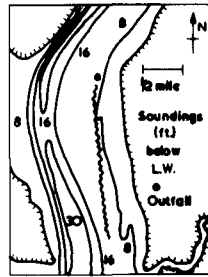
FIG. 9.   POTOMAC ESTUARY
SEDIMENT DISCHARGE POINT.

CONCENTRATION (ppm)

CONCENTRATION (ppm)

TIME AFTER INJECTION: 6 MINS.

TIME AFTER INJECTION: 43 MINS
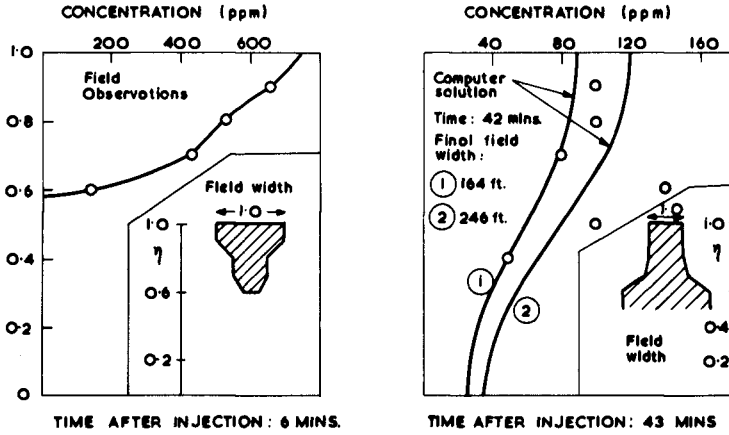
FIG. 8a. COMPARISON OF MODEL AND FIELD RESULTS FOR THE IRISH SEA.

CONCENTRATION (ppm)

VELOCITY (ft/sec)

TIME AFTER INJECTION: 53 mins.

VELOCITY PROFILE
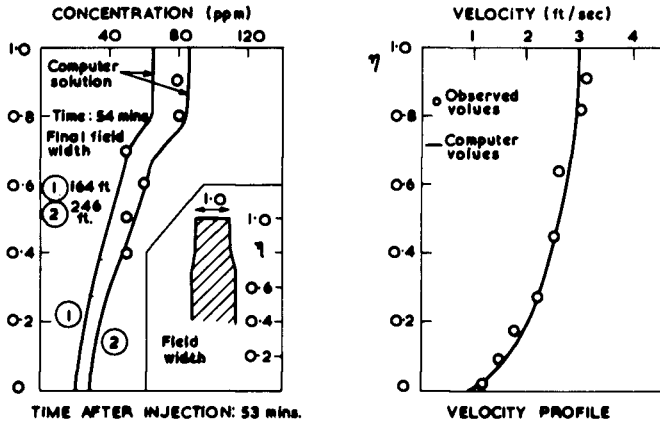
FIG. 8b. MODEL AND FIELD RESULTS FOR THE IRISH SEA TESTS.

CONCENTRATION (ppm)
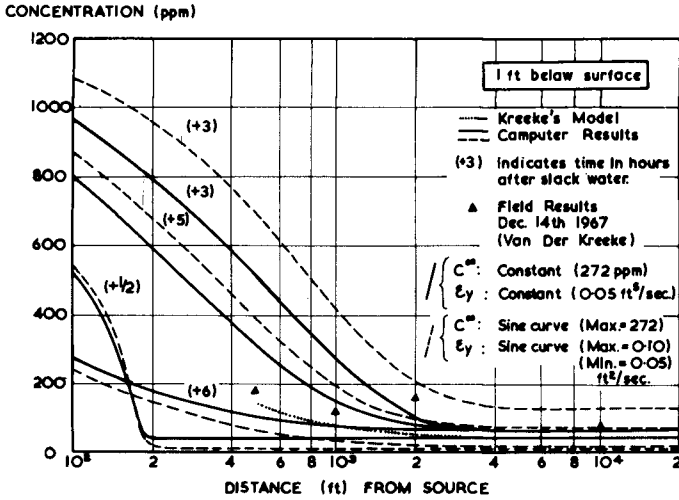
FIG. 10. COMPARISON OF FIELD AND MODEL RESULTS FOR POTOMAC ESTUARY : 1ft. BELOW SURFACE.
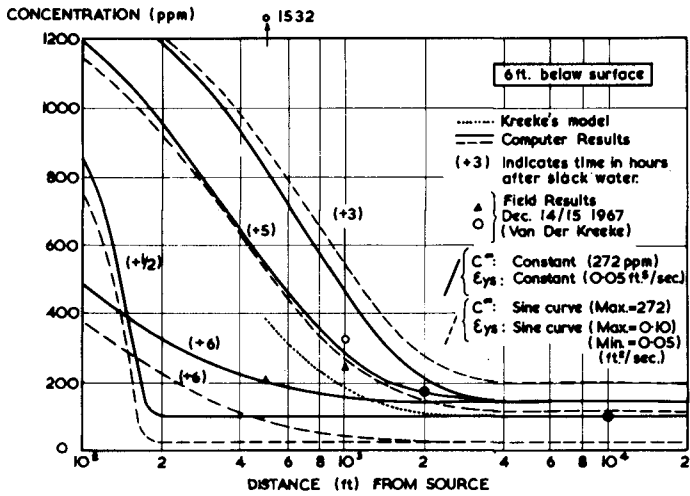
FIG. 11 COMPARISON OF FIELD AND MODEL RESULTS FOR POTOMAC ESTUARY : 6ft BELOW SURFACE.
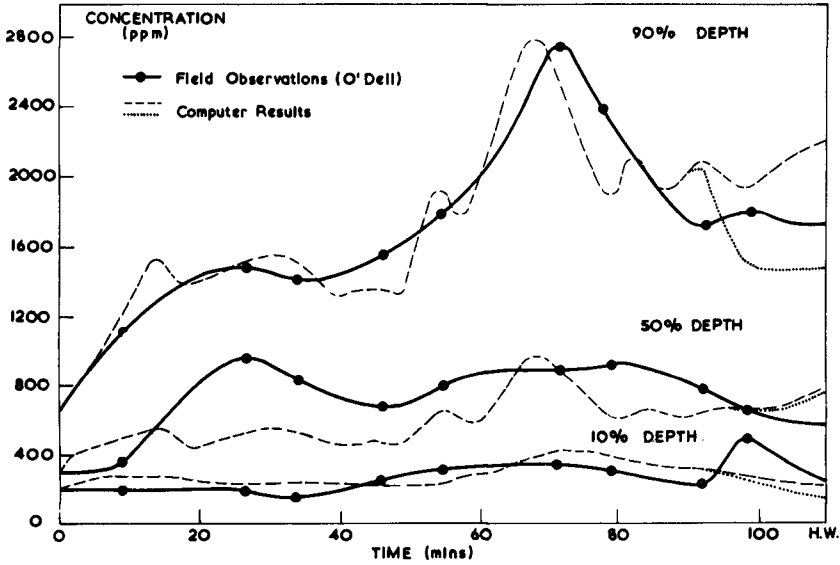
FIG. 12.   COMPARISON OF FIELD AND MODEL RESULTS – GLADSTONE LOCK.
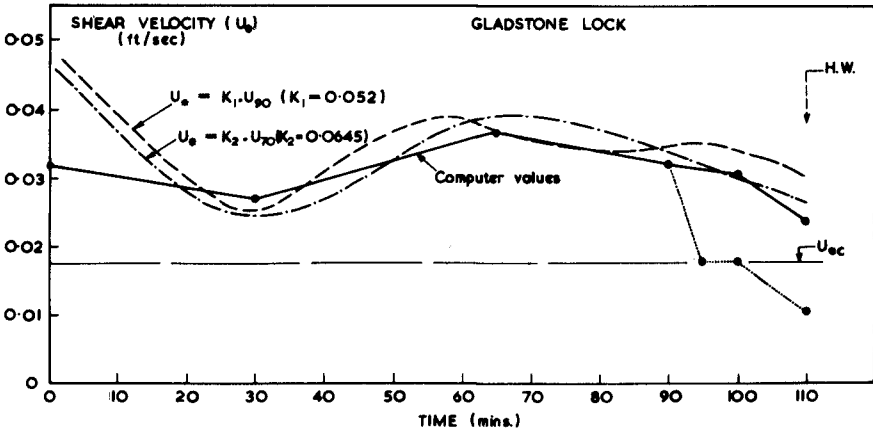
FIG. 13.   COMPARISON OF U_* VALUES USED IN THE COMPUTER MODEL WITH EQUATION 14.

CHAPTER 66

SAND CONCENTRATION IN AN OSCILLATORY FLOW
by W.T. Bakker[1]

0. Abstract.

In this paper first a numerical model is described con-
cerning the velocity distribution in an oscillatory flow, res-
pectively without and with resultant current. From the mo-
mentaneous velocity gradients eddy viscosities are derived.
Using the approach of VANONI [1], a numerical model is given
for the calculation of sediment concentration and suspended
sediment transport. In order to give reliable results, the
bed-load concentration should be known. This will be investi-
gated in the future; at the moment the model only provides
qualitative results.

1. Introduction.

This paper deals about the calculation of suspended
sediment transport in an oscillatory flow, with or without
resultant current. The approach is the same as the one of
VANONI [1], however unstationary effects have been taken into
account: the sediment transport is found by multiplying mo-
mentaneous concentrations with momentaneous velocities and
integrating these over the wave period.
The investigation only covers a part of a larger schedule for
research:
a. Computation of the velocity distribution in a horizontally
   oscillating flow, as occurs for instance in a oscillatory
   water tunnel. Assumptions and computations are given in ch.
   2.
b. From the velocity distributions the gradient of the velo-
   cities and the eddy viscosity is derived, after which the
   suspended load can be calculated. The method is treated in
   ch. 4.
c. For the solution given ad b, a boundary condition near the
   bottom is needed and therefore investigations have to be
   made about the bottom transport. These investigations still
   have to be carried out. As the sand concentration at the
   bottom determines the concentration in the higher layers,
   this means, that the present investigation only can give
   qualitative results.
d. The results of the mentioned computations should be checked
   in a oscillatory wave tunnel. Also this check still has to
   be made.

[1] Senior Scientific Officer, Techn. Univ. of Delft,
Head of Study Dept. Vlissingen, Rijkswaterstaat.

e. The following step is the adding of a constant additional
current. Ch. 3 deals with the computation.

f, g. Again the same procedure can be applied, including the cal-
culation of the sediment transport (f, chapter 4) and the
check in an oscillatory water tunnel (g).

h,i,j. Finally the three-dimensional problem has to be tackled:
waves and currents making an angle with each other. The
way of solving is in principle the same (h: investigation
water motion, i: investigation sediment motion), however
now checks in prototype and hydraulic model should be made
(j). The three-dimensional problem will not be treated
here: the paper ends with a conclusion (chapter 5).

2. Numerical computation of the velocity distribution in an os-
cillatory flow.

2.1. Assumptions.

2.1.1 Apart from turbulent fluctuations, the flow is assumed to
be horizontally directed and to be uniform in horizontal
direction. Hence, the velocity u is assumed to be only a
function of the vertical coordinate z and of the time t,
but no function of the horizontal coordinate x. The pres-
sure gradient is acting in horizontal direction; the
pressure is only a function of x and t.

2.1.2 In the inner part of the fluid, a turbulent shear stress
is assumed, according to the assumptions of PRANDTL [2]
equal to:

$$\tau = \rho l^2 \frac{\partial u}{\partial z} \left| \frac{\partial u}{\partial z} \right| \tag{1}$$

in which τ is the shear stress, taken positive when ac-
ting in positive x-direction from the upper layer to the
lower layer. ρ is the specific density of the fluid, l is
the mixing length, being according to von KARMAN [3] pro-
portional to the distance z from the theoretical bottom:

$$l = \varkappa z \tag{2}$$

$\varkappa$ being the von KARMAN constant.

2.1.3 With respect to the boundary conditions, two cases a and b
are considered:

a The fluid motion far from the bottom is such, that a har-
monic shear stress velocity at the bottom results;

b The velocity U of the fluid far from the bottom elapses
harmonically in course of time.
The bottom is assumed to be hydraulically rough. The velo-
city at a distance z_0 above the theoretical bottom level is
assumed to be zero, z_0 is assumed to be .03 times the
ripple height.

2.2. Derivation of the equation for the shear stress velocity.
The acceleration on a rectangular element of the fluid
is caused by the gradient of the shear stress in vertical

fig.1
Shear stress velocity p_* and velocity U_d^* as function of time t_* and level Z_*
(harmonic p_*)
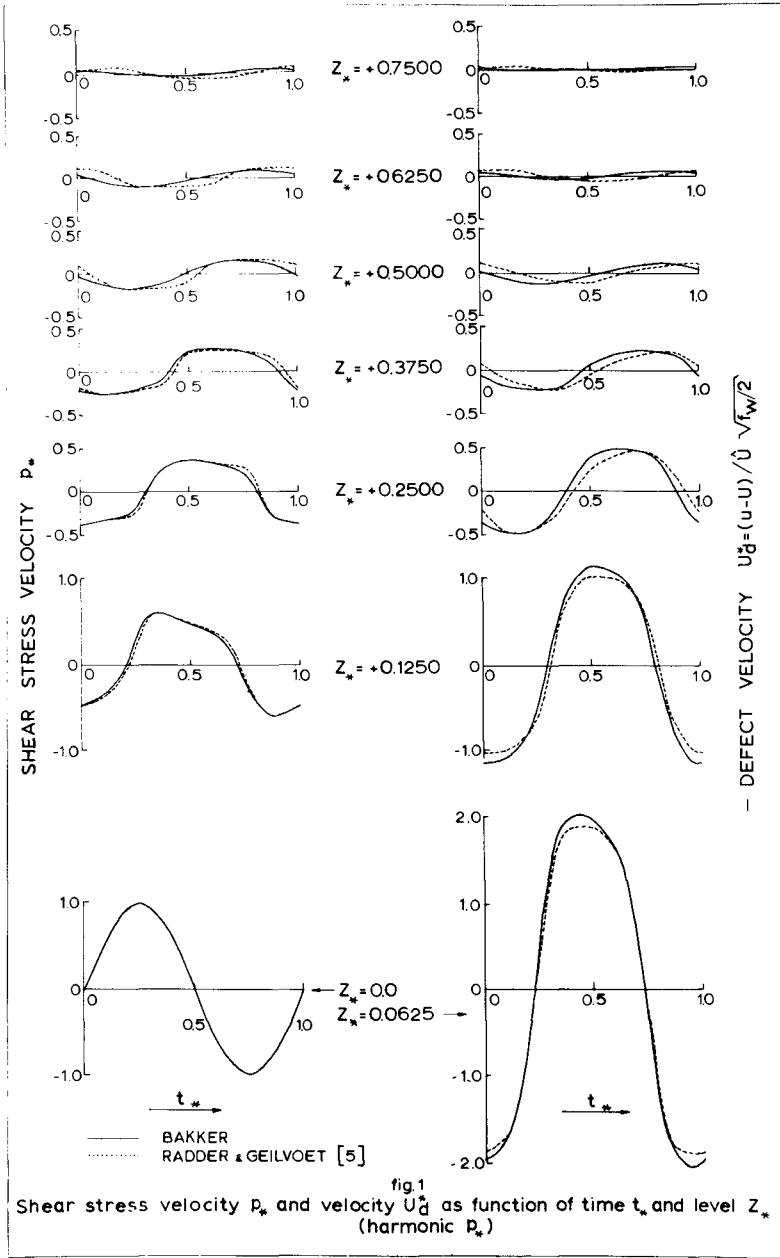
direction z and the gradient of the normal pressure p_r in horizontal direction x:

$$\rho \frac{\partial u}{\partial t} = \frac{\partial \tau}{\partial z} - \frac{\partial p_r}{\partial x} \tag{3}$$

Far from the bottom, the shear stress is reduced to zero, as well as $\frac{\partial \tau}{\partial z}$. There, according to (3), $\frac{\partial u}{\partial t}$ will be no function of z, as p_r is assumed to be no function of z.
The velocity far from the bottom, of which the variable part is only a function of t (not of z) will be called U, being determined by:

$$\rho \frac{\partial U}{\partial t} = -\frac{\partial p_r}{\partial x} \tag{4}$$

We assume U only a function of t in this section.
JONSSON [4] calls u-U the "defect velocity" defined by:

$$u_d = u - U \tag{5}$$

The defect velocity has a physical meaning: it is the velocity which occurs when considering the case of an oscillating plate in a fluid being at rest at infinity instead of the case of a moving fluid above a stable bottom. Subtracting (4) from (3) and substitution of u_d from (5) gives:

$$\frac{\partial u_d}{\partial t} = \frac{\partial(\tau/\rho)}{\partial z} \tag{6}$$

or, introducing (1) and (2):

$$\frac{\partial u_d}{\partial t} = \frac{\partial(xz \frac{\partial u}{\partial z} | xz \frac{\partial u}{\partial z} |)}{\partial z} \tag{7}$$

This equation can be transformed into an equation for the internal shear stress velocity. In this paper this will be denoted by p instead of U_*, as the star as index will be reserved for dimensionless quantaties. Define p as:

$$p = sign(\tau) . \sqrt{\tau/\rho} \tag{8}$$

From (1) and (2):

$$p = xz \frac{\partial u}{\partial z} \tag{9}$$

According to (5), U in (9) may be replaced by u_d, and hence, differentiation of eq (7), to z and multiplying by xz gives a differential equation for the internal shear stress velocity:

$$\frac{\partial p}{\partial t} = xz \frac{\partial^2(p|p|)}{\partial z^2} \tag{10}$$

This equation can be solved by numerical procedures, as will be shown in the appendix. For this goal, first the equation has been made dimensionless by introducing the dimensionless variables:

fig.2
Shear stress velocity P_* and velocity U_d^* as function of time t_* and level Z_*
(harmonic U)
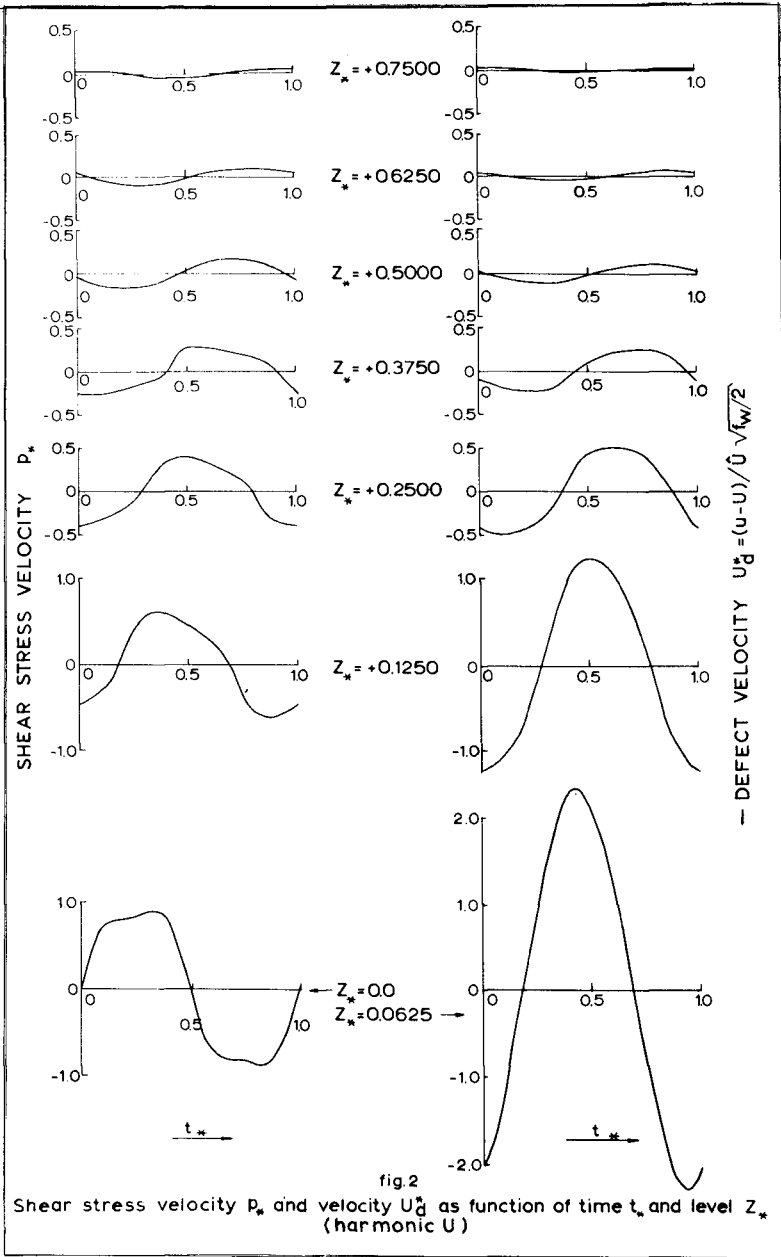
$p_* = p/\hat{p}_b$ where $\hat{p}_b$ = the maximum shear stress, exerted at the bottom

$t_* = t/T$ where T = the period of the periodical motion

$z_* = z/Z$ where $Z = x\hat{p}_b T$ = a reference length

Then eq (10) reduces to:

$$\frac{\partial p_*}{\partial t_*} = z_* \frac{\partial^2 (p_* |p_*|)}{\partial z_*^2} \tag{11}$$

The equation has first been solved with the assumption of a sinusoidal shear stress velocity p^*_b at the bottom, i.e. with the following boundary conditions:

$$p^*_b = \text{SIN } 2\pi t_* \quad \text{for} \quad z_* = 0 \tag{12}$$

and $p^* \equiv 0$ for $z_* = z^*_{max}$ (13)

The upper boundary should be $p_* = 0$ for z_* is infinite; however as this values is difficult to obtain numerically, it has been replaced by z^*_{max}. From an approximate analytical solution it was found that the maximum value of p_* at $z_* = 1$ was about $3^o/oo$ of the maximum value at the bottom; therefore for most computations $z^*_{max} = 1$ has been chosen. Also numerical computations with larger z^*_{max} always gave low values of p_* at $z_* = 1$.

2.3. The initial condition.
        As initial condition has been chosen:

$$p_* \equiv 0 \quad \text{for } t_* = 0 \tag{14}$$

Considering the symmetry of the motion, it is reasonable to assume, that for the final solution at every level and time is valid:

$$p_* (t_*) = -p_* (t_* + \tfrac{1}{2}) \tag{15}$$

As the initial condition does not coincide with the periodical solution of p_* at any time, the initial condition gives an initial disturbance, which fades away after a number of periods calculation. In order to fasten the process of convergence to the periodic solution, corrections were applied after each of the first calculated wave periods (up to half of the total number of calculated periods). If the calculated velocity after $(n+\tfrac{1}{2})$ T was a and after nT was b, a correction $(b-a)/2$ was applied. This way of correcting attenuated the initial effect very soon and after the first half number of periods the motion remained very well periodic during the computation.

2.4. Calculation of p and U.
        In the appendix an explicite method of numerical computation is described for solving eq (11). The solution has been checked by RADDER and GEILVOET, using an implicite method [5]. The implicite and the explicite method showed to be about equivalent, although illconditioned matrices

could make the implicite results less reliable when p_b was
about zero[5]. In fig. 1 (left-hand side) the results of the
explicite and implicite method are shown: for various levels
z_* curves are drawn indicating p_* as function of t_*. In fig.
5^a, left-hand side, curves are drawn showing p_* as function
of z_* for various values of t_*.

By numerical integration the dimensionless defect velo-
city $u_d^* = u_d/\hat{p}_b$ can be found. Using (9):

$$u_d^* = \frac{1}{x} \int_{z_*}^{\infty} \frac{p_*}{z_*} \, dz_* \tag{16}$$

For the lower boundary of integration z_* the various levels
on which p_* has been computed can be substituted. The right
hand side of fig. 1 shows u_d^* as function of t_*, at various
levels z_*, fig. 5^b gives u_d^* as function of z_* for various
values of t_*.

At a distance $z=z_0$, u equals zero, according assumption
2.1.3, and thus u_d^* equals $-U$, according to (5). By assuming
the values of z_* at the successive levels for which p_* has
been computed, equal to 0.03 $r^*=0.03$ r/Z, for the correspon-
ding values of the dimensionless ripple height r_* the dimen-
sionless velocity $U_*=U/\hat{p}_b$ far from the bottom can be found.
Then according to (5), $U_*=U/\hat{p}_b$ equals $u_d^* + U_*$. Fig. 5 shows
velocity profiles u_* for various t_*.

From the value of U_* a first-order approximation of the
friction coefficient can be derived.

A usual definition of the friction coefficient is (vide
for instance JONSSON [6], [7]:

$$f_w = \frac{\hat{\tau}}{\frac{1}{2}\rho \hat{U}_h^2} \tag{17}$$

where τ denotes the top shear stress, caused by a harmonic
velocity with amplitude U_h far from the bottom. Of course,
then τ is not harmonic in course of time.

As in the calculated case U does not elapse harmoni-
cally, it does not seem correct to replace (17) by:

$$f_w \overset{?}{=} \frac{2 \hat{p}_b^2}{\hat{U}_*^2}$$

Instead, the first and third harmonic U_1 and U_3 of U
have been calculated and for f_w the relationship has been
assumed:

$$f_w = \frac{3\pi}{8} \frac{2\hat{p}_b^2}{U_*^2} \tag{18}$$

The coefficient "$3\pi/8$" originates from the consideration,
that a schematized harmonic shear stress should have an
amplitude, equal to $8/3\pi$ times the top value of the real,
non-harmonic one in order to be equivalent with respect to the
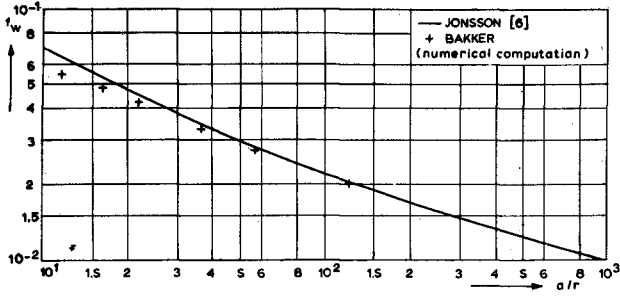
fig. 3 FRICTION COEFFICIENT f_w VERSUS RATIO STROKE LENGTH/RIPPLE HEIGHT
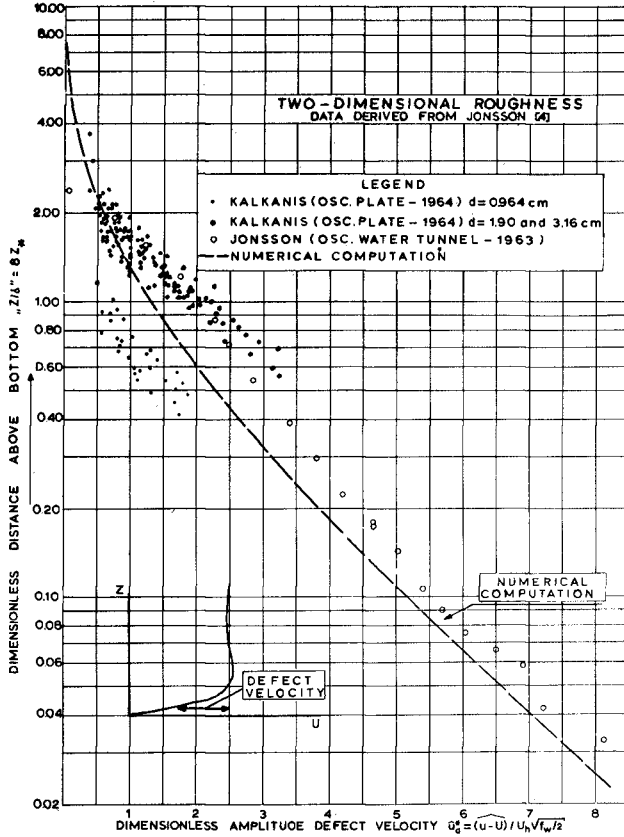
fig. 4 ENVELOPE OF DEFECT VELOCITY DISTRIBUTIONS
COMPARISON NUMERICAL RESULTS WITH DATA

energy dissipation [8], [9].

It will be reminded that in (18) $U_1/\hat{p}_b$ equals $U_1{}^*$. Thus, starting from a certain level on which p_* and U_* have been computed and assuming this level $z_o{}^*$ equal to $0.03r_*$, one finds f_w for $r_* = z_o{}^*/0.03$ from (18). On the other hand, $z_o{}^*$ can be expressed in the ratio stroke length /ripple height a/r:

$$z_o^* = 0.03 r_* = 0.03 \frac{r}{z} = 0.03 \frac{r}{x\hat{p}_b T} = \frac{0.03}{2\pi x \sqrt{f_w/2}} \cdot \frac{r}{UT/2\pi}$$

$$\frac{r}{a} = \frac{2\pi x \sqrt{f_w/2}}{0.03} \cdot z_o^* \qquad\qquad (19)$$

in which f_w is known from (18).

As $z_o{}^*$ can be, in principle every level for which u_* has been calculated, from one numerical computation (with a small Δz_*) a number of combinations of a/r and f_w can be found. These are given in fig. 3.

However, still the assumed coefficient $3\,\pi/8$ as well as the stated boundary condition (U in this way, that a harmonical shear stress velocity results) seems artificial and not quite logical. In a more elegant way, one can add a third harmonic to p_* ($\hat{p}_b$ then being defined as the amplitude of the first harmonic of p_b) and minimize by an iteration procedure the third harmonic of U_*, starting from u_d^* at a certain level $z_o{}^*$. Then f_w can be found as:

$$f_w = 2\frac{\hat{p}_b^{*2}}{\hat{U}_*^{2}} \qquad\qquad (20)$$

where $\hat{p}_b{}^*$ equals the top value of the combination of the first and third harmonic[1].

In fig. 2, analogous to fig. 1, a third harmonic equal to 17% of the first one and having a phase difference of 15° with the first one, has been added to the shear stress velocity.[2]

By this, the third harmonic of U_* at a level $z_* = 0.0625$ dropped to 1% of the first one (being originally 15%).

As in this particular case, the value of $\hat{p}_b$ appeared to be 10% smaller than $\hat{p}_b$, eq (20) gave considerable lower friction coefficients than (18). This is a reason for future researsch; now only the way of solution has been indicated.

As Z equals $x\hat{p}_b T$, i.e. $2\pi x\, a\sqrt{f_w/2}$, and f_w can be found from a/r, the dimensionless numerical model can be connected with the prototype.

---

[1] for reasons of symmetry of the motion the second harmonic of as well p_b^* as U_* should be zero.

[2] i.e. $p_b = \sin \omega t + 0.17 \sin(3\omega t + 15^o)$

fig. 5^a ATTENUATION OF SHEAR STRESS VELOCITY P_* IN Z_* DIRECTION

NO RESULTANT SHEAR STRESS VELOCITY

RESULTANT SHEAR STRESS VELOCITY $\overline{P_0}^* = 1$

fig.5^d MEAN DEFECT VELOCITY COMPARED WITH LOGARITHMIC PROFILE

LOWER ENVELOPE DEFECT VELOCITY PROFILES

UPPER ENVELOPE DEFECT VELOCITY PROFILES

MEAN DEFECT VELOCITY

LOGARITHMIC PROFILE

fig.5^b DEFECT VELOCITY PROFILES (NO RESULTANT CURRENT)

fig.5^c DEFECT VELOCITY PROFILES (RESULTANT CURRENT)

fig. 5^e VELOCITY PROFILES (NO RESULTANT CURRENT)

fig. 5^f VELOCITY PROFILES (RESULTANT CURRENT)

2.5. Comparison with measurements and other theories.
      Fig. 3 shows a comparison between the friction coeffi-
cient found by JONSSON [6] and the results of the numerical
computation. Fig. 4 shows a graph in which the data is plot-
ted collected by JONSSON [4] from his experiments described
in [6] and from experiments of KALKANIS [11].[1] Furthermore,
the amplitude of the dimensionless defect velocity u_d^* found
from the computer program is plotted versus the dimension-
less height above the bottom z_*.
The correspondence is quite satisfactory.
      In fig. 3 the obtained friction coefficients are com-
pared with the results of JONSSON [6] . For low values of
a/r the numerical model gives somewhat lower results.

3.   Oscillatory flow plus resultant current.

      A shear stress velocity, constant over the vertical and
in the time, results according to (16) into a logarithmic
velocity profile, being a good approximation of the velocity
profile of a stationary current. Therefore, the approximation
p=constant (say $\bar{p}_b$) was assumed to be good enough to repro-
duce the velocity profile in the layers of the fluid above
the turbulent boundary layer. In this section U (defined by
(4)) will be assumed to consist of a logarithmic part,
being zero at $z=z_{max}$ and an unstationary part U' being no
function of z. U' thus denotes the velocity at $z=z_{max}$:

$$U = \frac{\bar{p}_b}{\chi} \ln \frac{z}{z_{max}} + U'(t)$$

z_{max} is assumed to be so large, that $\frac{\partial \tau}{\partial z}$ in eq (3) can be
neglected. As in sect. 2.2 the defect velocity u_d will be
defined as the deviation of u from U, occuring in the tur-
bulent boundary layer, cf eq (5).
      The combination of an oscillatory flow plus a resul-
tant current has been simultated with the explicite com-
puter program by adding, after some wave periods of a normal
run, a constant shear stress velocity over the whole stretch
from bottom to $z*_{max}$. After that, the calculation was con-
tinued over a number of wave periods until a periodical
shear stress velocity resulted. The curves of p_* as function
of z_* for various t_* are plotted in fig. 5[a], together with
the analogous ones in the case that no resultant shear
stress is present. It shows, that the variation of the shear
stress velocity attenuates much more slowly in upward direc-
tion in the case with a resultant shear stress velocity than
in the case without and further more, that the envelope of
minimum shear stress velocity at each level tends faster to
the imposed constant shear stress velocity than the envelope

----

[1] "z/δ " in fig. 1[d] of [4] has been transferred to z_*.
     From [10] , eq (4.4), (4.14) and (4.18) it shows that
     $\delta =(0.04 \quad \pi a \quad \sqrt{f_w/2})/\chi$ and as $Z=2 \quad \pi \chi a \quad \sqrt{f_w/2}$, it
     appears that "z/δ "$= 8 z_*$, as $\chi = 0.4$.

of the maxima. Because of the last-mentioned feature, the mean
shear stress velocity inside the fluid differs from the mean
shear stress velocity, imposed in the beginning.

In fig. 5^a with a thick drawn line the mean shear stress
velocity has been indicated, with an interrupted line the im-
posed one.

Fig. 5^c shows the integration from p_* to U_d^* carried out
in the same way as done for oscillatory flow without current
in fig. 5^b, i.e. by integrating, according to (16), taking as
upper boundary $z_* = z_{max}^*$ [1]).

In fig. 5^d, analogous to fig. 5^c, with a thick drawn line
the mean value of u_d^* has been indicated, with an interrupted
line the logarithmic profile, resulting from a stationary
shear stress velocity equal to $\bar{p}_b$.

From fig. 5^c figure 5^f can be derived, by a parallel
shift of the velocity distributions, in this way, that the ve-
locity at a distance $z_o^* = 0.03\ r_*$ equals zero. This gives the
real velocity distribution for various times t_*. Also the line
of the mean value of u_d^* and the line of the logarithmic pro-
file are shifted (thick drawn-, resp. interrupted line in fig.
5^f) and one observes, that the time-average of the velocity
above the bottom will be larger than one would find from the
logarithmic profile (interrupted line), which would result
when leaving the variation in the shear stress velocity out
of consideration. Far from the bottom the interrupted line
and the drawn line will be parallel. This means, that for a
given value of the average mean shear stress velocity the
mean velocity over the depth will be larger with an oscilla-
tory motion than without. If the mean shear stress velocity
$\bar{p}_b$ equals the amplitude of the variation $\hat{p}_b$ [2]) from the nu-
merical computation it appeared that this increase is of the
same order as this shear stress velocity.

Furthermore, comparing fig. 5^b with fig. 5^c, it shows
that the same variation of the shear stress velocity $\hat{p}_b^*$ re-
sults in a much larger variation of u_d^* when a resultant cur-
rent is present than when there is not. This is the effect
of the deeper intrusion into the fluid of the variation of
the shear stress when a resultant current is present (cf.
fig. 5^a). This results in a larger variation of U (compare
fig. 5^e with fig. 5^f) with the same amplitude $\hat{p}_b$.
Summarizing and concluding:

In a stationary current without oscillatory flow U is
proportional to the bottom shear stress p_b:

$$\bar{U} = \sqrt{\frac{2}{f_c}}\ p_b \ ; \ \text{where} \ \sqrt{\frac{2}{f_c}} = \frac{1}{h} \int_o^h \frac{1}{x} \ln \frac{z}{z_o}\ dz = \frac{C_h}{\sqrt{g}}$$

C_h being the Chezy coefficient and g the acceleration of gravi-
ty. Of an oscillatory flow is present one finds:

_____

[1]) z_{max}^* has been chosen somewhat too small in fig. 5^c. This
is no matter of principle.

[2]) Note, that the top value of p_b equals $\bar{p}_b + \hat{p}_b$.

$$c_b = \frac{1}{\sqrt{2\pi}} \int\limits_{B_* \psi - \frac{1}{\tau_0}}^{\infty} e^{-z^{3/2}} \, dz$$

fig 6   SAND CONCENTRATION AT VARIOUS LEVELS
AS FUNCTION OF TIME
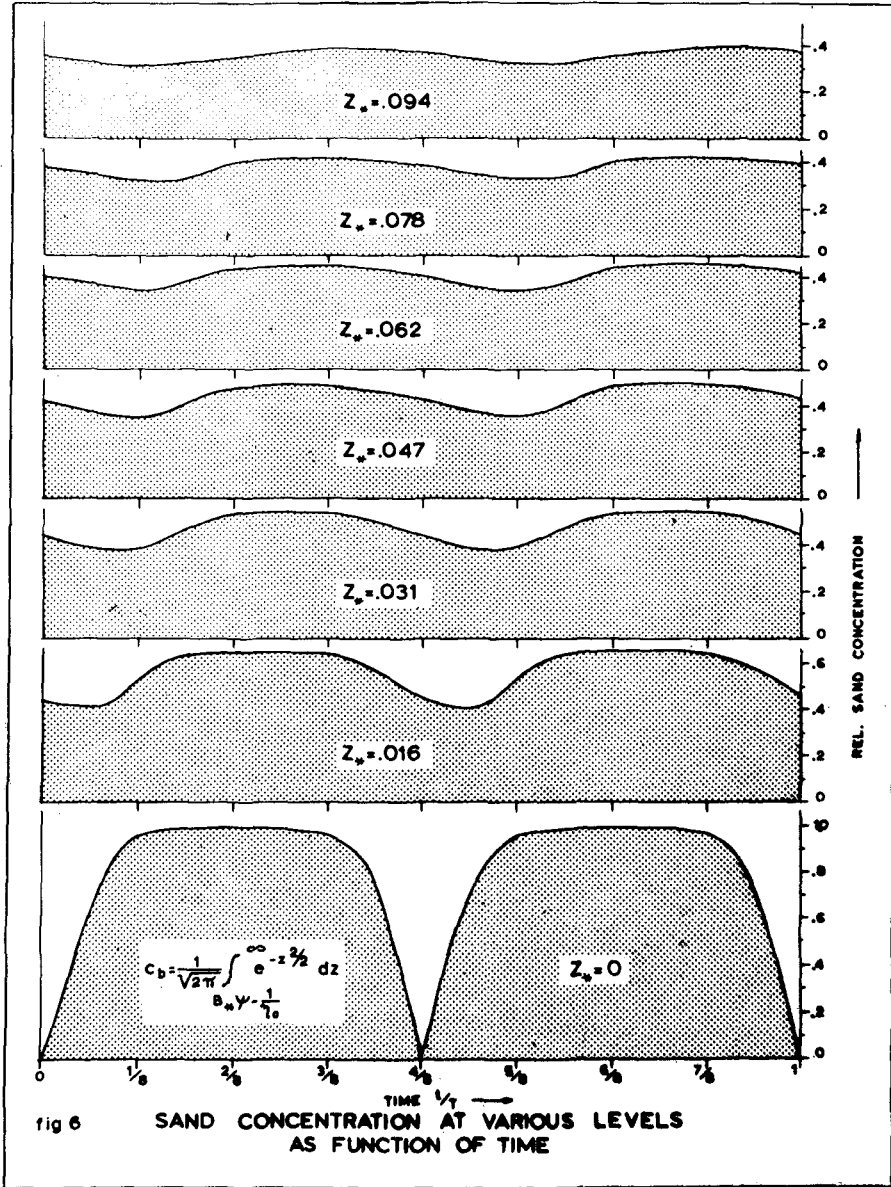
$$\bar{U} = \sqrt{\frac{2}{f_c}} \; \bar{p}_b + U_r$$

, where U_r is a positive residual velocity [1)]
U_r is a function of $\hat{p}_b/\bar{p}_b$ and of a/r. Thus U_r can be hidden in a decreasing coefficient f_c.

and $\hat{U} = \hat{p}_b \sqrt{\frac{2}{f_w}}$ f_w decrease when apart from the oscillatory flow a current is present [2)].

The average value over the wave period of the bottom shear stress equals, when $\hat{p}_b \leqslant \bar{p}_b$:

$$\bar{\tau} = \overline{\left\{ \bar{p}_b + \hat{p}_b \; \sin(\omega t + \varphi) \right\}^2} = \bar{p}_b^2 + \tfrac{1}{2} \hat{p}_b^2$$

$$\bar{\tau} = \tfrac{f_c}{2}(\bar{U} - U_r)^2 + \tfrac{f_w}{2} \hat{U}^2 \qquad\qquad (21)$$

Therefore, although the existance of U_r and the decrease of f_w, still an increase of the average shear stress can be expected by the presence of waves.

4. Sand concentration and sand transport.

The calculation of the sand concentration is based on the equation:

$$\frac{\partial c}{\partial t} = \frac{\partial}{\partial z}\left(\varepsilon \; \frac{\partial c}{\partial z} + wc\right) \qquad\qquad (22)$$

Eq (22) is a continuity equation for the sediment. The right-hand part between the parentheses indicates the sediment flux in a vertical downward direction, w being the settling velocity, positive in negative z-direction, the first term indicating the turbulent exchange, the second one the settling. c is the sediment concentration. The turbulent exchange factor has been taken equal to the eddy viscosity ε, defined by:

$$\frac{\tau}{\rho} = \varepsilon \frac{\partial u}{\partial z} \qquad\qquad (23)$$

where, according to (1) and (2):

$$\varepsilon = x^2 z^2 \left| \frac{\partial u}{\partial z} \right| \qquad\qquad (24)$$

In a dimensionless shape, eq (22) reads:

$$\frac{\partial c}{\partial t_*} = \frac{\partial}{\partial z_*}\left(\varepsilon_* \frac{\partial c}{\partial z_*} + w_* c\right) \qquad\qquad (25)$$

where $\varepsilon_* = \varepsilon/x^2 \hat{p}_b^2 \; T \; (= \varepsilon T/Z^2)$ \qquad\qquad (26)

[1)] from numerical computations it was found, that U_r is of the order of p_b, when $\hat{p}_b = \bar{p}_b$
[2)] Reductions of 30% may occur when $p_b = \hat{p}_b$
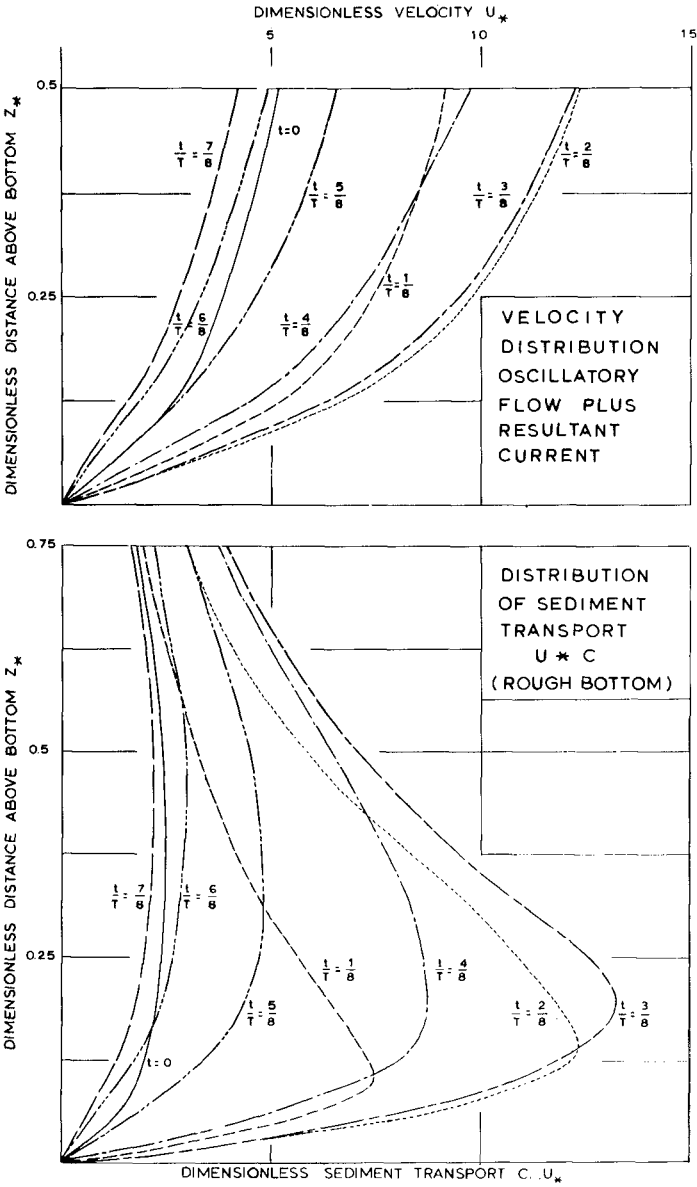
fig. 7 EXAMPLE OF VELOCITY DISTRIBUTION AND SEDIMENT TRANSPORT IN AN OSCILLATORY FLOW WITH RESULTANT CURRENT.

or, from (24): $\varepsilon_* = Y_* |p_*|$ (27)

and $w = w/x \, \hat{p}_b \; (= w T/Z)$ (28)

w_*, indicating the ratio between the falling distance of a grain in still water in a wave period on one hand and the decay distance Z of the shear stress on the other hand, also can be compared with "Z"="w/x V_*" as defined by EINSTEIN[12], where V_* is the shear stress velocity of a uniform flow with mean velocity $V_{\circ}$

From the differential equation (22) the difference equation (29) can be derived, in which c' denotes the concentration at time $t + \Delta t$ and c at time t:

$$\frac{c'(z_*) - c(z_*)}{\Delta t_*} = \varepsilon_*(z_*) \frac{c(z_* + \Delta z_*) - 2c(z_*) + c(z_* - \Delta z_*)}{(\Delta z_*)^2}$$

$$+ \frac{\varepsilon_*(z_* + \Delta z_*) - \varepsilon_*(z_* - \Delta z_*)}{2 \Delta z_*} + w_* \frac{c(z_* + \Delta z_*) - c(z_* - \Delta z_*)}{2 \Delta z_*} \quad (29)$$

The computation of c has been carried out in the same way as the calculation of p_*, described in appendix A. First p_* is calculated in all points of the wanted grids at a certain time t_*, and after that ε_* (from (27)) and c in the same way in the same points at the same time. Values of c smaller than zero are replaced by zero. As initial condition has been taken: $p_* = c \equiv 0$; the boundary condition at z^*_{max} is c=p≡o.

The bottom boundary condition remains a problem in its own, which will be investigated later on. In the exemple, given in fig. 6, some arbitrary function has been chosen. The concentration has been chosen equal to the probability that the lift force on a particle is larger than its own weight. For this probability p_r was found by KALKANIS[11] (using the well-known EINSTEIN-aproach[12]:

$$p_r = \frac{1}{\sqrt{2\pi}} \int_{B_* \psi - \frac{1}{\eta_\bullet}}^{\infty} e^{-z^2} dz \quad (30)$$

where ψ is proportional to the ratio between the lift force and the own weight:

$$\psi = \Delta \frac{gD}{u_n^2} \quad (31)$$

where Δ is the relative specific density $(\rho_s - \rho)/\rho$, D is the grain diameter and u_n is the velocity at a distance 0.35 D from the theoretical bed. Relating u_n with the shear stress velocity p, assuming a logarithmic velocity distribution, one finds for a rough bed: $u_n = 5.24 \, p'$ (vide [12], p. 35, eq (45) to (46)); where p' is the part of the bottom friction τ', exerted on the

grains.

If τ' is a fraction μ (ripplefactor) of the total shear stress, one finds:

$$\psi = \psi \min / p_*^2 \tag{32}$$

where

$$\psi \min = \frac{1}{(5.24)^2} \cdot \frac{\Delta}{\mu} \cdot \frac{gD}{p_b^2} \tag{33}$$

In (30) B_* has been taken 4 and $1/\eta_o$ equal to 1.5, following KALKANIS [11].

Fig. 6 shows the concentration at various levels as a function of time for an oscillatory flow without current. Fig. 7 shows the velocity distribution and the sediment transport, i.e. concentration times velocity for an oscillatory flow with resultant current.

5. Conclusion.

It may be expected, that the computer programs under development [1) may provide a powerful tool in the understanding of unstationary periodical water- and sediment motion. Careful testing on data will be obligatory. Already a better insight in the water motion of an oscillatory current with a resultant flow has been obtained (ch. 3).

Appendix A.

The numerical computation according to the explicit method.

The differential equation (11) can be written as the following difference equation, relating the value of p_* after one increment of time to the original value of p_* in the same point and in the two adjacent points.

$$p_* [z_*, t_* + \Delta t_*] = p_* [z_*, t_*] +$$

$$+ \frac{z_* (\Delta t_*)}{(\Delta z_*)^2} \quad p_* [z_* - \Delta z_*, t_*] \cdot \mathrm{abs} \, (p_* [z_* - \Delta z_*, t_*])$$

$$-2 \, p_* [z_*, t_*] \cdot \mathrm{abs} \, (p_* [z_*, t_*])$$

$$+ p_* [z_* + \Delta z_*, t_*] \cdot \mathrm{abs} \, (p_* [z_* + \Delta z_*, t_*]) \tag{A1}$$

In (A1) the factor $\Delta t_* / (\Delta z_*)^2$ can be chosen arbitrary, with the limitation, that numerical instabilities have to be avoided. From the solution of similar linear differential equations this appears to include the condition:

------

1) Details about the programs are given in the internal reports [8] and [13].

$$\Delta t_* \leq \frac{(\Delta z_*)^2_*}{2 \; p_{*max} \cdot z_{max}} \qquad \qquad (A2)$$

in which: p_{*max} =the maximum p_* which occurs. This maximum is
found at the bottom and equals 1.

z_{*max} =the maximum z_* for which the computation is
carried out. As stated in ch. 2, z^*_{max} mostly
equals 1.

As the boundary condition will be: U=0 at z=.03 times the
ripple height r, near the bottom a maximum grid height Δz=.03
r/Z=.03 r/2πx a√f$_*$/2 will be required. For a reasonable value
r/a=400 this would make Δz_* of the order 1/3 000. Then from
(A2) it appears, that a maximum Δt_* is required, equal to
$10^{-6}/18$. Calling a "basic calculation" the calculation of one
value of p_* [z_*, t_*+ Δt_*] according to (A1), the required num-
ber of basic calculations which have to be carried out for only
one wave period would be of the order 3 000x18x10^6= 54x10^9,
which is very much, even for a computer.

Therefore, a more economic way of computation had to be
developed, which is called: the method of the "pulsating grid".

	BOUNDARY CONDITION					HEIGHT ABOVE THE BOTTOM $z_*/\Delta z_*$	
	↓ 1	4	8	12	16	20 24	32
	1 2 3 4 5						
t	① ② ③ ④ ⑤						
(t/Δt divisible	I	II	III	IV	V		
by 8)	①		②		③	④	
t +Δt	1 2 3 4						
t + 2Δt	1 2 3 4 5						
	① ② ③ ④						
t + 3Δt	1 2 3 4						
t + 4Δt	1 2 3 4 5						
	① ② ③ ④ ⑤						
	I	II	III	IV			

fig. A1. Schedule of calculations according to the pulsating grid.

This system gives a high accuracy and much information near
the bottom and relatively less far from the bottom.

For this aim a small grid length Δz_* has been chosen near
the bottom (fig. A1), consisting of 5 points 1 to 5. When the
number of time steps n=$t_*/\Delta t_*$ was odd, calculations were
carried out in this grid. When the number n was divisible by
2 but not by 4 however, calculations were carried out also in
a grid with a double grid length, consisting also of 5 points

①to⑤(fig. A1). When n was divisible by 4 but not by 8, the width of the grid was doubled again (points I to V) and calculations were carried out in the smallest, the medium and the largest grid, etc.

Thus of the total number of grids equals m, the first four points of the last one cover the whole stretch from $z_* = 0$ to $z_* = 1$ and the first one has a length of $\frac{5}{4} \cdot 2^{-m+1}$. The distance Δz_* equals one fifth of the length of the smallest grid, i.e. 2^{-m-1}.

The maximum z_* of the smallest grid is $5 \times 2^{-m-1}$, and therefore, according to (A2), the maximum time step, which does not give instabilities will be:

$$\Delta t_* = 2^{-m-5} \text{ with } \Delta z_* = 2^{-m-1} \tag{A3}$$

Eq (A2) shows one of the advantages of the chosen system: because z^*_{max} is taken never more than 5 times Δz_*, Δt_* is proportional to Δz_* instead of proportional to $(\Delta z_*)^2$.

It can be easily shown[8], that when $\Delta t_* = 2^{-m-5}$, the number of basic calculations per wave period will be of the order $128/\Delta z_*$. In the case Δz_* equals 1/3 000, this number becomes 400 000, being a very small fraction of the original number of calculations. This indicates, that the more intricate way of programming is feasible.

The following schedule of computations is used (fig. A1). Assume the values of p_* in the points 1 to 5, ①to⑤ and I to V at time t are known and that t is divisible by 8.

At time $t + \Delta t$, the points 2, 3 and 4 are found from point 1, 2, 3, 4, 5 at time t, using eq (A1). Point 1 at time $t + \Delta t$ is found from the boundary condition, point 5 is not calculated.

At time $t + 2\Delta t$ the following calculations are carried out (fig. A1). Point 2, 3 are calculated from point 1, 2, 3, 4 at time $t + \Delta t$, using eq (A1); point ②③④ are found from point ①②③④⑤ at time t, using eq (A1) with double values of Δy and Δt. Point 1 at time $t + 2\Delta t$ is found from the boundary condition at the bottom; p_* at point① equals the calculated value in point 2 (fig. A1), point 4 equals point②, point 5 is found by extrapolating between②and③, using an extrapolation formula:

$$p_5 = (-p_3 + 4\tfrac{1}{8} p_② + 3\tfrac{1}{4} p_③ - \tfrac{3}{8} p_④)/6 \tag{A4}$$

(A4) relates the values of p_* in the smaller and the larger grids; all values apply for the same time. The index indicates the grid point. In (A4) the indices surrounded by a circle denote the values in a larger grid, the indices without a circle in a smaller grid.

Now the way of calculation will be clear: at time $t + 3\Delta t$ only calculations in the smallest grid are carried out; at time $t + 4\Delta t$ the same schedule of $t + 2\Delta t$ is followed, only up to one grid larger: the points II, III, IV are found from I, II, III, IV, V at time t, the points②,③ from point①②③④ at time $t + 2\Delta t$, the points 2, 3 from point 1, 2, 3, 4 at time $t + 3\Delta t$. Point④ equals point II, point⑤ is interpolated between II and III. Point 4 equals point②, point 5 is interpolated between② and③. Point① equals point 2, point I equals point②, point 1 is found from the boundary condition.
Now the following time step can be calculated, etc.

Literature.

[1] Vanoni V.A.
Transportation of suspended sediment by water.Trans.
Amer. Soc. Civ. Engrs. 111 p. 67-133   (1946)

[2] Prandtl, L.
Abrisz der Stromungslehre, Braunschweig, 3er Abschnitt (1931)

[3] Karman, Th. von
Mechanische Ahnlichkeit und Turbulenz. Proc. 3rd Int.
Congress for Appl. Mech. Vol I p. 85-92   (1930)

[4] Jonsson, I.G.
On the existence of universal velocity distributions in
an oscillatory, turbulent boundary layer. Techn. Univ. of
Denmark, Basic Res. Progress report no. 12   (1966)

[5] Radder, K.W. and Geilvoet, W.
Snelheidsverdeling in een oscillerende stroom (velocity
distribution in an oscillatory flow).Techn. Univ. of
Delft, M. Sc. Thesis (unpublished)   (1973)

[6] Jonsson, I.G.
Measurements in the turbulent wave boundary layer.10th
I.A.H.R. Congress, London I, p. 85-92   (1963)

[7] Jonsson, I.G.
Wave boundary layers and friction factors.Proc. 10th
Conf. Coastal Engng, Tokyo p. 127-149   (1967)

[8] Bakker, W.T.
Bottom friction and velocity distribution in an oscilla-
tory flow. Rijkswaterstaat, Dir. for Hydr. Res. and Water
Management, Dept. for Coastal Res., Memo 72-23^{b} (internal
report)   (1972)

[9] Proudman.
Dynamical Oceanography (§ 151)   (1953)

[10] Jonsson, I.G. and H. Lundgren,
Derivation of formulae for phenomena in the turbulent wave
boundary layer. Techn. Univ. of Denmark, Basic Res. Pro-
gress report no. 9   (1965)

[11] Kalkanis, G.
Transportation of bed material due to wave action. Coast.
Engng. Res. Center, Techn. Memo. no. 2.   (1964)

[12] Einstein, H.A.
The bed-load function for sediment transportation in open
channel flow. U.S.Dept. of Agr.; Techn. Bull. no. 1026 (1950)

[13] Bakker, W.T.
Sand concentration in an oscillatory flow. Rijkswater-
staat, Dir. for Hydr. Res. and Water Management , Dept.
for Coastal Res., Memo 72-28^{a} (int. rep.)   (1973)

[14] Kajiura, K.
A model of the bottom boundary layer in water waves.Bull.
Earthg. Res. Inst. 46, (pp) 75-123   (1968)

[15] Manohar, M.
Mechanics of bottom sediment movement due to wave action.
Beach Erosion Board, Techn. Mem. 75   (1955)

CHAPTER 67

FACTORS CONTROLLING CHANGES TO AN OPEN COAST BEACH

William N. Seelig[1]
and
Robert M. Sorensen[2]

ABSTRACT

A study of historical information and field measurements in
Sargent Beach, Texas, reveal that the shoreline is retreating with
historic rates increasing from -10 feet per year in the late 1800's
to -31 feet per year (-9.8 m/year) in the early 1970's. The cause of
this erosion is the lack of an adequate sand supply to the beach zone.
This sand deficiency is due to: a) reduced updrift sand input to the
coast by the Brazos River beginning in 1945 and caused by decreased
sediment transport capability of the river, b) increased sand storage
in the Brazos Delta encouraged by jetties and vegetation, and c) pos-
sible offshore losses of sand due to hurricane wave energy focusing
on the Brazos Delta in conjunction with river jetting during peak river
flows.

INTRODUCTION.

Sargent Beach, Texas is located on the western coast of the Gulf
of Mexico adjacent to Caney Creek, 70 miles (115 km) southwest of
Houston, Texas on a straight section of coastline (Figure 1). The
purpose of this study is to investigate medium to long term beach
changes and the factors causing these changes. Therefore, this study
included 26 miles (41 km) of coast updrift from Sargent Beach and 6
miles (9 km) downdrift of Sargent so that the overall pattern of
coastal change could be examined. The coast updrift of Sargent Beach
is of particular interest since it includes the Brazos River, which
has the highest sediment load of all Texas rivers, the Brazos Delta,
which stores a large volume of sediment at the mouth of the river, and
the Freeport Jetties at the former mouth of the Brazos River (Figure 1).

A more thorough discussion of many aspects of this work may be
found in Seelig and Sorensen (1973b), and studies on the Brazos

[1]Civil Engineer, Special Projects Branch, Coastal Engineering Research
Center, Ft. Belvoir, Virginia (formerly Research Assistant, Civil
Engineering Department, Texas A&M University, College Station, Texas).

[2]Chief, Special Projects Branch, Coastal Engineering Research Center,
Ft. Belvoir, Virginia (formerly Associate Professor, Civil
Engineering Department, Texas A&M University, College Station, Texas).
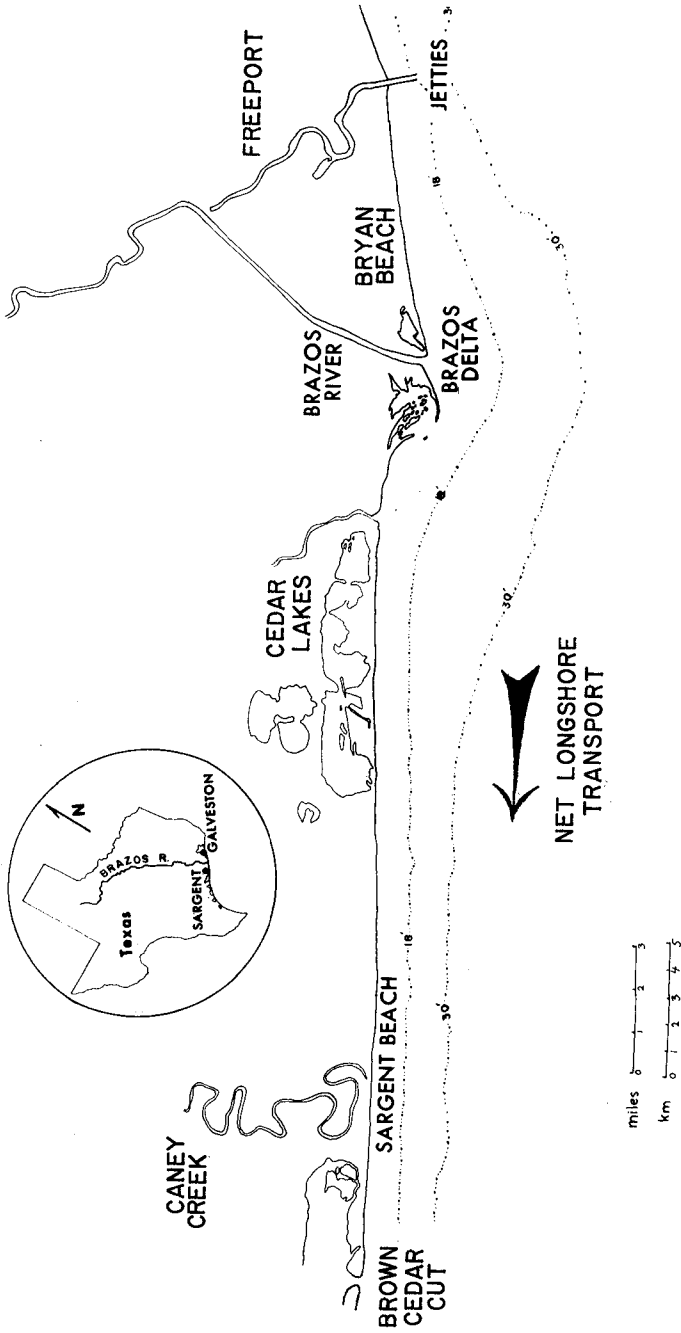
FIGURE 1. SARGENT BEACH AND VICINITY

Delta by Sealy (1974), and Odem (1953). An investigation of Brown
Cedar Cut, an inlet to the southwest of Sargent, is available in
Mason and Sorensen (1971).

HISTORICAL BACKGROUND.

    The study area, as illustrated in Figure 1, has undergone a
variety of large scale changes since the first surveys were made of
the coastal zone in 1852. While the net shoreline change for the
section of coast adjacent to and including Sargent Beach has undergone
large net shoreline retreat, the area adjacent to the Brazos River has
shown a more complex series of change.

    In the 1850's the Brazos River mouth in the old location had a
small delta with a straight coastline to either side (Figure 2). Due
to shoaling and navigation problems at the river mouth, jetties were
built and completed in 1899 which caused shoreline advances downdrift
of the jetties. By the 1930's this Brazos Delta had reached the
seaward end of the jetties (Figure 2). Due to continued navigation
problems in Freeport Harbor, a decision was made in 1929-1930 to
reroute the Brazos River mouth 6 miles (10 km) to the west. This
change caused a new delta to be built at the present location of the
river mouth with an associated erosion of the old delta. The new
delta reached its maximum length in 1948, then retreated while mi-
grating westward to the 1971 location (Figure 2).

BRAZOS RIVER   BRAZOS RIVER PRIOR
AFTER 1929-1930   TO 1929-1930

1852

1971   1933

1948

N

BRAZOS DELTAS   1 MILE
                                 1 KM
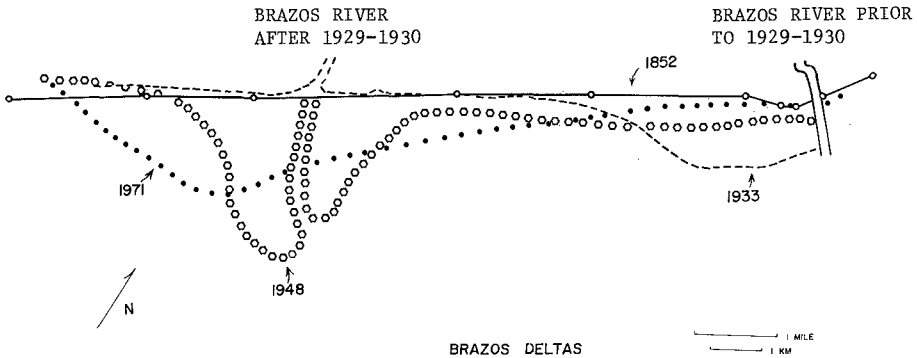
FIGURE 2

SARGENT BEACH CHANGES.

   Sargent Beach displays many of the classical characteristics of an
eroding beach. Sargent Beach is steeper and narrower than other beaches
in the area (e.g. Bryan Beach) with a scarp typically higher than 3
feet (1 m) and a concave beach seaward of the scarp. Oyster reefs,
clay outcrops and stumps are occasionally exposed on the beach face
suggesting that Sargent has been eroding throughout recent geologic
time (Figure 3).

FIGURE 3.   SARGENT BEACH   23 NOVEMBER 1972

   To determine historical shoreline changes for Sargent Beach
surveys, maps and photographs for the period 1852 to 1972 were analyzed.
They show the shoreline retreated 1800 feet (550 m) for this 120 year
period to give a mean shoreline change rate of -15 feet per year
(-4.5 m/year). A study of historical shoreline changes for the entire
Texas coast shows Sargent Beach to be retreating faster than 96 percent
of the Texas coast (Figure 4). Also note that 65 percent of the Texas
shoreline has retreat rates greater than zero feet per year so that
the Texas coast is predominantly erosive with Sargent Beach one of the
hardest hit area. A more detailed discussion of Texas coastal changes
is given in Seelig and Sorensen (1973a).
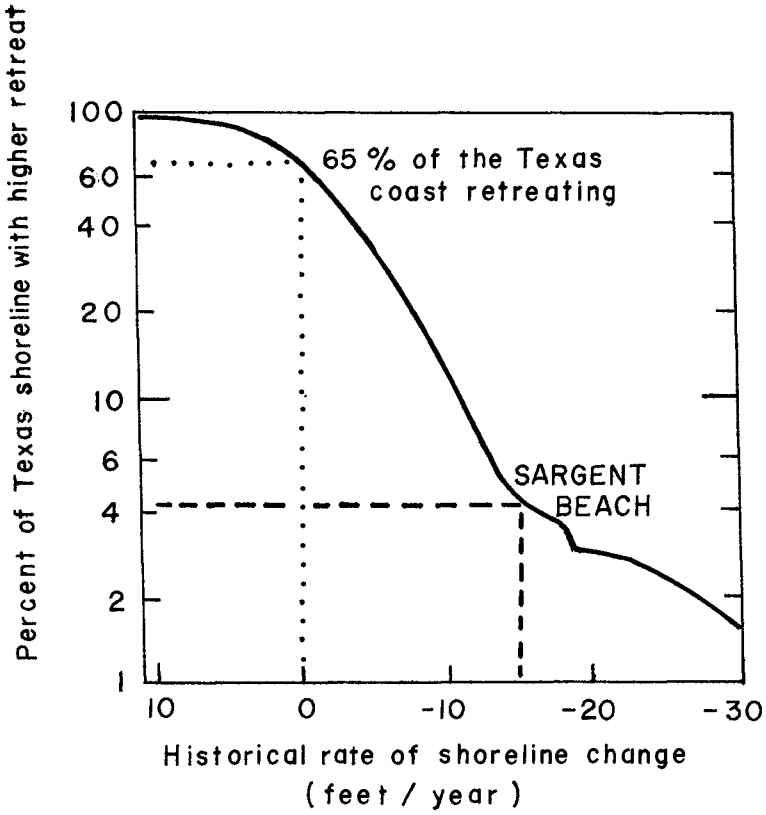
CUMULATIVE CURVE OF TEXAS
HISTORICAL SHORELINE CHANGES

FIGURE 4

The most striking result of the Sargent shoreline change is shown
in a chronological plot of shoreline position for the time period 1852
to 1972, which indicates a continual increase in the rate of shoreline
retreat or acceleration of beach losses (Figure 5). For example, in
the mid 1800's the shoreline retreat rate was approximately 10 feet
per year (3 m/year) which grew to 31 feet per year (9.8 m/year) for
1967 to 1973.
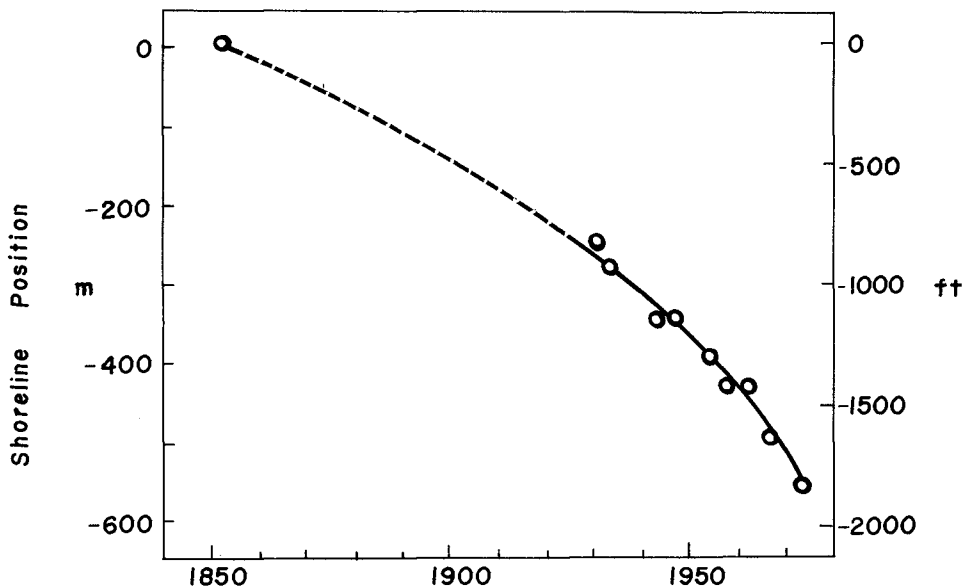
SARGENT BEACH SHORELINE LOCATION

FIGURE 5.

To investigate beach changes in greater detail, fifteen surveys
were made of four profiles at 1000 feet spacing on Sargent Beach for
the period 1967 to 1972 (surveys provided by Coastal Engineering
Research Center, Ft. Belvoir, Va.). Analysis of these profiles
includes location of the mean sea level intercept and determination of
volume change of the beach between the +5 and -5 feet contours
(Figure 6). The beach intercept retreated and the beach shape re-
mained relatively constant, so that the beach volume changes are
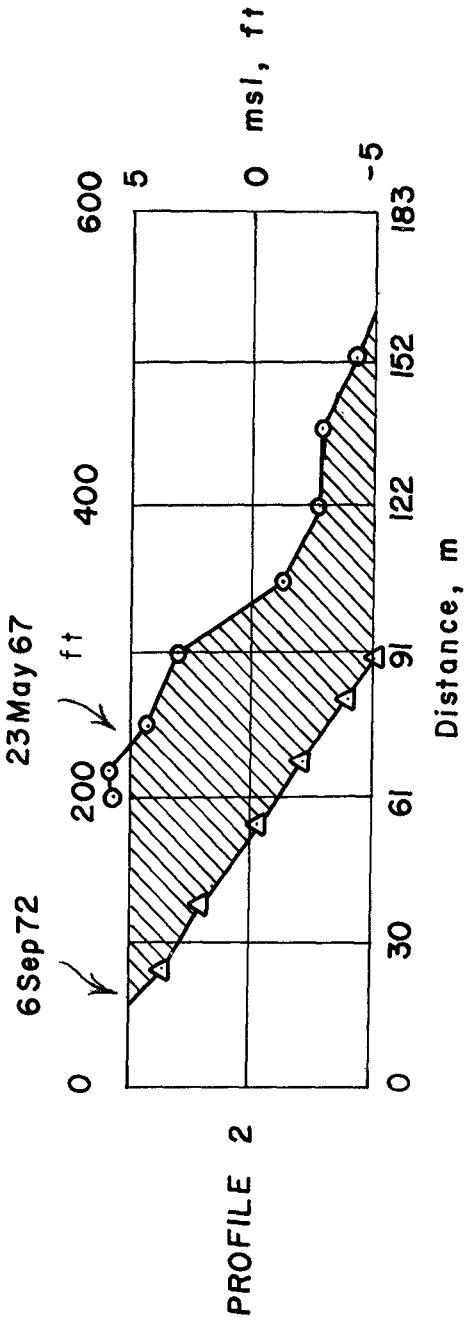
SAMPLE SARGENT BEACH PROFILES

FIGURE 6.

proportional to the intercept changes. Therefore, the beach can be
considered to be eroding continuously when using a three to six month
sampling interval (Figure 7).
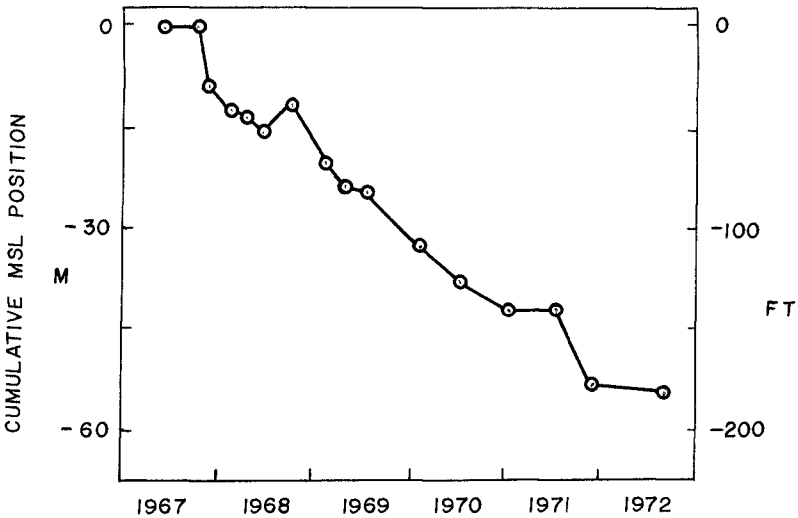
SARGENT SHORELINE CHANGES

FIGURE 7.

LONGSHORE TRANSPORT

   The net longshore transport of sand for the study area is from
east to west as determined from analyses of hindcast data for three
years off Caplan, Texas, growth of the Brazos deltas, and changes to
Brown Cedar Cut (Figure 1). Estimates of the transport rate vary
between 10,000 and 90,000 cubic yards per year depending on the data
and assumptions used (Mason and Sorensen, 1971, and Seelig and
Sorensen, 1973b). The gross rate is estimated to be between 250,000
to 1,000,000 cubic yards per year.

SUBSIDENCE

   Tide records indicate that much of the Texas coast is slowly
subsiding at varying rates (Hicks, 1972, and Swanson and Thurlow, 1972).
The recent subsidence rate for Freeport, the closest tide station to
Sargent Beach, has averaged .037 feet per year (.01 m/year). Assuming
a beach slope of 0.04, subsidence is estimated to cause approximately

5 feet (2 m) of beach retreat at Sargent Beach for the 5.3
year survey period. This 5 feet of shoreline retreat, estimated as
a first approximation of the shoreline change due to subsidence,
compared with a total observed shoreline retreat of 160 feet,
so subsidence is assumed to play a minor role in recent shoreline
changes.

SEDIMENT INPUT TO THE COAST

    The Brazos River has the highest sediment load of all
Texas rivers discharging directly into the Gulf of Mexico.
Measurements at the Richmond Bridge, 100 miles (160 km) from
the coast, include the river cross-section, daily water dis-
charge, suspended sediment measurements, and numerous size
analyses of suspended and bed load samples. These measurements,
in addition to work by Welborn (1973) and a Colby technique (1957),
are used to estimate the total suspended and unmeasured river
discharge of sand, where sand is defined as material greater
than or equal to 0.062 mm in diameter.

    Although the year-to-year river sand load may have a wide
random variation, a large scale pattern of sand discharge is
apparent when cumulative sand discharge for 1922 to 1972 is
plotted (Figure 8). The slope of this cumulative curve rep-
resents the mean long-term rate of sand input to the coast. As
can be seen in Figure 8, the slope (rate of sand discharge)
for the period 1922 to 1945 is approximately three times greater
than the sand discharge rate for 1945 to 1972. This drastic de-
crease in the sand load rate means that after 1945 only one-
third as much sand reached the coast in any given long period
of time as before 1945.

    A combination of factors caused this decreased sand load
to the coast after 1945. First, a dam on the Brazos River,
completed in the mid 1940's, alters the river hydraulics, which
directly effect the capability of the river to transport sand.
Calculations of sand transport for the Brazos River show that
65 percent of the sand reaching the coast is transported
during the highest 10 percent of water discharge periods, of
flood type conditions.   Similarly, 90 percent of the sand is
moved in the highest 25 percent river discharges. Since a purpose
of dams is to aid in flood control by reducing flood conditions,
even a small reduction in peak river discharge causes a
drop in the rate at which sand raches the coast. Sand is
further inhibited from reaching the coast due to reservoir
sedimentation.
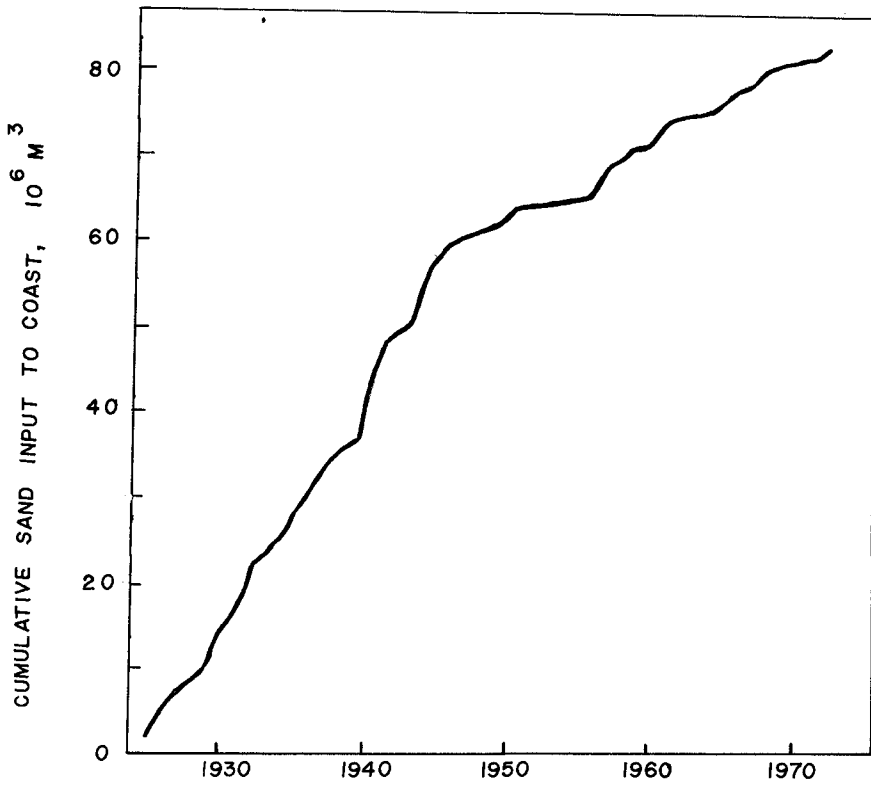
BRAZOS RIVER SAND LOAD
(CUMULATIVE)

FIGURE 8.

A drought in the 1950's for the Brazos area further decreased river discharge and therefore sand transported by the Brazos River.

Changes in the agriculture of the Brazos River watershed associated with World War II may have also changed runoff character-istics and river hydraulics, thereby reducing the river sand load.

SEDIMENT STORAGE

The Brazos Delta, at the mouth of the Brazos River, updrift from Sargent Beach, had a small subaerial portion in 1852 suggesting that only a small volume of sediment was stored in that area (Figure 2). The Freeport Jetties completed in 1899, however, provided a shadow zone downdrift of the jetties which encouraged the high Brazos sediment load to be deposited in the lee of the jetties (Figure 9). This old Brazos Delta largely disappeared when the river sediment supply was cut off in 1929-1930, suggesting that the old Brazos Delta was largely composed of river material.

When the river was rerouted to the west in 1929-1930, a large percentage of the sediment stored at the jetties was moved westward under the action of the predominant waves from the southeast. This unusually large mass of sand moving westward was trapped at the new river location to form the new delta nucleus. Continued high river sediment discharge en-couraged growth of the new Brazos Delta, which was quickly vegetated in the subtropical climate of the Texas coast. Aerial photography shows that this vegetation plays an impor-tant role in holding the delta together during hurricane periods.

The new Brazos Delta reached its maximum length in the mid 1940's, with retreat of the subaerial delta after the 1940's associated with the decreased river sand load. The symmetrical delta of 1948 also moved westward under the force of the westward longshore drift to the position shown in 1971 (Figure 2).
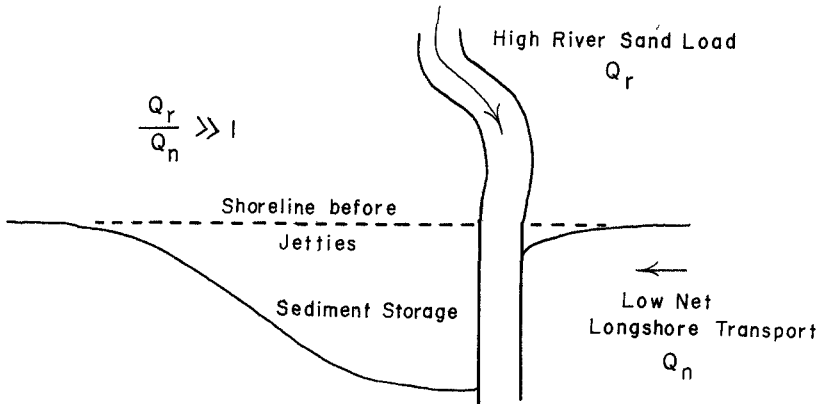
CONDITIONS FOR OLD BRAZOS DELTA FORMATION

FIGURE **9**

Hydrographic surveys for 1930 and 1972 were compared to determine the total net volume of sediment stored for both the old and new Brazos Deltas. Sediment size analyses of delta and offshore sediments by Odem (1953) and Nieneber (1963) were applied to this volume change to estimate the volume of sand stored, which indicates that one third of all Brazos River sands reaching the coast between 1930 and 1972 were stored in the Brazos Delta in 1972.

OFFSHORE LOSSES.

Hayes (1967) reports that hurricanes, such as Carla in 1961, move significant volumes of sediment out of the active beach zone and into deeper water where the sediment is effectively no longer available to the beach. It is believed that this process is encouraged by the Brazos deltas since a) their delta shapes focused wave energy, b) stored sand is available to be moved, and c) the jetting action of the Brazos River during flood conditions, also associated with hurricanes, will carry sediment offshore. Through this mechanism the delta is essentially acting as a system to bypass river sands from reaching the beach.

Surface sands found offshore of the Brazos Delta (Nienaber, 1963, Texas A&M Univ., Sea Dock Study, 1973) area are a sign that beach bypassing has taken place. Additional study of this mechanism is suggested.

CONCLUSIONS.

The large scale beach losses at Sargent Beach, now resulting in a net shoreline retreat of 31 feet per year, are due to a change in the delicate balance between supply and demand of sand. The simultaneous decrease in the sand load of the Brazos River after 1945 with the increase in storage in the Brazos Delta and improved possibility of offshore losses since 1930 means that much less sand is available to Sargent Beach from updrift sources. At the same time wave forces and associated longshore currents continue to remove sediment from Sargent Beach to give a net retreat and erosion of the beach (Figure 10).

ACKNOWLEDGMENTS
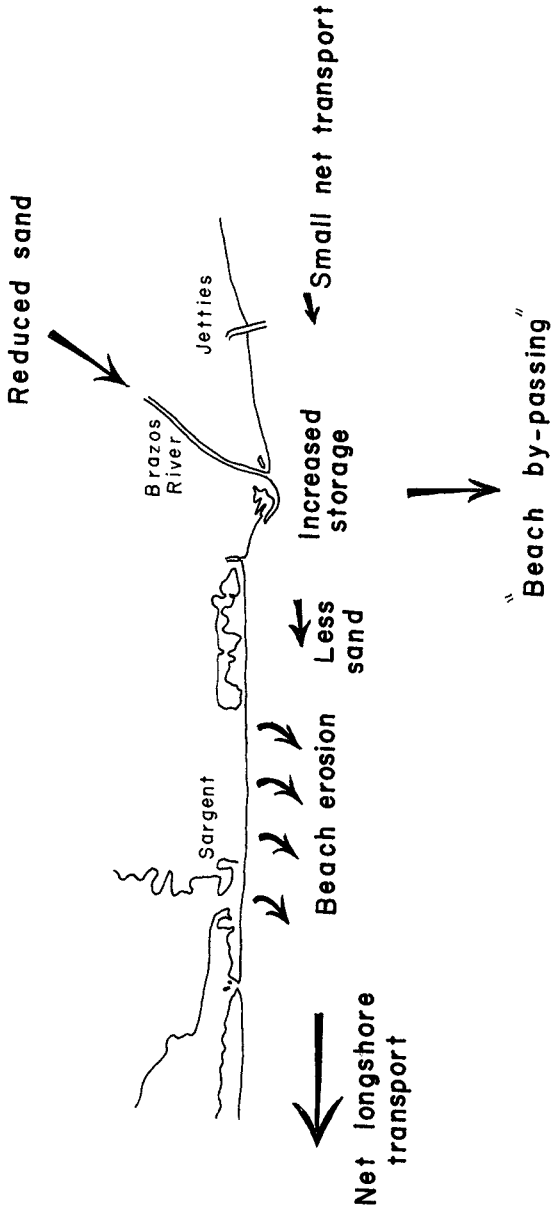
THE SAND BUDGET 1930's ~ 1970's

FIGURE 10.

REFERENCES

Colby, B. R., "Relationship of Unmeasured Sediment Discharge to Mean Velocity," Transactions, American Geophysical Union, Vol. 35, No. 5, Oct., 1957, pp. 708-717.

Hayes, M. O., "Hurricanes as Geologic Agents: Case Studies of Hurricanes Carla, 1961, and Cindy, 1963," Bureau of Economic Geology, Report Inv. 61, Univ. of Texas, Austin, Texas, 1967.

Hicks, S. D., "On the Classification and Trends on Long Period Sea Level Series," Shore and Beach, April, 1972.

Mason, C., and Sorensen, R. M., "Properties and Stability of a Texas Barrier Beach Inlet," Sea Grant Publication No. TAMU-SG-71-217, Texas A&M University, College Station, Texas, Aug., 1971.

Nienaber, J. H., "Shallow Marine Sediments Offshore From the Brazos River, Texas," Institute of Marine Science, Vol. 9, 1963, pp. 311-372.

Odem, W. I., "Delta of the Diverted Brazos River of Texas," Thesis in Geology, Univ. of Kansas, 1953, pp. 1-112.

Sealy, J. E., "A Mathematical Model for River Delta Development and Its Application to the New Brazos Delta at Freeport, Texas," M. S. Thesis in Geology, Texas A&M University, College Station, Texas, May 1974.

Seelig, W. N., and Sorensen, R. M., "Historic Shoreline Changes in Texas," Sea Grant Report TAMU-SG-73-206, Texas A&M University, College Station, Texas, April, 1973(a).

Seelig, W. N. and Sorensen, R. M., "Investigation of Shoreline Changes at Sargent Beach, Texas," Sea Grant Report TAMU-SG-73-212, Texas A&M University, College Station, Texas, 1973(b).

Swanson, R. L., and Thurlow, C. I., "Recent Subsidence Rates Along the Texas and Louisiana Coasts as Determined From Tide Measurements," National Ocean Survey, NOAA, Rockville, Maryland, 1972.

Welborn, C. T., unpublished notes on the Colby method for computing the unmeasured sediment load of the Brazos River at Richmond, Texas, U. S. Geological Survey, Austin, Texas, received 1973.

CHAPTER 68

PROTECTION OF SANDY COASTS IN DEPENDENCE OF
THE DUNE - BEACH - TYPE

by

Heie Focken Erchinger *)

ABSTRACT

Barrier dunes are the natural protective structures
against flooding the low-lying land during storm tides.
Their strength and resistance are to be estimated in
consideration of the total dune-beach-profile. For
standardization of dune-beach-profiles 3 types are to
be distinguished. For each of these types the
necessary and the possible actions for stabilization
of the barrier dunes and also of inshore dune areas
are described.

INTRODUCTION

On sandy coasts the ridges of sand dunes are often the
natural protective structures against flooding the
low-lying land, the villages or towns during storm
tides. The strength and resistance of these barrier
dunes, which are found just landward of the beach, is
to be estimated in consideration of the extent and the
height of the dunes as well as of the width, the height
and the stability of the beach. As in many cases on the
beach in consequence of altering sea and wave conditions
and different littoral drift the supposition for erosion
or aggradation varies, dunes and beaches have to be ob-
served constantly. The beginning of a considerable
erosion of the dunes has to be seen in connection with

---

*) Dipl.-Ing., Coastal Protection Department
   298 Norden/Ostfriesland, West-Germany
   P.O.-Box 102

the development of the beach. A systematical research
of the reasons and the further development has to be
done. The research has to include the total dune-beach-
profile.

STANDARDIZATION OF DUNE-BEACH-PROFILES

To find a system and to ease the discussion three
different dune-beach-types are to be distinguished.

Type 1   with surplus of sand and a filled up, wide
         and high beach,

Type 2   with a balanced statement of sand conditions,

Type 3   with sand deficiency and beach erosion.
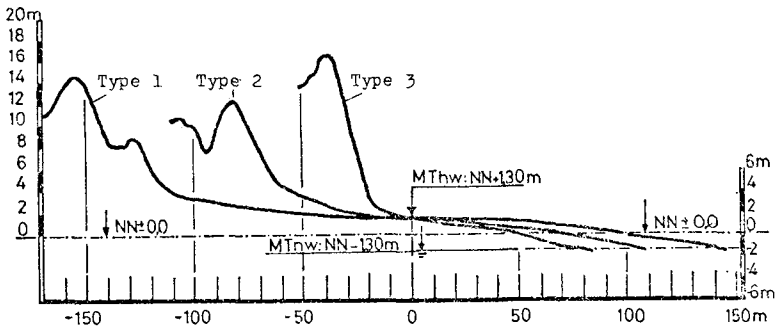
Fig. 1   Dune-Beach-Profiles of the Isle of Spiekeroog

Dune-Beach-Profiles of the Isle of Spiekeroog, one of
the East Friesian islands of the German North Sea
Coast, are chosen for examples of the single types of
the dune and beach. The main wind direction during
storm tides is about North-West. The dominant littoral

drift is from West to East. The sandbars pass the
inlets to the tidal flats in a curve, cambered to the
North. The point, where the bars reach the beach,
varies. On the eastside of this deposit point we have
a natural beach fill up, and on the westside a sand
deficiency as a rule.

Therefore, type 1 is to be found on the eastside and
type 3 on the westside of the deposit point of the
bars. (Fig. 2).

Type 1 is a high and wide beach filled up by surplus
of sand. The foredunes increase by aeolian deposited
sand. The new built dunes or the new sand layers are
stabilized with vegetation by nature.

Type 2 has a balanced statement of sand conditions
and, therefore, a less high and wide beach than Type 1.

Type 3 has a low and narrow beach and a cliff at the
seaside of the eroding dune. During storm surges it
runs up to a considerable eroding of the dune.

The following datas are typical for the dune-beach-
types with dune and beach sand grain size about 0.2 mm:

      TYPE 1   TYPE 2   TYPE 3
Inclination of the beach between MHW and MHW - 1 m
      1 on 90   1 on 60   1 on 40

Distance between MHW on the beach and the toe of the dune
      110 m   65 m   20 m

Inclination of the slope:
   of the natural deposited overgrown dune   1 on 2
   of the cliff   1 on 1.3
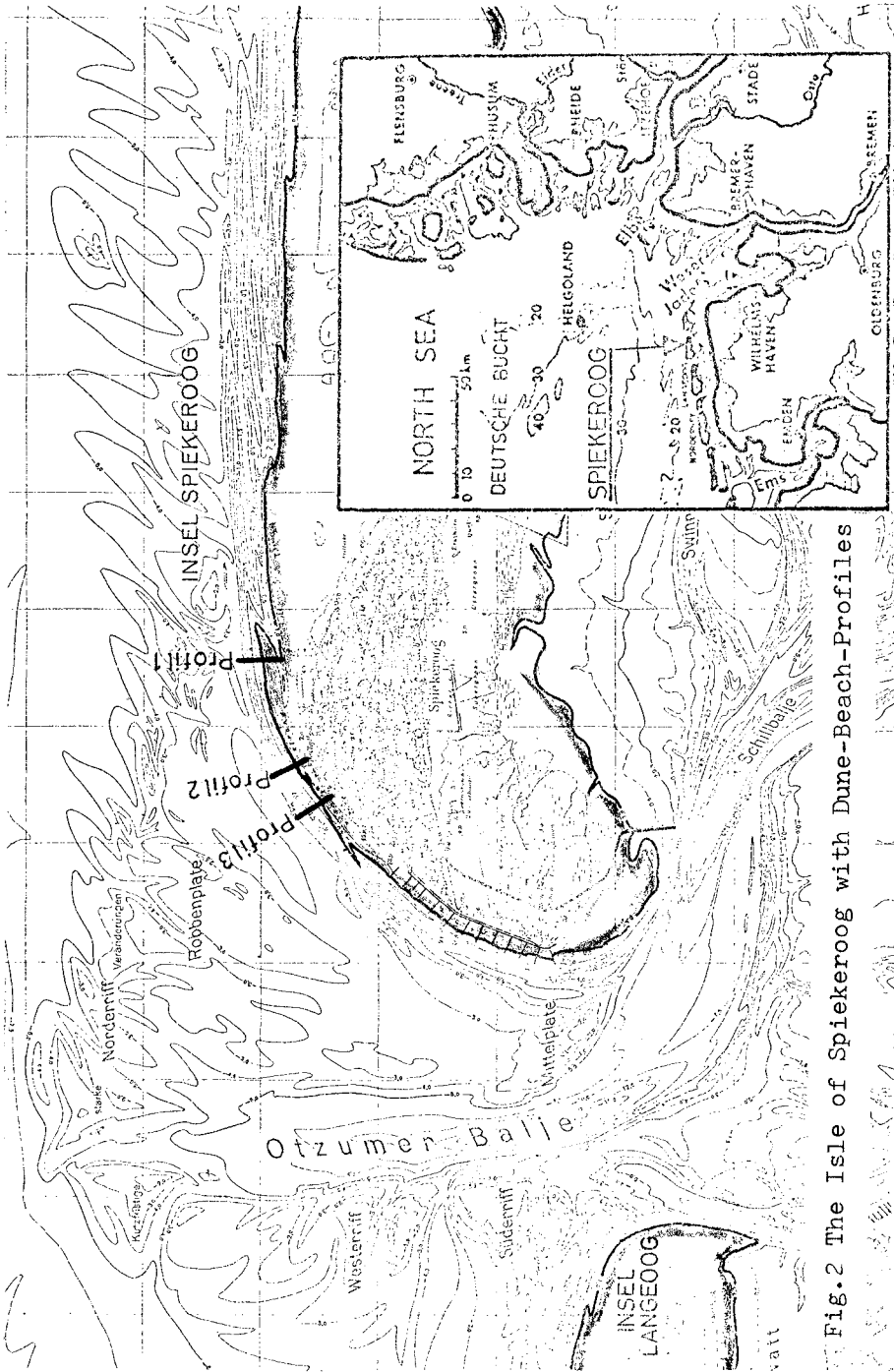
Fig.2 The Isle of Spiekeroog with Dune-Beach-Profiles

Dune Erosion in the Stormtides

Stormtides:

NN + 3.74 m   19.11.73
NN + 3.60 m   16.12.73
NN + 2.55 m   16.11.73
NN + 2.52 m   14.12.73
NN + 3.46 m   13.11.73

Accretion

MThw NN + 1.30 m

MTnw NN − 1.30 m

NN ± 0.00
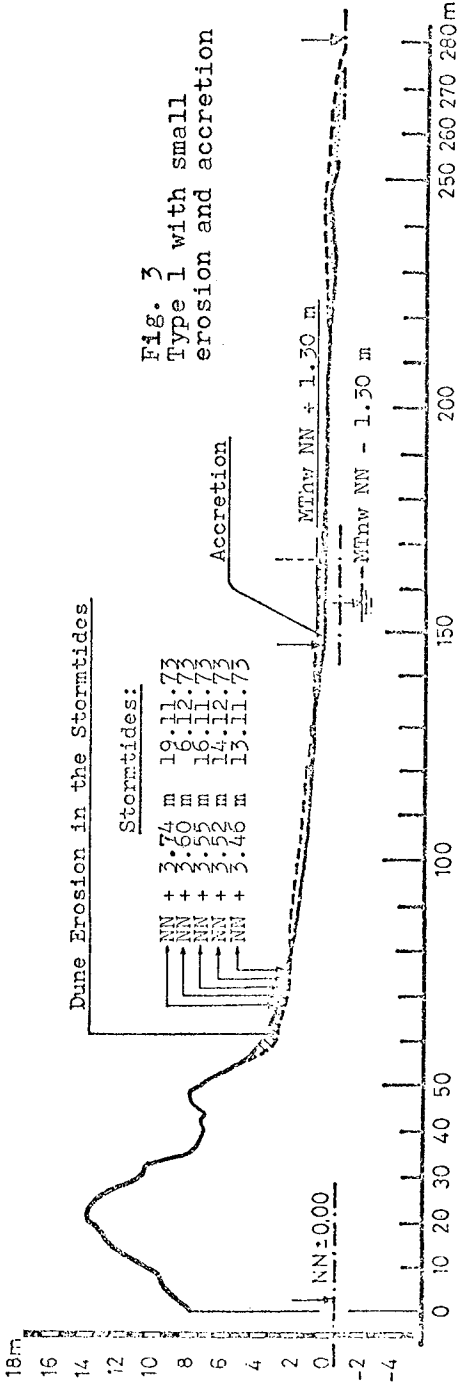
Fig. 3
Type 1 with small
erosion and accretion

Dune Erosion in the Stormtides

Stormtides:

NN + 3.74 m   19.11.73
NN + 3.60 m   16.12.73
NN + 2.55 m   16.11.73
NN + 2.52 m   14.12.73
NN + 3.46 m   13.11.73

Accretion

MThw NN+1.30m

MTnw NN −1.30m

NN ± 0.00

NN ± 0.00
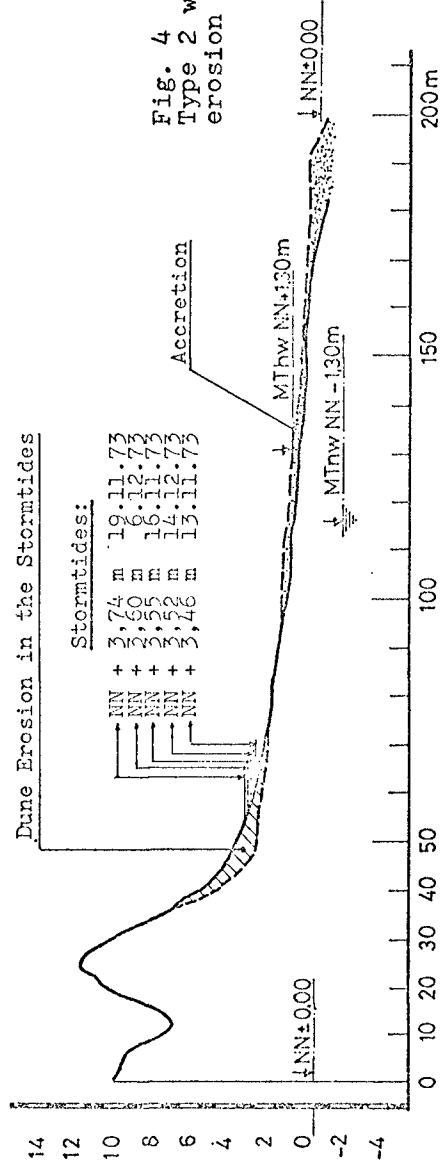
Fig. 4
Type 2 with moderated
erosion and accretion

In November/December 1973 21 storm tides attacked
our coast, 5 of them have been very high, about 2,5 m
higher than MHW. These storm tides result in a con-
siderable wave wash of the dunes and an accretion on
the beach especially on the beach sections of type 3.

On the dune beach type 1 only a very small effect
could be remarked (Fig. 3). On type 2 there was a
remarkable cliff, which meanwhile is filled up by
aeolian deposited sand (Fig. 4). In type 3 most of
the foredune was eroded with a width in the base of
about 20 m and about 230 m^3 loss per linear m. But
this sand nourished the beach, which increased con-
siderably (Fig. 5).
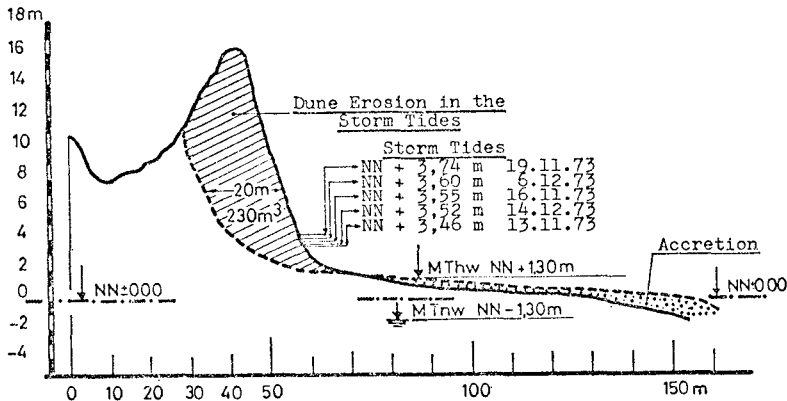
Fig. 5   Type 3 with considerable erosion and accretion

STABILIZATION OF BARRIER DUNES

And now the question, what is to do for stabilizing
sand dunes to prevent the loss of their protection,
for the sand dunes may provide more effective
protection at a lower cost than either a bulkhead
or seawall.

For each dune-beach-type there are different suitable
measures to be taken.

Type 1: The foredune at the landward side of the high
and wide beach increases by aeolian deposited sand.
The new built dunes or the new sand layers are
stabilized with vegetation by nature, in general with
two dune grasses: agropyron junceum at the toe of the
dune and the lower parts, and ammophila arenaria on
the slope and the higher parts. Protective actions
are not to be taken as a rule. To get uninterrupted
ridges of dunes it may be favourable to promote sand
deposition in lower parts by constructing sand fences
and planting dune grasses.

Type 2 has a less high and wide beach than Type 1.
As a rule in storm surges a small cliff at the toe
of the dune is created by wave action. It has to be
filled up by sand. For this fill up and the artificial
construction of dunes sand fences of brush or plastic
fabrics a.s.o. are to be placed on the beach. Formerly
sand fences have been constructed of natural products
like brush or reed mats. Nowadays plastic fabrics are
preferred. Plastic mats like foils or plates of poly-
ethylene (PE) 2 mm thick with holes about 2 times 8 cm
for coarse-grained sand are used (Fig. 6).

The plates are fastened on wooden piles or reinforcing
steel bars. The holes inclose 28 % of the surface.
Another plastic fabric is a polyester-web, known as
Trevira; it is preferred for fine-grained dune-sand
about 0.2 mm and fastened on wooden piles. This web
of small threads has openings about 70 % of the surface.
(Fig. 7). The height of these plastic sand fences
measures between 60 und 120 cm, they are cheaper than
brush fences and they are more durable and even nearly
imperishable.

Fig. 6   Sandfence of polyethylene

Fig. 7   Sandfence of the polyester-web
         "Trevira"

The fences are to construct parallel to the toe of
the dune in one or few lines with side spurs or
perpendicular fences between them.

Fig. 8   Sandfences at the toe of
          the barrier dune

After the sand has deposited it should be stabilized
with vegetation. The most satisfactory plants of dune
grasses, ammophila arenaria, are long-lived perennials,
with extensive root systems, spreading rapidly and
maintaining the surface increasing by farther deposits.
A rank growth of these dune grasses is to be expected
after steady new sand deposition as the plants get
the nutritive substance out of the sand. The dune
grasses are to be planted in lines with a distance
of about 30 cm and 30 cm distance between each plant
in the line. In spring, autumn and winter there is no
problem of growing up in the described climate region.

Type 3 has a low and narrow beach and a cliff at the
seaside of the eroding dune. During storm surges it
runs up to a considerable eroding of the dune (Fig. 9).

Fig. 9   Cliff of the barrier dune of type 3

There practically is no chance for any method of
artificial construction of dunes. Constructing sand
fences and planting dune grasses may be effectful,
only if aeolian sand deposition is to be expected
after a remarkable accretion in result of dune erosion
in a storm surge. Planting of dune grasses on the
steep cliff means no stabilizing against storm surges.
What can be done is to make the slope of the dune less
steep for rendering possible an aeolian redeposit of
the dune to cover the sand from loss by littoral
transport (Fig. 10). On the Isle of Spiekeroog an
inclination of the slope of the 12 m high cliff with
aeolian redeposit about 1 on 1.9 to 1.4 in the upper
part was found.
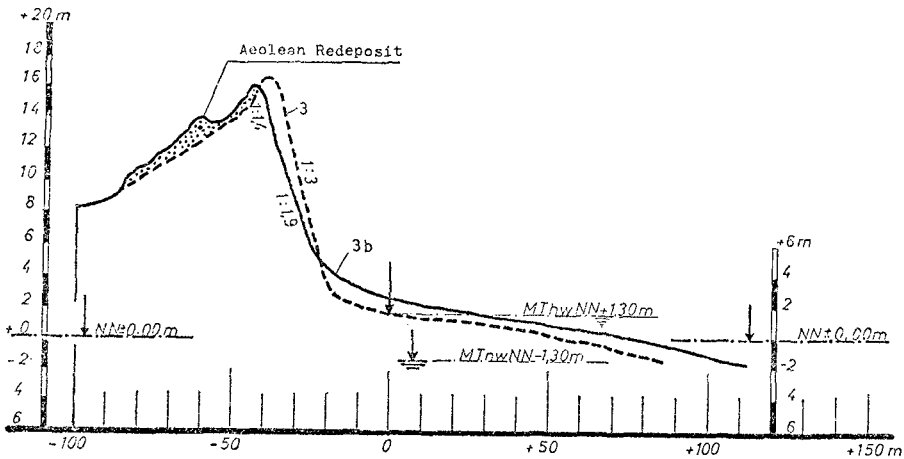
Fig. 10   Dune-beach-profile type 3 with
           aeolian redeposit

Another way of redeposition is proved in the Nether-
lands. On the Isle of Texel the eroding dune is
redeposited by bulldozers.

If in the case of farther eroding of the barrier dune
of type 3 human settlements, buildings a.s.o. would
be destroyed by the sea and the development of the
beach and the littoral drift remain unfavourable,
protective structures like groynes, seawalls or
revetments to the flattened slope of the dune have to
be carried out. A wide dune area at the beachside
kept free of any buildings provides that the eroding
of the dune can be borne for a long time before
suitable protective actions have to be taken. As there
are coasts with alternating phases of beach erosion
and aggradation, these areas without buildings can
render it possible to stand out without protective
actions. But if protective actions are inevitable,
massive constructions should only be built, if there

is no other possibility of protection, for such gearing
in the natural development of the beach can cause un-
welcome secondary effects and inefficacies like lee
erosion, wave reflection a.s.o. Protective actions
which are according to nature like artificial beach
fill up are to be preferred to massive constructions
like groynes and revetments as a rule.

STABILIZATION OF INSHORE DUNE AREAS

But not only the front but also the back of the fore-
dune has to be covered from aeolian erosion. At the
back of the barrier dune the dune area has often been
blown out onto the ground water level after the dune
vegetation has been destroyed. To prevent further
erosion sand fences are constructed reticularly over
the dune surface each field measuring 25 times 25 m.
Dune grasses are planted in the single fields in
reticular strips or the field at all (Fig. 11).

Fig. 11   Stabilization of inshore-dune-areas

By fences and plants the roughness of the surface
increases, so that wind, erosion and deposition are
influenced and wind movement is deflected or screened.
Then typical plants in this special location are to
be taken root and the dunes are stabilized by vegetation.

REFERENCES:

1) Dieren, J.W. van: Organogene Dünenbildung, Den Haag, 1934

2) Erchinger, H.F.:   Die Erhaltung der Dünen zum Schutze der Inseln in
                           Ostfriesland, Bauwirtschaftliche Informationen Nr. 11
                           Neumünster, 1970

3) Erchinger, H.F.:   Dünenschutzmaßnahmen und Versuche zur Dünenbegrünung
                           auf Norderney, Deutscher Rat für Landespflege Heft 14/1970

4) Erchinger, H.F.:   Kunststoffe im Dünenbau, Wasser und Boden Heft 11/1972

5) Führböter, A.:   A Refraction Groyne built by Sand, 14th Intern. Conference
                           on Coastal Engineering, Copenhagen, Paper 3.7-2

6) Kramer, J.:   Künstliche Wiederherstellung von Stränden unter besonderer
                           Berücksichtigung der Strandaufspülung Norderney 1951/52.
                           Bd. 9. Jahresbericht der Forschungsstelle Norderney 1957,
                           S. 53/92

7) Kramer, J., A. Führböter,   Sandbuhne vor Sylt zur Stranderhaltung
   R. Köster, J. Schwitters   Die Küste 20/1972 Nr. 23, S. 1/62
   u. J.Sindern:

8) Luck, G.:   Bericht über die zweite Strandaufspülung am Weststrand
                           von Norderney. Bd. 20. Jahresbericht der Forschungsstelle
                           Norderney 1968, S. 7/34

9) Lüders, K., A. Führböter   Neuartige Dünen- und Strandsicherung im Nordwesten der
   u. W. Rodloff: Insel Langeoog. Die Küste 20/1972 Nr. 23, S. 63/111

10) Lux, H.:   Die biologischen Grundlagen der Strandhaferpflanzung
                           und Silbergrasansaat im Dünenbau. In: Angewandte
                           Pflanzensoziologie (Stolzenau/Weser), H. 20/1964

11) Lux, H.:   Planmäßige Festlegung der schadhaften Binnendünen auf
                           den nordfriesischen Inseln Sylt und Amrum
                           Natur und Landschaft, H. 6/1969

12) Witte, H.-H.:   Die Schutzarbeiten auf den Ostfriesischen Inseln
                           Die Küste H. 19/1970

13) Zitscher, Fr.F.:   Kunststoffe für den Wasserbau. Verlag W. Ernst
                           u. Sohn, Berlin, München, Düsseldorf, 1971.

CHAPTER 69

BARRIER BEACHES AND SEDIMENT TRANSPORT IN

THE SOUTHERN GULF OF ST. LAWRENCE

by

E. H. Owens

Atlantic Geoscience Centre, Geological Survey of Canada,
Bedford Institute of Oceanography, Dartmouth, Nova Scotia.

ABSTRACT

Barrier islands and barrier beaches have developed across
structurally controlled estuaries and embayments in the southern Gulf
of St. Lawrence. The supply of sediments to the littoral zone and the
subsequent accumulation of barrier deposits is a result of the re-
working, transportation and longshore dispersal of sediments which are
moved landward by tidal and wave-induced currents from the adjacent
shallow sea floor. The size and stability of the barriers is controlled
by the shoreline orientation.

INTRODUCTION

Barrier islands and barrier beaches have developed across
structurally controlled embayments or estuaries in the southern Gulf of
St. Lawrence, Canada. Distinct regional variations in the geomorphology
of these barrier deposits are discussed in relation to shoreline
orientation and to sediment dispersal patterns in the littoral zone. It
is possible to explain the morphological variations in terms of the
coastal zone processes and the sediment transport systems of the littoral,
nearshore, and offshore zones. This synthesis of the barrier systems is
based on a reconnaissance survey of the coastal zone (Owens, 1974a; Owens

1177
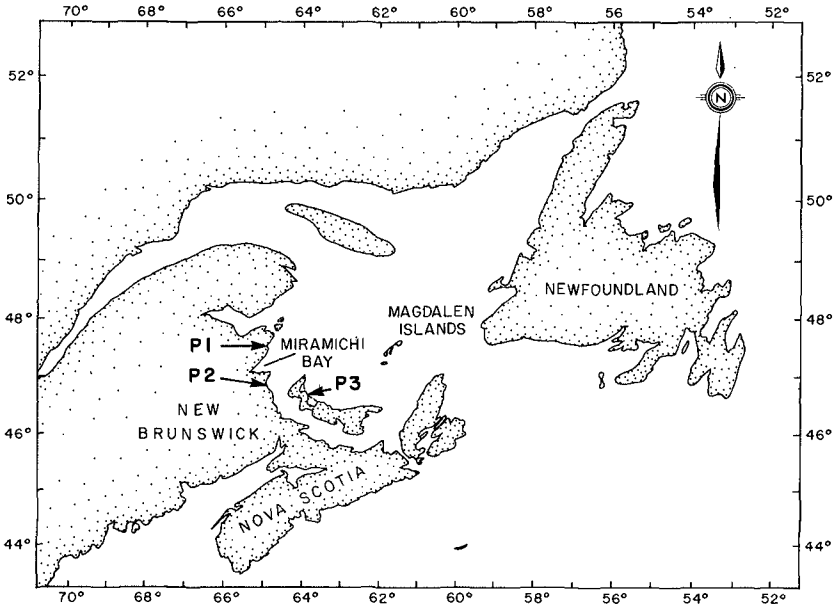
Figure 1: Location diagram of the Gulf of St. Lawrence, Canada. P1, P2, and P3 refer to the sites of profiles given in Figure 10.
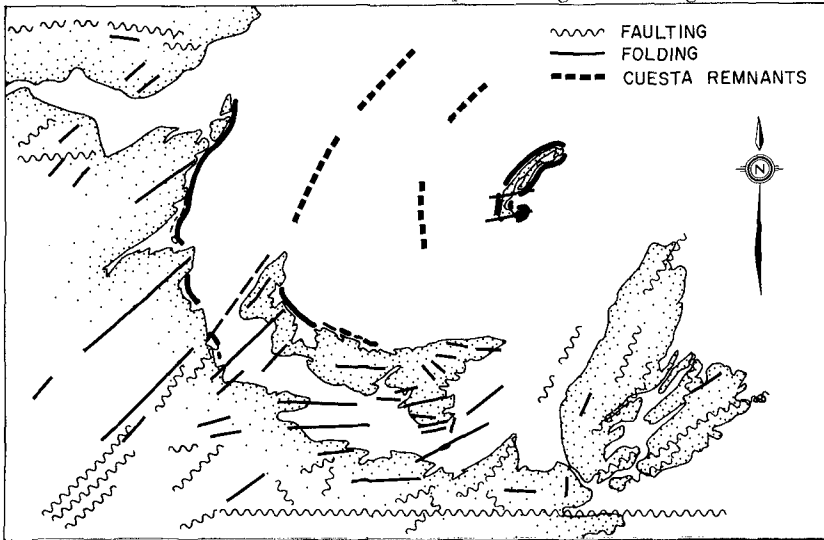
Figure 2: Major structural trends in the southern Gulf of St. Lawrence (after Owens, 1974a). Barrier beaches are indicated by a solid line parallel to the coast.

and Harper, 1972) and on a detailed sedimentological study of the Gulf of St. Lawrence (Loring and Nota, 1973).

The southern half of the Gulf of St. Lawrence is a shallow (< 200 m), semi-enclosed sea (Fig. 1) underlain by unresistant Permo-Carboniferous sandstones and shales which have been folded to form a broad northerly plunging synclinorium (Sheridan and Drake, 1968). The submarine morphology of this region is related to a preglacial drainage system which developed along lines of structural and lithological weaknesses. The Pleistocene ice sheets did not significantly modify this drainage pattern and the major effect of glaciation was the deposition of tills and moraines (Loring and Nota, 1973). After deglaciation the sea level was lowered to a maximum of -70 m as a result of isostatic readjustment. The glacial and fluvio-glacial sediments were then reworked during the subsequent marine trans-gression which followed the period of emergence. The present shoreline
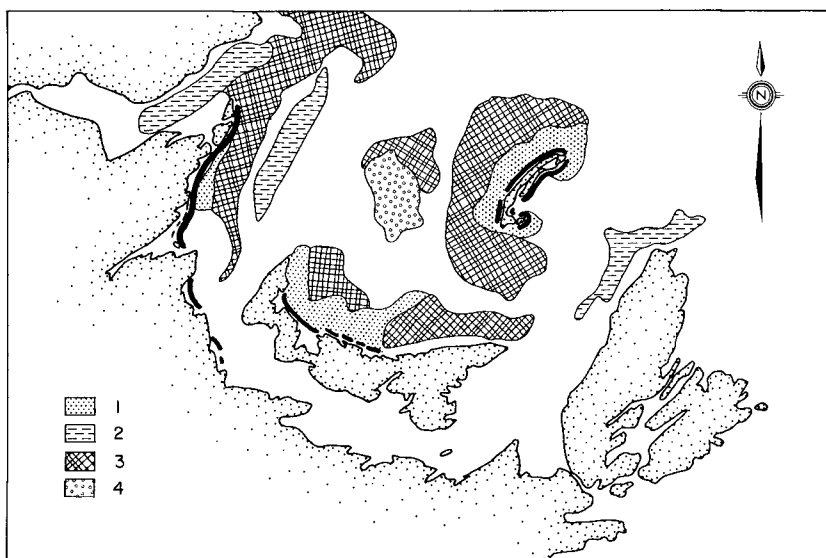
Figure 3: Sedimentary environments of the southern Gulf of St. Lawrence (from Loring and Nota, 1973).
1. Nearshore and coastal areas of active reworking and re-distribution
2. Active deposition of fine-grained sandy and very sandy pelites
3. Areas of non-deposition with local reworking and formation of lag deposits
4. Offshore areas of active reworking and redistribution
Blank areas are zones of transition.

results from the submergence of the cuesta lowland and the subsequent
development of barrier beaches across embayments and estuaries (Fig. 2)
(Johnson, 1925).

SEDIMENT SOURCES

          Where the unresistant sandstones and shales outcrop along the
coast they are rapidly eroded by wave action resulting in shoreline retreat
rates greater than 1 m/year. The supply of sediment from the sandstones is
limited by the low relief (the cliffs are usually less than 5 m high) and
by the short sections of the outcrops updrift of the barrier beaches (Owens,
1974a). Also, sediment from rivers which drain small catchment areas
often does not reach the littoral zone as the drowned estuaries act as
sediment traps. These terrestrial sources therefore do not supply large
volumes of sediment to the coastal zone at the present.

          Detailed analysis of bottom sediments in the southern gulf by Loring
and Nota (1973) shows that reworking and redistribution is taking place off-
shore. A map of sedimentary environments (Fig. 3) indicates zones where
glacial and fluvio-glacial deposits are being reworked (units 3 and 4).
Fine-grained sediments are transported and deposited in deeper water
(unit 2) while sands are redistributed landward (unit 1). Mineralogical
analysis of material from the littoral and offshore environments (Loring
and Nota, 1969) shows that these sediments are derived from the same
source. Direct evidence for movement of sediment on the sea-floor is pro-
vided by bottom photographs and side-scan sonar records, which show fields
of sand waves in water depths up to 54 m (Loring et al, 1970).

          The reworking, sorting, and redistribution of bottom sediments on
the shallow shelf results from tide- and wind-generated currents.
Lauzier (1967) reported landward residual drift on the sea-floor adjacent
to the coasts of eastern New Brunswick and northern Prince Edward Island
(Fig. 4). These bottom currents can be related to the prevailing and
dominant offshore winds along these coasts (Fig. 5) which cause a seaward
movement of surface waters and generate a counter residual drift toward
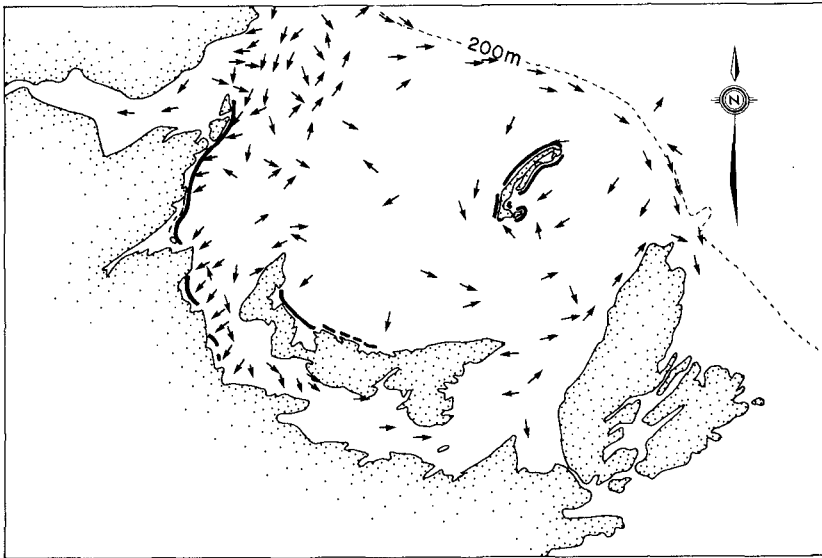
Figure 4: Bottom residual currents in the southern Gulf of St. Lawrence
(after Lauzier, 1967). Barrier beaches are indicated by a
solid line parallel to the coast.
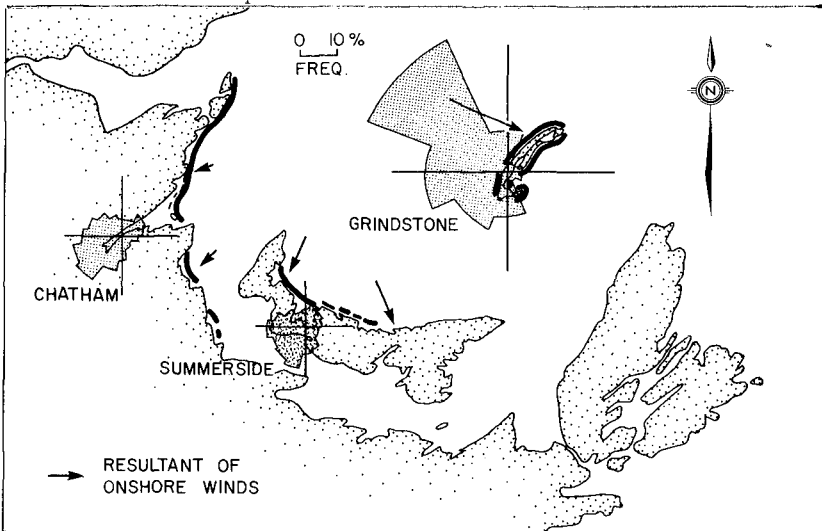
Figure 5: Wind frequency roses for Chatham, New Brunswick; Summerside,
Prince Edward Island; and Grindstone, Magdalen Islands. The
resultants of onshore winds are proportional. Barrier beaches
are indicated by a solid line parallel to the coast.

BARRIER BEACH TEXTURE ANALYSIS

|	INTERTIDAL			DUNE			
	n	$\bar{x}(\phi)$	σ	n	$\bar{x}(\phi)$	σ	UNIT
N.E. NEW BRUNSWICK	26	1.52	0.49	8	1.51	0.46	a
NEGUAC/MIRAMICHI	23	1.73	0.40	4	1.69	0.38	b
KOUCHIBOUGUAC	8	1.46	0.39	3	1.61	0.37	c
BUCTOUCHE	4	1.49	0.39	1	1.58	0.39	d
NORTH P.E.I.	6	1.93	0.38	7	2.09	0.38	e
ILES-MADELEINE (W)	15	1.67	0.32	6	1.67	0.37	f
ILES-MADELEINE (E)	17	1.87	0.36	5	1.95	0.36	g

Table 1: Summary of textural data for intertidal and dune sediment
samples. The location of the units is shown in Figure 6.

the land. This provides the mechanism for the transportation of sand
into the shallow nearshore zone where it is redistributed by tidal and
wave-induced currents.

Textural analyses of intertidal and dune samples from the barrier
beaches, collected at a 10 km interval (Owens, 1974b), show a high degree
of uniformity in mean size and sorting values (Table 1; Fig. 6). The
averaged mean grain size values for each unit range from 1.46ϕ to 1.93ϕ
(0.36 mm to 0.26 mm) for the intertidal samples and from 1.51ϕ to 2.09ϕ
(0.35 mm to 0.24 mm) for the dune samples. All the sorting values (σ)
fall within Folk's "very well sorted" (<0.35) or "well sorted" (0.35 -
0.49) categories. This uniformity of textural characteristics, combined
with the mineralogical homogeneity discussed by Loring and Nota (1969)
suggests a common source for the barrier sediments.

The barrier beaches developed initially during the marine trans-
gression and have migrated landward. The maintenance and extension of
the barriers is dependant on a continuing supply of sediment. A major
source of sand is onshore transportation from the adjacent nearshore
and offshore zones.

SEDIMENT DISPERSAL

The southern gulf is a semi-enclosed sea, largely protected from Atlantic swells, and the wave environment is dominated by short period, locally generated, storm waves. Two factors limit wave generation, the relatively short fetches (<700 km) and the presence of sea and beach-fast ice for up to four months each year (Owens, 1974a; 1974c). This is also a micro-tidal environment with mean tidal ranges less than 2 m.

Discussion of separate barrier systems is possible as each set of barriers has developed across a particular embayment or estuary and is usually bordered by a bedrock outcrop. For this discussion the barrier coasts have been divided into seven units (Fig. 6) on the basis of morphology and sediment dispersal characteristics.

The northeast coast of New Brunswick (unit a) and the Neguac-
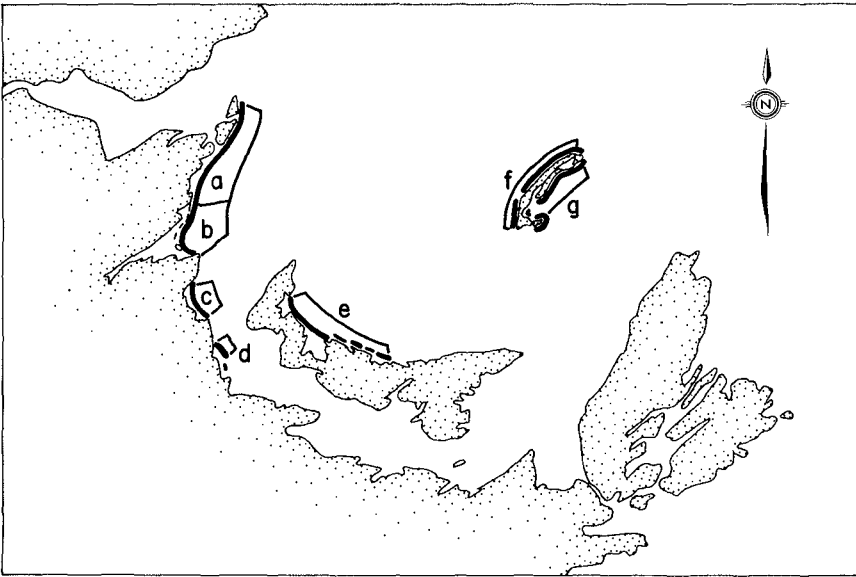
Figure 6: Barrier beach units in the southern Gulf of St. Lawrence.

    a. Northeast New Brunswick
    b. Neguac - Miramichi embayment
    c. Kouchibouguac embayment
    d. Buctouche Bar
    e. Northern Prince Edward Island
    f. Western Magdalen Islands
    g. Eastern Magdalen Islands

Miramichi embayment (unit b) together form one of the major barrier systems in the southern gulf. Sediment is supplied to the littoral and nearshore zones from the shallow offshore sea-floor and is redistributed along the coast. Meteorological data from Chatham (Fig. 5) shows the predominance of winds from the southwest in this area, that is offshore, with the on-shore wind vectors out of the northeast quadrant (Fig. 7). The direction of littoral transport is from north to south in response to wind-generated waves from the northeast quadrant (Owens, 1974a).

North of the Miramichi-Neguac embayment the barrier system is char-acterized by sediment bypassing and transport to the south. At Neguac, on the north shore of Miramichi Bay (Fig. 8) this dispersal pattern has led to rapid inlet migration and barrier extension (Owens, 1974d). A change in
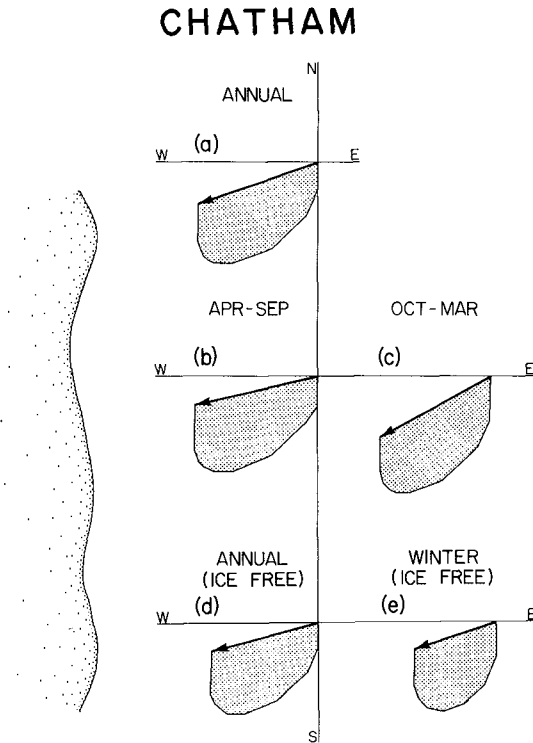
CHATHAM

Figure 7: Vectors of onshore winds for the coast of northeast New Brunswick and the Neguac-Miramichi embayment, based on data from Chatham, New Brunswick. Shoreline orientation is assumed to be north-south.
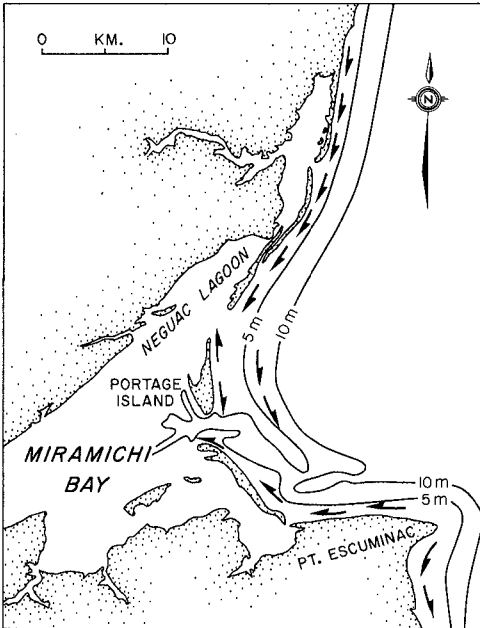
Figure 8: Generalized pattern of sediment dispersal (indicated by the arrows) in the littoral and near-shore zones of the Neguac - Miramichi embayment.
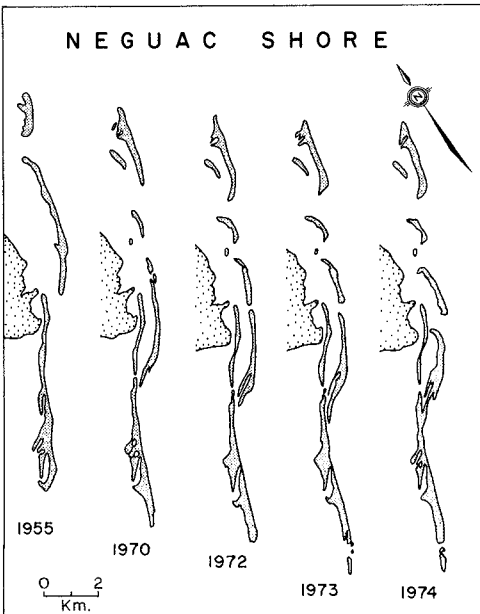
Figure 9: Shoreline changes at Neguac, New Brunswick, derived from vertical and oblique aerial photography. The location of this barrier system in relation to the adjacent coast is shown in Figure 8.

shoreline orientation at Neguac, due to the drowning of the Miramichi
estuary, has led to the development of overlapping barrier islands (Fig.
9). In addition to distal migration and extension of the larger barrier
islands, the smaller islands have reoriented to become more closely
aligned to waves approaching from the northeast. Miramichi Bay acts as
a sediment trap for material supplied by the river and for the southward
littoral drift along this coast. There is an area on the south shore of
the embayment where the drift is reversed (Fig. 8) as waves from the
northeast generate westerly and northwesterly longshore currents. At
Portage Island, although the prevailing direction of littoral drift is to
the south, a reversal to the north can occur depending on the direction
of wave approach.

        The barrier beaches of this coast are generally low, less than
3 m above mean high water (profile P-1; Fig. 10), and are frequently
washed over or breached by storm waves. Extension of the barriers at
Neguac appears to result from pulses of sediment which are moved along-
shore under storm-wave conditions, though no direct measurements have
been made to confirm this.

N.E. NEW BRUNSWICK
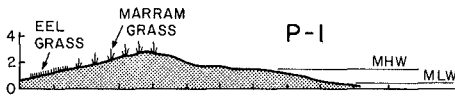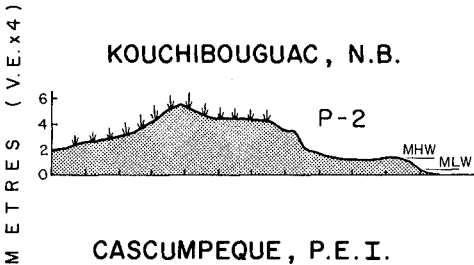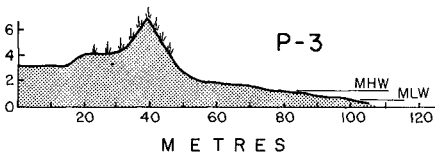
Figure 10: Selected profiles
           across three barrier
           beaches. These profiles
           are located in Figure 1.

Dates of profile survey:

P-1	10 June 1972
P-2	8 June 1972
P-3	1 August 1972

The barriers across the Kouchibouguac embayment (unit c: Fig. 6) are orientated to face the northeast and waves approach at a less acute angle to the shoreline as compared with the barrier systems to the north. As a result of this different orientation the longshore component of sediment movement is reduced, although littoral drift is still to the south. Sediment is supplied to the littoral zone by coastal erosion in updrift areas and by the onshore movement of material from the shallow offshore area (Kranck, 1967). Little sediment is lost from the embayment by littoral or nearshore drift around the rock headlands at the southern limit of this system because of a local drift reversal (Owens, 1974a; Fig. 13). The barrier beaches are up to 6 m above mean high water (profile P-2; Fig. 10) and are only infrequently breached by storm waves. This system is migrating landward (McCann and Bryant, 1972) but is relatively stable and is not undergoing major shoreline changes.

Buctouche Bar (unit d; Fig. 6) is a recurved spit which is growing southwards across a broad shallow estuary. Due to the relatively small fetch window created by Prince Edward Island the direction of wave approach is from the north. This induces a strong longshore drift component. The proximal section of the spit is very low and narrow, as this is a zone of sediment bypassing. The distal section is characterized by multiple, truncated recurved ridges which result from the southward and landward migration of the spit.

The extensive barrier islands and barrier beaches on the north coast of Prince Edward Island (unit e; Fig. 6) face the northeast and are characterized by relatively stable inlets and dunes up to 8 m above mean high water level (profile P-3; Fig. 10). This barrier system is similar in many ways to that of Kouchibouguac Bay. Sediment is supplied by the erosion of adjacent unresistant sandstone cliffs (Owens, 1974a; Fig. 8) and by onshore transport of reworked deposits from the shallow offshore zone (Fig. 3). The vectors of onshore winds, using data from Summerside, P.E.I. (Fig. 5), indicate the generation of littoral drift from northwest to southeast. Superimposed on this drift is a pattern of wave-induced currents which cause local reversals of longshore drift (Fig. 11). Longshore sediment movement is less than that for the northeast coast of New Brunswick as the angle of wave approach is not high
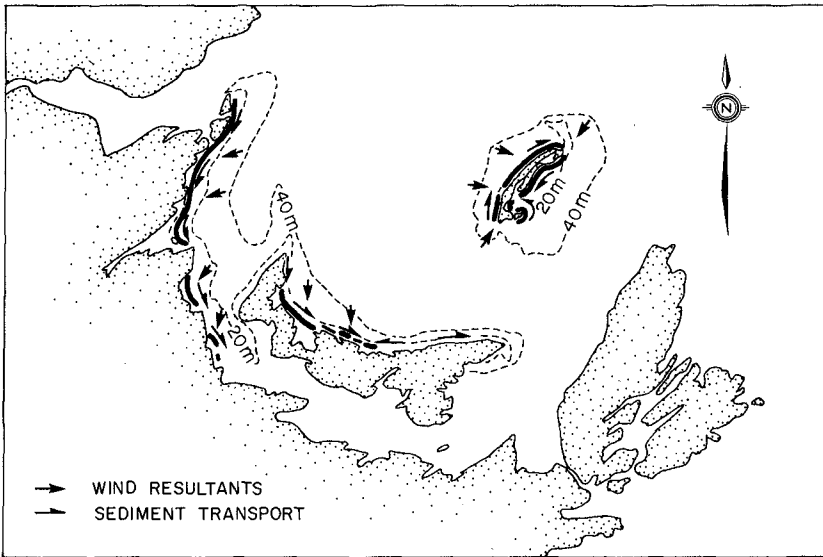
Figure 11: Onshore wind resultants and generalized pattern of sediment transport in the littoral zone of the southern Gulf of St. Lawrence.

due to refraction of the incoming waves across the shallow offshore sea-floor. There is a seasonal movement of sediment between the littoral and nearshore zones by the migration of submarine bars (McCann and Bryant, 1972).

The barrier beaches of the Magdalen Islands (units f and g; Fig. 6) are the largest single accumulation of littoral zone sediments in the Gulf of St. Lawrence and are exposed to waves generated from all wind directions. The prevailing and dominant winds are from the north-west quadrant (Fig. 5) and the east-facing coasts of the islands are a relatively sheltered environment, affected only by storm winds out of the northeast and by modified Atlantic swell waves which pass through Cabot Strait. The barriers and tombolos of the Magdalen Islands are anchored by a series of unresistant bedrock outcrops (Fig. 12) which are being rapidly eroded and supply sediment directly into the littoral zone. On the shallow shelf west of this barrier complex bottom sediments are being actively reworked and transported toward the Islands by wave-
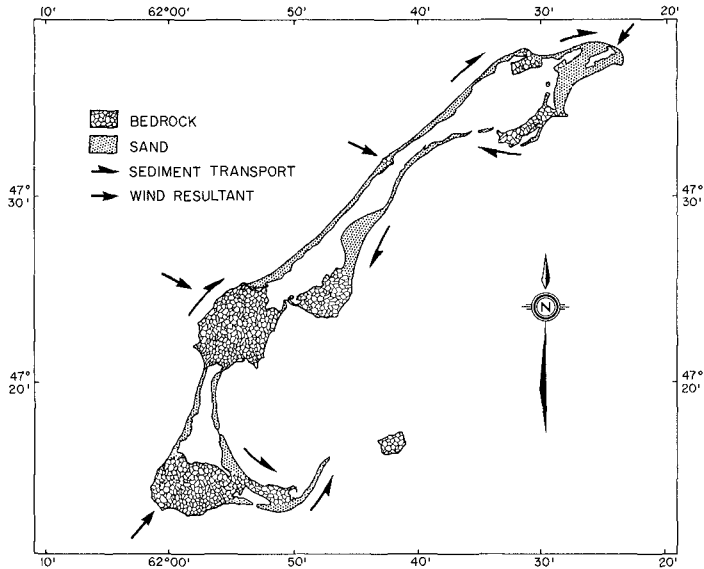
Figure 12: Onshore wind resultants and sediment dispersal around the
          Magdalen Islands, Quebec.

induced currents. Loring and Nota (1973) state that the bottom
sediments grade from gravelly, poorly sorted sands to gravelly well
sorted sands towards the west coast of the Islands (units 3 and 3c;
Fig. 13). Dispersal of these sediments around the northern and
southern extremities of the Islands leads to deposition of fine-grained
sediments (unit 2; Fig. 13) in a sheltered zone, protected from waves
out of the west and northwest.

        The west facing barriers of the Magdalen Islands are a zone of
sediment bypassing. Material fed into the nearshore zone from offshore
is transported to the north and northeast in a series of large submarine
bars and troughs. During periods of storm wave activity incoming waves
break on the outer bars and generate currents in excess of 1 m/sec in
the submarine troughs. Sediment is moved northward in these troughs as
a series of large assymetrical sand waves. The barriers on this coast
are relatively narrow, 500 to 1000 m wide, up to 6 m high, and are fre-
quently eroded by storm wave action. By contrast the barriers on the
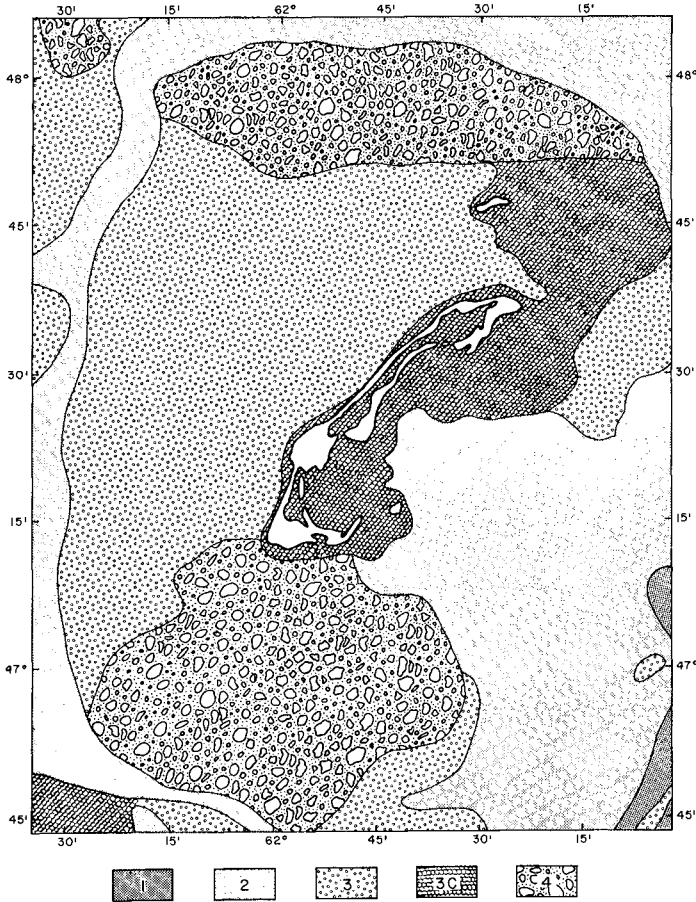
Figure 13: Distribution of surface sediments on the sea-floor adjacent
          to the Magdalen Islands (adapted from Loring and Nota, 1973).

          1. Sandy Pelite
          2. Fine Sand
          3. Coarse-medium grained Sand
         3c. Well sorted coarse-medium grained Sand
          4. Gravel/Gravelly Sand

east coast of the Islands are in a lower energy environment, affected
primarily by storm waves out of the northeast associated with the
passage of cyclonic depressions. The broad pattern of sediment transport

is from northeast to southwest with local reversals due to shoreline
orientation, particularly at the southern end of this east-facing coast.
The barriers are generally wider, up to a maximum of 2 km, and the near-
shore bars are less complex and of lower elevation than on the exposed
coast. This coast is a zone of sediment accumulation and beach prograda-
tion.

SUMMARY

        With the rise in sea-level since the Pleistocene, barriers have
migrated landward. As sea-level continues to rise this landward
migration is still evident as indicated by the numerous outcrops of
marsh and lagoonal deposits in the intertidal beach throughout the
southern gulf. In addition, barriers have developed by the growth of
spits across estuaries and embayments as sediment is transported along-
shore by wave-induced currents. The distribution of barrier islands is
related to the drowned lowland topography which has developed along
structural trends and lithological weaknesses. Evidence from sediment
studies in the offshore areas shows that bottom material is being
actively reworked and redistributed on the shallow shelves and sand is
transported into the nearshore zones for redistribution by nearshore
and littoral processes. Differences in barrier morphology are related
to the pattern of sediment dispersal along the coast which results from
the direction of wave approach and the orientation of the shoreline. On
coasts where the wave approach is at an angle to the shore, barriers are
low and subject to rapid change by storm waves as these are zones of
longshore transport and sediment bypassing. Where incoming waves are
adjusted to the shoreline trend, because of refraction or because of the
orientation of the coast, rates of longshore sediment transport are lower
and the barriers are more extensive and more stable.

        The barrier beaches of the southern Gulf of St. Lawrence are
similar to those found elsewhere in the world. Although the processes
and morphology are directly comparable with other barrier systems two
characteristics give this region its uniqueness. (1) The gulf is a
semi-enclosed sea and as a result the level of wave energy is much lower
and the rates of wave-induced sediment transport are lower than on open-

ocean coasts. In addition, this is a storm wave environment and there is a marked seasonal variation in energy levels. (2) Sea and beach-fast ice are present for up to four months each year (January to April). This prevents the operation of littoral processes during that period and any calculations of annual longshore sediment transport volumes must be reduced by at least 30 per cent. This is particularly important as severe storms are most frequent during the period between October and April.

REFERENCES

Johnson, D.W., 1925. The New England Acadian shoreline; Wiley and Sons, N.Y., 608 p., (Facsimile Ed.: Hafner, N.Y., 1967).

Kranck, K., 1967. Bedrock and sediments of Kouchibouguac Bay, New Brunswick; J. Fish. Res. Board Can., v. 24, p. 2241-2265.

Lauzier, L.M., 1967. Bottom residual drift on the continental shelf area of the Canadian Atlantic coast; J. Fish. Res. Board Can., v. 24, p. 1845-1859.

Loring, D.H., and Nota, D.J.G., 1969. Mineral dispersal patterns in the Gulf of St. Lawrence; Rev. Geogr., Montreal, v. 23, p. 289-305.

Loring, D.H., and Nota, D.J.G., 1973. Morphology and sediments of the Gulf of St. Lawrence; Fish. Res. Board Can., Bull. no. 182, 147 p.

Loring, D.H., Nota, D.J.G., Chesterman, W.D., and Wong, H.K., 1970. Sedimentary environments on the Magdalen Shelf, southern Gulf of St. Lawrence; Marine Geol., v. 8, p. 337-354.

McCann, S.B., and Bryant, E.A., 1972. Barrier islands, sand spits and dunes in the southern Gulf of St. Lawrence; Maritime Sediments, v. 8, p. 104-106.

Owens, E.H., 1974a. A framework for the definition of coastal environments in the southern Gulf of St. Lawrence; Geol. Surv. Can., Paper 74-30, Volume I (in press).

Owens, E.H., 1974b. Size analysis of surface samples from the coastal zone of the southern Gulf of St. Lawrence; Bedford Instit. of Oceanog. Rept. BI-D-74-1, 106 p.

Owens, E.H., 1974c. The effects of ice in the littoral zone at
        Richibucto Head, eastern New Brunswick; Proc. 1st. Symposium on
        the Geol. Action of Drift Ice, Quebec City, April 1974 (in press).

Owens, E.H., 1974d. Coastline changes in the southern Gulf of St.
        Lawrence; Geol. Surv. Can., Paper 74-1, Part A, p. 123-124.

Owens, E.H., and Harper, J.R., 1972. The coastal geomorphology of the
        southern Gulf of St. Lawrence: A reconnaissance; Maritime
        Sediments, v. 8, p. 61-64.

Sheridan, R.E., and Drake, C.L., 1968. Seaward extension of the
        Canadian Appalachians; Can. J. Earth Sci., v. 5, no. 3, Part 1,
        p. 337-373.

CHAPTER 70

Overwash Processes on Assateague Island

John S. Fisher[1]

Stephen P. Leatherman[2]

Capt. Frederick C. Perry[3]

Abstract

The primary barrier dune on the northern portion of
Assateague Island, Maryland is presently being scarped on its
seaward face and breached by storm-generated surges. During
storms, sediment-ladened water moves across the dune line
onto the barrier flats as overwash. The objective of this
project is to determine the role overwash plays in barrier
island sedimentary dynamics.

An overwash model has been suggested. The nonvegetated
overwash fan serves as a reservoir for the eventual distribution
of the storm-deposited sand. Eolian processes, after the
storm, determine the net contribution of overwash sand to each
of the different morphological features, i.e., dunes, marsh,
beach, etc.

[1]Assistant Professor, Department of Environmental Sciences,
  University of Virginia, Charlottesville, Virginia

[2]Research Assistant, Department of Environmental Sciences,
  University of Virginia, Charlottesville, Virginia

[3]Waterways Experiment Station, U. S. Army Corps of Engineers,
  Vicksburg, Mississippi

Introduction

Overwash in this discussion refers to the flow of swash and associated transported sediment across the frontal dune line onto the barrier flats during a storm or an unusually high tide. This process results in the characteristic breaching of the primary dune line, a feature apparent in field reconnaissance as well as identifiable from aerial photography. Relatively small-scale overwash deposits (the subject of this paper) have been monitored in which the breach in the dune is on the order of 40 ft (12 m). Much larger breaches have been observed, e.g., the March 1962 storm destroyed over 1000 ft (305 m) of primary dune at Cape Hatteras, N. C. The former features result in a fan-like deposit, while the latter are much more broad in character.

Overwash processes are of interest because of their role in the overall sediment budget of the barrier island. The temporal and spatial frequency of these events, as well as the storm parameters causing them, are poorly understood at present. From a coastal engineering viewpoint, an understanding of overwash dynamics is necessary for the evaluation of shoreline management alternatives. In particular, the policy of barrier dune construction and sand fencing projects precludes some understanding of overwash dynamics (Dolan, 1972).

This study was designed to observe and quantify the discrete overwash events, in order to begin to address the issues cited above.

Previous Investigations

With the present eustatic rise in sea level (Hicks, 1972), barrier islands are being encroached upon by the sea, and in many cases eroded, National Shoreline Study (1971). Kraft (1973), working on the Delaware coastline, concluded that the washover sands migrate landward across marsh and lagoonal sediments at the leading edge of the Holocene transgression. Dillon (1970) and Swift (1968) investigated the migration of the Rhode Island barrier and the process of coastal erosion and transgressive stratigraphy in the Bay of Fundy, respectively. These authors concluded that shore face erosion and washover was the dominant process responsible for landward migration.

Pierce (1970) investigated the dynamics of the overwash process suggesting that the velocity of the surge slows after it "overtops" the barrier. Deposition of the entrained sediment occurs on the tidal flats and near the bayside of the barrier. Concerning the sediment moved by overwash, Pierce (1973) concluded that the amount of material transported by this process is difficult to evaluate due to the lack of accurate periodic surveys, but that the size of the overwash fans in this area suggests a significant amount of sediment transport. Hayes (1967) and Perkins and Enos (1968) studied hurricane deposition. Aerial photography and field reconnaissance indicated that large volumes of sediment were washed onto and sometimes over the barrier by the hurricane surge.

Site Description

The northern end of Assateague Island, Maryland, was chosen as the field site for this study. This location overwashes several times each year, with the deposits characterized by the small fan-shape feature described above. The relatively small scale of these deposits makes a control volume approach to the computation of the sediment budget feasible. In addition, this area is relatively accessible during a storm with a reasonable degree of safety for the field crew. An analysis of historical charts and photography by several investigators, particularly Slaughter (1949) and Gawne (1966), indicates that the trend for Assateague has been seaside erosion and thus landward migration.

Figure 1 is a schematic of the study area. This section of Assateague Island contains many closely-spaced overwashes. The throat widths are about 40 ft (12 m), and the fans extend toward the bay for an average of 150 ft (46 m). Many of these fans are connected to the bay and thus drained by well-defined sluiceways or channels.

The sediment consists primarily of quartz sand with mean diameters of .25 mm on the fan, .20 in the dunes, and .30 mm on the beach, as determined by sieving. The overwash sediment is characterized by a high percentage of heavy minerals, chiefly ilmenite, rutile, and garnet.
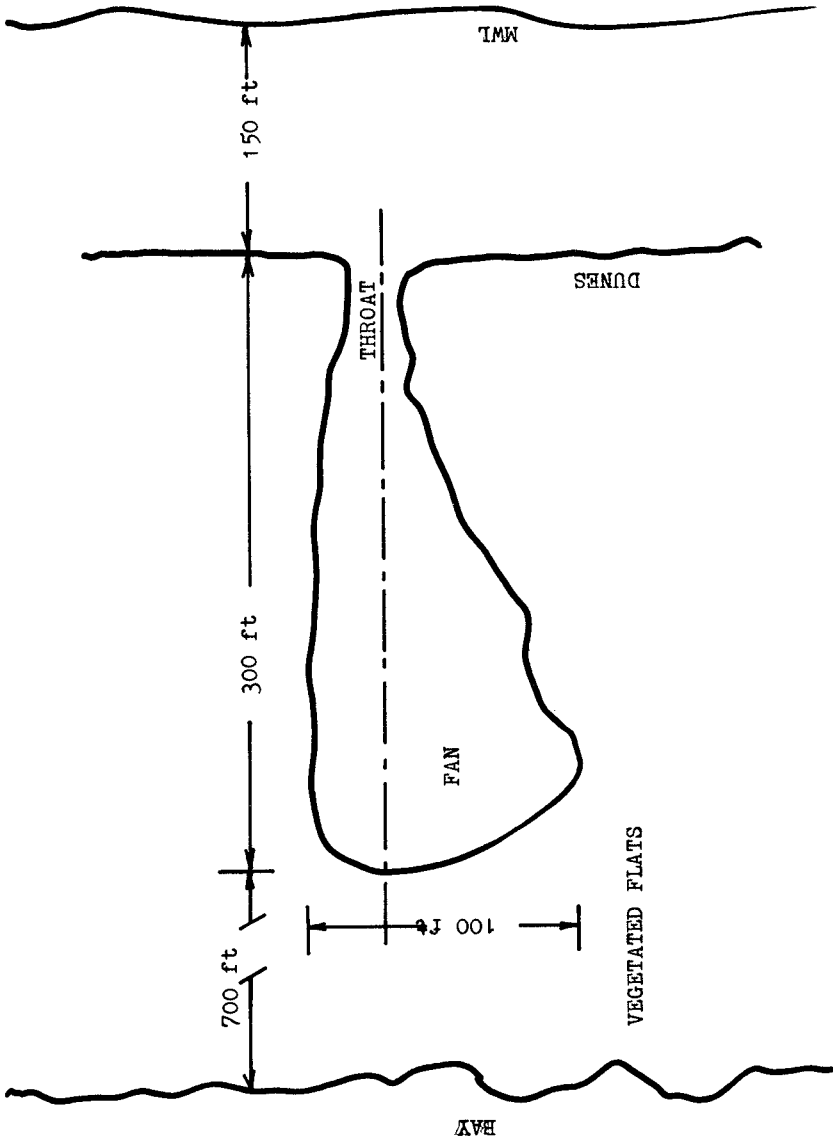
Figure 1, Schematic of Overwash Area

Details of the Present Study

     The present study began in February of 1973 with the
initiation of a monthly surveying program. A rectangular grid
has been superimposed on a transverse slice of the island from
the vegetated barrier flats seaward to the mean water line so
as to include a single overwash fan and adjacent barrier dunes.
Elevations are surveyed at each point along seven lines with
an accuracy of .05 ft (1.52 cm). Fixed markers are located only
along the baseline, in order to avoid artificial scour or fill
within the boundaries of the active fan.

     In addition to the systematic measurement of the elevation
changes, a technique is employed to monitor the depth of erosion
and thus the gross deposition, Figure 2. Plugs of painted sand
are placed level with the surface along the survey lines. After
an overwash, these plugs are sectioned such that the amount of
erosion, as well as the depth of post storm fill, can be deter-
mined.

     During storm conditions, quantification of overwash
hydraulics are attempted. The velocity of the surge through
the throat and the temporal frequency of the surges are recorded.
Suspended sediment samples are also collected.

Analysis of Data

     The field program outlined above has made possible the
detailed study of individual overwash events. Ideally, the
field site would be surveyed just before and immediately after
the storm-overwash period. In practice, there is often an
interval of several days before or after the storm, and thus the
analysis of data must consider the additional factor of eolian
transport of material.

     The first storm to be monitored in detail occurred on
March 22, 1973. This northeaster had deep water wave heights
reported greater than 30 ft (9 m) with surface winds of 65
knots (33 m/sec) at sea, NOAA (1973). At Ocean City, Maryland,
COSOP observations reported 6 ft (2 m) breaking waves, with
periods of 8 to 12 seconds out of the northeast, CERC (1973).
Figure 3 illustrates the sediment deposition pattern for this
storm. The maximum depth of erosion can be seen from the
elevation of the colored sand plugs. This erosion was con-
centrated in the forward or throat section of the overwash
feature. The net change after the storm was a deposition of

1.

LEVEL A [initial elevation]

PLUG OF DYED SAND

PRE-OVERWASH

2.

LEVEL A

EROSION LEVEL B

MAXIMUM DEPTH OF
OVERWASH EROSION

3.

LEVEL C [post storm]

LEVEL A

LEVEL B

POST OVERWASH
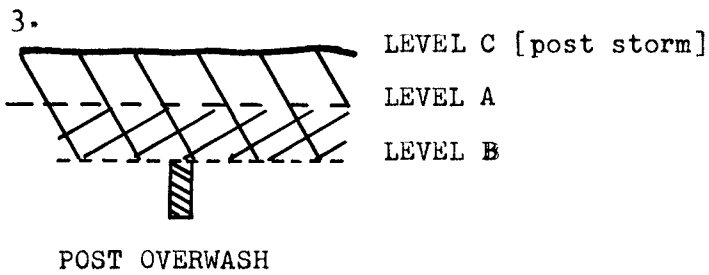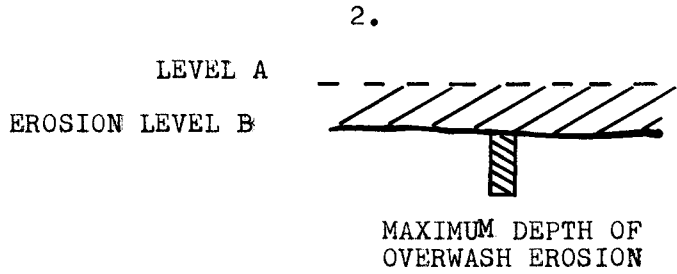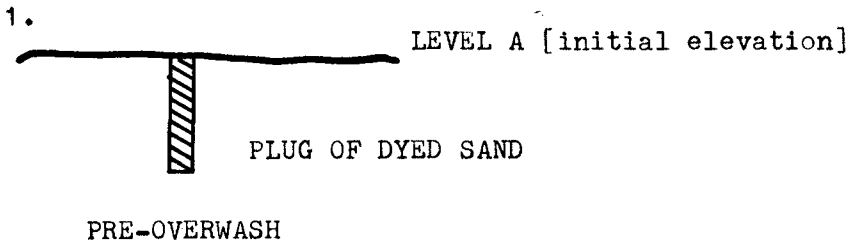
Figure 2, Method for Determining Erosion Depth
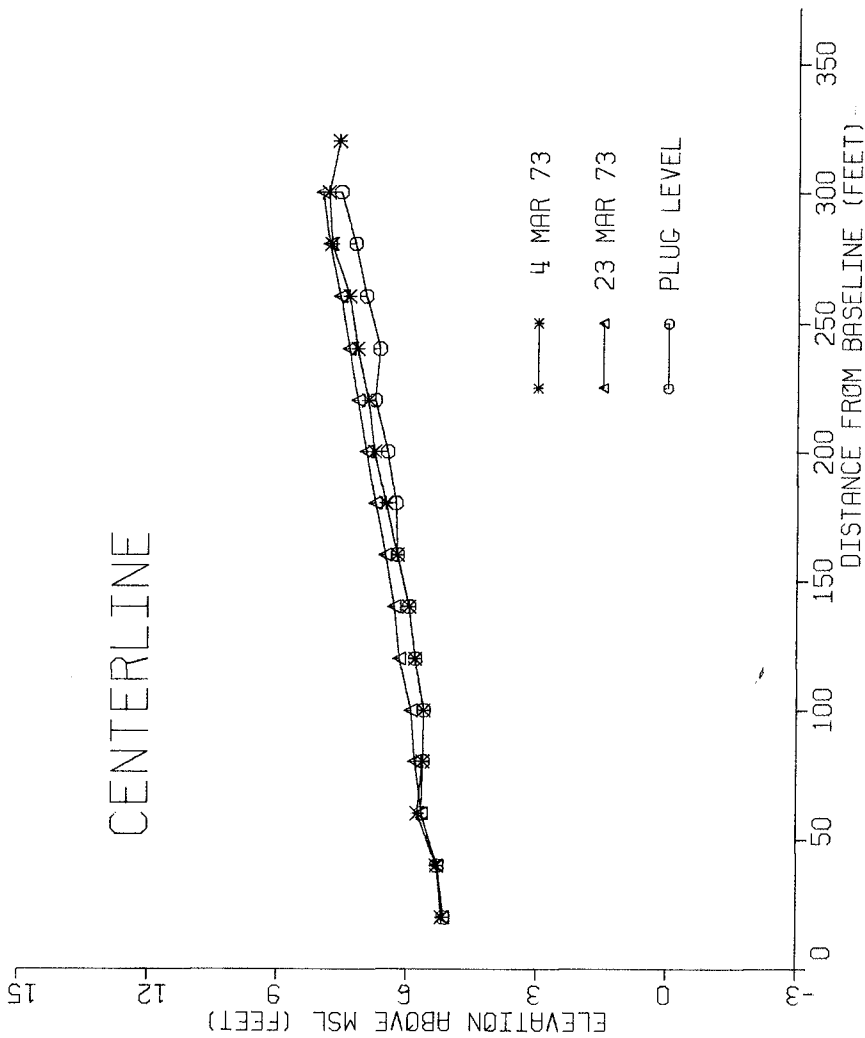
Figure 3, Centerline Profile Change, Northeaster, March 22, 1973

material over the fan, tapering off towards the marsh. This wedge-shaped deposit is typical of the overwashes observed on the island.

Velocities in the throat section were measured during the storm using a Gurley current meter. Maximum surge velocities were 8 ft/sec (2 m/sec) at 1 ft (.3 m) above the bottom of a 3 ft (1 m) deep surge. During a two hour period which corresponded to the peak of the storm, 130 surges were observed to cross the dune line with some surges penetrating the entire width of the island. Thus, approximately one surge per minute was recorded.

During this same period of observation, suspended sediment samples were obtained by hand-held collection bottles. These samples, collected at mid-depth in the overwash surge, had concentrations of about 50% sediment by weight.

A second overwash resulting in a significant volume of sediment transported onto the study site occurred on October 26-27, 1973. Tropical Storm Gilda generated 10 second, 6 ft (2 m) waves as observed on Assateague Island (BEP, 1974). Figure 4 shows the net sediment transport along the centerline from this storm. In this case, the area of erosion extended further back onto the fan, although in general the pattern is similar to the previous example. By integrating all seven survey lines over the entire deposit, the net volume change can be computed. For this storm, 83 cubic yards (64 m^3) were deposited.

Overwash Hypothesis

Based upon the analysis of data and observations made, a basic model of overwash on Assateague Island has been proposed. The storm parameters needed for overwash appear to include breaking waves in excess of 6 ft (2 m) with a storm tide of 1 ft (.3 m) or greater. Figures 5, 6, 7, and 8 illustrate the probable sequence of erosion and deposition during an overwash.

The initial stages of overwash are primarily erosional in nature, in the throat section of the fan. Sand is transported to the fan itself or flushed to the marsh via the sluiceway depending on the magnitude of the surge. Later, as the surge velocities decrease, during the later stages of the storm, new
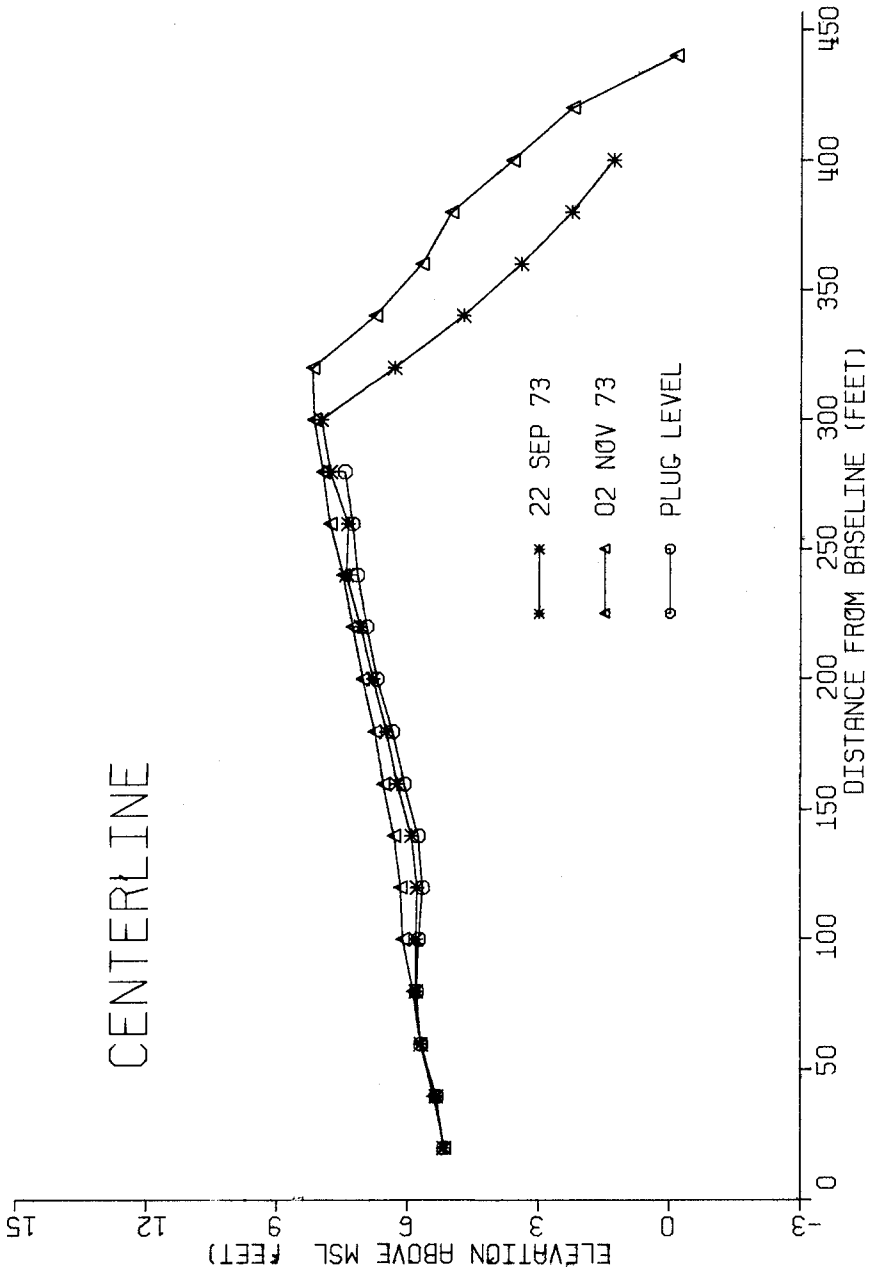
Figure 4, Centerline Profile Change, Tropical Storm Gilda, October 26, 1973
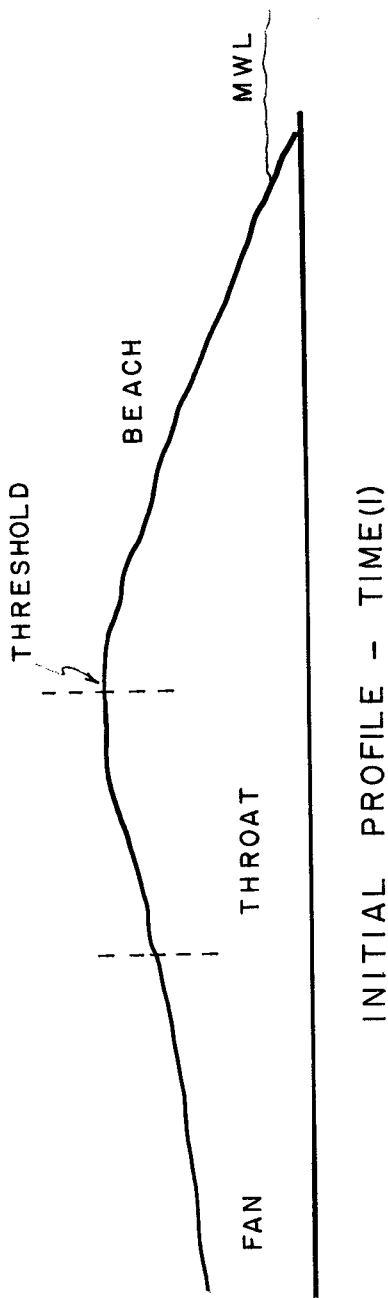
Figure 5, Overwash Model, Initial Conditions
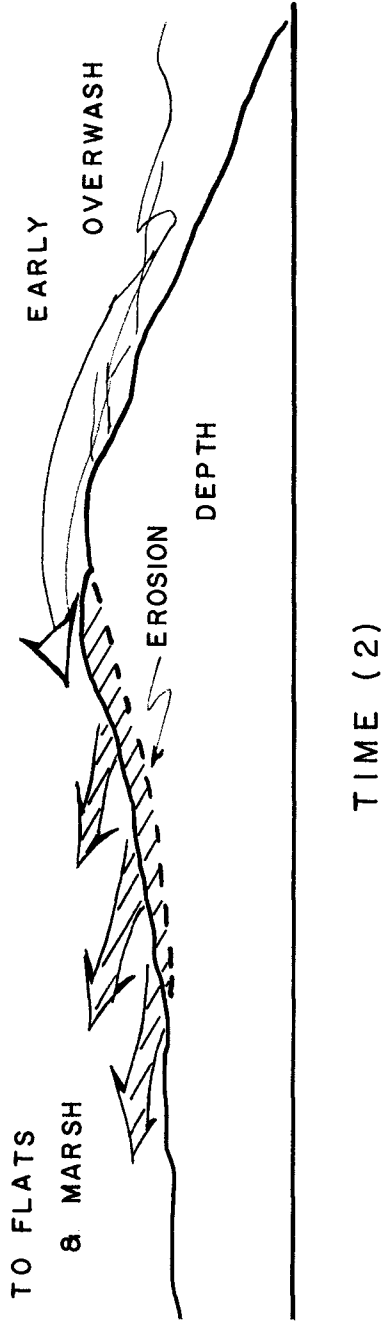
Figure 6, Overwash Model, Early Overwash Surges
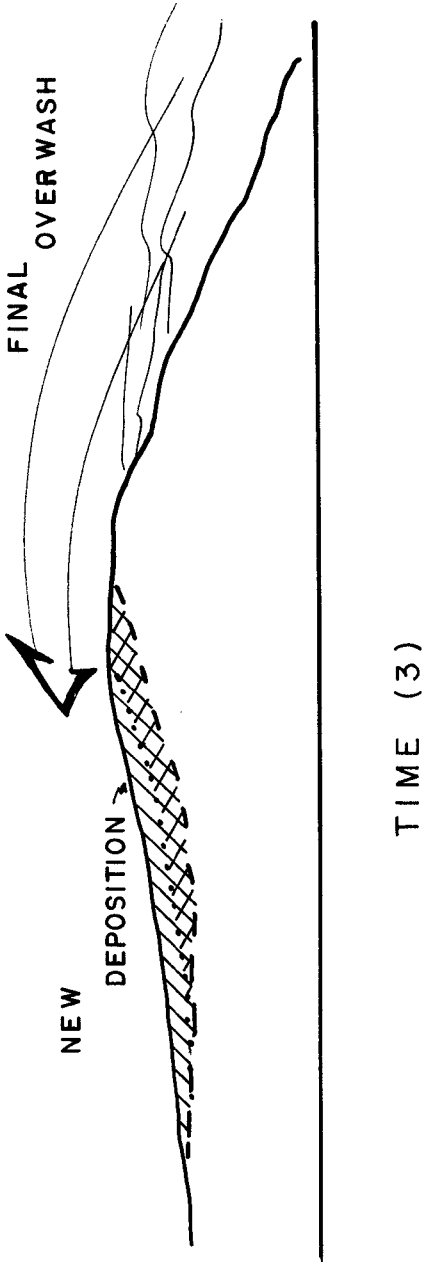
Figure 7, Overwash Model, Net Storm Deposition

FINAL OVER WASH

NEW DEPOSITION

TIME (3)
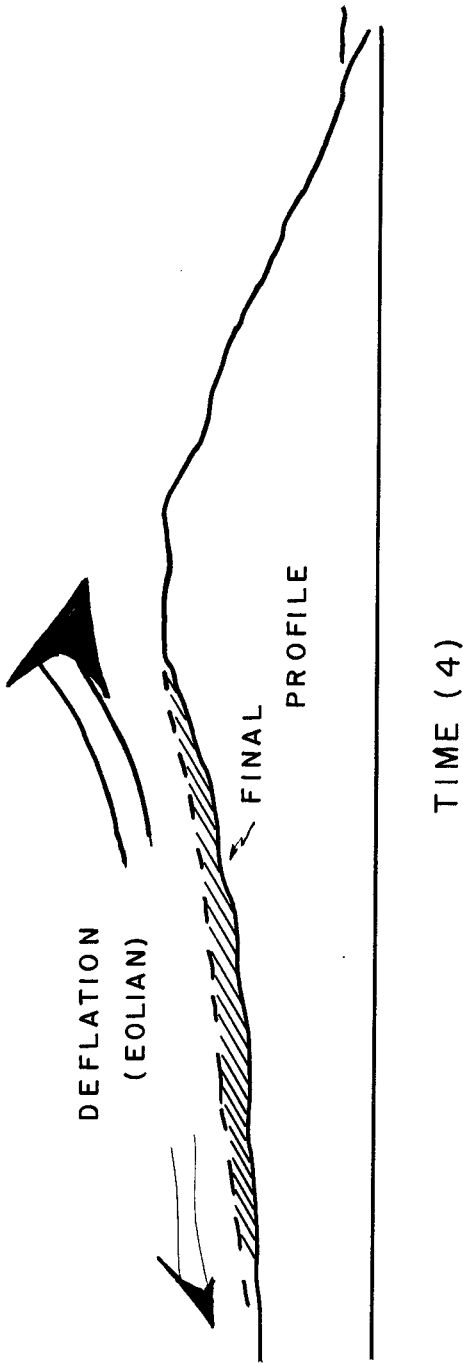
Figure 8, Overwash Model, Eolian Deflation of Fan and Throat

material is deposited over both the throat and fan sections.
Finally, after the storm has abated, the wind reworks the newly
deposited material. The net contribution of sand to each of
the morphological features, i.e., the dunes, marsh, flats or
beach depends on wind direction and magnitude.

Summary and Conclusions

After two years of continuous study of this transverse
slice of the island, some surprising initial conclusions can
be drawn. At least 4 storms are known to have caused overwash
at this site during the past two years. Our surveys, which
include the last two of these storms, indicate approximately
36 cubic meters or an average of 3.8 cm over the fan area of
net loss of sand at this site (Figure 9). Considering the
transient nature of this environment, this loss can be essentially
neglected, and the fan elevation considered stable.
The dune line has receded slightly by seaward scarping, consistent
with an eroding beach. Survey profiles for Northline 4 (Figure 10)
and Southline 4 (Figure 11) over the same 14 month period show
that the backside of the dunes are accreting. This sediment
has been derived from the overwash fan. The elevation of the
vegetated barrier flats and marsh have remained essentially
unchanged with respect to eolian action. This analysis indicates
that the beach is the chief recipient of the overwash material.

The throat width has been reduced 5 to 10 ft (1.5 to 3 m)
during the period of study. This latter figure suggests that
the overwash process at this level of storm intensity is not
competent to self-maintain the breaches in the dune line. Further
evidence supporting this conclusion can be obtained from an
analysis of historical photography.

In March 1962 a severe northeaster struck this area. Aerial
photographs of Assateague Island immediately after the storm
show that the overwash throat at the present research site was
approximately 100 ft (30 m) in width. The throat has sub-
sequently been reduced to 40 ft (12 m) which is consistent with
the five foot reduction per year calculated from the field data.

The program outlined above is being continued with the
addition of tide and wave gage data, as well as refinements in
the measurement program during the storms. This new data should
greatly improve the quantification of these overwash processes.
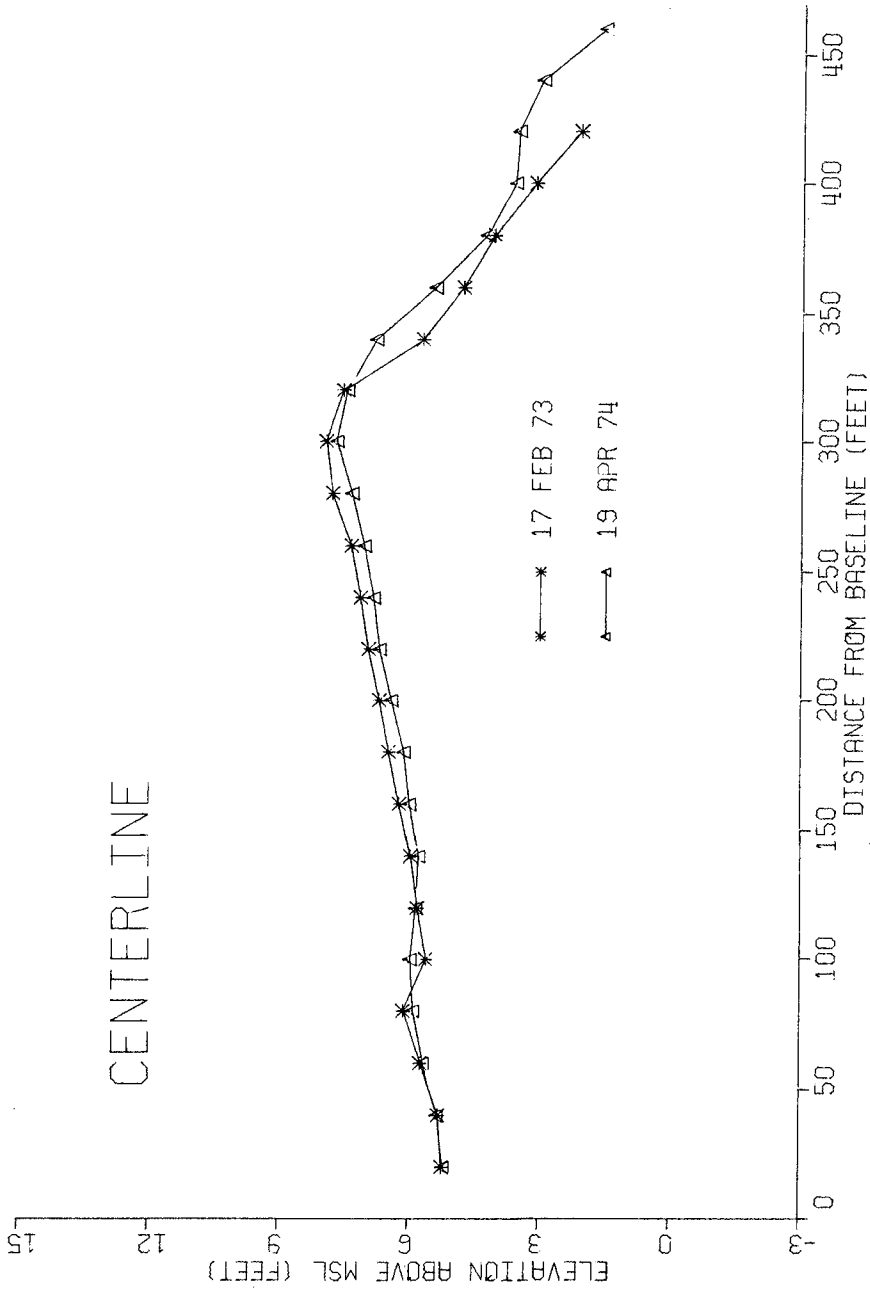
Figure 9, Net 2-year Change, Centerline
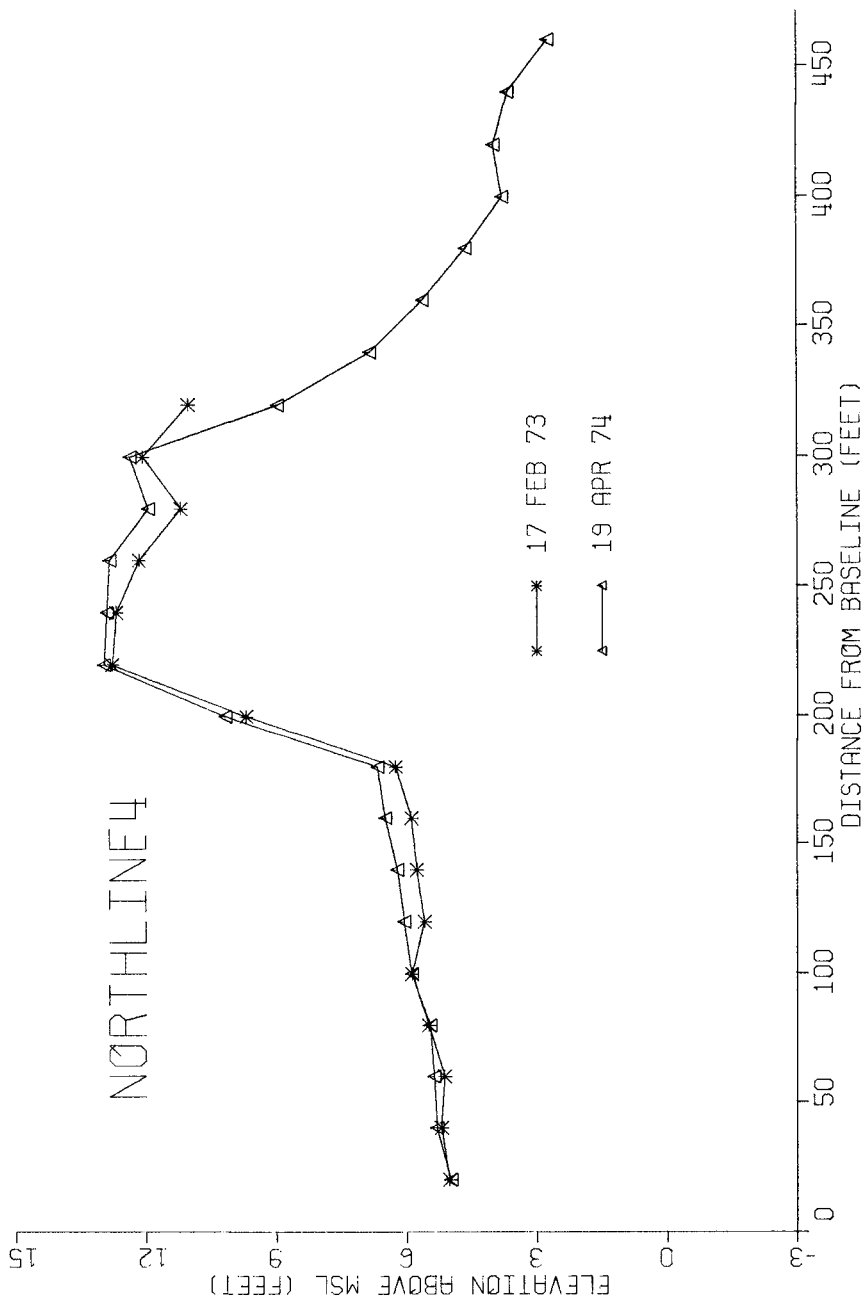
Figure 10, Net 2-year Change, 40 ft. north of Centerline

COASTAL ENGINEERING
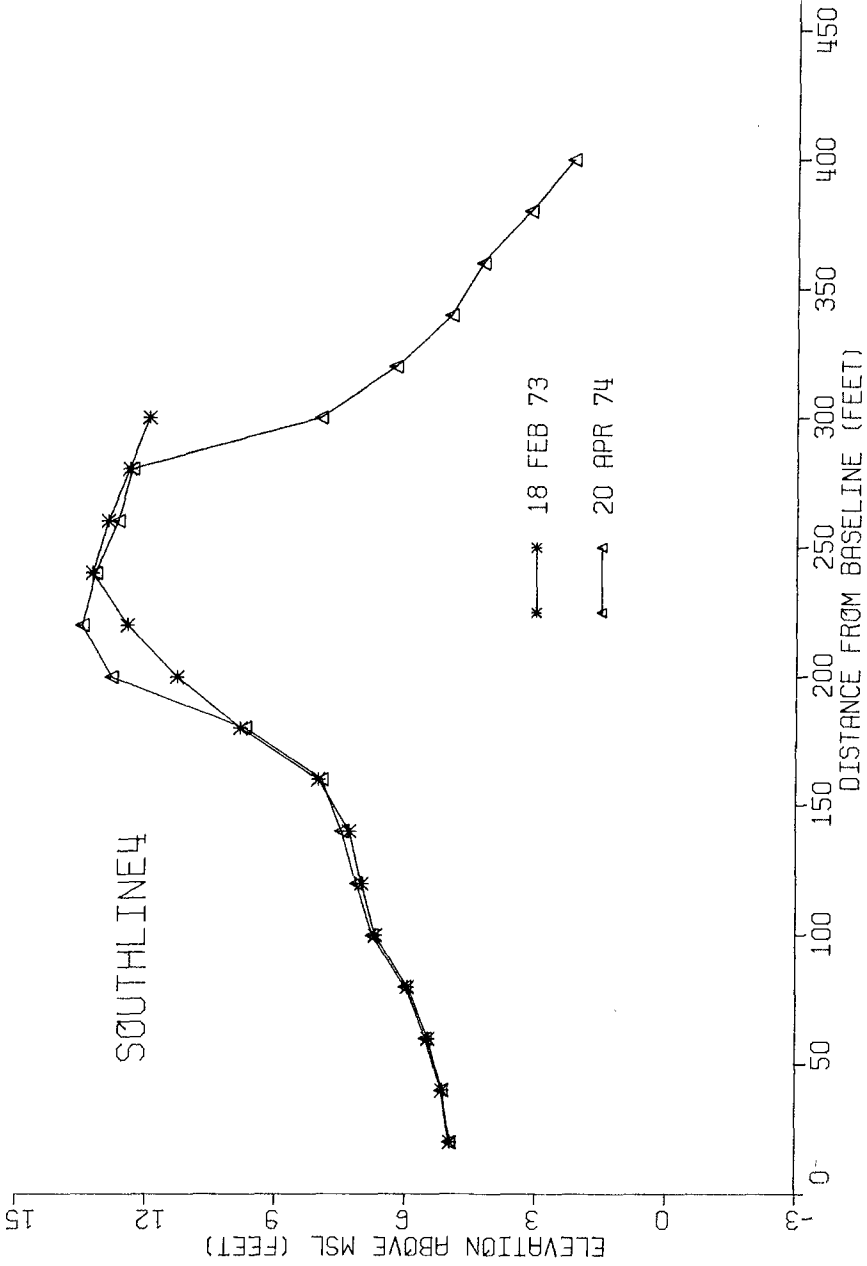
Figure 11, Net 2-year Change, 40 ft. south of Centerline

References

1. Coastal Engineering Research Center, Coastal Observations
    Program (COSOPS), Ocean City Coast Guard Station, 1972-1974.

2. Coastal Engineering Research Center, Beach Evaluation
    Program (BEP), Assateague Island, 1972-1974.

3. Corps of Engineers, Report on the National Shoreline Study,
    Washington, D. C., August 1971, p. 18-19.

4. Dillon, William P., 1970, Submergence Effects on a Rhode
    Island Barrier Lagoon and Inferences on Migration of
    Barriers, Journal of Geology, Vol. 78, p. 94-106.

5. Dolan, Robert, 1972, Barrier Dune System along the Outer
    Banks of North Carolina: A Reapprisal, Science, Vol. 176,
    p. 286-288.

6. Gawne, Constance Elaine, 1966, Shore Changes on Fenwick
    and Assateague Islands Maryland and Virginia, B.S. thesis,
    University of Illinois, 140p.

7. Hayes, Miles O., 1967, Hurricanes as Geological Agents:
    Case Studies of Hurricanes Carla, 1961, and Cindy, 1963,
    Texas Bureau of Economic Geology, Report of Investigation
    No. 61, 54p.

8. Hicks, Steacy D., 1972, On the Classification and Trends of
    Long Period Sea Level Series, Shore and Beach, p. 20-23.

9. Mariners Weather Log, National Oceanic and Atmospheric
    Administration, Vol. 18 , No. 2   , p. 108-109.

10. Kraft, John C. et al., 1973, Morphological and Vertical
    Sedimentary Sequence Models in Holocene Transgressive
    Barrier Systems, in Coastal Geomorphology, Donald R. Coates,
    editor, Publications in Geomorphology, State University
    of New York, p. 321-354.

11.   Perkins, R. D. and Enos, Paul, 1968, Hurricane Betsy in
      the Florida-Bahama Area -- Geologic Effects and Comparison
      with Hurricane Donna, Journal of Geology, Vol. 76, p. 710-717.

12.   Pierce, J. W., 1970, Tidal Inlets and Washover Fans, in
      Barrier Islands, Maurice L. Schwartz, editor, Dowden,
      Hutchinson and Ross, Inc., Stroudsburg, Pa., p. 334-339.

13.   Pierce, J. W., 1973, Sediment Budget Along a Barrier
      Island Chain, Sedimentary Geology, Vol. 3, p. 5-16.

14.   Slaughter, Turbit H., 1949, Shore Erosion in Tidewater
      Maryland, Maryland Department of Geology, Mines and Water
      Resources Bulletin No. 6, p. 109-115.

15.   Swift, Donald J. P., 1968, Coastal Erosion and Transgressive
      Stratigraphy, Journal of Geology, Vol. 76, p. 444-456.

CHAPTER 71

EROSION PROBLEMS OF THE DUTCH ISLAND OF GOEREE

by H.G.H. ten Hoopen and W.T. Bakker
Coastal Research Department, Rijkswaterstaat, The Hague
The Netherlands

ABSTRACT

At many places along the dutch coast especially at the West side of the islands, erosion occurs.
One of the islands where the erosion is severe, is Goeree, situated in the Delta area in the South-West of the Netherlands. (see fig. 1). This isle is recently connected with other islands by dams. (see fig.2). These dams built within the scope of the Deltaproject plans closing the tidal estuaries and to shorten the length of the coastline thus reducing the wave attack. This paper examines how the influences of the closure of the estuaries affect on the erosion of the neighbouring coast. To this end, the changes in vertical and horizontal tide caused by the closure as well as the wave induced littoral drift and the sand-transport caused by a combination of tidal currents and waves before and after the closure, are computed. On the basis of this computations, a few suitable solutions for the reduction of erosion are discussed.
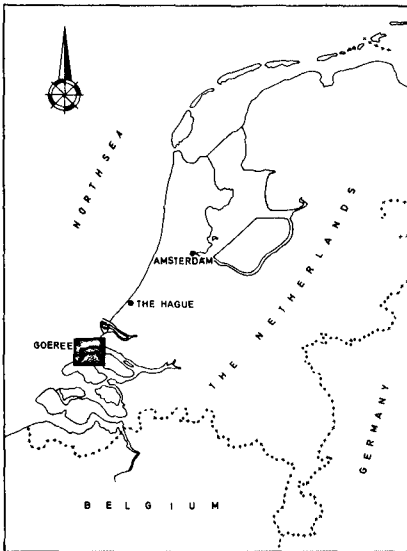
Figure 1 MAP OF THE NETHERLANDS SHOWING THE LOCATION OF THE ISLE OF GOEREE
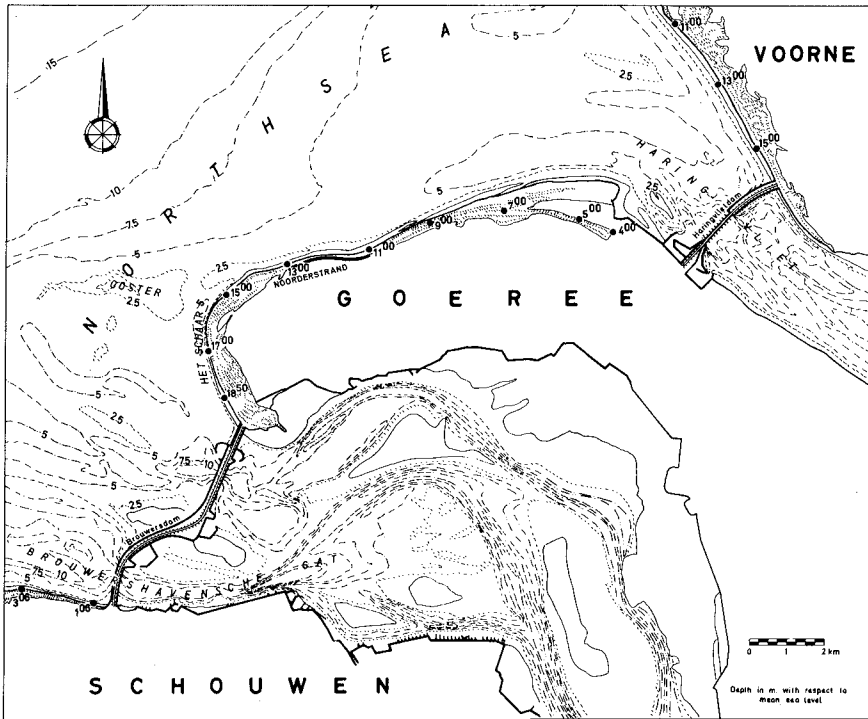
Figure 2 MAP OF THE WESTERN PART OF GOEREE WITH DEPTH CONTOURS

INTRODUCTION

Prior to the closure of the tidal estuaries, Haringvliet and the
Brouwershavensche Gat estuaries (see fig. 2), the westcoast of
the isle had already been subjected to severe erosion. In 1968
the regression of the dunes reached a maximum of about 20 m per
year with an annual loss of sand of about 400.000 m^3 whereas the
former mean loss was approximately 200.000 m^3. Because of this
alarming regression the following three sandsupplies have been
carried out since 1969.
1. In the winter of 1969, 400.000 m^3;
2. In the summer of 1971, 610.000 m^3;
3. At the beginning of 1974, 3.500.000 m^3 sand,

which 800.000 m^3 sand were used for the enforcement of the
dunes. (see also fig. 8).

It is obvious that with sandsupplies the regression of the origi-
nal dune ridge or coastline can be slowed down or even been hal-
ted. The disadvantage of these supplies is the need for supply-
ing sand over such a long time. Up till now sand that was used
for the above mentioned beach nourishment was pumped from a
neighbouring lake over a distance of maximum six kilometers,
for this reason the costs per m^3 sand were low. In the future,
because of environmental objections, no more sand can be pumped
from this lake, but has to be taken from attracting the sea,
against relative high costs. Because of the above mentioned
reasons the optimal solution to reduce the erosion is to be
found.

In order to determine the best measures against this severe
erosion the direction, distribution and order of magnitude of
the littoral drift along the island before and after the closure
of the Brouwershavensche Gat has to be known. Only the closure
of the Brouwershavensche Gat is mentioned here inasmuch as clo-
sing of the Haringvliet did not influence the westcoast erosion.
Erosion problems have been solved by means of model tests, here
however the sandmovement is calculated by means of mathematical
formulas.

WAVE INDUCED LITTORAL DRIFT ALONG THE ISLAND

Calculations are only possible if wind, wave and tidal data are
available.

The wind and wave data are based on data collected at the dutch
lightvessel Goeree [1] *. On this lightvessel the wave height,
periods and directions are estimated visually. The wave direc-
tions are combined into 30 degree sectors, (see fig. 3), the
wave heights are pat in groups with a half meter difference
between each and finally the wave periods are grouped into the
categories of duration shorter than 5 sec., between 5 and 7
sec., between 7 and 9 sec. and longer than 9 sec.

*) See list of references.

The number and percentages of the observations in each of the
above mentioned classes (categories) are known. As mentioned
before the wave heights are estimated visually on board of this
lightvessel. Measured wave height data acquired by means of a
wave recorder on board of the former drilling platform "Triton"
near The Hague are also available. A correlation is made between
the wave height recorded on the drilling platform by means of a
step gauge. For onshore winds (fetch limited)(see fig. 3) the
wave heights are calculated by means of wave generation graphs
from Thysse [2] and Bretschneider [3].

Explanation

················· M.S.L.
– – – – – – – M.S.L. – 5 m.
———·—— M.S.L. – 7.5 m.
——————— M.S.L. – 10 m.

0   1   2 km
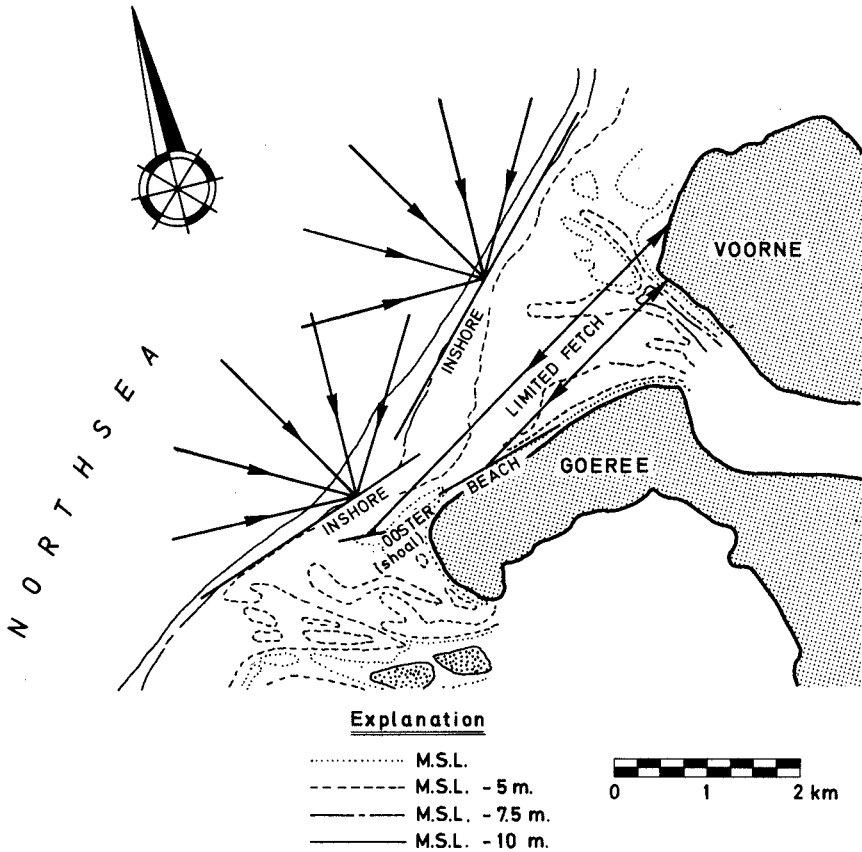
Figure 3 DIRECTION OF THE WAVE RAYS FOR WHICH THE WAVE INDUCED LITTORAL DRIFT
         IS COMPUTED ALONG OOSTERSHOAL AND NOORDERSTRAND
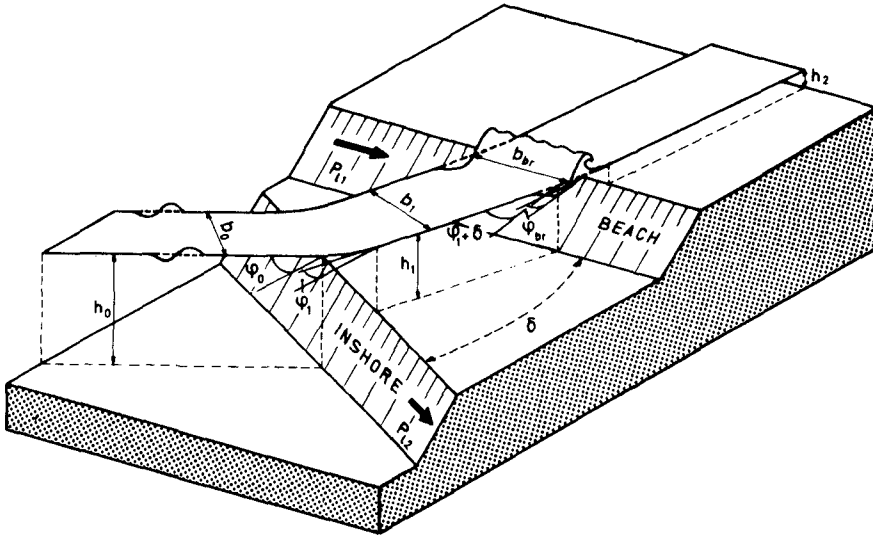
Figure 4 THREE DIMENSIONAL VIEW OF A BEACH PROFILE WITH A WAVE RAY APPROACHING THE BEACH
P_{l1}=LONGSHORE COMPONENT OF THE WAVE ENERGY ALONG THE BEACH
P_{l2}=LONGSHORE COMPONENT OF THE WAVE ENERGY ALONG THE INSHORE

For the computation of the wave induced littoral drift the
vertical tide is also introduced. To this end the mean tide
measured by tide gauge is used. From the correlation between
wave data from the drilling platform "Triton" and the light-
vessel "Goeree" it is found that the wave period estimated on
the lightvessel is one and a half times the measured mean period
on "Triton". The period showing the wave pattern as good as
possible seems to be that period where the energy/unit of area
and the energy transport/m' of the singular wave equals that of
the wave pattern (T_{eq}). Battjes [4] found that this period is
1,23 times the mean period. In this way the observed periods
can be substituted by T_{eq} = 0,82 T_{ge}, where T_{eq} = equivalent
wave period and T_{ge} = observed wave period on the lightvessel
"Goeree".

It is assumed that the waves are known at a depth of about 15 m
minus mean sea level (depth at the drilling platform). From this
depth the changing of the waves as a result of refraction and
shoaling at the breakerline is computed by assuming two groups
of parallel depth contours in front of the Noorderstrand (north-
coast) and the Ooster shoal, in this case called "inshore" and
"beach". (See fig. 3 and 4).
Along "inshore" and "beach" the longshore component of the
energy flux is computed with a simplified version of the Svasek
method. [5]. Svasek's method, a variation of the C.E.R.C. method
[6], assumes the littoral drift between two adjacent depth con-
tours to be proportional to the longshore component of energy
loss between these contours. The above mentioned simplification
is the reduction of depth contours to two groups of parallel
depth contours. [7] [8].
For this computation the following assumptions are made:
a) The sediment transport along a sandy coast is directly pro-
   portional to the longshore component of the loss of energy;
b) The sediment transport between two depth contours is directly
   proportional to the longshore component of energy loss between
   those contours;*
c) The waves are spilling breakers inside the breakerzone;
d) Refraction proceeds inside the breakerzone;
e) The loss of the wave energy is caused by breaking of the
   wave;
f) The loss of energy between deep water to breaking depth is
   negligible relative to the losses in the breakerzone;
g) The waves will be taken into consideration while ripcurrents
   are not considered;

* Although mathematically the given formulation is not correct
   as it is not even possible to take the longshore component of
   a scalar [9]. The meaning of the expression i.e. $\sin \varphi$ times
   the loss of wave energy (φ being the breaker angle) will be
   clear.

h) Wave phase velocity in the breakerzone is equal to wave group
   velocity and is dependent on depth only;

i) The depth contours are schematized to two groups of parallel
   depth contours that make an angle with each other;

j) When φ is angle of wave incidence, it is assumed that $\cos\varphi_{br}$
   equals 1 in the breakerzone. This assumption is based upon
   the consideration that in the case where the angle of wave
   incidence in deep water is 75°, the wave period is 7 seconds
   and the wave height 3,5 m, then the cosine of the angle at
   breaking point will be 0,867. This number is one of the
   smallest values this cosine can attain.

The longshore component of the flux of energy per m' along the
coast at the edge of the breakerzone can be given by:

$$P1 = nE_{br} \ c_{br} \ \sin\varphi_{br} \ \cos\varphi_{br} \qquad \cdots \cdots \cdots (1)$$

where n = group velocity/phase velocity

          $E_{br} = \frac{1}{8} \rho g H_{br}^{2}$ = energy per unit of water surface
               area [10].

          ρ = density of the water

          g = acceleration of gravity

          H_{br} = breaker height

          c_{br} = wave celerity in the breakerzone

          φ_{br} = angle of wave incidence at the breakerline

According to assumption j) we put $\cos\varphi_{br} = 1$

By assuming a narrow spectrum of frequency

$$\overline{H_{br}^{2}} = \frac{1}{2}(H_{sign})_{br}^{2} \qquad \cdots \cdots \cdots (2)$$

where $(H_{sign})_{br}$ = significant breakerheight

Further more is assumed that the ratio significant wave height
in the breakerzone and breakerdepth is a constant value (γ).

$$(H_{sign})_{br} = \gamma \, h_{br} \qquad \qquad \cdots \cdots \cdots \quad (3)$$

where h_{br} = breakerdepth

To compute the celerity in the breakerzone use is made of the
theory of Bernoulli, i.e. the second order approximation of the
solitary wave is used [11] and it is assumed that the wave cele-
rity is equal to the group velocity in the breakerzone.

$$c_{br} = \sqrt{g(h_{br} + H_{br})} \qquad \qquad \cdots \cdots \cdots \quad (4)$$

For parallel depth contours Snell's law is valid

$$\frac{\sin \varphi_o}{c_o} = \frac{\sin \varphi_{br}}{c_{br}} \qquad \qquad \cdots \cdots \cdots \quad (5)$$

where φ_o = angle of wave incidence in deep water

             c_o = celerity of the waves in deep water

Using the assumptions a).....j) and the mentioned formulas, the
longshore component of energy flux can be found.
a) If no shoals are present (h_2 = 0) and all depth contours are
   parallel (δ = 0)(see fig. 4 for declaration of symbols) then
   from formulas (1)....(5)

$$Pl_1 = K \, h_{br}^3 \, \frac{\sin \varphi_o}{c_o} \qquad \qquad \cdots \cdots \cdots \quad (6)$$

where $K = \frac{1}{16} \rho g^2 \gamma^2 (1 + \gamma)$

However if $h_2 > 0$ then a part of the energy passes the shoal and
is lost for the longshore component of energy flux along the
"beach".

Using the assumptions b), c) and d) one finds for the magnitude
of this energy loss:

$$K \, h_2^3 \, \frac{\sin \varphi_o}{c_o} \qquad \qquad \cdots \cdots \cdots \quad (7)$$

The wave energy flux Pl_1 along the beach is:

$$Pl_1 = K(h_{br}^3 - h_2^3) \, \frac{\sin \varphi_o}{c_o} \qquad \cdots \cdots \cdots \quad (8)$$

For two groups of parallel depth contours that make an angle δ
with each other the equations will be slightly different because
the longshore component of the energy flux is computed along the
"inshore" as well as the "beach". Moreover is the angle of wave
incidence at the "beach" (= φ_1') not to be calculated directly
with Snell's law. $\varphi_1' = \varphi_1 + \delta$ (see fig. 4) where φ_1 is computed
with Snell's law and δ can be positive as well as negative. In
figure 4 δ is positive.

b. If $h_{br} > h_1$, the waves are breaking from the "inshore" till
   the "beach".

The longshore component of wave energy flux along the "beach" is

$$Pl_1 = K(h_1^3 - h_2^3) \, \frac{\sin(\varphi_1 + \delta)}{c_1} \qquad \cdots \cdots \cdots \quad (9)$$

and along the "inshore":

$$Pl_2 = K(h_{br}^3 - h_1^3) \, \frac{\sin \varphi_o}{c_o} \qquad \cdots \cdots \cdots \quad (10)$$

c. If $h_2 < h_{br} < h_1$ then the waves only break on the "beach":

$$Pl_1 = K(h_{br}^3 - h_2)^3 \, \frac{\sin(\varphi_1 + \delta)}{c_1} \qquad \cdots \cdots \cdots \quad (11)$$

and

$$Pl_2 = 0$$

d. If $h_{br} < h_2$ then $Pl_1 = Pl_2 = 0$

As can be seen from these formulas the breakerdepth has to be
known to compute this longshore component of energy flux.
Computation of breakerdepth:
Take two wave rays lying a distance of 1 m apart from each other
at the coastline. The flux of energy between these rays is:

$$n_o c_o b_o E_o = n_1 c_1 b_1 E_1 = n_{br} c_{br} b_{br} E_{br} \qquad \cdots \cdots (12)$$

where   b = distance between two wave rays
indexes   o = at deep water
           1 = at depth h_1
           br = at breakerdepth

from equation (12):

$$\frac{1}{2} c_o b_o \frac{1}{8} \rho g H_o^2 = c_{br} b_{br} \frac{1}{8} \rho g H_{br}^2 \qquad \cdots \cdots (13)$$

If h_{br} is smaller than h_1 the waves break on the beach and
making the same assumptions as mentioned before one finds for
h_{br}:

$$h_{br} = \left[\frac{H_o^2 \, \text{sign} \, c_o}{2\gamma^2 \sqrt{(1+\gamma)g}} \cdot \frac{b_o}{b_{br}} \right]^{2/5}$$

where for two groups of parallel depth contours:

$$\frac{b_o}{b_1} = \frac{\cos \varphi_o}{\cos \varphi_1} \quad \text{and} \quad \frac{b_1}{b_{br}} = \frac{\cos(\varphi_1 + \delta)}{\cos \varphi_{br}}$$

(see fig. 4)

so $$\frac{b_o}{b_{br}} = \frac{\cos \varphi_o}{\cos \varphi_1} \frac{\cos(\varphi_1 + \delta)}{\cos \varphi_{br}}$$

If $h_{br} > h_1$ i.e. when the waves are breaking on the inshore the result is:

$$h_{br} = \left[\frac{H_{sign}^2 \cdot c_o}{2\gamma^2 \sqrt{(1+\gamma)g}} \cdot \frac{\cos \varphi_o}{\cos \varphi_{br}} \right]^{2/5}$$

In both cases $\cos \varphi_{br}$ is found by an iteration procedure.

For each occurring wave height, period, angle of wave incidence and waterlevel the breakerdepth and so the longshore component of wave energy is to be computed.
The resultant littoral drift is computed under the assumption that Q (=littoral drift) = 2000 Pl $\left[m^3 \text{ sand/year} \right]$. [5]
A computerprogram is developed to compute the resultant sand-drift with aid of the mentioned formulas in a relative short time.
Only along the Ooster(shoal) and the Noorderstrand (beach) this wave induced littoral drift is computed.
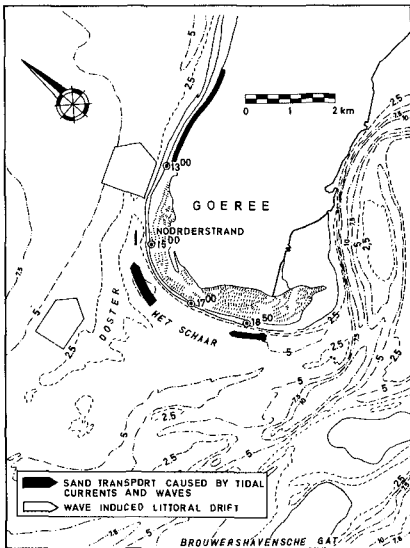
Figure 5 CALCULATED SEDIMENT TRANSPORT ALONG
THE ISLE OF GOEREE BEFORE THE CLOSURE
OF THE BROUWERSHAVENSCHE GAT
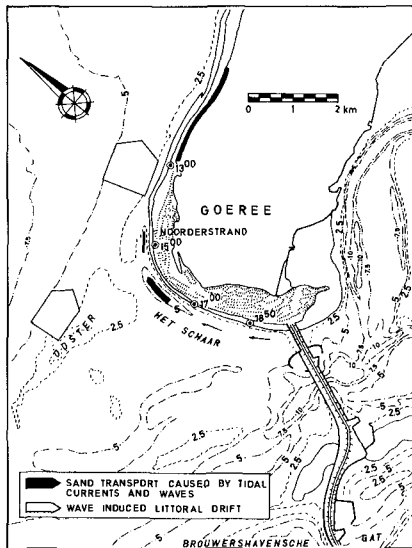
Figure 6 CALCULATED SEDIMENT TRANSPORT ALONG
THE ISLE OF GOEREE AFTER THE CLOSURE
OF THE BROUWERSHAVENSCHE GAT

In front of the beaches and shoals more to the south the depth
contours are too freakish to expect reliable results. However
here the transports are relatively small. The resultant drift
turned out to be more than 1 million m^3 sand/year along the
Ooster and about half a million more along the Noorderstrand
going in eastward direction (see fig. 5 and 6).

SAND TRANSPORT CAUSED BY TIDAL CURRENTS AND WAVES

While the order of magnitude of the wave induced littoral drift
is more or less independent of the closure of the estuaries
there is a big difference in the sandtransport caused by tidal
currents and waves before and after this closure.
A numerical two dimensional tidal computation according to the
Leendertse method [12] is made to compute the horizontal and
vertical tide round the westside of the island, before and after
closure of the Brouwershavensche Gat. Some data obtained from
this computation are used as boundary conditions for a more
detailed one dimensional tidal computation in the Schaar channel.
This is a channel with a maximum depth of 8 m in front of the
Westcoast (see fig. 2). For this purpose the Schaar channel is
schematized into five sections of different depth. In the sec-
tions the mean horizontal tide is computed. Between the two sec-
tions the waterlevel is known. Figure 7 shows the horizontal
tide before and after the closure. The biggest velocities are in
both cases directed to the north. After the closure however the
velocities are less, especially in the neighbourhood of the
Brouwersdam. The longshore transport caused by the interaction
of tidal currents and wave induced orbital velocities is
approached with Bijker's formula [13].
This formula is derived from the Kalinske-Frijlink formula [14].

TIDAL VELOCITIES ROUND THE ISLE OF GOEREE
BEFORE THE CLOSURE OF THE BROUWERSHAVENSCHE GAT

TIDAL VELOCITIES ROUND THE ISLE OF GOEREE
AFTER THE CLOSURE OF THE BROUWERSHAVENSCHE GAT

COURSE OF VELOCITIES IN:

————	GULLY PART 1
— — —	GULLY PART 2
—·—·—	GULLY PART 3
—··—··—	GULLY PART 4
············	GULLY PART 5
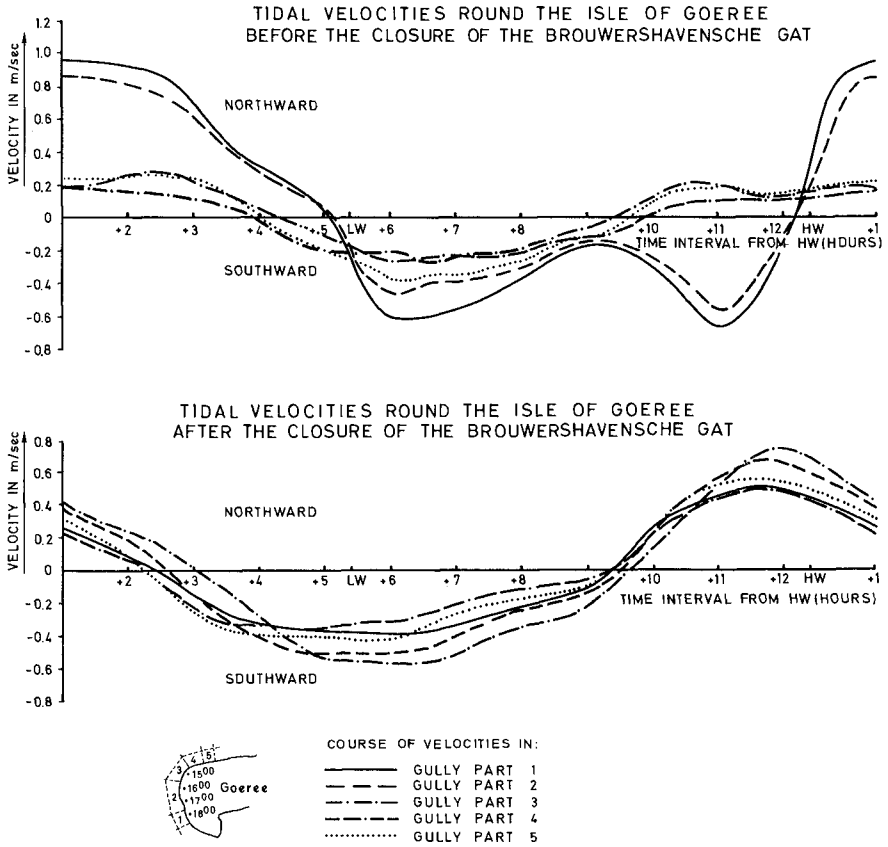
Figure 7

Bottom load:

$$S_b = 5\ D\ \frac{v}{C_r}\sqrt{g}\ e^{-0,27\ \dfrac{\Delta D C_r^{\,2}}{\mu v^2\ \left\{1+\frac{1}{2}(\xi\frac{u_b}{v})^2\right\}}}$$

where S_b = bottom load per unit of time

D = grain diameter

v = current velocity

C_r = resistance coefficient

g = accelaration of gravity

Δ = relative apparent density

μ = ripple coefficient

ξ = parameter

u_b = orbital velocity near the bottom

Suspended load:

$$S_s = 1.83 \; S_b \; (I_1 \ln \frac{33h}{k} + I_2)$$

where S_s = suspended load per unit of time

I_1 en I_2 = Einstein integrals [15]

h   = depth

k   = half the ripple height

By means of Bijker's formula, it is found that the transport
rate is increasing to the north (see fig. 5 and 6). From this
computations of the sandtransport in the Schaar channel the
magnitude as well as the location of the observed erosion in
prototype can be explained.

Before the closure of the Brouwershavensche Gat sand used to
come from this estuary. After the closure the sandfeed to the
Schaar channel coming from the estuary was cut off.
Though the sandtransport capacities after the closure are
smaller the erosion is larger because of the change in diffe-
rence of capacities. The order of magnitude of the mean sand-
losses in the erosion area found from the computation are about
200.000 to 300.000 m^3/year after the closure and about 150.000
to 200.000 m^3/year before the closure of the estuary. That is
about the same amount as the mean yearly losses in the prototype.
This resultant sanddrift feeds the Noorderstrand.

SOLUTIONS FOR REDUCING THE EROSION

Up till now sandsupplies have been carried out to reduce the
erosion. Figure 8 shows a cross section of the beach after the
sandsupply and the enforcement of the dunes in 1974.

See also the aerial photograph made a year after the sandsupply
in 1971.

By a very large sand nourishment the streamprofile of the Schaar
channel narrows down. This in turn causes higher flow velocities
resulting in an increasing loss of sand. Because of this a clo-
sure of the channel is considered in the future. This should be
done with a dam made of sand because the channel stops the sand-
feed of the Noorderstrand. The littoral drift along the sanddam
however can replace the sand that used to come from the Schaar
channel. This sanddam can be considered like a big sandsupply
(about 10 million m^3). Figure 9 shows a possible solution of
such a dam.

It will be clear that such a solution only has effect if one
does not prevent erosion of the sanddam, otherwise the erosion
would be replaced from the Westcoast of the island to the Noor-
derstrand.
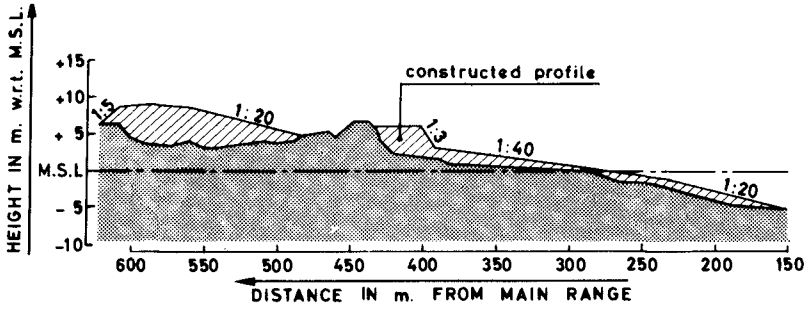
Figure 8 PROFILE OF THE DUNES AFTER THE SANDSUPPLY IN 1974
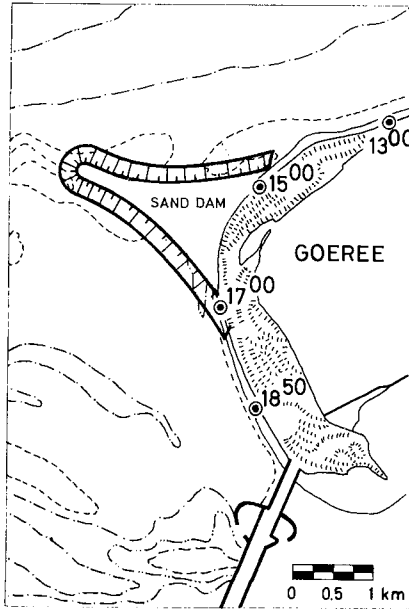
Figure 9ᵃ Location of the sand dam
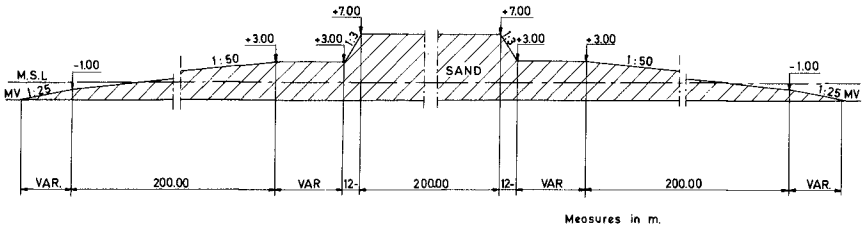
Figure 9ᵇ Cross section of the sand dam

Figure 9 EXAMPLE OF THE LOCATION AND THE DESIGN OF A SAND DAM TO CLOSE THE SCHAAR-GULLY

AERIAL PHOTOGRAPH OF THE WEST-COAST OF GOEREE. TAKEN 3 May 1972
(area where the sand supply was carried out)

REFERENCES

1. Wind and wave data of Netherlands lightvessels since 1949
   K.N.M.I., Med. en Verhand. no. 90 by R. Dorrestein.

2. Dimension of wind-generated waves. Report Gen. Assembly
   Int. Assoc. Phys. Oceanography, Ref. 2.80-81. Oslo 1948.

3. "Generation of wind waves over a shallow bottom" by C.L.
   Bretschneider; Technical Memorandum nr. 51, Oct. 1954,
   Beach Erosion Board Office of the Chief of Engineers.

4. Letter nr. 366/B/IV (19 march 1968) from J.A. Battjes
   (Technical University of Delft) to J.N. Svasek (Rijkswater-
   staat, Deltadienst).

5. Invloed van brekende golven op de stabiliteit van zandige
   kusten (The influence of breaking waves on the stability of
   sandy coasts), Rijkswaterstaat, Deltadienst, Waterloopkun-
   dige Afdeling, Nota W 68.083 by J.N. Svasek.

6. Shore Protection, Planning and Design, U.S. Army Coastal
   Engrng, Res. Center. Technical Report no. 4, 1966, pp. 175.

7. Computation of the wave induced littoral drift according to
   the Svasek-method adapted to parallel depth contours.
   Studyreport W.W.K. 71-2 by W.T. Bakker.

8. Berekening van het zandtransport volgens de methode Svasek
   bij een strand en een vooroever die een hoek met elkaar ma-
   ken. (Computation of the wave induced littoral drift accor-
   ding to Svasek's method adapted to two groups of parallel
   depth contours). Studyreport W.W.K. 71-18 by W.T. Bakker,
   H.G.H. ten Hoopen and G.R.H. Grieve.

9. Computation of set-up, longshore currents, run-up and over-
   topping due to wind-generated waves by J.A. Battjes.

10. On the statistical distribution of the heights of seawaves.
    Journal of Marine Research, Vol. XI, 1952, nr. 3 by
    M.S. Longuet-Higgins.

11. Water waves, pp. 342 and further Interscience Publishers -
    New York - London by J.J. Stoker.

12. Aspects of a computational model for long-period water wave
    propagation. The Rand Corporation R.M.-5294 - P.R.,
    may 1967 by J.J. Leendertse.

13. Some considerations about scales for coastal models with
    movable bed. Delft Hydraulics Laboratory, publ. nr. 50
    by E.W. Bijker.

14. Discussion des formules de débit solide de Kalinske,
    Einstein et Meyer-Peter et Mueler compte tenue des mesures
    récente de transport dans les rivières Néerlandaises.
    2me Journal Hydraulique Soc. Hydr. de France, Grenoble
    1952, pp. 98-103, by H.C. Frijlink.

15. The bed-load function for sediment transportation in open
    channel flows. U.S. Dept. of Agriculture, Washington D.C.,
    Technical Bulletin no. 1026, september 1950 by H.A. Einstein.

CHAPTER 72

ON THE DEPOSITIONAL PROPERTIES OF ESTUARINE SEDIMENTS

by

Ashish J. Mehta[1] and Emmanuel Partheniades[2]

ABSTRACT

The depositional characteristics of flocs of fine cohesive sediments in a turbulent flow field differ distinctly from those of a cohesionless material such as sand. This difference exists because the floc size and shear strength distributions depend on the sediment type as well as the flow condition itself; consequently, the problem of the depositional behavior of these flocs is rather complex, and not easily amenable to analytic treatment.

The present basic experimental study was carried out in a specially designed annular channel. The derived laws of deposition in relation to the time-rates as well as the steady-state concentrations are described and discussed. The reanalyzed results of other limited investigations agree well with the result of the study.

[1]Assistant Research Scientist, Coastal and Oceanographic Engineering Laboratory, University of Florida, Gainesville, Florida 32611.

[2]Professor of Hydraulic Structures, Aristotelian University of Thessaloniki, Thessaloniki, Greece; Professor, Department of Civil and Coastal Engineering, University of Florida, Gainesville, Florida 32611.

INTRODUCTION

Shoaling of fine cohesive sediments is often of considerable impor-
tance in characterizing the hydraulic as well as geomorphic regimen of
such coastal features as tidal entrances, bays and estuarine navigation
channels, where the presence of relatively high salinity and low flow
velocities results in the deposition of flocculated fine-grained sedi-
ments carried by the flow. The sediment itself may be derived from up-
stream river sources, or it may be transported into the estuary or bay
through the ocean entrance by the upstream salinity currents. When the
sediment load is heavy, dredging becomes necessary and, in general, a
costly operation. This and other problems, such as locating a safe area
for dumping of fines from dredge spoils,has created a significant inter-
est in investigating the laws governing the depositional behavior of co-
hesive sediments.

Until recently, most basic investigations dealing with elucidating
the laws of sediment transport were confined to studying cohesionless,
or coarse materials such as sand and gravel. Such was the case partly
because coarse particles have relatively well-defined physical and me-
chanical characteristics and therefore their behavior in a given flow
field is well-suited to an analytic description and experimental vari-
fication, as for example the bed-load function theory formulated by
Einstein (1950) indicates. Unfortunately, in contrast to coarse sedi-
ments, fine cohesive sediments exhibit a much more complex behavior in
a flow field, as the sequel points out.

Nature of Cohesive Sediments - The predominant constituents of
cohesive sediments are silt and clay, consisting of particles of sizes
less than about 60 microns. A significant characteristic of these par-
ticles, particularly those in the less than 2 micron range (clay fraction)
is their plate-like structure, with a large specific surface area (surface
area per unit weight) as compared with cohesionless particles, such that
the physico-chemical surface force acting on any such particle is in gen-
eral orders of magnitude stronger than the gravity force represented by the
submerged weight of the particle. Under the influence of certain minimum a-
mounts of ionic constituents such as salt, in an ambient medium such as water, the
physico-chemical forces become strongly attractive, and cause the particles
to cohere into aggregates, or flocs, when brought together by collisions,
in a turbulent shear flow field. The flocs often are orders of magnitude
larger than the individual particles, and are much more prone to settle-
ment in a given flow field, because of their relatively large settling
velocities.

Inasmuch as flocculation depends on the physico-chemical surface forces of the cohesive material, the ionic medium and on the flow condition, the floc size and shear strength distributions are expected to vary with the type of sediment-water suspension, as well as the flow itself. This makes the problem of the depositional behavior of flocculated cohesive sediments rather complex. Thus Partheniades (1971), in discussing the differential sediment continuity equation derived by McLaughlin (1961), has noted, that it is difficult to integrate this equation to obtain an analytic solution for the law of deposition, because the free surface and bottom boundary conditions are unknown functions involving the floc settling velocity and the turbulent diffusivity. As a consequence, studies on the depositional behavior of cohesive sediments have mainly been experimental.

Previous Studies - Krone (1962) conducted an important but limited series of tests on the measurement of rates of deposition of Bay mud from the San Francisco Bay in a straight flume, and essentially correlated his results with the bed shear stress. For suspended sediment concentrations less than 300 ppm, his measurements indicated an exponential decrease in the suspended concentration with time. For concentrations between 300 ppm and 10,000 ppm, a logarithmic relationship between concentration and time was obtained, whereas for concentrations in excess of 10,000 ppm, another logarithmic relationship was obtained, and the rate of deposition was found to be relatively slow. Krone also observed that there exists a critical shear stress τ_c above which no deposition can take place, while at lower shear stresses, all sediment must eventually deposit. From experimental measurements, τ_c, for the Bay mud suspension was found to be in the range of 0.60 to 0.78 dynes/cm^2.

The deposition tests of Partheniades (1965) were adjunct to his erosion studies on the Bay mud; he observed that in a given test, after a period of relatively rapid deposition, the suspended sediment eventually approached an apparent "equilibrium value". It was noted that two deposition runs, one of high and one of low initial suspended concentration resulted in nearly the same ratio of the apparent "equilibrium concentration" to the concentration at the beginning of the run. From this observation it was concluded that for a given flow condition, a constant proportion of the total initially suspended cohesive material (silt and clay) is always carried in suspension. Mehta (1973) used the data of Partheniades to derive a critical shear stress τ_c of 0.65 dynes/cm^2 which is consistent with the values obtained by Krone.

It is noteworthy that Partheniades obtained an "equilibrium concentration" for runs with shear stresses greater than τ_c whereas most of Krone's tests were conducted at shear stresses less than τ_c; therefore Krone did not observe the phenomenon associated with the equilibrium concentration, and erroneously postulated, as noted earlier, that no sediment deposition can take place for bed shear stress greater than τ_c.

Rosillon and Volkenborn (1964) studied the depositional behavior of Maracaibo sediment. They noted the effects of depth, initial suspended

concentration and salinity on the rate of deposition. In two of their
runs, the suspended sediment concentration apparently reached an "equi-
librium" value; however, an examination of their data reveals that some
of their runs were not carried out for long enough periods to determine
whether equilibrium concentrations would be attained; this fact limited
the possibility of a systematic analysis of their measurements.

The various studies described above were able to isolate some im-
portant factors affecting the rates of deposition, such as the bed shear
stress, depth of flow, type of sediment, initial suspended concentration
and salinity. However, the ranges of these variables studied were limited,
and therefore, no generalized conclusions could be drawn from the results.
It was further realized that straight flumes tend to disrupt the flocs
when they pass through the return pipe and diffusers. Primarily to ob-
viate this problem, a special annular rotating channel-ring assembly was
constructed at M.I.T. and experiments were conducted using kaolinite clay
in distilled water (Partheniades, Cross and Ayora, 1968). A major advan-
tage of this type of apparatus is that it can essentially generate a flow
that is uniform at every section, and is free from any floc-disrupting
elements. The present investigation was also carried out in a similar
but larger apparatus constructed at University of Florida and its attri-
butes will be discussed in the sequel.

OBJECTIVES

The investigation described here was to a certain extent a continua-
tion of tests initially conducted at M.I.T., but with a much broader scope.
The following were its main objectives:

1. A study of the effects of flow parameters on the rates of deposi-
tion of flocculated fine sediments under turbulent flow conditions, and
derivation of quantitative relationships describing these effects.

2. Generalization of the law relating the "equilibrium concentration"
to flow parameters.

3. Identification of physico-chemical parameter(s) which may be used
to characterize the cohesive characteristics of a given sediment.

EQUIPMENT AND TEST PROCEDURE

The components of the basic experimental equipment consisting essen-
tially of a system of rotating ring and annular channel (Fig. 1) are brief-
ly described below; a detailed description may be found elsewhere (Mehta
and Partheniades, 1973b).

The two main components were: (a) an annular fiberglass channel, 8 in.
wide, 18 in. deep and 60 in. in mean diameter containing the sediment sus-
pension and (b) an annular plexiglass ring of the same mean diameter as the
channel but slightly less than 8 in. wide. The ring could be positioned
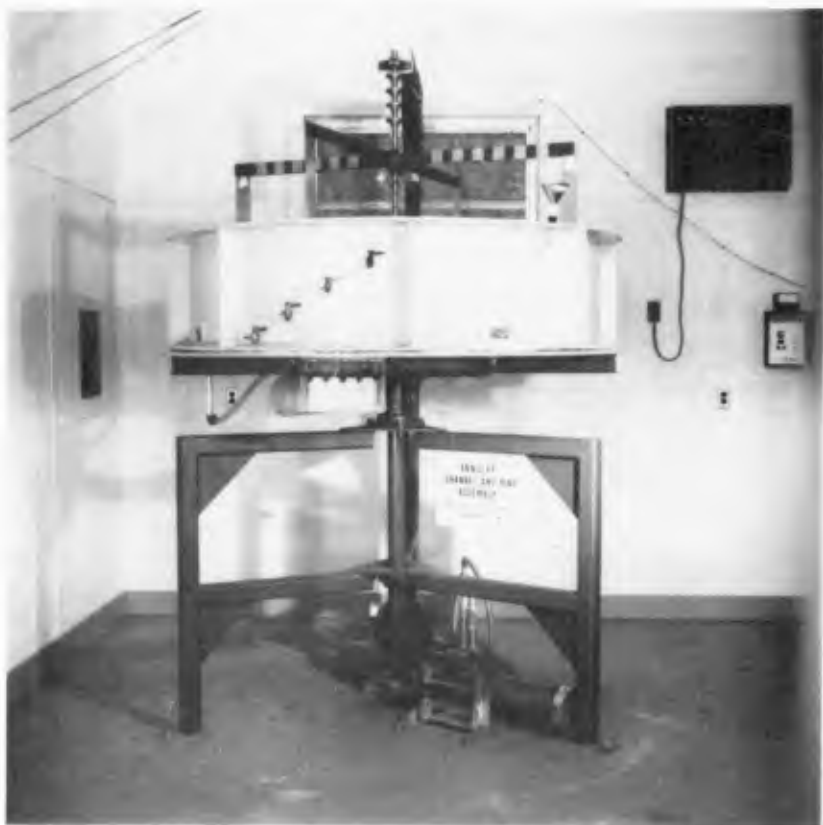
Fig. 1   Annular Channel and Ring Assembly.

within the channel so as to remain in contact with the water surface. A
uniform turbulent shear flow field could be generated by a simultaneous
rotation of the channel and the ring in opposite directions at a given
"operational speed" at which the radial secondary currents generated by
the channel were counter-balanced by corresponding currents caused by the
ring, in the opposite sense. An operational speed was determined by selec-
ting a channel speed, and then varying the ring speed until a number of
3/8" plastic beads with a specific gravity of 1.04 placed at the bottom of
the channel moved uniformly without shifting either towards the outer wall
or towards the inner wall of the channel. Later, the same procedure was
repeated using kaolite clay, and the uniformity of the deposited material
across the width of the channel was checked by measuring the depth of the
deposited bed. Four sample taps at different elevations were provided,
as shown in Fig. 1, to withdraw suspended sediment samples into bottles
on the rack attached below the channel. Water lost due to sample with-
drawal could be replenished from a funnel at the top of the channel. Be-
cause the ring had to stay on the water surface to generate flow, the
channel bed shear stress was measured by introducing a false annular
plexiglass bottom which was attached to the channel bottom by means of
steel blades with strain gages. Through proper calibration the bending
of the blades produced by a given shear stress on the false bottom was
registered by the strain gages on a meter outside the channel.

     Four types of sediments were studied, namely a) a kaolinite clay
from Bath, South Carolina, mined by Dixie Clay Company; this clay immed-
iately flocculates even in distilled water, b) San Francisco Bay mud,
whose predominant clay mineral constituent is montmorillonite, followed
by illite, kaolinite, halloysite and chlorite, as well as organic matter,
c) Maracaibo sediment from Venezuela, which contains an abundance of
quartz in the silt size range, and illite, followed by Kaolinite, mont-
morillonite and chlorite in the clay fraction; it also contains organic
matter, which, as in the case of Bay mud, imparts a greyish color to the
sediment, and finally d) a 50/50 mixture of kaolinite and Bay mud.

     Distilled water as well as salt water at sea water salinity were used
for tests with kaolinite, whereas the other three sediments were tested
in salt water only. The initial suspended sediment concentration C_0 was
varied from approximately 1,000 to 26,000 ppm, while the bed shear stress
τ_b was varied from 0 to approximately 11 dynes/cm^2. Flow depths of 6, 9,
12 and 13 in. were selected. The test procedure essentially consisted in
stirring the suspended sediment at a high speed, to break up any chunks of
sediment, and then rapidly lowering the speed to an "operational" value,
to allow deposition of the material to commence. From time to time the
suspended material was then withdrawn and its concentration determined
through vacuum-filtration of the sample.

TEST RESULTS

     The first extensive sets of tests were carried out with kaolinite in
distilled water. The primary purpose of these measurements was to inves-
tigate the hydrodynamic interaction between the settling flocs and the
flow, by keeping the sediment type and water quality constant.

Fig. 2 shows a typical set of time (t)-concentration (C) runs. These are all at C_0 = 1,005 ppm with a flow depth of 6 in., and τ_b varying from 0 to 3.55 dynes/cm^2. It is clearly observed from this figure that in each case, after a period of relatively rapid deposition, the suspended concentration C attains a constant steady-state value, which was previously referred to as "equilibrium concentration", C_{eq}. In what follows, these two aspects, namely, the time dependent part of the runs and the steady-state part of the runs represented by C_{eq}, are discussed.

Degree of Deposition - In Fig. 3, the ratio C_{eq}/C_0, such as may be obtained from Fig. 2, is plotted against the bed shear stress τ_b, for all the tests carried out with kaolinite in distilled water. Here, although runs at different values of C_0 have not been separated by different symbols, it was found, that the data points fall randomly about a single line; this for instance is clearly observed with respect to data taken at different depths of flow. This very interesting observation has the implication that for a flow at a given bed shear stress and sediment type, the ratio C_{eq}/C_0 remains constant, and is independent of the depth of flow or C_0. Thus for example, at τ_b = 3.1 dynes/cm^2, if C_0 is 2,000 ppm, then C_{eq} will be 1,000 ppm. If on the other hand, C_0 is 20,000 ppm, then C_{eq} will be 10,000 ppm. In other words, the amount of sediment that can be maintained in suspension at steady-state depends not on the flow condition, but is contingent upon the available initial quantity of suspended sediment. This behavior contrasts with the transport process for coarse cohesionless sediments, whose bed material transport is governed by an exchange of the sediment particles between the bed and the suspension, such that in a state of equilibrium the number of particles depositing per unit area per unit time equals the number eroding per unit area per unit time. Consequently, the equilibrium concentration of the coarse suspended bed material, depends not on the availability of suspended material of the same kind, but solely on the flow condition itself, inasmuch as the exchange rates themselves depend on the latter.

C_{eq} is thus not an equilibrium concentration but rather represents a constant amount that indefinitely remains in suspension at steady-state, at a given flow condition. This further implies that any exchange of particles between the bed and the suspension, as occurs in the case of cohesionless materials must be precluded for cohesive sediments; this is a fundamental difference between the hydrodynamic behavior of cohesionless and cohesive sediments. Partheniades, Cross and Ayora (1968) confirmed this conclusion directly by flushing the annular channel of the suspended material at steady-state. They found that, in this condition the bed exhibited no erosion and the flowing water above the bed remained clear.

Another interesting feature of Fig. 3 is the existence of a well-defined minimum shear stress, τ_{bmin}, below which no amount of material can remain in suspension indefinitely. This shear stress is the same as τ_c obtained by Krone (1962), but contrary to his postulation, it does not represent a shear stress above which no amount of material can deposit. From Fig. 3, τ_{bmin} = 1.80 dynes/cm^2 for the suspension of kaolinite in distilled water.
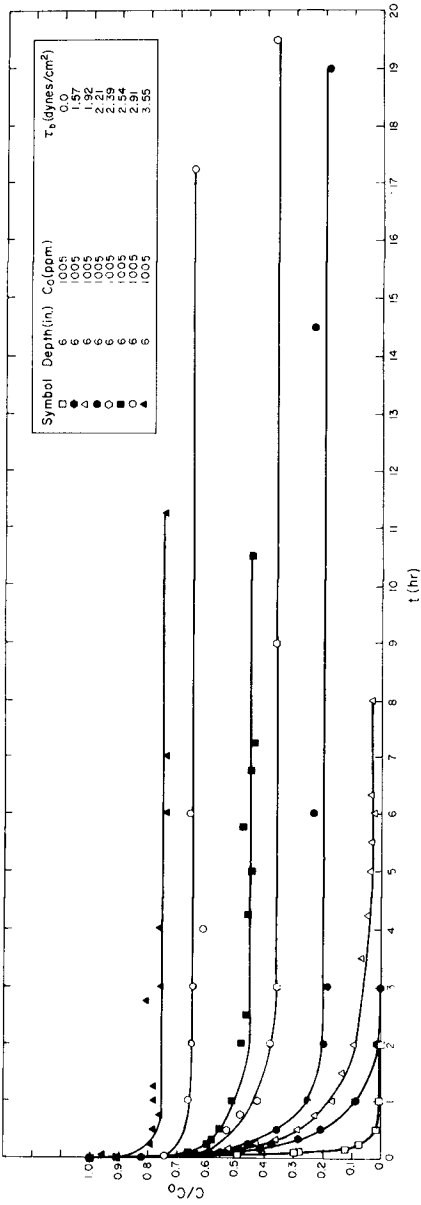
Fig. 2   Ratio C/C_0 of Instantaneous to Initial Suspended Concentration versus Time t for Tests using Kaolinite in Distilled Water.
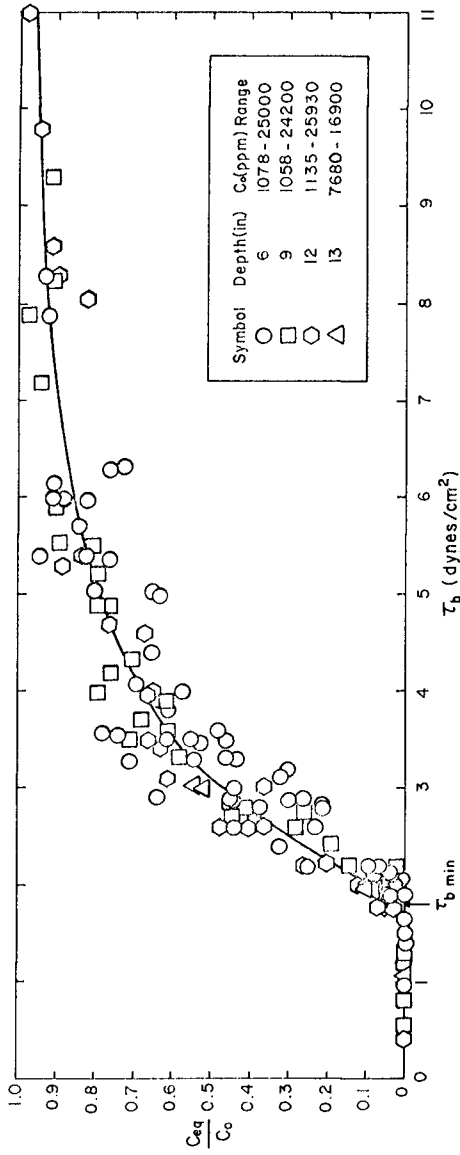
Fig. 3   Ratio C_{eq}/C_0 of Steady-State to Initial Suspended Concentration versus Bed Shear Stress τ_b.

It should be noted that the fraction $1 - C_{eq}/C_0$ represents the degree of deposition at steady-state. In Fig. 4, the data of Fig. 3 are plotted on a log-normal paper, in terms of $C^*_{eq} = C_{eq}/C_0$, in percent, as a function of the dimensionless parameter $\tau^*_b - 1$, where $\tau^*_b = \tau_b/\tau_{bmin}$. The straight line on the plot is represented by the expression

$$C^*_{eq} = \frac{1}{\sqrt{2\pi}} \int_{-\infty}^{y_a} e^{-w^2/2} \, dw \qquad (1)$$

where

$$y_a = \frac{1}{\sigma_1} \log[(\tau^*_b - 1)/(\tau^*_b - 1)_{50}] . \qquad (2)$$

Here, σ_1 is the standard deviation, $(\tau^*_b - 1)_{50}$ is the geometric mean of the log-normal relationship and w is a dummy variable. For the data of Fig. 4, $\sigma_1 = 0.49$ and $(\tau^*_b - 1)_{50} = 0.72$.

The plot of Fig. 5 is similar to Fig. 4, except that it is normalized with respect to the geometric mean $(\tau^*_b - 1)_{50}$. Here, Series A (at a depth of 6 in. and $C_0 = 6,140$ ppm) and Series B (at a depth of 9 in. and $C_0 = 10,270$ ppm) correspond to measurements using kaolinite in salt water in the annular apparatus. Series C is for the 50/50 mixture of kaolinite and Bay mud in salt water and Series D is using Bay mud in salt water. Measurements of Partheniades, Cross and Ayora (1968), Partheniades (1965) and Rosillon and Volkenborn (1964) are also included.

An interesting aspect of Fig. 5 is that even though values of τ_{bmin} and $(\tau^*_b - 1)_{50}$ are different for different suspensions, the value of $\sigma_1 = 0.49$ for the standard deviation is seen to hold for all the data; thus suggesting a universality of this coefficient. This implies that C^*_{eq}, and therefore, the degree of deposition is uniquely determined by the ratio of $(\tau^*_b - 1)/(\tau^*_b - 1)_{50}$, irrespective of the values of $(\tau^*_b - 1)_{50}$ or τ_{bmin}.

It has been shown elsewhere (Mehta and Partheniades, 1973a) that for measurements taken in salt water, $(\tau^*_b - 1)_{50}$ and τ_{bmin} are related, and therefore, only τ_{bmin} need be measured to obtain the degree of deposition of a given sediment. Further, it appears that under certain conditions, τ_{bmin} can in turn be related to the cation exchange capacity (CEC) of the sediment, which is a measurable quantity, and is representative of the cohesive property of the sediment itself.

Rates of Deposition - Since C_{eq} represents the amount of sediment that does not deposit, $C_0 - C_{eq}$ represents the amount that gets deposited, and the fraction $C^* = C_0 - C/C_0 - C_{eq}$ is the fraction of depositable sediment $(C_0 - C_{eq})$ which is deposited at any given time. C^* of course varies from zero when $C = C_0$, to unity, when $C = C_{eq}$.

Figs. 6, 7, and 8 show some of the experimental data (from Mehta, 1973) for kaolinite in distilled water, plotted in terms of C^* in percent versus t/t_{50}, where t_{50} is the time at which C^* is 50%. The data points indicate
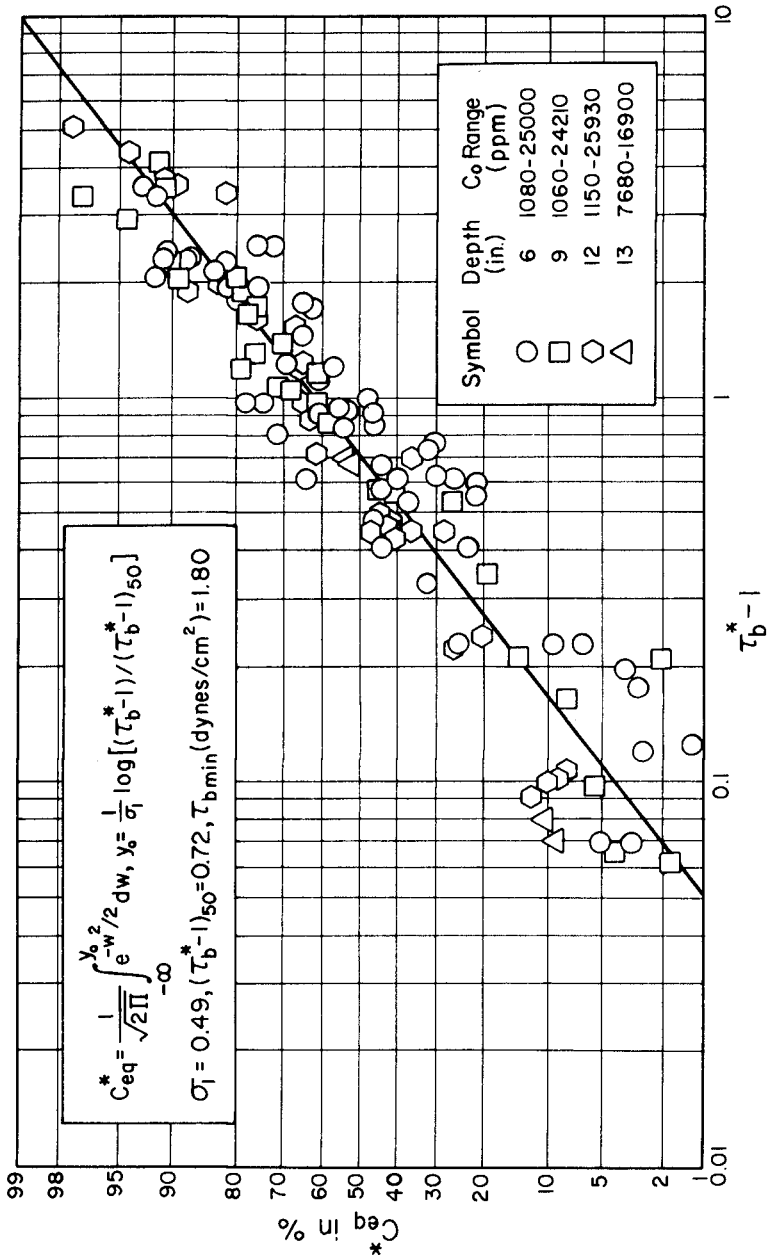
Fig. 4   Relative Steady-State Concentration $C_{eq}^* = C_{eq}/C_o$ versus Shear Stress Parameter τ_b^*-1 for Kaolinite in Distilled Water.
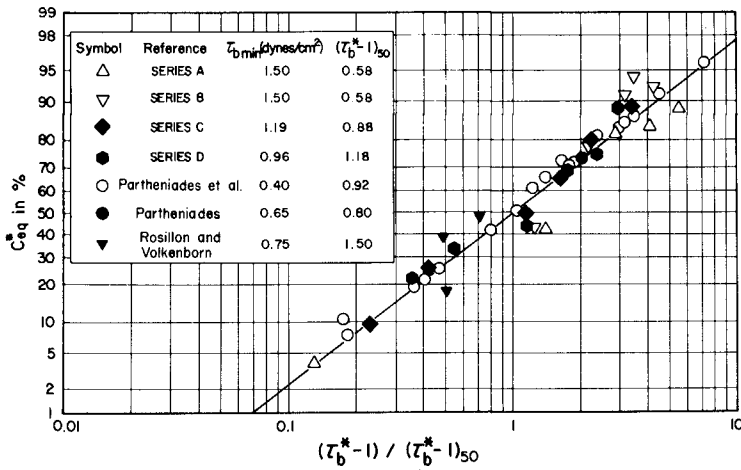
Fig. 5 C_{eq}^* versus Normalized Bed Shear Stress Parameter $(\tau_b^*-1)/$
$(\tau_b^*-1)_{50}$. Data Points are from Different Types of Suspensions
(Series A to D) and other Investigations.
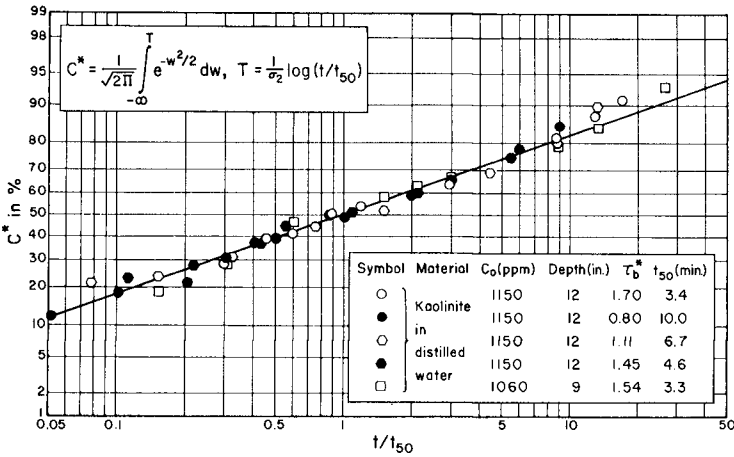
Fig. 6 Fraction of Depositable Suspended Concentration, C^*, versus
Normalized Time t/t_{50}, for Kaolinite in Distilled Water.
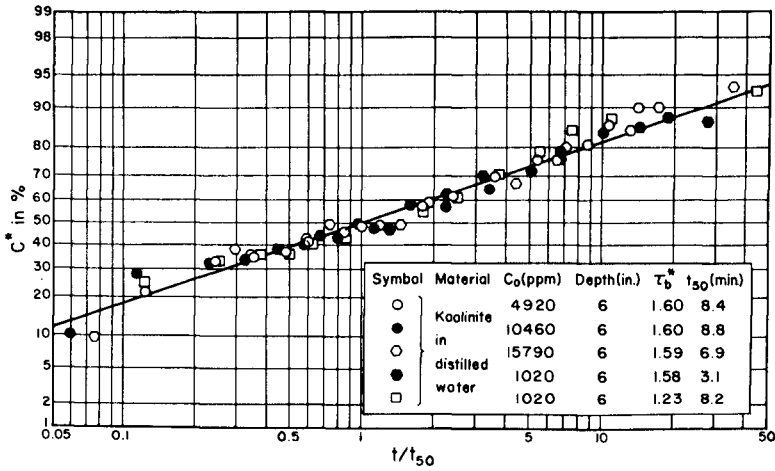
Fig. 7 Fraction of Depositable Suspended Concentration, C*, versus Normalized Time t/t₅₀ for Kaolinite in Distilled Water.
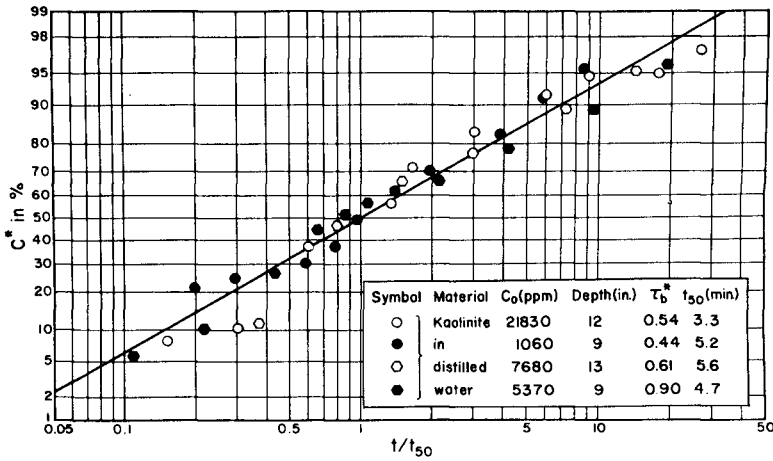
Fig. 8 Fraction of Depositable Suspended Concentration, C*, versus Normalized Time t/t₅₀ for Kaolinite in Distilled Water.

the following log-normal relationship for the decrease of suspended con-
centration with time:

$$C^* = \frac{1}{\sqrt{2\pi}} \int_{-\infty}^{T} e^{-w^2/2} \, dw \qquad (3)$$

where

$$T = \frac{1}{\sigma_2} \log[t/t_{50}] \quad . \qquad (4)$$

Here, σ_2 is the standard deviation, t_{50} is the geometric mean and w is a
dummy variable. It can be seen from the plots that the log-normal rela-
tionship holds for τ_b^* less than unity, i.e., $\tau_b < \tau_{bmin}$, as well as for
τ_b^* greater than unity, i.e., $\tau_b > \tau_{bmin}$. From Eqs. (3) and (4), the fol-
lowing expression can be derived for the time-rate of deposition:

$$\frac{dC^*}{dt} = \frac{0.434}{\sqrt{2\pi}\sigma_2} e^{-T^2/2} \frac{1}{t} \quad . \qquad (5)$$

Figs. 9 and 10 show examples of variations of the parameters σ_2 and
t_{50} with τ_b^*, depth of flow and initial concentration C_o, for kaolinite in
distilled water. In general, the trends are somewhat obscured by the
scatter of data points; however, the following broad conclusions may be
derived from these and other similar plots obtained by Mehta (1973):

1. The variation of σ_2 and t_{50} with τ_b^* is such that for a particular
τ_b^*, the rate of deposition reaches its lowest value. For kaolinite in
distilled water, this value of τ_b^* was found to vary between 1 and 2 dynes/
cm^2, depending on the value of C_o and the depth of flow. As τ_b^* decreases
below this particular value, the rates become higher, while as τ_b^* increases
above this value, the rate also increases, but less significantly.

2. The effect of depth for τ_b^* less than unity is such that increas-
ing the depth tends to increase the rate of deposition. For τ_b^* greater
than unity, the effect is less significant and less distinct.

3. The effect of C_o is such that in general, increasing C_o decreases
the rate of deposition.

Fig. 11 shows examples of some of the rates measured for kaolinite in
salt water (from Series B). These also indicate the law given by Eq. (5).
The rates are, however, in general slower than for kaolinite in distilled
water. Fig. 12 shows two sets of reanalyzed data of Rosillon and Volken-
born (1964) which indicate remarkable consistency with the log-normal law.
The rates were, however, much lower than those measured in the annular chan-
nel, as indicated by the relatively much higher values of t_{50}. Finally,
Fig. 13 shows reanalyzed data of Partheniades (1965) and Krone (1962) which
also agree with the log-normal law.

Symbol	Depth(in.)	C_0(ppm)
○	6	4920
◑	6	6310
■	9	5370
●	12	5280
△	13	7680
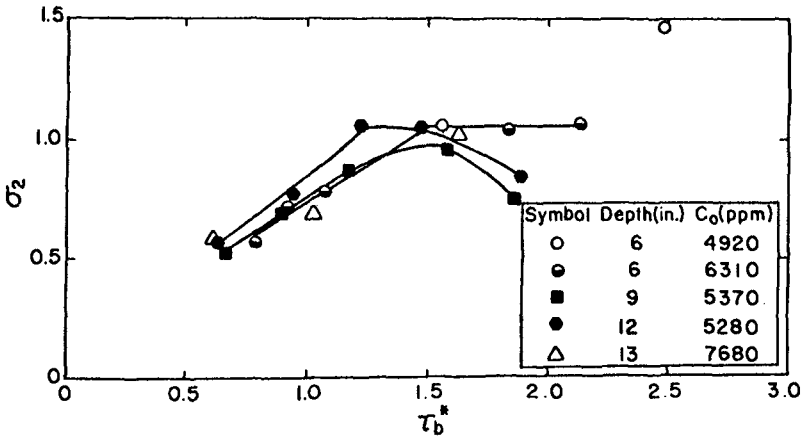
Fig. 9   Examples of Variation of σ_2 with τ_b^* for Kaolinite in Distilled Water.
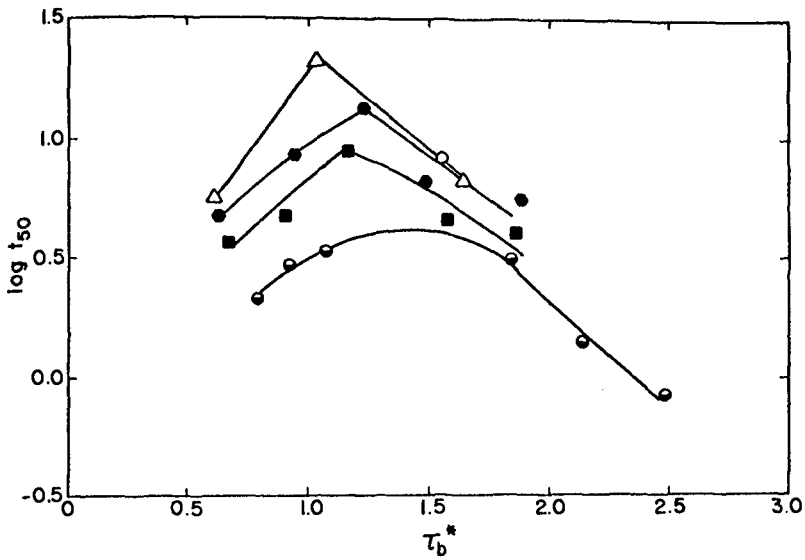
Fig. 10   Examples of Variation of Log t_{50} with τ_b^* for Kaolinite in Distilled Water.
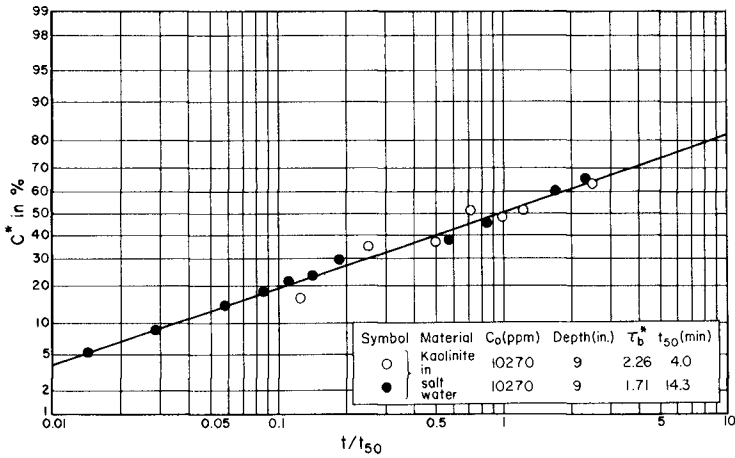
Fig. 11   Fraction of Depositable Suspended Concentration, C*,
           versus Normalized time t/t₅₀ for Kaolinite in Salt
           Water.
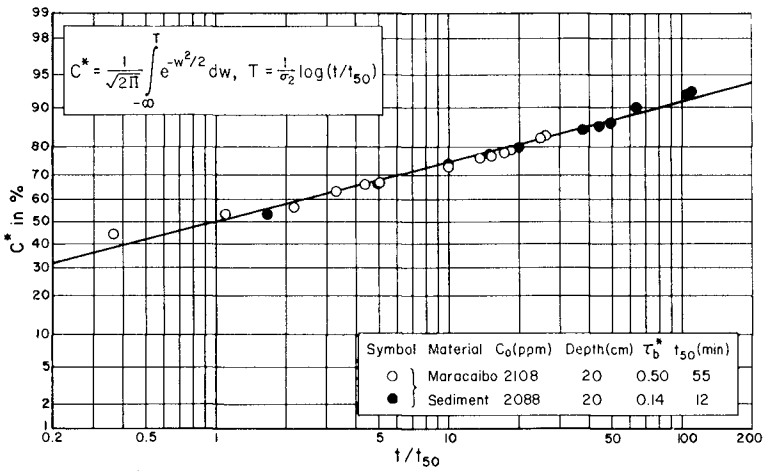
Fig. 12   Fraction of Depositable Suspended Concentration, C*,
           versus Normalized time t/t₅₀ for Maracaibo Sediment.
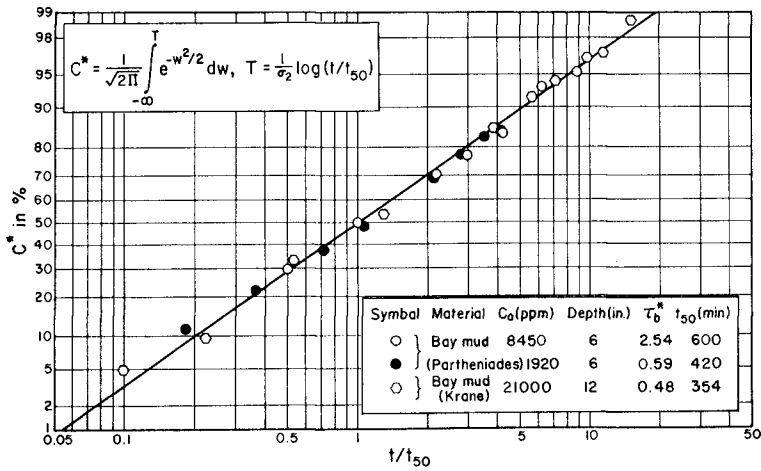
Fig. 13   Fraction of Depositable Suspended Concentration, C*,
          versus Normalized Time t/t$_{50}$. Data of Krone (1962)
          and Partheniades (1965).
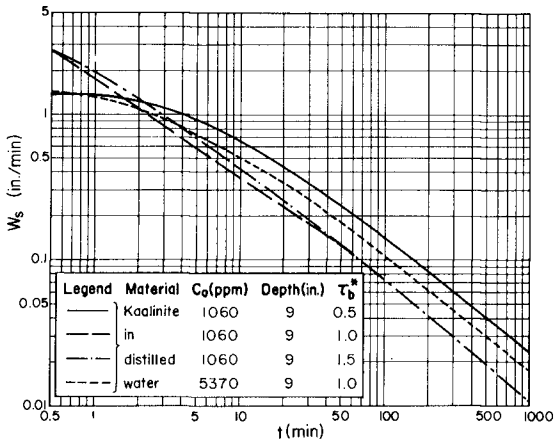
Fig. 14   Variation of Apparent Settling Velocity, W$_S$,
          versus time t for Kaolinite in Distilled
          Water.

It should be pointed out that inasmuch as it is desirable to be able to predict the rate of deposition of any given sediment under a given flow condition, the parameters σ_2 and t_{50} must be functionally related to τ_b^*, depth of flow and C_0, as well as a physico-chemical parameter such as the cation exchange capacity of the sediment. The scope of the present study was, however, limited to experimentally describing the relationships between σ_2 and t_{50} with τ_b^*, depth of flow and C_0 only.

Certain limits were observed in the applicability of the law of Eq. (5). Thus it was noted by Mehta (1973) that for high initial concentrations C_0, of the order of 25,000, Eq. (5) may still be used for τ_b^* > 1, but for τ_b^* less than unity, significant deviations begin to appear. It may further be noted that for τ_b^* of the order of 0.25 and less, for all concentrations, the data may exhibit deviations from Eq. (5).

SETTLING VELOCITIES

The scope of this paper precludes an extensive discussion of the results; such a discussion may be referred to elsewhere (Mehta and Partheniades, 1973b). It suffices to note that the process of deposition of the flocs appears to be controlled by the stochastic turbulent processes in the zone near the bed. There, the strongest shear and lift forces prevail, and these in turn control the size and shear strength distributions of the flocs in suspension. Thus a floc which is strong enough to withstand the maximum shearing force acting on it near the bed will settle on the bed and will attach itself to the bed by cohesive bonds. On the other hand, a floc with a relatively low shear strength will be broken into two or more smaller units and these will be reentrained in the suspension by the strong hydrodynamic lift forces. This hypothesis in fact implies that the steady-state suspension represented by C_{eq} contains flocs that are too weak and small to be able to withstand the shear stresses near the bed and deposit.

The settling velocities of the depositing flocs are of signficance, particularly from an engineering point of view. It is obvious from the foregoing presentation, that inasmuch as the sediment floc size distribution depends not only on the type of sediment-water suspension but also on the flow condition itself, the settling velocities of the flocs can not be derived from extrapolation of results, to smaller particles, obtained for sand grains.

A simple finite volume continuity principle for the sediment in the annular channel may be written as

$$\frac{dC^{**}}{dt} = -\frac{W_s}{h} C^{**} \tag{6}$$

where $C^{**} = 1 - C^* = C - C_{eq}/C_0 - C_{eq}$ represents the fraction of depositable sediment which is in suspension at any given time, h is the total depth of flow and W_s is the settling velocity. Since as noted the settling flocs are segregated by a stochastic selection process near the bed before some of them actually deposit on the bed, W_s may be viewed as an apparent settling velocity; it thus involves a probability of deposition, which

depends on the time-distribution of the turbulent bed shear stress
(Mehta, 1973). For a given test, the variation of C^{**} and dC^{**}/dt
with time can ultimately be obtained through Eqs. (3), (4) and (5);
Eq. (6) can therefore be utilized to determine the variation of W_s
with time. Four examples of this nature are given in Fig. 14, where
W_s (in/sec) is plotted against time t (min) for Kaolinite in distilled
water suspension at $C_o = 1,060$ ppm, depth h = 9 in. and τ_b^* varying from
0.5 to 1.5 dynes/cm^2. An interesting observation is that for t greater
than 10 minutes, the plots begin to exhibit an approximate exponential
decrease of W_s with time. Clearly, the settling velocity can not be
assumed to be a constant.

APPLICATION

      A few brief comments on the applicability of the derived law of de-
position in numerical models are in order.

      1. Although the law itself may be assumed to be applicable under
field conditions, the constants defining the log-normal relationships
must necessarily be evaluated through calibration using field data,
since the present state of the art does not permit ready determination
of these constants from known relationships; the use of the cation ex-
change capacity is only a first step toward this direction.

      2. Sediment dispersion was absent in the annular channel inasmuch
as there was no concentration gradient dC/dx in the direction of flow;
it is believed this term was also of secondary importance in the straight
flume experiments with which the data have been compared. Field appli-
cation of the law of deposition must be carried out in general in con-
junction with the one-dimensional transport-diffusion equation. In this
context it may be noted that although deposition is essentially a phe-
nomenon associated with the bottom boundary, in the transport-diffusion
equation, the law of deposition may be included as a sink term.

      3. Care must be taken in applying the law of deposition derived
under a steady flow situation to time varying flows.

ACKNOWLEDGEMENT

REFERENCES

Einstein, H. A., "The Bed-Load Function for Sediment Transportation in
Open Channel Flows," Tech. Bull., No. 1026, U. S. Dept. of Agriculture,
Soil Conservation Service, Washington, D. C., September, 1950.

Krone, R. B., "Flume Studies of the Transport of Sediment in Estuarial
Shoaling Processes," Final Rep.,Hydr. Engr. Lab. and Sanitary Engr. Res.
Lab., Univ. of California, Berkeley, June, 1962.

McLaughlin, R. T., "Settling Properties of Suspension," Trans. ASCE, Part I, Vol. 126, p. 1734, 1961.

Mehta, A. J., "Depositional Behavior of Cohesive Sediments," Ph.D. Dissertation, University of Florida, Gainesville, March, 1973.

Mehta, A. J. and Partheniades, E., "Effect of Physico-Chemical Properties of Fine Suspended Sediment on the Degree of Deposition," Proc. Int. Symp. on River Mech., Int. Assoc. for Hydr. Res., Vol. 1, p. 465, Bankok, January, 1973a.

Mehta, A. J., and Partheniades, E., "Depositional Behavior of Cohesive Sediments," Tech. Rep. No. 16, Coastal and Oceanographic Engineering Laboratory, University of Florida, Gainesville, March, 1973b.

Partheniades, E., "Erosion and Deposition of Cohesive Soils," J. Hydr. Div., Proc. ASCE, Vol. 91, No. HY1, Proc. Paper 4204, January, 1965.

Partheniades, E., Cross, R. H., and Ayora, A., "Further Results on the Deposition of Cohesive Sediments," Proc. 11th Conf. on Coastal Engr., Vol. 1, Ch. 47, p. 723, London, September, 1968.

Partheniades, E., "Erosion and Deposition of Cohesive Materials," Chapter 25, in River Mechanics, Edited by H. W. Shen, Colorado State University, Fort Collins, Colorado, 1971.

Rosillon, R., and Volkenborn, D., "Sedimentacion de Material Cohesivo en Agua Salada," Thesis, Univ. of Zulia, Maracaibo, Venezuela, November, 1964.

CHAPTER 73

STABILITY AND BEARING CAPACITY OF BOTTOM SEDIMENTS

by

R.J. Mitchell   and   J.A. Hull[2]

The results of model testing show that the strength and stability
of bottom sediments can be substantially reduced by the cyclic loading
pulses induced by wave action. The minimum soil strength is approximately
equal to the remoulded vane strength and the depth of wave remoulding
appears to be mainly a function of the wave characteristics. The
phenomenon of wave remoulding should be considered in the design of
offshore foundations as reductions in bearing capacity and lateral
shearing resistance can develop as a result of the action of storm waves.

Where bottom sediments are sloping such that the static factor of
safety against slope failure is less than the soil sensitivity, severe
storm conditions may lead to submarine landsliding. Wave induced submarine
landsliding has been reproduced in model tests and the results are
correlated with current analytical approaches to this problem.

INTRODUCTION

Most offshore construction and exploration activities are located in
coastal waters where wave characteristics and water depths are such that
the bottom sediments experience pressure pulses from passing waves. Under
storm conditions these pressure pulses have been considered to induce
catastrophic instabilities in soft gently sloping bottom sediments
(see, for example, Bea, 1971). The role of wave action in causing submarine
slope instabilities has been examined analytically by Henkel (1970) and by
Wright and Dunham (1972). Henkel considers circular arc sliding from an
upper bound moment equilibrium approach while Wright and Dunham carry out
stress analyses appropriate to an infinite slope type of failure. These
two possible modes of failure are shown on Figure 1. Both theoretical
treatments attempt to evaluate the driving forces (or stresses) exerted
in the soil mass by a standing wave. At failure, gravitational forces
together with driving forces due to wave action are assumed to overcome the
resisting forces derived from the undisturbed strength of the sediment.

---

[1]   Associate Professor, Department of Civil Engineering,
      Queen's University at Kingston, Ontario, Canada.

[2]   Geotechnical Engineer, H.Q. Golder Associates,
      Toronto, Ontario, Canada.

(a) Rotational Sliding (HENKEL, 1970)

(b) Infinite Slope Sliding (WRIGHT ‡ DUNHAM, 1972)
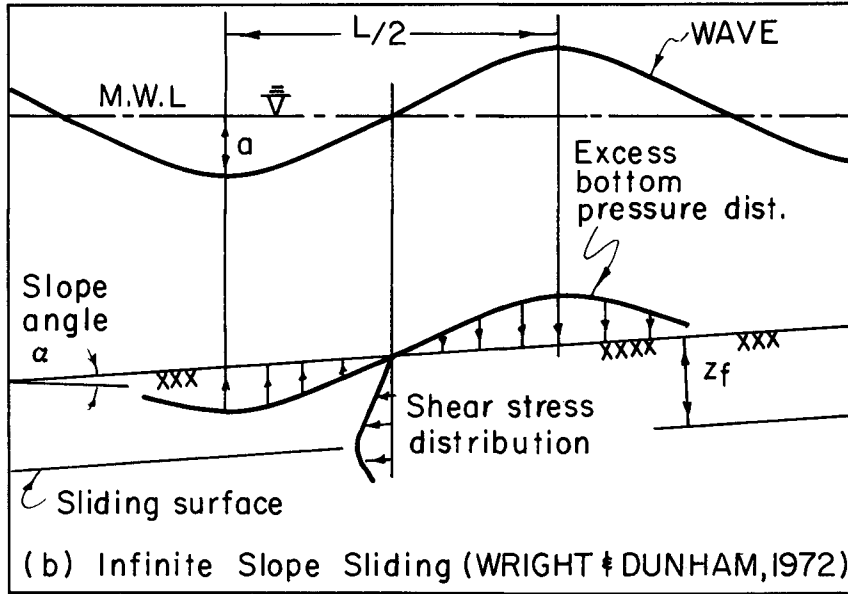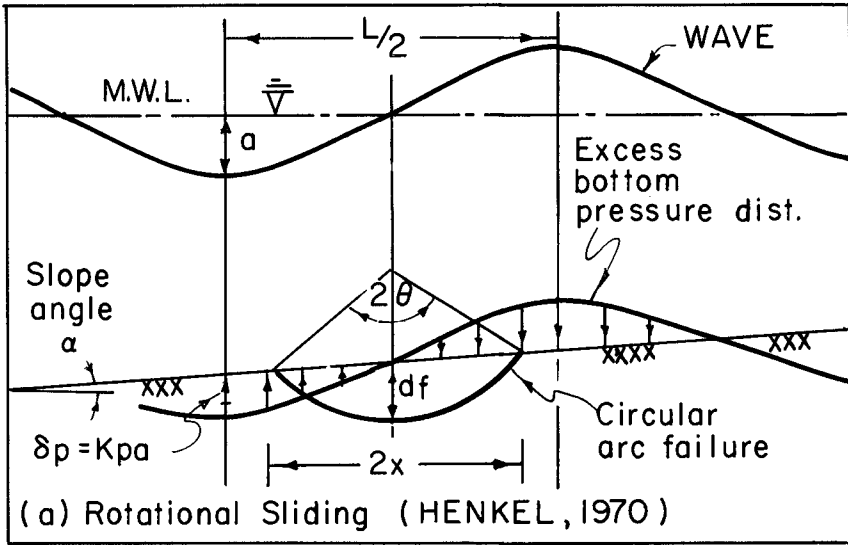
FIGURE 1 :   STATIC REPRESENTATION OF FAILURE MODES

Mitchell et al (1972) demonstrated that wave action was instrumental in initiating mass movements of submarine sediments in model studies but indicated little correlation between the model test results and previous analytical predictions. They suggest, from analysis of the model test results, that the driving forces in submarine landslides are primarily gravitational and that a progressive wave train initiates failure by reducing the soil strength (remoulding the soil).

In the design of offshore foundations the bearing capacity, lateral resistance (for piles) and stability of the bottom sediments must generally be evaluated. lf wave action causes loss of strength due to remoulding there will be an associated decrease in bearing capacity and lateral resistance as well as a potential for mass instability; these effects would be relatively independent of the direction of the storm wave progression. If waves produce only driving forces, stability against landsliding would be the main concern and the effect would vary depending on the direction of the wave train with respect to the dip of the sediment surface. The studies reported in this paper were carried out to investigate the effects of wave action on the strength of a marine sediment.

Strength of bottom sediments and depth of slope failures

Seasonal and long term variations in deposition rates and in the consistency of sedimenting materials complicates the problem of characterizing the strength-depth relations for marine sediments. In areas where sedimentation rates are relatively high, bottom sediments may remain unconsolidated (i.e. an excess pore water pressure gradient exists in the sediment due to high rates of accumulation and slow rates of consolidation) for long periods of time (see, for example, McClelland, 1967). Despite these complications, many marine sediments exhibit somewhat linear increases in undrained strength with depth although the upper portion of the profile often shows a nearly constant strength (see, for example, Sangrey, 1972).

In laboratory studies it is convenient to prepare a simply sedimented soil and it is necessary to examine the form of the strength vs. depth relation in such model sediments. Morgenstern (1967) suggests that the undrained strength profile for a simply sedimented soil may be approximated by

$$C_u = A \sigma_v' = AZ \overline{\gamma}' \qquad\qquad 1$$

where C_u = the undrained strength at depth Z

A   is a soil constant related primarily to the effective stress strength parameter ϕ' of the soil

σ_v' = $Z \overline{\gamma}'$ is the effective vertical stress at depth Z

$\overline{\gamma}'$ is the average effective unit weight of the overburden above depth Z .
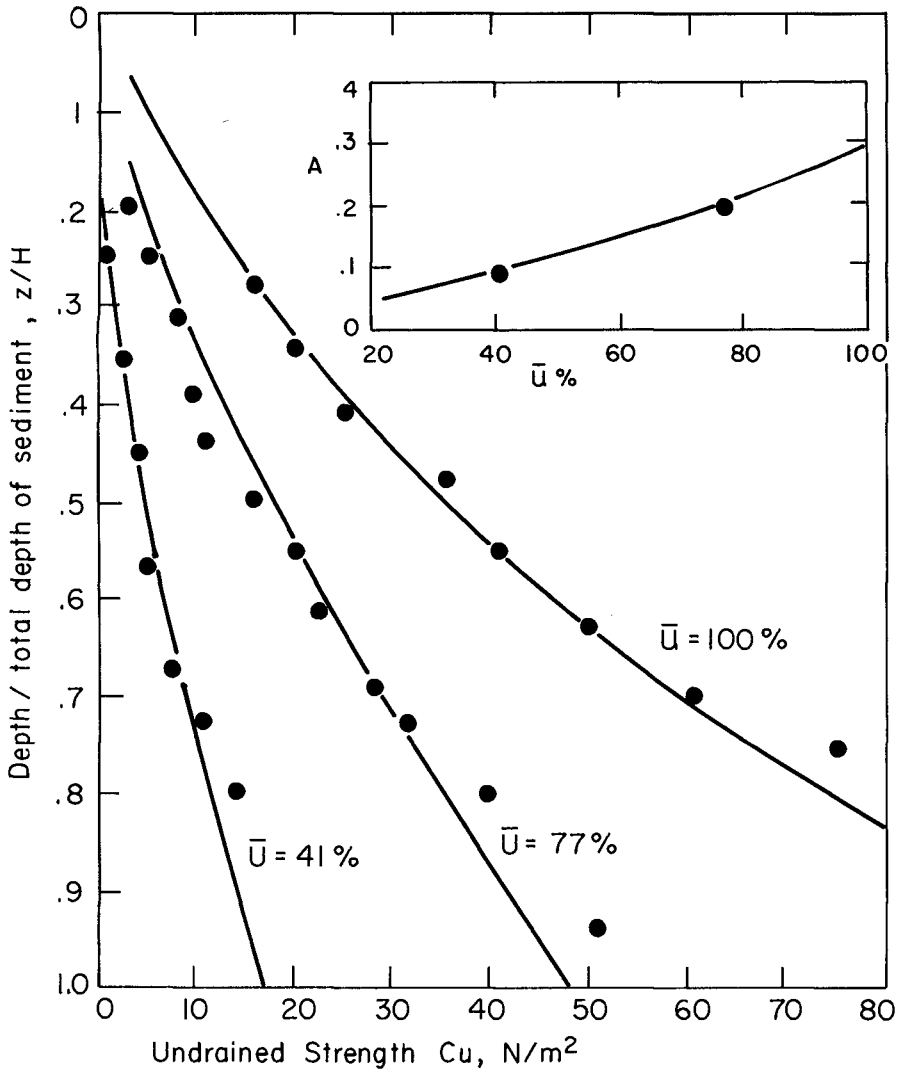
FIGURE 2 :   UNDRAINED STRENGTH PROFILES (DATA FROM TSUI,1972)

Detailed density and pore water pressure measurements carried out by Tsui (1970) and Hull (1973) show that laboratory sedimentation of a bentonite slurry results in the following characteristics:

$$\text{Unit weight, } \gamma = B + C Z$$

and excess pore water pressure, $\Delta u = D Z$

where   B, C and D are constants depending on the degree of consolidation.

From equation 1, the undrained strength profile is then predicted as:

$$C_u = A [B - (D + \gamma_\omega)] Z + \frac{CZ^2}{2} \qquad\qquad 2$$

Using experimental values of the constants B, C and D at various average degrees of consolidation, $\overline{U}\%$, equation 2 is fitted in Figure 2 to the vane strength data published by Mitchell et al (1972). The form of the profiles agrees with equation 2 and numerical correlation is obtained by using $A = F(\overline{U}\%)$ as shown inset on Figure 2. The value of A at $\overline{U} = 100\%$ agrees with the Mohr-Coulomb value $A = \sin \phi'/(1 + \sin \phi')$, for $\phi' = 24°$, a reasonable value for this clay. Since A does not remain constant it is concluded that the strength of underconsolidated sediments cannot be predicted from effective stress considerations alone; a more fundamental strength gain develops as the soil consolidates.

In prototype situations the gravitational stresses are proportionally higher (according to the linear scaling factor λ) and variations in density over the depth of the profile are likely to be less pronounced. Prototype strength profiles would then be expected to be more linear than those at the model scale.

The short term (undrained)factor of safety against gravitational failure of submerged slopes can be shown to be directly proportional to the C_u/σ'_v ratio (Gibson and Morgenstern, 1962) and for infinite slope sliding this factor of safety is given by

$$F.S. = \frac{2 C_u}{\overline{\gamma}' Z \sin 2\alpha} \qquad\qquad 3$$

where α is the slope angle. Thus at any given degree of consolidation the depth of failure is independent of the strength vs. depth relation providing it is of the form given in equation 1. Any contribution of wave characteristics to depth of failure should then be related in the model and prototype situations.

(A) PLAN

(B) SECTION A-A
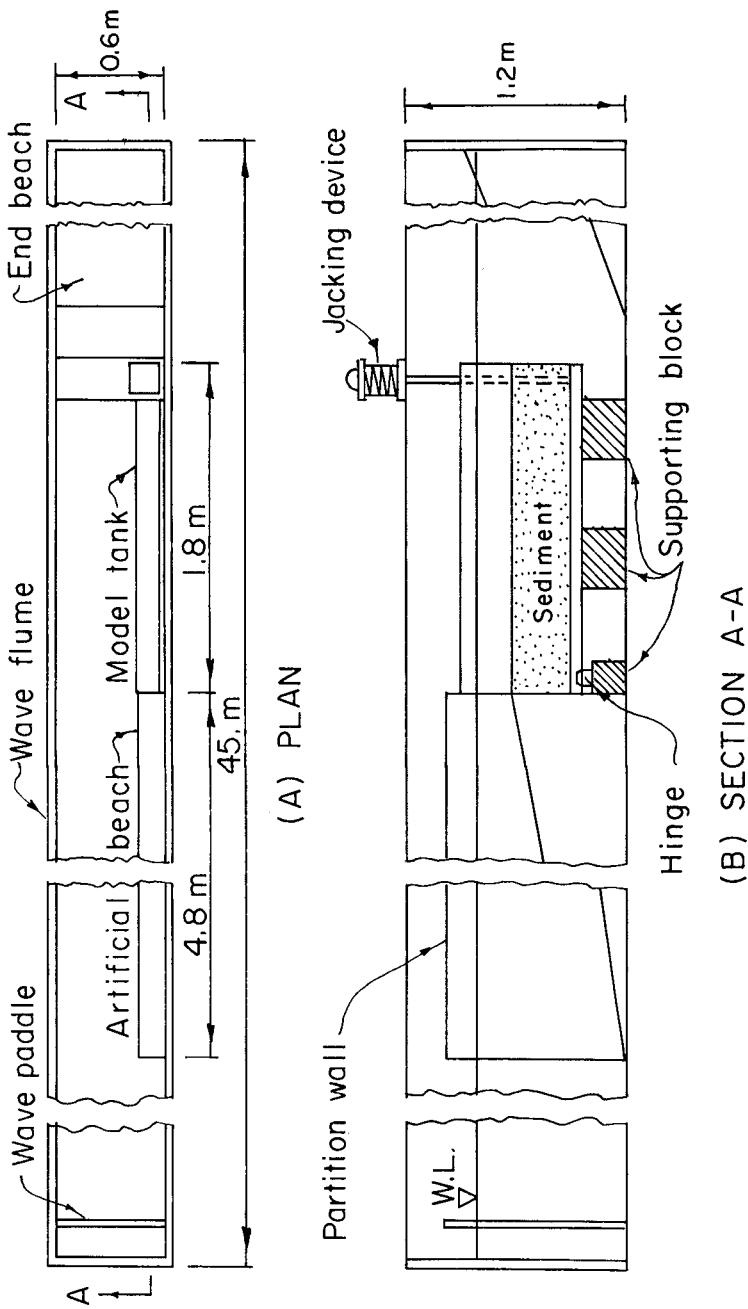
FIGURE 3 : MODEL TANK IN WAVE FLUME

MODEL STUDIES

        Model studies were carried out using the physical facilities
described by Mitchell et al (1972) to determine the effect of wave action
on the strength and stability of a bentonite clay sedimented in a marine
environment. Figure 3 shows the physical arrangements with the model tank
dimensions being 6 ft. long by 2 ft. deep by 0.5 ft. wide. A commercial
bentonite was used as the sediment and was prepared as a 10 percent by weight
suspension. Sea water was represented in the sediment and in the flume by a
mixture of 35 parts sodium chloride per thousand parts of water. Soil
movements were documented by sequential photographs of plastic markers
embedded in the sediment and visible through the plastic wall of the model
tank. For further details of the sediment preparation techniques the
reader is referred to Mitchell et al (1972) and Hull (1973).

        The current model studies incorporated more variations in test
conditions than earlier studies. In addition to passing progressive wave
trains over sediments tilted at various inclinations, static tilting tests
were carried out on sediments that had previously been subjected to wave
action. Laboratory vane strength measurements were carried out on the
sediments before and following wave action and/or tilting experiments. Model
tests were carried out under two different deep water wave lengths and the
depth of water to wave length ratio was varied between the limits of
practical influence.

        The bentonite used in these model studies differed from that used
in earlier model studies; sediment strengths were an order less in magnitude
than those reported by Mitchell et al (1972) and the sediment exhibited a
constant strength over the upper portion of the profile. A typical strength
profile from the sediment used in this study is shown in Figure 4 for
comparison to those in Figure 2.

Effect of wave action on the strength of bottom sediments

        The effect of wave action on reducing the strength of bottom
sediments was investigated by two methods: direct measurement using the
vane apparatus and indirect measurement in static tilting tests. Series of
vane strength measurements were carried out on sediments consolidated to a
given degree of consolidation. Undisturbed and remoulded vane strength
measurements were made prior to passing waves and following sequential
application of waves of different heights (wave length constant). Each
wave was allowed to act on the soil for several minutes prior to taking
strength measurements. It was found that progressive increases in wave
energy (wave height) remoulded the soil to increasing depths. Sinking of
the near surface plastic markers (G_s = 1.05) accompanied the remoulding
of the soil by wave action. Figure 5 shows typical undisturbed and
remoulded vane shear strength measurements.

        Static tilting tests were carried out by tilting the tank at a
rate of 3 degrees per minute. Displacement of the plastic markers during a
typical test are shown in Figure 6. Failure angles from static tilting tests
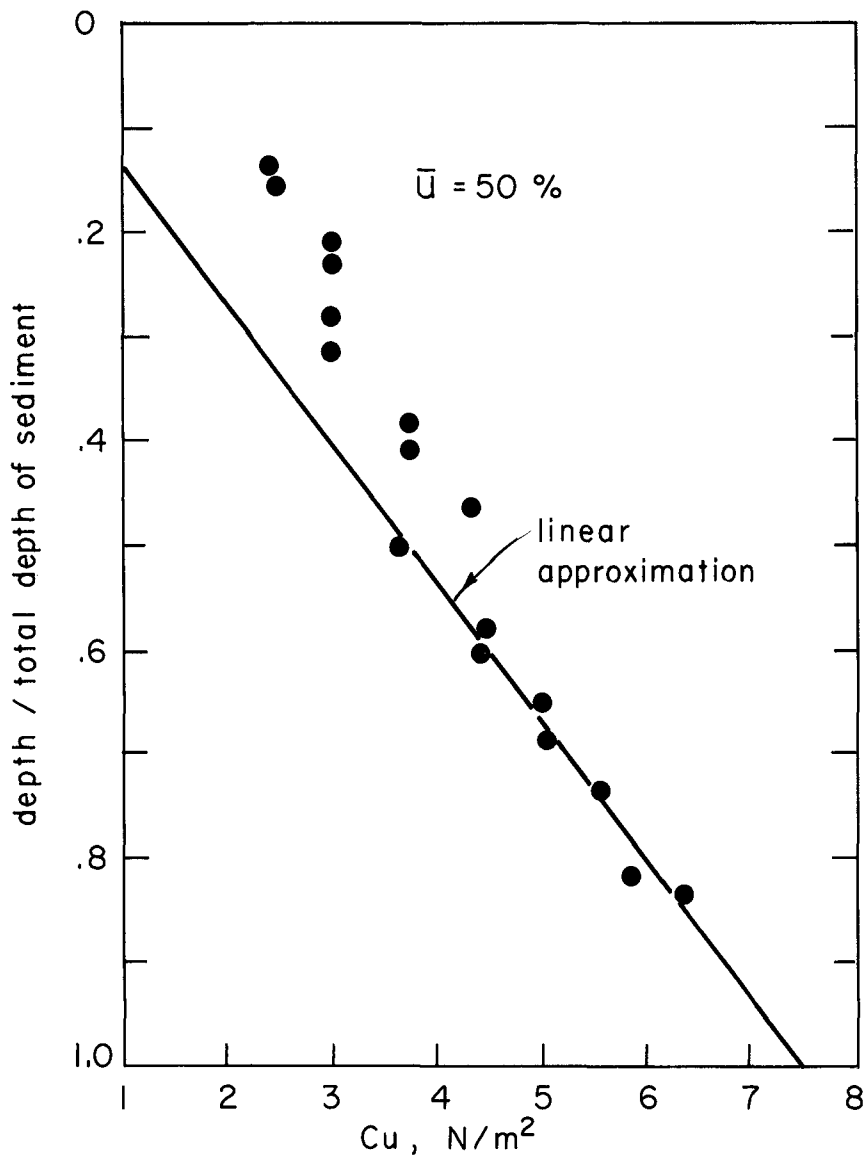
FIGURE 4 : UNDRAINED STRENGTH PROFILE, $\bar{U} = 50\%$
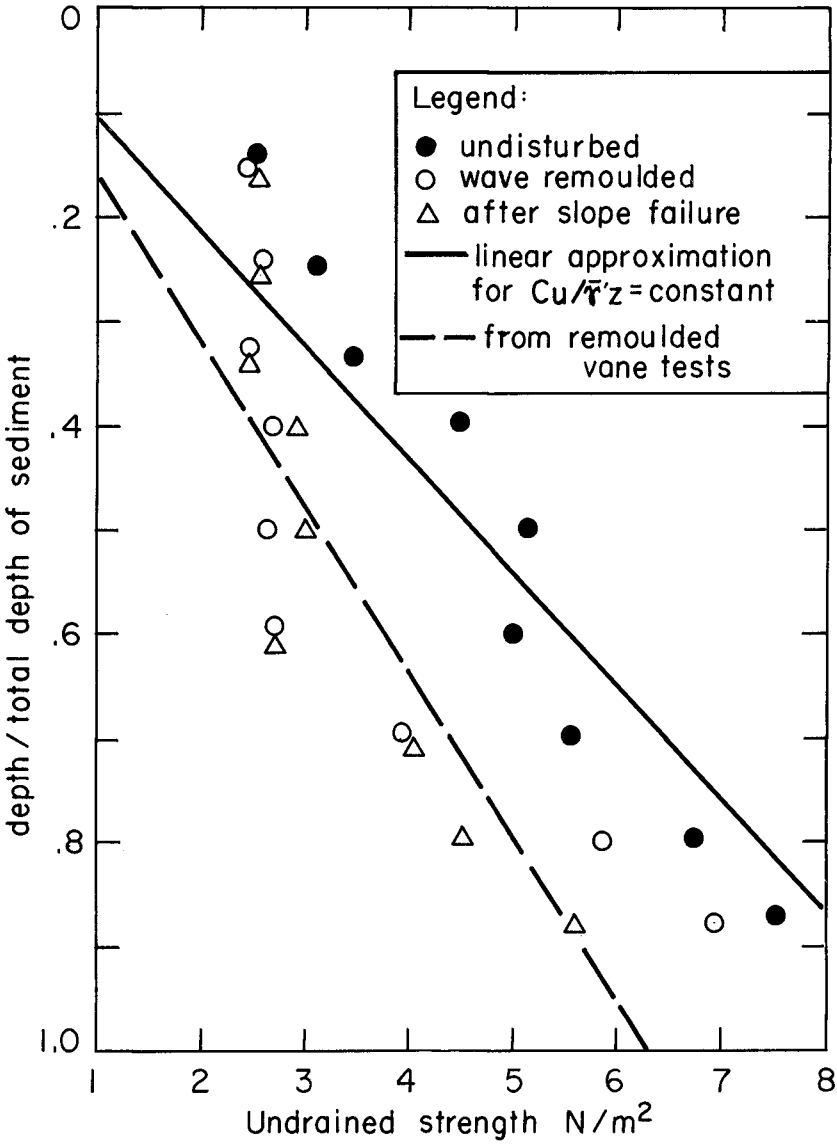
FIGURE 5 : VANE TEST RESULTS FOR $\bar{U} = 70\%$
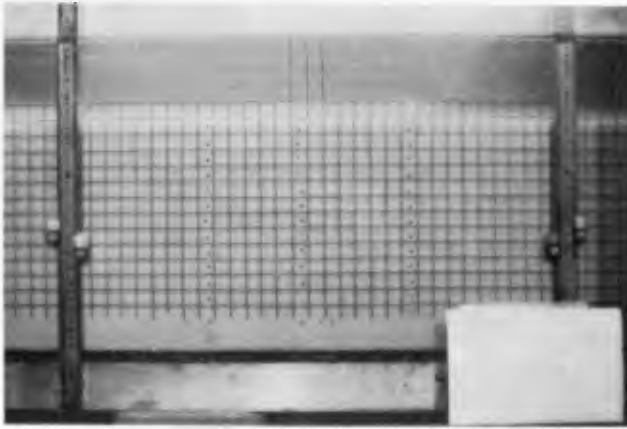
(A)   PRₗ ⊃R TO TILTING
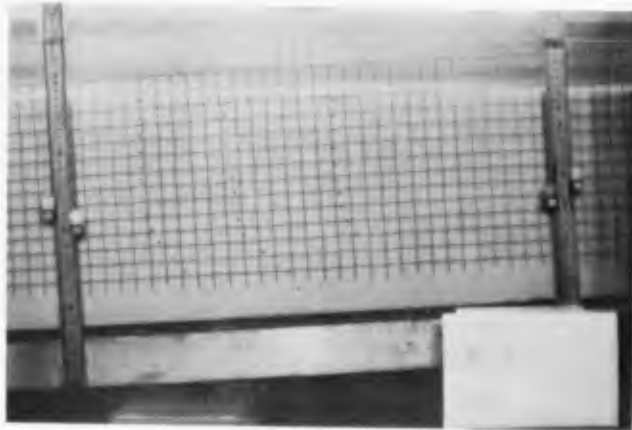
(B)   AT FAILURE

FIGURE 6 :   MARKER DISPLACEMENTS IN
STATIC TILT TEST, $\overline{U}$ = 30%
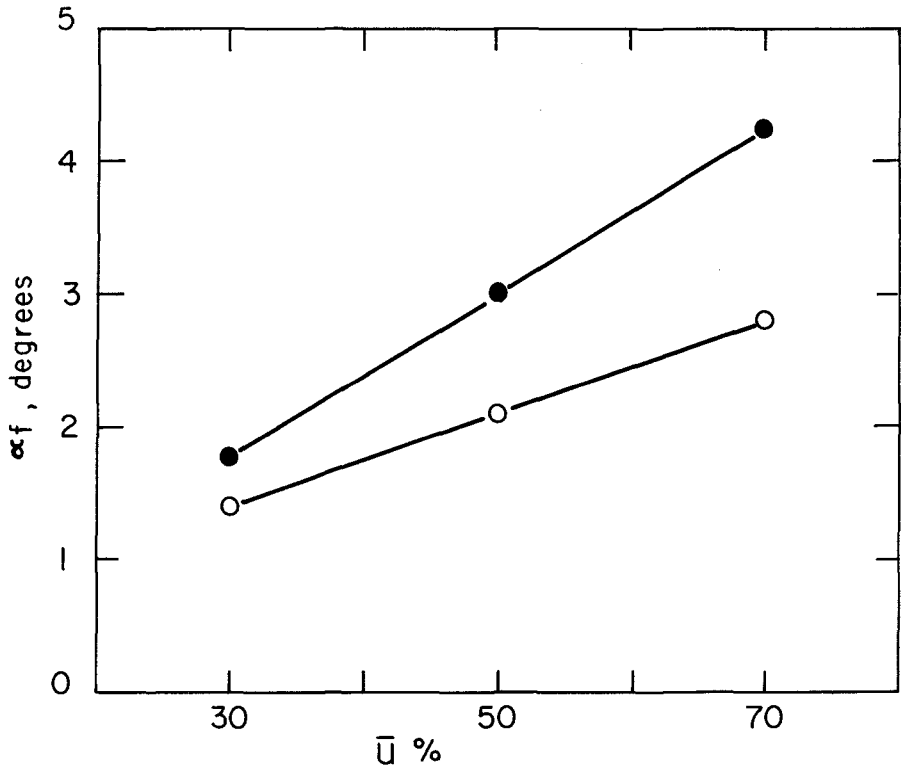
FIGURE 7 : FAILURE ANGLES IN STATIC TILTING TESTS

carried out without wave remoulding and after wave remoulding are shown in Figure 7. These measured angles were found to give a factor of safety approximately equal to unity in equation 3 for the undisturbed and remoulded strength profiles respectively.

From the data in Figure 7 and correlations such as shown in Figure 5 it is concluded that progressive waves can cause loss of strength in consolidating sediments. The minimum strength of the sediment after wave remoulding was found to be approximately equal to the remoulded vane strength. The ratio of undisturbed to remoulded strength (soil sensitivity) averaged about 1.5 in the laboratory sediments. In prototype situations soil sensitivities may be in the order of 10 (see, for example, Sangrey, 1972).

Effect of wave action on slope stability

Tilted sediments at known average degrees of consolidation and gravitational factors of safety, F.S., were subjected to incremented increases in wave height until failure of the slope occurred (wave length constant). These experiments were similar to those reported by Mitchell et al (1972) except that the depth of water to wave length ratio (d/L_o) was varied over a wide range and the sediment was substantially weaker. The subsurface pressure initiating a slope failure, δp_c , and the depth of failure, z_f , were of primary interest in each experiment. Movements of the plastic markers and pore water pressure changes were recorded after each wave train had acted on the sediment until an equilibrium was established. The time duration of each successive increment in wave height varied from about 3 minutes for initial waves to about 10 minutes for the penultimate wave. The wave defining the critical subsurface pressure, δp_c , was that wave under which continual downslope movements occurred.

Figure 8 shows typical marker displacement between successive increments of a test. For d/L_o ratios less than about 0.45 the marker displacements generally showed a well defined failure zone similar to earlier experiments; for d/L_o ratios greater than 0.45 the failure was usually poorly defined and extended to the sediment surface. Figures 9 and 10 show the marker displacement sequences for typical tests.

The model test results presented by Mitchell et al (1972) were carried out at a nearly constant value of $d/L_o = 0.35$ and indicated that the critical subsurface pressure, δp_c , (calculated from linear wave theory) was given by

$$\delta p_c = 2.40 \ S_r \qquad\qquad 4$$

where S_r is the reserve strength and is given by

$$S_r = (F.S. - 1) \ \bar{\gamma}' \ z \ \frac{\text{Sin } 2\alpha}{2} = C_u \ (1 - \frac{1}{F.S.}) \qquad\qquad 5$$
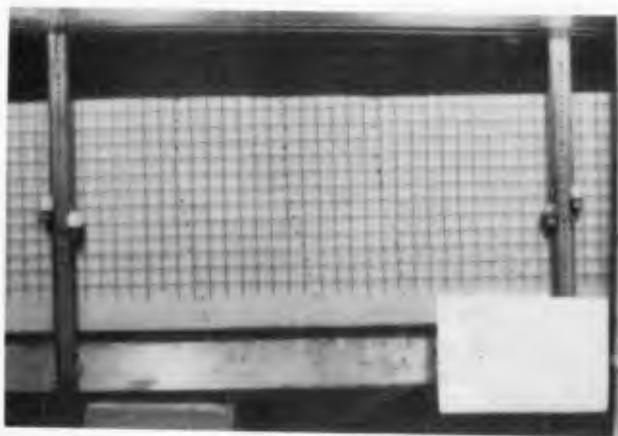
(A)   PEN-ULTIMATE WAVE
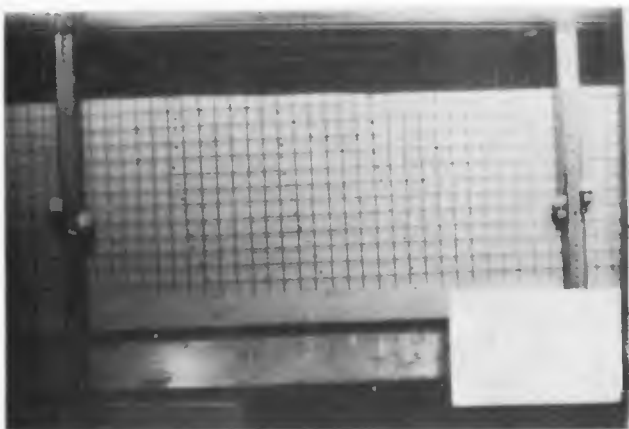
(A)   FAILURE WAVE

FIGURE 8 : MARKER DISPLACEMENTS DURING
WAVE INCREMENT, $\overline{U}$= 50% , d/Lo = 0.28

Curve	Comment
1	after tilt
2	before failure
3	failure
4	post failure
5	post failure
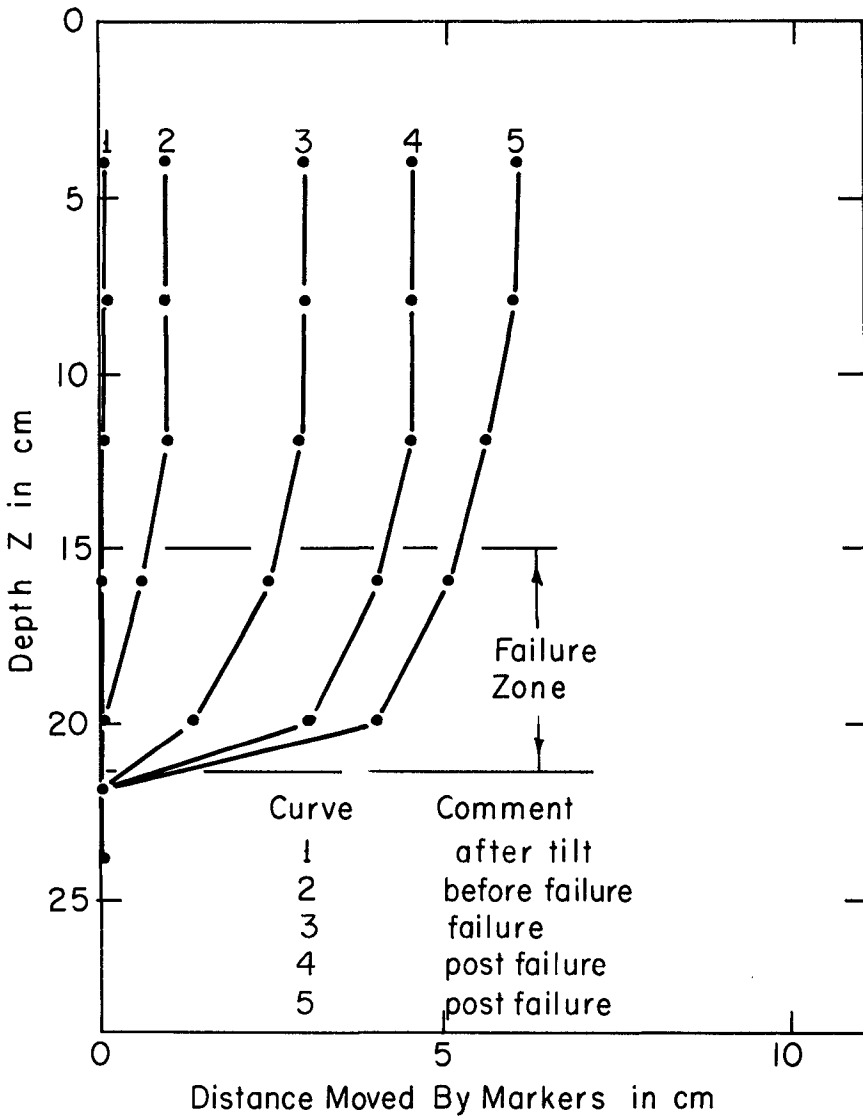
FIGURE 9 :   MARKER DISPLACEMENTS, d/L_o < 0.45
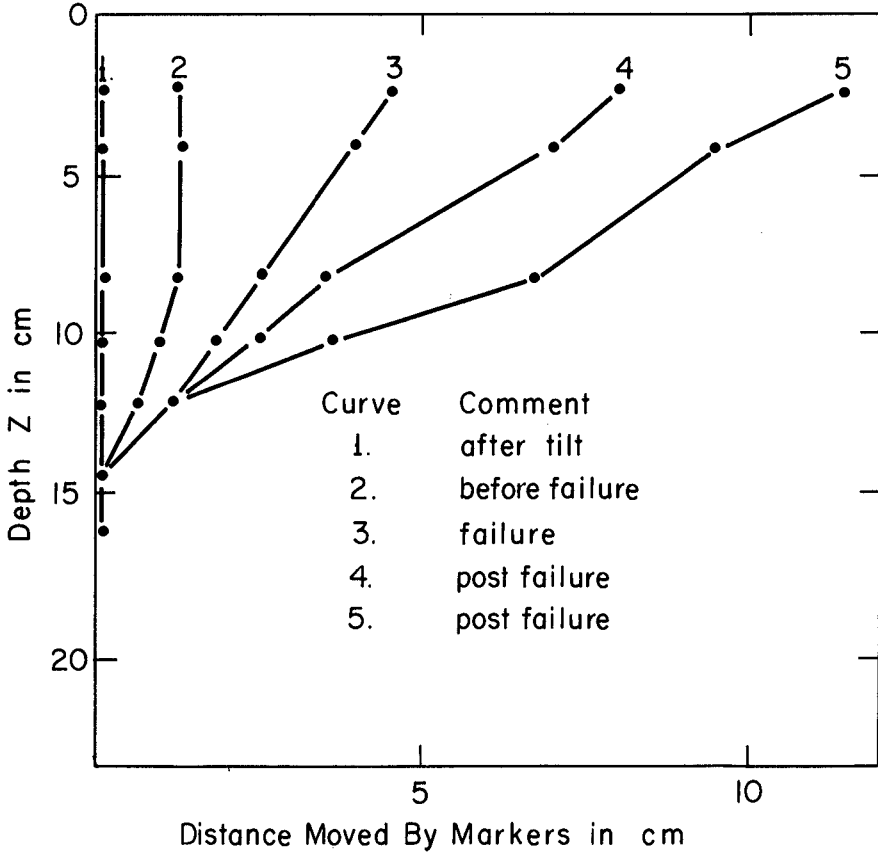
FIGURE 10 :   MARKER DISPLACEMENTS, d/L_o > 0.45

The reserve strength, S_r, may be considered as the strength remaining after the shearing stresses due to gravitational forces have been deducted from the soil strength. A summary of the tests in which wave induced failure occurred is contained in table 1. The values of $\delta p_c / S_r$ given in table 1 generally increase with increased depth of failure. The average value $\delta p_c = 2.5 \, S_r$ compares favourably with the earlier correlation. For static factors of safety in excess of 2.0 no well defined slope failures occurred but, under relatively high subsurface pressures the sediment surface gradually flattened by downslope movement of near surface materials. This observation supports the suggestion (Mitchell et al, 1972) that no mass failure will be initiated by waves if the static factor of safety is in excess of the sensitivity of the soil (this criterion follows directly from the concept that the slope failures are gravitational phenomenon and the wave action acts only to reduce the soil strength by remoulding).

Depth of slope failures

Theoretical analyses indicate that the depth of failure, z_f, in all cases will increase as the bottom pressure, δp, increases. Wright and Dunham (1972) conclude that failure will be limited to shallow depths and indicate a maximum failure depth of 0.19 L_o for soils of constant strength. Henkel (1970) produces a non-dimensional plot relating the depth of failure to wave length ratio, (z_f/L), to certain wave characteristics and the static factor of safety. Using reserve strength, S_r, to eliminate the variations in F.S. a plot similar to that produced by Henkel is shown in Figure 11. While earlier data (Tsui, 1972) supported the suggestion that the depth of failure is limited to about 0.2 L_o, the current tests show that the depth of failure does increase with the $\delta p_c / S_r$ ratio in general agreement with the relation derived by Henkel (1970). Tests conducted by Tsui (1972) were restricted to 0.32 < d/L_o < 0.42; extension of this range of d/L_o also indicates that depth of failure decreases with increasing water depth as shown on Figure 12. The lack of precise agreement between the two series of model studies, particularly with regard to failure depths, may be due to differences in the form of the strength profiles (compare Figures 2 and 4) and it must be concluded that the form of the in situ strength profile may influence the depth of failure in prototype situations.

As noted earlier, failures where d/L_o > 0.45 developed by gradual slope flattening with maximum movement at the mud line. This type of failure also developed in test No. 8 (see Table 1), where d/L_o < 0.45 but the factor of safety was large (F.S. = 2.0). In tests where d/L_o < 0.45 and F.S. < 2.0 zonal failures occurred (see Figure 10). Cyclic movements and fissure patterns approaching circular arcs were visible in the sediment just prior to the development of a zonal failure. This type of failure can

TEST No.	$\bar{U}$%	α_f	F.S.	d/L_o	z_f/L_o	$\delta p_d/S_r$
1	33	1.8	2.0	.52	.23	3.0
2	70	4.4	1.4	.616	.255	1.1
3	50	3.0	1.7	.566	.333	1.0
4	30	1.8	2.0	.510	.360	2.0
6	50	3.0	1.7	.41	.31	2.24
8	42	2.5	2.0	.294	.41	2.7
9	75	4.5	1.4	.368	.525	2.35
10	50	3.0	1.7	.315	.23	1.85
11	85	5.1	1.0	.338	.50	1.70
12	70	4.2	1.4	.333	.475	2.24
13	50	3.0	1.7	.28	.575	4.3
14	70	4.2	1.7	.324	.49	2.85
15	70	4.2	1.7	.282	.46	3.1
16	70	4.2	1.3	.195	.565	4.1

TABLE 1 - List of Slope Stability Tests
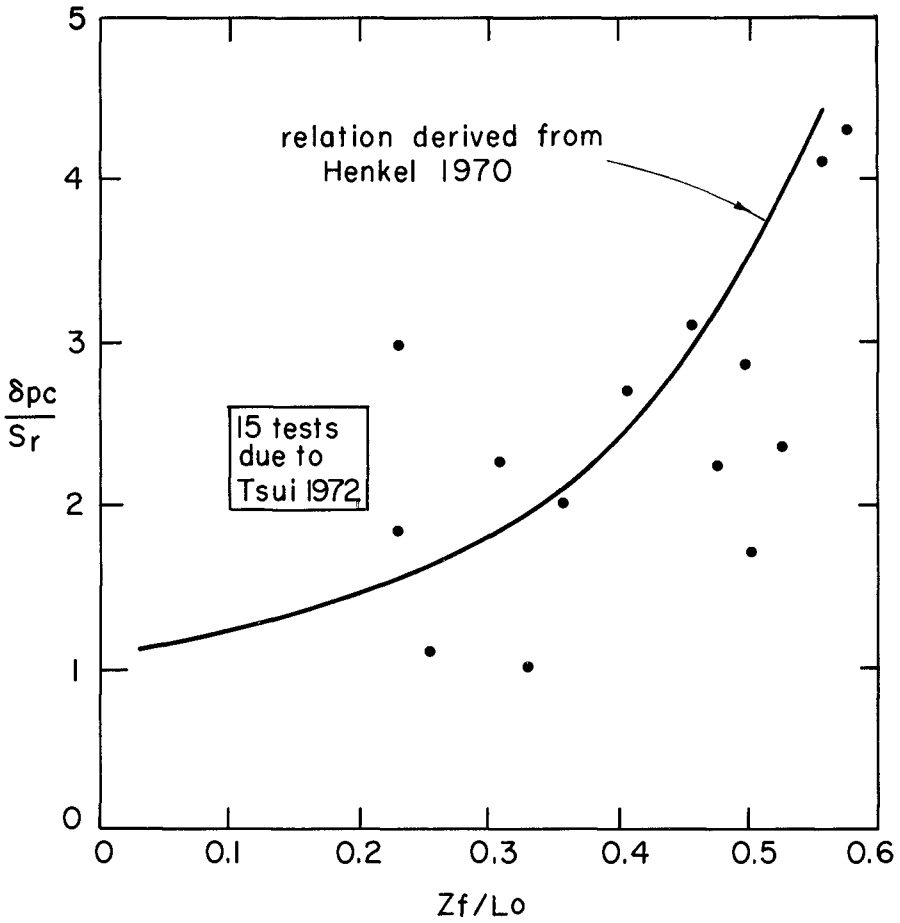
FIGURE 11 : RELATION BETWEEN BOTTOM PRESSURE, SOIL STRENGTH AND FAILURE DEPTH
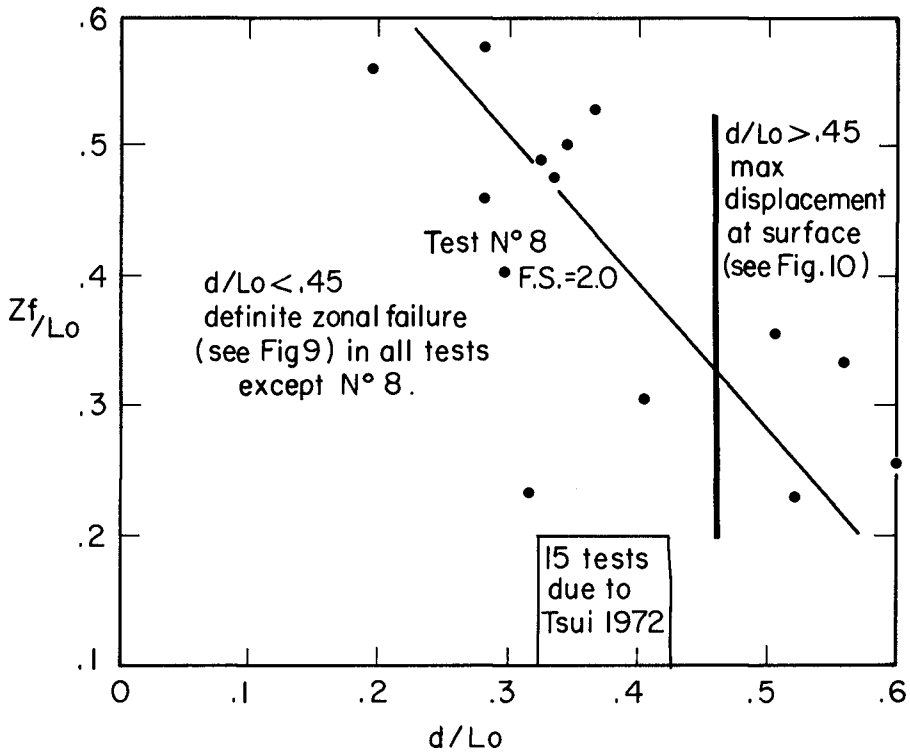
FIGURE 12 : RELATION BETWEEN WATER DEPTH AND FAILURE
DEPTH FOR CRITICAL WAVE CONDITIONS
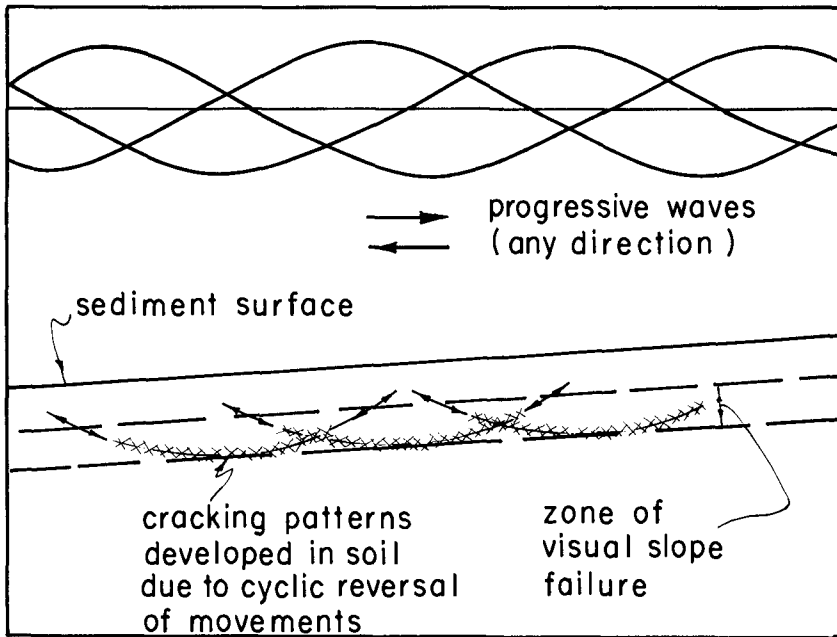
FIGURE 13 : FORMATION OF ZONAL FAILURE IN A SLOPE WHEN $d/L_o < 0.45$

be associated with an extension of the static rotational analysis
(see Figure 1) to the progressive wave situation as depicted in Figure 13.

Slight increases in pore water pressure were noted on the
standpipes (see Figure 8) when the sediment was subjected to wave action
but marked decreases in pore water pressures accompanied the actual slope
failure. Pore water pressure decreases were associated with the development
of zonal failure as shown on Figure 13. From these visual observations it
is concluded that the reversals in shearing strain (reversals in
rotational movements) causes remoulding of the soil. The depth of
remoulding was observed to increase with increasing subsurface pressure in
general agreement with the relations shown in Figures 11 and 12.

Conclusions

From the model tests and correlations presented in this paper the
following conclusions are advanced:

1. Cyclic subsurface pressures due to wave action can cause
   remoulding and loss of strength in fine grained
   submarine sediments. The depth of remoulding generally
   increases with increased subsurface pressure.

2. In sloping offshore sediments the remoulding due to wave
   action may lead to slope instabilities. The depth of
   potential slope failures increases with increased
   subsurface pressure in general accordance with the
   relation proposed by Henkel (1970). Deep failures are
   not considered possible unless the sensitivity of the
   soil is in excess of the static factor of safety of the
   slope.

While many advances in offshore sampling and in situ testing
techniques are being made in order to measure the undisturbed strength of
submerged soils, it is suggested that in situ measurement of remoulded
strength profiles should be considered an essential part of all offshore
subsurface investigations where water depths are less than the water wave
lengths during storm conditions. The possibility of wave action reducing
the sediment strength should be considered in the design of all permanent
offshore structures.

Acknowledgements

References

Bea, R.C. (1971),   How Sea-floor slides affect offshore structures,
        The Oil and Gas Journal, Nov. 1971 pp 88-92.

Gibson, R.E. and Morgenstern, N.   (1962), A note on the stability of
        cuttings in normally consolidated clays, Geotechnique 12:212-216.

Henkel, D.J.   (1970), The role of waves is causing submarine landslides,
        Geotechnique 20:1:75-80.

Hull, J.A.   (1973), Wave induced submarine slope instabilities, M.Sc.
        Thesis, Queen's University, Kingston, Ontario, Canada.

McClelland, B.   (1967), In Marine Geotechnique, University of Illinois
        Press, 1967 p 22-40.

Mitchell, R.J., Tsui, K.K. and Sangrey, D.A.   (1972), Failure of
        submarine slopes under wave action, 13th Int. Coastal Eng. Conf.,
        Vancouver, July 1972, Vol. 11, pp 1515-1539.

Morgenstern, N.R.   (1967), Submarine slumping and Initiation of Turbidity
        Currents,   p. 22-40 in Marine Geotechnique, University of
        Illinois Press.

Sangrey, D.A.   (1972), Obtaining strength profiles with depth for Marine
        Soil deposits using disturbed samples, A.S.T.M.   STP 501,
        pp 106-121.

Tsui, K.K.   (1972), Stability of submarine slopes, Ph.D. Thesis,
        Queen's University of Kingston, Ontario, Canada.

Wright, S.G., and R.S. Dunham (1972), Bottom stability under wave induced
        loading, Offshore Technology Conference, Dallas Texas,
        Paper No. OTC 1603.

CHAPTER 74

Morphological Changes in a Fine Sand Tidal Estuary
After Measures of River Improvement

by

Dr.-Ing. G. Hovers

Federal Ministry of Transport, Bonn
Federal Republic of Germany

Artificial shipping channels in fine sand tidal estuaries
are difficult to maintain. The attempt to stabilize the river
beds and thus the fairway in the upper reaches of the Outer
Weser by means of systems of river structures has been a
success. The further deepening of the fairway necessitated
the artificial narrowing of the river bed. The successes of
improvement achieved over a prolonged period have up to now
been satisfactory. Some explanations concerning the effects
of the river structures on the morphology are given in the
present report. In the improved river bed a continuous shifting
of sediments is taking place, which is mainly due to the inces-
sant action of the tidal currents. It is inevitable in this
process that sand is drifted into the deep excavated channel.
If one has a good knowledge of the natural shifting processes,
it is possible nowadays, by using suitable Hopper suction
dredgers, to employ to a certain extent methods of dynamic river
engineering by means of the proper artificial shifting of the
excavated soil within the cross sections of the river.

The capability of improvement of tidal rivers and their
estuaries is of great importance for the sea ports that are
situated on them. This is particularly true in a time when the
dimensions of sea-going ships are still increasing and the
countries are confronted with the problem of permanently having
to improve the approaches to their sea ports, if they want to
participate in overseas trade also in the future.

The reason why the improvement of fine sand tidal estuaries
is so difficult and so expensive, depending on the local hydro-
graphical and morphological conditions, is that the sediments
are continually shifted on account of the tidal currents which
are constantly changing in place and time and varying in their
force as well as on account of the motion of the sea and the
wash of the waves.

This renders the improvement, the maintenance, and the
marking of artificial fairways for ocean shipping rather diffi-
cult.

The safe and easy operation of such ships in narrow waters necessitates therefore <u>sufficiently deep and wide fairways</u> in <u>stable river beds</u>. In order to achieve this, river structures (groynes, training walls) may be employed and/or dredging operations undertaken.

It is precisely in the field of dredging that completely new aspects have developed during the past years with respect to the improvement and the maintenance of fairways in tidal river beds, owing to the construction and the employment of very big Hopper suction dredgers. This raises the question whether the conventional and extremely cost-intensive river structures using mats made of shrubbery or plastic material and stones can perhaps be dispensed with in the future in the improvement of fairways in morphologically instable tidal estuaries.

This report deals with the successes achieved in the improvement of the Outer Weser, the approach to the ports on the Lower Weser Bremen, Brake, Nordenham, and Bremerhaven, by means of artificial river structures.

A few sentences only on the area where the investigation was made :

The Weser together with the Jade and the Elbe flow on a rather small stretch of coast into the south-eastern part of the North Sea. From there tidal waves penetrate periodically into the estuaries of these rivers and in places produce flood and ebb tide velocities of up to 2.50 m/sec in the deep river beds at mean tidal amplitudes of up to 3.50 m (Fig. 1).

Decisive for the size of the river bed cross sections is the quantity of the mean tidal waters.

At ebb tide 151 million cubic metres of water flow through the cross section of the Weser at km 65 (Bremerhaven), to which the Weser river contributes about 15 million cubic metres. Owing to the water coming from the adjacent tidal flats the volume of water at ebb tide increases rapidly towards the sea and amounts to as much as 855 million cubic metres 35 km below Bremerhaven (km 100).

The relation between cross section and quantity of flow in the Outer Weser is the following :

$$c = \frac{F_{em}}{T_{em}} = 14,200$$

From this formula a cross-section preserving mean velocity of flow at ebb tide of <u>0.61 m/sec</u> can be derived. This relation is of great significance for the measures of improvement,

for it means that there is always a certain equilibrium
between the river bed cross section and the hydrodynamic
forces of the tidal currents. This equilibrium must be
taken into consideration for improvement measures. If it
is not possible to permanently increase the quantity of
flow in a river bed, then the deepening of the fairway,
which is necessary to enable shipping traffic, can only be
carried out, if the enlargement of the cross section in the
fairway is compensated by a reduction of the cross section
of the same volume in the lateral areas of the river. What
matters above all is that the hydraulic capacity of the
river bed cross section is maintained.

        In a bifurcation of a river conditions are different,
because here it is as a rule possible to influence the
respective quantities of flow in the individual river beds.

        In the Outer Weser both cases exist in the section of
improvement, namely the system of "one river bed" and that
of "several river beds". From km 65 to km 78 there is now-
adays only one single tidal river bed with adjacent tidal
flats of different size. Then, further out towards the sea,
a bifurcation follows. As a system with almost two parallel
river beds, which comprises several big sandbanks, the Weser
then flows into the sea.

        The factor which determines the morphological changes
in the section from km 65 to km 100 are the tidal currents.
The ebb tide is, as a rule, stronger on the slopes on the
right-hand side, seen in downstream direction. The flood
tide predominates, on the other hand, on the opposite slopes
and in the "lee-side" areas of the ebb behind the sands.
Apart from local influences also the effect of the Coriolis
forces manifests itself here. In all those areas where the
ebb tide is clearly stronger, a resulting shift of sediments
in the direction of the ebb tide must be reckoned with. A
shift of sediments in the direction of the flood tide will
result in all those places where the flood tide clearly pre-
dominates over the ebb tide.

        The resulting conditions of current must always be
taken into consideration in all measures of improvement and
maintenance in tidal currents and must already be taken into
account in the plannings; and what is more, they must be the
very basis of sensible river engineering planning.

        The estuary of the Outer Weser has considerably changed
during the past centuries due to tidal currents and the
motion of the sea. When in 1891 the first measures of river
improvement had to be carried out in the upper reaches of
the Outer Weser, because the big transatlantic passenger
steamers which the Norddeutsche Lloyd had taken into service
a couple of years earlier could reach Bremerhaven only with

difficulty and only at flood tide, the river bed between
km 65 and km 78 still had a natural width between the edges
of the tidal flats of between 1,300 m and 2,300 m (Fig. 2).
The mean depths of the river bed were between 4 m and 6 m.
The river bed was split in itself several times by middle
grounds. Bars hindered the passage of the big passenger
ships, so that they did not run according to schedule.

The first artificial measures of river improvement were
therefore intended to provide a continuous fairway with a
width of 200 m and a depth of 8 m below low water in the
Outer Weser below Bremerhaven. Owing to the steady develop-
ment of the sizes of ships a first attempt was made as early
as 1906 to deepen the fairway to 10 m below low water. This
aim could not be reached, however, on account of unfavourable
morphological developments in the seaward bifurcation of the
river. Neither river structures nor extensive dredging
operations were able to check the silting up in the Wurster
Arm, the eastern part of the river, which served as the main
channel until 1922. This situation compelled the competent
authorities in 1921 to abandon the fairway in the Wurster Arm
and to create a completely new fairway in the western part of
the river, the Fedderwarder Arm, which was in some way favoured
by nature.

This relocation of the fairway took place on the basis of
very extensive hydrographical investigations, from which the
future trends of the morphological changes in the inner area
of the Weser estuary could be deduced with sufficient pre-
cision.

In the realization that in a "one-river-bed" system an
artificial deepening of the fairway necessitates an artificial
lateral diminution of the river cross section and in the
"two-river-bed" system which follows in seaward direction an
immediate success of the river improvement measures can be
expected only if the quantity of flow in the new channel can
be considerably increased at the cost of the Wurster Arm,
river structures and dredging operations for the first time
carefully co-ordinated and harmonized in their effects were
made use of on a large scale. The function of the river
structures was to reduce the too wide river cross sections,
to stabilize the river beds in their position, and in the
area of the bifurcation also to influence the development of
the quantities of flow in favour of the new channel. The
dredging operations served in the first place to excavate a
new fairway and subsequently to remove the sand that had been
drifted again into this artificial fairway. The dredged soil
was without exception used as "building material" in the re-
shaping of the river bed cross sections.

The measures undertaken between 1922 and 1928 were a
complete success. After the damage in the fairway which was

mainly due to insufficient maintenance during World War II
had been repaired, the fairway in the Outer Weser could be
deepened without exception to 11.0 m below chart datum in
1965, after the system of river structures had been completed,
and in 1972 without particular effort even to 12.0 m below
chart datum.

        This success in river improvement is mainly due to the

                        - profile changing
                        - profile stabilizing and
                        - current influencing effect

of the many training walls and groynes, which were built as
the situation required and thus have gradually developed into
an effective system in the course of the past eighty years
(Fig. 3). Nowadays the river structures form the backbone of
an estuary which is instable by nature. Their effect was
above all that the shifting of sediments in the river bed
which was due to the current could be reduced and largely be
brought under control.

        The effects of the structures can be demonstrated qual-
itatively and to a certain extent also quantitatively in
various ways. Two examples have been chosen for this purpose :

        The first river structures in the Outer Weser were two
training walls opposite and below Bremerhaven. The function
of these walls was to dam detrimental minor channels up
against the main channel and to cause them to silt up. The
quantities of flow of the minor channels that had been dammed
up were to increase the scavenging effect of the tidal cur-
rents in the usable range of the main channel.

        From the comparison of the maps (Fig. 4) we can recognize
qualitatively that the silting up of the minor channels behind
the walls developed as expected. The natural improvement of
the depths which was expected in the usable range of the main
channel could not take place, however, to the degree as
desired, because the water displaced from the minor channels
had an erosive effect outside the usable range of the main
channel. This can be very well illustrated in the charts
showing the changes of depths. They show the resulting
shiftings of sediments due to the current in their full scope
and intensity. It must be borne in mind here, however, that
the positive development of the depths in the narrow usable
range of the main channel after 1898 was mainly achieved by
the employment of dredgers and that the dredged soil was dis-
charged in the minor channel which still existed below the
training wall on the left bank. This action accelerated the
silting up of the minor channel.

        It took as much as twenty years, namely until 1921, before
the minor channel west of the training wall built opposite

Bremerhaven was completely silted up. The position of the
sedimentation areas in the period from 1915 to 1921 shows the
tendency to further alluvia on the western tidal flat – and
what is particularly important – to sediments in the fairway
before the bifurcation Wurster Arm/Fedderwarder Arm, as well
as considerable hollows in the entrance to the Fedderwarder
Arm. Here the natural tendency to deepen the Fedderwarder Arm
becomes visible, which in 1921 made it necessary to abandon
the fairway in the Wurster Arm and to develop a completely new
fairway in the Fedderwarder Arm, which is obviously favoured
by nature.

     The river structures built in connexion with the reloca-
tion of the fairway between 1922 and 1928 with simultaneously
deepening the fairway to a depth of 10 m below chart datum
were above all groups of groynes on both sides of the river
in the upper section of improvement and, in addition to that,
training walls in the area of the bifurcation. The river
improving functions of the structures were very different,
depending on the local conditions.

     The groynes of km 72 and km 76.4 left bank, for example,
were intended to contribute in the first place to quickly and
definitely silting up a minor channel which was already in
the process of silting up, and secondly to further reduce the
width of the remaining main channel cross section. Therefore
the construction of the groyne km 72 left bank was made step
by step in accordance with the morphological development. The
function of all other groynes was primarily to fix the newly
determined lines of groyne heads and to actively reshape the
cross section of the river bed.

     The dredged material obtained from the fairway was dis-
charged in the first phase of improvement mainly before the
entrance to the Wurster Arm, in order to artificially raise
the bottom here and so to divert the water at ebb tide to the
west into the new channel. The training wall which was grad-
ually built out on the RSSt had in the first place the func-
tion of preventing the water from flowing into the wrong
channel. It was to prevent that too large quantities of water
at ebb tide were lost to the Wurster Arm.

     The effects of these constructional measures become
evident in the charts showing the changes of depths. The
author would like to use another method here, however, in
order to demonstrate the changing effect of river structures
on the morphology of the river beds :

     The changes in profile at km 72 (Fig. 5) :

     This diagram shows the complete morphological development
in the profile of km 72 over a period of 100 years. In 1921
the river bed in profile km 72 still had a width of 1,865 m,
a cross section below chart datum of 10,300 sq. metres, and a

mean depth of 5.5 m. The gradual building out of the groyne
at km 72 left bank by a total of 900 m (!) during the period
1922/1928, together with the development of a passive groyne
on the other bank opposite to it, worked within a few years
an amazing yet fully intended change in the profile. The
western edge of the tidal flats could be very rapidly ad-
vanced, thus reducing the width of the cross section to less
than 1,000 m and the cross section itself by about 2,000 sq.
metres, yet increasing the mean depth to as much as 8.2 m.
Owing to the deterioration of the cross-section stabilizing
groynes during World War II, the profile widened again
slightly after 1945, which immediately entailed a distinct
reduction of the mean depths. The reconstruction work on the
river structures after 1957 had at once a positive effect on
the profile depths, because the widths of the river bed could
be reduced again.

     Without going so far as to explain all the details, the
author will demonstrate in a combined comparison of map and
depth changes (Fig. 6) as well as by a selected chart showing
the changes in profile (km 81) (Fig. 7) the morphological
changes in the bifurcation Wurster Arm/Fedderwarder Arm, which
were influenced by river structures.

     After 1900 the middle section of the Wurster Arm begins
to deteriorate rapidly. The river bed shifts in westward
direction towards the Robbenplate and in this process divides
into two channels, in one of which the ebb tide predominates
and in the other the flood tide. The explanation of this
development lies in fundamental morphological changes in large
areas in the Weser estuary, which cause a natural scavenging
of the Fedderwarder Arm and ebb water is inevitably attracted
by this channel. This development can be recognized very
early in the charts showing the changes of depths, more clearly
even than in the comparison of maps.

     The attempt to stop the westward movement of the Wurster
Arm by artificially stabilizing the eastern part of the Robben-
plate is only of limited significance with respect to place
and time. These river structures and the simultaneous dredging
operations in the fairway cannot prevent the progressing
splitting of the Wurster Arm.

     The sole objective of the river improvement measures after
1921 is to develop a new fairway in the Fedderwarder Arm. Since
the Fedderwarder Arm had at that time no sufficient total cross
section, the improvement aim is in the first place to influence
the morphological development with a few structures and to drive
it in each development phase systematically into the desired
direction :

     - the training wall RSSt is to increase the quantity of
       flow at ebb tide in the Wurster Arm,

- the training wall LalüNSt is to prevent cross-
  currents and the drifting of sand from the estuary
  of the Fedderwarder Priel into the new channel,

- the training wall RNSt is to stop in this place the
  eastward movement of the Fedderwarder Arm.

  In the course of the following years this wall is to
  become a fixed point in the whole system of river
  structures.

The further development in the new channel shows that the
river structures in connexion with the dredging operations
fully achieve their effects. It is above all clearly recog-
nizable from the charts showing the changes of depths that now
large masses of soil are shifted in the new channel due to the
stronger tidal currents, which necessitates above all constant
and extensive maintenance dredging operations in the fairway.

The chart showing the changes in profile of km 81 (Fig. 7)
shows us the state of the Fedderwarder Arm when the relocation
of the fairway was set about in 1922. Accelerated by the
measures of river improvement, the widths and the cross sec-
tions in the Fedderwarder Arm increase rapidly, whereby the
westward movement of the deep river bed is tolerated for some
time, until the planned line of groyne heads along the western
tidal flats has been reached in a natural way. This was the
case in 1948. It was then begun to stop the further westward
movement of the Fedderwarder Arm by the construction of pas-
sive groynes along the Langlütjen tidal flats. The river bed
reacted as expected.

The purpose of the further raising of the training wall
RSSt in 1952 to 1 m above chart datum and then in 1964 to
1.5 m above chart datum was to divert larger quantities of ebb
water from the Wurster Arm to the Fedderwarder Arm. The result
was not quite what one had imagined, however; the additional
quantities of ebb water which had been gained for the Fedder-
warder Arm do not work within the usable range of the latter,
in its fairway that means, but outside of it, directly on the
training wall RSSt, and lead here to the formation of a new
minor channel and to an additional mobilization of large masses
of soil which make extra dredging operations in the fairway
necessary.

Which is now the realization to be gained from these maps
and diagrams?

- The river beds in the area of improvement could be
  stabilized in their position by means of river
  structures, which made it possible to dredge durable
  and solid channels in the river beds, to maintain
  these at reasonable cost, and to mark them by fixed
  aids to navigation.

- The river bed cross sections could be transformed,
  by means of active river structures, so as to comply
  with the requirements of shipping. Originally very
  wide and flat river beds which were split in them-
  selves, they could be provided with narrower but
  sufficiently deep cross sections. The limit of the
  capability of improvement of a river bed cross
  section is set by the volume of the tidal waters.
  This limit has not yet been gone beyond in the area
  of improvement in the Outer Weser.

This success in the stabilization and transformation would
not have been achieved by dredging operations and the selected
discharge of the dredged soil alone.

It was only through the effects of the system of river
structures with their markedly

- profile stabilizing,
- profile changing, and
- current influencing effect

that we succeeded in creating a fairway in the Outer Weser
which is capable of further development. The fact that the
dredged soil obtained from the improvement and maintenance work
was re-used properly, from the river engineering point of view,
contributed also to reaching the aim of improvement so quickly.

The principal objective of the improvement and maintenance
should be to keep the drifting of sand from the lateral areas
of a river bed into the artificial deep fairway as low as pos-
sible. Discharged soil from dredging operations must therefore
by no means interfere with the desired morphological develop-
ment of a river bed section or even influence it negatively;
neither should this soil drift back into the deep fairway, or
at least only as little of it as possible.

It is certainly wrong to remove the soil which is con-
tinually dredged from a river bed which is in equilibrium with
the cross-section preserving forces of the current, from the
cross section of that river bed. This would only cause an
excessive widening of the cross section of the tidal river bed.
The consequence would automatically be a new natural silting
up of the cross section, which would in turn necessitate new
dredging. It would be much better to leave the dredged soil
as far as possible in the cross section, but to distribute it
properly there.

This has become possible nowadays through the employment
of modern Hopper suction dredgers, provided that their draught
permits them to be employed in shallow water. If one has an
exact knowledge of the mechanisms of the natural shifting of
sediments in the tidal river beds which is due to the currents,
these dredgers make it possible to employ methods of dynamic

river engineering, the aim of which should be to effectively further the desired change or stabilization of the tidal river beds by properly transferring the dredged soil.

First experiments have been made in this direction in the Outer Weser during the past years. The qualitative results hitherto obtained speak in favour of a continuation and improvement of the active re-use in river improvement operations of the dredged soil. The dredged soil may then become a material in river engineering and may by no means be in every case removed from the range of a tidal river bed cross section, that is to say from the inner sediment cycle of the river bed. The author thinks that the question of sediment cycles within tidal river beds must be given more attention in the future, in order to avoid unnecessary expenses for maintenance work in fine sand tidal river beds.

The German tidal estuaries and
the area of investigation.
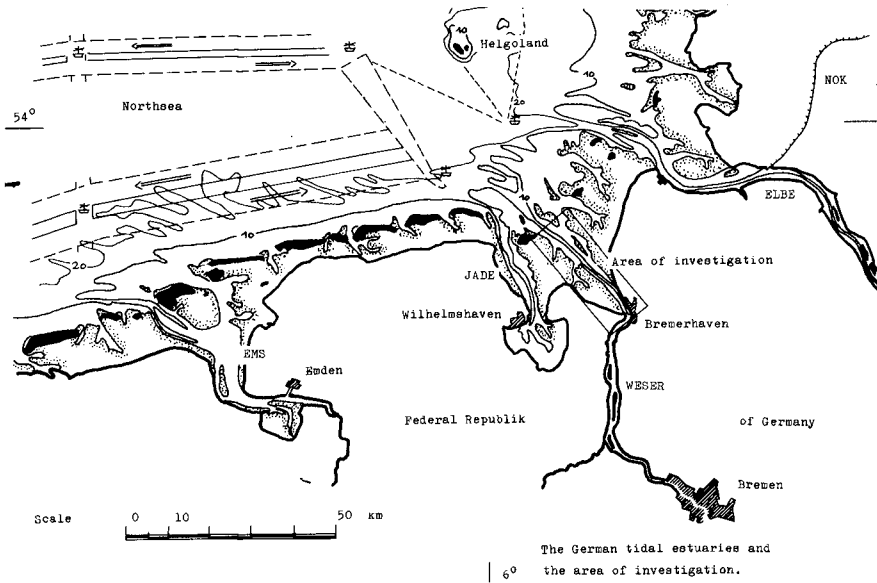
Fig. 1   The German tidal estuaries and the area of investigation
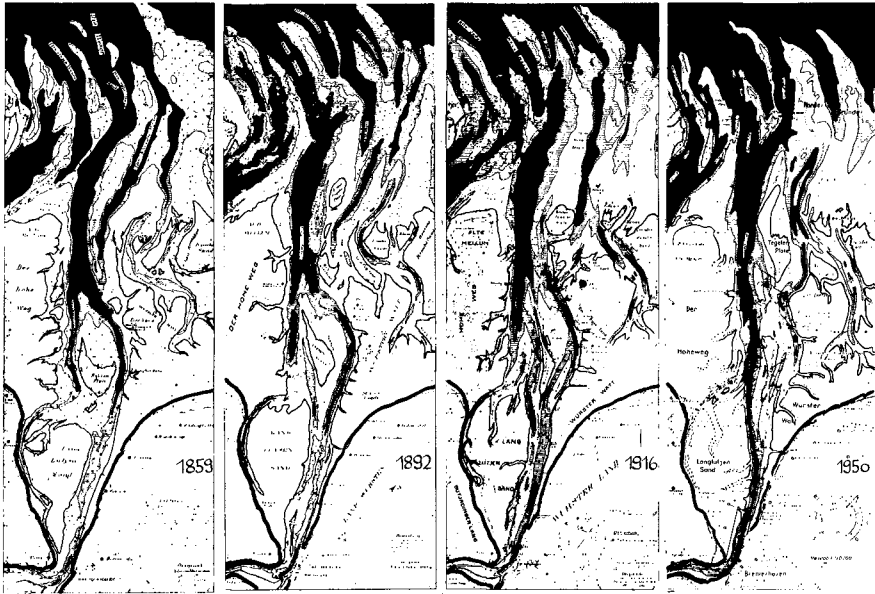
Fig. 2   The Outer Weser in 1859, 1892, 1916, 1950
          - a rough comparison of maps
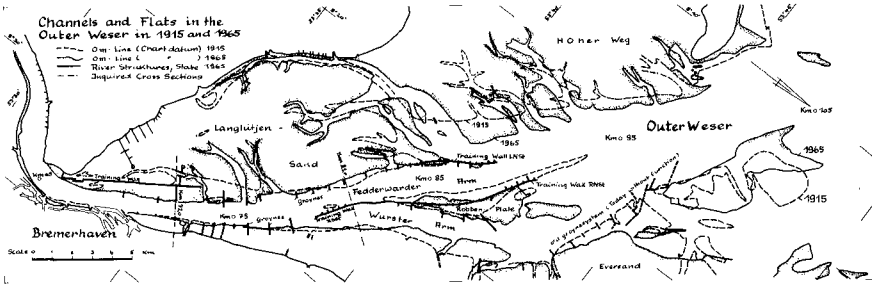
Fig. 3   River beds and tidal flats in the Outer Weser 1915 and 1965
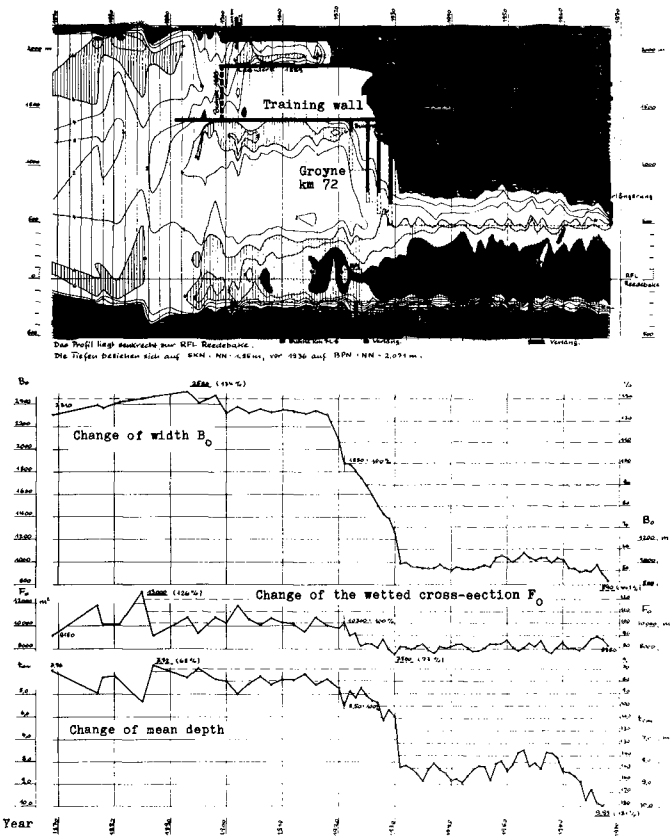
Fig. 5   Changes in the profile km 72, Outer Weser, 1869 - 1968
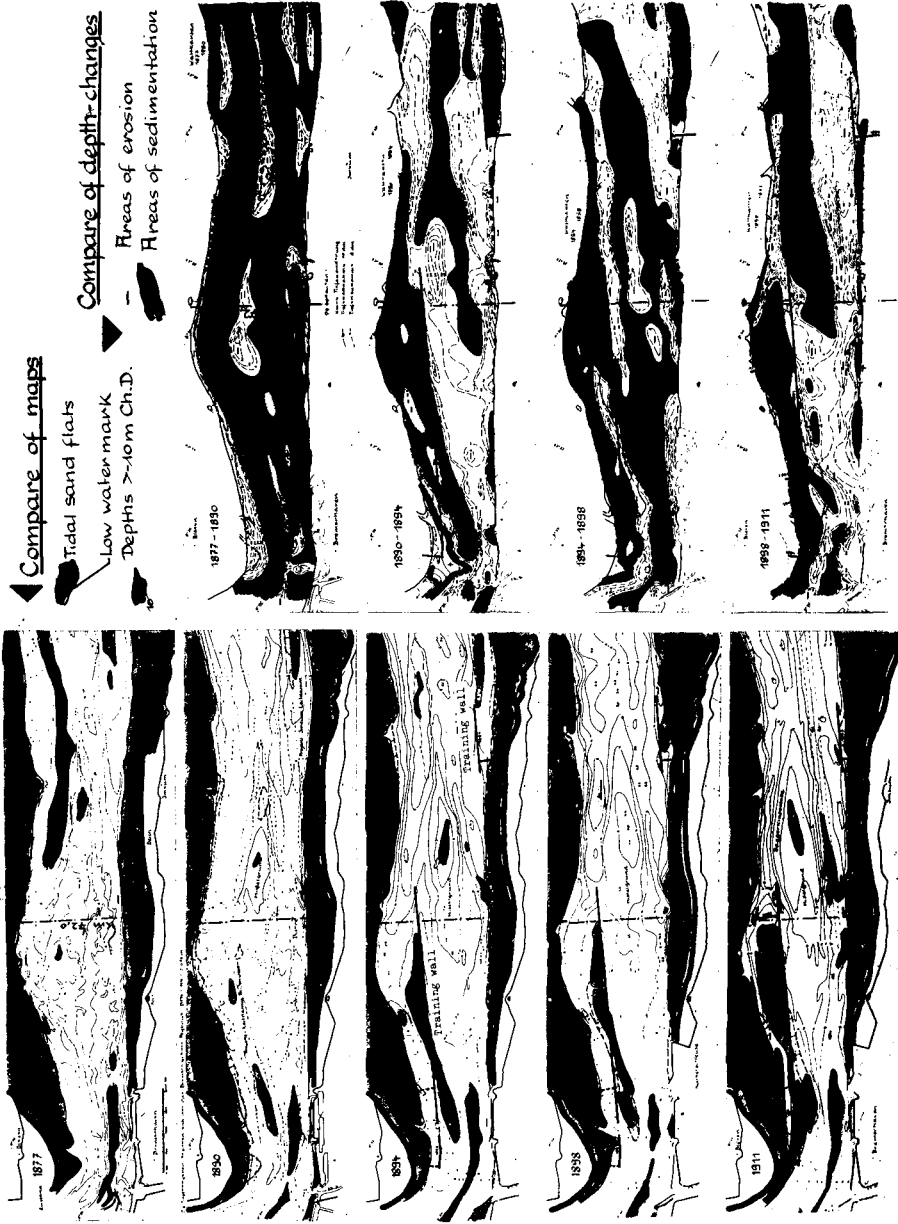
Fig. 4   Morphological changes after the construction of
         training walls in the section km 65 - 80
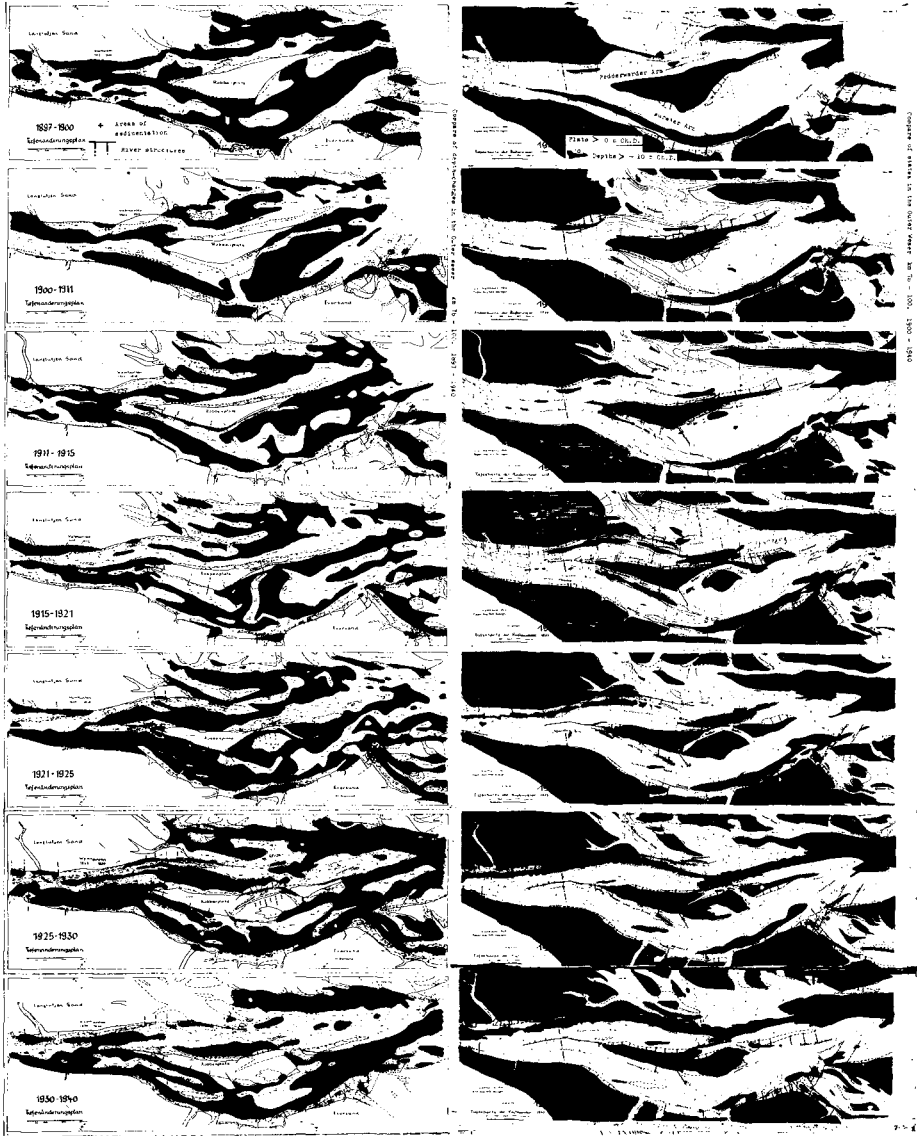
Fig. 6   Combined comparison of map and depth-changes,
          Outer Weser, km 78 - 100, 1900 - 1940
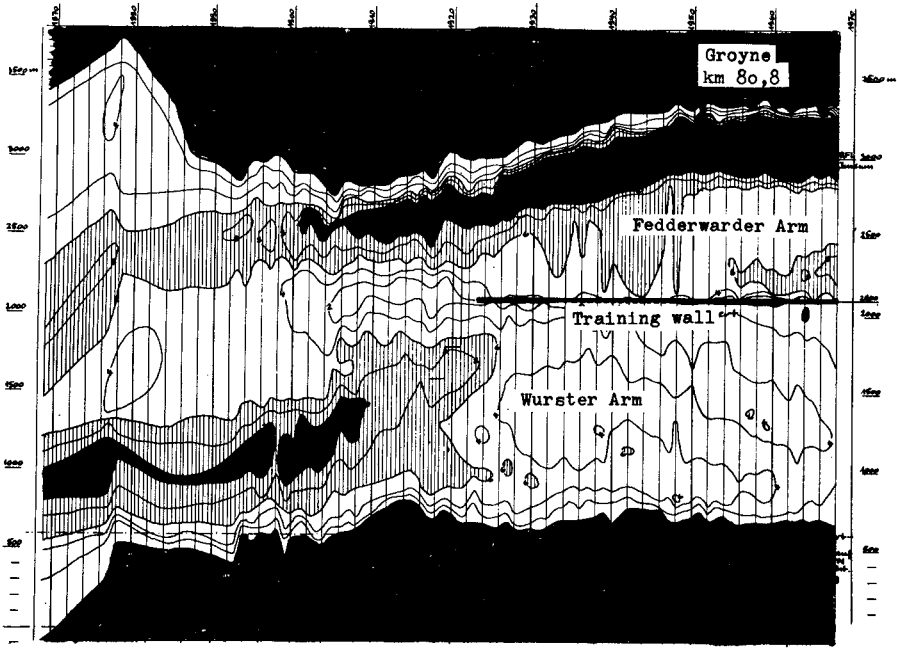
Fig. 7   Changes in the profile km 81, Outer Weser, 1869 - 1968

CHAPTER 75

PHYSICAL CHANGES IN ESTUARINE SEDIMENTS
ACCOMPANYING CHANNEL DREDGING

by

Charles K. Sollitt, Assistant Professor
Department of Civil Engineering, Oregon State University

and

Stephen D. Crane, Research Assistant
Ocean Engineering Programs, Oregon State University

ABSTRACT

The physical characteristics of estuarine sediments provide useful information
about sediment sources, the nature of bottom surface stresses and sediment
transport mechanisms. Changes in sediment composition and state are also use-
ful indicators for estimating the effects of unnatural stresses on dependent
chemical and biological activities. In this study, the changes in several sedi-
ment properties have been monitored for an isolated estuarine dredging project.

The effect of estuarine hopper dredge activities has been evaluated for an Army
Corps of Engineers project at Coos Bay, Oregon. The project included suction
head dredging at a shoal area within the navigation channel and in bay spoiling
at a deep section of channel one mile downstream from the dredge site. Core
samples were taken five days before dredging and two, thirteen and seventy days
after dredging at the dredge and spoil sites. Subsequent laboratory analysis of
the core samples revealed that dredging induced redistribution of bottom sedi-
ments produced significant changes in several physical characteristics of the
dredged material. Repeated resuspension of bottom sediments during the dredging
and spoiling operations caused a net loss of fine grained sediments and light
organic constituents. Several symptomatic changes were observed which validate
this finding, including: an increase in median grain size and decrease in uni-
formity of dredge spoils due to loss of fine fractions; a decrease in volatile
solids in the dredge spoils due to a net loss of organics; a decrease in poros-
ity at the spoils site due to the ability of the coarse grain sediments to resist
resuspension; and a decrease in hygroscopic moisture content due to loss of porous
organics and silt-clay material from the spoils.

Conditions following dredging were observed for a period of seventy days. Partial
recovery of the sediment system was observed after two weeks with no further re-
covery in two months. The initial recovery came about due to the availability of
local sources of resuspended sediment adjacent to the dredge site. This occured
under low flow conditions in early fall. Complete recovery of the system was not
observed and probably requires the relatively large sources of sediment which
accompany heavy winter and spring runoff. Thus, the immediate effects of dredging
may persist until the annual cycle of sediment erosion and deposition have oc-
curred.

INTRODUCTION

Equilibrium Conditions

Estuarine sediment systems tend towards boundary stability as a result of long term sediment transport equilibrium. Short term local events may cause erosion and accretion to be temporarily out of balance and observations over geologic time scales may reveal gradual sedimentation. However, the mean geometrical configuration of an estuary remains quite stable over time periods measured in years, decades and centuries. A complex system of channels, embayments, tidal flats and barriers of varying permeability compose this quasi-stable boundary configuration. The system is in harmony with the flushing patterns and the sediment sorting patterns which ultimately determine the distribution of biological activity within the estuary.

Dredging represents a perturbation in this trend towards boundary stability. Utilization of an estuary as a commercial resource often requires the creation of navigation channels in areas where natural sedimentation has produced shoals. Subsequent deposition of the spoils causes excess accretion in areas where erosion and accretion were previously in balance. As a result, the boundary configuration of the affected areas is changed from the equilibrium condition. The estuary responds by increased accretion in the dredged channels where a local increase in the cross section area reduces mean velocities and reduces the sediment load capacity of the flow. At the spoil sites, excess deposition reduces the flow area, increases the local velocity and causes erosion of the spoiled materials. Thus, the estuary attemps to restore the equilibrium condition and return to the stable boundary configuration. Sedimentation within the navigation channels necessitates further maintenance dredging and cycles of artificially induced erosion and accretion result.

The effects of these dredging induced changes on an estuarine ecosystem can not be determined without detailed information about temporal and spatial variation in important ecosystem descriptors. However, it can be postulated that if dredging activities represent a significant input to the total annual sediment budget for a given area, then some response in dependent physical, chemical and biological processes might be anticipated. Furthermore, if dredging is repeated on a regular basis or if dredge scheduling interfers with critical annual cycles such as spawning, then some long term changes in sensitive biota could occur.

The study described herein was undertaken to investigate some short term effects of a small scale dredging project in an estuary which is routinely dredged at an annual rate which approaches the estimated sediment flux from upstream water shed sources. Although other investigators within the interdisciplinary research group studied changes in sediment chemistry and benthic biological acticity, (i.e. Slotta, et al) this discussion is confined to observed changes in the physical characteristics of surface sediments.

Study Site

The study was conducted at Coos Bay, Oregon. Coos Bay is one of the most active timber ports in the world and is located 200 miles south of the Columbia River on the Oregon coast. The estuary surface area encompasses 10,000 acres, half of which is tideland. Waterborne commerce approaches four million tons annually, most of which is associated with the logging industry. The commercial area

of the estuary extends to river mile 17.

Annual maintenance dredging averages about 1.8 million cubic yards of
which approximately 30% is removed from the study site at river miles 12
through 15. Prior to the study, this region had not been dredged for more
than a year so that relatively undisturbed conditions could be assessed be-
fore dredging. A small shoal, 8,000 cubic yards, was removed via hopper
dredge from the confluence of the Coos River with Isthmus Slough at river
mile 14 to maintain a navigable depth of 30 feet. See Figure 1.

The dredged material was removed in 1800 or less cubic yard loads by the
U. S. Army Corps of Engineers' hopper dredge Chester Harding and spoiled in
mid-channel at River Mile 13 where the water depth exceeded 35 feet. Spoiling
occurred onan ebbing tide with maximum observed bottom currents of 1.5 feet
per second.

Hypothetical Dredge Disturbance

A dominant feature of hopper dredging activities is the resuspension of
bottom sediments. As a dredge suction head passes through a dredge site, sur-
face sediments are drawn into the head and pass to the hopper. Some of the
material around the suction head is disturbed mechanically and thrown into
suspension. Heavier particles settle out after the disturbance passes, while
lighter particles remain in suspension due to ambient turbulence and may be
transported from the original site by local currents. The material which
passes into the hopper is initially in suspension, but the heavier particles
settle to the hopper bottom. The lighter particles remain in suspension and
some are returned to the estuary water column via the hopper overflow. At the
spoil area, the contents of the hopper are released and settle to the bottom as
a slurry. Surface shear during descent and impact-induced mixing at the bottom
resuspend a portion of the material; again, the fines may be transported from
the spoil site. As a result of repeated resuspensioning and settling and the
subsequent loss of fines, it is hypothesized that dredge spoils may contain
smaller fractions of fines than occur at the dredge site. Furthermore, the
organic constituents within the sediment can be expected to wash out of the
spoil material if they have low specific gravities or small particle sizes.

If a net loss of fines and/or organic constituents does occur, then changes
in several physical parameters would include:

1. an increase in mean particle size at the spoil site due to loss
    of small particles;
2. a decrease in uniformity due to selective removal of fines;
3. an increase in porosity and water content due to slow consolida-
    tion rates and decreased uniformity;
4. a decrease in mean specific gravity due to loss of lighter frac-
    tions; and
5. a decrease in volatile solids due to loss of organics.

Sampling Program

In order to investigate changes in these parameters, bottom samples are
required from the dredge and spoil sites before and after dredging. Post-
dreding samples are also required to determine if a tendency exists to return
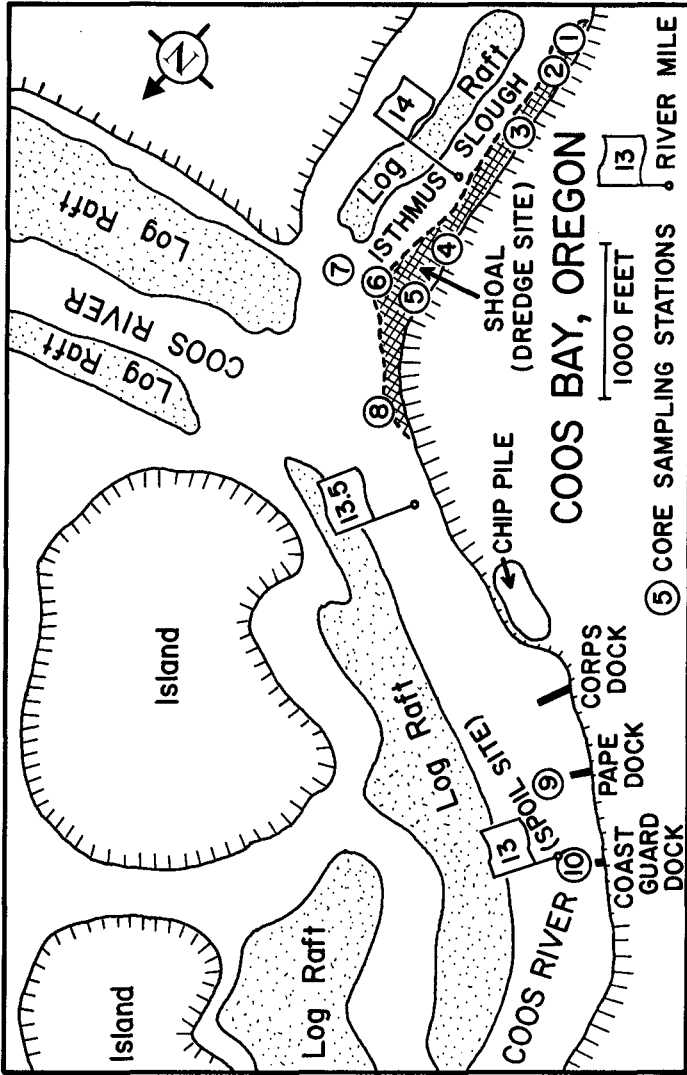
Figure 1. Coos Bay Oregon, River miles 13 to 14. Core sample station locations.

to initial conditions from natural erosion and sedimentation processes. Relatively large and undisturbed samples are required because of the number of tests to be run on each sample. In addition, some profile information is required to evaluate the depth dependence of the properties in question. To satisfy these requirements, the sampling program included:

1. gravity core sampling stations in the dredge and spoil areas to evaluate surface and subsurface physical properties of bottom sediments before and after dredging;

2. a line of sampling buckets along the longitudinal axis of the spoil site to evaluate spoil properties immediately after release from the hopper, and

3. sediment stakes alongside the buckets at the spoil site to investigate subsequent rate of erosion and/or deposition.

The locations of the ten core sampling stations are identified as circled arabic numerals on the chart in Figure 1. Seven of the stations are located in the dredging area (River Mile 13.8 to 14.2) to provide adequate sampling for a limited number of passes by the dredge over a relatively expansive area. Station Eight is two-tenths mile downstream from the dredge area (River Mile 13.6), Station Nine is at the center of the spoil site (River Mile 13.1) and Station Ten is at the downstream end of the spoil site (River Mile 13.0).

Core samples were taken 5 days before, 2 days after, 13 days after and 70 days after the dredge operation. Each sample was obtained with a 300-pound gravity corer constructed by the research team. Core liners (1-7/8 inch diameter acrylic tubing) were used; core lengths varied from 4 to 20 inches.

Twenty-five sampling buckets were placed at 100-foot centers along the assumed center line of the spoil area. Five-gallon paint cans were used with 30 pounds of concrete added as ballast. The buckets were tied to a common line for spacing and lowered from the surface with the sediment stakes attached. SCUBA divers were used to position the buckets and set the sediments stakes in place. SCUBA activities were hampered severely by limited visibility of 6 inches to a few feet. As a result some of the buckets and stakes were not placed properly before spoiling occurred.

The sediment stakes were fabricated from No. 3 reinforcing steel bars, 5-feet long. A 6-inch bar was welded on at the 2-foot level to support a plywood plate to resist penetration into the bottom. Tape rings were placed at one-tenth foot intervals to be used as depth indicators.

LABORATORY ANALYSIS

Sediment samples were stored for a period of two to six months before physical analyses were completed. Cores were kept sealed to prevent loss of pore water and shrinkage, but no attempt was made to stop chemical and biological reactions.

Samples were extruded from the cores in four-inch segments. Consequently, profile information is limited to averages over four-inch intervals. Individual samples were separated and dry prepared according to ASTM Designation D 421-58. Particle size analyses included sieving, hydrometer and hygroscopic moisture content analyses were conducted according to ASTM Designation D422-63 except

that wood chips larger than 0.589 mm (#30 sieve) were removed by sieving in preparation for particle size analysis.

Percent volatile solids were measured as the percent difference in weight after combustion at 600°C for four to six hours. This time was larger than the 15 minutes recommended by Standard Methods due to the large sizes of both the sample and the individual wood chips.

Specific gravity determinations were made in accordance with the procedure recommended by Lambe (1951). Tests were run on all surface samples at the spoil site and on random samples at the dredge site.

Porosity was calculated from the combined measurements of sample volume, oven dry weight and specific gravity. Due to uncertainties involved in sample partitioning and the subsequent volume determination, this quantity can be expected to have large standard deviations.

In the data analysis that follows, specific samples may be identified by number. The sample identification numbers may be interpreted as follows:

1. the first number refers to the station location (Figure 1)
2. the letter refers to the date the sample was taken; e.g.
                 A = 5 days before dredging
                 B = 2 days after dredging
                 C = 13 days after dredging
                 D = 70 days after dredging
3. the last number refers to the depth of the sample; e.g., 08 refers to a four-inch long sample extending from the four-inch level to a maximum depth of eight inches.

Thus, sample number 6C04 is from Station 6, thirteen days after dredging and extends from the water-bottom interface to a depth of four inches. Bucket samples are prefixed with a letter "B". Finally, a 12-inch core was taken by SCUBA divers at a mound near Bucket 16 seven days after dredging. The resulting four-inch long sub-samples of that core are designated 16-4, 16-8 and 16-12.

INTERPRETATION OF RESULTS

Repetitive samples were not taken at each station so a statistical analysis could not be performed to evaluate confidence intervals from the data. In lieu of a statistical analysis, the results are presented such that trends in the data for composite regions of interest are isolated. That is, data from individual stations are combined to produce regional characteristics for the dredge site and the spoil site. It should be recalled that Stations 1 through 7 were approximately within the dredge site. Stations 9 and 10 and the buckets were within the spoil site and Station 8 was in between the two regions, but closer to the dredge site.

Particle Size Distribution

Grain size analysis graphs for each sample are presented in the report by Slotta, et al. Three important parameters can be identified from these graphs. The first is the median grain size (D_{50}), which is defined as the

particle diameter which divides the sample into 50 percent portions by weight. This parameter is useful for classifying the gross features of the material as either predominantly sand, silt, or clay. The second is the effective grain size (D_{10}) which designates the particle diameter below which 10 percent of the sample is finer by weight. This parameter correlates well with the permeability of the material (Lambe, 1951) and indicates the ease with which fluid will flow through the sediment, e.g., large D_{10} values indicate less resistance to flow. The third parameter is the uniformity coefficient, defined as D_{60}/D_{10}. which expresses the relative homogeneity of the sediment sample; values less than 2 are termed uniform.

Changes in these parameters could be observed by plotting each parameter versus station number as a function of time. However, a more useful representation is formed by plotting two of the parameters against each other and noting segregation and change as a function of location, time and associated dredging activity. This type of graph also identifies functional relationships between variables.

The technique is illustrated in Figure 2, where the uniformity coefficient is plotted versus median grain size for surface samples five days before and two to seven days after dredging. Station numbers are printed adjacent to the appropriate point. Regional properties are identified by enclosing points with similar features. In Figure 2, it is shown that before dredging, surface samples (above a depth of four inches) at both the dredge and spoil sites grouped fairly well with an average median grain size of approximately 0.04 mm and an
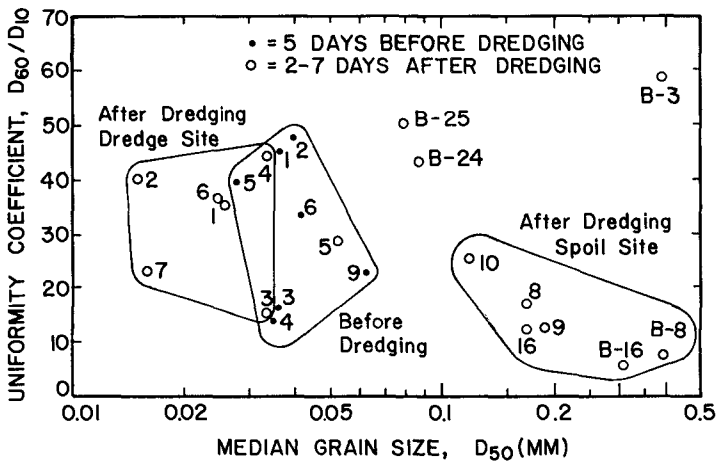
Figure 2. Uniformity coefficient versus median grain size.

average uniformity coefficient equal to 30. Two days after dredging, however, these parameters differed between the dredge and spoil areas. It is apparent from Figure 2 that an average six-fold increase in the median grain size occurred at the spoil site, while the dredge site experienced a decrease in median grain size by a factor of two. Associated with this change is decrease in uniformity at the spoil site.

The spoil site behaved in accordance with the hypothesis that repeated re-suspension of the sediment during dredging causes a net loss of fines. This process results in an increase in the median grain size and a more uniformly coarse material. Whereas the dredge material is classified as a well graded silt, the spoil material has the characteristics of a well graded fine sand. Exceptions to the noted trends are evident in spoil samples B-3, B-24 and B-25. This is probably due to the fact that these locations are at the extremes of the spoils area and are not completely indicative of spoil conditions.

The dredge site behavior appears to be an anomoly since a decrease in median grain size is experienced which is contrary to the anticipated effect of combined mechanical and hydraulic agitation of the surface sediment causing a loss of fines. The reason for this behavior is evident from an examination of Figure 3. In this figure, the uniformity coefficient is plotted versus median grain size for surface and subsurface samples at the dredge site before dredging. The graph clearly shows that the surface sediment is more coarse than the sub-surface sediments. Thus, the effect of dredging is to remove the surface sediments and expose the finer subsurface materials. The effect of hydromechanically disturbing these subsurface sediments is less significant. However, it is apparent from a comparison of Figures 2 and 3 that the exposed surface sediment properties after dredging are more vaiable than the pre-dredging subsurface properties. This is an indication of sporadic resuspension of the subsurface materials. The variability may be due to the fact that the dredge activities were limited so that uniform coverage of the dredge area was not possible.

The pre-dredge sediment profiles provide insight into the hydraulic and sediment transport characteristics of the system. A layering of sediments would be anticipated. However, one might expect also to find finer sediments near the surface in the summer and fall when low flow conditions permit the finer material to settle out of suspension. The profiles reveal the opposite trend; coarse material near the surface with finer material at depth as shown in Figure 3. This behavior indicates some additional destabilizing forces are working on the surface sediments which cause the fines to be washed into sus-pension and carried away. The source of these destabilizing forces can poss-ibly be traced to active commercial marine traffic in the navigation channels. Large lumber and wood chip ships frequent these channels and often drag anchors as they approach loading docks. In addition, prop wash from the screws of large vessels in the shallow channels could be sufficient to resuspend bottom sediment on a regular basis. Thus, any material deposited near the surface would probably be overturned and resuspended frequently and the fine sediments would be washed away by this unstable condition.

Figure 4 displays the tendency of the sediment properties to return to orig-inal conditions after dredging activities cease. Comparison with Figure 2 re-veals that within two weeks the median grain size at the spoil site had decreasea by a factor of two which indicates a natural deposition of material containing more fines than the spoils. At the dredge site, less variability is observed
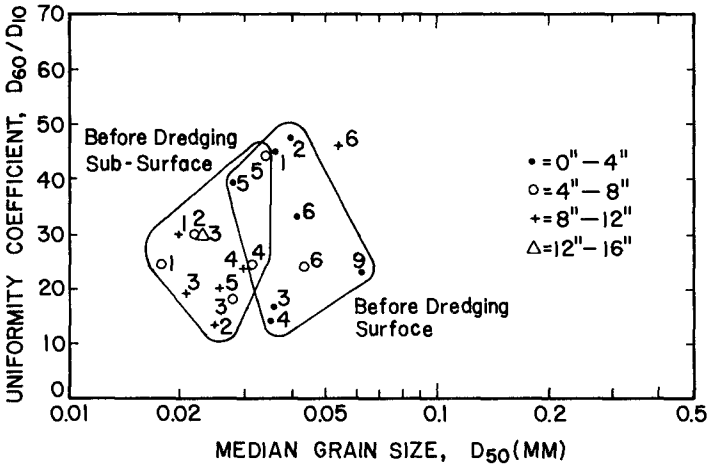
Figure 3.   Uniformity versus median grain size, depth dependence.
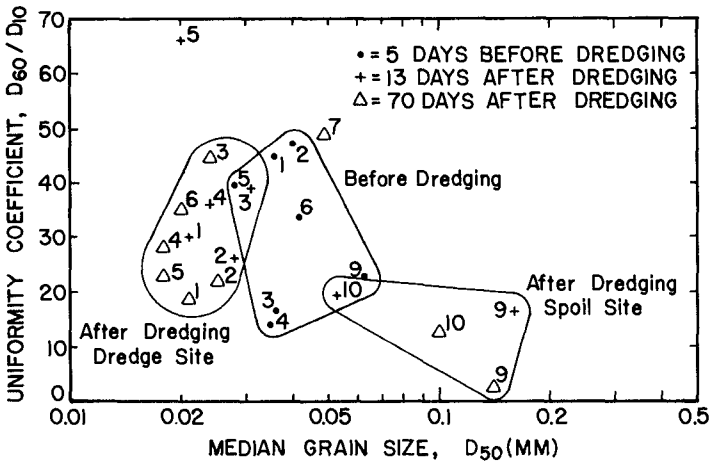
Figure 4.   Uniformity versus median grain size, return tendencies.

between stations. This is a further indication of overturning and mixing of
surface sediments by man-made and non man-made causes.

The return rate decreases sharply between the two week and two month sample
dates. The reason for this possibly is due to the fact that the greatest sources
of sediment occur with heavy winter and spring runoffs. During late fall, sedi-
ment sources are limited to resuspended materials adjacent to the dredge site.
Thus, a complete return to original conditions probably does not occur until the
annual cycle of sediment erosion and deposition has elapsed.

Volatile Solids

The change in volatile solids, a measure of organics content, is demonstra-
ted in Figure 5, wherein the percent volatile solids is plotted against median
grain size for surface samples five days before and two days after dreding. Seg-
regation by particle size permits the dredge and spoil sites to be distinguished.
Figure 5 also shows a change in mean volatile solids from 10 percent before
dredging to 8 percent after dredging. The trend is more demonstrable if Core 16
is ignored since it was acquired five days after the rest of the samples. The
behavior concurs with the hypothesis that the organics are composed of lighter
fractions which are more susceptible to flushing via resuspension than heavier
sediments particles.

The average volatile solids level of the natural sediment exceeds the 6.0
percent level established by the EPA for identification of polluted sediments.

Specific Gravity

Specific gravity determinations were made for all surface samples at the
spoil site and random samples throughout the dredge area. The results are plot-
ed in Figure 6, along with the median grain size. No measurable change in spe-
cific gravity is apparent. This can be explained in terms of the sample consti-
tuents. The sand, silt and clay fractions are minerals with a specific gravity
normally ranging from 2.6 to 2.7. The only light constituent is the organic
material which is largely composed of wood chip and wood fibers. The large wood
chips (greater than 0.589 mm) were removed by sieving before the specific grav-
ity tests were conducted. Consequently any change in organics (volatile solids)
is masked in the specific gravity measurements. In addition, the 2 percent av-
erage change observed in volatile solids would cause a decrease in specific grav-
ity by less than 0.06. The specific gravity results indicate that the mineral
constituents are typical for river or marine sediments.

Porosity

Core sample porosity is plotted with median grain size in Figure 7. Data
from surface samples five days before and two days after dredging are presented.
The results demonstrate a ten percent decrease in porosity for the dredge spoils.
This result was not anticipated because it was hypothesized that by losing the
fine grained material, voids would remain unfilled between the coarse particles.
The explanation for the observed behavior may be the same as that for the de-
crease in particle size below the surface. Specifically, the destabilizing ero-
sional forces are capable of keeping the finer sediments in a disturbed, less
consolidated state. The coarser sediments, on the other hand, are massive enough
to resist the erosional forces and are able to consolidate into a more compact
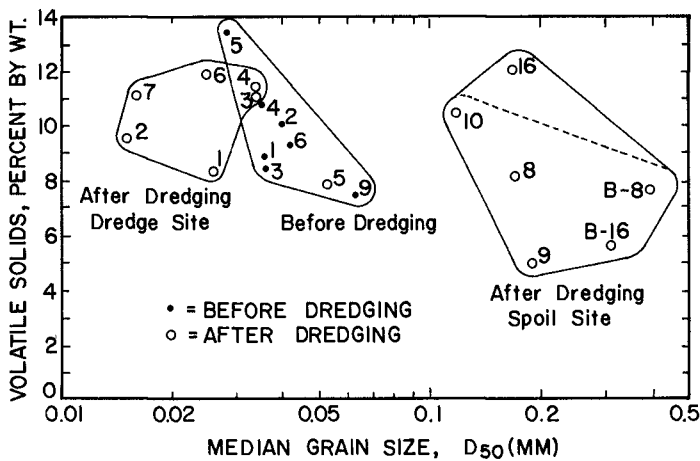
Figure 5.   Volatile solids versus median grain size.
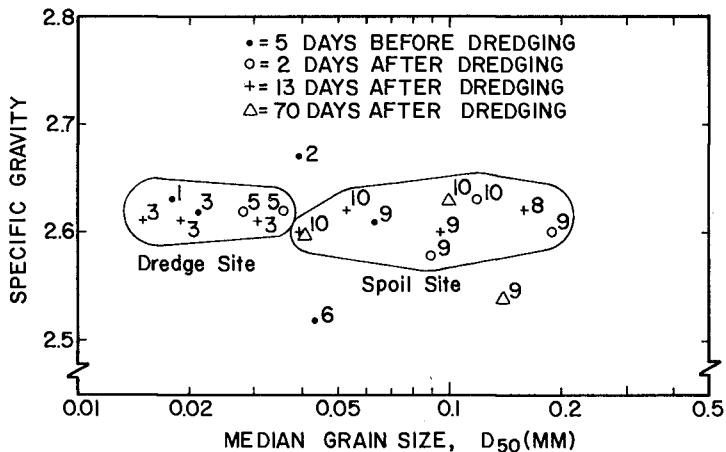
Figure 6.   Specific gravity versus median grain size.
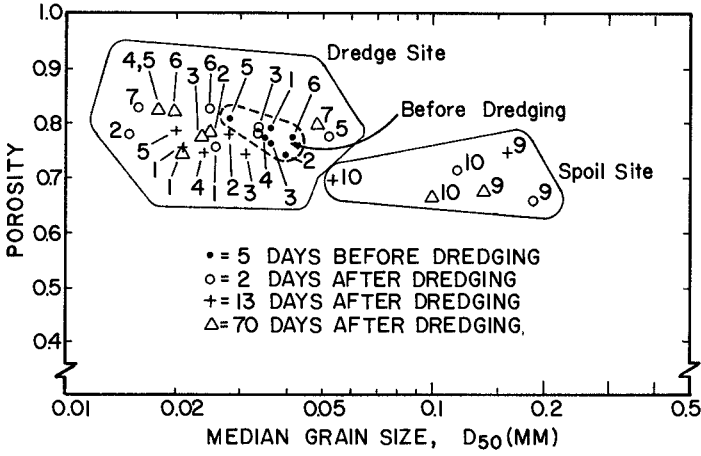
Figure 7.   Porosity versus median grain size.
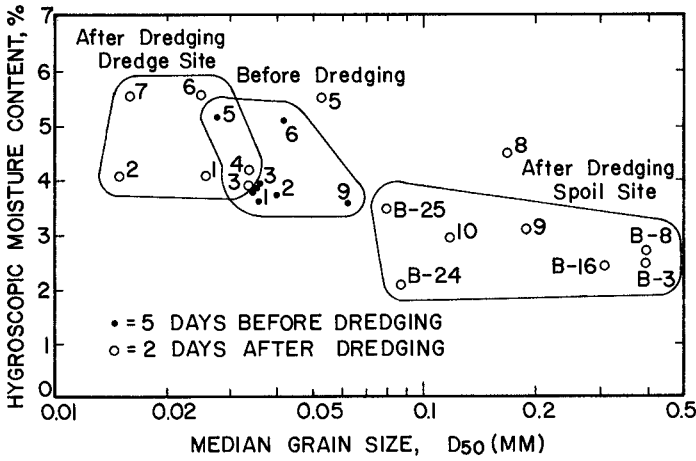
Figure 8.   Hygroscopic moisture content versus median grain size.

configuration. As a result, the coarse spoiled sediments are less porous.

Hygroscopic Moisture Content

The hygroscopic moisture content is a measure of the moisture contained within the pores of individual grains of sediment. These pores are to be distinguished from the voids between particles; the latter are accounted for in the porosity measurement. The hygroscopic moisture content is calculated as the water content fraction by weight remaining in the air dried sample at room temperature and humidity. This parameter is generally low for clean sands and high for silt, clay and organic materials. The change in this parameter accompanying dredging is shown in Figure 8, wherein hygroscopic moisture content is plotted versus median grain size for surface samples five days before and two days after dredging. Although the results vary somewhat due to daily changes in temperature and humidity, the trend in Figure 8 is readily apparent: the hygroscopic moisture content decreases significantly at the spoils site and increases slightly at the dredge site. Again, it appears that less clean sediments have been exposed at the dredge site and the fine fractions have been washed from the sediment at the spoil site.

Sediment Stake and Bucket Survey

Very limited success was experienced in determining deposition patterns with the bucket and stake array. Many difficulties were attributable to exceptionally poor visibility in the turbid waters. Approximately one-half of the buckets were either tipped over or missing after spoiling. This was an apparent reaction to the dredge and other marine traffic.

The placement of the linear bucket and stake array is shown in Figure 9.

Spoils were found in buckets ranging from #3 to #25 with some empty buckets in between. Heaviest depositions were found in and around bucket #16 where a 24-inch depth was recorded on the sediment stake. A large mound, 40 to 50 feet in diameter, surrounded the area. The composition of the material included approximately equal portions of wood chips and fine sand. This location coincided with the center of the spoils area. However, a large chip ship was berthed at the Pape Dock and forced the dredge to hold the bucket array to port during many of the downstream spoiling runs. This probably accounted for the sporadic empty buckets found during retrieval operations.

An analysis of the physical properties of the bucket samples was included in most of the foregoing figures. The properties were very similar to those of surface samples taken at Stations 9 and 10 two days after dredging. A large difference occurred in the volatile solids levels. The bucket samples are uniformly high (up to 65%) in volatile solids which concurs with the large percentage of wood chips found in the buckets. This behavior is probably a consequence of spoils falling from the hopper in a quasi-solid mass. The wood chips were trapped in the buckets with the rest of the material and were sheltered from local erosional forces. Around the bucket, the combined effect of currents and ship traffic may have resuspended and eroded the relatively light wood chips. Consequently, wood fragments were absent in core samples taken two or more days later. This is further evidence of unstable bottom conditions exisiting in this area of the Coos River.
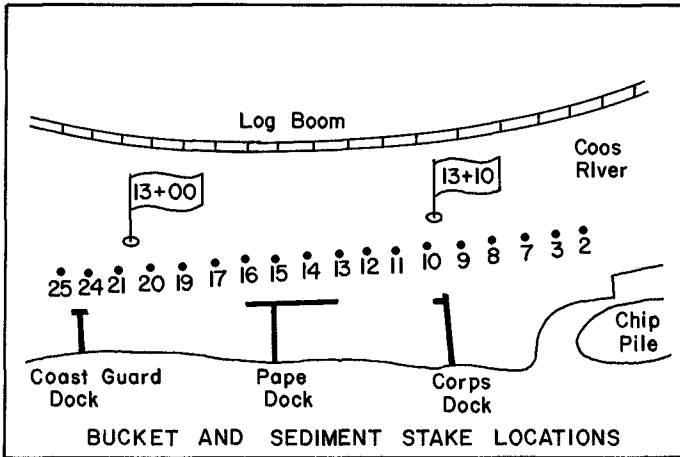
Figure 9.   Bucket and sediment stake locations.

SUMMARY

The data presented in the preceding paragraphs substantiate the hypothesis that hopper dredging promotes the resuspension and loss of lighter fractions of bottom sediment. It has been shown that after dredging the sediments:

1. increased in median grain size and decreased in uniformity at the spoil site due to loss of fines;
2. decreased in median grain size at the dredge site due to exposure of fine subsurface material;
3. decreased in porosity at the spoil site due to the ability of the coarse sediments to resist resuspension;
4. retained a constant specific gravity due to uniform density among the major constituents;
5. decreased in volatile solides in the dredge spoils due to the loss of light organics (with the exception that surface spoils were high in volatile solids immediately after spoiling before the wood chips were washed away);
6. decreased in hygroscopic moisture content due to loss of porous organics and silt-clay material.

The data further demonstrate that relatively unstable conditions exist in this reach of the estuary, probably aggrevated by marine traffic, causing frequent resuspension of surface sediments. Physical symptoms of the dredging disturbance persisted for more than two months after the dredging operation was completed even though a very small volume of sediment was removed and spoiled. The results indicate that changes in the physical characteristics of surface sediments may remain until significant natural erosion and deposition occur to mask the disturbance.

BIBLIOGRAPHY

1. Slotta, L. S., Sollitt, Bella, Hancock, McCauley and Parr, "Effects of Hopper Dredging and In Channel Spoiling in Coos Bay, Oregon," Final Report, Oregon State University, July 1973.

2. ASTM Standards, Part II, 1973 Annual Edition, pp. 203-213.

3. Standard Methods for the Examination of Water and Waste Water, APHA, AWWA, WPCF, 13th Edition, 1971.

4. Lambe, W. T., Soil Testing for Engineers. John Wiley and Sons, New York, 1951.

CHAPTER 76

GEOMORPHOLOGICAL STUDIES OF THE ESTUARY

OF RIVER NETRAVATI NEAR MANGALORE

E. J. John[1] and K. P. Cheryan[2]

ABSTRACT

A number of factors such as wave conditions, tides, river flows, sediment charge, and ocean currents affect the features of an estuary. The understanding of the morphology of an estuary is essential on purely scientific considerations as well as applied to harbours. An attempt is made to study these inter-related and unsteady features and their combined effect on an estuary qualitatively. The estuary selected for the study is the one near Mangalore on the West Coast of India at latitude 12° 51' north and longitude 74° 50' east, where two rivers, viz., river Netravati and river Gurpur meet together and join the sea. An effort is made to analyse the changes in the estuary in terms of prevailing wave conditions, river flows and sediment transport.

INTRODUCTION

The understanding of the behaviour of an estuary is essential on purely scientific considerations as well as applied to harbours. A number of factors are varying seasonally and year after year, which affect the condition of the estuary, and hence haphazard observations will not yield any accurate results. As a preliminary to comprehensive study of river estuary problems, it is desirable to investigate in a general manner the behaviour of a selected estuary, viz., the estuary of river Netravati and river Gurpur. During the monsoon period these rivers carry large quantity of discharge with good percentage of sediments. Ocean currents and waves are also predominant during this season. Most of the changes in an estuary occur during this period. Changes during the rest of the year are quite

----

[1] Assistant Professor, Department of Applied Mechanics and Hydraulics, Karnataka Regional Engineering College, Suratkal, India.

[2] Assistant Engineer, Neendakara Port, Quilon, India. Formerly post-graduate student at Karnataka Regional Engineering College, Suratkal, India.
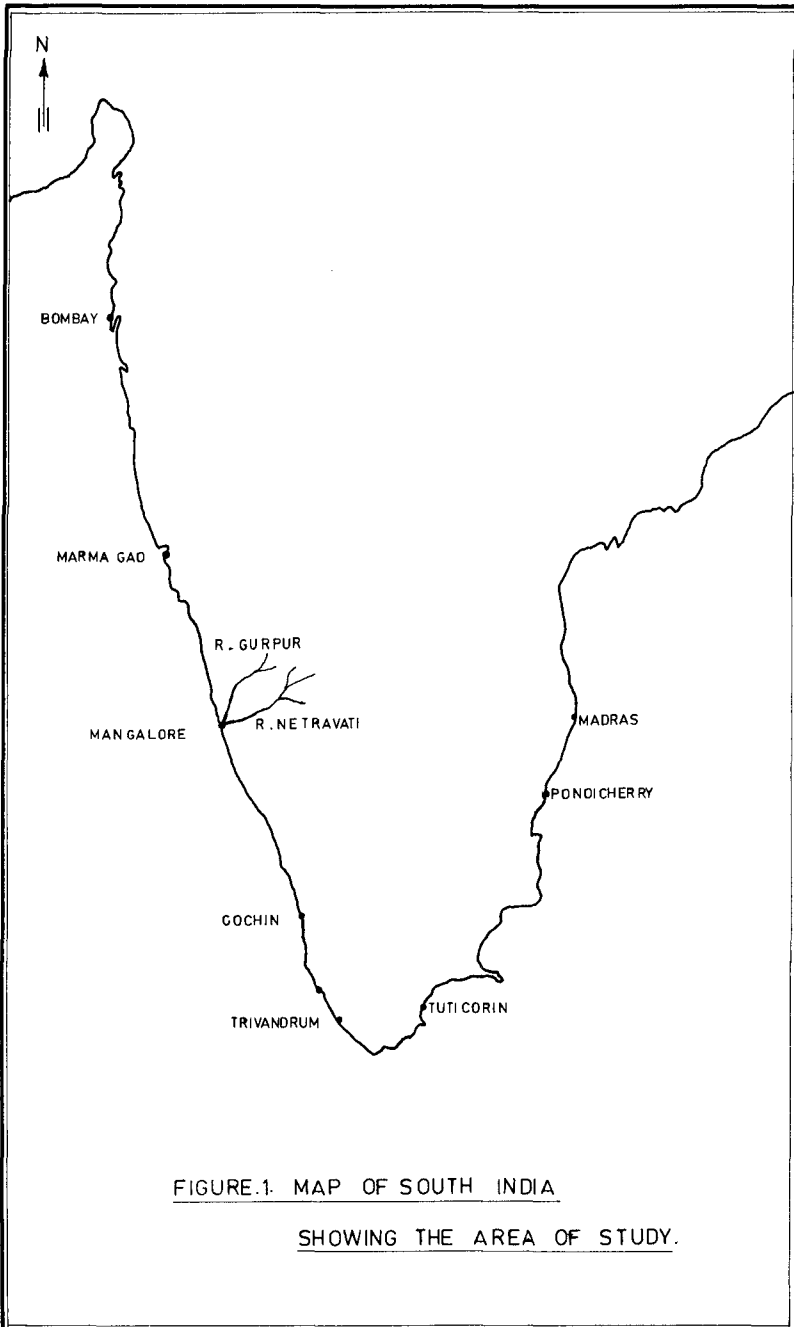
FIGURE.1. MAP OF SOUTH INDIA

SHOWING THE AREA OF STUDY.

insignificant.   Hence in this study it is proposed to
examine the general morphology of the estuary prior
to and after a monsoon period.   An effort is made to
analyse the changes in the estuary in terms of pre-
vailing wave conditions, river flows and sediment
transport.

        The estuary selected for the study is the
estuary near Mangalore at 12° 51' north and longitude
74° 50' east, where two rivers, viz., river Netravati
and river Gurpur meet and join the sea together.   The
river Netravati is having a catchment area of 3160 sq.
km. and a maximum discharge of 8170 m³/s. and the river
Gurpur is having a catchment area of 665 sq. km. and a
maximum discharge of 1140 m³/s.   A map of South India
showing the location of the area of study is given in
Fig. 1 and a detailed map of the estuary is given in
Fig. 2.

                        FIELD STUDY

        Some informations about the morphology of the
estuary can be obtained by studying the maps covering
the area under investigation.   Since these maps are
generally updated from time to time any change in the
morphology must be seen in these maps.   In the present
case, three maps (i) Geodetic traverse survey map prepared
in 1904 (ii) Hydrological survey map of Mangalore Port
prepared by Capt. G. P. Ranson in 1949 and (iii) a map
prepared in connection with Mangalore Port investigations
in 1953 were available for detailed study.   Since the
latest map referred only to 1953, it was found necessary
to prepare a fresh map of the area showing relevent
changes.   This map of the area was prepared with refe-
rence to three important land marks, which were all
shown in the earlier maps.   Contour maps of the area
within the estuary, near the river mouth and outside
the mouth into the sea were also prepared before and
after monsoon period, by taking soundings from a
country boat.   The position of the boat was fixed by
two theodolotes kept on either bank.   Sediment samples
were collected from the sea bottom, near the mouth of
the river and inside the estuary.

        River discharges were determined by establi-
shing river gauges in the two rivers beyond the tidal
zone.

        Tide records from the tide gauge set up with-
in the estuary were collected and studied.   The mixed
type of tide occurs at Mangalore.   Mixed tides are
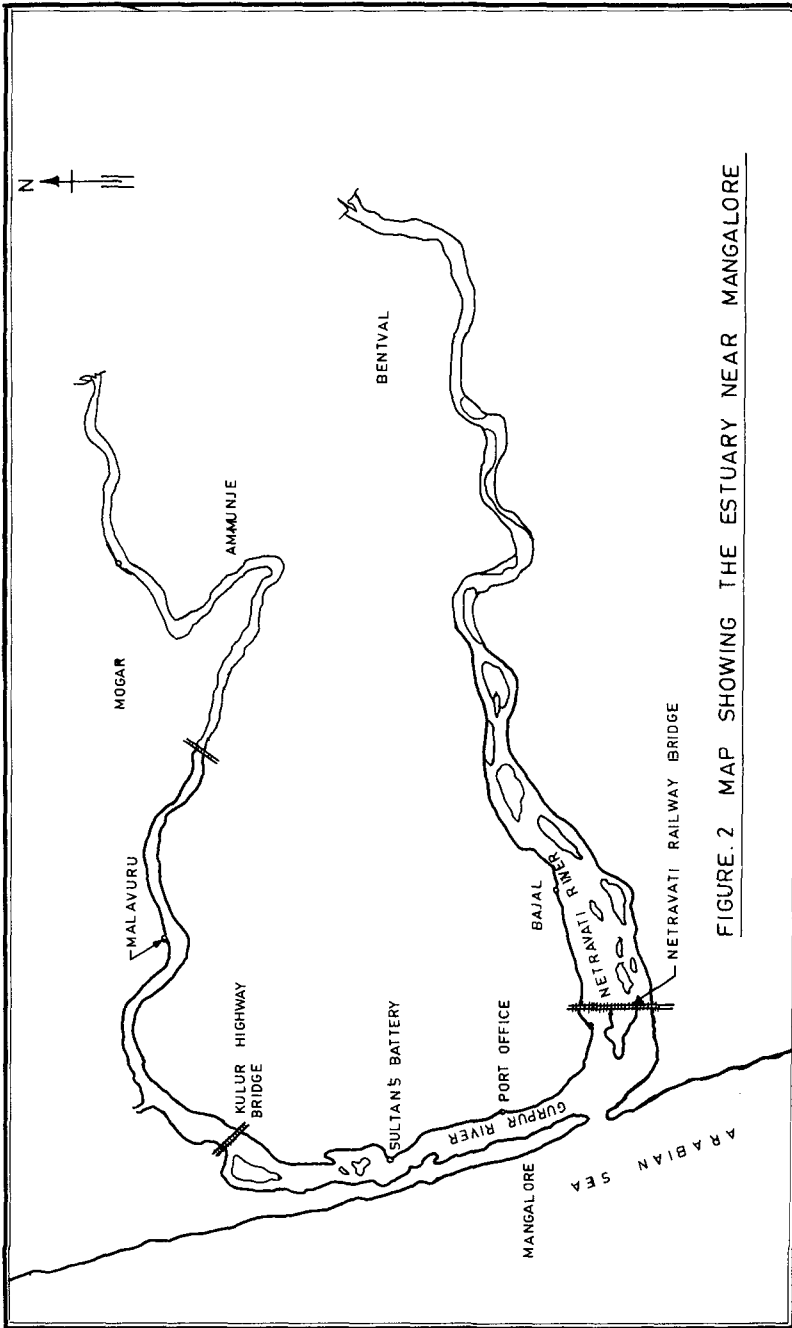
FIGURE. 2 MAP SHOWING THE ESTUARY NEAR MANGALORE
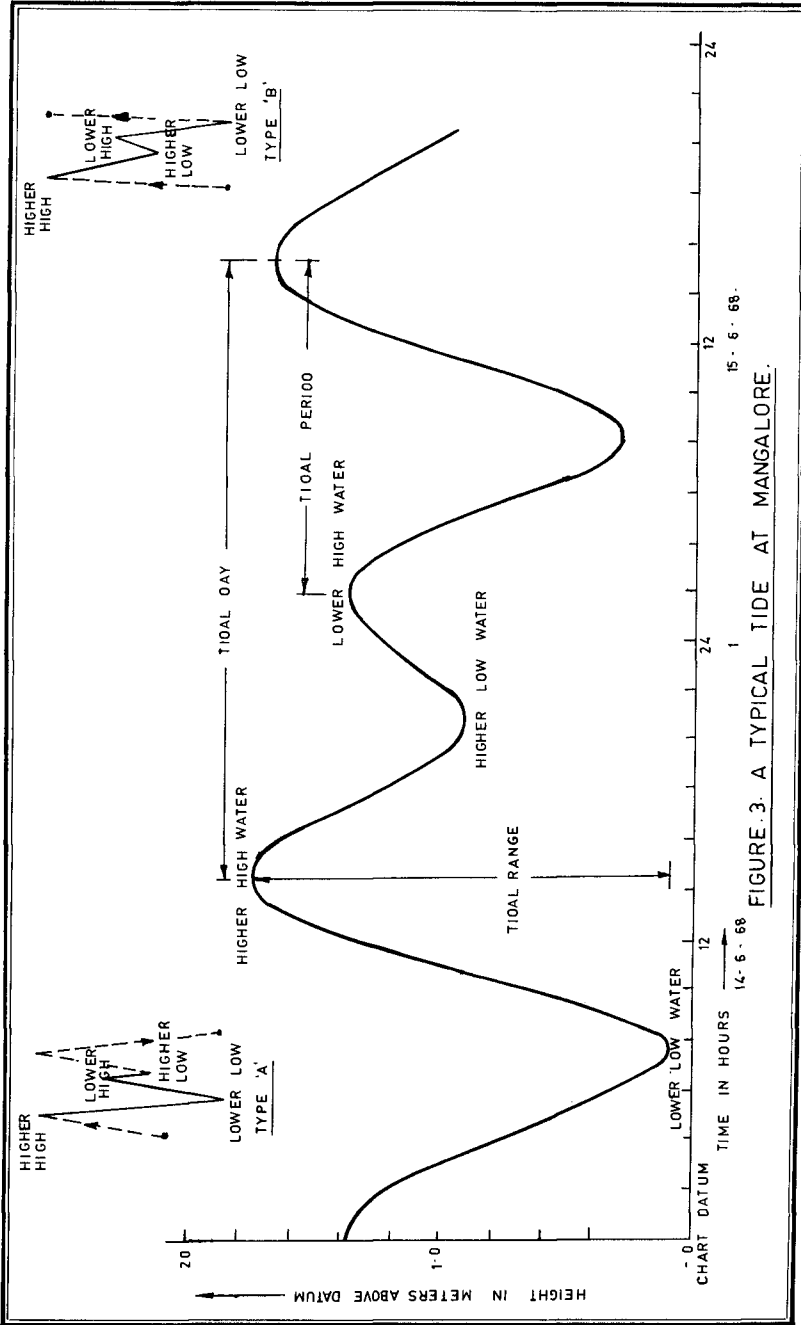
FIGURE. 3. A TYPICAL TIDE AT MANGALORE.

characterised by significantly unequal high waters and
low waters on most lunar days in a month. Salient
features of this type of tides are shown in Fig. 3.
The tides alternate from high water to low water.
There are two high waters and two low waters in a
tidal day. So we can distinguish them as a higher
high water and a lower high water. Similarly the low
waters may be classified as a higher low water and a
lower low water. Another aspect revealed on the exa-
mination of the tidal graph is that it has two definite
sequence of occurrences of high and low waters. These
sequences may be classified as type 'A' and type 'B'
and these are shown in Fig. 3. In type 'A' tides, a
higher high water is followed by a lower low and from
there to a lower high. From the lower high position,
the tides fall to a higher low and rise back to a
higher high. This cycle is repeated. In type 'B'
tides, a higher high water is followed by higher low
and from there to a lower high. From the lower high
position, the tides fall to a lower low and rise back
to a higher high. Type 'A' and type 'B' tides are
counted for the year 1968 and found to be totalling
111 and 240 respectively. On some days in July the
types could not be distinguished due to large fluctua-
tions in the river stages due to floods.

GENERAL MORPHOLOGY

From the morphological study conducted for
one season it will be difficult either to hindcast the
previous history or to forecast the future trends.
The first and foremost aspect that strikes an observer
is that the sand spits on either side of the river
mouth are entirely different in character and appearance.
The most striking differences are listed below:

Description	North Sand Spit	South Sand Spit
Beach material	Fine sand	Coarse sand
Colour of beach material	Fairly bleached	Reddish brown
Elevation of the spit	Low	High
Slope of the beach	Gentle	Steep
Topography	Slightly wavy, the waves being parallel to the coast	Permanent ridges and valleys. A few of them parallel to the coast and many at an angle
Width	500-600 meter wide, wider towards the river mouth	400 meters at the base narrowing towards river mouth
Habitation	Inhabited	Scarcely inhabited

SH -   RIVER SHOALS

P ·-   POOLS

SP -   RIDGES OR SPURS BUILT BY WAVES.

B -   BARS

FIGURE 4. FEATURES   OF   THE ESTUARY
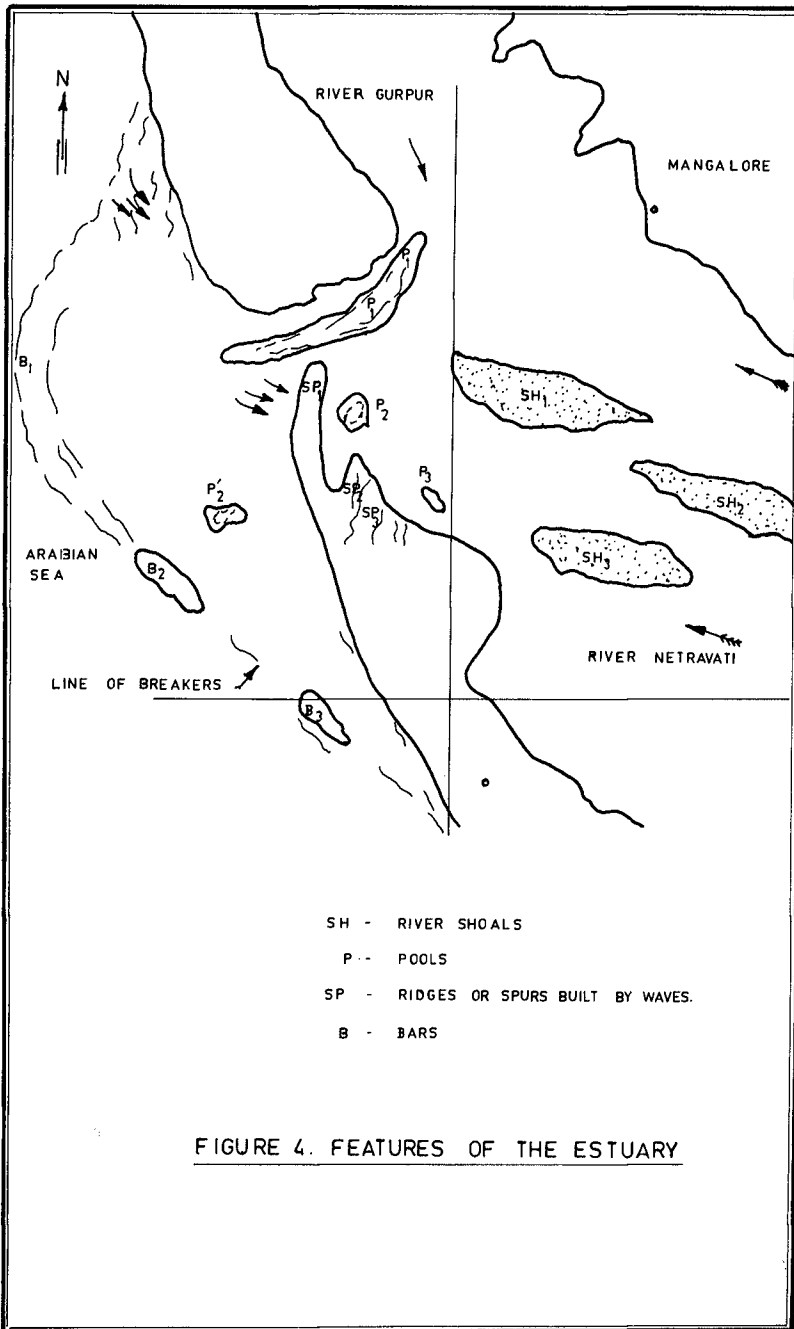
These evidences indicate that the source of the materials on these two sand spits are different. Further the mode and time of deposition may also be different.

The prominent features of the present position of the estuary are marked in Fig. 4. Starting from the river towards the sea, they are:

1. Sand deposition or shoal inside the estuary marked 'SH' acting as a guide bank for the present channel of the river.

2. Pool or area of large depth 'P' extending from just inside the river mouth, through the gut upto the bar.

3. The projecting spur on the southern sand spit marked 'SP', created by the west north-west wave action at the river mouth and

4. The off-shore bar marked 'B' formed at the present river mouth.

Now looking to the south of the present system, we can identify the discarded remnants of similar systems, the more southward they are, the less prominent. They are marked in Fig. 4 with the corresponding suffixes using the same notation. In the case of pools south of present gut, they are intruded by sand-spit, dividing them into two halves one inside the estuary and one in the sea. The features in the portion of the pool within the sea are fast disappearing due to constant action of waves. The features inside the rivers are also being distorted slowly. There are permanent ridges on the southern sand spit.

Examination of the geodetic traverse survey map shows that the southern bank of the river Netravati extends from the railway bridge towards west. This indicates that the river had a straighter course earlier. Now the south sand spit has been built up virtually across the river. The river now practically flows as a narrow channel close to the northern bank.

A comparison of maps prepared in 1905 (G.T.S.), in 1949 (G.P.Ranson), in 1953 (Mangalore Port authorities) and in 1968 (the authors) shown in Fig. 5 reveals that the river mouth is gradually migrating towards north.

N

74° 50' E

○
R ·C · CATHEDRAL

MANGALORE

FISH MARK BOAT
BUILOING   YARO

└HO

12°·50'

BOAT BUILDING YARD

x—x—x G·T·S· SURVEY 1905

———— RANSONS SURVEY 1949

●—o— MANGALORE   PORT SURVEY 1953

·—·—· PREMONSOON 1968 ⎫
                      ⎬ BY AUTHORS
———— POSTMONSOON 1968 ⎭

FIGURE·5· COMPARISON OF MAPS.
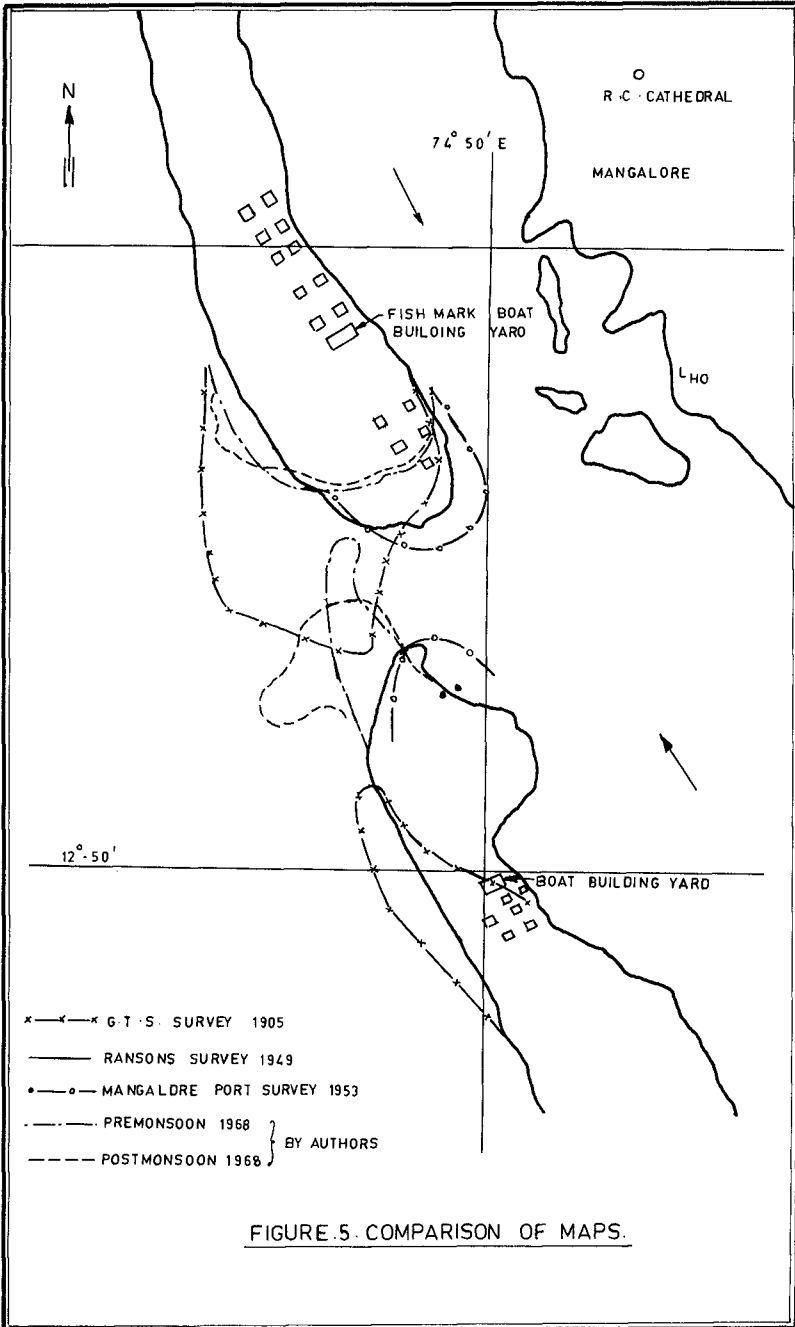
LITTORAL DRIFT

By the radioactive tracer studies and the flourescent sand studies conducted by the Mangalore Harbour Project and Central Water and Power Research Station, Poona (4), it has been concluded that the predominant direction of littoral drift in the region is from north to south.

The river discharges are deep brownish yellow in colour due to the admixture of lateritic ferrous compounds. When the coloured river water is ejected into the body of blue expanse of water one can easily observe the path taken by the river water into the sea, by mere visual observation of the contrasting colours. This aspect has been noticed during the study. This method of observation is quite useful to understand the diffusion pattern of the river into the sea waters at different stages of discharge. It is noticed that the river water is taking an abrupt southerly turn, as soon as it enters the sea.

The river Gurpur, is taking an abrupt turn southwards near Kulur leaving only a narrow land strip of 500-600 m. wide between the river and the sea (Fig.2). It would be natural to assume that the river Gurpur had once flown straight towards west at Kulur to join the sea and this inference has been confirmed by Cheryan (3). Between Kulur hills and Suratkal hillocks, there is a vast area of flat low-lying land. The river might have changed its course several times to build such a wide plain. The sand spit separating the Gurpur river and the sea exhibits certain curves at two places, one at Sultan's Battery and another south of it, indicative of former river mouths. Cheryan (3) while conducting geological and geotechnical studies at Panambur, reported evidences of an old river bed. All these indicate that the river Gurpur had a separate exit into the sea at first and later it was forced to flow southwards to join Netravati. This shifting might have taken place during a long period of time. It can only be the littoral drift that had contributed to the maximum for this shift.

MORPHOLOGY OF ESTUARY

During the major part of the year, fair weather prevails and the estuary is under the action of tides only as there is very little upland discharge. The tidal prism for Mangalore estuary for a spring tide of 1.77 m. is found to be 21 million m^3. and for an average tide of 1.25 m. it is 13 million m^3. The limit specified by Ippen (5) for a well-mixed estuary is to have the ratio

N

NORTH SANO SPIT

RIVER
GURPUR

SOUTH SANO
SPIT

RIVER
NETRAVATI

NOTE ——————②   2 METER CONTOUR BELOW CH·OATUM SHOWING THE
                 OUTLINE OF BAR JUST BEFORE MONSOON

     —·—②   2 METER CONTOUR OPENED UP OUE TO FLOOO FLOW
                 LEAVING A CHANNEL IN THE MIOOLE

     ————②   CLOSING UP OF 2M CONTOUR OUE   TO WAVE AFTER
                 MONSOON

     ——————▶   OIRECTION OF SAND   MOVEMENT OUE TO WAVES.

FIGURE·6. DEVELOPMENT OF BAR AT THE RIVER MOUTH
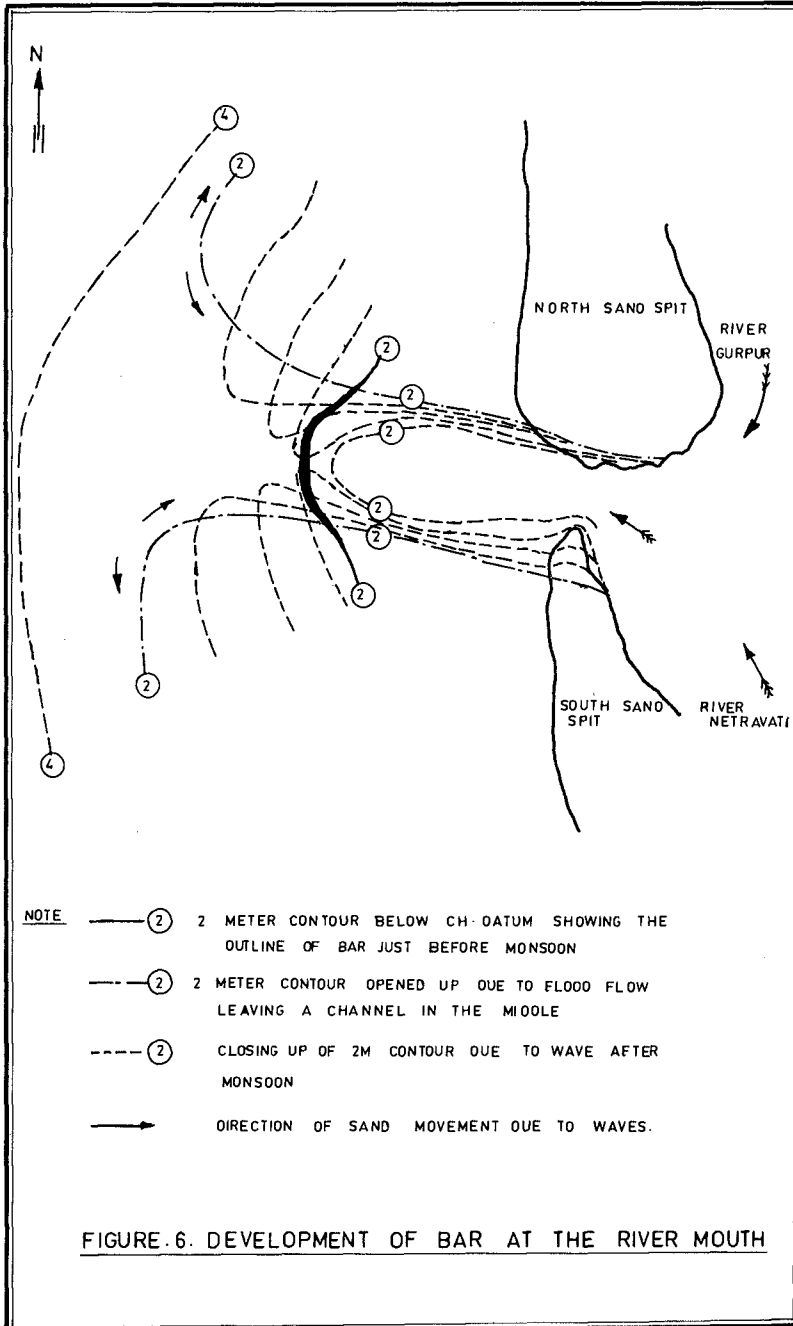
of fresh water discharge to tidal prism to be of the
order of 0.1 or less. This gives the values of 49 m^3/s.
and 24.5 m^3/s. for the discharge for a spring tide and
average tide respectively. The summer flows in both the
rivers are found to be obviously less than these quanti-
ties. Hence during most part of the year, i.e., from
November to end of May, the estuary is in a well-mixed
stage. During this period, the salinity is found to in-
trude about 20 km. in the river Netravati and to about
15 km. in the river Gurpur. Particularly no sediments
are being brought into the river from the catchment area,
outside the monsoon season. Also the bed materials of
the river are not affected by tidal velocities. But the
real problem to be considered at this time is not the
action of salinity on the upland sediments, but due to
the sediments brought in from the sea by tidal action.

        As explained earlier, there are two types of
tides, viz., type 'A' and type 'B' prevalent in the es-
tuary. It can be seen that for type 'A' the larger range
occurs from higher high to lower low. This means that
the larger velocities occur at the ebb flows in a tide.
In the case of type 'B' tides, the larger range is noti-
ced when the tide rises from a lower low to a higher
high. This means that for this type of tides, the flood
flow will have larger velocities. From the number of
different types of tides, already given, it can be seen
that for two-third portion of the year flood velocities
are predominant and for one-third portion of the year ebb
velocities are predominant. A similar type of study has
been conducted for the West Coast of U. S. (7). In this
estuary the flood currents are stronger than those during
the ebb. This aspect is a major factor which affects the
sedimentation in the estuary.

                    OFF-SHORE BAR

        The bar that is formed at the mouth of the
estuary is of the form as shown by the 2 m. contour in
Fig. 6. In the pre-monsoon survey it was like a wall
built across the gut. The floods had breached the bar and
a wide channel of 4 m. depth carved through the barrier.
The materials had spread out like a fan. No appreciable
changes in the 4 m. and 6 m. contours were noticed. The
bar is again rebuilt by the waves after the floods
receded. The extent to which the bar is broken depends
on the intensity of peak discharge during the monsoon
season.

                'PALIKE' OFF MANGALORE COAST

        'Palike' is a fascinating phenomenon observed
along the Mangalore Coast. The name 'Palike' is locally

used for the condition of the sea when it becomes calm
locally at some regions, when all other regions are rough.
These calm regions are noticed at certain locations, last-
ing for a few days only. The appearance of large quantity
of semi-decayed leaves and twigs is associated with the
formation of these calm regions. These leaves are frag-
ments say 1 cm. to 2 cm. in size. They are deposited on
the shore by the waves in large heaps, sometimes 1 m. to
1.5 m. in thickness. These leaves are partially decayed
and black in colour. At the surf zone the waves are stir-
ring up a huge quantity of leaves which gives a black tinge
to the water. Fishermen throng to such areas to fish in
the calm waters, as they find it hazardous to go elsewhere
into the sea due to rough weather.

        In this connection, the mud banks along Kerala
Coast (6) has to be mentioned. These mud banks get stir-
red up during heavy storms and the mud is thrown in sus-
pension creating a viscous medium. The waves passing
through this get dampened, thus creating a zone of rela-
tively calm area. But no report of the occurrence of
leaves has been made in this connection.

        Regarding 'Palike', the local people had differ-
ent versions of explanations and experiences to quote.
Some reported of having experienced a strong current lead-
ing into the calm region from one side and diffusing out
through the other sides. They explained that the leaves
are found at the exit of these currents. Some reported
the presence of clusters of leaves and clay which gave
a spongy reaction when prodded with a sounding rod. Lumps
of leaves loosely cemented together by clay particles are
seen floating on the water, and are washed ashore on the
beach.

        A possible explanation for the large deposition
of leaves would be that they are brought down by the
floods of the season and are deposited on the shore by
waves. But this seems highly improbable as the 'Palike'
leaves are in small pieces and separated from the twigs
and in a semidecayed condition.

        There are a number of rivers on the west coast
discharging an enormous quantity of water into the sea.
They carry bed load, suspended load and floating debris.
The suspended sediments and the floating debris do not
settle down fast. They are carried by the ocean currents.
When they reach regions with eddies, the suspended sedi-
ments and debris will be just sucked in. In such pockets
flocculation takes place and clay particles settle down.
In this downward movement, they stick to the leaves and
weigh them down. The large percentage of leaves inside
the clay mass prevents the development of cohesive bonds
between the particles. Deposits of this type may be

accumulated in a few isolated places. The violent storm
waves will stir up the heap of loosely held material.
The leaves will start floating in the water. The presence
of such large quantity of flaky pieces of leaves and clay
particles thrown into suspension will dampen the waves in
the area. Some of these leaves may be thrown off the
mass and carried to the shore. Thus the leaves brought
to the shore may be only a portion of a large mass, which
is situated away from shore.

CONCLUSIONS

The estuary is subjected to a number of pheno-
mena such as tides, ocean currents, littoral drift etc.
A qualitative study of these inter-related and unsteady
features and their combined effect on the estuary is made.
On the basis of the study, the following conclusions can
be drawn.

1. The river Gurpur might have joined the sea
independently at some place north of the present position.

2. After it has joined the river Netravati as at
present, the river mouth is migrating gradually towards
north, as is seen from the comparison of maps shown in
Fig. 2.

3. The limit specified by Ippen (5) for a well-
mixed estuary is satisfied by the estuary for most part of
the year.

4. A horse-shoe shaped submerged bar is formed
at the mouth of the estuary after the monsoon, which is
broken during the subsequent monsoon to allow flood waters.

5. 'Palike' (calm areas within a very rough
sea) is a fascinating phenomenon observed along the
Mangalore Coast.

to Prof. I. V. Nayak and Prof. G. Ranganna for their
encouragement and valuable suggestions. Permission of
the college authorities to publish this paper is appre-
ciated.

REFERENCES

1. Central Water and Power Research Station, Poona,
   'Specific notes on model study of Mangalore Port',
   specific note No. 321/1954, 373/1955, 374/1955 and
   395/1956.

2. Cheryan K. P., 'Site studies of river estuary at
   Mangalore during monsoon period 1968', thesis sub-
   mitted to the University of Mysore, at Mysore, India,
   in 1969, in partial fulfilment of the requirements
   for the Master of Technology in Marine Structures.

3. Cheryan Punnoose P., 'Geological and geotechnical
   study of boring profiles at Panambur', thesis sub-
   mitted to the University of Mysore, at Mysore, India,
   in 1968, in partial fulfilment of the requirements
   for the Master of Technology in Marine Structures.

4. Govt. of India, Ministry of Transport, 'Report on
   the development of a new all weather deep sea major
   port at Mangalore', Vol. I, Part I, March 1965.

5. Ippen A. T., 'Estuary and Coast line Hydrodynamics',
   McGraw-Hill Book Co. Inc., New York, 1966.

6. Moni N. S., 'Study of mud banks along the south
   west coast of India', Proceedings of the twelfth
   Coastal Engineering Conference, ASCE, Washington
   D. C., 1970.

7. Simmons H. B., 'Field experience in Estuaries',
   Chapter 16, 'Estuary and coastline hydrodynamics',
   Edited by A. T. Ippen, McGraw-Hill Book Co., Inc.,
   New York, 1966.

· · · · ·

CHAPTER 77

COMPATIBILITY OF BORROW MATERIAL FOR BEACH FILLS

by

R. G. Dean[1]

ABSTRACT

A simple method is presented for estimating the relative compati-
bility of borrow material being considered for beach fill purposes.
The method defines the "compatible" fraction of the material as that
coarser portion with the same mean diameter (in "phi" measure) as the
native material on the beach. A single graph is presented which allows
determination of the number of units of borrow material required to
obtain one unit of compatible material. Use of this method requires
that the size distributions be reasonably represented by the "log-
normal" relationship and also requires knowledge of the means of the
native and borrow materials and the standard deviation of the borrow
material (all in phi measure). This method overcomes shortcomings of
the Krumbein-James method published in 1965. Several examples are pre-
sented illustrating the application of the method presented in this
paper.

INTRODUCTION

The problem of arresting the wide-spread erosion along many of the
valuable shorelines of the world represents a major challenge to the
engineer and coastal planner. The recent evaluation of shoreline con-
ditions entitled "National Shoreline Study"(1) conducted by the U. S.
Army Corps of Engineers in 1972 established a first "remedial cost" of
1.8 billion dollars to restore the "critically eroded" beaches and an
annual maintenance cost of 56 million dollars thereafter. Due to the
accelerating development along the shoreline, this cost will continue
to increase in the future.

The value of high-quality beaches for recreation and protection
against extreme storm waves is well-established. For example, in Florida,
tourism is the largest industry representing an income of 3 billion
dollars a year. Surveys conducted by the Florida Department of Commerce
have shown that over 70% of the tourists cite beaches as the single
feature providing the greatest enjoyment during their stay. The pro-

---

[1]Professor, Coastal and Oceanographic Engineering Laboratory,
University of Florida, Gainesville, Florida 32611.

tection provided by a natural beach-dune system functions by providing a "reservoir" of sand which, under high wave attack, is eroded and transported offshore where it is alternately stored in a "storm bar". Although the formation of this bar is at the expense of the beach-dune system, the build-up of this bar is self-limiting. As the bar crest increases in elevation, it causes the incoming waves to break, thereby limiting the wave energy attacking the beach dune, see Figure 1. If a protective
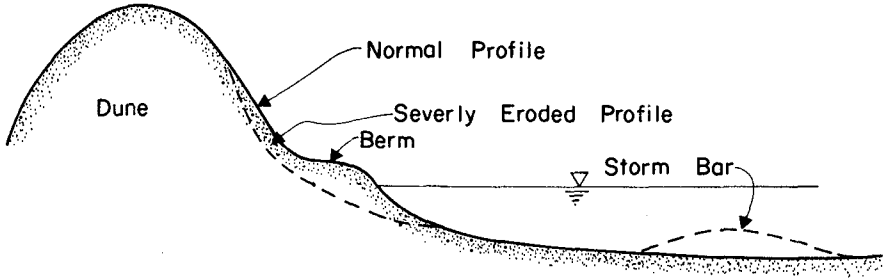
FIGURE 1   NORMAL AND SEVERLY ERODED BEACH PROFILES

beach and dune system are not present, and, if instead, a protective seawall is installed,there is no equivalent "reservoir" of sand and the storm waves will cause erosion immediately in front of the seawall. If there is insufficient material to build the bar, the waves will continue unattenuated to scour the foundation and may lead to eventual collapse. Following a storm, the ensuing normal wave conditions will cause the bar to be transported ashore with eventual rebuilding of the berm and, over several years, the combined action of long waves, high tides, onshore wind and vegetation will reconstruct and heal the dune system, thereby restoring the protective supply of beach material.

In many past cases, the policy of coping with beach erosion has been on a rather piece-meal basis in which individual home owners or small groups of home owners attempt to arrest their localized beach erosion problem. Generally, an unusually severe hurricane or other storm can cause major recession of the shoreline and significant loss to upland structures. The lack of effectiveness of these piece-meal efforts is evidenced in Florida by many lots platted in areas that are now underwater and by a number of landward displacements of the coastal highway which follows the shoreline. An extreme example is provided by the north end of Jupiter Island, where the average recession is 40 feet per year since St. Lucie Inlet was cut in 1892(2).

Recent planning inducates that more effective beach erosion control programs may be implemented within the present decade. Beach restoration and periodic nourishment maintenance is probably the most attractive method of beach erosion control. A number of such projects of limited

extent have been carried out. To date in Florida, there have been seven
such projects encompassing beach segments ranging from 0.6 miles to 3.2
miles in length. Ideally such projects should be based on a coastal
physiographic unit, such as between inlets or between headlands. Addi-
tionally it may be desirable (more economical) to include structural
stabilizing components as an integral part of the project to reduce
losses, especially at such places as inlets. Unfortunately beach res-
toration and maintenance projects, involving the placement of massive
volumes of sand on the beach, are expensive, usually costing on the
order of one-half to one million dollars per mile. The authorized Miami
Beach project is probably the most expensive planned to date and is
expected to cost between four and five million dollars per mile for a
ten mile segment of shoreline.

The high costs of beach restoration and the probable scale of
future nourishment programs, as indicated in the aforementioned National
Shoreline Study, demands a much better general understanding of littoral
processes and, in particular, a greatly improved capability to reliably
predict the performance of beach fills. Ideally, for a placed fill of
particular material characteristics and dimensions, one should be able
to predict the evolution of the shoreline and the transport and dis-
position of the fill material. Reliable prediction of beach fill per-
formance would aid the engineer and the public agency providing the
funds and would also lead to a more rational judgement regarding the
allocation of budgeted funds to additional fill vs. stabilization
structures. Needless to say, predictions are also necessary to allow
proper budgetary planning for future beach maintenance operations.

The present shortcomings in our ability to carry out such predic-
tions reflects not only an inadequate knowledge of littoral processes,
but a dearth of information regarding the "wave climate" affecting the
shoreline and the performance of existing beach fill projects; in
particular, data concerning wave direction are lacking. There have been
surprises in the expected vs. realized performance of beach fills and
the present capability to predict loss rates is probably only within
a factor of two or three. There are attempts(3),(4) to cast available
knowledge in the framework of numerical models to represent shoreline
response under prescribed wave conditions; however, at present such
efforts must be considered rudimentary and unverified.

One of the key elements in predicting beach fill performance is in
evaluating differences in transport rates between the placed ("borrow")
material and the "native" beach material. Present beach nourishment
projects generally plan to use offshore sources of material and while
material is generally plentiful, it is usually of a lesser quality
(i.e. finer) than the native beach sand. The problem then arises of
rationally selecting between a nearshore finer material or an alternate
more costly borrow area of more suitable size distribution.

This paper is concerned with the "compatibility" of beach sands
and presents a method for determining the amount of required borrow
material to yield one unit that is consistent with the native material.

While it is tempting to refer to this fraction as a retention percentage, this is misleading and is not the case; hence the term "compatibility" signifies consistency from consideration of correspondence with native sand characteristics.

REVIEW OF PREVIOUS WORK

Krumbein and James(5)(K-J) have developed a procedure for evaluating the compatibility of borrow materials which have certain properties relative to the native material. In particular, their method is applicable if the native sand is better sorted than the borrow material. There are features of the K-J approach which limit its use and which are not consistent with our knowledge of beach processes. First, if the borrow material is better sorted than the native material, the method simply does not apply. This may be the case where dune sand is being considered as the borrow sand or where an offshore bar or relic submerged beach of well-sorted material is being considered. Secondly, the compatibility as defined in the K-J model requires the portion of the retained borrow material to have exactly the same size distribution as the original native material. This assumption implies that both finer and coarser fractions of the borrow material will be "lost". It is this feature that is not consistent with knowledge of littoral processes and that results in an unrealistically pessimistic expectation of the suitability of borrow material which contains considerable quantities of material coarser than the native sand. In the following paragraphs, the method of K-J will be reviewed briefly.

Krumbein and James found it convenient to describe sand size in "phi" (ϕ) units, where

$$\text{Size in } \phi \text{ units} = -\log_2(D) \tag{1}$$

and D is the sand diameter in millimeters. Furthermore their method is applicable for sand size distributions, $f(\phi)$, which are reasonably well approximated by a so-called "lognormal" relationship, i.e.

$$f(\phi) = \frac{1}{\sigma\sqrt{2\pi}} e^{-(\phi-\mu)^2/2\sigma^2} \tag{2}$$

in which μ and σ represent the mean and standard deviation respectively of the sand size distribution, both measured in phi units. Figure 2 is reproduced from Krumbein-James and portrays the distributions of two sands and their lognormal approximations which are straight lines on the arithmetic probability paper.

As stated previously, the K-J model requires that the retained portion of the borrow material have exactly the same distribution as the native material. This leads to definition of a "critical phi ratio", $R_{\phi_{crit}}$ which represents the required placed weight units of borrow material to result in one weight unit of "retained" material with
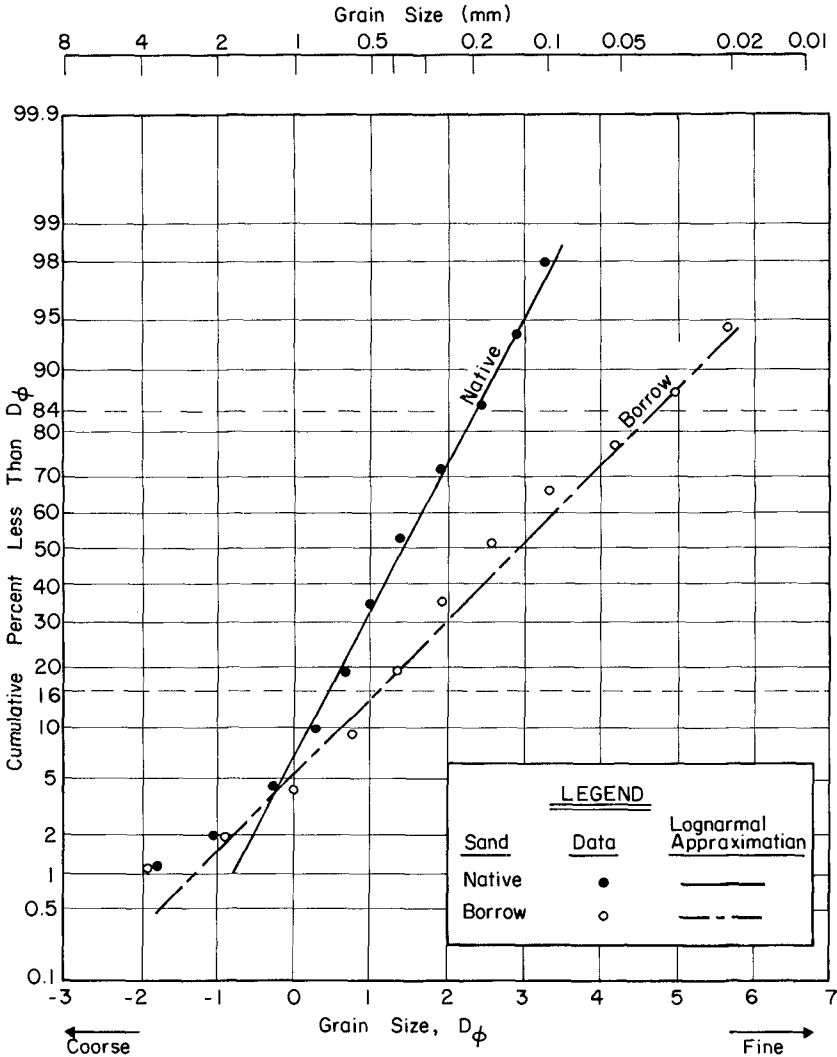
FIGURE 2   LOGNORMAL DISTRIBUTION APPROXIMATIONS TO NATIVE AND BORROW SANDS IN VIRGINIA BEACH, VIRGINIA NOURISHMENT PROJECT (FROM REFERENCE 5)

exactly the same distribution as the native material. This ratio can be shown to be

$$R_{\phi_{crit}} = \frac{\sigma_{\phi_b}}{\sigma_{\phi_n}} e^{-(\mu_{\phi_n} - \mu_{\phi_b})} /2(\sigma_{\phi_n}^2 - \sigma_{\phi_b}^2) \tag{3}$$

where the ϕ subscripts emphasize that μ and σ are in ϕ units. For the Virginia Beach, Virginia example presented in Figure 2, $R_{\phi_{crit}}$ is calculated to be

$$R_{\phi_{crit}} = 3.09$$

Figure 3 is a graphical presentation of the supposed effect on the borrow material to render it compatible with the native in accordance with the K-J method. It is noted that losses of the borrow material have occurred both in the coarse and fine fractions with the greater losses (for this case) in the finer components. The only diameter at which losses do not occur is at ϕ_{crit} where the original ratio of borrow to native distributions is 1:3.09. After the supposed losses occur, the ratio of retained borrow material to native material is 1:3.09 for all diameters. Of particular concern is the implied losses of the coarser fraction and this would be of greatest numerical significance in cases where the mean diameter of the borrow material (in millimeters) was greater than that of the native material. One of the objectives of the method to be described subsequently is to remove this unrealistic feature present in the K-J approach.

METHOD

The required method must establish a realistic equivalence between the native material and the retained fraction of the borrow material. In particular, the method should allow for losing the fine fraction of the borrow that is not present in the native material; however, the coarser fraction in the borrow will be considered to be "compatible". In general, the compatibility will be based on equivalence of the mean diameter of the altered borrow and native sands. In the following a lognormal distribution of the form of Equation (2) will be considered. The reader is cautioned that the μ and σ variables are in ϕ units.

The native and original borrow size distributions will be denoted as $f_n(\phi)$ and $f_b(\phi)$ respectively and the "altered" borrow distribution as $f_{b_a}(\phi)$. The consideration that the finer fractions of the borrow material will not be "compatible", results in the altered size distribution being expressed as

$$f_{b_a}(\phi) = \begin{cases} Kf_b(\phi) & , \quad \phi \leq \phi_* \\ 0 & , \quad \phi > \phi_* \end{cases} \tag{4}$$

a.) Sand Size Distributions (Native and Original and Altered Borrow)

Sand	μ^*	σ^*
Native	1.5	0.91
Borrow	2.96	1.76

* In Phi Units
$K_1 = 3.09$
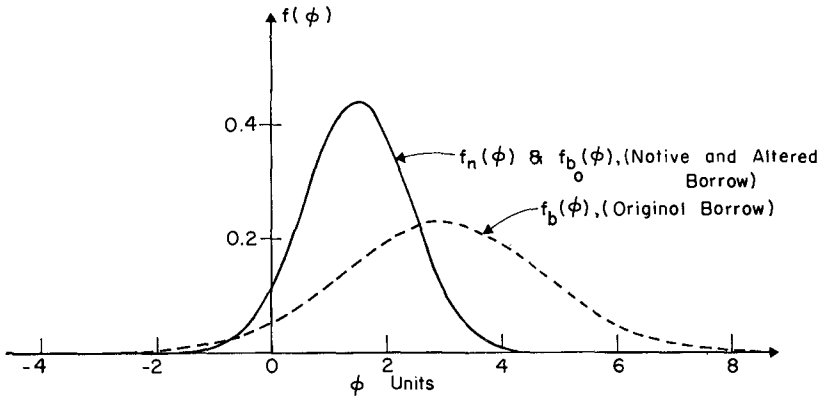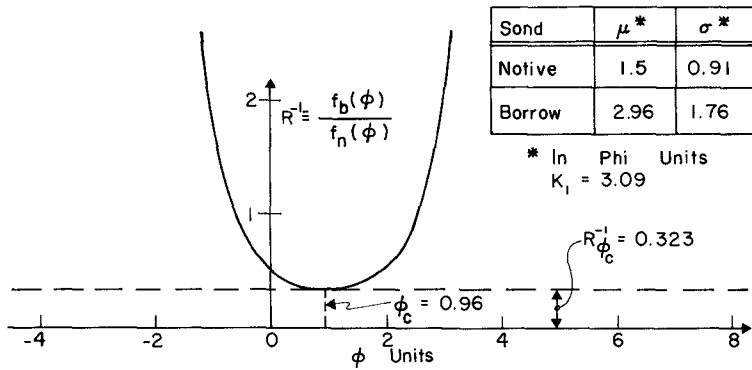
b.) Ratio of Sand Size Distributions

Coarse ← → Fine

FIGURE 3   EXAMPLE OF KRUMBEIN-JAMES METHOD APPLIED TO THE VIRGINIA BEACH FILL $(\sigma_b > \sigma_n)$

where K and ϕ_* are constants selected such that $f_{b_a}(\phi)$ represents a normalized distribution with the same mean diameter as the native sand. The problem posed is in establishing K and ϕ_* for any given native and original borrow sand size characteristics and in interpreting the results in terms of the compatible fraction of the borrow sand.

The normalized distribution requirement is expressed as

$$\int_{-\infty}^{\infty} f_{b_a}(\phi)d\phi = K \int_{-\infty}^{\phi_*} f_b(\phi)d\phi = \frac{K}{\sigma_b \sqrt{2\pi}} \int_{-\infty}^{\phi_*} e^{-(\phi-\mu_b)^2/2\sigma_b^2} d\phi = 1 \qquad (5)$$

and the requirement that the altered distribution mean diameter be at least as large as the native mean diameter is

$$\int_{-\infty}^{\infty} \phi \, f_{b_a}(\phi)d\phi \leq \mu_n$$

or

$$\frac{K}{\sigma_b \sqrt{2\pi}} \int_{-\infty}^{\phi_*} \phi \, e^{-(\phi-\mu_b)^2/2\sigma_b^2} d\phi \leq \mu_n \qquad (6)$$

For a given situation of fixed borrow and native sand characteristics, Equations (5) and (6) are two relationships involving the two unknowns, K, and ϕ_* associated with the altered borrow distributions. These equations include three parameters (μ_n, μ_b, σ_b) characterizing the native and borrow sands. It is useful to reduce the number of parameters to two by introducing dimensionless quantities defined by

$$\phi' \equiv \frac{\phi}{\sigma_b}$$

$$\mu' \equiv \frac{\mu}{\sigma_b}$$

Equations (5) and (6) can be rewritten in terms of dimensionless quantities and integrated to yield

$$\frac{K}{2}[1 + \text{erf}(\phi'_* - \mu'_b)] = 1 \qquad (7)$$

$$\frac{K}{\sqrt{2\pi}} e^{-(\phi'_* - \mu'_b)^2/2} \geq \mu'_b - \mu'_n \qquad (8)$$

where the error function "erf (x)" is defined as

$$\text{erf }(x) = \sqrt{\frac{2}{\pi}} \int_0^X e^{-t^2/2} \, dt$$

and t is a dummy variable of integration. It is noted that Equations (7) and (8) now involve only two dimensionless parameters, μ_b' and μ_n' characterizing the size distribution characteristics of the native and original borrow sands.

An iterative computer solution of Equations (7) and (8) was employed to determine K and ϕ_* for a fairly wide range of μ_b' and μ_n'. Although the parameter ϕ_* is determined in the solution, it is the quantity K that is of primary interest. It will be shown next that K represents the number of units of borrow material that must be placed in order to retain one unit of compatible fill.

Referring to Figure 4, the fraction of the original borrow material
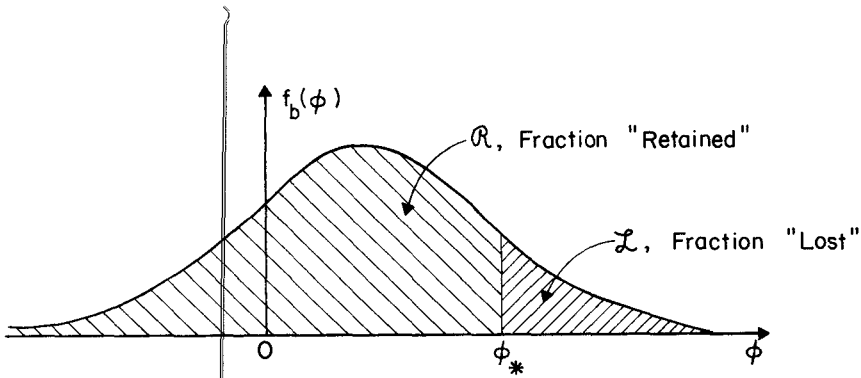
FIGURE 4   PORTIONS OF ORIGINAL BORROW MATERIAL
            "RETAINED" AND "LOST"

that is compatible with the native sand is defined as $\mathcal{R}$, where

$$\mathcal{R} \equiv \int_{-\infty}^{\phi_*} f_b(\phi) \, d\phi \tag{9}$$

but from Equation (5)

$$K\int_{-\infty}^{\phi\star} f_b(\phi)d\phi = 1 \tag{10}$$

These two equations establish the following reciprocal relationship between $\mathcal{R}$ and K, i.e.

$$\mathcal{R} = \frac{1}{K} \tag{11}$$

Therefore, for a particular example in which the native and borrow sands result in a value $K = 4$, only 25% of the borrow material is compatible. Stated differently, for this example it would be necessary to place 4 units of borrow material on the beach to yield one unit of material compatible with the native sand. In general, the quantity K represents the number of units of borrow material placed on the beach that is required to yield one unit of material compatible with the native material.

Figure 5 presents isolines of K as a function of μ_n' and μ_b'. The semi-logarithmic plot was chosen as it was found that each of the isolines of K on the semi-log plot is simply a vertically-displaced form of any of the other isolines. For $\mu_n' > \mu_b'$ (i.e. the borrow material is coarser than the native), 100% of the borrow material is compatible by the criterion utilized in this paper. In the case where the borrow mean diameter is less than the native, Figure 5 provides a useful means of determining the compatibility.

EXAMPLES ILLUSTRATING APPLICATION OF THE METHOD

Example 1

Consider the case of the beach fill at Virginia Beach, Virginia. The native and borrow material characteristics have been presented by Krumbein and James(5) as presented in Figure 2; these characteristics are also given in Table I for reference. Using the Krumbein-James method,

TABLE I

SIZE CHARACTERISTICS OF THE VIRGINIA BEACH, VIRGINIA
NATIVE AND BORROW SANDS

Sand	$\mu^\star$	$\sigma^\star$
Native	1.5	0.91
Borrow	2.96	1.76

$\star$ In Phi Units
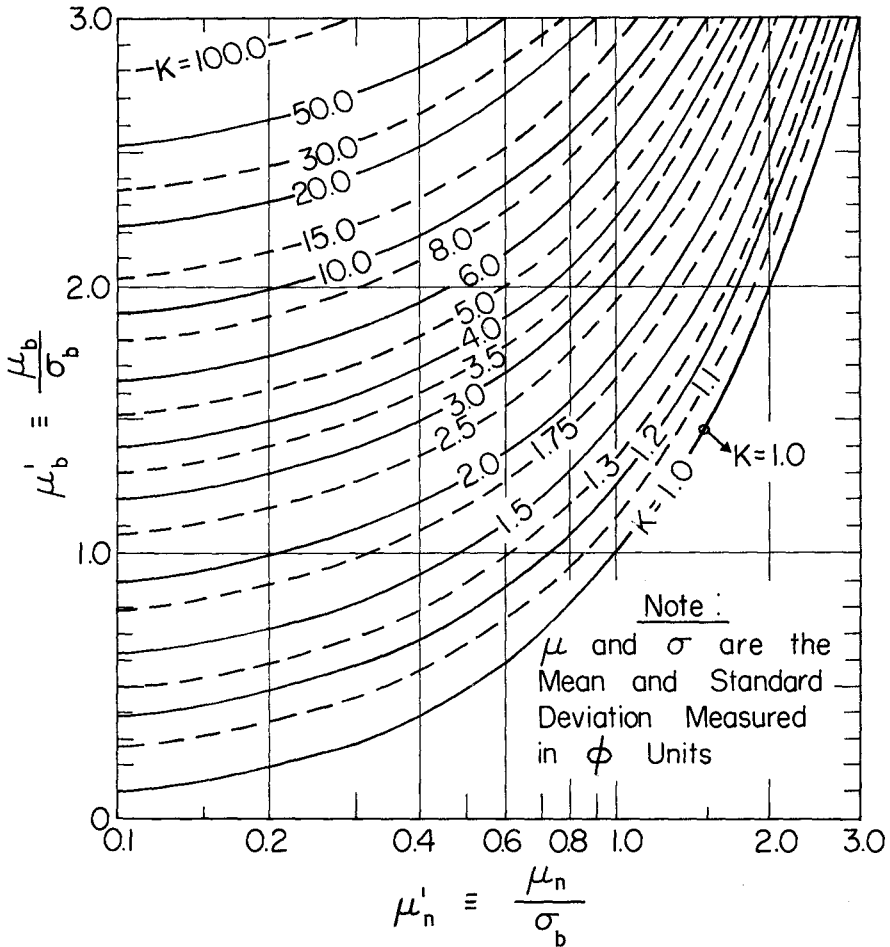
FIGURE 5 REQUIRED REPLACEMENT VOLUME, K, OF "BORROW" MATERIAL TO OBTAIN ONE UNIT OF "COMPATIBLE" BEACH MATERIAL

a required volume of 3.09 units of borrow material is indicated to retain one unit on the beach. For the method presented in this paper, a value of 2.05 is determined for K. It is recalled that the K-J method considers that portions of both the coarser and finer fractions are somehow winnowed out from the original material placed whereas the present method considers "losses" only from the finer fraction of the borrow material. These different considerations are primarily responsible for the spread from 2.05 to 3.09; differences of this magnitude could be important in evaluating the economic feasibility of a beach nourishment project.

Example 2

As a second example, consider the narrow beach north of St. Lucie Inlet, Florida (shown as the inset in Figure 6) and suppose that it is desired to consider two sand sources for possible fill purposes along the beach north of the inlet. The size characteristics of a sand sample taken from the beach face and degree of approximation by a lognormal distribution are presented in Figure 6. Figure 7 presents the lognormal distributions from two possible source areas in the inlet area. The table inset in Figure 7 presents the size characteristics of the native and borrow sands and the K values for the two borrow sands. It is seen that 1.4 units of Borrow "1" material would be required to result in one unit of compatible material; because the diameter of Borrow "2" material is greater (less in phi measure) than the native material, all this borrow material is compatible. If compatibility as defined in this paper were considered to be a measure of retention, these results would provide a good basis for evaluating the cost effectiveness of, for example, borrow sources which are more expensive on a unit volume basis but which possess better retention characteristics.

SUMMARY

A method has been presented for evaluating the compatibility of borrow material with the native sand on the beach. Compatibility as used here relates to that coarser fraction of the borrow material which has a mean diameter equal to or greater than the native material. The method also requires that the native and borrow sands be reasonably represented by a lognormal relationship and that the size characteristics of these sands be known. A single figure presents the number of units of borrow material required to yield one unit compatible with the native sand. Although the method does not address the important question of loss rate, it should be useful in providing a quantitative basis for evaluating various possible borrow areas for beach nourishment purposes.

ACKNOWLEDGEMENT
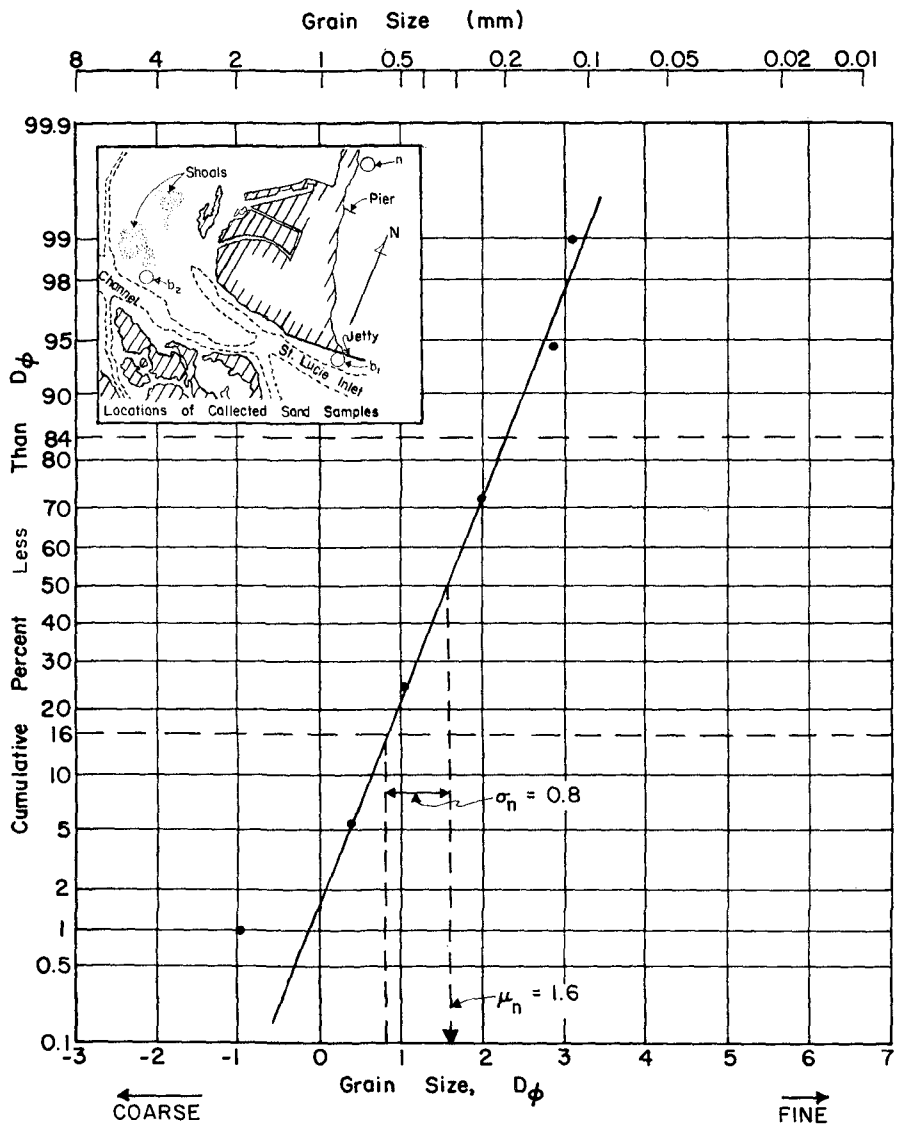
FIGURE 6 SAND SIZE DISTRIBUTION FOR "NATIVE" SAND
NEAR ST. LUCIE INLET, FLORIDA
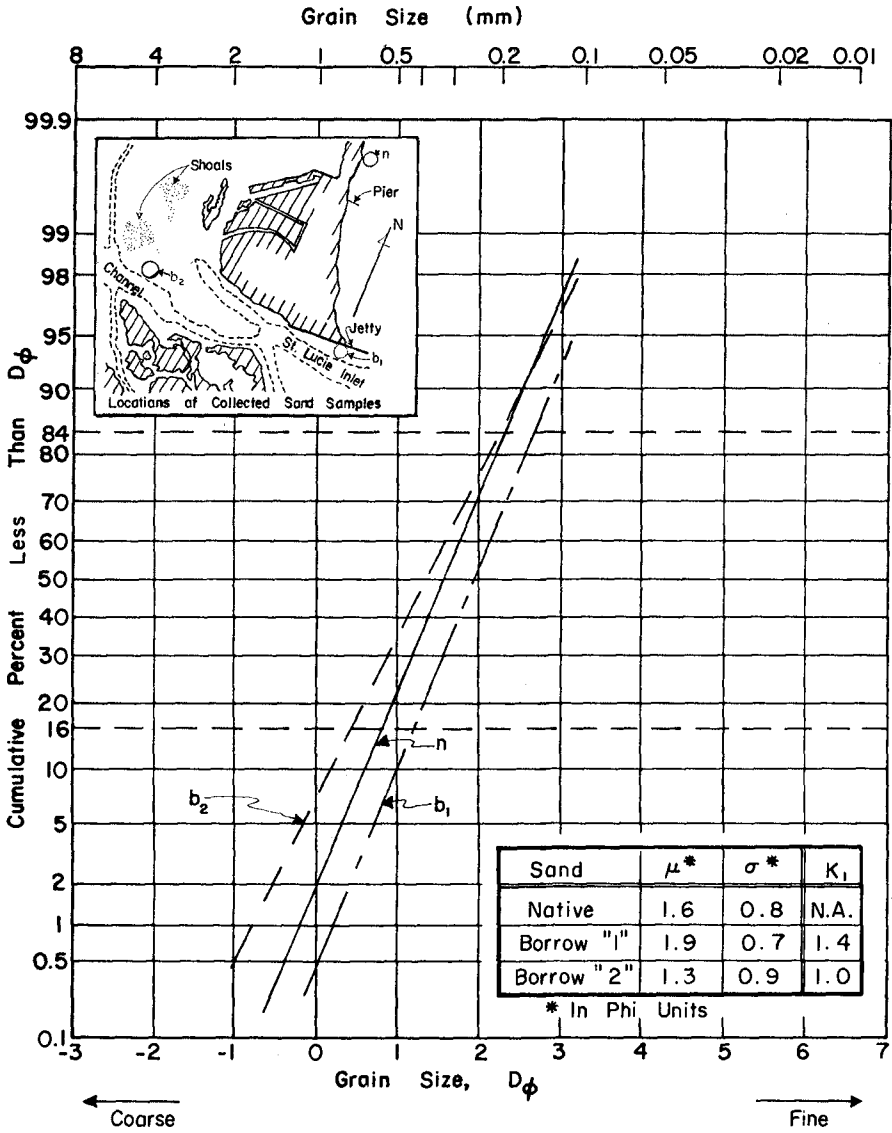
FIGURE 7   EVALUATION OF "COMPATIBILITY" OF TWO POSSIBLE BORROW MATERIALS WITH NATIVE BEACH SAND. AREA NEAR ST. LUCIE INLET, FLORIDA

REFERENCES

1. U. S. Army Corps of Engineers, "Report on the National Shoreline Study," Department of the Army, Washington, D. C., August 1971.

2. U. S. Army Corps of Engineers, "Survey Review Report on St. Lucie Inlet, Florida," Jacksonville District, August 1965.

3. Price, W. A., K. W. Tomlinson and D. H. Willis, "Predicting Change in the Plan Shape of Beaches," Chapter 72, Proceedings, Thirteenth Conference on Coastal Engineering, Vancouver, B. C., p. 1321-1330, 1972.

4. Le Blond, P. H., "Formation of Spiral Beaches," Chapter 73, Proceedings, Thirteenth International Conference on Coastal Engineering, Vancouver, B. C., p. 1331-1346, 1972.

5. Krumbein, W. C. and W. R. James, "A Lognormal Size Distribution Model For Estimating Stability of Beach Fill Material," Technical Memorandum No. 16, U. S. Army Coastal Engineering Research Center, Washington, D. C., November 1965.

CHAPTER 78

Beach Fill Stability and Borrow Material Texture

William R. James
U.S. Army Coastal Engineering Research Center
Kingman Building
Fort Belvoir, Virginia 22060

ABSTRACT

The dependence of beach fill stability on the textural properties of borrow material requires development of quantitative methods for use in selection of borrow areas and in prediction of possible maintenance costs associated with periodic renourishment. If a shore segment is viewed as a sediment mass transfer system, where grains of different size have different transport rates, then termination of natural sediment input to the shore segment will cause the beach to retreat and the materials in the active zone will become coarser. The ratio of retreat rates associated with a given borrow material texture to that associated with native material can be used in optimizing economic factors involved in selection among potential borrow zones.

With certain simplifying assumptions the relative retreat rate associated with a given borrow material texture can be predicted from observations of the modifications in textural properties of native material which occur during the eroding condition following termination of the natural supply of sediment. Further simplifying assumptions result in an analytical expression for relative retreat rates which may not require observations of the natural beach in the eroding condition.

The proposed method is in substantial agreement with qualitative guidelines provided in the Shore Protection Manual [2].

INTRODUCTION

Artificial beach nourishment is a commonly utilized approach for treatment of a beach or shore erosion problem. It is the most direct method for maintaining and improving recreational benefits in shore protection projects. It is also widely used for emergency storm protection in areas where source materials are readily available. This latter use is due primarily to favorable construction costs as compared to alternatives and the simplicity and speed of construction. However, the precise degree of effectiveness of beach fill utilized to stabilize a shore erosion problem is not always predictable. Some projects have suffered severe losses of fill material during the construction phase itself, with an end result of little or no improvement over the pre-existing conditions.

One of the major factors controlling the stability of a beach fill is the texture of the borrow material. Fine, well-sorted borrow material, such as that commonly found in bays, backshore dunes, or the bottom surface of the offshore zone, will generally respond rapidly to wave and current conditions, moving alongshore and offshore out of the project area. Material of this type is generally not suitable for use as beach fill. On

the other hand, coarse, more poorly-sorted material, such as that found in alluvial channels, glacial outwash, and sometimes in offshore shoals, tends to provide more stable beach fills, although the resulting beach is not always ideal for recreational purposes. Clearly, there is a need to develop means of predicting the relative stability of borrow material from potential sources.

DISCUSSION OF PREVIOUS WORK

An early attempt to develop such a method of prediction was made by Krumbein and James [1]. They proposed a simple mathematical model which bases predictions of grain size effects on a direct comparison between the grain size distribution of the native littoral zone materials and that of a potential borrow material. Their basic assumption is that the native material is essentially in equilibrium with local shore processes and hence can be used to predict the stable grain size distribution which will result from sorting modifications to the borrow material. They define a ratio quantity which represents the minimum volume of borrow material required to manufacture, through selective removal of borrow material from individual size classes, a unit volume of material having the same grain size distribution as the native material. Where both native and borrow materials are approximately lognormally distributed an analytical solution is presented, based on the phi means and phi sortings of the two distributions.

Qualitative and quantitative guidelines based on this model appear in the Shore Protection Manual [2], recently published by the U.S. Army Coastal Engineering Research Center. Figure 1, reproduced from the Shore Protection Manual, shows contours of predicted overfill ratios plotted against dimensionless scales of differences between phi means and phi sortings of native and borrow materials. (The phi grain size measure is the negative logarithm, to base 2, of grain diameter in millimeters, so that larger phi means indicates finer sand. The phi sorting is the square root of the central second moment of the grain size distribution on the phi scale). The horizontal axis represents the relative difference in phi means between borrow and native materials scaled by the phi sorting of the native material grain size distribution. The vertical axis, plotted on a logarithmic scale, represents the ratio of borrow material phi sorting to native material phi sorting. In this figure the origin, plotted at the center, represents the point at which phi means and phi sorting values for both native and borrow material grain size distributions are the same. The area to the right of the vertical axis represents the conditions in which borrow material has a finer, or higher, phi mean than the native material. Conversely, the condition in which borrow material is coarser than native material is represented by the region to the left of the vertical axis. The region above the horizontal axis represents the conditions in which borrow material is more poorly sorted, or more well graded, than the native material, and the region below the vertical axis represents the conditions in which borrow material is better sorted, or more poorly graded, than the native material. It should be noted that no curves are plotted for this latter condition. This is because it is not mathematically possible to
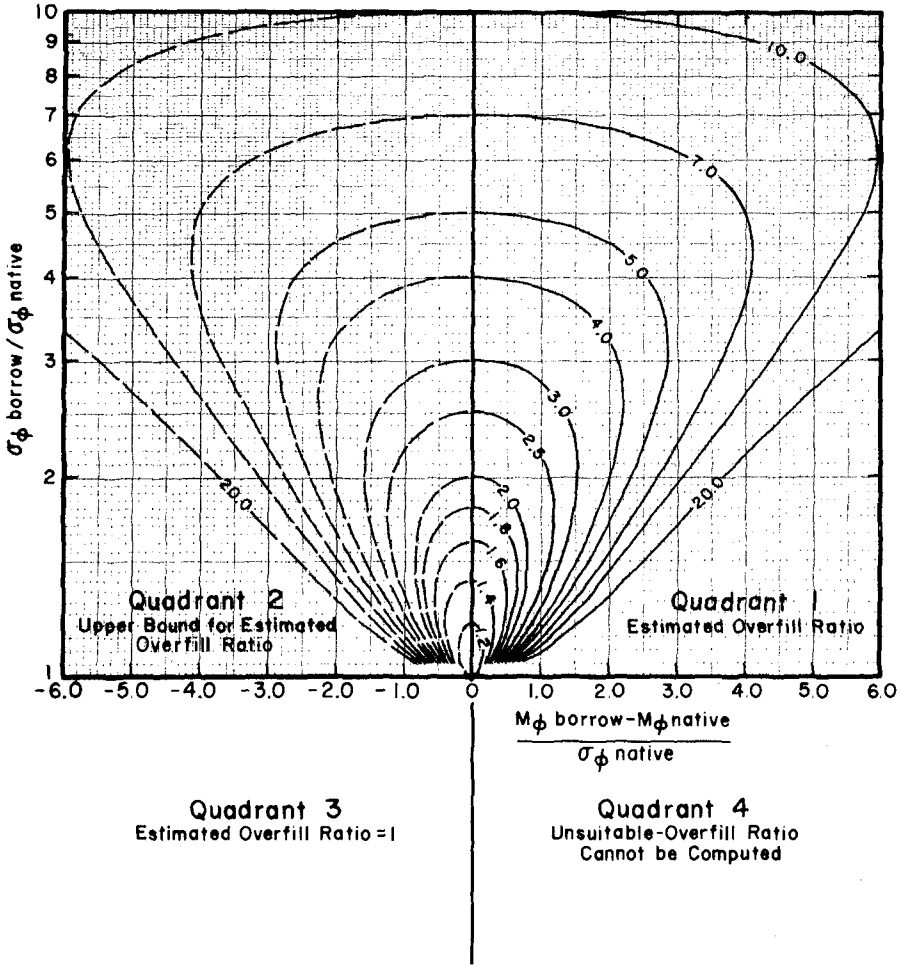
Figure 1. Overfill ratio curves plotted against relative difference
           in phi means and ratio of phi sorting of borrow and native
           materials (after SPM, 1974).

produce a lognormal grain size distribution with poorer sorting than that of the original material by selective removal of material. In a more practical sense it means that in the condition of well-sorted borrow material and poorly-sorted native material there will be size classes of the native material grain size distribution for which no material is available in the borrow material grain size distribution.

The inability of this model to predict overfill ratios in this condition represents a major shortcoming of the method. For well-sorted borrow materials the present guidelines are that if the borrow is coarser than native material, an overfill ratio of unity is assumed, and if borrow material is finer than native material it is deemed unstable or unsuitable. A similar difficulty arises in the condition where borrow material is more poorly sorted than native material. Note that the overfill ratio contours are symmetrical about the vertical axis. This means that the calculated overfill ratio is insensitive to the sign of the difference in phi means between borrow and native materials. This is to say, the calculated overfill ratio for a coarse borrow material will be the same as that calculated for fine borrow material if the absolute scaled value of the difference in phi means between borrow and native materials is the same. This is probably unrealistic. Experience has demonstrated that coarser fill tends to be more stable than finer fill. Note that the curves to the left of the vertical axis are dashed. Present guidelines state that calculated overfill ratios which fall in this quadrant are to be interpreted as upper bounds rather than actual estimates. Unfortunately, in many practical situations, the available borrow materials are either finer and better sorted than native material, or coarser and more poorly sorted, and in these cases the present quantitative guidelines cannot be applied.

The Krumbein and James model is based on the assumption that all of the fill material will be reworked and sorted by wave action. If the resultant fill is stable, this assumption is only valid if the sorting modifications keep pace with the construction phase of the project. This assumption is probably valid in the special case of feeder beach construction, where the fill is stockpiled updrift of the problem area and allowed to move downdrift by natural mechanisms. However, when the entire beach segment in a project is artificially nourished the construction usually occurs at a pace much greater than the natural sorting processes can fully keep up with. The result is construction of an artificial beach mass with textural properties much more similar to those of the borrow material than to those of the native beach material. In such circumstances only a limited portion of the fill will have been exposed to sorting processes if stability is attained. In such circumstances the overfill ratio will overestimate the excess fill required.

In addition to the above mentioned deficiencies of the Krumbein and James model there may be many situations where the basic assumption underlying their model may be quite inaccurate. When beach fill is used as a shore protection measure it is normally used to remedy an erosive condition rather than to improve a stable one. The erosive conditions may occur due to change in water level or wave climate, or due to the termination or sharp reduction of the natural supply of sediment to the eroding beach segment. The latter event may be due to natural causes or to the construction of littoral barriers such as jetties, breakwaters or groins. When a natural beach is in a state of erosion it may be unrealistic to assume that artificial

nourishment will provide a permanent solution. A wiser approach might be
to plan on periodic renourishment based on predicted erosion rates.
      In this paper a mathematical model is proposed for predicting the
ratio of renourishment requirements associated with a given borrow material
to those which would be associated with use of native material for a beach
fill, given that the natural supply of material to the problem area has
been terminated. This ratio, hereafter called the "relative retreat ratio"
can be used as a guide for evaluating the relative suitability of alternate
borrow sources in the same way as the overfill ratio, as described in the
Shore Protection Manual.

<div align="center">THE GENERAL MODEL</div>

      One may consider a stretch of beach as a sediment cell, with sediment
exchange occurring across the cell alongshore and offshore boundaries. The
mass of sediment within such a cell can be considered to lie within one of
two distinct zones, an active zone within which material is exposed to wave
and current action, and an inactive zone consisting of the backshore and
underlying bed materials. The inactive zone serves as a sediment reservoir
which is tapped as required to maintain an appropriate mass of material in
the active zone in circumstances where the sediment output rate exceeds the
input rate. A simple model for the mass-transfer system is based upon the
following two assumptions: (1) the mass of material acted upon by waves
and currents within the cell is solely determined by the littoral forces.
The mass of sediment comprising the active zone does not depend on the grain
size distribution of the constituent material. (2) The average amount of
time a sediment particle spends in the active zone within the cell depends
upon the size of the grain and the littoral forces acting upon it, but does
not depend on the distribution of grain sizes.
      An equilibrium condition for the mass-transfer system exists when the
mass input rate equals mass output rate for each grain size. In this con-
dition the grain size distribution of the active-zone material remains
constant, and no material is added to or removed from the backshore reservoir.
If this balance is upset, either by reduction in the supply of sediment to
the beach area, or by change in the wave climate or water level, the beach
will retreat or accrete by removal or addition of material to the inactive
reservoir.
      In this paper interest is restricted to the condition of erosion,
especially in the condition of severe erosion which typically follows the
emplacement of beach fill. The placement of fill material on a beach may
be viewed as the construction of an artificial headland, which has the
effect, at least initially, of terminating the natural supply of sediment
to the beach segment, and concentrating erosive wave action on it. The
face of the fill will suffer erosion, and the beach will experience a net
retreat. The grain size distribution of the active-zone material will
coarsen as the finer material is winnowed out at a higher rate than the
coarser material.
      This initial berm retreat is due in part to a natural profile adjust-
ment during which the offshore foundation of the fill is built by natural

mechanisms. However if no natural supply of sand is available, the fill
will continue to experience retreat after the initial profile adjustment.

If littoral processes remain constant, the grain size distribution
of the active material will approach a constant form, and the rate of
retreat of the beach will become constant. This condition is attained
when for each grain size, the system output rate, through winnowing action,
exactly matches the rate of incorporation from the reservoir. In order
to maintain constant mass in the active zone, the rate of incorporation of
material from the reservoir exactly matches the rate of loss through win-
nowing. Then the rate at which grains of a particular size enter the
active zone through incorporation from the reservoir is determined by the
total system output rate and the grain size distribution of the material
in the reservoir, which for the purposes of this application is the borrow
material grain size distribution. The effects of selection of alternative
borrow types can be estimated by comparison of the steady retreat rates
associated with the respective borrow material grain size distributions.

The general model described above can be mathematically represented
in the form of a finite-difference mass balance equation,

$$Mf(\phi,t+\Delta t) = Mf(\phi,t) - w(\phi)\Delta tMf(\phi,t) + f_b(\phi) \int w(\phi)\Delta tMf(\phi,t)d\phi, \qquad (1)$$

which describes the modification of the grain size distribution of active
zone material following emplacement of a fill. If M is the mass of material
in the active zone of the cell and $f(\phi,t)$ represents the grain size distri-
bution of this material at any time t, then the product represents the mass
of material of a given size in the active zone at time t. During the
passage of a time increment of duration Δt, material of various sizes is
removed at differing rates due to the winnowing processes. The function,
$w(\phi)$, here called the winnowing function, describes the differential rate
of erosion associated with particles of various sizes.

This winnowing function may be interpreted probablistically as follows:
the inverse of the winnowing function represents the expected time of
residence that a particle of size ϕ remains in the active zone following
incorporation from the reservoir, and prior to its passage out of the cell
through erosion. The second term on the right-hand side of Equation (1)
thus represents the mass of material of a given size in the active zone
which is removed during the time increment Δt.

The first assumption in the model requires that the mass of material
in the active zone remain constant, under constant littoral forces. There-
fore the amount of material which must be incorporated from the reservoir
in the time increment Δt is given by the integral of this term over all
grain sizes. Inasmuch as the grain size distribution of material in the
reservoir is the borrow-material grain size distribution, (which is not
the same as the active-zone material grain size distribution) the grain
size distribution of the active-zone material will be modified. This
grain size distribution will attain a constant form, and the retreat rate
will attain a constant value, when the material in the active zone attains
the grain size distribution which satisfies the condition given in Equation 2,

$$w(\phi)\, f'(\phi) \;=\; \frac{E}{M} \; f(\phi), \tag{2}$$

where $f'(\phi)$ is the steady-state active-zone grain size distribution associated with the backshore material having grain size distribution $f(\phi)$, and E is the steady retreat rate. This condition states that the product of the winnowing function and the stable active-zone grain size distribution, is proportional to the borrow or backshore material grain size distribution.

In absence of direct knowledge of the winnowing function, $w(\phi)$, and the active-zone cell mass, M, it is not possible to evaluate Equation 2 for the retreat rate, E, in a practical situation. Of course, it is not the intent here to use this model to predict an actual retreat rate, but rather to provide a basis for selection among various types of borrow material. In many situations where beach fill is considered, the beach area is experiencing erosion. In these cases one can use observations on the performance of the native material as a basis for predicting the performance of a proposed borrow material.

Suppose that in some given situation beach erosion is initiated by sharp reduction in, or termination of the natural supply of sediment to the beach area. This could be caused by the construction of jetties or groins, or by natural causes. If one observes the rate at which the beach retreats and the textural properties of the native backshore material and the active-zone materials following initiation of erosion, then one has sufficient information to use the proposed model to predict the performance of a borrow material.

This can be seen as follows. Using Equation 2, the winnowing function may be expressed in terms of the retreat rate associated with the native material, E_n, the grain size distribution of the native material in the backshore, $f_n(\phi)$, and the resulting modified grain size distribution of active-zone native material, $f_n'(\phi)$, as shown in Equation 3a,

$$w(\phi) \;=\; \frac{E_n}{M} \; \frac{f_n(\phi)}{f_n'(\phi)} \tag{3a}$$

Similarly, Equation 2 may be used to express the steady-state active-zone material grain size distribution associated with a borrow material having grain size distribution f_b as shown in Equation 3b,

$$f_b'(\phi) \;=\; \frac{E_b}{M} \; \frac{f_b(\phi)}{w(\phi)} \; . \tag{3b}$$

Substituting Equation 3a into 3b, and integrating over grain size, yields the relation expressed in Equation 4,

$$\frac{E_b}{E_n} = R_b = 1 \left/ \int \frac{f_b(\phi)\, f_n'(\phi)}{f_n(\phi)}\, d\phi \right. . \tag{4}$$

From this equation it is seen that the ratio of retreat rates associated
with borrow and native materials can be determined solely from knowledge
of the borrow material grain size distribution, the native material grain
size distribution, and the modified grain size distribution of native
material in the active zone, observed in the eroding state.

This ratio, here referred to as the relative retreat rate, R_b, can be
used for prediction of the economic consequences associated with use of any
particular borrow material. If for example, two sources of borrow material
are available, but differ greatly in their textural properties, and if one
of these sources of borrow material can be utilized with one half the con-
struction costs of the other, this does not necessarily imply that the less
expensive material is the most economic. The more costly material may be
more stable. Calculation of the relative retreat rates of the two materials
may indicate that the less costly material will retreat at three or four
times the rate of the more costly material, resulting in the requirement for
more frequent renourishment and a higher total maintenance cost.

A SPECIFIC MODEL

In many cases it may not be possible to obtain appropriate data on the
performance of the native material. This may occur where the beach fill is
planned to accompany construction of jetties or other littoral barriers. In
such instances the fill is often planned for the purpose of circumventing
initiation of an erosive condition downdrift of the engineering structure,
as well as for improvement of recreational facilities and shore protection
within the project area. Here the engineer cannot wait to observe the beach
in the erosive condition which he intends to prevent.

With certain simplifying assumptions, observation of the natural beach
in an eroding condition may not be necessary. If the native and borrow
material grain size distributions are approximately lognormal, and it is
assumed that the modified active-zone material grain size distribution will
also be lognormal, and that coarser particles have longer cell residence
times than finer particles, then the winnowing function must be of exponential
form on the phi scale. If the winnowing function is exponential, then the
relative retreat rate associated with a lognormal borrow material having phi
mean $M_{\phi b}$, and phi sorting $\sigma_{\phi b}$ is given by Equation 5,

$$\log(R_b) = \Delta \left(\frac{M_{\phi b} - M_{\phi n}}{\sigma_{\phi n}} \right) - \frac{\Delta^2}{2} \left(\frac{\sigma_{\phi b}^2}{\sigma_{\phi n}^2} - 1 \right), \tag{5}$$

where $M_{\phi n}$, $\sigma_{\phi n}$ are the phi mean and phi sorting of the native material, and Δ
is a dimensionless parameter which is a measure of the selectivity of the
sorting processes as expressed by the winnowing function. The interested
reader can find a derivation of this expression in the appendix.

The parameter Δ. As shown in the appendix, the dimensionless parameter,
Δ, represents the scaled difference between phi means of native active-zone
material observed both prior to and following the establishment of an
eroding condition. Its value reflects the selectivity of the sorting pro-
cesses. A low value means that the natural sorting processes are not highly

selective, and that consequently the predicted relative retreat rates
associated with different borrow materials do not differ greatly from
unity. Conversely, high values of the parameter indicate a high degree
of selectivity in the sorting processes and yield predicted relative
retreat rates which vary greatly over typical sources of potential borrow
materials. Hence it is important to estimate the value of this parameter
in order to apply the model.

There are several ways in which field data may be used to evaluate
this parameter. The most direct method is to observe the textural pro-
perties of active zone materials in an equilibrium state, and in an eroding
state following termination of natural sediment input. Equation A5 (in the
appendix) may then be used to directly estimate the value of Δ. Unfortunately
data of this type are not readily available.

An indirect method for evaluating this parameter involves comparison of
the grain size distribution of active-zone material in an equilibrium profile
condition with that of material caught in a downdrift sand trap. Inasmuch as
finer particles have higher transport rates than coarser particles, the mean
size of material trapped by a total littoral barrier will be finer than
material constituting the active portion of the profile updrift of the trap.
The trapped material grain size distribution will be proportional to the pro-
duct of the winnowing function times it active-zone material grain size
distribution. Using this relation it can be shown that

$$\Delta = \frac{M_{\phi t} - M_{\phi n}}{\sigma_n} ,$$ (6)

where $M_{\phi t}$ represents the phi mean of the trapped material. Data presented in
[3, p. C13, C14] were used to estimate the phi parameter of composite grain
size distributions of material caught in the sand trap behind the offshore
breakwater at Channel Islands Harbor, California, and along the active por-
tion of a profile updrift of this trap. The data are quite sketchy (only
three samples from the trap and only 6 from the profile) and hence only
give a crude indication of the Δ value. For these data the composite phi
sorting is on the order of unity for both profile and trap material, and
the composite phi means differ by something between .5 and .8ϕ, giving a
rough estimate of Δ between .5 and .8.

Eulerian tracer theory provides another indirect method for estimating
Δ. In an Eulerian sediment tracer experiment the tracer is injected con-
tinuously into the surf zone for a period of time sufficiently long to allow
thorough mixing of tagged grains with untagged grains at some appropriate
distance downdrift of the injection site. Sediment samples collected after
mixing is attained are analyzed for tracer concentration as a function of
grain size. The grain size distribution of the sampled tracer, normalized
by dividing by tracer injection rates for each size, represents the grain
size distribution of the material in transit (that which would be trapped
by a total littoral barrier). Hence Equation 6 may be used to estimate Δ,
comparing the mean grain size of the normalized tracer grain size distri-
bution with the composite mean of the samples from which tracer concentra-
tions were measured, assuming these samples adequately cover the active
zone of the transport system.

This technique was applied to the results of such a tracer experiment conducted in April, 1972, at the U.S. Army Coastal Engineering Research Center Prototype Experimental Groin site at Point Mugu, California. This experiment is fully described in [4]. Although sample coverage of the active-zone was not as complete as desired for the purposes of this paper, the estimated value of Δ from these experimental results is 0.66, which is consistent with the range of values indicated by the Channel Island Harbor data.

The two beach locations discussed above are quite similar both in textural properties of native materials and in wave climate. Hence the agreement in estimated Δ values is not overly surprising. Although data of the required type were not found for any other coastal area, an indication of a probable range of Δ values in a very different shore environment can be estimated from data collected in connection with beach fill behavior at Presque Isle Peninsula, on the southeastern shore of Lake Erie. The neck of the peninsula has been breached several times in this century and this has been a source of much concern because the peninsula protects a major Great Lakes port (Erie, Pennsylvania) from wave action. Seawalls, a groin field, and repeated beach fills have been constructed here as shore protection measures. Berg and Duane [5] report results of a beach fill experiment where a coarse, poorly sorted fill ($M_\phi = 0.4\phi$; $\sigma_\phi = 1.5\phi$) was placed in one groin cell adjacent to a fine fill ($M_\phi = 2.2\phi$; $\sigma_\phi = 0.66$) and the relative behavior of the fills observed. In a later report [6, p. 26] it was reported that on the average over a five year period, sand losses from the fine fill area exceeded those from the coarse fill area by a factor of 3 1/2 to 4. Using these numbers and Equation 5 one can deduce that the appropriate Δ value has the bounds $1.3\sigma_n < \Delta < 1.45\sigma_n$, where σ_n is the phi sorting of the composite native material grain size distribution. Unfortunately the history of repeated beach fill in this area makes it impossible to give an exact value to σ_n. However, the composite phi sorting for natural beaches from a wide variety of coastal environments usually lies between .4 and 1, limiting probable values of Δ to the range 0.5 to 1.5.

Of course it is quite possible that different coastal environments will differ in the selectivity of their associated sorting processes. Variability of wave climate differs radically with relative exposure of shore segments to predominant storm wave attack. Hence it may be necessary to conduct field experiments in a variety of circumstances to determine an appropriate Δ value for application to any given coastal segment. In any case it appears that an appropriate value of delta is on the order of unity. Hence a value of $\Delta = 1$ is adopted for the purposes of further discussions in this paper.

Comparison of Relative Retreat Rates and Overfill Ratios. Figure 2 is a plot of contours of relative retreat rates, (using $\Delta = 1$), plotted using the same abscissa and ordinate as used in Figure 1. The contours of the overfill ratio, as given in the Shore Protection Manual, are overlain in quadrant 1.

Ignoring for the moment the overfill ratio curves, it can be seen that the relative retreat rate can be calculated for any combination of native and borrow material textural parameters; hence contours appear in all four quadrants (relative retreat rates less than 1/7 or greater than 7 are not shown). It can also be seen that the relative retreat rate increases for an increasing difference between the phi means of native and borrow materials,
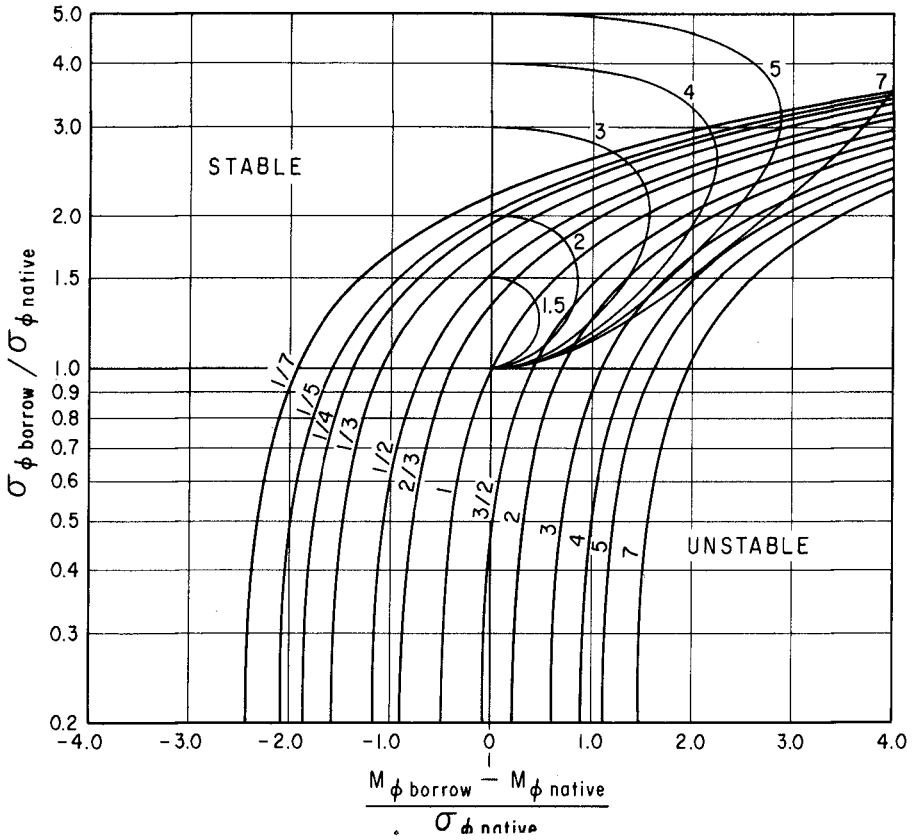
Figure 2. Relative retreat rate curves plotted against relative difference in phi means and ratio of phi sorting of borrow and native materials. For these curves a value of Δ=1 is assumed. In the upper right quadrant overfill ratio curves are also shown for purposes of comparison. Curves for relative retreat rates and overfill ratios exceeding seven are not shown.

and is sensitive to the sign of the difference; the finer the borrow
material, the higher the predicted relative-retreat rate. It can also
be seen in this figure that predicted retreat rates are sensitive to the
ratio of phi sorting between borrow and native material. More poorly-
sorted borrow material results in lower steady retreat rates. An intuitive
explanation of this relation is that more poorly sorted borrow material
contains a larger fraction of coarser material, which provides a more stable
armor. The central curve, passing through the origin, shows values of the
parameters for which the relative retreat rate is unity. Borrow materials
having phi means and sortings which plot on this line have a predicted
steady-retreat rate which is the same as that of the native material.
Borrow materials plotting to the right and below this curve have higher
predicted retreat rates than the native material, and borrow materials
plotting to the left and above this curve have lower predicted retreat
rates, or are more stable than the native material.

Comparison of relative retreat rate curves and the overfill ratio
curves in quadrant 1 indicates that there is very little quantitative agree-
ment between the two techniques. Relative retreat rates are everywhere
lower in value than the corresponding overfill ratios. In fact, the only
thing the two techniques appear to share, in quadrant 1, is a general
tendency to predict lower stability for finer borrow material. Hence it
can be said that the model proposed here represents a radical departure,
in a quantitative sense, from present guidelines for borrow material plotting
in this quadrant.

In contrast, the predictions based on the proposed model are remarkably
congruent with the interpretive text which accompanies the graph of this
type in the Shore Protection Manual. The Shore Protection Manual states
that borrow material plotting in the lower right hand quadrant (quadrant 4)
is generally to be considered unsuitable. The proposed model predicts the
most unstable fill types are those which plot in this quadrant. An advantage
of the proposed model is that it enables calculations to be performed in this
quadrant, and hence, in contrast to present guidelines, enables an estimation
of the degree of unsuitability. Similarly, the Shore Protection Manual states
that material plotting to the left of the vertical axis (quadrants 2 and 3)
will be stable, or more stable than predicted by overfill ratio calculations.
As can be seen in Figure 2, borrow material plotting to the left of the
vertical axis generally have predicted relative retreat rates less than
unity: that is, they are more stable than native material. Moreover, the
degree of stability can be calculated for borrow materials which are better
sorted than native materials.

CONCLUDING REMARKS

In the previous section a direct numerical comparison was presented
between relative retreat rates, as predicted by the proposed model, and
the overfill ratio, as predicted by the Krumbein and James model. It is
important to recall the justification for such a comparison because the
conceptual frameworks underlying the two methods differ radically. The
overfill ratio is calculated on the assumption that some portion of the
borrow material is absolutely stable and hence that a finite proportion of

the original material will remain on the beach indefinitely. The relative retreat rate is calculated on the opposing assumption that no material is absolutely stable, but that finer material is less stable than coarse material, and hence a coarse beach fill will require renourishment less frequently than a fine one. Overfill ratios can never be less than unity because a beach will not retain more material than is added to it. Relative retreat rates can be less than unity because a coarse fill might erode more slowly than native material.

The two methods can be compared only because they both ultimately attempt to predict the economic consequences associated with the utilization of potential borrow materials. In a monetary sense, the engineer can interpret the overfill ratio as a factor to be applied to the actual unit cost of obtaining a given borrow material in quantities sufficient to ultimately establish planned project dimensions. The relative retreat rate can be interpreted as a factor to be applied to the maintenance costs associated with periodic renourishment, when determination of these renourishment requirements is based on natural erosion rates associated with native material.

Both models are quite simple from a conceptual standpoint, thus it seems unlikely that either of them fully describes any real shore situation. However a subtle distinction can be made in the types of uses to which these methods are put. On one hand the engineer wishes to estimate the total cost associated with selection of a given borrow material. Application of the two methods will give some indication of the possible range of such values but strict use of either method seems unjustified, when the inherent simplicity of the models is weighed against the staggering complexities of the physical processes operating in the nearshore and beach environments. On the other hand, the engineer is usually limited to a few economically feasible sources of borrow material and he must choose one, regardless of the absolute accuracy of his predicted costs. The power of these methods to aid in such a decision seems greater than their absolute predictive powers. Indeed it is the very simplicity of the underlying concepts that allow the engineer to excercise independent judgement, based on his experience, in applying the methods and in finding an appropriate compromise between them when they provide very different results.

ACKNOWLEDGMENTS

REFERENCES

[1] Krumbein, W.C., and W.R. James, "A Lognormal Size Distribution Model for Estimating Stability of Beach Fill Material", Technical Memorandum No. 16, U.S. Army Coastal Engineering Research Center, November 1965.

[2] U.S. Army Coastal Engineering Research Center, Shore Protection Manual, Vol. II, 1974.

[3] U.S. Army Corps of Engineers, Los Angeles District, Three Year Report 1967-1969, Cooperative Research and Data Collection Program, Coast of Southern California, December 1970.

[4] James, W.R., "An Eulerian Sediment Tracer Experiment: Measurement of Littoral Drift at Point Mugu, California", Technical Memorandum, U.S. Army Coastal Engineering Research Center (in manuscript, number not yet assigned).

[5] Berg, D.W., and D.B. Duane, "Effects of Particle Size and Distribution on Stability of Artificially Filled Beach, Presque Isle Peninsula, Pennsylvania", Proceedings of the 11th Conference on Great Lakes Research, published by the International Association for Great Lakes Research, 1968, pp. 161-178.

[6] U.S. Army Corps of Engineers, Buffalo District, Review Report on Cooperative Beach Erosion Control Project at Presque Isle Peninsula, Erie, Pennsylvania, November 1973.

APPENDIX

Derivation of Equation 5

Assumptions:

1. Native and borrow material grain size distributions are lognormal:

$$f_n(\phi) = (1/\sqrt{2\pi}\sigma_n) \ \exp\{-(\phi-M_{\phi n})^2/2\sigma_n^2\}, \tag{A1a}$$

$$f_b(\phi) = (1/\sqrt{2\pi}\sigma_b) \ \exp\{-(\phi-M_{\phi b})^2/2\sigma_b^2\}. \tag{A1b}$$

2. The steady-state grain size distribution of active zone material observed in the eroding state is lognormal;

$$f_n'(\phi) = (1/\sqrt{2\pi}\sigma_n) \ \exp\{-(\phi-M_{\phi n}')^2/2\sigma_n'^2\}. \tag{A2}$$

3. The winnowing function monotonically increases with ϕ.

    Substituting equations A1a and A2 into equation 3a from the text, we have,

$$w(\phi) = \frac{E_n \sigma_n'}{M \sigma_n} \exp\left\{\frac{1}{2}\left(\frac{\phi-M_n'}{\sigma_n'}\right)^2 - \left(\frac{\phi-M_n}{\sigma_n}\right)^2\right\}. \tag{A3}$$

    Examination of equation A3 shows that assumption 3 above will only be satisfied if $\sigma_n' = \sigma_n$. Hence equation A3 may be rewritten as

$$w(\phi) = (E_n/M) \ \exp\{(M_{\phi n}'^2 - M_{\phi n}^2)/2\sigma_n^2\} \ \exp\{\phi(M_{\phi n} - M_{\phi n}')/\sigma_n^2\}. \tag{A4}$$

Let a dimensionless parameter Δ be defined as

$$\Delta = (M_{\phi n} - M'_{\phi n})/\sigma_n \ . \tag{A5}$$

Equating A4 and 3a, and using A5 to eliminate the appearance of $M'_{\phi n}$, we can write

$$\frac{f'_n(\phi)}{f_n(\phi)} = \exp\left\{\Delta\left(\frac{M_{\phi n}}{\sigma_n} - \frac{\Delta}{2}\right)\right\} \exp\left\{-\frac{\Delta\phi}{\sigma_n}\right\} . \tag{A6}$$

Multiplying by equation (A1b), completing the square in the exponent, integrating over grain size, and taking the inverse yields, (by equation 4 of the text),

$$R_b = \exp\left\{\Delta\left(\frac{M_{\phi b} - M_{\phi n}}{\sigma_n}\right) - \frac{\Delta^2}{2}\left(\frac{\sigma_b^2}{\sigma_n^2} - 1\right)\right\} ,$$

which completes the derivation.

CHAPTER 79

BEACH FILL PLANNING - BRUNSWICK COUNTY, NORTH CAROLINA

Limberios Vallianos, Chief, Coastal Engineering Studies Section,
Wilmington District, U.S. Army Coprs of Engineers

ABSTRACT

Planning has recently been completed for a shore protection project
along a 9-mile (14.5 km) reach of shoreline fronting the Towns of
Yaupon Beach and Long Beach in Brunswick County, North Carolina.
The investigative program related to this planning effort embodied
numerous interrelated elements which, on integration, resulted in a
rational engineering design having a continuous beach fill as the
central feature. Specifically, the investigation included: (a)
definition of the environment, viz, wind, waves, storm tide frequen-
cies, beach profile characteristics, shore processes, and ecological
habitats along the proposed project area as well as in potential
beach fill sources; (b) Designs and cost estimates including
establishment of various fill profile configurations, cost optimiza-
tion of fill positions, evaluation of the frequency of shoreline
retreat and the attendant displacement of fill materials, evaluation
of the compatability of materials from various fill sources with the
natural beach materials, environmental impact studies, and economic
studies; and (c) Final plan formulation arriving at the optimum
fill plan in terms of engineering functionality, economics, and
minimal adverse environmental impacts.

INTRODUCTION

The coastline of the State of North Carolina, U.S.A., is highly
exposed to the effects of storm tides and waves attendant with the
intense extratropical cyclones (hurricanes) that frequently pass
over or near this particular coastal margin which is characterized,
along its entire length, by a chain of low sandy barrier islands.
Additionally, many sections of this coastline experience severe
erosion problems even during relatively storm-free periods. Notwith-
standing the hazards associated with beach erosion and hurricane
generated tides and waves, development along the coast of North
Carolina has, in the past quarter of a century, grown at an unpre-
cedented high rate. It is remarked that similar conditions exist
throughout other sections of the U.S. Atlantic and Gulf coasts.
Accordingly, the Congress of the United States has authorized the
construction of numerous projects to eliminate or mitigate the
adverse effects created by major storms and/or beach erosion where
such problems exist along highly developed shorelines. One of the
sites for which a combined hurricane protection and beach erosion
control project was authorized is located along a 9-mile (14.5 km)
reach of shoreline fronting the Towns of Yaupon Beach and Long Beach
in Brunswick County, North Carolina (see vicinity map). Preliminary
planning for this project was accomplished in 1965 and resulted in
recommendations to restore the dunes and beach strands in the pro-

1350

ject area by the artificial placement of fills, and to maintain the
restored beach by a program of periodic beach replenishment. The
required beach fill for initial project construction and subsequent
replenishment was planned to be obtained from the marshlands backing
the barrier island in the project area.

In 1971, funds were made available for the detailed preconstruction
planning of the project for Yaupon Beach and Long Beach. At the
outset of preconstruction planning, it was evident that the initially
planned project would require extensive reevaluation due to changes
in conditions following project authorization. Particularly impor-
tant in this respect was the realization that beach-fill sources
originally planned for project construction and subsequent beach
replenishment would probably be unacceptable by current standards
pertaining to the preservation of important ecological systems.
These fill sources were exclusively located in biologically produc-
tive estuarine areas comprised essentially of intertidal marshlands.
In addition to the important issues concerning fill material acqui-
sition, another significant element favoring complete project re-
evaluation was the awareness that some fundamental changes in pro-
ject design could possibly be found desirable in light of the in-
creased knowledge and experience related to beach-fill design ac-
quired subsequent to project authorization. Accordingly, a detailed
assemblage of project alternatives was developed and fully examined
in arriving at the final project recommendations.

The preconstruction planning effort, a portion of which is described
in this paper, considered the feasibility of standard onshore engi-
neering works, viz., seawalls, groins, dune-beach restoration fills,
and combinations thereof. An examination of the possible extensive
use of seawalls on the low barrier island topography indicated that
such an approach would be too costly and esthetically undesirable.
It is remarked that any functional plan involving seawalls would also
require periodic beach replenishment as a minimum measure against
long-term shore erosion. In addition to seawalls, a reexamination
was made of the feasibility of using groins, exclusive of any other
protective measure, to compartment the entire beach strand fronting
Yaupon and Long Beaches. This approach was discounted due to the
strong possibility of aggravating existing erosion along the unpro-
tected shore situated immediately east of the project site. Further-
more, a groin system alone would provide only minimal protection
against the effects of major storms. Accordingly, the assemblage
of project alternatives developed for detailed examination involved,
as a central feature, the utilization of dune and/or beach fill.

A total of 12 basic alternatives and 7 feature alternatives were
completely analyzed during the investigation. These included:
plain dune-beach fills varying in elevation; dune-beach fills in
combination with groins; dune-beach fills and short seawalls at
select locations with and without groin systems; and the stabiliza-
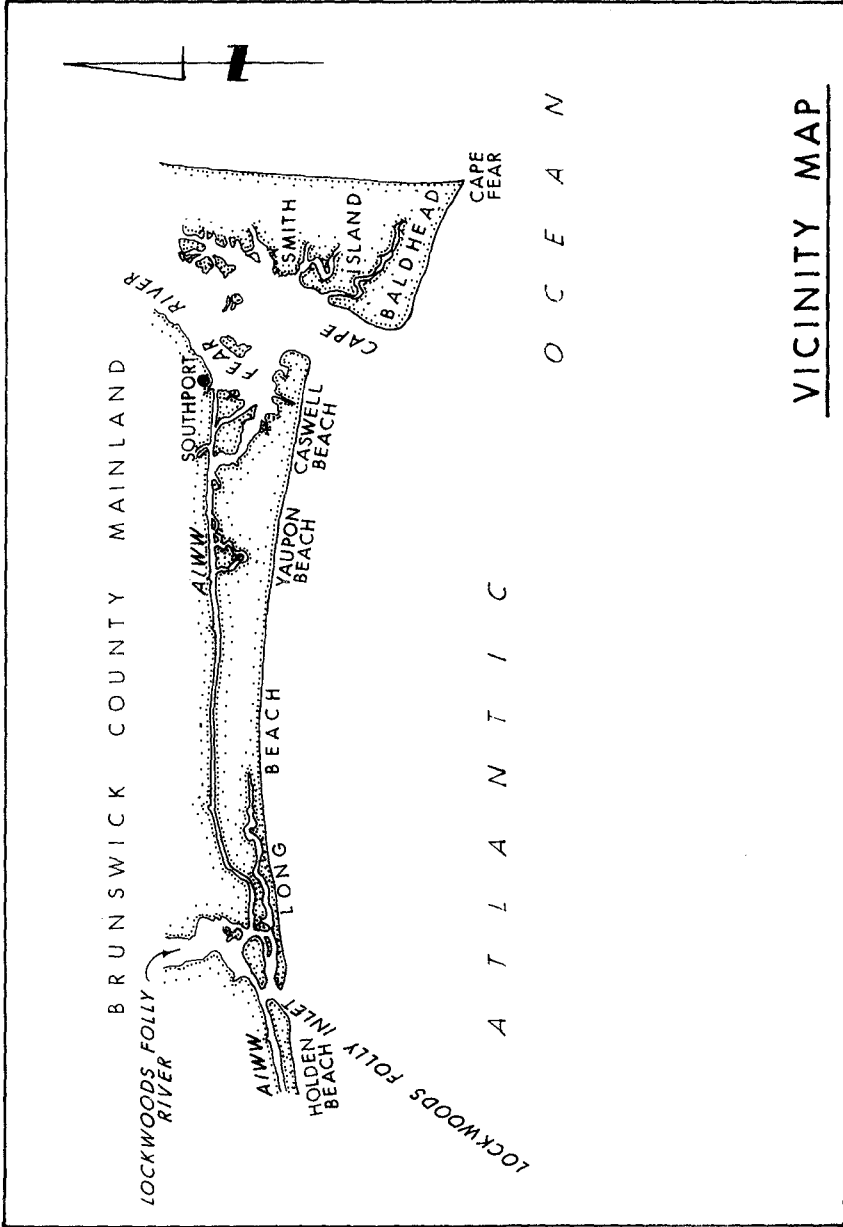
VICINITY MAP

tion of Lockwoods Folly Inlet (see vicinity map) by major control
structures in combination with the other shore protection project
alternatives. The project alternatives were evaluated vis-a-vis
nine potential sources of dune-beach fill, including two oceanic
sources, for which detailed assessments were conducted in regard to
the engineering quality of the sediments, cost of acquisition, and
environmental impacts related to the fill acquisition.

The investigation resulted in the recommendation to construct a
continuous dune and beach fill along the 9 miles (14.5 km) of pro-
ject shoreline through the artificial placement of approximately
11,000,000 cubic yards (9,200,000 cubic meters) of fill. The east
terminal of the fill would be stabilized by a system of 12 adjust-
able groin structures. Similarly, the west fill terminal would be
stabilized by 11 adjustable groins. The dune portion of the fill,
having an elevation of 15 feet (4.6 meters) above mean-sea-level,
would be planted with a suitable grass to prevent the intrusion of
wind-blown sands into the developed upland area. The project shore
would be stabilized against erosion by a program of periodic beach
fill replenishment involving fill placement at an average annual rate
of approximately 402,000 cubic yards (305,000 cubic meters). Two
basic sources of sediment have been selected for project construction
and subsequent replenishment. Environmental studies indicate that
there will be little or no adverse environmental impacts associated
with the use of these two areas and that some environmental enhance-
ment may result from the acquisition of the proposed fill by dredging
operations. A schematic diagram of the proposed plan is given on
Figure I. Note that the cross-sectional schematic shows four fill
configurations. The selected plan is designated as PLAN-BTG.

ENVIRONMENTAL FACTORS AND CONDITIONS

As mentioned above, the area germane to the project study described
herein is characterized by sandy barrier islands which back upon
elongated lagoons comprised of marshlands and reptilian networks of
tidal channels. These islands are narrow bands having widths vary-
ing from about 500 to 1500 feet (150 to 450 meters). The basic
topographic relief of the islands is low and in general does not
exceed an elevation of 10 feet (3 meters) above mean-sea-level
(m.s.l.), except for scattered dunes and the frontal duneline which
is hummocky and varies widely in elevation from 10 to 30 feet (3 to
9 meters) above m.s.l. The beach strands along the areas of particu-
lar interest here are narrow and offer only minimal protection to
the dense ocean front development, even under conditions prevailing
with moderate extratropical weather disturbances. Specifically,
the beach strand widths at Long Beach and Yaupon Beach are only 66
feet (20 meters) and 44 feet (13 meters), respectively, at the mean
stage of the astronomical tide. Typical conditions along the study
area are illustrated on PHOTO-PLATE I. Brief descriptions of
specific factors and conditions related to the beach and nearshore
zone in the project study area are given below.

PLAN VIEW
NO SCALE

CROSS-SECTIONAL VIEW
NO SCALE
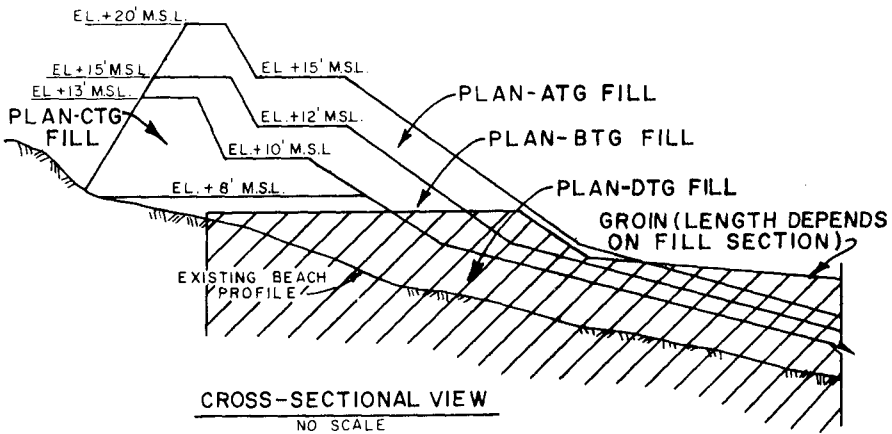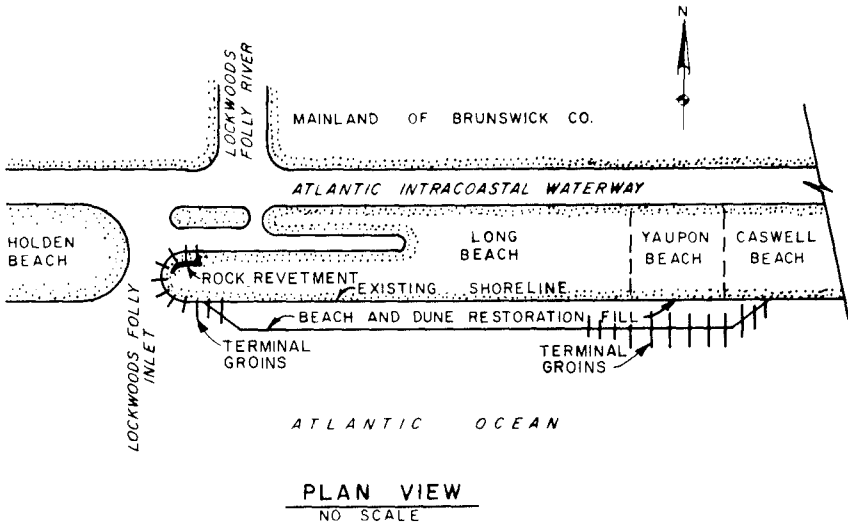
SCHEMATIZATION OF PLANS ATG THROUGH DTG

FIGURE I

LONG BEACH   APRIL , 1971

YAUPON BEACH   JUNE , 1972
PHOTO PLATE I

Beach Profile Characteristics. The natural beach berm in the study
area is generally located at an elevation of 8 feet (1.4 meters)
above m.s.l. The average geometric characteristics of the beach
profile seaward of the berm crest are given below. The active beach
profile terminates at a depth of approximately 28 feet (8.5 meters)

ELEVATION RANGE ± M.S.L.	+8 FT. TO M.S.L.	M.S.L. TO - 8 FT.	-8 FT. TO -18 FT.	-18 FT. TO -24 FT.	-24 FT. TO -30 FT.	-30 FT. TO -48 FT.
BEACH PROFILE SLOPE	IV:10H	IV:54H	IV:58H	IV:295H	IV:595H	IV:2,550H

below m.s.l. The granulometric properties of surficial sediments on
the beach profile are generally characterized by the following tab-
ulation of phi mean particle sizes and associated standard deviations.

Sample Profile Location in Feet ± M.S.L.	0	-4	-8	-12	-16	-20	-24	-28	-32
Sample Phi Mean Particle Size	1.45	1.68	1.42	2.16	2.45	1.99	1.26	1.11	1.57
Sample Phi Standard Deviations	0.51	0.47	0.48	0.51	0.45	0.67	0.51	0.46	0.51

Winds. On an annual basis, winds blow onshore 35.4 percent of the
time and offshore 35.1 percent of the time, the remaining 29.5 per-
cent of time accounts for alongshore winds or calm conditions. As
regards onshore winds, 45 percent occur from the southwest, 33 per-
cent from the south and 22 percent from the southeast. With respect to
onshore wind speeds, 96 percent are less than 20 knots, 65 percent
are less than 12 knots, and 33 percent are less than 7 knots.

Waves. Observed offshore wave data is well correlated with the
overall wind data, as approximately 36.5 percent of all observed
waves are directed onshore. The distribution of onshore deep water
waves in terms of direction is as follows: ESE - 10%; SSE - 19%;
S - 18%, SSW - 19%; and WSW - 34% . The percentage distribution of
deep water waves approaching shore with respect to all deepwater
waves in terms of wave height and period is given in the tabulation
below.

ONSHORE WAVE HEIGHTS (FEET)	ONSHORE WAVE PERIOD (SECONDS)						
	< 6	6-7	8-9	10-11	12-13	> 13	Total
	PERCENTAGE OF ALL DEEP WATER OBSERVATIONS						
< 3	8.35	1.03	0.32	.06	0.01	0.60	10.37
3-5	10.20	6.08	1.25	.34	0.08	0.14	18.09
5-8	0.85	2.37	1.75	.46	0.08	0.06	5.57
8-12	0.19	0.50	0.61	.30	0.17	0	1.77
12-18	0.04	0.19	0.14	.23	0.04	0.04	0.68
> 18	0.04	0	0	.02	0	0	0.06
Total	19.67	10.17	4.07	1.41	0.38	0.84	36.54

The above tabulation shows that 78 percent of the waves which
approach shore from deep water are equal to or less than 5 feet
(1.5 meters) in height, and that 82 percent of the wave periods are
equal to or less than 7 seconds.

Tides. The mean astronomical tide range in the study area is
approximately 4.2 feet (1.3 meters), with a spring tide range of
about 4.8 feet (1.5 meters). Tidal anomalies, particularly those
associated with tropical cyclones (hurricanes), can be quite severe.
For example, Hurricane "Hazel" (15 October 1954) generated a surge
in the study area which reached a still-water-elevation of approx-
imately 15 feet (4.6 meters) above m.s.l. Computed tide level-
frequency relationships for the area, calibrated with storms tides
of record, are given below.

TIDE LEVEL ABOVE M.S.L. (FT.)	4.3	4.7	6.5	9.2	11.2	12.4	13.5	14.8	15.6
PERCENT CHANGE OF OCCURRENCE ANNUALLY	30	20	10	5	2	1	0.5	0.2	0.1

STUDY INVESTIGATIONS

Investigations related to the study area and alternative solutions
to existing shore problems were conducted over a period of 2-years
and involved the following, briefly described elements.

Tide Level-Frequency Analysis. Hurricane-surge heights in the
study area were computed for various wind fields having central
pressure indices ranging from 27.36 to 29.00 inches (10.8 to 11.4 cm)
of mercury. In determining the generalized hypothetical hurricane
frequencies, consideration was given to the chance of occurrence of
the storm paths based on hurricane-track records dating from 1887.
Two basic paths of hurricane approach were established and tide
level-frequency curves were computed for each path. A composite
hypothetical curve was then obtained by adding the percent of
occurrences of the two curves for given water levels. Finally, the

composite curve was adjusted in accordance with the limited recorded
tide data that was available. Basic data from the adjusted com-
posite curve was presented in the previous section under "Tides".

Winds, Wave Climate, and Shore Processes. Wind data were only of
casual interest in this study as the hindcasting of wave character-
istics was not considered necessary due to the availability of suf-
ficient wave data. Records of the U.S. Weather Service Station at
Wilmington, N. C. were compiled for the period January 1948 through
June 1960. These data were found to be generally well correlated with
the direction of wave height data selected for use in the study. In
regard to wave data, 3 sources of information were analyzed to
obtain a representative wave climate for the study area. These
sources included: recorded and visually observed wave information
from a fixed lighttower located approximately 25 nautical miles
(46 kilometers) southeast of the study area; shipboard observations
from both a 1 degree and 10 degree offshore geodetic grid; and
surf observations from two onshore locations near the study area.
The information related to the 1° geodetic grid square $33^{\circ} - 34^{\circ}$ N.,
$77^{\circ} - 78^{\circ}$ W. was selected as the best representation of wave clima-
tology applicable to the study area. These wave data were utilized
for wave refraction and alongshore sediment transport analyses. The
wave refraction analysis resulted in the development of approximately
1,460 wave orthogonals. The area covered by the analysis extended
over a shoreline distance of 16 miles encompassing the study area.
Wave rays were refracted toward this shoreline reach from deepwater
directions E. 30° S., E. 60° S., South, S. 30° W., and S. 60° W.
with wave periods of 4, 6, 8, 10, 12, and 14 seconds. For each set
of refraction diagrams, representing a certain wave direction and
period, alongshore sediment transport curves were developed relating
the variability of sand transport to distance along the 16 miles
(26 kilometers) of shoreline studied. This analysis resulted in the
development of 144 sediment transport curves from which two composite
curves were obtained that gave, respectively, easterly and westerly
sediment transport quantities on an average annual basis. The sand
deficit derived from the computed longshore transport regime was
compared to a second and independent analytical computation of sand
sediment deficit based on the assumption of an equilibrium profile,
the magnitude of shoreline retrogression, and the attendant computed
volumetric losses. The computed alongshore transport deficit
added to the loss of sediment computed for the shore recession
associated with sea level rise compared closely to the total sand
deficit based on overall volumetric losses. Shore recession due to
sea level rise was determined generally in accordance with the
method proposed by Bruun, see reference 1.

Designs and Cost Estimates. Important elements of these investiga-
tions included: (1) Establishment of design fill profile config-
urations on the basis of existing natural profiles obtained by field
surveys; (2) cost optimization of the position of alternative pro-
ject fills considering cost impacts resulting from the interrela-
tionships of volumetric requirements, rights-of-way and relocations

and dune back-slope bulkheads for fill containment; (3) analytical
determination of the relationship of shoreline retreat to frequency
of occurrence (based on storm-tide frequency) for each basic
alternative fill; (4) analytical determination of frequency of
occurrence of volumetric displacement of fill material due to storm
action; (5) analytical determination of the probability of storm-
displaced fill returning to shore under poststorm wave action; (6)
wave overtopping on fill sections; (7) subsurface exploration
in potential fill source areas including six estaurine, one upland,
and two oceanic areas; (8) granulometric analysis of surficial
beach profile samples and potential sediment source samples; (9)
cost analysis of dredging from potential fill sources; (10) selection
of fill sources on basis of interrelated factors of cost, sediment
quality, and environmental considerations; (11) beach replenishment
cost studies in regard to plain beach fills and beach fills compart-
mented with groins; (12) designs and cost estimates for groins,
seawalls, and revetments; and (13) establishment of right-of-way
values and relocation costs.

Economic Analysis. The economic analysis involved the evaluation of:
(a) physical damages to structures prevented along the upland zone
by each of the basic project fill alternatives in accordance with
water level-frequency and water level-damage relationships established
for the study area; (b) benefits from recreational use of the re-
stored beach strand areas with respect to the diminishing benefits
from recreational use of the existing dry beach areas which are
presently eroding; (c) land loss prevention benefits for properties
which presently back the existing beach strands-these properties
would, in time, be subject to erosive conditions in the absence of
erosion-control measures depending on the rates of shoreline retro-
gression which are 3.6 feet (1.1 meters) and 5.7 feet (1.7 meters)
per year at Long Beach and Yaupon Beach, respectively; (d) benefits
resulting from a higher utilization of land in those areas in which
development is presently hindered by an obvious threat of beach
erosion; and (e) local redevelopment benefits computed as the
amortized value of wages of workers hired locally for initial pro-
ject construction and subsequent project operations.

Environmental Analysis. The environmental analysis involved the
results of investigations necessary to establish the characteristics
of the existing natural setting, the type and value of the natural
resources therein, and the impacts on the setting and its resources
as a result of project construction and operation. An extensive
resource inventory was developed by literature reviews, field studies,
and consultations with authoritative environmental interests. The
study area and its surroundings were divided into distinct units,
each of which was assessed in terms of ecological considerations
with respect to project-related influences. A significant amount of
the environmental analysis pertains to the evaluation of potential
project fill sources, leading to the selection of areas in which
acquisition of sediments for project construction and operation

would not result in unacceptable environmental impacts. For those
areas selected as fill sources, precautionary procedures related to
dredging operations were developed to protect adjacent areas from
possible adverse effects of dredge-generated turbidities. In
addition to fill acquisition, the environmental analysis assesses
all other aspects of project construction and operation including
the short- and long-term environmental impacts of fill placement on
the shorelines and the construction of groins.

FILL PLAN FORMULATION

The degree of protection afforded by a given fill depends on its
geometry in terms of elevation and volumetric characteristics. The
particular above-water configuration of a fill is chosen to approach
the basic shape of a natural beach; to wit, the fill profile is com-
prised of a high landward portion resembling a frontal dune and/or
a flat lower form which has the appearance of a natural beach strand.
Seaward of the limits of normal wave run-up on the beach face,
nothing can be done in the way of artificially shaping the fill
profiles, as this area is molded in accordance with the interaction
of wave forces and attendant nearshore circulations and the physical
characteristics of the fill materials. The designs of the restora-
tion fills are based on the concept that materials placed as fill
will be sorted, by wave action, into restricted size ranges along
the active profile in a fashion similar to that existing on the
natural beach profiles. The degree to which the sorted fills would
approach the same characteristics as the natural beach profiles de-
pends on the overall granulometric characteristics of the fills,
presuming there are no differences in the densities and particle
shapes of the fill and natural materials. All potential fill sources
investigated did possess those characteristics which would allow for
the natural development of profiles approaching those currently
existing along the shore and nearshore zones of the study area.
Accordingly, the design fill profiles were based on the natural
beach profile measurements conducted during the investigation. The
resulting average slope characteristics selected for design purposes
are those described under the preceding section entitled
"Environmental Factors and Conditions". The active beach profile in
the study area was found to extend to seaward depths of about 28
feet (8.5 meters) below m.s.l. Failure to provide sufficient ma-
terial volume for entire coverage of the active profile would result
in material being displaced from higher to lower portions of the in-
place fill (following initial placement) making it impossible to
develop the design profile. This would result in a recession of
the design fill shoreline and a reduction in the quantities of material
in the beach berm or dune sections of the fill. The net volumetric
quantity of material required to fulfill the needs of a particular
fill section depends on the desired amount of seaward advance of the
fill with respect to the existing profile. In the case where the
sorted fill is expected to develop characteristics similar to the
natural beach profile, a sufficient amount of net fill must be pro-

vided so that every point on the sorted fill profile will be equi-
distant from a corresponding profile point on the existing natural
profile. For example, if the design profile is to advance the
mean-water line a seaward distance of 100 feet, each point on the
active profile must also be advanced seaward a distance of 100 feet
in order to attain the design fill cross-sectional area. Though
this is a seemingly obvious conclusion, it is, more often than not,
overlooked in the design of beach fills.

The volumetric requirements and associated costs of each basic fill
alternative depend on the position of its landward limits. If, for
example, the landward toe of the dune fill were placed at the exist-
ing high-water line, the volume and associated cost of the fill would
be higher than if the toe of the fill were placed in the upland area.
On the other hand, if the landward toe of the dune is placed in the
upland areas, high costs are incurred due to the necessity to purchase
expensive rights-of-way, relocate structures, or to construct back-
slope bulkheads to retain the dune fill. In order to arrive at the
most economical position of each of the basic fill alternatives, a
cost optimization scheme was employed that involved a family of four
curves, three of which give, respectively, the relationships of cost
of fill, costs of rights-of-way and relocations, and cost of back-
slope bulkheads, each with respect to various positions of a given fill
as measured from an arbitrary index position. The fourth curve is a
composite of the three curves mentioned above, that is, the fourth
curve represents the total cost of the protective fill for any location.
The minimum point on the total cost curve gives the most economical
position of the restoration fill. An example of the optimization
scheme is given in FIGURE II.
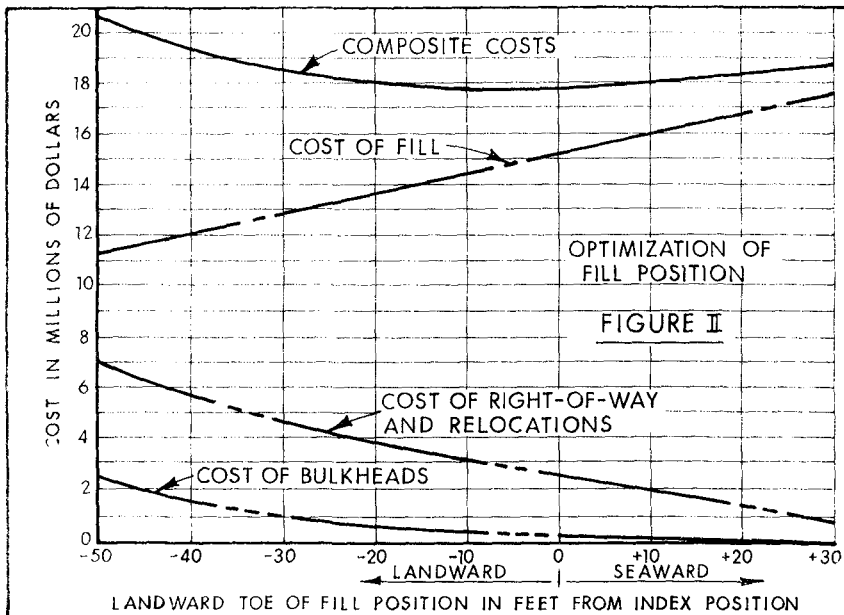
In regard to the degree of protection provided by each of the basic
alternative fills, this aspect of plan formulation was accomplished
by an analytical determination of the relationships of fill shore-
line retreat with respect to the frequency of occurrence of various
tide levels. The method utilized to determine shoreline retreat-
frequency relationships was similar to the procedure presented by
Edelman in 1968, see reference 2, revised in this case to fit local
conditions. These relationships are presented graphically in FIGURE
III. On the basis of FIGURE III, the alternative fill Plans ATG, BTG,
CTG and DTG have design capabilities associated with storm tide and
wave action having frequencies of occurrence of 0.2, 1.5, 4.0, and
8.0 percent per year, respectively. The short-term but large-scale
shoreline fluctuations occurring with storm action, as demonstrated
graphically on FIGURE III, are accompanied with the offshore dis-
placement of sediments. The relationships of volumetric displace-
ment with respect to frequency of occurrence of storm tides and waves
are given on FIGURE IV. It is of interest to note that analytical
results indicate that the volumetric displacement of dune and/or
beach material in an offshore direction is independent of the fill
configuration. These findings agree with general observations that
dunes function as sand reservoirs during storm retreat of beach
profiles and thereby reduce the recessions that would occur in the
absence of dunes. The frequency of volumetric displacements is
particularly important in determining project maintenance costs on
an average annual basis. Natural poststorm restoration is a well
known phenomenon. However, the degree of natural beach restoration
for a particular site is generally unknown. For the Yaupon and
Long Beach project, analytical investigations were conducted to
determine the capabilities of the normal wave climate to return ma-
terials to the shore following storm displacement. The analysis was
conducted in accordance with methods presented by Johnson and
Eagleson in reference 3. In this case it was found that, for all
practical purposes, materials displaced by storms would return to
the shores. Of course, the hydraulic restorative agents cannot
return materials to the higher portions of a dune and beach fill.
In a purely natural situation the lower beach forms are restored over
relatively short periods of time (several days to several months)
depending on the severity of a particular storm and the character-
istics of the poststorm wave action. The natural dunes generally
recover from storm effects at a slower rate than the lower beach
zone as their restoration is dependent on wind speed, direction,
and the availability of finer fractions of the beach sediments.
Since it would be desirable to attain project protection as soon
as possible following storm recessions, the average annual amounts
of material displaced from the basic alternative fill sections,
above the natural beach berm level of +8 ft. m.s.l., were determined
and costs computed to mechanically redistribute that material to the
higher portions of the design profiles.

Beach materials and fill sources. All potential sources of fill in
the general vicinity of the project site were investigated. These

SHORELINE RETREAT
vs
STORM FREQUENCY

—————— FILL PLAN ATG
— — — FILL PLAN BTG
– – – – FILL PLAN CTG
–·–·– FILL PLAN DTG

SHORELINE RETREAT IN FEET

PERCENT CHANCE OF OCCURRENCE PER YEAR

FIGURE III

OFFSHORE FILL DISPLACEMENT
vs
STORM FREQUENCY

OFFSHORE VOLUMETRIC FILL DISPLACEMENT
CUBIC YARDS PER LINEAL FOOT

PERCENT CHANCE OF OCCURRENCE PER YEAR
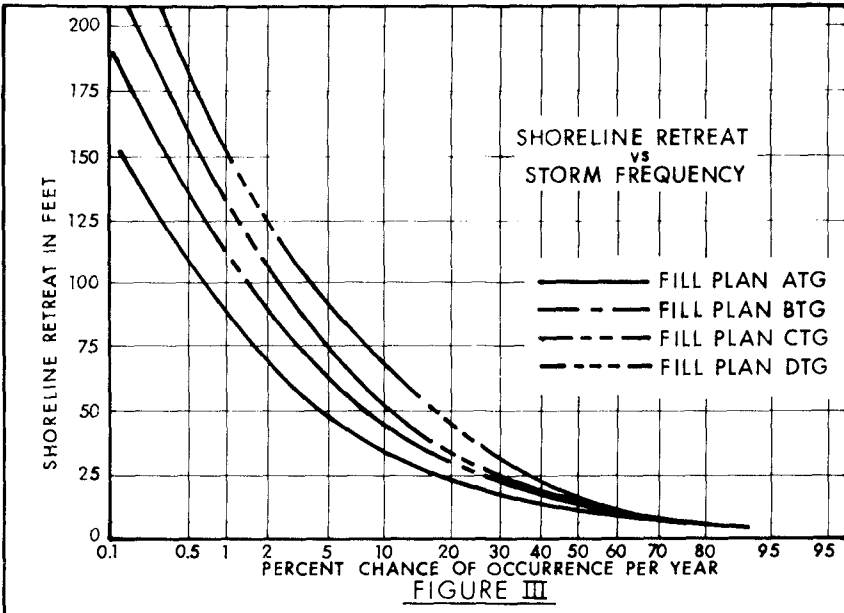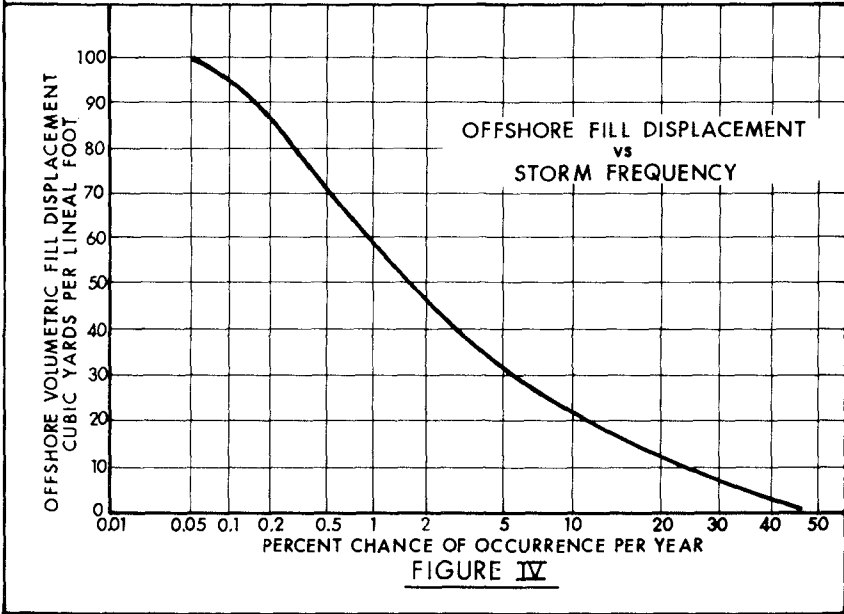
FIGURE IV

sources are referred to as potential borrow areas and are designated
by the abbreviation PBA. A total of nine potential borrow areas,
designated PBA-A through PBA-I, were involved in the investigation.
The subsurface exploration of materials contained in the various
potential borrow areas has been mentioned. The collection of a
representative set of material samples was required in order to con-
duct a comparative analysis between the granulometric properties of
the fill sources and the natural or native beach materials, and
thereby determine the compatibility of the fill materials with re-
spect to the nearshore environment. In this connection, the wave-
sorting phenomenon - involving the segregation of the discrete
particles comprising the beach and nearshore bottom into restricted
size ranges along the active profile - is of prime importance in the
conceptual formulation of beach fills. Since the natural beach,
including the nearshore bottom, is the end product of a distribution
process which acted upon a particular source of material over some
period of time, it is reasonable to assume that if a composite ma-
terial possessing the average characteristics of beach material
were placed along the shore, the prevailing hydraulic forces would
tend to sort that composite material into a distribution having the
characteristics observed on the natural beach. Accordingly, the
first part of the fill-source material analysis involves defining
the general characteristics of the native material. The second part
of the analysis involves the determination of the characteristics
of the various source materials and their compatibility with the
nearshore environment as reflected by the distribution character-
istics of the native beach material.

The native beach material characteristics were determined from 170
surficial samples obtained from 10 profile range lines spaced at
intervals of 6,000 feet (1.8 km) along the project and adjacent shore-
lines. The samples were obtained from 17 discrete profile points lo-
cated between the beach berm crest and the 32-foot m.s.l. depth con-
tour on each range line. Samples from the PBA's were obtained from 79
subsurface and submarine cores, from which 750 samples were selected
for laboratory analysis. Locations of submarine cores were deter-
mined by an analysis of a sonic geophysical survey. The basic
statistical parameters describing the characteristics of beach and
fill-source particle size distributions are mean particle size,
standard deviation, and variance. These parameters are applied to
the "Log Normal Size Distribution Model" (see reference 4) which
defines the compatibility of a particular fill material with respect
to beach material in terms of a value referred to as the "critical
ratio." This value is the ratio of the total volume of material
placed as fill to the net volume of fill remaining in-place after
natural hydraulic sorting action has taken place. In arriving at the
gross volume of material required from a given source to obtain a net
design volume in the fill section, it is also necessary to consider
the quantity of silts and clays within the basic material source that
would remain in suspension after discharge from the dredge pipeline
and not deposit within the fill section. Therefore, the quantity of

sandy material within the potential fill sources was determined and the respective "critical ratios" were based only on these settleable fractions of the source material. Accordingly, a net unit volume of material in the fill section, following initial placement and subsequent hydraulic sorting action, would require the removal of the number of unit volumes of source material given by the ratio "critical ratio"/fraction sandy material. For example, if the "critical ratio" is 1.4 and the percent sand (settleable material) in the fill source is 70 percent, approximately 2.0 cubic yards of source material are required to obtain 1.0 cubic yard of net fill in the design section. Therefore, if the unit cost of dredging and placing material on the project shore is $1.00 per cubic yard for a borrow area having the material characteristic described above, the cost of an effective unit volume of material from that borrow area would be $2.00 per cubic yard.

The selection of a source or combination of sources for the acquisition of project fill was dependent on environmental considerations as well as the cost and interrelated material suitability aspects mentioned above. The cost estimate computations involved a detailed analysis of each potential borrow area (PBA) including the cost of mobilization and demobilization of primary and booster pumping units and the direct cost of pumping on a unit cost basis. The cost of an effective unit volume for the design section was then determined for each PBA on the basis of the respective "critical ratios" and fraction of settleable materials. The full results of environmental investigations are too lengthy for explanation herein; however, it will suffice to state here that: (a) PBA's -E, -F, -G, -H, and -I are ecologically important to the natural resource base of the Southeastern Coastal Zone of North Carolina, and that acquisition of sediments in these areas for project construction and/or subsequent beach replenishment would be highly injurious to the ecosystems involved; and (b) PBA's -A, -B, -C, and -D are areas in which dredging activities would have little or no significant short- or long-term environmental impacts. A summary of the elements necessary for the rational selection of project fill sources is given below in table 1. On the basis of the information summarized in table 1, PBA's -A and -B were selected as the project fill sources.

TABLE 1

Potential borrow area (PBA)	Gross unit volumes of material per unit volume of net fill	Cost of an effective unit volume of net fill ($)	Adverse impacts on environmental resources if area is dredged
A	1.40	0.45	Not significant
B	1.24	0.81	Not significant
C	1.51	1.86	Not significant
D	4.93	2.66	Not significant
E	1.62	0.63	Significant
F	3.32	1.30	Significant
G	4.80	1.58	Significant
H	3.90	1.29	Significant
I	2.45	0.81	Significant

The gross volume of material available within PBA-A amounts to approximately 1,900,000 cubic yards. The remaining quantity of material required for a given basic alternative fill must be obtained from PBA-B. The volumetric relationships are given in table 2.

TABLE 2

Fill plan	Gross volumetric requirements (cu. yds.)	Gross volume of material in PBA-A (cu. yds.)	Gross fill requirement from PBA-B (cu. yds.)
ATG	17,620,000	1,900,000	15,720,000
BTG	11,000,000	1,900,000	9,100,000
CTG	8,670,000	1,900,000	6,770,000
DTG	8,350,000	1,900,000	6,450,000

Selection of fill plan BTG was based on the comparison of excess annual benefits of the various fill plans. Excess annual benefits are defined as the difference between total annual benefits and annual costs which include the capitalized cost of initial construction and annual operating costs.

Beach replenishment (nourishment). Beach nourishment requirements were determined on the basis of computed average annual shoreline recession rates. To convert shoreline recession to corresponding volumetric loss, the entire beach profile, extending from the berm crest to the 28 ft. m.s.l. offshore depth contour, was assumed to retrogress at the same rate as the shoreline. In other words, an equilibrium profile was assumed to exist. The assumption of the existence of an equilibrium profile condition was supported by the close comparison of the results of the two independent sediment deficit computations. The first computational approach utilized the

historic shoreline changes and the second approach combined along-
shore transport deficits with sediment losses due to a rise in sea
level. On the assumption of an equilibrium profile condition and
the average characteristics of profiles surveyed in the study area,
the computed loss of beach material attending a shoreline recession
of 1 foot is 1.54 cubic yards (1.2 cubic meters) per lineal foot
(0.3 m) of beachfront. Applying this volumetric loss quantity to
the average annual recession rates of 3.6 feet and 5.7 feet for
Long Beach and the general Yaupon Beach area, the respective average
annual volumetric losses are 5.54 cubic yards (4.2 cu.m.) and 8.78
cubic yards (6.7 cu.m.) per lineal foot of shore. On the basis of
shoreline distances, the average annual beach replenishment demand
would be 288,600 cubic yards (221,000 cu.m.) for a continuous fill
extending from Lockwoods Folly Inlet to and including the shores of
Yaupon Beach. The replenishment rate given above is based on the
existing shoreline, and in order for the estimated replenishment
value to be valid for a project fill, the fill must have an align-
ment which follows, as closely as possible, the natural shore align-
ment. The natural coastline configuration is the product of a long-
term process involving the interaction of sediments comprising the
shore and the nearshore hydraulic forces. If a fill alters the
basic coastline orientation, there will be a natural reaction tend-
ing to restore the shore to its prior alignment. Usually, such a
reaction results in higher erosion rates than had been experienced
by the natural shore. Accordingly, in positioning the basic alter-
native project fills, care was exercised in maintaining the same
shoreline configuration existing along the natural coast. However,
adherence to this basic approach is not possible at the extremeties
of a fill which must terminate at some point beyond which the natural
coast continues. At such a point, a transition to the natural coast
must be effected which necessarily requires a deviation from the
natural shore alignment. The differences in alongshore transport at
and near a fill transition were analyzed on the basis of fill tran-
sition and wave angularities. In general, if the fill transition is
very gradual the difference in alongshore processes between the na-
tural shore and the transition will be relatively small. Conversely,
a sharp transition results in significant changes in alongshore
transport rates resulting in rapid erosion of the transition.
However, the relationships of different transitions in terms of cost
are not simply functions of transition angularity with respect to
normal shore alignment. For example, a very gradual transition is
lengthy and the initial cost of fill to develop the transition is
high. Also, though the erosion rate per unit length of transition
may be only slightly higher than the normal shore erosion rate, the
large length of a gradual transition could require a considerable
periodic replenishment rate. On the other hand, a somewhat sharper
transition having a shorter length and lower initial costs could
also have a lower overall replenishment requirement due to its
shorter length, notwithstanding the possibility that the erosion rate
per unit length of this transition is greater than the more gradual
transition. In view of the possibilities mentioned above, a cost

optimization scheme was required to determine the most economical
fill transitions. The optimum east and west transitions of a con-
tinuous fill along the shores of Yaupon and Long Beaches were found
to be, respectively, 4,240 feet (1290 m.) and 4,000 feet (1220 m.) in
length and to have computed replenishment requirements of 87,200 cubic
yards and 115,000 cubic yards per year. The alternative to a plain
beach transition zone is to employ a small, tapered groin system
which allows for shortening of the transition sections. Such groin
systems were evaluated and found to be the most economic means of
effecting the fill transitions, based on the assumption that the
compartmented transition fills would adjust to normal shore align-
ments and, therefore, could be maintained by a beach replenishment
rate equivalent to the natural erosion rate in the vicinity of the
proposed transitions. Accordingly, terminal groin systems were
adopted for the overall fill plan. The total volumetric beach re-
plenishment needs for the proposed fill along Yaupon and Long Beaches,
amounts to 289,500 cubic yards (220,000 cu.m.) per year. Of this
amount, 30,000 cubic yards (23,000 cu.m.) would be obtained from
PBA-A which represents the estimated deposition of littoral materials
flushed to and deposited in that area by tidal flow through Lockwoods
Folly Inlet. The remaining 259,500 cubic yards (197,000 cu.m.) per
year would be obtained from materials in PBA-B. On the basis of the
material characteristics in PBA-B, the gross volume of material re-
quired to yield 259,500 cubic yards of sorted beach fill would be
321,800 cubic yards (245,000 cu.m.). Thus, the gross average annual
volume of beach replenishment materials to be obtained from PBA's –
A and B would amount to approximately 402,000 cubic yards (305,000
cu.m.). The tentative schedule is to accomplish periodic beach re-
plenishment at 3-year intervals, with each operation involving the
placement of 1,206,000 cubic yards along the project fill.

CONCLUSIONS

In the course of his professional practice, this writer has perused
numerous documents pertaining to the planning or design of large
beach fill projects. In so doing, it has, all too often, been evident
that many engineers have given little more consideration to such
plans than one would give to a common land-fill in a stable upland
area. This revelation is particularly dismaying on considering that
beach fills are generally major engineering works involving sizable
capital expenditures for initial construction and subsequent operation.

This paper has identified some of the important, complex, and inter-
related elements which can and should be evaluated by the engineer in
arriving at a rational plan to place a sedimentary fill for the pur-
pose of coastal protection. Admittedly, the present state of know-
ledge concerning shore processes, at best, allows for only rough
approximations of beach fill behavior; but, for this very reason, if
for no other, the engineer must exert every reasonable effort to es-
tablish a base of analyses from which sound judgments can be made.
Moreover, it is only through the comparison of rational initial

design assessments with actual beach fill behavior that the engineer
can fully evaluate a given fill performance, design future project
modifications if necessary, or define those areas in which future
research is needed to develop or refine engineering criteria.

REFERENCES

1. Bruun, P - Sea Level Rise as a Cause of Shore Erosion, Journal
    Waterways and Harbours Division, ASCE, February 1962

2. Edelman, T. - Dune Erosion During Storm Conditions, 11th
    Conference on Coastal Engineering, London, England, September 1968.

3. Johnson, J. W. and Eagleson, P. S. - Coastal Processes, Chapter
    9, Estuary and Coastline Hydrodynamics, edited by Arthur T.
    Ippen, McGraw Hill Inc., 1966

4. Krumbein, W. C. and James, W. R. - A Lognormal Size Distribution
    Model for Estimating Stability of Beach Fill Material, U. S.
    Army Coastal Engineering Research Center, Technical Memorandum
    No. 16, November 1965.

CHAPTER 80

BEHAVIOR OF BEACH FILL
AT ATLANTIC CITY, NEW JERSEY

by

Craig H. Everts[1]
Allan E. DeWall[2]
Martin T. Czerniak[3]

ABSTRACT

A beach monitoring program between 1962 and 1972 at Atlantic City, New Jersey was designed to observe the response of beaches to waves and tides of specific intensity and duration as a first step in developing a storm warning system for low-lying coastal communities. As a by-product of that study the behavior of beach sand following two beach replenishment projects in 1963, and again in 1970, was determined. Monitoring was done using repetitive beach surveys above mean sea level (MSL) at seven profile lines. Survey results show that following replenishment, losses of the fill material above MSL were between nine and twelve times the losses measured in adjacent non-fill areas. Loss rates were largest at the updrift end of the fill region. About two and one-half times more material appeared to move in a seasonal on-offshore direction than moved permanently alongshore and above MSL to the southwest. For each meter of beach retreat, 5 to 6 m^3/lineal meter of fill were lost.

INTRODUCTION

Protective and recreational beaches sometimes require a periodic artificial replenishment of sand. The high cost and often recurring need for such replenishment justifies a study of what happens to the sand emplaced as beach fill to determine the most effective and economical method to rehabilitate the beach in the future. In addition, general information may be acquired for improving the design of fill projects at other locations.

Effective beach fill design involves many physical factors. Among them are the selection of a suitable fill material, the method to be used in transporting the fill material from its source to the beach, and the

---

[1]Oceanographer, [2]Geologist, [3]Civil Engineer
Coastal Processes Branch
U.S. Army Coastal Engineering Research Center
Kingman Building, Ft. Belvoir, Virginia   22060

manner of placing the fill material on the beach. Fill placement is
the subject of this paper which is a by-product of an Atlantic City,
New Jersey study to observe beach changes in response to waves and
tides of specific intensity and duration as a first step in developing
a storm warning system for low-lying coastal communities (Galvin, 1968).
The study, a part of the Beach Evaluation Program of the Coastal Engi-
neering Research Center (CERC), included two beach replenishment pro-
jects in 1963 and 1970. Survey data were acquired only above mean sea
level (MSL). A beach loss using these data may, therefore, indicate an
accretion below MSL, or a real loss to the beach system by longshore
transport.

ATLANTIC CITY ENVIRONMENT

Physical Setting. Atlantic City is located on the New Jersey coast
about 130 km south of New York City (Figure 1). It lies on the northern
one-half of Absecon Island which is a 13.2-km long by 0.8 to 2.4-km wide
barrier island with an average ground elevation of less than 3 m above MSL.
Its beaches are characterized by berms averaging 80 m in width and 2.2 m
in elevation (Table 1). Natural dunes have been replaced by a boardwalk or
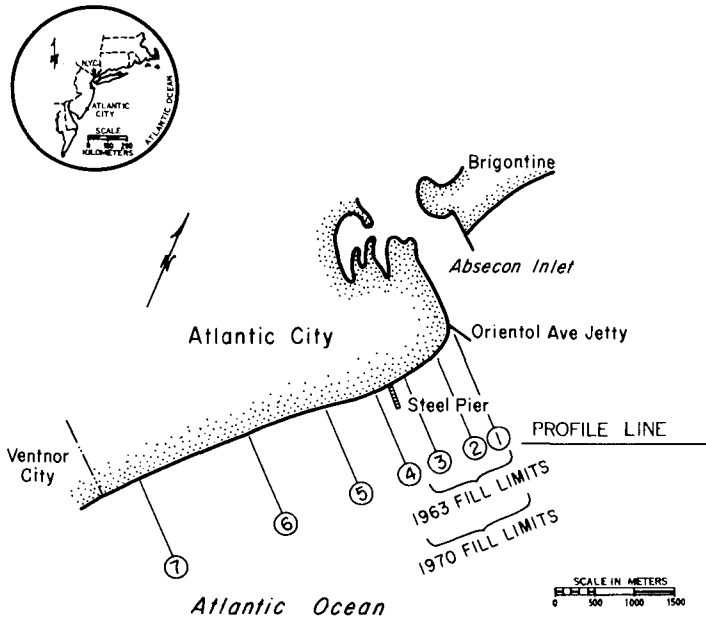
Figure 1. Location of Atlantic City Study Area and Profile Lines

seawall. The 5000 m northeast-southwest trending study reach includes the
entire Atlantic City beachfront from Absecon Inlet (Oriental Avenue) on
the north end to the Ventnor City limits. Approximately 94% of that shore-
front, one of the East coast's most popular recreational beaches, is publically
owned.

Table 1. NATURAL BERM CHARACTERISTICS - ATLANTIC CITY

Profile Line	Average Berm Width (from boardwalk in meters)	Average Berm Elevation (meters above MSL)	Average Foreshore Slope
1	180	1.3	.039
2	5	2.3	.066
3	75	3.0	.047
4	50	2.4	.046
5	60	2.2	.046
6	90	2.1	.039
7	110	2.0	.045

Beach Material. Natural beach material at Atlantic City is medium
to fine-grained sand (McMaster, 1954; and Ramsey and Galvin, 1971). Median
grain diameters range from 0.22 to 0.33 mm. McMaster found the sands to be
composed of approximately 98% well-rounded quartz.

Wave and Tide Data. Wave data were obtained at Atlantic City between
1957 and 1967 from a CERC staff gage located in 5.5 m of water on the Steel
Pier (Figure 1). Based on 18,132 observations, Thompson and Harris (1972)
determined the mean wave height at Atlantic City to be 0.9 m. Less than
1% of the waves exceeded 3 m. Figure 2 shows the weighted time duration,
in hours per month, of waves which exceeded a height of 1.2 m for the
survey years 1962-1967. The percent of the total monthly record which was
available is given in the upper center of each monthly record. Using the
mean monthly wave period of 8 sec, a wave height of 1.2 m results in a
wave steepness (wave height/wave length) of 0.021 at the gage.

Eight hundred twelve visual observations of the direction of wave
approach at the outer breaker zone were made at irregular time intervals
at Atlantic City between 1968 and 1973. A distribution of these data is
shown in Figure 3. The percent of the total monthly observations is given
for one of five possible sectors of wave approach identified in the upper
portion of the figure. Waves from Sectors 1 or 2, for example, approach
the shore at an angle north of the shore-normal orientation (Sector 3).

At Atlantic City, the mean tidal range is 1.2 m and the spring range
is 1.5 m. The maximum storm surge recorded was 2.0 m in 1951. In 1962,
1963, and 1964 the maximum storm surges were 1.3, 1.1, and 1.2 m, respectively.
In 1965 the maximum surge was 0.8 m, and in 1966, 1967, and 1968 the maximum
storm surges were 1.0, 0.9, and 0.8 m.
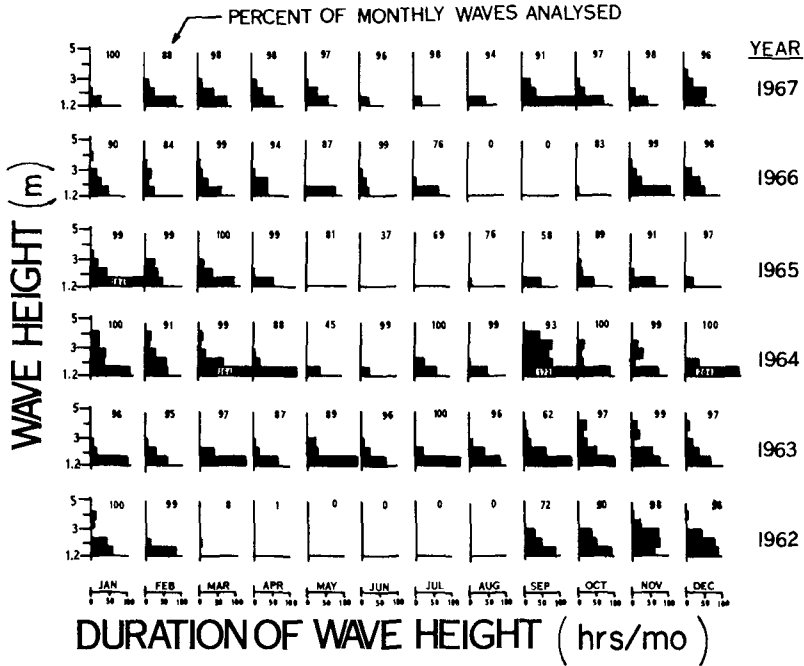
Figure 2. Monthly Time Duration of Waves which Exceeded 1.2 m at Atlantic
           City (1962-1967)

     Coastal Structures. In 1948 a 244-m long stone jetty (Oriental
Avenue jetty) was constructed on the north end of Atlantic City. Its
purpose was to stabilize Absecon Inlet which had migrated 183 m south-
west between 1840 and 1935. The jetty was extended to its present 359 m
length in 1961 and 1962. Groin construction at Atlantic City began in
1928 and since then twelve groins have been built on the northeastern
half of the study beach. Eight, which were built between 1930 and 1950,
are in existence today.

                        DATA COLLECTION AND ANALYSIS

     Field Procedure. Repeated surveys of the seven non-equally spaced
profile lines shown in Figure 1 were made between October 1962 and April 1972
on an irregular basis. A standard level and tape survey method was used.
Each profile began at a semi-permanent base station at the landward end
with data collected along a line normal to the shore at each change in
beach slope or every 15 m from the base station out to an elevation of
about -0.3 to -0.6 m MSL. Horizontal and vertical data were recorded to
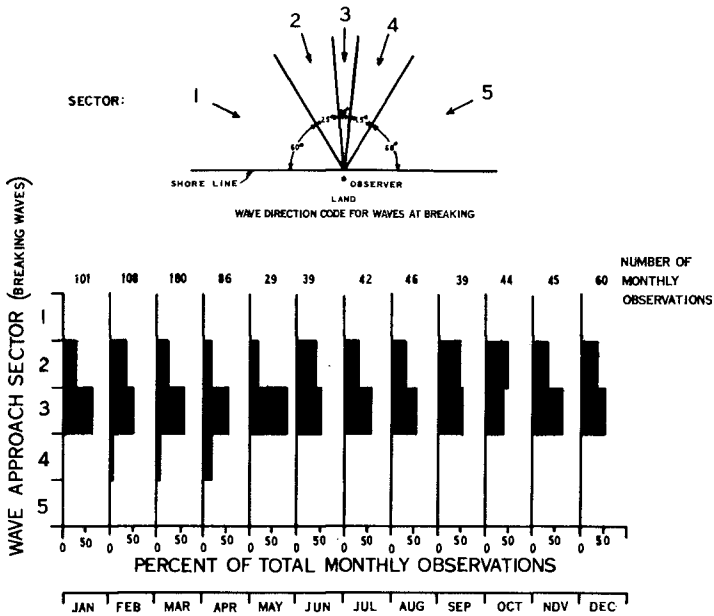
Figure 3.   Direction of Wave Approach, by Month, at Atlantic City

0.3 and 0.03 m, respectively.

Data Handling and Analysis. Survey data, recorded in standard note-
books in the field, were later transferred to plots or to optical scanning
forms and sent to CERC. Upon receipt, the data were automatically compiled,
edited, and put on magnetic tape. For each profile line, the data were
analyzed to obtain the sand volume (cross-sectional area under the profile
times a unit distance parallel to the coast) change between each survey and
the volume under the profile at the time of the first survey. Fixed bounds
in computing the volume change were the profile (upper bound), the MSL ele-
vation (lower bound), and the fixed base station (landward bound) near the
boardwalk. Few elevation changes occurred at the latter location so the
computed value is an accurate representation of the change in sand volume
above MSL. Changes in the position of the MSL shoreline were also computed.

BEACH FILL PROJECTS

     Two general procedures for artificial beach restoration and improve-
ment are stockpiling and direct placement (Hall and Watts, 1957). Stock-
piling is the establishment and periodic replenishment of a volume of
suitable beach material at the updrift sector of a problem area. Direct

fill placement is restoration by fill placed along the entire eroded sector.
The 1963 and 1970 Atlantic City projects were a combination of the two
procedures. In the northeast sector of the beach direct fill placement
was used. This material, however, acted as a stockpile and moved to the
southwest to nourish the downdrift beaches.

In February-May 1963, 430,000 m³ of fill, an average of 440 m³ per
lineal meter of beach (m³/m), were placed along 1160 m of beach southwest
of the Oriental Avenue jetty (Figure 1). The purpose of this fill was to
restore the beach after it was severely eroded by a March 1962 storm. The
beach deteriorated after the 1963 fill and in June and July of 1970 an
additional 610,000 m³ of material were placed on 1460 m of beach south-
west of the jetty (an average of 416 m³/m). Fill material in each case
was dredged from Absecon Inlet and pumped south to the beaches. It had a
mean grain size (0.3 mm) similar to that occurring naturally on the beach.

Profiles before and after fill placement are shown superimposed in
Figure 4. Surveys in 1963 indicated that 145, 246 and 168 m³/m on Profile
Lines 1, 2, and 3, respectively, were placed above MSL, or 43% of the total
volume of fill. Following the 1970 fill, 216, 183, and 193 m³/m were placed
above MSL on the same profile lines, or 48% of the total fill volume.

For both the 1963 and 1970 fills, the post-fill shape of the profile
varied considerably along the coast (Figure 4). However, the shape was
similar at each profile line. At Profile Line 1 fill was placed mainly on
top of the 137-m wide berm while it was placed seaward of the pre-fill

Figure 4. Cross-section of Beach from Profiles Taken Before and After
           Beach Nourishment in 1963 and 1970

berm on Profile Lines 2 and 3. The artificial berm elevations were 2.4
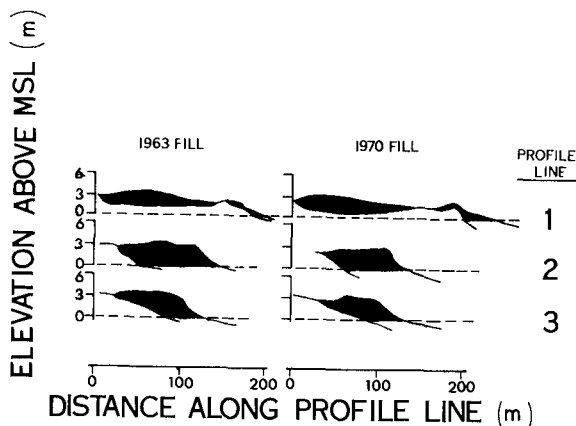to 3.0 m. The foreshore slope of the profiles varied from .02 (Profile
Line 1, 1963) to 0.11 (Profile Line 2, 1970).

<div align="center">RESULTS</div>

Changes Following Beach Replenishment. The volume loss rate of
sand from the fill region above MSL was greatest immediately following
placement. Thereafter the rate decreased with time in a consistant
manner. On individual profile lines, loss rates following the two fills
appear to be similar. This is shown in Figure 5 where the cumulative
change in sediment volume is plotted for the period 1962-1972. Note
that volume is related to the pre-fill datum volume = 0 of the initial
survey of 27 October 1962.

In the fill area the volume loss rate is also a function of distance
southwest of the Oriental Avenue jetty (Figure 6). At Profile Line 1 the
loss rate was rapid and constant until the profile line returned to the pre-
fill profile volume shown in Figure 5. Ninety percent of the fill volume
was lost at Profile Line 1 in six months following replenishment in 1963
and in eight months subsequent to the 1970 fill. These were mostly storm
changes with few accretional recoveries observed in the intervening periods.
Initially the loss rate on Profile Line 2 was similar to that on Profile
Line 1, but when 70% of the fill placed above MSL was lost the rate dropped
to less than one-half the initial rate. A maximum natural accretion of
10 m^3/m between surveys was measured before all of the fill above MSL was
lost. On Profile Line 3 the fill loss rate was uniformly low, however,
large natural recoveries of material were observed. For instance, during
the spring of 1965 a mean accretion above MSL of 51 m^3/m was calculated
which returned Profile Line 3 to near its maximum volume as measured at
the time of the fill. This situation was nearly duplicated in the
summer of 1967 when a recovery of 44 m^3/m was measured.

Following beach replenishment, steep artificial foreshore slopes
rapidly adjusted to the more gradual natural slope for that season of the
year. The adjustment frequently occurred at the expense of some fill sand
above MSL. The beach at Profile Line 2, for example, adjusted in less than
20 days to a more gradual slope which was maintained throughout the summer
of 1963. The slope flattening was accompanied by a sand loss of 11 m^3/m
from the subaerial beach.

Temporal Aspects of Beach Change. Three frequencies of beach change
can be identified in the survey data:

(1) *Changes Between Surveys (Including Storms).* Considerable vari-
ation was observed in the beach volume as a result of four storms for
which post-storm surveys were available (Table 2). The post-storm surveys
were usually made within two days following the storm. When weighted by
the distance between profile lines, these changes provide the average sand
loss for the entire Atlantic City coast as shown at the bottom of the table.
Maximum storm erosion occurred during the November 1963 storm (Hurricane
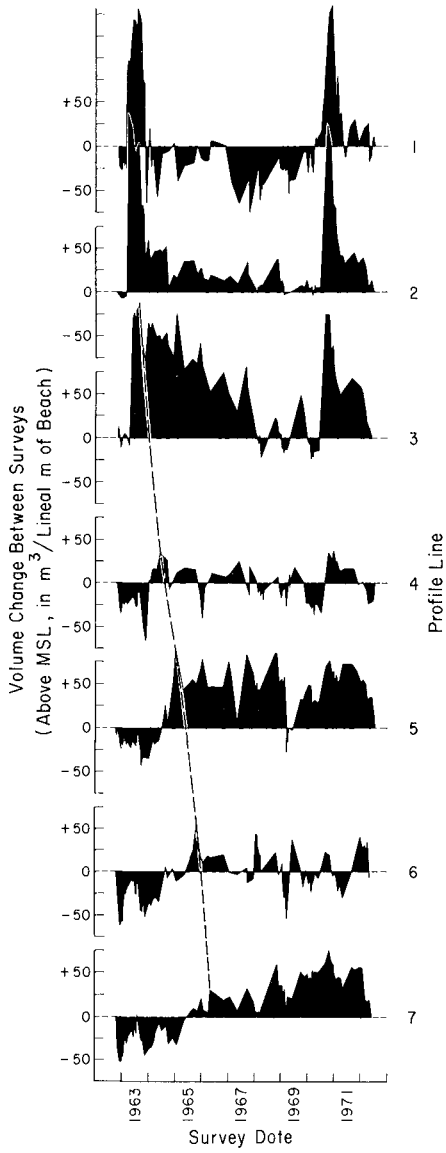
Figure 5. Change in Sediment Volume Between Surveys
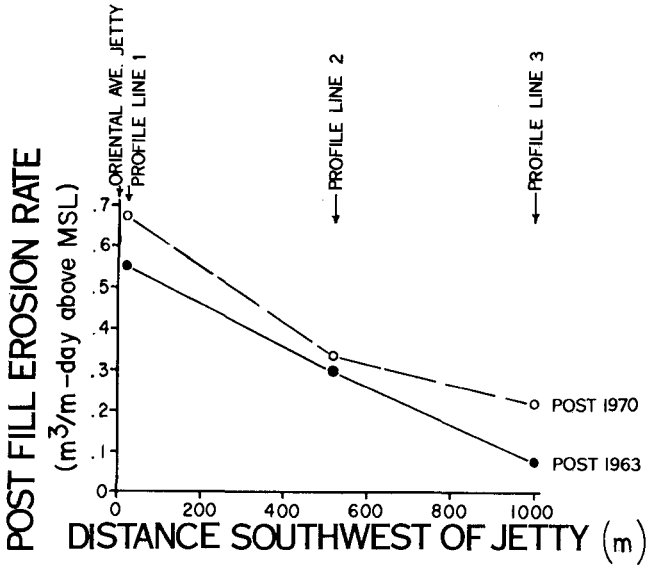
Figure 6.   Loss Rates Following the 1963 and 1970 Beach Fills During the
            Time Interval in which the Fill Volume was Reduced by 90 Percent
            Above MSL

Ginny) when an average 20 m^3/m, or 100,000 m^3 for the entire beach, was lost.
The average loss per lineal meter of beach for the four storms was 13 m^3/m.
Largest losses occurred on the northeast (fill) end of the study area.

     The largest volume loss measured between any two consecutive surveys,
which averaged about a month apart, is plotted in Figure 7 vs the associated
beach recession at MSL. The resulting volume loss above MSL per meter of
beach recession was 2.45 m^3/m. Maximum accretion between any two consecu-
tive surveys was of nearly the same magnitude as maximum erosion except on
Profile Lines 1 and 2, where maximum accretion values were only 32.6 and
27.6 m^3/m, respectively. The relationship with shoreline recession or pro-
gradation, as shown in Figure 7 was not always observed for lower volume
losses and gains.

     (2) *Seasonal Changes*. Clear trends of volume in storage above MSL
were evident when volume data are averaged by month. Figure 8 shows the
monthly sand volume, referenced to a mean zero datum, for all the profile
lines averaged for all survey years (1962-1972). The May-June interval
was a time of accretion above MSL while the period September - February is
one of sand loss. From June through October the subaerial beach lost an
average of 61 m^3/m of sand. The northeast beaches experienced the greatest
losses and gains of sand between months. Large variations between the

Table 2.   BEACH CHANGES ABOVE MSL (m^3/m) CAUSED BY STORMS AT ATLANTIC CITY

Profile Line			Storm Date		
	Nov 63	Dec 70	4 Feb 72	19 Feb 72	Average
1	−130	+52	+3.5	−43	−29
2	−61	−23	−20	−4.5	−27
3	−12	−24	−18	−7.0	−15
4	−19	+8.3	−12	−6.8	−7.4
5	−8.8	−18	−5.0	−19	−12.7
6	−7.5	+2.8	+3.3	−16	−4.3
7	−17	−9.0	−33	−22	−20
Average:	−20	−5.3	−10	−16	−13
Days Between Surveys:	36	9	8	7	
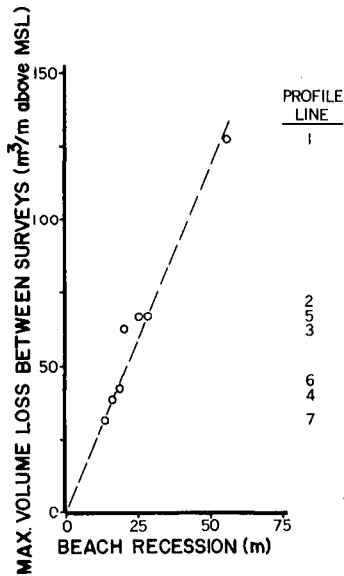
Figure 7.   Maximum Volume Losses on the Profile Lines vs Beach Recession
at MSL
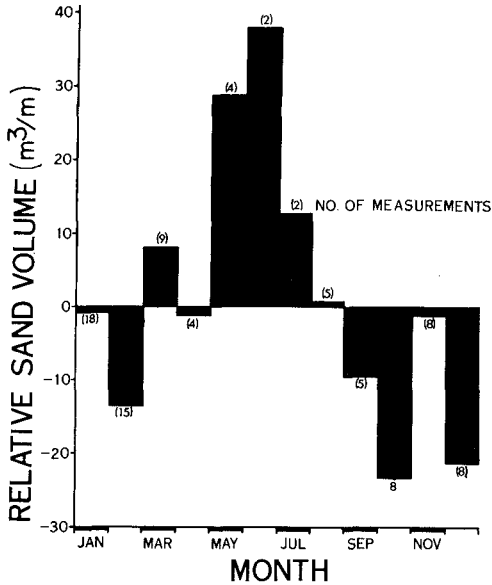
Figure 8.   Change in Sand Volume Above MSL on the Beach, by Month

same months occurred from one year to the next.

(3) *Yearly Variations*. Variations between years in the mean sand
volume on the beach were only partially related to the volume placed during
the fill projects. Figure 9 illustrates the average yearly volume change
relative to the beach volume in October 1962.

Alongshore Redistribution of Beach Material. Sand volumes on
beaches southwest of the nourished areas increased in a time ordered sequence
after the fill was placed while during the same period the nourished
beaches experienced erosion. Cumulative yearly mean volume change for
each profile line relative to the volume immediately after the beach was
nourished in 1963 is illustrated in Figure 10. Maximum accretion occurred
on Profile Line 4 in 1964, on Profile Line 5 in 1965, on Profile Line 6
in 1968 and on Profile Line 7 in 1969.

The dashed lines in Figure 5 also illustrates what appears to be a
progressive shift in beach volume maxima above MSL after the 1963 fill.
The migrating beach material, which caused the shoreline to prograde
seaward as it passed, decreased in volume with time and with distance
along the shore from Profile Line 3. The locus of the maximum loss, trailed,
in time, the peak accretion and also moved to the southwest.
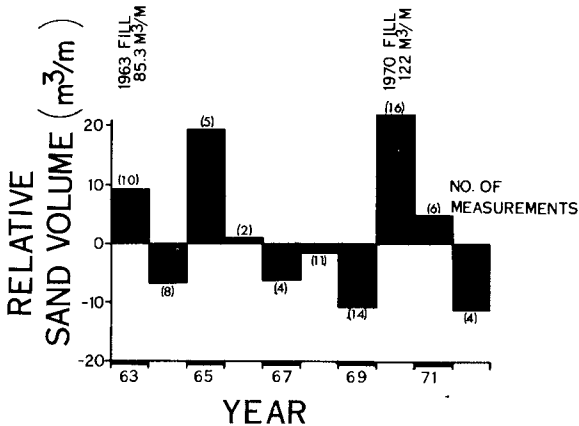
Figure 9.   Change in Sand Volume Above MSL on the Beach, by Year

DISCUSSION AND CONCLUSIONS

The behavior of fill material following nourishment projects at
Atlantic City in 1963 and 1970 was consistent. It was also in what
appears to be a qualitatively predictible manner. Beach survey data
and wave data provide the following information on where, when, and how
much artificial and natural beach material is eroded or deposited, and
in what direction it is transported:

(1) *Volume Loss vs Beach Retreat.* An estimate of the short and
long term beach volume fluctuations, especially those that accompany
shoreline retreat, is important in designing the safe width of a protective
beach. At Atlantic City the maximum measured volume loss above MSL per
meter of shoreline retreat at MSL was 2.45 m^3/m (Figure 7). Since 43 and
48%, respectively, of the fill was placed above MSL in 1963 and 1970, a
meter of beach retreat might be expected to be accompanied by an actual
loss of 5-6 m^3/m of fill material.

(2) *Beach Fill Losses.* Loss rates for fill material were much
larger than loss rates of adjacent natural material. Following the 1963
fill program 50,000 m^3 were lost in eight months, while 84,000 m^3 were
lost in 15 months subsequent to the 1970 fill. When averaged over the
fill area the loss rates were 65 and 47 m^3/m-yr, respectively, or twelve
and nine times the mean annual loss from the entire subaerial Atlantic
City beach.

(3) *Foreshore Slope Adjustment.* Foreshore slopes in the fill region
of Atlantic City adjusted rapidly to the natural slope of the season, and,
though other factors were involved, when the fill was placed on slopes
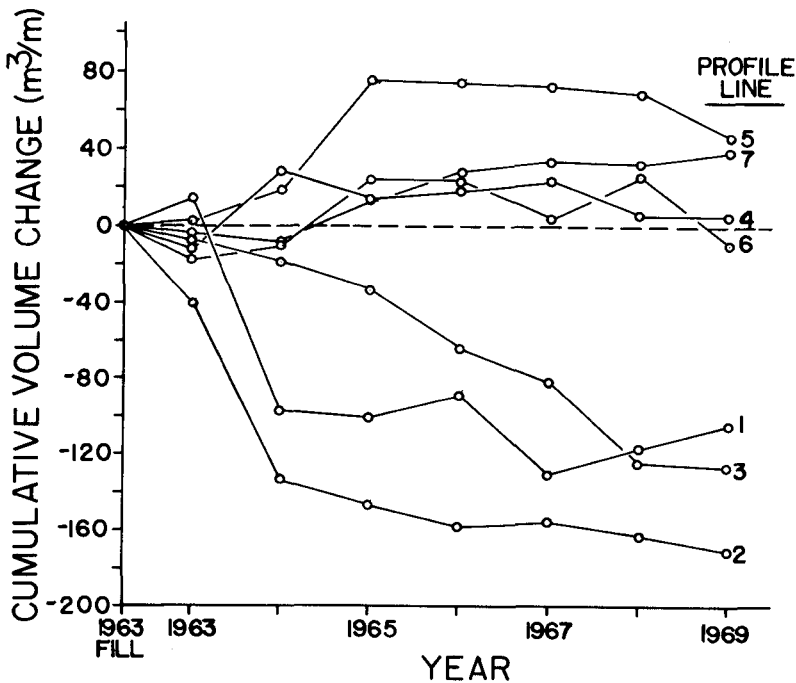
Figure 10. Yearly Change in Sand Volume Above MSL at each Profile Line

greater than the natural slope a small volume of sand (about 10 m^3/m) was
lost. Conversely, were the fill slope was less than the natural slopes,
the foreshore slope remained stable.

    (4) *Net Yearly Sand Loss*. Between the non-fill years 1965 and 1969
the mean annual sand loss from the entire 5000 m shoreline averaged 5.3
m^3/m-yr above MSL (Figure 9). This is the best approximation to the
natural beach loss available; however, the gain or loss of sand from one
year to the next was highly variable. Consequently, a useful expected
yearly sand loss, or gain, is difficult to predict.

    (5) *Annual Sand Losses*. The mean yearly gain or loss of sand to the
subaerial beach (Figure 9) appears fairly well characterized by the number
and severity of autumn and winter storms. In 1965, for example, a year of
few storms, 95,000 m^3 (19 m^3/m) of sand were added to the beaches. Con-
versely, in 1964, a year of frequent storms, 33,000 m^3 (6.6 m^3/m) of sand
were lost from the subaerial beach. The duration of waves that exceeded
a steepness of 0.021, which were usually associated with storms, was, in

1964, more than twice that of 1965 (Figure 2). A wave steepness of 0.021 was used because a steepness between 0.02 and 0.025 is frequently applied to the design of prototype beaches to designate the cutoff point between waves causing erosion and those causing accretion. Saville and Watts (1969), however, have pointed out that although these values are commonly used, they are derived mostly from laboratory studies and are doubtful when applied to a field situation. For the North Sea coast, Schijf (1959) observed a relation-ship between winter gales and their effect on beaches which was similar to that of Atlantic City.

(6) *Monthly Changes in Beach Volume.* Summer was the season of natural beach accretion and autumn and winter were predominately seasons of erosion (Figure 8). As observed with yearly changes, there was a direct relationship between monthly sand volume above MSL and the monthly frequency of waves greater than 1.2 m (Figure 2). Frequent high waves in the period September–February resulted in a low volume of sand in storage above MSL, while the absence of such waves between May–July allowed sand accretion. A mean 38 m^3/m above the average of all surveys was observed in June, and a mean 23 m^3/m less than the average was observed in October.

(7) *Storm Losses.* An average storm loss, based on four storms, for the entire Atlantic City beach above MSL, was 13 m^3/m (Table 2). The maximum loss for a single storm was 20 m^3/m averaged for the entire coast, and the minimum was 5.3 m^3/m. Losses on the nourished profile lines were two to five times greater than on other profile lines. The maximum loss on any profile line was 130 m^3/m (Profile Line 1) resulting in a MSL shoreline retreat of 53 m.

(8) *Beach Change Intervals.* An analysis of the survey data indicates that the long term erosion problem in the fill region was caused primarily by abrupt events (storms). These storm losses (Table 2), for which there was in-complete later recovery, accompany cyclic seasonal changes and yearly changes (Figure 8 and 9). Figure 11 summarizes beach volume changes measured during the 1962 and 1972 study period. For the entire study beach the magnitude of storm losses was greater than the sand volume change between years and less than that between months. Monthly changes were about twice the variation observed between years while yearly variations were two to three times as large as the mean annual loss for the 1965-1969 interval. These data may be of use in determining when it is necessary to artifically replenish the protective beach, and in determining when a natural recovery may be expected.

(9) *Direction of Alongshore Movement.* Periods of shoreline advance which alternated with periods of shoreline retreat indicate beach material moved alongshore (and above MSL) in "humps" or waves. These features have been observed elsewhere, e.g. Bruun (1954) along the North Sea coast. The time dependent movement of the sand volume maximum in Figures 5 and 10 also indicate transport to be in a net southwest direction. This movement was directly related to the direction anticipated using wave data (Figure 3). The mean direction of wave approach for all months except April was north-east of shore-normal which suggests that net alongshore currents should
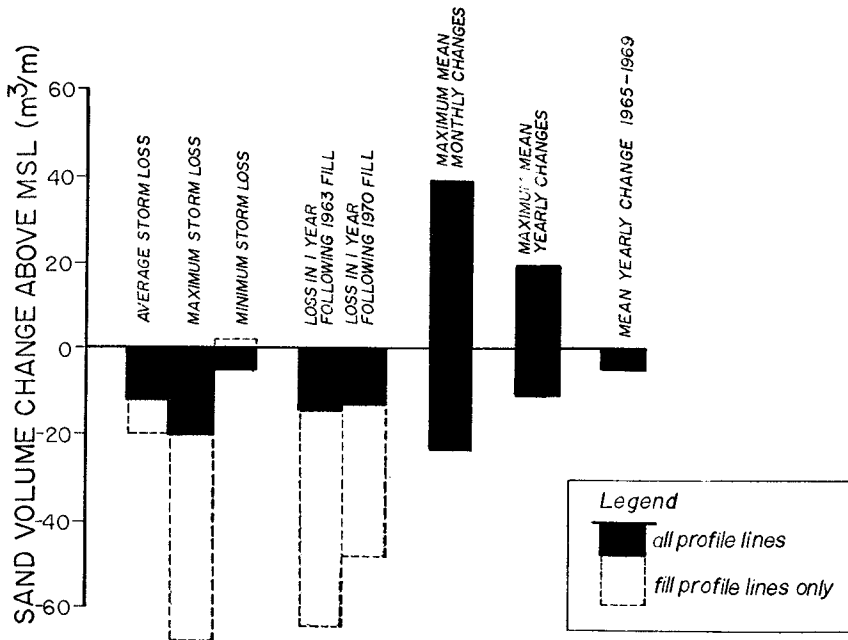
Figure 11. Maximum Volume Changes Above MSL Measured During the Period 1962-1972

be to the southwest. Waves from southwest of shore-normal were as common as those from the northeast during April. March and April were the only months in which a significant portion of the waves approached from south of shore-normal, and they were also the only months in which the survey data indicated a reversal in the direction of sand movement. Figure 10 reflects this reversal and shows the increase in volume at the Oriental Avenue jetty (Profile Line 1) measured during the second quarter in 1963 (Figure 5).

(10) *Rate of Alongshore Movement*. The migration rate of the volume maximum following the 1963 fill was 2 m/day while that following the 1970 fill was 3 m/day (Figure 5).

(11) *Volume of Alongshore Movement*. In 1964 the sand volume within the subaerial "hump" was 46 m^3/m above MSL, while in 1965 it was 40 m^3/m. At a southwestward rate of movement of 2 m/day, the maximum transport above MSL on Profile Line 4 in 1964 was 34,000 m^3/yr. This assumes that the entire "hump" was moving at a constant rate. In 1965, the maximum volume transported above MSL was 30,000 m^3/yr which indicates the volume decreased with time and distance from the date and location of the fill. Near Absecon Inlet, Caldwell (1966) estimated a net longshore transport rate to the south-

east, above and below MSL, of 76,000 m³/yr, or slightly over twice that
observed above MSL following the 1963 beach fill.

(12) *On-Offshore Sand Movement.* It is difficult to determine the
total volume of sand that moved in an on-offshore direction vs an along-
shore direction because surveys were not available below MSL. However,
since the difference in sand volume above MSL between summer and winter
was similar at all seven profile lines and relatively consistent from
year to year, much of the average 60 m³/m seasonal change must have been
the result of on-offshore exchange. Such on-offshore movement has been
noted by many observers, including Watts (1956) at Ocean City, New Jersey;
in Harrison County, Mississippi (1958); and at Virginia Beach, Virginia
(1959); and Perdikis (1961) on a number of replenished New England beaches
They found that fill material lost from the beach above MSL was transported
directly offshore. They also found that, subsequently, much of it was moved
onshore again or moved in an alongshore direction. Based on the available
data at Atlantic City, the on-offshore movement is about two and one-half
times the volume which moved alongshore and above MSL following the 1963
fill. The importance of the net longshore movement is that it results
in a permanent loss to the study beach while the on-offshore movement
is cyclic and mostly non-permanent.

GENERAL IMPLICATIONS

(1) A localized feeder beach near the jetty (Figure 1) would result
in the maximum residence time of fill sand on the problem beaches. Res-
idence time is the time interval that a unit volume of fill material re-
mains in the eroding beach region. Because the updrift fill areas nourish
fill areas to the southwest, fill loss rates above MSL decrease away from
the jetty and material placed at the most updrift location remains in the
problem beach system the longest. The beach near the jetty is, in addition,
closest to the present fill source at Absecon Inlet. The jetty inhibits
return flow of fill material to the inlet.

(2) The predominant sand movement to the offshore region appears to
occur between September and March. The greatest subaerial fill losses would
be expected to occur then and the residence time of fill placed during that
period would be less than for fill placed during the spring.

(3) When natural conditions are similar, large volume beach fills
placed within the reach of waves generally experience loss rates consider-
ably above the average non-fill loss rate. Smaller volumes of fill, placed
more frequently, would probably lessen the loss rate and increase the res-
idence time of fill on the problem beach.

(4) It appears that optimum feeder beach use at Atlantic City would
be after April when longshore current reversals are at a minimum. Follow-
ing April nearly all material that moves alongshore would be expected to
move and nourish the beaches to the southwest.

(5) The possibility of migrating accretional features, even three
or four years after the fill, should be considered when using surveys to

evaluate the total effectiveness of a beach fill project since the accretional phase at any location may not be permanent, but may be followed by an erosional phase.

(6) The offshore area should be surveyed to account, as much as possible, for the total sand budget.

(7) A survey made in the spring or summer will generally indicate a larger sand volume on the beach than one from the autumn or winter, even when the mean yearly volume is unchanging. One survey per season would provide a better means to determine net sand loss than a single survey per year.

REFERENCES

Bruun, Per, "Migrating Sand Waves and Sand Humps, with Special Reference
     to Investigations Carried Out on the Danish North Sea Coast," In
     Proceedings of Fifth Conference on Coastal Engineering, Grenoble,
     France, 1954, p. 269-295.

Caldwell, Joseph M., "Coastal Processes and Beach Erosion," Journal of
     the Society of Civil Engineers, Vol. 53, No. 2, 1966, p. 142-157.

Galvin, Cyril J., Jr., "CERC Beach Evaluation Program: 1962-1968,
     Background," Unpublished paper of the U.S. Army Coastal Engi-
     neering Research Center, 17 July 1968, 30 p.

Hall, Jay V. and George M. Watts, "Beach Rehabilitation by Fill and
     Nourishment," In ASCE Transactions, 1957, p. 155-177.

McMaster, Robert L., "Petrography and Genesis of the New Jersey Beach
     Sands," State of New Jersey Department of Conservation and
     Economic Development, Geology Series Bulletin No. 63, 1954, 239 p.

Perdikis, Harry S., "Behavior of Beach Fills In New England," In Journal
     of the Waterways and Harbors Division ASCE, V. 87, No. WW1, 1961,
     p. 75-110.

Ramsey, Michael D. and Cyril J. Galvin, Jr., "Size Analysis of Sand Samples
     from Three Southern New Jersey Beaches," unpublished paper, U. S. Army
     Coastal Engineering Research Center, Washington, DC, 1971, 47 p.

Schijf, J. B., "Generalities of Coastal Processes and Protection," In
     Journal of the Waterways and Harbors Division, ASCE, V. 85, No. WW3,
     1959, p. 1-12.

Saville, Thorndike, Jr., and George M. Watts, "Coastal Regime-Recent U. S.
     Experience," Coastal Engineering Research Center, Reprint 3-70, June 1969.

Thompson, Edward F., and D. Lee Harris, "A Wave Climatology for U. S.
     Coastal Waters," In Offshore Technology Conference, 4th, Houston, 1972,
     Paper No. 1693.

Watts, George M., "Behavior of Beach Fill at Ocean City, New Jersey,"
     Beach Erosion Board Technical Memorandum No. 77, 1956, 33 p.

Watts, George M., "Behavior of Beach Fill and Borrow Area at Harrison
     County, Mississippi," Beach Erosion Board Technical Memorandum No. 107,
     1958, 14 p.

Watts, George M., "Behavior of Beach Fill at Virginia Beach, Virginia,"
     Beach Erosion Board Technical Memorandum No. 113, 1959, 26 p.

Watts, George M., Limberios Vallianos, and Robert A. Jachowski,
     Paper S. II-2, XXIII International Navigation Congress,
     Brussels, 1973, 25 p.

CHAPTER 81

BEACH RESTORED BY ARTIFICIAL RENOURISHMENT

Douglas Edward Newman

Senior Scientific Officer
Hydraulics Research Station, Wallingford, England

ABSTRACT

This paper describes how a once popular pleasure beach became denuded by the abstraction of sand for industry and how, in more recent times, it was restored to its former levels. The history of the area has been studied in some detail, and it can be seen that the lowering of the beach caused progressive damage to the sea wall, eventually leading to flooding of some parts of the frontage.

In the 1960's a parapet was added to certain sections of the sea wall, and local flooding was alleviated, but the lower parts of the wall and apron suffered continuously from wave attack and the situation deteriorated to an extent where complete reconstruction of the sea defences had to be considered. It was shown that a scheme involving beach renourishment by the pumping of sand from offshore provided a more economical solution and the area now enjoys the amenities provided by the restored beach.

. . . .

History of the Area.

Portobello beach lies on the South Bank of the Firth of Forth, about five kilometres from the City Centre. (Fig 1)

An early plan, dated 1783, shows that much of the foreshore, about one mile in length, was privately owned and in some cases divided by fences erected by individual owners. A description of the beach in 1798(1) states that it consisted of golden sands and dunes, and that it was free of stone or boulders - it was, in fact, the selected bathing area of the city dwellers.

Even at this time there was some industry in Portobello, and it was described as a prominent centre for the manufacture of earthenware and tiles, and quantities of building bricks. In 1799, the population of the town was stated to be 300.

In 1824, there are records of a crystal and flint glass industry and ten years later the labour force attached to those works was about 600. From 1834 onwards, the output of the glass works was devoted to the making of bottles and this continued until at least the turn of the century.

The increase in the population of the town led to many changes and in particular to the administration of the beach and foreshore. In 1860 a Promenade was constructed along part of the frontage, the maintenance thereof being derived from Public Subscription.
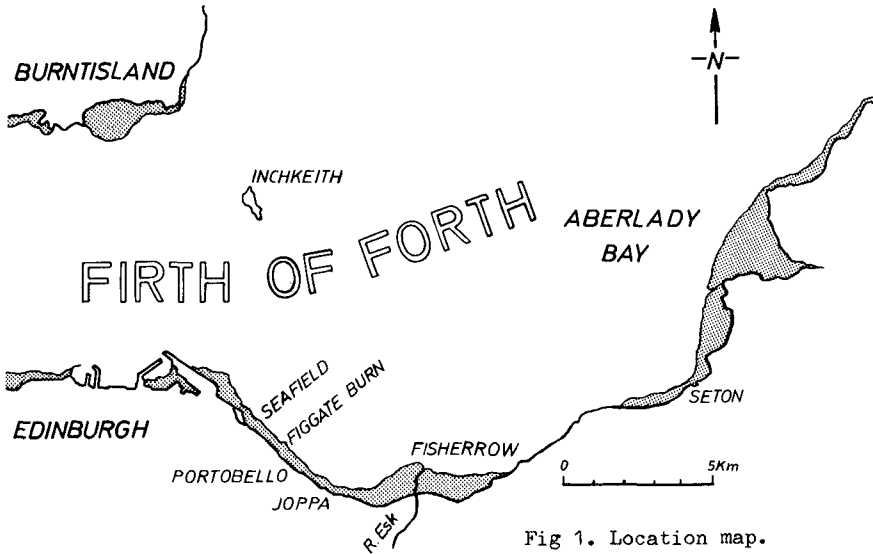
Fig 1. Location map.

    In 1871, a pleasure pier was built and by this time the area had
taken on the appearance of a resort, increasing in popularity year by
year.

    The glass industry prospered throughout these years, but the
continued removal of sand for the purpose went apparently unnoticed.
It is recorded that the Promenade was severely damaged by wave action
during storms on a number of occasions between 1877 and 1896, but it
was rebuilt and eventually extended over the entire frontage - a
distance of about 1 mile.

    It may be of interest to note that the bottle factory was at the
western end of the frontage where more recent research has shown a
net annual littoral drift of beach material from the east.   It could
be that the industry flourished partly on the feed of material towards
it, and partly at the expense of the foreshore which was being reduced
in level every year. We may never know the exact cause, but it is
significant that by 1926, thirty years later, the beach level was
possibly as much as two metres below the promenade level, and the wall
was exposed to heavy wave attack in times of storm.

Early remedial measures.

    An apron of loose rubble with a covering of cement mortar was
built up along parts of the wall, but successive periods of bad
weather made severe inroads on this structure. As a further precaution
steel sheet piling was driven at the toe of the apron, but this too
was occasionally undermined.

    The glass industry no longer existed but the building trade now
had an interest in the material of the beach, and it is known that the

practice of removal continued until at least the mid 1930's.   Photo-
graphic records of those days show lines of horses and carts filled
with sand and stones leaving the beach. It is clear from these pictures
that the foreshore had by this time been reduced to stones and muddy
sand. There had been a great change in 40 years.

     The records show that the apron was extended to other parts of the
Promenade in 1940, and that just after the war £30,000 was spent on
repairs to the frontage.

Flooding.

     In 1958, the City Engineer's Department consulted the Hydraulics
Research Station regarding the state of the beach and the danger of
flooding of some of the houses along the promenade. As a result, model
tests were performed to establish the most suitable design for a para-
pet to be added to parts of the sea wall, and a few years later
portions of the promenade were protected by this means. At the time,
however, it had become clear that most of the sea wall required some
maintenance and a major scheme would have to be put in hand.   Either
the sea wall would have to be rebuilt or some alternative scheme
sought. The feasibility of a beach nourishment scheme was considered,
but no adequate method could be suggested.

Reappraisal.

     In 1970, the feasibility of renourishment was again considered.
Amongst other considerations the study was based on the results of an
offshore survey of bed material carried out in 1970 at the direction
of the City Engineer.

     What little sand remained on the beach at Portobello was very fine
and similar to that found immediately offshore. It had a mean size of
0.20 mm. The beach slope was 1:42 and at the sea wall the sand level
was between 2 and 3 m from the level of the promenade and about 1 m
below the level of MHWS. The mean spring tidal range at Portobello is
5.3 m.

     Any attempt to replenish the beach at this site was considered to
have a better chance of success if the sand used was appreciably
coarser than that already remaining. The area was exposed to consider-
able wind fetch from the N.E. Under wave action, coarser sand tends
to move in the layers close to the bed. Here not only is the drift of
water normally towards the shore, but the orbital velocities are higher
towards the beach than away from it. Hence coarser material has a
greater tendency to move shoreward than finer material which can be
entrained in the mid-depth layers where the drift of water is away
from the beach. (2)

     At Fisherrow and Seton, to the east of Portobello, the beach slope
was 1:12 and was made up of a coarser sand of 0.38 mm - 0.52 mm.   The
 offshore survey showed considerable deposits of coarse sand (median
size 0.27 mm) about 1 kilometre offshore of Fisherrow. Here, according
to borehole samples the available volume of material would have been
600,000 cu.m. This was roughly three times the requirements of a beach
renourishment operation.

The Sand Replenishment Scheme

    The operation of sand replenishment started in June 1972.   A 'bucket dredger' was stationed off Fisherrow at the 'borrow area'(Fig 2).
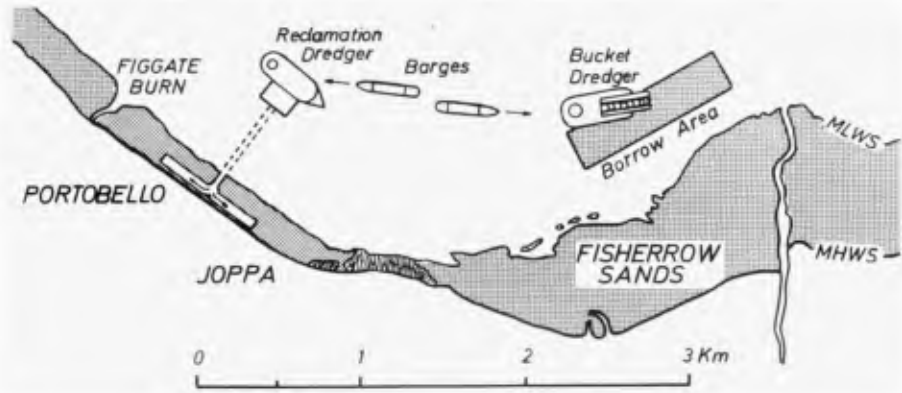
Fig 2. Renourishment scheme - general layout.

    This loaded self propelled barges (each having a capacity of 500 cu.m.) which conveyed the sand at the rate of 1 load per hour to a reclamation dredger positioned some 400 m off Portobello beach (Fig 3).

Fig 3. The reclamation dredger and pipeline.

The barges were unloaded by the suction head of the dredger and the sand transferred directly ashore via a 75 cm dia. submarine pipeline.

On the beach the pipeline was bifurcated at the middle point and valves were inserted into each leg so that pumping to either side of the beach could be controlled. The weather was generally calm through-out the operation which was completed in 4 weeks.

Six groynes, equally spaced throughout the length of the beach, were constructed to hold the sand from possible movement towards the west under the action of north-easterly gales.

The beach before renourishment stood at a slope of 1:42 and was composed of a median-sized sand of 0.20 mm. The restored beach was graded to a slope of 1:20, and after 18 months was standing at a slope of 1:23. The mean size of the sand was 0.27 mm (Fig 4).
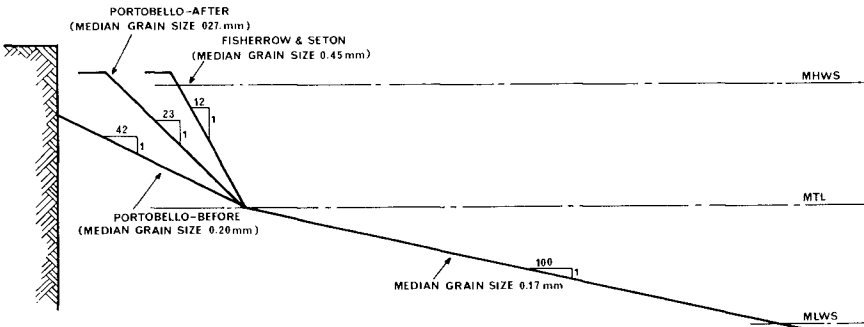
Fig 4. Beach slopes and median grain size.

Calculations on the volume of sand remaining in position show that after this period, which included nearly two winters, no loss of sand could be positively identified. The records are based on 30 cross sections throughout the total length of some $1\frac{1}{2}$ kilometres (Fig. 5).
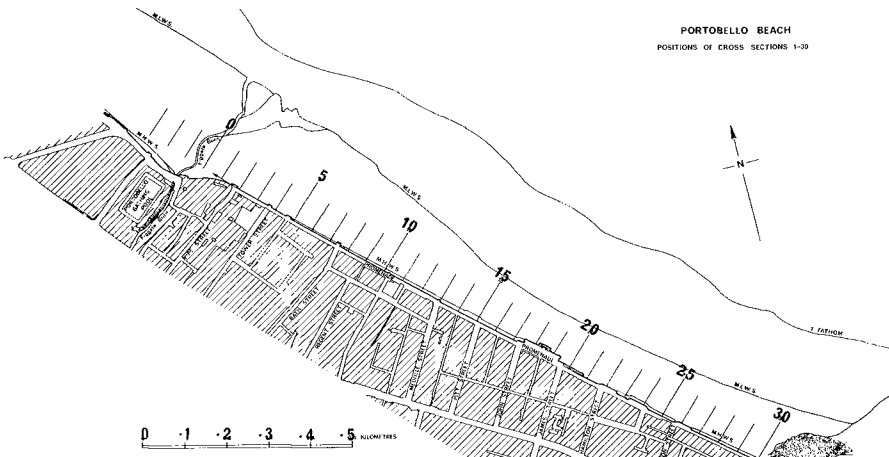
Fig 5. Plan view of beach sections 1-30.
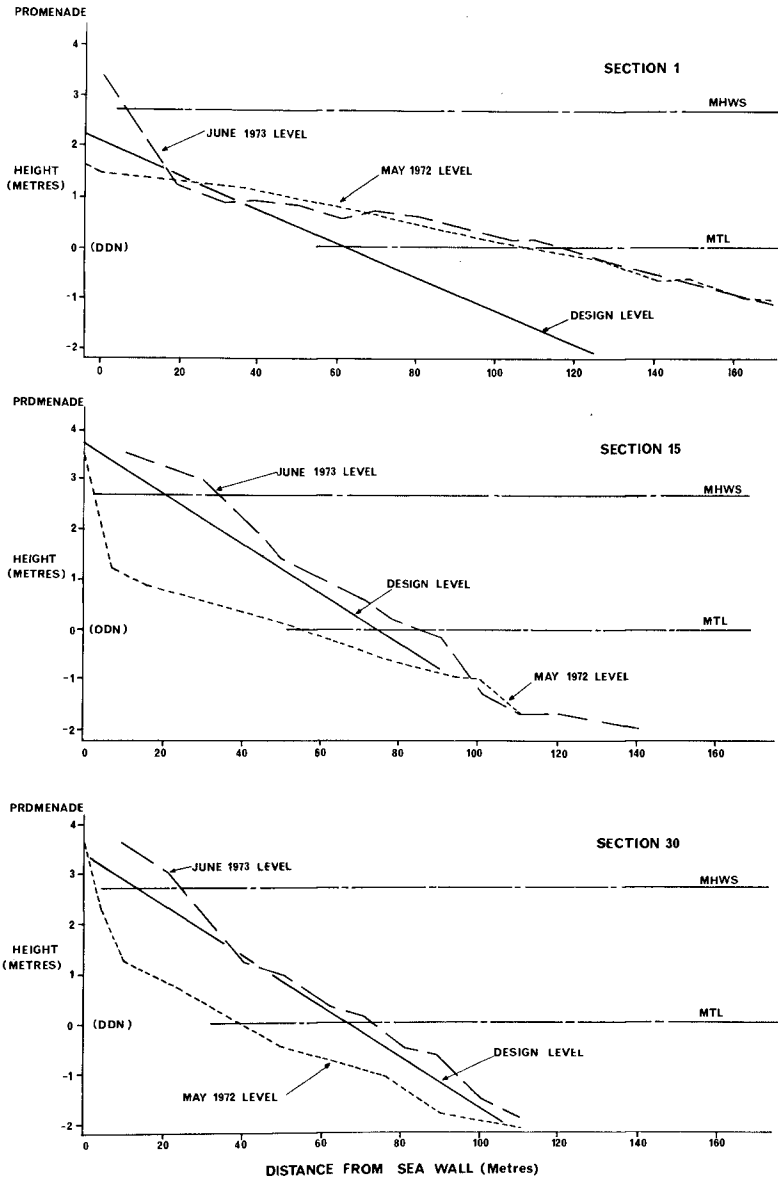
PORTOBELLO BEACH

Fig 6. Comparison of three beach sections.

(a) Intermediate Section before replenishment.

(b) Intermediate Section after replenishment.

Fig. 7. Portobello Beach.

(a)   Before renourishment.

(b)   After renourishment.

Fig 8. Portobello Beach near western limit.

(a) Before replenishment.

(b) After replenishment.

Fig 9. Portobello beach from the air.

and whereas it is evident that some spilling of the material has occurred at the ends of the restored beach, there is little sign of any appreciable movement offshore. Fig 6 shows the centre section and the terminal sections after 2, and Fig 4 the slopes and sand sizes of the neighbouring beaches compared with Portobello.

Figs 7 and 8 show two parts of the foreshore before and after the renourishment operation. Fig 9 is an aerial picture of the beach before and after the scheme commenced.

It is understood that the City Engineer's Department would want to replace sand losses from the new beach should they be greater than 10% of the volume placed. The quantities would be assessed on a calculation based on the beach profiles.

The cost of the scheme described in this paper was £300,000 for beach replenishment, and £60,000 for the construction of five timber (greenheart) groynes and one gabion (stone) groyne. Although the estimated littoral drift at Portobello is not considered to be high, it was thought that a 'spillover' of the newly won sand towards the West might create a dredging problem at the entrance to Leith Docks.

Recent measurements taken at groyne No. 1 (Section 1 Fig 5) show that there is an accumulation of sand on the East side and a difference in level of about 1 m across the groyne. The West side of the terminal groyne will be buttressed with stone to avoid further spillage.

References.

(1) BAIRD W. "The History of Duddingston and Portobello." Andrew Elliot, Edinburgh 1898.

(2) Unpublished report of work carried out at the Hydraulics Research Station, 1959.

CHAPTER 82

BEACH DEVELOPMENT BETWEEN HEADLAND BREAKWATERS

S.Y. Chew, Senior Principal Civil Engineer
Housing & Development Board, Republic of Singapore.

P.P. Wong, Lecturer, Department of Geography
University of Singapore, Republic of Singapore.

K.K. Chin, Associate Professor, Department of Civil Engineering
University of Singapore, Republic of Singapore.

ABSTRACT

Breakwaters in a series can be employed to protect sedimentary coasts. They are used to protect newly reclaimed land along the southeast coast of Singapore; they act as headlands between which sand beaches are formed. The development of these beaches takes place under conditions of low energy waves, a predominant wave direction from the southeast and an east-west littoral drift. The characteristics and development of three beaches over a one-year period are presented. Surveys of the reclaimed land show various beach types between the headland breakwaters. A relationship exists between berm orientation and headland breakwater orientation. Beach stability is tentatively indicated by the formation of a wide berm.

INTRODUCTION

One of the functions of the offshore breakwater is to protect the coast from wave action. By dissipating the wave energy along its entire length, the breakwater causes sediments in its lee to deposit and a shore salient is formed. If the breakwater is of sufficient length in relation to its distance from the shore and if the breakwater is built on a littoral drift coast, a tombolo will form joining the breakwater to the shore[1]. If the offshore breakwaters are placed in a series along a coast with a gentle offshore slope and a substantial littoral drift, tombolos will form behind the breakwaters between which bays will be sculptured by waves to form stable shapes[2]. These attached breakwaters would thus form a series of artificial headlands (Fig 1).

In nature, beaches between headlands are influenced by the position of the headlands. Where the headlands are closely spaced and a limited sediment supply exists, small pocket beaches are formed. Where the headlands are far apart and an adequate sediment supply exists, long and wide beaches are formed. Generally, between these two extremes most beaches between natural headlands take a shape that is related to the predominant wave approach; on the downcoast sector is a long and straight beach while on the upcoast end is curved beach. Such beaches

have been studied under various names; "zeta curve" bays (3), "half-
heart shape" bays (2), "headland-bay beaches" (4), "J-shaped curves" (5)
and "crenulate shaped bays" (6).

The curved segment of the beaches between natural or artificial
headlands has attracted much attention. Krumbein (7) suggested that
these beaches may approximate a logarithmic spiral. Yasso (4) confirmed
this observation in his study. Silvester (6) in his modal study estab-
lished a relationship between the logarithmic spiral constant and the
angle of predominant wave approach. A quasi-permanent shape was
reached when waves broke simultaneously around the model bay. As it is
difficult to measure the curved sector in nature, Silvester and Ho (8)
suggested the use of an indentation ratio to relate the bay's shape to
wave approach.

EAST COAST RECLAMATION SCHEME

The afore-mentioned concepts of headland breakwaters and beach
formation between them were applied in 1968 and are being applied on a
large scale along the southeast coast of Singapore, where a series of
headland breakwaters is used to protect newly reclaimed land. The
reclamation which is officially known as the "East Coast Reclamation
Scheme" is carried out by the Housing & Development Board which is a
statutory board responsible for public housing, in a number of phases
(Fig 2).

1   Phases I & II comprising 458 ha from Bedok to Tanjong Rhu were
reclaimed between April 1966 and May 1971. The fill came from the
nearby hills at Bedok and was conveyed to the sea by a continuous
conveyor belt system.

2   Phase III, which is west of Phase II, comprises an area of 67 ha
and involves the hydraulic placement of fill material behind an offshore
stone bulkhead. It was implemented in April 1971 and scheduled for
completion by the end of 1974.

3   Phase IV comprising 485 ha is an eastward extension of the
earlier two phases. It was implemented in April 1971 and will be
completed in early 1976. The same method of reclamation in the first
two phases is used here.

The headland breakwaters used in Phases I, II & IV to protect
the reclaimed land (Plate 1) are of two types:

a   Gabion breakwaters constructed on the foreshore of the newly
reclaimed land at low tide (Fig 3). The gabions used for the construc-
tion of breakwaters are PVC coated steel wire cages of 2x1x1 m, 3x1x1 m
and 3x1x$\frac{1}{2}$ m in capacity and filled with stones ranging from 0.3 m to
0.2 m in size. Each breakwater is built up with these gabions in three
layers rising from LWOST to approximately 0.9 m above HWOST. The length
of the gabion breakwaters varies between 28 m and 46 m depending on the
siting distance from the edge of the fill which is from 30 m to 60 m.
The minimum length of the gabion breakwater is in the order of 1$\frac{1}{2}$ wave
length. The breakwater spacing which varies from 120 m to 240 m is
determined by the allowable shoreline recession between headland break-
waters. The limit of recession was estimated on the assumption that

the downcoast sector of the beaches will be oriented with the predom-
inant wave approach. It varies from 25% to 30% of the headland
breakwater spacing.

b   Rip rap breakwaters constructed dry in the fill material along
a near straight edge of fill and subsequently become wet (Fig 4). The
area upon which each rip rap structure is to be constructed is first
overfilled, compacted and thereafter excavated in stages to form an
earth mound with a seaward slope of 1:2 and a landward slope of 1:1$\frac{1}{2}$.
A vynilon sheet used as a filtering medium to prevent removal of fill
material by wave action is then spread loosely over the entire mound.
On top of it are placed a 0.2 m layer of 0.15 m – 0.1 m stones, a
second 0.3 m layer of 0.3 m – 0.15 m stones, and lastly a layer of
0.5 m stones properly pitched. The rip rap structure extends 0.4 m
below LWOST to 1.6 m above HWOST. Subsequent wave action removes the
fill material to expose the rip rap breakwater which are spaced at
300 m to 360 m. The length of the rip rap breakwater varies from 55 m
to 67 m, which has to be such that it would not subsequently become an
"offshore island". This can be predetermined using the Silvester's
relationship between logarithmic spiral constant and the predominant
wave approach angle(6).

Plate 1. High aerial oblique of Phases I & II Reclamation

        Both types of headland breakwaters are used in Phases I & II.
The rip rap breakwater is being used in Phase IV.

        The objective of this paper is to present field data on beach
processes and development of the beaches between the headland break-
waters of the project. Data monitored at the first four headland
breakwaters of Phase IV from August 1972 to July 1973 are presented
(Plate 2). The one-year data are analysed for the northeast monsoon
(December 1972 – March 1973) and the remaining period (August 1972 –
November 1972, April 1973 – July 1973), as the variation between these
two periods is large. The results of the two surveys of Phases I & II
in April 1972 and February 1974 are also included.

Plate 2. Low aerial oblique of the studied area

BEACH PROCESSES

Winds

Winds were recorded at the Changi Aerodrome at a point 1.2 km
from the sea and 10 m above mean sea level. Sharp contrasts in
direction and velocity of winds were recorded for the northeast monsoon
and the other period (Fig 5). Winds during the northeast monsoon are
predominantly from N-NNE and are less than 5 m/s. Winds during the
other period are from the southeast quadrant with speeds of 2-3 m/s.

Tides

The tides are essentially semi-diurnal of a mixed type with a
mean range of approximately 2.64 m. The maximum range recorded was
3.49 m on 11 February 1974.

Waves

A resistance wave staff coupled to a battery operated Rustrak
recorder was used to record waves. The waves were measured in 3.5 m
water at the end of an open jetty; they were sampled once every 2 hours
between 0830 hours and 1700 hours during which their direction was also
determined by a compass. The data from August 1972 to July 1973 were
analysed in accordance with Draper(9) and reduced to deep water waves
by linear wave theory and refraction diagrams(10), an example of which
is given in Fig 6.

The cumulative distribution of significant wave height, H_s and
maximum wave height, H_{max} for the recorded period is shown in Fig 7.
This figure can be used to determine the proportion of time for which
H_s or H_{max} exceeded any given wave height.

The frequency distribution of H_S, H_{max} and zero-crossing period, T_z, are also given for the northeast monsoon and the other period (Fig 8). During the northeast monsoon the highest value of H_{max} was 1.1 m and for more than 65% of the time, H_{max} did not exceed 0.6 m. During the other period H_{max} exceeded 0.6 m for less than 10% of the time. 90% of T_z fell between 2.5 and 4 seconds during the northeast monsoon while T_z was predominantly around 3 seconds during the other period.

The relationship between H_S and T_z for the period of northerly winds and southeasterly winds are given in Fig 9. The numbers represent the number of occurrences which fell within the range of H_S and T_z values. The dashed lines represent wave steepness (H_S/L_o). For the northerly winds, 0.2 - 0.3 m and 3-4 second waves prevailed. For the southeasterly winds, 0.2 m and 2.75 second waves prevailed.

The frequency of occurrence of various significant wave heights H_S for one year is given in Fig 10 which shows that predominant wave approach is from the southeast quadrant resulting in a nett westward drift.

The relationships computed for wind speed, U, vs H_S and T_z suggest a stronger link between waves and southeasterly winds (ie onshore winds) than between waves and northerly winds (ie offshore winds) (Fig 11). This suggests that the southeast coast of Singapore is washed by refracted swell from the South China Sea.

For onshore winds, the empirical relationships

H_S = 0.087 U and

T_z = 3.154 $U^{-0.2}$

are being used for planning purposes on the southeast coast.

Currents

Drogue experiments and a current meter measurement were carried out at Phase IV. The details of the two types of drogues used are shown in Fig 12. The drogues were released from a boat and their movements were picked up by two theodolite stations from the shore. Their positions were later plotted on large scale plans and the velocity of current computed. Simultaneously, tide, waves and winds at hourly intervals were recorded throughout the period of observation.

May 2, 1973 experiment:

Drogues seeded 300 m offshore decelerated towards high tide and immediately after high tide they changed in direction and accelerated (Fig 13). The change in direction is clockwise.

May 3, 1973 experiment:

The change in direction was not immediately after high tide for drogues seeded 1000 m offshore (Fig 14). Within 50 m of the shore, the velocity of drogues fluctuated due to the effect of reflection of oblique waves from the headland breakwaters.

In-situ current measurement at 1000 m offshore and in 15 m depth of water was carried out for 25 hours on October 18, 1973 to determine the speed and direction of current at various depths. The current velocity was resolved into north and east components. These were plotted against time and smooth curves obtained. The north and east components of current at each lunar hour were extracted from the curves for the construction of a tidal current ellipse. An example for the current is in the east-west direction (Fig 15). The current flows eastward for approximately 11 hours with a maximum velocity of 1.1 m/s and westward for approximately 14 hours with a maximum velocity of 0.5 m/s. The values of the westward flow are of the same magnitude as those in the May 3, 1973 experiment.

From the data collected so far it appears that the tidal current in the Singapore Straits flows eastwards during the first main ebb between the highest high water and the lowest low water for about 11 hours and the remaining 25 hours the tidal current is westwards and that the change in current flow is not related to tide.

<center>BEACH DEVELOPMENT</center>

Grain Size

The fill material for Phases I, II & IV is Older Alluvium, which is of Quaternary age and consists of semi-consolidated gravels, sands and clays(11). Under wave action, the fines are removed leaving behind sands and gravels between the headland breakwaters.

The grain size characteristics of the fill material between the first four headland breakwaters (A-D) in Phase IV are given in Fig 16. The fill material was sampled along 20 stations on July 1972. The median size varied from 0.03 mm to 0.66 mm and the average median size along the three bays was 0.19 mm.

Subsequently, after wave action samples of beach material at mid-tide were taken on May 1973 and at the upper foreshore, mid-tide and lower foreshore on August 1973. The characteristics of these samples are shown in Fig 17.

May 1973 Mid-tides Samples:

The median size varies from 0.5 mm to 1.9 mm with an average of 0.97 mm. Coarser sediments are found around the headland breakwaters. Sorting is generally poor except between the headland breakwaters.

August 1973 Samples:

(a)   Upper foreshore: The median size varies from 0.26 mm to 0.4 mm with an average of 0.3 mm. The sediments are coarser at the headland breakwaters than between the breakwaters. Sorting is good varying from 1.2 to 1.6.

(b)   Mid tide: The median size varies from 0.4 mm to 1 mm with an average of 0.63 mm. Similarly, coarser sediments are found around the headland breakwaters. There is a slight improvement in sorting between the headland breakwaters.

(o) Lower foreshore: The median size varies from 0.25 mm to
1.9 mm with an average of 0.76 mm. In contrast, finer sediments are
found around the headland breakwaters. Sorting in this zone is poorer.

Beach & Offshore Changes

        Beach changes along the first four headland breakwaters in
Phase IV were monitored for a year. As the beach forms between each
pair of headland breakwaters a J-shaped bay develops. The beach
geometry varies along the bay and changes with the seasons. 20 beach
profiles along the beach between headland breakwater A and headland
breakwater D were surveyed on October 1972 and April and October 1973.
Data are given for profiles 14, 16 and 18 in the third bay (Fig 18) to
illustrate the following points:-

        (a) During the northeast monsoon, erosion across the foreshore
occurs at the upcoast section and accretion at the downcoast sector to
form a straight berm in each bay. The mean beach gradient on the up-
coast curved sector and downcoast straight sector is 1:10 and 1:8
respectively.

        (b) During the other period, erosion occurs at the downcoast
straight sector and accretion at the upcoast curved sector of the bay.
The mean beach gradient for both the upcoast and downcoast sectors is
generally 1:9.

        (o) There is marked alongshore variation in the maximum height
of the beach according to the seasons. At the end of the northeast
monsoon, the height of the beach at the downcoast straight sector is
0.5 m higher than the upcoast curved sector. During the other period,
the height of the beach at the downcoast end is 0.9 m lower; this
reflects the degree of exposure to wave action.

        The offshore topography also varies. Echo soundings were also
carried out in October 1972 and April and October 1973. The changes in
the offshore topography of the three bays between these periods are
given in Fig 19 and 20.

        A comparison between October 1972 and April 1973 seabed contours
shows erosion of the offshore during the northeast monsoon when
predominant waves arrive from the southeast quadrant. Further, due to
diffraction and refraction around the downcoast end of the headland
breakwater, the upcoast portion of the bay retrograded to form a
J-shaped bay (Fig 19).

        A comparison between April 1973 and October 1973 seabed contours
indicates a general accretion of the offshore topography in the period
after the northeast monsoon when waves come from the SSW to SE. The
shape of the bays remains unchanged (Fig 20.)

        Although the J-shaped bay prevails throughout the year between
each pair of headland breakwaters in Phase IV, changes in the beach
geometry and offshore topography suggest that an equilibrium shape has
not been reached. For land-use planning purposes, it is necessary to

determine the limit of erosion. Silvester(6) has suggested that the
relationship between the logarithmic spiral constant and the wave
obliquity can be used to determine the equilibrium shape of beaches
between headlands. The probable shapes based on this criterion of the
three bays for wave approach from the southeast are given in Fig 21.
This assumes that the westward littoral drift is reduced or cut off.

Beach Types

A survey of Phases I & II in April 1972 shows that beaches
between headland breakwaters take various shapes(12). Based on the
development of the beach, the formation of the berm, the shape of the
beach and the character of the sand projection behind the headland
breakwaters, several beach types were identified (Table 1). The
various shapes of the beaches reflect the complexity of other factors
at work such as the original position of the fill line in relation to
the headland breakwater alignment and the orientation of the headland
breakwaters to littoral drift and wave approach.

TABLE 1.   BEACH TYPES BETWEEN HEADLAND BREAKWATERS, PHASES I & II (12)

TYPES	FEATURES
NEW BEACHES	(1) Beach is not fully developed; marine clays underlying the sand prism are exposed. (2) Curvature of the bay is from crescentic to J shape. (3) Sand projection forms on the lee of the downcoast breakwater and is the nucleus for berm construction. (4) Scarp along the fill material is common.
DEVELOPING BEACHES	(1) Beach is sufficiently formed. (2) Typical curvature of the bay is J shape with a downcoast straight sector. (3) Berm develops from the downcoast breakwater towards the opposite end. It varies from a triangular form which tapers upcoast along the bay to an almost continuous formation between the breakwaters. (4) Scarp along the fill material varies from isolated sections to an almost continuous one along the bay.
BEACHES INTERRUPTED BY DRAINS	(1) As beach formation progresses, the drain becomes increasingly important; the sequences of beach development are as follows: (a) No effect by the drain on beach formation; the features are as for developing beaches. (b) Deposition becomes pronounced on the upcoast side of the drain. (c) Distinct development of an upcoast J-shaped bay and a downcoast straight sector, generally characterized by a scarp. (2) Silting in drains becomes an increasing problem as the upcoast sector develops, thus necessitating dredging.
DEVELOPED BEACHES	(1) Beach and berm are well formed. (2) Typical curvature of bay is a J shape with a long downcoast straight sector. (3) Berm varies in width along the bay. (4) Little or no sand transport in the lee of breakwaters.
UNBAYED BEACHES	(1) Beach is characterized by a well-formed berm with varying width. (2) Straightness of beach is interrupted by a (a) concavity when surface runoff impounded behind the berm cuts channels across it and the material from the foreshore is removed by the littoral drift; (b) convexity when eroded material from the berm and foreshore forms a small delta offshore.

Berm

In the April 1972 survey of Phases I & II, a relationship was found to exist between berm orientation and headland breakwater orientation (Fig 22). In February 1974, when an exceptional high tide occurred due to the moon, earth and sun ooming almost in a straight line, the beach geometry was modified. However, the relationship between berm orientation and headland breakwater orientation remains almost constant (Fig 22). Beaches with developed berms were less affected by this exceptional high tide.

CONCLUSION

The southeast coast of Singapore is a sheltered area and winds from the north during the northeast monsoon do not have a large influence except through refracted swell from the South China Sea. It is essentially a low energy coast throughout the year with the waves coming from the southeast quadrant, so that westward littoral drift is present.

Beach development between the headland breakwaters of the reclaimed land is therefore under a low energy regime and a westward littoral drift. Wave action effectively removes the fines and leaves ooarser material behind to form the beaches.

Under such conditions, headland breakwaters constructed in a series on a gentle sloping littoral drift shore provide an economic solution for the protection of the ooast and for the formation of beaches. While the headland breakwater system is effective in minimising littoral drift in this low energy environment, it can be effective as a shore protection measure in high energy area since the growth of bay to equilibrium is independent of wave period(13). Tentatively, beach stability between the headland breakwaters is suggested by the presenoe of a wide berm in the absence of an equilibrium shape determined according to the criteria of Silvester(6).

ACKNOWLEDGEMENT

REFERENCES

1 U.S. Army Coastal Engineering Research Centre (1966), "Shore Protection, Planning & Design", Technical Report No. 4, p. 236.

2 Silvester, R. (1960), "Stabilization of sedimentary coastlines" Nature Vol. 188, No. 4749, pp. 467-469.

3 Halligan (1960) reported in "Geographical Variation in Coastal Development", Davies, J.L. (1972), Oliver & Boyd, Edinburgh, p. 136.

4 Yasso, W.E. (1965), "Plan geometry of headland-bay beaches",
      Journal of Geology, Vol. 73, pp 702-714.

5 Swan, S.B. (1968), "Coastal classification with reference to the
      east coast of Malaya", Zeitschrift fur Geomorphologie, Neuw
      Folge, Suppl. Bd 7, pp 114-132.

6 Silvester, R. (1970), "Growth of crenulate shaped bays to equilibrium",
      Proceedings of the American Society of Civil Engineers, Journal
      of Waterways and Harbours Division, Vol. 96, No. WW2, pp 275-285.

7 Krumbein, W.C. (1947), reported in "Geographical Variation in Coastal
      Development", Davies, J.L. (1972), Oliver and Boyd, Edinburgh,
      p 137.

8 Silvester, R. & Ho, S.K. (1973), "Use of crenulate shaped bays to
      stabilise coasts", Proceedings of the 13th Conference on Coastal
      Engineering, American Society of Civil Engineer, pp 1347-1365.

9 Draper, L. (1966), "The analysis and presentation of wave data -
      a plea for uniformity", Proc. of 10th Conference on Coastal
      Engineering, American Society of Civil Engineers, pp 1-11.

10 Silvester, R. (1966), "An aid to constructing wave refraction
      diagrams" Trans I.E. Australia, CE 8, pp 123-127.

11 Alexander, F.E.S. (1950) "Report on the availability of granite on
      Singapore and the surrounding islands", Government Printing
      Office, Singapore.

12 Wong, P.P. (1973), "Beach formation between breakwaters, south-east
      coast of Singapore", Journal of Tropical Geography, Vol. 37,
      pp 68-73¢

13 Private discussion between Dr. Richard Silvester and the senior
      author.
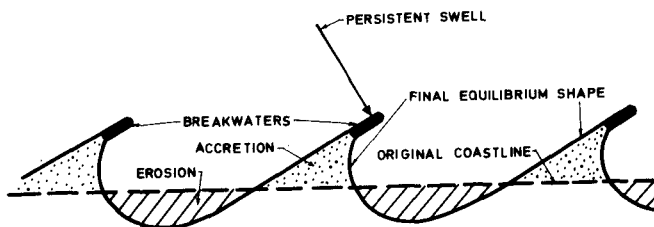
Fig 1   A METHOD OF PREVENTING LONG TERM MOVEMENT
         OF SEDIMENT ALONG THE COAST (AFTER SILVESTER, 1960)

Fig 2 ORIENTATION MAP SHOWING AREAS RECLAIMED & STUDIED AREA

a TYPICAL SECTION OF GABION BREAKWATER

b TYPICAL SECTION OF FORESHORE AND GABION BREAKWATER BEFORE TOMBOLO IS FORMED
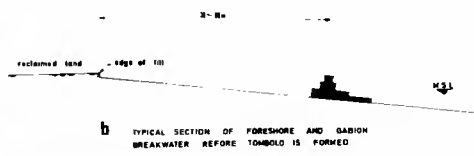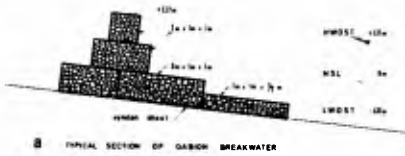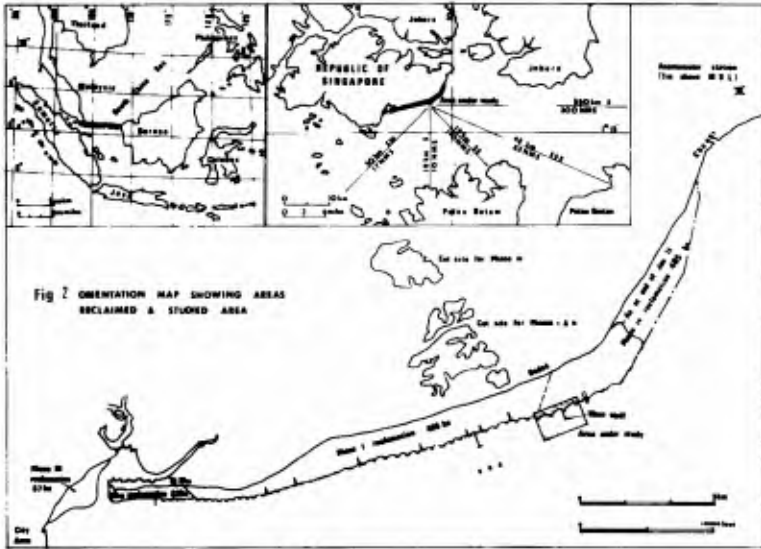
Fig 3 a, b and c. Gabion breakwater
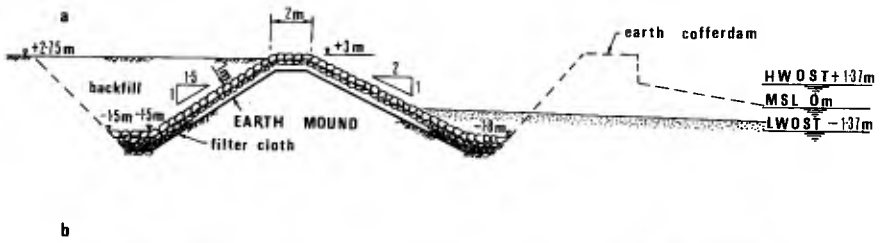
Fig 4 a and b.　Rip rap breakwater.
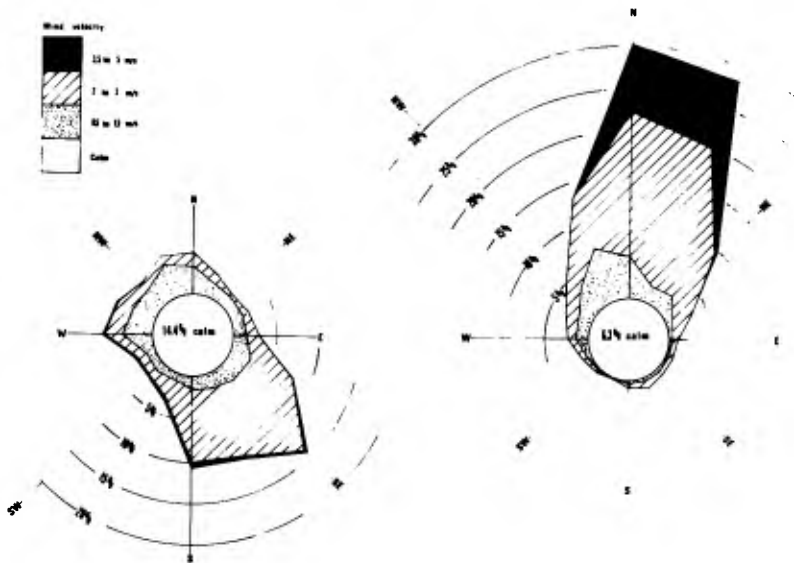
Fig 5　WIND ROSE FOR AUG. TO NOV 1972, APR. TO JULY 1973　　　WIND ROSE FOR DEC. 1972 JAN FEB AND MARCH 1973
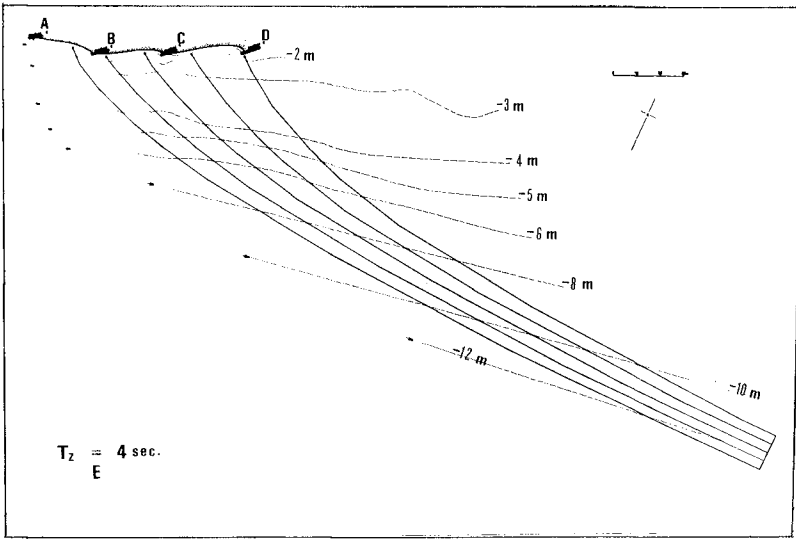
Fig 6. Refraction diagram
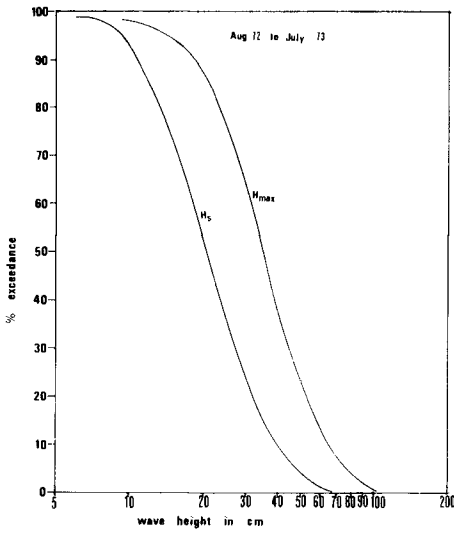
Fig 7   CUMULATIVE DISTRIBUTION OF SIGNIFICANT
         WAVE HEIGHT (H_s) AND   MAX. WAVE HEIGHT (H_{max})
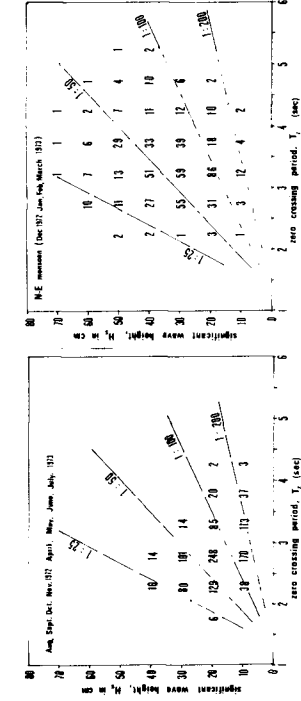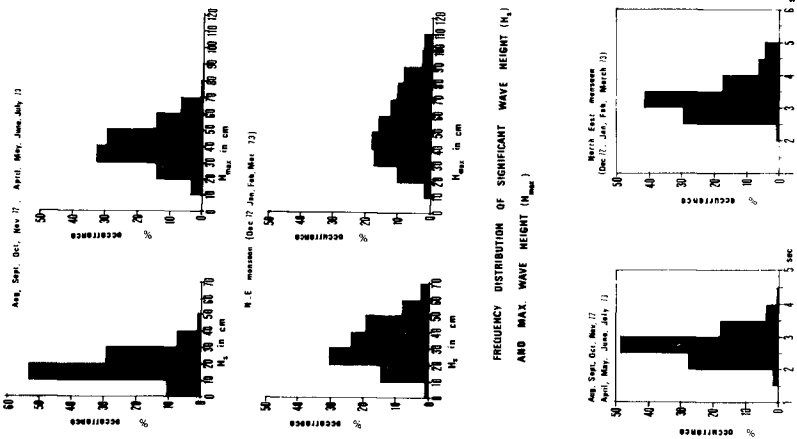
Fig. 9. Scatter plot of H_s vs T_z.
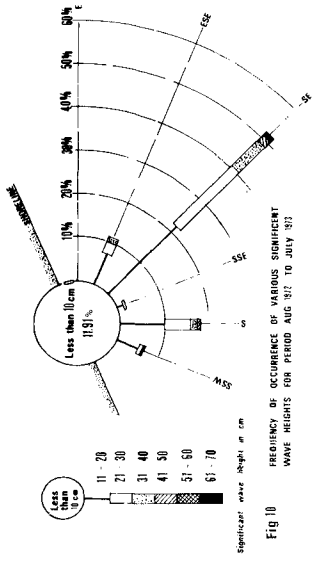
Fig 10   FREQUENCY OF OCCURRENCE OF VARIOUS SIGNIFICANT WAVE HEIGHTS FOR PERIOD AUG 1972 TO JULY 1973

FREQUENCY DISTRIBUTION OF SIGNIFICANT WAVE HEIGHT (H_s) AND MAX. WAVE HEIGHT (H_{max})

DISTRIBUTION OF ZERO-CROSSING PERIOD T_z
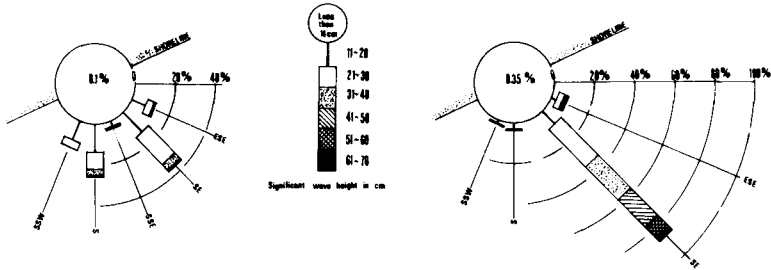
Fig 8. Frequency Distribution of H_s, H_{max} & T_z
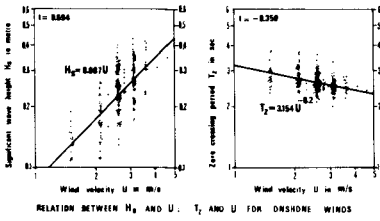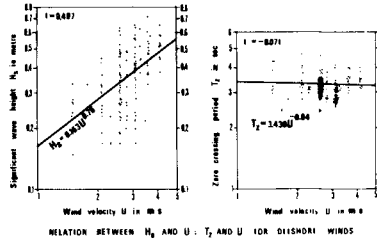
Fig 11. Relationships between H$_S$ and U; T$_Z$ and U
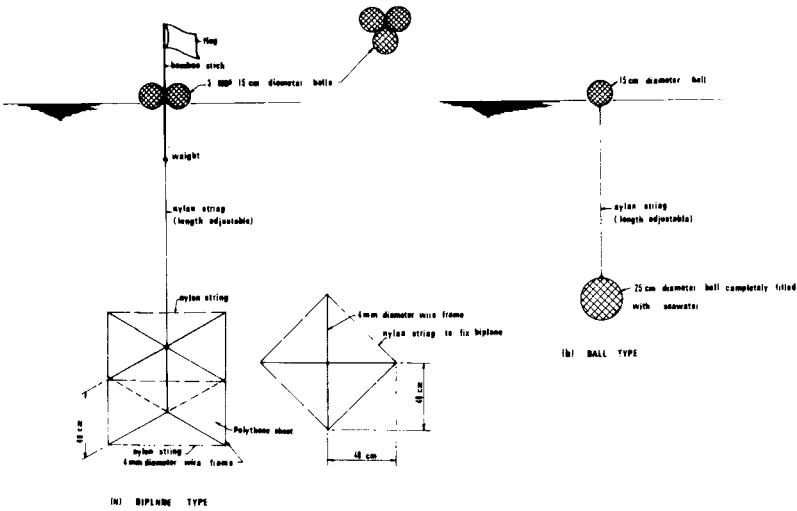
Fig 12. Details of Drogue
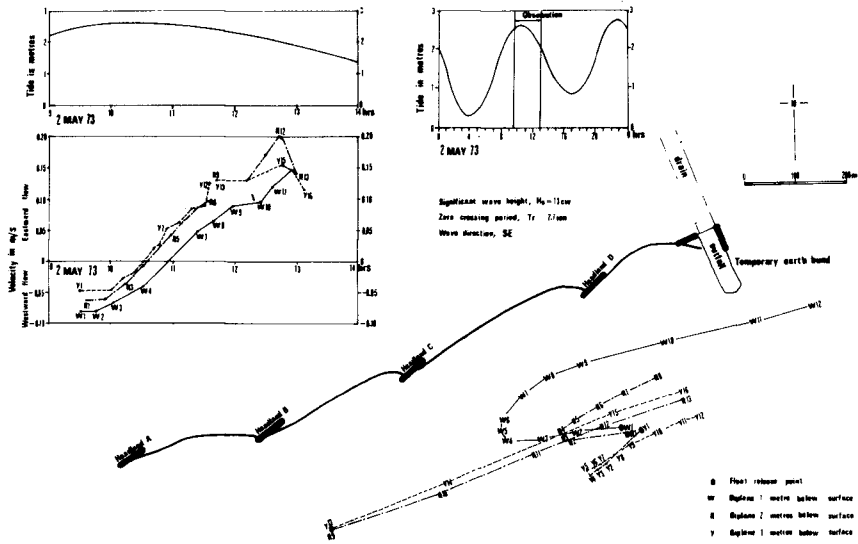
Fig 13   CURRENT OBSERVATION BY FLOATS ON 2 MAY 1973
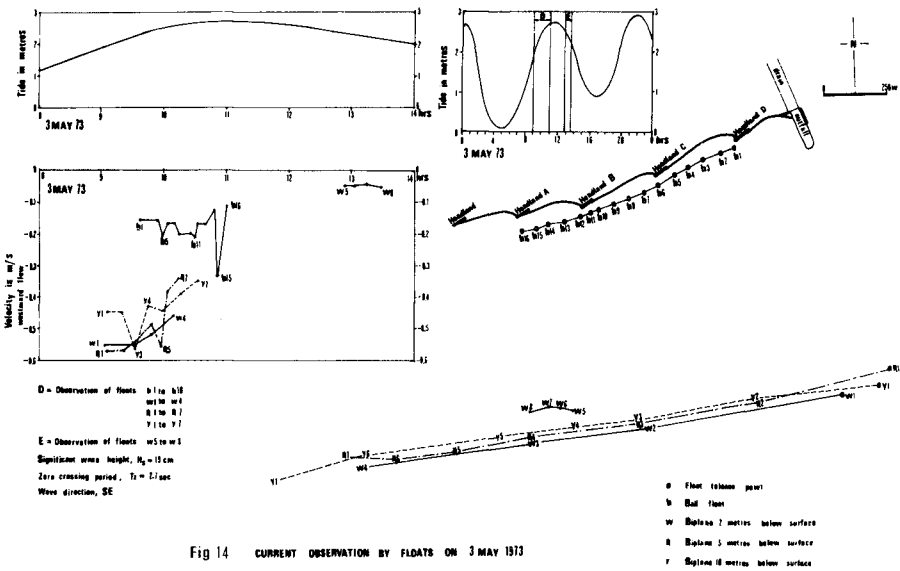
Fig 14   CURRENT OBSERVATION BY FLOATS ON 3 MAY 1973

Fig 16. Grain size characteristics of fill material.

Fig 15 FIXED POINT CURRENT OBSERVATION AT 1000 METRES OFFSHORE OF STUDIED AREA.
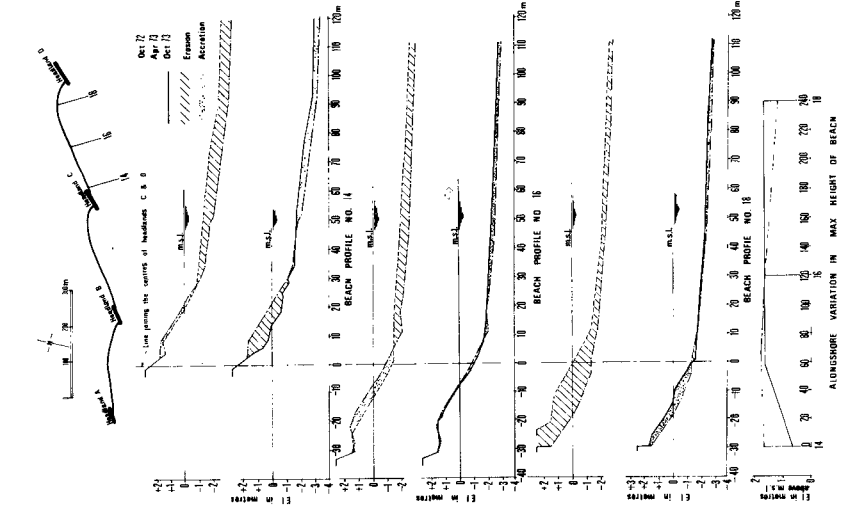
Fig 18. Beach profiles 14, 16 and 18.
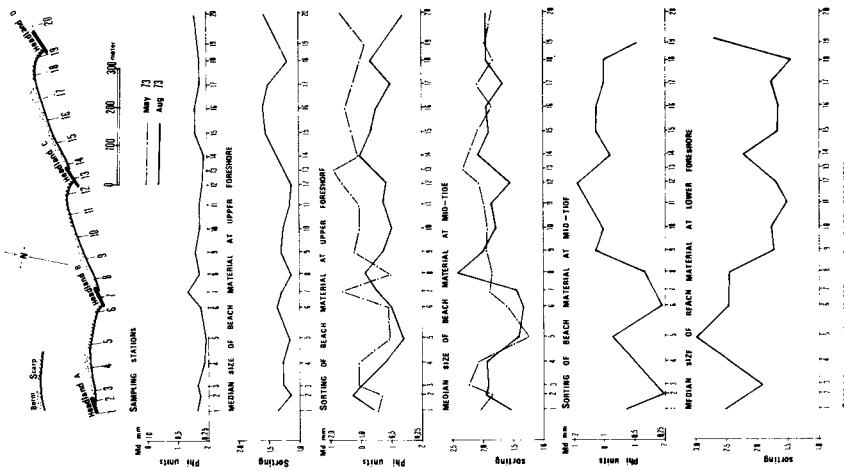
Fig 17. Characteristics of beach material.
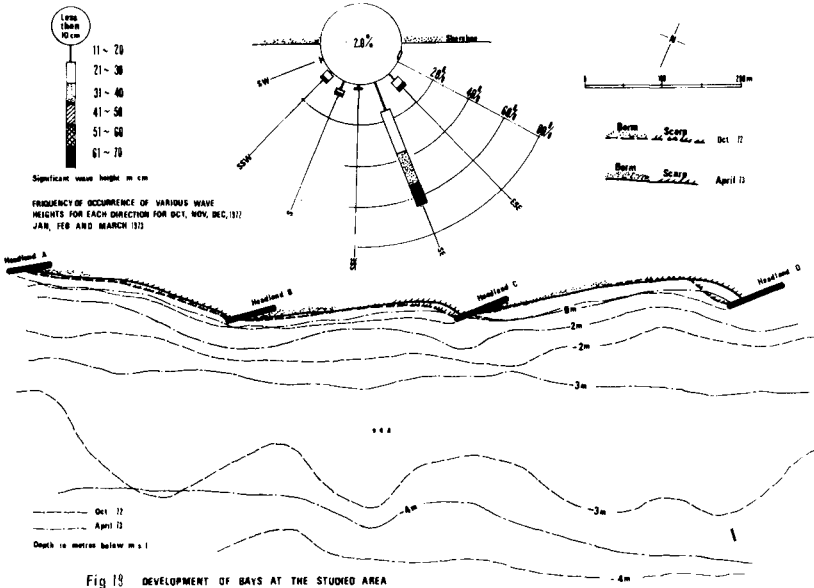
Fig 19 DEVELOPMENT OF BAYS AT THE STUDIED AREA
(Oct 72 to April 73)
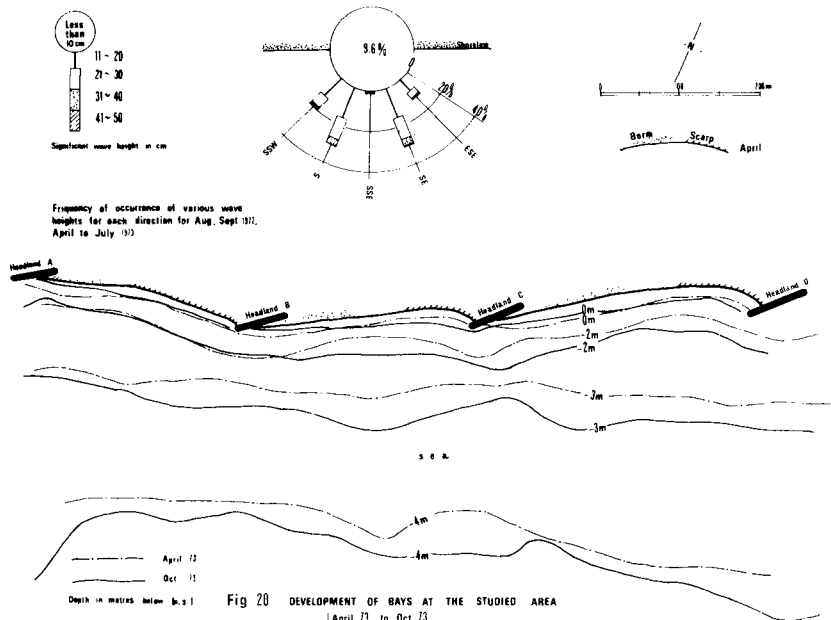
Fig 20 DEVELOPMENT OF BAYS AT THE STUDIED AREA
(April 73 to Oct 73)

FREQUENCY OF OCCURANCE OF VARIOUS SIGNIFICANT
WAVE HEIGHTS FOR PERIOD AUG 1972 TO JULY 1973

WAVE ORTHOGONAL
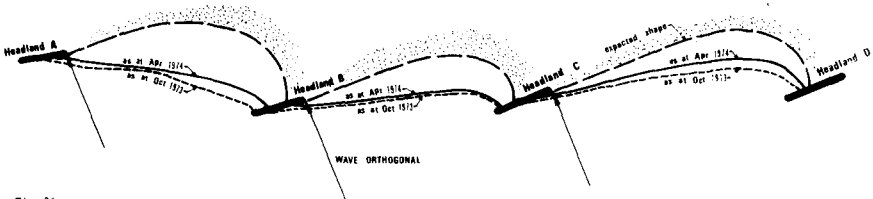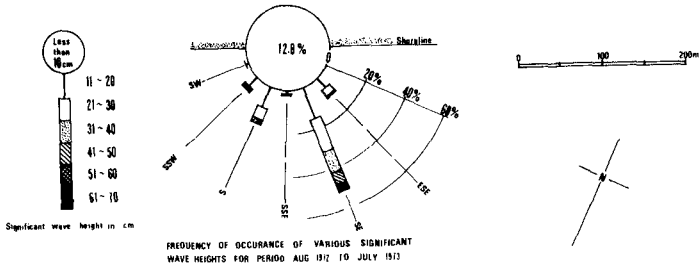
Fig 21
EXPECTED SHAPE OF BAY BETWEEN HEADLAND BREAKWATERS WHEN NETT WESTWARD DRIFT IS REDUCED/CUT OFF
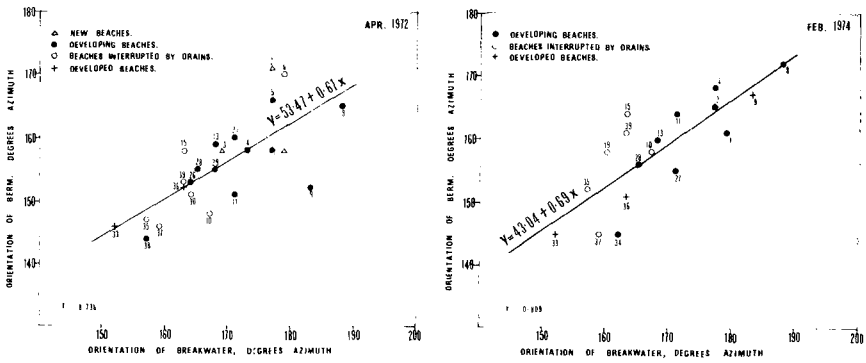
FIG. 22   RELATIONSHIP BETWEEN ORIENTATION OF BERMS AND ORIENTATION OF BREAKWATERS.

CHAPTER 83

DESIGN OF A DETACHED BREAKWATER SYSTEM

by

Osamu Toyoshima
Director, Sea Coast Division,
River Bureau,
Ministry of Construction,
JAPAN

ABSTRUCT

Beach erosion is one of the serious problem in Japan.   As a countermeasure against beach erosion, many preventive works, such as sea walls and groins, have been constructed during the past 20 or more years.   However, as the result of field investigations, it has become clear that sea walls and groins are not always effective on beach erosion prevention, and inversely, in some cases, they accelerate the beach erosion.

Based on the above cognition, the author has proposed and tried to apply the detached breakwater system as a measure against beach erosion for the last 8 years.   This is for the purpose of developing the sand deposition behined the breakwater.   Therefore several experimental works of the detached breakwater system were carried out under the guidance of the present author, and most of these tests were successful.

The design method of this system was composed by the author on the basis of the result of field investigations, which have been conducted for more than 8 years.

The numerous construction works of detached breakwaters have been carried out in accordance with the design method proposed in this paper, and the effectiveness of detached breakwaters has been proved on the several coasts in Japan where severe beach erosion occurs.

EXPERIMENTL WORKS OF THE DETACHED BREAKWATER SYSTEM

The oldest document on beach erosion in Japan was written in 833.   Since the 1950's, beach erosion has been increasingly severe in many coastal areas, not only on sandy beaches, but also on soft-rocky coasts.   The deterioration of rivers as a source of sediment supply to the coast, and the construction of shore protection works and harbor facilities have brought the erosion of the coast line all over the Japanese Islands.

Many groins have been construoted on many coasts, and the number of groins amounts to more than 8,000 at present.   More than half of them are still effective, but the remainders are ineffective. The reason of such ineffectiveness must be as follows. Before 1940's unilatteral littoral drift caused most of the beach erosion, but recentry, the straightly coming waves, the direction of which is almost perpendicular to the shore line, have been causing the severe beach erosion.

Owing to the above consideration, the author tried to apply the
detached breakwater system as a measure against beach erosion.   A
detached breakwater system consists of a group of breakwaters,
constructed in parallel with the shore line, and is normally located
in the surf zone.   The primary function of the detached breakwater is
to diffract and dissipate the incoming wave energy.
      The first experimental work of this system was carried out on
Ishizaki coast near Hakodate city Hokkaido Island.   Before 1960,
there were wide sandy beaches with 1 or 2 meters thickness of sand
on the rocky sea bed.   After finishing the sea wall construction
works, which were carried out early in the 1960's, the sandy beaches
have vanished.
      Then, the author proposed to construct detached breakwaters
there, and built trially the first one the nearshore of the rocky
bed in 1966.   Soon after the completion of the work, the tombolo
was formed in front of sea wall, and it grew larger gradualy.
      More than 10 breakwaters have been succeedingly constructed
during the following several years, and they were all effective.
According to later investigations, it has become clear that the
deposit sand was carried from offshore sea bed at a depth of about
4 meters, where a kind of seaweeds was newly found.   The seaweeds
can grew only on the rocky bed.   The length of a breakwater is
about 60 meters, and it was built by the 2 layer pile of the 3.5
ton hexa-leg-blocks.   The tombolos generated by the detached break-
water system exist even now, and the yield of seaweeds is on the
increase.
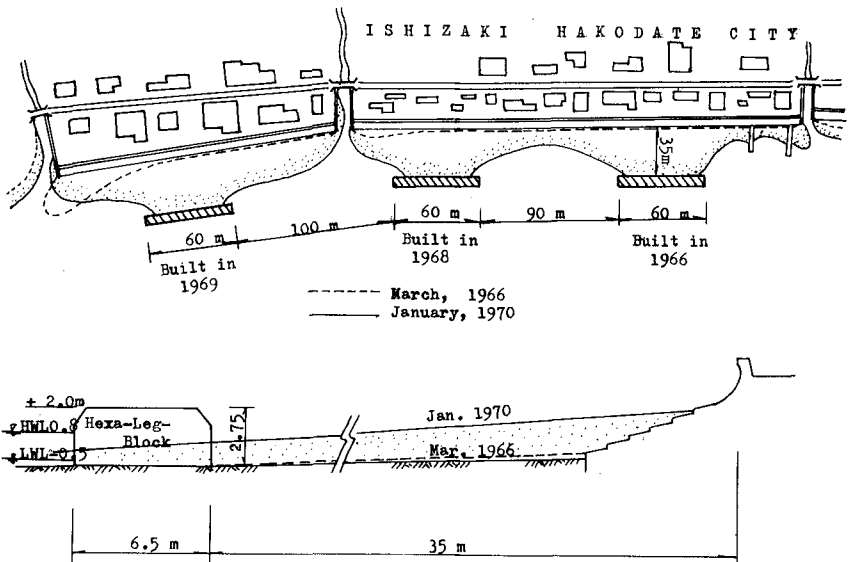
Fig. 1   The detached breakwaters on Ishizaki coast.

Pl. 1   The detached breakwaters on Ishizaki coast and the model of
        the hexa-leg-blocks

The second experimental work of this system was carried out on
West-Niigata coast, which is one of the most famous places in the
sense of severe beach erosion in Japan.   The coast has been eroded
since 1890, and the eroded distance amounts to more than 300 meters.
Therefore, its regression speed was about 6 to 10 meters per year.
The first breakwater construction was initiated in 1966, and the
additional three breakwaters have succeedingly constructed in later
2 years.
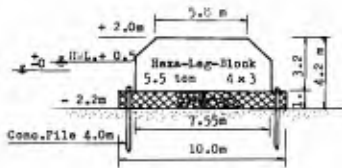
Fig. 2   The structure of the
         breakwater on West-
         Niigata coast

The length of the first breakwater is
400 meters.   The structure was const-
ructed on the sandy sea bed at the
depth of about 2.5 meters, and was
about 120 meters offshore from the
shore line.   The breakwater consists
of 2 layer pile of hexa-leg-blocks and
rubble mound covered with steel wire
cage.
        Since it was under construction,
the tombolo was formed behind the
breakwater, and the maximum advanced
distance of shore line was about 80 meters.   However, 2 years later
after the completion, the body of breakwater sunk about 1.8 meters,
and the tombolo reduced the size.   Reinforcement works for rising
the crown height of breakwater were carried out, and the tombolo
advanced again.
        Further experimental works have been carried out in the follow-
ing several years, and most of them have been successful as the
countermeasure against beach erosion.
        Then the author intended to establish a design criterion for
the detached breakwater system.   At first, the author analysed the
collected data of 86 samples of existing detached breakwaters.

STATISTICAL STUDY OF EXISTING DETACHED BREAKWATER

In 1969, the author has done a statistical study on the exist-

ing detached breakwaters.   At that time, there were 86 places where
breakwaters had been constructed, and the number of the breakwaters
was 217 in total, in which the breakwaters at 18 places constructed
under the author's supervision were included.   The following fac-
tors were investigated.
    1.   Classification of breakwater type (continuous, single, or
        group breakwaters)
    2.   Relationship between breakwater length and distance from
        shore line
    3.   Relationship between breakwater length and water depth
    4.   Relationship between distance from shore line and openning
        between the neighboring two breakwaters
    5.   Structure type and crown height above still water level
    6.   Relationship between sinking and foundation works
    7.   Primary factor for the sand deposition and tombolo formation
(1)   Classification of breakwaters
    The detached breakwaters were classified into several according
to the length of breakwaters.   Table 1 is the result of classifica-
tion.
      Table 1   Classification of existing detached breakwaters

Classification		Number of places	Number of breakwaters	Total length
Continuous breakwaters		10	10	12,743 m
Island type	Single breakwaters	34	34	4,093
or group	2 breakwaters	18	36	4,189
breakwaters	3 breakwaters	9	27	3,952
	4 breakwaters or more	15	110	8,243
Total		86	217	33,220 m

According to this table,
    1)   The number of places for continuous type is only 10 (12%),
        but the total length of them amounts to 38% of all, and the
        mean length of a breakwater exceeds 1,200 meters.
    2)   The number of places for single type amounts to 40%, but the
        mean length of a breakwater is only 120 meters.
    3)   Group breakwater, concist of 4 or more breakwaters, amounts
        to only 17% of the total number of places, but the number of
        breakwaters amounts to 51% of all, and the mean length of
        a breakwater is 75 meters.
(2)   Continuous breakwater
    According to the field investigations about the continuous
breakwaters,the following facts can be found:
    1)   Most of the breakwaters have been constructed before 1960.
    2)   They have never formed tombolos.
    3)   For the purpose of the sand deposition, the continuous break-
        water are not always better than the island type breakwaters.
    4)   For the purpose of dissipating wave energy, the continuous
        breakwaters are better than the island type.

(3)   Relationship between breakwater length and distance from shore
      line
    Fig. 3 shows the relationship stated above.   It is impossible
to find out any correlation between breakwater length and distance
from the shore line.
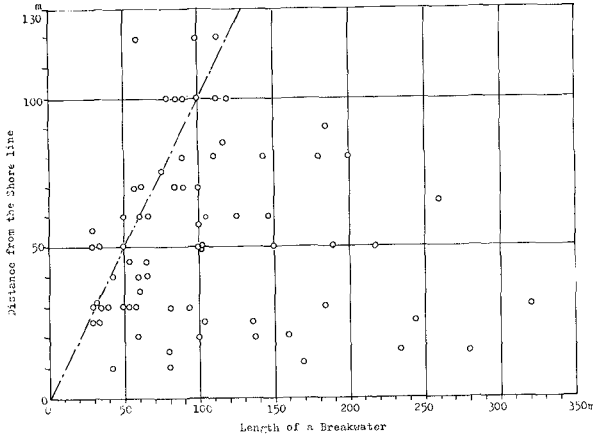
Fig.3   Breakwater length and distance from shore line

(4)   Relationship between breakwater length and water depth
    Fig. 4 shows that it is also impossible to find out a clear
correlation between the breakwater length and the depth where the
breakwaters are constructed.
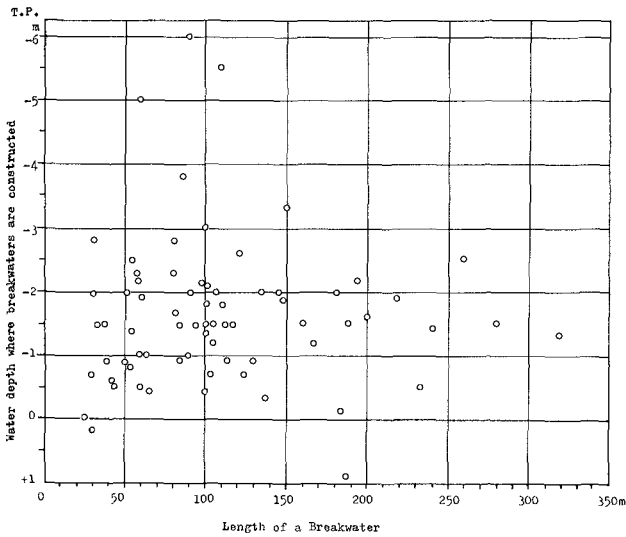
Fig.4   Breakwater length and water depth

Most of the breakwater were constructed at the water depth within
the range of 1 m to 2 m below T.P.(Tokyo Peil).
(5)   Relationship between distance from shore line and openning
     Fig. 5 shows that most of the openning between the neighboring
two breakwaters are less than 50 m, and they have no relationship
with the distance from the shore line.
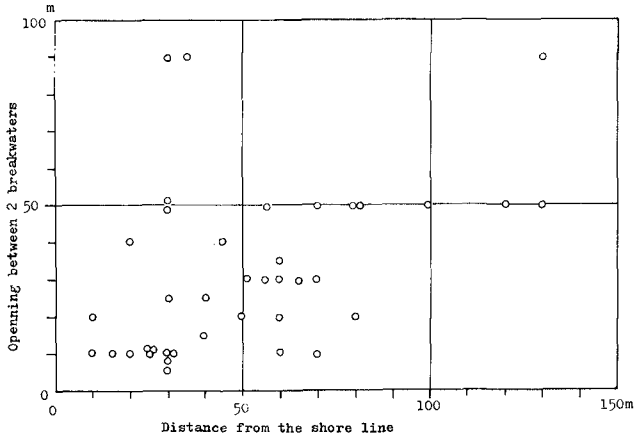
Fig. 5   Distance from the shore line and openning

(6)   Crown height of breakwater
     Fig. 6 shows that most of breakwater have the crown height of
1 to 2 m above the high water level.
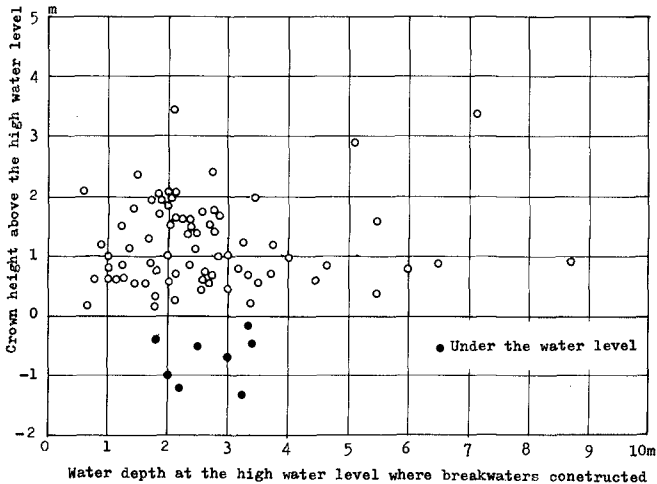
Fig. 6   Crown height of breakwaters above the high water level

(7)   Structure type of breakwater
     Table 2 shows the structure type of breakwaters classified for each age when breakwaters construction started.

Table 2   The structure type of detached breakwaters

Construction start / Structure		before 1955		1956-1965		after 1966		total	
		place	length	place	length	place	length	place	length
p e r m e a b l e	tetra-pods	2	2,750m	6	2,931m	9	4,005m	17	9,686m
	hexa-leg blocks	–	–	2	725	16	5,392	18	6,117
	hollow triangle	–	–	1	250	1	120	2	370
	akmon	–	–	–	–	1	279	1	279
	another blocks	–	–	–	–	2	248	2	248
	total	2	2,750m	9	3,906m	29	10,044m	40	16,700m
u n p e r m e a b l e	concrete blocks	7	4,594	4	1,950	1	238	12	6,782
	cellular blocks	2	485	–	–	3	187	5	672
	composit type	2	2,230	3	800	3	1,260	8	4,290
	rubble mound	3	1,040	4	887	5	1,320	12	3,247
	stone facing	6	871	2	367	1	291	9	1,529
	total	20	9,220m	13	4,004m	13	3,296m	46	16,520m
all total		22	11,970m	22	7,910m	42	13,340m	86	33,200m

According to this table, it is recognized that the structure type of of breakwaters has been changed with the age and the difficulty to get construction materials.   Very recentry, after the appearance of tetrapod, many kinds of armour blocks have been used as a construction material in general.   It is not clear that what type structure is most suitable for detached breakwaters, but the author pressumes that the permeable type has some merrit and generally better than un-permeable type.
(8)   Sinking and Foundation
     Most of the breakwaters have been sinking more or less, except those constructed on the rocky sea bed.   Several measures for prevention of sinking have been applied, however the effective foundation has not yet been found.
(9)   Factors for getting good sand deposition and tombolo formation
     The function of the existing 86 samples of detached breakwaters are devided into two groups, one is for wave dissipation and another is for sand deposition and tombolo formation.
Table 3 shows the purpose and function of detached breakwaters.

Table 3 Purpose and function of existing 86 breakwaters

Purpose	Number of place	Function for sand deposition			
		nothing	small	effective	tombolo
Wave dissipation	48	36	5	7	1*
Sand deposition	38	6	5	27	19*
Total	86	42	10	34	20*

* : Number of place where tombolos were formed are included in "effective".

In spite of that the breakwaters were constructed with wave dissipation purpose, the breakwaters are effective at 12 places for sand deposition.   Inversely, in spite of that the breakwaters were constructed with sand deposition purpose, the breakwaters at 11 places are ineffective.
In order to find out the factors for getting good sand deposition and tombolo formation, the author investigated the relationship among the breakwater length, distance from shore line, the crown height of breakwater, and water depth where the breakwaters were constructed.
Fig. 7 shows the correlation among these factors for island type breakwaters (except continuous type breakwaters) in non-dimension. However, as shown in this figure, any clear factor for sand deposition and tombolo formation can not be found.
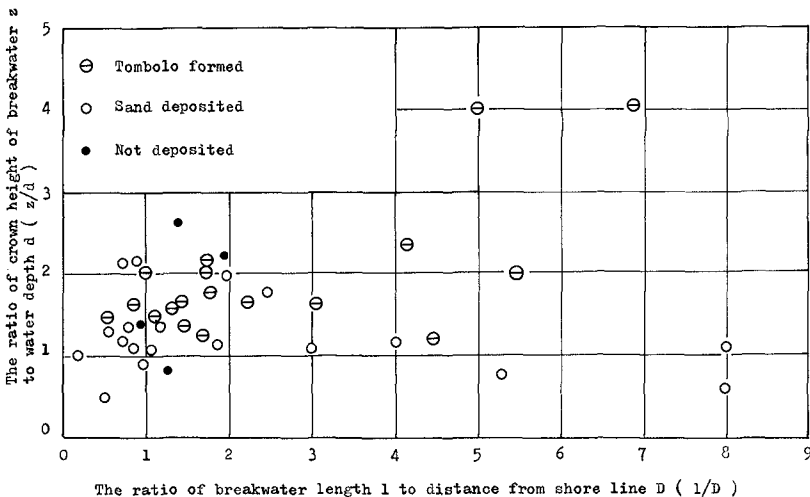
Fig. 7 Effect of breakwater location on sand deposition

DESIGN CRITERION OF THE DETACHED BREAKWATER SYSTEM

Since the statistical studies stated above could not find any clear factor for sand deposition, the author tried to make a tentative design criterion according to the results of investigation of statistical analyses and of the experience obtained through the experimental works described above.

First of all, the author proposed to classify the breakwater system into the following four systems according to the water depth of the breakwater location.

    1. The shore line system
    2. The shallow water depth system
    3. The median water depth system
    4. The deep water depth system

(1)   The shore line system

This type is normally to built the breakwaters near the shore line, and to be used in the following cases:
  1. the place where the beach slope being steep,
  2. sand deposition to be created being possibly sufficient even in a small scale,
  3. the main object being to prevent score in front of sea wall,
  4. to maintain the existing shore line as it is.
As for the type to be employed in such cases, the group island type shall be preferable because of following effects,
    1. flowing the sand through the openning of breakwaters,
    2. intercepting the littoral drift along the shore line caused by diffraction waves.
The length of a breakwater must be 2 or 3 times wave length, that is 40 to 60 meters, and the openning between the neighboring two breakwaters must be equall to one wave length, that is about 20 meters.
As to the structure type, a 2 layer pile of armour blocks is effective, wherein the foundation works are not particularly needed.
The inherent problems of this system may be the occurrence of a large scale scoure in front of the breakwaters, especially in the case of constructing a breakwater on the coasts confronting the open ocean.

(2)   The shallow water depth system

Breakwaters of the shallow water depth system are constructed at a water depth of less than 1 meter on a relatively gentle beach or on a beach where a big tidal range is expected, and the construction works are principally conducted by the use of the track-and crane method.
Deposition of sand is ensured by this system even though the amount of collected sand is not enough in many cases.
As for the type to be used in this case, the group island type breakwaters shall be preferable by the same reason as described in the shore line system.　When a continuous breakwater is applied, jetties should be constructed behind the breakwater at an appropriate interval.

The length of a breakwater must be equall to 3 to 5 times the wave length, that is 60 to 100 meters, and the openning between the

neighboring two breakwaters must be equall to one wave length, that
is about 20 meters.   In addition, the length of a breakwater should
not be longer than 10 times the wave length in the case of island
type.
        Though the distance from the shore line is most naturally
determined by the water depth of the breakwater location, too long
distance is not profitable.
As to the structure, an arranged pile of armour blocks is profit-
able, and the crown height of structure is extended to more than 1
to 1.5 meters, or a half wave height above the high water level.
Possible large scale sinking of the detached breakwater may be
prevented to some extent by means of proper foundation works such
as mat, rip rup and like, but depending upon the foundation condi-
tions after execution, an enforcement of armour blocks should
occasionally be considered.
        As a result of case study by using the data of previously done
works, the following seems to be the main reasons why the sand
deposition could not be achieved in this system.
   1. The structure is impermeable and built in olden age.
   2. The length of breakwater is too short in comparison with the
        distance from shore line, and the structure is located at the
        site of big tidal range.
   3. The structure is very high and is impermeable.
In designing and executing the breakwaters, therefore, the above
mentioned points should be fully considered beforehand.

(3)   The median water depth system

        This system is the most common one which is constructed by the
use of a floating plant.   The construction site should be selected
in the surf zone at the water depth of 2 to 4 meters normally, and
of 6 meters or more in particular case.
The purpose of this type is to reduce the wave energy and to produce
the accreation of sand behind the breakwater.
For the first purpose mentioned above a long continuous breakwater
is preferable, while for the second purpose an island type breakwater
or a group of short breakwaters is rather preferable.
        When a single island type breakwateris used, the breakwater
length should be 3 to 10 times the wave length, that is about 100 to
300 meters.   When a group of a breakwater is used, the length of
each breakwater should be 2 to 6 times the wave length, that is 60
to 200 meters, and the openning between the neighboring two break-
waters should be one wave length, that is 20 to 50 meters.
Although the distance from the shore line has a close relationship
with the depth of the breakwater location, it should be 0.3 to 1.0
times the length of breakwater as a standard.   In the case of cont-
inuous breakwater, the distance should be 1 to 3 times the wave
length, that is 30 to 100 meters.
        As for the structure type, there is a strong tendency to use
armour blocks, but in the case of that the water depth is rather
deep, some other works such as rubble mound breakwater, or composit
type breakwater etc. should be considered in design.
The crown height should be a half wave height, or 1.0 to 1.5 meters
above the high water level, the condition of which is the same as
the shallow water depth system.
The sinking of the breakwater body is one of the biggest problems

here. Several countermeasure have been tried, but any definite
solution has not been yet found.
Most of the cases in this system where sand could not be
deposited are situated on the unsuitable conditions for the sedimen-
tation and accumulation of sand. In other words, this situation may
be explained as follows. In those cases, the water surface behind
the breakwater is not calm enough to induce the sedimentation and
accumulation of sand. That is to say, the water surface in the
area is disturbed by the reflected waves which are generated from
the sea wall owing to the fact that the water depth in front of sea
wall is deep enough or the slope of sea bottom near the shore line
is steep enough.
Accordingly, in order to construct a detached breakwater at a place
as stated above aiming at the formation of sand deposit behind the
breakwater, the execution of foot protection works at the sea wall
should be considered in advance, and furthermore, if possible, beach
sand replenishment works should be simultaneously executed to
shallow the water depth in front of the sea wall as much as possi-
ble, for the purpose of reducing the reflection coefficient of waves
at the sea wall.

(4)   The deep water system

The breakwater in this type is located at the outside of the
surf zone, and is similar to the normal breakwaters, the function
of which is mainly to dissipate wave energy. Therefore, this type
of breakwater is effective in dissipating wave energy and stabiliz-
ing the bottom configlation in the surf zone, but is not effective
in bringing sand to the sheltered area from dther places.
The dimension of the breakwater determines the calmness in the
sheltered area. As for the structure type, a composite type break-
water or a vertical-face breakwater is profitable from the view of
construction cost, because the use of armour blocks is especially
expensive in this case.

THE LATER EXPERIMENTAL WORKS ON KAIKE COAST

Following the design criterion described here, more than 20
works were executed, and all of them were successful to accomplish
the main purpose.
The latest works have been executed on Kaike coast.
Kaike is one of the famous hot spring resorts places along the
Japan Sea, and the Kaike coast has been eroded since 1920's.
The regression distance amounts to 300 meters during the last 50
years. There were many hot spring hotels along the shore line,
but all of them were vanished into the sea.
First of all, several groins and sea wall were constructed as
the preventive works against beach erosion. However, groins became
ineffective gladually.
A large amount of armour blocks were installed in front of sea walls,
but violent winter waves attacked the sea wall, and over-topped
frequently . Therefore the housing area was ocassionally flooded
by sea water.
Then the author proposed to construct detached breakwaters as

a countermeasure.   During the period from 1971 to 1973, three
breakwaters were constructed.
The breakwaters were located 100 meters apart from the sea wall and
at the water depth of about 5 to 6 meters.   Each of these break-
waters is quite effective to bring back the sand and to form a
large tombolo.   The thickness of deposit sand is about 5 meters
at the head of tombolos, and about 2 to 3 meters in front of the
sea wall.
These tombolos have become larger or smaller according to the sea
condition, and they grow normally under violent wave condition in
winter.
Fig. 8 & 9 show the detached breakwaters and sand deposition at
Kaike coast.
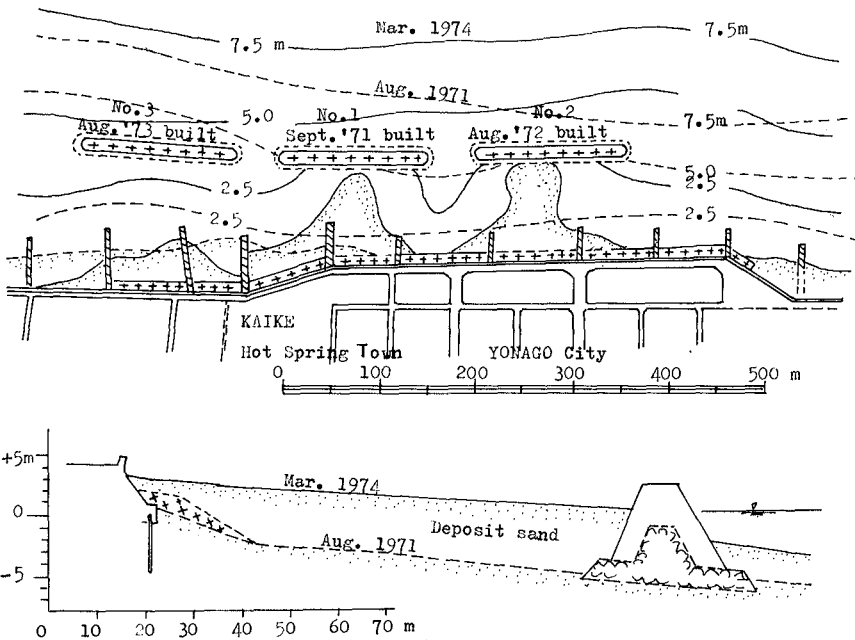
Fig. 8   The detached breakwater at Kaike coast
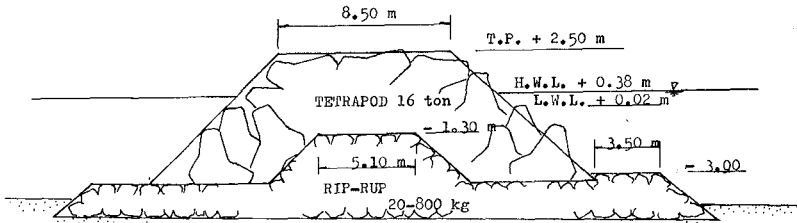
Fig. 9   The structure type of breakwater at Kaike coast

ADDITIONAL REMARK TO BE CONSIDERED IN THE DESIGN AND
EXECUTION OF THE DETACHED BREAKWATER SYSTEM

In addition, the following remarks should be taken into
consideration in designing and executing the detached breakwater
system.
1.   The detached breakwaters should, if possible, be const-
     ructed prior to the sea wall construction.
2.   It is impossible to prevent completly a fatal coast
     erosion even by means of detached breakwater works.
3.   When a breakwater is provided to form the sand deposition
     behind the breakwater, the measures to reduce the reflect-
     ion of waves from the shore line should be taken into
     consideration prior to the execution of a breakwater.
4.   As the shore line just beyond the openning between the
     neighboring two breakwaters is used to be scored, a
     counter-plan for shore protection should be considered
     before hand.

CHAPTER 84

FIELD AND MODEL STUDY ON THE PROTECTION OF
RECREATIONAL BEACH AGAINST WAVE ACTION

Shoji Sato and Norio Tanaka

Port and Harbor Research Institute, Ministry of Transport,
3-Chome, Nagase, Yokosuka, Japan

INTRODUCTION

The heightening of a sea wall is often proposed for the purpose of decreasing the amount of wave-overtopping. In a recreation beach, however, the heightening of sea wall is undesirable from the view-point of environmental preservation and beach utilization. In this paper, instead of it, a proposal is made of the sea wall with a wide frontal step as well as the widening of beach by artificial nourishment.

The frontal step is not only effective to decrease the amount of wave-overtopping, but also serves as a promenade for visitors. The widening of beach is known to serve to decrease wave-overtopping as well as to increase the utility for recreation. However, the protection of the nourished beach itself becomes sometimes a difficult problem. In this paper, the hydraulic characteristics of a wide frontal step and the effect of several protective measures for the nourished beach are described on the basis of model and field tests conducted for the improvement of Suma Beach.

Suma Beach is a recreational beach situated west of Kobe Port as shown in Fig. 1. The shore-line is about 2 km long and runs from east to west (Fig.11). The beach profile, as shown in Fig.2, has the narrow backshore at about 3 m above L.W.L. and a small step at about 1.5 m below L.W.L. The beach slope is 1/10 in the foreshore, 1/25-1/30 between 2 and 5 m below L.W.L and 1/60-1/80 in the offshore beyond about 6 m below L.W.L. The waves are predominant from the direction of SSW so that the beach materials tend to move eastward along the shore. The waves are in usual so small that most of them are less than 0.5 m in $H_{1/3}$ (significant wave height) and waves of more than 1.5 m in $H_{1/3}$ occour only a few times a year. But in the very rare cases, the beach have experienced the attack

of severe waves such as the later-described. The beach material is com-
posed of coarse sand in the foreshore and fine sand in the offshore,
except sand of a few millimeters in mean diameter at the bottom deeper
than 8 m. The appearence of the coarse sand in the offshore seems to
depend on the action of tidal currents of 1 - 1.5 knots in velocity. Also,
the tidal range is 1.7 m in mean spring tide.

WAVE-OVERTOPPING CHARACTERISTICS OF A FRONTAL STEP

In 1965, a big typhoon hit Suma Beach and gave damage to houses
behind of the beach. At that time, the significant wave was estimated to
be 4.7 m hihg and 10 sec. in period and the tidal level was estimated to
rise until 3.7 m above L.W.L. Therefore, model tests have been conducted
in a channel and the profile shown in Fig.3 has been recommended as a
future plan. The profile is obtained by adding a sand fill at the part
above -1.5 m deep, heightening the sea wall by 0.5 m and attaching a wide
frontal step of +3.5 m high to the original typical profile. Through
this model test, wave-overtopping characteristics of a wide frontal step
have been revealed as follows.

Measurement of wave-overtopping and calculation of expected rate of wave-overtopping

Test on wave-overtopping discharge has been conducted with a scale
of 1/50 in a wave channel of 22 m long, 0.6 m wide and 55 cm high shown
in Fig.4. In the model, the water topping over a sea wall due to wave
action is guided into a water-trap. The water in the trap is pumped up
by a vacuum pump in order to be measured in volume. For each test, the
total amount of water topping the sea wall by only seven consecutive waves
numbered from the 6th one of a regular wave train has been measured in
order to exclude the influence of re-reflection of waves from the other
end of the wave channel.

Fig.5 shows an example of the curve for overtopping discharge ob-
tained from the test. The condition of test is 3.7 m above L.W.L. in
water level and 10 sec. in wave peirod. From such curves, the expected
rate of overtopping discharge for waves of 4.7 m in $H_{1/3}$ has been
calculated as follows using Goda's method[1],[2]:

$$q_{exp} = \sum_{j=1}^{m} q_j(H_j) \varDelta p(H_j)$$

Fig.1 Situation of Suma Beach

Fig.2 Distribution of mean diameter of bed materials along the profile
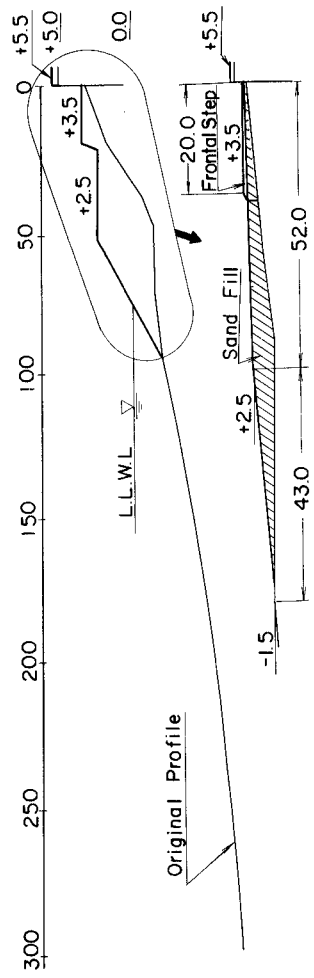
Fig.3 A recommended profile with a wide frontal step
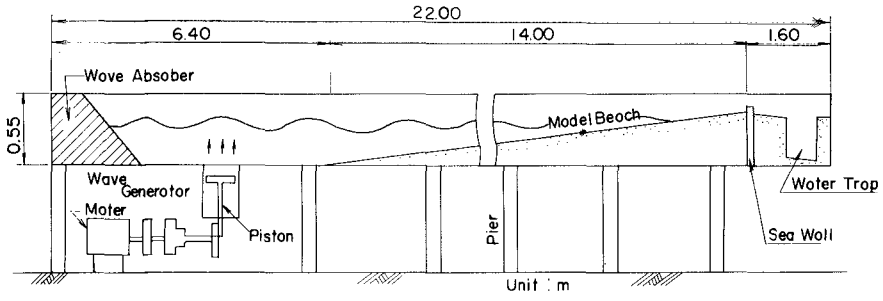
Fig. 4   A wave channel used for test on wave-overtopping
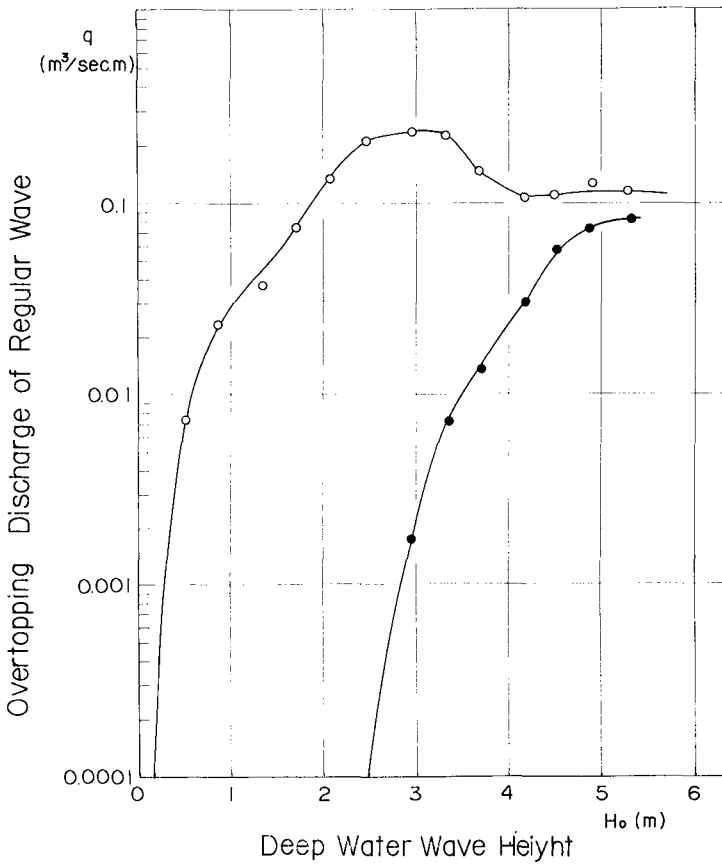
Fig. 5   Overtopping discharge of regular waves on the
present profile and the profile with sand fill
(Water Level: 3.7m above L.W.L.)

where q_{exp} is the expected rate of overtopping discharge, q_j is the rate of overtopping discharge of a regular wave of H_j in height, and $\Delta p(H_j)$ is the occurence probability due to the Rayleigh distribution of waves between ($H_j - \Delta H/2$) and ($H_j + \Delta H/2$) in a irregular wave group of 4.7 m in $H_{1/3}$. q_j is obtained from experimental data such as Fig.5. In this study, ΔH is taken to be 58 cm.

Effect of wide frontal step against wave-overtopping

Fig.6 shows the expected rate of wave overtopping discharge q_{exp} for sea walls with different frontal steps under the same condition of waves and water level as Fig.5 mentioned above. In the figure, "Present Profile" corresponds to the typical profile of Suma Beach shown in (a) of Fig.7 and "Only Sand Fill" to the profile added with sand fill to the typical profile as shown in (b) of Fig.7. "6 m Sea Wall" is a profile with the sand fill of which the sea wall has been heightened until +6 m above L.W.L. The other each profile has the same sand fill as Fig.7 in addition to the corresponding each step shown in Fig.6. The profile F corresponds to the recommended profile shown in Fig.3.

In this figure, the expected rates q_{exp} of wave overtopping of the profiles A, B, C and D are less than the profile of "Only Sand Fill". The profile of "Only Sand Fill" has the same sea wall of 5 m above L.W.L. as the profiles A, B, C and D, but has not a frontal step as seen from Fig.7. Also, the profiles of E and F are nearly equal in q_{exp} to the profile of " +6 m Sea Wall" though they are +5.5 m in the height of sea wall. These facts should be attributed to the effect of frontal step. That is, it is clear that the height of sea wall can be decreased by adding a frontal step without increasing the amount of wave-overtopping.

Effect of a parapet

In Fig.6, each profile of A, B, E and G has a parapet of 50 cm high in the seaward end of the frontal step. It is interested that the profile B is larger in q_{exp} than the profile D without a parapet. In order to make more clear this matter, q_{exp} is compared in Fig.8 between the profiles with and without a parapet. In this figure, black dots show the result of test conducted under the same condition as white dots of 10 sec in wave period except that the wave peirod is 8 sec. Also, in the figure, the fact that dots are plotted in the right side of the actual line of 45° against the abscissa shown that q_{exp} increases due to attaching of a
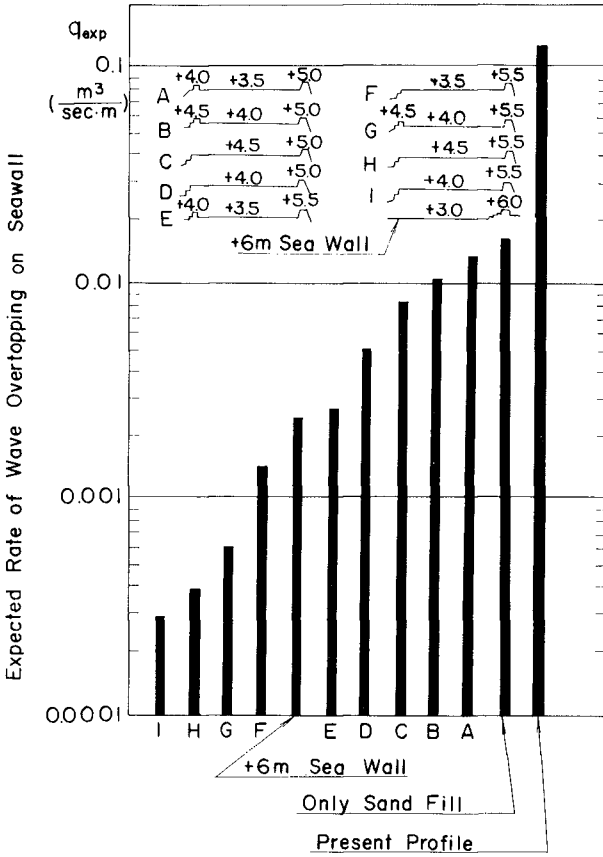
Fig.6   The comparison of the expected rates of wave-overtopping on different types of sea walls (h=3.7m, T=10sec, $H_{1/3}$=4.7m)
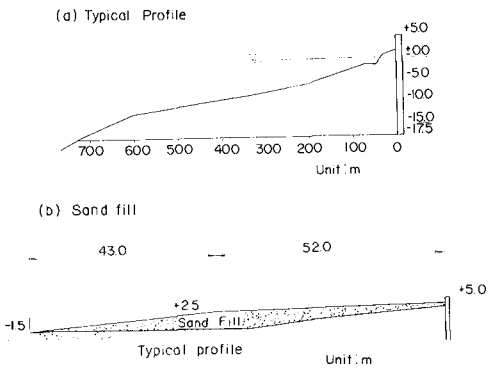
Fig.7   The typical profile and the sand fill

parapet of 50 cm high. All cases except the black dots of the profile D and B are plotted in the right side of the actual line. That is, in the most cases, the attaching of a parapet at the seaward end of a frontal step does not decrease the amount of wave overtopping, for the most cases it increases the amount. This depends on the fact that the wave running up the parapet disturbs the water filled between the parapet and the sea wall by the foregoing waves.

Effect of the height of a frontal step

In Fig.6, the comparison of q_{exp} between the profile F and H shows that the former with a lower frontal step is larger in q_{exp} than the latter with a higher one. But, the profile D is less in q_{exp} than the profile C, though the former is less in the height of a frontal step than latter. The difference of the height between the sea wall and the frontal step is one meter in the profile H and only 0.5 metres in the profile C. This seems to be the reason why the result of the comparison of q_{exp} between the profile F and H is different from between D and C. This shows that the waves running up the frontal step overtop easily the sea wall, unless the sea wall is so enough higher than the frontal step. Therefore, under the condition of a constant height of sea wall, the wave overtopping discharge does not always decrease with the increase of height of frontal step.

An additional test has been conducted to make more clear the above mentioned matter. In Fig.9, is shown the result of the test where the overtopping discharge of regular waves has been investigated for four profiles different in the height of frontal step under the condition of the sea water level of 3.4 m above L.W.L., the wave period of 10 sec and the crown elevation of sea wall of 5.5 m above L.W.L. The overtopping discharge q of regular waves of around 4.5 m high is the maximum for the profile R and the minimum for the profile P. Also, q of waves of around 5.5 m high is the maximum for the profile P and the minimum for the profile Q.

Though the effect of the height of frontal step on the wave over-topping discharge is not so simple as mentioned above, the expected rate q_{ecp} of wave overtopping for irregular waves of 4.7 m in $H_{1/3}$ is calculated on the basis of Fig.9 and shown in Fig.10. In the figure, F, I and H are for the cases that the waver level is 3.7 m above L.W.L. and also plotted on the basis of Fig.6. From the figure, in general, the wave
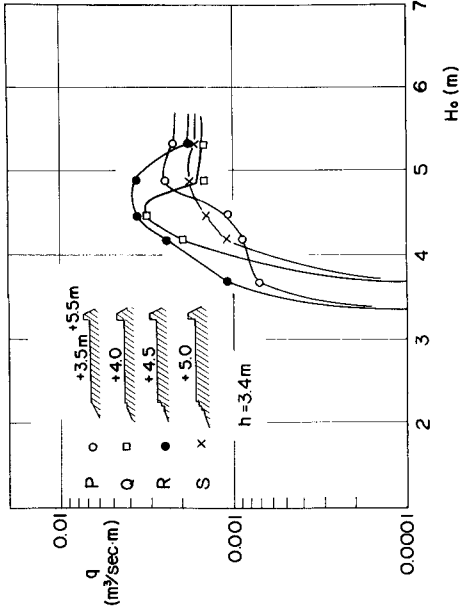
Fig.9 Overtopping discharge of regular waves against the profiles different in the height of frontal step (h=3.4m, T=10sec)
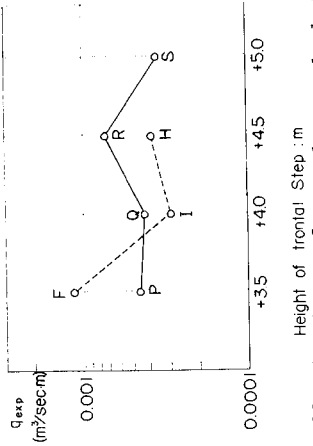
Fig.10 The change of q_{exp} due to the height of frontal step.
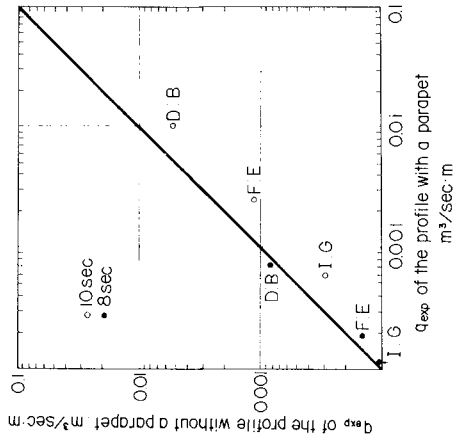
Fig.8 Comparison of expected rate of wave overtopping between the profiles with and without a parapet

overtopping discharge seems first to decrease, then to increase and again
to decrease as the height of the frontal step is heightened gradually from
the beach level. In the second step showing the increase of discharge
such as from Q to R, the decrease of the ability to prevent the wave run-
ning up on the frontal step from moreover overtopping the sea wall, which
is caused by the decrease of the relative height of sea wall against the
frontal step, seems to exceed the increase of the ability to prevent the
wave from running up on the frontal step by the heightening the frontal
step. In the last step showing the decrease of the discharge, the frontal
step is seemed to become so high as to decrease very much the volume of
waves running up on it, despite the decrease of the relative height of the
sea wall against the frontal step.

EFFECT OF PROTECTIVE MEASURES OF NOURISHED BEACH

In order to examin the stability of sand fill recommended above, a
foreshore part between two groins shown in Fig.11 was nourished on trial
with sand of 10,000 cubic meters in the summer of 1970, of which grain
size is shown in Fig.12. But in one year after the nourishment, the
foreshore was eroded by 4,000 cubic meters, despite there was no attack
of typhoon. Therefore, field and model tests have been conducted to find
out the measures suitable to protect the nourished beach against waves.

Model test

The model test has carried out in a wave basin with a scale of 1/50
in vertical and horizontal. Sand of 0.2 mm in mean diameter was used as
the material of the model beach. The area reproduced in the wave basin
is shown in Fig.11.

The experimental condition such as waves and water level in the
model should be determined so that the profile change in the prototype
is reproduced in the model as exactly as possible. Fig.13 shows the
comparison of equi-depth lines between just after the sand-filling in
1970 and about one year after it. The part above the equi-depth lines
os 1.5 m below L.W.L. is eroded except the portion near to the east-side
groin. The sand eroded during this one year amounts to about 4,000 cubic
meters, as mentioned above. But, the seaward-part of about 20 m long of
the both groins consists of steel piles built so as to coincide with the
slope of the nourished beach in the level of their frown. This may be
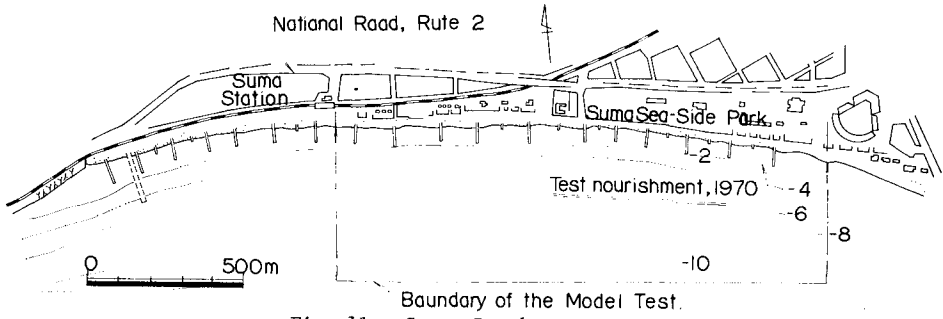
Fig. 11   Suma   Beach
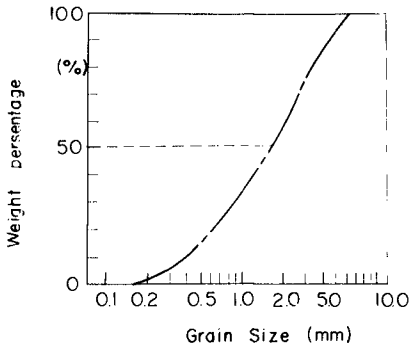
Fig.12   Grain size distribution
of the nourished sand
in the prototype
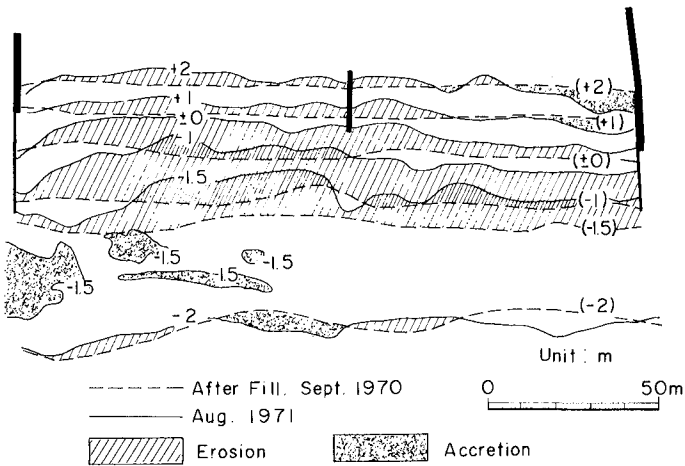
Fig. 13   The change of equi-depth lines in the section
nourished artificially in 1970

the main reason why the relatively large amount such as 4,000 cubic meters
has been eroded from the nourished beach in 1970. Anyhow, by the prelimi-
nary test, the wave of 3 cm high, 0.86 sec period and SSW direction with
the water level of 3 cm above L.W.L. has been selected as a model condition
suitable to reproduce the change of the equi-depth line in the prototype
shown in Fig.13. The model wave corresponds to the wave of 1.5 m high and
6 sec in the prototype and the model water level to 1.5 m above L.W.L. in
the prototype. The erosion corresponding to 4,000 cubic meters in the
field has occurred in 4 hours of wave action in the model, when the equi-
depth lines changed as shown in Fig.14. The change is approximately
similar to Fig.13, though the contrast between erosion and accretion is
stronger than the prototype.

     Then, at first, the extension of groins and the offshore breakwater
have been tested under the above selected wave and water level. In this
case, the extended part of groins corresponds to 60 m in length and 2 m
above L.W.L. for the seaward part of 20 m long and 3 m for the other part
in the crown elevation. The offshore breakwater corresponds to 3 m above
L.W.L. in the crown elevation. Fig.15 shows the change of bottom of four
sections in the central part of the model beach, where equi-depth lines
are shown by dotted lines for the initial profile and by actual lines for
one after the wave action of 4 hours. The material volume above L.W.L.
has been compared between before and after of the wave action, of which
the results is shown in the figure with the notion of "Erosion" or
"Accretion". From the figure, it is seen that the extension of groins is
not enough to protect the nourished beach only by itself from the waves
even the year of the normal weather condition without severe typhoons,
but that the addition of the offshore breakwater is enough to protect
the beach.

     However, the nourished beach should be retained even against the
large waves in the typhoons. Therefore, the model test for the waves of
3 m high and 8 sec has been carried out under the conditions of the same
wave direction and water level as the fore-going test. The results are
shown in Fig. 16, where the change of the material volume above L.W.L. in
the same as the fore-going test is also shown for each section. In the
test, the elevation of the submerged breakwater is 1.5 m below L.W.L. at
the crown. The followings are seen from the figure;

  (1) The offshore breakwater of the case 4 is the least in the erosion
of beach, and changes the shore line to be convex.

- - - - Originol Fill
———— After 300min of Wove Run
▨▨▨ Erosion
▨▨▨ Accretion
Unit of Woter Depth: m (in Prototype)

O   in Model   5 m
O   in Prototype   50m·
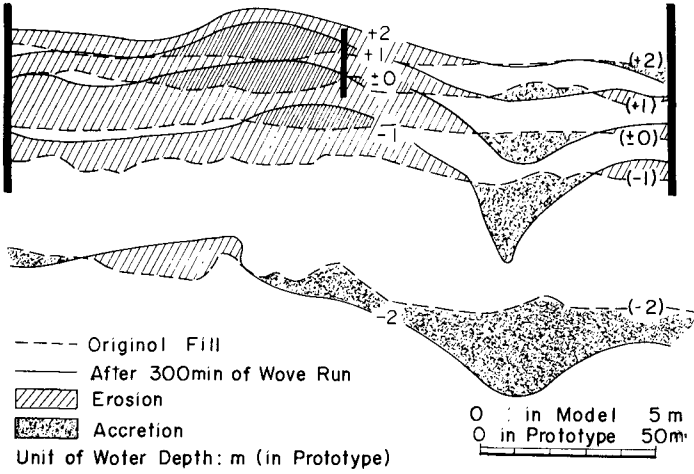
Fig. 14   The change of equi-depth line in 4 hours of wave
           action in the model (H=1.5m, T=6sec, h=1.5m)

(a) Case-1 Extension of Groins   ———— 4 hours of wave action
                                            - - - - Initial

(Erosion: 341 m³) | (Erosion: 710 m³) | (Erosion: 711 m³) | (Erosion: 1014 m³)
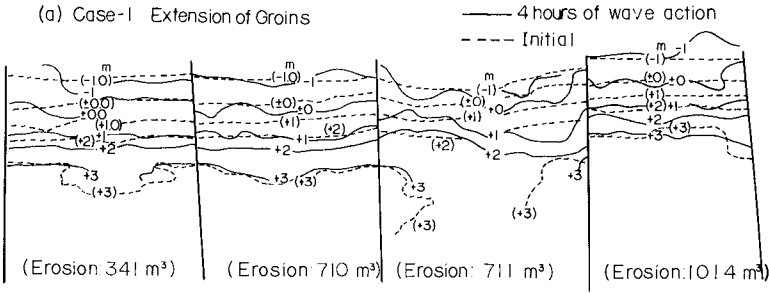
(b) Case-2 Offshore-Breakwater in Addition to Extension of Groins

(Accretion: 168m³) (Erosion 98m³) (Accretion: 464m³) (Accretion: 228m³)

SCALE   = = = Permeable type
O   50   100m   ——— Impermeabe type
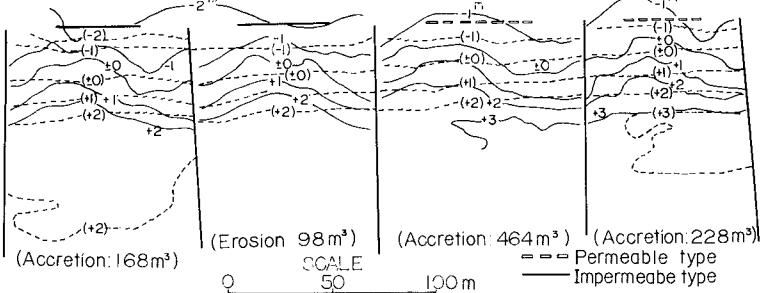
Fig. 15   The change of equi-depth lines due to the wave of
           H=1.5m and T=6sec in the model.
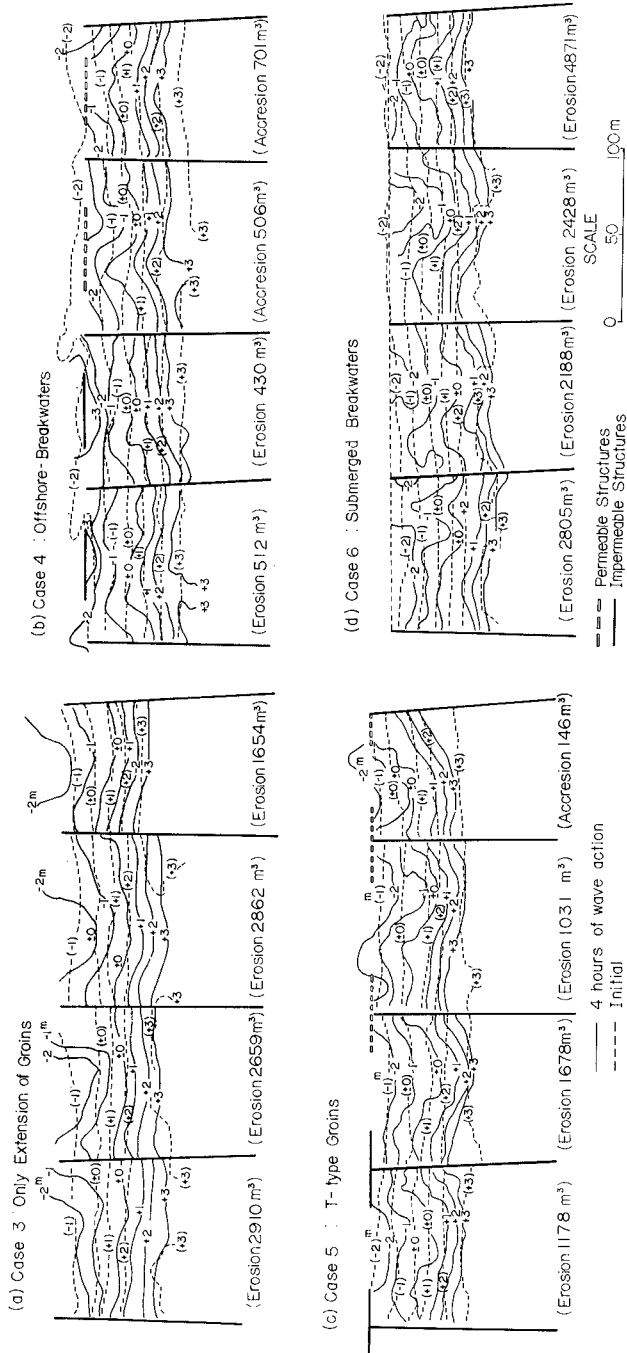
Fig. 16   The change of equi-depth lines due to the wave of H=3m and T=8sec in the model test

(2)   The T-type groin of the case 5 is inferior to the offshore
breakwater and superior to the submerged offshore breakwater in the
ability retaining the beach material, and changes the shore line to be
concave.

(3)   The shore line seems to be more straight at the offshore breakwater
than at the T-type groin.

Field test

On the other hand, in the summer of 1972, a T-type groins, a permeable
offshore breakwater and a submerged offshore breakwater have been construc-
ted in the field as shown in Fig.17, and each section has been nourished
with sand of 7,300, 6,600 and 8,000 cubic meters respectively.   The
structures of T-type groins, offshore breakwater and submerged breakwater
are impermeable, permeable and impermeable, respectively as shown in Fig.
17.

Fig. 18 shows the comparison of equi-depth lines between September
1972 and January 1974 for each section.   Fig. 19 shows the change of
profiles along each broken lines drawn in Fig. 18.   Moreover, Fig. 20
shows the volume change of each material above L.W.L. for each section,
where the change is expressed by the volume difference of each surveying
data against September 1972 which is just after the beach nourishment.
From these figures 18 to 20, are seen the follows:

(1)   The section of the offshore breakwater is less in the erosion of
beach than the T-type groins, as same as in the model tests (see Fig.20).

(2)   The section of the submerged breakwater is the most changeable
in the volume of beach material (see Fig. 20).   This means the submerged
breakwater is inferior to the other measures in the ability of protecting
beach.

(3)   The shore line is more straight in the section of the offshore
breakwater than the T-type groins, as same as in the model test.

(4)   The erosions has occured mainly in the foreshore which extends
from about $- 1 \sim -1.5$ to $+2.0 \sim +2.5$ m L.W.L. (see Fig.19).   This might be
relative to the fact that the beach nourishment have been conducted so as
to push out offshoreward the foreshore of -1.5 m L.W.L. to +3.0 m L.W.L.

(5)   In the section of T-type groins, the slope of foreshore tends to
be gentle in the center and steep in the both side (see Fig.19).   In the
section of offshore breakwater, it should be steep in the center and gentle
in the both side, but such a tendency have not appeared clearly.
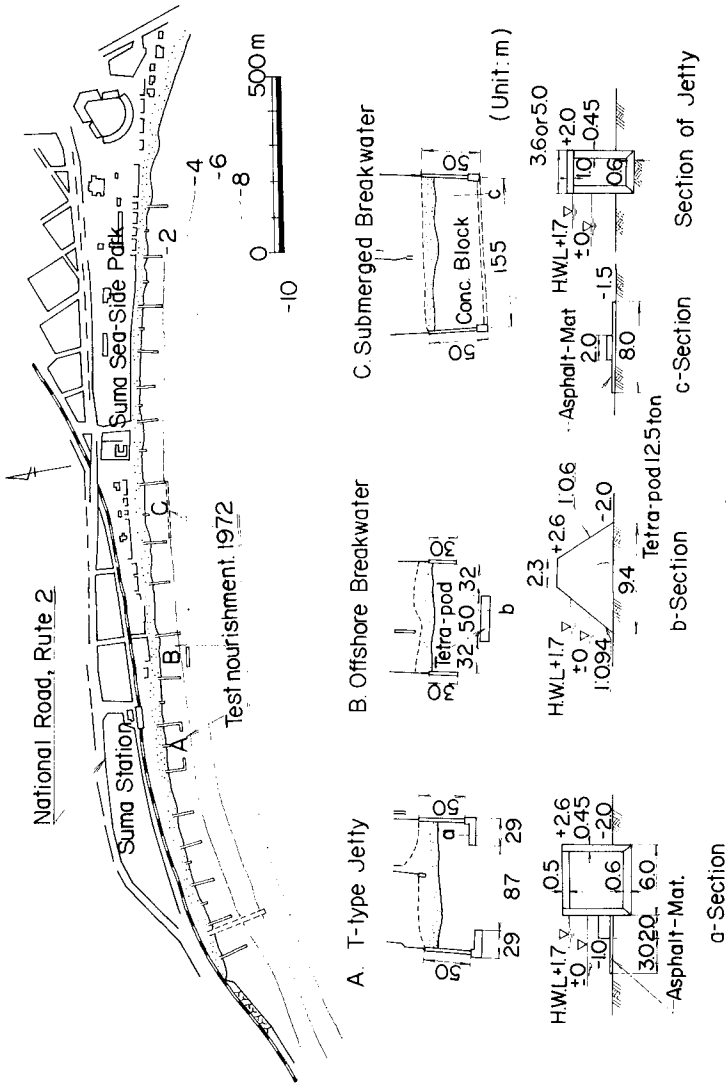
Fig. 17 Protective measures constructed in the field in 1972 for the comparison of their ability on beach protection
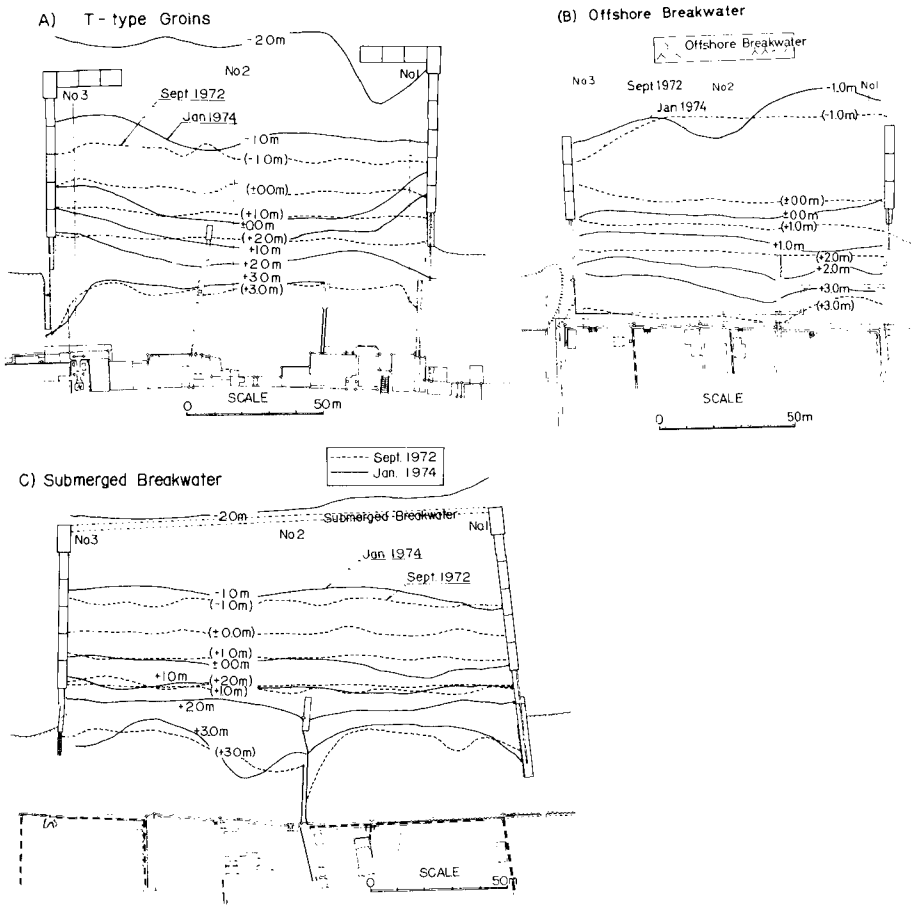
Fig. 18   The comparison of equi-depth lines between
           September of 1972 and January of 1974

Fig. 20　Volume change of the material on the beach above L.W.L.

Fig.19

The change of beach profile after sand-fill in the prototype

As seen from the above mentioned, the results of model test consides fairly well with the field test in the qualitative consideration. But it is difficult to compare the model test with the field test in the quantative consideration.

CONCLUSION

In a recreational beach, the heightening of sea wall is undesirable from the view-point of environmental preservation and beach utilization. Therefore, a proposal has been made of the sea wall with a wide frontal step as well as the widening of beach by artificial nourishment. And the follows have been made clear by the model and field tests.

On the wide frotal step;

(1) The height of sea wall can be decreased by adding a wide frontal step without increasing the amount of wave overtopping discharge.

(2) The attaching of a parapet of 50 cm high at the seaward end of a frontal step does not serve to decrease the amount of the wave overtopping; for the mose cases it increases the amount.

(3) The amount of wave overtopping first decreases, then increases and again decreases as the height of frontal step is raised from the beach level.

On the protective measures of the nourished beach;

(1) The offshore breakwater is superior to the T-type groins in the ability retaining the beach material. And T-type groins are superior to the submerged breakwater.

(2) The shore line changes into convex shape in the section of the off-shore breakwater and into concave shape in the section of the T-type groins.

(3) The shore line is kept more straight in the section of the offshore breakwater than the T-type groins.

(4) The results of model test coincide fairly with the field test in the qualitative consideration.

At last, the authors express their thanks to Mr. Tensetsu Hattori and Mr. Katsunori Sasaki in the same Institute as the authors for their cooperation in this works.

REFERENCES

1) Senri Tsuruta and Yoshimi Goda: Expected discharge of irregular wave
    overtopping, Proc. of 11th Conference on Coastal Engineering, Vol. II,
    Sept. 1968.

2) Yoshimi Goda: Expected rate of irregular wave overtopping of seawalls,
    Coastal Engineering in Japan, Vol. 14. J.S.C.E., Dec. 1971, pp.43 - 51.

CHAPTER 85

A REFRACTION GROYNE BUILT BY SAND

by Alfred FÜHRBÖTER [1]

ABSTRACT

The interaction between a normal groyne and waves mostly is by diffrac-
tion, i.e. the structure of the groyne, especially the width, is very
small in comparison to the wave length. But when a groyne is built with
lateral slopes comparable with normal beach slopes, also refraction
processes occur and surf zones are created nearly parallel to the center
line of the groyne. It can be shown that, for all directions of wave
approach, the longshore currents always are directed shoreward. So, when
such a groyne is built by sand, due to the erosion of the groyne an
artificial sand spit is formed and a beach nourishment at the adjacent
areas of the shore can be expected. Furthermore, sand originating from
the normal littoral drift can be caught by such a structure as it
happens in case of normal groynes.

In a field experiment at the shore of the city of Westerland on the
island Sylt/Germany, with 680,000 m^3 of sand such an artificial sand
groyne was built in 1972. One year later, this sand masses were grown
up to nearly 1,050,000 m^3. After a sequence of five heavy storm surges
in November and December 1973, still 770,000 m^3 could be detected before
the shore in 1974. The evaluation of the experiment is continued; the
aim of it is find out whether repeated beach nourishment is more
economic than protective works. For this reason the knowledge of the
"half decay time" of a beach nourishment is necessary.

---

[1] Prof. Dr.-Ing., Leichtweiß-Institut für Wasserbau of the Technical
University Braunschweig, Germany
Hydrodynamics and Coastal Engineering Division

1. ABOUT THE CONCEPT OF SAND GROYNES (REFRACTION GROYNES).

The main effect of normal sea groynes against approaching waves is by diffraction, i.e. the groynes are acting as an obstacle against wave motion. On the side of wave attack, waves may be broken and/or reflected; sometimes even MACH-stem reflection can be observed. The structures themselves can be regarded as more or less linear elements; their widths are small in comparison to wave lengths. Even when the cross sections are built with slopes on the sides, these slopes are very steep; waves do break on these slopes but no refraction process occurs.

However refraction will play an important roll when a groyne is built in the form of a large, flat and three-dimensional body in such a manner, that the lateral slopes and the head of the groyne are as flat as the natural beach. Such a groyne only can be constructed in sand itself because of the immense masses which are necessary for building it. Such an artificial sand spit may act partially also by diffraction like a normal groyne. It is of essential importance, however, that refraction processes are produced on the slopes and influence the surf and longshore currents along the beaches of the groyne (FÜHRBÖTER et al. 1972, FÜHRBÖTER 1973).

The refraction processes, their influence on the angle of wave approach at the breaker line and on the longshore currents caused by surf are shown schematically on Fig. 1. For each direction of wave approach there is a point of divergence at the head of the groyne; the longshore currents on the sides of the groyne are always directed shoreward. At the side of wave approach (left hand on Fig. 1), a nodal point is formed where the normal longshore current along the shore meets the longshore current caused by the surf on the slope of the groyne; on the other side (right hand on Fig. 1) there is a point where the energy due to the longshore current is nearly zero. So it is easy to explain that at the head of the groyne always erosion and in the nearshore sections of the groyne always sedimentation will occur. The same effect can be expected when wave approach is perpendicular to the shore.
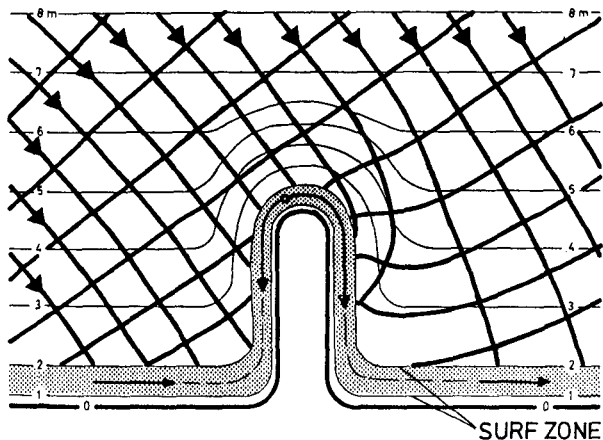
Fig. 1: Refraction processes and longshore
         currents upon a sand groyne
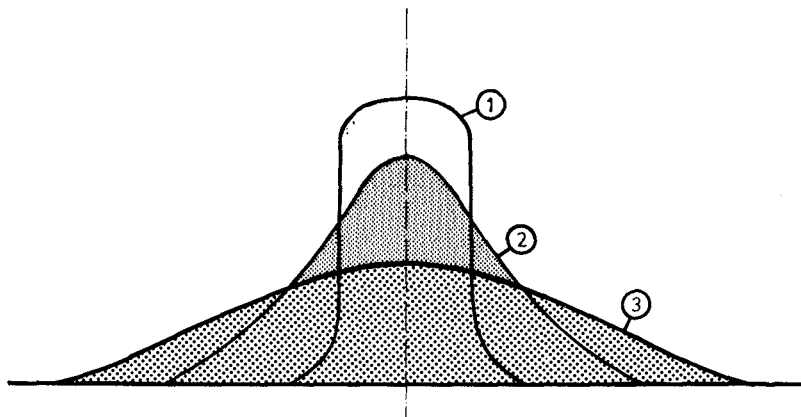
Fig. 2: Deformation of a sand groyne into an
         artificial sand spit by wave attack
         from all directions

The groyne as to be seen on Fig. 2 will be deformed continuously under
the assumption that waves are approaching from all directions. By the
process of erosion at the head, sediment transport upon the slopes at
both sides is caused and sedimentation occurs in the corners between
groyne and shore so that gradually the groyne changes into the con-
tour of a flat sand spit. During the phase of deformation, a reduction
in length of the groyne will be compensated by increasing width at the
shorelines besides it (Fig. 2). This process is very complex in the
detail due to the interactions between waves, longshore currents and
beach profiles.

After deformation into a sand spit, the system of longshore currents
will have another pattern, too, as to be seen on Fig. 3 for the case of
a small angle of wave approach. There are no more points of divergence
at the head of the groyne. But Fig. 3 also shows two zones with re-
markable reduction of the longshore component in comparison to that on
Fig. 1.

According to the predominant wave direction of the season the groyne
or spit will change the form according to the scheme on Fig. 4. Similar
to a tidal dune, a certain amount of sand will move from one slope to
the other but without leaving the system.

The model presented here is simplified and qualitative but it demon-
strates that an effect on shore stabilisation can be expected from such
a structure. Moreover it is possible that sand from the natural long-
shore transport can be caught in the sedimentation zones of the groyne
here acting like a normal groyne. With regard to the flat form of the
sand body, it can be expected that no lee erosion will occur.

It should be noticed that the concept of a depot nourishment in form
of a sand groyne as described here is only applicable for coasts with
wave action occurring from nearly all directions. For predominat wave
attack from one direction only, this concept has to be modified.
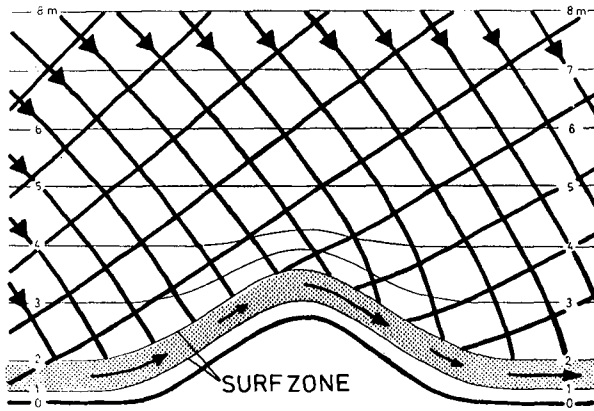
Fig. 3: Refraction processes and longshore
currents upon an artificial sand spit

Fig. 4: Changing of the form of the spit due according
to the prevailing wave direction

2.   FIRST APPLICATION OF THE SAND GROYNE CONCEPT BEFORE WESTERLAND/SYLT.

The island of Sylt before the west coast of Schleswig-Holstein/Germany suffers from strong wave erosion by the North Sea. In the average, in the last century an annual erosion of nearly 1 m was started; a comprehensive study of this problem is given by LAMPRECHT (1955).

Especially at the site of the city and well known recreation place of the island, Westerland, already at the beginning of this century a protection work in form of a seawall became necessary in order to prevent further dune erosion. The further development of these defense structures is described on Fig. 5; no comment is necessary here, it is the normal process at all places where a coastline under erosion is fixed. Even supported by a system of heavy groynes,the erosion could not be stopped; the groyne effect is less because of the fact that the average of wave approach is nearly perpendicular to the shoreline here.

Fig. 6 shall may give an impression of the strength of wave attack against the seawall (storm flood in 1954). By the reflection of wave energy at the nearly vertical defense works the natural erosion process is superimposed by human made erosion additionally.

At the top of Fig. 7, the morphological development of the area before the shore is illustrated. The longshore bar (Fig. 7) is a typical feature along the west coast of Sylt.

About 1970, it became necessary to design a further toe protection of the seawall due to the danger of underscour; this measure would have been the third toe protection (see Fig. 5). Because of the increasing costs of construction and maintenance of the works and because of the fact that erosion could not be delayed but was even accelerated due to the vertical face of the structure, alternative solutions were discussed and an artificial beach nourishment was taken into consideration.

1912-1922

▼ HHThw

▼ MThw

|— 30 m —|

1938-1940

▼ HHThw

▼ MThw

|— 30 m —|

1960-1961

▼ HHThw

▼ MThw

|— 30 m —|

1965-1966

▼ HHThw

▼ MThw

|— 30 m —|

?
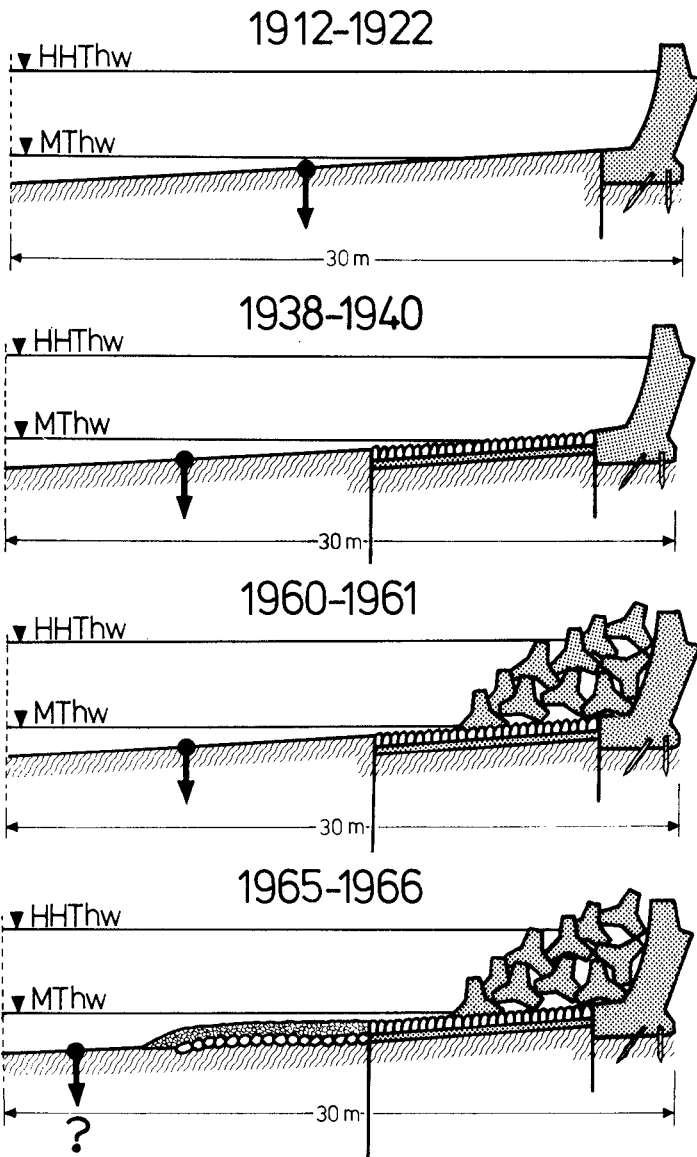
Fig. 5: Developement of the coastal defense works before
         Westerland/Sylt

19.5.1953

13.3.1973

21.4.1972

17.5.1973

11.10.1972

28.2.1974

20.12.1972
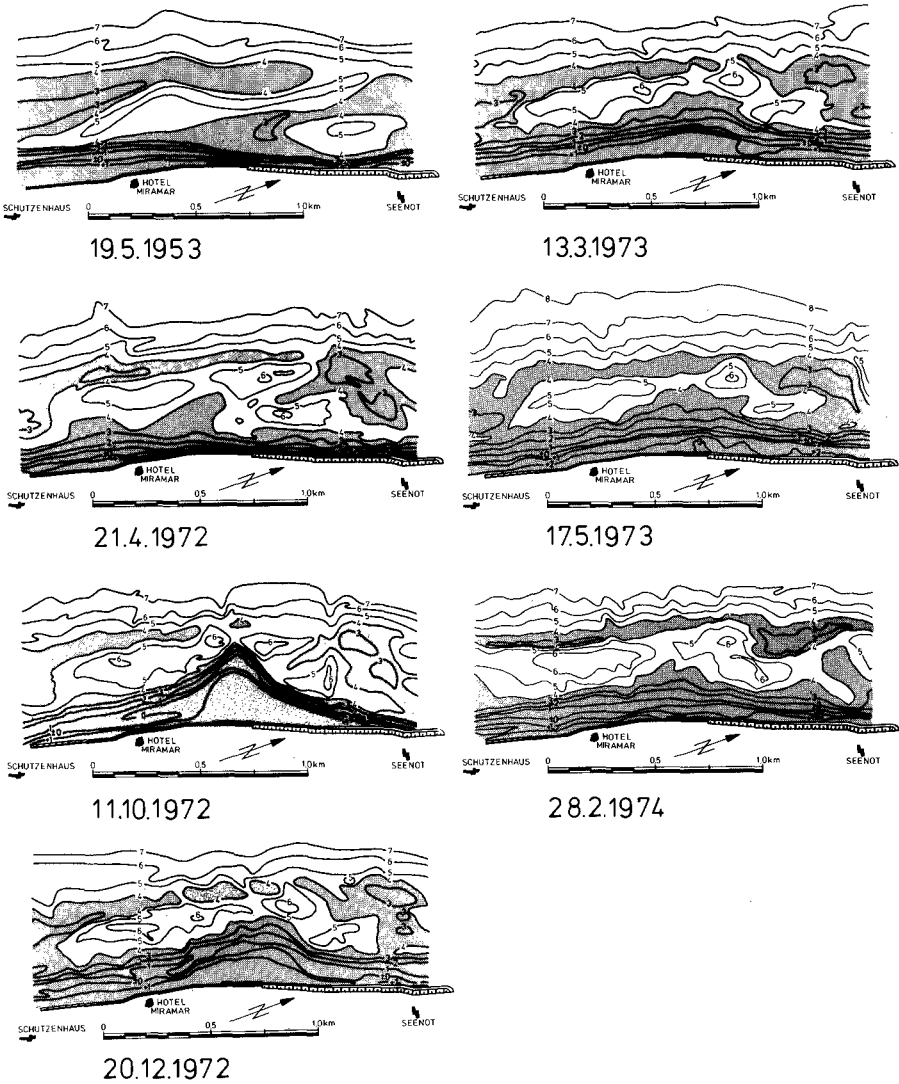
Fig. 7:   Development of coastal morphology before Westerland/Sylt since
          1953 (after surveys of the AMT FÜR LAND- UND WASSERWIRTSCHAFT
          HUSUM)

Fig. 6: Wave attack at the seawall of Westerland/Sylt during a storm surge in 1954 (after LAMPRECHT 1955)

Although being aware that such a measure would have to be repeated after several years this solution seemed to be more economical than further reinforcements of the existing structures and their toe protections. An exact calculation for economy, however, only can be carried out with the knowledge of the time when the nourishment has to be repeated.

In a first plan, a field experiment was considered with a normal beach nourishment along the shoreline where toes of the defense works had to be protected. By this "linear" fill-up an artificial beach slope due to the sedimentation process of hydraulic transport would have been created which is not in response to the wave-beach-profile. During change of the profile, with longshore currents additionally perhaps, an important loss of sand masses cannot be avoided.

Therefore here the concept of a depot nourishment in form of such a sand groyne was planned as a field experiment with the scale 1 to 1 (FÜHRBÖTER et al. 1972, KRAMER 1972). For observation of the full scale experiment, a comprehensive measuring and survey program was carried out by the AMT FÜR LAND- UND WASSERWIRTSCHAFT HUSUM together with university institutes, amongst it the LEICHTWEISS-INSTITUT FÜR WASSERBAU of the Technical University of Braunschweig with a wave and current measuring program (FÜHRBÖTER et al. 1972, BÜSCHING and FÜHRBÖTER 1974, DETTE and FÜHRBÖTER 1974).

After surveys and investigations on the shore before the beach nourishment, in summer 1972 an additional mass of nearly 700,000 m^3 was deposited before the center of the defense works from Westerland. Only one feeder pipeline was used for it being lengthened perpendicularily to the shore across the surf zone.

The grain size of the sand deposited at the beach was nearly similar to that of the natural beach sand; from the nearly 1,000,000 m^3 excavated in the wadden sea behind the island, about 300,000 m^3 with grain diameter less than .2 mm were lost; this is in good agreement with other beach nourishments on the german coast of the North Sea where about 30 % were estimated as spoil loss during beach fill process (KRAMER 1972).

Because of heavy wave action even during summer season, the sand groyne was formed into an artifical sand spit already during construction. The survey from 11.10.1972 shows the form of the spit with the additional mass of 700,000 m^3 of sand (Fig. 7).

Fig. 7 shows the further development of this sand spit; Fig. B shows the wave climate of the 3 winters after the nourishment (measured about 1,300 m ashore at a water depth of about 8 m below MSL). Additionally, on Fig. 9 the change of the distribution of the additional sand masses in m^3/100 m shoreline for a length of 1.7 km around the center line of the sand groyne and for the whole length of B km is given.

Winter Season
 1971/1972
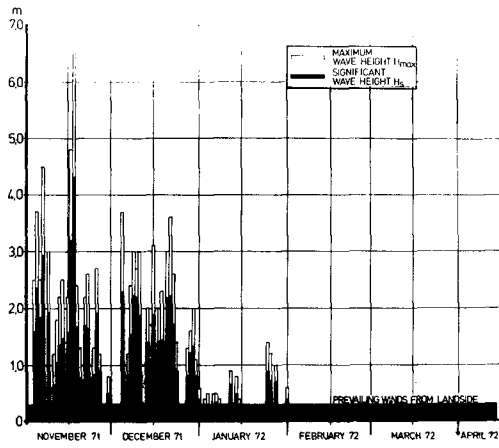
Winter Season
 1972/1973
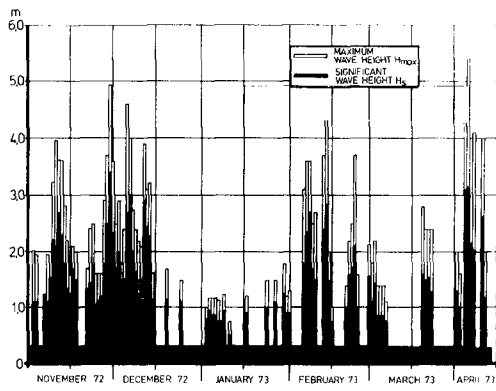
Winter Season
 1973/1974
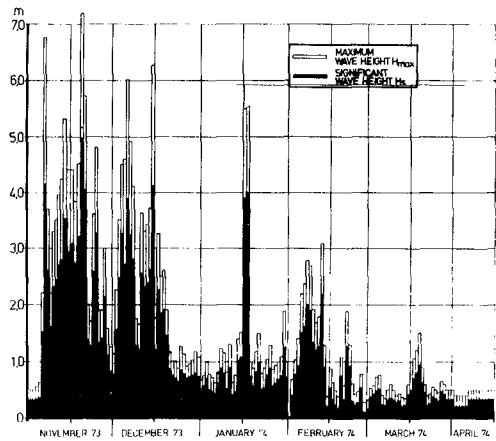
Fig.8: Wave climate before
       Westerland/Sylt from
       1971 to 1974
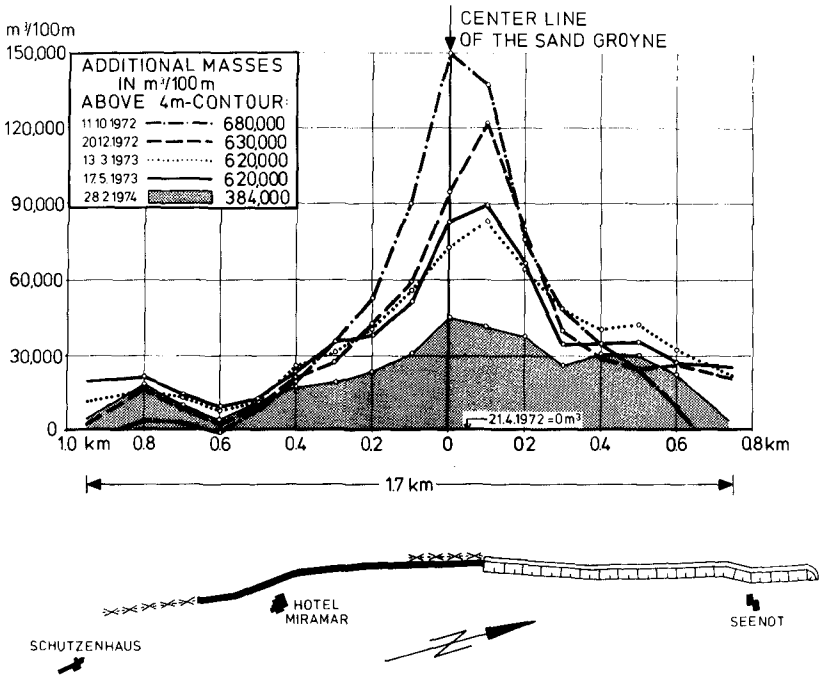
Fig. 9: Distribution of the additional sand masses near the center line of the sand groyne (length 1.7 km)
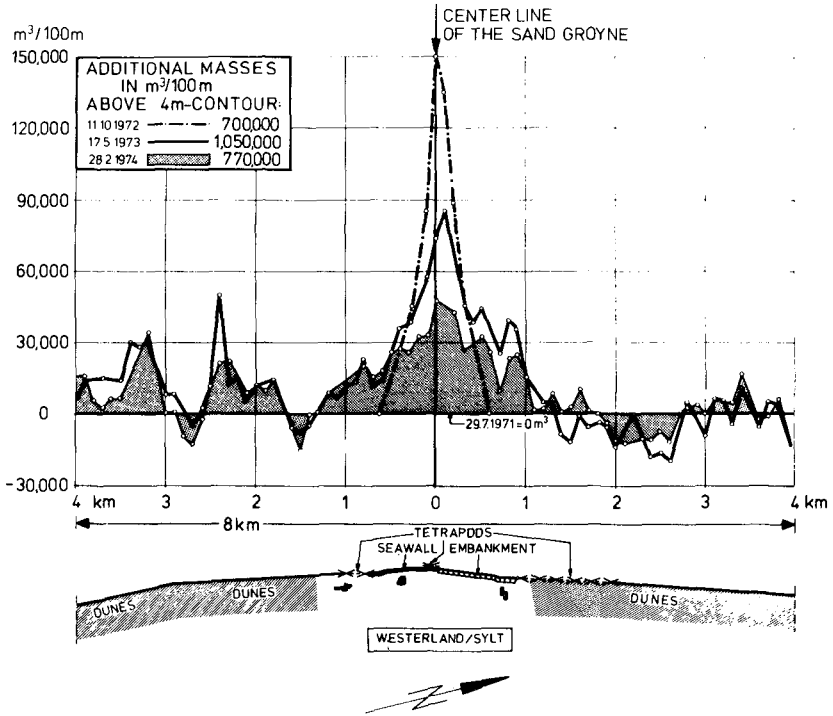
Fig. 10: Distribution of the additional sand masses near the center
        line of the sand groyne (length 8.0 km)

The results from Fig. 7, 9 and 10 can be summarized as followes:

    a.   Even during the relative weak storm
           season of winter 1972/1973 the changes
           of the shape of the artificial sand
           spit were more significant than in the
           following winter with stronger storm
           action.

    b.   The change of the form of the sand
           groyne as predicted in the scheme on
           Fig. 2 was verified by the field
           experiment.

    c.   After construction, only a length of
           about 1 km was protected by the sand
           depot at both sides of the center line
           of the groyne. However after one winter
           season already the waves and their long-
           shore currents had distributed the sand
           over the whole length of the protection
           works.

In the area near the center line (length 1.7 km), sand losses from
680,000 m^3 in October 1972 to 385,000 m^3 in February 1974 occurred.
With regard to the length of 8 km, however, the masses increased to
1,050,000 m^3 in May 1973; this is surely due to the deposition of addi-
tional sand from the natural longshore current due to the sand spit
acting like a single groyne. During winter season 1973/1974 with very
heavy wave action (Fig. 8) and 5 extreme storm surges, the masses de-
creased to 770,000 m^3; this is still 90,000 m^3 more than the 680,000 m^3
after construction in October 1972 (Fig. 9 and 10).

3. BEACH NOURISHMENT AND HALF DECAY TIME

It is a rule of experience for artificial beach nourishments, espe-
cially losses of material per unit of time(monthly or annually) are
predominant just after the beach fill than later on (KRAMER 1958,

LUCK 1968). This is due to the necessary accomodation of the artificial
spoil beach slope to the wave equilibrium profile.

It seems that in this case the law of half decay time from nuclear
physics can be used

$$V = V_o \cdot 2^{-\frac{t}{t_H}}$$

V = Volume of additional sand masses at the
      time t

V_o = Volume of beach fill after the nourishment
      (t = 0)

t = time

t_H = half decay time

On Fig. 11, the reduction of a beach fill (V_o = 98,000 m^3) at the
Baltic Sea (Sierksdorf) during one winter season is illustrated in
linear and logarithmic scale. The straight line in the logarithmic pre-
sentation shows a quite good agreement with the expontial law. Further
surveys were not available for this case study.

With a digital program also used for Fig. 9 the sand losses in the
area near the centerline of the sand groyne (length 1.7 km, Fig. 9)
were computed for the additional masses above different levels
from MSL - 4 m till MSL + 1 m; with 680,000 m^3 = 100 % on 11.10.1972
the decrease of the beach till near the centerline is to be seen on Fig.12
with a linear time scale.

According to the occurrence of waves, for the use of the concept of half
decay time a distorted scale of time should be used. Instead of time the
sums of wave energy is plotted against the sand losses (Fig. 12); the
total wave energy in kWh/per m shoreline was calculated by application
of linear wave theory from the continuous wave records (Fig. 8) and
taking the significant heights.
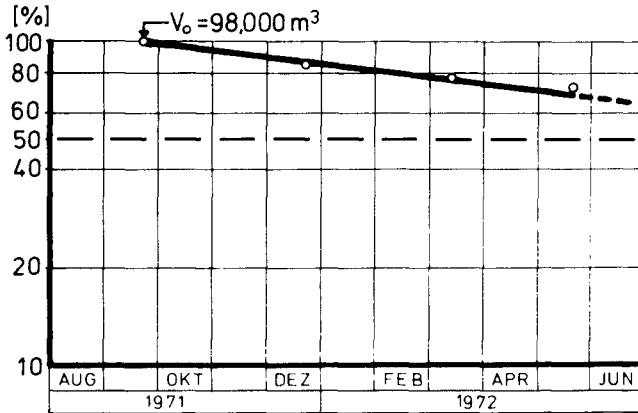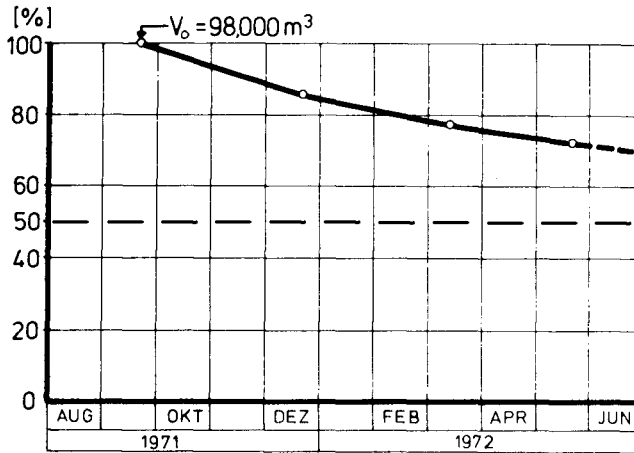
Fig. 11: Sand losses of a beach nourishment during one winter season
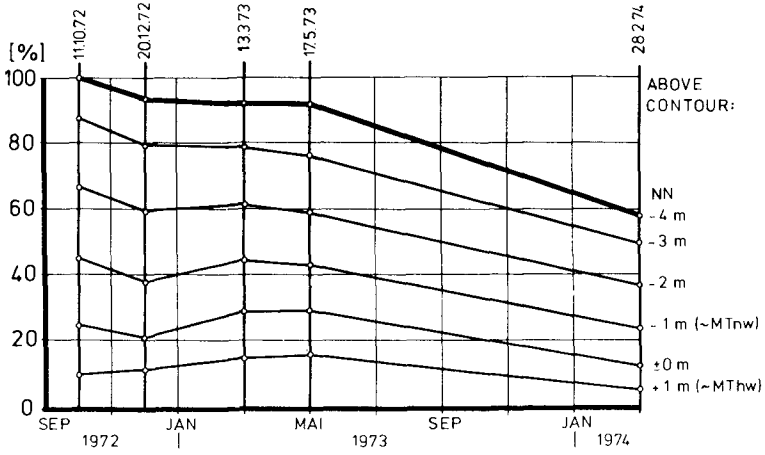
Fig. 12: Sand losses in the area near the center line (length 1.7 km,
see Fig. 9) in dependence of time
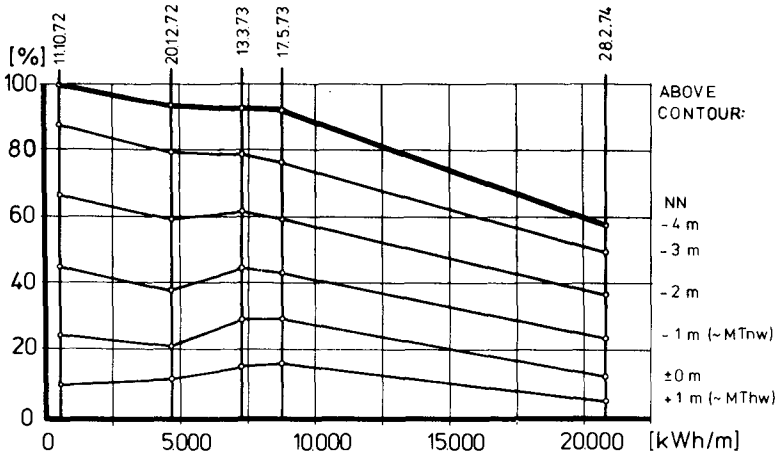
Fig. 13: Sand losses in the area near the center line (length 1.7 km,
see Fig. 9) in dependence of the sum of wave energy

In both cases the plotting of Fig. 12 and Fig. 13 do not give such a clear picture like Fig. 11. This is mainly due to the fact that the length of 1.7 km is not representative for the whole length improved by the nourishment. For 8 km of shoreline (Fig.10) the result of the surveys is as already mentioned before:

11.10.1972	680,000 m^3
17. 5.1973	1,050,000 m^3
28. 2.1974	770,000 m^3

Because the surveys are expensive in costs, time, personal and evaluation and strongly dependent upon weather conditions, only a restricted number of them could be carried out. Seasonal changes or the effect of single storm surges therefore cannot be selected here. So the reduction of masses on Fig. 12 and Fig. 13 cannot be regarded as real losses because the lateral shorelines have their benefit from them (Fig. 10).

4. CONCLUSIONS

The time and number of surveys (nearly 3 years) do not allow up to today an exact extrapolation of the half decay time for the artificial sand spit. The morphological development, however, shows that a sort of stabilisation of it can be stated which also remainde during the very strong storm and wave action of the winter 1973/1974 (Fig. 7, 9 and 10). Further surveys and investigation will help to allow a judgement about the feasibility of the concept. The results seem so far to be of high interest for further planning and design in future.

4. REFERENCES

BÜSCHING, F. FÜHRBÖTER, A.	1974	Wave Measuring Instrumentation for Field Investigations Internat. Symposium On Ocean Wave Measurement and Analysics Braniff Place, New Orleans, USA
DETTE, H.H. FÜHRBÖTER, A.	1974	Field Measurements in Surf Zones Summaries, 14th. Internat. Conference on Coastal Eng., Copenhagen, Dänemark,
FÜHRBÖTER, A. KÖSTER, R. KRAMER, J. SCHWITTERS, J. SINDERN, J.	1972	Sandbuhne vor Sylt zur Stranderhaltung "Die Küste", Heft 23
FÜHRBÖTER, A.	1973	Eine Refraktionsbuhne aus Sand vor Sylt Wasser und Boden, 25 (1973) Nr. 12
KRAMER, J.	1958	Die Strandaufspülung Norderney 1951-1952 und ein Plan zu ihrer Fortführung. "Die Küste",Jahrgang 7
KRAMER, J.	1972	Coastal Protection by Beach Nourishment Proc. XIIIth Internat. Conference on Coastal Eng., Vancouver, 1972
LAMPRECHT, H.O.	1955	Brandung und Uferveränderungen an der Westküste von Sylt Mitt. d. Franzius-Institutes, Heft 8
LUCK, G.	1968	Bericht über die zweite Strandaufspülung am Westrand von Norderney. Forschungsstelle Norderney, Jahresbericht 1968, Band XX.

CHAPTER 86

PERFORMANCE OF A JETTY-WEIR INLET IMPROVEMENT PLAN

by

J. A. Purpura[1], B. C. Beechley[2]

C. W. Baskette, Jr.[3], J. C. Roberge[4]

ABSTRACT

Comprehensive monitoring has been carried out since 1970 to determine the performance and effects of a navigation and inlet stabilization project at Ponce de Leon Inlet, Florida. The improvement plan at the tidal inlet included construction of two jetties, a weir sand by-pass system, and dredging of a navigable channel (Figure 1). An evaluation was made of the general current patterns, the relative refracted wave energy distribution, and the volumetric beach and hydrographic fluctuations associated with the inlet. An analysis of this data was used to interpret the dramatic and unexpected changes which have resulted along the adjacent coastline and within the inlet after the completion of the inlet improvements.

BACKGROUND AND DESCRIPTION OF INLET SYSTEM

Ponce de Leon Inlet is located in Volusia County on the east coast of Florida, about 65 miles south of St. Augustine Harbor and about 57 miles north of Canaveral Harbor. The inlet connects the Atlantic Ocean with the Halifax River and the Indian River North which are used extensively by commercial and recreational vessels (Figure 1). The mean tidal range is 4.1 ft. in the ocean and 2.3 ft. inside the inlet channel, with an estimated mean tidal prism of about 12,000 acre-feet.

Past records (1, 2)* indicate an average annual recession of the mean low water line in the 2-mile reach immediately north of the inlet of

---

[1]Professor, Civil and Coastal Engineering Department, University of Florida, Gainesville, Florida 32611, USA.

[2]Engineer, Fred R. Harris, Inc., Great Neck, New York, 11021, USA.

[3]Civil Engineer, Water Resources Planning, U. S. Army Engineer District, Norfolk, Virginia 23510, USA.

[4]Engineer, Waterways Experiment Station, U. S. Army Corps of Engineers, Vicksburg, Mississippi 39180, USA.

*Numbers in parentheses indicate references at the end of the paper.

PROJECT: An entrance channel 15 feet deep and 200 feet wide across the ocean bar and thence 12 by 200 feet and 12 by 100 feet to Indian River North, thence 12 by 100 feet southward to the Inter-coastal Waterway; 7 by 100 feet in Halifax River northward to the IWW; ocean jetties about 4,200 feet long and about 2,700 feet long on the north and south sides of the inlet, respectively; a weir in the north jetty and an impoundment basin inside the weir for transfer of littoral drift across the inlet by use of a pipeline dredge. Length of the project is about 5 miles.

MEAN TIDAL RANGE: 4.0 feet at entrance, 2.3 feet of the Coast Guard Station inside the inlet and 4.1 feet in the ocean at Daytona Beach.

PONCE DE LEON INLET
FLORIDA
SCALE IN FEET
1000 0   1000 2000 3000

N

ATLANTIC

OCEAN

EASTERLY LIMIT OF FEDERAL PROJECT

0.2 MI.

PONCE DE LEON INLET

SOUTHERLY LIMIT OF FEDERAL PROJECT

1.4 MI.

18'

12'

6'

18'

12'

6'

WEIR N. JETTY

S. JETTY

6'

1.0 MI.

U.S.C.G. LIGHTHOUSE

IMPOUNDMENT BASIN

(12' x 125')

INTRACOASTAL

WATERWAY

2.0 MI.

6'

2.7 MI.
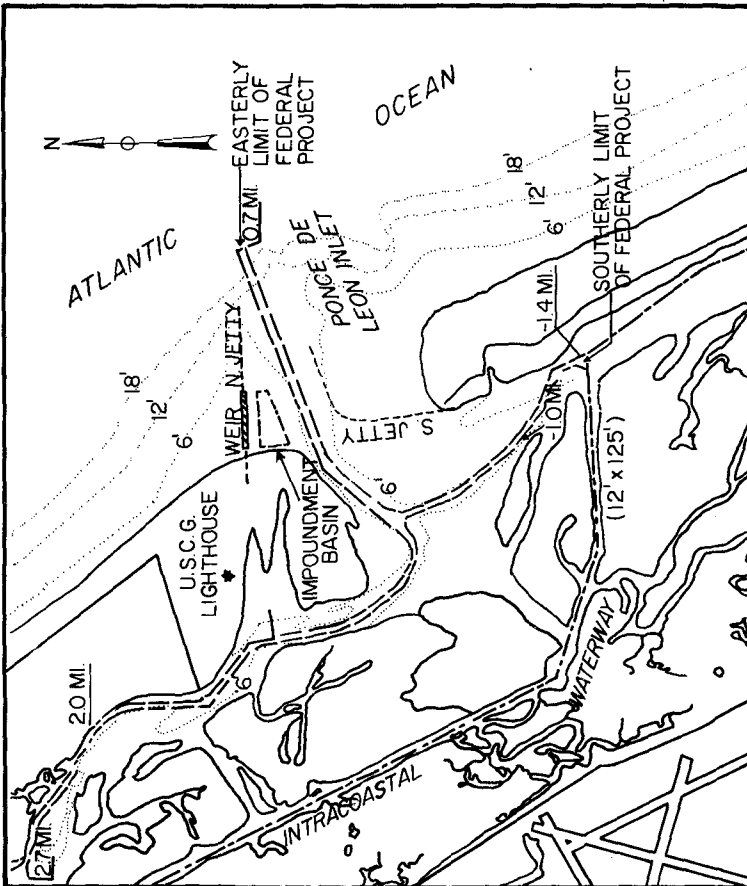
GENERAL PLAN OF IMPROVEMENT

FIGURE 1

about 7 ft. per year. For the 4-mile reach immediately below the inlet, shoreline recession is accompanied by accretion of the offshore portion of the profile. The net average annual littoral transport rate in the vicinity of Ponce de Leon Inlet has been estimated to be in the neighborhood of 500,000 cubic yards southerly and 100,000 cubic yards northerly.

Navigation through the original natural inlet had always been difficult and hazardous. A typical fan-shaped sandbar characterized the ocean entrance over which intense wave breaking took place. Inadequate depths across the bar and continuous shifting of the channel crossing that bar caused the principal difficulties and hazards to navigation.

In July 1968, the Jacksonville District, U. S. Army Corps of Engineers undertook the construction of an inlet stabilization system consisting of an entrance channel, a pair of jetties and an impoundment basin south of the north jetty. The north jetty contained a submerged weir section to allow the southward moving sand to pass over it and deposit in the impoundment basin. This basin would then be dredged periodically with the material being placed on the beach south of the inlet. This design was based on (a) the previously mentioned mean annual rate of southerly littoral drift, (b) an expected rapid accretion north of the north jetty, (c) negligible accretion immediately south of the South jetty, and (d) beach erosion further south of the inlet.

PLAN OF IMPROVEMENT

The north jetty called for in the improvement plan (3) is composed of 500 ft. of prestressed concrete sheet piling, 1800 ft. of king pile weir panels, and 1750 ft. of rubble mound section. The first 300 ft. of the weir crest are at an elevation of +4.00 ft. while the crest elevation of the remaining 1500 ft. of the weir is 0.00, which is taken at mean low water level. The crest elevation of the 1750 ft. of the rubble mound offshore section of the jetty is +7.00 ft.

The south jetty has a total length of about 3800 ft. It is entirely rubble mound construction of variable composition (3). The impoundment basin, (Figure 2), has a horizontal area of about 600,000 ft.^{2} and it is to be dredged to a depth of -20.00 ft. Initial dredging of the basin corresponded to about 400,000 cu. yds. of dredged material. The outlined design was based on an amount of littoral drift of 310,000 cu. yds. expected to pass over the weir annually.

A 7200 ft. long entrance channel leads from the ocean to the Halifax and Indian River north, where it divides into two inner channels following these two rivers (Figure 1). The entrance channel has been designed with a width of 200 ft., a depth of 12 and 15 ft., an over-depth of 2 ft. and a side slope (vertical over horizontal) 1 on 5.

Of interest to the present work is that material excavated from the entrance channel and the impoundment basin was to be disposed immediately south of the south jetty in order to assure a strong land connection between the west end of the south jetty and the existing barrier beach.
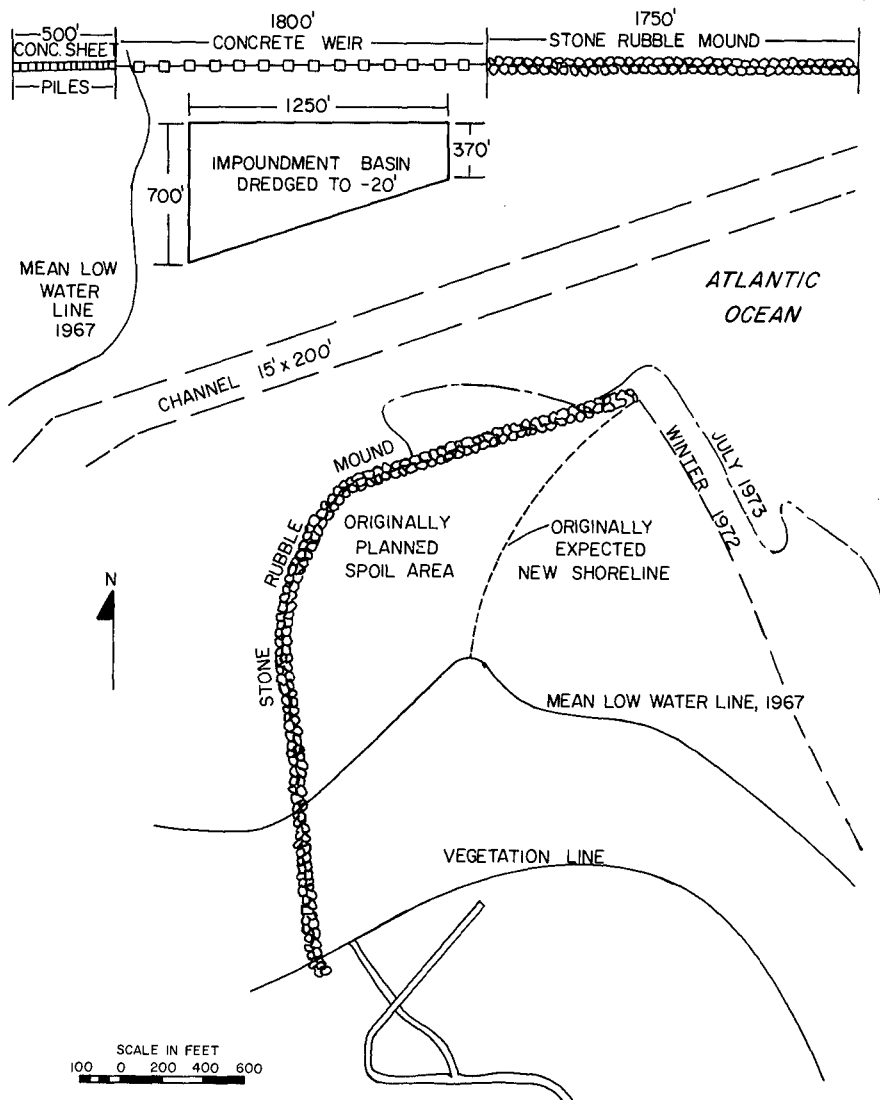
FIGURE 2 Outline of the Ponce de Leon Stabilization System

Figure 2 shows an outline of the July 1973 shoreline and M.L.W. and of the originally expected new shoreline after the dredge disposal.

STUDIES AND INVESTIGATION OF IMPROVEMENT SYSTEM

Extensive historical records of the Ponce de Leon Inlet area (4) have been utilized to produce a quantitative study of sand movement as influenced by the jetty-weir-impoundment basin system. In general, relative volumetric fluctuations for each beach, offshore and basin section influenced by the inlet improvement project were determined. The entire study area was analyzed according to location: Beach South of South Jetty (extending approximately 5000 feet south of the inlet); Offshore South of South Jetty (same); Beach North of North Jetty (extending approximately 4000 feet north of the inlet); Offshore North of North Jetty (same); Outer Basin (area between jetties including the impoundment basin and channel); and Impoundment Basin. Detailed inquiries as to the movement of sand within the study area must be referred to Reference (6).

South of South Jetty

Construction of the south jetty was begun in July 1968 and was completed in October 1969. Rapid accretion in the area immediately south of the south jetty became evident soon after completion. This area was to be used as the primary spoil area for material dredged from the impoundment basin and navigation channels. Immediately preceeding any spoil deposition (August 1971), it is estimated that about 2,000,000 cu. yds. of sand had accreted in this area since construction was completed. This amount surpasses the littoral drift estimates for this area, hence the theory was put forward that the offshore, by-pass bar was migrating westward due to the influence of construction (5). The effect of this migration was to deposit vast amounts of sand in this area.

The beach section of the area immediately south of the south jetty has continued to accrete gaining 1,260,000 cu. yds. between August 1971 and July 1973, including deposition of dredge spoil.

Between August 1971 and July 1973 the offshore volumes have shown a loss of some 80,000 cu. yds. The total volume (beach and offshore) for this same period therefore has increased 1,180,000 cu. yds.

The latest trend between May 1973 and July 1973 shows that the beach has lost almost 300,000 cu. yds. of sand. However, the offshore volume during this same period gained some 240,000 cu. yds.

It therefore appears that the beach-offshore areas south of the south jetty seem to be approaching a quasi-steady state.

Accretion reached the eastern tip of the south jetty in the summer of 1971. Since that time a prominent bulge has formed on the beach and continually grown seaward. This promontory appears to be the remnants of the offshore by-pass bar, and in fact has taken on the orientation of

a northerly growing by-pass bar. Examination of recent records (4) indi-
cated growing trend of a bar encroaching towards the channel to the north.
Continued growth would of course have a direct influence on navigation.

It is pointed out that beach areas from the south jetty extending
approximately 2400 ft. southerly have generally been accreting since
September 1967, however, beach areas, an additional 1600 ft. southerly,
from this point, have decreased in volume from August 1971 to September
1972 but have generally accreted from September 1972 to July 1973.
Part of this accretion may be due to the seasonal variation. Looking at
the offshore volumes it can be seen that from the south jetty to a point
approximately 1600 feet south there has been a very slight decrease and
from the offshore area of the southernmost reaches of the study area
there has been a slight increase in volume. The very small fluctuations
in these areas surely support the theory of an approaching quasi-steady
state in the southern reaches of the study area.

North of North Jetty

The north jetty was constructed in several stages beginning in
September, 1968 and ending with the final placing of the horizontal weir
sections in July 1971. Coastline changes north of the north jetty have
been most severe.

Prior to and during construction of the north jetty, the general
area presently occupied by that rubble mound structure was characterized
by extensive shoals. After the completion of the north jetty and weir
in July 1971, the area just north of the north jetty experienced dramatic
accretion of sand as was expected. The sections of beach farther north,
for the most part have experienced continuing erosion ever since the
final placing of the weir sections. The beach section 4000 to 2000 ft.
north of the jetty-weir lost almost 390,000 cu. yds. of sand between
August 1971 (just after construction), and July 1973. During this same
time period the offshore section of the same area gained over 265,000
cu. yds. This creates a total deficit of some 125,000 cu. yds., some of
which deposited in the fillet north of the north jetty.

Between February 1973 and July 1973 the beach, extending 4000 ft.
north of the jetty, lost some 248,000 cu. yds. and the offshore volumes
gaines 428,000 cu. yds. creating a total gain of approximately 180,000
cu. yds.

It is evident from these volumetric fluctuations that the beach
areas north of the north jetty, continue to lose material, while, the
latest trend seems to be a stabilization pattern, perhaps attributable
to seasonal fluctuations. Although the loss of material from the beach
area is quite significant, it is even more dramatic because of the loss
of dunes and beachline recession of up to 200 ft. On the other hand,
there has been a continual gain of material in the offshore areas during
the same time periods. The net effect when comparing the beach and off-
shore volumes has been a gain of sand in the area north of the north
jetty. Moreover, the trend is a continual buildup of material on the

offshore areas. Hence the sand is apparently not being lost to the
system but is moving offshore.

It is felt that the jetties per se were not the cause of the upland
(beach area) erosion to the north, but rather a combination of factors.
Historically the area north of the inlet has suffered from accumulation-
erosion cycles (1, 3). More recently the general area has suffered from
some rather severe storms and erosion to the dunes has been apparent for
long stretches of the coastline north of the inlet. It is also felt that
the construction sequence also contributed in part to the upland erosion
north of the north jetty.

The north jetty seems to be "anchoring" the offshore material as
evidenced by the volumetric comparisons. This action will undoubtedly in
time progressively improve the beach areas. There is, however, evidence
that a by-passing bar around the inlet is once more being established.
Unfortunately quantitative measurements of this bar were beyond the limits
of this study.

Outer Basin

The area defined in this study as the outer basin was characterized
by extensive shoals before construction was begun. During construction,
this area continued to accrete, gaining approximately 19,000 cu. yds. of
sand between September 1967 and August 1971, which was deposited on the
shoal just inside and adjacent to the north jetty. During construction,
(July 1968 - July 1971), not only did the outer basin accrete, but an
extensive shoal developed in the south interior portion of the inlet,
indicating much greater deposition than appears in the outer basin vol-
umetric estimates. The spit on the well-developed north interior shoal
continued to grow inward.

The land mass immediately south of the inlet has a seaward offset
with respect to the north side. This seemingly does not support the
theory of a predominant southerly drift of littoral material. Historical
information however, shows that accumulated material to the north period-
ically "detached" and moved to the south beach (1, 3).

Upon completion of the rubble mound jetties, a fairly well defined
channel was formed due to constriction of the inlet's outer cross-section
and resulting increased velocities. Evident throughout the construction
sequence was the typical offshore by-pass bar around the mouth of the
inlet. This appears to have been partly dissipated due perhaps to the
improved flushing characteristics of the inlet.

The volume of sand in the outer basin has fluctuated somewhat since
construction of the jetties was completed. These fluctuations are attri-
butable to dredging operations and to several storms which hit the area.

In August 1972, the impoundment basin was dredged, removing slightly
more than 400,000 cu. yds. During this time natural flushing had removed

what remained of the outer shoal just inside the north jetty.

Intense erosion of the beach section just south of the north jetty
on the north shoal became evident just after completion of the north
jetty. This phenomenon continues to the present, resulting in the growth
of a spit westerly along the north side of the channel. In Febuary 1973,
under the influence of a strong northeast storm, dramatic erosion took
place causing the complete deterioration of this beach section and the
breaching of an old channel on the north side of the north shoal. In-
tense shoaling of the interior portions of this channel is taking place,
with inner shoals reportedly hampering navigation to marinas located at
its extreme interior portion. The closure of this channel now seems to
be taking place, however this process should be expedited with the use
of dredge spoil or by other means.

In June 1972, it became apparent that sand began blowing over,
washing through, or circumventing the south jetty and depositing just
inside the basin on the north side of the south jetty. Around December
1972, a shoal began forming at the inner seaward extremity of the south
jetty. The shoal continued to grow in size and migrate westward on into
the inlet. It is felt that the growth of this shoal has influenced, and
is continuing to influence, the channel orientation. This shoal will be
continually nourished by sand passing through or around the south jetty.

Between February 1973 and July 1973 the amount of material in the
outer basin appears to have remained fairly constant. However, due to
local complaints, maintenance dredging in the entrance channel was com-
pleted during March-April 1973. Approximately 95,000 cu. yds. was dredged
by a hopper dredge and 27,000 cu. yds. by a side caster.

Since completion of the dredging, the channel has been affected by
shoaling. As mentioned above, the growth of the shoal on the north side
of the south jetty has, and is presently, influencing a northerly migra-
tion of the channel. In addition, the growth of an offshore bar around
the tip of the north jetty is also influencing the navigation channel.
The combined effect of this offshore bar and inner shoal is to force the
outer portion of the channel southward and the mid-section of the channel
northward toward the impoundment basin, resulting in a clockwise shifting
of the outer portions of the channel. In connection with the navigation
channel, it should be noted that the throat section of the inlet between
the extensive inner north and south shoals appear to be reaching an ap-
parent equilibrium. It must be noted that this equilibrium cross-sec-
tional area has shown a tendency to move southward, due to the influence
of the growing spit on the inner north shoal.

It is felt that the immediate future tendencies for the outer basin
are: (a) the continued deflection of the navigation channel as explained
above; (b) continued growth and westward migration of the outer south
shoal; (c) eventual filling of the breached north channel with slight
replenishment of that beach section; and (d) continued equilibrium trends
in the throat section.

Impoundment Basin

The impoundment basin is situated immediately inside and parallel
to the weir section in the north jetty (Figures 1, 2). The basin itself
is approximately 700 ft. x 1250 ft. x 370 ft., and dredged to a depth of
-20 ft. below M.L.W. The original dredging of this basin called for the
removal of slightly more than 400,000 cu. yds. of material. As mentioned
previously, it was anticipated that the littoral drift passing over the
weir annually would amount to about 310,000 cu. yds., or 620,000 cu. yds.
every two years. These figures were founded on gross annual drift rates
estimated to be about 600,000 cu. yds., southerly and 100,000 cu. yds.
northerly, resulting in a net southerly drift of 500,000 cu. yds. The
validity of these estimates has since been questioned. Walton (6) has
recently estimated the drift to be about 386,000 cu. yds. southerly and
309,000 cu. yds. northerly leading to a net southerly drift of 77,000 cu.
yds.

Dredging of the impoundment basin was completed in August 1972.
Though slightly more than 400,000 cu. yds. was removed in constructing
the basin, the capacity of the basin was estimated at 620,000 cu. yds.
allowing the overflow into adjacent areas. As previously noted, estimates
called for dredging of the impoundment basin every two years.

As of February 1973 there had been a deposition of approximately
200,000 cu. yds. of drift material in the impoundment basin since July
1972. Further examination shows the deposition of an additional 100,000
cu. yds. as of July 1973. This has taken place over a one year span, and
seemingly corroborates the rate of deposition in the basin as estimated
in the design.

The above estimates of deposition do not validate the littoral drift
estimates, however. The southerly growth of an offshore bar around the
tip of the north jetty (4), indicates the deposition of littoral material
at this point. The growth of this bar as mentioned previously influenc-
ing the outer section of the navigation channel, and may have an effect
on the operation of the weir-impoundment basin system. Further monitor-
ing of this bar growth is desirable.

R. R. Clark (7) estimates the flow of sand moving across the throat
section of the inlet over one flood cycle to be around 21,000 cu. yds.,
while the growth of the shoal on the north side of the south jetty indi-
cates the input of northerly drift into the inner basin. In addition,
intense erosion has taken place just south of the north jetty resulting
in a breakthrough of the old channel. Regardless of the source, it is
evident that vast amounts of sand are within the inner basin itself.
Vast amounts of sand which could have helped fill the impoundment basin,
while the southerly drift contributes to the growth of the aforementioned
bar sand around the north jetty tip.

Dye tests carried out on June 29, 1973 indicate strong tidal flows
over the weir on both ebb and flood flow. Scuba observations in the im-
poundment basin area, noted relatively strong bottom currents and sand
motion attributable to the interaction of tidal currents and wave activity.

An examination of contour maps (4) shows a flattening of the basin adjacent to the weir, probably a result of the current activity.

It must be concluded that the sand deposition in the impoundment basin can not be totally attributed to the flow over the weir. It is evident, from above, that other sources of sand within the system are most likely contributing to the impoundment basin. Rate of filling of various areas of the impoundment basin may offer some clues as to source. Future sand tracing experiments may also be a help as well as comprehensive sand sampling and analysis. Growth of the offshore bar around the north jetty must also be observed and evaluated.

CURRENT PATTERNS

In order to help evaluate the mechanisms associated with the physical shoreline and hydrographic changes being experienced in the vicinity of Ponce de Leon Inlet, an understanding of the flow patterns through the inlet was attempted. A dye tracer test was conducted to determine flow patterns in the inlet during the peak discharges of ebb and flood flow.

Water-tight dye packets were floated at predetermined locations within and immediately outside of the inlet. At the estimated peak discharge of ebb and flood flow, respectively, the dye packets were opened, and distinct, continuous streamlines of green dye resulted. Aerial observation of the streamlines depicted the relative magnitude, strength, and direction of the current flows at various locations within the inlet. Figures 3 and 4 indicate the predominant flow direction and relative magnitude observed during each cycle.

The relative length of the tracer streamlines in these figures indicate the location of higher current. In the throat section, the dye pattern reveals a stronger flood current against the north edge of the channel. The friction loss over the shallower south bank explains the lower current on the south half of the channel. Seawater overtopping the north jetty weir section at flood tends to hug the north boundary of the channel and enter the Halifax River, whereas flow entering between the heads of the north and south jetty seem to be diverted into both Rockhouse Creek and the Indian River North. During ebb flow, through the throat section, the dye streak on the south bank is longer than that on the north side, indicating stronger velocities. The ebbing current was measured across the channel on a different occasion and the results showed a slightly stronger current on the south half of the channel. This is probably due to the strong ebb flow from the Halifax River which cannot make the abrupt bend into the inlet, and thus is thrust against the south bank. Also, the flow is concentrated into a smaller cross-section during ebb and is not allowed to flow across the extensive shoals to the south.

Figure 3 denotes a strong current overtopping the weir section during flood flow. There is also a very strong southerly flow evident along and parallel to the beach just north of the weir. It should be noted that this strong current is independent of any visible wave induced current

FIGURE 3
CURRENT PATTERNS
FLOOD FLOW

SCALE: I INCH = 800 FEET

FIGURE 4
CURRENT PATTERNS
EBB FLOW

SCALE I INCH = 800 FEET

ATLANTIC
OCEAN

HALIFAX RIVER

INDIAN RIVER NORTH
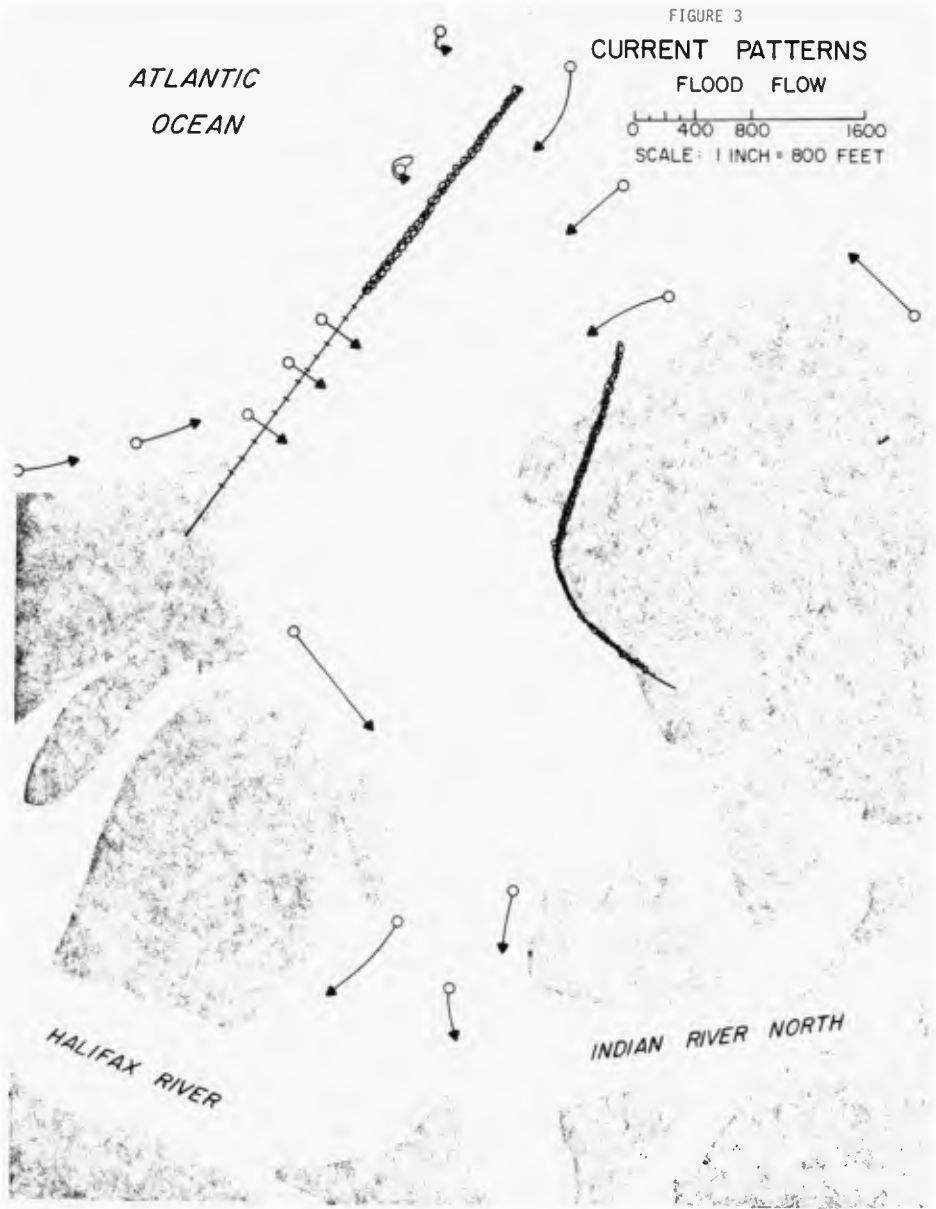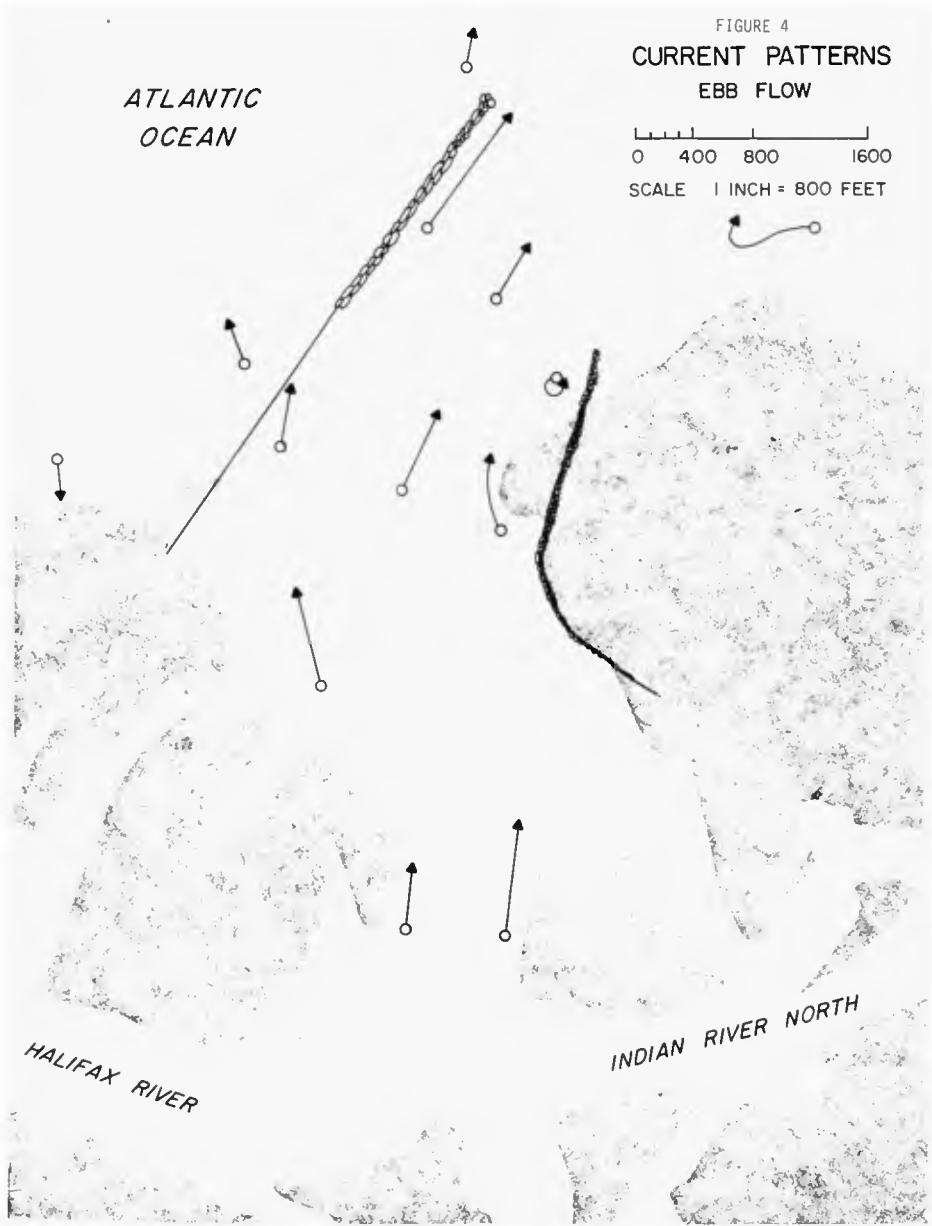
since the dye tests were made on a day with very minimal wave activity
while later, at slack water, there was a negligible longshore current.
On ebb flow, at a time when the tide level is approaching the level of
the weir section, a strong flow is observed both across the weir and
along the north jetty. Divers have observed that the current across the
weir section to the northeast is quite strong during the ebb cycle. The
weir section effects the inlet hydraulics by increasing the flow area
during the flood cycle, while somewhat constricting the flow to within
the two jetties during the extreme ebb flows. Another interesting phen-
omena may be observed in Figure 4 where the dye released to the north of
the weir and just seaward of the breakers progresses shoreward during
the ebb cycle.

Current patterns at the seaward end of the channel indicate a
stronger current during ebb than at flood due to the above mentioned con-
striction. Due to the configuration of the jetty system whereby the
project channel is constructed closer to the north jetty than to the
south jetty, the currents tend to be greater and more concentrated on
the north side of the entrance during both the ebb and flood cycles.
Dye released along the north side of the north jetty indicate negligible
flow outside of the channel.

In Figure 4 a large eddy is observed during ebb current which tends
to circulate clockwise moving water and sediment back into the inlet.
This is a classical example of an inlet performing as a sediment sink on
ebb flow as well as during flood. Sediment is rounding the south jetty
and contributing to the large shoal extending from the south jetty. As
this shoal progrades further into the channel, a more constricted channel
flow results. Hydrographic surveys reveal this shoal to be migrating
westward toward the large inner shoal area south of the throat. It is
interesting that this shoal has aligned itself directly opposite the
north jetty.

The dye study reveals many things not readily apparent to casual ob-
servation. Although certain limitations are evident, a general pattern
of the surface currents may be reasonably described. In that channel
depths are very small in comparison with the channel width and length,
the circulation shown by the surface currents is a good indication of the
general circulation of the bottom currents. From these current patterns
a better understanding of the sediment movement and shoal formation and
migration is accomplished.

WAVE REFRACTION ANALYSIS

In order to evaluate the significance of the physical changes taking
place at Ponce de Leon Inlet, and to obtain a broad overview of the ef-
fects of wave forces on the erosion patterns and littoral drift character-
istics, a refraction analysis of deepwater waves approaching the shore in
the vicinity of the inlet was conducted. It is not intended to infer that
refraction of wave energy is the primary cause for these changes, but
rather a contributing process which should be investigated and evaluated.

Computation and construction of the refracted wave rays was achieved through the use of a computer program developed by the Coastal Engineering Research Center (8), a digital computer, and an incremental plotter. Deepwater waves with periods of 4, 7 and 12 seconds were directed toward the inlet from directions both perpendicular and at 45° angles to the shoreline. Wave refraction diagrams (4) were plotted for each of the above conditions, two of which are shown on Figures 5 and 6. These diagrams illustratively portrayed the effect of the irregular bathymetry in the vicinity of Ponce de Leon Inlet on the refraction of wave energy. Locations of concentrated wave energy could be observed for the particular conditions assumed.

Wave energy distributions were also obtained from the refraction diagrams and plotted on a relative basis (Figure 7 and 8) from which could be determined the areas displaying a general tendency for energy concentration or reduction. It was noted that the larger storm waves caused greater concentrations of energy at certain points along the shoreline than the more normal waves. Also, by observing the resultant angle of wave approach at the shoreline, it was concluded that for an equal distribution of waves originating from different directions, a net southerly drift predominance would result to the north of the inlet and a varying drift predominance to the south.

The wave rays generated in deepwater and converging on the inlet were then superimposed on a smaller grid encompassing the immediate inlet area, and refracted shoreward. Figure 6 shows a typical nearshore wave refraction pattern which was developed. From these diagrams, distinct locations of energy concentration and tendencies toward physical shoreline changes were determined. It appears that the existence and growth of the large promontory located just to the south of the south jetty is a result of a localized reversal of drift to the north associated with the refraction wave energy. Also, waves entering the entrance of the inlet tend to be refracted toward the north jetty and shoreline to which it is attached, thence enhancing the significant erosion which is being experienced in this area. Lastly, it was noted that, with respect to the region just north of the inlet, regardless of the wave characteristics, the rays are everywhere bent toward the inlet. It was therefore concluded that along the shoreline to the north side of the inlet there exist a predominant tendency for drift toward the inlet.

CONCLUSIONS

It was the objective of this study to determine the performance and effects of the Ponce de Leon Inlet Improvement Plan. In doing so, an evaluation was made of the general current patterns, the relative refracted wave energy distribution, and the volumetric beach and hydrographic fluctuations associated with the inlet. These analyses resulted in the following conclusions:

1. Since construction of the inlet stabilization system and navigation project at Ponce de Leon Inlet, dramatic changes have resulted along the adjacent coastline and within the inlet.
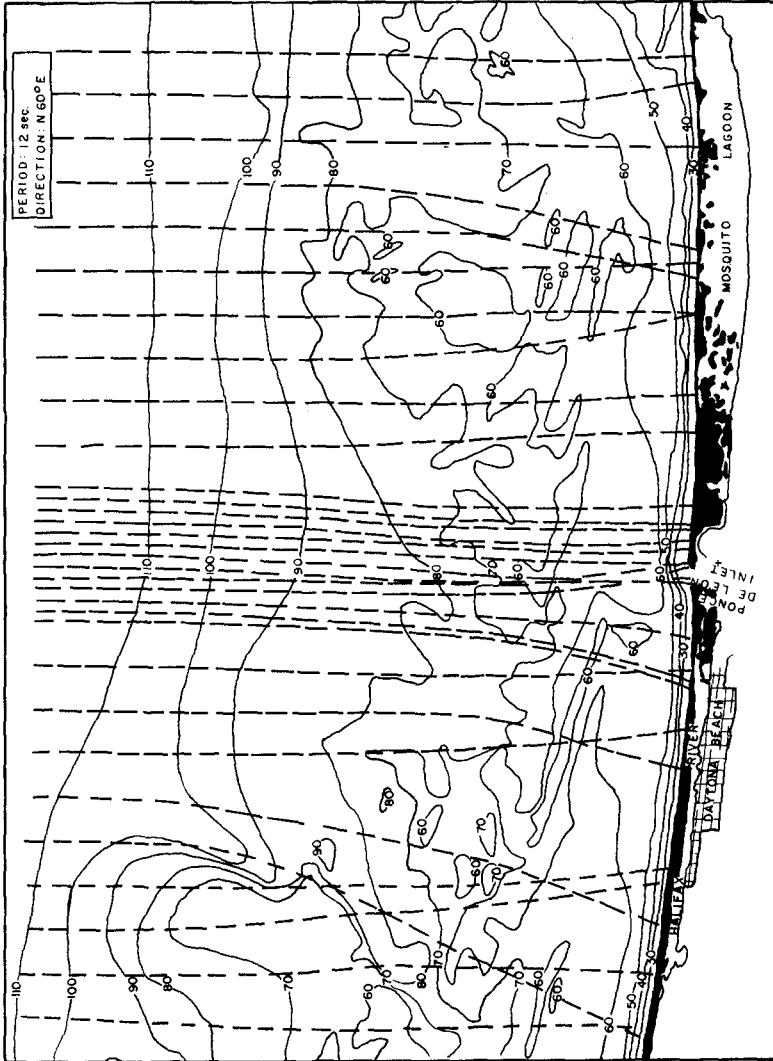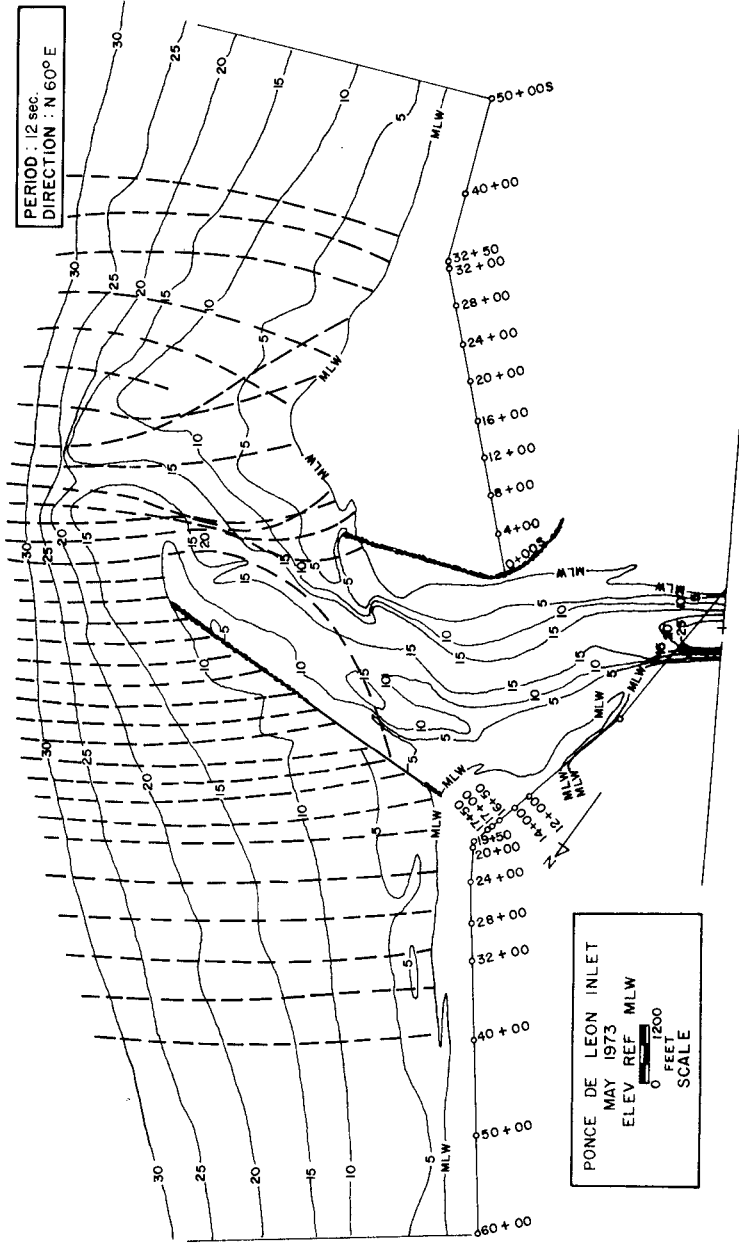
FIGURE 5
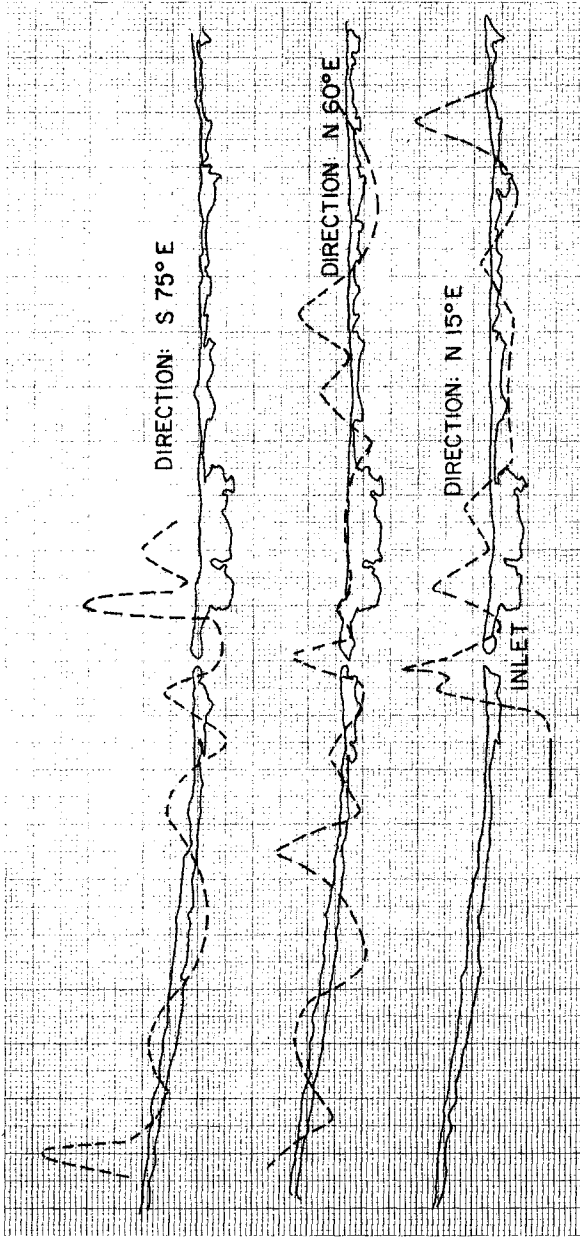
FIGURE 6

FIGURE 7

WAVE ENERGY DISTRIBUTIONS ON SHORELINE FOR 12 SEC. WAVES

FIGURE 8

2.   Rapid sand accretion has been experienced south of the south
jetty. This growth began during construction and has persisted to date.
The rate of this rapid growth has led some to conclude that the large net
annual littoral drift rate assumed in the design of the stabilization sys-
tem was in error, and a more balanced drift condition may exist. This
theory was seemingly substantiated by the simultaneous erosion being ex-
perienced on the beaches north of the inlet. However, results of this study
indicate the former estimate is more logical and that other factors related
to the construction of the jetties and weir system to be the major cause.
It was noted that, since construction, the significant offshore bypass bar
across the entrance to the inlet has tended to move shoreward, bringing
with it a large volume of sand. Also during this construction period,
relatively few northeast storms were experienced affording favorable con-
ditions for net northward littoral drift transport, which was in turn
trapped by the south jetty. Recent hydrographic data indicate this area
just south of the south jetty is reaching a relative quasi-steady state
equilibrium condition, with the only major changes being the continued
growth of the offshore bypass bar system, and the passage of sand around
and over the south jetty forming a significant shoal in the heart of the
inlet.

3.   Associated with this rapid accretion to the south of the inlet
was a significant dune erosion to the north of the inlet. This is believed
to be due in part to the sequence of construction. With the south and
north rubble mound jetties being constructed first, a free, unobstructed
flow of longshore drift was diverted through the opening where the weir
was to be. This change was noted by the progression of the beach profile
toward shore immediately north of the inlet during this construction
period. Likewise, the erosion condition was worsened with the elimination
of northward moving drift by the south jetty. However, since construction
of the weir section, the offshore profile north of the inlet began to grow
seaward again, indicating an entrapment of material. Volumetric compari-
sons show that beach plus offshore areas have shown a net, albeit, small
gain in material since inlet improvement. Nonetheless, erosion still per-
sists along the shoreline well north of the inlet. This erosion is felt
to be due more to the storms experienced during the recent past rather
than to the effects of the inlet improvements. The stretch of beach north
to Daytona has a history of erosion prior to any inlet improvements.

4.   The erosion of the shore immediately inside the north jetty can
be expected to continue until an equilibrium condition is reached. Un-
fortunately, the limits of this eventual erosion cannot easily be deter-
mined, but it is not believed that the entire north shoal will dissipate.

5.   Monitoring of the weir-impoundment basin, indicates that approxi-
mately 75 percent of the material dredged from the basin in August 1972
has been replaced. It was determined that the impoundment basin presently
contains approximately 50 percent of its maximum expected volume. This
would indicate that the estimated net southerly drift rate, designed basin
dimensions, and scheduled maintenance intervals set forth in the design
memorandum are of the proper magnitude. However, it is also noted that
significant longshore drift material appears to be moving sufficiently
offshore so as to miss the weir section and to enhance the development of

an entrance bar growing around the tip of the north jetty.

      6. Appreciable littoral transport, by-passing the weir section and impoundment basin and contributing to the growth of a spit on the south side of the inner north shoal is gradually pushing the inner channel cross-section to the south. This is a slow process and is showing some signs of abatement. However, the portion of the channel between the impoundment basin and south jetty is still in a condition of flux. Tendencies have been for the channel to move northward toward the basin and north jetty in this region, due to the naturally deep water of the basin and the expanding shoal adjacent to the south jetty. It should be noted that once the deposition basin is dredged again, the northward tendency for movement will be enhanced, with a possible adverse affect to the north jetty. As the channel approaches the ocean entrance, the shoal bar circumventing the north jetty is pushing the channel to the southeast. Again, this condition may be expected to continue as the by-passing bar grows. In summary, the channel is seemingly following a closkwise alignment, succumbing to the pressure of littoral transport and deposition.

REFERENCES

1.   U. S. Army Engineer District, Jacksonville, Corps of Engineers, Jacksonville, Florida, "Survey Review Report on Ponce de Leon Inlet, Florida," Serial No. 61, September 30, 1963.

2.   U. S. Army Engineer Division, South Atlantic Corps of Engineers, Atlanta, Georgia, "National Shoreline Study and Regional Inventory Report, South Atlantic-Gulf Region, Puerto Rico and Virgin Islands," August 1971.

3.   Department of the Army, Jacksonville District, Corps of Engineers, Jacksonville, Florida, "General and Detail Design Memorandum, Ponce de Leon Inlet, Florida," Serial No. 17, November 29, 1967.

4.   U. S. Army Engineer District, Jacksonville, Corps of Engineers, Jacksonville, Florida, "Report on the Performance of the Ponce de Leon Inlet, Florida Improvement System," Coastal and Oceanographic Engineering Laboratory, Florida Engineering and Industrial Experiment Station, University of Florida, Gainesville, Florida, September, 1973.

5.   Partheniades, E., and J. A. Purpura, "Coastline Changes Near A Tidal Inlet," Thirteenth Coastal Engineering Conference, American Society of Civil Engineers, New York, N. Y., July 1972.

6. Walton, T. L., Jr., "Littoral Drift Computations Along the Coast
    of Florida by use of Ship Wave Observations," Thesis presented to
    the University of Florida in Partial Fulfillment of the Requirements
    for the Degree of Master of Science in Coastal and Oceanographic
    Engineering, June 1972.

7. Clark, R. R., "Hydraulic Characteristics of Ponce de Loen Inlet,"
    Unpublished Manuscript, University of Florida Civil and Coastal
    Engineering Department.

8. U. S. Army Coastal Engineering Research Center, "A Method for
    Calculating and Plotting Surface Wave Rays," TECH. MEMO NO. 17,
    February 1966.

CHAPTER 87

PERFORMANCE ASSESSMENT OF SELF-DREDGING HARBOUR ENTRANCES

by

J.W. Carmichael [1] and I. MacInnis [2]

ABSTRACT

This provides further information and assessment of the three harbour entrance wave traps at Dingwall, Inverness and Pleasant Bay located in Canada. These were constructed to reduce the amount of maintenance dredging required in the entrance channels.

Wave climate data and littoral material analysis are presented.

Observations on the performance of each structure are given and conclusions drawn as to restrictions and constraints on applicability.

PURPOSE

This is a follow-up to the paper presented by Donnelly and MacInnis at the Eleventh Conference on Coastal Engineering in 1968 which should be read as background material for this paper.

Since 1968 data has been produced on wave climate and littoral drift and further experience gained in the effectiveness of the rubble mound four-armed wave traps at Dingwall, Inverness and Pleasant Bay, all located in the Cape Breton area of the province of Nova Scotia, Canada.

WAVE CLIMATE

The deep water wave climate has been estimated for the three locations. However, refraction and diffraction has not been included in the analysis.

The hindcasting routine used to provide the wave data from the hour-by-hour wind data is based on the deep water curves of Sverdrup-Munk-Bretschneider as revised by Bretschneider in 1970 (Look Laboratory Quarterly, June 1970). The wind data was recorded at Cap-aux-Meules in the Magdalen Islands (Gulf of St. Lawrence) and was used for the three sites. This data was obtained during the ice-free period (excluding January, February and March) in 1969, 1970, 1971.

Figs. 1, 2, 3 and 4 show the percentage of time that the significant wave height or significant wave period exceeds the specific values for the given directions or for all directions summed together. For example, at Dingwall, 3% of the time the waves from the S.E. direction exceed 7 feet in height.

1. Engineering Program Officer, Department of Public Works, Ottawa, Canada.
2. Atlantic Region Coastal Engineer, Dept. of Public Works, Halifax, Canada.

LITTORAL MATERIAL

        The grain size distribution of sea bed material taken at the harbour
entrances is shown in Fig. 5. This shows the marked differences at the
three locations. At Inverness it is mainly a fine sand while at Dingwall
the sand ranges from medium to coarse. In the case of Pleasant Bay it runs
from coarse sand through fine and coarse gravel. While the curve does not
show it, the fact is known that the material runs to cobbles of 6-inch
diameter.

SHORELINE AND ORIENTATION

        Dingwall is located on a large crescent-shaped bay which extends
between two rocky headlands approximately nine miles apart. The bay extends
in about 4½ miles. The axis of the bay is oriented approximately N80°E.
Inverness is located on a reasonably straight shoreline which runs approximately
N.E. - S.W. Pleasant Bay is in a bay or bight approximately four miles wide
and 3/4 miles deep. The shore is oriented approximately the same as Inverness.

        Fig. 6, 7 and 8 are aerial photos of the three locations showing
the entrance structures at the harbours and their orientation and layout.

        The sea bottom profile extending from the low water mark to the 18'
contour is as shown below:

                    Dingwall   -   1: 65
                    Inverness   -   1:100
                    Pleasant Bay -   1: 35

STRUCTURE DATA

        Some historical information and physical data relating to the three
structures are given in the following table.

		Design Dimensions of Entrance			Max. Width of Trap Basin (approx)	Equilibrium Depth (approx) ft.
		Width		Depth at		
Location	Date Completed	H.W. Level	Bottom	L.W.		
Dingwall (a) Entrance Structure	- 1962	129'	80'	12'	600'	5
(b) Groynes	- 1964					
Inverness	1965	119'	90'	5'	300'	2
Pleasant Bay	1967	156'	100'	10'	400'	Variable depending on severity of storms

OBSERVATIONS

(a) Dingwall –
    This structure is considered to be reasonably successful with an
    equilibrium depth at low tide of approximately 5'.   Dredging has
    been carried out to 10' depth every five years in order to straighten
    and improve the channel. This represents a marked improvement in
    contrast to conditions which prevailed before the wave trap was built
    when one could walk across the harbour mouth in the dry at high tide
    and that only two years after having a dredged channel 26' deep at
    L.W.

    A shoal has developed approximately 250' outside the seaward
    breakwater which maintains approximately 6' depth at L.W.   This,
    of course, is beyond the control of the flushing action of the wave
    trap.

    This structure had the advantage of being specifically designed from
    a model study at the National Research Council based on the specific
    environment prevailing at Dingwall.

(b) Inverness –
    This structure is only moderately successful with an equilibrium depth
    of approximately 2' at L.W. in the wave trap channel and requiring
    almost annual dredging but of a lesser amount than formerly.   Aerial
    photos show a large amount of material in suspension around the entrance
    to the wave trap. Indications are that the outer breakwater should
    be approximately 300' farther seaward in a depth of 12' of water in
    order to maintain a 5' depth in the wave trap.

    A further reason for the limited flushing action appears to be linked
    to the permeability of the boundaries of the wave trap.   As the
    flushing action is dependent on the development of a hydraulic head
    within the wave trap, any permeability of the trap walls diminishes
    this head. This would indicate that grouting of the voids in the
    trap walls would improve its effectiveness.

(c) Pleasant Bay –
    This structure can not be considered to be successful as at times the
    trap plugs almost completely with beach gravel and sand. The principal
    reason for this lack of success is because the steep slope of the bottom
    allows large waves to break near the mouth and carry in the coarse
    gravel and cobbles which the flushing current is unable to disgorge
    from the mouth.

CONCLUSIONS

1. It is evident that a slope or gradient of the bottom to seaward from
    within the trap is essential to permit it to operate successfully.   Based
    on the experience with Dingwall and Inverness, it appears that the ratio
    of the depth just seaward of the head of the trap to the equilibrium
    depth in the trap is approximately 2.4 to 1 i.e. to maintain a depth of
    5' in the trap channel, the seaward breakwaters should be located to
    have the head in 2.4 x 5 = 12' depth.

2. As resonance is important in the functioning of the wave trap, it is
    essential that the trap dimensions be in tune with the predominant

influences in the wave climate. This is evident from the performance
of the Dingwall structure, the design of which was developed from an
hydraulic model study. The Inverness and Pleasant Bay structures
did not have this advantage.

3.   The four armed wave trap of rubble mound design is an effective means
      of maintaining entrances to harbours where 5 to 6 feet depth is required
      and littoral material in the fine to coarse sand sizes is a problem.
      It does however require careful attention to wave trap dimensions and
      should be based on hydraulic model tests.

REFERENCE

1.   Donnelly, P. and MacInnis, I.
      "Experience with Self-Dredging Harbour Entrances". ASCE Proceedings
      11th Conference on Coastal Engineering
      p.p. 1283 - 1294, 1968.
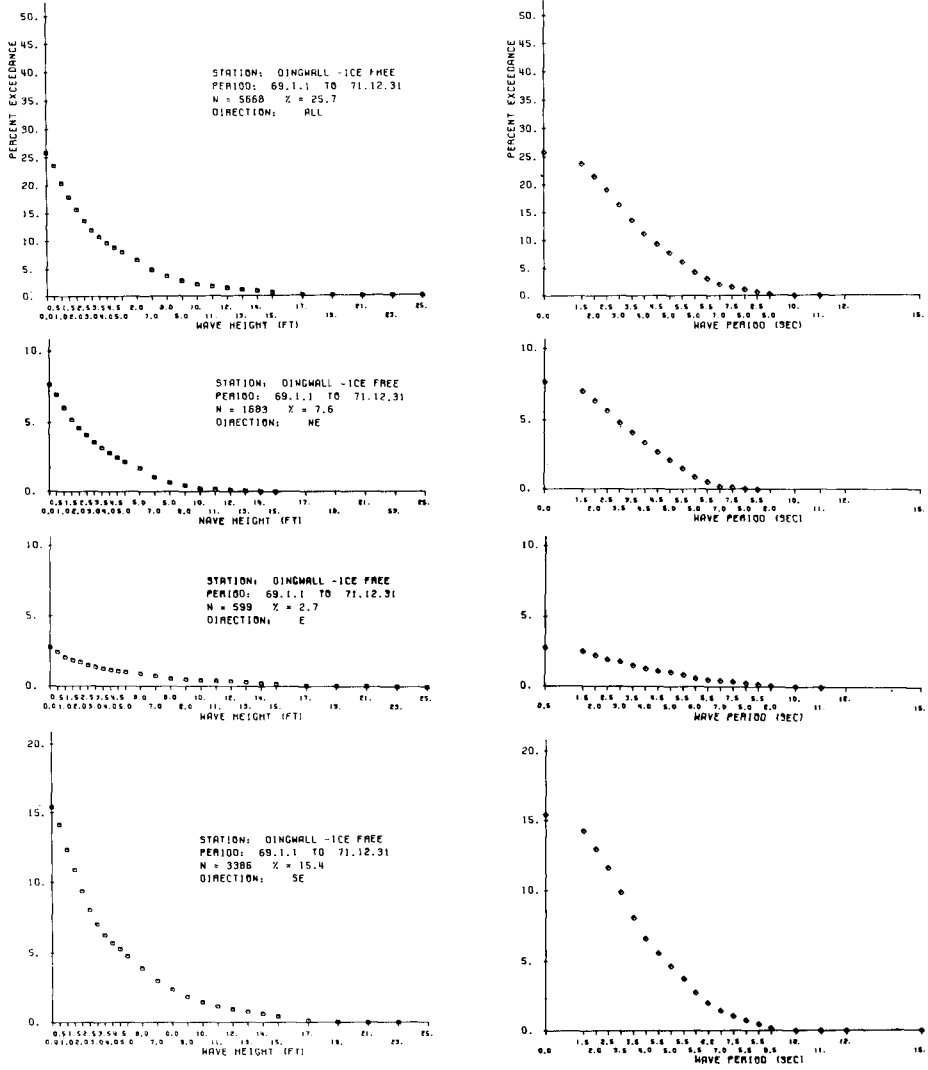
Fig. 1   WAVE CLIMATE DATA FOR DINGWALL

Fig. 2 WAVE CLIMATE DATA FOR INVERNESS

Fig.3   WAVE CLIMATE DATA FOR INVERNESS

STATION: INVERNESS-ICE FREE
PERIOD: 69.4.1 TO 71.12.31
N = 5017   X = 25.3
DIRECTION: NW

STATION: INVERNESS-ICE FREE
PERIOD: 69.4.1 TO 71.12.31
N = 1270   X = 6.4
DIRECTION: N

STATION: INVERNESS-ICE FREE
PERIOD: 69.4.1 TO 71.12.31
N = 1605   X = 8.1
DIRECTION: W

STATION: INVERNESS-ICE FREE
PERIOD: 69.4.1 TO 71.12.31
N = 4607   X = 23.3
DIRECTION: SW
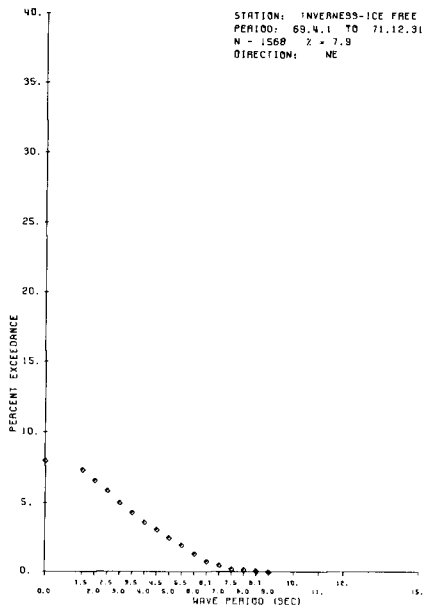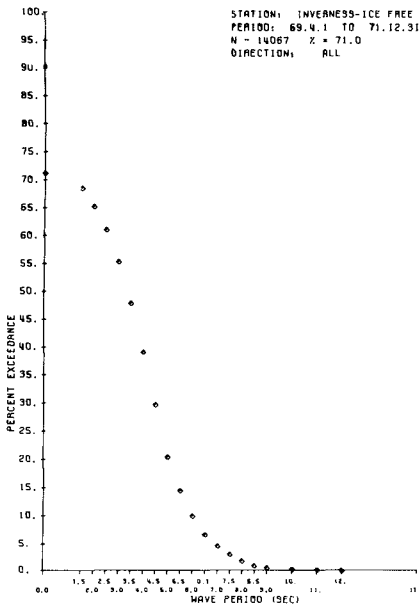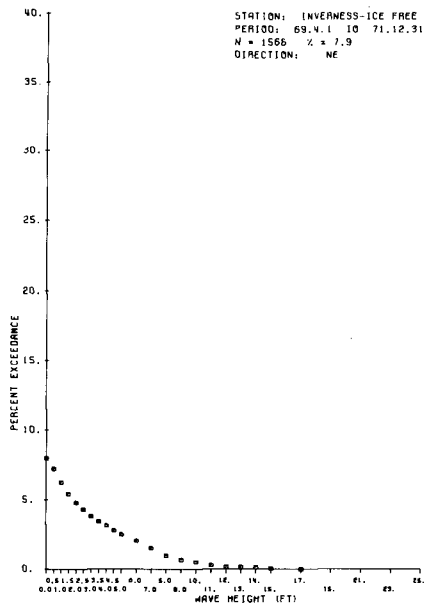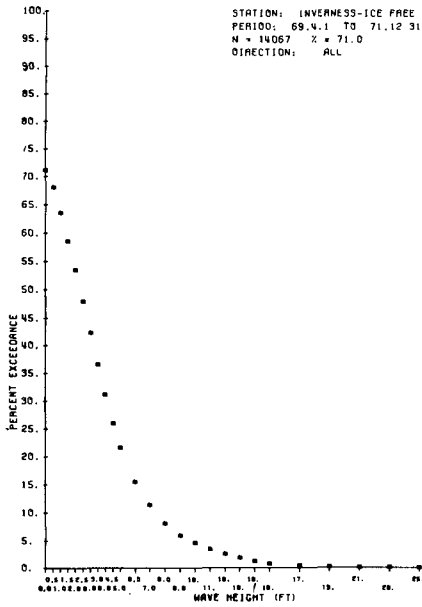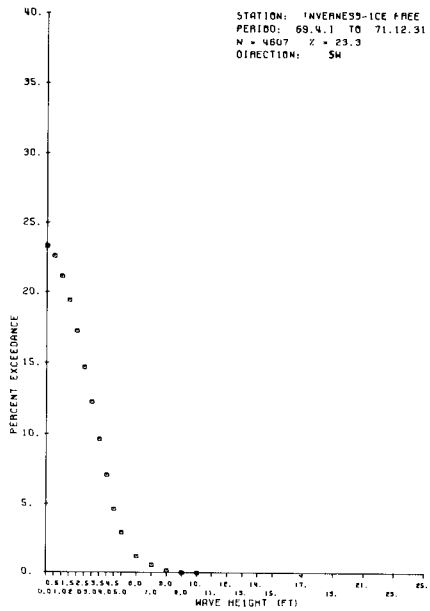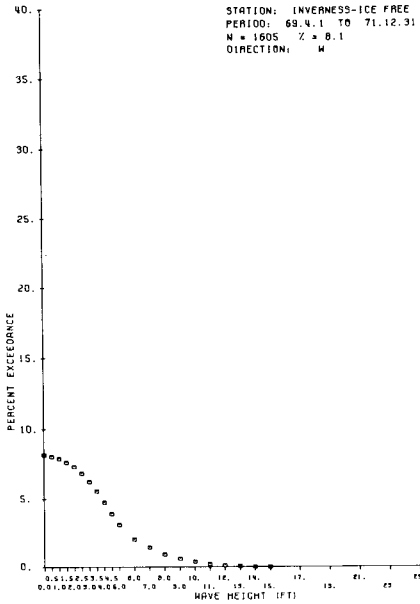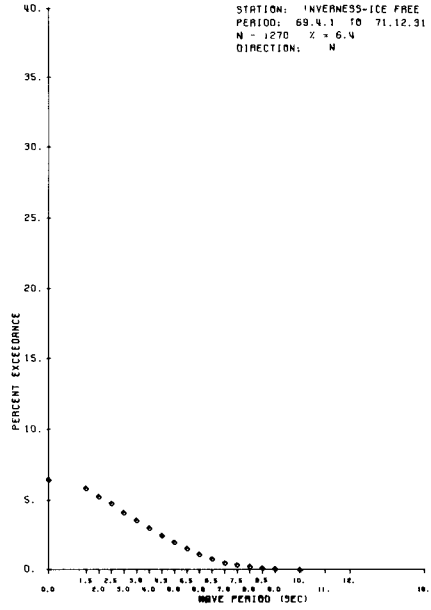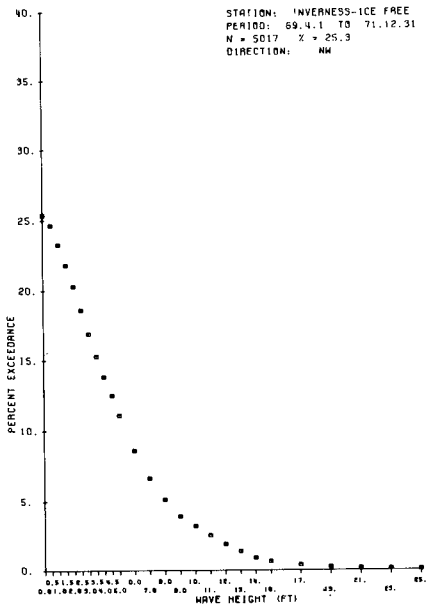
Fig. 4   WAVE CLIMATE DATA FOR INVERNESS

Fig. 5
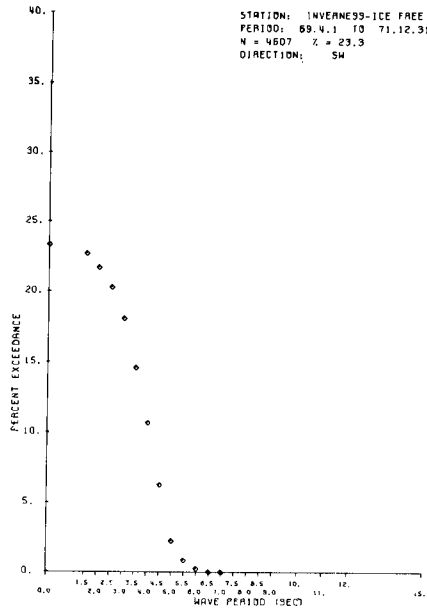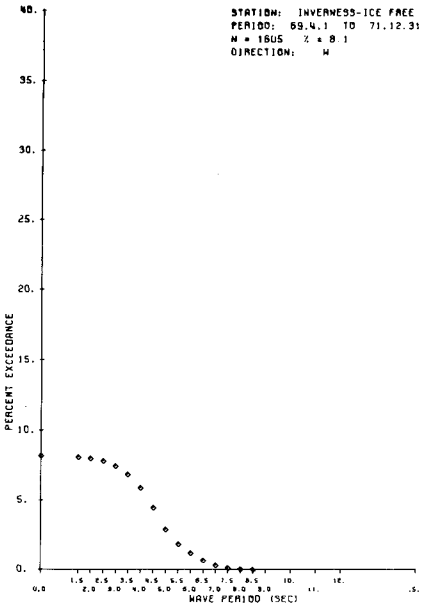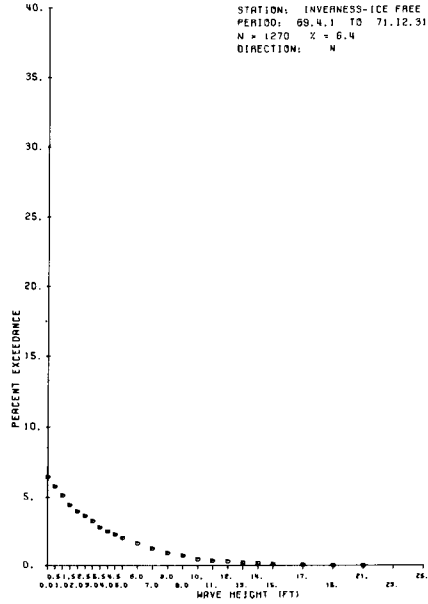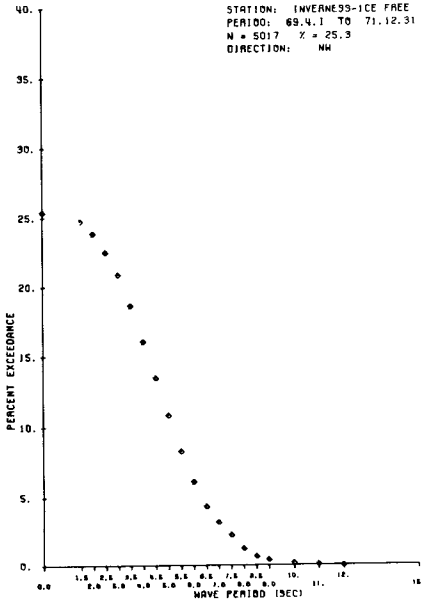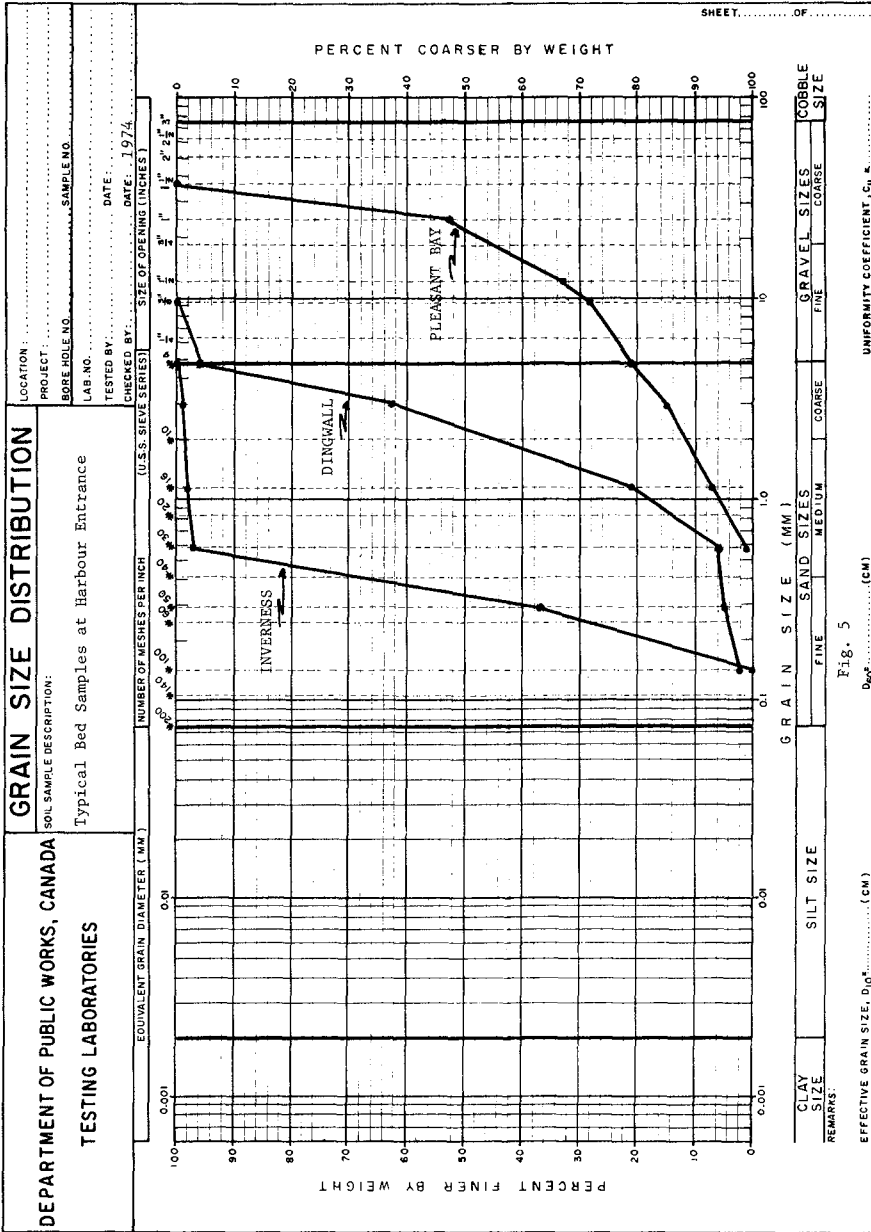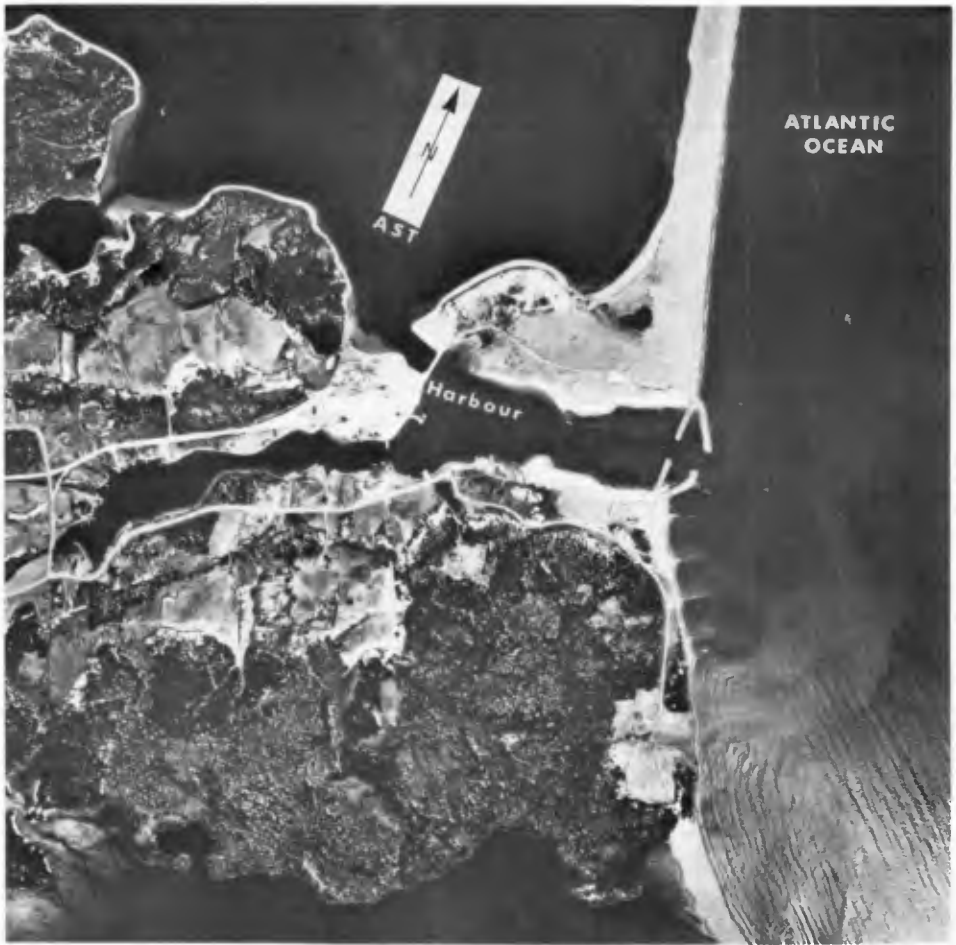
Fig. 6 Aerial Photograph
of
OINSWALL, NOVA SCOTIA

Scale (approx.)

1000   0   1000′   2000′
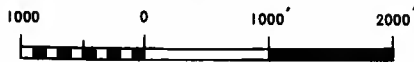
Fig. **7** Aerial Photograph
of
INVERNESS, NOVA SCOTIA

Scale (approx.)

1500   0   1500   3000

Fig. 8 Aerial Photograph
of
PLEASANT BAY, NOVA SCOTIA

Scale (approx.)

CHAPTER 88

FIELD AND MODEL STUDIES FOR VISAKHAPATNAM HARBOR

by

Simon Ince* and W. W. Jamieson**

ABSTRACT

Model studies and analysis of oceanographic and littoral drift data were undertaken to advise Howe India (Private) Ltd. on littoral drift, siltation and shore erosion problems to be encountered during and after the construction of Visakhapatnam Outer Harbor Project.

Distorted fixed-bed and movable-bed models with a horizontal scale of 1:300 and a vertical scale of 1:80 were calibrated to reproduce the integrated net effect of an average southwest and northeast monsoon season. Experiments were conducted to assess and predict seasonal changes resulting from the construction of the system of breakwaters under normal and extreme conditions. Recommendations were made concerning breakwater and sand trap location, shore protection, dredging and disposal of dredged material.

INTRODUCTION

Visakhapatnam is situated in latitude 17°-41'-34", longitude 83°-17'-45" on the Bay on Bengal almost midway along the thousand mile length of coast between Calcutta and Madras (Fig. 1). Before 1933, a limited volume of sea trade was carried out by means of lighters plying between the shore and ships anchored offshore. This was a dangerous operation during the monsoon seasons due to waves breaking over the sandbar in front of the narrow entrance channel. In 1933, the existing harbor at Visakhapatnam was completed by dredging a 26 ft. outer channel through the sandbar. The depth of the entrance channel was increased over the years to 38 ft. The problem of maintaining the dredged depth was complicated by the existence of a large amount of littoral drift along India's coastline on the Bay of Bengal averaging about a million tons a year in a northerly direction. To prevent the silting of the entrance channel and the erosion of the shoreline north of the entrance channel, the following solution was evolved. An island breakwater of about 1000 ft. length on the southern side of the entrance channel was constructed by scuttling 2 merchant ships, filling them with sand, boulders and concrete and protecting them on the weather and lee sides by boulders. This breakwater was so aligned as to allow the littoral drift to pass through the gap between it and Dolphin's Nose and to settle in a sand trap in the lee of the breakwater, where a dredger could operate a good portion of the time during the southwest monsoon season. Part of the dredged material was discharged by means of a floating pipeline to the north of the entrance channel, thus maintaining continuity of littoral drift and the remainder was hoppered out to the dumping grounds. Figure 2 shows these two locations of sand disposal and the existing layout of approaches to Visakhapatnam Inner Harbor.

---

* University of Arizona, Tucson, Arizona, U.S.A., 85721.

** National Research Council of Canada, Ottawa, Canada
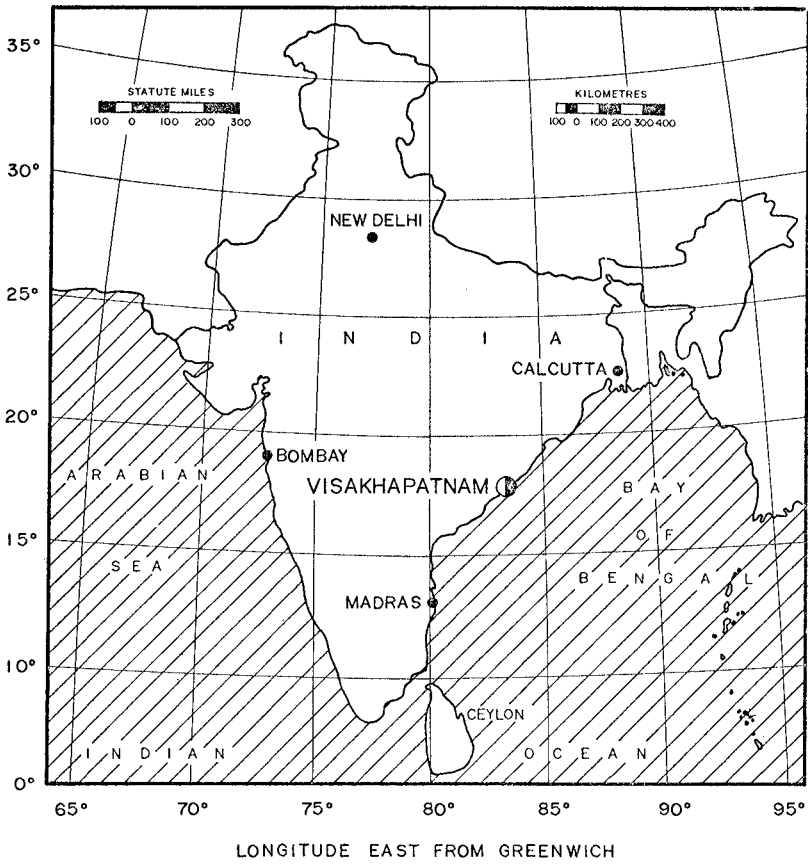
FIG. I LOCATION MAP
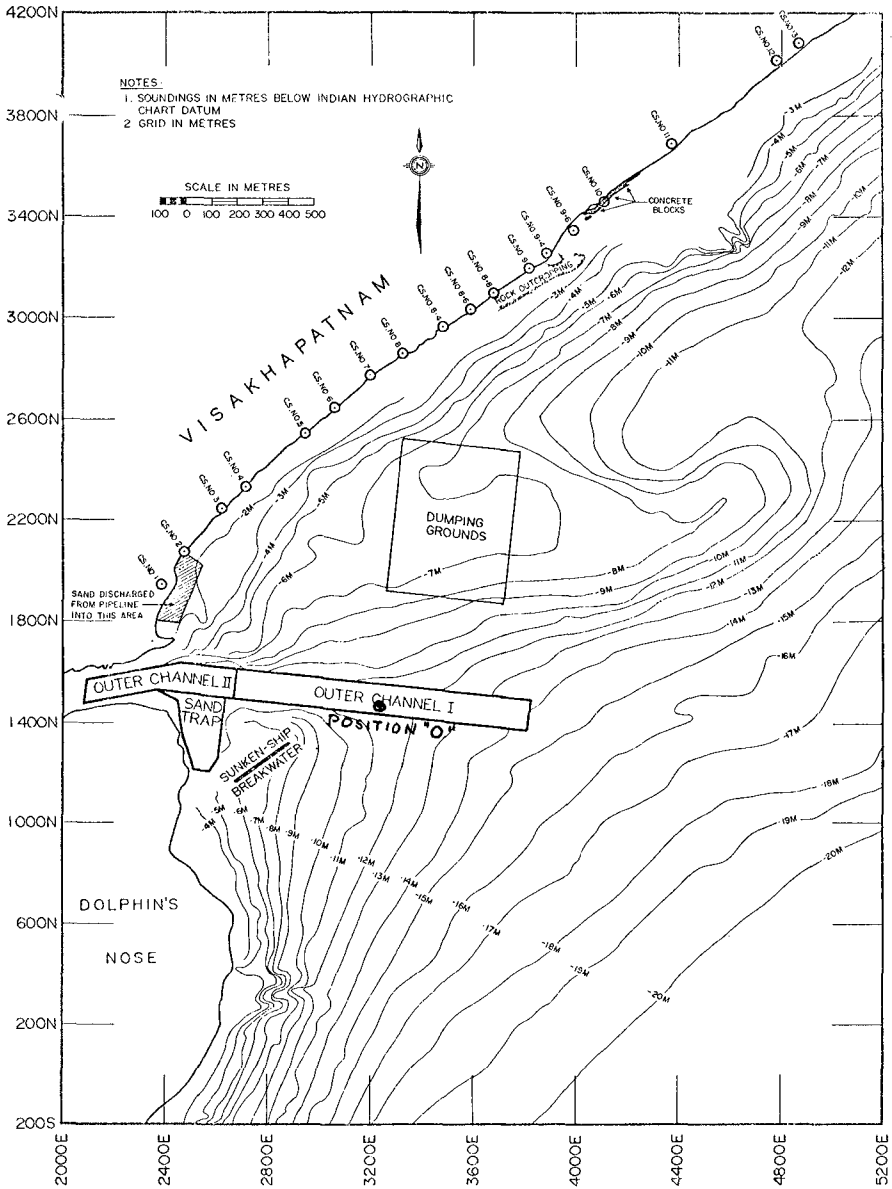
FIG. 2 EXISTING CONDITIONS AT VISAKHAPATNAM
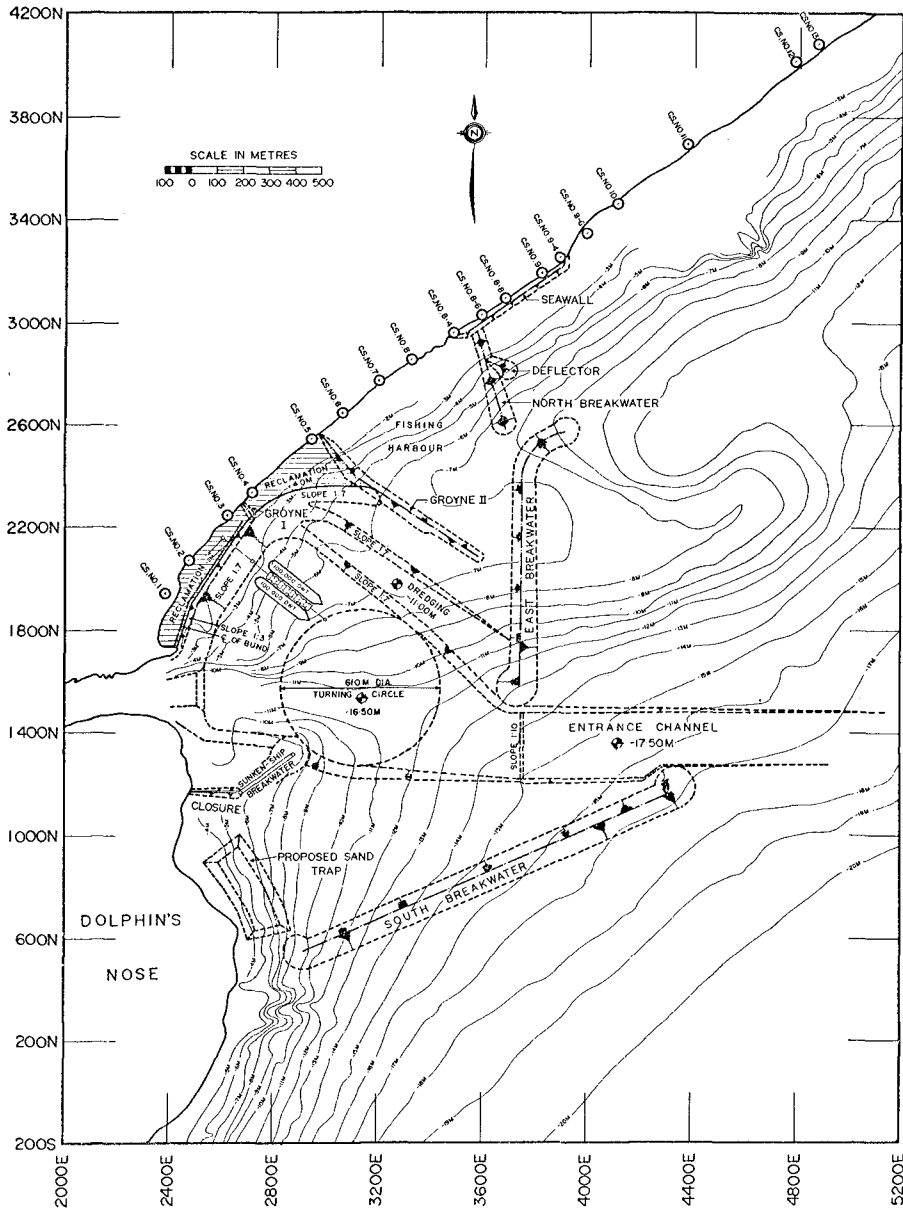
FIG. 3 FINAL LAYOUT OF VISAKHAPATNAM OUTER HARBOUR

VISAKHAPATNAM OUTER HARBOR PROJECT

Over the years the volume of cargo handled through the Port of Visakha-
patnam has gradually increased, and the export of ore through the Port of
Visakhapatnam is expected to reach 12 million tons annually. The maximum
ship size which can be accommodated at the existing loading facility is
33,000 DWT. From an economic point of view it has become essential to use
ore carriers of 100,000 DWT and larger.

In accordance with these requirements, the consulting engineers, Howe
India (Private) Ltd., prepared plans for an Outer Harbor Development which
could eventually provide berthing and loading facilities for ore carriers up
to 200,000 DWT. The final layout is shown in Fig. 3.

Since the problems of littoral drift, channel siltation and shore erosion
arising from the effects of the cyclic southwest and northeast monsoon seasons
were well known, the consulting engineers asked the Hydraulics Section of the
National Research Council of Canada to conduct - in collaboration with the
Central Water and Power Research Station in Poona - oceanographic data analysis
and hydraulic model studies concerning the Visakhapatnam Outer Harbor Project.
The studies provided answers to the following points:

1. Determination of the optimum clearance between the coast and the head
   of the south breakwater considering passage of littoral material, the
   deposition in the sand trap and wave energy through these gaps.
2. Location and configuration of new sand trap.
3. Quantity of sand deposited in the sand trap and the interior of
   the harbor under various conditions.
4. Suitable dumping grounds for dredged material.
5. Quantity of sand which will have to be dredged and pumped to the
   northern shore on the average and during extreme conditions.
6. Optimum discharge zone for the sand-bypass pipeline.
7. Quantity of sand which may be deposited in the entrance channel
   on the average and during extreme conditions.
8. Effect of the Outer Harbor Construction on the coastline north
   of the North Breakwater.

Some of the problems are discussed in this paper.

METEOROLOGICAL AND OCEANOGRAPHIC CONDITIONS

The climate of Visakhapatnam is dominated by the monsoons, which divide
the year approximately into four seasons:

a) The northeast monsoon from the end of November to the end of
   February with predominantly northeasterly winds.
b) The premonsoon period from March to May when the winds have shifted
   to a southwesterly direction and cyclones are frequent.
c) The southwest monsoon from the middle of May to the middle of October
   with predominantly southwesterly winds.
d) The postmonsoon period from the middle of October to the end of
   November with variable weather and greatest frequency of cyclones.

Wave observations were made by the Visakhapatnam Port Trust from 1934 onward at position 0 marked on Fig. 2. During the months of November, December and January the predominant direction of approach of waves at position 0 is from the sector E to ESE, whereas during March, April, May, June, July, August and September the predominant direction is from the sector S to SSE. The predominant period of the waves, disregarding the 0-2 sec. periods, is between 8 and 10 seconds. The average yearly wave height rose is shown in Fig. 4.

The currents which are of concern to construction problems at Visakhapatnam are the longshore currents in the surf zone. The general circulation in the Bay of Bengal and tidal currents are of minor importance.

The longshore currents at Visakhapatnam are in a northerly direction during the southwest monsoon season, and in a southerly direction during the northeast monsoon as indicated by measurements and observations of beach changes due to littoral drift. This is a confirmation of results obtained from wave refraction diagrams, where the angle between the wave front in the breaker zone and the shoreline gives an indication of the direction of the longshore currents.

Of particular interest are currents in the existing sand trap region, where they are not only a function of waves breaking at an angle with the shoreline but are also influenced by wave reflection and diffraction, partly due to the rocky shoreline, but in large measure due to the presence of the sunken-ship breakwater. Moreover, the intensity and direction of currents are greatly influenced by the amount and configuration of the accumulated sand. It has been observed by personnel of the Visakhapatnam Port Trust, for example, that currents across the entrance channel increase in magnitude as the sand trap fills up, and currents of 1 to 2 ft./sec. exist when the sand trap is nearly full. Measurements on the fixed-bed model have indeed confirmed these observations.

The littoral drift and shore erosion problems were briefly touched on earlier. The harbor layout with the sand trap and the floating pipeline sand by-passing scheme has been quite successful in maintaining the required depths in the entrance channel. Over the years this depth has been increased from 26 ft to 38 ft.

The problem of controlling shore erosion north of the entrance channel, however, has not been as successful. The reason for this is simply that the sand by-passing scheme, which as a principle of maintaining the mass continuity of the natural littoral drift is an excellent idea, has not been fully and continuously utilized. With the increase in ship traffic the floating pipeline has been disconnected for extended periods. Thus pumping of the sand to the north of the entrance channel (Fig. 2) has decreased considerably due to these frequent interruptions. Instead, the sand settling in the sand trap and O.C.II has been more and more hoppered out to the dumping grounds.

Over the years, there has been a gradual cutback of the shoreline north of the entrance channel, much of it taking place since 1933. In some places the shoreline recession is as much as 100 meters. It is, of course, not always easy to separate shoreline changes due to natural causes from those
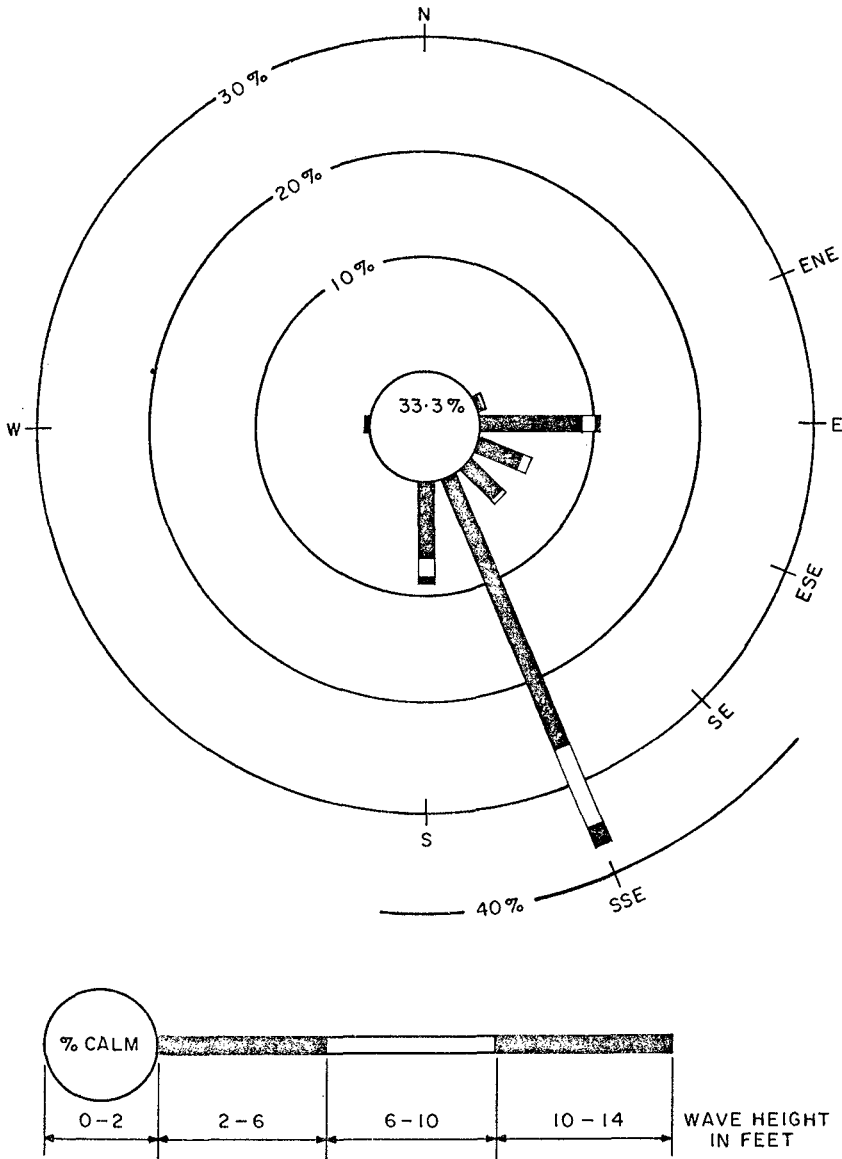
FIG. 4 AVERAGE YEARLY ROSE DIAGRAM FOR WAVE HEIGHTS
AT POSITION O

occurring as a result of man-made interferences. On a geological time scale
nearly all beaches are in an evolutionary stage, whereas on a human time
scale they appear to be in quasi-equilibrium. Even so, a few very stormy
years can and do cause appreciable changes in the shoreline lasting for a
number of years, while over a longer period the original conditions might
be nearly restored without apparent change. There are also the seasonal
changes affecting the shoreline and the beach profiles. At Visakhapatnam,
for example, the shoreline at C.S.9 varies by about 50 meters during one year

Having said all this, the inescapable fact still remains that erosion of
the shoreline north of the entrance channel has taken place since the cons-
truction of the harbor above and beyond the measure that might have occurred
naturally, since the sand by-passing has not been complete and the beaches
to the north have been starved over the years. Observations by the Visakha-
patnam Port Trust indicate that when the quantity of sand pumped to the north
of the entrance channel remained constant for a few years, the shoreline
assumed a new average equilibrium position. As the quantities of sand by-
passing decreased, however, it became necessary to protect an extending portic
of the shore by dumping large quantities of rock and concrete blocks (Fig. 5).

Thus, it becomes absolutely imperative in the planning of the Outer
Harbor Project, to evaluate the quantities of littoral drift at Visakhapatnam
and to design an effective sand by-passing system which can maintain the con-
tinuity of littoral drift across the harbor. In this manner one can be sure
that at least no adverse effects will be caused by the construction of the
Outer Harbor.

The main source of qualitative and quantitative information about littora
drift is the extensive dredging records maintained by the Visakhapatnam Port
Trust. The records over the years 1941 to 1965 show that on the average, the
yearly quantity of sand dredged from the sand trap, O.C.I and O.C.II is
approximately 725,000 cu. yd.

Dredging is done throughout the year and does not, therefore, reflect
the seasonal accumulation in the sand trap and the outer channels I and II.
It was thought useful to analyze 6 years' (1964-1969) records and sounding
charts in greater detail to determine at what times and where deposition took
place in the sand trap and outer channel II. The resulting mass curve for
1969 is shown in Fig. 6. The most salient feature of this plot is the obvious
fact that almost all the material is settling in the sand trap and outer
channel II during the period from April to November, which is essentially the
southwest monsoon period. The conclusion can be drawn, then, that nearly all
the quantities dredged from the sand trap and outer channel represent the
littoral drift resulting from wave action during the southwest monsoon season.
The mean annual dredging quantity of 725,000 cu. yd. represents the proportion
of mean annual northerly littoral drift settling in the S.T., O.C.I, and O.C.I
The mean annual southerly littoral transport is estimated at 165,000 cu. yd.,
and the average annual net drift may be estimated to be around 560,000 cu. yd.
to the north.

The seasonal changes in the direction of the littoral drift with the
southwest and northeast monsoons causes cyclic variations all along the beach,
more obvious at some points than at others. The monthly variation of the

FIGURE 5
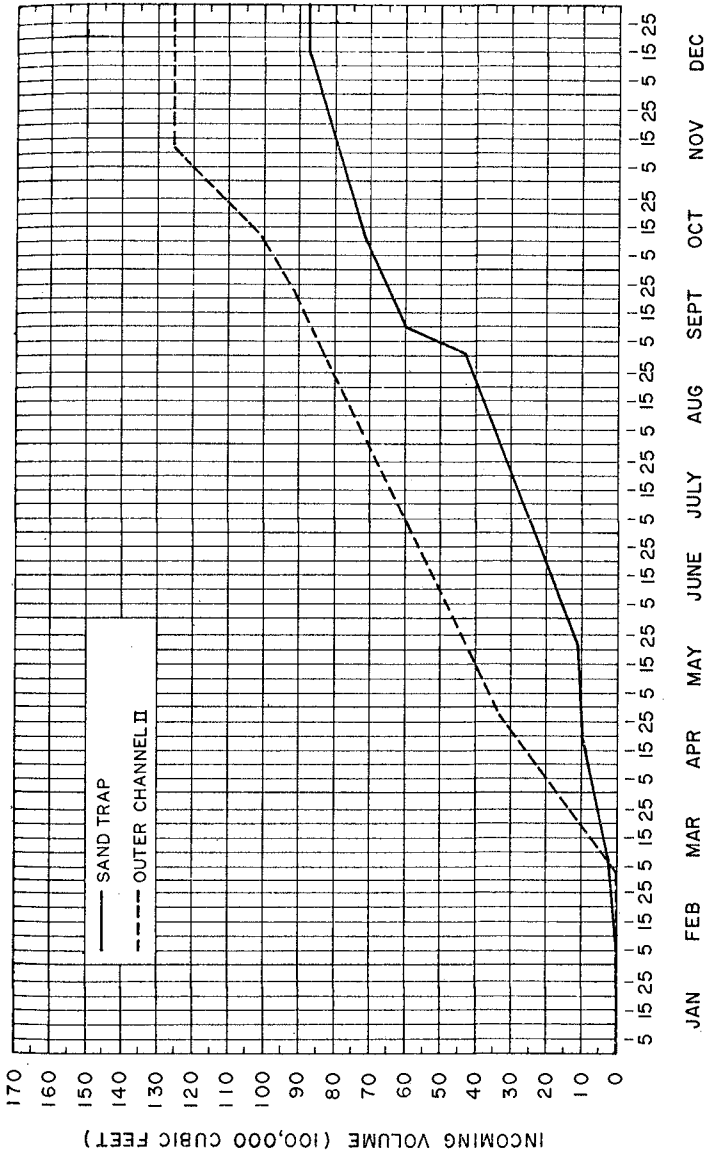
FIG. 6   MASS CURVES FOR 1969
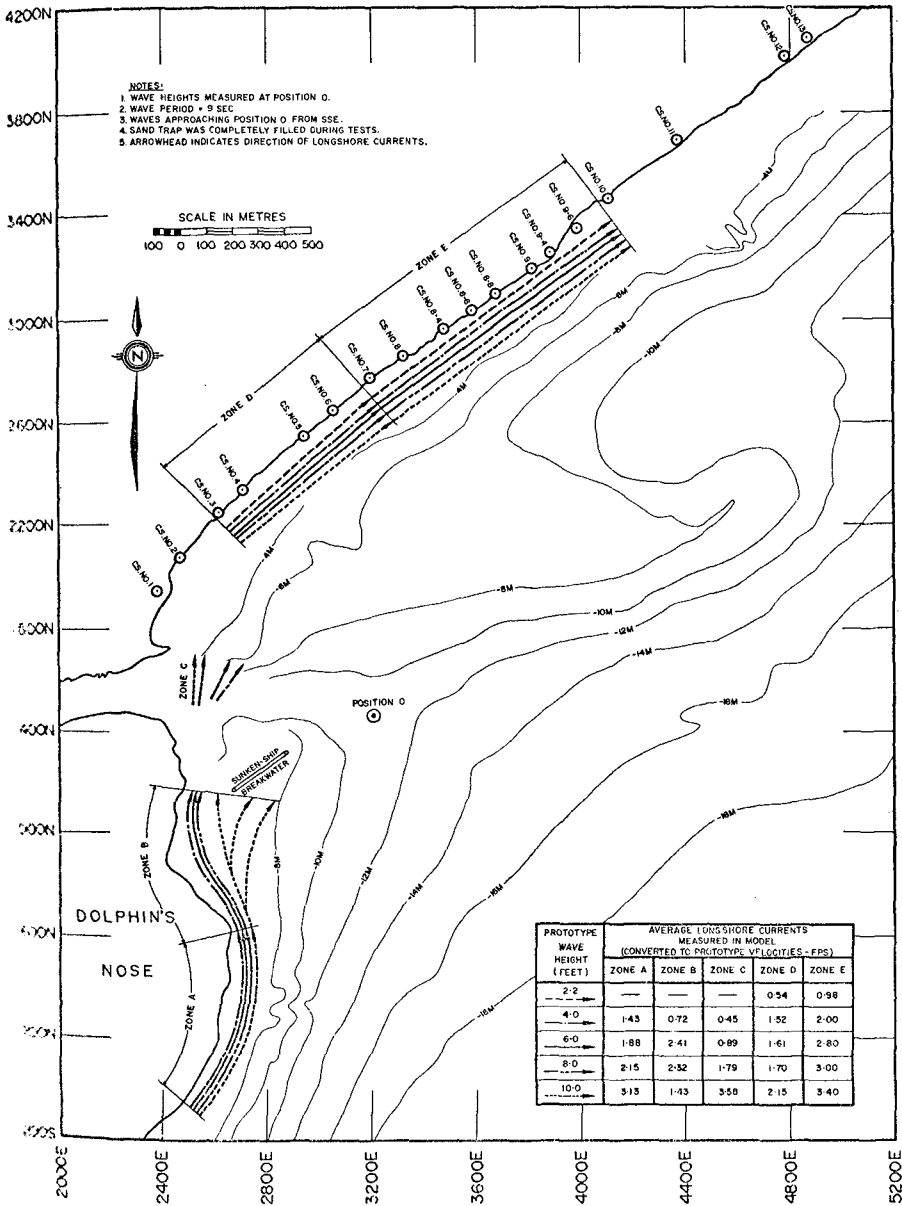
FIG. 7 LONGSHORE CURRENTS

shoreline (MHWST) at C.S.9 and C.S.10 is shown in Fig. 8. C.S.9 and C.S.10
show a most interesting feature beyond the annual cycle of cutback and build-
up, which ordinarily would not be as pronounced. The effects of the south-
west and northeast monsoons are magnified due to the existence of the rock
outcropping between C.S.9 and C.S.10 (Fig. 2). This rock outcropping has beer
exposed more and more over the years as the quantity of sand pumped to the
foreshore has decreased, and acts now as a groyne. During the southwest
monsoon season accretion occurs on the updrift side (C.S.9) and erosion takes
place on the downdrift side (C.S.10). During the northeast monsoon season
the conditions are reversed. This point of discontinuity plays an important
role in the coastal regime at Visakhapatnam.

MODEL INVESTIGATIONS

     Fixed-bed and movable-bed model tests were undertaken to assist the
consulting engineers with design information according to the terms of refer-
ence. Phase I of the investigation was conducted on a fixed-bed model in
order to verify the general littoral drift current magnitudes and directions,
the zone of effective littoral movements, and the general pattern of depositio
in the sand trap and entrance channel.

     The fixed-bed model was constructed to a horizontal scale of 1:300 and
a vertical scale of 1:80. The limits of the model were chosen to reproduce
correctly the refraction phenomena of waves approaching the shoreline from
any direction. The length of shoreline reproduced on the model was long
enough to give a reasonable representation of the longshore current pattern.

     The longshore current measurements done on the model and in the field
agreed reasonably well. (Fig. 7)

     The comparison of current measurements in the area of the sand trap and
O.C.II show a greater variability in both direction and magnitude (Fig. 9).
This is essentially due to conditions in the sand trap. When the sand trap is
full, there are strong currents across the entrance channel whereas with
completely dredged sand trap these currents are small. Since an exact com-
parison of currents would depend on the condition of the sand trap at the time
of the measurements, these differences are to be expected. The overall patter
of currents is in line with the observations.

     Although the fixed-bed model gave a good indication of the currents
in the littoral transport zone, the complete study of erosion and deposition
problems for the Visakhapatnam Outer Harbor required the use of a movable-
bed model.

     The fixed-bed model with a horizontal scale of 1:300 and a vertical
scale of 1:80 was converted to a partially movable-bed model of the same
scales by excavating the cement and molding the submarine topography with
crushed bakelite in the areas along the beach. Experiments with a number
of model bed material samples with different D_{50} values and distributions
indicated that the crushed bakelite ($D_{50} = 0.7$ mm) gave the most reasonable
calibration conditions.
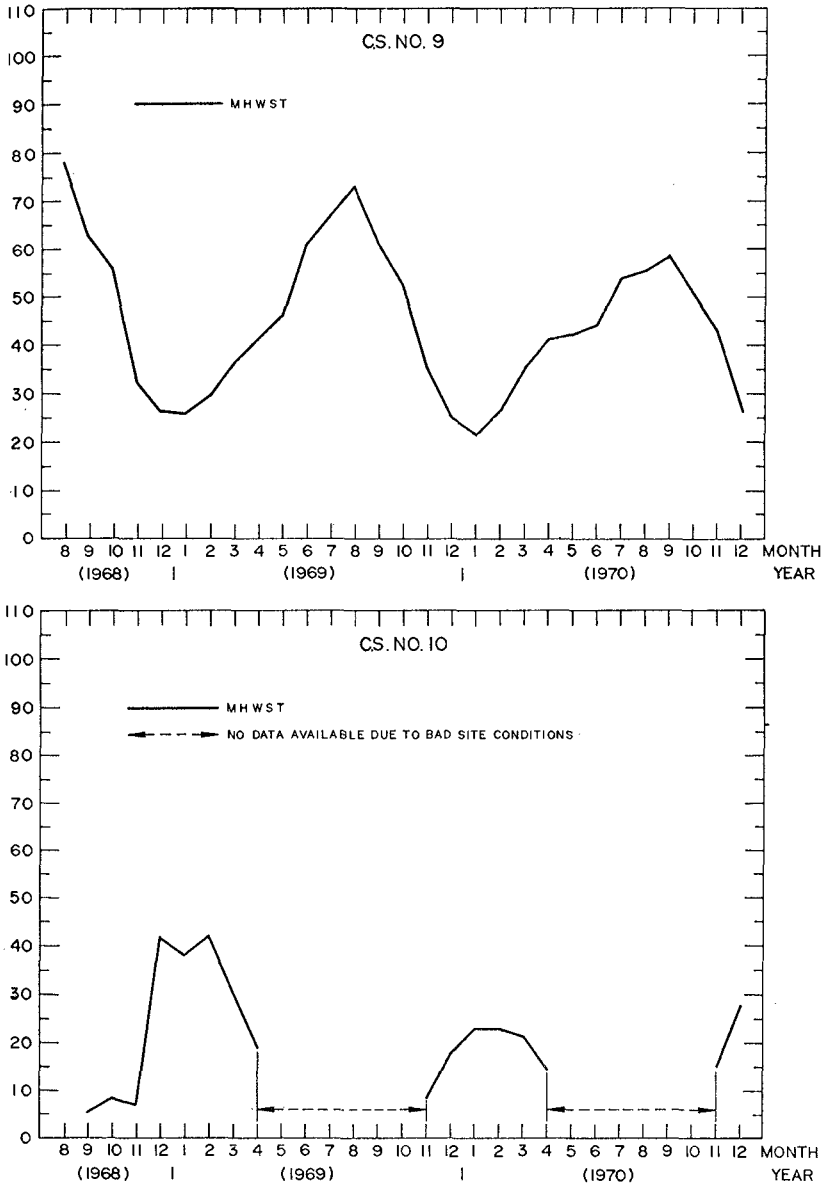
FIG. 8   MONTHLY VARIATION OF THE SHORELINE
AT C.S. 9 AND C.S. 10
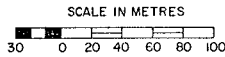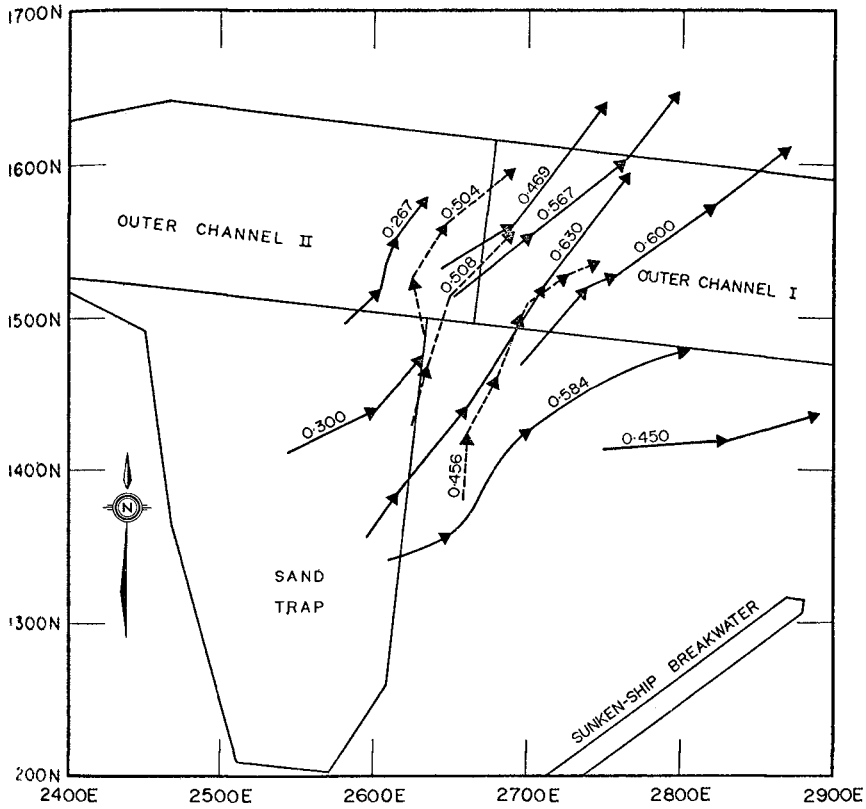
FIG. 9   CURRENTS IN THE SAND TRAP
AND THE OUTER CHANNEL

The period from April 20-September 9, 1969 was used for calibrating the model for the southwest monsoon. The April profiles of C.S.1 to C.S.13 were reproduced in the model to the -6 m depth. Wave direction, wave height and wave period were so adjusted that after a certain interval of time the erosion and deposition patterns and quantities in nature were reproduced in the model.

From the dredging records supplied by the Visakhapatnam Port Trust, it was calculated that in the period April 20 to September 9, the following quantities of sand were deposited in various locations in and south of the entrance channel (Figs. 6, 10 and 11):

Sand Trap	180,000 cu. yd.	(43.5%)
O.C.II	220,000 cu. yd.	(53.0%)
O.C.I	14,000 cu. yd	(3.5%)
	414,000 cu. yd.	100.0%

The quantity of sand pumped to the foreshore around C.S.1 during this period was about 120,000 cu. yd.

The erosion and buildup of the shore north of the entrance channel is given by the profiles at C.S.1 to C.S.13.

The calibration procedure consisted in finding a physically reasonable and acceptable combination of wave direction, wave height and wave period which, when applied over an interval of time would reproduce the natural events as observed at Visakhapatnam from April to September.

After a considerable number of calibration tests it was found that deep water waves of 7 ft. height and 8 sec. period (prototype values) approaching the harbor from SSE (H = 5.5 ft. at position 0 due to refraction and shoaling) and acting for 150 minutes reproduced reasonably well the sequence of events at Visakhapatnam during the 143-day period from April 20 to September 9.

The historical scale for the model was thus established at 150 minutes for the movement and deposition of around 420,000 cu. yd. of sand in the sand trap, O.C.II and O.C.I.

The April and September shorelines (MHWST) in the model were used as a base test with which results of other tests are compared. The repeatability of the calibration runs was in general quite good, except at C.S.8, C.S.9, C.S.9-6 and C.S.10 where variations of up to ± 25% were observed. This is essentially due to the sensitivity of the littoral processes to the influence of the rock outcropping.

Figure 12 shows the deposition pattern in the sand trap and in O.C.II. It should be noted that during the period April 20 to September 9, 1969, no substantial dredging took place in the sand trap until the first part of September; for obvious reasons, O.C.II was being continuously dredged during this period. The model results in Fig. 11 show no dredging in the sand trap and in O.C.II. Other tests have been performed where the movable-bed material was continuously removed from O.C.II corresponding to dredging in nature. It should be noted that the deposition pattern is similar in model and proto- type. The dotted areas indicate the deposition of the finer sand.
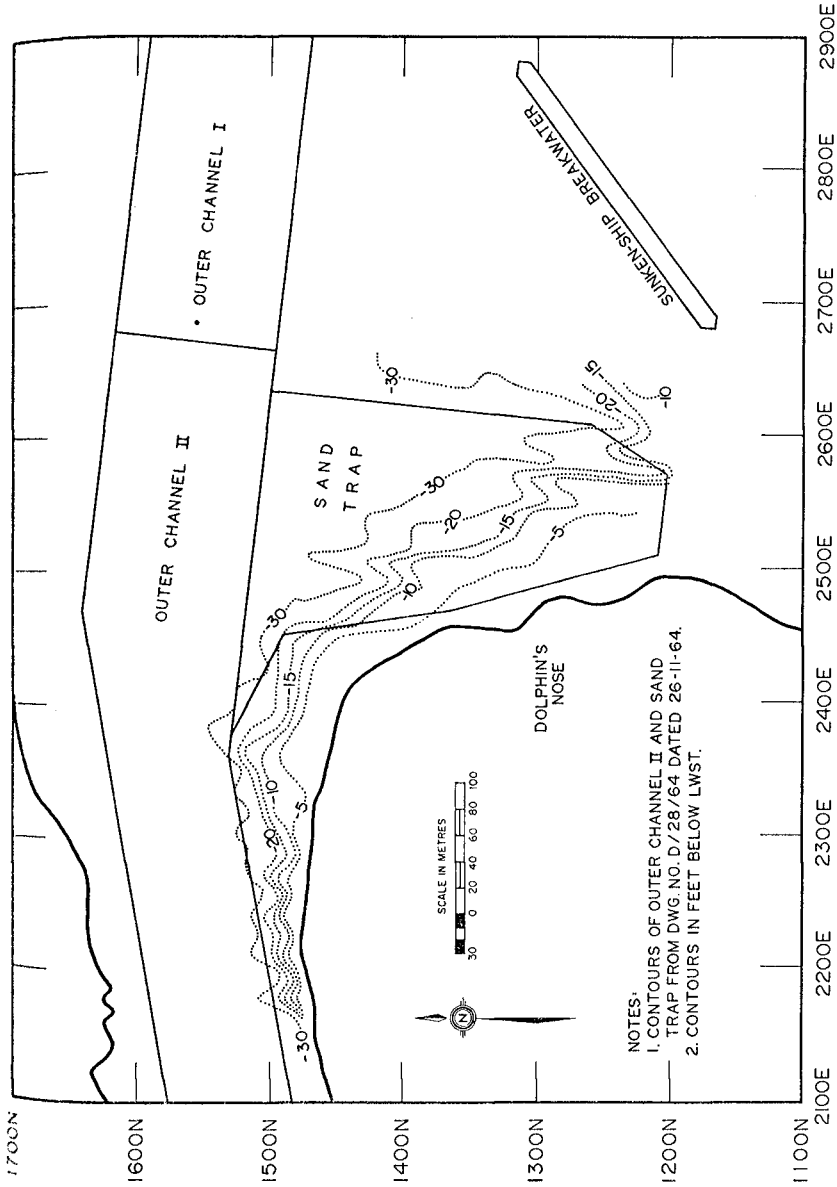
FIG. 10 DEPOSITION PATTERN IN THE SAND TRAP (PROTOTYPE)

OUTER CHANNEL I

OUTER CHANNEL II

SUNKEN-SHIP BREAKWATER

SAND TRAP

DOLPHIN'S NOSE

SCALE IN METRES

30 0 20 40 60 80 100

N

NOTES·
1. CONTOURS OF OUTER CHANNEL II AND SAND
   TRAP FROM DWG. NO. D/28/64 DATED 26-11-64.
2. CONTOURS IN FEET BELOW LWST.

To represent the 414,000 cu. yd. of sand deposited in the prototype, 1.6 cu. ft. of crushed bakelite (≃ 425,000 cu. yd.) was injected into the model along the 2300E coordinate line between the -6 m contour and the shore. After 150 minutes, the pattern shown in Fig. 11 was obtained with the following quantities:

Sand Trap	170,000 cu. yd.	(40.0%)
O.C.II	220,000 cu. yd.	(51.8%)
O.C.I	10,000 cu. yd.	(2.4%)
	400,000 cu. yd.	94.2%

The rest of the material is unaccounted for; some of the finer material deposited in the lee of the sunken-ship breakwater and the remainder was probably distributed in the region seaward around Dolphin's Nose.

The April and September profiles of C.S.1 to C.S.13 were reproduced in the model and compared with those of the prototype. The correspondence - although not perfect - was acceptable. It should be remarked that it is very difficult to match one season's profile in the model and prototype, because the model deals with average and uniform conditions over a season, while the prototype is subject to the non-uniform effects of storms.

The model was also calibrated for the northeast monsoon conditions for the period November 8, 1969 to February 8, 1970. After a considerable number of tests it was found that 2.5 ft., 6 sec. waves (prototype values) arriving at position 0 from S38E and acting for 40 minutes gave the best results. The repeatability was again reasonably good. However, at C.S.8, C.S.9 and C.S.11 there are discrepancies between model and prototype amounting to as much as 30% and the repeatability was no better than $\pm 25\%$. All model results have therefore confidence limits of $\pm 25\%$.

The new harbor layout is shown in Fig. 3. The starting point for all tests was the April 1969 conditions. The model was operated for 180 minutes for the southwest monsoon season corresponding to a slightly below average year for sand deposition in the sand trap, O.C.II and O.C.I (≈520,000 cu. yd.). For simulation of the northeast monsoon season the model was operated for 40 minutes corresponding to a southerly drift of 100,000 cu. yd. All resulting changes are compared to 1969 April and/or September conditions in the model.

The length and general alignment of the south breakwater was located by the consulting engineers in collaboration with the Central Water and Power Research Station Laboratories. While optimum harbor tranquility was one of the main considerations, it was required to adjust the gap between the shore-line at Dolphin's Nose and the head of the breakwater to achieve a trade-off between wave agitation in the harbor and effective longshore sand transport through the gap. The Hydraulics Section of the National Research Council was not involved in harbor tranquility studies, but did perform tests with various gap dimensions concerning trap efficiency. The gap location and width adopted by the consulting engineers shown in Fig. 3 was found to be satisfactory. The effect of a slightly wider gap was not discernible on the movable-bed model but would have injected more wave energy into the harbor. Placing the head of the breakwater closer to shore did interfere to some degree with the
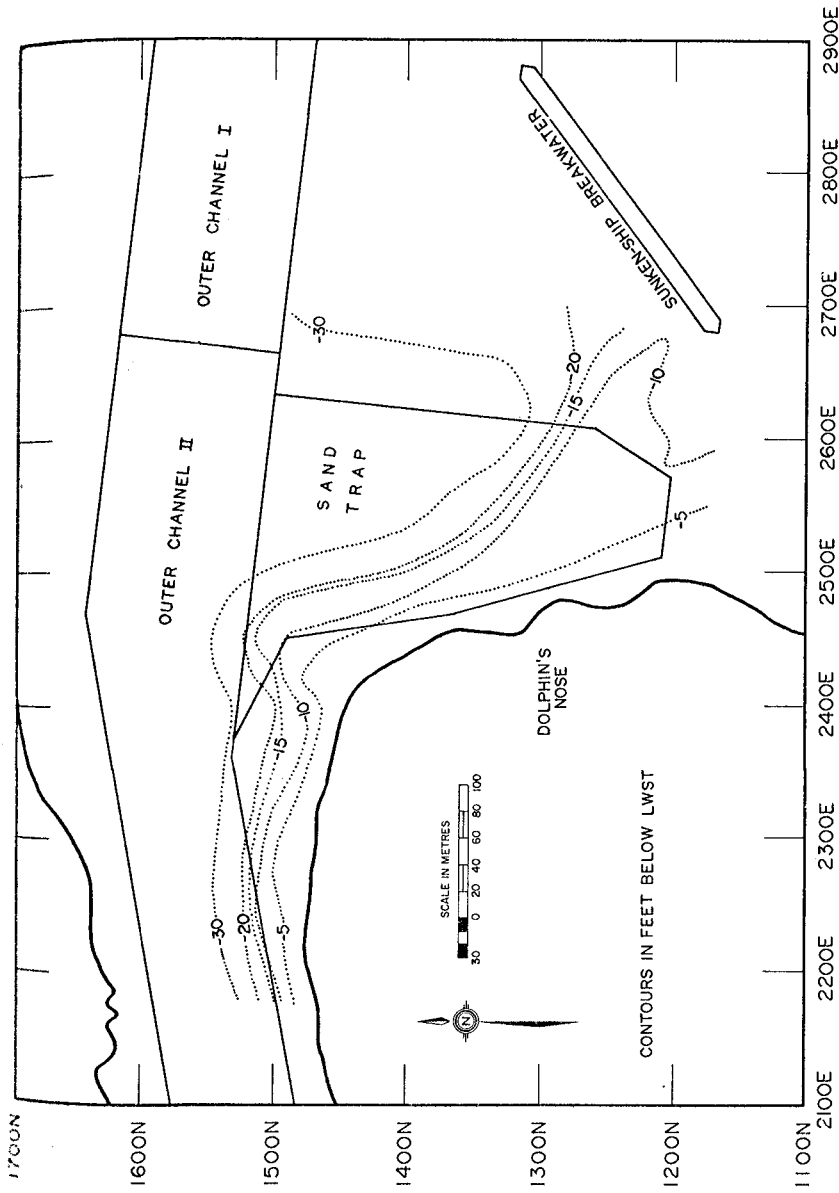
FIG. 11 DEPOSITION PATTERN IN THE SAND TRAP (MODEL)

sand transport, but not beyond the limits of accuracy of the experiments. In other words, the displacement of the breakwater head ±25 m in either direction did not indicate significant changes of littoral transport through the gap. The optimum location, size and dimensions of the new sand trap was established after considerable experimentation. The choice was dictated by conditions of littoral transport as well as limitations imposed by the rock contours. The bottom of the sand trap was set at an average of -18 m. Three fundamental tests were conducted to determine the efficiency of the sand trap and the conditions under which the gap would be blocked. Only one is reported here.

Southwest Monsoon Season

Northerly Littoral Drift: 650,000 cu. yd.

The deposition pattern around the gap, the head of the south breakwater, in the sand trap and in the harbor area is shown in Figs. 12 and 13. The types and quantities of sedimentary material deposited in various general regions are as follows:

Zone	Type	Quantity (cu.yd.)	Percent of Total
I	Coarse)		
II	Fine)	430,000	66.1
III	Coarse-Medium	40,000	6.2
IV	Fine	50,000	7.7
V	Coarse-Fine	90,000	13.8
VI	Fine	35,000	5.4
		645,000	99.2
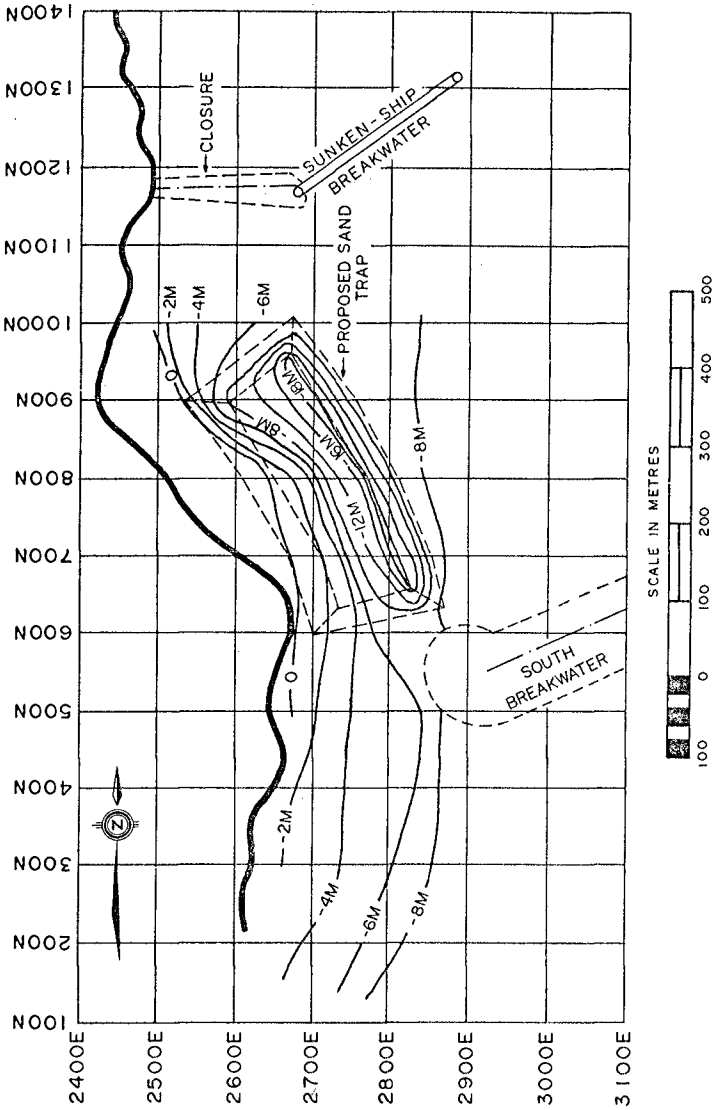
FIG. 12 DEPOSITION PATTERN AROUND THE GAP AND THE NEW SAND TRAP DURING THE SW MONSOON SEASON (LITTORAL DRIFT: 650,000 CU YD)
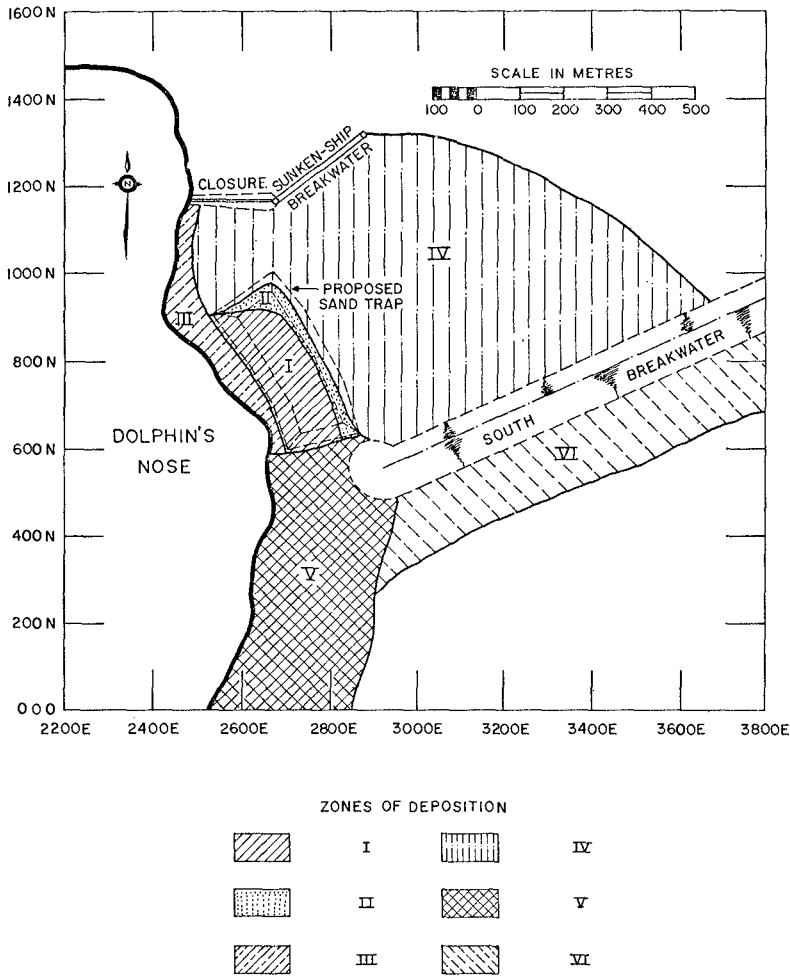
FIG. 13 ZONES OF DEPOSITION AROUND THE SOUTH BREAKWATER
AND THE SAND TRAP

CHAPTER 89

HYDRAULICS OF TIDAL INLETS ON SANDY COASTS

by

Ramiro Mayor-Mora, Dr. Eng.*

ABSTRACT

A series of laboratory experiements was carried out on an idealized ocean-inlet-bay system subjected to reversing flows caused by tidal and surface wave actions. The testing was done in a rectangular basin simulating a "bay" or "lagoon" and separated from an "ocean" basin by a sand barrier across which inlet pilot channels of varying cross sections and lengths were cut prior to starting each run; the ocean side of the barrier formed a 1:30 flat beach throughout the tests. Disturbances in the ocean were created by tide and wave generators. Their effects in the bay and inlet channel were measured by water level and current velocity recording units. Experimental measurements are presented here in normalized form in order to determine the relationships governing the hydraulic behaviour of a tidal inlet. These results are also compared to those obtained from a numerical approximation (the lumped parameter approach), all as functions of a proposed coefficient that includes the ocean-inlet-bay system characteristics. The experimental findings are further compared to available field data. Investigation of the effects of surface waves, controlling jetties, and fresh water inflow into the bay on the dimensionless parameters are also explored.

1. INTRODUCTION

Physical model studies are one of the alternatives to field data gathering in order to meet the need for understanding general processes occurring at and in the vicinity of tidal inlets on sandy coasts and for assessing the relative importance of the hydraulic parameters involved.

This paper summarizes major findings resulting from a laboratory investigation (1) carried out using a simplified model to reduce the complexity of the inlet, processes and their analysis. The model did not take account of inlet channel stability, sediment transport rates, salt water effects, flow patterns or littoral drift. The study included: the testing of movable-bed inlets with varying geometric characteristics, subjected to combinations of tides and surface waves whose effects are the generation of reversing flows that shape the inlet channels; the simultaneous measurement of the fluctuating water levels in the ocean, bay and inlet, and current velocities; the measurement of channel geometry at the end of each run; correlation of the parameters defining the hydraulic behaviour of the inlets; and comparison of the experimental results with those predicted by a numerical approximation and to some available field data.

* Senior Hydraulic and Coastal Engineering Specialist,
  SNC INC. (Consultants), Montreal, Canada.

2. THE LUMPED PARAMETER APPROACH

The simplifications adopted to solve the simultaneous differential equations defining the hydraulics of a tidal inlet with fixed channel have decreased in number since Keulegan formulated his theoretical analysis (2). Huval and Wintergerst have included various important refinements to that analysis in a numerical solution known as "lumped parameter approach" (3) which accounts for non-sinusoidal ocean tide, variable bay surface area, variable inlet depth and cross sectional area throughout a tidal cycle due to sloping inlet banks and variable water levels, fresh water inflow into the bay and flow accelerations in the non-prismatic inlet channel.

The lumped parameter approach integrates the ordinary differential equations determining the water surface fluctuations:

$$h_o - h_b = \frac{1}{2g} \cdot (k_{en} + k_{ex} + \frac{fL}{4R}) \cdot |V| \cdot V + \frac{L}{g} \cdot \frac{\partial V}{\partial t} \qquad \text{Eq. 1}$$

and

$$\frac{\partial h_b}{\partial t} = \frac{A \cdot V + Q_f}{AB} \qquad \text{Eq. 2}$$

where, h_o and h_b are the water surface elevations in the ocean and in the bay respectively at time t, k_{en} and k_{ex} are the coefficients of energy losses due to channel entrance and exit, f the Darcy-Weisbach friction coefficient, L the length of the equivalent prismatic channel, R its hydraulic radius at time t, V the mean current velocity through A, the flow cross section, AB the bay surface area and Q_f the fresh water discharge into the bay. All parameters in Eq. 2 are functions of time.

In addition to a quadratic flow resistance assumption, Huval and Wintergerst assumed $k_{en} + k_{ex} = 1$ and f a function of Manning's coefficient.

For comparison to the experimental results, the computer program developed by Huval and Wintergerst was modified so that

$$k_{en} + k_{ex} + \frac{fL}{4R} = F \qquad \text{Eq. 3}$$

where F, the inlet energy losses coefficient determined from measurements, became an input to the program as explained below.

3. TESTING PROGRAM AND DATA REDUCTION

A systematic series of 36 experimental runs was carried out on idealized ocean-inlet-bay systems involving reversing flows caused by tidal and uniform surface wave actions, at the Engineering Field Station of the University of California, Berkeley.
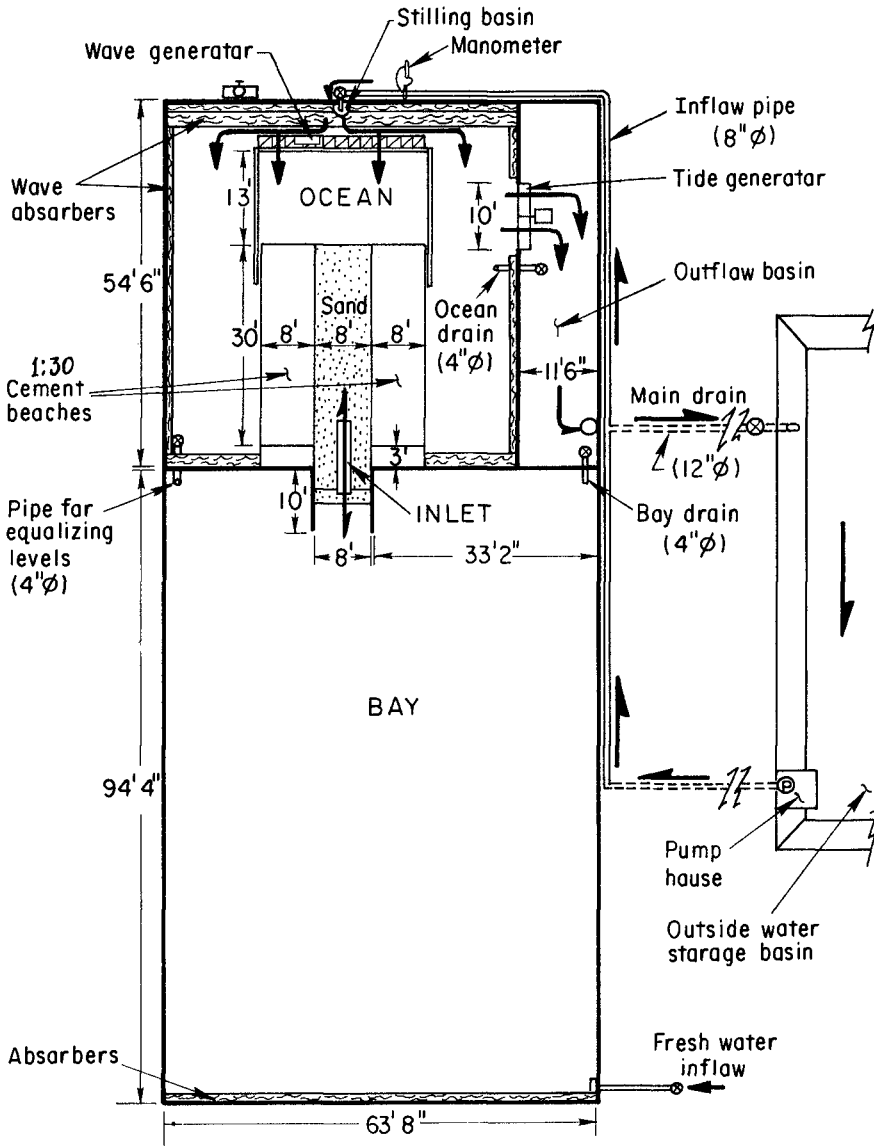
Fig. 1 - Schematic view of the testing facilities.

Fig. 1 illustrates the dimensions and components of the facilities. These
were complemented by units continuously recording water level fluctuations,
wave characteristics and current velocities, and devices for measuring
and recording the inlet geometries. Fig. 2 shows the grain size character-
istics of the sand used throughout the testing program to form a sloping
barrier (1:30 on the ocean side) between the two basins.

Detailed descriptions of the facilities, equipment, instruments, testing
procedures and resulting data have been reported elsehwere (1). Briefly,
a typical run consisted in cutting a prismatic pilot channel through the
sand barrier, activating the tide generator set at a tidal period of 20 to
60 minutes until a periodic hay tide motion was attained for several cycles
at which time the run was terminated. The resulting inlet geometry was
noted. A second part of the run was initiated by resuming the tidal action
for a few cycles, followed by the introduction of uniform surface waves
perpendicular to the initial inlet channel alignment as shown in Fig. 3.
The photographs illustrate the behaviour of a short, deep inlet throughout
a complete tidal cycle once periodic conditions were reached everywhere
in the system. Inlet characteristics were again fully documented. Duration of
each part of the run ranged from 4 to 25 hours.

Throughout the testing program, the following items were kept constant:
surface area of the bay basin, beach slope, pilot channel bank slopes, and
relative location of the walls defining the ocean basin, sand barrier and
the bay.
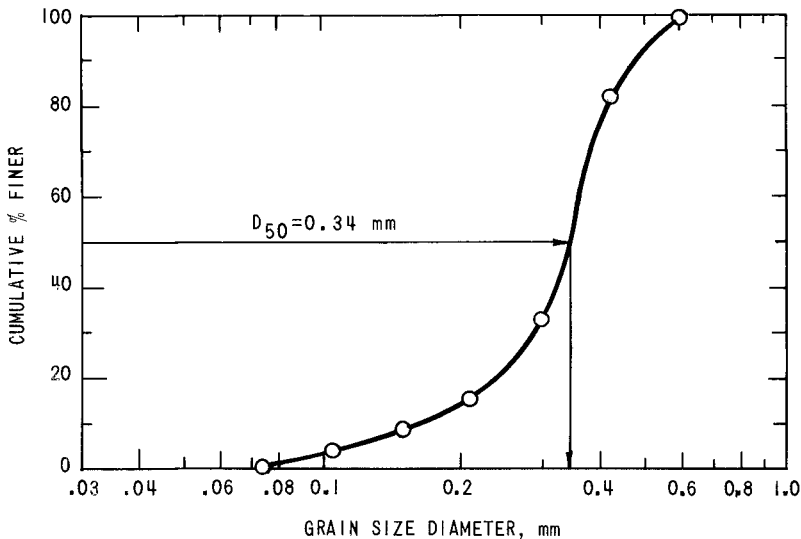
Fig. 2 — Sieve analysis of sand used in the testing.

Runs were also carried out to assess the effects of steeper surface waves (the rest of the runs with wave steepness under 0.024), parallel smooth-wall jetties (controlled condition) and fresh-water inflow into the bay (10.2 gpm).

Tide records were used for determining mean ocean and bay levels (MOL and MBL), ocean and bay ranges (RO and RB), time lags between ocean and bay high and low waters (EH and EL), duration of ebb and flood flows, as well as the slope of the bay tide curve at maximum discharge (dh_b/dt) and the ocean, inlet and bay water surface elevations (h_o, h_i and h_b, respectively) corresponding to that instant. Cross sectional areas (AMOL), surface widths (WMOL) and wetted perimeters (PMOL), were referred to the mean ocean level. In the case of runs with tidal action only, average values of the latter three parameters were computed whereas for runs with waves the throat region (vicinity of the cross section presenting the minimum flow area below MOL) was used for their computation. Clarification regarding all this parameters can be obtained by examining Fig. 4.

It has been shown (1) that repletion coefficients K, at maximum discharges ($dV/dt \approx 0$) can be obtained from measured parameters as follows:

$$K_f = \frac{T}{\eta \sqrt{2\,RO \cdot (h_o - h_b)_f}} \cdot \frac{1}{\alpha_f} \cdot \left(\frac{\partial h_b}{\partial t}\right)_f^{max} \qquad \text{Eq. 4}$$

for flood flow, and

$$K_e = \frac{T}{\eta \sqrt{2\,RO \cdot (h_b - h_o)_e}} \cdot \frac{1}{\alpha_e} \cdot \left(\frac{\partial h_b}{\partial t}\right)_e^{max} \qquad \text{Eq. 5}$$

for ebb flow, where T is the ocean tidal period and

$$\alpha = A/AMOL = 1 + [(WMOL + ETA \cdot h_i) \cdot h_i / AMOL] \qquad \text{Eq. 6}$$

Accordingly, two values of K were computed for each inlet thus identifying the corresponding run. Using Keulegan's (1) definition of K, values of the inlet energy losses coefficient are obtained:

$$F_f = \left(\frac{\sqrt{g} \cdot T}{\eta \sqrt{RO}} \cdot \frac{AMOL}{AB} \cdot \frac{1}{K_f}\right)^2 \qquad \text{Eq. 7}$$

for maximum flood discharge, and

$$F_e = \left(\frac{\sqrt{g}\ T}{\eta \sqrt{RO}} \cdot \frac{AMOL}{AB} \cdot \frac{1}{K_e}\right)^2 \qquad \text{Eq. 8}$$

for maximum ebb discharge.

From equations 7 and 8 the expression

$$G = K_f \sqrt{F_f} = K_e \sqrt{F_e} = \frac{\sqrt{g} \cdot T}{\eta \sqrt{RO}} \cdot \frac{AMOL}{AB} \qquad \text{Eq. 9}$$

Bed at end of run   **t = 0 min.**   **t = 7·5 min**
            (start of ebb)

0   1   2 ft.

t = 13 min.   **t = 17 min.**   **t = 22.5 min.**
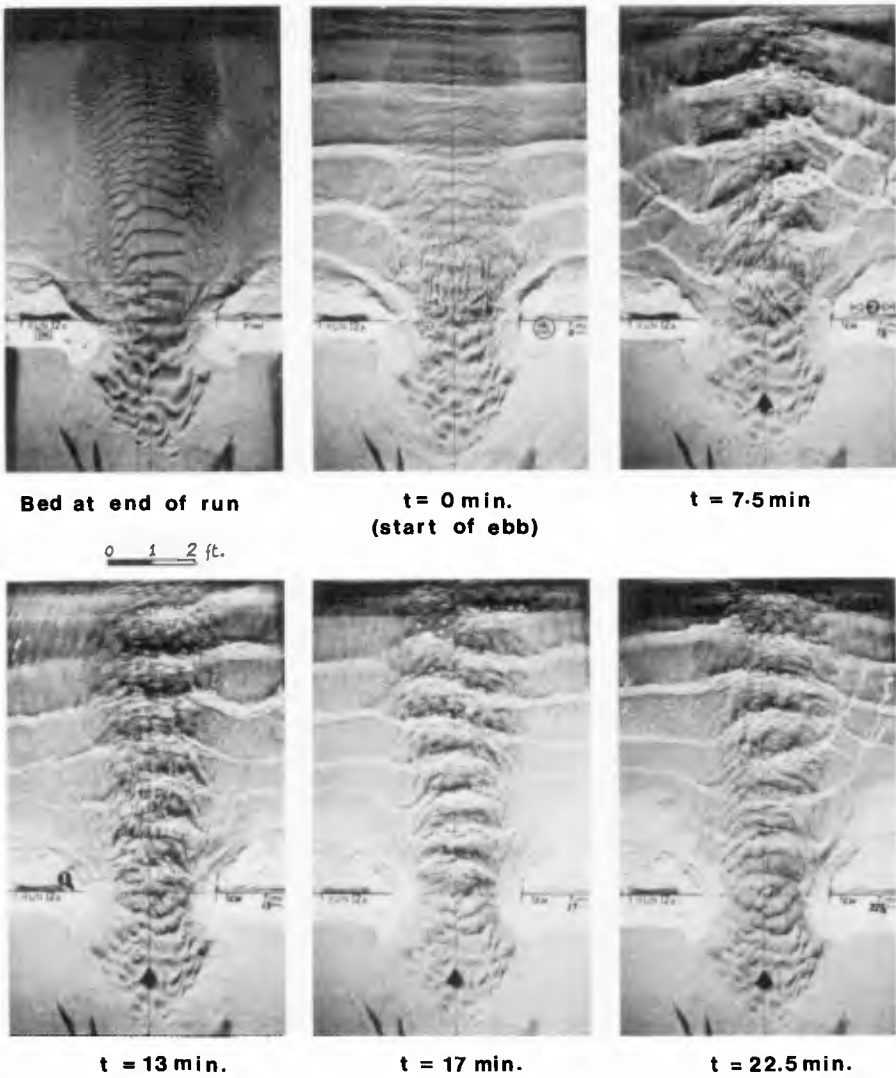
Fig. 3 — Model inlet under a 60-min. tidal cycle and 0.75-sec. uniform waves. EBBING.

t ≅ 30 min.   t = 37.5 min.   t = 43 min.
(start of flood)

t = 47 min.   t = 52.5 min   t = 60 min.
                                                               (end of flood)
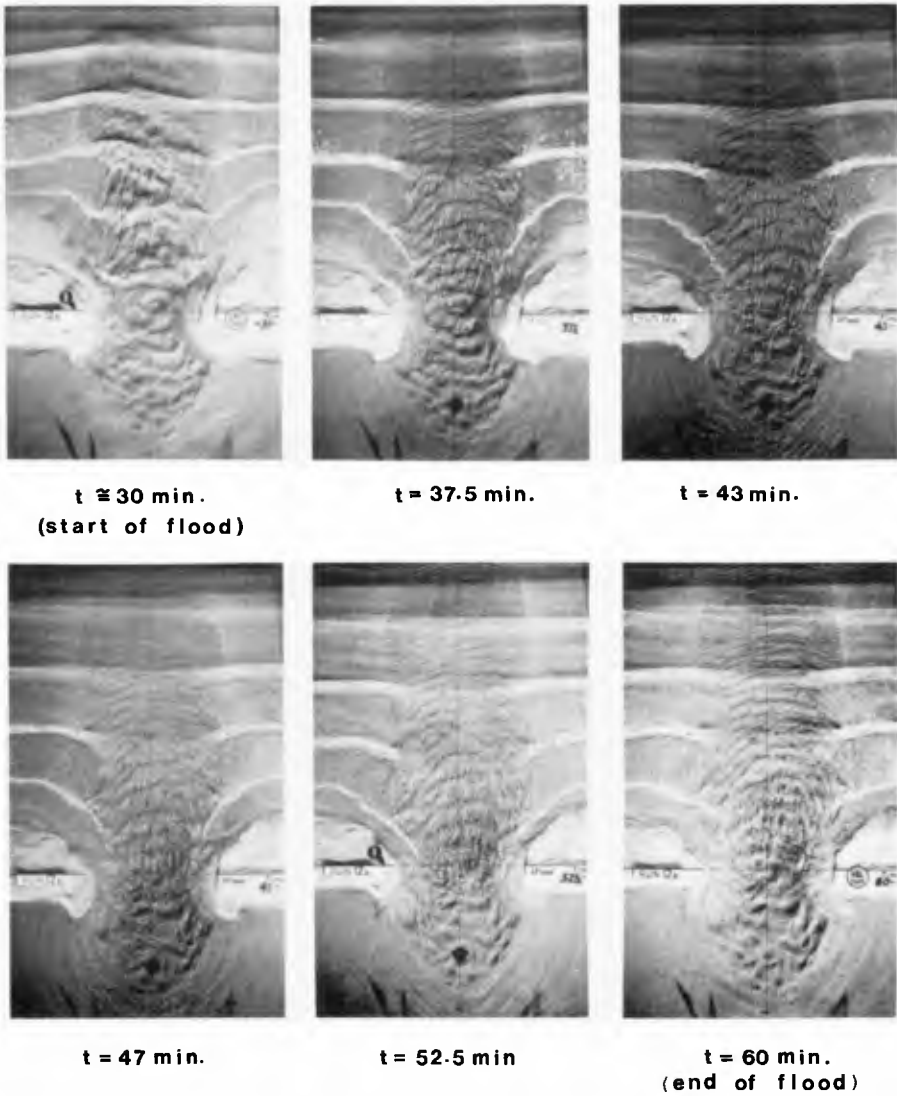
Fig. 3 — (cont'd) Model inlet under a 60-min. tidal cycle and uniform waves. FLODDING.
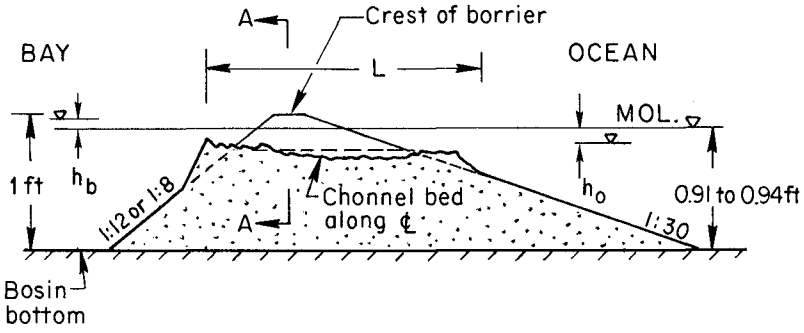
b) Typical sand barrier profile along channel center line.
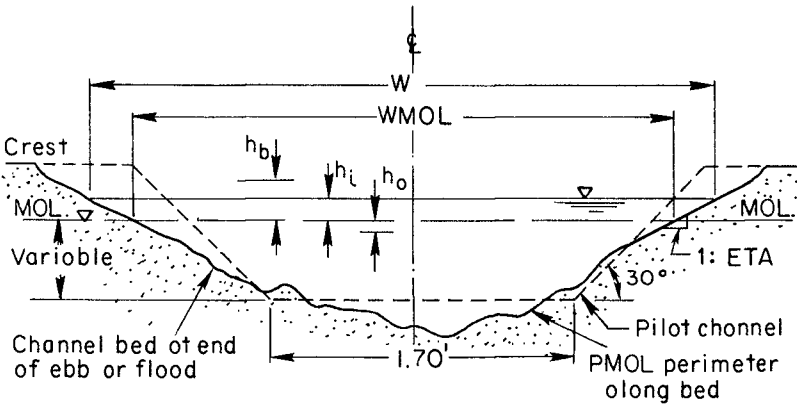
a) A-A Section: Typical flow cross section perpendicular to channel alignment.

Fig. 4 – Longitudinal and transverse profiles of a typical sand barrier.

is obtained. G represents a dimensionless number, constant throughout a
tidal cycle, defining the inlet characteristics and those of the ocean tide.
G is a useful variable since its computation is based on quantities measur-
able both in the laboratory and in the field, making it unnecessary to
estimate friction coefficients, exit and entrance energy loss coefficients
or length of channel.

4.   DIMENSIONLESS HYDRAULIC PARAMETERS VS. G.

Computations based on measurements yielded rough estimates of f at maximum
discharges ranging from 0.01 to 0.65 but most of them from 0.05 to 0.20.
Corresponding estimates of n ranged from 0.006 to 0.049, most of them within
the 0.013 - 0.030 range.

For comparison to experimental results, data for each run were input to the
lumped parameter program, the procedure for their treatment being: in
the interest of time sinusoidal ocean tides were assumed with measured RO
and T; values of V and h_b were adopted as initial conditions, as well as
time intervals and the approximate number of tidal cycles necessary for
the results to show a periodic bay tide; values of n were then computed
corresponding to maximum discharges for both ebb and flood flows. Two
solutions were obtained (assuming that the roughness coefficients mentioned
remain constant throughout the tidal cycle) but only that one corresponding
to ebb flow roughness was retained for comparison because it showed closer
agreement between actual measured parameters and results from the analytical
solution; the reason for this probably being, among others, that a closer
approximation to open channel flow (theoretical assumption) is evident during
the ebb flow, the inlet behaving more like an orifice during flood. Computed
values of n for ebb ranged from 0.016 to 0.049, most of them from 0.020 to
0.027.

Therefore, each run provided the absolute results as illustrated in Fig. 5
showing computer plots of ocean and bay tides, mean velocities and discharges
during a cycle according to the lumpted parameter approach compared to
measured values of the first three variables. It should be pointed out that
the measured velocity is a local one at the centre of the flow section, thus
greater than the computed average. The case illustrated corresponds to a long
and shallow inlet under tidal action, the analytical results based on an
ebb flow value of n.

In addition to plots of absolute parameters, output included combinations
of the results for all runs presented in dimensionless form thus allowing
generalization of the findings as shown in the following figures, where
the smooth curves are either best-fits or envelopes of the analytical results
by the lumped parameter approach for uncontrolled inlets under either tidal
action or simultaneous tidal and mild wave actions.

a. Ocean Tide Damping

The ratio of the bay and ocean tide ranges (Fig. 6) may be interpreted as a
measure of the ability of an inlet to filter the ocean tide, where a high
value indicates low damping efficiency. This ratio is very well predicted
by the theory in the case of tidal action, and in a minor degree for the
combined tidal and wave actions. Although not conclusive, it seems that
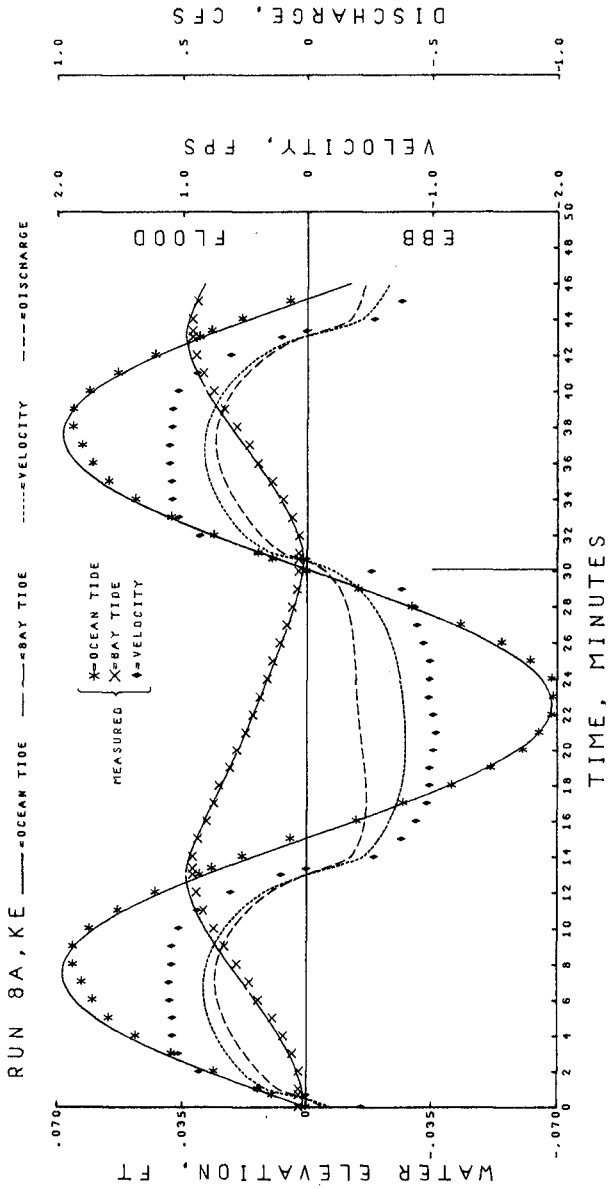
Fig. 5 – Comparison of measured parameters and theoretical solution by the lumped parameter approach, throughout a tidal cycle. K = 0.179.
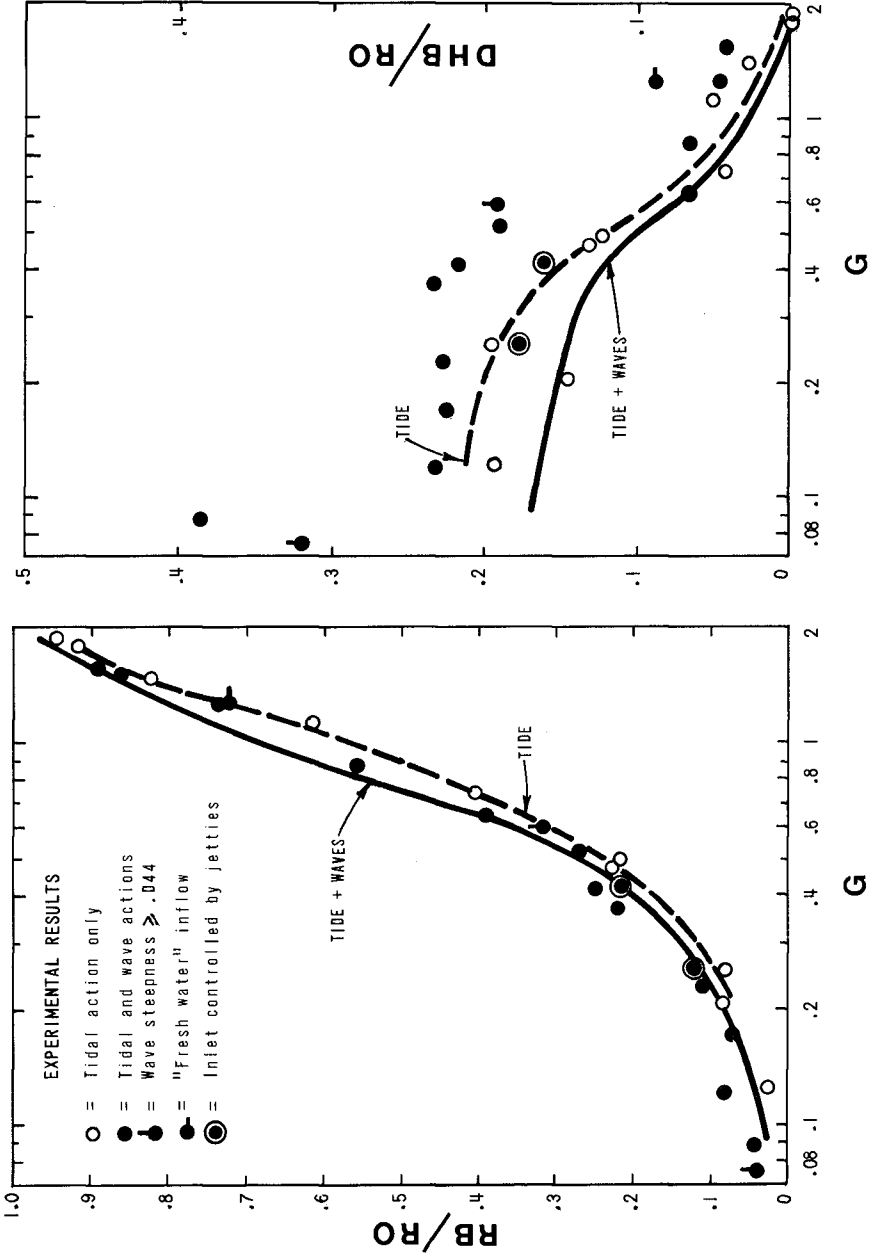
a given inlet, steeper waves do not affect greatly the results obtained
milder waves. But the effect of waves on damping of the tide as
)ared to tidal inlets without much wave action is an increase in the
il range of the bay, as predicted by the numerical approach and confirmed
the experiments. This effect appears to be reduced in the case of bays
l fresh water inflows.

il damping ratios are found to be very sensitive to changes in the values
G (that is, changes in the bay and flow area characteristics for a given
ation) larger than 0.5, as evidenced by the steep sections of the curves.

Bay Superelevation

. 6 also shows the difference between bay and ocean mean elevations
perelevation or DHB) divided by the ocean range and related to G.
superelevation predicted by the numerical method is longer under
al action than under tidal and wave actions, specially for low G
ues, whereas experimental measurements indicate just the opposite, in
ition to their large scatter. The mean bay waters are always above
but the difference in the ratio decreases with increasing G. It is
eresting to note that the inflexion points in the two sets of curves
tide and wave action shown in Fig. 6 appear to occur at about the same
ue of G. Highest predicted values of superelevation are around 20% of
tidal range whereas values close to 40% were measured. Keulegan's
ory (2) did not predict bay superelevation.

Dimensionless Maximum Mean Current Velocity

maximum mean velocity across a flow section, VMAX, can be approximated
by

$$VMAX = \frac{QMAX}{AMOL \cdot \alpha}$$ Eq. 10

re QMAX is the maximum discharge through the inlet obtained by multiply-
AB by the maximum slope of the recorded bay tide. Dimensionless values
maximum current velocities, AVMAX, are expressed as

$$AVMAX = \frac{QMAX}{\pi \cdot AB \cdot RO/T}$$ Eq. 11

shown in Fig. 7 for both ocean conditions and for ebb and flood flows.

t of the results based on experimental measurements are well predicted
the lumped parameter solution for inlets under tidal action only, the
uracy of the prediction being smaller in the case including waves. The
ory shows that for a given inlet AVMAX for flood is always higher than
ebb value, fact that is confirmed by the experiments. However, it
uld be pointed out that this is not necessarily the case of absolute
imum mean velocities since the maximum velocity during ebb flow could
greater than that during flood.
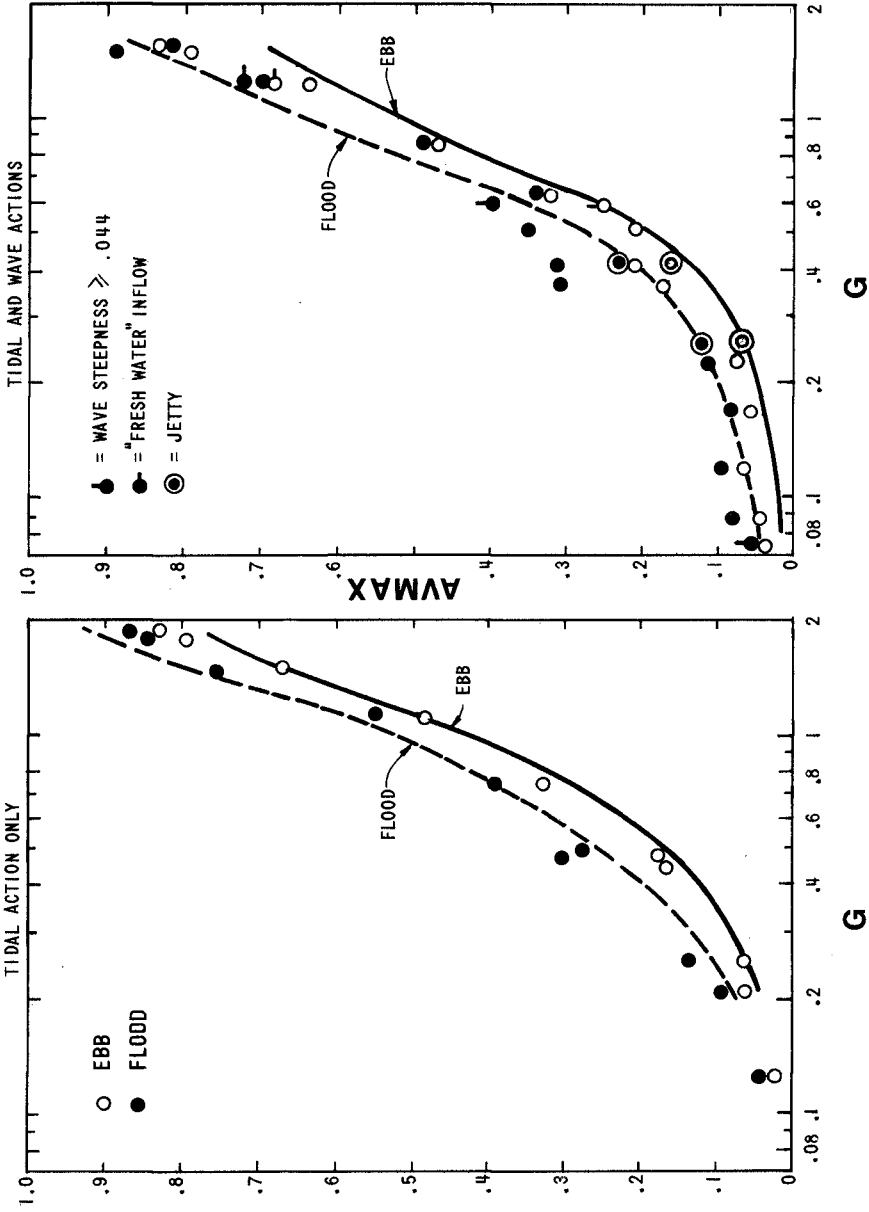
Fig. 7 – Dimensionless maximum mean current velocities as functions of the inlet G. Comparison of model measurements to the lumped parameter approach.
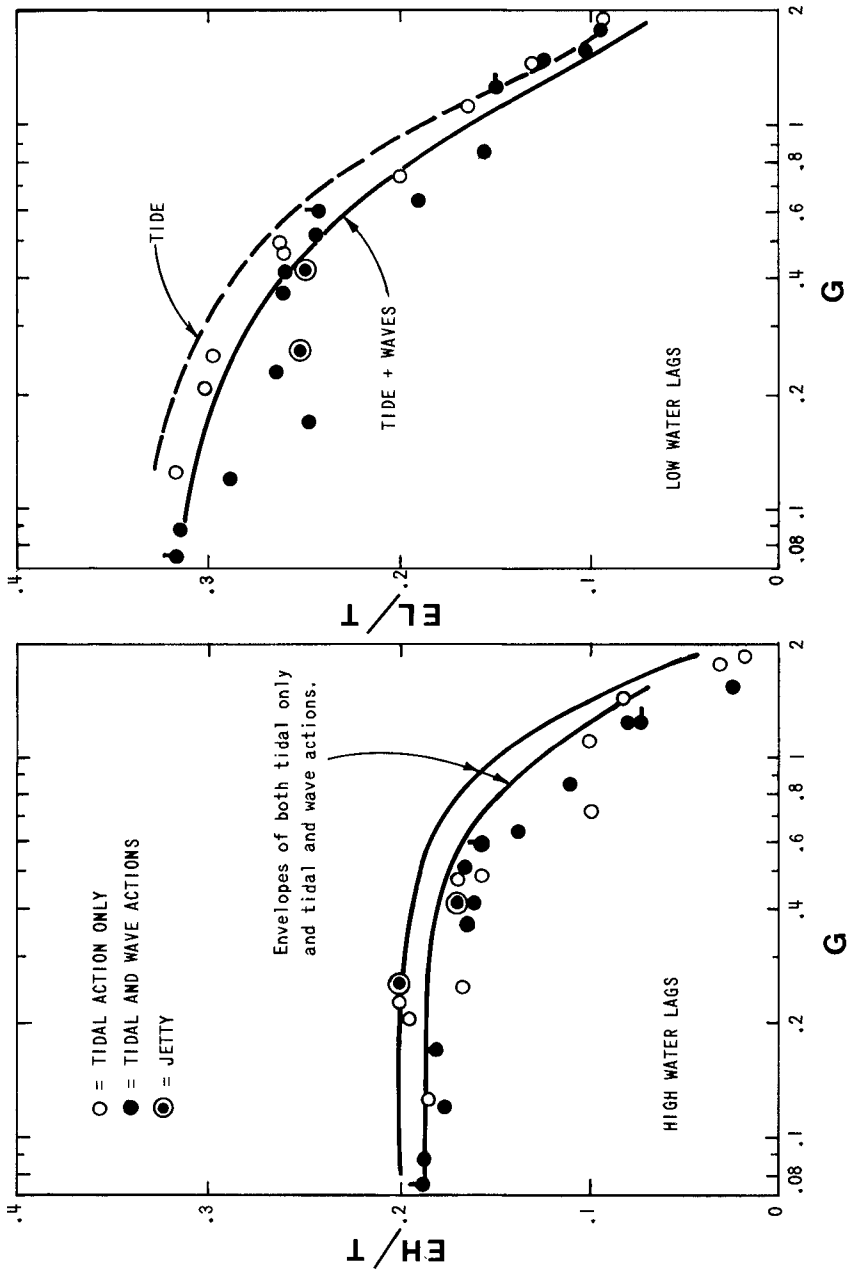
Fig. 8 — Dimensionless time lags between ocean and bay waters as functions of the inlet G. Comparison of model measurements to the lumped parameter approach.

d.   Time Lags

The dimensionless time lags between ocean and bay high and low waters are
shown as functions of G in Fig. 8. Lags between high waters are shorter
than those between low waters in all types of inlets but the difference
decreases as G increases. It could be said that, in general, the theory
slightly overestimates the values of time lags. The high water lag results
indicate that they reach an upper limit of close to 0.20 for G smaller than
about 0.50, according to the lumped parameter approach. For high waters,
the introduction of waves does not seem to affect the values of the lag,
whereas it decreases somewhat the lag between low waters, as shown by both
theoretical and experimental results. In other words, wave action
accelerates the transmission of the ocean low water into the bay, specially
in the case of inlets with low G values.

The above is visualized by the trends obtained from the tests and shown in
Fig. 9: the dimensionless time lag between ocean and bay low waters (minima)
is always longer than that corresponding to high waters (maxima). The
45° line in this figure corresponds to the basic Keulegan's development (2),
the measurements for the tidal and wave action case being somewhat closer
to such line.

e.   Ebb and Flood Duration

Fig. 10 shows the duration of both ebb and flood, i.e., the periods of time
between slack waters at the inlet channel. In general, durations of ebb flow
decrease with increases in G. These ebb durations are reduced when waves
are introduced, up to values of G of about 0.50, whereas wave action does
not seem to affect much the durations in the case of inlets with larger G
coefficients. Keulegan's approximation (2) implied equal ebb and flow
durations for any inlet.

f.   Inlet Energy Loss Coefficient

F can be regarded as a measure of the resistance to flow presented by an
inlet system at the instant of peak discharges in the channel. Experimental
values of F (from Eqs. 7 and 8) are correlated with G as shown in Fig. 11,
most of them being below 10. Inlets present a greater resistance to flow
during the emptying of the bays than they do during the flood flow, the
latter occuring at higher channel stages that diminish the effects from the
rippled beds. These unit energy losses during the ebb flow are greater
in the case of wave action specially for values of G smaller than about
0.60. On the other hand,unit losses during flood are not much affected by waves.

5.   JETTIES, STEEP WAVES AND INFLOW INTO THE BAY

Regarding the exploratory tests, superelevations seem to decrease when
controlling jetties are introduced but their influence on bay tidal range
and dimensionless maximum mean velocities and lags is minor. Steeper waves
cause somewhat higher bay superelevations and maximum mean velocities, but
their effects on time lags are similar to those found for milder waves. As
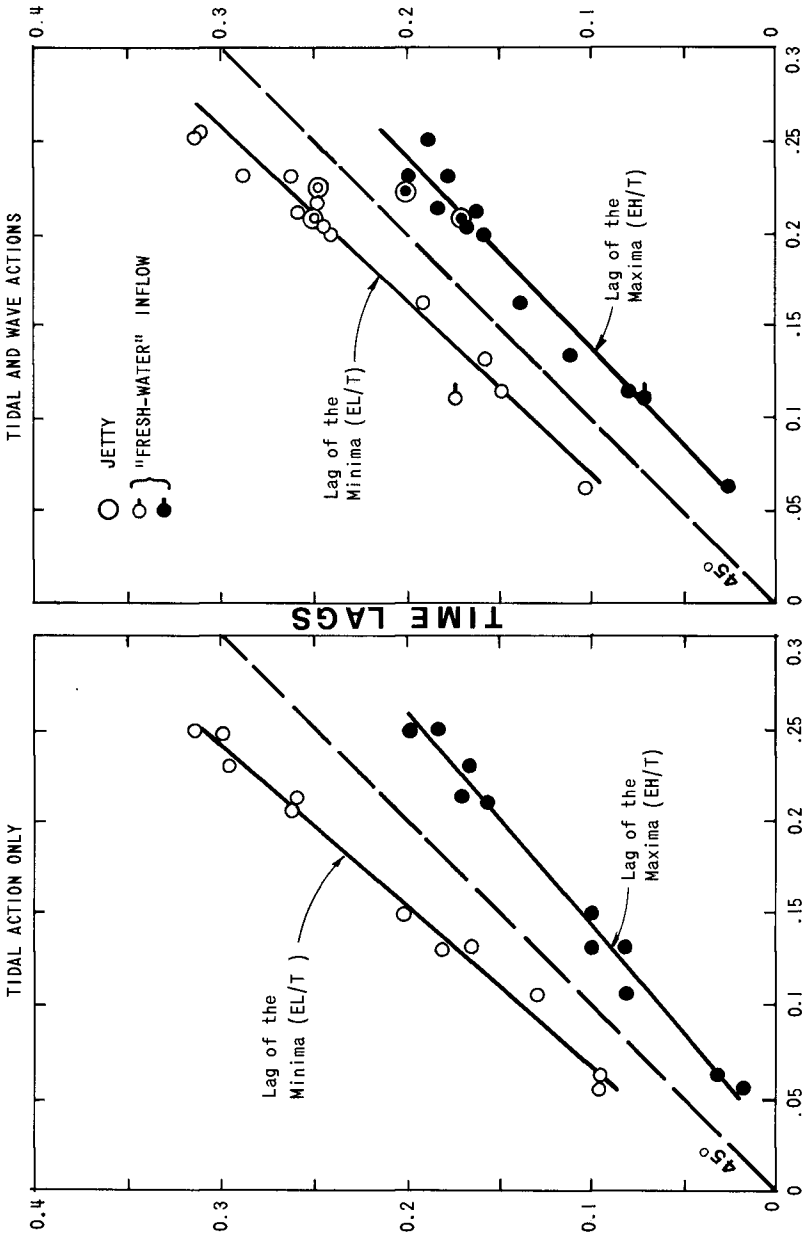
Fig. 9 — Dimensionless time lags compared to average time lags for a tidal cycle, and trends obtained from experimental measurements.
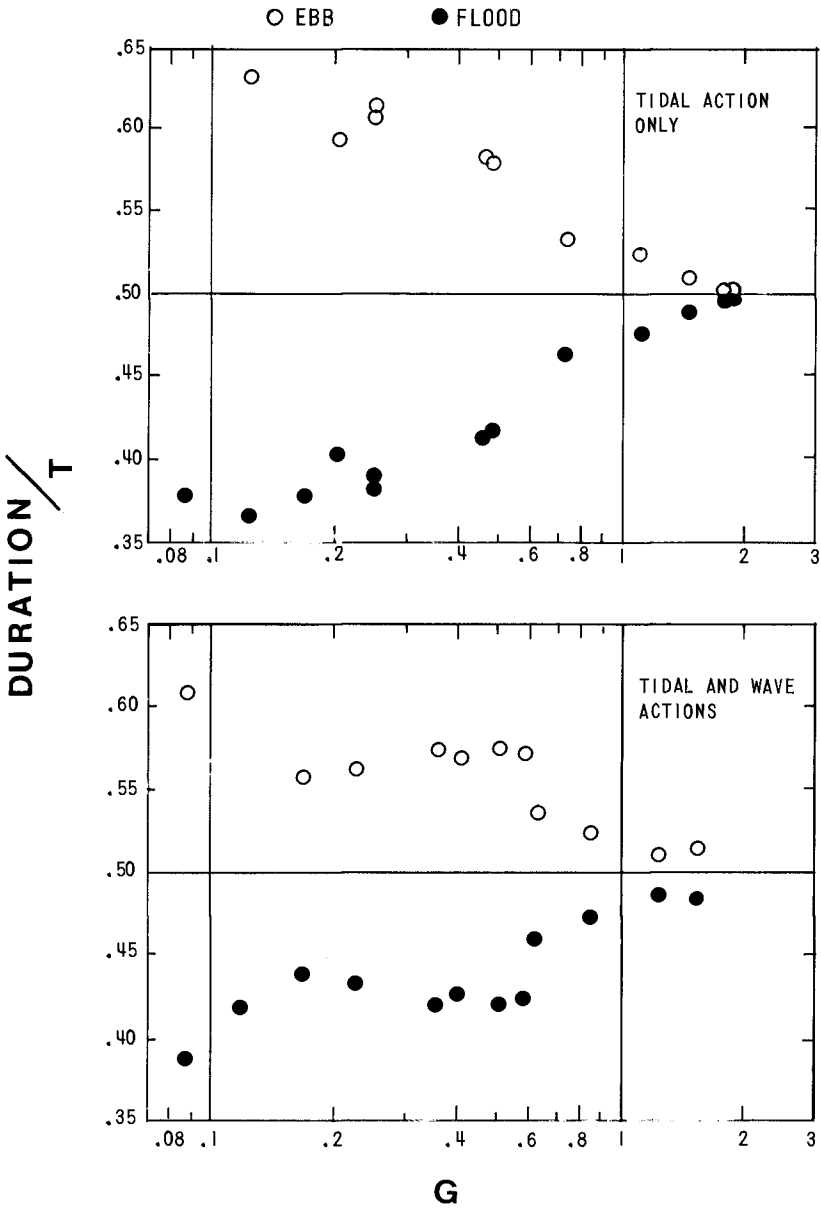
Fig. 10 — Dimensionless durations of ebb and flood as functions of the inlet G, obtained from experimental measurements.
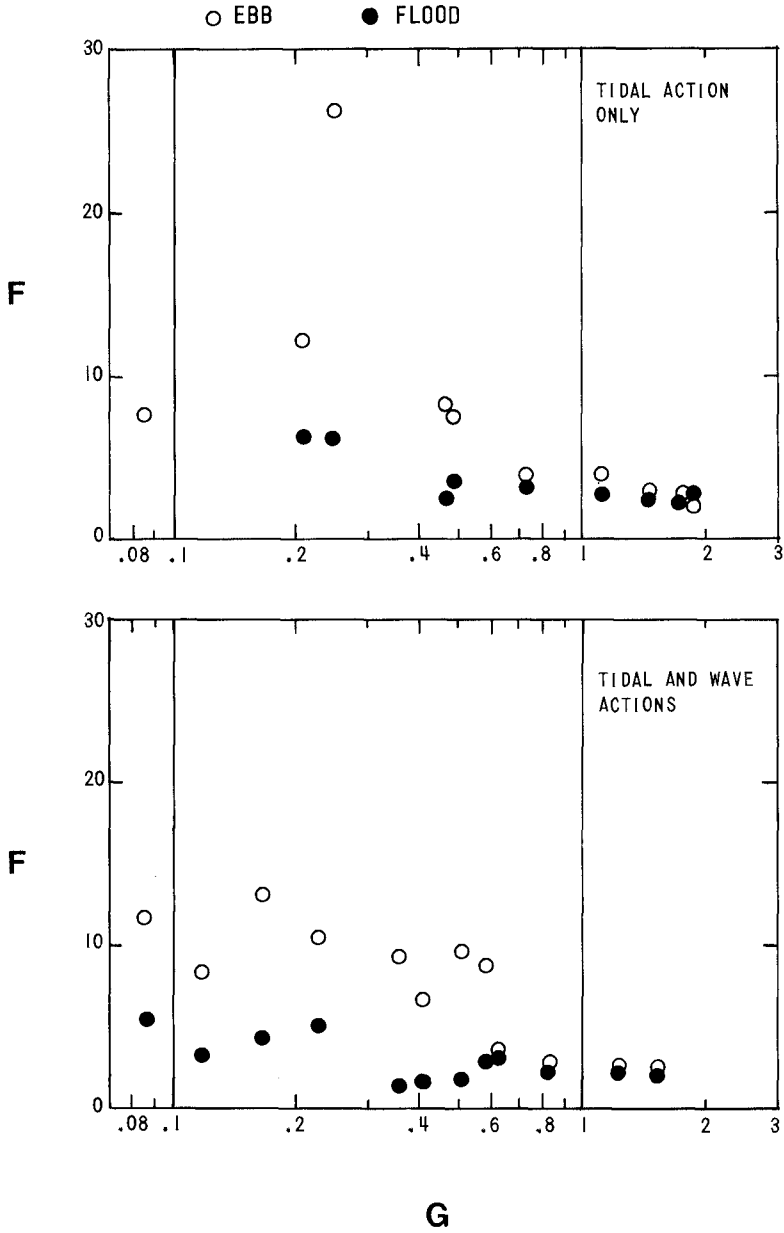
Fig. 11 — Inlet total loss coefficients (F) as functions of the inlet G, obtained from experimental measurements of uncontrolled inlets.

expected, fresh water inflow into the bay causes higher superelevations, lower values of dimensionless flood velocities and higher for those corresponding to ebb, whereas low water time lags are longer than those for similar bays with no fresh water inflows. Of course, more systematic research is needed for a complete assessment of all these effects.

6.   TIDAL PRISM AND MINIMUM FLOW AREA

Since the requirement imposed by assuming that the water surface elevation was uniform throughout the bay was met in all runs (the ratio of the tidal wave length to the distance from the inlet to the bay furthermost point varied from 65 to 200), for all practical purposes the bay water level moved up and down as a horizontal plane (1). The basin walls being vertical the experimental tidal prism P can be computed as

$$P = AB \cdot RB \qquad\qquad \text{Eq. 12}$$

Tidal prisms on mean range for prototype inlets (1) and those for the model inlets are related to throat flow areas below MOL in Fig. 12. It is noted that the extension of the curve of experimental inlets with wave and tide action interacts prototype inlet conditions so model and field data seem to be governed by the same law regarding tidal prisms and minimum flow areas. However, the importance of the field data scatter is evidenced by the scale of relative differences shown in the figure. A further comparison is shown in Fig. 13 for unimproved inlets, including data from Nayak and Lin (1) for model inlets subjected to constant ebb flow only and field data for inlets without jetties and with one jetty not affecting the characteristics of the throat region.

7.   CONCLUSION

With this simplified model it has been possible to further the knowledge of tidal inlet behaviour through the correlation of the various hydraulic para- meters presented here as functions of the variable G. Most of the relation- ships are predicted by the lumped parameter approach with the exception of some of them related to combined tidal and wave actions. It should, however, be kept in mind that the numerical solution does not take into account wave effects. The relations between absolute tidal prisms and minimum inlet flow areas for both model and prototype were investigated, although the gap between field and laboratory measurements is still great.

The effects of controlling jetties, fresh water inflow into the bay and steep surface waves on the inlet hydraulics were explored. Much remains to be done in the investigations of these particular cases.
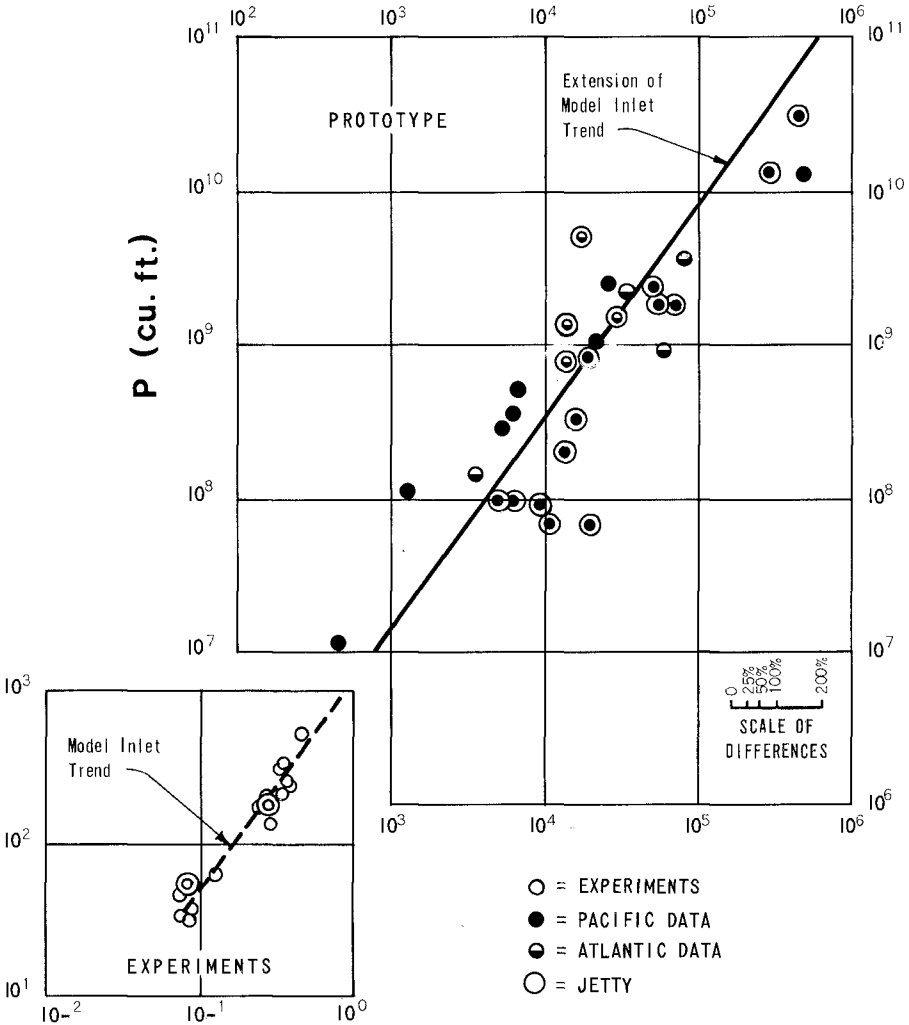
Fig. 12 — Relationship between minimum flow area and tidal prism (P)
for some North American inlets and model inlets under
tidal and wave actions.
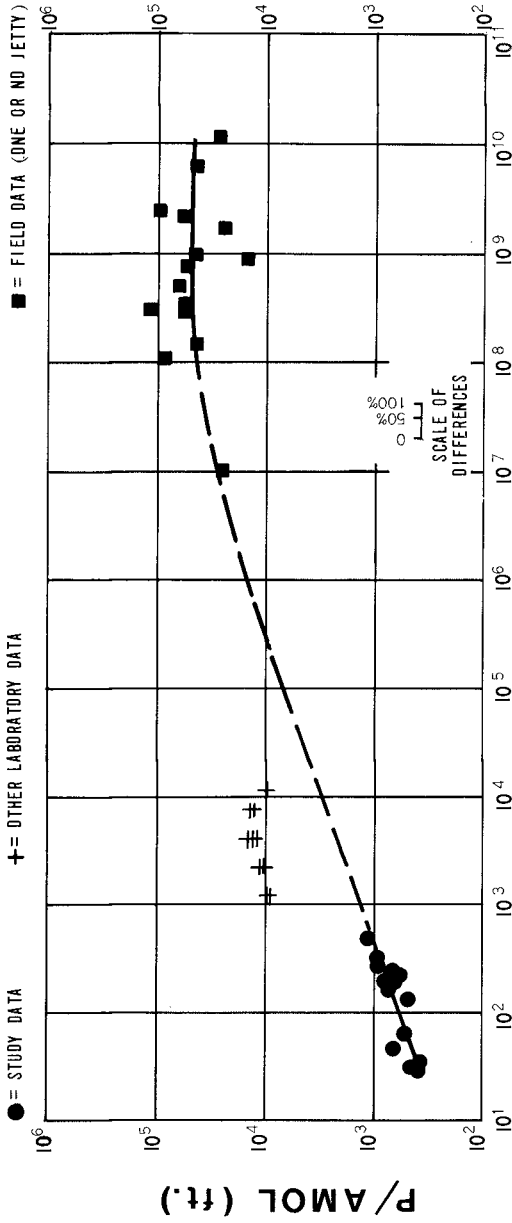
Fig. 13 — Ratio of tidal prism (P) to minimum flow area as a function of the tidal prism. Comparison of laboratory and field data. Dashed line is a rough extrapolation of model and field trends.

REFERENCES

1. Mayor-Mora, R., "Hydraulics of Tidal Inlets on Sandy Coasts",
    University of California, Berkeley, Hydraulic Engineering
    Lab. Report HEL 24-16, August 1973.

2. Keulegan, G.H., "Tidal Flow in Entrances. Water Level Fluctuations
    of Basins in Communication with Seas," U.S. Army Corps of Engineers
    Tech. Bull. No. 14, of the Committee on Tidal Hydraulics, July 1967.

3. Huval, C.J., and Wintergerst, G.L., "Numerical Modeling of Tidal
    Inlet Hydraulics by the Lumped Parameter Approach", U.S. Army Corps
    of Engineers, Waterways Experiment Station, Vicksburg, Miss., January
    1973 (Report draft).

CHAPTER 90

HYDRAULIC CONSTANTS OF TIDAL ENTRANCES

M. P. O'Brien[1] and R. R. Clark[2]

ABSTRACT

Data contained in the Tide Tables, Current Tables and navigation charts of National Ocean Survey pertaining to tidal entrances along the coasts of the continental United States are analyzed to obtain flow coefficients defined by a simple hydraulic equation. The evaluation of the published data indicates that the data are sufficiently accurate and representative, despite some unexplained anomalies, to permit determination of the approximate discharge coefficients and, more importantly, to identify categories of flow regimes of inlets. A few conclusions are:

1. The Keulegan approach and similar analyses of inlet hydraulics provide a useful qualitative framework for ordering data but they apply quantitatively only to small inlets and lagoons with simple inlet channel geometry.

2. The lag of slack water in the entrance channel after HW and LW is a powerful tool in the analysis of the hydraulic regime. It is easily measured in the field and should become an identifying characteristic of each entrance.

3. The resistance coefficient F represents the overall impedance and exit losses, reflections from the lagoon shore, fresh water discharge and the configuration of the channel between the inner and outer bars. It may be determined from measurements of lag and maximum velocity at the throat and the range of ocean tide.

[1]Professor/Consultant, Coastal and Oceanographic Engineering Laboratory, University of Florida; Dean Emeritus, College of Engineering, University of California, Berkeley.

[2]Engineer, Division of Beaches and Shores, Department of Natural Resources, State of Florida, Tallahassee; Formerly - Graduate Student, Civil and Coastal Engineering Department, University of Florida.

1. The tide in the lagoon continues to rise after high water in the ocean. Slack water occurs when the two curves intersect, and high waters and low waters around the lagoon occur at the same time. With reference to the definitions of Figure 1 the relevant equations are:

$$\eta_0 \;=\; \text{elevation of ocean tide} \;=\; a_0 \cos \sigma t \tag{1}$$

$$\eta_B \;=\; \text{elevation of tide in lagoon} \;=\; a_B \cos (\sigma t - \varepsilon)$$
$$=\; a_0 \cos \varepsilon \cos (\sigma t - \varepsilon) \tag{2}$$

$$2a_B \;=\; \text{range in lagoon} \;=\; 2a_0 \cos \varepsilon \tag{3}$$

Here, a_0 and a_B are the ocean and lagoon tidal amplitudes and $\sigma (= 2\pi/T)$ is the angular frequency of the tidal period T.

2. The driving head at any time t during the tidal cycle is:

$$\eta_0 - \eta_B \;=\; a_0 \cos \sigma t - a_0 \cos \varepsilon \cos (\sigma t - \varepsilon)$$
$$=\; a_0 \left[\cos \sigma t - \cos \varepsilon \cos (\sigma t - \varepsilon)\right] \tag{4}$$

Slack water occurs at $\sigma t = \varepsilon$
Maximum head occurs at $\sigma t = \varepsilon + \frac{\pi}{2}$
Maximum head = $(\eta_0 - \eta_B)_{max} = a_0 \sin \varepsilon$

These relationships follow directly from the assumption that the tide curves in the lagoon and the ocean are sinusoidal. If the friction loss in the entrance channel is quadratic, the maximum value of the velocity, averaged over the flow area, A_c, becomes

$$\overline{V}_{max} \;=\; \left[\frac{2g\, a_0 \sin \varepsilon}{F}\right]^{1/2} \tag{5}$$

where

$$F \;=\; k_i + k_e + \frac{fL_c}{4R_c} \tag{6}$$

Here, k_i and k_e are the inlet entrance and exit loss coefficients respectively, f the Darcy-Weisbach friction coefficient, R_c the hydraulic radius for the flow area, A_c and g is the acceleration of gravity.

The entrance and exit loss coefficients approximate unity. The quantity, L_c, is the length of a channel of area A_c which would have the same overall friction loss as the real channel. If the real channel with a length X_L has reasonably well defined boundaries, a value for L_c may be estimated as

$$L_c \;=\; \int_0^{X_L} \left(\frac{R_c}{R_x}\right)\left(\frac{A_c}{A_x}\right)^2 dx \tag{7}$$

$$f = (F - 1) \frac{4R_c}{L_c} \tag{8}$$

$$n = 1.48 R_c^{1/6} (\frac{f}{8g})^{1/2} \text{(Manning's coefficient).} \tag{9}$$

Keulegan (1967) recognized that quadratic friction causes the tide curve in the lagoon to depart from sinusoidal. He represented his results as functions of a repletion coefficient K defined as

$$K = \frac{T}{2\pi a_0} \frac{A_c}{A_B} (\frac{2ga_0}{F})^{1/2} \tag{10}$$

where A_B is the surface area of the lagoon. The quantities comprising K are the primary variables which must be known in order to determine the flow conditions in an inlet.

The quantity F, computed from Equation (5) employing measured values of $\overline{V}_{max}$, ε, and a_0, represents the effect of all influences restricting the flow and not merely the entrance and exit losses and the bottom friction. It should thus be regarded as the overall impedance of the inlet.

SOURCES OF DATA

Ideally, the data used to determine the hydraulic constants should include:

1. Measurements of the velocity across the throat section (representing the minimum cross-sectional area of the inlet) to fix the time of slack water after HW and LW and the average velocity over the throat area A_c at the time of strength of flood and ebb.

2. Concurrent measurements of the tide in the ocean sufficiently far from the inlet to avoid the effect of local drawdown.

3. Survey of the inlet channel at the time of velocity measurements.

There are very few entrances for which such complete sets of concurrent data are available.

The NOS (National Ocean Survey) Tide Tables and Current Tables are intended primarily as aids to navigation. They include the tide at only a limited number of stations on the open coast. Current data pertain to the navigation channel, usually the deepest part of the cross-section; however, the location of this current measurement may not have been at the throat. Evidently, these data are not ideal for determining the hydraulic coefficients but they do have virtue of representing the results of extended periods of measurement and of rigorous processing to obtain representative average values.

The tabulated tide and current data were analyzed as follows:

1. The tabulated strengths of ebb and flood currents (V_{max}) were averaged and multiplied by 0.85* to obtain $\overline{V}_{max}$, the maximum average velocity over the inlet cross-section.

2. The tide ranges at stations on the open coast were plotted against distance along the coast, and the ocean tide range applicable to each inlet was obtained by interpolation.

3. The times of HW and LW at the throat section were obtained by applying the tabulated time differences from the reference station.

4. The lags of slack water after HW and LW were determined by combining the data in the Tide Tables and Current Tables. At the primary stations, the lags were averaged over a period of one month; at the secondary stations, over a period of one week. The characteristics of the entrances selected for study are listed in Tables 1 and 2.

Equation (5) was employed to compute two sets of values of F as follows:

a. F was based on the mean range of tide, the average lag of slack water after HW and LW, and the average of the strengths of flood and ebb currents.

b. Daily predictions of tides and currents were used to determine the range, the strength of current, and the lag for the flood and ebb phases separately, in order to obtain values F_F (flood) and F_E (ebb) for each tidal cycle. Tables 3 and 4 show values of F_F and F_E averaged over a number of tidal cycles.

Entrances on the coast of the Gulf of Mexico were studied, and some data pertaining to them are included in the tables. However, the variability of tide range and the lag of slack water were too great to permit calculation of the hydraulic constants using the velocity data given in the Current Tables.

EVALUATION OF RESULTS

Friction Coefficients

Unfortunately, there are few entrances which have sufficiently regular channels to justify calculation of L_c, from Equation (7) and f and n from Equations (8) and (9). The seven entrances listed in Table 5 are the only entrances included in this study for which the configuration of the channel seemed to justify calculation of L_c.

---

*An estimate based on measurements in unidirectional open channel flow.

TABLE 1

ENTRANCE GEOMETRY AND TIDES FOR REFERENCE STATIONS

ENTRANCE	JETTIES	OCEAN TIDE MEAN RANGE $2a_o$ (ft)	THROAT SECTION AREA (MWL) A_c (ft²)	THROAT SECTION WIDTH W (ft)	THROAT SECTION MEAN DEPTH (ft)	THROAT SECTION MAX. DEPTH (ft)	RATIO OF WIDTH TO HYDR. RADIUS W/R_c	BAY (LAGOON) AREA (MWL) A_B (ft²)	BAY TIDE MEAN RANGE $2a_B$ (ft)
NARROWS	Bridge	4.5	305920	5000	61	103	82	N. A.	4.5
DELAWARE		4.4	2454900	64300	38	N. A.	1683	N. A.	4.9
CHESAPEAKE	Bridge	3.5	1890000	76000	25	60	3065	N. A.	2.4
CHARLESTON	2 Jetties	5.2	73450	2800	26	38	107	N. A.	5.2
SAVANNAH	2 Jetties	6.9	41050	1670	26	39	65	N. A.	7.4
ST. JOHNS R.	2 Jetties	5.4	49230	1580	31	36	51	N. A.	4.5
MIAMI	2 Jetties	2.5	18690	950	20	33	48	N. A.	4.5
MOBILE	Natural	1.3^a	228000	15300	15	60	1040	1.34×10^{10}	1.5
GALVESTON	2 Jetties	2.1^b	232920	6875	34	38	203	1.60×10^{10}	1.2
GRAYS	2 Jetties	6.4	262520	10200	26	48	397	(1.89×10^9)	7.2
HUMBOLT	2 Jetties	4.3	51900	2200	34	42	134	(5.67×10^8)	6.8
SAN FRANCISCO	Bridge	4.2	(931000)	(5270)	(177)	N. A.	30	N. A.	4.2
SAN DIEGO	1 Jetty	3.7	63670	1855	41	48	47	(4.75×10^8)	4.0

N. A. - Not Available

( ) - Data from other sources

a - Diurnal

b - Mixed

TABLE 2

ENTRANCE GEOMETRY AND TIDES FOR SECONDARY STATIONS

ENTRANCE	JETTIES	OCEAN TIDE MEAN RANGE $2a_o$ (ft)	THROAT SECTION				RATIO OF WIDTH TO HYDR. RADIUS W/R_c	BAY (LAGOON) AREA (MWL) A_B (ft²)	BAY TIDE MEAN RANGE $2a_B$ (ft)
			AREA (MWL) A_c (ft)	WIDTH W (ft)	MEAN DEPTH (ft)	MAX. DEPTH (ft)			
FIRE ISLAND	1 Jetty	4.1	35500	2600	14	18	188	2.45×10^9	0.7
SHINNECOCK	2 Jetties	3.0	5520	800	7	N. A.	116	3.14×10^8	N. A.
JONES	1 Jetty	4.2	28900	2500	13	24	195	4.78×10^8	2.4
E. ROCKAWAY	1 Jetty	4.5	10735	680	14	22	50	N. A.	3.9
ROCKAWAY	1 Jetty	4.5	82300	3060	27	48	114	6.27×10^8	5.2
MANASQUAN	2 Jetties	4.3	3530	360	10	N. A.	37	5.80×10^7	3.3
BARNEGAT	2 Jetties	4.3	12700	950	13	28	71	N. A.	0.6
INDIAN R.	2 Jetties	4.1	(5300)	500	11	N. A.	47	N. A.	0.9
HATTERAS	Natural	3.6	43050	8800	5	N. A.	1796	N. A.	<0.5
OCRACOKE	Natural	3.6	82200	6750	12	53	553	N. A.	<0.5
NEW RIVER N.C.	Natural	3.7	7950	600	11	N. A.	57	1.01×10^9	<0.5
ST. MARYS	2 Jetties	5.8	111440	3400	33	71	104	8.89×10^7	6.0
PORT ROYAL	Natural	6.4	513020	12830	40	60	321	N. A.	7.1
FT. PIERCE	2 Jetties	3.1	8950	900	10	23	91	1.27×10^9	0.7
LAKE WORTH	2 Jetties	2.8	19300	870	21	33	42	4.00×10^8	2.6
PORT EVERGLADES	2 Jetties	2.6	16600	800	27	N. A.	30	7.53×10^7	2.3
PENSACOLA	Natural	1.2^a	82850	2400	35	52	70	3.34×10^9	1.5

TABLE 3

INLET HYDRAULICS FOR REFERENCE STATIONS

ENTRANCE	$\bar{V}_{max}$ (NOS Current Tables) FLOOD (ft/sec)	EBB (ft/sec)	TIDAL PRISM HYDRAULIC - P_H (ft³)	VOLUMETRIC - P_V (ft³)	LAG OF SLACK - ϵ (°) ϵ_F	ϵ_E	ϵ AVG	IMPEDANCE - F F_F	F_E	F AVG
NARROWS	2.87	3.38	1.43×10^{10}	N. A.	67.1	66.8	67.0	22.9	16.4	19.2
DELAWARE	3.04	3.21	$\{9.29 \times 10^{10}$ (11.1×10^{10})	N. A.	35.5	42.8	39.2	13.3	13.5	13.4
CHESAPEAKE	1.69	2.54	6.30×10^{10}	N. A.	110.2	113.8	112	51.6	20.7	31.0
CHARLESTON	3.04	3.04	2.71×10^{9}	N. A.	27.8	27.0	24.4	7.4	6.3	6.8
SAVANNAH	2.70	4.39	1.76×10^{9}	N. A.	29.8	40.9	35.3	21.4	10.9	14.6
ST. JOHNS R.	3.21	3.89	3.03×10^{9}	N. A.	92.2	93.4	92.3	20.9	14.9	17.5
MIAMI	3.21	3.55	9.12×10^{8}	N. A.	55.1	58.1	56.7	9.3	7.0	8.0
GRAYS	3.21	4.73	1.26×10^{10}	1.36×10^{10}	15.1	20.3	17.7	7.9	5.1	6.0
HUMBOLT	2.70	3.80	2.50×10^{9}	$\{3.86 \times 10^{9}$ (3.03×10^{9})	11.5	18.4	14.9	4.6	5.5	5.1
SAN FRANCISCO	4.90	5.75	6.00×10^{10}	$\{$N. A. (5.1×10^{10}) 1.90×10^{9}	49.5	64.4	56.9	5.7	5.2	5.5
SAN DIEGO	2.03	2.54	1.97×10^{9}	1.90×10^{9}	8.5	13.9	11.2	6.2	7.0	6.7

( ) - Data from other sources

TABLE 4

INLET HYDRAULICS FOR SECONDARY STATIONS

ENTRANCE	$\overline{V}_{max}$ (NOS Current Tables)		TIDAL PRISM		LAG OF SLACK (°) ϵ AVG	IMPEDANCE F AVG
	FLOOD (ft/sec)	EBB (ft/sec)	HYDRAULIC - P_H (ft³)	VOLUMETRIC - P_V (ft³)		
FIRE ISLAND	4.06	4.06	$\begin{cases} 2.42 \times 10^9 \\ (2.23 \times 10^9) \end{cases}$	1.72×10^9	93.5	16.0
SHINNECOCK	4.23	3.89	$\begin{cases} 3.15 \times 10^8 \\ (3.06 \times 10^8) \\ 2.03 \times 10^9 \end{cases}$	N. A.	78.9	11.5
JONES	5.24	4.39		$\begin{cases} 1.15 \times 10^9 \\ (1.5 \times 10^9) \end{cases}$	48.7	8.8
E. ROCKAWAY	3.72	3.89	5.79×10^8	N. A.	31.7	10.5
ROCKAWAY	3.04	4.56	4.13×10^9	3.26×10^9	17.9	6.2
MANASQUAN	2.87	3.04	$\begin{cases} 1.52 \times 10^8 \\ (1.74 \times 10^8) \end{cases}$	1.91×10^8	50.6	16.9
BARNEGAT	3.72	4.23	7.40×10^8	N. A.	94.9	12.1
INDIAN R.	3.04	3.55	2.96×10^8	N. A.	65.8	15.3
HATTERAS	3.55	3.38	2.23×10^9	N. A.	103.8	13.0
OCRACOKE	2.87	4.06	4.26×10^9	N. A.	96.9	13.3
NEW RIVER, N.C.	1.86	3.04	2.90×10^8	$<5 \times 10^8$	112.4	24.4
ST. MARYS	3.89	4.39	5.58×10^9	5.33×10^9	30.2	7.6
PORT ROYAL	3.04	3.04	1.89×10^{10}	N. A.	31.3	16.6
FT. PIERCE	4.39	5.24	6.42×10^8	8.89×10^8	87.3	7.2
LAKE WORTH	4.06	6.08	1.34×10^9	1.04×10^9	57.7	5.9

TABLE 5

ENTRANCE FRICTION COEFFICIENTS

ENTRANCE	L_C (ft)	R_C (ft)	F	f	n
FIRE ISLAND	33100	13.8	16.0	0.025	0.022
E. ROCKAWAY	11100	13.7	10.5	0.047	0.022
INDIAN R.	4200	10.6	15.3	0.143	0.051
ST. MARYS	15200	32.8	7.6	0.057	0.039
LAKE WORTH	1900	20.9	5.9	0.220	0.071
HUMBOLDT	2690	17.9	5.1	0.110	0.049
SAN DIEGO	18860	40.9	6.7	0.049	0.038

The values of f and n listed in Table 5 are high as compared with the values frequently assumed in calculating hydraulic friction losses in tidal waterways. In this connection, the data for Indian River Inlet are of particular interest because Keulegan (1967) found f = 0.098 and n = 0.046 from velocity and surface elevation measurements there in the relatively uniform channel between the ends of the jetties and the seaward side of the bridge. The values listed in Table 4 (f = 0.143; n = 0.051) for Indian River Inlet include the losses at the jetty ends, through bridge piers, and in the irregular channel between the bridge and the bay, in addition to the losses in the channel where Keulegan obtained his data. The value of f obtained is inversely proportional to the computed value of L_c which is subject to considerable error because the end-points are seldom well defined.

Tidal Prism

An indication of the validity of the values of $\overline{V}_{max}$ used in determining F is provided by a comparison of the tidal prism computed from:

    a. The surface area and range of tide in the lagoon.

    b. Integration over the ebb or flood phase of the average velocity times the flow area, as given by Keulegan (1967):

$$P_H = \frac{\overline{V}_{max} \cdot A_c \cdot T}{C_K \cdot \pi} \tag{11}$$

The value of C_K as a function of K ranges from 0.81 to unity. Keulegan and Hall (1950) found that $C_K \approx 0.86$ gave good agreement with tidal prisms determined by velocity measurements. Applying this equaiton, the tidal prisms in Table 3 and 4 were computed. Comparison of the value of P_H with that determined volumetrically, P_V, gives:

Location		P_H/P_V
St. Marys		1.04
San Diego		1.04
Grays Harbor		0.93
Manasquan	(0.91)	0.79
Rockaway		1.26
Lake Worth		1.29
Fort Pierce		0.72
Mobile		0.63
Galveston		1.36
Fire Island	(1.30)	1.40
Humboldt Bay	(0.83)	0.65
Jones Inlet	(1.35)	1.77
Average	(1.06)	1.07

The values in parentheses are data from sources other than the Current Tables and Tide Tables, believed to be valid. The large discrepancy in the case of

Jones Inlet has not been explained; using a value of P_V supplied by the Long Island State Park Commission this ratio would become 1.35.

The average difference of 7 percent in the preceeding table is perhaps of little significance since P_H and P_V differ in some cases by as much as a factor of two. However, the sources of errors in each quantity should be recalled in assessing the results.

Regarding the accuracy of P_H, the velocity in the Current Tables (V_{max}) was multiplied in all cases by 0.85 to obtain the average velocity; the velocity may not have been measured at the throat section; and the flow area may have changed between the times of the survey and of the current measurements. For example, the flow area at the throat at Humboldt Bay entrance changed as follows:

Year	A_c
1911	51900 ft^2
1917	46480 ft^2
1935	66840 ft^2
1937	56510 ft^2

The ratio of the maximum (1935) to minimum (1917) area is 1.44.

The tidal prism based on lagoon area and tide range (P_V) is subject to considerable error because of the difficulty in determining the surface area at LW. The line of HW is clearly delineated on the charts but its position may be in error where the surveyor interpolated between tide gages - especially in flat terrain and with a decreasing tide range away from the inlet. Not all of the inlets studied could be included in this list, either because the low water area was ill defined or because of interconnections between lagoons.

Ratio of Ranges

The usual assumptions made in the hydraulic analysis of inlets include a sinusoidal ocean tide and a horizontal water surface in the lagoon. If these assumptions are satisfied, the ratio of ranges (a_B/a_0) should equal the cosine of the average lag of slack water (Equation (3)). A measure of the degree to which this assumption is satisfied is the difference in these quantities

$$\Delta = \frac{a_B}{a_0} - \cos \varepsilon \tag{12}$$

Figure 2 shows these data. The absolute size of the entrance is represented by the dimensionless ratio (A_c/a_0^2).

For small entrances, the values of Δ scatter around zero randomly, but there is an upward trend (dashed line) with absolute size and all of the large entrances show large positive values of Δ. Noteworthy is the fact that the range of tide inside but adjacent to the inlet equaled or exceeded the ocean range in a large number of the entrances studied. This

phenomenon was observed at the Narrows, Rockaway Inlet, Delaware Bay, Charleston Harbor, Savannah River Entrance, St. Marys River Entrance, Port Royal Sound, Pensacola Bay, Mobile Bay, Grays Harbor, Humboldt Bay, San Francisco Bay and San Diego Bay. This list includes entrances covering a wide range in absolute size, range of tide, overall resistance coefficient (impedance), and configuration of the inlet channel.

In all cases where the ratio of ranges (a_B/a_0) equaled or exceeded unity, cos ε did approach unity with the following exceptions:

Location	cos ε
The Narrows	0.39
Delaware Bay	0.77
San Francisco Bay	0.55

If the lag of slack water approaches 90°, the range of tide inside should approach zero, according to the hydraulic theory. Examples of entrances where the flow conditions differ markedly from this relationship area:

Location	Lag ε (deg)	cos ε	a_B/a_0
Chesapeake Bay	112	-0.37	0.68
St. Johns River	92	-0.04	0.83

Clearly, these entrances follow a regime differing fundamentally from that assumed in the hydraulic theory.

Times of HW and LW in Lagoon

If the water surface in the lagoon remains approximately horizontal during the tidal cycle, high waters should occur at the same time at all tide stations at the shores of the lagoon and concurrently with slack water after HW in the inlet channel; this same statement should be true for the times of LW. Examination of the data in Tide Tables shows that this phase relationship occurs at very few inlets, and that the usual situation is one in which the tide is not in phase across the lagoon. Consequently, the effective elevation of the water surface in the lagoon, a_B, differs from that obtained from continuity assuming a level surface. Compuations of the tidal prism on the basis of surface area and tidal ranges would require consideration of these phase differences.

Tractive Stress

An estimate of the maximum average tractive stress may be made for inlet channels which are sufficiently regular to permit computation of Manning's n as follows:

$$\tau_{max} = \gamma RS = \gamma \frac{\overline{V}^2_{max}}{C^2}$$

$$= \frac{\gamma}{2.21} \cdot \frac{n^2 \overline{V}^2_{max}}{R^{1/3}} \qquad (13)$$

Values of maximum tractive stress τ_{max} (where γ is the specific weight of water, C the Chézy coefficient, R the hydraulic radius and S the slope fo the enrgy grade line at the time of maximum velocity) computed by Equation (13) are:

Location	$\overline{V}_{max}$(ft/sec)	n	τ_{max}(lb/ft^2)
Fire Island	3.45	0.022	0.07
East Rockaway	3.23	0.022	0.06
Indian River	3.29	0.510	0.37
St. Marys	3.52	0.039	0.17
Lake Worth	5.07	0.071	1.37
Humboldt	3.25	0.049	0.28
San Diego	1.94	0.038	0.05

Reported values of the maximum tractive stress in the main channels of estuaries are in the range of 0.03 to 0.20; at the throat section, somewhat higher values probably occur. At Lake Worth entrance, the maximum tractive stress is high but this is so because the maximum velocity there is unusually strong. The other values seem reasonable, considering the nature of the data employed and the fact that effects other than friction resistance are lumped into Manning's n as determined in this study.

CATEGORIES OF ENTRANCES

The configuration of entrances on sandy coasts represents a dynamic equilibrium in response to influences which vary seasonally, annually, and over long periods. Wave climate, littoral transport, river sediment, range of tide, fresh-water runoff, wind drift, and even biological growth, superimpose shifts in this configuration upon the long range geological trend of change due to subsidence, uplift and sea-level change. Engineering works - jetties, dredging, river regulation, new inlets - initiate the approach to new equilibrium conditions. In a sense, each inlet is unique in its hydrodynamic and morphological regime, and generalizations about details of inlet behavior are dangerous - at least in the present state of our knowledge. However, this study has identified a few characteristics which permit a rough classification of inlets. Some examples of inlets in these categories will illustrate this point.

Inlets Exhibiting Simple Hydraulic Flow

The two inlets used to illustrate the analysis of the hydraulic flow regime - Absecon by E. I. Brown (1928) and Indian River by Keulegan (1967) - were very different in configuration and hydraulic characteristics. The approach developed in this paper will be applied both to compare the methods

and the quantitative results.

Absecon Inlet is not listed in the Current Tables, and this analysis is based on Brown's measurements. Brown determined the tidal prism, the maximum velocity, and the lag of tidal events in the lagoon by current measurement and found that the measurements agreed closely with his predicted values.

The ratio of the ranges of lagoon and ocean tides, assumed by Brown to be effectively the same for both channels, was 0.74; the theoretical values, equal to cos ε, were 0.70 for Absecon Channel and 0.74 for the Main Channel.

Absecon Inlet connects the ocean to a highly irregular system of channels and bays. At the time of Brown's study the inlet was unimproved and consisted of two channels - the Main or Thorofare Channel and the Absecon Channel. Quantities scaled from charts or measured at the throat section were:

	Absecon Channel	Main Channel
A_c (ft^2)	17,750	12,000
R_c (ft)	19.5	6.62
ε (°)	46.6	42.4
$2a_0$ (ft)	3.8	3.8
$2a_B$ (ft)	2.8	2.8
$\overline{V}_{max}$ (ft/sec)	3.00	2.46
L_c (ft)	35,000	10,000

The calculated resistance characteristics are:

	Absecon Channel	Main Channel
F	9.65	13.54
f	0.019	0.033
n	0.020	0.020
C (Chézy)	121	92

These values seem reasonable. Brown used C = 116 for the Absecon Channel and C = 85 for the Main Channel in calculating the tidal prism.

Indian River Inlet connects the ocean to Indian River Bay, which in turn is connected to Rehoboth Bay. The inlet channel is stabilized by two jetties, 1530 ft. in length; bridge piers obstruct the channel 1400 ft. from the seaward ends of the jetties. The study by Keulegan (1967) of this inlet was based on surveys and current measurements made prior to 1950. The data in the tide and current tables and published charts are of uncertain but later dates. There has been considerable shoaling in the inlet channel since Keulegan's study.

Oata listed in the 1973 Tide Tables and Tidal Current Tables and the derived coefficients are:

$$\bar{V}_{max} = 3.30 \text{ ft/sec (average of flood and ebb)}$$
$$\varepsilon = 65.8°$$
$$2a_o = 4.1 \text{ ft}$$
$$F = 15.30$$
$$f = 0.143$$
$$n = 0.051$$

These values of f and n are high as compared with other inlets, but they do include the loss through the bridge piers. If F and ε are constant characteristics of an inlet, the equation for $\bar{V}_{max}$ may be simplified for each inlet; for Indian River Inlet, $\bar{V}_{max} = (2ga_o \sin \varepsilon/F)^{1/2} = 0.24 \sqrt{2ga_o}$. This coefficient is exactly the same as that obtained by Keulegan. As noted previously, Keulegan computed the values of f and n for the channel between the ocean and the bridge, not including the friction and shock losses through the bridge piers using current measurements made from the bridge and tide records on the seaward side of the bridge. He obtained f = 0.098 and n = 0.046. These values are in reasonably close agreement with those obtained in this study.

Abnormal Tide Ranges in the Lagoon

As noted earlier, if the lagoon fills by "hydraulic flow", the ratio of the amplitude in the bay to that in the ocean should follow the relationship $a_B/a_o = \cos \varepsilon$ from Equation (3). This ratio should always be less than unity if the assumptions underlying the theory are fulfilled. Figure 2 shows that the discrepancy between a_B/a_o and $\cos \varepsilon$ is substantial at a majority of the inlets studied; in fact, few inlets exhibit good agreement in this respect.

There are many entrances and lagoons at which the range inside exceeds that in the ocean. One example of this effect is San Francisco Bay where the tide range at all points around the Bay proper exceeds that in the ocean. A smaller entrance showing the same effect is St. Marys River Entrance on the border of Florida and Georgia, where the ranges are as follows:

Location	Range	Oistance from Throat (n.m.)
Ocean	5.8	-
St. Marys	6.0	7

The hydraulic coefficients of this entrance are not unusual.

The cause of this behavior has not been determined. Convergence and shoaling of the channels, and resonance are possible causes. In any event, tide ranges in the lagoon exceeding the range in the ocean are a clear warning that the hydraulic regime does not conform to the "hydraulic flow" relationships; if the range in the lagoon is less than that in the ocean, this
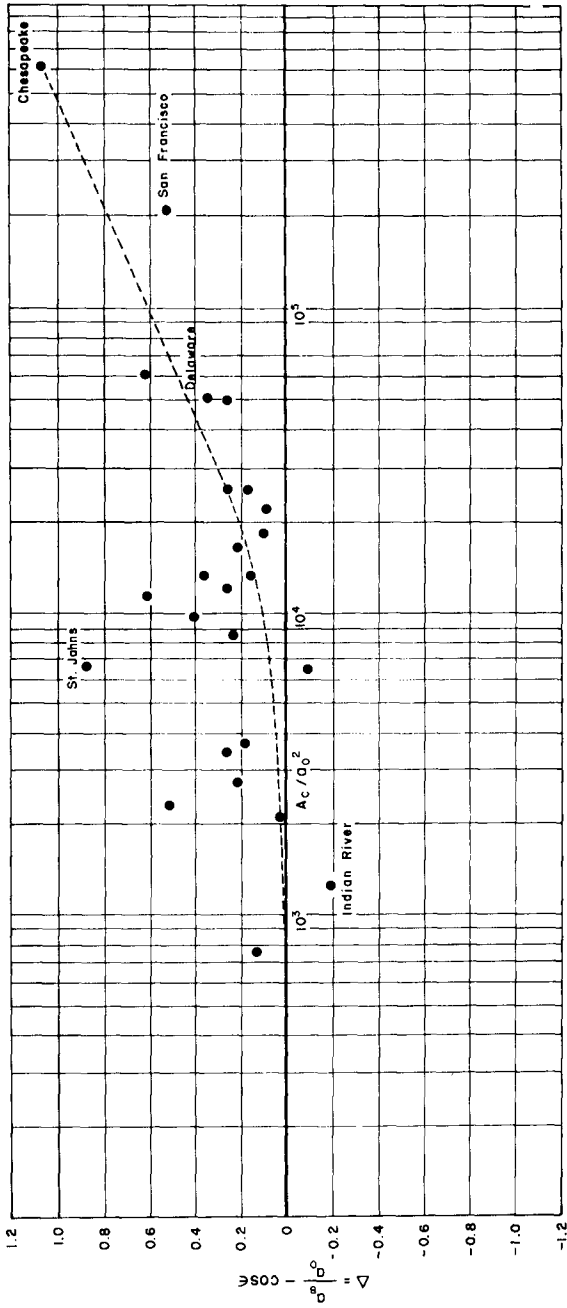
Figure 2   Degree of Deviation from "Hydraulic Flow" Represented by $\hat{\Delta}$, as a Function of $A_c/\hat{a}_0^2$.

effect may nevertheless be present and may increase the range above the theoretical value.

These facts lead to the conclusion that the ratio of ranges is not, in general, a reliable indicator of the flow conditions in an entrance.

Very Large Lagoon Area

If the ratio of the surface area of the lagoon to the flow area of the inlet (A_B/A_C) is very large, the repletion coefficient (Equation (10)) should be small, the lag of slack water should approach 90 degrees, and the range of tide in the lagoon should approach zero. The effective surface area A_B may be only a fraction of the total surface area of the lagoon if the lagoon is shallow; each element of the tide wave advances across the lagoon at the celerity $\sqrt{gh}$ (where h is the depth) and the tidal prism is bounded by the amplitude a_B and a horizontal dimension equal approximately to $T\sqrt{gh}/4$. Flow through the inlet is limited by a backwater effect induced by the limited depths.

The inlets to Pamlico Sound (Oregon, Hatteras, Ocracoke, and others) exemplify this type of flow regime. The hydraulic characteristics of two of these inlets are:

Location	Mean Ocean Range (ft)	Lagoon Range (ft)	$\overline{V}_{max}$ (average flood and ebb) (ft/sec)	ϵ (deg)	F
Hatteras	3.6	<0.5	2.05	104	13
Ocracoke	3.6	<0.5	2.05	97	13

These two inlet differ greatly in width and depth.

Flow Through the Entrance as a Shallow Water Wave

Under the assumption of hydraulic flow through an entrance, the range of tide inside should decrease as the lag of slack water after HW increases towards 90 degrees. Conversely, if the propagation of the tide through an entrance has the properties of a shallow-water wave, the lag of slack water should be approximately 90 degrees, and the range should not be reduced in passing through the inlet; strength of current should occur at approximately HW and LW.

St. Johns River Entrance (Florida) is an example of flow through an entrance which is of a fundamentally different character from the "hydraulic flow" usually assumed. The width and depth of the river for some miles above the mouth are approximately constant; apparently, the tide advances through the entrance as a wave with the strength of ebb and flood currents occurring at LW and HW almost exactly.

As Figure 2 shows, the degree of departure from hydraulic flow increases with absolute size of the entrance. Probably, all but the smallest entrances exhibit a mixed flow regime with both "tide-wave" and "hydraulic" effects present in the current velocity tide range re-lationships.

REFERENCES

Brown, E. I., "Inlets on Sandy Coasts," Proc. ASCE, Vol. 54, p. 505, 1928.

Castãner, P. F., "Selected Bibliography on the Engineering Characteristics of Coastal Inlets," HEL-24-7, Hydr. Engr. Lab., U. C. Berkeley, Aug., 1971.

Chapman, S., "Fluctuation of Water-Level in a Tidal Power Reservoir," Phil. Mag. Sixth Series, Vol. 49, p. 501, 1923.

Dean, R. G., "Hydraulics of Inlets," U. of Florida (Unpublished), 1971.

Keulegan, G. H., and Hall, J. V., Jr., "A Formula for the Calculation of Tidal Discharge Through an Inlet," B. E. B. Bulletin, Vol. 4, No. 4, July, 1950.

Keulegan, G. H., "Tidal Flow in Entrances: Water Level Fluctuations of Basins in Communication with the Seas," Tech. Bull. No. 14, Committee on Tidal Hy-draulics, Waterways Experiment Station, July, 1967.

CHAPTER 91

EVALUATION OF OVERALL ENTRANCE
STABILITY OF TIDAL ENTRANCES

P. Bruun[1], F. Gerritsen[2] and N.P. Bhakta[3]

ABSTRACT

This paper is written in continuation of earlier published
material (2, 4, 5) dealing with stability of tidal inlets on
littoral drift shores. The experience available at that time
was responsible for the introduction of two parameters:
$V_{mean\ max}$, defined as the mean max. velocity in the gorge at
spring tide and the Ω/M_{tot} ratio (tidal prism at spring tide
divided by material transport to the entrance from the ad-
joining shores) as the most pertinent parameters for descrip-
tion of overall stability. A more detailed justification for
this choice is given in this paper, based on computation of
the relative sediment transport at various tidal phases.
Examples of earlier date (4) and twelve new examples from
India are given.

DISCUSSION ON THE JUSTIFICATION OF
DESCRIBING THE RELATIVE ENTRANCE STABILITY OF TIDAL INLETS
IN ALLUVIAL MATERIAL BY $V_{mean\ max}$ AND THE Ω/M_{tot} RATIO

$V_{mean\ max}$ is equal to Q_{max}/A where Q_{max} is the mean maximum
discharge at spring tide and A is the cross sectional gorge
area at M.S.L. The Ω/M_{tot} ratio (Ω = tidal prism at spring
tide, M_{tot} = the total quantity of drift carried to the en-
trance per year or other time period) is related to the over-
all stability of the channel (2, 4, 5). There is an almost
linear relationship between $V_{mean\ max}$ and A. According to
experiences (2, 4) large Ω/M_{tot} ratios make the entrance
channel flush well, while low Ω/M_{tot} ratios cause the build-
up of entrance bar(s) for material which is bypassing.

The question is: Do these two criteria for the description
of stability present an oversimplification of a complex pro-
blem of the same character as some other (exponential) rela-
tion between the tidal prism and gorge cross-sectional area,
ignoring the obvious relation between flow and sediment
transport?

While the first method of approach ($V_{mean\ max}$ and Ω/M_{tot}) may
be expanded to give more details relating these factors to
more detailed parameters, the second approach (tidal prism Ω
versus gorge area A) cannot possibly give reliable results
although they are convenient for a first approximation and
easy to "prove" repeatedly. Another drawback is that such
overall considerations must disclose odd cases which do not
fit into the picture. Two entrances with the same general

[1]Dept. of Ocean Engineering, The Norwegian Institute of
 Technology, Trondheim
[2]Dept. of Ocean Engineering, The Univ. of Hawaii, Honolulu
[3]Director, Preinvestment Study of Fishing Ports, FAO, UN,
 Bangalore, India

flow characteristics, but with different inputs from the sea, cannot be expected to have the same degree of stability because small sediment inputs to the channel obviously does not call for the same "effort" by inlet currents to flush the channel for these sediments as large inputs, for which more flow energy is needed for the "cleaning-action". Material in a tidal entrance is flushed out at either end of the channel and comes to rest on shoals on the bay side, and also often on the sea side or on both sides. If there were no input of littoral drift material to the channel, the channel would gradually approach a non-scouring condition (2). If the input of littoral drift material is heavy nature must administer the available flow energy to ensure that the cross-section is maintained most economically with minimum loss of flow energy.

GENERAL DISCUSSION OF STABILITY

With reference to Figure 1, the stability of an inlet at location (x) may be defined by

$$\frac{\partial S}{\partial x} = 0 \tag{1}$$

in which S is the bed material transport. This criterion may be utilized to analyse the conditions for stability.

In order to do this it is advantageous to use the total concentration of sediment load as a transport parameter and to write

$$S = Q\, c_T \tag{2}$$

whereby c_T is the total average sediment concentration in a given cross-section.

Applying the stability criterion $\frac{\partial S}{\partial x} = 0$ to this expression we find

$$\frac{\partial S}{\partial x} = Q\, \frac{\partial c_T}{\partial x} + c_T\, \frac{\partial Q}{\partial x} = 0 \tag{3}$$

This expression can now be further developed.

If waves have little or no influence on the magnitude of the total sediment transport, it is attractive to use Yang's unit stream power concept for the computation of the sediment transport.

In Yang's paper (12) an expression for the total sediment concentration is submitted:

$$\log c_T = \alpha + \beta \log(VS - VS_{cr}) \tag{4}$$

in which α and β are coefficients. Using V (average velocity), S (slope), and A (cross-section) as independent parameters, and assuming that VS_{cr} (critical unit stream power per sec) is small compared to VS, under maximum flow conditions, equation (4) may be reduced to

$$-\frac{1}{A}\frac{\partial A}{\partial x} + 3 c_T \beta\frac{\partial v}{\partial x} + c_T \frac{\partial v}{\partial x} = 0 \tag{5}$$

The solution of this equation requires some additional information (input) regarding the shape of the inlet ($A_x = f(x)$) and the supply of sediments from the littoral drift (c_T at $x = 0$).

Further analysis leads to a relationship of the following type

$$V_m = \frac{Q_m}{A} = f(\eta, x, S_m, (V_o c_{T_o}),) \tag{6}$$

in which

Q_m = maximum discharge
η = shape factor (e.g. $A = A_o e^{-\eta x}$)
x = distance from entrance
S_m = slope of water level during maximum current conditions
$V_o c_{T_o}$ = sediment discharge at $x = 0$ per unit of surface area

Since $S_m = \frac{\tau_m}{\rho g h}$ the slope component also represents the maximum bottom shear stress in the cross-section.

Of particular interest in this relationship is the dependency of V_m (stable conditions) on $\frac{\tau_m}{h}$ and $V_o c_{T_o}$, the first representing the shear stress per unit of volume and the second representing a measure of input of sediment into the inlet at $x = 0$ (the entrance). This is discussed later in the paper. The parameter τ_m/h indicates that the depth of the inlet channel may affect the stability shear stress as defined in earlier papers (2, 4) and proved earlier in the slight dependency of $V_{mean\ max}$ upon depth (4, p 133).

In the entrance current and wave action join forces in the transport. (This mechanism, discussed earlier (4, p 114), will be mentioned in detail in a paper in progress. It has been omitted for reasons of space).

Gorges are usually protected to some extent against wave action for which reason it is the tidal (and other) currents which are the main flushing agents. This is well demonstrated at many tidal entrances, e.g. in the Thyborøn Channel on the Danish North Sea Coast (2, 4). This inlet, cut by nature in 1862, and navigable a few years later, was continuously bothered by a large offshore bar with a controlling depth of only about 10 ft. The bar was the result of heavy wave action and heavy littoral drift to the inlet entrance from both sides. Close to one million cubic meters of sand material a year is transported into the inlet and deposited on extensive bay shoals.

Fig. 2 shows the variation of gorge sections I of the inlet
during the period 1887 to 1970. After 1892 important dredg-
ing operations were started on the outer bar. This is clearly
reflected in the increasing cross-section. Since it became
difficult to keep up with the extremely heavy littoral-drift
deposits, a different strategy was adopted. Dredging was
transferred to the bay shoal main channel(s). The result was
that the controlling depth on the outer bar increased to 15
feet and is now at least 20 feet and mostly close to 30 feet
or more. Construction in the early 1920's of a 3,000-foot-
long jetty on the northern barrier of the inlet further im-
proved this situation.

The inlet channel gradually adjusted itself to the actual
current and wave situation. Table 1 shows some cross-sectional
areas of varying exposure to wave action (Fig. 2). Comparing
characteristics of gorge section I to similar entrances (2, 3,
4, 5) it may be noted that the gorge area is below average size.
Taking into account that almost one million cubic meters of
sand material is carried through each year this cross-section
for depositing on inlet shoals, it seems likely that normal
stability velocities may have increased a little because of
the heavy material load. Since the gorge has very steep slopes,
its shape factor, as compared to other inlets, has apparently
improved, too.

The relative stability of cross-sectional entrance areas is as
mentioned in ref. 4, a result of combined wave and current
action producing shear stresses which determine the cross-
sectional area and its stability under varying wave and current
exposure.

TABLE 1   CROSS-SECTIONAL AREAS OF THYBORØN CHANNEL (FIG. 2)

Approximate cross-sectional areas (m^2)
$V_{mean\ max}$ (m/sec)

	I GORGE	II	III
m^2	5,000	5,500	8,000
Material load per year	~3/4 million cu.m	~3/4 million cu.m	~3/4 to one million cu.m
Wave action during storms	light to moderate	moderate	heavy
$V_{mean\ max}$ m/sec	~1,05	~0,95	~0,65
T_s kg/m^2	~0,5 kg	~0,4 kg	~0,2 kg

The variation of cross-sectional area of improved inlet channels
is dealt with in Fig. 3 (2) where, for a number of American in-
lets with parallel jetties, the cross-section has been plotted
along the length of the inlet channel in a dimensionless diagram.
Information on actual data is given in Table 2 of ref. 2. The

cross-sections (A) at different locations have been divided
by the cross-section at the entrance (A_O) to obtain a dimen-
sionless ratio, using the relative distance from the seaward
end (x/L) as the second parameter.

From Fig. 3 it may be seen that the entrance cross-sections
generally are greater than the cross-sections in other parts
of the channel. The presence of wave action apparently de-
creased the bottom stability because orbital velocities due
to the wave action increased bottom shear stresses., resulting
in greater cross-sections near the entrance of the channel and
thereby a smaller "apparent" stability velocity and shear stress
corresponding to the tidal flow only (ref. 4 gives details of this).

Fig. 3 reveals that Fernandina Harbor (St. Marys River entrance,
North Florida) does not follow "normal practice". The jetties
protecting the entrance are parallel in length for 2,500 ft, but
diverge further inland. In Fig. 3 the length "L" of the jetties
refers only to the parallel sections in the entrance, which
differ from the other inlets in that the width is very large
(3,900 ft) in comparison to the length of the parallel part.
Waves, therefore, can easily enter the harbor and the energy
loss towards the entrance jetties and beaches along the channel
is therefore relatively small.

These examples clearly demonstrate - just as in the case of
Thyborøn Channel - the importance of the bottom shear veloci-
ties for material movement. The input of material to the ent-
rance from the adjoining ocean shores must therefore also be an
important factor.

The question which hereafter arises is that velocities are
defines as "mean max". It is therefore of interest to appraise
the error which may result by computing bed load transport based
on a criterion only considering a mean velocity occuring at one
particular time when it attains its maximum value at springtide.

$V_{mean\ max}$ - The situation apparently is: First we say V_{mean}
next $V_{mean\ max}$ and finally we define $V_{mean\ max}$ at spring tide.
Regarding V_{mean}: Consider a schematic cross-section of a tidal
entrance, Fig. 4. A few isovels have been drawn and shear
stresses acting on the bottom may be computed. Splitting the
cross-section in these parts and assuming an average velocity of
1 m/sec over the entire cross-section shown in Fig. 4, the average
velocity may approximate 0.9 m/sec in the section closest to the
bank and 1.1 m/sec in the middle. As velocities along the slop-
ing banks are smallest, this section carries relatively less
bed load transport per unit width of bottom.

Assuming (according to eq. (7) mentioned later) that bed load
transport $\sim V^5$, the error by using 1 m/sec instead of an inte-
grated V^5 over the entire bottom may be evaluated by an expres-
sion like

$$V^5_1 \quad + \quad V^5_2 \quad + \quad V^5_3$$

$$\frac{\text{bank} \quad \text{middle} \quad \text{center}}{\text{section} \quad \text{section} \quad \text{section}}$$
$$3$$

which for

$$V_1 = 0.9, \quad V_2 = 1.1 \text{ and } V_3 = 1.1 \text{ m/sec}$$

is 1.07 or 7% increase compared to $V_{ave} = 1$ m/sec or about
15% increase of the bottom shear stress. If the difference
between side and middle section is as much as 0.4 m (1.2 –
0.8) the error is about 27% for the shear stress. Smaller
deviations from the 1 m/sec average velocity will only cause
minor deviations. In all cases the increase in velocity needed
to flush away the surplus material will be of the order of
magnitude mentioned above, 5 to 10%, corresponding to an in-
crease in bottom shear stress of 10 to 20%, which means that
the error obtained by using the average velocity for the entire
cross-section will only be small. This is true whether $V_{mean\ max}$
is 0.9 m/sec, 1.0 m/sec or 1.1 m/sec. Reference is made to
the following section on Ω/M_{tot}.

$V_{mean\ max}$ is in this connection defined as the mean of the max
current over a certain period of time (2-3 hours) at spring
tide conditions and it always seems to be in the range of av.
0.9 m/sec to ab. 1.1 m/sec. The explanation of the ab. 1 m/sec
is partly given in refs. (2), (4) and (5) as a result of the
fact that a sand bottom for these velocities becomes "smooth"
i.e. ripples disappear and low dunes develop which become in-
creasingly lower with increasing velocity until finally anti-
dunes develop. $V_{mean\ max} = 1$ m/sec is located in that part
of the "transition zone" when ripples have vanished and dunes
still developing smoother with increase of velocity, appear.
This situation is discussed below.

Next: Why only use the max velocity? This question obviously
must be discussed in relation to the sediment transport in the
channel.

The problem of start of bed load transport has been dealt with
in numereous publications referring to stream flow (1). At
tidal inlets in alluvials the situation is that bottom material
is derived from shores and beaches on either side of the ocean
entrances. Sand matcrial of 0.1 - 0.3 mm will therefore begin
to move when mean velocities close to the bottom are about
0.3 m/sec (1 ft/sec). This velocity depends to some extent
upon grain size and depth (2, 10). At 0.3 m/sec bottom starts
developing ripple marks.

When the velocity exceeds about 0.6 m/sec (2 ft/sec) ripples
become flatter and are gradually replaced by dunes until the
bottom becomes almost flat at 0.9 m/sec - 1.2 m/sec (3-4 ft/sec).
During that process bed load transport increases very rapidly as
the full shear stress at a still increasing extent is exerted
directly upon the bottom (2, 4). For example, bed load transport

increases from approximately 100 pp m to 3,000 pp m (4,
Fig. 38) when velocity increases from 0.5 m/sec to 1.0 m/
sec.

The ASCE Committee on Sedimentation discusses various sedi-
ment discharge formulas (1). These formulas are not idential
in detail but a feature that those which the Committee con-
siders being the most reliable have in common (e.g. those by
Engelund and Hansen, Toffaletti and Colby), is that the sedi-
ment discharge is largely a function of the bed shear stress
raised to the 2.5 power, although this relationship may not
be expressed directly. For example the Engelund-Hansen for-
mula states:

$$g_s = 0.05 \; \gamma_s V^2 \sqrt{\frac{d_{50}}{g(\frac{\gamma_s}{\gamma}-1)}} \left[\frac{T_o}{(\gamma_s-\gamma)d_{50}}\right]^{3/2} \tag{7}$$

when g_s = sediment transport per unit width per unit time
      V = mean velocity
      T_o = bed shear stress = $\rho u_*^2 = \frac{\rho g V^2}{C^2}$
      γ_s = specific gravity of sediment
      γ = specific gravity of fluid
      d_{50}= mean full diameter of bed sediment
      g = acceleration of gravity
      C = Chezy's friction coefficient

Engelund and Hansen, however, do not recommend their formula
for cases in which the median size of the sediment is less
than o.15 mm; the geometric, standard deviation of the grain
size is greater than approximately 2 and T_* is less than 0.15
kg/m². These conditions are undoubtedly fulfilled for all
tidal inlets on alluvial shores when grain size usually ranges
from 0.15 - 0.3 mm; sand is well graded and T_* is somewhere
between 0.04 and 0.06 kg/m².

For tidal entrances subjected to flow due to simple harmonic
semi-diurnal tides, and in cases when the connecting channel
has a simple geometry, the velocity of the flow is approxi-
mately proportional to $\sqrt{\sin\theta}$ when θ is the tidal phase angle.
The sediment discharge therefore depends approximately upon
$\sin^2\theta\sqrt{\sin\theta}$. Integrating this expression for various phase
intervals it may be noted that about 80% of the sediment
transport takes place between the velocity phase angles 70
and 110 degrees, when velocities vary between about 85 to 90%
and 100% of the peak velocity occurring at the 90 degree
velocity phase angle. This general result indicates that the
mean max velocity occurring for about one hour and a quarter
on either side of the peak velocity may be considered an im-
portant flow parameter in describing the equilibrium condition
between flow and sediment movement, and consequently for de-
scription of bottom stability. The situation, needless to say,
depends upon details of the actual tidal fluctuations and the
specific time interval during which velocities are equal to or

exceed about 85 to 90% of the peak velocity. During that
period the "stable" entrance channel is flushed for all or
for the larger part of the material which was deposited in
the entrance during the slack water period. Normally most
or all of this material is derived from the littoral drift
zone on one or on either side of the entrance. $V_{mean\ max}$,
however, refers to spring tide (2, 4).

Tidal range for spring tide conditions is usually of the
order of 30 to 50 per cent higher than for mean tidal range
conditions, but these conditions are subjected to seasonal
variations with max range at the two equinoxes. The max
current velocities may then increase 10 to 15 per cent and
the tidal prism perhaps a little more. This in turn means
that bed load transport during the peak period may be twice
as high as during mean tidal conditions. This situation
lasts a few days only during the 28 days moon cycle. One
may expect the gorge cross-sectional area increases slightly
during this period, which to some minor extent compensates
for the increase in velocity. It is probably not essential
whether "normal mean high" or "spring mean high" velocities
are used for description of the stability. If this were the
case the effect could be expected to be relatively largest
for entrances with small tidal range which should then demon-
strate somewhat higher mean max velocities. Based on the
presently available survey material such effect has not (yet)
been noted. It may be within the range of a number of other
deviations. Consequently, it must also be less important
whether it is the mean Ω at spring tide or the high Ω at max
spring tide that has to be considered; the important conside-
ration is that it has to be the same general tidal conditions
for all entrances to make comparisons possible.

The conclusion is apparently that $V_{mean\ max}$ at spring tide
seems to be a useful parameter for description of the cross-
sectional stability of a tidal inlet entrance channel.

Ω/M_{tot} - An evaluation of the Ω/M_{tot} ratio must of necessity
include an evaluation of the overall material transport in the
gorge. The general rule is that in the gorge almost all trans-
port of sand > about 0.01 mm takes place as bed load transport
while finer particles < 0.06 mm including silt and clay, if
present, may be transported mainly in suspension.

Consider a tidal entrance which is subjected to input of
littoral drift from the adjoining shores.

Mathematically the situation may be described as:

$$\frac{dS}{dt} = \frac{dM}{dt} \tag{8}$$

which expresses that the increase in sediment transport shall
be equal to the increase in input of sediments from the seashore,
M. This definition implies that the quantity of sediment trans-
port in the inlet channel as well as the input of littoral
transport to the channel (eq. 3) is known.

With regard to channel transport the situation is: When flow
velocity increases beyond the limiting velocity for material
movement bed load transport starts and the entire surface layer
of the bottom moves forwards and backwards with the ebb and
the flood current. In a stable channel currents have to <u>carry
away</u> the surplus material which is deposited during slack
water and which is attempting to choke the channel. In numeri-
cal form eq. (8) be written:

$$\Delta S(t) = \Delta M(t) \tag{9}$$

where ΔS is the increase in sediment transport per unit time
which is necessary to cope with the input per unit time of
sediment from the littoral drift zone of the adjoining shores.
"Unit time" may for e.g. be chosen to be a tidal period. The
number of those per year for semi-diurnal conditions is approxi-
mately 680. Consider an input of littoral drift material to
the entrance,350,000 m^3/year,the quantity of material is a
practical figure referring to conditions on the US East Coast
and at many places elsewhere. This material which has to be
removed during each half tidal cycle is approximately 500 m or

$$\Delta S \sim 500 \ m^3$$

The cross-sectional area may under simplified conditions be
computed as:

$$A = \frac{\pi \Omega C_2}{T} \tag{10}$$

when Ω is the tidal prism, C_2 is a coefficient varying between
0.8 and 1.0 and T is the tidal period (7).

As mentioned earlier, experience shows that the Ω/M ratio for
a relatively stable gorge channel is > 150 (2, 4). With Ω/M =
150, Ω would be 150·350,000 = 5.3·10^7 corresponding to a A =
$Q_{mean \ max}$ (mean max discharge at springtime) = $\frac{\Omega C_2 \pi}{T} \approx 3,400 \ m^2$
assuming that the mean max $\sim$ 1 m/sec (2, 4). No general figure
can be given for the depth over width ratio. For the improved
inlets in Florida it is 0.03 - 0.04. For the unimproved ent-
rances it is of the order 0.01 - 0.02. Assuming a ratio of
0.02 for A = 3,400 m^2 this corresponds to a gorge of about
500 meters wide and 8 m deep (4, Table 18). The increase in
sediment transport due to the input of littoral drift material
must be approximately 1 m^3 (500/500) per meter per tidal cycle.
1 m^3 $\sim$ 2 tons of sand.

Using a mean max velocity of approximately 1 m/sec in the
Engelund-Hansen formula, eq. (7) one has with $d_{50} \sim$ 0.0002 m,
γ_s = 2.65 gr/cm^3, γ = 1 gr/cm^3, g_s = 0.5 kg/sec/m

As mentioned above, high velocity flows (about 0.9 - 1.1 m/sec)
run for about 2 - 3 hours in each half tidal cycle, which
means that a total of 60·60·0.5·2.5 = 4.5 tons is transported
per 2.5 hour period per meter. If this quantity is increased
by another 2 tons the current velocity obviously must be
increased. The increase must correspond to an increase in

transport of about 45%. As bed load transport depends upon the bottom shear stress in about the 2.5th power (1) this means that the mean bottom shear stress must increase about 20%. If this is correct one should be able to detect that kind of difference in mean max velocity which, however, only needs to be about 10% higher when comparing non-protected tidal entrances with jetty protected entrances.

It is therefore very interesting to note the situation at some hydraulically rather well defined tidal entrances mentioned in Table 2 (Table 18 of ref. 2).

TABLE 2   COMPARISON BETWEEN THE MEAN MAX VELOCITY IN JETTY
          PROTECTED AND IN ENTRANCES WITHOUT JETTIES (2)

Entrance	T mean max	in kg/m²
Grays Harbor, Wash.	0.49	jetties
Port Aransas, Texas	0.46	-
Calcasieu Pass, La.	0.45	-
Thyborøn, Denmark	0.49	- Ave. 0.47
Longbout Pass, Fla.	0.55	no jetties
Big Pass, Fla.	0.55	-
East Pass, Fla.	0.54	-
Ponce De Leon, Fla.	(0.48)[x]	- Ave. 0.55
		(0.53)

[x] (large shoals - jetties built in 1970-1972)

Although the material in Table 2 is meager, there is probably an indication that the mean max bottom shear stress for stable conditions are somewhat (about 10 - 15 per cent) lower for jetty protected entrances than for non-protected. This corresponds to an increase of bed load transport of about 35 - 40 per cent against 45% mentioned above. In the case considered, about 350,000 m³ is transported by ebb and by flood currents every year. With about 40% increase this means that 140,000 m³ extra is flushed and consequently about 140,000 m³ or conversly about 40% has to be kept back by jetties or transferred mechanically if the extra flushing is to be avoided or is unobtainable.

Table 3 of ref. (4) lists a few practical examples from Florida (inf. by the U.S. Army Corps of Engineers, Jacksonville District, Florida). It may be noted that inlets with long jetties bypass 80% (by ebb currents mainly), inlets with short or medium about 40% and inlets with "very short" jetties about 20%.

These figures are interesting in that it may be seen how inlets with jetties are able to bypass by flushing relatively more material after they have been protected by jetties which on the one hand retain part of the surplus littoral drift which bothered the gorge channel and on the other hand concentrate the flow. In the latter case wave action was helpful in bypassing or otherwise leaving the material where the stream power was higher than on the shores of the channel, thereby increasing the rate of flushing.

TABLE 3   PREDOMINANT DRIFT QUANTITY AND BYPASSING DRIFT
          FOR SOME JETTY-PROTECTED INLETS IN FLORIDA (4)

Inlet	Jetty Length	Drift Total per year	Drift Bypassed per year	Bypassed Total max.	Bypassed or flushed by tidal flow
Jupiter	very short	225,000	150,000	60%	ab. 20%
Sebastian	short	300,000	200,000	60%	30% to 50%
South Lake Worth	medium	180,000	ab. 90,000 flushed sea- and bayward	50%	ab. 50%
Palm Beach[x]	long	225,000	ab. 175,000 flushed sea- and bayward	(80%)	(ab. 80%)
Ft. Pierce	very long	250,000	200,000	80%	ab. 80%

[x]Condition 1964-1965

From the above-mentioned and numerous similar cases it may
be concluded that generally the major part of the sediment
transport in a tidal inlet is "native inlet material" which
is moved forwards and backwards with the tidal currents.   In
addition littoral drift material which moves in "from the
side" is being flushed by the inlet currents.   The question
still remains: Is the Ω/M_{tot} ratio a useful parameter for
describing the relative stability of the inlet gorge channel?

As explained in detail in ref. (4), the quantity of material
transported as bed load is independent of depth when the mean
velocity is about 1 m/sec (See Fig. 5 from ref. (4)).

This in turn means that the total sediment transport (bed load)
is proportional to the width (W) of the gorge channel (cross-
sections of similar geometry considered).   As explained earlier,
an average of 80% of the transport takes place when the max
velocity is between 85% to 90% and 100% of the peak velocity.
For wide inlet channels of mean depth D one has:

$$S + M \sim W \tag{11}$$

or drift of "native material" plus input of littoral drift
material is proportional to the width of the channel.

But $W \cdot D = A \ (=\frac{\pi \Omega C}{T}^2)$

$W \sim D$ for similar cross-section
$W^2 \sim \Omega$
$W = S + M \sim \sqrt{\Omega}$

$$\frac{\Omega}{M} \sim \frac{(M+S)^2}{M} \tag{12}$$

From this expression it may be seen that Ω/M_{tot} is high when
M << S and Ω/M is low when M >> S.   From this follows that the
Ω/M ratio may be expected to be a useful parameter to describe
the relative stability of the gorge cross-sectional area for

wider channels. This is also true for narrower channels when
S + M is rather proportional to A ~ Ω which means that Ω/M ~
M + S/M = 1 + S/M, which supports the conclusion for wide
channels.

The following section considers some practical $V_{mean\ max}$ and
Ω/M_{tot} ratios.

EXAMPLES OF THE USE OF THE $V_{mean\ max}$ AND Ω/M_{tot}
CRITERIA IN SOME TIDAL INLETS IN INDIA'
THE UNITED STATES AND EUROPE

Table 4 lists tidal entrances in India located on the
Arabian Sea as well as on the Bay of Bengal. These inlets
were all studied under the Preinvestment Study of Fishing
Ports, a joint project of the Indian Government and the
Food and Agricultural Organization of the United Nations.
Some of the information was derived from existing sources,
e.g. the Poona laboratory.

In some cases e.g. at Beypore, data on tidal prism and flow
were available from earlier surveys. In others, e.g. at
Malpe, new surveys were undertaken. Half of the cases which
are listed in Table 4, however, were not surveyed and esti-
mates therefore were based on local information and overall
inspections. The results from these cases must therefore be
considered with some reservation with respect to reliability.
All figures refer to the situation at the gorge channel and
its immediate vicinity and not to offshore conditions when the
influence of tidal currents have vanished.

It is interesting to note, however, that the mean max velocity
for the inlets which have been surveyed in detail or at least
to some extent varies from 0.9 to 1.2 m/sec. The average of
five gorges which were surveyed in more detail is 1.02 m. In
no case - whether surveyed in detail or not - was the mean max
velocity lower than 0.9 m/sec or higher than about 1.2 m/sec
refering to the situation(s) mentioned in Table 4. It is
necessary to distinguish between monsoon and non-monsoon
periods.

Consider the Ω/M_{tot} ratio it may be noted that entrance
conditions may be classified in three main groups: Those (11
and 12) which are protected by rock reefs functioning as break-
waters, for which reason they are not bothered by heavy littoral
drift deposits. Their Ω/M ratio is 100-150 even if tidal prism
is only medium. The next catagory which has Ω/M ratios of 50-
100 has in some cases large offshore bars (1, 3, 7, 8) but
these bars can usually still be passed by shallow draft vessels,
including fishing boats. These entrances have medium to large
tidal prisms.

The third catagory (2, 4, 5, 6, 9, 10) is characterized by
comprehensive bars with very shallow depth. They are "bar-
bypassers". Almost all of them have relatively small tidal
prisms and $\Omega/M < 50$ and mostly even ≤ 20. Some depend upon

flushing during the monsoon, and are closed during the non-
monsoon period. Others are mainly stable during the non-
monsoon period when littoral drift is minimum. All cases
refer to the relatively most stable condition of the entrance
not the offshore channel during the seasons. Averaging
figures over e.g. one year makes no sense under the climatic
conditions in India. Comparison is made with the entrances
listed in Table 5 (Table 13 of ref. 2) comprising a number
of tidal inlets in the United States and in Europe.

In Table 5 entrances with relatively satisfactory and stable
entrance conditions (1, 2, 5, 6, 7, 8, 10, 11, 12, 13, 14,
15, 16, 17, 18, 21, 22, 23) all have $\Omega/M > 150$. Those with
"fair conditions" have $100 \leq \Omega/M \leq 150$ (3, 22). Entrances
with conditions between "fair" and "poor" (19) have $50 \leq$
$\Omega/M \leq 100$ and those with "poor" conditions (4, 9, 20) have
$\Omega/M < 50$. Of these, Brielse Mass has been closed, Figueira
Da Foz has been improved by jetties and Ponce De Leon has
been improved by jetties and a submerged weir in the north
jetty. There therefore seems to be good agreement between
"the Indian experience" listed in Table 4 and the combined
"European-American experience" listed in Table 5.

The conclusion of these investigations, therefore, is that the
Ω/M_{tot} ratio seems to be a fairly reliable parameter for the
description of the overall stability of a tidal entrance on
an alluvial shore. Reference is still only made to the sta-
bility of the gorge channel and not to the outer part of the
channel which does not carry concentrated channel flow.
This problem will be dealt with in a forthcoming paper. This
outer part of the channel may be subjected to deposits carried
to the entrance by offshore shore-parallel currents or flushed
out by ebb currents. This is typical for a number of tidal
inlets in India, e.g. for Nos. 1 and 8 of Table 4. Wave
action, however, will as demonstrated in the above-mentioned
Thyborøen Inlet in Denmark and at inlets in Florida and else-
where, be able to assist the tidal currents in keeping the
outer part of the channel free of deposits (4). Still, there
is the possibility that a moderate-size bar may form where
entrance tidal currents meet sediment laden longshore currents.
This is mainly characteristic for entrances with $\Omega/M_{(tot)}$
ratios of 100 to 150 and relatively larger inputs of sediments.
As proven by Shemdin and Dane (9), a bar may also cause a pile
up of water (changes of slope) in the lower part of the outlet.
This, in turn, decreases the discharge and contributes to
further deterioration of the entrance.

Design procedure - With respect to design procedure for improve-
ment one must distinguish between preliminary and detailed de-
sign. For preliminary design one may proceed as follows (4, 5):

(1) Secure all available information on Ω (tidal prism),
$Q_{mean\ max}$ (mean max discharge under spring tide conditions).
Compare Ω, $Q_{mean\ max}$ and other Q's by computation and current

velocity measurements in the gorge channel. Evaluate bay
(lagoon) tidal range based on experience from cases of
similar tidal range and similar geometry of bay (or lagoon).

(2) In layout, use straight or almost straight channel
boundaries to avoid scour on one side and deposits on the
other side of the channel in bends.

(3) Evaluate M_{tot} as closely as possible e.g. based on
experience from neighbouring shores. Check the Ω/M ratio.
Observe its seasonal changes and pay particular attention to
its lowest value(s). If littoral drift formulas are used,
check with 2 - 3 of them.

(4) Evaluate the most likely $V_{mean\ max}$ based on experience,
considering the local littoral drift capacity.

$$V_{mean\ max} = 1 \text{ m/sec} \pm \alpha \text{ m/sec} \quad \alpha = 0.1 \text{ to } 0.2 \text{ m/sec}$$

(5) Initially, use an overall relationship between tidal prism
and cross-sectional area of gorge:

$$A = \frac{\Omega}{V_{max}} \frac{C_2 \pi}{T} \qquad C_2 \approx 0.9$$

Compute $Q_{max} = A V_{mean\ max}$

(6) Design cross-section, horizontal bottom, slope 1 in 5
(sand bottom) or 1:X, X = slope of training wall or jetty.

(7) Check velocity distribution. Use one of the available
theories (as e.g. explained in refs. 2, 4 with references).

(8) Check $V_{mean\ max}$ again. Adjust gorge area to selected
$V_{mean\ max}$ in greater detail with respect to velocity distri-
bution.

(9) Check Q_{max} and Ω by detailed computation.

(10) If Ω thereby decreases below acceptable value consider-
ing the Ω/M_{tot} ratio, try to increase Ω by increasing A and
repeat computations listed above. Observe the seasonal changes
in Ω/M_{tot} with special reference to low values.

(11) If Ω cannot possibly be increased, try to decrease the
active M_{tot} by jetties, traps, or by an entrance geometry
better suited for effective flushing, if possible. For de-
tailed design model experiments may be advantageous or neces-
sary to secure the most desirable velocity distribution in the
inlet channel as a whole, as well as in the cross-section.

(12) In the case of improvement of an existing inlet, use
tracer experiments to clarify littoral drift pattern and if
necessary also the littoral drift quantity, the latter being
subject to long-time experiments. Use experience values if
available or energy flux considerations as mentioned in pre-
vious section.

(13) One may finally try to compute the bed load transport
in the gorge channel e.g. by using Engelund and Hansens (7)
procedures for bed-load transport and compare quantity with
littoral drift quantity.

When it comes to detailed design, the tidal hydraulics
computations may be undertaken according to Dr. Dronker's
theories (4). Owing hysteresis effect (4, Fig. 35), the time
period when the bottom is covered by well developed ripples
is relatively short and it may be assumed that the bottom is
smooth or only slightly undulated for velocities exceeding
0.5 m/sec (assuming fine and medium size sand). Friction
factors of C = about 45 $m^{+\frac{1}{2}}$ sec^{-1} therefore prevail for at
least two thirds of the tidal cycle and C = about 35 $m^{\frac{1}{2}}$ sec^{-1}
for the remaining period.

Most often the detailed design of a tidal inlet on a littoral
drift shore depends upon the results of a hydraulic model
study. For fixed bed flow studies adequate model laws are
available. This is not yet the case for movable bed studies.
One is here faced with a tedious calibration procedure which
may be based on a known time-history and/or the results of
tracer experiments and other results of sediment transport or
semi-theoretical investigations or procedures. The general
knowledge on the behaviour of tidal inlets as described above
is helpful, however, in determining the reliability of the
model and its reproduction of conditions in the prototype.
Field studies, however, are all important. From them we learn
generalizations and their variances.

LIST OF REFERENCES

(1)   ASCE, Task Committee on Sedimenttransport, 1971, "Sediment
              Transporation Mechanics: Sediment Discharge
              Formulas", Proc. ASCE, Journ.Hyd.Div. No. HY4,
              pp 523-567.
(2)   Bruun, P. and Gerritsen, F., 1960, "Stability of Tidal
              Inlets", North Holland Publishing Company, 130 pp.
(3)   Bruun, P. and Battjes, J., 1963, "Tidal Inlets and Littoral
              Drift", Proceedings IAHR, London 1963, Paper 117
(4)   Bruun, P., 1967, "Tidal Inlets and Littoral Drift",
              University Book Company, Oslo, 220 pp.
(5)   Bruun, P., 1973, "Port Engineering", Chapter 8 on "Tidal
              Inlets", Gulf Publishing Co., Houston, 440 pp.
(6)   Haynie, R.M. and Simons, P.B., 1968, "Design of stable
              channels alluvial streams", Proceedings ASCE,
              Journ.Hyd.Div. No. HY6, pp 1399-1420.
(7)   Keulegan, G., 1951, "Third Progress Report on Tidal Flow in
              Entrances", Nat.Bureau of Standards, Rep.No. 1147.
(8)   Philpott, K.L., 1963, "Basic experiments on the development
              of coastal inlets with and without wave action",
              Internat.Association of Hydraulic Research
              Congress, London 1963, Paper 1.39.
(9)   Shemdin, O.H. and Dane, K.A., 1971, "Laboratory simulation
              of formation and flushing of sand bars at river
              mouths", Proceedings, 14th IAHR congress, Paris.
(10) Simons, D.B., Stevens, M.A. and Duke, J.H., "Predicting
              Stages on Sand-Bed Rivers", Proceedings ASCE, Journ.
              of the Waterways, Harbors and Coastal Engineering
              Division, Vol. 99 No. WW2, May 1973, pp 231-243.
(11) Vollmers, H., 1973, "NATO advanced study institute on
              Estuary Dynamics", Seminar, Lisbon June-July 1973.
(12) Yang, C.T.Y., "Unit stream power and sediment transport"
              Journal of the Hydraulics Division, Proceedings
              American Society of Civil Engineers, Vol. 9.8,
              No. HY 10, October 1972, pp 1805-1026.

TABLE 4

TIDAL ENTRANCES AT INDIA
HYDRAULIC AND CROSS SECTIONAL CHARACTERISTICS RELATED TO OVERALL STABILITY

m = monsoon
n = non-monsoon
su = surveyed
e = estimated by computation
s = spring

Name of entrance or inlet	Tidal range s spring n normal m	Ω 10⁶ m³	A m² at MSL	Q_max m³/sec	M 10⁶ m³ per year net total Drift is almost uni-directional M - M_tot	V mean max	Depths, m gorge MLW	Depths, m bar MLW	Note m/M	
(1) Beypore (estuary)		16 m, 5 nm (e+su)	1,000 / 300		0,2	1,0 (su)	6-7 / 5-6	1,5-2	~ 80 m	Comprehensive bar
(2) Chandipur (estuary)	s 4	5 (e)			0,25	1,2 (e)		0,9-1,2	~ 20	Comprehensive bar very shallow
(3) Honavar (estuary)		≤ 20 (su)	800 nm, 1400 m, 1,000 su		0,2	1,2 su	5-7 su	2 su	50-100	Bar
(4) Kalingapatam (estuary)		1 nm (e)		1,000 su	0,1 (nearshore)	-			10-20	Comprehensive bar very shallow
(5) Krishnapatam (estuary)		(10) (e)	500 m, 500 ± nm		0,5-0,7	1,2 m	(0,5-1)	~ 0,5	10-20	Comprehensive bar very shallow
(6) Machilipatam (estuary)		10 (e+su)			0,2 (nearshore)	-	~ 2	~ 1	20-50	Comprehensive bar very shallow
(7) Malpe (estuary)	s 1,2	5,8 (su)	350 ± su	350 su	0,1	1,0 su	2-3 su	1-1,5 su	~ 60	Bar
(8) Neandakara (estuary)		(9) (e+su)	(600)		0,2	0,9 (su)			~ 50	Bar
(9) Nizampatam (estuary)		1-1,5 (su)	~ 70 × su		0,1 (nearshore) 0,3-0,4	1,0 su	3 su	max 1,5 su	10-20	Comprehensive bar very shallow
(10) Ponnani (estuary)		~ 3 (e)	300 m + nm		0,2			0,5-1 m / 2-2,5 nm	10-20	Comprehensive bar very shallow
(11) Sapati (estuary)	s 4,0	~ 15 (e)			0,1 to the entrance		3		100-150	Protected by rock reefs
(12) Versova (estuary)		~ 6 (e)	400 ±	0,05-0,1	0,05-0,1	0,9 (e)	3-4		100-150	Protected by shore rock
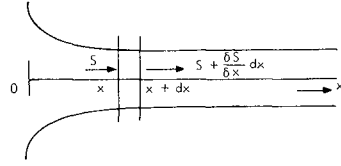
Fig. 1   Tidal Entrance Equilibrium.Schematics
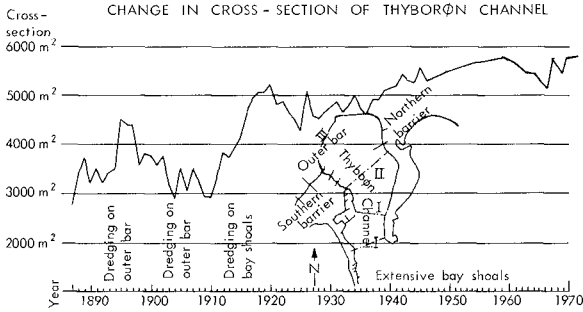
FIG. 2. DEVELOPMENT OE THE GORGE OF THYBORØN INLET ON THE
DANISH NORT SEA COAST. (ref.2)
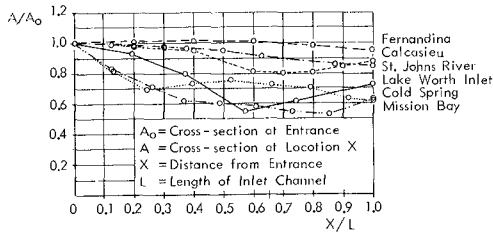
FIG. 3. CROSS - SECTION AREAS BELOW M.L.W. FOR SOME
JETTYIMPROVED INLETS. (ref.2)

TABLE 5   FLOW AND LITTORAL DRIFT CHARACTERISTICS FOR SOME
TIDAL INLETS IN THE UNITED STATES AND EUROPE (2)

	Inlet (Kind of Improvement)	Ω^{*} Tidal Prism cu yd/half cycle	Q_{max} Maximum Discharge cu yd/sec	M^{**} Littoral Drift cu yd/year	$\frac{\Omega}{M}$
(1)	Amelandse Gat, Holland (Bank stabilization on north side)	600×10^6	36,600	1.0×10^6	~600
(2)	Aveiro, Portugal (jetties)	80×10^5	$5,000^{1)}$	$1,3 \times 10^6$	~60
(3)	Big Pass, Florida (None)	12×10^6	700	$<0.1 \times 10^6$	>120
(4)	Brielse Mass, Holland before closing (Closed)	40×10^6	2,700	1.0×10^6	~40
(5)	Brouwershaven Gat, Holland (before closing, closed)	430×10^6	30,000	1.0×10^6	~430
(6)	Calcasieu Pass, La. (diurnal) (Jetties and Dredging)	110×10^6	2,600	0.1×10^6	$~550^{2)}$
(7)	East Pass, Florida (diurnal) (Dredging)	60×10^6	1,720	0.1×10^6	$~300^{2)}$
(8)	Eyerlandse Gat, Holland (None)	270×10^6	19,000	1.0×10^6	~270
(9)	Figueira Da Foz, Portugal (Dredging)	20×10^6	1,200	0.5×10^6	~40
(10)	Fort Pierce Inlet, Florida (Jetties and Dredging)	80×10^6	3,700	0.25×10^6	~320
(11)	Gasparilla Pass, Florida (None)	15×10^6	900	$<0.1 \times 10^6$	>150
(12)	Grays Harbor, Washington (Jetties and Dredging)	700×10^6	48,000	1.0×10^6	~700
(13)	Haringvliet, Holland (before closing, closed)	350×10^6	25,000	1.0×10^6	~350
(14)	Inlet of Texel, Holland (Stabilization on south side)	1400×10^6	115,000	1.0×10^6	~1400
(15)	Inlet of Vlie, Holland (None)	1400×10^6	110,000	1.0×10^6	~1400
(16)	Longboat Pass, Florida (None)	30×10^6	1,400	$<0.1 \times 10^6$	>300
(17)	Mission Bay, California before dredging (Jetties and Dredging)	15×10^6	1,100	0.1×10^6	~150
(18)	Oosterschelde, Holland (Will be closed)	1400×10^6	100,000	1.0×10^6	~1400
(19)	Oregon Inlet, N.Carolina (Occasional Dreging)	80×10^6	5,100	1.0×10^6	~80
(20)	Ponce De Leon Inlet, Fla. (before improvment)	20×10^6	1,500	0.5×10^6	~40
(21)	Port Aransas, Texas (diurnal) (Jetties and Dredging)	60×10^6	1,900	0.1×10^6	$325^{2)}$
(22)	Thyborøn, Denmark (Minor Dredging)	140×10^6	7,500	1.0×10^6	~140
(23)	Westerschelde, Holland (Some dredging)	1600×10^6	115,000	1.0×10^6	~1600

* Total amount of littoral drift interfering with the inlet may
deviate from this value if drift direction is too predominant
or if the inlet is improved by long jetties and/or bypassing
* Spring tide   1) Increasing   2) $\Omega/2M$, diurnal tide

FIG. 4. Tidal channel with a few Isolines for
Velocities drawn. Schematics.
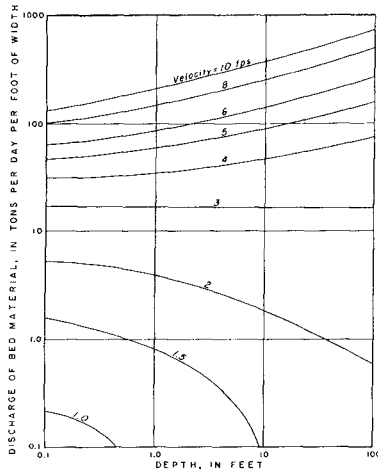
Fig. 5   Effect of Depth on the Relationship
between Mean Velocity and Empirically Determined
Discharges of Bed Material (0.3 mm medium diameter)
at 60 degrees F.   (Ref. 3, Colby, 1964)

CHAPTER 92

Channel Stability in Tidal Inlets: A Case Study

Robert J. Byrne
Virginia Institute of Marine Science
Gloucester Point, Virginia, U.S.A.

Joseph T. DeAlteris
Dames and Moore, Inc.
Cranford, New Jersey, U.S.A.

Paul A. Bullock
Institute of Financial Planning
Omaha, Nebraska, U.S.A.

Abstract: Wachapreague Inlet, a downdrift offset inlet in the barrier island complex of the mid-Atlantic U.S. coast was studied during the period 1971-1973. Elements of the study included: (1) the inlet morphometric history (120 years), (2) assessment of surficial and sub-bottom sediments within the inlet complex, (3) response of the channel cross-sectional area to short-term variations in wave activity and tidal volumes, and (4) the distribution of tidal flows within the channel.
    It is concluded that: (1) a qualitative correlation exists between short-term channel cross-sectional area change and the ratio of ebb tidal power to wave power. It is inferred that the important element is the direct wave activity on the ebb-tidal delta; (2) duration differences in rising and falling phases of the tide (flood longer than ebb) lead to an ebb dominence in bedload capacity at the inlet with the result that this inlet has a natural flushing ability; (3) there is pronounced sand circulation within the inlet complex via a sediment flow loop which is driven by wave refraction and lateral inflow on the up-drift side. The sand volumes thus delivered annually to the inlet channel from the ebb delta appears to far exceed the estimated littoral drift. The local sand circulation should, therefore, be considered in engineering design for inlet control structures.

I INTRODUCTION

Although the behavior of tidal inlets has been widely studied there are many knowledge gaps which preclude predicting the details of behavior for any given natural inlet [2, 3, 7, 15]. In general the cross-sectional stability of an inlet is understood to represent a balance between the advection of sand by littoral drift to the inlet and the scouring capability of the hydraulic currents generated at the inlet. Most of the previous work has cast the problem in terms of regional littoral drift rates and gross hydraulic characteristics. The objectives of the present study are:

1.) To document the short-term response in the inlet channel cross-sectional area as effected by variations in wave activity and tidal prism which arise from storm activity and fortnightly variations in tide range, and to relate the responses to these process variables [13, 14].

2.) To develop a qualitative model for sediment circulation within the inlet complex which is internally consistent with both the short-term channel response and the recent history (120 years).

Wachapreague Inlet, in the barrier island chain of the lower Delmarva Peninsula (Figs. 1 and 2), was selected as it has had a relatively stable and well defined channel for the past century and it appears to be a good example of the offset inlets common to this barrier chain.

II METHODS

In order to ascertain the changes in cross-section areas at different positions in the inlet channel range lines were established on the north shore of Parramore Island at an interval of 200 meters (Fig. 3). During operations the sounding boat progressed across the inlet on a range line while distances from the shore were recorded as horizontal angles, the baseline of which was 400 meters. Repetitive surveys over 10 range lines were conducted 46 times during the thirteen month study period August 1971 through September 1972. Since the position of the inlet throat changed with time three ranges (2, 22, 22A) were established to accommodate the shifts in position. The echo sounder was calibrated for each survey using a bar check and all soundings were corrected to mean tide level.

The precision of the profiling technique was tested by running ten consecutive profiles within a one hour time span at Range 22. The mean area was 4,596 m^2 with standard deviation of 62 m^2.

Additional input data to the study consisted of continuous current velocities at one point in the inlet throat (0.6 depth) and tide gage recordings at the inlet and at the town of Wachapreague. Daily visual wave observations were obtained from the Coastal Engineering Research Center (U.S. Army Corps) observers on Assateague Island, some 45 km to the north.

Discharge gaging was performed at Ranges 22 (inlet throat) and 8. Six buoyed stations were occupied at each range throughout the tidal cycle and the mean velocity over the vertical was sampled at each station every 0.5 hr.

The storage system with which the inlet interacts is complex as there are channels connecting with the adjacent inlets: the leakage to adjacent inlets is small, however. Even more important is the fact that the storage area does not remain constant with increase in tide stage since channels, tidal flats and lagoons and then extensive marshes become sequentially flooded. In order to determine the storage characteristics the area serviced by the inlet (Fig. 4) was sequentially photographed from low to high water using black-white infra-red film. Flooded area was thus determined as a function of tide stage. The stored water volume as a function of tide stage at the town of Wachapreague is shown in Fig. 5. The tidal prism for any given tide could then be estimated as the difference in volume stored at high and low water.

III CHARACTERISTICS OF THE SYSTEM

Inlet Morphology, Recent History and Sediments. Wachapreague Inlet is a downdrift offset inlet with a well-developed crescentic ebb tidal delta which has remained unchanged in position and development over the last 120 years. The flood induced deposits on the interior of the throat have diminished over the last 120 years, particularly since 1934. The channel axis has migrated to the south over the last
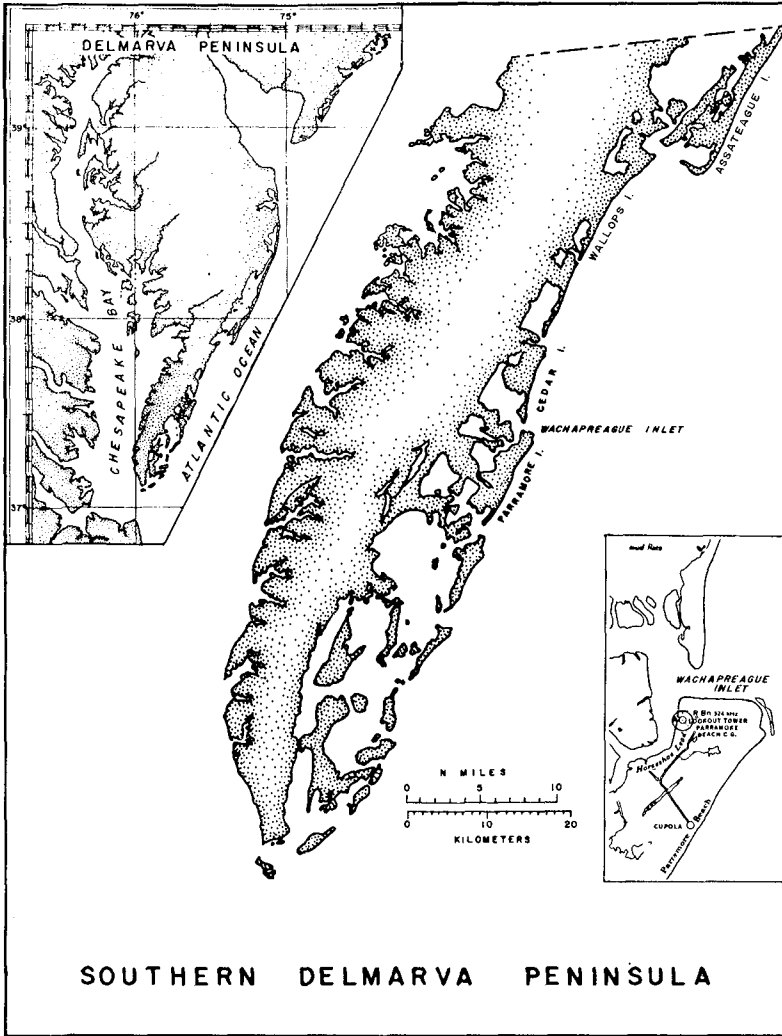
Figure 1. Lower Delmarva Peninsula. Extreme upper is lower
           Assateague Island and Fishing Point, a recurved spit.
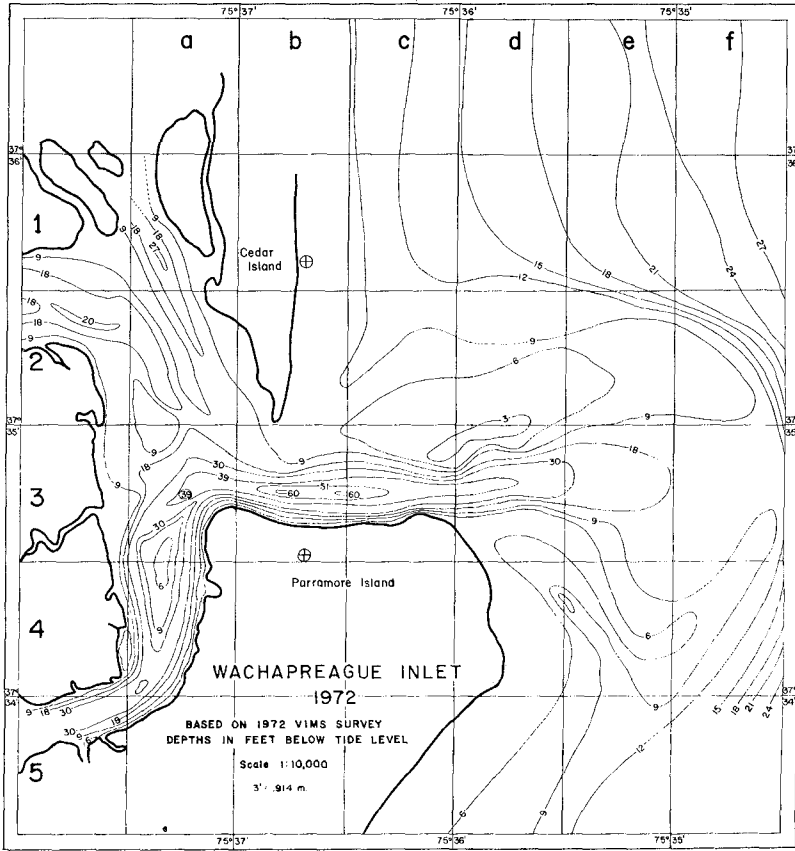
Figure 2. Wachapreague Inlet complex, 1972 survey. 1 minute of latitude = 1.83 km (6,000 ft.).
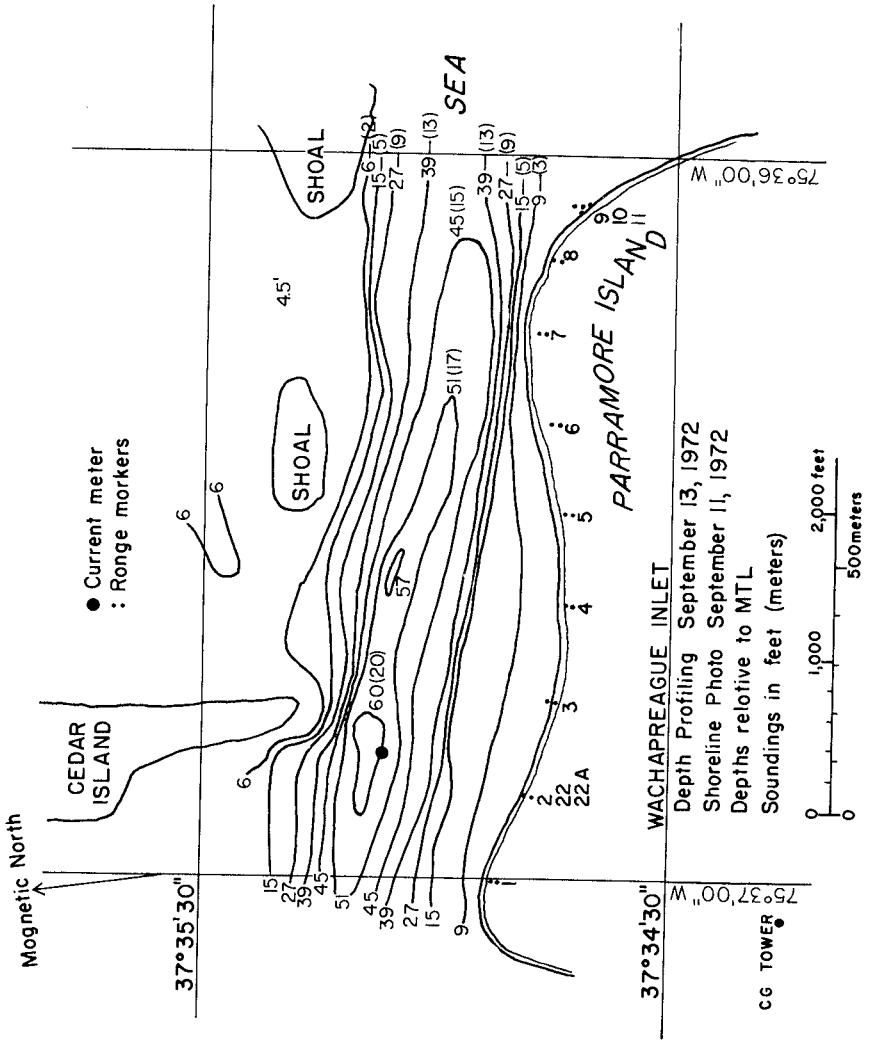
Figure 3. Wachapreague Inlet channel. Note shelf on south and asymmetry of channel cross-section. Numbers on south shoreline are survey range line positions, 1 through 11.
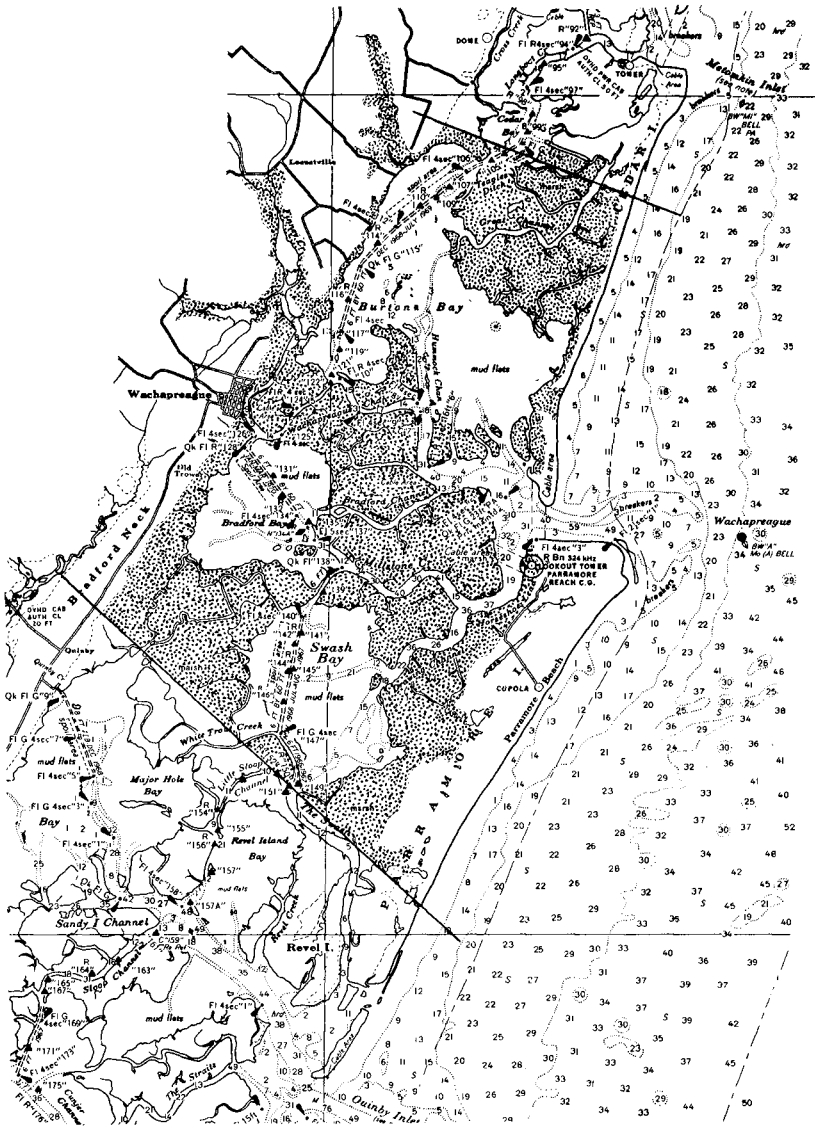
Figure 4.   Wachapreague Inlet storage system.   Stippled areas are
marsh.   Distance between latitude coordinates = 18.3 km.
From U.S.C. & G.S. Chart 1221.
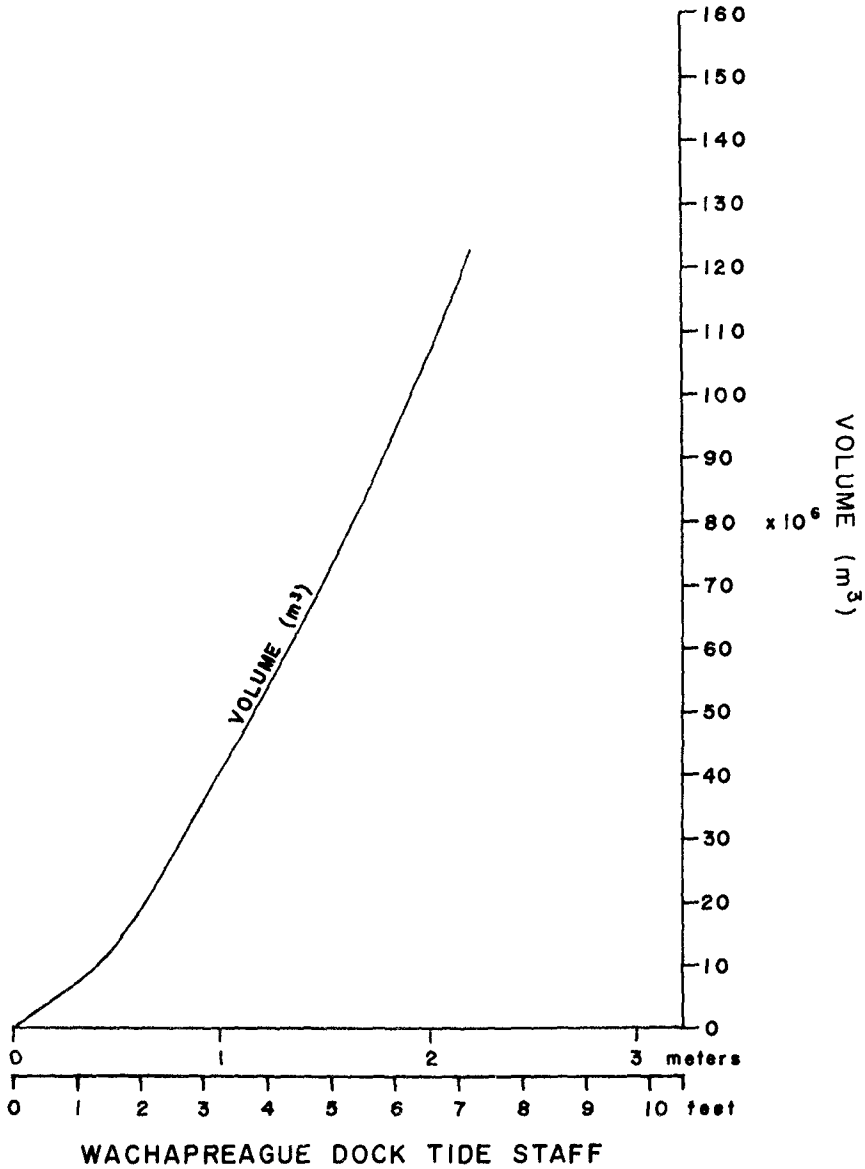
Figure 5. Storage volume relative to tidal elevations
           at town of Wachapreague. Mean tide level
           = 4.36 ft.

century (1 m/yr) and increased in length (1660 m in 1852 to 3050 m in 1972) due to the retreat of Cedar Island and accretion of sand on the northern ocean face of Parramore Island. The northern side of the channel thus represents an advancing sand wedge: based upon historical surveys the average annual accumulation is about 75 x 10 m³/yr.

Investigation of the subsurface sediments indicates the north flank of the channel is a wedge of fine sand deposited (average slope 3.5°) during the southerly migration of the channel. The steep south flank (average slope 30°) of the channel is composed of firm cohesive lagoonal muds and the bottom of the channel is a hard clay-silt with gravel horizons. The surficial sediments of the inlet complex vary from patches of shells, gravels and cobbles in the throat to very well sorted fine sand on the ebb delta. The channel bottom is covered with a thin traction carpet of shells and gravel. It appears that the long-term erosional process has been that of abrasion of the bottom and slumping of the south flank. Additional details of the geologic setting are given elsewhere [6].

The northern side of the inlet channel is flanked by ephemeral shoals which control the magnitude of lateral inflow and outflow. Historical charts and aerial photographs indicate cyclic removal and regeneration of these features. In the course of the 13 month channel response study the shoals degenerated from complete development to virtual absence (Fig. 6), with a loss of 1.5 x 10⁶ m³ of sand between the period June 1971 and Sept. 1973.

Tide and Basin Storage Characteristics. The regional tides are semi-diurnal with a mean ocean range of 1.16 m. Limited drogue studies indicate the coastal tidal flow is northerly during ebb flow in the inlet. The tide range on the inside of the inlet is the same as the ocean range and at Wachapreague the range is 5 cm larger; thus the inlet gates the full potential tidal volumes to the interior system. The phase lag between high and low waters between the inlet and the town of Wachapreague, approximately 12 km distant via channels, is -0.6 hr and -0.7 hr, respectively. There is virtually no fresh water inflow to the system. Relative to annual mean tide level the prisms for mean and spring tidal ranges are 77 x 10⁶ m³ and 91 x 10⁶ m³, respectively.

The existing storage characteristics generate distortions in the basin tides which result in a difference in duration of rising and falling water level with the rising duration being longer by 0.4 hr. This was verified by comparison between a nine month record at the Wachapreague reference gage and the ocean gage at Wallops Island (30 km north) where the mean duration difference was only 0.05 hr. Since the full potential prism is realized and the inlet area is large the duration difference should be reflected in the duration of ebb and flood currents in the inlet. Verification was obtained by comparing one month's data between the inlet currents and the reference station tides; the duration differences were 0.35 hr and 0.45 hr, respectively. Given a longer average flood duration over ebb, the mean ebb discharge will be somewhat larger than the flood and the tendency for net outward sediment transport can be expected. This is discussed later.

Due to the pertaining storage characteristics of the interior system the discharge maxima in the inlet are shifted toward the time of high water. Limited gaging information at the inlet indicates that slack water follows the extremes of the tide by about 0.4 hr.
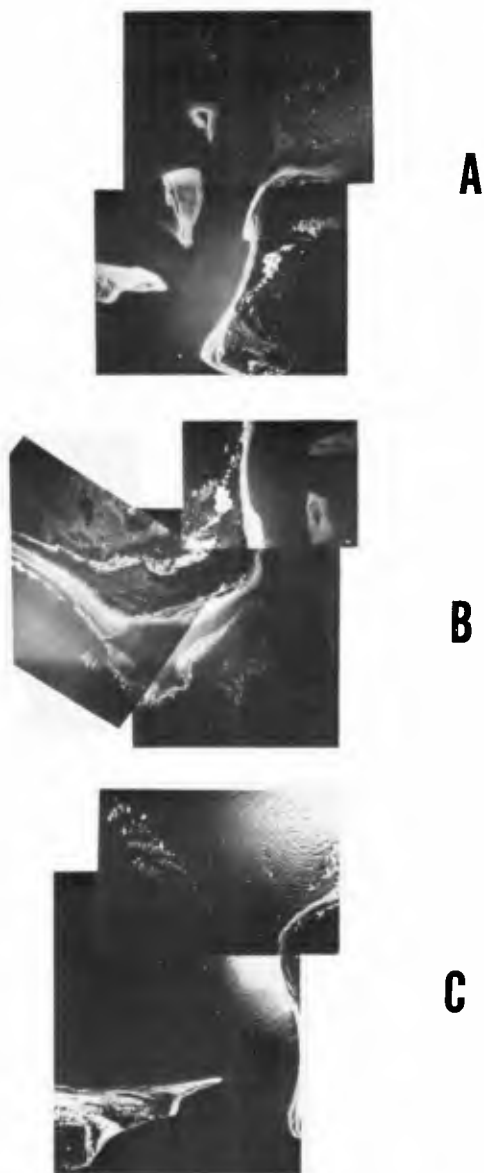
Figure 6. Diminuation of north flanking shoals controlling lateral
           inflow and outflow. A, Sept. 1971; B, Feb. 1972; C,
           Sept. 1972. NASA-Wallops photographs.

Mean tide level shows significant variations in absolute level during the year as a result of steric fluctuations and atmospheric pressure patterns [16]. An analysis of Wachapreague tides for a three year period [1] showed mean tide levels are lowest in January and February while the highest occur in September, October, and November. Mean tide levels for the survey period are shown in Fig. 8 wherein it is to be noted that the October level is .3 m higher than the January level. The importance of this phenomena in complex storage systems is evident if a spring tide range (1.43 m) is considered at these times. Calculations using the storage relationship indicates the October prism is 18% larger than January. Thus the period of enhanced prisms coincides with the advent of the northeast storm season on the east U.S. coast. During these months the largest longshore drift may be expected as the seasonal reduction in beach volumes occur. Were it not for the enhanced prisms occurring simultaneously more severe inlet shoaling would occur.

Flow Conditions in the Inlet Channel. The distribution of ebb and flood flow along the inlet channel is controlled by the degree of development of the lateral shoals flanking the north side of the channel as well as the character of the entrance. In a very generalized sense the flood flow behaves as a radial inflow to a point sink whereas the ebb flow is more channalized and then issues as a plane jet over the ebb delta system. In order to discern the flow patterns in the channel flow gaging was performed simultaneously for a 26 hour period at Ranges 22 and 8 (Fig. 3) in September 1972 when the flanking shoals on the north had diminished and were at 1 m (MLW) depth (Fig. 6). Comparison of the flood prism at Ranges 8 and 22 indicated that 35% of the total prism passing the throat (Range 22) occurred as lateral inflow over the north flank of the channel while during ebb about 15% of the prism exited as lateral outflow.

At Range 22 itself the ebb and flood flows in the channel are similarly distributed but the ebb velocities are somewhat higher. This is due to the fact that about 10% of the flood prism passes over the shelf area on the southern flank. On ebb, however, only 4% of the prism passes over the shelf.

At Range 8, some 1,200 m to the east, the flood discharge is less than the ebb, the difference being a function of the magnitude of lateral inflow, which in turn depends on the degree of development of the shoals. The ebb flow distribution is strongly skewed with higher speeds on the south side whereas during flood the flow is slightly skewed with the higher velocities on the north side. Thus, during times when the north flanking shoals are well developed and lateral inflow is reduced there is the potential for a net inward sand transport on the north side of the channel.

IV RESULTS AND DISCUSSION

Results. The results of the repetitive cross-sectional area measurements are shown in Fig. 7. Virtually all of the area modulations were the result of change in the volume of sand on the north side of the inlet channel. The 8 m contour on the steep south flank remained within ±7 m of the mean position in 91% of the cases; these were not real shifts but instead represent the range of positioning errors on the steep slope. Variation of maximum depth at each range line was small;
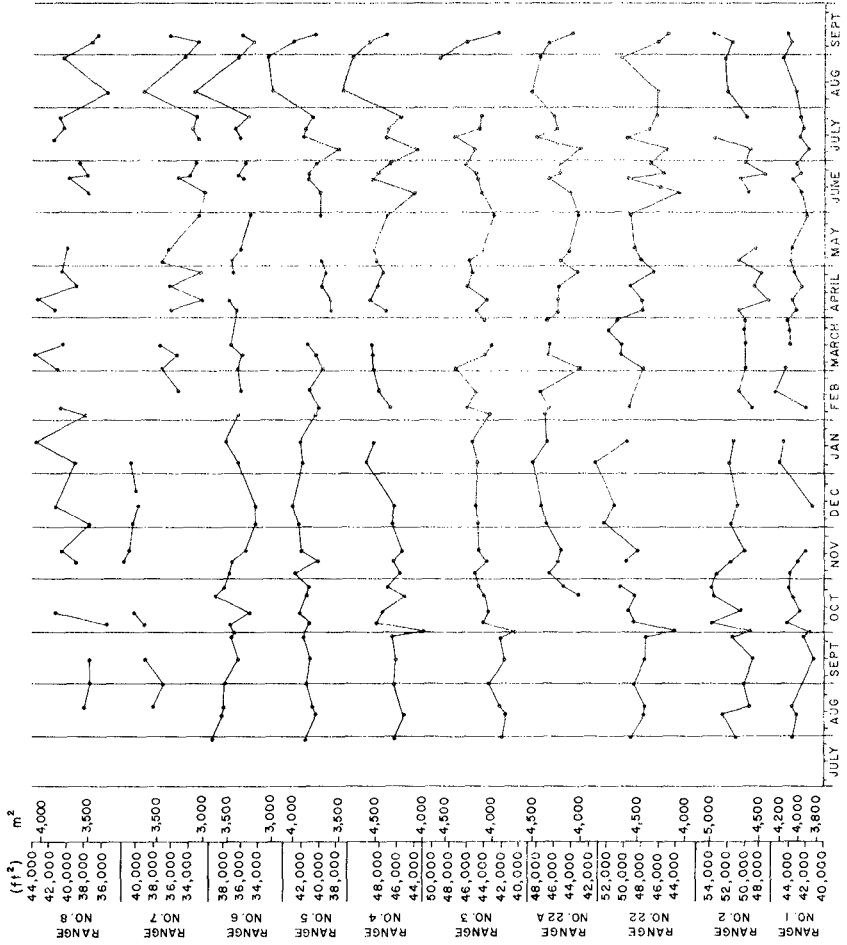
Figure 7. Cross-sectional area changes at Ranges 1 through 8, 1971-1972. Time ticks within months are 5th, 15th and 25th of month.

83% of the maximum depths fell within ±0.5 m of their means. Range 1
showed the greatest depth variation with a decrease of 2 m between
mid-January and mid-February, 1972. The horizontal position of maxi-
mum depth for each range remained stable; for all ranges and cases the
position of maximum depth fell within ±15 m of their means 83% of the
time.

   The results indicate that adjustments in inlet cross-section
can take place very rapidly. A case of rapid response is illustrated
by the surveys of 28 Sept., 1 Oct. and 6 Oct., 1971. Between the first
two dates Tropical Storm Ginger stagnated off the Virginia Coast during
the waning of neap tides. The heavy northeast seas presumably resulted
in large longshore sand transport and a consequent reduction in area
throughout most of the channel. The throat (Range 22) was reduced in
area by 7.2% between 28 Sept. and 1 Oct. Then spring tides and residual
storm surge resulted in very large tidal prisms which expanded the
cross-sections beyond the pre-storm condition. The throat was expanded
in area by 10.4% between 1 Oct. and 6 Oct.

   The largest average cross-sectional area change occurred at
the throat and at ranges 7 and 8 while the least response was evidenced
at Range 1. The throat (22, 22A) and Range 7 and 8 also exhibited the
highest percentage of large area changes ($> 93 m^2$). The coherence be-
tween ranges in the sense of the area changes (±) was generally high
for large storms or large prisms. Examination of Fig. 7 suggested
that the ranges could be grouped in sets representing the throat (Ranges
2, 22, 22A), the seaward section just before the flair of the ebb tidal
delta (Ranges 7, 8) and the center section (Ranges 3, 4, 5, 6). The
averaged response for these sections is shown in Fig. 9. During the
period Aug. 1971 to mid-March 1972 there is very poor coherence between
the throat and Ranges 7, 8; when the throat expanded the outer section
generally closed. This was prior to the complete removal of the shoals
flanking the channel on the north. After the reduction of the shoals
there was generally high coherence between all three sections.

   It is particularly interesting to note the behavior of Range
7 which exhibited a dramatic (17%) reduction in area by February 1972
which persisted with modulations through Sept. 1972. This reduction
occurred as a result of the formation of a lateral inflow induced delta
deposit on the north which was time coincident with the diminuation of
the large lateral shoal (Fig. 6). It is interesting to note that the
other ranges did not reflect this dramatic reduction in area.

   Discussion. The tidal characteristics of the system result
in a duration difference between rising and falling tidephases such
that the mean ebb discharge is expected to be somewhat greater than the
flood. To qualitatively assess the potential significance of this the
net transport tendency during the study was calculated. The sediment
transport rate was assumed to be proportional to the cube of the mean
discharge which was determined using the prism calculated from the
storage function, Fig. 5. The net sediment transport in the inlet
channel for a given period is then given by:

$$\text{Net sediment transport} \quad \alpha \; \Sigma(\frac{P_F}{\Delta t_F})^3 \; \Delta t_F - \Sigma \; (\frac{P_E}{\Delta t_E})^3 \; \Delta t_E$$

where P_F and P_E are flood and ebb prism and Δt_F and Δt_E are flood and
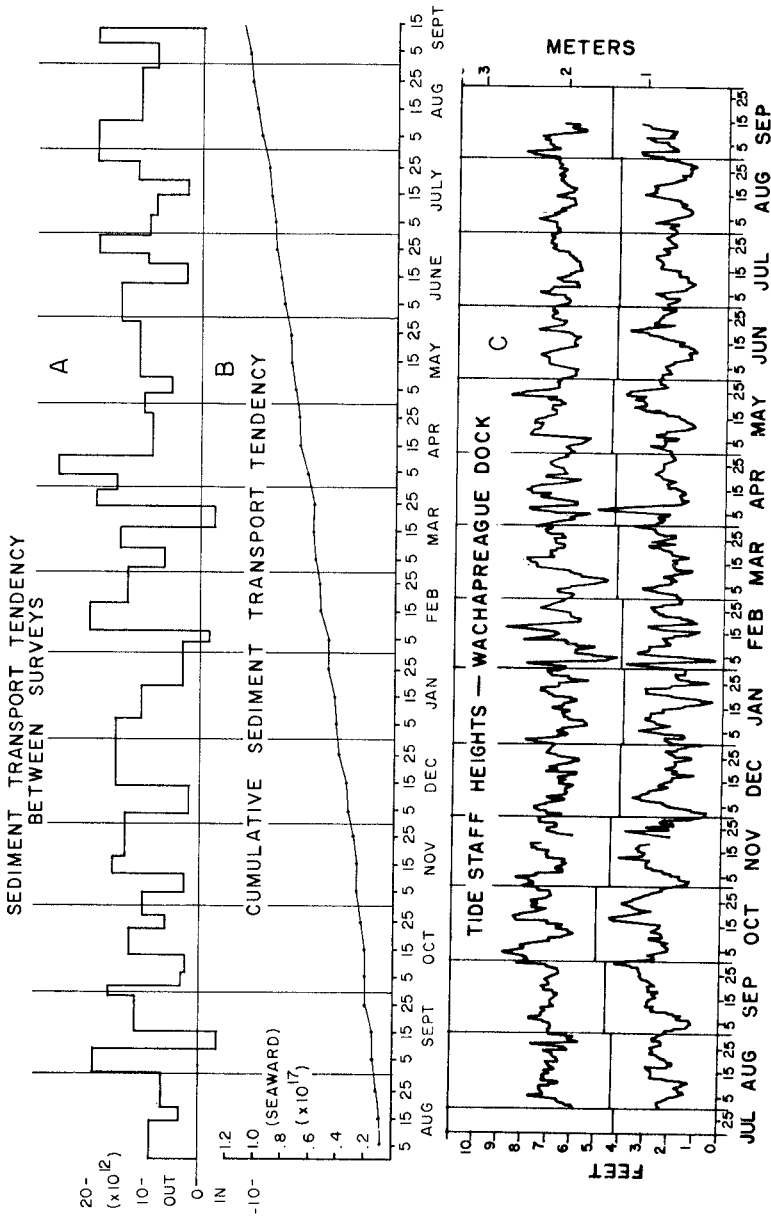
Figure 8. Net sediment transport tendency: A, average during cross-section area sampling intervals; B, cumulative transport tendency. C, Daily extremes of tide elevation and monthly mean tide levels.

ebb durations. The cumulative transport for the year is shown in Fig. 8 as is the average daily net transport within survey periods. Although there were periods of net inward transport the cumulative tendency over the long term is a net outward transport. These results agree with the analysis of Mota Oliveira [11] and King [9] which predict an ebb transport dominance for storage systems with sloping banks. This characteristic of the system offers an explanation for the absence of flood delta growth in recent times (120 years) and the maintenance of the highly developed ebb tidal delta system. This evidence and an examination of the morphology of the other deep inlets to the south along this reach of coast indicate that relatively small volumes of sand are trapped on the interior of the inlets. Caldwell [4], in contrast, finds that the flood deltas of the inlets of the New Jersey, U.S.A., coast trap about 25% of the sand in the littoral drift system.

       Most workers in tidal inlet problems consider the long-term cross-sectional stability to be controlled by the balance between the magnitude of littoral drift and the flushing power of the inlet currents [10]. In order to examine the short-term channel area response to these parameters the ebb tidal power and wave power were cast as a ratio following O'Brien [14] and Nayak [12]. The storage function was used to calculate the average daily ebb tidal power and the daily visual wave observations by CERC on Assateague Island were used to calculate breaking wave power. Since the wave observation program does not discriminate wave direction for small wave angles the ratio was weighted using the U.S. Coast Guard wave direction observations at Chesapeake Light, some 35 km off the mouth of Chesapeake Bay. The resulting ratio is proportional to the ebb tidal power and the shallow water wave power.

$$\text{Channel maintenance ratio} \quad \alpha \quad \frac{\bar{Q}_E R_E}{H^{5/2} F}$$

where $\bar{Q}_E$ = mean ebb discharge (prism ÷ duration of ebb)
        R_E = ebb tide range
        H = wave height
        F = wave duration weighting factor

            F = 3 waves approach 0 to 70° true
            F = 2 waves approach 80° to 110°
            F = 1 wave approaches 110° to 180°

The wave direction weighting factor, although arbitrary in its limit, was designed to increase the weight given to waves from the northeast, the dominant direction of storm conditions [17]. Since the sediment transport relationships for the tidal flow and littoral drift are imperfectly known the ratio has meaning only in a qualitative sense; that is, when the tidal power dominates an increase in cross-section might be expected relative to those times when wave power dominates.

       The comparison between the channel maintenance ratio, averaged over the sampling periods, and averaged channel response is shown in Fig. 9. There is general qualitative agreement between the sense of area change in the throat section and the sense of the change in the maintenance ratio in 20 of 31 cases compared. The hiatus in the calculated values for the maintenance ratio between December through March is due to the absence of wave information. In those 19 cases where an
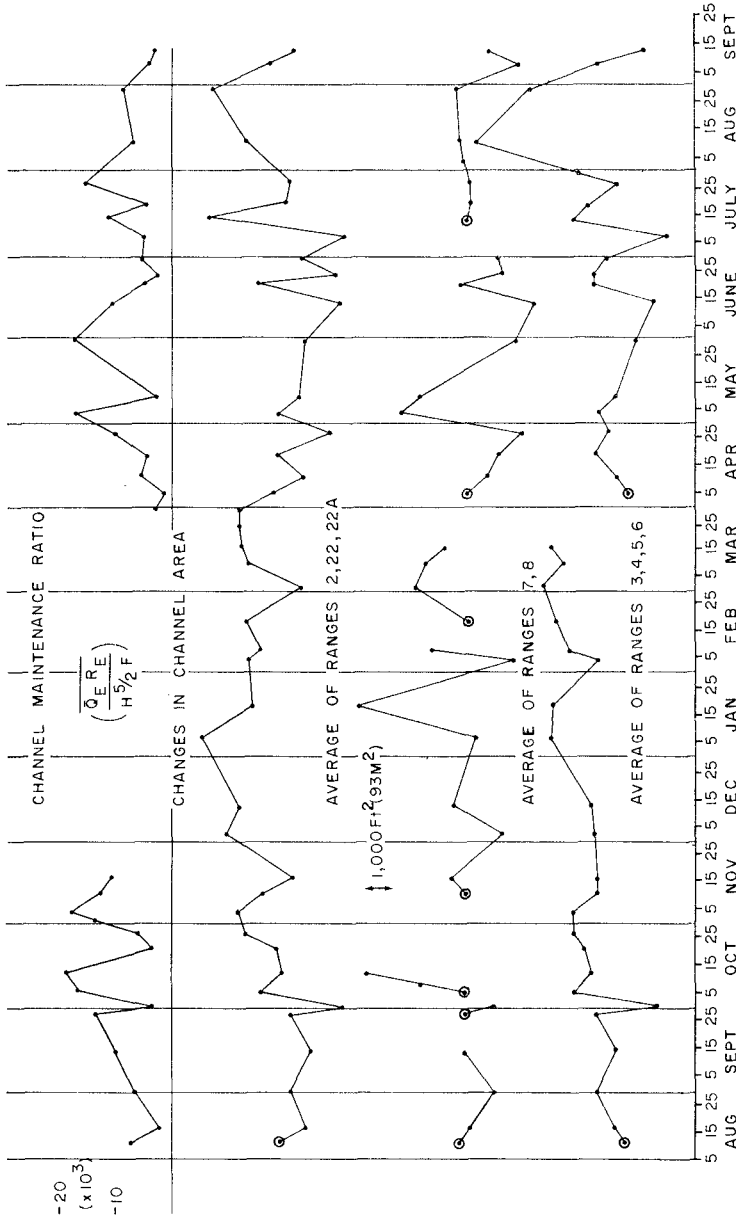
Figure 9. Comparison of channel maintenance ratio with changes in channel cross-sectional area. Circled points indicate starting position. Where gaps in data exist plots were restarted.

area change greater than 93 m^2 occurred 14 agree with the sense of change in the ratio. However, it is of interest to note that the same ratio unweighted for wave direction agrees with the sense of area changes in 21 of the 31 cases and in 13 of the 19 cases where large (> 93 m^2) changes occurred. Thus essentially no improvements in the correlation resulted using the weighting scheme for wave direction. We will return to this point.

It may be concluded that the ratio of ebb tidal power to wave power is a potentially useful parameter to characterize short-term inlet channel response. Since most of the dramatic area reduction occurred during wave activity from the northeast or east it is appealing to interpret the general correlation between the channel response and the maintenance ratio as indicating that channel closure is largely due to longshore drift from the north. However, there are several factors which indicate that the short-term modulations in cross-sectional area were due, to large degree, to a sand exchange between the channel and the ebb tidal delta complex. These elements of evidence are:

1.) As previously mentioned the correlation between the channel maintenance ratio and channel was insensitive to weighting for wave direction. This element of evidence is simply suggestive since the weighting scheme used was arbitrary.

2.) Addition of the incremental sand volumes deposited and removed within the segment of the channel surveyed over the 13 month period total to a minimum of 2 x 10^6 m^3. Considerations of what is known of longshore drift rates in the region preclude the conclusion that the sand deposited in the inlet is due solely to input via longshore drift. For example, the Corps of Engineers [5] estimates that .46 x 10^6 m^3/yr drifts to south along northern Assateague Island and that .3 x 10^6 m^3/yr is trapped in the growth of Fishing Point at the southern terminus of Assateague. Consideration of the recession rates from 1852-1962 of the island chain between Wachapreague Inlet and Assateague Island indicate a sand volume loss of .33 x 10^6 m^3/yr if the eroding marsh barrier islands are composed of 25% sand (probably an overestimate). Thus a reasonable estimate for maximum southerly drift to the inlet is .5 x 10^6 m^3/yr. The results of computed wave refraction [8] and field observations indicate that wave refraction patterns allow only small volumes of northerly drift for waves from the southerly quadrants. Recognizing the considerable risk in comparing events over a one year period with averages based on decades, the estimate of drift versus the observed volumes deposited strongly suggests that a large fraction of the sand volume modulation in the inlet channel is due to adjustments between the channel and the ebb delta system.

3.) As previously mentioned approximately 1.5 x 10^6 m^3 of sand was lost from the shoals flanking the north side of the channel in the course of the 13 month survey. Existing knowledge of the tidal flows near the inlet indicates that virtually all of this material must have been driven into the channel and subsequently flushed onto the ebb delta complex and/or into the interior.

4.) Particular cases during the survey period indicate that southeast wave activity also can result in channel area reduction, particularly during low or moderate prisms and either an inward or low outward net sand transport conditions (14-19-26 July, 1972). In contrast, a case

(26 July - 10 Aug. 1972) with similar wave conditions and a somewhat larger prism but with a calculated strong net outward transport the channel widened dramatically (ratio predicted decrease in area). Finally, it is noteworthy that Range 1 exhibited a depth decrease during mid-Jan. to mid-Feb. 1972, a time of sustained low net outward transport. These data suggest that the net sand transport character- istics during the given period also play a significant role in the modulation of channel area.

In summary it appears that the qualitative agreement between the channel response and the "maintenance ratio" reflects the import- ance of wave activity on the ebb delta complex, regardless of wave di- rections, as well as generalized net southerly advection of sand along the coast on the littoral drift system.

Given the totality of evidence presented it is possible to formulate a qualitative model for sediment circulation within the in- let complex which is consistent with both the short-term channel re- sponse and the recent history of the inlet. The main element of the model is the inferred existance of a sediment flow loop on the north side of the inlet complex (shown schematically in Fig. 10). The system is driven by the combined influence of wave refraction, the regional tidal flow and the flow distribution within the channel:

1.) Wave refraction tends to drive sand to the west from the northeast flank of the ebb delta. Evidence of this is shown in Fig. 5 where the lateral shoals accrete by a succession of spits [6, 8].

2.) The regional tidal flow is northerly during ebb in the channel which would tend to drive material carried over the delta to the north.

3.) As previously discussed the ebb flow at Ranges 6, 7, 8 is concen- trated on the south side of the channel and during periods of low lateral inflow the flood currents on the north flank at Range 6, 7, 8 are as large or larger than ebb, so that a sediment transport loop within the channel itself is possible. During times of high lateral inflow the flood currents cascade sand into the channel (i.e., Range 7 response) part of which is derived in the loop via steps 1 and 2. During periods of large prism the ebb velocities in the channel are sufficient to scour the north flank of the channel.

During northeast storms the wind induced circulation most likely overrides the regional tidal flow with resultant intensive sediment flow to the south flank of the delta. Whatever sand is re- introduced into the channel from the south is scoured by the concen- trated ebb flow.

The recent, longer term, history of the inlet appears to be dominated by the characteristics of the littoral drift supply, the basin morphology and the geologic controls on the inlet:

1.) Study of regional and local wave refraction diagrams [8] indicate a strong net littoral drift to the south. Moreover, the local wave refraction for wave approaches from all quarters favors the enhance- ment of the ebb delta and storage of bypassed sand on the north ocean face of Parramore Island. The updrift coast is an eroding marsh island sequence with an estimated maximum annual drift of .5 x 10^6 m^3/yr. Thus the area is one with moderate to low littoral drift supply.

2.) The basin morphology and frictional characteristics appear to re- sult in a net seaward transport of bed load material. Consequently
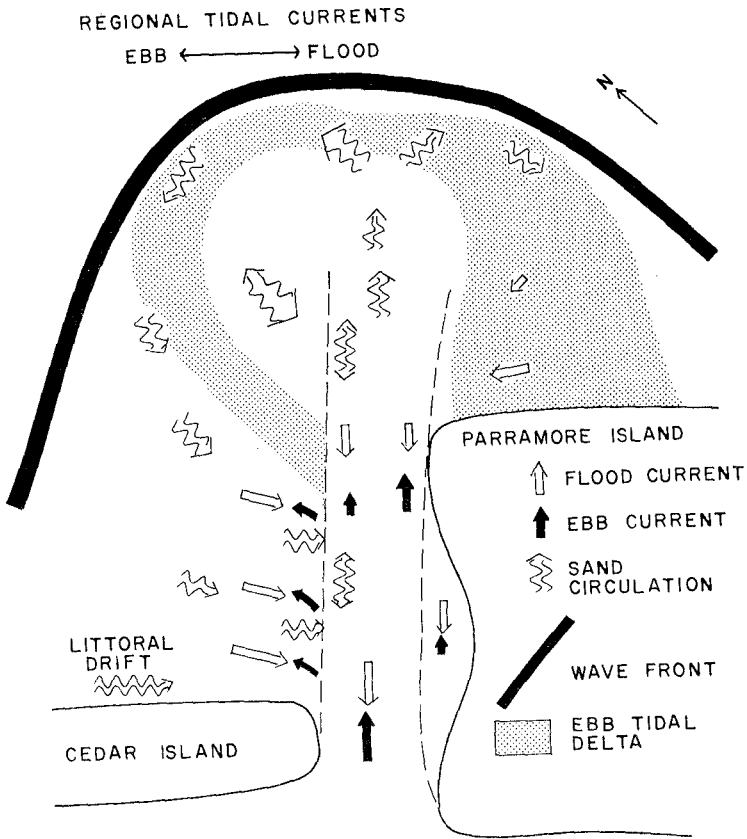
Figure 10. Model showing sand circulation loop between channel and
           ebb tidal delta and schematic of gross current flow
           characteristics within the channel.

flood induced interior deposits have not enlarged during the last
century and the channel must act in a bypassing mode.
3.) Due to sedimentological controls and the strong net southerly
littoral drift the inlet channel has slowly migrated south as the
south wall slumps and the inlet floor is abraded by the traction
carpet. In the process of migration a wedge of sand is deposited on
the north side of the channel.
        The results of this study have ramifications on engineering
design practices since the collective evidence indicates pronounced
sand circulation between the ebb delta system and the channel. While
these results should have general applicability to offset inlets they
also probably apply to inlets in general. Thus, any engineering de-
sign should consider the local effects within the inlet complex as
well as the littoral drift rates. For example, jetty-weir sand by-pass
design considerations should include the question whether local sand
circulation from the ebb delta will necessitate a larger impoundment
basin or increased dredging frequency. If such circulation does occur
there may be a reduction in sand volumes on the ebb delta due to im-
poundment and mechanical by-passing.

REFERENCES

1. Boon, J.D., III, 1974. Sediment transport processes in a salt
        marsh drainage system. Unpublished Ph.D. dissertation,
        School of Marine Science, College of William and Mary,
        Williamsburg, Virginia, U.S.A.

2. Brown, E.I., 1928. Inlets on sandy coasts. Proceedings ASCE,
        54(2)505-553.

3. Bruun, P., 1967. Tidal inlets housekeeping. Journal, Hydraulics
        Div., ASCE, 93(HY5)167-184.

4. Caldwell, J.M., 1966. Coastal processes and beach erosion.
        Journal Boston Soc. Civil Engr., 53(2)142-157.

5. Corps of Engineers, 1973. Survey report, Atlantic Coast of Mary-
        land and Assateague Island, Va. U.S. Corps of Engineers,
        Baltimore District (report in preparation).

6. DeAlteris, J.T., and Byrne, R.J., 1973. The recent history of
        Wachapreague Inlet, Virginia. The Second International
        Estuarine Research Conf., Myrtle Beach, S.C., 15-18 Oct.

7. Escoffier, F.F., 1940. The stability of tidal inlets. Shore and
        Beach, 8(4)114-115.

8. Goldsmith, V., Byrne, R.J., Sallenger, A.H., and Drucker, D.H.,
        1973. The influence of waves on the origin and development
        of the offset coastal inlets of the southern Delmarva Penin-
        sula. The Second International Estuarine Res. Conf., Myrtle
        Beach, S.C., 15-18 Oct.

9. King, D.B., Jr., 1974. The dynamics of inlets and bays. Tech.
        Rpt. No. 22, College of Engr., Univ. of Florida, Gainesville,
        82 p.

10. Johnson, J.W., 1973. Characteristics and behavior of Pacific coast
        tidal inlets, Journal of Waterways, Harbors and Coastal Engn.
        Div., Proc. ASCE, v. 99, No. WW3, August, 325-339.

11. Mota Oliveira, I.B., 1970. Natural flushing ability of tidal in-
        lets. Proc. 12th Conf. Coastal Engineering, 1827-1845.

12. Nayak, I.V., 1971. Tidal prism-area relationship in a model inlet.
        Univ. of Calif., Hydr. Engr. Lab., Berkeley, Tech, Rept. No.
        HEL-24-1, 72 p.

13. O'Brien, M.P., 1969. Dynamics of tidal inlets. In Coastal Lagoons,
        a Symposium, 397-407 (ed. Castanares, A.A., and Phleger, F.B.),
        Universidad Nacional Autonoma de Mexico.

14. O'Brien, M.P., 1970. Notes on tidal inlets on sandy shores. Univ.
        of Calif., Hydr. Engr. Lab., Berkeley, Report HEL-24-5.

15. O'Brien, M.P. and Dean, R.G., 1972. Hydraulics and sedimentary
        stability of coastal inlets. Proc. 13th Conf. Coastal Engr.,
        761-780.

16. Pattulo, J., Munk, W., Revelle, R., and Strong, E., 1955. The
        seasonal oscillation in sea level. Journal of Marine Research,
        14(1)88-156.

17. Saville, T., Jr., 1954. North Atlantic coast wave statistics
        hindcast by Bretschneider-revised Sverdrup-Munk method.
        Beach Erosion Board, U.S. Army Corps of Engineers, Tech.
        Memo No. 55.

CHAPTER 93

STABILITY CRITERIA FOR TIDAL BASINS

by

Eberhard Renger[1]   and   Hans-Werner Partenscky[2]

ABSTRACT

The contribution deals with the morphologic examinati-
ons and calculations for a deep-water harbour which is to be
constructed in the tidal flats of the Elbe estuary near the
North Sea islands of Scharhörn and Neuwerk. An attempt is
made to examine the stability of tidal channels (gullies)and
tidal flats which may be disturbed to a greater or lesser
extent by the various proposals for the connecting dike be-
tween the industrial area near the harbour and the coastline.

The underlying logic for the determination of the equi-
librium of the flats and the quantitative solution for the
sand-balance is as follows:

It has been shown in several empirical investigations
that the increase of the relative volume of the tidal basin
(V/V_{MLW}), referenced to the gully volume for MLW, can be de-
termined as a simple function to the base $(\bar{a})$ logarithm of the
geodetic elevation (z^*) between MLW and any higher contour
level up to MHW. Furthermore it can be shown that (V_{MLW}) is
also a function of the tidal drainage area (E).

The base $(\bar{a})$ has been related to the size of the tidal
drainage area (E), because this area is subject to consider-
able modification by offshore structures such as dikes and
causeways.

---

[1] Scientific Associate, Franzius-Institute,Hannover, West-
Germany

[2] Director of the Franzius-Institute, Technical University
of Hannover

A comparison of the volumes of the tidal basins for the si-
tuation before and after construction can be made.

This   inturn leads to the sand balance which can be
applied to the given and expected volumes of the tidal basin,
so that the sand removed or added can be predicted.

INTRODUCTION

In case of major man-made constructions in the reach of
tidal flats and tidal gully systems, changes in the tidal re-
gime as well as in the morphology of the tidal basins must be
expected. However, due to the mutual interaction between ti-
dal currents and velocities and sediment transport a new state
of equilibrium will eventually be reached.

Although the coastal engineer in general is mainly in-
terested in the changes of the tidal characteristics (tidal
range, current velocities and directions) which will be
caused by constructions such as dams, dikes, etc., the modi-
fications in the morphological structure of the tidal basins
concerned (erosion and sedimentation) might become an impor-
tant aspect with respect to navigation. The prediction of the
changes to be expected in the cross-sectional area of existing
navigation channels as well as the prediction of sand balan-
ces is therefore of vital interest in areas where navigation
has an important role.

In this contribution an attempt is made to examine the
stability behavior of existing tidal basins along the German
Bay between the Netherlands and Denmark. The stability cri-
teria obtained by means of a semi-empiric approach are then
applied to predict morphologic changes to be expected due to
a proposed dam to the deep-water harbor Neuwerk/Scharhörn of
the City of Hamburg which is to be constructed in the tidal
flats of the ELBE estuary.

STABILITY BEHAVIOR OF TIDAL BASINS

It has been shown by several authors that a relation-
ship exists between the tidal volume, and also the area of
the tidal basin (E), and the outflow cross-sectional area
(F) on the seaward side. (Bruun, Gerritsen(1958),Hensen(1971)
O'Brien (1969), Rodloff (1970), Walther (1972)). However,
this two-dimensional approach appears to be somewhat limited

for a detailed and, moreover, quantitative description of
the actual three-dimensional situation.

In the present study, the usual method for the descripti-
on of the morphologic state of the tidal basin by means of
characteristic vertical cross-sections was therefore aban-
doned and replaced by an approach in which horizontal layers
were used to describe the volume capacity of the tidal gully
system (Renger, E. und Partenscky, H.W., 1974).

The contour-enclosed surface area of each layer corres-
ponding to a well-defined geodetic level was evaluated by
means of a planimeter by using contour lines of existing sea-
charts (1:10000). The characteristic relationships between
the contour-enclosed areas of a given tidal basin and the ge-
odetic elevation referred to MLW is shown on figure 1a.
Figure 1b shows the typical volume curve of the tidal basin
which was obtained by numerical integration from curve a).
For the mathematical description the volume values are re-
lated to a reference volume of the tidal channel at MLW
(figure 1c).

A total of 22 tidal basins on the German Bay (along the
North Sea coast) were systematically studied. First, the in-
crease in the horizontal contour-enclosed area open to the
sea was determined as a function of increasing contour ele-
vation (see fig. 1a). Then, by stepwise integration, the re-
lative volume of the tidal basin (V/V_{MLW}), referenced to the
gully volume for MLW, was calculated (see figure 1c).

The determination of the reference volume (V_{MLW}) as a
function of the area of the tidal basin (E) gave for the
22 tidal basins a relation of the form (fig. 2):

$$V_{MLW} = 8 \cdot 10^{-3} E^2 \qquad (1)$$

An appropriate expression may be obtained for the size of
the reference area enclosed by the MLW contour (O_{MLW}) by
way of the following empirical equation (fig. 3):

$$O_{MLW} = 2.5 \cdot 10^{-2} E^{3/2} \qquad (2)$$

The mathematical approximation to the data for relative
volume of the tidal basin (V/V_{MLW}) (See Fig.1c) is given
by the logarithmic function

$$z^* = \log_{\bar{a}} (V/V_{MLW}) \qquad (3)$$

where the parameter $(\bar{a})$ is dependent on the size of the

tidal area (E) as follows (see fig. 4):

$$\bar{a} = 5 \cdot E^{-0.272} \qquad\qquad (4)$$

The parameter ($\bar{a}$) characterizes the volume-distribution of the tidal basin between MLW and any higher contour level up to MHW, i.e. for $z^* \geq 0$.

By means of Eqs. (1) and (4) a relationship for volumes of the tidal basin is established between the area of the tidal basin (E) and the geodetic elevation (z^*) in the following form:

$$V = V_{MLW}(\bar{a})^{z^*} = 8 \cdot 10^{-3} \quad E^2 (5 \ E^{-0.272})^{z^*} = f(z^*, E) \qquad (5)$$

where V = volume of the tidal basin in $10^6 \cdot m^3$
       E = area of the tidal basin in km^2
       z^* = geodetic elevation referenced to MLW in m.

The relation expressed by Eq. (5) demonstrates clearly that the tidal gully systems of the German Bay exhibit a stability that is readily described.

   How much the tidal range and the composition of the bed material may influence the stability of a tidal gully system as expressed in Eq. (5), can not as yet be determined, since the mean tidal range of the tidal basins evaluated falls only between 2,5 m and 3,5 m and the mean grain diameter of the bed material lies between 0,16 mm and 0,20 mm.

APPLICATION OF THE RESULTS OBTAINED TO THE DEEP-WATER HARBOR PROJECT NEUWERK/SCHARHÖRN

1. General layout of the harbor

   In the following, the results obtained from the general study on the stability of tidal basins are applied to the project of the planned deep-water harbor Neuwerk/Scharhörn of the city of Hamburg. This harbor is to be constructed in the tidal flats of the Elbe estuary near the North Sea islands of Scharhörn and Neuwerk (fig. 5). An industrial area of about 12 km^2 around the harbor shall be connected with the coast by means of an earthdam. Figure 6 shows the general layout of the planned harbor with different alternatives for the dams in the southern range of the Elbe estuary and the existing morphology of the tidal channel system. (Partenscky, H.W. und Renger, E., 1974).

The project has been studied on a hydraulic fixed-
bed model at the FRANZIUS-INSTITUTE of the Technical
University of Hannover in order to determine the changes
in the tidal characteristics to be expected by the con-
struction of the dams (model boundary on Fig. 5).

The important question as to what extent the stability
of the existing tidal basins might be disturbed by the
dams could not be answered by the model tests. However,
a prediction of the morphological changes was possible by
using the results of the general study as outlined above:

In general it is assumed that the existing equilibri-
um of the tidal basins will more or less be disturbed by
the planned dams and shifted to a new equilibrium state.

2. Morphologic changes north of the planned dams

For several reasons, the southern layout of the
connecting dam (fig. 6, Alternative C) was finally se-
lected. The areas of the three northern tidal basins
Buchtloch, Eitzenbalje and Hundebalje$_2$(see Fig.6) shall
be enlarged by an area of about 25 km^2, i.e. about 50%
of their initial area. This shall consequently lead to
an enlargement of the volume of the tidal basin and
therefore to erosion. As a result a certain percentage
of the eroded sand will be transported by the tidal
currents and be deposited outside the seaward boundary
of the tidal basins near the important international
waterway ELBE - river.

Some secondary dams following the existing watershed
were therefore planned to reduce this effect in the
northern tidal flats. The danger of sedimentation in the
navigation channel could so be kept as small as possible.

3. Morphological changes south of the planned dams

Due to the planned dam (Alternative C, fig. 6), the
tidal basin of the TILL is considerably reduced in its
area. Fig. 7 shows a simplified sketch of the situation.
The area of the tidal basin TILL is shown by the dotted
line with different limits for the seaward boundary,
labelled by TILL - (11), - (12) and - (13). The pattern
of the tidal channels is presented by means of the MLW-
contour line.

The total area of the tidal basin TILL shall be re-

duced in its northern tidal flats and gullies from about
12o km^2 to 9O km^2 (skrashed area on Fig. 8d. A reduction
in the drainage area of a tidal basin is usually followed
by a shrinking of its volume, i.e. sedimentation in the
tidal gullies concerned must be cxpeeted.

The graphs on Fig. 8a to e show on the ordinate thc
geodetic elevation z* referred to the reference level at
MLW. On the right hand side (fig. 8c), the relative vo-
lume of the TILL is shown within the three selected boun-
daries (11), (12) and (13), whieh were mentioncd above.
The eharacteristie parameters (ā) of the logarithmic
approximation curve are labelled by the corresponding
numbers on Fig. 4 . The points (11), (12) and (13) follow
quite well the general tendency even for different limits
of the seaward boundary. This rather good agreement makes
a relatively independent choice of the seaward boundary
possible and keeps the results of the calculations within
the gencral tendeneies.

For thc predicted new equilibrium of the TILL with
its reduced area of thc tidal basin, a distribution curve
of the relative volume was found by means of interpola-
tion between the three eurvcs (11), (12) and (13) (see
fig. 8c).The corresponding distribution eurvc of the con-
tour-enclosed areas for the predieted eondition of the
reduced TILL is shown on fig. 8a. The existing eondition
is labelled by (13) on figurc 8a.

In fig. 8b on the right-hand side, the distribution
of the contour-encloscd areas ΔO north which had been
cut off by the dam from thc tidal basin TILL, is presen-
ted. Thesc contour-enclosed areas were added to the
northern tidal flats and had to be subtraeted from those
of the existing equilibrium. The remaining distribution
of the contour-enelosed areas of the rcdueed area of the
TILL is given by the curve on the left-hand of figurc 8a,
whieh is labclled "existing condition with dam".

The vertical distribution of thc shrinking of the
eontour-enclosed arcas is shown on the left-hand side of
Fig. 8b (ΔO, south).

This distribution is calculated as the differcnce
of the contour-enelosed areas of the "existing condition
with dam" and that of the "predicted cquilibrium". The
dottcd area (fig. 8a and b) represents a mcasure for the
predicted sedimentation in the TILL. Numerically it was
found that a volume of about 38 Million m^3 of sand must
be expected as sedimentation in thc tidal basin TILL due
to the planned construetion of the southern dam.

CONCLUSIONS

A semi-empirical method has been employed to describe the morphologic structure of tidal basins observed in the German Bay/North Sea. The objective of the study was to determine the vertical distribution of the volume of a tidal basin by analytical expressions.

It could be shown that a well defined relationship between the different parameters such as reference area by MLW-contour (O_{MLW}), reference gully-volume V_{MLW}, characteristic parameter ($\bar{a}$) of the relative volume V/V_{MLW} and the area of the tidal basin (E) exists.

The results enable the coastal engineer to predict morphological changes in the tidal basins which must be expected by the construction of greater offshore structures such as dikes and causeways. By comparing the volumes of the tidal basins before and after the construction (new equilibrium), the sand removed or added can be calculated.

The stability criteria obtained by means of the semi-empiric approach were applied to predict morphologic changes to be expected due to a proposed dam to the deep-water harbor Neuwerk/Scharhörn of the city of Hamburg which is to be constructed in the tidal flats of the ELBE estuary.

How much the tidal range and the composition of the bed material may influence the stability of a tidal basin as expressed in equation (5) can not as yet be predicted, since the mean tidal range of the tidal basins evaluated falls only between 2,5 m and 3,5 m and the mean grain diameter of the bed material lies between 0,16 and 0,20 mm.

REFERENCES

1. Bruun, P. and Gerritsen,F. "Stability of Coastal Inlets". J. Waterways Harbors Division, ASCE,84, WW3, Paper No 1644, (May,1958).

2. Hensen, W., "Ausbau der seewärtigen Zufahrten zu den deutschen Nordseehäfen.A.Die wissenschaftlichen Aspekte". HANSA-Schiffahrt-Schiffbau-Hafen.108.Jahrgang, 1971, Nr. 15.

3. O'Brien,M.P.,"Equilibrium Flow Areas of Inlets on Sandy Coasts."Journal of the Waterways and Harbours Division. Proc. of the American Society of Civil Engineers. Vol.96,No. WW1, Feb.1969.

4. Partenscky, H.-W. und Renger, E., "Modelluntersuchungen für den geplanten Tiefwasserhafen Neuwerk/Scharhörn", Schiff & Hafen, Heft 5/1974, 26. Jahrgang S.447-456.

5. Renger, E. und Partenscky, H.-W., "Stabilitätsverhalten von Watteinzugsgebieten", Die Küste, H.25, 1974.

6. Renger, E., "Untersuchungen von Watteinzugsgebieten", Mitteilungen des Franzius-Instituts für Wasserbau und Küsteningenieurwesen der Technischen Universität Hannover, Heft 40, 1974.

7. Rodloff, W., "Über Wattwasserläufe", Mitteilungen des Franzius-Instituts der Technischen Universität Hannover, Heft 34, S. 1 bis 88, 1970.

8. Walther, Fr., "Zusammenhänge zwischen der Größe der ostfriesischen Seegaten mit ihren Wattgebieten sowie den Gezeiten und Strömungen", Jahresbericht 1971. Bd. XXIII der Forschungsstelle Norderney der Niedersächsischen Wasserwirtschaftsverwaltung. 1971.
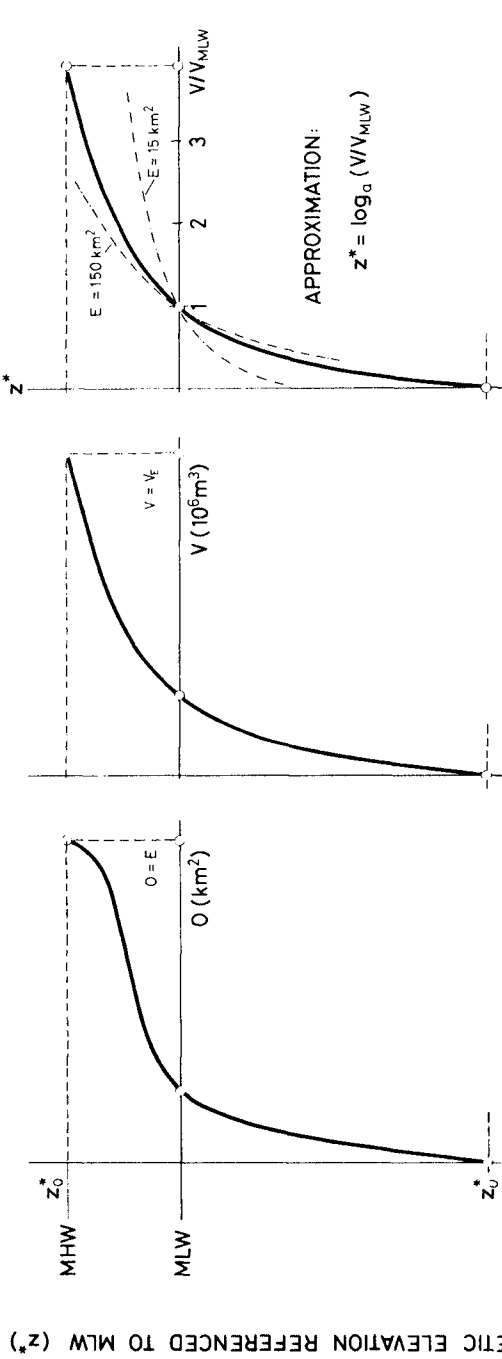
a) CONTOUR - ENCLOSED
AREA $\bar{O} = f(z^*)$

b) VOLUME $V = f(z^*)$
OF THE TIDAL BASIN

c) RELATIVE VOLUME $V/V_{MLW} = f(z^*)$

Fig. 1 Typical example of the Morphologic characteristics of
a tidal basin in the German Bay/North Sea.

$$O_{MLW} = 2.5 \cdot 10^{-2} \cdot E^{3/2}$$

Fig. 3

$$V_{MLW} = 8 \cdot 10^{-3} \cdot E^{2}$$
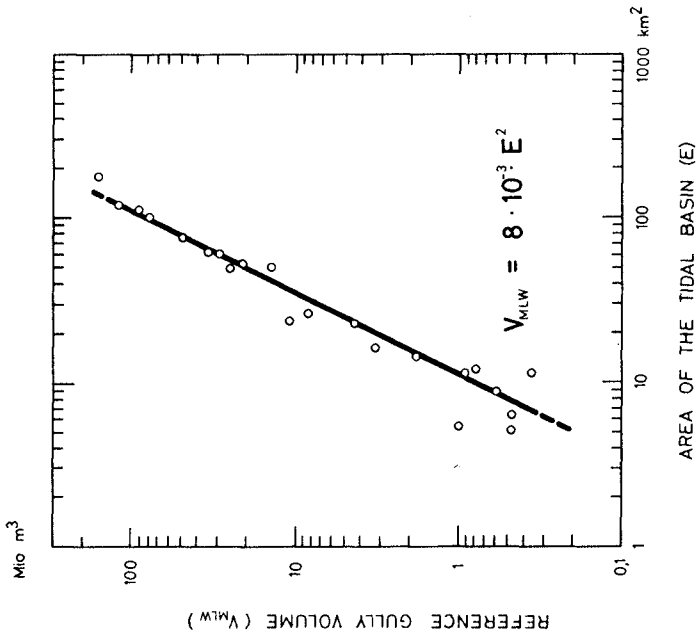
Fig. 2
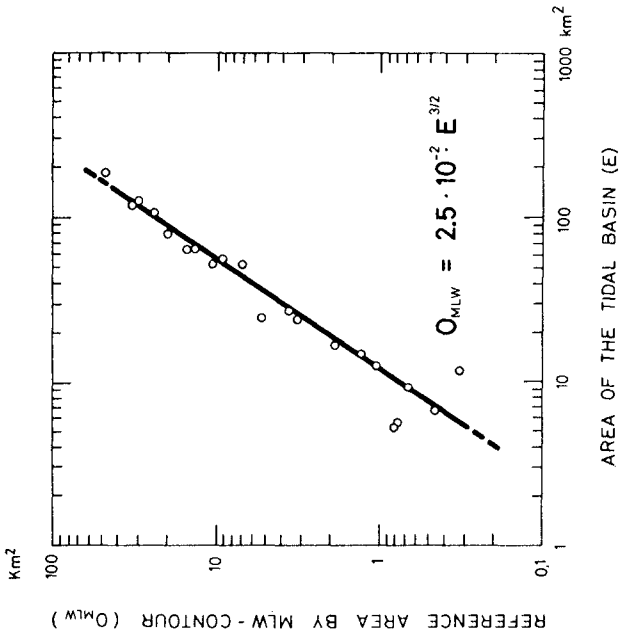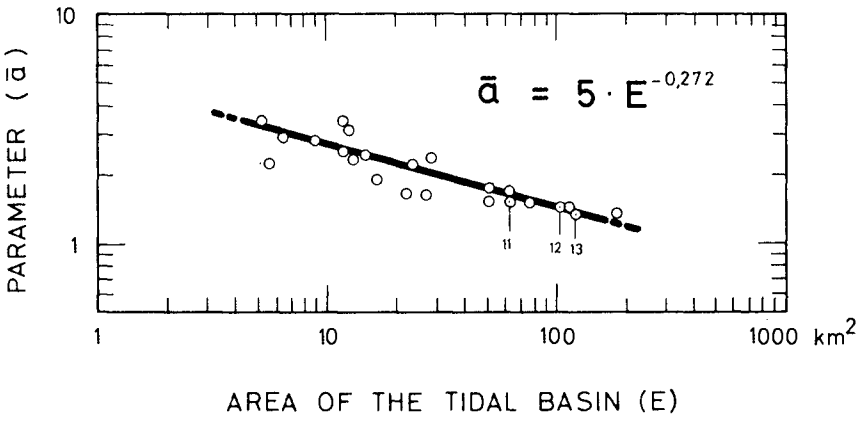
Fig. 4
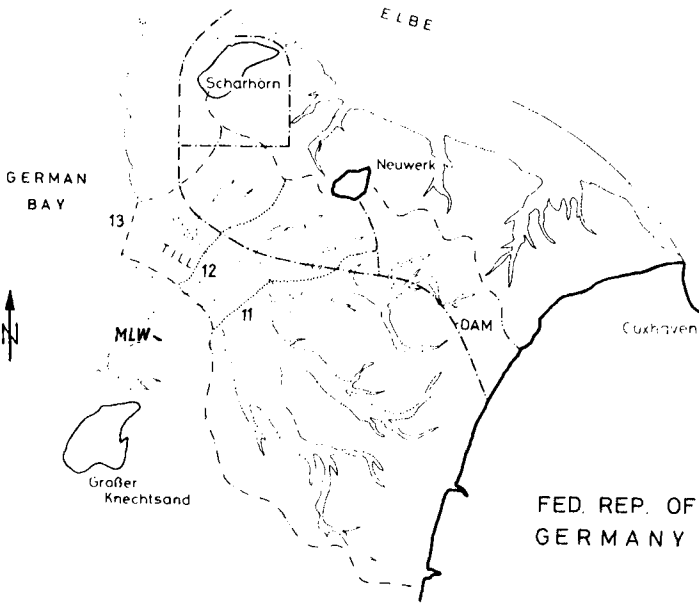
Fig. 7   Simplified sketch of the tidal area
Neuwerker Watt (the area of the tidal
basin TILL is shown by the dotted line).
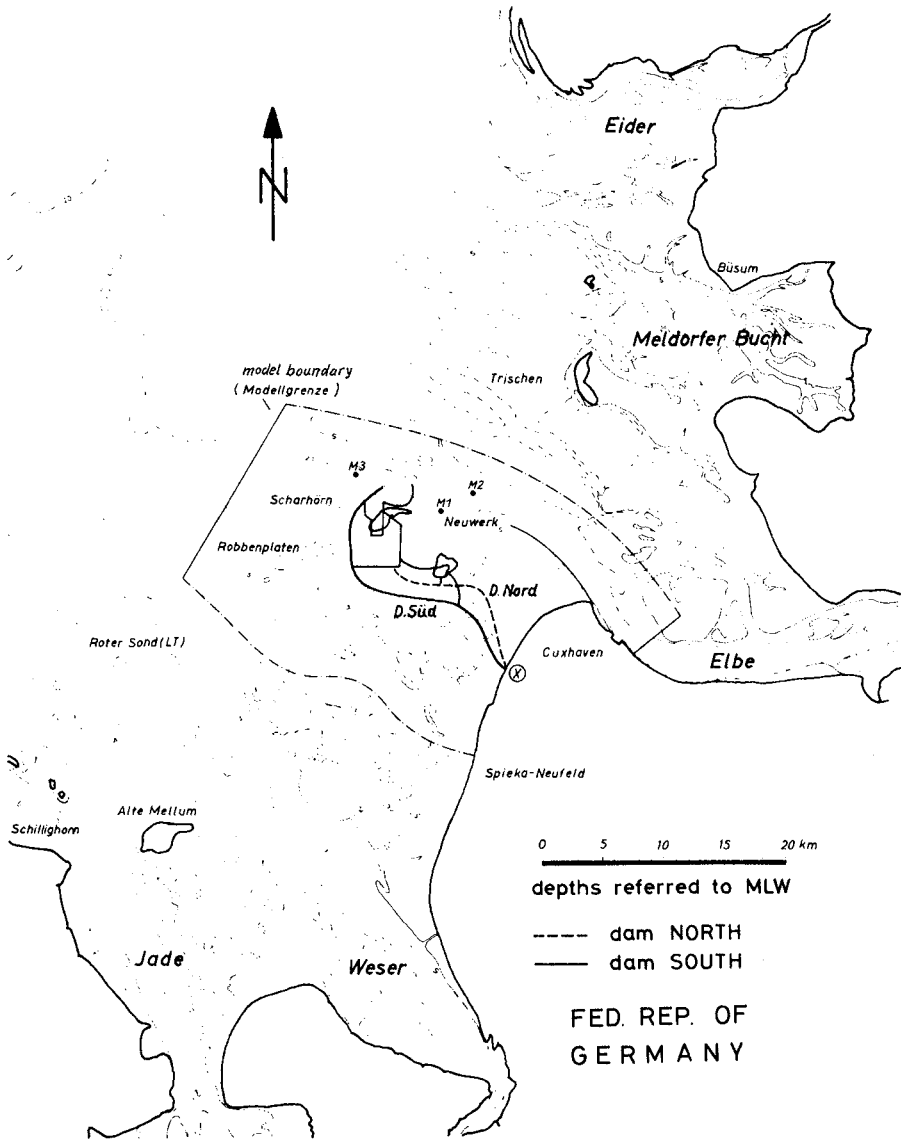
Fig. 5   Tidal basins and tidal channel systems
          in the German Bay/North Sea.
          General layout of the deep-water harbor
          Neuwerk/Scharhörn.

Fig. 6 General layout of the planned deep-water harbor Neuwerk/Scharhörn with
different alternatives A,B,C,D for the dams in the southern range of
the Elbe estuary and existing morphology of the tidal flats.
(Contours referred to MLW).
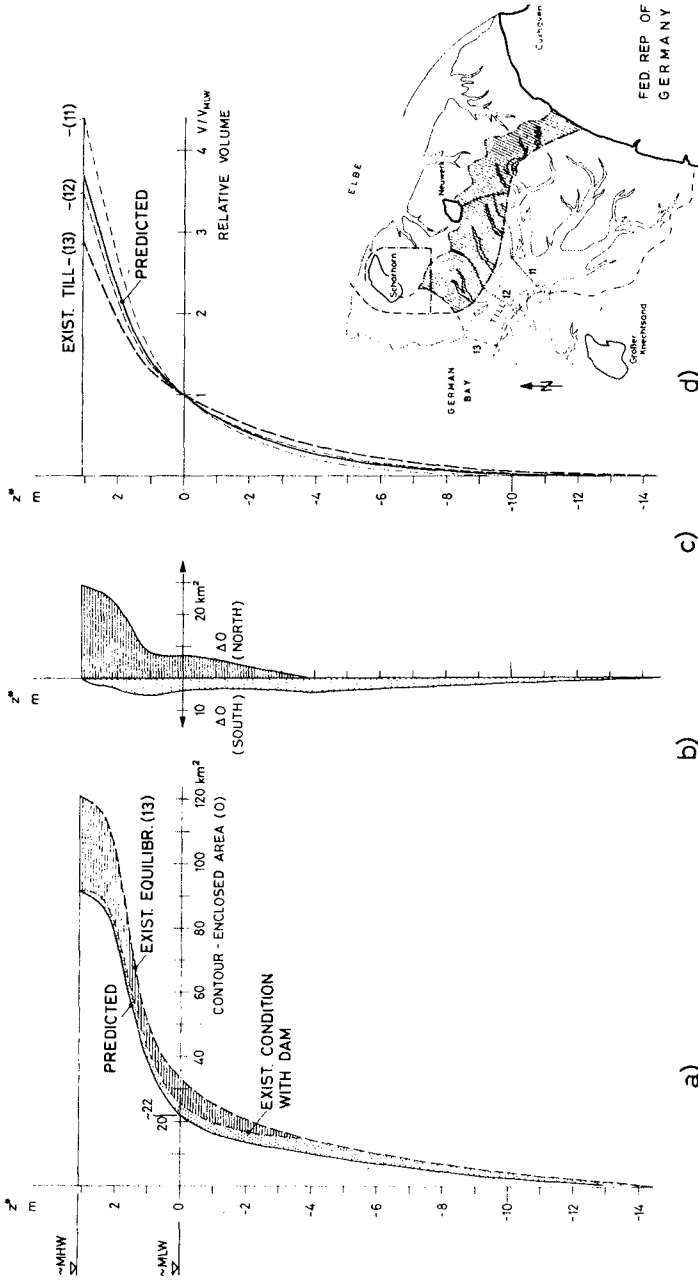
Fig. 8   Results of morphologic calculations for the tidal basin TILL
          (German Bay/North Sea)

CHAPTER 94

COMPUTING EOLIAN SAND TRANSPORT FROM ROUTINE WEATHER DATA

S. A. Hsu
Coastal Studies Institute, Louisiana State University
Baton Rouge, Louisiana 70803

ABSTRACT

    Extensive wind profile measurements have been made over beaches, tidal flats, and small dune fields in Barbados, Ecuador, Florida, Texas, and on Alaskan Arctic coasts by the author and his associates during the past several years. The linear relationship between shear and wind velocities was further verified by these measurements, in conjunction with Bagnold's data from experiments in a Libyan desert. From these measurements, a simple method is developed for computing eolian transport of the most common sand particle sizes which occur on coasts and deserts by using only routinely available wind observations from nearby weather stations.

INTRODUCTION

    In the coastal environment one of the main unsolved problems of sand supply and loss is that of calculating the rate of sand transport by wind action. Recently, Hsu (1971a) introduced a method based on limited field measurements by which this rate can be scaled using a special Froude number. Extensive wind profile measurements have been made over beaches, tidal flats, and small dune fields in Ecuador, Florida, Texas, and on Alaskan Arctic coasts by the author and his associates during the past several years. The linear relationship between shear and wind velocities was further verified by these measurements and also by Bagnold's (1941) data from experiments in a Libyan desert (Hsu, 1973).

    To add to the measurements previously obtained, an experiment to measure the wind stress on the air-beach interface of an island beach was conducted on Barbados, West Indies, during July-August 1973. The results are synthesized in this paper, along with those from similar experiments on continental coasts (Hsu, 1973). These results are related to routine wind observations from weather stations, so that anyone who is interested in computing the rate of eolian sand transport can use the simple formula provided in this paper for general application. The necessity for complicated measurements of atmospheric shear velocity is eliminated.

DEVELOPMENT OF THE METHOD

    The relationship formulated by Hsu (1971a) for computing the rate of sand transported by the wind is (see Fig. 1)

$$q = K \cdot Fr^3 = K \left[\frac{U_*}{(gD)^{1/2}} \right]^3 \tag{1}$$
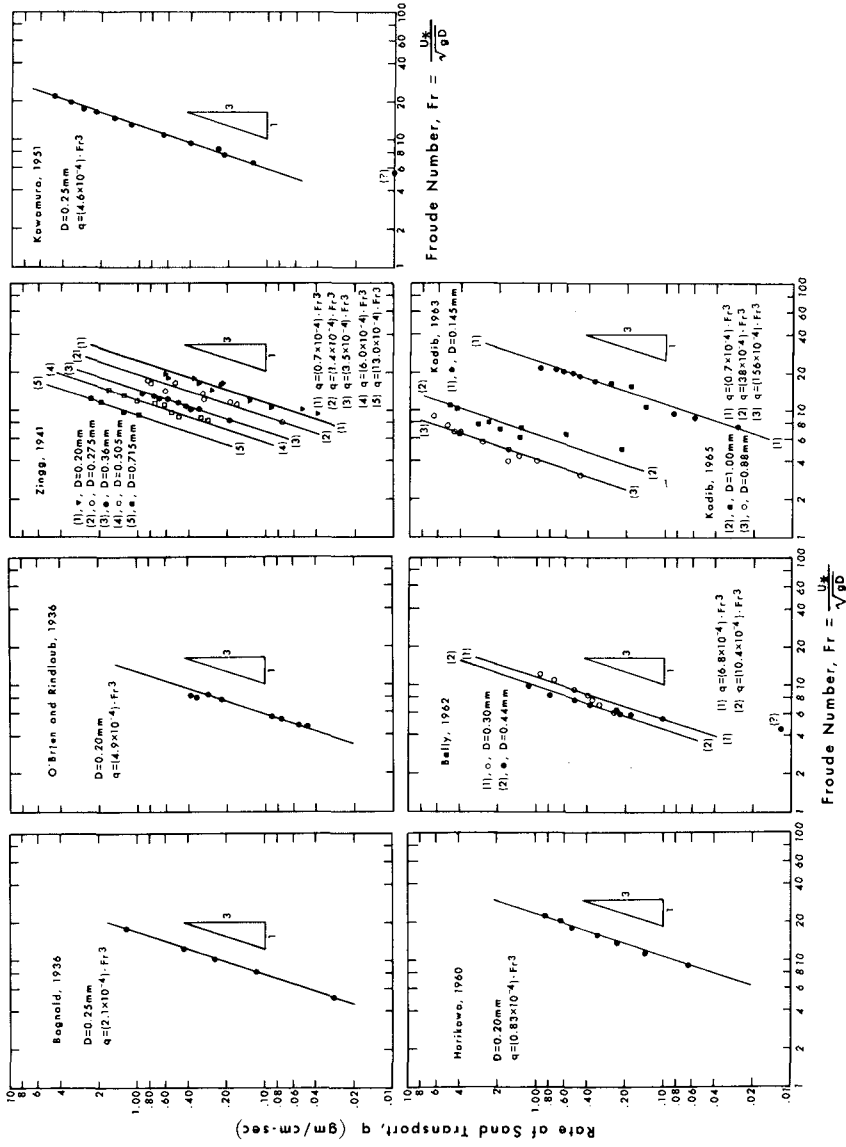
Figure 1. Froude number scaling in the rate of eolian sand transport (from Hsu, 1971a).

where q (gm/cm-sec) is the rate of sand transported by the wind and Fr is a special Froude number. Fr is a function of the atmospheric shear velocity U_* (cm/sec), the acceleration of gravity g (980 cm/sec^2), and the mean grain size of the sand particles D (mm). K is defined as the dimensional eolian sand transport coefficient and has the same dimensions as q. The values of K are delineated in Fig. 2. The value of Fr is explicitly determined by the bracketed term in equation (1).

If the value of U_* is known, the rate of eolian sand transport can be computed. In order to utilize routine wind observations to compute U_* values, the following procedure was developed.

In the lowest turbulent layer of the atmosphere over land, under homogeneous steady-state conditions, the logarithmic horizontal wind velocity increase with height has been observed over beaches (Hsu, 1971b), over tidal flats (Hsu, 1972), over deserts (Bagnold, 1941), and in laboratory channels (Kadib, 1965).

The logarithmic wind profile law states that

$$\bar{U}_z = \frac{U_*}{\kappa} \ln \frac{z}{z_0} \quad , \qquad (2)$$

where $\bar{U}_z$ is the mean horizontal wind velocity at any given height z, U_* is the shear (or friction velocity, equivalent to $[\tau/\rho]^{1/2}$, where τ is the surface wind stress and ρ is the air density), κ is the von Kármán constant (≈ 0.4), and z_0 is the aerodynamic roughness length defined under the boundary condition that $\bar{U}_z = 0$ at $z = z_0$. The value of z_0 depends upon the characteristics of the underlying surface.

Figure 2. Determination of eolian sand transport coefficient from mean grain size of sand particle (from Hsu, 1971a)

Under eolian sand transport conditions, however, equation (2) should be modified such that

$$\bar{U}_z - U_t = \frac{U_*}{\kappa} \ln \frac{z}{z_{ot}} \quad , \qquad (3)$$

where U_t is the threshold velocity (see Bagnold, 1941) and z_{ot} is the roughness length defined under the boundary condition that $\bar{U}_z = U_t$ at $z = z_{ot}$. The value of z_{ot} depends upon the mean grain size of the surface sand under question.

Figure 3 verifies the validity of equation (3) on coasts and in deserts by showing some examples of wind profile measurements under eolian sand transport conditions. For instrumentation and wind data reduction and analysis procedures on coasts and in deserts, see Hsu (1971b, 1972) and Bagnold (1941), respectively. Similar criteria have been used in investigations in laboratory channels (e.g., see Kadib, 1965).

Figure 3. Examples of observed wind velocity vertical
distribution over sand surfaces when the sand was in
motion. The data lines are indicated by H-E, H-T, and
B for measurements made by Hsu over a beach near Playas,
Ecuador, by Hsu over a beach on northern Padre Island,
Texas, and by Bagnold in the Libyan desert (from Hsu,
1973).

Figure 4 shows that the linear relationship between shear and wind velocities is further verified by wind profile measurements for eolian transport of sands with mean diameters ranging from 0.2 to 0.3 mm. This relationship was derived using data collected from a variety of environments, including those over beaches, tidal flats, and small dune fields in Barbados, Ecuador, Florida, and Texas by Hsu (1971a, 1972, and unpublished data), over an Arctic beach by Walters (1973), and in the Libyan desert by Bagnold (1941). Some detailed information was given in Hsu (1973, 1974).

Thus the rate of eolian sand transport can be computed by a given value of D and wind speed at 2 m above the surface by using Figs. 2 and 4. However, it is not always convenient for an anemometer to be located 2 m above the surface. In this case, equation (3) may be used. At heights $z = 2$ m and 10 m we obtain from equation (3) and Fig. 4 the following set of equations to calculate U_* as a function of U_{10m}:

$$U_{10m} - U_t = \frac{U_*}{\kappa} \ln \frac{1000}{z_{ot}} \qquad (4a)$$

$$U_{2m} - U_t = \frac{U_*}{\kappa} \ln \frac{200}{z_{ot}} \qquad (4b)$$

$$U_* = 0.044 \ U_{2m} \qquad (4c)$$

Equation (4) yields

$$U_* = 0.037 \ U_{10m} \ . \qquad (5)$$

Note that the difference between equations (4c) and (5) is rather small. Because an anemometer at a height between 2 and 10 m is usually available at nearby weather stations, for general applications the average of equations (4c) and (5) may be useful:

$$U_* \ (cm/sec) = 4.0 \ U \ (m/sec) \qquad (6)$$

where U is the known hourly averaged wind velocity in the constant direction of transport at an anemometer height between 2 and 10 m.

Therefore, by using Fig. 2 in conjunction with equation (6), the rate of eolian sand transport can easily be computed for a given value of D. An example is given in the following section.

APPLICATION OF THE METHOD

It is simple to apply the method developed in the previous section. For example, to compute the most commonly occurring and well-sorted standard
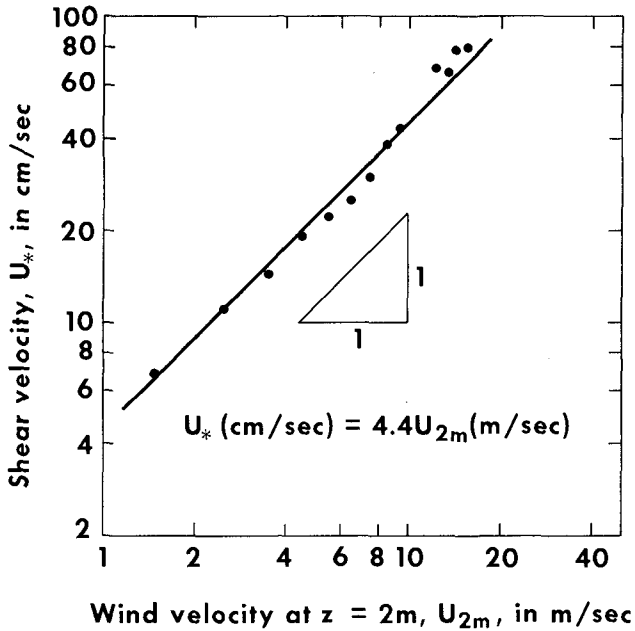
Figure 4. Relationship between shear and wind velocities
synthesized from many measurements, ranging from tropical
to arctic continental coasts (for details see Hsu, 1973
and 1974) and the Libyan desert, as well as a windward
beach near Bath, on the island of Barbados, West Indies.

sand particle size D (= 0.25 mm; see, e.g., Bagnold, 1941), the following
steps may be followed:

1. From Fig. 2 we have K = 2.17 x 10^{-4} by setting D = 0.25 mm.

2. Substituting values of K, g, D, and equation (6) into
    equation (1) we get

$$q = 1.16 \times 10^{-4} \ U^3 \ .\qquad\qquad(7)$$

Equation (7) is shown in Fig. 5.

     The accuracy of this simple method should be within the experimental
error arising from field and laboratory measurements because equation (7)
is developed from the data sets. For those sand particle sizes not well
sorted, Bagnold's correction criterion may be used. For nonstandard sizes,
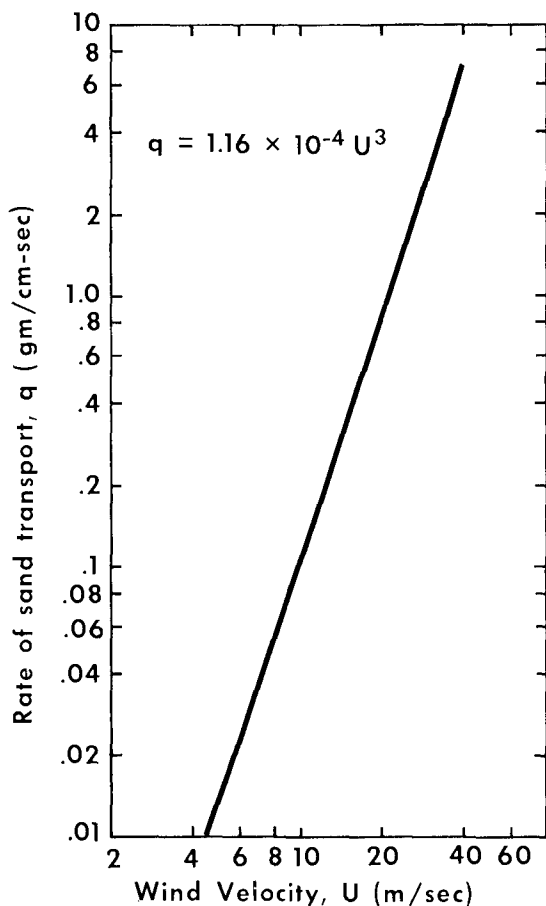
Figure 5. Computation of eolian sand transport for standard
particle size (D = 0.25 mm) from routine wind observations at
height 2 to 10 m above the ground obtained from nearby weather
stations. U is the known hourly averaged wind velocity in the
constant direction of transport.

it is recommended that Kadib's collection of U_t and z_{ot} be applied to the
computation of U_*, which will be used in conjunction with K to calculate q.
Further research should be conducted on the transport mechanism in the wet
sand environment (e.g., swash zone) and sand movement around manmade coastal
structures.

REFERENCES

Bagnold, R. A., 1941, The physics of blown sand and desert dunes. New York
      (Morrow), 265 pp.

Hsu, S. A., 1971a, Wind stress criteria in eolian sand transport. J. Geophys.
      Res., 76:8684-8686.

_____, 1971b, Measurement of shear stress and roughness length on a beach.
      J. Geophys. Res., 76:2880-2885.

_____, 1972, Boundary-layer trade-wind profile and stress on a tropical
      windward coast. Boundary-Layer Meteorol., 2:284-289.

_____, 1973, Computing eolian sand transport from shear velocity measure-
      ments. J. Geol., 81:739-743.

_____, 1974, Experimental results of the drag-coefficient estimation for
      air-coast interfaces. Boundary-Layer Meteorol., 6:505-507.

Kadib, A. A., 1965, A function of sand movement by wind. University of
      California, Berkeley, Tech. Rept. HEL-2-12, 91 pp.

Walters, C. D., 1973, Atmospheric surface boundary layer wind structure
      studies on an Alaskan Arctic Coast during the winter and summer
      seasons. Unpublished Master's thesis, Louisiana State University,
      45 pp.

CHAPTER 95

SCOUR UNDER A VERTICALLY OSCILLATING LEG

by

Richard Silvester
Department of Civil Engineering
The University of Western Australia
Nedlands. W.A.

ABSTRACT

Mishaps with jack-up oil rigs could be caused
by scour beneath their legs as they oscillate
vertically, either on site or when being shifted to
or from site.   This action was replicated in the
laboratory by moving cylindrical feet to and from a
sandy bed at frequencies appropriate to the scale of
the model.   By retaining equal Reynolds numbers for
the sand grains, whose size was commensurate with
prototype material, the period of oscillation had to
vary with the leg diameter.   By adopting a suitable
size scale, a range of periods was determined from
knowledge of resonant motions of rigs in relatively
deep water.   Erosion was recorded which appeared
sufficient to cause mal-distribution of load in the
structure.   Even when oscillations occurred in a
leg penetrating the bed, no support was available
due to liquifaction of the soil.   The two pilot
studies herein described indicate the need for a
comprehensive research program on the subject, due
to the large investments in jeopardy.

INTRODUCTION

Among the various offshore mobile drilling units, the jack-up
rig has become increasingly popular.   From a survey by Howe in
1968[1] there were 92 such units in a total of 192 at that time.
However, this form of rig has suffered a high incidence of mishaps.
As seen in Table 1 they have accounted for 60% of the major accidents,
excluding those due to blowouts.   In this context a major accident
is defined as damage of at least US$1.0M or total loss.   Of these
half were suffered on site, through storm action, normal conditions
or moving on or off site, the last accounting for two thirds of this
category.

Howe stated: "A problem plaguing early pile-supported jack-up
rigs was excessive leg penetration in soft soils.   At least 2 of
these rigs tipped over because of apparent soil failures while
preparing to move off location".

1627

TABLE I.   Mishap incidence with oil rigs 1949-68 - after Howe[1]

Type of Rig		Submersible	Jack-up	Ships & Barges	Semi-Submersible	Totals
On Location	Blowouts	1	3	1	-	5
	Severe Storm	2	1	2	2	7
	Normal Conditions	1	2	-	-	3
	Moving On or Off	1	6	-	-	7
Under Tow		-	6	1	1	8
Totals		5	18	4	3	30
% of Total Accidents (Ex-Blowouts)		16	60	12	12	100
% of Total Exposure		29	43	23	5	100

It appears that motion of the legs near the seabed can produce an
unstable condition. Rigs are particularly prone to this when load is
being partially taken by a floating carrier, but even when in position such
a structure can suffer resonant swaying, which can lift legs from the bed a
matter of centimeters.   It will be shown in this paper that these
oscillations, with periods from 3 to 10 seconds, can scour significant holes
beneath legs, even in non-cohesive soils of large grain size.

PROTOTYPE LEG MOTIONS

Harleman et. al[2] have stated that the first modal frequencies of tall
offshore towers are 0.1 cps or higher, or a period of 10 seconds or less.
This is based upon the motion of structures fixed at the bed as might apply
to a piled structure (see Figure 1A).   Jack-up rigs are normally founded
on the seabed, or if tied by piles will be free to oscillate when being
shifted on or off site.   In this event a certain degree of rocking can ensue
which causes repeated lifting of the legs from the floor.

This resonant motion is depicted in Figure 1B, the frequency of which can be determined simply if it is assumed that the mass of the structure is concentrated at the deck and small angles of tilt are considered.   The equation of motion is then

$$\frac{d^2\theta}{dt^2} = \pm \frac{B\,g}{2[L^2+B^2/4]} \qquad\qquad ---\;(1)$$

where θ = instantaneous angle of tilt from the vertical

         L = height of the deck centre of gravity from the sea bed

         B = horizontal distance between legs

         g = acceleration due to gravity

         t = time

This represents a periodic, but not simple harmonic motion, the period of which is given by

$$T = 8[(L^2 + B^2/4)\theta'/Bg]^{\frac{1}{2}} \qquad\qquad ---\quad(2)$$

where θ' is the extreme angle of tilt in radians (see Figure 1B).

Typical dimensions for deep-water jack-up rigs according to Howe[1] are: L = 100 metres, B = 50 metres, giving $T = 37.3\,\sqrt{\theta'}$.   For a leg to rise 0.5 metre from the bed $\theta' = 0.01$ radians (0.57°), so that T = 3.7 secs.

The resonant input to produce such rocking could be provided by normal wind generated waves.   For example 10 second waves propagating through this 50 metre wide structure in say ?? metre depth of water would exert sequential forces on the legs with a period of 3.7 seconds.

Larger vertical lifts of the legs could take place with longer periods of oscillation.

WATER PARTICLE VELOCITIES

Assuming that a leg moves vertically from the bed to some height 2A above it, this implies an amplitude of oscillation A with some period T. As seen in Figure 2 some scour (S) will ensue the size of which must be defined at some radius;   in this case it was taken at the periphery of the leg.   Maximum scour occurred between this radius and the centre of the leg.

If it is also assumed that the vertical velocity of the water adjacent to the foot is equal to that of the foot, is zero at the bed, and is linearly distributed between, the horizontal water velocity (U) at the radius r is then given by (3)

$$U = -Vr/2R \qquad \qquad --- (3)$$

where   R = height of the foot above the bed at any instant.

It is seen from Figure 2 that

$$R = S + A(1 + \sin 2\pi t/T) \qquad \qquad --- (4)$$

if sinusoidal oscillation is assumed and t is the instantaneous time from the mean level
The vertical velocity of the foot $V = \partial R/\partial t$ which from equation (4) becomes

$$V = (2\pi A/T) \cos 2\pi t/T \qquad \qquad --- (5)$$

Substituting for R and V into equation (3) gives

$$U = - \frac{\pi r}{T} \left[\frac{\cos 2\pi t/T}{(S/A) + 1 + \sin 2\pi/T} \right] \qquad --- (6)$$

By differentiating equation (6) with respect to t and equating to zero the maximum velocity becomes

$$U_{max} = \pm \frac{\pi D}{2T} \Big/ \sqrt{(\frac{S}{A} + 1)^2 - 1} \qquad \qquad --- (7)$$

where   D = diameter of the leg

The relationship of U_{max}, D/T and S/A is illustrated in Figure 3. It is seen that as soon depth increases so maximum velocity decreases, indicating that some equilibrium will be reached when particles are no longer disturbed.

Equation (7) is dimensionally homogeneous, but it is worthwhile to approach the parameter problem from dimensional analysis, from which it can be shown that the following terms are relevant

$$\pi_1 = S/D, \quad \pi_2 = A/D, \quad \pi_3 = d_s/D, \quad \pi_4 = Dd_s/\nu T,$$

$$\pi_5 = (S_s-1)gd_s^3 /\nu^2$$

where d_s = median diameter of the sediment

ν = kinematic viscosity of the water

S_s = specific gravity of the sediment (assuming that of the fluid is unity)

so that $S/A = f(A/D, Dd_s/vT, d_s/D, (S_s-1)gd_s^2/v^2)$ - - - (8)

If equation (7) is approximated by

$U_{max} = \pm \pi DA/2TS$ - - - (9)

the Reynolds number of flow for the sediment particles is

$R_n = \dfrac{\pi DAd_s}{2TSv}$ - - - (10)

indicating that $S/A = f(Dd_s/vt)$, which is similar to π_4 above.

SCALING LAWS

From equation (7) it is seen that similar S/A ratios will ensue in model and prototype if $(D/T)/U_{max}$ ratios are similar. For sediments of similar characteristics in prototype and model similar U_{max} values should be employed. This demands that $(D/T)_r = 1$. A similar conclusion is reached from equation (10) if d_s/v is to remain constant.

It was necessary to decide on a prototype diameter which any model leg purported to represent. In tests at the Asian Institute of Technology[4] a scale of 1:50 was assumed, so that legs of diameter 2.54, 5.08, and 7.62 cms represented prototype values of 1.27, 2.54 and 3.81 metres respectively. Amplitudes used were 2.11, 3.71, 5.56 and 7.5 mm, representing prototype values of 10.55, 18.55, 27.80 and 37.50 cms.

As noted already, the prototype periods of oscillation can vary up to 10 seconds. A range of 2.5 to 10 was tested which, because of the 1:50 scale and $(D/T)_r = 1$, became 0.05 to 0.2 seconds. The AIT tests were also conducted with three sediments of median diameter 0.018, 0.043 and 0.085 cms. Fresh water was used throughout for which the average ambient temperature of 30°C gave $v = 0.0085$ stokes.

At the University of Western Australia[5] legs of larger diameter were used, namely 8.05, 10.62, 13.13 and 15.78 cms, which were oscillated over a similar range of A/D values as for the former tests (i.e. 0.0276 to 0.219). If these purported to represent the same prototype legs as before the scale approximates 1:20. The periods of oscillation were thus in the same prototype range as previously.

Only one median diameter of sand (0.0177 cms) was used but two different water densities of 1.155 and 1.194 were obtained by the addition of salt. The kinematic viscosities were altered very little. As will be seen, insufficient runs were made from which to draw any conclusions on the influence of the (S_s-1) and v terms in the π_5 parameter.

EXPERIMENTAL PROCEDURE

The legs were attached to a sliding shaft which was activated by a crank arm off a rotating wheel.   The amplitude and speed of motion could be varied through a variable speed drive.   The number of oscillations were recorded by a tachometer and speed setting by stroboscope.   Initial tests were conducted to find the time necessary for equilibrium scour profiles to be reached. This is an important element in such tests with sediment and might be the source of some of the scatter encountered in the results.

Prior to oscillating the legs the 7 cms thick sand bed was compacted by tamping under saturated conditions.   The leg was attached with its minimum level set at the sand surface.   The scour profile was subsequently measured by means of a horizontally traversing pointer gauge.   A typical set of profiles is illustrated in Figure 4.   At very high frequencies the profile became conical, in which case the movement of sand particles was intense and the resultant slope of the hole (from the leg periphery inwards) was at the angle of repose for the soil.   These holes have been omitted from the analysis since the scouring conditions are quite different from the remainder of the tests.   This is not to infer that this phenomenon does not warrant investigation, but the present study centered on incipient motion of particles in the equilibrium profile.

RESULTS

The obvious dependent ratio from equation (7) is S/A since it entered into the calculation of U_{max}.   This was then tested against dimensionless parameters $Dd_s/\nu T$, A/D, d_s/D and $(S_s-1)gd_s^3/\nu^2$.   As already noted too few results were obtained on these pilot studies to check the last parameter adequately.   A regression analysis conducted on data from both test series resulted in an equation.

$$\frac{S}{A} = f\left\{\left(\frac{Dd_s}{\nu T}\right)^{1.061}\left(\frac{A}{D}\right)^{0.224}\left[\frac{(S_s-1)gd_s^3}{\nu^2}\right]^{-0.700}\right\} \quad - - - (11)$$

which was then approximated to

$$\frac{S}{A} = f\left\{\left(\frac{Dd_s}{\nu T}\right)\left(\frac{A}{D}\right)^{\frac{1}{4}}\left[\frac{(S_s-1)gd_s^3}{\nu^2}\right]^{-\frac{2}{3}}\right\} \quad - - - (12)$$

Results are plotted in Figures 5 and 6.   The bulk of the data for d_s = 0.0177 and 0.018 are shown in Figure 5, where it is seen that the small change in median diameter produces a cluster around lines at slightly different slopes.   The kinematic viscosities were 0.0113 and 0.0085 stokes respectively. At this stage it does not warrant the determination of an equation for either of these curves, only to note that scour can range from A to 7A.   In terms of the prototype equivalents this could range from 10 to 200 cms for the diameters implied.

The few results for larger diameter particles are well defined by the two lines drawn in Figure 6. They indicate that for coarser sediments slight increases in the combined parameter, as occasioned by larger diameters or greater frequencies of oscillation, could result in excessive scouring for any given leg amplitude. The few points for (S_s-1) changes are inconclusive since they provided scatter similar to the results for $d_s = 0.0177$ in Figure 5.

It may be thought that this scouring action could be compared directly with incipient bed movement due to waves, of which Silvester and Mogridge[6] collected the many formulae derived. However, there is one significant difference in the conditions in that positive and negative pressures are exerted on the soil under the leg, which according to Bagnold[7] has a greater disturbing influence on larger sized grains. As the leg rises so is a suction applied to the surface of the bed and the particles placed in suspension are then forced outwards with the water in the subsequent downward motion. It does not take a great frequency to have the bed beneath the leg hidden within a fog of suspended sand.

FURTHER OBSERVATIONS

Although the apparent scour dimensions as given above do not appear to be disastrous, they would provide a distribution of load on the legs quite different from those for which they and the whole frame were designed. But it should be remembered that in the current tests the leg oscillated only down to the original bed level. In practice a leg could well follow its scour hole down and so keep digging. In fact a test was conducted in which an oscillating leg was lowered into the sand surface with no apparent increase in its resistance to motion. The boiling of the soil indicated that liquifaction was taking place. This action probably prompted Howe's statement quoted in the introduction. It can be envisaged that coarse sand would suffer this loss of load carrying capacity more than fine sediment which would resist this fluctuating dispersion of water. However, prior to this buried condition the fine sediment would be scoured more by any given oscillating condition.

A curve developed for the time required to reach equilibrium scour (4) indicated that in one half to two days in prototype conditions a continuous oscillation could produce the results as indicated. This is well within the realms of storm duration when resonant oscillation could be set up.

Another phenomenon observed in the tests was a vortex generated up the sides of the leg. As illustrated in Figure 7 this had an upward velocity adjacent to the leg with a less well defined return flow out from this surface. This water motion carried sediment, placed in suspension by the suction and high velocities beneath the foot, up the sides of the leg and outwards to some radius before its fall velocity exceeded the upward stream. The radius of the scour equated that of the observed horizontal dimension of the vortex plus the radius of the leg. For finer sediments the mound radius exceeded this sum and for coarser material it was smaller.

The generation of this vortex is possibly due to the pressure
fluctuations produced at the outer periphery of the foot.   As the leg
moves upwards water is drawn in with a maximum horizontal velocity at the
foot level.   As the leg decelerates on its upward journey the pressure
becomes positive, so forcing water out from the base of the foot.   This
outward flow interacts with the previous inward current, to force fluid up
the side of the leg.   By this circulation material is removed from the
vicinity of the leg and placed in a mount surrounding it.   Perhaps the
volume of sediment removed may be a better criterion to correlate with leg
characteristics rather than scour at the periphery of the leg.

TOPICS FOR FURTHER RESEARCH

The two pilot studies can only be instrumental in directing attention
to this important problem.   All the variables tested need much more data
on which to draw conclusions and derive relationships.   But the exigencies
of natural oceanic conditions must not be forgotten, such as wave action
with its mass-transport current near the bed boundary layer and ocean
currents which create their own vortex structure.   Posey[8] has alluded to
the turbulent structure produced by wave action within the space frames of
oil rigs and similar structures, which can scour major depressions under
them.   All these actions need to be researched in concert before any
solution can be contemplated.   Metering of sediment suspension around
existing rigs would be a worthy investment.   This would necessarily have
to be carried out with sampling tubes fixed to the legs at the outset.

Specific problems requiring attention are :-

1.   The actual motion of structures rocking on a floor require analysis
     and measurement since the sinusoidal oscillation used herein may
     distort the scouring action greatly, either through under-rating or
     in over-rating it.

2.   More tests are required to find the influence of A/D, d_s/D,
     $(S_s-1)gd_s^3/\nu^2$ by using sediments of varying diameter and density
     with larger scale models.

3.   The phenomenon of liquifaction needs researching since its influence
     could overshadow any scouring that takes place.

4.   Future tests should incorporate measurements of velocities and
     pressures on the base of the foot and on the bed beneath it.   This
     latter could be accomplished by a fixed bed shaped as a scour hole.

5.   Experiments should be conducted in the presence of waves and currents,
     firstly with single cylindrical legs and later with the rig structure
     as a whole.

CONCLUSIONS

1.   The history of mishaps with structures resting on the seabed would
     indicate a foundation source of failure which to date has not been
     fully appreciated.

2. The possible resonant oscillation of oil rig structures, with
    consequent lifting of feet from the floor, could produce scouring
    or liquifaction of the soil which can result in a dangerous load
    redistribution.

3. Water particle velocities and pressure fluctuations beneath a leg
    oscillating vertically, with frequencies experienced in nature, can
    be sufficient to remove sediment from beneath the foot.

4. Scour can be related to leg dimensions and sediment characteristics
    by suitable dimensionless parameters, the final form of which requires
    much more experimental investigation.

5. The scaling criterion would appear to be the Reynolds number for
    fluid velocity past the sand grains, which for similar model-prototype
    sediment and fluid results in a diameter to period ratio of unity.

6. The time to produce equilibrium scour profiles is well within the
    period during which storms can be experienced.

7. The removal of sediment by the vortex generated up the sides of an
    oscillating leg determines in part the diameter of the resulting
    mound.

8. There are many facets to the problem of scour beneath space frames
    in the very turbulent medium of the sea which require urgent attention
    from the oil industry.

9. Metering of sediment suspension near the sea floor could provide an
    immediate indicator of foundation problems.

ACKNOWLEDGEMENTS

REFERENCES

1. Howe, R.J.   "Offshore Mobile Drilling Units", Ocean Industry,
                        $\underline{3}$ (7), 1968.

2. Harleman, D.R.F., Nolan, W.C. and Honsinger, V.C., "Dynamic Analysis
                        of Offshore Structures", Proc. 8th. Conf. Coastal
                        Eng., 1963, 482-499.

3. Svendsen, I.A.   "On the forces induced on a rectangular cylinder
                        by a forced heave motion with draught depth ratio
                        close to unity", J. Hyd. Res. $\underline{6}$ (4), 1968,
                        335-360.

4. Barradell-Smith, J.M., "Scour under offshore mobile jack-up rig legs".
                        M.Eng. Thesis No.324 Asian Institute of Technology,
                        Bangkok, 1970.

5.   Taneerananon, P.   "Scour under oil rig legs", B.E(Hons) Thesis,
                              University of Western Australia, 1972.

6.   Silvester, R. and Mogridge, G.R., "Reach of waves to the bed of the
                              continental shelf", Proc. 12th Conf. Coastal Eng.
                              2, 1970, 651-667.

7.   Bagnold, R.A.   "Motion of waves in shallow water - interaction
                              between waves and sand bottoms", Proc. Roy. Soc.,
                              A187, 1946, 1-18.

8.   Posey, C.J.   "Protection of offshore structures against underscour"
                              Proc. ASCE 97 (HY7) 1971, 1011-1016.
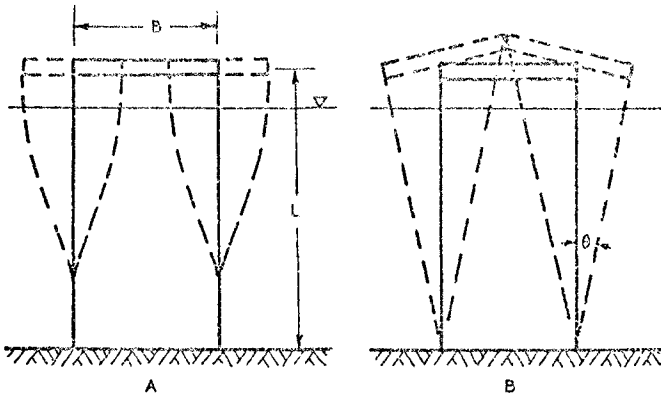
Figure 1 - Possible motions of structures in deep
         water.

Figure 2 - Definition sketch of leg oscillation and scour.
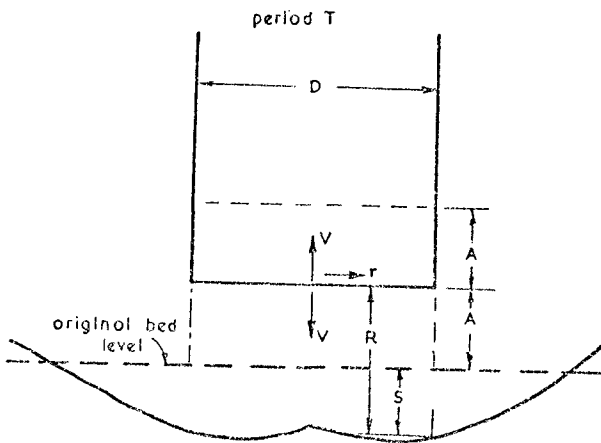
Figure 3 - Relationship between U_{max}, D/T and S/A.
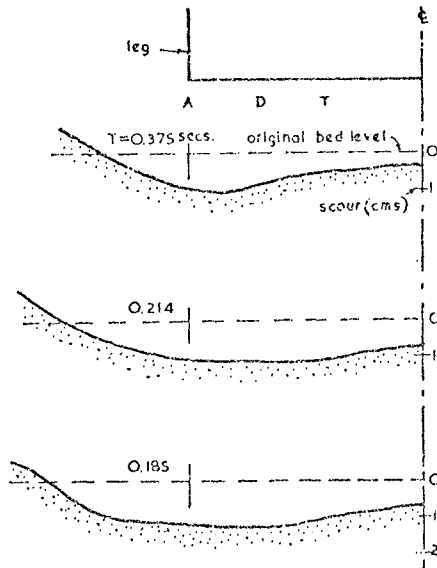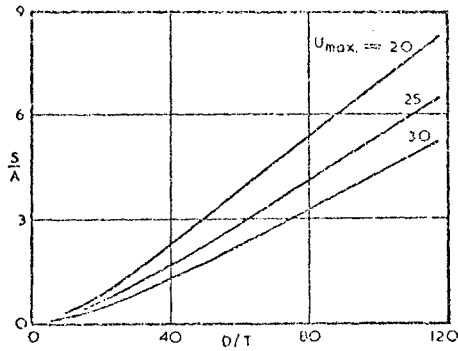
Figure 4 - Typical set of scour profiles for d_s = 0.0177 cms, A = 0.502 cms, D = 13.13 cms and T as shown.

Figure 5 - Scour ratio S/A versus a combined
           dimensionless parameter for the bulk
           of data.
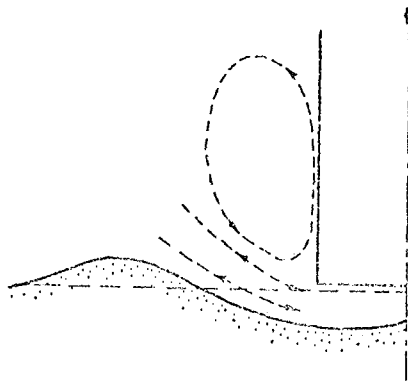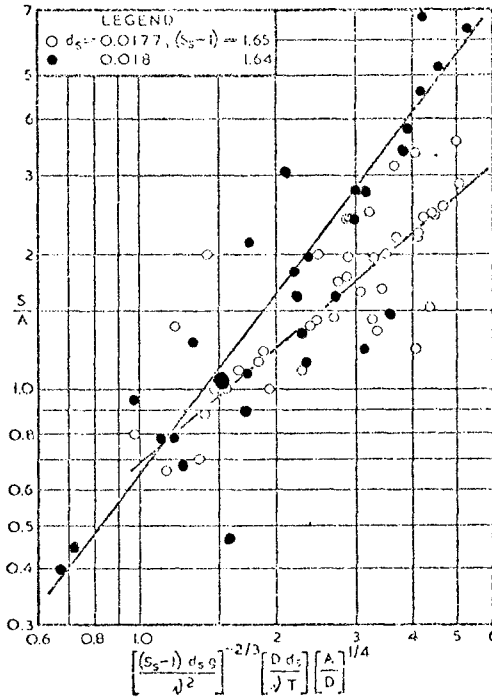
Figure 7 - Vortex formation around circular leg.
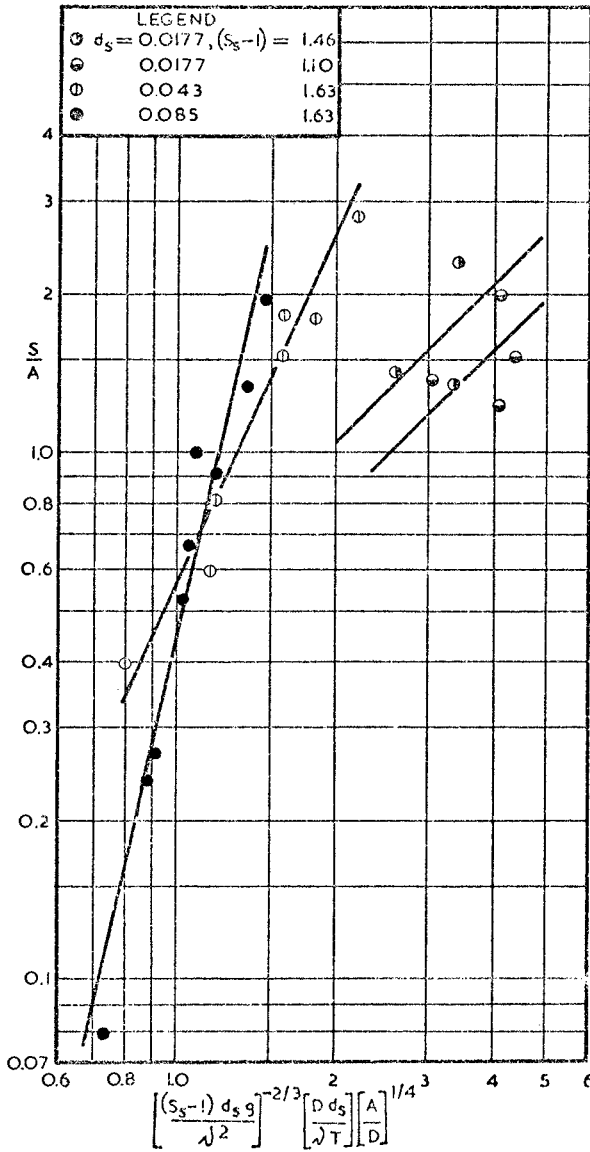
Figure 6 - Scour ratio S/A versus a combined dimensionless
          parameter for variations in d_s and ν.

CHAPTER 96

EXPERIMENTAL INVESTIGATION OF TURBULENCE NEAR CYLINDERS

by

Torkild CARSTENS [x]
Søren Peter KJELDSEN [xx]
Ola GJØRSVIK [xx]

ABSTRACT

Model tests with locally generated turbulence near hori-
zontal and vertical cylinders are reported.

Turbulence is measured with newly developed ultra-sonic
probes, and spectral density functions and auto-correlation
functions are given.

Tests are carried out in uniform currents, in sinusoidal
waves, and in combinations of current and waves.

Results are given for a viscous laminar boundary layer
corresponding to a very fine sediment, and for a turbulent
boundary layer corresponding to a hydraulically rough bottom.

In Norway recent scour research, initiated by the North Sea
oil operations, has been guided in three directions:

1) Scour around big gravity structures

2) Distribution of pore pressures in the ground under
    wave loads.

3) Local scour near unburied pipelines.

---

[x] Chief of research, [xx] senior research engineers, River
     and Harbour Laboratory at the Society for Industrial
     and Technical Research at the Technical University of
     Norway

The unburied pipeline and therefore an extensive research work
on possibilities for scour, and forces on the pipeline during
different scour stages has been carried out.

This has been reported by KJELDSEN, GJØRSVIK, BRINGAKER,
JACOBSEN 1973 (1), and as a result of this a practical relation
has been given from which scour depths near unburied pipelines
can be estimated.

With E as a scour Euler number and F as a pipeline Froude
number the scour depth can be found from the equation

$$E = 4/5 \cdot F^{4/5} \tag{1}$$

This equation is based on tests in uniform currents with
pipeline Reynolds numbers in the interval:

$$1 \cdot 10^4 \leq R \leq 2 \cdot 10^5 \tag{2}$$

15 tests were carried out and a regression analysis gave a
correlation coefficient 0,98 to eq. (1).

From this investigation it was clear that it was the energy
in the locally generated turbulence that was responsible both
for the scour and for the forces on the pipelines.

The conclusion was drawn that no more knowledge about scour
and pressure distributions around cylinders could be obtained
using "all over parameters".

Therefore the investigation reported here with observations
and analysis of locally generated turbulence, was initiated.

EXPERIMENTAL SET-UP

Two ultra-sonic probes were available for the turbulence
measurements.

These are "transit time difference velocity meters".

The instruments are shown in Figure 1. The first one has
four piezo-electrical crystals and uses two ultrasonic sound
beams. The frequency used in the sound beams is 300 Hz.

ULTRA - SONIC PROBES

G II

PROBE ANGLE θ

PROBE

CRYSTAL

VELOCITY

FLUME

3,4 mm

SOUND BEAM

WAKE

40 mm

60 mm

G III

PROBE ANGLE θ

WAKE

PROBE

VELOCITY

2,4 mm

SOUND BEAM

FLUME

34 mm

40 mm
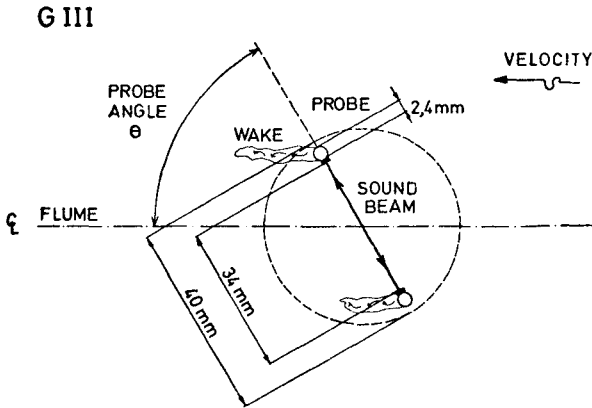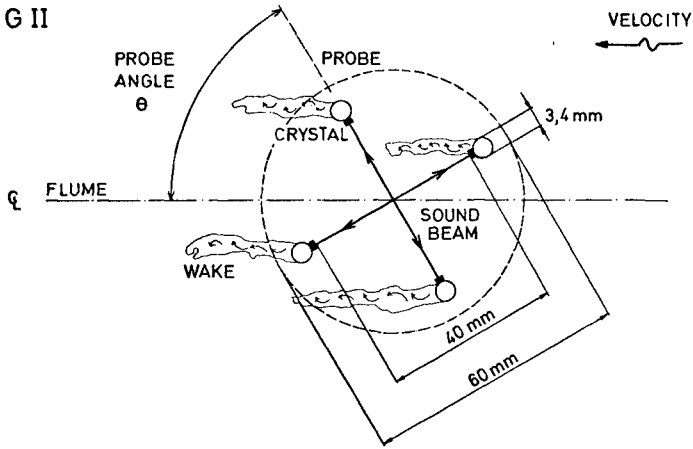
Fig. 1

The second one has two crystals and uses one ultrasonic sound beam. From recorded time differences of the sound beams travelling through the water, the flow velocity can be evaluated.

The first probe gives the velocity vector in a (horizontal or vertical) plane, while the other gives one component of the velocity vector only.

One particular advantage is, that the probes are very efficient in two phase-flow with heavy sediment transport.

A comprehensive description of the instruments and the calibration procedure is given by AUDUNSON, GYTRE, LAUKHOLM (2).

The probes were placed immediately upstream and downstream of the actual structures.

Two series of tests were performed, as shown in table 1.

In the first test series, no scour action took place and only turbulence was recorded.

The tests were performed in a 26 m long, 0.75 m wide and 0.60 m deep flume with a bottom of shingles with a mean grain diameter $d_{50}=16$ mm giving a hydraulically rough bottom and a very strong turbulence, which was extremely useful for the testing and calibration of the signal from the probes.

For verification of the results runs with uniform currents on a plane bottom, and different water depths were performed.

The probes were placed on different positions along the flume to check the growth of the boundary layer and to give the position of the fully developed velocity profile.

After this, the same verifications were done with sinus-oidal waves and combinations of waves and currents.

After turbulence recordings were taken for all these situations, a horizontal cylinder with a diameter of 6 cm was placed on the bottom and the turbulence recorded just ahead and just behind.

Similarly a vertical cylinder with the same diamter were placed on the bottom and the turbulence near it was recorded.

For comparison another test series was performed. Here the "clear water scour case" was examined, where no grain movement takes place on an undisturbed bottom while scour action starts ahead of an unburied pipeline.

These tests were performed in a 33 m long, 0.5 m wide and 2 m deep flume, with a silty bottom, with a material with a mean grain diameter $d_{50}=0.074$ mm which is very similar to bottom materials found in the North Sea.

T E S T   T A B L E   1

RUN No.	Flume (m)	Structure	Diameter (cm)	Bottom (mm)	Flow	Mean flow velocities (m/s)	Waves (m)(sec)	Water depth (m)	Scour	Probe
—	—	—	—	—	—	—	—	—	—	—
1-22	Length:26 Width:0.6 Depth:0.75	Unburied pipeline Vertical pile	6.0 6.0	Shingles d₅₀=16	Uniform current Sinusoidal waves Current and waves	0.10 0.20	T=1.0-2.5 H=0.015- 13.2	0.20 0.30 0.50	No scour. Turbulence recordings only.	G III Ultrasonic current meter One channel
52-56	Length:33 Width:0.5 Depth:2.0	Unburied pipeline	50.0 22.5 6.0	Silt d₅₀ = 0.074	Uniform current	0.20 0.25	—	1.50	Start of "Clear water scour" observed	G II Ultrasonic current meter Two channels

The viscous boundary layer in this flume was laminar, and tests were performed with pipelines with diameters 50 cm, 22.5 cm and 6 cm.

Only tests in uniform currents were performed in this flume.

The scour action was recorded and some results from the test series will be given, but further work has to be carried out, as correct turbulence recordings on a hydraulically smooth bottom are very difficult to obtain.

Possibilities for a digital as well as for an analogue analysis of the recorded turbulent signal existed.

The measuring period was 3 - 6 minutes.

Modification of the signal from the probe was done by a specially designed box ("ULTRA-GYTRE"). From there the signal was taken to a tape recorder (TANDBERG 100) and to a plotter (SANBORN).

From the tape recordings the measured signal was converted to digital form with a frequency of 10 Hz, giving a Nyquist frequency of 5 Hz, and anlysed on a computer.

Further the signal was taken to a wave analyser (NORTRONIC) and an xy-plotter (GÖERZ), which allowed us to make an analogue analysis of the frequency distribution in the measured signal.

As the noise level from the probe for higher frequencies was quite high, it was decided to base the analysis on the digital signal only.

From the converted data, a turbulent data base was obtained.

A fast Fourier analysis gave spectral density functions as well as autocorrelation functions.

SPECTRAL DENSITY FUNCTIONS

Spectral density functions were obtained for all tests mentioned in table 1, and as an example fig. 2 is given.

The measuring period varied in the different tests from 3 - 6 minutes.

To get more confidence in the obtained spectral density function, the signal was divided into 4 blocks overlapping each other, and each consisting of a measuring period of 102.4 sec.

SERIES: GII RUN 52

PROBE AHEAD OF PIPELINE

PIPELINE DIAMETER: D = 0,50 m

MEAN FLOW VELOCITY: V = 0,20 m/sec.

Components recorded in mean flow direction:

Mean velocity at probe level

(2,5 cm over bottom): $\bar{U}$ = 4,49 cm/sec.

Turbulence intensity: $\hat{u}$ = 11,90 cm/sec.

Relative turbulence intensity: $\frac{\hat{u}}{\bar{U}}$ = 264 %

Components recorded perpendicular to flow direction:

Mean velocity: $\bar{U}$ = 1,02 · 10^{-1} cm/sec.

Turbulence intensity: $\hat{u}$ = 2,05 · 10^{-1} cm/sec.

Relative turbulence intensity: $\frac{\hat{u}}{\bar{U}}$ = 200 %
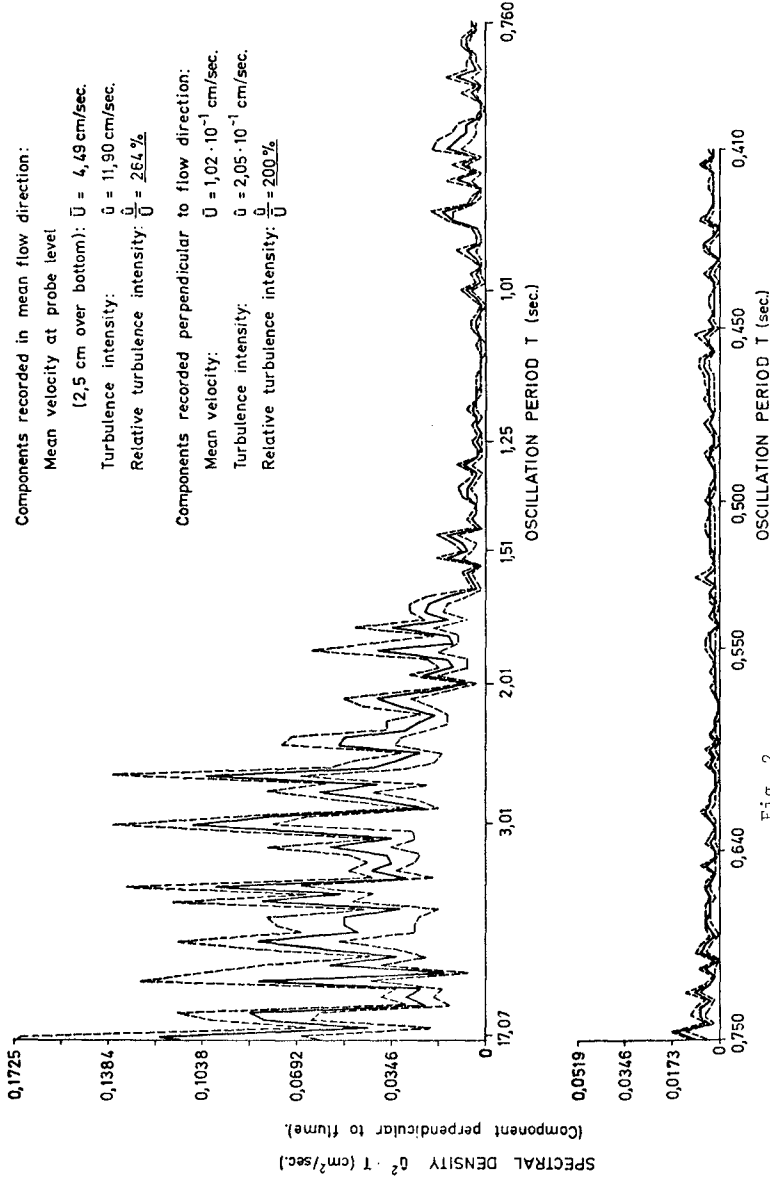
Fig. 2

The Fourier analysis was made on each block, and the mean values of the spectral density from the four blocks was calculated for each oscillation period and drawn as a full curve in fig. 2.

In addition the variance in the mean value for each oscillation period was calculated. The variance is added to and subtracted from the mean value, and shown in fig. 2 as dotted lines.

The lower limit for oscillations that could be recorded is given by the measuring period for the blocks, 102.4 sec, but to get confidence in the curve the lowest oscillations were omitted, and the lowest oscillation given in fig. 2 is the sixth harmonic, corresponding to period T=17.07 sec.

It is obvious from the results given in fig. 2, that the turbulence is clearly anisotrop, with a component perpendicular to the flume wall, that is negligible, compared with the component along the mean flow direction.

The turbulence is thus "two-dimensional", however, we were only able to measure the horizontal component.

Fig. 1 shows that in the "two-dimensional" case the distance in the mean flow direction between the probes on the current meter can be reduced, if the current meter makes an angle with the mean flow direction. The measurements can be obtained with a probe with one channel only, as shown in fig. 1. In the test series with G III the probe angle was 60°, thus giving a probe distance of 17 mm in the mean flow direction and a theoretical cut-off of turbulence at 8 Hz in a flow with a mean flow velocity of 0.20 m/sec.

A good deal of noise occurred in the signal, so in practice we got an upper limit of 2.5 Hz corresponding to an oscillation period of 0.4 sec.

The digital technique gives a reliable value up to this limit, since 2.5 Hz is half the Nyquist frequency.

The bandwidth actually obtained with the instrumentation and analysis used thus became

$$17.07 \overset{<}{=} T \overset{<}{=} 0.41 \text{ sec.} \tag{3}$$

AUTOCORRELATION FUNCTIONS

The difference in the turbulence between the various tests performed, is best illustrated by the obtained autocorrelation functions.

Fig. 3 illustrates the situation in a uniform current with a mean flow velocity of 0.20 m/sec.

SERIES: G III RUN 3

V = 0,20 m/s
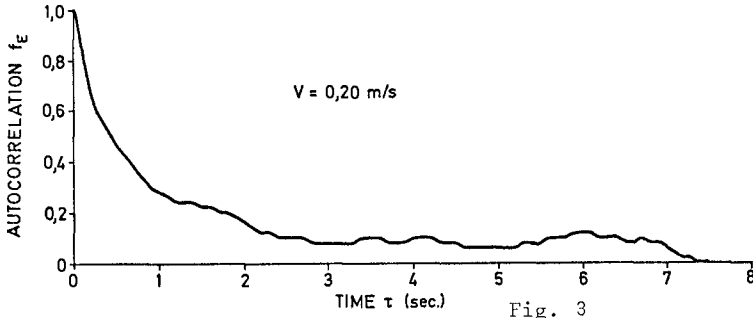
Fig. 3

SERIES: G III RUN 7

WAVE: T = 2,5 sec.
H = 0,13 m

Fig. 4

SERIES: G III RUN 4

WAVE: T = 2,5 sec.
H = 0,015 m

V = 0,20 m/s
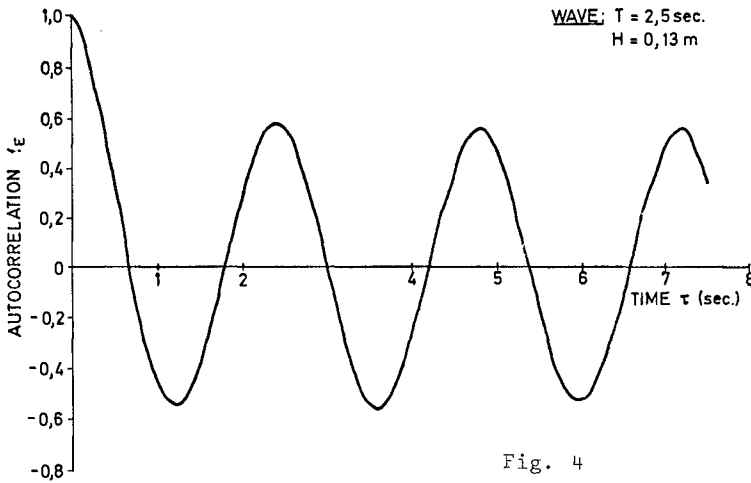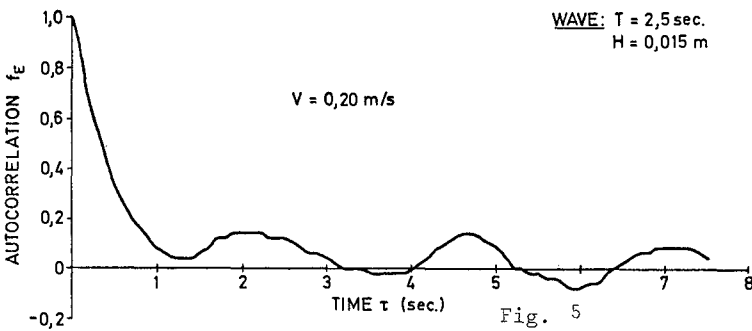
Fig. 5

     The curve has an obvious negative exponential form, and
thus gives another verification of the obtained data.

     Fig. 4 illustrates the situation for a wave with period
2.5 sec and height 0.13 m.

     Fig. 5 illustrates the situation with a combined flow of
a current with mean velocity 0.20 m/sec and a wave with period
2.5 sec and height 0.015 m.

     In fig. 6 the effect of an obstruction is shown. Here the
probe is placed just ahead of a pipeline in a wave with a period
1.75 sec and a height 0.12 m, and it is observed, that the auto-
correlation function is changed significantly.

     Fig. 7 shows the autocorrelation function for the probe
placed behind the pipeline in a uniform current with mean flow
velocity 0.20 m/s.

     Fig. 8 shows the function obtained with the probe behind
the pipeline in a combined action of a current with mean flow
velocity 0.10 m/s and a wave with period 2.5 sec and height
0.12 m, propagating in the same direction as the current.

     Fig. 9 gives the autocorrelation function near a vertical
cylindrical pile for comparison. Here the current was 0.20 m/sec
and the wave had a period of 2.5 sec and a height of 0.12 m. The
locally generated turbulence was in this case much less than in
the former case with the horizontal pipeline.

     All curves were obtained on a hydraulically rough bottom
with a water depth 0.50 m.

     For the uniform current case, curves were obtained with
the probes in several different positions along the flume, and
good agreement was found between the individual correlation func-
tions, which is another verification of the obtained data.

SERIES: G III   RUN 10

PROBE AHEAD OF PIPELINE   WAVE: T = 1,75 sec.
                                       H = 0,12 m

Fig. 6

SERIES: G III   RUN 15

PROBE BEHIND PIPELINE
V = 0,20 m/s

Fig. 7

SERIES: G III   RUN 14

PROBE BEHIND PIPELINE   WAVE: T = 2,5 sec.
V = 0,10 m/s   H = 0,12 m

Fig. 8

SERIES: G III   RUN 19

Fig. 9
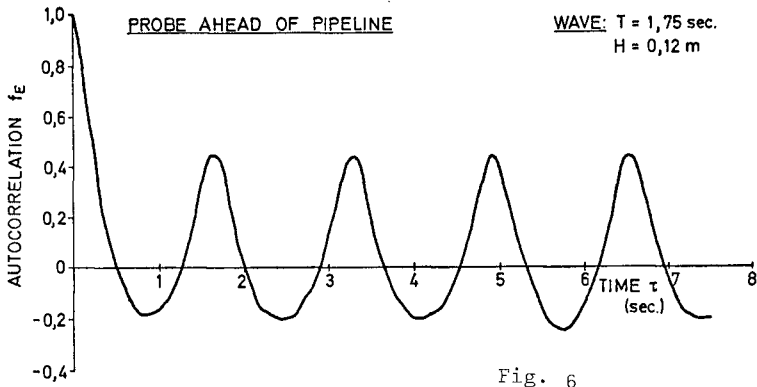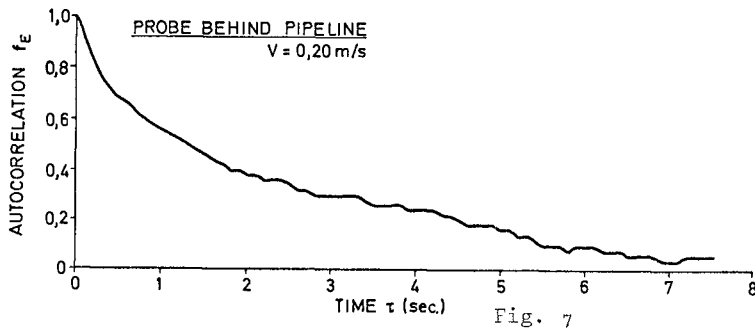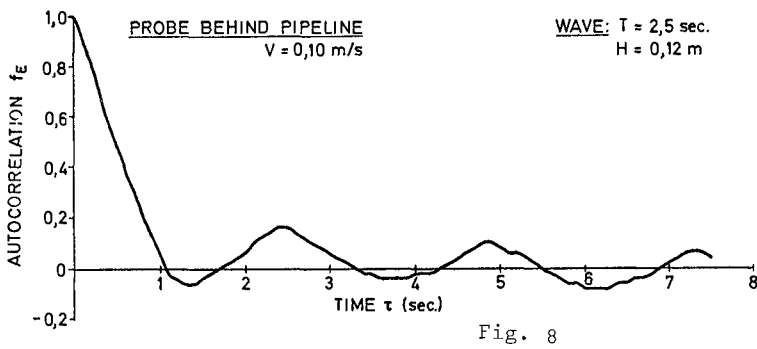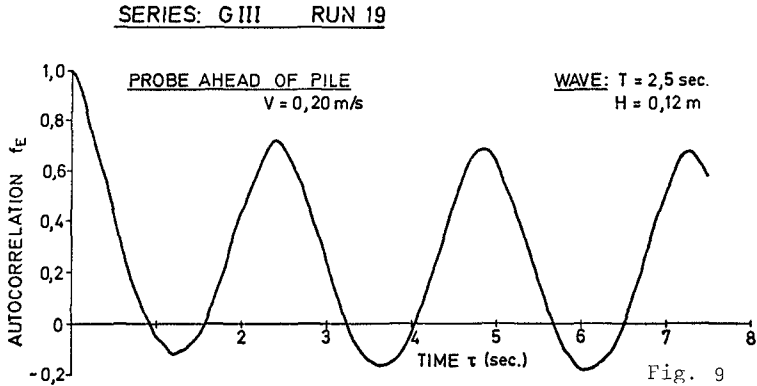
CONCLUSIONS

From this investigation it can be concluded that the new ultrasonic velocity meter delivers a reliable signal, and thus gives very good opportunities for measurement of turbulence characteristics.

A very clear demonstration is given of the modification of autocorrelation functions for the recorded velocity, compared with autocorrelation functions for undisturbed flows due to uniform currents, sinusoidal waves, and combinations of waves and currents.

Applications of the new instrument, other than in scour research, may well include important problems of fluid loading on cylinders.

REFERENCES

(1)   KJELDSEN, S.P.   "Local scour near offshore pipelines."
       GJØRSVIK, O.   Proc. second intern. Conf. on Port and
       BRINGAKER, K.G.   Ocean Eng. under Arctic Conditions.
       JACOBSEN, J.:   University of Iceland 1973

(2)   AUDUNSON, T.   "Measuring Fluid Flow by an Acoustic
       GYTRE, T.   Velocity Meter."
       LAUKHOLM, A: (To be published)

Thyborøn Inlet, Denmark

PART III

COASTAL STRUCTURES AND RELATED PROBLEMS,

Agger, Denmark

CHAPTER 97

DAMAGES TO COASTAL STRUCTURES
by
Orville T. Magoon[1], M. ASCE,
Robert L. Sloan[2], M. ASCE,
and
Gary L. Foote[3], A.M. ASCE

ABSTRACT

Coastal Engineering literature contains many references to
coastal structures in the design or construction stage but few refer-
ences to these same structures concerning their maintenance effective-
ness subsequent to completion. This paper describes a successful
long-term maintenance history of major coastal public structures in
the State of California, U.S.A. It is concluded that proper design
combined with prudent maintenance will result in effective coastal
structures with long economic lifetimes.

INTRODUCTION

This paper is in partial response to the suggestions of Dean
M. P. O'Brien and others at the Vancouver Coastal Engineering
Conference, 1972, for information on the maintenance of coastal struc-
tures in order to determine the efficacy of coastal designs. In
reviewing the material available on history and maintenance of coastal
structures along the California, U.S.A. coastline, a sufficiently
large quantity of material was developed that could not be reported
in one paper. It is expected that additional information on this
subject will be published subsequently. For the purposes of this
paper, however, damage of certain key structures which represent

---

[1] Civil Engineer, U.S. Army Engineer Division, South Pacific, Planning
Division, Chief, Coastal Engineering Branch, San Francisco, California,
U.S.A.

[2] Civil Engineer, U.S. Army Engineer District, Engineering Division,
Assistant Chief, Water Resources and Urban Planning Branch, San
Francisco, California, U.S.A.

[3] Civil Engineer, U.S. Army Engineer Division, South Pacific,
Construction-Operations Division, Operations and Maintenance Branch,
San Francisco, California, U.S.A.

structural types commonly found on exposed coasts will be presented.
Material used has been referenced with exception of extensive use of
the annual reports of the Chief of Engineers. All three of the authors
have been associated with the design, construction, maintenance for
inspection of these structures for approximately 20 years.

The reach of coast under consideration and the location of the
structures discussed in this paper is shown on Figure 2. The exposed
portion of the California Coastline is over 1,300 miles in length and
includes a great variety of coastal shoreline types. It is interesting
to note that a vast portion of California's coastal shoreline is
retrograding and is therefore being lost by natural geologic processes
of erosion. In some areas, such as the entrance to Humboldt Bay,
jetties are used to stabilize the entrance through a barrier beach.
Other areas are rocky coasts, and breakwaters are needed to provide
harbors and safe mooring areas. In still other areas, seawalls are
used to provide protection of eroding coastlines. The wave climate
in the northerly portion of the California Coast is severe. It is
exposed to the full force of north Pacific winter storms, usually
occurring during the period from November to March. Generally, the
severe storms at this location are produced by extra tropical cyclones,
which originate near Japan and move generally eastward toward Alaska.
When the "Pacific high pressure area" moves southward, the stronger
and rapidly moving low pressure of frontal systems produce severe
storms which produce high waves along the coast.

For example, a storm in February, 1960, resulted in a significant
deepwater wave height of 32 feet, as determined by hindcasting. Such
waves, when combined with refraction and shoaling, at a particular
location produce design waves of up to 40 feet, breaking. Lesser waves
were experienced in most other coastal locations studied.

For reasons of economic feasibility, a majority of the structures
under consideration are of rubble-mound (flexible) construction,
although several of these have concrete armor unit layers protecting
areas of severe wave attack. The most common maintenance efforts on
rubble-mound structures appear to be necessitated by a loss of material
due to structural settlement and flattening of the seaward slopes or
loss of material on the landward side due to overtopping. A few
instances have been noted where settlement of the flexible portions
of a rubble-mound structure with a concrete cap has resulted in a hole
or gap under the rigid cap. This has occurred both at the Crescent
City outer breakwater and the Noyo Harbor north jetty, the latter
located near Fort Bragg. In structures with a relatively low cap,
loss of armor layers on the landward slopes has also been reported.

Concrete armor units of modern design have been successfully used
at three Northern California locations at the Santa Cruz jetties,
(quadripods), the Humboldt jetties (cubes, tetrahedrons, and dolosse),
and Crescent City (tetrapods and dolosse). Concrete armor units have
been damaged by several mechanisms including (1) movement of the unit
and subsequent impact, and (2) abrasion of the unit by continued
movement and/or rocking action. Damage to concrete armor units at
other locations is discussed in references (4) and (5). As the dolos

unit has been in service for only a relatively short period of time,
no conclusions can be drawn concerning this unit; however, over 10
years of experience with the tetrapod and quadripod units indicates
that where these units are placed in accordance with model study
results or by use of the Hudson stability equation, a stable, service-
able structure results. In one instance where 25 ton concrete units
were subjected to extreme motion and impact by large flying armor
stones, breakage of the units occurred. Similar movements have also
been observed in model studies of structures conducted at the Corps
of Engineers' Waterways Experiment Station Vicksburg, Mississippi.

As shown on Figure 1, selected sections of coastal structures
may experience concentrated wave action (even under relatively mild
wave attack) due to local bathymetric effects. These areas of severe
wave attack have probably produced points of initial failure. Designers
of coastal structures should pay particular attention to localized
effects where appropriate.

CRESCENT CITY HARBOR

Crescent City Harbor is protected by a rubble-mound outer
breakwater extending S 27° E for approximately 3,700 feet and S 80° E
for approximately 1,000 feet (see Figure 3). This latter portion is
called the realigned extension. The outer portion of the Crescent
City main breakwater was built of 12 ton per average (armor stone)
with slopes of from 2-1/2 to 1 through 4 on 1.

Originally, it had been planned to extend the structure along
the S 27° E alignment toward Round Rock. However, as shown in Figure
4, about 500 feet of breakwater was extensively damaged during the
winter of 1950 to 1951 and a realigned 1,000 foot extension was con-
structed during 1954 to 1957, as shown in Figure 5.

During the winter of 1956-1957, the stone section of the break-
water extension from Station 36+70 to 39+10 suffered a loss of armor
stone and as sufficient stone could not be obtained from local quarries,
one hundred and forty 25-ton tetrapods identical to the tetrapods
placed in this section were placed in two layers from approximately
Station 37+10 to 38+10 and were placed one layer from approximately
Station 38+10 to 39+10 (see Figure 6). These repairs were completed
in June 1957.

This section was extensively damaged during a severe storm in
February, 1960, which resulted in the movement along the breakwater
of 25-ton tetrapod units of distances of at least 100 feet (see Figure
7) and extensive breakage of tetrapods (see Figure 8). At the present
time, approximately half of the tetrapods are damaged or broken,
caused apparently either by movement or impact of large stone units
or broken concrete fragments. The breakwater is also subject to
severe overtopping (see Figure 9). This often results in a steepening
in the back side of the breakwater and, in some instances, in the
formation of a wave trench (see Figure 10). Two hundred and forty-six

40-ton dolosse were placed as repair between Stations 35+00 and 37+00 (area of maximum overtopping in Figure 9) in late 1973 (see Figure 22).

HUMBOLDT JETTIES

The Humboldt jetties (1), shown on Figure 12 have probably experienced the most severe wave attack and necessitated the greatest amount of maintenance of any structure studied. The structures were initiated in 1889, and, although the exact quantities of new construction and maintenance stone cannot be determined exactly, the quantity of stone placed for repair has been greater than the quantity placed in the initial construction (more than 1,000,000 tons). Documented storm attack on the structure (see Figure 11) has indicated that waves completely cover the seaward portions of the structure, with an average dock elevation of 26 feet MLLW. Several types of failure have been repeatedly experienced at the Humboldt jetties. Damage by uplift pressures is shown in Figures 13 and 14. In an effort to prevent slope failure by overtopping, portions of the back sides of the structure were covered with concrete. As shown in Figures 15 and 16, initial cracking of this concrete eventually breaks up completely.

During the 1960s, a concrete monolith was constructed at the seaward head of the North Jetty. A ringing levee was placed around the head, with the intention of pouring mass concrete into the area surrounding the existing head. However, wave action through the ring levee resulted in washing away of the concrete as it was poured. Soon after construction, the ring levee was washed away resulting in an overhanging concrete mass shown in Figure 17. This subsequently collapsed, resulting in large broken pieces as shown in Figure 18. In efforts to stabilize the heads of these structures, a great number of concrete blocks (see Figure 19) with maximum weights of 100 tons have been placed along the sides of the jetties. Essentially all of these blocks have been dislodged. Many of the blocks and supporting stones have been displaced landward and moved landward (see Figure 20).

As described by Magoon and Shimizu (2), both the North and South Jetty heads have been repaired with 42 and 43-ton concrete dolosse armor units (see Figure 21). Most of these units are reinforced; however, as shown in Figure 22, unreinforced and fiber reinforced (3) units have been placed at both the Humboldt jetties and at the Crescent City outer breakwater (see Figure 22). Based on the available inspections which do not include those units placed under water, about 12% of the unreinforced units are broken, 0.4% of the conventionally reinforced units are broken and none of the fiber reinforced units are broken.

NOYO HARBOR

The small jetties at Noyo Harbor (see Figure 23) demonstrate

a classical failure of composite structures which results from
consolidation of the rubble structure and subsequent removal of the
material below the concrete cap, leaving the cap in the form of a
bridge (see Figure 23). Rigid coastal structures often fail by loss
of protective material at the toe and subsequently collapse or topple
over. Photographs of Figures 7 and 27 are left to right reversed.

CONCLUSIONS

   Modes of failure of flexible coastal structures under severe
wave attack have been presented. It is believed that engineering
solutions to all of the above failures, many initiated in the early
20th century when rational solutions may not have been available,
can now be understood and corrective solutions be found.

ACKNOWLEDGEMENT

REFERENCES

1. WHITTEMORE, GEORGE F., "Construction of Humboldt Bay Jetties,"
    The Military Engineer, Volume XVIII, No. 97, February 1926,
    pp. 60-63.

2. MAGOON, O.T. and SHIMIZU, N., "Use of Dolos Armor Units in
    Rubble-Mound Structures, e.g., for Conditions in the Arctic,"
    Proceedings from the First International Conference on Port and
    Ocean Engineering Under Arctic Conditions, Technical University
    of Norway, Trondheim, Norway, Volume II, 1971, pp. 1089-1108
    (also as CERC Reprint 1-73).

3. BARAB, SAUL and HANSON, DEAN, "Investigation of Fiber Reinforced
    Breakwater Armor Units," Proceedings, American Concrete Institute,
    International Symposium: Fiber Reinforced Concrete, Publication
    SP-44, 1974, pp. 415-434.

4. MORAIS, C.C. and ABECASIS, F., "Storm Surge Effects at Leixoes,"
    Proceedings, Fourteenth International Conference on Coastal
    Engineering, Copenhagen, Denmark (in press).

5. U.S. ARMY PACIFIC OCEAN DIVISION, Technical Report No. HED 74-1,
    "Report on Kahului Breakwater Surveillance Program, March, 1974,
    Fort Armstrong, Honolulu, Hawaii.

FIGURE 1. Wave attack on Crescent City
Outer Breakwater.

STATE OF CALIFORNIA
U.S.A.
COASTAL PROJECT SITES

FIGURE 2

CRESCENT CITY HARBOR
CALIFORNIA

SCALE IN FEET

U. S. ARMY ENGINEER DISTRICT, SAN FRANCISCO
CORPS OF ENGINEERS
SAN FRANCISCO, CALIFORNIA
31 DECEMBER 1967   FIGURE 3
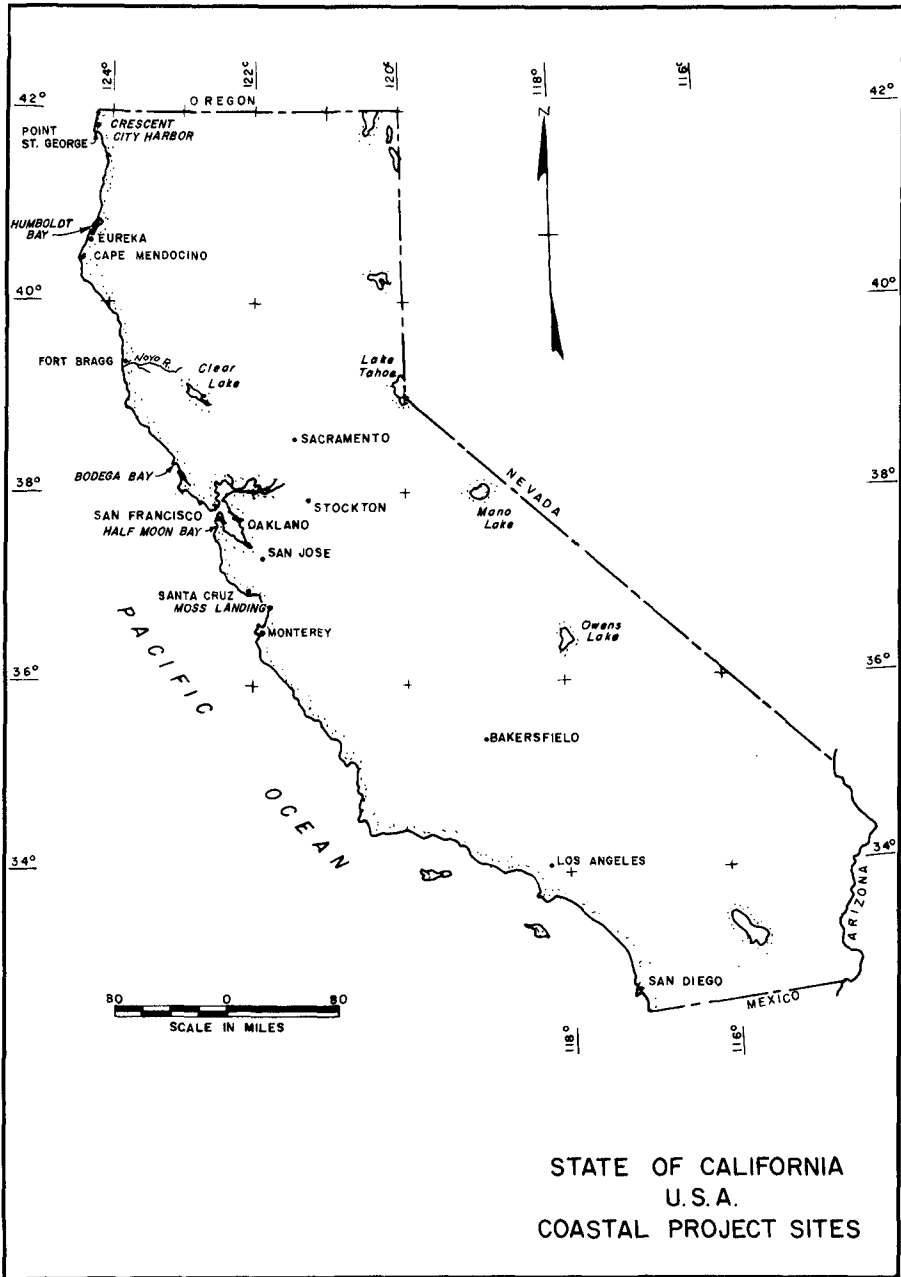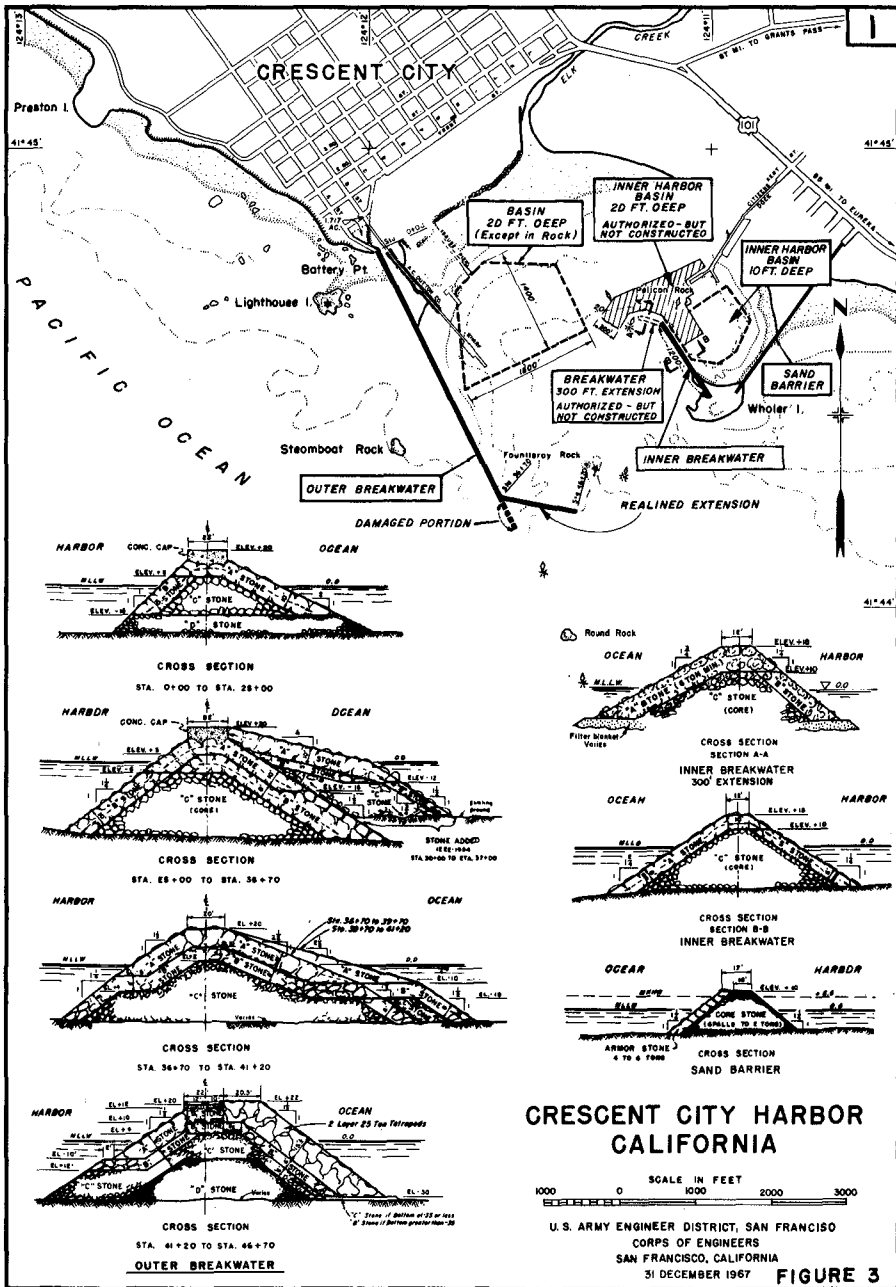
FIGURE 4.   Damaged original extension of
             Crescent City Outer Breakwater--
             viewed from Station 36+70 with
             Round Rock in distance(upper right).

FIGURE 5.   Realigned extension of Crescent
             City Outer Breakwater.
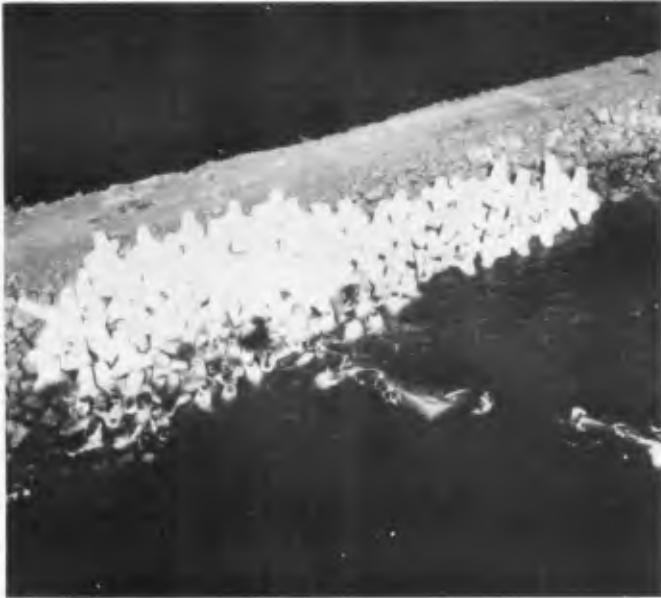
FIGURE 6. Tetrapod repairs to realigned extension of Crescent City Outer Breakwater.

FIGURE 7. Storm wave displacement of originally submerged tetrapod from repaired area shown on Fig.6.

FIGURE 8.   Tetrapod damaged by storm wave
            attack on repaired area shown on
            Fig.6.

FIGURE 9.   Wave overtopping--Crescent City
            Outer Breakwater.

FIGURE 10.   Wave trench resulting from the
             overtopping shown on Fig. 9--
             Crescent City Outer Breakwater.
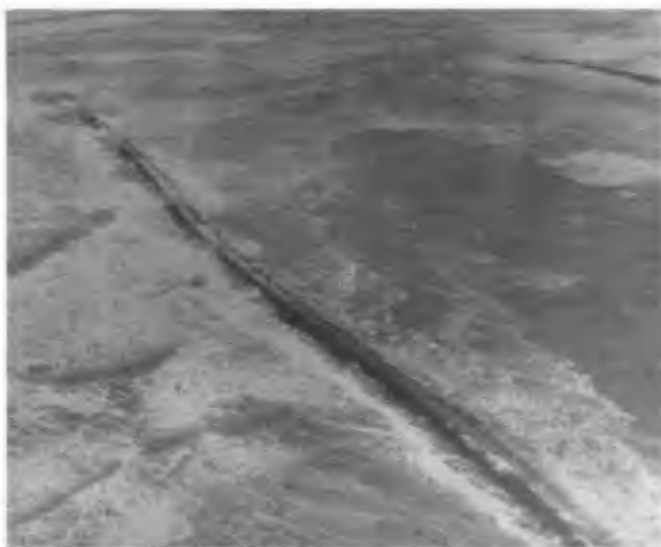
FIGURE 11.   Jettied entrance to Humboldt
             Harbor and Bay during storm
             activity of February 1960.

HUMBOLDT HARBOR AND BAY, CALIFORNIA

U.S. ARMY ENGINEER DISTRICT, SAN FRANCISCO
CORPS OF ENGINEERS
SAN FRANCISCO, CALIFORNIA
30 AUGUST 1968 FIGURE 12
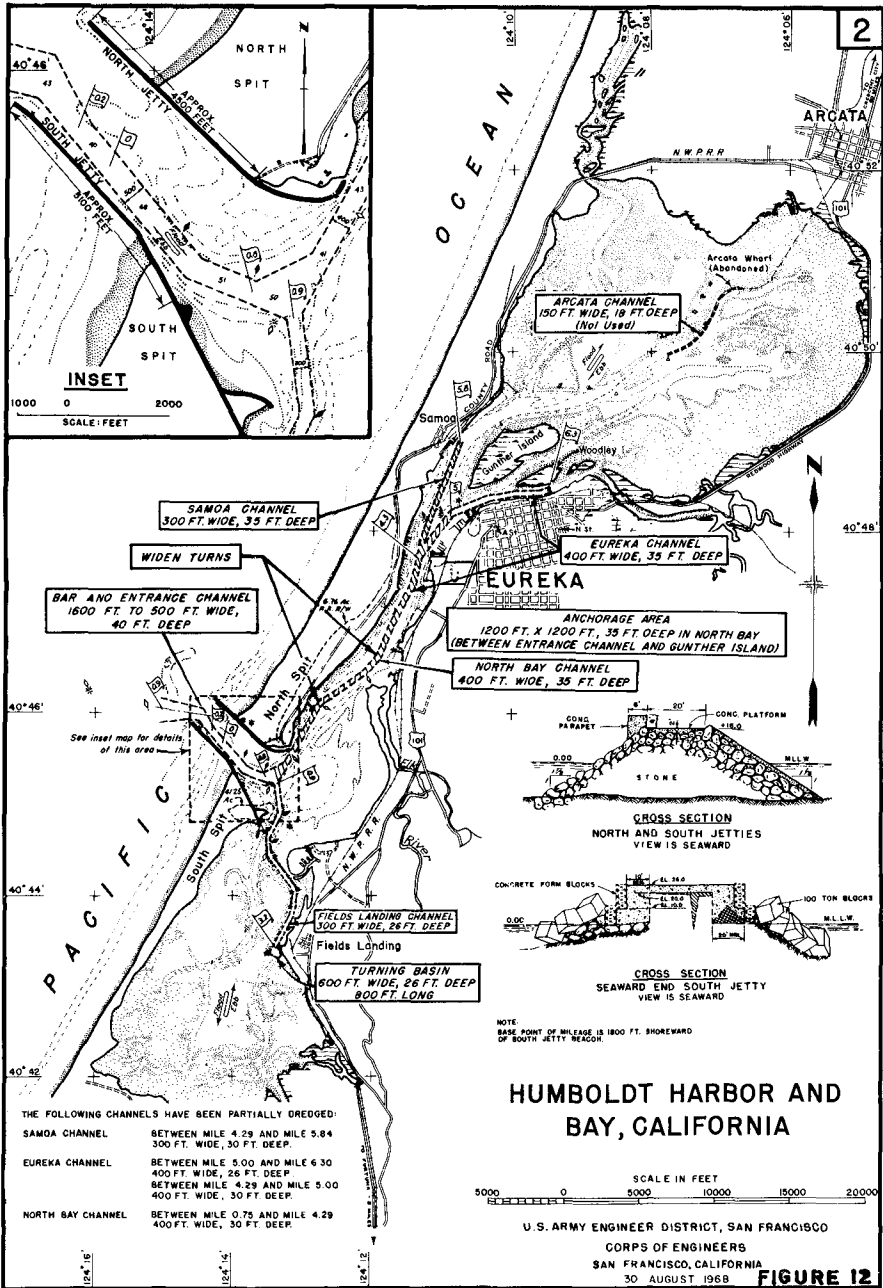
FIGURE 13.   Uplift pressure failure--Humboldt
             Harbor and Bay North Jetty.

FIGURE 14.   Advanced stages of uplift pres-
             sure failure--Humboldt Harbor and
             Bay North Jetty.

FIGURE 15.   Beginning of slope separation
              failure--Humboldt Harbor and Bay
              South Jetty.

FIGURE 16.   Advanced slope separation failure--
              Humboldt Harbor and Bay South
              Jetty.

FIGURE 17. Displacement of ring dike and
lack of concrete penetration--
seaward head of Humboldt Harbor
and Bay North Jetty.

FIGURE 18. Monolithic breakup--Humboldt
Harbor and Bay North Jetty.

FIGURE 19. 20-ton pre-cast concrete blocks circa 1932--seaward face of Humboldt Harbor and Bay South Jetty.

FIGURE 20. Stones displaced from seaward head of Humboldt Harbor and Bay North Jetty showing extensive rounding due to impact and abrasion.

FIGURE 21. Wave dissipation in Dolos armor
units--rehabilitated Humboldt
Harbor and Bay North Jetty.

DOLOS ARMOR UNITS(5)
CALIFORNIA, USA

	UNREINFORCED		CONVENTIONAL REINFORCED		FIBER REINFORCED		TOTAL
	Total	Broken(1)	Total	Broken(1)	Total	Broken(1)	
Humboldt Jetty North	4(2)	0	2238	9	17	0	2259
Humboldt Jetty South	22	9	2513(3)	9	0	–	2533
Crescent City	246	22(4)	0	–	0	–	246

NOTES:

(1) Based on visual count. Units under water or in underlayers not always counted.

(2) Placed in relatively protected location or trunk.

(3) I estimate 1/4 are exposed similar to unreinforced dolosse.

(4) Includes underlayer breakage, and breakage by wave action during construction.

(5) Does not include those used in destructive tests.

FIGURE 22
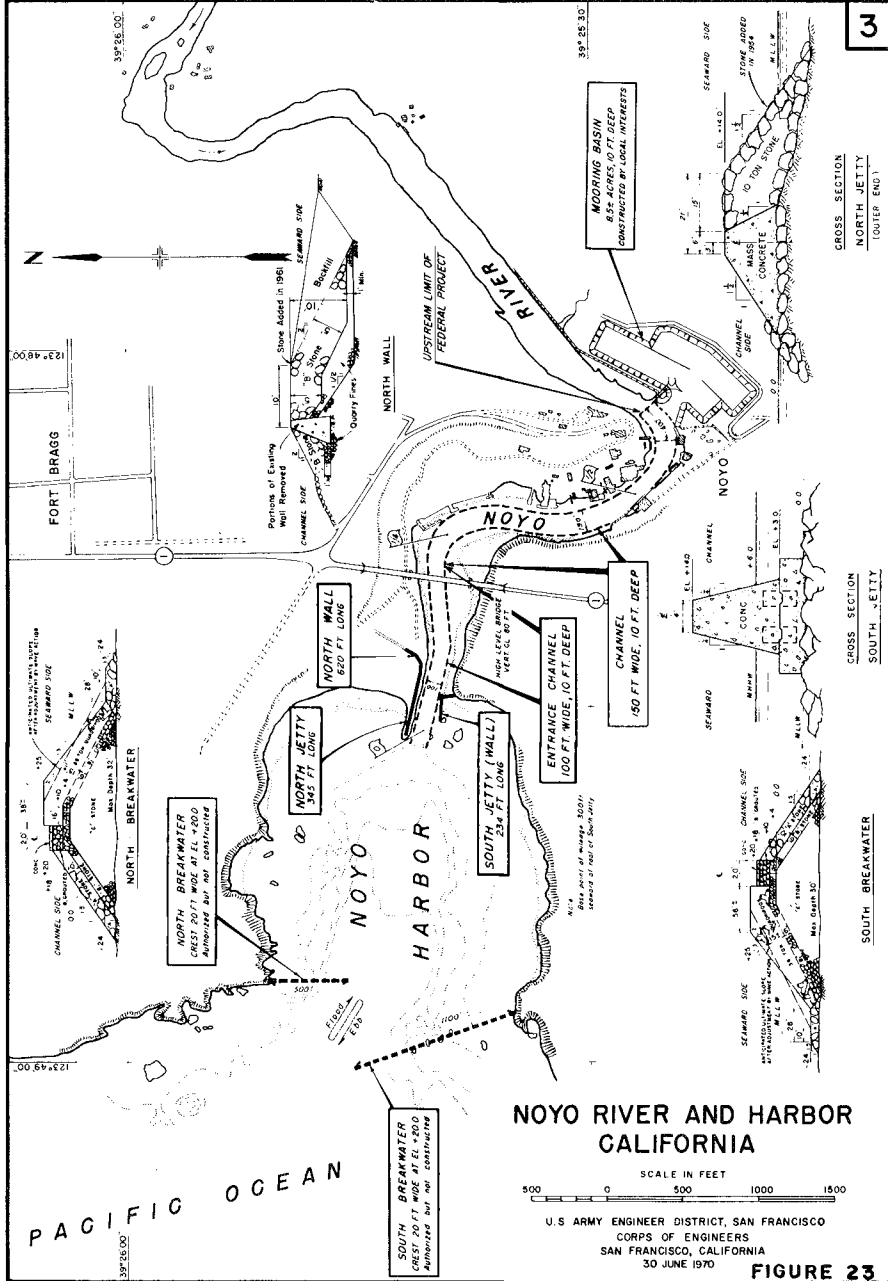
NOYO RIVER AND HARBOR
CALIFORNIA

SCALE IN FEET

U.S ARMY ENGINEER DISTRICT, SAN FRANCISCO
CORPS OF ENGINEERS
SAN FRANCISCO, CALIFORNIA
30 JUNE 1970

FIGURE 23

FIGURE 24.   Failure of rigid structure due to
             undermining--Noyo River and Harbor
             North Wall and Jetty.

FIGURE 25.   Advanced failure of rigid structure
             due to undermining--Noyo River and
             Harbor North Wall and Jetty.

CHAPTER 98

IRREGULAR WAVE ATTACK ON A DOLOS BREAKWATER

by C. Campos Morais

Research Officer LNEC (Laboratório Nacional de
Engenharia Civil), Lisboa, Portugal

ABSTRACT

The paper deals with two-dimensional tests on a scale model of
a dolos breakwater. It is related with the construction of a large
harbour at Sines for tankers with up to 1 million dwt, ore ships with
up to 300,000 dwt, general cargo, etc. The main breakwater is design
ed with 40 t dolos, in order to withstand waves with up to 11 m si-
gnificant wave height(100 years return period).

Considerations on wave data and on modelling the spectrum
(Pierson-Moskowitz) precede the presentation of three sets of tests
on LNEC's irregular wave flume. Main results are compared with
those from regular wave tests.

The most important conclusions are stressed: influence of pla
cement on dolos damages, irrelevance of maintenance, importance of
the singular zone of the dolos support base, disadjustment of Hudson's
formula for calculation of dolos weight using H as significant wave
height,and importance of individual movements for the risk of break-
ing of individual blocks.

1. INTRODUCTION

The use of dolos in the construction of breakwaters is in per-
manent expansion. After its presentation by Merrifield and Zwam-
born [1] , [2] , a few studies on the subject appeared [3], but we
can say that the principal reason for its use is the heigh damage coe
fficient presented and the consequent low weight of the block compar
ed with others when the same design wave is considered. But the
high interlocking power of every block gives to that kind of break-
waters some characteristics not identical to classical ones: return
period of waves must be larger, individual movements risk to provoke
breaking damages, placement of dolos is a complexe job, etc.

Hydraulic model studies using irregular waves and connected with
the present construction of a large oil harbour in Sines are the sub
ject of this paper.

2 - SINES PROJECT

The location of Sines is on the portuguese western coast,south
of Lisbon (fig. 1). The future port, under construction, will be

built in a zone limited by a cape and a bay (fig. 2) with no impor-
tant littoral mouvements. Before the construction of the new har-
bour only a small fishing harbour (fig. 3)and a recreational beach
(fig. 4) existed there.
      The project embodies the construction of a new town, for a
population expected to be near 100,000 people during the early eigh-
ties, and a lot of new industries, usually related with port areas:
oil refineries, steel mills, shipyards, petrochemicals, oil and ore tran
shipment, etc [4] . So the port has to deliver sheltered conditions
for super-tankers and ore ships. Main features and dates of the ma
ritime undertaking are as follows:

      - Oil refinary for 10-12 million tons/year of crude
      - Sheltered berthing for tankers up to 1 million dwt and ore
        carriers up to 350,000 dwt
      - Physical characteristics of the harbour:
        Max. depth of water (head of main break.): -50 m
        Total length of main breakwater: 2 km
        Max. height   "   "   "
        (from bottom to crest)   : 70 m
        Crest level of curtain wall   : +19 m
        Total vol. of concrete   : 860,000 m^3
        Total vol. of rock   : 8,500,000 m^3
        Weight of dolos   : 40 t
      - Beginning of project   :~March 72
      - Work contract   : August 73
      - Installation of contractor yard   : August 73/June 74
      - Expected dates of completion :
        for the small construction harbour: June 74
        Berth nº 3 (100,000 dwt)   : April 75
        Berth nº 2 (250 to 350,000 dwt) : August 75
        Berth nº 1 (500 to 100,000 dwt) : August 76
        Final conclusion   : April 77

      Fig. 5 shows the lay-out of the harbour scheme with the main
breakwater reaching, at the head, 50 m deep water and sheltering
the three berths: for up to 100,000 dwt tankers,for up to 350,000
dwt tankers and for up to 1,000,000 dwt tankers.
      The study, from the maritime hydraulic point of view, of the
cross section of this main breakwater, was the subject of several
studies at LNEC. Fig.s 6, 7 and 8 show the three cross sections
consecutively considered on LNEC's studies: the one formerly consider
ed, the variant presented by the contractor when he won the public
competition and the cross section under study at present.

3 - LABORATORY STUDY OF MARITIME HYDRAULIC PRO-
    BLEMS FOR SINES

      Besides tests on wave agitation, long period waves and wave
data computation, hydraulic tests using the cross section were done.
      Fig. 9 summarises the most important problems studied. From

those, the more important results related with the stability of dolos are presented in this paper.

4 - WAVE DATA, SPECTRUM MODELLING AND IRREGULAR WAVE SIMULATION

4.1 - Wave data

Data used for the Sines study are based on six years visual observations (with optical device) that were made at Figueira da Foz [5] and on a two years set of records made by a Datawell wave-rider buoy (accelerometer) off Sines. Figueira da Foz data were extrapolated to Sines after reciprocal comparison and thus a valid wave climate was defined for the Sines Harbour design.

Using the exponential, log-normal, Weibull and Weibull- Battjes distributions extreme values were computed, appearing the most probable values for significant wave heights:

$$\text{Once in} \quad 1 \text{ year} : \quad H_s^Z = 6.5 \text{ m}$$
$$"\quad"\quad 10 \text{ years:} \quad = 8.5 \text{ m}$$
$$"\quad"\quad 30 \text{ years:} \quad = 9.5 \text{ m}$$
$$"\quad"\quad 100 \text{ years:} \quad = 11.0 \text{ m}$$

4.2 - Modelling the spectre

In order to simulate adequate spectra for use in model tests the Pierson-Moskowitz expression was used as follows:

$$W(\omega) = \frac{\alpha g^2}{\omega^5} e^{-\beta (\omega_0/\omega)^4}$$

or

$$P(f) = \pi \frac{\alpha g^2}{\omega^5} e^{-\beta (\omega_0/\omega)^4} \quad \text{as} \quad W(\omega) = \frac{1}{\pi} P(f)$$

f : frequency; ω : angular frequency

$P(f)$: spectral density

$\alpha = 8.1 \times 10^{-3}$

$\beta = 0.74$

$g = 9.8 \text{ m s}^{-2}$

Note: $\omega_0 = \dfrac{g}{U}$

$$U = \sqrt{\frac{H_s \times 10^2}{2.12}}$$

U : wind force, measured 19.5 m above sea level, necessary for the generation of a F.A.S. with H_s

Fig. 10 shows a sequence of different theoretical P-M spectra corresponding each one to a given H_s.

Fig. 11 shows actual spectra as an example of the growth of a storm, recorded on the 16th - 17th December 1973 by the Sines Datawell buoy.

4.3 - Irregular wave simulation

LNEC's irregular wave flume has been described in several previous papers [6] , [7]. It is 50 m long, 1.6 m wide and 0.80 m maximum depth of water (fig. 12). The system of signal generator is through filtering white noise, feeding a servo-controlled hydraulic-actuator. The data acquisition system is based in a Hewlett Packard analog-to-digital converter (fig. 13).

5 - TESTS WITH IRREGULAR WAVES

The duration of each test was 90 minutes and tide was reproduced (+0.20 to +3,80 m). Thirty ton dolos were used.

Three series of tests with irregular waves are presented. In the first two series (Nº 2000 and 4000) cross section from fig. 6 was tested. In the third one conditions were similar but the dolos layer did not lay on the toe rock and was rather indefinitely extended until it lied on the flume floor.

Fig.s 14, 15 and 16 show simulated spectra for each test.

Cumulative damage curves are shown for 2nd series (fig. 17) and 3rd series (fig. 18)

It should be noted:

- The scatter of results, although the experimental conditions were the same

- The way damages grow is practically uniform. During the first part of the test (low water) damages grow rather steeply and then settle (with the exception of test nº 4011, in which damages would still grow if the test were extended in time)

In the following table individual results for tests nº 4000 are presented, together with correspondent values of H_s, H_{max} and percentage of damages (total values and values for the upper, middle and lower zone of dolos layer)

Test nº	H_s (m)	H_{max} (m)	% damages			
			total	upper	middle	lower
4004	8.8	21	22	12	40	48
4005	8.8	21	35	1	40	59
4006	8.8	20	9	8	39	53
4007	8.9	18.5	9	0	63	37
4008	7.8	18.5	10	10	50	40
4009	8.8	18	11	14	53	33
4010	8.6	18	5	0	38	62
4011	8.5	19	18	0	32	68
4012	8.5	18	5	0	63	37
4013	7.9	16.5	19	10	39	51
4014	8.0	17	9	3	18	79

In the 2000 series, with 3 tests, damages were between 6 and 7.5 %.

6 - JOINT COMPARISON OF RESULTS USING REGULAR AND IRREGULAR WAVES

The most important results of tests with regular waves[8], on the same cross section, are summarised in fig. 19.

Let us see, in the following table, a joint comparison of results, using regular and irregular waves.

JOINT COMPARISON OF RESULTS				
IRREGULAR WAVES	H_s(m)	H_s^z(m)	H_{max} (m)	% damages[*]
1) Tests no 2000	8.8	10-11	16	6-7.5
2) Tests no 4000	8.9	10-11	18-20	5-35
3) Indefinite dolos layer		(9.5)	18-20	4-6
REGULAR WAVES	H(m)			% damages[**]
Criterium of damages: (*) blocks displaced from original position	10.5			1
	12.5			5
(**)blocks displaced from dolos layer	13			10

The main conclusion is that the significant wave heigth should not be used as equivalent parameter for regular and irregular waves. Results are not enough to allow the definition of another parameter, which however should be an exceedance quantile greater than $H_{1/3}$ ($H_{13.3\%}$) but lower than $H_{1/100}$ ($H_{1\%}$).

In the evaluation of results there are three important details that should be taken into account because they contribute to make it difficult to interpret them:

- The large scatter of experimental results
- The different criteria of considering damages in tests with regular and irregular waves (blocks displaced from dolos layer or blocks displaced from original position)
- Rather important variations in the density of the concrete used in the models of dolos:

2.53 t/m³ (prototype)
2.47 (correct value on model, using 1.03 t/m³ to sea water)
2.24 (actual value on LNEC model tests)

7 - FINAL DESIGN OF DOLOS WEIGHT

The criterion used by the designer for establishing the design wave is mentioned [9]:

1 - Only oscillations for a storm with 10 years of return period ($H_s^Z = 8.5$ m)

2 - Beginning of dolos displacements for a storm with 30 years of return period ($H_s^Z = 9.5$ m)

3 - Damages up to 1% for a storm with 100 years of return period ($H_s^Z = 11$ m)

As the test results did not obey the design wave criterion   it was decided to use 40 t instead of 30 t dolos. Later tests with 40 t have shown that this weight produced results in agreement with the adopted design wave criterion.

According to recently published results by HUDSON, 1974 [10], the weight theoretically compatible with the utilized parameters should be 33 t for $K_D = 22$. The excess weight will minimize individual block movement and thus breaking risks will be smaller.

8 - FINAL REMARKS

Taking into account these results and results published by other authors some final remarks will be made on the use of dolos in rubble-mound breakwaters:

1 - One of the most important aspects in the investigation of model and prototype behaviour of dolos is the large dependance of the amount and growth of damages upon the way the blocks are placed. This is shown by the scatter in the experimental results and it is feared that the behaviour of a structure will depend on the way it was built

2 - Owing to the interlocking capacity of the dolos, such break waters do not allow recharges, and so, to avoid maintenance, it is necessary to design them for large return periods in order that the percentage of damages is low

3 - The singular zone of the dolos support base, either in what concerns its depth, is intimately linked with the regular or the irregular characteristics of the simulated waves, and when they are irregular, with the respective extreme values distribution, as is readily understood.

4 - As previously mentioned the significant wave height parameter does not seam to be suitable for the design of break-waters through the use of Hudson-type formula.

5 - The individual movements of the blocks which, if large, may determine unwanted breaks, can only be minimized if an increase in the dolos weight is used, above the value that from the hydraulic stand point is considered satisfactory. Other people prefer to use reinforced blocks as it was the case at Humboldt Bay Harbour [11] .

9 - MAIN PARTICIPANTS IN THE PROJECT OF SINES MARI-
TIME UNDERTAKING

Gabinete da Area de Sines (GAS) - Direct overall responsability
(Governamental Department).

Bertlin/Consulmar/'Lusotecna - Designers of maritime project.

Mrs Castanho, R. Carvalho, Vera-Cruz - Sea wave basic data
study.

Societá Italiana per Condotte d'Acqua - Contractor.

Laboratório Nacional de Engenharia Civil (LNEC) - model test
studies (tests with regular waves by Mr. Vera-Cruz).

The permission to publish this paper, which was granted by GAS,
is gratefully acknowledged.

REFERENCES

[1] MERRIFIELD, E.M. and ZWAMBORN, J.A. - The economic
value of a new breakwater armour unit "dolos", 10th Conf. on
Coastal Engineering, Tokyo, Japan, 1966, pp. 885-912.

[2] MERRIFIELD - Dolos concrete armour protection, Civil Engineer
ing - ASCE Dec., 1968.

[3] OUELLET, Y. - Considerations on factors in breakwater mo-
del tests, 13th Conf. on Coastal Engineering, Vancouver, Ca-
nada, 1972 Vol III pp. 1809-1826.

[4] GAS (PRESIDENCIA DO CONSELHO) - Plano Geral da Area
de Sines, Lisboa 1973.

[5] CARVALHO, J.R. and BARCELÓ, J. - Agitação marítima
na costa oeste de Portugal Metropolitano, Memória nº 290 do
LNEC, Lisboa, 1966.

[6] CARVALHO, M.; RAMOS, S. and MORAIS, C. - Spectral com
putations on pressure wave gauge records, 12th Conf. on Coas-
tal Engineering, Washington, U.S.A. 1970, Vol. I pp 65-83.

[7] MORAIS, C., RAMOS, S. and CARVALHO, M. - Waves induced
by non-permanent paddle movements, 13th Conf. on Coastal
Engineering, Vancouver, Canada, Jul. 1972. Vol. I, pp. 707-722.

[8] LNEC - Molhe oeste do porto de Sines - Ensaios em canal de
um perfil-tipo (muro-cortina de face curva), Report by Vera-
-Cruz, Lisbon, Jan. 1973.

[9] BERTLIN, CONSULMAR, LUSOTECNA - Dados de Base do
Anteprojecto, Vol. II.

[10] HUDSON, R.Y. - Concrete armor units for protection against
wave attack - Report of ad hoc committee on artificial armor
units for coastal structures, U.S.Army Engineer Waterways
Experiment Station, Hydraulics Laboratory, Vickburg, Mississipi,
Misc. Paper H-74-2, Jan. 1974.

[11] MAGOON, O. and SHIMIZU, N. - Use of dolos armor units in
rubble-mound structures e.g. for conditions in the Artic, 1st
International Conf. on Port and Ocean Engineering under Artic
Conditions, Vol II, pp 1089-1108, Norway 1971.

Fig. 1 - Location of Sines   Fig. 2 - Sines surroundings
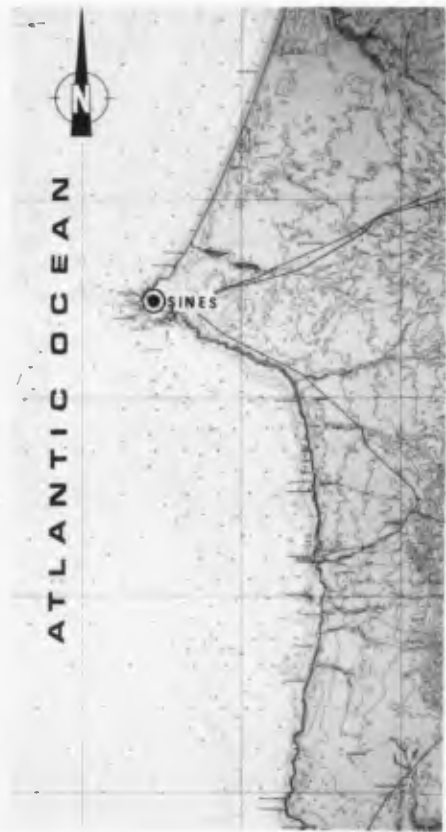
Fig. 3 - Old small fishing harbour   Fig. 4 - Bay and beach
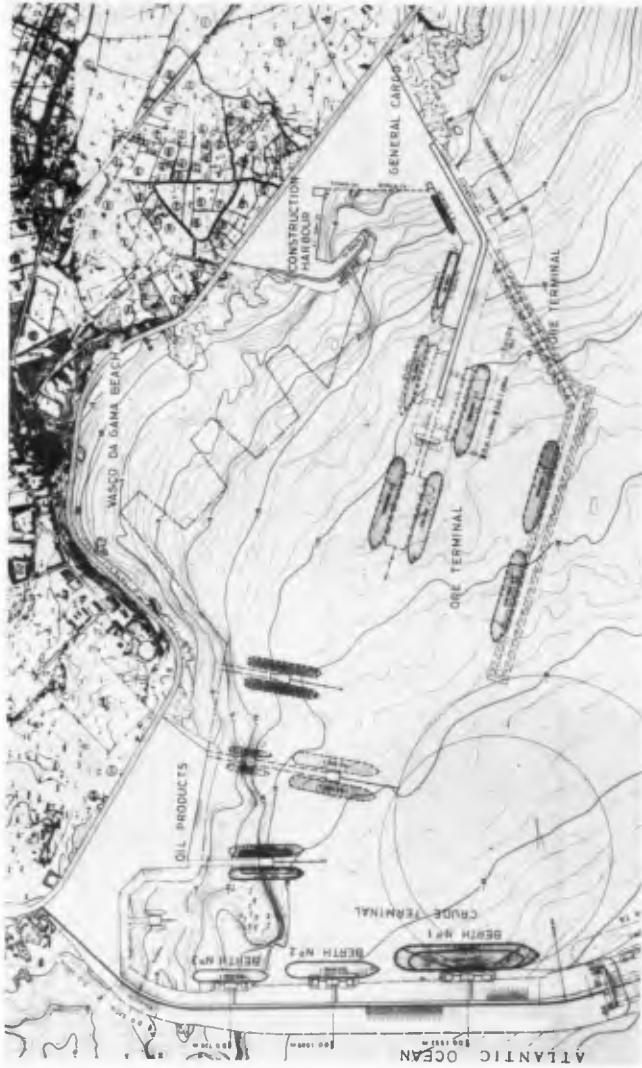
Fig. 5 – Lay out of the harbour
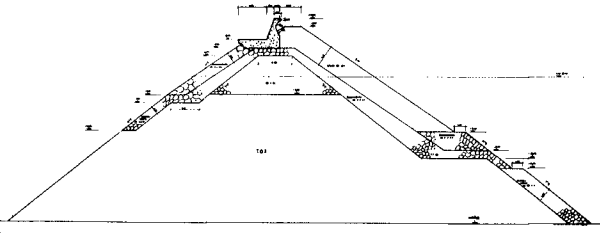
Fig. 6 - Cross section formerly considered
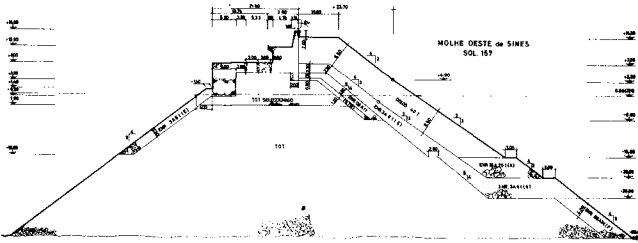
Fig. 7 - Variant presented by the contractor
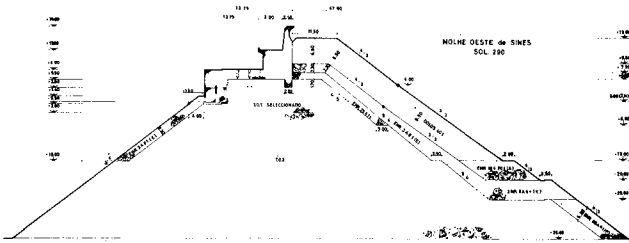
Fig. 8 - Cross section under study
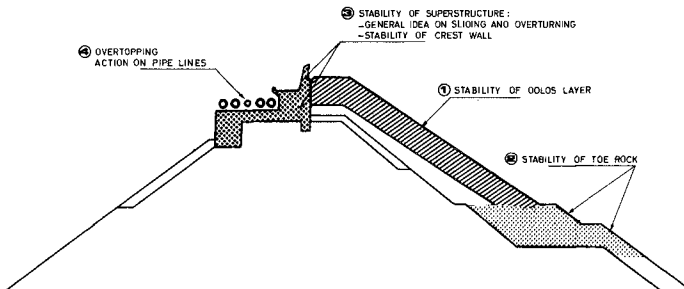
Fig. 9 - Problems under study
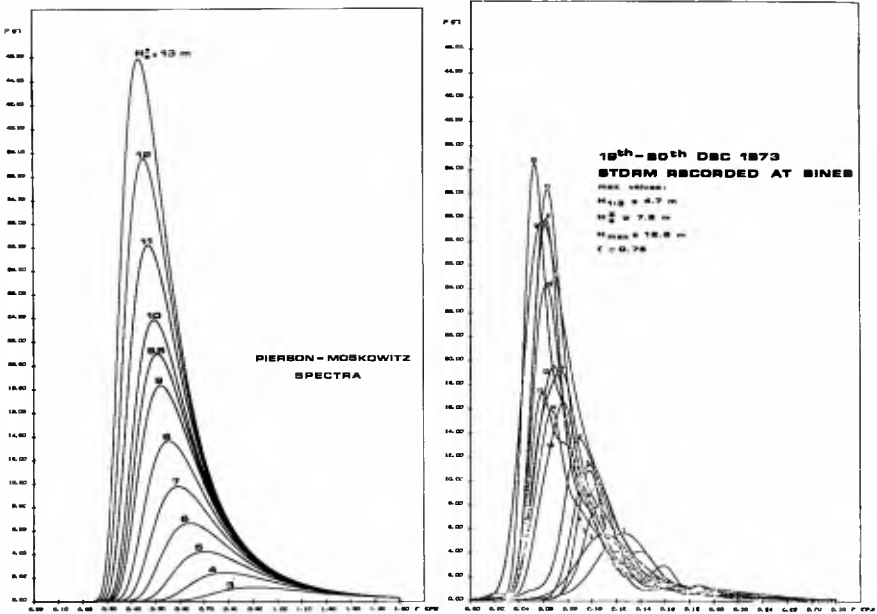
Fig. 10 - Theoretical Pierson-
- Moskowitz spectra

Fig. 11 - Spectra from a storm

Fig. 12 - LNEC irregular wave flume
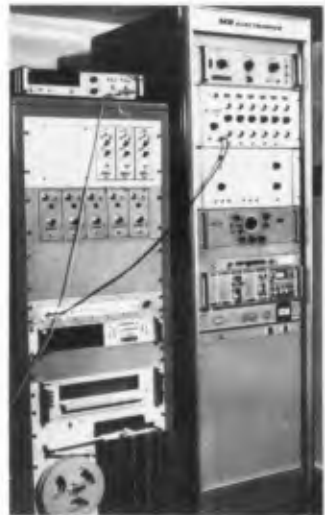
Fig. 13 - Instrumentation
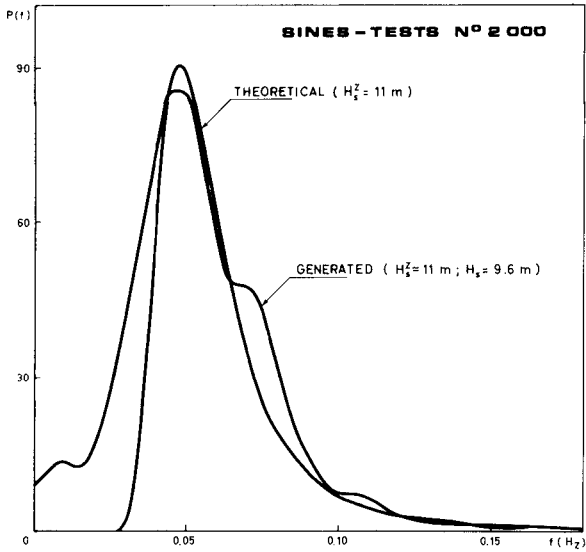
Fig. 14 - Theoretical and simulated spectra
(tests nº 2000 - 1st serie)
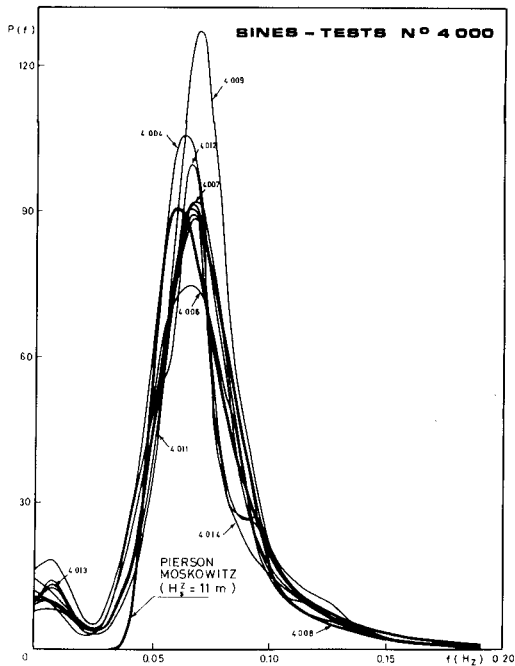
Fig. 15 - Theoretical and simulated spectra
(tests nº 4000 - 2nd serie)
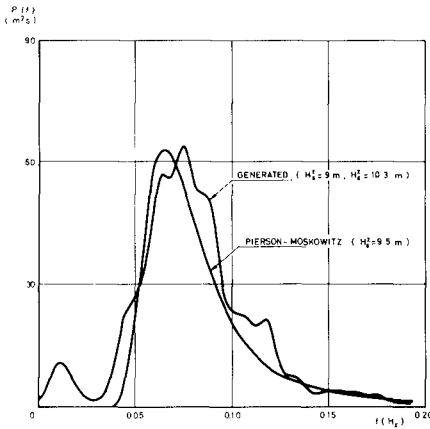
Fig. 16 - Theoretical and simulated spectra
          (3rd serie)
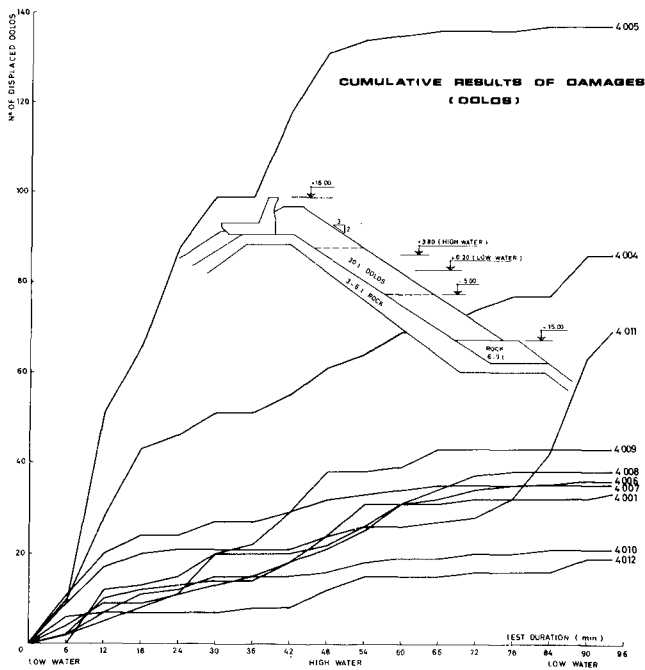
Fig. 17 - Cumulative results of damages (2nd serie)
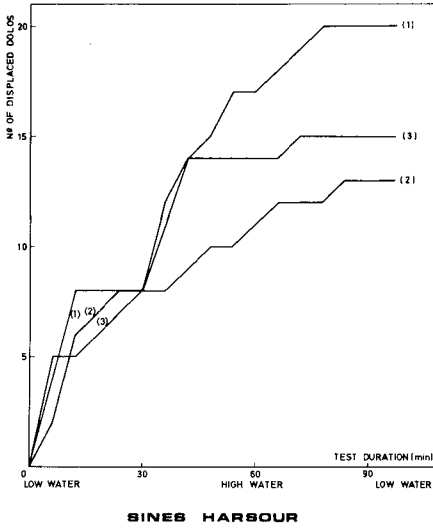
Fig. 18 - Cumulative results of
damages (3rd serie)
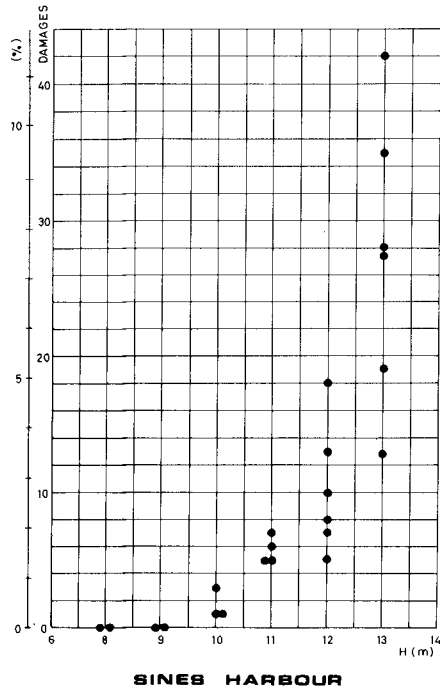
Fig. 19 - Regular wave
test results

CHAPTER 99

STABILITY OF DOLOS SLOPES

by
Michael Brorsen, M.Sc., res.eng.
H.F. Burcharth, professor
Torben Larsen, M.Sc., res.eng.

Hydraulics Laboratory
Danish Engineering Academy – Aalborg University
DK-9000 Aalborg, Denmark

Abstract

The stability of dolos armour blocks against wave attack has
been investigated in wave model studies.

Simple definitions to describe the block movements are intro-
duced and the following results are discussed:

1. The stability of dolos slopes against regular waves and
    the influence of the slope.

2. The stability of dolos slopes against irregular waves that
    are not Rayleigh distributed.

3. Comparison between the stability of dolos, natural stones
    and cubes.

4. The influence of the surface roughness of the dolos model
    blocks.

5. The applicability of Hudson's formula.

Introduction

This paper includes results from model tests which have been
carried out in the Hydraulics Laboratory at the Danish Engi-
neering Academy in Aalborg, Denmark. The paper also includes
results from tests carried out by two former students at the
Engineering Academy Mr. Springborg and Mr Jepsen. Below, the
most important data of the experimental set up are summarized:

Dolos height	4,5 cm
Dolos, cube and natural stone weight	38 g
Dolos and cube density	2,3 t/m³
Natural stone density	2,65 t/m³
Water depth	25-40 cm
Wave period	0,7-1,2 sec
Wave flume bottom	horizontal
Number of block layers	2
Under layer	broken stones

Definitions of damage

After some initial tests it was decided to describe the dolos
movements by the following terms:

    1st degree   No movements at all.

    2nd degree   Blocks can rock, but will not move from
                       mean position.

    3rd degree   A few blocks will move, but the armour
                       layer remains stable.

    4th degree   Blocks are moved continuously until the
                       armour layer is destroyed.

    5th degree   The armour layer is destroyed in a short
                       time.

This system of definitions is almost the same as the system
applied by Hydraulics Research Station [7] and Paul and Baird
[5].

1st and 2nd degree do not require further explanation, but in
the 3rd degree it was remarked that at the start of the test a
few blocks were removed, but later on nothing more happened,
and this was valid for both regular and irregular waves.

In 4th degree the armour layer is unstable, but the blocks are
moved slowly one by one. For prototype conditions it would be
expected that the slope would still be able to resist smaller
waves after a short storm with waves corresponding to 4th de-
gree. For 5th degree total failure will occur in a short time.

It is natural to try to compare these definitions with the
wellknown percentage of damage. The 0-percentage is found on
the transition between 2nd and 3rd degree. The 3rd degree will
be equal to approximately 2-4% damage, but in the 4th and 5th
degree the damage is dependent on time and therefore the per-
centage of damage will increase with increasing duration of the
test.

Influence of slope

Figure no 1 shows the stability conditions due to regular wave
attack perpendicular to the slope. H is the wave height, h is
the dolos height and a is the slope defined as cotangent to the
angel between horizontal and the slope. The grey screen on the
figur in the transition between the degrees of damage indicates
the inaccuracy of the tests. The figur includes own results and
results from the accessible literature. All the tests have been
carried out with almost the same density, so it was possible to
use the simple parameter H/h to compare the results. It is re-
markable that the stability is independent of the slope if the
accuracy is considered.
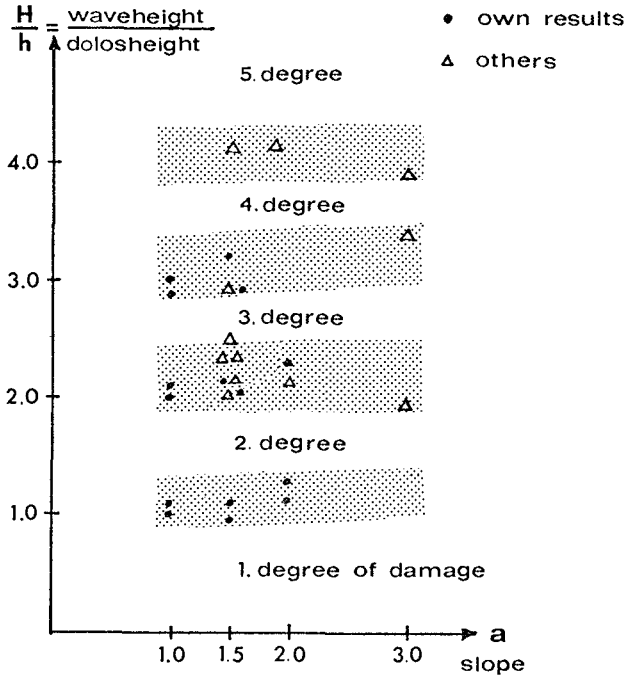
Fig. no 1

Irregular waves

Figur no 2 shows the waveheight distribution obtained in irregular wave tests. H_s is the significant waveheight defined as the average height of the highest third part of the waves. $\bar{H}$ is the average waveheight. ε is the spectral width parameter defined as $\varepsilon^2 = 1 - (T_c/T_z)^2$ where T_c is the top-top period and T_z the zero upcrossing period. It is remarkable that the distribution differs from the Rayleigh-distribution especially for the higher part of the waves.

The wavespectrum was not recorded, but the wavegenerator was fed
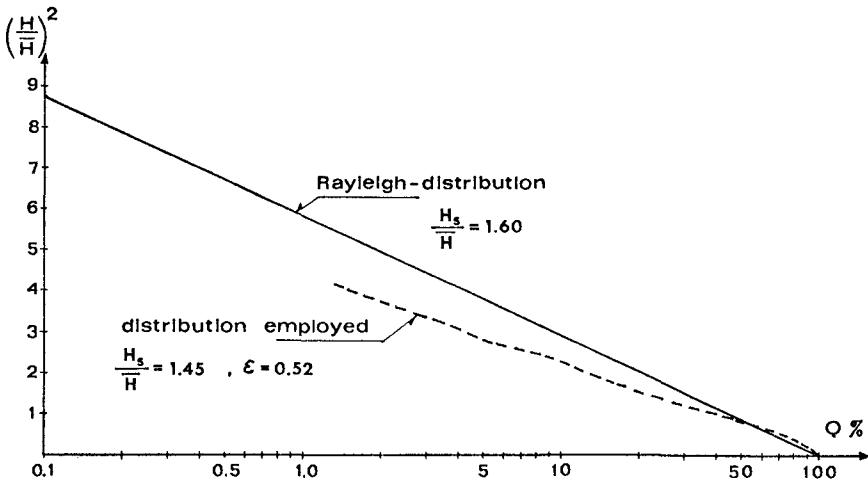
Fig. no 2

with a signal which was estimated to give a Moskowitz spectrum in front of the wavegenerator. The electrical inputsignal consisted of 10 discrete frequencies and the transferfunction was estimated after Biesels small amplitude wavegeneration theory.

Figur no 3 illustrates the general result obtained when the effect of regular and irregular waves was compared.

The result was that irregular waves with a significant waveheight H_s will cause the same damage as regular waves with the height $H = 0,8\ H_s$ and the factor 0,8 was the same for all slopes and blocks compared if the accuracy was considered. The conclusion is therefore that in the sphere of the tests regular waves are probably satisfactory to compare the stability of different slopes and blocks relativly.

Refference [7] and [12] have found that the ratio between regular wave height and significant irregular wave height causing the same damage was equal to 1.0. The explanation of this devia-

DOLOS CONCRETE

a = 1.5
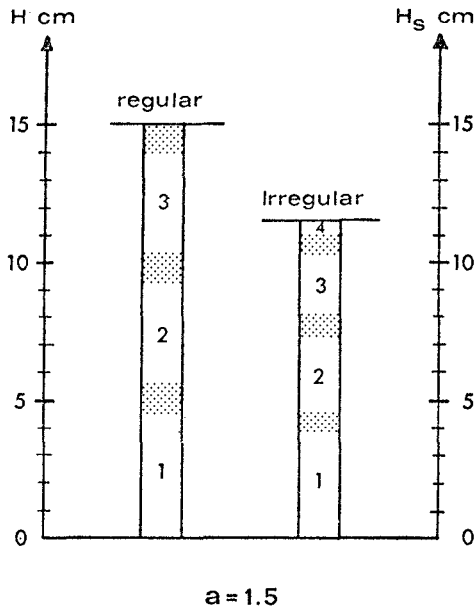
Fig. no 3

tion between the results proberly is due to the differens in waveheight distribution used in the different tests.

Dolos, natural stones and concrete cubes

The stability of dolos, natural stones and concrete cubes has been directly compared in the model test by having the different blocks simultanously attacked by the same waves. Figur no 4 shows the results of the tests. The blockweight was 38 g for all the blocks and the density of the concrete dolos and cubes

was 2,3 t/m^3 and density of the natural stones was 2,65 t/m^3 corresponding to prototype conditions.
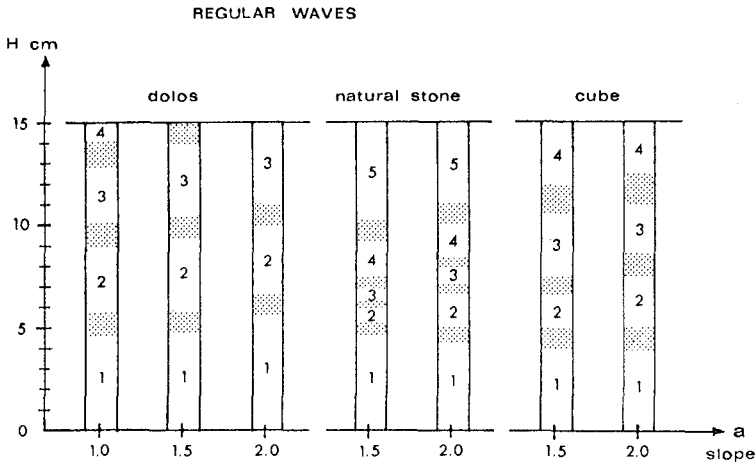
Fig. no 4

The results of the stability of natural stones and cube are in good agreement with results from the literature.

First figur no 4 shows the better stability of the dolos. Moreover it is significant that dolosslopes are less sensitive to overloading than e.g. natural stones.

The results in figur no 4 can be transfered to other scales by use of Froudes model scale law simply by multiplying the waveheight by the scale and multiplying the blockweight by the third power of the scale.

Concrete and plastic modelblocks

Fig. no 5 shows the stability of concrete and plastic model

IRREGULAR WAVES
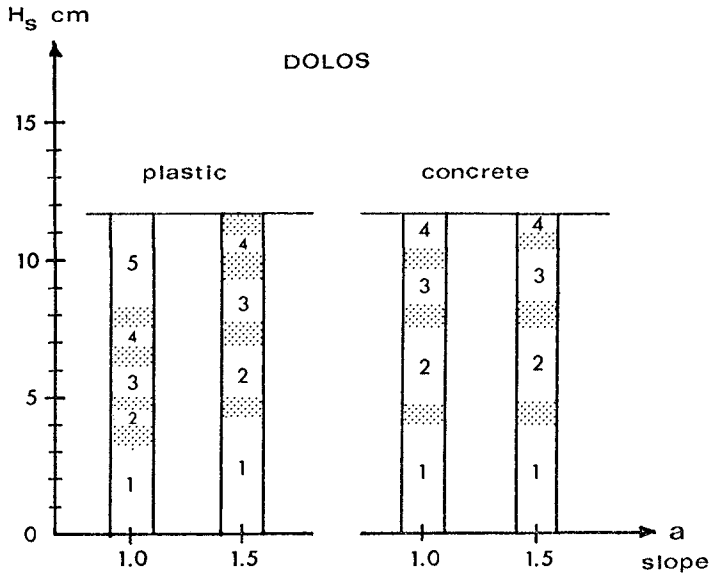
Fig. no 5

blocks. A significant lower stability for plastic-dolos can be observed at the 1 in 1 slope.

A satisfactory unique physical explanation of this cannot be given at the moment. But it can directly be observed that wet plastic dolos are much more smooth than the concrete ones and a reduction of the friction between the blocks will of course reduce the stability, especially a reduction of the interlocking capability should be expected to be important.

The influence of the surface roughness seems to be important in certain circumstances and in the authors opinion further research on this point is recommendable.

Hudson's formula

In fig. no 6 calculations of the stability factor K in Hudson's wellknown formula is plotted against the slope.
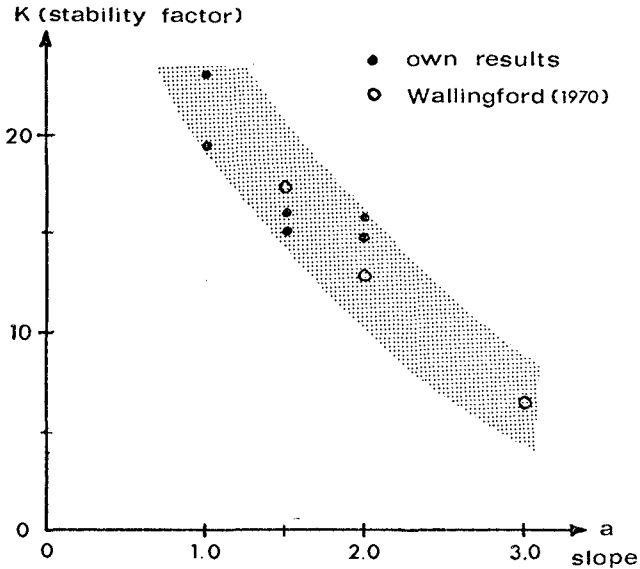
Fig. no 6

In spite of the considerable inaccuracy in the tests, which is strongly amplified by the third power-influence of the wave-height in the stability factor, it is clear that Hudson's formula does not describe the stability of dolos slopes satisfactory. The reason for this is probably the interlocking between the blocks and the high porosity of the armour layer.

As the results show that other forces are involved than assumed for the set up of Hudson's formula, the stability as function of the density cannot be expected to be the same as expressed by Hudson's formula.

The dependence of the third power on the waveheight is of course
not affected if the Froudes scalelaw is assumed to be valid.

Fieldinvestigation by photogrammetry

In order to follow up abovementioned modeltest a fieldinvesti-
gation of the dolos-breakwater in Hirtshals harbour, Northjut-
land, Denmark was started in 1973. The purpose of the investi-
gation which is in progress is to registrate both damage and
small movements of the blocks in the armour layer. At the same
time the waveheight is measured. The block movements are de-
termined after photogrammetrical records from a height of
approximately 300 m. In this case it is possible to registrate
movements with a mean error of 1,5 cm.

Literature

[1]   Merrifield, E.M., Zwamborn, J.A. (1966): "The economic
       value of a new breakwater armour unit Dolos", Proc. of
       10th Conf. on Coastal Eng. Tokoy 1966.

[2]   Merrifield, E.M. (1968): "Dolos concrete armour protec-
       tion", Civil Engineering, Dec. 1968.

[3]   Merrifield, E.M. (1970): "Dolos - a new breakwater and
       coastal protection block", The Dock and Harbour Autho-
       rity, April 1970.

[4]   Mangoon, O.T., Shimizu, N. (1971): "Use of Dolos Armour
       units in rubble-mound structures e.g. for conditions in
       the arctic", Proc. of 1st int. conf. on port and ocean
       eng. under arctic conditions. Trondheim 1971.

[5]   Paul, M.W., Baird, W.F. (1971): "Discussion on breakwa-
       ter armour units", Proc. of 1st int. conf. on port and
       ocean eng. under arctic conditions. Trondheim 1971.

[6]   Paape, A., Walther, A.W. (1962): "Akmon armour unit for
       cover layers of rubble mound breakwaters", Hydraulics
       Laboratory Delft, publ. no 27, 1962.

[7]   Hydraulics Research Station, Wallingford (1970): "High
       Island water scheme - Hong Kong. A study on the use of
       dolos armour units for wave protection on the seaward
       face of the Eastern Dam", Report no EX 532.

[8]   Hudson, R.Y. (1959): "Laboratory investigation of rubble-
       mound breakwaters", Proc. A.S.C.E., Waterways and Har-
       bours division, sept. 1959.

[9]   Brorsen, M., Burcharth, H.F., Larsen, T. (1973): "Sta-
       bility of dolos slopes" (in Danish), Hydraulics Labora-
       tory, Bulletin no 3, Danish Engineering Academy, Aalborg,
       Denmark.

[10]   Zwamborn, J.A., Beute, I. (1972): "Stability of dolos
       armour units", ECOR symposium, Stellenbosch, nov. 1972.

[11]   Jepsen, H.S., Springborg, N.J. (1974): "Model test on
       the stability of dolos slopes" (in Danish), Master the-
       sis, Danish Engineering Academy, Aalborg, Denmark.

[12]   Quellet, Y. (1972): "Effects of irregular wave trains
       on rubble-mound breakwaters", Proc. A.S.C.E., Waterways,
       Harbours and Coastal Engineering Division, feb. 1972.

CHAPTER 100

NEW WAVE PRESSURE FORMULAE FOR COMPOSITE BREAKWATERS

By

Yoshimi Goda

Marine Hydrodynamics Division

Port and Harbour Research Institute, Ministry of Transport

Nagase, Yokosuka, Japan

ABSTRACT

A proposal is made for new wave pressure formulae, which
can be applied for the whole ranges of wave action from non-
breaking to postbreaking waves with smooth transition between
them. The design wave height is specified as the maximum wave
height possible at the site of breakwater.

The new formulae as well as the existing formulae of Hiroi,
Sainflou, and Minikin have been calibrated with the cases of
21 slidings and 13 nonslidings of the upright sections of proto-
type breakwaters. The calibration establishes that the new
formulae are the most accurate ones.

I. INTRODUCTION

Japan is currently constructing breakwaters with the rate of 30,000
to 40,000 m per year to protect her commercial ports, which count one
thousand in total number. Most of these breakwaters are built with concrete
caissons rested upon low rubble mounds, thus being subject to wave pressures
upon vertical faces. They are designed mostly for the so-called breaking
wave condition because their construction sites are relatively shallow in
comparison with the design wave heights. In recent years, however,
breakwaters have been extended to the water depths of 15 to 20 m or more,
and the so-called standing wave condition has become applicable.
Figure 1 is such an example, showing a plan of Kashima Port and its
breakwaters. A question arises in the design of such breakwaters: i.e.,
how the discontinuity in the calculated wave pressure at the transition
from breaking to standing wave conditions should be treated, because
the discontinuity inevitably appears somewhere in the long stretch of
a breakwater extending from the shallow to relatively deep waters.

As every harbor engineer knows, existing wave pressure formulae are
for either the breaking wave condition or the standing wave condition except
for Ito's formula [1] to the author's knowledge. And at the threshold
between the breaking to standing waves, the calculated wave pressure
decreases suddenly. The standard method of wave pressure calculation in
Japan is no exception. As shown in Fig. 2, the wave height for the calcul-
ation of pressure is specified as the significant height, $H_{1/3}$. When the
water depth above the mound of a breakwater, d, is less than $2 H_{1/3}$, the
formula by Hiroi [2] for breaking waves is employed; this gives $p_b = 1.5 w_o H$.
Otherwise, the simplified Sainflou's formulae [3] with a partial application
of Hiroi's pressure around the still water level are used. The application

1702
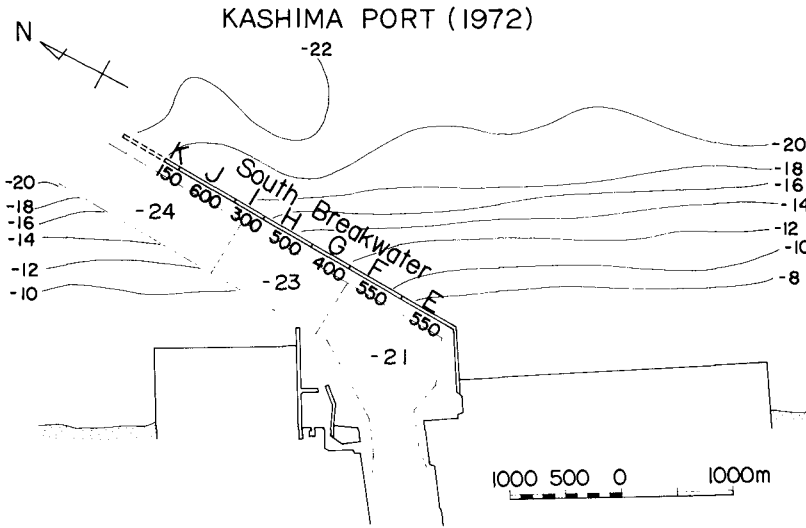
KASHIMA PORT (1972)

Fig. 1   Plan of Kashima Port
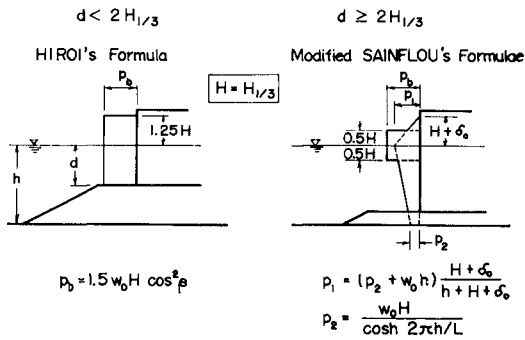
Fig. 2   Standard wave pressure formulae in Japan

of p_b in the range of $\pm 0.5\,H$ has been conceived partly for a possible partial breaking of wind waves and partly for the precaution against the attack of individual waves higher than $H_{1/3}$. Even with the partial application of p_b, a decrease of about 30 per cent in the total wave pressure is observed across the condition of $d = 2\,H_{1/3}$. The employment of Minikin's formulae [4] instead of Hiroi's formula will cause a larger change in the wave pressure across the threshold water depth.

The rationality of engineers calls for a smooth transition of wave pressure from breaking to standing waves, which will yield a gradual variation in the design width of breakwater caissons in a layout such as shown in Fig. 1. The present paper answers for the call by proposing new wave pressure formulae which cover the ranges of standing, breaking, and postbreaking waves with a single expression [5]. The new formulae are also characterized with the employment of the maximum wave height, H_{max}, at the design site. This reflects the design principle that an upright section of breakwater must withstand the attack of largest wave thrust expected. The followings are the details of the new formulae and the result of their calibration with 34 case studies of the performance of prototype breakwaters during high seas around the coasts of Japan.

II. FORMULATION OF THE NEW METHOD OF WAVE PRESSURE ESTIMATION

Wave pressures exerted upon a vertical wall is a complicated phenomenon, and the presence of a rubble mound makes the problem more difficult. Many investigations, theoretical, experimental, and of field observations, have been undertaken to clarify the phenomenon of wave pressures, and they have yielded a number of wave pressure formulae. But most of previous studies set their objects on either breaking waves or standing waves. These studies provide no solution for the question of a smooth transition from breaking to standing waves. By this reason, the author conducted his own experiments which covered the ranges of standing, breaking, and postbreaking waves by the increase of incident wave heights at several preselected wave periods (see [6,7] for details).

Figure 3 is an example of the distribution of maximum and minimum wave pressures along a vertical wall. The bottom of test flume had the gradient of 1 on 100, and the flume was gradually narrowed from the width of 80 cm to that of 50 cm over the distance of 18.5 m so as to secure the condition of postbreaking waves at a fixed test section. Figure 3 shows that wave pressures are almost proportional to the incident wave heights without exhibiting impulsive breaking wave pressures of high intensities. Though the occurrence of impulsive breaking wave pressure is much feared in the design of vertical-faced breakwaters, it is realized only when wave conditions and dimensions of breakwater satisfy a set of certain requirements. It is a rare phenomenon for prototype breakwaters, which are built on the sea bed of gentle gradient and subject to the action of irregular waves with medium to large wave steepness (cf. Mitsuyasu's experiments [8]). Furthermore, it can be proved that the finite forward momentum of breaking wave front limits the wave load effective for sliding of an upright section resting on the nonlinear vibration system of the rubble mound and foundation to the mean pressure of about $(2 \sim 3)\,w_0\,H_b$, even if the exerting wave pressure itself may amount to $10\,w_0\,H_b$ or more [9].
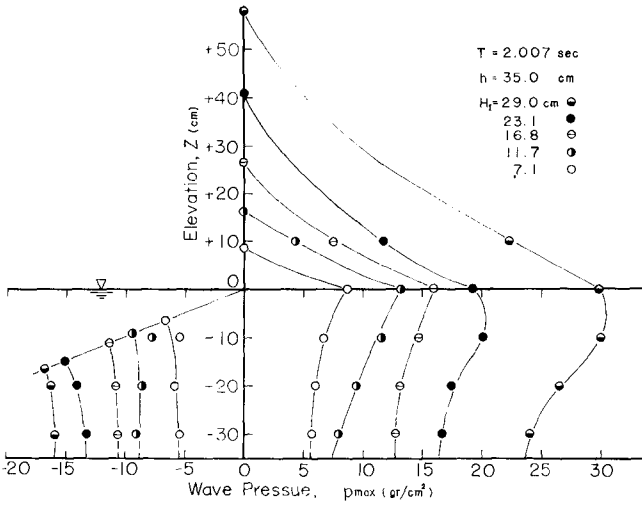
Fig. 3   Distribution of maximum and minimum wave
         pressures along a vertical wall
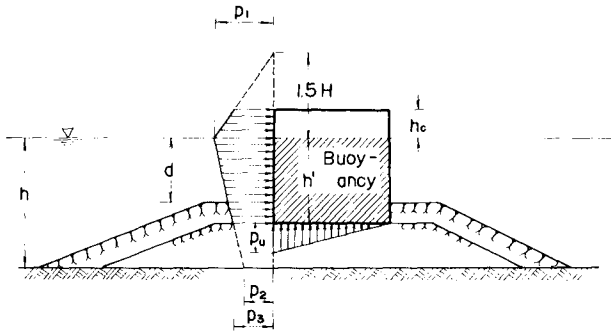
Fig. 4   Distribution of design wave pressure

The results of the experiments and the estimation of effective wave load as well as the requirement of simplicity in the application of formulae have brought the author to propose the distribution of design wave pressure as shown in Fig. 4. It has the largest intensity of p_1 at the still water level, and extends to the elevation of $1.5\,H$ above the still water level. The imaginary wave pressure of p_2 at the elevation of sea bottom is proportional to p_1. The distribution is given by a straight line connecting p_1 and p_2, and another between p_1 and $p = 0$ at $z = 1.5\,H$. The wave overtopping due to a low crest height of breakwater is assumed to exercise no effect on the distribution and intensity of wave pressures for the sake of simplicity.

The intensities of wave pressures, p_1, p_2, and p_3, are calculated with the following formulae:

$$p_1 = w_0\,H_D\,(\alpha_1 + \alpha_2 \cos^2\beta) \tag{1}$$

$$p_2 = \frac{p_1}{\cosh\,2\pi h/L} \tag{2}$$

$$p_3 = \alpha_3\,p_1 \tag{3}$$

where,

$$\alpha_1 = 0.6 + \frac{1}{2}\left[\frac{4\,h/L}{\sinh\,4\pi h/L}\right]^2 \tag{4}$$

$$\alpha_2 = \min\left\{\frac{h_b - d}{3\,h_b}\left[\frac{H_D}{d}\right]^2,\ \frac{2\,d}{H_D}\right\} \tag{5}$$

$$\alpha_3 = 1 - \frac{h'}{h}\left[1 - \frac{1}{\cosh\,2\pi h/L}\right] \tag{6}$$

H_D : design wave height (see Eq. 8 hereafter)
w_0 : specific weight of sea water
L : wavelength of design wave
$\min\{a,b\}$: smaller one of a or b
β : angle of wave approach
h_b : water depth at which the breaker height is to be evaluated (see Eq. 10).

The pressure factors of α_1 and α_2 have been determined empirically on the basis of experimental data and the calibration of new formulae with the case studies of prototype breakwaters. Comparison of the pressure intensity p_1 with experimental data is shown in Fig. 5 for a vertical wall without a rubble mound and in Fig. 6 for a vertical wall rested on a rubble mound. The pressure intensities by experiments are not the raw data of measurements but the results of calculation from the total pressures using the distribution of Fig. 4. The pressure intensity calculated with the above formulae is shown with dash-dot lines. The curves in full lines in Fig. 5 represent the theoretical values of finite amplitude standing waves of fourth order approximation [10,11]. For a vertical wall without a rubble mound, the factor of α_2 is almost nil, and the nondimensional wave pressure of p_1/w_0H_D is regarded constant. The effect of a rubble mound on wave pressure is represented with the factor of α_2, which increases parabolically with the relative wave height of H_I/h. The second term in the expression
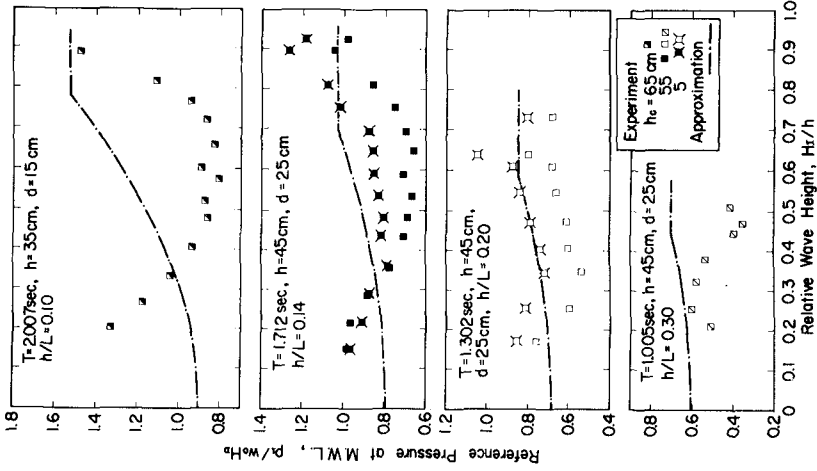
Fig. 6 Pressure intensity of p_1 on a vertical wall rested on a rubble mound
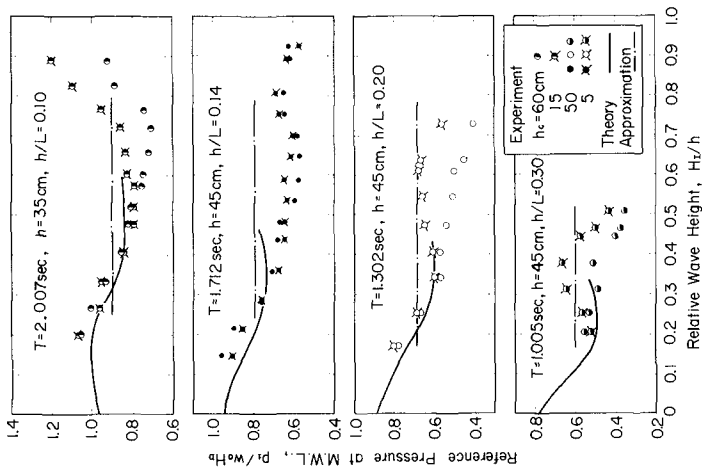
Fig. 5 Pressure intensity of p_1 on a vertical wall without a rubble mound

for α_2, or $2d/H_D$, is so incorporated to avoid the excessive increase of α_2 for $d \to 0$. (This term is not employed in Fig. 6, where α_2 is taken constant for postbreaking waves.) Though the agreement between the formulae and the laboratory data is not excellent, the difference may be disregarded for the purpose of general formulation of wave pressure estimation.

For the calculation of uplift pressure acting beneath the bottom of upright section, the triangular distribution is assumed irrespective of wave overtopping. The intensity of toe uplift is given by:

$$P_u = \alpha_1 \, \alpha_3 \, w_o \, H_D \tag{7}$$

The omission of α_2 term is the consequence of expectation that the part of the wave pressure represented with α_2 is of short duration and will not contribute much to the total uplift. The buoyancy is calculated for the volume of upright section beneath the still water level even if its crest is low enough to cause wave overtopping. This method of buoyancy and uplift calculation, which is a departure from the standard method in Japan, was first proposed by Ito [1].

The design wave height, H_D, is the highest wave height expected under the given wave condition. It is the smaller one of $1.8\,H_{1/3}$ or H_b, which is the limiting breaker height. The height of H_b is to be estimated not at the site but at the place in the distance of $5\,H_{1/3}$ toward the offshore from the breakwater. That is,

$$H_D = H_{max} \simeq \min\{\, 1.8\,H_{1/3}\,,\ H_b \,\} \tag{8}$$

$$H_b = 0.17\,L_o\{\ 1 - \exp[\,-1.5\frac{h_b}{L_o}\,(1 + 15\,\tan^{4/3}\theta)\,]\} \tag{9}$$

$$h_b = h + 5\,H_{1/3}\,\tan\theta \tag{10}$$

where L_o is the deepwater wavelength of $gT^2/2\pi$ and $\tan\theta$ denotes the mean gradient of sea bottom. Equation 9 for H_b is an empirical formulation of the breaker index prepared by the author [12], based on the compilation of laboratory data from various sources. The value of H_b/h_b by Eq. 9 is governed by both the gradient of sea bottom and the relative water depth of h_b/L_o as shown in Fig. 7.

The period of design wave is T_{max}, which can be taken as the same with $T_{1/3}$ on the basis of the statistical analysis of a number of surface wave records [13].

III. CALIBRATION WITH PROTOTYPE BREAKWATERS

The new method has been tested with the data of slidings of model breakwaters by regular and irregular waves, and it has succeeded in predicting their slidings [5]. The real test of any wave pressure formula, however, is the one with the data of the performance of prototype break-waters during heavy seas. The analysis of slidings alone is not sufficient, but the analysis of nonsliding cases should also accompany the former for cross-examination of the accuracy of proposed formulae.
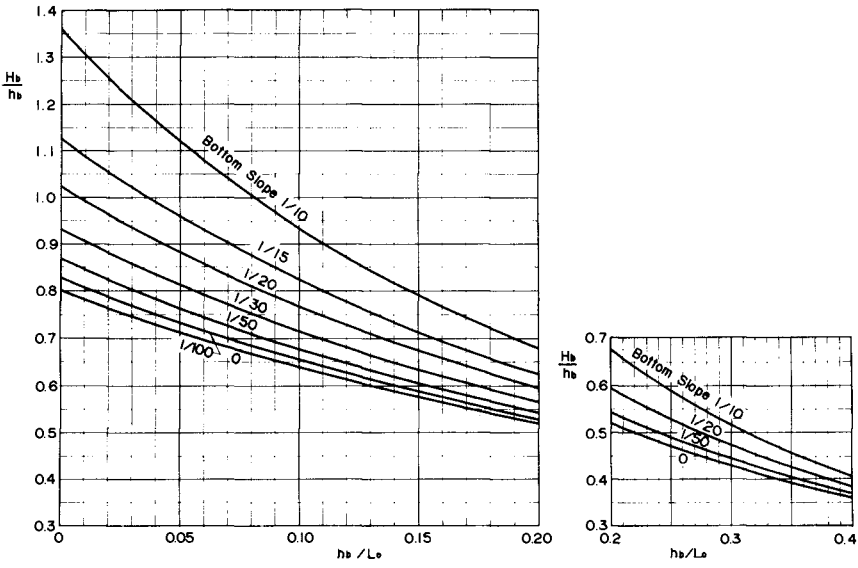
Fig. 7   diagram of limiting breaker height
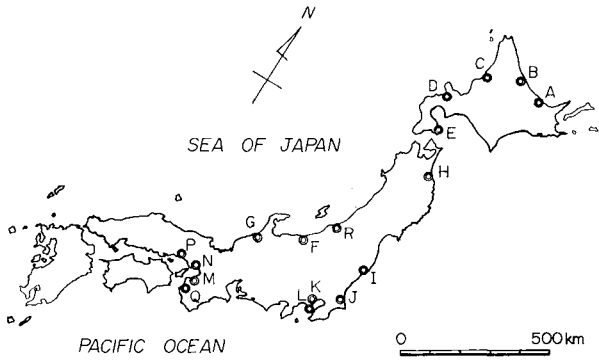
Fig. 8   Location map of the ports for the study of breakwater stability

Being the country with the longest stretch of composite breakwaters in the world, Japan can provide a long list of the performance of composite breakwaters during heavy seas. Slidings of upright sections, however, are relatively few in spite of large quantities of breakwater construction. The author searched for the cases of slidings of breakwaters in various reports and documents, and then investigated these cases if there might be breakwaters in the neighborhood which withstood the same storms without damage. Reportings of the observation of largest waves in record often provided excellent data of nonsliding cases. Existence of a large number of wave observation stations at the offices of harbor construction around Japan was most helpful in estimating the magnitude of high seas. For the cases in the past before modern wave observations became available, various techniques of wave hindcasting have been employed. In total, 21 cases of slidings and 13 cases of nonslidings at 17 ports shown in Table 1 and Fig. 8 have been selected for the calibration of wave pressure formulae.

An example of analysis is the case of the south breakwater (H-section) of Kashima Port, the cross section of which is shown in Fig. 9. When a storm passed by the port on January 9, 1972, twelve caissons of the H-section were slided by 0.2 to 1.8 m by the waves of $H_{1/3} = 6.5$ m and $T_{1/3} = 14$ sec (estimated values). The total wave pressures were estimated by four formulae: i.e., the standard method in Japan, the new method, Sainflou's formulae with $H_D = H_{max}$, and Minikin's formulae with $H_D = H_{max}$. The calculated pressures varied from 150.6 t/m by the standard method to 523.7 t/m by Minikin's formulae. With the weight of caisson being 278.9 t/m at the condition of full submergence, the pressures yield the safety factor of 1.11 to 0.33 against the sliding. (The full buoyancy for all the volume without the uplift pressure was assumed in the application of Sainflou's formulae, while the calculation same as the new method was applied for Minikin's formulae.) Since the caissons of the H-section actually slided, the safety factor of 1.11 by the standard method in Japan is contradictory with the reality. On the other hand, the safety factor of 0.33 by Minikin's formulae is considered too small, judging from the fact that nearly two-thirds of the caissons remained at their original positions.

Another example is the case of the west breakwater of Mega Harbor, Himeji Port, shown in Fig. 10. When the typhoon No. 6420 approached the area, a part of the breakwater near the tip was without crown concrete, while the middle part was with cap concrete to the elevation of +2.0 m and the part near the bend to the jetty which connected the breakwater and the shore was just after completion. After the passage of the estimated waves of $H_{1/3} = 3.6$ m and $T_{1/3} = 6.8$ sec, the part without crown concrete was found in sliding by 0.17 to 1.12 m, whereas the other parts were almost unslided. The analysis of the safety factor against sliding with the four formulae has resulted in the values less than 1.0 for both the sliding and nonsliding. This may have been caused by an overestimation of wave heights or by some other factors. But attention is called for the difference between the safety factors of sliding and nonsliding cases. Though the non-sliding case should show the safety factor higher than the sliding case, the wave pressure formulae except for the new method fail to satisfy the expectation.

KASHIMA PORT   South Breakwater (H-Section)
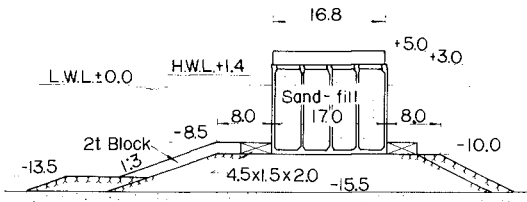
Sliding : $H_{1/3}$= 6.5m, $T_{1/3}$= 14.0 sec

Formulae	H_D (m)	P (ton/m)	S.F. against sliding
Standard	6.5	150.6	1.11
New	11.7	185.7	0.84
Sainflou	11.7	183.3	0.91
Minikin	11.7	523.7	0.33

Fig. 9   Case study of breakwater stability (1)

MEGA HARBOR   West Breakwater
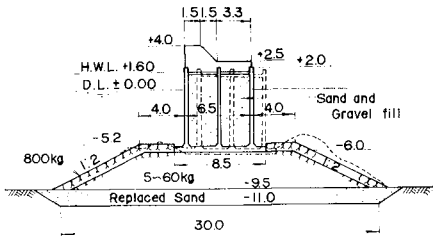
$H_{1/3}$ = 3.6 m, $T_{1/3}$ = 6.8 sec

Formulae	H_D (m)	Sliding		Nonsliding	
		P(t/m)	S.F.	P(t/m)	S.F.
Standard	3.6	44.6	0.78	55.8	0.74
New	6.5	36.1	0.75	45.7	0.82
Sainflou	6.5	46.2	0.74	58.4	0.71
Minikin	6.5	173.3	0.15	311.0	0.12

Fig. 10   Case study of breakwater stability (2)

Table 1. List of Breakwaters under Examination

No	Port	Breakwater (section)	(1)	(2)	Extent of damage if any (3)	(4)
A	Abashiri	North B. (T)	1927	'27.12 - '28.1	about 4	43 (all)
B-1	Monbetsu	East B.	c*	'65.1.9	about 3	7 among 20
B-2	do	North B.	1930	do	[0]	none
C-1	Rumoi	South B. (B)	c	'21.11.7	0.5	5 (all)
C-2	do	do (A)	c	'21.12.4	[0]	none
D	Iwanai	West B. (C)	c	'65.12.15	0.3	2 among 6
E-1	Todohokke	East B. (H)	c	'59.9.27	about 1.5	3
E-2	do	do (G)	1955	'60.10.22	[0]	none
F-1	Himekawa	West B. (B)	1969	'70.2.1	5.4	3
F-2	do	do (E)	1972	'72.12.1	[0]	none
G-1	Kanazawa	West B. (C)	c	'67.12.15	0.4	9 among 10
G-2	do	do (E)	c	'70.2.1	[0]	none
H-1	Hachinohe	North B.(8th)	c	'66.12.15	3.7	6 among 8
H-2	do	do (10th)	c	'71.1.17	1.4	28 among 30
I-1	Onahama	2nd West B.(A)	c	'70.2.1	0.9	8 among 13
I-2	do	1st West B.(E)	1969	'71.4.29	about 0.6	7 among 120
I-3	do	do	1969	'70.2.1	[0]	none
I-4	do	2nd West B.(A)	1971	'71.4.29	[0]	none
J-1	Kashima	South B. (H)	1970	'72.1.9	about 1	12 among 33
J-2	do	do (J)	c	do	about 0.5	8 among 40
J-3	do	do (K)	c	'72.12.25	1.4	10 (all)
J-4	do	do (G)	1970	'72.1.9	[0]	none
J-5	do	do (I)	1971	do	[0]	none
J-6	do	do (J)	1972	'72.12.25	[0]	none
K-1	Yokohama	Kanagawa B.	c	'38.9.1	about 1	10 (all)
K-2	do	North B.	1935	'49.8.31	[0]	none
L	Kurihama	F₂-Seawall	c	'58.1.27	about 5	6 (all)
M	Kaizuka	West B.	1960	'61.9.16	about 8	9 among 10
N	Kobe	3rd B.	1937	'64.9.25	0.05	2
P-1	Mega	West B. (C)	c	'64.9.25	0.4	11 among 13
P-2	do	do (A)	1964	do	[0]	none
Q-1	Wakayama	Secondary B.	c	'64.9.25	0.4	5 (all)
Q-2	do	West B.	1961	'65.9.10	about 0.6	19 among 86
R	Niigata	West B. (F)	c	'70.2.1	[0]	none

Note:
       * : "c" stands for "under construction."
    (1) : Year of construction
    (2) : Date of occurrence of high seas
    (3) : Root-mean-square distance of sliding (m)
    (4) : Numbers of slided caissons.

Table 2. Analysis of the Slidings of Caissons of Composite Breakwaters

No	Port	Water level (m)	Waves Hmax (m)	H1/3 (m)	T1/3 (s)	β (°)	Dimensions of Breakwater (1) (m)	(2)	(3) (m)	(4) (m)	(5) (m)	(6) (m)	(7) (t/m)	Safety Factor against sliding (a)	(b)	(c)	(d)	No
A	Abashiri	+1.5	8.7	5.2	9.0	0	-10.9	1/50	-5.0	-7.3	+2.4	11.5	142.6	1.11	0.84	1.04	0.28	A
B	Monbetsu	+1.6	7.8	4.5	8.0	40	-10.0	1/50	-6.0	-7.5	+1.0	9.0	77.3	1.34	0.70	0.76	0.37	B
C-1	Rumoi	+1.5	8.5	4.7	9.0	0	-14.5	1/200	-5.4	-7.3	+0.6	10.6	109.0	1.14	0.78	1.03	0.55	C-1
D	Iwanai	+1.0	8.1	4.5	9.0	0	-12.0	1/100	-7.0	-8.5	+0.5	11.5	113.9	1.09	0.83	0.98	0.37	D
E-1	Todohokke	+1.3	5.5	4.0	9.7	0	-5.5	1/50	-2.1	-5.0	+4.2	7.5	67.6	0.71	0.57	0.80	0.44	E-1
F-1	Himekawa	+0.8	11.3	6.3	11.1	0	-8.8	1/7	-4.5	-6.0	+4.5	15.0	177.9	1.04	0.47	0.86	0.28	F-1
G-1	Kanazawa	+0.5	6.7	5.0	9.0	0	-9.0	1/100	-3.0	-4.5	+1.0	15.0	94.8	1.34	0.65	1.47	0.52	G-1
H-1	Hachinohe	+1.5	6.0	5.0	10.0	10	-6.5	1/120	-2.5	-4.5	+2.5	10.5	80.9	0.93	0.76	1.11	0.46	H-1
H-2	do	+1.5	7.6	6.1	11.5	10	-8.8	1/150	-4.5	-6.5	+3.5	16.0	175.6	1.16	1.13	1.32	0.53	H-2
I-1	Onahama	+1.4	9.9	5.5	10.0	0	-17.0	1/500	-7.0	-8.5	+2.5	15.0	203.4	1.31	1.00	0.99	0.36	I-1
I-2	do	+1.4	9.8	6.0	11.0	14	-13.0	1/500	-6.0	-7.0	+5.0	13.0	195.9	1.12	0.95	1.14	0.33	I-2
J-1	Kashima	+1.4	11.7	6.5	14.0	0	-15.5	1/100	-8.5	-10.0	+5.0	17.0	278.9	1.11	0.84	0.91	0.33	J-1
J-2	do	+1.4	11.7	6.5	14.0	0	-19.0	1/100	-12.5	-14.0	+3.8	17.0	333.1	1.49	0.91	0.94	0.29	J-2
J-3	do	+1.4	11.7	6.5	14.0	0	-21.0	1/100	-12.5	-14.0	+3.8	17.0	333.1	1.49	0.96	0.94	0.31	J-3
K-1	Yokohama	+2.1	5.8	3.2	6.0	0	-11.7	1/500	-6.5	-6.5	+2.2	9.0	43.3	0.98	0.71	0.62	0.09	K-1
L	Kurihama	+2.0	5.7	3.5	8.5	0	-6.0	1/100	-4.5	-4.5	+2.5	8.0	63.2	1.00	0.87	0.94	0.21	L
M	Kaizuka	+3.0	4.7	3.0	5.5	25	-5.5	1/100	-1.5	-3.0	+3.5	5.0	32.8	0.80	0.79	0.73	0.17	M
N	Kobe	+3.2	5.9	3.3	6.0	0	-11.2	1/500	-4.9	-4.9	+3.0	6.9	49.1	1.19	0.88	0.75	0.16	N
P-1	Mega	+2.0	6.5	3.6	6.8	0	-9.5	1/500	-5.2	-6.0	+2.0	6.5	57.8	0.78	0.74	0.75	0.15	P-1
Q-1	Wakayama	+2.8	9.2	6.0	11.0	0	-10.0	1/100	-6.1	-8.1	+2.4	14.0	167.9	1.04	0.81	1.05	0.41	Q-1
Q-2	do	+2.0	8.6	6.3	12.0	0	-9.4	1/100	-5.0	-7.0	+5.0	12.0	162.5	0.84	0.80	0.92	0.34	Q-2

Note: See Table 3 for the explanation of (1) (7) and (a) (d).

Table 3.   Analysis of the Nonslidings of Breakwater Caissons under High Seas

No	Port	Water level (m)	Waves Hmax (m)	H1/3 (m)	T1/3 (s)	β (°)	Dimensions of Breakwater (1) (m)	(2)	(3) (m)	(4) (m)	(5) (m)	(6) (m)	(7) (t/m)	Safety Factor against sliding (a)	(b)	(c)	(d)	No
B-2	Monbetsu	+1.6	6.7	4.5	8.0	30	-7.5	1/40	-6.0	-7.5	+3.6	10.5	137.4	1.19	1.10	0.97	0.24	B-2
C-2	Rumoi	+1.5	9.5	5.8	9.0	0	-13.9	1/200	-13.9	-7.3	+1.7	10.6	122.6	1.25	0.94	0.89	0.10	C-2
E-2	Todohokke	+1.3	5.3	5.0	10.0	0	-5.5	1/80	-4.0	-5.0	+4.2	9.0	79.7	0.67	0.95	0.98	0.35	E-2
F-2	Himekawa	+0.6	10.8	6.0	11.0	0	-16.0	1/7	-8.5	-10.0	+5.0	16.5	277.9	1.20	1.06	1.04	0.35	F-2
G-2	Kanazawa	+0.6	7.7	7.2	11.4	15	-9.5	1/100	-5.0	-6.5	+4.0	15.0	181.4	1.00	1.23	1.32	0.63	G-2
I-3	Onahama	+1.4	9.4	5.5	10.0	20	-13.0	1/500	-6.0	-7.0	+5.0	13.0	195.9	1.31	1.10	1.05	0.37	I-3
I-4	do	+1.4	10.8	6.0	11.0	20	-17.0	1/500	-7.0	-8.5	+5.0	15.0	247.9	1.35	1.01	1.02	0.39	I-4
J-4	Kashima	+1.4	11.5	6.5	14.0	0	-14.0	1/100	-8.5	-10.0	+5.0	17.0	278.9	1.11	0.87	0.93	0.32	J-4
J-5	do	+1.4	11.7	6.5	14.0	0	-17.5	1/100	-10.5	-12.0	+5.0	17.0	319.5	1.12	0.92	0.94	0.32	J-5
J-6	do	+1.4	11.7	6.5	14.0	0	-19.0	1/100	-12.5	-14.0	+5.0	17.0	358.8	1.50	1.04	0.96	0.32	J-6
K-2	Yokohama	+2.2	6.3	3.5	7.3	0	-11.7	1/500	-5.2	-6.5	+3.5	9.0	89.7	1.43	1.06	0.94	0.20	K-2
P-2	Mega	+2.0	6.5	3.6	6.8	0	-9.5	1/500	-5.2	-6.0	+4.0	6.5	69.2	0.74	0.82	0.71	0.12	P-2
R	Niigata	+0.7	10.1	7.1	12.5	17	-13.0	1/100	-8.0	-9.5	+4.0	16.0	241.6	1.07	1.00	1.04	0.37	R

Note: (1) Elevation of sea bottom below the datum
(2) Gradient of sea bottom
(3) Elevation of the crest of armour stones or blocks of rubble mound below the datum
(4) Elevation of the base of caisson below the datum
(5) Elevation of the brest of breakwater above the datum
(6) Width of caisson at its base
(7) Submerged weight of caisson

(a) by the standard formulae in Japan
(b) by the new formulae
(c) by Sainflou's formulae with H_{max}
(d) by Minikin's formulae with H_{max}

The results of similar analysis for the remaining cases of slidings and nonslidings are summarized in Tables 2 and 3. The safety factors against sliding calculated with the four formulae are shown in Figs. 11 to 13 with open circles for nonsliding cases and closed circles for sliding cases. Figure 11 is the comparison of the standard formulae with the new method, while Figs. 12 and 13 exhibit the safety factors by Sainflou's and Minikin's formulae, respectively. If the open circles for nonslidings are found all above the line of S.F. = 1.0 while the closed circles for slidings are all below that line, the formulae under examination can be judged most accurate. From this point of view, the standard formulae in Japan do not perform well as evidenced by the existence of nonsliding data below the line of 1.0 (E and P) and that of sliding data above the line of 1.0 (B, G, I, J, and others). On the contrary, the new formulae produce only a minor intermixing of sliding and nonsliding data, and a line of boundary can be drawn around S.F. = 0.95.
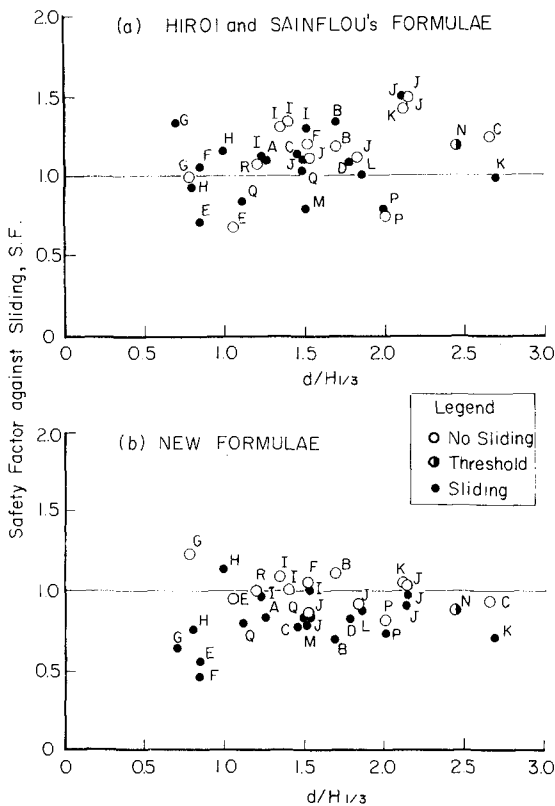
Fig. 11 Safety factors against sliding by the standard formulae
         and the new ones

The performance of Sainflou's formulae in Fig. 12 is fairly well, even though most of the breakwaters under study do not satisfy the so-called standing wave condition. A close examination of Fig. 12 reveals however that several nonsliding data have the safety factors smaller than those of sliding data at the same ports as in the cases of C, G, I, and P.
The result with Minikin's formulae is poor with a total mixing of sliding and nonsliding data at very low level of safety factor. This indicates that Minikin's formulae predict wave pressures far larger than actual values. The employment of $H_{1/3}$ instead of H_{max} increases the absolute values of safety factor, but the extent of mixing of data is not improved.
The formula proposed by Ito [1] for composite breakwaters was also examined, but the result was inferior to the new formulae.

The results of the analysis of the performance of prototype breakwaters establish that the new wave pressure formulae are the best ones for practical calculation of wave pressures upon composite breakwaters and for the analysis of the stability of upright sections against wave actions.
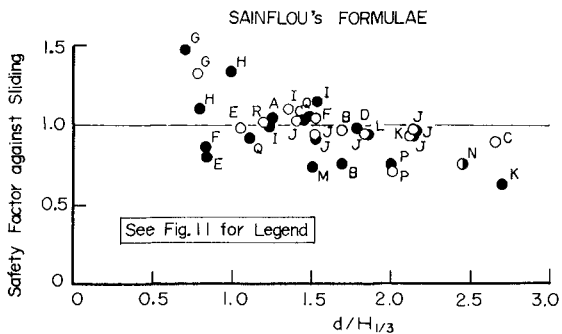
Fig. 12   Safety factor against sliding by Sainflou's formulae
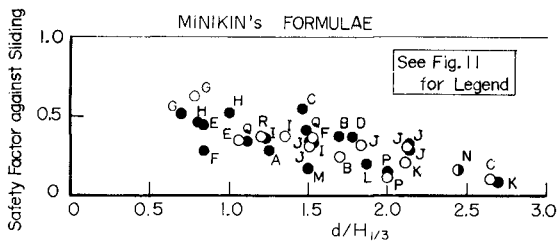
Fig. 13   Safety factor against sliding by Minikin's formulae

IV.   CALCULATION OF THE WIDTH OF BREAKWATER CAISSON

The new wave pressure formulae are applied for the calculation of the width of breakwater caisson for illustration. The following assumptions are made:

gradient of sea bottom   : $\tan\theta$ = 1/100
crest height of breakwater   : h_c = 0.6 $(H_{1/3})_0$
crest height of caisson   : h_c' = 1.0 m
specific weight of caisson with sand filling : γ = 2.1 t/m
specific weight of crown concrete   : γ = 2.3 t/m
thickness of armour stones   : $h' - d$ = 1.5 m
safety factor against sliding   : S.F. = 1.2
frictional coefficient between caisson and
        rubble mound   : μ = 0.6

The significant wave height at the site of breakwater is taken same as the deepwater value of $(H_{1/3})_0$ or 0.65 h if the former exceeds the latter. The limitation of $(H_{1/3})_{max}$ = 0.65 h is due to the results of wave observation around the coasts of Japan.

The results of calculation are shown in Figs. 14 to 16. The first figure exhibits the effect of the height of rubble mound on the caisson width. As the rubble mound becomes thick, a larger width of caisson is required as the result of the increase in wave pressure expressed with the factor of α_2. The effect of wave height is shown in Fig. 15. The wave period is so selected that the deepwater wave steepness will be in the range of $(H_{1/3})_0 / L_0$ = 0.03 ~ 0.04. In the shallow waters, the caisson width does not vary much with the increase in wave height, because
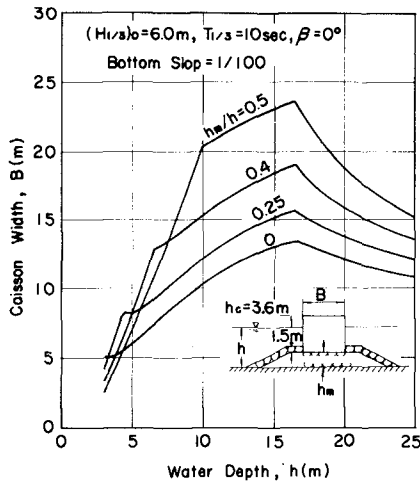
Fig. 14   Effect of rubble mound on the width of caisson
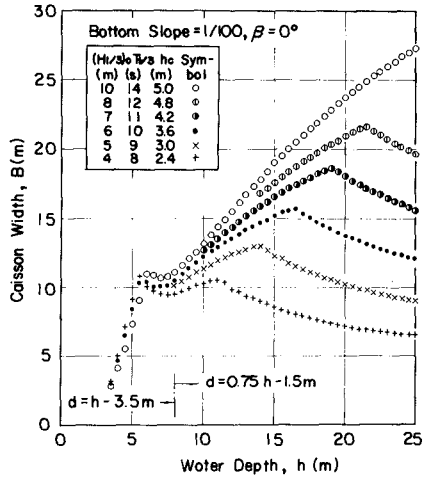
Fig. 15   Effect of wave height on the width of caisson
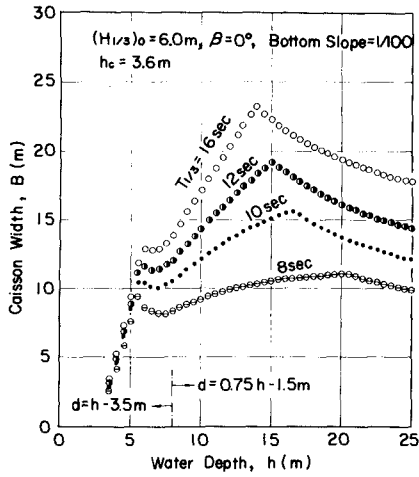
Fig. 16   Effect of wave period on the width of caisson

H_{max} is limited by the water depth. As the water becomes deep, however, the magnitude of wave height directly affects the caisson width. Therefore, the selection of design wave height in relatively deep waters is crucial for the safety of breakwater caissons.

The new wave pressure formulae indicate a strong influence of wave period on the wave pressure as shown in Fig. 16, where the wave period is increased from $T_{1/3}$ = 8 to 16 sec while the wave height is fixed at $(H_{1/3})_0$ = 6.0 m. In the waters deeper than h = 6.0 m, the caisson width is almost proportional to the wave period. The effect of wave period on the wave pressure is due to the two reasons. The first is that the breaker height increases as the wave period becomes long as indicated in Fig. 7. The second is that the intensity of wave pressure increases with the increase in wave period as represented with the factors of α_1 and α_3. Thus, the swells with long periods are more dangerous than wind waves with the same heights.

V. SUMMARIES

The new wave pressure formulae have the following characteristics:

(1) The design wave height is specified as the maximum wave height possible at the site of breakwater.

(2) The changes of wave pressures from standing through breaking to postbreaking waves are smooth, being calculated with a single expression.

(3) The uplift pressure is applied irrespective of the occurrence of wave overtopping, while the buoyancy is calculated for the volume of upright section beneath the still water level.

(4) The effects of the wave period and the gradient of sea bottom are incorporated in the estimation of wave pressure.

The new formulae have been calibrated with the cases of 21 slidings and 13 nonslidings of the upright sections of prototype breakwaters in Japan. The calibration establishes that the new formulae are the most accurate ones among various wave pressure formulae. With the new formulae, engineers will be able to design composite breakwaters under any wave condition with the consistent principles.

REFERENCES

1) Ito, Y.: Stability of mixed-type breakwater - a method of probable
        sliding distance - , Coastal Engineering in Japan, Vol. 14,
        JSCE, 1971, pp.53-61.
2) Hiroi, I.: The force and power of waves, Engineering, Aug., 1920.
3) Sainflou, G.: Essai sur les diques maritimes verticales, Annales des
        Ponts et Chausees, Vol. 98, No. 4, 1928.
4) Minikin, R. R.: Wind, Waves and Maritime Structures, Charles Griffin
        and Co., Ltd., 1950, p.39.

5) Goda, Y.: A new method of wave pressure calculation for the design
        of composite breakwaters, Rept. Port and Harbour Res. Inst.,
        Vol. 12, No. 3, 1973, pp.31-69 (in Japanese).
6) Goda, Y. and T. Fukumori: Laboratory investigation of wave pressures
        exerted upon vertical and composite walls, Rept. Port and Harbour
        Res. Inst., Vol. 11, No. 2, 1972, pp.3-45 (in Japanese).
7) Goda, Y.: Experiments on the transition from nonbreaking to post-
        breaking wave pressures, Coastal Engineering in Japan, Vol. 15,
        JSCE, 1972, pp.81-90.
8) Mitsuyasu, H.: Experimental study on wave force against a wall,
        Coastal Engineering in Japan, Vol. 5, JSCE, 1962, pp.23-47.
9) Goda, Y.: Motion of composite breakwater on elastic foundation under
        the action of impulsive breaking wave pressure, Rept. Port and
        Harbour Res. Inst., Vol. 12, No. 3, 1973, pp.3-29 (in Japanese).
10) Goda, Y. and S. Kakizaki: Study on finite amplitude standing waves and
        their pressures upon a vertical walls, Rept. Port and Harbour
        Res. Inst., Vol. 5, No. 10, 1966, 57p (in Japanese).
11) Goda, Y.: The fourth order approximation to the pressure of standing
        waves, Coastal Engineering in Japan, Vol. 10, JSCE, 1967, pp.1-11.
12) Goda, Y.: A synthesis of breaker indices, Trans. Japan Soc. Civil
        Engrs., Vol. 2, Part 2, 1970, pp.227-230.
13) Goda, Y. and K. Nagai: Investigation of the statistical properties of
        sea waves with field and simulated data, Rept. Port and Harbour
        Res. Inst. Vol. 13, No. 1, 1974, pp.3-37 (in Japanese).

CHAPTER 101

INVESTIGATIONS OF WAVE-PRESSURE FORMULAS
DUE TO DAMAGES OF BREAKWATERS

by

Shoshichiro Nagai*

and

Katsuhiko Kurata**

ABSTRACT

The wave-pressure formulas derived in our laboratory have been
verified by the investigations of the slide of the vertical walls of
composite-type breakwaters due to severe waves during heavy storms which
have attacked numerous harbors in Japan since 1959. Some of the exam-
ples are shown in this paper.

INTRODUCTION

Formulas to predict the values of the maximum simultaneous pres-
sures exerted by breaking waves and partial breaking waves on the
vertical walls of composite-type breakwaters of various shapes have been
derived by one of the authors since 1960[1], [2]. Those wave-pressure
formulas have been proven by model experiments[3] of 1/20 and 1/10
scales which were conducted in a large wave tank with a length of 60 m,
a width of 2 m, and a depth of 2 m, and partly compared with wave
pressures measured at the Harbor of Haboro in the Japan Sea in 1957 and
1958[2].

Since 1959 several typhoons and severe storms have hit a number of
breakwaters in Japan in the Pacific Ocean and the Japan Sea to cause
damages, and most of the damages were the slide of the vertical walls of
composite-type breakwaters.

Although there were no measurement of wave pressures exerted by

* Professor of Hydraulic Engineering, Faculty of Engineering,
  Osaka City University, Osaka, Japan

** Research Associate of Hydraulic Engineering, Faculty of
   Engineering, Osaka City University, Osaka, Japan

storm waves on the vertical walls of the composite-type breakwaters
which were slid during the storms, the maximum simultaneous pressures
which would have been exerted during the storms on the vertical walls
were calculated by the wave-pressure formulas derived in our laboratcry,
and those maximum pressures calculated could explain the reason of the
slide of the vertical walls in most of the breakwaters damaged. Some of
the examples including composite-type breakwaters with low and wide
rubble-mounds as well as high and narrow rubble-mounds are presented
herein.

DESIGN CRITERIA FOR COMPOSITE-TYPE BREAKWATERS

A breakwater is generally designed by the characteristics of the
design wave, the topography of the sea bottom, the soil condition of the
sea bottom, and the topography of the harbor. The main parts of the
breakwater design are the optimum design of the cross-section, determi-
nation of the optimum length and orientation of the proposed breakwater.
Only the basic problems needed for the optimum design of the cross-
section of a composite-type breakwater are described in this paper.

1. Design-Wave Height

What kind of wave heights should be used would be one of the most
important problems for the design of breakwaters. The selection of the
design-wave height should be different between a composite-type break-
water and a rubble-mound type one. Since a few meters of slide of the
vertical wall of a composite-type breakwater generally would threaten
the stability of the vertical wall, and the failure of the vertical wall
will result in the complete loss of protection, the highest one-tenth-
wave height, $H_{1/10}$, should be used for the design of a composite-type
breakwater. Even if $H_{1/10}$ is used, and say, $T_{1/10} = 10$ sec, about 14 to
15 higher waves than $H_{1/10}$ would hit the breakwater only for an hour,
because the probability of occurrence of waves with larger height than
$H_{1/10}$ is about 4 percent. If $H_{1/3}$ is used, and say, $T_{1/3}$ is 10 sec,
about 50 waves with larger height than $H_{1/3}$ would attack the breakwater
for an hour, and then the breakwater generally could not withstand for
more than an hour because it would be very difficult in most of compo-
site-type breakwaters that the factor of safety for the design is taken
larger than 1.3 to 1.5.

The design-wave height for a rubble-mound type structure could be

the significant wave height, $H_{1/3}$, because any failure that may occur
due to higher waves in the wave train is progressive and the displace-
ment of some numbers of an individual armor unit will not result in the
complete loss of protection.

2. Buoyancy exerted on the Vertical Wall

If H_c defines the height from the design sea level to the crown of
the vertical wall, and $\gamma H_{1/10}$ denotes the height from the design sea
level to the point at which the maximum simultaneous pressure exerted on
the vertical wall becomes zero, the buoyancy should be considered to act
on the whole body of the vertical wall when $H_c \leqq \gamma H_{1/10}$.

3. Selection of Up-lift Pressures exerted on the Bottom

The up-lift pressures exerted on the bottom of the vertical wall is
assumed that the maximum up-lift pressure, $(p_u)_{max}$, is exerted on the
seaward-side edge of the bottom and the intensity of p_u diminishes line-
arly towards the harbor-side edge of the bottom to become zero there, i.
e. the up-lift pressures on the bottom of the vertical wall distribute
triangularly.

The value of $(p_u)_{max}$ is assumed as follows;
(a) When the cover-concrete-blocks or cover-stones placed at the sea-
ward-side and in front of the vertical wall are not dislocated by waves,
$(p_u)_{max} = 1.0$ to 1.5 t/m^2.
(b) When the cover-concrete-blocks or cover-stones are dislocated by
waves, $(p_u)_{max} = 2$ to 3 t/m^2.

According to the results of the experiments[4] and our experiences
in prototype, the up-lift pressures distribute triangularly on the bot-
tom of the vertical wall of composite-type breakwater in most of the
breakwaters, and the values of $(p_u)_{max}$ depend mainly upon the cover-
blocks or cover-stones placed at the seaward-side and in front of the
vertical wall, with no direct relation to the intensities of the hori-
zontal wave pressures exerted near the bottom of the vertical wall.
Therefore, in the design of a breakwater the careful placement of the
sufficiently large cover-concrete blocks or cover-stones is especially
required to reduce the uplift pressures exerted on the bottom of the
vertical wall.

4. Selection of the Coefficient of Friction between the Vertical Wall
and the Rubble-Mound

The value of the coefficient of friction, f, between the vertical

wall and rubble-mound of composite-type breakwater is influenced mainly by the thickness and width of the cover-concrete blocks or cover-stones placed at the harbor-side and sea-side of the vertical wall. It may be decisively stated that the main factors to insure the stability against slide of the vertical wall of a composite-type breakwater are the dead weight and width of the vertical wall and the cover-layers placed at the both sides of the vertical wall.

According to the results of the experiments[4] and our experiences in prototype, the critical values of the coefficient of friction, f_{cr}, when the vertical wall is about to be slid due to waves should be taken as follows;

(a) When the vertical wall of composite-type breakwater is completed one to two years ago, and the cover-concrete-blocks or cover-stones were dislocated during a storm, f_{cr} = 0.65 to 0.70.

(b) When it passes more than about two years after completion of the vertical wall of a breakwater, and the cover-blocks or cover-stones were dislocated during a storm, f_{cr} = 0.70 to 0.75.

(c) When it passes more than about two years after completion of the vertical wall, and the cover-blocks or cover-stones were not dislocated during a storm, f_{cr} = 0.80 to 0.90.

The value of the coefficient of friction to be used for the design of the breakwaters must be taken to be smaller than the critical values above mentioned, f_{cr}. It is a long-experienced general rule in Japan that f is taken 0.60 for the design.

5. Wave-Pressure Formulas and Their Regions Applicable

The wave-pressure formulas derived in our laboratory for composite-type breakwaters can be divided into two scopes; one group is available to composite-type breakwaters with high rubble-mounds, the criteria for which is the ratio of h_1 and h_2, h_1/h_2, to be smaller than 0.40 to 0.50, and the other group is applicable for those with low rubble-mounds, the criteria for which is 0.40 to 0.50 $\leq h_1/h_2 <$ 0.75, in which h_1 defines water depth above the top of the rubble-mound and h_2 denotes water depth at the toe of the sea-side slope of the rubble-mound. The formulas belonging to the first group were presented in Ref.(1) and those to the second group were described in Ref.(2).

When the rubble-mounds of composite-type breakwaters are so low that $h_1/h_2 \geq$ 0.75, and $h_2/H \geq$ 1.80, in which H defines the design wave

height, standing waves are always formed in front of the breakwaters, regardless of the top-width of the rubble-mound, B. The pressures exerted by perfect and partial standing waves on vertical walls can be obtained with sufficient accuracy for design purposes by the use of formulas [5], [6]

<div align="center">

VERIFICATION OF WAVE-PRESSURE FORMULAS
DUE TO DAMAGES OF BREAKWATERS
</div>

1. The Port of Kashima

This port, the plan of which is shown in Fig. 1, is one of the biggest industrial ports in Japan, and was recently built on a long straight sandy coast directly exposed to the Pacific Ocean.
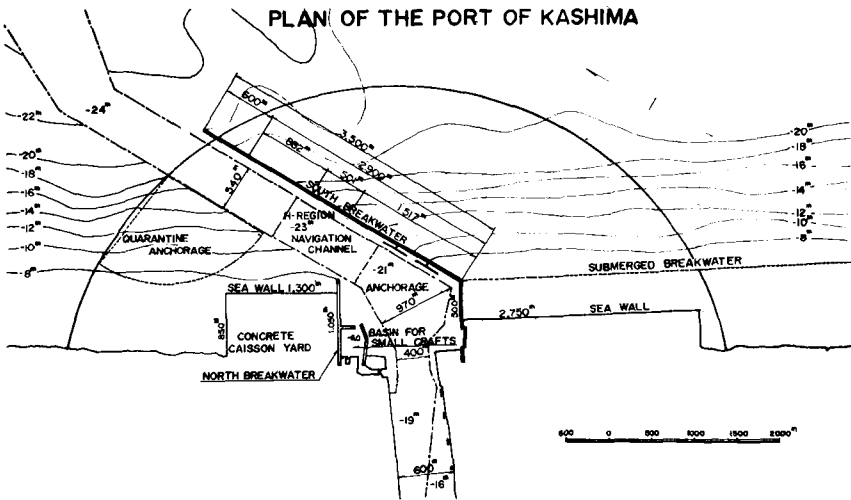
Fig. 1. - THE PLAN OF THE PORT OF KASHIMA

2,900 m in length of the South Breakwater located from a depth of water about 9 m below the Datum Line (D.L.) to a water depth of about 20 m below D.L. was severely hit by storm waves of January in 1970, the wave characteristics during which were hindcast $H_{1/10} = 10$ m and $T_{1/10} = 10$ sec to 12 sec, and the vertical wall of reinforced concrete caisson, shown in Fig. 2, were slid by 0.24 m to 1.81 m. Since the water depths during the storm, $h_1 = 9.9$ m, $h_2 = 16.9$ m, and $h = 18$ m, which defines a

water depth about three wave lengths offshore from the breakwater, at
H.W.L. (D.L. + 1.40 m),

   $h_1/h_2 = 0.59$, $h/L = 18/117 = 0.15$ to $18/146 = 0.12$, $h_2/H = 16.9/10$
   $= 1.7$, $h_1/H = 1.0$, and $H/L = 0.085$ to 0.068,

it is known that the waves broke in front of the vertical wall of the
breakwater, and the maximum simultaneous pressures exerted by the break-
ing waves is obtained by the formula[2]

$$P = \alpha \ w_0 \ H \ (\ h_1 \ \frac{\tanh\beta}{\beta} + \frac{1}{2} \ \gamma \ H \ )$$
$$= 1.7 \times 1.03 \times 10 \ (\ 9.9 \times \frac{\tanh 1.0}{1.0} + \frac{1}{2} \times 0.83 \times 10 \ ) \qquad \Bigg\} \ (1)$$
$$= 204 \ t/m.$$

SOUTH BREAKWATER, PORT OF KASHIMA
H-SECTION
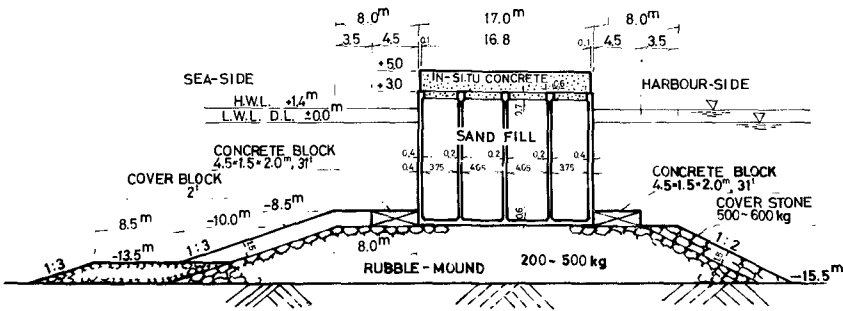
Fig. 2. - CROSS-SECTION OF H-REGION, KASHIMA HARBOR

   Subtracting the pressure acting above the crown level of the verti-
cal wall (D.L. + 5.00 m), the net resultant pressure is

   $P = 204 - 23.3 = 181 \ t/m.$ \hfill (2)

Since the height from the H.W.L. (D.L. + 1.40 m) to the crown level of
the vertical wall (D.L. + 5.00 m), H_c, is 3.60 m, and H_c is much smaller
than $\gamma H = 0.83 \times 10 = 8.3$ m, a large amount of wave overtopping is esti-
mated to be caused when the waves hit the breakwater. Therefore, it may
be adequate to consider that the breakwater was submerged into water
when the waves hit. The dead weight of the vertical wall when submerged

S. Nagai et al.

into water is 275 t/m. In view of the fact that the cover concrete
blocks placed in front of and at the foot of the vertical wall were dis-
located by the waves, the uplift pressure at the sea-side edge of the
bottom of the vertical wall, p_u, may be estimated 3 t/m^2, and the re-
sultant of the uplift pressures on the bottom of the vertical wall is

$$P_u = \frac{1}{2} \times 3 \times 17 = 25.5 \text{ t/m.} \tag{3}$$

Since the breakwater was completed only one year prior to the
storm, the critical value of the coefficient of friction, f_{cr}, would be
estimated from 0.65 to 0.70, and the resisting force of the vertical
wall against slide would be at most

R = 0.70 (275 - 25.5) = 175 t/m, or

R = 163 t/m for f_{cr} = 0.65. $\Big\}$ (4)

The calculation shown above proves that the vertical wall should be
slid due to the pressures of the waves, because P is 3 to 10 percent
larger than R.

Experiments were performed to know the maximum simultaneous pres-
sures exerted on the vertical wall of the breakwater by various kinds of
breaking waves with heights of about 9 m to 12 m and periods of 8 sec to
14 sec by the use of a 1/25-model in a wave channel with a wind blower,
100 m long, 2 m deep, and 1.2 m wide.

The results of the experiment showed that the maximum resultant
P_e = 193 t/m of the maximum simultaneous pressures was exerted by a wave
with H = 9.6 m and T = 8 sec when the sea level was D.L. $\pm$ 0 m, as shown
in Fig. 3, and P_e = 140 t/m by the same wave when the sea level was
D.L. + 1.40 m.

The resultants of the maximum simultaneous pressures exerted by the
breaker of the same wave are obtained by the formula as follows:

For the sea level of D.L. $\pm$ 0 m, α = 2.4, β = 1.36, and γ = 0.65,
hence

$$P_{cal} = 2.4 \times 1.03 \times 9.6 \left(8.5 \times \frac{\tanh 1.36}{1.36} + \frac{1}{2} \times 0.65 \times 9.6 \right)$$

$$= 204 \text{ t/m,} \tag{5}$$

and for the sea level of D.L. + 1.40 m, α = 1.5, β = 0.90, and γ = 0.88,
hence

$$P_{cal} = 1.5 \times 1.03 \times 9.6 \left(9.9 \times \frac{\tanh 0.90}{0.90} + \frac{1}{2} \times 0.88 \times 9.6 \right)$$

$$= 180 \text{ t/m.} \tag{6}$$

S. Nagai et al.

Subtracting the pressures acting above the crown of the vertical wall from the resultants, P_{cal} = 202 t/m for the sea level of D.L. $\pm$ 0 m, which corresponds to P_e = 193 t/m, and for the sea level of D.L. + 1.40 m P_{cal} = 157 t/m, which corresponds to P_e = 140 t/m. The experimental and calculated values of the resultant of the maximum simultaneous pressures, P_e = 193 t/m and P_{cal} = 202 t/m, may be said to be in a fairy good agreement, and about 10 to 16 percent larger than R = 175 t/m.

If Hiroi's formula is used to obtain the maximum resultant pressure,

$$P = 1.5 \ w_0 \ H_{1/10} \ (h_1 + H_c) = 1.5 \times 1.03 \times 10 \ (9.9 + 3.6)$$
$$= 209 \ t/m. \tag{7}$$

$$T = 8.0 \quad sec \qquad H/L - 0.10 \qquad h_1/h_2 - 0.55$$
$$H = 9.6 \quad m \qquad h/L = 0.323 \qquad B/h_2 = 0.52$$
$$L = 96.4 \ m \qquad h_2/H = 1.61$$
$$V = 38 \quad m/sec \qquad\qquad SCALE = 1/25$$
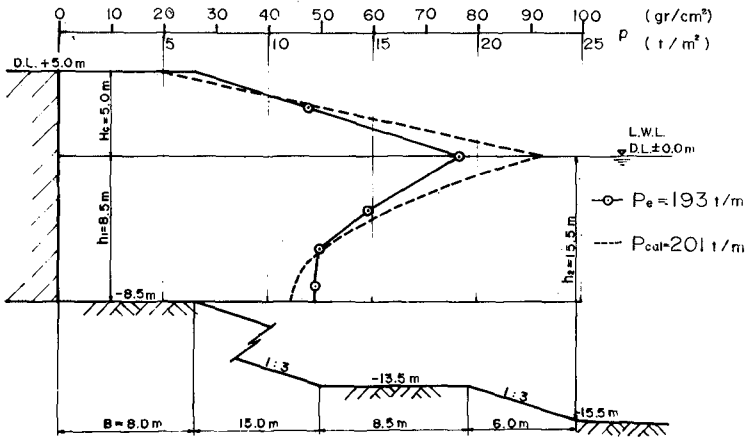
Fig. 3. - P_e AND P_{cal}-CURVES OF H-SECTION, KASHIMA HARBOR

This value is very close to P of Eq. 1, and this case proves that Hiroi's formula is in some cases to be adequate to be used for obtaining the maximum resultant pressure when there is a large overtopping of waves over the vertical wall of composite-type breakwater, as it has been proven in prototype and experiments in Japan[1].

Minikin's formula is quite inapplicable to such a case, showing P_{cal} = 529 to 437 t/m at H.W.L., and P_{cal} = 464 to 383 t/m at L.W.L. for the same waves with $H_{1/10}$ = 10 m, $T_{1/10}$ = 10 sec to 12 sec.

2. The Port of Hachinohe

A part, 318 m long, of the 1,400 m long breakwater which is located at depths about 6 m to 9 m below L.W.L. (D.L. + 0.30 m), as shown in Fig. 4, was severely damaged and slid 6 m at maximum by storm waves of January, 1971. The slid part of the breakwater is located at a water depth of about 8.5 m below L.W.L., as shown in Fig. 5, and the storm waves offshore from the breakwater were hindcast $H_{1/10}$ = 7.8 m to 8.0 m and $T_{1/10}$ = 8 sec to 12 sec from wave data recorded at a water depth of 10 m in the vicinity of the breakwater during the storm.

PLAN OF THE PORT
OF HACHINOHE

Fig. 4. - PLAN OF THE PORT OF HACHINOHE

NORTH BREAKWATER
PORT OF HACHINOHE
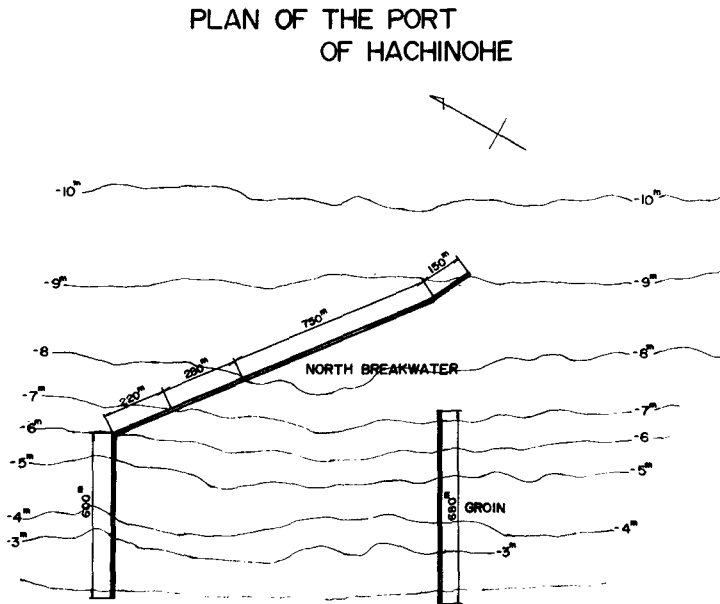
SEA - SIDE   HARBOUR-SIDE
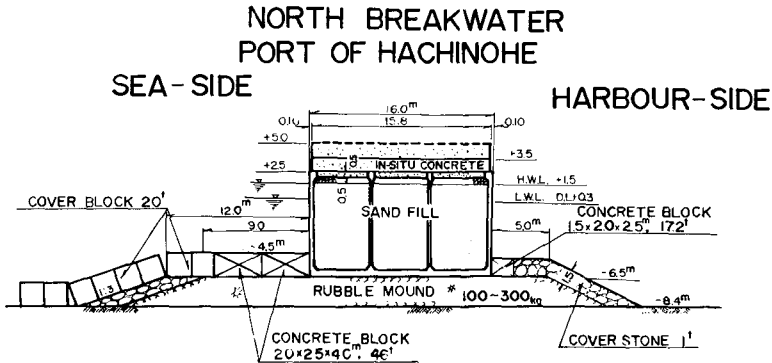
Fig. 5. - CROSS-SECTION OF THE BREAKWATER, HACHINOHE HARBOR

When the tidal level is L.W.L. (D.L. + 0.30 m), $h_1 = 4.8$ m, $h_2 =$ 8.7 m, hence $h_1/h_2 = 0.55$, and $h_2/H = 1.1$ for $H = 8.0$ m. Therefore, the waves decisively break in front of the breakwater. By using the diagram[2] of α for $h_2/H = 1.5$, the value of α is assumed $\alpha \approx 4.0$, hence $\beta = 2.1$ is obtained. Since the values of h/L are approximately 0.19 to 0.14 for waves of $T_{1/10} = 8$ sec to 10 sec, the value of γ is obtained 0.50. Then the resultant of the maximum simultaneous pressures exerted by the wave of $H = 8.0$ m and $T = 8$ sec to 10 sec is obtained

$$P = 4.0 \times 1.03 \times 8.0 \left(4.8 \times \frac{\tanh 2.1}{2.1} + \frac{1}{2} \times 0.50 \times 8.0 \right)$$

$$= 139.3 \approx 140 \text{ t/m}. \tag{8}$$

Since $H_c = 3.2$ m and $\gamma H = 4.0$ m, decrease in the pressures due to overtopping, ΔP, is negligible small, and the vertical wall of the breakwater should be considered to have been submerged into water when the waves hit the breakwater.

Judging from the damages of the breakwater that the maximum slide of the vertical wall was 6 m, and the four reinforced concrete caissons suffered some cracks on the walls, it may be assumed that cover-concrete blocks placed at the feet of the vertical walls would probably have been dislocated by the waves prior to occurrence of the slide of the vertical walls, therefore, the uplift pressure at the seaward-side edge of the bottom of the vertical wall may be assumed $p_u = 3.0$ t/m^2, and the resultant of the uplift pressures exerted on the bottom of the vertical

S. Nagai et al.

wall will be

$$P_u = \frac{1}{2} \times 3.0 \times 16 = 24 \text{ t/m.} \tag{9}$$

Since the value of f_{cr} may be assumed 0.65 to 0.70 from the lapse
of only about two years after completion of the breakwater, the resist-
ing force of the vertical wall against slide would be at most

$$R = 0.7 (176 - 24) \simeq 106 \text{ t/m.} \tag{10}$$

The results of the calculation of Eqs. 8 and 10 that the value of P
is 32 percent larger than R may be said to prove a large amount of slide
of the vertical wall.

In order to investigate the maximum simultaneous pressures which
would be exerted by the highest waves that are possible to be generated
offshore the breakwater at the sea level of L.W.L., experiments were
conducted by using a 1/25-model in the 100-meter long wave channel. The
maximum resultant pressures, P_e, measured in the experiments were as
follows:

At the tidal level of L.W.L. (D.L. + 0.3 m)

  H = 8.3 m, T = 8 sec, P_e = 147 t/m, P_{cal} = 144 t/m,

  H = 7.1 m, T = 9 sec, P_e = 103 t/m, P_{cal} = 116 t/m,

  H = 8.2 m, T = 9 sec, P_e = 165 t/m, P_{cal} = 142 t/m,

  H = 7.4 m, T = 10 sec, P_e = 108 t/m, P_{cal} = 113 t/m,

  H = 8.3 m, T = 10 sec, P_e = 139 t/m, P_{cal} = 142 t/m.

The results of the experiments showed:

(1) Very large waves with H $\simeq$ 8 m to 8.3 m and T = 8 sec to 10 sec, the
steepnesses of which were as steep as 0.077 to 0.10, could be generated
within at least several wave-lengths offshore from the breakwater due to
the superposition of large reflecting waves from the breakwater on in-
coming waves.

(2) Those very steep waves severely broke against the breakwater, exert-
ing large resultants of pressures of about 140 t/m to 165 t/m on the
vertical wall of the breakwater.

The values of the resultants of the maximum simultaneous pressures
calculated and measured in the experiments, P_{cal} and P_e, are in a good
agreement, and they may be stated to prove well the severe damages of
the breakwater.

The wave-records measured at a water depth of 10 m below L.W.L.
offshore from a breakwater located at the east district of the Harbor of

Hachinohe showed $H_{1/3}$ = 6.05 m and $T_{1/3}$ = 11.5 sec, although the wave recorder did not act during the severest hours of the storm. Therefore, it would be estimated that the $H_{1/10}$ during the severest hours of the storm was larger than approximately 7.8 m, and the H_{max} was about 10 m which was nearly equal to the depth of water where the wave recorder was located. As was mentioned above, such extremely high and steep waves were also generated offshore from the breakwater in the 1/25-scale model experiment.

If Hiroi's formula is used, P = 98.9 t/m for the same wave, which is a little smaller than R. Minikin's formula is quite inapplicable to such a case.

3. The Port of Himeji

The Port of Himeji is situated about 60 km west of the Port of Kobe, and located on the northern coast of the Seto Inland Sea. This harbor was hit on the 24th of August and 25th of September in 1964 by typhoons, and especially the latter one caused damages to the break-waters of the harbor.

A wave recorder of pressure-type set on the bottom of the sea with a water depth of 12 m below D.L. $\pm$ 0 m recorded well waves during the August-24th typhoon, and the significant wave was $H_{1/3}$ = 3.50 m and $T_{1/3}$ = 6.1 sec. The ratios of $H_{max}/H_{1/3}$ and $H_{1/10}/H_{1/3}$ were 1.43 and 1.29, respectively. The significant wave at the site of the wave recorder estimated by SMB-method from the winds measured during the typhoon was $H_{1/3}$ = 3.2 m and $T_{1/3}$ = 6.6 sec.

Although the wave recorder did not act well during the September-25th typhoon, the waves during the typhoon could be estimated suffi-ciently by SMB-method from the winds measured during the typhoon and by the use of the wave data obtained during the August-24th typhoon as mentioned above. The waves thus estimated at the site of the wave re-corder were as follows:

$$H_{1/3} = 3.50 \times \frac{3.50}{3.20} = 3.80 \text{ m}, \quad T_{1/3} = 7.0 \text{ sec},$$

$$H_{1/10} = 1.29 \times 3.8 = 4.90 \text{ m} \simeq 5.0 \text{ m}, \quad T_{1/10} = 7.5 \text{ sec}.$$

The breakwater, the cross-section of which is shown in Fig. 6, was under construction when the typhoon hit the harbor, and some portion of the breakwater was not completed, being left the parapet-wall from D.L. + 2.50 m to D.L. + 4.00 m to be constructed, and the other portion of

S. Nagai et al.

the breakwater was just completed up to the crown of the parapet-wall of
D.L. + 4.00 m.

WEST BREAKWATER, MEGA HARBOUR, PORT OF HIMEJI
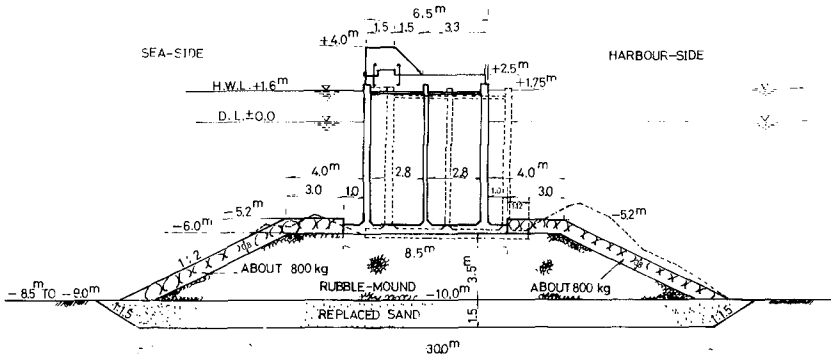
Fig. 6. - CROSS-SECTION OF THE BREAKWATER, HIMEJI HARBOR

The completed part of the breakwater could withstand with no dam-
ages against the waves, but the uncompleted portion was slid about one
meter toward the harbor-side, as shown in Fig. 6 by a broken line, and
somewhat subsided.

Although the highest tidal level during the typhoon was D.L. + 2.00
m, it was estimated that the largest wave pressures during the typhoon
would have been exerted on the breakwaters at a tidal level of about
D.L. $\pm$ 0 m, because the crown levels of the uncompleted and the com-
pleted breakwaters were so low as D.L. + 2.50 m and D.L. + 4.00 m, re-
spectively, against $H_{1/10} = 5.0$ m.

Since the depth of water, h, at the tidal level was about 10 m at
the sea about three times of the length of the incoming wave with a pe-
riod of $T_{1/10} = 7.5$ sec from the breakwater, the steepness of the in-
coming wave is $H_{1/10}/L_{1/10} = 5.0/65 = 0.078$. The deep-water wave was
hindcast by SMB-method to be $T_0 = 7.8$ sec and $L_0 = 95$ m, and then the
height of the deep-water wave was calculated $H_0 = 5.4$ m from $H/H_0 = 0.93$
for $h/L_0 = 10/95 = 0.11$. The depth of water at the breaking point of
the incoming wave, h_b, was obtained about 7.3 m from $h_b/H_0 = 1.35$ on an

S. Nagai et al.

average for $H_0/L_0 = 0.058$.

Judging from the ratios of $h_1/h_b = 5.2/7.3 = 0.70$, $h_2/h_b = 8.5/7.3$
$= 1.2$ to $9.5/7.3 = 1.3$, and $H_{1/10}/L_{1/10} = 0.078$, the incoming wave may
decisively be estimated to have broken on the rubble-mounds of the
breakwaters. Therefore, the resultant of the maximum simultaneous pres-
sures[2] exerted on the vertical walls by the breaking wave, P, is ob-
tained as follows:

From the values of $h_2/H_{1/10} = 8.5/5.0 = 1.7$, $B/h_2 = 4.0/8.5 = 0.47$,
$h_1/h_2 = 0.55$, $\alpha = 1.5$ is obtained[2], then $\beta = 1.1$ and $\gamma = 0.88$ are ob-
tained. Finally P is obtained by

$$P = 1.5 \times 1.03 \times 5.0 \ (\ 5.2 \times \frac{\tanh 1.1}{1.1} + \frac{1}{2} \times 0.88 \times 5.0 \ )$$

$$= 7.73 \ (\ 3.78 + 2.20 \ ) = 46.23 \ \text{t/m}. \tag{11}$$

Subtracting the pressures acting above the crown level of the
breakwater (D.L. + 2.50 m), the net resultant of the maximum pressures
which would have acted on the vertical wall of the uncompleted break-
water is

$$P = 46.23 - 3.17 = 43.06 \simeq 43.1 \ \text{t/m}. \tag{12}$$

Judging from the fact that the breakwater was under construction
when the typhoon hit the harbor, and the thickness of the cover layer of
rubble at the seaward-side foot of the vertical wall was only 0.80 m
without any cover concrete block, the up-lift pressure at the seaward-
side edge of the bottom of the vertical wall may be estimated at least
$p_u = 3$ t/m^2, and the resultant of the up-lift pressure on the bottom is

$$P_u = \frac{1}{2} \times 3.0 \times 8.5 = 12.8 \ \text{t/m}. \tag{13}$$

The critical value of the coefficient of friction against slide
between the vertical wall and the rubble-mound may be estimated $f_{cr} =$
0.70 at most, because the breakwater was under construction and the
thickness of the cover layer of rubble was only 0.80 m. Since $H_c = 2.50$
m was smaller than $\gamma H_{1/10} = 0.88 \times 5.0 = 4.4$ m, the breakwater should be
considered to have been completely under water when the $H_{1/10}$-wave hit
it. Therefore, the resisting force of the vertical wall against slide
would be at most

$$R = 0.70 \ (\ 62.1 - 12.8 \ ) = 34.5 \ \text{t/m}, \tag{14}$$

in which 62.1 t/m denotes the dead weight in water of the vertical wall
of the uncompleted breakwater.

The result of the calculation that the value of P is about 25 per-
cent larger than R may be said to prove the slide of the vertical wall.

The resisting force of the vertical wall of the completed break-
water against slide would be

$$R = 0.70 \ (\ 79.5 \ - \ 12.8 \ ) \ = \ 46.7 \ t/m, \tag{15}$$

in which 79.5 t/m denotes the dead weight in water of the vertical wall
of the completed breakwater.

Since $\gamma H_{1/10} = 4.4$ m is a little larger than $H_c = 4.0$ m for the
completed breakwater, decrease in the maximum simultaneous pressures due
to overtopping is 0.14 t/m, hence the net resultant pressure is

$$P = 46.23 \ - \ 0.14 \ = \ 46.09 \ \underset{\sim}{} \ 46.1 \ t/m. \tag{16}$$

From Eqs. 15 and 16, the value of R is a little bit larger than P.   This
may be stated to show that the completed portion of the breakwater would
have been near the critical state of the stability of the vertical wall.

Although Minikin's formula is inapplicable to this case, if it is
used for reference, the resultant of the maximum wave pressures is

$$P = \frac{1}{3} \ p_{max} \ H \ + \frac{1}{2} \ w_0 \ H \ (\ \frac{H}{4} + h_1 \ )$$

$$= \frac{1}{3} \ \{ \ 102.4 \ \times \ 5.2 \ (\ 1 \ + \frac{5.2}{9.5}) \ \times \ 0.078 \ \} \ \times \ 5.0 \ + \frac{1}{2} \times \ 1.03 \ \times \ 5$$

$$\times \ (\ \frac{5}{4} + \ 5.2 \ )$$

$$= \ 106 \ + \ 16.6 \ = \ 122.6 \ t/m. \tag{17}$$

(Actually such a difference of hydrostatic pressure between the seaward-
side and harbor-side as 16.6 t/m does not exist.)

Since the value of P is much larger than R = 34.5 t/m and 46.7 t/m, both
the uncompleted and the completed breakwaters would have been slid to a
comparatively large distance toward the harbor-side.   This is contrary
to the fact.

If Hiroi's formula is used, the resultant of the wave pressures on
the completed breakwater is

$$P = 1.5 \ \times \ 1.03 \ \times \ 5.0 \ \times \ 9.2 \ = \ 71 \ t/m. \tag{18}$$

Since the value of P is larger than R = 46.7 t/m, the completed break-
water must be slid by the wave of $H_{1/10} = 5$ m.   This is also contrary to
the fact.

4. The Port of Kada

This harbor is a small commercial and fishery harbor located on the
northernmost eastside coast of the Kii Channel which connects with the

Pacific Ocean at the southern end, and protected by small islands from waves coming from the west and by a cape from waves coming from the south. Therefore, a small breakwater of about 67 m in length was constructed to protect the harbor from waves coming in by diffracting the cape from the south west.

    This breakwater, which has two kinds of cross-section, as shown in Fig. 7, was hit by storm waves during Isewan Typhoon which was one of the biggest typhoons passing over the Japanese Archipelago and passed about 100 km south of harbor on the 26th of September in 1959.

    The middle portion of about 40 m in length of the breakwater, the cross-section of which is shown as B-B section in Fig. 7, was slid toward the harbor-side from 4 cm to 30 cm and subsided from 4 cm to 13 cm at the crown, but the head portion of the breakwater, the cross-section of which is shown as A-A section in Fig. 7, was not slid.

    The tidal level of the sea when the waves were the severest during the typhoon was estimated D.L. + 2.10 m. Since the sea-side feet of the vertical walls of the A-A and B-B sections were well covered by a concrete block and rubbles, the up-lift pressures acting on the sea-side edges of the bottoms of the vertical walls are assumed p_u = 1.0 t/m^2 to 1.5 t/m^2.

KADA HARBOUR
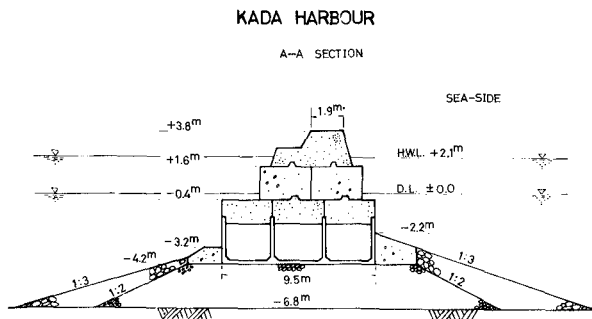
A-A SECTION

Fig. 7. - CROSS-SECTION OF THE BREAKWATER, KADA HARBOR

(A-A section)

S. Nagai et al.

KADA HARBOUR
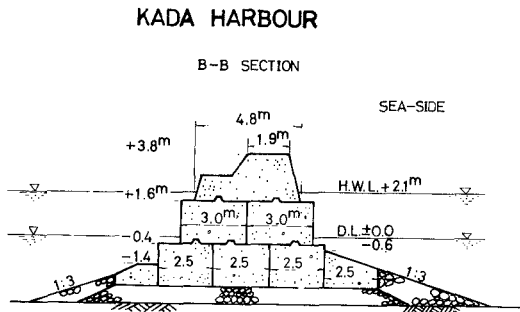
B-B SECTION

Fig. 7. - CROSS-SECTION OF THE BREAKWATER, KADA HARBOR

(B-B section)

Judging from the fact that the breakwater was constructed more than two years before the typhoon hit it, and the cover-concrete blocks and rubbles placed at the seaward sides of the vertical walls were not dislocated by the waves during the storm, the critical coefficient of friction may assumed f_{cr} = 0.90. Therefore, the resisting forces against slide due to the waves would be assumed for the A-A section

$$R_A = 0.90 \ (\ 63.75 - 4.5 \ ) \ = 53.3 \ t/m \ for \ p_u = 1.0 \ t/m^2,$$
$$\text{and } R_A = 51.3 \ t/m \ for \ p_u = 1.5 \ t/m^2, \qquad\qquad \} \ (19)$$

and for the B-B section

$$R_B = 0.90 \ (\ 49.71 - 3.75 \ ) \ = 41.4 \ t/m \ for \ p_u = 1.0 \ t/m^2,$$
$$\text{and } R_B = 39.7 \ t/m \ for \ p_u = 1.5 \ t/m^2, \qquad\qquad \} \ (20)$$

in which the values of 63.75 t/m and 49.71 t/m are the dead weights in water of the A-A and B-B sections, respectively.

The $H_{1/10}$ in Kada Harbor during the severest waves of the typhoon was estimated about 4 m to 4.5 m and $T_{1/10}$ from 10 sec to 12 sec, from the wave data recorded during the typhoon in the Port of Wakayama which is located several kilometers south of the Kada Harbor.

Judging from the fact that the depths of water in front of the vertical walls of the B-B and A-A sections were h_1 = 2.7 m and 4.3 m, which were smaller than or nearly equal to the estimated $H_{1/10}$ = 4.0 m to 4.5 m, and the seaward slopes of the rubble-mounds of the breakwaters were equally 1:3, and moreover, the rubble-mounds did not have a flat crown in front of the vertical walls, i.e., B = 0, it is decisively estimated

S. Nagai et al.

that the waves would have broken in a state of plunging breaker just in front of the vertical walls and the vertical distribution of the maximum simultaneous pressures exerted by the breaking waves was the C-type[1].

The maximum pressure of the breaking waves is estimated $p_{max} = 20$ t/m^2 to 26 t/m^2 from the values of $h_1 \frac{h_1}{h} \frac{H}{L} \simeq 0.040$ to 0.12, but $p_{max} = 20$ t/m^2 will be adequate for the breakwater which is well protected from severe waves coming in from the Kii Channel[1]. Therefore, the result-ant of the maximum simultaneous pressures is obtained by

$$P = \frac{1}{2} p_{max} H_{1/10} \simeq \frac{1}{2} \times 20 \times 4.5 = 45 \text{ t/m.} \qquad (21)$$

It may be understood from Eqs. 19 to 21 that the B-B section of the breakwater would be slid only by a short distance by the wave of H = 4.5 m and T = 10 sec to 12 sec, but that the A-A section, i.e. the break-water head, would not be slid by the wave.

If Hiroi's formula is used, the limiting wave heights required for the slide of the breakwater are H = 5.53 m to 5.75 m for the A-A sec-tion, while H = 5.83 m to 6.08 m for the B-B section. This means that the A-A section would be slid by smaller waves in height than those which can slide the B-B section. This is quite contrary to the fact.

If Minikin's formula is used, p_{max} for the A-A section is obtained by

$$p_{max} = 102.4 \times 4.3 \left(1 + \frac{4.3}{8.9} \right) \frac{4.5}{84} = 35.0 \text{ t/m}^2, \qquad (22)$$

and the resultant of the maximum pressure exerted by the wave of 4.5 m in height is

$$P = \frac{1}{3} \times 35.0 \times 4.5 + 1.03 \times \frac{4.5}{2} \left(4.3 + \frac{4.5}{4} \right)$$

$$= 52.6 + 5.1 = 57.7 \text{ t/m,} \qquad (23)$$

which is larger than $R_A = 53.3$ t/m of Eq. 19. Therefore, the breakwater head must be slid by the wave. This is contrary to the fact.

If $H_{1/10}$ is estimated 4.0 m, $p_{max} = 31.2$ t/m^2, and P = 41.6 + 10.9 = 52.5 t/m. This value of P is a little bit smaller than $R_A = 53.3$ t/m, and about 27 percent larger than $R_B = 41.4$ t/m. This may mean that ac-cording to Minikin's formula the B-B section must be slid at a compara-tively large distance toward the harbor-side and the A-A section was at a critical state of stability when the wave of $H_{1/10} = 4.0$ m attacked the breakwater. This is a little different from the fact.

CONCLUSIONS

The optimum design of the cross-section of a breakwater is to de-
sign such a cross-section as to meet the requirements of the breakwater
at the proposed construction site at a minimum of costs. The costs in-
clude those for design and construction, and the capitalized costs of
repairs of estimated damages due to waves. In general, since a harbor
has been requiring a larger and deeper water basin, the cross-section of
the breakwater which protects the water basin from the design wave has
been becoming larger, and more important and expensive. Therefore, it
may be stated common practice through the world for the design of such
a breakwater to conduct a three-dimensional model experiment to study
the optimum length and orientation of the proposed breakwater, and more-
over, a two-dimensional stability model study to determine the optimum
cross-section of the breakwater. At the same time the optimum design of
the cross-section of a projected breakwater is especially required to
know the construction cost of the breakwater at the first stage of the
planning of a harbor and to verify the result of a two-dimensional model
study.

The optimum design of the cross-section of a projected composite-
type breakwater requires the selections of the values or formulas of the
five design factors at least mentioned in this paper. Although those
values of the design factors have been studied by using numerous model
experiments of different scales of 1/10 to 1/25 during more than twenty
years in our laboratory, such investigations have also been carried out
for practical design purposes by the use of damages of composite-type
breakwaters which have been suffered with severe waves during typhoons
hitting the Japanese Archipelago since 1959.

It may therefore be stated from those investigations that the
values of the design factors and the wave-pressure formulas presented in
this paper would be applicable with sufficient reliability for the opti-
mum design of the cross-section of a composite-type breakwater.

REFERENCES

(1) Nagai, S.; "Shock Pressures exerted by Breaking Waves on Break-
            waters", Journal of the Waterways and Harbors Div.,
            ASCE., June, 1960.

(2) Nagai, S. and Otsubo, T.; "Pressures by Breaking Waves on Composite-
        type Breakwaters", Proceedings of the Eleventh Coastal
        Engineering Conf., 1968, London.

(3) Nagai, S.; "Sliding of Composite-type Breakwaters by Breaking
        Waves", Journal of the Waterways and Harbors Div., ASCE.,
        Feb., 1963.

(4) Nagai, S., Tamai, S. and Kubo, S.; "Slide of the Vertical Wall of
        Composite-type Breakwater and Up-lift Pressures on the
        Bottom of the Vertical Wall", Proc. of the 7th Conf. on
        Coastal Eng. in Japan, 1960.

(5) Nagai, S.; "Pressures of Standing Waves on a Vertical Wall", Journal
        of the Waterways and Harbors Div., ASCE., Feb., 1969.

(6) Nagai, S.; "The Pressures of Partial Standing Waves", Journal of the
        Waterways and Harbors Div., ASCE., Aug., 1968.

CHAPTER 102

BREAKING WAVE FORCES ON A LARGE DIAMETER CELL

Akira Watanabe
Lecturer
and
Kiyoshi Horikawa
Professor

Department of Civil Engineering
University of Tokyo
Tokyo, Japan

ABSTRACT

Experiments have been carried out by using non-break-
ing waves and breaking waves to investigate the wave forces
on a vertical circular cell located in the shallow water.
Based on the experimental data, the drag coefficient and
the inertia coefficient of a circular cylinder and the
curling factor of breaking waves are estimated, and the
computation methods of wave forces are examined. As a
result, it is shown that the phase lag of inertia forces
behind the accelerations of water particles should be con-
sidered for the estimation of the drag coefficient as well
as the inertia coefficient. In addition the previous
formula of the maximum breaking wave forces acting on a
cell or a pile is revised by introducing the effects of
the above-mentioned phase lag and another phase difference,
both of which are functions of the ratio of the cell diam-
eter to the wave length. It is confirmed that the pro-
posed formula is applicable even to the large cell with
the diameter comparable to the wave length.

INTRODUCTION

Many studies have been done on the impulsive pressures
acting on a vertical wall, but there has been very little
investigation of breaking wave forces on a cell-type struc-
ture. The breaking wave forces should be taken into con-
sideration all the same in the design of pile-type or
cell-type structures in nearshore area, because breaking
waves cause extreme shock pressures on a cell structure as

well as on a vertical wall.

Hall(1958) reported experimental data of the breaking
wave forces on a circular pile located on a sloping beach.
Goda *et al*.(1966) applied von Kármán's theory on the impact
of the seaplane float during its landing to the estimation
of the impact force of breaking waves, and they proposed
the computation method of the impulsive breaking wave
forces acting on the total length of a pile. It was a
great step in the present problem, but whether their for-
mula can be applied to the large diameter cell has been
uncertain.

In the present paper it is shown that the ratio of
the cell diameter to the wave length is one of the impor-
tant parameters for the estimation of wave forces in the
range of wave conditions from non-breaking to after-break-
ing, and a revised formula for the maximum breaking wave
force acting on a large diameter cell is proposed.

PREVIOUS STUDIES OF WAVE FORCES
ACTING ON A CIRCULAR CYLINDER

Non-breaking Wave Forces

The total force F_T exerted on a vertical circular
pile by non-breaking waves is usually expressed as the sum
of the drag force and the inertia force in the following
form:

$$F_T = \frac{w_o}{2g} D \int_{-h}^{\eta} C_D u |u| dz + \frac{w_o}{g} \frac{\pi D^2}{4} \int_{-h}^{\eta} C_M \dot{u} dz \qquad (1)$$

where w_o is the specific weight of water, g is the accel-
eration of gravity, D is the pile diameter, u is the hori-
zontal velocity of water particles, $\dot{u}$ is the horizontal
acceleration of water particles, η is the surface elevation
above the still water level, h is the water depth, and C_D
and C_M are called the drag coefficient and the inertia co-
efficient respectively.

If the phase difference between the water particle
acceleration and the inertia force as well as between the
velocity and the drag force is assumed to be negligibly
small, the total wave force F_T and the maximum value $(F_T)_{max}$
are represented as follows:

$$F_T(\theta) = (F_D)_{max}\sin^2\theta + (F_M)_{max}\cos\theta \qquad\qquad (2)$$

$$(F_T)_{max} = (F_D)_{max} + (F_M)^2_{max}/4(F_D)_{max} \qquad\quad \Bigg\}$$
$$\text{for } 2(F_D)_{max} > (F_M)_{max} \qquad\Bigg\} \qquad (3)$$
$$= (F_M)_{max} \quad \text{for } 2(F_D)_{max} < (F_M)_{max} \Bigg\}$$

where $(F_D)_{max}$ and $(F_M)_{max}$ are the maximum values of the drag force and the inertia force respectively, and θ is the phase angle which is zero at the instant when the water surface crosses the still water level upwards.

Breaking Wave Forces

When breaking waves act on a pile, an impact force is added to the drag force and the inertia force. Goda *et al.*(1966) assumed that the impact force is the result of the change in momentum of the water mass of a vertical wave front which has the height of $\lambda\eta_c$ and the velocity equal to breaking wave celerity c_b, and they expressed the total impact force on a pile as follows:

$$F_I = w_o D H_b{}^2 K_B \lambda (1-t/\tau_B) \qquad 0\leq t \leq \tau_B \qquad (4)$$

$$K_B = \pi c_b{}^2 \eta_c/2gH_b{}^2 \;:\; \text{Impulsive force factor} \Bigg\}$$
$$\tau_B = D/2c_b \;:\; \text{Duration time of impact force} \Bigg\} \qquad (5)$$

where H_b is the breaking wave height, η_c is the crest height above the still water level and λ is the curling factor of breaking waves. The values of the curling factor were determined experimentally and were presented as a function of the bottom slope and the relative depth at the breaking point.

Since the duration time of the impact force is very short, the resultant stress in a structure or the measured value of the impact force depends not only upon the magnitude of the impact force itself, but also upon the natural frequency of the structure. Goda *et al.* have simplified the actual pile as a single-degree of freedom oscillatory system, and have shown that the effective impact force on an actual pile $(F_I)_e$ is expressed by $(F_I)_e = X_{max}F_I$, where X_{max} is the impact response factor which depends on both the duration time τ_B and the natural frequency as a func-

tion of their product.

By assuming that the wave profile ahead the vertical wave front is approximated as $\eta = \eta_c \sin\theta$, the phase angle θ_B at the collision of wave front can be given by $\sin^{-1}(1-\lambda)$, because $\eta = (1-\lambda)\eta_c$ at the phase of breaking. Therefore the drag force and the inertia force which should be added to the above impact force are expressed as follows:

$$(F_D)_B = (F_D)_{max}(1-\lambda)^2 \qquad\qquad (6)$$

$$(F_M)_B = (F_M)_{max}\sqrt{1-(1-\lambda)^2} \qquad\qquad (7)$$

Goda *et al.* have confirmed the validity of their model by means of their experimental data for four test piles. It has been, however, uncertain whether their formula is applicable to the large diameter cell or not.

EXPERIMENTAL APPARATUS AND PROCEDURES

Wave Force Measuring Apparatus

In order to examine the applicability of the above-mentioned formulae to the large diameter cell, the authors performed laboratory experiments for two test cells with the diameters of 13 cm and 50 cm respectively.

The force measuring apparatus for the cell with the diameter of 50 cm is sketched out in Fig. 1. The test cell made of duralumin is supported by slide bearings and is able to move parallel to the wave direction with very little friction. The wave force acting on this test cell is transmitted to two strain plates upper and lower (300 mm center to center), through steel rods. Therefore we can determine the total wave force and the height of action point by measuring strains of these strain plates. The strain plates and the slide bearings are fixed on the foundation, which has sufficiently high rigidity and large weight and is bolted to the base buried in the concrete bottom.

The test cell with the diameter of 13 cm is structurally similar to the one shown in Fig. 1. Table 1 shows the characteristics of these test cells.

Experimental Procedures

A wave basin, 40 m long, 25 m wide, from 0.6 to 1.1 m deep, was used for the present experiments (Fig. 2). Training walls were placed in this basin in order to divide the width of wave channel at 6 m, and a sloping bottom of 1 to 30 was settled between them.

The still water depth at the front of the cell was always kept 20 cm, and the wave period was varied from 1.0 to 2.0 sec at 0.25 sec intervals. In order to investigate also the values of the inertia coefficient and the drag coefficient for the large diameter cell, the wave height was also changed from about 2 cm to after-breaking condition for each wave period. The experimental wave conditions are shown in Table 2.

The incident wave height and the wave height at the location of the cell were measured by resistance type wave gages with two parallel copper wires. Another wave gage was settled at the location of 60 to 100 cm ahead the cell in order to measure the wave celerity. In addition, six current meters of miniature propeller type were set on a vertical beam at intervals of 5 cm so as to measure the distributions of horizontal velocities. A small light source and a photo-transistor are mounted on these current meters, and when the propeller rotates, the four blades of it cut off the light beam; thus each rotation of the propeller produces four pulse signals. The orbital velocities under wave crest are supposed to be purely horizontal, so we can evaluate these maximum orbital velocities from the closest time interval of pulse signals by using the calibration curve gained by the uniform flow perpendicular to the meters.

The breaker forms were observed to be spilling type for the wave period less than 1.5 sec and plunging type for the period greater than 1.75 sec. It was difficult to detect breaker heights by the wave gage on account of fluctuations of the breaking position, but the mean values of recorded breaker heights coincided nearly to the evaluated ones from the new breaker index proposed by Goda(1970). In the present analysis the authors employed this breaker index for the evaluation of the breaker height H_b, the breaker depth h_b, and the crest height above the bottom Y_b.

Figure 3 shows one example of breaking wave force on the large diameter cell. A typical impact force with

duration time of about 0.2 sec can be recognized.

EXPERIMENTAL RESULTS

Wave Celerity and Horizontal Velocity

    The wave celerities were estimated from the wave re-
cords obtained by two wave gages located with interval
from 60 to 100 cm nearby the test cell. The ratio of this
actual wave celerity c to the one given by the small ampli-
tude wave theory c_A is shown in Fig. 4 in relation to the
steepness of deep water waves.

    According to the pulse records of orbital velocities,
the maximum horizontal velocities were observed to occur
almost under the wave crest except in the vicinity of the
bottom where the maximum velocities lag behind the wave
crest about 0.08 sec at maximum. Ignoring these lags,
the authors have chosen the maximum values at each eleva-
tion as the maximum velocities under the wave crest.

    Goda(1964) has expressed this maximum velocities u_{max}
by the product of orbital velocities of the small amplitude
wave theory and a velocity factor K which represents the
finite amplitude effect in the following form:

$$\left. \begin{aligned} u_{max}(z) &= K\frac{\pi H}{T} \cdot \frac{\cosh k(h+z)}{\sinh kh} \\[2ex] K &= \sqrt{1 + \alpha\left(\frac{H}{h}\right)^{1/2} \cdot \left(1+\frac{z}{h}\right)^3} \ , \quad k = \frac{2\pi}{L_A} \end{aligned} \right\} \qquad (8)$$

where L_A is the wave length given by the small amplitude
wave theory, and a factor α is a function of only the rela-
tive water depth h/L_A. Goda has calculated the values
of α by using the Iversen's breaker index on the assumption
that the horizontal velocities at the breaker crest, that
is $u_{max}(Y_b-h)$ in Eq.(8), should be equal to the breaking
wave celerity c_b. The values of α for the present condi-
tion have been calculated by using the Goda's new breaker
index and the measured breaking wave celerity, and are
shown in Table 3.

    Figure 5 shows the comparison of the vertical distri-
butions of the measured velocities and the values calcu-
lated with the use of Eq.(8) and the factor α given in

Table 3. The calculated values exceed the measured ones in the neighborhood of the wave crest as the wave height increases, but the difference between them is not so great as a whole. It is also similar in the cases of other wave periods.

The Inertia Coefficient

A number of laboratory investigations have been conducted in order to determine the magnitudes of the inertia coefficient and the drag coefficient. Most of these studies are depending on the expression of the total force shown in Eq.(2); in other words, they are based on the assumption that is sufficiently small the phase difference between the water particle acceleration and the inertia force as well as between the particle velocity and the drag force.

MacCamy and Fuchs(1954) have examined the inertia force on a single pile by a diffraction approach. According to their investigation, the inertia force $F_M(\theta)$ is given by

$$F_M(\theta) = (F_M)_{max}\cos(\theta - \varepsilon)$$

$$= \frac{w_o}{g}\,\frac{\pi D^2}{4}\hat{C}_M\int_{-h}^{\eta}\dot{u}_{max}\cos(\theta - \varepsilon)\,dz \qquad (9)$$

$$\hat{C}_M = \frac{4}{\pi\delta^2\sqrt{J_1'(\delta)^2 + Y_1'(\delta)^2}}, \quad \varepsilon = \tan^{-1}\frac{J_1'(\delta)}{Y_1'(\delta)}, \quad \delta = \frac{\pi D}{L} \qquad (10)$$

which shows that the inertia force lags behind the particle acceleration by the phase angle ε, and that this phase lag and inertia coefficient $\hat{C}_M$ depend on the ratio of the pile diameter D to the wave length L. These quantities are presented by solid lines in Fig. 6.

By introducing the phase lag ε and by assuming that there is no phase difference between the horizontal velocity and the drag force, Eq.(2) for the total force is modified to the following equation:

$$F_T(\theta) = (F_D)_{max}\sin^2\theta + (F_M)_{max}\cos(\theta - \varepsilon) \qquad (11)$$

Therefore the estimation of the inertia coefficients through the relation $F_T(0)=(F_M)_{max}$, which is deduced from

Eq.(2), has a risk of underestimation of them.

The inertia coefficients derived from the measured non-breaking wave forces are plotted in Fig. 6. The quantities $(C_M)_o$ are based on the relation $F_T(0)=(F_M)_{max}$ and show a tendency to be less than the theoretical values given by Eq.(10). In the case of the large cell with the diameter of 50 cm, since the values of $(F_D)_{max}$ are only 10 per cent of $(F_M)_{max}$ and the phase difference ε is about 20 degrees at the most, so the error due to neglect of the drag force in the neighborhood of the phase $\theta=\varepsilon$ is less than 1 per cent; hence $(F_T)_{max}$ is supposed to be equal to $(F_M)_{max}$. The quantities $(C_M)_T$ in Fig. 2 are thus evaluated from the maximum total wave force $(F_T)_{max}$, and they have a tendency to be slightly greater than the theoretical values. This fact seems to be caused by the reason that the accelerations of water particles have been estimated by the small amplitude wave theory. In the case of the diameter of 13 cm, since the drag force is not so small, the values of $(C_M)_T$ have not been calculated.

The Drag Coefficient

The drag coefficients are usually estimated on the basis of the assumption that the drag force reaches the maximum and no inertia force is present under the wave crest ($\theta=\pi/2$). Equation(11) means, however, the inertia force is not zero at the phase $\theta=\pi/2$. In this paper the authors have estimated the values of the drag coefficient from the maximum drag force $(F_D)_{max}$ given by

$$(F_D)_{max} = F_T(\pi/2+\varepsilon)/\cos^2\varepsilon \qquad\qquad (12)$$

and from the measured velocities.

The drag coefficients C_D thus computed are shown by solid circles and solid triangles in Fig. 7 in relation to Reynolds number $R_e = u_o D/\nu$, where u_o is orbital velocity under the wave crest at the still water level computed from Eq.(8). These values C_D agree well with the steady flow data expressed as NPL curve given by Goldstein. The values C_D' in the same figure are the drag coefficients evaluated on the basis of the relation $(F_D)_{max} = F_T(\pi/2)$ without the phase difference ε. Figure 7 implies that the phase lag of the inertia force should be considered for the estimation of the drag coefficient as well as the inertia coefficient.

The Curling Factor of Breaking Waves

The curling factor λ of breaking waves is defined in the above-mentioned impact force model as the ratio of the vertical wave front height to the crest height above the still water level. But the vertical wave front is a hypothetical idea, and it is difficult to estimate this factor λ by using the actual shape of the breaking wave front. In practice λ is to be determined from the impact force records through the following equation;

$$(F_I)_e = X_{max} \ \frac{\pi}{2} \ \frac{w_0}{g} \ Dc_b{}^2 \lambda \eta_c \qquad\qquad (\ 13\ )$$

which is the expression of the maximum value of effective impact force reduced from Eqs.(4) and (5). In the present analysis the authors have regarded the peak value above the starting value of the sharp spike in the impulsive force records as the maximum impact force $(F_I)_e$ as shown in Fig. 8. The impact response factor X_{max} has been given by Goda *et al.*(1966) as a function of the product of impact duration time τ_B, which can be calculated from Eq.(5) by using the measured wave celerity c_b, and natural frequency of a cell in water.

Figure 9 shows the relation between the curling factor and the relative water depth h_b/L_A for the present case of the bottom slope of 1 to 30 together with the data given by Goda *et al.* for the bottom slope of 1 to 10 and 1 to 100 respectively. The magnitudes of the curling factor show a decreasing trend with increasing relative depth or with decreasing bottom slope. This is well understood as the effect of change of the breaker type from plunging to spilling type.

COMPARISON OF MEASURED WAVE FORCES AND CALCULATED ONES

Computation Methods of Wave Forces

The above-mentioned examinations confirm that the wave forces of non-breaking waves are to be given well by the following equation in considering the phase lag ε of the inertia force rather than by Eq.(2).

$$F_T(\theta) = (F_D)_{max}\sin^2\theta + (F_M)_{max}\cos(\theta-\varepsilon) \qquad\qquad (\ 14\ )$$

$$(F_D)_{max} = \frac{w_o}{2g} \, D C_D \int_{-h}^{\eta_c} u_{max}{}^2 dz \tag{15}$$

$$(F_M)_{max} = \frac{w_o}{g} \, \frac{\pi D^2}{4} \, C_M \int_{-h}^{\eta_c} \dot{u}_{max} dz \tag{16}$$

In general, therefore, the maximum value of the total wave force $(F_T)_{max}$ cannot be given by Eq.(3).

According to Goda *et al.*, the maximum breaking wave force is formulated as:

$$F_B = (F_I)_e + (F_D)_{max} \sin^2 \theta_B + (F_M)_{max} \cos \theta_B \tag{17}$$

where $\theta_B = \sin^{-1}(1-\lambda)$.

While the impact force is assumed to occur at the instant when the vertical wave front impinges on the front of the cell in the above equation, the expressions of the drag force and the inertia force are based on the phase corresponding to the center line of the cell. Hence we must consider the phase difference of the water surface elevations between at the front of the cell and at the center line of the cell. By assuming that the wave profile can be expressed by a sinusoidal form for simplicity, this phase difference is expressed by $\delta_B = \pi D/L_b$. In addition to this phase difference, it is necessary to introduce the phase lag ε of the inertia force in order to revise Eq.(17) for the large diameter cell. Based on these considerations, the general formula of breaking waves acting on a pile or a cell is proposed as follows:

$$F_B = (F_I)_e + (F_D)_{max} \sin(\theta_B - \delta_B) |\sin(\theta_B - \delta_B)|$$

$$+ (F_M)_{max} \cos(\theta_B - \delta_B - \varepsilon) \tag{18}$$

where $\delta_B = \pi D/L_b, \ \theta_B = \sin^{-1}(1-\lambda)$.

Comparison of Measured Values and Calculated Ones

The best way to examine these computation methods is to compare the measured wave forces to the computed ones. Figures 10 and 11 show this comparison for each wave period for the cases in which the cell diameter is 50 cm and 13 cm respectively. The ordinate $(F_T)_{max}$ is the maximum value of total force, the abscissa H_o means the reduced wave height in deep water, and small numbers in these figures indicate the wave height at the depth of the test cell.

The solid circles are the measured values of $(F_T)_{max}$, which are the averaged values for each sequence of wave force records. Each figure shows that as the offshore wave height H_O becomes large, the total wave force also increases first until it reaches a maximum value, and then decreases rapidly. This corresponds to the change of wave conditions from non-breaking to just-breaking, and finally to after-breaking.

According to Eq.(14), the maximum value of non-breaking wave force is not represented by Eq.(3). It is, however, reasonable to calculate $(F_T)_{max}$ by Eq.(3) under the present experimental conditions. In the case of the cell diameter of 13 cm, the phase difference ε is about 5 degrees at the most and $\sin^2\varepsilon$ is less than 0.01, and therefore the error owing to the use of Eq.(3) in computation of $(F_T)_{max}$ is less than 1 per cent. On the other hand in the case of 50 cm diameter, although the value of $\sin^2\varepsilon$ reaches 0.12, the value of $(F_D)_{max}$ is only 10 per cent of $(F_M)_{max}$, and the error due to the use of Eq.(3) is also 1 per cent at the most.

In the present analysis the computations of total forces are based on the following quantities. The inertia coefficient and the phase lag are the values given by the diffraction theory, that is Eq.(10). The drag coefficient are given by the NPL curve corresponding to the steady flow as shown in Fig. 7. The horizontal velocities under the wave crest are estimated with Eq.(8) and the values of α given in Table 3. The water particle accelerations are evaluated from the small amplitude wave theory by using the measured wave heights.

The open circles in Figs. 10 and 11 are the non-breaking wave forces computed thus by Eq.(3). The open squares and the solid triangles indicate the values of breaking wave forces computed by Eq.(17) without the phase difference, and by Eq.(18) in consideration of the phase differences, respectively.

In the range of non-breaking waves, the agreements between the measured forces and the computed ones by Eq.(3) are fairly good in both cases of the large diameter and the small diameter. As for the impulsive forces of just-breaking and immediately-after-breaking waves it is as follows. In the first cases where the cell diameter is 50 cm, the calculated values by Eq.(17), which has been proposed by Goda *et al.*, are rather small in comparison

with the observed ones. Besides they are smaller than
even the values by Eq.(3), which does not include the im-
pact force component, for wave period $T \leq 1.75$ sec. On the
contrary, Eq.(18) proposed by introducing both the impact
force and the phase differences gives reasonable values in
this range. For $T \leq 1.5$ sec, Eq.(3) yields the best agree-
ments with the observed values, but it cannot manifest the
impulsive characteristics observed clearly in the wave
force records. This result implies that it is better to
use Eq.(18) rather than Eq.(3) in the range of breaking
waves even for these wave periods, although it is necessa-
ry to obtain more reliable values of various coefficients
used in Eq.(18).

       In the next cases where the cell diameter is 13 cm,
the phase differences δ_B and ε are so small that Eq.(17)
and Eq.(18) give almost the same values, and these values
agree well with the observed ones in the range where the
measured wave forces reach their maximum. For $T=2.0$ sec
the measured values of breaking wave forces are rather
small in comparison with the calculated ones. This fact
is supposed to be caused by the lack of the data of just-
breaking wave forces in this experiments. It is necessa-
ry to accumulate much more data and to examine them.

       The after-breaking wave forces could not be investi-
gated thoroughly on account of the irregular form of their
records which seems to be indicative of turbulence in the
after-breaking waves, and because of scattering of wave
height data. The measured values have a tendency to fall
between the calculated values by Eq.(3) and by Eq.(18).

Supplements on Wave Force Records

       The above-mentioned analyses are based on the averaged
wave forces for each sequence of wave force records under
the same condition. The maximum values of breaking wave
forces have shown remarkable variations in the present
experiments in the same way as the breaking wave forces on
a vertical wall. Such variations are due to the fluctu-
ations of the breaking position, the breaker height and
the wave form.

       Figure 12 shows one example of the histograph of
breaking wave forces acting on the large diameter cell.
The distribution is not Gaussian and the most probable
value is less than the mean value. The maximum value
reaches almost two times the minimum value. In the pres-

ent cases the histograph trends to approach Gaussian dis-
tribution as the wave period becomes short. In all cases
the occurence probability of wave forces less than 1.5 times
the mean value amounts to 90 to 100 per cent.

     The authors have also obtained some data for the ver-
tical distribution of the wave forces by using the partial
wave force meters which are structurally similar to the
total force meter and consist of eight sliced cylindrical
cells. Figure 13 shows the vertical distributions of the
breaking wave forces acting on the large diameter cell.
In each case the maximum value occurs in the vicinity of
the still water level.

                    CONCLUDING REMARKS

     On the basis of the experimental data on the wave
forces exerted on a circular cell by non-breaking waves
and by breaking waves, the computation methods of wave
forces and the various coefficients have been investigated.
The major conclusions are as follows:
   1)   The phase difference between the accelerations of
the water particles and the inertia forces must be consid-
ered for the estimation of the drag coefficient as well as
the inertia coefficient.
   2)   The formula proposed in the present paper, Eq.(18),
is satisfactory to calculate the impulsive breaking wave
forces even on the large cell with the diameter comparable
to the wave length.

     There are some problems unsolved in the application
of the present formula to the estimation of the actual
wave forces. The first problem is how to determine the
various coefficients used in this formula. The curling
factor of breaking waves has not yet been formulated in
the universal form as the function of breaker character-
istics. The authors are not confident whether the so-
called scale effect on the values of this factor is present
or not. It is necessary to devote much efforts continu-
ously to accumulate the experimental data on this factor
under various conditions. Whether the scale effect exists
or not is not clear at present also as to the values of the
drag coefficient. But in the design of the large diameter
cell-structures, it seems not so important since the drag
force component is much less than the inertia force. The
third problem is how to determine the impact response
factor; in other words the estimation of the natural fre-

quency of the actual structures. In the actual design,
not only the natural frequency of the structure itself but
also that of the foundation or the ground and the effect
of the connection between them are important and difficult
to estimate. The expression of the phase difference δ_B
in Eq.(18) seems reasonable as the first approximation but
is probably too simple to formulate the complicated real
phenomena. It is desirable to improve also the value of
this phase difference in future.

REFERENCES

Goda, Y. (1964): "Wave forces on a vertical circular
      cylinder; Experiments and proposed method of wave
      force computation", Rept. Port and Harbour Res. Inst.,
      Ministry of Transport, Japan, No. 8, 74 p.

Goda, Y. (1970): "A synthethis of breaker indices", Proc.
      Japan Soc. Civil Engrs., No. 180, pp. 39-49. (in
      Japanese)

Goda, Y., S. Haranaka and M. Kitahata (1966): "Study of
      impulsive breaking wave forces on piles", Rept. Port
      and Harbour Res. Inst., Ministry of Transport, Japan,
      Vol. 5, No. 6, 30 p. (in Japanese)

Hall, M. A. (1958): "Laboratory study of breaking wave
      forces on piles", Beach Erosion Board, Tech. Memo.,
      No. 106, 24 p.

MacCamy, R. C. and R. A. Fuchs (1954): "Wave forces on
      piles; A diffraction theory", Beach Erosion Board,
      Tech. Memo., No. 69, 17 p.
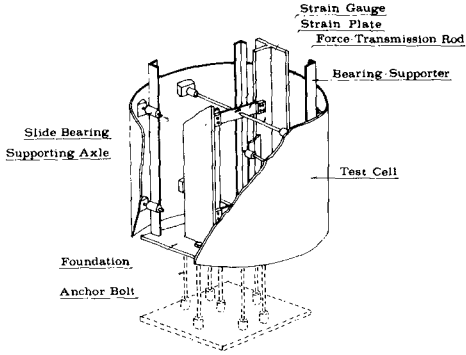
Fig. 1   Wave force measuring apparatus.

Table 1.   Characteristic values of wave force meters.

Diameter (cm)	Height (cm)	Weight of Cell (kg)	Natural Frequency (Hz) in the air	in water	Sensitivity (10^{-6} strain/kg)
50	40	11.2	85	39	33
13	40	2.0	88	40	88
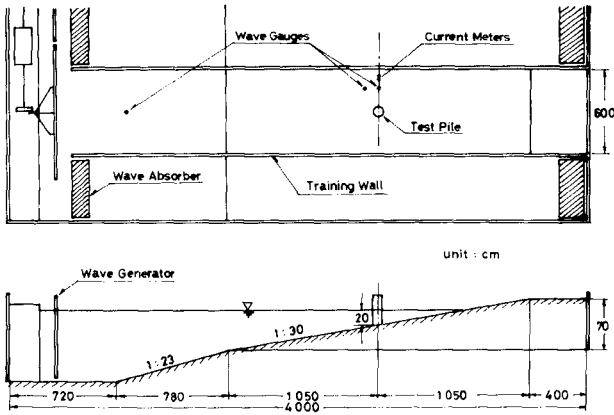
Fig. 2   Wave channel and instrumentations.

Table 2. Experimental conditions.

T (sec)	H_O (cm)	H_S (cm)	D/L D=50 cm	D=13 cm
1.00	3.0 – 13.4	2.7 – 13.1	0.35 – 0.41	0.092 – 0.110
1.25	2.6 – 14.3	2.4 – 14.5	0.26 – 0.31	0.067 – 0.080
1.50	2.7 – 17.7	2.7 – 16.0	0.20 – 0.25	0.052 – 0.064
1.75	2.2 – 17.5	2.3 – 18.2	0.16 – 0.21	0.041 – 0.055
2.00	2.4 – 19.3	2.7 – 20.1	0.14 – 0.18	0.037 – 0.048

H_O : Reduced offshore wave height
H_S : Wave height at the location of the cell
$L = cT$, c : Wave celerity measured at the location of the cell
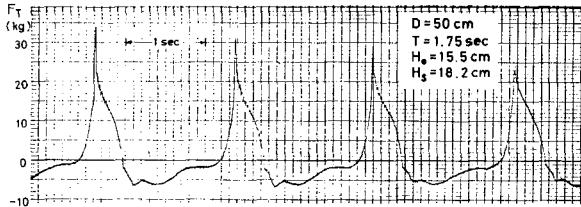
Fig. 3 Typical record of breaking wave force on a cell.
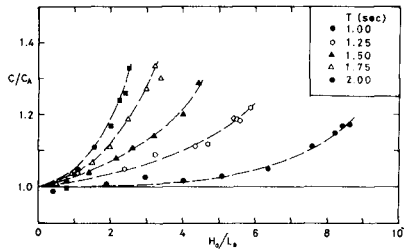
Fig. 4 Relation between wave celerity and wave steepness.

Table 3. Breaker characteristics and a factor α

T (sec)	h/L_A	H_b/h	Y_b/h	L_b/L_A	α
1.00	0.165	0.655	1.47	1.16	0.813
1.25	0.125	0.715	1.53	1.19	1.025
1.50	0.101	0.800	1.60	1.22	0.913
1.75	0.085	0.910	1.70	1.34	0.767
2.00	0.074	0.980	1.77	1.33	0.601
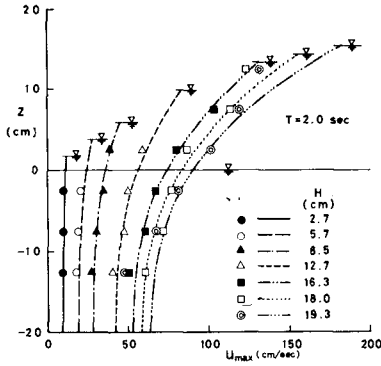
Fig. 5 Vertical distributions of horizontal velocity under wave crest.
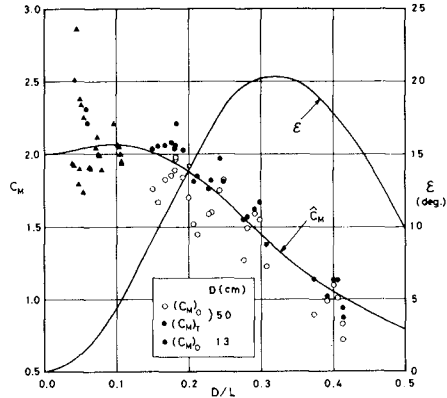
Fig. 6 Inertia coefficient and phase lag of inertia force.
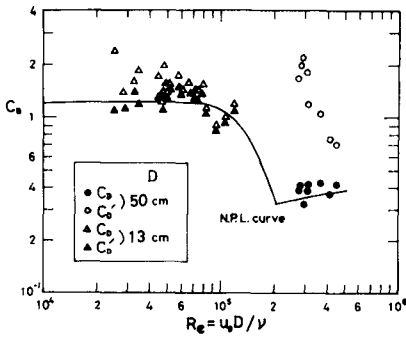
Fig. 7 Relation between drag coefficient and Reynolds number.
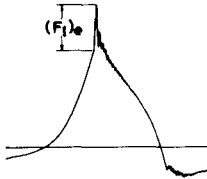
Fig. 8 Effective impact force.
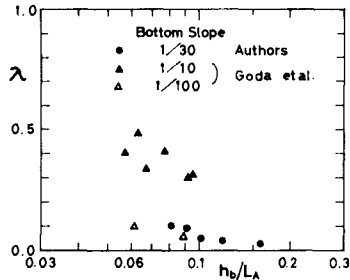
Fig. 9 Relation between curling factor and relative depth.
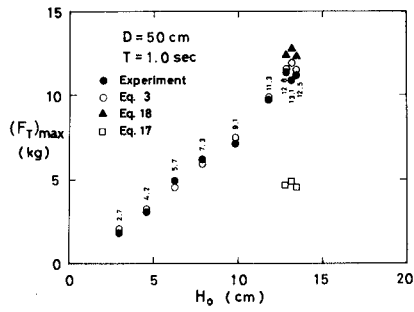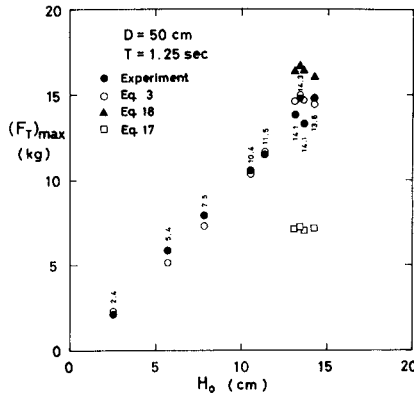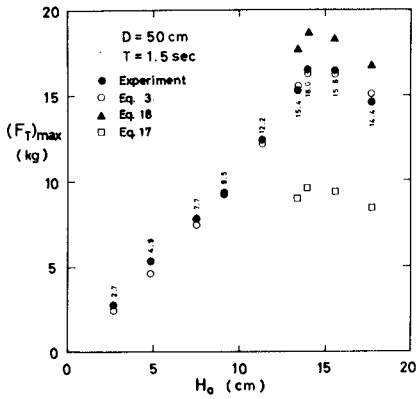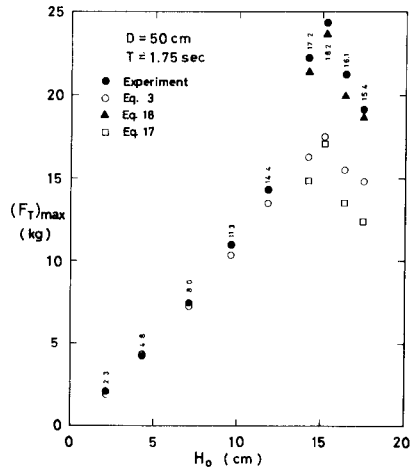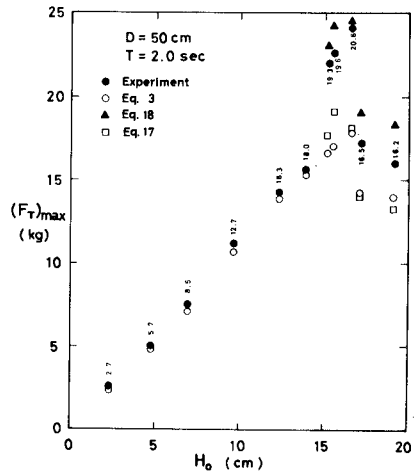
Fig. 10   Comparison of measured wave forces and calculated ones. (D = 50 cm)
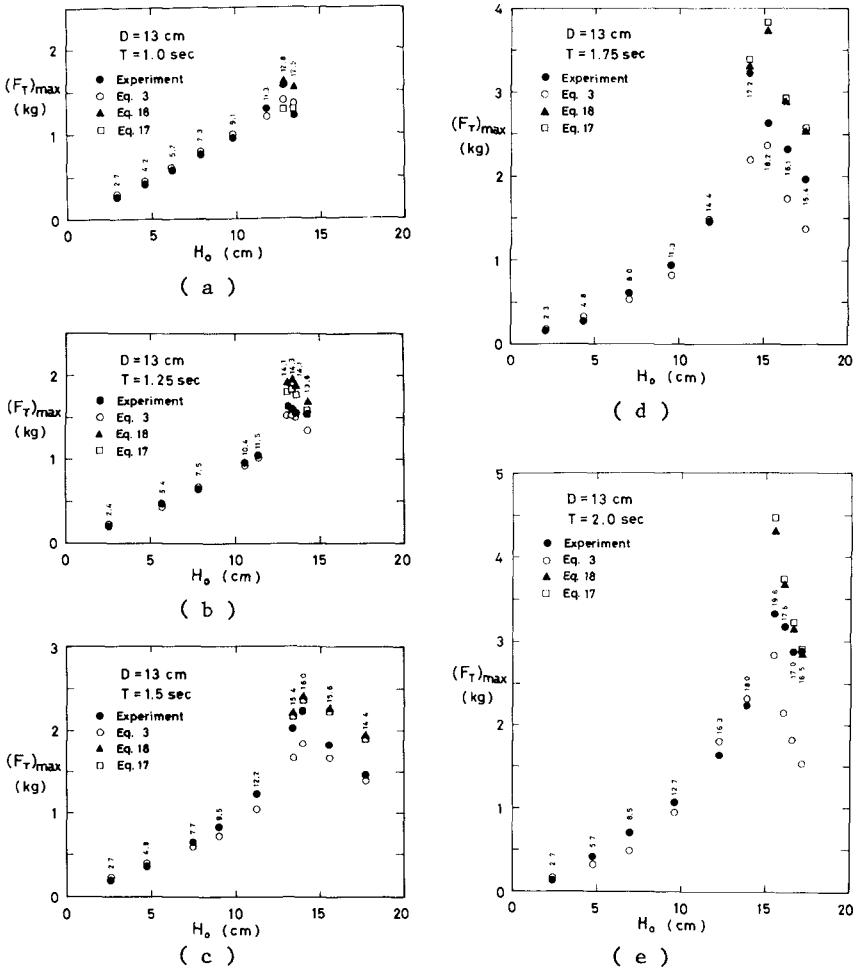
Fig. 11 Comparison of measured wave forces and calculated ones.
($D = 13$ cm)
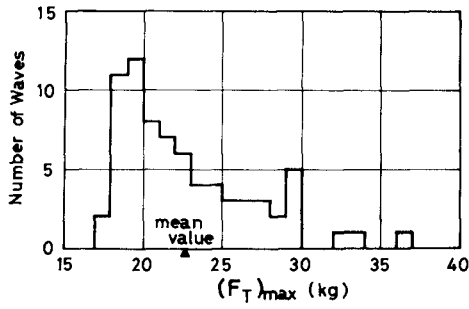
Fig. 12   Histograph of breaking wave force.
($D = 50$ cm, $T = 2.0$ sec, $H_g = 19.6$ cm)
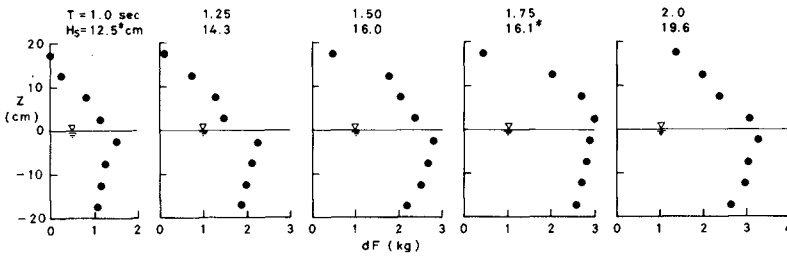
Fig. 13   Vertical distributions of breaking wave forces.
($D = 50$ cm, $*$: after-breaking wave height)

CHAPTER 103

FIELD MEASUREMENTS OF IMPACT PRESSURES IN SURF

R. L. Miller[1], S. Leverette[2], J. O'Sullivan[2],

J. Tochko[2] and K. Theriault[2]

ABSTRACT

Field measurements were made of the vertical distribution of impact pressures exerted by breaking waves. Four distinct types are recognized and compared. These are near-breaking wave, plunging breaker, spilling breaker and post-breaking bore. The measurements were obtained by placing a 6 foot aluminum flat plate, backed by a cylinder in the surf zone, so that the flat faced the approaching breakers. Five sensors were placed at one foot intervals on the flat. The sensors consisted of strain gage mounted aluminum diaphragms.

Results indicated that impact pressure is significantly influenced by breaker type. The bore generated the largest impact pressures, followed in decreasing order by plunging breaker, spilling breaker and near breaking wave. In the vertical array, the largest impact pressures were recorded at or near the top, except for the bore where the reverse occurred. A qualitative explanation is given of various phenomena associated with impact pressures, by considering breaker mechanics.

INTRODUCTION

As waves travel toward the shore and eventually break, they either dissipate on a sloping beach or strike a fixed object sometimes with forces which significantly exceed those of non-breaking waves. The resisting solid may be a cliff or a man-made structure. Thus interest in the phenomenon of breaking wave impact forces may range from coastal erosion to the design and protection of coastal structures.

The pressure-time pattern recorded when a breaking wave strikes a rigid object typically consists of two parts, a long period pressure of relatively low intensity, and superimposed on the initial pressure rise, a relatively high very short period pressure, of the order of milliseconds associated with the impact of the free surface. See figure 1.

[1] The University of Chicago and Woods Hole Oceanographic Institute.

[2] Massachusetts Institute of Technology and Woods Hole Oceanographic Institute.

Fig. 1

OSCILLOSCOPE PRESSURE PATTERNS
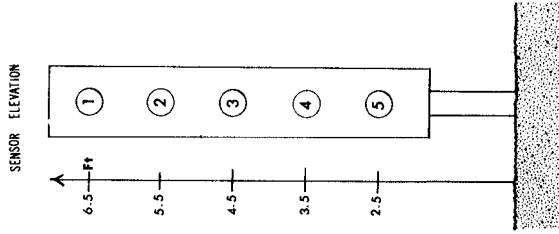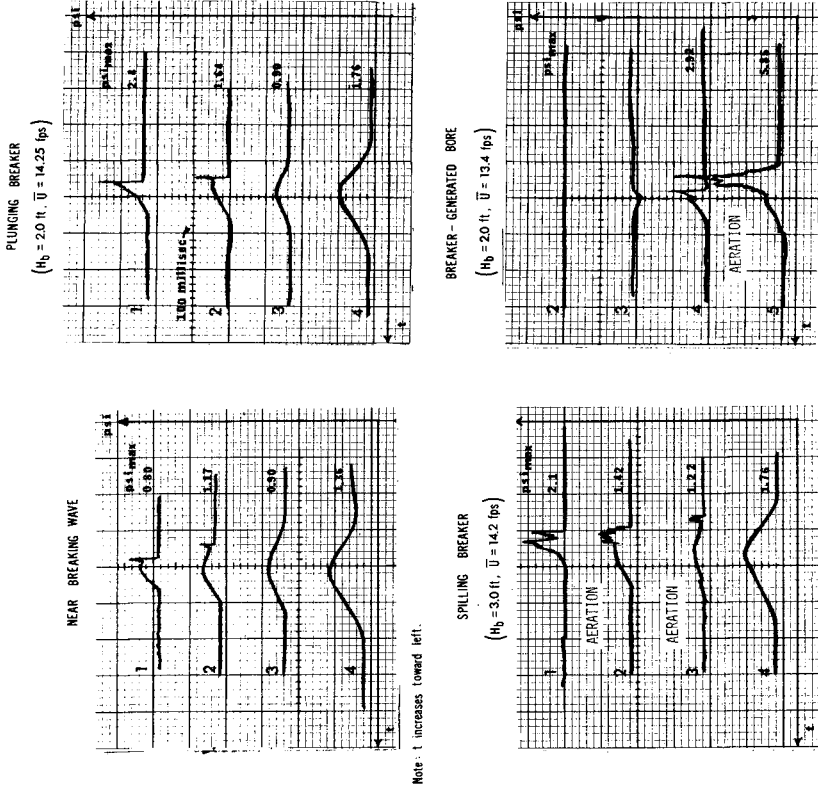
In this paper, attention is focused on the "impact pressure" portion of the total force. "Impact pressure" Wiegel (1964), Weggel, (1968), refers to the impact of the free surface of a translatory mass of water against a rigid surface. These pressures are distinguished by relatively large magnitude and short duration. The phenomenon is also referred to as "shock pressure" but in this paper the less ambiguous term, "impact pressure" will be used.

Impact pressures have been investigated extensively in the laboratory. These include Bagnold (1939), Denny (1951), Ross (1955), Hayashi and Hattori (1958), Nagai (1960) and Weggel (1968) among others.

Full scale studies in the field are notably lacking. The well-known work of Gaillard (1904) and Molitor (1934) did not include sensing devices capable of recording the transient, high magnitude signals associated with impact pressures. As far as we know, the only published data on full scale impact pressures at several points along a vertical gradient, is that of Rouville, Besson, and Petry (1938) at Dieppe. A field study reported by Morison, Johnson, and O'Brien (1954) recorded the total force exerted by breaking waves on a pile. Although outside the scope of the present study, their paper contains relevant results and is referred to later.

An examination of the above literature indicated wide disagreement in the interpretation of results and a serious lack of field data. Accordingly a field program was planned with the following aims: 1. To measure impact pressures generated by full-scale breakers under field conditions. 2. To obtain a vertical gradient by using an array of simultaneously recording sensors, whose exposed faces are small relative to wave height. 3. To identify and record the breaker types generating the impact as the data is taken. 4. To compare the results with published laboratory and field data. 5. To eliminate any effect due to the Bagnold air cushion which has been observed only in laboratory channels with confining sidewalls.

<center>THE EXPERIMENTAL DESIGN</center>

A. Choice of field site. The outer shore of Cape Cod proved to be an ideal location. The summer topography consists of a rather steep foreshore with an extensive tide-flat of approximately $1^o - 3^o$ slope exposed at low tide by the 10-12 feet tide range. The typical sea-state in August consists of regular swell with periods of the order of 8 seconds. High frequency secondary waves due to local wind are usually absent.

B. Strategy. The sensor system was emplaced at low tide on the
exposed flat. Figure 2 illustrates structural details of the sys-
tem. A 10 ft. vertical pipe fastened to the top of the cylinder
served to keep the conducting cables high above the surf and splash.
The conducting cables, which were used for power in and signal back,
were then carried horizontally through the air to the beach area.

As the tide began to rise, the first impact pressures were gen-
erated by bores created by waves breaking seaward of the sensor sys-
tem. As the tide continued to rise, the sensing system received the
impact of plunging or spilling breakers. Finally at high tide, forces
due to a series of near breaking waves were recorded by the sensor sys-
tem. On the falling tide the reverse sequence occurred. In this way
it was possible to get two complete sets of data per tide cycle.

C. The sensing and recording system. The basic support structure con-
sisted of a 6 ft. aluminum cylinder. A portion of the curvature of the
cylinder was removed down the full length and an aluminum flat face
clamped on as shown in figure 2. At 1 ft. intervals along the vertical
length of the flat, two inch diameter openings were cut. A thin alu-
minum disc was then clamped over each opening, to serve as an impact
sensor in the form of a strain-gage mounted diaphragm. Calibration
of the strain-gage mounted diaphragm-amplifier unit was accomplished
by static loading. Dynamic calibration was also carried out. Details
are given in Tech. Rept. no. 14, 1974, Miller et al.

The water-tight cylinder contained the required wiring, strain
gage amplification and associated electronics. The structure was sup-
ported by three turnbuckle-tightened cables leading from anchors buried
in the sand flat. The base was supported by a steel rod driven 3 feet
into the sand. The resulting structure offered a rigid, stable, support
for the vertical array of sensors.

Signals passed through the conducting cable to the shore to be re-
corded by a 4-channel oscilloscope with polaroid camera attachment. A
switching box enabled us to monitor 4 of the 5 sensors simultaneously.
Power was supplied by a 5 KW portable generator.

For each recorded breaker, an observer noted 1) the elapsed time
for the wave to travel from a staff 50 ft. seaward, to the sensor sys-
tem; 2) the breaker height using a scale painted on the cylinder and
3) the breaker type.

RESULTS

The oscilloscope records are illustrated in figure 1. Simul-
taneous traces from four sensors are shown for a single wave. Each
trace is identified by a number corresponding to a particular sensor

INSTRUMENTED
CYLINDER
CONDUCTING CABLE TO SHORE
ALUMINUM FACE PLATE
PRESSURE TRANSDUCERS
ALUMINUM CYLINDER
SUPPORT WIRE
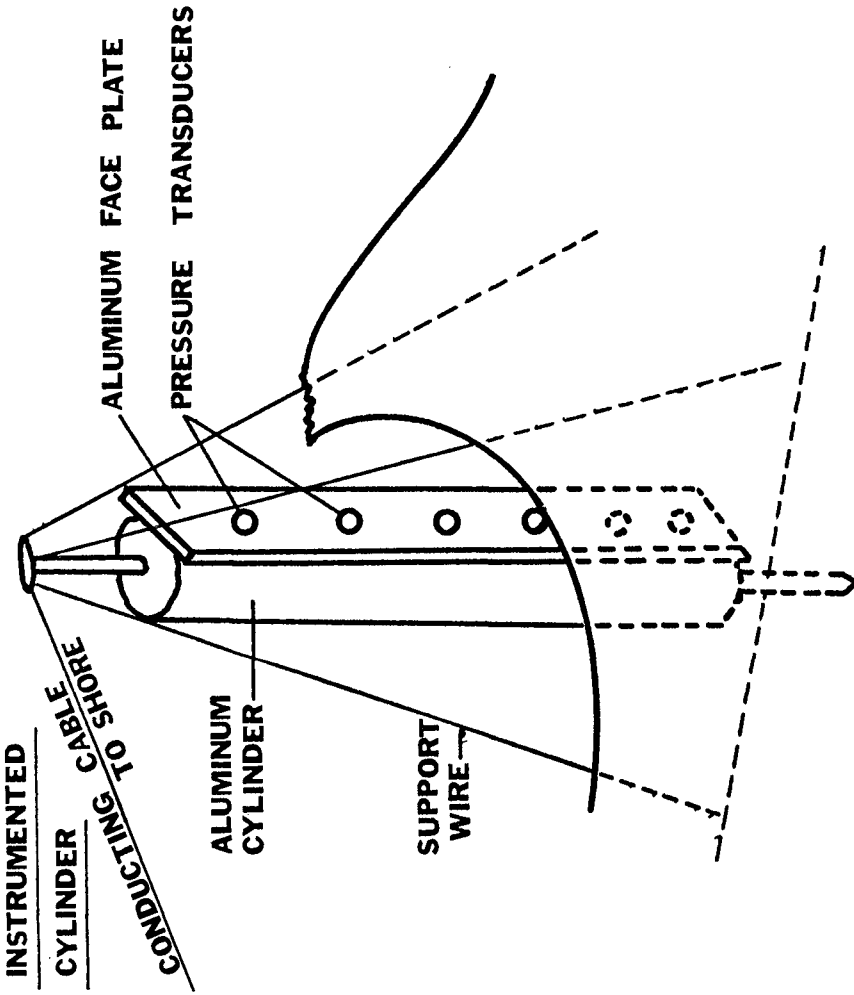
Fig. 2

whose position above the bottom is indicated at the left. Time is read from right to left. Typical records were selected, one for each of the breaker types. Although the magnitudes vary, the shape of the traces are repeated with little variation for other waves within each breaker type category. It thus appears that the pressure-time trace is a diagnostic property.

1. <u>Near breaking wave</u>. Impact pressure consists of a small but distinct single "spike" confined to the upper portion of the vertical gradient, as the wave strikes the sensor structure. A relatively large phase lag between the first arrival of the wave at sensor 2 and the later arrival at sensor 1, reflects the wave slope at the time of impact. The local inclination of the free surface in the vicinity of the sensor face also affects the magnitude of the impact pressure. With respect to this factor, the maximum impact will occur when the free surface of the wave strikes all parts of the sensor face simultaneously. The impact pressure magnitude is less, depending upon the degree of departure from this criterion.

2. <u>Plunging breaker</u>. Impact pressure is relatively large and distinct, consisting of a single spike which dominates the total pattern in the upper part of the gradient. Air entrainment is not yet present in the near breaking and plunging breaker, as shown by the single distinct trace in the impact region. In contrast to the near breaking wave, the phase lag for "impact spikes" between sensor 2 and sensor 1 is much smaller, indicating a near-vertical forward face. In several of the plunging breaker records the first arrival is recorded at the upper sensor. This indicates that the traces were recorded at the early overturning stage of the front face of the plunging breaker.

3. <u>Spilling breaker</u>. The upper two sensors show compound partly blurred, impact pressure spikes due to the presence of significant amounts of entrained air, as is characteristic of the spilling breaker. The maximum impact pressure is recorded at the upper part of the vertical gradient, as is also the case for plunging breakers and near-breaking waves.

4. <u>Post-breaking bore</u>. Records at fewer sensors in the vertical array reflects the drop in height as the bore is formed from the breaking wave. Compound impact pressure spikes due to aeration are noted, as in the case of the spilling breaker. The impact pressure gradient is reversed however.

The maximum impact pressure for each breaker type is given in frequency distribution form in figure 3. Although there is insufficient data for statistical estimates of the mean and standard deviation, the available data shows a progression in average maximum impact pressure from near breaking, through spilling and plunging breakers to post-breaking bores.

FREQUENCY OF MAXIMUM IMPACT PRESSURES

NEAR BREAKING
AV.= 1.55 PSI

PLUNGING
Av.= 2.63 PSI

SPILLING
Av.= 2.20 PSI
Av.= 1.74 PSI

BORE
Av.= 2.75 PSI

0   .5   1   1.5   2   2.5   3   3.5   4   4.5   5   5.5   6   6.5   7   psi
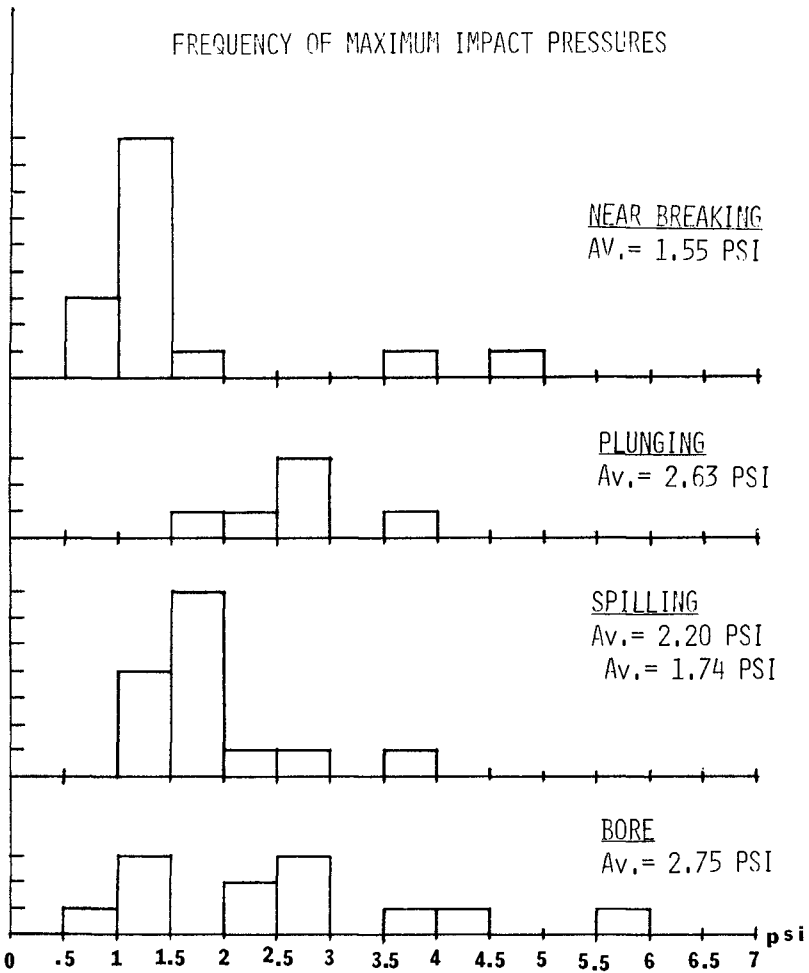
Fig. 3

Dynamic pressure vs. wave velocity

The dynamic pressure of waves in general may be expressed as $p/w = (f) \ U^2/2g$ where p/w is the pressure head, $U^2/2g$ is the head of the fluid at impact and f is a coefficient, w is unit weight of water and U is wave velocity. A large number of equations for both waves and breakers can be expressed in this manner by adjusting (f) to fit the particular equation. This relationship is shown by Hayashi and Hattori (1958) who list more than 10 equations published by various authors. Hayashi and Hattori present these equations rearranged in the form given above, with the appropriate value of (f). They plot p/w vs. $U^2/2g$ comparing their experimental data with a line at $(f) = 4$ as well as several other lines, including $(f) = 2$, Hiroi (1920) and others.

We have expanded their figure to include other model data and full scale field data, (figure 4) and added a line representing Bagnold's 1939 equation, $p_{max} = 0.54 \ \rho U^2 H/D$, where D is the thickness of the Bagnold air cushion, and H is the crest to trough wave height. Converting to the general form, one obtains $p_{max}/w = (1.08 \ H/D) \ U^2/2g$. According to Bagnold the air cushion thickness D is of the order of 0.4 (H) at maximum. It is thus possible to evaluate the coefficient $(f) = (1.08 \ H/D)$, as 2.70. For comparison, a line at $(f) = 10$ is plotted which passes through Hayashi and Hattori's recorded laboratory data at small values of $U^2/2g$ and also through the much larger values of $U^2/2g$ calculated from the full scale Dieppe data.

The Cape Cod data for full scale breakers appear to follow the trend of $p/w = (f) \ U^2/2g$, with spilling breakers plotting roughly along the $(f) = 1.6$ line and plunging breakers along the $(f) = 2$ line. The Cape Cod bore and the Dieppe data points however do not follow the trend of $p/w = (f)U^2/2g$ at all.

Impact pressure vs. wave height

Intuitively it would appear that a simple functional relationship should exist between wave force and wave height. In this regard all available published laboratory and field data has been plotted in figure 5. The ordinate is impact pressure in units of pounds per square inch and the abscissa is breaker height (H_b) in inches. It is not clear in the solitary wave studies of Bagnold and subsequently Denny, whether the wave height is taken at near-breaking or just breaking stage.

The data points consist of laboratory or full scale magnitudes either for individual observations or averages, as indicated. Several points are derived from Bagnold (1939, fig. 21), who gives curves based on experiments which predict the time-history of pressure impulses assuming adiabatic compression of the enclosed air cushion. The maxima are plotted for three values of D, thickness of the air cushion.
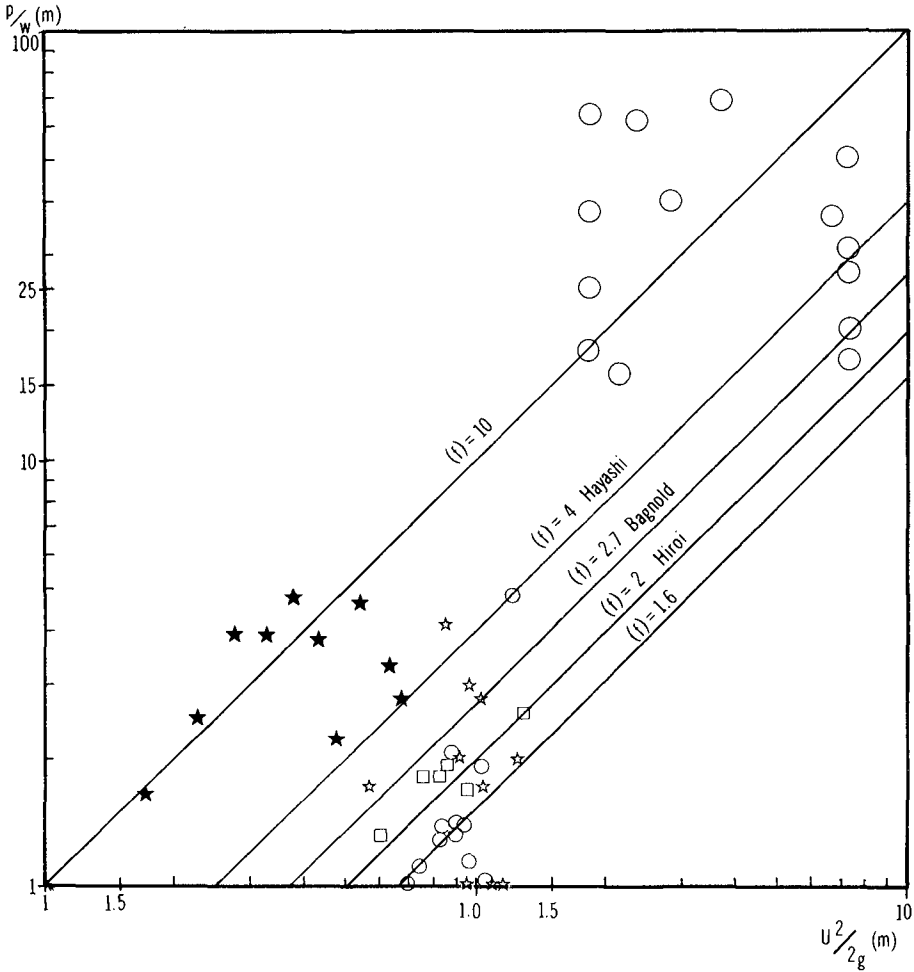
Figure 4.   Dynamic pressure vs. wave velocity.

○ Dieppe.   Rouville et al.

☆ Bore

□ Plunging Breaker   } Cape Cod data.

○ Spilling Breaker

★ Lab (Solitary) Hayashi et al.
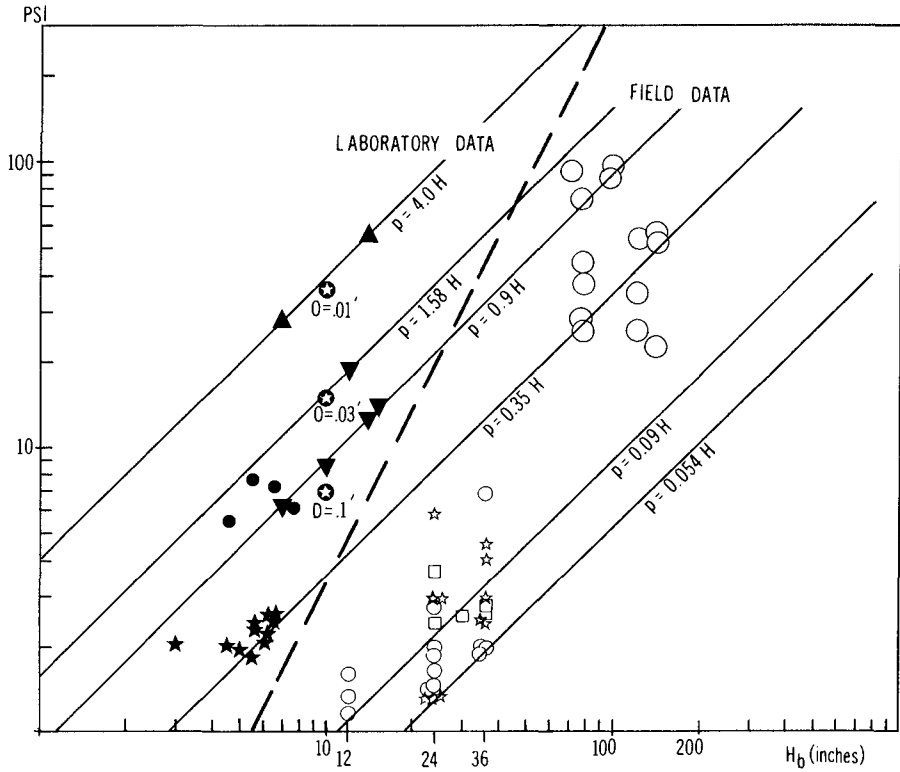
Figure 5. PSI vs. Breaker height.

Laboratory   ● Ross (av. "First Wave")

                 ▲ Denny max.

                 ▼ Denny most freq. calm water

                 ▼ Denny most freq. disturbed water

                 ★ Nagai

                 ✪ Bagnold

Field   ◯ Dieppe

                 ☆ Bore

                 ☐ Plunging Breaker   Cape Cod data.

                 ◯ Spilling Breaker

In addition to the various data points, several lines of the form
$p = (K\gamma)H$ are shown, where K is a numerical coefficient and γ is the
unit weight of water. Hiroi (1920) was the first to propose this simple
linear equation in the form $p = 1.5\gamma H$ or $PSI = 0.054$ H (inches). The
upper three lines are due to Denny and are based on empirical fit to
very large numbers of experimented results. The line $PSI = 0.09H_b$ is
an empirical fit to the Dieppe data.

It can be seen that the full scale field data gives much lower
values for impact pressure than would be expected from the model studies.
The suitability of a single linear equation for H vs. p seems also open
to question. These points will be covered in the discussion section.

DISCUSSION

Morison, Johnson and O'Brien (1954) conducted a field study in which
breakers are distinguished from near breaking waves and from the breaker
generated bore. They measured wave forces on a $3\frac{1}{2}$ inch pile hinged at
the base. A plot of wave height vs. wave force indicates that for given
height the magnitude of the force is correlated with the wave or breaker
type. These are arranged in decreasing order with respect to wave force.

Designation by Morison, et al.	Probable Breaker Type according to Miller et al.	Comment
"Foam line"	Bore	greatest forces recorded
"Breaker with some foam"	Bore?	
"Breaker"	Plunging Breaker	magnitudes overlap with bores
"Sharp peak swell starting to break"	Spilling Breaker	magnitudes overlap with plunging breakers
"Sharp peak swell"	near breaking wave	lowest forces recorded

Wiegel (1964) commenting on the field data of Morison et al and also on
laboratory observations notes that "the forces exerted on a pile by a
'foam line' of a certain height were considerably higher than the forces
for a breaking wave of the same height."

Although our field data is recorded at individual points in a ver-
tical gradient rather than for an entire piling, the results are strikingly
similar to those of Morison et al, in one respect. The same progression in
magnitude vs. wave or breaker type was found in our field experiments, as
shown in figures 2 and 3. We have attempted a qualitative interpretation
of breaker mechanics.

I. Post-breaker bores

On the average the bore appears to generate the highest impact pressure but the data shows a wide scatter. The vertical distribution of impact pressures is consistently maximum at the lowest sensor, decreasing upward.

A. Bore generated by plunging breaker

The abrupt collapse of the plunging breaker is accompanied by a sharp decrease in height and significant increase in celerity. The new wave-form is that of a bore. The large scale vortices and associated air entrainment results in a rapid dissipation of the initial energy of the bore. However, the impact pressure is recorded just after generation. It is reasonable to expect a higher impact pressure than in the parent plunging breaker. The form of the bore typically consists of a steep face and flat top . The horizontal velocity of water particles in the vicinity of the entire front face is at or near that of the bore velocity. The upper portion of the face consists of a turbulent mixture of air and water containing as high as 20-30% air bubbles per unit volume. Miller 1972, Fuhrboter (1970). The base of the bore-face contains little or no air bubbles. The difference in local density leads to significantly higher momentum at the lower portion of the bore face. The net result is maximum impact pressures at the base of the bore.

B. Bore generated by Spilling breaker

The spilling breaker also transforms into a bore during the gradual decrease in wave height after breaking. Since the spilling breaker is characterized by initial small scale breaking just at the crest, it is some time before the fully developed bore is generated. The slow loss in wave height is accompanied by energy dissipation at such a rate that the celerity does not show abrupt or significant increase over that of the initial spilling breaker. The maximum impact pressure is at the base of the front face, as in all bores.

The preceding discussion leads to an expectation of:

1. Maximum impact pressure at the lowest recording sensor.

2. A wide variation in impact pressure magnitudes but with maximum values higher than those due to plunging or spilling breakers.

II. Plunging breaker

The plunging breaker may result in relatively high impact pressures due to the following:

1. The free surface has not yet begun the process of air entrainment, thus the mass per unit volume of the moving fluid is that of water.

2. During the early stages of breaking a large portion of the face
   is essentially vertical, and may impact simultaneously over the
   area of the sensor. The water particle velocity in the upper
   portion of the face is close to that of the wave velocity.
   This leads to high values in the middle or top of the instrument
   array.

3. The jet-like overturning crest may impact the uppermost sensor
   leading to large values at the top of the instrumented section.

Spilling breaker

   The initial celerity of the spilling breaker is not signifi-
cantly different than that of the plunging breaker. The breaking
process begins in a small region at the crest, and expands gradually
as the wave subsides, thus the steep to vertical front face so charac-
teristic of the plunging wave does not develop on a large scale. Con-
sistent with this, the fluid particle velocity is equal to that of the
wave velocity, only in the vicinity of the crest. Since the free sur-
face does not impact the full sensor face simultaneously, the expectation
is that the impact pressures will be less than those of the plunging
breaker, and will be similar in magnitude to those due to the near-
breaking wave.

   The vertical distribution of impact forces is presented in summary
in figure 6. Two graphs are given for each of three categories: Bore,
Plunging breaker and Spilling breaker. The ordinate indicates the sen-
sor position. One graph presents results for three simultaneously re-
cording sensors, and one graph presents results for two simultaneously
recording sensors. The abscissa gives the ratio of the observed impact
pressure to the maximum observed for a given wave. The patterns show
consistent maximum at the lowest sensor for bores, and the reverse for
spilling and plunging breakers. One additional pattern found in both
plunging and spilling breaker data shows the maximum at the middle of
the gradient. To facilitate comparisons a straight line connects average
values, by sensor level.

   The Dieppe data (Rouville et al) represents the only available field
data recorded in a manner similar to ours, although it is for much larger
breakers. Although Rouville et al did not indicate breaker shape, it is
striking to note that with the exception of two runs, all of their data
fit the bore pattern, with maximum value at the lowest sensor. This
leads to the inference that most of the Dieppe data for exceptionally
large impact pressures, was generated by bores from waves breaking just
seaward of the sea wall.

   Nagai (1960) carried out model studies and developed empirical pre-
dictions for maximum impact pressure based on consideration of break-
water shape, changes in wave height, and incident wave steepness. He
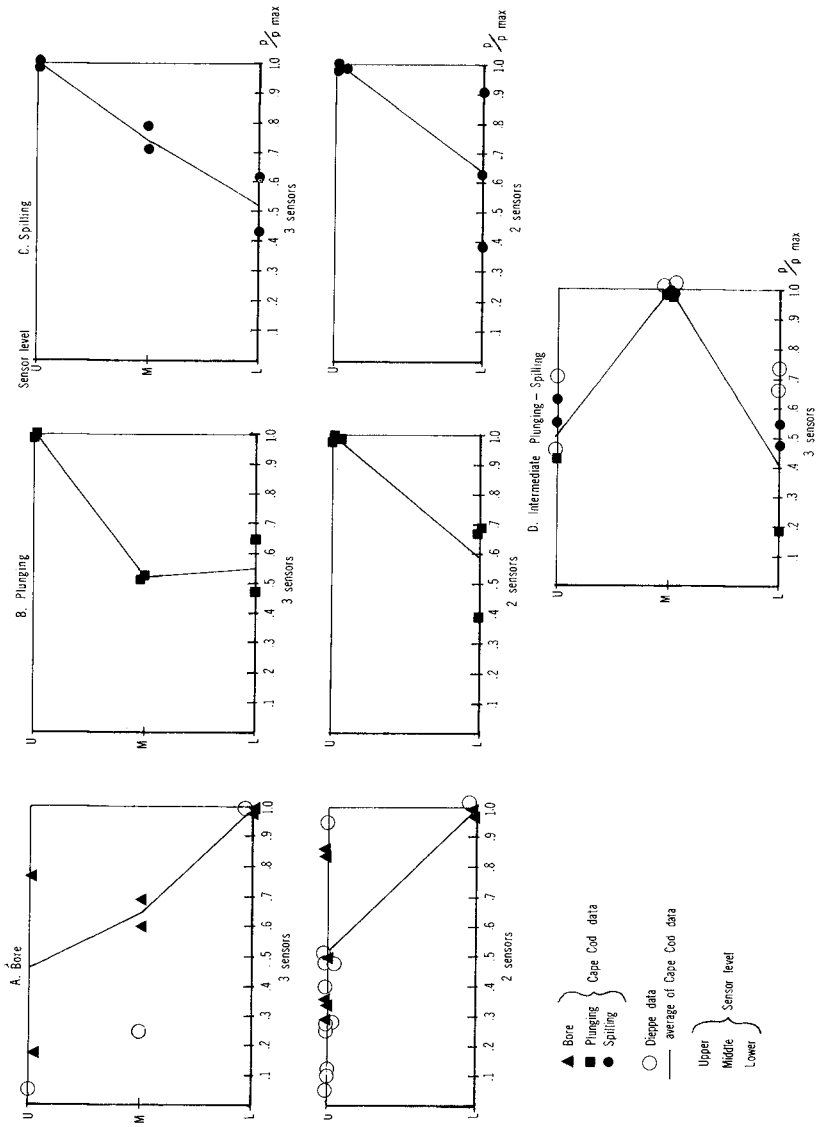
Figure 6.   Vertical distribution of impact pressure.

fits predicted impact pressures to the Dieppe data with some success.
Although he does not consider breaker shape explicitly, his "Type C"
is suggestive of the post-breaker bore.

     The evidence accumulated in figure 5 indicates that a single
linear equation for impact pressure as a function of wave or breaker
height is insufficient to yield reliable predictions. Bagnold (1939)
observed that linear scaling of his model study results gave full-scale
values more than ten times too high when compared with the Dieppe field
data. Our Cape Cod data also plotted in figure 5 shows the same effect.
He attributed the discrepancy to rarity of occurrence of the air pocket,
irregularity of the surface of waves in nature, and most importantly to
the presence of air in the water -- "the ultimate limit to the intensity
of shock pressures .... is set by the quantity of air locked in and on
the surface of the wave before impact." Denny (1951) draws similar con-
clusions but his experiments stress that a disturbed free surface will
result in lower impact pressures, as shown in figure 5. Weggel (1968)
also stresses the importance of air in the mechanics of wave impact.

     We feel that the explanations given above are all valid, but the
key lies in recognizing that different breaker types give different im-
pact pressures. Air entrainment is insignificant in the near breaking
and early plunging wave, but the degree to which the free surface is
irregular, is important. On the other hand air entrainment is of great
significance in the spilling breaker and post-breaker bore. Further-
more, the vertical distribution of impact loading for these two breaker
types is significantly dependent on the vertical distribution of air
in the water.

     Figure 4 gives some evidence that recognition of breaker types
may lead to a family of prediction equations of the general form $p/w =$
$(f)U^2/2g$ as discussed earlier. Collection of large numbers of field
observations of impact pressures for the various breaker types is
needed before reliable prediction equations can be devised.

                              CONCLUSIONS

I. Full scale data taken at Cape Cod support the initial premise that
the nature and magnitude of impact pressure is directly related to
breaker shape. Analysis of published studies support this conclusion.

a. The strong bore formed just after the collapse of the plunging
    breaker generates the largest impact pressures. Weak bores gener-
    ated by spilling breakers on the other hand, do not generate large
    impact pressures. This results in a wide scatter of data for this
    breaker type.

b. The maximum impact pressure in the vertical gradient is at the
    base of the bore.

c. The next largest impact pressures are due to plunging breakers,
    but the gradient is reversed, with maximum at the top.

d. The spilling breaker is similar in vertical gradient, but smaller
    in magnitude.

e. Although the near-breaking wave generates the smallest impact
    pressures, impact "spikes" are noted when the wave surface strikes
    the sensor face.

II. The role of entrained air and of the angle of impact of the free
surface, are reasonably explained when breaker shapes are taken into
account.

III. Typical time-pressure patterns were found to characterize the
various breaker types. Thus the time-pressure pattern is a diagnostic
property.

IV. Extreme shock pressure due to entrapped air did not occur. In
view of the geometry of our sensor structure, these pressures were not
expected. We feel that confining sidewalls as in the laboratory studies
of Bagnold and of Denny or in full scale waves striking an I beam, Wiegel,
Beebe and Moon (1957) are required before the Bagnold air pocket phenom-
enon can occur.

REFERENCES

Bagnold, R. A. 1939, Interim report on wave-pressure research. Jour.
     Inst. Civil Eng. June. pp. 202-226.
de Rouville, A., P. Besson, and P. Petry, 1938. Etat actuel des Etudes
     internationales sur les Efforts dus aux Lames Ann. Ponts et
     Chaussees, vol. 108 II, pp.
Denny, D. F., 1951, Further experiments on wave pressures. Jour. Inst.
     Civil Eng. Feb. pp. 330-345.
Fuhrboter, A., 1970, Air entrainment and energy dissipation in breakers.
     Proc. 12th Coastal Engineer. Conf., Washington, D. C., pp. 391-398.
Caillard, D. D., 1904, Wave action in relation to engineering structures.
     Ft. Belvoir, Va.: U. S. Army Corps of Engineers, The Engineer School
     (reprinted 1935).

Hayashi, T. and M. Hattori, 1958, <u>Pressure of the breaker against a vertical wall</u>. Coastal Eng. in Japan, Vol. 1, pp. 25-37.

Hiroi, I., 1920, <u>The force and power of waves</u> Engineer, pp. 184-185.

Miller, R. L., 1972, <u>Study of air entrainment in breaking waves</u>. EOS Vol. 53, no. 4, p. 426.

Miller, R. L., S. Leverette, J. O'Sullivan, J. Tochko and K. Theriault, 1974, <u>The effect of breaker shape on impact pressures in surf</u>. Tech. Rept. No. 14. Fluid Dynamics and Sed. Transp. Lab., Dept. of the Geophys. Sci, University of Chicago.

Molitor, D. A., 1935, <u>Wave pressures on seawalls and breakwaters</u>. Trans. ASCE, Vol. 100, pp. 984-1002.

Morison, J. R., J. W. Johnson, and M. P. O'Brien, 1953, <u>Experimental studies of forces on piles</u>. Proc. Fourth Conf. on Coastal Eng. (Chicago) pp. 340-370.

Nagai, S. 1960, <u>Shock pressures exerted by breaking waves on break-waters</u>. Trans. ASCE, paper no. 3261, pp. 772-809.

Ross, C. W., 1955, <u>Laboratory study of shock pressures of breaking waves</u>. Beach Erosion Board, Tech. Memo. 59, U. S. Army Corps of Engineers, 22 pp.

Weggel, J. R., 1968, <u>The impact pressures of breaking waves</u>. Ph.D. Thesis, Dept. Civil Eng. Univ. of Illinois, Urbana, Ill., 190 pp.

Wiegel, R. L. 1957, K. E. Beebe, and J. Moon, <u>Ocean wave forces on circular cylindrical piles</u>, J. Hydr. Div. ASCE, vol. 83, HY2 Paper 1199.

Wiegel, R. L. 1964, <u>Oceanographical Engineering</u>, Prentice-Hall, Inc., Englewood Cliffs, N. J., 532 pp.

CHAPTER 104

IMPACT PRESSURES PRODUCED BY BREAKING WAVES

by

Norbert L. Ackermann
Professor of Water Resources Engineering
Asian Institute of Technology

and

Ping-Ho Chen
Graduate Student
Asian Institute of Technology

ABSTRACT

Experiments were conducted in a vacuum tank in order to investigate the effect which entrained air has on impact loads which are produced when waves break upon a structure. In these experiments a flat plate was dropped onto a still water surface in an environment where the ambient pressure of the surrounding air could be controlled. Rings of varying height were fixed to the surface of the falling plate in order to trap different volumes of air between the falling plate and the water. Experimentally determined values were obtained of the maximum pressure p_{max} when the plate struck the water surface for various ring heights δ and ambient pressures p_o in the vacuum tank.

Experimental results indicate that the pressure rise or shock pressure $p_s = (p_{max}-p_o)$ decreased with reductions in the ambient pressure and volume of entrapped air. Even when air was removed such that the absolute pressure in the tank was equal to the vapor pressure of the water, water hammer conditions, where the peak pressures depend upon the celerity of sound waves in the media, were never found to occur.

INTRODUCTION

The spatial distribution of the magnitude and duration of impact loads produced by waves breaking against a structure are little understood at the present time. Design procedures for such conditions are based on empirical relationships[1][2] that have little basis on a rational analysis of the hydrodynamic features that produce these impact loads. Most experimental investigations on the problem of shock pressures produced by waves breaking upon a structure have been conducted in wave channels[3][4][5][6][7]. The advantage of such an experimental arrangement is that the relationship between the wave characteristics and the impact loads can be studied directly. In a wave channel considerable experimental difficulties have been experienced however in arranging for the wave to impinge upon the structure at the moment of breaking. It is difficult, if not impossible, to control in a systematic manner the impact conditions; such as the velocity of impact, the volume of entrained air, the ambient pressure and area of impact.

1778

In order to identify the dynamic features of the impact loads other than by specifying the wave conditions in the channel that produced these loads, experimental tests were conducted in which a plate was used to strike a water surface. As described by Wang[8], this could be made equivalent, in a dynamic sense, to a column of water striking a flat surface. Predetermined volumes of air could be trapped between the water and the plate through the use of small cups or rings fixed to the face of the falling plate. Prior to impact, the ambient pressure of the air in these rings could be controlled by reducing the pressure within the test chamber using a vacuum pump.

Kamal[9] had conducted experiments using an apparatus which was somewhat similar but which differed most significantly from that used in the present study in that the apparatus used by Kamal could not control the ambient pressure or density of the air trapped between the plate and the water surface. Bagnold[3] suggested that the impact pressures produced by a wave breaking against a vertical wall depended upon the amount of air trapped between the wave and the structure. If no air were present water hammer pressures were believed to occur, water hammer pressures have therefore often been suggested in the literature as a reasonable upper limit for the peak pressures which could exist when a wave would break against a structure. Such pressures were never recorded experimentally however. Explanations have been given that the situation where water hammer pressures would occur were statistically extremely small and that even small amounts of entrained would air greatly reduce the celerity of the pressure wave and consequently the magnitude of the peak pressure.

THEORETICAL CONSIDERATIONS

Fig.1 is a schematic diagram showing entrapped air within a cylindrical chamber. The air is compressed by a column or piston of water having an initial velocity V_0. This compression of the entrapped mass of air was suggested by Bagnold[3] to be representative of the mechanism that created impact pressures when a breaking wave struck a vertical wall. If it is assumed that the air is compressed adiabatically the equation of motion of the water column can be expressed as

$$\rho_w K \frac{d^2 x}{dt^2} - p_o \left(\frac{\delta}{x}\right) + p_o = 0 \tag{1}$$

In Eq.(1), ρ_w is the density of water, δ is the height of the air chamber, γ is the adiabatic gas constant, x and t are the distance and time coordinates, respectively, and K is the length of the impinging mass of the water column whose motion is described by the x,t coordinates. Eq.(1) originally proposed by Bagnold also can be used to describe the compression of a volume of air trapped in a cylindrical chamber which is attached to a flat plate which strikes the still water surface. The mass of the falling plate should be large so that the velocity of the moving plate is not influenced by the pressure forces in the chamber. For this condition, the value of K represents the length of an effective water column whose motion can be described by the x,t coordinates. The mass of this water column can be considered for purposes of convenience as a virtual mass equal to

$$\text{virtual mass} = \rho_w K \frac{\pi D^2}{4} \tag{2}$$

where D is the diameter of the cylindrical chamber attached to the falling plate.

Using Eq.(1) Mitsuyasu[10] determined the relationship describing the maximum pressure p_{max} as

$$\frac{\rho_w V_o^2}{5 p_o} (\frac{K}{\delta}) + 1.4 - (\frac{p_{max}}{p_o})^{0.4/1.4} - 0.4(\frac{p_{max}}{p_o})^{-1.0/1.4} = 0 \qquad (3)$$

The ratio K/δ can be considered as a geometrical property of the cylinder-piston mechanism used in the modeling concept. Fig.2 shows the theoretical relationship as predicted by Eq.(3), between the maximum pressure rise or shock pressure $p_s = (p_m - p_o)$ and the ambient pressure p_o for various values of K/δ. This figure is constructed for a constant value of $\rho_w V_o^2$. As the initial volume of the entrapped air reduces, the shock pressure p_s increases. As δ approaches zero, the maximum pressure p_s becomes infinite as can be seen from an inspection of Eq.(3). Such an analysis assumes however that the water is incompressible. If the compressibility of the water is considered, the upper limit of the impact pressure against a rigid structure will be governed by the water hammer equation.

$$p_{max} = \rho_w V_o C \qquad (4)$$

In Eq.(4) C is the celerity of a pressure wave in the media. The air leakage models proposed by Mitsuyasu[10] and Verhagen[11] show that an air pocket will always exist at the condition of maximum shock pressure. Only by completely removing the air from the water-structure environment could impact pressures conceivably be produced of the magnitude indicated by Eq.(4). In the present study, it was attempted to produce such a condition by conducting the experiments in a vacuum tank from which the air could be removed. Impact pressures were experimentally determined under conditions in which the ambient air pressure varied from atmospheric pressure to the vapor pressure of water. By substituting data from the experimental results into Eq.(1) or Eq.(3), the value of K could be calculated. This value was then computed for the theoretical value of K which would exist if the effective mass of the water was equal to the virtual mass of a disk in a semi-infinite fluid having a diameter equal to that of the cup shaped cylinder attached to the face of the falling plate. The value of K corresponding to such a hypothesis would yield $K = 2D/3\pi$.

EXPERIMENTAL INVESTIGATION

Two mechanical systems were constructed which permitted a falling plate to strike a water surface in a tank where the ambient pressure could be controlled.

System 1: Hinged Plate

The plate shown in Fig.3 was hinged about one of its edges. A pressure transducer having a frequency response of 5,500 Hz was mounted flush with the surface of a protruding part of the plate that had a diameter of 10 cm as shown in the figure. Small rings used to trap air between the plate and the water could be mounted on the plate. The transducer was spatially prepared to operate in a range of pressure of $\pm$ 15 psi gage. The maximum overload pressure was 75 psi. A recording oscillograph manufactured by Consolidated Electrodynamics Corporation Type 5-124 having a galvanometer with a frequency response of 2000 Hz was used to record the pressure response.

The maximum velocity of the plate, at the location of the pressure transducer, prior to impact was approximately 10.0 ft/sec. Fig.4 shows the relationship between the measured shock pressure, the height of the cylindrical disks or rings attached to the face of the falling plate and the ambient pressure in the vacuum tank. Both alcohol and water were used as the liquids in the vacuum tank.

System 2: Vertically Falling Plate

The plate used in system 2 was circular having a diameter of 30 cm as shown in Fig.5. The pressure transducer and recording oscillograph was the same as that described in system 1. The plate had a vertical motion with a maximum fall velocity prior to impact of 4.87 ft/sec. Fig.6 shows the relationship between the experimentally determined values of the shock pressure, ambient pressure in the vacuum tank and the height of the rings mounted on the face of the falling plate. The rings had a diameter of 5/8 inch.

DISCUSSION OF RESULTS

System 1

As shown in Fig.4, the maximum pressures produced at impact, for each combination of ambient pressure and ring size, exhibited an increasing degree of scatter about the average value for each series of 25 tests, as the ambient pressure in the vacuum tank and the height of the "air-rings" were reduced. However, as the pressure in the tank approached the vapor pressure of the water, the impact pressures produced by the plate striking the water surface never approached the magnitudes which would have occurred if water hammer conditions existed. It appeared that the entrapped air always governed the impact producing forces even though the ambient pressure in the tank was reduced as low as the vapor pressure of the water.

When water was replaced by alcohol, the measured pressures increased in proportion to the density change of the liquids. Such a variation would be predicted however by both water hammer theory as well as the equations which described the air pocket as the predominate mechanism dictating the magnitude of the impact pressures. Table 1 presents the average shock pressure measured for tests with both alcohol and water. In these tests the depth of the liquid in the tank was 7 inches and the ambient pressure was atmospheric. Twenty five tests were conducted for each ring height.

Table 1 – Average Value of Impact Pressures in Tank Using Both Alcohol and Water

Ring Height δ	Ave.Value of 25 Measurements of Shock Pressure		$\dfrac{\rho_{water}}{P_{alcohol}}$	$\dfrac{\rho_{water}}{\rho_{alcohol}}$
	in water P_{water}	in alcohol $P_{alcohol}$		
0 in	10.12	7.67	1.32	1.27
0.125 in	8.69	6.89	1.26	1.27
0.250 in	7.53	5.97	1.26	1.27
0.375 in	6.23	5.18	1.20	1.27
(Ambient Air Pressure Atmospheric)		Average	1.26	1.27

The average pressure increased by a factor of 1.26 when using water instead
of alcohol. This ratio was approximately equal to the respective increase
in density of the two liquids which was 1.27.

System 2

The experimentally determined data for the plate which fell vertically
onto the water surface is shown in Fig.6. In this figure the shock pressure
is presented as a function of the ambient air pressure in the tank for differing
heights of air rings which were attached to the plate. The data showed
increasing scatter as the air ring height was reduced. The greatest variation
in experimental data resulted when $\delta = 0$. Such a behavior is understandable
since, as δ decreases, the volume of air trapped between the water and the
plate for each test would become more variable. When $\delta = 0$ however the maximum
impact pressure was still an order of magnitude less than that which would have
existed if water hammer pressures occurred. The pressure $p = \rho_w V_o C$ was 322 psi;
more than four times the allowable overload pressure of the pressure transducer.
After each series of tests the transducer was recalibrated. There was no
indication that any time the pressure transducer had been loaded beyond its
overload capacity.

In order to insure that the results were not in error as a result of a
possible non coplanar alignment of the water-plate interface at the moment of
impact, the face of the plate was later machined to a wedge or conical shape
form shown in Fig.5. This change in the geometry of the plate did not produce
a significant change in the experimentally determined values.

The values of K computed from Eq.(3) using the experimentally determined
data is shown in Fig.7. When the ambient pressure was atmospheric and the
ring heights were 1/8 inch or larger, the value of K could be approximated
reasonably well by considering that the water mass used in Eq.(1) was equal
to 1/2 of the virtual mass of a circular disk in an infinite fluid having a
diameter equal to that of the rings which were attached to the falling plate.
The factor of 1/2 was used since the virtual mass of a disk (virtual mass =
$\rho D^3/3$) in an infinite fluid is computed assuming that fluid completely surrounds
the disk. In the present experiments the fluid is only exposed to one face
of the disk shaped opening of the air pockets at the moment of impact. The
value of K is seen to increase with decreasing ambient pressure. This result
seems reasonable since with a decrease in the ambient pressure the mass of
decelerating water increases as more of the liquid enters the cylindrical
shaped air pockets or rings.

CONCLUSIONS

Bagnolds[3] model describing shock pressures caused by the adiabatic
compression of air pockets formed between a breaking wave and vertical wall
was investigated:

(i) For cylindrical shaped air pockets originally at atmospheric conditions
having a diameter of 5/8 inch and a length of 1/8" or greater, the effective
mass of fluid which could be considered to behave as a piston compressing the
air trapped in the cylindrical shaped pocket could be approximated by using
one half of the theoretically determined value of the virtual mass of a disk

in an infinite fluid. The diameter of this disk should be equal to that of
the cylindrical shaped air ring or pocket attached to the falling plate.

(ii) The maximum recorded shock pressures, for conditions where the
ambient air pressures in the tank varied between atmospheric and the vapor
pressure of the water, were always an order of magnitude less than water hammer
pressures.

It therefore appears that shock pressures produced by a wave breaking
against a structure in field conditions could never produce pressures that would
approach those predicted by water hammer theory.

REFERENCES

(1) Minikin, R.R., "Wind, Waves and Maritime Structures", London, England:
     Charles Griffin and Co., Ltd., 1963, 2nd revised edition.

(2) Hiroi, I., "The Force and Power of Waves", The Engineer, 20 August 1920,
     pp.184-185.

(3) Bagnold, R.A., "Interim Report on Wave-Pressure Research", Journal
     Institution of Civil Engineers, Vol.12, No.7, June 1939, pp.202-226.

(4) Denny, D.F., "Further Experiments on Wave Pressure", Journal Institution
     of Civil Engineers, Vol.35, No.4, Paper No.5804, February 1951, pp.330-345.

(5) Nagai, S., "Shock Pressures Exerted by Breaking Waves on Breakwaters",
     ASCE, Waterways and Harbors Division, Journal, Vol.86, WW2, June 1960, pp.1-38.

(6) Hayashi, T. and Hattori, M., "Pressure of the Breaker Against a Vertical
     Wall", Coastal Engineering in Japan, Committee on Coastal Engineering,
     Japan Society of Civil Engineers, Tokyo, Japan, Vol.1, 1958, pp.25-37.

(7) Garcia, W.J., "An Experimental Study of Breaking-Wave Pressure", U.S. Army
     Engineer Waterways Experiment Station, Corps of Engineers, Research
     Report H-68-1, September 1968.

(8) Wang, M.S., "Wave Impact Pressures", Thesis No.664, Asian Institute of
     Technology, Bangkok, Thailand, 1974.

(9) Kamal, A.M., "Shock Pressure on Coastal Structures", ASCE, Waterways and
     Harbors Division, Journal, WW3, August 1970, pp.689-700.

(10) Mitsuyasu, H., "Shock Pressure of Breaking Wave", Proceedings, Tenth
      Conference on Coastal Engineering, Vol.1, 1966, pp.268-283.

(11) Verhagen, J.H.G., "The Impact of a Flat Plate on a Water Surface", Journal
      of Ship Research, Vol.11, No.4, pp.211-223.

LIST OF SYMBOLS

C	velocity of sound in water
D	diameter
K	length
p	pressure
p_{max}	maximum pressure
p_o	ambient pressure
p_s	shock pressure or pressure rise
V_o	velocity
t	time
x	length coordinate
γ	adiabatic gas constant
δ	height of ring
ρ_w	density of water
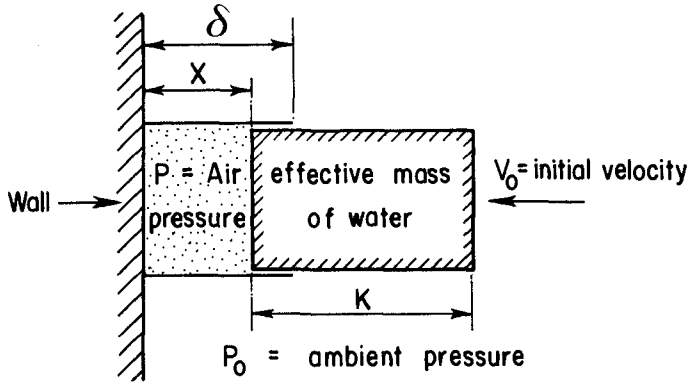
Fig. I   Schematic   diagram   of   column   of
          compressed   air   and   piston   of   water
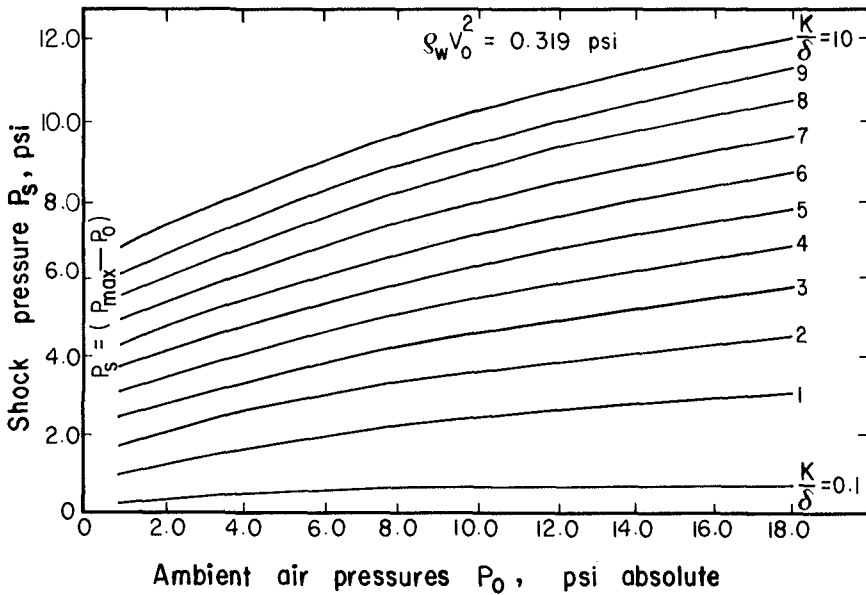
Fig. 2   Theoretical   relationship   between   shock   pressures   and
          ambient   air   pressure   derived   from   Bagnold's   model
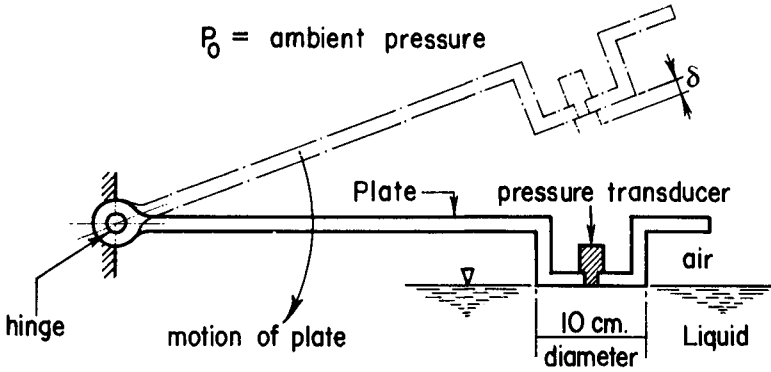
Fig.3   Schematic diagram of hinged plate with pressure transducer which struck water surface

Height of air ring δ, inches
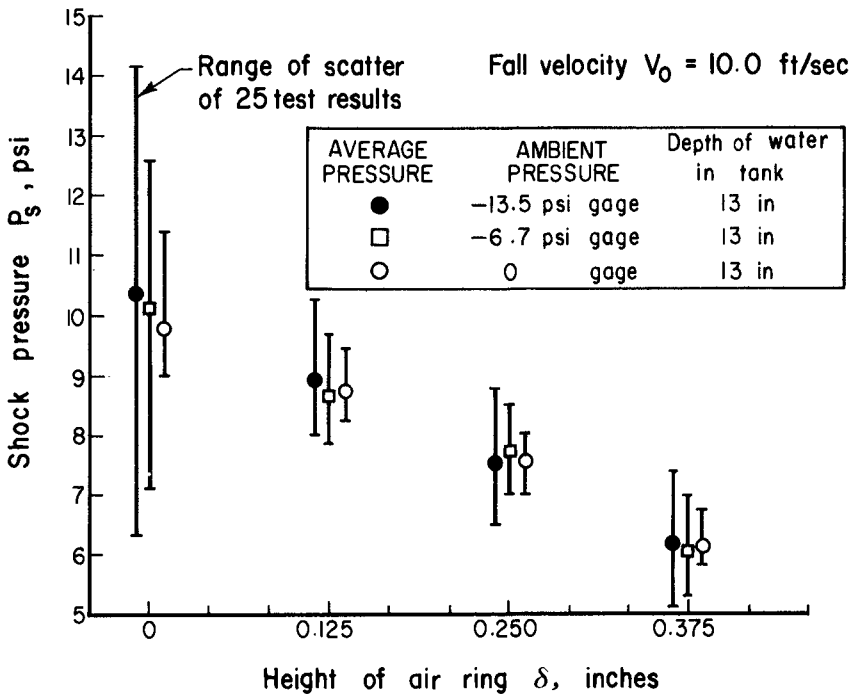
Fig. 4   Relationship between shock pressure and height of air ring for different ambient air pressures
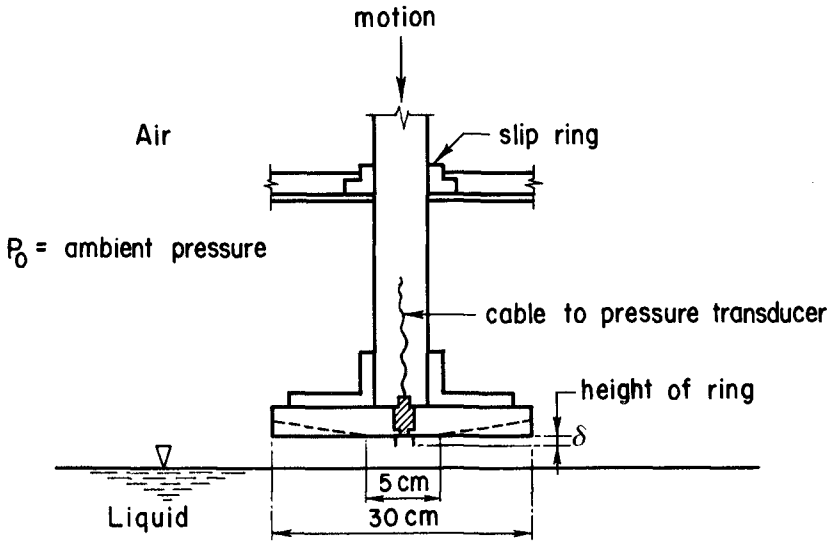
Fig.5 Schematic diagram of circular plate and pressure
        transducer which struck water surface
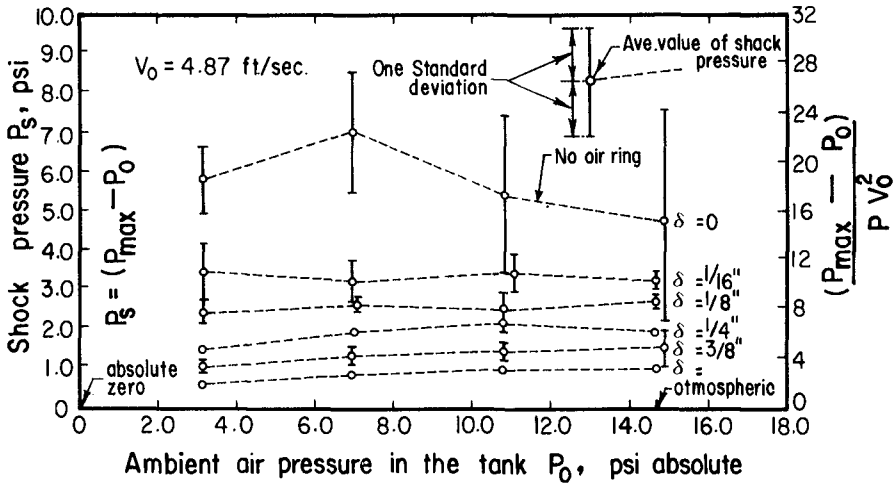
Fig.6 Experimentally determined relationship between shock
        pressure and ambient air pressure for constant value
        of impact velocity V_0
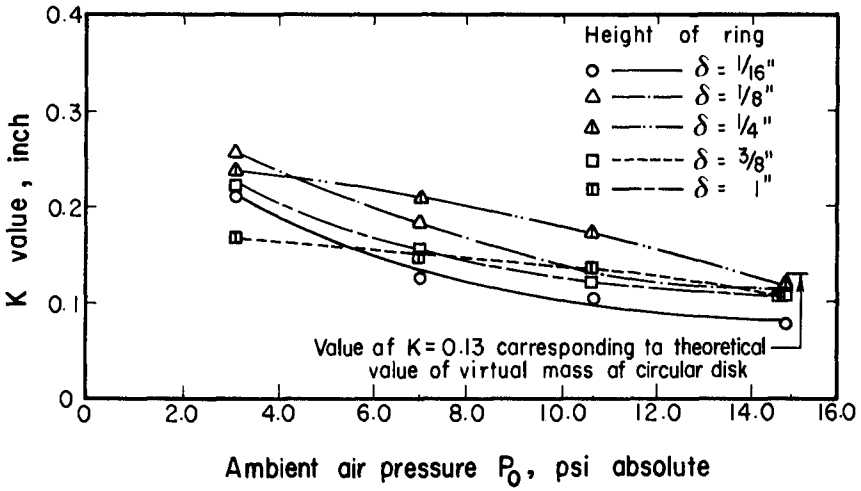
Fig. 7   Relationship between K values and ambient air pressures

CHAPTER 105

TOTAL WAVE FORCE ON A VERTICAL CIRCULAR CYLINDRICAL PILE

Yoshito Tsuchiya
Professor of Coastal Engineering

and

Masataka Yamaguchi
Assistant Professor of Coastal Engineering
Disaster Prevention Research Institute, Kyoto University
Kyoto, Japan

ABSTRACT

This paper deals with the estimation of total wave force on a vertical
circular cylindrical pile. Firstly, finite amplitude wave theories such as
those of Stokes waves and cnoidal waves are recalculated by the Stokes second
definition of wave celerity and the applicability of the theories for wave crest
height above the still water level, wave celerity and horizontal water particle
velocity is briefly discussed. Secondly, the drag and inertia coefficients are
estimated respectively from the results of experiments for total wave force by
the authors and by other researchers, based on the Morison wave force equation
applying the theories and characteristics of the coefficients are considered
in relation to the wave characteristics and pile dimension. Lastly, the appli-
cability of the wave force equation proposed is investigated in comparison with
experimental and theoretical results for time variation of total wave force and
maximum total wave force.

INTRODUCTION

It is needless to say that accurate estimation of wave force on ocean
structures in the design is of very importance. In present state, the two
methods as a practical approach are usually used for the estimation of wave
force acting on a rigid circular cylindrical pile by nonbreaking waves. The
one is based on the theory of wave diffraction (MacCamy-Fuchs, 1954 and Yama-
guchi-Tsuchiya, 1974) of which solution is obtained from the boundary value
problem under the assumption of inviscid fluid and irrotational motion. The
other is the so-called Morison wave force equation (Morison, 1950) which ex-
presses each component of wave force divided into the drag force and the inertia
force with characteristics of incident waves, assuming that the wave motion is
not essentially disturbed by the existence of the pile.

It is important factors in calculating the wave force by the Morison wave
force equation to estimate accurately the wave crest height above the still
water level, water particle velocity and water particle acceleration and to
select properly the drag and inertia coefficients.

In this paper, from this point of view, some examinations are made.
Based on the finite amplitude wave theories and the wave-pile characteristics,
a relation between the drag and inertia coefficients estimated from many exper-

imental results is established as well as the applicability of the theories to
the wave force equation. Also, the validity of the wave force equation proposed
is examined comparing the theoretical results of total wave force with the ex-
perimental ones. In this investigation, the total wave force on a pile by non-
breaking finite amplitude waves is discussed under the assumption that the dia-
meter of pile is small compared with the wave length and consequently the effect
of wave diffraction by the pile on the total wave force can be neglected.

FINITE AMPLITUDE WAVE THEORIES AND WAVE FORCE EQUATION

(1) Finite Amplitude Wave Theories (Tsuchiya-Yamaguchi, 1972) For the
estimation of wave force, there are many fruitful theories of finite amplitude
waves such as Stokes waves and cnoidal waves. The wave theories however have been
derived by using either of two physical definitions of wave celerity (Stokes,
1880). The one is the so-called Stokes first definition of wave celerity, which
means that the average horizontal water particle velocity over a wave length is
vanished, and it is given as

$$c = \frac{\int_0^L (c + u)dx}{\int_0^L dx} \quad \dotfill (1)$$

in which c is the wave celerity, L the wave length, u the horizontal water
particle velocity and x the horizontal coordinate at the still water level.
The other is the Stokes second definition, which is given as

$$c = \frac{\int_0^L \int_{-h}^{\eta} (c + u)dzdx}{\int_0^L \int_{-h}^{\eta} dzdx} \quad \dotfill (2)$$

in which h is the depth of water, η the surface displacement from the still
water level and z the vertical coordinate being taken positive upward from the
still water level. According to this definition, the average momemtum over a
wave length is vanished by addition of a unform motion.

Table 1 shows a classification of such wave theories by the definition of
wave celerity. For the analytical solution of Stokes waves, there are so many
theories, but they all use the first definition. On the contrary, for the
cnoidal waves, there are three theories; the Chappelear theory is derived by the
first definition and the others are done by the second one. In this section,
the Stokes wave theory by Skjelbreia and Hendrickson (1960) and the cnoidal
wave theory by Chappelear (1962) are recalculated using the second definition.

If the moving coordinate system with the wave celerity as shown in Fig. 1
is used for an irrotational steady periodic waves and the dimensionless quanti-
ties are defined by

$$\left. \begin{aligned} &\bar{\phi} = \frac{k\phi}{c\lambda}, \quad \bar{X} = kX, \quad \bar{z} = kz, \quad \bar{\eta} = \frac{k\eta}{\lambda}, \quad \bar{h} = kh, \quad \bar{c} = \sqrt{\frac{k}{g}} c \\ &\bar{Q} = \frac{kQ}{\lambda^2}, \quad \bar{u} = \frac{u}{c\lambda}, \quad \bar{w} = \frac{w}{c\lambda} \end{aligned} \right\} \quad \dots\dots (3)$$

the basic equation can be expressed as

$$\frac{\partial^2 \bar{\phi}}{\partial \bar{X}^2} + \frac{\partial^2 \bar{\phi}}{\partial \bar{z}^2} = 0 \quad \dotfill (4)$$

in which ϕ the velocity potential, k the wave number, λ a small expansion para-

Table 1   Classification of finite amplitude wave theories by
the definition of wave celerity

Wave Theory	Definition of Wave Celerity	
	The first definition	The second definition
Analytical solution (Stokes waves)	Stokes (2nd approx., 1880) Tanaka (3rd approx., 1953) De (5th approx., 1955) Skjelbreia (3rd approx., 1959) Skjelbreia & Hendrickson (5th approx., 1960) Bretschneider (5th approx., 1960)	Authors (4th approx., 1972)
Analytical solution (Cnoidal waves)	Chappelear (3rd approx., 1962)	Keulegan & Patterson (1st approx., 1940) Laitone (2nd approx., 1961) Authors (3rd approx., 1972)
Numerical solution (Stokes waves)	Chappelear (1961) Dean (1965)	von Schwind & Reid (1972)

meter which will be determined later, g the acceleration of gravity, Q the Bernoulli constant, w the vertical water particle velocity and X the abscissa in the steady state coordinate system. The dimensionless velocity potential $\bar{\phi}$ is defined as

$$\bar{u} = \frac{\partial \bar{\phi}}{\partial \bar{X}}, \quad \bar{w} = \frac{\partial \bar{\phi}}{\partial \bar{z}} \quad \dots\dots\dots\dots\dots\dots(5)$$

The boundary conditions at the bottom and at the water surface are given respectively as

$$\frac{\partial \bar{\phi}}{\partial \bar{z}} = 0 ; \quad \bar{z} = -\bar{h} \quad \dots\dots\dots\dots\dots\dots(6)$$

$$\frac{\partial \bar{\phi}}{\partial \bar{z}} + \frac{\partial \bar{\eta}}{\partial \bar{X}} - \lambda \frac{\partial \bar{\eta}}{\partial \bar{X}} \frac{\partial \bar{\phi}}{\partial \bar{X}} = 0 ; \quad \bar{z} = \lambda \bar{\eta} \quad \dots\dots\dots(7)$$

$$-\bar{c}^2 \frac{\partial \bar{\phi}}{\partial \bar{X}} + \bar{\eta} + \lambda \Big[\frac{1}{2} \bar{c}^2 \Big\{ \Big(\frac{\partial \bar{\phi}}{\partial \bar{X}}\Big)^2$$

$$+ \Big(\frac{\partial \bar{\phi}}{\partial \bar{z}}\Big)^2 \Big\} + \bar{Q} \Big] = 0 ; \quad \bar{z} = \lambda \bar{\eta} \quad \dots\dots\dots\dots(8)$$
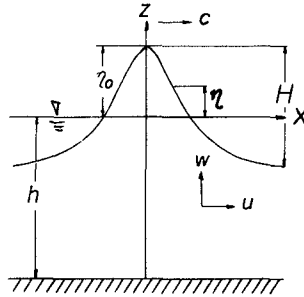
Fig. 1   Definition sketch of coordinate system used

The perturbation method is able to be applied in order to obtain the approximate solution, as a small parameter λ is included in the above equations. According to the perturbation method of Skjelbreia and Hendrickson, the velocity potential in a series form satisfying the Laplace equation and the boundary condition at the bottom as well as the corresponding wave profile are assumed to the fourth order approximation as follows:

$$\bar{\phi} = (A_{01} + \lambda A_{02} + \lambda^2 A_{03} + \lambda^3 A_{04}) \bar{X} + (A_{11} + \lambda^2 A_{15}) \cosh(\bar{h} + \bar{z}) \sin \bar{X}$$

$$+ (\lambda A_{22} + \lambda^3 A_{24}) \cosh 2 (\bar{h} + \bar{z}) \sin 2\bar{X} + \lambda^2 A_{33} \cosh 3 (\bar{h} + \bar{z}) \sin 3 \bar{X} + \lambda^3 A_{44} \cosh 4 (\bar{h} + \bar{z}) \sin 4 \bar{X} \cdots (9)$$

$$\bar{\eta} = \cos \bar{X} + (\lambda B_{22} + \lambda^3 B_{24}) \cos 2\bar{X} + \lambda^2 B_{33} \cos 3\bar{X} + \lambda^3 B_{44} \cos 4 \bar{X} \quad \dots\dots\dots\dots\dots\dots\dots\dots\dots\dots\dots(10)$$

in which A_{ij} and B_{ij} are the coefficients to be determined. The first term in Eq. (9) being also harmonic function is different from the assumption by Skjelbreia and Hendrickson as already pointed out by Stokes (1880). Furthermore, the following equations are assumed for the Bernoulli constant and the wave celerity

$$\bar{Q} = C_3 + \lambda^2 C_4 \quad \dots\dots\dots\dots\dots\dots\dots\dots\dots\dots\dots\dots\dots\dots(11)$$

$$\bar{c}^2 = C_0^2 (1 + \lambda^2 C_1) \quad \dots\dots\dots\dots\dots\dots\dots\dots\dots\dots\dots\dots\dots(12)$$

in which C_i is the coefficient to be determined.

If Eqs. (9), (10), (11) and (12) are substituted into a set of the boundary condition at the free surface, Eqs. (7) and (8), the coefficients A_{ij}, B_{ij} and C_i are determined from the grouped powers of λ and sub-grouped powers of $\cos(nX)$ and $\sin(nX)$ according to the procedure of Skjelbreia and Hendrickson. The coefficients are finally determined as

$$A_{01} = 0, \quad A_{03} = 0, \quad A_{11} = \frac{1}{\sinh kh}, \quad A_{13} = -\frac{(5 \cosh^2 kh + 1) \cosh^2 kn}{8 \sinh^5 kh} - \frac{A_{02}}{\sinh kh}$$

$$A_{22} = \frac{3}{8 \sinh^4 kh}, \quad A_{24} = \frac{192 \cosh^8 kh - 424 \cosh^6 kh - 312 \cosh^4 kh + 480 \cosh^2 kh - 17}{768 \sinh^{10} kh}$$

$$- \frac{3 A_{02}}{8 \sinh^4 kh}, \quad A_{33} = \frac{-4 \cosh^2 kh + 13}{64 \sinh^7 kh}$$

$$A_{44} = \frac{80 \cosh^6 kh - 816 \cosh^4 kh + 1338 \cosh^2 kh - 197}{1536 (-1 + 6 \cosh^2 kh) \sinh^{10} kh}$$

$$\left. \right\} \,..(13)$$

$$B_{22} = \frac{(2 \cosh^2 kh + 1) \cosh kh}{4 \sinh^3 kh}$$

$$B_{24} = \frac{272 \cosh^9 kh - 504 \cosh^7 kh - 192 \cosh^5 kh + 322 \cosh^3 kh + 21 \cosh kh}{384 \sinh^9 kh}$$

$$B_{33} = \frac{24 \cosh^6 kh + 3}{64 \sinh^6 kh}$$

$$B_{44} = \frac{768 \cosh^{11} kh - 448 \cosh^9 kh - 48 \cosh^7 kh + 48 \cosh^5 kh + 106 \cosh^3 kh - 21 \cosh kh}{384 (6 \cosh^2 kh - 1) \sinh^9 kh}$$

$$\left. \right\} \,..(14)$$

$$C_0^2 = \tanh kh, \quad C_1 = \frac{8 \cosh^4 kh - 8 \cosh^2 kh + 9}{8 \sinh^4 kh} + 2 A_{02}$$

$$C_3 = -\frac{1}{4 \sinh kh \cosh kh} + \frac{\sinh kh}{\cosh kh} A_{02}$$

$$C_4 = \frac{4 \cosh^6 kh + 16 \cosh^4 kh - 38 \cosh^2 kh + 9}{64 \sinh^7 kh \cosh kh} + \frac{4 \cosh^4 kh + 5}{8 \sinh^3 kh \cosh kh} A_{02}$$

$$+ \frac{2 \sinh kh}{\cosh kh} A_{02}^2 + \frac{\sinh kh}{\cosh kh} A_{04}$$

$$\left. \right\} \,...(15)$$

The above formulation by the authors coincides with the one by Skjelbreia and Hendrickson, if the terms of A_{02} and A_{04} are vanished.

Applying the Stokes second definition of wave celerity expressed by Eq. (2) to determine the coefficients A_{02} and A_{04}, the calculation finally yields

$$A_{02} = -\frac{\cosh kh}{2 kh \sinh kh}$$

$$A_{04} = \frac{4 \cosh^7 kh - 20 \cosh^5 kh + 16 \cosh^3 kh - 9 \cosh kh}{32 kh \sinh^7 kh} - \left(\frac{\cosh kh}{2 kh \sinh kh} \right)^2$$

$$\left. \right\} \dots\dots\dots\dots(16)$$

Therefore, the wave celerity and the horizontal and vertical water particle velocities are written respectively as

$$\frac{c}{\sqrt{gh}} = \sqrt{\frac{\tanh kh}{kh}(1+\lambda^2 C_1)} \quad \cdots\cdots\cdots\cdots\cdots\cdots\cdots\cdots\cdots\cdots\cdots\cdots\cdots\cdots\cdots\cdots (17)$$

$$\frac{u}{c} = \lambda^2 A_{02} + \lambda^4 A_{04} + (\lambda A_{11} + \lambda^3 A_{13})\cosh h(h+z)\cos kX + 2(\lambda^2 A_{22} + \lambda^4 A_{24})\cosh 2k(h+z)\cos 2kX$$

$$+ 3\lambda^3 A_{33}\cosh 3k(h+z)\cos 3kX + 4\lambda^4 A_{44}\cosh 4k(h+z)\cos 4kX \quad \cdots\cdots\cdots\cdots (18)$$

$$\frac{w}{c} = (\lambda A_{11} + \lambda^3 A_{13})\sinh k(h+z)\sin kX + 2(\lambda^2 A_{22} + \lambda^4 A_{24})\sinh 2k(h+z)\sin 2kX$$

$$+ 3\lambda^3 A_{33}\sinh 3k(h+z)\sin 3kX + 4\lambda^4 A_{44}\sinh 4k(h+z)\sin 4kX \quad \cdots\cdots\cdots\cdots\cdots (19)$$

The small parameter λ is also expressed as

$$2(\lambda + \lambda^3 B_{33}) = kH \quad \cdots\cdots\cdots\cdots\cdots\cdots\cdots\cdots\cdots\cdots\cdots\cdots\cdots\cdots\cdots\cdots\cdots\cdots\cdots (20)$$

in which H is the wave height. It is apparent from the definition of wave celerity that the wave celerity by both the definitions coincides in deep water waves. The horizontal water particle velocity corresponds to the one to be superposed the steady current of higher order term in the wave theory, in which the average mass transport vanishes, on the periodic motion of water particle.

On the other hand, the Chappelear cnoidal wave theory by the first definition to the third approximation is transformed into the theory by the second definition, if only substituting the expressions for horizontal water particle velocity and surface profile into Eq. (2) through a tedious calculation. The calculation yields

$$\begin{aligned}
\frac{c}{\sqrt{gh}} = 1 &+ (L_3 + L_0\kappa^2 S_1) + \Big[-\frac{1}{4}L_0^2\kappa^2 + \Big\{5L_0 L_3\kappa^2 + \frac{3}{2}L_0^2\kappa^2(1+\kappa^2)\Big\}S_1 \\
&- \frac{3}{4}L_0^2\kappa^4 S_2 + L_0^2\kappa^4 S_1^2\Big] + \Big[-\frac{63}{80}L_0^3\kappa^2(1+\kappa^2) - \frac{9}{4}L_0^2 L_3\kappa^2 + \Big\{10 L_0 L_3^2\kappa^2 \\
&+ \frac{27}{2}L_0^2 L_3\kappa^2(1+\kappa^2) + \frac{12}{5}L_0^3\kappa^2(1+\kappa^2)^2 + \frac{1}{80}L_0^3\kappa^2(46+119\kappa^2 \\
&+ 46\kappa^4)\Big\}S_1 + \Big\{-\frac{27}{4}L_0^2 L_3\kappa^4 - \frac{241}{80}L_0^3\kappa^4(1+\kappa^2)\Big\}S_2 + \frac{101}{80}L_0^3\kappa^6 S_3 \\
&+ \Big\{9L_0^2 L_3\kappa^4 + 3L_0^3\kappa^4(1+\kappa^2)\Big\}S_1^2 - \frac{3}{2}L_0^3\kappa^6 S_1 S_2 + L_0^3\kappa^6 S_1^3\Big]
\end{aligned} \quad \cdots\cdots\cdots\cdots (21)$$

in which κ is the modulus of Jacobian elliptic function, L_0 and L_3 the expansion parameters which are calculated from the following equation for the second approximation.

$$\begin{aligned}
\frac{H}{h} &= \kappa^2 L_0\Big\{1 + \frac{1}{4}L_0(10 + 7\kappa^2) + 6L_3\Big\} \\
2L_3 &+ L_0\Big(\kappa^2 + \frac{E}{K}\Big) + L_0^2\Big\{-\frac{1}{5}(1-6\kappa^2-9\kappa^4) + 2(1+\kappa^2)\frac{E}{K}\Big\} + 6L_0 L_3\Big(\kappa^2 + \frac{E}{K}\Big) + L_3^2 = 0
\end{aligned} \quad \cdots (22)$$

And S_1, S_2 and S_3 are given as

$$\begin{aligned}
S_1 &= \frac{1}{L}\int_0^L \mathrm{sn}^2\Big(\frac{\sqrt{3L_0}}{2h}X\Big)dX = \frac{1}{\kappa^2}\Big(1 - \frac{E}{K}\Big) \\
S_2 &= \frac{1}{L}\int_0^L \mathrm{sn}^4\Big(\frac{\sqrt{3L_0}}{2h}X\Big)dX = \frac{1}{3\kappa^4}\Big\{-2(1+\kappa^2)\frac{E}{K} + \kappa^2 + 2\Big\} \\
S_3 &= \frac{1}{L}\int_0^L \mathrm{sn}^6\Big(\frac{\sqrt{3L_0}}{2h}X\Big)dX = \frac{1}{15\kappa^6}\Big\{(-8\kappa^4 - 7\kappa^2 - 8)\frac{E}{K} + 4\kappa^4 + 3\kappa^2 + 8\Big\}
\end{aligned} \quad \cdots\cdots\cdots\cdots (23)$$

in which K and E are the complete elliptic integrals of the first and the second kind respectively. In the limiting case where $\kappa = 1$, the cnoidal waves become the solitary wave and the wave celerity by both the definitions coincides as

$$\frac{c}{\sqrt{gh}} = 1 + (L_3 + L_0) + (3L_0^2 + 5L_0L_3) + \left(10L_0L_3^2 + 27L_0^2L_3 + \frac{57}{5}L_0^3\right) \quad \dots \dots \dots \dots (24)$$

The other wave characteristics in the steady state are the same as those by the first definition.

   In addition, it is found that the expressions for wave characteristics of the second order approximate solution of cnoidal wave theory by Chappelear using the second definition agree exactly with those by Laitone (1965), if the expansion
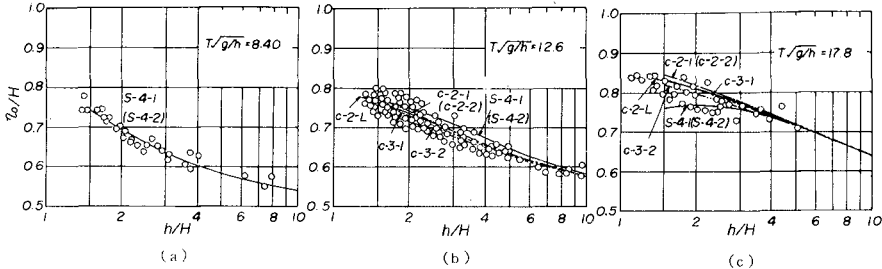
Fig. 2   Comparison for wave crest height above still water level

parameters L_0 and L_3 in the Chappelear theory are expanded into the power series of H/h and the expression is rewritten into the power series of H/h to the second order of H/h (Yamaguchi-Tsuchiya, 1974).
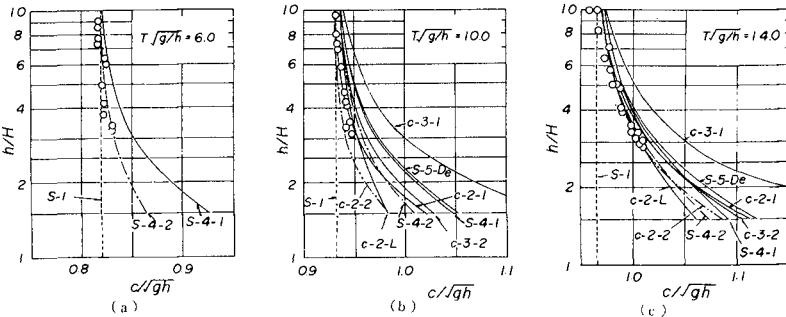
Fig. 3   Comparison for wave celerity(Experimental values shown were
             obtained by Iwagaki and Yamaguchi, 1967)

   Figs. 2, 3 and 4 show the comparisons between the theoretical curves and the experimental results for wave crest height above the still water level, wave celerity and vertical distribution of horizontal water particle velocity at phase of wave crest respectively, in which η_0 is the wave crest height above the still water level and T the wave period.   In these figures, the notation S-1 indicates the theoretical curves for the Airy waves, S-4-1 and S-4-2 those for the Stokes waves of the fourth order approximation by the first and the second definition, S-5-De for the Stokes waves of the fifth order approximation by De (1955), c-2-1, c-2-2, c-3-1 and c-3-2 for the Chappelear cnoidal waves of the second and the third approximation by both the definitions, and c-2-L for the cnoidal waves of the second approximation by the second definition which Laitone (1965) converted from the depth below the wave trough to the mean water depth, respectively.   The experimental results tend to agree more better with the theoretical curves by the second definition, although it is not capable of making clear enough which defini-

tion in the wave theory is more applicable for the estimation of horizontal
water particle velocity, because of much scatter of the experimental values. It
is however concluded from many examples of the comparison that the fourth order
approximate solution of Stokes waves and the second one of cnoidal waves calcu-
lated using the second definition of wave celerity are more applicable for the
estimation of wave characteristics. Therefore, these theories are used in the
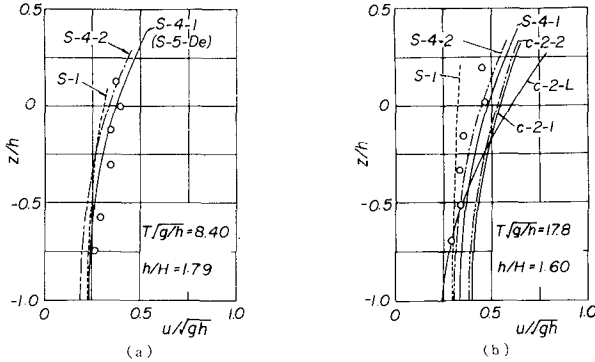
Fig. 4 Comparison for vertical distribution of horizontal water
        particle velocity at phase of wave crest

calculation of wave force in this paper.

    (2) Wave Force Equation With the frame of
reference shown in Fig. 5, the horizontal wave
force dF on a segment dz of a pile can be
expressed as

$$dF = \frac{\rho}{2} C_D A\, u|u|\,dz + \rho C_M\, V\, \frac{du}{dt}\, dz \quad \ldots \ldots \ldots (25)$$

in which ρ is the density of fluid, C_D the drag
coefficient, C_M the inertia coefficient, du/dt
the horizontal water particle acceleration, A
the projected area perpendicular to the hori-
zontal water particle velocity and V the dis-
placed volume of the fluid. For a vertical
circular cylindrical pile of the diameter D,

Fig. 5 Schematic diagram of wave
        force system used

A and V are given by A = D and V = $\pi D^2/4$ respectively. This is well-known as the
Morison wave force equation (Morison, 1950). The first term indicates the drag
force and the second the inertia force. Then, the total wave force is obtained
by integrating Eq. (25) from the bottom to the water surface as

$$F = \int_{h}^{\eta} \frac{\rho}{2} C_D\, A\, u|u|\,dz + \int_{h}^{\eta} \rho C_M\, V\, \frac{du}{dt}\, dz \quad \cdots\cdots\cdots\cdots\cdots\cdots\cdots\cdots\cdots\cdots\cdots (26)$$

    The horizontal water particle acceleration by the Stokes waves using the
second definition at phase of x = 0 can be calculated by Eq. (18) as

$$\frac{du}{dt} = -c\sigma \Big[\{ F_1 \cosh k(h+\eta) - F_0 F_1 \cosh k(h+\eta) - \frac{1}{2} F_1 F_2 \cosh 3k(h+\eta) \} \sin \sigma t + \{ 2F_2 \cosh 2k(h+\eta)$$

$$- 2F_0 F_2 \cosh 2k(h+\eta) - \frac{1}{2} F_1^2 + F_1 F_3 \cosh 4k(h+\eta) \} \sin 2\sigma t + \{ 3F_3 \cosh 3k(h+\eta) - \frac{3}{2} F_1 F_2$$

$$\cosh k(h+\eta) \} \sin 3\sigma t + \{ 4F_4 \cosh 4k(h+\eta) - 2F_1 F_3 \cosh 2k(h+\eta) - F_2^2 \} \sin 4\sigma t \Big] \ldots (27)$$

in which

$$F_0 = \lambda^2 A_{02} + \lambda^4 A_{04} \ , \quad F_1 = \lambda A_{11} + \lambda^3 A_{13} \ , \quad F_2 = 2(\lambda^2 A_{22} + \lambda^4 A_{24}) \ , \quad F_3 = 3\lambda^3 A_{33} \ , \quad F_4 = 4\lambda^4 A_{44} \dots (28)$$

and $\sigma(=2\pi/T)$ is the angular frequency.

If the inertia coefficient is assumed to be constant over a water depth, the total inertia force F_I is expressed by substituting Eq. (25) into the second term of Eq. (26) and integrating it from the bottom to the water surface as

$$F_I = -\rho C_M V c^2 \left[\{ F_1 \sinh k(h+\eta) - F_0 F_1 \sinh k(h+\eta) - \frac{1}{6} F_1 F_2 \sinh 3k(h+\eta) \} \sin \sigma t \right.$$

$$+ \{ F_2 \sinh 2k(h+\eta) - F_0 F_2 \sinh 2k(h+\eta) - \frac{1}{2} F_1^2 k(h+\eta)$$

$$\left. - \frac{1}{4} F_1 F_3 \sinh 4k(h+\eta) \} \sin 2\sigma t + \{ F_3 \sinh 3k(h+\eta) - \frac{3}{2} F_1 F_2 \sinh k(h+\eta) \} \sin 3\sigma t \right\} \dots (29)$$

$$+ \{ F_4 \sinh 4k(h+\eta) - F_1 F_3 \sinh 2k(h+\eta) - F_2^2 k(h+\eta) \} \sin 4\sigma t$$

The total drag force F_D can be computed by integrating the following equation according to the Simpson rule, as the mathematical formulation for the total drag force is difficult.

$$F_D = \frac{\rho}{2} C_D A \int_{-h}^{\eta} u|u| dz \quad \dots (30)$$

After all, the total wave force F is given as the sum of the drag force by Eq. (30) and the inertia force by Eq. (29).

$$F = F_D + F_I \quad \dots (31)$$

On the contrary, if the second order approximate solution of cnoidal waves is used in place of the Stokes waves, the total inertia force can be written as

$$F_I = -\rho C_M V \frac{4K\sqrt{gh}}{T} h \left(1 + \frac{\eta}{h} \right) \text{sn} \gamma t \, \text{cn} \gamma t \, \text{dn} \gamma t \left[L_0 \kappa^2 + L_0^2 \kappa^2 (1+\kappa^2) + 5 L_0 L_3 \kappa^2 + 2 L_0^2 \kappa^4 \text{sn}^2 \gamma t \right.$$

$$+ \frac{1}{2} \{ L_0^2 \kappa^2 (1+\kappa^2) - 3 L_0^2 \kappa^4 \text{sn}^2 \gamma t \} \left(1 + \frac{\eta}{h} \right)^2 - \left(\frac{c}{\sqrt{gh}} \right)^{-1} \{ L_0^2 \kappa^2 \left(1 - \frac{E}{K} \right) - L_0^2 \kappa^4 \text{sn}^2 \gamma t \} \right] \cdot (32)$$

in which sn, cn and dn are the Jacobian elliptic functions with a real period and

$$\frac{\eta}{h} = 2L_3 + L_0(1+\kappa^2) - L_0 \kappa^2 \text{sn}^2 \gamma t + L_3^2 + \frac{3}{20} L_0^2 (12 + 23\kappa^2 + 12\kappa^4) + 6L_0 L_3 (1+\kappa^2)$$

$$- \frac{5}{2} L_0^2 \kappa^2 (1+\kappa^2) \text{sn}^2 \gamma t - 6 \kappa^2 L_0 L_3 \text{sn}^2 \gamma t + \frac{3}{4} L_0^2 \kappa^4 \text{sn}^4 \gamma t \quad \dots (33)$$

$$\frac{c}{\sqrt{gh}} = 1 + L_3 + \left(1 - \frac{E}{K} \right) \{ L_0 + (2 + \kappa^2 - \frac{E}{K}) L_0^2 + 5 L_0 L_3 \} \ , \quad \gamma = \frac{2K}{T}$$

The total drag force can be obtained by the similar numerical integration to the case of the Stokes waves described already.

(3) Estimation of Drag and Inertia Coefficients If the drag and inertia coefficients are assumed to be constant over a wave period and the vertical direction in water depth, they can be estimated respectively by the following equations using the experimental results of the time variations of total wave force and the corresponding water surface displacement. For the estimation of the drag coefficient, it can be expressed as

$$C_D = \frac{F_{\eta_0}}{(\rho/2) A \int_{-h}^{\eta_0} u|u| dz} \quad \dots\dots\dots\dots\dots\dots\dots\dots\dots\dots\dots\dots\dots (34)$$

in which F_{η_0} is the total wave force measured at phase of wave crest.

Using the finite amplitude wave theories, the inertia force can not be separated from the total wave force unlike the method of estimation by the small amplitude wave theory, because the phase of zero points in the time variations of water surface displacement and horizontal water particle velocities does not coincide each other and the phase of the latter changes slightly with a location in water. Accordingly, for the estimation of the inertia coefficient, it can be expressed as

$$C_M = \frac{F_{\eta=0} - (\rho/2) C_D A \int_{-h}^{0} u|u| dz}{\rho V \int_{-h}^{0} (du/dt) dz} \quad \dots\dots\dots\dots\dots\dots\dots\dots\dots\dots\dots (35)$$

in which $F_{\eta=0}$ is the total wave force measured at phase of zero point in the time variation $\eta=0$ of water surface displacement.

Furthermore, for the representation of the drag coefficient, the Keulegan-Carpenter number (1958) which shows unsteadiness of wave motion is taken in addition to the wave Reynolds number. The Reynolds number R_e and the Keulegan-Carpenter number KC are defined respectively as

$$Re = \frac{\sqrt{u_c^{2*}}\, D}{\nu}, \qquad KC = \frac{\sqrt{u_c^{2*}}\, T}{D} \quad \dots\dots\dots\dots\dots\dots\dots\dots\dots\dots (36)$$

in which ν is the kinematic viscosity and u_c^{2*} the averaged value of squared horizontal water particle velocity at phase of wave crest on an instantaneous water depth, which is also defined as

$$u_c^{2*} = \frac{\int_{-h}^{\eta_0} u^2\, dz}{h + \eta_0} \quad \dots\dots\dots\dots\dots\dots\dots\dots\dots\dots\dots\dots\dots (37)$$

CHARACTERISTICS OF DRAG AND INERTIA COEFFICIENTS

(1) Experimental Apparatus and Procedure The wave tank used in the experiment is 78 m long, 1.0 m wide and 1.5 m deep which has the sloping model beach of 1/100, 45 m long. The experimental apparatus is composed of the measurement system of wave force and a test pile set on the rigid frame at the location of about 53 m distance from the wave generator. The measurement system of wave force is to measure total wave force from the difference of the strain at two points on a pile generated by an action of waves. In the experiment, time variations of total wave force on a pile and surface displacement were measured in the wide range of wave characteristics. The wave characteristics used in the experiment are tabulated in Table 2. The previous experimental and observed results in addition to the experimental result of the authors are considered, as their outlines are shown in Table 3.

(2) Drag Coefficient Fig. 6 shows a relation between the drag coefficient and the wave Reynolds number. The coefficients were estimated by the fourth order approximate solution of Stokes waves as shown in Fig. 6 (a) and by the second approximate solution of cnoidal waves in Fig. 6 (b). In the figure, the experimental results by the authors, Goda, Burton et al., Jen and Ross and the observed ones by Morison et al. and Wiegel et al. are indicated. In the results by Ross and Morison et al., the maximum wave force was given only. However, the drag force was predominant taking into account of the wave-pile characteristics, so that the drag coefficient could be estimated from the maximum

Table 2 Wave characteristics used in experiment

Wave period T sec	Depth of water h cm	T√g/h	Diameter of pile D cm	Wave height H cm
1.5	55.6	6.30	14.0	9.3 ~ 37.5
1.5	55.6	6.30	28.0	12.4 ~ 34.2
2.0	55.6	8.40	14.0	7.8 ~ 40.9
2.0	55.6	8.40	21.0	6.6 ~ 33.4
2.0	55.6	8.40	28.0	6.9 ~ 40.7
2.5	55.6	10.5	14.0	5.4 ~ 43.2
2.5	55.6	10.5	21.0	5.6 ~ 36.6
2.5	55.6	10.5	28.0	7.7 ~ 47.6
3.0	55.6	12.6	7.0	4.9 ~ 44.2
3.0	55.6	12.6	14.0	4.7 ~ 46.9
3.0	55.6	12.6	21.0	4.5 ~ 37.4
3.0	55.6	12.6	28.0	4.7 ~ 46.9
2.5	27.8	14.8	7.0	5.3 ~ 23.6
2.5	27.8	14.8	14.0	4.9 ~ 23.6
3.0	27.8	17.8	7.0	4.2 ~ 21.2
2.6	41.7	12.6	7.0	5.5 ~ 31.6
1.8	14.0	12.6	7.0	5.0 ~ 12.7

Table 3 Outline of previous results of experiment and observation of wave force on a pile

Researcher	Year	Wave period T sec	Depth of water h cm	Wave height H cm	Diameter of pile D cm	Wave Reynolds number Re×10⁻⁴
Morison et al.	1953	4.2 ~ 13.3	91.4 ~ 160.6	18.3 ~ 110.0	8.9	2.72~ 20.4
Hademan et al.	1955	1.0 ~ 1.49	30.5 ~ 124.1	12.2 ~ 25.6	1.27 ~ 15.2	0.48~ 8.1
Wiegel et al.	1957	9.1 ~ 18.6	1400.0 ~ 1500.0	134.2 ~ 625.0	32.4 , 61.0	19.0 ~ 130.0
Ross	1959	3.75 ~ 16.0	153.0 ~ 458.0	58.0 ~ 235.0	32.4	21.0~ 86.0
Goda	1964	1.37 ~ 7.96	100.0 , 130.0	9.3 ~ 80.1	7.6 , 14.0	1.43~ 21.8
Jen	1967	0.91 ~ 5.30	91.4	2.1 ~ 18.3	15.2	0.38~ 5.7
Burton et al.	1970	0.81 ~ 1.67	61.0	1.0 ~ 25.4	9.4 ~ 10.2	0.67~ 5.1

wave force. Also, the drag coefficients by the authors, Jen and Burton et al. are limited in the case where the drag force is more than about 15 % of the maximum total wave force. The curves shown in the figure are the drag coefficient in a uniform flow by Vennard, Goldstein and Fage et al. respectively which differs each other corresponding to the extent of turbulence intensity near the critical Reynolds number. There is hardly prominent difference on the whole trend between the results by the Stokes waves and those by the cnoidal waves. It is found from the figure, in spite of large scatter of the results that the drag coefficient tends to decrease with the increase of the wave Reynolds number in the ranges of $R_e < 2 \times 10^5$ and $R_e > 10^5$. Accordingly, the drag coefficient is considerably different at the same Reynolds number. This may be not only due to the scatter caused by experimental error but also due to the dependence on the other parameter affecting the drag coefficient of a pile in wave motion, in addition to the wave

Fig. 7 Relation between drag coefficient and wave Reynolds number (2)

Fig. 6 Relation between drag coefficient and wave Reynolds number (1)

Reynolds number.

Fig. 7 shows the similar results to Fig. 6, in the case where the fourth order approximate solution of the Stokes wave theory by the first definition and the Airy wave theory were used. In this figure, the drag coefficient C_{D41} was obtained by the Stokes wave theory and C_{D1} by the Airy wave theory. The drag coefficient estimated using the Stokes wave theory by the first definition becomes slightly smaller than the one by the second definition and there is little difference in the relation with the wave Reynolds number. On the contrary, the drag coefficient by the Airy wave theory is larger than the results by the finite amplitude wave theories and the range of scatter is wider, because the wave crest height above the still water level and the horizontal water particle velocity are underestimated.

The Keulegan-Carpenter number is well-known as one of the dimensionless pararmeters to be described the unsteadiness of wave motion. Figs. 8 and 9 are the drag coefficient described in relation to the wave Reynolds number and the Keulegan-Carpenter number. The curve indicated by broken line was obtained being classified the data into some intervals of the wave Reynolds number and the Keulegan-Carpenter number and averaged. Although the experimental values of drag coefficient are scattered as shown in Figs. 6 and 7, the drag coefficient at a constant wave Reynolds number generally decreases with the increase of the Keulegan-Carpenter number. It is supposed refering to the Bidde (1970) experiment that the reason can be explained as; the trend in the small value of the Keulegan-Carpenter number approaches the Vennard curve in a uniform flow with small turbulence intensity and the trend in large value corresponds to the Fage and Warsap curve in a uniform flow with large turbulence

(a)

(b)

Fig. 8   Relation between drag coefficient and wave Reynolds number with Keulegan-Carpenter number (1)

intensity. There is similar
trend in the relation between
the drag coefficient estimated
by the cnoidal waves and the
above parameters.

(3) Inertia Coefficient
Fig. 10 is a relation between
the inertia coefficient and
the ratio of wave height to
pile diameter. The upper
figure was obtained using the
Stokes wave theory by the second
definition and the lower by the
cnoidal waves. The curve shows
a general trend obtained by
averaging experimental values.
The coefficient by both the
theories tends to decrease
slightly with the increase of
the ratio, except for the observed
values by Wiegel et al. (1957). The
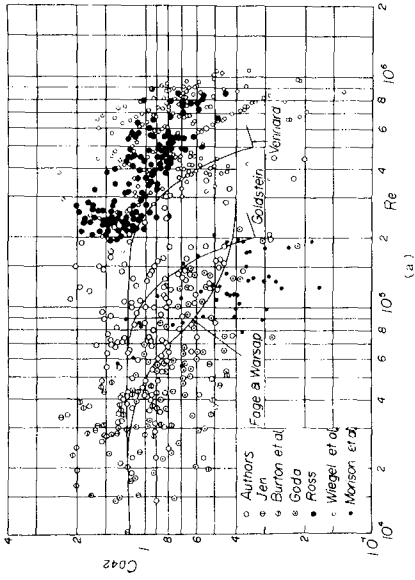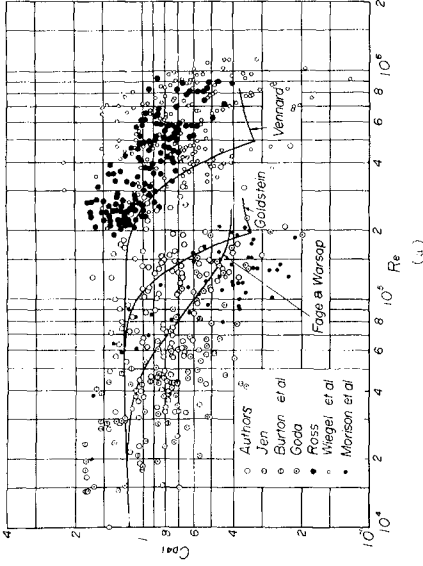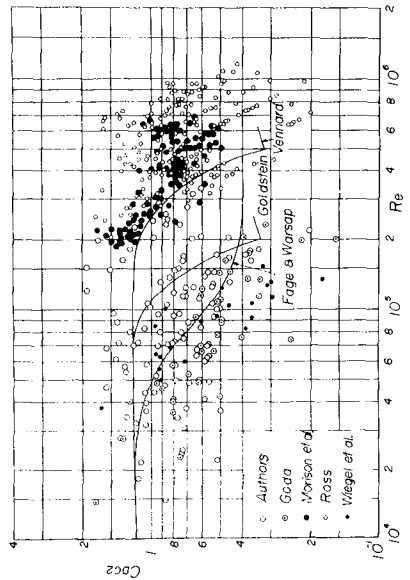

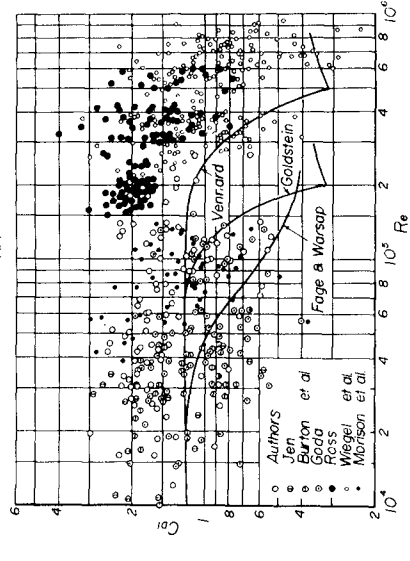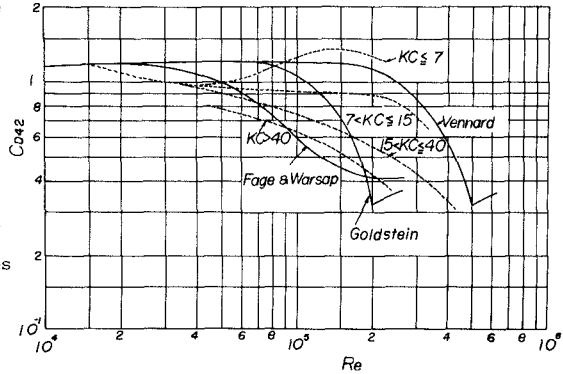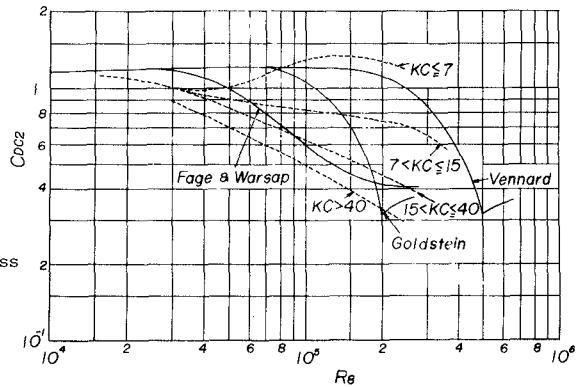Fig. 9 Relation between drag coefficient
and wave Reynolds number with
Keulegan-Carpenter number (2)

increase of the ratio means the increase of drag force in the total wave force.
Therefore, this may be due to the vortex shedding behind the pile in the pre-
dominant region of drag force, according to the Sarpkaya and Garrison (1963)
study on the inertia coefficient of a pile in a unidirectional accelerated flow.

Fig. 11 is also the similar relation. The wave theories used in the esti-
mation of the coefficient are the Stokes wave theory by the first definition of
which result is shown in Fig. 11(a) and the Airy wave theory in Fig. 11(b),
respectively. It is clear from the comparison between Figs. 10 and 11 that there
is hardly prominent influence of wave nonlinearity on the inertia coefficient,
because the inertia coefficient is changed nothing but slightly larger than the
one by the finite amplitude wave theories.
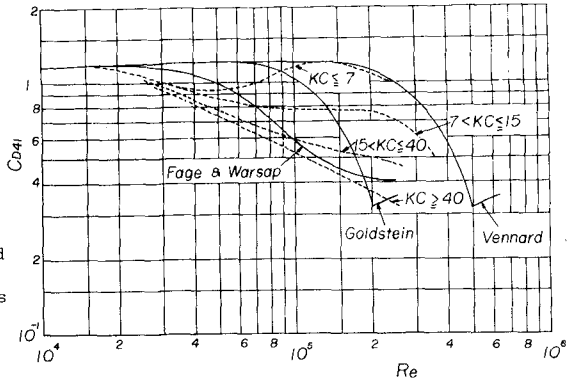
TOTAL WAVE FORCE

(1) Time Variations of Total Wave Force   Keulegan and Carpenter (1958)
estimated the phase variation of the drag and inertia coefficients from the
results of experiment of wave force on a horizontal circular pile using the
Airy wave theory. In so far as the finite amplitude wave theories are used,
however, such an analysis is so difficult that the effect of the phase variation
of the coefficients on the time variation of total wave force is investigated
from comparison between the theoretical curves and the experimental results of
the time variation of total wave force. In this case, the coefficients are
assumed to be constant over a wave period.

Some examples of the comparison are shown in Fig. 12 of which the upper
figure is the corresponding time variation in the water surface displacement.
In this figure, the solid line indicates the theoretical total wave force by
the Stokes waves, the two-dotted chain line the one by the cnoidal waves and
the broken line and the one-dotted chain line indicate respectively the theore-
tical drag and inertia force by the Stokes waves. The coefficients in themselves
estimated directly from the experimental results by the method mentioned previous-
ly were used in the theoretical computation of total wave force. The experimetal
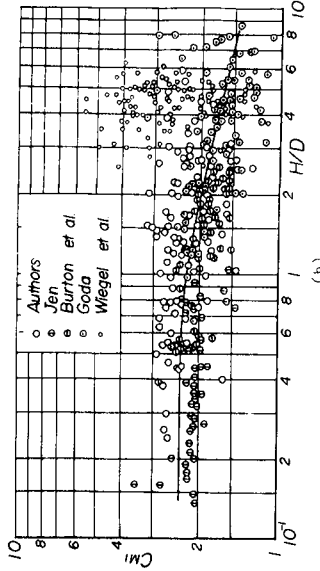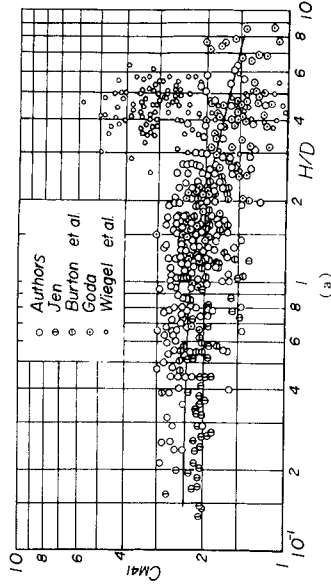
Fig. 11 Relation between inertia coefficient and ratio of wave height to pile diameter (2)
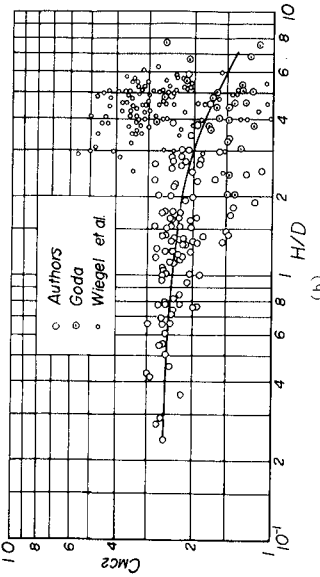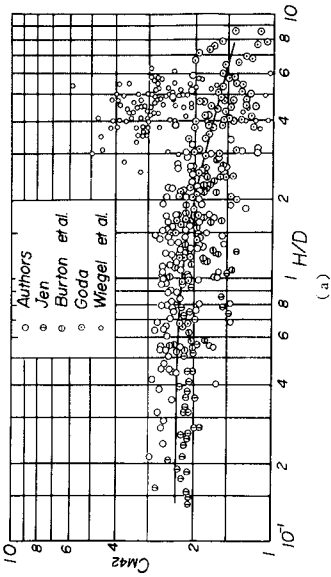
Fig. 10 Relation between inertia coefficient and ratio of wave height to pile diameter (1)
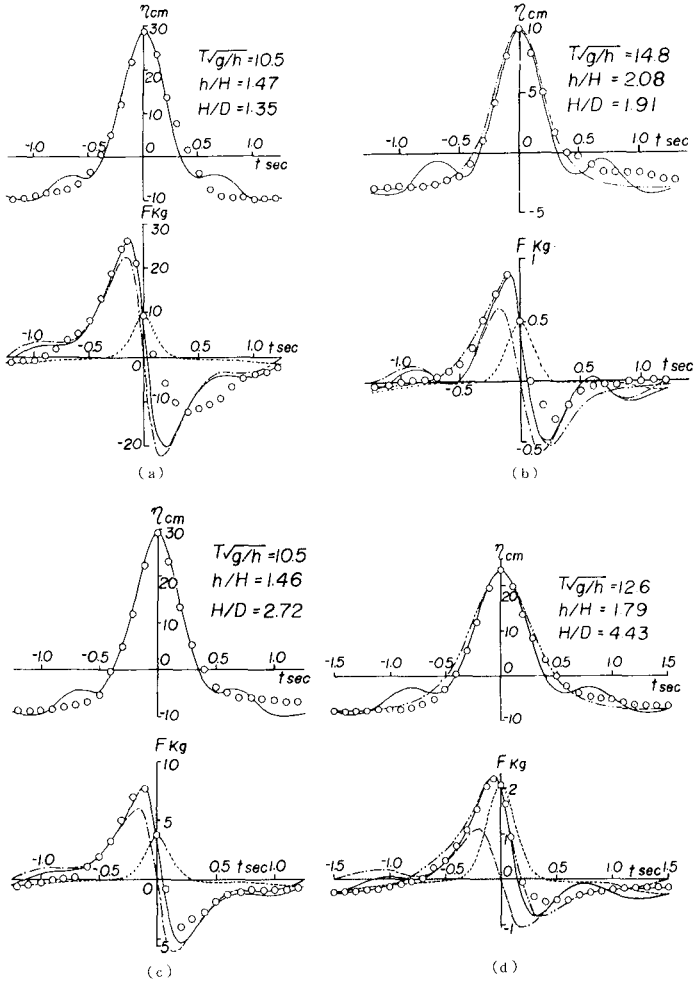
Fig. 12   Time variations of water surface displacement and total
          wave force in comparison with theories

time variation of total wave force and the corresponding water surface displace-
ment agree well with the theoretical curves by the Stokes waves within the range
of $T\sqrt{g/h} \leq 12.6$ and those by the cnoidal waves within the range of $T\sqrt{g/h} \geq 14.8$.
From the above consideration, it is expected that the phase variation of the
coefficients has not so serious effect on the computed results of total wave force.

Fig. 13 is another comparison of the
time variation of total wave force. In this
figure, the solid line indicates the theore-
tical total wave force including the effect of
the convective term in water particle acceler-
ation and the broken line the one not including
the convective term.   The influence of the
convective term on the total wave force is
only a few percent at most, but it would
affect the maximum total wave force when the
inertia force becomes predominant.

(2)   Maximum Total Wave Force   The ap-
plicability of the total wave force equation
by finite amplitude wave theories to the
estimation of maximum total wave force is
investigated.   In this case, the wave theo-
ries used are such as the Airy wave, Stokes
wave and cnoidal wave theories explained
already.

Fig. 14 shows one of the comparisons,
where the abscisa gives the measured wave
force or bottom moment and the ordinate is
the computed one.   In this figure, the
fourth order approximate solution of the
Stokes waves by the second definition of
wave celerity, the one by the first defini-
tion and the cnoidal wave theory were used
respectively with the constant drag and
inertia coefficients. There is relatively
good correspondence between them, except for
the experimental values by Goda (1964), in
which the computed results show larger values
than the experimental ones, because the drag
force is predominant in the most of his
experiment and moreover the estimated drag
coefficient is smaller than 1.0 in most
cases. Taking into account of the poor
correspondence between the theoretical
results applying the Airy wave theory and
the experimental ones, as shown in Fig. 15,
the results mentioned above describe the
good efficiency of the wave force equation applying the finite amplitude wave
theories and the appropriateness of selected values of the coefficients in prac-
tical purposes.

(a)

(b)

(c)

Fig. 13   Influence of convective
term in water particle
acceleration on total wave
force

The comparison in the case where both the drag and inertia coefficients were
estimated respectively from the relations proposed by the authors is shown in
Fig. 16.   Although there are some cases where the correspondence becomes poorer
in comparison with Fig. 14, if the inertia coefficient is determined from the
relations proposed, the mutual correspondence becomes better and the range of
scatter narrower in general cases.   It may be worthwhile recommending from the

(a)

(b)

(c)

Fig. 14 Comparison between exper-
imental and computed max-
imum total wave forces (1)
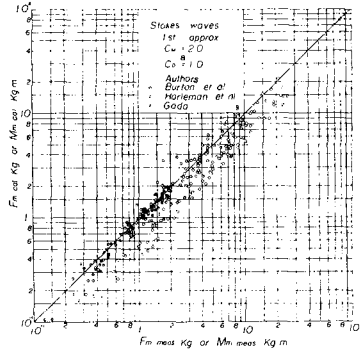
Fig. 15 Comparison between experimental
and computed maximum total wave
forces (2)

above consideration that the estimation of
wave force on a pile by such a method is
more hopeful.

CONCLUSIONS

The Stokes wave theory of the fourth
order approximation by Skjelbreia and Hend-
rickson and the cnoidal wave theory of the
third approximation by Chappelear were re-
calculated using the Stokes second defini-
tion of wave celerity and it was found from
the compariaon with the experimental results
that these theories are more applicable for
the estimation of wave characteristics.

The theories were applied to the wave
force equation by Morison and the drag and
inertia coefficients were estimated from many
experimental results including the previous
studies of wave force on a pile. As a result,
relations between the drag and inertia coef-
ficients and the wave-pile characteristics
were established respectively.

It was shown that the wave force equation
using either the Stokes wave theory or the
cnoidal wave theory and the drag and inertia
coefficients proposed, is very effective to
estimate the maximum total wave force on a
pile due to finite amplitude but nonbreaking
waves.

(a)

(b)

(c)
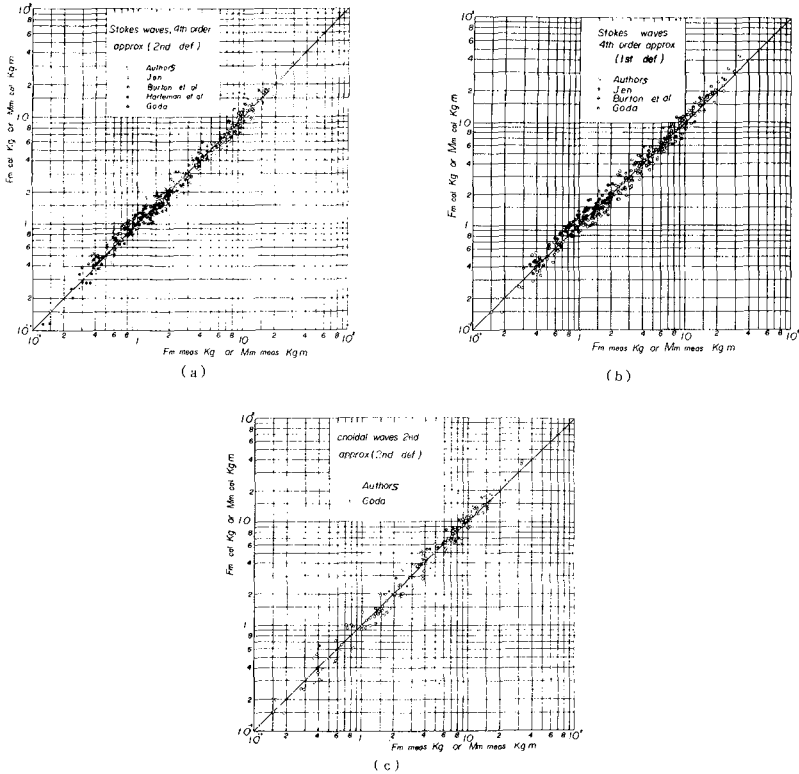
Fig. 16   Comparison between experimental and computed maximum
total wave forces (3)

Although a practical method was proposed for the estimation of total wave force on a vertical circular cylindrical pile within the range of experiment, further investigations should be carried out for the range of higher wave Reynolds number.

REFERENCES

Bidde, D. D. (1970). Wave Forces on a Circular Pile Due to Eddy Shedding, Univ.
    of California, Berkeley, Hydraulic Engg. Laboratory, Tech. Report, HEL 9-16,
    pp. 1-141.
Burton, W. J. and Sorensen, R. M. (1970). The Effects of Surface Roughness on the
    Wave Forces on a Circular Cylindrical Pile, Texas A & M Univ., COE Report,
    No. 121, pp. 1-37.
Chappelear, J. E. (1962). Shallow-Water Waves, Jour. Geophys. Res., Vol. 67,
    No. 12, pp. 4693-4704.
De, S. C. (1955). Contributions to the Theory of Stokes Waves, Proc. Cambridge
    Phil. Soc., No. 51, pp. 713-736.
Goda, Y. (1964). Wave Forces on a Vertical Circular Cylinder; Experiments and a
    Proposed Method of Wave Force Computation, Report of Port & Harbour Tech.
    Res. Inst., No. 8, pp. 1-74.
Harleman, D. R. F. and Shapiro, W. C. (1955). Experimental and Analytical Studies
    of Wave Forces on Offshore Structure, Part 1, MIT Hydrodynamics Laboratory,
    Tech. Report, No. 19, pp. 1-55.
Iwagaki, Y. and Yamaguchi, M. (1967). On the Limiting Condition of Stokes Waves
    and Cnoidal Waves, Proc. 14th Conf. on Coastal Engg., JSCE, pp. 8-16(in
    Japanese).
Jen, Y. (1967). Wave Forces on Circular Cylindrical Piles Used in Coastal Structure,
    Univ. of California, Berkeley, Hydraulic Engg. Laboratory, Tech. Report, HEL
    9-11, pp. 1-94.
Keulegan, G. H. and Carpenter, L. H. (1958). Forces on Cyliders and Plates in
    an Oscillating Fluid, Jour. Res. NBS, Vol. 60, No. 5, pp. 423-440.
Laitone, E. V. (1961). The Second Approximation to Cnoidal and Solitary Waves,
    Jour. Fluid Mech., Vol. 9, pp. 430-444.
Laitone, E. V. (1965). Series Solutions for Shallow Water Waves, Jour. Geophys.
    Res., Vol. 70, No. 4, pp. 995-998.
MacCamy, R. C. and Fuchs, R. A. (1954). Wave Forces on Piles; A Diffraction
    Theory, Tech. Memo. BEB, No. 69, pp. 1-17.
Morison, J. R. (1950). Design of Piling, Proc. 1st Conf. on Coastal Engg., pp.
    254-258.
Morison, J. R., Johnson, J. W. and O'Brien, M. P. (1953). Experimental Studies of
    Forces on Piles, Proc. 4th Conf. on Coastal Engg., pp. 340-370.
Ross, C. W. (1959). Large-Scale Tests of Wave Forces on Piling, Tech. Memo. BEB,
    No. 111, pp. 1-9.
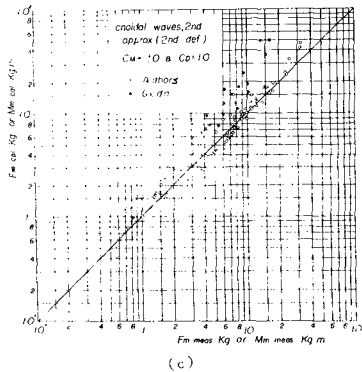Sarpkaya, T. and Garrison, C. J. (1963). Vortex Formation and Resistance in
    Unsteady Flow, Jour. Applied Mech., Vol. 30, No. 1, pp. 16-24.
Skjelbreia, L. and Hendrickson, J. A. (1960). Fifth Order Gravity Wave Theory,
    Proc. 7th Conf. on Coastal Engg., pp. 184-197.
Stokes, G. G. (1880). On the Theory of Oscillatory Waves, Math. Phys. Paper, Vol.
    8, pp. 197-229.
Tsuchiya, Y. and Yamaguchi, M. (1972). Some Considerations on Water Particle
    Velocities of Finite Amplitude Wave Theories, Coastal Engg. in Japan, Vol.
    15, pp. 43-57.
Wiegel, R. L., Beebe, K. E. and Moon, J. (1957). Ocean Wave Forces on Circular
    Cylindrical Piles, Proc. ASCE, Vol. 83, HY2, pp. 89-119.
Yamaguchi, M. and Tsuchiya, Y. (1974). Nonlinear Effect of Waves on Wave Pressure
    and Wave Force on a Large Cylindrical Pile, Proc. JSCE, No. 229, pp. 151-
    163(in Japanese).
Yamaguchi, M. and Tsuchiya, Y. (1974). Relation between Wave Characteristics of
    Cnoidal Wave Theory Derived by Laitone and by Chappelear, Bull. DPRI, Kyoto
    Univ., Vol. 24, Part 3(in preparation).

CHAPTER 106

FORCES FROM FLUID FLOW AROUND OBJECTS

By John H. Nath[1] and Tokuo Yamamoto[2]

Abstract

All hydrodynamic forces on submerged objects are shown to
be due to the acceleration effects of the fluid flow. However,
it is useful to consider separately the influence from the var-
ious ambient flow and local flow conditions. At times certain
aspects of the flow can be ignored, which simplifies the analysis.
Examples are developed for circular cylinders near a plane bound-
ary with a flow direction parallel to the boundary and perpendic-
ular to the cylinder. Potential flow theory predicts that large
vertical forces exist away from the boundary when the cylinder
is against the boundary and that large negative forces exist to-
ward the boundary when the cylinder is positioned a small distance
from the boundary, when the viscous effects are small. When the
cylinder is near the boundary, the added mass coefficient is the
same regardless of the direction of the flow, providing the flow
is perpendicular to the cylinder. In addition, the added mass
coefficient is much larger for cylinders near the boundary than
when they are in a free stream. Good agreement between theory
and laboratory experimentation was obtained for various coeffi-
cients with waves on horizontal cylinders near a plane boundary.

INTRODUCTION

There is an increasing need for accurate information on how
to analyze the fluid dynamic forces on objects constructed for
various types of ocean engineering projects. Structures such as
piers, drill rigs, semi-submersibles, pipe lines, cables, buoy-
ancy elements, ships, barges and so forth, require realistic infor-
mation as to the forces from the major loading activities of the
wind, waves and current. Such forces originate from the fluid mo-
tion or the object motion, or both. Certain amounts of information
exist in the literature on such fluid motions, but much of it is
difficult to understand by the average design engineer.

---

[1]Professor and Director, Environmental Fluid Dynamics Lab. O.S.U.
and Principal, Nath-Eager and Associates, Corvallis, Oregon

[2]Research Engineer, Oregon State University, Corvallis, Oregon, USA

Ideally, one should consider the submerged object to be a part of the boundary conditions for the flow regime. The general pressure distribution is then determined, if possible, for the entire flow regime and then evaluated on the surface of the object. Closed mathematical solutions are obtained whenever possible, which usually involves determining the velocity potential or stream function in the governing equations of fluid motion, (when viscous effects can be ignored), or a solution to some form of the Navier-Stokes equations is at least tried. However, closed solutions are rarely obtained, so that numerical models may be required. In addition, measurements from a prototype structure and/or physical scale model study in the laboratory give the analyst an opportunity to validate a theoretical model or to establish an empirical model for complicated flows that do not yield to analysis.

OVERVIEW OF ANALYSIS

Models of the physical processes involved can be developed from one or more of the following: closed mathematical solutions, numerical solutions, and physical model studies. The usefulness of all these should be considered for any given problem. In addition, the analyst should try to present the results of his analysis in a form that is relatively easy to understand by the designer, who usually is not the same person.

The flow regimes are sometimes very complicated and depend on many things, some of which are the ambient velocity distribution, free stream turbulence, wake characteristics, boundary and initial conditions, the total acceleration, the phase relationships between the various actions and the motion of the object itself, and the interaction of the object motion with the flow. Consequently, no general design criteria are available and many theoretical works on this subject are based on simplifying assumptions.

In general, an analysis should be concerned with the following:

Potential flow theory (ideal fluids)

1. Uniform steady ambient flow or the steady linear motion of the object.

2. Non-uniform flow due to boundary irregularities, curvilinear motion of the body, free surface conditions, skewed axis bodies, etc.

3. Unsteady, non-uniform flow, such as periodic motion, impulsive motion and aperiodic motion (random fluctuations).

Viscous flow (real fluids)

1. Free stream turbulence.

2. Boundary layer development on the object (skin friction
    drag).

3. Submergence of the object in a boundary layer developed
    on a nearby surface.

4. Wake formation (Boundary separation, form drag and
    vortex shedding).

Topics for differences that occur between simplifying assump-
tions and the conditions in nature

1. Irregular boundaries.

2. Aperiodic nature of the flow.

3. The shape and motion of the actual wave compared to the
    wave theory assumed.

4. Three-dimensional aspects of the flow versus a two-di-
    mensional analysis.

5. Unknown oceanographic conditions.

It is sometimes useful to consider the forces from a com-
plicated, time dependent flow to be the result from the super-
position of more than one relatively simple terms. Thus, the
Morison equation was established as an empirical relationship
to explain the phenomena of wave forces on vertical piling. (8).
They stated that the wave force was due to an accelerative force
(proportional to the virtual mass coefficient and the water part-
icle temporal acceleration evaluated at the pile center) and a
drag force (proportional to the drag coefficient and the square
of the water particle horizontal velocity). The approach was
simple and easy to use, with an attempt at a physical explanation
for such forces. However, in subsequent years, evaluations of
the coefficients displayed a great deal of scatter. This was
sometimes due to the inclusion of several modifying flow effects
into the determination of C_D and C_M; whereas, certain effects
should be considered separately, as discussed in this paper.

Some basic shortcomings of the Morison equation approach
include:

1. The forces from diffracted and reflected waves are not
    considered, which is necessary when the cylinder diameter
    to wave length ratio is large (4).

2. The convective acceleration components of the ambient
    flow are not included.

3. The evaluation of C_D and C_M depends on the wave theory
    used, and phase relationship between the ambient
    fluid velocity and the drag force is not taken into
    account. The importance of this is illustrated
    in Figure 1 which depicts the surface stress distribu-
    tion on a circular cylinder oscillating in a harmonic
    manner, such that laminar flow, without separation,
    results. The total drag force is $\pi/4$ out of phase
    with the cylinder velocity. For turbulent flow, in-
    cluding a wake formation, a similar, albeit unknown,
    phase difference will exist between the drag force
    and the relative motion between cylinder and fluid.
    Thus, the evaluation of the virtual mass coefficient
    may be in error when it is assumed that the drag force
    is zero when the relative velocity between the cylinder
    and ambient fluid is supposed to be zero.

4. Another shortcoming is that the Morison equation may
    give a misconception that drag forces are not due to
    acceleration effects.

To illustrate the last point for a real fluid, consider
Figs. 2 and 3. Figure 2 depicts steady uniform flow around a
cylinder such that form drag predominates. Figure 3 depicts
shear flow on a thin, flat place such that skin friction drag
predominates, a manifestation of which is the development of
the boundary layer thickness. In both cases a wake is formed.
We assume the pressure gradient is zero in each case (steady
unconfined flow) and that shear stresses do not exist on the
surface of the control volumes. Thus, the only forces acting
on each control volume one due to the cylinder in one case,
and the flat plate in the other, which represent the two ex-
tremes of form drag and skin friction drag.

The general momentum equation applied to the surface of
the control volume will determine the force exerted on the con-
trol volume by the object. In general, for any control volume,

$$\Sigma \vec{F} = \frac{d\vec{M}}{dt} = \frac{\partial M}{\partial t} + \vec{u} \cdot \nabla \vec{M} \qquad (1)$$

or

$$\Sigma \vec{F} = \frac{\partial \vec{M}}{\partial t} + \int_s \rho \vec{u} \ \vec{u} \cdot \vec{n} ds \qquad (2)$$

where

$$\vec{M} = \int_V \rho \vec{u} dV \qquad (3)$$

is the total momentum within the control volume, $\vec{u}$ is the velo-
city vector, $\vec{i}u + \vec{j}v + \vec{k}w$, $\vec{n}$ is the unit normal vector directed
outward from the control volume, ρ is the fluid mass density, s
indicates the surface of the control volume and V is the volume.

The fluid is incompressible so ρ is constant and Eqs. 1
and 2 are readily recognizable in terms of acceleration. The
first term on the rhs of Eq. 2 is the temporal term and the
second is the convective term. Thus, even for cases where the
viscous effects on the force completely predominate, it is seen
that they should be considered as acceleration effects. For a
circular cylinder in uniform flow where vortices are being
shed, the convective term of the acceleration is time dependent,
since the ambient velocity, U_∞, is constant. When the ambient
velocity is changing with respect to time, the first term on
the rhs of Eq. 2 is non-zero.

It is well known that in real fluids the potential flow
considerations are quite valid in many conditions except where
the viscous effects make modifications through boundary layer
development, vortex shedding and other viscous wake manifesta-
tions and free stream turbulence.

In many cases the viscous effects are neglibible. For ex-
ample, in the impulsive motion of a circular cylinder "instanta-
neously" to the velocity, U, perpendicular to its axis, the
viscous effects are initially very small until the wake has had
time to build. The drag coefficient for the laminar case is
shown in Fig. 4, which appears in Sarpkaya (12) for a Reynolds
number of from 0.15 to 1.2×10^5. Thus when the fluid travel is
less than about 0.4D the wake has not yet formed. Likewise, it
is infered that in waves, if the water particle displacements
are less than this amount, separation effects will be negligible.

Another interesting aspect of Fig. 4 is that the drag coef-
ficient reaches the value of 1.55 at Ut/D = 4, whereas for
steady flow at this Reynolds number it has the value of about
1.1 to 1.2. For this condition twin vortices have been formed
in the wake of the cylinder and have not yet been shed. When
the vortices are finally shed, a stable alternating of shedding
is set up into the familiar Karman vortex trail.

Thus, if considerations for wake formation can be neglected
a potential flow solution is possible. If not, we are usually
dependent on testing. Theoretically, if the wake shape and time
characteristics can be closely approximated, a modified shape of
the object can be assumed and a potential flow solution is still
possible, using the modified shape for the object. Several re-
cent cases have been presented in the literature where the viscous
effects can be neglected, some of which are in (1, 2, 3, 4, 5,
9, 10, 11, 13, and 14).

It is well known that the conditions of nature may not coincide closely with the simplified assumptions made in an analysis. For example, a pipeline placed on the sea bottom may not really approximate the condition of a cylinder near a plane boundary because of bottom irregularities. Thus, the spacing between the pipe and boundary may change with regard to positions on the pipeline. The designer should be aware of the maximum irregularities that can occur and try to conservatively estimate the differences in forces acting so as to obtain an envelope of conditions to which the pipeline is likely to be subjected. This paper will show that small differences in clearance under a pipeline can make large differences in the forces acting on the pipe.

In addition, flow conditions are not likely to be steady, nor periodic. For the case of ocean waves the random nature of the water surface elevation and wave frequencies may be taken into account (10), particularly for linear systems. However, in many areas the waves are multi-directional, although a particular direction may predominate. Considerations must be given to the differences between these simplified analytical conditions and the actual conditions provided by nature.

Laboratory experimentation is viewed with mixed emotions by the profession. The usually large dissimilarity between the Reynolds number in the laboratory and in nature prompt many engineers to feel that the laboratory work is only academic in nature and that realistic forces cannot be obtained. However, when Reynolds number dissimilarity is important, the drag coefficients that are determined from laboratory work are usually larger than would be the case for natural conditions, and the use of them would therefore result in conservatively large forces for design. However, the considerations for the ambient acceleration aspects of the flow may completely predominate the total force condition such that the viscous effects are negligible. Thus, for some pipes subjected to certain wave frequencies and heights, the Reynolds number has negligible influence and, therefore, the undesirable scale effects between laboratory and prototype conditions are non-existant. This is true when Froude number is important and Reynolds is not, indicating that the surface wave generated by the object is important but that the wake formation is not. The results determined from such laboratory experimentation are directly applicable to prototype conditions. In general, for conditions where wake formation is not important, and where surface tension is also not important, laboratory results are directly applicable to prototype conditions providing the load conditions in nature can be reproduced in the laboratory.

THEORETICAL EXAMPLE

Analytical developments for wave forces on cylinders near
a plane boundary were compared to laboratory results with some
success. First considerations have been given to rigid cylin-
ders with the flow perpendicular to the cylinder axis.

The proximity of the plane boundary will have an influence
on the viscous effects. Vortex shedding and wake size are in-
fluenced as indicated in Fig. 5, which shows drawings, inter-
preted from photographs of positions of a 2-inch cylinder near
the boundary in a birefringent fluid. The photographs (taken
with polarized light) showed that vortex shedding begins to be
suppressed when the cylinder is within one diameter of the bot-
tom and that the wake size is considerably increased when the
cylinder is on the bottom where vortex shedding is nearly stop-
ped, indicating a possible increase in drag coefficient. The
flow Reynolds number was 1.7×10^4. In addition, for conditions
where the wake formation is important, as in Fig. 5, the lift
forces may always be positive, because of the nearby plane
boundary, instead of negative when wake formation is negligible
This will be discussed in more detail later.

The free surface effects (or the surface waves generated
by the presence of the cylinder) can be examined with the use
of potential flow theories. For uniform steady horizontal flow
Havelock (5) developed a linearized second-order solution in a
complicated series that would not be usable by the usual designer.
The results are summarized in (15). However, a translation of
the results into graph form is shown in Figs. 6 and 7. They show
that the surface effects on the forces on a cylinder submerged
in a uniform flow are negligible if the submergence is greater
than about four cylinder diameters. Recently Tuck (14) solved
the problem in non-linear second-order form and showed that the
non-linear effects are significant in some cases.

Likewise, Ogilvie (11) derived the forces acting on a cyl-
inder while it is oscillating near the surface. The solution
for the added mass coefficient is again a series solution and
is summarized in Fig. 8. It can be seen that if the cylinder
is submerged 3 or 4 diameters that the added mass coefficient
from the free surface effects (which are frequency dependent)
are negligible. Actually, for a cylinder submerged as little
as one diameter the forces from the free surface effects are
small.

For this experimental work, only oscillatory forces were
considered and the cylinders were submerged at least one diam-
eter and usually more. In addition, wave particle motion was
calculated to be less than 0.4D so that viscous effects were
negligible. Thus, the study reduced to investigating the

effects of the nearby plane boundary on the wave forces on
cylinders, with potential flow theories. Comparisons were
made with laboratory measurements.

The uniform potential flow for a cylinder near a plane
boundary is mathematically equivalent to that for two equal
cylinders in a uniform flow. The complex potential for two
cylinders in a uniform stream was determined with Milne-
Thompson's circle theorem. (We have since expanded this to
N number of cylinders in a uniform, unsteady stream, each
moving individually.) The method of images applied to two
cylinders is also reviewed in (1) and (9). An image solution
in three dimensions for an ellipsoid travelling parallel to its
major axis is presented by Eisenberg (2). The result for this
work is detailed in (15). The total forces on the cylinder
were then found from the Blasius theorem as

$$X - iY = \tfrac{1}{2} i \rho \oint \left(\frac{dw}{dz}\right)^2 dz - i \rho\frac{\partial}{\partial t} \oint \bar{w}\, d\bar{z} \qquad (4)$$

where X and Y are the forces in the x and y directions and
$w = \phi + i\Psi$, the complex potential.

In Eq. 4 the first term on the rhs accounts for the con-
vective acceleration and the second term for the temporal ac-
celeration.

Uniform, steady potential flow, parallel to the plane
boundary, was considered first as shown in Fig. 9. No net
drag force results parallel to the wall. However, a "lift"
force on the cylinder, perpendicular to the wall, due to the
convective acceleration effects of the steady local flow, does
result. The potential flow solution is in terms of an infi-
nite series of doublets distributed from the center of the
cylinder on the radius, toward the wall. It is reviewed in (15)
and will be detailed in a future paper. The result for the
lift force is, for s > a (see Fig. 9):

$$F_L = -4\pi\rho U^2 a \sum_{j=1}^{\infty} \sum_{k=1}^{\infty} \frac{m_j\, m_k}{\left[\dfrac{2s}{a} - q_j - q_k\right]^3} \quad, \quad e > a \qquad (5)$$

where

$$m_n = q_2^2 \, q_3^2 \, \cdots \, q_n^2 , \qquad\qquad m_1 = 1 \qquad (6)$$

$$q_n = \frac{1}{\dfrac{2s}{a} - q_{n-1}}, \qquad\qquad q_1 = 0 \qquad (7)$$

The results for this case are also given in terms of bi-polar coordinate variables in Ref. 9. At the wall (s = a), the lift force per unit length of cylinder is given in closed form by Müller (9) as

$$F_L = \rho U^2 \, a \, \frac{\pi}{9} \, (\pi^2 + 3) . \qquad (8)$$

The lift coefficient is defined as

$$C_L = \frac{F_L}{\tfrac{1}{2}\rho U^2 D} . \qquad (9)$$

The lift coefficient, C_L, was calculated as a function of the gap between the cylinder and the bottom boundary using the first 40 images and it is plotted in Fig. 10. When the gap, e, is equal to one cylinder diameter, the lift coefficient is very small and may be neglected for many design problems. Figure 10 also shows that (for the theoretical potential flow case) if the gap is very small then a very large negative force exists toward the wall. However, when the cylinder touches the wall a positive lift force is experienced. Therefore, a severe reversal of lift force is possible for some cylinders that are not securely anchored down and where the submerged weight of the pipe is less than the positive force when the cylinder touches the bottom. Boundary layers on both the wall and the cylinder will alter the results from the potential flow theory.

Another simple loading condition of great interest is for uniform ambient flow that is accelerating either perpendicular to, or parallel to, the plane boundary. The added mass coefficients in such cases will be the same as for a cylinder accelerating in the same direction in a still fluid. The result is given below and the derivation, which again is dependent on an infinite destribution of doublets on the cylinder radius, will be detailed in a future publication.

For a cylinder accelerating parallel to a near by plane boundary (the x direction) with a temporal acceleration of $\dot{u}$, the Blasius theorem results in hydrodynamic forces on the cylinder of

$$X = -\rho \pi a^2 C_M \dot{u} \tag{10}$$

and

$$Y = +\rho C_L a u^2 \tag{11}$$

where

$$C_M = 1 + 2 \sum_{j=1}^{\infty} \frac{m_j}{m_1}^2 \tag{12}$$

or

$$C_M = 1 + 2 \sum_{j=2}^{\infty} (q_2^2 q_3^2 \ldots q_j^2)^2 \tag{13}$$

and for C_L the developments in Eqs. 5 through 9 are valid. Thus, for $e > a$ there is an attractive force between the cylinder and the plane boundary.

For a cylinder accelerating perpendicular to the plane boundary,

$$X \approx 0 \tag{14}$$

and

$$Y \approx -\rho \pi a^2 C_M \dot{v} + \rho C_L a v^2 \tag{15}$$

The added mass and lift coefficients are determined the same way as for Eqs. 10 and 11. Thus, whether the cylinder is accelerating toward or away from the boundary, there is an attractive force between the cylinder and the boundary which is proportional to the square of the velocity. Actually, for a cylinder accelerating on a line at any angle with the boundary, the lift force will be determined in the same manner and will be proportional to the square of the absolute value of the cylinder velocity and the added mass force will also be the same as before and proportional to, and colinear with, the cylinder acceleration. The added mass coefficient, C_M, as determined from Eq. 13 is plotted in Fig. 11.

The above developments can be applied to cylinders subjected to waves if the velocity and acceleration gradients are negligible over the diameter of the cylinder as indicated in Fig. 12 and if the wake development is negligible. That is, the uniform, potential flow assumptions must be valid in order for these developments to be applicable. This restricts the usefulness of the theoretical developments, but these cases are important. The solutions for non-uniform, unsteady flow, and for cases of significant wake formation, are being developed in order to remove this restriction and they will be presented in a future paper.

EXPERIMENTAL EXAMPLE

Laboratory testing was accomplished on 2", 4½" and 6" diameter cylinders at various spacings from a nearby plane boundary and for various water depths. The test set-up is indicated in plain view in Figure 13. Typical wave and force records are shown in Figs. 14 and 15. A complete summary of the original results is given in Ref. 15.

In most cases the cylinders were submerged at least two cylinder diameters below the free surface. In a few cases, about one diameter submergence was obtained. For oscillatory flow, therefore, the free surface effects should be small, as indicated in Fig. 8. So, as a first approximation the free surface effects were ignored. In addition, the wave heights and lengths, in conjunction with the water depths produced particle displacements that were small with respect to the cylinder diameter, so that the viscous effects could be ignored.

When a wave crest is over a cylinder the water particle acceleration acts downward on the cylinder. In addition, the horizontal velocity is maximum at that point so that the "lift" force from it is maximum and negative, adding to the vertical particle acceleration force. When a wave trough is over a cylinder the water particle acceleration acts upward, in opposition to the lift force. These effects are clearly in evidence in Fig. 14 where the space beneath the cylinder is about 0.02 times the diameter, but they do not appear in Fig. 15 where the space is 0.05 times the diameter. One might predict this result from Fig. 10, although keeping in mind that he is comparing oscillatory flow to steady flow. Evidently they are closely comparable in this case because the lift force was derived from the records from

$$F_L = \tfrac{1}{2} \left(- \left| F_{crest} \right| - \left| F_{trough} \right| \right) \qquad\qquad (16)$$

Likewise, the vertical temporal acceleration force was approximated from

$$F_{VA} = \frac{1}{2} \left(- \left| F_{crest} \right| + \left| F_{trough} \right| \right)$$ (17)

Such data were plotted for several runs and examples of some of the results are given in Figs. 16 and 17. The slope of the line in Fig. 16 gives the lift coefficient and the slope of the line in Fig. 17 yields the added mass coefficient. Figure 18 shows similar results for the horizontal temporal acceleration forces, which were obtained from the raw data at times when the horizontal acceleration was computed to be maximum. Linear wave theory was assumed, again as a first approximation, since wave steepness was small.

The results of all the testing are shown in Figs. 10 and 11. In addition, the testing results, replotted from Schiller (11) are shown. Agreement in the lift coefficient between uniform flow theory and experimental wave results were suprisingly close. Considerable scatter exists for the added mass coefficient and is probably due to some influence from drag (or simply a wake formation), the use of Airy wave theory, the inappropriateness of comparing uniform flow to non-uniform flow and experimental error. In addition, the accurate measurement of forces when the cylinder touches the plane boundary is very difficult.

CONCLUSIONS

The influence of a nearby plane boundary on the hydrodynamic forces on a cylinder is clear when there is no wake formation. Figure 11 shows that the added mass coefficient for a cylinder on the boundary is more than twice as large as for a cylinder in a free stream. Similarly the lift coefficient is about +4.5 when the cylinder rests on the boundary and is zero in the free stream (except for viscous flow modifications from vortex shedding). However, when a small gap exists between the cylinder and the boundary a very large and negative lift coefficient exists for the cylinder.

Sometimes relatively simple solutions can yield adequate results for design work providing the constriants implicit with the simplifications are completely recognized. Thus, the diffraction theory approach may not be necessary if surface waves are not caused by the presence of the object, which is the case for cylinders when the submergence is greater than four cylinder diameters. In addition, if velocity gradients are not large over the cylinder diameter, uniform flow solutions may be useful.

Additional work is necessary to include non-uniform flow. In addition, the viscous effects need clarification, particularly with regard to their influence on the potential flow developments, and accurate knowledge of the phase shift between the ambient flow and drag force fluctuations need to be known. The influence of cylinder skew angles and roughness, when near the boundary, are also topics for future investigations.

All forces acting on submerged objects should be considered to be acceleration forces. Analyses should consider the potential flow effects and the viscous effects. Most viscous effects must be determined in the laboratory; however, mathematical solutions for laminar flow may be tractable. In addition, many acceleration (particularly including gravitational) effects can be investigated in the laboratory with little or no deleterious effects from scale dissimilarities. Because the viscous effects were small, the results given here are directly applicable to similar prototype conditions. High Reynolds number testing will be conducted in the future at the OSU Wave Research Facility that is capable of producing waves with heights up to five-feet high and breaking.

It is hoped that the results presented here have been put into a form that is readily useable by designers for problems where the wake development is negligible.

ACKNOWLEDGEMENTS

REFERENCES

1. Carpenter, L. H., "On the motion of Two Cylinders in an Ideal Fluid", Journal of Research of the National Bureau of Standards, Vol. 61, 1958, pp. 83-87.

2. Eisenberg,Phillip, "An Approximate Solution for Incompressible Flow About an Ellipsoid Near a Plane Wall", Journal of Applied Mechanics, June, 1950.

3. Garrison, C. J. and Roa, V. S., "Interaction of Waves with
    Submerged Objects", Journal of the Waterways, Harbors and
    Coastal Engineering Division Journal, ASCE, Vol. 97, No.
    WWZ, May, 1971.

4. Garrison, C. J. and Chow, P. Y., "Wave Forces on Submerged
    Bodies", Journal of the Waterways, Harbors and Coastal
    Engineering Division Journal, ASCE, Vol. 98, No. WW3, Aug-
    ust, 1972.

5. Havelock, T. H., "The Forces on a Cylinder Submerged in a
    Uniform Stream", Proceedings of the Royal Society, London,
    Ser A157, pp. 526-534, 1936.

6. McCamy, R. C. and Fuchs, R. A., "Wave Forces on Piles: A
    Diffraction Theory", Technical Memo No. 69, Beach Erosion
    Board, U.S. Army Corps of Engineers, 1954.

7. Milne-Thomson, L. M., "Theoretical Hydrodynamics", 5th ed.,
    MacMillan, New York, 1968.

8. Morison, J. R., et al, "The Force Exerted by Surface Waves
    on Piles", Petroleum Transactions, AIME, Vol. 189, 1950.

9. Müller, von Wilhelm, "Systeme von Doppelquellen in der
    ebenen Stromung, insbegondere die Stromung um zwei
    Kreisylinder", Ztschr. f. angew. Math. und Mech., Band 9,
    Helf 3, pp. 200-213, June 1929.

10. Nath, J. H. and Harleman, D. R. F., "Dynamics of Fixed
    Towers in Deep water Random Waves", Journal of Waterways
    and Harbors Division, ASCE, November, 1969.

11. Ogilvie, J. F., "First and Second Order Forces on a Cyl-
    inder Submerged Under a Free Surface", Journal of Fluid
    Mechanics, Vol. 16, Part 3, pp. 451-472, July 1963.

12. Sarpkaya, T., "Separated Flow About Lifting Bodies and
    Impulsive Flow About Cylinders", AIAA Journal, Vol 4, No. 3,
    March, 1966.

13. Schiller, F. C., "Wave Forces on a Submerged Horizontal
    Cylinder", M.S. Thesis, Naval Postgraduate School, Monterey,
    California, June, 1971.

14. Tuck, E. O., "The Effect of Non-linearity at the Free Sur-
    face on Flow Past a Submerged Cylinder", Journal of Fluid
    Mechanics, Vol. 22, 1965.

15. Yamamoto, T., Nath, J. H. and Slotta, L. S., "Yet Another
    Report on Cylinder Drag or Wave Forces on Horizontal Cyl-
    inders," Bulletin No. 47, Engineering Experiment Station,
    Oregon State University, April, 1973.
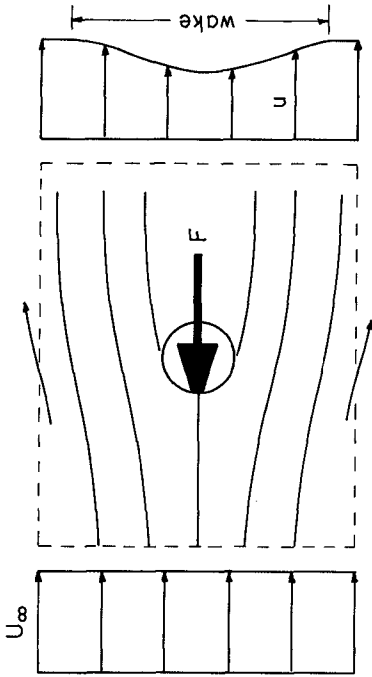
Fig. 2 – Example of Profile Drag
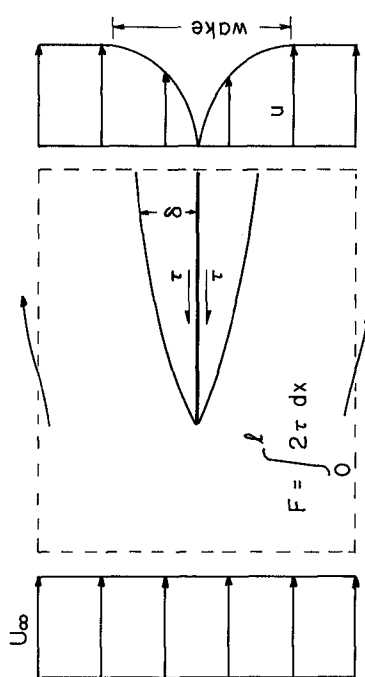
Fig. 3 – Example of Shear Drag
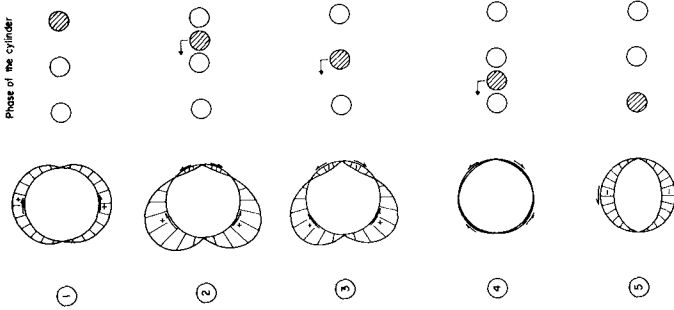
Fig. 1 – Laminar Flow Surface Drag
for an Oscillating Cylinder
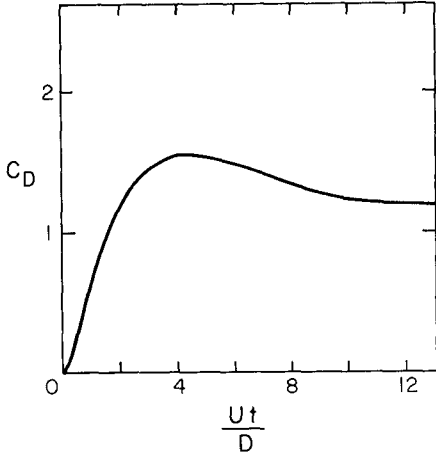
Fig. 4 – Drag Coefficient for Impulsive Motion of a Circular Cylinder (From Rosenhead)
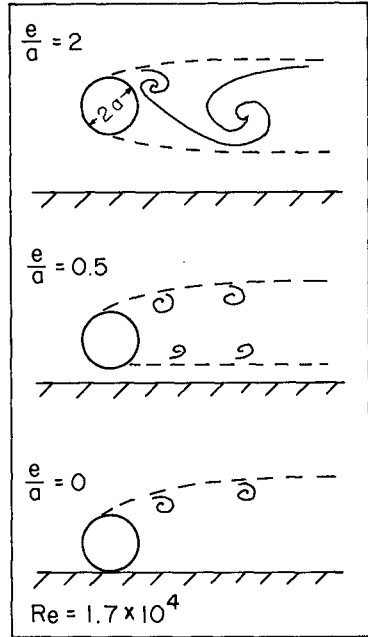
Fig. 5 – Wake Interpretations from Flow Visualization
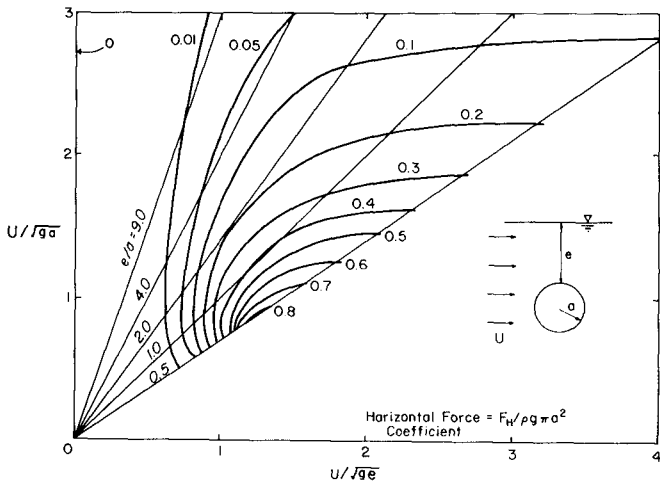
Fig. 6 – Free Surface Effect on Drag Force on a Circular Cylinder (Computed from Havelock(1936)).
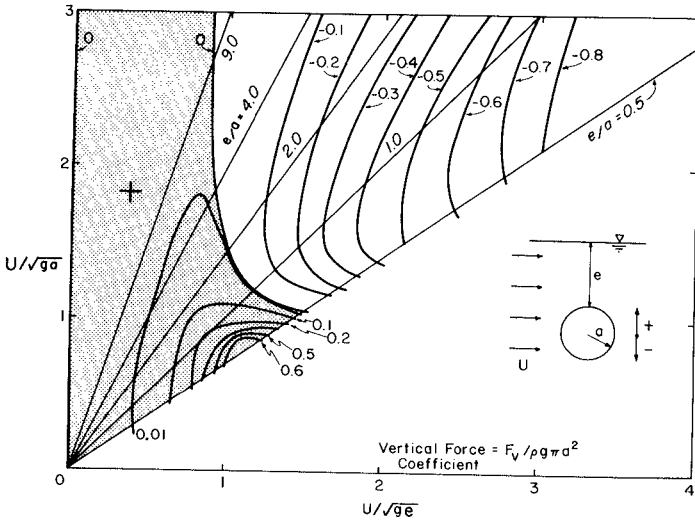
Fig. 7 - Free Surface Effect on Lift Force on a
Circular Cylinder (Computed from Havelock (1936)).

Fig. 9 - Cylinder in Cross
Flow with Nearby Plane
Boundary

Fig. 8 - Free Surface Effect on Added Mass of a
Circular Cylinder (Computed from Ogilvie (1963)).
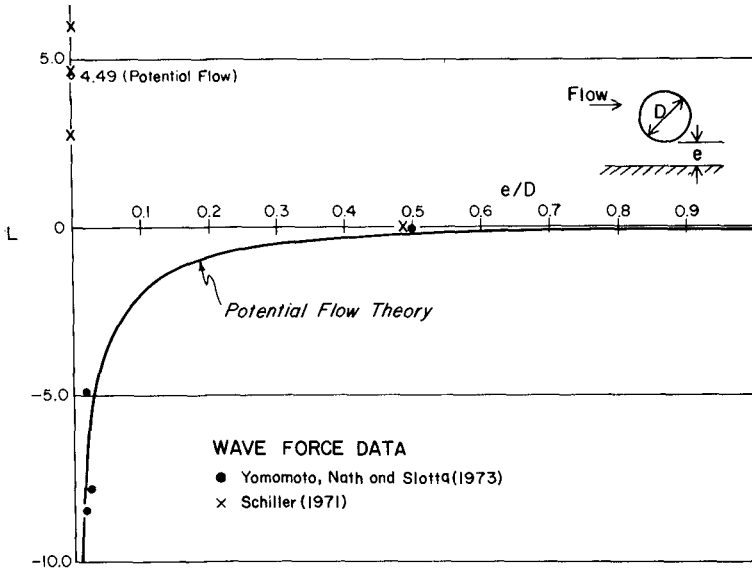
Fig. 10 - Lift Coefficient of Circular Cylinders
Near a Plane Boundary
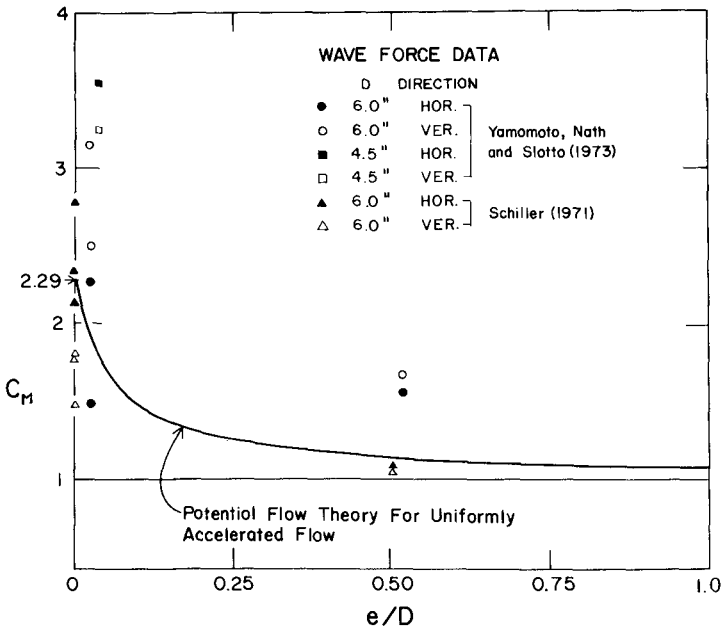
Fig. 11 - Added Mass Coefficients for Circular Cylinders
Accelerating Near a Plane Boundary
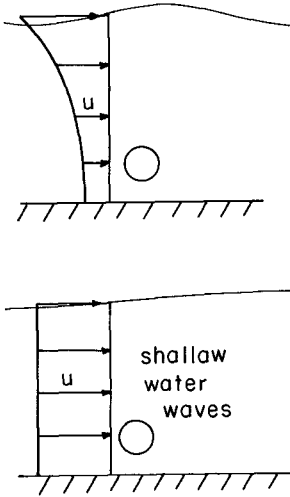
Fig. 12 - Uniform Flow
Approximation to Non-
Uniform Flow
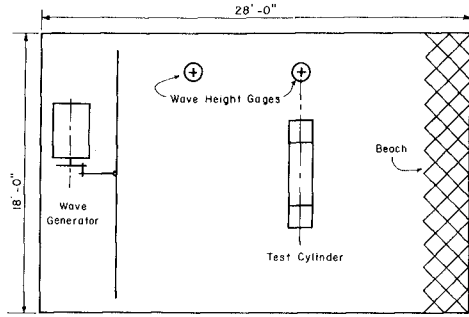
Fig. 13 - Schematic Illustration
of Wave Basin and Experimental
Setup
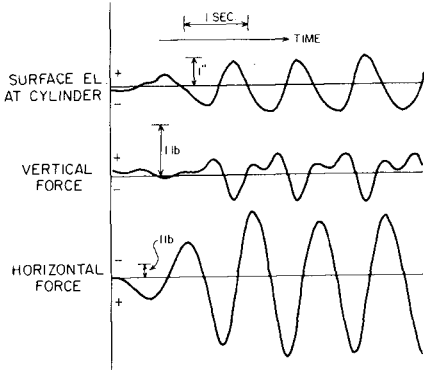
Fig. 14 - Example Data for D = 6",
e = 1/8", h = 10"
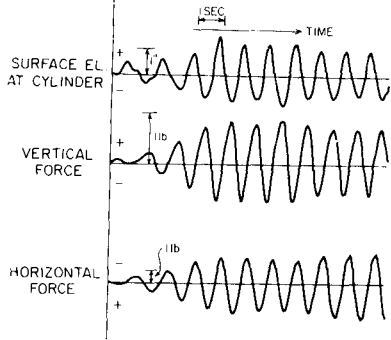
Fig. 15 - Example Data for
D = 6", e = 3", h = 14-1/8"
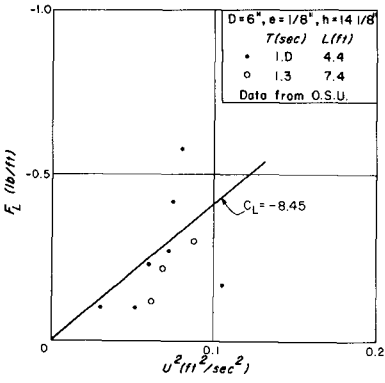
Fig. 16 – Lift Force vs.
Horizontal Velocity Squared
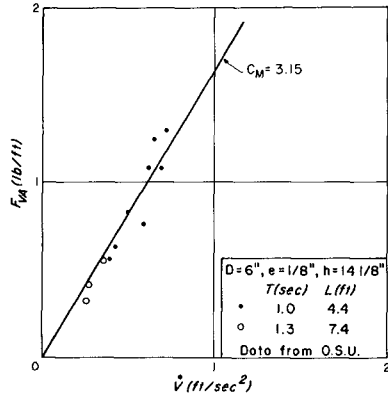
Fig. 17 – Vertical Acceleration
Force vs. Vertical Acceleration
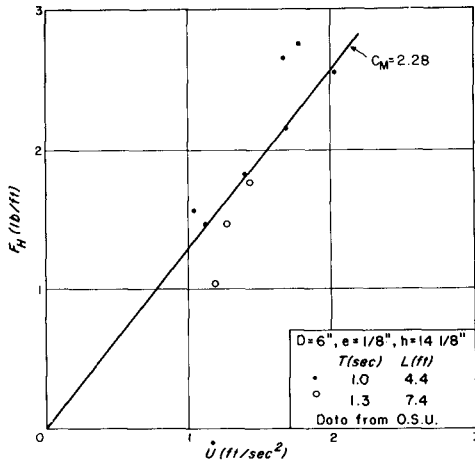
Fig. 18 – Horizontal Force vs. Horizontal
Acceleration

CHAPTER 107

INTERACTION OF PLANE WAVES WITH

VERTICAL CYLINDERS

by

Bradford H. Spring
Assistant Professor of Civil Engineering
Valparaiso University, Valparaiso, Indiana

and

Peter L. Monkmeyer
Professor of Civil and Environmental Engineering
University of Wisconsin, Madison, Wisconsin

ABSTRACT

This study deals with the interaction of linear, plane water waves with stationary groups of rigid, vertical, circular cylinders under conditions in which the inertial forces on the cylinders dominate over the drag forces. A direct matrix solution as well as multiple scattering as suggested by Twersky (1952) are used to obtain the velocity potential in the vicinity of the cylinders. The groups may consist of a number of cylinders having any geometric arrangement, may have Dirichlet, Neumann, or mixed boundary conditions, and need not have identical diameters. The study represents an extension of the single-cylinder case presented by MacCamy and Fuchs in 1954.

Basic scattering coefficients for 192 different arrangements of two cylinders are obtained with the aid of a Bessel coordinate transformation and a matrix inversion procedure. The resulting potential function is then applied to calculate force components in the direction of wave advance and orthogonal to it. For the cases considered the former departs as much as 65% from the force on a single cylinder and the mass coefficient is found to range from 1.19 to 3.38 - a not insignificant departure from the often used value of 2.0. Furthermore the orthogonal force may be as large as 67% of the single-cylinder force.

INTRODUCTION

As off-shore construction continues to expand around the world, the need for an improved understanding of the effects of water waves on various structures in the sea becomes increasingly evident. Basic to many such problems is the fundamental

one involving plane, periodic waves and vertical, circular cyl-
inders, since many such structures include one or more cylindri-
cal legs.

In the present study a general approach to the problem of
describing the interaction of linear, plane waves with station-
ary groups of rigid, vertical circular cylinders is examined.
In particular cylinders located in intermediate or deep water
and having relatively large diameters (when compared with wave
height) are considered in as much as they are representative of
a type of off-shore construction that has received much atten-
tion recently.

Dean and Harleman (see Ippen (1966)) demonstrate that as
the ratio of wave height to cylinder diameter, H/D, diminishes
and the ratio of water depth to wave length, h/L, grows, the
ratio of inertial force to drag force as described by the
Morison Equation (Morison, et al (1950)) increases. For exam-
ple, if H/D = 1.00 and h/L = 0.40, the inertial force will be
ten times as large as the drag force. Many off-shore struc-
tures, and in particular those considered in the present study,
are therefore subject primarily to inertial forces with drag
effect considered negligible.

Under these circumstances classical diffraction theory,
which presupposes a frictionless fluid and therefore neglects
drag seems to be ideally suited to the solution of problems
involving the interaction of plane waves with large cylinders
in deep or intermediate-depth water. MacCamy and Fuchs (1954)
were the first investigators to apply diffraction theory to this
interaction problem. Their study of the diffraction of periodic
plane waves about a single circular cylinder led to a new
approach to the problem of predicting wave forces on structures.

The present study is an attempt to extend the work of
MacCamy and Fuchs to a consideration of wave interaction with
more than one vertical cylinder. One approach to the solution
of such problems is multiple scattering as suggested by
Twersky (1952). A direct matrix method appears to offer more
rapid and reliable solutions and is therefore emphasized herein.

THEORETICAL ANALYSIS

Problem Statement. The problem under consideration is the inter-
action between incoming plane water waves and an arbitrary col-
lection of vertical circular cylinders located in the path of
the waves. The following conditions are assumed to prevail:

1. The waves are linear (small amplitude theory), and are not
    breaking.

2. The bottom is horizontal and impermeable with a depth suffi-
    cient for deep water or intermediate depth wave conditions.

3. The cylinders are circular, rigid, vertical, stationary, impermeable and have a relatively large diameter with respect to the wave height.

4. Drag effects are negligible (i.e. the water behaves as an ideal fluid).

   A general procedure for determining the velocity potential for any number of cylinders is outlined first and then the specific case of two cylinders, Fig. 1, is analyzed more completely. Details of the analytical procedure are omitted herein, but are described by Spring (1973).
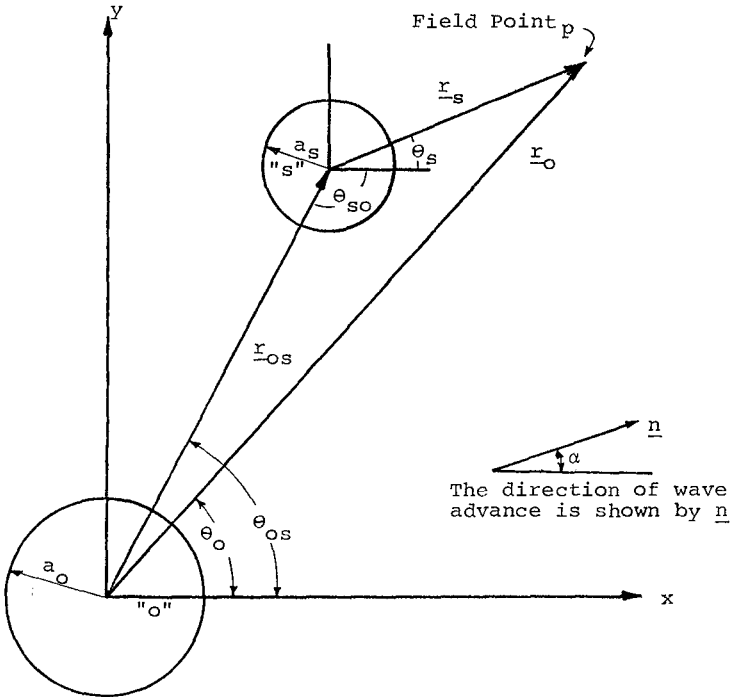
Figure 1. Definition Sketch for Cylinder "o" and Cylinder "s"

   The approaching plane waves are conveniently expressed in terms of cylindrical coordinates since circular cylinders are under study. Thus in terms of the coordinate center "s" the

incoming wave may be written (see Twersky (1952) and MacCamy
and Fuchs (1954)

$$\emptyset_{in}(r_s,\theta_s) = -\text{Re}\Big[f(z,t) \exp(ikr_{os} \cos(\theta_{os}-\alpha))$$

$$\cdot \sum_{n=-\infty}^{\infty} J_n(kr_s) \exp(in(\theta_s-\alpha+\pi/2))\Big] \tag{1}$$

where the symbols are as defined in Fig. 1, $J_n(kr_s)$ is the
Bessel function of the first kind, of order "n" and

$$f(z,t) = \frac{gH}{2\sigma} \frac{\cosh[k(h+z)]}{\cosh kh} e^{-i\sigma t} \tag{2}$$

where   g = the acceleration due to gravity

            H = the wave height

            h = the depth of water from the still water
                level to the bottom

            k = the wave number, $2\pi/L$

            L = the wave length

            T = the period

            z = the vertical coordinate, measured positive
                upward from the still water level

            σ = the frequency, $2\pi/T$

     The waves scattered by the cylinders have as yet undeter-
mined amplitude but must vanish at large distances from the
cylinders due to circular dispersion. Also the waves must be
outgoing rather than incoming. Thirdly, the scattered wave
expression must be rather general to provide enough flexibility
to account for the non-symmetrical scattering of the waves from
the cylinder or cylinders. With negative sign on the time expo-
nential, the Hankel function of the first kind (see MacCamy and
Fuchs (1954),

$$H_p^1(kr) = J_p(kr) + iY_p(kr) \tag{3}$$

will adequately express the radial dependence of the scattered
waves. Since there will be no need for any Hankel function of
the second kind (which describes incoming circular waves), the
superscript on $H_p^1(kr)$ will be dropped and it will be understood
that $H_p(kr)$ = Hankel function of the first kind with argument kr.

     The scattered wave from the "sth" cylinder will then be

$$\emptyset_{sc}(r_s,\Theta_s) = \mathrm{Re}\left[f(z,t) \sum_{n=-\infty}^{\infty} A_n^s H_n(kr_s) e^{in\Theta_s}\right] \qquad (4)$$

and for the cylinder located at "o"

$$\emptyset_{sc}(r_o,\Theta_o) = \mathrm{Re}\left[f(z,t) \sum_{n=-\infty}^{\infty} A_n^o H_n(kr_o) e^{in\Theta_o}\right] \qquad (5)$$

where the A_n's are complex constants (as yet unknown) of the form $a_n + ib_n$, with appropriate superscript.

Since linear waves (small amplitude wave theory) are being considered, the velocity potential at any field point "p" may now be represented by superposing the various wave components to give

$$\emptyset_p = \mathrm{Re}\left[f(z,t)\left[\exp(ikr_{os}\cos(\Theta_{os}-\alpha))\right.\right.$$

$$\cdot \sum_{n=-\infty}^{\infty} -J_n(kr_s)\exp(in(\Theta_s-\alpha+\pi/2))$$

$$\left.\left.+ \sum_{j=1}^{Q}\sum_{n=-\infty}^{\infty} A_n^j H_n(kr_j) e^{in\Theta_j}\right]\right] \qquad (6)$$

where the summation term on j accounts for the potential of the scattered waves from all cylinders present (Q being the number of such cylinders).

The potential function described by Eq. 6 is difficult to handle since each scattered wave is expressed in terms of a different coordinate center. There is however, a Bessel "addition theorem" or coordinate transformation available to express all wave components in terms of one selected coordinate center (see Watson (1966) pp. 359-61, or Abramowitz and Stegun (1965) p.363).

Referring to Fig. 2, the Bessel coordinate transformation of $C_\nu(\tilde{w})$ (which may be any one of the cylinder functions – J,Y, H^1, H^2 or a derivative or linear combination thereof) from coordinate center 1 to a new coordinate center 2 is given by

$$C_\nu(\tilde{w}) \; e^{\pm i\nu\psi} = \sum_{m=-\infty}^{\infty} C_{\nu+m}(Z) \; J_m \; (z) \; e^{\pm im\emptyset} \tag{7}$$

with the restriction that $\left| z \; e^{\pm i\emptyset} \right| < \left| Z \right|$

It should be noted that the restriction is lifted if ν is an integer or zero and the only functions involved are of the first kind.
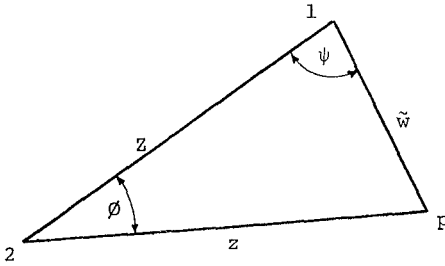
Figure 2. Definition Sketch for Bessel Coordinate Transformation

Direct Solution Versus Multiple Scattering. The final step in the derivation of the velocity potential is the application of the reflection or Neumann boundary conditions at the surface of the rigid, impermeable circular cylinders. These conditions are given by

$$\frac{\partial \emptyset_p}{\partial r_s} = 0 \text{ @ } r_s = a \tag{8}$$

for each cylinder and must be applied to evaluate the coefficients A_n^j in Eq. (6). In the instance of water waves scattered by impermeable vertical cylinders, the Neumann condition is applied on each cylinder. It should be noted however, that the method does not require all boundary conditions to be of the same type.

The fundamental difference between the direct approach used herein and the procedure suggested by Twersky (1952) is in the method of application of the cylinder boundary conditions. In the "direct" approach the boundary conditions on all cylinders are applied simultaneously and all unknowns are obtained by means of a single matrix inversion of a set of simultaneous equations. The number of equations increases with the number of cylinders

involved in the problem (except for such special cases as an
infinite row of cylinders of the same size and spacing); and
with the number of terms taken in the summations. The practical
limit on the method is therefore the limit of the matrix size
which can reasonably be handled by the digital computer available.

    In contrast, the multiple scattering approach takes one cyl-
inder at a time and sequentially solves for the scattering coef-
ficients. The sum of the multiple scattering coefficients for a
particular cylinder approaches the direct solution if enough
orders of scattering are considered.

The Two-Cylinder Problem. The general method described above
will be applied in this section to the case of two cylinders as
shown on Fig. 1. The two-cylinder case is used as an illustra-
tion of the techniques involved. Three, four, six, or more cyl-
inders could likewise be considered. On the other hand it
should be noted that the size, orientation and spacing of the
cylinders and the direction of wave approach are all arbitrary
and can be selected later to make computations for a particular
situation.

    The velocity potential at any field point "p" in terms of
cylinder "s" may be formed by superposing the velocity poten-
tials for the incoming plane wave, the scattered wave from cyl-
inder "s" and the scattered wave from cylinder "o" as suggested
by Eq. (6). The Bessel coordinate transformation from "o" to
"s" and the cylinder boundary on "s" are then applied and the
resulting complex expressions are separated into real and imag-
inary parts, while noting that $A = a + ib$, $H = J + iY$ and $H' =
J' + iY'$. This results in two sets of equations in the four
sets of unknowns a_p^s, b_p^s, a_p^o, b_p^o, as follows:

$$-J'_{-m}(ka_s) \cos\left[(kr_{os} \cos(\theta_{os}-\alpha)) - m(-\alpha+\pi/2)\right]$$

$$+ (a_{-m}^s J'_{-m}(ka_s) - b_{-m}^s Y'_{-m}(ka_s))$$

$$+ \sum_{n=-\infty}^{\infty} J'_m(ka_s)\left[(a_n^o J_{n+m}(kl_{os}) - b_n^o Y_{n+m}(kl_{os})) \cos(n\theta_{os} + m\theta_{so})\right.$$

$$\left. -(b_n^o J_{n+m}(kl_{os}) + a_n^o Y_{n+m}(kl_{os})) \sin(n\theta_{os} + m\theta_{so})\right] = 0 . \qquad (9a)$$

and

$$-J'_{-m}(ka_s) \; \sin\left[(kr_{os} \cos (\theta_{os}-\alpha)) - m(-\alpha+\pi/2)\right]$$

$$+ \; (b^S_{-m} \; J'_{-m}(ka_s) + a^S_{-m} \; Y'_{-m}(ka_s))$$

$$+ \; \sum_{n=-\infty}^{\infty} J'_m(ka_s)\left[(b^O_n \; J_{n+m}(kl_{os}) + a^O_n \; Y_{n+m}(kl_{os})) \; \cos(n\theta_{os} + m\theta_{so})\right.$$

$$+ \; (a^O_n \; J_{n+m}(kl_{os}) - b^O_n \; Y_{n+m}(kl_{os})) \; \sin(n\theta_{os} + m\theta_{so})\Big] = 0 \qquad (9b)$$

where $m = 0, \pm1, \pm2, \; \ldots\ldots$

In similar fashion the Bessel coordinate transformation from "s" to "o" and boundary condition on cylinder "o" are applied, producing two more equation sets in the same four sets of unknowns a^s_p, b^s_p, a^o_p, b^o_p, as follows

$$-J'_{-m}(ka_o) \; \cos\left[-m(-\alpha+\pi/2)\right] + (a^O_{-m} \; J'_{-m}(ka_o) - b^O_{-m} \; Y'_{-m}(ka_o))$$

$$+ \; \sum_{n=-\infty}^{\infty} J'_m(ka_o)\left[(a^S_n \; J_{n+m}(kl_{os}) - b^S_n \; Y_{n+m}(kl_{os})) \; \cos(n\theta_{so} + m\theta_{os})\right.$$

$$- (b^S_n \; J_{n+m}(kl_{os}) + a^S_n Y_{n+m}(kl_{os})) \; \sin(n\theta_{so} + m\theta_{os})\Big] = 0 \qquad (10a)$$

and

$$-J'_{-m}(ka_o) \; \sin\left[-m(-\alpha+\pi/2)\right] + (b^O_{-m} \; J'_{-m}(ka_o) + a^O_{-m} \; Y'_{-m}(ka_o))$$

$$+ \; \sum_{n=-\infty}^{\infty} J'_m(ka_o)\left[(b^S_n \; J_{n+m}(kl_{os}) + a^S_n \; Y_{n+m}(kl_{os})) \; \cos(n\theta_{so} + m\theta_{os})\right.$$

$$+ \; a^S_n \; J_{n+m}(kl_{os}) - b^S_n \; Y_{n+m}(kl_{os})) \; \sin(n\theta_{so} + m\theta_{os})\Big] = 0 \qquad (10b)$$

In order to reduce the coefficients and the equations to a finite number, m and n are given a range of $-M$ to $+M$ where the value of M required to maintain a specified precision increases with increasing ka_s and ka_o and decreasing kl_{os}. For the two-cylinder problem this will therefore result in $8M+4$ equations and unknowns.

Once the coefficients have been computed the final velocity potential is obtained. In functional form, therefore,

$$\emptyset = f(z) \sum_m (f_m \cos(m\theta+\sigma t) + g_m \sin(m\theta+\sigma t)) \qquad (11)$$

where f_m and g_m are functions of r, and

$$f(z) = \frac{gH}{2} \frac{\cosh[k(h+z)]}{\cosh kh}$$

Pressure on the Cylinder Face. The pressure field may be determined with the aid of the generalized Bernoulli Equation

$$\frac{\partial \emptyset}{\partial t} + gz + \frac{P}{\rho} + \frac{1}{2}(\nabla\emptyset)^2 = 0 \qquad (12)$$

Neglecting the kinetic energy and considering only the dynamic pressure, P_d, one obtains

$$P_d = -\frac{\partial \emptyset}{\partial t} = \rho\sigma \, f(z) \sum_m (f_m \sin(m\theta+\sigma t) - g_m \cos(m\theta+\sigma t)) \qquad (13)$$

For the pressure on a cylinder face f_m and g_m must be evaluated at the appropriate radial distance.

Horizontal Force Components on the Cylinder Face. By integrating the dynamic pressure over the entire cylinder face the horizontal force is obtained. In general functional form the force components may be expressed as follows:

$$F_x = \frac{\pi H \rho \sigma}{2} f(z) \, R_x \cos(\sigma t+\delta_x) \qquad (14a)$$

and

$$F_y = \frac{\pi H \rho \sigma}{2} f(z) \, R_y \cos(\sigma t+\delta_y) \qquad (14b)$$

where R_x, R_y, δ_x and δ_y are amplitudes and phase angles which depend on ka_s, ka_o, kl_{os}, and θ_{os}.

ANALYSIS OF THE DATA

Computer Procedure. It is readily apparent that the solution of Eqs. (9) and (10) by matrix inversion requires the services of high speed computers. In this case the UNIVAC 1108 of the Madison Academic Computing Center and the Datacraft 6024 of the Engineering Computing Laboratory, both at the University of Wisconsin-Madison, were employed. The flow diagram describing the program for the solution of the two-cylinder problem is presented in Fig. 3.

Specify cylinder size parameters, ka_1 and ka_2, and cylinder separation parameter kl_{os}.

Calculate Bessel functions of the 1st and 2nd kinds and their derivatives on ka_1, ka_2, and kl_{os}.

Specify horizontal angle θ_{os}

Calculate matrix elements (coefficients of the unknowns a_n and b_n).
Matrix subroutine solves for the scattering coefficients a_n and b_n.

Calculate multiple scattering coefficients up to 9th order. Compare summation of the first nine orders with the a_n and b_n obtained above.

Use scattering coefficients to verify cylinder boundary conditions on the cylinder faces, $r_1 = a_1$, and $r_2 = a_2$.

Calculate the pressure modulus and phase on both cylinder faces at $20°$ increments and the ratio to single cylinder pressure.

Calculate horizontal force components (modulus and phase), ratio to single cylinder force, and C_m.

Specify new angle θ_{os}

Specify new cylinder separation kl_{os}

Figure 3.   Computer Flow Diagram: Two Cylinders

Calculations were aimed at the determination of the pressure distribution on the faces of the cylinders and the horizontal force components per unit depth. Pressures and forces were also calculated for the single isolated cylinder case of MacCamy and Fuchs (1954). Thus the pressures and forces which are presented herein are expressed as ratios to the single cylinder pressures and forces. These ratios clearly reveal the effect that the presence of the auxiliary cylinder has on the cylinder of interest.

All calculations were accomplished in non-dimensional form in terms of the parameters describing wave length and cylinder size, spacing, and orientation: ka_1, ka_2, kl_{os}, and θ_{os} (where a_1 and a_2 are the radii of cylinders 1 and 2 respectively).

The Two-Cylinder Solution. The primary objectives in studying the two-cylinder case are to illustrate the technique involved, to compare the direct method with the multiple scattering approach, and to lay the groundwork for future extensions. Thus the full range of cylinder sizes and spacings is not considered here.

Two series of calculations were made, both with the incident waves moving in the positive "x" direction ($\alpha = 0°$). In the first series the two cylinders were of equal size, $ka_1 = ka_2 = 0.40$. The horizontal spacing between cylinders, kl_{os}, was varied from 0.80 (cylinders touching) to 9.5 (approximately 1.5 wavelengths apart) in twenty steps, and the angular position of the second cylinder, θ_{os}, was varied from 0° to 90° in steps of 30°. Thus eighty combinations of angle and distance were considered.

In the second series cylinders of unequal size ($ka_1 = 0.40$, $ka_2 = 0.60$) were considered. The parameter kl_{os} was varied between 1.00 and 8.0 while the angular position of the second cylinder was varied between 0° (cylinder one leading) and 180° (cylinder two leading) in steps of 30°, providing 112 different locations of cylinder two in relation to cylinder one. For each of these situations the following items were calculated:

1. Basic scattering coefficients, by both the direct method and the multiple scattering approach.

2. Pressure amplitude and phase angles at 20° increments around the cylinder.

3. Ratio of pressure amplitude to the pressure amplitude on an isolated cylinder at 20° increments around the cylinder.

4. Force components in the two horizontal directions.

5. Ratio of force to that of a single cylinder (x-component only).

6. Equivalent mass coefficient (x-component) as defined by Morison, et al (1950).

Horizontal Force Components. Amplitudes and phase angles of the
horizontal force components (R_x, R_y, δ_x, δ_y as given in Eqs.
(14)) were calculated along with the ratio to the force on a
single cylinder (x-component only). Typical results for two
equal diameter cylinders and two unequal diameter cylinders are
in Tables 1 and 2, respectively. Furthermore force ratios for
the same two cases are shown graphically as follows:

Figure 4: $\theta_{os} = 0°$ and $180°$ Figure 6: $\theta_{os} = 60°$ and $120°$

Figure 5: $\theta_{os} = 30°$ and $150°$ Figure 7: $\theta_{os} = 90°$

The force ratios for both equal- and unequal-size cylinders
appear in each figure for easy comparison. Moreover in Fig. 7
force ratios for an infinite row of cylinders (ka = 0.400, $\theta_{os} = \pm 90°$) are included.

   The orthogonal or y-component of force was also calculated
(see Tables 1 and 2), and in one case rose to 67 percent of the
x-component force ($ka_1 = 0.400$, $ka_2 = 0.600$, $kl_{os} = 1.00$, $\theta_{os} = 30°$). Although the effect on the maximum resultant was gener-
ally less than 10 percent, partly due to the phase differences
between the x and y components, in one case the maximum resul-
tant was increased by 50 percent. From a design point of view,
either static or dynamic, both force components may be significant.

The Mass Coefficient. The force ratio mentioned above and in
Tables 1 and 2 can also be interpreted as the ratio of the mass
coefficient for one of two cylinders to the mass coefficient of a
single isolated cylinder. Therefore independent calculation of
the latter using the equations derived by MacCamy and Fuchs
(1954), permits determination of the former. Such values of C_m
are also included in Tables 1 and 2.

   It is of interest to note that C_m may differ significantly
from 2.0. In the limited range of this study C_m varies from
1.192 to 3.380 as shown in Table 2.

General Observations. The following general observations can be
made about the cases studied:

1. The force ratios are periodic in the spacing parameter kl_{os},
    with attenuated amplitude, not unlike that of Bessel functions.
2. The effect of a neighboring cylinder on the force of the first
    cylinder is very significant with as much as a 59 percent
    increase for two cylinders of equal size at $\theta_{os} = 90°$ and in
    contact; and up to 42 percent decrease in the instance of two
    unequal cylinders at $\theta_{os} = 0°$ and in contact.
3. Cylinders lined up in the direction of wave advance generally
    exhibit greater variation in the x-component of force than do
    cylinders lined up orthogonal to the wave advance vector.

Table 1. THEORETICAL FORCE: TWO EQUAL-DIAMETER CYLINDERS   ka(1) = ka(2) = 0.400

Cylinder Separation kl$_{os}$	Horizontal Angle θ$_{os}$	Cylinder No. 1						Cylinder No. 2					
		Force R$_x$	Phase δ$_x$	Coeff C$_m$	Force R$_y$	Phase δ$_y$	Force Ratio	Force R$_x$	Phase δ$_x$	Coeff C$_m$	Force R$_y$	Phase δ$_y$	Force Ratio
0.3000	0°	0.5904	178.9	1.476	0.0000	----	0.7187	0.6829	123.9	1.707	0.0000	----	0.8313
	30	0.7113	164.7	1.778	0.3084	- 51.5	0.8659	0.8396	130.8	2.099	0.3036	- 55.9	1.0220
	60	1.0731	153.6	2.683	0.2937	- 33.1	1.3063	1.1625	143.5	2.906	0.3374	- 56.7	1.4151
	90	1.3045	157.9	3.261	0.1075	78.2	1.5880	1.3045	157.9	3.261	0.1075	-101.8	1.5880
1.0000	0	0.6368	-177.2	1.592	0.0000	----	0.7752	0.7395	111.8	1.849	0.0000	----	0.9002
	30	0.6719	172.9	1.630	0.1702	- 56.2	0.8179	0.8032	121.7	2.008	0.1428	- 56.4	0.9777
	60	0.8493	161.1	2.123	0.1694	- 28.2	1.0339	0.9525	141.9	2.381	0.1704	- 64.2	1.1594
	90	1.0052	163.7	2.513	0.0922	67.3	1.2236	1.0052	163.7	2.513	0.0922	-112.7	1.2236
1.3000	0	0.7212	-174.1	1.803	0.0000	----	0.8780	0.7937	94.5	1.984	0.0000	----	0.9661
	30	0.7001	178.9	1.750	0.1201	- 73.5	0.8523	0.8165	106.8	2.041	0.0767	- 59.8	0.9940
	60	0.7594	166.0	1.924	0.1269	- 36.8	0.9366	0.8916	134.5	2.229	0.0980	- 78.8	1.0854
	90	0.9000	166.1	2.250	0.0811	50.6	1.0955	0.9000	166.1	2.250	0.0811	-129.5	1.0955
1.6000	0	0.8158	-174.1	2.039	0.0000	----	0.9930	0.8249	76.9	2.062	0.0000	----	1.0041
	30	0.7605	-178.2	1.901	0.0987	- 95.7	0.9258	0.8289	91.4	2.072	0.0501	- 58.7	1.0090
	60	0.7460	170.2	1.865	0.1091	- 52.2	0.9081	0.8702	126.1	2.175	0.0621	- 93.6	1.0593
	90	0.8545	167.5	2.136	0.0736	32.6	1.0402	0.8545	167.5	2.136	0.0736	-147.4	1.0402
2.0000	0	0.9217	-178.3	2.304	0.0000	----	1.1219	0.8417	53.2	2.104	0.0000	----	1.0245
	30	0.8505	-178.7	2.126	0.0830	-130.1	1.0352	0.8340	70.8	2.085	0.0411	- 57.1	1.0151
	60	0.7558	174.3	1.890	0.0954	- 78.3	0.9200	0.8553	114.5	2.138	0.0354	-108.1	1.0411
	90	0.8233	168.9	2.058	0.0654	7.6	1.0021	0.8233	168.9	2.058	0.0654	-172.4	1.0021
2.5000	0	0.9675	173.6	2.419	0.0000	----	1.1778	0.8363	24.0	2.091	0.0000	----	1.0180
	30	0.9195	176.4	2.299	0.0703	-177.0	1.1193	0.8247	45.3	2.062	0.0423	- 74.8	1.0039
	60	0.7971	176.6	1.993	0.0833	-115.2	0.9703	0.8407	100.0	2.102	0.0227	-110.6	1.0234
	90	0.8046	170.4	2.011	0.0560	- 23.8	0.9794	0.8046	170.4	2.011	0.0560	156.2	0.9794
3.0000	0	0.9102	166.7	2.276	0.0000	----	1.1080	0.8212	- 4.2	2.053	0.0000	----	0.9997
	30	0.9143	170.7	2.285	0.0612	134.6	1.1130	0.8101	20.7	2.025	0.0410	-106.4	0.9861
	60	0.8377	176.2	2.094	0.0741	-153.6	1.0197	0.8280	85.7	2.070	0.0237	-119.6	1.0079
	90	0.7977	171.7	1.994	0.0477	- 53.8	0.9711	0.7977	171.7	1.994	0.0477	126.2	0.9711

Table 2.   THEORETICAL FORCE: TWO CYLINDERS OF UNEQUAL DIAMETER   ka(1) = 0.400, ka(2) = 0.600

Cylinder Separation kl_{os}	Horizontal Angle θ_{os}	Cylinder No. 1						Cylinder No. 2					
		Force R_x	Phase δ_x	Coeff C_m	Force R_y	Phase δ_y	Force Ratio	Force R_x	Phase δ_x	Coeff C_m	Force R_y	Phase δ_y	Force Ratio
1.0000	0°	0.4769	-166.3	1.192	0.0000	-----	0.5805	1.0569	109.1	1.761	0.0000	-----	0.9184
	30	0.5629	166.6	1.407	0.3784	- 56.5	0.6852	1.1717	116.7	1.953	0.2551	- 79.4	1.0182
	60	1.0151	146.0	2.538	0.3651	- 35.6	1.2356	1.4176	132.2	2.363	0.3274	- 82.2	1.2319
	90	1.3521	150.7	3.380	0.1729	73.7	1.6459	1.5049	150.6	2.508	0.1529	-110.1	1.3077
	120	1.2106	161.2	3.026	0.4658	139.3	1.4736	1.2571	175.8	2.095	0.2516	155.1	1.0923
	150	0.8065	166.2	2.016	0.4175	159.2	0.9818	0.9769	-148.1	1.628	0.2951	149.4	0.8489
	180	0.6035	164.3	1.509	0.0000	-----	0.7346	0.9421	-127.7	1.570	0.0000	-----	0.8187
1.3000	0	0.6560	-159.9	1.640	0.0000	-----	0.7985	1.1445	90.4	1.908	0.0000	-----	0.9946
	30	0.5943	-174.1	1.486	0.2244	- 70.5	0.7235	1.1702	101.8	1.950	0.0927	- 83.7	1.0168
	60	0.7279	158.7	1.820	0.2364	- 35.9	0.8860	1.2561	127.8	2.093	0.1549	-100.8	1.0915
	90	0.9750	158.9	2.437	0.1582	54.9	1.1868	1.2560	158.1	2.093	0.1352	-129.2	1.0914
	120	0.9539	168.4	2.385	0.2307	136.0	1.1612	1.0783	-165.1	1.797	0.1583	170.3	0.9370
	150	0.7833	168.1	1.958	0.1887	174.6	0.9535	0.9983	-124.2	1.664	0.1695	155.7	0.8675
	180	0.7179	163.3	1.795	0.0000	-----	0.8739	1.0417	-106.9	1.736	0.0000	-----	0.9052
1.7000	0	0.9009	-164.3	2.252	0.0000	-----	1.0967	1.2088	65.3	2.015	0.0000	-----	1.0504
	30	0.7717	-168.5	1.929	0.1774	-101.9	0.9394	1.1979	80.3	1.996	0.0403	- 59.3	1.0409
	60	0.6695	170.3	1.674	0.2015	- 56.9	0.8150	1.2216	116.8	2.036	0.0738	-128.8	1.0615
	90	0.8581	162.8	2.145	0.1462	29.6	1.0445	1.1751	160.9	1.958	0.1209	-156.6	1.0211
	120	0.8959	170.2	2.240	0.1347	128.4	1.0905	1.0372	-147.2	1.729	0.1354	164.4	0.9013
	150	0.8109	167.4	2.027	0.1125	-166.3	0.9871	1.1038	-100.7	1.848	0.1314	147.7	0.9635
	180	0.8016	162.3	2.004	0.0000	-----	0.9758	1.2083	- 84.6	2.014	0.0000	-----	1.0499
2.1000	0	1.0662	-175.0	2.666	0.0000	-----	1.2979	1.2184	40.2	2.031	0.0000	-----	1.0587
	30	0.9366	-173.4	2.342	0.1525	-139.0	1.1412	1.1961	58.6	1.994	0.0538	- 46.0	1.0394
	60	0.7121	173.1	1.780	0.1808	- 85.3	0.8669	1.2042	104.9	2.007	0.0270	-147.4	1.0464
	90	0.8071	165.6	2.018	0.1318	3.5	0.9825	1.1416	162.6	1.903	0.1069	174.7	0.9920
	120	0.8703	170.4	2.177	0.0861	125.1	1.0600	1.0626	-131.6	1.771	0.1229	149.2	0.9234
	150	0.8160	166.1	2.040	0.0950	-149.5	0.9934	1.2251	- 82.5	2.042	0.1120	132.4	1.0645
	180	0.8294	160.9	2.073	0.0000	-----	1.0096	1.3313	67.1	2.219	0.0000	-----	1.1569

Figure 4. Force Ratio Versus Cylinder Separation, Two Cylinders, $\theta_{os} = 0°$ and $180°$
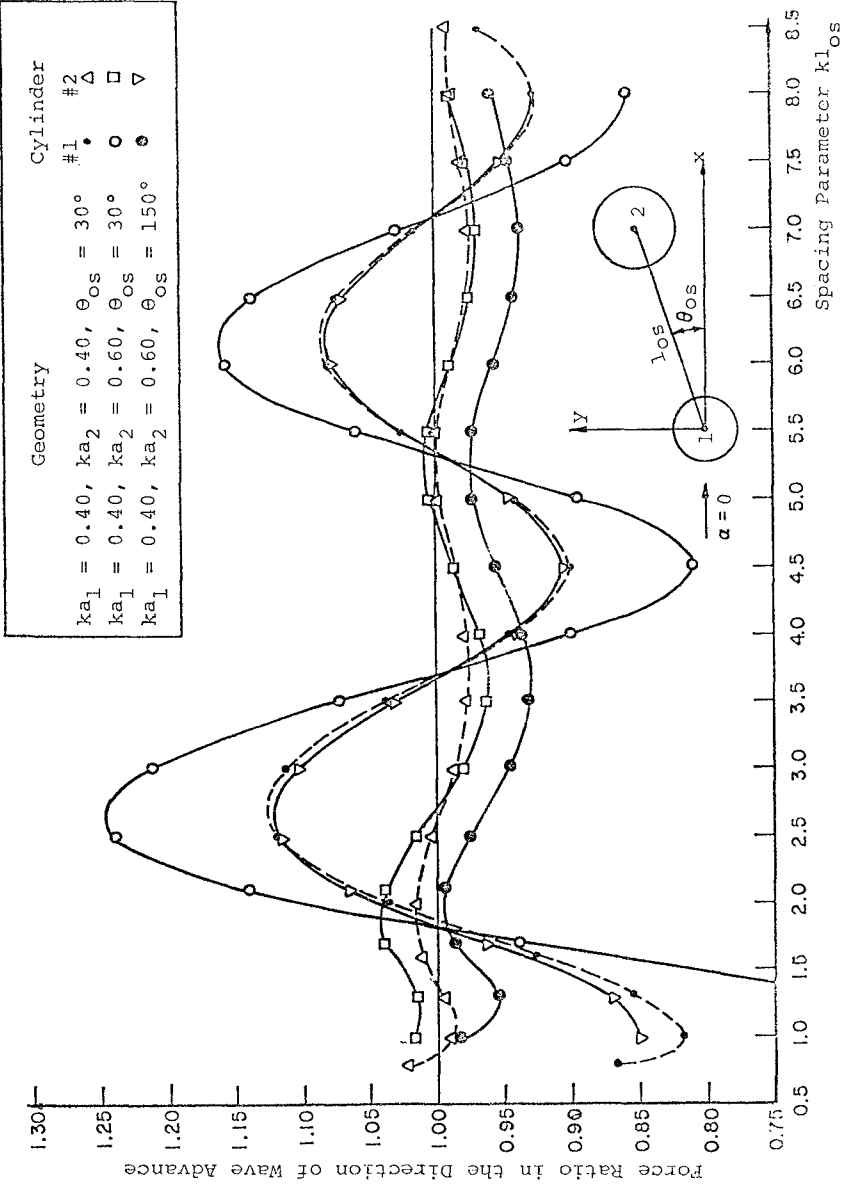
Figure 5. Force Ratio Versus Cylinder Separation, Two Cylinders, $\theta_{os} = 30°$ and $150°$
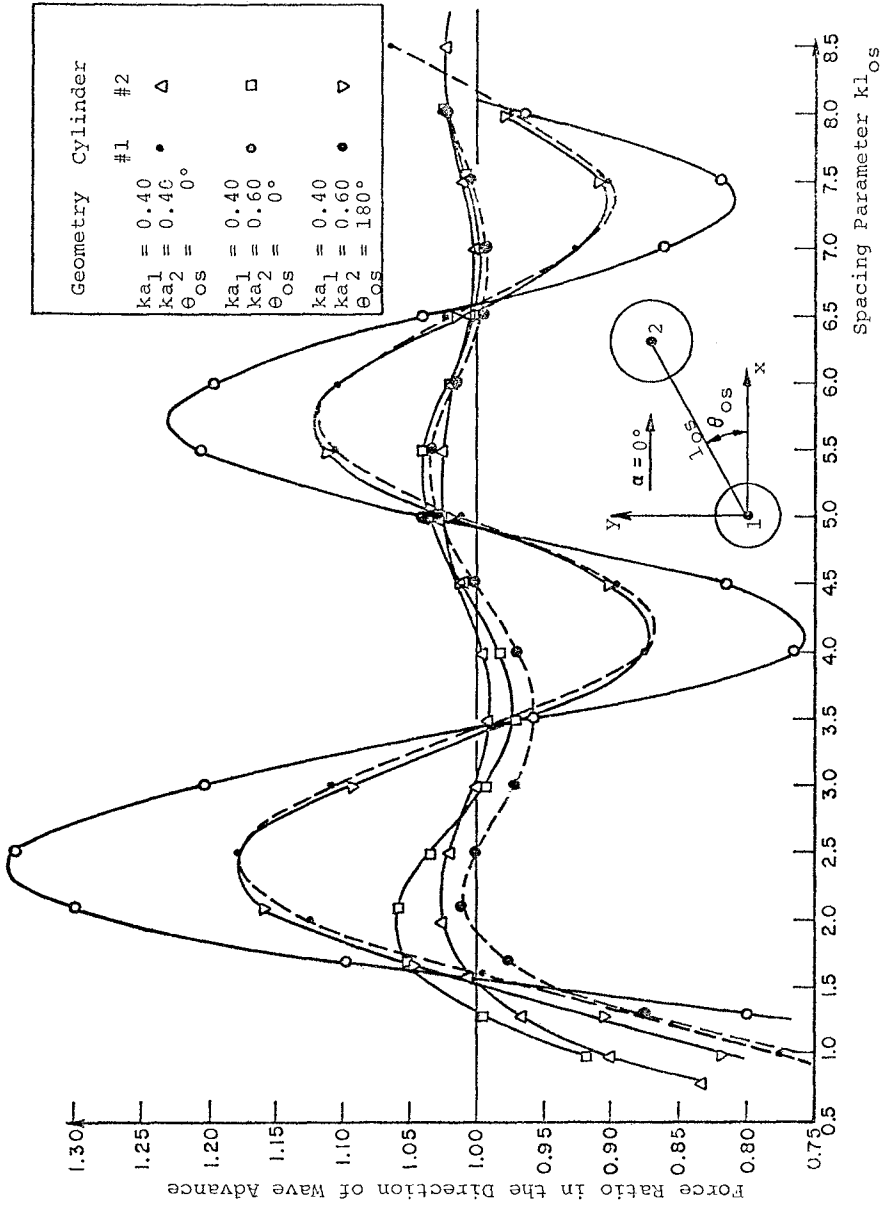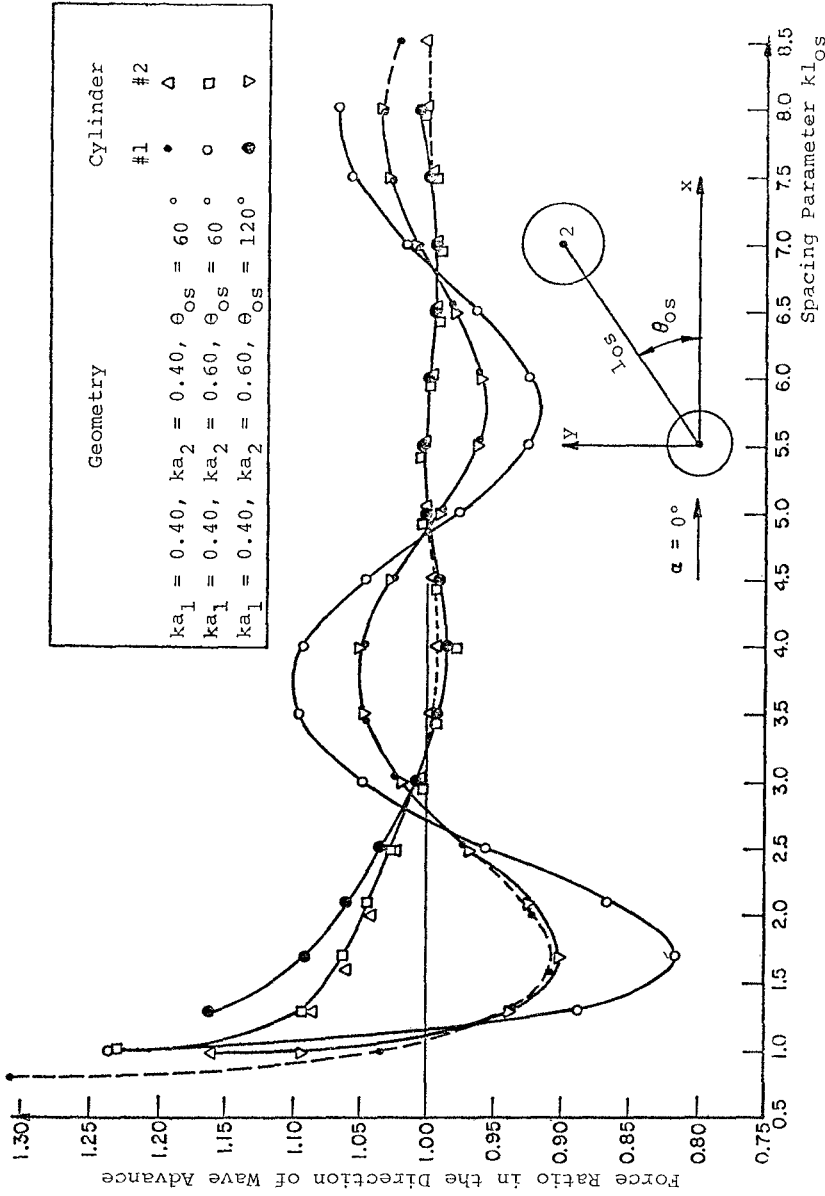
Figure 6. Force Ratio Versus Cylinder Separation, Two Cylinders, $\theta = 60°$ and $120°$
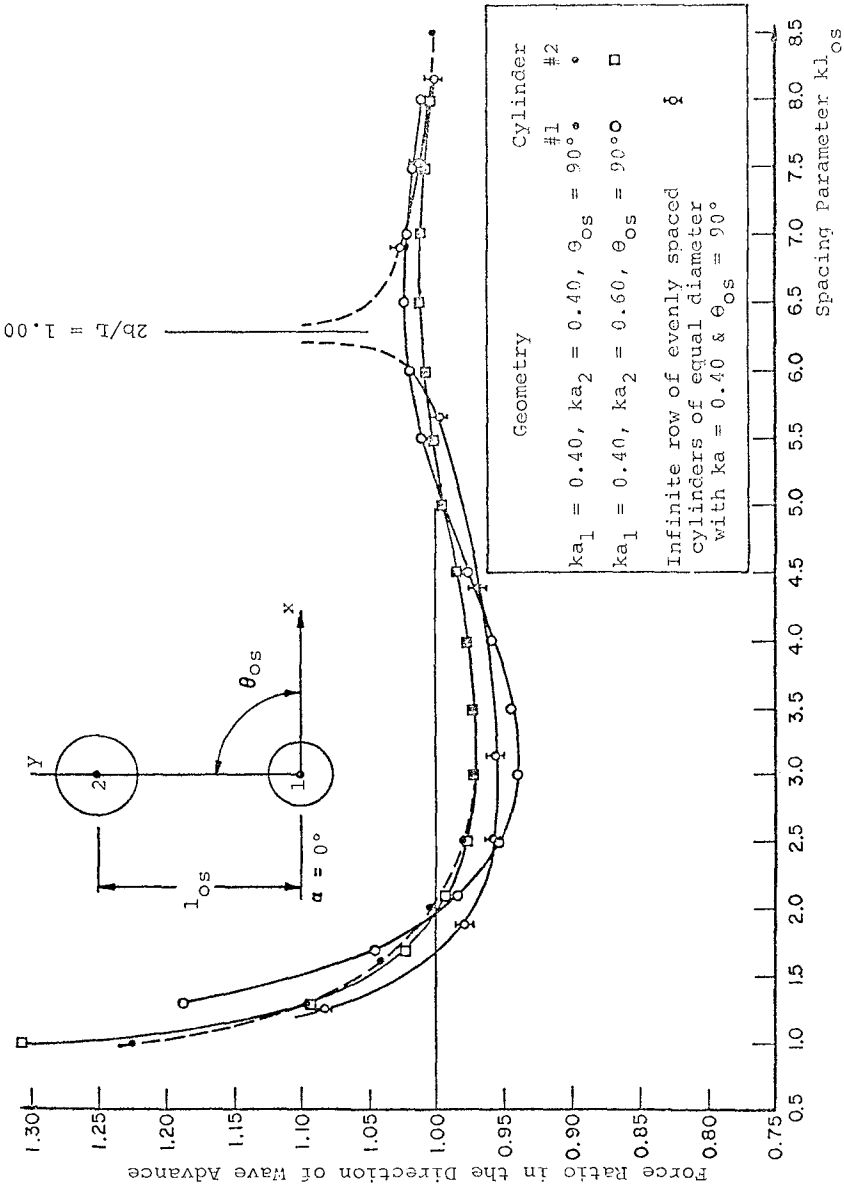
Figure 7.   Force Ratio Versus Cylinder Separation,
           Two Cylinders, $\theta_{os} = 90°$

Single Isolated Cylinder Pressure and Force. By way of verifica-
tion, the pressure amplitudes for single, isolated cylinders with
ka = .5 and ka = 1.0 were checked against those published by
Wiener (1947) for sound diffraction by a single rigid cylinder.
Agreement to the 4th decimal place was obtained.

CONCLUSIONS

1. A means of calculating the pressures and forces on a cluster
    of vertical circular cylinders is developed. The method
    employs diffraction theory, but avoids multiple scattering
    techniques, in favor of a direct, matrix solution.

2. Theoretical calculations for the force in the direction of
    wave advance reveal as much as a 60% departure from the force
    on a single isolated cylinder in the instance of two equal-
    diameter cylinders and as much as a 65% departure for two
    cylinders of unequal diameter. The force on a given cylinder
    is thus significantly affected by the presence of neighboring
    cylinders. The mass coefficient, C_M, is found to range from
    1.19 to 3.38, significant departures from the often assumed
    value of 2.0

3. The component of force perpendicular to the direction of wave
    advance is found to be very significant when the cylinders
    are close together, rising in one case to 67% of the force
    component in the direction of wave advance. Although the
    effect on the maximum resultant is generally less than 10%, in
    one case a 50% increase is found. Both force components may
    be significant for design of cylinders used for offshore tower
    supports.

4. The method is not restricted to water waves, but can also be
    applied to other cases of scalar scattering in acoustics or
    electromagnetics.

ACKNOWLEDGEMENTS

REFERENCES

Abramowitz, Milton, and Irene A. Stegun, (1965), Handbook of
    Mathematical Functions, National Bureau of Standards, 1964,
    or Dover 1965.

Ippen, Arthur T., (1966), Estuary and Coastline Hydrodynamics,
    McGraw-Hill.

MacCamy, R.C., and R.A. Fuchs, (1954), Wave Force on Piles: A
    Diffraction Theory, U.S. Army Coastal Engineering Research
    Center (formerly Beach Erosion Board), Technical Memorandum
    No. 69.

Morison, J.R., M.P. O'Brien, R.W. Johnson, and S.A. Schaaf,
    (1950), "The Force Exerted by Surface Waves on Piles,"
    Petroleum Transactions, American Institute of Mining and
    Metallurgical Engineers, Vol. 189, pp. 149-154.

Spring, Bradford H., (1973), Interaction of Plane Water Waves
    With Vertical Circular Cylinders, Unpublished doctoral
    thesis, Department of Civil and Environmental Engineering,
    University of Wisconsin-Madison.

Twersky, Victor, (1952), "Multiple Scattering of Radiation by an
    Arbitrary Configuration of Parallel Cylinders," Journal of
    the Acoustical Society of America, Vol. 24, January 1952,
    pp. 42-46.

Watson, G.N., (1966), A Treatise on the Theory of Bessel Func-
    tions, Cambridge University Press, First paperback edition.

Wiener, Francis M., (1947), "Sound Diffraction by Rigid Spheres
    and Circular Cylinders," Journal of the Acoustical Society
    of America, Vol. 19, pp. 444-451.

CHAPTER 108

LAMINAR BOUNDARY LAYER AROUND A CIRCULAR CYLINDER
UNDER OSCILLATORY WAVES

Yuichi Iwagaki
Professor

and

Hajime Ishida
Graduate Student

Department of Civil Engineering
Kyoto University
Kyoto, Japan

ABSTRACT

A solution of water particle velocities in the boundary layer developed by monochromatic waves on the surface of a circular cylinder is obtained by applying the boundary layer approximations and perturbation method to the Navier-Stokes and continuity equations represented in the cylindrical coordinates. Since, in this process, it is necessary to give the velocity outside the boundary layer, the water particle velocities of diffracted waves around the cylinder are derived from MacCamy-Fuchs' velocity potential. Moreover, the occurrence of laminar flow separation is explained by using this solution.

On the other hand, using a hydrogen bubble tracer some experiments have been performed about the water particle velocities of diffracted waves, velocity profiles in the boundary layer and occurrence of wake vortices. These results are compared with theoretical ones.

INTRODUCTION

In estimation of the wave force on a circular cylinder, the Morison equation expressed as the sum of the inertia and drag forces is generally used. However, concerning the mechanism how the drag force is induced by wave motions, few papers have been reported yet, and therefore, it is right to say that the relationship between the drag coefficients under wave motion and in steady state flow is not clear yet.

On the other hand, in the diffraction theory presented by MacCamy and Fuchs[1] to estimate the wave force on a large-diameter pile, since the drag force due to flow separation and subsequent vortex formation can not be contained because of neglecting the viscosity of the fluid, an applicable range of their theory is limited.

Therefore, in order to estimate the wave force more correctly, it is necessary to make progress in the study based on an idea of making clear the interaction between waves and the pile, that is, investigating the effect of the pile on the waves, and next, making clear the internal mechanism of the affected waves, and finally, evaluating the force on the pile in such velocity and pressure fields. From this viewpoint, the present study deals with the laminar boundary layer on the surface of a circular cylinder developed by monochromatic waves.

The concept of boundary layer was introduced by Prandtl in 1904, and studies of the laminar flow around a circular cylinder in steady state have been made by Blasius, Karman, Hiementz, Porlhausen, Howarth and many other investigators. As a result, a lot of important facts were found about separation point, pressure distribution, characteristics of the drag coefficient and so on[2],[3]. With respect to the laminar boundary layer on an oscillating circular cylinder in still water, Schlichting solved the boundary layer equation using successive approximations, and explained the existence of mass transport velocity outside the boundary layer[3].

On the other hand, Keulegan and Carpenter investigated experimentally the relationship between the flow pattern around a horizontal cylinder installed under the nodal area of standing waves and the wave force acting on the cylinder, and found that the case when Keulegan-Carpenter's number is equal to 15 is a critical condition yielding the lowest value of the inertia coefficient and the largest value of the drag coefficient[4]. The authors also investigated variations of the drag and inertia coefficients with Keulegan-Carpenter's number for progressive waves[5]. However, these are not mentioned in this paper.

THEORY

The coordinate system is shown in Fig.1, in which $(\theta, \hbar, z)$ and (x, y, z) denote the cylindrical coordinates and boundary layer coordinates respectively.

(1) Water Particle Velocity around Circular Cylinder

The water particle velocity in the boundary layer must connect with the potential velocity outside the boundary layer that is the water particle velocity of diffracted waves.

Let U, V and W be the water particle velocities of diffracted waves in the direction of the coordinates θ, $\hbar$ and z respectively. These are determined by MacCamy-Fuchs' velocity potential Φ[1] as follows:
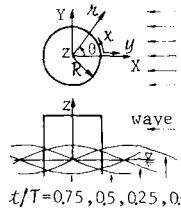
Fig.1 Coordinate system.

$$U = \frac{1}{\hbar}\frac{\partial \Phi}{\partial \theta} = \frac{\pi H}{T} \cdot \frac{\cosh kh(1+z/h)}{k\hbar \; \sinh kh} \left[-\sum_{n=0}^{\infty} E_n n \{J_n(k\hbar) - \frac{J_n'(kR)}{H_n^{(2)}(kR)} H_n^{(2)}(k\hbar)\} \sin(n\theta)\right] e^{i\sigma t} \quad , \cdots (1)$$

$$V = \frac{\partial \Phi}{\partial \hbar} = \frac{\pi H}{T} \cdot \frac{\cosh kh(1+z/h)}{\sinh kh} \left[\sum_{n=0}^{\infty} E_n \{J_n'(k\hbar) - \frac{J_n'(kR)}{H_n^{(2)}(kR)} H_n^{(2)}(k\hbar)\} \cos(n\theta)\right] e^{i\sigma t} \quad , \cdots (2)$$

$$W = \frac{\partial \Phi}{\partial z} = \frac{\pi H}{T} \cdot \frac{\sinh kh(1+z/h)}{\sinh kh} \left[\sum_{n=0}^{\infty} E_n \{J_n(k\hbar) - \frac{J_n'(kR)}{H_n^{(2)}(kR)} H_n^{(2)}(k\hbar)\} \cos(n\theta)\right] e^{i\sigma t} \quad , \cdots (3)$$

in which H:wave height, T:wave period, h:water depth, k:wave number, σ:angular frequency, R:radius of cylinder, t:time, J_n, $H_n^{(2)}$ and J_n', $H_n^{(2)'}$ denote Bessel function of order n, Hankel function of second kind of order n and their derivatives respectively, and $E_0 = 1$ when n=0 and $E_n = 2(i)^n$ when n≥1.

(2) Three Dimensional Laminar Boundary Layer Theory on Circular Cylinder

Using the relations $\theta = x/R$ and $\hbar = R+y$, the Navier-Stokes and continuity equations expressed by the cylindrical coordinates θ, $\hbar$ and z are represented in the boundary layer coordinates x, y and z as follows:

$$
\left.\begin{array}{l}
u_t + (uu_x + uv/R)/(1+y/R) + vu_y + wu_z = -(1/\rho)p_x/(1+y/R) \\[4pt]
\quad + \nu\{u_{yy} + u_y/R(1+y/R) + (u_{xx} - u/R^2 + 2v_x/R)/(1+y/R)^2 + u_{zz}\}\quad , \\[10pt]
w_t + uw_x/(1+y/R) + vw_y + ww_z = -g - (1/\rho)p_z \\[4pt]
\quad + \nu\{w_{yy} + w_y/R(1+y/R) + w_{xx}/(1+y/R)^2 + w_{zz}\}\quad , \\[10pt]
u_x/(1+y/R) + v/R(1+y/R) + v_y + w_z = 0\quad ,
\end{array}\right\}\quad \cdots\cdots\cdots\cdots(4)
$$

in which u, v and w denote the water particle velocities in the direction of coordinates x, y and z respectively, and ρ:density, p:pressure, g:acceleration of gravity, ν:kinematic viscosity.

Taking $U_M = \pi H/T$ as a representative velocity and the wave length $L = 2\pi/k$ as a representative length, the quantities containing in Eq.(4) are replaced in the following dimensionless forms:

$$
\left.\begin{array}{l}
x' = kx,\qquad y' = \sqrt{Re}\,ky,\qquad z' = kz,\qquad t' = \sigma t,\qquad Re = c/(k\nu), \\[8pt]
u' = u/U_M,\qquad v' = \sqrt{Re}\,v/U_M,\qquad w' = w/U_M,\qquad p' = (p+\rho gz)/(\rho c U_M),
\end{array}\right\}\quad \cdots\cdots\cdots\cdots(5)
$$

in which c:celerity and Re is a convenient Reynolds number to magnify the coordinate y in the boundary layer. Hereafter, however, for the sake of convenience, dimensionless quantities are denoted without prime.

Rearranging Eq.(4) by substituting Eq.(5), the following dimensionless equations are obtained with respect to dimensionless velocities and pressure, containing the parameters U_M/c, $1/kR\sqrt{Re}$ and $1/Re$:

$$
\left.\begin{array}{l}
u_t + (U_M/c)\{(uu_x + uv/kR\sqrt{Re})/(1+y/kR\sqrt{Re}) + vu_y + wu_z\} \\[4pt]
\quad = -p_x/(1+y/kR\sqrt{Re}) + u_{yy} + u_y/\{kR\sqrt{Re}(1+y/kR\sqrt{Re})\} \\[4pt]
\quad\quad + \{u_{xx}/Re - u/(kR\sqrt{Re})^2 + 2v_x/RekR\sqrt{Re}\}/(1+y/kR\sqrt{Re})^2 + u_{zz}/Re\quad , \\[10pt]
w_t + (U_M/c)\{uw_x/(1+y/kR\sqrt{Re}) + vw_y + ww_z\} \\[4pt]
\quad = -p_z + w_{yy} + w_y/\{kR\sqrt{Re}(1+y/kR\sqrt{Re})\} + w_{xx}/\{Re(1+y/kR\sqrt{Re})^2\} + w_{zz}/Re\quad , \\[10pt]
(u_x + v/kR\sqrt{Re})/(1+y/kR\sqrt{Re}) + v_y + w_z = 0\quad ,
\end{array}\right\}\quad \cdots(4')
$$

in which $U_M/c = \pi H/L$ is of the order of the wave steepness in magnitude, and is generally supposed to be a very small quantity. Therefore, denoting it by ε_1 as

$$\varepsilon_1 = U_M/c = \pi H/L \ll 1 , \qquad \cdots\cdots\cdots\cdots\cdots\cdots\cdots (6)$$

the dimensionless velocities u, v and w are expanded into power series of ε_1 as follows:

$$u = u_0 + \varepsilon_1 u_1 + \varepsilon_1^2 u_2 + \cdots, \quad v = v_0 + \varepsilon_1 v_1 + \varepsilon_1^2 v_2 + \cdots, \quad w = w_0 + \varepsilon_1 w_1 + \varepsilon_1^2 w_2 + \cdots . \quad \cdots (7)$$

Also, $1/kR\sqrt{Re} = \sqrt{\nu T/2\pi}/R$ is of the order of the ratio of the boundary layer thickness to the radius of cylinder in magnitude, which may generally be very small. Therefore, denoting it by ε_2 as

$$\varepsilon_2 = 1/kR\sqrt{Re} = \sqrt{\nu T/2\pi}/R \ll 1 , \qquad \cdots\cdots\cdots\cdots\cdots\cdots\cdots (8)$$

the following approximate series can be introduced:

$$1/(1 + y/kR\sqrt{Re}) = 1/(1 + \varepsilon_2 y) = 1 - \varepsilon_2 y + \varepsilon_2^2 y^2 - \cdots . \qquad \cdots\cdots\cdots\cdots\cdots (9)$$

In this paper, it is supposed that the order of ε_2 in magnitude is the same as ε_1 or smaller than ε_1. Moreover, the condition is limited within the range of $kR = 2\pi R/L \lesssim 1$, and accordingly the order of $1/Re$ is smaller than that of the square of ε_2 since the relation $1/Re = (kR)^2 \varepsilon_2^2 \lesssim \varepsilon_2^2$ is established.

Then, it is supposed that the velocities outside the boundary layer are represented in terms of the water particle velocities of diffracted waves on the surface of the cylinder obtained by substituting $\kappa = R$ into Eqs.(1) and (3). Designating them by U_R and W_R after dividing by U_M, these can be written in the following dimensionless forms:

$$U_R = \frac{\cosh(kh+z)}{\sinh kh} \frac{2i}{\pi(kR)^2} \left[\sum_{n=0}^{\infty} \frac{n \cdot E_n}{H_n^{(2)'}(kR)} \sin\frac{nx}{kR} \right] e^{it} \quad , \qquad \cdots\cdots\cdots\cdots (10)$$

$$W_R = \frac{\sinh(kh+z)}{\sinh kh} \frac{2i}{\pi \cdot kR} \left[\sum_{n=0}^{\infty} \frac{n \cdot E_n}{H_n^{(2)'}(kR)} \cos\frac{nx}{kR} \right] e^{it} \quad . \qquad \cdots\cdots\cdots\cdots (11)$$

The dimensionless pressure gradients are approximately expressed by using Eqs.(10) and (11)

$$-p_x = U_{R_t} + \varepsilon_1 (U_R U_{R_x} + W_R U_{R_z}) \quad , \qquad -p_z = W_{R_t} + \varepsilon_1 (U_R W_{R_x} + W_R W_{R_z}) \quad . \qquad \cdots\cdots\cdots\cdots (12)$$

By rearranging Eq.(4´) with respect to the powers of ε_1 after substituting Eqs.(5) to (11) into Eq.(4´), the first approximate equations concerning ε_1^0 (order of the zeroth power of ε_1) are obtained as follows:

$$u_{0_t} - u_{0_{yy}} = U_{R_t} , \quad w_{0_t} - w_{0_{yy}} = W_{R_t} , \quad u_{0_x} + v_{0_y} + w_{0_z} = 0 . \qquad \cdots\cdots\cdots\cdots (13)$$

The boundary conditions are given as

$$y = 0: \ u_0 = v_0 = w_0 = 0 , \qquad y = \infty: \ u_0 = U_R, \ w_0 = W_R . \qquad \cdots\cdots\cdots\cdots (14)$$

The solutions of Eq.(13) satisfying Eq.(14), that is, the first approximate solutions can be obtained in the similar manner to that by Schlichting[3], as follows:

$$u_{1st} = u_0 = \zeta_0' U_0 e^{it}, \quad w_{1st} = w_0 = \zeta_0' W_0 e^{it}, \quad v_{1st} = v_0 = -\zeta_0 (U_{0_x} + W_{0_z}) e^{it}, \quad \cdots \cdots (15)$$

in which

$$\zeta_0' = 1 - e^{-(1+i)y/\sqrt{2}}, \qquad \zeta_0 = y - \frac{1-i}{\sqrt{2}} \{1 - e^{-(1+i)y/\sqrt{2}}\},$$
$$U_0 = U_R/e^{it}, \qquad W_0 = W_R/e^{it}. \qquad \left.\begin{array}{l} \\ \\ \end{array}\right\} \quad \cdots \cdots (16)$$

Although U_0 and W_0 are real functions in the case of oscillating flow, they are complex functions in the case of wave motion as recognized from Eqs.(10) and (11). Therefore, the actual water particle velocities are given by the real parts in Eq.(15).

The second approximate equations concerning $\varepsilon_1{}^1$ (order of the first power of ε_1) are obtained as

$$u_{1_t} - u_{1_{yy}} = (U_R U_{R_x} + W_R U_{R_z}) - (u_0 u_{0_x} + v_0 u_{0_y} + w_0 u_{0_z}) + (\varepsilon_2/\varepsilon_1) u_{0_y},$$
$$w_{1_t} - w_{1_{yy}} = (U_R W_{R_x} + W_R W_{R_z}) - (u_0 w_{0_x} + v_0 u_{0_y} + w_0 w_{0_z}) + (\varepsilon_2/\varepsilon_1) w_{0_y}, \left.\begin{array}{l} \\ \\ \\ \end{array}\right\} \quad \cdots \cdots (17)$$
$$u_{1_x} + v_{1_y} + w_{1_z} = (\varepsilon_2/\varepsilon_1)(y u_{0_x} - v_0),$$

and the boundary conditions are given by

$$y=0: \ u_1 = v_1 = w_1 = 0, \qquad y=\infty: \ u_{1_y} = 0, \ w_{1_y} = 0. \qquad \cdots \cdots \cdots \cdots \cdots (18)$$

Among the solutions of Eq.(17) satisfying Eq.(18), u_1 is described as follows:

$$u_1 = (\varepsilon_2/\varepsilon_1) \zeta_1' U_0 e^{i\sigma t}$$
$$+ \zeta_{1a}' (U_0 U_{0_x} + W_0 W_{0_z}) e^{2i\sigma t} + \zeta_{1d}' (U_0 W_{0_z} - W_0 U_{0_z}) e^{2i\sigma t}$$
$$+ \zeta_{1b}' \{ (\hat{U}_0 \hat{U}_{0_x} + \check{U}_0 \check{U}_{0_x}) + (\hat{W}_0 \hat{U}_{0_z} + \check{W}_0 \check{U}_{0_z}) \}$$
$$+ \zeta_{1c}' \{ (\hat{U}_0 \check{U}_{0_x} - \check{U}_0 \hat{U}_{0_x}) + (\hat{U}_0 \check{W}_{0_z} - \check{U}_0 \hat{W}_{0_z}) \}$$
$$+ \zeta_{1e}' \{ (\hat{U}_0 \hat{W}_{0_z} + \check{U}_0 \check{W}_{0_z}) - (\hat{W}_0 \hat{U}_{0_z} + \check{W}_0 \check{U}_{0_z}) \} \qquad , \qquad \cdots \cdots \cdots \cdots (19)$$

in which

$$\zeta_1' = \frac{1}{\sqrt{2}} \eta' e^{-(1+i)\eta'},$$
$$\zeta_{1a}' = -\frac{i}{2} e^{-\sqrt{2}(1+i)\eta'} + \frac{i}{2} e^{-(1+i)\eta'} + \frac{1-i}{2} \eta' e^{-(1+i)\eta'},$$
$$\zeta_{1d}' = -\frac{7i}{4} e^{-\sqrt{2}(1+i)\eta'} + \frac{3i}{2} e^{-(1+i)\eta'} + \frac{1-i}{2} \eta' e^{-(1+i)\eta'} + \frac{i}{4} e^{-2(1+i)\eta'}, \left.\begin{array}{l} \\ \\ \\ \\ \end{array}\right\} \quad \cdots (20)$$

$$\zeta_{1b}^{\prime}=-\frac{3}{4}+\frac{1}{4}e^{-2\eta^{\prime}}+e^{-\eta^{\prime}}(\frac{1}{2}\cos\eta^{\prime}+2\sin\eta^{\prime})-\frac{\eta^{\prime}}{2}e^{-\eta^{\prime}}(\cos\eta^{\prime}-\sin\eta^{\prime}) ,$$

$$\zeta_{1c}^{\prime}=-\frac{3}{4}-\frac{1}{4}e^{-2\eta^{\prime}}+e^{-\eta^{\prime}}(\cos\eta^{\prime}-\frac{1}{2}\sin\eta^{\prime})+\frac{\eta^{\prime}}{2}e^{-\eta^{\prime}}(\cos\eta^{\prime}+\sin\eta^{\prime}) ,$$

$$\zeta_{1e}^{\prime}=-\frac{1}{2}+e^{-\eta^{\prime}}(\frac{1}{2}\cos\eta^{\prime}+\sin\eta^{\prime})-\frac{\eta^{\prime}}{2}e^{-\eta^{\prime}}(\cos\eta^{\prime}-\sin\eta^{\prime}) ,$$

$$\Biggr\} \quad \cdots\cdot(20)$$

and $\eta^{\prime}=y/\sqrt{2}$, and $\wedge$ and $\vee$ indicate real and imaginary parts respectively.
The form of Eq.(19) was identically determined under consideration that the right-
hand side of Eq.(17) contains the products of complex number, and unknown functions
contained in Eq.(19), shown by Eq.(20), were obtained as the sum of homogeneous
solution and paticular one, in the same manner as for the first approximate solu-
tions. The second approximate solution of u is indicated by using Eqs.(15) and
(19) as

$$u_{2nd}=u_0+\varepsilon_1 u_1 . \qquad \cdots\cdots\cdots\cdots\cdots\cdots\cdots\cdots(21)$$

It is recognized that the second approximate solution contains the second harmonic
component and the mass transport velocity in addition to the fundamental component.
The actual velocity is given by the real part in Eq.(21). $\zeta_0^{\prime}$, $\zeta_{1a}^{\prime}$ and $\zeta_{1b}^{\prime}$ are the
same as those obtained by Schlichting[3], and however, $\zeta_1^{\prime}$, $\zeta_{1c}^{\prime}$, $\zeta_{1d}^{\prime}$ and $\zeta_{1e}^{\prime}$ appear
as new functions in this study because the boundary layer is treated as three
dimensional, the curvature of the circular cylinder is taken into account and the
velocities outside the boundary layer are given by the water particle velocities
of not oscillating flow but waves.

COMPUTATIONS AND DISCUSSIONS

    Fig.2 shows the ratio of the water particle velocity of diffracted waves U
calculated by Eq.(1) to the maximum value of the water particle velocity of pro-
gressive waves under the condition $\theta=90°$ and $t/T=0.25$. It is found from this
figure that the water particle velocity of diffracted waves on the surface of
cylinder $(r/R=1)$ is twice as large as the velocity of progressive waves under the
condition that the radius of cylinder is small compared with the wave length
$(kR\lesssim0.5)$, and this result corresponds to the theoretical fact that the potential
velocity on the surface of cylinder at $\theta=90°$ is twice as large as the current
velocity in steady flow[3]. The velocity decreases rapidly far from the cylinder,
and agrees roughly with that of progressive waves under the condition $r/R\gtrsim5$.
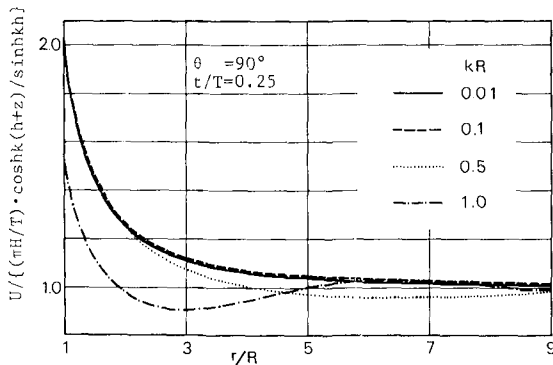

Fig.2 Computed water
particle velocities of
diffracted waves around
circular cylinder.

Concerning the velocity profile in the boundary layer, some results of calculation of the second approximation u_{2nd} represented by Eq.(21) are shown. The value of u_{2nd} is determined by giving the values of the following four parameters kh, kR, $\varepsilon_1 = \pi H/L$ and $\varepsilon_2 = \sqrt{\nu T/2\pi}/R$ besides the coordinate variables θ, y/R, z/h and t/T.

$\underline{Fig.3}$ shows the variation of the velocity profiles with increase in ε_1. It is understood from this figure that the more ε_1 increases, the more the difference between u_{2nd} and the potential velocity U_R shown by a broken line increases, and therefore, the connection of u_{2nd} with U_R outside the boundary layer does not become smooth. This is due to the fact that in deriving the second approximation, the boundary condition on the cylinder surface is taken in preference to that outside the boundary layer. If this approximate solution is appropriate, it is expected in the real phenomenon that an abrupt velocity gradient appears in the neighborhood of outside of the boundary layer as the wave height increases, and therefore, small eddies which rotate in the opposite direction to the wake vortex may occur even when the wake vortex does not appear. Such a phenomenon as to support this expectation is seen in $\underline{Photo.1}$.
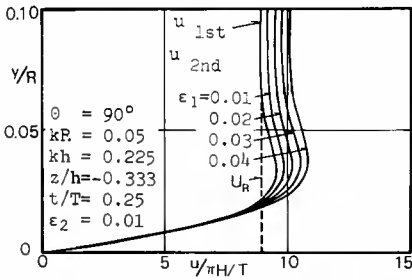
Fig.3 Variation of u_{2nd} with ε_1.

Photo.1 Hydrogen bubble lines in boundary layer.

Fig.4 shows the variation of the velocity profile with change of ε_2 only which is equivarent to change of ν. It is found from this figure that as ε_2 increases, the boundary layer thickness increases.

Fig.5 shows the variation of the velocity profile with change of the radius of cylinder R only which results in changes of both kR and ε_2. It is found from this figure that in the case when the radius of cylinder is as small compared with the wave length as $kR=0.01$, the separation occurs already at $\theta=110°$. In this case, Keulegan-Carpenter's number[4] (denoted by K.C. hereafter) is

$$K.C.=\frac{u_{max}\cdot T}{2R}=\frac{\pi\varepsilon_1}{kR}\cdot\frac{\cosh\ kh(1+z/h)}{\sinh\ kh}=14.5$$

As mentioned later, even when K.C. is smaller than 14.5, the vortex formation is seen, and therefore, it is reasonable that the separation occurs in this example.

Fig.4 Variation of u_{2nd} with ε_2.

kh=0.45 z/h=-0.167 t/T=0.25 ε_1=0.02

Fig.5 Variation of u_{2nd} with kR and ε_2.

EXPERIMENTS AND DISCUSSIONS

In order to examine, first of all, the water particle velocity of diffracted waves, a circular cylinder made of Lucite with the radius of 10cm was 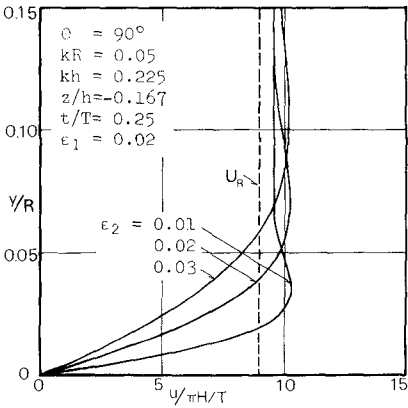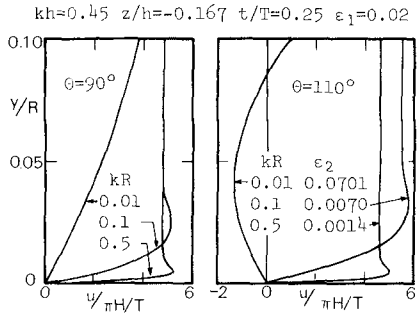installed in the center of the wave tank, which is 17.5m long, 1.5m wide and 75cm deep. Using a pulse generator, a train of hydrogen bubble lines was generated from a platinum wire with a diameter of 0.1mm stretched horizontally from the surface of the cylinder, and photographs are taken from above the water surface. The sketch of this experimental apparatus is shown in **Fig.6**.

The platinum wire was painted at intervals of about 1cm so as to recognize the coordinates $\hbar$ and θ of hydrogen bubbles from photographs, an example of which is shown in <u>Photo.2</u>. Thus, the velocities U and V were measured by means of dividing the distances of hydrogen bubbles in the directions of θ and $\hbar$ by the time interval of pulse repeated.

θ   =30°
kR =0.162
t/T=0.31
T =2.0sec
H =5.3cm
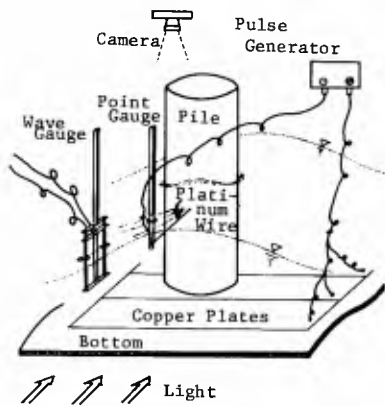
<u>Fig.6</u> Sketch of experimental apparatus
        (in case of diffracted waves).

<u>Photo.2</u> Hydrogen bubble lines
          of diffracted waves
          around circular cylinder.

Figs.7 (a)-(e) show comparisons between experimental values of water particle velocities and theoretical curves calculated by Eqs.(1) and (2) denoted by solid lines. It is found from these figures that concerning U, experimental values are generally smaller than theoretical ones, in which both resemble each other in shape in front of the cylinder ($\theta<90°$), but differ in rear of the cylinder ($\theta>90°$), and that concerning V, both agree roughly. In the analysis of these experimental data, however, it is afraid of containing errors in some extent due to neglecting the change of velocity field in space and time.

(a) $\theta=30°$

(b) $\theta=60°$

(c) $\theta=90°$

(d) $\theta=120°$

(e) $\theta=150°$
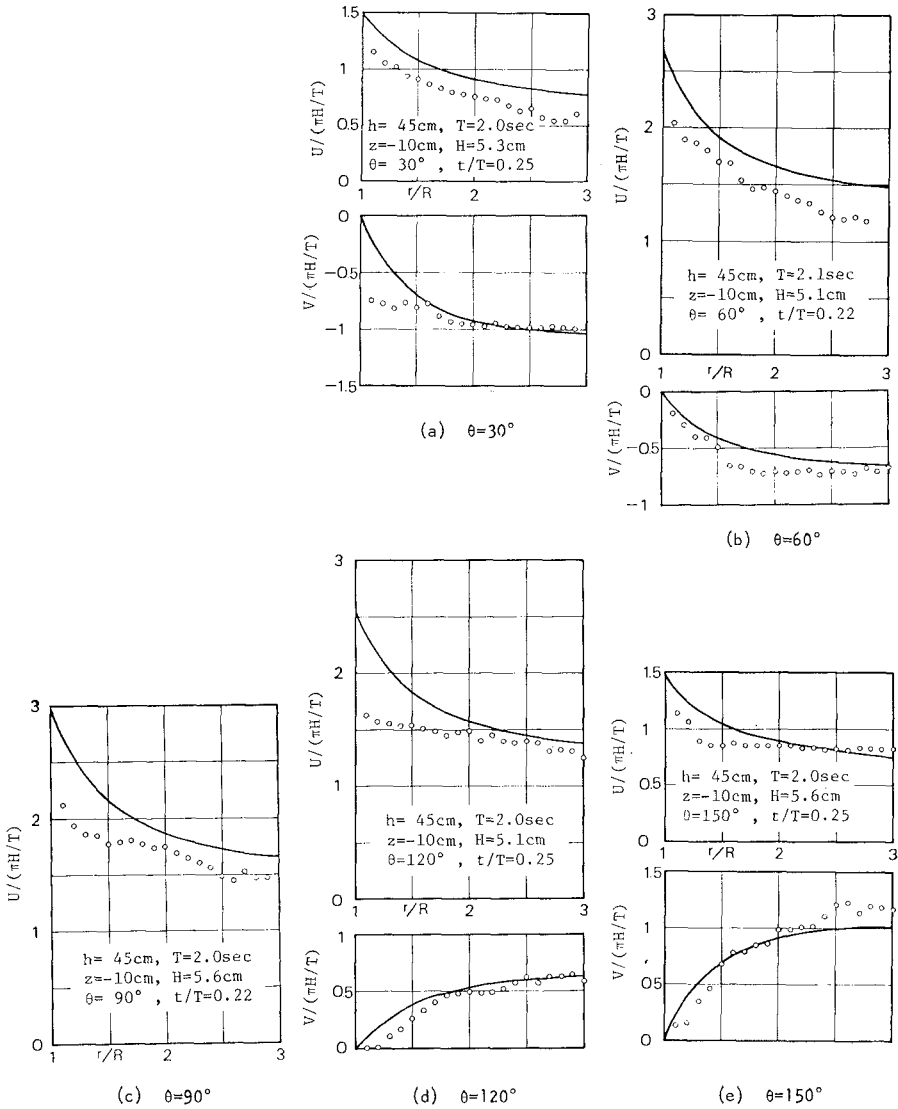
Fig.7   Comparison of water particle velocities of diffracted waves
around circular cylinder between theory and experiment.

In order to measure the velocity profile in the boundary layer, a semi-circular cylinder with a radius of 10cm was attached to the side wall of the wave tank which is 27m long, 50cm wide and 70cm deep as shown in Fig.8, and photographs of hydrogen bubble lines generated from the platinum wire with a diameter of 0.05 mm were taken through the glass bottom.
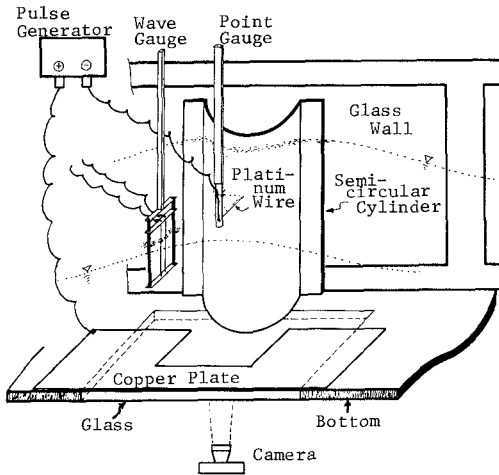
Fig.8 Sketch of experimental apparatus
(in case of boundary layer).

The experimental conditions are as follows:

h=45cm, z=-15cm, θ=90° and 110°, T:1 to 10sec, H:1 to 4cm, ν=1.204X10^{-2}cm^2/sec.

Some examples of the photographs in the boundary layer are shown in Photo.3, and some results of this experiment are shown in Fig.9. In these figures, theoretical velocity profiles of the first and second approximations are also shown by dotted and solid lines respectively. Within the range of the experiment, flow separation were not recognized both in the experiment and the theory. It is found from the figures that measured values are generally smaller than theoretical ones. One of the reasons may be that water particle velocities of diffracted waves in the experiment have a tendency to become smaller than in the potential theory as mentioned above, and in addition, in the boundary layer theory presented in this study, the water particle velocity outside the boundary layer with a finite thickness is given by the value on the surface of cylinder calculated from Eq.(1), which means that the boundary layer thickness is neglected.

On the other hand, it is recognized from Photo.3-(b) or Fig.9-(b) that the phase angle of water particle velocities in the boundary layer precedes more than outside the boundary layer.
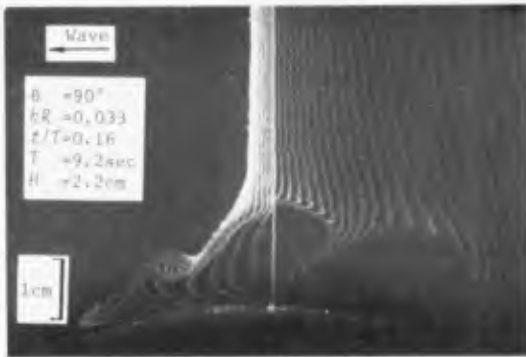
(a)
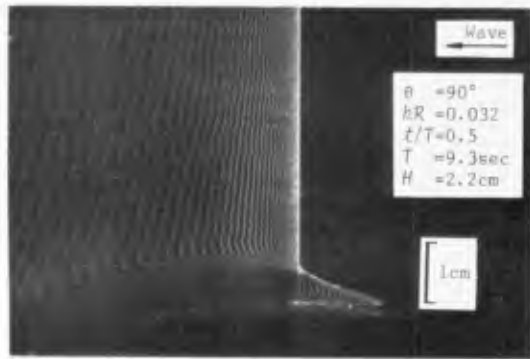
(b)
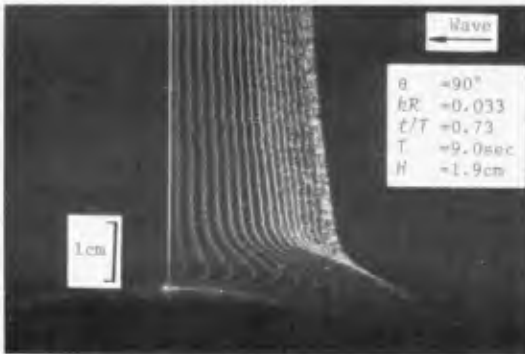
(c)

Photo.3 Hydrogen bubble lines in boundary layer.
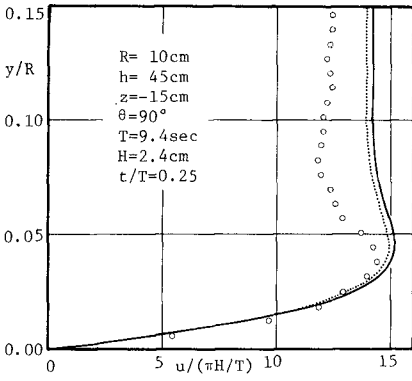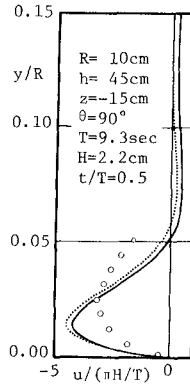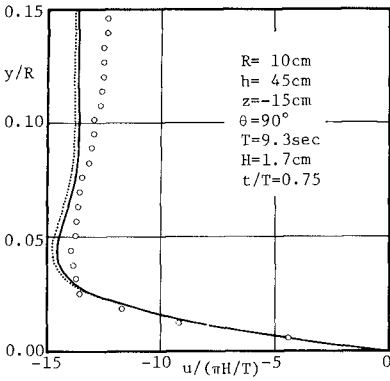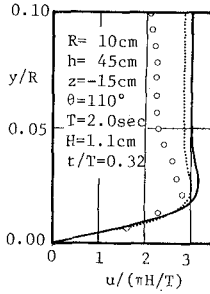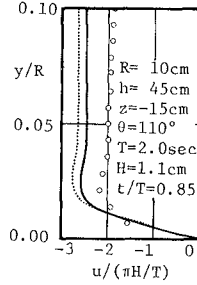
Fig.9 Velocity profiles in laminar boundary layer
around circular cylinder due to waves.

Finally, in order to examine the occurrence of wake vortices, photographs were also taken of hydrogen bubble lines produced from the platinum wire stretched in front of a brass pile with a radius of 1cm, an example of which is shown in Photo.4.

Fig.10 shows a trace of the photograph taken after the wave crest passed over the pile, and Fig.11 shows velocity profiles of the second approximation calculated in the same case as in Fig.10. From these figures, the occurrence of laminar flow separation and subsequent development of wake vortices can be recognized. In this case, the location of separation point is derived theoretically as $\theta=102°$, which is almost identical to that in steady flow[2],[3], and $K.C.$ is equal to 10.7 and the Reynolds number is approximately 1200.

This fact of vortex formation at $K.C.=10.7$ is consistent with the experimental results obtained by Keulegan and Carpenter[4]. Resently, Sarpkaya investigated experimentally the variation of the drag and inertia coefficients with $K.C.$ in oscillating flow[6]. It is found from his results that at $K.C.=12$, the drag coefficient reaches to the largest value and the inertia coefficient decreases to the lowest value, which corresponds to the critical condition $K.C.=15$ obtained by Keulegan and Carpenter[4]. They stated that at $K.C.=12.5$, a single eddy is formed and is separated during a half cycle of fluid motion, and the process of eddy shedding has a very significant bearing on the variations of the drag and inertia coefficients[4]. Considering their studies, therefore, further investigations are necessary about the time variation of wake vortices under progressive waves.

Photo.4 Occurrence of wake vortices behind pile due to waves. ($R=1$cm)

Fig.10 Occurrence of wake vortices behind pile due to waves.

R=1cm, h=45cm, z=-5cm, T=3sec, H=3cm, t/T=0.25
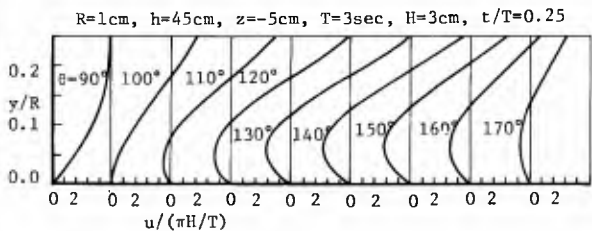
Fig.11 Separation of laminar boundary layer around pile due to waves.

CONCLUSION

In this paper, first of all, the water particle velocities of diffracted waves around a circular cylinder have been discussed, and next, the velocity profiles in the boundary layer on the surface of cylinder have been derived theoretically and compared with the experimental results, and finally, the occurrence of flow separation have been discussed.

Summarizing the results of this study, the following statements are made:

1. Theoretical values of the water particle velocity around a circular cylinder are generally smaller than experimental ones, but both are resemble in velocity profile in front of the cylinder.

2. The second approximate solution of the water particle velocity in the boundary layer explains various characteristics of the boundary layer, that is, boundary layer thickness, precedence of phase angle of water particle velocity in the boundary layer, existence of mass transport velocity in the neighborhood of outside of the boundary layer, and occurrence of flow separation.

3. In order to discuss quantitatively the validity of the second approximate solution, it is necessary to obtain more accurate data, over a wide range, of water particle velocities both in the boundary layer and of diffracted waves.

4. Considering the relationship between flow patterns and wave forces, it is also important to investigate the criterion for flow separation, subsequent vortex formation and vortex shedding under various conditions, and to measure the pressure distribution on the surface of cylinder especially when the wake vortex is formed.

ACKNOWLEDGEMENT

REFERENCES

1) MacCamy,R.C.,and R.A.Fuchs: Wave forces on piles: Diffraction theory, Tech. Memo., No.69, B.E.B., 1954.

2) Chia-Shun Yih: Fluid Mechanics, McGraw-Hill, 1969.

3) Schlichting,H.: Boundary Layer Theory, McGraw-Hill, 1968.

4) Keulegan,G.H.,and L.H.Carpenter: Forces on cylinder and plates in an oscillating fluid, Jour. Res. Nat. Bur. Stand., Vol.60, No.5, pp.423-440, May 1958.

5) Iwagaki,Y., H.Ishida and T.Senda: Wave forces on a pile under irregular waves, Proc. 20th Conf. Coastal Eng. in Japan, pp.1-5, Nov.1973. (in Japanese)

6) Sarpkaya,T.: Wave forces and periodic flow about cylinder, Summaries of 14th Conf. Coastal Eng., pp.271-274, June 1974.

CHAPTER 109

WAVE FORCES ON PIPELINES

by Dr. M. Fadhil Al-Kazily[*]
Arab Projects & Development
A Research & Consulting Institute, Beirut, Lebanon

ABSTRACT

Water waves exert a force on a pipeline which is placed within the zone of wave influence. This force is made up of a periodic force which is composed of a drag and an inertial force, and a non-periodic second order force which acts upward.

The coefficients of mass C_M and drag C_D as defined by the "Morison equation" were evaluated for many wave and depth conditions and it was found that the coefficients vary with the wave heights, wave length, depth of the cylinder below still water surface, and within the wave cycle.

WAVE FORCE ANALYSIS

The forces exerted on a circular cylinder by unbroken surface waves, assuming the cylinder is sufficiently far from the bottom are made up of two components:

1. Inertial force which is proportional to the acceleration exerted on the mass of the water displaced by the cylinder.

2. Drag force which is proportional to the square of the water particle velocity.

In designing vertical piles it is necessary to compute only the horizontal and lift forces, as these are the only important forces acting on such a cylinder. But when designing a horizontal structural member subjected to wave action it is necessary to find the horizontal, vertical, uplift and transverse forces.

Considering a long and slender horizontal cylinder with its axis at right angles to the wave crest, only the vertical (sinusoidal), uplift and transverse force (due to eddy sheddings) are of importance. But when the cylinder is parallel to the wave crest then the vertical and horizontal components of the force become important. In addition the uplift and transverse may be of importance. For simplicity in the analysis of the data of this study, and because other theories do not necessarily yield better results, the linear theory is used.

The water surface elevation, Fig. 1, is given by:

$$\eta(x,t) = \frac{H}{2} \cos 2\pi \left(\frac{x}{L} - \frac{t}{T} \right) \tag{1}$$

---

[*] Formerly, Senior Engineer, Bechtel Inc., San Francisco, California

and the water particle velocity and acceleration is given by:

$$u_{(z)} = \frac{\pi H}{T} \frac{\text{Cosh } kz}{\text{Sinh } kd} \text{ Cos } 2\pi \left(\frac{x}{L} - \frac{t}{T}\right) \qquad (2)$$

$$v_{(z)} = \frac{\pi H}{T} \frac{\text{Sinh } kz}{\text{Sinh } kd} \text{ Sin } 2\pi \left(\frac{x}{L} - \frac{t}{T}\right) \qquad (3)$$

$$\frac{\partial u}{\partial t} (z) = \frac{2\pi^2 H}{T^2} \frac{\text{Cosh } kz}{\text{Sinh } kd} \text{ Sin } 2\pi \left(\frac{x}{L} - \frac{t}{T}\right) \qquad (4)$$

$$\frac{\partial v}{\partial t} (z) = -\frac{2\pi^2 H}{T^2} \frac{\text{Sinh } kz}{\text{Sinh } kd} \text{ Cos } 2\pi \left(\frac{x}{L} - \frac{t}{T}\right) \qquad (5)$$

The center of the force meter is assumed to be fixed at $x = 0$, and for this location Eqs. (1) through (5) become:

$$\eta_{(t)} = \frac{H}{2} \text{ Cos } \omega t \qquad (6)$$

$$u_{(z)} = \frac{\pi H}{T} \frac{\text{Cosh } kz}{\text{Sinh } kd} \text{ Cos } \omega t \qquad (7)$$

$$v_{(z)} = -\frac{\pi H}{T} \frac{\text{Sinh } kz}{\text{Sinh } kd} \text{ Sin } \omega t \qquad (8)$$

$$\frac{\partial u}{\partial t} = -\frac{2\pi^2 H}{T^2} \frac{\text{Cosh } kz}{\text{Sinh } kd} \text{ Sin } \omega t \qquad (9)$$

$$\frac{\partial v}{\partial t} = -\frac{2\pi^2 H}{T^2} \frac{\text{Sinh } kz}{\text{Sinh } kd} \text{ Cos } \omega t \qquad (10)$$

$$\text{where } \omega = \frac{2\pi}{T}$$

1. Vertical Forces

The force per unit length due to surface waves is given by the Morison Equation:

$$F_{(z,t)} = C_M V\rho \frac{\partial v}{\partial t} + \frac{1}{2} C_D \rho A v |v| \qquad (11)$$

where

$$V = \frac{D^2 \pi}{4} = \text{the volume of the displaced fluid per unit length.}$$

$$A = D = \text{the projected area of the cylinder, per unit length, in the direction of flow.}$$

v and $\partial v/\partial t$ are given by Eqs. (8) and (10). Figure (2) is a sketch showing the sign convention of η_t, drag and inertia forces and $F_{(z,t)}$. Upward force is considered positive.

Using Eqs. (8) and (10) in Eq. (11) and:

$$F_{MV} = \frac{D^2}{2} \rho \frac{\pi^3 H}{T^2} \frac{\text{Sinh } kz}{\text{Sinh } kd} \tag{12}$$

and

$$F_{DV} = \rho \frac{D}{2} \left(\frac{\pi H}{T} \frac{\text{Sinh } kz}{\text{Sinh } kd} \right)^2 \tag{13}$$

then for a horizontal cylinder parallel to the wave crest, or a very short segment of a cylinder placed at right angles to the wave crest at $x = 0$, the equation can be written:

$$- F_{(t,z)} = + C_M F_{MV} \cos \omega t + C_D F_{DV} \sin \omega t |\sin \omega t| \tag{14}$$

Equation (14) and Fig. 2 show that the Maximum downward force occurs at $0 \leq t \leq \frac{T}{4}$, and the maximum upward force occurs at $\frac{T}{2} \leq t \leq \frac{3T}{4}$.

2. Horizontal Forces

By a similar analogy, the Morison Equation for a force acting horizontally on a horizontal cylinder with its axis parallel to the wave crest is:

$$F_{(z,t)} = - C_M F_M \sin \omega t + C_D F_D \cos \omega t |\cos \omega t| \tag{15}$$

where

$$F_M = \frac{\pi^3 D^2}{2} \rho \frac{H}{T^2} \frac{\text{Cosh } kz}{\text{Sinh } kd} \tag{16}$$

and

$$F_D = \rho \frac{D}{2} \left(\frac{\pi H}{T} \frac{\text{Cosh } kz}{\text{Sinh } kd} \right)^2 \tag{17}$$

Figure 3 is a sketch showing the sign convention of $\eta(t)$, drag and inertial forces and $F_{(z,t)}$ for the horizontal forces. Force is positive in the direction of wave advance. Equation (15) and Fig. 3 show that the maximum horizontal component force in the direction of wave propogation occurs when $\frac{3}{4}T \le t \le T$ and the maximum negative force occurs at $\frac{1}{4}T \le t \le \frac{1}{2}T$.

Examining Eqs. (20) and (21) it can be seen that the maximum horizontal force occurs at $\frac{T}{4}$ seconds after the maximum vertical force (both in the positive and negative directions), assuming the coefficients of drag and mass (C_D and C_M) remain constant throughout the wave cycle.

3. Coefficients of Mass and Drag (C_M and C_D)

One of the problems in the design of structural elements to withstand the dynamic forces of waves is to find and use the appropriate values of C_M and C_D.

The compute C_M and C_D from force measurements consider Eq. (14) which can be written (for $t \le \frac{T}{4}$):

$$- F_{(z,t)} = C_M \, F_{MV} \, \text{Cos} \, \omega t + C_D \, F_{DV} \, \text{Sin}^2 \, \omega t \tag{18}$$

The maximum downward force occurs at $\dfrac{\partial - F_{(z,t)}}{\partial t} = 0$

That is, $C_M \, F_{MV} \, \omega \text{Sin} \, \omega t = 2C_D \, F_{DV} \, \omega \text{Sin} \, \omega t \, \text{Cos} \, \omega t$

$$\text{Cos} \, \omega t_1 = \frac{C_M \, F_{MV}}{2C_D \, F_{DV}} \tag{19}$$

t_1 is the time phase of the maximum downward force relative to the crest, that is the maximum downward force leads the crest by t_1. Therefore the maximum force is given by Eq. (18) as evaluated at t_1. That is:

$$- F_{(z,t_1)} = C_M \, F_{MV} \, \text{Cos} \, \omega t_1 + C_D \, F_{DV} \, \text{Sin}^2 \, \omega t_1 \tag{20}$$

which could be written as

$$- F_{(z,t_1)} = \frac{C_M^2 \, F_{MV}^2 + 4 \, C_D^2 \, F_{DV}^2}{4 \, C_D \, F_{DV}} \tag{21}$$

This procedure assumes that C_M and C_D are constants, at least for $0 \leq t \leq \frac{T}{4}$.

Solving Eqs. (19) and (20) for C_M and C_D gives:

$$C_M = \frac{-2 \, F_{(z,t_1)}}{F_{MV}(1 + \cos \omega t_1)} \tag{22}$$

$$C_D = \frac{-F_{(z,t_1)}}{F_{DV}(1 + \cos \omega t_1)} \tag{23}$$

Similarly for the horizontal force, consider Eq. (15) at $\frac{T}{4} \leq t \leq \frac{T}{2}$ which becomes:

$$- F_{(z,t)} = C_M \, F_M \sin \omega t + C_D \, F_D \cos^2 \omega t \tag{24}$$

for maximum force

$$\frac{\partial (-F_{(z,t)})}{\partial t} = 0$$

that is:

$$C_M \, F_M \, \omega \cos \omega t = 2 C_D \, F_D \, \omega \sin \omega t \, \cos \omega t$$

$$\sin \omega t_1 = \frac{C_M \, F_M}{2 C_D \, F_D} \tag{25}$$

t_1 here is the time phase of the maximum negative horizontal force relative to the crest. The maximum negative force is then given by:

$$- F_{(z,t_1)} = C_M \, F_M \sin \omega t_1 + C_D \, F_D \cos^2 \omega t_1 \tag{26}$$

or

$$- F_{(z,t_1)} = \frac{C_M^2 \, F_M^2 + 4 C_D^2 \, F_D^2}{4 C_D \, F_D} \tag{27}$$

Here C_D and C_M are assumed constant for $\frac{T}{4} \leq t \leq \frac{T}{2}$. Solving Eqs. (25) and (26) for C_M and C_D gives:

$$C_M = \frac{-2 \, F_{(z,t_1)} \, \text{Sin} \, \omega t_1}{F_M(1 + \text{Sin}^2 \, \omega t_1)} \tag{28}$$

$$C_D = \frac{-F_{(z,t_1)}}{F_D(1 + \text{Sin}^2 \, \omega t_1)} \tag{29}$$

Computing C_M at t=0 and $t = \frac{T}{2}$ and C_D at $t = \frac{T}{4}$ and $\frac{3}{4}T$ does not require making the assumption that C_M and C_D are time independent. C_M and C_D are empirical coefficients, they were found to be a function of t, by Keulegan and Carpenter (1958), and of z, by Jen (1968).

4. C_M and C_D as functions of time.

Consider a case in which the time history of the wave, $\eta_{(t)}$, and the time history of the force, $F_{(z,t)}$ are known (Eqs. 6 and 14). Then for each time, t, we have an equation for C_M and C_D of the form:

$$A = B \cdot C_M + E \cdot C_D \tag{30}$$

where A, B and E are constants and could be computed from the time history of the wave characteristic and the cylinder diameter. Therefore if Eq. 26 is evaluated at t_1, t_2, t_3, t_4...etc. and any two consecutive equations are solved simultaneously, vales of C_M and C_D at $t = \frac{t_1 + t_2}{2}$ etc. could be computed. These will show any dependence of C_M and C_D on time within the wave cycle.

5. Force on an Inclined Cylinder.

Consider a cylinder inclined at an angle θ to the vertical, in a vertical plane that is normal to the wave crests, Fig. 4. The velocity and acceleration components which exert the maximum force on the cylinder at any time, t, are those which are at right angles to the cylinder.

From Eqs. (7) and (8) the component of water particle velocity (R_u) perpendicular to the cylinder becomes:

$$R_u = \frac{\pi H}{T^2} \, \frac{1}{\text{Sinh} \, kd} \, \{\text{Cosh} \, kz \, \text{Cos} \, \omega t \, \text{Cos} \, \theta - \text{Sinh} \, kz \, \text{Sin} \, \omega t \, \text{Sin} \, \theta\} \tag{31}$$
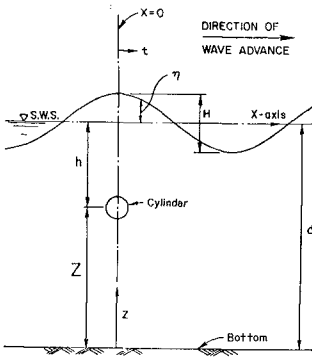
Fig. 1 Definition Sketch
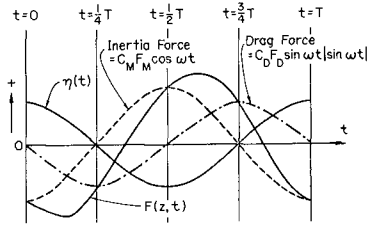
Fig. 2 Sign Convention of $\eta(t)$, and the Vertical Forces
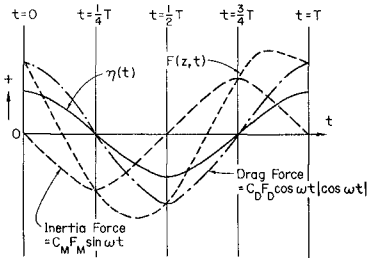
Fig. 3 Sign Convention of $\eta(t)$ and the Horizontal Forces
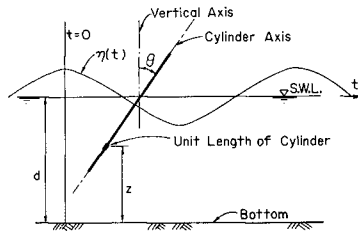
Fig. 4 Inclined Cylinder Configuration

Similarly the perpendicular acceleration (R_A) obtained from Eqs. (9) and (10) is:

$$R_A = \frac{-2\pi^2 H}{T^2} \quad \frac{1}{Sinh\ kd} \quad \{Cosh\ kz\ Sin\ \omega t\ Cos\theta + Sinh\ kz\ Cos\quad \omega t\ Sin\theta\} \qquad (32)$$

Using Eqs. (22) and (23) in Eq. (11) for $0 \leq t \leq \frac{T}{4}$ one can obtain the force per unit length acting on the inclined cylinder, $F(z,t,\theta)$.

$$F_{(z,t,\theta)} = + C_M \{F_M\ Cos\ \theta\ Sin\ \omega t + F_{MV}\ Sin\ \theta\ Cos\ \omega t\}$$

$$+ C_D \{F_D\ Cos^2\ \theta\ Cos^2\ \omega t + F_{DV}\ Sin^2\ \theta\ Sin^2\ \omega t$$

$$- \tfrac{1}{2}\sqrt{F_D \cdot F_{DV}} \quad Cos2\theta\ Sin\ 2\ \omega t\} \qquad (33)$$

F_M, F_{MV}, F_D and F_{DV} have been defined previously. In Eq. (33) $F_{(z,t,\theta)}$ is considered positive if its horizontal component is in the direction of wave advance and its vertical component is downwards.

Assuming deep water conditions (i.e., $\frac{d}{L} < 0.5$), $Cos\ kz \rightarrow Sinh\ kz$, $F_M \rightarrow F_{MV}$; and $F_D \rightarrow F_{DV}$. Then Eq. (8) becomes

$$F_{(z,t,\theta)} = C_M F_M\ Sin(\omega t + \theta) + C_D F_D\ Cos^2\ (\omega t + \theta) \qquad (34)$$

For maximum Force:

$$\frac{\partial F}{\partial t}(z,t,\theta) = C_M F_M\ \omega Cos(\omega t + \theta) - 2C_D F_D\omega Sin(\omega t + \theta)Cos(\omega t + \theta) = 0$$

therefore

$$Sin(\omega t_1 + \theta) = \frac{C_M\ F_M}{2C_D F_D} \qquad (35)$$

Thus the maximum force occurs at t_1 when Eq. (35) is satisfied, and it is:

$$F_{(z,t_1,\theta)max} = C_M F_M\ Sin(\omega t_1 + \theta) + C_D F_D\ Cos^2(\omega t_1 + \theta) \qquad (36)$$

Substitution Eq. (35) in Eq. (36) one can obtain

$$F_{(z,t_1,\theta)} + \frac{C_M^2\ F_M^2 + 4C_D^2\ F_D^2}{4C_D F_D} \qquad (37)$$

From Eqs. (35) and (36) it is seen that the magnitude of the maximum force per unit length on an inclined cylinder is independent of the inclination angle θ; that is, it is equal for all values of θ. The only thing that changes with the angle of inclination is the time phase at which the maximum force occurs. In shallow water conditions that maximum force per unit length occurs when the cylinder is vertical, and in any other position the force will be smaller. This could be explained by the orbital path of the water particles, which is elliptic.

UPLIFT FORCES

A non-periodic upward force was observed during the early stages of the laboratory experiments. When a wave passed over a horizontal cylinder, rigidly fixed at right angles to the wave crest, a constant upward force was produced.

Explanation

The Stokes second order equation for pressure is given by:

$$\frac{P}{\rho g} + y = \frac{H}{2} \frac{\text{Cosh } kz}{\text{Cosh } kd} \text{ Cos } 2\pi \left(\frac{x}{L} - \frac{t}{T} \right)$$

$$+ \frac{3}{8} \frac{\pi H^2}{L} \frac{\text{Tanh } kd}{\text{Sinh}^2 kd} \frac{\text{Cosh } 2kz}{\text{Sinh}^2 kd} - \frac{1}{3} \text{ Cos } 4\pi \left(\frac{x}{L} - \frac{t}{T} \right)$$

$$- \frac{1}{8} \frac{\pi H^2}{L} \frac{\text{Tanh } kd}{\text{Sinh}^2 kd} \text{ Cosh } 2kz \qquad\qquad (38)$$

where: P is the pressure at any point x,y in the fluid and all other symbols have been defined previously, (Wiegel, 1964).

The mean pressure throughout the wave cycle is given by:

$$p = \frac{1}{T} \int_0^T \left(\frac{p}{\rho g} - y \right) dt$$

Therefore

$$p = \frac{1}{8} \frac{\pi H^2}{L} \frac{\text{Tanh } kd}{\text{Sinh}^2 kd} \text{ Cosh } 2kz \qquad\qquad (39)$$

As the pressure in a fluid is the same in all direction, and acts normal to the cylinder, the uplift force per unit length on a circular cylinder, mounted horizontally and parallel to the wave crest, is given by integrating the vertical component of the pressure as given in Eq. (39) around the circumference of the cylinder. See Fig. 5. Therefore:
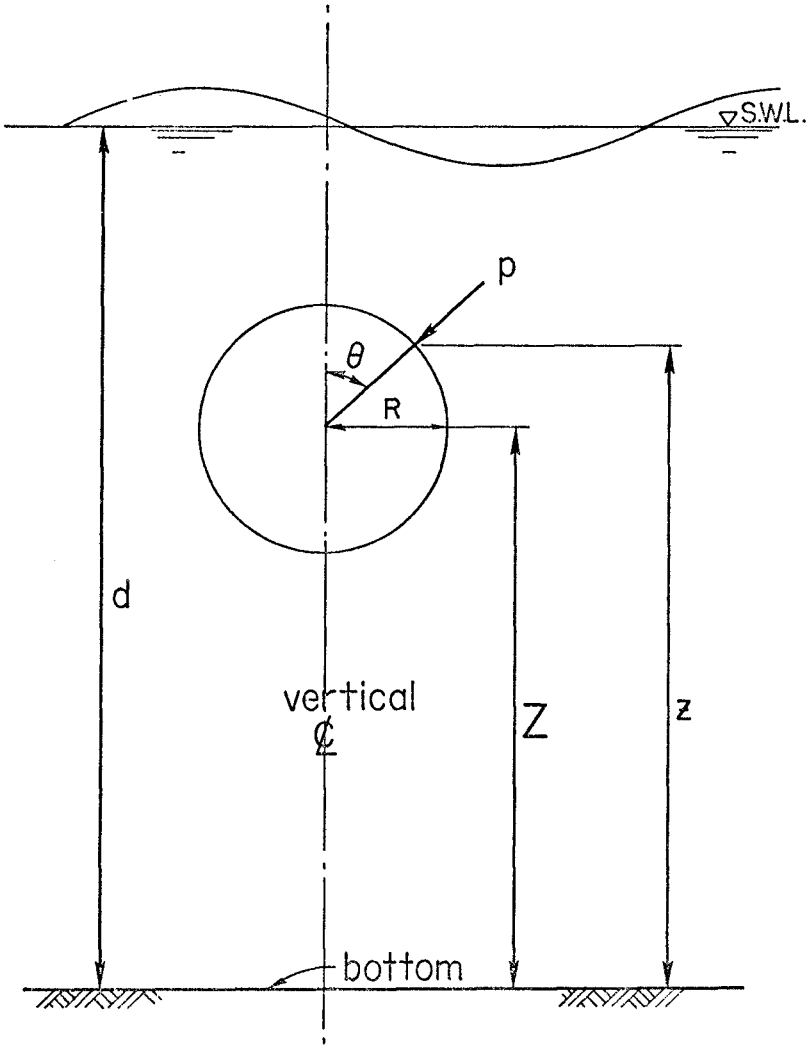
Fig. 5   Definition Sketch Showing Pressure on the Cylinder

$$\text{uplift} = \frac{1}{8} \frac{\pi H^2}{L} \frac{\text{Tanh kd}}{\text{Sinh}^2 kd} \cdot 2 \int_0^\pi \text{Cosh 2kz Cos}\theta \cdot R d\theta$$

and $z = Z + R\text{Cos}\theta$ (see Fig. 5)

Therefore:

$$\text{uplift} = \frac{1}{4} \frac{\pi H^2}{L} \frac{\text{Tanh kd}}{\text{Sinh}^2 kd} \int_0^\pi R\text{Cos}\theta \text{ Cosh } 2k(Z + R\text{Cos}\theta) d\theta$$

Then the uplift per unit length is reduced to:

$$\text{uplift} = \frac{1}{8} \frac{\pi^2 H^2}{L} \frac{\text{Sinh 2kZ}}{\text{Sinh 2kd}} \cdot R \cdot I_1 (2kR) \tag{40}$$

The units of this uplift is in unit of pressure head. To change it to units of force it should be multiplied by ρg, then the uplift equation becomes:

$$\text{uplift/unit length} = \frac{1}{8} \rho g \frac{\pi^2 H^2}{L} \frac{\text{Sinh 2kZ}}{\text{Sinh 2kd}} \cdot R \cdot I_1 (2kR) \tag{41}$$

where:

> R = radius of the cylinder.
>
> Z = the distance between the center of the cylinder and the sea floor.

I_1 (2kR) = Bessel's Function of the first kind.

When all the lengths are measured in feet and ρg is taken to equal 62.4 lb/ft^3, the uplift force is then given in lb/ft. Equation (40) is true also for a cylinder fixed at right angles to the wave crest.

DATA ANALYSIS

Data:

Three force meters were used in this study. Two of the force meters were mounted horizontally, parallel to the wave crest. One of these was 1.5 inch O.D. circular cylinder and the other was a 4.0 inch O.D. circular cylinder; both were 11.25 inches long. 606 runs were made with the 1.5 inch O.D. force meter, forces being measured only in the vertical direction. The force meter was mounted at various depths beneath the still-water surface between 3.5 inches and 19.31 inches, for wave periods varying from 0.47 sec. to 1.32 secs. and wave heights from 0.075 ft. to 0.0160 ft. With the 4 inch O.D. force meter 934 runs were made to measure forces in the vertical direction and 755 runs to measure forces in the horizontal direction. The depth of the cylinder below the still-water surface was varied from 4.42 inches to 22.88 inches, the wave period from 0.47 sec. to 1.33 secs., and the wave height from 0.08 ft. to 0.215 ft.

Figure 6 shows a sample record obtained using the 1.0 inch segment, 2.0 inches O.D. force meter (shown in Fig. (7)) which was placed at right angles to the wave crest. Six sets of records were made with the force meter located at distances from 3.0 inches to 17.0 inches beneath the still-water surface. Each set consisted of many runs, with wave periods varying from 0.41 sec. to 1.32 secs., and wave heights from 0.067 ft. to 0.243 ft. Eight sets of records were also made with the last mentioned force meter placed at a number of different angles to the horizontal (Fig. 4). The axis of the cylinder was always in a plane at right angles to the wave crest. Each of these sets consist of 33 runs.

Data Reduction

1. Sinusoidal Wave Force - Mass and Drag Coefficients:

Two methods were used to compute values of the coefficient of mass and the coefficient of drag at specific points in the wave cycle. The first was to evaluate C_M and C_D at the time when the maximum force occurred. The other was to evaluate C_M when the vertical or horizontal component of the water particle velocity was zero (depending on whether the vertical or horizontal forces were being considered) and C_D when the vertical or horizontal component of the acceleration was zero.

To evaluate C_M and C_D at the time of the maximum force, the wave periods (T), the wave heights (H), the maximum force (F_{t_1}), and the phase lag (t_1) at which this maximum force occurred were found from the records of the experiments. Then C_M and C_D are evaluated from the vertical force records using Eqs. (22) and (23). Similarly C_M and C_D are computed from the horizontal force records using Eqs. (28) and (29).

To evaluate C_M and C_D at the zero horizontal or vertical component of water particle velocity and acceleration, the maximum inertia force (I.F.) and the maximum drag force (D.F.) were measured from the oscilograph records. Then using Eqs. (18) and (15) C_M and C_D can be evaluated as follows, for vertical forces:

$$C_M = \frac{I.F.}{F_{MV}} \quad \text{and} \quad C_D = \frac{D.F.}{F_{DV}} \tag{42}$$

and for horizontal forces:

$$C_M = \frac{I.F.}{F_M} \quad \text{and} \quad C_D = \frac{D.F.}{F_D} \tag{43}$$

C_M and C_D were evaluated by these two methods for force meter diameters of 4.0 inches and 2.0 inches, for many wave conditions.

C_M and C_D were also evaluated at regular intervals throughout the wave cycle for one set of records. A sample plot of C_M and C_D as they vary within the wave cycle is shown in Figs. 8 and 9.

FIG. 6 SAMPLE RECORD – VERTICAL FORCE
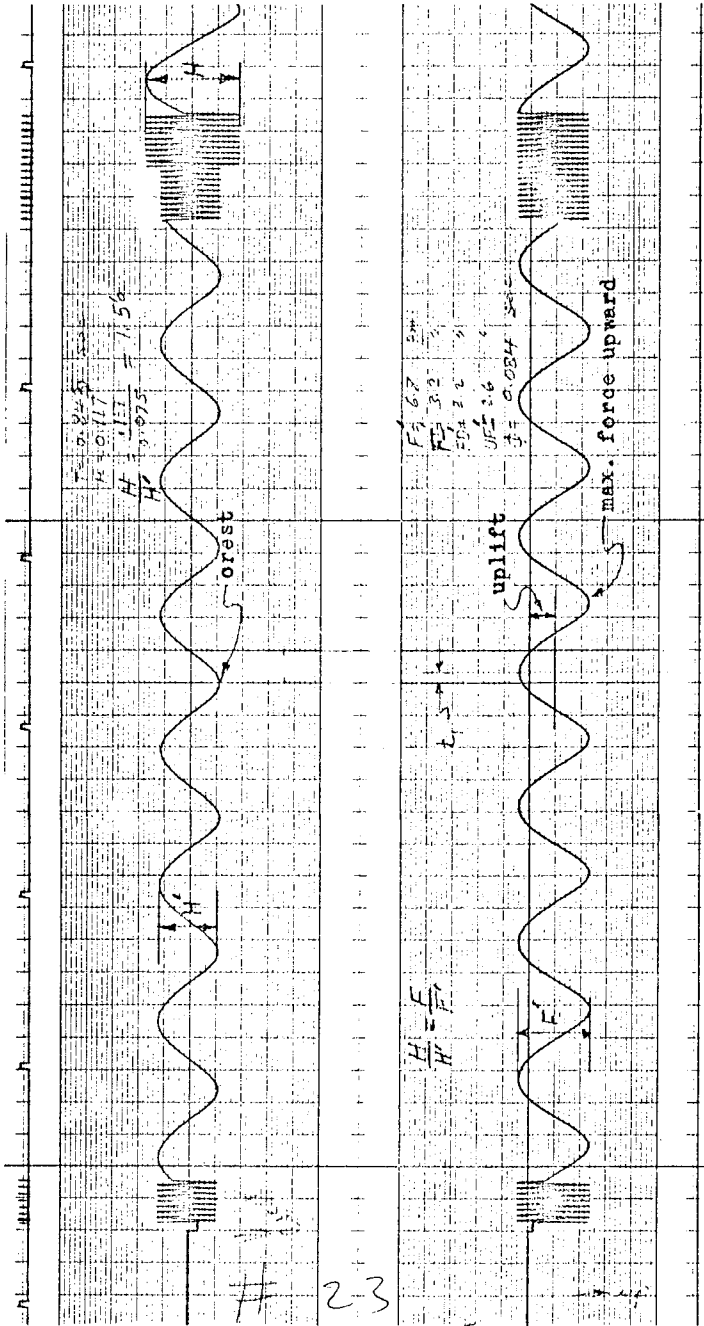
T = 0.85 sec., H = 0.117 ft., F = 10.95 gm., t_{II} = 0.08 sec., IF = 5.15 gm., DF = 3.54 gm., Uplift = 2.6 gm., Cylinder O.D. = 2.0 in., d = 2.13 ft., h = 3.0 in., Cylinder length = 1.0 in. (Set Nº 1, Record Nº 6, Run Nº 2)
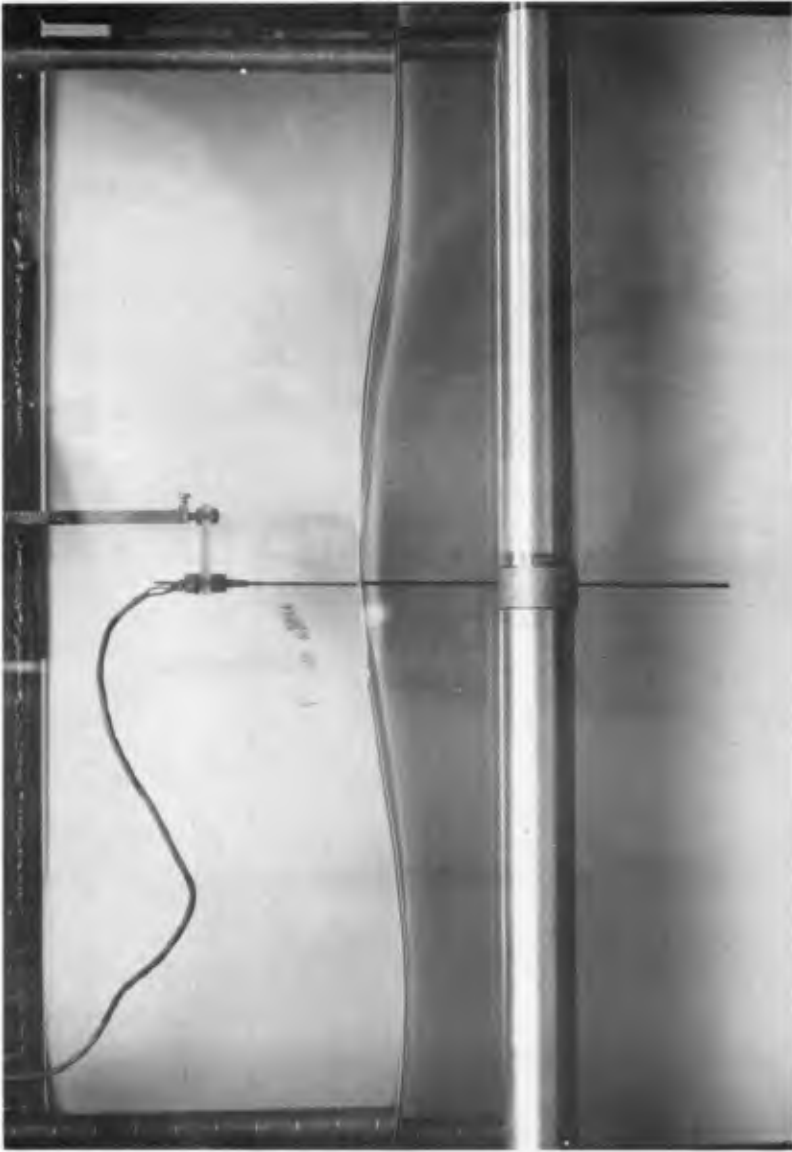
FIG. 7   FORCE METER

RESULTS AND DISCUSSION

The Coefficients of Mass and Drag

The coefficient of mass, C_M, and the coefficient of drag, C_D, were computed at two points in the wave cycle for the 4.0 inch O.D. cylinder, both for horizontal and vertical forces, and for the 2.0 inch O.D. cylinder placed at right angles to the wave crest. The two specific points are at the time when the maximum force occurs, and when the drag force or the inertial force is zero.

The following characteristics were observed for C_M:

1. C_M decreases as the wave height increases, if the wave period remains the same. This agrees with the results obtained by Evans (1970).

2. C_M increases as the depth of the cylinder beneath the still-water surface increases, if the wave characteristics remain the same. This differs from the findings of Shell Oil Company who conducted an analysis on wave and force data obtained in the Gulf of Mexico, on a vertical pile. They found that C_M decreased as the distance beneath the still-water surface increased (Evans, 1970).

3. C_M increases as the wave period, T, increases, if the wave height remains the same.

4. C_M computed from the vertical forces on the 4.0 inch O.D. cylinder was slightly smaller than that computed from the horizontal forces for the same wave conditions.

However, a definite relationship seems to exist between C_M and D_{pv}, the ratio of the vertical diameter of the orbit of the water particle to the diameter of the cylinder, this relationship is shown in Figure 10. A similar relationship exists between C_M and D_{pH}, the ratio of the horizontal diameter of the orbit of the water particle to the diameter of the cylinder, D.

2. Uplift Forces (None-Periodic)

The non-periodic uplift force was measured for all runs when the cylinder was at right angles to the wave crest. (No uplift force was detected for cylinders parallel to the wave crest.) Then the uplift force per unit length of cylinder was computed from Eq. (41). The computed uplift force was found to be always smaller than the measured force. An empirical coefficient, C, was then obtained by dividing the measured uplift force by the computed value. This coefficient was then plotted against the wave steepness, (H/L). Figure 11 shows this relationship.

Thus, the uplift equation becomes:

$$\text{Uplift} = \frac{1}{8}C \cdot \rho g \ \frac{\pi^2 H^2}{L} \ \frac{\text{Sinh } 2kx}{\text{Sinh } 2kd} \cdot R \cdot I_1 \ (2kR) \tag{44}$$

This uplift was also evaluated for all runs made with the 2 inch O.D. force meter.

The uplift force was also evaluated using Goodman's equation for uplift which is:

$$\text{Uplift}_G = \frac{1}{2} \pi^3 \frac{\rho H^2 D^2}{T^2} k \, e^{-2kh} \, \alpha_1(kR) \tag{45}$$

where h is the depth of the cylinder center line beneath the still water surface, R is the radius of the cylinder and $\alpha_1(kR)$ is evaluated for each kR. This uplift was also smaller than the measured values. A coefficient (C_g) was obtained by dividing the measured uplift by that computed using Eq. (45) and it was plotted against H/L, Figure 12. The relationship was found to be similar to that between C and H/L. The modified Goodman's Eq. (45) becomes

$$\text{Uplift}_G = \frac{1}{2} C_g \pi^3 \rho \frac{H^2 D^2}{T^2} k \, e^{-2kh} \, \alpha_1(kR) \tag{46}$$

3. Forces on an Inclined Cylinder

The maximum force on an included circular cylinder for a specific wave was obtained from the oscillograph records. The maximum sinusoidal force for a specific wave length and wave height was plotted against the angle of inclination of the cylinder to the vertical. Figure 13 shows such plots. (Here, WH = wave height and WL = wave length.)

It appears on theoretical grounds that, for deep water waves (circular water particle paths), the maximum force on a unit length of cylinder is not changed in magnitude by changing the angle of inclination of the cylinder, if the wave characteristics remain constant, and if that unit length of cylinder remains at the same depth below the still-water surface. However the time phase at which the maximum force occurs does change. Figure 14 shows the change of t_1/T with the angle of inclination of the cylinder with the vertical (θ) as defined in Figure 4.

CONCLUSIONS

The following conclusions are drawn from this study:

1. The maximum force, time phase solution for C_M and C_D, which is defined by the Morison equation, is a useful method of evaluating C_M and C_D for a cylinder subjected to wave action as it yields the values of C_M and C_D at a time of maximum force. This value of CM is larger than that computed when the drag force is zero in both the vertical and horizontal direction.

2. Once CM and CD are found the sinusoidal force amplitude can be computed accurately from 21 for the vertical force, and from 27 for the horizontal force.

3. The coefficient of mass, CM, is not constant and it varies with the wave height, wave period, depth of cylinder beneath the still-water surface and the diameter of the cylinder. It also varies within the wave cycle when all the previously mentioned variable are held constant. CD also appears to vary with wave height, wave period, cylinder depth below still water level and the diameter of the cylinder. It also varies within the wave cycle.
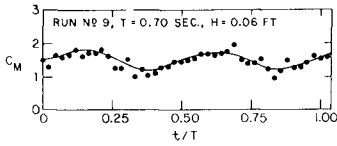
FIG. 8 COEFFICIENT OF MASS C_M VERSUS t/T
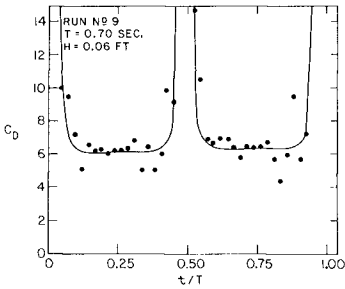
FIG. 9 COEFFICIENT OF DRAG C_D VERSUS t/T
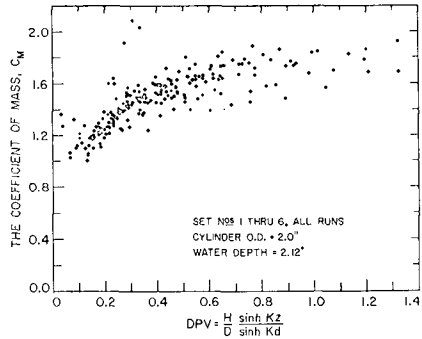
FIG. 10 THE COEFFICIENT OF MASS VS THE RATIO OF ORBITAL PATH DIAMETER TO THE O.D. OF THE CYLINDER (DPV)
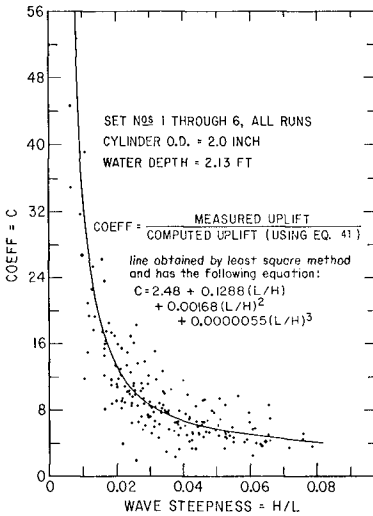
FIG. 11 UPLIFT COEFFICIENT (COEFF) VS WAVE STEEPNESS
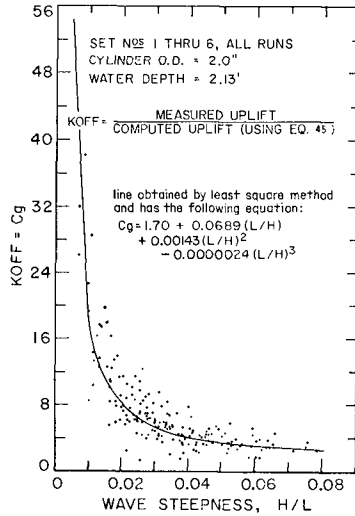
FIG. 12 UPLIFT COEFFICIENT (KOFF) VS WAVE STEEPNESS, H/L

WH = 0.11 FT.   WL = 6.00 FT.

WH = 0.12 FT.   WL = 6.00 FT.

WH 0.13 FT.   WL = 6.00 FT.

WH = 0.14 FT.   WL = 6.00 FT.

WH = 0.15 FT.   WL = 6.00 FT.

WH = 0.16 FT.   WL = 6.00 FT.
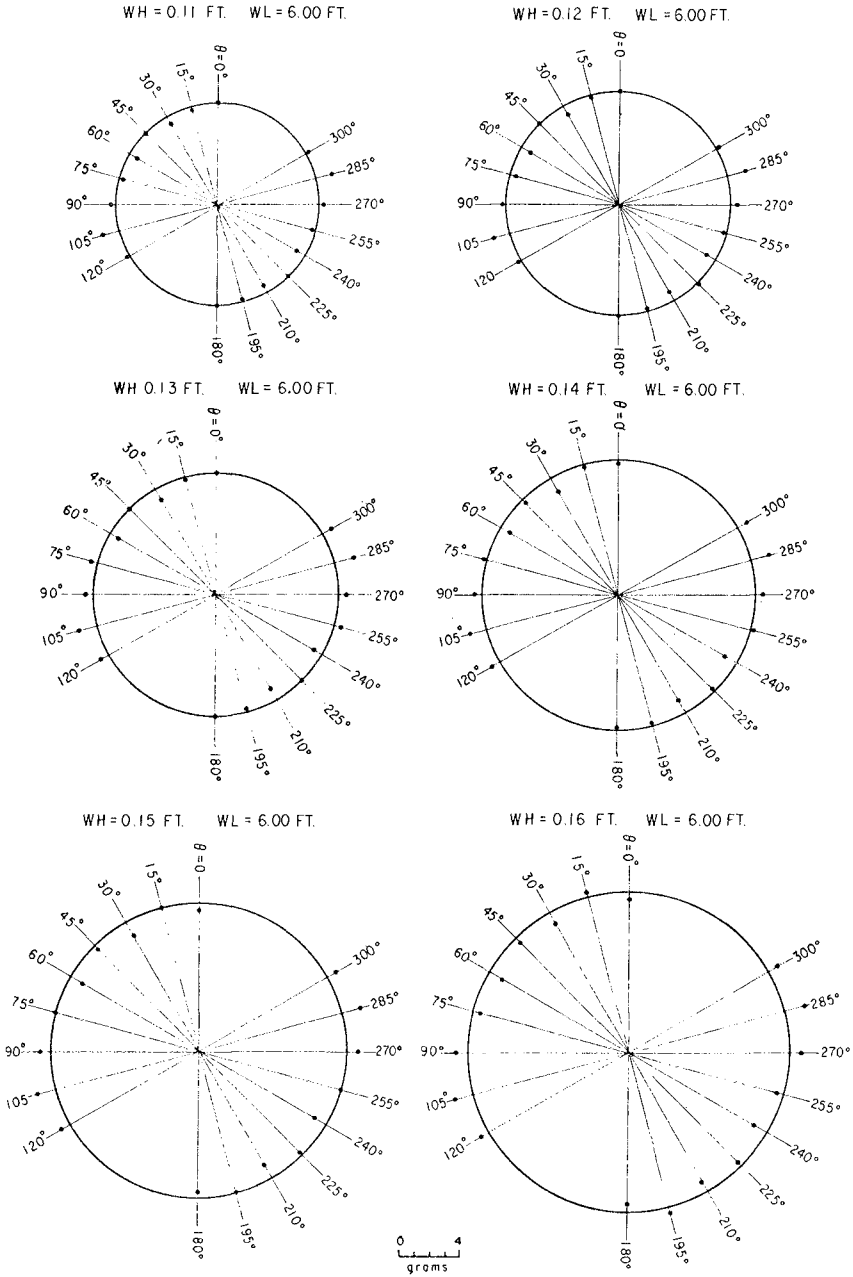
FIG. 13 FORCE VS. ANGLE OF INCLINATION
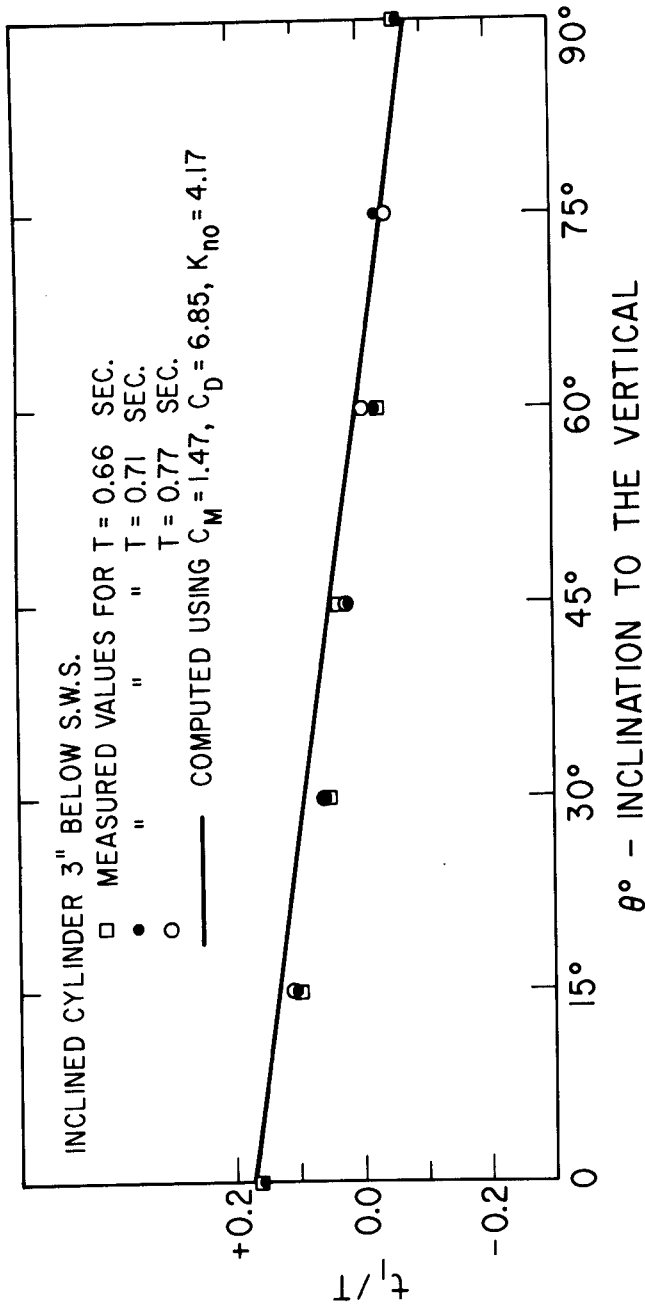
FIG. 14   DIMENSIONLESS TIME PHASE VS. INCLINATION ANGLE

4.   The method used to evaluate CM and CD within the wave cycle is a very useful method to show the variation of C_M and C_D within the wave cycle.

5.   The coefficient of mass, CM, varies with the time in the wave cycle in the shape of a sinusoid with frequency twice that of the wave causing it.   CM is always positive.

6.   When the cylinder is at right angles to the wave crest, it experiences a non-periodic uplift force of appreciable magnitude.

7.   The magnitude of this uplift force could be estimated reasonably well using Eqs. (44) and (46), provided the empirical coefficient C or Cg are known.

8.   For the cases studied the coefficients C and Cg seem to have a definite relationship with the wave steepness.

9.   For deep-water conditions (d > L/2) the magnitude of the sinusoidal force amplitude does not change when the inclination of the cylinder to the horizontal is changed, but the phase time at which this maximum force occurs, relative to the wave crest, does change.

10. $A_{max} T^2/D$ appears to be a useful parameter to correlate with CM.

11.   The ratio of the diameter of the water particle orbital path to the cylinder diameter, $\left(\frac{H \; Sinh \; kz}{D \; Sinh \; kd}\right)$ in the vertical direction or $\left(\frac{H \; Cosh \; kz}{D \; Sinh \; kd}\right)$ in the horizontal direction also appears to be a useful parameter to correlate with CM.

REFERENCES

1. Abramowitz, M. and I. A. Stegum (editors); Handbook of Mathematical
    Functions, National Bureau of Standards Applied Mathematics Series, 55,
    seventh printing, May 1968, pp. 375.

2. Al-Kazily, M. F. and E. Scott; "The Variation of CM and CD through One
    Wave Cycle," to be published, 1972.

3. Anonymous; "A Beach from the Deep," Shore and Beach, Vol. 37, No. 2,
    October 1969.

4. Anonymous; Energy in Western Europe, Report No. 367, Stanford Research
    Institute, Menlo Park, Ca., Jan. 1969.

5. Anonymous; International Petroleum Encyclopedia, Petroleum Publishing
    Company, Tulsa, Oklahoma, 1968, pp. 10-30

6. Anonymous; "National Petroleum Councils Report on U.S. Energy Outlook,"
    Ocean Industry, Jan. 1972, Vol. 7, No. 1, pp. 19.

7. Arie, Milio and Maaru Kiya; "Lift of a Cylinder in Shear Flow Subject to
    an Interference of a Plane Wall," Transactions of the Japan Society of
    Mechanical Engineers, Vol. 33, No. 246, Feb. 1967.

8. Bidde, Devidas D., "Laboratory Study of Lift Forces on Circular Piles,"
    Journal of the Waterways, Harbors and Coastal Engineering Division,
    Proceedings of ASCE, No.v 1971, pp. 595-614, Vol. 97.

9. Bretschneider, C. L., Evaluation of Drag and Inertial Coefficient from
    Maximum Range of Total Wave Force, Technical Report 55-5, Texas A & M,
    College Station, Texas, May 1967.

10. Dean, R. G. and P. M. Aagaard, "Wave Forces Data Analysis and Engineering
    Calculation Method," Journal of Petroleum Technology, March 1970, pp. 368-
    375, Vol. 22.

11. Dean, R. G. and D. R. F. Harleman, "Interaction of Structures and Waves,"
    Estuary and Coastal Engineering Hydrodynamics, edited by Arthur T. Ippen,
    Mc Graw-Hill, Chapter 8, pp. 341-403, 1966.

12. Evans, D. J., "Analysis of Wave Force Data", Journal of Petroleum Technology
    March 1970, pp. 347-358.

13. Ewing, M., "Some Results of Deep Ocean Drilling", Proceedings, 1969
    Offshore Technical Conference, Vol. 1, Houston, Texas, May 1969, pp. 43-49.

14. Gee, H. C., "Beach Nourishment from Offshore Sources", Journal of Water
    Ways and Harbors Division, Proceedings of ASCE, August 1965.

15. Goodman, Theodore, R., "Forces on a Hovering Slender Body of Revolution
    Submerged under Waves of Moderate Wave Lengths", Developments in Mechanics,
    by S. Ostrach and R. Scanlan, Vol. 2, Part 1, Fluid Mechanics, Pergamon Press
    Inc., 1965, pp. 525-549.

16. Grace, R. A., "The Effect of Clearance and Orientation on Wave Induced
     Forces on Pipe Lines: Results of Laboratory Experiments". Technical
     Report No. 15, University of Hawaii – Look – LAB – 71 – 15, April 1971.

17. Huston, John, "Dredging Fundamentals", Journal of the Waterways and Harbor
     Division, Proceedings of the ASCE, Vol. 93, No. WW3, August 1967, p. 45.

18. Jen, Yuan, "Laboratory Study of Inertia Forces on Piles", Journal of the
     Waterways and Harbors Division, Proceedings of the ASCE, Feb. 1968, pp. 59–76.

19. Jensen, W. C., Energy in Europe, University Printing House, Cambridge,
     England, 1967.

20. Johnson, Ronald E., "Regression Model of Wave Forces on Ocean Outfalls",
     Journal of the Waterways and Harbors Division, ASCE, May 1970, pp. 289–305.

21. Kaplan, P. and P. N. Hu, "Virtual Mass and Slender Body Theory in Waves",
     Proceedings Sixth Annual Conference on Fluid Mechanics, Sept. 1959,
     pp. 183–197.

22. Keulegan, Carbis H. and Lloyed H. Carpenter, "Forces on Cylinders and
     Plates in an Oscillating Fluid", Journal of Research, National Bureau
     of Standards, Vol. 60, No. 5, May 1958, pp. 423–440.

23. LaMotte, Clyde, "Cas and Oil Activity will Soar in 1970's", Ocean
     Industry, Feb. 1970, Vol. 5, No. 2, p. 7.

24. MacCamy, R. C. and R. A. Fuchs, Wave Forces on Piles: a Diffraction
     Theory, U.S. Army Corps of Engineers, Beach Erosion Board, Technical
     Memo No. 69, Dec. 1954.

25. Morison, J. R., M. P. O'Brien, J. W. Johnson, and S. A. Schaaf, "The
     Forces Exerted by Surface Waves on Piles", Petroleum Transactions, AIME,
     Vol. 189, 1950, pp. 149–154.

26. Ogilvie, T. Francis, "First and Second Order Forces on a Cylinder Sub-
     merged under a Free Surface", Journal of Fluid Mechanics, Vol. 16,
     Part 3, July 1963, pp. 451–472.

27. Savage, C. H., The Design and Analysis of a Submerged Buoyant Anchored
     Pipeline for the Transportation of Natural Gas through the Deep Ocean,
     Ph.D. thesis, Stanford University, 1970.

28. Savage, G. H., S. M. Sullivan, R. L. Street, and P. L. Boutin, The Design
     of a Submerged, Buoyant, Anchored Transoceanic Pipeline for Transporting
     Natural Gas, Paper No. SPE 3021, American Institute of Mining, Metallurgical
     and Petroleum Engineers, Inc., 1970.

29. Thrasher, L. W. and P. M. Aagaard, "Measured Wave Force Data on Offshore
     Platforms", Journal of Petroleum Technology, March 1970, pp. 339–346.

30. Ursell, F., "The Expansion of Water-wave Potentials at Great Distances",
     Proceedings Cambridge Philosophical Society, Vol. 64, 1968, pp. 811–826.

31. Ursell, F., "Surface Waves on Deep Water in the Presence of a Submerged
     Circular Cylinder", I and II. Proceedings, Cambridge Philosophical
     Society, Vol. 46, 1950, pp. 143–158.

32. Wheeler, J. D., "Method for Calculating Forces Produced by Irregular Waves", Journal of Petroleum Technology, March 1970.

33. Wiegel, R. L., Oceanographic Engineering, Prentice-Hall, Inc., Englewood Cliffs, N. J., 1964.

34. Wiegel, R. L., "Parallel Wire Resistance Wave Meter", Proceedings of the First Conference on Coastal Engineering Instruments, Council on Wave Research, The Engineering Foundation, 1953, pp. 39-43.

35. Wiegel, R. L., K. E. Beebe and J. Moon, "Ocean Wave Forces on Circular Cylindrical Piles", Journal of Hydraulics Division, Proc. ASCE, Vol. 83, No. HY2, Paper #1199, April 1957.

36. Wilson, James F. and Hartley M. Caldwell, "Force and Stability Measurements on Models of Submerged Pipelines". Preprints, 1970 Offshore Technology Conference, April 1970, Houston, Texas, Vol. 1, Paper No. OTC 1224.

CHAPTER 110

WAVE SCATTERING BY PERMEABLE AND IMPERMEABLE
BREAKWATER OF ARBITRARY SHAPE

Takeshi IJIMA, Chung Ren CHOU and Yasu YUMURA
Professor, Doctor Course Student and Research Associate
Faculty of Engineering, Kyushu University, Fukuoka 812, Japan

Abstract

This paper deals with a theoretical method of calculation of the fluid motion, when a sinusoidal plane wave incidents to a permeable breakwater of arbitrary shape at constant water depth and shows that the problem for impermeable breakwater is solved as a special case of this method.

The method described here is the extension of the author's method[1] of solution for two-dimensional permeable breakwater by the method of continuation of velocity potentials for two different fluid regions into three-dimensional problems by means of Green functions.

Here, the analytical process of calculation is presented and as representative examples, wave height distributions and wave forces around an isolated elliptic- and rectangular breakwater are calculated and compared with experiments in wave channel.

The principle of this method is also applied to the analysis of submerged and semi-immersed fixed cylinder and the motions of floating body of arbitrary shape.

Introduction

We have many investigations on wave scattering problem for impermeable, straight breakwater, but few of permeable one, especially, of arbitrary shape. Here, we show a method of calculation for fluid motion around as isolated permeable and impermeable breakwater of arbitrary shape.

Assuming the fluid resistance to be proprotional to the fluid velocity, the fluid motion in a permeable breakwater regions has a velocity potential. And the motion in outer region of breakwater has also another velocity potential. These velocity potentials are developed into infinite series of orthogonal functions in terms of the depth z from still water surfaces, with eigenvalues determined by free surface and bottom boundary conditions in both fluid regions. And the coefficients of terms in these infinite series are the functions of horizontal coorinates (x,y) and satisfy Helmholtz's

equations inherent to their own eigenvalues. Hence, by Green's identity for-
mula, these coefficients at any point (x,y) in fluid region are expressed by
their boundary values and normal derivatives to the boundary. Moreover, ow-
ing to the singularity of Green functions on the boundary, the boundary valu-
es and their normal derivatives of these coefficients are related by integral
equations. Then, dividing the boundary into small elements and taking the
sum, these integral equations are transformed into linear summation equations,
which relate the values and their normal derivatives of coefficients on the
boundary.

On the other hand, by the conditions of mechanical continuities of mass
and energy flux through the boundary surface induced by fluid motions in out-
er and inner regions, the values and normal derivatives of above coefficients
for outer region are linearly related to those for inner region.

Thus, we have two kinds of linear relations between the codfficients and
their normal derivatives on the boundary and by solving these equations
simnltaneously, we obtain the boundary values and derivatives of coefficients.
Then, by Green's identity formula, the velocity potentials and so the fluid
motion at any point (x,y) in both regions are completely obtained.

As for the impermeable breakwater, the velocity potential in outer region
is expressed by only two terms because of identical vanishing of scattering
terms in infinite series and also normal derivatives of the coefficients
vanish by the kinematical condition on the boundary. Hence the coefficients
are determined by only one integral equation, from which velocity potential
is easily determined.

I Analysis for Permeable Breakwater

A sinuoidal plane wave of frequency $\sigma(=2\pi/T$: T is wave period) is assum-
ed to incident to a permeable breakwater of arbitrary shape at constant water
depth h: As shown in Fig.1, the origine of cooridinate system is fixed at
still water surface, x and y axes are taken in horizont, and z axis is ver-
tically upwards. The cross-section of breakwater is indicated by a closed
curve D, which shows the boundary between outer and inner fluid regions.
Fluid motion in outer region I is assumed to be small amplitude wave motion
in ideal, imcompressible fluid, and the one in inner region II to be Darcy's
flow in porous material of void V with fluid resistance proportion is μ.

Then, fluid motions in both regions have velocity potential $\Phi(x,y,z)\exp(-i\sigma t)$ and wave function satisfies the following Laplace's equation.

$$\frac{\partial^2 \phi}{\partial x^2} + \frac{\partial^2 \phi}{\partial y^2} + \frac{\partial^2 \phi}{\partial z^2} = 0 \tag{1.1}$$

(i) Wave function $\phi_1(x,y,z)$ in region I

The general solution of Eq.(1.1) which satisfy free surface and bottom boundary conditions and radiation condition is expressed as follows:

$$\phi_1(x,y,z) = \frac{g\zeta_0}{\sigma}[\{f_0(x,y)+f_1(x,y)\}\frac{\cosh k(z+h)}{\cosh kh} + \sum_{n=1}^{\infty} f_2^{(n)}(x,y)\frac{\cos k_n(z+h)}{\cos k_n h}] \tag{1.2}$$

where g is gravity acceleration and ζ_0 is the amplitude of incident wave which is given by $\zeta_i = \zeta_0 \cos[k(x\cos\omega + y\sin\omega)+\sigma t]$, where ω is the incident angle with x axis. k and k_n are roots of the following equation.

$$kh \tanh kh = -k_n h \tan k_n h = \sigma^2 h/g \tag{1.3}$$

$f_0(x,y)$ corresponds to the incident wave potential and is expressed by the real part of the following equation.

$$f_0(x,y) = -i \exp[-ik(x\cos\omega + y\sin\omega)] \tag{1.4}$$

$f_1(x,y)$ and $f_2^{(n)}(x,y)$ are unknown functions which satisfy the following Helmholtz's equations.

$$\frac{\partial^2 f_1}{\partial x^2} + \frac{\partial^2 f_1}{\partial y^2} + k^2 f_1 = 0 \quad , \quad \frac{\partial^2 f_2^{(n)}}{\partial x^2} + \frac{\partial^2 f_2^{(n)}}{\partial y^2} - k_n^2 f_2^{(n)} = 0 \tag{1.5}$$

(ii) Wave function $\phi_2(x,y,z)$ in region II

Fluid motion in permeable material with void V and resistance coefficient μ is determined by wave function ϕ_2. Fluid velocity components u_i (i=1,2,3) and pressure intensity p are given as follows:

$$u_i = \frac{\partial \phi_2}{\partial x_i} e^{-i\sigma t} \quad , \quad p/\zeta = i\frac{\sigma}{V}(1+i\mu V/\sigma) \phi_2 e^{-i\sigma t} -gz \tag{1.6}$$

And $\phi_2(x,y,z)$ which satisfies free surface and bottom boundary condition is expressed as follows:

$$\Phi_2(x,y,z) = \frac{g\zeta_0}{\sigma} \sum_{s=1}^{\infty} f_3^{(s)}(x,y) \frac{\cosh \bar{k}_s(z+h)}{\cosh \bar{k}_s h} \tag{1.7}$$

where $\bar{k}_s$ are the complex roots of the following equation.

$$\bar{k}_s h \tanh \bar{k}_s h = (1+i\mu V/\sigma) \sigma^2 h/g \qquad , (s=1,2,3,4,\ldots\ldots) \tag{1.8}$$

$f_3^{(s)}(x,y)$ are unknown functions to satisfy next equation.

$$\frac{\partial^2 f_3^{(s)}}{\partial x^2} + \frac{\partial^2 f_3^{(s)}}{\partial y^2} + \bar{k}_s^2 f_3^{(s)} = 0 \tag{1.9}$$

(iii)   Respresentation of f_1, $f_2^{(n)}$, $f_3^{(s)}$ by means of Green's identity formula

Indicating the point on the boundary D by (ξ,η) and the point in fluid region I and II by (x,y), the distance between them is

$$r(x,y:\xi,\eta) = r(\xi,\eta:x,y) = \sqrt{(x-\xi)^2 + (y-\eta)^2} \tag{1.10}$$

Green functions which are particular solutions of Eq.(1.5) and (1.9) with singularities of order log r when r tends to zero and satisfy Sommerfeld's[2] radiation condition when r tends to infinity are $-\frac{i}{2}H_0^{(1)}(kr)$ for f_1, $-K_0(k_n r)/\pi$ for $f_2^{(n)}$ and $-\frac{i}{2}H_0^{(1)}(\bar{k}_s r)$ for $f_3^{(s)}$, where $H_0^{(1)}$ and K_0 are Hankel function of the first kind and modified Bessel function of order zero, respectively. Then, following to Green's identity formula, $f_1(x,y)$, $f_2^{(n)}(x,y)$ and $f_3^{(s)}(x,y)$ are represented by their values $f_1(\xi,\eta)$, $f_2^{(n)}(\xi,\eta)$, $f_3^{(s)}(\xi,\eta)$ and their normal derivatives $\bar{f}_1(\xi,\eta) = \partial f_1(\xi,\eta)/k\partial\nu$, $\bar{f}_2^{(n)}(\xi,\eta) = \partial f_3^{(s)}(\xi,\eta)/k\partial\nu$, $\bar{f}_3^{(s)}(\xi,\eta) = \partial f_3^{(s)}(\xi,\eta)/k\partial\nu$ on the boundary D as follows:

$$f_1(x,y) = -\frac{1}{2}\int_D [f_1(\xi,\eta)\frac{\partial}{\partial\nu}(-\frac{i}{2}H_0^{(1)}(kr)) - (-\frac{i}{2}kH_0^{(1)}(kr))\bar{f}_1(\xi,\eta)]ds \tag{1.11}$$

$$f_2^{(n)}(x,y) = -\frac{1}{2}\int_D [f_2^{(n)}(\xi,\eta)\frac{\partial}{\partial\nu}(-K_0(k_n r)/\pi) - (-kK_0(k_n r)/\pi)\bar{f}_2^{(n)}(\xi,\eta)]ds \tag{1.12}$$

$$f_3^{(s)}(x,y) = \frac{1}{2}\int_D [f_3^{(s)}(\xi,\eta)\frac{\partial}{\partial\nu}(-\frac{i}{2}H_0^{(1)}(\bar{k}_s r)) - (-\frac{i}{2}kH_0^{(1)}(\bar{k}_s r))\bar{f}_3^{(s)}(\xi,\eta)]ds \tag{1.13}$$

where ν is outward normal to the boundary and integral is the line integral taken in counter-clockwise direction along the boundary D.

Taking the limit when point (x,y) tends to any point (ξ',η') on the

boundary, Eq.(1.11) (1.12) (1.13) give the following integral equations.

$$f_1(\xi',\eta') = -\int_D [f_1(\xi,\eta)\frac{\partial}{\partial\nu}(-\frac{i}{2}H_0^{(1)}(kR)) - (-\frac{i}{2}kH_0^{(1)}(kR))\bar{f}_1(\xi,\eta)]ds \qquad (1.14)$$

$$f_2^{(n)}(\xi',\eta') = -\int_D [f_2^{(n)}(\xi,\eta)\frac{\partial}{\partial\nu}(-K_0(k_nR)/\pi) - (-kK_0(k_nR)/\pi)\bar{f}_2(\xi,\eta)]ds \qquad (1.15)$$

$$f_3^{(s)}(\xi',\eta') = \int_D [f_3^{(s)}(\xi,\eta)\frac{\partial}{\partial\nu}(-\frac{i}{2}H_0^{(1)}(\bar{k}_sR)) - (-\frac{i}{2}kH_0^{(1)}(\bar{k}_sR))\bar{f}_3^{(s)}(\xi,\eta)]ds \quad (1.16)$$

where $R = \sqrt{(\xi'-\xi)^2 + (\eta'-\eta)^2}$

(iv) Tramsform of line integral to summation

Dividing the boundary curve D into small N segments S_j (j=1,2,3,..N) by N points and indicating the central point of each segment by (ξ_j,η_j), the line integral along D is replaced by summation as follow, for example:

$$\int_D f_1(\xi,\eta)\frac{\partial}{\partial\nu}(-\frac{i}{2}H_0^{(1)}(kR))ds = \sum_{j=1}^{N} f_1(\xi,\eta)\int_{\Delta S_j}\frac{\partial}{\partial\nu}(-\frac{i}{2}H_0^{(1)}(kR_{ij}))ds \qquad (1.17)$$

where $R_{ij} = \sqrt{(\xi_j-\xi_i)^2 + (\eta_j-\eta_i)^2}$ and (ξ_i,η_i) is any fixed point corresponding to (ξ',η').

Thus, Eq.(1.14)(1.15)(1.16) are written by the following summation equations.

$$f_1(i) + \sum_{j=1}^{N}\{\bar{A}_{ij}f_1(j) - A_{ij}\bar{f}_1(j)\} = 0 \qquad (1.18)$$

$$f_2^{(n)}(i) + \sum_{j=1}^{N}\{\bar{B}_{ij}^{(n)}f_2^{(n)}(j) - B_{ij}^{(n)}\bar{f}_2^{(n)}(j)\} = 0 \qquad (1.19)$$

$$f_3^{(s)}(i) - \sum_{j=1}^{N}\{\bar{E}_{ij}^{(s)}f_3^{(s)}(j) - E_{ij}^{(s)}\bar{f}_3^{(s)}(j)\} = 0 \qquad (1.20)$$

where $f_1(j)$, $\bar{f}_1(j)$,...... etc. represent $f_1(\xi_j,\eta_j)$, $\bar{f}_1(\xi_j,\eta_j)$,.... etc..and

$$A_{ij} = \int_{\Delta S_j}(-\frac{i}{2}kH_0^{(1)}(kR_{ij}))ds \quad , \quad \bar{A}_{ij} = \int_{\Delta S_j}\frac{\partial}{\partial\nu}(-\frac{i}{2}H_0^{(1)}(kR_{ij}))ds$$

$$B_{ij}^{(n)} = \int_{\Delta S_j}(-kK_0(k_nR_{ij})/\pi)ds \quad , \quad \bar{B}ij = \int_{\Delta S_j}\frac{\partial}{\partial\nu}(-K_0(k_nR_{ij})/\pi)ds$$

$$E_{ij}^{(s)} = \int_{\Delta S_j} (-\frac{i}{2}kH_0^{(1)}(\bar{k}_s R_{ij}))ds \quad , \quad \bar{E}_{ij}^{(s)} = \int_{\Delta S_j} \frac{\partial}{\partial \nu}(-\frac{i}{2}H_0^{(1)}(\bar{k}_s R_{ij}))ds \quad (1.21)$$

$$R_{ij} = \sqrt{(\xi_j-\xi_i)^2 + (\eta_j-\eta_i)^2}$$

(v) Mechanical continuity conditions along boundary D

Mass and energy flux induced by fluid motions in inner and outer regions should be continuous through the immersed surface of breakwater. These conditions are satisfied by the continuities of fluid velocities normal to the boundary D and of the fluid pressure intensities at the boundary. Fluid pressure in outer and inner regions p_1 and p_2 are given as follows[3]:

$$p_1/\zeta = i\Phi_1(x,y,z)e^{-i\sigma t} \quad , \quad p_2/\zeta = i\sigma\frac{1+i\mu V/\sigma}{V}\Phi_2(x,y,z)e^{-i\sigma t} \quad (1.22)$$

Therefore, the continuity conditions are expressed as follows:

$$\partial\Phi_1(\xi,\eta,z)/\partial\nu = \partial\Phi_2(\xi,\eta,z)/\partial\nu \quad , \quad \Phi_1(\xi,\eta,z) = \frac{1+i\mu V/\sigma}{V}\Phi_2(\xi,\eta,z) \quad (1.23)$$

Substituting Eq.(1.2) and (1.7) into above equations, we obtain

$$\{\bar{f}_0(\xi,\eta)+\bar{f}_1(\xi,\eta)\}\frac{\cosh k(z+h)}{\cosh kh} + \sum_{n=1}^{\infty}\bar{f}_2^{(n)}(\xi,\eta)\frac{\cos k_n(z+h)}{\cos k_n h} = \sum_{s=1}^{\infty}\bar{f}_3^{(s)}(\xi,\eta)\frac{\cosh\bar{k}_s(z+h)}{\cosh\bar{k}_s h}$$
$$\cdots\cdots\cdots\cdots\cdots\cdots\cdots\cdots\cdots\cdots\cdots\cdots\cdots\cdots\cdots\cdots\cdots\cdots(1.24)$$

$$\{f_0(\xi,\eta)+f_1(\xi,\eta)\}\frac{\cosh k(z+h)}{\cosh kh} + \sum_{n=1}^{\infty}f_2^{(n)}(\xi,\eta)\frac{\cos k_n(z+h)}{\cos k_n h} =$$

$$\frac{1+i\mu V/\sigma}{V}\sum_{s=1}^{\infty}f_3^{(s)}(\xi,\eta)\frac{\cosh\bar{k}_s(z+h)}{\cosh\bar{k}_s h} \quad\cdots\cdots\cdots\cdots\cdots\cdots\cdots (1.25)$$

Multiplying each term of above equations by $\cosh k(z+h)$ and $\cos k_n(z+h)$, and integrating from $z=-h$ to $z=0$, we have next relations.

$$f_1(\xi,\eta) = -[f_0(\xi,\eta) + \frac{\alpha}{N_0}\sum_{s=1}^{\infty}\frac{f_3^{(s)}(\xi,\eta)}{1-(\bar{\lambda}_s/\lambda_0)^2}] \quad (1.26)$$

$$f_2^{(n)}(\xi,\eta) = -\frac{\beta}{N_n}\sum_{s=1}^{\infty}\frac{f_3^{(s)}(\xi,\eta)}{1+(\bar{\lambda}_s+\lambda_n)^2} \quad (1.27)$$

$$\bar{f}_1(\xi,\eta) = -[\bar{f}_0(\xi,\eta) + \frac{\alpha}{N_0} \sum_{s=1}^{\infty} \frac{\bar{f}_3^{(s)}(\xi,\eta)}{1-(\bar{\lambda}_s/\lambda_0)^2}] \tag{1.28}$$

$$\bar{f}_2^{(n)}(\xi,\eta) = -\frac{\beta}{N_n} \sum_{s=1}^{\infty} \frac{\bar{f}_2^{(s)}(\xi,\eta)}{1+(\bar{\lambda}_s/\lambda_n)^2} \tag{1.29}$$

$$\alpha = i\frac{\mu}{\sigma}(1+i\mu V/\sigma), \quad \beta = i\mu V/\sigma, \quad \lambda_0 = kh, \quad \lambda_n = k_n h, \quad \bar{\lambda}_s = \bar{k}_s h$$

$$N_0 = \frac{1}{2}(1+2\lambda_0/\sinh 2\lambda_0), \quad N_n = \frac{1}{2}(1+2\lambda_n/\sin 2\lambda_n), \quad \bar{f}_0(\xi,\eta) = \partial f_0(\xi,\eta)/k\partial\nu \tag{1.30}$$

(vi)　Determination of f_1, $f_2^{(n)}$, $f_3^{(s)}$ .... etc. on the boundary D

Eq.(1.18)(1.19)(1.20) and (1.26)(1.27)(1.28).(1.29) are the relations to determine f_1, $f_2^{(n)}$,........ on the boundary.

From Eq. (1.20), $\bar{f}_3^{(s)}(\xi_i,\eta_i)$ is expressed by $f_3^{(s)}(\xi_j,\eta_j)$ as follows:

$$\bar{f}_3^{(s)}(i) = \sum_{j=1}^{N} M_{ij}^{(s)} f_3^{(s)}(j) \text{ where } M_{ij}^{(s)} = \frac{1}{\Delta(s)} \sum_{k=1}^{N} \gamma_{kj}^{(s)} \Delta_{ki}^{(s)} \tag{1.31}$$

where $\Delta(s)$ is the matrix by $E_{ij}^{(s)}$, $\Delta_{ki}^{(s)}$ is the determinant, given by removing the "k"th row and the "i"th column from $\Delta(s)$ and then multiplying $(-1)^{k+i}$ and $\gamma_{kj}^{(s)} = \delta_{kj} + \bar{A}_{kj}^{(s)}$, δ_{kj} is Kronecker's delta, i.e. $\delta_{kj}=0 (k\neq j) : =1(k=j)$.

Substituting Eq.(1.26)(1.29) into Eq.(1.18)(1.19), and then eliminating $\bar{f}_3^{(s)}$ by Eq.(1.31), we have next linear simultaneous equations in term of $f_3^{(s)}$.

$$\sum_{s=1}^{\infty} \frac{1}{1-(\bar{\lambda}_s/\lambda_0)^2} [f_3^{(s)}(i) + \sum_{j=1}^{N} \bar{A}_{ij} f_3^{(s)}(j) - A_{ij} \cdot \sum_{k=1}^{N} M_{jk}^{(s)} f_3^{(s)}(k)]$$

$$= -N_0 [f_0(i) + \sum_{j=1}^{N} \bar{A}_{ij} f_0(j) - A_{ij} \bar{f}_0(j)] \tag{1.32}$$

$$\sum_{s=1}^{\infty} \frac{1}{1+(\bar{\lambda}_s/\lambda_n)^2} [f_3^{(s)}(i) + \sum_{j=1}^{N} \bar{B}_{ij}^{(n)} f_3^{(s)}(j) - B_{ij}^{(n)} \sum_{k=1}^{N} M_{jk}^{(s)} f_3^{(s)}(k)]$$

$$= 0 \quad , \quad (n=1,2,3,\ldots\ldots\ldots)$$

Above equations are applied to i=1,2,3,...N. If we take n ans s to n*

and s*,respectively, we have $(n*+1)N$ equations for $s*N$ unknown $f_3^{(s)}$. There-
fore, taking $s*=n*+1$, all of $f_3^{(s)}$ $(s=1,2\ldots s*)$ are determined by solving
Eq.(1.32) and then $\bar{f}_3^{(s)}$, f_1, $\bar{f}_1$, $f_2^{(n)}$, $\bar{f}_2^{(n)}$ are obtained by Eq.(1.31)(1.26)
(1.27)(1.28)(1.29),respectively.

(vii) Determination of $f_1(x,y)$, $f_2^{(n)}(x,y)$ and $f_3^{(s)}(x,y)$

$f_1(x,y)$, $f_2^{(n)}(x,y)$ and $f_3^{(s)}(x,y)$ at any point of fluid region are calcu-
lated by Eq.(1.10)(1.12)(1.13) as follows:

$$f_1(x,y)=-\frac{1}{2}\sum_{j=1}^{N}[\bar{A}_{xj}f(j)-A_{xj}\bar{f}(j)], \quad f_2^{(n)}(x,y)=-\frac{1}{2}\sum_{j=1}^{N}[\bar{B}_{xj}^{(n)}f_2^{(n)}(j)-B_{xj}^{(n)}\bar{f}_2^{(n)}(j)]$$

$$f_3^{(s)}(x,y)=\frac{1}{2}\sum_{j=1}^{N}[\bar{E}_{xj}^{(s)}f_3^{(s)}(j)-E_{xj}^{(s)}\bar{f}_3^{(s)}(j)] \tag{1.33}$$

where A_{xj}, $\bar{A}_{xj}$,.... are those which are given in Eq.(1.21) by replacing
(ξ_i,η_i) by (x,y).

Thus, wave function $\phi_1(x,y,z)$ and $\phi_2(x,y,z)$ are completely determined and
the fluid motions are fully made clear.

(viii) Numerical evalulation

A_{ij} and $\bar{A}_{ij}$ in Eq.(1.21) are calculated numerically, after Lee(1971),[4]
in the following way.

$$R_{ij}=\sqrt{(\xi_j-\xi_i)^2+(\eta_j-\eta_i)^2} \quad , \quad S_j=\sqrt{(\Delta\xi_j)^2+(\Delta\eta_j)^2}$$

$$\Delta\xi_j=\frac{1}{2}(\xi_{j+1}-\xi_{j-1}) \qquad\qquad \Delta\eta_j=\frac{1}{2}(\eta_{j+1}-\eta_{j-1}) \tag{1.34}$$

Noting that when kr tends to zero,

$$H_0^{(1)}(kr)\doteqdot 1+2i(\log\frac{kr}{2}+r)/\pi \quad , \quad H_1^{(1)}(kr)\doteqdot-2\frac{i}{\pi}\frac{1}{kr}$$

$\gamma=0.577216\ldots\ldots$ (Eluer's constant)
for $j\neq i$, we obtain

$$A_{ij}=-\frac{1}{2}H_0^{(1)}(kR_{ij})k\Delta S_j$$

$$\bar{A}_{ij}=\frac{i}{2}H_1^{(1)}(kR_{ij})(\frac{\xi_j-\xi_i}{R_{ij}}k\Delta\eta_j-\frac{\eta_j-\eta_i}{R_{ij}}k\Delta\xi_j)$$

for $j=i$

$$A_{ii} = \frac{1}{\pi}(\gamma - 1 + \log\frac{k\Delta S_i}{4} - i\pi/2)$$

$$\bar{A}_{ii} = \frac{1}{2\pi}(\xi_s \eta_{ss} - \xi_{ss}\eta_s)_i \Delta S_i$$

(1.37)

where

$$\xi_s = \frac{\xi_{i+1} - \xi_{i-1}}{2\Delta S_i} \quad , \quad \xi_{ss} = \frac{6}{\Delta S_{i+1} + \Delta S_i + \Delta S_{i-1}}[\frac{\xi_{i+1} - \xi_i}{\Delta S_{i+1} + \Delta S_i} - \frac{\xi_i - \xi_{i-1}}{\Delta S_i + \Delta S_{i-1}}]$$

(1.38)

$$\eta_s = \frac{\eta_{i+1} - \eta_{i-1}}{2\Delta S_i} \qquad \eta_{ss} = \frac{6}{\Delta S_{i+1} + \Delta S_i + \Delta S_{i-1}}[\frac{\eta_{i+1} - \eta_i}{\Delta S_{i+1} + \Delta S_i} - \frac{\eta_i - \eta_{i-1}}{\Delta S_i + \Delta S_{i-1}}]$$

Similary, other terms in Eq.(1.21) are as follows:

$$B_{ij}^{(n)} = -\frac{1}{\pi}K_0(k_n R_{ij})k\Delta S_j \quad , \quad B_{ii}^{(n)} = \frac{1}{\pi}(\gamma - 1 + \log\frac{k_n\Delta S_i}{4})k\Delta S_i$$

$$\bar{B}_{ij}^{(n)} = \frac{1}{\pi}K_1(k_n R_{ij})(\frac{\xi_j - \xi_i}{R_{ij}}k_n\Delta\eta_j - \frac{\eta_j - \eta_i}{R_{ij}}k_n\Delta\xi_j)$$

(1.39)

$$E_{ij}^{(s)} = -\frac{i}{2}H_0^{(1)}(\bar{k}_s R_{ij})k\Delta S_j \quad , \quad E_{ii}^{(s)} = \frac{1}{\pi}(\gamma - 1 + \log\frac{\bar{k}_s\Delta S_i}{4} - i\pi/2)k\Delta S_i$$

$$\bar{E}_{ij}^{(s)} = \frac{i}{2}H_0^{(1)}(\bar{k}_s R_{ij})(\frac{\xi_j - \xi_i}{R_{ij}}\bar{k}_s\Delta\eta_j - \frac{\eta_j - \eta_i}{R_{ij}}\bar{k}_s\Delta\xi_j)$$

(1.40)

$\bar{B}_{ii}^{(n)}$ and $\bar{E}_{ii}^{(s)}$ are the same as $\bar{A}_{ii}$. And $f_0(j)$ and $\bar{f}_0(j)$ are as follows:

$$f_0(j) = -i\exp\{-ik(\xi_j\cos\omega + \eta_j\sin\omega)\}$$

$$\bar{f}_0(j) = \frac{\Delta\xi_j\sin\omega - \Delta\eta_j\cos\omega}{\Delta S_j}\exp\{-ik(\xi_j\cos\omega + \eta_j\sin\omega)\}$$

(1.41)

(ix) Convergence of the infinite series in ϕ_1 and ϕ_2

For the existence of wave function ϕ_1 and ϕ_2, infinite series in the righthand sides of Eq.(1.2) and (1.7) must be uniformly convergent in x,y,z. It is difficult for the authors to prove the convergence but it is estimated in the following way.

For large value of n in Eq.(1.2), we have

$$k_n h \doteqdot n\pi - \frac{1}{n\pi}\frac{\sigma^2 h}{g} \quad \text{and} \quad \sum_n^\infty f_2^{(n)}(x,y)\frac{\cos k_n(z+h)}{\cos k_n h} = \sum_n^\infty f_2^{(n)}(x,y)\cos k_n z \quad (1.42)$$

Above series is convergent for $0 \geq z \geq -h$, if series $\sum\limits_{n}^{\infty} f_2^{(n)}(x,y)$ is convergent. While, sequence $B_{xj}^{(n)}$ and $\bar{B}_{xj}^{(n)}$ in Eq.(1.33) are monotonic decrease for increasing n at any point (x,y), so that if the series $\sum\limits_{n}^{\infty} f_2^{(n)}(\xi,\eta)$ and $\sum\limits_{n}^{\infty} \bar{f}_2^{(n)}(\xi,\eta)$ converges, series $\sum\limits_{n}^{\infty} f_2^{(n)}(x,y)$ also converges. Similarly, if series $\sum\limits_{s}^{\infty} f_3^{(s)}(\xi,\eta)$ converges, series $\sum\limits_{s}^{\infty} f_3^{(s)}(x,y) \cdot \cosh \bar{k}_s(z+h)/\cosh \bar{k}_s h$ also converges.

We have

$$N_n \doteq -\frac{(n\pi)^2}{2\sigma^2 h/g} , \qquad \bar{\lambda}_s \doteq \frac{\sigma^2 h}{g} \frac{\nu\mu}{\sigma} \frac{1}{s\pi} + i(s\pi - \frac{1}{s\pi} \frac{\sigma^2 h}{g}) \tag{1.44}$$

for large n and s. Therefore, in Eq.(1.27)

$$\sum\limits_{n}^{\infty} \sum\limits_{s}^{\infty} \frac{f_3^{(s)}(\xi,\eta)}{N_n\{1+(\bar{\lambda}_s/\lambda_n)^2\}} \doteq -\frac{2\alpha}{\pi^2} \frac{\sigma^2 h}{g} \sum\limits_{n}^{\infty} \sum\limits_{s}^{\infty} \frac{f_3^{(s)}(\xi,\eta)}{n^2 - s^2 + 2i\frac{1}{\pi^2} \frac{\mu\nu}{\sigma} \sigma^2 h/g} \tag{1.45}$$

Above series are convergent, if series $\sum\limits_{s}^{\infty} f_3^{(s)}(\xi,\eta)$ converges, and then $\sum\limits_{n}^{\infty} f_2^{(n)}(\xi,\eta)$ converges.

Moreover, from Eq.(1.40), $E_{ij}^{(s)} \ll E_{ii}^{(s)}$ and $\bar{E}_{ij}^{(s)} \ll \bar{E}_{ii}^{(s)}$ for large s. Therefore, Eq.(1.20) approaches to the following equation for large s.

$$(1-\bar{E}_{ii}^{(s)})f_3^{(s)}(i) + E_{ii}^{(s)}\bar{f}_3^{(s)}(i) = 0 ,$$

from which

$$\bar{f}_3^{(s)}(i) = -\frac{1-\bar{E}_{ii}^{(s)}}{E_{ii}^{(s)}} f_3^{(s)}(i) \tag{1.46}$$

where $\bar{E}_{ii}^{(s)}$ is indepentent on s and $E_{ii}^{(s)}$ is approximated as follows:

$$E_{ii}^{(s)} \doteq \frac{k\Delta S_i}{\pi} \{-1+i(\frac{s\pi\Delta S_i}{4h} -\pi/2)\} \tag{1.47}$$

$E_{ii}^{(s)}$ increases with increasing s, so that from Eq.(1.46), $\sum\limits_{s}^{\infty} \bar{f}_3^{(s)}(\xi,\eta)$ converges, if $\sum\limits_{s}^{\infty} f_3^{(s)}(\xi,\eta)$ converges.

Thus, if $\sum\limits_{s}^{\infty} f_3^{(s)}(\xi,\eta)$ converges, $\sum\limits_{s}^{\infty} \bar{f}_3^{(s)}(\xi,\eta)$, $\sum\limits_{n}^{\infty} f_2^{(n)}(\xi,\eta)$ and $\sum\limits_{n}^{\infty} \bar{f}_2^{(n)}(\xi,\eta)$ are convergent, and wave cunctions $\Phi_1(x,y,z)$ and $\Phi_2(x,y,z)$ exist. But it is difficult to prove mathematically the convergency of $\sum\limits_{s}^{\infty} f_3^{(s)}(\xi,\eta)$ and is estimated numerically, as shown in later example.

In practical calculations, infinite series are replaced by finite series,

Hence, the accuracy of calculation should be tested by the agreement of both sides of Eq.(1.24)(1.25) for any value of z at any point (ξ,η).

(x)   Wave height distribution and wave forces to breakwater

Wave profiles ζ_I and ζ_{II} at any point in outer and inner regions are given by following equations.

$$\zeta_I = i\zeta_0 \Phi_1(x,y,z) e^{-i\sigma t} \quad , \quad \zeta_{II} = i\zeta_0 \Phi_2(x,y,z) e^{-i\sigma t} \tag{1.48}$$

And   the ratios of wave height in both regions to incident wave height $K_d^{(1)}$ and $K_d^{(2)}$ are calculated as follows:

$$K_d^{(1)} = \left| f_0(x,y) + f_1(x,y) + \sum_{n=1}^{\infty} f_2^{(n)}(x,y) \right| \quad , K_d^{(2)} = \left| \frac{1+i\mu V/\sigma}{V} \sum_{s=1}^{\infty} f_3^{(s)}(x,y) \right| \tag{1.49}$$

Wave forces F_x and F_y to breakwater in positive x and y directions are calculated as follows:

$$\frac{F_x}{\rho g \zeta_0 h^2} = -i \, e^{-i\sigma t} \, \frac{\sigma^2 h}{g} \, \frac{(1+i\mu V/\sigma)^2}{V} \, \sum_{s=1}^{\infty} \sum_{j=1}^{N} \frac{f_3^{(s)}(j)}{\lambda_0(\overline{\lambda}_s)^2} \, k\Delta\eta_j \tag{1.50}$$

$$\frac{F_y}{\rho g \zeta_0 h^2} = i \, e^{-i\sigma t} \, \frac{\sigma^2 h}{g} \, \frac{(1+i\mu V/\sigma)^2}{V} \, \sum_{s=1}^{\infty} \sum_{j=1}^{N} \frac{f_3^{(s)}(j)}{\lambda_0(\overline{\lambda}_s)^2} \, k\Delta\xi_j \tag{1.51}$$

II   Analysis for Impermeable Breakwater

For impermeable breakwater, the scattering terms $f_2^{(n)}(x,y)$ in Eq.(1.2) vanish identically and wave function $\Phi_1(x,y,z)$ becomes simple as follows:

$$\Phi_1(x,y,z) = \frac{g\zeta_0}{\sigma} \{f_0(x,y) + f_1(x,y)\} \frac{\cosh k(z+h)}{\cosh kh} \tag{2.1}$$

On the boundary D, fluid velocity normal to D should vanish, so that

$$\partial\Phi_1(\xi,\eta,z)/\partial\nu = 0 \quad , \text{ and so } \quad \partial f_1(\xi,\eta)/\partial\nu = -\partial f_0(\xi,\eta)/\partial\nu \tag{2.2}$$

Substituting this relation into Eq.(1.14), we have next integral

equation to determine $f_1(\xi,\eta)$

$$f_1(\xi',\eta') + \int_D f_1(\xi,\eta) \frac{\partial}{\partial\nu}(-\frac{i}{2}H_0^{(1)}(kR))ds = -\int_D (-\frac{i}{2}kH_0^{(1)}(kR))\bar{f}_0(\xi,\eta)ds \qquad (2.3)$$

from which, f_1 is determined by the following linear equations.

$$f_1(i) + \sum_{j=1}^{N} \bar{A}_{ij}f_1(j) = - \sum_{j=1}^{N} A_{ij}\bar{f}_0(j) \qquad , \quad (i=1,2,3,\ldots,N) \qquad (2.4)$$

And the first equation in Eq.(1.33), $f_1(x,y)$ and hence $\Phi_1(x,y,z)$ are determined.

Distribution of wave height ratios and wave forces to breakwater are calculated by the following equations.

$$K_d = |f_0(x,y) + f_1(x,y)| \qquad (2.5)$$

$$\frac{F_x}{\rho g \zeta_0 h^2} = -ie^{-i\sigma t} \frac{\sigma^2 h}{g} \frac{1}{\lambda_0^3} \sum_{j=1}^{N} [f_0(x,y) + f_1(x,y)]k\Delta\eta_j$$

$$\qquad (2.6)$$

$$\frac{F_y}{\rho g \zeta_0 h^2} = ie^{-i\sigma t} \frac{\sigma^2 h}{g} \frac{1}{\lambda_0^3} \sum_{j=1}^{N} [f_0(x,y) + f_1(x,y)]k\Delta\xi_j$$

III Numerical calculation

Here, breakwaters of elliptic and rectangular shape, where x and y radii are 2a and 2b, and x-side and y-side are 2a and 2b, respectively, calculate the case when a/b=0.2, b/h=2.5, for wave of $\sigma^2 h/g=0.5$, kh=0.772(kb=1.93).

In general, it is desired to make distance ΔS_j between successive calculation points in the boundary be shorter than about one eighth of wave length. Hence, in these calculations, twenty claculation points are distributed along the boundary as shown in Fig.2 where the largest distance between successive points is about 0.13L(L:wave length).

(i) Convergence of the series

As an example, taking n*=3,s*=4, the numerical values of $f_1(j), f_2^{(n)}(j)$ and $f_3^{(s)}(j)$ at every calculation points are shown in Table-1 for elliptic

breakwater of V=0.5, $\mu V/\sigma$=1.0 for wave of $\sigma^2 h/g$=0.5, ω=0°. (For the case of
ω=0°, values at symmetrical points with respect to x axis are the same, so
that, values at j=11~19 are the same as those at j=1~9, respectively.)

From the results, it is found that the convergence of the series dis-
cussed in II(vii) is satisfactory and n*=3,s*=4 are sufficient for practical
calculation of this case.

(ii)   Exactness of calculation

The exactness of calculation are determined numerically by testing how
accurately the continuity conditions Eq.(1.24) and (1.25) are satisfied.
Table-2 shows the numerical comparisons of both sides of Eq.(1.24) and(1.25)
at depth of z/h= 0.-0.2,-0.4,..., -1.0 at point j=10 and15 in above case.
From the results, it is found that the exactness of calculation is sufficient.

(iii)   Wave height distribution

Fig.3~6 are calculated wave height distributions by Eq.(1.49) for perme-
able breakwater with V=0.5, $\mu V/\sigma$ =1.0 and by Eq.(2.5) for impermeable break-
water, where the former are shown by broken curves and latter by full curves.

Fig. 7~10 are those for the case when b/h=2.5(kb=1.93), a/b=0.5, $\sigma^2 h/g$=
0.5(kh=0.772) and V=0.5, $\mu V/\sigma$=1.0.

From these distributions, it can be seen that:
(a)   The differences between rectangular and elliptic breakwater arise from
the apexes of rectangle and clearly appear for ω=0° and almost disappear
for ω=90°.
(b)   The longer becomes the breakwater, the more clearly appears the standing
wave in front of breakwater, for ω=0° in case of b/h=1.0, the standing wave
almost disappears.
(c)   The wave height in front of permeable breakwater is always smaller than
that of impermeable one. And wave height behind permeable breakwater is
smaller than the one behind impermeable breakwater for the case of short
breakwater but is adverse for the case of long breakwater. This is due to
fact that for short breakwater, waves behind it are mainly diffracted waves
and behind permeable breakwater they are smaller than those behind impermeable
one, and for long breakwater, waves behind permeable one aremainly transmitted
waves through breakwater but those behind impermeable one are mainly diffract-
ed waves and become smaller for longer breakwater.

(iv) Wave Forces

Calculated wave forces by (1.50),(1.51) and(2.6) are as shown in Table-3.

(v) Comparisons with experiments

For comparisons of analysis with experiments, rectangular and elliptic breakwater models are placed in wave channel of length 25m, width 1m and depth 0.6m with flap-type wave generator as shown in Fig.11.

Impermeable models are made of concrete and permeable models are of wire screen filled by small concrete blocks, of which the average void is 0.40, and b/h=1.0, a/b≈0.5. The water depth is 20cm, wave period is kept constant as 1.28 sec.($\sigma^2 h/g=0.5$)

Considering the effect of reflection by channel walls, wave height distributions are calculated, taking V=0.50, μ/σ=2.0, for the boundary conditions as shown in fig.11, that is, at imaginary boundary W_2 and W_4 far from breakwater waves progess from right to left without reflection waves and at channel walls W_1 and W_3, normal velocity of fluid motion vanishes.

And under the same conditions, wave heights are measured. The results of calculations and experiments are shown in Fig. 12~15, where left and right parts are by calculations and experiments, respectively. From these figures, it is found that results of calculation agree fairly well with those of experiments.

IV Conclusions

In above calculations, we assumed V=0.5, μ/σ=2.0 and found that theory and experiments are in good argument. In this analysis V and μ/σ are interpretted as virtual quantities related to void and fluid resistance of breakwater. Hence they are not necessarily the same as the actual values, but are to be selected so as to obtain agreement of theory and experiments.

The method of analysis described in this paper can be applied to the calculations not only for elliptical and rectangular shapes but also for arbitrary shapes. And the same principle is avaiable to the analysis of permeable quay wall, and also of fixed semi-immersed, of submerged cylinders.

Reference

(1) Takeshi IJIMA, Yasuhiko EGUCHI, Akira KOBAYASHI (1971):
     "Theory and Experiment on Permeable Breakwater and Quay Wall", Proc.
     18th Conf. Coast Eng. Janpan (in Janpanese)
(2) John, Fritz(1950): " On the motion of Floating Bodies II ", Communica-
     tions on Pure and Applie Mathematics, Vol.III No. 1∿4, pp. 45∿100
(3) same as (1)
(4) Lee,Jiin-Jen (1970): "Wave-induced Oscillations in Harbors of Arbi-
     trary Shape", Calif. Inst. for Technology

Table 1
Successive values of f_1, $f_2^{(n)}$, and $f_3^{(s)}$ for $\sigma^2 h/g = 0.5$

j	f_1	$f_2(1)$	$f_2(2)$	$f_2(3)$
20	-0.5171 -0.1911i	0.0105 +0.0168i	-0.0376 +0.0191i	-0.0002 -0.0001i
1	-0.3172 -0.0438i	0.0066 +0.0171i	-0.0027 +0.0043i	-0.0010 +0.0006i
2	-0.2138 +0.0105i	-0.0230 -0.0074i	0.0007 +0.0049i	0.0010 +0.0020i
3	-0.0780 -0.0137i	-0.0127 -0.0010i	0.0018 +0.0037i	0.0012 +0.0017i
4	-0.0101 -0.0317i	-0.1112 -0.0012i	0.0018 +0.0029i	0.0011 +0.0014i
5	0.0504 -0.0589i	-0.0123 -0.0032i	0.0016 +0.0027i	0.0011 +0.0012i
6	0.1107 -0.0934i	-0.0166 -0.0069i	0.0015 +0.0032i	0.0013 +0.0013i
7	0.1550 -0.1113i	-0.0259 -0.0146i	0.0009 +0.0044i	0.0016 +0.0013i
8	0.2485 -0.1828i	-0.0974 -0.0710i	-0.0150 +0.0123i	0.0028 +0.0011i
9	0.3379 -0.2024i	0.0195 +0.0155i	-0.0161 +0.0127i	0.0029 -0.0005i
10	0.4492 -0.2315i	0.0357 +0.0003i	0.0094 -0.0042i	0.0060 -0.0044i

j	$f_3(1)$	$f_3(2)$	$f_3(3)$	$f_3(4)$
20	0.1560 -0.0287i	0.0022 -0.0157i	-0.0060 +0.0101i	-0.0004 -0.0017i
1	0.2331 -0.0647i	-0.0029 -0.0227i	-0.0021 -0.0042i	-0.0012 -0.0022i
2	0.2640 -0.0971i	-0.0203 -0.0247i	-0.0020 -0.0050i	-0.0008 -0.0024i
3	0.2834 -0.1605i	-0.0233 -0.0273i	-0.0038 -0.0060i	-0.0016 -0.0027i
4	0.2917 -0.1939i	-0.0267 -0.0285i	-0.0049 -0.0063i	-0.0021 -0.0028i
5	0.2937 -0.2299i	-0.0315 -0.0286i	-0.0059 -0.0062i	-0.0025 -0.0028i
6	0.2927 -0.2677i	-0.0377 -0.0282i	-0.0068 -0.0058i	-0.0029 -0.0027i
7	0.2916 -0.2948i	-0.0450 -0.0275i	-0.0073 -0.0050i	-0.0031 -0.0026i
8	0.2821 -0.3610i	-0.0848 -0.0223i	-0.0108 +0.0026i	-0.0034 -0.0023i
9	0.2825 -0.3998i	-0.0377 -0.0296i	-0.0122 +0.0013i	-0.0043 -0.0033i
10	0.2775 -0.4542i	-0.0431 -0.0366i	-0.0117 -0.0090i	-0.0037 -0.0049i

Table 2

Numerical check on the boundary conditions

(i)   Continuity of fluid pressure

j	z/h	Region I	Region II
10	0.0	0.3821 +0.2298i	0.3755 +0.2317i
	-0.2	0.3716 +0.1859i	0.3738 +0.1823i
	-0.4	0.3795 +0.1442i	0.3786 +0.1464i
	-0.6	0.3542 +0.1264i	0.3525 +0.1261i
	-0.8	0.2944 +0.1348i	0.2950 +0.1338i
	-1.0	0.2637 +0.1432i	0.2628 +0.1447i
15	0.0	1.0487 -0.0582i	1.0421 -0.0282i
	-0.2	0.9485 -0.0562i	0.9479 -0.0659i
	-0.4	0.8825 -0.0552i	0.8828 -0.0483i
	-0.6	0.8428 -0.0469i	0.8428 -0.0477i
	-0.8	0.8209 -0.0415i	0.8207 -0.0443i
	-1.0	0.8131 -0.0402i	0.8134 -0.0360i

(ii)   Continuity of fluid velocity

j	z/h	Region I	Region II
10	0.0	-0.0746 +0.0076i	-0.0750 +0.0052i
	-0.2	-0.0362 +0.0688i	-0.0362 +0.0670i
	-0.4	-0.0154 +0.2579i	-0.0153 +0.2575i
	-0.6	-0.1214 +0.5515i	-0.1214 +0.5515i
	-0.8	-0.3093 +0.8383i	-0.3094 +0.8386i
	-1.0	-0.4047 +0.9596i	-0.4047 +0.9592i
15	0.0	0.0415 -0.0359i	0.0428 -0.0349i
	-0.2	0.0630 +0.0020i	0.0625 +0.0018i
	-0.4	0.0725 +0.0372i	0.0748 +0.0373i
	-0.6	0.0326 +0.0200i	0.0326 +0.0199i
	-0.8	0.0087 +0.0104i	0.0085 +0.0104i
	-1.0	0.0112 +0.0177i	0.0115 +0.0177i

Table 3

Calculated Results for Wave Forces

Shape		Ellipse			Rectangle			Remarks
Cross-section Area		πab			$4ab$			
Angle of Incident ω		0°	45°	90°	0°	45°	90°	
$\sigma^2 h/g = 0.5$, $kb = 1.93$								
$\dfrac{F_x}{\rho g \zeta_o h^2}$	a/b= 0.2	9.146	5.374	0.0	9.641	5.447	0.0	Imperm.
		4.208	2.427	0.0	4.802	2.561	0.0	Perm.
	a/b= 0.5	8.562	5.074	0.0	9.184	5.564	0.0	Imperm.
		6.184	3.626	0.0	6.956	3.784	0.0	Perm.
$\dfrac{F_y}{\rho g \zeta_o h^2}$	a/b= 0.2	0.0	1.371	1.508	0.0	1.644	1.417	Imperm.
		0.0	1.280	1.411	0.0	1.736	1.604	Perm.
	a/b= 0.5	0.0	3.210	3.673	0.0	3.973	3.466	Imperm.
		0.0	2.894	3.273	0.0	3.433	3.403	Perm.
$\sigma^2 h/g = 1.0$, $kb = 3.00$								
$\dfrac{F_x}{\rho g \zeta_o h^2}$	a/b= 0.2	6.431	2.773	0.0	6.774	2.534	0.0	Imperm.
		4.033	1.595	0.0	4.546	1.400	0.0	Perm.
	a/b= 0.5	6.571	2.418	0.0	6.952	2.175	0.0	Imperm.
		5.023	1.821	0.0	5.651	1.247	0.0	Perm.
$\dfrac{F_y}{\rho g \zeta_o h^2}$	a/b= 0.2	0.0	1.148	0.687	0.0	1.122	0.479	Imperm.
		0.0	1.002	0.552	0.0	1.103	0.404	Perm.
	a/b= 0.5	0.0	2.560	1.797	0.0	2.752	2.893	Imperm.
		0.0	2.082	1.412	0.0	2.117	1.948	Perm.
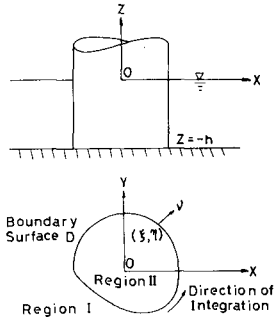
Fig.1   Definition   Sketch
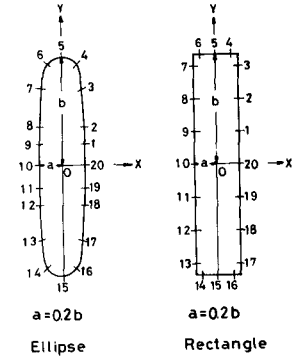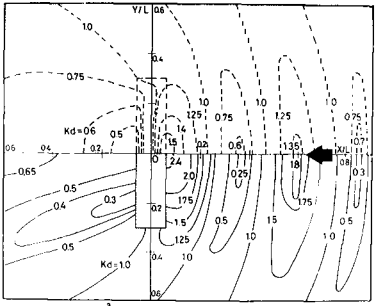
a = 0.2b   a = 0.2b

Ellipse   Rectangle

Fig.2 Distribution of Calculation Points

$\sigma^2 h/g = 0.5$ Kb=1.93   b/h = 2.5   a/b = 0.2

Fig.3   Distribution of Kd for Rectangle

$\sigma^2 h/g = 0.5$ Kb=1.93   b/h = 2.5   a/b = 0.2

Fig.4   Distribution of Kd for Ellipse

$\sigma^2 h/g = 1.0$ Kb=3.00   b/h = 2.5   a/b = 0.2
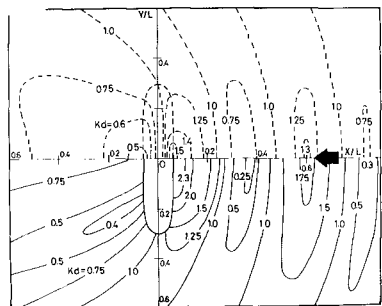
Fig.5   Distribution of Kd for Rectangle

$\sigma^2 h/g = 1.0$ Kb=3.00   b/h = 2.5   a/b = 0.2

Fig.6   Distribution of Kd for Ellipse
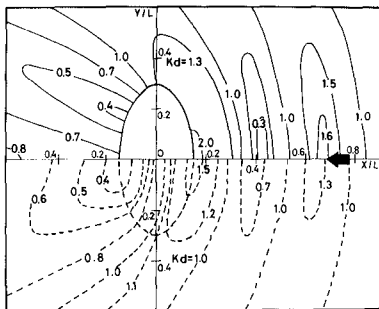
$\sigma^2 h/g = 0.5$ $Kb = 1.93$ $b/h = 2.5$ $a/b = 0.5$
Fig. 7   Distribution of Kd for Ellipse
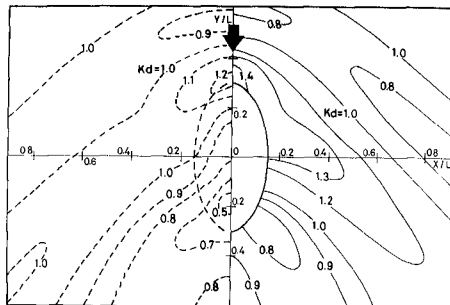
$\sigma^2 h/g = 0.5$ $Kb = 1.93$ $b/h = 2.5$ $a/b = 0.5$
Fig. 8   Distribution of Kd for Ellipse
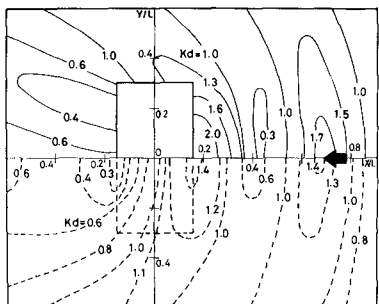
$\sigma^2 h/g = 0.5$ $Kb = 1.93$ $b/h = 2.5$ $a/b = 0.5$
Fig. 9   Distribution of Kd for Rectangle
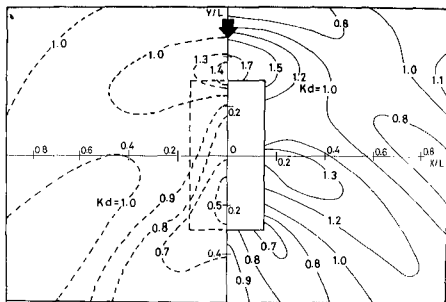
$\sigma^2 h/g = 0.5$ $Kb = 1.93$ $b/h = 2.5$ $a/b = 0.5$
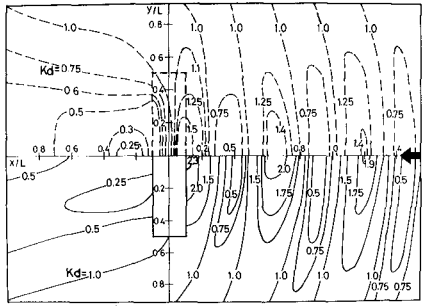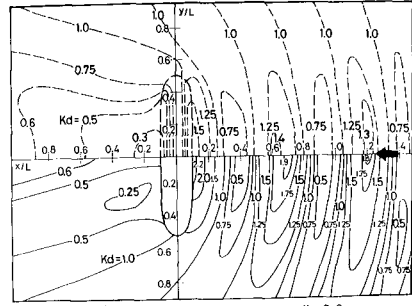Fig. 10   Distribution of Kd for Rectangle
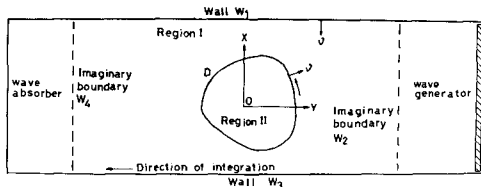
Fig. 11 Definition   Sketch
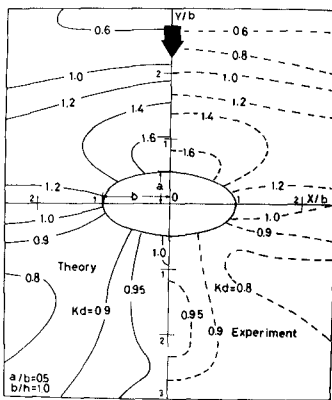
Fig 12 $\sigma^2 h/g = 0.5$, Distribution of Kd for
Impermeable Ellipse
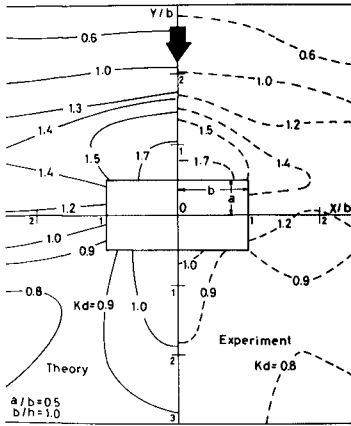
Fig.13 $\sigma^2 h/g = 0.5$, Distribution of Kd for Impermeable Rectangle
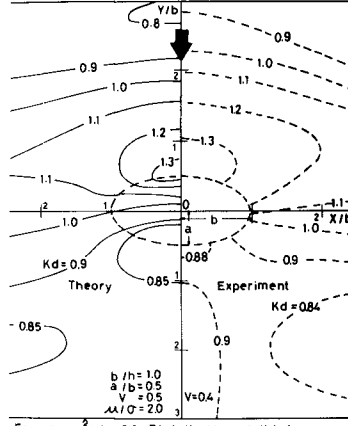
Fig.14 $\sigma^2 h/g = 0.5$, Distribution of Kd for Permeable Ellipse
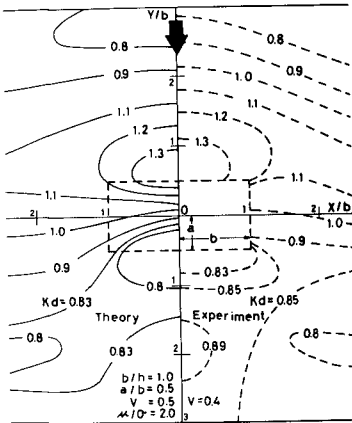
Fig.15 $\sigma^2 h/g = 0.5$, Distribution of Kd for Permeable Rectangle

CHAPTER 111

WAVE TRANSMISSION
THROUGH VERTICAL SLOTTED WALLS

by

Joachim Grüne [1]

and

Sören Kohlhase [2]

ABSTRACT

This paper deals with the wave transmission through a
vertical slotted wall. In an experimental study the
transmission coefficient has been investigated as a
function of the shape of the wall elements (rectangular
shape and H-beam shape), of the ratio of solid wall to
total wall lenght (wall-element ratio) and of the wave
approach direction.

The test results for a wave direction perpendicular to
the wall are compared with previous investigations and
theoretical derivations. For an oblique wave approach
the test results are described by a semi-empirical for-
mula. This formula, combined with a theoretical solution
for perpendicular wave approach is used to describe the
transmission coefficient for any angle of wave approach.

[1] Dipl.-Ing.   "Franzius-Institut für Wasserbau
                             und Küsteningenieurwesen"

[2] Dr.-Ing.   Technical University of Hannover,
                             Germany

INTRODUCTION

For solving certain coastal engineering problems, some
times an artificial construction is wanted, which should
be permeable with respect to currents and sedimentation
problems, on the other hand the same construction should
give a sufficient protection against wave action. Such
a construction could be a vertical slotted wall.

The general physical process, when a wave passes a verti-
cal slotted wall, is shown in Fig. 1. The energy balance
can be stated as follows:

$$E_I = E_T + E_R + E_V$$

where E_I = wave energy of the incident wave
         E_T = wave energy of the transmitted wave
         E_R = wave energy of the reflected wave
         E_V = wave energy loss

The wave damping effect may be described only by the
transmitted wave energy compared with the incident wave
energy or (instead of wave energy) by the transmitted wave
height compared with the incident wave height.

The purpose of the study described in this paper, there-
fore was to obtain the "wave transmission characteristics"
for vertical slotted walls with respect to

  1. the ratio of the impermeable part of the wall to the
     total wall

  2. the shape of the wall elements

  3. the wave approach direction

DEFINITIONS AND NOTATIONS

The transmission coefficient κ_T is defined as the ratio of the transmitted wave height H_T to the incident wave height H_I:

$$\kappa_T = \frac{H_T}{H_I}$$

The wave height after passing the slotted wall, also will be influenced by diffraction due to the geometry of the basin behind the wall. Therefore the transmitted wave height H_T must be defined directly behind the wall as shown in Fig. 2 which also shows some possible configurations of a slotted wall combined with adjacent impermeable walls.

The gaps extend over the total water depth (Fig. 1). Therefore the "wall-element ratio" W is given by (Fig.3):

$$W = \frac{b}{e}$$

where b is the width of each wall element and e is the centerline space of the elements. $100 \cdot W$ gives the relative wall-element ratio in %.

The direction of wave approach to the wall is defined by the angle ß as shown in Fig. 4.

EXPERIMENTAL EQUIPMENT AND PROCEDURE

The experiments were conducted in a wave basin 0.5 m deep, 6.7 m wide and 35 m long (Fig. 5). The test area was 6.7 m wide and 25 m long. The basin was equipped with a combined flap- and piston type wave generator for regular waves. The upper and lower strokes could be adjusted independently to reproduce the horizontal particle velocity distribution for any desired wave period and wave height as accurate as possible.
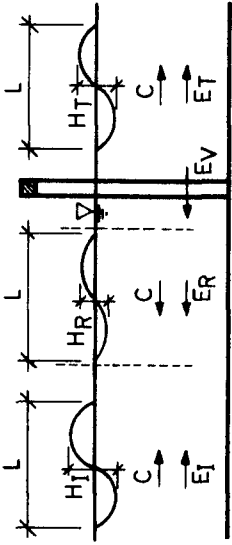
FIG. 1 WAVE TRANSMISSION
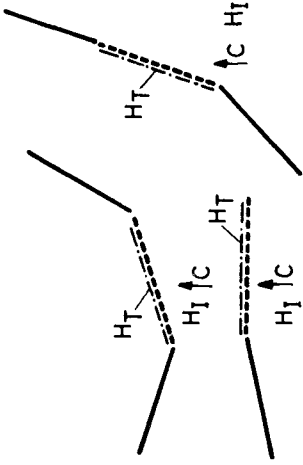
FIG. 2 DEFINITION OF THE
TRANSMITTED WAVE HEIGHT H_T
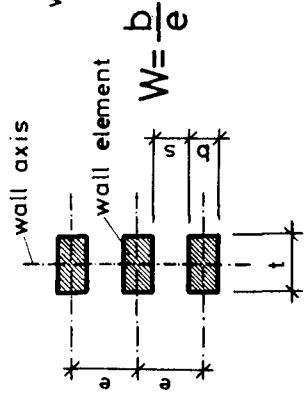
FIG. 3 NOTATION FOR WALL-ELEMENTS
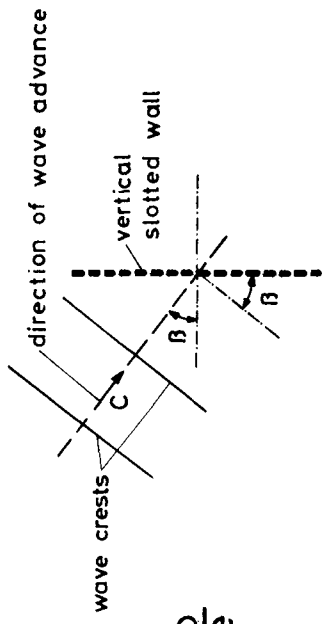
FIG. 4 NOTATION FOR WAVE APPROACH

plan view

elevation
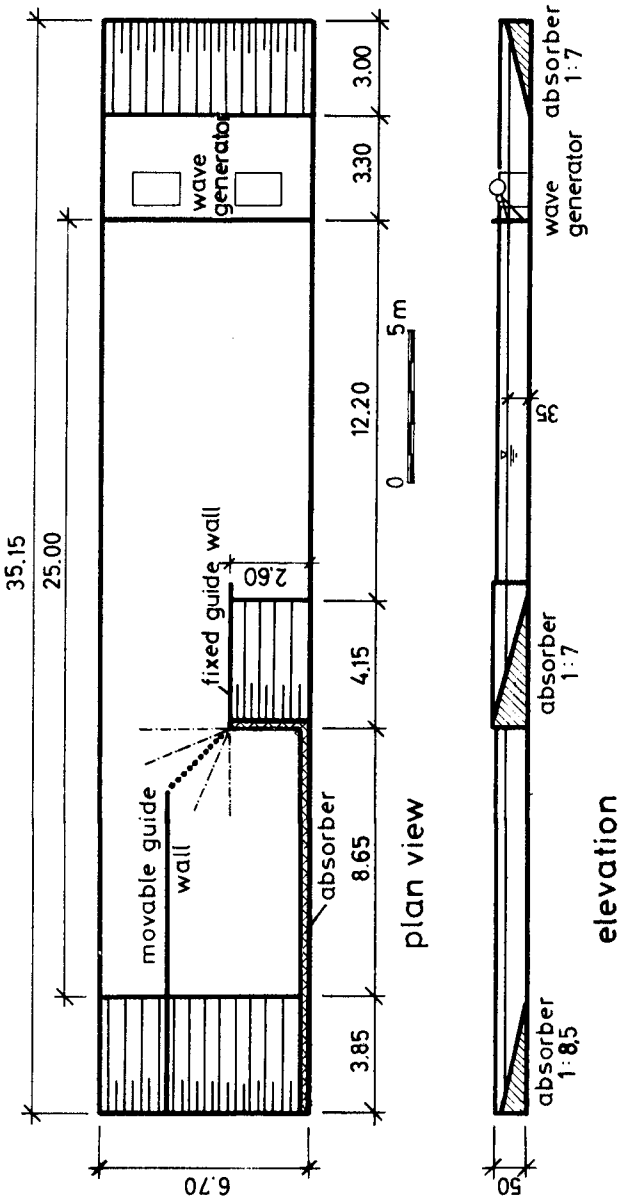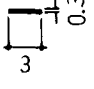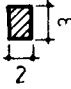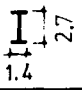
FIG. 5   THE WAVE BASIN

At one side of the vertical slotted wall a wave absorber
was placed which separated a wave basin behind the wall.
At the other side of the slotted wall the transmitted
wave was separated from the incident wave by a movable
impermeable guide wall. For the wave direction $\beta = 0^\circ$
(perpendicular to the wall) these guide walls were situated
on both sides of the slotted wall to ensure a constant
width. The wave directions β included 0°, 45°, 67.5° and
90°.

The shapes and the dimensions of the wall elements are
listed in the following table:

shape of the wall-element	rectangular b:t = 1:0.1			rectangular b:t = 1:1.5			rectangular b:t =		rectangular b:t =		H-beam b:t=1:2	
Dimensions [cm]							1:0.75	1:0.5	1:0.66	1:1.33		
W	0.5	0.6	0.75	0.4	0.5	0.68	0.68		0.6	0.75	0.425	0.61

Each test series (with a constant wave direction β, a
constant wall-element ratio W and a given shape of the
wall-elements) comprised about 12 runs, each with a
different wave. The parameters of these waves were varied
in steps in the range of:

wave height H_I:	4 cm	to	14 cm	
wave lenght L:	80 cm	to	300 cm	
wave period T:	0.7 sec	to	1.7 sec	
wave steepness $\frac{H_I}{L}$:	1 : 12	to	1 : 40	

The water depht of 35 cm was held constant for all tests.

The waves were measured with a movable parallel-wire
resistance type wave gauge. Both the incident wave H_I and
the transmitted wave H_T were measured and averaged in
cross-sectional profiles, the incident wave H_I about 5 m
in front of the slotted wall, the transmitted wave H_T

directly behind the slotted wall (Fig. 2). The incident
wave also was measured in a longitudinal section profile,
to separate the reflexion effect. In the case of wave
direction ß > 45° for the calculation of transmitted wave
height mean values, about 0.5 m of the total wall lenght
on the wave absorber side has not been considered to
eliminate second order effects due to diffraction exten-
sively.

EXPERIMENTAL RESULTS

In the first instance the transmission coefficient κ_T was
plotted as a function of the wave steepness $\frac{H_I}{L}$. As an
illustration Fig. 6 shows some results of 4 test series
for a H-beam shape wall element with a constant wall-
element ratio W = 0.61. The scattering of the data may
be influenced additionally by the effect of re-reflection
and second order effects caused by diffraction.

A straight line has been fitted to the data, which then
has been used for other computations and plots. Fig. 6
also shows a slight decrease of the transmission coeffi-
cient with increasing wave steepness. The influence of
the relative water depth d/L is found to be negligible
for these test conditions, which is also in agreement
with previons investigations [1].

1. RESULTS FOR WAVE DIRECTION ß = 0°

   Fig. 7 shows the effect of different shapes of wall
   elements and wall-element ratios W. It can be seen,
   that the shape of the wall elements has only a small
   influence.

   Fig. 8 shows the effect of the thickness t of the
   wall. As expected, κ_T decreases with increasing thick-
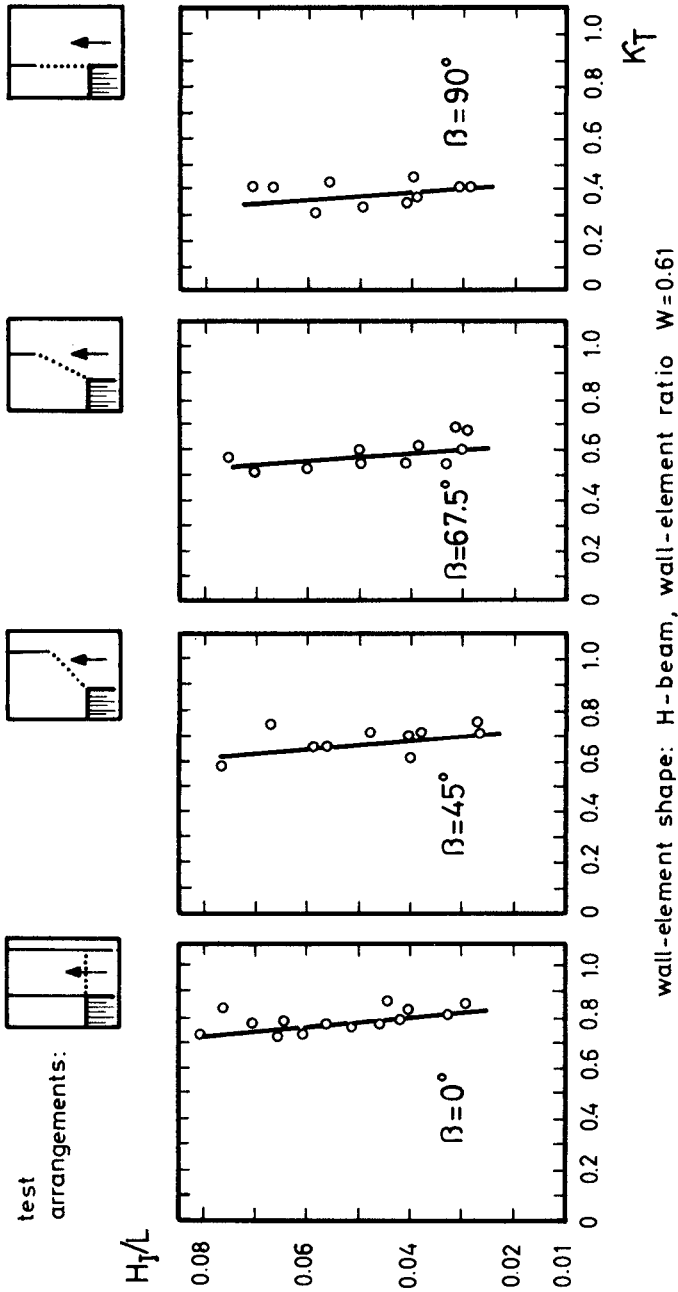
FIG, 6   TRANSMISSION COEFFICIENT K_T VERSUS WAVE STEEPNESS H_I/L
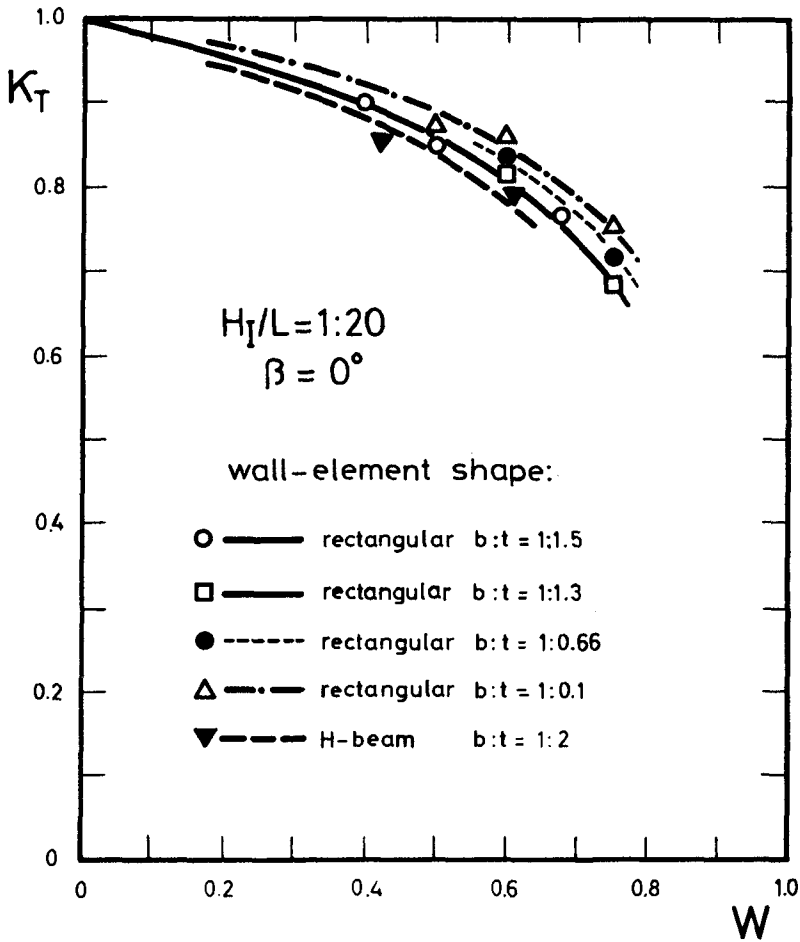
FIG. 7 TRANSMISSION COEFFICIENT K_T VERSUS WALL-ELEMENT RATIO W
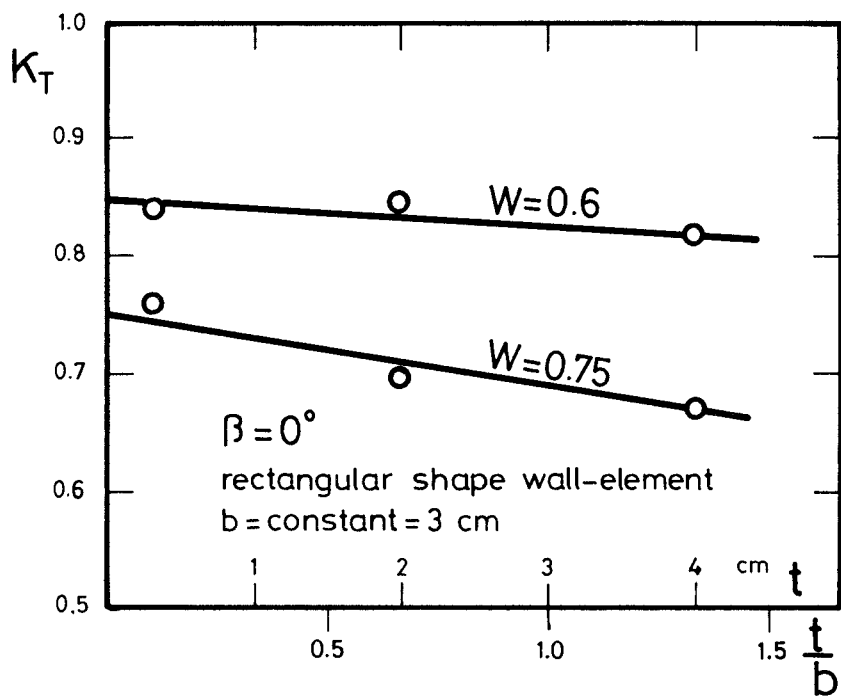
FIG, 8 TRANSMISSION COEFFICIENT K_T VERSUS WALL THICKNESS T

ness. It should be noted, that this effect is
strengthened with increasing wall-element ratio W.
However, the influence of the thickness, which is
proportional to the wall friction aréa,is small.

2. RESULTS FOR WAVE DIRECTION $0^O < \beta \leq 90^O$

For wave directions $\beta > 0^O$ the influence of the shape
of the wall elements is more important than for $\beta = 0^O$.
Figs. 9 and 10 show the results for κ_T as a function
of the wave direction for different ratios W and shapes
of the wall elements.

In all cases with wave direction $\beta = 90^O$ the trans-
mission coefficient κ_T has about half the value of
that for $\beta = 0^O$. This can readily be explained by the
effects of diffraction due to the presence of the
adjacent solid wall on one side (wave absorber), which
can be seen as a semi-infinite impermeable breakwater.

Generally it must be considered, that the transmission
coefficient κ_T for $\beta \gg 0^O$ (especially for $\beta > 75^O$)
contains a part of the diffraction effects. These
diffraction effects depend on the relative wall
lenght ℓ/L (wall lenght ℓ compared to wave lenght L),
which in this study has been in the range $1.0 < \ell/L < 3.75$.

The test results shown in Figs. 9 and 10 can be
described by the following semi-empirical formula:

$$\kappa_{T\beta} = 0.5 \ \kappa_{TO} \cdot (1+\cos^a\beta)$$

were $\kappa_{T\beta}$ = transmission coefficient for any wave
         direction β

   κ_{TO} = transmission coefficient for the wave
         direction $\beta = 0^O$

   a   = shape coefficient of the wall element
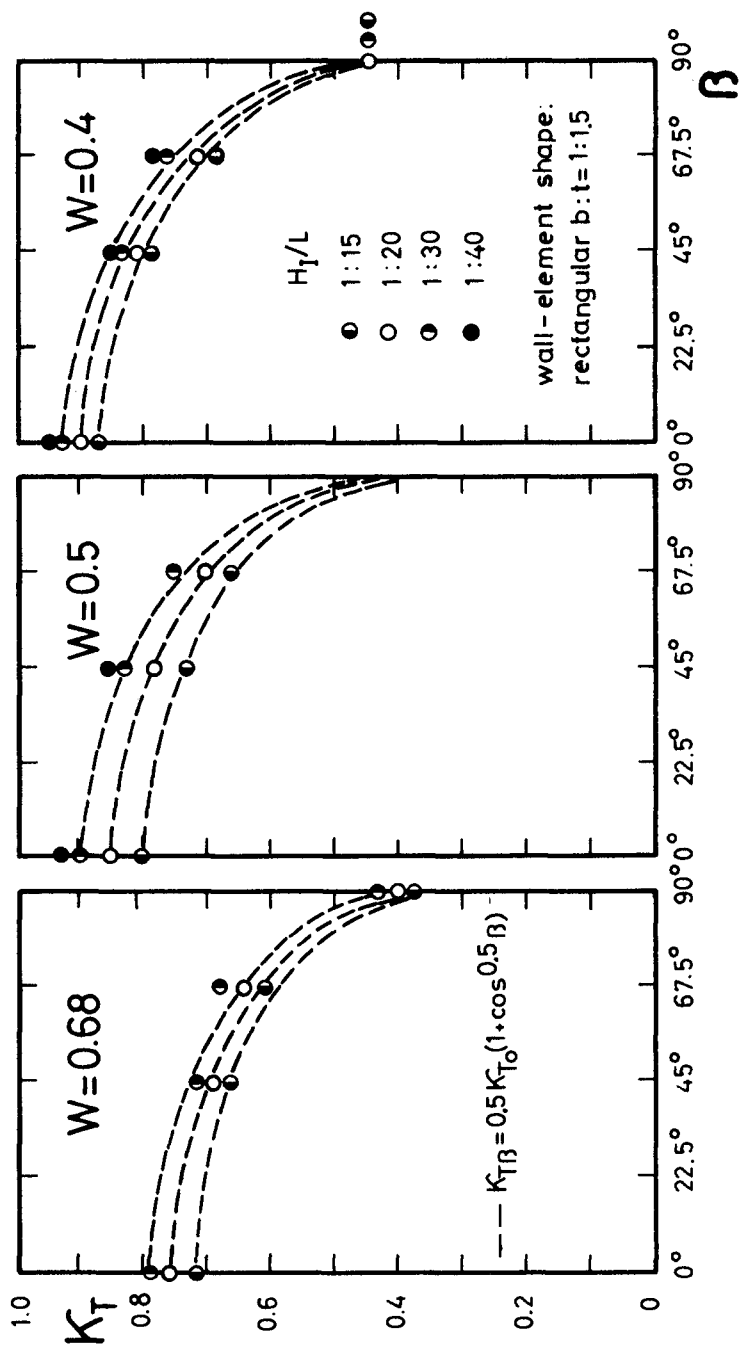
FIG. 9 TRANSMISSION COEFFICIENT K_T VERSUS WAVE DIRECTION
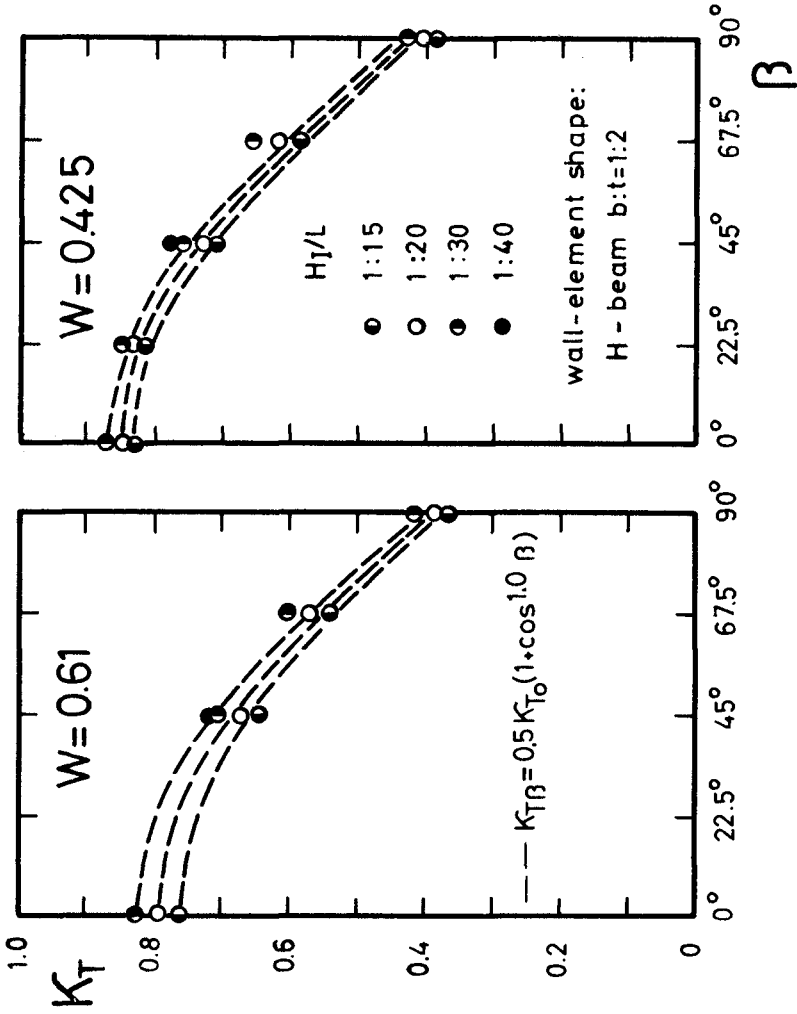
FIG. 10   TRANSMISSION COEFFICIENT K_T VERSUS WAVE DIRECTION

The values for the shape coefficient were found to be

a = 0.5 for rectangular shape b:t = 1:1.5
a = 1.0 for H - beam   shape b:t = 1:2

The differences in κ_T comparing the tested wall-element shapes especially for $\beta = 67.5^\circ$, probably are generated by eddy formation behind the wall of the H-beam type.

BRIEF REVIEW OF EALIER STUDIES AND COMPARISON OF THE RESULTS

Only for a wave direction $\beta = 0^\circ$ previous work on wave transmission throughvertical slotted walls was published.

For perpendicular wave approach test results were obtained by HARTMANN [1] for rectangular-section elements, HAYASHI [2] [3] et.al. and WIEGEL [4] for circular-section elements, which are in a fair agreement with the author's results as shown in Fig. 11.

WIEGEL, HAYASHY et.al. and HARTMANN have also derived theoretical equations for the wave direction $\beta = 0^\circ$.

WIEGEL [4] developed a formula for the transmission coefficient κ_T as a funktion of the wall-element ratio W as follows:

$$\kappa_T = \sqrt{1 - W}$$

The values calculated from this formula are about 25 % smaller than the measured values.

HAYASHY et.al. [2] [3] studied the transmission effects for the range W = 0.8 to 1.0. He developed the following formula [2] :

$$\kappa_T = 4 \frac{d}{H_I} \epsilon \left[- \epsilon + \sqrt{\epsilon^2 + \frac{H_I}{2d}} \right]$$

where

$$\varepsilon = C \ \left(\frac{s}{b+s}\right) \ \bigg/ \ \sqrt{1 - \left(\frac{s}{b+s}\right)^2} \quad \text{and } C = 0.9 \text{ to } 1.0 \ .$$

This formula can be transformed to

$$\kappa_T = 4 \ \frac{d/L}{H_I/L} \ \varepsilon \left[-\varepsilon + \sqrt{\varepsilon^2 + \frac{H_I/L}{2d/L}} \ \right]$$

where

$$\varepsilon = C \ (1-W) \ \bigg/ \ \sqrt{1 - (1-W)^2}$$

The values calculated by this formula for the range $W < 0.8$ are more dependent on the relative depht d/L than is suggested by the experiments.

A modification of this derivation for shallow water waves of small amplitude results in the formula [3]

$$\kappa_T = 4 \ \frac{d/L}{H_o/L} \ \varepsilon \ \frac{a^2 \ kd}{\alpha \ \tanh \ kd} \left[-\varepsilon + \sqrt{\varepsilon^2 + \frac{H_o/L}{2d/L} \ \frac{\tanh \ kd}{a^2 \ kd}} \ \right]$$

where $a = 1.1$ and $\alpha = \left(\frac{kd}{\sinh \ kd}\right)^2 (1 + \frac{\sinh^2 \ kd}{3})$

HARTMANN [1] derived a formula by means of the energy transferability method of GODA and IPPEN for a wave dissipator composed of wire mesh screens. With appropriate assumptions he obtains

$$\kappa_T = \sqrt{1 - w^2}$$

This formula is in very good agreement with all experimental results (Fig.11).
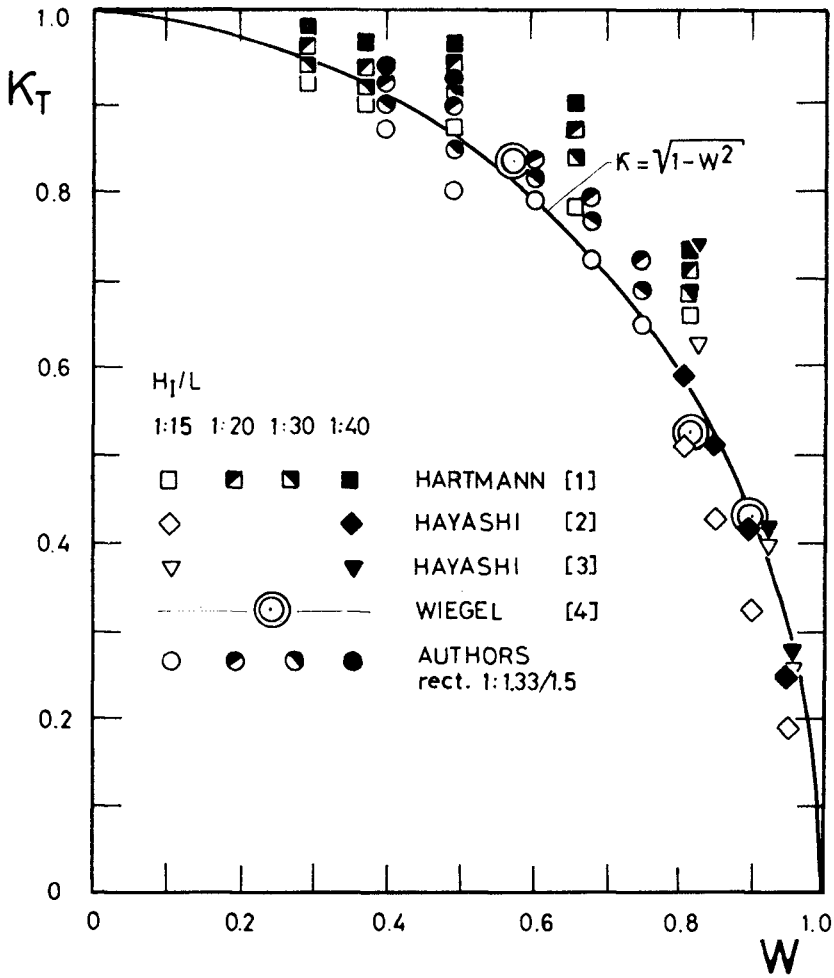
FIG. 11 COMPARISON OF THE RESULTS FOR WAVE DIRECTION $\beta = 0^\circ$

CONCLUSION

The experimental results and the comparison with the
results for the wave direction $\beta = 0^{\circ}$ of other authors
have shown, that the transmission coefficient κ_T depends
only slightly on the relative water depht d/L and the
wall-element thickness t. More important factors are
besides the wave steepness H/L and the shape of the wall
elements mainly the wall-element ratio W and the wave
direction β.

For a wave direction $\beta > 0^{\circ}$ it was found, that the in-
fluence of the wall-element shape is more important than
for a wave direction perpendicular to the wall ($\beta = 0^{\circ}$).

For the wave direction $0 \leq \beta \leq 90^{\circ}$ the following formula
describes the test results:

$$\kappa_{T\beta} = 0.5 \ \kappa_{To} \ (1+\cos^a \beta)$$

With that formula, combined with the equation for $\beta = 0^{\circ}$
derived by HARTMANN, the transmission coefficient κ_T for
any wave direction may be described by the following
formula:

$$\kappa_T = 0.5 \ \sqrt{1 - W^2} \ (1+\cos^a \beta)$$

REFERENCES

[1] HARTMANN
Das Stabgitter in instationärer
Strömungsbewegung
Mitt. des Instituts für Wasser-
bau und Wasserwirtschaft
TU Berlin
Heft 69, 1969

[2] HAYASHI et.al.
Hydraulic Research on the Closely
Spaced Pile Breakwater
Coastal Engineering in Japan
Vol. 9, 1966

[3] HAYASHI et.al.
Closely Spaced Pile Breakwater
as a Protection Structure against
Beach Erosion
Coastal Engineering in Japan
Vol. 11, 1968

[4] WIEGEL
Closely Spaced Piles as a Break-
water
Dock and Harbour Authority
Sept. 1961

CHAPTER 112

TRANSMISSION OF REGULAR WAVES PAST FLOATING PLATES

by

Uygur Şendil, Asst. Prof. of Civil Engrg.
Middle East Technical University, Ankara, Turkey

and

W.H.Graf, Assoc. Prof. of Civil Engrg.
Lehigh University, Bethlehem, Pa., USA
presently, Guest Professor, EPF, Lausanne, Switzerland

ABSTRACT

Theoretical solutions for the transmission beyond and reflection of waves from fixed and floating plates are based upon linear wave theory, as put forth by John (1949), and Stoker (1957), according to which the flow is irrotational, the fluid is incompressible and frictionless, and the waves are of small amplitude. The resulting theoretical relations are rather complicated, and furthermore, it is assumed that the water depth is very small in comparison to the wave length.

Wave transmissions beyond floating horizontal plates are studied in a laboratory wave flume. Regular (harmonic) waves of different heights and periods are generated. The experiments are carried out over a range of wave heights from 0.21 to 8.17 cm (0.007 to 0.268 ft), and wave periods from 0.60 to 4.00 seconds in water depth of 15.2, 30.5, and 45.7 cm (0.5, 1.0 and 1.5 ft). Floating plates of 61, 91 and 122 cm (2, 3 and 4 ft) long were used.

From the analyses of regular waves it was found that: (1) the transmission coefficients, H_T/H_I, obtained from the experiments are usually less than those obtained from the theory. This is due to the energy dissipation by the plate, which is not considered in the theory. (2) John's (1949) theory predicts the transmission coefficients, H_T/H_I, reasonably well for a floating plywood plate, moored to the bottom and under the action of non-breaking incident waves of finite amplitude. (3) a floating plate is less effective in damping the incident waves than a fixed plate of the same length.

INTRODUCTION

Floating horizontal plates are being constructed as breakwaters. When waves meet a horizontal plate, part of the wave energy is reflected by the plate, part of it is transmitted beyond the plate, part is transformed into flow energy as water flowing over the plate, and part

of it is absorbed by the plate and its supports. Earlier experiments by
Wiegel et al. (1962), Wiegel (1964), Chen and Wiegel (1970), and others
with horizontal objects showed that transmitted waves are of complicated
form.

John (1949) and Stoker (1957) have theoretically determined the
transmission of wave energy from a fixed or floating plate by consider-
ing a boundary value problem of a potential flow. Stoker (1957) derived
an approximate theory for freely floating and fixed obstacles in shal-
low water. While Stoker's theory is rather useful for the fixed plate
problem, it is too involved a theory for the present problem. In the
study by Stoker (1957, p.448) on floating elastic breakwaters, it was
indicated that the wave reflection and transmission is an irregular
function of wave length, L, and the structure length, λ. In this theo-
retical study the wave energy was either transmitted or reflected, i.e.
no energy dissipation was considered. The theory is derived from the
exact hydro-dynamical linear theory for gravity water waves of small
surface amplitude by making the simplifying assumption that the wave
length, L, is sufficiently large compared with the depth, d, of the
water such that the ratio L/d is of the order eight to ten. In fact it
is possible to formulate a mathematical theory without making such a
restrictive assumption regarding the ratio of wave length to depth; for
example, a theory has been worked out by John (1949) for floating rigid
bodies having simple harmonic motions, but no solutions could be found
in the case of interest in practice.

John (1949) investigated theoretically the effect of an infi-
nitely thin floating cylinder on an incoming wave and derived the
reflection coefficient as:

$$C_R = \frac{H_R}{H_I} = \frac{(\pi D/L)^5}{45 \left[(1-.4(\frac{\pi D}{L})^2)^2 + (\frac{\pi D}{L})^2 (1 - \frac{(\pi D/L)^2}{15})^2 \right]^{1/2}} \times$$

$$\times \frac{1}{\left[(1 - \frac{(\pi D/L)^2}{3} + (\frac{\pi D}{L})^2 \right]^{1/2}}$$

(1)

where D is the diameter of the cylinder at the still water line. Further-
more, the transmission coefficient, H_T/H_I, can be obtained by using
the law of conservation of energy, $(H_T/H_I)^2 + (H_R/H_I)^2 = 1$. Reflection
coefficients for a floating cylinder obtained by using Eq.1 are smaller
than reflection coefficients for a fixed cylinder of the same diameter,
see John (1949).

Wiegel (1964, p.142) studied in a model basin the effects of
periodic waves on a plastic bag 3.05 m by 3.05 m by 10 cm thick (10 ft
by 10 ft by 4 inch) filled with water. It was seen that a bag twice the
wave length should be fairly effective as a breakwater. In another study
by Wiegel et al. (1962) six bags were lashed side by side to form a 7.31
m by 6.10 m by 1.22 m deep (24 ft by 20 ft by 4 ft) breakwater. The bags
were moored in San Francisco Bay and filled with Bay water. The bags
were subjected to wind waves with periods 1 to 2 seconds and heights 15
to 46 cm (0.5 to 1.5 ft). Energy spectrums of the incident and trans-
mitted waves were obtained; it was concluded that the hovering breakwater
is effective for damping the incident waves.

Other experiments with floating objects such as pontoon type break-
waters, floating tires, etc. were carried out by Homma et al. (1964),
Kamel et al. (1968) and Kato et al. (1969). Recently Wen and Shinozuka
(1972) considered a large floating plate to represent a future offshore
airport and formulated its response to random incoming waves.

Floating breakwaters are designed to have larger natural periods
of roll, pitch, and heave than the expected wave periods. Furthermore,
Chen and Wiegel (1970) report that to obtain a long natural period, the
floating breakwaters should have a large mass but small elasticity.

Floating breakwaters compared to fixed breakwaters are simple in
fabrication and placement. Their size depends on the wave length, wave
height, direction of waves, and degree of protection required at the
leeward side. However, there is one important problem in connection with
the design of floating breakwaters, that is the forces exerted on the
mooring lines. The wave forces exerted on the mooring lines are very
complicated and at times considerable (see Wilson and Garbaccio, 1969;
Tudor, 1968). Therefore, the application of the floating breakwater is
limited to smaller bodies of water (see Frederiksen, 1971). However,
they may be used in oceans for small chop during short construction
operations or cargo handling.

The present investigation concerns itself with the prediction of
the wave energy before and after a floating plate. Tests were carried
out with regular waves having different wave heights and periods.

THE EXPERIMENT

The wave flume was of uniform cross section, 0.61 m (2 ft) wide,
0.61 m (2 ft) deep, and 20.58 m (67.5 ft) long. It is shown in Fig.1.
The flume is constructed with a steel and aluminum frame; the sides are
made of glass. Two energy absorbers built with four thin perforated
aluminum sheets were placed at both ends of the flume. These sheets,
separated by 6 mm (1/4-inch) spacers, are bolted to an 8 mm (5/16-inch)
aluminum impermeable plate. The downstream absorber is inclined at 15°
to the horizontal, whereas the upstream absorber (A), located behind
the wave generator, is inclined at 45°. To conduct tests with regular
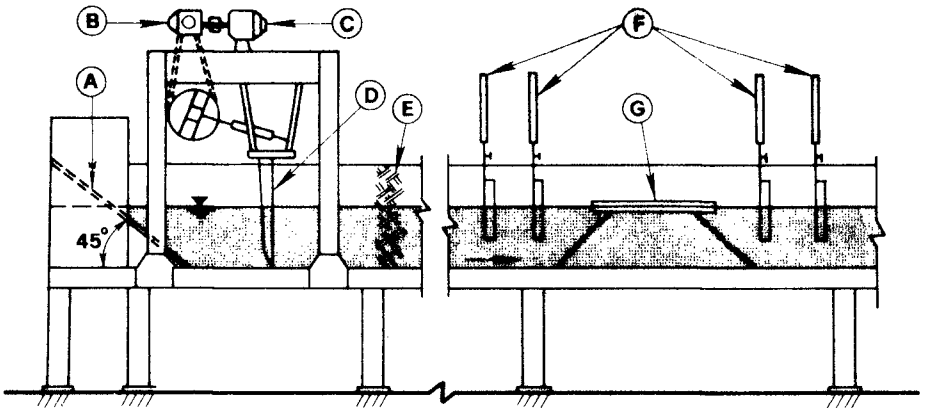
A. Upstream Absorber   E : Wire Mesh Filter
B : Hydraulic Transmission   F : Wave Gages
C : Motor   G : Plate(Marine Plywood 3/16 inch thick)
D : Wave Generator Paddle

Fig. 1 Experimental Set-Up for Regular Wave (not to scale)

waves, a paddle type wave generator (D) was installed at one end of the
wave flume. A wire mesh filter (E) was put in front of the generator
paddle to smooth the generated waves and to absorb reflected wave energy
from the generator paddle.

The set-up for the floating plate (G) is shown in Fig.1. The
mooring of the plate was provided by light chains and hooks. Floating
plates of three different sizes were used, having the following length,
width, and thickness respectively: 61 by 61 by 0.48 cm (24 by 24 by
3/16 inch), 91 by 61 by 0.48 cm (36 by 24 by 3/16 inch), and 122 by 61
by 0.48 cm (48 by 24 by 3/16 inch).

The wave generator consists of an oscillating plate, hydraulic transmission, and AC electric motor. The generator is capable of producing frequencies in the range of 0 to 5 cps. The speed of the motor could be adjusted to obtain the desired wave period while different wave heights could be obtained through stroke adjustment. The water surface fluctuations were measured by capacitive type wave gages, described by Killen (1956) and Sendil (1973). The signals from the wave gages were recorded on a 6-channel Model BL-520 Brush recorder.

Floating plates were positioned at 13.57 m (44.5 ft) from the upstream end of the flume. The waves were measured at four positions, namely 4.57 m (15 ft) and 6.10 m (20 ft) to the front of the plate and at about 1.22 m (4 ft) and 2.44 m (8 ft) to the rear of the plate.

Table 1 gives a tabulation of the tests; 138 runs were carried out for the floating plate experiments that are given in Sendil (1973, Appendix B).

Table 1
Number of Runs for Different Plate Lengths, λ
(Run No. 379 to 516)

T (sec)	λ=2 ft d (ft)			λ=3 ft d (ft)			λ=4 ft d (ft)		
	0.5	1.0	1.5	0.5	1.0	1.5	0.5	1.0	1.5
0.6	4	–	3	5	5	5	5	5	6
1.0	5	5	5	6	6	5	5	5	6
2.0	5	5	5	–	–	–	–	–	–
4.0	4	4	4	4	5	4	3	4	5

The data obtained were analyzed by using the method of dimensional analysis.

Fig.2 shows a definition sketch of the horizontal plate with the incident and transmitted waves progressing in water of constant depth, d. For a horizontal plate interacting with regular waves, the following variables are of importance: (1) Wave parameters -- H_I, incident wave height; H_T, transmitted wave height; L, wave length; $\bar{T}$, wave period. (2) Plate parameters -- λ, length of the plate; b, width of the plate;

s, thickness of the plate; ε, roughness of the plate. (3) Flow parameters
-- g, gravitational acceleration; U, horizontal component of orbital velo-
city; d, still water depth; k', roughness of the bottom. (4) Fluid param-
eters -- ρ, fluid density; μ, fluid viscosity.
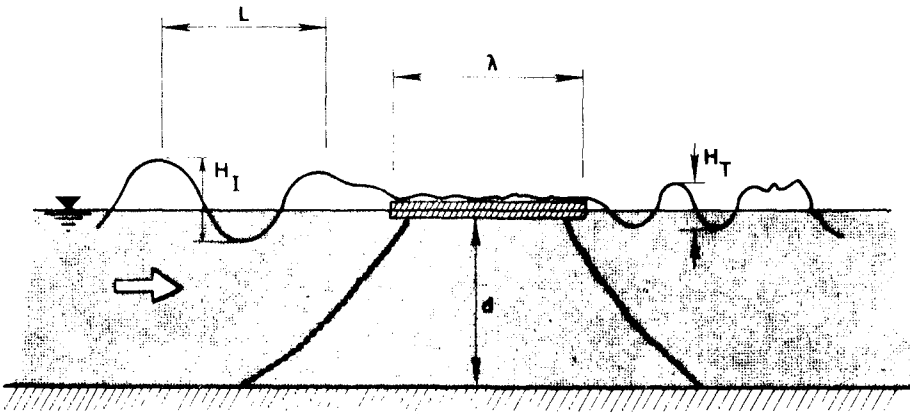
Fig. 2 Definition Sketch for Regular Waves

In the present experiments the roughness of the channel bottom,
k', and the roughness of the top and bottom surface of the plate, ε,
were held constant. Furthermore, the plate thickness s, was small so
that its effect on wave reflections was assumed to be negligible. Then,
for the two dimensional (b=1) case of a very wide plate, the variables
pertaining to the present problem may be written as

$$f(H_I, H_T, L, T, \lambda, g, U, d, \rho, \mu) = 0 \tag{2}$$

Grouping these variables into dimensionless parameters yields:

$$\frac{H_T}{H_I} = f(\frac{H_I}{L}, \frac{d}{L}, \frac{\lambda}{L}, \frac{U_m T}{\lambda}, Re, Fr)$$ (3)

where $U_m T/\lambda$ is another form of Keulegan-Carpenter's (1958) period param-
eter, with U_m as the maximum horizontal component of orbital velocity.

PRESENTATION OF RESULTS

The important parameters obtained from dimensional analysis for
the wave transmission beyond a floating plate were expressed by Eq.3. In
search for a meaningful relationship, the various arguments in Eq.3 were
plotted; this was done by Sendil (1973). The findings are briefly summa-
rized as:

(a) Plotted were the transmitted wave height, H_T, against the
incident wave height, H_I, with the relative plate length, λ/L, as
parameter for two different d values. It was concluded that H_T, H_I, and
λ/L are important parameters.

(b) Plotted were the transmission coefficient, H_T/H_I, against the
wave steepness, H_I/L, with the relative plate length, λ/L, as parameter
for three different λ values. It was concluded that H_T/H_I, H_I/L and λ/L
are important parameters.

(c) Plotted were the transmission coefficient, H_T/H_I, against the
Reynolds number, Re, with the relative plate length, λ/L, as parameter
for three different λ values. The present experiments showed that the
Reynolds number is not an important parameter.

(d) Plotted were the transmission coefficient, H_T/H_I, against the
Froude number, Fr, with the relative plate length, λ/L, as parameter for
three different λ values. The present experiments showed that the Froude
number is not an important parameter.

(e) The transmission coefficient, H_T/H_I, was plotted against the
period parameter, $U_m T/\lambda$, with relative depth, d/L, as parameter for
three different λ values. The present experiments indicated that, $U_m T/\lambda$
is not an important parameter.

In summary, it is believed that the following parameters play an
important role: H_T/H_I, H_I/L, λ/L, and d/L. Eq.3 can now be written as:

$$\frac{H_T}{H_I} = f(\frac{H_I}{L}, \frac{\lambda}{L}, \frac{d}{L})$$ (4)

It can be noticed that the significant parameters for the floating plate, given by Eq.4, are the same as the significant parameters for the fixed plate, obtained by Sendil (1973).

A comparison of the floating plate experiments of this study was made with John's (1949) theory (see Eq.1) and is presented in Fig.3. However, it should be pointed out that in John's (1949) theory, the plate length, λ, is represented by the diameter, D, of a flat cylinder. It is believed that this does not present a problem when comparing theory with experiments. The experimental data of Wiegel et al. (1962) and of Wiegel (1964, p.141) are also included. It can be seen from Fig.3 that there is some agreement of the present data with John's (1949) theory.

Wiegel et al.'s (1962) data for a 3.05 m by 3.05 m by 10 cm bag (10 ft by 10 ft by 4 inch) filled with water under pressure also seem to follow the general trend of the theoretical curve of John (1949). Their incident wave heights ranged from 2.80 to 6.70 cm (0.092 to 0.220 ft) and the wave periods ranged from 0.72 to 3.94 seconds.

Experimental data from Wiegel (1964, p.141) for plastic and rubber sheets fall above the theoretical curve, whereas the data for plywood fall below the curve. This indicates that materials of large mass and small elasticity are apparently more effective in damping the waves than materials of small mass and large elasticity. Hence, the plywood damped the waves more effectively than the plastic sheets. The plywood and plastic sheets used by Wiegel (1964) were 152 cm (5 ft) in length, with holes, and subjected to wind generated waves in a water depth of 15.2 cm (0.5 ft).

The relative depth, d/L, was used as parameter in Fig.3. There was no evident dependence of H_T/H_I upon d/L. However, in general, larger d/L ratios are associated with larger λ/L ratios and smaller transmission coefficients, H_T/H_I, whereas smaller d/L ratios are associated with smaller λ/L ratios and larger transmission coefficients, H_T/H_I.

Comparing floating plates with fixed plates (see Sendil, 1973; p.112) it was concluded that a floating plate is less effective in damping the incident waves than a fixed plate of the same length.

As it can be seen in Fig.3, the present data compare favorably with John's (1949) theory for floating plates. However, a further correlation was made by proposing the following relation:
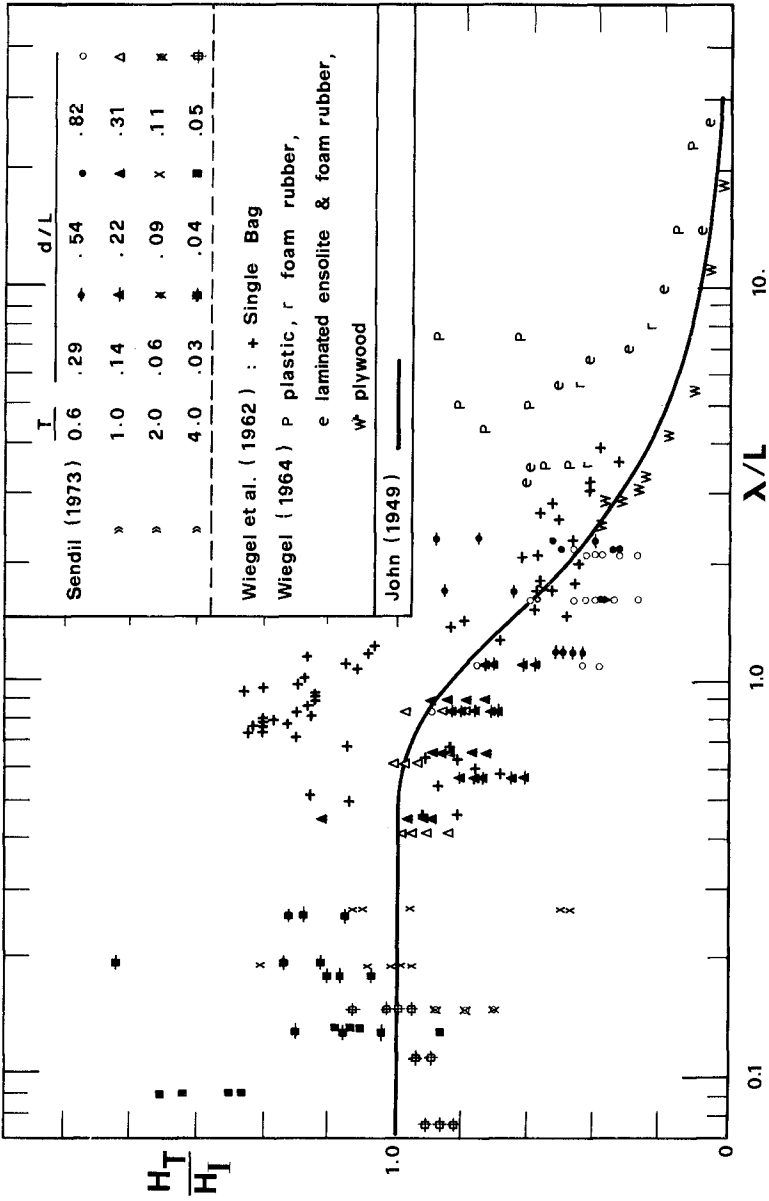
Fig. 3   Transmission Coefficient, H_T/H_I, vs. Relative Plate Length, λ/L; d/L as Parameter   (Floating Plate)

$$\frac{H_T}{H_I} = \alpha_1 \cdot C_T \tag{5}$$

where α_1 is a correction factor depending upon the wave steepness, H_T/L, and C_T is the transmission coefficient from John's (1949) theory, which can be obtained by using Eq.1 and the law of conservation of energy. Values of α_1 are plotted against wave steepness on a logarithmic paper in Fig.4. The plate lengths included in this plot are 61, 91, and 122 cm (2, 3, and 4 ft).

A linear curve is eye-fitted to the plotted points in Fig.4. For a very small wave height, H_I, and/or a very long wave length, L, or for $H_I/L \to 0$, it can be deduced that John's (1949) theory should be valid and hence $\alpha_1 \to 1$. Therefore, α_1 must pass through unity. As it can be seen in Fig.4, there is a very weak relationship between α_1 and H_I/L — that means the present data and John's (1949) theory agree well, which already was noticed in Fig.3. This in turn indicates that John's theory predicts wave transmission coefficient, H_T/H_I, satisfactorily.

A weak relationship between α_1 and H_I/L is again seen when Wiegel et al.'s (1962) data for the 10 ft single bag are plotted; see Fig.5.

In summary, the wave steepness, H_I/L, yields a weak relationship, and the relative depth, d/L, does not yield a detectable relationship with the wave transmission coefficient, H_T/H_I, for floating plates. Therefore, Eq.4 can be written as:

$$\frac{H_T}{H_I} = f(\frac{\lambda}{L}) \tag{6}$$

which is made up of the same significant parameters as used in John's (1949) theory.

CONCLUSIONS

The present investigation was concerned with the study of wave height and energy transmitted beyond a floating horizontal plate. Experiments were carried out with regular waves having different heights and periods. The following conclusions may be drawn from the experimental results.

(i) A comparison of Şendil's (1973) data with John's (1949) theory (see Fig.3) showed that the transmission coefficients, H_T/H_I, obtained from the present experiments are in overall agreement with the theoretical values.
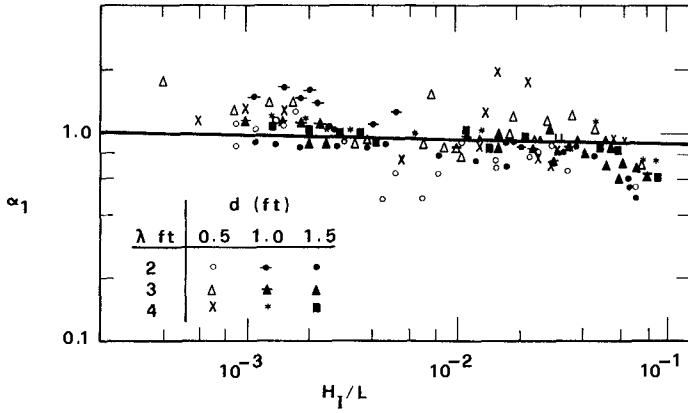
Fig. 4 α_1 vs. H_I/L for Floating Plate
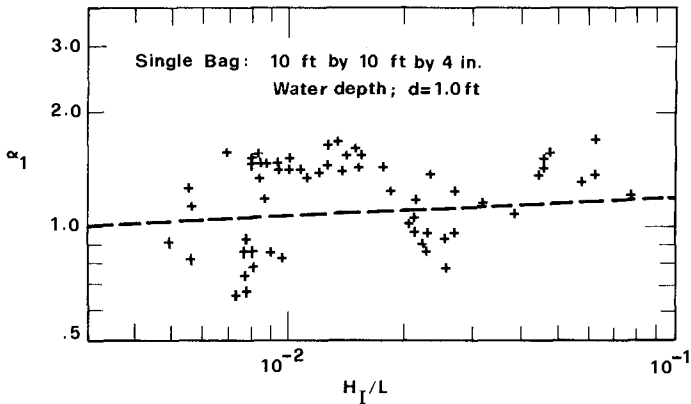
Fig. 5 α_1 vs. H_I/L for Floating Bag

(After Wiegel et al.,1962)

   (ii) John's (1949) theory predicts the transmission coefficient, H_T/H_I, -- Eq.1 -- reasonably well for a plywood plate, moored to the bottom and subjected to non-breaking incident waves of finite amplitude.

   (iii) A floating plate is less effective in damping the incident waves than a fixed plate of the same length (see Sendil 1973). A floating plate will have an effective damping of the incident waves if its length is several times the incident wave length.

REFERENCES

1. Chen, K. and Wiegel, R.L., "Floating Breakwater for Reservoir Marinas," Proceedings 12th International Conference on Coastal Engrg. Vol.3, 1970, pp.1647-66.

2. Frederiksen, H.D., "Wave Attenuation by Fluid Filled Bags", Proceedings, ASCE, Vol.97, No.WW1, Feb. 1971, pp. 73-90.

3. Homma, M., et al., "An Experimental Study on Floating Breakwaters", Coastal Engineering in Japan, Vol.7, 1964, pp.85-94.

4. John, Fritz, "On the Motion of Floating Bodies I", Communications on Pure and Applied Math., Vol.2, 1949, pp.13-57.

5. Kamel, A.M., and Davidson, D.D., "Hydraulic Characteristics of Mobile Breakwaters Composed of Tires or Spheres," T.R. H-69-2, U.S. Army Engineers, Waterways Experiment Station, Vicksburg, Mississippi, June, 1968.

6. Kato, J. et al., "Damping Effect of Floating Breakwater", Proceedings, ASCE, Vol.95, WW3, August 1969, pp.337-344.

7. Sendil, U., "Transmission of Water Waves Past Horizontal Plates", Ph.D. Dissertation, Lehigh University, Bethlehem, Pa., 1973.

8. Stoker, J.J., "Water Waves", Interscience Publishers, Inc., New York, 1957, pp.415-449.

9. Tudor, W.J., "Mooring and Anchoring of Deep Ocean Platforms", Proceedings, Conf. on Civil Engineering in the Oceans, ASCE Conf. September 1967, San Francisco, 1968, pp.351-300.

10. Wen, Y. and Shinozuka, M., "Analysis of Floating Plate Under Ocean Waves", Proceedings, ASCE, Vol.98, WW2, May 1972, pp.177-190.

11. Wiegel, R.L., "Oceanographical Engineering", Prentice-Hall, Inc., Englewood Cliffs, New Jersey, 1964.

12. Wiegel, R.L., et al., "Hovering Breakwater", Proceedings, ASCE, Vol.88, WW2, May 1962, pp.23-50.

13. Wilson, B.W., and Garbaccio, D.H., "Dynamics of Ship Anchor-Lines in Waves and Current", Proceedings, ASCE, Vol.95, WW4, November 1969, pp.449-465.

NOTATIONS

Fr	=	Froude number defined as $U_m/\sqrt{gd}$
g	=	gravitational acceleration
H_I	=	incident wave height
H_R	=	reflected wave height
H_T	=	transmitted wave height
H_R/H_I	=	reflection coefficient
H_T/H_I	=	transmission coefficient
k'	=	roughness of the bottom of the wave flume
L	=	local wave length
L_o	=	deep water wave length
Re	=	plate Reynolds number defined as $(U_m\lambda/\nu)$
s	=	thickness of plate
T	=	wave period
U	=	horizontal component of orbital velocity
U_m	=	maximum horizontal component of orbital velocity
α_1	=	a correction factor, defined by Eq. 5
ε	=	roughness of plate
λ	=	length of plate
μ	=	fluid viscosity
ρ	=	fluid density

CHAPTER 113

RUN-UP DUE TO BREAKING AND NON-BREAKING WAVES

by

F. Raichlen[1] and J. L. Hammack, Jr.[2]

ABSTRACT

This study was conducted to investigate the effect of incident wave parameters on run-up for both a smooth-faced structure and a structure armored with quarry-stone. The ratio of the depth-to-wave length (the relative depth) was found to be important in defining wave run-up for both cases. The relative run-up (expressed as the ratio of the run-up elevation above still water level to the incident wave height) for waves which break at the toe of the structure was less than the maximum relative run-up for non-breaking waves for the same relative depth. For both structures, the maximum relative run-up for experiments with long waves occurred at a value of the modified Ursell number, $(1/2\pi)^2 (HL^2/h^3)$, of order unity which indicates that the nonlinear and linear effects are approximately equal in the incident wave.

INTRODUCTION

The objective of the present fundamental study, some results of which are presented herein, is to investigate the effect on run-up of certain basic parameters which describe the incident wave system. In addition, two structures with the same slope were used in the laboratory to evaluate several effects of the characteristics of the structure on run-up: a smooth slope and a slope armored with a quarry-stone. Relative to the present investigation it is of interest to discuss briefly three previous run-up studies which are also fundamental in emphasis.

Saville (1956) investigated run-up on smooth-faced structures of various slopes with a beach (slope of 1:10) constructed seaward of the toe of the structure. All run-up data were normalized with respect to the unrefracted deep water wave height and plotted as a function of the ratio of this wave height to the square of the wave period without detailed attention to the ratio of the depth to the wave length. (The ratio of the wave height to the square of the wave period is directly proportional to the wave steepness.) As noted by Saville the data exhibited scatter (less than ±20%), and the experimental curves which were presented were fitted through the average of these data.

---

[1] Professor of Civil Engineering, W. M. Keck Laboratory of Hydraulics and Water Resources, California Institute of Technology, Pasadena, California U.S.A.

[2] Research Fellow in Civil Engineering, W. M. Keck Laboratory of Hydraulics and Water Resources, California Institute of Technology, Pasadena, California, U.S.A.

Hudson (1959) presents experimental results for run-up on rubble-mound structures of various slopes constructed in a constant depth wave tank and exposed to periodic non-breaking waves. The experiments were conducted for variable wave heights and with constant values of the ratio of depth-to-wave length varying from 0.1 to 0.5. The run-up data were presented as the relative run-up, i.e., the run-up normalized by the wave height without the structure in place, plotted as a function of the wave steepness (wave height divided by wave length) for constant depth-to-wave length ratios. Since it was difficult to find trends of data for given values of depth-to-wave length, experimental curves were presented which were envelopes of the data. (The experimental curves obtained from these data and from Saville (1956) are also presented by CERC (1966).)

Grantham (1953) shows limited data which demonstrate the importance of structure slope, wave steepness, depth-to-wave length, and porosity of the structure on run-up. With relation to the present study, Grantham found that for the three structures studied, there was an increase in relative run-up as the ratio of depth-to-wave length decreased for a given wave steepness.

ANALYTICAL CONSIDERATIONS

A definition sketch describing the problem under consideration is presented in Figure 1 showing the run-up defined as the maximum vertical distance from the still-water surface to the position on the face of the structure to which the water surface rises during wave attack. For convenience the wave height, H, is indicated on the figure; however, the wave height which is used in describing the incident wave system is that which exists at the location of the toe of the slope without the structure in place. (This will be discussed later in connection with the experimental procedure.) For both the smooth-slope and the rubble-mound structure no over-topping is permitted. In fact, the latter structure is constructed on an impermeable base; hence, there is only run-up on the structure without associated transmission of wave energy either through or over the structure.

The problem of run-up has not been amenable to a complete theoretical treatment due to the difficulty in analytically describing the many factors involved. Therefore, dimensional analysis will be employed (similar to Hudson (1958)) to define the important non-dimensional parameters which describe the problem. Referring to Figure 1, if a functional relationship exists between the run-up and the description of the incident wave system and the structure, for regular waves impinging on a breakwater face at normal incidence to the structure, this relationship can be expressed as:

$$f(H, T, h, 1/m, R, \rho_w, \mu, g, \alpha, \psi) = 0 \qquad (1)$$

where f( ) indicates a "function of".

The first four variables of Equation (1) define the incident wave characteristics, R is the run-up on the structure face measured vertically from the still water level, ρ_w is the fluid density, μ is the dynamic fluid viscosity, g is the acceleration of gravity, and α is the slope of the face of the structure with respect to the bed. The last variable, ψ, (assumed to be non-dimensional) describes the physical characteristics of the breakwater
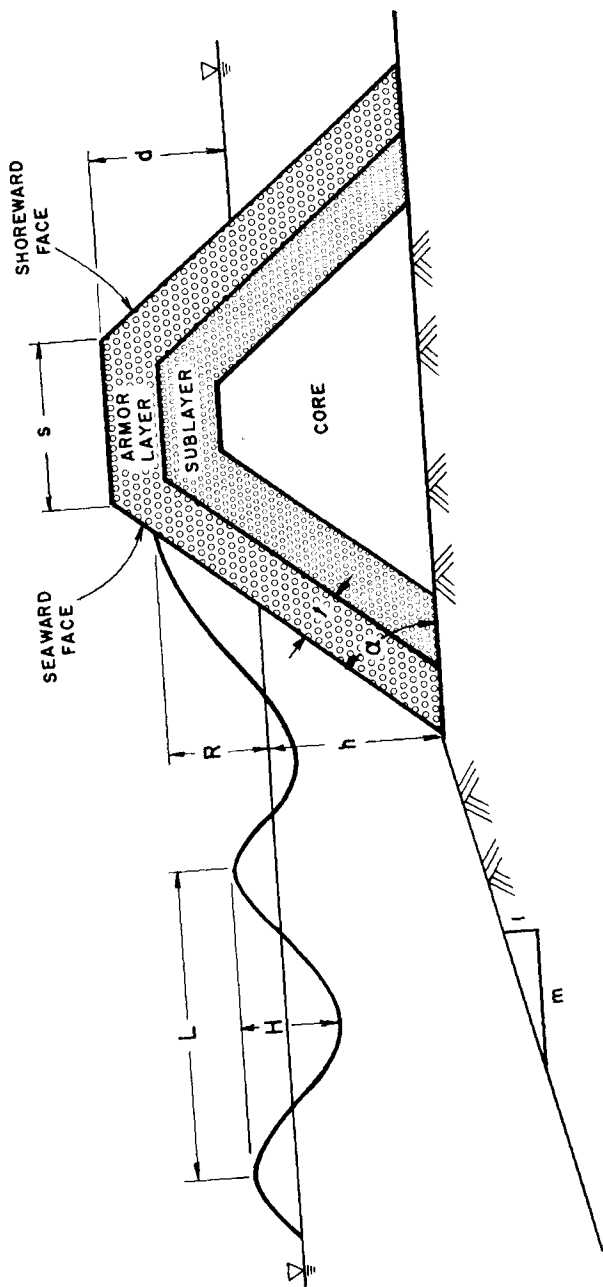
Figure 1. Definition Sketch of a Rubble-Mound Structure.

face which affect run-up, and would be a function of such factors as: the
shape of the armor units, the roughness of the face, the permeability of the
armor layer, the characteristics of the underlying material, the method and
type of construction, etc. Hence, ψ describes features of the breakwater,
relevant to run-up, which demonstrate the difficulty of developing universal
run-up characteristics for rubble-mounds. (In the case of a structure with
a smooth impermeable face, the parameter ψ becomes relatively unimportant
in defining run-up.) The variables ρ_w, g, and h are used in non-dimension-
alizing Equation (1) which results in the following:

$$f(\frac{H}{h}, \frac{T^2 g}{h}, \frac{1}{m}, \frac{R}{h}, \frac{\mu/\rho_w}{\sqrt{gh}\ h}, \alpha, \psi) = 0. \tag{2}$$

The second term in Equation (2) is proportional to the ratio of the wave
length to the depth, L/h; the fifth term is an inverse Reynolds number with
the velocity equal to the shallow water wave celerity. By a suitable com-
bination of terms in Equation (2) it can be shown that the length dimension
in the Reynolds number can be expressed as the characteristic dimension of
an armor unit and the velocity can be expressed as the water particle ve-
locity. Therefore Equation (2) can be rewritten as:

$$\frac{R}{H} = \phi(\frac{H}{h}, \frac{L}{h}, \frac{1}{m}, R_e, \alpha, \psi) \tag{3}$$

where as mentioned, the Reynolds number, R_e, is a function of the water
particle velocity and a linear dimension of the armor. In Equation (3) the
relative run-up (expressed as the run-up elevation divided by the wave
height) is considered a function of the wave characteristics as embodied in
the ratio of wave height-to-depth and the ratio of the wave length-to-depth
as well as the off-shore slope, 1/m. It is noted that these three parameters
define the characteristics of long-waves and the latter becomes most impor-
tant in defining the shape of the breaking or incipient breaking wave. As
mentioned previously, when comparing experiments for smooth-faced structures
the variable ψ can be eliminated; of course, this parameter is less
important when investigating the action of various incident wave systems
on a particular rubble-mound slope. (The distance of the structure from
the wave source may be important in laboratory tests due to the effect of
distance on the evolution of nonlinear waves. This distance is not in-
cluded in the present discussion.)

The breakwater face armored with quarry-stone represents a hydro-
dynamically rough surface; hence, for sufficiently large Reynolds number,
the dependence of run-up on the Reynolds number as shown in Equation (3)
should be minimal. Therefore, the list of variables shown in Equation (3)
can be reduced to:

$$\frac{R}{H} = \phi(\frac{H}{h}, \frac{L}{h}, \frac{1}{m}, \alpha, \psi) \tag{4}$$

Corrections for the effect of Reynolds number must be applied to the results
of laboratory experiments to investigate run-up on prototype structures, if
the scale of the experiments is not large enough.

In the case of deep water waves Equation (4) can be rewritten in terms
of the incident wave steepness as:

$$\frac{R}{H} = \phi(\frac{H}{L}, \frac{L}{h}, \frac{1}{m}, \alpha, \psi) \ . \tag{5a}$$

Since neither the relative depth, h/L, nor the bottom slope, 1/m, are im-
portant when the wave is not affected by the bottom (the condition of deep
water waves), the non-dimensional variables in Equation (5a) can be further
reduced to:

$$\frac{R}{H} = \phi(\frac{H}{L}, \alpha, \psi) \ . \tag{5b}$$

Equation (5b) is most applicable for steep structures; for structures with
relatively small slopes (say 1:10 and less) the waves would in all proba-
bility shoal on the structure leading to an influence of water depth above
the face of the structure.

   Still a third way of presenting the non-dimensional variables which
affect run-up is to combine the first two terms in Equation (4) such that
the following expression is obtained:

$$\frac{R}{H} = \phi(\frac{HL^2}{h^3}, \frac{L}{h}, \frac{1}{m}, \alpha, \psi) \ . \tag{6a}$$

   The first term on the right-hand side of Equation (6a) is commonly re-
ferred to as the Ursell number which describes the relative importance of
nonlinear and linear effects in an incident long wave. This expression
results since nonlinear effects are proportional to the ratio of the ampli-
tude to the depth and the linear effects of frequency dispersion are pro-
portional to the square of the ratio of the depth to a characteristic length
in the direction of propagation. The characteristic length shown in Equa-
tion (6a) is the wave length; however, the characteristic length should be
associated with a local property of the wave, since the effect of frequency
dispersion would be greatest in regions of large curvature of the water
surface. Therefore, an appropriate horizontal length is: $\ell = (\eta_o/\eta_x)$ where
η_o is the total change of wave amplitude in a region along the wave, e.g.,
between two points of zero slope, and η_x is the maximum slope of the water
surface in that region. (See Hammack (1973) for a more detailed discussion
of local length scales for irregular waves.) If, for convenience, the small
amplitude wave theory is used, the characteristic length dimension corres-
ponding to this definition is: $\ell = L/2\pi$. Therefore, a modified Ursell
number may be given as: $(1/2\pi)^2(HL^2/h^3)$. For solitary waves where nonlinear
and linear effects are balanced, the same type of definition of the horizontal
length yields a numerical value of the Ursell number of approximately 2.3;
hence, when the modified Ursell number is about 2 to 3, nonlinear effects
should be approximately equal to linear effects. To comply with this defi-
nition of the Ursell number Equation (6a) can be rewritten as:

$$\frac{R}{H} = \phi\left\{\left[\frac{1}{2\pi}\right]^2 \frac{HL^2}{h^3}, \frac{L}{h}, \frac{1}{m}, \alpha, \psi\right\} \tag{6b}$$

   It should be emphasized that Equation (6b) like Equation (4) is applic-
able for long waves and the use of these equations to describe run-up of
short waves is not strictly correct. On the other hand, the non-dimensional

variable $(1/2\pi)^2$ (HL^2/h^3) in Equation (6b) can be used to separate the data
and to demonstrate the importance of h/L in the description of the problem.
These features will be explored in detail in a later section.

EXPERIMENTAL EQUIPMENT AND PROCEDURES

Experiments were conducted in a wave tank 36.5 meters long, 91.5 cm wide,
and 91.5 cm deep. The walls of the wave tank are constructed of glass
throughout and the bottom is constructed of stainless steel built to within
$\pm$ 0.8 mm of a plane surface. A periodic wave generator is mounted to the
wave tank at one end and the tank is supported by a center hinge and motorized
jacks upstream and downstream of the hinge point. Through this arrangement
the slope of the wave tank can be changed from horizontal to a maximum of 1
vertical for 50 horizontal. Since the wave machine is attached to the wave
tank, waves can be generated which propagate into water with a decreasing
depth as the tank is tilted. Hence, breaking waves can be produced at a
particular location in the wave tank for a given wave period simply by in-
creasing the stroke of the wave machine incrementally.

In these experiments the slope of the wave tank was maintained at 1
vertical for 200 horizontal and the incident wave characteristics were
measured using a parallel wire resistance wave gage at the location where
the toe of the structure would be placed. The water surface variations were
recorded until reflections from the end of the tank returned to the gage
location. From an average of approximately five waves, the stroke setting of
the wave machine was determined which would generate the desired incident wave
height at that location and wave tank slope without the structure in place.

The wave run-up on two structures was investigated. Both structures
had a slope of 1 vertical to 2 horizontal, and in the case of the smooth and
impermeable face, the slope was constructed of plywood treated with an epoxy
paint. The second structure (also with a slope of 1 vertical to 2 horizontal)
had a fitted rock face with two underlayers of material placed on the same
plywood face. In both cases the toe of the structure was located approxi-
mately 20 m from the wave generator in a water depth of 25.8 cm.

A schematic drawing of the rubble-mound structure used in this study
and the size distributions of the armor layer material ("A" rock) and the
sublayer material ("B" rock) are presented in Figure 2; the ordinate is the
weight of the individual rock and the abscissa is the percent by weight of
the sample which is finer than the indicated ordinate value. The mean
weight of the armor material is approximately 460 grams and the sublayer
material has a mean weight of approximately 50 grams. (The rock utilized
was "block-like" and obtained from the Fisher Quarry of the Umpqua River &
Navigation Company, Camus, Oregon.)

This structure was built as a model of a breakwater to a scale of 1/40
in three layers starting with a crushed rock layer (0.8 mm mean size)
approximately 15.2 cm thick placed directly on the plywood slope described
previously with a sublayer of "B" rock 6.9 cm thick placed on top of this and
followed by the armor layer of "A" rock one layer thick (approximately 8.6
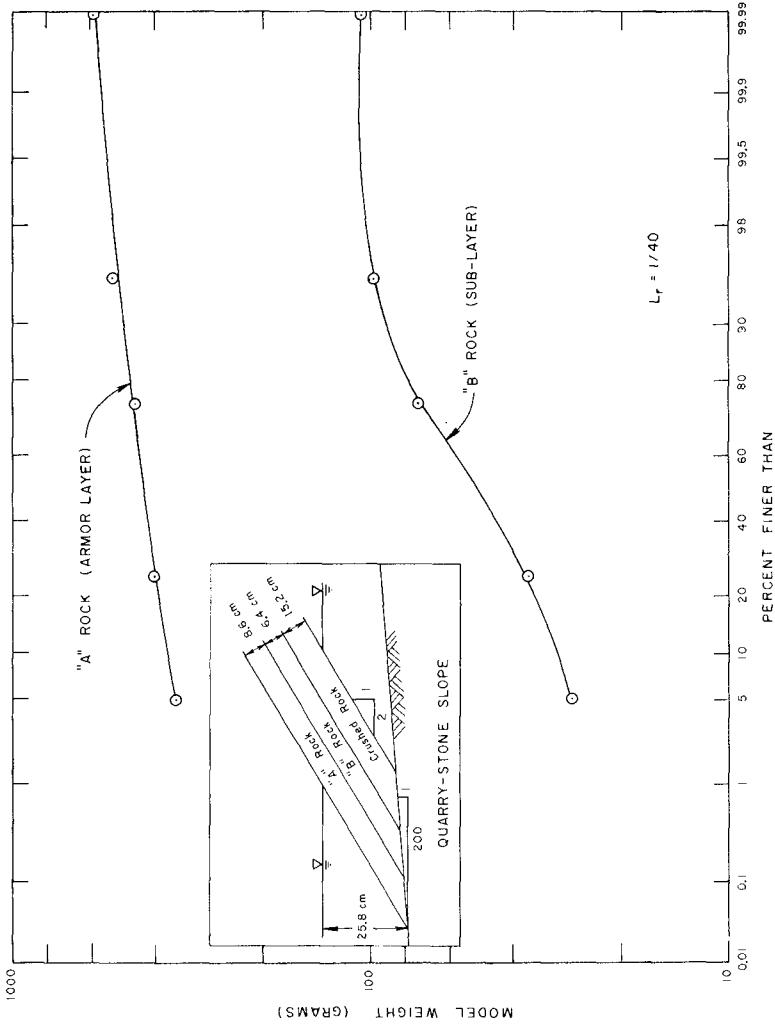cm). Between the underlayer and the sand a thin filter layer of gravel with

Figure 2. Rock Size Distribution and Schematic Drawing of Rubble-Mound Structure.

a 6 mm nominal diameter was used to prevent the sand from migrating through
the rock layers.   The armor rock was fitted from the bottom of the flume
through the maximum elevation with the long axis of the rock perpendicular
to the slope.   Hence, this is not a true scale model since the rock below
the mean water level ordinarily would be randomly placed with fitted rock
placed only above mean water level.   However, this was considered a satis-
factory method of construction, since it was of interest to provide a rubble-
mound with a surface roughness and permeability vastly different from the
smooth slope yet relatively uniform throughout.   A photograph of the face of
the structure is presented in Figure 3 which shows the fitted nature of the
surface.

A continuous record of run-up as a function of time was obtained in
these studies using two miniaturized staff gages mounted parallel to the
slope and to each other for both the smooth slope and the quarry-stone slope
experiments.   The gages mounted approximately 15 cm apart above the quarry
stone are shown in Figure 3.   The instrument operates as a step gage with
56 equally spaced pins giving a step voltage output which is linearly pro-
portional to the wetted length of the gage.   A drawing of the gage is pre-
sented in Figure 4a; the main body of the gage which supports the pins is
approximately 1 cm square and contains 56 conductors, one for each pin.
The pins are 1.38 cm apart and each pin is approximately 1.6 cm long; the
innermost 1.1 cm electrically insulated with only the outer 5 mm exposed.
Mounted parallel to the rod which supports the pins is a stainless steel
conductor which forms a reference ground for the system.   Essentially the
pins with the associated electronics work as 56 switches, each switch actu-
ated when a threshold limit of conductivity is reached between the pins and
the conductor rod which is caused when the water immerses the pin and the
conductor simultaneously.   To reduce the effect of the splash on the
response of the instrument, the electronic logic insures that before a
voltage level corresponding to the highest wetted pin is indicated, the two
next lower pins must be wetted simultaneously.

In the case of the smooth slope the gage was mounted so that the center-
line of the pins was approximately 5 mm above the surface of the structure.
For the quarry-stone slope the run-up gage was placed parallel to the slope
and as close as possible to the slope (see Figure 3).   An obvious disadvan-
tage in measuring the run-up in this manner is that the run-up is measured
a fixed distance away from the slope.   Thus, the gage location will tend to
give a run-up which may be somewhat less than the intersection of the run-up
tongue with the slope.   Nevertheless, all measurements will be consistent,
assuming the shape of the run-up tongue is similar for the experiments, and
a comparison of the results for different value of h/L and between the two
types of slope should be valid.   The major advantage of such a gage is that
a real time record of run-up and run-down can be obtained.

The gages were placed on the structure so that the pins on one gage
faced those on the other (see Figure 3) with the gages staggered in the di-
rection of wave propagation such that a pin on one gage was located midway
between the opposite pins on the other gage.   Since these gages were only
approximately 15 cm apart, it was possible to average the run-up spacially
between these two gages with an accuracy of + one-half the gage pin spacing.
(Of course, to obtain a better spacial average more run-up gages of this type
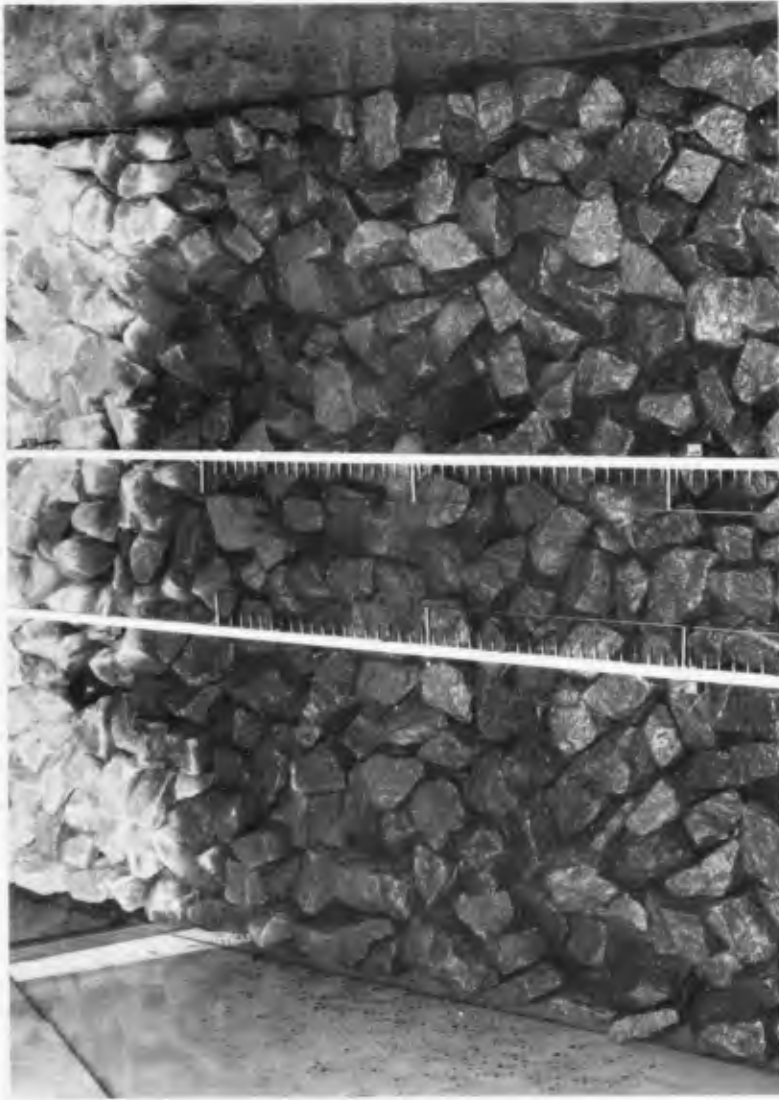placed across the slope would be preferable.)

Figure 3. Photograph of Face of Rubble-Mound Structure Showing Run-Up Gages in Place.
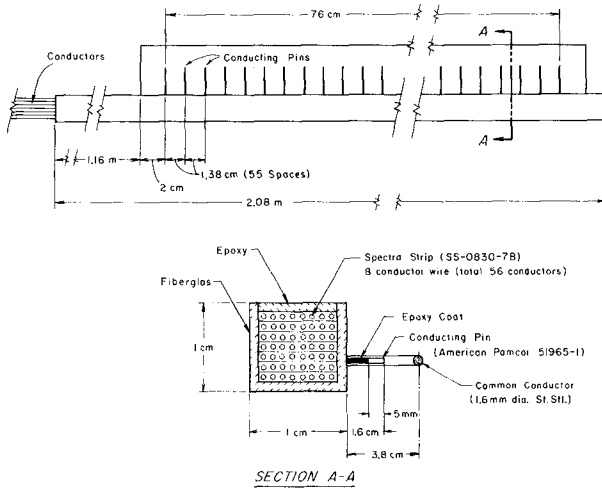
Figure 4a.   Drawing of Run-Up Gage.
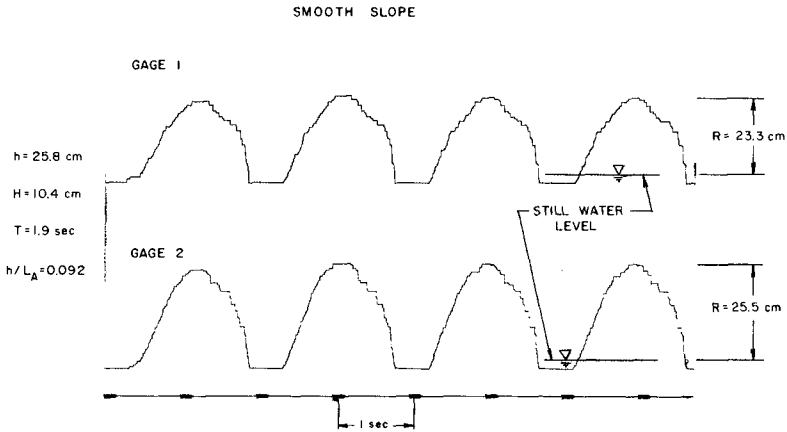
SMOOTH SLOPE

Figure 4b.   Typical Record of Run-Up as a Function of Time.

A typical record of run-up as a function of time is shown in Figure 4b
for the indicated wave conditions. These measurements were made on the
smooth slope, and it is seen that due to the length of the run-up gage it
was not possible to measure the run-down with this gage location; the mini-
mum level indicated is the voltage level with the lowest pin out of the
water.

The experimental procedure for both the smooth and the quarry-stone
slope was as follows. Waves were generated at the desired wave period and
wave height and the run-up recorded continuously. The wave generator was
turned off before the first wave which had been generated and reflected
from the structure reached the wave machine. Hence, depending upon the
wave period, from five to eleven run-up maxima were averaged to give the
time averaged run-up for each gage. As mentioned previously, the time
averaged values of maximum run-up obtained with each of the two gages were
then averaged to give a temporal and spacial average of the run-up on the
structure for the given wave conditions. A deviation of $\pm$ one-half a pin
spacing (measured vertically) was then assigned to the average run-up
readings; hence, the run-up elevation could be measured accurately to within
$\pm$ 3.1 mm. Since the run-up gages consist essentially of 56 switches which
can only record an "on-off" condition they were calibrated by electronically
connecting the pins in increments of 6, 12, 18, ..., 48, 54 pins. Point
gage measurements were used to locate the pins on the slope both vertically
and horizontally; hence, the voltage level associated with each group of
six pins could be related to a run-up elevation. Such calibrations were
conducted before and after experimental series corresponding to each wave
period, and the gages were found to be reproducible and stable over the
duration of an experiment.

PRESENTATION AND DISCUSSION OF RESULTS

Experiments have been conducted at six different depth-to-wave-length
ratios for the smooth and quarry-stone slopes and at wave heights which
include incipient breaking waves at the toe of the structure. (The wave
length used in the definition of relative depth has been determined from
the linear dispersion relation based on the incident wave period and the
water depth at the toe of the structure and is denoted hereafter as L_A.)
For all cases the slope of the wave tank was maintained at 1 vertical to
200 horizontal; hence, considering Equations (4), (5) and (6) the non-
dimensional parameters which describe run-up in the experiments with the
smooth or the quarry-stone slopes are: L_A/h and H/h or H/L_A or HL_A^2/h^3.

In this way the effect on the relative run-up of two parameters dependent on
the incident wave system is investigated.

The results for the smooth slope are presented in Figure 5 where the
abscissa is the modified Ursell number, $(1/2\pi)^2(HL_A^2/h^3)$, and the ordinate is
the relative run-up, R/H. The waves represented by the data in Figure 5 range
from deep water to shallow water waves. The limits of the accuracy of the
run-up gage ($\pm$ 3.1 mm) are indicated on each data point in terms of the
relative run-up; hence, as the absolute run-up increases the accuracy of
the gage expressed in a relative sense improves. Experimental curves have
been fitted to the data corresponding to each relative depth using a
second-order curve-fitting procedure tempered by judgment.
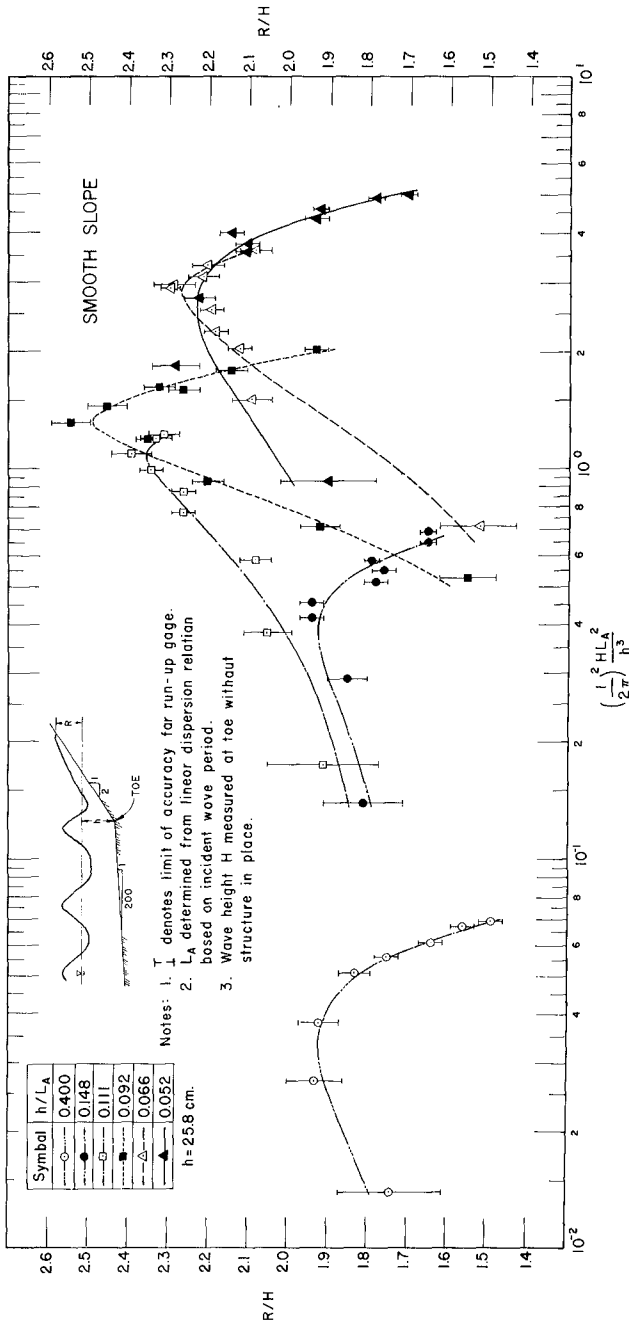
Figure 5.   Relative Run-Up on a Smooth Slope for Various Ratios
            of Depth-to-Wavelength.

There are several features of the data of Figure 5 which should be emphasized. The range of the modified Ursell number which is covered by the experiments is from approximately 10^{-2} to 10; however, this parameter arises in connection with long wave (shallow water wave) theory so that strictly speaking its significance in describing the relative importance of nonlinear effects to linear effects in the incident wave is applicable to these data primarily for $h/L_A = 0.066$ and 0.052. Nevertheless, this parameter does tend to sort all the data in a rational manner. For each relative depth (h/L_A) the relative run-up increases to a maximum and then decreases with increasing Ursell number. Since the data point at the largest value of the modified Ursell number for each relative depth corresponds to an incipient breaking wave at the toe of the structure, it is evident that the relative run-up for incipient breaking waves on the smooth slope is considerably less than the maximum run-up for non-breaking waves.

As the relative depth, h/L_A, decreases the maximum relative run-up increases to a maximum and then decreases. The maximum relative run-up associated with the two shortest waves are approximately equal as are the maximum relative run-up for the two cases with shallow water waves ($h/L_A = 0.066$ and 0.052). In the latter case the maximum relative run-up occurs at a modified Ursell number of order unity, i.e., approximately 2.5; hence, it appears that the maximum run-up for long waves occurs when nonlinear and linear effects in the incident wave are approximately equal.

The relative run-up for the quarry-stone slope is presented in Figure 6 in an identical manner as the data in Figure 5 for the smooth slope. The first obvious difference between Figure 5 and Figure 6 is the reduction of the relative run-up by nearly a factor of two for identical waves incident upon the quarry-stone slope compared to the smooth slope. At first glance, although the data separate according to the value of the relative depth, some of the trends noted easily in Figure 5 are not immediately apparent. Nevertheless, when the data corresponding to each depth-to-wave length are analyzed separately, trends similar to the smooth slope case are observed. For example, at each relative depth, as the modified Ursell number increases the relative run-up reaches a maximum and then decreases to that corresponding to the incipient breaking wave; however, the variation is not as great as that observed for the experiments with the smooth slope. In the case of the quarry-stone slope, as the relative depth decreases the maximum relative run-up appears to increase monotonically. The maximum relative run-up for the two longest waves investigated ($h/L_A = 0.066$ and 0.052) is again approximately the same and occurs at a magnitude of the modified Ursell number of approximate 2.5.

In Figure 7 the relative run-up is presented as a function of the relative depth h/L_A for the smooth slope and the quarry-stone slope. The relative run-up shown for the non-breaking waves is the maximum run-up observed for the indicated h/L_A. For convenience of interpretation, the data corresponding to incipient breaking waves are shown in shaded areas. The effect of h/L_A is readily apparent in Figure 7; R/H reaches a maximum value of approximately 2.5 for the smooth slope at $h/L_A = 0.92$ for non-breaking waves. The relative run-up for the quarry-stone slope generally increases with decreasing h/L_A and is approximately one-half the corresponding maximum relative run-up for the smooth slope with non-breaking waves. When waves
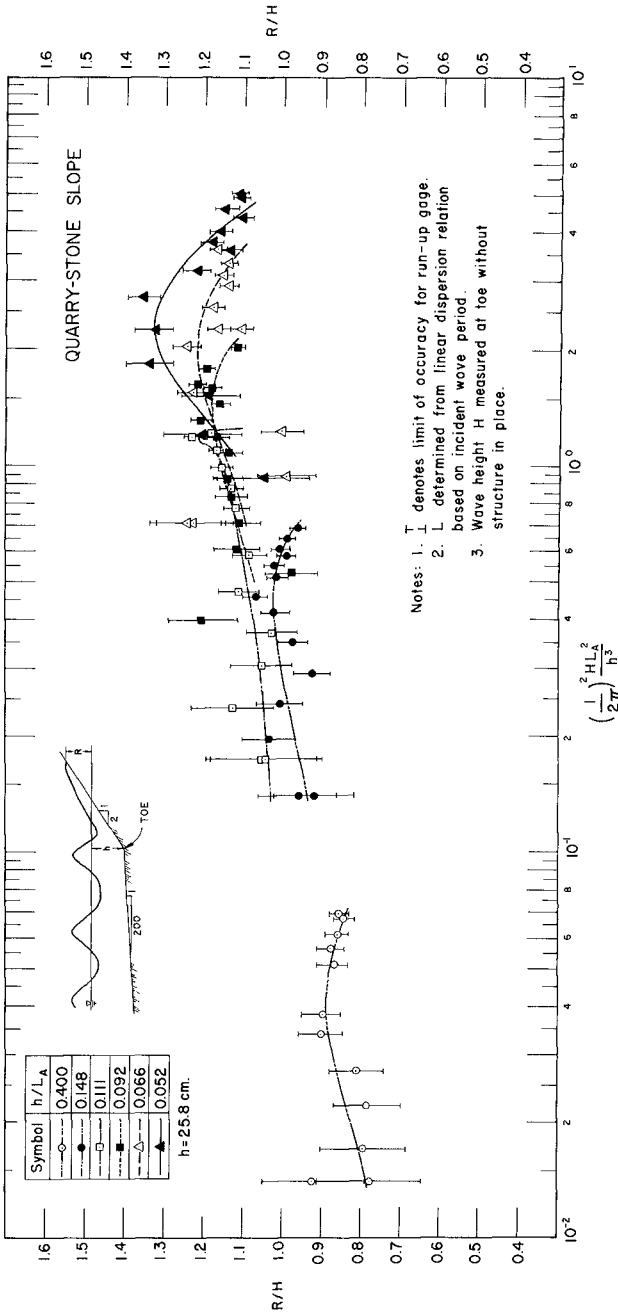
Figure 6.   Relative Run-Up on a Quarry-Stone Slope for Various Ratios
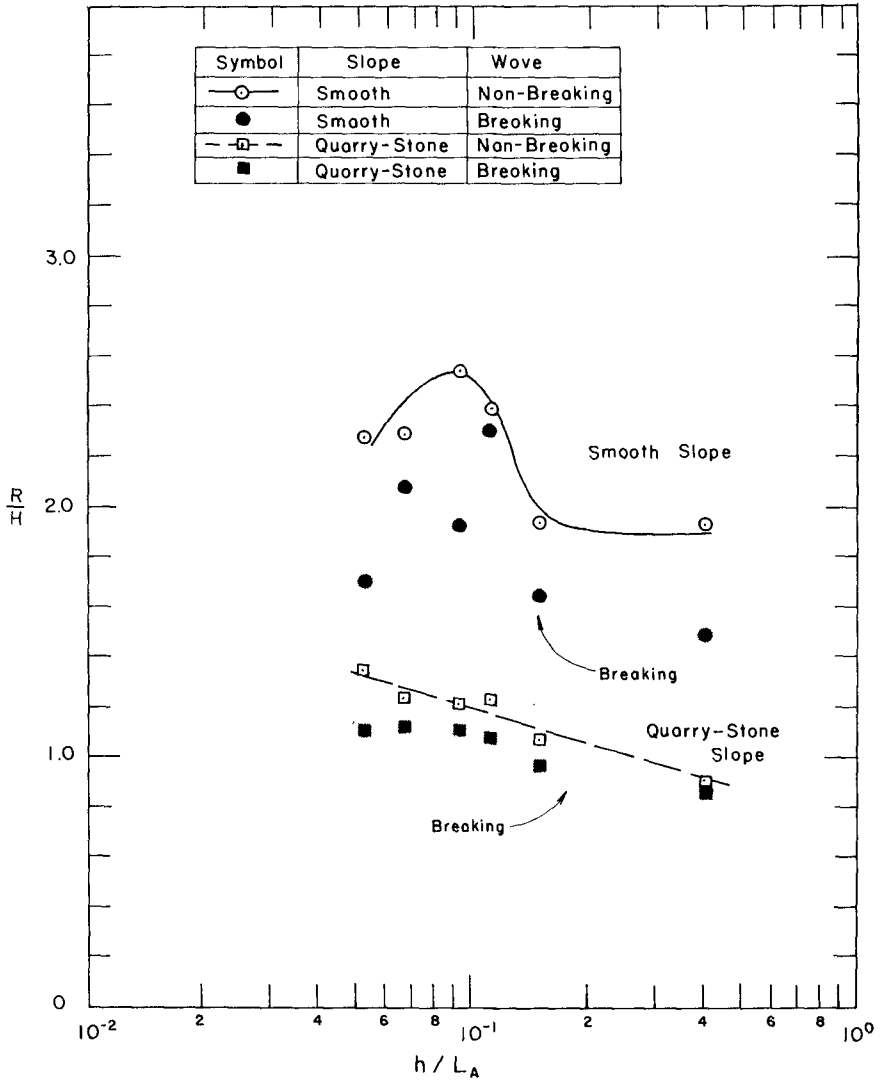of Depth-to-Wavelength.

Figure 7. Maximum Relative Run-Up for Non-Breaking and Breaking Waves
          as a Function of Relative Depth.

break at the toe of the structure the relative run-up is always less than that corresponding to the maximum for non-breaking waves; the reduction is significantly greater on the smooth slope than on the quarry-stone slope. Therefore, it appears that the relative depth, h/L_A, is indeed an important parameter in defining run-up for these experimental conditions.

The same relative run-up data shown in Figure 7 have been replotted and are presented in Figure 8 as a function of the ratio of the incident wave height to the depth at the toe of the structure for each relative depth. (It should be realized that this type of presentation is more applicable for the long waves since the ratio of wave-height-to-depth is more important for these waves.) Again the breaking wave data are enclosed in shaded areas for each structure. A definite trend in the data is apparent if one progresses from data which correspond to the shortest wave length to those corresponding to the longest wave length; this can be seen from the data for both non-breaking and breaking waves. Hence, what first appears to be scatter of data is apparently an ordered behavior of the data when examined closely. This presentation emphasizes that the maximum run-up on both the smooth and the quarry-stone slopes for a given relative depth is greatest for non-breaking waves.

These data can be presented in a somewhat different manner as shown in Figure 9, where the maximum relative run-up is plotted as a function of the parameter H/gT^2 on the abscissa. Hence, the relative run-up is expressed as a function of the wave steepness, and is most applicable for waves which are nearly deep water waves. (As in Figures 7 and 8 the data which correspond to breaking waves are enclosed in shaded areas.) Included for convenience are the corresponding curves presented by CERC (1966) for smooth and quarry-stone structures with slopes of 1:2. It is seen for the deep water waves the data in both cases agree well with the curves. As the ratio of the depth-to-wave length decreases the data deviate from these experimental curves. Again, the importance of the ratio of depth-to-wave length can be seen by progressing with the data from the shortest to the longest waves, and for both the smooth slope and the quarry-stone slope, a trend appears to exist.

CONCLUSIONS

The following major conclusions can be drawn from this study:

1. The ratio of depth-to-wave length is an important parameter in defining relative run-up, R/H. In fact, the scatter of data which is usually attributed to experimental error in some run-up studies may indeed represent the effect of relative depth.

2. The maximum relative run-up for both the smooth slope and the quarry-stone armored slope is always greater than the relative run-up associated with waves which break at the toe of the structure.

3. The maximum relative run-up for long waves occurs at a modified Ursell number of between two and three for both slopes. This Ursell number corresponds to an incident wave where non-linear and linear effects are approximately equal.
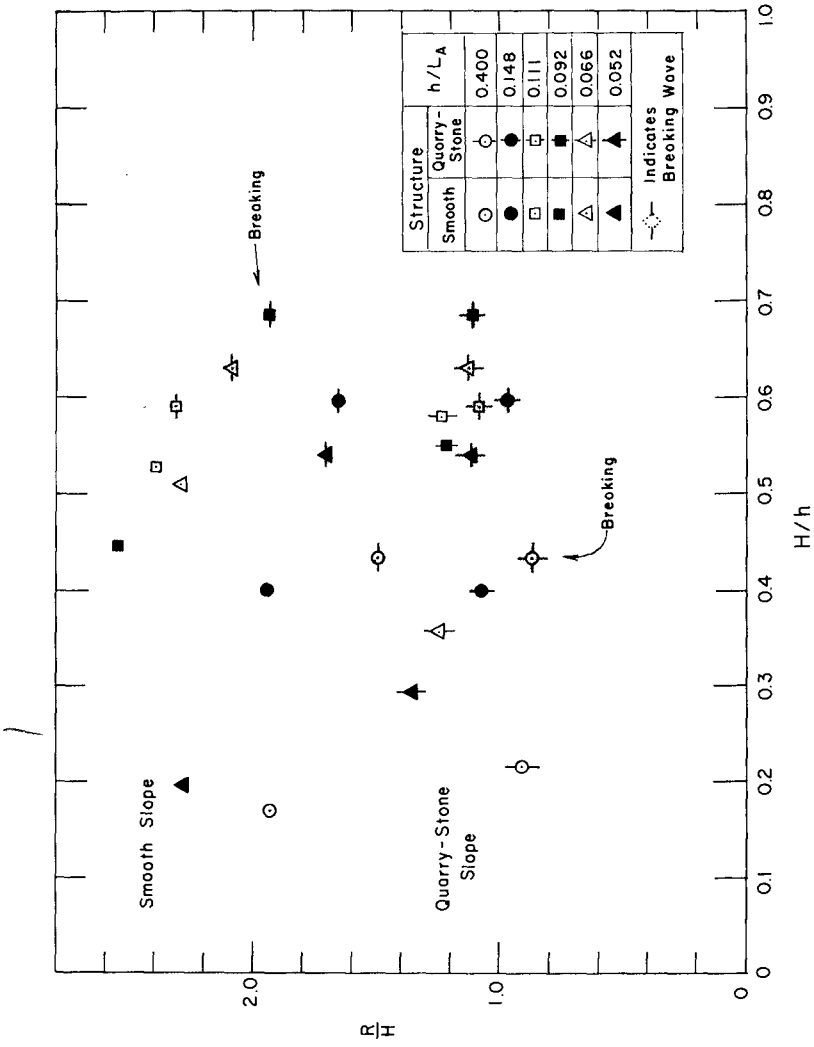
Figure 8. Maximum Relative Run-Up for Non-Breaking and Breaking Waves as a Function of H/h.
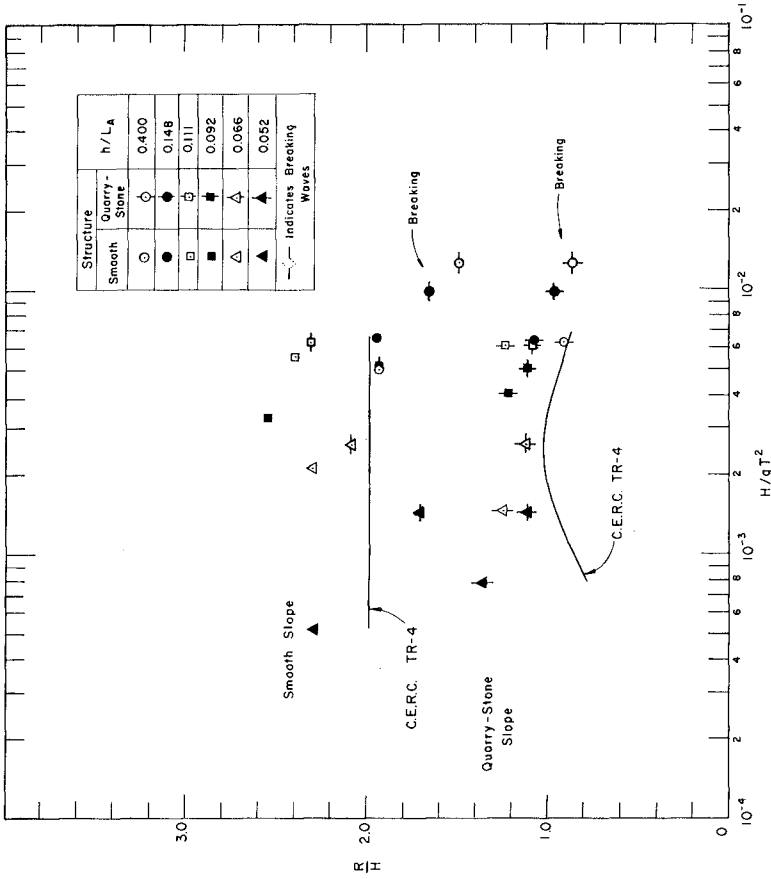
Figure 9. Maximum Relative Run-Up for Non-Breaking and Breaking Waves
as a Function of H/gT^2.

4. The Experimental curves for run-up on smooth and quarry-stone
    slopes from CERC (1966) exhibit somewhat less relative run-up for
    the same wave steepness when compared to these results. Part of
    the reason for the difference for the quarry-stone slope may be
    attributed to differences in the method of construction and part
    may be the effect of relative depth described previously.

REFERENCES

C. E. R. C. (Coastal Engineering Research Center), Technical Report No. 4,
    1966.

Grantham, K. N., "Wave Run-Up on Sloping Structures", _Trans. A.G.U._,
    Vol. 34, No. 5, October, 1953.

Hammack, J. L., "A Note on Tsunamis: Their Generation and Propagation
    in an Ocean of Uniform Depth", _Journal of Fluid Mechanics_, Vol. 60,
    Part 4, 1973.

Hudson, R. Y., "Design of Quarry-Stone Cover Layers for Rubble-Mound
    Breakwaters", Res. Rpt. 2-2, _U.S. Army Engineers Waterways Exp._
    Stat., Vicksburg, Miss., July, 1958.

Saville, T. Jr., "Wave Run-Up on Shore Structures", _ASCE, JWWH_, WW2,
    April, 1956.

CHAPTER 114

COMPUTER ALGORITHM OF WAVE RUNUP ON BEACHES

by

Flora Chu Wang[1] A. M. ASCE, James A. Purpura[2] M. ASCE

Tsao-Yi Chiu[3] and Yu-Hwa Wang[4] A. M. ASCE

ABSTRACT

An efficient computer program for predicting wave runup on beach profiles is presented. The solution is derived through the IBM 370/165 of the Computing Center, University of Florida.

The wave runup data utilized in this study is based on the labora-tory-derived curve obtained from the experimental work of Saville, and expressed as linear regression; the historical storm frequency data is furnished by National Oceanic and Atmospheric Administration; and the surveyed beach profile is supplied by the field program of Coastal and Oceanographic Engineering Laboratory, University of Florida.

A broad spectrum of waves are selected to simulate hurricanes ap-proaching the coast. The results thus obtained should provide useful guidelines in establishing the Coastal Construction Setback Line, and to the design criterion of Coastal Structures.

---

[1] Civil Engineer Consultant, 741 N. W. 36th Street, Gainesville, Florida.

[2] Professor of Civil & Coastal Engineering Department, University of Florida, Gainesville, Florida.

[3] Associate Engineer of Coastal & Oceanographic Engineering Laboratory, University of Florida, Gainesville, Florida.

[4] Assistant Professor of Civil & Coastal Engineering Department, University of Florida, Gainesville, Florida.

INTRODUCTION

In 1971, the Legislature of the State of Florida (8) enacted that the Department of Natural Resources shall establish a Coastal Construction Setback Line along the sand beaches of the State fronting on the Atlantic Ocean and the Gulf of Mexico.

The law provides that the establishing of such setback line shall be based on data determined from comprehensive engineering and topo-graphic surveys which include dune elevations, foreshore slopes, offshore slopes, beach profiles, upland development and vegetation-bluff lines; and from historical storm and hurricane tides, the beach erosion trends, and the predicted wave runup.

The present study is attempted to develop an efficient computer algorithm for predicting wave uprush upon a complicated beach surface with changing slopes, and to facilitate the decision-making process in establishing of the construction of the setback line along the beaches.

BACKGROUND

Theory of Breaking Waves

No generally applicable wave runup theory exists for breaking waves. Breaking is known as a non-conservative process, and breaking point is a mathematical singularity.

LeMéhauté and Koh (2) concluded that the runup of breaking waves has been determined by theory only in the case of solitary waves, but the problem becomes increasingly difficult as the wave period decreases (or as the wave steepness increases) due to the influence of the back-wash on the following waves.

The Bore runup theory elucidated by Shen and Meyer (9) which allows breaking is based on the first-order nonlinear long wave equations, the runup according to this theory depends very weakly on the slope of the beach, hence the analysis thus derived is of academic interest, and cannot be used for calculating the runup for the practical applications.

Experimental Investigations

Theory has not yet been able to give an accurate estimate of run-up caused by waves on sloping beaches or structures, many experiments have been performed systematically to supplement the principle. An ex-cellent qualitative description of the experimental findings has been summarized by the Beach Erosion Board Technical Report No. 4 (10).

Saville (6) performed a large number of experiments and found that wave runup R, the vertical height to which water from a breaking wave will rise on the structure face, increased with water depth d at the

toe of the structure until a water depth-wave height ratio of between 1 and 3 was reached. His results were presented graphically showing the relative runup R/H_o' as a function of structure slope α, structure depth d and wave steepness H_o'/T^2, where H_o' referred to the equivalent deep water wave height and T the wave period.

Savage (5) furthered the experiments of Saville by including the effects of roughness and permeability. The recent experimental study of Machemehl and Herbich (3) on the effect of slope roughness on wave runup showed that the relative runup was reduced approximately 15% and 30% for regular and irregular wave tests respectively.

The work of Saville has been used for a number of years with reliability, hence his laboratory test data of relative runup is utilized in this study as a part of computer input.

Methods for Determining Wave Runup

Numerical analysis based on the method of characteristics has been developed by Freeman and LéMehauté (1) to calculate the runup of solitary waves and its effect due to bottom slopes. The predictions based on this method unfortunately depend on the chosen value of a constant which is somehow based on experience.

Wagges (12) proposed an empirical relationship between the breaker height-breaking depth ratio, wave steepness and the beach slopes. The proposed equations are approximations to what is usually scattered laboratory breaker data.

An approximate method for determining wave runup on composite slopes from laboratory-derived curves for single slopes was first presented by Saville (7). His method was one of successive approximations which involved the replacement of the actual composite slope with a hypothetical slope obtained from the breaking depth d_b, and an estimated wave runup R value. Saville found that the wave runup predicted by his method to be generally within 90% of experimental values except for the largest berms tested. The indications were that, after a horizontal berm had reached a certain width, further widening had no significant effect in reducing wave runup.

There is at present no proven technique to adequately describe a breaking wave in mathematical form, the approximate method of Saville's uprush prediction is adapted in the current analysis as a part of computer algorithm.

DESCRIPTION OF INPUT DATA

Laboratory-Derived Runup Curve

A typical laboratory-derived runup curve by Saville (7) is shown
in Fig. 1. It delineates the model-determined relation between relative
runup R/H_o' and structure slope $\cot\alpha$ as a function of wave steepness H_o'/T^2.

Data are read from the curve and are presented in Table 1, and have
been used as an input for linear regression analysis. Their functional
relationships have thus been obtained for different values of wave steep-
ness. Many examples have demonstrated the frequency dealing with waves of
H_o'/T^2 between 0.04 and 0.15 and practically never with values less than
0.005 or greater than 0.4; they have also exhibited that the computed
hypothetical slopes are always in the range of 1 on 4 and 1 on 10 or flat-
ter. Therefore, their lower and upper bounds, and linear logarithmic
functional relationships displayed in Table 1 are justified under the
practical considerations, and have been incorporated in the computer al-
gorithm for ease of handling input data.

Topographic Surveyed Beach Profile

Fig. 2 shows the location map of a part of the study area and range
lines for St. Lucie County, Florida.

The surveyed beach and offshore profiles range number 36 are displayed
in Fig. 3 which are supplied by the field program of the University of
Florida (4). The profile lines are begun behind the dune where existing
and are extended seaward to wading depth. The profile input data are read
in an increasing order of horizontal distance X associated with the ele-
vation Y from the mean sea level. Due to the core storage requirement,
the maximum of 50 stations are designed for each profile; and a maximum of
30 beach profiles can be included in the program as a single computer run.

Historical Storm Frequency Data

No reliable storm surge records are available of water levels on the
open coast of Florida during major hurricanes which have occurred in the
past few decades.

In a study of storm tide in Florida (11), the Department of Coastal
and Oceanographic Engineering, University of Florida has analyzed the
normal yearly high tides and high water levels caused by hurricanes and
expressed the results as frequency of occurrence for a certain water level
to be equaled or exceeded. Due to the lack of available data for the study
area, the surge frequency curve thus derived indicates a much higher trend
than the information newly furnished by National Oceanic and Atmospheric
Administration (NOAA). Both surge elevation frequency curves are shown in
Fig. 4.
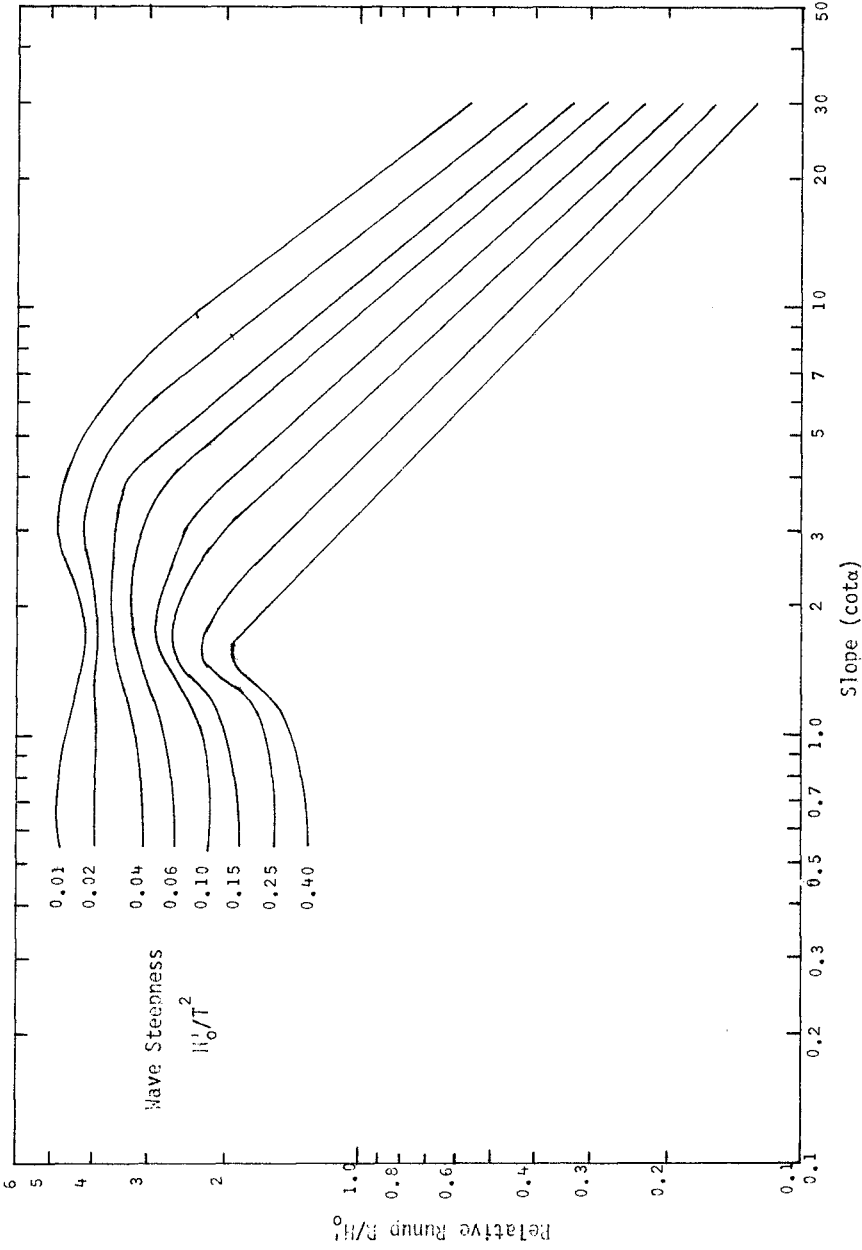
FIG. 1. - Relative Runup for Specific Values of Wave Steepness (After Saville, 1958)

TABLE 1. - Experimental Data of Relative Runup Read from Fig.1

Slope cotα \ Wave Steepness H'_o/T^2	Relatvie Runup R/H'_o							
	(1) 0.40	(2) 0.25	(3) 0.15	(4) 0.10	(5) 0.06	(6) 0.04	(7) 0.02	(8) 0.01
1.9	1.70 (a)							
2.5	1.27	1.64 (a)						
3.3	0.98	1.25	1.85 (a)	2.40 (a)				
4.0	0.83	1.05	1.51	1.95	2.80 (a)	3.40 (a)		
6.0	0.56	0.72	0.99	1.27	1.74	2.10	3.00 (a)	
8.0	0.43	0.54	0.73	0.93	1.25	1.59	2.10	3.00 (a)
10.0	0.35	0.44	0.58	0.74	0.97	1.16	1.60	2.27
15.0	0.24	0.30	0.38	0.48	0.61	0.73	0.90	1.35
20.0	0.18	0.23	0.28	0.35	0.44	0.52	0.68	0.92
25.0	0.15	0.19	0.22	0.28	0.34	0.40	0.52	0.69
30.0	0.13	0.16	0.18	0.23	0.28	0.32	0.41	0.55
38.5	0.10 (b)	0.12	0.14	0.18	0.21	0.24	0.31	0.40
48.5		0.10 (b)	0.11	0.14	0.16	0.19	0.23	0.29
53.0			0.10 (b)	0.13	0.15	0.17	0.21	0.26
66.0				0.10 (b)	0.11	0.13	0.16	0.20
73.0					0.10 (b)	0.12	0.14	0.17
83.0						0.10 (b)	0.13	0.15
95.0							0.10 (b)	0.12

Note:
(a) Preset upper bound of relative runup for linear logarithmic interpolation
(b) Preset lower bound of relative runup for linear logarithmic interpolation
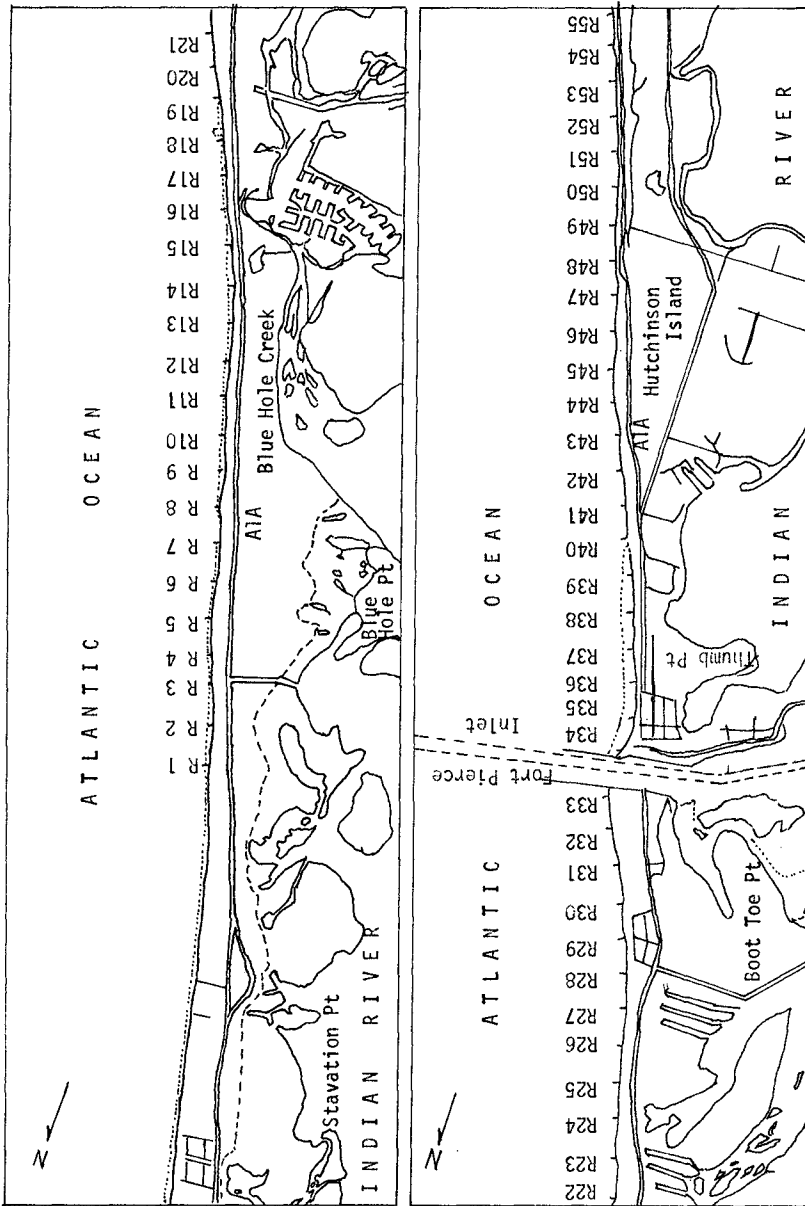
FIG. 2. – Location Map of Study Area and Range Lines, St. Luice County, Florida
(After University of Florida,1972)
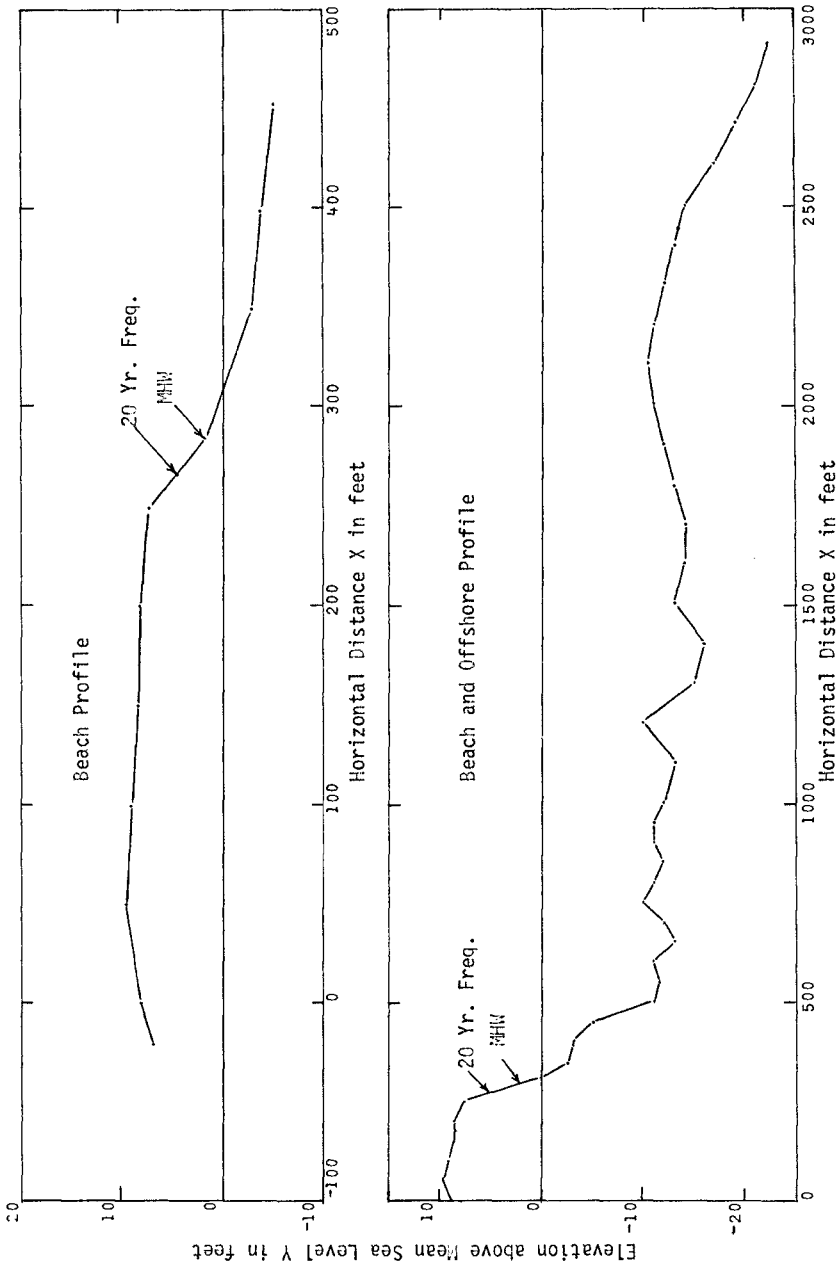
FIG. 3. – Surveyed Beach and Offshore Profiles Range Number 36, St. Luice County, Florida (After University of Florida, 1972)
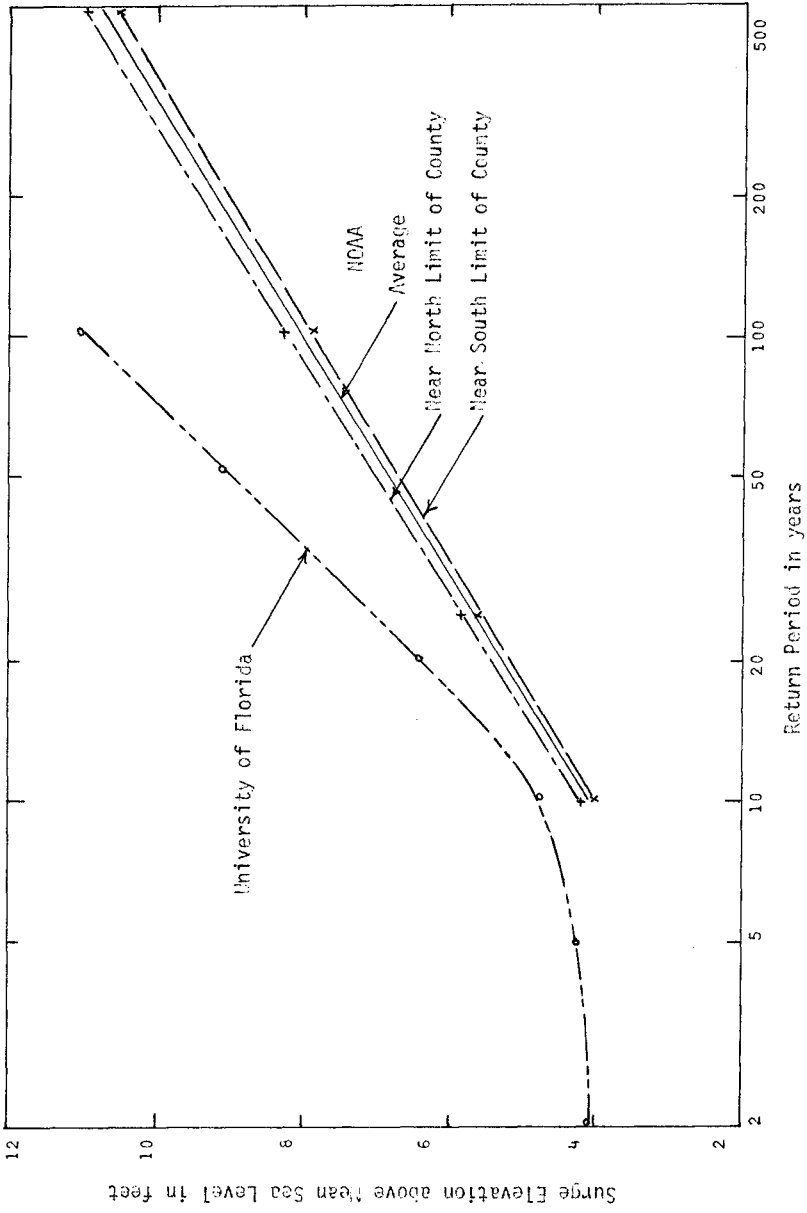
FIG. 4. - Storm Surge Elevation Frequency Curves, St. Lucie County, Florida
(After NOAA, 1972 and University of Florida, 1962)

The NOAA's data are utilized in the present study. For example, with a return period of 20 years, a 5.3 ft. of storm surge is read directly from the curve, superimposed with an estimated 2.0 ft. of wave setup and a predicted mean high tide level of 1.9 ft., the total of 9.2 ft. still water level can be used in the study to simulate a hurricane approaching the coast. Similarly, a 4.5 ft. still water level could also be used to represent a condition under normal weather but with heavy action caused by remote storms.

Wave Heights and Wave Periods

The wave forecasting procedures may be used to translate the comprehensive offshore wind speed and direction data into wave data. With the advent of high-speed computers, a broad spectrum of waves can be examined for the responses of each beach profile. Wave heights range from 2 ft. to 26 ft. and wave periods from 4 to 16 seconds have been tested to estimate the wave uprush upon the surveyed beach profiles. Six combinations of wave height and wave period for each value of still water level are designed as one set of input data on wave condition.

DEVELOPMENT OF COMPUTER ALGORITHM

Initial Estimation of Wave Runup Profile

The initial wave runup at each beach station is estimated by assuming a hypothetical slope extending from the breaking point to the point of the station. The relationships between the estimated slope $\cot\alpha_i$ at the station i and breaking depth d_b are

$$\cot\alpha_i = \frac{X_{db} - X_i}{Y_i - Y_{db}} \quad \dots\dots\dots\dots\dots\dots\dots\dots\dots(1)$$

wherein (X_i, Y_i) are the coordinates at beach station i and (X_{db}, Y_{db}) are the coordinates of breaking depth d_b intercepted with beach profile and computed by the solitary wave equation for a given set of wave height H_o' and wave period T,

$$d_b = \frac{H_o'}{1.5(H_o'/T^2)^{1/3}} \quad \dots\dots\dots\dots\dots\dots\dots\dots\dots(2)$$

Using this computed hypothetical slope and a known wave steepness, a value of initial runup R_i at station i can be determined from the linear regression of laboratory-derived runup curve. Thereby, for a chosen still water level WTL, the vertical coordinate of runup Y_i' can be expressed as

$$Y_i' = R_i + WTL \quad \dots\dots\dots\dots\dots\dots\dots\dots\dots(3)$$

The runup of other stations are also routed, the initial wave runup pro-
file can thus be predicted.

Search for Feasible Wave Runup

The previous step provides a logical estimation of initial wave run-
up profile. From then on, three possible cases can be identified:

(a) All runup are above their beach stations, no feasible runup;
(b) all runup are below their beach stations, no solution either;
(c) some runup are above their beach stations and some are below,
     a feasible solution exists.

Based upon the theory of linearity, the refined algorithm is initiated,
it says: For any two successive beach stations, if runup of first point is
above its beach station while the second one is below, or vice versa, then
there exists a feasible solution. Such solution can be found by the
iterative procedure presented as follows:

(a) Find the linear equation of two successive beach stations
     (X_i, Y_i) and (X_{i+1}, Y_{i+1}) exhibiting alternative runup;
(b) find the linear equation of these two alternative runups
     (X_i, Y_i') and (X_{i+1}, Y_{i+1}');
(c) find the intersection (X_r, Y_r) of the above two linear equations,
     which can be easily varified as:

$$X_r = \frac{X_i(Y_{i+1} - Y_{i+1}') + X_{i+1}(Y_i' - Y_i)}{(Y_i' - Y_1) + (Y_{i+1} - Y_{i+1}')} \quad \dots\dots\dots\dots\dots\dots(4)$$

$$Y_r = \frac{Y_i(Y_{i+1} - Y_{i+1}') + Y_{i+1}(Y_i' - Y_i)}{(Y_1' - Y_i) + (Y_{i+1} - Y_{i+1}')} \quad \dots\dots\dots\dots\dots\dots(5)$$

(d) compute the hypothetical slope extending from the breaking point
     (X_{db}, Y_{db}) to the point of intersection (X_r, Y_r);
(e) determine the new runup R_n by known regression function;
(f) if the difference of new runup with initial estemated one is
     less than a tolerance limit TL, say 0.05 feet, then the feasible
     runup has been obtained;
(g) otherwise, repeat the process by substituting

$$X_{i+1} = X_r$$
$$Y_{i+1} = Y_r \qquad\qquad \dots\dots\dots\dots\dots\dots(6)$$
$$Y_{i+1}' = R_n + WTL$$

and find the new intersection point which in turn determines
a new runup.

Final Recommendation of Wave Runup

The above algorithm further provides a multiple choice of feasible runup for a beach surface with changing slopes. This information is extremely valuable to the designer from a coastal engineering point of view. In the present computer model, the final recommended runup R_f for a given wave condition is taken as that feasible runup with maximum X distance, that is, the one which is closest to the offshore.

FORMULATION OF COMPUTER PROGRAM

The preceeding algorithms have been translated into a FORTRAN IV program for use with the University of Florida IBM 370/165 computer, and consists of a main routine and 9 subroutines. The main program MAI is designed to read in all input data, to initiate calling a series of subroutines, and to print out the detailed results and summary tables.

The input are designed with up to 30 beach profiles and up to 50 stations for each profile. Each wave condition, designed as 6 combinations of wave height and wave period associated with one still water level, is treated as a new sub-problem, therefore, no limitation on number of wave conditions has been imposed.

The functions of each subroutine are described briefly as follows:

(a) Subroutine STA is designed to find the lowest station of the beach profile;
(b) subroutine BXY is developed to compute the wave steepness, the breaking depth and its coordinates intercepting with the beach profile;
(c) subroutine STL is used to find the still water level which intercepts the beach profile;
(d) subroutine INT is designed to interpolate the known regression equation of relative runup;
(e) subroutine RNI is developed to estimate the initial wave runup profile;
(f) subroutine RNF is used to search for the feasible runup;
(g) subroutine RNR is designed to recommend the final computed runup;
(h) subroutine OPD is developed to pring out the detailed results for each beach profile, and reprint the input data to facilitate checking; and
(i) subroutine OPS is used to print out the summary results for a group of 12 beach profiles under one wave condition.

The program logic and the sequence in which individual steps performed are displayed in Fig. 5. The program requires 21,584 bytes of storage; 1,218 bytes for the main program, and 20,366 bytes for 9 subroutines.

START

Read County Name CONTY
No. of Ranges NR & Wave Condition NW

Read Range Number NRS
No. of Stations NS, Coordinates (X,Y)

IW = 1   (1st wave condition)

Read Wave Condition WTL, H, T

IR = 1   (1st range)

Call Subroutine STA (find the lowest station)

IHT = 1   (1st pair of H and T)

Call Subroutine BXY (compute breaking depth)

Call Subroutine STL (find index station of WTL)

Call Subroutine INT (interpolate linear regression)

Call Subroutine RNI (estimate initial runup profile)

Call Subroutine RNF (search for feasible runup)

Call Subroutine RNR (recommend final computed runup)

No   IHT = IHT + 1
          Test: IHT > 6

Yes

Call Subroutine OPD (print the detailed results)

Yes   IR = IR + 1
           Test: IR ≤ 12

No

Call Subroutine OPS (print the summary table)

No   IW = IW + 1
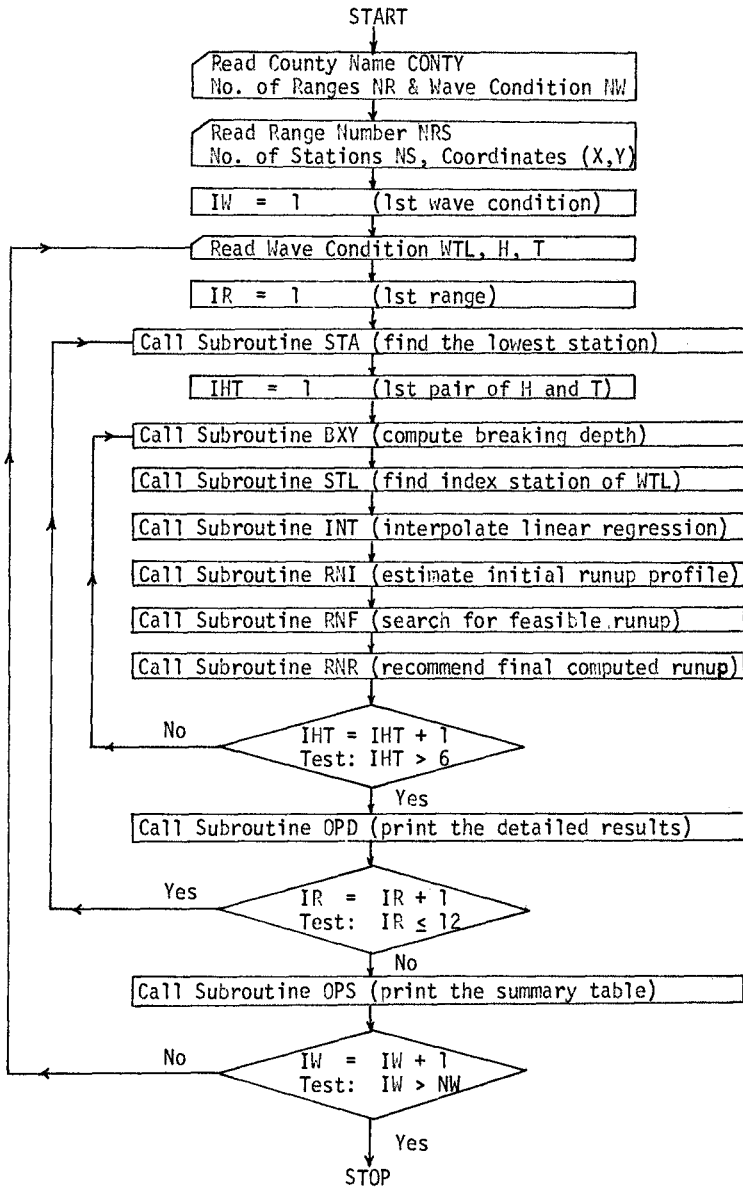   Test: IW > NW

Yes

STOP

FIG. 5. - Flow Chart for the Wave Runup FORTRAN Computer Program

SAMPLE PROBLEM AND COMPUTER RESULTS

The beach profile range number 7 of St. Lucie County, Florida is used for an example problem. The profile consists of 12 beach stations. Still water level of 9.2 feet is used in conjunction with waves of 4, 6, 8 and 10 feet in height and 6, 8 and 10 seconds in period. A sample input data is illustrated in Fig. 6.

Detailed computer results from a series of calculations of wave runup on beach profiles are shown in Table 2. All essential input data are also printed in Table 2.

The summary results for a group of 12 beach profiles are printed in a tabular form which makes it a relatively easy task for analyzing by the design engineer. Table 3 is a typical computer summary output.

Fig. 7 shows the engineering significance of all message output in a graphical form. The computer plotting is currently being developed at the Department of Civil and Coastal Engineering, University of Florida.

CONCLUSIONS AND RECOMMENDATIONS

For examining the response of the 24 beach profiles to a variety of waves, eighteen combinations of still water level, wave height, and wave period are used to compute the wave runup. For these 432 study cases, the total computer execution time is 13.79 seconds CPU on IBM 370/165. The results of these studies show that:

(a) The extreme high waves do not cause high runup due to the fact that they break far from the shorelines;

(b) lower waves (or reformed waves) with longer periods produce much higher runup;

(c) because of the low dune elevation in the study area of St. Lucie County, over 90% of the beach profiles are overtopped with the 9.2 ft. still water level and wave of 6 ft. in height and 8 seconds in period. Even with the 4.5 ft. still water level, some low profiles are overtopped by the low and long waves.

The computer program developed herein is mainly for the computations of wave uprush on beach profiles. The results thus obtained are essential to the design criterion in setting up coastal construction setback lines. At the certain time interval, with new surveyed data which in turn makes the new computer results available, the establishment of such setback line could be subject to review by the Department of Natural Resources.

The methodology of this computer program in the prediction of wave runup can be equally applied to the design crest elevation of protective structures subject to wave action such as breakwaters, seawalls, beach fills, and dams. It is hoped that the current computer approach could be served as a viable tool in the design and analysis processes.

Card A: County Name, Number of Beach Profile and Wave Condition (10A4,2I10)

CONTY   NR   NW

ST. LUICE | COUNTY | 1 | 1

Card B: Beach Profile Range Number, and Number of Beach Stations (2I10)

NRS   NS

7 | 12

Card C: Beach Station Coordinates (11F7.0)

X	Y	X	Y	X	Y	X	Y	X	Y	X
-80.0	-50.0	11.04	10.73	0.0	0.6	12.19	12.24	50.0	75.0	9.09	100.0
11.27	130.0	130.0	10.69	133.0	3.73	150.0	200.0	6.28	1.48	250.0	-1.77
280.0	-4.07

Card D: Wave Condition (F5.0,5x,12F5.0)

WTL   H T   H T   H T   H T   H T   H T   H T   H T

9.20 | 4.0 6.0 | 6.0 6.0 | 4.0 4.0 | 6.0 8.0 | 6.0 10.0 | 10.0 10.0

FIG. 6. – Input Data Form of Wave Runup Computer Program

TABLE 2. - Detailed Results of Wave Runup Computer Program

ST. LUICE COUNTY

WAVE RUNUP ON BEACHES

STILL WATER LEVEL = 9.20 FEET

RANGE NUMBER 7

STA NO.	DIST X FT.	ELEV Y FT.	H = 4.0 FT. T = 6.0 SEC.			H = 6.0 FT. T = 6.0 SEC.			H = 4.0 FT. T = 8.0 SEC.			H = 6.0 FT. T = 8.0 SEC.			H = 8.0 FT. T = 10.0 SEC.			H = 10.0 FT. T = 10.0 SEC.		
			DB 5.54	XDB 177.3	YDB 3.66	DB 7.26	XDB 195.3	YDB 1.94	DB 6.71	XDB 189.5	YDB 2.49	DB 8.80	XDB 216.6	YDB 0.40	DB 12.4	XDB 268.2	YDB 3.17	DB 14.4	XDB *	YDB *
			R	XR	YR	R	XR	YR	R	XR	YR	R	XR	YR	R	XR	YR	R	XR	YR
1	-80.0	11.04	0.78	-	-	1.08	-	-	1.05	-	-	1.49	-	-	2.27	+	+	*	*	*
2	-50.0	10.73	0.85	-	-	1.18	-	-	1.15	-	-	1.59	-55.8	10.79	2.44	+	+	*	*	*
3	0.0	12.19	1.35	-	-	1.76	-	-	1.81	-	-	1.69	-44.4	10.89	3.26	+	+	*	*	*
4	50.0	12.24	1.94	-	-	2.41	-	-	2.58	-	-	3.04	50.0	12.24	4.07	+	+	*	*	*
5	75.0	9.09	1.76	60.1	10.96	2.32	55.7	11.52	2.49	54.3	11.69	2.63	+	+	3.63	+	+	*	*	*
6	100.0	11.07	2.82	+	+	3.31	+	+	3.71	+	+	4.02	+	+	4.94	+	+	*	*	*
7	130.0	10.69	4.49	+	+	4.71	+	+	5.62	+	+	5.31	+	+	5.91	+	+	*	*	*
8	133.3	8.73	3.40	+	+	3.80	+	+	4.37	+	+	4.42	+	+	5.16	+	+	*	*	*

NOTE:
" - " = RUNUP IS BELOW THE STATION
" + " = RUNUP IS OVER TOPPING
" * " = BREAKING DEPTH IS LOWER THAN THE LOWEST STATION

TABLE 3. - Summary Results of Wave Runup Computer Program

			ST. LUICE COUNTY			
STILL WATER LEVEL = 9.20 FEET				WAVE RUNUP ON BEACHES		
RANGE NUMBER	H= 4.0 FT T= 6.0 SEC	H= 6.0 FT T= 6.0 SEC	H= 4.0 FT T= 8.0 SEC	H= 6.0 FT T= 8.0 SEC	H= 8.0 FT T=10.0 SEC	H=10.0 FT T=10.0 SEC
2	R= 2.24 FT X= 22.6 FT Y=11.44 FT	R= 1.75 FT X=-28.1 FT Y=10.95 FT	R= 1.71 FT X=-34.5 FT Y=10.91 FT	R= 5.47 FT + +	R= 6.03 FT + +	* * *
3	R= 1.05 FT X= 50.0 FT Y=10.25 FT	P= 1.09 FT X=-15.1 FT Y=10.29 FT	R= 1.07 FT X=-11.8 FT Y=10.27 FT	R= 1.14 FT X=-102.4FT Y=10.34 FT	R= 1.81 FT X=-122.4FT Y=11.01 FT	* * *
4	R= 0.59 FT X=-83.3 FT Y= 9.79 FT	R= 0.84 FT X=-97.7 FT Y=10.04 FT	R= 0.79 FT X=-94.8 FT Y= 9.99 FT	R= 4.52 FT + +	R= 6.44 FT + +	* * *
5	R= 7.94 FT + +	R= 6.17 FT + +	R= 8.08 FT + +	R= 6.63 FT + +	R= 7.27 FT + +	R= 8.07 FT + +
6	R= 1.99 FT X=114.2 FT Y=11.19 FT	R= 1.60 FT X= 61.5 FT Y=10.80 FT	R= 1.57 FT X= 57.2 FT Y=10.77 FT	R= 1.88 FT X= 27.8 FT Y=11.08 FT	R= 2.03 FT X=-72.9 FT Y=11.23 FT	* * *
7	P= 1.76 FT X= 60.1 FT Y=10.96 FT	R= 2.32 FT X= 55.7 FT Y=11.52 FT	R= 2.49 FT X= 54.3 FT Y=11.69 FT	R= 3.04 FT X= 50.0 FT Y=12.24 FT	R= 5.16 FT + +	* * *
8	R= 1.62 FT X= 5.9 FT Y=10.82 FT	R= 1.41 FT X=-54.6 FT Y=10.61 FT	R= 1.41 FT X=-54.4 FT Y=10.61 FT	R= 1.89 FT X=-69.6 FT Y=11.09 FT	R= 2.69 FT X=-94.8 FT Y=11.89 FT	* * *
9	P= 1.80 FT X= 20.4 FT Y=11.00 FT	R= 2.42 FT X= 17.3 FT Y=11.82 FT	R= 2.43 FT X= 8.7 FT Y=11.63 FT	R= 3.57 FT + +	R= 4.30 FT + +	* * *
10	R= 1.66 FT X= 29.6 FT Y=10.86 FT	R= 2.10 FT X= 19.2 FT Y=11.30 FT	R= 2.19 FT X= 17.2 FT Y=11.39 FT	R= 2.74 FT X= 4.2 FT Y=11.94 FT	R= 2.88 FT X=-26.8 FT Y=12.08 FT	* * *
11	R= 2.24 FT X= 36.3 FT Y=11.44 FT	R= 2.85 FT X= 31.2 FT Y=12.05 FT	R= 2.90 FT X= 20.9 FT Y=12.10 FT	R= 2.82 FT X= -5.4 FT Y=12.02 FT	R= 3.52 FT X=-28.9 FT Y=12.72 FT	* * *
13	R= 2.50 FT X=109.4 FT Y=11.70 FT	R= 2.94 FT X=106.9 FT Y=12.14 FT	R= 3.39 FT X=104.4 FT Y=12.59 FT	R= 3.86 FT X=101.8 FT Y=13.06 FT	R= 4.26 FT X= 80.1 FT Y=13.46 FT	* * *
14	R= 3.26 FT X= 75.5 FT Y=12.46 FT	R= 3.79 FT X= 72.2 FT Y=12.99 FT	P= 4.45 FT X= 68.2 FT Y=13.65 FT	R= 4.94 FT X= 65.3 FT Y=14.14 FT	R= 5.67 FT X= 52.8 FT Y=14.87 FT	* * *

NOTE: " + " = ALL RUNUP ARE OVER TOPPING
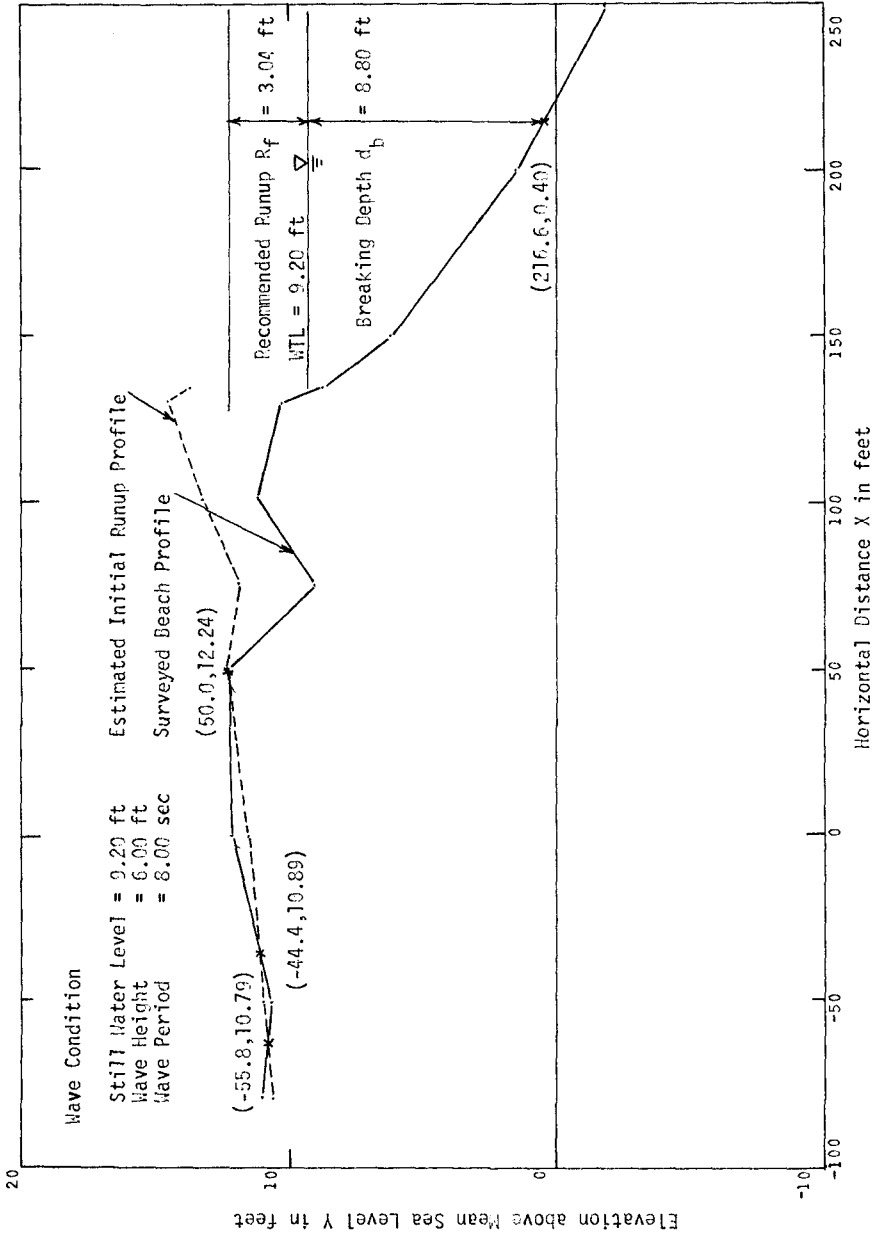   " * " = BREAKING DEPTH IS LOWER THAN THE LOWEST STATION

FIG. 7. - Surveyed Beach and Estimated Initial Runup Progiles, Range Number 7, St. Luice County, Florida

APPENDIX I. - REFERENCES

1. Freeman, J. C., and LeMéhauté, "Wave Breakers on a Beach and Surges on a Dry Bed," Journal of the Hydraulics Division, ASCE, Vol. 90, No. HY2, Proc. Paper 3834, March, 1964.

2. LéMehauté, B., Koh, Robert C. Y., and Hwang, Li-San, "A Synthesis on Wave Run-up," Journal of the Waterways and Harbors Division, ASCE, Vol. 94, No. WW1, Proc. Paper 5807, February, 1968.

3. Machemehl, J. L., and Herbich, J. B., "Effects of Slope Roughness on Wave Run-up on Composite Slopes," Coastal Engineering Department, Texas A & M University, Report No. 129, August, 1970.

4. "Recommended Coastal Setback Line for St. Lucie County, Florida," Department of Coastal and Oceanographic Engineering, Engineering and Industrial Experiment Station, College of Engineering, University of Florida, Gainesville, June, 1972.

5. Savage, R. P., "Wave Run-up on Roughened and Permeable Slopes," Journal of the Waterways and Harbors Division, ASCE, Vol. 84, No. WW3, Proc. Paper 1640, May, 1958.

6. Saville, T., Jr., "Wave Run-up on Shore Structures," Journal of the Waterways and Harbors Division, ASCE, Vol. 82, No. WW2, Proc. Paper 925, April, 1956.

7. Saville, T., Jr., "Wave Run-up on Composite Slopes," Proceedings, 6th Conference on Coastal Engineering, Council on Wave Research, University of California, 1958.

8. Section 161.053, Coastal Construction and Excavation, Florida Statutes, Enacted by the Legislature of the State of Florida, June, 1971.

9. Shen, M. C., and Meyer, R. E., "Climb of a Bore on a Beach, Part 3, Run-up," Journal of Fluid Mechanics, Vol. 16, 1963, pp. 113-125.

10. "Shore Protection, Planning and Design," Technical Report No. 4, 3rd edition, Beach Erosion Board, Corps of Engineers, U. S. Department of the Army, Washington, D. C., 1966.

11. "Storm Tides in Florida as Related to Coastal Topography," Bulletin Series No. 109, Florida Engineering and Industrial Experiment Station, University of Florida, Gainesville, 1962.

12. Weggel, J. R., "Maximum Breaker Height," Journal of Waterways and Harbors Division, ASCE, Vol. 98, No. WW4, Proc. Paper 9384, November, 1972.

APPENDIX II. - NOTATION

The following symbols are used in this paper:

d = water depth at the toe of the structure;

d_b = breaking depth measured from still water level;

H_o' = equivalent deep water wave height;

R = wave runup, the vertical height above still water level;

R_f = recommended runup;

R_i = initial estimated runup at station i;

R_n = new estimated runup;

T = wave period;

TL = tolerance limit;

X = horizontal distance;

X_i = X-coordinate of beach station i;

X_r = X-coordinate of intersection point;

X_{db} = X-coordinate of breaking depth;

Y = elevation above mean sea level;

Y_i = Y-coordinate of beach station i;

Y_i' = Y-coordinate of runup at station i;

Y_r = Y-coordinate of intersection point;

Y_{db} = Y-coordinate of breaking depth;

WTL = still water level;

α = structure slope.

CHAPTER 115

WAVE SET-UP AND WAVE GENERATED CURRENTS
IN THE LEE OF A BREAKWATER OR HEADLAND

Michael R. Gourlay
Department of Civil Engineering
University of Queensland, St. Lucia, Australia

ABSTRACT

Field and model observations indicate the existence of wave generated currents in the lee of breakwaters and headlands. It is shown by an idealised laboratory experiment that such currents could be produced by an alongshore gradient of breaker height with wave crests parallel to the beach. The mechanism for the generation of the current is explained together with some of its characteristics including its interaction with the wave set-up which causes it. It is further shown that it is possible to calculate by simple methods the hydraulic conditions causing the current. Currents produced by this mechanism appear to be of practical importance in determining the local plan shape of beaches close to breakwaters and headlands.

1. INTRODUCTION

The generation of unidirectional currents by waves in shallow water is now recognised as one of the fundamental mechanisms involved in the shaping of sedimentary coastlines. The action of waves breaking at an angle to a coast and so producing a current parallel to the shore and consequent alongshore movement of sand or littoral drift, has been widely known for many years. More recently the influence of mass transport currents induced by non breaking waves has also been recognised as a significant factor in coastal processes. Not so widely known is the process whereby currents may be generated parallel to the shoreline by breaking waves whose crests are also parallel to the beach.

Twenty-five years ago Irribarren (1) described a situation where a current was generated by swell waves whose breaking crests were parallel to the beach in a bay. Refraction analysis confirmed the visual observation that the breaker height decreased along the beach as the beach became more sheltered. The observed current flowed in the direction of decreasing breaker height. Although Irribarren was able to show the significance of this lateral expansion current, as he called it, in the interaction between coastal and fluvial processes at the mouth of a river at the sheltered end of the beach, it does not seem that much attention was paid to this process of current generation in the years immediately following the publication of his observations. However several years ago the present author was involved in conducting model investigations for several proposed small boat harbours in Queensland and nearby islands. During these tests it was observed that in many situations wave generated currents of considerable magnitude occurred. Closer analysis of some simple measurements and observations showed that while these currents generally increased with the magnitude of the breaking waves, it was quite obvious that they were not always formed by the classical littoral current mechanism of waves breaking at an angle to the shore.

2. SOME ACTUAL CASES

Since the publication of the observations made in fixed bed models (2a, 2b) some further situations where currents caused by alongshore gradients in breaker height occur have been studied. These situations, which include both field and.model studies, give further information concerning both the nature and effects of such currents.

One situation is shown on figure 1. A rather steep beach (1 in 11 to 1 in 12) of medium to coarse sand (0.6 to 1.0 mm) is located on the weather side of a large enclosed bay where the tide range (approx. 2 m) is comparatively large in comparison to the height of the waves which break upon the beach. For winds from the predominant direction as shown, the southern end of the beach is sheltered from the resultant wave action. Wave refraction and diffraction produce an alongshore gradient in breaker height which may under certain conditions produce a reverse eddy current in the lee of the headland as shown in fig. 1. Further along the beach the effect of the breaker height gradient is balanced by the breaker angle effect tending to generate the classical littoral current. Consequently there is a null point of zero alongshore velocity at a place where the wave height is less than its value along the exposed portion of the beach.

In the preceding case the reverse current does not appear to be of great importance in the overall beach system behaviour. In figure 2 is shown a larger scale situation at Currumbin on the exposed southern coast of Queensland, Australia. The original situation is shown in figure 2b. Waves refracting and diffracting around the offshore rock had a noticeable angle with the shore and caused a sandspit to grow northward and push the mouth of the creek northwards until floodwaters cut a new channel near the headland and the process repeated itself. Experiments in a moveable bed model (figure 2a) showed that the building of a breakwater connecting the rock to the mainland reversed the current direction near the creek mouth causing a spit to grow southwards instead of northwards. Similar behaviour occurred when a connecting breakwater was built in the prototype.

The third example has already been discussed in reference 2b. Fig. 3a shows model observations of currents in the lee of a headland on the Queensland coast. An eddy was again observed and appears to be responsible for the formation of the shoal on the western side of the river mouth. Figure 3b shows that wave refraction will cause an alongshore gradient of breaker height which could generate such a current as suggested by the previous examples. On the other hand there is a second current generated along the northern side of the headland by waves breaking at an angle to the shore and it is possible that the circulating current is an eddy induced by momentum transfer from this second current. The process of current generation in the lee of a headland or structure is thus a complicated phenomenon dependent upon the local topography and wave conditions and intimately connected with variations in height, direction and location of the breaking waves.

3. WAVE SET-UP AND RADIATION STRESS THEORY

At about the same time as the observations described in reference (2a, 2b) were being made the phenomenon of wave set-up was beginning to receive attention by various investigators. It appears to have been first noticed in a

comparison of storm surge levels between sheltered and exposed areas during a
hurricane (3). Subsequent field observations by Dorrestein (4) and laboratory
studies reported by Saville (3) showed that significant increases in mean water-
level occurred within the surf zone landward of the breakpoint. A smaller
decrease in mean water level or set-down was also observed in the zone just
seaward of the breakpoint. Subsequently increases in mean water level caused
by the wave action were observed in lagoons and coral atolls and behind permeable
breakwaters (5).

     A theoretical explanation of the phenomenon of wave set-up and set-down
as well as a unified approach to wave generated currents has been made possible
by the work of Longuet-Higgins and Stewart (6 and 7) who introduced the concept
of the "radiation stress" resulting from the changes in momentum flux within
the wave system as the waves propagate over a shoaling bottom. The theory which
is essentially a consideration of second order terms in the equations of motion,
was put forward independently in a different form by Lundgren (8).

     Subsequent laboratory experiments on a plane beach by Bowen, Inman and
Simmons (9) showed that the theory of Longuet-Higgins and Stewart could be
applied to the calculation of the set-down offshore of the breakpoint with the
qualification that the maximum measured set-down was somewhat less than the
theoretical due to the limitations of first order theory. Inshore of the break-
point the set-up slope was found to be related to the beach slope and the mean
ratio of wave-height to water depth within the surf zone. The magnitude of the
set-up increases with the height of the breaking waves.

     Moreover in recent years the radiation stress theory has been applied to
several wave generated current and related problems. For instance Bowen (10)
has considered the generation of longshore currents on a plane beach and the
occurrence of rip currents (11). Longuet-Higgins (12 and 13) has also studied
the longshore current problem, while O'Rourke and Le Blond (14) have calculated
longshore currents in a semi-circular bay. The set-up within a coral atoll
caused by waves breaking on the fringing reef has been treated by Tait (15).
Longshore sand transport has also been investigated using this approach by Komar
(16), while Bakker (17 and 18) has further considered the longshore sand transport
problem in the situation where waves both break at an angle to the shore and have
a longshore variation in wave height. Komar (19) has used the theory to explain
how a stable equilibrium beach cusp formation can be maintained by a balance
between the radiation stress component caused by waves breaking at an angle to
the shoreline and the component caused by an alongshore gradient in breaker
height.

4. LABORATORY INVESTIGATION

4.1. Purpose and Scope of Experiments.

     Consideration of the various observations made in particular situations
suggested that if the process of alongshore current generation by breaker height
gradients were to be fully understood it would be necessary to make some
systematic observations in a simplified situation where other current generating
mechanisms were absent. The situation adopted for study after consideration of
various alternatives was one in which an alongshore gradient of breaker height
was obtained by diffraction of waves behind a semi-infinite breakwater parallel
to the wave crests. The beach behind the breakwater was formed of concrete and
was parallel to the undiffracted wave crests in the exposed zone outside the
geometric shadow of the breakwater while in the sheltered zone behind the break-
water it wascurved with a constant radius centred on the breakwater tip.
Since the diffracted wave crests have theoretical curves which can be approximated
by a circle the influence of waves breaking at an angle to the beach was almost

completely eliminated. The general arrangement is shown in figure 4.

In this investigation the primary variable, the breaker height was measured for both the two dimensional (sheltered area blocked off) and the three dimensional system for several different incident wave heights at periods of 1.0 and 1.5 seconds. The water depth offshore of the beach was maintained at 20 cm in all cases. At the same time the resulting wave set-up was determined, together with the velocity and pattern of the unidirectional current flowing into the sheltered area. It was intended to treat the analysis of the system in two parts - one involving the relationship between the breaking wave characteristics and wave set-up and the other involving the "steady" non uniform flow relationship between the wave set-up and the current.

It should be particularly noted that the experimental arrangement permitted the study of a complete current system and so avoided some of the problems associated with studies of longshore currents where it is impossible to obtain the ideally desirable infinitely long beach and wave generator.

4.2. Measurement methods

Wave heights were measured using capacitance wave height meters of the insulated wire type, the wave trace being recorded on a twin channel pen recorder. Wave set-up was measured using 39 piezometers located at fixed points within the beach both offshore along lines perpendicular to the beach and inshore along the still water line. Piezometers were connected through a series of manifolds to an 8 tube air-water differential manometer in which the mean water level in the beach area could be obtained relative to that in the horizontal offshore section of the basin. Additional measurements of wave set-up were made at other locations using a probe made of 2 mm stainless steel tube which was placed normal to the beach and very close to it so that the opening was within the bottom boundary layer.

The wave generated current was observed and recorded using photographic methods. A movie camera was suspended above the test basin pointing vertically downwards and the paths of coloured floats recorded during a period of 2 to 2.5 minutes. A large number of almost neutrally buoyant floats were photographed in each sequence to cover the field of view. Selected float paths were then plotted from coordinates read off the film using a film analyser and current surface velocities deduced from the plotted data after the influence of the orbital velocities had been eliminated. All velocities quoted or shown on the various figures are average values determined over one or more wave periods.

In all cases the accuracy and consistency of the measurements were influenced by the fact that the test basin was located outdoors and so was subjected to uncontrollable variations in conditions due to the weather. In particular a close watch had to be kept on the water level and the effects of leakage and evaporation made good at approximate intervals.

4.3. Experimental Results

In this paper results are presented for a single incident wave condition ($H_I = 9.0$ cm, $T = 1.50$s), and the general characteristics of the current system are outlined together with various conclusions concerning its nature. The effects upon the current system of varying the incident wave conditions will be treated in a subsequent paper.

4.3.1. Wave Height and Wave Set-up.

        The variation of wave height within the beach system is shown on figure 5.
It is immediately evident from a study of the wave height contours that, while
the wave height generally varies as would be expected from diffraction theory,
there are also other factors influencing its magnitude. For instance in the
exposed zone the occurrence of interference maxima and minima as predicted by
diffraction theory can be recognised. However superimposed upon these is the
effect of the wave reflected from the beach causing a pattern of nodes and
antinodes more or less at right angles to the interference lines. Similar less
recognisable effects occur in the sheltered zone. Nevertheless it is quite obvious
that there is a very considerable alongshore gradient in breaker height.

        The corresponding variation of mean water level within the system is shown
on figure 6 and wave set-up profiles normal to the beach along four lines, are
plotted on figure 7. It can be seen that the mean water level variations are of
a larger order of magnitude within the surf zone compared with those offshore of
the plunge point of the waves. Moreover variations in mean water level offshore
of the breakpoint are consistent with those to be expected from application of
"radiation stress" theory. In particular set-down occurs off the exposed portion
of the beach and set-up within the sheltered area. Within the surf zone the wave
set-up profile is straight and rises from the plunge point of the waves with a
slope less than that of the beach.

        Comparison of figures 5 and 6 immediately suggests that the wave set-up is
generally proportional to the breaker height as was in fact found in two
dimensional tests. Figure 8 shows the resultant alongshore gradients of breaker
height and wave set-up within the surf zone. It is evident that the alongshore
gradient of mean water level created by the wave breaking process provides the
driving force for a current flowing into the sheltered area.

4.3.2. Wave Generated Current System

        The current system itself is depicted on figure 9. The system is both
simple in general form and complex in detail. The alongshore current commences
within the surf zone in the exposed area outside the geometric shadow of the
breakwater. It then flows parallel to the shore into the sheltered area after
which it is deflected by the breakwater to flow back into the exposed zone to
form a complete closed circuit. At the same time a smaller secondary eddy forms
in the stagnation area near where the beach and breakwater intersect while the
whole mass of water inside the main eddy is set in motion by the primary wave
generated current.

        Considered in more detail it is found that the extent of the wave generated
current system coincides with the area affected by diffraction extending as far
into the exposed zone as the first interference maximum of the wave height
(figure 5). As figure 8 indicates this means that the wave generated current
commences in the vicinity of the point where both wave height and mean water
level have a maximum value. Outside this zone the interference effect causes
variations in wave height and mean water level which result in the formation of a
rip current as indicated in figure 9. In these experiments the characteristics
of this rip current have not been investigated as its form is obviously modified
by the side wall of the model basin.

        The actual zone where water flows into the surf zone is located outside
the geometric shadow of the breakwater. Here the water transported landward
by mass transport currents offshore is projected by the breakers into the surf
zone where the maximum alongshore gradient of mean water level exists. Both
the velocity and discharge of the current increases up to a maximum in the vicinity

of the line of the geometric shadow of the breakwater where the primary current
is still confined inshore of the break point (figure 10). Once inside the
sheltered zone the current flows parallel to the beach until deflected at the
stagnation point in the corner.

Typical horizontal velocity profiles are shown in figure 11. These are
of surface velocities and any variation in surface velocity between crest and
trough of the waves has been averaged out in the drawing of the profiles. Four
profiles have been selected, one from the zone where the current is developing
(profile 1), the others from the zone between where the current has reached its
maximum discharge (profile 2) and where the maximum velocity passes offshore of
the plunge point (profile 4). Each profile clearly shows how the current is
concentrated parallel to the shore in the vicinity of the surf zone with a maxi-
mum velocity several times that of the induced eddy inside the primary current.

At profile 1 the current is completely confined inshore of the plunge
point. However at profile 2, along the line of the geometric shadow of the
breakwater, the primary current extends seaward as far as the breakpoint while
the peak of the current is inshore of the plunge point. At profile 3, the primary
current extends offshore of the break point. However the peak current velocity
still occurs landward of the plunge point and since the latter has moved inshore
and the depth has decreased the maximum velocity is greater. However, at profile
4 the situation appears to have reached a point of instability where the maximum
current velocity oscillates between a point just inshore of the plunge point and
a point offshore near the breakpoint. The inshore position of the maximum
velocity appears to coincide with the uprush phase of the surf zone cycle and
the offshore position with the backwash phase.   This oscillation has not been
investigated in detail but it was found (figure 10) that the maximum current
velocity attains its greatest value just before it passes offshore of the plunge
point. Furthermore while within the surf zone the maximum current velocity has
a Froude number of the order of unity and a longitudinal section along the line
of maximum velocity (figure 10) suggests a flow profile and energy gradient rather
similar to a broadcrested weir with a drowned hydraulic jump on the downstream
face in the vicinity of the breaker plunge point.

Observation of the flow and float paths also leads to the conclusion that
a helicoidal secondary current is present within the main flow system. This
appears to be generated in the zone where the current reaches its maximum discharge,
i.e., near the geometric shadow of the breakwater, as the uprush and backwash of
the breaking waves are carried alongshore by the primary wave generated current.
A similar effect with rip feeder currents has been observed in the field by Eliot (20).

4.3.3. Summary of Wave Generated Current Types

The current system induced by diffraction at the breakwater produces four
distinct types of unidirectional current. These are:-
- the initial inflow normal to the beach in the zone where the waves break and
release their energy;
- the primary surf zone current which follows an approximate logarithmic spiral
path in plan and has a helicoidal secondary current superimposed upon it;
- the induced secondary eddies within the sheltered zone, one within the main
primary current circulation, the other within the stagnation zone near the base
of the breakwater;
- the offshore mass transport current of the waves which is very greatly distorted
by the circulatory current.

5. APPLICATION OF EXPERIMENTAL RESULTS

5.1. Simple Computation of Wave Generated Current

        It is desirable for engineering purposes that the magnitude of the along-
shore current can be calculated so that estimates of its significance as a sand
transporting agent can be made. To do this it is necessary to be able to determine
the following relationships:-
- the height and location of the breakers along the shore as a function of
geometry and incident wave conditions;
- the wave set-up as a function of the breaker height;
- the current velocity as a function of the alongshore gradient in mean water level.

5.1.1. Computation of break point location

        The variation in wave height within this system is a consequence of
combined diffraction and shoaling. A first estimate of this phenomenon has been
obtained using the generalised diffraction diagram for the case of the semi-
infinite breakwater (figure 21 of reference 21) combined with small amplitude
theory for computing shoaling effects.

        The procedure adopted was to commence with the generalised diffraction
diagram for constant water depth upon which are shown wave crests at intervals
of one wave length and contours of the diffraction coefficient. Small amplitude
theory was used to calculate the travel time of a wave crest of a given period up
the beach, the calculation being made for small increments of distance x. From
the latter computation, the positions of the wave crests at successive time intervals
of one wave periodwere calculated taking the initial position as that of the
breakwater tip. These distances were plotted upon tracing paper overlying the
generalised diffraction diagram and the diffraction coefficient contours replotted
in their correct relative positions along the relocated wave crests. The combined
diffraction-shoaling coefficient K_{ds} was obtained by multiplying the value of K_d
by the shoaling coefficient K_s appropriate to the depth in question. For conven-
ience, this was done at points defined by the intersection of a given depth
contour with a given K_d contour and the final combined diffraction shoaling diagram
shown on figure 12 obtained by drawing contours of K_{ds}.

        The combined diffraction-shoaling diagram shown as figure 12 is for a
period of 1.0 seconds which is not the same as that used in the test reported
in the preceding part of the paper, i.e., 1.5 seconds. Unfortunately limitations
of the generalised diffraction diagram prevent its application in a system where
only one or two wave lengths occur which is the case for the test results with
1.5s wave period. Moreover as discussed subsequently other questions arise which
make it difficult to predict the location of the break point for these particular
results. However, figure 12 has been used with empirical wave breaking data as
correlated by Goda (22) to predict the location of the break point for waves of
one second period and an incident height of 6.5 cm.

        For comparison breakpoint locations observed on three separate occasions
in the test basin with waves of similar height and period are also shown. The
agreement is quite good in the exposed zone and the influence of the interference
maximum upon the breakpoint location is similar in both cases. Discrepancies
however appear in the exposed zone where the rip current flows seaward and in the
sheltered zone where the alongshore current spreads out of the surf zone. Such
discrepancies are not unexpected in these places.

5.1.2. Computation of wave set-up

In principle once the breaker location and height is known, the resulting wave set-up at the still water line, $\bar{\eta}_{swl}$, can then be calculated for a beach of a given slope as has been done for spilling breakers by Bakker (18). In practice there are problems. Firstly in the cases considered in this investigation all breakers in the zone of maximum alongshore gradient were plunging breakers. As shown on figure 7 wave set-up for this type of breaker begins at the plunge point and not at the breakpoint. It is thus necessary to be able to calculate the distance between breakpoint and plunge point x_p as well as to choose a suitable value of the breaker index $\gamma = \dfrac{H_b}{d_b}$.

Experimental data of Galvin (23) gives an estimate of the plunge point distance as a function of breaker height and beach slope. The following empirical equation relating these variables was obtained by Galvin.

$$\frac{x_p}{H_b} = 4.0 - 9.25 \tan \beta \tag{1}$$

Using this equation and assuming a constant set-down between breakpoint and plunge point and shallow water conditions, consideration of simple geometry as was done by Bakker (18), gives the following relationship for $\bar{\eta}_{swl}$ referred to deepwater conditions.

$$\frac{\bar{\eta}_{swl}}{H_b} = \frac{\left\{ 3C^2 \left[1 - (4.0 - 9.25 \tan \beta) \gamma \tan \beta \right] - \frac{1}{2} \right\} \gamma}{3C^2 \gamma^2 + 8} \tag{2}$$

where $\gamma = \dfrac{H_b}{d_b}$

C is a factor defined by $\gamma' = C\gamma$ where γ applies at the breakpoint and γ' within the surf zone. β is the beach slope.

Application of the preceding equation to the test situation is complicated by the fact that the reference level for mean water level is different while the magnitudes of C, γ and the numerical constants are all subject to uncertainty. To avoid the influence of inaccuracies in the reference level in the test basin equation (2) can be modified to give the set-up relative to the mean water level at the breakpoint, $\bar{\eta}'_{swl}$

Thus

$$\frac{\bar{\eta}'_{swl}}{H_b} = \frac{3C^2 \gamma \left[1 - (4.0 - 9.25 \tan \beta) \gamma \tan \beta \right]}{3C^2 \gamma + 8} \tag{3}$$

$\dfrac{\bar{\eta}'_{swl}}{H_b}$ as calculated from equation (3) is shown as a function of γ in figure 13, the constant C being assumed equal to unity. Experimental points from two dimensional tests at periods of 1.0 and 1.5s and various wave heights are also shown. The theoretical curve in general yields values of $\dfrac{\bar{\eta}'_{swl}}{H_b}$ about 10% below the experimental values. This can be considered to be quite good agreement in view of the large scatter in the selected experimental data used by Galvin to obtain equation (1).

Galvin (23), considering the kinematics of the plunging wave crest, also predicted theoretically that $\frac{x_p}{H_b}$ would be of the order of 2. Modification of equation (3) using $x_p = 2H_b$ gives

$$\frac{\bar{\eta}'_{swl}}{H_b} = \frac{3C^2\gamma \left[1 - 2\gamma \tan \beta\right]}{3C^2\gamma + 8} \qquad (4)$$

When plotted on figure 13, equation (4) coincides with the upper bound to the experimental data. Hence for these tests an average value of $x_p = 2.5\ H_b$ gives a fair estimate of the dimensionless wave set-up $\frac{\bar{\eta}'_{swl}}{H_b}$. Indeed, the relatively small influence of γ can well be neglected and a constant value of 0.2 assumed for $\frac{\bar{\eta}'_{swl}}{H_b}$, at least as a first approximation. The alongshore gradient of mean water level is thus theoretically calculable. The second step of determining the magnitude of the wave generated current from this gradient then follows.

5.1.3. Interaction between current and wave set-up

It has been found however that the relationship between breaker height and actual wave set-up is rather more complicated than it would first appear. Analysis of the experimental data indicates that the surf zone wave set-up in the system studied is the sum of at least four separate components. These are as follows:-

(i)   equivalent two dimensional set-up for a given breaker height;
(ii) offshore set-up in the sheltered zone;
(iii) current set-up or superelevation resulting from centrifugal acceleration;
(iv) a displacement effect when the current is flowing within the surf zone caused by the wave uprush and backwash being carried along the beach by the current.

To these flow components which can be observed in the model must be added the effect of the alongshore gradient of radiation stress at the breakpoint which results in a further contribution to the wave set-up. The separation of these various factors influencing the wave set-up is dependent upon a knowledge of the alongshore primary current. Complete analysis of the test data for the case described in this paper is not yet available. Furthermore it appears that this particular set of data is subject to other complications due to the occurence of secondary waves which produce a further discrepancy between the two and three dimensional wave set-up in the exposed zone. It thus seems that it will be necessary to analyse the results of other wave conditions in more detail before a reasonable simplified method of calculation of the wave generated current can be evolved.

5.2. Inferences concerning Beach Morphology

From the point of view of sand movement and beach morphology it may be inferred that the circulatory wave generated current behind a breakwater or headland is a primary agent in determining the well known logarithmic spiral shape of beaches. In particular, erosion of the foreshore can be expected to occur in the zone just outside the geometric shadow of the breakwater where the

current is accelerating while accretion of the foreshore can be expected in the zone of deceleration associated with the stagnation eddy. Deposition is also likely outside the surf zone towards the centre of the induced eddy.

As in all sediment transporting systems changes in the bed configuration will induce changes in the hydraulic system until an equilibrium is set up. In this situation this may well include the development of an adverse bed gradient along the current path which will oppose the transporting action of the current on the bed material. Moreover the offshore contours and planform of the beach may be modified in such a way that the waves within the sheltered zone break at an angle to the shoreline and so provide a balancing dynamic force component to oppose the original alongshore current generated by the alongshore gradient of breaker height. This part of the process has not yet been investigated.

However in considering the morphological significance of these currents it is important that the relative scale of the system be considered. For the tests described in this investigation the input wave length is of the order of $\frac{1}{2}$ to $1/3$ the size of the breakwater - beach system. This means that many of the factors influencing the current may well be exaggerated compared with conditions existing behind a real breakwater or headland. In this latter case then it is quite possible that simplified calculations may prove to be quite adequate to determine the magnitude of wave set-up and current velocity as the magnitudes of the interactions between the current and the waves will be quite small. On the other hand if groynes are under consideration then it can be expected that many of the interaction factors will be present and will need to be allowed for.

Finally it should be emphasised that this type of current does not produce the large scale log spiral beach plan forms discussed by Silvester (24) which result from an interaction between littoral drift and wave refraction when waves break at an angle to an initially straight beach. Such systems will however be modified by local alongshore variations in breaker height. These currents do however significantly influence the beach shape in the lee of any fixed structure or other fixed point and so shape the section of beach with greatest curvature. With no sediment supply coming round the breakwater or headland they will determine the beach shape completely. When sediment does come round the headland as in figure 2a the lateral expansion current will contribute to the development of the equilibrium plan form. When the latter is obtained however the reverse eddy will presumably disappear being replaced by a littoral current in the opposite direction with a transport capacity equal to the sediment supply.

6. CONCLUSION

The generation of currents of the lateral expansion type behind a breakwater by an alongshore gradient of breaker height when the wave crests are parallel to the beach has been reproduced in the laboratory. The basic mechanism producing the current has been shown to be an alongshore gradient of wave set-up within the surf zone. The resulting current is found to have a path in plan which appears to be log spiral in form and there is evidence of significant interaction between the current and the hydraulic conditions causing it.

Using a combination of theoretical and empirical methods it has been shown that it is possible to calculate the break point location for the particular test geometry considered and also to estimate the wave set-up from the breaker height for two dimensional plunging breakers. It thus appears that it should be possible to calculate the alongshore current in such a situation but full confirmation of this conclusion awaits the analysis of the complete test data.

It is evident that a current system of this type may be of primary importance in determining the alignment of a beach in the immediate vicinity of a breakwater, groyne or headland. Moreover it should be realised that the effects of breaker angle in generating a littoral current are always subject to modification by an alongshore gradient in breaker height regardless of the mechanism causing this gradient.

REFERENCES

1.　　Irribarren Cavanilles, R.　Corrientes y transportes de arena originades por el oleaje. Revista de Obras Publicas, May - June 1947. French translation in Bull. de l'Association Internationale Permanente des Congrès de Navigation Vol. 23, 1949, pp. 100-132.

2(a)　Gourlay, M.R.　Wave generated currents - some observations made in fixed bed hydraulic models. Procs 2nd Australasian Conference on Hydraulics and Fluid Mechanics, Auckland, Dec. 1965.
 (b)　Also published in revised form as Univ. of Qld. Dept. Civil Engineering Bull. No. 7 Nov. 1965.

3.　　Saville, T.　Experimental determination of wave set-up. Procs 2nd conference on Hurricanes, Miami, June 1961. U.S. Weather Bureau, National Hurricane Research Project Rep. No. 50, Mar. 1962.

4.　　Dorrestein, R.　Wave set-up on a beach. Procs 2nd conference on Hurricanes, Miami, June 1961, U.S. Weather Bureau, National Hurricane Research Project Rep. No. 50, Mar. 1962.

5.　　Diskin, M.H., Vajda, M.L. and Amir, J.　Piling-up behind low and submerged permeable breakwaters. Procs ASCE Vol. 96, no. WW2, May 1970 pp. 359-372.

6.　　Longuet-Higgins, M.S. and Stewart, R.W.　Radiation stresses in water waves; a physical discussion with applications. Deep-Sea Research Vol. 11, 1964, pp. 529-562.

7.　　Longuet-Higgins, M.S. and Stewart, R.W.　A note on wave set-up. J. Mar. Res. Vol. 21, 1963, pp. 4-10.

8.　　Lundgren, H.　Wave thrust and wave energy level. Procs 10th I.A.H.R. Congress, London, 1963, Vol. 1, pp. 147-151.

9.　　Bowen, A.J., Inman D.L. and Simmons, V.P.　Wave "set-down" and set-up. J. Geophys. Res. Vol. 73, 1968, pp. 2569-2577.

10.　　Bowen, A.J.　The generation of longshore currents on a plane beach. J. Mar. Res. Vol. 27, 1969, pp. 206-215.

11(a)　Bowen, A.J.　Rip currents 1. Theoretical Investigations.
　(b)　Bowen, A.J. and Inman D.L.　Rip currents 2. Laboratory and field observations. J. Geophys. Res. Vol. 74, 1969, pp. 5467-5490.

12.　　Longuet-Higgins, M.S.　Longshore currents generated by obliquely incident sea waves. J. Geophys. Res. Vol. 75, 1970, pp. 6778-6801.

13.　　Longuet-Higgins, M.S.　Recent progress in the study of longshore currents. Chapter in Waves on beaches and resulting sediment transport. Ed. R.E. Meyer Academic Press, 1972, pp. 203-248.

14.   O'Rourke, J.C. and Le Blond, P.H.   Longshore currents in a semicircular
       bay.   J. Geophys. Res. Vol. 77, 1972, pp. 444-452.

15.   Tait, R.J.   Wave set-up on coral reefs.   J. Geophys. Res. Vol. 77, 1972
       pp. 2207-2211.

16.   Komar, P.D.   The mechanics of sand transport on beaches.   J. Geophys.
       Res. Vol. 76, 1971, pp. 713-721.

17.   Bakker, W.T.   Littoral drift in the surf zone.   Rijkswaterstaat,
       Directorate for Water Management and Hydraulic Research, Department for
       Coastal Research.   Study Report WWK 70-16, 1970.

18.   Bakker, W.T.   The influence of longshore variation of the wave height on
       the littoral drift.   Rijswaterstaat, Directorate for Water Management and
       Hydraulic Research, Department for Coastal Research.   Study Report WWK 71-19,
       1971.

19.   Komar, P.D.   Nearshore currents and the equilibrium cuspate shoreline.
       Oregon State Univ., Dept. Oceanogr. Tech. Rep. 239, May 1972.

20.   Eliot, J.   The persistance of rip current patterns on sandy beaches.
       Engineering Dynamics of the Coastal Zone.   I.E. Aust., 1st Australian
       Conference on Coastal Engineering, Sydney May 1973, pp.29-34

21.   Shore Protection, Planning and Design.   U.S. Army Coastal Engineering
       Research Center.   Tech. Rep. No. 4. 3rd. ed. 1966.

22.   Goda, Y.   A synthesis of breaker indices.
       Trans. J.S.C.E., Vol. 2, Part 2, 1970, pp. 227-230.

23.   Galvin, C.J.   Breaker travel and choice of design wave height.
       Procs A.S.C.E., Vol. 95, No. WW2, May 1969, pp. 175-200.

24.   Silvester, R.   Stabilization of sedimentary coastlines.
       Nature, Vol. 188, 1960, pp. 467-469.

LIST OF SYMBOLS

d - water depth d_b - water depth at breakpoint

H - wave height H_b - wave height at breakpoint

H_I- wave height incident to breakwater - in this case measured in water depth d
      = 20 cm

H_o- deepwater wave height

$K_d = \dfrac{H}{H_I}$ - diffraction coefficient

$K_s = \dfrac{H}{H_I}$ - shoaling coefficient relative to water depth d = 20 cm

$K_{ds} = K_d \cdot K_s$ - combined diffraction-shoaling coefficient relative to water depth
          d = 20 cm

T = wave period

x_p= distance between breakpoint and plunge point

β = beach slope angle

$\gamma = \dfrac{H_b}{d_b}$ - breaker index

$\gamma' = C\gamma = \dfrac{H}{d}$ within surf zone landward of plunge point

$\bar{\eta}_{swl}$ - wave set-up at still water line relative to still water level in deep
        water

$\bar{\eta}'_{swl}$ - wave set-up at still water line relative to mean water level at
        breakpoint.

Figure 1

(a)

(b)

After Breakwater Construction   Before Breakwater Construction

Figure 2

(a) Wave Generated Currents   (b) Refraction Diagram

Figure 3

Figure 4

WAVE HEIGHT CONTOURS
in centimetres

Exposed zone

Sheltered zone

Run-up Limit

Plunge point
Break point

T = 1·5 s   H = 9·1 m
d = 20 cm

Figure 5

WAVE SET-UP CONTOURS
in centimeters

Exposed zone

Sheltered zone

Run-up Limit

Plunge point
Break point

T = 1·5 s   H = 9·1 cm
d = 20 cm

Figure 6

H_I = 9·1cm   T = 1·5 s
Beach slope   1 in 10
Set-up slope   1 in 26

Profile A

Profile B

Profile C

Profile D

Distance from S.W.L. in metres

Figure 7

Figure 8

Figure 9

Figure 10

H_I = 9·1 cm

T = 1·5 s

Profile 1

Profile 2

Profile 3

Profile 4
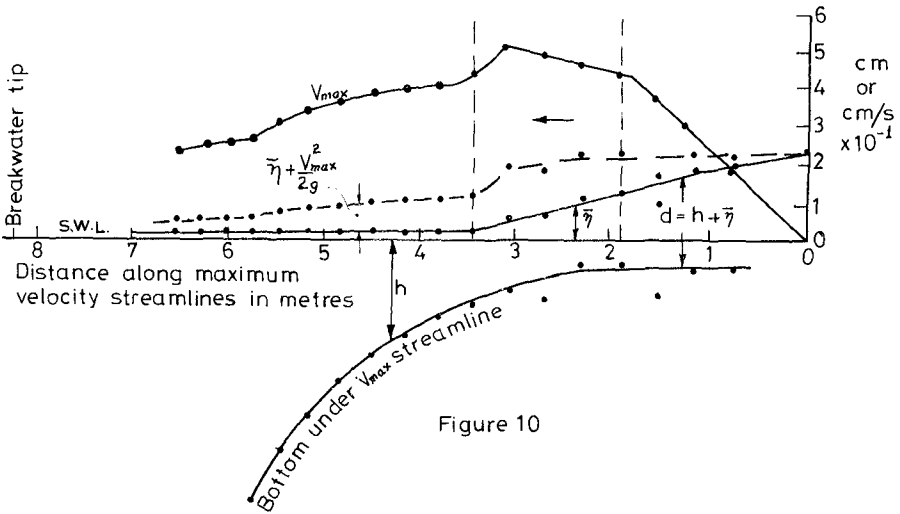
Distance from S.W.L. in metres
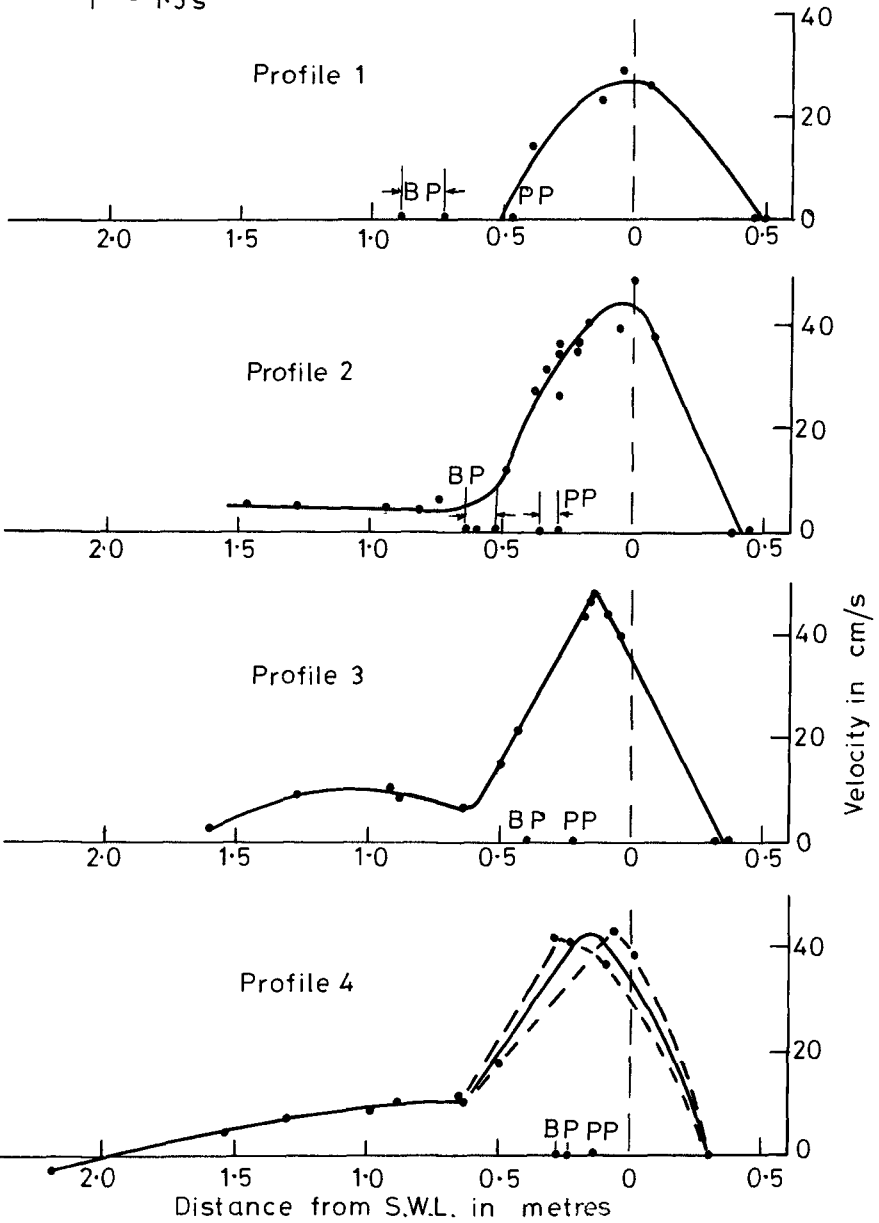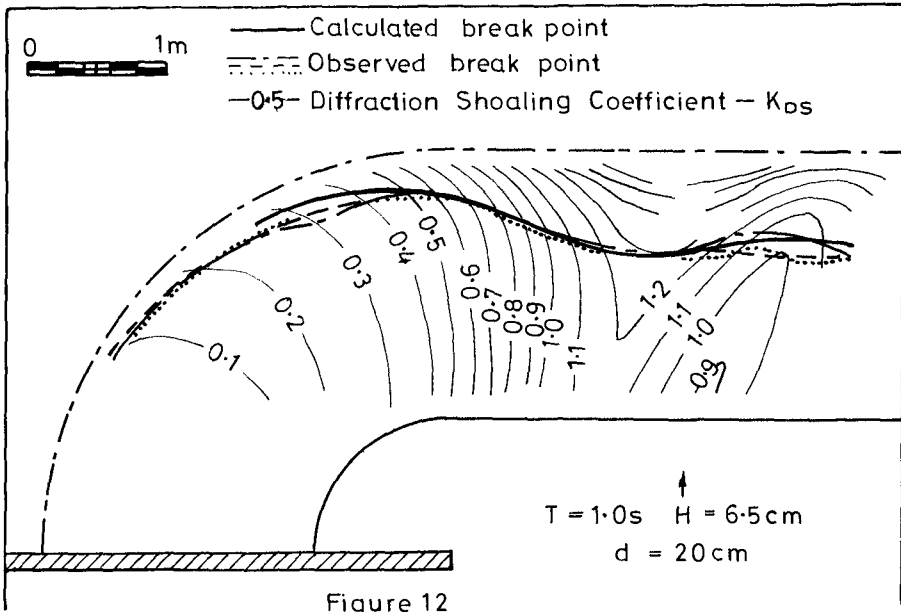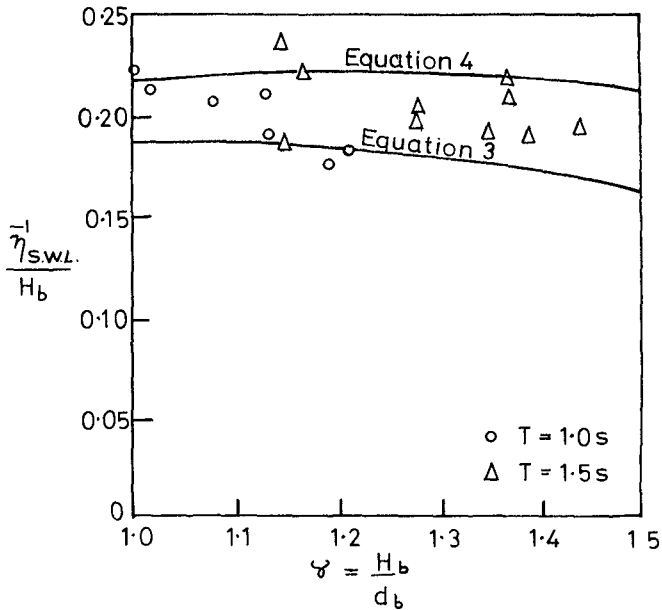
Figure 11

Figure 12

Figure 13

CHAPTER 116

ESTIMATION OF WAVE OVERTOPPING
QUANTITY OVER SEA-WALLS

by

Akira Takada

Associate Professor, Department of Civil Engineering,
Chubu Institute of Technology
Kasugai, Japan

ABSTRACT

This paper tried to formulate the wave overtopping quantity by using a model of overtopping mechanism. Namely, the author investigated the problem by applying the "Calculation method for discharge of overflow weirs" i.e. the method of Fukui et al. (1963) and Shi-igai et al. (1970)[2].

INTRODUCTION

Actually it is very difficult to prevent perfectly the wave overtopping caused by irregular waves. Therefore, the sea-wall must be designed based on the conception of allowable wave overtopping quantity, on the premise that a drain system is constructed behind the sea-wall.

The conventional method of determining the crest height of sea-walls is based on the height of wave run-up. Recently, however, there is a tendency to introduce the wave overtopping quantity as the design criteria of sea-walls. Therefore, it is urgently required to establish a method of calculating the wave overtopping quantity.

According to previous researches, it has been disclosed that the wave overtopping quantity on a sea-wall has a close correlation with the spatial profile of wave run-up and the time history of surface elevation on a vertical sea-wall. At present, efforts are paid for finding out response functions of the above-mentioned factors and the quantity of the wave overtopping[1]~[4].

The author proposed the calculation formula of the wave overtopping quantity by using the spatial profile of wave run-up at the 13th Conference on Coastal Engineering in 1972[3]. The said calculation formula comprise a controversial problem in the determination of the spatial profile of wave run-up for the complicated cross-sectional shape of sea-walls. Here, as a calculation formula that is free from any unreasonable point as a physical model and involves general applicable features, the author investigated the problem by applying the "Calculation method for discharge of overflow weirs" i.e. the method of Fukui et al.(1963) and Shi-igai et al.(1970)[2].

Namely, overtopping waves on vertical sea-walls are regarded as complete overflows at sharp crest weirs[2] and the characteristics of the discharge coefficient of overtopping waves to the vertical sea-walls were investigated empirically.

This paper tried to formulate wave run-up height and wave overtopping quantity on vertical sea-walls in the bottom slope of 1/10.

THE CALUCULATION FORMURA OF WAVE
RUN-UP HEIGHT ON VERTICAL SEA-WALLS

1. THE CLASSIFICATION OF THE WATER DEPTH AT THE TOE OF SEA-WALLS

The experiments made so far show that the water depth at the toe of sea-walls where causes the maximum run-up height corresponds nearly to the breaking point of progressive waves are approximately given by Eq.(1) proposed by Miche (1944)[5].

$$(H_b/L_b)_p = 0.142 \tanh 2\pi(h_b/L_b)_p, \tag{1}$$

for the sea-bottom slope of 1/10,
Where $(h_b)_p$ is the water depth of breaking of progressive waves, $(L_b)_p$ is the wave length at $(h_b)_p$ and $(H_b)_p$ is the wave height at $(h_b)_p$.
The calculated values of Eq.(1) are shown in the solid line of Fig.1. The solid line of Fig.1 shows the relation between the equivalent deep-water-wave steepness H_0'/L_0 and $(h_b)_p/L_0$.
When the wave after breaking hits a vertical sea-wall, however, there occur large amount of spray. The water depth at the toe of sea-walls where the spray height of wave run-up become a maximum for a given H_0'/L_0 value may be given by experiments as Eq.(2).

$$H_0'/L_0 = 0.21 \tanh (2\pi h_{R'max}/L_0), \tag{2}$$

for the sea-bottom slope of 1/10,

Where H_0' is the equivalent deep-water-wave height, L_0 is the wave length in deep water and $h_{R'max}$ is the water depth at the toe of a sea-wall where the spray height of wave run-up becomes a maximum.

The calculated values of Eq.(2) are shown in the dotted line of Fig.1.

2. THE CALCULATION FORMURA OF WAVE RUN-UP HEIGHT

By arranging the experimental values of wave run-up height with $(h_b)_p$ as boundary, the calculational formula may be such as follows.

2.1 The region of $h \gtreqqless (h_b)_p$

In this region, the wave run-up height is thus nearly equal to the wave crest height of the standing wave. The wave crest height of the second-order approximation solution for finite amplitude standing wave is given by Eq.(3) proposed by Miche (1944)[5].

$$\frac{R}{H_0'} = \left[1 + \frac{\pi}{4} \frac{H}{L} \left\{ 3 \coth^3(2\pi\frac{h}{L}) + \tanh(2\pi\frac{h}{L}) \right\} \right] S, \tag{3}$$

Where R is the wave run-up height from the still water level, h is the water depth at the toe of a sea-wall, H is the incident wave height at h, L is the incident wave length at h, and S is the shoaling factor at h.
The S values are given by Eq.(4) from the small amplitude wave theory.

$$S = \frac{H}{H_0'} = \sqrt{\frac{(\sinh 4\pi\frac{h}{L})(\coth 2\pi\frac{h}{L})}{\sinh 4\pi\frac{h}{L} + 4\pi\frac{h}{L}}} \quad , \tag{4}$$

The other hand, the relation between H_0'/L_0 and H/L, and the relation between h/L_0 and h/L can be expressed as Eq.(5) and Eq.(6) by the small amplitude wave theory, respectively.

$$\frac{H}{L} = \left(\frac{\sinh 4\pi\frac{h}{L}}{\sinh 4\pi\frac{h}{L} + 4\pi\frac{h}{L}}\right)^{1/2} (\coth 2\pi\frac{h}{L})^{3/2} \frac{H_0'}{L_0}, \tag{5}$$

$$\frac{h/L}{\tanh(2\pi\, h/L)} = h/L_0 \quad , \tag{6}$$

The calculated values of Eq.(3) either give wave run-up height close to the experimental values, or values somewhat over the experimental values[3),4)].

2.2   The region of $h = 0\sim(h_b)_p$

(1)   The essential run-up height of wave, R

In the region under researches, it is known experimentally that the R values are almost proportional to the h values[6)].
In consequence, if the R values on the vertical sea-walls are obtained, the calculational formula in this region will then be given as Eq.(7) by approximation.

$$\frac{R}{H_0'} = \left\{\frac{(R_b)_p}{H_0'} - \frac{R_0}{H_0'}\right\} \frac{h}{(h_b)_p} + \frac{R_0}{H_0'} \quad , \tag{7}$$

where $(R_b)_p$ is wave run-up height on vertical sea-walls for $h = (h_b)_p$ and R_0 is wave run-up height on vertical sea-walls for beach line (h = 0).
The experimental values of R/H_0' for the sea-bottom slope of 1/10 is shown in Fig.2.   The experimental values represented in the solid line, as shown, by approximation, may be expressed by Eq.(8).

$$R_0/H_0' = 0.18 \ (H_0'/L_0)^{-1/2} \quad , \tag{8}$$

for the sea-bottom slope of 1/10,

The $(R_b)_p/H_0'$ values can be calculated by Eq.(9) from Eq.(3).

$$\frac{(R_b)_p}{H_0'} = \left[1 + \frac{\pi}{4} (\frac{H_b}{L_b})_p \left\{ 3 \coth^3 2\pi(\frac{h_b}{L_b})_p \right.\right.$$
$$\left.\left. + \tanh 2\pi(\frac{h_b}{L_b})_p \right\} \right] (S_b)_p, \tag{9}$$

Where $(S_b)_p$ is the shoaling factor for $h = (h_b)_p$ and can be calculated by Eq.(4). The $(S_b)_p$ values are also obtainable with Eq.(10).

$$(S_b)_p = \frac{(H_b)_p}{H_0'} = \frac{(H_b/L_b)_p}{H_0'/L_0} \cdot \frac{(h_b)_p/L_0}{(h_b/L_b)_p} \quad , \tag{10}$$

(2) The spray height of wave run-up, R'

a) The region of $h = h_{R'max} \sim (h_b)_p$

The calculated values of Eq.(3) were found to explain fairly well the experimental R' values in the region. Calculation of the R' values may thus be approximately by Eq.(11) from Eq.(3).

$$\frac{R'}{H_0'} = \left[1 + \frac{\pi}{4} \frac{H}{L} \left\{ 3\coth^3(2\pi\frac{h}{L}) + \tanh(2\pi\frac{h}{L}) \right\} \right] S \quad , \tag{11}$$

b) The region of $h = 0 \sim h_{R'max}$

The results of author's experimental research show that in the region the R'/H_0' values are obtainable approximately by Eq.(12).

$$\frac{R'}{H_0'} = \left(\frac{R'_{max}}{H_0'} - \frac{R_0'}{H_0'} \right) \left(\frac{h}{h_{R'max}} \right)^2 + \frac{R'_0}{H_0'} \quad , \tag{12}$$

Where R'_{max} is the maximum spray height of wave run-up for the wave of a given H_0'/L_0 value. R'_{max} can be calculated by Eq.(13) from Eq.(11).

$$\frac{R'_{max}}{H_0'} = \left[1 + \frac{\pi}{4} \left(\frac{H}{L} \right)_{R'max} \left\{ 3\coth^3 2\pi \left(\frac{h}{L} \right)_{R'max} \right. \right.$$

$$\left. \left. + \tanh 2\pi \left(\frac{h}{L} \right)_{R'max} \right\} \right] S_{R'max} \quad , \tag{13}$$

where $S_{R'max}$ is the shoaling factor for $h = h_{R'max}$ and can be calculated by Eq.(4). The $S_{R'max}$ values are also obtainable with Eq.(14).

$$S_{R'max} = \frac{H_{R'max}}{H_0'} = \frac{(H/L)_{R'max}}{H_0' / L_0} \cdot \frac{h_{R'max}/L_0}{(h/L)_{R'max}} \quad , \tag{14}$$

where $(H/L)_{R'max}$ is shallow-water-wave steepness for $h = h_{R'max}$, and R_0'/H_0' is the spray height of wave run-up on vertical sea-walls for beach line $(h = o)$.

The experimental values of R_0'/H_0' for the sea-bottom slope of 1/10 are shown in Fig.2. The experimental values represented in the dotted line, as shown, by approximation, may be expressed by Eq.(15).

$$R_0'/H_0' = 0.22(H_0'/L_0)^{-1/2} \quad , \tag{15}$$

for the sea-bottom slope of 1/10,

(3) Adaptability of the calculational formula

Fig.3 shows the comparison between calculated values and experimental values[4],[6]~[8]. The solid line is the calculated values of R/H_0' and the dotted line is the calculated values of R/H_0'. As described, the calculational formula exhibits good fitness to the experimental results. It is, therefore, well adaptable for actual problem.

In the region after breaking waves, the wave set-up has to be taken into consideration. This was, however, neglected in the present research. Taking account of the phenomenon, accuracy of the calculational formula should be improved still further.

CALCULATIONAL FORMURA OF THE WAVE OVERTOPPING QUANTITY OVER VERTICAL SEA-WALLS

1.   APPLICATION OF THE WEIR DISCHARGE CALCULATIONAL METHOD[1],[2]

As indicated in Fig.4, the discharge calculational method for a sharp crest weir will be applied to obtain the quantity of wave overtopping[1],[2].

The quantity of wave overtopping Q of width B per a wave period is represented by Eq.(16) by using the method of Shi-igai et al. (1970)[2].

$$Q = \int_{t_u}^{t_d} q(t)dt = \frac{2}{3}\sqrt{2g}\ B\int_{t_u}^{t_d} C(t)$$

$$\times \left[\left\{\eta^*(t) + h_a - H_c\right\}^{3/2} - (h_a)^{3/2}\right] dt, \qquad (16)$$

where $q(t)$ is the discharge of wave overtopping per a unit time at time t, H_c is the crown height of a sea-wall from the still water level, $C(t)$ is the discharge coefficient of overtopping wave at time t, $\eta^*(t)$ is the time history of the surface elevation for a vertical sea-wall at the wave over-topping time, (h_a) is the water head of approach velocity, (t_u) is time when a wave of a given period start overtopping, (t_d) is the time when the overtopping is terminated, and g is the acceleration of gravity.

Here, for convenienc' sake of practical use, (h_a) is disregarded and the time history of surface elevation $\eta(t)$ on a vertical sea-wall for non-overtopping wave is used instead of $\eta^*(t)$, and erros caused from above assumptions are considered to be included in $C(t)$. On the other hand, assuming that an average value of times is used for $C(t)$ which is defined by a constant K, Q is given by Eq.(17), as proposed by Shi-igai et al. (1970)[2].

$$Q = \frac{2}{3}\sqrt{2g}\ BK\int_{t_u}^{t_d} \left\{\eta(t) - H_c\right\}^{3/2} dt, \qquad (17)$$

where K is the average coefficient of wave overtopping discharge.

Here, as shown in Fig.5, $\eta(t)$ is assumed to have approximately a trapezoidal profile, then Q is further given by follows, as proposed by the author (1972)[4].

$$Q = \frac{2}{3}\sqrt{2g}\ BK \left[2\int_{t_u}^{t_d} \left\{\frac{(t - t_u)R}{(t_R)_u - t_u} - H_c\right\}^{3/2} dt\right.$$

$$\left. +\int_{(t_R)_u}^{(t_R)_d} (R - H_c)^{3/2} dt, \right. \qquad (18)$$

$$= \frac{4}{15} \sqrt{2g} \; BK(R - H_c)^{3/2} \left\{ (1 - \frac{H_c}{R})(t_{oo} - t_{RR}) \right.$$

$$\left. + \frac{5}{2} t_{RR} \right\} , \tag{19}$$

(t_{RR}) varies with H/L and h/L. Here, the values of (t_{RR}) are assumed to have approximately 0.05T. Therefore, the calculational formula of Q is expressed by Eq.(20), as proposed by the author (1972)[4].

$$Q = \frac{4}{15} \sqrt{2g} \; BK \; (R - H_c)^{3/2} \left\{ (1 - \frac{H_c}{R})(\frac{t_{oo}}{T} - 0.05) \right.$$

$$\left. + 0.125 \right\} T , \tag{20}$$

where T is a wave period, and (t_{oo}) is shown in Fig.5. The (t_{oo}) values are expressed by follows[4].

(1)   The (t_{oo}) values for h > 0

$$t_{oo}/T = (t_o/T)_d - (t_o/T)_u , \tag{21}$$

$$= 2(t_o/T), \; \text{for} \; \frac{1}{8} < t_o/T < \frac{1}{4} , \tag{22}$$

Here, the values of t_o/T are calculated from $\eta(t)$. Eq.(23) is $\eta(t)$ by the second-order approximation solution of finite amplitude standing wave.

$$\eta(t) = H\cos 2\pi\frac{t}{T} + \frac{\pi}{4} \frac{H}{L} H(3\coth^3 2\pi\frac{h}{L}$$

$$- \coth 2\pi\frac{h}{L})\cos 4\pi\frac{t}{T} + \frac{\pi}{4} \frac{H}{L} H\coth 4\pi\frac{h}{L} , \tag{23}$$

with $\eta(t) = 0$ in Eq.(23), the values of t_o/T are calculated from Eq.(24).

$$\cos(2\pi\frac{t_o}{T}) = \frac{1}{\pi\frac{H}{L}} \left[\left\{ 1 + \frac{\pi^2}{2}(\frac{H}{L})^2 \; MN\tanh 2\pi\frac{h}{L} \right\}^{1/2} - 1 \right] , \tag{24}$$

where

$$M = \left\{ 3 \coth^2(2\pi h/L) - 1 \right\} \coth(2\pi h/L) , \tag{25}$$

$$N = 3 \coth^4(2\pi h/L) - 2 \coth^2(2\pi h/L) - 1 , \tag{26}$$

The (t_{oo}/T) values are then such as in Fig.6.

(2)   The (t_{oo}) value for beach line (h = 0)

$$t_{oo}/T = 0.25 , \tag{27}$$

2. EXPERIMENTAL RESULTS OF THE K VALUES

(1) The classification of the h values

By the experiments performed, the K values are known to differ largely with the (h) values[4]. The K values were thus studied for three regions, i.e. the region of $h > (h_b)_s$, the region of $h = (h_b)_p \sim (h_b)_s$ and the region of $h = 0 \sim (h_b)_p$, as shown in Fig.7.

Here, $(h_b)_s$ is the water depth of breaking for standing waves and can be calculated from Eq.(28) proposed by Kishi (1959)[10].

$$\left(\frac{H_b}{L_b}\right)_s = \frac{-\coth 2\pi \left(\frac{h_b}{L_b}\right)_s + \sqrt{\coth^2 2\pi \left(\frac{h_b}{L_b}\right)_s + 0.350 \operatorname{cosech}^2 2\pi \left(\frac{h_b}{L_b}\right)_s}}{0.592\pi \operatorname{cosech}^2 2\pi (h_b/L_b)_s} \quad , \quad (28)$$

where $(H_b)_s$ is the height of the incident wave which causes breaking of standing waves and $(L_b)_s$ is the wave length for $h = (h_b)_s$.

(2) Experimental results and the discussions

The K values were calculated with Eq.(29) from the Q_{exp} values and Eq.(20).

$$K = \frac{Q_{exp}(R - H_c)^{-3/2}}{\frac{4}{15}\sqrt{2g} \ B \left\{ (1 - \frac{H_c}{R})(\frac{t_{oo}}{T} - 0.05) + 0.125 \right\} T} \ , \quad (29)$$

where Q_{exp} are experimental values of wave overtopping quantity.
Here, for the R and (t_{oo}) values in Eq.(29), those by calculational formula mentioned were used.
Fig.8 (a) shows the relation between K_s and H_0'/L_0 for the region $h > (h_b)_s$. As in Fig.8 (a), the K_s values are not much influenced by H_0'/L_0. Though the experimental values are in considerable scattering, the average value can be taken approximately as $K_s = 0.38$. Therefore, the K_s values are smaller than the value of the discharge coefficient of sharp crest weirs ($K \fallingdotseq 0.65$).
Fig.8 (b) shows the relation between K_s and H_c/H_0' for the region of $h > (h_b)_s$. The K_s values are not much influenced by H_c/H_0', as shown in Fig.8 (b), and the K_s value in average is approximately 0.38.
Fig.9 (a) shows the relation between K_p and H_0'/L_0 for the region of $h = 0 \sim (h_b)_p$. The K_p values are not much influenced by the H_0'/L_0 values, as shown in Fig.9 (a).
Fig.9 (b) shows the relation between K_p and H_c/H_0' for the region of $h = 0 \sim (h_b)_p$. It is thus seen that, though the scattering in experimental values are fairly large, the K_p values become smaller with larger H_c/H_0' values. And the K_p values are generally smaller than the K_s values. If, then, the K_p values are represented by a solid line as in Fig.9 (b), the calculational formula for the K_p values is Eq.(30).

$$\log_{10} K_p = -(0.523 + 0.699 \frac{H_c}{H_0'}) \ , \quad (30)$$

(3) The calculation formula of the K values

From these experiment and the discussions, the K calculation formula are obtained by the following equations.

a) The region of standing waves $\left[h > (h_b)_s \right]$

$$K_s = 0.38 \ , \tag{31}$$

b) The region of transition into breaking waves
waves $\left[h = (h_b)_p \sim (h_b)_s \right]$

$$K_b = (K_s - K_p)\left\{ \frac{h - (h_b)_p}{(h_b)_s - (h_b)_p} \right\}^2 + K_p \ , \tag{32}$$

c) The region after breaking waves $\left[h = 0 \sim (h_b)_p \right]$

$$\log_{10} K_p = -(0.523 + 0.699 \frac{H_c}{H_0}) \ , \tag{30}$$

for the sea bottom slope of 1/10,

(4) Adaptability of the K calculational formulas

Fig.10 shows the comparison between calculated values and experimental values[3],[4],[9]. It is thus seen that, though the scattering in experimental values are fairly large, the calculated values indicate fairly accurately the tendency of the experimental values. However, it is for future study to improve the accuracy of these calculation formulas.

CONCLUSIONS

The author could experimentally obtain the calculation formulas both for wave run-up height and wave overtopping quantity on vertical sea-walls in the sea-bottom slope of 1/10.
The result obtained by the present study may be summarized as follows.

(1) In the region of $h > (h_b)_p$, the calculation formula of wave run-up height is given by Eq.(3).

(2) In the region of $h = 0 \sim (h_b)_p$, the calculation formula of wave run-up height is experimentally given by Eq.(7). And the calculation formulas of spray height of wave run-up are experimentally given by Eq.(11) and Eq.(12).

(3) The calculation formula of the wave overtopping quantity is given by Eq.(20).

(4) The average coefficients of wave overtopping discharge are generally smaller than the average value of the discharge coefficient for a sharp crest weir.

(5) The calculation formulas of the K values in Eq.(20) are given approximately Eq.(30)~Eq.(32).

ACKNOLEDGMENTS

APPENDIXES

      The method employed in this study is similar to those of Fukui et al.
(1963)[1] and Shi-igai et al. (1970)[2].

      The method of analysing the wave overtopping by approximating it
with the steady weir overflow was originally presented by Fukui et al.
in their study "On the Tsunami Wave Overtopping" (1963)[1].
Later, Shi-igai et al. (1970)[2], by applying this method to their study
"On the Overtopping of Short-periodic Waves," investigated the character-
istics of the virtual wave run-up, in which the time history curve of
surface elevation of a triangular waveform and a constant discharge
coefficient of wave overtopping were assumed.
With all the results these studies have attained, some important points
still remain opened to further studies.

Namely:
1.   The results are insufficient for the quantitative interpretation of
the characteristics of the height of run-up, the time histories of surface
elevation, and the discharge coefficient of wave overtopping.

2.   A constant discharge coefficient of wave overtopping was assumed.
Actually, however, it varies significantly with several parameters such
as: the water depth at the toe of sea-walls; the crown height of sea-
walls; wave steepness; sea-bottom slopes; the slope of sea-walls and
others.

3.   The formula for the wave overtopping calculation affords neither
enough accuracy nor wide applicability.

4.   The triangular approximation by Shi-igai et al. (1970)[2] for the
time histories of surface elevation does not show good agreements with
observations. Besides, in this study, the fundamental wave form assumes
small amplitudes, which is inadequate for analysing such an involved
phenomena as wave overtopping.

5.   Shi-igai et al. (1970)[2] presented the virtual wave run-up concept
and studied the characteristics of this phenomena. However, this
approach could not permit positive utilization of the results of other
studies previously performed.

Thus, intending to solve these problems, after examing extensive·experi-
mental results, the authors have presented the formula for the calcula-
tion of the height of wave run-up and the quantity of wave overtopping
on vertical sea-walls.

REFERENCES

1) Fukui, Y., M. Nakamura, H. Shiraishi and Y. Sasaki: Hydraulic
   study on tsunami, Coastal Engineering in Japan, Vol. VI, 1963,
   pp. 68 ~ 82.

2) Shi-igai, H. and T. Kono: Anaytical approach on wave overtopping
   on levees, Proc. 12th Coastal Engineering Conference, 1970,
   pp. 563 ~ 573.

3) Nagai, S. and A. Takada: Relations between run-up and overtopping
   of waves, Proc. 13th Coastal Engineering Conference, 1970, pp.
   1975 ~ 1992.

4) Takada, A: Wave overtopping quantity correlated to the surface
   elevation of finite amplitude clapotis, Proc. JSCE, Vol. 201,
   1972, pp. 61 ~ 76 (in Japanese).

5) Miche, M.: Movements ondulatoires de la mer en profondeur constante
   ou decrissant (I~IV), Amales des Ponts et Chaussées, Vol. 121,
   1944, pp. 25 ~ 78, 131 ~ 164, 270 ~ 292, 367 ~ 406.

6) Toyoshima, O., N. Shuto and H. Hashimoto: Wave run-up on Coastal
   structures, Coastal Engineering in Japan, Vol. IX, 1966, pp.
   119 ~ 126.

7) Saville, T. Jr.: Wave run-up shore structures, Trans, ASCE, Vol.
   123, 1958, pp. 139 ~ 150.

8) Ishihara, T., Y. Iwagaki and Y. Suzuki: Design of sea-walls ——
   Specially its effective height ———— , Coastal Engineering in
   Japan, Vol. 2, 1955, pp. 57 ~ 70.

9) Iwagaki, Y., A. Shima and M. Inoue: Effects on wave height and
   sea water level or wave overtopping and wave run-up, Coastal
   Engineering in Japan, Vol. VIII, 1965, pp. 141 ~ 151.

10) Kishi, T.: The possible height gravity waves in shallow water,
    Coastal Engineering in Japan, Vol. II, 1959, pp. 9 ~ 16.
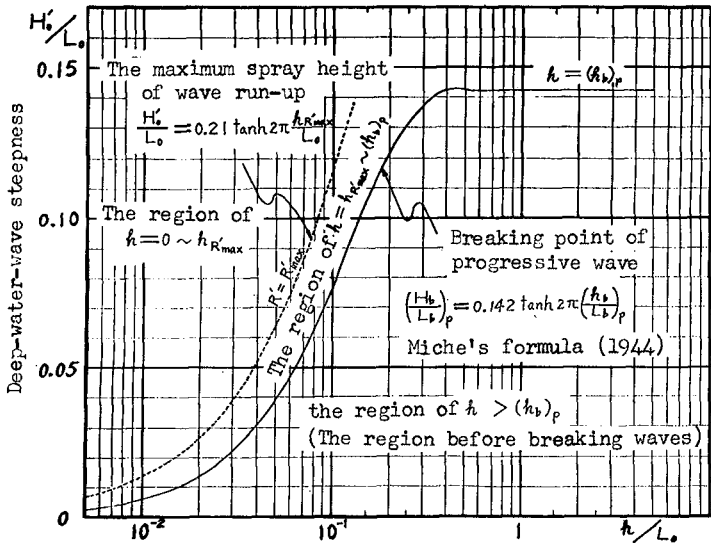
Fig. 1. The classification of the water depth at the toe of
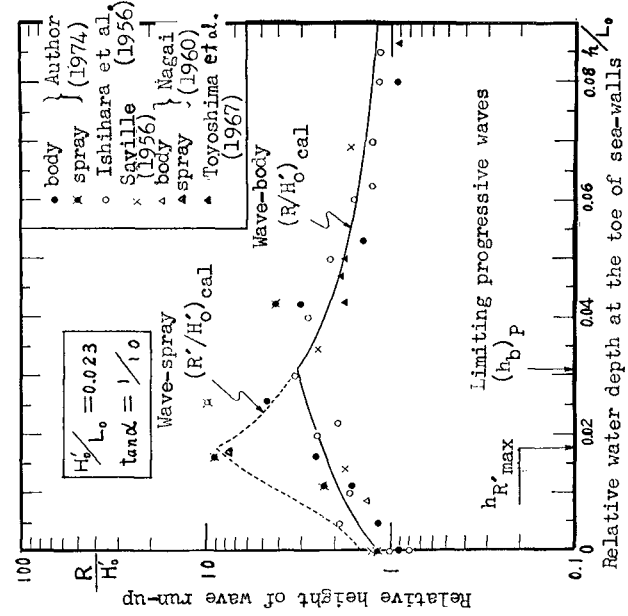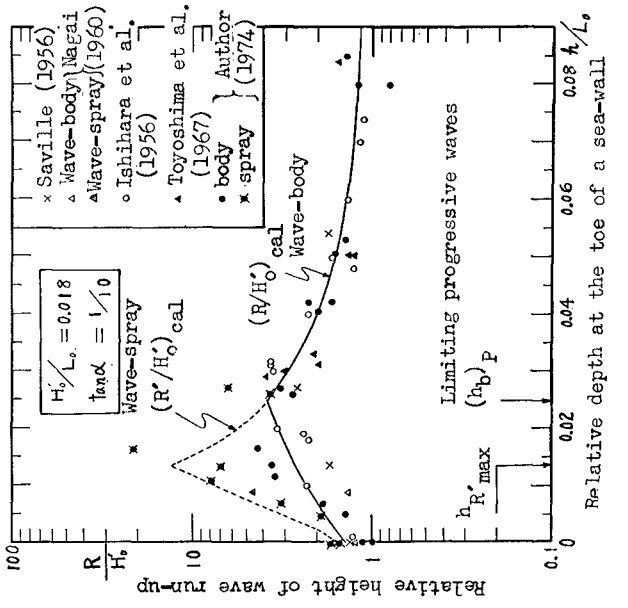vertical sea-walls for the bottom slope of 1/10.
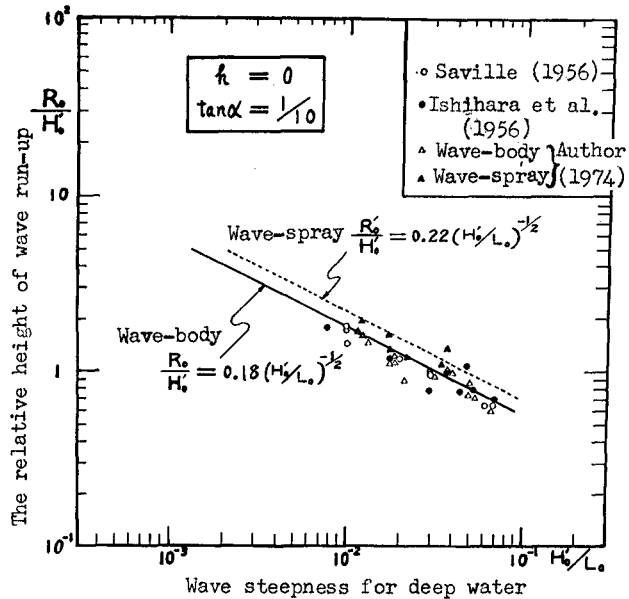
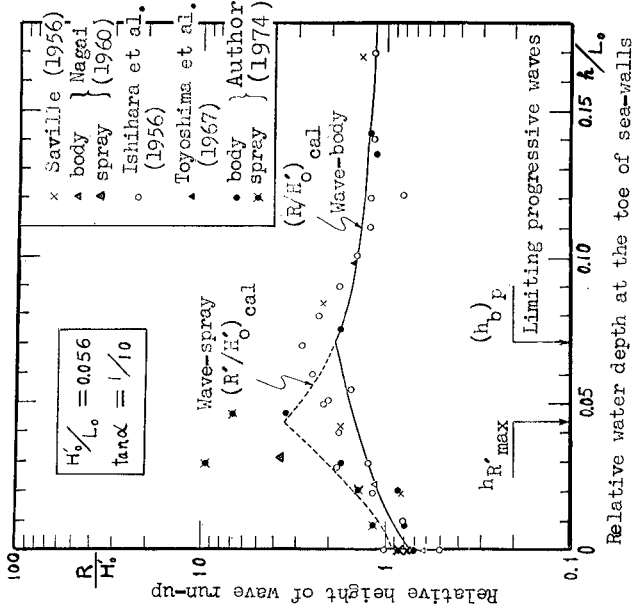Fig. 2. Relations between R/H'_0 and H'_0/L_0 for $h = 0$.

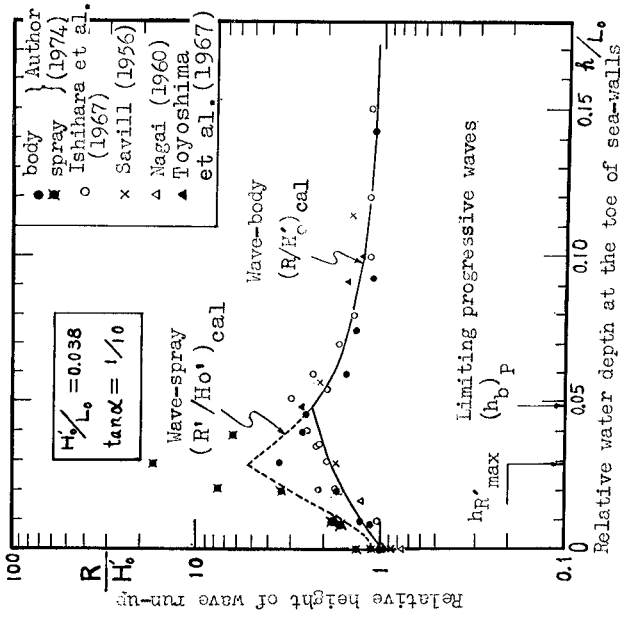(a) Results for $H_o'/L_o = 0.018$ and the bottom slope of 1/10

(b) Results for $H_o'/L_o = 0.023$ and the bottom slope of 1/10

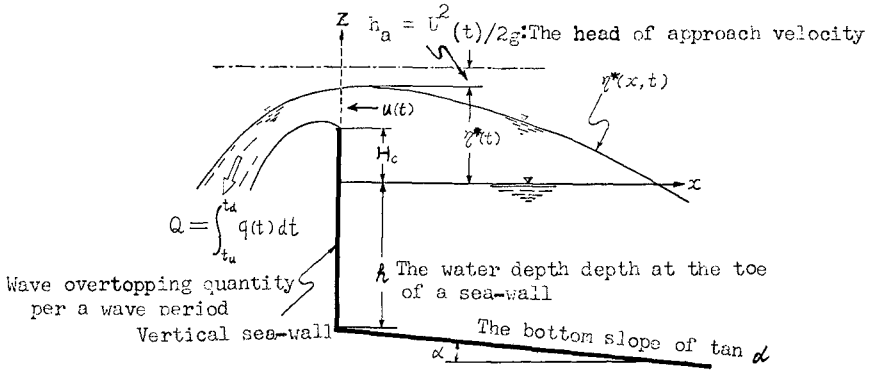Fig. 3. Comparison between calculated and experimental values of the height of wave run-up for vertical sea-walls.

(c) Results for $H_o'/L_o = 0.038$ and the bottom slope of 1/10

(d) Results for $H_o'/L_o = 0.056$ and the bottom slope of 1/10

Fig. 3. Comparison between calculated and experimental values of the height of wave run-up for vertical sea-walls.

Fig. 4(a). Application of the discharge calculation method of the overflow weir for wave overtopping quantity.[2)]
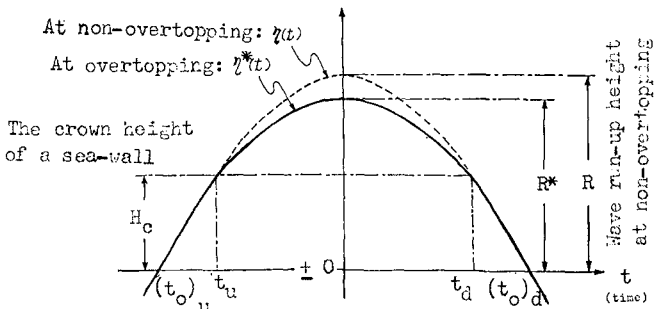
Fig. 4(b). Sketch of time history of the surface elevation at wave run-up.
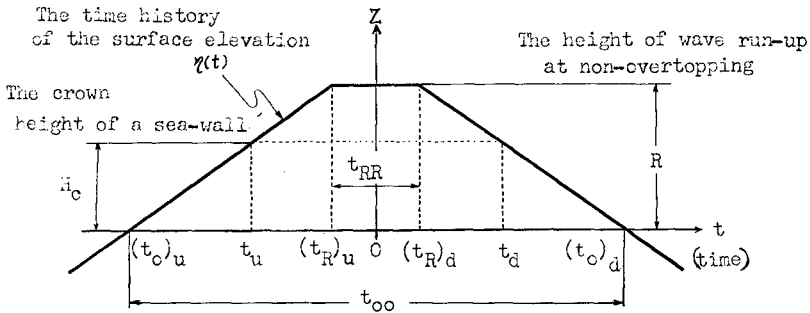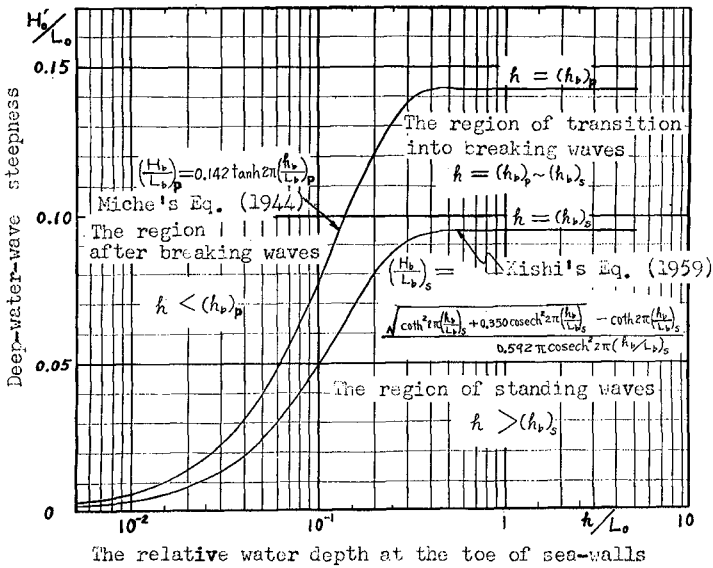

Fig. 5. The assumption of the time history of the surface elevation.
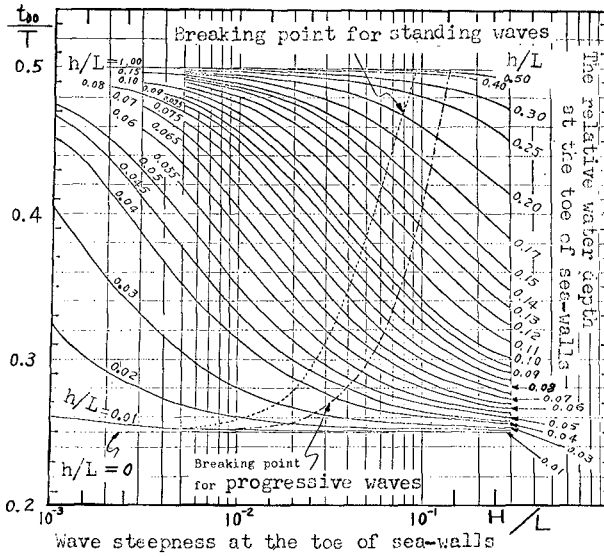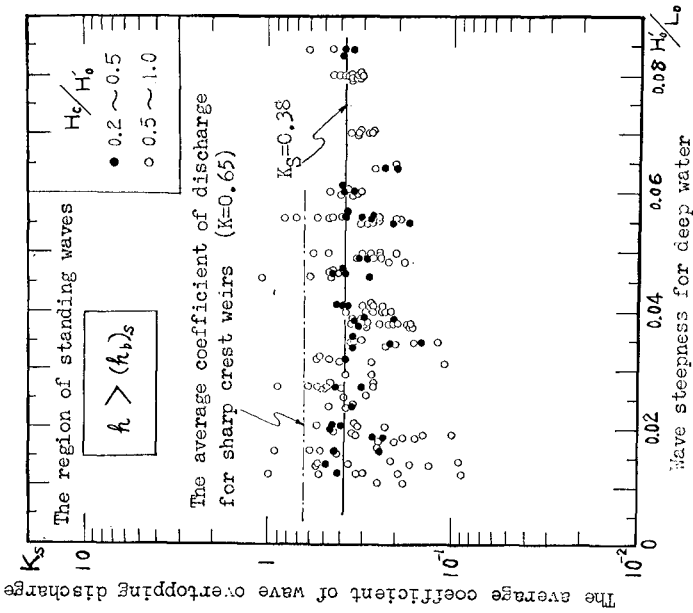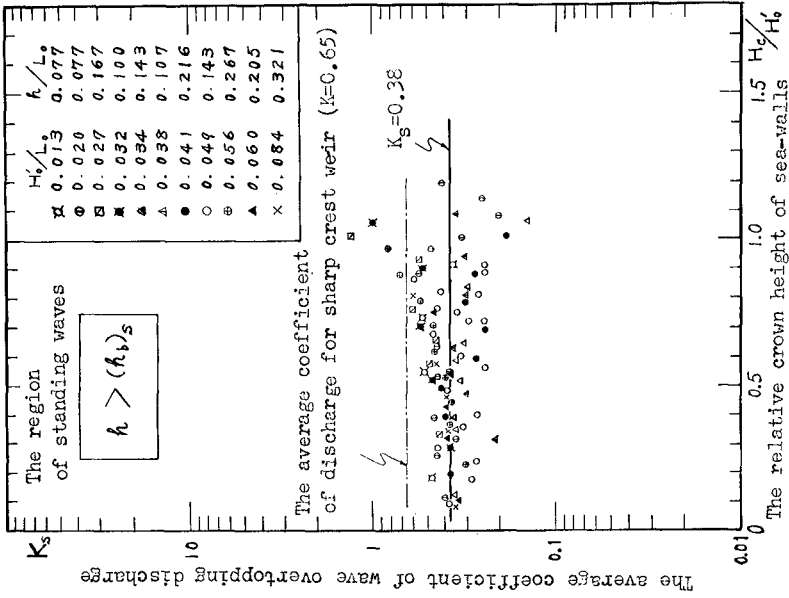
Fig. 6.   Calculated value of t_{oo}/T.

Fig. 7.   The classification of the water depth at the toe of vertical sea-walls for the bottom slope of 1/10.

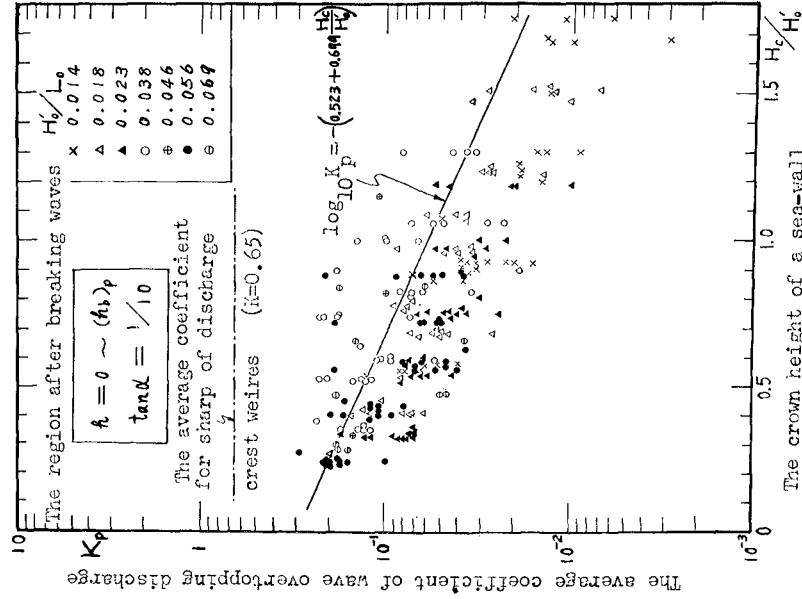(b) Relations between K_S and the crown height of vertical sea-walls

(a) Relations between K_S and wave steepness

Fig. 8. Experimental results of the average coefficient of wave overtopping discharge for $h \geqq (h_b)_S$.
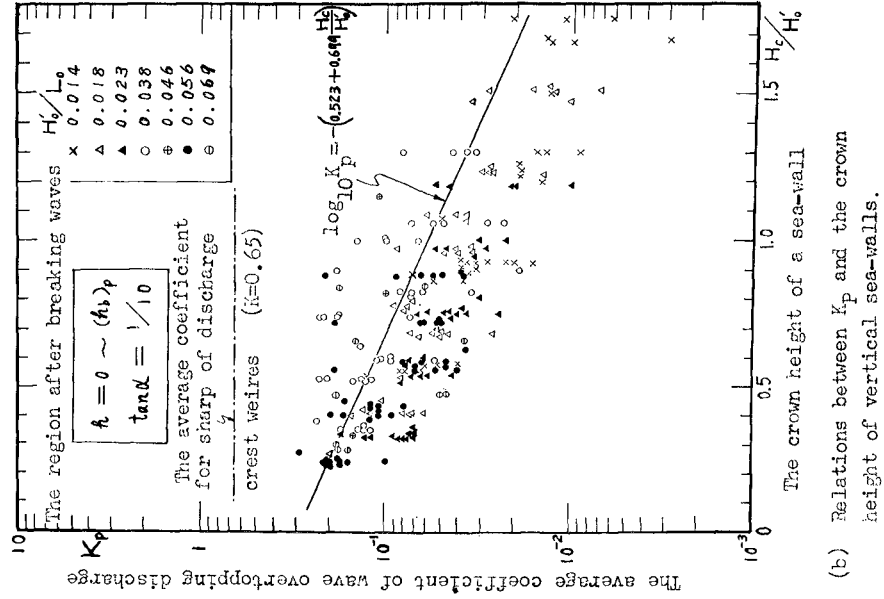
(b) Relations between K_p and the crown
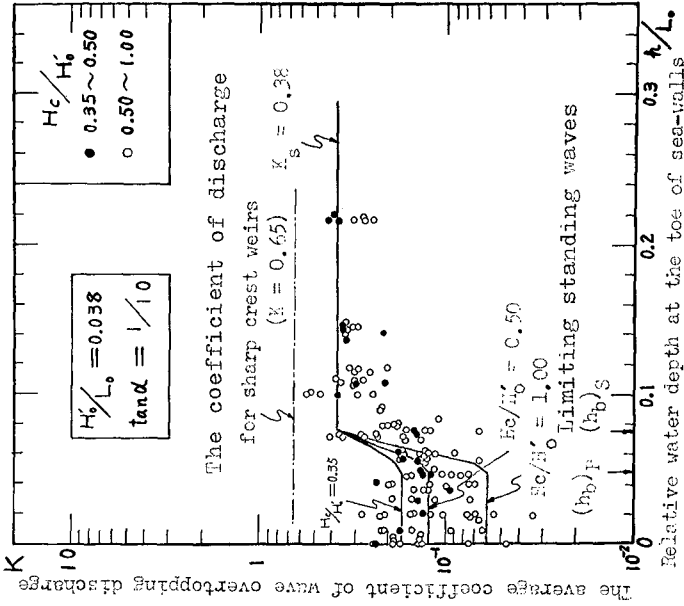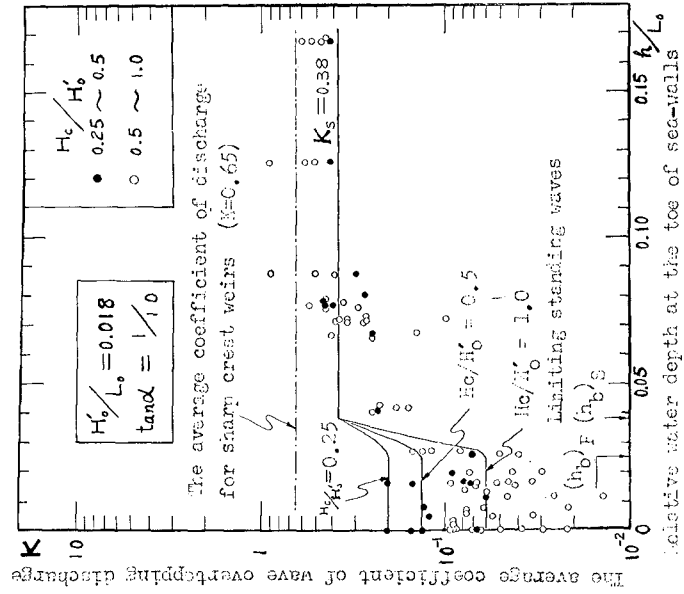   height of vertical sea-walls.

(a) Relations between K_p and wave steepness

Fig. 9.   Experimental results of the average
          coefficient of wave overtopping
          discharge for $h = 0 \sim (h_b)_p$.

(b) Results for $H_o'/L_o = 0.038$ and the bottom slope of $1/10$

(a) Results for $H_o'/L_o = 0.018$ and the bottom slope of $1/10$

Fig. 10. Comparison between calculated and experimental values of the average coefficient of wave overtopping discharge for vertical sea-walls.
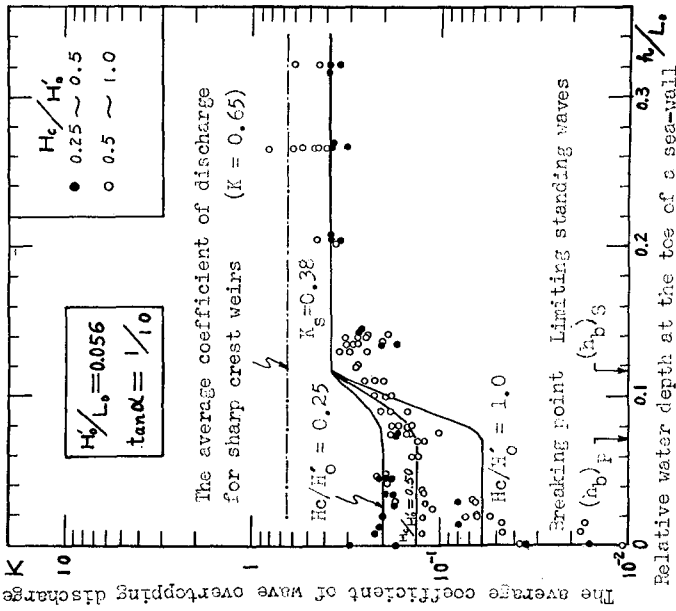
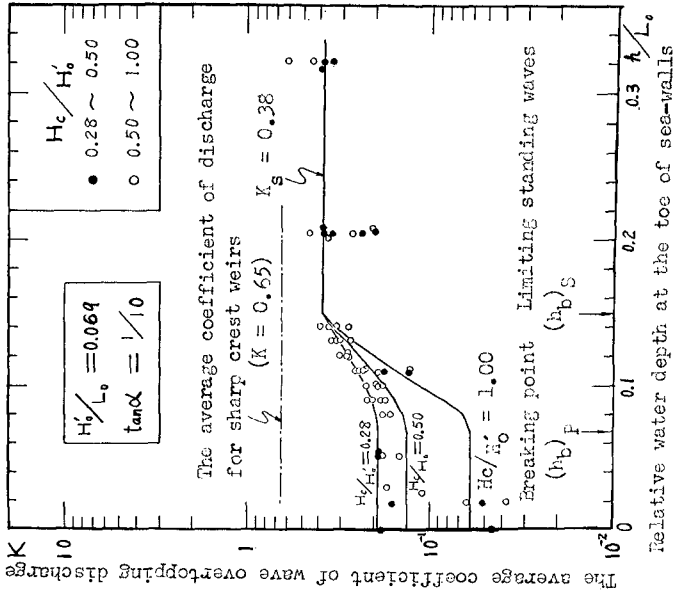(c) Results for $H_0'/L_0 = 0.056$ and the bottom slope of 1/10

(d) Results for $H_0'/L_0 = 0.069$ and the bottom slope of 1/10

Fig. 10.   Comparison between calculated and experimental values of the average coefficient of wave overtopping discharge for vertical sea-walls.

CHAPTER 117

WAVE OSCILLATIONS IN AN OFFSHORE OIL STORAGE TANK

By Hooshang Raissi[1]

INTRODUCTION

The rapidly incrasing demand to exploit known offshore oil fields throughout the world, and the costly conventional method of piping the oil to the shore have given support to the concept of offshore storage terminals located in the immediate vicinity of the field. The Khazzan Dubai oil storage tanks at Fateh field, off-shore from Dubai (Chamberlin, 1970), the Pazargad one million-bbl crude-oil storage barge at Syrus field, Iran, offshore in the Persian Gulf (Feizy and McDonald, 1972), and the new offshore reinforced-concrete million-bbl oil storage tank at the Ekofisk field in the North Sea (Ocean Industry, 1972), show the new attitude which the offshore oil-production industry has developed toward this system.

A closed floating, or pile-supported, bottomless barrier might provide an effective solution for storing oil offshore or containing an oil spill.

The crude oil coming from the production platform is in-jected at the sea level inside the closed bottomless barrier, it dispalces the water inside, and remains above the water as a result of its density. The oscillations of the internal wave at the interface of oil and water and the surface waves resulting from different incident waves in such a container were studied in this work.

THEORETICAL ANALYSIS

Suppose that a homogenous layer of fluid of density ρ_1 (oil) of thickness h lies over another homogeneous layer of fluid of density ρ_2 (water) of thickness H-h (see Fig. 1). The two fluids are immiscible, and the surface tension and viscosity of the fluids will not be taken into account.

1. Assistant Professor University of Tehran - Iran

The boundary conditions at the interface are as follows:

a.   Vertical velocity is the same in both fluids:

$$\phi_{1z} = \phi_{2z} = \eta_{2z} \quad \text{at} \quad Z = + h \tag{1}$$

b.   Pressure is continuous at the interface:

$$P_1 = \rho_1 \, (\phi_{1t} + g(h - \eta_2))$$

$$P_2 = \rho_2 \, (\phi_{2t} + g(h - \eta_2))$$

so that

$$\rho_2 \, (\phi_{2t} + g(h - \eta_2)) = \rho_2 (\phi_{1t} + g(h - \eta_2)) \tag{2}$$

Taking the partial derivative of Eq. (2) with respect to t gives

$$\rho_2 \phi_{2tt} - \rho_1 \, \phi_{1tt} - g(\rho_2 - \rho_1) \, \eta_{2t} = 0 \tag{3}$$

The free-surface boundary condition is

$$\tag{4}$$

$$\phi_{tt} + g \, \phi_{1z} = 0 \text{ at } Z = 0$$

The bottom boundary condition is

$$\phi_{2z} = 0 \quad \text{at} \quad Z = H \tag{5}$$

From the continuity equation for an incompressible fluid,
$\vec{\nabla} \vec{u} = 0$, and the definition of the velocity potential, Laplace's
equation is obtained:

$$\nabla^2 \phi_1 = 0 \tag{6}$$

$$\nabla^2 \phi_2 = 0 \tag{7}$$

Therefore, the problem is to find the velocity potentials ϕ_1 ,
and ϕ_2 , which satisfy Laplace's equations, Eqs. (6) and (7),
subject to a number of prescribed boundary conditions. Using
the method of separation of variables, we will get to the
following equation, (wehausen 1970).

$$-\frac{\sigma^2}{gk} = \frac{\rho_2(\text{ coth } kh+1)+\{\rho_2(\text{coth } kh-1)+2\rho_1\}}{2\{\rho_2 \quad \text{coth } kh \quad + \quad \rho_1\}} \qquad (8)$$

for(+)

$$\frac{\sigma^2}{gk} = 1.0 \qquad (9)$$

for(-)

$$\frac{\sigma^2}{gk} = \frac{\rho_2 - \rho_1}{\rho_2 \text{ coth } kh + \rho_1} \qquad (10)$$

From Eq. (g) we have

$$\qquad (11)$$

$$\eta_1 = (a \text{ Coskx } + b \text{ Sinkk}) \text{ Sin } (\sigma t + \tau)$$

$$\eta_2 = e^{-kh}(a \text{ Coskx } + b \text{ Sinkx}) \text{ Sin } (\sigma t + \tau) \qquad (12)$$

and from Eq. (10) we have

$$\eta_1 = (a \text{ Coskx } + b \text{ Sinkx }) \text{ Sin } (\sigma t + \tau) \qquad (13)$$

and

$$\eta_2 = \frac{\rho_1}{\rho_2 - \rho_1} e^{kh} (a \text{ Coskx } + b \text{ Sinkx}) \text{ Sin } (\sigma t + \tau) \qquad (14)$$

Two-Dimensional Case (A Rectangular Bottomless Container)

For the case of two barriers extending from the surface to a given depth (D) , assuming that the depth of immersion of the barriers are bigger than half of the surface wavelength.   In order to have a resonance motion within the container, we must have

$$\frac{nL}{2} = B \tag{15}$$

where n is the number of half-wavelengths, and B is the distance between the barriers. From Eq.(15),

$$K = \frac{\pi n}{B}$$

Then Eq. (9) becomes:

$$\frac{\sigma^2 B}{\pi g} = n \tag{16}$$

and

$$\eta_1 = A \ Cos \ \frac{\pi n}{B} \ Sin \ (\ \sigma t + \tau)$$

$$\eta_2 = A \ e^{-kh} \ Cos \ \frac{\pi n}{B} \ Sin \ (\sigma t + \tau)$$

Then Eq (10) becomes:

$$\frac{\sigma^2 B}{\pi g} = n \ \frac{1 - \dfrac{\rho_1}{\rho_2}}{Coth \ \dfrac{\pi n h}{B} + \dfrac{\rho_1}{\rho_2}} \tag{17}$$

and

$$\eta_1 = A \ Cos \ \frac{\pi n}{B} \quad Sin \ (\ \sigma t + \tau)$$

$$\eta_2 = - A \ \frac{\rho_1}{\rho_2 - \rho_1} \ e^{kh} \ Cos \ \frac{\pi n}{B} \ Sin \ (\sigma t + \tau)$$

There will be resonance with a large surface wave whenever

$$\frac{\sigma^2 B}{\pi g} = 1, 2, 3, \ldots$$ (18)

There will be resonance with a large internal wave whenever

$$\frac{\sigma^2 B}{\pi g} = \frac{1 - \frac{\rho_1}{\rho_2}}{\coth\frac{\pi h}{B} + \frac{\rho_1}{\rho_2}}, \quad 2\frac{1 - \frac{\rho_1}{\rho_2}}{\coth\frac{2\pi h}{B} + \frac{\rho_1}{\rho_2}} + \ldots,$$ (19)

This is not the exact solution of the problem, because the barriers were assumed to extend to a depth which is more than half a surface wave length and also the water depth H was considered to be infinite. For this reason the experimental wave height of the internal waves and surface waves were compared with the numerical solution of this problem, Based on a varitional form of the equation for steady oscillatory irrotational motion of an inviscid incompressible fluid (Bai, 1972).

Three-Dimensional Case (Circular Bottomless Container)

The amplitude variation in polar coordinates in the case of oscillation in a circular basin of constant depth is described by the following expression (Lamb, 1932):

$$\eta = \Sigma_m \, C_m \, J_m \, (Kr) \, \cos m\theta \, \cos \sigma t$$ (20)

For oscillation inside a cylinder, the following boundary condition should be satisfied:

$$\frac{\partial \eta}{\partial r} = 0 \quad \text{at} \quad r = a$$ (21)

(periphery of basin)

This is identical to stating that the normal velocity at the
boundary is zero, from Eq.

$$J'_m (Ka) = 0 \tag{22}$$

This means a maximum or a minimum (a crest or a trough)
should exist at the outer edge of the cylinder.

The lowest symmetrical mode of oscillation is the first root
of $J_0(Ka)$ $Ka = 3.832$

This gives one nodal circle located at $r/a = 0.688$.

The period of the wave which causes this mode of oscillation
at the interface of oil and water can be obtained by substituting Eq.
(22) into Eq. (10). This gives:

$$\frac{\sigma^2 R}{g} = 3.832 \frac{1 - \dfrac{\rho_1}{\rho_2}}{\coth(3.832 \frac{h}{a}) + \dfrac{\rho_1}{\rho_2}} \tag{23}$$

The condition for the same mode of oscillation to occur at
the surface of the oil can be obtained by substituting Eq. (22) into
Eq. (9), giving

$$\frac{\sigma^2 a}{g} = 3.832 \tag{24}$$

The same calculation is being carried for other modes of
oscillation.

EXPERIMENTAL EQUIPMENT AND ARRANGEMENTS

Two-Dimensional Model

The two-dimensional model studies were performed in a wave channel that is 1 ft. wide by 3 ft. deep by 100 ft. long (Fig 5).

At one end of the channel there is a flapper-type generator; at the other end a beach was installed to absorb wave energy and minimize wave reflection. Also shown in the figure is a wave filter located in front of the wave machine. A rectangular bottomless container 1 ft. wide by 1.5 ft. deep by 2.33 ft. long was constructed of 1/4 inch lucite, simulating a perfectly reflecting rigid barrier.

Two types of wave gages were used to measure the wave amplitude, one for the internal waves at interface of oil and water, and the other for measuring the surface oil waves inside the container.

For the first type, parallel-wire resistance wave gages were used (Wiegel, 1953). Since oil is a very poor electric conductor compared with tap water only the depth of the immersion of wires in water is proportional to the probe conductivity.

For measuring the surface oil waves inside the container, a capacitance type wave recorder was used . The capacitor has a definite initial capacitance which depends on the probe length, distance between the probes, and the dielectric of the material between the capacitor "plates".

In addition, motion pictures were taken through the glass walls of the channel (while the container had oil inside) of several experimental runs. The camera was mounted so that its line of sight was perpendicular to the side of the flume and level with the undisturbed oil and water interface. A grid on the glass wall of the wave channel, permitted the measurement of the surface and internal waves inside the containers.

Three-Dimensional Modle

This experiment was conducted in an ripple-tank.
The tank is 20 feet long, 49½ inches wide, and 4 inches deep. Periodic
waves were generated by a mechanical wave flap driven by an electric
motor (Fig. 6).

A wave filter was located in front of the wave generator,
and circualr Lucite cylinder was used as a model of a circualr oil
container.

A section of the bottom ot the ripple tank was made of
plate glass, underneath the glass bottom was a plane mirror mounted at
45 degrees to the horizontal. A strong light source was reflected by
the mirror through the glass bottom. The light beams were converged
by wave crests and diverged by wave troughs. This permitted visual
observations of the wave patterns on a horizontally mounted tracing-
paper screen above the tank. Pictures were taken of the wave patterns
inside the cylinder at different incident-wave conditions by a camera
located above the tracing-paper screen (Fig.1).

PRESENTATION AND DISCUSSION OF RESULTS

Two-Dimensional Model Study

Experimental studies were conducted to measure the periods
of waves causing oscillations at the interface of oil and water, and
also at the surface of the water.

Measurements were also made of the distribution of maximum
internal and surface-wave amplitudes, inside the two-dimensional oil
container. Three different liquids with specific gravities of $S = 0.685$,
and 0.830 and 0.910 were used to substitute for oil inside the model.
The experiments were run for only one depth, $H = 1.5$ ft., and one immersion
depth of the barriers, $D = 0.5$ ft.   An oil layer of thickness $h = 0.3$
was used inside the oil container (Fig. 1) for all the experiments.

The theoretical solution described in Theoretical Section Eqs. (18 and 19)   was used to predict the frequencies associated with surface and internal wave oscillations. Figures 2 to 4 illustrate the theoretical and experimental values of $\sigma^2 B/\pi g$ for any mode of surface - and internal-wave oscillation.

Although the mathematical treatment was carried out under the assumption that the depths of the immersion of the barriers are larger than $1/2$ the surface wavelength ($D \geqslant 1/2$ L), the experimental results correspond very well with the theory for all ranges of wave periods (T = 3.8 to 0.65 sec.).

A small difference could be detected between the theoretical values of circular wave frequency and the experimental ones for the surface-wave oscillations. The experimental values were higher than the theoretical ones, especially for the first mode of oscillation which is associated with longer waves. This difference is due to the change in wave number associated with surface wave oscillation caused by insufficient immersion depth of barriers, which makes the theoretical solution only approximate.

However, this effect is not important for higher modes of surface oscillations and internal-wave oscillations owing to the short wave lengths causing them. In this case the theoretical assumption $D \geqslant 1/2$ L is valid.

Comparison of Figs. 2   , 3 and   4 show that the change in oil density does not have any significant effect on the period of waves causing the oil-surface oscillations, but that it has a significant effect on the wave periods causing the internal-wave oscillations. The greater the density of the oil, the larger the wave period corresponding to any mode of oscillation.

The computer numerical technique (Bai. 1972), was used to calculate Amplification Factors for comparison with the experimental measurements, (Figs 7 and 8).. The amplification factor (A) for the surface waves is the ratio of the maximum wave height to the incident-wave height, and for the internal waves it is the ratio of the maximum internal-wave height to the incident-wave height. The experimental results for the internal waves agree well with the theory. However, the experiment results show a higher amplification factor for the surface wave than is predicted by theory. This might be due to an insufficient number of internal boundary segments being used along the interface of oil and water for the numerical calculations. An effect of the oil density on the internal - and surface-wave heights during the oscillations could be seen by comparing Figs. 7 and 8. Both show the internal - and surface-wave heights for the first mode of internal-wave oscillation. The internal-wave heights for oil with a density of 0.83 gr/cm^3 are higher than the ones for oil with a density of 0.685 gr/cm^3.

It should be noted that the incident waves that cause oscillations of the higher-density oil are the longer waves, and that the higher internal-wave oscillations are partially due to the higher wave energy which can penetrate inside the bottomless storage tank. Figure 7 also shows a lower surface-wave height for oil with higher density for the first mode of internal-wave oscillation. This might be due to the fact that the wave period causing the first mode of internal-wave oscillation for oil with lower density, is nearer to the zero mode of oscillation of the surface wave.

Three-Dimensional Study

This experiment was conducted for a water depth of H =3.5 in.
The immersion depth of the one-foot diameter circualr oil container was
D = 2 in.   An oil layer thickness of h = 1in. was used inside the oil
container.   Figure   11   shows photographs taken   of the differen. modes
of oscillation at the interface of the water and oil with an oil
density of 0.80 gr/cm^3 .   The theoretical solution Eqs.(23 and 24)
predicts the frequencies associated with any mode of surface - and
internal-wave oscillation.

Figures 9 and 10 show the theoretical and experimental
values of σ^2 D/g for any mode of internal - and surface-wave oscillation.

CONCLUSIONS

From the study the following major conclusions are drawn:

1.   The prediction from the theory of resonant frequencies for
        internal and surface waves corresponds very well with the
        experimental results.

2.   A change in oil density does not have any significant effect
        on the period of the waves need to cause surface-wave oscillation.
        It does have a significant effect on the period of the waves
        needed to cause internal-wave oscillation; the higher the
        density of oil, the higher the wave period needed to generate a
        particualr mode of oscillatior.

3.   The experimental results for the internal-wave amplification
        factors correspond closely to the numerical results. However,
        the experimental results give higher amplification factors than
        the theory for the surface waves within the tank.

4.   The internal-wave heights are higher for oils with higher density,
        all other conditions being equal.

REFERENCES

1. Bai, Kwang, June, "A Variational Method in Potentail Flows with a Free Surface, "Ph.D. Thesis in Naval Architecture, University of California, Berkeley, California, 1972.

2. Chamberlin, R. S., "Khazzan Dubai, Design, Construction and Installation, "Chicago Bridge and Iron Co. Paper No. OTC 1492, Preceedings of Second Offshore Technology Conference, Dallas, Texas, April 1970.

3. Feizy, G., and McDonald, J. E., "Pazargad-World's Largest Crude Oil Storage Barge, "Iran Pan American Oil Cc. Paper No. OTC 1526, Proceedings of Fourth Offshore Technology Conference, Houston, Texas, May 1972.

4. Lamb, H., Hydrodynamics, Sixth Edition, Dover Publications, New York, 1945.

5. Ocean Industry, "North Sea Report, "Phillips Ekofisk Million Barrel Oil Storage Tank Near Completion, PP. 35-35, July 1972.

6. Wiegel, Robert, Parallel Wire Resistance Wave Meter, Coastal Engineering Instruments, Council on Wave Research, The Engineering Foundation, 1953, PP. 39-43.
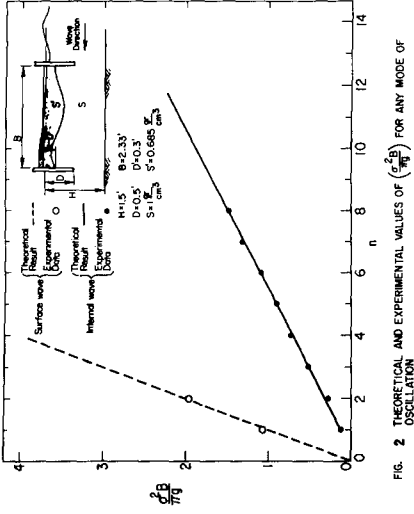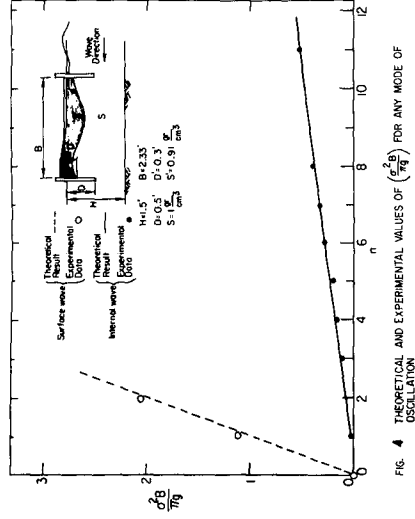
FIG. 2 THEORETICAL AND EXPERIMENTAL VALUES OF $\left(\frac{\sigma^2 B}{\pi g}\right)$ FOR ANY MODE OF OSCILLATION

FIG. 4 THEORETICAL AND EXPERIMENTAL VALUES OF $\left(\frac{\sigma^2 B}{\pi g}\right)$ FOR ANY MODE OF OSCILLATION

FIG. 1 DEFINITION SKETCH OF OIL-WATER COORDINATE SYSTEM

FIG. 3 THEORETICAL AND EXPERIMENTAL VALUES OF $\left(\frac{\sigma^2 B}{\pi g}\right)$ FOR ANY MODE OF OSCILLATION
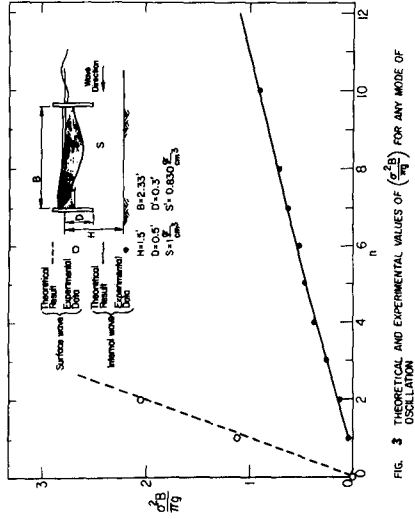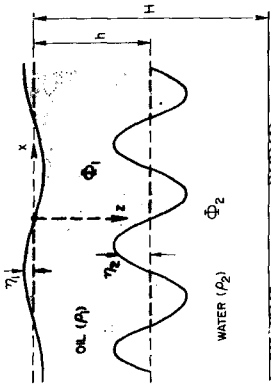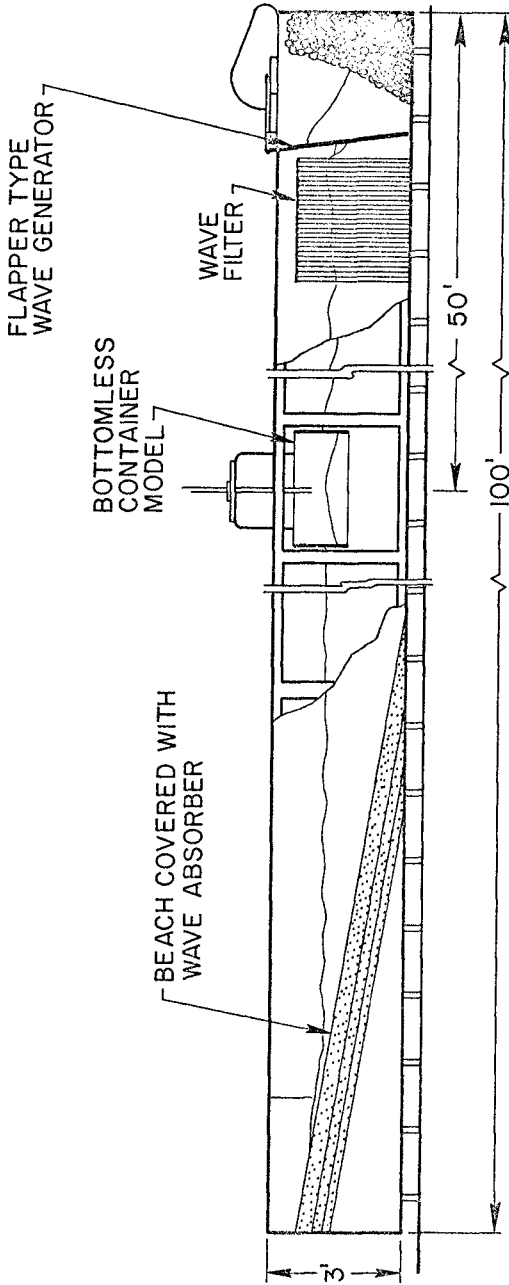
FIG. 5   DRAWING OF THE WAVE CHANNEL

CAMERA

ELECTRIC MOTOR

TRACING PAPER SCREEN

GEAR

WAVE FLAP

WAVE FILTER

$\frac{1}{10}$ FT NET GRID

OIL

WAVE ABSORBING BEACH

BOTTOMLESS OIL CONTAINER

WATER

GLASS BOTTOM

MIRROR

45°

LIGHT SOURCE

WAVE ABSORBER

POLISHED ALUMINUM

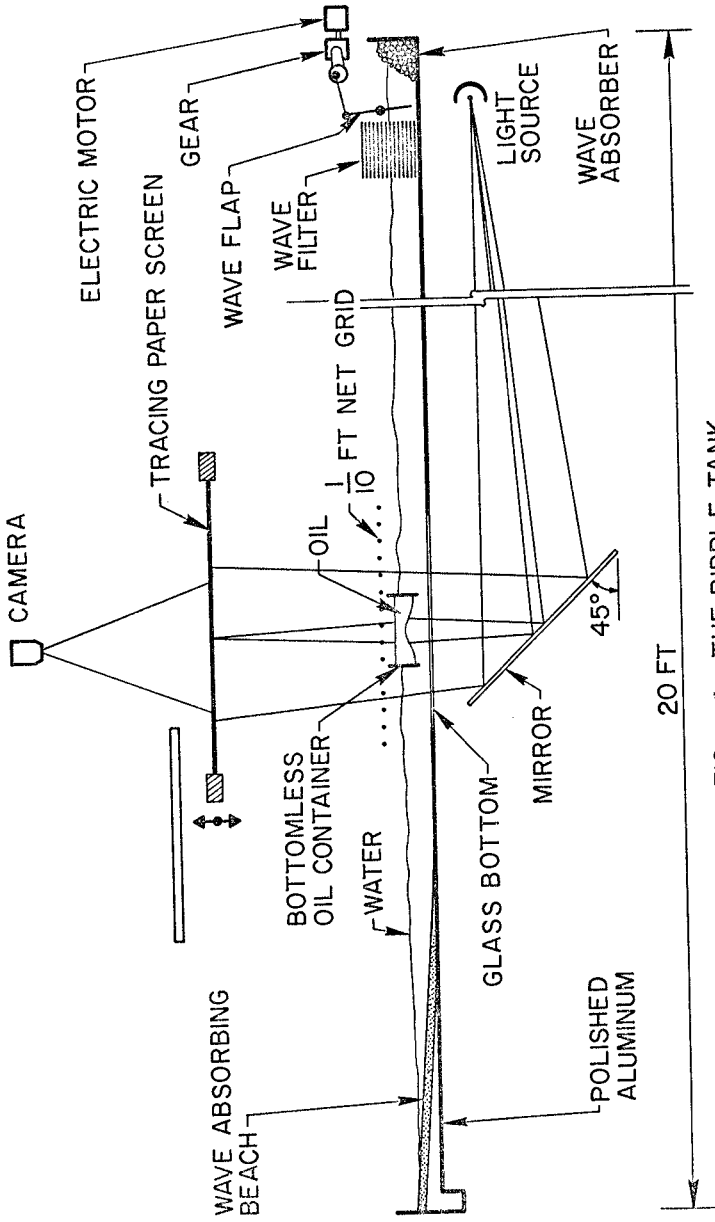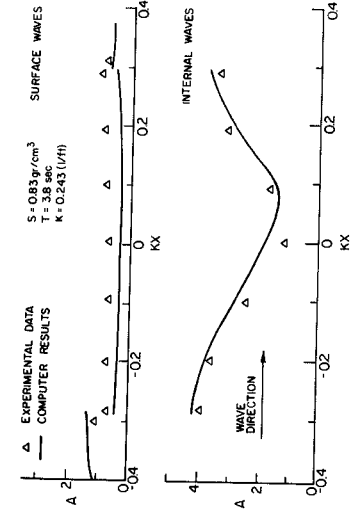20 FT

FIG. 6 THE RIPPLE TANK

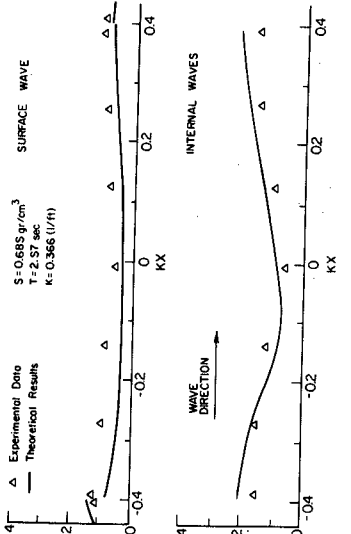FIG. 7 MAXIMUM WAVE AMPLITUDES OF INTERNAL AND SURFACE WAVES

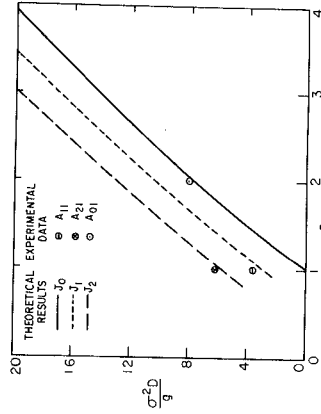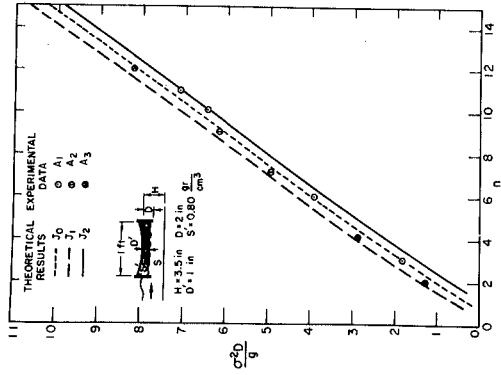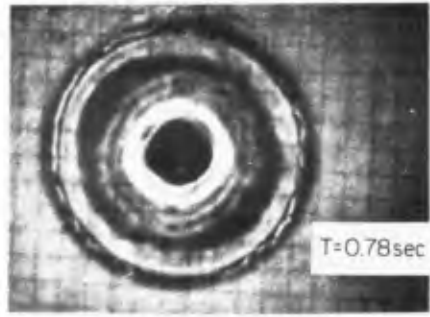FIG. 8 MAXIMUM WAVE AMPLITUDES OF INTERNAL AND SURFACE WAVES

FIG. 9 INTERNAL WAVE OSCILLATION

FIG. 10 SURFACE WAVE OSCILLATION
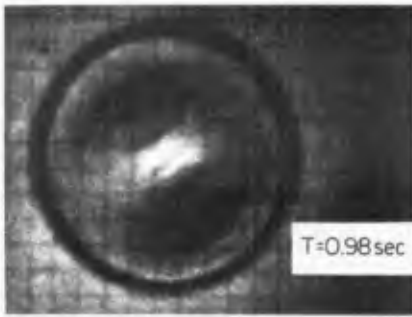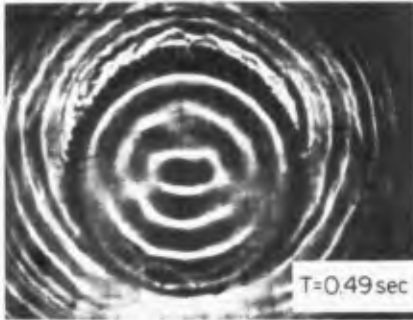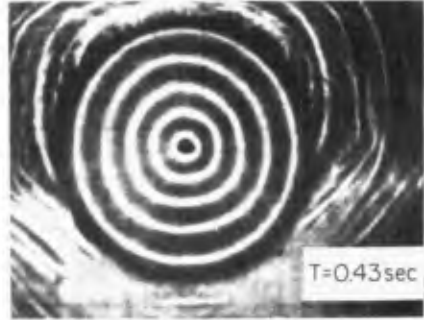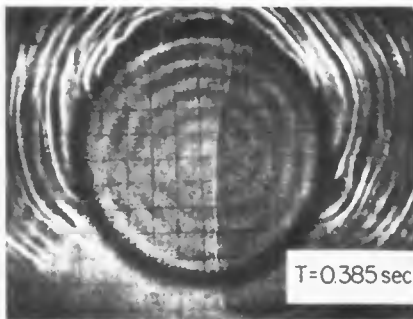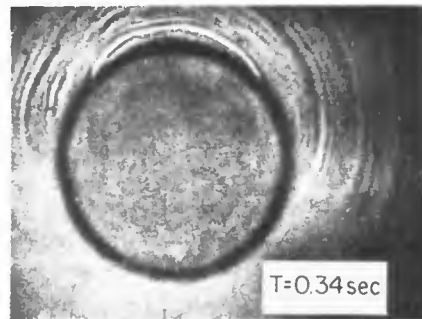
FIG.11 INTERNAL WAVE PATTERN INSIDE THE CIRCULAR
BOTTOMLESS OIL CONTAINER

CHAPTER 118

ECONOMIC APPROACH TO OPTIMIZING DESIGN PARAMETERS

W. Edgar Watt   and   Kenneth C. Wilson [1]

ABSTRACT

    For coastal engineering works, as for other structures, the
designer must search for the economic optimum point. This point
represents the minimum in the sum of direct cost and cost of possible
future damage. By setting up functional representations of these costs
the optimum can be obtained directly. This approach is illustrated by
models developed independently in the Netherlands and in Canada. At
this stage the output of the models may be denoted as the 'perfect
knowledge' optimum, in the sense that parameters of the cost functions
are assumed to be known with complete accuracy.

    In the 'real world' case, however, the estimated values of the
parameters will be subject to considerable uncertainty. It is shown
that because of this uncertainty the 'real world' design optimum will
generally be shifted to give a structure larger than that indicated by
the 'perfect knowledge' assumption. The novel contribution of the
present paper consists of analyzing this shift to obtain simple
expressions for the apparent overdesign due to uncertainty and for the
resulting cost increase. An illustrative example is presented.

---

[1]   Associate Professors, Queen's University at Kingston, Canada.

INTRODUCTION

Structures which must resist natural forces are generally
designed to withstand a potential damage event which can be defined by
a specific return period. For most coastal engineering works damage
can be associated with wave action. Although a rigorous description of
potentially damaging waves would involve spectral analysis, in common
practice it is found that a single wave height parameter is sufficient
to quantify a potential damage event, i.e. a given storm. The wave
height can then be combined with the appropriate tide height to yield
the height parameter h . This parameter is taken to be a random
variable which has a probability density function f(h) (Figure 1)
and cumulative distribution function F(h) . Engineers commonly use
the exceedance probability, $p = 1 - F(h)$, or its reciprocal, the
return period T , as indices of the magnitude of the event.
Selecting a specific value of the height parameter as the design
height, H_d , is equivalent to fixing the return period, T , of the
potential damage event which the structure is to withstand. Conversely,
specification of a return period defines the design height.

In principle, the optimum design can be obtained by economic
analysis. With small T (and H_d) the initial outlay for construction
will be low, but the cost of probable future damage will be large. On
the other hand with large T (and H_d) probable future damage will be
small but construction cost will be greatly increased. The optimum
return period, $\hat{T}$, which lies between these extremes, produces a
minimum in the sum of construction cost plus cost of probable future
damage. Figure 2 shows this optimum point.

The optimization process can be carried out by successive trial
designs but this is tedious, and in many cases a valuable simplification
can be made by approximating both the construction cost and the cost
of probable future damage by mathematical functions. In particular,
this approach provides a suitable method for dealing with groups of
similar structures. Although some design studies may be required to
determine the numerical values of coefficients included in the
functions, the optimum point can now be obtained directly by
differentiating the total cost for a minimum. This approach to the
optimum design of coastal works was pioneered in studies made in the
Netherlands. An analysis developed independently in Canada for flood-
control works in inland waters is conceptually similar and provides a
valuable alternate formulation for coastal structures. In both cases
the expressions obtained for the optimum show the effects of the
regional probability function and the type of structure. In addition,
the importance of economic factors such as interest rate is taken into
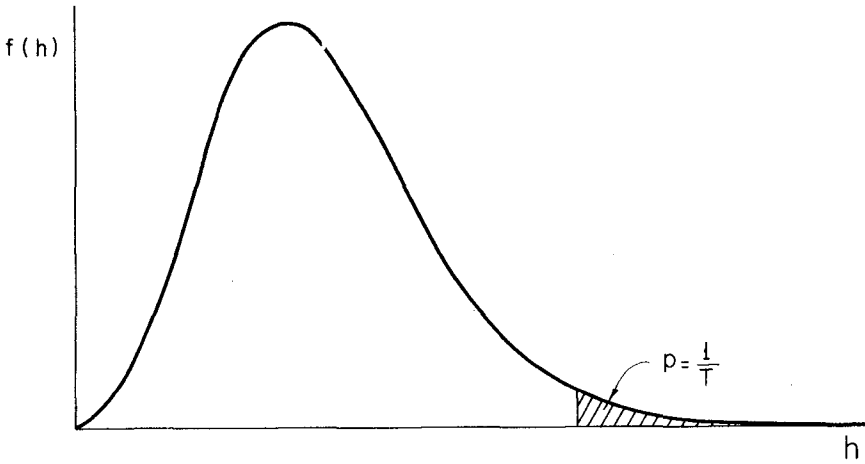account.
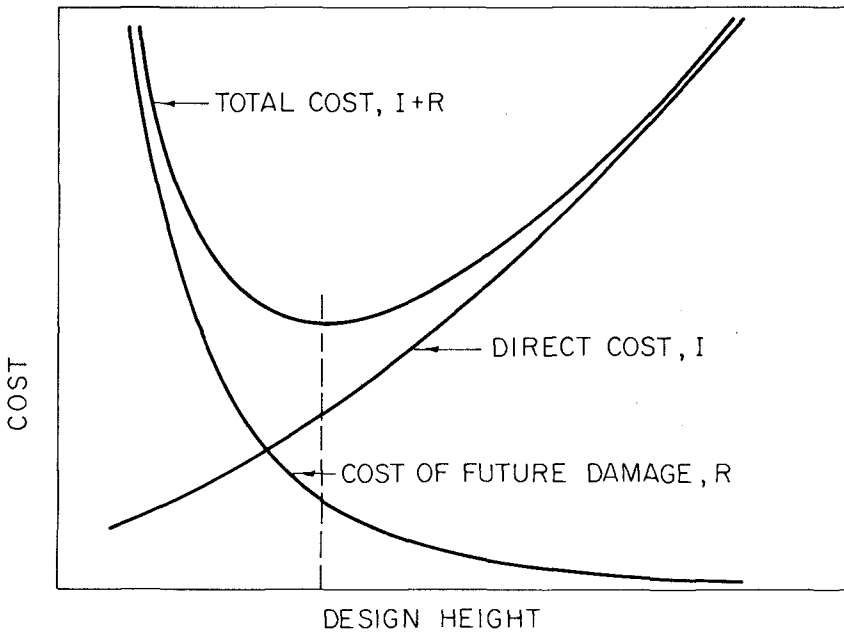
FIGURE 1　　PROBABILITY DENSITY FUNCTION FOR h

FIGURE 2　COST RELATIONS FOR COASTAL STRUCTURES

'PERFECT KNOWLEDGE' OPTIMIZATION

Overall Concept

The development of the analytical model is carried out in two stages. In the first stage the relations leading to the economic optimum design for a typical structure are set up to yield the common return period for a regional aggregate. In dealing with these relations it is assumed that all the required parameters, including the characteristics of the regional probability function, are known with complete accuracy. This may be termed the 'perfect knowledge' case, on the understanding that the knowledge of extreme events extends only to the statistics of their distribution and not to their particular values in specific future years.

This first stage -- the 'perfect knowledge' model -- is outlined below. In the second stage, which will be dealt with in subsequent sections, the analysis is modified to take account of the effects of uncertainties in the input data, including uncertainty in the assumed regional probability function.

Cost Functions

As mentioned previously, economic analysis could be carried out by determining direct cost and damage cost for a series of trial designs. However, greater insight can be obtained by using continuous cost functions rather than discrete trial values. The functions for direct cost and damage cost are expressed in terms of an appropriate variable, denoted as X , which is known as the scope of the trial design. In coastal engineering problems X would represent the height of a dike or breakwater above some datum level. Note that here the scope X is quite distinct from the height parameter h . The lower the value of X which is selected, the greater is the probability of overtopping, and hence of damage.

The specific relations linking direct cost and damage cost to the scope X are somewhat different in the Netherlands and the Canadian models. These relations are set out in Table 1. However, in the text below these relations are given in general functional form. Whenever possible, the nomenclature used in the Netherlands study has been adopted.

Direct Cost: The direct cost, I , comprises construction cost plus capitalized cost of annual maintenance over the lifetime of the structure. Therefore, I is an increasing function of the scope of the trial design, which may be written as

$$I = \phi_1 (X) \qquad\qquad (1)$$

TABLE 1

SUMMARY OF PERFECT KNOWLEDGE OPTIMIZATION

Relation		Netherlands Model	Canadian Model
Scope	X	$X = H - H_o$	$X = Q - Q_o$
Direct Cost	$I = \phi_1(X)$	$I = I_o + I'X$	$I = K_1 X^m$ *
Exceedance Probability	$p = \dfrac{1}{T} = \phi_2(X)$	$p = p_o e^{-\alpha X}$	$p = (X/A)^{-q}$
Damage Cost per Event	$\phi_3(X)$	W	$K_3 X^r$ **
Present Value Function	$\psi(\delta, L)$	$1/\delta$	$f = ((1+\delta)^L - 1)/\delta$
Cost of Probable Future Damage	$R = \psi(\delta,L)\phi_2(X)\phi_3(X)$	$R = R_o e^{-\alpha X}$ $(R_o = p_o W / \delta)$	$R = K_2 X^{-n}$ $\begin{bmatrix} n = q - r \\ K_2 = f K_3 A^q \end{bmatrix}$
Optimum Scope	$\hat{X}$	$\hat{X} = \dfrac{1}{\alpha} \ln \dfrac{R_o \alpha}{I'}$	$\hat{X} = \left(\dfrac{n K_2}{m K_1} \right)^{1/(m+n)}$
Optimum Return Period	$\hat{T} = 1/\phi_2(\hat{X})$	$\hat{T} = \dfrac{1}{p_o} e^{\alpha \hat{X}}$	$\hat{T} = (\hat{X}/A)^q$
Relative Loss	$D = \phi_4(y)$	$D = e^{-y} - 1 + y$	$D = \dfrac{n}{m} (e^{my/q}-1) + (e^{-ny/q}-1)$

$$\begin{bmatrix} D = \dfrac{(I+R) - (\hat{I+R})}{\hat{R}} \\ y = \ln (T/\hat{T}) \end{bmatrix}$$

*   In the Canadian model the direct cost can also be expressed in the more general form $I = I_o + K_1 X^m$.   This change does not affect the other equations given above.

**   The expression given here for 'damage cost per event' is one of the possible formulations studied in the Canadian model. For further information see reference 4. Note that when $r = 0$, $X^r = 1$ and K_3 corresponds to W of the Netherlands model.

Cost of Probable Future Damage: The cost of probable future
damage or future losses, R ,
is the total present worth of possible damage events during the service
life. Hence, R equals the product of two factors; the first is the
present worth function of the interest rate and the service life,
ψ (δ, L) , and the second is the probable cost of damage in any
individual year. The second factor, in turn, is given by the product
of the probability of a damage event, ϕ_2 (X) , and the ensuing
damage cost, ϕ_3 (X) .

$$R = \psi (\delta, L) \cdot \phi_2 (X) \cdot \phi_3 (X) \tag{2}$$

Optimum Scope and Optimum Return Period

The optimum scope, $\hat{X}$, which is associated with the minimum in
the total cost can be determined by differentiating equations 1 and 2
with respect to X and equating the sum of the derivatives to zero.
The corresponding optimum return period is obtained from the reciprocal
of the exceedance probability.

$$\hat{T} = 1 / \phi_2 (\hat{X}) \tag{3}$$

Relative Loss

The difference between the total cost, 1 + R , for any value of
X and the total cost for $\hat{X}$ can be defined as a loss due to lack of
optimization. This loss, divided by some typical cost (say $\hat{R}$) , is
denoted as the relative loss, D . In this work D is expressed not
in terms of (X - $\hat{X}$) but in terms of the relative return period T/$\hat{T}$
or, to be more specific, its natural logarithm, denoted here by y.

$$D = \phi_4 (y) \tag{4}$$

Figure 3 shows the form of this function.

CONSEQUENCES OF UNCERTAINTY

The optimization process dealt with in the previous section was
based on the assumption that all the required parameters were known
exactly. In the 'real world' situation, however, the values employed
necessarily represent estimates made from available data. These
estimates are, of course, subject to significant uncertainty.

On initial inspection it might be thought that such uncertainty
would not influence the design return period, which could still be taken
as the 'perfect knowledge' optimum, $\hat{T}$. However, further consideration

will show that this is not generally the case. The total cost function is not symmetric about its minimum point, and for structures of the type considered here the left hand limb of the curve rises much more rapidly than the right hand limb, as illustrated by Figure 2. It follows that the penalty for underdesign is greater than that for an equivalent overdesign. If the 'perfect knowledge' optimum were adopted for design, then cases of both underdesign and overdesign would occur, but the total penalty, or financial loss, for the cases of underdesign would exceed that for the cases of overdesign. In these circumstances the total loss can be reduced by the strategy of adopting a design return period larger than the 'perfect knowledge' optimum. The analysis of the 'real world' case which is given below relates this apparent overdesign to the degree of uncertainty and other parameters.

It may be remarked that the analysis of such an apparent overdesign in terms of degree of uncertainty represents the formal expression of a concept which is implicit in the traditional factor of safety. The apparent or 'perfect knowledge' optimum design for most simple structures represents the boundary between underdesign, which results in failure, and overdesign, which adds excess material. Here again, the penalty for underdesign exceeds that for equivalent overdesign, and this is taken into account in practice by apparent overdesign inherent in the use of the factor of safety. It is an old truism that the factor of safety might well be called the 'factor of ignorance'. This is demonstrated by the increased factor of safety used in situations of increased uncertainty. For example, a large factor of safety will be applied for a natural material with highly variable properties, but a smaller factor will be applied for a manufactured material of controlled quality.

<center>OPTIMIZATION UNDER UNCERTAINTY</center>

Probability Distribution for Optimum Return Period

As noted above, in the 'real world' case, the various quantities included in the expression for $\hat{T}$ are not known with absolute certainty, but must be considered as probabilistic in the sense that during the design process their values can only be estimated within some margin of variation or uncertainty. Therefore, if the best present estimates of the various quantities are substituted into equation 3, the result will be affected by these uncertainties. It follows that the estimated optimum return period $\hat{T}$ (based on the 'perfect knowledge' formulation) can be expected to differ from the true optimum $\hat{T}_o$ by some amount which represents the combined effect of the uncertainties of all the components.

Therefore, the value of the true optimum, $\hat{T}_o$, can only be expressed by means of a probability statement. This statement would
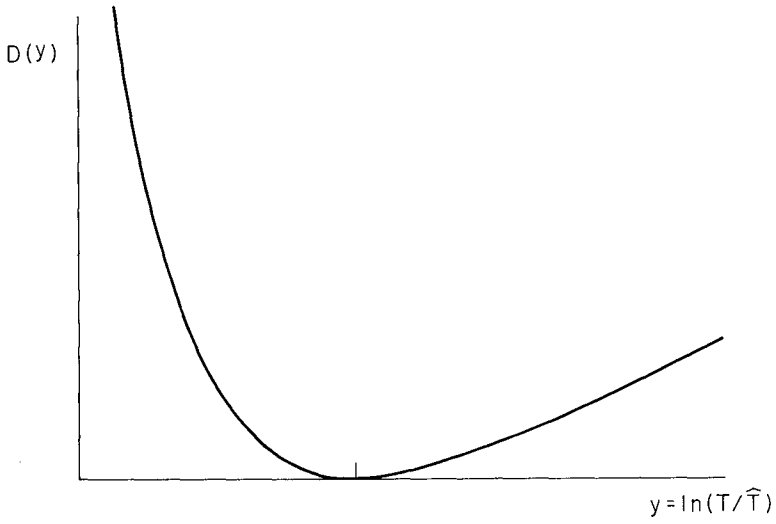
$$y = \ln(T/\widehat{T})$$

FIGURE 3 RELATIVE LOSS FUNCTION

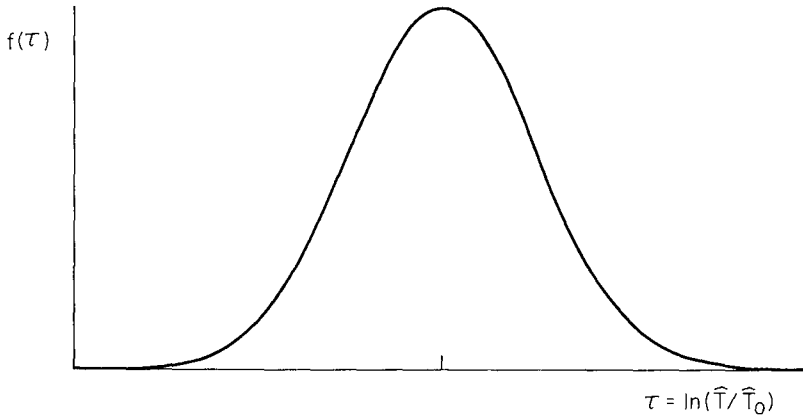$$\tau = \ln(\widehat{T}/\widehat{T}_0)$$

FIGURE 4 PDF FOR OPTIMUM RETURN PERIOD

normally take the form of a cumulative distribution function or its
derivative, the probability density function (pdf) . The pdf for
$\hat{T}_o$ could be determined by a Monte Carlo type analysis, using Equation 3,
if information were available on the pdf for each of the variables.
In the present analysis, $\hat{T}_o$ was assumed to be lognormally distributed
about its estimated value $\hat{T}$ (i.e.   ln $(\hat{T}/\hat{T}_o) = \tau = N (0, \sigma_\tau)$).
This is shown on Figure 4. The standard deviation, σ_τ , of this
distribution is then an index of the uncertainty which results from the
combined effect of the uncertainties in the various economic and
physical factors included in the expression for the optimum return
period.

Minimization of Expected Loss

The uncertainties in estimating the optimum return period which
have been dealt with above imply that for a given installation, $\hat{T}$ is
either greater or less than the true value $\hat{T}_o$. Hence a design based
on $\hat{T}$ $(T_d = \hat{T})$ will result in total cost greater than the minimum,
and this excess cost can be considered as a penalty or loss. Because
of the uncertainties inherent in the 'real world' case, this loss
cannot be completely eliminated. The expected loss is defined as the
summation of the product of loss and probability density over the full
range of relative return period.

$$EL = \int_{-\infty}^{\infty} D(y) \cdot \hat{R} \cdot f(\tau) \cdot d\tau \tag{5}$$

As a result of the asymmetry of the total cost function, and
hence $D(y)$, the penalty for underdesign is greater than that for an
equivalent overdesign, and it follows that the expected loss can be
minimized by selecting a design return period greater than the
'perfect knowledge' optimum. As shown on Figure 5, this can be
visualized as a shift of the pdf, $f(\tau)$, relative to the loss curve,
$D(y)$. The amount of this shift is denoted by a (i.e. $a = y - \tau$
where $a = \ln T_d/\hat{T}$, $y = \ln T_d/\hat{T}_o$ and $\tau = \ln \hat{T}/\hat{T}_o$) . The value
of a required to minimize the expected loss (see Figure 6) can be
written functionally as

$$a = \phi_5 (D(y), f(\tau)) \tag{6}$$
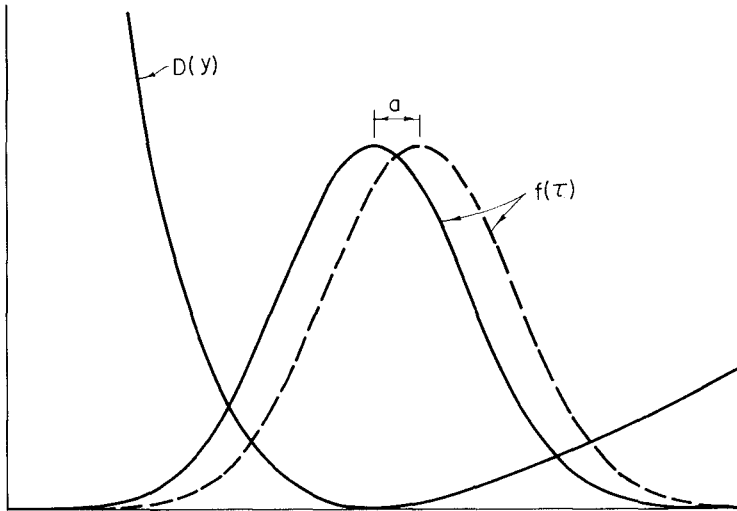
FIGURE 5 SHIFT TO MINIMIZE EXPECTED LOSS
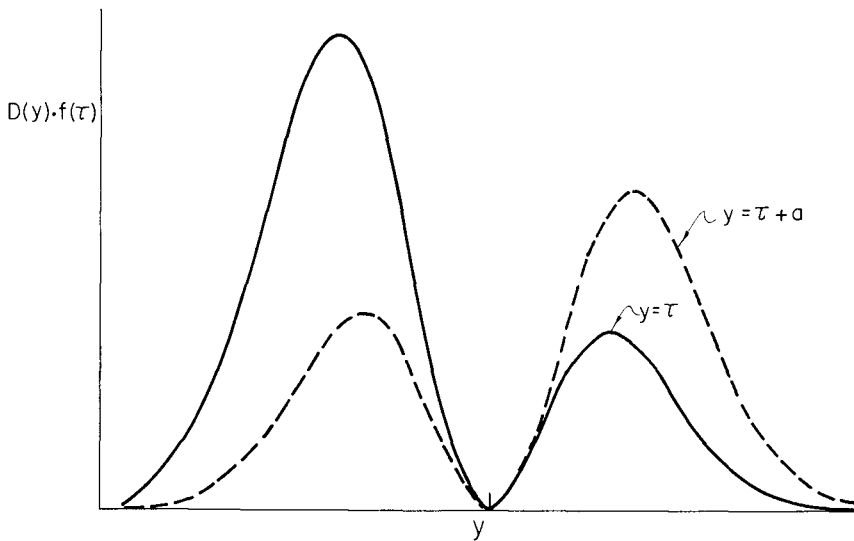
FIGURE 6 EFFECT OF SHIFT ON EXPECTED LOSS

Overdesign Factor

On substituting the particular functions for $D(y)$ given in Table 1 into equation 5 and differentiating for a minimum, one obtains the relations shown below for a.

For the Netherlands Model:

$$a = \sigma_\tau^2 / 2 \tag{7a}$$

For the Canadian Model:

$$a = (1 - (r + m) / q) \cdot \sigma_\tau^2 / 2 \tag{7b}$$

Here r, m, and q are exponents used in R-X, I-X and p-X relations respectively.

As an alternative formulation, it may be useful to express this shift in terms of the design scope X (i.e. dike height above some datum level) and its uncertainty as given by σ_X or $\sigma_{\ln X}$. In this case, using the scope-return period relation (equation 3) the following expressions are found for the Netherlands and Canadian models respectively.

$$X_d = \hat{X} + \frac{\alpha}{2} \sigma_X^2 \tag{8a}$$

$$\ln X_d = \ln \hat{X} + \frac{q-r-m}{2} \sigma_{\ln X}^2 \tag{8b}$$

Minimum Expected Loss

Substitution of the values for a (equation 7) into equation 5 yields the minimum value for the expected loss. As with D, a dimensionless form (L_{min}) is obtained by dividing this value by $\hat{R}$. The resulting expressions for L_{min} are as follows.

For the Netherlands Model:

$$L_{min} = \sigma_\tau^2 / 2 \tag{9a}$$

For the Canadian Model (ignoring certain higher-order terms):

$$L_{min} = \frac{n(n + m)}{q^2} \sigma_\tau^2 / 2 \tag{9b}$$

SIGNIFICANCE OF FUNCTIONAL MODELLING

The principal outputs of the two functional models of economic optimization have been presented above. Although the 'perfect knowledge' sections of the two models were developed completely independently, they show considerable basic similarity. The Netherlands model specifically assumes a straight line relation for construction cost and because of this linearization and the shape assumed for the regional probability distribution, it is able to use a minimum number of parameters. The Canadian model is not constrained in this fashion, and thus is more versatile. At the same time, however, it requires more parameters.

Under the conditions for which the Netherlands model was developed, it would appear that the results of the two models are virtually equivalent. This is illustrated in the appendix, using the data to which the Netherlands model was originally applied. It is seen that the calculated 'perfect knowledge' dike height is 5.97 m for the Netherlands Model and 5.92 m for the Canadian Model.

The more recent developments of functional modelling in Canada have been directed to the effect of uncertainty, as noted in a previous section. This work comprises the extension of both the original Netherlands model and the Canadian model to allow for uncertain data, and it has been shown that in this 'real world' case the design scope should be larger than the 'perfect knowledge' optimum. The fact that the functional representation of optimum design can provide simple quantitative expressions for this 'apparent overdesign' or 'factor of ignorance' demonstrates the advantages of this technique over the conventional trial design method.

The figures shown in the appendix again indicate that the two models give similar results, with the 'real world' optimum design heights being 6.14 m and 6.09 m for the Netherlands and Canadian formulations, respectively. For the data used in this particular example the difference in dike height may not be large, but nevertheless the increase in construction cost over the 'perfect knowledge' optimum amounts to about 7 000 000 guilders for both models. By including the effect of data uncertainty in the analysis, the 'real world' modelling has shown that this extra construction cost is justified by a reduction in the probable cost of future damage.

The loss or extra cost due to uncertainty, which equals or exceeds the increase in construction cost noted above, can potentially be reduced by improved data-gathering systems and prediction techniques. In this connection the estimates of this loss provided by the 'real world' functional modelling can provide a rational basis for allocating resources to field measurement and analytic studies directed to reducing uncertainty.

REFERENCES

1.   van Dantzig, D. and Hemelrijk, J.   "Extrapolation of the
         Frequency Curve of the Levels of High Tide at Hook of
         Holland by means of Selected Storms", Report of the
         Delta Committee 3 II.1, 7-56, 1960.

2.   Van Dantzig, D. and Kriens, J. "The Economic Decision
         Problem Concerning the Security of the Netherlands
         Against Storm Surges", Report of the Delta Committee 3
         II.2, 57-110, 1960.

3.   Wilson, K.C.   "Benefit-Accuracy Relationship for Small Structure
         Design Floods", Water Resources Research 8 (2),
         508-512, 1972.

4.   Wilson, K.C. and Watt, W.E.   "Optimizing Design Parameters
         for Small Flood-Control Structures", Proceedings of the
         First Canadian Hydraulics Symposium, Edmonton, 544-563,
         1973.

APPENDIX

EXAMPLE CALCULATIONS WITH NETHERLANDS AND CANADIAN MODELS

Data

The data given below have been abstracted from the Report of the Delta Committee cited in the list of references.

Annual exceedance probability of levels h metres above MSL given by

$$p = 2.63 \, e^{-2.97 \, (h-1.70)}$$

with estimated uncertainty (expressed in σ_τ units) of

$$\sigma_\tau = 0.23 \, (h-1.70)$$

Effective annual interest rate (interest minus inflation), 0.015

Costs, expressed in Mf (1 Mf = 10^6 guilders)

Washout Cost,   W = 24 200 Mf

Direct Cost,   I = 110 Mf at H_d = 5.00 m

                 1 = 150 Mf at H_d = 6.00 m

'Perfect Knowledge' Optimization

a) Netherlands Model   In this case X has an arbitrary origin. It
                         will be taken as $X = H_d$ - 5.00. Also, from
    above α = 2.97. The resulting expressions for I and R , in Mf,
    are

$$1 = 110 + 40 \, X \quad \text{and} \quad R = 242 \, e^{-2.97 \, X}$$

$$\therefore \quad X = \frac{1}{\alpha} \, \ln \frac{R_o \alpha}{1'} = 0.97 \text{ m}$$

$$\hat{H}_d = 5.00 + \hat{X} = 5.97 \text{ m}$$

$$\hat{I} = 148.8 \quad \text{and} \quad \hat{R} = 13.4$$

b) Canadian Model   In this case the origin of X is taken as the
                      same as that of the height distribution, i.e.

$$X = H_d - 1.70$$

Equating direct and damage costs to the values at H = 5.00 m and
6.00 m (X = 3.3 and 4.3) gives m = 1.17. With r = 0, q = n =
11.15. Thus

$$I = 27.2 (X)^{1.17} \quad \text{and} \quad R = 1.46 \times 10^8 (X)^{-11.15}$$

$$\therefore \quad \hat{X} = \left[\frac{n K_2}{m K_1}\right]^{1/(m+n)} = 4.22 \text{ m}$$

$$\hat{H}_d = 1.70 + \hat{X} = 5.92 \text{ m}$$

$$\hat{I} = 146.6 \quad \text{and} \quad \hat{R} = 15.4$$

Effect of 'Real World' Uncertainty

a) <u>Netherlands Model</u>   Since $H_d \simeq 6$ m, σ_τ should be evaluated at this point.

i.e. $\sigma_\tau = 0.23 (6 - 1.7) \simeq 1.0$

$$\sigma_X = \frac{\sigma_\tau}{\alpha} = .337$$

$$X_d = \hat{X} + \frac{\alpha}{2} \sigma_X^2 = 0.97 + 0.17 = 1.14 \text{ m}$$

$$H_d = 5.00 + X_d = 6.14 \text{ m}$$

$$I_d = 155.5$$

$$\text{Loss due to uncertainty} = L_{min} \hat{R} = \frac{\sigma_\tau^2}{2} \hat{R} = 6.7$$

b) <u>Canadian Model</u>   Again, $\sigma_\tau = 1.0$, and, thus

$$\sigma_{\ln X} = \frac{\sigma_\tau}{q} = .0897$$

$$\ln X_d = \ln \hat{X} + \frac{q-r-m}{2} \sigma_{\ln X}^2 = 1.440 + .040 = 1.480$$

$$\therefore \quad X_d = 4.39 \text{ m}$$

$$H_d = 1.70 + X_d = 6.09 \text{ m}$$

$$I_d = 153.6$$

$$\text{Loss due to uncertainty} = L_{min} \hat{R}$$

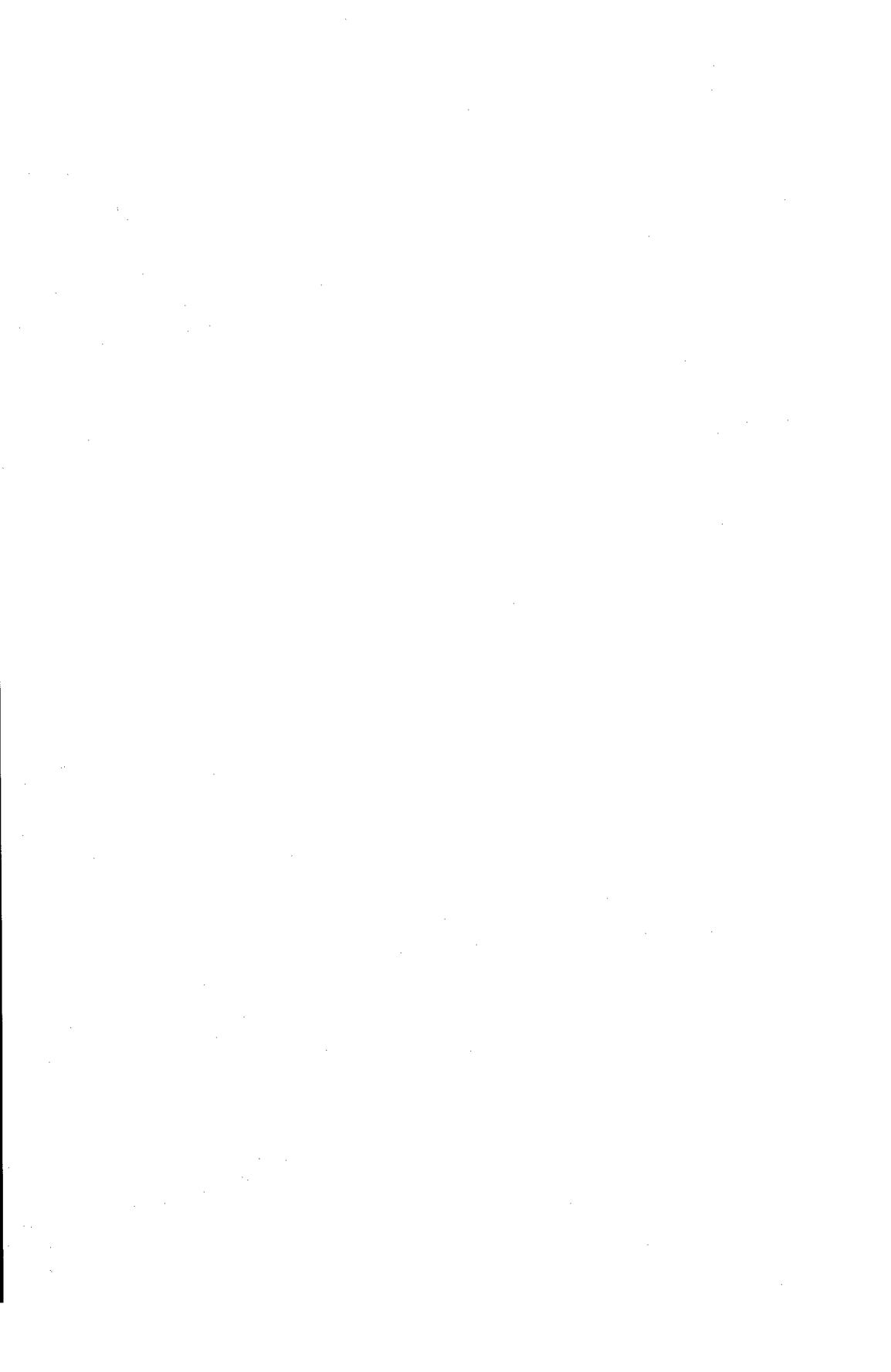$$= \frac{n(n+m)}{q^2} \frac{\sigma_\tau^2}{2} \hat{R} = 8.5$$

Hvide Sande Inlet, Denmark

PART IV

COASTAL, ESTUARINE, AND ENVIRONMENTAL PROBLEMS

Ferring Lake, Denmark

CHAPTER 119

ANCIENT AND MODERN HARBORS: A REPEATING PHYLOGENY

by

Douglas L. Inman

Scripps Institution of Oceanography, University of California

La Jolla, California 92037

ABSTRACT

The Minoans and Phoenicians appear to have developed a very
superior "lay" understanding of waves and currents, which led to the
development of remarkable concepts in working with natural forces in
their coastal engineering works. For example, the Phoenicians developed
a "continuous self-flushing" harbor at Tyre and possibly a "flushable"
harbor for the removal of sand and silt at Sidon. It would appear that
developments of this type were the outgrowth of the close association
with and acute observation of nature that occurs where a coastal people
learn to work with currents and sail, in the absence of technology for
harnessing large amounts of power. However, harbor design became markedly
stereotyped following the development of large engineering corps with the
capacity for rapid and massive construction. The earlier innovative,
natural concepts in harbor design appear to have become obscured by the
end of the Roman era, and have remained relatively unused to this day.

In view of man's present extensive intervention in the coastal
zone, mostly based on "brute force" technology, a careful study of the
ancients' ability to work with nature provides valuable insight for
today's problems.

INTRODUCTION

Maritime activity began in the Mediterranean Sea about 4,000 years
ago. It is here that the first rudimentary sea-going ships appeared,
which in time led to the development of significant maritime commerce
and the associated technology for building docking facilities and harbors.
The evolution of marine technology, its adjustment to man's socio-economic
needs, and the impact of natural catastrophies, are all recorded in the
remains of sunken ships and the ruins of the many ancient harbors that
border the Mediterranean Sea (Figure 1). Fortunately, a number of excel-
lent treatise on ancient ships, harbors, and cities in the Mediterranean
have been published (e.g., Casson, 1959; Flemming, 1969, 1971).

It seems that the earliest mariners landed and beached their boats.
They also used the natural protection afforded by rivers, headlands, and
embayments to moore and anchor in protected waters. The numerous small
islands of the Aegean Sea were ideally situated for protecting early
mariners. However, as ships became larger and their number increased,
the development of docking and harbor facilities became essential. It is
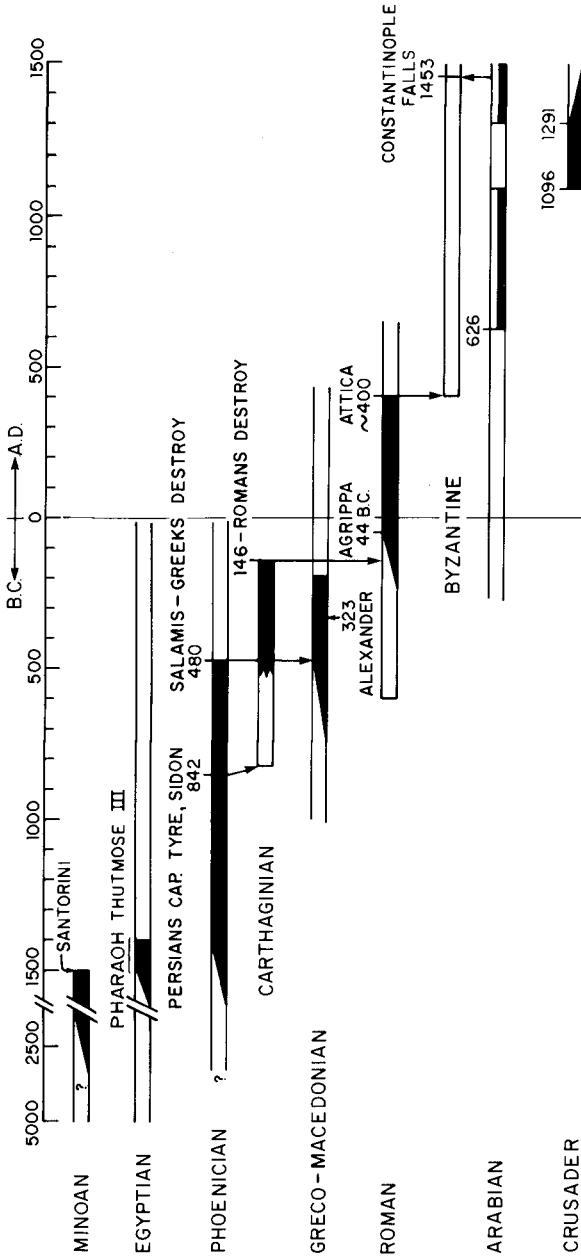apparent that by 1500 BC the Minoans were constructing protected wharfs

Figure 1.   Chronology of civilizations' influence on Mediterranean harbors and ships.

and berthing facilities by excavating them into the sandstone rocks at Nirou Khani, Crete. The perfection of protected anchoring basins with quay-side berthing facilities appears to have been a Phoenician development as illustrated by harbors at Sidon, Tyre, Akko (Acre), and Atlit along the coasts of Lebanon and Israel.

The present location of ancient harbor sites is markedly influenced by sea level changes, coastal tectonics, and the erosion and depositional history of the coast. Sea level has risen at rates of about 10 to 15 centimeters per century during the past 3,500 years, leading to what would appear to be a submergence of the coastline relative to sea level of about 3 to 5 meters. In the absence of other factors, one can expect to find that ancient harbor sites are submerged, and indeed a large number of them are (Flemming, 1969b; 1971). Coastal tectonics may accelerate this effect by submerging the coast, or alternatively, decreasing the submergence or completely overcoming it by raising ancient sites above present sea level. Finally, erosion and deposition alter the coastline so that ancient sites may now be far at sea, or buried some distance inland from the present shoreline. The latter case is typical of coasts where rivers have prograded the shoreline and filled former embayments. Typical examples of landlocked sites are Luni, Aquileia, and Ostia in Italy (Figure 2).

MINOAN HARBORS

The Minoans were the first people to whom history ascribes an extensive maritime commerce and a navy. They conquered and colonized the Isles of the Aegean, and through their fleet maintained control over much of the eastern Mediterranean from prehistoric times to 1500 BC. Principal centers of Minoan civilization appear to have been on the islands of Crete and Thera (Santorini), thus protecting them from invasion, except by sea. Their ships protected the islands and therefore their cities needed no stone walls (Casson, 1959).

The Minoan dominance of the Mediterranean appears to have ended abruptly in 1500 BC with the explosion of Santorini volcano and the subsequent tsunami that destroyed the major Minoan cities (Figure 3). It seems that the Minoans were about to embark on war with Egypt and Greece when the Santorini explosion intervened, demolishing the Minoan empire and causing extensive damage in Greece and Egypt (Galomopoulus and Bacon, 1969, p 19; Chadwick, 1972). In excavations near Heraklion Crete, Marinatos (1926) found buildings filled with pumice and ash, and in one instance found where massive blocks from a Minoan wall had been moved over 18 meters, apparently by catastrophic wave action.

The explosion of Santorini was far greater than the eruption of Vesuvius that destroyed Pompeii in 79 AD, and several times more powerful than the explosion that destroyed Krakatoa in 1883. The Santorini explosion blew out 83 square kilometers from the center of the island, and formed dense ash clouds whose deposits are now found as volcanic ash layers in sea floor cores from the eastern Mediterranean (Figure 3).

Thus, it appears that a great sea empire vanished almost overnight. This event made a vivid imprint on the minds of the Mediterranean peoples.

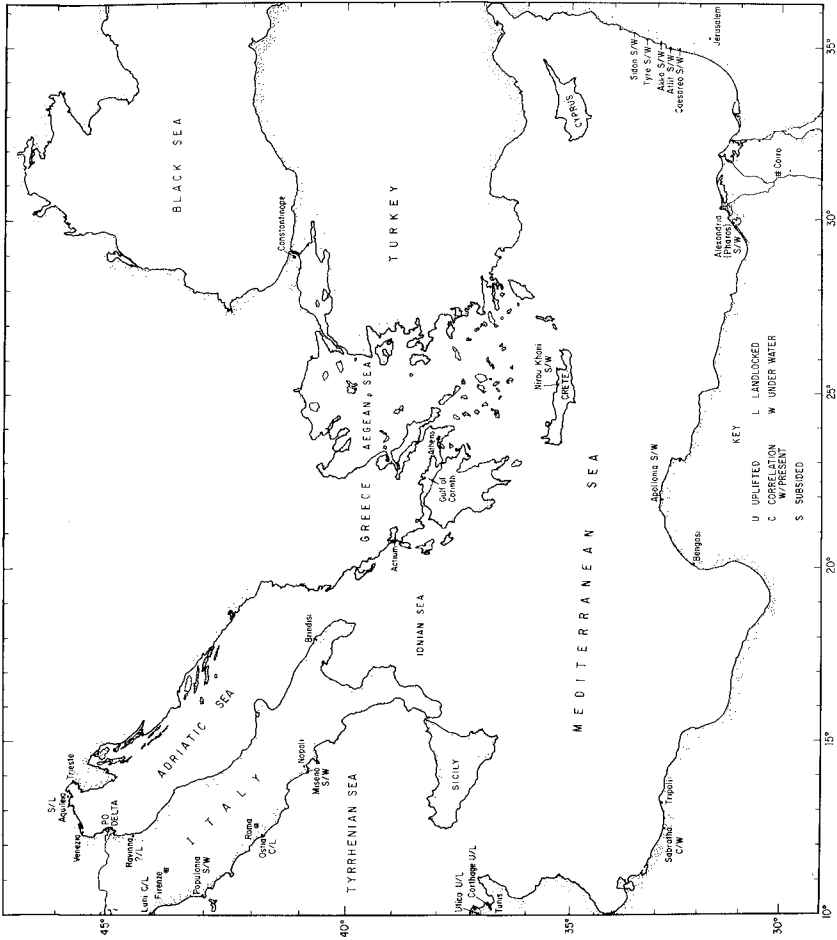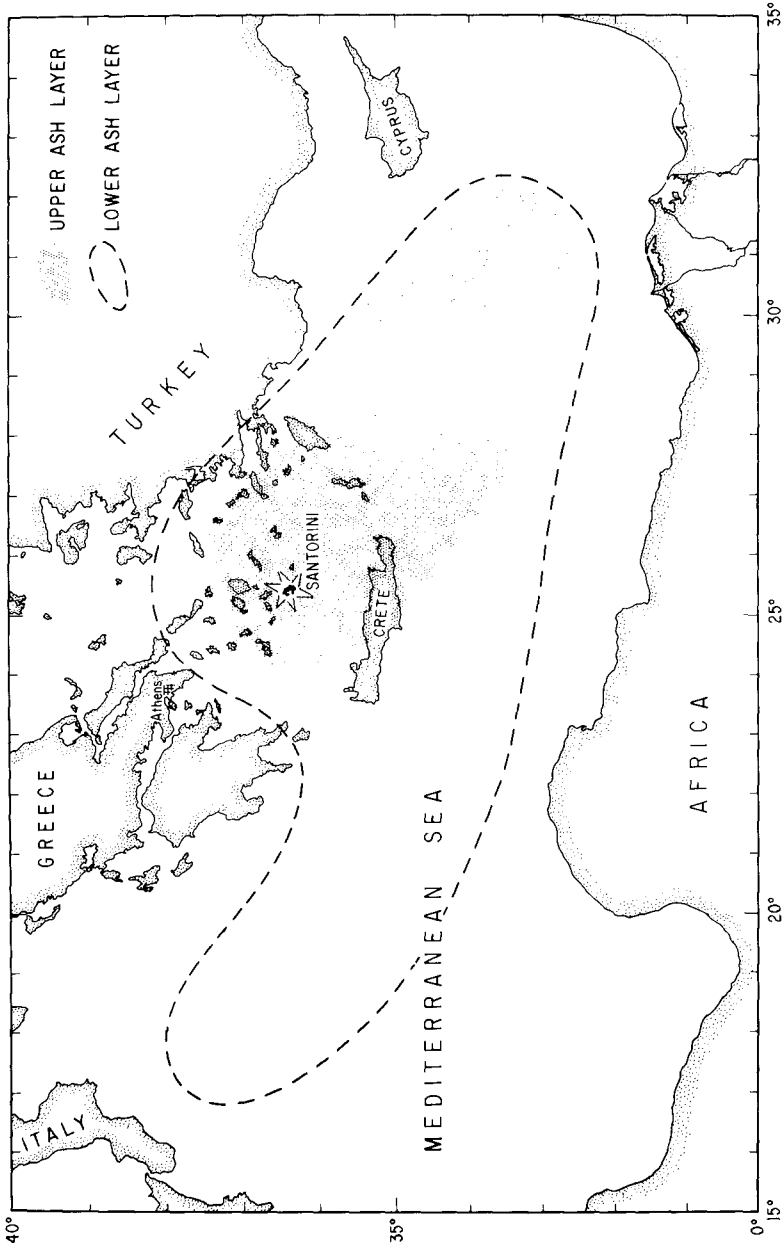Figure 2. Some ancient harbor sites in the eastern Mediterranean.

Figure 3. Extent of the distributions of two deep sea layers of volcanic as from explosion of Santorini volcano. The lower ash layer is older than 25,000 years, while the upper ash layer appears to correlate with the explosion of 1500 BC that coincides with the decline of the Minoan civilization (after Nickovich and Heezen, 1967).

Plato, who traveled extensively in Egypt as well as Greece, appears to have used the legend of a lost civilization on a continent sinking beneath the sea as a setting for his Timaeus and Critias. Thus, about 360 BC Plato recorded for posterity the myth of Atlantis (Mavor, 1969, p 12).

The principle harbor for the city of Knossos on Crete was probably at Amnissos, near the present harbor of Heraklion. This has been largely destroyed or covered by subsequent structures. An ancient sea port was established near Heraklion by the Saracens in the 9th century BC. This was rebuilt and fortified by the Genoese in the 9th century, and enlarged and strengthened by the Venetians in the 12th century. The Venetian harbor remains as the inner basin of the modern harbor of Heraklion.

The first harbor that dates from Minoan times was found at Nirou Khani about 12 kilometers east of Heraklion (Marinatos, 1929). It consists of several slips cut into the dune rock of the small headland forming the western end of the beach fronting the Knossos Beach Hotel (Figure 4). In plan, the major excavation consists of a single rectangular cut, 43 meters long and 11 3/4 meters wide, with a masonry rock wall 3/4 meters thick running the entire length of the excavation and dividing it into two long channels 6 x 43 meters and 5 x 43 meters. The excavation is on the sheltered lee side of the headland, and is associated with numerous walls that are both parallel and orthogonal to the excavation. On the landward side of the excavation is a 6 meter wide level area as though it had formerly been a wharf.

Both the wharf area and the masonry wall are now near sea level or 10 to 20 cm above sea level. Thus, it seems that the sea has risen at least one meter relative to land since the Minoan wharf was built. The excavated portion of the tank has a sand bottom with a maximum depth of 2 meters below sea level, but the excavation and wall appear to go deeper than this. The northwest or windward side of the headland contains a quarry area which appears to have been used for obtaining stone for the structures now found on the lee side.

It is of interest to note that the two harbor berths at Nirou Khani, which are 43 meters long by about 6 meters wide, would easily have accomodated two of the well known Greek trireme of a later age. The trireme is reported to have had a length of 35 meters, beam width of 3.7 meters, and a draft of 1.1 meters (Galanopoulos and Bacon, 1969, p 129).

PHOENICIAN HARBORS

Initially the Phoenician civilization occupied what is now roughly Syria, Lebanon and Israel. The Phoenicians were one of the great peoples of the world and were noted for their sailing, navigating, trading and colonizing. The alphabet of the western world, as well as the Greek and Roman alphabets, were derived from that of the Phoenicians. The Phoenicians were well known to the Egyptians as early as 2900 BC, but it wasn't until about 1400 BC, following the fall of the Minoan empire, that they became a great sea power.
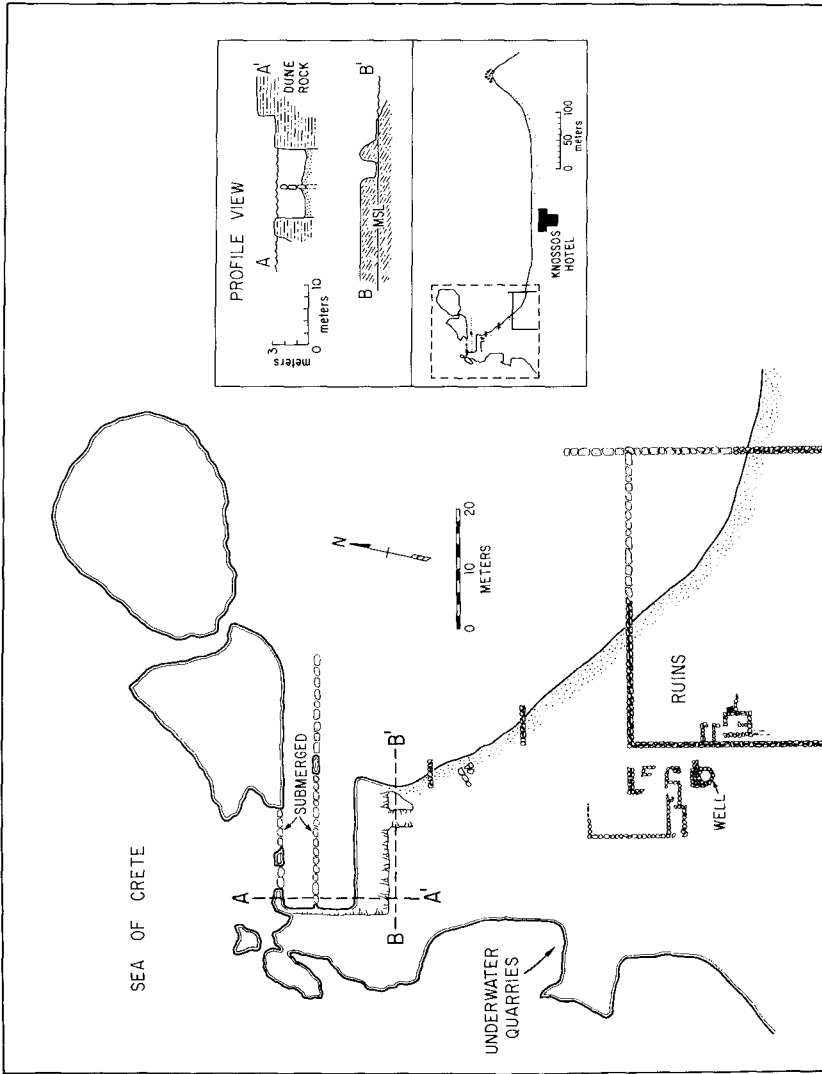
Figure 4. Minoan harbor and market place (circa 1500 BC) at Nirou Khani, 12 km east of Heraklion, Crete. Details of the two 40 m long harbor slips measured by author in October 1972; archaeology from Marinatos (1926).

        In 1500 BC Phoenicia became a frontier province of Egypt and by
1400 BC had regained independence. It remained at the height of its
power and influence for the next 400 years. From 1200 to 800 BC the
Mediterranean became a "Phoenician Lake". The Phoenicians established
colonies along the African and Spanish coasts of the Mediterranean and
along the Atlantic coast of Africa and Portugal. Their decline as a
world power began in 842 BC when the Assyrians captured the principle
Phoenician cities of Tyre and Sidon. However, they remained a great
naval power under Persian rule until the fleet was destroyed by the Greeks
in the battle of Salamis in 480 BC. Phoenicia came under Greco-Macadonian
rule in 323 BC when Alexander the Great took Tyre and Sidon and destroyed
the Persian Empire. Later,in the first century BC,the Romans seized
Carthage, and Tyre and Sidon also fell to Roman rule. Tyre and Sidon
remained Roman centers of learning and continued to prosper until the area
fell to the Moslem invasion in 626 AD.

        Probably one of the earliest Phoenician harbors was constructed
more than a milenium BC in the Naaman River, and is now buried under a
portion of the City of Akko (Acre) in Israel. The increasing importance
of Phoenicia as a maritime people, however, soon led to the development
of protected harbors with large anchorages and elaborate piers and quays
for handling cargo. The well preserved ruins of the ancient harbors of
Sidon, Tyre, Akko, and Atlit provide ample testimony to the high develop-
ment of harbor engineering by the Phoenicians. The harbor of Tyre was
originally separated from the mainland, and was considered to be self-
flushing. The present tombolo connecting the harbor to land was construc-
ted by Alexander the Great during the seige of Tyre in 323 BC. It is
claimed that large reservoirs were built into the harbor of Sidon so that
it could be flushed by opening sluice gates (Frost, 1963).

        The harbor of Akko is the best example of a Phoenician harbor that
has survived, with almost continued use, to the present (Figure 5). The
original Phoenician base for the breakwater and lighthouse is still
available for inspection by divers. Upon this foundation, and clearly
identifiable by the unique construction techniques of the various civiliza-
tions, one recognizes the efforts of Hellenic, Roman, Crusader, and modern
engineers.

        The following description of the southern breakwater and the Tower
of Flies (lighthouse) is based on a diving reconnaissance by me lead by
Abner Raban,and the written account of Elisha Linder (1971). The break-
water closes the natural harbor and forms excellent protection from the
frequent storms from the southwest. The south breakwater originally had
a length of 340 meters, a width of 12 meters, and its base is on a sandy
bottom. It is constructed of 4 layers of stone, the lower of which is
Phoenician and is now 2.8 meters below sea level. The Phoenician and
Hellenic layer above it are built in the "rashin" manner of cut stone
pieces, about 0.6 x 0.6 x 1.5 meters in length. The Roman construction,
which extends from just below sea level to about 1.5 meters above,consists
of massive cut sandstone pieces, 2 x 2 x 12 meters in length, typical of
the construction blocks used in the time of Herod the Great (73-4 BC).
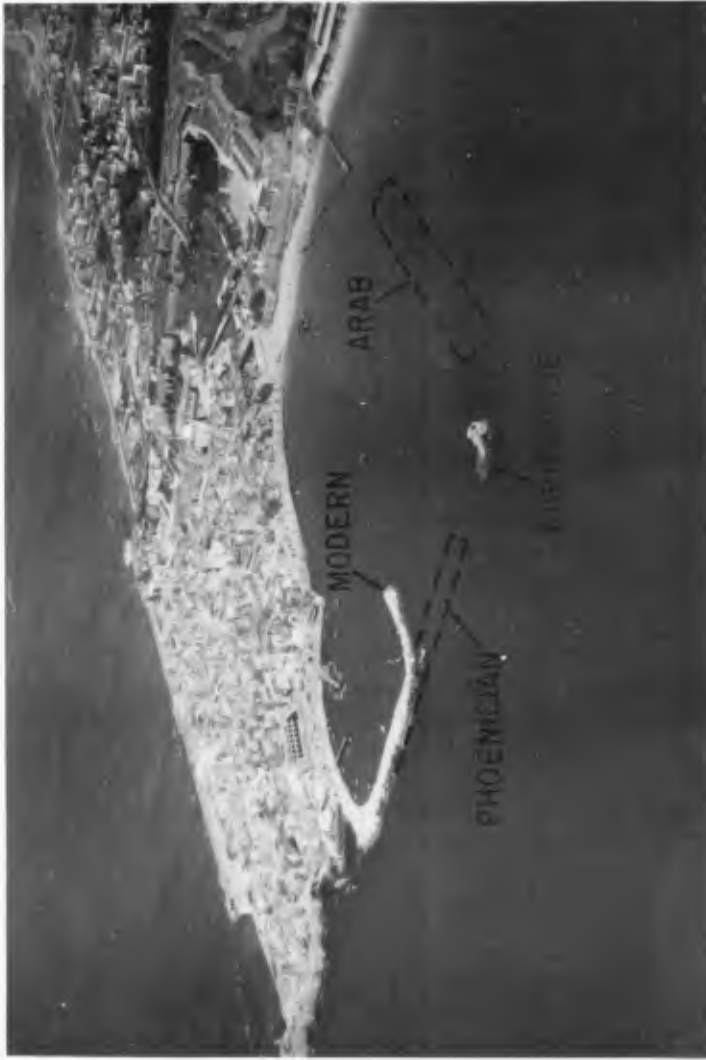The Crusader layer,above the Roman,consists of cut stone pieces, about

Figure 5. Air photograph of the harbor at Akko (Acre) looking northwest. The modern rouble mound breakwater lays on a submerged foundation of Phoenecian, Roman, and Crusader construction. The submerged Arab breakwater dates from 900 A.D.

10 x 20 x 20 centimeters, that form a wall which was backfilled with rubble. The modern (highest) level consists of a large size rubble mound placed randomly on top of the ancient breakwater (Figure 5).

The Tower of the Flies is also known as El Minara, "The Tower of Light". Its lower construction is similar to that of the south breakwater except that it rests on natural rock. The lower level consists of elongated stones whose dimensions are 0.6 x 0.6 x 2 meters. It is built by the same method of "rashin" which makes up a line of stairs that starts at the natural rock bottom,which is at a depth of 5 1/2 meters.

The remnants of a submerged rubble mound breakwater are visible between the Tower of Flies and the shore. This was placed about 900 AD by the Arabs who sunk barges loaded with stone.

The tops of the breakwater and quay of the Phoenician harbor of Atlit are now just at sea level. They are constructed of very uniform rectangular cut stone pieces with dimensions of 0.4 x 0.4 x 1.4 meters. The stone slabs are offset and interlocked where the breakwater joins the quay wall (Figure 6).

The Phoenicians achieved a very high level of technology for submarine construction. The Phoenician stones are relatively small and don't have the lead connection used during Roman periods, or the iron connections which were used during the Crusader times. We do not know the methods they used to place the stones underwater, nor how they positioned and assembled the stones into the smooth walls which have withstood the effects of waves and currents for 25 centuries.

ROMAN HARBORS

The Roman Age began about 600 BC when the Etruscans began domination of much of Italy. In 509 BC,the last of the Etruscan kings were overthrown and Rome became a city-state and then a republic. It flourished and grew on previous and contemporary Greek teaching and thinking. The Greeks were the thinkers and the Romans were the doers. Originally, Rome was not a sea power, but became one in 260 BC during the Punic Wars (against Phoenicia) when Rome interferred with the affairs of Carthage, a Phoenician colony. It is reported that Rome became a naval power by making 100 copies of a Private warship in 60 days (Casson, 1959, p 159).

Early Roman harbors were carefully planned and well constructed. A good example is the port of Aquiliea which was built in 181 BC as an outpost on the northeastern frontier. Aquiliea was a river harbor designed to take ships about 35 meters long. It was unique in that its quays had two loading levels, one for high and one for low water levels (Figure 7). The mooring ports are constructed of three beautifully cut stones, morticed together with metal straps to form a round opening (Figure 8). It is not clear whether the opening was intended for a bollard to be used in mooring, or for a davit used in handling cargo, or both. The mooring ports are placed at intervals of about 34 meters along the quay wall.

Figure 6. Phoenecian quay at Atlit showing interlocked and offset slabs where the breakwater joins the quay wall.

Figure 7. Stone quay in river port of Aquileia, Italy (circa 180 B.C.).
 Quay had landing stages at two levels (for varying river levels?).
 Note protruding mooring stones shown in Figure 8.

Figure 8. Details of mooring port shown in Figure 7. Port is
constructed of three cut stones, morticed together with metal straps.

Julius Caesar, who was proconsular of the Roman Senate, actually became in effect a dictator. Members of the senate, filled with foreboding, killed Julius Caesar on the Ides of March in 44 BC. Civil war followed, until Octavian finally defeated the Egyptians under Mark Anthony at Actium on 31 BC. Following the civil war, Octavian, Julius Caesar's heir, consolidated the country into the first Roman Empire and assumed the title Augustus, reigning from 27 BC to 14 AD. Under Augustus the Roman Empire attained its maximum size, and the only further expansion was the conquest of Britain during the rein of Emperor Claudius (41 AD 54 AD).

The Romans became a great sea power under Agrippa, who was Octavian's (later called Augustus) lieutenant. Also, about this time the Romans attained the summit of their technological skill as harbor engineers. Agrippa constructed the harbor of Miseno near Naples in 31 BC, and it became the main base of the Roman fleet. In 79 AD, Pliny the Elder, who was then commander of the Roman fleet, sailed from Miseno in a futile attempt to save the people of Herculaneum and Pompeii, and lost his life by suffication from the fumes of Versuvius.

The main breakwater at Miseno is constructed of a double row of Roman arches, joined and capped at the top to form a single solid wall (Fig 9). The arches are staggered so that each support column of the inner row stands opposite an arch of the outer row. This construction technique, borrowed from the very successful use of the Roman arch for aquaducts and bridges, had a number of advantages when employed as a breakwater. The arch concept enabled breakwaters to be constructed in deep water with a minimum amount of stone. The open-but-staggered columns permitted currents to flow freely through the structure, while protecting the harbor from wave action. This novel construction was highly successful at Miseno, where siltation was not a problem. The submerged remnants of the support columns for the staggered arches are still in place and the outer row is available for inspection by divers. However, a modern rubble mound breakwater has been placed over the inner row of arches.

Staggered, double rows of underwater arches became a favored method of breakwater construction by the Romans, and although not always successful, they were used extensively. For example, Caludius' Port at Ostia near Rome was constructed of staggered arches in 54 AD, as was Sabratha in Africa about 200 AD.

Caesarea was an outstanding example of Roman influence on harbor engineering. The harbor was built on the site of a previous Phoenician harbor by Harod the Great, and was completed in 10 BC (Figure 10). It is described by Josephus Flavius (Antiq. XV 9.6) who wrote, "the harbor is free always from the waves of the sea". It was constructed by reinforcing two reefs, which stretched seaward, with vast stone blocks. A quay encircled the whole harbor, and on the quay were arches "where the mariners dwelt". The underwater ruins of the harbor were studied in 1960 by a group headed by Edwin Link. The main breakwater is in the shape of an arc that extends 450 meters seaward from the shore, then curves to the north for 370 meters along the shore. The entrance is between the main breakwater

Figure 9. Roman arches supporting the aquaduct leading to Ceaserea, constructed about 20 B.C.. Staggered double rows of underwater arches were a favored method of breakwater construction by the Romans.
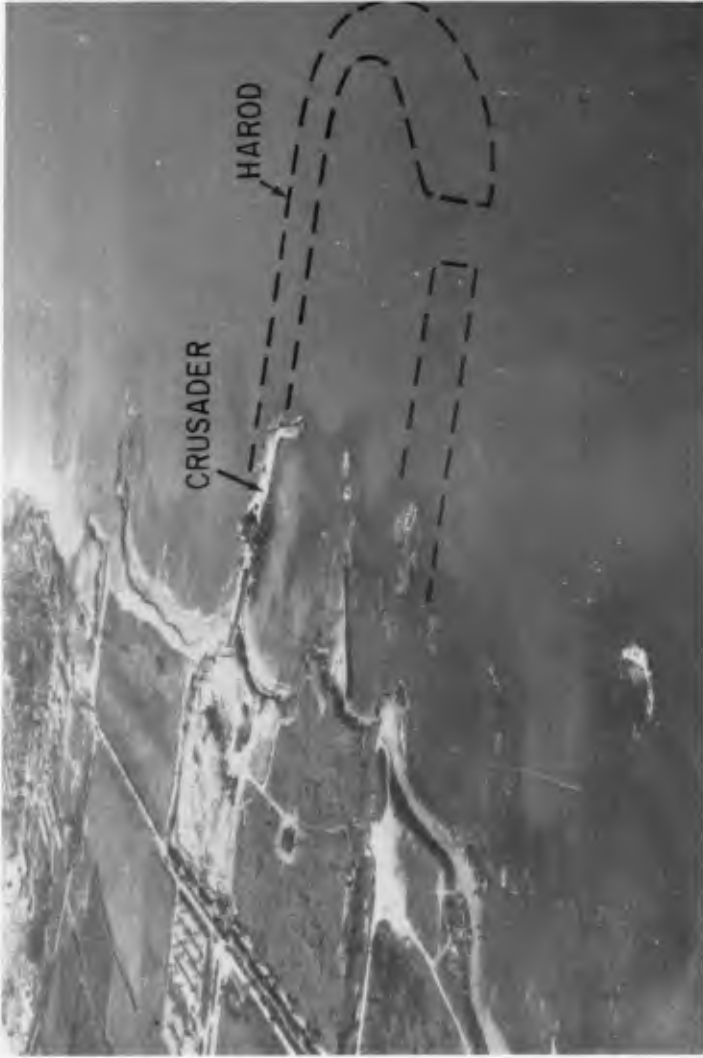
Figure 10. Reconstructed city of Ceaserea and the crusader breakwater and harbor looking south. Dashed line outlines the large harbor constructed by Herod the Great in 10 B.C.

and the north breakwater and is open to the north, which is the direction
of the least waves. The average width of the breakwater is 50 meters and
the depth is over 7 meters. The size of stone is surprising. The largest
stones are 2 1/2 x 3 x 15 meters, and each one weighs about 30 tons
(Linder, 1971). Some stones were joined by lead and wood caulking, and others
were sealed by molton lead poured in the spaces between the stones. In
water deeper than 7 meters, the Romans built up a layered platform of
smaller stones for the large stones to rest upon. In water 6 meters or
less, they rested the hugh pillars directly on the bottom. Caesarea fell
to the Moslems in 638 AD and its sea power faded. It was partially revised
under the Crusaders, when it was taken by Baldwin I in 1101. The
Crusaders rebuilt and walled about one-tenth of the Roman City, and rebuilt
about one-eighth of the harbor (Figure 10). The city was further strengthened
by Richard I (1191). It again fell to the Moslems and was demolished in
1265. Stones from its ruins were transported to Akko and Jaffa for
building purposes.

Ostia, the port of Rome built near the Tiber, is said to have been
one of the finest examples of Roman harbor engineering. The harbor construc-
tion was begun by Claudius in 42 AD, and completed by Nero in 54 AD. The
principle of the staggered Roman arch was used for the main breakwaters.
Although the harbor was magnificently constructed and huge, with an area
of 850,000 square meters, it proved not to be safe from waves and was
subject to siltation. A storm in 62 AD caused the loss of many ships, and
the harbor was eventually abandoned in preference of the hexagonal shaped
basin that was built in 98 - 117 AD by Trajan. The ruins of Claudius'
harbor are landlocked and have not been excavated. The ruins of Trajan's
harbor are landlocked and easily visible from the air (Schmiedt, 1964).

Harbor design became progressively more stereotyped during the
last half of the Roman era, and their construction was characterized by
massive structures that required large armies of workmen. Innovative
concepts in design, and attempts to work with natural elements, appear to
be absent. As a result there were a greater number of failures. The
Roman empire gradually declined and experienced a series of serious invasions
by the Huns beginning in 406 AD. The Huns under Atillia invaded again in
433-55 AD. In 455 AD, the vandal king, Gaiseric, built a fleet that began
the domination of the Mediterranean from the west, and caused the Roman
empire to be restricted to the eastern Mediterranean. There was a brief
resurgence of the Roman Empire in 600 AD, but by 626 AD, Egypt and the
western Mediterranean fell to Islam, and a Byzantine empire replaced the
Roman in the central and eastern Mediterranean.

CRITIQUE

Most of the world's population has always lived near the coast
where the seas are the means of transportation and a source of food. This
close association with nature gave the Minoans and Phoenicians a very
superior "lay" understanding of waves and currents which is evident in
their coastal engineering works. Since they lacked the technology for
harnessing large amounts of power, they developed remarkable concepts in
working with natural forces, as can be seen by an inspection of the ruins
of their ancient harbors.

These natural approaches and the resulting "gentle architecture" carried through to Roman times. The Romans developed staggered, double rows of underwater arches as a favored method of breakwater construction. The staggered arches provided baffles for dissipating waves, while permitting currents to flush the harbor. However, harbor design became markedly stereotyped following the development of large engineering corps with the capacity for rapid and massive construction. The earlier innovative, natural concepts in harbor design appear to have become obscured by the end of the Roman era, and have remained relatively unused to this day.

Harbor technology had brief resurgences during the Crusader times, when Genoese and Venetians constructed some remarkable harbors including that at Heraklion, Crete. Following this,there was a general decline in technology until the beginning of the age of world exploration in the 15th century AD. However, it now appears that we have again passed through a zenith in harbor technology and are now in what would be equivalent to a "second Roman decline". This is attested to by the numerous "white elephants" that line our coasts. In view of man's present extensive intervention in the coastal zone, mostly based on "brute force" technology, a careful study of the ancients' ability to work with nature provides valuable insight for today's problems.

ACKNOWLEDGMENTS

REFERENCES

Casson, L., 1959, The Ancient Mariners; Sea farers and Sea Fighters of the Mediterranean in Ancient Times, The Macmillan Co., New York, 286 pp (paperback Minerva Press M16).

Chadwick, J., 1972, "Life in Mycenaean Greece", Scientific American, vol 227, no 4, p 36-44.

Flemming, N. C., 1969a, "Sunken cities and forgotten wrecks", p 123-171 in G. E. R. Deacon (ed) Oceans, an atlas-history of man's exploration of the deep, Paul Hamlyn, London, New York, 295 pp.

Flemming, N. C., 1969b, "Archaeological evidence for eustatic change of sea level and earth movements in the western Mediterranean during the last 2,000 years", Geological Society of America, Special Paper 109, 125 pp.

Flemming, N. C., 1971, Cities in the Sea, Doubleday & Co.Inc., Gasden
        City, New York, 222 pp (refer to p 34-48).

Frost, H., 1963, Under the Mediterranean, Routlege & Kegan Paul Ltd.,
        London, 278 pp.

Frost, H., 1971, "Recent observations on the submerged harbor works at
        Tyre", Bulletin du Musee de Beyrouth, vol 24, p 103-111, 2 plates.

Galanopoulos, A. G. and E. Bacon, 1969, Atlantis; The Truth Behind the
        Legend, Bobbs-Merril Co., New York, 216 pp.

Linder, 1971, "Underwater archaeology, a new dimension in the study of
        Israel in antiquity", Qadmoniot, vol 4, no 2, p 44-55 (in Hebrew).

Marinatos, S., 1926, "Excavations at Nirou Khani, Crete", Practika
        Archaeologikis Etaireias Athinon, p 141-147.

Marinatos, S., 1929, "Excavations in Crete", Practika Archaeologikis
        Etaireias Athinon, p 94-95.

Marinatos, S., 1972, "Thera: key to the riddle of Minos", National
        Geographic, vol 141, no 5, p 702-726.

Mavor, J. W., Jr., 1969, Voyage to Atlantis, G. P. Putnam's Sons, New
        York, 320 pp.

Nickovich, D. and B. D. Heezen, 1967, "Physical and chemical properties
        of volcanic glass shards from Pozzuolana Ash, Thera Island, and
        from upper and lower ash layers in Eastern Mediterranean deep sea
        sediments", Nature, vol 213, p 582-584.

Schmiedt, G., 1964, "Contributo della foto-interpretazione alla riconstruz-
        icnne della situazione geografico-topografica dei porti antichi in
        Italia", Coi Tippi dell' Instituto Geografico Militare Firenze,
        Italia, 81 pp, 58 figs.

CHAPTER 120

WAVE ATTENUATION AND CONCENTRATION ASSOCIATED WITH HARBOUR
APPROACH CHANNELS

by

J.A. Zwamborn[*] and G. Grieve[**]

ABSTRACT

Modern bulk carriers require deeper and wider harbour entrances.   As a
result long approach channels have to be dredged outside the breakwaters.
These large channels cause considerable changes in the waves due to
refraction and diffraction which effect the wave conditions in the
harbour entrance.

    As part of the Richards Bay harbour entrance studies, two phenomena
were found to considerably effect the design of the entrance layout,
namely:

(i)   wave attenuation for waves travelling near parallel to the
        channel axis, caused by refraction of wave energy away from
        the channel, and

(ii)   wave concentration on the channel side slopes, also mainly due
        to refraction, reaching a maximum for a critical approach
        direction of about 25° relative to the channel axis.

As a result of the wave attenuation, waves travelling within an angle
of 20° either side of the channel axis were found to cause no problems
whatsoever with regard to wave penetration into the harbour.

    Unacceptable wave penetration was, however, experienced for wave
directions close to the critical direction.   A great number of variations
to the entrance layout were tested to minimise this problem.   The results
showed the superiority of a flat channel slope of 1 in 100 above steeper
side slopes and the beneficial effect of a Vee-shaped channel bottom.
Also test results with irregular waves with regard to height, period
and directions were found to be significantly different from those
with uniform waves which considerably exaggerate the wave concentration
phenomenon.

---

[*]   Head: Coastal Engineering and Hydraulics Division, National Research
       Institute for Oceanology, South African Council for Scientific and
       Industrial Research, Stellenbosch.

[**]   Research Officer, Coastal Engineering and Hydraulics Division, South
       African Council for Scientific and Industrial Research, Stellenbosch
       (formerly).

INTRODUCTION

As a result of ever increasing ship sizes, greater channel depths and widths have to be allowed for in modern harbour entrance design.

Entrance channel depths of between 22 and 25 m are required for 150 000 dwt loaded ships whereas 250 000 to 300 000 dwt bulk carriers may require depths of between 25 and 28 m. Due to the limited depths which exist in most of the world's coastal areas, entrance channels become several kilometres long and, under these circumstances, it becomes impractical to protect the entrance channels by breakwaters over their entire length.

Moreover, safe manoeuvring of these huge vessels requires sufficiently wide entrance channels with widths varying between 300 and 600 m and preferably straight approach channels to avoid sudden course corrections in the channel.

As a result the conventional two-arm system of breakwaters is not very effective in reducing wave heights in harbours which incorporate these deep and wide entrance channels. Relatively short breakwaters sufficiently long to avoid excessive sediment deposition in the harbour entrance should therefore normally suffice.

This means that an approach channel of several kilometres long has to be dredged and maintained *outside* the protection of the breakwaters. During the studies for the design of the deep water port which is being constructed at present at Richards Bay in Natal (approximately 160 km north of Durban) it was found that the approach channel has a considerable influence on the wave conditions in the harbour entrance.

WAVE TRANSFORMATIONS EFFECTING HARBOUR ENTRANCE DESIGN

Wave directions and heights change due to wave refraction, diffraction, shoaling, bottom friction and percolation, as waves move into transitional and shallow water. Although bottom friction has been found to effect the wave heights and wave energy spectra in shallow water[1,2], wave refraction and diffraction are by far the most important wave transformations in harbour entrance design. The effect on wave height due to shoaling only becomes important in very shallow water ($d/L_o = 0,05$, where d = water depth and L_o = deep water wave length) and the shoaling coefficient viz. $k_s = H/H_o$ (H_o being the wave height in a water depth d and H_o in deep water), can readily be determined for a given wave length and water depth[3]. On the other hand, the effect of wave refraction and diffraction differ from case to case and can only be determined for a particular harbour layout by extensive hydraulic model testing or, in cases, with relatively simple boundary conditions, by calculation, i.e. mathematical modelling.

Conventional harbour layouts

Before the advent of the super class ships conventional harbours usually
consisted of twin-armed breakwaters enclosing a sufficiently large area
for mooring ships or protecting a river mouth or lagoon entrance in the
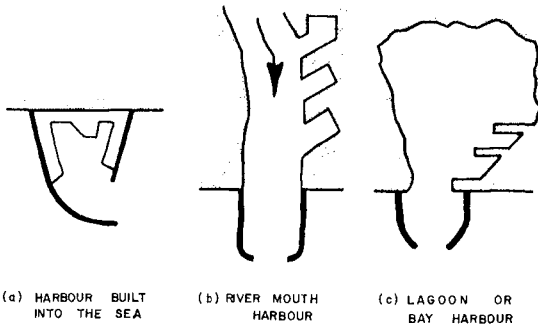case of inland harbours (see Figure 1).

Examples of the first
type can be found at
Kashima (Japan), Gordons
Bay, Port Elizabeth, Cape
Town (South Africa) and
of the second type at
Ijmuiden, Rotterdam
(Holland), East London,
Durban (South Africa).

The main purpose of
the double breakwaters
in the convential harbour
design was to reduce the
wave heights in the harbour
basin to acceptable limits
and, in the case of sandy
coasts, to protect the
harbour entrance from
excessive siltation.

(a) HARBOUR BUILT   (b) RIVER MOUTH   (c) LAGOON   OR
    INTO THE SEA   HARBOUR   BAY HARBOUR

Fig. 1.   Conventional type harbours.

To facilitate the reduction of wave heights the entrance widths were
made relatively small, i.e. 50 to 200 m, which was acceptable in view
of the high manoeuvrability of the smaller ships using these harbours.

Although in certain cases, for example Durban harbour, some dredging
was necessary outside the breakwaters to maintain the required water
depth in the harbour entrance the breakwaters usually extended to such
a depth that no extensive outside dredging was necessary. For the
design of these harbour entrances, including the breakwater structures,
deep sea wave conditions could thus be converted to the harbour entrance
area by standard refraction techniques and wave heights inside the
harbour could be determined using diffraction diagrams[3] or on a hydraulic
model.

Harbour entrances for super ships

The enormous increase in the size of super tankers has introduced a new
dimension in harbour design. Where in the past the main emphasis was
on providing sufficient entrance width between the breakwaters for ships
to pass through, with the 17 to 22 m draught of the 150 000 to
300 000 dwt ships, deep and wide entrance channels have to be provided
over considerable distances out to sea. Although sedimentation problems
still play a role in the design of such channels[4] the channel alignment,
width and depth are mainly determined by navigation requirements[5]. Prefer-
ably, the approach channel should be straight for easy manoeuvring and
it has to be dredged out to sea to the point where the depth is equal
to the required channel depth. Where the channel meets the shore rela-
tively short breakwaters are provided to protect the channel against
siltation caused by littoral drift and, to some extent, from wave
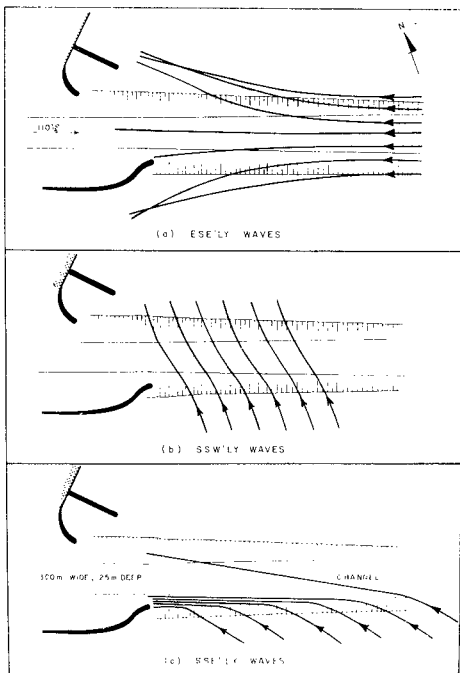penetration.

Fig. 2. Wave refraction caused by
         channel slopes.

The presence of a deep approach channel, however, considerably changes the local wave regime in the entrance area, mainly as a result of wave refraction caused by the channel.

As an example the basic layout of the Richards Bay harbour is shown schematically in Figure 2. This figure indicates for waves travelling in the direction of the channel a reduction in wave height in the entrance area near the breakwaters, Figure 2(a) for waves crossing the channel very little change, Figure 2(b) and for waves approaching the channel at a 'critical' oblique angle a considerable concentration of wave energy which may cause serious problems, Figure 2(c).

WAVE ATTENUATION

Based on conventional diffraction theory there would virtually be *no* reduction in wave heights inside a harbour with a large entrance channel as shown in Figure 2 for waves running in line with the channel axis. For instance for a 12 s period ESE'ly wave (i.e. almost parallel to the channel axis) the wave height inside the harbour would still be about 60 per cent of the incident height.

Tests on a 1 in 100 scale model showed considerably greater reduction in wave heights caused by refraction and diffraction in the approach channel. For the above wave condition the model gave a wave height in the harbour of only about 20 per cent which effectively solved the problem of the potentially difficult wave direction parallel to the channel axis!

Effect of dredged channels

The effects of a relatively deep dredged channel on the incident waves may be separated as follows:

(i)   A difference in wave celerity between the waves travelling in
       the channel and adjacent to the channel causes a considerable
       phase difference, resulting in wave diffraction on the channel edges;

(ii)   waves travelling on the channel slopes are refracted away from
       the channel.

Due to the difference in depth the part of the wave travelling in the
channel will move faster than that in the shallower surrounding area.
For example when the channel is 25 m deep and the surrounding sea
bottom depth is 20 m the wave celerities for a 12 s period wave are
13,8 and 12,7 m/s respectively. Thus the wave in the channel would be
180° out of phase after it has travelled over 955 m in the channel
(see Figure 3). Due to the difference in phase a mixed wave pattern
will result. Assuming
vertical channel sides
and constant water depth
the resulting wave
pattern could perhaps be
approximated using con-
ventional diffraction
theory, i.e. the wave
travelling in the channel
will diffract out of the
channel and the wave on
the sides will diffract
into the channel. The
resulting waves are the
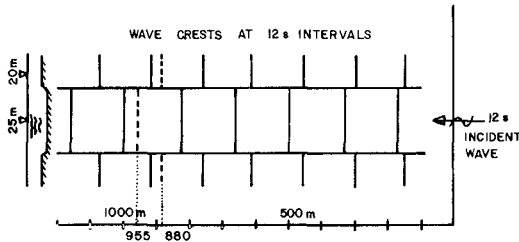sum of the two diffrac-
ted waves.

Fig. 3.   Wave advance in dredged channel.

       Preliminary tests in a wave basin, however, showed that with a
phase difference of about 90° the waves break up into waves with
individual crests inside and next to the channel and the average wave
height at a distance of 700 m from the channel entrance was reduced by
about 40 per cent for 12,0 s waves.

       In practice the channel side slopes will not be vertical but will
have a slope varying between 1 in 20 and 1 in 100. In addition to the
diffraction effect, waves travelling on or near the side slopes will
therefore refract away from the channel (see Figure 2(a)).

                    Richards Bay Harbour entrance

The proposed layout of the Richards Bay harbour entrance, which is
designed for 150 000 dwt ships entering under virtually all conditions,
is shown in Figure 4 [5,6]. The layout includes a 3,5 km long, 300 to 400 m
wide and 25 m deep dredged approach channel and a 1,2 km long main break-
water.

       Wave penetration studies formed an important part of the design of
the Richards Bay harbour entrance. Tests were carried out on a 1 in 100
scale model to determine the wave heights in the harbour for all possible
wave directions between SSW and ENE. As expected, the wave penetration
for ESE'ly waves running parallel with the channel axis was greatly
reduced due to diffraction and refraction in the entrance channel (see
Figure 5) whereas normally this wave direction would have caused the
worst wave penetration.

Fig. 4.   Layout Richards Bay Harbour Entrance.

Fig. 5. Wave attenuation in entrance
channel for ESE, 12 s waves.

Relative wave heights, as measured in the model for 12 s period ESE'ly waves, are shown in Figure 6. For an incident wave height at the model boundary of 100 per cent, the wave height in the approach channel is reduced to about 50 per cent, further reducing to only about 15 per cent inside the harbour. High waves exceeding 130 per cent are seen to occur on the top of the 1 in 100 south channel slope.
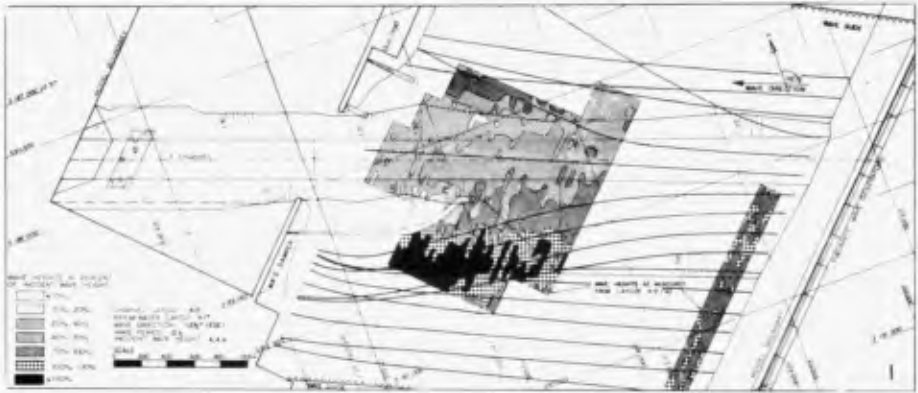
Fig. 6. Richards Bay, final layout, wave attenuation for
         $112\frac{1}{2}^{\circ}$ (ESE) 12 s waves.

Wave refraction lines calculated by computer are super-imposed on the
wave penetration diagram in Figure 6. The agreement, both qualitively
(wave pattern) as well as quantitatively (wave heights) is seen to be
remarkably good.

WAVE CONCENTRATION

Wave penetration tests in the Richards Bay harbour model were initially
done only for the wave directions E, ESE, SE, SSE and S $(22\frac{1}{2}^{\circ}$ direction
sectors) and wave penetration was found to be acceptable for all these
directions[6].   At a later stage of the investigation, however, it was
decided to test several directions between SE and SSE and it was found
that unacceptable wave penetration occurred over a narrow direction
sector of 10° to 20°, with a mean angle of approach relative to the
channel axis of about 25° (or 35° relative to the corresponding deep
sea wave direction).

This wave concentration caused a serious problem in the design of
the Richards Bay harbour entrance layout. For the initially accepted
layout[6] it caused wave heights considerably in excess of the prescribed
0,9 m maximum inside the harbour, it caused high waves in the harbour
entrance creating problems to navigation and it resulted in very high
waves on the south breakwater head.

Wave concentration on Richards Bay south channel slope

The wave concentration problem can be explained by *refraction theory*.
As is shown in Figure 2(c), there is a 'critical angle' of approach
when the waves will refract just enough to remain on the channel slope
causing a large increase in wave height until a state of instability is
reached and the waves move sideway across the channel. This can be
seen clearly from Figure 7 which also shows the large areas where the
wave heights exceed the incident heights by more than 30 per cent (the
layout used for this test had a slope on the south side of the channel
of 1 in 20 compared with 1 in 100 shown in Figure 4).

Fig. 7.   Relative wave heights in entrance channel without
          breakwaters.

Again for a channel depth of 25 m and a depth of 20 m for the surrounding
area the 'critical' refraction angle, which is the angle of wave approach
resulting in a refracted direction parallel to the channel axis for a
12 s wave, is found as follows:

$$\sin \alpha = \frac{C_{si}}{C_{ch}} = \frac{12,7}{13,8} = 0,92 \quad \text{or} \quad \alpha = 67^{\circ}$$

where: α = angle between normal to orthogonal and channel axis

        C_{si} = wave celerity to the side of the channel

        C_{ch} = wave celerity in the channel

Thus the critical angle of wave approach is 23° or with the 111° channel
direction the critical direction of wave approach at the channel entrance
becomes 134°, which corresponds to a deep sea wave direction of about
141° (between SE and SSE). This agrees very closely with the average
critical direction found from the various model tests on the Richards
Bay model which was found to be about 25° (see Figure 8).

Although the wave concen-
tration caused by the Richards
Bay south channel slope can
thus be explained effectively
by refraction theory it is
clear that wave heights will
reach a limiting value where
the assumption of *no* trans-
verse energy transfer does not
hold any more. Particularly
for a relatively flat channel

Fig. 8: Wave concentration on channel slope
        for SSE, 12 s waves.

slope, in the initial wave height build up, diffraction will play a minor role only but as the waves get higher and the difference in water depths becomes greater near the shore, diffraction becomes more important.

As may be seen from Figure 7 a point of instability is reached where the high waves leave the channel slope. In this particular case the maximum wave height on the channel slope before it crossed into the channel was 1,6 times the incident wave height.

Similar problems can be anticipated where long entrance channels have to be dredged outside the breakwaters.

Examples may be found at Le Havre with its 12,5 km long 300 m wide entrance channel and at Europort with its 12 km long by 600 to 400 m wide channel. In the latter case, unexpected damage occurred to the north breakwater which is probably caused by similar wave concentration on the channel side slope.

Methods to reduce wave concentration

Although the wave concentration occurs only for a small wave direction sector at Richards Bay, this sector is in the dominant wave direction and ways to reduce the concentration had to be explored. Theoretical studies as well as extensive model testing were carried out using different channel slopes, widths, degree of channel tapering (widening towards the seaward end), breakwater shapes and channel bottom configurations[7].

Standard wave penetration tests were carried out for various layouts for all the wave directions in the critical range between SE and SSE. The effects of the changes were judged from relative wave height diagrams and from the average wave height inside the harbour opposite Sandy Point (see Figure 4).

The effect of *channel slope* was investigated by changing the south channel slope, which was responsible for the wave concentration, from the maximum stable slope of 1 in 20 to 1 in 30, 1 in 60, 1 in 80 and 1 in 100 respectively. Various composite slopes were also tested. Some of the test results are shown in Figures 9 to 12.
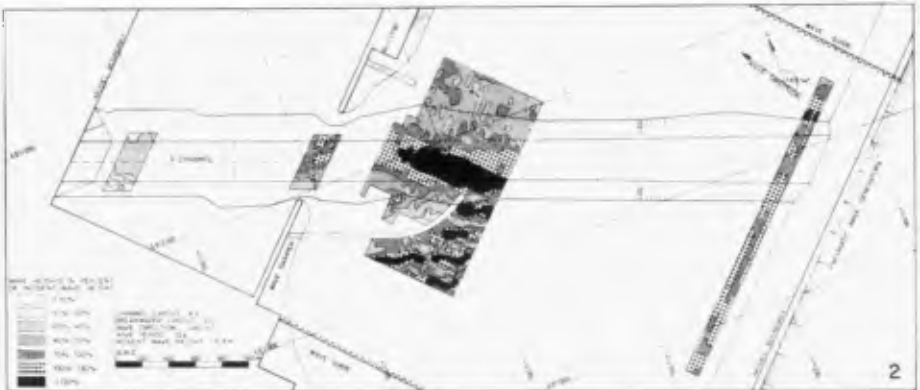

Fig. 9. Wave penetration diagram, 1:20 slope, $146\frac{1}{4}^{\circ}$, 12 s waves.

Fig. 10. Wave penetration diagram, 1:60 slope, $146\frac{1}{4}^{O}$, 12 s waves.

Fig. 11. Wave penetration diagram, 1:100 slope, $146\frac{1}{4}^{O}$, 12 s waves
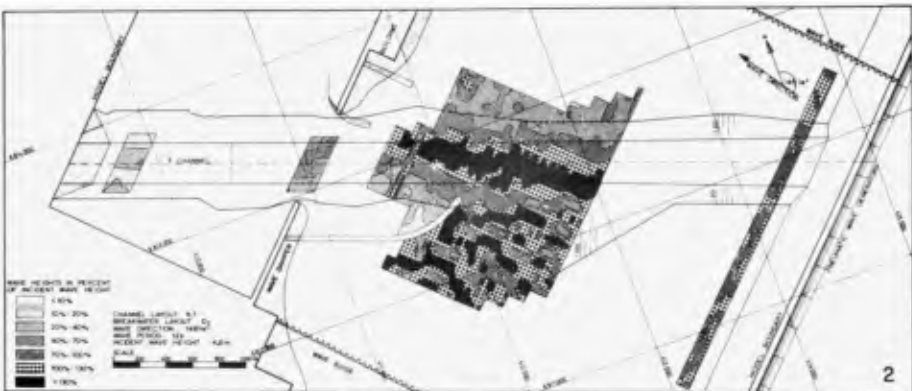

Fig. 12. Wave penetration diagram, 1:20/1:100 Composite slope, $146\frac{1}{4}^{O}$, 12 s waves.

As may be expected, the wave concentration spreads out as the slope decreases but only for a 1 in 100 slope was a satisfactory reduction obtained in the wave heights in the entrance channel (see Figure 11). To reduce dredging costs, composite slopes were also tried but were found to be ineffective, as can be seen from the example in Figure 12.

Fig. 13. Wave penetration at Sandy Point for various channel layouts.
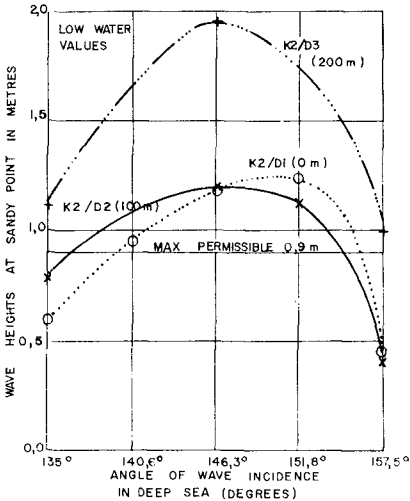
Fig. 14. Wave penetration at Sandy Point for various distances of breakwater tip to channel edge.

The wave heights inside the harbour are shown in Figure 13. The change of slope from 1 in 20 to 1 in 100, involving 4×10^6 m^3 extra dredging, is not too significant whereas the 1 in 60 and the composite slopes are considerably worse. The wave heights in the entrance channel, however, were much lower with the 1 in 100 slope (see Figures 9 and 11) and in later tests with different breakwater configurations it was found that the 1 in 100 slope was also superior with regard to wave penetration at Sandy Point.

The 1 in 100 south channel slope was therefore accepted as the best solution for the Richards Bay channel layout.

The effect of the *distance* of the breakwater tip to the channel side (bottom side) was also studied. The basic layout used was the same as shown in Figure 9 and wave penetration for distances of 0, 100 and 200 m respectively are shown in Figure 14. From the navigation point of view the breakwater tip should be as far as possible away from the channel side and the optimum distance is thus 100 m because wave penetration was found to increase significantly for greater values.

The effect of *channel tapering* was also tested. The increase in channel width from 300 m to 400 m shown in Figure 4 at the seaward end of the channel is required to compensate for the reduction in accuracy of navigational aids for greater distances offshore. Although no improvement was expected, a channel layout tapering from 300 m to 700 m was tested, but the results showed
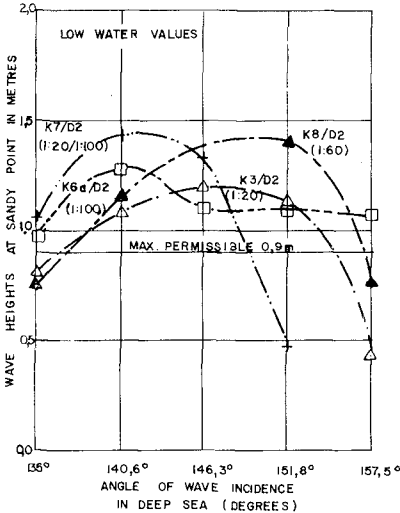
a threefold increase in the frequency of occurrence of wave heights
in excess of the maximum possible 0,9 m inside the harbour. This in-
crease is due to additional wave energy converging towards the entrance
area and the entrance channel should therefore have the minimum accep-
table widening towards it's deep end.

Breakwaters 1,2, 1,7 and 2,2 km long respectively were tested to
study the effect on wave concentration of *breakwater length*. For the
particular approach channel length at Richards Bay (about 4,5 km total)
a 2,2 km breakwater length was found to be needed to avoid excessive
wave build up on the channel slope. Although a long breakwater will
thus provide a solution the high cost will in most cases be prohibitive.

Different south breakwater *shapes* were tested in a further attempt
to reduce wave penetrations due to concentration on the channel slope.
It was found that conditions inside the harbour improved significantly
for a breakwater with a short section parallel to the channel axis,
as can be seen from a comparison of Figures 11 and 15. Larger sections
of the breakwater parallel to the channel were not acceptable because
of considerable reflection of E'ly waves into the channel and the
'short kink' breakwater shown in Figure 15 was concluded to be the best
layout.

Fig. 15.   Wave penetration diagram, short kink breakwater,
           $146\frac{1}{4}°$, 12 s waves.

A very effective way to reduce the wave heights in the entrance
channel, was found to be the provision of a *Vee-bottom* in the channel.
The effect of the Vee-bottom is to refract the wave energy towards the
channel sides where it moves out of the channel, or is dissipated
against the sides. Two different conditions were tested using the
basic layout shown in Figure 4, namely:

(a) A Vee-bottom was provided over the approximately 1 km transition
     section from -25 m to -19,5 m channel depth (centre line depth
     was made -25 m and at the channel edges -20 m);

(b) the above Vee-bottom was extended into the inner channel over
     a further 1,5 km (centre line depth -25 m, edges -18,5 m).

The test results in Figure 16 show a considerable reduction in wave penetration, even for the 1 km Vee-bottom which involves only $0,5 \times 10^6$ m^3 extra dredging. Although there are obvious practical disadvantages, this solution is very effective and in the case of wide entrance channels it is probably the only solution to the wave penetration problem.
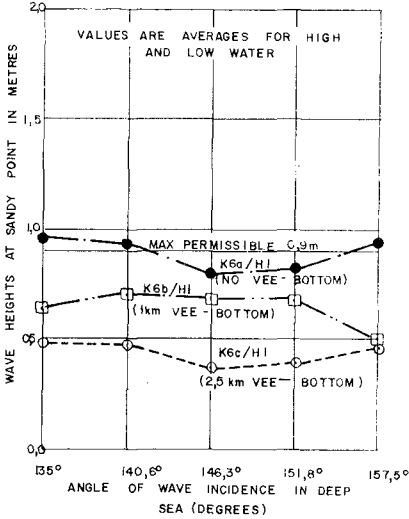
In certain cases a Vee-bottom can also be provided in the outer part of the channel to reduce the wave heights in the harbour entrance area. In fact, in the case of a harbour entrance for a marina at Muizenberg near Cape Town one proposed solution involved the provision of a specially shaped offshore depression combined with relatively short breakwaters which was found to reduce wave penetration to acceptable limits and, at the same time, improved entry conditions[8]

Fig. 16.   Wave penetration at
          Sandy Point for various
          Vee-bottom channel beds.

Wave penetration Richards Bay proposed layout

The final layout for the Richards Bay harbour entrance arrived at after some two and a half years research into the wave concentration problem is shown in Figure 4. Relative wave heights for ESE'ly waves are shown in Figure 6, which shows the considerable wave attenuation for the direction parallel to the channel, and for the 'critical' direction of $146\frac{1}{4}^\circ$ in Figure 17, which shows the remaining wave concentration on the south channel slope.

Figure 18 gives the SE'ly wave condition, which results in far the worst wave attack on the South breakwater, causing serious problems to the stability of breakwater armouring. Figure 19 gives the 'critical' wave direction of 77° for the north slope of the channel (77° deep sea or 90° at the seaward end of the channel). Although some concentration is noted on the north channel slope this causes no problems whatsoever.

Wave *orthogonals*, based on conventional refraction theory, are superimposed on the wave penetration diagrams of Figures 17, 18 and 19. The *agreement* between model tests and refraction theory is again seen to be very good, both qualitatively as well as quantitatively.

Fig. 17.   Richards Bay final layout wave penetration for $146\frac{1}{4}^{\circ}$,
           12 s waves.

Fig. 18.   Richards Bay final layout, wave penetration for 135° (SE)
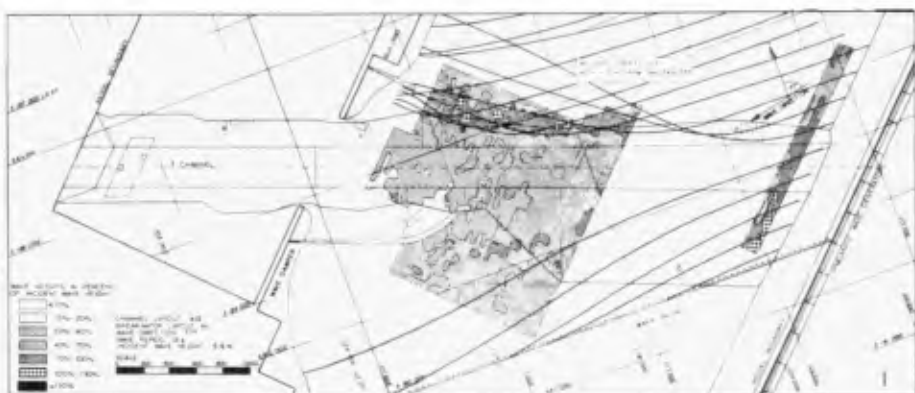

Fig. 19.   Richards Bay final layout, wave penetration for 77°,
           12 s waves.

The wave penetration inside the harbour opposite Sandy Point is shown
in Figure 20 for 12 s waves and all directions tested.   Wave conditions
inside the harbour were not to exceed 0,9 m more often than once in 10
years.   As may be seen from Figure 20 this requirement, however, was
not met for the layout shown in Figure 4.   The only way to further
reduce the wave penetration was found to be a 1 km long Vee-bottom
(see Figure 16).
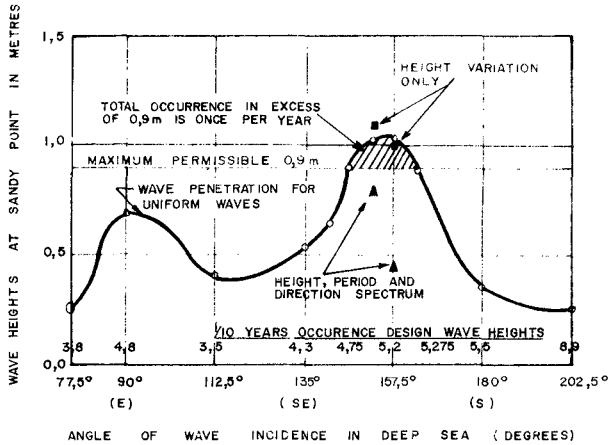
Fig. 20.   Wave penetration at Sandy Point for
            Richards Bay final layout.

EFFECT OF IRREGULAR WAVES

The above considerations are all based on uniform waves which seldom
occur in nature. Since the wave concentration only occurred in a
narrow direction band it was decided to investigate the effect of irre-
gular wave spectra particularly of a *direction spectrum.*

With the available wave generating equipment it was possible to
generate pseudo-random waves both with varying wave heights only as
well as with simultaneous direction, height and period variations.
Tests were carried out with the basic wave directions of $152°$ and $157\frac{1}{2}°$,
which are in the critical direction sector, and a dominant wave period
of 12 s.   The direction spread achieved was $7°$ (model input) which can
be accepted to occur under most conditions found in nature[9].

Obviously, the wave measuring method used for the uniform waves,
which was done for 10 s intervals on a close grid of 0,35 m by 1 m,
could not be used for the irregular wave tests. Instead, the incident
waves and the waves inside the harbour were measured simultaneously at
six points for a 10 minute period.   Simultaneously recorded 1 minute
sections of the records were spectrally analysed on a Varian 620.L.100
computer and the average ratio of Sandy Point and model input H^*_{mo} values

***

$^*H_{mo} = 4 \sigma \simeq H_s$,   where σ is the root of the variance and H_s the
                    significant wave height.

were calculated to determine the wave penetration. The results, shown as
point values in Figure 20 show very close agreement between uniform wave
results and the wave height spectrum only. However, the wave height,
period *and* direction spectrum cases show a considerable reduction in
wave penetration, particularly for the $157\frac{1}{2}^{o}$ case, for which the re-
duction is more than 50 per cent! Thus, provided it can be confirmed
that for the critical wave directions at Richards Bay the minimum wave
direction spread is at least 7° the entrance layout shown in Figure 4
is completely satisfactory.

     The above results prove that the wave concentration problem is,
in accordance with refraction theory, caused by a critical wave
direction which focusses the wave energy onto the channel slope.

     *It also follows that the tests with uniform uni-directional waves
greatly exaggerate the wave concentrating and that, for situations
similar to the Richards Bay one, it will be necessary to tests with a
spectrum of wave heights, periods and directions.*

CONCLUSIONS

Modern bulk carriers require wide and deep harbour entrances which
could result in serious wave penetration problems for waves running
near parallel to the entrance channel axis. However, due to the
existence of a 3,5 km long approach channel at Richards Bay this problem
was completely eliminated because these waves were considerably reduced
in height due to wave transformation in the approach channel. In the
case of Richards Bay, this applied to all wave directions within about
20° either side of the direction of the channel axis.

     Since the avoidance of beam waves also improves the navigability of
the entrance [10]it thus follows that the *direction of the entrance channel*
should preferably coincide with the *dominant wave directions* to minimise
wave penetration.

     Particularly, when the incident waves are limited to a relatively
small direction sector *selective offshore dredging* can thus be utilised
to reduce wave heights in a harbour entrance considerably reducing the
problem of wave penetration.

     At Richards Bay the channel alignment had to be made 111° because
of the existence of a sub-bottom gorge in the base rock and also to limit
the length of the approach channel, which did not agree with the dominant
wave approach of 158°.   In any case, recorded wave directions covered a
direction sector of about 80° (in the channel area) which is much larger
than the above $2 \times 20^{o} = 40^{o}$ sector. For the angles of wave approach
in excess of 20° relative to the channel axis, serious *wave concentration*
was found to occur on the *channel slopes* particularly when the angle
was close to the 'critical' value.

     From a comparison of model test results and wave orthogonals based
on refraction theory, it was established that the wave concentration is
mainly caused by *wave refraction* on the channel slope.

     Based on extensive model tests it was found that this problem could
be minimised for the Richards Bay harbour layout by providing a flat
1 in 100 south channel slope, by using a short kink at the end of the
south breakwater and by dredging a Vee-shaped channel bottom. The
optimum distance from the breakwater foot to the channel edge was found

to be 100 m and the channel should have a minimum widening towards
it's seaward end. The wave concentration of course, can be avoided
by lengthening the breakwaters but in most cases this would be
uneconomical.

As a result of the wave concentration on the channel slopes, special
attention had to be given to the *stability of the breakwaters* which
experienced wave heights greatly in excess of the incident wave heights
used in the design.

It was found recently that the wave concentration and resulting wave
penetration were considerably reduced when a wave height, period and
direction spectrum was introduced in the Richards Bay model. It is
thus clear that, in similar studies, not only should a large number
of wave directions, possibly with only $5°$ in between, be used in the
tests but *preferably irregular waves with regard to wave height period
and direction should be used to avoid considerable errors in the
results obtained from tests with uniform waves.*

Measurements of prototype directional spectra thus becomes a
prerequisite for accurate reproduction in the model of prototype condi-
tions. Moreover, model wave machines which can cope with directional
wave spectra should be employed for these studies.

REFERENCE

1. BRETSCHNEIDER, C.L. and REID, R.O. "Modification of wave height
    due to Bottom Friction, Percolation and Wave Refractions"
    B.E.B., Tech. Memo No. 45, 1954.

2. VAN IEPEREN, M.P. "The bottom friction of the sea bed off Melkbos-
    strand - A comparison of a quadratic with a linear friction model".
    Stellenbosch, June, 1974.

3. CERC. "Shore protection, planning and design". Technical Report
    No. 4. Third Edition, Washington, June, 1966.

4. BRUUN, Per. "The future port and sedimentation problems". Schiff
    und Hafen, Heft 2/1971.

5. ZWAMBORN, J.A. "Richards Bay Harbour Entrance Design". ECOR
    Symposium paper S71,Stellenbosch, November, 1972.

6. ZWAMBORN, J.A. and ROSSOUW, J. "Design of Richards Bay Harbour
    Entrance". CSIR Report MEG 1034, Stellenbosch, July, 1971.

7. GRIEVE, G. and ZWAMBORN, J.A. "Design of Richards Bay Harbour
    Entrance : Wave model tests on entrance layout". CSIR Report
    C/Sea 74/2, Stellenbosch, March, 1974.

8. NICHOLSON, J.M.C. "Muizenberg Marina Project - Wave model studies".
    CSIR Report ME 1156, Stellenbosch, October 1972.

9. HICKS, A.B. et al. "Investigations for the Garden Island Causeway,
    Western Australia. Proc. XXIII 2nd International Navigation Congress,
    Section II, Subject b, Ottawa, 1973.

10. HOPPE, K.G. "Design of Richards Bay Harbour Entrance : Manoeuvring
    tests with a 150 000 dwt bulk carrier ship". CSIR Report ME 1223,
    Stellenbosch, September, 1973.

CHAPTER 121

PRACTICAL SCALING OF COASTAL MODELS

by

J.W. Kamphuis

Professor of Civil Engineering
Queen's University at Kingston
Kingston, Ontario, Canada.

ABSTRACT

In this paper the practical design of coastal mobile bed models is
considered. The semi-theoretical approach expressed by the author in
earlier publications (9,10,11,12) is extended and used to classify and
design coastal models. Fixed bed coastal models are discussed first to
form a basis for the argument. Subsequently, mobile bed models are
classified according to criteria of dynamic similarity satisfied in their
design and scale effects present in their operation. Basic scale laws are
next derived for all classifications of coastal models. This is done for
both inshore and offshore models, the distinction being brought about by
adjusting the velocity scales for unidirectional (and long wave) motion.
Time and sediment transport scales are next derived and some well known
models are compared. The presence of bedform and model distortion is also
treated. The work is compared with that of other authors.

FIXED BED COASTAL MODELS

For fixed bed short wave models (12) the basic model scales, where
distortion is allowed, are

$$n_H = n_L = n_d = n_z = n_a = n$$

$$n_u = n_t = n_T = n^{1/2} \qquad\qquad (1)$$

$$n_x = n_y = Nn$$

Here n is the model scale (prototype over model value) and N is the
model distortion. The subscripts refer to wave height (H), wave length
(L), depth of water (d), vertical scale (z), wave orbital amplitude (a),
orbital velocity (u), time (t), wave period (T), and the horizontal
scales $(x$ and $y)$. Where no subscript appears, n refers to the basic
(vertical) scale. Here it is considered that water is used as the fluid

medium, i.e. the scales for gravity, fluid viscosity and density are unity.

When motion within the boundary layer is of interest the model behaviour must be rough turbulent (9). For this case additional scales may be derived (9,10,11) using boundary layer equations and a number of assumptions.

Work by Riedel et al (22) and Kamphuis (14) on shear stresses below waves has further shown that for rough turbulent flow, i.e.

$$\frac{\hat{v}_* k_S}{\nu} > 200 \quad \text{and} \quad \frac{k_S}{a_\delta} > 0.01 \tag{2}$$

$$\frac{\hat{v}_*^2}{\hat{u}_\delta^2} = 0.2 \left(\frac{k_S}{a_\delta}\right)^{3/4} \tag{3}$$

Their research indicates that this expression is also approximately valid in the transition region

$$15 < \frac{\hat{v}_* k_S}{\nu} < 200 \tag{4}$$

Here v_* is the shear velocity ($= \sqrt{\tau_0/\rho}$) , τ_0 is the shear stress at the bottom, ρ is the fluid density, k_S is the "sand grain" bottom roughness, ν is the kinematic viscosity of the fluid, a_δ is the wave orbital amplitude at the bottom, u_δ is the wave orbital velocity at the bottom and $\hat{}$ denotes the maximum value.

Equations 1 and 3 yield a practical shear stress scale

$$n_{\hat{\tau}_0} = n N_{k_S}^{3/4} \tag{5}$$

where N_{k_S} is the roughness distortion normally necessary in practical models

$$N_{k_S} = n_{k_S}/n \tag{6}$$

The effect of distortion of roughness is quite considerable. Equation 5 is of importance when determining friction losses for waves travelling substantial distances in models as well as when determining shear stresses on a mobile bed.

For the laminar boundary layer, experimental evidence (14,22)

shows that

$$\frac{\hat{v}_*}{\hat{u}_\delta} = \frac{1}{RE^{1/4}} \tag{7}$$

where RE is the wave Reynolds Number ($= \hat{u}_\delta \, a_\delta \, / \, \nu$) . This expression yields

$$_w n_{\hat{\tau}_0} = n^{1/4} \tag{8}$$

In this case the bottom material has no effect and the scale may be thought of as a result of the scaling down of the waves only - hence the subscript w . If for rough turbulent flow the waves only are scaled down, i.e. the bottom material remains the same, then Eq. 5 reduces to Eq. 8.

For the unidirectional (and tidal) flow aspects of a coastal model the following scales may be derived (9,10)

$$n_U = n^{1/2}$$

$$n_x = n_y = {}_\ell n_L = Nn \tag{9}$$

$$_\ell n_T = {}_\ell n_t = Nn^{1/2}$$

$$n_f = n_S = N^{-1}$$

Here U is the average flow velocity, f is the friction factor and S the surface slope. Subscript ℓ refers to long waves.

The friction factor scale requires a total shear stress which is a function of model distortion, in order to achieve correct current patterns in the model

$$_\ell n_\tau = n \, N^{-1} \tag{10}$$

where τ is the shear stress required for unidirectional (or tidal) flow. If a logarithmic velocity profile is assumed, an expression for the shear stress on the bottom may be found.

$$_\ell n_{\tau_0} = n_U^2 \, N_{k_s}^{1/4} \tag{11}$$

Equations 10 and 11 may be satisfied simultaneously by making $N_{k_s} = N^{-4}$.

This would, however, totally destroy any reasonable wave simulation near the bottom. Thus for combination models, combining short waves and unidirectional flow (or long waves), additional roughness in the form of vertical roughness strips must be supplied. For the model, the additional shear stress required is

$$\tau_a = \tau - \tau_o = \frac{\tau_p}{n} (N - N_{k_s}^{-1/4}) \tag{12}$$

where τ_p is the prototype shear stress.

Most model studies assume inherently that the velocity scales are equal to the shear velocity scales so that velocities may be used in model analysis, rather than shear velocities or shear stresses. Examination of Eqs. 1, 5, 9 and 11 indicate that normally this is incorrect since

$$n_{\hat{v}_*} = n_u N_{k_s}^{3/8} \quad \text{and} \quad {}_\ell n_{v_*} = n_U N_{k_s}^{1/8} \tag{13}$$

MOBILE BED COASTAL MODELS

CRITERIA FOR DYNAMIC SIMILARITY

In mobile bed models the upper region, the boundary layer, the bottom configuration and the sediment motion must be modelled simultaneously. The criteria for dynamic similarity in modelling mobile beds have been discussed earlier (9,10,11) and may be summarised as

$$n_{R_*} = \frac{n_{v_*} \, n_D}{n_\nu} \tag{14}$$

$$n_{F_*} = \frac{n_\rho \, n_{v_*}^2}{n_{\gamma_s} \, n_D} = \frac{n_\rho}{n_{(\rho_s - \rho)}} \cdot \frac{n_{v_*}^2}{n_g \, n_D} = 1 \tag{15}$$

$$\frac{n_{\rho_s}}{n_\rho} = 1 \tag{16}$$

$$\frac{n_{a_\delta}}{n_D} = 1 \tag{17}$$

where R_* is the grain size Reynolds Number, F_* the densimetric Froude Number, D the particle size, ρ the fluid density, ρ_s the particle density and γ_s the underwater specific weight $= (\rho_s - \rho)g$.

MODEL CLASSIFICATION

It is impossible to satisfy Eqs. 14 through 17 simultaneously but for R_* > 2 it would not be unreasonable to drop Eq. 14 (10, Fig. 1). This would result in a scale effect at low shear velocities, i.e. at flow reversals. The type of model where Eq. 14 only is ignored will be called the "Best Model" (BM) for ease of reference and in Table 1, the criteria satisfied and the scale effects present if criteria are not satisfied may be found for this type of model.

Unless the prototype particle size is very large, it is impossible to satisfy Eq. 17. The model material resulting from Eq. 17 would become too small and the mode of material transport would change from bed load to suspended load transport. This is unacceptable and Eq. 17 is out of necessity quickly ignored. Two possibilities now present themselves. The first is the use of sand as a model material. This meets Eq. 16, but now Eq. 15 cannot be quite satisfied, while for most practical purposes Eq. 14 cannot be satisfied either. The scale effects resulting from the disregard of Eqs. 14, 15 and 17 for this "Sand Model" (SM) may be found in Table 1. It may be noted that unless the prototype transport is very small, adjustments need not be made in connection with F_* .

The second possibility is to ignore Eq. 16 resulting in a model with lightweight material. It is now possible to satisfy Eqs. 14 and 15 simultaneously. This model will be referred to as a "Light Weight Model" (LWM). Ignoring Eq. 16 involves additional scale effect shown in Table 1.

Because scale selection for LWM is rather restricted, laboratory studies may be carried out, still counting on the fact that for R_* > 2 , Eq. 14 may be ignored. This type of model will be referred to as the "Densimetric Froude Model" (DFM) since only Eq. 15 is satisfied, ensuring that F_* is correct.

Finally, all too often, the last step is taken and none of Eqs. 14 through 17 are satisfied. This will be referred to as the "Nothing Model" (NM). In this case it is often ensured that sediment transport does occur in the model, by artificial means such as exaggerating wave heights and current velocities. This simply ensures that F_* in the model is greater than critical. Any similarity between model and prototype is strictly forced by adjusting model quantities until the model approximates prototype situations.

SCALE LAWS FOR SEDIMENT MOTION OVER FLAT BED

Consider first the sediment motion over a flat mobile bed. For this case, Kamphuis (13) states it is not unreasonable to assume that

$$n_{k_s} = n_D \qquad (18)$$

TABLE 1

MODEL CLASSIFICATION

CRITERIA	CRITERIA SATISFIED					SCALE EFFECT (if criterion is not satisfied)
	BM	SM	LWM	DFM	NM	
$n_{R_*} = 1$	x	x	✓	x	x	transport is not similar at low velocities and velocity reversals
$n_{F_*} = 1$	✓	x	✓	✓	x	initiation and transport of material may now be totally different in model and prototype, requiring extensive adjustment
$n_{\frac{\rho_S}{\rho}} = 1$	✓	✓	x	x	x	particle ballistics are no longer correct. particle motion above water at the shore is incorrect
$n_{\frac{a_\delta}{D}} = 1$	✓	x	x	x	x	transport scale varies with depth

For BM , Eqs. 5, 11 and 15 to 18 yield the scales for D , γ_s , $\hat{\tau}_o$ and $_\ell\tau_o$, if it assumed that equations developed for flow without sediment transport are valid for flow with sediment transport. This is not an unreasonable assumption since in most cases the sediment transport is purposely kept small to prevent suspension of the bottom material.

It may be seen that for the Froude velocity scale $(= n^{1/2})$, the shear stress resulting from unidirectional (or long wave) motion is scaled down the same as the shear stress from wave motion. The current pattern condition (Eq. 10) may be satisfied by additional roughness similar to the fixed bed model, however, this model meets the additional requirement that bottom shear stresses from wave and current motion are scaled down the same. This is summarised in the first line of Table 2, cols 1 to 6.

For SM Eqs. 5, 11, 16 and 18 yield the second line (cols 1 to 6) in Table 2. It must be noted that the shear stress scales resulting from waves and currents may now be forced equal only by adjusting the velocity scale for unidirectional flow (col 5) which will be no longer Froudian. The current pattern condition, Eq. 10 may once again be satisfied by added roughness (col 6).

In most cases, however, the condition of simultaneously correct bottom shear and correct current patterns cannot be brought about simply by adding roughness (τ_a becomes negative). In this instance, the model may be distorted (col 7) to achieve shear and current similarity. But for mobile bed models the maximum distortion must normally be rather small as a result of other considerations such as stability of slopes and positions of beaches (19). This means that col 7 often is not a feasible solution and, either the bottom shear stress scale for unidirectional (or long wave) flow is made the same as the bottom shear stress scale for the short wave portion of the model (col 5), resulting in an incorrect current pattern or the current pattern can be forced to be correct (col 8) causing unequal shear stress scales at the bottom. This is done by adjusting the velocity scale for unidirectional (long wave) action.

Inherent in this adjustment is a philosophical decision that a coastal model is a waves model with currents and long waves added, i.e. adjustable to give the required similarity. This is not the same philosophical decision as made by Fan and Le Méhauté (4).

For inshore areas, e.g. in a littoral drift study, the shear resulting from wave motion normally greatly exceeds the shear from current action. To model these areas correctly, the governing velocity scale would need to be as in col 8. In offshore areas, e.g. around deep-sea gravity structures, where material is moved by combined wave and current action, the velocity scale should be as in col 5. Distortions normally do not matter in these latter studies and exact current patterns can be brought about by baffles. In either case, the answer will be slightly incorrect because of a scale effect resulting from not modelling either current patterns or shear stresses correctly as well as from ignoring Eqs. 14, 15 and 17 (discussed earlier). For convenience these two types of models will be labelled Inshore Models (IM) and Offshore Models (OM) .

TABLE 2

BASIC SCALE LAWS

MODEL TYPE	n_D (1)	n_{γ_s} (2)	n_{τ_o} (3)	$\ell^{n_{\tau_o}}$ 2) (4)	For $\ell^{n_{\tau_o}} = n_{\tau_o}$, SHEAR FROM CURRENTS = SHEAR FROM WAVES	For $\ell^{n_{\tau_o}} = \ell^{n_T} = n_{\tau_o}$, SHEAR FROM CURRENTS = SHEAR FROM WAVES, CURRENT PATTERNS CORRECT		For $\ell^{n_{\tau_o}} = \ell^{n_T}$, CORRECT CURRENT PATTERN
					n_U (5)	τ_a (6) or	N (7) or	n_U (8)
BM	n	1	n	n	$n^{1/2}$	$\frac{\tau_p}{n}(N-1)$	-	-
SM	$*$ 1)	1	$n^{1/4} n_D^{3/4}$	$n^{3/4} n_D^{1/4}$	$n^{1/4} n_D^{1/4}$	$\frac{\tau_p}{n}(N-n^{3/4} n_D^{-3/4})$	$n^{3/4} n_D^{-3/4}$	$\dfrac{n^{5/8}}{N^{1/2} n_D^{1/8}}$
LWM	$n^{-1/11}$	$n^{3/11}$	$n^{2/11}$	$n^{8/11}$	$n^{5/22}$	$\frac{\tau_p}{n}(N-n^{9/11})$	$n^{9/11}$	$\dfrac{n^{7/11}}{N^{1/2}}$
DFM or DFM	$*$	$n^{1/4} n_D^{-1/4}$	$n^{1/4} n_D^{3/4}$	$n^{3/4} n_D^{1/4}$	$n^{1/4} n_D^{1/4}$	$\frac{\tau_p}{n}(N-n^{3/4} n_D^{-3/4})$	$n^{3/4} n_D^{-3/4}$	$\dfrac{n^{5/8}}{N^{1/2} n_D^{1/8}}$
	$n\, n_{\gamma_s}^{-4}$	$*$	$n\, n_{\gamma_s}^{-3}$	$n\, n_{\gamma_s}^{-1}$	$n^{1/2} n_{\gamma_s}^{-1}$	$\frac{\tau_p}{n}(N-n_{\gamma_s}^3)$	$n_{\gamma_s}^3$	$\dfrac{n^{1/2} n_{\gamma_s}^{1/2}}{N^{1/2}}$
NM	$*$	$*$	$n^{1/4} n_D^{3/4}$	$n^{3/4} n_D^{1/4}$	$n^{1/4} n_D^{1/4}$	$\frac{\tau_p}{n}(N-n^{3/4} n_D^{-3/4})$	$n^{3/4} n_D^{-3/4}$	$\dfrac{n^{5/8}}{N^{1/2} n_D^{1/8}}$
					CM			IM

1) $*$ denotes free choice

2) long wave shear stress for Froude velocity scale $n_U = n^{1/2}$

For LWM , Eqs. 14 and 15 express a relationship between v_* , D and γ_s and Eqs. 5, 11 and 18 yield the third line in Table 2. Columns 6 and 7 are now very unlikely and it is imperative to make a choice between modelling the bottom shear stress resulting from unidirectional (or tidal) flow correctly or modelling current patterns correctly. Similar relationships for DFM and NM have been derived.

Table 2 shows that in most cases a choice must be made with respect to correct bottom shear and correct current patterns. For correct bottom shear resulting from unidirectional (or long wave) flow (i.e. a deep water sediment transport model) - OM condition,

$$n_U = n^{1/4} n_D^{1/4} \tag{19}$$

while for correct current patterns (inshore models) the IM condition is

$$n_U = n^{5/8} N^{-1/2} n_D^{-1/8} \tag{20}$$

PRESENCE OF BEDFORM

The above discussion refers totally to mobile bed models with a flat bottom. Many models and almost all prototypes have bedform, in the way of ripples and dunes, on the bottom. In the absence of research results on shear stresses resulting from bedform below waves, it is assumed that as in unidirectional flow

$$\tau_\Delta = \frac{\rho U^2 \Delta^2}{\Lambda d} \tag{21}$$

where Δ is the height and Λ the length of the bedform, while τ_Δ is the shear stress resulting from bedform presence only. Mogridge (17) has found that for waves

$$n_\Delta = n_\Lambda = n \quad \text{for} \quad \frac{\rho \hat{u}_\delta^2}{\gamma_s D} < 40 \tag{22}$$

This results in a shear stress scale for a model with bedform of

$$n_{\tau_\Delta} = n_U^2 = n_u^2 = n \tag{23}$$

This is the same as the flat bed (or grain) shear stress scales in BM , but

it is considerably greater than the shear stress scales in the other models where the grain size is distorted. Thus grain shear is certainly exaggerated in these models relative to the shear generated by the bedform. The total shear is of course a combination of the two. In models where the bedform generated shear predominates, it will be possible to use additional roughness strips (as in BM) and to satisfy the current pattern and shear conditions simultaneously.

Under waves, results obtained by Inman and Bowen (6) and Carstens et al (2) indicate that Eq. 21 underestimates the actual shear stresses by at least one order. This does not necessarily mean that Eq. 23 is incorrect. Until accurate shear stress measurements over bedform under waves have been made, Eq. 23 must be used.

This leaves one further problem. On a bed with bedform the direction of sediment transport must be the same in model as in prototype. This depends a great deal on the phase difference between the rise of the eddies from the lea of the bedform and the main orbital motion. A number of papers have been written on this subject and an interesting recent discussion may be found in Ref. 7.

SEDIMENT TRANSPORT AND TIME SCALES

Most coastal mobile bed models are built to determine coastal morphology in the future. For this it is necessary to determine sediment transport scales and time scales for bed morphology.

From Ref. 11 it may be seen that the relationship for flat bed sediment transport under two dimensional wave action is

$$\frac{q_s}{v_* D} = \phi \left(R_* , F_* , \frac{\rho_s}{\rho} , \frac{a}{D} , \alpha \right) \tag{24}$$

where q_s is the volume of material transported per unit width and α is the asymmetry of wave motion. Normally α is the same in model and prototype if Eq. 1 is satisfied.

The sediment transport scale may then be derived as

$$n_{q_s} = m \, n_{v_*} \, n_D \tag{25}$$

where the scale effect m is a function of all the dimensionless ratios of Eq. 24 ignored in the model design, as well as of the bedform present in model and prototype.

Normally in offshore coastal models, the sediment transport is governed by the wave motion rather than the currents (i.e. the currents modify the transport resulting from wave action) and thus Eq. 25 can be considered an adequate approximation of the sediment transport scale. The corresponding time scale may be derived as

$$n_{t_s} = \frac{N \, n^2}{m \, n_{V_*} \, n_D} \, n_{(1-p)} \qquad (26)$$

where p is the material porosity, i.e. volume of voids over total volume. Both n_{q_s} and n_{t_s} are given in Table 3 as a function of model type.

To obtain a sediment transport scale for littoral transport in a nearshore coastal model, it is postulated that the waves stir up the material and the nearshore current pattern moves it along. Using the approach first used by Bagnold (25) and assuming wave shear stress and unidirectional velocities interact, the scale for littoral drift is

$$n_{Q_\ell} = M \, N \, n \, n_{\hat{\tau}_o} \, n_U \, n_{\gamma_s}^{-1} \qquad (27)$$

The time scale for coastal morphology may be derived as

$$n_{t_m} = \frac{N \, n^2 \, n_{\gamma_s}}{M \, n_{\hat{\tau}_o} \, n_U} \, n_{(1-p)} \qquad (28)$$

Here M is the scale effect for littoral transport which is a function of all the parameters ignored from Eq. 24. In addition M includes the non-similarity of fall velocity, but more importantly, M includes the non-similarity of wave climate. When a survey is made of some model studies performed, one quickly recognises that the sediment transport and time scales are defined very subjectively. The model wave climate may vary from monochromatic waves from one direction to several waves from several directions. These represent all sorts of prototype wave climates from short term monsoon conditions to many years of net transport where the gross transport is in both directions.

Both the littoral drift and time scales are given in Table 3 as a function of model type. Table 4 gives a comparison of scales for a limited number of models. It may be seen that M is very sensitive to the similarity of wave climate.

SCALES DERIVED BY OTHER AUTHORS

For fixed bed models, there is general agreement among the various authors, but for mobile bed models certain differences in basic philosophy are evident.

Valembois (23) derives scales for mobile bed motion which are similar to LWM without the substitution of Eq. 18.

TABLE 3

SEDIMENT TRANSPORT AND TIME SCALES

MODEL TYPE	OFFSHORE MODEL (OM)		INSHORE MODEL (IM)	
	n_{q_s}	n_{t_s}	n_{Q_ℓ}	n_{t_m}
BM	$m\, n^{3/2}$	$N\, n^{1/2} \cdot \dfrac{n(1-p)}{m}$	$M\, N\, n^{5/2}$	$N\, n^{1/2} \cdot \dfrac{n(1-p)}{M}$
SM	$m\, n^{1/8}\, n_D^{11/8}$	$\dfrac{N\, n^{15/8}}{n_D^{11/8}} \cdot \dfrac{n(1-p)}{m}$	$M\, N^{1/2}\, n^{15/8}\, n_D^{5/8}$	$\dfrac{N^{3/2}\, n^{9/8}}{n_D^{5/8}} \cdot \dfrac{n(1-p)}{M}$
LAM	m	$N\, n^{2} \cdot \dfrac{n(1-p)}{m}$	$M\, N^{1/2}\, n^{17/11}$	$N^{3/2}\, n^{16/11} \cdot \dfrac{n(1-p)}{M}$
DFM or DFM	$m\, n^{1/8}\, n_D^{11/8}$	$\dfrac{N\, n^{15/8}}{n_D^{11/8}} \cdot \dfrac{n(1-p)}{m}$	$M\, n^{1/2}\, n^{13/8}\, n_D^{7/8}$	$\dfrac{N^{3/2}\, n^{11/8}}{n_D^{7/8}} \cdot \dfrac{n(1-p)}{M}$
	$m\, n^{3/2}\, n_{Y_s}^{-11/2}$	$N\, n^{1/2}\, n_{Y_s}^{11/2} \cdot \dfrac{n(1-p)}{m}$	$\dfrac{M\, N^{1/2}\, n^{5/2}}{n_{Y_s}^{7/2}}$	$N^{3/2}\, n^{1/2}\, n_{Y_s}^{7/2} \cdot \dfrac{n(1-p)}{M}$
NM	$m\, n^{1/8}\, n_D^{11/8}$	$\dfrac{N\, n^{15/8}}{n_D^{11/8}} \cdot \dfrac{n(1-p)}{m}$	$\dfrac{M\, N^{1/2}\, n^{15/8}\, n_D^{5/8}}{n_{Y_s}}$	$\dfrac{N^{3/2}\, n^{9/8}\, n_{Y_s}}{n_D^{5/8}} \cdot \dfrac{n(1-p)}{M}$

TABLE 4

COMPARISON OF COASTAL MODELS

MODEL	Ref	n	N	n_{Y_s}	n_0	TYPE	n_U	n_{t_m}	n_t	M	COMMENTS
Cobourg	15	60	3.33	55	.14	NM	$n^{1/2}$	$\dfrac{133,000}{M}$	21,000	6.4	25 minutes = 1 year; waves from one direction; wave height exaggerated by 2; thin layer of bed material
Durban	8	100	3	1	1	SM	$n^{1/2}$	$\dfrac{950}{M}$	2,200	.43	4 hrs = 1 yr; 4 different waves in cyclical pattern
									65	14.6	4 hrs = 65 hrs; waves from one direction
Newcastle	16	100	2	1	1	SM	$n^{1/2}$	$\dfrac{630}{M}$	1,825	.35	3 days = 12 - 17 years; two different waves from same direction
Scheveningen	3	25	6	1	1	SM	2.5	$\dfrac{670}{M}$	730	.91	12 hrs = 1 yr; waves from one direction
									440	1.53	20 hrs = 1 yr; waves from two directions
Thyborøn	20	40	6.25	4.71	.11	NM	$n^{1/2}$	$\dfrac{15,500}{M}$	17,500	.90	prior to 1900; 80 hrs = 16 years
									4,400	3.5	after 1900; 80 hrs = 40 years
Visakhapatnam	5	80	3.75	4.18	.71	NM	$n^{1/2}$	$\dfrac{5,200}{M}$	1,375	3.8	150 mins = 143 days during monsoon
									3,300	1.6	40 mins = 92 days during monsoon

Bijker (1) specifies four similarity conditions which may be reduced to Eqs. 10 and 15 plus the condition that the shear velocity scale is the same as the orbital velocity scale. The last condition would appear to be incorrect except for BM .

Fan and Le Méhauté (4) satisfy Eqs. 14 and 15 like in LWM , but use the unidirectional (or long wave) considerations as basic and assume all roughness to be bottom roughness (i.e. no vertical roughness elements). This causes a coastal model to be an extension of a unidirectional flow model (waves are added). In this paper it is argued that a coastal model is a waves model and the unidirectional portion is adjusted to suit the wave conditions. This is a little more realistic since the wave shear stresses normally dominate and unidirectional (long wave) components can then be adjusted to yield an inshore model (current patterns correct) or an offshore model (shear stresses the same for unidirectional and wave phases). Fan and Le Méhauté also propose a morphology time scale which differs considerably from Eq. 28.

Yalin (24) differs from the present analysis only in the extent of the argument (he also deals mainly with LWM). He proposes a distortion equal to n .

REFERENCES

1. Bijker, E.W., "Some Considerations about Scales for Coastal Models with Movable Bed", *Delft Hydraulics Laboratory,* Publication No. 50

2. Carstens, M.R., Neilson, F.M. and Altinbeck, H.D., "Bedforms Generated in the Laboratory under an Oscillatory Flow", *Coastal Engineering Research Centre,* Technical Memo 28, U.S. Corps of Engineers, Washington, 1969

3. Delft Hydraulics Laboratory, private communication

4. Fan, L.N. and Le Méhauté, B., "Coastal Movable Bed Scale Model Technology", *Tetra Tech.* Report No. TC-131

5. Ince, S. and Jamieson, W.W., Internal Report, *National Research Council,* Ottawa, 1972

6.   Inman, D.L. and Bowen, A.J., "Flume Experiments on Sand Transport
         by Waves and Currents", *Proceedings 8th Coastal Engineering
         Conference,* Mexico, 1963, pp 137-150

7.   Inman, D.L. and Tunstall, E.B., "Phase Dependent Roughness
         Control of Sand Movement", *Proceedings 13th Coastal
         Engineering Conference,* Vancouver, 1972, pp 1155-1171

8.   Jordaan, J.M., "Study of Durban Harbour Silting and Beach Erosion",
         Proceedings 12th Coastal Engineering Conference, Washington,
         1970, pp 1097-1116

9.   Kamphuis, J.W., "Scale Selection for Wave Models", *Queen's
         University C.E. Report No. 71,* 1971

10.   Kamphuis, J.W., "Scale Selection for Mobile Bed Wave Models",
         Proceedings 13th Coastal Engineering Conference, Vancouver,
         1972, pp 1173-1196

11.   Kamphuis, J.W., "Sediment Transport by Waves over a Flat Bed",
         Engineering Dynamics of the Coastal Zone, *The Institution of
         Engineers of Australia,* Sydney, 1973, pp 228-233

12.   Kamphuis, J.W., "Wave Models with Fixed Bed", *Waterways, Harbours
         and Coastal Engineering Journal, A.S.C.E.,* Vol. 99, WW 4,
         Nov. 1973, pp 471-483

13.   Kamphuis, J.W., "Determination of Sand Roughness for Fixed Beds",
         Accepted for publication to *Journal I.A.H.R.,* 1974

14.   "Wave Friction", To be published

15.   Le Méhauté, B. and Collins, J.I., "A Model Investigation of
         Cobourg Harbour", *Queen's University Civil Engineering
         Report No. 17,* Kingston, 1961

16.   Lucas, A.H. and Anderson, P.G., "Newcastle Harbour Entrance Shoal
         Wave Model and Sand Tracing", *Engineering Dynamics of the
         Coastal Zone,* Sydney, 1973, pp 89-98

17.   Mogridge, G.R., "Wave Generated Bed Forms", *Queen's University,*
         Ph.D. Thesis, 1973

18.   Noda, E., "Coastal Movable-Bed Scale-Model Relationship",
         Tetra Tech Report No. TC-191

19.   Paul, M.J., Kamphuis, J.W., and Brebner, A., "Similarity of
         Equilibrium Beach Profiles", *Proceedings 13th Coastal
         Engineering Conference,* Vancouver, 1972, pp 1217-1236

20.   Reinalda, R., "Scale Effects in Models with Littoral Sand Drift",
         Delft Pub No 22, 1960

21.   Riedel, H.P., "Direct Measurement of Bed Shear Stress under Waves",
           Queen's University, Ph.D. Thesis, 1972

22.   Riedel, H.P., Kamphuis, J.W., and Brebner, A.,
           "Measurement of Bed Shear Stress Under Waves",
           Proceedings 13th Coastal Engineering Conference,
           Vancouver, 1972, pp 587-604

23.   Valembois, J., "Etude sur Modele du Transport Littoral Conditions
           de Similitude", *Proceedings 7th Coastal Engineering
           Conference,* The Hague, 1961, pp 307-377

24.   Yalin, M.S., *"Mechanics of Sediment Transport",* Pergamon Press,
           London, 1971

25.   Yalin, M.S., *"Theory of Hydraulic Models",* MacMillan, London, 1971

CHAPTER 122

DESIGN OF DISTORTED HARBOR WAVE MODELS

By

R. W. Whalin and C. E. Chatham

U. S. ARMY ENGINEER WATERWAYS EXPERIMENT STATION, VICKSBURG, MISSISSIPPI

ABSTRACT

An investigation of errors incurred by scale distortion for fixed-bed harbor wave models has been performed and results of this study applied to the design, construction, and operation of a model of Los Angeles and Long Beach Harbors. Objectives of the model investigation must be clearly prescribed in order that each phenomenon affected by scale distortion can be analyzed. In some cases, if study objectives are too broad, a distorted model may be incompatible with these objectives; however, it will be found that in many circumstances a distorted model will produce valid data with considerable time and cost savings in construction and operation.

INTRODUCTION

The design of scale model harbors for the investigation of wave phenomena can be divided into two basic categories consisting of the type problem under study. These two areas are (1) harbor oscillations which are of major importance for large commercial harbors due to the potential for moored ship surging and (2) excessive wave heights from the normal wind waves which are of paramount importance for small-craft harbors and of some importance for commercial harbors. There are certainly other types of harbor problems such as tidal flushing, transport of cold and warm water discharges, and tsunami effects that warrant investigation in distorted wave models; however, the scale model design for this class of problem is considerably more elementary because of the validity of the long-wave assumption for tides and tsunamis. The two classes of problems under investigation in this paper encompass the intermediate wave period range for which neither the long nor short wave assumption is valid.

Quantitative data can be obtained from distorted harbor wave models provided the model design is conducted on a comprehensive basis. Some of the more important wave phenomena which may be effected either directly or indirectly by model scale distortion are refraction, diffraction, energy transmission through breakwaters and other structures, reflection from the shoreline and coastal structures, viscous friction at the bottom, harbor resonance, reflections within the harbor, breaking height, breaking depth, wave steepness, longshore currents, runup, and mass transport. It becomes immediately obvious that study objectives must be well defined if one has any hope of intelligently analyzing those phenomena which are important. An example of the application of the principles enumerated in this paper are applied to a model of Los Angeles and Long Beach Harbors.

DESIGN CONSIDERATIONS

This section discusses some of the more important phenomena in design considerations for harbor wave models. It always is desirable for wave action models to be constructed to an undistorted scale if time, cost, and space allow.

Viscous Friction Effects

The viscous dissipation of energy at the model bottom can become an extremely important consideration in models involving large prototype areas of relatively shallow water. In the United States this can be a problem in models of areas on the East and Gulf Coasts and in some areas in the Great Lakes. In the prototype, viscous dissipation of energy at the bottom is practically nil (almost always being less than one percent); however, if the model scale is too small and propagation distances are large, then this can result in a considerable scale effect in the model. Since scale distortion acts to improve this particular scale effect (use of a horizontal scale ratio smaller than the vertical scale ratio will reduce the relative amount of excessive energy dissipation in the model), the greater the distortion the less the scale effect. Computations on the viscous dissipation of energy at the bottom can be based on the original work of Keulegan (1950). The effect of viscous dissipation of energy at the bottom on the wave height is given by

$$H_2 = H_1 \, e^{-\int_o^X \delta dX} \tag{1}$$

over a propagation distance of X where H_1 is the wave height at X = 0 and H_2 is the height after the wave has traveled a distance, X, in water of depth, d, and

$$\delta = \frac{5\Pi \sqrt{\Pi \nu T}}{L^2 \{\sinh \frac{4\Pi d}{L} + \frac{4\Pi d}{L}\}} \tag{2}$$

Actually the calculation of viscous energy dissipation must be performed along wave orthogonals. It is possible that complicated offshore topographies could result in different amounts of viscous dissipation of energy near the shoreline. This must be analyzed in detail for each specific case.

Wave Refraction

Refraction effects are a function of d/L only; thus, if it is required that $(d/L)_m = (d/L)_p$, then linear wave refraction is correctly reproduced in the model and the result is that the ratio of the model to prototype wave period is proportional to one divided by the square root of the vertical length scale. Any other scaling method will result in errors in the wave refraction pattern and coefficients. Therefore, the choice of any other scaling method will necessitate the detailed investigation of errors introduced into the refraction pattern. This is accomplished by computing wave refraction patterns for the undistorted case and repeating the computation

for the distorted model scales and the scaled wave periods. A comparison of the wave front positions and the refraction coefficients will yield the desired information.

Wave Diffraction

Similitude of linear wave diffraction effects from model to prototype requires that $(x/L)_m = (x/L)_p$ where x is a horizontal distance and L is the wavelength. The scale effect present in the diffraction pattern for a distorted scale model depends upon the similitude relation chosen to determine the wave period. If diffraction is the major phenomena of interest then the diffraction effects can be preserved when the time scale is proportional to the square root of the horizontal length scale. Of course, the longer the wavelength the less important are diffraction scale effects.

Wave Reflections

Two types of wave reflections should be considered in analyzing the effect of model distortion. Reflections from breakwaters or other structures and from the shoreline comprise one type and the other is the cumulative reflection from bottom slopes as the wave propagates from deep water to the shoreline. The scale effect arising from increased reflections from distorted bottom slopes is a function of the existing bottom slope. If the bottom slope is very gradual, there will probably be an extremely small scale effect; however, if the bottom slope is relatively steep or the distortion too large, quite significant scale effects can result. The latter reflection problem mentioned above occurs from the position of the wave generator to the point of breaking nearshore.

The magnitude of waves reflecting from slopes is a function of the slope, the wave steepness, and the type of material comprising the slope. An estimate of the reflection coefficient from the breakwater or the shoreline can be obtained, to a first order of approximation, by the classicial theory of Miche. Keeping in mind that the theory is applicable only for small reflections and small amplitude waves (linear theory) and realizing that the theory over-estimates the reflection coefficient (at least when it is large), application of the theory can determine if scale effects relative to reflections must be contended with. The reflection coefficient R is given by

$$R = \frac{H_r}{H_i} = \rho R' = \frac{H_o/L_{o_{max}} \quad \text{theory}}{H_o/L_o} = \rho \, \frac{2\alpha}{\Pi} \, \frac{\sin^2\alpha}{\Pi} \, \frac{1}{H_o/L_o} \qquad (3)$$

where α is the average beach slope in radians and ρ is an empirical coefficient estimated to be 0.8 for smooth impermeable slopes (such as a fixed-bed wave action model). Analysis of the cumulative wave reflection during propagation over the variable bottom topography can be estimated from the theory of Rosseau (1952). Usually there will be a negligible reflection scale effect due to this phenomenon.

Wave Breaking Location

If the time scale for a distorted scale model is determined on the basis of obtaining the correct refraction pattern (requiring that $d_m/L_m = d_p/L_p$), the ratio of a vertical to a horizontal length will be correct presuming each is indeed to scale. The implication is significant; that is, the wave steepness ratio ($H_m/L_m = H_p/L_p$) also is correct provided that the wave height is modeled correctly. This means that when all factors affecting the wave height (refraction, shoaling, bottom friction, reflections, diffraction, and bottom percolation) are either modeled correctly, or made to be compensatory, the wave steepness will be modeled correctly. The effects of these factors, briefly stated, are as follows:

a. Refraction. Refraction effects are modeled correctly by requiring that $d_m/L_m = d_p/L_p$.

b. Shoaling. Wave shoaling is a function of d/L only; thus, shoaling is modeled correctly if refraction is correctly modeled.

c. Bottom friction. The greater the distortion factor the nearer one comes to modeling the correct prototype bottom friction. It can be demonstrated that an increase in the incident wave height can compensate for the excessive loss in wave energy due to bottom friction. Thus, by the time the model waves reach the shoreline their height can be correctly reproduced.

d. Reflections. The problem of wave reflection was discussed and it was ascertained that an estimate of the increased wave reflection from the shoreline and from offshore structures could be made. These scale effects, if significant can be compensated for by performing some wave flume tests to design the model breakwaters and shoreline from some material which will yield the proper reflection coefficient. It also was ascertained that reflection scale effects from the underwater topography were probably negligible but could be calculated and if significant could be compensated for by an increase in the incident wave height at the generator.

e. Diffraction. Since, to the first order of approximation, diffraction effects are a function of the ratio of a horizontal distance to the wavelength, the requirement that $d_m/L_m = d_p/L_p$ to produce the correct refraction and shoaling effects, introduces an error into the diffraction pattern. Each case must be analyzed in detail to determine the magnitude of this error and to ascertain if it is acceptable. Should diffraction effects be the phenomenon of major importance, then the time scale can be based on similitude of linear wave diffraction.

f. Bottom percolation. Bottom percolation acts to reduce the wave height in the same manner as bottom friction; however, this effect is less than the attenuation due to bottom friction in the prototype and is negligible in most instances.

In view of the above considerations, one realizes that the wave steepness at the breaking location will be correct provided the incident wave is increased at the wave generator to compensate for any excessive model wave height attenuation due to bottom friction and bottom reflection scale effects. Thus, one comes directly to the conclusion that wave breaking characteristics will be correct (both depth of breaking and angle of breaking) regardless of whether or not the breaking is depth dependent or steepness dependent. The only factor which might cause an error is that breaking is somewhat dependent on the bottom slope (Street, 1966); however, for the slopes and distortions usually considered in harbor wave models there will be a small error due to the slope dependence of the breaking location.

Longshore Velocity

In order to analyze the possible scale effect due to model distortion on the longshore velocity, it will be assumed that for any scale model in which longshore velocity is of paramount importance, the time scale must be predicated on the relation $(d/L)_m = (d/L)_p$ which has as the consequence of producing the correct breaking location as previously discussed. We will resort to the following analytically derived equation given by Johnson and Eagleson, in Ippen (1966):

$$V_L^2 = \frac{3}{8} \frac{g H_b^2 n_b}{d_b} \frac{\sin \alpha \sin \Theta_b \sin 2\Theta_b}{f} \tag{4}$$

where

V_L = longshore velocity component

H_b = breaking wave height

n_b = ratio of group to phase velocity at the breaker

d_b = depth at breaking

Θ_b = angle of breaking

α = average beach slope

f = Darcy-Weisbach coefficient

f is computed using the Kármán-Prandtl resistance equation for steady uniform flow in a rough conduit

$$f = [2 \log_{10} \frac{d_b}{k_e} + 1.74]^{-2} \tag{5}$$

where k_e is the absolute bottom roughness. k_e for natural sand is assumed to be 0.0033 ft, 0.0010 ft for sheet metal or smooth cement, and 0.0208 ft for pea gravel. For the model computation we will assume $k_e = 0.0010$ ft since it is constructed of smooth cement.

Thus the longshore velocity can be written as

$$V_L = (\tfrac{3}{8}) \; [g \; (\frac{H_b}{d_b}) \; H_b \; n_b]^{\frac{1}{2}} \; \frac{[\sin \alpha \; \sin \Theta_b \; \sin 2\Theta_b]^{\frac{1}{2}}}{[2 \; \log_{10} \frac{d_b}{k_e} + 1.74]^{-1}} \tag{6}$$

or

$$V_L = (\tfrac{3}{8})^{\frac{1}{2}} \; [g \; \frac{H_b}{d_b} \; H_b \; n_b]^{\frac{1}{2}} \; [2 \; \log_{10} \frac{d_b}{k_e} + 1.74] \; [\sin \alpha \; \sin \Theta_b \; \sin 2\Theta_b]^{\frac{1}{2}}$$

$$\frac{V_{L_m}}{V_{L_p}} = \frac{[H_b \; n_b \; \sin \alpha]^{\frac{1}{2}}_m}{[H_b \; n_b \; \sin \alpha]^{\frac{1}{2}}_p} \; \frac{[2 \; \log_{10} \frac{d_b}{k_e} + 1.74]_m}{[2 \; \log_{10} \frac{d_b}{k_e} + 1.74]_p} \tag{7}$$

since $(H_b/d_b)_m = (H_b/d_b)_p$ and $(\Theta_b)_m = (\Theta_b)_p$ assuming that the angle of breaking and breaking height and depth are modeled correctly as discussed in previous section. Thus, the scale effects can be analyzed on the basis of the variation of the second term below from 1

$$\frac{(V_L)_m}{(V_L)_p} = \frac{(H_b)_m}{(H_b)_p}^{\frac{1}{2}} \; \frac{(n_b \; \sin \alpha)^{\frac{1}{2}}_m}{(n_b \; \sin \alpha)^{\frac{1}{2}}_p} \; \frac{(2 \; \log_{10} \frac{d_b}{k_e} + 1.74)_m}{(2 \; \log_{10} \frac{d_b}{k_e} + 1.74)_p} \tag{8}$$

since by the scaling requirement that $d_m/L_m = d_p/L_p$ one obtains that the velocity ratio is determined by the square root of the vertical scale ratio (i.e. $(H_{b_m}/H_{b_p})^{\frac{1}{2}}$). Thus, if we compute the variation of the second term above from 1 as a function of model and prototype wave characteristics, we can ascertain the model scale effects due to distortion.

It can be shown that

$$n_b = \frac{1}{2} \ [1 + \frac{2k_b \ d_b}{\sinh \ 2k_b \ d_b}] = \frac{1}{2} \ [1 + \frac{\frac{4\Pi d_b}{L_b}}{\sinh \ \frac{4\Pi d_b}{L_b}}] \qquad (9)$$

Thus, since our scaling relation requires that $d_m/L_m = d_p/L_p$ for reproduction of wave refraction effects,

$$\frac{(n_b)_m}{(n_b)_p} = 1 \qquad (10)$$

and, if we let $V_{L_{se}}$ represent the scale effect in the longshore velocity,

$$V_{L_{se}} = \frac{(\sin \ \alpha)_m^{\frac{1}{2}}}{(\sin \ \alpha)_p^{\frac{1}{2}}} \ \frac{(2 \ \log_{10} \frac{d_b}{k_e} + 1.74)_m}{(2 \ \log_{10} \frac{d_b}{k_e} + 1.74)_p} - 1 \qquad (11)$$

The first term represents that portion of the scale effect due to the distortion of the beach slopes, which tends to increase the model longshore velocity. The second term representes that portion of the scale effect due to increased bottom friction, which tends to decrease the model longshore velocity.

Wave Transmission through Structures

One problem of extreme importance for distorted harbor wave models is energy transmission through the protective structures. The structure must be built to the geometrically distorted scale of the model. The only reliable manner in which to insure that no adverse scale effects are present is to perform wave transmission tests through a model test section of the prototype breakwater in a wave flume at an undistorted scale sufficiently large so that no Reynolds number scale effects occur. Usually a scale of 1:20 to 1:30 is sufficient for this purpose. Subsequently, two-dimensional flume tests must be conducted for a cross section of the distorted scale model breakwater in order to insure that approximately the correct transmission coefficient is obtained.

DESIGN OF LOS ANGELES AND LONG BEACH HARBORS MODEL

In the case (Los Angeles and Long Beach Harbors, see fig. 1) under
detailed study, the objective was to determine the effect of planned major
revisions and improvements to the harbors (channel deepening and construction
of additional basins and piers, see fig. 2) in order to insure that satis-
factory mooring conditions will obtain with respect to wave and current conditions
and their effects on ship surge. Also, it is desired to determine whether the
proposed construction plans will increase wave and surge action conditions in
the existing harbor areas and whether tidal flushing of the harbor areas will
be adversely affected by the proposed expansion. While primary interest is
focused on wave periods in the range from 20 seconds to 2 minutes, it is
suspected that long-period swell could be a problem for some of the proposed
harbor revisions; thus, it is desired to obtain accurate model data for prototype
wave periods at least as small as 15 seconds. If possible, it also is desirable
to investigate tsunami effects. Since harbor and basin resonance is undoubtedly
the major problem, it must be prescribed that wavelengths within the harbor
are correct (i.e. relative to the horizontal scale of the model). It should
be noted that this requirement will produce some scale effect errors in both
the model refraction and diffraction. Wave periods will be based on the
following relationship for intermediate water depths:

$$T_m = T_p \; [\frac{\ell_{hm}}{\ell_{hp}}]^{\frac{1}{2}} \quad [\frac{\tanh \frac{2\Pi}{\Omega} \frac{d_m}{L_m}}{\tanh 2\Pi \frac{d_m}{L_m}}]^{\frac{1}{2}} \tag{12}$$

where, T_m = model wave period

T_p = prototype wave period

ℓ_{hm} = horizontal length scale in the model

ℓ_{hp} = horizontal length scale in the prototype

Ω = distortion

d_m = model depth of the inner harbor

L_m = model wavelength

Refraction diagrams constructed from open ocean directions between west
and southeast indicated that significant long-period wave energy can penetrate
to the harbor site only from the south. A typical refraction diagram for
60-second prototype waves is shown in fig. 3. The refraction diagram showed a
strong convergence zone (caustic) due to the shape of the underwater contours
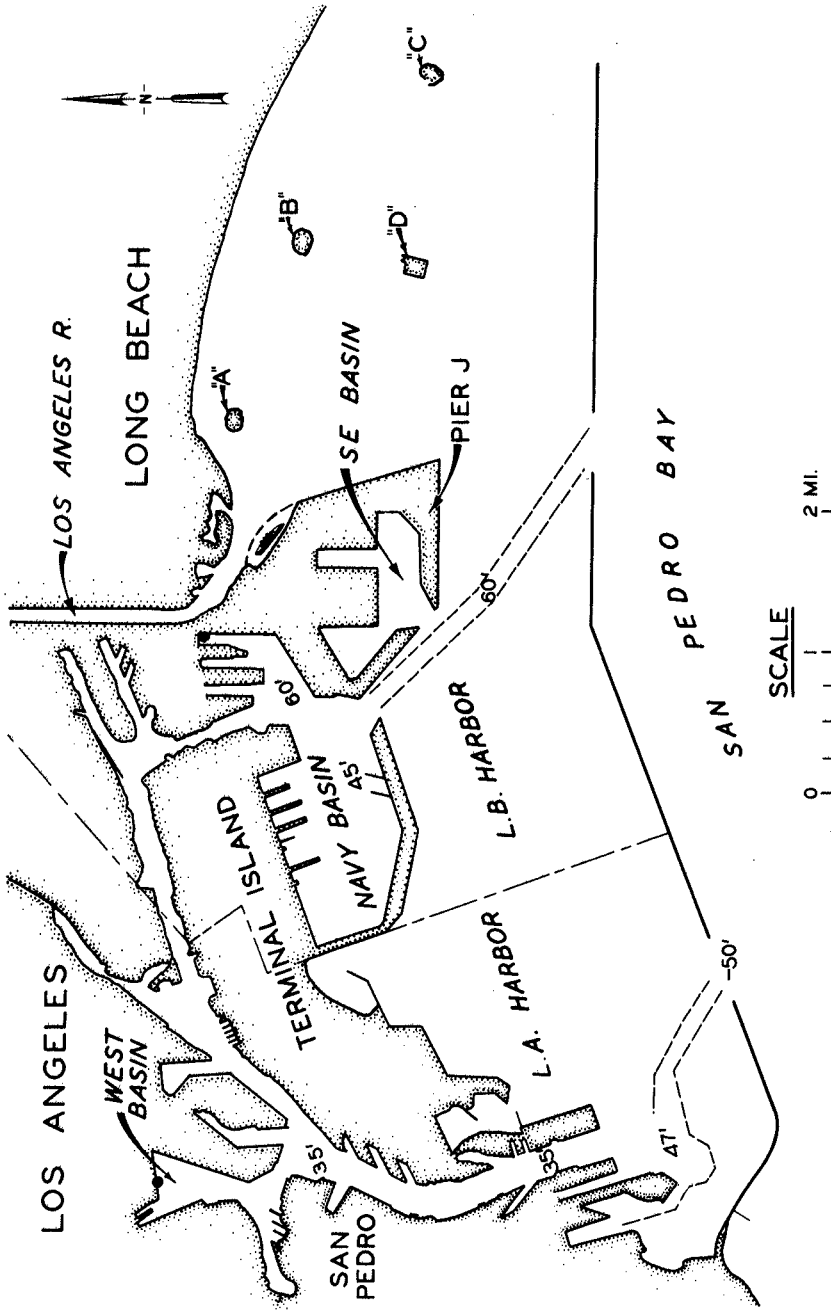seaward of the harbor site. Since presently available refraction theory is

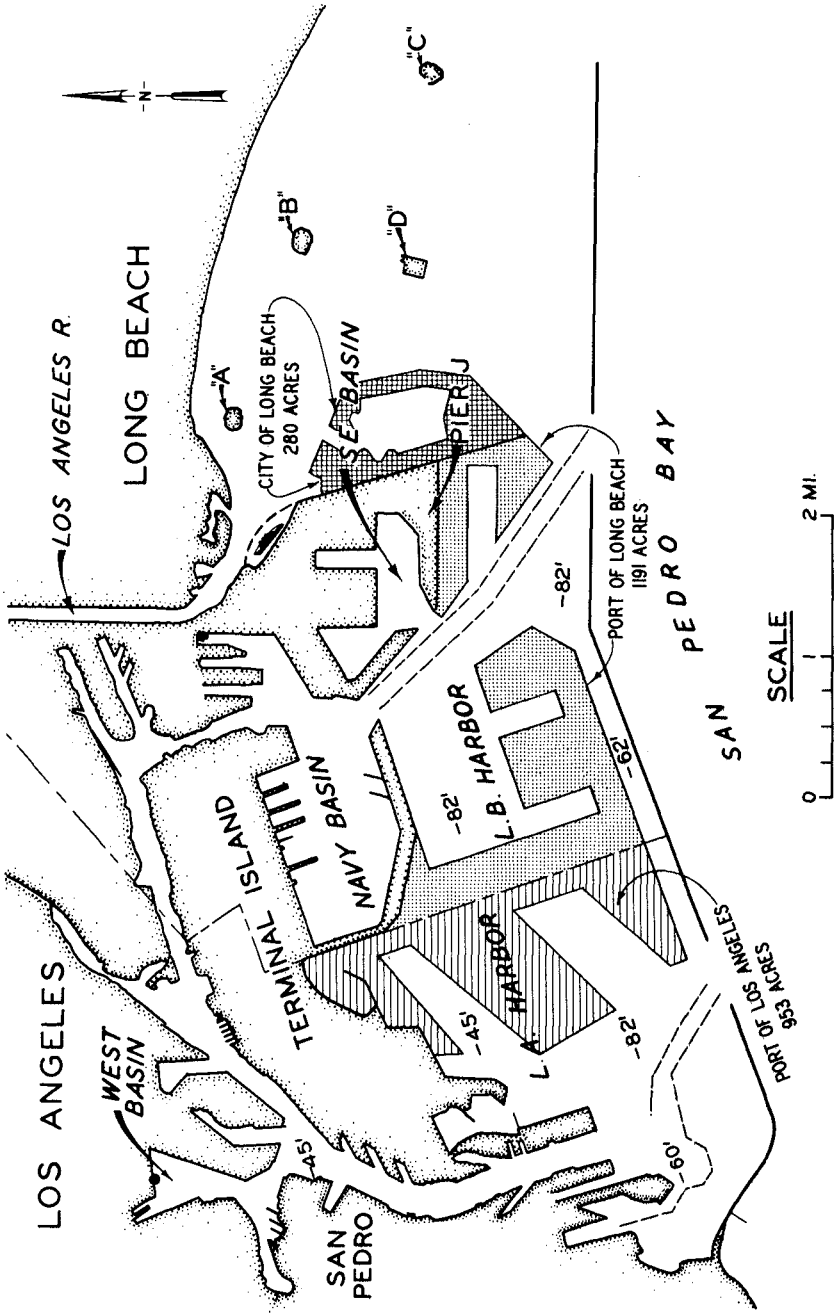Figure 1. Los Angeles-Long Beach Harbors; Existing Conditions.

Figure 2. Los Angeles-Long Beach Harbors; Proposed Revisions.
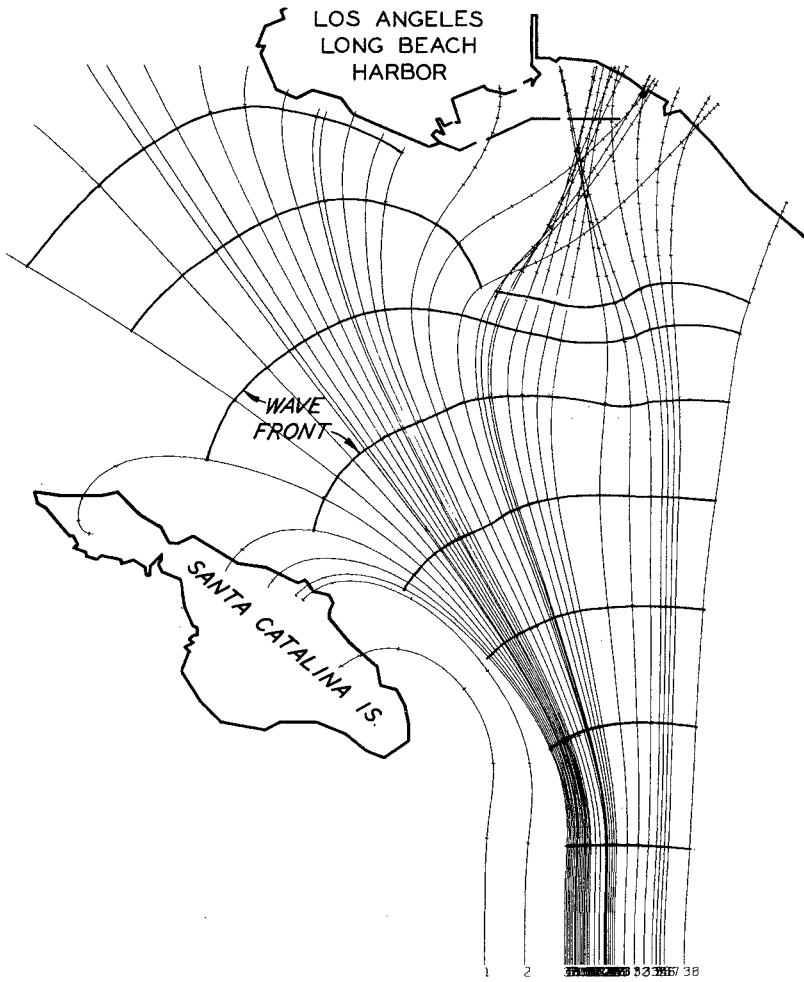
Figure 3.   Refraction Diagram for 60-Second Wave Period.

not able to accurately predict what happens in strong convergence zones, it
was necessary to reproduce this area in the model so that wave fronts approaching
the harbor would be correct. Consequently, underwater contours were reproduced
in the model to a prototype depth of 300 feet.

The wave front at the -300 contour (ranging from a straight line for 15-
second waves to an "S" shaped curve for 360-second waves) will be reproduced
by a 200-foot-long hydraulic piston-type wave generator with time synchronized
sections. By varying the individual machine settings, the wave height can be
varied along the wave front (to allow for convergence or divergence which has
taken place due to refraction seaward of the -300-foot contour).

To evaluate the effects of distortion, refraction diagrams were constructed
for representative wave periods for the following cases:

Vertical scale	Horizontal scale	Distortion
1:1	1:1	None
1:100	1:200	2
1:100	1:300	3
1:100	1:400	4
1:64	1:256	4

A comparison of these diagrams indicated no significant differences between
the distorted and undistorted cases for wave periods of one minute (prototype)
or above. For the shorter wave periods (15-30 seconds prototype) there were
some differences in direction and energy content, but adjustments will be made
in the initial wave generator position and stroke setting to compensate for
these. Model scales of 1:100 (vertical) and 1:400 (horizontal) were selected
based on the refraction analysis (distortion = 4).

The model viscous friction effect was evaluated using Keulegan's equation
for wave-height attenuation. The computations made are included in the following
table:

Horizontal Scale	Vertical Scale	Distortion	H_x for $T = 15$ sec	H_x for $T = 360$ sec
1:200	1:100	2	.8925	.9438
1:300	1:100	3	.9642	.9545
1:400	1:100	4	.9833	.9595
1:256	1:64	4	.9816	.9705

These computations indicate that for a given vertical scale, viscous friction
decreases as distortion increases because the travel distance is less. For
the selected model scales (1:100 vertical and 1:400 horizontal) and the range
of wave periods to be tested (15-360 seconds prototype), attenuation due to
viscous friction would be from 2 to 4% in the extreme reaches of the model.
A small correction for this scale effect can easily be applied to the wave data.

The rubble-mound breakwaters protecting the harbor are relatively porous and considerable long period wave energy passes through the voids of these structures. Two-dimensional tests of typical breakwater sections were conducted at undistorted scales of 1:20 (large enough to have negligible scale effects) to determine the wave transmission and wave reflection characteristics. A typical breakwater section is shown in fig. 4. Two-dimensional tests were then conducted using different sizes of rock in the distorted breakwater section until the correct wave transmission and reflection were duplicated. Figure 5 shows a typical plot of wave transmission versus wave period. It was found that using the vertical scale (1:100) to geometrically scale the rock sizes would produce the correct wave transmission through the breakwater structures. A typical section of the model breakwater is shown in fig. 6.

Reflections from underwater topography seaward of the breakwaters for the natural and distorted cases were calculated using the theory of Rosseau (1952). The practical application of this theory requires a fitting to the actual bottom of the parametric representation of the Rosseau bottom contour. That is, given depths d_1 and d_2, one must determine the best γ which produces a good fit to the bottom. As $\gamma \to \Pi/2$ the bottom contour approaches a step and as $\gamma \to 0$ the bottom approaches a constant depth. The reflection coefficient is given by:

$$C_R = \frac{\tanh \Pi S_1 - \tanh \Pi S_2}{\tanh \Pi S_1 + \tanh \Pi S_2} \tag{13}$$

where S_1 and S_2 are solutions of

$$S_1 \tanh \frac{\Pi S_1}{N} - \frac{N F_1}{\Pi} = 0,$$

$$S_2 \tanh \frac{\Pi S_2}{N} - \frac{N F_1}{\Pi \rho} = 0, \tag{14}$$

$$F_1 = \frac{\omega \, d_1}{g}, \text{ and } \gamma = \Pi/N$$

where ω = wave frequency

ρ = water density

For the contours seaward of the Los Angeles-Long Beach Harbors breakwater and for the range of wave periods (15-360 seconds, prototype) under consideration, reflections would be one percent or less for the undistorted case. For the distorted model contours, reflections would range from 0 to about 28 percent for the steeper slopes. Fortunately the steeper slopes are oriented so that the waves will be reflected toward the model side wall and not back toward the wave generator. A rubberized fiber wave absorber will be installed around the
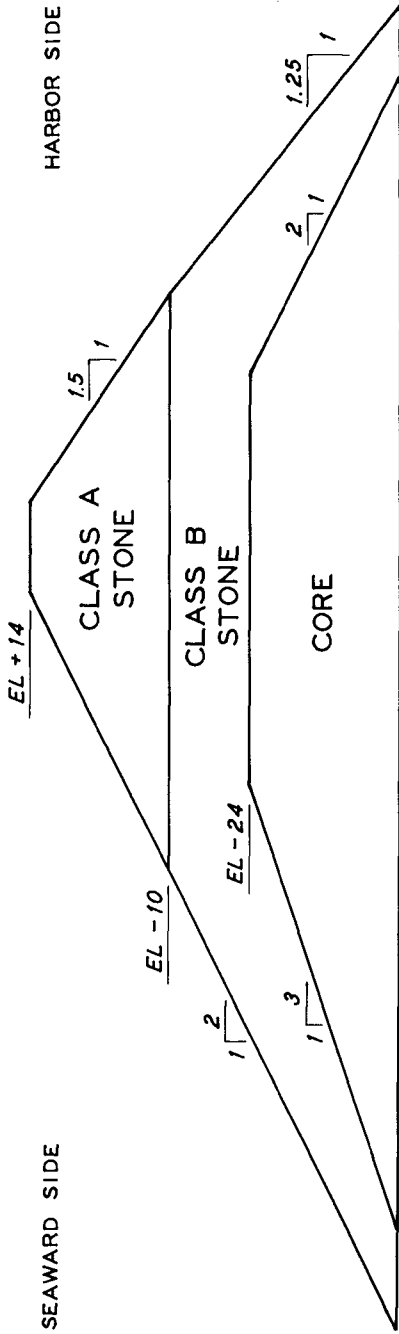
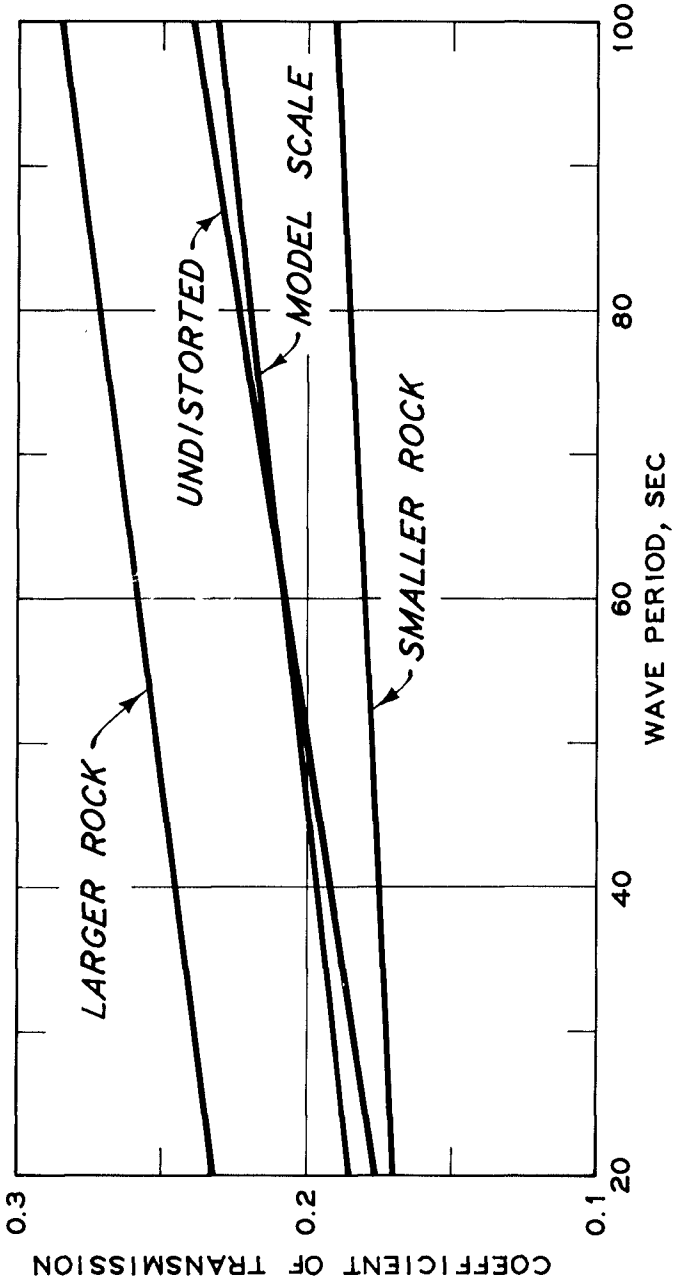Figure 4. Typical Section of Los Angeles-Long Beach Harbors Breakwater.

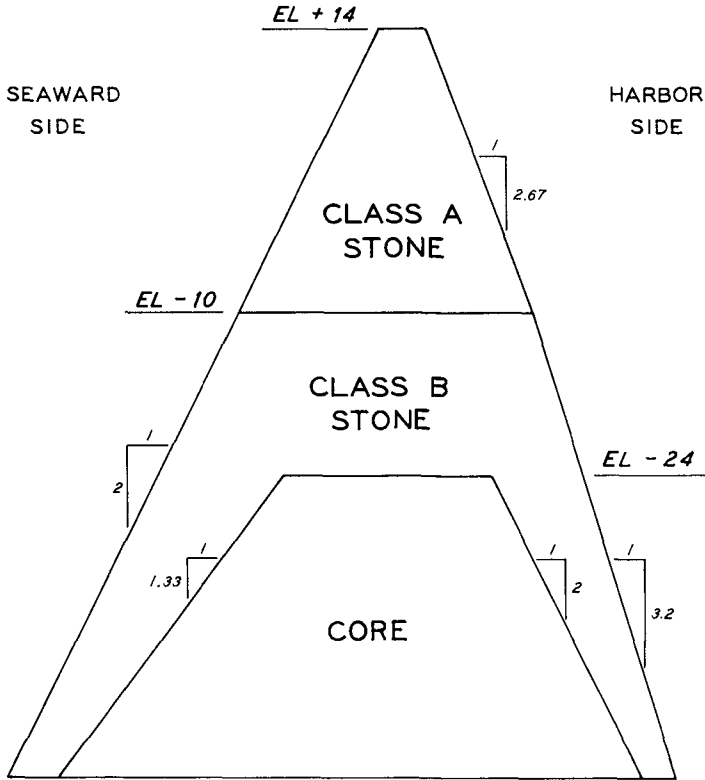Figure 5.　Comparison of Breakwater Transmission for Distorted and Undistorted Sections.

Figure 6. Typical Section of Model Breakwater; Distortion = 4; Rock Sizes Scaled Using Vertical Scale (1:100).

model perimeter walls and a wave filter of the same material will be installed
in front of the wave generator to dampen waves which would be re-reflected
from the wave generator.

Reflections from the sides of the harbor basins were studied two-dimensionally
for the distorted and undistorted cases. These sides have an average slope of
1v on 1.5H and reflection coefficients for the undistorted case ranged from
about 0.3 to 0.6. The distorted slopes increased the reflection coefficients
about 10 to 20 percent (ranged from about 0.4 to 0.7). This increase was not
considered significant enough to warrant addition of artificial roughness or
wave absorbers around the basin sides.

CONCLUSIONS

After consideration of the various items described above, it was concluded
that valid data can be obtained from the Los Angeles and Long Beach Harbors
model for a vertical length scale of 1:100 and a distortion of 4.0. However,
every time model distortion is considered, an analysis of all phenomena relevant
to the study objectives must be carefully conducted. Since no two study
objectives or prototype conditions will be identical, it is impossible to
state specific conclusions of universal applicability. Construction of the
Los Angeles and Long Beach Harbors model has been completed and model operation
is underway. The model area is 44,000 square feet which represents the largest
wave model constructed in the United States (see figs. 7 and 8).
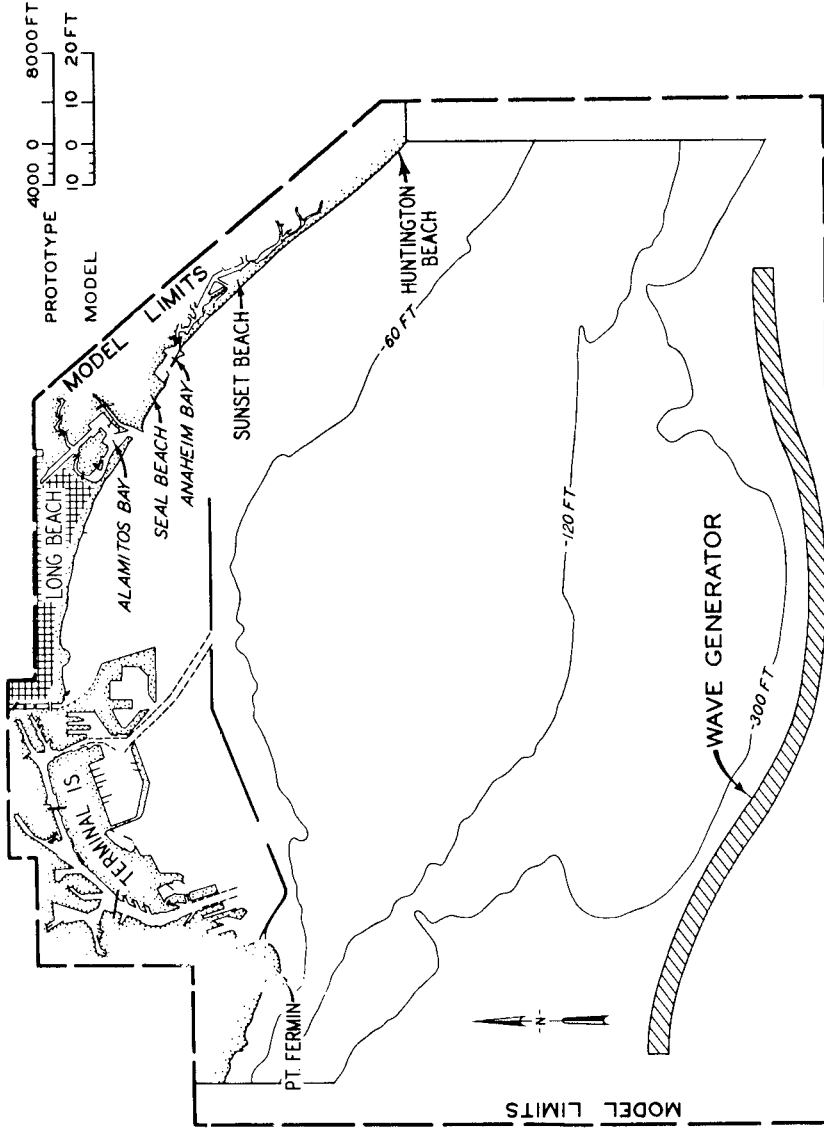
ACKNOWLEDGEMENTS

Figure 7. Los Angeles-Long Beach Harbors Model Layout.

Figure 8. General View of Los Angeles-Long Beach Harbors Model.

REFERENCES

IPPEN, A. T., 1966, Estuary and Coastline Hydrodynamics. McGraw-Hill
    Book Co., Inc., 744 pp.

KEULEGAN, G. H., 1950, The Gradual Damping of a Progressive Oscillatory Wave
    with Distance in a Prismatic Rectangular Channel. NH. Bur. Stds. Rept.
    75 pp.

ROSSEAU, M., 1952, Contribution a la theorie des ondes liquides de gravite
    en profondeur variable. Publ. Sci., et Tech. du Ministere de l'Air
    No. 275; 73 pp.

STREET, R. L. and F. E. CAMFIELD, 1966, Observations and Experiments on
    Solitary Wave Deformation. Proceedings of 10th Conference on Coastal
    Engineering, Vol. 1, American Society of Civil Engineering, 25 pp.

CHAPTER 123

ESTIMATION OF BOUNDARY CONDITIONS FOR COASTAL MODELS

by

S. K. Liu,[1] J. J. Leendertse,[1] and J. Voogt[2]

ABSTRACT

In this study, frequency response and transfer function techniques
are used together with cross-spectral and fast Fourier transform methods
to determine the proper boundary values for computing the flow field of
a coastal sea. Tide data containing considerable perturbations from
swell and meteorological disturbances are analyzed.

In computing the frequency response estimates, the effect of noise
in the input is treated by a cancelling technique and by the choice of
a reference station to evaluate the interdependencies among the other
stations at the boundary. The usefulness of the network frequency response
function is threefold: (1) future conditions can be simulated using
observed water levels at any single location, (2) boundary information
for models of different grid size can be obtained by interpolation, and
(3) missing data at a given location can be estimated optimally using
data at neighboring stations and the network response function. The
paper discusses an example of such an application, the determination of
a boundary of a two-dimensional model of Jamaica Bay, New York City,
U.S.A.

INTRODUCTION

One of the major difficulties in coastal and estuarine hydrodynamic
computation is obtaining good boundary information. For example, the
computation requires the time histories of water levels at open boundaries
as one of the major input forcing functions from which is derived the
internal flow field. Field measurements at boundaries, as well as within
the prototype, are also needed during various phases of model development
and adjustment. However, such field data often contain noise generated by
instruments, meteorological disturbances, or short-period waves. Often,
part of the records of the critical period may even be missing. This
paper deals mainly with problems such as these encountered frequently in
hydrodynamic and water quality modeling. The analyses used are the esti-
mation of network frequency response function, cross-spectral computation,
noise cancellation, and numerical convolution.

---

[1]The Rand Corporation, Santa Monica, California 90406 U.S.A.

[2]Rijkswaterstaat, Dienst Informatieverwerking, The Hague, The
Netherlands.

ESTIMATION OF NETWORK FREQUENCY RESPONSE FUNCTIONS

The frequency response function H(f), as its name indicates, describes the amplitude and phase relationship between one fluctuation with a certain frequency f as input and the resulting fluctuation as output.

In determining network frequency response relationships, the statistical approach using cross-spectral estimates is used instead of the classic method employing the deterministic Fourier or Laplace transforms, because the sampling variability, confidence limits, and the phase of the frequency response function can only be estimated using cross-spectral procedures.

A description of the computational method used in this paper is presented by Liu,[1] and by Leendertse and Liu.[2,3] Reference is also made to the handbook of Jenkins and Watts[4] and the thesis of Goodman[5] on this subject. A brief outline of the computational method is given below.

With respect to the interdependency (or the lack of it) between two random time series, x_t and y_t, we see that if the random processes are jointly stationary such that the joint distribution depends only on time differences, then the degree of interdependency can be measured by the cross-covariance function. In discrete time this is defined as

$$\hat{\gamma}_{xy}(k) = \frac{1}{n - k} \sum_{t=1}^{n-k} (x_t - \bar{x}) (y_{t+k} - \bar{y})$$

$$\hat{\gamma}_{yx}(k) = \frac{1}{n - k} \sum_{t=1}^{n-k} (y_t - \bar{y}) (x_{t-k} - \bar{x})$$

(1)

for k = 0, 1, 2, ... m, where m is the largest time lag chosen, n the total number of data points, and $\bar{x}, \bar{y}$ the mean values of the series {x},{y}.

The relationship between these two stochastic processes can also be expressed by the integral equation

$$y(t) - \mu = \int_0^\infty h(\tau) [X(t - \tau) - \mu_x] \, d\tau + N(t)$$

(2)

where $h(\tau)$ is the impulse response function, μ_x, μ_y are the mean values of the two processes, and N(t) is the uncorrelated error term.

Wiener[6] showed that the optimal estimates of $h(\tau)$ should satisfy the following integral equation:

$$\gamma_{xy}(t) = \int_0^\infty \hat{h}(\tau) \, \gamma_{xx}(t - \tau) \, d\tau$$

(3)

The solution to Eq. (3) may be obtained by Fourier transformation. Because covariance function and spectral density function form a Fourier transform pair, thus

$$P_{xy}(f) = H(f) \cdot P_{xx}(f) \quad \text{or} \quad H(f) = P_{xy}(f)/P_{xx}(f) \tag{4}$$

where $P_{xy}(f)$ is the cross-spectrum between $x(t)$ and $y(t)$, $P_{xx}(f)$ is the auto-spectrum of $x(t)$, and the complex valued function $H(f)$ is the frequency response function. The possibility of using a statistical approach using spectral densities to give the frequency response was suggested by Lee.[7] However, it was later[5] that a quantitative basis for applying the method with finite sample records corrupted by measurement noise became available.

For computing the cross-spectral density function estimate by a numerical Fourier transform, the even and odd parts of the cross-covariance function are determined by

$$\hat{A}(k) = \tfrac{1}{2}[\gamma_{xy}(k) + \gamma_{yx}(k)] \tag{5}$$

$$\hat{B}(k) = \tfrac{1}{2}[\gamma_{xy}(k) - \gamma_{yx}(k)] \tag{6}$$

from which the co-spectral density function is estimated:

$$\hat{C}_{xy}(f) = 2\tau\left[\hat{A}(o) + 2\sum_{k=1}^{k=m-1} \hat{A}(k) \cos(2\pi f k\tau) + \hat{A}(m) \cos(2\pi f m\tau)\right] \tag{7}$$

The quadrature spectral density function is estimated by

$$\hat{Q}_{xy}(f) = 2\tau\left[2\sum_{k=1}^{k=m-1} \hat{B}(k) \sin(2\pi f k\tau) + \hat{B}(m) \sin(2\pi f k\tau)\right] \tag{8}$$

The spectral density functions of input and output are determined in a similar manner. If, in Eq. (1), the output series is replaced by the input series, we obtain the auto-covariance function of the input,

$$\gamma_{xx}(k) = \frac{1}{n-k} \sum_{t=1}^{t=n-k} (x_t - \bar{x})(x_{t+k} - \bar{x}) \tag{9}$$

from which the input spectral density function is determined:

$$\hat{P}_{xx}(k) = 2\tau\left[\gamma_{xx}(0) + 2\sum_{k=1}^{k=m-1} \gamma_{xx}(k) \cos(2\pi f k\tau) + \gamma_{xx}(m) \cos(2\pi f m\tau)\right] \tag{10}$$

The output spectral density function is determined similarly.

The time interval τ used in the analysis influences the highest frequency that can be determined by the analysis method. At least two samples per cycle are required to define a frequency component in a data set; thus the highest frequency determined is

$$f_c = \frac{1}{2\tau} \tag{11}$$

This frequency is the so-called Nyquist frequency. If higher frequencies are present in the data, these are aliased as lower frequencies.

The spectral density functions are determined for particular frequencies f. These frequencies are calculated only at the special discrete frequencies of harmonic number k, where

$$f = \frac{kf_c}{m} \quad k = 0, 1, 2, 3 \ldots m \tag{12}$$

The total number of discrete frequencies determined depends on the maximum lag mτ.

For each spectral function, the discrete value found is a kind of average value in a certain range or band. The bandwidth for the computations is

$$B = \frac{1}{m\tau} \tag{13}$$

One would tend to determine the spectral functions with small bandwidth -- thus in much detail -- by choosing a large value for m. Unfortunately, this considerably affects the accuracy of the result.

It should be understood that the analysis method gives estimates of the function only. Since we are dealing with data that is not deterministic, each sample record used for analysis differs from another and the results obtained from these records will also differ somewhat.

The estimates of spectral density functions described above are so-called "raw" estimates, which have certain undesirable properties. If a strong periodic component is present, the analysis may show small positive and negative values in the frequency bands adjacent to that in which the periodic component is present. This phenomenon is called "leakage," and the negative values it produces are particularly bothersome. To counter it, frequency smoothing is used, by which the estimate at a particular frequency is computed as a weighted average of the particular frequency and the adjacent frequency.

For example, the smoothed co-spectral density function can be taken as

$$\bar{C}_{xy}(f) = \bar{C}_{xy}\left(\frac{kf_c}{m}\right) = .25\hat{C}_{xy}\left(\frac{(k-1)f_c}{m}\right) + .5\hat{C}_{xy}\left(\frac{kf_c}{m}\right) + .25\hat{C}_{xy}\left(\frac{(k+1)f_c}{m}\right)$$
$$\tag{14}$$

This frequency smoothing is called "hanning," which is equivalent to the Tukey lag window.[4] Other methods of minimizing the effect of leakage are available,[1,4] but these are not applied in this investigation.

For the absolute value of the smoothed cross-spectral density we obtain the following estimate:

$$|\bar{\hat{P}}_{xy}(f)| = \left(\bar{\hat{C}}_{xy}(f)^2 + \bar{\hat{Q}}_{xy}(f)^2\right)^{\frac{1}{2}} \tag{15}$$

Subsequently, the estimated amplitude of the frequency response function is

$$|\hat{H}(f)| = \bar{\hat{P}}_{xy}(f) / \bar{\hat{P}}_{xx}(f) = \hat{A}_{xy}(f) \tag{16}$$

and its estimated phase spectrum is

$$\hat{\phi}(f) = \tan^{-1}\left[\bar{\hat{Q}}_{xy}(f) / \bar{\hat{C}}_{xy}(f)\right] \tag{17}$$

The frequency response function thus obtained is an optimal estimate (in a least square sense), assuming that the system is linear. Even if we assume that we have a linear system whose input $\{x\}$ may be measured exactly, the output may still contain measurement errors. In the case analyzed here, the output may be influenced by wind and system nonlinearities. The measured output then contains the transformed input signal plus measurement noise, etc. (in our case noise caused by wind and nonlinearities).

It is now possible to introduce a measure of the linear relation between the two series, called the coherency function $\Omega_{xy}(f)$. The squared coherency is estimated to be

$$\Omega^2_{xy}(f) = \frac{|\bar{\hat{P}}_{xy}(f)|^2}{\bar{\hat{P}}_{xx}(f) \ \bar{\hat{P}}_{yy}(f)} \tag{18}$$

If the system is completely linear, the squared coherency is unity; if the two time series are completely uncorrelated, then the coherency would be zero. If the coherency is less than unity but greater than zero, then there is noise in the measurements, the system is not linear, or the output $\{y\}$ of the system is due to an input $\{x\}$ as well as other inputs.

In determining the behavior of a system it is often useful to see how the noise is distributed over the frequency range. The estimated spectral density function of the noise is expressed by

$$\bar{\hat{P}}_{x\Delta y}(f) = [1 - \Omega^2_{xy}(f)] \ \bar{\hat{P}}_{yy}(f) \tag{19}$$

In a strict sense, when the cross-spectral estimates $\hat{P}_{xy}(f)$ are used to determine the frequency response function, the measurement noise at the input will cause the frequency response function to be underestimated, as can be seen from the equation

$$\hat{H}(f) = \bar{\hat{P}}_{xy}(f) / \bar{\hat{P}}_{xx}(f) = \bar{\hat{P}}_{xy}(f) / [P_{xx}(f) + P_{nnx}(f)] < H(f) \tag{20}$$

in which $P_{xx}(f)$ is the true value of input spectra and $P_{nnx}(f)$ is the spectrum of extraneous noise components in the input. Notice that the uncorrelated noise at the output does not cause bias.

The amount of measurement noise and the error due to it can be estimated by computing the amplitude function forward and backward between two sets of records (i.e., switching x series and y series in the computational sequence). By going from y to x, the noise in y would cause the transfer from y to x to be underestimated, which is equivalent to the overestimation of x in the relative amplification factor. However, by going from x to y, the noise in y no longer influences the value of backward transfer, but the noise in x is now the important factor. In each direction the transfer function is underestimated. Therefore, the best estimate of the transfer function from y to x is

$$\tfrac{1}{2}[1/A_{yx}(f) + A_{xy}(f)] \qquad\qquad\qquad (21)$$

The error would be cancelled out if the random measurement noise level in both records were about the same.

The computed coherency $\hat{\Omega}^2_{xy}(f)$ also contains some bias if the phase difference between two stations is appreciable. This bias can be reduced by a process called alignment (see Ref. 4 for details), using the peak of the cross-covariance as a guide to make the required shift.

DATA ANALYSIS

One of the applications of the network frequency response analysis is estimating open boundary conditions for a two-dimensional mathematical model of the Netherlands coast in the North Sea (Fig. 1). In order to determine the proper boundary conditions for the model, 29 bottom pressure recorders were installed by the Netherlands Rijkswaterstaat during the months of May and June 1971. Hourly water level data were first analyzed without astronomical prejudices, thus allowing for all possible frequencies and their higher harmonics that were present.

The frequency domain mapping was carried out using arbitrary-radix algorithms of fast Fourier transforms. During the transformation, Tukey's[8] interim data taper window was applied to eliminate leakage from the peaks. The Fourier line spectra for stations U (reference station) and A_1 are shown in Fig. 2. The contribution from the meteorological disturbances, located in the frequency range below 0.04 per hour, and the higher harmonic components induced by the diurnal-semidiurnal components can be noted in the graphs.

Frequency response analyses and cross-spectral computations were then carried out between the reference station U and the 21 stations located at the model open boundary. The graphic results from a typical analysis are shown in Fig. 3. In the top row the adjusted bottom pressures at station A are shown. The computed spectra at station A are also shown. It will be noted that the higher harmonics of the lunar component, which are the quarter-diurnal tide (M_4 at f = .16 hr^{-1}) and the sixth-diurnal
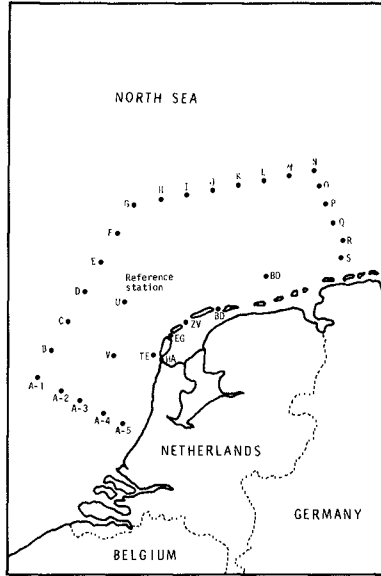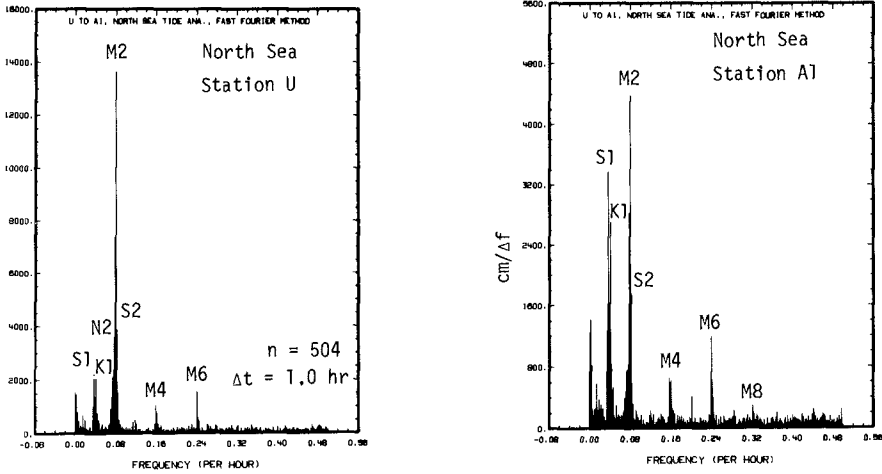
Figure 1   Relative location of tide gauges

Figure 2   Analysis of tidal components and other oscillations in the observed
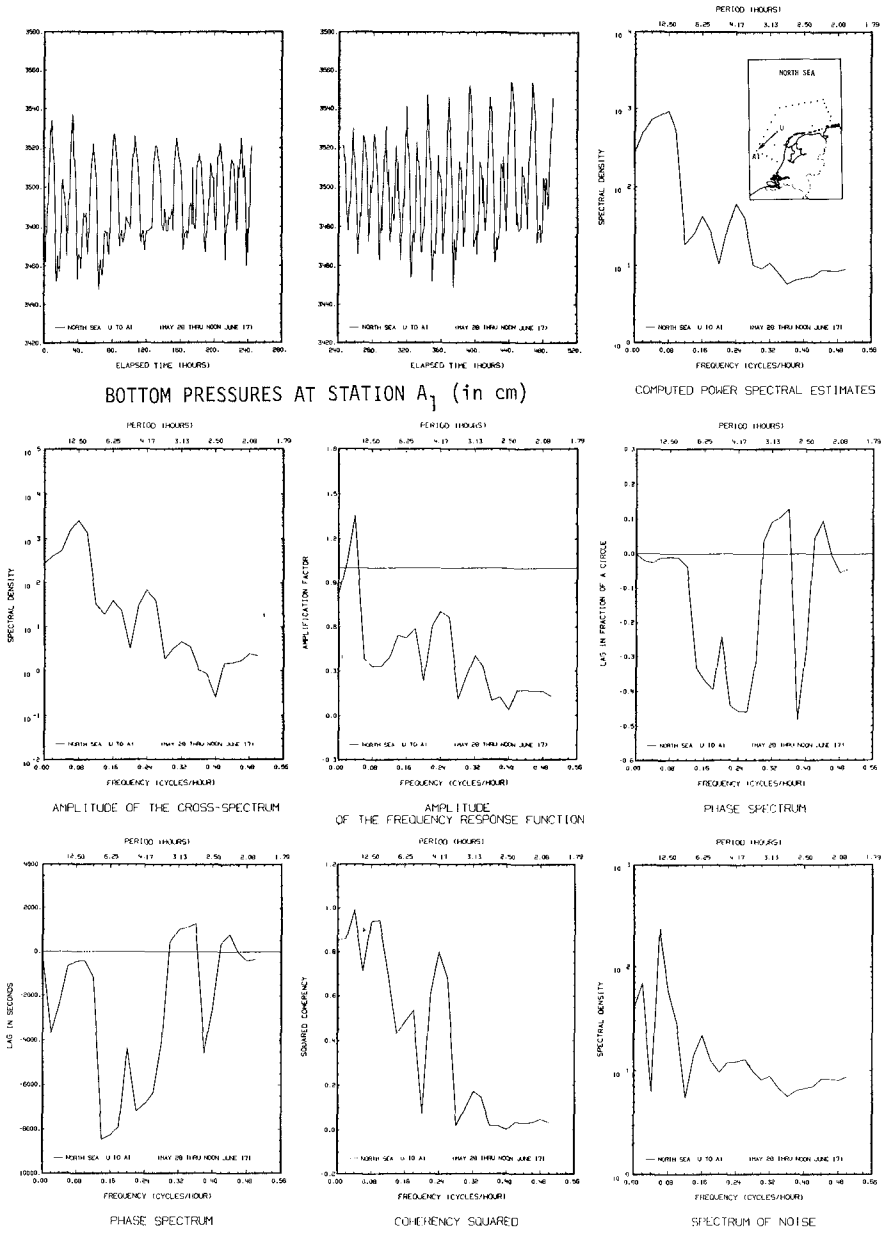data using fast Fourier transform and cosine data tapering filter

BOTTOM PRESSURES AT STATION A₁ (in cm)

COMPUTED POWER SPECTRAL ESTIMATES

AMPLITUDE OF THE CROSS-SPECTRUM

AMPLITUDE
OF THE FREQUENCY RESPONSE FUNCTION

PHASE SPECTRUM

PHASE SPECTRUM

COHERENCY SQUARED

SPECTRUM OF NOISE

Figure 3   Frequency response analysis between Station U
(reference station) and Station A1

tide (M_6 at f = .24 hr^{-1}), contain much less energy than the semi-diurnal tide at f = .08 hr^{-1}. This can also be found in the cross-spectrum between the reference station U and A_1 in the first graph in the second row of Fig. 3. The amplitude of the frequency response estimate between U and A_1 shown in the middle graph, indicates that the amplification factor is 1.36 for the diurnal tide (f = 0.04), but only 0.3 for the semi-diurnal tide (f = 0.08). The phase of the response function is shown in the third graph of the second row in fractions of a circle. The phase is also shown in the bottom row as the lag in seconds. The computed square coherency and the spectrum of the uncorrelated components are shown in the bottom row.

The spatial distribution of the amplitude and phase of the frequency response function and the spatial distribution of the coherency of the records for the semidiurnal component from the reference station U and the boundary stations are shown in Fig. 4. The decrease in amplification near station A_2 indicates the passing of the amphidromic point located approximately halfway between the English and Dutch coasts (see Proudman and Doodson, Fig. 5, Ref. 9). The amplitude, phase, and squared coherency of the computed frequency response function for the quarter-diurnal harmonic (f = 0.16/hr) along the boundary network are shown in Fig. 6.

Frequency response function for points between gauges can be interpolated for models of different grid size. The impulse response function $h(k)$ between the reference station U and the boundary stations is obtained by inverse Fourier transform from the co-, quad-, and auto-spectra of the reference station.

$$\hat{h}(k) = \frac{\Delta f}{2} \left\{ \sum_{h=0}^{m} \left[\hat{\overline{C}}_{sy}(h)/\hat{\overline{P}}_{xx}(h) \right] \cos \frac{hk\pi}{m} \right.$$

$$\left. + \sum_{h=0}^{m} \left[\hat{\overline{Q}}_{xy}(h)/\hat{\overline{P}}_{xx}(h) \right] \sin \frac{hk\pi}{m} \right\} \tag{22}$$

for k = 0, 1, 2, 3 ... m
    h = 0, ... m

The water levels at these boundary points for any future condition can then be generated optimally from the measured information at station U (or from any other single station) by the convolution formula:

$$\hat{y}(n\Delta t) = \Delta t \sum_{k=0}^{n} x(k\Delta t) \, \hat{h}(n\Delta t - k\Delta t) \tag{23}$$

RECONSTRUCTION OF BOUNDARY INFORMATION

The aforementioned approach was used for reconstructing the open boundary information of a two-dimensional mathematical model of Jamaica Bay, New York City, U.S.A., as shown in Fig. 7.[2] During a large-scale field observation of water quality for comparing simulated with observed
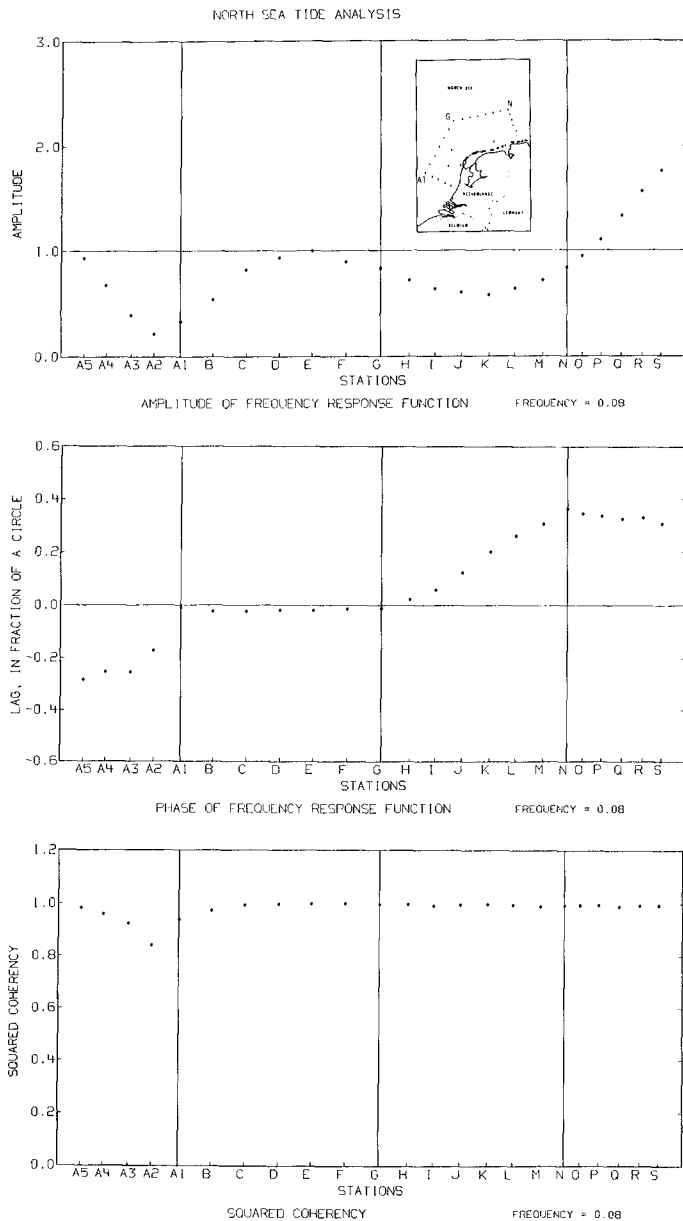
Figure 4   Amplitude, phase, and squared coherency of the computed
            frequency response function for the semi-diurnal
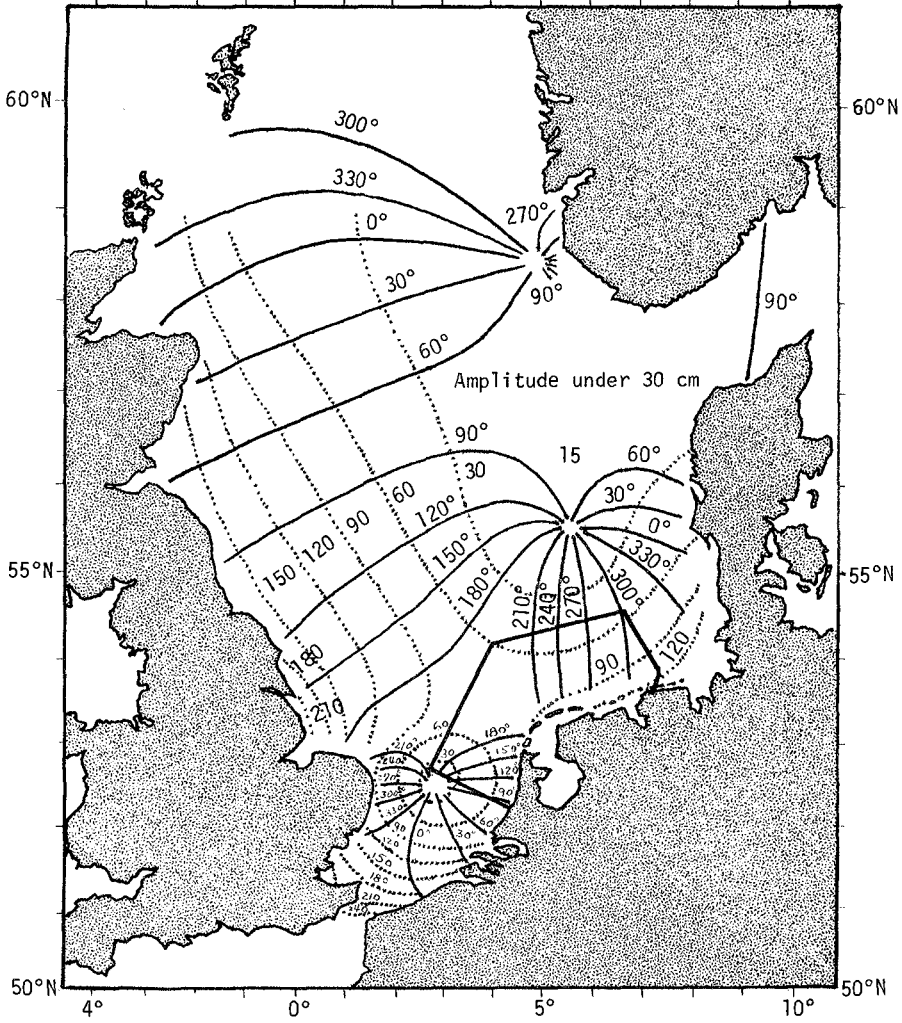   tidal component (frequency = 0.08/hr)

Figure 5   Cotidal times, observed amplitudes, and amphidromic points
near the area of the coastal model for the M_2 component
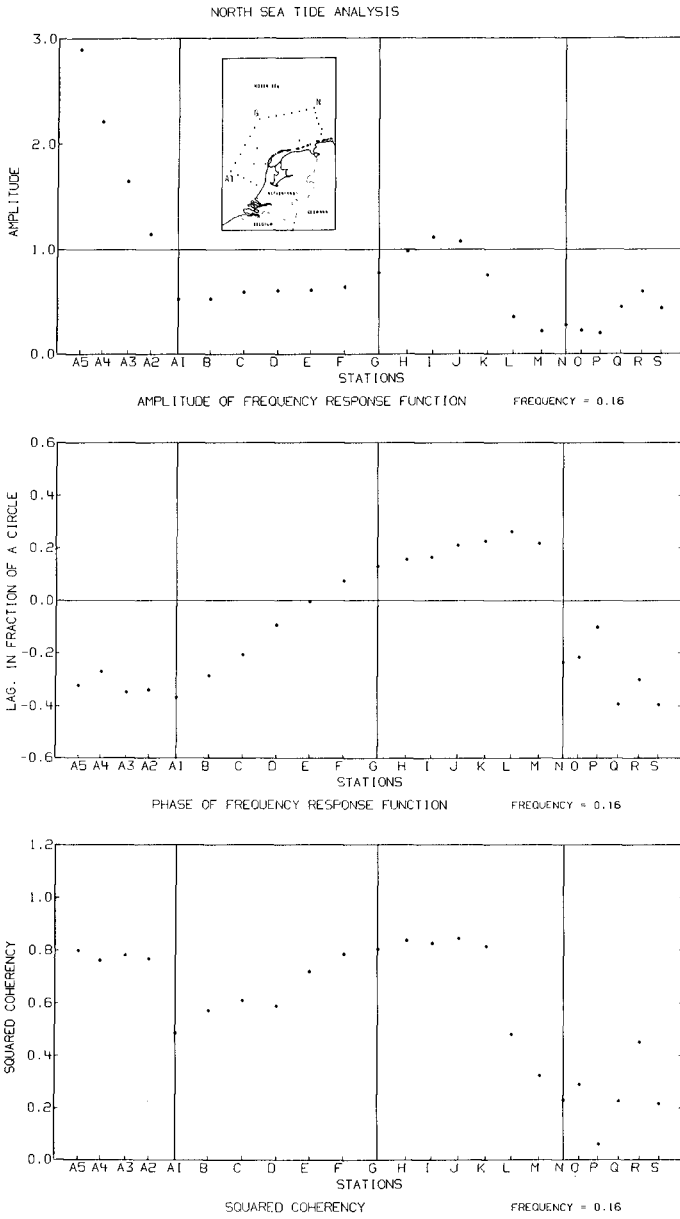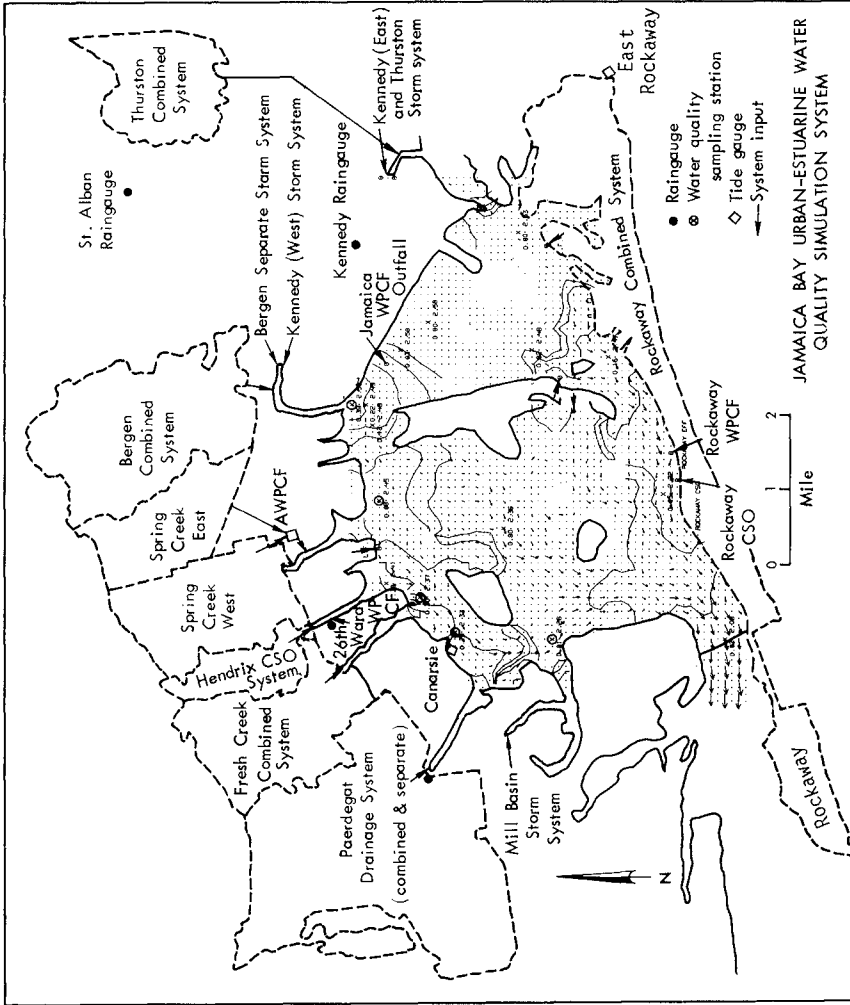(from Proudman and Doodson, 1924)

Figure 6   Amplitude, phase, and squared coherency of the computed frequency response function for the quarter-diurnal tidal component (frequency = 0.16/hr)

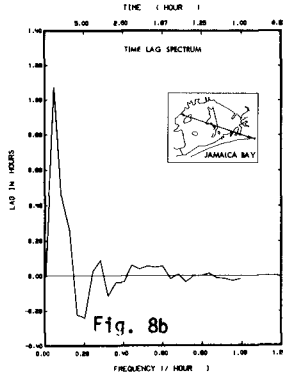Figure 7   Jamaica Bay Urban-estuarine Water Quality Simulation System (Ref. 2)

pollutant distribution after a rainstorm, the tide gauge in the bay at
Canarsie (northwestern corner of Fig. 7) malfunctioned without being
detected until after the entire field operation was completed. It was
found that the gauge became inoperative just before the sampling started
with a few days of usable data prior to that period. Without tide
information, no meaningful simulation could be made. Rather than request
another survey, it was decided to reconstruct the missing water level time
history. The nearest available tide data covering the entire period was
the East Rockaway gauge located on Long Island (southeast corner of map).
The only way for making the simulation is to derive the response (transfer)
function from East Rockaway to Canarsie with the mutually available data
before the experiment. Secondly, response function can be derived between
Canarsie and Rockaway (open boundary) with data collected in October 1970
with high accuracy. Once these response functions are determined, the
time history of the water levels at the open boundary can be reconstructed
(either in the frequency domain by transformation or in the time domain by
convolution) for the water quality simulation period.

Figures 8a, 8b, and 8c are the computed frequency response functions
between Canarsie and East Rockaway using the group of data just prior to
May 31, 1972. Figures 8d, 8e, and 8f are the response functions between
Rockaway and Canarsie using October 1970 data (dotted lines). The solid
lines in this set of graphs are results derived from another numerical
simulation of tidal flows between these two stations. Figure 8g is the
reconstructed water level (by transformation) at the model boundary
using data observed from May 31 through June 3, 1972, at East Rockaway.

With the boundary information determined, the water quality simulation
can then be carried out. A typical constituent distribution map is shown
in Fig. 9. Detailed discussion of this particular simulation can be
found in Leendertse and Liu.[2]

                                SUMMARY

The usefulness of the network response function in numerical simulation
is threefold: (1) future conditions can be simulated using observed water
levels at any single location; (2) boundary information for models of
different grid size can be obtained by spatial interpolation along the
boundary line; and (3) missing data at any location can be estimated
optimally (in a least square error sense) using data at neighboring station
and the network response functions. The uses of response function and
cross-spectral density function to make numerical or hydraulic model
adjustment are discussed elsewhere.[2,3]

Figure 8a

Fig. 8b

Fig. 8c

Fig. 8d

Fig. 8e

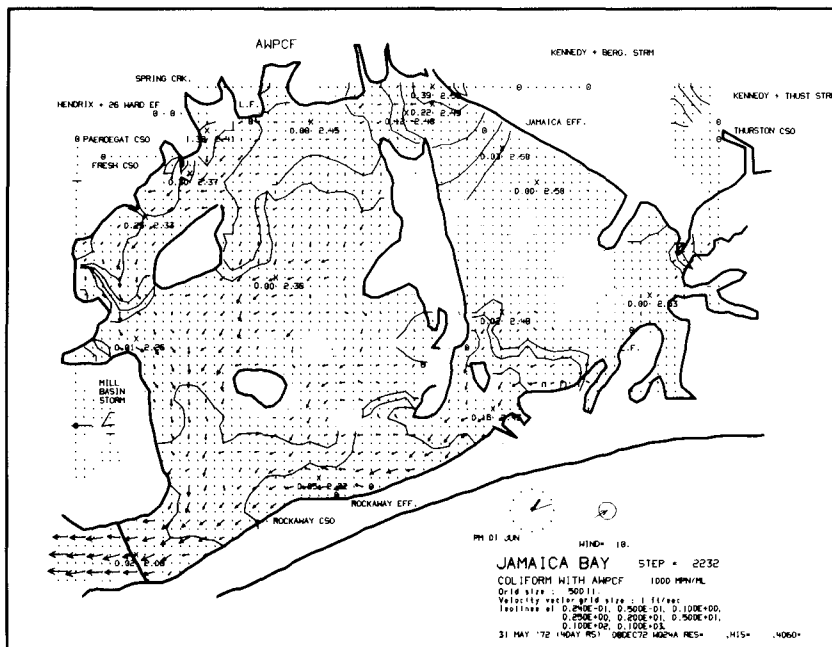Fig. 8f

Fig. 8g
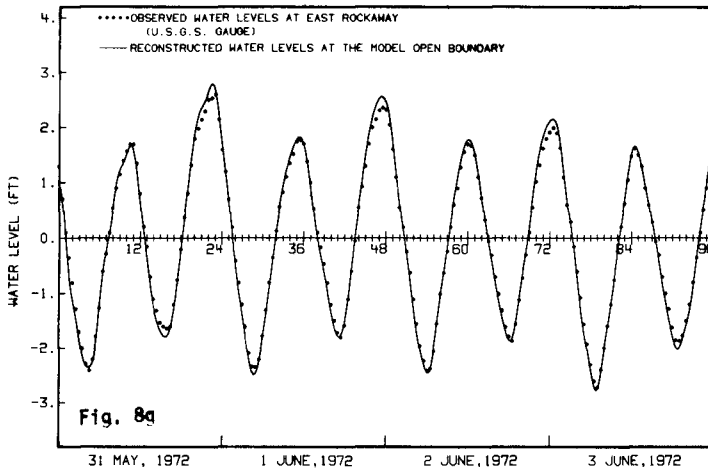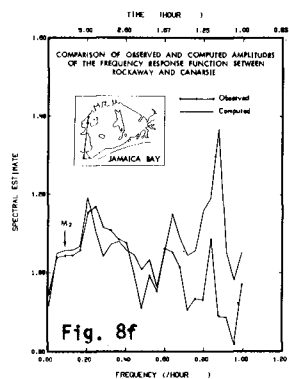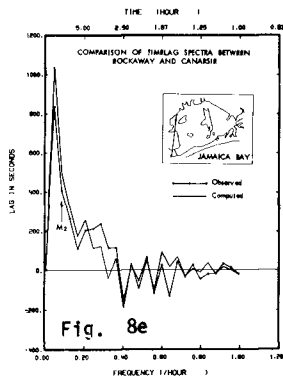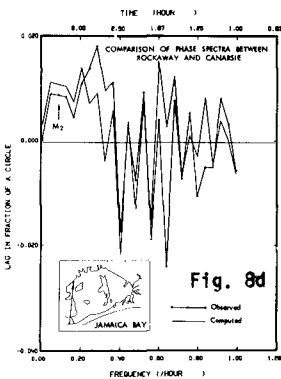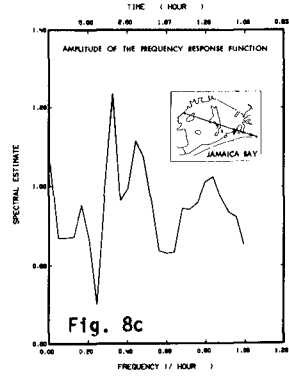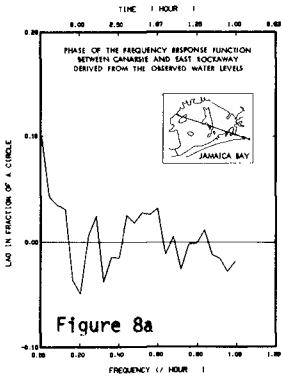
Figure 9   A typical constituent distribution map of water quality simulation
           as generated by the Integrated Graphic System (IGS) developed at
           Rand

REFERENCES

1. Liu, Shiao-Kung, *Stochastic Simulation and Control of Urban-Estuarine Water Quality Systems*, The Rand Corporation, R-1622-NYC (in preparation).

2. Leendertse, Jan J., and Shiao-Kung Liu, *A Water-Quality Simulation Model for Well Mixed Estuaries and Coastal Seas: Vol. VI, Simulation, Observation, and State Estimation*, The Rand Corporation, R-1586-NYC, September 1974.

3. Leendertse, Jan J., and Shiao-Kung Liu, *Comparison of Observed Estuarine Tide Data with Hydraulic Model Data by Use of Cross-Spectral Density Functions*, The Rand Corporation, R-1612-NYC, September 1974.

4. Jenkins, G. M., and D. G. Watts, *Spectral Analysis and its Applications*, Holden-Day, 1968.

5. Goodman, N. R., *On the Joint Estimation of the Spectra, Co-Spectrum and Quadrature Spectrum of a Two-Dimensional Stationary Gaussian Process*, Engineering Statistic Laboratory Scientific Paper 10, New York University, 1957.

6. Wiener, N., *The Extrapolation, Interpolation and Smoothing of Stationary Time Series with Engineering Applications*, John Wiley & Sons, Inc., New York, 1949.

7. Lee, Y. W., *Application of Statistical Methods to Communication Problems*, Lincoln Laboratory, Technical Report 181, 1950.

8. Tukey, J. W., "An Introduction to the Calculation of Numerical Spectrum Analysis," in *Spectral Analysis of Time Series*, Bernard Harnes, ed., John Wiley & Sons, Inc., New York, 1967, pp. 25-46.

9. Proudman, J., and A. T. Doodson, "The Principal Constituent of the Tides of the North Sea," *Phil. Trans. Roy. Soc.* A224 (London, 1924).

CHAPTER 124

RESEARCH ON THE MODEL SHELTERING

INVESTIGATION OF A HARBOR

Ho-Shong Hou[*]

[*]Lecturer, National Chung Hsing University, C. E. Dept., Taiwan, R.O.C.
Principal Investigator, Taichung Harbor Construction Bureau, R.O.C.
Ph.D. Graduate Student, Civil and Coastal Engr., Univ. of Fla., Gaines-
ville, Fla. U.S.A.

ABSTRACT

The Model Sheltering Experiment deals with the planning arrangement of
the proposed harbor and is done by the worst wave condition (with respect to
wave direction, wave height, and wave period) which probably occurred on the
proposed harbor. The objectives of this experiment are to get the wave pat-
tern of the harbor basin and to understand the various phenomena of the wave
refraction, diffraction, and reflection caused by model test due to different
harbor arrangement, and to comprehend the sheltering effect of the outer
breakwaters. From the analysis of these test results, harbor planning of the
most effective arrangement - the most economic length of breakwaters and the
most ideal width of harbor entrance could be selected. For the purpose of
analyzing results of model tests; comparison of theoretical wave diffraction
calculation is proposed.

INTRODUCTION

Here is research of the outer breakwater arrangement of a big harbour.
Taichung Harbor is pending to be constructed as an international commercial
harbor on the mid-western coast of Taiwan. It is a pure artificial harbor.

2139

The wave sheltering effect is most important of all. For obtaining safe

navigation, especially easy maneuverability of the ship and calm harbor

basin for normal operation. The optimal arrangement was required. For

getting the optimum result, a large-scale model experiment was necessary

to check and compare all proposed arrangements.

The author was in charge of the model investigation of Taichung Har-

bor. However, he wished to appreciate the direction of Ito (Head of Hydrau-

lic Engr. Division, Port and Harbour Research Institute, Japan) and Tang

(Professor and Chairman of Hydraulic Engr. Dept., National Cheng Kung

University, Taiwan, R.O.C.). Hence, he could get the better achievement

of harbor planning.

1.   ELEMENTS OF THE SHELTERING MODEL EXPERIMENT

1.1   The Model Construction and The Test Method

On the test basin, at first, the mortar model of the whole harbor area

including the harbor basin, inner harbor arrangement, outer breakwater ar-

rangement, and topography of seaward up to 50 M deep was made. The navi-

gation chart is 1970. The undistorted model was constructed by the scale

of 1/150. The model was referred to fixed bed model. For the convenience

of measurement, contours were painted white to determine depth of the head

of breakwaters. Fresh water was pumped into the test basin from outer reser-

voir. The required water level is measured by point gauge.

Before model test pr-ocessed, the rating curve of wave period vs. wave

height was calibrated by neon tube wavemeter and step resistance wavemeter,

separately. Incident wave height were checked by wave meter.   Since the

plunger type wave generator is autocontrollable by the motor and the gear,

therefore different wave directions of the test were got done. From wave

height measurement in the wide area harbor region, the diffraction coef-
ficients (ratio of wave height in the harbor region to incident wave
height) were got. Then, from all equal wave height ratio lines, the wave
pattern of the harbor region was obtained. The figure is called wave dif-
fraction diagram. From this diagram, different sheltering effect of each
arrangement of the outer breakwaters against the intruding waves was realized.
Such an experiment is known as the Sheltering Model Experiment.

In this Sheltering Model Experiment the phenomena of wave shoaling and
refraction due to water depth change could be got further informations.
Simultaneously, those of wave overtopping and wave reflection through the
breakwater when waves attached, were perceptible from the model test and
could be noted down for the references of the structure design and section
stability test.

1.2 Purpose of Sheltering Model Experiment

The purpose of this test was to compare wave sheltering effects of
harbor basin of eight proposed outer breakwater arrangements, and decide
the optimal arrangement of the wave sheltering effect.

1.3 Model Scale

The scale of this undistorted model was determined by the harbor area
and the size of the test basin. Whence, the horizontal plane and vertical
scale was chosen as $n_H = n_V = 1/150$.

1.4 Test Conditions

A. Wave conditions

Wave conditions were based on recent 10 year records of wind (including
typhoon and monsoon) and waves and selected by the largest typhoon and the
strongest monsoon.

According to the analysis of typhoon data, the largest two typhoons
were Elsie typhoon and Pamela typhoon. From the calculations of Wilson

moving fetch method, the largest waves which could occur around the coast of Taichung harbor shown as Table 1.

Table 1. Wave Conditions of Taichung Harbor

Wave Direction	Wave Height $H_{1/3}$ (m)	Wave Period $T_{1/3}$ (sec)	Remarks
NNE	4.9	10	Elsie (at depth -15 m)
N	5.8	12.4	Pamela (at depth -10 m)
NNW	5.4	10.2	Pamela (at depth -10 m)
NW	5.0	11.2	Pamela (at depth -10 m)
WNW	3.9	8.6	Elsie (at depth -15 m)
W	4.2	9	Elsie (at depth -15 m)
WSW	3.3	12.2	Elsie (at depth -15 m)
SW	3.1	11.2	Pamela (at depth -10 m)

During the monsoon of the winter, the wave which occurred frequently was in deep water $H_0 = 2.78$ m, $T_0 = 7.9$ sec

Wave direction: NNE

From above data, therefore the selected waves for model test were showed below:

(1) N direction: H = 6 m, T = 12 sec was the largest significant wave of N direction caused by typhoon or strong monsoon of the winter season.

(2) N direction: H = 3 m, T = 8 sec was the wave of monsoon of

the winter season during storm time.

(3) WNW direction: H = 4.5 m, T = 9 sec was the largest incident

wave due to typhoon intruded from WNW direction, just opposite to

the direction of the harbor entrance.

(4) WSW direction: H = 3.5 m, T = 9 sec was the largest signifi-

cant wave caused by typhoon intruded from WSW direction.

B. Tide

The tide of Taichung Harbor is semi-diurnal, but after 5 or 15 days

there is a high tide or a low tide only, the tidal difference of each day

is very obvious.

Because Taichung Harbor is located in the middle of the Taiwan Strait,

therefore, its tidal range is particularly large. The maximum tidal range

is 5.5 meters or so. According to tide statistical analysis of recent ten

years the tide of Taichung Harbor is shown as follows:

Mean Tide Level (M.T.L.): +2.90 m

High Water of Spring Tide (H.W.O.S.T.): +5.00 m

Low Water of Spring Tide (L.W.O.S.T.): +0.40 m.

For the Sheltering Model investigation, H.W.O.S.T. is used, therefore

tide level was selected as +5.00 m, as model water level: +3.33 cm.

1.5 Element of Waves of Model Experiment

Table 2. Model Waves vs Actual Waves

Items	Scale	Prototype	Model
Wave Period	$\dfrac{1}{\sqrt{150}}$	12 Sec	0.98 Sec.
		10 Sec	0.84 Sec.
$T_{\frac{1}{3}}$	$= \dfrac{1}{12.2}$	9 Sec	0.75 Sec.
		8 Sec.	0.65 Sec.
Wave Height	$\dfrac{1}{150}$	6 m	4.00 cm
		4.5 m	3.00 cm
$H_{\frac{1}{3}}$		3.5 m	2.33 cm
		3 m	2.00 cm

2. SIMILARITY OF MODEL EXPERIMENT

2.1 Similarity of Wave Motion

Now if the factors of bottom friction and wave transformation of the model are neglected and Cartesian Coordinate is used, then the equation of motion could be written as:

$$\frac{\partial u}{\partial t} + u\frac{\partial u}{\partial x} + v\frac{\partial u}{\partial y} + w\frac{\partial u}{\partial z} = -\frac{1}{\rho}\frac{\partial p}{\partial x} \qquad (2.1)$$

$$\frac{\partial v}{\partial t} + u\frac{\partial v}{\partial x} + v\frac{\partial v}{\partial y} + w\frac{\partial v}{\partial z} = -\frac{1}{\rho}\frac{\partial p}{\partial y} \qquad (2.2)$$

$$\frac{\partial w}{\partial t} + u\frac{\partial w}{\partial x} + v\frac{\partial w}{\partial y} + w\frac{\partial w}{\partial z} = -g -\frac{1}{\rho}\frac{\partial p}{\partial z} \qquad (2.3)$$

where

U, V and W are velocity components of x, y and z respectively. p is pressure.

Here, in order to make kinematic similarity between model and prototype, therefore from the ratio of each term of equation of motion of prototype with respect to each term of equation of motion of model, correspondingly, the term of prototype is marked subscript   "p". Likewise, the term of model is marked "m" on the subscript   , too. From equation (2.1) the following equivalent equation is got

$$\frac{u_p/t_p}{u_m/t_m} = \frac{u_p^2/x_p}{u_m^2/x_m} = \frac{v_p u_p/y_p}{v_m u_m/y_m} = \frac{w_p u_p/z_p}{w_m u_m/z_m} = \frac{p_p/\rho_p x_p}{p_m/\rho_m x_m} \qquad (2.4)$$

In the test basin, fresh water is used, but in the prototype, the fluid is sea water. Here $\rho_p \approx \rho_m$ is assumed. Therefore, from the first term and the second term of eq. (2.4). The following equation is obtained.

$$\frac{u_p/t_p}{u_m/t_m} = \frac{u_p^2/x_p}{u_m^2/x_m} \quad \therefore \frac{t_m}{t_p} = \frac{u_p}{u_m}\frac{x_m}{x_p}, \therefore \frac{u_p}{u_m} = \frac{x_p/x_m}{t_p/t_m} \qquad (2.5)$$

Simultaneously from the first term and the third term, and from the first

and the fourth term, the following two equations are obtained.

$$\frac{V_p}{V_m} = \frac{\gamma_p/\gamma_m}{t_p/t_m} \qquad (2.6)$$

$$\frac{W_p}{W_m} = \frac{\gamma_p/\gamma_m}{t_p/t_m} \qquad (2.7)$$

From the second and the fifth term, the following equation is got, too.

$$\frac{P_p}{P_m} = \frac{U_p^2}{U_m^2} \qquad (2.8)$$

Similarly from the third term and the fifth term of equation (2.2) yields

$$\frac{P_p}{P_m} = \frac{V_p^2}{V_m^2} \qquad (2.9)$$

Then, from the fourth term and the sixth term of equation (2.3) yields

$$\frac{P_p}{P_m} = \frac{W_p^2}{W_m^2} \qquad (2.10)$$

Furthermore, from the second term of the left hand side and the first term

of the right hand side of equation (2.3) yields

$$\frac{U_p W_p/x_p}{U_m W_m/x_m} = \frac{\gamma_p}{\gamma_m}$$

because $\gamma_p = \gamma_m$ $\qquad \therefore \qquad \dfrac{U_p W_p}{x_p} = \dfrac{U_m W_m}{x_m} \qquad (2.11)$

Likewise, from the third term and the fourth term of equation (2.3) with

respect to the first term of the right hand side of equation (2.3) the fol-

lowing two equations are obtained

$$\frac{V_p W_p}{\gamma_p} = \frac{V_m W_m}{\gamma_m} \qquad (2.12)$$

$$\frac{W_p^2}{z_p} = \frac{W_m^2}{z_m} \qquad (2.13)$$

The above equations are concluded that from equations of (2.8), (2.9) and (2.10)

$$\frac{U_p}{U_m} = \frac{V_p}{V_m} = \frac{W_p}{W_m} = \frac{V_p}{V_m} \qquad (2.14)$$

From equations of (2.11), (2.12) and (2.13)

$$\frac{U_p W_p}{U_m W_m} = \frac{x_p}{x_m} \quad , \quad \frac{V_p W_p}{V_m W_m} = \frac{y_p}{y_m} \quad , \quad \frac{W_p^2}{W_m^2} = \frac{z_p}{z_m} \quad (2.15)$$

The relationship between eq. (2.14) and eq. (2.15) yields

$$\frac{x_p}{x_m} = \frac{y_p}{y_m} = \frac{z_p}{z_m} = \frac{\ell_p}{\ell_m} \qquad (2.16)$$

Thus, from the relationship of equation (2.14) and equation (2.16), then

equation (2.15) can be expressed as

$$\frac{V_p}{V_m} = \left(\frac{\ell_p}{\ell_m}\right)^{\frac{1}{2}} \qquad (2.17)$$

Above form can be reduced as

$$\left(\frac{\ell_p}{\ell_m}\right)^{\frac{1}{2}} = \frac{\ell_p/\ell_m}{t_p/t_m}$$

or

$$\frac{t_p}{t_m} = \left(\frac{\ell_p}{\ell_m}\right)^{\frac{1}{2}} \qquad (2.18)$$

Therefore, the scales of wave (short period) motion of model experiment

are determined as follows.

   (1) From equation (2.16), the horizontal scale and the vertical

   scale must be equal to each other.

   (2) From equation (2.14) and equation (2.17), velocity scale is

   the root of length scale.

   (3) From equation (2.18), time scale is the root of length scale.

   (4) From equation (2.8), (2.9) and (2.17), the scale of the pressure

force per unit area is equal to length scale.

2.2 Similarity of Wave Refraction and Wave Diffraction

   A. Similarity of the variation of wave height due to refraction effect

   Wave refraction phenomena is caused by wave propagates into different

water depth and celerity is changed, then wave is transformed.

From the finite amplitude wave theory.

$$C = \sqrt{\frac{gL}{2\pi} \tanh \frac{2\pi h}{L}} \qquad (2.19)$$

Where g, L, h are gravity acceleration, wave length and water depth.
If the celerity of prototype is similar to that of model, then wave refraction phenomena is kept the same with each other.

From

$$\frac{C_p}{C_m} = \frac{\sqrt{\frac{gL_p}{2\pi} \tanh \frac{2\pi h_p}{L_p}}}{\sqrt{\frac{g_m L_m}{2\pi} \tanh \frac{2\pi h_m}{L_m}}} \qquad (2.20)$$

$L = L_0 \tanh \frac{2\pi h}{L} = \frac{gT^2}{2\pi} \tanh \frac{2\pi h}{L}$ & $Let \frac{g_p}{g_m} \approx 1$, be substituted into above
equation yield

$$\frac{C_p}{C_m} = \frac{T_p \tanh \frac{2\pi h_p}{L_p}}{T_m \tanh \frac{2\pi h_m}{L_m}}$$

or

$$\frac{C_p}{C_m} \times \frac{T_m}{T_p} = \frac{\tanh \frac{2\pi h_p}{L_p}}{\tanh \frac{2\pi h_m}{L_m}}$$

Because $for\ "Shallow\ water"\ condition,\ \tanh \frac{2\pi h}{L} \approx \frac{2\pi h}{L}$

$$\therefore \quad \frac{C_p}{C_m} \times \frac{T_m}{T_p} = \frac{h_p L_m}{h_m L_p}$$

hence

$$\frac{C_p}{C_m} \times \frac{T_m}{T_p} \times \frac{L_p}{L_m} = \frac{h_p}{h_m} \qquad (2.20\,a.)$$

Otherwise, from

$$\frac{L_p}{L_m} = \frac{L_{op}}{L_{om}} = \frac{T_p^2}{T_m^2} \qquad (2.20.b.i)$$

and

$$\frac{C_p}{C_m} = \frac{L_p/T_p}{L_m/T_m} = \frac{T_m}{T_p} \times \frac{L_p}{L_m}$$

$$(2.20.b\text{-}ii)$$

$$\therefore \frac{C_p}{C_m} = \frac{T_m}{T_p} \times \frac{T_p^2}{T_m^2} = \frac{T_p}{T_m}$$

$$(2.20.b\text{-}iii)$$

Equations (2.20b) be substituted into equation (2.20a) yields

$$\frac{T_p}{T_m} \times \frac{T_m}{T_p} \times \frac{T_p^2}{T_m} = \frac{h_p}{h_m}$$

$$\therefore \frac{T_p}{T_m} = \sqrt{\frac{h_p}{h_m}}$$

$$(2.21)$$

For "deep water" $h/L > \frac{1}{2}$; $\tanh \frac{2\pi h}{L} = 1$. $\therefore C^2 = \frac{gL}{2\pi}$, thus

$$\frac{C_p}{C_m} = \sqrt{\frac{L_p}{L_m}} \; ; \quad at \text{ the stage, no required on } L_p/L_m \;.$$

Therefore, the scale of wave period be selected as the root of the

scale of water depth, then the similarity of wave refraction is obtained.

   B. Similarity of the variation of wave height due to diffraction effect

   Wave diffraction means diffusion of wave energy along the parallel direc-

tion of wave crest. Therefore, in order to get the similarity of wave length

must be met. Thus, the scale of wave period must be chosen as the root of the

scale of wave length. Shown as following:

$$\frac{L_p}{L_m} = \frac{\frac{g_p T_p^2}{2\pi} \tanh \frac{2\pi h_p}{L_p}}{\frac{g_m T_m^2}{2\pi} \tanh \frac{2\pi h_m}{L_m}}$$

$$(2.22)$$

(i) If distorted model is used, Let $(L_H)_r = \frac{(L_H)_p}{(L_H)_m}$; $(L_v)_r = \frac{(L_v)_p}{(L_v)_m}$

Thus, $(L_H)_r \neq (L_v)_r$, Now $L_r = (L_H)_r$, where $L_r = L_p/L_m$

For "Shallow Water" $C = \sqrt{gh}$. $\therefore C_r = (h_r)^{1/2} = (L_v)_r^{1/2}$

$C = \frac{\Delta x}{\Delta t} = \frac{L}{T}$; $\therefore L_r/T_r = (L_v)_r^{1/2}$. $\therefore T_r = (L_H)_r/(L_v)_r^{1/2}$

For "Intermediate Water" $L_r = T_r^2 \dfrac{\tanh 2\pi h_p/L_p}{\tanh\left(2\pi \frac{h_m}{(L_v)_r} \cdot \frac{L_v}{L_m} \cdot \frac{(L_v)_r}{(L_H)_r}\right)}$

$\therefore L_r = (L_H)_r = T_r^2 \dfrac{\tanh \frac{2\pi h_p}{L_p}}{\tanh\left(2\pi \frac{h_p}{L_p} \cdot \frac{(L_H)_r}{(L_v)_r}\right)}$

For "Deep Water" $T_r = L_r^{1/2} = (L_H)_r^{1/2}$.

(ii). If undistorted model is used, then $(L_H)_r = (L_v)_r$. From Eqn (2.22)

Thus, $\dfrac{T_p}{T_m} = \sqrt{\dfrac{L_p}{L_m}}$

$$(2.23)$$

3. SCOPE OF MODEL AND FACILITIES

3.1 Scope of Model

The Sheltering Model Experiment of Taichung Harbor was accomplished
in the Large Test Basin of the Taichung Harbor Hydraulic Laboratory. The
size of the Large Test Basin is 60 meters long, 43 meters wide and 1 meter
high.

The scope of model was based on the harbor area of Taichung Harbor
10 year development main plan and was constructed with the topography of
the harbor entrance area, water depth reached to -50 m. According to this
range, the undistorted model scale 1/150 was used and the fixed-bed model
was made of mortar in order to match Geometric Similarity between the
model and the prototype.

3.2 Experimental Facilities

The main equipment of the Sheltering Model Experiment are listed as
below:

3.2.1 Wave Generator

The plunger type wave generator was used in the Sheltering Model Ex-
periment. Its plunger is 30 meters long, therefore, it could produce regular
waves within 30 meter wide area. The wave generator was composed of motor,
accelerator, eccentric roller, gear box and wave-making plunger. Its power
is 30 horsepower. When the power switch is turned on, its motor makes the
accelerator and eccentric roller operating, and causes the shaft to bring
the plunger move upward and downward periodically. Then the waves are pro-
duced. Wave height is determined by the eccentric distance of the eccentric
roller, its maximum range is 150 mm. Wave period is adjusted by the accel-
erated ratio of the accelerator, its period range is from 0.55 sec/cycle to
2.2 sec/cycle.

The wave generator was installed on the semi-circular gear rail and
regular rails, therefore it could be moved along the semi-circular trail
and changed its position, then the waves from different direction were
produced.   The wave producing situation is shown as Fig. 3.1..

3.2.2 Wavemeter

Two kinds of wavemeter were used in the experiment.   One was Neon-tube
type wavemeter, the other was Step-resistance type wave meter.   The former
was used to determine the wave height of the position of wave generator, the
latter was used to measure incident wave heights and wave heights of the har-
bor basin.

A.   Neon-tube type Wavemeter

The Neon-tube Wavemeter is composed of pick-up and neon-tube indicator.
Shown as Fig. 3.2.   During the experiment, the pick-up was put on the measured
point of the test basin, it was connected to the neon-tube indicator, then the
indicator was connected with AC power.   Therefore, the pick-up neon-tube indic-
ator and water of the test basin composed a close circuit.   Each neon-tube cir-
cuit of the indicator with respect to each circuit of the pick-up was formed as
a parallel series.   Therefore, when water waves reached the pick-up, electric
current passed through the circuits of the underwater part of the pick-up.   Then
the lights of the neon-tube indicator are shown.   Due to oscillation of wave
crest and wave trough, the number of the lights showing would be increased and
decreased correspondingly.   By the difference of the number of the lights show-
ing, wave height was calculated.

B.   Step-resistance type Wavemeter

The Step-resistance type wavemeter is composed of pick-up with electric
resistance box (See Fig. 3.3), electric power control box, and pen-oscillograph

(1) Pick-up: Its section has knife-like shape and is made of acrylic
material. A lot of metallic points which were used to connected circuits,
were attached to the acrylic material. The clearance of the metallic point
is 2 mm. The upper part of the pick-up was electric resistance box. Each
circuit of the resistance box, was connected with the circuit of the pick-up
and formed as parallel series, respectively. Pick-up was connected into elec-
tric power control Box by cable.

(2) Pen-Oscillograph: By using electric power control Box as a center
part, then Pen-Oscillograph was connected into the control Box by cable.
When a series of waves caused water particles move up and down then electric
resistances of the whole circuit of the pick-up decreased and increased respec-
tively. Therefore, electric current occurred opposite to the effect of resis-
tance. The effect of electric current is conducted by cable to electric power
control box, then be strengthened and amplified by control box, later conducted
to Pen-Oscillograph which writes the wave fluctuation pattern on the record
paper.

3.2.3 Point Gauge

For determining and fixing water level of model test, point gauge is usu-
ally used. When the wall of the test basin connects with water surface, due
to surface tension, the connecting point is higher than real water level. The
purpose to use point gauge is to avoid the error. A point gauge is fixed by
the wall of the basin and kept a little distance with the wall. When it is
operated, at first horizontal level is adjusted by turning the triangular screws,
then the measuring pole is moved up or down to make sure the expected water
level. Outer side of the measuring pole, a rectangluar-type of timber is in-
stalled a little lower than the water surface. The rectangular timber box can
prevent oscillation of water waves, therefore the point gauge can determine and

fix the expected water level accurately.

4. WAVE DIFFRACTION THEORY

Penny and Price (1944; 1952) showed that the Sommerfield solution of the diffraction of light is also a solution of the water wave diffraction phenomenon.

When incident waves are moving toward the coastal structure, they will be reflected, or break, or both, whereas the poriton propagating past the tip of the structure will be the source of a flow of energy in the direction essentially along the wave crest and into the region in the lee of the structure. The "end" of the wave will act somewhat as a potential source and the wave in the lee of the breakwater will spread out in approximately a circular arc with the amplitude decreasing exponentially along this arc. The same phenomenon will also occur in the reflected portion of the wave.

This complicates the physical picture considerably, as part of the wave energy associated with the "radial" wave being generated from the end of the reflected wave will travel into the harbor region. The two sets of waves, cylindrical and radial, reinforce and cancel each other in such a manner as to cause an irregular wave height in this region. This physical phenomenon is known as diffraction.

4.1 Definition of the Diffraction Coefficient

The surface elevation of the linear water wave theory can be expressed as

$$\eta_s = \frac{A i k c}{g} e^{i k c t} \cosh k d \cdot F(x, z) \tag{4.1.1}$$

where the real part of the expression on the right is used.

For the case of progressive waves travelling in the direction of the x axis with no structure present, $F(x,z) = e^{-ikx}$, therefore

$$\eta_s = \frac{A i k c}{g} e^{i k (c t - x)} \cosh k d$$
$$= a \cdot \sin k (c t - x) \tag{4.1.2}$$

The diffraction coefficient, K', is defined as the ratio of the wave
height in the area affected by diffraction to the wave height in the area
unaffected by diffraction; it is the ratio of the amplitude of Eq. (4.1) to
(4.2). Therefore, K' is expressed by the modulus of F(x,z) for the diffracted
wave as

$$K' = |F(x,z)| \qquad\qquad (4.1.3)$$

4.2 Diffraction Calculation of Arrangement of Breakwaters

Diffraction situation of waves intruding into the harbor region, and
sheltering effect of breakwaters, can be calculated by mathematical model solu-
tions for the case of water areas of the navigational channel and the harbor
entrance of same depth.

Now, the head of the breakwater is considered as the origin of the polar
coordinate and the line of the breakwater is referred to the polar axis. Shown
as Fig. 4.1.
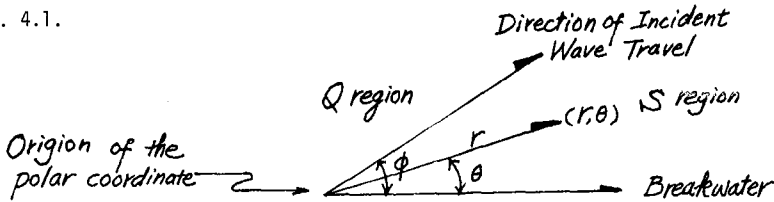
Fig. 4.1 Nomenclature for Wave Diffraction Calculation at the Breakwater Head.

Therefore, the diffraciton coefficient K' of any point (r,θ) of the harbor
basin, can be calculated by the following equation

$$K' = |A + iB| = \sqrt{A^2 + B^2} \qquad\qquad (4.2.1)$$

Here, K' indicates the ratio of the wave height H of any point (affected by
diffraction) of the harbor basin to the incident wave height H_0 (Unaffected by
diffraction) of the harbor entrance.

In the shelter area, i.e. in the lee of the breakwater, region S as Fig. 4.1

shown.

$$A = U_1 \cos[Kr\cos(\theta-\phi)] + U_2 \cos[Kr\cos(\theta+\phi)]$$
$$+ W_1 \sin[Kr\cos(\theta-\phi)] + W_2 \sin[Kr\cos(\theta+\phi)] \qquad (4.2.2)$$

$$B = W_1 \cos[Kr\cos(\theta-\phi)] + W_2 \cos[Kr\cos(\theta+\phi)]$$
$$- U_1 \sin[Kr\cos(\theta-\phi)] - U_2 \sin[Kr\cos(\theta+\phi)] \qquad (4.2.3)$$

If the point (r,θ) in the area of the wave intruding direction, i.e. in region Q as Fig. 4.1 shown.

$$A = \cos[Kr\cos(\theta-\phi)] - U_1 \cos[Kr\cos(\theta-\phi)] + U_2 \cos[Kr\cos(\theta+\phi)]$$
$$- W_1 \sin[Kr\cos(\theta-\phi)] + W_2 \sin[Kr\cos(\theta+\phi)] \qquad (4.2.4)$$

$$B = -\sin[Kr\cos(\theta-\phi)] - W_1 \cos[Kr\cos(\theta-\phi)] + W_2 \cos[Kr\cos(\theta+\phi)]$$
$$+ U_1 \sin[Kr\cos(\theta-\phi)] - U_2 \sin[Kr\cos(\theta+\phi)] \qquad (4.2.5)$$

where $K = 2\pi/L$, L: Wave Length

ϕ: the angle of the breakwater line with the direction of incident wave travel.

$$U_{1,2} = \frac{1}{2}\left[\int_0^{\sigma_{1,2}} \cos(\tfrac{\pi}{2}\sigma^2)d\sigma + \int_0^{\sigma_{1,2}} \sin(\tfrac{\pi}{2}\sigma^2)d\sigma\right] \qquad (4.2.6)$$

$$W_{1,2} = \frac{1}{2}\left[\int_0^{\sigma_{1,2}} \cos(\tfrac{\pi}{2}\sigma^2)d\sigma - \int_0^{\sigma_{1,2}} \sin(\tfrac{\pi}{2}\sigma^2)d\sigma\right] \qquad (4.2.7)$$

$$\sigma_1 = 2\sqrt{\tfrac{Kr}{\pi}} \sin[\tfrac{1}{2}(\theta-\phi)] \qquad (4.2.8)$$

$$\sigma_2 = -2\sqrt{\tfrac{Kr}{\pi}} \sin[\tfrac{1}{2}(\theta+\phi)] \qquad (4.2.9)$$

Diffraction procedure of waves intruding into the harbor region, from Eq. (4.2.1) to (4.2.9), could be rewritten as Flow Chart shown in the following.

START

Input 1: *The Calculated elements* ($F.B.E\ D\phi, DD, DP,\ \phi max, Dmax, Pmax, J$)

Input 2 : *The Polar Coordinate of calculated points* ($R(I), A(I), I=1, J$)

Output 1: *The proper Title*

$\phi = F$

(10)

$\phi = \phi + D\phi$

$ST\phi P$ — Yes — $\phi > \phi m$

(12)

$D = B$

(13)

$D = D + DP$

$D > Dm$ — Yes

$P = E$

$P = P + DP$

$P > Pm$ — Yes

$I = 1$

(100)

$I = I + 1$

$I > J$ — Yes — (23)

$n\phi$

(100)

Caculating The Wave Length By approximated polynomial : $Wal = Wal\ (D, P)\ (\S 1)$

(100)

$RW = R\ (I)\ /\ Wal$

$TH\phi = 0.001743 * \phi$
$THA = 0.001743 * A\ (I)$

Preparation for the calculation of Diffraction (§2)
$Sig\ 1 = Sig\ 1\ (RW. Tha, Th\phi)$
$Sig\ 2 = Sig\ 2\ (RW, Tha, Th\phi)$
$Alp = Alp\ (RW, Tha, Th\phi)$
$Bet = Bet\ (RW, Tha, Th\phi)$

Three region of Diffracted plane Determined by Sig 1 & Sig 2,

$Sig\ 1 \gtreqless 0$ — $n\phi$ / Yes

$Sig\ 2 \gtreqless 0$ — Yes — (35) — Yes — $Sig\ 2 \gtreqless 0$

$n\phi$

Reflecting region

Sheltering Region — (92)

Proceeding Region — (102)

$K = 1$ — Index number — $K = 2$

Call FCS ($C1, S1, Sig\ 1$)
$U_1 = .5 * (1 - S1 - C1)$
$W_1 = .5 * (S1 - C1)$
Call FCS ($C2, S2, Sig\ 2$)
$U_2 = .5 * (1 - S2 - C2)$
$W_2 = .5 * (S2 - C2)$
$AK = AK\ (ALP, Bet\ U_1, U_2, W_1, W_2)$
$BK = BK\ (ALP, Bet\ U_1, U_2, W_1, W_2)$

Call FCS ($C1, S1, Sig\ 1$)
$U_1 = .5 * (1 - S1 - C1)$
$W_1 = .5 * (S1 - C1)$
Call FCS ($C2, S2, Sig\ 2$)
$U_2 = .5 * (1 - S2 - C2)$
$W_2 = .5 * (S2 - C2)$
$AK = AK\ (ALP, Bet, U_1, U_2, W_1, W_2)$
$BK = BK\ (ALP, Bet, U_1, U_2, W_1, W_2)$

(35)

(109)

$C\phi DK = SQRT\ (AK^2 + BK^2)$

Output 2 : $\phi, D, P, R(I), A$ $RW, C\phi DK, K, J$

5. THE PROPOSED EIGHT ARRANGEMENTS OF OUTER BREAKWATERS AND TEST RESULTS:

5.1 Experiments of N wave direction

For the test condition of N direction: Wave height was 6 M, wave period was 12 sec. The arrangements and test results were shown from Fig. 5-1, *5-2*, Fig. 5-1-1 **to** 5-1-8.

Case 1: The pier head of north breakwater reached up to -12 M water depth.

Test result: The waves of the harbor mouth were very confused, the wave height of outer harbor basin was above one meter. Since the distance which north breakwater overlapped south breakwater was not long enough, waves easily intruded into harbor basin. Waves diffracted from the north pier head, travelled to the south pier head and reflected. Due to these effects, the harbor entrance was disturbed. Therefore, wave sheltering effect was bad.

Case 2: The pier head of north breakwater of Case 1 was prolonged along its original direction up to -20 M water depth. South breakwater was kept the same as Case I.

Test result: Wave sheltering effect was quite good. Harbor basin was almost calm. The effective width of harbor entrance became a little smaller. Ship navigation should be changed to a curved course.

Case 3: Based on the arrangement of Case 2, the north pier head part of water depth from -15 M to -20 M, its total length was 150 meters to be shifted northward, and this part was made to be parallel to WNW direction.

Test result: Wave sheltering effect was not so good as that of Case 2. Waves passed through the north pier head, then intruded along south breakwater obviously. However, navigational course was suitable for ship being maneuvered.

Case 4: The oblique parts of outer breakwaters was parallel shifted landward, the north pier head reached to water depth -10 M, and the south pier head

reached to water depth ~7 M. The distance between the north pier head and
the south pier head is 220 meters.

Test result: Wave sheltering effect was not good because water depths
of the pier heads were not deep enough.

Case 5: The direction and width of harbor entrance was kept the same as
that of Case 1 and the oblique part of north breakwater was turned northward,
and let the angle between the straight part and the inclined part be 20°30',
the north pier head was prolonged to water depth -20 M.

Test result: Wave heights of the harbour mouth showed a little small,
comparing to Case 4, but outer harbor basin existed oscillation of stationary
waves. Its wave sheltering effect was not really good.

Case 6: The position of the head point of north breakwater was fixed as
Case 5. The straight part of north breakwater was kept the same as Case 5.
The middle part of north breakwater was turned 10°15' southward with the straight
part. The pier-head part, 240 meters long, was turned southward, and the head
was matched with water depth of -20 M. The direction, position and length of
south breakwater was kept the same as those of Case 1.

Test result: Its wave sheltering effect seemed a little better, wave
heights of outer harbor basin were below one meter. It looked good.

Case 7: The straight part of north breakwater was based on Case 1 and
prolonged 210 meters seaward, then turned southward. The oblique part of north
breakwater was kept parallel with that of Case 1, but the pier head part, which
was deeper than -20 M, was 46 meters. South breakwater was the same as Case 1.

Test result: Its wave sheltering effect was better than that of Case 6,
even not so good as that of Case 2. However, wave heights of harbor basin except
those of harbor mouth, were below one meter. It met the requirement of operation.

Case 8: The arrangement of this case was almost the same as Case 7. The only difference is, the pier head part of north breakwater was cut down 46 meters, so that the pier head reached to water depth -20 M.

Test result: Its wave sheltering effect was not so good, compared with that of Case 7, and its width of harbour mouth showed a little large.

5.2 Theoretical calculation of N wave direction for the selected five arrangements

Based on flow chart of wave diffraction coefficients for Case 1, 2, 5, 6 and 7 were calculated by Digital-Computer. From calculating results showed that wave sheltering effects of Case 2 and Case 7 were quite good, the same trend as that of model experiment. Shown from Fig. 5-2-1 to Fig. 5-2-5.

When test results being compared with theoretical calculations, it could be found out that the wave heights in the outer harbor entrance measured from model test were larger than the calculated figures, and that the wave heights in the inner harbor entrance were smaller than the calculated values. The difference is due to the following reasons: (1) There were boundaries such as reinforced concrete walls of the test basin, timber plates for the wave guiders etc. in the model test; these often produced reflection of waves. The basin of the outer harbor entrance was easily influenced by these reflections. Therefore, the wave heights in this area of the model test were larger than those of the theoretical results. (2) The theoretical wave heights were based on waves in irrotational, inviscid flow, whereas there was a viscosity effect in the model, as well as bottom friction; viscosity and bottom friction in the model were relatively much larger than in the prototype for the shallow harbor basin areas, but for those deep basin areas such as navigational channel, etc. Their viscosity and bottom friction could not be in scale by model law.

For above reasons, the theoretical wave heights in the outer harbor entrance and navigational channel may be considered to be more accurate than those of the

model. Wave heights in the inner side of the breakwater and waves in the
shallower water depths of the harbor basin were selected from the results of
the model test, because the effects near to real phenomena were considered.
The wave heights of the inner harbor entrance and its surrounding basin area
were between the model and the theoretical values.

5.3 Experiment of Waves from WNW and WSW directions

The objective of the experiments of WNW and WSW directions was to check
whether the ship could be safely anchored in the dock and controllably maneuvered
in the navigational channel or not during the worst weather of hurricane intruding.

Therefore, except the experiment of N direction, the experiments of WNW
and WSW were required to test and investigate. Here the most ideal case among
those arrangements were selected to process these experiments. How much of waves
intruding the harbor mouth and harbor basin during waves from WNW and WSW direc-
tions were measured. Test results were shown from Fig. 5-3-1 to Fig. 5-3-4.

From test results, they showed waves from WSW direction, the wave heights
of the inner harbor basin occurred below one meter, and did not affect the opera-
tion of navigation. But waves from WNW direction, the wave heights of the inner
harbor basin were high above one meter, they could not meet the requirements of
operation. In order to reduce wave heights of inner harbor basin, the quay
wall against the harbor entrance direction should be designed for wave-energy
absorbent function, and the width of inner harbor entrance should be reduced
some quantity. Of course, the width of inner harbor entrance could not diminish
too much. For the concept of "harbor paradox", the condition of small mouth and
large basin easily caused harbor resonance, since that the inner harbor entrance
need to be reduced suitably so that it could prevent waves intruding from outer
basin, and it can also resease the waves of inner basin out of inner entrance.

6. CONCLUSION

1. From above results of wave sheltering model investigation, we could select the optimal sheltering effect of harbor arrangement. As above mentioned arrangements, Case 2 was the best; however Case 3, Case 6, and Case 7 could also meet the requirements. It should however be noted that although Case 2 appears to offer the optimal solution of sheltering effect of the harbor arrangement, but because of other effects such as those related to sand prevention and maneuverability of navigation, the final arrangement selected was that close to Case 7.

2. For the selected arrangement the inner side of outer breakwaters, and north quay which opposed againse harbor mouth should be designed for wave energy absorption function to prevent waves from WNW direction caused by hurricane.

3. Because experimental results and theoretical calculations showed the same trend, therefore we could obtain the better achievement of harbor planning.

References

1. Hou, H. S. "Research of Model Experiment on Outer-Breakwater Arrangement of Taichung Harbor", Research Report of National Science Council, Taipei, Rep. of China; June, 1973

2. Hou, H. S. "A Study of the Wave, Alongshore Current, and Littoral Drift in South-eastern Taiwan", Journal of Civil Engineering, Vol. 14, No. 1 p. 1 - p. 28, Taipei, R. O. C., Aug, 1971.

3. Johnson, J. W. "Generalized wave diffraction diagrams", Proceeding of First Conference on Coastal Engineering, 1951.

4. Johnson, J. W. "Engineering aspects of diffraction and refraction", Proc. A.S.C.E. Vol. 118, 1953.

5. Penny-Price: "Diffraction of Sea Waves by breakwaters", Artificial Harbours, Dire. Misc. Weapon Develop. Tech. His. No. 26, 1944.

6. Wiegel, R. L.: "Diffraction of waves by semi-infinite breakwater", Proc. A.S.C.E. Vol. 88, No. HY1, part, 1962.

Fig. 5.1. The Plunger-Type Wave Generator
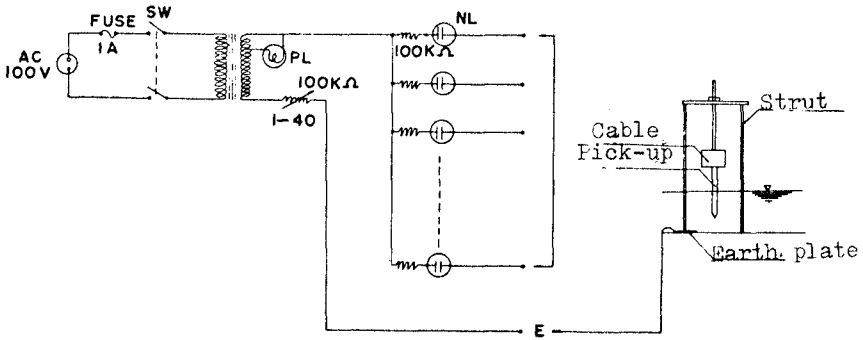
Fig. 3.2. The Principle of Connected Diagram
of Neon-Tube Wavemeter.
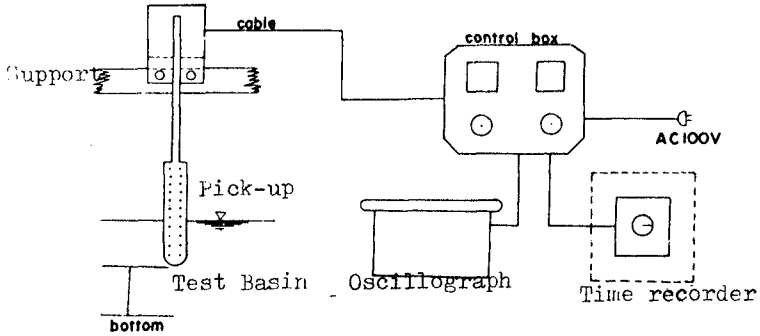
Fig. 3.3. The Principle of Connected Diagram
of Step-Resistance Wavemeter.
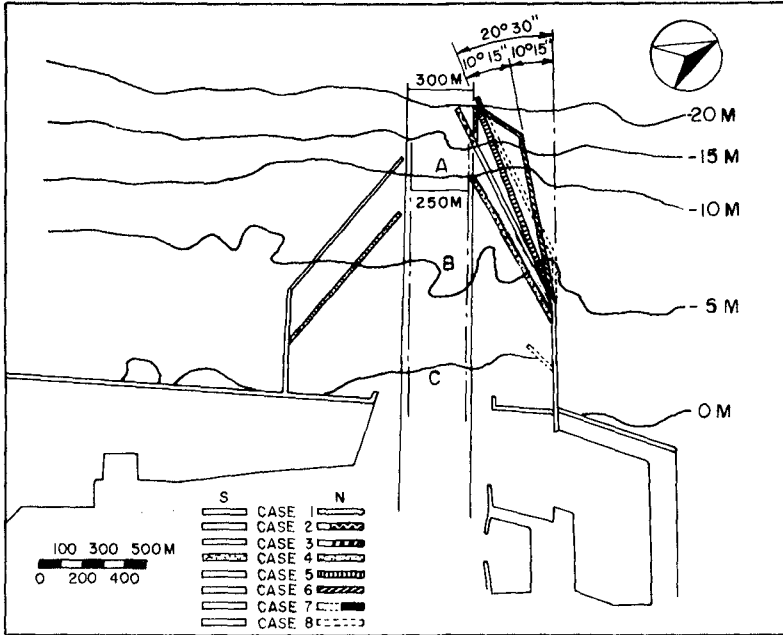
FIG.5.1. THE OUTER-BREAKWATER ARRANGEMENTS OF 8 DIFFERENT CASES
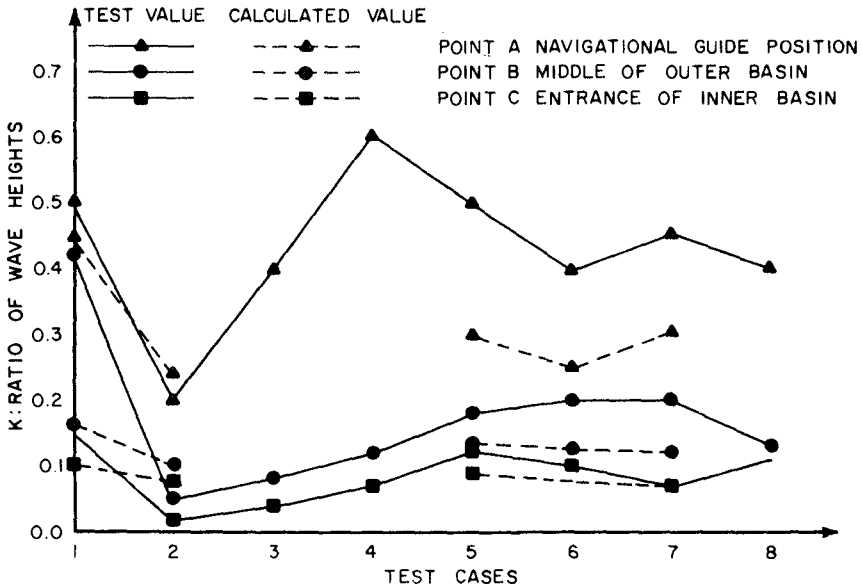
FIG.5.2. COMPARISON ON RATIO OF WAVE AGAINST INCIDENT WAVE AMONG DIFFERENT CASES

Case 1.
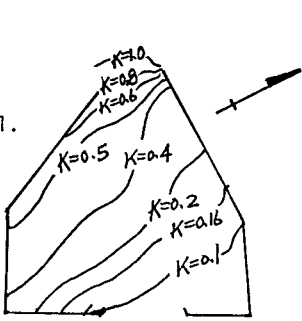
Fig.5-1-1

Case 2.
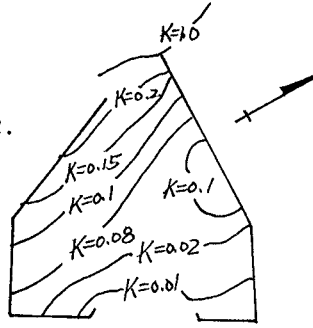
Fig.5-1-2

Case 3.
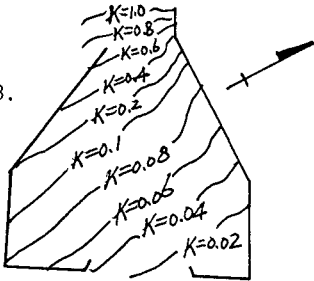
Fig.5-1-3

Case 4.
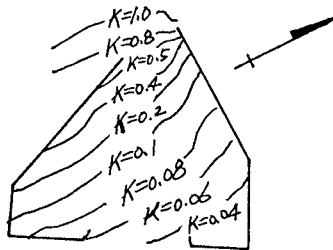
Fig.5-1-4

Case 5.
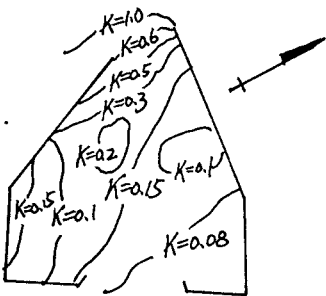
Fig.5-1-5

Case 6.
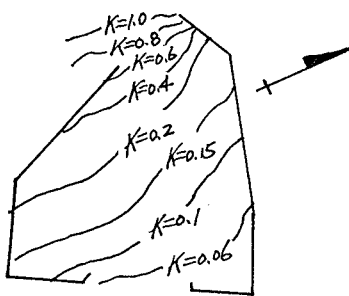
Fig.5-1-6
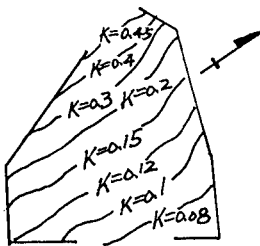
Wave Patterns of Test Results of N Dir.

Fig.5-1-7 Wave Pattern   Fig.5-1-8 Wave Pattern
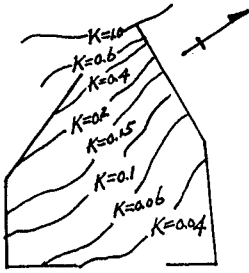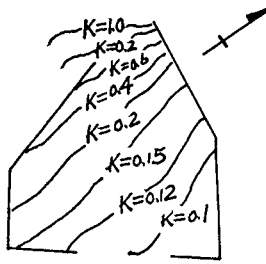
Fig.5-1-1 to Fig.5-1-8 Test Results of N Wave Direction.

Case 1.   Case 2.   Case 5.
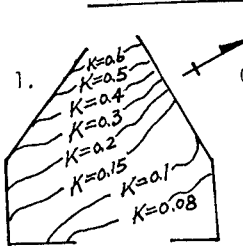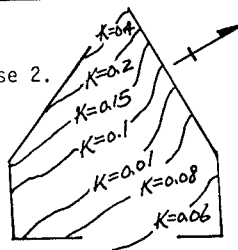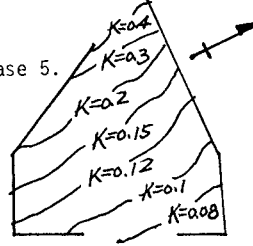
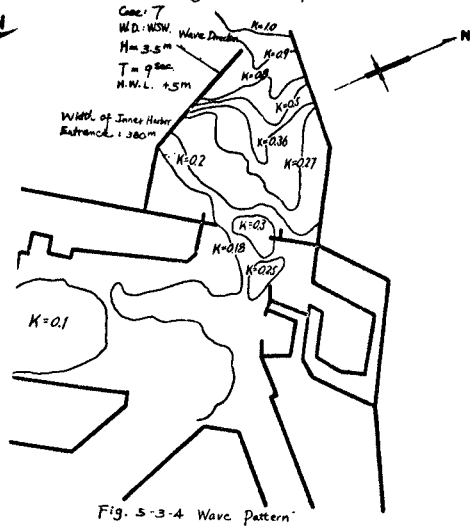Fig.5-2-1   Fig.5-2-2   Fig.5-2-3
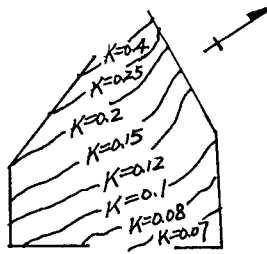
Fig.5-2-4   Fig.5-2-5

Fig.5-2-1 to Fig.5-2 -5 Calculated Diffraction Diagram.

Case: 7.
Wave Dir. : WNW
H = 4.5 m
T = 9 sec.
H.W.L. : +5 m
Width of Inner Harbor Entrance is 560 m.

Fig. 5-3-1 Wave Pattern

Case : 7
Wave Dir. : NNW
H = 4.5 m
T = 9 sec.
H.W.L. : +5 m
Width of Inner Harbor Entrance : 380 m

Fig. 5-3-2 Wave Pattern

Case : 7
W.D. : WSW
H = 3.5 m
T = 9 sec.
H.W.L. : +5 m.
Width of Inner Harbor Entrance : 560 m

Fig. 5-3-3 Wave Pattern

Case : 7
W.D. : WSW.
H = 3.5 m
T = 9 sec.
H.W.L. : +5 m
Width of Inner Harbor Entrance : 380 m

Fig. 5-3-4 Wave Pattern
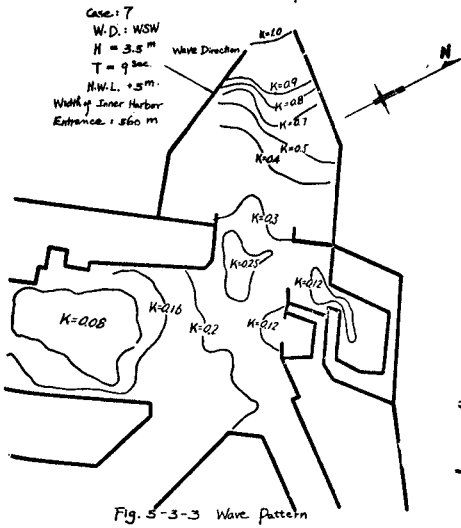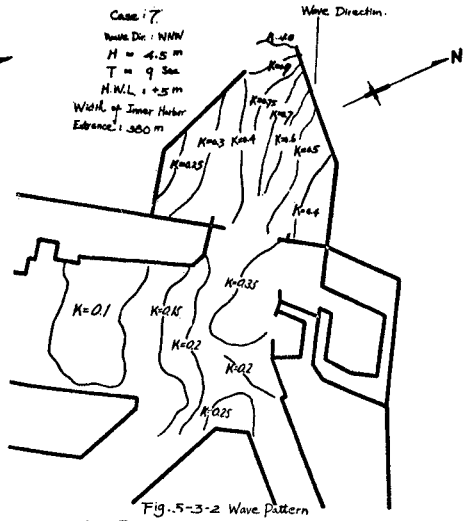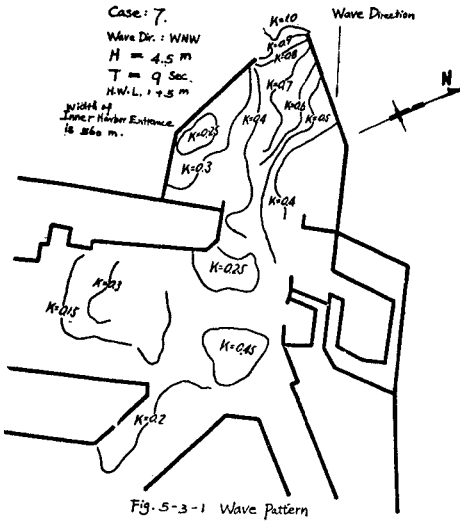
CHAPTER 125

AMPLIFICATION OF LONG WAVES IN MARINA DEL REY

by Jiin-Jen Lee

Assistant Professor of Civil Engineering
University of Southern California

ABSTRACT

Water surface oscillations in a man-made marina--Marina del Rey, California--have been studied through prototype experiments and theoretical analysis. The prototype experiments are conducted by using both the floating gauge and pressure type gauge. The field data show that a distinct mode of oscillation with wave periods between 45 minutes and 50 minutes are naturally present almost all the time. Such resonant wave periods also agree well with the theoretical results.

INTRODUCTION

Waves which propagate from the open-sea across the continental shelf into bays and harbors usually experience changes in propagating direction, wave profile due to local bathymetry and horizontal geometry of the embayment. The geographical configuration of a harbor can cause significant amplification or attenuation of the incident wave system especially for the long period waves. The phenomenon of large amplifications of long period waves in harbors or bays is well documented, e.g., Raichlen (1966), Wilson (1972), and Miles (1974).

The present work contains some prototype long period wave measurements in a man-made marina--Marina del Rey, California. In order to understand and explain the measured result, the theoretical results calculated by using the theory developed by Lee and Raichlen (1972), are compared.

Marina del Rey is the largest man-made small craft harbor in the United States. It is located approximately 15 miles west of central Los Angeles. At the present time there are approximately 6000 small boats which are moored inside the marina.

In the following, a brief outline of the theoretical analysis

will be presented followed by a description of the experimental
equipment.   The data obtained from the field measurements will
be compared with the theoretical results.

THEORETICAL ANALYSIS

For the theoretical analysis, the flow is assumed irrota-
tional and the fluid incompressible, thus one can define a velocity
potential Φ such that the fluid particle velocity vector can be ex-
pressed as the gradient of the potential.   In order to simplify the
problem, the horizontal layout of Marina del Rey (as shown in
Fig. 1) is approximated by only the main channel with the entrance
open to the open-sea region.   The water depth in the marina is
considered to be constant. This assumption plus the linearized
free surface condition at the water surface and the no-flow con-
dition at the bottom will enable one to find the velocity potential
in the form of:

$$\Phi(x, y, z, t) = \frac{1}{i\sigma} \quad \frac{A\, g\, \cosh k\,(h+z)}{\cosh kh} \quad f(x, y)\, e^{-i\sigma t} \qquad (1)$$

where $i = \sqrt{-1}$, σ is 2π/period, k is 2π/wave length, h is the
water depth, z is the vertical coordinates which originate from
the water surface, x and y are the horizontal coordinates.   The
function $f(x, y)$ must satisfy the Helmholtz's equation:

$$\frac{\partial^2 f}{\partial x^2} + \frac{\partial^2 f}{\partial y^2} + k^2 f = 0, \qquad (2)$$

and the boundary conditions that $\partial f/\partial n = 0$ along all solid boun-
daries and the radiation condition.

To solve for $f(x, y)$ in the harbor, the total domain of con-
sideration is divided into three regions: the open-sea region,
the region bounded by MNOP, and the region bounded by OPQR
(see Fig. 1).

The function f in any position (x, y) in Region I is expressed
as:

$$f(x, y) = -\frac{i}{4} \int_S \left[f(x_o, y_o) \frac{\partial}{\partial n} \left[H_o^{(1)}(kr) \right] - \right.$$

$$\left. H_o^{(1)}(kr) \frac{\partial}{\partial n} f(x_o, y_o) \right] ds \qquad (3)$$
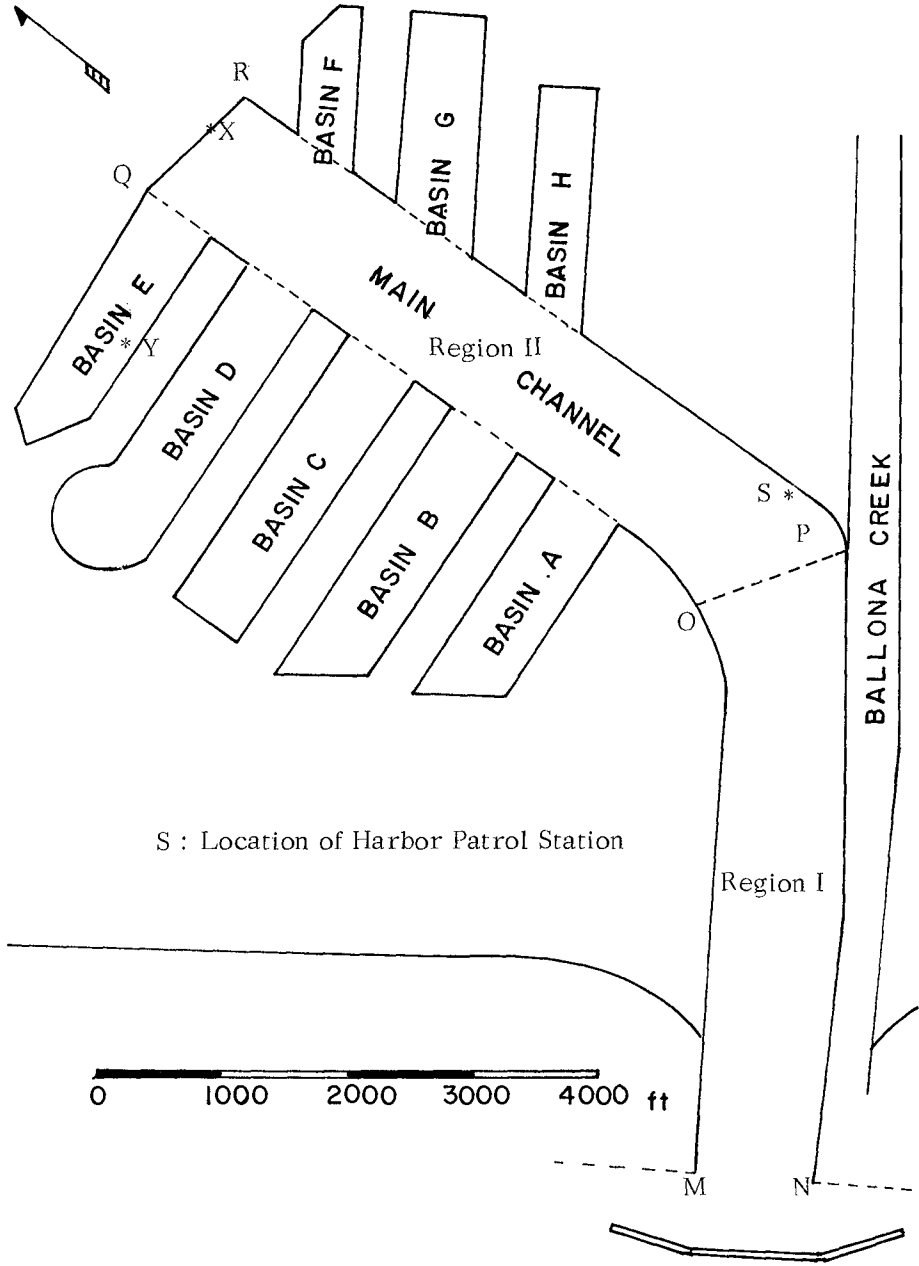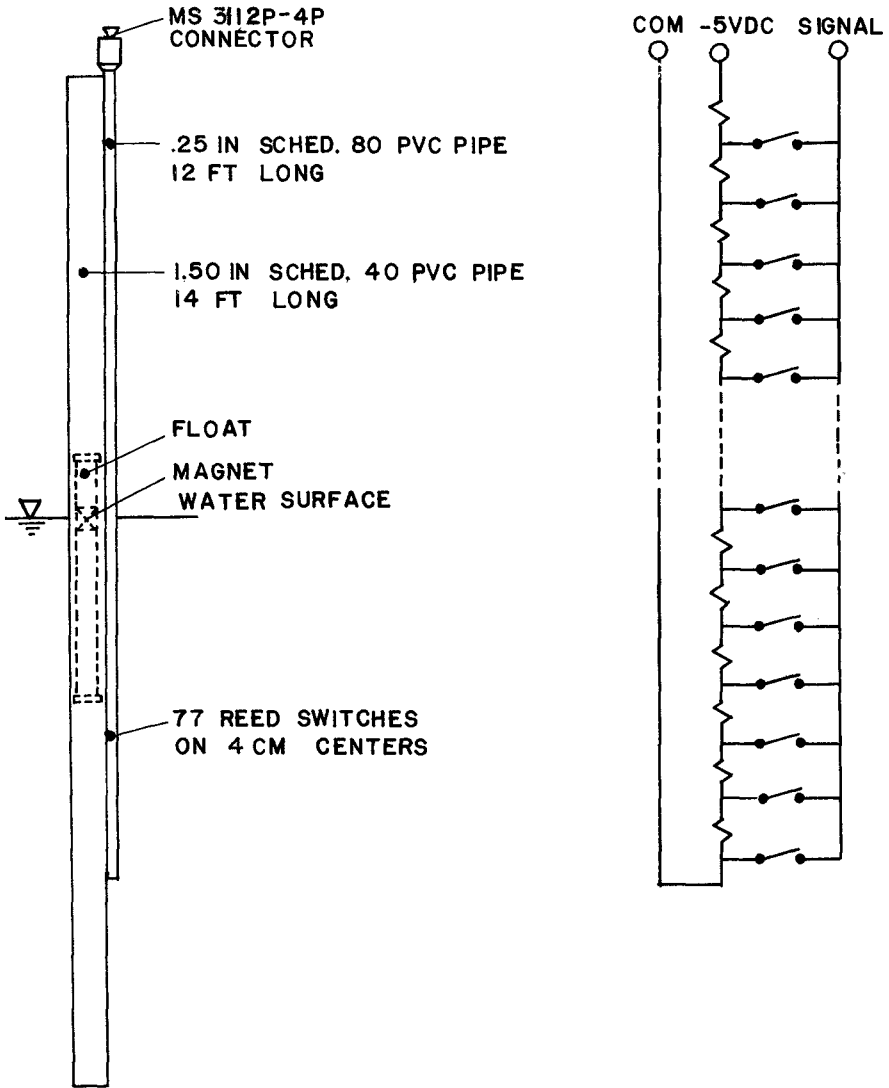
Fig. 1 Layout of the Marina del Rey Model

Fig. 2. Surface Gauge for Long Wave Measurement

where x_0, y_0 is the position of the boundary point, r is the dis-
tance between (x, y) and (x_0, y_0), n is directional normal of the
boundary.   If (x, y) is allowed to approach the boundary at (x_i, y_i),
then an integral equation can be formed from Eq. (3).   The
integral equation so formed can become matrix equation by approx-
imating the line integral with a discrete summation from divided
boundary segments:

$$\underline{F} = G_n \cdot \underline{F} - GF_{-n} \tag{4}$$

where $\underline{F}$ represents a vector of the value of f at each of the boun-
dary segments, F_n is a vector representing the value of $\partial f / \partial n$ at
each boundary point. G_n and G are both matrixes, the size of the
matrix is the number of segments into which the boundary is di-
vided.   Eq. (4) can be further reduced to a matrix equation with
$\underline{F}$ expressed only in terms of the unknown normal derivative of
$\overline{\partial f} / \partial n$ at the harbor entrance (MN) and the common boundary OP.

Following the same procedure, the solution of f in Region
II can be expressed in terms of $\partial f / \partial n$ at the common boundary OP.
These unknown values of $\partial f / \partial n$ at the common boundaries (MN and
OP) can be solved by using the continuity condition, i. e. , water
surface elevation as well as the horizontal velocity must be con-
tinuous at these boundaries.

EXPERIMENTAL EQUIPMENT AND PROCEDURES

The field data were obtained using two types of long-per-
iod wave gauges.   The first type of gauge is called the floating
gauge; a schematic diagram of the floating gauge is shown in Fig.
2.   It is seen that the gauge consists of a stilling well which is
constructed of 1 1/2 inches I. D. schedule 40 PVC pipe of 14 feet
long.   Inside the stilling well a water surface float equipped with
a permanent magnet is placed.   A tube (constructed of 1/4 inch
l. D. schedule 80 PVC pipe of 12 feet long) which contained a re-
sistive voltage divider and 80 reed switches evenly spaced at 4
centimeter centers, was attached to the outside of the stilling
well.   The permanent magnet in the float which moves with the
changes in water surface elevation closed the magnetic reed
switch nearest to it and taped off a voltage which was proportional
to the water surface elevation.

The second type of gauge was a strain gauge pressure
transducer and signal conditioner mounted in a waterproof pres-
sure protected case which was placed on the sea floor.   The
pressure variations at the sea floor were calibrated to corres-

pond to variations in water surface elevation. The signals were
transmitted to the recording station located on shore through the
undersea cable. This underwater instrument is primarily used
in locations where surface obstruction must be avoided such as
the location at the center of the marina entrance. The electronic
signal is recorded on a Honeywell-Brown "Electronic" Servo-re-
corder.

RESULTS AND DISCUSSION

Numerically determined response of the simplified Marina-
del Rey model to periodic incident waves is presented in Fig. 3.
As mentioned earlier, the results are obtained by dividing the total
region of consideration into three sub-regions: Open-sea Region,
Region I, and Region II with the final results obtained by matching
solution at all of the common boundaries. The ordinate in Fig. 3
represents the amplification factor which is defined as the maximum
wave height within the marina divided by the standing wave height
at the entrance if the marina is closed. The abscissa is the dimen-
sionless wave number (kl) where k is the wave number and l is
the length of the main channel. In prototype dimension l is 11,000 ft.
If one use the mean depth of 12 ft. , the wave period for the first
resonant mode (kl= 1.49) is approximately 40 minutes. The wave
period for the second resonant mode is 13 minutes (kl equals 4.57)
, for the third mode the period is 7.5 minutes. Attention is also
directed to the results of large amplification of wave amplitude for
the first mode. The mode shape for each of the resonant mode is
presented in Fig. 4. It is clear that for the first mode the water
surface elevation is quite uniformly distributed except the region
near the harbor entrance. This resonant mode is referred to as
Helmholtz mode or pumping mode. For the second mode there exi-
sts one nodal line so that as part of the basin is in positive displace-
ment the other part is in negative displacement. For the third mode
of oscillation there are two nodal lines, and the shape of water
surface elevation is relatively more complicated.

The observed long period wave amplitude in the marina
varied from day to day, but were approximately 10 inches for the
first mode, 2-4 inches for the second mode and perhaps 1 inch for
the third mode. Here, only the first mode data will be compared
with surface wave gages and the theoretical predictions. An exam-
ple of large amplification of long period wave within the marina is
shown in Fig. 5. The upper curve in Fig. 5 is the water surface
history at the marina entrance taken by the pressure gage placed
at the bottom. Other than the tide, long period waves are not obvi-
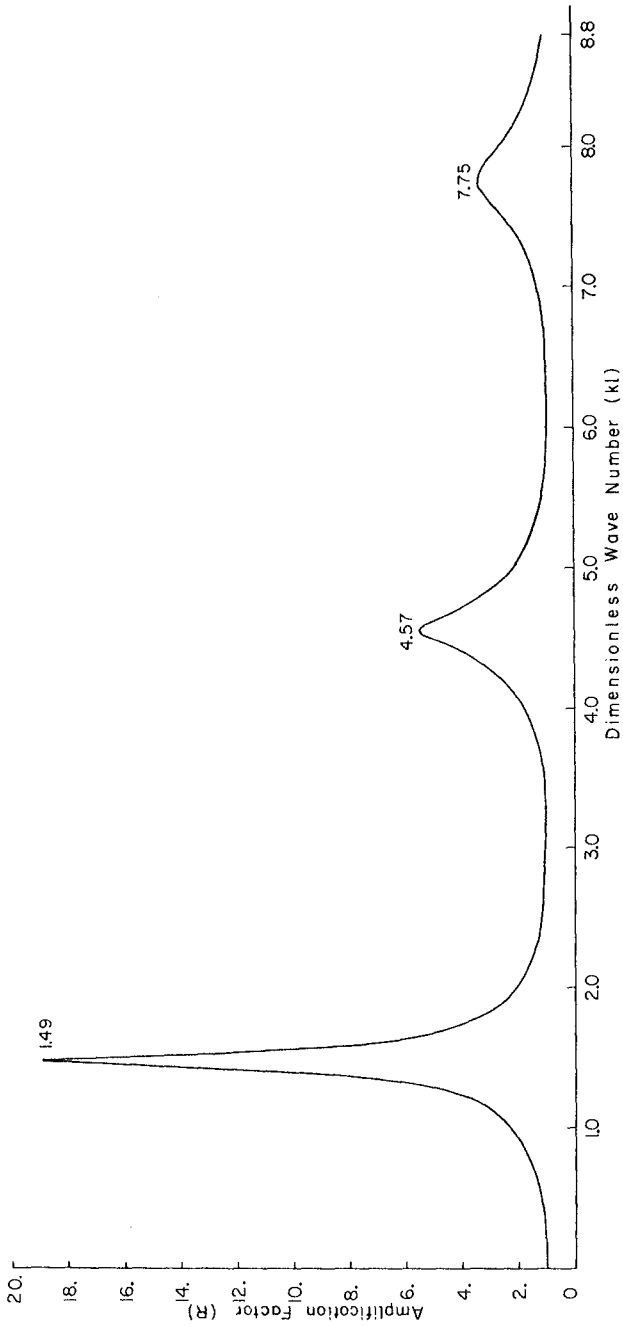ous. The lower curve in Fig. 5 represents the water surface history

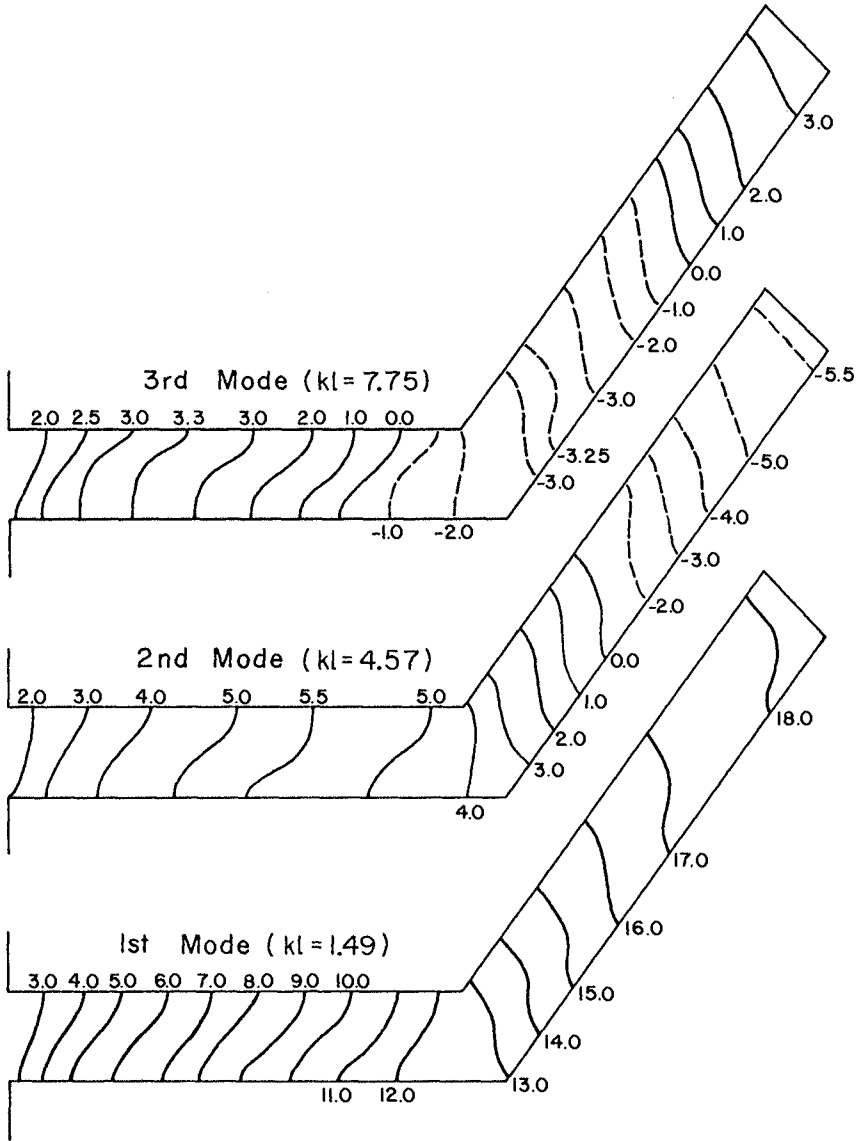Fig. 3. Response Curve at Marina del Rey, Calif.
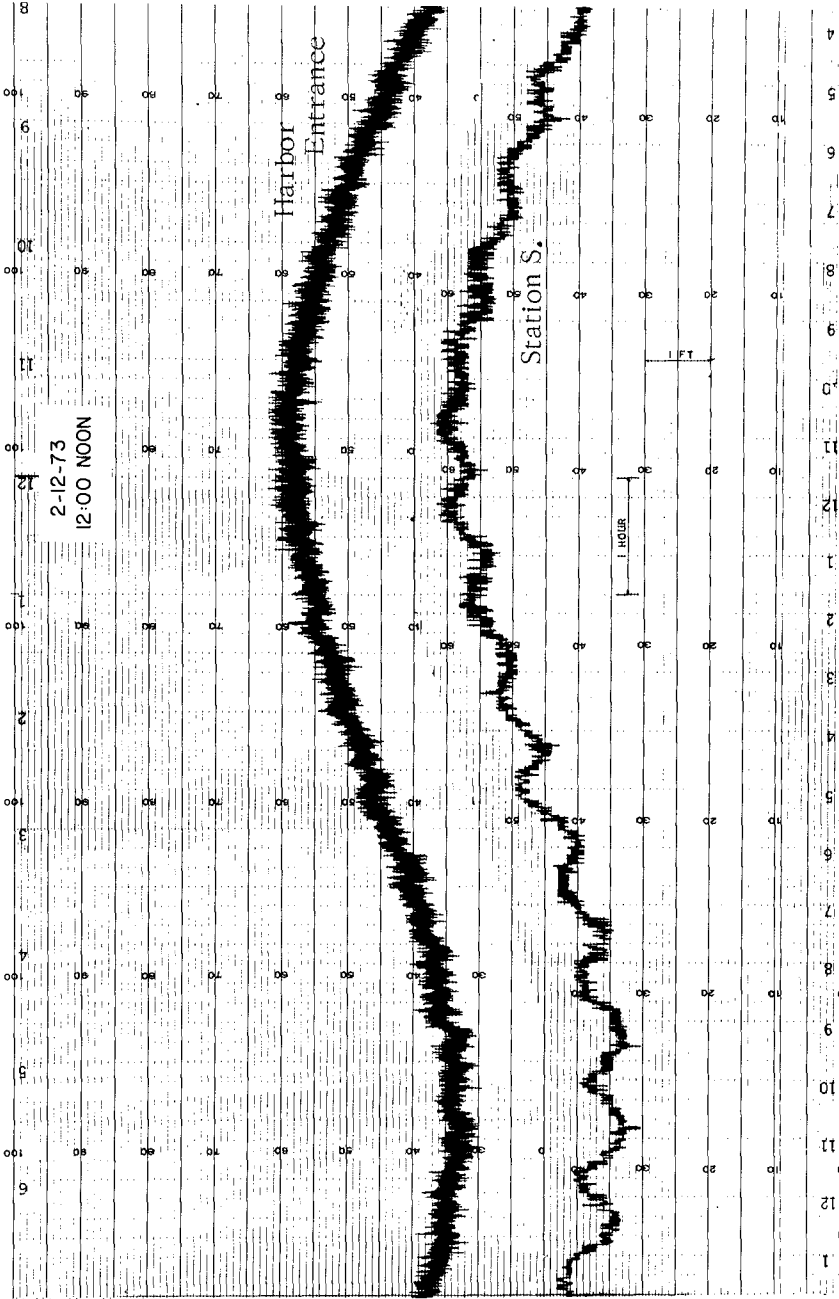
Fig. 4. Mode Shape of the First Three Modes

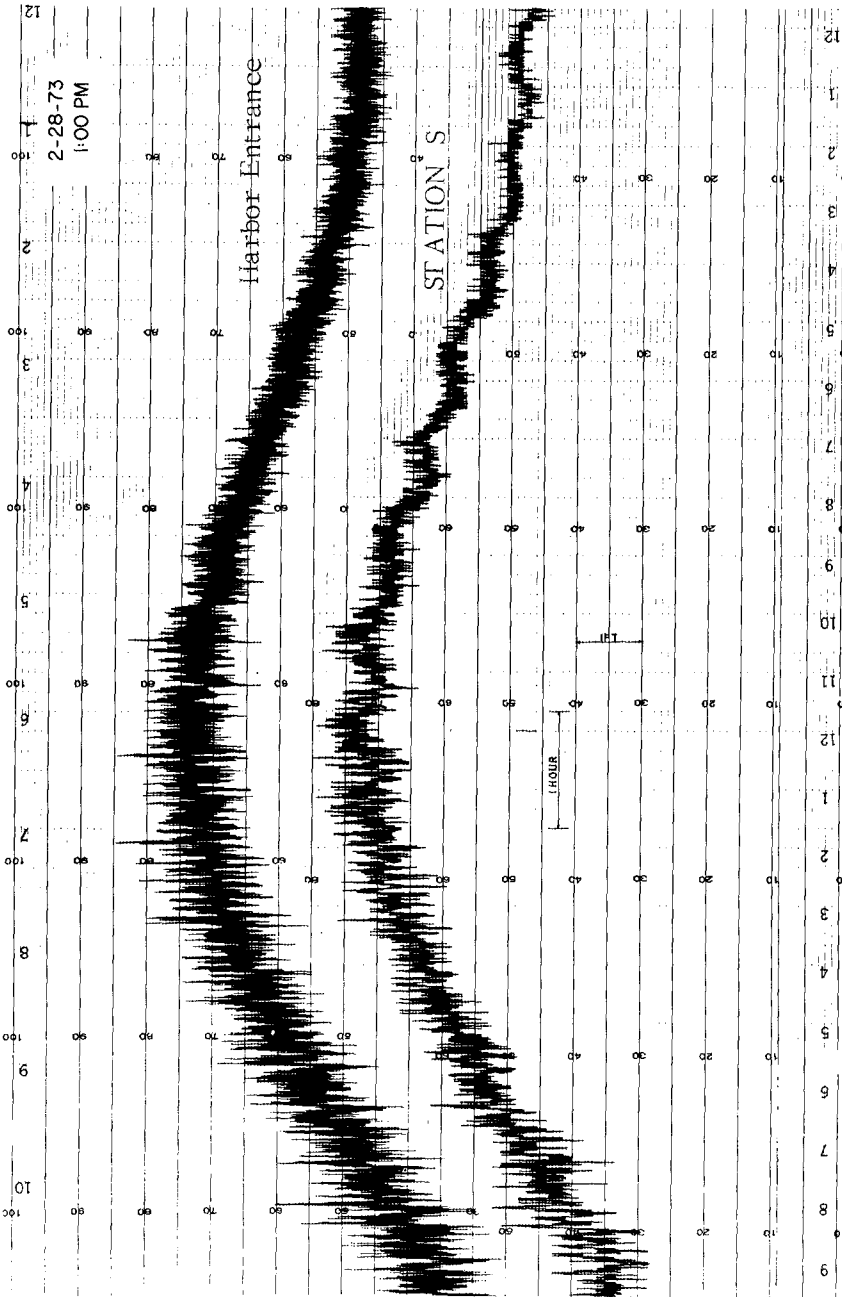Fig. 5 Water Surface History at Two Locations in side the Marina

Fig. 6, Water Surface History at Two Location inside the Marina

at the harbor patrol station (Station S shown in Fig. 1.) taken by
the float gage. In addition to the tidal fluctuation it is clearly seen
that long period waves of approximately 45 minutes period also
exist. The wave height of this wave is about 0.8 ft. It is interesting
to note that the observed wave period is very close to that of the
first mode (kl=1.49) shown in Figs. 3 and 4. The amplification
factor based on the field results is not known because no estimate
of the incident wave amplitude at this period can be made.   However
one may obtain the approximate ratio of the relative amplitude bet-
ween the lower curve and the upper curve for this period. This
ratio is about six, which agree reasonably well with that indicated
in the lower curve of Fig. 4.   Thus, it appears that the field data
agree well with the theoretical prediction at least for the first mode.

        Fig. 6 shows the wave records for the same respective loca-
tions as that shown in Fig. 5 . These data were taken during a sea
storm on Feb. 28, 1973. A significant difference between Fig. 5 &
Fig. 6 is that the amplitude of higher frequencies waves is smaller
at Station S than that at the marina entrance. Thus the marina do
damp out waves with higher frequencies although they do amplify
certain long period waves.

        In order to more fully demonstrate the nature of the first
mode of oscillation   within the marina, records taken from three
measuring devices placed at three different locations within the
marina is shown in Fig. 7. These three locations are: Station S (
harbor patrol station), Station X (the end of the main channel),
and Station Y (inside the Basin E). Records from the Station X
are taken by means of the hydrodynamically filtered pressure gauge
placed at the bottom, while at the other two locations the digital
type surface gages are used. It can be seen that the records are in
phase at these locations for the first mode. The amplitude of first
mode of oscillation at Stations X and Y are larger than that at
Station S as was predicted in the theoretical calculation.

                        CONCLUSIONS

        Results from the field experiment conducted at Marina del
Rey, Los Angeles, California clearly showed the phenomenon of
long period oscillation within the marina. The wave period of the
first mode is approximately 45 minutes - 50 minutes. Such mode
is naturally present almost at all time. Theoretical results have
also been shown to agree reasonably well with the field experiments.
It will be of great interest to investigate further the source of
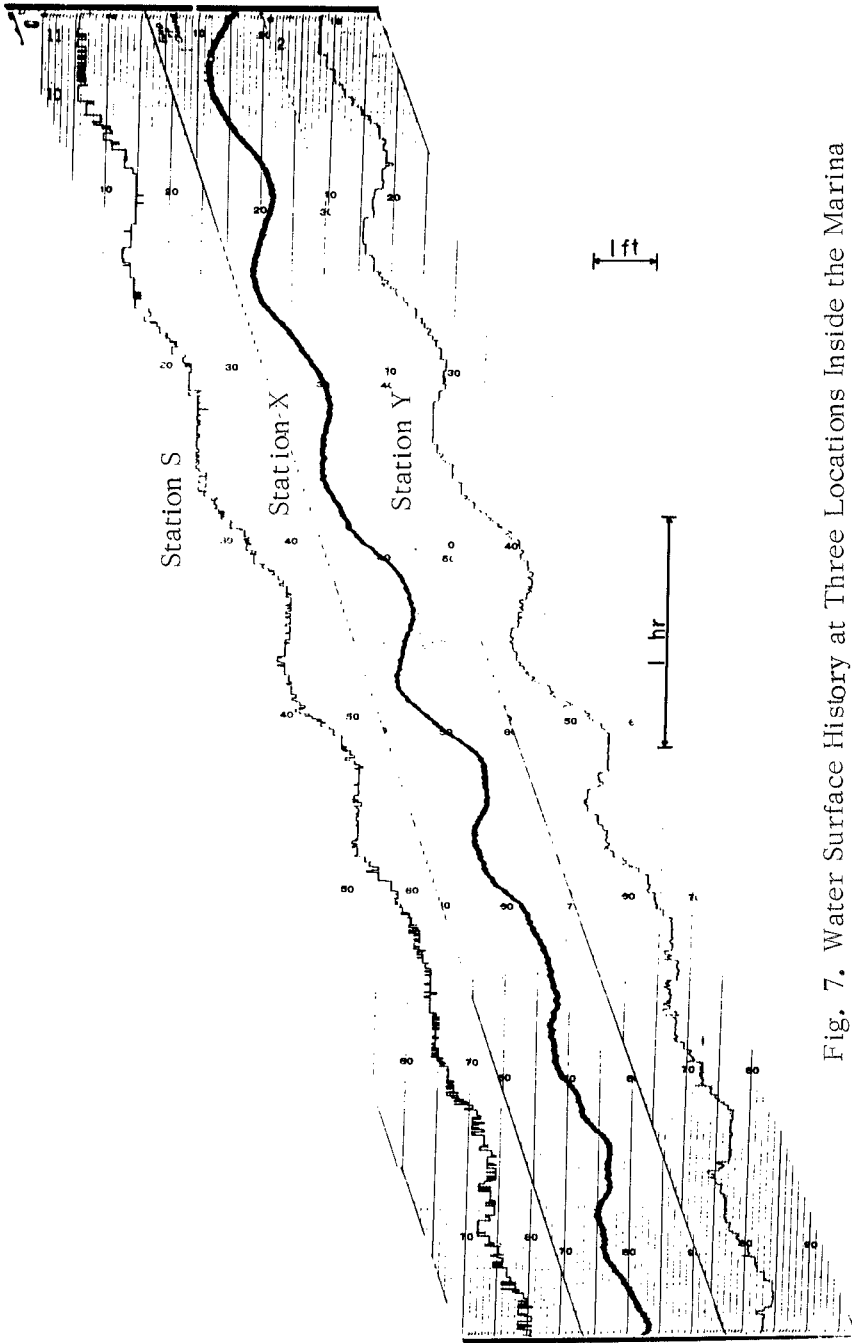excitation of such long waves.

Fig. 7. Water Surface History at Three Locations Inside the Marina

ACKNOWLEDGEMENT

LIST OF REFERENCES

Lee, J.-J. and Raichlen, F. " Wave Induced Oscillation in Harbor with Connected Basins ", Journal of Waterways , Harbor, and Coastal Engineering, ASCE, Vol. 98, No. WW3, 1972, pp. 311-332.

Miles, J.   " Harbor Seiching ", Annual Review of Fluid Mechanics, Vol. 6, 1974, pp. 17-35.

Raichlen, F. " Harbor Resonance ", Estuary and Coastline Hydro-dynamics, Edited by A. T. Ippen, Chapter 7, 1966, McGraw Hill Book Co..

Wilson, B. W. " Seiches " , Advances in Hydroscience, Vol. 8, 1972, pp. 1-94.

CHAPTER 126

BUOYANT DISCHARGES FROM SUBMERGED MULTIPORT DIFFUSERS

by

Donald R.F. Harleman* and Gerhard H. Jirka**

ABSTRACT

    The application of submerged multiport diffusers for the discharge of
degradable liquid wastes and of heated cooling water from electric power
generation forms an important aspect of coastal zone management. Previous
buoyant jet models for submerged diffuser discharge have been developed for
the limiting case of discharge in unconfined deep water in the form of rising
buoyant jets. These models can be used for sewage diffusers, but are not
applicable for diffusers in shallow receiving water with low buoyancy, the
type used for thermal discharges ("thermal diffusers"). A multiport diffuser
will produce a general three-dimensional flow. Yet the predominantly two-
dimensional flow which exists in the center portion of the three-dimensional
diffuser can be analyzed as a two-dimensional "channel model". Theoretical
solutions for diffuser-induced dilutions are derived for the two-dimensional
case and verified experimentally. Furthermore, the theory can be applied to
the three-dimensional situation by requiring equivalency of far-field effects,
that is the frictional resistance governing the diffuser-induced motion at
larger distances from the diffuser line.

INTRODUCTION

    In designing a system for the discharge of waste heat from electric energy
production the engineer has various alternatives at hand to control the thermal
effects within the receiving water. The choice of alternatives is influenced
by engineering, economic and environmental objectives, and may typically range
from low velocity surface discharges maximizing the heat transfer to the
atmosphere to high velocity submerged discharges maximizing the local mixing.
The increasing application of the latter type, in the form of a submerged multi-
port diffuser, stems primarily from the implementation of water quality standards
which require high dilutions within a limited mixing zone. The purpose of this
strategy of environmental conservation is to constrain the impact of heated
discharges to a small area.

---

*
Professor of Civil Engineering and Director, R.M. Parsons Laboratory for Water
   Resources and Hydrodynamics, M.I.T., Cambridge, Massachusetts, U.S.A.

**
Lecturer in Civil Engineering and Research Engineer, M.I.T. Energy Laboratory,
   Cambridge, Massachusetts, U.S.A.

CHARACTERISTICS OF MULTIPORT DIFFUSERS

A submerged multiport diffuser is essentially a pipeline laid on the bottom
of the receiving water. The heated water is discharged in the form of round
turbulent jets through ports or nozzles which are spaced along the pipeline.
The jets actively entrain ambient water through shear effects at the jet
boundaries. An important feature is the interference of the individual round
jets of diameter D, spacing ℓ and velocity U_o a relatively short distance away
from the nozzles to form a two-dimensional jet, as shown in Figure 1. In usual
temperature prediction problems the major interest does not lie in the initial
region close to the nozzles, but rather farther away, for example at the surface
of the receiving water. It has been demonstrated (Reference 1) that outside
the initial region the jet dilution of the multiport diffuser is similar to an
"equivalent slot diffuser" with slot width

$$B = \frac{\pi D^2}{4\ell}$$

and equal discharge velocity U_o. Using the concept of the "equivalent slot
diffuser" reduces the number of dimensionless parameters characterizing a
multiport diffuser and thus provides a means to compare different diffuser
designs and applications.

For several decades coastal cities have utilized submerged multiport
diffusers for the discharge of municipal sewage water. Noteworthy aspects of
these "sewage diffusers" are: 1) Water quality standards dictate dilution
requirements in the order of 100 and higher when sewage water id discharged.
As a consequence these diffusers are limited to fairly deep water (more than
100 feet deep). 2) The buoyancy of the discharged water is significant. The
relative density difference between sewage water and ocean water is about 2.5%.

Only in very recent years have multiport diffusers been used for the
discharge of heated condenser cooling water from thermal power plants. Depend-
ing on the water quality classification of the receiving water and on the
cooling water temperature rise, dilutions between about 5 and 20 are required
within a specified mixing area. This dilution requirement frequently rules out
relatively simple disposal schemes, such as discharge by means of a surface
channel or a single submerged pipe. On the other hand, multiport diffusers
can be placed in relatively shallow water (considerably less than 100 feet deep)
and still attain the required dilutions. The economic advantage in keeping
the conveyance distance from the shoreline might be substantial, in particular
in lakes, estuaries or coastal waters with extended shallow nearshore zones.
"Thermal diffusers" have these characteristics: 1) They may be located in
relatively shallow water. 2) The buoyancy of the discharged water is low.
Initial density differences are in the order of 0.3% corresponding to a
temperature differential of about $20^\circ F$, an average value for thermal power
plants.

The difference in performance between "sewage" and "thermal" diffusers is
illustrated qualitatively in Figure 2. Figures 2a and 2c show the deep water
diffuser with high buoyancy which produces a distinct jet region with a stable
surface layer. Dilution prediction for this   situation   may be determined
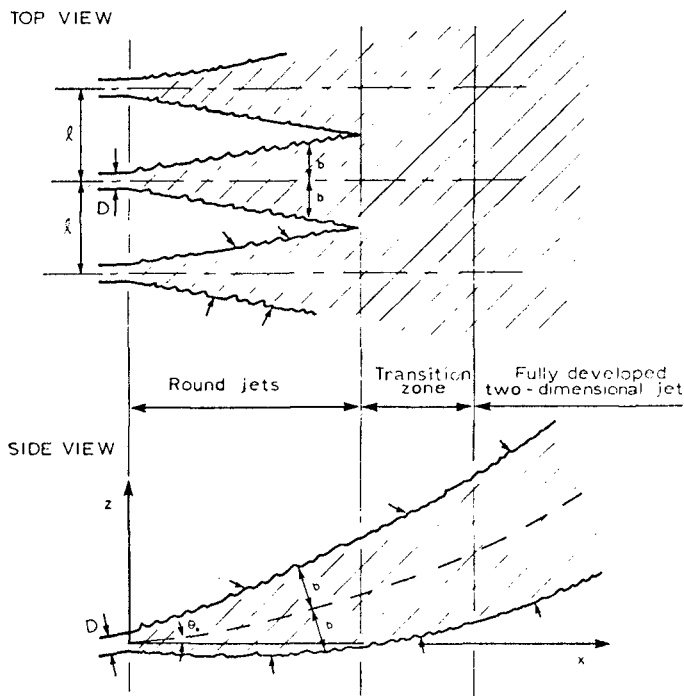
Figure 1:   Jet Interference for a Submerged Multiport Diffuser

using well-established buoyant jet models, such as Abraham (2), Fan and Brooks
(3), Hirst (4), in which the thickness of the surface layer is not a signifi-
cant portion of the total depth. On the other hand, diffusers in shallow water
with low buoyancy (Figures 2b and 2d) may not create a stable surface layer.
Subsequently, already mixed water is re-entrained into the jets decreasing the
dilution as would be predicted from buoyant jet models. As an extreme case of
boundary effects in shallow water a fully mixed flow zone may be established as
shown in Figure 2d.

    A theoretical and experimental investigation of the mechanics of multiport
diffusers in shallow water has been performed by Jirka and Harleman (5). The
study was concerned with a) The establishment of criteria which describe whether
stable or unstable near-field conditions will result, b) The development of a
predictive model for the case of an unstable near-field ("thermal diffuser")
and c) The investigation of three-dimensional circulations produced by a diffuser
of finite length in the receiving water which is either stagnant or flowing.
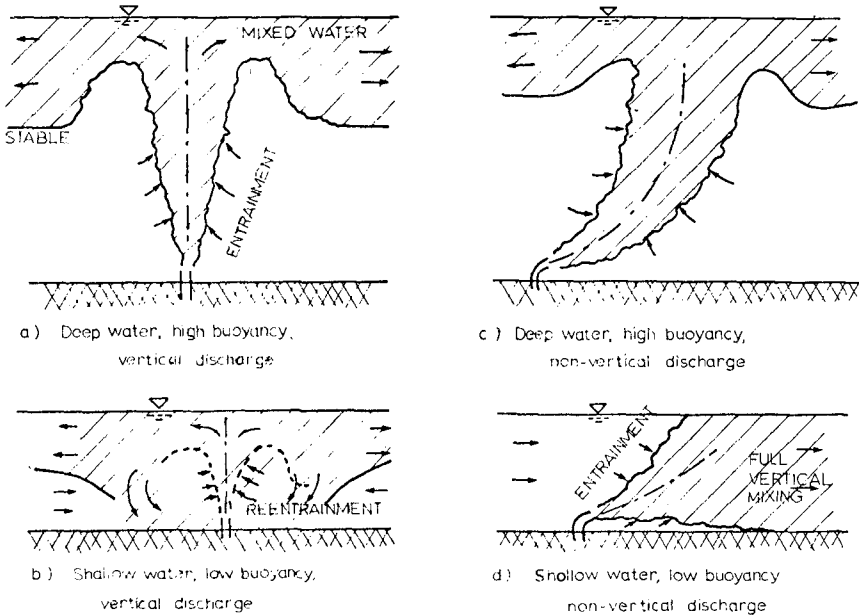
Figure 2:   Qualitative Illustration of Vertical Flow Field in
            Diffuser Vicinity for Various Discharge Conditions

ANALYSIS

A multiport diffuser of length $2L_D$ will produce a three-dimensional flow
field as depicted in Figure 3. Yet the predominantly two-dimensional flow
which exists in the centerportion of the three-dimensional diffuser can be
analyzed as a two-dimensional "channel model". The "channel model" consists
of a diffuser section bounded by channel walls of length 2L and opening at both
ends into a large reservoir (Figure 4).

The observed vertical structure of the flow field for a diffuser discharge
within the two-dimensional channel is indicated in Figure 4 for the case of a
stable near-field zone without re-entrainment. Four flow regions can be
discerned in this general case:
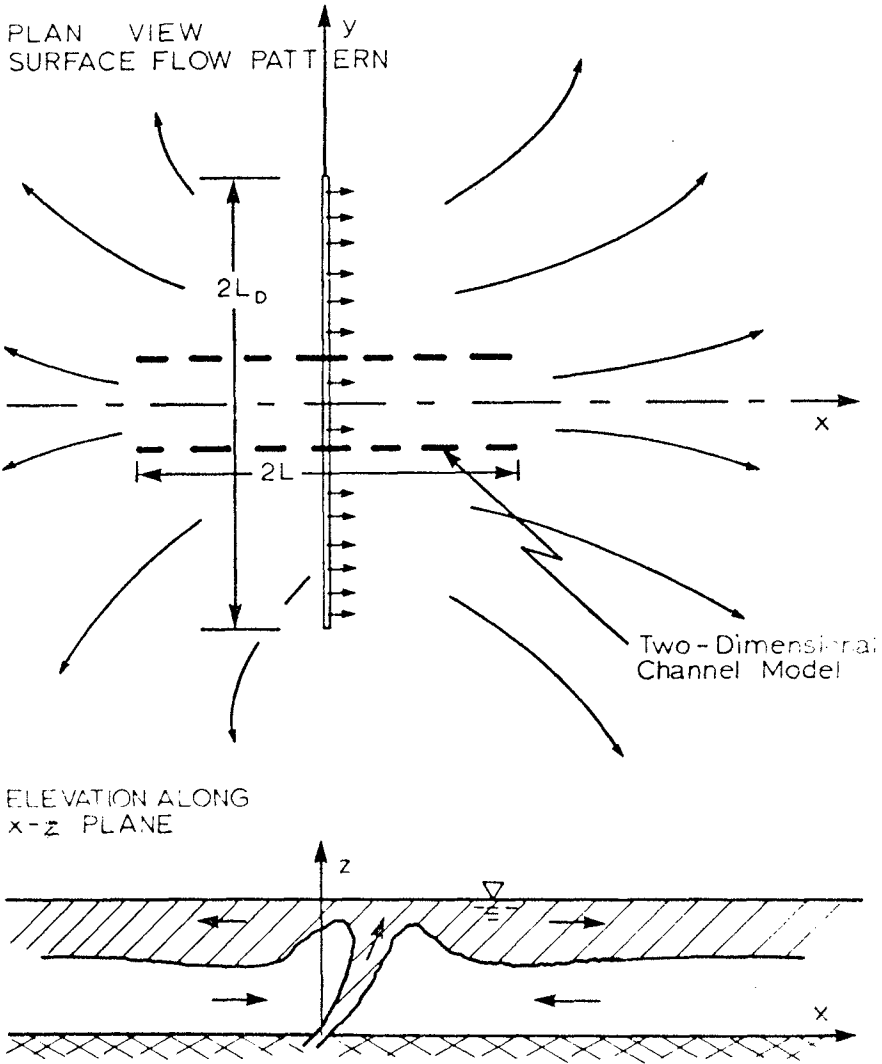
PLAN   VIEW
SURFACE FLOW PATTERN

$2L_D$

$2L$

Two-Dimensional
Channel Model

ELEVATION ALONG
x-z PLANE

Figure 3:   Three-Dimensional Flow Field for a Submerged
            Diffuser with Two-Dimensional Behaviour in
            Centerportion

1) <u>Buoyant Jet Region</u>: Forced by its initial momentum and under the action of gravity, the two-dimensional slot jet rises towards the surface entraining ambient water.

2) <u>Surface Impingement Region</u>: The presence of the free surface, with its density discontinuity, diverts the impinging jet in the horizontal directions.

3) <u>Hydraulic Jump Region</u>: An abrupt transition between the high velocity flow in the surface impingement region to lower velocities in the flow away zone is provided by an internal hydraulic jump.

4) <u>Stratified Counterflow Region</u>: A counterflow system is set up as a buoyancy-driven current in the upper layer and an entrainment-induced current in the lower layer.

Regions 1, 2 and 3 constitute the near-field zone; region 4 and the water body outside the channel, the far-field zone. The governing equations can be developed for each region accounting for its distinct hydrodynamic properties. Matching the solution for all regions provides an overall prediction of the diffuser induced flow field.

① Buoyant Jet Region
② Surface Impingement Region
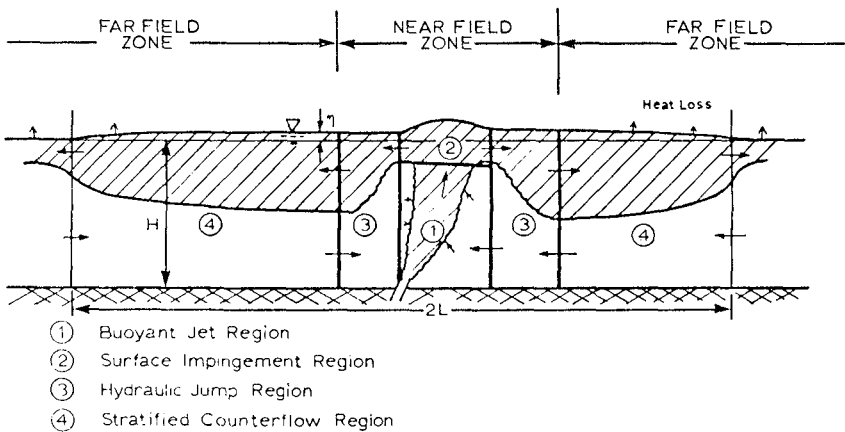③ Hydraulic Jump Region
④ Stratified Counterflow Region

Figure 4: General Vertical Structure of Diffuser Induced
           Flow Field (Two-Dimensional Channel Model)

Inspectional analysis of the governing equations shows that the following four dimensionless parameters characterize the multiport diffuser (equivalent slot B):

Densimetric Froude Number $\quad F_s = \dfrac{U_o}{\sqrt{\dfrac{\Delta\rho_o}{\rho_a}\, gB}}$

Relative Submergence $\qquad \dfrac{H}{B}$

Angle of Discharge $\qquad \theta_o$

Far-Field Parameter $\qquad \Phi = f_o\, \dfrac{L}{H}$

where

ρ_a = ambient density

$\Delta\rho_o$ = initial density difference

g = gravitational acceleration

H = water depth

f_o = bottom friction factor

Table 1 provides a survey of typical values of these parameters for both sewage and thermal diffusers.

THEORETICAL PREDICTIONS OF SURFACE DILUTIONS

Figure 5 gives theoretical prediction for surface dilutions as a function of F_s and H/B for the case of a vertical diffuser discharge ($\theta_o = 90^o$) with $\Phi = 1.0$. A criterion line divides the parameter range into two regions: diffusers with a stable near-field and diffusers with an unstable near-field. This is further illustrated in Figure 6. Diffusers with stable near-field have a distinct jet entrainment zone and the transition to the far-field is given by either a normal or a submerged internal hydraulic jump. Dilutions produced are essentially due to jet entrainment. In contrast, no internal hydraulic jump exists for diffusers with an unstable near-field. As a consequence, a local mixing zone with vertical recirculation is established and overall dilutions are governed by far-field effects: a dynamic equilibrium between buoyancy forces accelerating the flow away from the mixing zone and frictional forces retarding it.
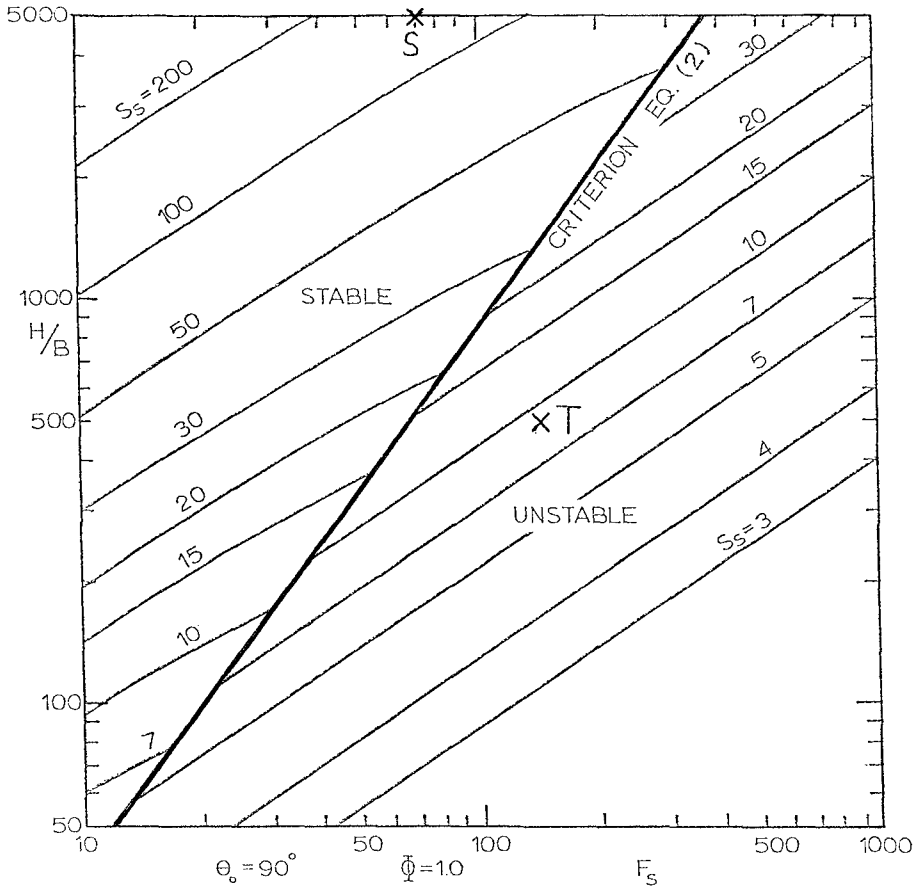
Figure 5: Surface Dilutions S_s as a Function of F_s, H/B Vertical Diffuser (Typical values from Table 1 are indicated for a sewage diffuser S and a thermal diffuser T)

A) STABLE NEAR-FIELD

1. Normal Internal Jump

CHANNEL
END
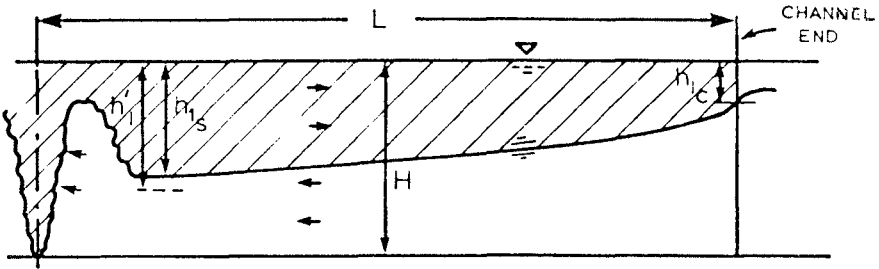
2. Submerged Internal Jump
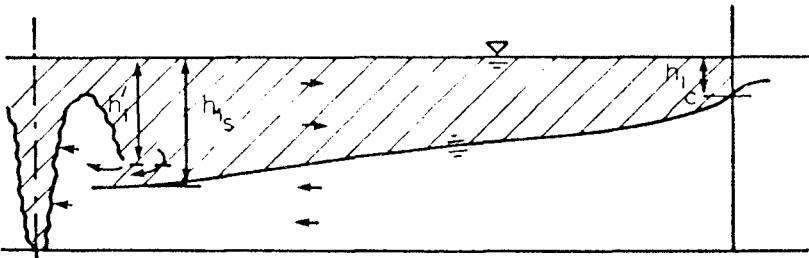
B) UNSTABLE NEAR-FIELD

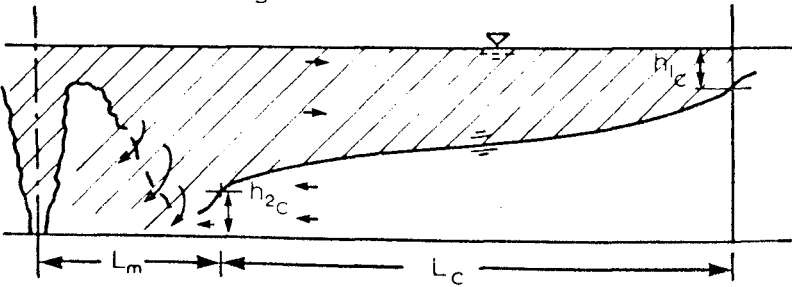Local Mixing and Reentrainment

Figure 6:   Vertical Flow Conditions for Different Combi-
            nations of Near-Field Stability and Far-
            Field Effects

Table 1

Variables	Sewage Diffuser	Thermal Diffuser
Water depth, H (ft.)	100	20
Total discharge, Q_o (cfs)	400	1000
$\Delta\rho/\rho_a$	0.025	0.003
	(fresh-salt water)	($\Delta T_o \sim 20°F$)
Total Diffuser Length,		
$2L_D$ (ft.)	3000	3000
Nozzle Diameter, D (ft.)	0.5	1.0
Nozzle Spacing, ℓ (ft.)	10	20
Discharge Velocity, U_o (fps)	6.8	8.5
Bottom Friction Coefficient, f_o	0.02	0.02
Equivalent Slot Width, B (ft.)	0.02	0.04
Dimensionless Parameters:		
F_s	70	140
H/B	5000	500
θ_o	variable	variable
Φ	0.1	1.5

The equation of the criterion line between stable and unstable conditions is

$$\frac{H}{B} = 1.84 \ F_s^{4/3} \tag{1}$$

The surface dilutions S_s in the stable parameter range are obtained from buoyant jet theory accounting for the thickness of the surface layer which is about 1/6 of the total depth. The surface dilutions S_s in the unstable parameter range are determined by stratified flow theory (far-field effects) and can be written as

$$S_s = 1.6 \ (\frac{k}{F_s})^{2/3} \ \frac{H}{B} \tag{2}$$

where k is a function of the far-field parameter Φ and may be tabulated over the range of interest.

Table 2

Φ	0	0.1	0.5	1.0
k =	0.25	0.225	0.187	0.17

The parameter values for a typical sewage diffuser (5) and a typical thermal diffuser (T) from Table 1 are indicated in Figure 5. The different hydrodynamic conditions and resultant surface dilution for the two diffuser types are clearly evident. For the thermal diffuser a dilution of 9 is predicted.

The dilution predictions of Figure 5 can be compared to Figure 7, in which buoyant jet theory (accounting for surface layer thickness) has been used over the whole parameter range. A dilution of 14 would be predicted for the thermal diffuser. This considerably higher prediction is due to the fact that the presence of the local mixing zone and re-entrainment has not been considered and would lead to drastically erroneous designs.

The results of the vertical discharge (θ_o = 90°) are also applicable to diffusers with alternating nozzles which do not have any net horizontal momentum and produce a similar symmetric flow field. Analysis and results for non-vertical discharges are also given in Reference 5. The theoretical results have been verified in an extensive series of experiments.

THREE-DIMENSIONAL ASPECTS OF THERMAL DIFFUSERS

The deep water, high buoyancy type diffuser with stable near-field always produces a well-stratified flow away from the diffuser line in all directions (see Figure 2). A contrasting behaviour can be observed in thermal diffusers in shallow water with low buoyancy as shown in Figure 8 for a vertical discharge: The presence of the entrainment mechanisms in combination with the near-field instability gives rise to a strong current which sweeps along the diffuser axis toward the center of the diffuser and then departs perpendicular to the diffuser line. The presence of this circulation leads to undesirable repeated re-entrainment and reduced dilutions. The circulation can be prevented by providing some discharge momentum along the diffuser axis through use of alternating nozzle with variable horizontal orientation β. In particular the orientation

$$\beta(y) = \cot^{-1}\left[\frac{1}{\pi} \log \frac{(1 + \frac{y}{L_D})}{(1 - \frac{y}{L_D})}\right] \qquad (3)$$

where y = distance along diffuser axis (Figure 8) was derived to provide stratified conditions with flow-away in the upper layer in all directions and maximum dilution.

Figure 9 shows experimental results from a three-dimensional diffuser located in a laboratory basin. The lower basin boundary is the symmetry line perpendicular to the diffuser axis: a mirror image can be assumed below this line. Horizontal dimensions x, y are normalized by the water depth H. Figures
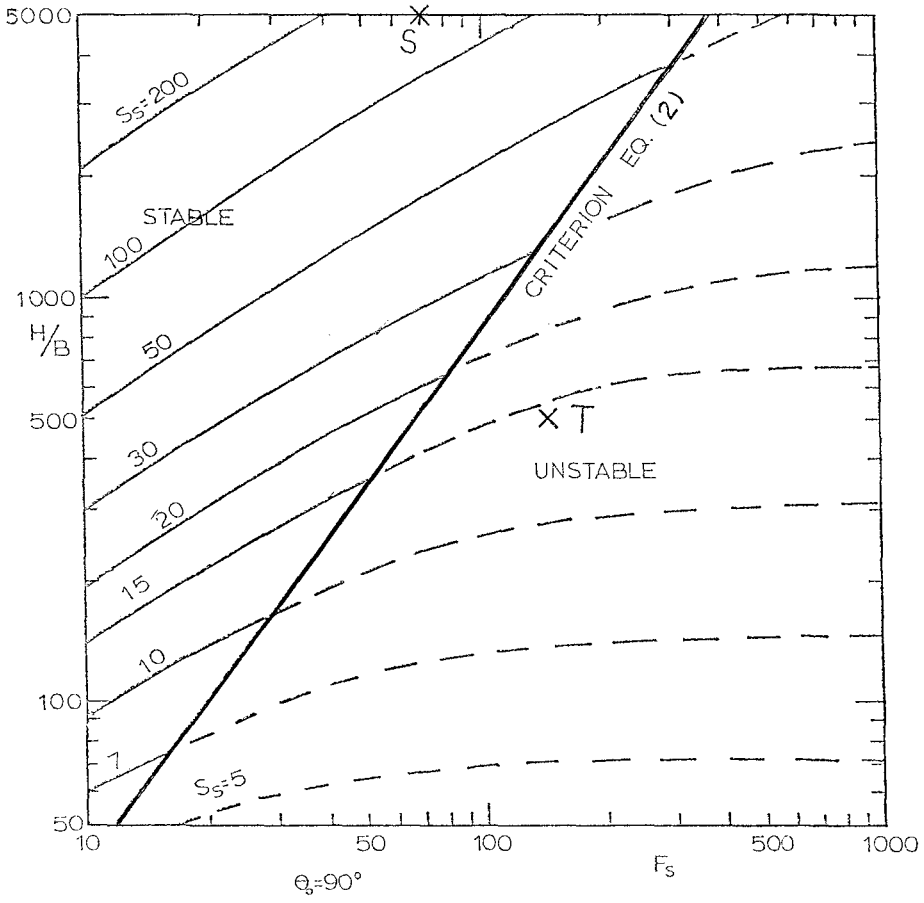
Figure 7: Theoretical Surface Dilutions S_s Assuming Buoyant Jet Theory Over the Whole Parameter Range (typical values from Table 1 are indicated for a sewage diffuser S and a thermal diffuser T)
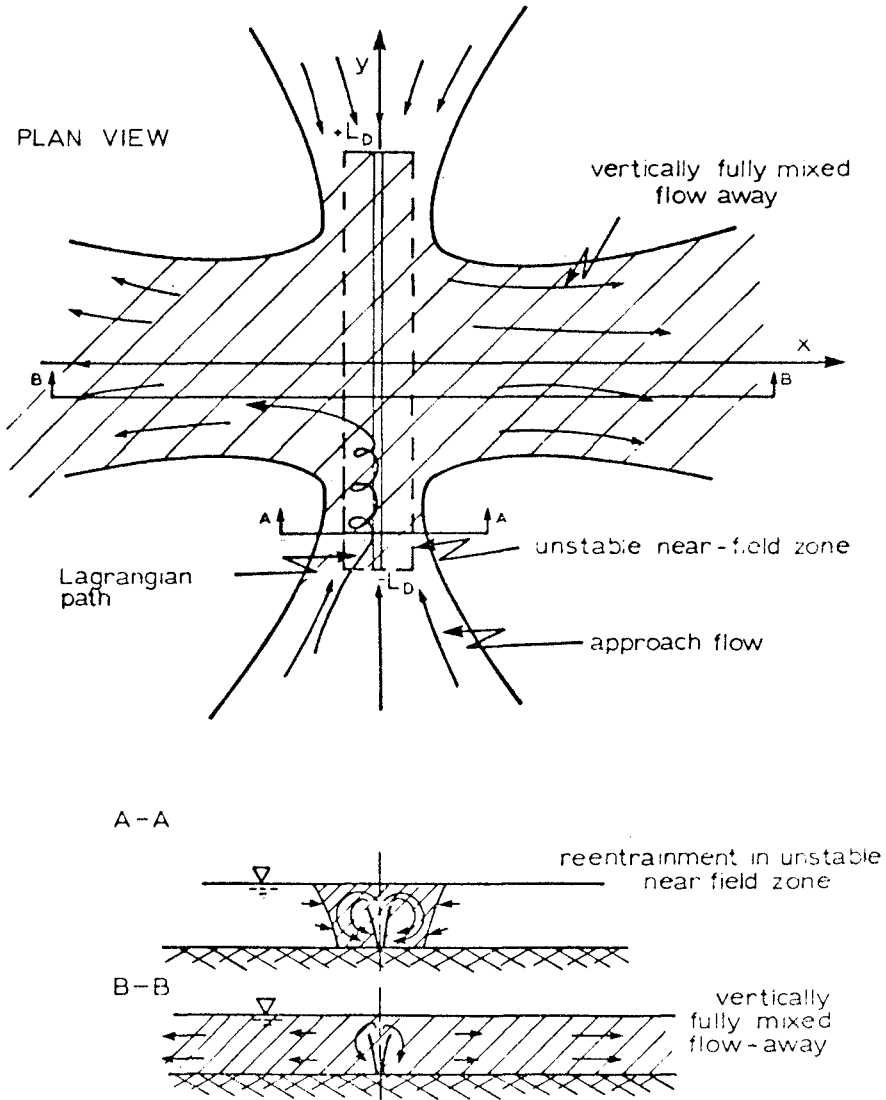
Figure 8: Three-Dimensional Flow Field for a Multi-port Diffuser in Shallow Water with Low Buoyancy and Vertical Discharge (No Control)
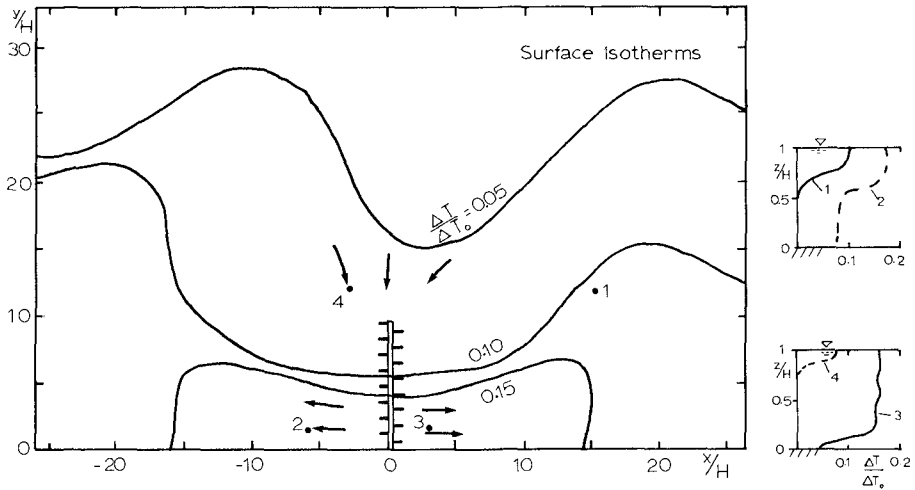
Figure 9a: Nozzle Orientation Normal to Diffuser Axis, F_s = 158, H/B = 628, Φ = 0.9

Figure 9b: Nozzle Orientation Variable Along Diffuser Axis (Equation 3), F_s = 160, H/B = 628, Φ = 0.9

Figure 9:   Experimental Results for a Multiport Diffuser with Alternating Nozzles in Stagnant Water. Shows Effect of Horizontal Nozzle Orientation on Horizontal and Vertical Temperature Distributions. Arrows Indicate Surface Currents.

9a and 9b show the normalized surface isotherms $\frac{\Delta T}{\Delta T_o}$, where ΔT_o = initial temperature difference, ΔT = temperature difference at the surface, and observed surface flow patterns for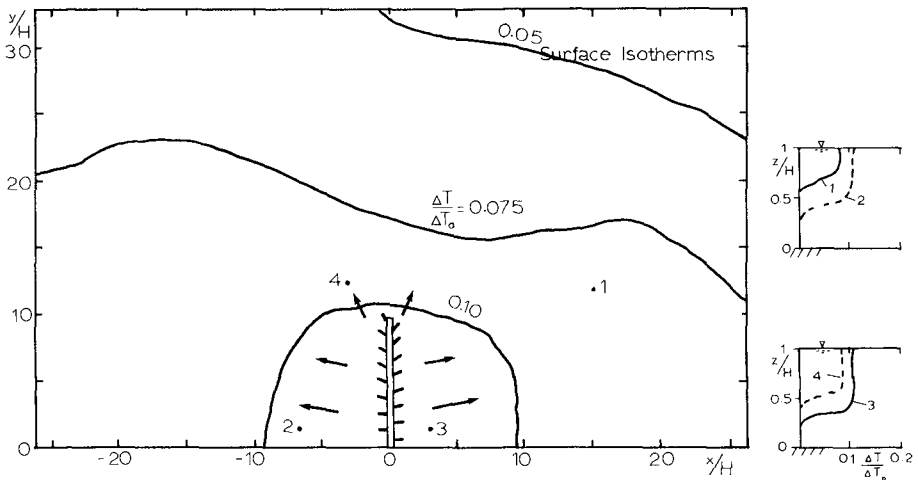 different horizontal nozzle orientations, but otherwise identical discharge conditions (same F_s, H/B and Φ). In Figure 9a the diffuser has alternating nozzles all normal to the axis thus providing no control and giving rise to a horizontal circulation. In Figure 9b the alternating diffuser nozzles are oriented according to Equation (3) thus preventing the horizontal circulations. The difference in stratification can be seen from the vertical temperature profiles at four points in the diffuser vicinity. The diffuser with control guarantees considerably better dilutions.

Under conditions of a controlled three-dimensional flow field the dilution prediction of the two-dimensional "channel model" can also be applied to the three-dimensional diffuser case provided that $L \stackrel{\sim}{\sim} L_D$ in the definition of the far field parameter Φ. In other words, the dilution in the two-dimensional channel will be equivalent to the three-dimensional diffuser if the channel length is taken about equal to the diffuser length.

EFFECT OF CROSSFLOW

If a multiport diffuser is placed in a steady cross current with magnitude u_a (see Figure 10) then the diffuser-induced flow field is modified by the crossflow. Two additional dimensionless parameters are needed to characterize the problem:

Volume flux ratio $V = \dfrac{u_a H}{U_o B}$

Angle of diffuser
with direction of γ
crossflow

Extremal cases of crossflow are V = 0 (stagnant conditions, as treated in the previous paragraphs) and V = large, such as in river applications, which result in full mixing, so that the dilution S_s = V. The diffuser was studied under moderate crossflow conditions which are important in lakes or coastal applications. A strong dependence on diffuser angle γ was found: Diffusers parallel to the crossflow ($\gamma = 0°$) in general produce lower dilutions as compared to diffusers perpendicular to the crossflow ($\gamma = 90°$). Figure 11 shows an example for a diffuser with alternating nozzles and nozzle orientation given by Equation (3): the extent of the $\Delta T/\Delta T_o$ = 0.075 isotherm is considerably smaller for the perpendicular diffuser (Figure 11a).

DESIGN CONSIDERATIONS

Practical thermal diffuser design involves the geometric outlay and dimensioning of a diffuser for a discharge flow Q_o, a temperature rise T_o and subject to an allowable surface temperature rise at the edge of some mixing zone, $T_{s\ max.}$ The required minimum surface dilution is then

$$S_{s\ min} = \frac{\Delta T_o}{\Delta T_{s\ max}} \tag{4}$$

The designing engineer usually has to choose between a diffuser with alternating
nozzles (zero net horizontal momentum) and a diffuser with unidirectional nozzles
(net horizontal momentum). This choice is dependent on the ambient current system
and bathymetry. From experimental observations it appears that, unless the
ambient currents are steady and strong and/or the bathymetry has a significant
offshore slope, unidirectional diffusers always tend to produce circulations in
the diffuser area which cause undesirable re-entrainment of already heated water.
Alternating diffusers on the other hand tend to produce a stratified flow
(except within the unstable near-field zone) with a reduced tendency for re-
entrainment.   As most sites are characterized by unsteady, possibly reversing
currents (tidal or wind-driven) and by extended shallow near-shore flats, the
installation of an alternating diffuser system seems to have certain advantages.

     As it is recognized that thermal diffusers will as a consequence of their
dynamic characteristics always produce an unstable near-field, the following
design considerations for alternating diffusers can be given:

     a) The temperature field should be uniform along the diffuser line. Theory
indicates that in case of variable depth the discharge per unit length should be
varied proportional to the 3/2 power of depth to produce uniform surface dilutions.

     b) Currents should be prevented from sweeping along the diffuser line. In
case of weak or no currents the nozzle orientation should be varied along the
line (Equation (3)). In case of stronger currents alignment of the diffuser axis
parallel to the current direction should be avoided.
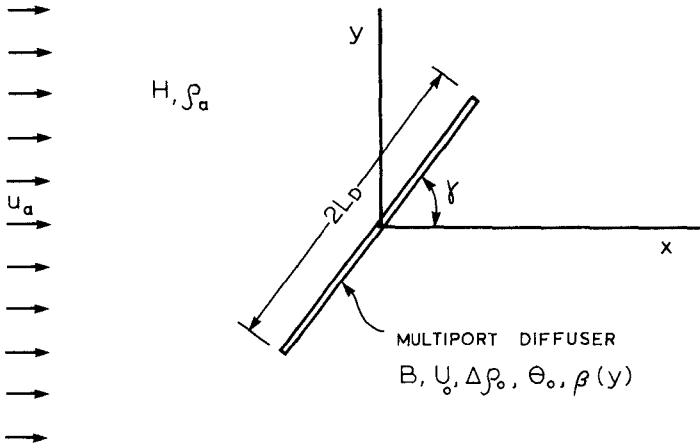
Figure 10: Multiport Diffuser in Ambient Crossflow

Figure 11a: Diffuser Axis Perpendicular to Cross Current
              F_s = 69, H/B = 558, Φ = 0.4, $\beta(y)$ Eq. (3), V = 14.0, γ = 90°
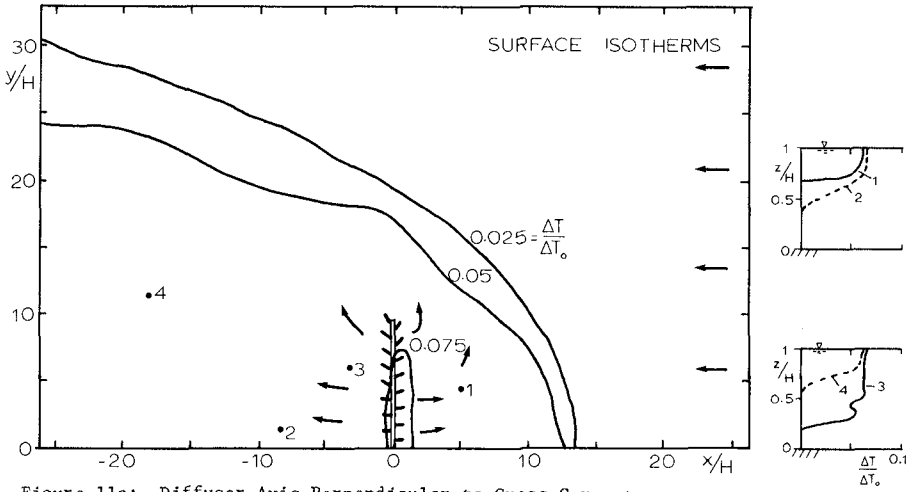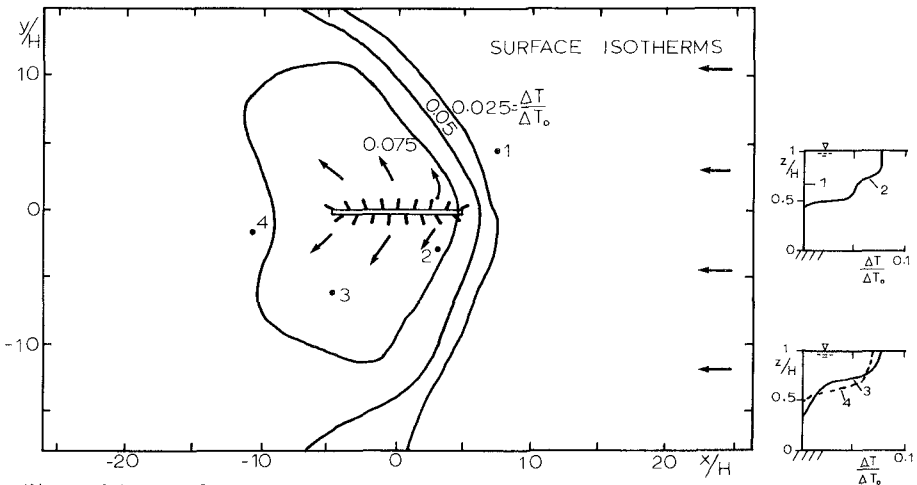
Figure 11b: Diffuser Axis Parallel to Cross-Current
              F_s = 66, H/B = 558, Φ = 0.2, $\beta(y)$ Eq. (3), V = 12.4, γ = 0°

Figure 11:   Experimental Results for a Multiport Diffuser with Alternating
              Nozzles in a Cross-Current.   Shows Effect of Diffuser Alignment.

c) In case of variable ambient conditions (such as unsteady wind-driven or tidal currents) it is desirable to use a diffuser which promotes stratification and is effective for both current directions. This objective is met by using diffusers with alternating nozzles (no net horizontal momentum). For these diffusers the required total length, $2L_D$, can be estimated by virtue of Equation (2) as

$$2L_D = \frac{Q_o}{\left(\frac{\Delta\rho_o}{\rho_a} g H_{ave}^3\right)^{1/2}} \frac{S_{s\ min}^{3/2}}{(4k)^{1/2}} \tag{5}$$

where H_{ave} = average depth in the discharge area and k is given in Table 2 as a function of $\Phi = f_o L_D/H$.

If the plant characteristics, Q_o and ΔT_o, and the water depth, H_{ave}, are taken as fixed, then Equation (5) states the attained dilution, $S_{s\ min}$, is uniquely dependent on the length, $2L_D$. Considering Figure 7, this places the design along an isoline S_s = const, for the example of Table 1, S_s = 9. The final position on the isoline is dependent on the choice of the secondary diffuser characteristics, namely discharge velocity, U_o and dimension, B. It is desirable to place the design close to the stable region in order to promote stratification by minimizing the intensity of the vertical recirculating eddy in the near-field. Shifting the diffuser design close to the stable region, however, necessitates lowering of the discharge velocity, U_o. A practical lower limit on U_o is about 5 fps due to the fact that lower discharge velocities require large diffuser pipes in order to maintain uniformity of discharge along the diffuser line. Thus from the point of view of discharge velocity, the thermal diffuser (T) of Figure 7 and Table 1 is about optimal (U_o = 8.5 fps). Another interesting consequence of Equation (5) is the fact that the diffuser design depends only on the total waste heat rejection, H_R, of the power plant (dependent on plant efficiency) and not on the particular condenser design (i.e. choice of Q_o and ΔT_o). Using the expression for the waste heat rejection

$$H_R = \rho c_p Q_o \Delta T_o$$

and a linear density-temperature relationship

$$\frac{\Delta\rho_o}{\rho_a} = |\beta\Delta T_o|$$

where β is the coefficient of thermal expansion, Equation (5) can be re-written in the form

$$2L_D = \frac{H_R/\rho c_p}{(\beta g H_{ave}^3)^{1/2} (4k)^{1/2}} \frac{1}{(\Delta T_{max})^{3/2}} \tag{6}$$

In summary, Equation (6) indicates that the required diffuser length of an alternating diffuser is only a function of the waste heat rejection, H_R, the available water depth, H_{ave}, the far-field condition, k, and the imposed temperature standard, ΔT_{max}.

With proper schematization of the site geometry, the theoretical predictions of Reference 5 can be used to provide a diffuser design or preliminary design estimate for the screening of alternative discharge schemes and/or for further investigation in a hydraulic scale model.

REFERENCES

1. Cederwall, K., "Buoyant Slot Jets Into Stagnant or Flowing Environments", W.M. Keck Laboratory for Water Resources and Hydraulics, Report No. KH-R-25, California Institute of Technology, April (1971)

2. Abraham, G., "Jet Diffusion in Stagnant Ambient Fluid", Delft Hydraulics Laboratory, Publ. No. 29 (1963)

3. Fan, L.-N. and Brooks, N.H., "Numerical Solution of Turbulent Buoyant Jet Problems", W.M. Keck Laboratory, California Institute of Technology, Report No. KH-R-18, January (1969)

4. Hirst, E., "Buoyant Jets Discharged to Quiescent Stratified Ambients", J. of Geophys. Res., Vol. 76, No. 30, October (1971)

5. Jirka, G.H. and Harleman, D.R.F., "The Mechanics of Submerged Multiport Diffusers for Buoyant Discharges in Shallow Water", Technical Report No. 169, Ralph M. Parsons Laboratory for Water Resources and Hydrodynamics, Department of Civil Engineering, M.I.T., March (1973)

CHAPTER 127

WAVE EFFECTS ON BUOYANT PLUMES

by

Nobuo Shuto

Chuo University, Tokyo, Japan

and

Le Huu Ti

Asian Institute of Technology

Bangkok, Thailand

Abstract

When a buoyant plume is discharged into water where
wave motions exist, the axis of plume is bent over and
horizontally fluctuated.   The dilution rate of the plume
is affected by this motion.   Experiments are carried out
to investigate the dilution rate of plumes when they
arrive at the free surface.   An analogy to the case of
buoyant plumes discharged into uniform steady cross streams
is applied to analyse the experimental data.   Within the
experimental range, it is found that the dilution rate is
inversely proportional to the square of the ratio of the
water depth to the diameter of outlet and is proportional
to the ratio of the discharge velocity to a characteristic
horizontal velocity of the ambient fluid.   The entrainment
coefficient is given as a function of a densimetric Froude
number for small Froude number and is a constant, 0.28, for
bigger Froude number than 4.3.

Introduction

It is well known that the buoyant plume discharged from

a point source into a cross stream shows a different dilution
rate compared with that into still water.   The difference
is considered due mainly to two causes.   The first cause
is that the total length of the plume is longer in a cross
stream than in still water.   Consequently, the plume in a
cross stream has a bigger chance to be diluted by the clean
ambient fluid.   The second reason is that the section of
the plume in a cross stream can not be approximated by a
circle, but by a "horse shoe" shape which is a result of the
bigger upward motion near the central part of the section.
In the plume of this kind, the entrainment of ambient fluid
is caused not only by the turbulence due to plume motion
but also by this upwards motion, while in case of a plume
in still water the turbulence is only one major cause of
entrainment.

Several researchers have treated buoyant plumes in
uniform steady cross streams.   The present paper reports
experimental results of buoyant plumes discharged into water
waves.

Theoretical consideration

It is assumed that the axis of the plume is nearly
horizontal, and that the horizontal movement of the plume
is almost equal to that of the ambient fluid.   The vertical
movement of the plume is, however, governed by the buoyancy
due to the density difference and the initial momentum, and
is quite different from that of the ambient fluid.   The
difference in the vertical velocities is the main cause to
yield the turbulence and entrain the ambient fluid.   The
entrainment is expressed by a coefficient α which is the
ratio of the entrainment velocity to the velocity difference.

The present paper does not treat a detailed structure
of the plume, but only discusses values on the axis of the
plume, which are considered important from the practical
point of view.

Sections of the plume are assumed circle. The velocity and density distributions are assumed to take the "top-hat" shape and follow a similarity law. Caution is needed to the difference bet ween these assumptions and the reality. Although we have just mentioned that the upward motion of water near the center of the plume was one of the main causes of bigger entrainment, no consideration of the phenomenon is taken into the above assumptions. All the effects are included in values of a which is to be experimentally determined.

The following four equations, integrated over a section of the plume, are basic equations which still contain the unsteady terms.

Equation of continuity

$$\frac{\partial D^2}{\partial t} + U\frac{\partial D^2}{\partial x} = 4aDw \tag{1}$$

Equation of motion in vertical direction

$$\frac{\partial(D^2 w)}{\partial t} + U\frac{\partial(D^2 w)}{\partial x} = \frac{\Delta\rho}{\rho} gD^2 \tag{2}$$

Equation of conservation of density defficiency

$$\frac{\partial(D^2\Delta\rho)}{\partial t} + U\frac{\partial(D^2\Delta\rho)}{\partial x} = 0 \tag{3}$$

Path of plume

$$\frac{\partial y}{\partial x} = \frac{w}{U} \tag{4}$$

in which a denotes the entrainment coefficient, D the diameter of the section of plume, w the vertical velocity in the plume, U the horizontal velocity of the ambient fluid, ρ the density and $\Delta\rho$ the density difference.

Since it is not easy to solve these equations analytically, the following consideration is introduced to obtain approximate expressions.

The plume discharged while the ambient fluid is flowing rightwards will rise diagonally rightwards. Then, the direction of motion of the ambient fluid changes leftwards. The plume, too, changes the direction of its ascent. New part of the plume which now begins to be discharged locates

below the old part of the plume, and these two parts of the
plume do not interact each other.   If the old part of the
plume is reflected with respect to a vertical line at which
the plume arrives at the end of the rightward movement, the
whole plume is regarded similar to the plume in a unidirec-
tional stream.   Accordingly, if a characteristic velocity
of the ambient fluid is well defined, the theoretical
considerations used in the analysis of plumes in a cross
stream can be applied with a sufficient accuracy to the
present case in order to estimate the dilution rate of the
plume at the free surface.

    We select the mean velocity U averaged over a half
wave period as a representative velocity. Within the range
that the wave motion is approximated by long waves, the
horizontal velocity is vertically uniform.

    These assumptions are used in averaging the above set
of equations. Such terms as D and w which vary periodical-
ly with respect to time may have some contributions through
the interaction terms such as D^2w to the analysis.   For
example, the initial velocity, w_0 , of the plume can vary
periodically.   The discharge of the plume is determined by
the piezometric head between the constant head tank and
the outlet of the plume at the bottom of channel.   Water
pressure in the channel fluctuates to some extent due to
wave motion, and the term D^2w does not vanish after the
averaging.   The fluctuation is, however, considered small
enough to be neglected in the analysis.   Thus, contribu-
tions of such terms are included in the value α , which can
be a function of F_{rU} or F_{rw_0} due to this approximation.

    Averaging the equations (1) to (4), we have the same
set of equations as in the case of the plume in a uniform
cross stream, and the solutions are given in the reference
(4).

    Dilution rate at the free surface is given by

$$\frac{\Delta\rho}{\Delta\rho_0} = \frac{1}{4\alpha^2} k \left(\frac{h}{D_0}\right)^{-2}$$

(5)

where h denotes the water depth and D_0 the diameter of the outlet.

Experimental equipment and procedure

A channel, 7.4 m long, 75 cm high and 50 cm wide, at the Asian Institute of Technology was used in the experiment. Two piston-type wave generators placed at each end of the channel can be operated synchronously to generate standing waves.   The channel was filled with salt water.

Fresh water is storaged in the two tanks, each with a capacity of 180 litres and pumped up to the constant head tank, from which fresh water is discharged through a 5/8 in. pipe.   Water overflowed the constant head tank returns to the storage tank and is repumped up.

The outlet is placed at the point where we have the maximum horizontal velocity under standing wave motion. Diameters of the outlet used in the experiments are 0.5 cm, 0.75 cm and 1.0 cm.

The discharge is determined by measuring the decrease of water quantity in the storage tank.

In order to know the dilution rate, samples were taken near the water surface, and their salinity and concentration of chromium were measured.   Initial   concentration   of chromium of the fresh water was 5000 $\mu g/l$.

A spectrophotometer was used to determine the concentration of chromium of the samples, and as the accuracy of this method was better than that of the measurement of salinity, only the results obtained by the spectrophoto-analysis are used in the following analysis.

The samples are taken from three points; one point just above the outlet, two points 50 cm apart from this point up- and downstream along wave direction.   After having examined that the experimental condition arrived at steady condition and having stopped the wave generator,   water samples were taken.   Thickness of the surface layer which

was composed of the diluted plume were 3 to 5 cm, and the
inlets of the samplers were inserted at 1-2 cm below the
free surface.   Intake velocity was controlled not to
entrain the water from the lower layer.   No sampling was
carried out at deeper points because the sampling only from
the plume itself is impossible due to the horizontal fluc-
tuation of the path of the plume caused by wave motion.

 Wave periods were determined from the rotation of the
wave generator, and wave height was measured from its
spacial distribution recorded along the side wall.

 A mixture whose density is the same as that of water
was made from benzene and carbon tetrachloride, and small
particles of the mixture were introduced in the tank to
measure the maximum excursion distance.   Theoretical
estimate of the excursion distance given by the theory of
long waves of small amplitude agreed very well with the
experimental results.

 Although standing waves were used in the experiment,
it is possible to transfer the present results to that
under progressive waves, because the excursion length is
so small compared with the wave length that the spacial
variations of horizontal velocity do not affect so much
the dilution of the plumes.

 Experimental conditions were as follows.

$h = 12.5, \ 25, \ 35 \, \text{cm}$

$h/D_0 = 12.5 \sim 70$

$F_{rU} = 1 \sim 7$

$k = \dfrac{w_0}{U} = 3 \sim 30$

$w_0 = 0.32 \sim 3.00 \, \text{m/sec}$

$\Delta\rho_0 = 0.01 \sim 0.05 \, \text{g/cc.}$

$H = 1.4 \sim 5 \, \text{cm}$

$T = 2.9 \sim 6.0 \, \text{sec}$

where F_{rU} is a densimetric Froude number defined with the
horizontal velocity U, H the wave height of progressive
waves and T the wave period.

Experimental results and discussions

(1). Classification of plumes.

Plumes are classified according to how many times the wave motion is repeated until they arrive at the free surface. A plume is called "nearly vertical" if the plume reaches the free surface within one half wave period. An "intermediate" plume is one that reaches the free surface within one wave period. Others are called "nearly horizontal". Thickness of the surface layer produced by the "nearly vertical" plume was the smallest, and the "nearly horizontal" plume gave the thickest surface layer. Figure 1 shows the classification of the plume in terms of the initial velocity of the plume, the horizontal velocity of the ambient fluid, the diameter of the outlet and the water depth. Except for the cases of smaller relative depth than 30, major factor which determines the type of plume is the relative velocity.

(2). Dilution rate of the plume at the free surface.

Abraham gave a formula of dilution for plume in still water as follows;

$$\frac{\Delta\rho}{\Delta\rho_0} = 9.7 F_{rw_0}^{2/3} \left(\frac{h}{D_0} + 2\right)^{-5/3} \tag{6}$$

which might be a good approximation for the case that the plume rises nearly vertically under small or negligible effects of the horizontal velocity of the ambient fluid. If the phenomenon is well approximated by the plume in a cross stream, the ratio $\Delta\rho/\Delta\rho_0$ may be proportional to $(h/D_0)^{-2}$.

The least scatter of experimental results obtained is shown in Fig.2, where the empirical relationship is

$$\frac{\Delta\rho}{\Delta\rho_0} = 0.17 F_{rw_0}^2 k^{-1} \left(\frac{h}{D_0}\right)^{-2} \tag{7}$$

or

$$\frac{\Delta\rho}{\Delta\rho_0} = 0.17 F_{r_U}^2 k \left(\frac{h}{D_0}\right)^{-2} \tag{8}$$

Comparison with Eq.(5) gives

$$\alpha = 1.21 F_{rU}^{-1} \tag{9}$$

In the above equations, F_{rU} and F_{rw_0} are the densimetric Froude number, with respect to the horizontal velocity of the ambient fluid U, and the initial velocity of the plume w_0, respectively.

(3). Entrainment coefficient.

Figure 3 shows α as a function of F_{rU}, after evaluating it by Eq.(5). For large values of F_{rU}, α is better approximated by a constant, 0.28, which is a little smaller than 0.33 for cases of the plume in a cross stream.

The major reason of this difference seems to depend on the difference of the definition of U.

For smaller values of F_{rU}, α is expressed as a function of F_{rU}. Fan gave

$$\alpha = f(k F_{rw_0}^{5/8}) \tag{10}$$

but in our cases, it is discovered more appropriate to express α as function of F_{rU}.

Cares are needed when we use the results given in Fig. 3. For α is bigger than unity, for very small values of F_{rU}. The coefficient α is the ratio of the entrainment velocity to the velocity which excites the entrainment. It is, therefore, physically impossible that α can exceed unity without any amplification mechanism. This fact tells that our model fails.

In addition, caution should be paid on the fact that values of α scatter very much for $h/D_0 < 16$. In the vicinity of the outlet, no similarity law is applicable due to the effect of high initial velocity. This affects the values of α, too.

Even with these faults, results shown in Fig.3 are practically applicable to compute the dilution rate of the plume.

(4). Empirical formula of the dilution of the plume.

Within the present experimental range where wave motion is sufficiently approximated by long waves of small amplitude, U in Eq.(8) is rewritten in terms of h and H and we have

$$\frac{\Delta\rho}{\Delta\rho_0} = \frac{1}{1.27} \frac{1}{\alpha^2} \frac{w_0}{\sqrt{gh}} \frac{h}{H} \left(\frac{h}{D_0}\right)^{-2}$$
$$\alpha = 1.21 F_{rU}^{-1} \quad F_{rU} \leqq 4.3$$
$$= 0.28 \quad F_{rU} \geqq 4.3$$

$$(11)$$

Conclusions

An empirical formula, Eq.(11), is established to compute the dilution rate of the plume discharged into wave motion which can be approximated by long waves.

Entrainment coefficient, α , is also given by Eq.(11), but caution is needed because the physical basis of α for small Froude number is ambiguous.

Nevertheless Eq.(11) is sufficient enough for practical purposes.

References

1. Abraham, G. (1960): Jet diffusion in liquid of greater density, J. Hyd.,Div., Proc. ASCE,Vol.86, HY 6, pp.1-13.
2. Fan,L.N. (1967): Turbulent buoyant jets into stratified or flowing ambient fluids, Rep. KH-R-15, W. Keck Lab., California Institute of Technology.
3. Morton,B.R. et al. (1956): Turbulent gravitational convection from maintained and instantaneous sources, Proc. Roy. Soc. London, Ser.A, Vol.234, pp.1-23.
4. Shuto,N. (1971): Buoyant plume in a cross stream, Coastal Engineering in Japan, Vol.14, pp.167-173.
5. Slawson,P.R. and G.T. Csanady (1967): On the mean path of buoyant, bent-over chimney plumes, J. Fluid Mech., Vol. 28, Part 2, pp.311-322.
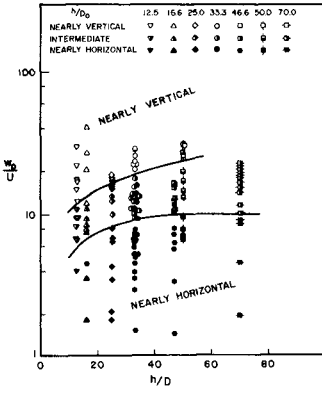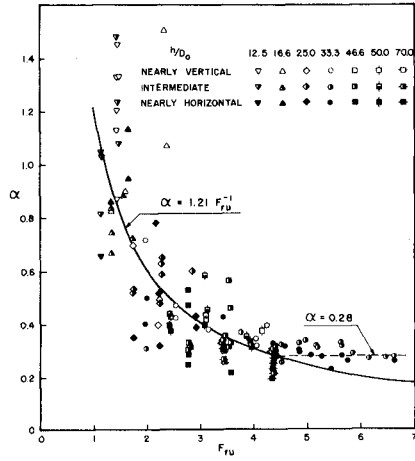
Fig.1 Classification
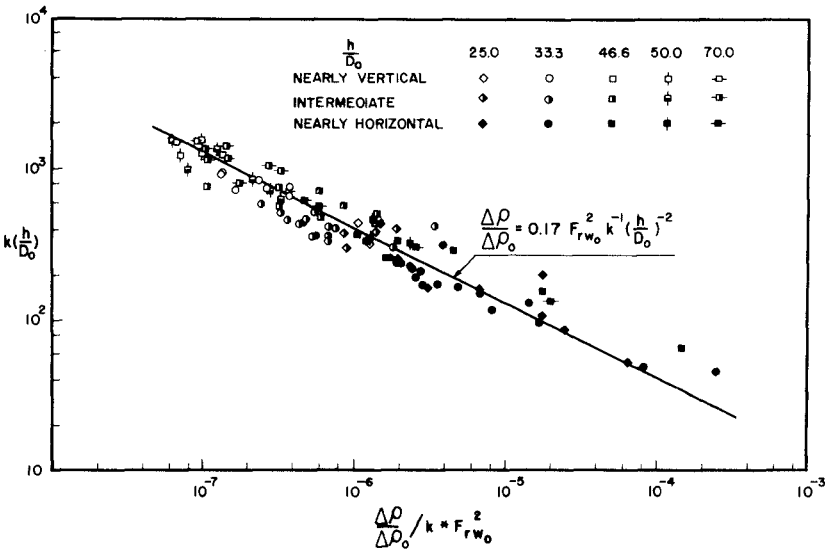   of plumes

Fig.3 Entrainment coefficient

Fig.2 Dilution rate of plumes at free surface

CHAPTER 128

ANALYSIS OF AIR-BUBBLE PLUMES

John D. Ditmars[1]
and
Klas Cederwall[2]

Abstract

    Models are developed to describe the gross behavior of air-bubble
plumes generated by point and line sources of air-bubbles released in
stagnant water bodies of uniform density. The models predict plume
width, velocities, and induced flow rates as a function of elevation
above the source.

    The analysis is confined to the plume mechanics and does not
include the horizontal flow created at the surface by the plume. An
integral similarity approach, similar to that used for single-phase
buoyant plumes, is employed. Governing equations are found by applying
conservation of mass, momentum, and buoyancy. The compressibility
of the air and the differential velocity between the rising air bubbles
and water are introduced in the buoyancy flux equation. Generalized
solutions to the normalized governing equations are presented for both
point and line sources of air-bubbles.

    The results of the analyses are compared with existing large-scale
experimental data. The comparisons indicate that the models predict
the gross behavior of plumes well and yield estimates of the entrain-
ment coefficients and lateral spreading ratios.

[1]Assistant Professor of Civil Engineering and Marine Studies,
University of Delaware, Newark, Delaware, U.S.A.

[2]Assistant Professor, Division of Hydraulics, Chalmers University
of Technology, Göteborg, Sweden.

Introduction

Air-bubble plumes have had a variety of applications in coastal
waters including the inhibition of ice formation, pneumatic breakwaters,
barriers to minimize salt water intrusion in locks, containment of
oil spills, and mixing for water quality control. While air-bubble
systems are often easily constructed and their application wide-spread,
a description of their hydrodynamic performance is required. The
details of such a two-phase flow are complex, but the gross hydro-
dynamic features of air-bubble plume are important for design purposes.
The models developed here describe the gross behavior of air-bubble
plumes generated by point and line sources of air-bubbles released in
stagnant water bodies of uniform density. These models predict the
plume width, velocities, and induced flow rates as a function of
elevation above the source.

The discharge of air-bubbles into water creates a turbulent plume
of an upward rising mixture of air and water by reducing the local bulk
density of water. The rising plume entrains water from over the depth
until it reaches the surface region, where as shown in Figure 1, a
horizontal current is created. This study is restricted to the region
below the influence of horizontal flow, and provides predictions of
the flow delivered to this surface region. Experimental evidence
indicates that the region of horizontal flow is approximately 0.25 of
the water depth above a line source and somewhat less for a point
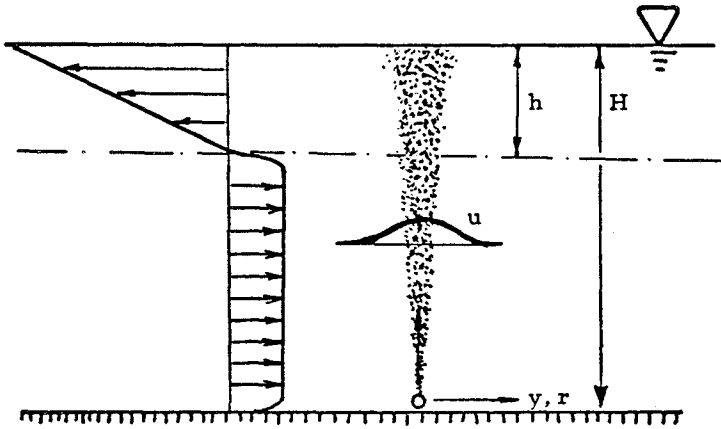source.

As air is discharged into water from a nozzle it breaks up into
bubbles of discrete size. A study of the formation of gas bubbles in
liquids has been reported by Davidson and Schüler (1). The rise and
motion of individual gas bubbles in liquids have been investigated in
many studies, and for example, Haberman and Morton (2), have reported
on a comprehensive study on the rise velocity of single air bubbles in
still water.

The similarity between the air-bubble plume and a single phase
buoyant plume was first pointed out by Taylor (3) in a discussion of
pneumatic breakwaters. He noted that the similarity existed only if
the air bubbles were so small that their rise velocity relative to the
induced plume velocity was negligible. The present study relaxes this
restriction and attempts to account for the existence of such relative
motion. Bulson (4,5) found semi-empirical relations for the maximum
velocity and thickness of the layer of horizontal surface flow.
Sjöberg (6) and Kobus (7) have investigated, both experimentally and
analytically, air-bubble plumes using the concepts of jet and plume
mixing.

Analysis and Model Development

The analysis of air-bubble plumes requires knowledge of the
following system parameters:

q_o volume rate of air discharged at atmospheric pressure
     (volume rate/unit length for a line source)
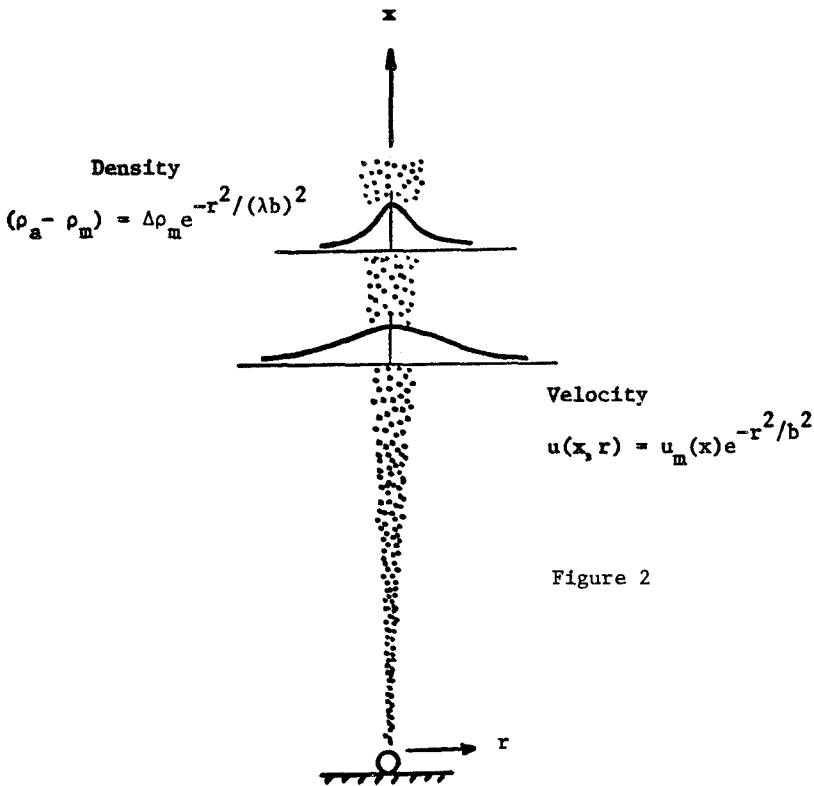
Velocity field close to the air-bubble plume.

Figure 1

Density

$$(\rho_a - \rho_m) = \Delta\rho_m e^{-r^2/(\lambda b)^2}$$

Velocity

$$u(x, r) = u_m(x) e^{-r^2/b^2}$$

Figure 2

u_b velocity of the air bubbles relative to the gross
       plume velocity

H   depth above the air source

H_o piezometric head equivalent of atmospheric pressure

It is assumed that for a first approximation u_b is equal to the terminal
rise velocity of an air-bubble in a stagnant water environment and
that the terminal value remains constant throughout the depth and is
characteristic of all bubbles in the system. This approximation is
reasonable, despite the fact that the bubbles probably vary in size
in the plume, as u_b values for bubbles with diameters ranging from
10^{-3} to 10^{-2}m range only from about 0.2-0.3m/s (2). The expansion of
the air bubbles as they rise through the water causes the driving force
for the system, buoyancy, to vary and must be accounted for. This
expansion is likely neither adiabatic nor truly isothermal but an
intermediate process. The choice of expansion law does not signifi-
cantly affect the results and the isothermal expansion is employed.
Thus, if x is the vertical coordinate originating from the source
(Figure 2) and q(x) is the local volume rate of air flow at x

$$q(x) \ (H_o + H - x) = q_o H_o \qquad\qquad (1)$$

and in particular at the source

$$q(o) = q_o \ \frac{H_o}{H_o + H} \qquad\qquad (2)$$

The air-bubble plume is analyzed following the similarity
assumptions and integral techniques proposed by Morton et al. (8) for
single-phase buoyant plumes. However, the effects of bubble "slip"
relative to the plume motion and the changing buoyancy due to bubble
expansion are included. The plume motion is assumed to be turbulent,
and laterial profiles of plume velocity and density deficiency are
assumed similar at all elevations and approximated by Gaussian dis-
tributions. The analyses for point and line sources are similar and
the case of a point source is discussed in detail below.

A Point Source

As indicated in Figure 2, the velocity of the rising plume is
given by

$$u(x,r) = u_m(x) \ e^{-r^2/b^2} \qquad\qquad (3)$$

where u is the local mean velocity and u_m is the centerline velocity
for this axisymmetric case. The characteristic lateral dimensional
of the plume is b(x) which is related to the standard deviation, σ,
of the lateral velocity distribution by

$$\sigma = b/\sqrt{2} \tag{4}$$

The distribution of density deficiency between the plume and surrounding water is

$$(\rho_a - \rho_m) = \Delta\rho_m \, e^{-r^2/(\lambda b)^2} \tag{5}$$

where ρ_m is the local density of the air-water mixture and ρ_a the density of the ambient fluid. $\Delta\rho_m(x)$ is then the centerline density difference between ambient water and air-water mixture within the plume at a particular level. $1/\lambda^2$ is the turbulent Schmidt number and λ may be thought of as the ratio of lateral spread of density deficiency to momentum.

Following Morton et al. (8), the rate of entrainment of water into the plume is assumed to be directly proportional to the mean centerline velocity. The Boussinesq assumption that density differences may be neglected except in the buoyancy terms allows mass conservation in terms of volume flux. The volume at any elevation x is

$$Q = \int_0^\infty 2\pi \, u \, r \, dr = 2\pi u_m \int_0^\infty e^{-r^2/b^2} r \, dr = \pi u_m \, b^2 \tag{6}$$

The rate of entrainment, $\dfrac{dQ}{dx}$, is assumed to be

$$\frac{dQ}{dx} = 2\pi \, b \, \alpha \, u_m \tag{7}$$

where α is the coefficient of entrainment assumed constant.

Thus,

$$\frac{d}{dx}(u_m b^2) = 2 \, \alpha \, u_m \, b \tag{8}$$

The buoyancy flux of the air-water flow at any x is

$$B = \int_0^\infty 2\pi(u+u_b)(\rho_a-\rho_m)r \, dr = \pi u_m \Delta\rho_m \frac{\lambda^2 b^2}{1+\lambda^2} + \pi u_b \Delta\rho_m \lambda^2 b^2 \tag{9}$$

The buoyancy passes any level x with the velocity $(u + u_b)$, since it is due to the air bubbles which move relative to the plume. This formulation differs from that of Kobus (7) where the transport rate of buoyancy was determined from experimental data as a function of air discharge rate and bubble size. Equation (9) requires only knowledge of the bubble rise velocity relative to still water. The buoyancy flux at any level x is found using Eq. (1) to be

$$B = q_o(\rho_a - \rho_{air}) \frac{H_o}{H_o + H - x} \tag{10}$$

As $\rho_{air} \ll \rho_a$, B may be written

$$B = q_o \, \rho_a \frac{H_o}{H_o + H - x} \tag{11}$$

and hence the buoyancy flux relation is

$$\pi u_m \Delta\rho_m \frac{\lambda^2 b^2}{1+\lambda^2} + \pi u_b \Delta\rho_m \lambda^2 b^2 = q_o \rho_a \frac{H_o}{H_o + H - x} \quad . \tag{12}$$

Similarly, for the momentum flux with $\rho_m \approx \rho_a$ according to Boussinesq assumption

$$M = \int_0^\infty 2\pi u^2 \, \rho_a \, r \, dr = \frac{\pi u_m^2 \rho_a b^2}{2} \quad . \tag{13}$$

The driving force of the plume is the buoyancy, and the momentum flux equation is

$$\frac{dM}{dx} = \int_0^\infty 2\pi (\rho_a - \rho_m) g \, r \, dr = \pi g \, \Delta \rho_m \lambda^2 b^2 \tag{14}$$

which combined with Eq. (13) yields

$$\frac{d(u_m^2 b^2)}{dx} = 2g \frac{\Delta \rho_m}{\rho_a} \lambda^2 b^2 \quad . \tag{15}$$

Substitution of $\frac{\Delta \rho_m}{\rho_a}$ from Eq. (15) into Eq. (12) gives two equations to solve

$$\frac{d(u_m b^2)}{dx} = 2 \, \alpha \, u_m \, b \tag{16}$$

$$\frac{d(u_m^2 b^2)}{dx} = \frac{2 \, g \, q_o H_o}{\pi (H_o + H - x) \left[\frac{u_m}{1+\lambda^2} + u_b \right]} \quad . \tag{17}$$

Eqs. (16) and (17) must be solved to obtain the centerline values u_m and b as a function of x and $\Delta \rho_m$ can be found from Eq. (12). The discharge of water or the volume flux of the plume at any elevation can be found from Eq. (6).

Since a solution to the differential equations cannot be obtained in closed analytical form, a numerical integration has to be carried out. The numerical solution follows from a direct step-by-step integration of the equations

$$\frac{d \, u_m}{dx} = \frac{2 \, g \, q_o H_o}{\pi u_m b^2 (H_o + H - x) \left[\frac{u_m}{1+\lambda^2} + u_b \right]} - \frac{2\alpha u_m}{b} \tag{18}$$

$$\frac{db}{dx} = 2 \, \alpha - \frac{g \, q_o H_o}{\pi u_m^2 b (H_o + H - x) \left[\frac{u_m}{1+\lambda^2} + u_b \right]} \tag{19}$$

Near $x = 0$, $u_m \gg u_b$ and hence Eqs. (18) and (19) take the following form

$$\frac{du_m}{dx} = \frac{2 \, g \, q_o H_o (1+\lambda^2)}{\pi u_m^2 b^2 (H_o + H - x)} - \frac{2\alpha u_m}{b} \, .$$ (20)

$$\frac{db}{dx} = 2 \, \alpha - \frac{g \, q_o H (1+\lambda^2)}{\pi u_m^3 b (H_o + H - x)}$$ (21)

These are the governing equations for a simple plume due to a source of buoyancy only, and their closed form solution provides the starting conditions for the numerical integration

$$b = \frac{6}{5} \, \alpha \, x$$ (22)

$$u_m = \left[\frac{25 \, g \, q_o H_o (1+\lambda^2)}{24 \, \alpha^2 \, \pi (H_o + H)} \right]^{1/3} x^{-1/3}$$ (23)

where $x = 0$ corresponds to the "mathematical origin." This "mathematical" or "virtual" source, as in single phase-plume analyses, is usually located below the real source of finite dimension.

A Line Source

The analysis of a two-dimensional air-bubble plume from a line source (which may be generated by a row of closely spaced orifices) is similar to that for the point source. For a lateral coordinate y, the velocity and density deficiency similarity profiles are given by

$$u(x,y) = u_m(x) \, e^{-y^2/b^2}$$ (24)

$$(\rho_a - \rho_m) = \Delta\rho_m \, e^{-y^2/(\lambda b)^2}$$ (25)

respectively.

The air discharge, q_o, has units of volume flux/unit length of source for this case and the volume flux/unit length at any elevation in the plume is

$$Q = \int_{-\infty}^{\infty} u \, dy = \sqrt{\pi} \, u_m b$$ (26)

The integral forms of the conservation of mass, buoyancy, and momentum, applied as for the point source case, yield the governing equations,

$$\frac{d}{dx} (u_m b) = \frac{2}{\sqrt{\pi}} \alpha u_m \qquad (27)$$

$$\frac{d}{dx} (u^2_m b) = \frac{\sqrt{2} \, g \, q_o \, H_o}{\sqrt{\pi}(H_o + H - x)\left[\dfrac{u_m}{\sqrt{1+\lambda^2}} + u_b\right]} \cdot \qquad (28)$$

Reduced for quadrature these are

$$\frac{du_m}{dx} = -\frac{2 \, \alpha \, u_m}{\sqrt{\pi} \, b} + \frac{\sqrt{2} \, g \, q_o \, H_o}{\sqrt{\pi}\left[\dfrac{u_m}{(1+\lambda^2)^{\frac{1}{2}}} + u_b\right](H_o + H - x)u_m \, b} \qquad (29)$$

$$\frac{db}{dx} = \frac{4\alpha}{\sqrt{\pi}} - \frac{\sqrt{2}}{\sqrt{\pi}} \frac{g \, q_o \, H_o}{\left[\dfrac{u_m}{(1+\lambda^2)^{\frac{1}{2}}} + u_b\right](H_o + H - x) \, u^2_m} \cdot \qquad (30)$$

As for the point source case, near x = 0, $u_m \gg u_b$, and the equations reduce to the simple two-dimensional plume equations which have the following solutions which provide the starting conditions for the numerical integration of Eqs. (29) and (30),

$$u_m = \left[\frac{g \, q_o H_o \, \sqrt{1+\lambda^2}}{\sqrt{2} \, \alpha(H_o + H)}\right]^{1/3} \qquad (31)$$

$$b = \frac{2}{\sqrt{\pi}} \alpha x \cdot \qquad (32)$$

Generalized Solutions to the Governing Equations

The governing equations for both the point and line source cases considered above require numerical integration to determine the centerline velocity, u_m, and the characteristic lateral dimension, b, and thus the plume width and volume flux at any elevation x. The governing equations and starting conditions for both cases were normalized using the system parameters to yield equations in terms of a dimensionless square root of the momentum flux, v, and a dimensionless mass flux, w, as shown in Table 1. The two governing independent parameters for each case G, a source parameter, and P, a scaling parameter for the water depth, are defined in Table 1.

Solutions of numerical integration of the normalized equations for a range G values of practical interest for a point source are given in Figure 3. Figure 3a shows the variation of the dimensionless centerline velocity v^2/w with dimensionless height above the source z, where

Air-Bubble Plumes in Homogeneous Environment

Case	Normalized Differential Eqs.	Starting Conditions	Parameters and Boundary Conditions
General Case, Point Source	$\dfrac{dw}{dz} = -2Gv$ $\dfrac{dv}{dz} = \dfrac{w}{z(v^3 + wv)}$	$w = \dfrac{6}{5}\left(\dfrac{9}{5}\right)^{\frac{1}{3}} G^{4/3}(1-z)^{5/3}$ $v = \left(\dfrac{9}{5}\right)^{\frac{1}{3}} G^{1/3}(1-z)^{2/3}$ $v^3 > w$	$G = \pi^{\frac{1}{2}} \dfrac{(H_o+H)\,\alpha\,(1+\lambda^2)\,u_b^{3/2}}{(g\,q_o\,H_o)^{\frac{1}{2}}}$ $z = 1$ to $z = P = H_o/(H_o+H)$
General Case, Line Source	$\dfrac{dw}{dz} = -G\dfrac{v}{w}$ $\dfrac{dv}{dz} = -\dfrac{w}{z(v+w)}$	$w = 2^{1/6}\, G^{2/3}\,(1-z)$ $v = 2^{1/3}\, G^{1/3}\,(1-z)$ $v > w;\ G < \sqrt{2}$	$G = 2^{\frac{1}{2}} \dfrac{(H_o+H)\,\alpha\,(1+\lambda^2)\,u_b^3}{g\,q_o\,H_o}$ $z = 1$ to $z = P = H_o/(H_o+H)$

Table 1

Figure 3
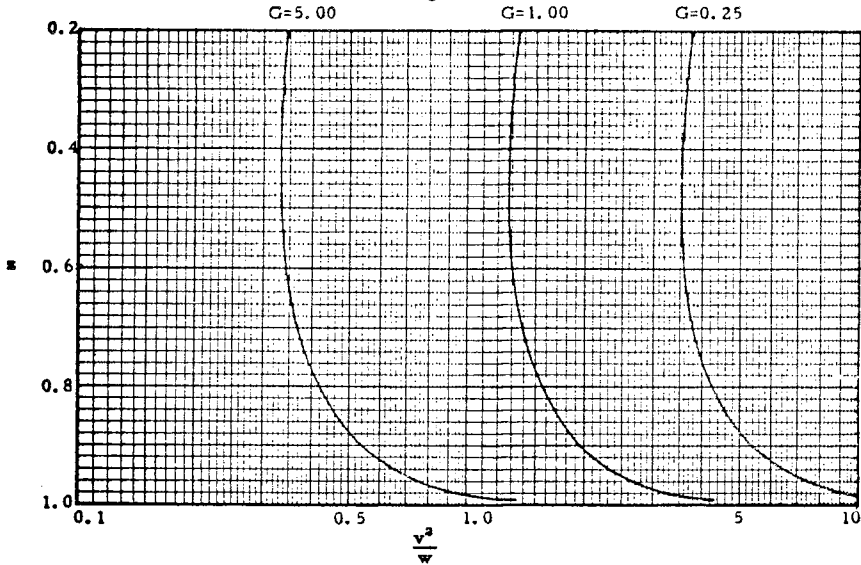
(a) **General** solution of the three-dimensional air-bubble plume for G equal 0.25,

·1.0 and 5.00. The centerline velocity $u_m = (1+\lambda^2) u_b \frac{v^2}{w}$.
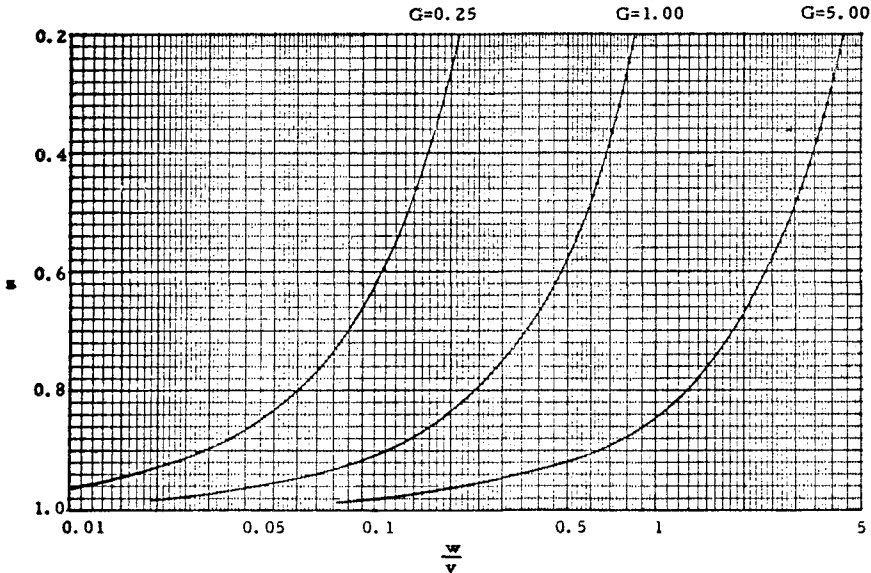
(b) General solution of the three-dimensional air-bubble plume for G equal

0.25, 1.00 and 5.00. The nominal half-width $b = \left[\frac{g q_o H_o}{\pi}\right]^{\frac{1}{2}} (1+\lambda^2)^{-1} u_b^{-3/2} \frac{w}{v}$.

$$z = \frac{H_O + H - x}{H_O + H} \tag{33}$$

and
$$u_m = (1+\lambda^2)u_b \frac{v^2}{w} \quad . \tag{34}$$

Figure 3b shows the variation of the dimensionless lateral dimension w/v with z, where

$$b = \left| \frac{g \, q_o H_o}{\pi} \right|^{\frac{1}{2}} (1+\lambda^2)^{-1} u_b^{-3/2} \frac{w}{v} \quad . \tag{35}$$

Similar solution curves are given in Figure 4 for a line source of air bubbles. Figures 4a and 4b show the variation of the dimensionless velocity, v/w, and the dimensionless lateral dimension, w^2/v, with depth, z, respectively. For the line source, the dimensional parameters are found from

$$u_m = (1+\lambda^2)^{\frac{1}{2}} u_b \frac{v}{w} \tag{36}$$

and
$$b = \frac{\sqrt{2} \, g \, q_o H_o}{\sqrt{\pi}(1+\lambda^2)u_b^3} \frac{w^2}{v} \quad . \tag{37}$$

The application of these generalized results requires, in addition to the system characteristics, determination of appropriate values of the entrainment coefficient, α, and the spreading ratio coefficient, λ, for both point and line air-bubble sources. Also, the location of the "virtual" source below the real source must be determined. Application of the plume models to experimental data was undertaken for verification of the model predictions and determination of these mixing parameters.

Comparison With Experimental Data

Large-scale laboratory experiments with both point and line source air-bubble plumes have been reported by Kobus (7). The point sources were located in 4.5m of water and consisted of orifices ranging from 0.05 cm to 0.5 cm in diameter with an air discharge range of 130 cm^3/s to 6200 cm^3/sec. The line sources were located in 2m and 4.3m of water and consisted of 0.1 cm diameter orifices spaced 10 cm apart with an air discharge range of 3000 cm^3/s-m to 10,000 cm^3/s-m. Kobus measured velocity profiles in the plumes with a current meter and reported these results for a variety of air discharges. The lateral velocity profiles indicated that the Gaussian profiles assumed in the analyses were a good approximation to the data.

The models developed above for point and line air-bubble plumes were applied to the experimental systems reported by Kobus (7), and predictions of centerline velocity and lateral spreading were made for a range of values of the entrainment coefficient and the lateral spreading ratio to determine best fits to the data (9). The location for the virtual source was found to be 0.8m below the real source for

Figure 4
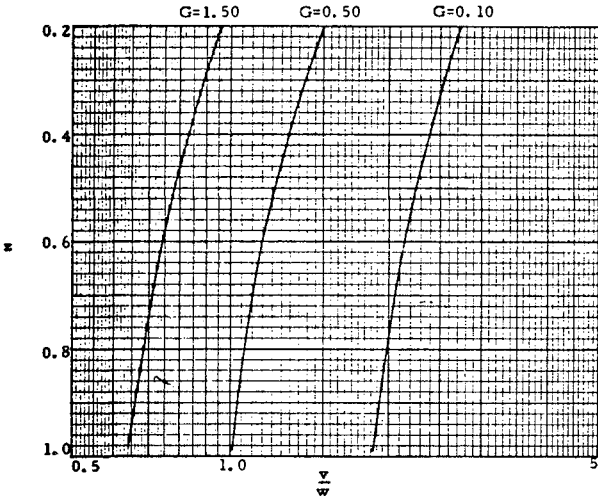
(a) **General** solution of the two-dimensional air-bubble plume for G equal 0.10, 0.50 and 1.50. The centerline velocity

$$u_m = (1+\lambda^2)^{\frac{1}{2}} u_b \frac{v}{w} .$$
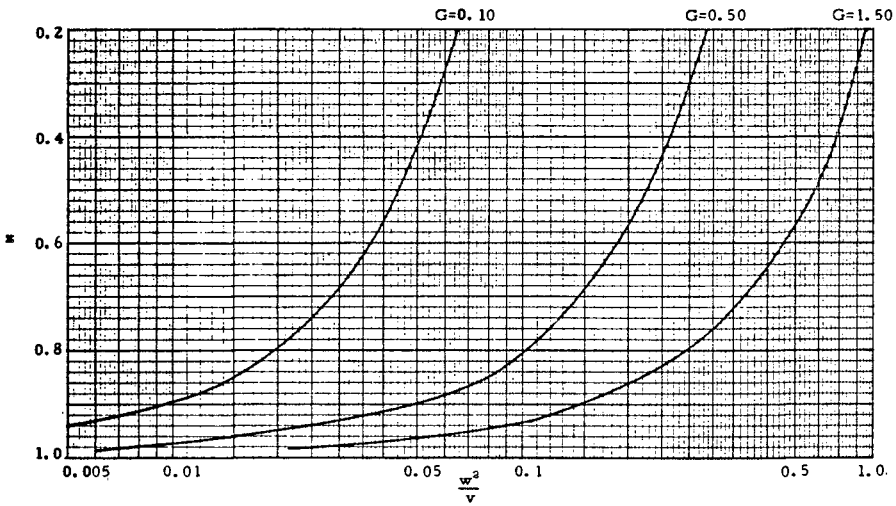
(b) **General** solution of the two-dimensional air-bubble plume for G equal 0.1, 0.5 and 1.5.

The nominal half-width $b = \dfrac{\sqrt{2}\, g\, q_o\, H_o}{\sqrt{\pi}\,(1+\lambda^2)\, u_b^3} \quad \dfrac{w^2}{v} .$

the range of Kobus' experimental data.

An example of the agreement between predicted and experimental centerline velocities and plume widths as a function of elevation for a point source are shown in Figures 5a and 5b, respectively. The good agreement of velocity values in the near-source region manifests the difference between the formulation of the buoyancy flux term presented here and that of Kobus' analysis (7) which results in centerline velocities approaching zero in this region. The effect of the relative motion of the bubbles within the plume is demonstrated in Figure 5a. Curve 1 represents a solution which includes the bubble rise velocity u_b = 0.30m/s (representative of the size range of bubbles in most plumes, as discussed previously) and curve 2 a solution where bubble expansion is included but u_b neglected. The "slip" of the bubbles results in smaller plume velocities, and, of course, the most efficient plumes, from the water moving standpoint, are those with small bubbles which have small rise velocities.

Comparisons of velocity predictions and data for line sources are shown in Figures 6a and 6b. The experimental data for the line source were more scattered than for the point source as the air curtain apparently created seiching in the tank. The effects of varying the values of α and u_b in the model are shown by the three model predictions.

The comparisons of model predictions and Kobus' data for eight sets of point source data and three sets of line source data indicated that the model predicts air-bubble plume behavior well with the appropriate choices of u_b, λ, and α (9). The value of u_b = 0.30 m/s was found to be appropriate for Kobus' data and was consistent with rise velocity data in still water for bubbles 10^{-3}m to 10^{-2}m in diameter (2). The effect of variations in u_b on plume characteristics was relatively small as shown in Figure 6. The lateral spreading ratio value of λ = 0.2 was indicated with no significant variation in results with values of 0.1 and 0.3. The typical value of λ for single-phase buoyant plume systems is about 1.0 or slightly larger. For air-bubble systems the bubbles remain close to the plume centerline, and thus, relative to momentum, density deficiency is diffused laterally to a lesser degree. The entrainment coefficient, α, was found to vary with the rate of air discharge as shown in Figure 7. The value of α for a point source approaches 0.08 for large air flow rates. For single-phase simple plumes Rouse et al. (10) found α = 0.082. The entrainment process depends on the turbulent structure of the plume, and α is known to vary from 0.057 from point source momentum jets to 0.082 for point source buoyant plumes (11). Apparently, over the range of air discharge rates used in the experiments the mixing environment, and thus α, changed and approached that of a simple plume for large q_o. The data for the line source case are limited, but Figure 7 indicates values of α less than that of 0.16 reported by Lee and Emmons (12) for single-phase line source plumes. However, the data were for small range of air discharge and increased with increasing q_o. Further experimental results are needed to determine the value of α over a wider range of air discharges; however, Figure 7 can be used as a guide with the likely upper limits on α of 0.082 and 0.16 for point and line sources, respectively.
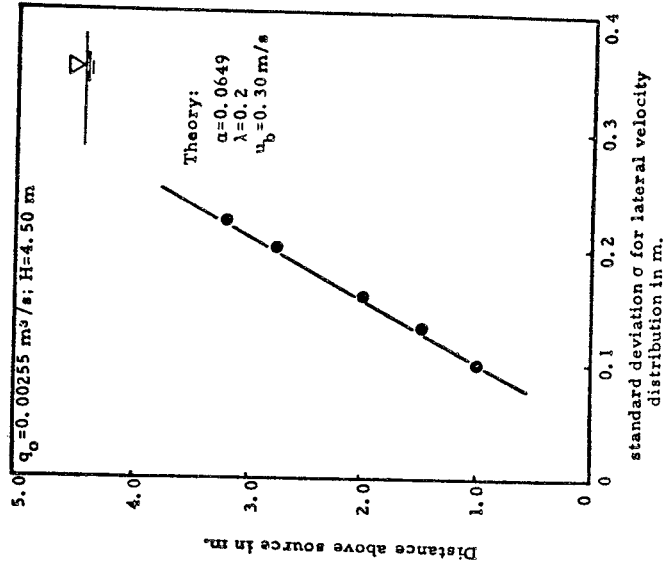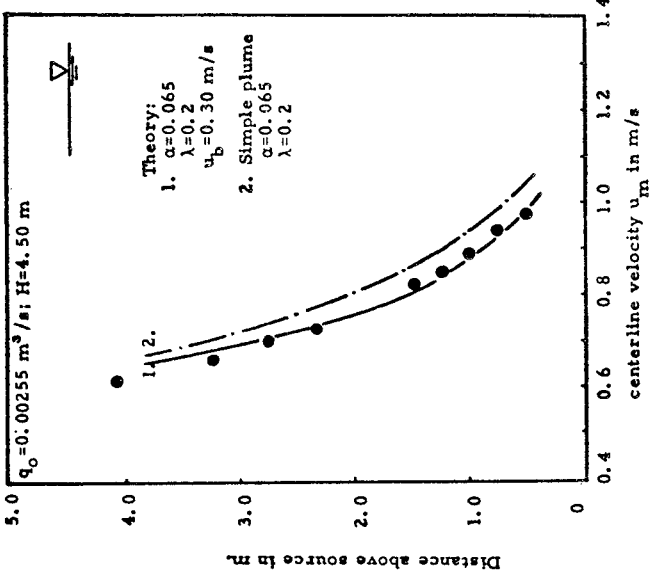
(b) Observed and predicted rate of growth of the lateral velocity profile with the distance above the (real) source. Experimental data by Kobus (1968).

(a) Observed and predicted variation of centerline velocity with distance above the (real) source. Experimental data given by Kobus (1968).
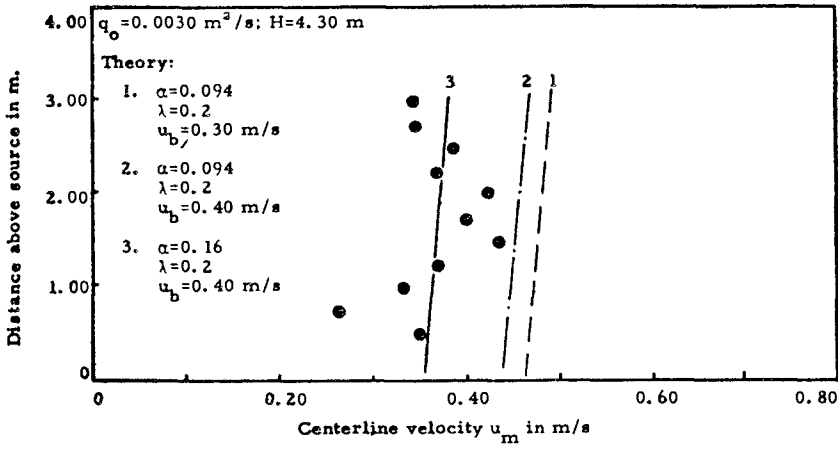
Figure 5

Figure 6

(a) **Observed and predicted variation of centerline velocity with distance above the (real) source. Experimental data by Kobus (1968).**

(b) **Observed and predicted variation of centerline velocity with distance above the (real) source. Experimental data given by Kobus (1968).**
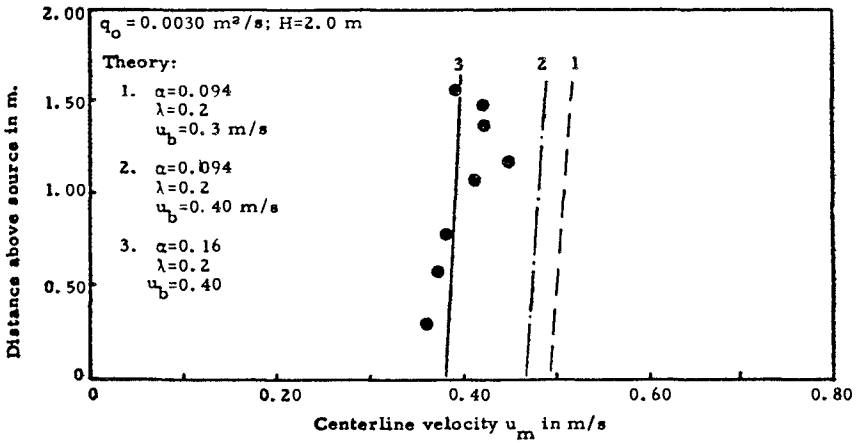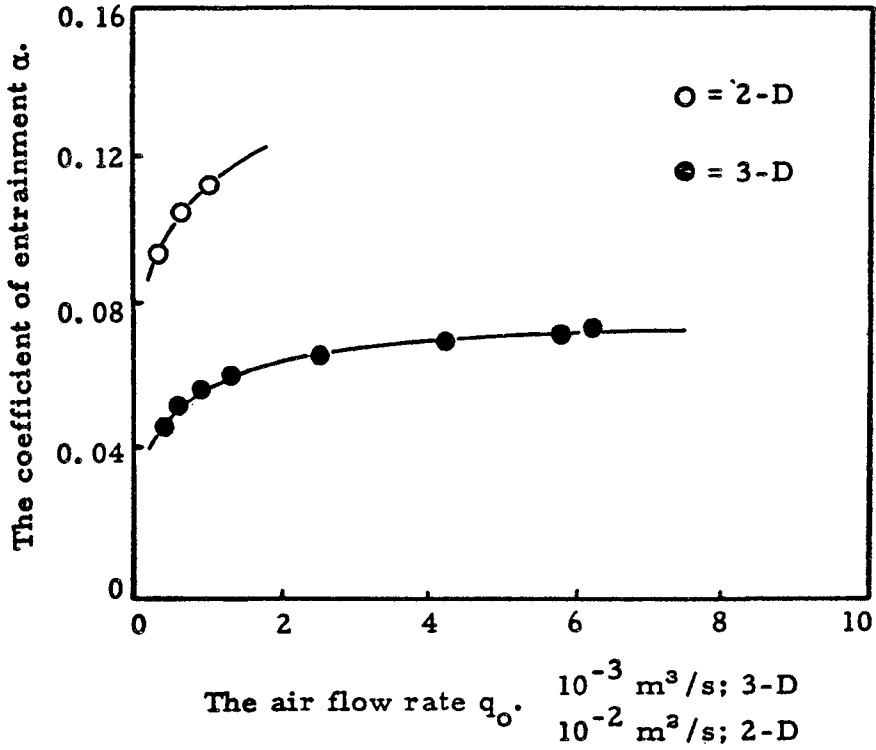
Figure 7

The coefficient of entrainment as a function of the air flow rate for two- and three-dimensional air-bubble plumes. Experimental data by Kobus (1968).

Conclusions

    The analyses and generalized solutions for the cases of point
source and line source air-bubble plumes provide predictions of the
gross hydrodynamic features of such systems. These features are the
velocity, width, and volume flux as a function of distance above the
source. Comparisons of the analyses with large-scale experimental
results indicated good agreement and yielded values for the lateral
spreading ratio parameter and the entrainment coefficients. Application
of the results requires that, in addition to the air discharge rate
and description of the receiving water environment, only an estimate
of the bubble rise velocity in still water be provided. Such estimates
are available as a function of bubble size (2).

References

1. Davidson, J. F. and Schüler, B.O.G., "Bubble Formation at an
    Orifice in a Viscous Liquid," Trans. of the Inst. of Chem. Eng.,
    Vol. 38, p. 144, 1960.

2. Haberman, W. L. and Morton, R. K., "An Experimental Study of
    Bubbles Moving in Liquids," ASCE Proc., Vol. 80, No. 387, Eng.
    Mech. Div., 1954.

3. Taylor, G. I., "The Action of a Surface Current Used as a Break-
    water," Proc. Roy. Soc. A, Vol. 231, p. 466, 1955.

4. Bulson, P. S., "Bubble Breakwater with Intermittent Air Supply,"
    Res. Rept. 9-2, Military Eng. Exper. Estab., Christchurch,
    Hampshire, England, 1962.

5. Bulson, P. S., "Large Scale Bubble Breakwater Experiments," Res.
    Rept. 9-3, Military Eng. Exper. Estab., Christchurch, Hampshire,
    England, 1962.

6. Sjöberg, A., "Strömnigshastigheter kring luft-bubbelrida i
    täthetshomogent och stillastäende vatten (in Swedish)," Chalmers
    Inst. of Tech., Hydr. Div., Rept. No. 39, 1967.

7. Kobus, H. E., "Analysis of the Flow Induced by Air-Bubble Systems,"
    Coastal Eng. Conf., London, Vol. II, p. 1016, 1968.

8. Morton, B. R. et al., "Turbulent Gravitational Convection from
    Maintained and Instantaneous Sources," Proc. Roy. Soc. A, Vol.
    234, p.1, 1956.

9. Cederwall, K. and Ditmars, J. D., "Analysis of Air-Bubble Plumes,"
    W. M. Keck Lab. of Hydraulics and Water Resources, Calif. Inst.
    of Tech., KH-R-24, 1970.

10. Rouse, H. et al., "Gravitational Convection from a Boundary
    Source," Tellus, Vol. 4, p. 201, 1952.

11. List, E. J. and Imberger, J., "Turbulent Entrainment in Buoyant
    Jets and Plumes," Proc. ASCE, Jour. Hydr. Div., Vol. 99, p. 1461,
    1973.

12. Lee, S. L. and Emmons, H. W., "Study of Natural Convection Above
    a Line Fire," Jour. Fluid Mech., Vol. 11, p. 353, 1951.

CHAPTER 129

NUMERICAL SIMULATION OF OIL SLICK TRANSPORT IN BAYS

by

Shen Wang and Li-San Hwang

Tetra Tech, Inc.

Pasadena, California

ABSTRACT

A computer model for simulating oil spreading and transport has been developed. The model can be utilized as a useful tool in providing advance information and thus may guide decisions for an effective response in control and clean-up once an accidental spill occurs. The spreading motion is simulated according to the physical properties of oil and its characteristics at the air-oil-water interfaces. The transport movement is handled by superimposing the spreading with a drift motion caused by winds and tidal currents. By considering an oil slick as a summation of many elementary patches and applying the principle of superposition, the model is capable of predicting the oil size, shape, and movement as a function of time after a spill originates. Field experiments using either cardboard markers or soybean oil to simulate a spill were conducted at the Long Beach Harbor. Computer predictions showed good agreement with the field traces.

1. INTRODUCTION

The rapid growth of offshore oil production and marine oil transport has led to an increasing danger of oil contamination of the coastal environment. Consequently, there is a growing worldwide concern over possible environmental damage caused by accidental oil spills.

The present study has been aimed at developing a computer model which is capable of predicting oil slick transport in harbors and bays. By means of numerical approximation, the model is able to simulate the spreading and movement of oil slicks on the ocean surface and to predict their destinations.

2227

The movement of an oil slick is simulated as a combination of the various phenomena which affect the spreading and transport. The simulation of the spreading process is governed by the physical properties of oil and its characteristics at the air-oil and oil-water interfaces. The spreading motion is then superimposed on the drift motion caused by winds and tidal currents to give the total movement. By considering the slick as a summation of many elementary patches in its numerical scheme and applying the principle of superposition to each individual patch, the model is capable of simulating the slick's shape distortion as a result of the relative shear motion produced by the non-uniformity of tidal currents and wind drifts on the water surface.

Sample computations have been conducted using the Long Beach Harbor-San Pedro Bay area as a test case. Several field tests using either cardboard markers or soybean oil to simulate a spill were also conducted in this area. Computer predictions using input obtained from field information show good agreement with the field traces and the validity of the computer model for field operation is substantially confirmed.

A dedicated small computer system is useful to accommodate the model for use in port offices. The geographical data and the oceanographic environment of the harbor can be pre-fed into the system. Wind information may be fed constantly to the system from remote sensors in the field. In the event of an accidental spill occurring in this area, one may press the keyboards to supply very simple data such as the time of the spill, type of oil, location and volume of the spill, and from this input the model will predict the oil size, shape, and movement as a function of time. The model may provide a moment-to-moment update of critical conditions. The model may predict the arrival time of the oil slick at various portions of the shoreline along with its spreading and transport well ahead of the true slick's arrival. This advance information of arrival time, location, and size would be extremely useful in guiding the decisions of engineers and operational personnel for an effective response in control and clean-up, and therefore, the model can be a very effective tool to minimize the environmental impact on shorelines.

2.   OIL SPREADING ON CALM WATER SURFACE

Only a sudden release of oil is considered in this paper. The site of spill is considered inside a harbor or inside the breakwater protection of a bay where the effect of the waves are generally negligible and the water may be regarded as calm.

The basic mechanism affecting the spreading of oil slicks over calm water includes inertia, gravity, viscosity and surface tension. At the initial stage, the primary driving force is due to gravity and the rate of spreading is governed by a balance between the gravitational pressure and the oil inertia. As the spreading proceeds, the oil slick becomes thinner and the viscous effect becomes more evident. Quickly, the oil thickness becomes thin enough so that the inertia

effect becomes negligible and the spreading enters into its second
phase while the gravitational spreading force is primarily balanced by
the water's viscous retardation. The gravity oriented body force gradu-
ally becomes less important as compared to the air-water-oil inter-
facial effect when the film thickness becomes even thinner, typically
on the order of milimeters. Finally, surface tension becomes domi-
nant as the major driving mechanism and responsible for the final phase
of spreading. The spreading rate at this phase is therefore determined
by a balance between the surface tension spreading force and the vis-
cous drag.

By balancing the various combination of forces, Fay [1] derived
the governing equations for various regimes. The actual spreading
processes at various regimes were also investigated experimentally
and results were compared with analytical predictions (Hoult [2]).
While the experiments show that the theory predicts correctly in terms
of the functional relationship among the governing parameters, discrep-
ancies exist on the magnitude of the proportionality constants. Waldman
et al [3], also recommended their values of these proportionality con-
stants based upon an analytical prediction performed by Fannelop and
Waldman [4]. Their values in some cases differ as much as 50% from
Fay's recommendation. In the following, the governing equations for
radial spreading derived by Fay are summarized. With the understanding
that large discrepancies exist between theories and experiments, the
proportionality constants were chosen mainly based upon fitting of em-
pirical data.

1.   Inertial Spreading

$$r = 1.14 \, (g \Delta V)^{1/4} \, t^{1/2} \qquad\qquad (1)$$

2.   Viscous Spreading

$$r = 1.45 \left[\frac{\Delta g \, V^2 \, t^{3/2}}{\nu^{1/2}} \right]^{1/6} \qquad\qquad (2)$$

3.   Surface Tension Spreading

$$r = 2.30 \left[\frac{\sigma^2 \, t^3}{\rho^2 \, \nu} \right]^{1/4} \qquad\qquad (3)$$

where

r =   radius of circular patch of oil

g =   gravitational constant

Δ = $\dfrac{\rho_{water} - \rho_{oil}}{\rho_{water}}$

V   =   volume of spill

t   =   time

ν =   kinematic viscosity of water

σ =   spreading coefficient (net surface tension at
                      air-oil-water interface)

ρ =   density

        For a small volume spill, only the third phase is of significance
as the first two phases last only a very short period in the entire spread-
ing history. For instance, in a 10,000 gallon spill the inertial phase
lasts only 20 minutes and the viscous spreading process should complete
in 40 minutes. Consequently, Equation (3) alone is sufficient to describe
the spreading almost entirely except in the very first hour after the spill
starts.

        Equation (3) also shows that within the surface tension process,
the leading edge of the oil spreading is independent of the volume spilled.
There is no question, however, that the final area of the film does de-
pend on the volume of the oil spill. Theoretical determination of the
final area would involve the knowledge of various physical properties of
oil in water, such as the change of the spreading coefficient, the diffusi-
vity, and the solubility. For practical purpose, however, an overall
estimate proposed by Fay [5] is used; the relationship is given as follows:

$$A = 10^5 \, V^{3/4} \tag{4}$$

Here the final area A is in square meters and the spill volume is in
cubic meters. The expression seems much over-simplified; it relates
with only one single parameter, the spill volume. Nevertheless, it
does fit the field data very closely.

        Nominal values for the physical properties of water and crude
oil are used in the entire study; they are listed as follows:

ρ_{water} = 1.94 slug/ft^3

ρ_{oil} = 1.84 slug/ft^3

ν = 1.296 x 10^{-5}ft^2/sec

σ = 0.65 x 10^{-3}lb/ft

Based upon these nominal values, calculations of the slick growth for spill volumes of 10^3, 10^4, 10^5, and 10^6 gallons are presented as a function of time in Figure 1. Since the slick size is independent of volume in the surface tension phase of spreading, all patches propagate along the same path line until they reach their final dimensions and cease to spread. This figure clearly shows that in small volume spills the surface tension phase is dominant during the entire spreading history.
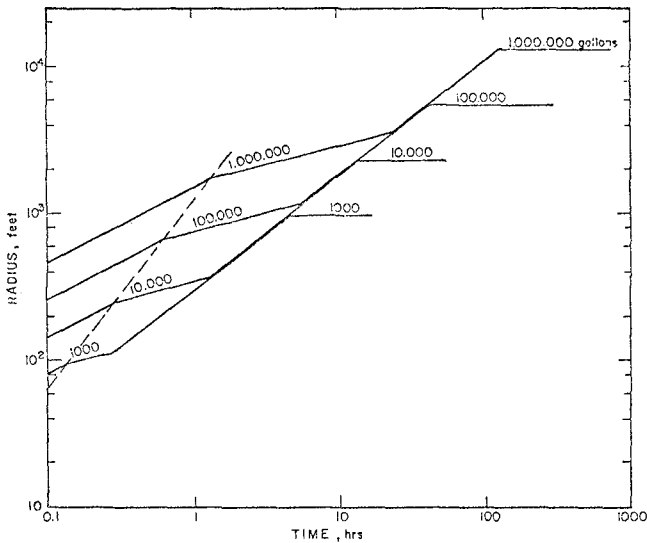

Figure 1. Slick Radius Increase as a Function of Time for Various Size Spills

The thickness of the oil slick varies from its center to its edge. The exact thickness distribution of a slick can only be obtained through proper modeling of the spreading dynamics during its growth. In order to give an order of magnitude idea about the slick thickness during the various phases of spreading, however, Figure 2 has been prepared by

assuming uniform thickness distribution for all cases at all times. The figure shows the nominal thickness variation as a function of time for the same four spills.

Figure 2. Nominal Thickness Decrease as a Function of Time
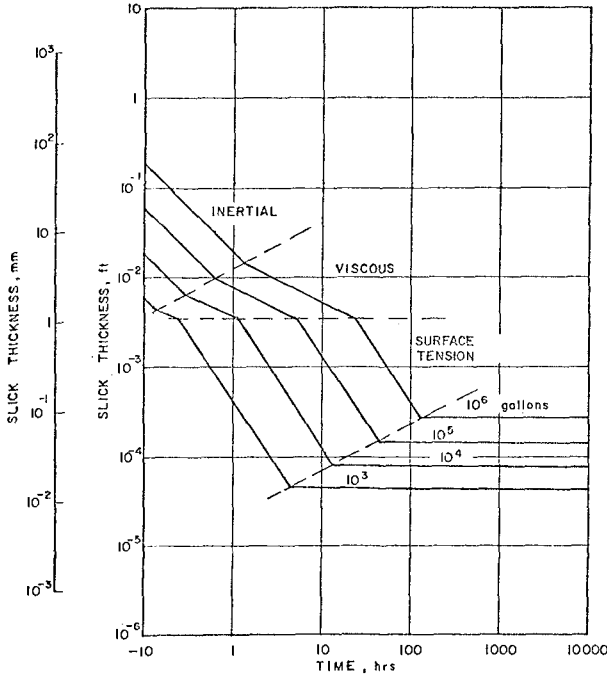
3. OIL TRANSPORT IN HARBOR

The primary factors affecting the movement of an oil slick are winds, tidal currents and waves. In the foregoing discussion on the spreading process, the water surface has been assumed calm without any effect due to water circulation or perturbation. In describing the transport process, the assumption is simply extended that the drifting

motion of an oil slick caused by winds, currents and waves can be
superimposed on the spreading motion of the slick on calm water as
described in the previous section.

The direct drift caused by the wind shear stress over the
water surface is generally agreed to be on the order of 3% of the
over-water wind speed. There is disagreement as to the direction,
however. For instance the experiments of Teeson and Schenck [6]
and the analysis of Warner, et al [7] suggests that an angular dis-
placement on the surface drift due to the effect of earth rotation
must be considered, whereas the analysis of the Torrey Canyon Oil
Slick Movement [8] shows good agreement by assuming the oil drift
always aligned with the wind direction.

It is anticipated that Coriolis force will affect the course of
transport if an oil slick is in movement under a steady wind over a
large distance on an open sea. While inside a harbor as opposed to
an open sea, the winds are highly local and unsteady in some cases
and the Coriolis effect can hardly be developed fully in a short time
scale; nevertheless, a partial development of the Coriolis effect may
be significantly responsible for oil transport.

The effects of surface waves are generally negligible because
of their oscillatory nature which produces little net force affecting
the spreading motion. Certainly, nonlinear effects of wave inter-
action may produce surface drift due to second order mass transport.
On the other hand, however, there is a retardation effect caused by
waves on surface drifts because of the presence of wind shadow on
the lee side of the wave crest. Schwartzberg [9] found that the en-
hancement and the retardation in surface drift caused by waves are
approximately of the same order of magnitude and cancel each other.
The apparent wind drift can factually be regarded as a constant, and
no net effect caused by waves needs to be considered.

The magnitude and direction of the tidal current are assumed,
in the present work, either calculable or measurable with required
accuracy. In the numerical example given in the later part of this
report, the tidal currents were calculated as a function of time and
space with the tidal stage as the input data.

In summary, the transport process of an oil slick is handled
as follows:

(1)   The effects of wind and current are assumed uncoupled
        with the spreading dynamics and they are superim-
        posable on the spreading motion of an oil slick on calm
        water.

(2)   The effects of waves on surface drift are considered
        negligible.

(3)   The tidal currents are obtained from either calcula-
         tions or measurements. They are input data varying
         as a function of time and space.

(4)   The wind induced surface drift is assumed to have a
         magnitude of 3% of the wind speed. Its angle of devia-
         tion from the wind direction is to be provided as a
         part of the input information.

4.   NUMERICAL SIMULATION

        The two-dimensional field of a harbor is constructed by a set
of perpendicular grids of equal grid spacings. At each grid point, the
field characteristic, ie., land or water, is identified by information
fed from input data. Each grid point represents a rectangular area of
Δ s x Δ s, where Δ s is the grid spacing. Whenever the grid point re-
presents water in the field, the local water depth should also be speci-
fied. In the two-dimensional field, the tidal current and the wind
driven current are each represented by a two-dimensional velocity
vector at each grid point. The variation in magnitude and direction of
these vectors from one grid point to another signifies the surface cur-
rent distributions. Similarly, if there are oil slicks in the field, the
local film thickness (averaging over a Δ s square) will be specified at
the corresponding grid points.

        The spreading of an oil slick consists of three distinct phases
as discussed in Section 2. The relationships governing the spreading
phenomenon in different phases presented in Section 2 provide funda-
mental information of circular spreading for an oil slick on a calm
water surface. When the oil slick is on water of uniform current, the
effect of the water movement may simply be superimposed to the
spreading motion. When the film is subject to non-uniform distur-
bances resulting from tide, wind, and others, the slick shape would be
distorted and appear irregular. To solve the exact problem concern-
ing spreading and transport in an arbitrary velocity field requires a
detail analysis of forces on elementary slick segments. The analysis
would very likely result in a set of differential equations similar to the
convective diffusion type equations with a tensor of air-oil-water inter-
face spreading, equivalent to a tensor of turbulent mixing relating
mass transfer between streamlines in the pollutant transport problem.
Assuming that this spreading coefficient could be specified as a func-
tion of space and time, there should be no difficulty in general to write
a computer program to determine the movement and spreading of an
oil slick in a given environment as well as the slick thickness distribu-
tion as a function of space and time. Nevertheless, even with modern
computers such an attempt would be too expensive to be practical in
terms of computing time, if not just ambitious.

        Instead of solving the exact problem, the present model simu-
lates the spreading and transport phenomena numerically by means
of superposition. The oil film is fictitiously divided into patches

according to the already established two-dimensional grids; each patch occupies an area of Δ s square centered at the grid point. The concept is to follow the motion of the center of these patches and to superimpose their motion together with a spreading. The process is carried out in appropriate time intervals. At the end of each time step, the average thickness of each patch is obtained by summing up the overlapping layers, resulting from spreading and transport at each grid point. The concept is similar to that adopted by Fischer [10] in predicting pollutant transport in water. As a result of carrying out this concept, the center of the slick is thicker initially, but the gradient of the film surface decreases gradually until a limiting thickness governed by the spreading mechanism is reached.

In numerical computations dealing with the diffusion type equations, the time step and grid spacing must be kept in appropriate limits, depending upon the magnitude of the diffusion coefficient, in order to assure the solution to be stable. Similarly, in the present numerical scheme, the correct simulation of the spreading mechanism requires an appropriate choice of the grid size and the time step. The selection of them depends mainly on the spreading coefficient and the spill volume.

The model is designed for predicting oil slick movement in a harbor or nearshore area. The primary input, therefore, is the information of the land boundaries. Land and water are identified by different code numbers. Wherever the region is identified as water, a water depth must also be specified. For a given bay area the above mentioned data are constant and seldom changed. It is therefore convenient that these data are stored on a magnetic tape file in a pre-arranged order.

The tidal current data should be input as a function of time and space. They can be obtained either through numerical computation from a separate tidal program or by compiling the observed information. In the present study, a separate hydrodynamic program is used for current data generation. This program takes the same boundary specification as the oil slick movement model. It requires the temporal information of the tidal stage as input. The current magnitude and direction are computed for every half hour interval and given as a function of location. These data are stored on a magnetic tape in a prescribed order and chronological sequence.

Other information, such as the site of spill, the quantity of spill, the oil properties, the wind speed and direction, etc. , varies from case to case. They must be updated each time the program is operated.

5.   AN EXAMPLE PROBLEM

This section presents some sample computations of oil slick transport using San Pedro Bay as an example. A typical diurnal tide used for this study is shown in Figure 3. The 25 hour cycle tidal

current was generated external to the system, but stored on a magnetic
tape in sequence of every half hour intervals. Figure 4 shows only one
plot of a continuous series of the calculated current velocity vectors in
the bay, with a wind of 5 knots blowing from the northwest being imposed.
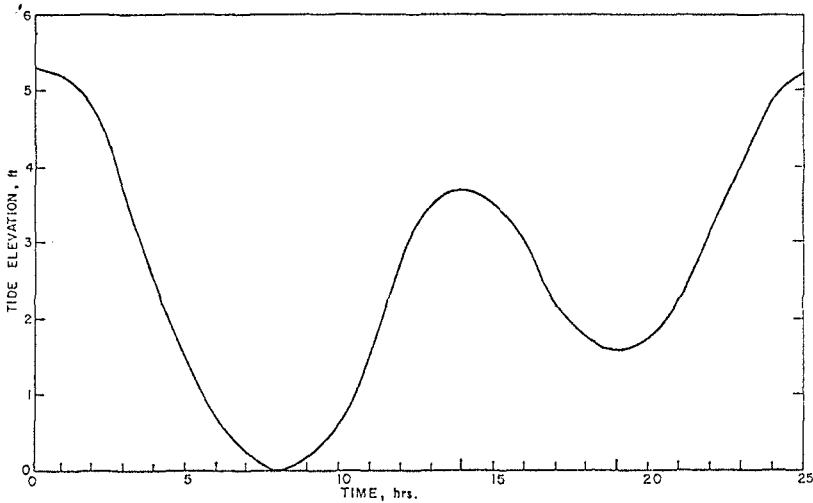

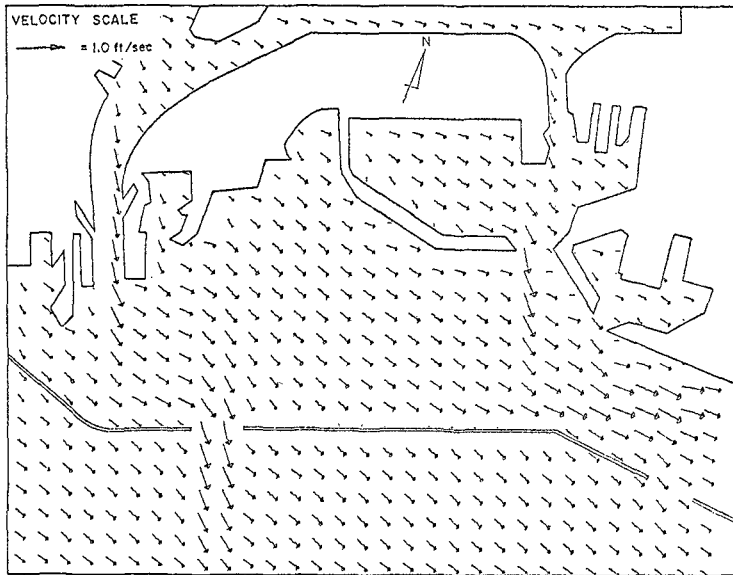Figure 3. Typical Tidal Fluctuation in San Pedro Bay

Figure 4. Current Field in San Pedro Bay at Referenced
Hour 3.5, Wind Speed 5 Knots, Direction 284.5°

Numerical experiments were conducted in the system to simulate spreading and transport for a sudden release of 100,000 gallons of crude oil. The results have been reported in [11]. Figure 5 shows only a typical computer output corresponding to 36 hours after the 100,000 gallons of oil is released at the location (12, 16) with no wind being taken into account. The asterisks in the plot stand for land or ocean boundaries; the numbers at each grid point indicate the thickness of the oil film in 10^{-2} mm, averaged over an area of 10^6 ft^2 around that point. The entire grid space under these numerals indicate the area covered by oil on the water surface at a particular time.

6. FIELD TESTS AND MODEL VERIFICATION

In order to verify the numerical model there were, in total, five field tests and demonstrations conducted at San Pedro Bay. The first two tests were made with 3' x 3' cardboards to simulate the oil transport. In the last three tests, soy bean oil was dumped at various locations. These tests covered a wide range of wind speed and direction and they were conducted at various stages with regard to tidal circulations. The complete test results and their comparisons with their numerical predictions have been reported in [11]. In the following, only the test procedures and two typical sets of the results are presented.

(1) CARDBOARD TESTS

The floating markers were made of 3' x 3', 1/16" thick posterboard and were sealed with paraffin on their edges in order to prevent them soaking between the layers. They were coated with florescent paint of a bright red-orange color and each board was identified by a number painted in black. In one test conducted on October 5, 1973, three cardboards were launched approximately 1000 feet apart from each other from a 25-ft. Bertram class motor boat, which has a fiberglass hull and wooden deck finishing. The cardboard markers behaved extremely well on the water surface; they were flexible and moved harmonically with the surface waves. The positions of the markers were fixed by a Cubic Autotape DM-40 electronic positioning system. The system includes a two-range interrogator on board the boat and two responders at fixed locations on shore. The Autotape employs microwave to measure the ranges between the moving boat and the two fixed sites where the two responders were located. The interrogator visually displays these ranges once per second in 5 metric units. These ranges were also simultaneously recorded on a paper printer.

In the October 5th test, one responder was put at the east end of Terminal Island and the second one was at Pier F

THICKNESS OF OILFILM IN CM/1000, AT END OF HOUR 36
OIL INSIDE THE BAY= 100000 GALLONS

Figure 5. Computer Output of Simulated Results for Oil Slick Distribution at End of Hour 36, No Wind
Grid Spacing = 1000 ft

of the Long Beach Harbor.   During the test, the locations of the
markers were traced and the   distances of each marker from
the two responders were recorded as a function of time.   The
paths of the markers were then determined by fixing their posi-
tions using two range lines.

        Wind information was obtained by means of an anemo-
meter and a magnetic compass on shore.   Wind speed and direc-
tion were recorded every 15 minutes; the records are shown in
Figure 6.   Taking wind speed as a constant of 8 knots but up-
dating the wind direction every half hour, the routes of the three
markers were calculated and compared with the field traces as
shown in Figure 7.   It is noted that because Marker 2 was
generally following the same path as Marker 3, Marker 2 was
relocated to a new location at 2:15 PM.   The computation used
a 500 ft. grid space and a one hour time step.   The total simu-
lation time was four hours for Markers 1 and 3, and two hours
for Marker 2 beginning at the relocated position.   The compu-
tation considered zero angle deflection with regard to the wind
drift current.   The agreement of the calculated results with the
field data appears to suggest that the markers were essentially
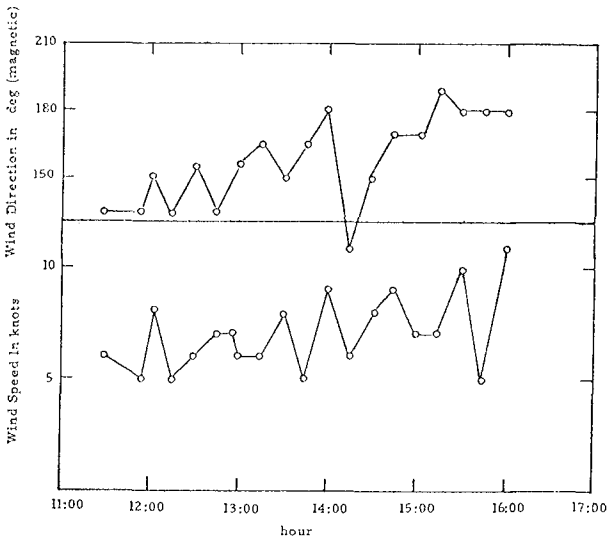moving along the direction of the wind.
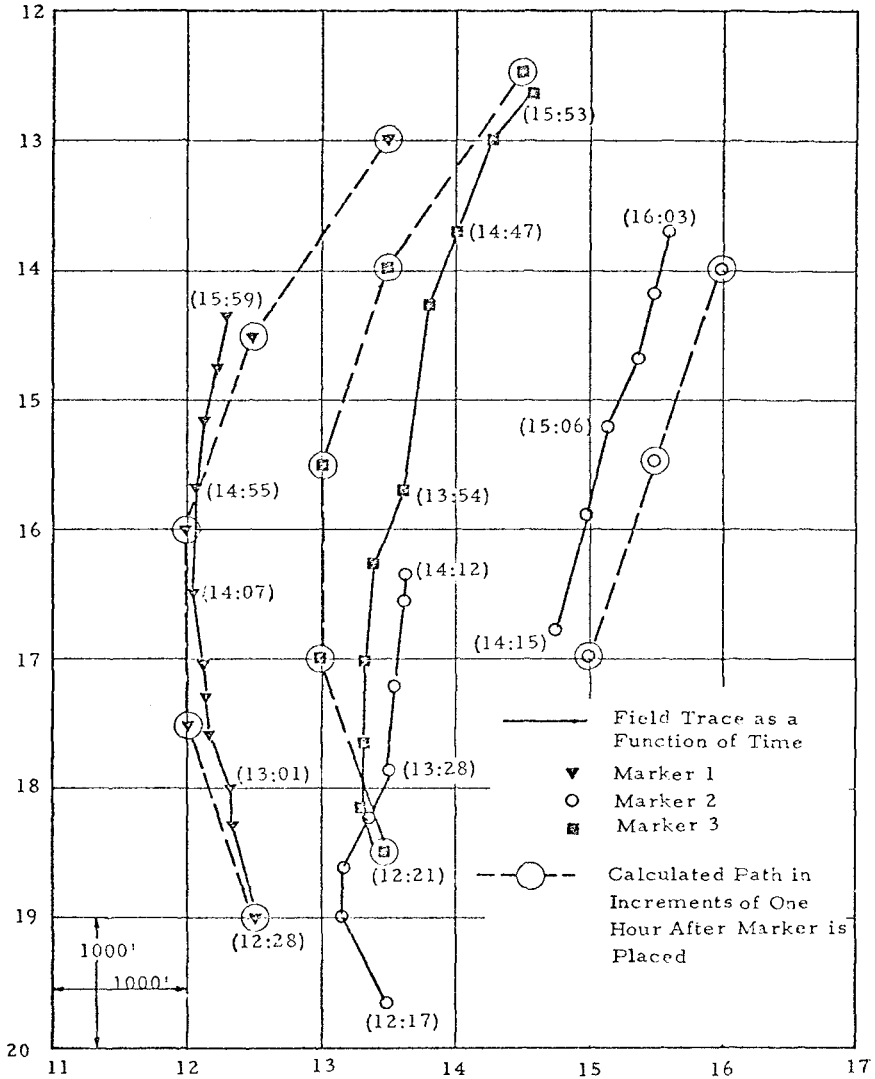

Figure 6. Wind Records

Figure 7. Calculated Paths and Field Traces of Markers
(Refer to Figure 5 for Grid Locations)

(2)   SOYBEAN OIL SPILL TESTS

        While the cardboard tests were essentially to show the
credibility of the model for analysis using field information,
the next three tests with soybean oil were to show the capability
of the model for forecasting with the initial information and the
capability of updating when better information becomes avail-
able.

        Instead of using the Cubic Autotape, a Motorola Mini-
Ranger System was used for oil slick positioning. Four re-
sponders were stationed onshore. The oil dumping position
fixing group was on a Coast Guard 40-ft. steel-hull boat. The
forecasting group was stationed onshore and equipped with a
portable teleprinter linked to the Control Data Kronos Time-
Sharing System by means of a regular telephone line.

        In one test conducted on February 11, 1974, five
gallons of soybean oil were dumped at 12:15 PM inside the
west end of the middle breakwater close to the Los Angeles
Harbor Main Channel. Because of its closeness to the main
channel traffic, the slick was unfortunately disturbed by a
passing ship, supertanker ESSO BERLIN, and no accurate
trace could possibly be made. Despite this unsuccessful
start, a second dumping of about ten gallons was made at a
new location at 2:13 PM. The dumping site and the initial
wind condition were transmitted from boat to shore through
walkie-talkie type radio communication. The shore group
immediately fed these data into the computer and obtained a
two-hour prediction.

        The wind information received at 2:13 PM was 9
knots and 215° (magnetic). Prediction based upon this in-
formation showed an approximate 10 degree discrepancy
with the traced data obtained later on. It appeared that a
10 degree wind drift deflection had to be included in the
computation for better agreement. This correction was also
confirmed in a subsequent test conducted on the following
day as reported in [11]. With this correction included in
the computation model, the predicted oil movement is shown
in Figure 8 together with the field traces.
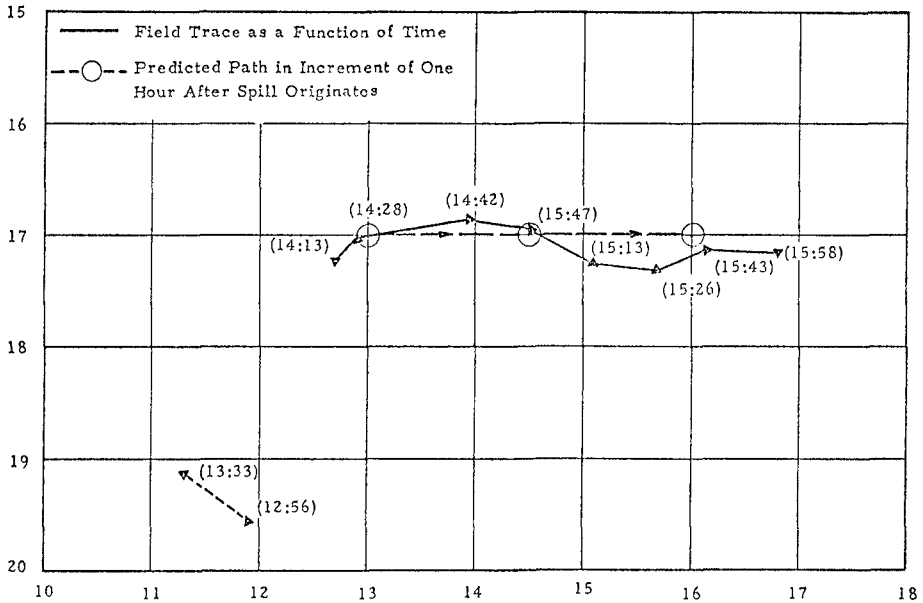
Figure 8. Predicted Path and Field Traces of the Slick Centroid
(10° Wind Drift Deflection Included in Prediction)

7.   DISCUSSION AND CONCLUSION

     While field observations of drift markers and small scale oil
slick movements have essentially validated the present model, some im-
portant assumptions applied herein deserve more detailed discussions.
The most important approximation is the spreading process simulation.
The numerical procedure is an attempt to represent the effect of the
pressure gradient over the slick boundary of the elementary patches.
The concept assumes that each patch of oil slick will locally spread and
diffuse over a circular field whose radius is stretched approximately
by one grid space during one time step before the final area of the slick
is reached. At the end of each time step, a superposition of the over-
lapping patches takes place. It is obvious that the grid size and the
time step are necessarily governed by the spill volume and the spread-
ing characteristics in order that the spreading process is properly
simulated. This is equivalent to the grid size and the time step being
controlled by the diffusion coefficient in solving convective-diffusion
equations by a finite difference technique.

     While the necessity of adjusting the grid size and the time step

is fundamental for a proper simulation of spreading, the application of the numerical program is not limited by these restrictions. From an operational point of view, the total spreading process is generally too short to be important. In other words, the impact of slick transport is generally more significant than the consequence of spreading in affecting decision on directing protective actions and control. Consequently, the grid size and time step may not necessarily tie up to the type and volume of the oil spill; they may be chosen essentially for convenience. The program then adopts a simple procedure to provide advance information on the slick's area and shape as a function of time.

The adopted concept of superimposing a transport motion on a spreading motion in calm water signifies that the mechanism for spreading and dispersion is essentially isotropic, which is known as not supported by observations. Field observations often find oil slicks pronouncedly stretched in the direction of drift. This phenomenon may be taken into consideration in the numerical scheme by including the directional property in the spreading coefficient, provided that sufficiently reliable data are available in this regard.

In regard to the wind drift information, it is anticipated that the Coriolis force may play an important role in altering the course of an oil slick only if it is transported over a long distance. Inside a harbor over a short time span, one should expect the wind drift deflection to be negligible. Nevertheless, the field test of soybean oil in San Pedro Bay showed an approximate 10 degree clockwise deflection in wind induced drift. There are no sufficient data available with regard to the wind drift deflection in harbors. Field surveys are necessary to obtain this information.

8.   REFERENCES

[1] Fay, J. A. , "The Spread of Oil Slicks on a Calm Sea, "
         in OIL ON THE SEA, ed. D. P. Hoult, 53-63, New
         York; Plenum, 1969

[2] Hoult, D. P. , "Oil Spreading on the Sea, " Annual Review
         of Fluid Mechanics, vol. 4, 1972

[3] Waldeman, G. A. , R. A. Johnson & R. C. Smith, "The
         Spreading and Transport of Oil Slicks on the Open
         Ocean in the Presence of Wind, Waves and Currents, "
         AVCO Corp. , Report AVSD-0068-73-RR, July 1973

[4] Fannelop, T. K. , and G. D. Waldman, "Dynamics of
         Oil Slicks, " AIAA Journal, vol. 10, pp 506-510,
         April 1972

[5] Fay, J. A., "Physical Processes in the Spread of Oil on
    a Water Surface," American Petroleum Institute,
    Proc. Joint Conference on Prevention and Control
    of Oil Spills, Washington, D. C., pp 463-467, June
    1971

[6] Teeson, D. and H. Schenck, "Studies of the Simulation
    of Drifting Oil by Polyethylene Sheets," Ocean Engi-
    neering, vol. 2, No. 1, pp 1-11, Sept. 1970

[7] Warner, J. L., J. W. Graham and R. G. Dean, "Pre-
    diction of the Movement of an Oil Spill on the Surface
    of the Water," Offshore Technology Conference,
    Dallas, Texas, Paper 155, 1972

[8] Smith, J. E., Editor, Torrey Canyon Pollution and
    Marine Life, Cambridge Univ. Press, New York 1968

[9] Schwartzberg, H. G., "The Movement of Oil Spills,"
    American Petroleum Institute, Proc. Joint Confer-
    ence on Prevention and Control of Oil Spills, Washing-
    ton, D. C., pp 489-494, June 1971

[10] Fischer, H. B., "A Method for Predicting Pollutant
     Transport in Tidal Waters," Water Resources Center
     Contribution No. 132, Hydraulic Laboratory, Univ.
     of California, Berkeley, March 1970

[11] Wang, S. and L. Hwang, "A Numerical Model for
     Simulation of Oil Spreading and Transport and its
     Application for Predicting Oil Slick Movement in
     Bays," Tetra Tech Report TT-P-345-74-1, Febru-
     ary 1974

CHAPTER 130

OIL SLICK FATE IN A REGION OF STRONG TIDAL CURRENTS

G. Drapeau[1], W. Harrison[2], W. Bien[3], & P. Leinonen[4]

ABSTRACT

This study examines the drifting, spreading and aging of small slicks of crude oil in the middle St. Lawrence Estuary. This region was chosen because it is well documented with field measurements, hydraulic scale models, and mathematical models; and also because it is becoming a strategic area for the development of supertanker ports for 300,000 and possibly 500,000 ton tankers.

Two controled releases of Venezuelan crude (370 and 800 litres) were made in November 1972, as ice began to form in the St. Lawrence Estuary. The experiments were supported by the Canada Centre for Remote Sensing which carried out extensive airborne monitoring.

The results indicate that it is impossible either to recover or to disperse small spills of oil in this region of strong tidal currents. Models also predict slick motion poorly. The alternative is to construct slick-drift roses that will indicate areas of expected beaching and assist in deployment of oil-spill clean-up technology.

INTRODUCTION

Concern with the fate of oil in the St. Lawrence Estuary was prompted by the planning of supertanker ports to accomodate 300,000 and possibly 500,000 ton vessels. The St. Lawrence Seaway is an important sea route for petroleum products (Fig. 1). Supertankers of any tonnage could reach the Saguenay area. The

---

[1] INRS-Océanologie, Université du Québec, Rimouski, Québec.

[2] Dept. of Geography, Erindale College, University of Toronto, Mississauga, Ont.

[3] Dept. of Geography, University of Toronto, Toronto, Ontario.

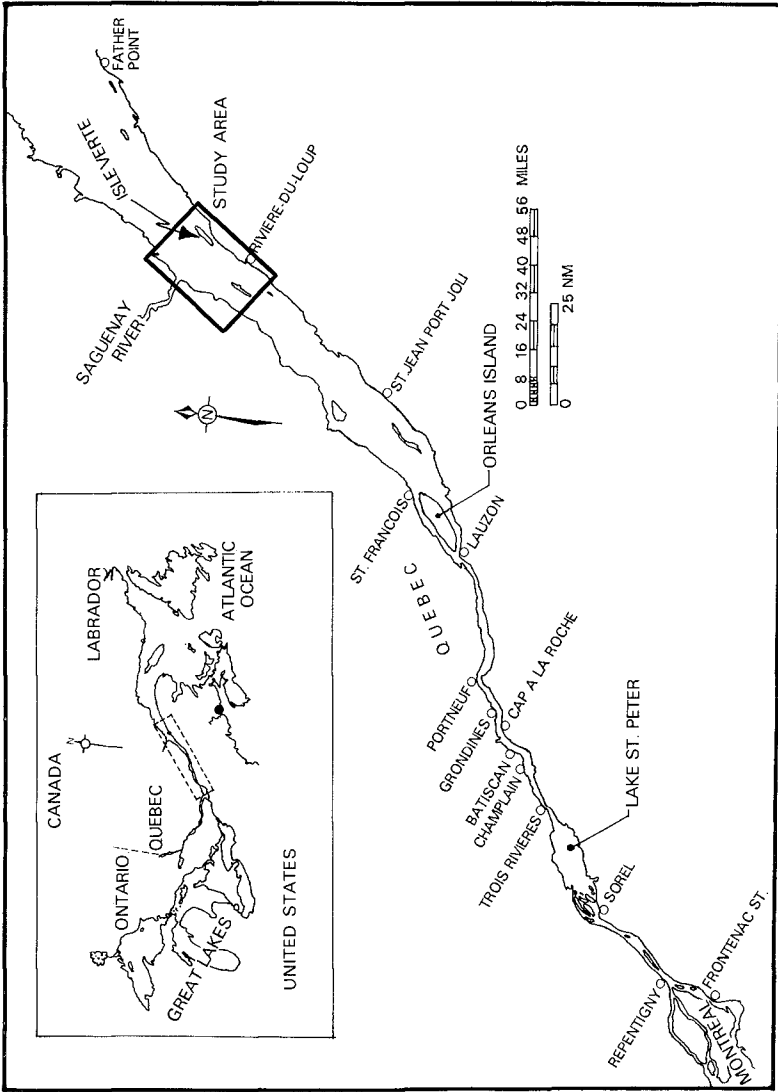[4] Dept. of Chemical Engineering, University of Toronto, Toronto, Ont.

FIG. 1 Location of the study area in the Middle St. Lawrence Estuary.

promoters of a supertanker port in the study area contend that, in addition of the economic advantage, pollution risks are lesser with fewer larger vessels than with smaller tankers sailing further up the river.

The Saguenay area of the St. Lawrence Estuary was chosen as a site for experimenting with oil slicks because tides generate strong currents in that area and also because the experiments could be carried out in late November at the time when ice begins to form in the Estuary, thus providing a good simulation for Arctic conditions. Furthermore, this area is well documented with measurements of surface currents (Canadian Hydrographic Service, 1939; Clarke, 1973) and analyses of tidal transports and streams (Forrester, 1969), with simulations based on one-dimensional (Kamphuis, 1970) and two-dimensional numerical models (Prandle and Crookshank, 1972) as well as with a hydraulic scale model built by the National Research Council of Canada. Logistics were also relatively simple and ship and aircraft surveys were easily coordinated.

ENVIRONMENT

Salinity in the area where experiments were carried out varies at the surface between 15°/oo in May and 29°/oo in September. Cold ocean water migrates upstream at the bottom of the Laurentian Trough and contributes to keep the water mass cool even during the summer months where it average 7^oC at the surface (El Sabh, 1974).

Waves in this part of the Estuary are not conspicuous because of the short fetch. For instance during one experiment waves of a period of approximately 4 seconds reached a height of one meter after the wind had been blowing at 10 to 15 m/sec for half a day.

Tides are the dominant oceanographic phenomenon in the Estuary. They are semi-diurnal and show considerable monthly variations. In the sutdy area, the spring tides reach a maximum of 4.6 metres (Canadian Hydrographic Service, 1972).

Tidal currents which are in the order of 1 m/sec (2 knots) in the lower Estuary become stronger and more intricate in the Saguenay area because of the complexity of the bottom topography, the inflow of deep "ocean" water from the Laurentian Trough, and the fresh water outflow of some 1500 m^3/sec from the Saguenay River. Currents of 3 m/sec are experienced locally. The currents in the study area are far from being uniform either in direction or intensity as can be seen on Fig. 2 which shows the distribution of surface currents at high tide. Tidal currents occasionally form gyres as shows the path of the oil slick offshore of Isle-Verte (Fig. 3).
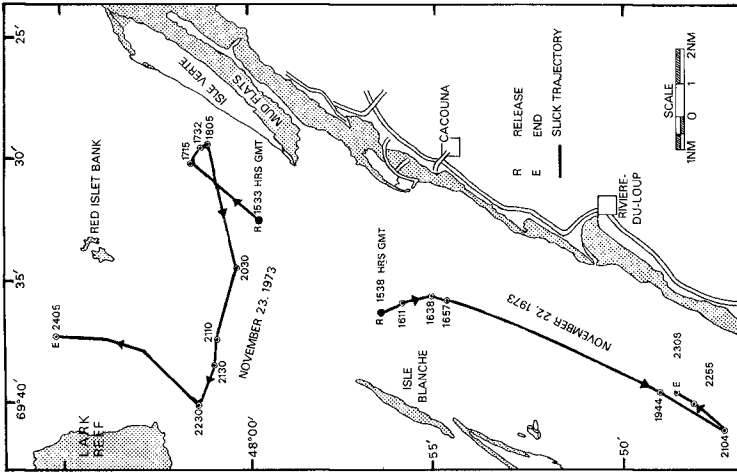
FIG. 3 Oil slick trajectories observed for the two experiments carried out in the St. Lawrence Estuary.
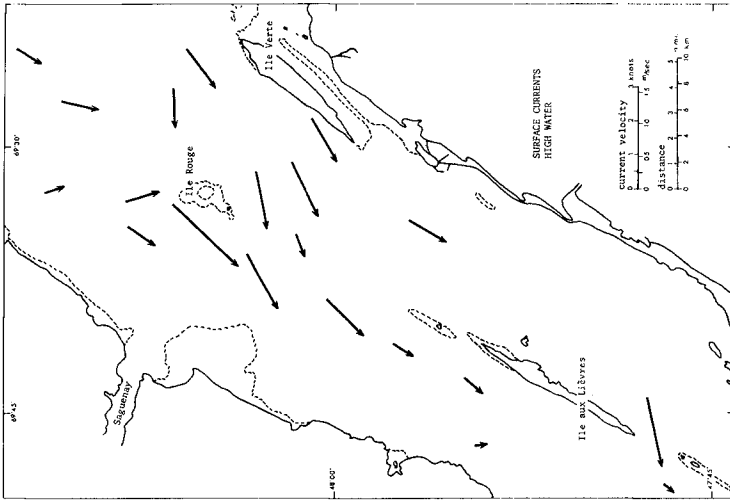

FIG. 2 Surface currents at high tide in the study area. Arrows show direction and relative intensity of currents.

EXPERIMENTS

The experiments were carried out as follows. Field work was conducted aboard the research vessel LE QUEBECOIS, a 28 metre stern trawler. Two releases of Venezuelan crude oil were performed using a domestic fuel tank to produce a uniform splashless spill by tilting the tank at the water surface. Slick imagery was accomplished by airborne sensors provided by the Canada Centre for Remote Sensing. Serial sampling of slicks for physico-chemical analysis was accomplished from a small inflated boat in order not to interfere with the displacement and spreading of the slick.

Some 370 litres (80 gal.) of crude oil (Fig. 3) were spilled for the first experiment, on November 22, 1972, under moderate and steady wind conditions (8 m/sec) in an area offshore of Rivière-du-Loup where tidal streams reach a speed of 1.5 m/sec and follow a simple reversing pattern of flood and ebb currents. The resulting oil slick was followed for 7 hr. 24 min. over a distance of 27.2 km and reached during that time a maximum drifting speed of 1.2 m/sec. Twice as much oil was spilled, (800 litres) for the second experiment, on November 23rd, under more severe wind conditions (15 m/sec) in an area where tidal streams follow complex rotational patterns and reach speeds of 3 m/sec. The second slick was followed for 9 hr. 12 min. over a distance of 37 km. The rate of drifting varied considerably during that experiment and reached a maximum speed of 2.85 m/sec. The path of the spilled oil was tracked by following the slicks and obtaining fixes of the ship position by radar. At the same time, surface drifters of different configurations were released, and some were found to follow the slicks very closely. One type of surface drifter was made of crossed pieces of plywood. The drifters that followed the slick most closely were simply made of floating pieces of plywood loosely tied together. These are very stable as they adjust to the shape of waves.

The Canada Centre for Remote Sensing participated actively in the experiments by flying two aircraft at one hour intervals during all the time that lasted the two experiments. Primary and secondary sensor platforms were a C-47 Dakota transport aircraft and a Falcon executive jet transport, respectively. Operational altitude of the aircraft ranged from 275 to 610 metres above sea level. The flight lines coincided with the longest slick axis and attempted to include as a photographic reference point the study vessel LE QUEBECOIS.

The C-47 aircraft was equiped with four vertical Vinten 70 mm cameras, one Zeiss RMK 8.5/23 camera (9" x 9" format), and one Deadalus infrared line scanner. The Dakota was also used at night to test laser induced fluorescence using a Helium-Cadmium laser operating at 441.6 nanometres (O'Neil et al., 1973). The laser
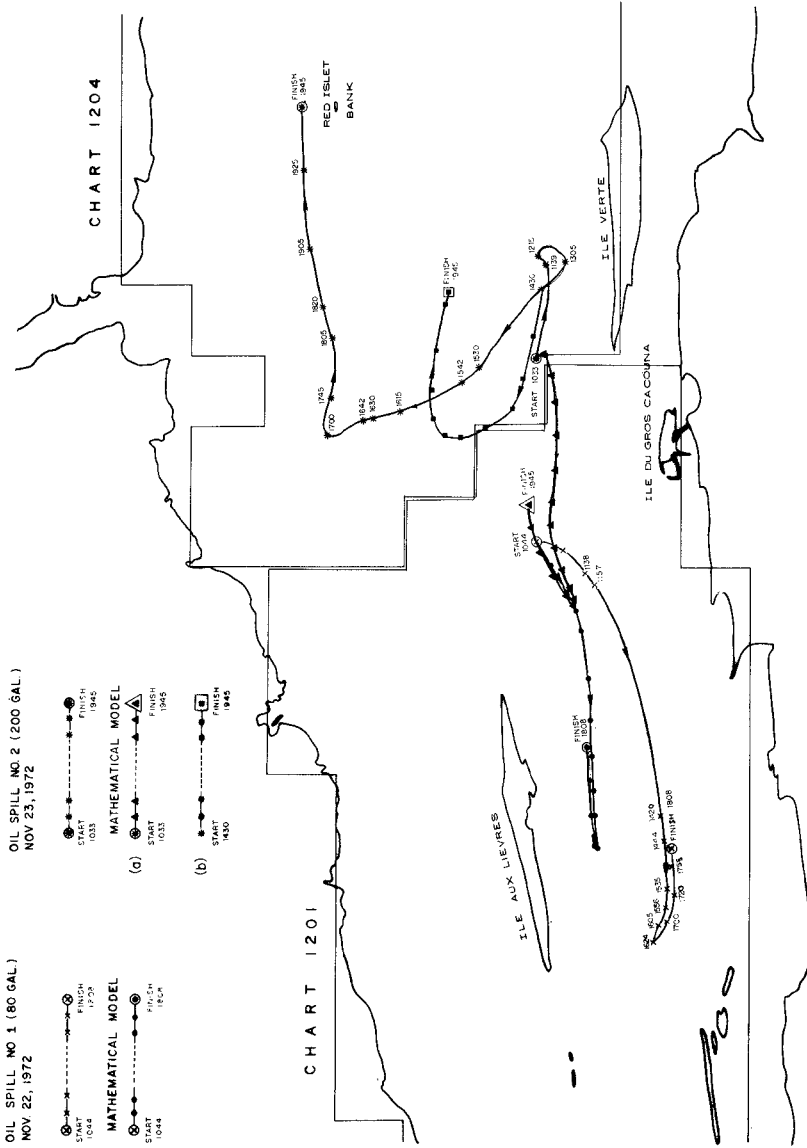
FIG. 4 Simulation of oil slick trajectories obtained from a two-dimensional mathematical model developed by the National Research Council of Canada.
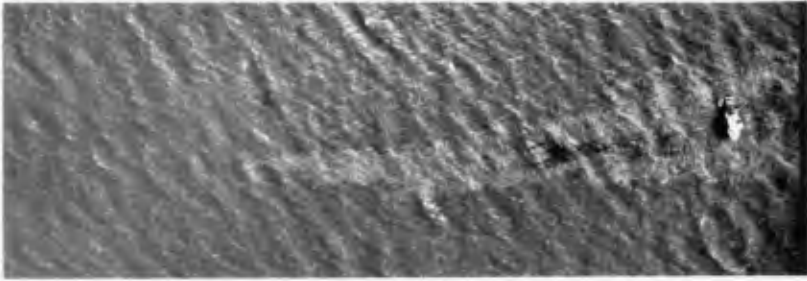
FIG. 5 Oil slick (800 litres) 24 minutes after its release. Wind
speed was 10 m/sec and current speed was 1 m/sec. Photograph taken
with a Wild RC-10 88-mm camera, fitted with a PAN 500 filter at f/5.6,
t: 1/150, on Double-X Aerographic film at an altitute of 305 metres.
The ship on the right side of the photograph is 28 metres long.
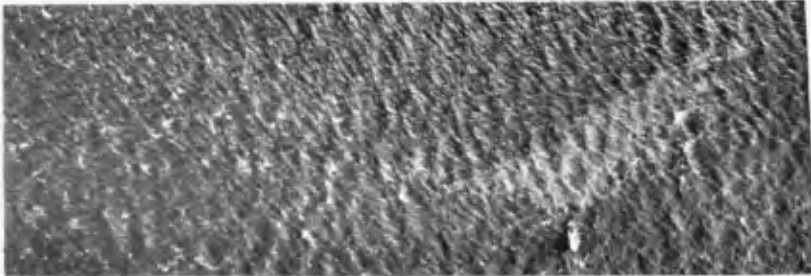
FIG. 6 Part of same oil slick as above 1 hr. 21 min. after its release;
same photographic settings at an altitude of 455 metres. The dark yolk
visible on the first photograph has disappeared.

FIG. 7 Part of the same oil slick 3 hr. 17 min. after its release; same
photographic setting at an altitude of 335 metres. The slick is shredded
due to wind action and had by that time spreaded over an area of some
80,000 square metres.
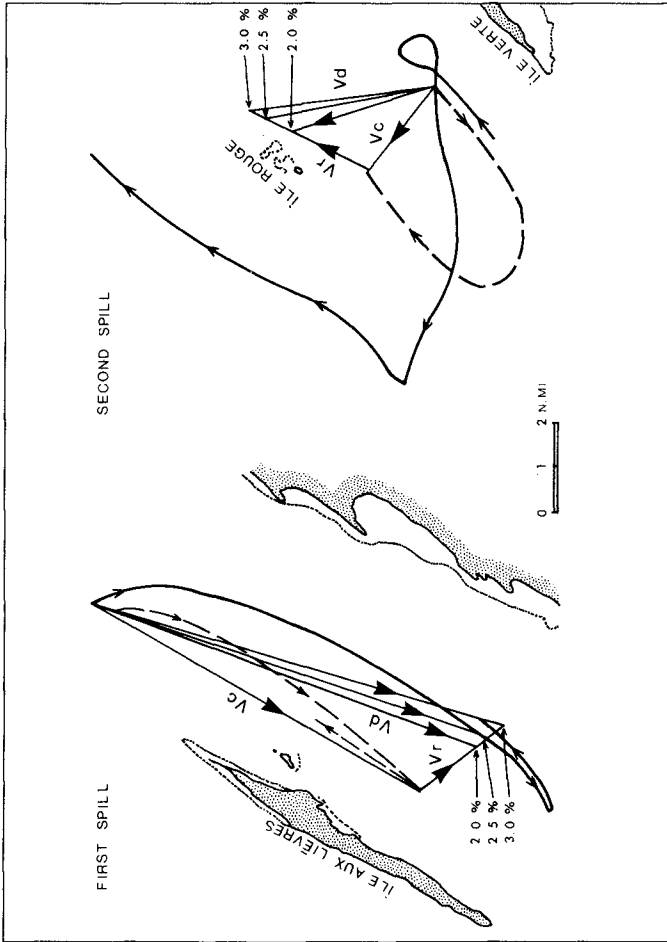
FIG. 8 Drift simulation based on vectorial addition of wind and current components of oil slick drift. The observed drifts are outlined by solid lines and the dotted lines show the computed tidal drift based on a two-dimensional mathematical model. The surface current component is then represented by the vector Vc and the wind effect on the oil slick by the vector Vr. The simulated displacement is outlined by vector Vd which is the resultant vector of Vc + Vr. The length of vector Vr varies according to the wind factor used. Lengths of vector Vr are shown for wind factor of 2.0, 2.5 and 3.0%. For the first spill, the simulation is good particularly if allowance were made for a drift angle towards the right. For the second spill, the drift simulation is unrealistic because a two-dimensional mathematical model is inadequate for surface current simulations in that area.

detector was at the development stage at the time of the experiments.
The Falcon aircraft was equiped with a RS14 infrared line scanner
system (fitted with a UV detector) and a Wild RC-10, 88-mm camera.

Film/filter combinations on the Vinten cameras were as
follows: 1) Aerochrome Infrared (2443) with filter W12{f/2.8 at
1/1000 sec}, 2) Ektachrome M.S. Aerochrome (2448) with no filter
{f/2.8 at 1/1000 sec}, 3) Double-X Aerographic (2405) film with
filter 58{f/2.8 at 1/1000 sec}, and 4) 2405 film with a Wratten 47
filter {f/4 at 1/1000 sec}. Aerocolour negative (2445) film was used
in the Zeiss camera at f/4, 1/100 sec, and Double-X Aerographic film
was used in the Wild RC-10 at f/5.6, 1/150 sec. (Fig. 5, 6, and 7).

The Deadalus infrared line scanner used cooled mercury-
cadmium telluride and indium-antinomide detectors having spectral
resolutions ranging between 8-14 um and 3-5 um, respectively.
After about 20-30 minutes oil and water had come to nearly identical
temperatures and the infrared line scans lost their usefulness for
imagining the oil slicks.

RESULTS

a) Drifiting of oil:

Drifting of oil on the surface of water results from the
combined action of wind and surface currents. The interesting point
is to establish to what extent these two parameters can be evaluated
and combined to predict the path of an oil slick in a specific area.
Wind direction and intensity over the spill were measured from the
research ship at 15-minute intervals. As for data on surface currents
along the drift path of the slicks, it was possible to have water
surface movements calculated by the National Research Council on the
basis of the two-dimensional numerical model (Fig. 4). The simulation
from the mathematical model and the actual drift were not expected to
coincide for many reasons. Firstly the mathematical model is two-
dimensional and assumes vertical homogeneity in terms of density and
velocity, an assumption which is not correct for the study area.
Assuming vertical homogeneity results, in most cases, in under-
estimating the velocity of surface currents. The numerical model
does not integrate the effect of the wind on the slick drift. When
compensation is made for the effect of the wind it is possible to
evaluate the capability of the two-dimensional model to simulate oil
drifting. It can be seen on Figure 8 that in the case of the first
spill, which took place in an area where tidal currents are simply
reversing, a two dimensional model is realistic in predicting the
displacement of an oil slick, particularly if one allows for a drift
angle towards the right. Obviously drift simulation with a
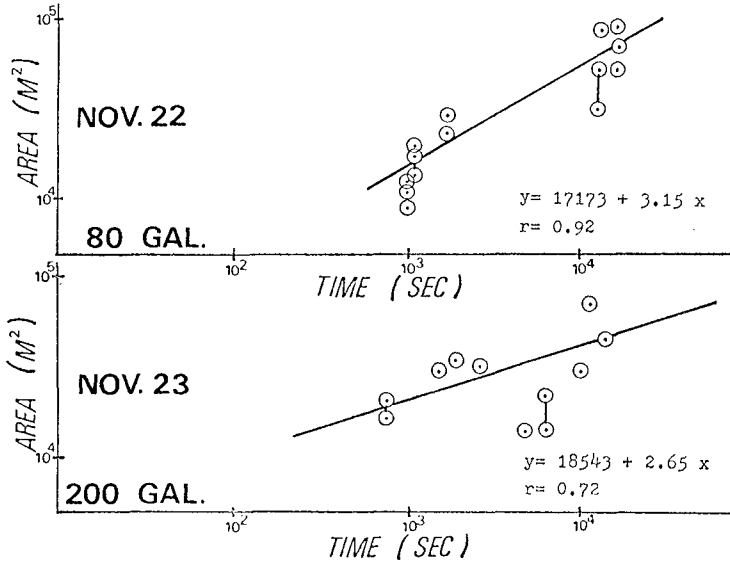
FIG. 9 Oil slick area versus time plotted on a log-log scale.
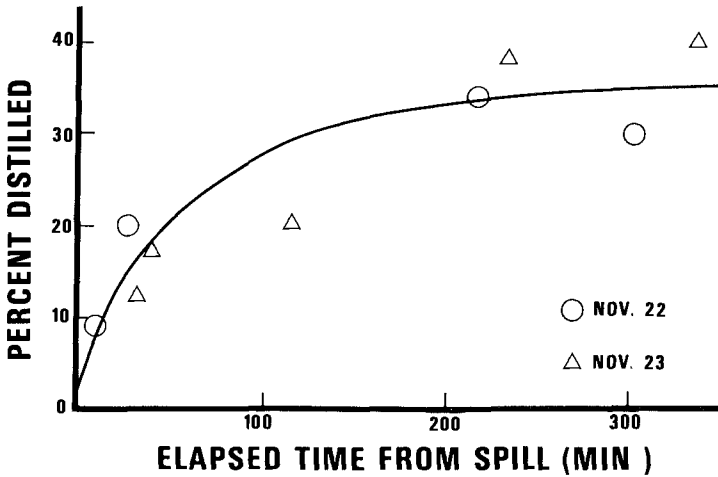
FIG. 10 Percent distilled fraction of crude oil versus elapsed time from spill.

two-dimensional model is not as succesful where tidal currents
are rotational and asymetric as it was the case for the second
experiment. In the latter case addition of the wind effect does
not improve the solution substantially.

b) Spreading:

The aerial photographs taken by the Canada Centre for
Remote Sensing permitted accurate measurements of oil slick
spreading. Image of M/V LE QUEBECOIS (27.4 metres long) served
as a length reference. The error in planimetering amounted to
approximately one per cent of a given determination of slick area.
In some cases however it was difficult to delineate exactly the
edge of a slick (Bien, 1973). The figures 5, 6, and 7 show
different stage of slick spreading of an initial spill of 800
litres. Areas of each slick were plotted on a log-log scale in
Figure 9. In the case of the first experiment, the slick was
estimated to cover an area of some 20,000 m^2 15 minutes after the
release, and to have spread over an area of 49,000 m^2 two and
one half hours later. The rate of spreading was slightly less
during the second experiment.

c) Aging:

The Venezuelan crude oil spilled during the experiments
underwent major physico-chemical alterations during the few hours
following the spilling. The physical appearance of the spilled oil
rapidly changed to form a viscous spongy type of "crocodile skin"
as shown on Figure 12. It resembles what is described as
"chocolate mousse" in the literature. Two hours after the spill,
emulsions of water in oil as shown in Figure 11, already contained
71 percent water and had reached a viscosity of 2040 centipoises
(Paquin and Lebel, 1975).

Oil slicks samples were collected every hour during the
experiment, stored, and later analyzed with a gas chromatograph.
The chromatograms from oil slick samples were compared to a series
of chromatograms obtained from laboratory distilled samples of
the same crude oil. The "percent distilled" values of the spill
samples are plotted as a function of time from the spill on
Figure 10. The results indicate that under the prevailing
environmental conditions, approximately 60 percent of the 6 hour
evaporation, that is 25% of the total sample, occurs within the
first hours after the spill. This is very important because the
more soluble and toxic components such a benzene, are included in
this first fraction.

FIG. 11 Microphotograph of emulsion of water in oil.
The largest droplets are 500 microns in diameter.
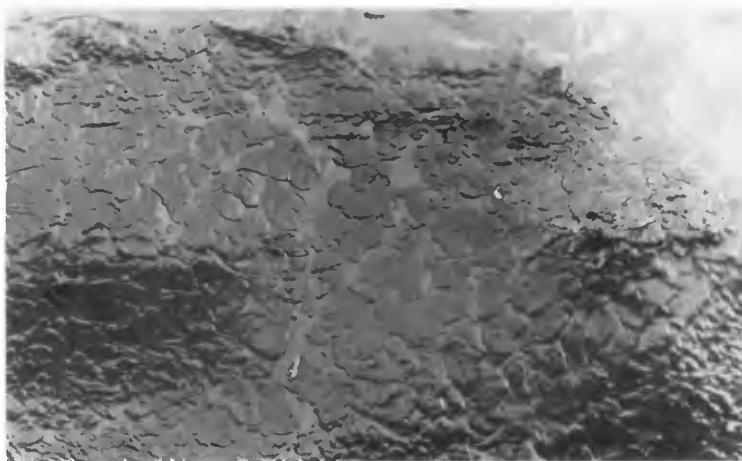
FIG. 12 Oil emulsion with "crocodile skin" texture.
Photograph taken three hours after the spilling of crude oil.
The area photographed is approximately 3 x 2 metres.

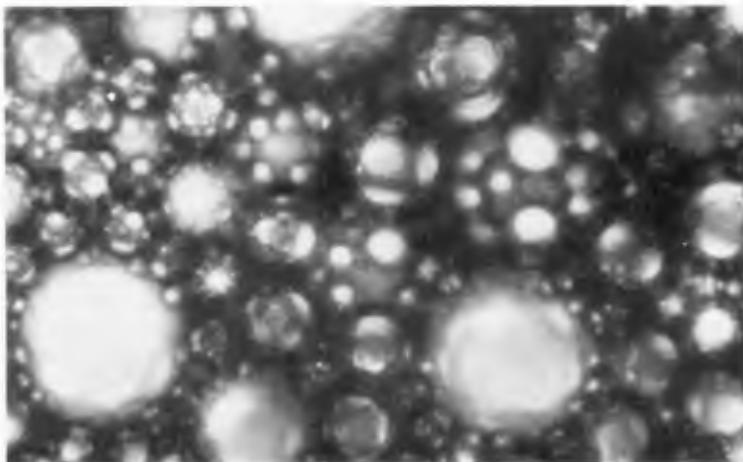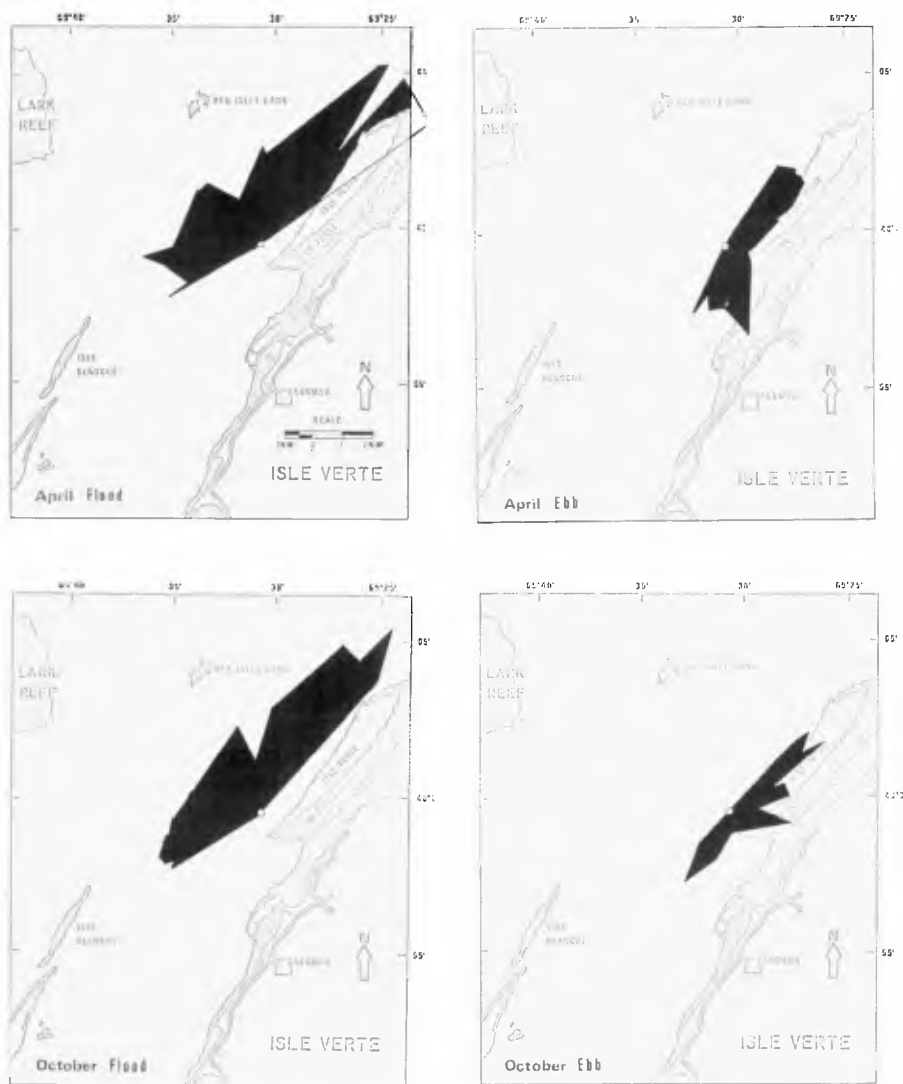FIG. 13 Slick drift roses for the months of April and October, covering
the conditions of spillage occuring during high-water (flood) and low-
water (ebb) slack.

CONCLUSIONS

        In a region of strong tidal currents, it is virtually
impossible to recover oil after it has been lost. During the first
experiment for instance, 370 litres of crude oil have spread over
an area of 20,000 m² only 15 minutes after it has been spilled.
This 20,000 m² slick doubled in area in less than two hours and
became shredded in long streaks, which makes dispersants physically
impossible to use. The rapid formation of emulsions is also a
major handicap because it makes either burning or absorption
impossible. As it is unfeasible to either recover the oil or
disperse it the other alternative is to attempt to minimize the
damages by predicting where the oil will eventually end. In an
area of strong tidal currents it is difficult to predict every
details of the path of a slick, but it is possible to take into
consideration the combined effect of drifting, spreading and aging
to predict the "reach" of spilled oil. For that purpose slick-drift
roses are constructed for different phases of the tide and different
wind conditions (Harrison, 1975). Construction of monthly slick-
drift roses involves summation of estuarine-current and wind-
transport vectors. In the present study the wind vectors used in
monthly rose constructions were those corresponding to extreme
wind persistence values found in a compilation of two consecutive
year's worth of information for Rivière-du-Loup, the meteorological
station closest to Isle-Verte (Fig. 3). The tidal-current values
used for the current vectors were those associated with spring tides.
Thus, the wind and tidal data used represented extreme conditions.
Environmental impact analysis should in general be based upon the
worst possible conditions. Monthly vectors for extreme wind
persistence and for strongest tidal currents were determined,
added, and the net vectors plotted for each of 12 points of the compass.
The ends of the vectors were then connected by straight lines. The
final result is a "rose" that shows the extreme limits of potential
slick motion that can be expected from small spills originating at a
given point during a given month. A series of 24 monthly slick-drift
roses was prepared for a potential offshore bunker site for a super-
tanker port at Isle-Verte. Twelve roses cover the condition of oil
spillage at high-water slack and the other 12 cover the condition of
spillage at low-water slack (that is, "slack current before flood").
Figure 13, for the months of April and October, shows unfavorable
slick-drift roses for the condition of spillage at high- and low-
water slack.

REFERENCES

BIEN, W., 1973; Modeling Petroleum Spills at Supertanker Ports:
        Master of Arts Thesis, University of Toronto, 122 p.

CANADIAN HYDROGRAPHIC SERVICE, 1939; Tidal Current Charts,
        St. Lawrence Estuary, Orleans Island to Father's Point.

CANADIAN HUDROGRAPHIC SERVICE, 1972; Canadian Tide and Current Tables,
        Vol. 3. St. Lawrence and Saguenay Rivers. 55 p.

CLARKE, J.R., 1973; Comparison of model and ptorotype velocities -
        St. Lawrence Estuary; Hydraulics Lab. Rept. LTR-HY-37,
        National Research Council of Canada, 17 p.

EL-SABH, M.I., 1974; Water Masses and Circulation in the Maritime
        Estuary of the St. Lawrence (in preparation) Am. Geophy. Un.
        Fall Meeting, San Francisco, December 1974.

FORRESTER, W.D., 1969; Tidal Transports and Streams in the St. Lawrence
        River and Estuary, Rept. BI 69-2 Bedford Institute of
        Oceanography, 14 p.

HARRISON, W., 1975: Environmental Analysis for Bahamas Supertanker
        Port: Proceedings of the 14th International Conference on
        Coastal Engineering, Copenhagen, June 24-28, 1974 (in press).

KAMPHUIS, J.W., 1970; Mathematical tidal study of St. Lawrence River:
        Journal of Hydraulics Div., ASCE, Vol. 96, No NY3, Proc.
        Paper 7141, March 70, pp. 643-664.

O'NEIL, R.A., A.R. Davis, H.G. Gross, J. Kruus, 1973; A remote
        sensing laser fluorometer: Manuscript, Inland Water Directorate.

PAQUIN, Y., and J. Lebel, 1975; Some aspects of formation of oil
        emulsions in the St. Lawrence Estuary (in preparation).

PRANDLE, D. and N. Crookshank, 1972; Numerical Model Studies of the
        St. Lawrence River, Hydraulics Lab. Rept. MH-109, National
        Research Council of Canada, 104 p.

CHAPTER 131

OIL SPREADING ON COASTAL WATERS

by

Young C. Kim*

ABSTRACT

The area of oil spread was measured in the laboratory and the
predictable model was established in determining the spreading area of
oil on coastal waters. The relationship between the oil slick and the
Reynolds, Froude, and Weber numbers was examined and the influence of
wind, currents, and waves on the spread area was investigated. The
effects on the changes in water depth and the alteration of the net
spreading coefficient on oil spreading capacity were also examined.
Comparison between the existing field measurements and the laboratory
work was made.

INTRODUCTION

The problem of oil spillage in the coastal zone has been one of
great magnitude and concern to the public, to industry, and to the fed-
eral government, particularly in this period of ecological awareness.
The Torrey Canyon disaster in 1967, the 1969 Santa Barbara Channel blow-
outs which discharged 336,000 gallons of crude oil, and recent accidental
spills caused by collision of marine vessels are examples of major sources
of spilled oil on coastal waters. When such a crisis of oil spill arises,
there is an immediate need to determine how fast the oil will spread and
how far it will go in a given time so that a reasonable plan for contain-
ment and collection of oil can be carried out.

---

*Professor of Civil Engineering, California State University, Los Angeles,
Los Angeles, California, U.S.A.

The present study is focused on the problem when the volume of spilled oil is relatively small and the water depth is shallow as in the coastal zone. The objectives of the study are to investigate (1) the oil spreading phenomena on the shallow coastal waters with sloping bottom (2) the effects of wind, waves, and currents and their relative magnitude of influence on oil spreading (3) influence of beach slope, and (4) obtain a predictable equation for oil slick transport on the coastal waters.

THEORETICAL CONSIDERATIONS

This complex phenomena of spreading of oil on coastal waters should be considered under three possible conditions: the first, spreading of oil in tranquil water; the second, convection by winds, waves, and tidal currents; and the third, transformation of waves due to change in water depths. However, in nature the oil slick is greatly displaced either by strong winds and weak currents or relatively strong tidal currents.

Basic assumptions are needed to study this complex phenomena. It is assumed that the principle of superposition for fluid velocities due to wind, waves, and currents is still valid and that the viscosity and surface tension force predominate since the amount of spill is relatively small. All oil slicks are quite thin; hence oil is in hydrostatic equilibrium in the vertical direction. Lastly the properties of oil do not vary with time and evaporation, dissolution of the soluable components and biological degradation of oil are absent.

A dimensional analysis of the pertinent parameters involved in the problem is carried out and the area of oil spread including the effects of wind, tidal currents, waves, and change in depths is expressed as

$$\ell = h \int \left[R, F, W, \frac{u}{U_w}, \frac{u}{U_c}, \frac{u}{U_m} \right]$$

where ℓ is the diameter of oil spread, h is the water depth, R is the
Reynolds number, F is the Froude number, W is the Weber number, u is the
volume flow rate per unit area, and U_w, U_c, and U_{wa} are the velocities
of wind, currents, and waves respectively.

For the spreading of oil in tranquil water, Fay (1) describes the
regimes of oil spreading as (a) the beginning phase in which only gravity
and inertia forces are important, (b) an intermediate phase in which
gravity and viscous forces dominate, and (c) a final phase in which
surface tension is balanced by viscous forces. The final area of oil
spreading in calm water in the tension regime is given as

$$\ell = \left(\frac{\alpha^2 t^3}{\rho^2 \nu} \right)^{\frac{1}{4}}$$

in which ℓ is the final area, α is the net surface tension, t is the
time, ρ is mass density, and ν is the kinematic viscosity of the water.
It is significant to note that in the inertial and viscous regimes, the
rate of spread is proportional to one-fourth and one-third power of the
volume released respectively, and in the surface-tension regime, the
final area is independent of the released volume of oil.

The drift due to wind can be estimated because the turbulent shear
stress at the water interface is the same in both the air and the water.
Furthermore the velocity of water is approximately three percent of the
wind velocity and the drift due to tidal currents can be estimated as
the velocity of water itself. Hoult (2) assumed that the two-velocity
vectors can be added when both wind-driven currents and tidal currents
are present. The drift due to waves may not be the significant factor
in the inertial regime; however, in the surface tension regime, the rate
of drift may be influence by the waves as the water depth changes in
coastal areas. For shallow water waves the situation is much more complex,
particularly where the bottom is sloping. In water which decreases in
depth in the direction of wave propagation, the phase velocity also de-
creases with distance. At the same time, the amplitude increases so
that fluid velocity increases rapidly. For similar reasons, mass trans-

port velocity increases rapidly and as breaking is approached, the phase
velocity, instantaneous particle velocity, and net particle velocity
approach each other in magnitude and direction.

EXPERIMENTAL INVESTIGATION AND DISCUSSION OF RESULTS

The tests have been conducted in a plexiglass tank 6 inches wide,
5 feet long, and 1 foot deep with adjustable bottom slope and water
depths. Oil has been introduced at the upstream and oil velocity and
arrival time have been measured by photocell technique. Three photo-
cells were placed on the bottom 2 feet apart. Variation of water levels
from 6 to 3 inches and the change of bottom slope of 2 to 5 percent were
used. The tests were conducted in the following three situations:
(a) oil spreading by wind, (b) oil spreading by waves, and (c) oil
spreading by current.

Dimensionless velocities, oil velocity to wind velocity, vs. Reynolds
number and the bottom slope were plotted as shown in Figure 1. Comparison
has been made by superimposing the results obtained by Keulegan and O'Brien
in the flume tests. The following comments are of particular significance
from the plot. The experiments show that the oil velocity on the water
surface is basically the same as the water particle velocity and that
the oil velocity induced by the wind is independent of density and vis-
cosity of oil. Moreover, both velocities, velocities of oil and water,
tend to increase with the wind velocity and water depth. The relative
velocity lies between 2 to 4 percent as the Reynolds number varies from
10^3 to 10^5. It can be seen that oil velocity is nearly 3 percent of the
mean wind velocity for low Reynolds number and is less than 4 percent of
the mean velocity at Reynolds number greater than 10^4. The tests also
show that at Reynolds number greater than 10^5, u over U ratio tends to
be constant. A comparison of measured oil slick size to experimentally
obtained oil spreading length in a sloping channel has been made and
plotted in Figure 2. Case (1) is the displaced length of oil when the
wind and waves were superimposed and case (2) is the displaced length

of oil when the currents and waves were superimposed. Obviously oil
slick transport on the coastal water is greatly influenced by the wind
rather than currents on the shallow water.

CONCLUSIONS

The findings of the study reported here may be summarized as follows:

1. When a small volume of oil is spilled in shallow coastal waters,
    the rate of spread is much greater than in deep water. Any assump-
    tion that oil spreading on the coastal water is the same as in
    tranquil water gives too conservative an estimate of spreading
    length.

2. Oil spreading in shallow coastal water is greatly influenced by
    wind, waves, and currents. Moreover, the currents induced by waves
    can not be neglected in shallow coastal waters.

3. Assuming that the concept of superposition is valid, the oil slick
    velocity due to wind and waves seems to be greater than the velocity
    due to waves and currents.

4. Effect of changing depth or beach slope has very little influence on
    oil slick velocity in coastal waters. Particularly, for wind gener-
    ated waves, the changing depth has no influence on the velocity of
    oil spreading.

5. There is a need for more scientifically controlled investigation on
    oil slick transport, particularly in the determination of true wind,
    waves, and current velocities. Further research is needed in devel-
    oping more realistic solutions to the three-dimensional oil spreadin-
    phenomena.

REFERENCES

(1) Fay, J. A., "The Spread of Oil Slicks on a Calm Sea," in <u>Oil on the</u>
     <u>Sea</u> (D. Hoult, ed.), Plenum Press, New York, 1969.

(2) Hoult, David P., "Oil Spreading on the Sea," <u>Annual Review of Fluid</u>
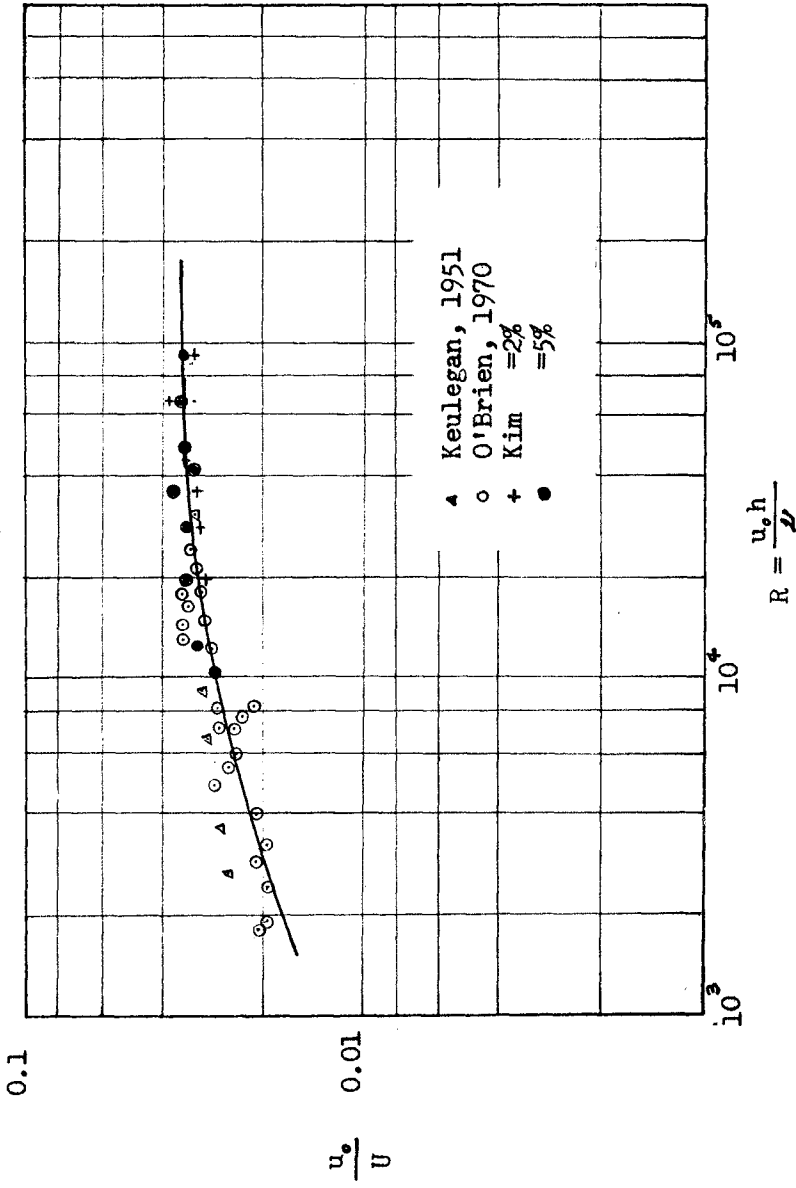   <u>Mechanics</u>, Vol. 4, 1972.

Fig. 1- $\frac{u_o}{U}$ vs. Reynolds Number and α
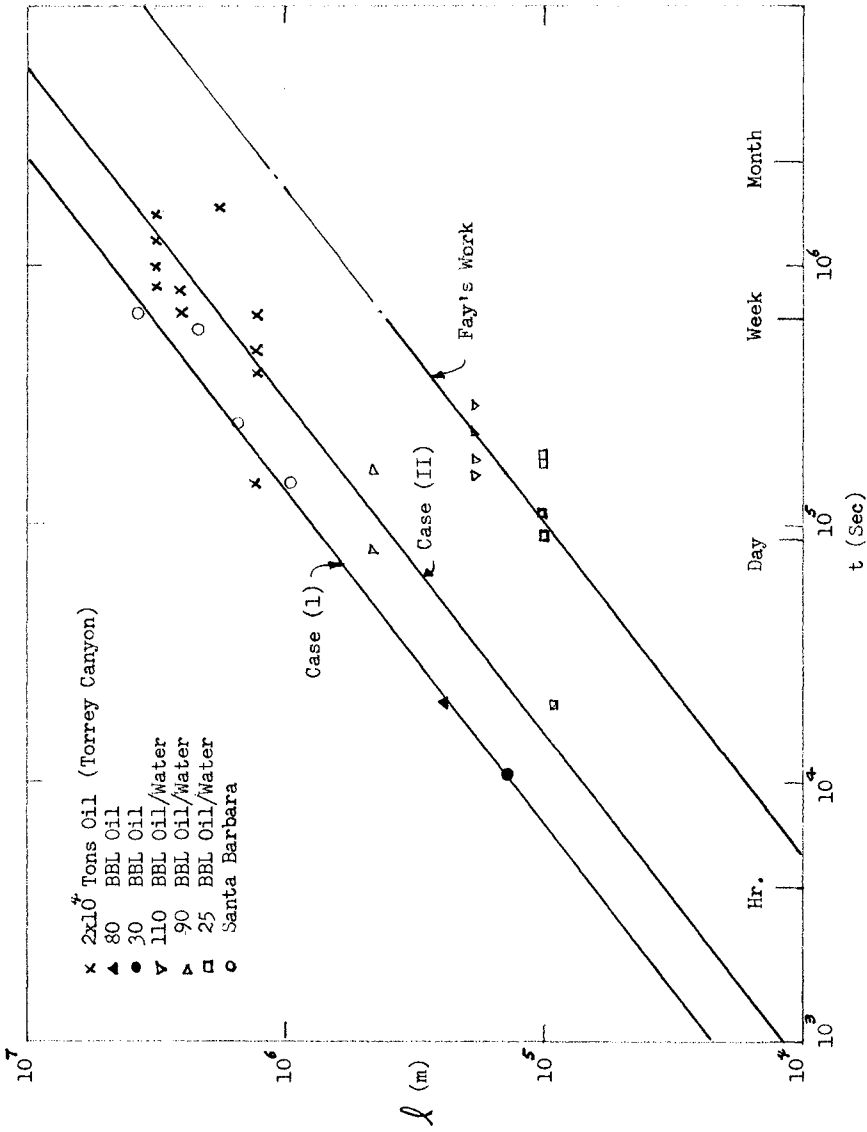
Fig. 2– A Comparison of Measured Oil Slick Size and the Experimentally Obtained Oil Spreading Length in a Sloping Channel

CHAPTER 132

EXCHANGE CHARACTERISTICS OF TIDAL INLETS

by

R. B. Taylor[1] and R. G. Dean[2]

ABSTRACT

Measurements of the exchange characteristics at tidal inlets are presented and interpreted in the framework of an idealized conceptual model. The conceptual model considers the primary cause of exchange to be the result of the differences in flow patterns away from and toward an inlet. The efflux from an inlet is considered to occur as a separated flow whereas a sink-type attached pattern is assumed for flow toward the inlet. The combined results of these two patterns is an effective lateral mixing. Field measurements were conducted from an anchored boat and a dye injection and monitoring approach were utilized. The measured results, expressed as "Basin Mixing Coefficients" are presented for three inlets and are interpreted in terms of the geometric and flow characteristics of the inlet and adjacent waters.

INTRODUCTION

One of the most difficult problems that must be addressed by investigators working with computer simulation models of long wave dispersive hydromechanics of bay systems and estuaries is the mixing and flushing mechanisms associated with the various inlets connecting a basin to the open ocean and at the interfaces to the various connected sub-basin regions. Unfortunately little information is available to obtain a predictive capability in this area. This paper describes a field measurement program designed to: (1) obtain specific information regarding the exchange characteristics of the tidal inlets of the Lower Biscayne Bay System for use in a computer simulation model of the bay, and (2) provide insight into the physical parameters governing tidal inlet exchange characteristics. In addition to a discussion of the field measurement program and the techniques used for data analysis, the mixing mechanism of an idealized tidal exchange cycle through an inlet is presented which provides some insight into the effects of inlet geometry and basin bathymetry on the exchange characteristics of the system.

---

[1]Florida Coastal Engineers, Jacksonville, Florida; formerly same affiliation as below.

[2]Coastal and Oceanographic Engineering Laboratory, University of Florida, Gainesville, Florida 32611.

Background

The work described herein is part of a study of the circulation, mixing, and flushing characteristics of the Lower Biscayne Bay System being conducted by the Coastal and Oceanographic Engineering Laboratory, University of Florida, for the Florida Power and Light Company, see Figure 1. Results of the field measurement program are being incorporated in the University of Florida's two dimensional numerical modeling system, described in References 1, 2, and 3, to provide adequate treatment of the exchange characteristics across the boundaries of the Card Sound sub-basin within the bay system. The Card Sound Basin is of particular interst to the overall study because at one time, consideration was given to the discharge of cooling water from the Florida Power and Light Company's Turkey Point facility into this basin.

A total of three inlets were selected for the injection of Rhodamine-WT fluorescent dye used as the tracer material for the experiment. The locations of these inlets are shown in Figure 1. The data were collected over a three month period during the Summer of 1972.

Discussion of the Problem

The flushing and exchange characteristics of a bay system or sub-basin are normally considered on a time scale of one or more complete tidal cycles. The mechanism for this net mass transport across an interfacial region, such as an inlet, from one mixing basin, such as a bay, to another mixing basin, such as the ocean, is the integrated effect of the mixing which occurs between the inflow volume of water crossing the interface during one-half of a tidal cycle and the water within the receiving mixing basin. The mixing characteristics of each basin can be expressed in terms of a single parameter, the Basin Mixing Coefficient, M, defined as

$$M = \frac{\Psi_{mb}}{\Omega} \tag{1}$$

where,

Ψ_{mb} = volume of water in the receiving basin that mixes with the inflow tidal prism

Ω = tidal prism

The net mass transport of a substance to or from a mixing basin over a period of time encompassing one or more tidal cycles depends on the Basin Mixing Coefficients for the two basins and the concentration of substance within the basin mixing volume and the inflow tidal exchange volume. Therefore, if a Transport Coefficient, R, is defined as
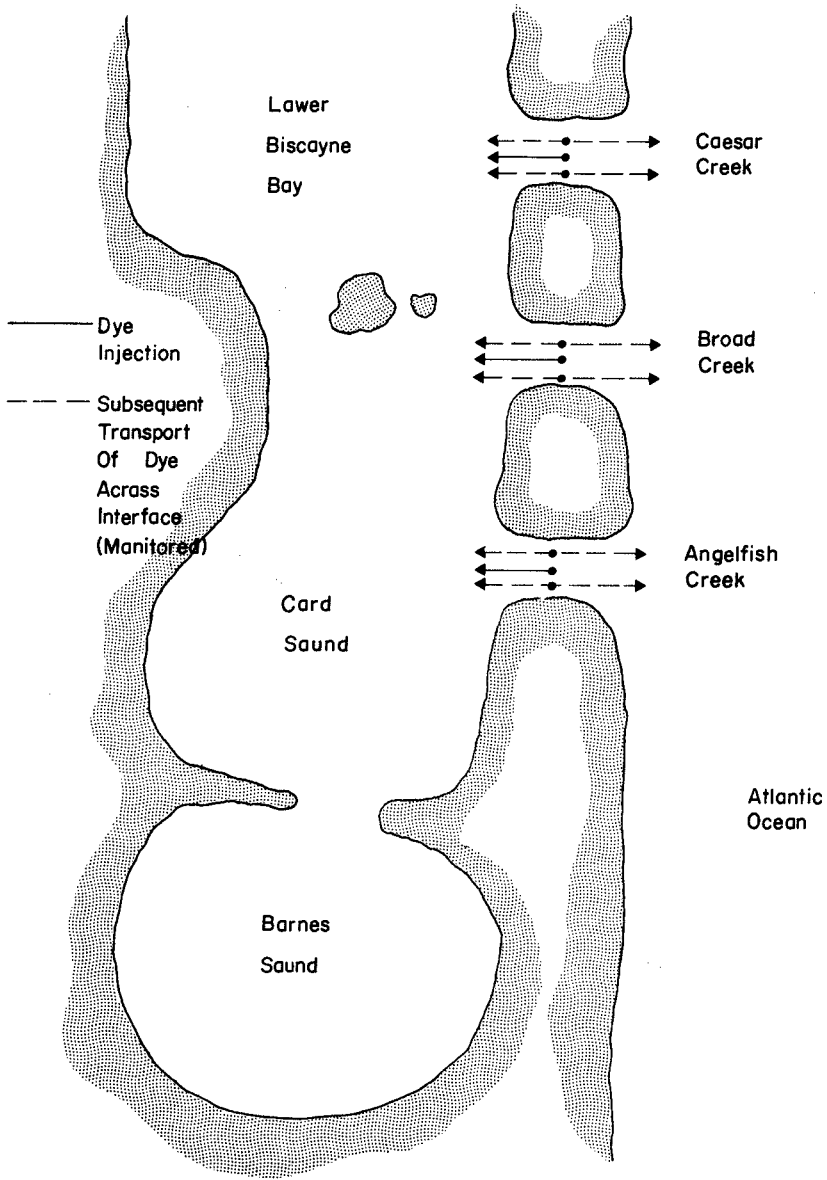
$$R = \frac{\Omega_{do}}{\Omega_{dI}} \tag{2}$$

FIGURE I SCHEMATIC OF LOWER BISCAYNE BAY SYSTEM
FOR EXCHANGE COEFFICIENT MEASUREMENTS
TEST

where,

Ω_{dI} = volume of substance transported across interface during one half of a tidal cycle of <u>inflow</u> to mixing basin

Ω_{do} = volume of substance transported across interface during one-half of a tidal cycle of <u>outflow</u> from mixing basin immediately following inflow.

then R must be expressible as a function of M, and the concentration of substance in the basin mixing volume, and the inflow tidal exchange volume. This will be shown to be true later in the paper. It should be noted from Eq. (2) that values of R>1 signify a net transport of substance <u>out</u> of the mixing basin during the tidal cycle whereas values of R<1 signify a net transport of substance <u>into</u> the mixing basin during the tidal cycle.

Significant differences exist between the Basin Mixing Coefficient and the Transport Coefficient. The Basin Mixing Coefficient characterizes the mixing capacity of the basin for the existing conditions of tide, wind, basin geometry, etc. and should therefore remain reasonably unchanged as long as these conditions hold. The Transport Coefficient, however, should reflect the time-varying nature of the concentration of substance within the basin in addition to the mixing capacity of the basin. If the concentration of substance in the basin mixing volume changes significantly from one tidal cycle to the next then R should also be expected to change.

As an aid in understanding the differences between M and R and their physical significance, consider the time series of events shown in Figures 2a - 2g following the injection of tracer during the flood tide in a tidal inlet connecting a small bay with the ocean. In this example the ocean represents one mixing basin, the small bay the other and the tidal inlet the interfacial region connecting the two. As shown in Figure 2 the characteristic mixing volume, Ψ_{Mb}, of the bay is of limited extent and remains essentially constant with time. The corresponding volume in the ocean and the energy available for mixing, however, are much larger and therefore provide a greater dilution of the substance transported across the interface in the tidal prism, Ω. Thus, these figures illustrate qualitatively how the Basin Mixing Coefficient, M, represents the characteristic mixing capacity of a basin. The net mass transport of substance over a complete tidal cycle from bay to ocean or from ocean to bay is also qualitatively shown in Figure 2. This is seen to depend not only on the Basin Mixing Coefficient, M, but also on the concentration of substance existing in the inflow tidal prism, Ω, and the basin mixing volume. Using the key for concentration level provided in Figure 2 the following is observed:

(1) <u>Bay</u> - For sequence 2a - 2c the transport coefficient, R, is <1 signifying a net transport of substance <u>into</u> the bay. For sequence 2e - 2g, R>1 signifying a net transport of substance <u>out</u> of the bay.

a. INJECTION

b. BAY MIXING

c. OUTFLOW FROM BAY /
   INFLOW TO OCEAN

d. OCEAN MIXING

e. INFLOW TO BAY /
   OUTFLOW FROM OCEAN

f. BAY MIXING

g. OUTFLOW FROM BAY /
   INFLOW TO OCEAN

CONCENTRATION LEVELS
HIGH TO LOW

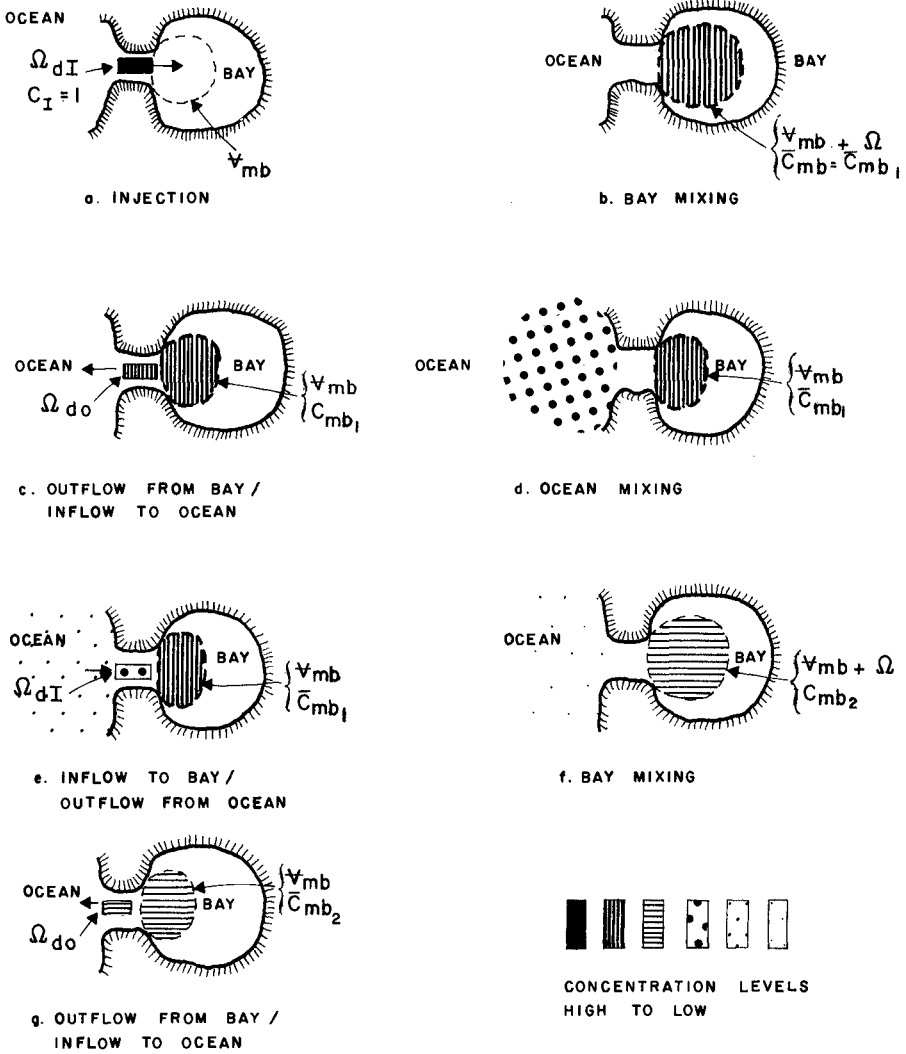FIGURE 2　SEQUENCE OF MIXING AND EXCHANGE
PROCESSES AFTER INITIAL INJECTION,
IDEALIZED DESCRIPTION

(2) Ocean - For sequence 2c - 2e and subsequent tidal cycles
     the Transport Coefficient, R, is >1 signifying a net
     transport of substance into the ocean. This is the result
     of two factors: (1) The characteristic mixing volume of
     the ocean is large relative to the tidal exchange volume;
     and (2) The high energy characteristics of the open coast
     resulting from wind, wave, and tidal activity cause a rela-
     tively rapid decay of concentration levels with the mixing
     volume.

    In the remaining portions of this paper these concepts are
developed more fully and are applied in the analysis of data obtained
from the three locations shown in Figure 1. However, while the Basin
Mixing and Transport Coefficients are useful parameters for describing
the exchange and flushing characteristics of a particular system, they
do not provide a basis for understanding the exchange mechanism. There-
fore, as previously mentioned, a conceptual model will be developed
for idealized representation of Mixing Basin Coefficients.

FIELD MEASUREMENT PROGRAM

    The field measurements were conducted from a 31 ft. houseboat
anchored by a two point moor at each of the three locations described
previously. The houseboat served as a mobile equipment platform,
field station, and living quarters for the field party.

    Rhodamine-WT fluorescent dye was chosen for the tracer material
to be used in these experiments because of its ability to be detected
in concentrations as low as 0.1 ppb and also because of its minimum
biological uptake.

    To commence a run of the experiment, dye was continuously injected
from the anchored houseboat for one half of a tidal cycle during which
the flow across the interface was into the Card Sound Basin (approxi-
mately 6.2 hours). The dye was injected by means of a hand siphon
arrangement running from a dye container on deck to a point just below
the surface of the water. The rate of injection was controlled by
means of a screw clamp on the end of the siphon hose. Injection rates
were periodically monitored and adjusted to a value of approximately
20 ml/min. Visual observations of the dye plume were made, both from
above and below the water surface. These observations demonstrated
the presence of large horizontal eddies and confirmed that the injected
dye was quickly mixed over the cross section of the inlet and vertically
over the water column.

    To establish background levels of fluorescence due to natural
causes existing in the Bay System and offshore waters, a series of
readings was made for the two mixing basins connected by the inlet
into which dye was to be injected. These readings were made prior to
injection at each test site and the values recorded for future use.

    The monitoring phase of each experimental run was begun at the
end of the initial injection phase, i.e. when slack water was observed

following the flow of water into Card Sound. During this phase, read-
ings of dye concentration, c, and water particle velocity, u, were
taken every 30 minutes at the same location (houseboat achorage) for
periods up to 63 hours (5 tidal cycles) following dye injection. Sample
plots of the measured u and c values versus time are shown in Figures
3 and 4.

Water particle velocity readings were obtained from a sensor
suspended from the houseboat at a fixed depth with a remote direct
readout located inside the houseboat. Water samples for monitoring
dye concentrations were obtained by pumping water through a continuous
flow sampling door on a G. K. Turner Model 111 Fluorometer. Lengths
of garden hose were used to route the water from the intake, located
approximately four feet below the water surface, inside the houseboat
to the pump and fluorometer, and finally outside again and over the
side. This arrangement proved to be very efficient allowing all equip-
ment to be centralized at one location protected from the weather.
This is particularly critical for the proper operation of the Turner
fluorometer which is sensitive to ambient lighting conditions and im-
proper ventilation.

Weather conditions during the conduct of the measurements at
Broad, Angelfish and Caesar Creeks were generally fair with light pre-
vailing winds from the northeast.

IDEALIZED CONSIDERATIONS AND DATA ANALYSIS

Idealized Considerations of Exchange Across Tidal Inlets

The renewal of waters in a bay system occurs due to flow into the
bay from upland sources, direct precipitation, and through exchange at
inlets connecting the bay to the adjacent ocean. The general case of
exchange at an inlet includes effects of stratification and possibly a
net flow through the inlet.

In discussing the mechanics of exchange across an inlet, the
primary problem of concern here will be that pertinent to the Biscayne
Bay - Card Sound system in which there is little apparent net flow and
in which the stratification characteristics are believed to be minimal.
Two components of the mixing responsible for the exchange are: (1) the
lateral effects in which flow toward the inlet occurs as a sink-type
flow, however flow away from the inlet occurs similar to a separated
jet, and (2) the vertical effects due to the velocity shear which is
similar to the transport that would occur in an oscillating flow in a
straight and uniform channel. In the following paragraphs, the contri-
butions to mixing from lateral effects will be discussed.

Mixing Due to Lateral Effects - Consider the situation shown in
Figure 5(a) in which separated flow is occurring away from the inlet
into the bay. The flow separation is due primarily to the direction
of the momentum of the exiting water and represents a jet-type flow
with the jet expanding away from the inlet due to a decrease in velocity

Caesar Creek (8/19/72 – 8/21/72)
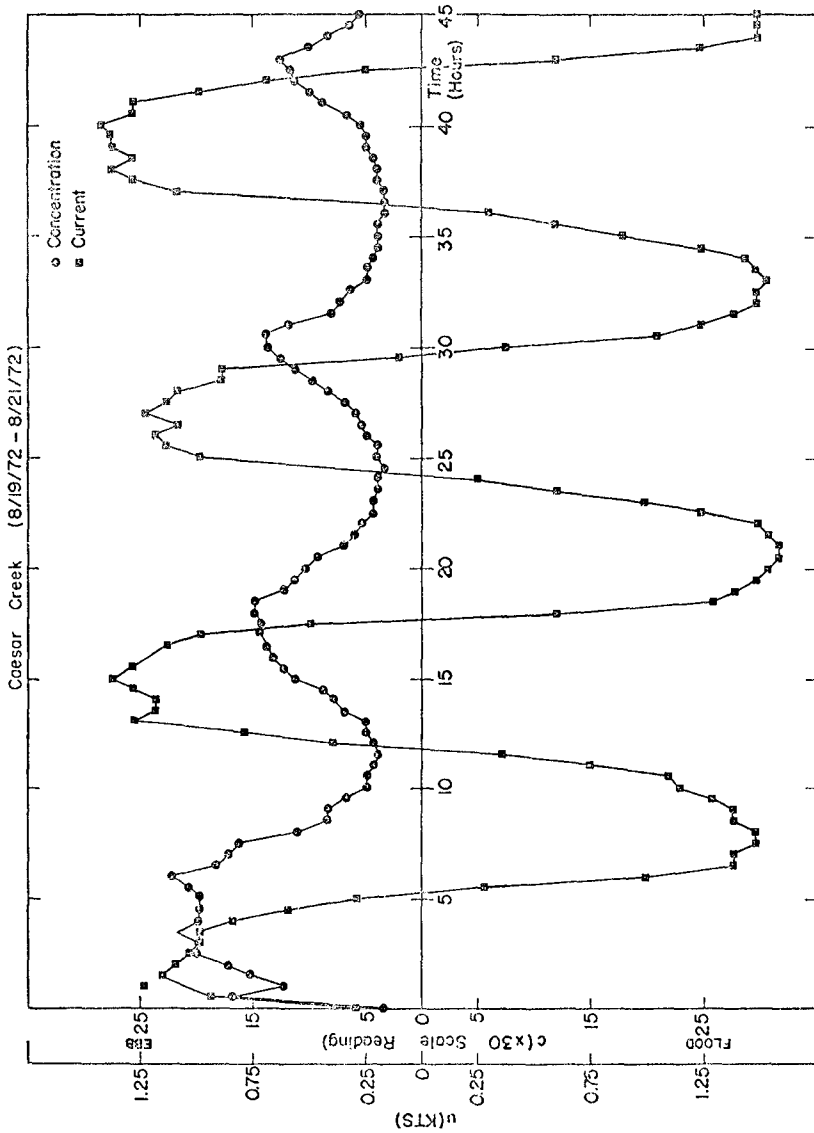
FIGURE 3 PLOT OF MEASURED u AND c VALUES FOR RUN NUMBERS IO, IOa, IOb, IOc OF EXCHANGE COEFFICIENT MEASUREMENTS TEST
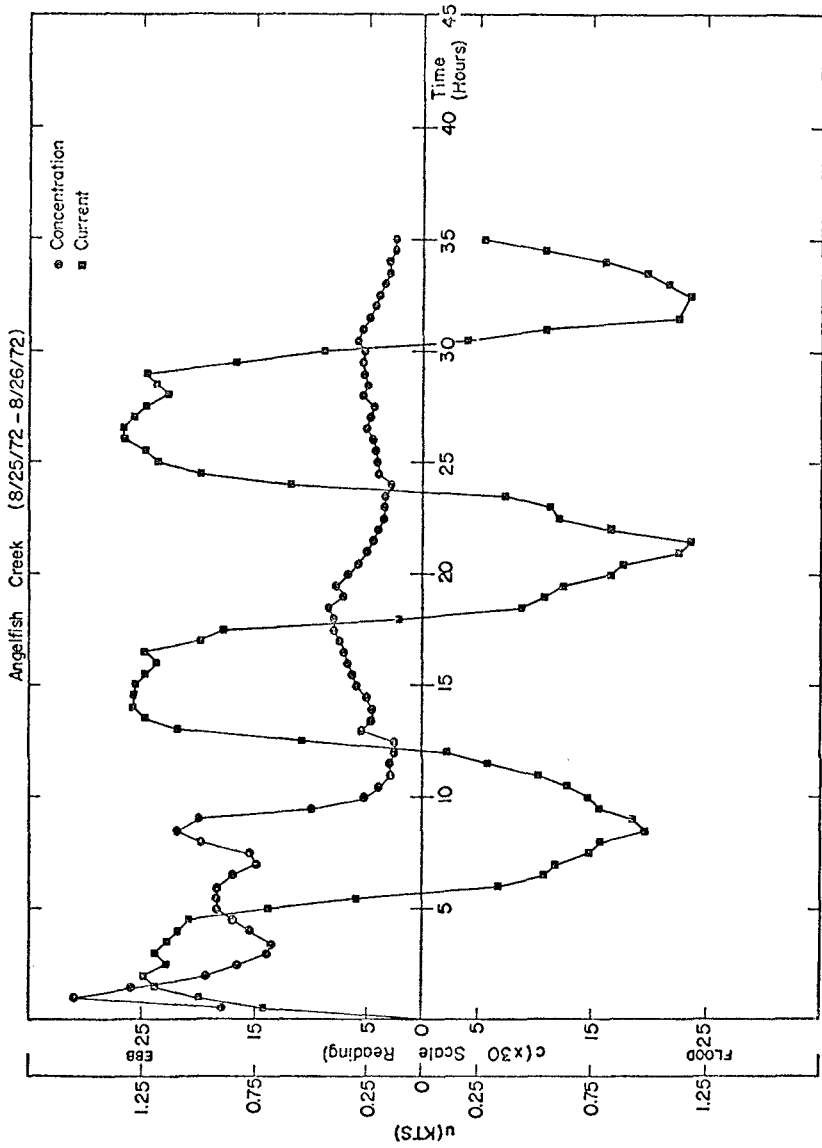
FIGURE   4   PLOT OF MEASURED u AND c VALUES FOR RUN NUMBERS 12, 12a, 12b
               OF EXCHANGE COEFFICIENT MEASUREMENTS TEST

o) Seporoted Flow During Outflow
From Inlet

b) Sink — Type Flow During Inflow
To Inlet

c) Volume Common To Inflow
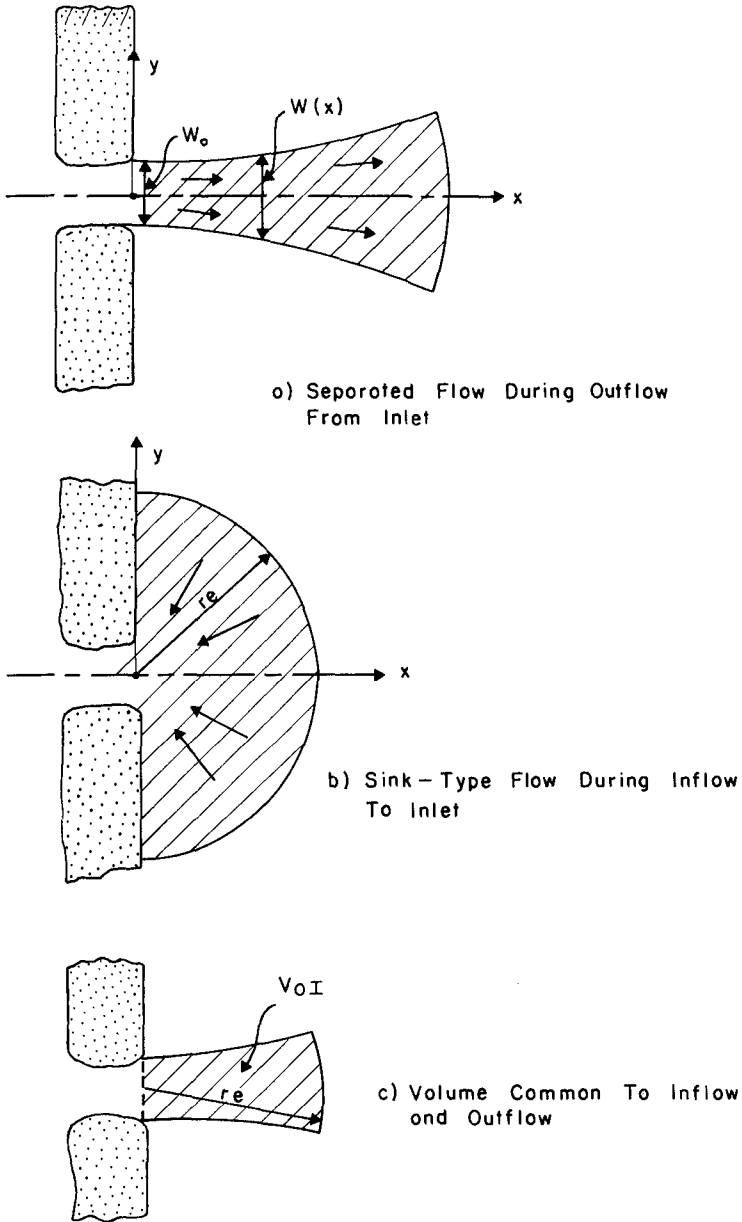ond Outflow

FIGURE 5   IDEALIZED   MECHANICS   OF   INLET   EXCHANGE   DUE
TO   DIFFERING   OUTFLOW   AND   INFLOW   PATTERNS

through a lateral momentum transfer to the adjacent water by shear
and through a vertical transfer of momentum to the bottom through
friction. For flow from the bay toward the inlet; however, the flow
features occur in a sink-like manner as presented in Figure 5(b).
Denoting the outflow volume as Ω_o, the inflow volume as Ω_I and the
volume common to the two as V_{oI}, considerations of the proportional
dilution of V_{oI} by bay water yields the following expression for M_B

$$M_B = \frac{\Omega_o - V_{oI}}{V_{oI}} = \frac{\Omega_o}{V_{oI}} - 1 \tag{3}$$

where it is assumed that $\Omega_o = \Omega_I$. This provides a qualitative descrip-
tion of one component of the exchange mechanism at an inlet. It is
noted that the flow patterns considered away from and toward an inlet
are in reasonable qualitative accord with some observations. A similar
definition and qualitative description would apply for the ocean mixing
coefficient, M_o.

    This description presented can be extended somewhat further to
obtain a crude formulation of the exchange coefficient. Consider the
flow away from the inlet to be governed by the following vertically
integrated equation of motion

$$\frac{\partial q_x^2}{\partial x} + \frac{\partial (q_x q_y)}{\partial y} = \frac{f|q|q_x}{8h} - gh\frac{\partial \eta}{\partial x} + \frac{h}{\rho}\frac{\partial \tau}{\partial y} \tag{4}$$

in which the motion has been considered to be steady, f = Darcy Weis-
bach friction coefficient, h and η are the water depth and tidal eleva-
tion and τ is the average lateral shear stress acting on the water
column to retard its flow. This shear stress represents a lateral
(y-direction) flux of momentum from the jet to the adjacent waters.
The quantities q_x and q_y represent the transport components per unit
width in the x and y directions and q is the transport magnitude per
unit width. In order to proceed further with this formulation, the
following simplifications will be made:

$$\frac{\partial (q_x q_y)}{\partial y} \ , \ \frac{\partial \eta}{\partial x} \ , \ \frac{\partial \tau}{\partial y} \quad \text{are assumed negligible}$$

$$q_x \approx q$$

The resulting equation is

$$\frac{\partial q^2}{\partial x} = - \frac{fq^2}{8h} \tag{5}$$

and the solution is

$$q(x) = q_o \, e^{-\left(\frac{f}{16}\frac{x}{h}\right)} \tag{6}$$

which, through continuity and the assumption of no entrainment, yields an equation for the width, $w(x)$, of the jet

$$w(x) = w_o \, e^{\frac{f}{16}\frac{x}{h}} \tag{7}$$

The flow toward an inlet is considered to be governed by sink flow in which

$$\Omega_I = \frac{\pi r_e^2 h}{2} \tag{8}$$

and an approximate expression for the Basin Mixing Coefficient, M, is determined from Eq. (3) as

$$M \approx \frac{\pi r_e^2 f}{32 h w_o \left(e^{\frac{f}{16}\frac{r_e}{h}} - 1\right)} - 1 \tag{9}$$

Unfortunately, the form above is not readily interpreted due to the many factors involved. Therefore computations were carried out to demonstrate the effect of depth, h, Darcy-Weisbach friction factor, f and tidal prism, Ω. The computations required values of Ω, and w_o, etc. Values were selected which are reasonably representative for the three inlets studied. The approximate values of Ω and w_o and the values selected for computation are presented in Table I.

TABLE I

Inlet	h_o (ft.)	w_o (ft.)	Ω* (ft.)^3
Broad Creek	7	2180	0.9×10^9
Caeser Creek	10	1800	1.3×10^9
Angelfish Creek	12	750	2×10^8
Base Value Used in Computations	Not Required	2000	1×10^9

* Based on O'Brien's Equilibrium Cross-Section
  Tidal Prism Relationship (Reference 5)

Effect of water depth on mixing coefficient - The effect of water
depth was investigated by fixing all other variables equal to values
which are considered realistic for the measurements and calculating M
for h = 5, 8, and 10 ft. The values for the other variables used are:
f = 0.02, Ω = 1 x 10^9 ft.^{3}, and w_0 = 2000 ft., thereby reducing Eqs. (8)
and (9) to

$$M \simeq \frac{1}{1.6 \times 10^{-3} h^2 (e^{31/h^{3/2}} - 1)} - 1 \qquad (10)$$

The effect of varying h is shown in Table II where it is seen that
smaller water depths tend to inhibit mixing.

<div align="center">

TABLE II

EFFECT OF BASIN WATER DEPTH, h,

ON MIXING COEFFICIENTS, M.

</div>

Water Depth, h (ft.)	Basin Mixing Coefficient, M
5	0.67
8	2.33
10	2.75

Effect of friction coefficient on mixing coefficient - The same
procedure was followed to investigate the effect of variations in the
friction coefficient as was described previously for the water depth.
The fixed values were: h = 6 ft., Ω = 1 x 10^9 ft.^{3}, and w_0 = 2000 ft.
resulting in the approximate equation

$$M \simeq \frac{f}{1.2 \times 10^{-3} (e^{107f} - 1)} - 1 \qquad (11)$$

The effects of varying friction coefficient are presented in Table
III where it is seen that a large friction coefficient causes the ebb
jet to be retarded close to the inlet and to widen. Reference to Figure
5 will demonstrate that this results in a reduced mixing.

TABLE III

EFFECT OF FRICTION COEFFICIENT, f

ON MIXING COEFFICIENT, M.

Darcy - Weisbach Friction Coefficient, f	Basin Mixing Coefficient, M
0.01	3.35
0.02	1.22
0.03	0.05

Effect of tidal prism of mixing coefficient - Repeating the described procedure for the tidal prism, Ω, as the variable and f = 0.02, w_o = 2000 ft., and h = 6 ft. as the fixed variables

$$M \simeq \frac{\Omega}{60 \times 10^6 \, (e^{0.7 \times 10^{-4}\sqrt{\Omega}} - 1)} - 1 \qquad (12)$$

and, as shown in Table IV, the Basin Mixing Coefficient is a maximum for $\Omega \simeq 5 \times 10^8$ ft.^{3}. It should be recalled that although the Basin Mixing Coefficient decreases with increasing Ω (> 5×10^8 ft.^{3}), the volume of mixing water increases due to the definition of M being normalized by Ω.

TABLE IV

EFFECT OF TIDAL PRISM, Ω,

ON MIXING COEFFICIENT, M.

Tidal Prism Ω (ft.^{3})	Basin Mixing Coefficient, M
1×10^8	0.64
5×10^8	1.20
1×10^9	1.05

It is noted that the equations based on the conceptual model are very approximate. Use of some ranges of values in these equations can result in negative M values. For example, small h values will result in negative M values when used in Eq. (10).

Data Analysis

As discussed previously, the data consisted of water velocity, u, and dye concentration readings, c, which, under ideal circumstances, were taken every one-half hour.

To analyze the recorded data, values of u and the product of u and c for each half-hourly reading were multiplied by the time interval between readings and the resulting values summed for each half tidal cycle. These sums represent approximations of the tidal prism and volume of dye respectively crossing the interface in each half tidal cycle. This is shown to be the case if it is assumed that the total instantaneous discharge, $Q(ft.^3/sec.)$, across the interface at any time, t, is proportional to the velocity , $u(ft./sec.)$, measured at a point, i.e.

$$Q = Ku \qquad\qquad (13)$$

where,

$$K = constant, (ft.^2)$$

If the assumption stated by Eq. (13) is valid, then the tidal prism, Ω, is given by

$$\Omega = \int_0^{T/2} Q\,dt$$

$$= \lim_{\Delta t \to 0} \sum_{i=1}^{N} Q_i \Delta t_i$$

$$= \lim_{\Delta t \to 0} \sum_{i=1}^{N} Ku_i \Delta t_i$$

and since K is assumed to be constant

$$\Omega \simeq K \sum_{i=1}^{N} u_i \Delta t_i \qquad\qquad (14)$$

where,

T = tidal period, 12.4 hrs.

N = number of measurement intervals in one half of a tidal cycle (T/2)

In a similar manner it may be shown that the volume of dye, Ω_d,

crossing the interface in one half tidal cycle is given by

$$\Omega_d \simeq K \sum_{i=1}^{N} u_i c_i \Delta t_i \tag{15}$$

Upon examination of the values of u, it was found that in most cases the measured water particle velocities were significantly greater during one half of the tidal cycle as compared to the other half. This fact was dramatically displayed by the values of Ω computed using Eq. (14) which indicated that the tidal exchange volumes passing across the interfacial regions varied by as much as a factor of 4. Based upon results obtained from the calibrated numerical model (Reference 1), which indicate that the ebb and flood tidal exchange volumes are with 0.5% of being equal, it was concluded that the assumption given by Eq. (13) was not valid, and therefore the measured values of u could not be used. As an alternative approach to obtaining values for u suitable for use in Eqs. (14) and (15), sinusoidal velocities were generated by adjusting the amplitude of the velocity such that

$$\left\{ \sum_{i=1}^{N} u_i \Delta t_i \right\}_{ebb} = \left\{ \sum_{i=1}^{N} u_i \Delta t_i \right\}_{flood} \tag{16}$$

for each tidal cycle and having the same times of slack water as the observed velocity. In effect, this approach loses whatever difference there may be between the ebb and flood tidal exchange volumes while preserving the phase relationship between u and c.

Values for Ω and Ω_d obtained using generated velocities, u, and measured dye concentration, c, were then applied to a mass balance of the dye during one tidal period. The mass balance considers the volume of dye crossing the interface during one half of a tidal cycle mixing with a volume of water containing a given concentration of fluorescence, and the resulting mixture crossing the interface in the opposite direction. From the mass balance, a "Basin Mixing Coefficient" is calculated which represents the mixing and flushing characteristics of the interfacial region, i.e. the Basin Mixing Coefficient, M, is expressed as

$$M \equiv \frac{\Psi_{mb}}{\Omega_I} = \frac{\bar{c}_I - \bar{c}_0}{\bar{c}_0 - \bar{c}_{mb}} \tag{17}$$

where

$$c_I \equiv \frac{\Omega_{dI}}{\Omega_I} \tag{18}$$

It is noted from Eq. (17) that calculation of a basin mixing coefficient requires knowledge of, $\bar{c}_{mb}$, the effective concentration of the basin waters which mix with the waters flowing into that basin. With the exception of initial background fluorescent levels, no attempt was made to determine $\bar{c}_{mb}$. In fact, its determination would prove to be a difficult task because it is an _effective_ value that is required. To rationally utilize Eq. (17), the following procedure was developed to estimate the time-varying value of $\bar{c}_{mb}$ from the field measurements.

The expression utilized to describe $\bar{c}_{mb}(t)$ is

$$\frac{dc_{mb}}{dt} = \underbrace{\lambda_I' (c_I - c_{mb})}_{\substack{\text{Rate of increase} \\ \text{of } c_{mb} \text{ due to mixing} \\ \text{with inflow tidal} \\ \text{exchange volume}}} - \underbrace{\lambda_{mb}' c_{mb}}_{\substack{\text{Rate of decrease of} \\ c_{mb} \text{ due to mixing of} \\ \text{high localized con-} \\ \text{centrations with} \\ \text{adjacent bay waters}}} \qquad (19)$$

where

λ_I' = decay constant for the mixing of basin water with inflow tidal exchange volume (t^{-1})

c_I = effective constituent concentration in water crossing interface into mixing basin

λ_{mb}' = constant representing decrease rate due to mixing with adjacent bay waters

For purposes of analysis; it is simpler and does not affect the results if the following equation is employed

$$\frac{dc_{mb}}{dt} = \lambda_I c_I - \lambda_{mb} c_{mb} \qquad (19)$$

where the definitions of λ_I and λ_{mb} are altered accordingly. Eq. (19) was solved using the following approximation for c_I

$$c_I(t) = c_{Io} e^{-\lambda_I t} \qquad (20)$$

where c_{Io} represents the effective constituent concentration at the interface for $t = 0$. Inserting Eq. (20) into (19), yields as a solution

$$c_{mb}(t) = c_{mbo} + \frac{c_{Io}\lambda_I}{\lambda_{mb}-\lambda_I} \left(e^{-\lambda_I t} - e^{-\lambda_{mb} t}\right) \tag{21}$$

The three unknowns (λ_I, λ_{mb}, c_{Io}) in the above equation were determined by requiring that the basin mixing coefficient, M, always be positive. Restating Eq. (17)

$$M = \frac{\bar{c}_I - \bar{c}_o}{\bar{c}_o - \bar{c}_{mb}} \tag{22}$$

it is seen that the sign of M can be positive or negative, depending on

Situation 1:

  $M > 0$ { $\bar{c}_I > \bar{c}_o$ and $\bar{c}_o > \bar{c}_{mb}$, or if $\bar{c}_I < \bar{c}_o$ and $\bar{c}_o < \bar{c}_{mb}$ }

Situation 2:

  $M < 0$ { $\bar{c}_I < \bar{c}_o$ and $\bar{c}_o > \bar{c}_{mb}$, or if $\bar{c}_I > \bar{c}_o$ and $\bar{c}_o < \bar{c}_{mb}$ }

The basis for utilizing the data collected to determine λ_I, λ_{mb} and c_{Io}, and hence c_{mb} and M is that M should be positive. The procedure then involves selecting trial values of the 3 unknowns along with the constraint $M > 0$. This procedure is explained more fully in Reference 3. A graphical illustration of the constraints which the procedure places on $c_{mb}(t)$ is presented in Figure 6. It is seen that the values of λ_I, λ_{mb} and c_{Io} define the curve for $c_{mb}(t)$ within a fairly limited range. Considering the Bay Mixing Coefficient, M_B, during the initial period when $\bar{c}_I > \bar{c}_o$, an upper limit is established for $\bar{c}_{mb}$. In later phases of the testing program, after a significant buildup of dye in the bay has occurred, $\bar{c}_o > \bar{c}_I$ and a lower limit on $\bar{c}_{mb}$ is established. Using various trial values of the unknowns to meet these limits, a relationship for $\bar{c}_{mb}$ is obtained which appears reasonable as shown in Figure 6.

RESULTS

For the three inlets, Broad Creek, Caeser Creek and Angelfish Creek (shown in Figure 1), measurements of basin mixing coefficients were carried out for a total of thirteen tidal cycles or portions of tidal cycles. As discussed previously these coefficients represent the number of tidal prisms of basin water mixing with the incoming water
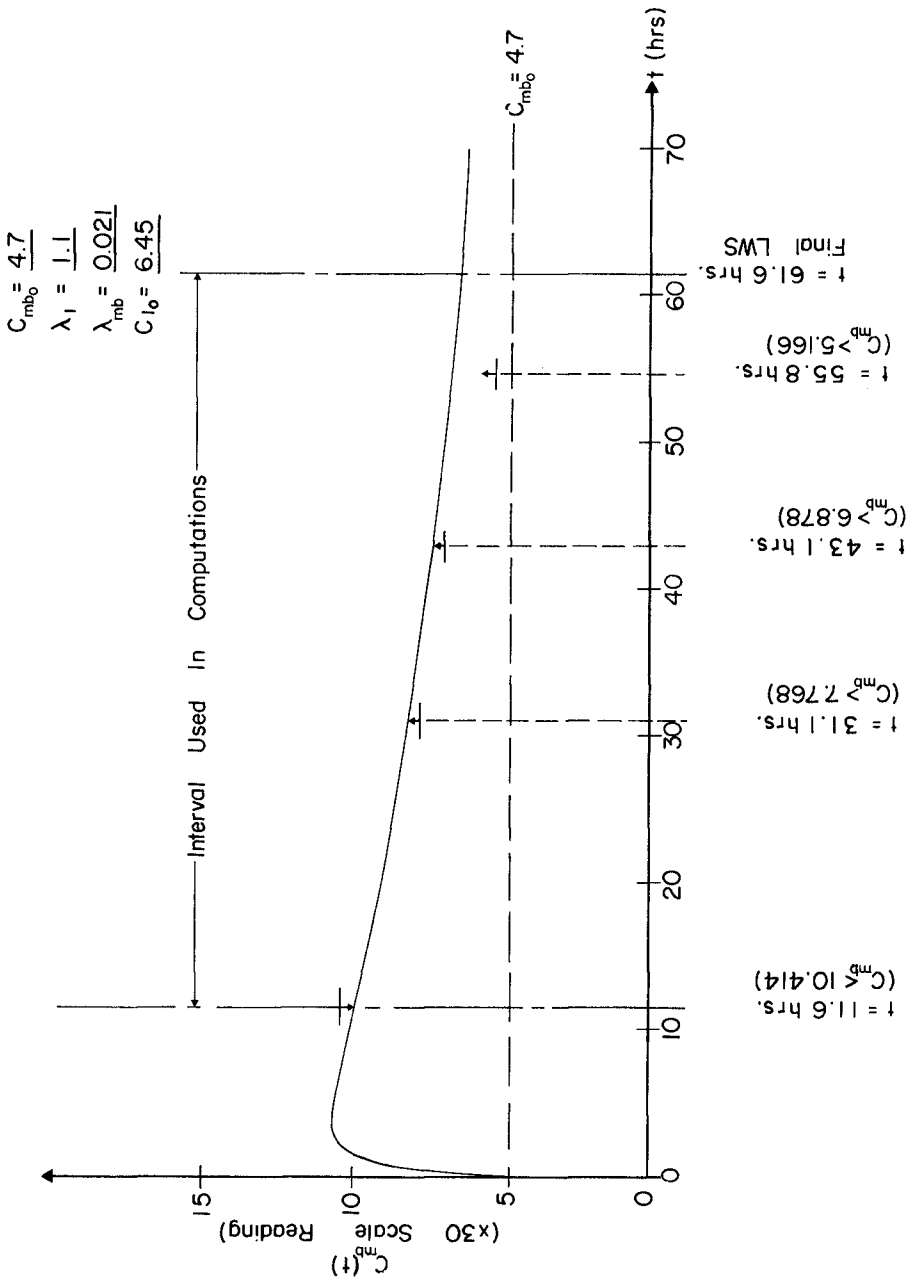
FIGURE   6   PLOT   OF $C_{mb}(t)$ VS t FOR   BAY   SIDE   CAESAR   CREEK

prior to outflow through the inlet. As used in this context, the word
"basin" can represent either the bay or the ocean.

     An example of measured dye concentration and inlet velocities is
presented in Figure 3 for Caeser Creek and Runs 10, 10a, 10b, and 10c.
The dye was injected on the flood cycle with monitoring commencing on
the first following ebb cycle. Very briefly it is seen that there is
considerable residual dye retained in the bay after injection as
evidenced by the maximum dye concentration approximately coinciding
with the end of each ebb cycle. Moreover, it is seen that the minimum
dye concentration corresponds more or less with the completion of the
flood cycle. The slow rate of decay is secondarily due to the low Bay
and Ocean mixing coefficients, but is primarily due to the residual
dye retained in the Bay following the injection and subsequently being
partly released on each ebb cycle. Both the bay and ocean shoals of
Caeser Creek are very substantial with the ocean shoals off Caeser
Creek extending 3 nautical miles offshore and the bay shoals extending
approximately one nautical mile bayward. These shoals tend to inhibit
mixing of the tidal prism, thereby resulting in low values of the
basin mixing coefficients.

     The Basin Mixing Coefficients are presented in Table V for the
three inlets studied. Only the Ocean Mixing Coefficients were obtained
for Broad Creek because this was the first inlet studied and in those
early phases of the measurement program, the measurements were limited
to determination of the Ocean Mixing Coefficients. The asterisked data
in Table V indicates that measured dye concentrations used to calculate
these points were close to the ambient concentration. The denominator
and numerator of Eq. (22) are therefore small and the accuracy of these
results is questionable.

     It is noted that during the measurements there was some variation
in the reasonably constant light northeast wind conditions. Moreover
any secondary longshore currents in the Bay or Ocean could result in
"sweeping" the residual dye away from the influence of the inlet.
This is believed to be of particular significance on the ocean side of
the inlets where the proximity (5 miles) of the Gulf Stream is known
to cause erratic nearshore currents parallel to the shoreline.

SUMMARY AND CONCLUSIONS

Summary

     Basin Mixing Coefficients have been defined as a measure of the
proportional mixing that occurs with the return portion of the tidal
prism flowing into that basin. A conceptual model is proposed based
on the effective lateral mixing resulting from the different flow
patterns that occur on the inflow and outflow portions of the cycle.
The flow away from the inlet is considered to occur as a separated
flow whereas a sink-type pattern is assumed to prevail during the flow
toward the inlet. Based on this simple concept a relationship is

TABLE V

SUMMARY OF BAY AND OCEAN

MIXING COEFFICIENTS

Inlet	Run No.	Ocean Mixing Coefficient, M_o	Bay Mixing Coefficient, M_b
Broad Creek	6	1.53	-
	7	4.40	-
	8	1.91	-
		(Avg.: 2.61)	
Caeser Creek	10	0.86	0.68
	10a	0.71	1.07
	10b	0.73	1.97
	10c	1.32	0.46
	10d	0.41	
		(Avg.: 0.81)	(Avg.: 1.05)
Angelfish Creek	11	2.10	10.02*
	11a	-	-
	12	0.53	4.59
	12a	0.52	0.28*
	12b	0.47*	
		(Avg.: 0.91)	(Avg.: 4.96)

* Indicates value subject to considerable error

developed for the Basin Mixing Coefficient, M. Measurements were carried out at three inlets in South Florida and the resulting Bay and Ocean Mixing Coefficients are reported.

Conclusions

The field measurements suggest, and the conceptual model supports the importance of shoals in inhibiting mixing of the tidal prism in a basin. Additional measurements of the type reported here are needed to: (1) provide necessary exchange characteristics for numerical modeling of constituent transport in any particular area, and (2) extend the data base to different tidal prisms, bathymetries and climatic conditions.

REFERENCES

1. Dean, R. G. and R. B. Taylor, "Numerical Modeling of Hydromechanics of Biscayne Bay/Card Sound System. Part I: Non-Dispersive Characteristics," Department of Coastal and Oceanographic Engineering, University of Florida, August, 1971.

2. Taylor, R. B. and R. G. Dean, "Numerical Modeling of Hydromechanics of Biscayne Bay/Card Sound System. Part II: Dispersive Characteristics," Department of Coastal and Oceanographic Engineering, University of Florida, July, 1972.

3. Taylor, R. B. and R. G. Dean, "Field Investigations of The Mixing and Flushing Characteristics of the Biscayne Bay/Card Sound System," Coastal and Oceanographic Engineering Laboratory, University of Florida, June, 1973.

4. O'Brien, M. P., "Equilibrium Flow Areas of Inlets on Sandy Coasts," Journal of the Waterways and Harbors Division, ASCE, February, 1969.

CHAPTER 133

TIDE-INDUCED MASS TRANSPORT IN LACOON-INLET SYSTEMS[1]

J. van de Kreeke[2] and D. C. Cotter[3]

ABSTRACT

   This paper examines the tide-induced net discharge in lagoon-inlet
systems. In particular, attention is given to the role inlets play in
inducing a steady current.
   The flow in the lagoon is described by the one-dimensional long wave
equations, the flow in the inlets is described by a semi-empirical equation.
Both numerical and analytical techniques are employed to solve for the net
discharge.

   The results of the study indicate that 1) the net discharge can be
significant provided the tidal amplitude to depth ratio is not small 2) the
net discharge can be considerably increased by the proper selection of the
inlet dimensions.

INTRODUCTION

   In an earlier publication van de Kreeke[8]has pointed out the possibility
of increasing the tide-induced flushing of lagoons and coastal channels by
proper selection of the inlet dimensions. This concept of using inlets for
environmental controls was discussed in a wider context by Lockwood and
Carothers [3] who in their paper also incorporated the possibility of
salinity control. In a recent paper by Mei, Liu and Ippen [5], an example
of increasing the tidal flushing by introducing two narrow asymetric con-
strictions near each entrance of a coastal channel with opposite orientation
is presented.

   The material presented here constitutes an elaboration of the concepts
set forth in the previously quoted papers. The practical significance of
the tide-induced net discharge is discussed and the role of the inlets in
inducing a/ steady current in coastal channels and lagoons is examined.

[1]Contribution from the Rosenstiel School of Marine and Atmospheric Science,
 University of Miami, Florida 33149

[2]Associate Professor, Division of Ocean Engineering, Rosenstiel School of
 Marine and Atmospheric Science, University of Miami.

[3]Graduate Assistant, Division of Ocean Engineering, Rosenstiel School of
 Marine and Atmospheric Science, University of Miami.

2290

EQUATIONS

A definition sketch of the lagoon-inlet system is presented in Figure 1.

The equations used to describe the flow in the lagoon are

Continuity
$$b \frac{\partial \eta}{\partial t} + \frac{\partial Q}{\partial x} = 0 \tag{1}$$

Momentum
$$\frac{\partial Q}{\partial t} + gA \frac{\partial \eta}{\partial x} + \frac{1}{A} \frac{\partial Q^2}{\partial x} = \frac{-F \, Q|Q|b}{A^2} \tag{2}$$

b = the width of the lagoon (assumed constant)

η = water surface elevation with respect to still water

t = time

Q = discharge

x = horizontal Cartesian coordinate

g = gravitational acceleration

A = $b(h+\eta)$ = cross-sectional area

h = depth with respect to still water

F = resistance coefficient

In deriving Equations (1) and (2) terms of $O(\frac{a}{h}^2)$ have been retained.

The equation used to describe the flow in the inlets is the semi-empirical relation

$$gA \frac{\partial \eta}{\partial x} = \frac{-F_i Q|Q|b}{A^2} \tag{3}$$

in which F_i is an inlet coefficient accounting for friction and exit and entrance losses and b and A refer to the width and cross-sectional area of the inlet.

NUMERICAL SOLUTION

A feeling for the order of magnitude and the effects of the inlets on the net discharge is obtained by solving Equations (1) - (3) for Q and η numerically and integrating Q over a tidal cycle. The computations are carried out for various combinations of inlet and lagoon dimensions, phase angles and amplitudes of the ocean tides. The lagoon and inlet dimensions
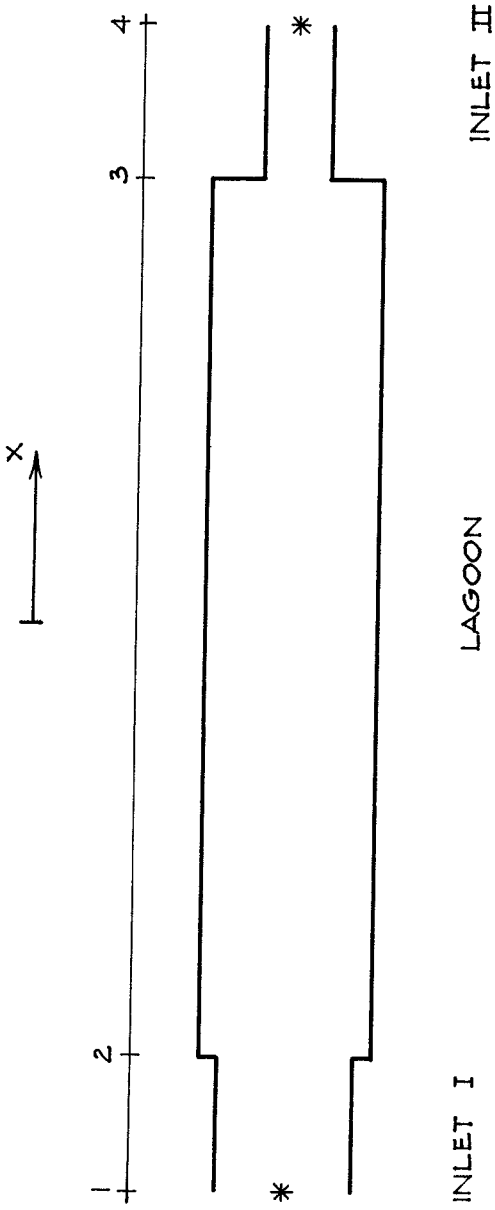
FIGURE 1   LAGOON — INLET SYSTEM ; PLAN VIEW.

used in the computations are typical for those found along the Florida
Atlantic and Gulf of Mexico coastline, i.e., for the lagoons the length
is O(10,000 ft) the width is O(1,000 ft) and the depth is O(10 ft), for
the inlets the length and width are O(1,000 ft) and the depth is O(10 ft).

   As an example the results of the computations for the lagoon-inlet
system indicated in Figure 1 with values of pertinent parameters listed
in Table 1 are presented. An explicit finite difference scheme is used
in the computations; see Reid and Bodine [6] and van de Kreeke [7]. The
time and space step are respectively $\Delta t = 100$ sec and $\Delta x = 5,000$ ft.

<div align="center">

TABLE 1
NUMERICAL VALUES USED IN COMPUTATIONS
</div>

BOUNDARY CONDITIONS

$$\eta_1 = a_1 \cos(\sigma t + \delta)$$
$$\eta_4 = a_4 \cos(\sigma t)$$
$$a_1 = a_4 = 1.3 \text{ ft } \delta = 0^o$$

The subscripts refer to stations indicated in Figure 1.

GEOMETRY OF LAGOON

   h = 10 ft, b = 2,500 ft, L = 80,000 ft

GEOMETRY OF INLET I

   h = 10 ft, b = 800 ft, L = 2,500 ft

GEOMETRY OF INLET II

The following combinations of depth, width and length are used for Inlet II

   h = 2 → 10 ft   b = 800 ft   L = 2,500 ft

   h = 10 ft   b = 100 → 2,500 ft L = 2,500 ft

   h = 10 ft   b = 800 ft   L = 0 → 10,000 ft

   No computations were carried out for depths of Inlet II smaller than 2
feet and widths of Inlet II smaller than 100 feet. For small depth, Inlet II
will be dry for part of the tidal cycle. For small width the depth to width
ratio of Inlet II is no longer small, a condition for Equation (3) to be valid.

   The net discharge as a function of depth, width and length of Inlet II
is plotted in respectively Figures 2a, 2b and 2c. The results show a zero
net discharge for Inlet II closed,(i.e. width = 0, depth = 0, length = ∞ (not
indicated in Figure 2c)) and for Inlet II being identical to Inlet I (symmetri-
cal lagoon-inlet system). The magnitude of the net discharge depends on the
relative dimensions of the inlets and can be either positive or negative.
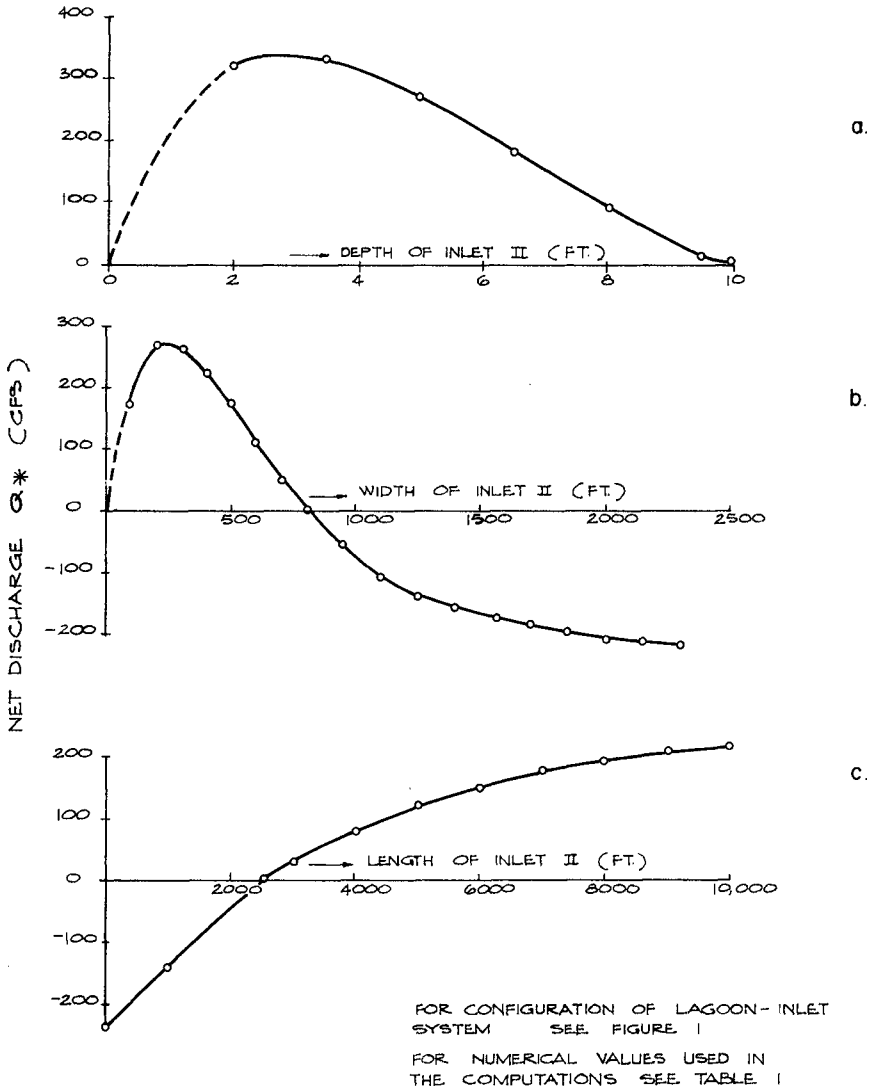
FIGURE 2   VARIATION IN NET DISCHARGE WITH
            DEPTH, WIDTH AND LENGTH OF INLET II

The results of the numerical computations provided enough incentive to attack the more complicated task of finding an analytic solution for the purpose of

1) obtaining a better understanding of the physics of the phenomenon of the tide-induced net discharge

2) to delineate the effects of the inlets on the net discharge

In particular the latter would be helpful when contemplating possible man-made modifications to existing lagoon-inlet systems.

ANALYTIC SOLUTION; PHYSICAL INTERPRETATION

Because the nonlinear friction term is of the same order as the linear terms, the long wave equations do not lend itself very well to an analytic solution. Therefore in the following treatment the friction term is linearized, realizing that in doing so the resulting solution can at best be an approximation. Linearization is accomplished by assuming a linear relation between bottom stress and mean velocity. The mechanics of the linearization process are described in detail in van de Kreeke [8] and Dronkers [2].

Upon introduction of the linearized friction term Equations(1) - (3) become

$$b \frac{\partial \eta}{\partial t} + \frac{\partial Q}{\partial x} = 0 \tag{4}$$

$$\frac{\partial Q}{\partial t} + gA \frac{\partial \eta}{\partial x} + \frac{1}{A} \frac{\partial Q^2}{\partial x} = - \frac{F_\ell Q b}{A} \tag{5}$$

$$gA \frac{\partial \eta}{\partial x} = \frac{-F_{i_\ell} Q b}{A} \tag{6}$$

in which F_ℓ = "linear" resistance coefficient

                F_{i_ℓ} = "linear" inlet coefficient

Substituting $A = b(h+\eta)$ in Equations (4) - (6) and neglecting terms of $0(\frac{a}{h})^3$

$$b \frac{\partial \eta}{\partial t} + \frac{\partial Q}{\partial x} = 0 \tag{7}$$

$$\frac{\partial Q}{\partial t} + gbh \frac{\partial \eta}{\partial x} = \frac{-F_\ell Q}{h} + \frac{F_\ell Q \eta}{h^2} - gb\eta \frac{\partial \eta}{\partial x} - \frac{1}{bh} \frac{\partial Q^2}{\partial x} \tag{8}$$

$$gbh \frac{\partial \eta}{\partial x} = \frac{-F_{i_\ell} Q}{h} + \frac{F_{i_\ell} Q \eta}{h^2} - gb\eta \frac{\partial \eta}{\partial x} \tag{9}$$

Because the nonlinear terms in Equations (7) - (9) are of $0(\frac{a^2}{h})$, a first order solution for the water levels and discharges is found by considering only the linear terms in the equations. The resulting first order expressions for the water levels and discharges, designated respectively η_ℓ and Q_ℓ are periodic in time and space and have the same frequency as the ocean tide. An expression for the net discharge, Q_*, in the lagoon-inlet system may be found by substituting in the complete Equations (7) - (9), including the nonlinear terms, a trial solution of the form

$$\eta = \eta_*(x) + \eta_\ell(x,t)$$

$$Q = Q_*(x) + Q_\ell(x,t)$$

in which $\eta_* = $ mean water surface elevation.

Averaging over a tidal period and neglecting terms of $0(\frac{a^3}{h})$ and higher, this results in

$$Q_* = \text{constant}$$

$$\frac{\partial}{\partial x} \left[\overline{\frac{Q_\ell^2}{bh}} + gbh\eta_* + \frac{gb}{2} \overline{\eta_\ell^2} + \int \frac{F_\ell Q_*}{h} dx \right.$$

$$\left. - \int \frac{F_\ell \overline{Q_\ell \eta_\ell}}{h^2} dx \right] = 0 \tag{11}$$

pertains to lagoon

$$\frac{\partial}{\partial x} \left[gbh\eta_* + \frac{gb}{2} \overline{\eta_\ell^2} + \int \frac{F_{i_\ell} Q_*}{h} dx - \int \frac{F_{i_\ell} \overline{Q\eta}}{h^2} dx \right] = 0 \tag{12}$$

pertains to inlet

The bar denotes averaging over a tidal cycle.

Applying Equations (10)-(12) to the lagoon-inlet system in Figure 1, integrating with respect to x, setting $\eta_{*_1} = \eta_{*_4}$ and eliminating η_{*_2} and η_{*_3} (1, ...4 refer to station locations, see Figure 1) yields the following expression for Q_*

$$Q_* \left[\frac{F_{i_\ell} L}{gbh^2_{\ I}} + \frac{F_\ell L}{gbh^2_{LAG}} + \frac{F_{i_\ell} L}{gbh^2_{\ II}} \right] = -\int_1^2 f_I(x)\,dx$$

$$-\int_2^3 f_{LAG}(x)\,dx - \int_3^4 f_{II}(x)\,dx \qquad (13)$$

where $\quad f_I(x) = \left[\frac{1}{h} \ \overline{\eta_\ell \frac{\delta\eta_\ell}{\delta x}} \right]_I$

$$f_{LAG}(x) = \left[\frac{1}{h} \ \overline{\eta_\ell \frac{\delta\eta_\ell}{\delta x}} + \frac{1}{gb^2 h^2} \ \overline{\frac{\delta Q_\ell^2}{\delta x}} - \frac{\overline{F_\ell Q_\ell \eta_\ell}}{gbh^3} \right]_{LAG}$$

$$f_{II}(x) = \left[\frac{1}{h} \ \overline{\eta_\ell \frac{\delta\eta_\ell}{\delta x}} \right]_{II}$$

The subscripts I, LAG and II refer to respectively Inlet I, the Lagoon and Inlet II.

The right side of Equation (13) has been evaluated by Cotter [1]. The resulting expressions are very lengthy and complex and to a large extent defy the purpose of the analytic solution. Therefore, the complete results of Cotter's [1] analysis will not be presented here.

As a matter of academic interest and to build faith in the numerical model, analytically and numerically computed net discharges for the lagoon-inlet system under consideration are compared in Figure 3. The net discharges computed with both methods show similar trends and orders of magnitude, however, the differences are too large to neglect. Since the process of linearizing the friction term is suspected of causing this discrepancy, a finite difference technique, similar to the one used in solving the equations including the quadratic friction term, is applied to the equations on which the analytic solution is based, i.e., Equations (4), (5) and (6). The time step and space step used in the computations are $\Delta t = 100$ seconds and $\Delta x = 5,000$ feet. The results of the finite difference computations for the linearized equations along with the analytic results presented earlier in Figure 3 are presented in Figure 4. From this figure it is seen that the two sets of results are

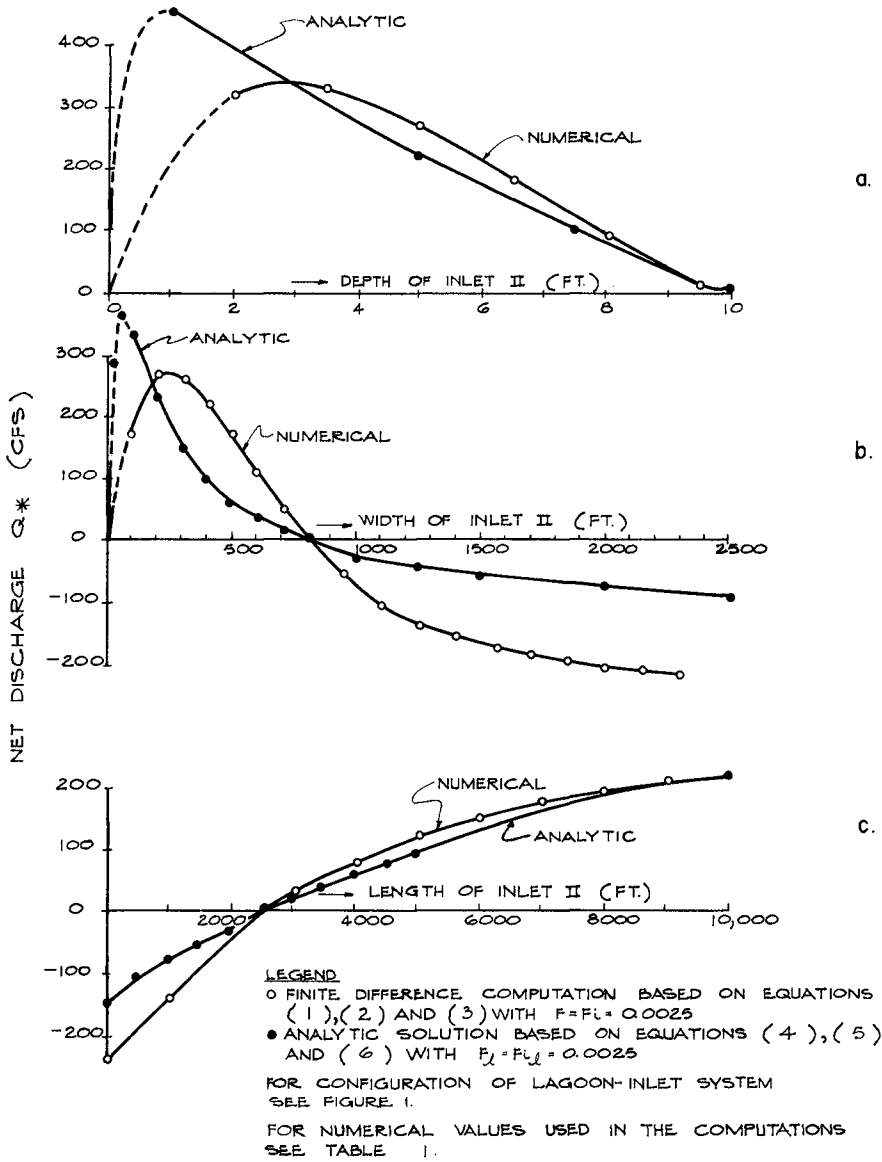FIGURE 3   COMPARISON   BETWEEN   NUMERICALLY AND
                 ANALYTICALLY   COMPUTED   NET   DISCHARGE.
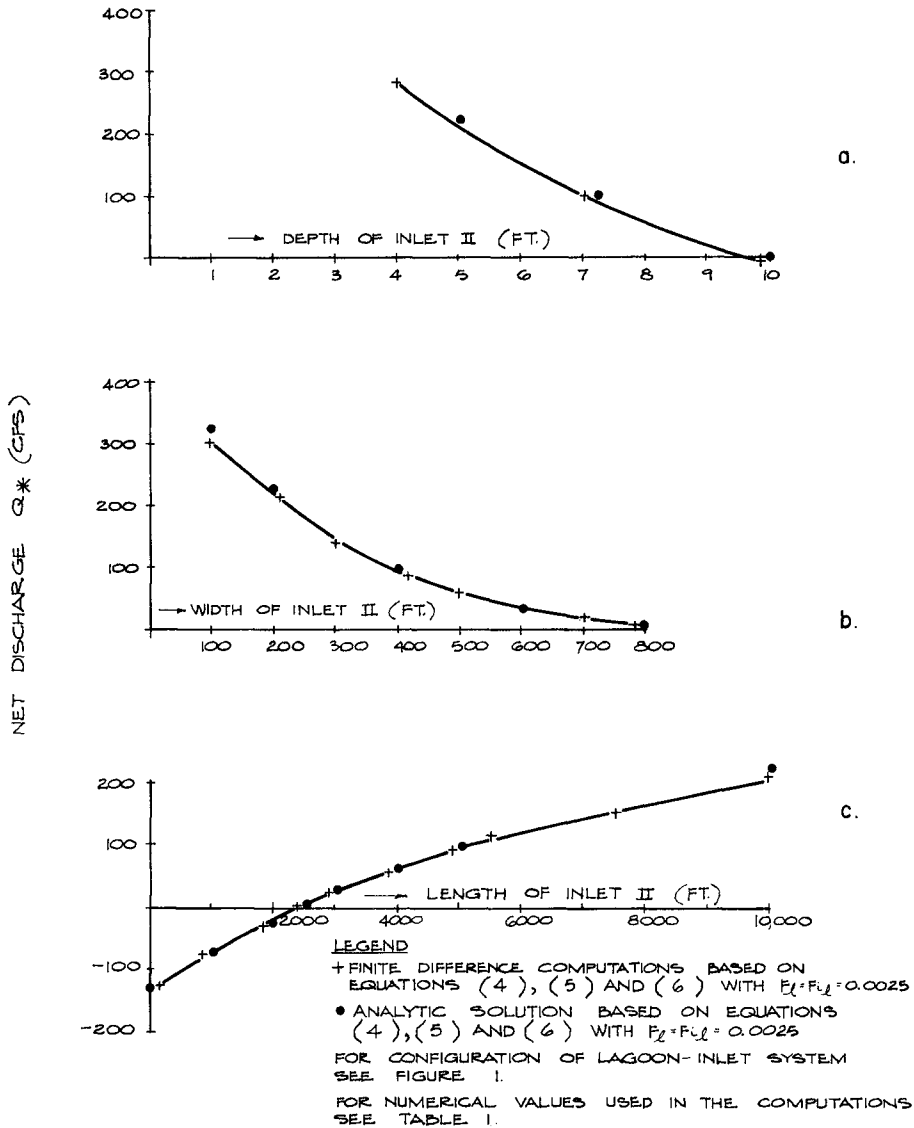
FIGURE   4   NUMERICALLY   COMPUTED   NET
                     DISCHARGE   USING "LINEARIZED" FRICTION.

similar in every respect. This leads to the conclusion that the differences between the numerical and analytic solution evident in Figure 3 arise from the linearization of the friction term employed in the analytic solution.

For a physical explanation of the tide-induced net discharge it seems best to return to Equations (11) and (12). These equations are the time averaged conservation of momentum equations for respectively the lagoon and the inlets. In Equation (11), the first three terms constitute the momentum flux across a vertical plane in the lagoon (or equivalently the radiation stress, Longuet-Higgins and Stewart [4], the last two terms constitute the momentum flux across the bottom (or equivalently the bottom stress). A similar physical interpretation can be given for the terms in Equation (12). In both the lagoon and inlets the excess momentum flux associated with the wave motion is balanced by momentum flux associated with a net discharge Q_* and a momentum flux (or equivalently a pressure) associated with a change in mean water level η_*. Note also that the relation between the slope in mean sea level and the net discharge is not the simple relation known from steady state hydraulics.

SUMMARY AND CONCLUSIONS

The tide-induced net discharge in a schematized lagoon-inlet system is determined by solving the system of governing long wave equations and inlet equations numerically and integrating the discharge over a tidal cycle. The results of the computations show that 1) the net discharge can be of a magnitude that is important when considering the renewal of the waters of the lagoon and 2) the magnitude of the net discharge is strongly affected by the inlet dimensions. The last conclusion suggests that a considerable increase in net discharge can be obtained by properly designing the inlets.

The physics underlying the net discharge is generally obscured when applying numerical techniques to solve the governing equations and therefore an analytical solution is sought to delineate the causes and principles behind the net discharge. Unfortunately, the analytic expression for the net discharge turns out to be rather complicated and therefore provides little physical insight in the role of the inlets with respect to the magnitude of the net discharge. In addition, it appears from comparison with numerical results that because of the linearization process applied to the friction term, the analytic solution yields at best an approximate value of the net discharge. Therefore, for accurate results recourse should be taken to numerical techniques.

Physical insight can best be obtained from the time-averaged conservation of momentum equations for the lagoon and inlets. These equations express the balance between the excess momentum flux across a vertical plane and across the bottom associated with the long wave traveling in the lagoon-inlet system, and the momentum flux associated with the net discharge and the change in mean water level.

Because the net discharge results from the nonlinear (second order) terms in the governing equations, significant net discharge should only be expected for large values of $\frac{a}{h}$ (a = amplitude h = depth). Also, the study presented in this paper pertains to schematized lagoon-inlet systems with a homogeneous fluid and merely serves to illustrate a concept. When dealing with actual lagoon-inlet systems, it should be realized that second order effects such as the net discharge can be easily obscured by the geometric irregularities in the lagoons and inlets and by gravity currents, fresh water inflow and by wind-induced currents.

REFERENCES

1. Cotter, D.C. Tide-Induced Net Discharge in Lagoon-Inlet Systems. Masters Thesis, University of Miami, Department of Ocean Engineering June, 1974.

2. Dronkers, J.J., Tidal Computations in Rivers and Coastal Waters, North Holland Publishing Company, 1964.

3. Lockwood, M.G. and Carothers, H.P., Preservation of Estuaries by Tidal Inlets, Journal of the Waterways and Harbors Division, ASCE, Vol 93, No. WW4, November, 1967.

4. Longuet-Higgins, M.S. and R. W.Stewart, Radiation Stresses in Water Waves; a Physical Discussion with Applications. Deep Sea Research, Vol. II, pp. 529-562, 1964.

5. Mei, C.C., P.L.F. Liu and A.T. Ippen, Quadratic Loss and Scattering of Long Waves, Journal of the Waterways Harbors and Coastal Engineering Division, ASCE, Vol. 100 No. WW3, August, 1974.

6. Reid, R.O. and B.R.Bodine, Numerical Model for Storm Surges in Galveston Bay, Journal of the Waterways and Harbors Division, ASCE, Vol. 94, No. WW1, February, 1969.

7. van de Kreeke, J., A Numerical Model for the Hydromechanics of Lagoons. Proceedings, XIIIth Conference on Coastal Engineering, Vancouver, 1972.

8. van de Kreeke, J., Tide-Induced Mass Transport in Shallow Lagoons, Department of coastal and Oceanographic Engineering, University of Florida, Technical Report No. 8, October, 1971.

CHAPTER 134

MATHEMATICAL MODEL OF SALINITY INTRUSION IN THE DELTA OF THE PO RIVER

by

Renzo Dazzi - Mario Tomasino

ABSTRACT

A general numerical model capable of reproducing long inter
nal waves in stratified fluids has been constructed with the aim   of
investigating the salt wedge penetration in the Delta of the Po river,
where the installation of a 2640 MW thermo-electric plant is   fore-
seen.

The working hypothesis of the model, in accordance with the
actual phenomenology of the river, is the one-dimensional homoge-
neous motion of two fluid layers of different density.

The main original aspects of the numerical computation are:

1) - The use of two different space steps (1 km for the fresh wa-
     ter layer; 200 m for salt water) simultaneously allowing   a
     good description of internal waves (the velocity of which   is
     much smaller than that of the external ones)   and making it
     possible to work with economic (100 sec) time steps.
2) - The straightforward description of the wedge head, obtained
     by making it always freely correspond to one of the grid points.

The model, which has been tested on actual events, reprodu-
ces reality with a very good approximation; it also gives evidence
of the small relevance of the interfacial stress coefficient in unstea
dy tidal generated motion of the salt wedge.

Renzo Dazzi - C.N.R. - Laboratorio per lo Studio della Dinamica
            delle Grandi Masse - 1364 S.Polo - Venice - Italy
Mario Tomasino - ENEL/C.R.I.S.-Servizio Idrologico- Corso del
            Popolo 245 - Venice - Italy

2302

1) INTRODUCTION

Two years ago the Italian National Authority for Electric Energy (ENEL) decided to construct a thermo-electric plant with a large productive capacity (2640 MW) in the zone of the Delta of the river Po (fig. 1). This zone was chosen for both technical and social reasons, with the scope of giving a contribution to industrialisation and raising the standard of living of the inhabitants of the underdeveloped Delta region. The technical reasons of the choise are obvious, considering that this estuarine site, which collects 24% of the Italian water flow, completely satisfies the cooling water necessities of such a plant.

The installation is foreseen on the main branch of the Delta, (5 km from the sea - fig. 2) with two intakes and two outfalls on the river and on an adjacent lagoon. The cooling of the station will necessitate a variable withdrawal from 80 m^3/sec to 320 m^3/sec when the plant is fully operative.

The mean year discharge of the river Po at Pontelagoscuro (the main observation station along the river) (fig. 1) is 1500 m^3/sec; the Pila branch, where the intakes will be located, has only about 50% of this discharge. The natural discharge of this branch is therefore comparable with the foreseen withdrawals, consequently the probability of a modification of the fluvial régime due to the installation is not so remote.

In order to investigate and predict the possible changes we developed an ordinary numerical hydrodynamical one-dimensional homogenous model, which simulated the network of the Delta from Pontelagoscuro to the sea (a length of 92 km of the main course of the river, as well as 160 km of the lateral branches).

This model gave very good results /1,2/ in the hindcasting of events with normal and high (up to 6000 m^3/sec) Pila discharge, but failed for Pila mean discharge lower than 500 m^3/sec, particularly during spring tides, when amplitude in the open sea facing the Delta is about 80 cm. .In fact during spring tides which occur at low discharge, the model gave a strong overevaluation of the upstream (negative) discharge (fig. 3).

Field measurements made in these conditions show that return currents are present and a salt wedge is formed; salt and fresh water flows are well identified and the stratification is very strong as the sharp interruption in the measured vertical profiles of salinity shows (fig. 4); it was revealed that the wedge under the fresh water penetrated up to 10 km from the river mouth (fig.2). These were the reasons why the homogenous model did not work correctly, its construction hypothesis being far away from the actual motion.

Fig. 1 - Delta of Po River

Fig. 2 - Thermoelectric plant location and longitudinal
         profile of the river bed
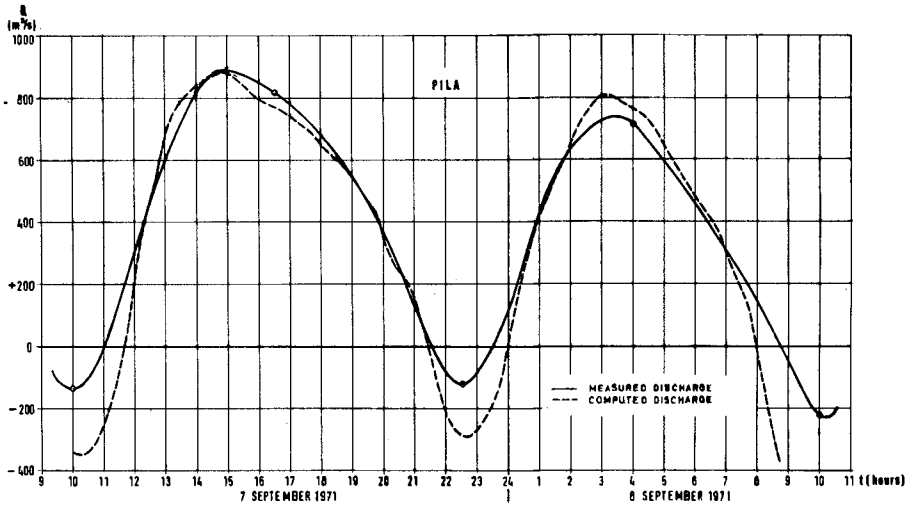
Fig. 3 - Simulation with density return currents

SEA

0   3 m
        ———— DEPTH
0   60 cm s
        ———— VELOCITY
0   30 ‰
        ------- SALINITY
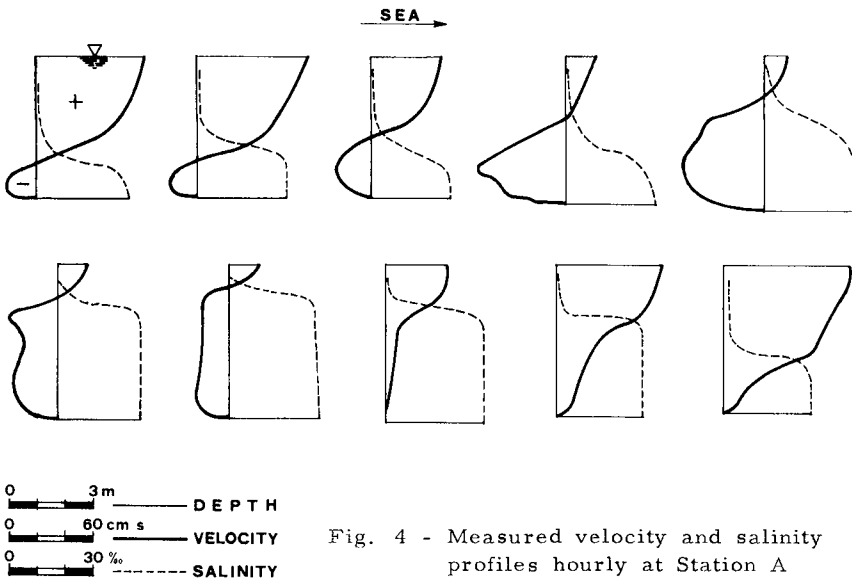
Fig. 4 - Measured velocity and salinity
         profiles hourly at Station A

It was therefore decided to build a model capable of reproducing the physical flow patterns and the sea water penetration in the river, with the aim of answering the main water quality questions (salinity and partially temperature) involved in the probable modification of the existing salt wedge behaviour.

It would be worthwhile briefly summarizing the possible consequences of this change:

	Effect	Damage
Environment modifications	1) Marine biota modification	Fish and plancton destruction
	2) Salt penetration in underground aquifers	Agricultural damage
	3) Sedimentation (flocculation) rate increase	Dredging
Technical effects	4) Recirculation of cooling water	Increase in water temperature

2) PHYSICAL FOUNDATIONS

The evidence of strong stratification enables the fluvial motion to be treated with the schematization of two homogenous layers, each with a constant density, considering the salt or mass transfer from one layer to the other as negligible: the two layers only interact by momentum exchange along the interface and reciprocal pressure effects.

With these hypotheses[*], which are fully justified by the measurements, the hydrodynamical equations for both layers are the same as for the homogenous one-layered flow, plus:

1) - one term in the continuity equation of the upper layer wich describes the discharge contribution of the lower layer
2) - one term in the momentum equation of the lower layer which takes into account the pressure exerted by the upper layer on the lower one
3) - a couple of terms in both the momentum equations which represent the interfacial stresses

---

[*]In these assumptions also the hydrostatic hypothesis is made for both layers, pratically generating /3/ a vertical integrated model of flow, which is only valid for long waves (this is precisely our field'of interest)

$$\frac{\partial u_1}{\partial t}+u_1\frac{\partial u_1}{\partial x}+g\frac{\partial Z_1}{\partial x}+\frac{\lambda}{8\,R_1}\left(u_1-u_2\right)\left|u_1-u_2\right|+\frac{g\,u_1\left|u_1\right|}{C^2\,R_1'}=0$$

momentum equations

$$\frac{\partial u_2}{\partial t}+u_2\frac{\partial u_2}{\partial x}+g\frac{\partial Z_2}{\partial x}+g\frac{\varrho_1}{\varrho_2}\frac{\partial Z_1}{\partial x}-\frac{\lambda}{8\,R_2}\left(u_1-u_2\right)\left|u_1-u_2\right|+\frac{g\,u_2\left|u_2\right|}{C^2\,R_2'}=0$$

$$\frac{\partial Z_1}{\partial t}B_1-\frac{\partial Z_2}{\partial t}B_2+\frac{\partial u_1}{\partial x}A_1=0$$

continuity equations

$$\frac{\partial Z_2}{\partial t}B_2+\frac{\partial u_2}{\partial x}A_2=0$$
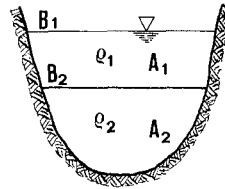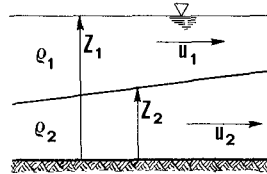
where:

t   = time
x   = distance coordinate
g   = gravity acceleration
ϱ_1,ϱ_2 = densities of the layers
u_1,u_2 = current mean velocities
Z_1,Z_2 = levels of the free surface and of the interface
B_1,B_2 = width of the free surface and of the interface
A_1,A_2 = cross section areas
R_1,R_2,R_1',R_2' = hydraulic radius given by the ratio between the
            cross section areas and the length of the friction
            contour
$C=\left[m^{1/2}/sec\right]$ Chézy coefficient
λ = dimensionless Darcy-Weisbach coefficient

(Quantities with index 1 refer to upper layer and with index 2 to
the lower layer)

    The head losses in the momentum equations are expressed:

1) - the bottom stress by the Chézy formula:

$$v=C\sqrt{R\,i}$$

2) - the interfacial stress by the Darcy-Weisbach formula

$$v = \sqrt{\frac{8\,g\,R\,i}{\lambda}}$$

where i represents the surface slope.

The set of four equations, which were firstly investigated for infinitely wide currents by Schijf and Schönfeld in 1953 /4/, defines two kinds of propagation velocity for small disturbances: one for the external waves i.e. surface waves, the other for internal waves i.e. the interface waves. These velocities can be easily determined /5/ by applying the Cauchy-Kowalewsky theorem to the set, putting:

$$A_x - c \cdot A_t = 0$$

where:
c   = wave propagation speed
A_x = matrix of the space derivative coefficients
A_t = matrix of the time derivative coefficients

This equation, still in the case of infinitely wide flows, produces a fourth degree equation:

$$\left(c - V_1\right)^2 \cdot \left(c - V_2\right)^2 - g\,h_2\left(c - V_1\right)^2 - g\,h_1\left(c - V_2\right)^2 + \varepsilon\,g^2\,h_1\,h_2 = 0$$

where:
h_1, h_2 = depth of the two layers

$$\varepsilon = \frac{\varrho_1 - \varrho_2}{\varrho_2}$$

whose four roots are the above mentioned propagation velocities of small perturbations in the fluid /6/.

Assuming the flow velocities as negligible, c_e (velocity of the external waves) and c_i (velocity of the internal waves) become:

$$c_e = \pm \sqrt{\frac{g\left(h_1 + h_2\right)}{2} + \frac{g}{2}\sqrt{\left(h_1 + h_2\right)^2 - 4\,\varepsilon\,h_1\,h_2}}$$

$$c_i = \pm \sqrt{\frac{g\left(h_1 + h_2\right)}{2} - \frac{g}{2}\sqrt{\left(h_1 + h_2\right)^2 - 4\,\varepsilon\,h_1\,h_2}}$$

If ε is small (as in the case of fresh water over salt water)

the two expressions can be approximated by:

$$c_e \simeq \pm \sqrt{g \left(h_1 + h_2\right)}$$

$$c_i \simeq \pm \sqrt{\varepsilon\, g \, \frac{h_1\, h_2}{\left(h_1 + h_2\right)}}$$

It immediately ensues that external wave velocity is very clo se to $\sqrt{g\,h}$, i.e. the propagation velocity in the one-layer homogene-ous flow; and in ratio, it results larger in magnitude than the inter nal wave velocity, being:

$$\frac{c_e}{c_i} \gtrsim \frac{2}{\sqrt{\varepsilon}}$$

The definition of c_i, c_e and the ratio $\frac{c_e}{c_i}$, whose physical meanings are clearly understood, is the most important aspect for what concerns the definition of the boundary conditions and the inte gration space step of the finite difference scheme used for solving the set of differential equations.

Another important feature which immediately descends from the definition of the propagation velocities, is that the two layered flow can be internally or externally sub or supercritical, depending upon whether it is possible for an internal or external wave to mo ve both up and downstream.
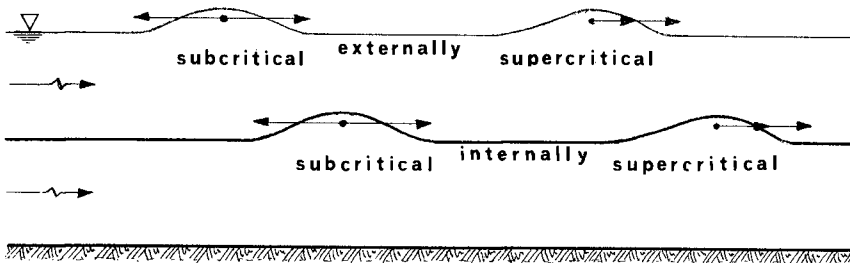
This behaviour is connected with the densimetric Froude num ber definition (in analogy with the one-layer flow) which individuates the internal sub or supercritical status of the flow /4/. Even though the densimetric Froude number is important in characterising the flow, it will not explicitly be used in the construction of the model.

3) THE FINITE DIFFERENCE SCHEME

The set of partial differential equations was integrated using a finite difference scheme, staggered both in space and time and expressing all the derivatives in the central form. All the terms present in the four equations are strictly written in this way, only neglecting the convective acceleration terms in the momentum equations. This is usual practice in hydrodynamic subcritical numerical computations and is permitted by the small relevance of these terms in the global balance of the momentum equations.

Defining the difference operator in such a straightforward way we assumed also a linear variation of all the variables, (both in time and space) expressing, when needed, the value in an intermediate point or instant as the mean between the precedent and the following values.

The geometry of the river bed is introduced into the model by defining the values of B_*, A_*, R_*, R_*' (*) as functions of the levels Z_* in every computation section and using a particular subprogram operating on the contour of the cross sections given by points. Hereafter $F(Z_*)$ will indicate the general level depending functions B_*, A_*, R_*, R_*'.

Defining:
Z1, Z2, U1, U2, B1, B2, A1, A2, R1, R2, R1', R2' as the same variables defined as $Z_1, Z_2, u_1, u_2, B_1, B_2, A_1, A_2, R_1, R_2, R_1', R_2'$ in the set of differential equations,
T = integration time step
X = integration space step
m = index defining the computation instant, so t = m · T
n = index defining the computation section, so x = n · X
and considering that Z1, Z2 are evaluated corresponding to integer values of m and n whilst U1, U2 are evaluated in correspondence to:

$$t = \left(m + \frac{1}{2} \right) \cdot T \qquad\qquad x = \left(n + \frac{1}{2} \right) \cdot X$$

the continuity equations are discretized as follows:

$$Z1_{m,n} = Z1_{m-1,n} + \left(\frac{B2}{B1} \right)_{m-\frac{1}{2},n} \cdot \left(Z2_{m,n} - Z2_{m-1,n} \right) +$$

$$+ \frac{T}{X} \cdot \frac{1}{B1_{m-\frac{1}{2},n}} \cdot \left[\left(A1 \cdot U1 \right)_{n-\frac{1}{2}} - \left(A1 \cdot U1 \right)_{n+\frac{1}{2}} \right]_{m-\frac{1}{2}}$$

(*) The asterisk represents 1 or 2.

$$Z2_{m,n} = Z2_{m-1,n} + \frac{T}{X} \cdot \frac{1}{B2}_{m-\frac{1}{2},n} \cdot \left[\left(A2 \cdot U2 \right)_{n-\frac{1}{2}} - \left(A2 \cdot U2 \right)_{n+\frac{1}{2}} \right]_{m-\frac{1}{2}}$$

where:

$$A2_{m-\frac{1}{2},n-\frac{1}{2}} = F \left(\frac{Z2_{m,n} + Z2_{m,n-1} + Z2_{m-1,n} + Z2_{m-1,n-1}}{4} \right)$$

$$A2_{m-\frac{1}{2},n+\frac{1}{2}} = F \left(\frac{Z2_{m,n+1} + Z2_{m,n} + Z2_{m-1,n+1} + Z2_{m-1,n}}{4} \right)$$

$$A1_{m-\frac{1}{2},n-\frac{1}{2}} = F \left(\frac{Z1_{m,n} + Z1_{m,n-1} + Z1_{m-1,n} + Z1_{m-1,n-1}}{4}, A2_{m-\frac{1}{2},n-\frac{1}{2}} \right)$$

$$A1_{m-\frac{1}{2},n+\frac{1}{2}} = F \left(\frac{Z1_{m,n+1} + Z1_{m,n} + Z1_{m-1,n+1} + Z1_{m-1,n}}{4}, A2_{m-\frac{1}{2} , n+\frac{1}{2}} \right)$$

$$B*_{m-\frac{1}{2},n} = F \left(\frac{Z*_{m,n} + Z*_{m-1,n}}{2} \right)$$

The finite difference scheme is partially implicit because in the continuity equations the unknown Z1 or Z2, in one point, depends on the unknown values of the same variable Z1 or Z2 in the surrounding points in the same instant. This requires a simultaneous solution of the set of continuity equations for each layer. In solving them, the lower layer set is tackled first in order to furnish known values of the lower layer discharge contribution to the upper layer set. Both the sets of nonlinear algebraic equations obtained by discretizing the continuity equations are solved by iterative procedures.

The momentum equations are discretized as follows:

$$U1_{m+\frac{1}{2},n+\frac{1}{2}} = U1_{m-\frac{1}{2},n+\frac{1}{2}} - \frac{g \cdot T}{X} \left(Z1_{n+1} - Z_n \right)_m - \frac{\lambda \cdot T}{8 \cdot R1_{m,n+\frac{1}{2}}} \cdot \frac{1}{4} \cdot$$

$$\cdot \left(U1_{m+\frac{1}{2}} + U1_{m-\frac{1}{2}} - U2_{m+\frac{1}{2}} - U2_{m-\frac{1}{2}} \right)_{n+\frac{1}{2}} \cdot \left| U1_{m+\frac{1}{2}} + U1_{m-\frac{1}{2}} - U2_{m+\frac{1}{2}} - U2_{m-\frac{1}{2}} \right|_{n+\frac{1}{2}}$$

$$- \frac{g \cdot T}{C^2 \cdot R1'_{m,n+\frac{1}{2}}} \cdot \frac{1}{4} \left(U1_{m+\frac{1}{2}} + U1_{m-\frac{1}{2}} \right)_{n+\frac{1}{2}} \cdot \left| U1_{m+\frac{1}{2}} + U1_{m-\frac{1}{2}} \right|_{n+\frac{1}{2}}$$

$$U2_{m+\frac{1}{2},n+\frac{1}{2}} = U2_{m-\frac{1}{2},n+\frac{1}{2}} - \frac{g \cdot T}{X} \cdot \left(Z2_{n+1} - Z2_n\right)_m - \frac{g \cdot T}{X} \cdot \frac{\varrho_1}{\varrho_2} \cdot \left(Z1_{n+1} - Z1_n\right)_m +$$

$$+ \frac{\lambda \cdot T}{8 \cdot R2_{m,n+\frac{1}{2}}} \cdot \frac{1}{4} \left(U1_{m+\frac{1}{2}} + U1_{m-\frac{1}{2}} - U2_{m+\frac{1}{2}} - U2_{m-\frac{1}{2}}\right)_{n+\frac{1}{2}} \cdot \left|U1_{m+\frac{1}{2}} +\right.$$

$$+ U1_{m-\frac{1}{2}} - U2_{m+\frac{1}{2}} - U2_{m-\frac{1}{2}}\bigg|_{n+\frac{1}{2}} - \frac{g \cdot T}{C^2 \cdot R2'_{m,n+\frac{1}{2}}} \cdot \frac{1}{4} \cdot$$

$$\cdot \left(U2_{m+\frac{1}{2}} + U2_{m-\frac{1}{2}}\right)_{n+\frac{1}{2}} \cdot \left|U2_{m+\frac{1}{2}} + U2_{m-\frac{1}{2}}\right|_{n+\frac{1}{2}}$$

where:

$$R2, R2' = F\left(\frac{Z2_{m,n} + Z2_{m,n+1}}{2}\right)$$

$$R1, R1' = F\left(\frac{Z2_{m,n} + Z2_{m,n+1}}{2}, \frac{Z1_{m,n} + Z1_{m,n+1}}{2}\right)$$

These equations link together the values of each U1 and U2 which are relative to the same point, due to the fact that the interfacial stress is expressed as a function of them both; then, for each grid point, the values of U1 and U2 are simultaneously determined by iteratively solving the two momentum equations of the upper and lower layer.

The difference scheme did not prove unconditionally stable in the practical simulations and slightly exceeded (in a version which also took into account the frictional terms), the theoretical values of the time steps allowed by the usual criterion of stability:

$$\frac{X}{T} \geq c$$

In this case we consider c_e as c, as the external wave velocity is more restrictive in respect to the criterion.

4) MODEL CONSTRUCTION

Steps

The practical realisation of the model began with the choice of the space step, i.e. by the definition of the density of level and velocity computation points. The choice was conditioned by the ratio

$\frac{c_e}{c_i}$, which in our case, being $\varrho_1 \simeq 1g/cm^3$ and $\varrho_2 \simeq 1.025 \ g/cm^3$,

gives $c_e \gtrsim \frac{2}{\sqrt{\varepsilon}} \cdot c_i \simeq 12 \cdot c_i$

The internal wave velocity is less than $\frac{1}{12}$ of that of the external wave; the ratio between wave lengths of internal and external waves of the same period can, in first approximation, be considered the same.

The most relevant tidal component in the Delta is M2, with a period of 12h 25', and an approximative 280 km wave length, as evaluated on the basis of the mean Po Delta depth of 4 m [*]. The overtide generation (i.e. higher harmonics) originating from the shallow water propagation does not attain (probably being overcome by dissipative phenomena) valuable effects for harmonics higher than the third one. Difference schemes of the same type as ours need about 30 points per wave length to give an almost perfect reproduction of a long wave propagation both in phase and amplitude /7/.

The step used in our previous one-layer model was 1 km, from which an accurate representation until the M2 fourth harmonic was obtained; as shown this is more than needed. A description of the internal wave with the same accuracy of the external one would require a space step of at least 1/12 of the previous one; considering that the external wave 1 km step was even too small, we adopted a 200 m step for this model, retaining it adequate to describe the tide induced penetration of the wedge in the river.

The first simulations made with this space step were revealed as uneconomical from the machine-time point of view, as they gave unstable results for time steps higher than 50 sec. This is explained considering that the mathematical velocity, i.e. $\frac{X}{T}$, in this case is lower than the physical one of the external wave; in fact:

$$\frac{X}{T} = \frac{200}{50} = 4 < 6.26 = \sqrt{9.81 \cdot 4} = \sqrt{g \ h} \simeq c_e$$

The Courant-Friedrichs-Lewy criterion for the stability condition of a finite difference scheme ($\frac{X}{T} \geq \sqrt{g \ h}$) is strictly valid for the linear case /7/, but it empirically proved valid for this one too.

---

[*] To evaluate the wave propagation speed it is necessary to take into account the depth, averaged on the whole of each cross section of the river.

FRESH LAYER GRID POINTS ▶ ⊙   +   ⊙   +   ⊙

SALT LAYER GRID POINTS ▶ ⊙ + ○ + ○ + ○ + ○ + ○ + ⊙ + ○ + ○ + ○ + ○ + ⊙

○ **level   + velocity**

       As the instabilities took origin in the surface waves, we decided
to adopt a wider step of 1 km again, for the upper layer only,
contemporarily obtaining the same degree of accuracy for the upper
and lower flow representation and having the possibility of working
with larger (more economical) time steps.

   Convergence

       At this point the quality of the lower flow representation,
obtained by using different steps for the two layers, was examined.
This was achieved by comparing the results of two simulation made
with the same time step (50 sec only in order to satisfy stability
requirements) and different space steps (200 m and 100 m).   The
simulations referred to a 2 km extension of a typical section of the
river bed and used actual hydrological data as input.

       The Godunov-Ryabenki theorem /8/, which affirms the
convergence of a finite difference scheme once its stability is
ensured, gives a tool with which to decide when a step is small
enough to well represent a certain perturbation. This is the case for
the 100 m and 200 m steps: in fact both simulations provide similar
results as regards shape and velocity propagation of the wedge (fig. 5);
the head velocity is almost the same and the more irregular
longitudinal profile of the wedge reveals the presence of higher
frequencies in the 100 m simulation. This is logical if considered in
relation with the sharp input used(abrupt raising of the salt water
level at sea) because it already contains high frequencies which are
only reproducible in a denser grid. Fig. 5 only represents the wedge
penetration; retraction occurs with a very slow decrease of salt level
at sea, and in this case the two simulations produce closely
resembling profiles. We then judged the 200 m step as sufficient for
the simulation of the wedge in the river.

       Hence, we finally adopted space steps of 1 km for the fresh
water layer and 200 m for salt water; it was then easy to work with
time steps of 100 sec, which are reasonable for computer time.

       This scheme is not valid if the last seaward section of the
model is completely occupied with salt water (in this case there

would be a one-layer motion, the computation of which would require
a 1 km space step for a time step of 100 sec); this has never
happened during field measurements.

Boundaries

The boundary conditions which are mathematically required by
the two-layer flow set of differential equations are defined, as
previously mentioned, by internal and external wave velocity at
upstream and downstream boundaries of the model. The number of
conditions to be imposed is given by the number of perturbations
entering the model through each boundary, as the theory of
characteristics /5/, /11/ illustrates. For a subcritical flow there
are two conditions (only one internal and one external wave can enter
the model) at each boundary.

In order to allow the model to reproduce the wedge penetration,
the upstream boundary has been placed far enough away from the sea
to ensure that it cannot be reached by the wedge head.

Therefore only one upstream boundary condition (one-layer
subcritical flow) is needed: the recorded fresh water level was used
in the simulations. At the downstream boundary we presumed the
motion as both internally and externally subcritical. This implies the
use of two boundary conditions, which were the fresh and salt water
level at the river mouth. However, when the salt wedge retracts and
disappears, the fresh water level is sufficient to enable the model
to work. Consequently two different kinds of motion can be reproduced:
one layer for the normal flow of the river or two layers in presence
of the wedge.

□ **boundary conditions**
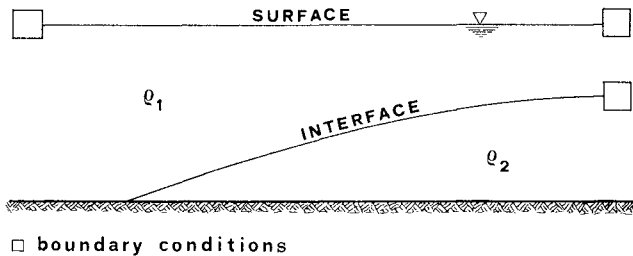
Using the internal critical condition of the motion in
correspondence with the widening of the river cross section /9/ it is
possible to avoid defining two boundary conditions at the mouth,
because it univocally links the salt water level to that of the fresh
water. For the sake of simplicity it has been used by several.authors
/10/. It has not been used in this model for three reasons:

1) - to have the possibility of testing the model simulations must
     deal with actual events; the lowest recording gauge in the river
     is placed before the widening of the river cross section; this is
     the only available downstream input.
2) - In our opinion the individuation of the critical section from the
     river morphology is very difficult. Moreover, as personally
     evidenced (presence of well marked surface fronts), in unsteady
     motion, the passage to critical conditions does not occur in a
     fixed point, instead the critical section migrates along the river
     following the tidal evolution.
3) - Furthermore, the main aim of the model is to predict the
     effects of future interventions on the river; therefore it is
     necessary to place the boundary conditions far enough away to
     render them independent from inner model events. So the
     critical conditions should be introduced into the model, allowing
     them to feel the consequences of fluvial régime modifications.

     In conclusion the model boundary conditions allowed us to
construct a physically respondent scheme, which overcame the
comparison with reality.

     As regards prediction, the seaward boundary conditions
require another solution which will consist of introducing a small
bi-dimensional model of the sea in front of the mouth, in order to
have an input that is only dependent on tide level.

Wedge head

     The motion of the wedge head has been modelled in the
simplest way: its position, which is in fact a movable inner boundary
in the model, always corresponds to one of the lower grid points,
where it vanishes. Two situations are then possible:

1) - if the upper flow is oriented downwards, the head can only
     advance if its slope (the pressure of the upper layer is less
     important) prevails on the interfacial friction. Viceversa if
     the slope is too weak, the head diminishes in volume and
     when the interface reaches the bottom it retracts by one space
     step and so on;
2) - if the upper flow is oriented upwards, the head advances one
     space step for each time step, fastly decreasing in amplitude,
     then rapidly becoming negligible.

     It is interesting to point out that this procedure is exactly the
same as for normal one-layer homogeneous models. In fact, if we
consider a linearised model with constant depth and use a time step
which is too large to verify the identity between physical and
mathematical velocity, it is well known that the numerical wave
(which propagates one space step for each time step) travels faster

than the real wave, but its amplitude rapidly decreases.

This form of modelling only identifies the position of the head relative. to the space step dimension i.e. with an approximation of 200 m. It is not important to get a higher precision, as made with more complicated schematisations /5/, because the head position is defined in correspondence with the small thickness of the lower layer, where the physical processes /12/ are not exactly the same as those formulated by the equations. For these reasons the lower flow velocity is left free on the head region to overcome the critical value (internal critical velocity tends to zero as the thickness of the layer decreases). However the head velocity in this scheme, as said before, is a purely "numerical" velocity and therefore it is logically free from physical bonds.

Interfacial stress

The friction between the layers, which is expressed by the Darcy-Weisbach formula, depends on the values of the coefficient λ. This coefficient is usually given as a function of the Reynolds and Froude numbers; many formulae and experimental laboratory results furnish a wide series of values, ranging from 10^{-3} to 10^{-1} /13, 14, 15/.

As a first simple hypothesis we made several computations assuming λ as a constant, and examining its effect on the wedge behaviour. As order of magnitude of λ , we assumed the values which were found valid in other wedge computations /10, 16/. Simulations were made for an arrested wedge, i.e. in a steady condition, imposing a slope of 5 cm in 3 km to the free surface. The results of fig. 6 show that the length of penetration of the arrested wedge is very sensitive to λ variations from 0.003 to 0.006, changing the penetration length from 2800 to 2000 m. Thus a precise definition of the coefficient would appear very important.

In the actual régime of the Delta an arrested wedge has never been recognised by field measurements. The possibility of its occurrance is really doubtful: in fact a steady condition in the tidal zone could only last for a few hours. The small propagation velocity of the internal wave causes the wedge to feel for a long time the influx of the initial unsteady condition. We then verified the effects of different values of λ simulating an unsteady motion on the true river geometry and using actual data as input. Fig. 7, showing the maximum penetration extent of the wedge, illustrates how the different values of λ scarcely affect the wedge.

The small relevance of the friction coefficient in these simulations is not only explained by the particular shape of the longitudinal profile of the river, which presents a relatively steep
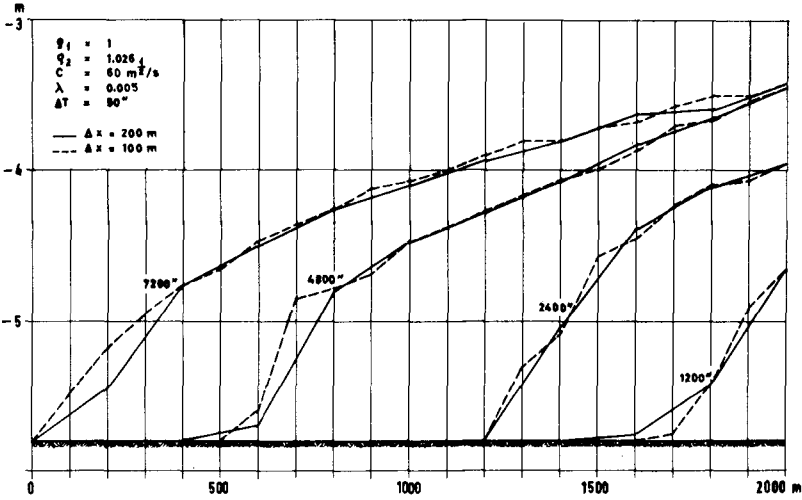
Fig. 5 - Effects of different space steps on the computed
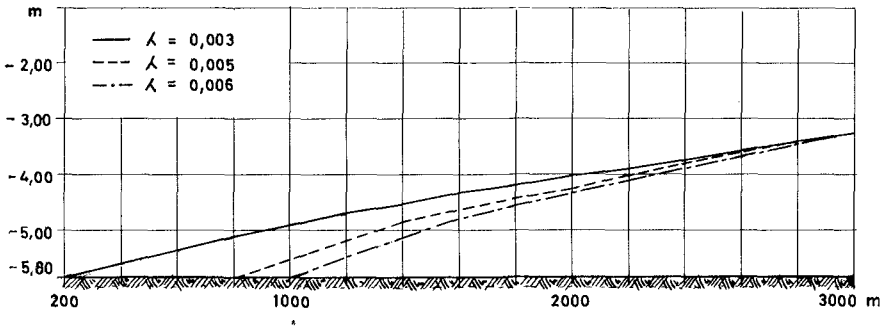   salt wedge profile

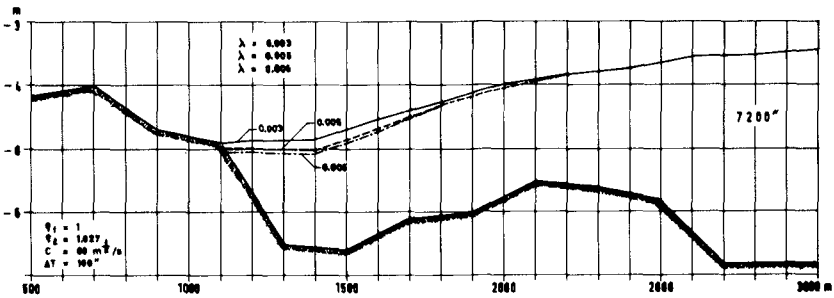Fig. 6 - Arrested wedge

Fig. 7 - Variations of Darcy-Weisbach coefficient effects on
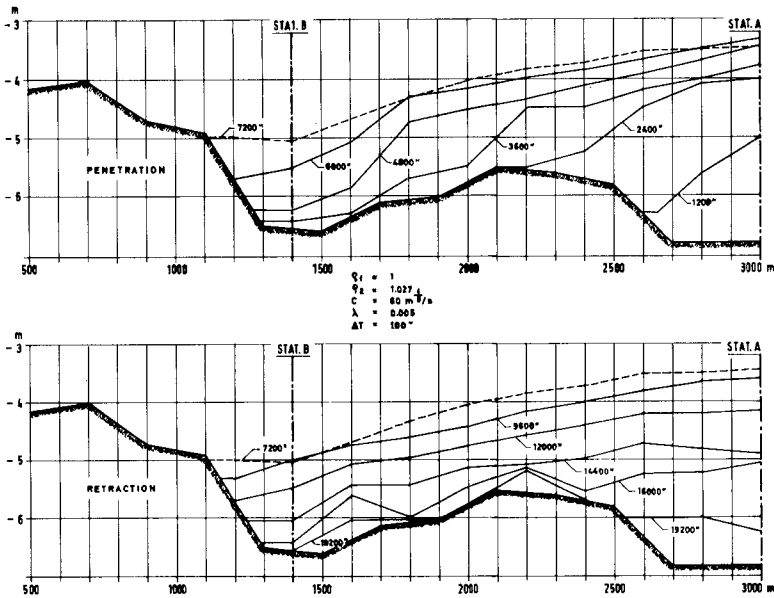   the maximum extent of the salt wedge

Fig. 8 - Simulation of the event of 22nd January 1974 –
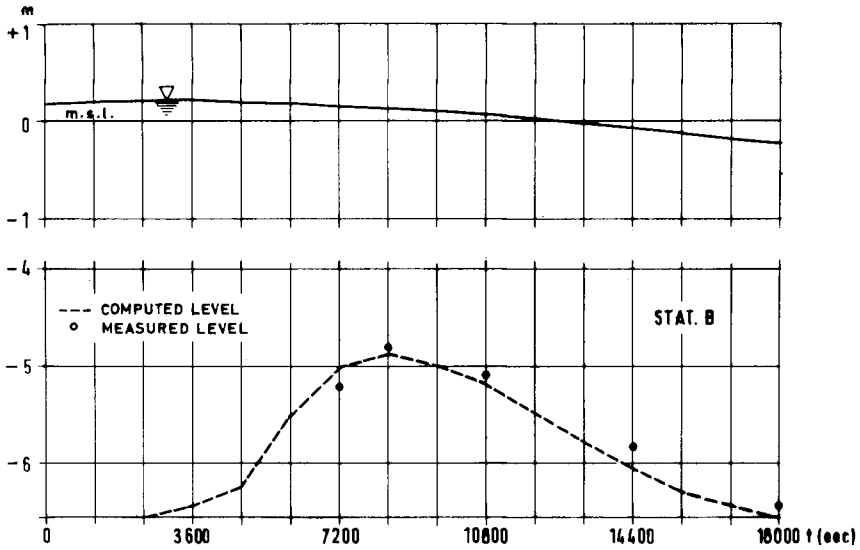Computed longitudinal profile of the salinity intrusion

Fig. 9 - Simulation of the event of 22nd January 1974 –
Computed and measured salt water level

bottom slope in correspondence with the extreme positions of the wedge head. In fact in the dynamic process of wedge penetration the friction between the layers plays a smaller role than the lower layer slope, which constitutes the main propulsive force for the wedge mo tion.

On the other hand, during penetration, both the upper and lower flow are oriented upwards, therefore diminishing the frictional effect which is in full action when the upper layer inverts its direction and blocks the salt water. For these reasons the interfacial stress coefficient does not need a sophisticated evaluation and therefore it has been considered a constant.

5) RESULTS AND CONCLUSIONS

On the basis of the previous considerations, the model has been applied to actual events for which sufficient information was available. The bottom friction coefficient (Chézy formula) was evaluated by a set of simulations in absence of salt water. Its value /1,2/ is well defined (60 $m^{1/2}$/sec) and its individuation was immediate.

Thereafter the interfacial friction coefficient was individuated by attempts as the one which best fitted the measurements. Figs. 8 and 9 show the results of a simulation of an event during which the wedge only penetrated for about 3 km upstream from station A (fig. 2). The simulation well reproduces (fig. 9) the sudden raising and the milder lowering of the salt water level, which is one of the main characteristics of the wedge. These results clearly demonstrate the reliability of the model in its present structure, in reproducing the two-layer motion.

Two main problems still remain open, both connected with the physical properties of the two-layer motion. First the interfacial processes: as seen, we solved them considering λ as a constant and the interface as impermeable. Actually the interface, whose phenomeno logy determine the value of λ is not impermeable. In fact, as the relative velocity between the two layers increases the small perturbations of the inter face grow in the form of billows which for higher velocity degenerate in eddies penetrating both layers /17/ in form of an interlayer. The time scale of the wedge phenomenology (6 hours) does not allow the interlayer to extend to the whole depth; therefore the two-layer schem atization remains valid, even if it generates a more complex flow pattern. The second point is more important to enable the model to predict. As said before, the downstream passage to critical condition has to be introduced into the model. In doing so it must be noted that the critical condition activates not-yet completely known mixing process es between salt and fresh water. These processes can not be described by the two-layer approximation only. Then the mere introduction in a model of internal supercritical flows /18/ is physically insufficient to represent the actual estuarine hydrodynamics.

REFERENCES

/1/ - Dazzi R. and Tomasino M. (1973), "Modello matematico per lo studio di un estuario o delta",
L'Energia Elettrica No 8, p. 477-486

/2/ - Tomasino M. and Dazzi R., "Il modello matematico del delta del Po", L'Energia Elettrica
(In print)

/3/ - Vreugdenhil C.8. (1970), "Computation of gravity currents in estuaries", Delft Hydraulics
Laboratory, publication No 96

/4/ - Schijf J.B. and Schönfeld J.C. (1953), "Theoretical consideration on the motion of salt and
fresh water", Proc. Minnesota International Hydraulics Convention Joined Meeting I.A.H.R.
and Hydraulics Division A.S.C.E., p. 321-333

/5/ - Boulot F., Braconnot P. and Marvaud Ph. (1967), "Détermination numérique des mouvements
d'un coin salé", La Houille Blanche No 8, p. 871-877

/6/ - Poggi 8. (1959), "Sul moto delle correnti stratificate", L'Energia Elettrica No 3,
p. 197-208

/7/ - Leendertse J. (1967), "Aspects of a computational model for long period water wave
propagation", The RAND Corporation, Santa Monica - California, memorandum RM 5294-PR

/8/ - Godunov S.K. and Ryabenki V.S. (1964), "The theory of difference schemes", North Holland
Publishing Company - Amsterdam

/9/ - Stommel H. and Farmer H.G. (1952), "Abrupt change in width in two-layer open channel flow",
Journal of Marine Research 11-2. p.205-214

/10/- Boulot F. and Daubert A. (1969), "Modèle mathématique de la remontée de la salinité sous
une forme stratifiée en régime non permanent", XIII Congrès de l'A.I.R.H., Kioto

/11/- Landau L.D. and Lifshitz F.M. (1959), "Fluid mechanics ", Vol. 6 of Course of theoretical
Physics, Pergamon Press, Oxford

/12/- Abraham G. and Vreugdenhil C.8. (1971), "Discontinuities in stratified flows", Journal of
Hydraulic Research No 3, o. 293-308

/13/- Abraham G. and Eysink W.D. (1971), "Magnitude of interfacial shear in exchange flow",
Journal of Hydraulic Research No 2, p. 125-151

/14/- Pedersen 8. (1972), "The friction factor for a two-layer stratified flow, immiscible and
miscible fluids", Rep. 27 , p. 3-13, Tech. Univ. Denmark

/15/- Shi-Igai and Sawamoto M. (1969), "Experimental and theoretical modeling of saline wedge",
I.A.H.R., Kioto p. 29-35

/16/- Vreugdenhil C.8. (1969), "Numerical computation of fully stratified flow", I.A.H.R., Kioto

/17/- Keulegan G.H. (1966), "The mechanism of an arrested saline wedge", Estuary and Coastline
Hydrodynamics, Mc Graw and Hill p. 546-574, Ippen editor

/18/- Grubert J.P. and Abbott M.8. (1972), "Numerical computation of stratified nearly horizontal
flows ", Journal of the Hydraulics Division, ASCE, oct. 1972

CHAPTER 135

THREE DESIGN SYSTEMS FOR APPLICATIONS IN COASTAL ENGINEERING

M.B. Abbott,
International Courses, Oude Delft 95, Delft, Netherlands;
Computational Hydraulics Centre, Danish Hydraulic Institute, Øster
Voldgade 10, 1350 Copenhagen K, Denmark;

J. Aa. Bertelsen, Aa. Damsgaard, P.I. Hinstrup, G.S. Rodenhuis and
R.I. Warren,
Computational Hydraulics Centre, Danish Hydraulic Institute, Øster
Voldgade 10, 1350 Copenhagen K, Denmark;

and A. Verwey,
International Courses, Oude Delft 95, Delft, Netherlands.

1. INTRODUCTION

The Computational Hydraulics Centre in Copenhagen has developed three
design systems for applications in hydraulics, coastal and offshore
engineering. Each system constitutes a software - documentation entity
that automatically constructs and runs mathematical models of a speci-
fic class when presented only with the model description. The systems
concerned are as follows:

> System 11, "Siva", is restricted to 1-dimensional flows
> of 1-layer (vertically homogeneous) fluids.

> System 21, "Jupiter", applies to 2-dimensional flows of
> 1-layer fluids.

> Systems 12/13 and 22/23, "Neptune", apply to 1-dimensional
> flows with 2 or 3 layers for the 12/13 and 2-dimensional
> flows with 2 or 3 layers for the 22/23.

Brief descriptions of these systems follow.

2. SYSTEM 11, "SIVA"

This system can be used to describe unsteady nearly-horizontal flows in
any system of channels, taking account of changes in flow section with
elevation and related effects on mean flow paths, resistances, dis-
persion etc. The system is built upon the equations of conservation of
mass and momentum, together with transport - dispersion - dilution -
reaction equations for salt, BOD and oxygen, as follows:

$$b_s\frac{\partial h}{\partial t} + \frac{\partial Q}{\partial x} = q \tag{1}$$

$$\rho\frac{\partial Q}{\partial t} + \frac{\partial}{\partial x}\frac{(\alpha\rho Q^2)}{A} + \rho g A\frac{\partial h}{\partial x} + \frac{\rho g Q|Q|}{C^2 AR} - \rho_q q|v|\cos\emptyset$$

$$+ \frac{Q\partial\rho}{\partial t} + \frac{f(h)\partial\rho}{\partial x} = 0 \tag{2}$$

$$A_v\frac{\partial c}{\partial t} + Q\frac{\partial c}{\partial x} - \frac{\partial}{\partial x}\frac{(AD\partial c)}{\partial x} = q(c_q-c) \tag{3}$$

$$A_v\frac{\partial L}{\partial t} + Q\frac{\partial L}{\partial x} - \frac{\partial}{\partial x}\frac{(AD\partial L)}{\partial x} + (K_1 - K_3)A_v L = q(L_q-L) \tag{4}$$

$$A_v\frac{\partial I}{\partial x} + Q\frac{\partial I}{\partial x} - \frac{\partial}{\partial x}\frac{(AD\partial I)}{\partial x} + K_1 A_v L - K_2 A_v(I_3-I) = q(I_q-I) \tag{5}$$

Equations similar to (3, 4, 5) can be introduced to describe polluti
due to heat and various chemicals. Fig.1-2 shows some properties of
the model constructed for field testing the system on the Limfjord,
in Northern Denmark.

3. SYSTEM 21, "JUPITER"

The "Jupiter" is applied to investigations in seas, more complicated
estuaries, harbour, lakes and similar bodies of water. The equations
of mass and momentum solved by the system read as follows:

$$\frac{\partial(\rho h)}{\partial t} + \frac{\partial(\rho p)}{\partial x} + \frac{\partial(\rho q)}{\partial y} = 0 \tag{6}$$

$$\frac{\partial}{\partial t}(\rho p) + \frac{\partial}{\partial x}\frac{(\rho p^2)}{h} + \frac{\partial}{\partial y}\frac{(\rho pq)}{h} + gh\frac{\partial}{\partial x}(\rho(h-H))$$

$$- \Omega\rho q + \frac{\rho g}{C^2 h}\sqrt{p^2+q^2}\cdot p - W_x\rho = 0 \tag{7}$$

$$\frac{\partial}{\partial t}(\rho q) + \frac{\partial}{\partial y}\frac{(\rho q^2)}{h} + \frac{\partial}{\partial x}\frac{(\rho pq)}{h} + gh\frac{\partial}{\partial y}(\rho(h+H))$$

$$+ \Omega\rho p + \frac{\partial g}{C^2 h}\sqrt{p^2+q^2}\cdot q - W_y\rho = 0 \tag{8}$$

Further, equations generalised from (3, 4, 5) can be superimposed, to constitute a "pollution superstructure".

The Jupiter has been extensively developed in several versions, referred to as "Marks". In the Mark 1, special forms of equations (6, 7, 8) are used along grid lines running adjacent to coasts, so that the model topography is resolved to a high level of accuracy — comparable with the "free grid" of the finite-element method. In the Mark 2 further facilities are introduced to allow flooding and drying within the model. The Mark 3 allows, in addition, several changes of scale within a single model, with step-down ratios in grid size of 2 or 3 at each change. The version carrying the pollution super-structure is called the Mark 4. Finally there is a Mark 5 that suppresses the special forms of (6, 7, 8) along beaches, so as to work in "minimum configuration". The identifiers can be combined, to give, for example, a Mark 52 or a Mark 53.

The Marks 1, 2 and 52 have been used extensively over the last three years while the Mark 53 has been field tested. Some results are shown in Fig. 3-5.

4. SYSTEMS 12/13 AND 22/23, "NEPTUNE"

The hydrodynamic "platform" program of the 12/13 is built upon equations of conservation of mass, linear momentum and density defect. For the System 12 these equations read as follows:

$$\frac{\partial}{\partial t}(\rho_1 h_1) + \frac{\partial}{\partial x}(\rho_1 u_1 h_1 + (\rho_0 q_0 - \rho_1 q_1) = 0 \tag{9}$$

$$\frac{\partial}{\partial t}(\rho_0 h_0) + \frac{\partial}{\partial x}(\rho_0 u_0 h_0) + (\rho_1 q_1 - \rho_0 q_0) = 0 \tag{10}$$

$$\frac{\partial}{\partial t}(\rho_1 u_1 h_1) + \frac{\partial}{\partial x}(\rho_1 u_1{}^2 h_1) + \rho_1 g h_1 \frac{\partial}{\partial x}(H + h_1 + h_0)$$

$$+ (\rho_0 q_0 u_0 - \rho_1 q_1 u_1) = 0 \tag{11}$$

$$\frac{\partial}{\partial t}(\rho_0 u_0 h_0) + \frac{\partial}{\partial x}(\rho_0 u_0{}^2 h_0) + \rho_0 g h^0 \frac{\partial}{\partial x}(H + \frac{\rho_1 h_1}{\rho_0} + h_0)$$

$$- (\rho_1 q_1 u_1 - \rho_0 q_0 u_0) = 0 \tag{12}$$

$$\frac{\partial \rho_1}{\partial t} + u_1 \frac{\partial \rho_1}{\partial x} - \frac{\rho_1}{\rho_w} \frac{\partial^2 \rho_1}{\partial x^2} + \frac{q_0 (\rho_0 - \rho_1)}{h_0} = 0 \tag{13}$$

$$\frac{\partial \rho_0}{\partial t} + \frac{u_0 \partial \rho_0}{\partial x} - \frac{\rho_0}{\rho_w} \frac{\partial^2 \rho_0}{\partial x^2} - \frac{q_1(\rho_1 - \rho_0)}{h_0} = 0 \qquad (14)$$

In addition, a bed stress, a surface (wind) stress and an interfacial stress may be introduced. The equations generalise easily to three layers and also to two dimensions. The systems can be used for three-dimensional modelling, when h_0, h_1 and h_2, for three layers, correspond to vertical Lagrangian coordinates, but the rate of vertical mixing in the physical and numerical stabilising processes remains unclear.

In both 12/13 and 22/23, pollution "superstructures" can be mounted, to describe the transport, dispersion, reaction etc. of various substances. Fig. 6 shows some results from field tests of the System 12 on the Gota river in South Sweden

5. CONCLUSIONS

The System 21, "Jupiter" is now a well tried instrument in coastal engineering, providing considerable economics in field investigations. The System 11, "Siva", and the 12/13 part of the "Neptune" are currently becoming operational on a commercial basis while the 22/23 is the subject of intensive development and should be available commercially during 1975.

6. NOTATION

b_s	(m)	storage width
c		salt concentration
f(h)	(m^4/s^2)	function of the depth squared integrated over the crosssection
g	(m/s^2)	acceleration due to gravity
h	(m)	level above arbitrary horizontal reference level
k_1	(s^{-1})	coefficient of BOD decay due to oxidation
k_2	(s^{-1})	coefficient of reaeration
k_3	(s^{-1})	coeeficient of BOD decay due to other processes
q	(m^2/s)	lateral inflow
t	(s)	time
u	(m/s)	velocity in x-direction
v	(m/s)	lateral inflow velocity, velocity in y-direction
x	(m)	coordinate along the river, West-East coordinate
Y	(m)	South-North coordinate
A	(m^2)	flow area perpendicular to the stream

A_v (m^2)   storage area perpendicular to the stream
                (integral of b_s over depth)
C   ($m^{\frac{1}{2}}/s$)   Chezy resistance value
D   (m^2/s)   coefficient of longitudinal dispersion
H   (m)   elevation of bed, above datum
I   dissolved oxygen concentration
I_s saturation concentration of dissolved oxygen
L   BOD concentration
Q   (m^3/s)   volume flux of fluid
R   (m)   hydraulic radius
α crosssectional velocity distribution co-
                efficient.
ρ (kg/m^3)   fluid density

System 11 figures.

Hydrodynamic Model of the Limfjord, North Jutland.
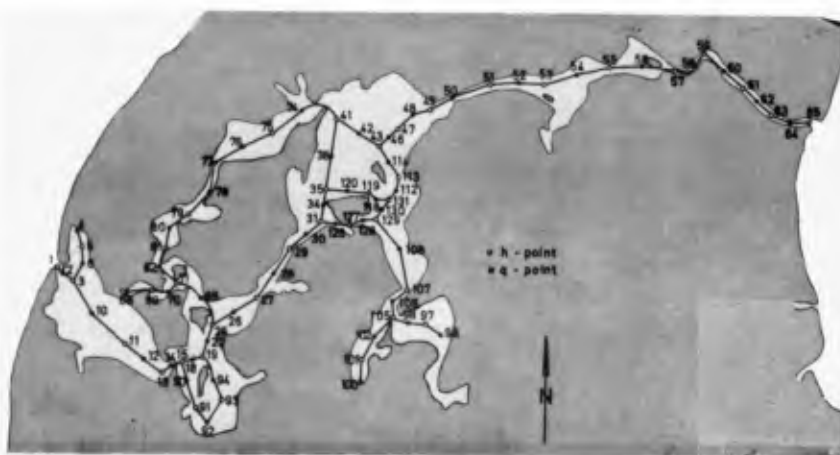
APPLICATION OF SYSTEM 11, SIVA   LIMFJORD, NORTH JUTLAND, DENMARK: COMPUTATIONAL GRID
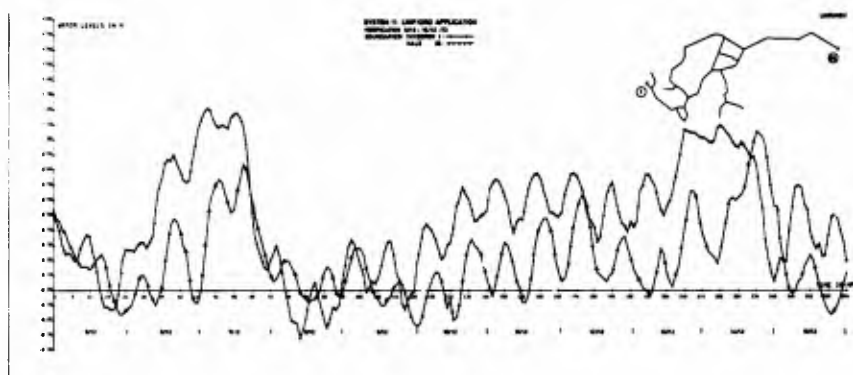
Fig. 1A

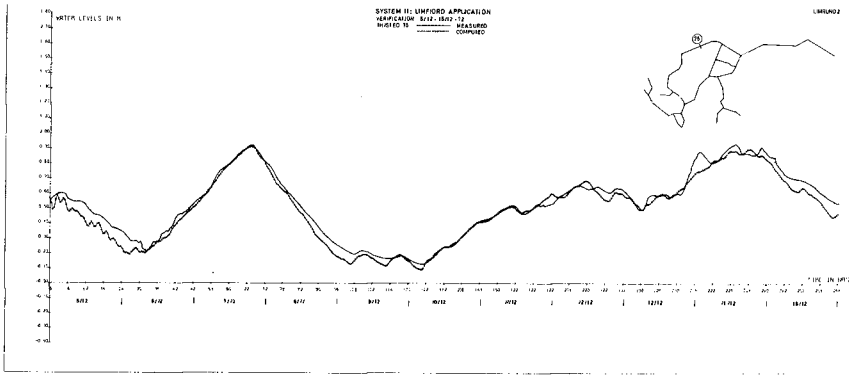Computational Grid

Fig. 1B

Water levels at Boundaries

Fig. 1C . Computed and Recorded Water Levels

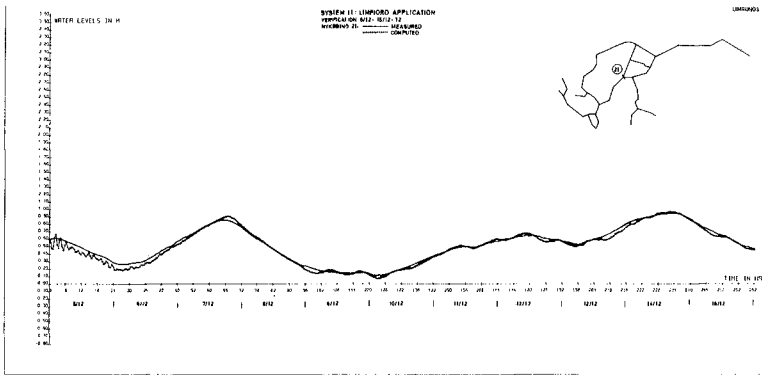

Fig. 1D

Computed and Recorded Water Levels

Fig. 1E   Computed and Recorded Discharges

Transport-Dispersion Model
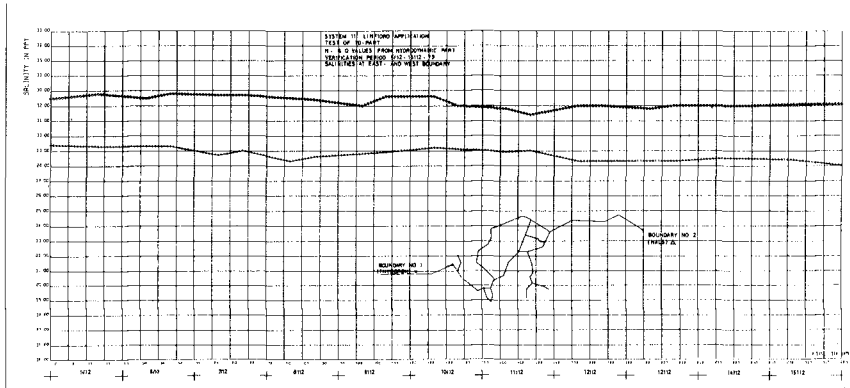
Fig. 2A

Recorded Salinities at Boundaries
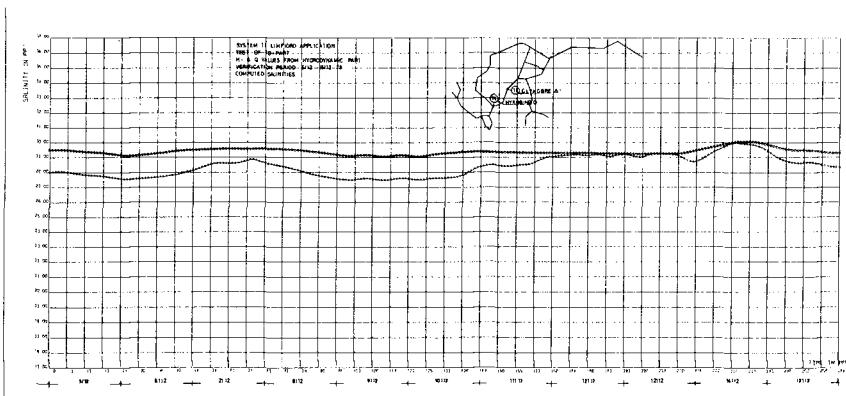
Fig. 2B

Computed Salinities

System 21   figures.

Model of Hurricane Surges in Key Biscayne, Florida
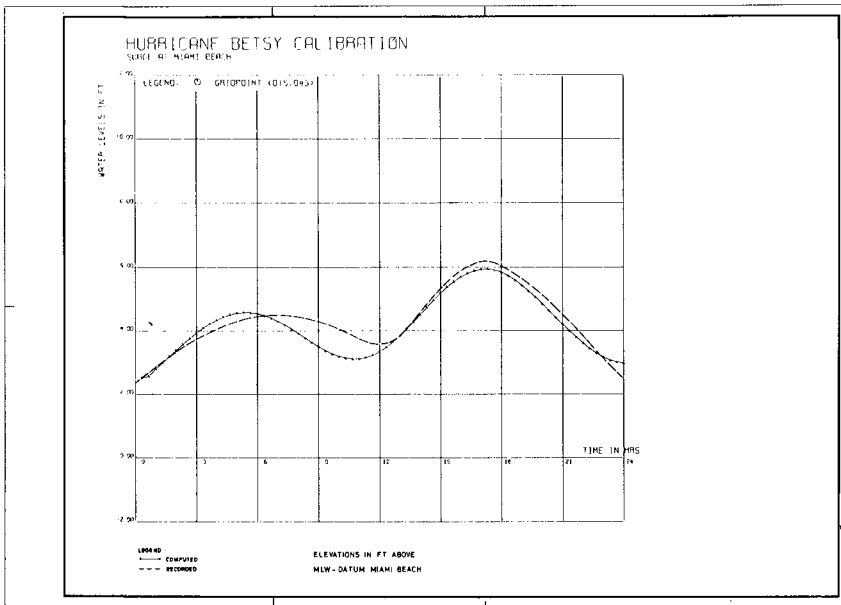
Fig. 3a
Calibration of the model using Hurricane "Betsy" data.

19 HRS
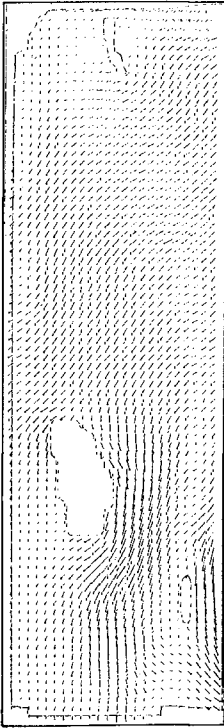
19 HRS
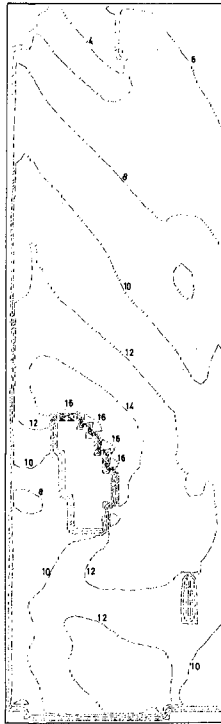
Fig. 3b
Plot of fluxes$(ft^2 \cdot s^{-1})$
19 hrs. after start of
test.

Fig. 3c
Plot of water level contours (ft)
19 hrs. after start of test.

Model of an Instantaneous Dam Failure.
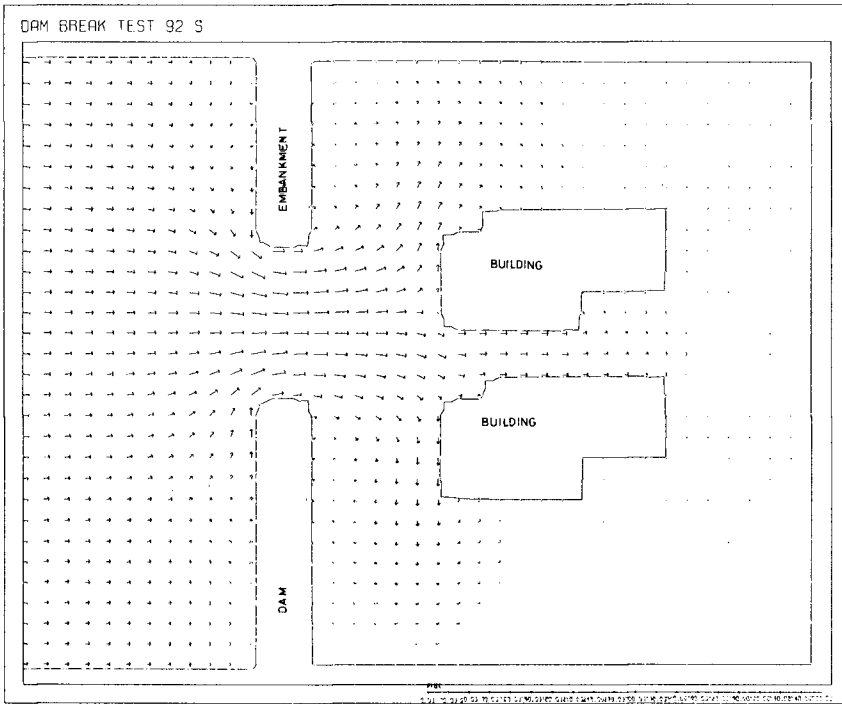
Fig. 4a
Plot of fluxes ($m^2 \cdot s^{-1}$)
92 sec. after failure.
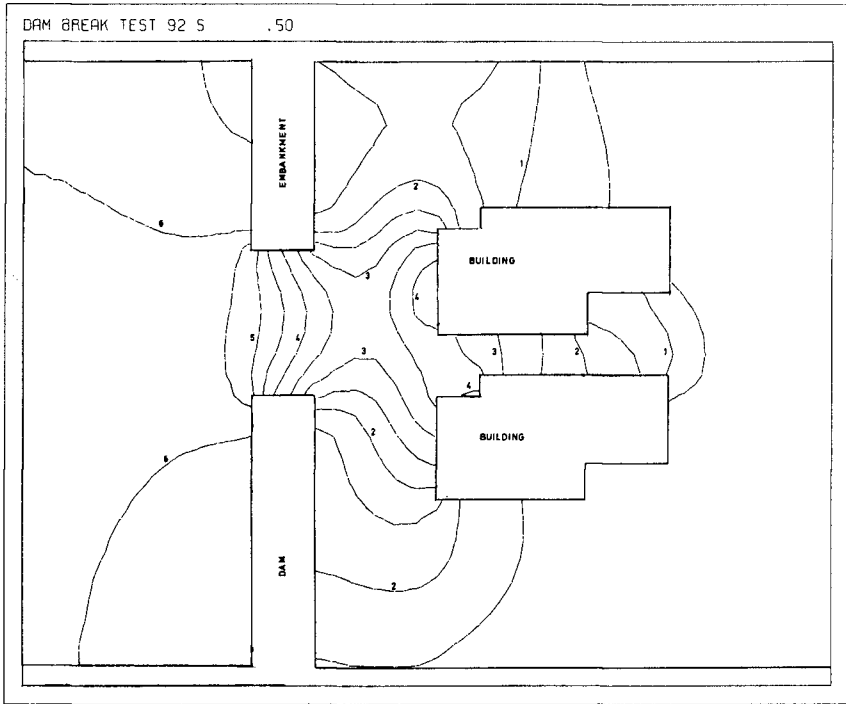
Fig. 4b
Plot of water level contours (m)
92 sec. after failure.

Model of Harbour Seiches.
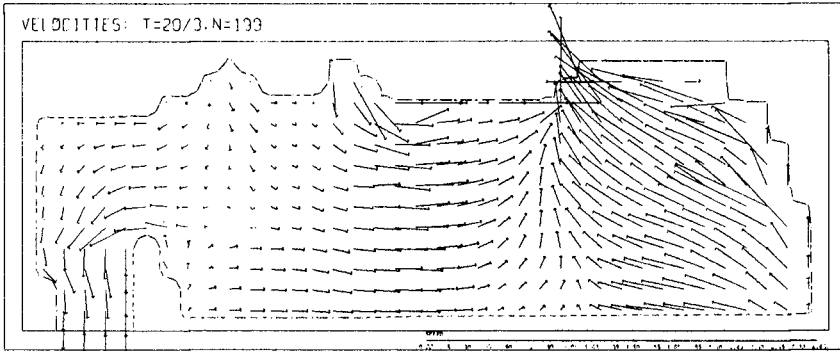
Fig. 5A
Plot of fluxes $(m^2 \cdot s^{-1})$ at an instant during a
full wave mode of oscillation.
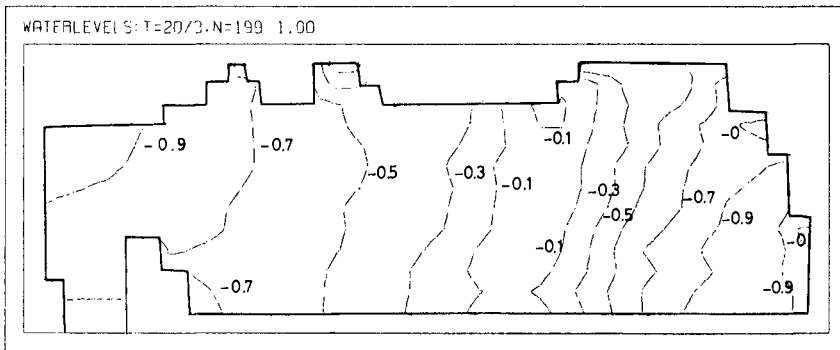
Fig. 5B
Plot of water level contours (m) at an instant
during a full wave mode of oscillation.

System 12   figures.

Model of the Göta River, Sweden
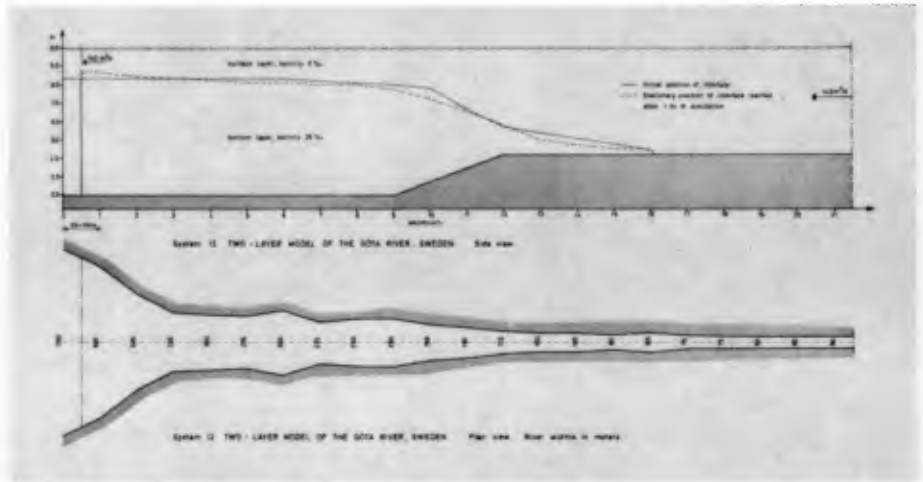
Fig. 6

Computed Positions of Interface

CHAPTER 136

A THREEDIMENSIONAL MODEL OF A HOMOGENEOUS ESTUARY

by

Jürgen S ü n d e r m a n n [1]

Summary

Basing on HANSEN's hydrodynamical-numerical method a
threedimensional model of wind and tidally generated pro-
cesses in a homogeneous estuary is developed. The model in-
cludes an arbitrary depth distribution and the simulation
of a boundary layer near the bottom. Some numerical examp-
les demonstrate the applicability for practical purposes.

1. Introduction

Mathematical models of the dynamics in homogeneous estuaries,
coastal waters and shallow seas are presently in a worldwide
practical use. Commonly they are based on the vertically inte-
grated hydrodynamical differential equations. Thus, the vertical
structure of the circulation field is not considered. This
procedure turned out to be sufficient for many purposes, so
for the investigation of tidal processes or the global wind
generated circulation.

On the other side, vertically averaged stream velocities are
of little evidence in the case of those propagation and trans-
port processes which are essentially vertically structured, e.g.
the movement of solid material.

The left part of fig. 1 shows a stream profile corresponding
to the empirical exponential law, the assumption of a constant
horizontal velocity gives a rather good approximation.

---

1) Professor, Technical University, Hanover, W. Germany

z

ū

x,u

u=u(z)

a

z

x,u

u(z)

ū=0

b
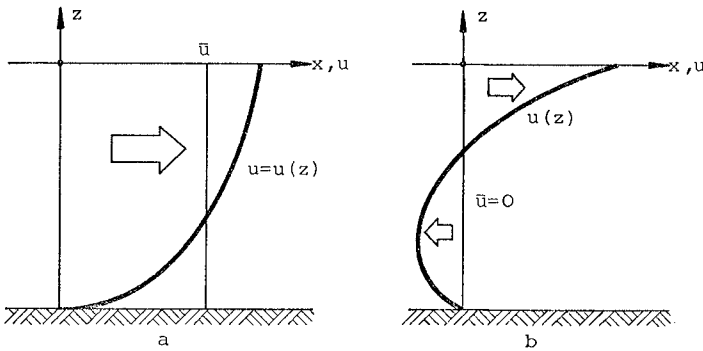
Fig. 1. Schematical vertical profiles of the stream velocity generated by tides (a) and by the wind stress (b)

Near the coastline, however, the real velocity distribution can deviate remarkably from a vertical mean. The right picture shows the typical vertical structure of a wind generated stream: the movement in the wind direction at the surface and a compensating countercurrent near the bottom. Although the mean velocity vanishes in this case, a considerable circulation occurs which may be connected with transport processes of dissolved constituents or sand. These processes can not be reproduced by the vertically integrated equations. Hence, its modelling requires the development of threedimensional models.

Vertically structured models are already used, especially in the field of physical oceanography, since several years (FRIEDRICH /1/). They have been developed, however for the baroclinic conditions of the deep ocean which are essentially different from the situation in coastal engineering.

Therefore, a specific threedimensional model has been developed (SÜNDERMANN /2/) which is presently being applied to the North Sea.

2. The model

The mathematical model is based on the following differential equations.

$$\frac{\partial u}{\partial t} + u \frac{\partial u}{\partial x} + v \frac{\partial u}{\partial y} + w \frac{\partial u}{\partial z} = -g \frac{\partial \zeta}{\partial x} + fv + \frac{\partial}{\partial z} \left(A_v \frac{\partial u}{\partial z} \right)$$

$$\frac{\partial v}{\partial t} + u \frac{\partial v}{\partial x} + v \frac{\partial v}{\partial z} + w \frac{\partial v}{\partial z} = -g \frac{\partial \zeta}{\partial y} - fu + \frac{\partial}{\partial z} \left(A_v \frac{\partial v}{\partial z} \right)$$

$$\frac{\partial \zeta}{\partial t} + u_s \frac{\partial \zeta}{\partial x} + v_s \frac{\partial \zeta}{\partial y} - w_s = 0$$

$$\frac{\partial u}{\partial x} + \frac{\partial v}{\partial y} + \frac{\partial w}{\partial z} = 0$$

ζ is the water level; u, v, w are the components of the velo-
city vector in a Cartesian system with coordinates x,y,z;
f is the Coriolis parameter; g the earth's acceleration and
A_V the vertical eddy coefficient. The index s refers to the
surface.

The first two equations are obtained from the NAVIER-STOKES
equation of motion with the assumption of a hydrostatic pressure
distribution and the BOUSSINESQ approximation for the turbulent
REYNOLDS stresses. The third equation is the formulation of the
kinematic boundary condition at the surface. The last equation
is the continuity equation for an incompressible medium.

In some cases, instead of the kinematic boundary condition, the
vertically integrated continuity equation has been used. A
horizontal turbulent exchange of momentum was introduced only if
it was necessary for reasons of numerical stability and
stationarity.

This system of hyperbolic partial differential equations is non-
linear and hence particularly suited to shallow water dynamics.

In addition, the following boundary conditions are added.

(a) $A_V \left. \frac{\partial u}{\partial z} \right|_s = \tau_s^{(x)}$, $A_V \left. \frac{\partial v}{\partial z} \right|_s = \tau_s^{(y)}$ at the surface, where $\tau_s^{(x)}$,
$\tau_s^{(y)}$ are the components of the wind stress at the water surface.

(b) The normal component of the velocity vector vanishes at solid
boundaries (coastline, bottom).

(c) The tangential component of the velocity vector vanishes at
solid boundaries (non slip condition).

(d) Prescribed water elevations or stream velocities at the lateral
open boundaries.

As initial condition a state of rest is assumed.

The discretization is carried out by means of a cubic grid net
which is especially adapted to the structure of the basic diffe-
rential equations, see fig. 2. It is related to the schemes of
HANSEN /3/ and LEENDERTSE /4/.
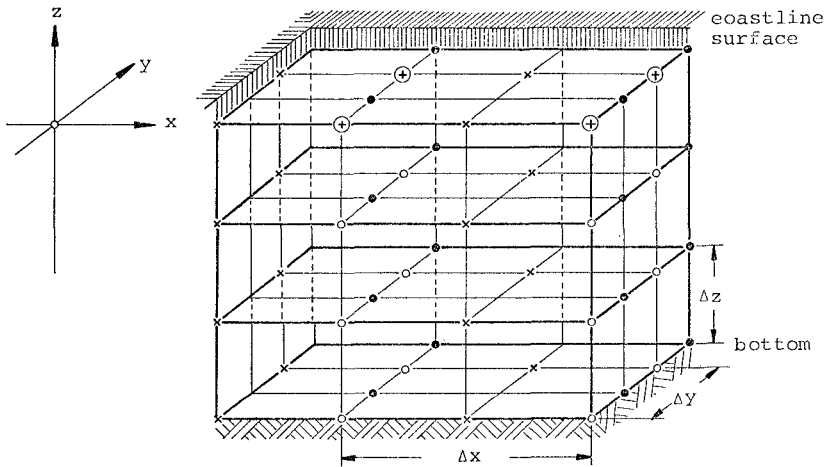
Fig. 2. Three dimensional computational grid. The unknowns are
calculated in the following points

+ ζ   × u   ● v   ○ w   ⊕ ζ and w

The horizontal space steps Δx and Δy are choosen equidistant.
Indeed, this is not necessary in principle, but it simplifica-
tes the discretizised equations.

The vertical grid distance Δz, however, should remain variable
in any case, for an arbitrary refinement of the grid is impossible
due to the enormously increasing core memory demand. On the
other hand, a relatively fine diseretization is required at in-
terfaces (e.g. surface and bottom). For the same reason it is
desirable to design the size of the grid elements near the sur-
face or the bottom to be variable, in order to include the free
moving surface and a variable depth distribution.

To fit the vertical velocity profiles as observed in nature, it
is necessary to consider a boundary layer near the bottom. This
can be modeled by introducing a coefficient of vertical eddy
viscosity dependent on the depth. In the model presented here
the relationship given by KAGAN /5/ has been used (fig. 3, upper
picture).

Analytical relationship (KAGAN 1968)

$$A_V(z) = \begin{cases} A_V^* \text{ , if } 0 \geq z \geq -h+d \\[2mm] \dfrac{z+h}{d} A_V^* \text{, if } -h+d \geq z \geq -h \end{cases}$$

Numerical realization

$k=1$

$k=K-2$ $u_{K-2} = (1+\kappa) \; u_{K-1}$

$k=K-1$ $\kappa = \dfrac{\overline{A_V} \; \Delta z}{A_V^* \; d}$

$k=K$
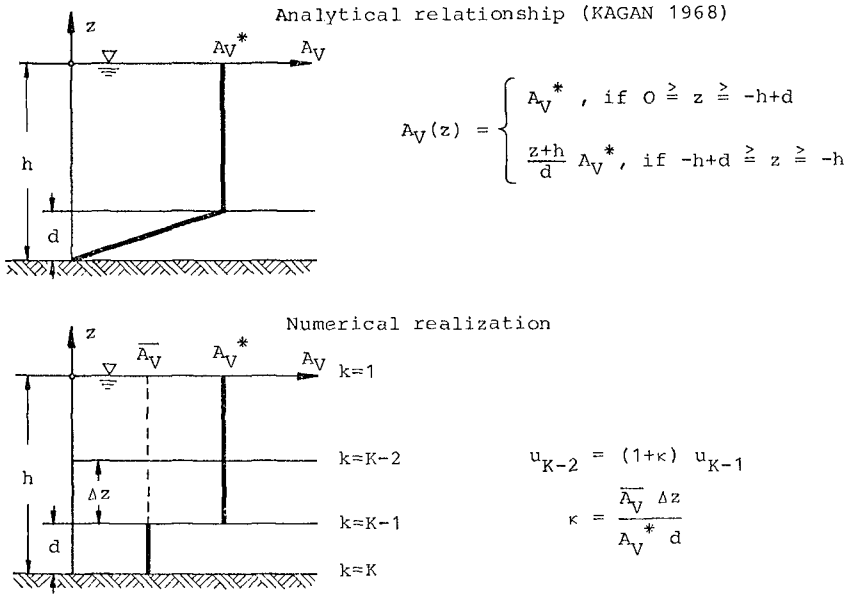
Fig. 3. The dependence of the vertical eddy coefficient A_V on the water depth z

This relationship can be parametrizised by means of a dimension-less quantity κ with a value of 0,2 to 0,3 (fig. 3, lower picture).

Fig. 4. demonstrates that the best approximation of the empirical exponential profile will be reached for a value of $\kappa = 0,3$. For comparison, the profile is also drawn for a constant eddy coefficient (this assumption results in a more linear velocity profile).
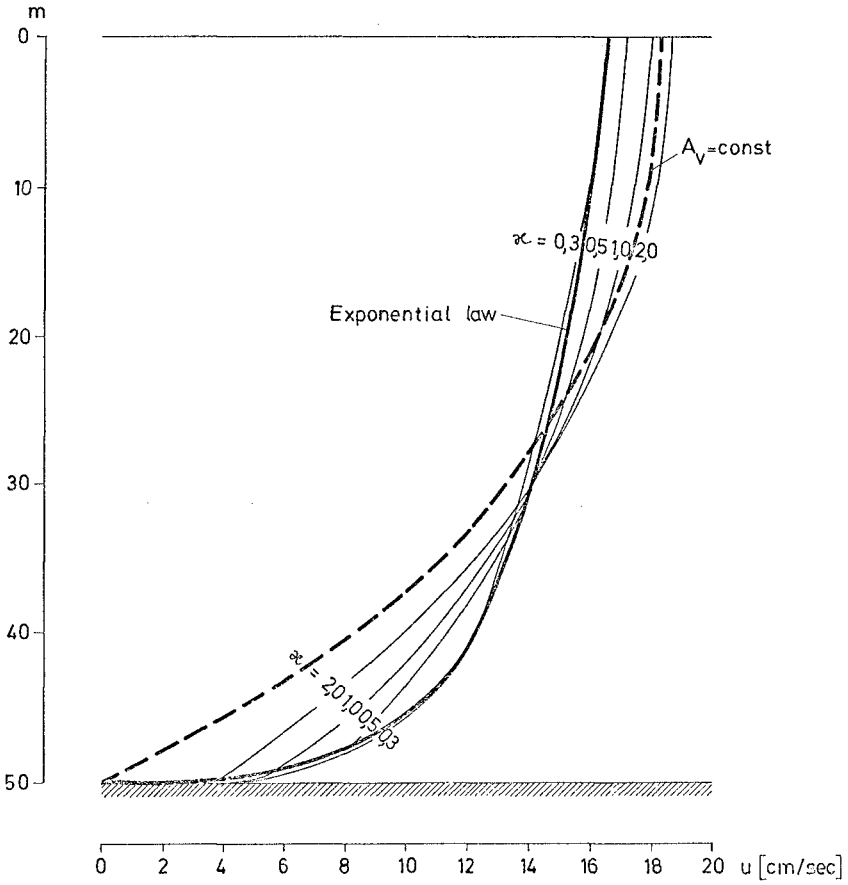
Fig. 4. Computed vertical profiles of tidal stream velocity for different models of the vertical eddy viscosity compared with the empirical exponential law.

The numerieal solution of the differential equations is ob-
tained by means of a finite difference method, firstly by using
the explicit scheme of HANSEN for both, the horizontal and the
vertical direction. As it turns out, the restrictions for
numerical stability are given not so much by the well-known
criterium of COURANT - FRIEDRICHS - LEWY:

$$\Delta t \; \overset{\le}{} \; \frac{\Delta x}{\sqrt{gh}} \; ,$$

but by an additional condition for the vertical grid distance:

$$\Delta^2 z \; \overset{\le}{} \; 2A_V \Delta t.$$

For instance, with $A_V = 0,1 \; m^2 \; sec^{-1}$ and $\Delta t = 300$ sec the verti-
cal grid distance should be choosen as

$$\Delta z \; \overset{\ge}{} \; 7,75 \; m.$$

Such a large grid cannot be accepted when investigating boundary
layer phenomena.

In order to overcome this difficulty the well-known implieit
procedure of CRANK - NICOLSON has been used for approximating
the vertical diffusive term. This procedure allows one to choose
the vertical grid distance Δz arbitrary. The technique also acts
to stabilize the numerical computation to such an extent that
the COURANT-criterium can be slightly extended.

If, for a given spatial discretization, the COURANT-criterium
leads to an unsuitable computational effort, the equations of
motion must also be solved by an implicit proeedure for the
horizontal direction. This can be achieved by type of alternating
direction method combining the equations of motion and the ver-
tically integrated eontinuity equation.

3. Some results for schematic models
The presented model is applied, firstly, to tidal and wind induced
threedimensional eirculation processes in schematic canals and
basins. The following examples are based on a eanal of constant
depth (50 m) and a length of about 100 km or on a basin with
100 km length, 50 km width and 50 m depth. The models have an
open boundary in the case of an incoming tidal wave (100 cm
amplitude),they are closed in the ease of wind generated motions
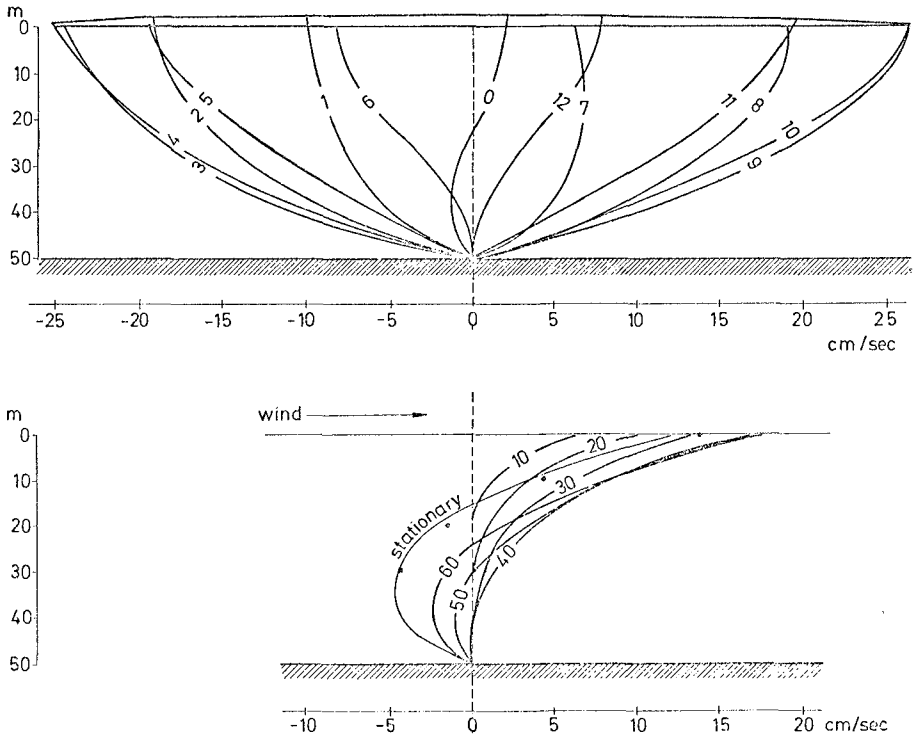
Fig. 5. Computed vertical velocity profiles in a canal of constant depth.

Upper picture: Tidal generated motion. The numbers are hours.
Lower picture: Wind generated motion. The numbers are minutes
                after the beginning of the wind.

(20 m/sec wind speed). Further values are:

$$A_V = 0,1 \text{ m}^2 \text{ sec}^{-1} \text{ and } f = 1,2 \cdot 10^{-4} \text{ sec}^{-1}$$

Fig. 5 shows some typical vertical velocity profiles for a point situated in the middle of a 50 m deep canal. In the upper picture the tidal flow for different tidal phases (in hours) has been drawn. It may be clearly seen that the alternation of the stream direction within the tidal cycle begins firstly in the deeper layer. The maximum velocities occur, generally, at the surface.

The lower picture shows the time dependent development of the velocity distribution under a stationary wind. The numbers are in minutes after the beginning of the wind's action. The counter-current near the bottom is formed after only 40 minutes. The points mark the analytical solution for the stationary linear case.

Fig. 6 shows, for the above considered example, the stationary circulation system along a longitudinal section. The upper figure demonstrates the corresponding water elevation.

wind ⟹ 20 (m/sec)
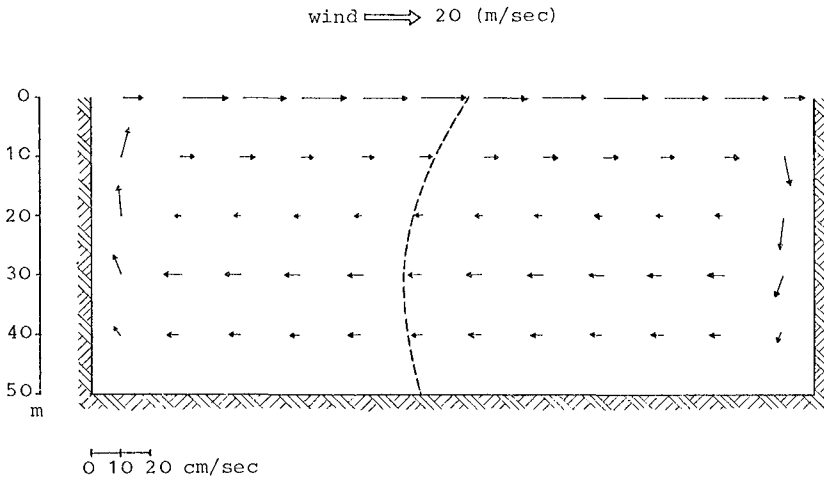
Fig. 6. Wind generated circulation field in a closed channel
of constant depth. The dashed curve shows a vertical stream
profile.

In fig. 7 the stationary stream fields are drawn for a
constant Northerly wind at different depths, namely at
the surface and for 10, 20, 30, 40, 50 m water depth. It is
assumed, in this case, that even at the bottom a nonvanishing
velocity can appear which generates an energy dissipation
according to a quadratic friction law. One can clearly see a
reduction and turning to the right, of the velocity vector
with increasing depth.
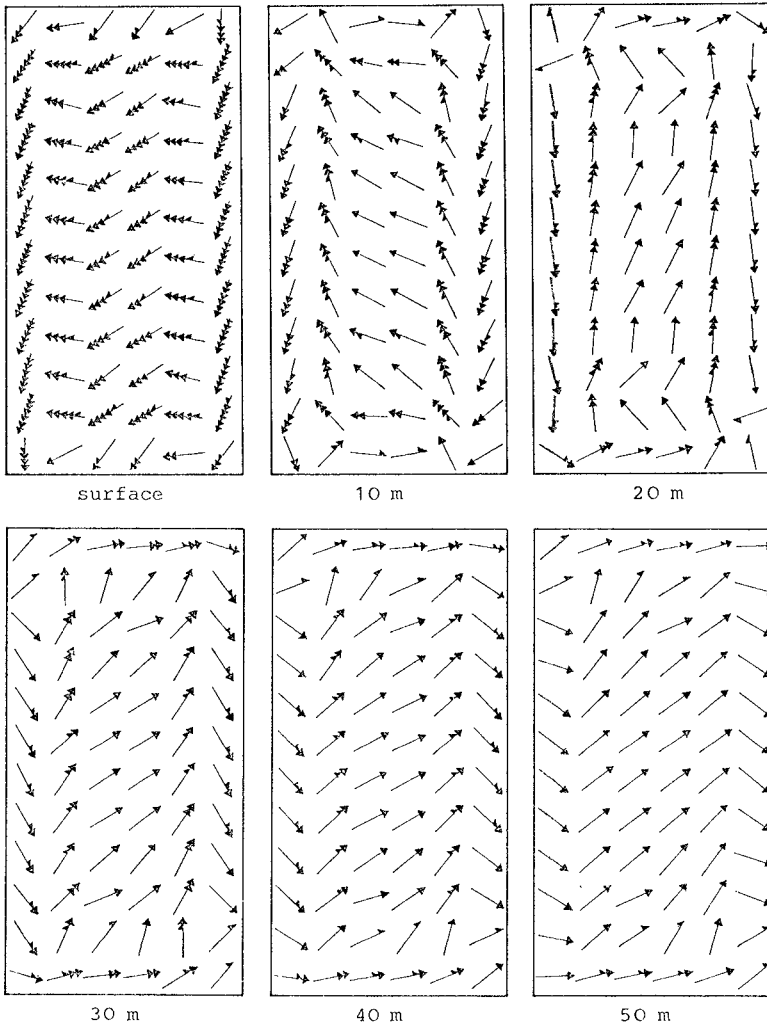
Fig. 7. Wind generated horizontal circulation field in a
        closed basin of constant depth for 6 horizons.

This fact suggests a comparison with the EKMAN theory of wind driven currents. Fig. 8 shows the velocity vectors for different depths for a point in the middle of the basin. The enveloping curve of the arrows should agree, in the ideal case, with the well-known EKMAN spiral (see the small sketch in the lower right corner). The theoretical EKMAN frictional depth

$$D = \pi\sqrt{\frac{2A_v}{f}} \simeq 40,7 \text{ m}$$

is in a good agreement with the computed value in the inner basin.
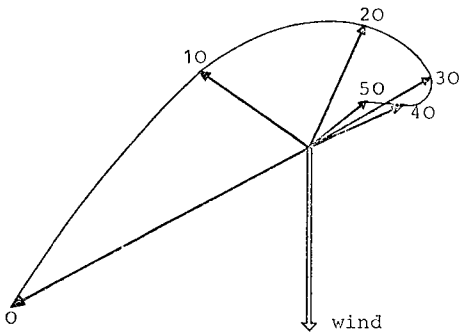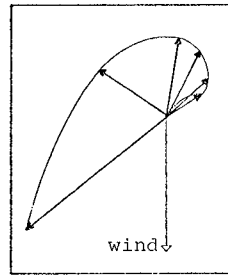
numerical computation   EKMAN theory
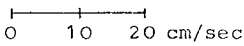
Fig. 8. The EKMAN spiral of the velocity vector for a
        Northerly wind over a basin of constant depth
        (the numbers are depths in meters).

It may also be seen from the last picture that for this depth
the direction of the current is just opposite to the surface
stream (which is the definition of the frictional depth).

Fig. 9 demonstrates a comparison with the unstationary
EKMAN theory. This theory states that the right-hand devia-
tion of the surface vector (at the Northern hemisphere)
converges to the 45° direction in the form of a CORNU spiral
(see the sketch in the lower right corner). The numbers are
hours after the beginning of the wind. The agreement of the
both hodographs is remarkable.

numerical computation   EKMAN theory

0   10   20 cm/sec
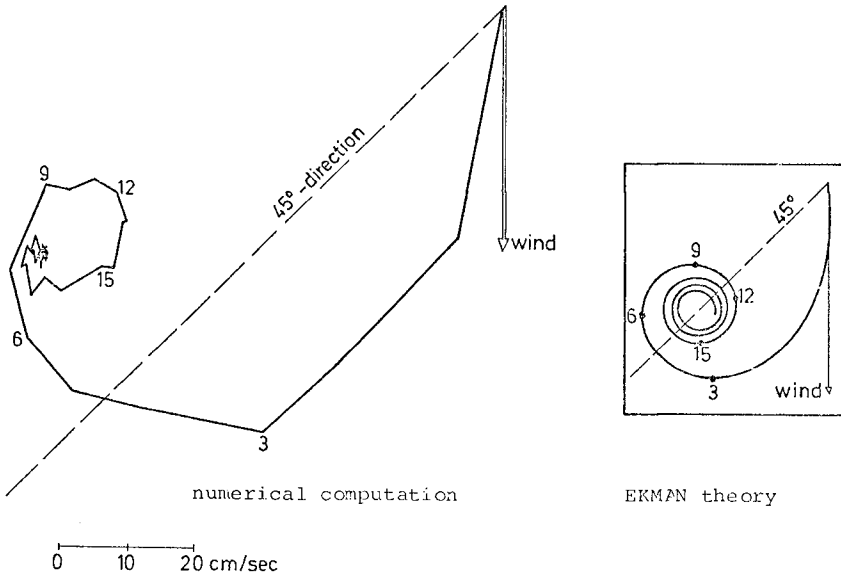
Fig. 9. The hodograph of the velocity vector at the surface
        for a Northerly wind over a basin of constant depth
        (the numbers are hours)

We shall deal now with tidal processes in schematic sea areas.
Fig. 10 shows a longitudinal section with the tidal generated
stream field in a canal for two tidal phases separated by a
half tidal period. The tides are controled by the boundary con-
ditions at the right boundary.
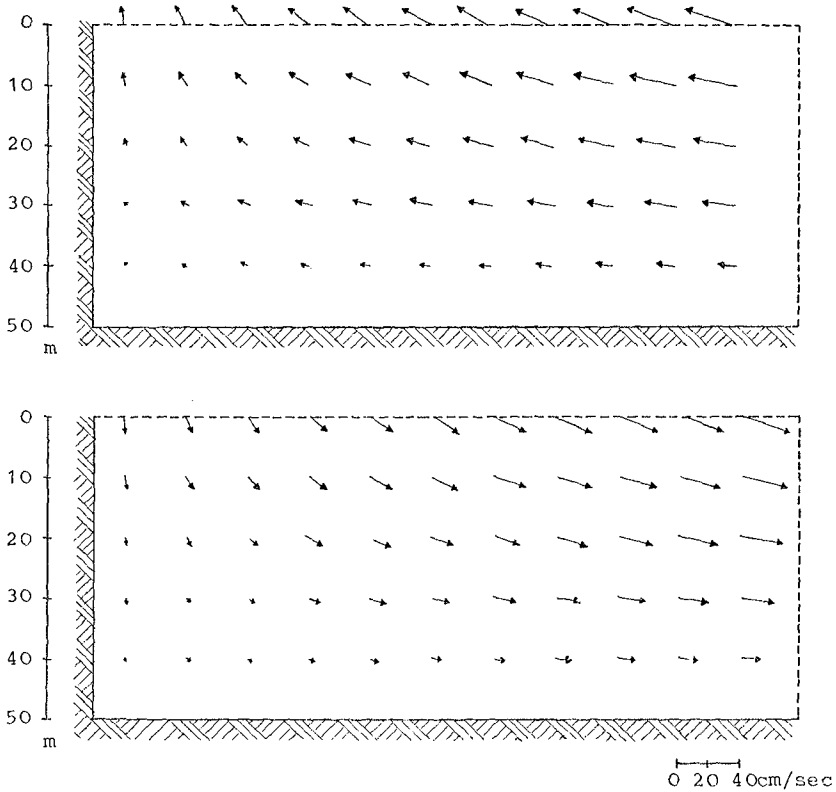
Fig. 10. Tide generated circulation field in an open channel
         of constant depth for two different phases.

It can be seen from the fig. 11 that also in the case
of a variable depth distribution - here with a simple submarine
barrier - reasonable velocity distributions are calculated.
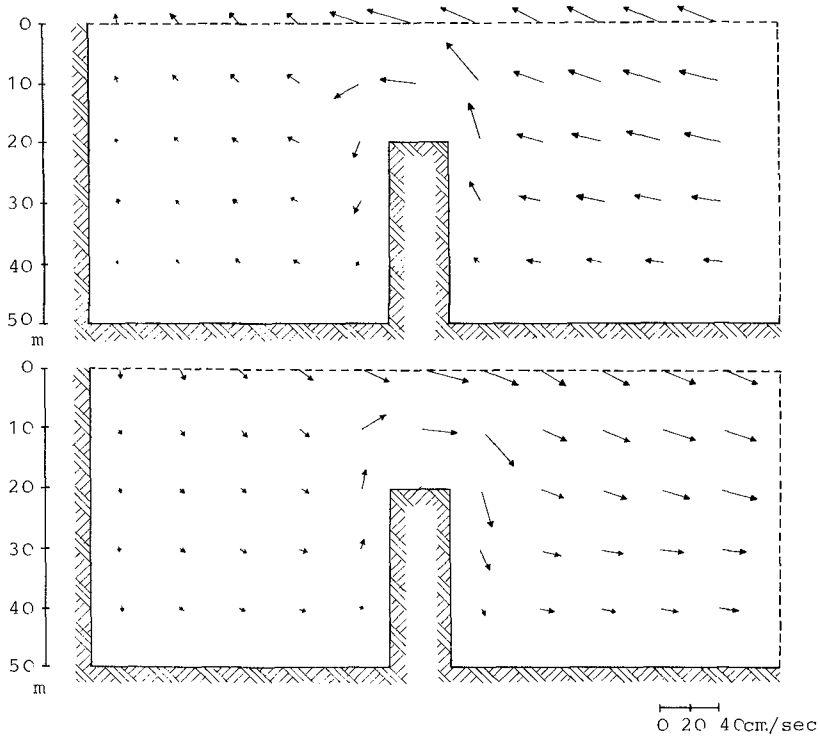
Fig. 11. Tide generated circulation field in an open channel with
a submarine barrier for two different phases.

Summarizing it can be stated that with the presented results
concerning the dynamics of schematic threedimensional bays the

developed numerical method has been suffieiently tested. The
assumption of simple geometrieal forms seems to be meaningful
and neeessary for the test stage of a new model. On the other
hand, by the introduction of a variable depth distribution
and of a boundary layer near the bottom the model elearly
approximates more natural eonditions. A first applieation to
a real sea basin is given for the following North Sea model.

4. The North Sea Model

The starting point for the discretization was a horizontal
grid net with a grid distanee of 37 km as has been used for
several years at the Institute for Oceanography of the Uni-
versity of Hamburg. This model has been extended, as shown
above, to a threedimensional model by the addition of further
10 eomputational planes in the vertieal direetion. This grid
planes are situated at the surfaee, at a depth of 3, 6, 10,
25, 50, 150, 220, 300 meters and at 3 and 1 m above the bottom
and the bottom itself. This diseretization ineludes that for
small depths (e.g. in the Southern part of the North Sea)
eertain grid planes are absent.

The model which has been developed by P. SCHÄFER /6/ is presently
in a testing stage. The next three pietures show some prelimi-
nary results eoncerning the main semidiurnal M_2-tide.

Fig. 12 gives the eomputed co-range and eo-tidal lines (in em
and hours after the moon's transit at the Greenwich meridian,
resp.). As a eomparison the known result of a vertieally integra-
ted model is presented simultaneously. The differenees are, in
general, quite small.

The tidal streams at the different depths, however, show partially
a remarkable variation and hence deviation from the mean inte-
grated value. In the area near the coast of the middle part of
the British Isles even the phenomenum oecurs that the orienta-
tion of the stream figures is ehanged. That means that the velo-
city veetor at the deeper layers is rotating in the opposite sense
of that one of the surface.
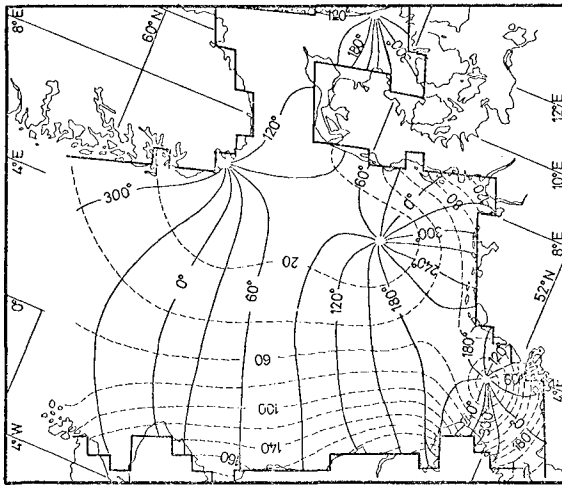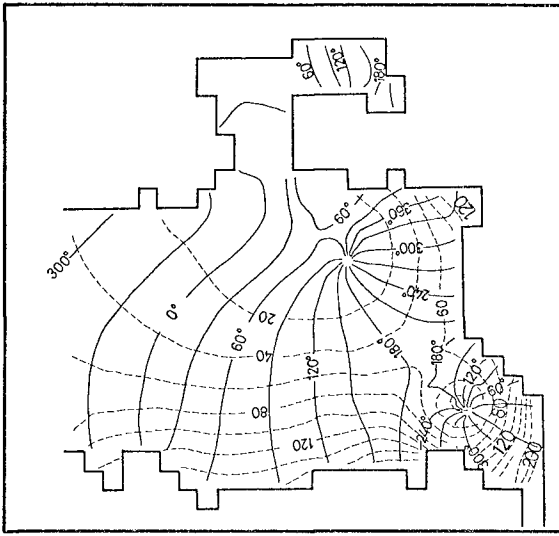
M$_2$-tide in the North Sea

Fig. 12. Co-tidal lines related to Greenwich (————) and co-range
lines in cm (-----) for a twodimensional (uper picture)
and a threedimensional model with 11 layers (lower picture).

The figures 13 and 14, finally, demonstrate the computed stream
figures for the depth horizons 10 m and 50 m of the Southern
and Western part of the North Sea, resp.

Those numerical results may considerably extend our knowledge
on the dynamics of this sea area. They open the possibility
of a coupling with transport models describing the propagation
of dissolved constituents and the movement of solid materials.
It is intended to investigate the motion processes in real bays
and estuaries in the same way. If this homogeneous models
are tested sufficiently the distribution of salinity, tempera-
ture and density will be included in the model.

References

/1/   FRIEDRICH, H. Preliminary results from a numerical multi-
      layer model for the circulation in the North Atlantic,
      Deutsche Hydrographische Zeitschrift 23, 4, 1970

/2/   SÜNDERMANN, J. Die hydrodynamisch-numerische Berechnung
      der Vertikalstruktur von Bewegungsvorgängen in Kanälen
      und Becken, Mitt. Inst. Meereskd. Univ. Hamb. 19, 1971

/3/   HANSEN, W. Hydrodynamical methods applied to oceano-
      graphic problems, Mitt. Inst. Meereskd. Univ. Hamb. 1, 1962

/4/   LEENDERTSE, J.J. Aspects of the computational model
      for longperiod water wave progagation, RAND Memorandum 5294,
      Delft, 1967

/5/   KAGAN, B.A. Hydrodynamical models of ocean tides (in Russian),
      Gidrometeoroizdat, Leningrad, 1968

/6/   SCHÄFER, P. Ein dreidimensionales diagnostisches Nordsee-
      modell zur Untersuchung großräumiger barokliner Bewegungs-
      vorgänge, Doctor Thesis, University of Hamburg, 1974
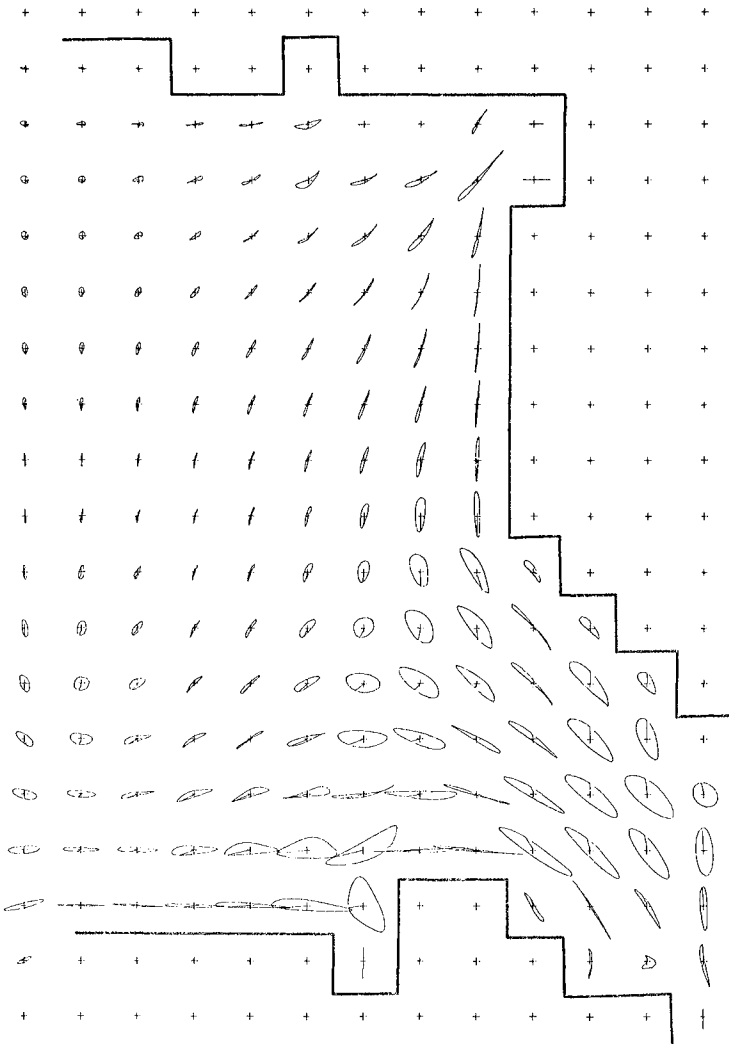
Fig. 13. M_2-tide in the North Sea.
Stream figures for 10m depth (Southern part)
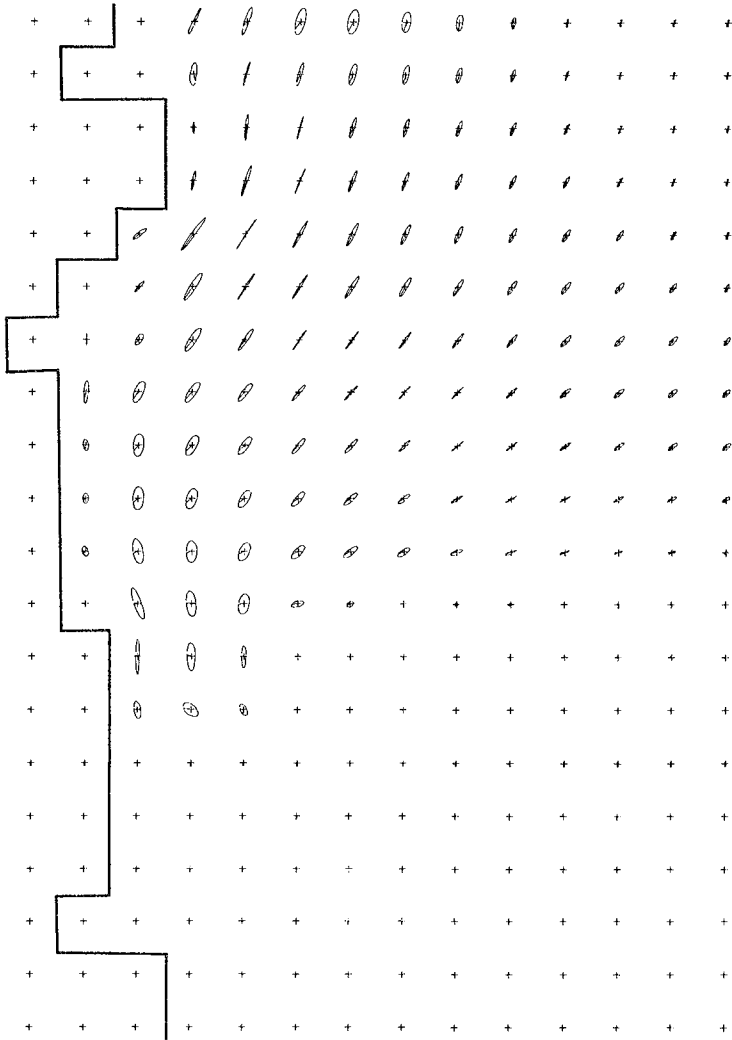
Fig. 14. M$_2$-tide in the North Sea.
        Stream figures for 50 m depth (Western part)

CHAPTER 137

FIELD AND MODEL DATA OF SPREADING IN ESTUARIES

F. Ohlmeyer[1], D. Berndt[2]

F. Ohlmeyer[1], D. Berndt[2]

INTRODUCTION

The coastal regions in the highly industrialized zones of
western Europe and other comparable parts of the world are a
preferable field of new industrial settling. The economic
reasons are: 1. Situation on deep water reachable by big ves-
sels and 2. The increasing of the units of power plants and
chemical industries demands for great quantities of water.
For instance 200 up to 500 m^3/s are no longer utopic today.
Generally such great quantities are not available but in
coastal regions especially on estuaries where the water move-
ment is governed mainly by tidal action. Fig. 1 shows new
industries and power plants in the region of the German Bay
the shaded areas are consisting tidal models.

In order to avoid environmental damages by pollution of in-
dustrial or thermal wastes and to diminish the recirculation
effects of power plant, it is necessary to get correct in-
formation of the concentration rates resp. temperatures that
will appear in these regions.

The ways to get this information are well-known:
1. Direct measurements in prototype, 2. Mathematic models,
3. Hydraulic models or hybride models. Direct measurement
is to some degree a necessary presumption to the latter two
ways, but furthermore it afterwards gives information of the
accordance of the model predictions. But often there is no
money to do so.

Of course it is not necessary to measure the whole area -
that would mean model investigations scaled 1:1 - but some
specific data will be sufficient.

1) Dipl.-Ing.   )   Bundesanstalt für Wasserbau
2) Dipl.-Ing.   )   Hamburg, Germany

Such comparisons could be made by the Bundesanstalt für Was-
serbau, Fed.Rep. of Germany, who carried out model investiga-
tions and field measurements in estuaries of the Elbe and
the Ems which belong to the well mixed types with a tidal
range of 2.5 up to 3.5 m.

RECIRCULATION EFFECTS

One subject of investigation was the recirculation of cool-
ing water. Fig. 2 shows the scheme of the thermal circuit;
during half a tidal cycle recirculation is nearly unavoid-
able. The temperature rise was in one case about $5^{\circ}C$, where
the heat output at the condenser was $\Delta T_o = 10^{\circ}C$. The re-
circulation rate $\varsigma = \frac{\Delta Ti}{\Delta T_o}$ (ΔT_i is the temperature rise at
the intake after the first cycle) can be expressed as $\varsigma = \frac{\varsigma_\infty}{1+\varsigma_\infty}$
where $\varsigma_\infty = \frac{\Delta Ti_\infty}{\Delta T_o}$ and $\Delta T_{i\infty}$ is the maximum possible tempe-
rature rise. For $\Delta T_{i\infty} = 5^{\circ}C$, $\varsigma = 0,33$ results. This rela-
tion is derived from the geometrical progression $\varsigma_\infty = \sum\limits_{n=1}^{\infty} \varsigma^n$.

The recirculation rates can also be regarded as a mixing
factor. The temperature curves (Fig. 3) show two peaks
which appear just after and before slack tide respectively
when the longitudinal flow velocity in the ambient estuary
water approaches zero, and thus the lateral spreading be-
comes dominant. Without mixing there would be complete re-
circulation ($\varsigma = 1$).

With the aid of model investigations it could be achieved
to diminish the recirculation rate of a power plant from
0.52 to 0.23 i.e. more than 50 %. The solution was a sheet-
piling of 30 m length beneath the outlet structure. The
situation of the inlet and outlet structures is shown in
Fig. 4, a bird's view picture of the power plant in model.
From left to right: inlet, outlet of the nuclear station;
inlet, outlet of the oil fired station.

In order to seperate the influence of one power plant to
the other, Rhodamine-B-Tracer was used. By this way the
influence of the indirect recirculation from earlier tidal
cycles could be eliminated too.

SPREADING MECHANISM

During the slack tide, a remarkably large lateral spreading
can be observed which apparently is caused by larger ini-
tial jet spreading. Therefore the plume of the pollutant
shows a special shape which is depicted in Fig. 5. Fig. 6
demonstrates the enlargement of the plume at lower fluvial
velocities. But the lateral spreading in a free stream is
also substantially larger during the slack tide than in
times of a higher velocity, and originates from intensified
convective lateral transport, resulting from large volume
eddies. The interaction between convection and turbulent
diffusion largely governs the spreading process in the tidal
region.

MODEL INVESTIGATIONS

A good accordance between model and prototype presumes a
correct simultation of the velocity field as well as a fair-
ly good turbulent diffusion all over the tidal cycle.

The latter is only possible with a specific distortion,
where the depth scale has to be

$$\lambda_2 = \lambda_1^{3/4}$$

relation of distortion
for turbulent flow in the rough
region

λ_1 = length scale

This relation is derived, with the aid of dimensional ana-
lysis, from Kolmogoroff's equation (1), the turbulent dif-
fusion equation (2) and the roughness condition $\lambda_r = 1$
through the application of the Manning-Strickler formula (3)
valid for turbulent flow in the rough region (Reynolds'
Number Re > 1200).

(1) $E = c \cdot G^{1/3} \cdot \ell^{4/3}$ (Kolmogoroff)

E = diffusion coefficient

G = energy dissipation per unit
    mass

ℓ = characteristic length of eddies

c = a constant

(2) $\frac{\partial c}{\partial t} + u \frac{\partial c}{\partial x} + v \frac{\partial c}{\partial y} = \frac{\partial}{\partial x} \partial\left(D_x \frac{\partial c}{\partial x}\right) + \frac{\partial}{\partial y} \partial\left(D_y \frac{\partial c}{\partial y}\right)$

(3) $u = \frac{1}{n} R^{2/3} J^{1/2}$ (Manning-Strickler)

The energy dissipation and the turbulent friction are in
this region only dependent upon $\frac{h}{d}$ (h = roughness height),
(d = depth), i.e. geometric parameters that are easily to
simulate in the model. Models scaled 1:100 (depth) and
1:500 (length and width) fullfill this condition und have
shown good results.

COMPARISON OF MODEL DATA WITH MEASUREMENT IN PROTOTYPE
Various field measurements were performed to verify model
experiments on lateral spreading of the polluted plume.
Fig. 7 shows the lateral distribution of the spreaded plume
1 1/2 hours before low water, 90 m below the outlet, 3 m
under the surface (near field test). Temperatures as well as
concentrations rates of Rhodamine were measured in prototype
and model. To indicate Rhodamine concentration a Turner
Fluorometer was used. The field results are almost identical
with the model results. Comparisons between the spreading
of a dye patch in prototype and model is shown by the graph
on Fig. 8 (far field test). Fig. 9 depicts the dye patch of
Rhodamine from an airplane.

The recording of time dependent temperature or concentration
values has been shown to be advantageous for the estimation
of the effect of an inflow (Fig. 10), since here maximum
and minimum values are recorded. By this way it is possible
to separate the influence from earlier tides. The oscilla-
tion is due to tidal action only and after 5 to 10 tidal
periods there will be an equilibrium.

APPLICABILITY OF PHYSICAL MODELS
It can be confirmed by comparison between model and proto-
type data that it is possible to simulate not only the dis-
persion in the far field area where the mixing process is
governed by free turbulent structures and the velocity

field of the stream but also the initial spreading of the
penetrating jet in the near field and the transition zone.
In this region it is necessary to record the width of the
polluted plume in the correct way at all tidal phases. This
is possible by using artificial roughness elements at the
outlet point.

In addition to the report of Dr. Schwarze (7.3.) one should
point out, that the distortion of the model is not only a
good thing in simulating thermal losses (thermal decay) but
besides it is a necessary presumption of recording the dis-
persion process in a physical model. The choice of scales
is not free but fixed to a specific relation.

The usage of the "characteristic length" in Kolmogoroff's
equation in passage 4 is only a mere thing of comparison
without knowing the real value of it. It is used only in
the dimensionless sense in the applicated analysis. In rea-
lity the "characteristic length" is equal to the diameter
of the largest eddies, which may fill the width of the
stream.

DECAY OF A POLLUTANT

Waste water, radioactive pollutants and cooling water are
subject to decay. This decay can't be simulated in the phy-
sical model if one is using a conservative tracer. But the-
re is a method to calculate this decay when getting the con-
centration rates due to the mere spreading process of tur-
bulent diffusion and convection from the model.

Furthermore, a decay curve has to be known (Fig. 11). Ac-
cording to the demonstrated figure a pollution only over a
one tide cycle is simulated. The occurring concentration
levels have to be reduced by multiplying them by the rate
of decay. An integration then gives the desired curve of a
non-conservative pollutant at the estimated point of the
estuary. The time increment of integration in this opera-
tion is just one tidal cycle.

CONCLUSIONS

Froudian tidal modelling besides two dimensional mathemati-
cal representation has proved to be a useful method to get
information about the concentration levels of pollutants
spreading into an area with tidal actions. The decay of
non-conservative pollutants can be evaluated by using a
decay curve. Distortion with scales of 1:500/1:100 and the
use of special artificial roughness elements seem to coun-
terbalance the effects of a differently turbulent diffusion
in vertical and horizontal directions which is predicted by
theory. The flow pattern in a model should be rough turbu-
lent.

REFERENCES

[1] CRICKMORE, 1972, Tracer tests of eddy diffusion in
        field and model, Proc. of the ASCE HY 10.

[2] OHLMEYER/VOLLMERS, 1973, Thermal and sewage pollution
        in tidal areas, Proc. of the 15th IAHR Congress,
        Vol. 2, Istanbul.

FIG 1
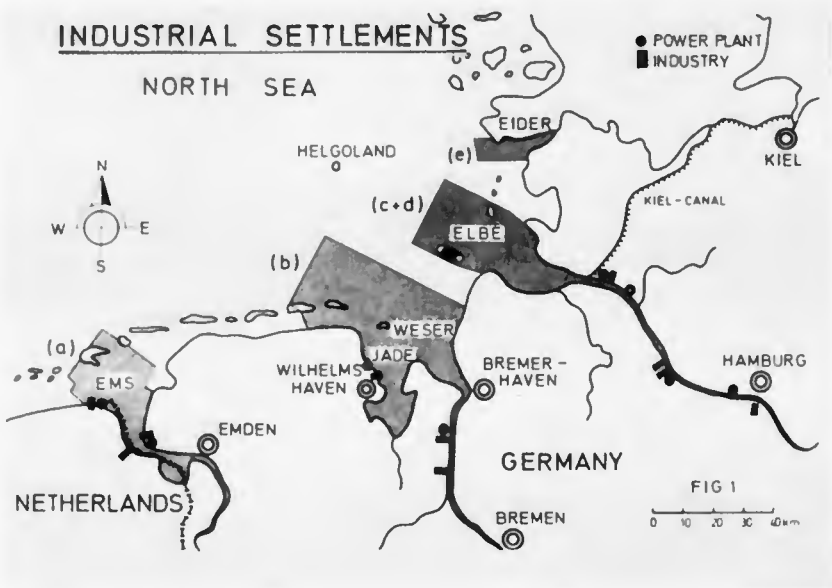
DIRECT RECIRCULATION
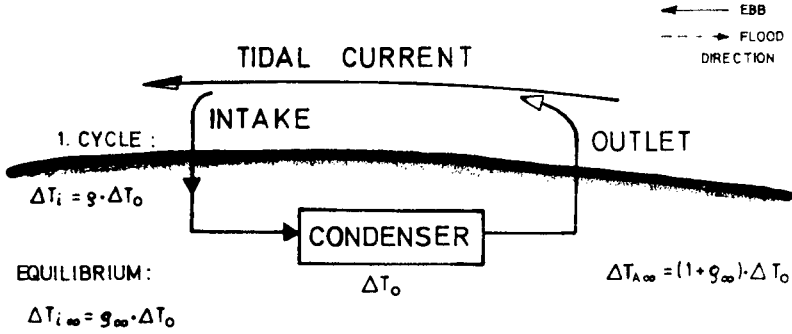
FIG. 2 THERMAL CIRCUIT OF A POWER PLANT
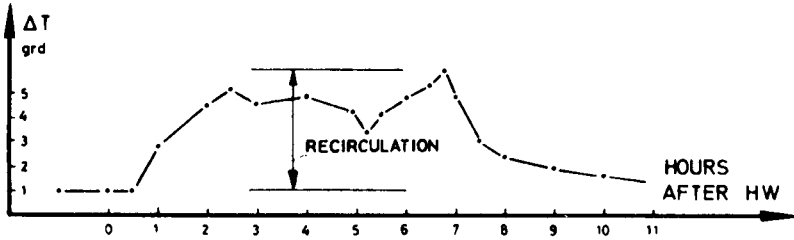
FIG. 3 INCREASING TEMPERATURES DURING EBB CURRENT
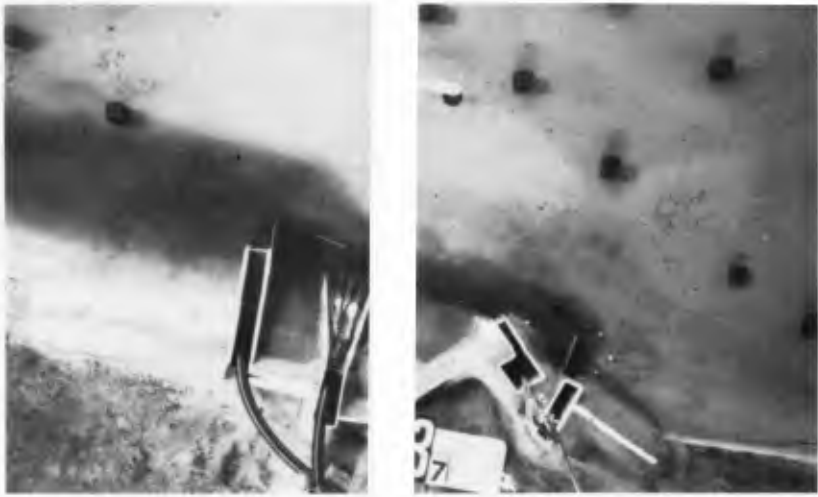
FIG. 4   THE POWER PLANTS   MODEL
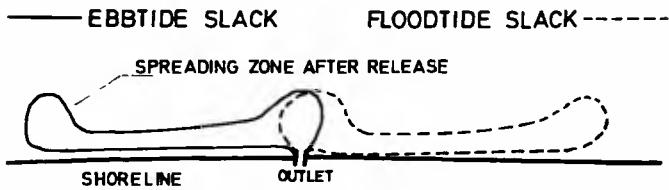
FIG. 5   THE SHAPE OF THE PLUME
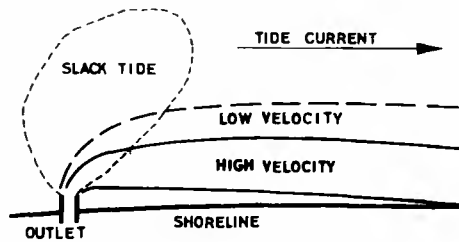
FIG. 6   THE PLUME AT VARIOUS TIDE PHASES
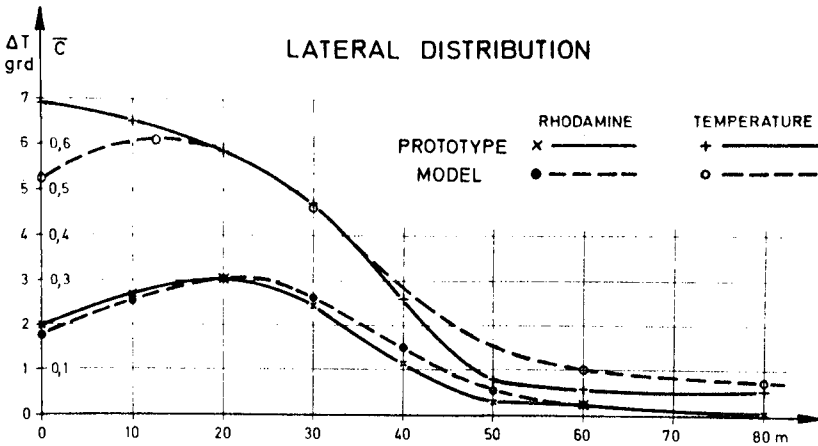
FIG. 7   LATERAL DISTRIBUTION CURVES 1 1/2 h BEFORE LW

$$\bar{C} = \frac{1}{1 + \frac{2\dot{r}}{a^2}\ (at + \dot{r}t^2)}$$

$\dot{r} = 2.1 \ m/min$

$a = 200 \ m$

O MODEL DATA
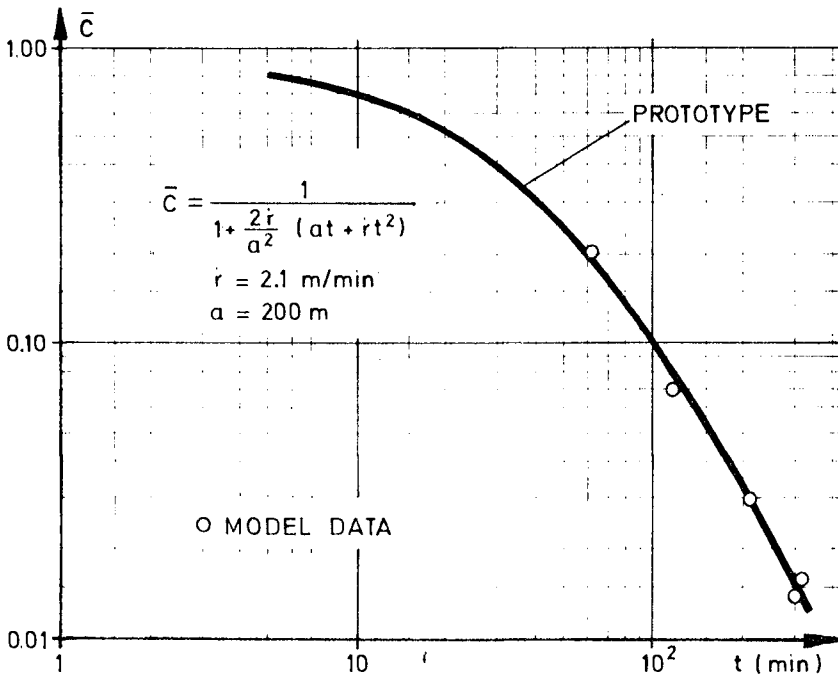
FIG. 8   DECREASING CONCENTRATION MAXIMUM OF A DYE PATCH
IN PROTOTYPE AND MODEL

FIG. 9   THE DYE PATCH FROM 600 ft HIGHT
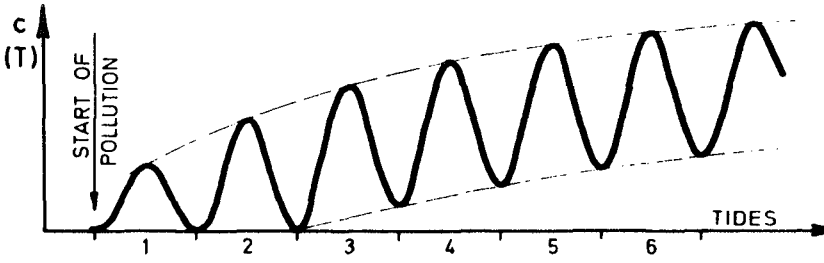
FIG. 10 INCREASING CONCENTRATION (OR TEMPERATURE) CURVE
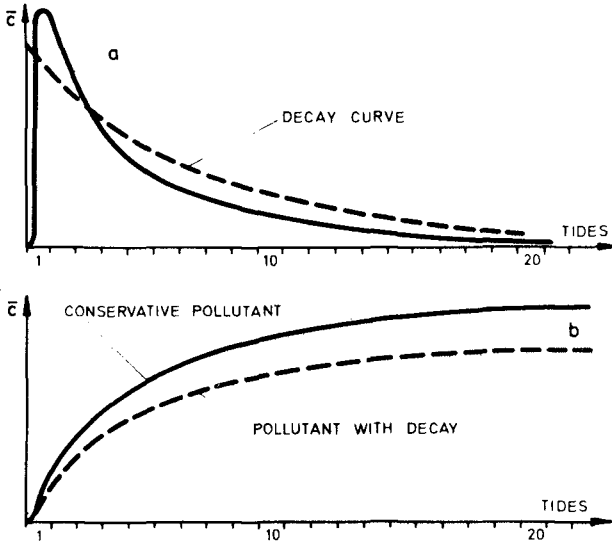
FIG. 11 CONCENTRATION CURVE WITH ONE TIDE CYCLE
POLLUTION

CHAPTER 138

Experimental Studies of Tidal Flow and Diffusion

in the Seto Inland Sea

by

Haruo Higuchi[1], Tamotsu Fukuda[2], Hiroshi Ihara[2], Norio Hayakawa[2]

Abstract

The paper describes the environmental problem of the Seto Inland Sea of Japan. A number of model studies of tidal flow and effluent diffusion of this sea are presented. In particular the similarity law that has been developed to model turbulent diffusion is delineated.

Introduction

During the post-war period, Japan has achieved a rapid industrilization which brought her prosperity as well as extensive environmental pollution problems. The Seto Inland Sea is one of the scenic areas of the country suffering from environmental pollution due to tremendous urbanization and industrialization of the surrounding region. In order to study water pollution of this sea, the senior author has undertaken two hydraulic model studies. On the basis of these studies, a model similarity law of turbulent diffusion has been established and an enormous hydraulic model of the entire sea was constructed.

The Seto Inland Sea

The Seto Inland Sea is a narrow passage of approximately 500 km long and 60 km wide and is squeezed by three major islands of Japan (Fig. 1). It is a shallow sea, most of the area less than 60 meters deep, and is sprinkled with more than 5000 islands. It covers the area of about 21,400 square kilometers and has three openings to the outside oceans. The surrounding area supports about 30 million people and the coastal region is heavily industrialized. Fig. 2 gives surface

---

1. Ehime University, Matsuyama, Japan.
2. Chugoku Institute of Industrial Technology, Hiromachi, Kure, Japan
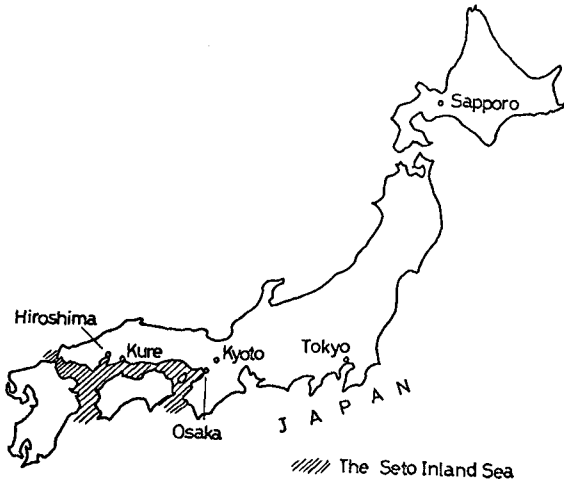
Fig. 1. Japan Islands and the Seto Inland Sea.
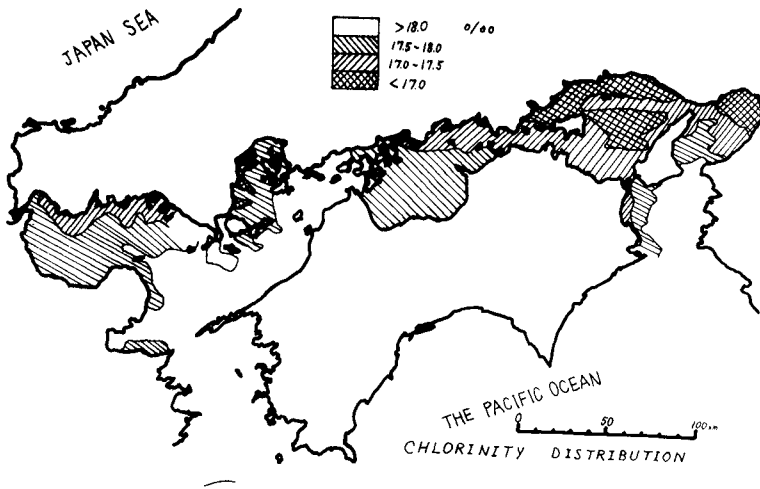
Fig. 2. Chlorinity Distribution of the Surface Water.

chlorinity measurement (1) of the sea which indicates that the sea
contains water only slightly less brine than oceanic sea water.
One measure of the water pollution is given in Fig. 3 as tranxparency
measurement.   Another indication is shown in Fig. 4 as one of COD
measurement of the surface water.   These two figures indicate that
substantial portion of the sea is judged as polluted and that the
most polluted area is where it is innermost, enclosed and coastal area.
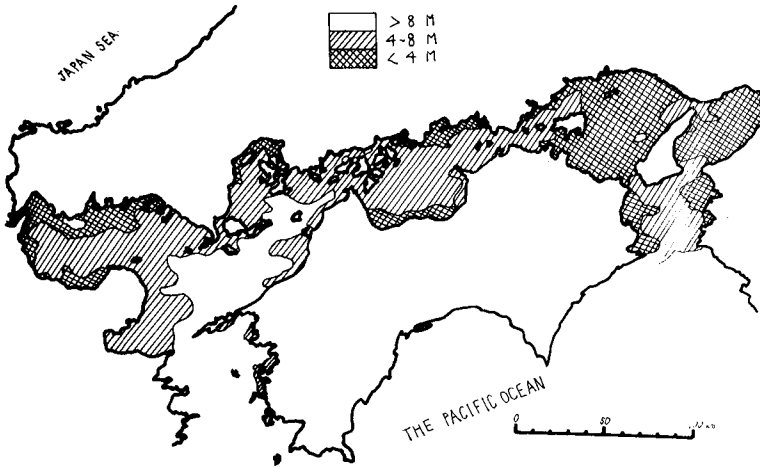
Fig. 3. Measured Transparency
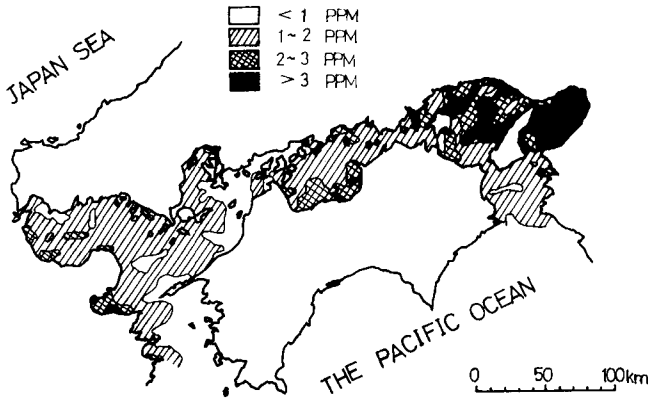
May. 22,1972
COD (Surface Layer)

Fig. 4 COD distribution

It is to this problem that the senior author undertook a hydraulic model study of this sea (2).   The plan view of this model is shown in Fig. 5.   Its horizontal and vertical length scale ratios are 1 to 10,000 and 1 to 1,000 respectively.   The model tide generated at one end of the Fig. 5 propagated into the model through branched channels whose lengths were adjusted in such a way that the phase difference at the openings is obtained.   The study carried out with this model includes existence of the tidal residual flow and effluent diffusion-dispersion pattern which is followed up to a period of several years.

    The smallness of the model and uncertainty on modelling turbulent diffusion, however, were limiting factors of this study.   The latter problem is discussed in the following section.
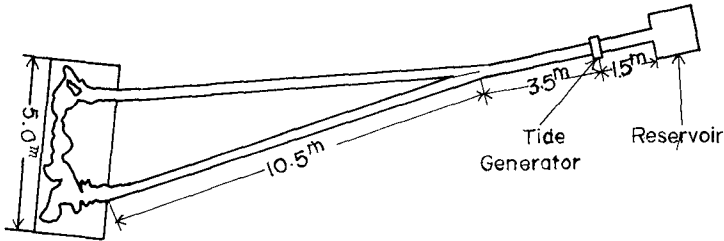
Fig. 5. Plan View of the Small Scale Model.

The Similarity Law

    To simulate the dynamical behavior of the tidal flow phenomenon in the model, the well-known Froude's law is invoked to give the following:

$$t_r = x_r h_r^{-\frac{1}{2}} \qquad\qquad (1)$$

where t_r, x_r and h_r are time, horizontal length and vertical length scale ratios of model to prototype respectively.   Further, the friction coefficient of the sea bed surface has to be scaled as follows:

$$C_r = x_r^{-1} h_r \qquad\qquad (2)$$

where C is the friction coefficient.   Inpractice length scale ratios x_r and h_r have to be given in advance of construction of the model

and the model bed surface is modified with roughness elements to satisfy
Eq. (2).   It is herewith proposed to model turbulent diffusion by
invoking the Richardson's power law on turbulent diffusivity,K, given as

$$K = \epsilon^{1/3} l^{4/3} \qquad (3)$$

where ϵ is the energy dissipation and l is the horizontal length
scale.   Equating the scale ratio for K derived from this power law
and the one from the dimensional viewpoint, and observing that ϵ
remains constant for wide range of length scale leads to the following:

$$K_r = x_r^{4/3} = x_r^2 t_r^{-1} \qquad (4)$$

where K_r is the scale ratio for the turbulent diffusion coefficient.
Eq. (4) is further reduced to the following:

$$t_r = x_r^{2/3} \qquad (5)$$

Substitution of Eq. (5) into Eq. (1) gives

$$h_r = x_r^{2/3} \qquad (6)$$

These last two equations imply that once the horizontal length scale
ratio is chosen, then the vertical length and the time scale ratios
follow.
      Validity of this law is observed in Fig. 6 which gives a plot
of diffusivity measurements in various tidal flow models and correspond-
ing prototype data.
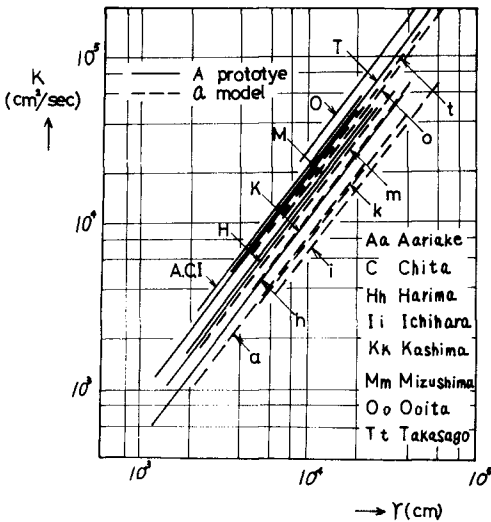
Fig. 6. Comparison of
Measured Diffusivity,
K, versus Length Scale
r .
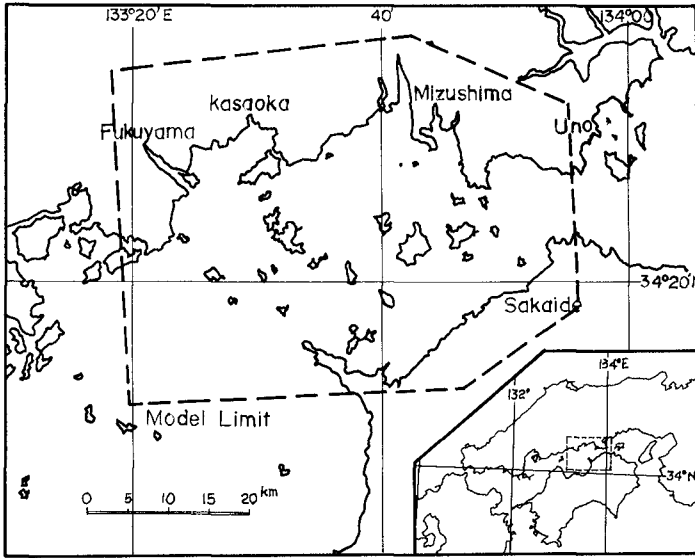
Fig. 7.   Plan View of the Mizushima Bay Area.
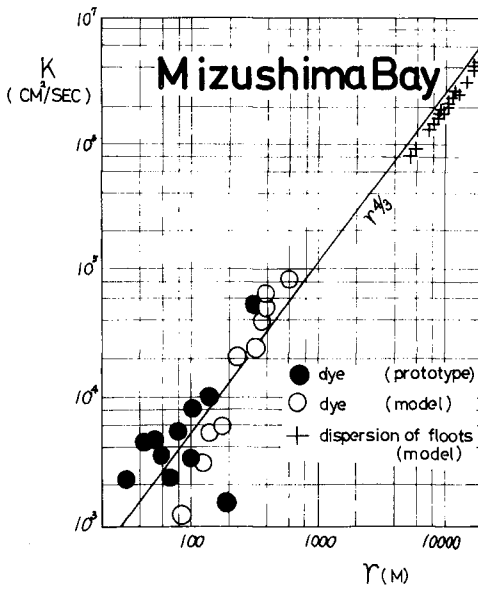
Fig. 8.   Measured Diffusivity of the Mizushima Bay Study.

Fig. 6 indicates that   can be regarded as constant for wide range
of length scale.
        More detailed study based on this similarity law was the Mizushima
Bay model study (3).   The model area is shown in Fig. 7.   This bay
is a small part of the whole Seto Inland Sea.   The horizontal length
scale ratio was chosen as   1   to   2,000.   According to Eqs. (5) and
(6) h_r = t_r = 1/160.   Fig. 8 gives comparison of measured diffusi-
vity   in   the model and prototype.

The Seto Inland Sea Hydraulic Model

        On the basis of the preliminary studies described in the preceding
sections, the Seto Inland Sea Hydraulic Model which covers the entire
region was constructed in 1973.   The model scale ratios are 1/2,000 in
the horizontal direction and 1/160 in the vertical direction according
to the similarity law Eqs (5) and (6).   It is housed in a building of
230 m x 100 m (Fig. 9).   The model is equipped with three separate
tide-generating facilities of weir type which are operated centrally
at the control room.   The tide generating system is equipped with an
electric computer which can generate complex functions to simulate
tidal motion and handle data processing devices.   The model includes
more than seventy rivers on which regulated flow mixed with dye solu-
tion to simulate the diffusion of pollutant is discharged.   Major
facilities of the model include two sets of cranes: observation stations
and water sampling stations.   The former consist of four traveling
cranes carrying eight camera-mounted, gondola-shaped stations   15 meters
above the model surface.   The latter is made up of two steel grills
of 10 m by   10 m hung by two traveling cranes.   These grills can travel
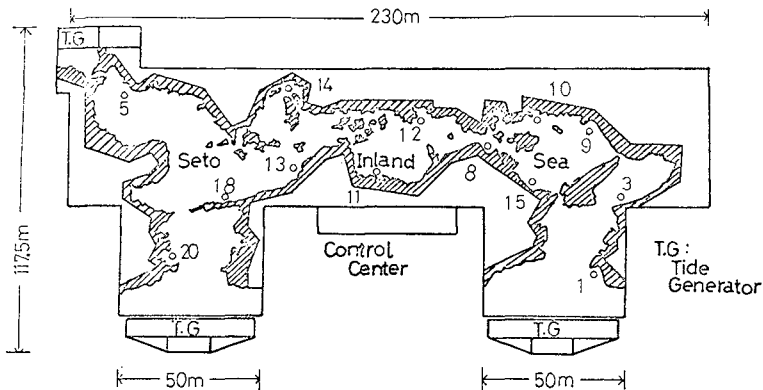
Plan view of the tidal flow model.   Numbered circles
indicate locations of wave gauges.

Fig. 9

in all three directions as well as rotate around its vertical axis and
can be brought at any desired position above the model surface in order
to extract water sample without disturbing the flow.

     Tidal oscillation of the model water surface is recorded with
specially designed wave gauges.   In Fig. 10 is shown amplitudes and
phase lags of these wave records when the semi-diurnal (M_2) tide is
given.   Their location is indicated as numbered circles in Fig. 9.
Field data are also entered in Fig. 10 for comparison.   The figure
shows that amplitude increases as much as three times and phase lags
as much as 6 hours inside of the inland sea.   Model-to-prototype
correspondence of better than twelve per cent is achieved everywhere
without adding any roughness element on the bed surface which has
trowel finished with mortar.   Further verification study is in progress
by adding roughness element on the model surface.

     In Fig. 11 is shown preliminary study of dye diffusion.   It conforms
with earlier studies including Mizushima Bay Model Study.
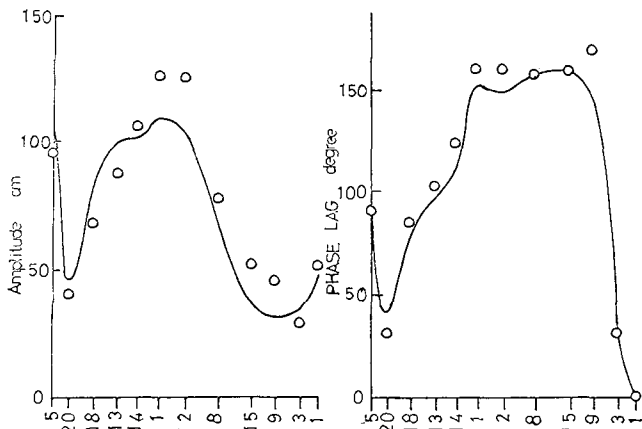
Fig. 10.

Amplitude (left) and Phase lag(right)distribution.
Circles relate to experimental data of wave gauges
whose localities are given as numbers in abscissa.
Solid lines relate to field gauge station data.

Fig. 11. Measured Diffu-
sivity of the Seto
Inland Sea Model.
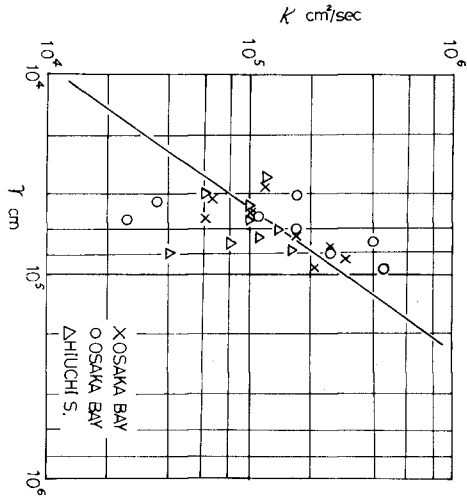
Conclusion

Polluted state of the Seto Inland Sea is reported herein.   As a
means to find an effective abatement program of water pollution and to
assess future impact on the aquatic environment, use of hydraulic model
is asserted.   In particular, a new similarity law of turbulent diffusion
is proposed and its validity and usefulness has been demonstrated with
respect to the results of number of hydraulic model studies.

An outcome of this background, an enormous hydraulic model of the
Seto Inland Sea is described and some of the preliminary results are
presented.

Acknowledgement

References

(1) Figs. 2 through 4 are extracted from large-scale survey of the
Seto Inland Sea undertaken by Environmental Agency of Japan in 1972.

(2) T. Sugimoto and H. Higuchi,"Experimental Studies on the Tidal
Mixing in the Seto Inland Sea (I)", Bulletin of Disaster Prevention
Institute, Kyoto University, No.14B, 1971,pp.435.

(3) H. Higuchi and T .Sugimoto,"On the Hydraulic Model Experiment on
the Diffusion due to the Tidal Current", Bulletin of Disaster Prevent-
ion Institute, Kyoto University, No.12B,1969,pp.633.

CHAPTER 139

HORIZONTAL DIFFUSION IN A TIDAL MODEL

by

Haruo Higuchi

Professor of Physical Oceanography
Department of Ocean Engineering
Ehime University
Matsuyama, Japan

and

Tetsuo Yanagi

Research Assistant
Department of Ocean Engineering
Ehime University
Matsuyama, Japan

Abstract

   The effect of the tidal residual flow on the horizontal diffusion
in a shallow tidal bay is investigated through a hydraulic model experiment,
for which Mikawa Bay in central Japan was used as a prototype.

   A hydraulic model of about 20 x 30 m including Mikawa Bay and neigh-
boring sea area, with a horizontal and vertical scale of 1/2000 and 1/160
respectively, was used, and a semi-diurnal tide was provided for it.
Experiments have shown that tide and tidal current are well reproduced
in the model.   The tidal locus does not close, that means the existence
of the residual flow.   The distribution of the concentration of the dye,
which is discharged from the bay bottom, corresponds to the pattern of
the residual flow.

   The diffusion coefficient in the bay obtained through one dimensional
analysis is the order of 10^5 cm^2/sec and that through two dimensional
analysis is less by one order and the dispersion coefficient becomes 10^5
cm^2/sec.   It is concluded that the dispersion due to the residual flow
plays more important role on the distribution of the material in the
shallow bay, as Mikawa Bay, than the diffusion due to the tidal current
itself.

1. Introduction

        There are many kinds of current depending on various motive forces
in the nearshore sea area.   Among these the most predominant current
through all seasons in the bays and inlets in Japan is the tidal current.
The so-called tidal current, which is directly generated by the tide
generating force, generates the minor scale currents such as the compen-
sating current and eddy current under the influence of the geographical
configuration such as headland and island as well as the bottom topography
and the smaller eddy currents due to the bottom stresses.

        In the existing shallow sea area, although the water particle goes
and returns during flood and ebb, the locus does not close after one tidal
cycle.   This displacement is called as "the tidal residue".   When the
vectors of such tidal residues are at random, it is considered that there
exists the turbulence, and when the vectors are uniform, there is the
constant flow.   The so-called constant flow is what is defined as the mean
value of the current during one tidal cycle at a fixed point, therefore,
this is a phenomenon seen from Eulerian standpoint.   On the other hand, the
residual flow is that seen from Lagrangean standpoint.   Although it seems
that both flows are different from each other, it is considered to be the same
phenomenon essentially.   The constant flow is also mainly caused by the
geographical configuration, and it forms the horizontal circulation often
in a bay.

        The pollutants discharged into the sea are diffused initially by small
eddies, and then it begins to be affected by larger eddies gradually depending
on the scale of the patch.   Beside the diffusion due to such eddies, the
distribution of pollutants is affected by the advection due to the current
of larger scale such as the constant flow.   The relationship between
diffusion and advection is discussed on the base of the results of a
hydraulic model experiment.

2. Prototype

        Mikawa Bay is in the central part of Japan, which is surrounded by both
Atsumi and Chita peninsula, and connected with the Pacific Ocean through
the southern part of Ise Bay. (Fig.1.)   The bay is about 30 km long
east to west and 20 km north to south, 500 km^2 in area, and 12 m deep.

        The tidal wave comes into the bay from the Pacific Ocean through
Irako Straits.   The spring tidal range in the bay is about 1.9 m, which
is 1.43 times of the Pacific coast.   The phase difference of M_2 con-
stituent is 12 degree.   The maximum flood current appears 3 hours
before high water in the bay and maximum ebb current 3 hours after
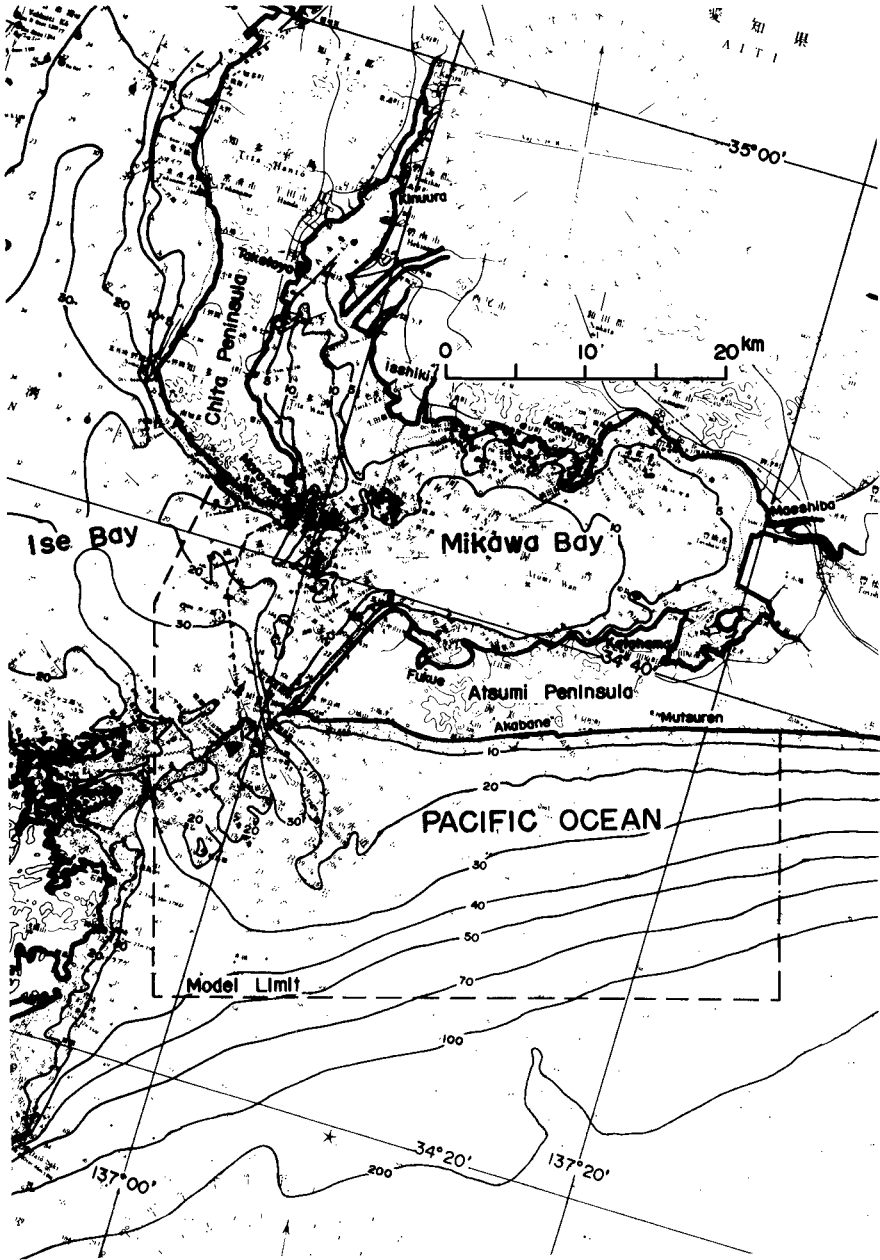
Fig.1   Bathygraphic chart of Mikawa Bay

that.   The mean value of the maximum current is about 30 cm/sec in the bay.

3. Similitude[1]

In the hydraulic model experiment for the tidal current, it is necessary for the following equations to be valid in order to hold a dynamical similitude between the prototype and the model,

$$t_r = x_r \ h_r^{-1/2},\tag{1}$$

$$C_r = x_r^{-1} \ h_r,\tag{2}$$

where x is the horizontal length, h the vertical length, t the time, C the friction factor, and suffix r shows the ratio of the quantity in the prototype and the model.

From the comparison of both equations of diffusion in the prototype and the model, the following equation is obtained,

$$K_r = x_r^2 \ t_r^{-1},\tag{3}$$

where K is the horizontal diffusivity.   On the other hand, the horizontal diffusivity is expressed as follows,

$$K = \varepsilon^{1/3} \ l^{4/3},\tag{4}$$

where ε is the rate of energy dissipation and l the scale of the phenomenon.   Therefore, the ratio of the diffusivity is written as follows,

$$K_r = \varepsilon_r^{1/3} \ l_r^{4/3}.\tag{5}$$

Assuming that the rate of energy dissipation in the model is equal to that in the prototype, that is, $\varepsilon_r = 1$, we obtain

$$K_r = x_r^{4/3},\tag{6}$$

since $l_r = x_r$.   From the equation (3) and (6), we get

$$t_r = x_r^{2/3}.\tag{7}$$

From the equation (1), (2), and (7), we obtain

$$h_r = x_r^{2/3},\tag{8}$$

$$C_r = x_r^{-1/3}. \tag{9}$$

Consequently, the scale ratios for the time, vertical length, and friction factor are determined only by that for horizontal length.   When the friction factor determined by the equation (9) is reasonal value, these scale ratios are acceptable.

4. Experiment

A hydraulic model of about 20 x 30 m including Mikawa Bay and neiboring sea area, of which the model limit is shown by broken lines in Fig.1, was constructed.   The horizontal scale is 1/2000, the vertical and time scales are 1/160, which are determined by the equations (7) and (8).   A semi-diurnal tide of the period of 280 sec was provided for it by an automatically controlled pneumatic tide generator.

The distribution of the tidal range in the model agrees well with that in the prototype.   The flow patterns in the flood and ebb also agree with those in the prototype.   From these two results, it is considered that the dynamical similitude for the tidal current holds well.

The loci of floats are shown in Fig.2.   A float moves along the solid line during the flood and then it does along the broken line during the ebb.   Generally, as shown in this figure, a float does not come back to the initial location after one tidal cycle, that is, the tidal locus does not close.   This suggests the existence of the constant flow caused by the geographical configuration.   This residue is called as "the tidal residue" and the current causing such a residue is called "the residual flow".   Such a residual flow forms several horizontal circulation in the bay.   An example is shown in Fig.3.   The velocity of the residual flow is several percent of the tidal current.

The horizontal distribution of the concentration of the dye, which was continuously released from the coast, at 90 tidal cycle after the commencement of release is shown in Fig.4.   The numeral shows the concentration in per mill (o/oo) of that of released dyed water.   The concentration is the mean value of the water column from the surface to the bottom.   In comparing Fig.4 with Fig.3, the distribution of the concentration seems to highly depend on the residual flow.

5. Consideration

a) One dimensional analysis
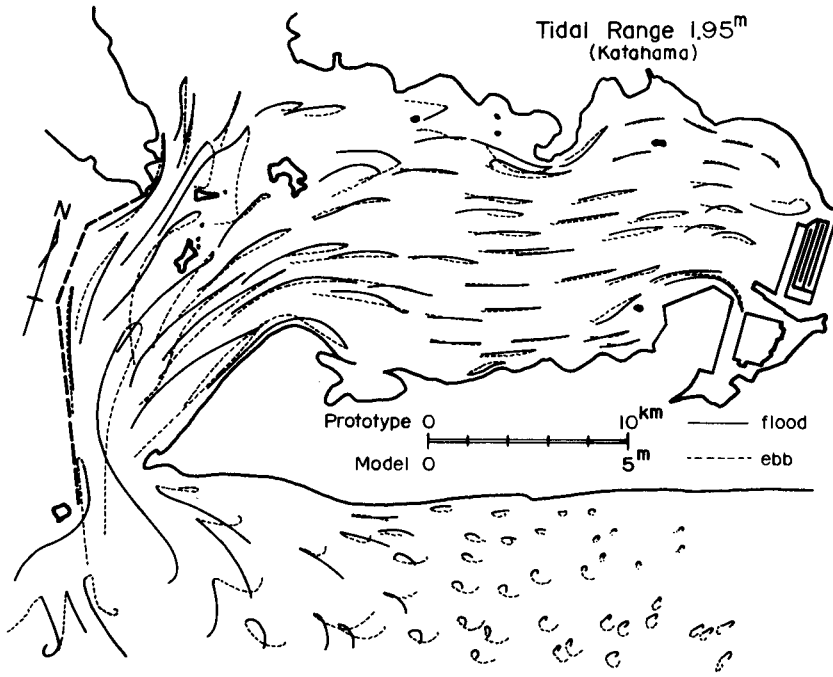
Fig.2　Tidal locus
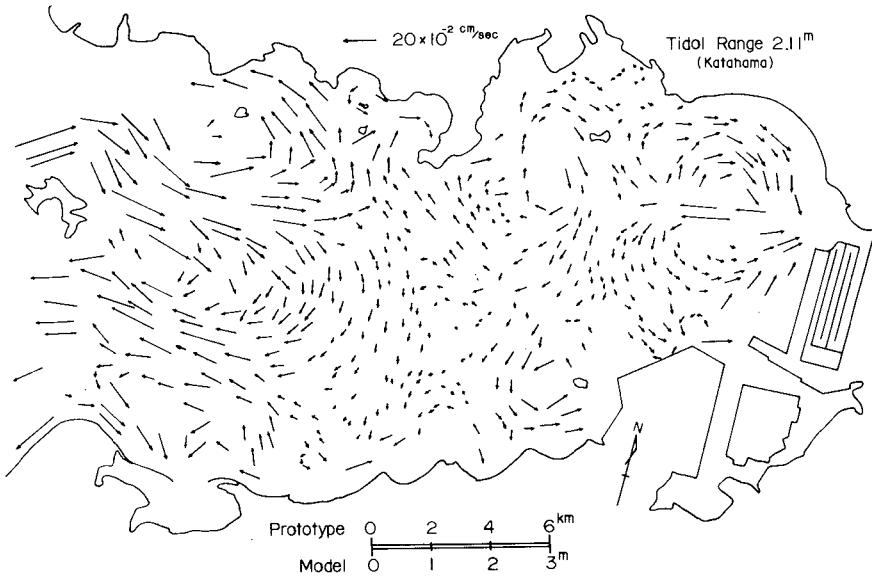
Fig. 3   Residual flow
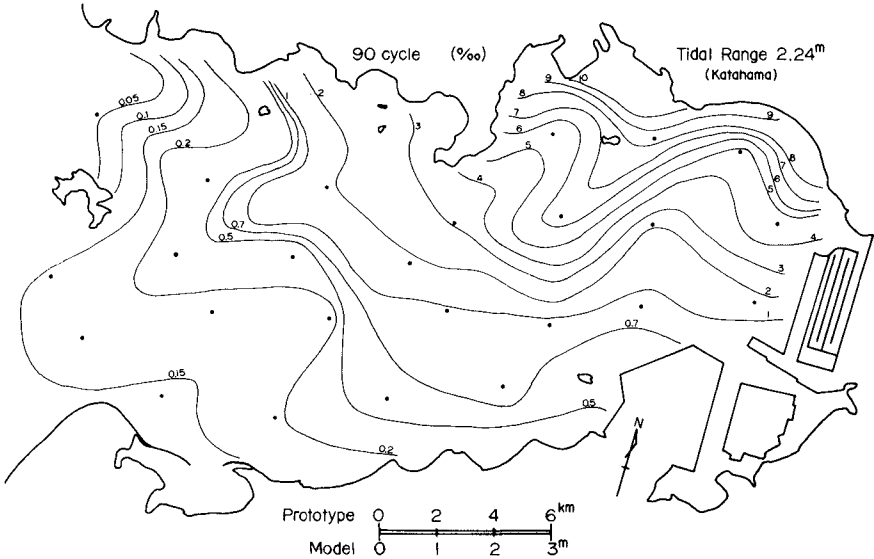
Fig.4   Horizontal distribution of dye concentration

The bay is divided into several sections along the center line as shown in Fig.5, where the point A is the releasing point and the dot means the sampling point.

The one dimensional equation of diffusion is as follows,

$$A \frac{\partial C}{\partial t} + Q \frac{\partial C}{\partial x} = \frac{\partial}{\partial x} \left(A \cdot K \cdot \frac{\partial C}{\partial x} \right) \tag{10}$$

wher A is the cross-sectional area, C the concentration, Q the rate of flow of the dyed water, K the diffusion coefficient. The diffusion coefficient is expressed in the form of difference as follows,

$$K = \frac{A \cdot \Delta x \cdot \frac{\Delta C}{\Delta t} + Q \cdot \Delta C}{A \cdot \frac{\Delta C}{\Delta x}} \tag{11}$$

The one dimensional diffusion coefficient is shown in Table 1, which is calculated from the mean concentration in each section and the increment of the concentration from 80 to 100 cycles after the commencement of release of the dyed water. The average value of the diffusion coefficient in the whole bay is 2.7×10^5 cm^2/sec.

b) Two dimensional analysis

The two dimensional equation of diffusion is as follows,

$$\frac{\partial C}{\partial t} = -\nabla \cdot (uC) + \nabla \cdot (K \nabla C), \tag{12}$$

where u is the velocity of the constant flow. The diffusion coefficient is caluclated in a box model enclosed by vertical planes parallel with the major (x) and minor (y) axis of tidal ellipse (Fig.6). Equation (12) is rewritten in the form of the difference as follows,

$$V \frac{\Delta C_5}{\Delta t} = S_1 u_1 C_1 - S_2 u_2 C_2 + S_3 u_3 C_3 - S_4 u_4 C_4$$
$$+ S_1 K_x \frac{\Delta C_1}{\Delta x} - S_2 K_x \frac{\Delta C_2}{\Delta x} + S_3 K_y \frac{\Delta C_3}{\Delta y} - S_4 K_y \frac{\Delta C_4}{\Delta y} \tag{13}$$

where V is the volume of the box, S the area of the side wall, u and v the velocity of the constant flow in x and y direction respectively. Assuming the same value of K_x and K_y respectively in the neighboring boxes, we obtain $K = 4.7 \times 10^4$ cm^2/sec and $K_y = 1.7 \times 10^4$ cm^2/sec in the central part of the bay. The length of the box is 4 km, the width 1.5 km. The mean water depth is 13 m and the maximum velocity of the tidal current is 20 cm/sec in the box. The two dimensional diffusion coeffi-
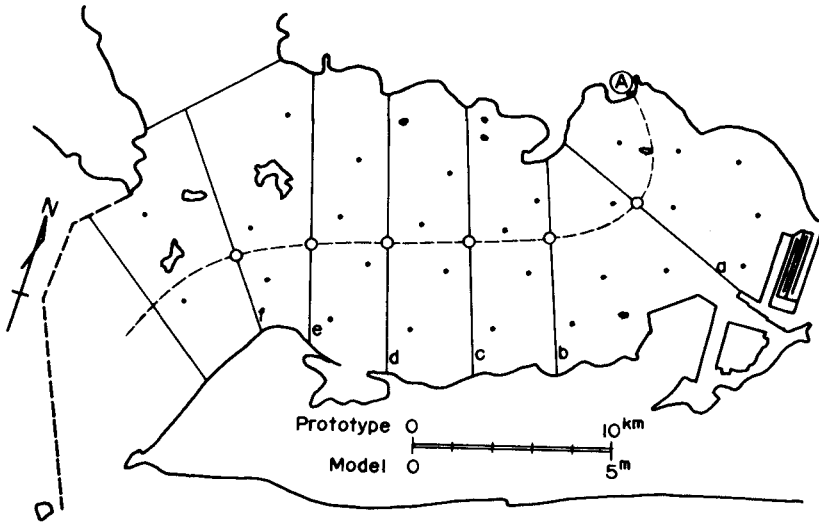
Fig.5   Section used for averaging

Table 1   Diffusion coefficient K in one dimensional model and
            dispersion coefficient D_1 in two dimensional
            model $(x\ 10^5\ cm^2/sec)$

Area	a	b	c	d	e	f
K	1.49	5.03	1.28	1.26	4.03	3.13
D_1	1.03	2.93	0.28	—	3.38	
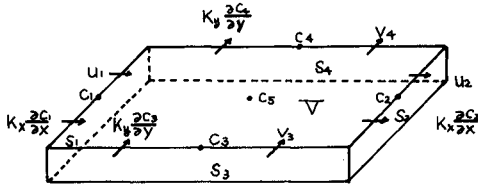
Fig.6   Box model
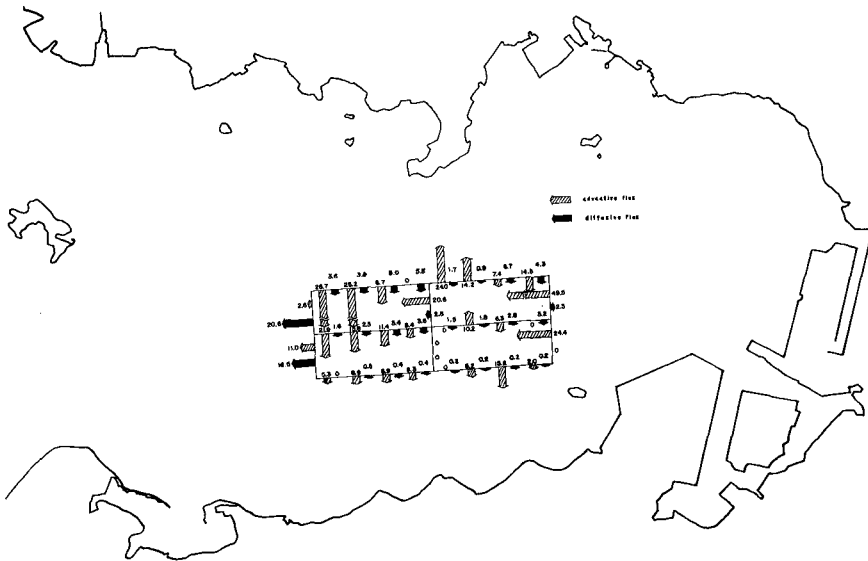
Fig.7   Advective flux and duffusive flux

cient is smaller by one order than one dimensional one.

The diffusive flux of the dye due to the tidal current and the advective flux due to the residual flow are shown in Fig.7, in which the black arrow shows the diffusive flux and dark one the advective flux.   From this figure it becomes to be clear that the advective flux is much larger than the diffusive flux.

We devide the current velocity into 4 parts, after Fisher's model[2],

$$U(x,y,t) = u_0(x) + u_1(x,t) + u_s(x,y) + u'(x,y,t),\qquad(14)$$

where u is the velocity,
    x the horizontal length from the bay bottom to the mouth,
    y the lateral length,
    u_0 the cross-sectional mean velocity of the dyed water, $u_0 = \langle \bar{u} \rangle$
    $^-$ shows the mean value in the cross-section.
    $\langle \ \rangle$ the mean velocity of the tidal current in the cross-section,
$$u_1 = \bar{u} - u_0,$$
    u_s the velocity of the residual current, $\bar{u}_s = 0,$
    u' the deviation of the velocity, $\bar{u}' = \langle u' \rangle = 0.$

The concentration of the dye is expressed in the same way as the velocity.

$$C(x,y,t) = C_0(x) + C_1(x,t) + C_s(x,y) + C'(x,y,t)\qquad(15)$$

The flux of the dye passing through a cross-section is expressed as follows,

$$M = \frac{1}{T}\int_0^T \int_A (uC)\ dA\ dt,\qquad(16)$$

where T is the tidal period, A the cross-sectional area.   Assuming that the change of the cross-sectional area due to the tide is small and $\langle u_1 C_1 \rangle \fallingdotseq 0$, equation (16) is rewritten as follows,

$$M = C_0 Q_0 + A_0(\overline{u_s C_s} + \langle \overline{u'C'} \rangle),\qquad(17)$$

where Q is the rate of flow of the dyed water, A_0 the mean cross-sectional area during one tidal cycle. $C_0 Q_0$ corresponds to the advective flux in one dimensional equation of diffusion.   The flux of dye is shown by dark arrows in Fig.8, where the white arrow shows the rate of flow due to the residual flow.

The dispersion coefficient, after Fisher, is as follows,

$$D_1 = \frac{1}{(dC_0/dx)} \cdot \overline{u_s C_s}.\qquad(18)$$
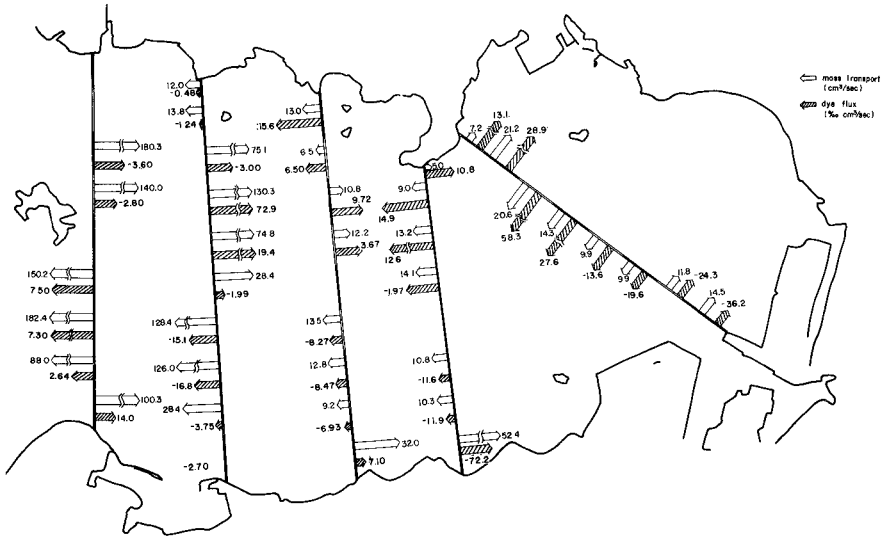
Fig.8   Rate of flow(mass transport) and dye flux

The value is shown in Table 1.   From this table, it becomes to be clear that
the one dimensional diffusion coefficient mainly consists of the dispersion
due to the residual flow.

6. Conclusion

     The mean value of the diffusion coefficient in Mikawa Bay is 2.7×10^5
cm^2/sec, which is obtained by one dimensional analysis from the distribution
of the concentration of the dye released continuously from the bay bottom.
The diffusion coefficient in a box model in the central part of the bay is
smaller by one order than it, which is obtained by two dimensional analysis of
the balance of the dye in the box.   The mean value of the dispersion coeffi-
cient due to the constant flow is 1.9×10^5 cm^2/sec.   The one dimensional
diffusion is almost understood as the dispersion due to the constant flow.

     In conclusion, the dispersion due to the constant flow plays more impor-
tant role on the distribution of the material in the shallow tidal bay, as
Mikawa Bay, than the diffusion due to the tidal current itself.

                              Referance

1)   Higuchi,H. and Sugimoto, T. : Experimental study on the horizontal
          diffusion due to the tidal current, Paper No.29: Symposium on "The
          physical process responsible for the dispersal of pollutants in the
          sea with special reference to nearshore zone"   Aarhus/University,
          Denmark, July 1972

2)   Fisher,H.B.: Mass transport mechanisms in partially stratified estuaries,
          Journal of Fluid Mechanics vol.53, pp.671-687, 1972

CHAPTER 140

THE EFFECT OF WIND ON CURRENTS
AND DIFFUSION IN COASTAL SEA AREAS

by   B. QUETIN*

--

ABSTRACT

The calculation of turbulent flow using Navier's equations assumes
the introduction of a turbulent viscosity coefficient the value of
which is normally constant, conforming with Boussinesq's hypothesis.

It was shown that setting aside this hypothesis, a velocity profile
quite different to that resulting from the classic theory is
obtained in the case of flow induced by wind. This result appears
to be confirmed by the tests carried out in the Mediterranean. The
advantage of this method is that it gives the vertical turbulent
diffusion which is of particular interest to pollution studies.

During the studies and experiments carried out in the Mediterranean
sea on pollution, we had envisaged estimating the diffusion of a
rhodamine stain by aerial photography.

The difficulties of interpreting coloured stains leaving indications
of high speed-gradients near the surface, which will be discussed
later, led us to reconsider the method of calculating currents due
to wind.

The classic EKMAN theory is based on the simplified BOUSSINESQ
theory. This theory can now be set aside owing to recent work on
turbulent flow, in particular that by Messrs. Biesel, Huffenus
and Gauthier at SOGREAH.

---

* Engineer in SOGREAH's Applied Mathematics Department

Two supplementary equations have to be treated which require nume-
rical treatment with a computer. The results obtained from this
program, called the EOLE program, are confirmed by our measurements
in the Mediterranean and by certain work at present being carried
out in French universities and offer new information.

It is well known that the transposition of the Navier equation :

$$\frac{\partial v}{\partial t} + V.\nabla V = -\frac{1}{p} \text{ grad } P + \nu \Delta V$$

to turbulent flow, by substituting $V = \overline{V} + v$, involves terms account-
ing for internal tension called Reynolds forces :

$$\frac{\partial \overline{V}}{\partial t} + \overline{V} \nabla \overline{V} = -\frac{1}{p} \text{ grad } P + \text{div } (\nu \text{ grad } \overline{V} - \overline{v_i v_j})$$

BOUSSINESQ's theory compares these forces to viscous forces which
leads to the kinematic viscosity of water being replaced by a much
higher turbulent viscosity : the eddy viscosity μ which has a totally
empirical value. In each case, the applications require physical
measurements.

$$\frac{\partial \overline{V}}{\partial t} + \overline{V}.\nabla \overline{V} = -\frac{1}{p} \text{ grad } P + \text{div } (\mu \text{ grad } \overline{V})$$

$\mu \quad >> \quad \nu$

The problem is therefore to define a more precise approach to the
phenomenon of turbulence. In the wake of extensive research work,
SOGREAH developed programs based on a first order schematic represent-
ation of turbulence. Although semi-empirical, the representation is
largely justified by the better conformity of results calculated
from these measurements.

This method of calculation consists of representing the viscosity by
a function of two parameters :

.   the turbulent energy dissipated locally,

.   a length defining the scale of turbulence.

which are included in the Navier equation, the first establishing the turbulent energy balance, the second defining the scale of turbulence.

In the case of flow induced by the wind the equations become :

$$\frac{\partial V}{\partial t} = - gi + \nu \frac{\partial}{\partial z} \left[(1 + k_1 R_T) \frac{\partial V}{\partial z} \right]$$

$$\frac{\partial E}{\partial t} = k_1 \nu R_T \frac{\partial^2 V}{\partial z^2} - \nu (k_3 + k_4 R_T) \frac{E}{1^2} + \nu \frac{\partial}{\partial z} \left[(\frac{5}{3} + k_2 R_T) \frac{\partial E}{\partial z} \right]$$

$$1 = k_5 z / \sqrt{1 + k_6 R_T}$$

$$R_T = 1 \sqrt{E/\nu}$$

where :

V	= local flow velocity
i	= slope of the sea surface
z	= depth
ν	= kinematic viscosity
E	= turbulent energy
1	= eddy scale
k_1 to k_6	= numerical coefficients
R_T	= Reynold's Number.

The boundary conditions express the shearing forces due to the action of the wind on the surface of the sea and the rugosity of the wall on the sea bed.

The program itself determine a variable distribution of calculation points in Z, which is indispensable for taking into account boundary layers. First of all, it solves the last two equations then calculates the velocity profile with the aid of the first equation.

The first EOLE program, deliberately simplified, was written to
verify the validity of the calculation method. It assumes that the
wind direction, the speed of water and the line with the steepest
slope to the surface of the water are all in the same vertical plane.
It calculates the speed of water as a function of the depth assuming
an established permanent regime. It will be immediately pointed out
that its extension to three dimensions, the consideration of Coriolis'
forces and the putting into operation of the model are at present in
progress.

In its initial form, the EOLE program is applied to two boundary
cases :

   .   the first case is where the wind is parallel to a rectilinear
       coastline. The surface of the sea is then horizontal and there
       is a general flow in the direction of the wind.

   .   In the second case the wind is assumed perpendicular to the shore.
       Simple considerations of continuity show that the flow of the
       surface bounded by the coast should be compensated by a deep
       inversed current. In permanent regime, the total discharge along
       the vertical is zero. The free surface of the sea presents an
       inclination.

In spite of its initial simplified nature, the EOLE program throws
new light on the present knowledge of the subject.

In all cases, the speed profile is very different to that obtained
by the classic theories. A rapid decrease of the speed in the upper
boundary layer is always observed. In addition, the speed at
lower levels decreases almost lineraly.

Graph 1 shows the parabolic speed profile, calculated assuming
constant eddy viscosity, and that obtained with the EOLE program
when the wind is perpendicular to the coast. It will be noted that
the return current is a maximum at a short distance from the bed.

Graph 2 shows the same comparison but with the wind parallel to the
coast.

The eddy viscosity is not as uniform as is shown in Graph 3. It
also varies in a notable manner as a function of the general flow
conditions.

This questions EKMAN's theory of depth friction and all the
conclusions from it, particularly in the field of overall
transport. It is found that the EKMAN depth is always of the
order of the real depth in shallow water.

In spite of the enormous difficulty of measuring the current at low
speeds, the measurements made in the Mediterranean confirm the
shape of the speed profile Graph 4. It should be pointed out that
measurements were only made at the surface and down to 10 metres.
The depth of the test area was around 50 metres.

The results are of particular interest to the study of transport and
diffusion with respect to the problems of pollution. The average
transport will be very different depending on the thickness of the
polluted layer. In addition, the measurement of velocity with the
aid of a very thin float is only significant of the upper boundary
layer and not of the transport of the mass.

The eddy viscosity is a measure of the rate of exchange between the
various flowing layers ; it strictely defines the vertical
coefficient of eddy diffusion. Its high variation with depth will
give very different effects on dilution depending on the thickness
of the polluted layer. Obtaining the vertical diffusion by
calculation could reduce experimental work in the sea.

At the begining of this review, I mentioned the difficulties of
interpreting diffusion from a rhodamine cloud, followed by aerial
photograph. The images of the rhodamine cloud show a sharp front
whereas the rear is diffuse and descends progressively. With due
consideration being given to the results given ahove, this
phenomenon is easily explained.

The cloud is highly sheared by the variations in velocity at the
surface. In the fastest surface layer the turbulent diffusion is
zero which explains why the front of the cloud is always well
defined. On the other hand, diffusion of the rear of the rhodamine
cloud increase depth since turbulent diffusion increases with depth.

This does not work for longitudinal and vertical diffusion for
which transport and velocity profile considerations have to be
made. This is only possible using highly sophisticated
mathematical models. SOGREAH is, at present in the process of
finishing such a model.

Sea pollution studies assume a more and more refined knowledge of
circulation in coastal waters where flow due to wind is often
preponderant. We wanted to show that the application of the most
advanced theories to the calculation of turbulent flow has
thrown new light on the subject. In particular results from the
EKMAN theory are considerably complemented by directly obtaining
the vertical diffusion value.

BIBLIOGRAPHY

–

Lacombe   : Cours d'Océanographie physique (Gauthier Villard
                   1965)

Biesel   : Conférence Générale – 14ème Congrès de l'AIRH
                   (Paris 1971)

Gauthier   : A Mathematical model for Laminar and Turbulent
                   Flow – (Von Karman Institute, mars 1971)

Huffenus   : Calculs d'écoulements en fluide réèl (La Houille
                   Blanche, n° 6, 1969)

Daly and Harlow : Inclusion of Turbulence Effects in Numerical Fluid
                   Dynamics (Los Alamos Scientific Laboratory
                   LA – DC – 11113)

D.B. Spalding   : Numerical Methods in Fluid Mechanics and Heat
                   Transfer (Imperial College EF/TN/A/34 – déc 1970)

Johnson   : The Effect of wind and wave action on the mixing
                   and dispersion of Wastes. (First International
                   Conference on waste disposal in the marine
                   environment – Berkeley 1959).

oOo

1.Velocity profile when the wind is perpendicular to the coast.

+———+ calculated by EOLE

———— with constant eddy viscosity
(Velocity of wind : 6,6 m/s)

2. Velocity profile when the wind is parallel to the coast.

+———+   calculated by EOLE
— — —   with constant eddy viscosity.
(Velocity of wind : 6,6 m/s)

$\bar{x} = 174,5$

3. Vertical eddy viscosity
with the EOLE program.
(Velocity of wind: 6,6 m/s)
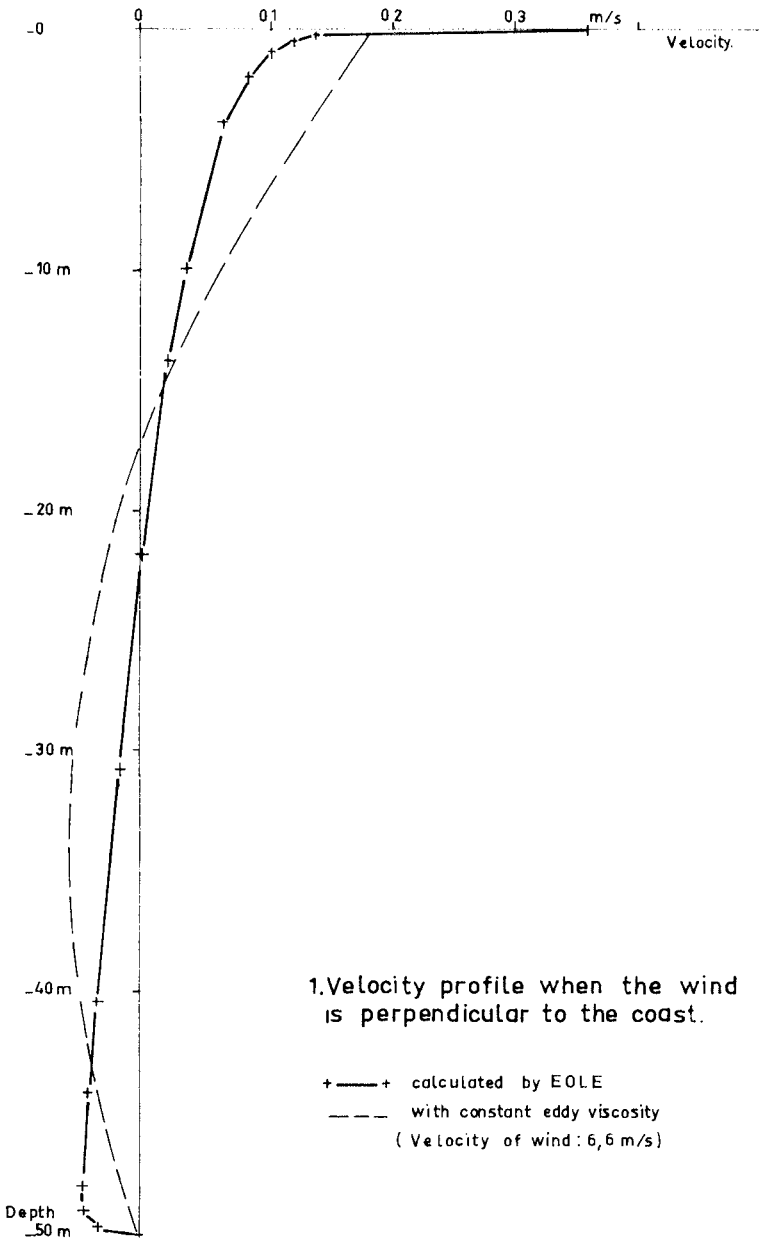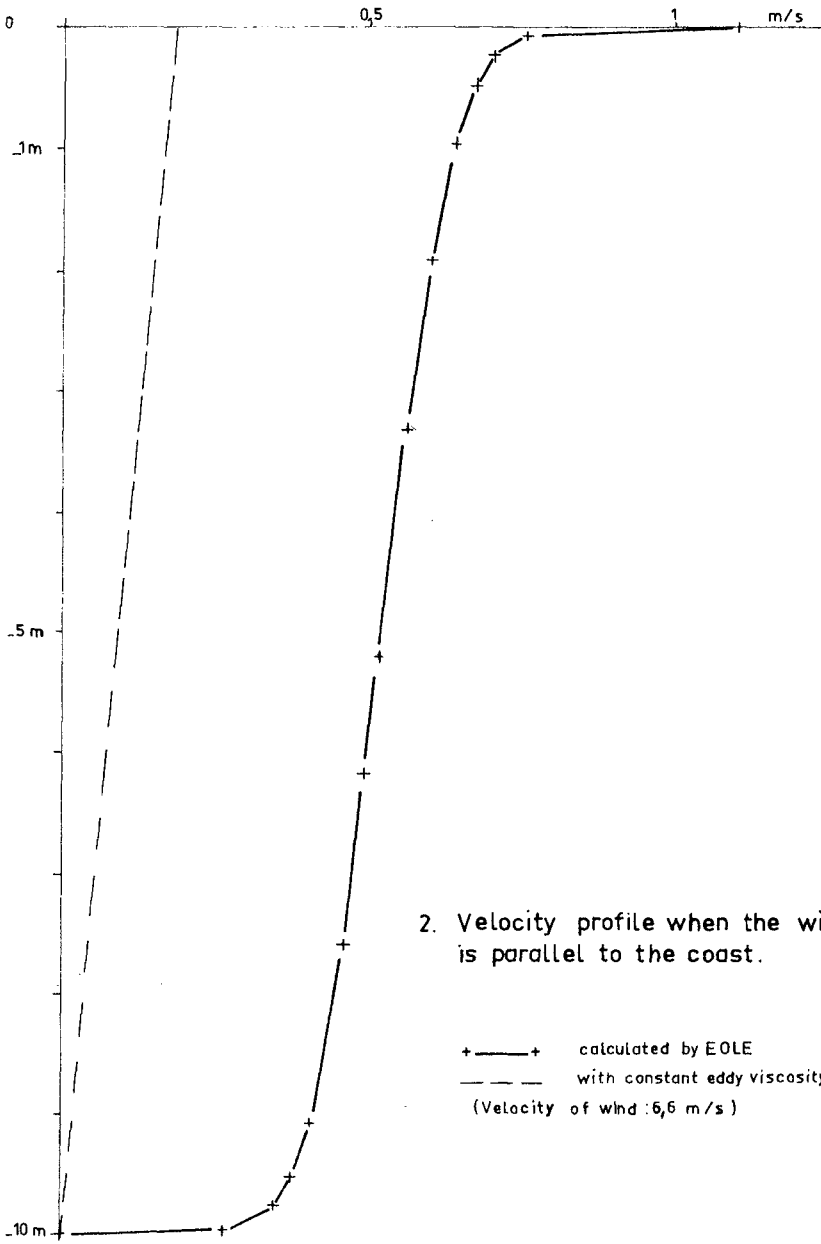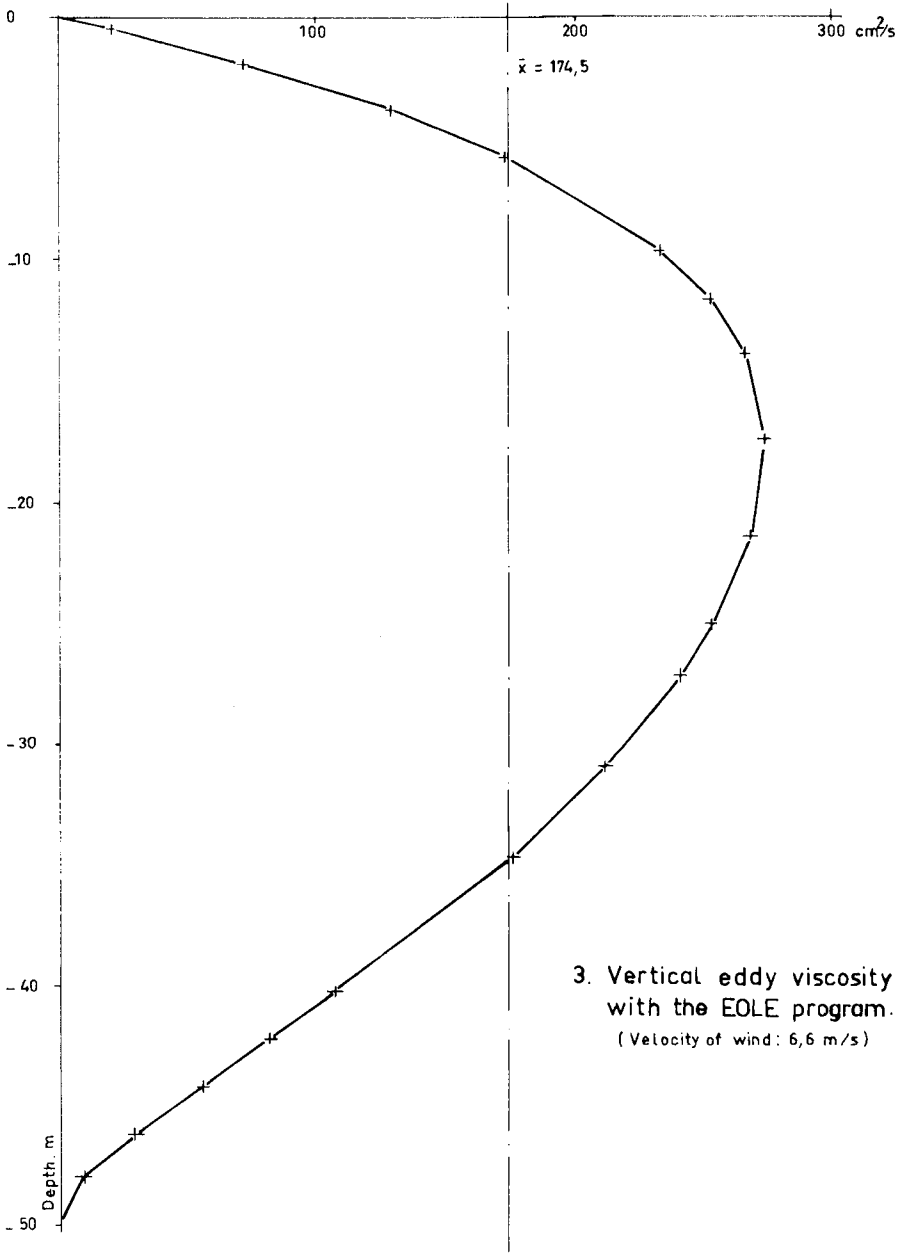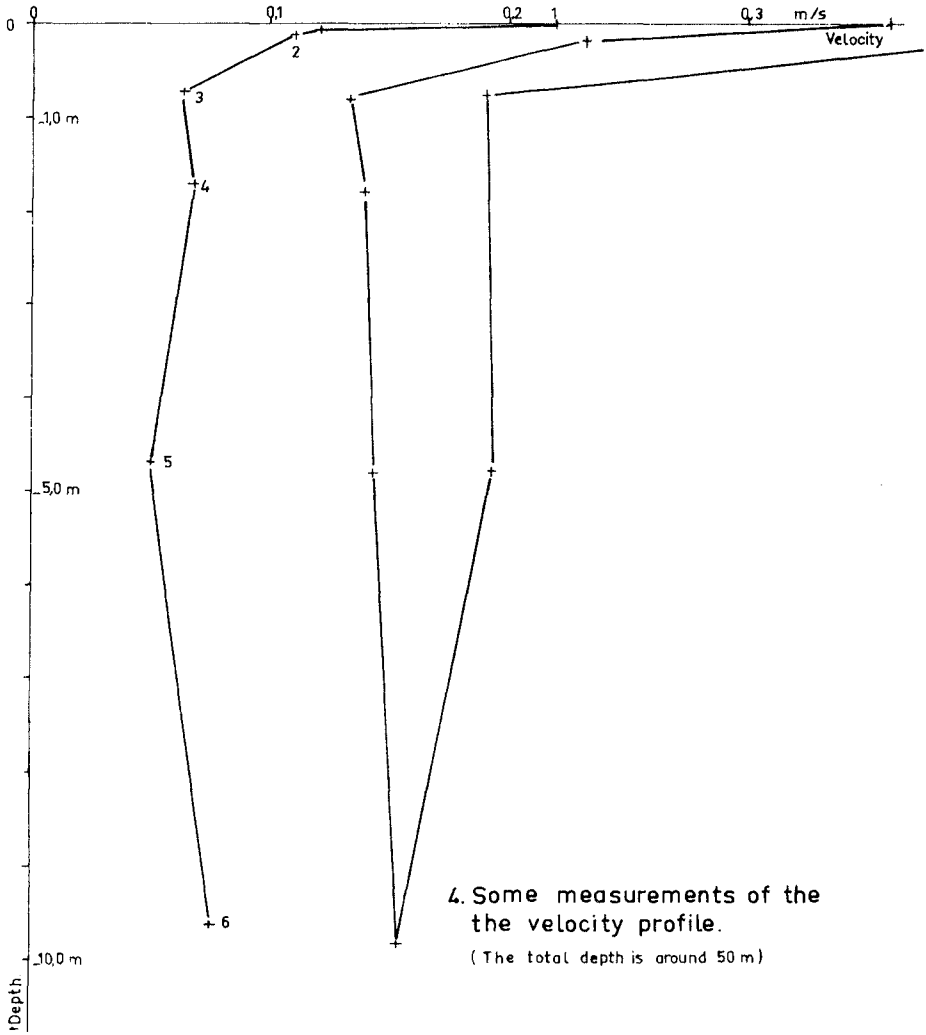
4. Some measurements of the
the velocity profile.
(The total depth is around 50 m)

CHAPTER 141

FINITE ELEMENT MODEL OF TWO LAYER

COASTAL CIRCULATION

by

JOHN D. WANG [1]

JEROME J. CONNOR [2]

ABSTRACT

A set of "averaged" partial differential equations for the circula-
tion in a two layered coastal water is established by assuming each layer
to be vertically homogeneous and by performing a vertical integration over
the layer thicknesses. Since the phenomena to be investigated typically
consist of long waves such as a tidal wave, the hydrostatic pressure as-
sumption is also introduced. The finite element method is employed to
transform the partial differential equations to a discrete system of or-
dinary differential equations which are solved using an implicit time
stepping method similar to the trapezoidal rule, but with the variables
(elevation and flows) staggered in time. A linear stability analysis
shows the initial value problem to be unconditionally stable. In prac-
tice, instability due to boundary conditions and non-linearity sets in.

Comparisons between computed and analytical solutions for simple
cases give good agreement. The tidal excitation of Massachusetts Bay,
represented as a rectangular basin with opening on one side is presented
as an illustrative example.

INTRODUCTION

The rapidly increasing development of our coastal areas has generated
the need for a better understanding of the physical processes in a coastal
water body and for methods to predict the effect of man-made changes. In
particular, significant effort has been directed at determining flow pat-
terns and mass transport [1, 7, 8, 10, 13]. For complex phenomena such as
these, one usually has to resort to physical or numerical models to obtain
solutions. This paper describes a numerical technique, based on the finite
element method, to predict tide and wind driven circulation for a stable
stratified water body in which two distinct layers can be distinguished, a
condition often found in coastal waters during summer time. Due to the

---

1) Graduate Student, R.M. Parsons Laboratory for Water Resources and Hydro-
   dynamics, M.I.T., Cambridge, Massachusetts, U.S.A.
2) Professor of Civil Engineering, R.M. Parsons Laboratory for Water Resources
   and Hydrodynamics, M.I.T., Cambridge, Massachusetts, U.S.A.

increased solar radiation a warmer, lighter surface layer forms with a rather abrupt density change between layers. It is reasonable to approximate the problem as consisting of two vertically homogeneous layers, thereby reducing the degree of complexity.

Until recently, numerical models of coastal circulation have been almost exclusively of the finite difference type. In previous works by the authors [4] a rigorous formulation and solution strategy for 2-dimensional one layer flow using the finite element method has been presented. This method is particularly attractive with respect to formulation and specifying boundary conditions. However, the error and stability aspects for hyperbolic and elliptic boundary value problems treated with finite element methods are not completely resolved. A stability analysis of the linearized system is presented here for some simple schemes. Apart from numerical problems, there are unresolved questions concerning the actual physical processes such as momentum and mass transfer between layers and at open boundaries. These are areas where much more research is needed before truly predictive capabilities are at hand.

MATHEMATICAL FORMULATION

The two layer flow problem is governed by the conservation of mass and momentum requirements. For illustration, it is useful to look at the one layer case first. Assuming that the water column is fairly well mixed it is reasonable to simplify the problem by performing a vertical integration using Leibnitz's rule and the boundary conditions on the surface and bottom. Fig. 1 shows a definition sketch with a horizontal x-y coordinate system, z vertically upwards, surface elevation η and bottom at z=-h. The dependent variables are the total water depth H (or alternatively η) and the total volume flows per unit width in x and y directions.

$$H = h + \eta \tag{1}$$

$$q_x = \int_{-h}^{\eta} u\,dz \tag{2}$$

$$q_y = \int_{-h}^{\eta} v\,dz$$

The form of the governing equations have been shown to be [4]:

$$\frac{\partial}{\partial t}(\rho H) + \frac{\partial}{\partial x}q_x + \frac{\partial}{\partial y}q_y = q_I \tag{3}$$

$$\frac{\partial}{\partial t}q_x + \frac{\partial}{\partial x}(\bar{u}q_x) + \frac{\partial}{\partial y}(\bar{u}q_y) = fq_y + B_x + \frac{\partial}{\partial x}(F_{xx} - F_p) + \frac{\partial}{\partial y}F_{yx}$$

$$\frac{\partial}{\partial t}q_y + \frac{\partial}{\partial x}(\bar{v}q_x) + \frac{\partial}{\partial y}(\bar{v}q_y) = -fq_x + B_y + \frac{\partial}{\partial x}F_{xy} + \frac{\partial}{\partial y}(F_{yy} - F_p) \tag{4}$$
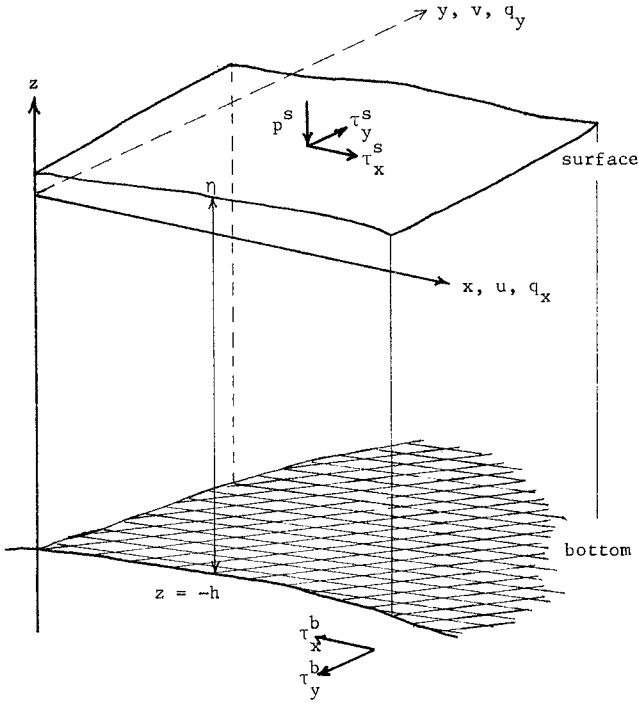
Fig. 1. Definition sketch for one layer flow.

here

$$F_p = \frac{1}{\rho_o} \int_{-h}^{\eta} p\,dz - \frac{1}{2} gh^2$$

$$= g(h\eta + \frac{1}{2}\eta^2) + \frac{1}{2} \frac{\Delta\rho}{\rho_o} gH^2 + \frac{p^s}{\rho_o} H \tag{5}$$

$$B_{x_i} = \frac{1}{\rho_o}(p^s \frac{\partial H}{\partial x_i} + \Delta\rho gH\frac{\partial h}{\partial x_i} + \rho_o gy\frac{\partial h}{\partial x_i} + \tau^s_{x_i} - \tau^b_{x_i}); \ i = 1,2 \tag{6}$$

and q_I denotes an internal source, $f = 2\Omega\sin\phi$ is the Coriolis parameter, (F_{xx}, F_{xy}, F_{yy}) are internal stresses; $\bar{u}$ and $\bar{v}$ are average velocities; F_p is the excess integrated pressure, p^s is the barometric pressure on the surface; and τ^s, τ^b are surface and bottom shear stresses. For convenience we frequently write x_1, x_2 for x, y. The mass density $\rho = \rho_o + \Delta\rho$ is replaced by the constant mean value ρ_o everywhere except in the hydrostatic pressure (5). This is known as the Boussinesque approximation.

The internal stress terms F_{xx}, F_{xy}, F_{yy} represent the specific momentum transfers due to viscosity, turbulence and vertical shear. Their general form is:

$$F_{x_i x_j} = \int_{-h}^{\eta} \left\{ \tau^{\mathbf{3}}_{x_i x_j}/\rho_o - <(u'_i\, u'_j) + (u''_i \cdot u''_j)>\text{ensemble} \right. $$
$$\left. - u''_i\, u''_j \right\} dz \qquad i,j = 1, 2 \tag{7}$$

where $\tau^{\mathbf{3}}$ is the molecular stress term; u' is the turbulent fluctuation of the velocity, u'' is the velocity deviation from the vertical mean value $\bar{u}$, and $u'^{''}$ is the deviation of the turbulent fluctuation. As indicated in (7) all turbulent fluctuations are ensemble averaged.

U = instantaneous velocity
u = ensemble average of U
$\bar{u}$ = vertical average of u
u'= turbulent fluctuation of U
$\overline{u'}$ = vertical average of u'
u"= vertical deviation of u
u'"= vertical deviation of u'
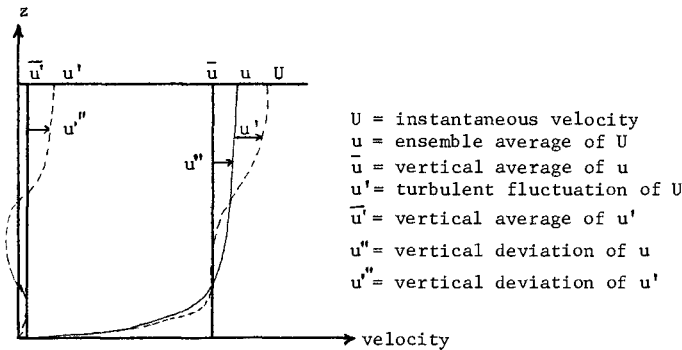
Fig. 2. Velocity distribution in the vertical and its components.

One of the most significant difficulties with an averaged or integrated formulation is the occurrence of additional variables due to the non-linear terms. In turbulence theory, these variables give rise to the so-called Reynolds stresses and the phenomenon is often called the closure problem because there are more variables than equations. For our approach, we have lumped all these apparent stresses together with viscous stresses in the internal specific force measures (force per unit width and density) F_{xx}, F_{xy}, F_{yy}. An engineering solution has been to interpret the apparent stresses as momentum transfer and represent them by a diffusion process analogous to Newton's law for viscous shear. Following this approach, we express the force measures as

$$F_{x_i x_j} = E_{ij} \left(\frac{\partial q_j}{\partial x_i} + \frac{\partial q_i}{\partial x_j} \right) \qquad \text{no summing over i, j} \qquad (8)$$

Once the "eddy diffusion" coefficient matrix E_{ij} is specified, the problem is closed. However, contrary to molecular viscosity which is a fluid property, the E_{ij}'s are functions of the flow field. More specifically they can depend on the flow, shear stresses on bottom and surface, depth and time. By definition $F_{ij} = F_{ji}$ and therefore E_{ij} must be symmetric. If E_{ij} is taken as anisotropic, the principal directions should usually be defined along and perpendicular to the local velocity direction. The effect of the internal stresses is to dissipate or generate energy depending on whether E_{ij} is positive or negative [5,11]. At present little is known about the validity of (8), in particular what is the relationship for E_{ij} in terms of flow parameters. It will be shown later that positive eddy viscosity improves numerical stability, mainly by dissipating high frequency energy.

The equations governing vertically integrated layered flow follow by generalizing (3), (4) and are written as

$$\frac{\partial H_k}{\partial t} + \frac{\partial}{\partial x} q_{xk} + \frac{\partial}{\partial y} q_{yk} = q_k \qquad (9)$$

$$\frac{\partial q_{xk}}{\partial t} + \frac{\partial}{\partial x}(\bar{u}_k q_{xk}) + \frac{\partial}{\partial y}(\bar{u}_k q_{yk})$$

$$= fq_{yk} + \frac{\partial}{\partial x}(F_{xxk} - F_{pk}) + \frac{\partial}{\partial y}F_{yxk} + \frac{1}{\rho_k} \left\{ \tau_{xk} - \tau_{xk-1} \right.$$

$$\left. + p_k \frac{\partial \eta_k}{\partial x} - p_{k-1} \frac{\partial \eta_{k-1}}{\partial x} \right\} \qquad (10)$$

$$\frac{\partial q_{yk}}{\partial t} + \frac{\partial}{\partial x}(\bar{v}_k q_{xk}) + \frac{\partial}{\partial y}(\bar{v}_k q_{yk})$$

$$= -f q_{xk} + \frac{\partial}{\partial x} F_{xyk} + \frac{\partial}{\partial y}(F_{yyk} - F_{pk}) + \frac{1}{\rho_k}\left\{\tau_{yk} - \tau_{yk-1}\right.$$
$$+ p_k \frac{\partial \eta_k}{\partial y} - p_{k-1}\frac{\partial \eta_{k-1}}{\partial y}\left.\right\}$$

where the notation for layer k is defined in Figure (3).
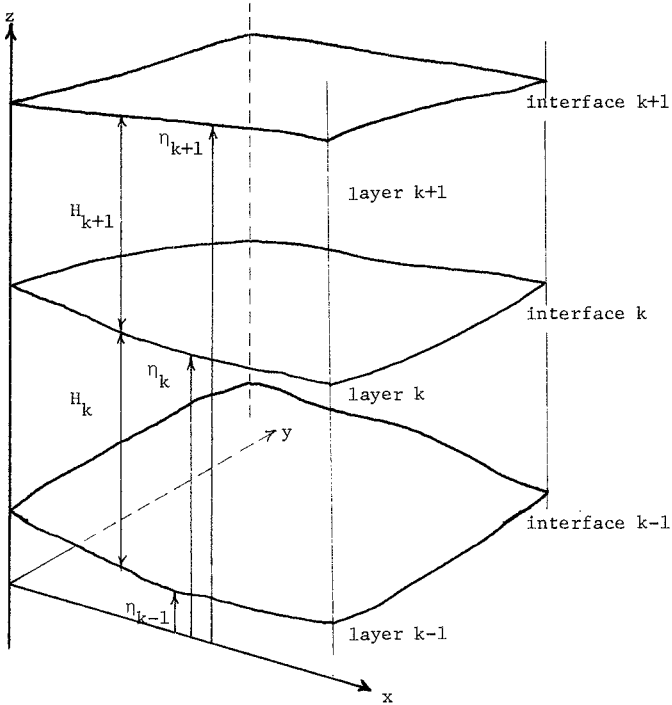
Fig. 3. Definition sketch for multilayered flow.

We still assume hydrostatic pressure, i.e., the pressure at the k'th
interface is given by $p_{k-1} - p_k = \rho_k g H_k$ (11)

For two-layer flow, $p_2 \approx$ atmospheric pressure

The equilibrium equations on the boundary take the following forms:
$$F_{nnk} = F^*_{nnk} \quad \text{on } S_k \tag{12}$$

where F^*_{nnk} is the prescribed specific force measure normal to the bound-
ary on layer k, S_k.

Conservation of mass (continuity) is satisfied when

$$q_{nk} = q^*_{nk} \text{ on } S_k \tag{13}$$

Here q^*_{nk} is the prescribed normal boundary flux for layer k. When the
eddy viscosity terms are retained in the formulation, additional equil-
ibrium conditions on tangential forces
$$F_{nsk} = F^*_{nsk} \tag{14}$$
and flows
$$q_s = q^*_s \tag{15}$$
can be specified.

The interfacial shear stresses are evaluated with the most common-
ly used relation:

$$\begin{Bmatrix} \tau_{xk} \\ \tau_{yk} \end{Bmatrix} = \begin{Bmatrix} \bar{u}_k - \bar{u}_{k-1} \\ \bar{v}_k - \bar{v}_{k-1} \end{Bmatrix} \rho_k C_{fk} [(\bar{u}_k - \bar{u}_{k-1})^2 + (\bar{v}_k - \bar{v}_{k-1})^2]^{\frac{1}{2}} \tag{16}$$

Investigations have shown the dimensionless friction factor, C_{fk}, to be
dependent on at least Reynolds number and densimetric Froude number
(Richardson number) [2].

Summarizing the formulation, the dependent variables are the volume
flows per unit width in each layer, q_{xk}, q_{yk} and the layer thicknesses H_k.
The governing equations are given by (9) – (10) which apply in the inter-
ior and (12) – (13) on the boundaries.

THE WEAK FORM

There has been considerable recent effort by mathematicians directed
at proving that the solutions obtained from the flow equations, notably
the Navier Stokes equations, are unique [6]. In one approach, the dif-
ferential equations are transformed to an integral expression which is
called the weak or Galerkin form [9, 12]. When the weak form has a uni-
que solution, this will also be the unique solution of the original

equations, and the weak form is then called the generalized form. Thus, the mathematical problem reduces to showing that the weak form has a unique solution. There are indications [6, 12] that the generalized equations constitute the well-posed form of the problem In what follows, we cast the problem into its weak form and use this as the basis for the finite element approximation. No attempt is made here to present a mathematical proof of uniqueness. However, we do present comparisons with analytical solutions.

The weak form is derived by weighting the continuity and equilibrium equations, and integrating over the total area.

$$\iint_{A_k} \left\{ \frac{\partial H}{\partial t} + \frac{\partial q_x}{\partial x} + \frac{\partial q_y}{\partial y} - q \right\}_k \cdot \Delta H_k \, dA$$

$$+ \int_{S_k} \left\{ q_n - q_n^* \right\}_k \cdot \Delta H_k \, ds = 0 \tag{17}$$

$$\iint_{A_k} [\left\{ \frac{\partial q_x}{\partial t} + \frac{\partial}{\partial x}(\bar{u}q_x) + \frac{\partial}{\partial y}(\bar{u}q_y) - fq_y \right.$$

$$+ \frac{\partial}{\partial x}(F_p - F_{xx}) - \frac{\partial}{\partial y}F_{yx} - \tau_x - p\frac{\partial \eta}{\partial x} \Big\}_k$$

$$+ \left\{ \tau_x + p\frac{\partial \eta}{\partial x} \right\}_{k-1}] \Delta q_{xk} \, dA$$

$$+ \int_{S_k} \left\{ F_{nx} - F_{nk}^* \right\}_k \Delta q_{xk} \, ds = 0 \tag{18}$$

$$\iint_{A_k} [\left\{ \frac{\partial q_y}{\partial t} + \frac{\partial}{\partial x}(\bar{v}q_x) + \frac{\partial}{\partial y}(\bar{v}q_y) + fq_x - \frac{\partial}{\partial x}F_{xy} \right.$$

$$+ \frac{\partial}{\partial y}(F_p - F_{yy}) - \tau_y - p\frac{\partial \eta}{\partial y} \Big\}_k$$

$$+ \left\{ \tau_y + p\frac{\partial \eta}{\partial y} \right\}_{k-1}] \, \Delta q_{yk} \, dA$$

$$+ \int_{S_k} \left\{ F_{ny} - F^*_{ny} \right\}_k \Delta q_{yk} \, ds = 0$$

where ΔH, Δq_x, Δq_y are arbitrary finite continuous functions and F^*_{nx}, F^*_{ny} are the prescribed values of the x and y components of the normal specific force measure. Applying Gauss's theorem for partial integration to the momentum equations yields the desired form:

$$\iint_{A_k} [(\left\{ \frac{\partial q_x}{\partial t} + \frac{\partial}{\partial x}(\bar{u}q_x) + \frac{\partial}{\partial y}(\bar{u}q_y) - f q_y - \tau_x - p\frac{\partial \eta}{\partial x} \right\}_k$$

$$+ \left\{ \tau_x + p\frac{\partial \eta}{\partial x} \right\}_{k-1}) \, \Delta q_{xk} + \left\{ (F_{xx} - F_p)\frac{\partial \Delta q_x}{\partial x} \right.$$

$$\left. + F_{yx}\frac{\partial \Delta q_x}{\partial y} \right\}_k] \, dA$$

$$- \int_{S_k} \left\{ F^*_{nx} \, \Delta q_x \right\}_k ds = 0 \qquad\qquad (19)$$

$$\iint_A [(\left\{ \frac{\partial q_y}{\partial t} + \frac{\partial}{\partial x}(\bar{v}q_x) + \frac{\partial}{\partial y}(\bar{v}q_y) + f q_x - \tau_y - p\frac{\partial \eta}{\partial y} \right\}_k$$

$$+ \left\{ \tau_y + p\frac{\partial \eta}{\partial y} \right\}_{k-1}) \, \Delta q_{yk} + \left\{ F_{xy}\frac{\partial \Delta q_y}{\partial x} \right.$$

$$\left. + (F_{yy} - F_p)\frac{\partial \Delta q_y}{\partial y} \right\}_k] \, dA$$

$$- \int_S \left\{ F^*_{ny} \, \Delta q_y \right\}_k ds = 0$$

FINITE ELEMENT DISCRETIZATION

The discretization in space is obtained by applying the finite el-
ement technique, which allows for a flexible grid configuration, easy
handling of complex boundaries and topography, and straightforward math-
ematical representation.

A boundary segment is classified according to the boundary condition
for the segment. On S_o, the open ocean boundary, the layer depths are
prescribed. On S_q, which can be either a land boundary or across a stream,
the normal flux is prescribed.
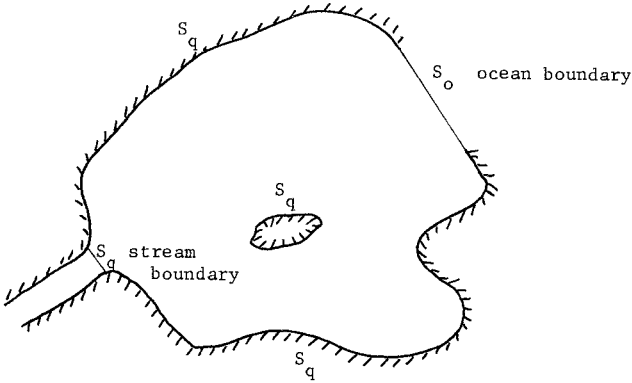
Fig. 4. Boundary classification.

When eddy viscosity is included, lateral shear can exist and the
tangential forces and fluxes on the boundaries must also be matched.
Prescribing the tangential flow, usually as a no-slip condition, does
not cause any conceptual problems. However, the need to know both nor-
mal and tangential forces presents a serious data acquisition problem
since layer depths can no longer be used as a replacement for the pressure
force.

The weak form is the natural basis for the finite element method. We
require the weighting functions ΔH, Δq_x, Δq_y to be admissible, that is,
described by the same shape functions as the dependent variables and sat-
isfying the homogeneous boundary conditions. With these restrictions,
ΔH, Δq_x, Δq_y can be interpreted as admissible variations of H, q_x, q_y.

The integrals

$$\int_{S_k} \left\{ q_n - q_n^* \right\}_k \Delta H_k \, ds \quad , \tag{a}$$

$$\int_{Sq_k} \left\{ -F_{nx}^* \right\}_k \Delta q_{xk} \, ds \quad , $$

$$\int_{Sq_k} \left\{ -F_{ny}^* \right\}_k \Delta q_{yk} \, ds \tag{b}$$

vanish and we are left with

$$\iint_{A_k} \left\{ \frac{\partial H}{\partial t} + \frac{\partial q_x}{\partial x} + \frac{\partial q_y}{\partial y} - q \right\}_k \Delta H_k \, dA = 0 \tag{20}$$

$$\iint_{A_k} \left[\left(\left\{ \frac{\partial q_x}{\partial t} + \frac{\partial}{\partial x}(\bar{u}q_x) + \frac{\partial}{\partial y}(\bar{u}q_y) - fq_y - \tau_x - p\frac{\partial \eta}{\partial x} \right\}_k \right. \right.$$

$$+ \left. \left\{ \tau_x + p\frac{\partial \eta}{\partial x} \right\}_{k-1} \right) \Delta q_{xk} + \left\{ (F_{xx} - F_p) \frac{\partial \Delta q_x}{\partial x} \right.$$

$$+ \left. \left. F_{yx} \frac{\partial \Delta q_x}{\partial y} \right\}_k \right] dA$$

$$- \int_{S_{ok}} \left\{ F_{nx}^* \, \Delta q_x \right\}_k \, ds = 0$$

$$\iint_{A_k} \left[\left(\left\{ \frac{\partial q_y}{\partial t} + \frac{\partial}{\partial x}(\bar{v}q_x) + \frac{\partial}{\partial y}(\bar{v}q_y) + fq_x - \tau_y - p\frac{\partial \eta}{\partial y} \right\}_k \right. \right. \tag{21}$$

$$+ \left. \left\{ \tau_y + p\frac{\partial \eta}{\partial y} \right\}_{k-1} \right) \Delta q_y + \left\{ F_{yx} \frac{\partial \Delta q_y}{\partial x} \right.$$

$$+ (F_{yy} - F_p) \frac{\partial \Delta q_y}{\partial y} \Big\}_{\cdot k}] dA$$

$$- \int_{S_{ok}} \Big\{ F_{\eta y}^* \, \Delta q_y \Big\}_k ds = 0$$

We have found that, under normal circumstances, the force integrals (b) on the prescribed flow boundary which, in theory, vanish have to be retained as a correction in practical application. This is due to the fact that the normal direction chosen for a boundary node point is the average direction for the adjacent segments, and specifying $q_n = 0$ for the node does not (unless the sides are parallel) result in $q_n = 0$ for the segments. This correction tends to zero as the grid is refined; but for practical grid sizes, (20) and (19) should be used.

All variables are now expressed in terms of the element nodal values and functions defining the spatial variation over the element domain,

$$f = \phi_i \, F_i \tag{22}$$

F_i are the nodal values and ϕ_i are prescribed functions of x and y.

Substituting (22) in (19) - (20) results in a system of ordinary differential equations relating the nodal variables

$$M_H \dot{H} + DQ = P_H \tag{23}$$

$$M_Q \dot{Q} - D^T H + CQ + EQ = P_Q \tag{24}$$

where H is a vector containing the nodal values of layer thickness, Q contains the nodal fluxes listed as $[q_{x_1} \; q_{y_1} \cdots q_{x_i} \; q_{x_i} \cdots q_{x_n} \; q_{y_n}]$ with i being the node number; the dot denotes time differentiation, P_H and P_Q are vectors containing non-linear and forcing terms. Although the elements of the coefficient matrices depend on grid and element type, they do have certain invariant properties: M and E (eddy viscosity) are symmetric and positive definite, and C (Coriolis) is skewsymmetric.

TIME INTEGRATION

Integration of (23) - (24) through time is carried out with the trapezoidal rule, a simple implicit scheme. The assumption is made that non-linear, Coriolis, and eddy viscosity terms are of relatively minor importance, hence a simple backward difference approximation is used for them. Our starting point is

$$\underset{\sim H}{M} \dot{\underset{\sim}{H}} + \underset{\sim}{D} \underset{\sim}{Q} = \underset{\sim H}{P} \tag{25}$$

$$\underset{\sim Q}{M} \dot{\underset{\sim}{Q}} - \underset{\sim}{D}^T \underset{\sim}{H} = \underset{\sim Q}{P} - \underset{\sim}{C} \underset{\sim}{Q} - \underset{\sim}{E} \underset{\sim}{Q} \tag{26}$$

A direct application of the trapezoidal rule is possible. However, storage requirements are excessive since one has to solve for all 3N (N is number of nodes) unknowns at the same time, and furthermore the coefficient matrix is unsymmetric. 18N·BW words of storage are required where BW is the minimum bandwidth.

To circumvent the storage problem a split-time scheme was devised. The variables H and Q are staggered in time such that H is defined at time t, t + Δt, and Q is defined at t $-\frac{1}{2}\Delta$t, t $+\frac{1}{2}\Delta$t etc. In this way, we can write (25) as

$$\underset{\sim H}{M} \dot{\underset{\sim}{H}} = \underset{\sim H}{P} - \underset{\sim}{D} \underset{\sim}{Q} \tag{27}$$

$$\underset{\sim Q}{M} \dot{\underset{\sim}{Q}} = \underset{\sim Q}{P} - \underset{\sim}{C} \underset{\sim}{Q} - \underset{\sim}{E} \underset{\sim}{Q} + \underset{\sim}{D}^T \underset{\sim}{H} \tag{28}$$

and solve (27) and (28) in successive order. The coefficient matrices remain symmetric, and required storage is reduced to 5N·BW words. In addition the accuracy is improved because the difference approximations are central rather than backward, and also significant economy in computation time is realized.

The stability of the linearised, homogeneous initial value problems can be investigated with the matrix method. We define

$$\underset{\sim 1}{M} = \underset{\sim Q}{M} + \theta \Delta t \underset{\sim}{E} \tag{29}$$

$$\underset{\sim 2}{M} = \underset{\sim Q}{M} - (1-\theta)\Delta t \underset{\sim}{E} \tag{30}$$

and write (27) - (28) as:

$$(\underset{\sim 1}{M} + \theta \Delta t \underset{\sim}{C}) \underset{\sim n+\frac{1}{2}}{Q} = (\underset{\sim 2}{M} - (1-\theta)\Delta t \underset{\sim}{C}) \underset{\sim n-\frac{1}{2}}{Q} + \Delta t \underset{\sim}{D}^T \underset{\sim n}{H} + \Delta t \underset{\sim H}{P} \tag{31}$$

$$\underset{\sim H}{M} \underset{\sim n+1}{H} = -\Delta t \underset{\sim}{D} \underset{\sim n+\frac{1}{2}}{Q} + \underset{\sim H}{M} \underset{\sim n}{H} + \Delta t \underset{\sim H}{P} \tag{32}$$

Their combined form is

$$\begin{Bmatrix} \underset{\sim 1}{M} + \theta \Delta t \underset{\sim}{C} & \underset{\sim}{0} \\ \Delta t \underset{\sim}{D} & \underset{\sim H}{M} \end{Bmatrix} \begin{Bmatrix} \underset{\sim n+\frac{1}{2}}{Q} \\ \underset{\sim n+1}{H} \end{Bmatrix} = \begin{Bmatrix} \underset{\sim 2}{M} - (1-\theta)\Delta t \underset{\sim}{C} & \Delta t \underset{\sim}{D}^T \\ \underset{\sim}{0} & \underset{\sim H}{M} \end{Bmatrix} \begin{Bmatrix} \underset{\sim n-\frac{1}{2}}{Q} \\ \underset{\sim n}{H} \end{Bmatrix} + \Delta t \begin{Bmatrix} \underset{\sim Q}{P} \\ \underset{\sim H}{P} \end{Bmatrix} \tag{33}$$

Taking θ equal to 1 corresponds to a fully implicit treatment of Coriolis and eddy viscosity, and θ equal to 0 is equivalent to a completely explicit

treatment. Values between 0 and 1 are also possible. We use $\theta = 0$ in our "split-time" scheme.
    By defining

$$X_{\sim n+1} = \begin{Bmatrix} Q_{\sim n+\frac{1}{2}} \\ H_{\sim n+1} \end{Bmatrix} \tag{34}$$

(33) takes a more convenient form,

$$(\bar{M}_{\sim 1} + \theta \bar{C} + \bar{D})\, X_{\sim n+1} = (\bar{M}_{\sim 2} + (1-\theta)\bar{C} + D^T)\, X_{\sim n} \tag{35}$$

Expressing $X_{\sim n+1}$ as

$$X_{\sim n+1} = \lambda X_{\sim n} \tag{36}$$

and substituting (36) in (35) leads to

$$\lambda = \frac{m + \Delta t[(1-\theta)(-e) + d_s] - i\Delta t[d_{ss} + (1-\theta)c_{ss}]}{m + \Delta t[\theta(e) + d_s] = i\Delta t[d_{ss} + \theta c_{ss}]} \tag{37}$$

where $i = \sqrt{-1}$; $m>0$; $e>0$; subscript s signifies that the value stems from the symmetric part of the matrix; and ss denotes the skew symmetric contribution.
    For $\theta = 0$, we obtain

$$\lambda = \frac{m + \Delta t d_s - \Delta t e - i\Delta t[d_{ss} + c_{ss}]}{m + \Delta t d_s + i\Delta t d_{ss}} \tag{38}$$

When eddy viscosity and Coriolis terms are neglected, (38) reduced to

$$|\lambda| = \left| \frac{m + \Delta t d_s - i\Delta t d_{ss}}{m + \Delta t d_s + i\Delta t d_{ss}} \right| = 1 \tag{39}$$

    Therefore, under the given assumptions, the $\theta = 0$ split-time scheme is unconditionally stable. However, application of the method has revealed that instability sets in at Courant numbers larger than approximately 1.5. An explanation is not yet known, but possible sources of instability are non-linear effects, boundary conditions and bottom variation. This is obviously an area where more research is needed.

RESULTS. VERIFICATION STUDIES

    The most desirable verification of a numerical model is a comparison with an "exact" analytical solution of the same system of equations. Fortunely, the analytical solution of standing waves in a 2-layered infinitely wide channel of length is known and we use this as a basis for verification. Figure 5 shows a side view of the channel and plans of two grid configurations.

Side view of channel

Plan view of channel with grid. $\Delta x=50$ m; $\Delta y=50$ m; $\Delta t=2.5$ sec.

Plan view of channel with fine grid. $\Delta x=25$ m; $\Delta y=50$ m; $\Delta t=1.25$ sec.
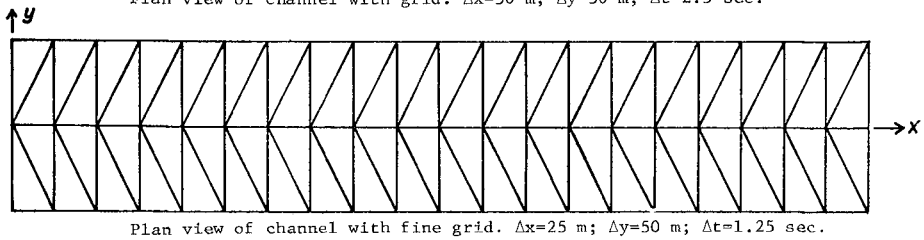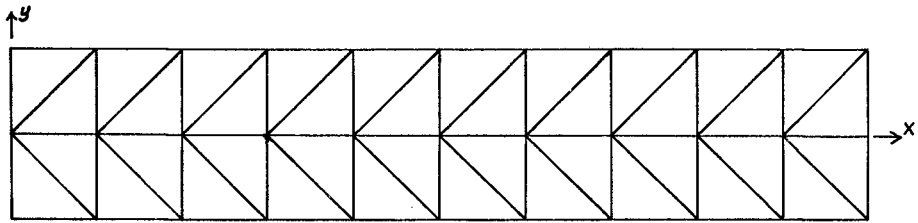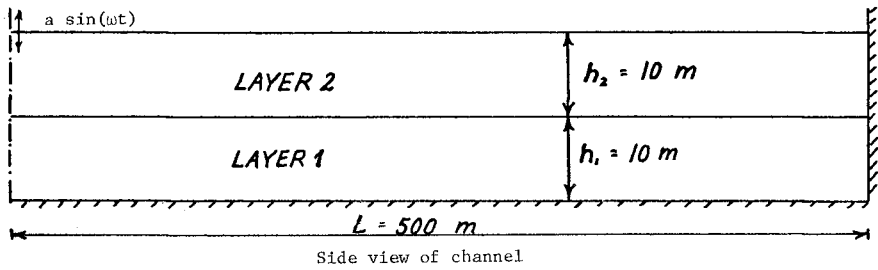
Fig. 5. Sketch of first comparison study. Rectangular channel.

The solution for the surface and interface displacements η_2, η_1 with a forcing consisting of sinusoidal oscillation (amplitude a) of the surface and no movement of the interface at the entrance is given by

$$\eta_1 = \left\{ A(1 - \frac{gh_2}{\omega^2} k_1^2) \cos k_1 x + B(1-\frac{gh_2}{\omega^2} k_2^2) \cos k_2 x \right\} \sin\omega t \qquad (40)$$

$$\eta_2 = \left\{ A \cos k_1 x + B \cos k_2 x \right\} \sin\omega t \qquad (41)$$

with

$$A = \frac{a(1 - \frac{gh_2}{\omega^2}k^2)}{(k_1^2 - k_2^2) - \frac{gh_2}{\omega^2}\cos k_1 L}; \quad B = \frac{a(\frac{gh_1}{\omega^2}k_1^2 - 1)}{(k_1^2 - k_2^2)\frac{gh_2}{\omega^2}\cos k_2 L} \qquad (42)$$

$$\begin{Bmatrix} k_1 \\ k_2 \end{Bmatrix} = [\frac{1}{2}\frac{\rho_1}{\Delta\rho}\frac{(h_1 + h_2)}{gh_1 h_2}\omega^2 \pm \omega^2\sqrt{(\frac{1}{2}\frac{\rho_1}{\Delta\rho}\frac{(h_1 + h_2)}{gh_1 h_2})^2 - \frac{\rho_1}{\Delta\rho}\frac{1}{gh_1 gh_2}}]^{\frac{1}{2}} \qquad (43)$$

The numerical model was initialised with the correct values of elevations at maximum displacement (velocities zero) and then run with the forcing for several tidal periods (T = 500 sec).

The analytical results and absolute error in the numerical solution are plotted in figure 6. The agreement for the fine grid is reasonable although not impressive.

The forcing period T was increased to 1000 sec., so that the number of short waves in the channel is approximately 1. Results are plotted in figure 7 and show very good agreement. This indicated that about 20 points per full wave length are necessary with the linear element for an accurate representation.

The second comparison is only qualitative, since it is impossible to satisfy the same boundary conditions in analytical and numerical models. The problem involved determining of the harmonic oscillation in a rectangular basin with an opening on one side. The dimensions of the basin are chosen so as to approximate the Massachusetts Bay on the east coast of the U.S.

The analytical solution of this problem is developed in [3] and is expressed in terms of infinite Fourier series. Collocation was used to specify the boundary conditions as discussed in the reference. In the numerical computation, the free surface was subjected to a tidal excitation, and the interface surface was fixed at its initial position. A sample plot of layer velocities is shown in figure 8, which compares favorably with the analytical results in figure 9.

CONCLUSION

The value of a model is determined by its ability to describe actual physical processes. For this type of evaluation, much more data is needed. The finite element method appears advantageous with respect to flexible spatial discretization and treatment of boundary conditions. The formulation is independent of grid configuration and choice of element type, since the structure of the equations remains the same. Compared with well-known finite difference models, the bandwidth of the finite element coefficient matrix is usually larger but the finite element model requires less nodes, i.e., less unknowns. Thus storage requirements are usually somewhat less, but the finite element method might require more computations. Additional research needs to be done on the time integration in order to increase the time step. The ocean boundary conditions are extremely important and additional work is needed to determine those properly.
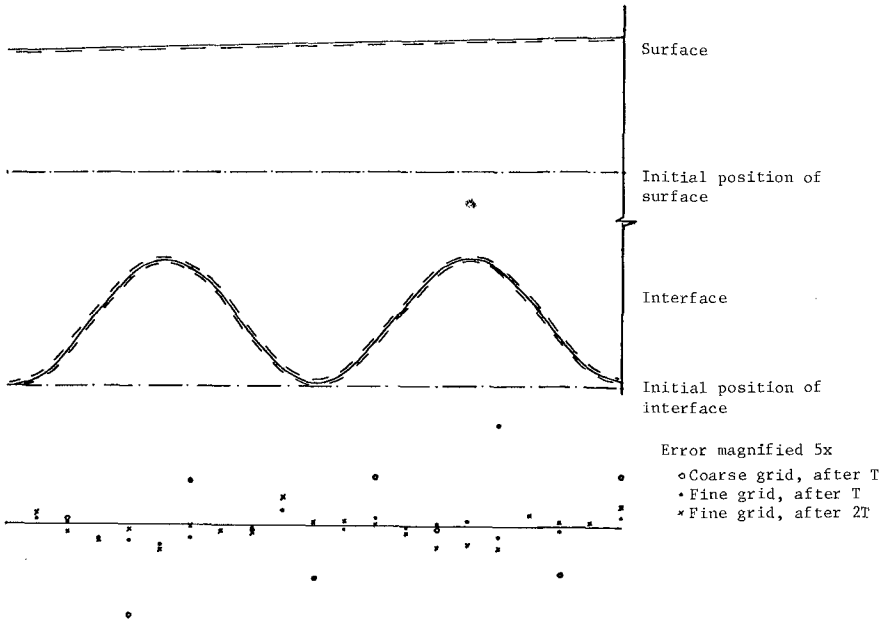
Fig 6. Comparison of solutions for rectangular channel. T=500sec.
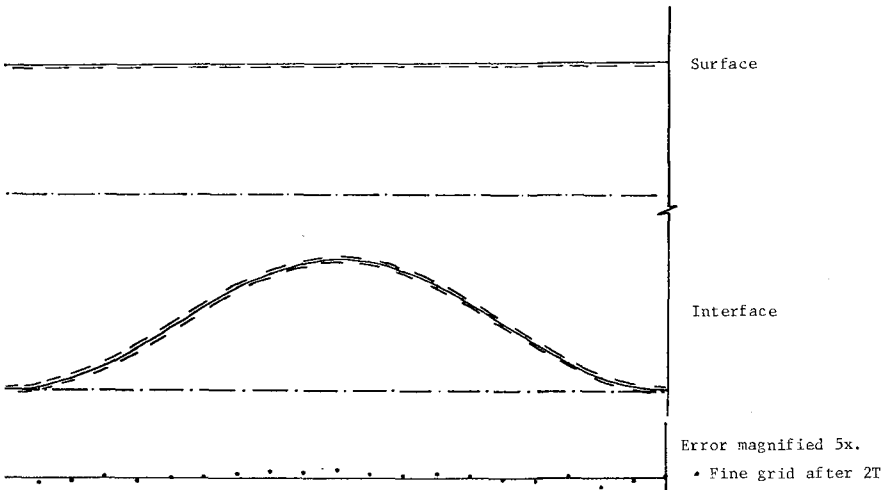
Fig. 7. Comparison of solutions for rectangular channel. T=1000 sec.

Fig. 8. Computed velocity field for two layered approximation of Massachusetts Bay.
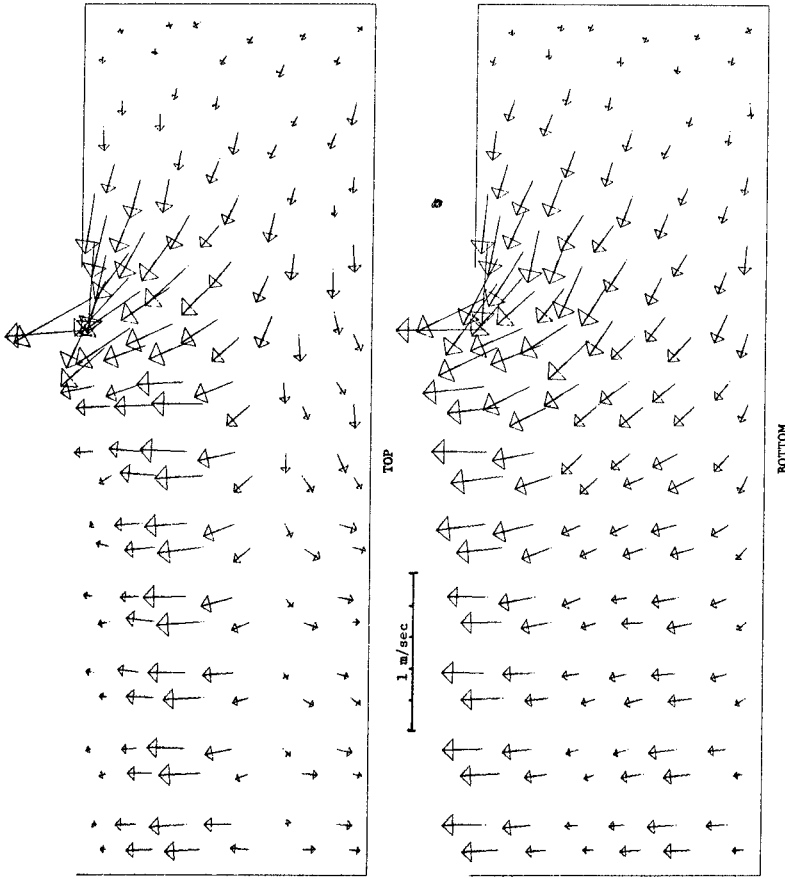
Rectangular approximation of Massachusetts Bay. 94 Node grid. Current velocities, 4.3 T (192500 sec.) after startup.

TOP

BOTTOM

1 m/sec
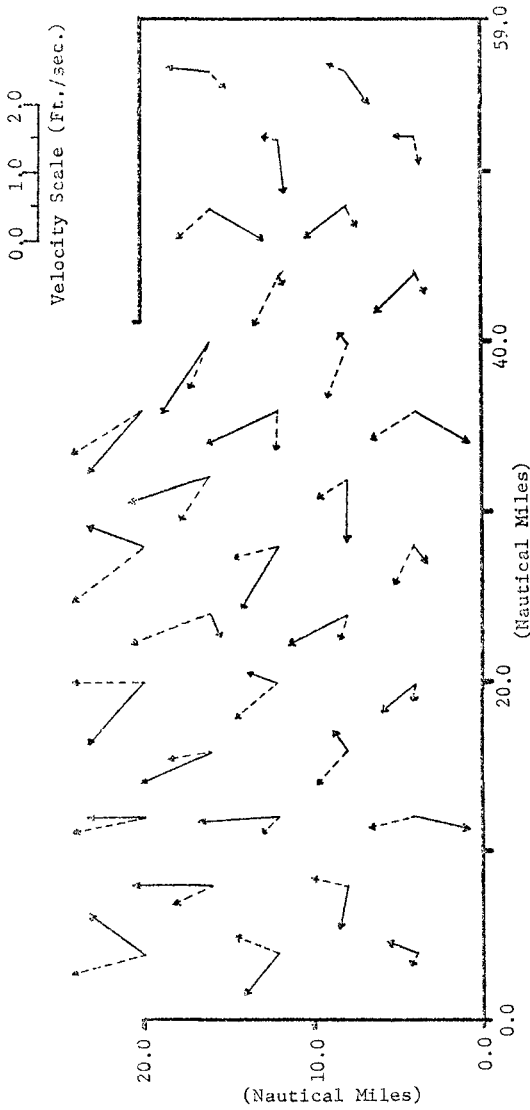
Figure 4-D: Two Layer Model of Massachusetts Bay.
Velocities at Maximum Ebb in Ft./sec.

Fig. 9. Velocity field from analytical solution in ref. [3].

REFERENCES

1. Abbot, M.B., Gruber, J.P., "Towards a design system for stratified flows", Int. Symp. on Stratified Flows, IAHR, Novosibirsk, 1972.

2. Abraham, G., Eysink, W.D., "Magnitude of interfacial shear in exchange flow", J. Hydraulic Research, AlHR, Vol. 9, No.2, 1971.

3. Briggs, D.A., Madsen, O.S., "Analytical models for one- and two layer systems in rectangular basins", TR 172, part Il, R.M.Parsons Laboratory for Water Resources and Hydrodynamics, M.I.T., 1973.

4. Connor, J.J., Wang, J.D., "Finite element modeling of two-dimensional hydrodynamic circulation", TR 172, part 1, R.M.Parsons Laboratory for Water Resources and Hydrodynamics, M.I.T., 1973.

5. Csanady, G.T., "Turbulent diffusion in the environment", Geophysics and astrophysics monographs, D. Reidel Publishing Co., 1973.

6. Ladyzhenskaya, O.A., "The mathematical theory of viscous incompressible flow", Gordon and Breach, 2nd edition, 1969.

7. Leendertse, J.J., Alexander, R.C., Liu, L.-K., "A three-dimensional model for estuaries and coastal seas, Vol. I : Principles of computation, Rand Corp. 1973.

8. Loziuk, L.A., Anderson, U.C., Belytschko, T., "Transient hydrothermal analysis of small lakes", J. Power Division, ASCE, PO2, Nov. 1973.

9. Mikhlin, S.G., "Variational methods in mathematical physics", Pergamon Press, 1964,

10. Simons, T.J., "Development of three-dimensional numerical models of the great lakes", Canada Centre for Inland Waters, Scientific Report, 1971.

11. Starr, V.P., "Physics of negative viscosity", McGraw-Hill, 1968.

12. Strang, G., Fix, G.J., "An analysis of the finite element method", Prentice-Hall, 1973.

13. Wada, A., "Study of thermal diffusion in a two layer sea caused by outfall of cooling water", Int. Symp. on Stratified Flows, IAHR, Novosibirsk, 1972.

CHAPTER 142

SIMILARITY CONDITIONS FOR THERMAL-HYDRAULIC
MODEL TESTS OF TIDAL ESTUARIES

by

Gerd Flügge[1] and Horst Schwarze[2]

INTRODUCTION

In connection with the design of proposed nuclear power plants on the Lower Weser River and on the Lower Elbe River in Germany, tidal models were constructed and tests carried out at the Franzius-Institute of the Technical University of Hannover for the purpose of studying the mixing and spreading of the hot water discharge. Thermal-hydraulic models are today still the most reliable method for the prediction of temperature distributions in the total area of temperature increase, especially in tidal regions.

Hydraulic models with free surface flow are in general based on the FROUDE scaling law. The flow fields in both the hydraulic model and in the prototype show a dynamic similitude when the FROUDE numbers of the flow in the model and in the nature are equal at corresponding points, i.e.:

$$\mathbb{F}_M = \mathbb{F}_N$$

$$\text{or:} \quad \frac{v_M}{\sqrt{g \cdot h_M}} = \frac{v_N}{\sqrt{g \cdot h_N}}$$

In case differences of density exist in zones, in which there is not yet a complete mixing of the heated cooling water with the ambient river water, one must apply the densimetric FROUDE scaling law:

[1]Dipl.-Ing., Scientific Assistant, Franzius-Institute of the Technical University of Hannover, Germany

[2]Dr.-Ing., Chief Engineer, Franzius-Institute of the Technical University of Hannover, Germany

$$F_{dM} \quad = \quad F_{dN}$$

or:
$$\frac{v_M}{\sqrt{g \cdot h_M \cdot \left(\frac{\Delta \rho}{\rho}\right)_M}} = \frac{v_N}{\sqrt{g \cdot h_N \cdot \left(\frac{\Delta \rho}{\rho}\right)_N}}$$

with v = mean velocity

      h = mean water depth

      g = acceleration of gravity

     $\frac{\Delta \rho}{\rho}$ = relative density difference between the cooling water and the ambient river water

In thermal-hydraulic models the same fluid (water) as in nature will be normally used. The physical values of the density ρ and of the specific heat c, as well as temperature differences ΔT , too, must therefore be equal in the model and in the nature, i.e.

$$\frac{\rho_N}{\rho_M} = 1 \; ; \quad \frac{c_N}{c_M} = 1 \; ; \quad \frac{\Delta T_N}{\Delta T_M} = 1 \; .$$

By applying the FROUDE scaling law, friction forces cannot be considered, so that the REYNOLDS number depends on the depth scale of the model as follows:

$$\frac{\mathbb{R}_N}{\mathbb{R}_M} = \frac{\dfrac{v_N \cdot h_N}{\nu_N}}{\dfrac{v_M \cdot h_M}{\nu_M}} = \lambda_V^{1/2} \cdot \lambda_V = \lambda_V^{3/2}$$

with λ_V = vertical scale of the water depths,

    $\lambda_V^{1/2}$ = scale of the velocities

    $\nu_N : \nu_M \approx 1$

Turbulent flow under prototype conditions can only be repro-
duced in the model, when the vertical model scale is suffi-
ciently large to guarantee turbulent flow in the model too.
The choice of the depth scale must therefore depend on a se-
lected turbulence level.

The length scale for a model of the tidal area of an
estuary as for example the Lower Weser River or the Lower
Elbe River, depends on the availability of space for the mo-
del in the laboratory.

From these two conditions follows, that the length scale
must be greater than the depth scale; i.e.

$$\lambda_H > \lambda_V$$

This means that a tidal model is in general distorted:

$$\kappa = \frac{\lambda_H}{\lambda_V} .$$

However, in as much as the spreading components of a model
should not be distorted, the horizontal dissipation of heat
in a distorted model is exaggerated with respect to the ver-
tical dissipation. For this reason, only a limited scale
distortion may be chosen for thermal-hydraulic models.

As a consequence of the comments made above, a dis-
tortion of $\kappa = 3$ as a maximum was chosen for the thermal-
hydraulic tidal model studies in the Franzius-Institute.

But there is another problem in handling a thermal-
hydraulic model:

Temperature distributions not only depend on the degree
of turbulence in the flow, they depend in a high degree
on the heat exchange between the water surface and the ad-
jacent atmosphere. This heat exchange at the water surface
does not depend on the hydrodynamic conditions of the river
flow or of the cooling water discharge. It will be rather
influenced by the increase of temperature at the water sur-
face compared with the equilibrium temperature of the river
and by the meteorological conditions, such as evaporation,
conduction and solar radiation. The heat exchange is charac-
terized by the heat exchange coefficient.

The phenomenon of heat exchange at the water surface
exists as well as in nature as in a thermal-hydraulic model.

Therefore special attention must be paid to the similitude of the heat exchange in the model.

The physical processes concerning the heat exchange at the water surface are the same in the prototype and in the model. It is therefore not possible to determine a scale for the heat exchange coefficient on the base of the FROUDE scaling law.

Beyond that, it is too expensive to reproduce in the laboratory the different meteorological conditions, such as relative humidity, atmospheric pressure, temperature, wind speed and wind direction.

Therefore, one must find a special relationship between the temperature distribution in the model, depending on the meteorological conditions of the laboratory and that climate in the nature, for which temperature distributions in the nature would be the same as measured in the model. By comparison of the scales for the heat input into the model and for the heat, transferred at the water surface into the atmosphere of the laboratory, one can find a factor for the heat exchange coefficient.

SCALE FOR THE HEAT INPUT

The waste heat of a power plant is injected with the cooling water discharge. The heat input is

$$H_i = Q \cdot \Delta T_C \cdot c \tag{1}$$

with Q = cooling water discharge

ΔT_C = temperature increase at the condenser

c = specific heat of water

With the FROUDE scaling law, the scale of the heat input is

$$\frac{H_{i_N}}{H_{i_M}} = \frac{Q_N}{Q_M} \cdot \frac{T_{CN}}{T_{cM}} \cdot \frac{c_N}{c_M} = \frac{Q_N}{Q_M} \cdot 1 \cdot 1 \tag{2}$$

With the scale for the horizontal lengths

$$\frac{\ell_{HN}}{\ell_{HM}} = \lambda_H$$

and for the vertical lengths

$$\frac{\ell_{VN}}{\ell_{VM}} = \lambda_V$$

the scale for the heat input becomes

$$\frac{H_{i_N}}{H_{i_M}} = \lambda_H \cdot \lambda_V^{3/2} \quad (=\text{scale for the discharge)} \qquad (2a)$$

for a distorted model

and $$\frac{H_{i_N}}{H_{i_M}} = \lambda^{5/2}$$

for an undistorted model with $\lambda_H = \lambda_V = \lambda$.

SCALE FOR THE HEAT EXCHANGE

It is supposed, that the heat input into the river flow is essentially given off by a heat exchange between the water surface and the adjacent atmosphere. The heat transfer at the bottom of the model is negligable.

The heat exchange at the water surface is given by:

$$H_e = K \cdot A \cdot \Delta T \qquad (3)$$

with K = heat exchange coefficient
     A = water surface, available for the heat exchange
     ΔT = temperature increase over the equilibrium
         temperature.

The scale of the heat exchange is $(K_N = K_M)$

$$\frac{H_{e_N}}{H_{e_M}} = \frac{K_N}{K_M} \cdot \frac{A_N}{A_M} \cdot \frac{T_N}{T_M} = \frac{A_N}{A_M} \cdot 1 \cdot 1 \qquad (4)$$

and with

$$\frac{\ell_{HN}}{\ell_{HM}} = \lambda_H$$

$$\frac{H_{e_N}}{H_{e_M}} = \lambda_H^2 \qquad \begin{array}{l}(=\text{scale for the} \\ \text{water surface})\end{array} \qquad (4a)$$

for a distorted and for an undistorted model.

REDUCTION FACTOR

The scale of the heat input (i.e. discharge) into a model is given by $\lambda^{5/2}$ and the scale of the heat exchange (i.e. the water surface) is given by λ^2.

This means that in thermal-hydraulic models the heat transferred at the water surface is less reduced than the heat input. The heat exchange depends linearly on the available water surface A and on the heat exchange coefficient K (equ. 3). The ratio of the scales for the heat input and for the heat exchange can be used in order to determine that heat exchange coefficient, which corresponds to the temperature distributions in prototype, which were obtained from the model on the basis of the FROUDE scaling law.

The reduction factor is given by:

$$\frac{\dfrac{H_{i_N}}{H_{i_M}}}{\dfrac{H_{e_N}}{H_{e_M}}} = \frac{\lambda_H \cdot \lambda_V^{3/2}}{\lambda_H^2} = \frac{\lambda_V^{3/2}}{\lambda_H} \cdot \frac{K_N}{K_M} \qquad (5)$$

in a distorted model, or

$$\frac{\dfrac{H_{i_N}}{H_{i_M}}}{\dfrac{H_{e_N}}{H_{e_M}}} = \frac{\lambda^{5/2}}{\lambda^2} = \lambda^{1/2} = \frac{K_N}{K_M} \qquad (5)$$

in an undistorted model. It depends on the geometrical scales of the model, as shown in figure 1.

HEAT EXCHANGE COEFFICIENT IN THE LABORATORY

For the critical judgement of temperature distributions obtained in thermal-hydraulic models, the heat exchange coefficient of the laboratory must be taken into account. Therefore, in the model the heat exchange between the water surface and the adjacent atmosphere is determined by means of systematic measurements in a special isolated basin with a free surface, which should be located directly beside the model.

In these tests the time-dependent cooling of the artificially heated water volume with a wellknown water surface and water depth of the basin leads to the calculation of a heat exchange coefficient (Fig. 2):

$$K = \frac{H_e}{A \cdot \Delta T_o}$$

with K = heat exchange coefficient in $W/m^2 \cdot {}^{\circ}C$

H_e = heat exchange at the water surface

  = $\dfrac{V \cdot \Delta T \cdot c}{\Delta t} \cdot 4,18 \cdot 10^6$ in W

c = specific heat of water

  = 1 $Mcal/m^3 \cdot {}^{\circ}C$

V = water volume of the basin in m^3
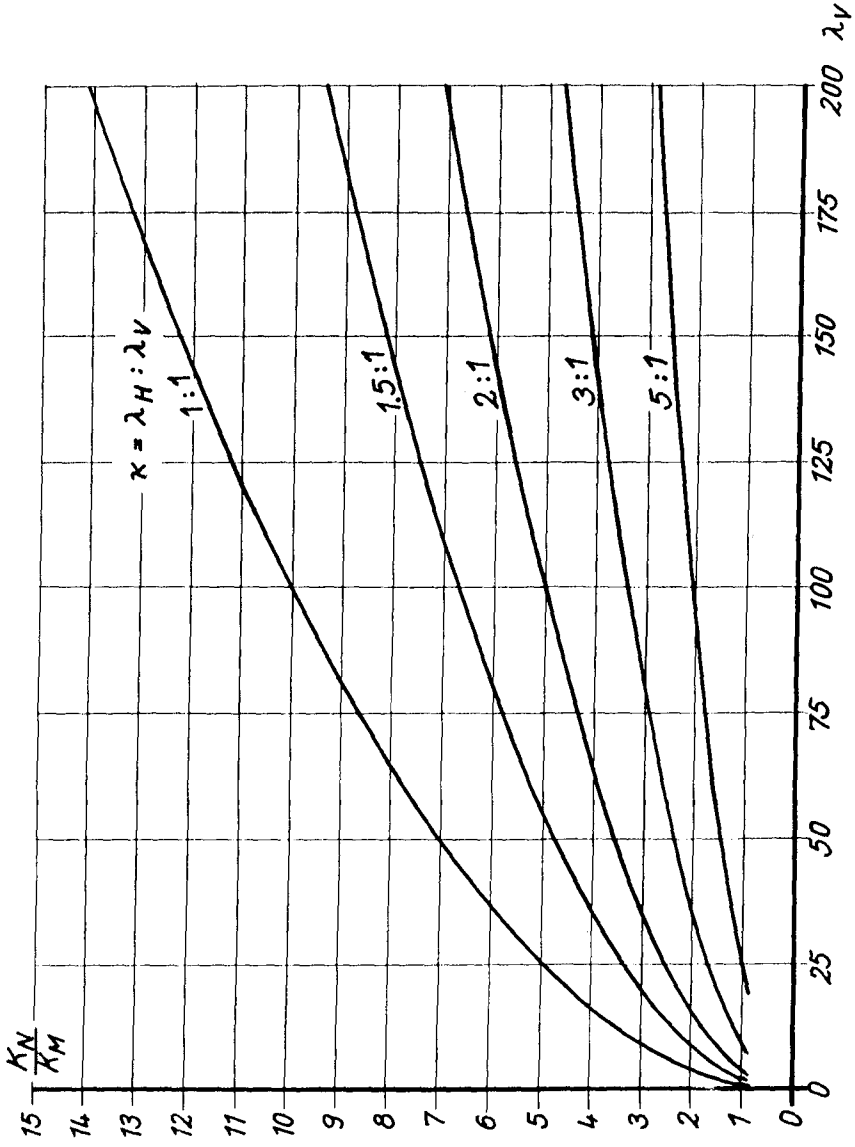
Fig. 1 Vertical scale λ_V versus reduction factor $K_N : K_M$ for different distortions κ

ΔT = decrease of the water temperature in the time interval Δt in $^{\circ}C$

Δt = time interval in sec

$4,18 \cdot 10^{6} W$ = 1 Mcal/sec

A = water surface of the basin in m^{2}

ΔT_{o} = $T - T_{E}$ in $^{\circ}C$

T = mean water temperature in the time interval Δt in $^{\circ}C$

T_{E} = equilibrium temperature of the water in the basin in $^{\circ}C$
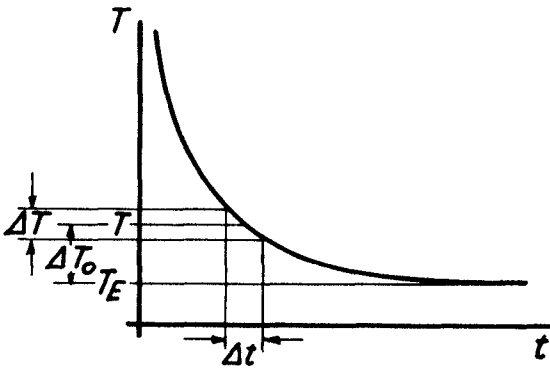
Fig. 2   Time dependent cooling in the basin

For example, for laboratory conditions during the tests, heat exchange coefficients K_M = 10 to 15 W/m^2.$^{\circ}$C (42 to 63 BTU/s . ft^2 .$^{\circ}$F) were found. In nature, however, it is much more difficult to determine the heat exchange coefficient K_N. In the German estuarine areas one assumes heat exchange coefficients of K = 50 to 100 W/m^2.$^{\circ}$C for the summer months (210 to 420 BTU/s) and K = 20 to 50 W/m^2.$^{\circ}$C (84 to 210 BTU/s . ft^2.$^{\circ}$F) for the winter period.

In the Franzius-Institute in Hannover, systematic field measurement programs in the Lower Weser River and in the Elbe River near Hamburg are planned in order to obtain better knowledge of the heat exchange coefficients and of the spreading of the heated water discharges in the special areas of the German estuaries.

CONCLUSIONS

With the present state of knowledge one can carry out thermal-hydraulic model tests in such a way, that one can expect reliable results about temperature distributions in the total area of temperature increase by cooling water injections. The choice of suitable scales for the model and especially the consideration of the heat exchange at the water surface guarantee the similarity of model and prototype flow conditions in thermal-hydraulic model studies.

CHAPTER 143

HYDROTHERMAL MONITORING: SURRY NUCLEAR POWER PLANT

C. S. Fang, G. Parker and W. Harrison[*]
Department of Physical Oceanography and Hydraulics
Virginia Institute of Marine Science
Gloucester Point, Virginia 23062

ABSTRACT

A hydrothermal monitoring program has been designed and deployed to gather data on the temperature distribution in the tidal James River near the outfall of the Surry Nuclear Power Plant at Surry, Virginia, U.S.A.

Monitoring to date has included two years of background data (1971 and 1972) taken prior to plant operation, and one year (1973) of data with the plant in operation.

The results of the first year post operational monitoring effort has been compared with the pre-operation background data and with the thermal effects that were predicted from studies by Carpenter and Pritchard on the James River Hydraulic Model at Vicksburg, Mississippi.

INTRODUCTION

The primary objective of this study is to thoroughly document waste heat distribution and related phenomena for the James River estuary due to the thermal discharge from the Surry Nuclear Power Plant. Results obtained to date will be compared to those predicted by the Hydraulic Model (Pritchard and Carpenter, 1967).

Circulating water for the Surry Nuclear Power Plant is taken from the James River on the downstream side of the site, transported through the condensers, and discharged into the river on the upstream side. The shoreline distance between intake and discharge points is about 5.7 miles; the overland distance across the peninsula, about 1.9 miles.

The plant discharges water by open channel flow to the

*Present address: University of Toronto, Ontario, Canada.

James River. This discharge, due to its free surface
nature, is a source of both momentum and buoyancy, spread-
ing vertically, laterally, and longitudinally due to
turbulent diffusion and density driven motions.

The first unit (822 Mw) of the Surry Nuclear Power
Plant began operation December 27, 1972; the second unit
(also 822 Mw) began operation in March 1973. Prior to
these times, two years of background data were obtained.
Both pre-operational and post-operational data collection
were accomplished using a moving boat sampling system.

INSTRUMENTATION, DATA COLLECTION, AND REDUCTION

To adequately define a thermal plume in three dimen-
sions, procedures and instrumentation have been designed
to allow a large area to be covered rapidly while sampling
temperature as a function of depth. Bolus et.al. (1971)
have given a detailed description of the design and oper-
ation of the data acquisition system, calibration procedures,
regression equations, and derived calibration curves.
Photographs of the equipment utilized in the study are
contained in a report by Chia et.al. (1972). Calculated
instrument accuracy and an analysis of boat position error
are discussed by Shearls et.al. (1973).

A schematic diagram of the basic information gathering
and recording system used on the boat is shown in Figure 1.
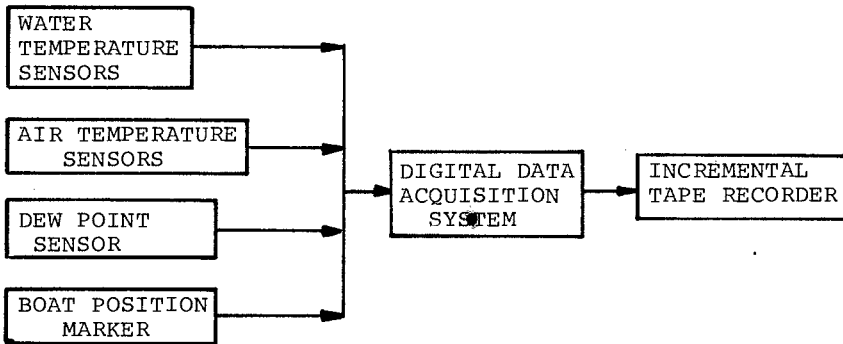
Figure 1.   Data Acquisition System for Survey
            Boat.

Thermistors were used as water and air temperature
sensors. Water temperatures were obtained at 0.5, 3, and
6 feet below the surface by mounting thermistors on a
submerged boom attached to the boat. Thermistors were
mounted in fan ventilated housings on the boat at 3 feet

and 6 feet above the water surface to measure air tempera-
tures. Dew point temperatures were measured using a
hygrometer mounted in a special housing attached to the
boat.

These data, along with a zero reference voltage, a
high voltage reference, and a boat position marker, were
sampled sequentially every 6 seconds and multiplexed by a
digital data acquisition system, then recorded on IBM
compatible tape by a high speed incremental tape recorder,
as the research vessel moved at constant speed along the
sampling transects. A computer program was developed to
reduce the field data to final form.

During each sampling run surface and bottom water
samples were taken at several fixed stations and brought
back to the lab for DO and salinity analysis.

This data acquisition system allows approximately
1000 samplings of all sensors to be taken during the one
hour and forty minutes required to traverse the designated
transects.

After the data has been reduced, isothermal maps are
made by equally spacing the data for each transect between
the end points of that transect. Isothermal lines are then
drawn by hand.

Instrument and system accuracy are presented in Table
1.

Table 1. Instrument and System Accuracy

Measurement	Instrument Accuracy	System Accuracy
Water Temperature	$0.2^{O}F$	$0.5^{O}F$
Air Temperature	$0.2^{O}F$	$0.5^{O}F$
Dew Point Hygrometer	$1.0^{O}F$	$1.5^{O}F$

The survey transects are shown in Figure 2.

RESULTS OF 1973 FIELD SURVEYS

Water Temperatures

Monthly average surface water temperatures for 1973
showed a steady rise from $56.8^{O}F$ in March to $81.8^{O}F$ in
June, continued to rise through July ($83.3^{O}F$) and peaked
in August at $84.4^{O}F$. Temperatures then declined slowly to
82.6 in September, and dropped rapidly to $72.4^{O}F$ in
October. In 1971 and 1972 average temperatures (see Shearls,
et.al., 1973) were above $80^{O}F$ only in July and August, July
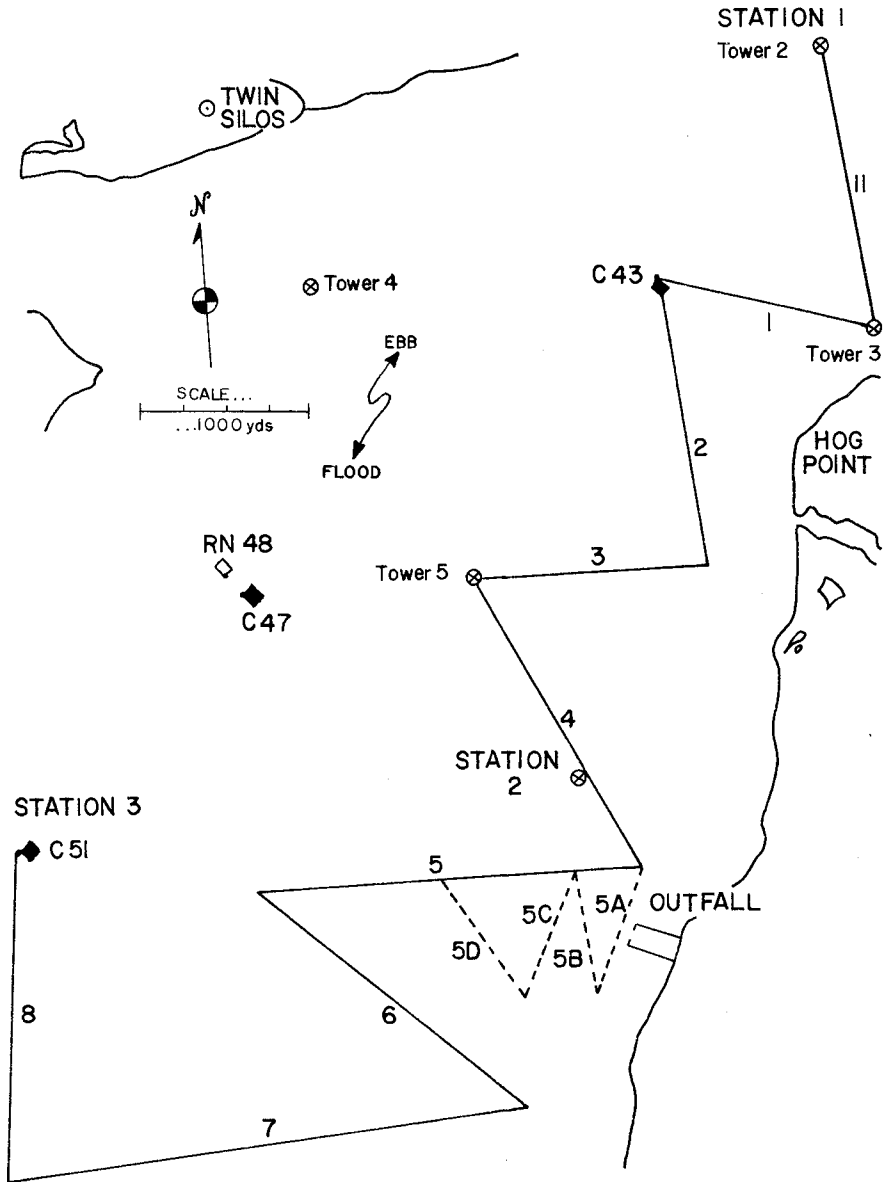
Figure 2.   Survey area showing transects monitored
             and D.O. and salinity stations. Dashed lines
             are the near field transects added in July
             1973.

being the peak month; while in 1973, temperatures exceeded
80°F from June - September inclusive, with the peak in
August. Furthermore, October temperatures were approxi-
mately 5°F and 12°F hotter in 1973 than in 1971 and 1972
respectively, and May 1973 temperatures were 2-3°F hotter
than in 1971 and 1972.

The rate of excess water surface temperature decrease
with distance from the plant outfall is presented in figure
3. In this Figure, T represents the surface water tempera-
ture at distance x from the outfall. T_a represents ambient
surface water temperature, and T_O represents initial outfall
temperature. Data plotted in Figure 3 was obtained from
isothermal maps from 5 different dates during July-September
1973. The position of the plume centerline was estimated.

This figure shows that temperatures decrease to
ambient conditions generally within 1200 yards of the out-
fall. The line drawn in Figure 3 represents a rough linear
approximation to the temperature decrease.

Table 2 lists average monthly values of surface water
temperature (^{O}F) for each transect during the three year
sampling period. Beginning with July 1973, transects 5A,
B, C, D are included in addition to transect #5. Values
for transect #11, initiated in 1973, are also included
in Table 2. No temperature averages for March 1971 are
presented because sampling did not begin until April of
that year. During 1972 transect #8 was not sampled during
the March runs, and therefore is not shown.

Water Stratification

Background data from 1971 and 1972 indicate a slight
thermal stratification (approximately 1^{O}F cooler three to
six feet below the water surface) during May through
September. The water column during the rest of the year
showed little temperature stratification within the top 6
feet.

Figure 4A, B, and C show the isothermal lines for
July 24, 1973 at the surface, 3 feet, and 6 feet, respec-
tively. These isothermal plots indicate that in the
vicinity of the outfall the area covered by the 84° - 89°
isotherms was larger at a depth of three feet than at the
surface, and was greatest for the 6 feet depth. In the
region of Hog Point, temperature isotherms show that water
temperatures at 3 feet were the same as at the surface, and
that 6 feet water temperatures were lower.

Figure 5 shows the water temperature profiles for
October 18 at several selected stations. The station
locations are shown in Figure 6. On October 18, only one
unit was operating at 93%, the discharge rate was approx-
mately 1900 cfs, air temperature was 67.0^{O}F, dew point

Figure 3. Water temperature decrease along plume centerline.

$$T - T_a = (T_O - T_a) - .00081 (T_O - T_a) X$$
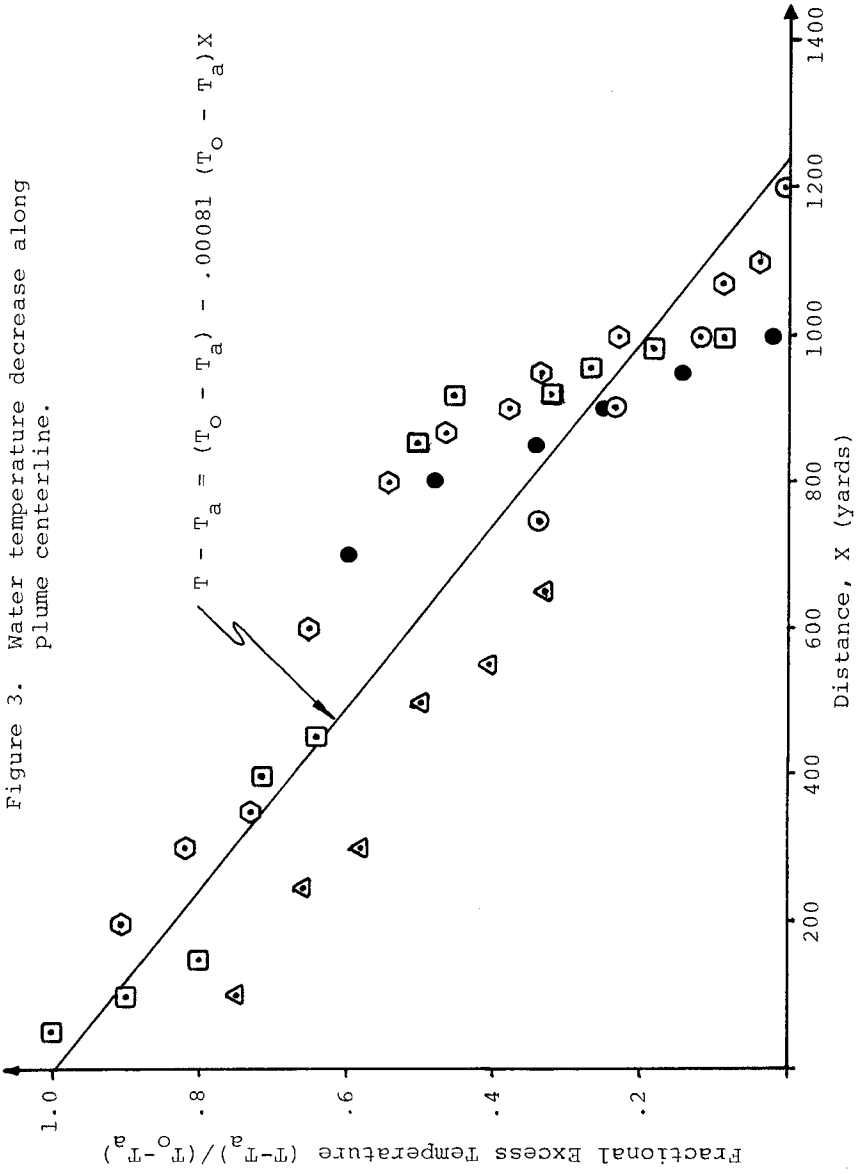
Table 2.   Monthly Averages of Surface Temperature/Transect, °F

Transect		March	April	May	June	July	Aug.	Sept.	Oct.	Nov.
1	(1971)	–	57.8	66.4	76.0	81.0	80.9	77.1	67.2	58.5
	(1972)	50.4	58.2	68.2	73.1	80.6	80.2	76.0	60.1	54.7
	(1973)	51.7	56.7	71.0	82.2	83.7	84.1	82.7	71.8	–
2	(1971)	–	57.8	66.6	74.8	81.6	80.7	77.5	67.6	58.4
	(1972)	50.6	58.7	68.0	73.0	80.8	80.4	76.2	60.2	54.6
	(1973)	52.6	56.8	71.6	82.6	83.5	84.7	82.6	71.8	–
3	(1971)	–	57.9	67.2	75.5	82.1	80.7	77.8	67.5	58.9
	(1972)	50.6	58.3	68.2	73.2	80.9	80.5	76.3	60.3	54.3
	(1973)	53.0	56.5	71.4	81.8	82.9	84.3	81.8	71.8	–
4	(1971)	–	58.3	67.6	75.9	82.3	81.0	77.9	67.7	58.6
	(1972)	50.5	58.6	68.4	73.6	81.2	80.7	76.4	60.3	54.4
	(1973)	52.4	56.6	70.3	81.9	83.1	83.7	82.4	71.9	–
5A	(1973)	–	–	–	–	83.8	85.3	84.4	75.2	–
5B	(1973)			–	–	83.9	85.3	83.7	72.5	–
5C	(1973)			–	–	85.0	85.3	83.7	73.0	–
5D	(1973)			–	–	83.2	85.1	83.3	72.7	–
5	(1971)	–	58.5	68.2	76.1	82.6	81.2	77.9	67.8	58.6
	(1972)	50.7	59.1	68.5	73.8	81.2	80.6	76.3	60.4	54.4
	(1973)	52.8	56.4	70.1	82.1	83.0	83.6	81.6	72.0	–
6	(1971)	–	59.0	68.2	76.4	83.0	81.1	78.0	68.0	58.3
	(1972)	50.8	59.5	68.4	73.8	81.2	80.7	76.4	60.4	54.5
	(1973)	53.2	56.6	70.4	81.8	83.2	84.5	82.0	72.4	–
7	(1971)	–	59.0	68.2	76.8	83.3	81.3	78.2	68.2	58.2
	(1972)	50.7	59.4	68.6	73.8	81.4	80.6	76.4	60.2	54.5
	(1973)	52.2	57.0	–	81.4	82.8	84.6	82.4	72.1	–
8	(1972)	–	59.0	68.5	73.7	81.5	80.5	76.2	60.3	54.4
	(1973)	51.4	57.0	–	80.5	82.8	83.6	82.2	72.1	–
11	(1973)	–	–	–	81.9	83.2	83.4	82.1	71.7	–
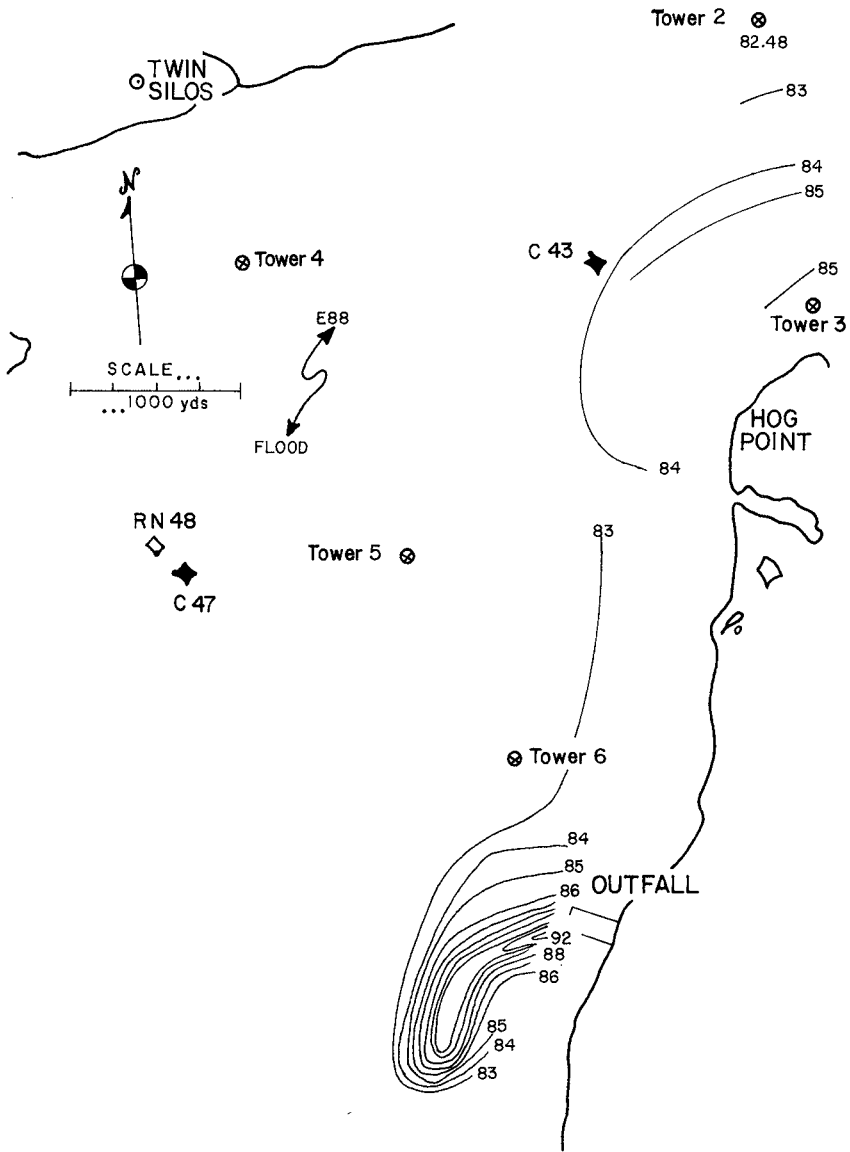
Figure 4A. Isothermal plot for July 24, 1973, flood, at a depth of 1/2 foot.
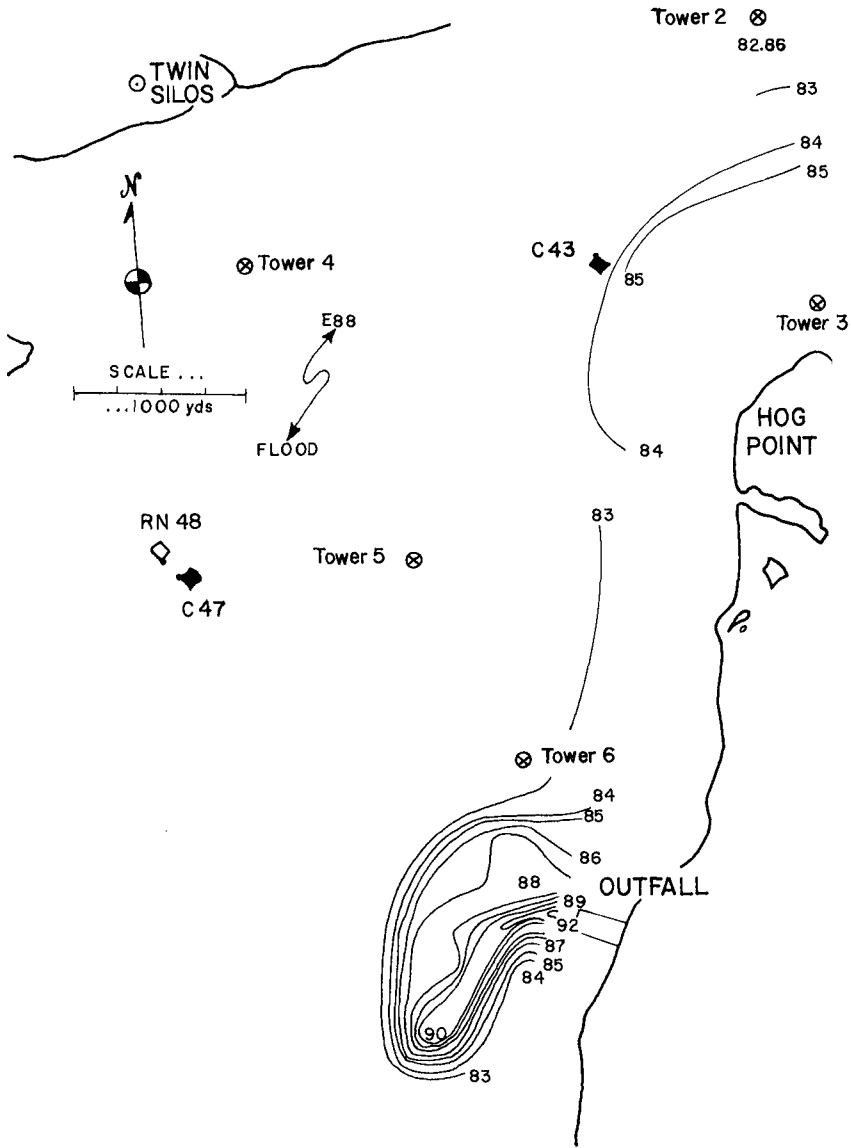
Figure 4B. Isothermal plot for July 24, 1973, flood, at a depth of 3 feet.
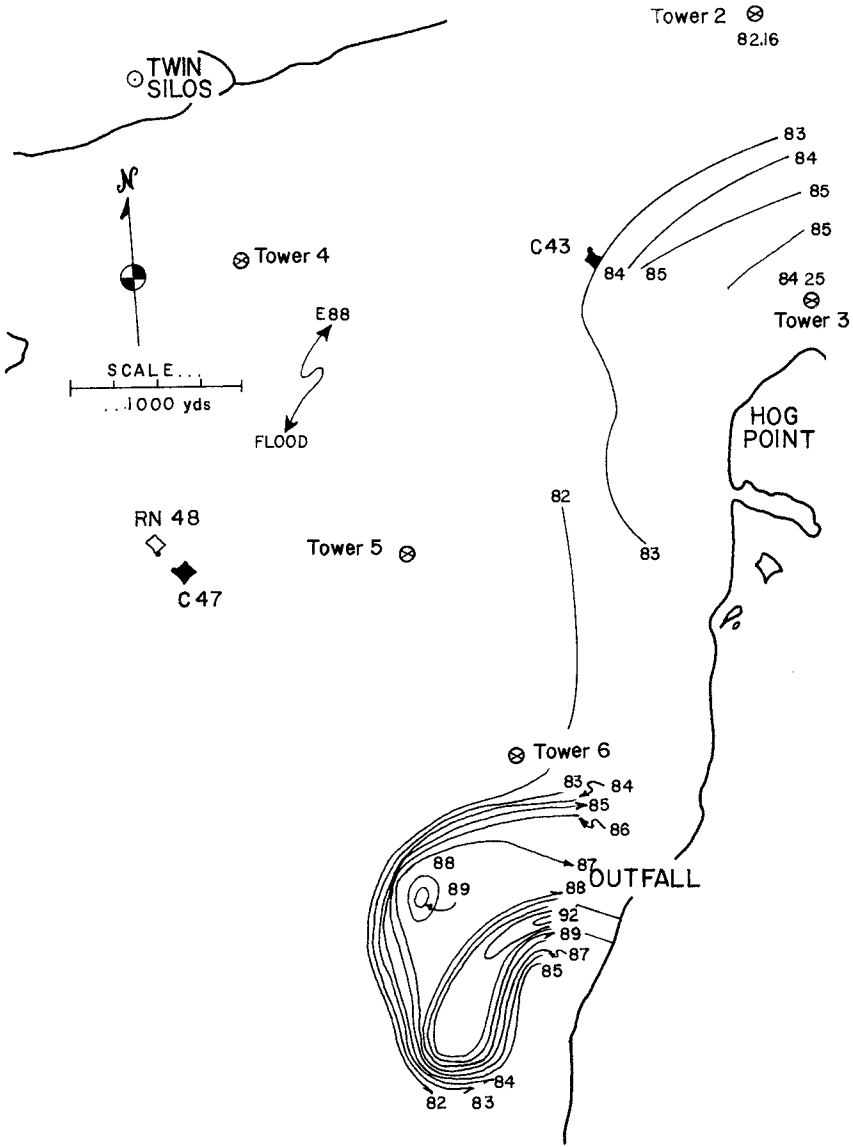
Figure 4C.   Isothermal plot for July 24, 1973, flood,
             at a depth of 6 feet.
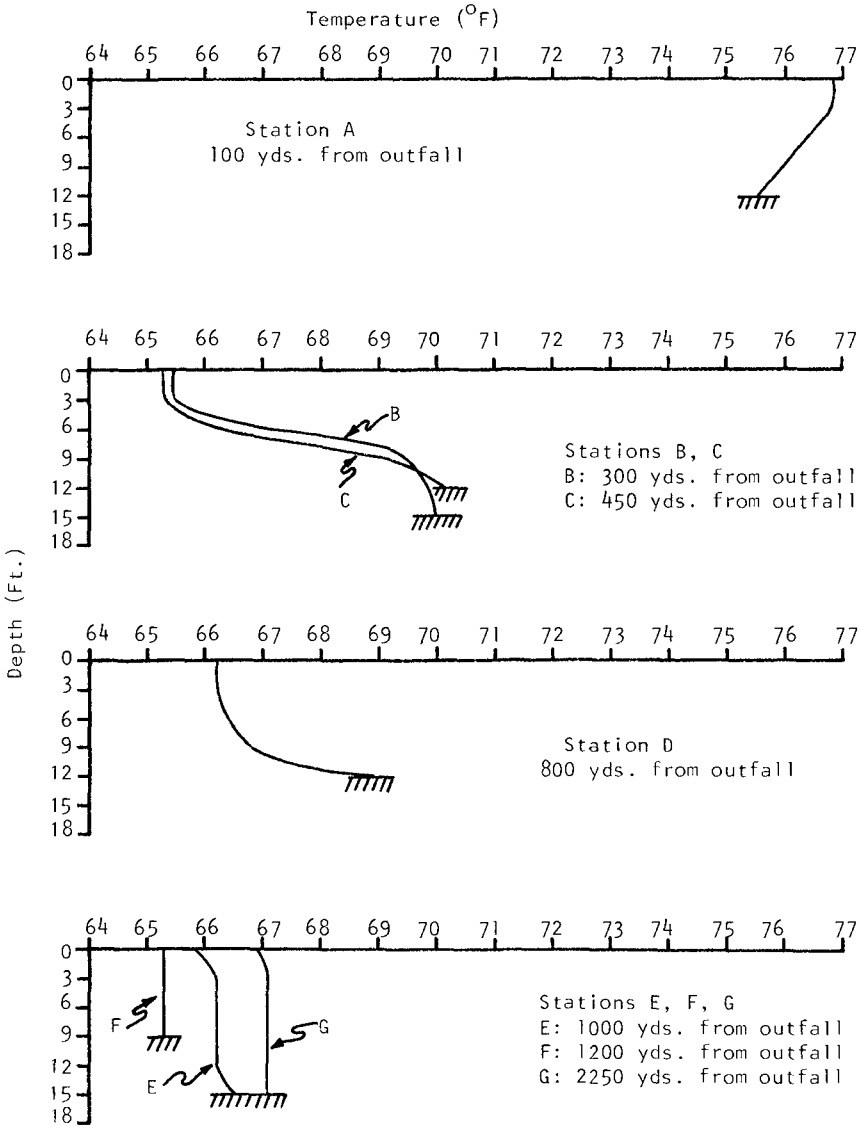
Figure 5.   Water temperature profiles for October 18
            at selected stations (see Figure 6).
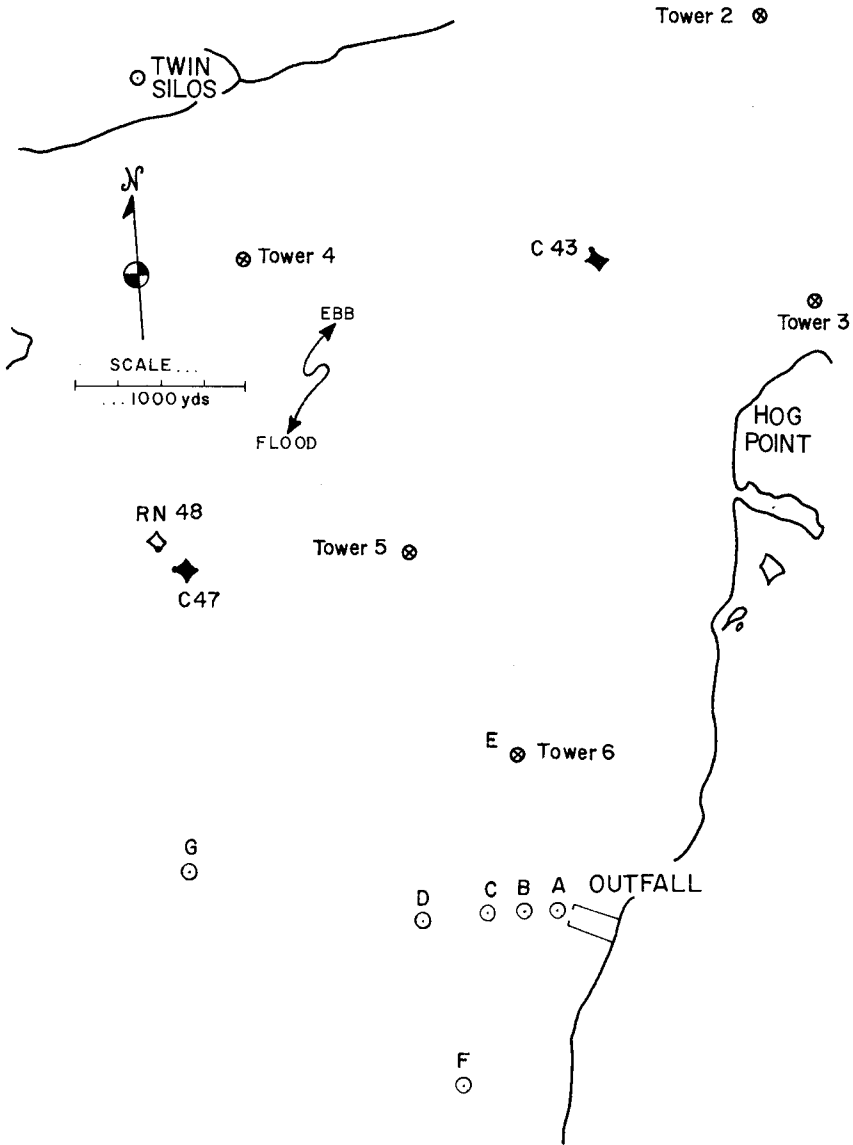
Figure 6.   Station locations for temperature profiles
            (Figure 5) on October 18.

temperature was 36.0^{O}F, and the winds were 5-10 MPH from
the southwest.

The water temperature profile for station A, approxi-
mately 100 yards from the mouth along the axis of the dis-
charge, shows that the water surface temperatures are
76.8^{O}F while the water temperature at the bottom (12 feet
depth) are 75.5^{O}F. At station B and C, 300 and 450 yards
from the discharge respectively, the surface water tempera-
tures are considerably lower, at approximately 65.4^{O}F.
Water temperatures at the 3 feet depth are the same as at
the surface. From the 3 feet depth water temperatures
steadily increase to approximately 70°F at the bottom. At
these stations, water temperatures at the 6 feet depth,
the deepest depth normally sampled by the boat system, were
only 1^O - 1.5^{O}F above surface temperatures. Station D, 800
yards from the discharge, shows the same pattern as stations
B and C, but in this case, bottom temperatures reach a
maximum of 68.8^{O}F.

Of the last three stations, E, F, and G, only station
E, 1000 yards from the mouth of the discharge and 850 yards
downstream, shows warmer waters at the bottom. In this
case, water temperatures from 3 feet to 12 feet are constant
at 66.2^{O}F and are a maximum of 66.5^{O}F at the 15 feet depth
of the bottom.

These water temperature profiles indicate that in the
near field region of the outfall water temperatures in the
top 3 feet decrease rapidly, but that below this depth the
temperature decrease is less rapid. This would indicate
that the plume was sinking in the near field region. This
"sinking" plume phenomena was apparently a result of
salinity differences between the discharge waters and sur-
rounding waters. On the occasions when outfall salinity
samples have been taken, the salinity of the discharge
waters has been 1ppt - 2ppt higher than salinity samples
taken at Tower 6. Within the ranges of salinities and
temperatures found in this area, an increase in temperature
of 6.3^{O}F has the same effect on the density of the water
as a decrease in 1 ppt in the salinity. This means that
water which had a salinity which was 1 ppt greater than
ambient water would have to be 6.3^{O}F warmer than the
ambient water to have the same density. A simplified
temperature-salinity-σ_T (density) diagram, Figure 7 shows
this clearly.

Starting at point C, a decrease in salinity of 1 ppt
at constant temperature results in point A, where σ_T
(density) is σ_t . Starting at C and increasing temperature
6.3^{O}F at constant salinity results in point B, where σ_t
is also σ_t . Therefore, if A represents ambient conditions,
an increase in 1 ppt salinity must be accompanied by an
increase in temperature of 6.3^{O}F in order for the densities
to remain the same.
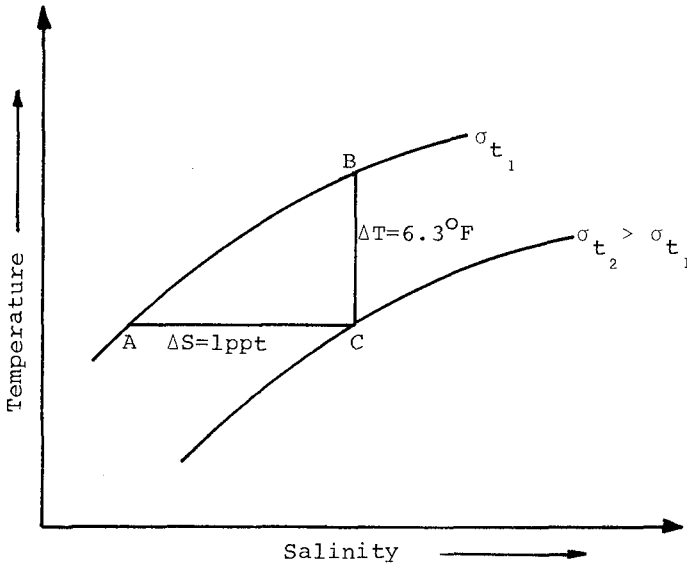
Figure 7. Temperature-Salinity-Density (σ_T) Diagram.

The plume reaches a point at which the temperature decrease more than compensates for the decrease in salinity due to mixing, and the denser plume waters sink with respect to the surrounding waters. This is generally a near field effect and occurs within a maximum radius of approximately 1000 yards from the outfall.

Dissolved Oxygen (DO) Concentrations

During 1972 DO concentrations in the area ranged from a low of 5.0 - 7.5 mg/ℓ during the hottest months (July and August) to a high of 11 mg/ℓ and over during the cooler months.

Of 366 total D.O. samples taken at all stations during 1972, only two bottom samples had D.O. concentration less than 5 mg/ℓ.

D.O. concentrations during 1973 showed the same trend as for 1972, with concentrations of 6.0 - 8.0 mg/ℓ during the summer and concentrations over 11 mg/ℓ during the cooler months.

In 1973 five of 98 surface samples and four of 97 bottom samples had D.O. concentrations below 5 mg/ℓ.
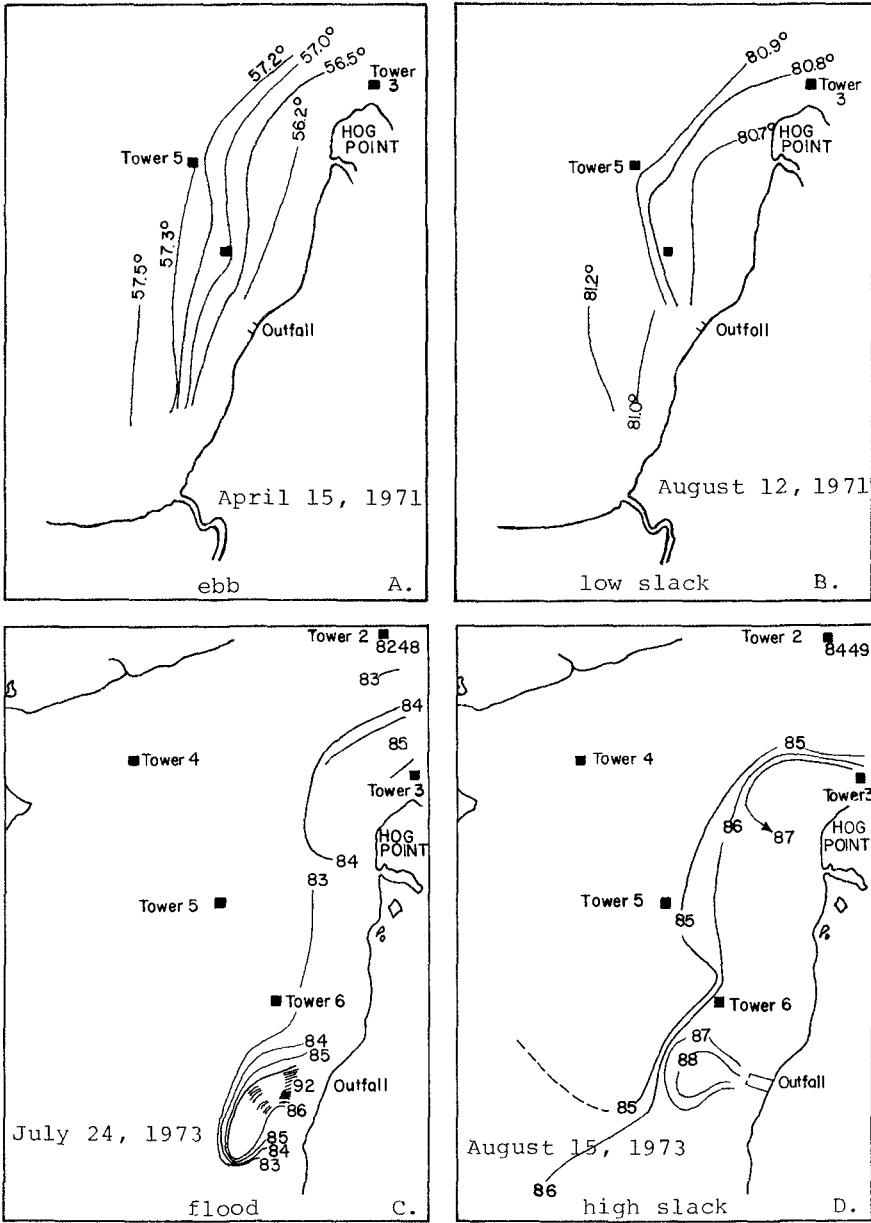
Figure 8.   Typical isotherms for the Hog Point region
            under natural conditions (A,B) and after
            plant operation (C,D).

Salinity

     Data from 1971 and 1972 indicates that average
salinities varied from 0.10 to 4.42 ppt in the downstream
part of the study area and from 0.10 to 2.63 ppt in the
upstream part. The minimum values were attained between
December and March and peak salinities usually occurred
in September. During 1973 salinities averaged 0.2 - 4.0
ppt higher than in 1971 or 1972 from June through October
due to lower fresh water discharge in 1973.

COMPARISON OF PRE- AND POST-OPERATIONAL TEMPERATURE
                    DISTRIBUTION

     Typical isothermal plots for the Hog Point region
under natural conditions, i.e. prior to plant operation,
are shown in Figure 8. These plots indicate that surface
water temperature gradients were small in the survey area
and the water can be considered horizontally homogeneous.
Temperatures generally varied less than 1°F throughout
the area.

     Typical isothermal plots for the area during 1973,
with the power plant in operation also are shown in
Figure 8. The temperature gradients in the area have been
greatly enhanced due to the thermal effluent.

     The greatest temperature gradients occur in the near
field region of the outfall and between towers 2 and 3 at
Hog Point. Temperatures increase towards shore, and
temperature variations in the far field region are generally
within the range 2° - 4°F. Near field temperature
variations are higher, usually within the range 5° - 9°F.

     The isothermal plots for 1973 indicate that the 1°F,
2°F, and to a lesser extent, the 3°F excess temperature
isotherms generally remained fairly constant in their
position throughout the tidal cycle. At low slack they
extended around Hog Point. During flood stage they were
pushed upstream slightly until at high slack they reached
their maximum upstream position. Ebb tidal stages showed
them again extending farther toward Hog Point. The 1°,
2°, and 3°F excess temperature isotherms, then, describe an
area affected by the heated effluent at all stages of the
tide and can be regarded as a secondary or permanent plume.
The region occupied by excess temperature isotherms of 4°
or higher showed greater movement with the tidal flow.
These isotherms were more closely spaced than those for
the permanent plume and showed a definite downstream
trend during ebb and low slack water, and a definite up-
stream direction during flood and high slack water. These
isotherms represent the area of greatest heat dissipation
of the heated effluent and can be considered the primary
plume.

COMPARISON OF FIELD RESULTS WITH PREDICTIONS MADE
FROM THE HYDRAULIC MODEL

Studies conducted by Carpenter and Pritchard on the
hydraulic model of the James River estuary resulted in
predictions of excess temperature distribution which would
result from the discharge of waste heat by the Surry Nuclear
Power Station. One of the purposes of this study was to
compare these predictions to actual temperature distributions
observed in the field in order to determine the reliability
of hydraulic modeling as a method of predicting the effects
of man made systems on the natural environment.

Carpenter and Pritchard did their experiments under
various conditions of river flow and heat rejection. The
conditions which are most applicable for comparison with
field data are for river discharges of 2000 and 6000 cfs
and a heat rejection of 12×10^9 Btu/hr. Their results
were presented as a series of isothermal maps of tempera-
ture distribution throughout a tidal cycle. In order to
compare prototype and model data, a planimeter was used to
determine the areas within each excess temperature isotherm
for a run during 1973 and a comparable hydraulic model run.

On five of the days sampled during 1973 the power plant
was operating at 90% capacity or above, with a heat rejec-
tion of 11×10^9 Btu/hr or above. These days obcurred
during the end of August and the first half of September.
During this period the river discharge averaged 1900 cfs.

These five days represent the closest agreement be-
tween actual fresh water discharge and heat rejection and
modeled fresh water discharge and heat rejection and are
the most directly comparable.

Table 3 shows comparison between the areas within
equivalent excess temperature isotherms for the hydraulic
model and the prototype for a river flow of 1900 cfs.

Table 4 shows a comparison between the areas within
equivalent excess temperature isotherms for the hydraulic
model and the prototype for a river flow of 7200 cfs.

Comparing results between prototype temperature
distribution and model temperature distribution for two
river flow conditions indicate that the model predictions
were more accurate for the higher river flow conditions.

Lower values for heat rejection in the prototype
were partially responsible for the smaller areas within
each excess temperature isotherm. Heat rejection values
on the days compared with hydraulic model predictions
were from 8-14% lower than the modeled heat rejection.
If it is assumed that at full plant capacity the areas in

Table 3.　Comparison between predicted areas from the hydraulic model and areas found in the prototype for river flow of 1900 cfs.

Prototype Date	Area $(\times 10^7 \text{ft}^2)$ within Equivalent Isotherms					
	Hyd. Mod. 2°C	Proto. 2°C	Hyd. Mod. 3°C	Proto. 3°C	Hyd. Mod. 5°C	Proto. 5°C
8-29-73	6.85	4.12	2.88	0.48	0.72	.076
9-10-73	5.94	2.67	5.04	0.17	0.36	.049
9-18-73	4.68	0.80	2.34	0.24	0.72	.028
8-29-73	3.32	0.24	1.80	0.70	0.54	.024
9-5-73		1.00		0.062		.035
9-7-73		1.83		0.26		.056
Average	5.17	1.78	3.02	0.21	0.59	.045

Table 4.　Comparison between predicted areas from the hydraulic model and areas found in the prototype for river flow of 7200 cfs.

Prototype Date	Area $(\times 10^7 \text{ft}^2)$ within Equivalent Isotherms					
	Hyd. Mod. 2°C	Proto. 2°C	Hyd. Mod. 3°C	Proto. 3°C	Hyd. Mod. 5°C	Proto. 5°C
6-25-73	6.12	1.04	4.14	0.15	0.36	-
6-28-73		2.47		0.92		-
6-20-73	4.32	2.29	3.24	0.27	0.36	-
6-22-73	7.75	4.36	1.80	0.73	0.18	-
6-25-73	4.18	1.33	2.32	0.92	0.36	-
Average	5.59	2.30	2.88	0.60	0.32	-

the prototype would have been 10-20% larger, which is probably an over-estimation, the differences between the model predictions and the prototype would still have been significant.

　　Qualitatively, the temperature distributions in the field are similar to those predicted by the model in that the heated waters are carried downstream during the ebb tidal cycle and are carried upstream on the flood tide.

CONCLUSIONS

1) Ambient water temperatures for 1973 ranged from 1.2^O–
    5.1^OF higher than for 1971 and 1972. The pre-operational
    data indicates that ambient temperatures varied by as
    much as 8^OF. The higher ambient temperatures for 1973
    could be due to natural heating, since air temperatures
    were higher for 1973 than either 1971 or 1972 except
    for the month of July.

2) Salinities were from .2 - 4 ppt higher than in 1971
    or 1972 from June through October due to the lower
    fresh water discharge. The pumping of more saline
    downstream waters through the plant increased the
    salinities at tower 6.

3) Dissolved oxygen concentration has not been adversely
    affected in the survey region. Only on two of the
    days sampled were bottom salinities below 5 mg/ℓ at
    any station.

4) Water temperatures decrease very rapidly within 1000–
    1500 yards from the outfall. In several instances the
    water on the bottom had higher temperatures than the
    surface waters, due to the higher salinity of the
    discharge water.

5) Data that has been collected to date does not indicate
    that there are any extreme temperatures, outside the
    near field region of the outfall, that could cause
    biological damage. Outside the outfall region, heated
    water is generally confined to the upper 6' of the
    water column. Heated waters generally do not cover
    more than half of the width of the estuary at it's
    narrowest point.

6) The James River Hydraulic Model, due to it's distorted
    scale, is best suited for far field analysis of the
    thermal effluent. The attempt to model all three
    regions with this model leads to quantitative values
    for temperature distributions which were higher than
    those values found in the field. Qualitatively the
    model predictions of plume movement with the tides
    are in close agreement with the prototype plume
    movement. Higher plant production will increase the
    agreement between prototype and model temperature
    distributions, but model values will probably still
    be higher than the temperature distributions found
    in the field.

7) Plant operation during 1973 averaged only 67% of
    capacity on the days monitored. In order to draw
    definitive conclusions concerning the maximum extent
    of the thermal effects or the agreement between
    hydraulic model and prototype temperature distributions,
    plant operation should be at a continuously high per-
    centage of capacity. Indications as to the effects of
    the thermal discharge can be drawn from the 1973 data,
    but no definitive conclusions can be made without
    further monitoring.

ACKNOWLEDGEMENTS

REFERENCES

Bolus, R. L., S. N. Chia and C. S. Fang. "The Design of
    the Monitoring System for the Thermal Effect Study of
    the Surry Nuclear Power Plant on the James River"
    VIMS SRAMSOE No. 16, Gloucester Point, Va. October
    1971.

Chia, S. N., C. S. Fang, R. L. Bolus and W. J. Hargis, Jr.,
    "Thermal Effects of the Surry Nuclear Power Plant
    on the James River, Virginia, Part II. Results of
    Monitoring Physical Parameters of the Environment
    Prior to Plant Operation" VIMS SRAMSOE No. 21,
    Gloucester Point, Va. February, 1972.

Pritchard, D. W., and J. H. Carpenter. "Temperature
    Distribution in the James River Estuary Which Will
    Result From the Discharge of Waste Heat From the
    Surry Nuclear Power Station", A Report Prepared for
    Virginia Electric and Power Company, Richmond,
    Virginia, 1967.

Shearls, E. A., S. N. Chia, W. J. Hargis, Jr., C. S. Fang,
    and R. N. Lobecker. "Thermal Effects of the Surry
    Nuclear Power Plant on the James River, Virginia,
    Part III. Results of Monitoring Physical Parameters
    of the Environment Prior to Plant Operation", VIMS
    SRAMSOE No. 33, Gloucester Point, Va. February, 1973.

CHAPTER 144

EFFECTS OF FLOODING ON A COASTAL PLAIN ESTUARY

Evon P. Ruzecki[1], William J. Hargis, Jr.[2]
and Ching S. Fang[3]
Virginia Institute of Marine Science
Gloucester Point, Virginia 23062

ABSTRACT

Rains from Tropical Storm Agnes resulted in unprec-
edented flooding of the Chesapeake Bay drainage basin in
June of 1972. A monitoring program was established to
follow the effects of the flood in the Chesapeake estuarine
system and contiguous continental shelf waters.

Financial and logistic assistance was solicited and
obtained from several federal and state agencies. The
monitoring program, called "Operation Agnes" offered
scientists a unique opportunity to watch the progress of
the flood.

Results of investigations into the effects of the
flood show that salinity structure exhibited a four stage
reaction, tides in the lower reaches of the estuaries were
essentially uneffected and currents returned to normal
after a short period of continuous ebbing. Total recovery
of the salinity distribution was affected within one
hundred days of flood crest at the fall line.

I.   INTRODUCTION

On 14 June 1972 a tropical depression developed over
the Yucatan Peninsula. It intensified to hurricane strength
in the Gulf of Mexico, traveled north, made landfall on
the Florida panhandle at noon on 19 June, dissipated to
tropical depression intensity as it passed northeast over
Georgia and the Carolinas, traversed the southeastern
corner of Virginia, moved out to sea near the mouth of

Chesapeake Bay, intensified to a tropical storm as it
moved northward parallel to the Delmarva Peninsula, made
a second landfall near New York City on the afternoon of
22 June and curved cyclonically into north central Penn-
sylvania where it began dissipating as an extratropical
depression on 23 June before turning eastward and moving
out to sea once more (DeAngelis and Hodge, 1972).   The
storm, first of the 1972 Hurricane season, was named
Agnes.   Wind and wave damage from Agnes reached $40 million
in Florida; however, greatest losses were due to flooding
in the Chesapeake Bay drainage basin where damage was
estimated to exceed $2 billion (NOAA, 1972).

        During the period 21 to 23 June, the entire Chesa-
peake Bay watershed area was subjected to measured rainfall
in excess of six inches, with approximately one-third of
the region receiving more than twelve inches of water and
isolated locations recording eighteen inches.   This deluge,
on a watershed which had been subjected to an exceptionally
wet spring, resulted in immediate flooding.   By 22 June,
it was evident that the Chesapeake Bay region had fallen
victim to Agnes.   The enormity of the catastrophy could
not be judged at that early date but the formulation of a
plan to follow the passage of flood waters through trib-
utary estuaries, the Bay, and out onto the continental
shelf had begun.   This paper describes the administrative
effort required to mobilize federal, and state agencies
and scientific institutions to monitor a natural disaster
and the results of the monitoring program.

        II.   ADMINISTRATIVE AND LOGISTICAL ACTIVITIES

        All local field activities of the Virginia Institute
of Marine Science (VIMS) were cancelled on 23 June and
efforts were redirected to monitor the effects of flood
waters from Agnes on the James, York and Rappahannock
Rivers, and lower Chesapeake Bay (south of the Potomac
River).   A sampling program was established which required
measurement of various parameters in each major Virginia
tributary to the Bay, the lower portion of Chesapeake Bay
and contiguous continental shelf waters.   The program
included the following physical measurements:

1)   Continuous measure of surface to bottom currents at no
     fewer than five stations at the mouth of Chesapeake
     Bay, four stations across the Bay near the mouth of
     the Potomac River, two stations near the mouth of the
     James River and two stations at the general head of
     the salt intrusion in the James, one station near the
     mouth of the York River and one station where the York
     is formed by the confluence of the Mattaponi and Pamun-
     key Rivers and one station near the mouth of the Rappa-
     hannock River.

2) Daily "same slack" sampling runs in the lower portion of the Bay and each of the three major Virginia tributaries were to provide surface to bottom measures of temperature, salinity, dissolved oxygen and sus- pended sediments at intervals of no more than five nautical miles in the rivers and ten nautical miles in the lower Bay.

3) No fewer than two cruises a month on the continental shelf to measure temperature and salinity at selected stations between Cape Charles, Virginia and Cape Hatteras, North Carolina.

4) Simultaneous weekly occupation of all current meter stations on any particular transect to obtain hourly measures of surface to bottom temperature, salinity, dissolved oxygen and suspended sediments for no fewer than 25 continuous hours.

Thus "Operation Agnes" was begun. It was evident that although the operation was an extremely ambitious undertaking for VIMS, there was much more that should be done, particularly in the upper portions of the Bay. Con- sequently, the directors of the Chesapeake Bay Institute (CBI) of The Johns Hopkins University in Baltimore, Maryland and the Chesapeake Biological Laboratory (CBL) of the University of Maryland's Natural Resources Institute were contacted, informed of our plans and urged to estab- lish flood effect monitoring programs in the Maryland portion of the Bay.

The inventory of oceanographic equipment at VIMS was sufficient to undertake Operation Agnes but allowed for only minimal down time on most gear. The Institute's staff was adequate to execute the Operation, but would require many twelve-hour days in both field and laboratory. We lacked a sufficient fleet of crewed sampling vessels and had no immediately apparent source of funds to scien- tifically monitor the impending disaster.

Federal and Virginia State Agencies were called on to assist in our sampling platform needs. Responses were, in almost all cases, immediate and most negotiating was accomplished by telephone. Table I list agencies and institutions which furnished logistic and coordinating support to VIMS during Operation Agnes.

Securing funds to pay for the collection, processing and analysis of samples was a more difficult task. Funding agencies are justifiably reluctant to commit resources to spur of the moment research efforts with somewhat loosely defined goals. Nonetheless, after several weeks of negotiating, numerous federal agencies responded with grants and contracts to help pay for Operation Agnes.

They are listed in Table II and we are grateful for
their response and cooperation.

Table I

Agencies Furnishing Logistic and Coordinating
          Support During Operation Agnes

A. Manned Vessels
    NOAA - National Ocean Survey and National
            Marine Fisheries Service
    U.S. Navy - Naval Oceanographic Office, Naval
                Ordinance Laboratory and Atlantic
                Fleet
    U.S. Army - Corps of Engineers, Norfolk and,
                Transportation Corps, Ft. Eustis
    U.S. Coast Guard - Coast Guard Training Center,
                       Yorktown, Va., and 5th Coast
                       Guard District
    Virginia Marine Resources Commission
    Virginia Pilots Association

B. Aircraft
    NASA - Headquarters, Washington, D.C.; Langley
            Research Center and Wallops Station
    U.S. Air Force - Langley Field

C. Other
    NASA - Langley Research Center (Instrumentation)
    U.S. Coast Guard - (Sampling from Light Stations)
    Virginia Department of Health - (bacteriological
                                    assessment)
    Virginia Water Control Board - (water quality,
                                    damage assessment)
    Virginia Division of Water Resources - (streamflow)

D. Coordination
    NOAA Headquarters
    U.S. Army Corps of Engineers, Chief's Office
    NASA Headquarters

Table II

Agencies Contributing Funding to Operation Agnes

National Oceanic and Atmospheric Administration
National Science Foundation
U. S. Army Corps of Engineers (Philadelphia,
  Baltimore and Norfolk Districts)
Environmental Protection Agency
Food and Drug Administration
Office of Emergency Preparedness

Intensive sampling during Operation Agnes persisted from 23 June to 31 August 1972 with monthly sampling extending to November 1972. The sampling program produced over 20 thousand hours of current meter records and over 25 thousand samples to be analyzed for salinity, dissolved oxygen and suspended sediment. Results of these analyses produced a comprehensive picture of the physical environmental effects of the most severe flood in the Chesapeake Bay region in recorded history.

III. SCIENTIFIC RESULTS OF OPERATION AGNES

In this paper, Chesapeake Bay is defined as the body of water between 37° and 38° North Latitude which is formed by the confluence of estuarine portions of the Susquehanna and smaller rivers from the north, the estuaries of the Potomac, Rappahannock, York, James and smaller rivers from the west and several small rivers from the east as shown in Figure 1. This definition will, no doubt, be disputed by some but best fits the discussions which follow.

A. River Flow

The deluge from Tropical Storm Agnes, on a saturated watershed, resulted in immediate flooding of the major tributaries to Chesapeake Bay. Most rivers crested at levels higher than previously noted in some two hundred years of record. Table III lists average flows for the month of June as well as average daily flows and instantaneous peak discharges for major tributaries to Chesapeake Bay for the period 20 to 27 June, 1972. These flows were measured (or estimated) at the furthest downstream gauging station in each river (usually just upstream of the region of tidal influence).

From 21 to 30 June, 1972, the Susquehanna River, usually responsible for 61% of the fresh water contributed to Chesapeake Bay in June, had flows averaging 15.5 times greater than normal. This river accounted for 64% of the fresh inflow to the Bay for the ten-day period and resulted in a 30 nautical mile translation of fresh water downstream (based on the movement of the 5 ppt isohaline) (Schubel, Carter and Cronin, 1974). Had Chesapeake Bay been a reservoir, the water level in the Bay and all its tidal tributaries would have been increased by approximately two feet from the ten-day Agnes-induced flooding of all major tributaries.

The relative effect of Agnes flooding on each major tributary becomes apparent when flows are normalized to average June flows. Figure 2 shows daily normalized flows for the major tributaries to the Bay during the period 20 June - 5 July 1972. Normalized peak instantaneous flows are also shown. From this figure, it is apparent
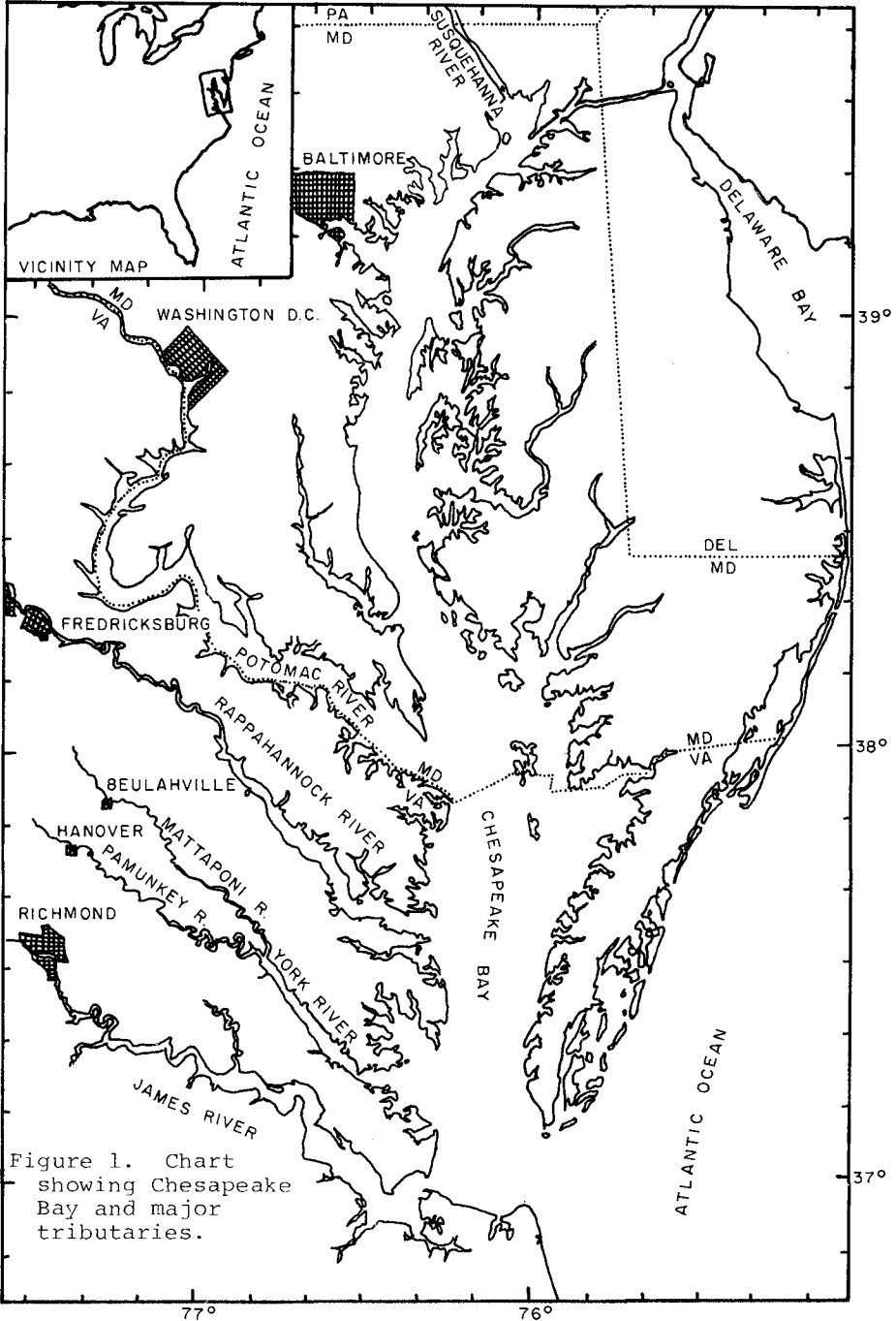
Figure 1. Chart showing Chesapeake Bay and major tributaries.

Table III

Gauged Flows for Major Tributaries to Chesapeake Bay
During Flooding from Tropical Storm Agnes
(Numbers in parenthesis indicate instantaneous peak flows)

River (Gauging Station)	Normal Avg. June Flows (cfs)[1]	Average daily flows (cfs)[1] for June, 1972							
		20	21	22	23	24	25	26	27
Susquehanna (Conowingo, Md.)	35,000	48,600	50,400	445,000	1,040,000	1,120,000 (1,130,000)	1,010,000	696,000	418,000
Potomac (Washington, D.C.)	8,020	7,160	12,000	172,000	268,000	334,000 (359,000)	200,000	79,800	35,600
Rappahannock (Fredericksburg, Va.)	1,240	1,090	6,380	84,200 (107,000)	44,500	18,200	7,410	5,100	4,600
York (Beulahville, Va.) (Hanover, Va.)	859	1,793	3,091	10,460	30,730 (35,630)[2]	34,300	32,500 (33,200)[2]	28,700	21,480
James (Richmond, Va.)	4,650	9,220	14,300	136,000	296,000 (313,000)	210,000	88,700	28,700	19,900

Note: 1 - cfs = cubic feet per second.

2 - The York River has two major tributaries where furthest downstream gauging stations are located: On the Mattaponi River, the gauging station at Beulahville, Va. recorded a peak instantaneous flow of 16,900 cfs on 25 June; on the Pamunkey River the gauging station near Hanover, Va. recorded a peak instantaneous flow of 29,900 cfs on 23 June. These instantaneous peak flows, combined with average daily flows in the associated York tributary gave combined peak flows into the York system as shown.
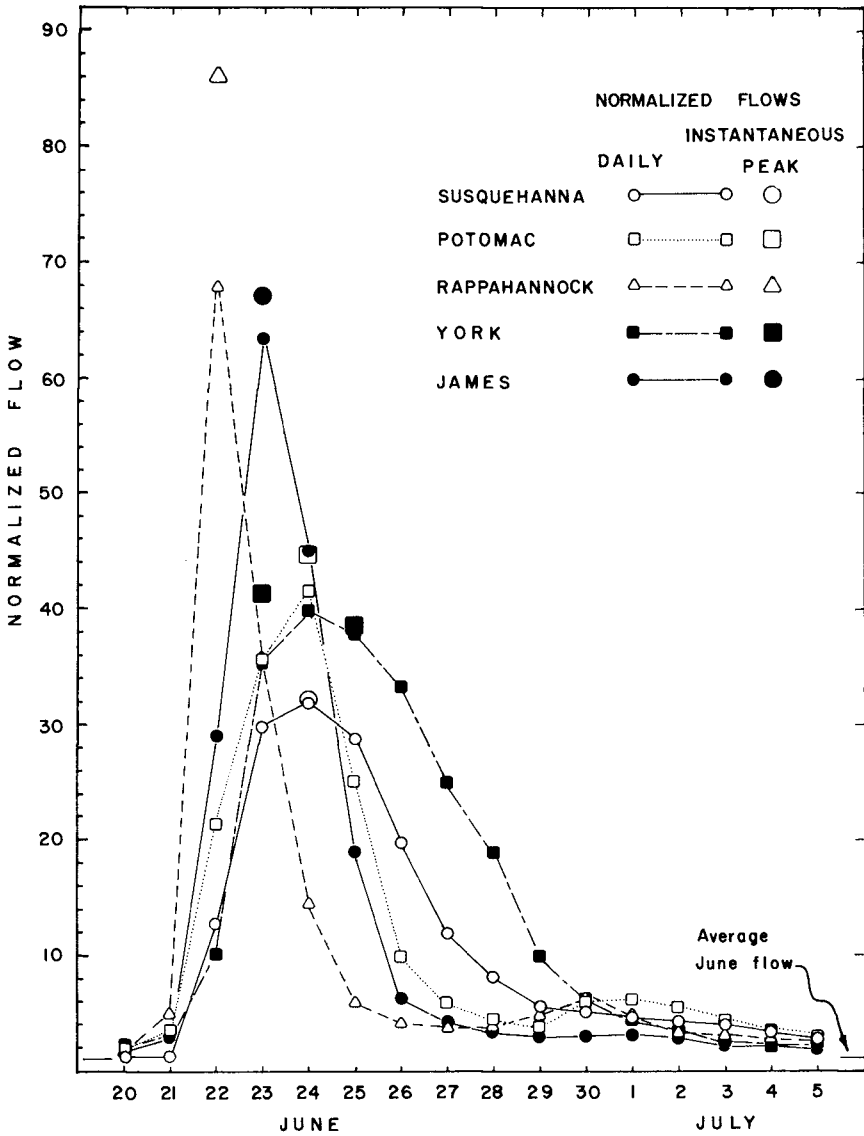
Figure 2. Normalized flows for major tributaries to Chesapeake Bay during flooding from Tropical Storm Agnes (1972).

that two forms of flooding occurred: (1) an abrupt flow
increase in excess of 60 times normal, followed by an
equally abrupt decrease in flow back to approximately six
times normal as is illustrated by the James and Rappa-
hannock Rivers, and (2) a somewhat slower increase in
flow to 30 or 40 times normal followed by a decrease in
flow which took twice as long as the increase as is illus-
trated by the Susquehanna and York Rivers. The normalized
record for the Potomac River falls somewhere between these
two. Table IV illustrates that for normalized flows,
flooding in the York River was most severe. When actual
volumes of water are considered, however, flooding in the
York was least severe because of the low flows usually
experienced in June (see Table III). Of all major trib-
utaries to the Bay, the York was least affected by Agnes
induced flooding.

Table IV

Normalized Flows for Major Tributaries to
Chesapeake Bay for Various Periods of
Flooding Due to Tropical Storm Agnes
(flows are normalized to the long term
average June flow).

| River | Normalized Flows (1972) | | |
	7 Days 21 to 27 June	10 Days 21 to 30 June	15 Days 21 June to 5 July
Susquehanna	19.5	15.5	11.6
Potomac	19.7	15.4	9.2
Rappahannock	19.6	15.2	11.3
York	25.3	21.2	15.2
James	24.4	18.0	12.8
Total	22.2	17.3	12.4

B. Effects of Flood Waters on the Salinity Distribution
    in Chesapeake Bay, It's Major Tributaries and
    Contiguous Continental Shelf

     Prior to the Agnes flood, Chesapeake Bay was in an
unusual hydrographic condition. Whereas water tempera-
ture was similar to that expected in late spring or early
summer, the salinity distribution was most akin to that
expected in mid-spring owing to greater than average
flows during the preceding winter and spring. Hence,
salinity was depressed more than in June of a year of
more normal rainfall.

     Chesapeake Bay and each of its major tributaries
showed similar reactions to Agnes flooding. Generally,

four stages were observed by Kuo and Ruzecki (1974)
and are shown in Figure 3.

1) Initially, flood waters forced surface salinities
   downstream several miles while bottom salinities
   remained somewhat constant, producing highly strati-
   fied estuaries. Distance and duration of the dis-
   placement were dependent on the dimensions of each
   particular basin and the magnitude of flooding within
   that basin.

2) The second stage of reaction to the flood was similar
   to the first but operated on bottom rather than sur-
   face waters shifting them downstream. This resulted
   in vertically homogeneous estuaries of very low
   salinity.

3) The third stage was essentially a reaction to the
   first two and is presumed to be the result of gravi-
   tational circulation. During this stage, there was a
   net transport of salt up the estuaries. This trans-
   port started in the lower layers, eventually acted
   on surface water and, particularly in the lower layers,
   moved salt water upstream substantially beyond the
   pre-Agnes position.

4) The final stage was vertical mixing between surface
   and bottom waters which resulted in salinity structure
   similar to that expected during a "normal" summer.
   This final stage of the reaction to Agnes-induced
   flooding was generally underway, for the Chesapeake
   Bay system, by the end of September, approximately
   100 days after the flood waters crested at the fall
   line.

     The generalized sequence of events described above
was evident to some extent in the Bay and all major
tributary estuaries but was most pronounced in the Bay
and the James and York Rivers. The remaining major
tributaries showed the first two (downstream directed)
stages but were subjected to Bay-tributary interactions
during the third (upstream directed) stage. At the time
the Potomac and Rappahannock rivers went through the third
stage, the up-Bay encroachment of high salinity water had
not reached their mouths. The result was an upstream
movement of slightly salty water into these rivers from
the northernmost portion of the Bay. This situation did
not occur in the James and York rivers because of their
proximity to the ocean.

     The Bay was subjected to a cascade of flooding from
the Susquehanna and Potomac. The early effect is shown
in Figure 4 which illustrates surface salinities for the
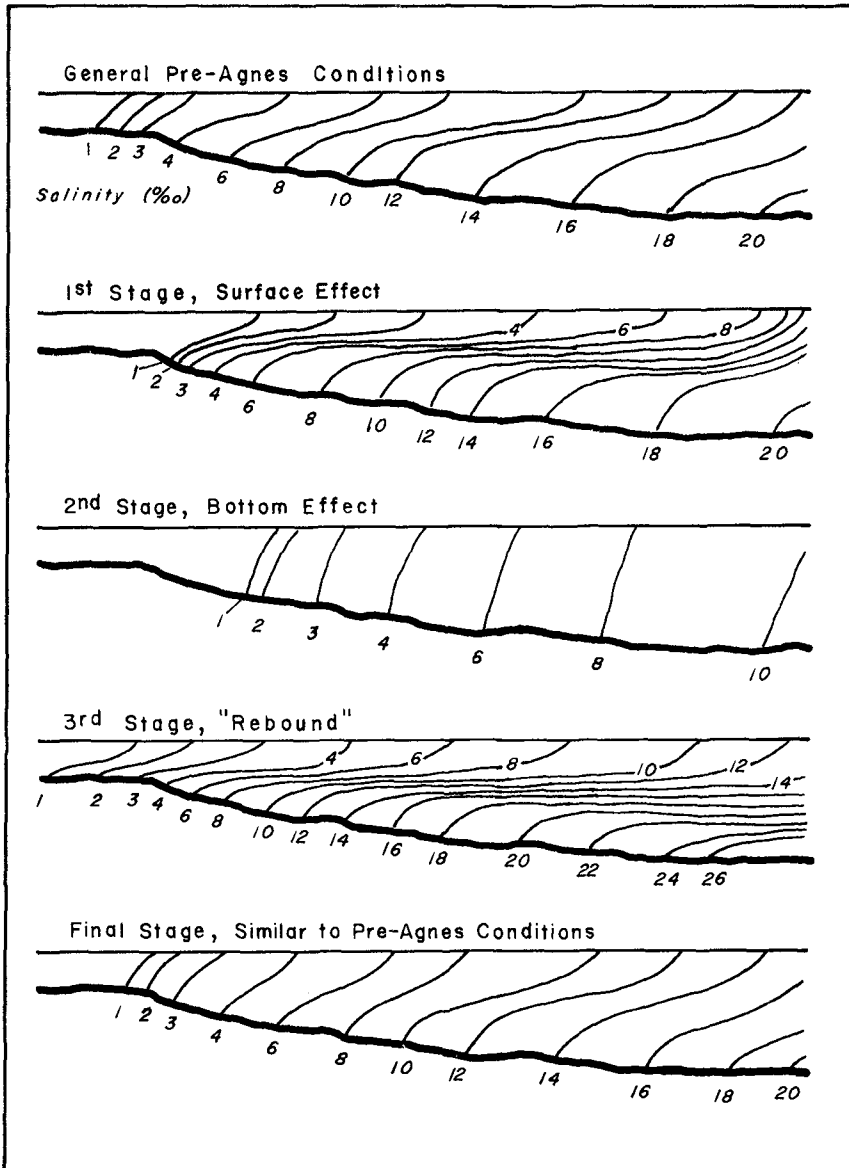period 29 June to 3 July. Flood waters from the

Figure 3. Schematic representation of sequential isohaline configuration in major estuaries of the Chesapeake Bay System resulting from flooding due to Tropical Storm Agnes.
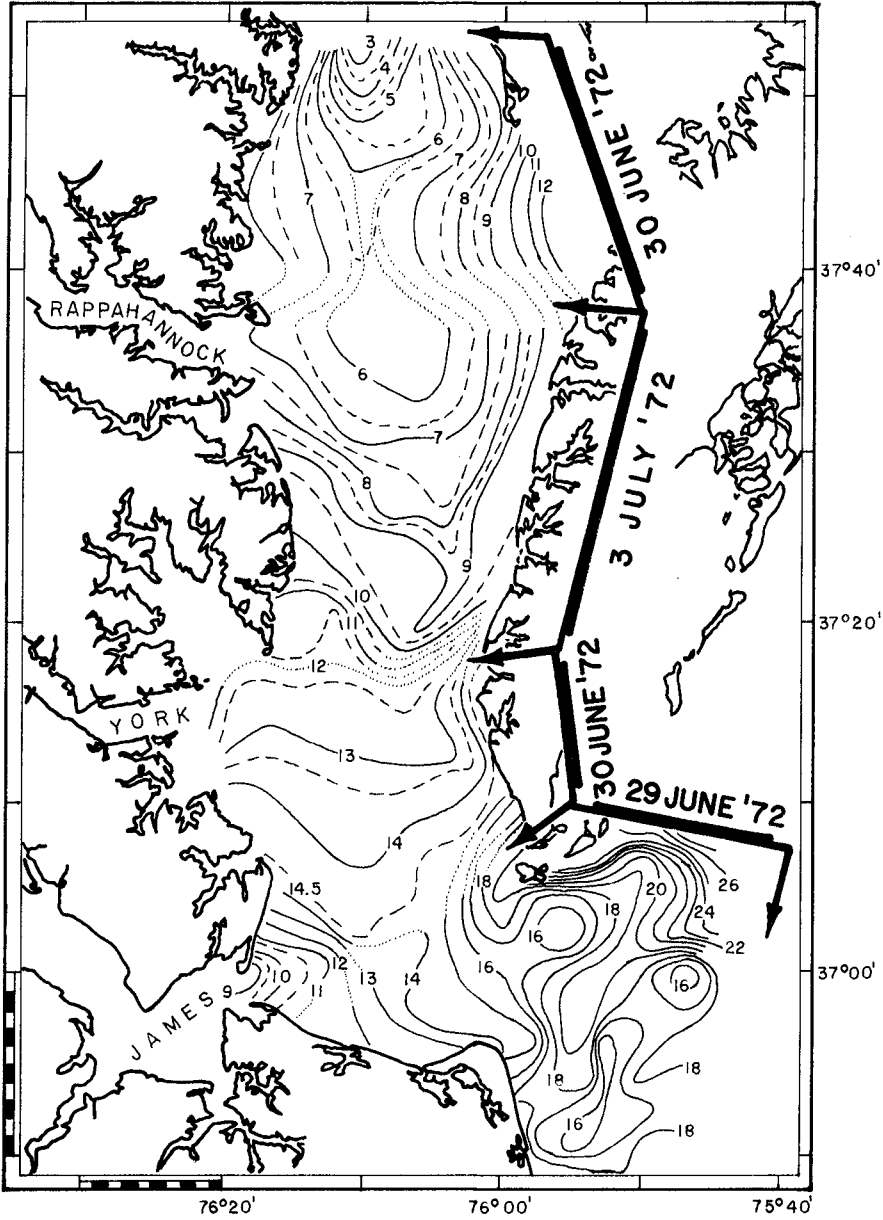
Figure 4. Surface salinities of Chesapeake Bay taken 29 June to 3 July 1972 approximately one week after flood waters from Tropical Storm Agnes crested at the fall line.

Susquehanna and Potomac coursed down the center of the Bay
bypassing pockets of higher salinity water in smaller
tributaries on either side. Sampling on 30 June and 3
July occurred at approximately the same tidal stage and
results show a 12.5 nautical mile downstream excursion
of the 6 part per thousand isohaline. The combined
effects of wind and tide resulted in the pulsing of
small patches of 16 ppt surface water from the Bay mouth.
Approximately seven days later, large patches of freshened
water from the Potomac and Rappahannock had progressed some
distance downstream from their mouths. At the same time,
high salinity water had begun moving up the Bay along its
eastern side. By 15 September, surface salinities in the
lower portion of the Bay (south of the mouth of the York
River) appeared to be recovering towards more normal
conditions as shown in Figure 5. For comparison, more
"normal" surface salinities are shown in Figure 6 which
covers the period 16-17 July 1973. Figures 4, 5, and 6
are each the result of surface water samples taken by
helicopter on a square grid with station spacing of
approximately 2 nautical miles.

     Analyses of over 120 sampling runs conducted on the
James, York, and Rappahannock Rivers indicate that these
tributaries to the Bay were subjected to internal seiches
which were generated by the flood shock. These internal
oscillations with periods from four to fifteen days helped
to vertically mix the estuaries (Hyer and Ruzecki, 1974).

     Location of measurements of tide and currents and
surface to bottom water sampling points are shown in
Figure 7. Tide and current measurements discussed below
were made at locations which have closed symbols in
Figure 7.

     Current and tide data from the James River analyzed
by Jacobson and Fang (1974) indicate the following:

1) Rise in water level was slight in the tidal rivers
    when compared with that experienced above the fall
    line. Water level elevations of approximately 6
    feet occurred in the upper portions of the tidal
    rivers, but no change was discernable at the mouths.
    Passage of the storm's low pressure center caused an
    increase in water level of a few inches. These
    features are illustrated in Figure 8a and b which
    resulted from tidal records at Hopewell and Norfolk
    (Seawells Point).

2) The normal tidal current pattern was disrupted, there
    being a continuously ebbing current for several days
    as far downstream as the zone of transition from fresh
    to salt water. Downstream of that zone, surface waters
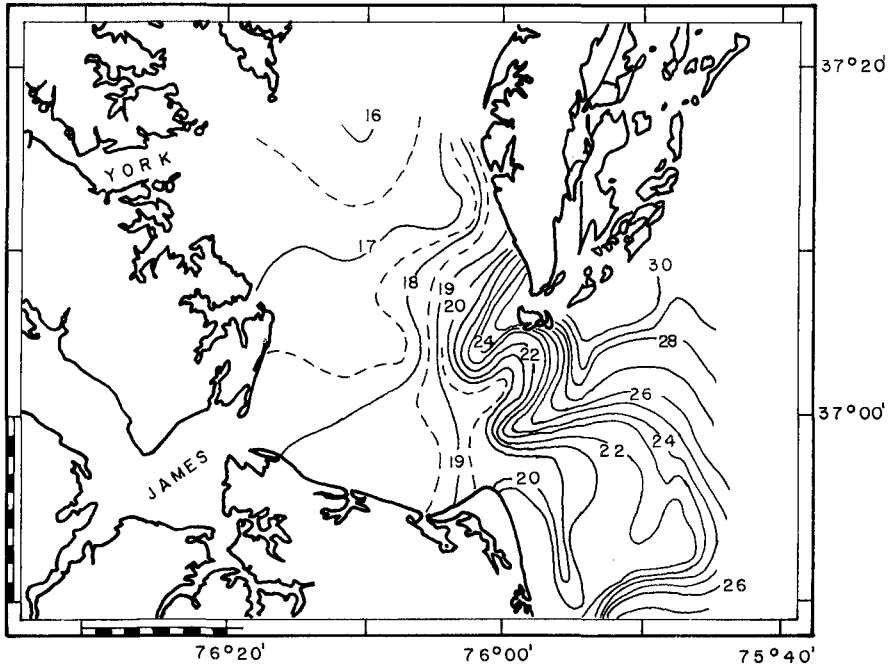
Figure 5.   Surface salinities of Lower Chesapeake Bay
             and adjacent continental shelf taken on 13
             September 1972, approximately 3 months after
             flood crest from Tropical Storm Agnes passed
             the fall line.

        ebbed continuously for three days after the flood
        crest passed Richmond, but lower layers showed normal
        ebb and flood current oscillations.

        Movement of Agnes flood waters onto the continental
shelf was traced with one cruise by the Chesapeake Bay
Institute and five cruises by the Virginia Institute of
Marine Science and is described by Kuo, Ruzecki and Fang
(1974).   Flood waters leaving the mouth of the Bay moved
southward along the coast.   Freshened water remained in
the upper 10 meters of the water column and was broken into
large patches by tidal motion at the Bay mouth.   Mixing of
the patches of fresh water with ocean water was most promi-
nent on their eastern boundaries, there being little
vertical or north-south mixing.
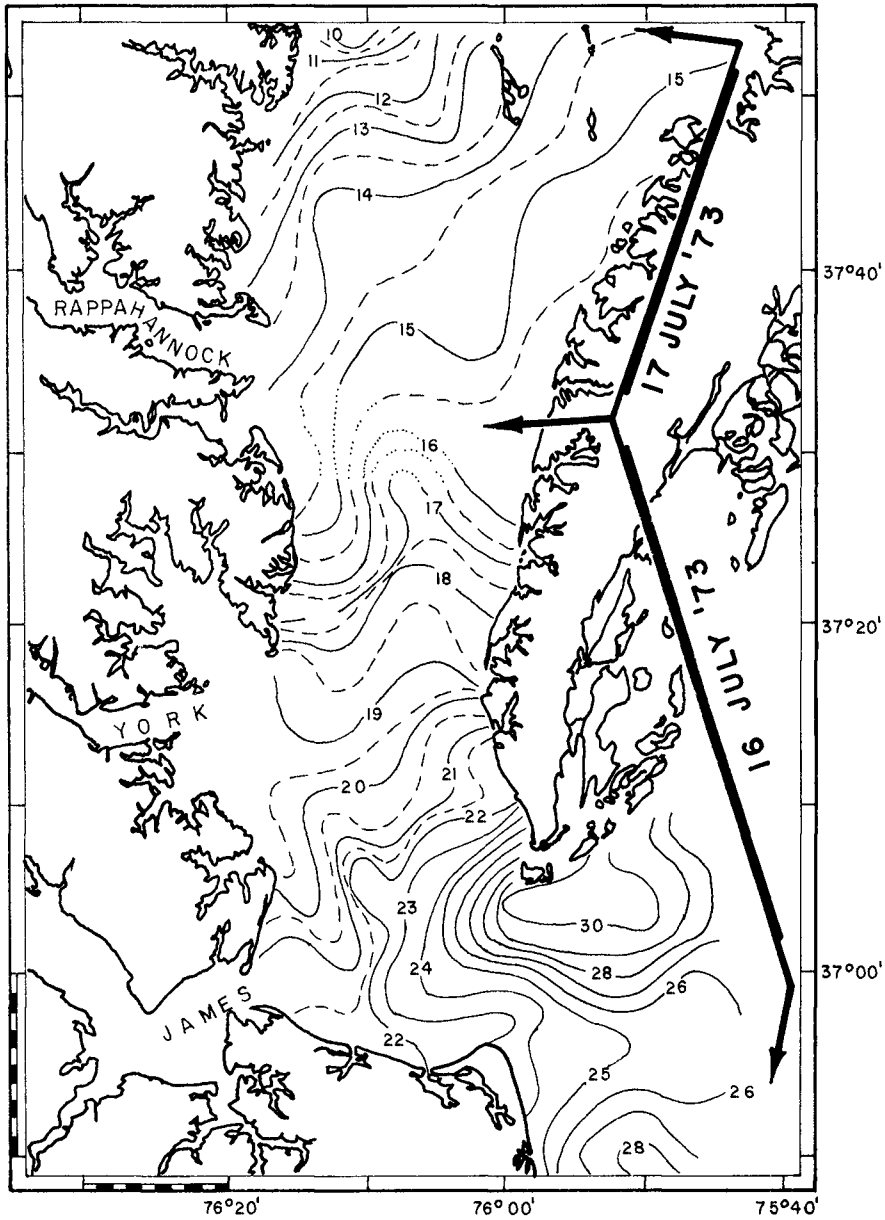
Figure 6.   Surface salinities of Chesapeake Bay during
            July 1973.
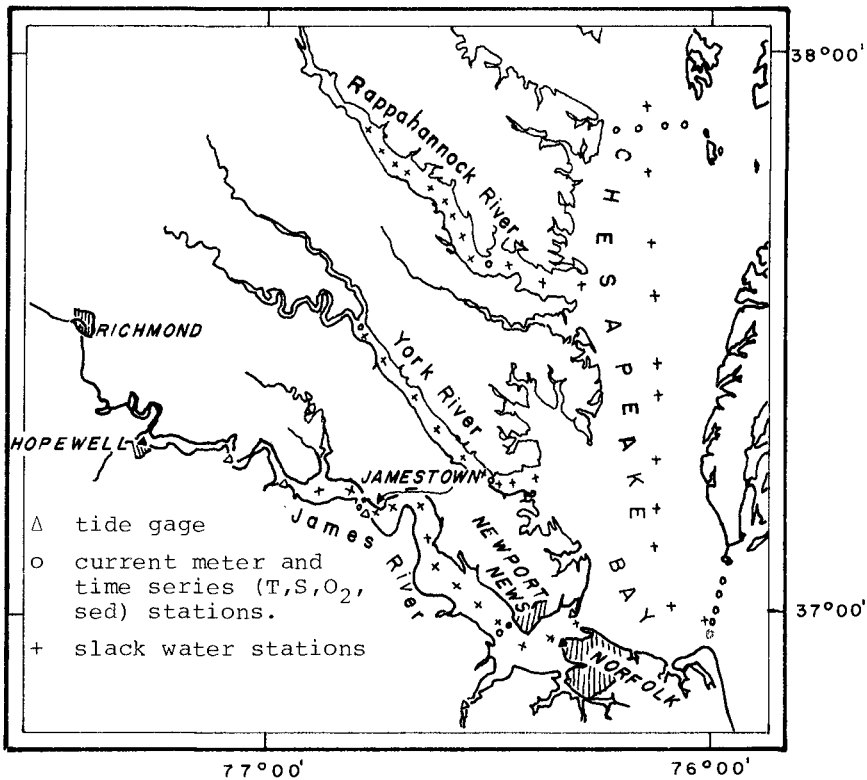
Figure 7.   Locations of slack water and current meter
            stations and James River tide gages occupied
            during Operation Agnes June-Sept. 1972.

C.   Effects of Agnes Flooding on Smaller Tributaries to
     Chesapeake Bay

     In general, small tributaries to the Bay became
reverse estuaries after the passage of the Agnes flood.
Their normal source of salt water, the Bay, became sub-
stantially fresher than these small rivers. Fresh water
moved upstream from the mouth in the surface layers and
saltier water moved from the upstream reaches toward the
mouth in the lower layers. These conditions persisted for
varying lengths of time depending on the recovery of ad-
jacent portions of the Bay. Seiche conditions similar to
those observed in the large tributaries were evident as
surface phenomena and were attributed to wind set-up rather
than freshwater flooding.
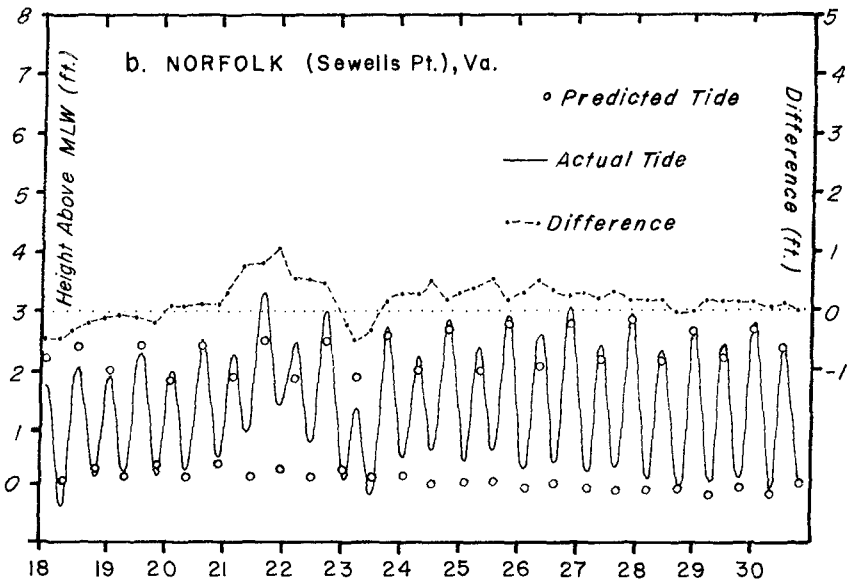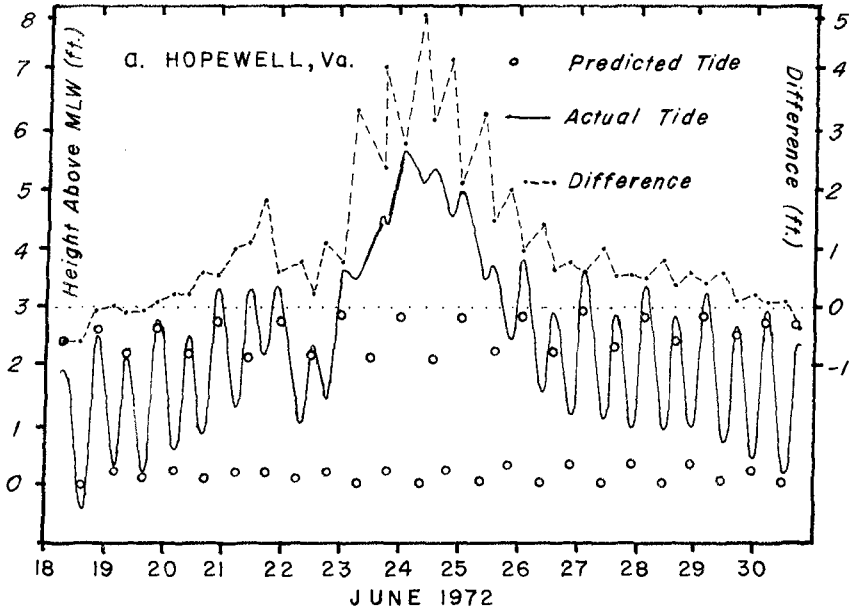
Figure 8. Predicted, and measured tides and their difference for a) Hopewell, (near the fall line) and b) Norfolk (near the mouth) in the James River during the period of flooding from Tropical Storm Agnes (Jacobson & Fang, 1974).

D. Recovery of the System

Flooding from Tropical Storm Agnes was catastrophic in the Chesapeake Bay drainage system. However, the effect on tides, currents and the distribution of sea salt within the estuarine portion of the system was short lived. Tidal fluctuations in the lower reaches of the James River estuary were only slightly effected by the flood waters. All tide gages in that river were recording normal fluctuations within a week of passage of the flood crest at the fall line. Predicted values of ebb and flood currents were matched within ten days. Salinities returned to normal within 100 days.

This rapid recovery progressed upstream, was initiated in the lower layers of all monitored portions of the system and was primarily the result of the "reaction" to the first two stages of the flood effect. If the Chesapeake Bay estuarine system had been subjected to the same volume of flood water over a substantially longer period of time, recovery of salinities would have taken much longer because the upstream surge of highly saline bottom water would have been much less intense.

E. Summary

It has not been possible to describe all of Operation Agnes, especially as it relates to the operations conducted in the upper portion of the Chesapeake Bay and its tributaries. Left for another communication must be descriptions of the efforts of the Chesapeake Bay Institute, the Chesapeake Biological Laboratory, the National Marine Fisheries Service, Laboratory at Oxford and the Environmental Protection Agency Laboratory at Annapolis. All participated and added much.

We have presented some details of the massive field and laboratory operations which evolved quickly to examine the various effects of Tropical Storm Agnes on this complex tidal system and adjacent coastal waters.

This multidisciplinary operation was designed to examine 1) physical, chemical and geological effects and attendant biological and social effects, and 2) the cycle of recovery.

It has been shown that the Chesapeake, itself, and its principal Virginia tributaries, behaved similarly. Smaller tributaries showed different responses.

In summary, the Bay and the Potomac, Rappahannock, York and James Rivers showed four stages:

a) Severe vertical stratification produced a large downstream displacement of surface isohalines.

b) Displacement of bottom isohalines downstream, elimi-
    nating the vertical stratification.

c) Net upstream transport of salt water in the lower
    layers to positions further upstream than before the
    flood.

d) Recovery, to normal isohaline patterns after vertical
    mixing. This last stage was reached within about 100
    days after the floods.

     There was some variation to this pattern depending
upon proximity to the ocean.

     Smaller tributaries became reverse estuaries with
salt water moving out at the bottom while fresh water
moved upstream on the top.

     Water height observations showed that water levels
in the tidal system did not rise a great deal on the
average as compared with the situation at and along the
fall line area. However, levels were much higher below
the fall line and diminished downstream until no change
was detected at tide gages located in the lower estuaries.

     Tidal current patterns were disrupted. A continuous
ebb occurred in the area above the salt water zone.
Below the salt water transition zone surface water ebbed
continuously for three days while the lower layers showed
normal ebb and flood current oscillations.

     The results are interesting since they represent a
picture of a great tidal system under conditions of
extreme fresh water stress and the phenomena related
thereto. It is noteworthy that Agnes produced certain
biological effects which have had severe economic and
social repercussions. For example, much of the Chesapeake
was closed to "body contact" sports and to direct harvest-
ing of shellfish as a result of the high bacterial counts
which occurred or of the threat of bacterial contamination.

     Additionally, severely depressed salinities killed
economically important oysters and soft clams over a wide
area. This produced immediate damage to the associated
fishery activities. Too, evidence is strong that Agnes
prevented the setting and survival of oyster larvae and
"spat" (immediate post-setting stages). Thus, the effects
on the oyster industries of the Bay were immediate as
well as of long duration.

     Populations and the fishery have not as yet re-
covered--two years later.

     As a result of the physical work and associated
fishery observations, it was possible to justify economic

assistance to public and private sectors of the oyster industry. To our knowledge, this is the first time that this has occurred in a situation of this nature. Thus, the physical research has not only yielded new insights into natural phenomena but has also produced immediate economic and sociological benefits.

IV.   REFERENCES

DeAngelis, Richard M., and William T. Hodge. 1972. Preliminary Climatic Data Report: Hurricane Agnes, June 14-23, 1972, U. S. Dept. Commerce, N.O.A.A. Technical Memorandum EDS NCC-1. iv + 62 pp.

Hyer, Paul V., and E. P. Ruzecki. 1974. Changes in Salinity Structure of the James, York and Rappahannock Estuaries Resulting from the Effects of Tropical Storm Agnes. (In Press).

Jacobson, John P., and C. S. Fang. 1974. Flood Wave-Tide Wave Interaction on the James River During the Agnes Flood. (In Press).

Kuo, Albert Y., E. P. Ruzecki and C. S. Fang. 1974. The Effects of Agnes Flood on the Salinity Structure of the Lower Chesapeake Bay and Contiguous Waters. (In Press).

N.O.A.A. 1972. Storm Data, Vol. 14, No. 6.

Schubel, J. R., H. H. Carter and W. B. Cronin. 1974. Effects of Agnes on the Distribution of Salinity Along the Main Axis of the Bay and in Contiguous Shelf Waters. (In Press).

CHAPTER 145

EFFECTS OF BANK RAISING ALONG THE THAMES

Anthony J. Bowen[1] and Sally J. Pinless[2]

ABSTRACT

  A one-dimensional numerical model was used to estimate the
location and volumes of water flooding over the banks of the
Thames Estuary under several combinations of bank levels and
possible storm surges. An assessment of the probable damage
resulting from each of these floods enabled a comparison to
be made between the various possible schemes for bank improve-
ment and, indeed, showed that there was a serious need for
such improvement even though a start on the construction of
the Thames Barrier was imminent. In an estuary such as the
Thames the overflow may provide a significant turn in the
continuity equation and the effect must therefore be pro-
grammed as an integral part of the model; one obvious effect
of the overspill is to limit the maximum levels to about 0.2 m
above the banks in the upper Thames, almost irrespective of
the size of the surge.
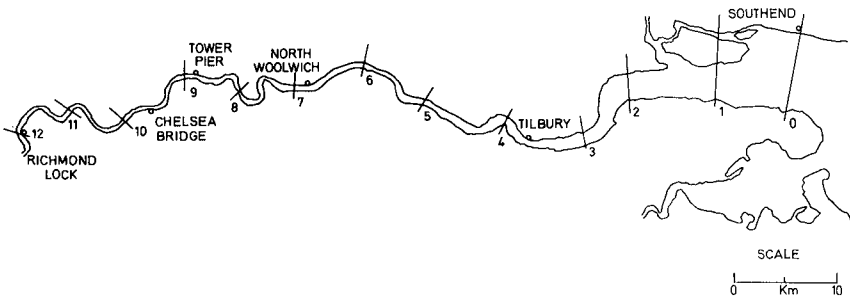
Figure 1.   The Thames Estuary, showing the cross-sections
at which surface elevation is computed in the numerical
model.

1. Department of Oceanography, Dalhousie University, Halifax,
    N. S.

2. Institute of Oceanographic Sciences, Bidston, Cheshire.

INTRODUCTION

Much of the City of London stands on what was, at one time, the flood plain of the River Thames. The growth of the city has led to increasing reclamation of areas, lying below even the level of high tides, which must be permanently protected by embankments. As the mean sea level at the mouth of the estuary is rising relative to the land at about 30 cm/century and the mean high water level in Central London appears to be increasing at more than twice this rate, the standard of the existing defensive works has in effect been slowly downgraded since their construction.

In January 1953, exceptional meteorological conditions over the North Sea resulted in a storm surge reaching extreme levels which equalled or just exceeded the flood defences in Central London. However, the river banks in the seaward reaches of the estuary were overtopped and, in some cases, breached: an area of some 120 km^2 was seriously flooded. During the rebuilding, the banks of the lower estuary were strengthened and raised to prevent a recurrence of the 1953 disaster. However the flood defences in Central London were not improved at this time, partly because the attempts made to estimate the reduction in the maximum levels reached in Central London due to the extensive overflow from the lower reaches tended to suggest that the maximum levels would not have been much higher (no more than 10 cm higher) had no flooding occurred (Allen, Price and Inglis, 1954).

However during the initial, hydrodynamic investigations for the Thames Barrier it became clear that these older estimates of the effect of overflow were seriously in error. If a surge of the magnitude of the 1953 storm surge was contained by the improved defences in the lower estuary, the results from both the numerical model at Bidston and the large hydraulic model of the estuary at the Hydraulics Research Station, Wallingford, predicted that the statutory defence levels in Central London would be exceeded by 20-25 cms. Although it was obvious that the problem would cease to exist when the Thames Barrier became operational, the question remained as to whether any bank raising was indicated to provide interim protection during the eight years it would take to complete the barrier construction.

THE NUMERICAL STUDIES

     To provide a cost-effectiveness study of the benefits
of various possible investments in improved defences in the
upper estuary, essentially four stages were required in the
analysis.

     i)   the design and costing of a variety of bank levels.

     ii)   the quantification of the location and volume of
water that would flood over into the City during storm surges
of various intensities (a variety of extreme levels) for each
set of bank levels.

     iii)   a costing of the damage which would result from the
predicted flooding.

     iv)   an analysis of the resulting data, the cost of the
defences against the cost of the flood damage, in terms of the
estimated chance of occurrence of a storm surge of given
magnitude. (Data on the return period of surges was already
available from the general oceanographic study for the Thames
Barrier, for example for the 1953 surge the estimated return
period is 80 years, that is, in any year there is a one in
eighty chance of a storm surge of this particular size occurring.
The chance of its occurrence over the eight year period required
to complete the complete barrier system is therefore one in ten.)

     A sophisticated, one-dimensional numerical model of the
Thames Estuary was used to study item (ii), the location and
volume of flooding which would result from a given combination
of surge and defensive scheme.

     The basic numerical model was proved on normal tides without
any flood effects (Rossiter and Lennon, 1965); the extension to
storm surges led to the results, previously mentioned, that
without flooding the levels in the upper Thames would have been
about 25 cms higher than those actually observed. To reproduce
the effects of flooding out of the river the details of the bank
levels along the river were programmed into the model. As the
overflow into adjacent land seriously alters the actual level in
the river, this effect has to be included in the continuity
equation of the basic numerical model. An 'overspill-section'
was defined as running from each half-section to half-section of
the model and was referenced by the number of the midway section
where the water elevation is calculated (Fig. 1). The bank
levels were split into sets of equal level and the total length
of bank at a particular level in each section was input to the
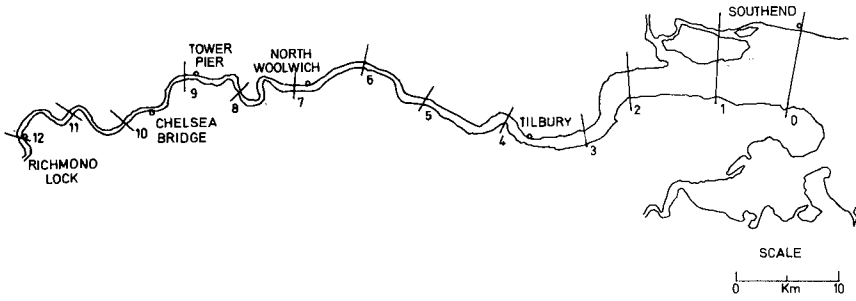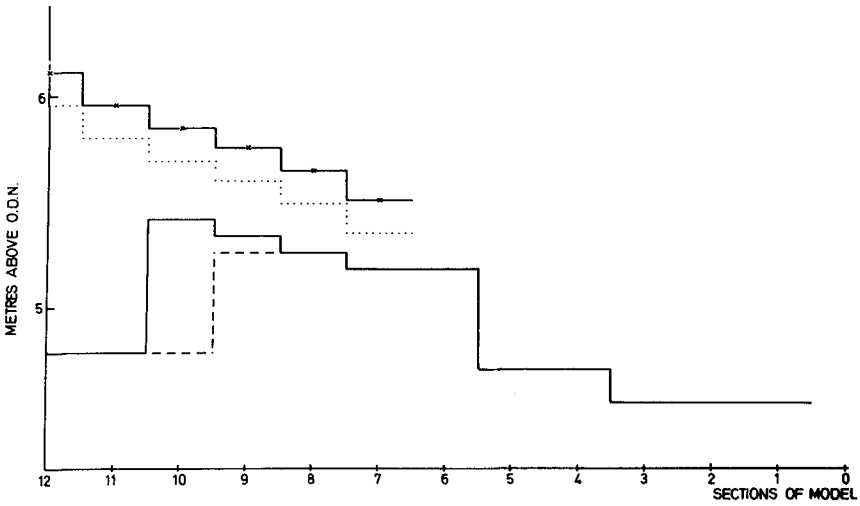
Figure 2. The lowest bank level at each section of the model. The levels in sections 1-6 are approximately those of 1953, by 1970 the bank levels here were sufficiently high that no flooding occurred in the surges used in the study.
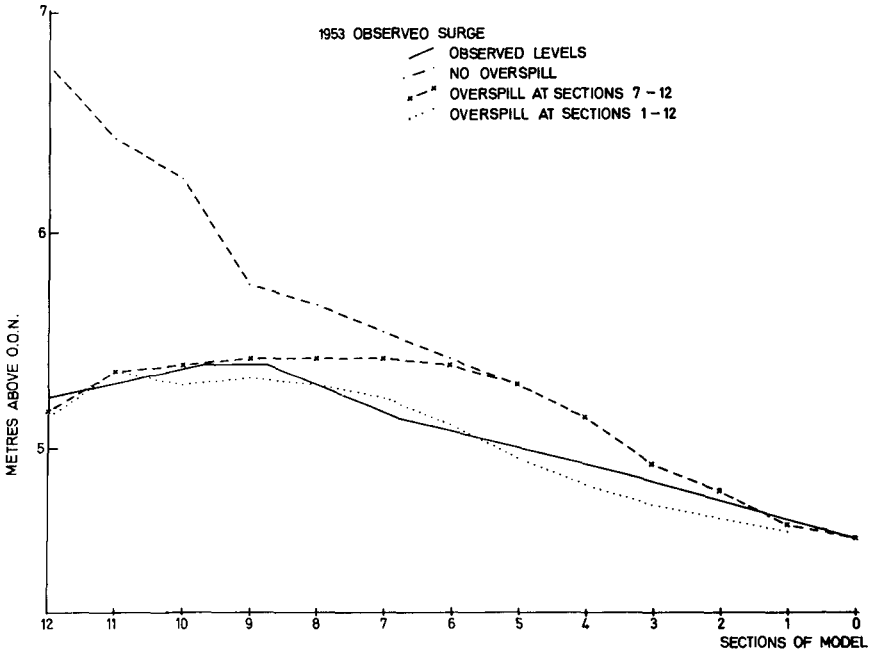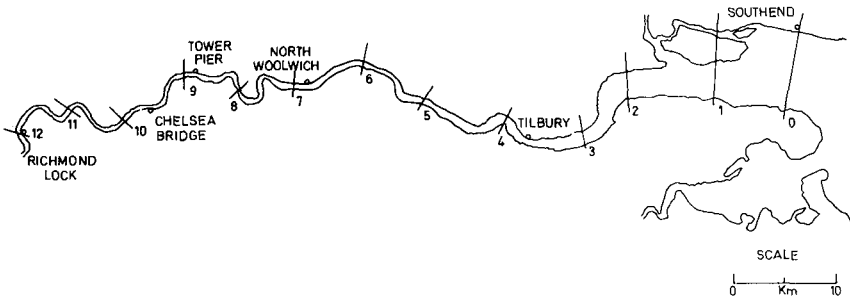
Figure 3. Maximum water levels reached along the river,
bank levels I (1953) for overspill at all sections, I (1970)
restricting the flooding to the upper river.

model. At every time step of the calculations the rate of
discharge over the north and south banks of each 'overspill-
section' was separately computed using the formula (Ven Te
Chow, 1959),

$$Q = C \sum_{i=1}^{N} L_i (z_{n,m} - h_i)^{3/2}$$

where   Q   = rate of discharge

         L_i = length of bank at level h_i

         N   = number of different bank levels in section

         $z_{n,m}$ = elevation at section n and time step m

         C   = coefficient of discharge, taken at 3.0

The total rate of discharge over the two banks was then computed
and used to obtain the new elevation, $z_{n,m+1}$, by the inclusion
of this additional term in the equation of continuity. Fortun-
ately the basic method of solution, an explicit, finite differ-
ence scheme allows such modifications to be made without
difficulty.

     Three sets of bank levels were used, levels I were derived
from the 1953 statutory defence levels for sections 1-6 and a
detailed survey (by the Greater London Council as part of the
design process for the improved defences) of the bank levels in
the upper river, sections 7-12. This survey provided 1970
levels but these were essentially still the same here as they
had been in 1953. Levels II and III represented two alternative
improvements for the upper river, approximately an increase of
0.30 m and 0.45 m on the existing levels. Figure 2 shows the
lowest level in the set of bank levels associated with each
section of the model for the various schemes.

     Level I (1953) provided a close approximation of the bank
conditions during the 1953 storm surge. Using the water levels
observed at Southerd during this surge as input, the model was
over with unlimited flooding (no account was taken at this stage
of the fact that the capacity of the flood plain might be ex-
ceeded). The resulting spill of water over the river banks
reduced the maximum water levels reached during the surge to
values very similar to those measured in 1953 (Fig. 3).

The distribution and volume of the flooding was also similar to that actually observed in 1953; some difference was expected as several banks were breached during the surge and this type of failure was not represented in the model. The assumption that the capacity of the flood plain at any section was not exceeded was checked after the complete calculation by comparing the total volume of flow over a section with the surveyed volume of the surrounding area. These results seemed to provide an adequate validation of the basic assumptions and method of solution used in the model.

Following the 1953 surge, the banks in the lower estuary (sections 1-6) had to be rebuilt and the opportunity was taken to raise the levels. By 1970, therefore, these banks, designed to withstand a surge 0.6 m higher than that of 1953 were complete. The banks of the upper river remained at essentially their previous level. The model results showed that were a 1953 surge to re-occur, although the maximum water levels reached in the river (Fig. 3) would not be dissimilar from those of 1953, the pattern of flooding undoubtedly would, the overspill of water being concentrated in Central London (Table 1). Although the total flood volume would be less (37.2×10^6 m^3 was the calculated overflow from sections 1-6 for 1953 conditions), it would be concentrated in a much more susceptible area for flood damage. The case for considering some bank improvements was certainly established.

It is interesting to note that even a surge 30 cm lower than the 1953 (53- in Table 1) would, in 1970, produce almost exactly the same flooding in the upper river as the larger surge did in 1953. However the damage in the upper river in 1953 was quite minor.

Larger surges, 30 cms (53+) and 60 cm (53++), give for the 1970 bank levels very similar maximum water levels in London to the 53. In fact, the highest surge loses so much water by overspill in sections 7 and 8 (Table I) that the maximum level reached at the head of the river is actually less than that of the smaller surges (Fig. 4).

Although the chance of the co-occurrence of a major surge and a major fresh water flood is small, it was of interest to compute the relative importance of the two effects. A value of 283 m^3/sec corresponds roughly to the maximum recorded fresh water flow in the Thames, 566 m^3/s to the estimated maximum

TABLE I

Overspill volumes at each section. ($\times 10^6$ m^3)

Surge	River Flow	Bank Level	7	8	9	10	11
53	–	I (1970)	2.33	2.62	0.52	1.15	2.27
53	–	I (1953)	0.10	0.23	0.05	0.78	1.72
53	283 m^3/s	I (1970)	2.66	3.45	0.91	1.51	3.94
53	566 m^3/s	I (1970)	3.05	4.06	1.00	1.65	4.74
53–	–	I (1970)	0.14	0.25	0.08	0.67	1.48
53+	–	I (1970)	7.00	6.25	1.14	1.87	3.14
53++	–	I (1970)	15.5	10.2	1.72	2.56	3.14
53	–	II	1.03	0.50	0.09	0.54	1.92
53	–	III	–	–	–	0.56	1.42
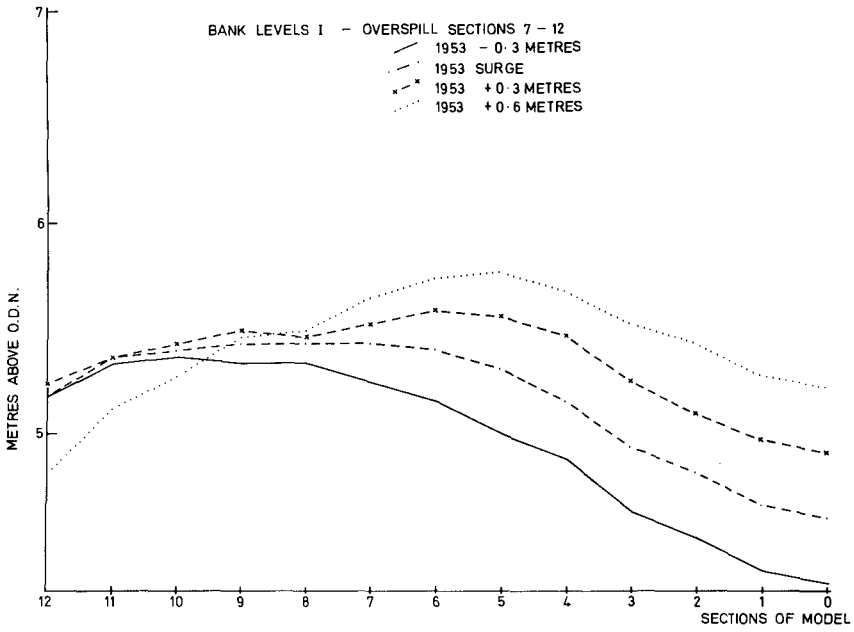
Figure 4. Maximum water levels reached along the river,
bank conditions I (1970), surges 53-, 53, 53+, 53++.

■ PONDED AREAS

▒ AREAS LIABLE TO TRANSIENT FLOW
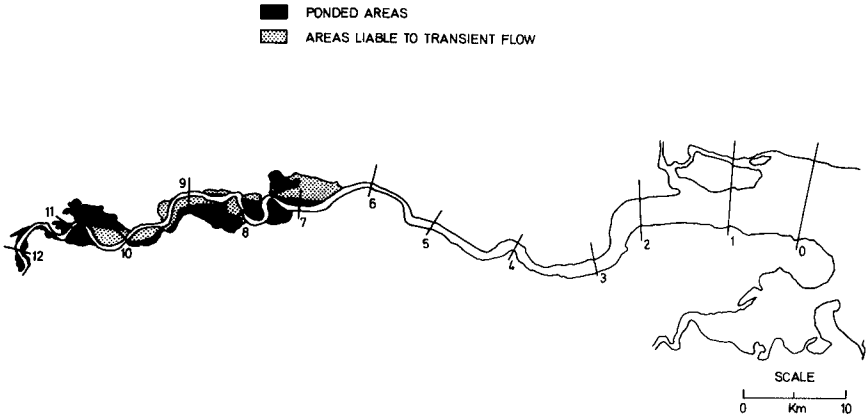
Figure 5.   Areas likely to be flooded by a repetition of
the 1953 surge after the bank improvements in the lower
estuary, bank conditions I (1970).
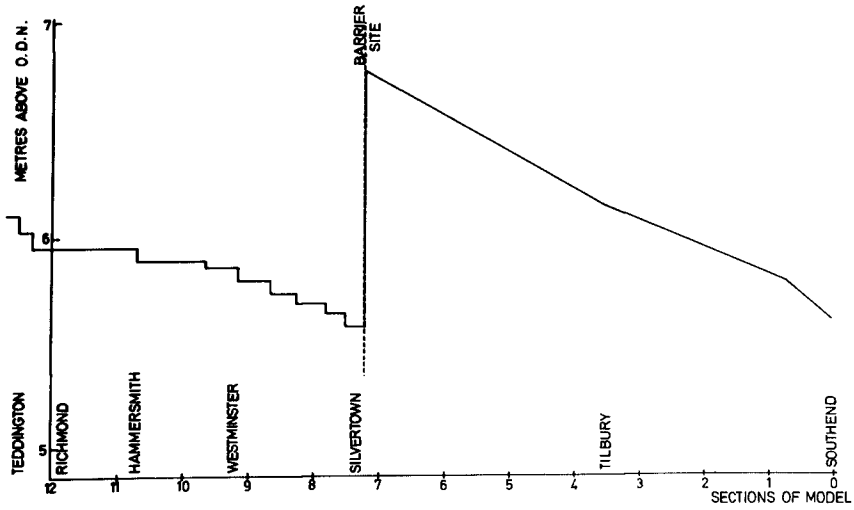
Figure 6.   Design bank levels for the Thames.   Construction
to the standard designated landward of the barrier site was
largely completed in 1973

conceivable flow. In either case the flooding is sub-
stantially increased along the whole upper river, however
it can be seen in Table I that this effect is relatively
small compared to the increase in flooding that occurs with
the higher surges.

ESTIMATION OF FLOOD DAMAGE

     The basic physical processes of the model having been
established, a series of experiments were run for combinations
of various surges, bank levels and fresh water flows.   Some
typical results are included in Table I.   In all these cases
the banks in the lower estuary were not overtopped; the
flooding was confined to the upper river.   The flood volumes
at each section were normally determined in terms of the flow
over the north and south banks (in general different due to
differing bank levels).   This data, the location and volume of
water flooding over either bank, enabled the engineers of the
Thames Barrier Project team of the Greater London Council to
estimate the route of the flood water and consequent depth of
flooding in the areas of ponding.   Figure 5 shows these areas
for a surge of the 1953 level at Southerd with the 1970 bank
levels, it also shows areas where transient flow would pass
through the streets on the way to drains and lower areas.   It
was thus possible to assess and cost the probably extent of
flood damage in Greater London for a variety of surge con-
ditions and bank levels along the Thames Estuary.   The results
clearly showed that an increase in the defense levels in the
upper river by some 0.45 m could be justified, in terms of a
cost-effectiveness analysis, to provide an interim protection
while the Thames Barrier is under construction.   The bank
raising meet the new standards, illustrated in Figure 6, was
largely completed in 1973.

CONCLUSIONS

     The inclusion of bank levels into the numerical model
not only provided detailed, predictive information on flood
volumes and locations for input to the cost-effectiveness
study for improved defences, it also illustrated some fund-
amental problems in the relation between the extreme levels
of the surge and the flood volumes.   In Figure 4 it is clear
that the flow of water over the banks restricts the maximum
level reached to some 0.2 m above the banks.   This pre-
sumably represents a balance between the flow up the estuary
and the overflow.   It is obvious that any prediction of
extreme levels at Richmond, at the head of the estuary,would
be pointless unless it included details of the existing bank

levels. An interesting question emerges as to how far sea-
wards one must go before estimates, for example in terms of
return periods, of the levels associated with major surges
can be reasonably made without including the effects of
coastal flooding.

ACKNOWLEDGEMENTS.

REFERENCES.

Allen, F. H., Price, W. A. and Sir Claude Inglis. 1954.
Model-experiments of the storm surge of 1953 in the Thames
Estuary and the reduction of future surges. Proc. Instn.
Civ. Engrs., Hydraulics Paper 5, 27 pp.

Rossiter J. R. and G. W. Lennon. 1965. Computation of tidal
conditions in the Thames Estuary by the initial value method.
Proc. Instn. Civ. Engrs., 31, 25-56.

Ven Te Chow. 1959. Open Channel Hydraulics. McGraw-Hill,
New York.

CHAPTER 146

RESEARCH IN THE HARINGVLIET ESTUARY

By A.W. Walther   M.Sc.Eng.

Abstract

After the closure of the Haringvliet estuary,
part of the Netherlands Delta Project,
morphological changes have occurred.
Until now it was impossible to give a
completely satisfactory forecast of such
changes, however, with the aid of the
Leendertse tidal computations a good picture
of the tidal flow in the estuary can be
obtained.
In the paper a short description is given of
both the tidal flow and the morphology of the
Haringvliet estuary related with some problems
of the practising engineers.

Introduction

    The socalled Delta region, situated in the south-western
part of the Netherlands, consists of a number of islands
separated by estuaries with gullies having a depth between
10 and 30 metres. The seaward side of the islands is
composed of sand; the gullies, probably being the result of
breaches in a continuous dune coast, were formed many
centuries ago. In the western part the rivers Rhine and Meuse
and in the south the Scheldt river discharge into the delta
and North Sea. The sediment transport of these rivers is not
large which means that from a geological point of view this
coast is not to be classified as a "delta" coast.
    The Delta region was often subjected to severe storm
surges and the flooding caused by the storm surge of
February 1953 was the direct motive for the decision to close
the four sea-arms comprised in the Delta Project, with the
purpose to protect the low-lying area against future storm
surges. The Haringvliet closure (see fig. 1) in 1969 was part
of this project. A large sluice complex in the middle of the
dam which, apart of negligible discharges during most of the
year, can be opened during periods of high discharge of the
Rhine river. In this way the original tidal volume in the
Haringvliet of 300 million cu.m. was reduced to one eighth.
It was expected that the morphological changes resulting
from the above reduction would mean increased sedimentation

in the entire area with possible scour in some locations.
     The need to keep a channel for the discharge of large
quantities of Rhine water (at the time of very high
discharges) and the requirement to maintain a fairway for
shipping towards the locks next to the sluices it was
desirable to predict the extent of the sedimentation.
     With respect to the coastal protection the possibility
of erosion of the adjacent sandy coasts had to be
investigated; moreover it was necessary to answer the
questions concerning the possibility for the construction
of artificial islands and for dredging sand in the area.
     In general it can be said that for all morphological
changes in this area a better insight was needed.
Different methods were used to predict such changes
(Dronkers, J.J. 1970)[1] but, as was also recognized by him
it is not yet possible to obtain a satisfactory forecast.
     Notwithstanding the above enough information
regarding hydraulic conditions and morphology could be
obtained as to answer the questions of the practising
engineers.

Tidal flow
     For the research into the tidal flow of the Haringvliet
estuary the tidal computations by the Leendertse method)[2]
have been used in most cases.
     Such computations have been carried out in close
cooperation with and the aid of the Rijkswaterstaat
Computer Centre in The Hague, the Elliot 503 and Philips
P 1400 have been used to this end.
     At first the existing situation had to be reproduced.

     The computations initially covered a large area along
the Delta coast using a net with squares of 1600 m each.
Boundary conditions were obtained from simultaneous
measurements by anchored ships, "flachsee" remote
measuring devices and sea-level measurements by fixed
gauging stations also along the coast. With the aid of
the large model the boundary conditions for the
Haringvliet model were obtained which used a net with
squares 400 m each.
     From fig. 1 it can be seen that the tidal range
increases when going south in the North Sea. The tidal
range at the mouth of the Haringvliet estuary is about
1,8 meter.
     An overall picture of the resulting maximum ebb and
flood flow for Ha 1 (1964 situation) is shown in fig. 2.
A detailed comparison of the model and prototype
measurements showed that in general a good agreement is
reached if the sea bed is reproduced in sufficient detail.
     In some places instabilities with the model will
occur namely fluctuations of velocities and waterlevels.
By reducing the time step these instabilities in general
will disappear; if not, a closer inspection of the

boundary conditions may reveal that instabilities are
generated from the boundaries of the model. This
condition however can also appear in prototype.
    Fig. 2 also shows the velocities for the Ha 2 model in
which the Ha 1 situation is repeated, however with a closed
dam and a maximum discharge of 12,000 m3/s through the
sluice gates. Fig. 3 shows the Ha 3 model without any
discharge.
    In order to be able to draw conclusions from the results
of the tidal computations it is necessary to know the
frequencies of exceedance of the discharges through the
Haringvliet sluices. For one of the possible programs
(NLP 70), set up with regard to the water control, shipping
and safety, the discharges of the Rhine were related to the
sluice discharge(s). The result is given below (table 1)

Rhine discharge cub.meters/sec.	Frequency of exceedance of Rhine discharge	Maximum discharge Haringvliet m3/s
3,000	55 days/annum	2,700
5,000	11 "	8,200
6,000	5 "	12,200
12,000	1 day/25 yrs	16,000
18,000	1 day/3000 yrs	19,000

Table 1. Frequency of exceedance of the Haringvliet and
         river Rhine discharges for program NLP 70.

    From the table it is clear that due to the few times that
the sluices are used, the discharged water can be disregarded
insofar the morphology is concerned almost the entire year.
Only in about 15% of the ebb conditions the discharge through
the sluices affects the sediment movement.
    The table also shows that the maximum ebb discharge no
longer reaches the original average value of 23,000 m3/s.
Particularly during the recent very low discharge values
of the Rhine (1971, 1972 and 1973) the reduction of the
discharges was very noticeable.
    In the period subsequent to the closure operations up to
and including 1973 the discharge values of the Rhine exceeded
3,600 m3/s only during 36 days while the value of 5,000 m3/s
was never exceeded.
    Insofar the morphology is concerned the results of the
Ha 3 model (fig. 3) may be considered a representative
average condition.
    Fig. 3 also shows the results of computation Ha 22 in
which model a sand dam starting at Europort Harbour and
extending to the south is used. This model is an example
of one of a number of proposed dams, islands and harbour
extensions, the effects of which were investigated by means
of Leendertse computations. In the Ha 22 model the wide
mouth of the estuary is narrowed considerably in order to
regulate the tidal flow. The average velocities in the main
channel are increased in order to reduce sedimentation and

consequently the need for future dredging. In addition to
the above advantage the current velocities near the southern
Europort beach are reduced which in turn decreases erosion.
      At present no final conclusion with regard to the
execution of the work can yet been drawn.

Morphology
      In the Haringvliet estuary (see fig. 4), just outside
the dam two channels are present: Rak van Scheelhoek in the
north and Slijkgat in the south. The Rak van Scheelhoek
splits up into the northern Gat van de Hawk and in the
middle of the outer estuary the Bokkegat. The point of
bifurcation moved in the last ten years before final
closure between 2,000 and 3,000 meters seaward. (compare
figs. 4 and 5).
      In the northern part of the outer estuary, during the
same 10 year period mentioned before, considerable
sedimentation was observed and a large sand flat was formed
(see fig. 5).
      Figure 6 shows both sedimentation and erosion after the
closure of the Haringvliet up to 1974. Considerable
sedimentation took place in the inner channels. The sediment
is composed of silt and silty sand.
      Near the Goeree coast both local scour and sedimentation
took place, the overall balance however was stable. The   *
coast of Voorne shows little erosion whereas at the western
point A (indicated by arrow on fig. 6) of the coast the
scour remained almost constant. Fig. 7, showing the recession
of various depth lines with time, clearly illustrates this
statement.
      This figure also shows that until now no influence can be
attributed to the closure of the Haringvliet dam in November
1969 insofar scour on this part of the Voorne coast is
concerned.
      In the central part of the inner estuary a pit was
dredged having a maximum depth of 15 meters (see fig. 6).
Sand dredged outside in the North Sea could be dumped there.
When required smaller dredgers could reclaim this sand and
pump it further inland. This work has been temporarily
stopped. The situation of the pit was chosen with regard to
both the flow during high discharges and the stability of the
sluices.

Conclusion
      Although only a general insight could be obtained into
the morphology of the Haringvliet estuary after closure of
the dam, most questions of the practising engineers could be
answered so far. The Leendertse method for tidal computations
proved to be a reliable tool. Further work on the forecasting
methods mentioned by Dronkers is necessary, especially the
relation between tidal flow and sediment movement, and the
influence of waves.

References
1. Dronkers, J.J., Research for the coastal area of the delta
                   region of the Netherlands 12th Coastal
                   Engineering Conference Washington, 1970.
2. Leendertse, J., Aspects of a computational model for
                   long-period water wave propagation
                   The Rand Corporation; Santa Monica
                   California, 1967.
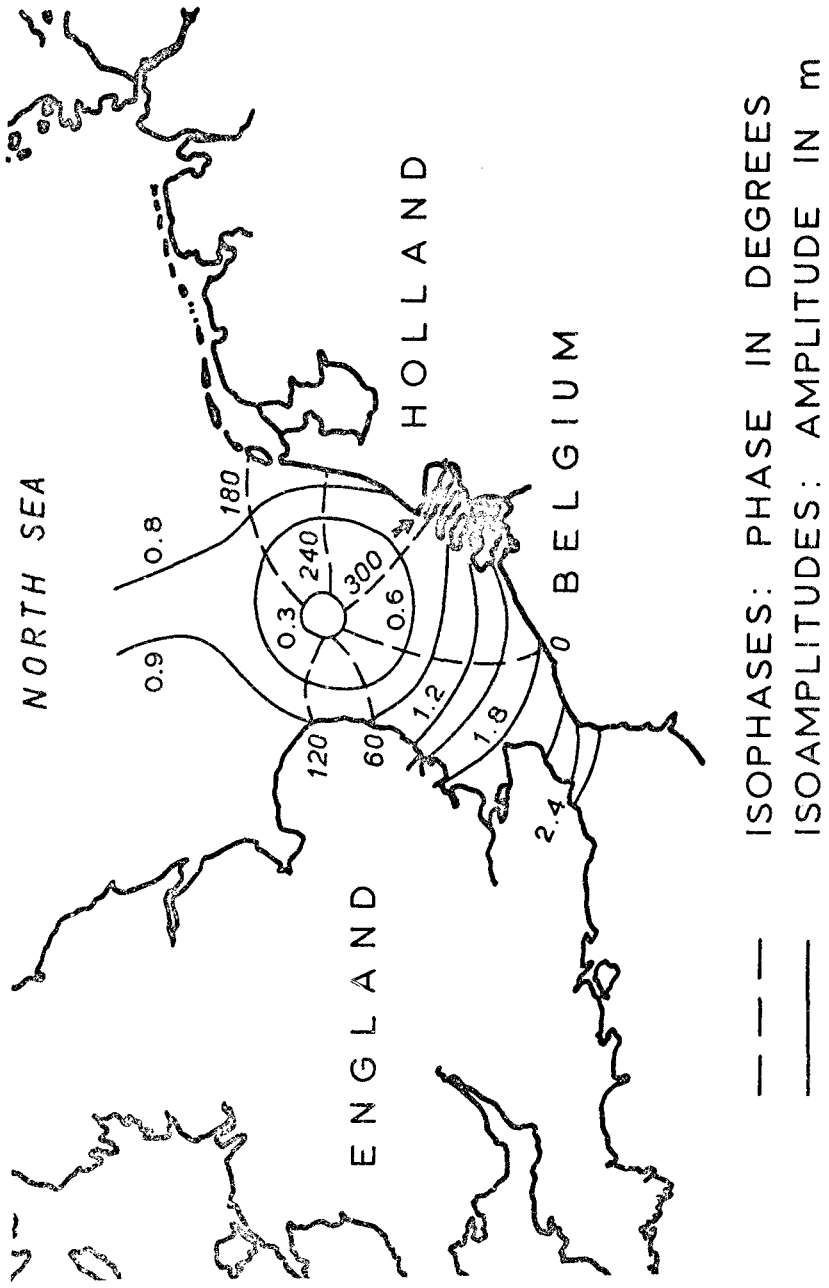
FIG.1   TIDAL CONDITIONS IN THE SOUTHERN NORTH SEA
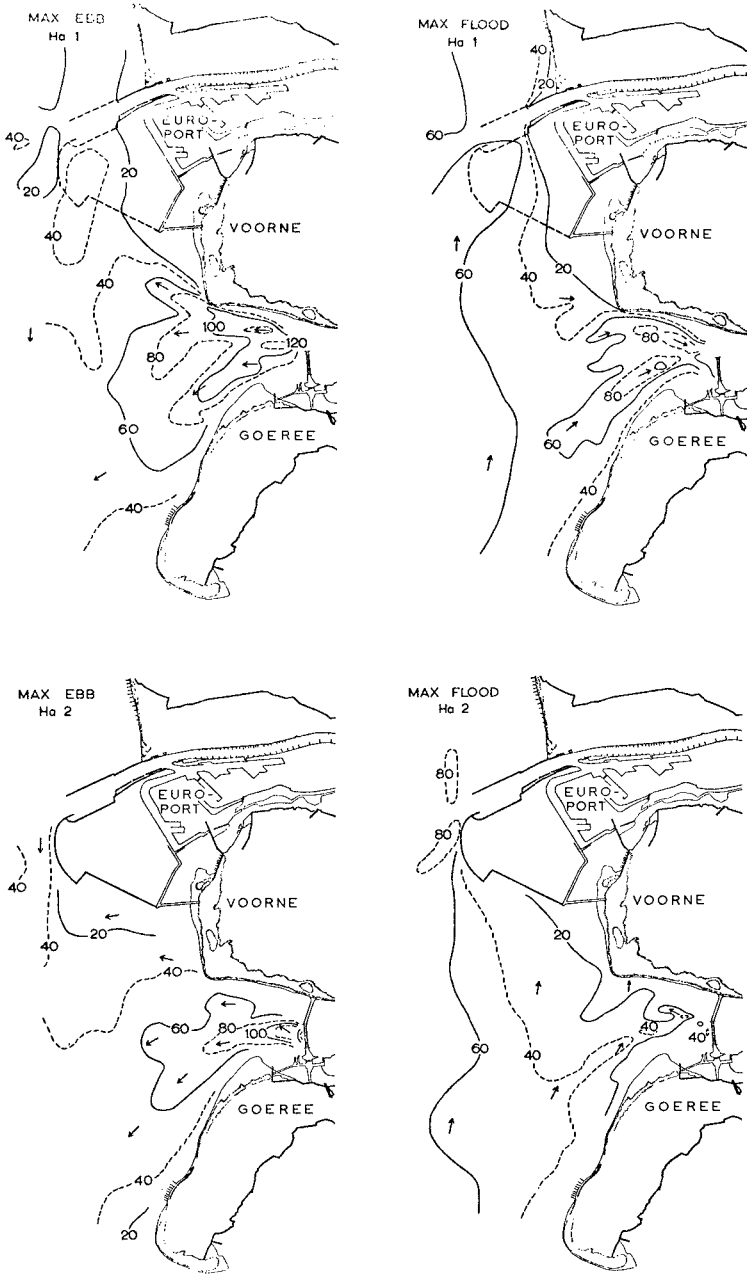
FIG. 2   LINES OF EQUAL VELOCITIES (cm/sec)
Ha 1   AND   Ha 2
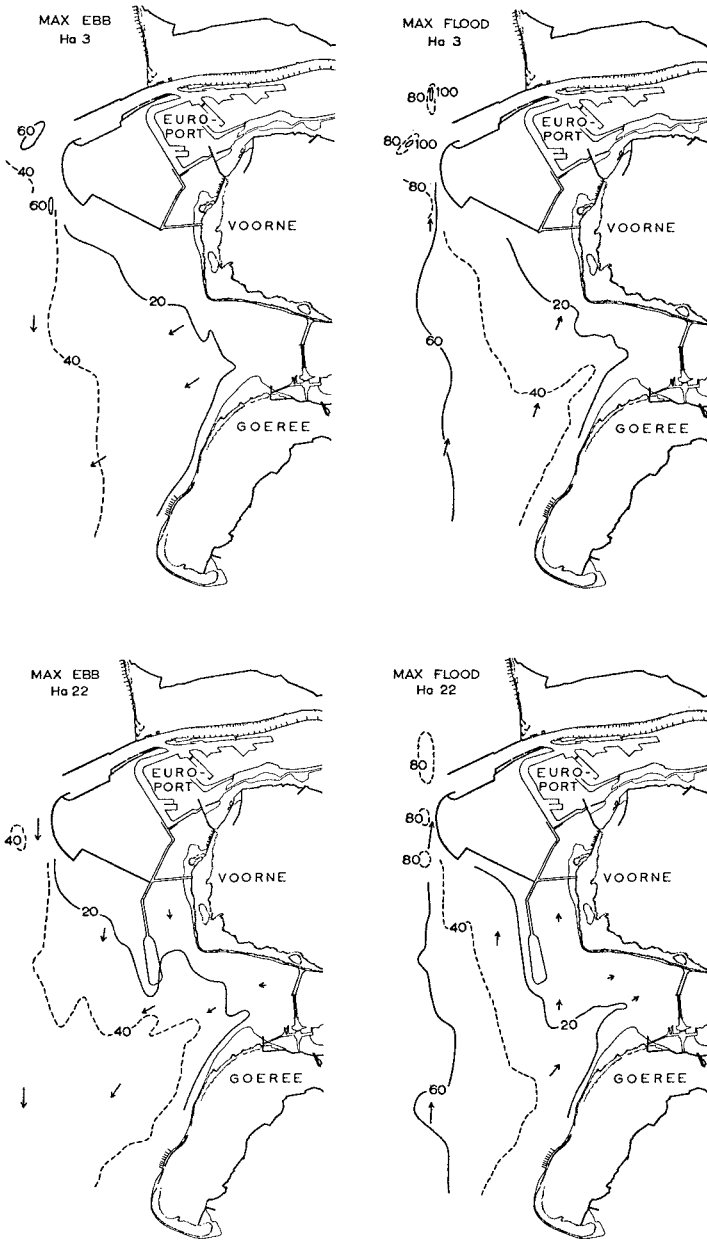
FIG. 3   LINES OF EQUAL   VELOCITIES (cm/sec)
Ha 3   AND   Ha 22
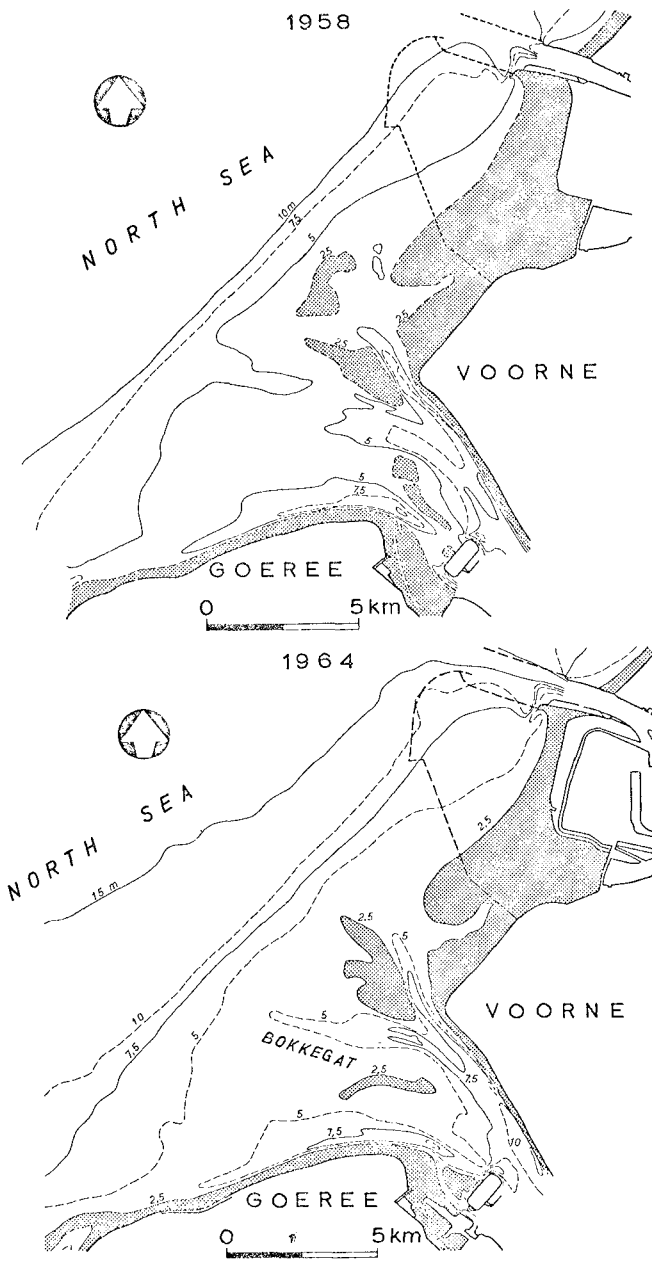
FIG. 4   SITUATION 1958 AND 1964
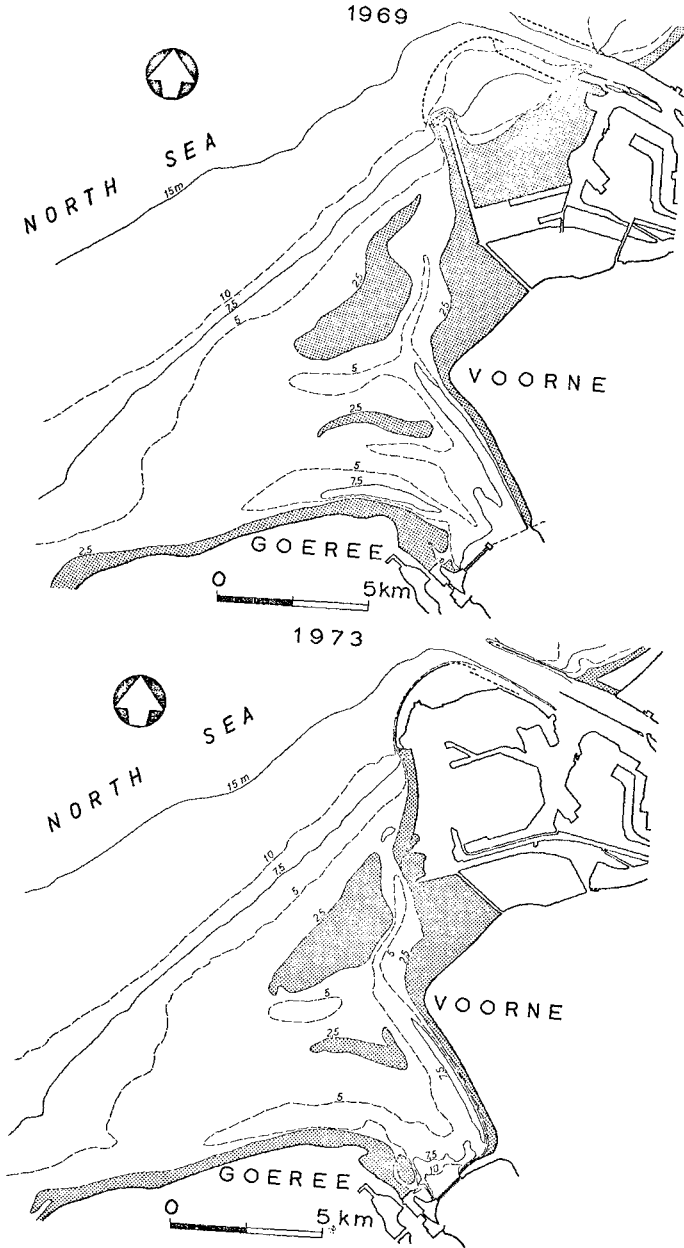
FIG. 5 SITUATION 1969 AND 1973
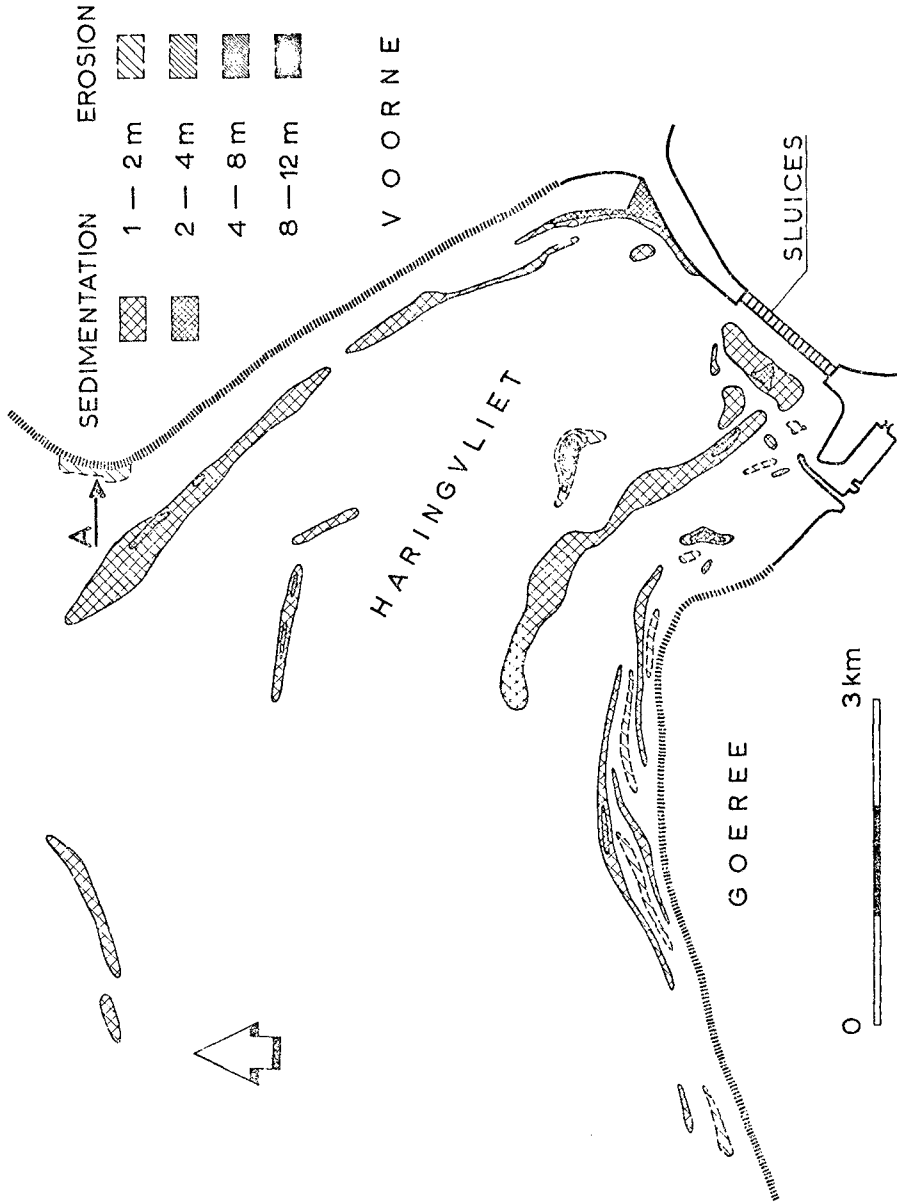
FIG. 6 MORPHOLOGICAL CHANGES 1969-1973
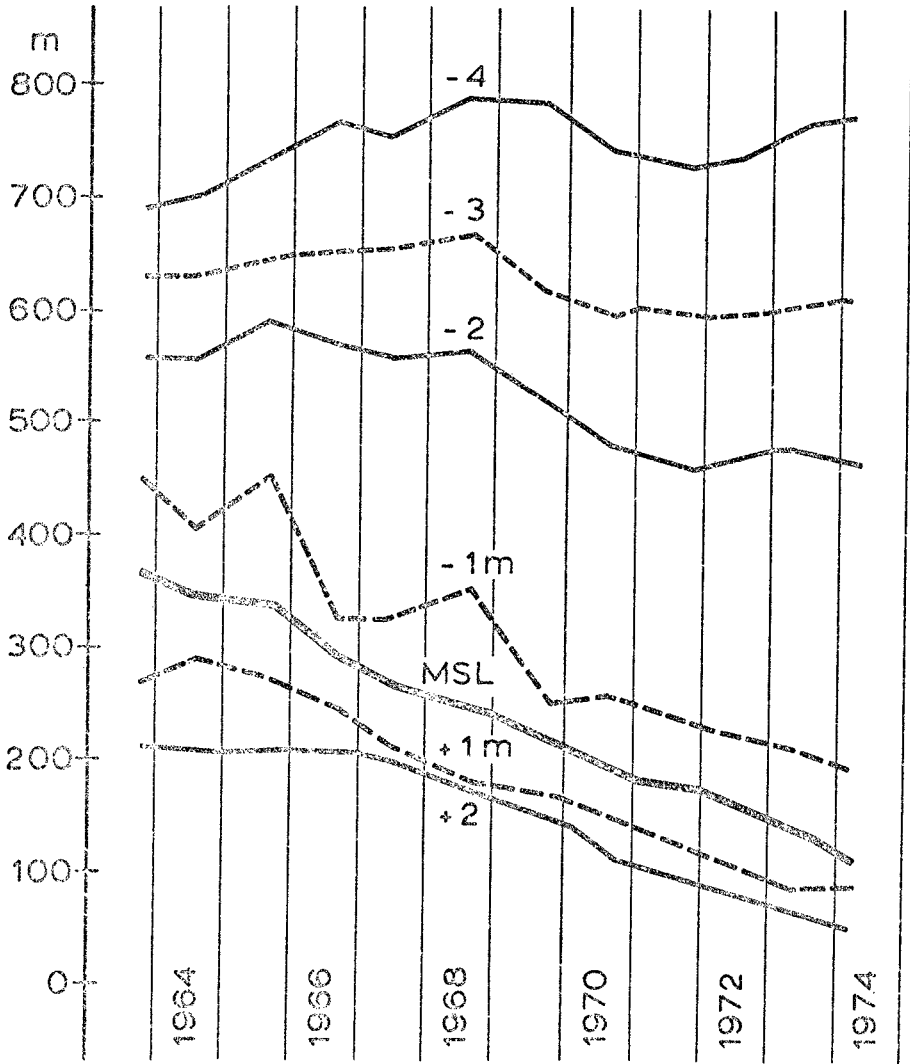
FIG. 7 EROSION OF VOORNE COAST
(POINT A OF FIG.6)

CHAPTER 147

NEW METHOD TO CLOSE TIDAL RIVERS

Hans-Gerhard Kniess
Wasser- und Schiffahrtsdirektion
Kiel, West Germany

The closing of tidal rivers is still a risky project as the
tidal flow alternates periodically its direction,velocity
and level.
On the last essential section of the Eider dam project a
new method for closing tidal rivers was invented and sucess-
ful operated.Contrary to common methods the main channel of
the river was closed only by hydraulic placement of sand
under protection of two permeable pile walls with perfora-
ted steel panels.

1.Construction site

About halfway between the Elbe estuary and the Danish border
the Eider River enters the North Sea.The Eider river forms
the most important outlet of water for the lower region of
Schleswig-Holstein with a drainage area of 2.000 sq.km.From
1967 to 1973 the estuarine mouth was closed by a 5 km long
dam with a 200 m wide sluice in order to get a safer protec-
tion against storm surges and more advantageous draining and
shipping.In the summer of 1972 the main channel south of the
completed sluice was to be closed.The opened sluice caused
only a little relief of the main channel in which the tidal
flow got a flood velocity up to 3 m/s.The tidal volume amoun-
ted to 45 million cu.m with an average range of 3.2o m.The
subgrade soil and bottom consists of silty finesand with in-
cluded clay.

2.Method

At first it was projected to close the main channel with two
walls out of stony material,but it became more advisable to
use only sand by hydraulic placement so that an easy and
quick reaction could become possible if any unexpected bot-
tom erosion would happen.It was necessary to invent a method
that protects the placed sand against the tidal race.The de-
mands were :   a safe and quick technical feasibility,
                 a kind flexibility to bottom erosion,
                 a low loading by impact of current and
                 waves and
                 little loss of sand.

2495

The solution : two rows of steel piles should be driven
through the river bed and between them perforated steel
panels should be installed so that sand could be deposi-
ted even during strong tidal flow.
In a second step the main construction characteristics
were investigated in a model test (Technical University
Hannover). The fig. 1 shows the main result : the optimal
shielding was to be expected with a perforation of the
panels between 20 and 30 per cent and with a distance of
the two pile walls between 15 and 20 m. For the further
design of the steel construction the static and dynamic
pressure of water, current and waves was estimated to a
loading of 1 Mp/sq.m.

3. Closing
In respect to the investigated characteristics the two
pile walls were constructed in a distance of 16 m to half-
frames which gave a good substructure for transport system
of material, machinery and other equipment. The perforated
steel panels were formed out of light steel sheet piles
in which holes of 10 cm diameter were stamped. The fig. 2
shows the schematic method in operation. The panels were
installed by portal cranes between the rammed piles so
that they reached just 2 m above the actual bottom level
inside of the pile walls. The filling sand was pumped by
a dustpan-dredger out of a depth between 30 and 40 m sea
level via two distribution carriages which alternately
connected with the central delivery pipeline. In this way
the filling sand could bei placed at the bottom with a
solid matter concentration of about 30 per cent and with
an output of 1.000 cu.m per hour of solid material. The
used sand consisted mainly of finesand with a mean grain
diameter of 0.2 mm.
Fig. 3 shows the current velocity distribution during the
closing operation. It shows a well distinguished sector
of the weakened current : inside of these shielding
sectors the sand settled and was demixed corresponding
to the respective flow velocity of its sedimentation.

FIG. 1

velocity distribution
by use of 2 perforated plates
(15 m distance)

within the hatched fields the specified current
velocity is lessend during n percent of the
the tide period

perforated plate   70% closure

n % of the tide period

current velocity
v < 30 cm/s

v < 20 cm/s

v < 10 cm/s

depth of filling
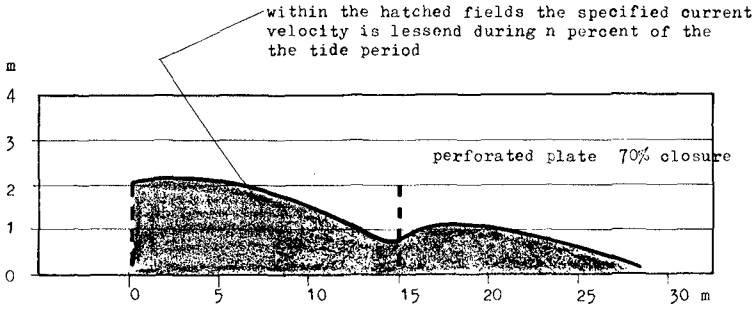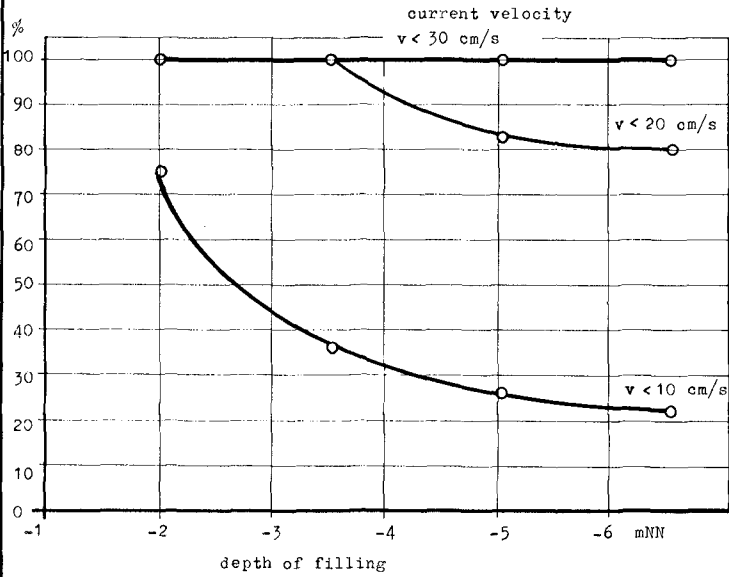
(NN = mean sea level)

FIG. 2
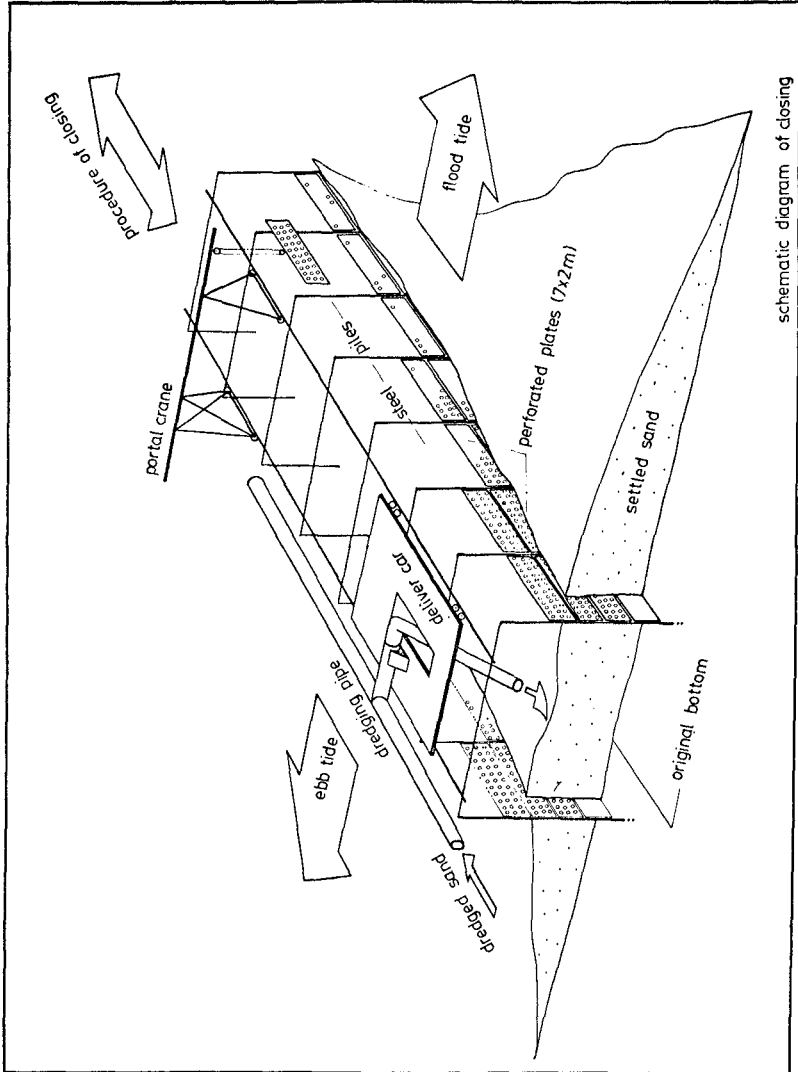
schematic diagram of closing

procedure of closing

flood tide

portal crane

steel piles

perforated plates (7x2m)

settled sand

deliver car

dredging pipe

ebb tide

dredged sand

original bottom

FIG. 3

current velocity
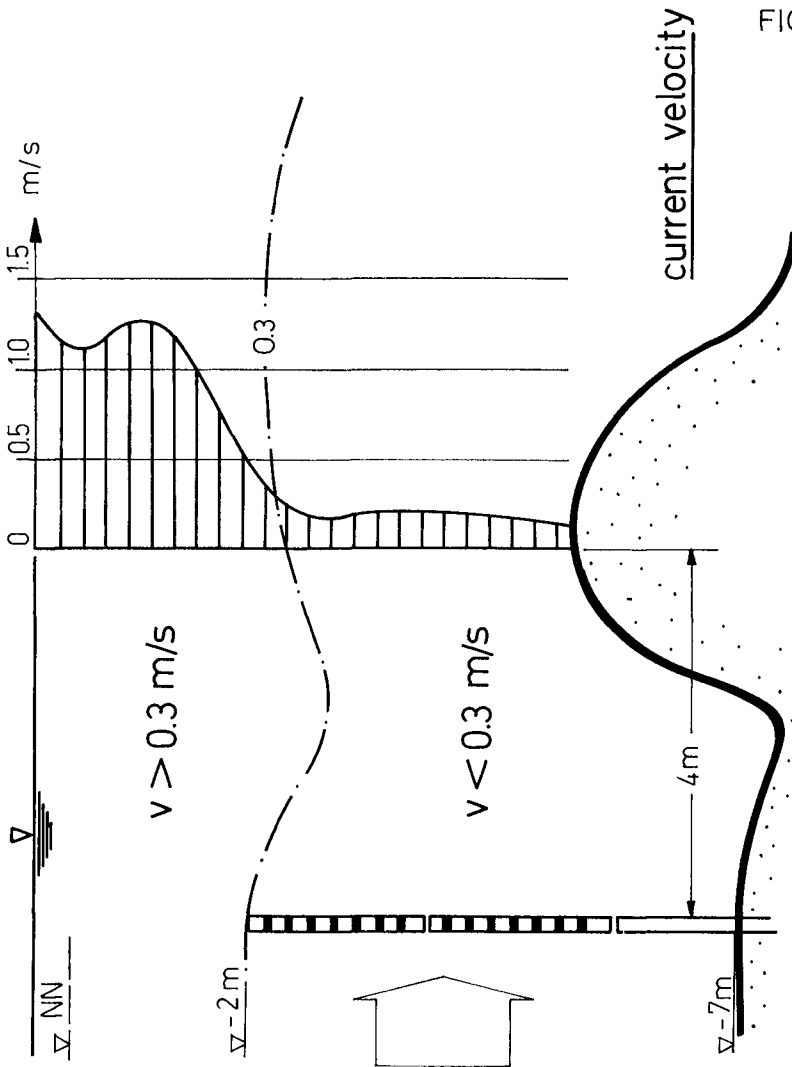
The under water slopes outside of the pile walls became
a good indication of the coincidence between model test
and nature. The fig. 4 shows in a cross-section the slopes
at two different times of closing.
The sequence of closing from the original bottom to high
water tide is shown in the fig. 5. The under water slopes
varied their inclination corresponding to the height of
closure and to their depths. To demonstrate this variation
the slopes in the sections of 10, 8 and 5 m under mean
sea level were separated and are shown in the fig. 6 as a
relation between height of closure and depth of section.
The slopes flattened after installation of panels, became
steeper with filling of sand and finally stabilized with
an inclination between 1:10 and 1:20 - corresponding to
the mean grain diameter of sand.

The main channel was closed within 6 weeks up to high
water tide with about 600.000 cu.m of sand inside and
outside of the pile walls. A saving of about 40 per cent
to other common methods could be achieved. This point
may emphasise the practical use and technical feasibility
of this method.

FIG. 4

FIG. 5

Temporary sequence of closing

FIG. 6

height of
closure

(mean sea level)

slope inclination

5 —— slope inclination between NN-4m and NN-5m
8 —— " " NN-7m " NN-8m
10 —— " " NN-9m " NN-10m

a = sea side , b = inner side
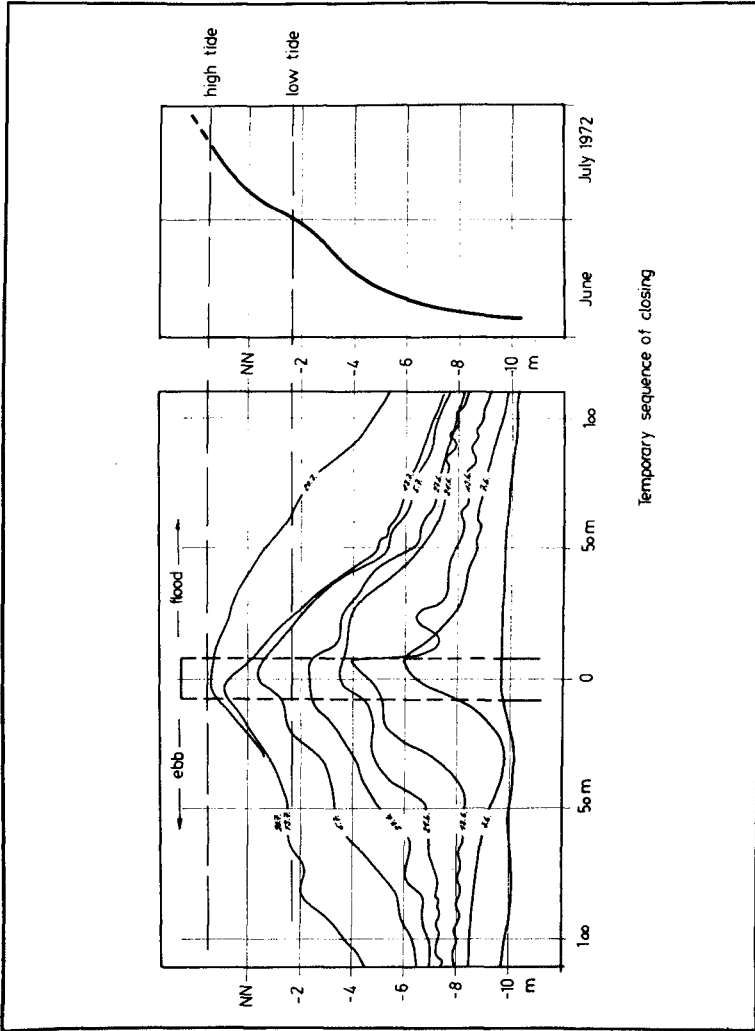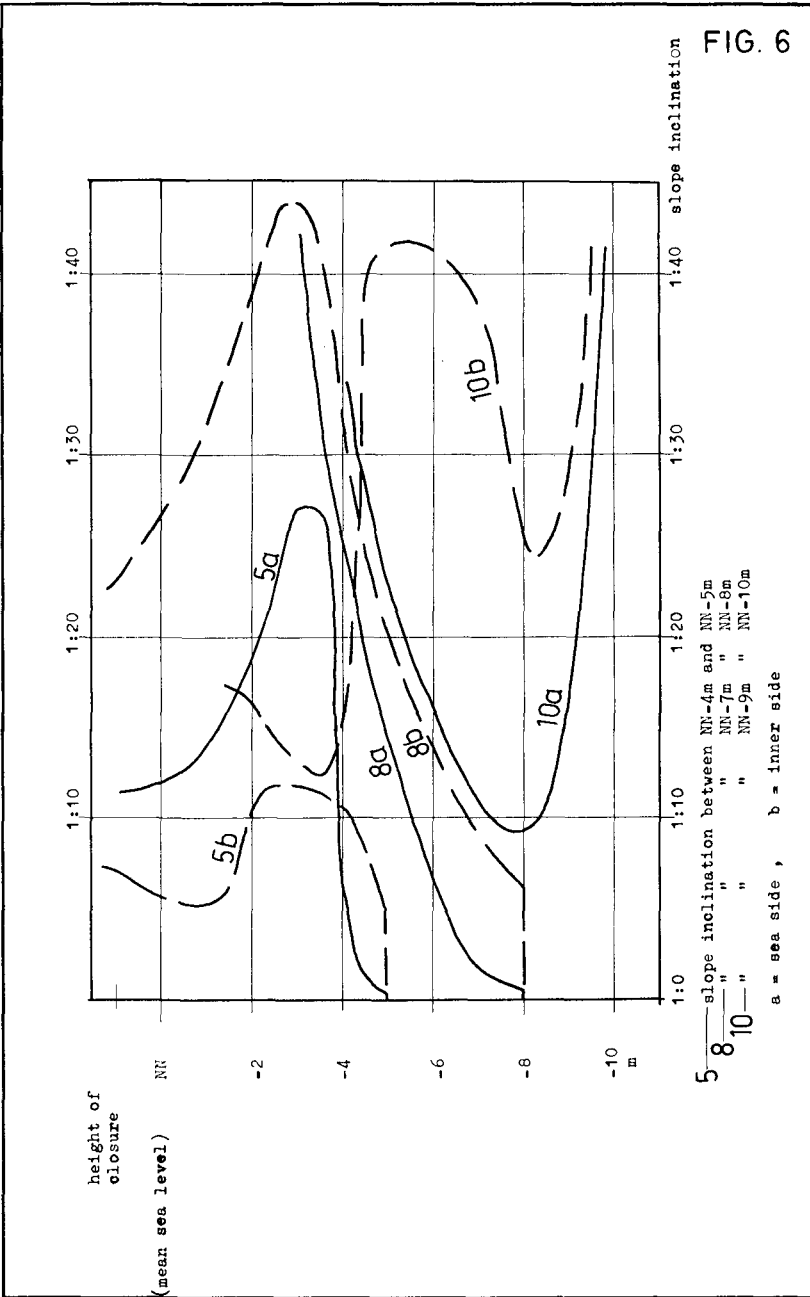
CHAPTER 148

AERIAL PHOTOGRAPHIC WATERLINE|SURVEY OF AN ESTUARY

by

J. Sindern and G.E. Schröder,

Wasser- und Schiffahrtsdirektion Kiel,
D23 Kiel, Hindenburgufer 247, Germany.

Abstract.

The project of a barrage across an estuary in
Northern Germany was accompanied by a programme to
monitor the hydrologic and morphologic situation.
This became necessary in order to avoid dangers
resulting from the sensitivity of the shallow wadden
area to human interference.
Various methods to record the morphology were tested.
The aerial photographic waterline survey proved
superior as it supplies a complete and economic
record and allows accurate analysis of the topography.
                          The principle consists in
taking aerial photographs at short time intervals
between low water and high water, each photo showing
a different waterline. The scale chosen was 1:18000,
corresponding to a flight altitude of 2700 metres.
Rectification of the distorted photos requires
reference markers to be distributed over the survey
area which measures about 140 km^2. By using simultaneous
tide gauge records, contour lines can be constructed
from the photographed waterlines.
This morphologic record is supplemented by submarine
survey of the estuary. It is expected that details of
sediment transport and of tidal prism changes may be
revealed. Predicted and actual effects of the barrage
will be compared, which might lead to a better under-
standing of such coasts.

1. <u>The necessity of monitoring morphologic changes.</u>

Aerial photography is certainly not new in coastal engineering. Here we shall have a closer look at the waterline method which differs from the conventional aerial photographic survey in several respects. Since 1965 the Wasser- und Schiffahrtsverwaltung (i.e. Federal Waterways Administration) in Germany applies this method, so that it should be possible now to report on its suitability.

In order to appreciate the need for monitoring an estuary, a brief look at the area concerned might be helpful. (Figure 1). Off the German North Sea Coast spreads an instable and shallow wadden area. Tidal flats, sand banks and channels shift frequently, especially in the funnel-shaped mouths of four major rivers. The tide is semi-diurnal and has a mean range in the order of three metres.

The particulars of the wadden area affect the tidal characteristics, the sediment transport as far as it is related to the tides, as well as energy and direction of waves attacking sea walls and eroding beaches. Thus, changes in the wadden area may result in an increased threat to the shore. Morphologic changes are important for shipping, too, which in this region is confined to a few navigable channels.

Some changes of the local morphology are expected as a result of a barrage built across the Eider estuary and completed in 1973.(Figures 2 and 3). It is about 5 kilometres long and allows to control the discharge of the river. Thus it is hoped to maintain a cross section required for draining the low marshes upriver. In addition, it serves as a flood barrier. Before the planning and hydraulic model tests started, the existing hydrologic and morphologic situation had to be recorded. During constructing changes had to be detected in time in order to allow the prevention of dangerous developments. And now, after completion, the actual effects of this interference with nature will be established and compared with the predictions as supplied by the model tests. Observations will continue until we can be sure that unfavourable changes are no longer likely to occur.

2. <u>Requirements and methods of morphologic monitoring.</u>

Morphologic monitoring is concerned with :

Fig. 1   Location of the Eider estuary.

Fig. 2   Location of the survey area and distribution of reference markers.

(Part of Chart D 103, with kind permission of Deutsches Hydrographisches Institut, Hamburg)

Fig. 3   The Eider flood barrier.

1. location, shape and elevation of those tidal flats
   lying above a certain level (in this case NN, which
   is the general reference datum, minus two metres).
2. location, shape and depth of channels.

The first requirement is to detect rapid changes in
the wadden area equally rapidly, because of their
potentially dangerous consequences. The necessary
qualitative information is supplied about every three
months by aerial photography at low water. The shape
of the waterline is compared with that on earlier
photographs to reveal changes. (Figure 4). Secondly,
a quantitative record of surface and submarine topography
should be obtained economically, and with some reliabi-
lity. It might be mentioned that the wadden area is
extended, but shows small height differences only. The
accessibility depends on the tide, and so a boat is
required in most cases. It is those particulars which
determine the suitability of the various survey methods,
mainly:
1. levelling,
2. aerial photography for stereophotogrammetric survey,
3. aerial photographic waterline survey,
for channels: echo-sounding with radio position-fixing.

With levelling, the stations are 100 to 150 metres apart.
The rate of progress depends largely on accessibility and
thus on the tide. About 0,5 km^2 may be covered per tide,
according to Lolezal (1952). The results are fairly
accurate, unless the factor t i m e is considered. For
in that case it becomes obvious that, with reasonable
expense, levelling cannot be accomplished as fast as a
tidal flat sometimes shifts or changes its shape. Thus it
is hardly ever possible to record the shape of the whole
area as at a certain time. Further uncertainty arises
from the difficulty to definitely derive shape and position
of contour lines from the heights of solitary points.
(Figure 5).

Stereophotogrammetric evaluation of aerial photographs
does not supply a true topographic record either. Lack
of contrast, in addition to an often nearly horizontal
surface, almost prevents the successful use of the
stereoplanigraph. Furthermore, unfavourable illumination
of a wet wadden surface sometimes reverses the grey shades
and causes misinterpretation of the relief. These
difficulties may be overcome only by flying rather low,
or by a considerable amount of additional levelling,
both of which make the whole operation too expensive.
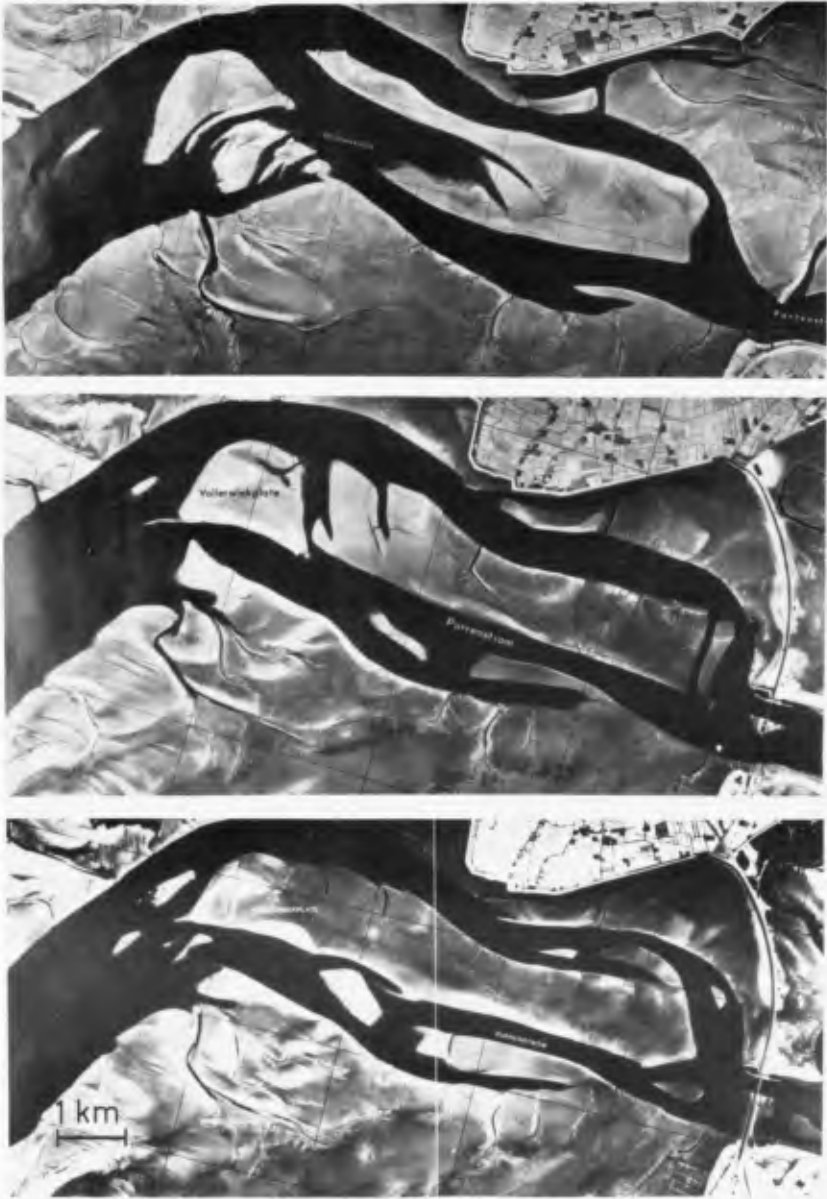
Photos: A.Hüpke

Fig. 4   Low water photographs of the Eider estuary in
          1966, September (top)
          1972, March   (middle)
          1973, May   (bottom).
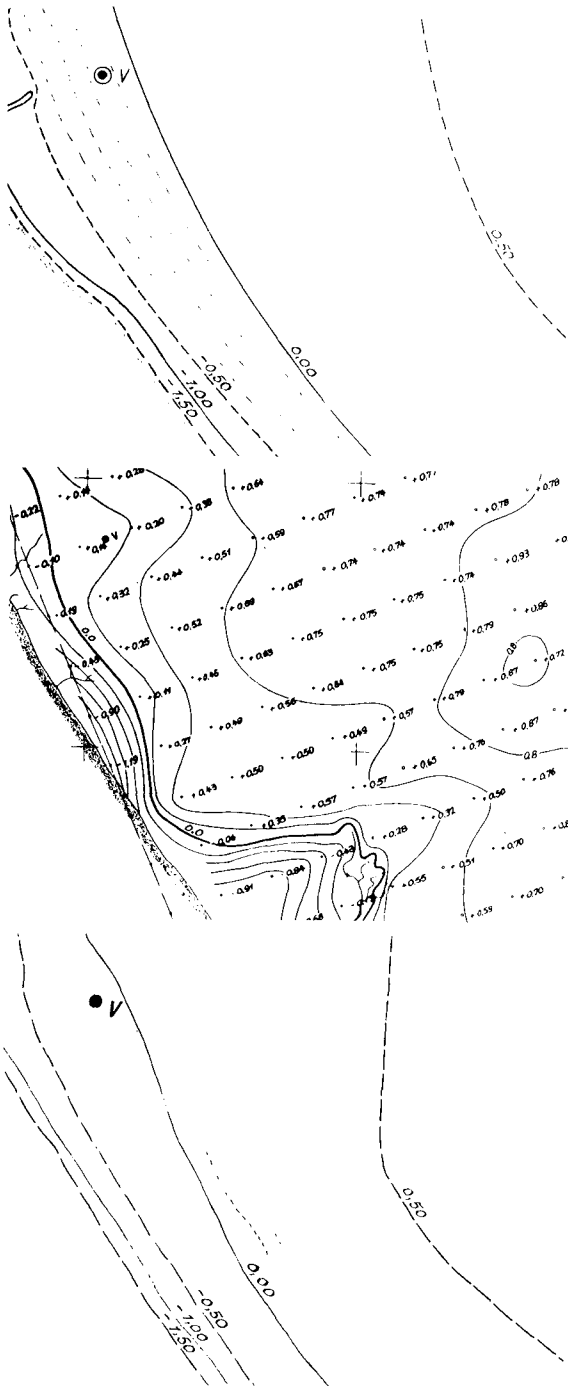
Fig. 5   Contour lines of the same area, constructed
          from data provided by
             levelling   (top)
             aerial photo,stereophotogrammetric survey (middle)
             aerial photographic waterline survey   (bottom).

3. Aerial photographic waterline survey.

Because of these drawbacks we looked for a method
allowing to record the topography completely and
instantaneously, and yielding reliable contour lines.
The publication "Mapping the low water line of the
Mississippi Delta" by William Shofnos and Bennett Jones
in 1960 encouraged us to do some experiments. They led
to the waterline method as it is used now for surveying
the Eider estuary every second year.

The principle is straight forward. Beginning at low
water, aerial photographs from the survey area are
taken at short time intervals until the flood tide
has covered the tidal flats. Each series of photos
shows a different waterline. (Figure 6). With the help
of tide gauge records horizontal contour lines can be
derived from the waterlines.

The survey area measures about 21 by 6,5 km. (Figure 2).
Figure 2 shows also the location of the reference points.
At least three, preferably four of them should be visible
on each single photograph in order to enable rectification
of the distorted photos. Accordingly, their maximum
distance depends on size, scale, and degree of over-
lapping of the pictures. In the present case, distances
vary between 1,7 and 3,2 km, according to the suitabili-
ty of the locations. The coordinates are determined
conventionally. On the photographs the reference points
should allow to be identified clearly, both against the
light background of a sandy surface and against darker
mud. Unfortunately, only very few sufficiently conspicuous
natural points are available, so that a number of arti-
ficial markers has to be set out. Their design was
chosen with easy identification and handling in mind.
(Figure 7). A shape of three white discs in triangular
arrangement on steel tubes stuck into the ground
proved suitable, i.e. reasonably portable, robust and
cheap. Erecting and surveying the twenty-odd markers
takes about two weeks.

For the evaluation later on the sea level heights at the
time of photographing will be required. The density of
the stations should be such that accuracy does not
suffer from the assumption of a linear sea level slope
between two adjacent tide gauges. Therefore, the five
permanent gauges are augmented by five to six provisional
portable ones, also self-recording. The coordinates are
established by conventional survey. To transfer the
reference datum to a gauge turned out to be a good
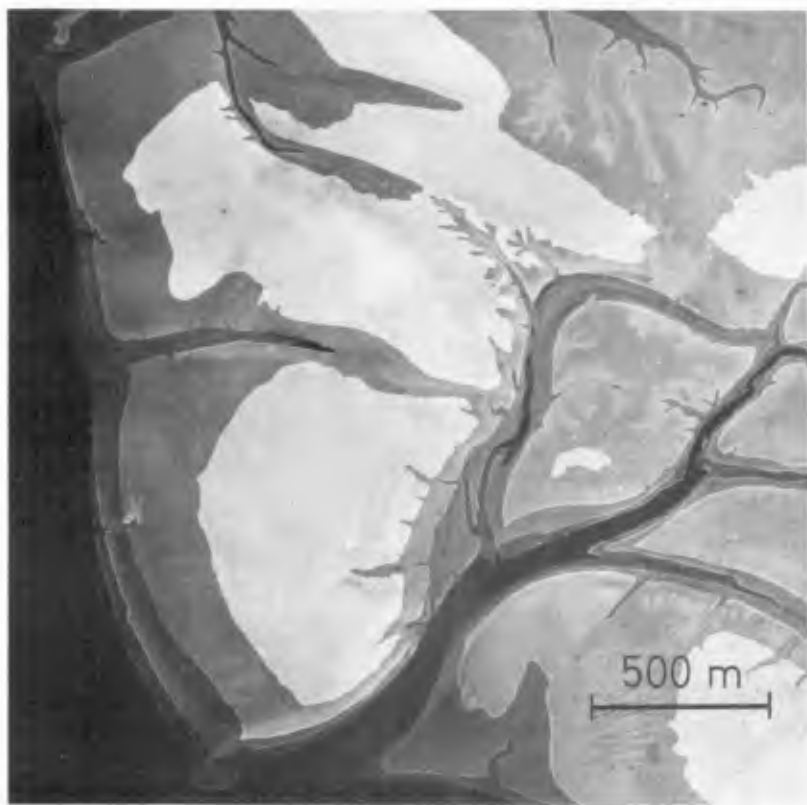
Fig. 6   The waterline, photographed
          at 45-min-intervals.
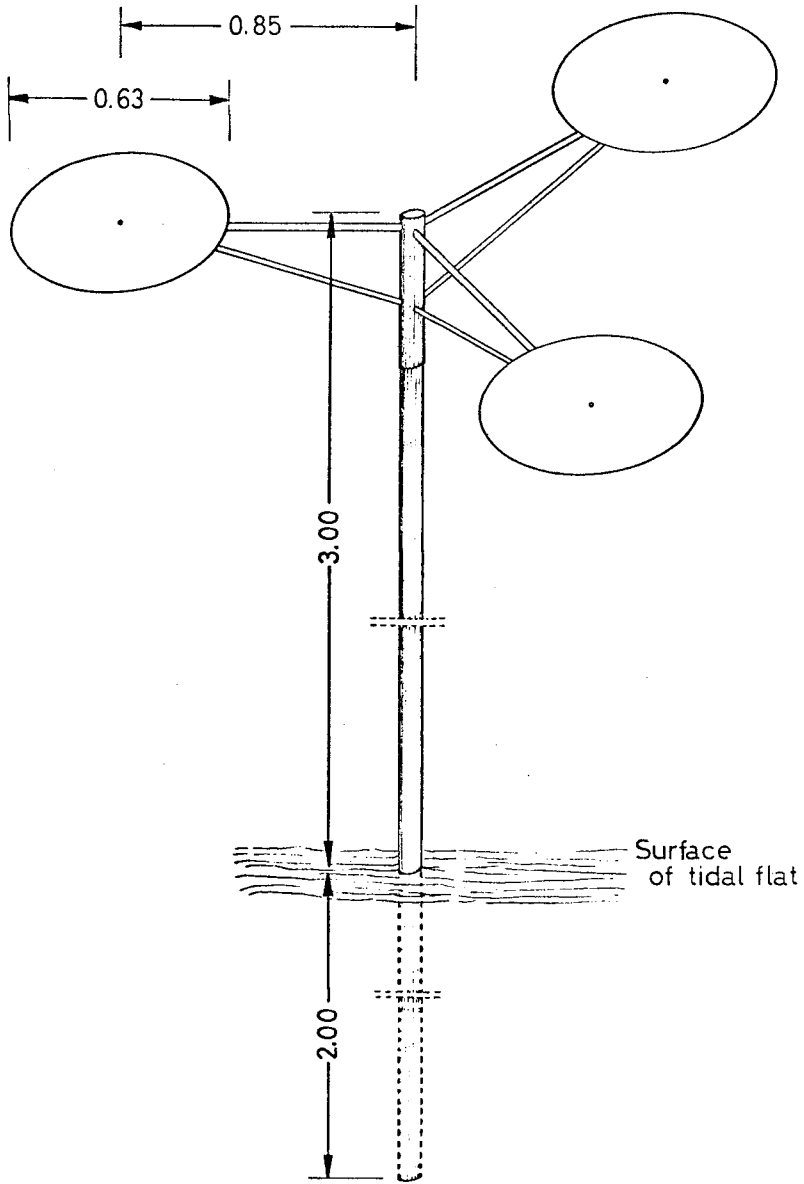
Fig. 7   A reference marker

opportunity to measure the heights on the way for
additional checks.

The quality of the photographs depends also on the
types of film and camera. Infrared film is used,
because even thin layers of water are shown completely
black, and cloud shadows and slight haze are suppressed.
Very accurate exposure and developing are essential,
however. The pictures are taken with an automatic
serial camera with Pleogon objective and a focal
distance of 15 cm. The negatives measure 23 cm square.

To choose the scale usually means to accept a compromise
between accuracy and economy. Experiments have shown
that at a flight height equivalent to a scale 1 : 20 000
the quality of the photos is already affected by an
omnipresent layer of slight haze, even if infrared film
is used. At the other end of the range a scale of
1 : 6 000 supplies excellent pictures. Here, however,
the expense for more reference markers and evaluation
of a great number of photographs makes scales as large
as that less economic. We ended up with 1 : 18 000.
Then the resolution of the film allows good enlargements
to the working scale 1 : 10 000. Longitudinal overlapping
varies between 60 and 80%, laterally the pictures taken
along two flight stripes overlap by about 20%.

The flight date can be fixed in advance only provision-
ally. Sometimes it requires a bit of patience to wait
for the day with favourable conditions. Because of the
length of daylight the months from April to September
are more suitable in this latitude. The entry of low
water and the position of the sun determine the start
of photographing. A complete flight programme takes up
to four hours, so that sunshine and a clear sky should
last as long, because of their importance for the quali-
ty of the photos. If there is too much wind, flights are
better postponed, as even small waves reduce the
distinctness of the waterline. Direct communication
between field crew (three men on a shallow-draught
survey launch) and aircraft crew are of great value.
Immediately before the flight, the field crew checks
the reference markers and the tide gauges. Via VHF
telephone the tide gauge clocks are then compared with
the camera clock.

Evaluation consists mainly in rectifying the photos
and constructing contour lines. After the flight, the
contractor who made the photos submits contact copies

on which we try to identify the reference points. Then
the contractor rectifies the distorted photos, using
the coordinates of the points, and supplies selected
enlargements on special sheets insensitive to variations
of humidity and temperature.

The next step is the construction of the contour lines.
(Figure 8). Provisional contour lines are obtained from
the photographed waterlines together with the lines of
equal sea level heights as derived from the tide gauge
records. Of course both must refer to the same time.
However, a lateral downward slope of the sea level in the
immediate vicinity of the waterline has not yet been
taken into account. As it varies spatially and tem-
porally, recording and analysing would be too expensive
for the purpose dealt with here. Instead, a few additional
profiles are levelled to establish the final location
of the contour lines, the shapes of which are already
known. These profiles are about four kilometres apart,
with stations every 20-50 metres. This survey immedia-
tely after the flight takes about a week.

4. Survey of channels.

The assessment of the morphologic situation requires
the knowledge of the submarine topography as well.
For this purpose the underwater forms are surveyed by
recording echo-sounder while the launch navigates along
the hyperbolae of a radio position-fixing system. The
results of this survey, too, are transferred onto the
working maps mentioned earlier.

5. Result and further work.

Finally, proper charts in the scale 1 : 25 000 are
prepared on the basis of the working maps. They supple-
ment existing but less accurate charts of the adjacent
coastline and will perhaps replace them in due course.
(Figure 9).

With these new charts it should be possible to monitor
sediment transfer and changes of the tidal prism more
accurately and over long periods. In the case of the
Eider barrage, the predicted and actual effects can be
compared. If it were possible then to more closely relate
hydrologic and geologic data to the morphologic history
of this type of coast, the nature of their inter-
dependence might become clearer.

Reference:

Sindern,J., und Kathage,F.,
Das Wasserlinienverfahren (Serien-Einzelbildmessung) -
            eine neue Art der Wattvermessung,
Deutsche Gewässerkundliche Mitteilungen, 6/1966,p.182-189.
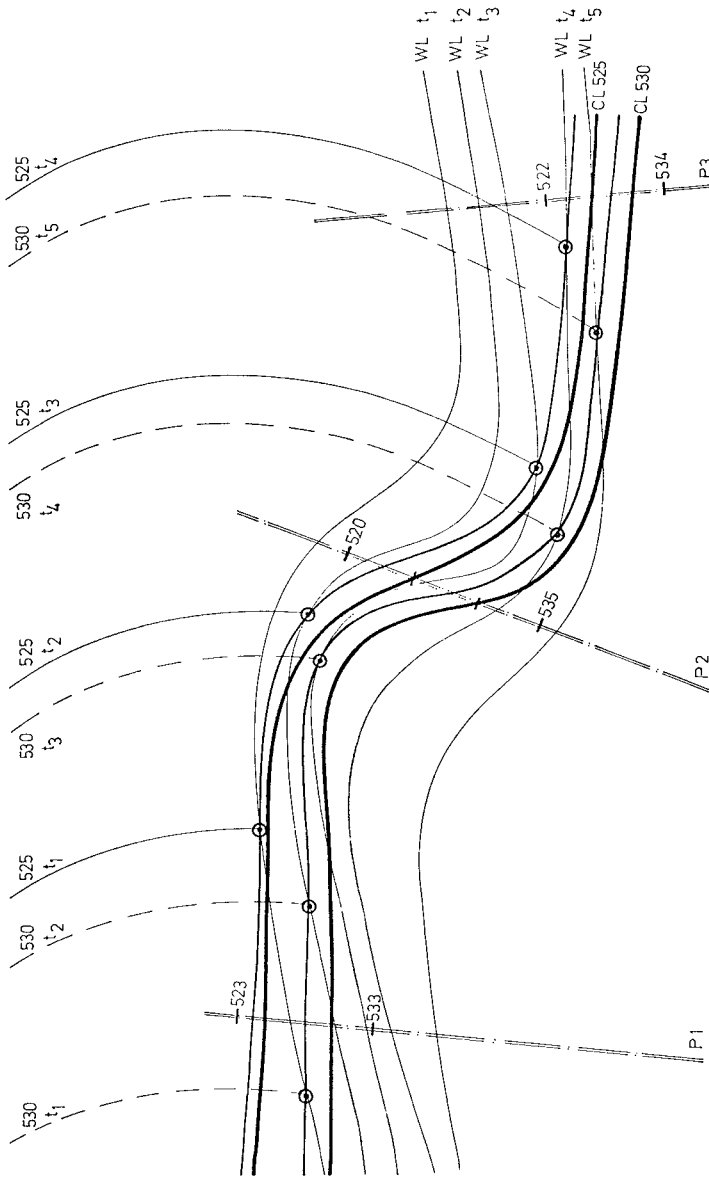
WL Waterline

CL Contour line

P Levelled profile

Fig. 8   Construction of contour lines from
         sea level heights at different times t_n,
         waterlines at different times t_n,
         and additional levelled profiles.

Fig. 9   Part of the final chart of the
Eider estuary as in July 1966.
Black dots indicate positions of tide gauges.

CHAPTER 149

SEA-LEVEL MEASUREMENTS IN THE WASH BAY

1. Introduction

A report (Binnie and Partners, 1965) on the water resources of the Great Ouse Basin put forward proposals for storage in the Wash of fresh water from the four rivers draining into the bay. The scheme suggested was to take the form of a barrage, enclosing about a third of the area of the bay, behind which fresh water would be stored in raised impoundments. Four years later (Binnie and Partners, 1970) this proposal was superseded by a scheme for storage in bunded reservoirs built on the foreshore at the head of the bay. The current Wash Feasibility Study (commenced in 1971) is expected to highlight the most suitable scheme of this sort following a programme which includes field data collection, hydraulic and mathematical model testing and site investigations. The scheme as currently envisaged would take the form of bunded reservoirs built (largely from dredged sea bed material) on the foreshore close to the outfall of the river Great Ouse and connected by tunnel to intakes on that river, and later on the river Nene. To meet increasing demand further impoundments could be built along the foreshore to store water drawn from the other rivers draining into the Wash. Figure 1 shows a possible reservoir scheme which is among those being considered. Continuous sea level observations have been made at 4 points in the Wash bay (figure 1) using automatic level recorders. The purpose was to provide information on tides and surges in connection with the feasibility study.

2. Description of the Wash

The Wash is a bay on the east coast of England facing the North Sea. Almost all the drainage into the bay is carried by the four principal rivers (Figure 1) which debouch at its head. Nearly one sixth of the catchment area of these rivers lies below high water of ordinary spring tides and consists of alluvial deposits resulting from successive reclamation works dating from Roman times, and from settlement of suspended solids in the bay water. All the four rivers are navigable for a considerable distance inland from their outfalls but virtually all marine commercial traffic now goes to King's Lynn on the Great Ouse, Boston on the Witham or Wisbech on the Nene.

Apart from a few kilometers of cliffs on the north-east shore, the Wash is almost entirely bounded by man-made coastal defence works. Extensive sand and mud flats have formed on the foreshores and from time to time new land is reclaimed to agriculture by construction of a new sea defence bank.

The bay is about 28 km long and 25 km wide. It narrows at the mouth to about 20 km. The volume of sea water entering past the mouth is about 3500 million m^3 on a mean spring tide (whose range at the mouth is almost 6m). Spring ranges of 8 m or more occur from time to time.

1. Institute of Oceanographic Sciences, Bidston Observatory, Birkenhead, Merseyside, England.

2. Binnie & Partners, Artillery House, Artillery Row, Westminster, London, England.
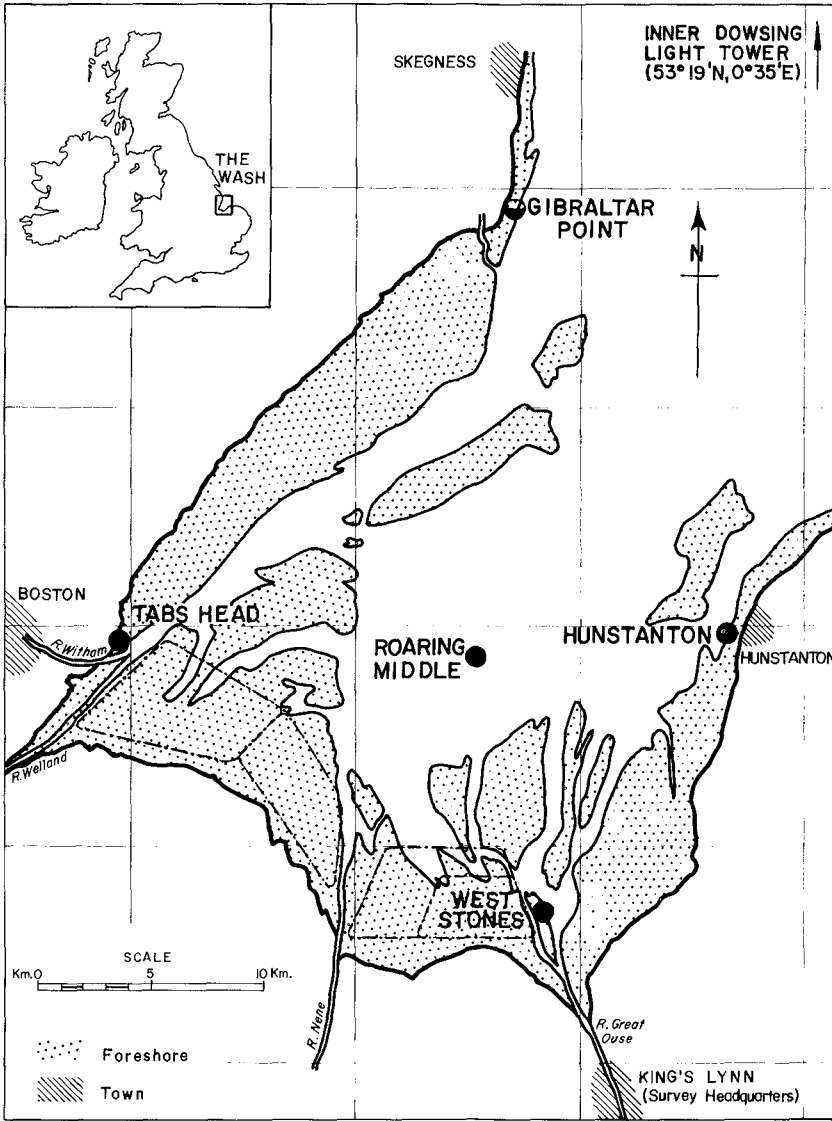
FIG.1 : LOCATIONS OF TIDE RECORDING STATIONS

High water is almost simultaneous throughout the Wash bay, being about 10 minutes earlier at Gibraltar Point than at West Stones and Hunstanton. The difference between high water levels measured at the head of the bay and those at its mouth is typically about $\frac{1}{2}$m (springs) or $\frac{1}{4}$m (neaps).

3.   Requirements for tidal recording

The level recording instruments were chosen and sited to provide information relevant to several aspects of the scheme including the following:-

    i.   mathematical models of the Wash bay and of the
             tidal portion of the river Great Ouse

   ii.   hydraulic model (1:100V, 1:1250H) of the Wash bay

  iii.   sea bed survey relating to design and construction

   iv.   design and construction of the enclosing bunds from
             dredged sea-bed material with the highest possible
             use of local materials for surface protection

    v.   measurement of the effect on water levels in the
             Wash of local wind set-up and of North Sea surges

   vi.   programming of the final closure of each reservoir
             bund against the tide

  vii.   prediction of sea-bed changes in the bay consequent
             upon construction operations and reservoir location.

The nearest permanent gauge on the North Sea coast is at Immingham, about 70 km north of the Wash entrance. There are automatic recording gauges at King's Lynn, Boston and Sutton Bridge but they are not well placed for the purposes of study. The King's Lynn record has, however, helped in analysing the progress of certain North Sea surges, including that of 1953 which was associated with disasters in both England and the Netherlands. Tides are predicted from Immingham predictions, for certain points within the bay on the basis of observations lasting about a month. The most recent series of such observations was carried out by the Hydrographer to the Navy in 1968 at Skegness, Hunstanton and Tabs Head. The resulting predictions are accepted as adequate for navigation purposes but were not good enough for the feasibility study.

In order to understand the existing tidal circulation in the bay and obtain sufficient information about predicted tides and surges at the most important points, there was a need for accurate records at the mouth of the Wash bay, along its coasts and at the proposed construction sites. At least one year's record from each of these places was needed to evaluate the main tidal constants, to analyse the incidence of storm surges, and to judge the local effects of the sea bed shape on both tide and surge. Initial proposals were based on a single deep-water recording gauge at a site in the Wash mouth with two more gauges on the edge of the bay but considerations of cost, accessibility and operation resulted in the choice of West Stones, Tabs Head, Hunstanton and Roaring Middle as automatic recorder sites.

At Gibraltar Point, which is on the North Sea coast adjacent
to the Wash entrance, sea levels were observed against a line of
six tide poles at 15 minute intervals continuously for a month by
a team of six and completed the geographical coverage of simultan-
eous observations.

The accuracy required in measurement of levels was determined
by the hydraulic model and was of the order of $\pm$ 0.025 m. While
this is not difficult in calm conditions, it is very demanding in
a stormy area such as the Wash and was an important consideration
in the choice of instrument.

4.   Selection of instrument type and recorder sites

The principal considerations which governed the type of
instrument chosen are listed in table 1 which shows how each of
the commercially available types compared.

The Wash is an area of intense inshore fishing activity and
the main river outfall channels are important seaways for vessels
up to 3000 tons. The areas of greatest interest in engineering
terms are dry or covered to only shallow depths during most of
each tide. Any deep water channel which might have seemed
attractive as a site for a pile-mounted recorder of the stilling-
well type was inevitably part of a channel on which inshore
fishermen depended at low water. Accordingly, there would have
been strong opposition to any system dependent on piles in deep
water. It was an important factor leading to selection of a
pneumatic instrument which can be mounted out of the deep channels
and needs only a very small and innocuous sensor below the low-
water mark.

Apart from the navigational considerations, any solution
which involved a pile in water deep enough to allow the whole
tidal cycle to be monitored was bound to be much more expensive
to support than one on a sand bank, because of the greater
unsupported length in water. This cost penalty would be even
greater if a mechanical system were used so that verticality of
the pile became important. There was a reluctance too, in the
light of experience in similar waters elsewhere, to rely on any
form of electrical or rigid mechanical link between sensor and
recorder. Repairs to such links can be costly and time-consuming
as would be the initial installation. A gas-filled tube, on the
other hand, although no less vulnerable, offered the following
advantages:-

a cut or leak in the tube would merely cause the pen to
move to zero on the chart with no serious damage,

a replacement tube length would be both cheap and easily
stored with the recorder,

replacement or reconnection could be carried out even in
moderately choppy weather provided access could be had to
the severed part attached to the sensor; once the tube
link was restored, the system could be quickly brought
back into service by purging the tube with gas.

Feature	Type of instrument		
	Stilling Well	Seabed mounted	Pneumatic
Accuracy	Good if carefully designed & maintained	Unknown	Good – but system parameters
Cost	Relatively low but pile expensive	High	High but accurate alignment unnecessary
Navigational obstacle	Yes	No	No
Vulnerability	Fairly High	Fairly High	High (tube and sensor only)
Repair costs	High	Very High	Low
Accessibility	Boat need at all locations		Boat needed at only two of four locations
Degree of Development (in 1971)	High	High (overseas model). Well advanced but not commercially available (UK)	Basic design well established but relatively untried at remote coastal location
Dependent on density of water	Yes (Lennon, 1971)	Yes	Yes

Table 1 – Considerations governing choice of instrument

Location	West Stones	Roaring Middle
Design wind speed (m/s)	46	46
Design wave height (m)	3.5	4.0
Design tidal velocity (m/s)	2.5	1.7
(kts)	4.5	3.0
Pile diameter (mm)	353	406
Wall thickness (mm)	9.5	9.5
Depth (m) to which jetted	10	$10\frac{1}{2}$
	(ie. $\frac{1}{2}$m into clay stratum underlying sand)	(into sand: driven by hammer for last 3m)
Sea bed level (m O.D.) at site	–1.0	–2.5
Lengths (m) of pile sections		
Upper	9.5	14.0
Lower	9.0	

Table 2 – Pile Design

Having established that a pneumatic instrument might be
suitable for local acceptability at any site combined with
accuracy and ease of installation and access, there remained
the limitation that the maximum length of tubing ruled out any
site not close to a sandbank or an existing firm structure on
which to mount the recorder. In all cases but one it proved
possible to select a site at which a manageable tube length
could be combined with a useful sea level record; the exception
was Hunstanton, where the problem of friction loss in the
bubbler tube was overcome by using two tubes, one to carry the
gas and the other to feed back the pressure signal (see Section
5).   Table 4 summarises the essential physical details of each
of the selected sites shown on figure 1.

All five stations contributed data to the physical and
mathematical models of the Wash and certain served other functions
as follows:-

West Stones :   Monitored sea levels in the area in which
construction would probably commence and which was therefore
also the scene of related studies such as trial bank construction,
site investigation and wave recording.   This site was also the
most seaward of a chain of 10 stations on the river Great Ouse
which provided tidal data for a mathematical model of the river.

Hunstanton :   as work on the R. Great Ouse mathematical
model proceeded, the decision was made to site the seaward origin
of the model further out than West Stones, it having been
established by this time that the fluvial outflow passing West
Stones was largely contained between drying sandbanks for another
8-10 km.   The commercial entertainment pier at Hunstanton afforded
the only location of the S.E. shore of the Wash at which a record
could be obtained without the expense of a third offshore pile-
mounted recorder.

Roaring Middle :   this site was the closest approach practicable
to a "deep water" record at the Wash mouth.   Roaring Middle is a
sandbank which dries about $\frac{1}{2}$m at low water springs.   The recorder
was mounted on a pile near the southern extremity of the bank
where survey showed the sand to be most stable and the length of
tubing would be shortest.

Use of the Roaring Middle site enabled monitoring of the full
tidal range at a site in deep water away from fluvial effect.

Tabs Head :   monitored sea levels in the SW corner of the
Wash into which later stages of the water storage scheme could
extend.

5.   Principles of pneumatic gauge design

The physics of pneumatic pressure tide gauges has been
discussed in detail elsewhere (Pugh, 1971, 1972); in this
section we summarise the essential theory and present formulae
for determining basic system parameters for coastal installations.
In the bubbling system compressed gas from a cylinder is reduced
in pressure through one or two valves so that there is a small
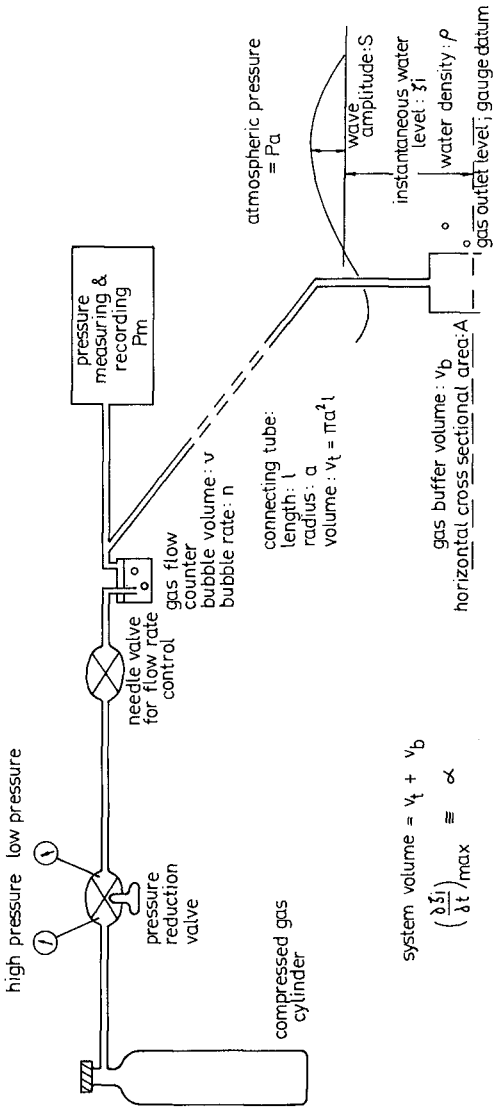
DETAILS OF PARAMETERS USED IN THEORETICAL TREATMENT OF PNEUMATIC SYSTEM

**FIG 2 : PNEUMATIC GAUGE SYSTEM
THEORETICAL PARAMETERS**

steady flow down a connecting tube to escape through an orifice
in an underwater canister or 'pressure point', (figure 3). At
this underwater outlet, for low rates of gas escape the gas
pressure is equal to the water pressure. The pressure of gas
in the system is measured and recorded at the shore end so that,
apart from small pressure gradients in the connecting tube, the
measured pressure, P_m is related to the water level above the
outlet by the elementary hydrostatic relationship:

$$P_m = \rho g \, \xi_i + P_a \tag{1}$$

where P_a is the atmospheric pressure at the water surface, g is
the gravitational acceleration, ρ is the mean water density and
ξ_i the instantaneous water level above the outlet. The flow of
gas along the tube will be driven by a pressure gradient so that
the measured pressure is higher than the true water pressure by
an amount which depends upon the tube dimensions and the rate of
gas flow. This flow rate, which is usually monitored through a
liquid filled bubble counter as illustrated, should therefore be
kept low to minimise the pressure gradient error and to conserve
the supply of gas. However, if the rate of supply of gas is too
low, the pressure in the system may be unable to increase as
rapidly as pressure change at the outlet due to increasing water
depth. Consequently water will be forced into the system until
the pressure balance and the recorded pressure is not then
related to the bubbler outlet datum.

   For any pneumatic system the three primary design constraints
are: the required accuracy, the tidal range to be measured and the
maximum rate of water level increase, $\alpha \equiv \left(\delta\xi_i/\delta t\right)$ max. For the Wash
measurements the required accuracy, γ , was 0.025 m, the range to
be measured allowing two metres for surges on a tidal range of
less than 8.0 m was 10.0 m with a maximum rate of water level
increase of 2.4 metres per hour. The two remaining design
constraints, which may be optimised by suitable site selection
are the maximum wave amplitude, and the length of the connecting
tube from the shore installation to the underwater outlet. It is
important to select a site which requires as short a connecting
tube as possible. The maximum expected wave amplitude may be
reduced by picking a sheltered site, but care should be taken to
ensure that the site chosen is well connected hydraulically to
the location for which the measurements are to be representative.
In practice, as shown by the previous discussion of site selection
in the Wash, the choice is limited, particularly when suitable
recorder housing and access are considered.

   As the system pressure increases, the bubbling rate usually
drops. The minimum rate, n_0 , at which gas should be supplied
from the high pressure source through the bubble counting chamber
at zero water head to avoid water entering the system is:-

$$n_0 v \;\geqslant\; \frac{V}{600} \, \alpha \tag{2}$$

where v is the volume of each bubble passing through the counter (given approximately by $\frac{4}{3}\pi c^3$, assuming spherical bubbles of radius equal to the radius, c, of the submerged orifice in the counter), and V is the total system of volume including both the tube and wave buffer volume, α is in metres per hour and n_0 in bubbles per minute.

When the maximum wave amplitudes are represented by:-

$$\xi_s + s(1 + \sin \omega t) \qquad\qquad (3)$$

where s is the maximum wave amplitude in metres, the period is $\frac{2\pi}{\omega}$ secs, ξ_s is the height (m) of the wave trough above the gauge outlet and the atmospheric pressure is taken as 10 m of water head equivalent to sufficient accuracy the minimum wave buffer volume is:-

$$V_b = \beta V_t \qquad\qquad (4)$$

where $\beta = \dfrac{2s}{\xi_s + 10}$ and V_t is the tube volume.

The gas volume in the measuring system is considered negligible and, for design purposes, the time constant of the tube is ignored. Because water enters the buffer volume during the wave cycle, the recorded pressure differs from the mean water head pressure by:-

$$\frac{V}{A}\frac{\beta}{2} \qquad\qquad (5)$$

where A is the horizontal cross sectional area of the buffer volume which should therefore be sufficiently large to satisfy the accuracy requirements - note that using an unbuffered open ended tube gives very large wave corrections. Since (5) is independent of wave period it may also be applied for tidal changes of level if the tidal amplitude is substituted for and the buffer volume is sufficiently large: if this is done, then the flow of gas is not necessary and the gauge operates in a non-bubbling mode so that the pressure drop is substantially reduced - see Pugh (1972) for further details.

When the minimum gas flow rate and wave buffer volume are applied, the maximum water head equivalent pressure drop across the connecting tube is:-

$$\Delta\xi = \frac{1}{\rho g}\ \frac{8\eta}{10}\ \frac{\alpha \cdot}{3600}\ \left(\frac{\ell}{a}\right)^2\ \phi \qquad\qquad (6)$$

where η is the gas viscosity at the system temperature ($\eta = 17\cdot5 \times 10^{-6} NM^{-2}$ for air at 10^0C) and a is the tube radius.

$$\phi = \beta + \tfrac{3}{2} \qquad \text{for bubbler gauge}$$

$$\phi = \tfrac{1}{2} \qquad \text{for non - bubbler gauge}$$

This shows that the error due to tube pressure gradient increases as the square of the tube length; for lengths less than about 200 metres the error is small but for greater lengths careful design is necessary.

Where the pressure point is mounted near the sea bed the optimum design parameters for the straightforward bubbler system may be estimated using the following formulae:-

cylindrical buffer volume   radius $= 0.4a \left(\dfrac{\ell}{\gamma}\right)^{\frac{1}{2}} \times 10^{-3}$ m

$\qquad\qquad\qquad\qquad\qquad\qquad$ depth $= 1.6\ \gamma$ m

minimum flow rate $\qquad\quad n_0 v\ = 0.0065[\alpha a^2 \ell]$ cc/minute

maximum total head loss
$\qquad\qquad$ (in tube) $\qquad\qquad\quad = 0.7 \times \left(\dfrac{\ell}{a}\right)^2 \times 10^{-6}$ metres

where the tube length ℓ is in metres, the internal radius a is in mm, the design accuracy γ is in metres, and the maximum rate of water level increase is in metres per hour. This assumes a value of 0.25 for β .

For installations where the gauge is mounted more than 20 m above the underwater gas outlet, for example on an oil rig, a correction for the static pressure head in the tube may be required, but this was not necessary in the Wash.

It is possible to design a system which has the low tube head loss of the non-bubbler gauge, yet avoids the necessity of the non-bubbler correction. This is done by using two tubes from the shore to the underwater outlet: air is forced along one tube so that the buffer volume is full of air, while the outlet pressure is transmitted through the second tube, in which there is no net flow of gas, to the recorder. This system was used for the Hunstanton gauge because the outlet was 440 m from the recorder.

6.   Description of gauges : installation

For these measurements the commercially available Neyrpic 'Telimnip' gauge was selected because it has the required datum stability since it records pressure using a mercury manometer – the necessary stability was not possible using electronic transducers. Another advantage of this instrument is the automatic elimination of atmospheric pressure and its variations by leaving one side of the manometer open to the atmosphere, and applying the pressure in the pneumatic system (equation (1)) to the other side. In effect a column of mercury is balanced against the column of water to be measured. A chart speed of 20 mm per hour was adopted as compatible with the required accuracy and operating range of 10 m. The scaling of the recorder gave nearly 25 mm of chart for each metre of water head. Each instrument was calibrated against a dead weight pressure standard.

Table 3 gives the design parameters calculated for the four gauges. A tube radius of 1.9 mm was adopted as standard as larger tubes used too much gas. Only at Hunstanton was the length of tube great enough to make these parameters critical; Hunstanton values are given for the single tube bubbler, the non-bubbler and two tube systems: it was eventually decided to use the two-tube system for direct accurate logging of water head pressures.

PARAMETER	Maximum rate of water level increase α (*)	Tube length ℓ (*)	Tube radius a	Tube volume $V_t = \pi a^2 \ell$	Wave maximum amplitude factor $\left(\beta = \frac{2s}{\sqrt{s}+10}\right)$	Minimum buffer volume (†) $v_b = \beta v_t$	Minimum cross sectional area of buffer volume $A = \frac{v_B}{2 \times \text{accuracy}}$ from (5) (†)	Total system volume $V = V_t + V_b$	Minimum flow rate (†) $\eta_0 \tilde{v}$ from (2)	Approximate life of scuba cylinder containing $1.5\ m^3$	ϕ^{η} from (7)	Maximum tube pressure drop error: $\Delta \xi$ max from (6) (†)
West Stones	2.4 m/hr	25 m	1.9 mm	.00028 m	$\frac{4}{15} = .27$	.00008 m³	.00194 m²	.00036 m³	1.5 cu/min	694 days	1.77	.001 m
Roaring Middle bubbler	2.0	50	1.9	.00068	$\frac{4}{18} = .22$	.00015	.00365	.00083	2.8	372	1.72	.001
Tabs Head bubbler	2.4	50	1.9	.00056	$\frac{4}{18} = .22$	.00012	.00308	.00070	2.8	372	1.72	.001
Hunstanton bubbler	2.2	440	1.9	.00499	$\frac{4}{15} = .27$	.00134	.03180	.00633	23.2	45	1.77	.081
non-bubbler	2.2	440	1.9	.00499	$\frac{12}{10} = 1.2$	.00599	not strictly applicable .06 m² gives suitable $\frac{V}{A}$	.01098	not required	–	0.5	.023
2-tube system	2.2	440 + 440	1.9	.00998	.27	.00268	.06360	.01266	46.4	22.5	0.5	.023

Table 3   Imposed (*) and computed (†) design parameters for pneumatic gauges in the Wash. (Design accuracy τ is 0.025 m)

The recorders at Tabs Head and Hunstanton were easily
mounted in small huts erected on a sea defence bank and on
an entertainment pier respectively. Those at Roaring Middle
and West Stones were mounted in steel cabins on circular steel
piles. The principal design details at these sites are listed
in table 2. The steel cabins each weighed nearly half a ton;
there would clearly be advantages in design modifications to
reduce the weight without sacrifice of protection from the
weather and wave attack. At both sites the piles were installed
in two sections, the lower of these being jetted into the sea
bed; sea water was pumped through two 1 inch pipes welded
inside the pile. The two sections were connected by bolt-and-
flange joints. Before installation, while still in the work-
shops, the piles and cabins were coated with an epoxy resin
and sacrificial zinc anodes were attached, one below the joint
and one above; these measures proved adequate to prevent
corrosion during the period of record. The cabins in which
the recorders were mounted were in each case about a metre
square and nearly two metres high. They provided sufficient
space for routine work on the instruments but it was sometimes
found a little inconvenient to have the entrance in the form of
a trapdoor in the floor, particularly when renewing the gas
cylinders. The pile designs were chosen to avoid vibration due
to tidal streams of up to 4-5 knots, with reference to the work
of Sainsbury and King (1971).

The sensors were in every case attached to screw pickets which
were screwed $\frac{1}{2}$ to 1 m into the sea bed. In each case it was
possible to do this by hand at a time of low water springs, but
at Hunstanton divers were used.

After inserting a picket the sensor, already linked to its
tube, was attached to the picket by a clamp and wing nuts. The
tube was purged by compressed gas when the recorder had been
installed. In the case of Hunstanton the twin tubes had to be
purged separately and divers were used to operate valves at the
seaward end of the system. A marker buoy was attached to each
picket. The bubbler tubes were attached at frequent intervals
to a chain laid on the sea bed. As a result of sea action,
these chains were buried to a depth of 5 - 10 cm. quite quickly
and thus hid the tubes from view while at the same time protecting
them from tensional loads in rough sea conditions.

At West Stones and Tabs Head, the effects of river discharge
on water density were significant. At West Stones the density
varied between 1003 kg m^{-3} at low water to 1024 kg m^{-3} at high
water. For subsequent calculation of water head from the
recorded pressures, the required accuracy was maintained by
expressing water density as a function of the water head.
Because the error introduced by incorrect density is proportional
to the water level being determined (e.g. 0.025 m accuracy
requires the density to be within 2.5% at 1.0 m but within 0.3%
at 7.5 m) the linear elevation/density relationship was weighted
to give the best fit at the higher water levels.

7.   Datum levels

     All water levels were reduced to Ordnance Datum Newlyn (0.D.).
In the Wash mean sea level is approximately 0.1 m above this
datum. However, because the Roaring Middle gauge was sited more
than 11 km from the nearest shore, conventional levelling
techniques could not be used. Hydrostatic levelling using a
liquid filled connecting tube was considered too expensive, so
a technique of hydrodynamic levelling was developed for using
simultaneous elevation measurements at Roaring Middle and
Hunstanton and readings from intermediate internally recording
current metres (Alcock and Pugh, 1974).

     The water level difference terms fall into three groups:-

     a.   Those which depend on the dynamics of the inter-
            mediate water, i.e. acceleration gradients in time
            and space, and Coriolis effects,

     b.   those which depend on conditions at the two sites,
            i.e. kinetic energy, atmosphere pressure and water
            density,

and c.   stress terms due to bottom friction and surface
            winds.

Average water levels at the two sites were estimated to differ
by less than 0.04 m with the main uncertainty arising from
determination of the advective and bottom stress terms. The
datum level at Roaring Middle was determined by this means to
be -3.43 m O.D.

8.   Operating and maintenance experience : costs

     During a period of 6 months the West Stones recorder was
in operation alone and the experience gained was valuable in
preparing for the more inaccessible and exposed location at
Roaring Middle. Problems arising at West Stones and overcome
during this period included:-

     a.   Wind vibration
            The frequency was about 1-2 c/s. There is some
            likelihood that it amplified a troublesome chart-
            slippage problem. Flexible mountings were tried
            to insulate the recorder from the vibrating
            housing but ultimately it was found that adjust-
            ment of the chart guides cured the problem completely.

     b.   High temperatures
            Apart from discomfort experienced during maintenance
            visits there was concern for the stability of the
            chart paper. Temperatures were monitored at West
            Stones and were found to range from 5 to 25°C
            typically. They were subsequently controlled within
            acceptable limits by painting the housing white,
            adding a hood mounted a few centimetres above the
            roof and coating the interior walls with insulating
            tiles.

Site	Sensor Location and Level	Recorder Location and Level	Means of access	Interval between maintenance visits		Installation cost	Approx. annual running cost	Physical reasons for choice of site	% acceptable data return from instrument
				Average	Maximum				
West Stones	In main Gt. Ouse navigation channel at toe of training wall. level −2.59 m OD ± 0.01 m	In steel housing on pile 9½ m high and jetted 10 m into sand at −1 m OD behind training wall. Pile diameter 356 mm and wall thickness 9.5 mm	By boat 1 hour from King's Lynn docks	7 days	23 days	£3,500 ($ 8,750)	£2,900 ($ 7,250)	Deep water with short run of tubing; also close to existing navigation beacon	89
Roaring Middle	On NW side of long sandbank. Level determined hydro-dynamically to be −3.43 m OD± 0.05 m	In steel housing on pile 14 m high and jetted 10½ m into sand at −2.5 m OD (highest point of sand bank). Pile diameter 406 mm and wall thickness 9.5 mm	By boat 3-4 hours from King's Lynn docks	10 days	20 days	£4,700 ($ 11,750)	£4,200 ($ 10,500)	Most feasible "mid-Wash" site (in deep water). Site of pile just dries at lowest low waters	86
Tabs Head	In main Witham navigation channel at toe of stone pitching. level −3.01 m OD ± 0.01 m	In concrete hut on top of levee at 7 m OD	By road and track ½ hour from Harbour Master's office at Boston	6 days	20 days	£1,500 ($ 3,750)	£1,700 ($ 4,250)	As West Stones, also close to existing staff gauge which forms basis of existing predictions	84
Hunstanton	½ km offshore of Hunstanton on line of pier at a level of −3.19 m OD	In wooden hut on concourse at end of entertainment pier at 9 m OD	Short walk along pier	4 days	16 days	£1,500 ($ 3,750)	£1,800 ($ 4,500)	Only practicable site on east side of Wash avoiding use of a third pile	69
Gibraltar Point	Line of 6 tide poles running out to springs low water mark from eastward−facing beach			Manned continuously for one month			£1,200*	Site previously used for observation of individual tides for model data collection	—

*cost of one-month exercise

Table 4 — The Wash: Details of Tide Recorder Sites

c.   Humidity

Ventilation during maintenance visits was improved
by cutting a 10 cm. diameter hole centrally in the
roof below the hood to improve the flow of air.

The lowest parts of spring tide curves were lost at West Stones
later in the study when sand began to accumulate in such a way
as to retain a low-water "pool" around the sensor.   Since
dredging was not practical the loss (about 0.3 m at most) was
overcome by sketching in the missing part of the curve with
reference to complete curves for similar tides obtained earlier
in the study.

Table 4 shows that the average data return from the four
gauges was 82% over a period from July 1972 to November 1973.
The below average return from Hunstanton was due to the
vulnerability of the long length of tubing on a holiday beach
and to the subsequent difficulty of purging water from a two-
tube system: purging air tended to flow down the tube which
was already free of water.   Future two tube systems would
avoid this by connecting each tube directly into the top of
the underwater outlet canister and purging each line separately.
Although some difficulty was experienced at West Stones and
Roaring Middle due to irregular chart drive speeds and drive
failure, it should be made clear that the gauges were not
designed to operate in the relatively severe vibration conditions
at the top of the piles.

On average the gauges were visited weekly, when standard
checks for zero stability, elevation and timing accuracy were
made.   As the Roaring Middle gauge was difficult to reach, it
was inspected less often than the others: the high data return
from such an inaccessible site is very satisfactory.

After removal from the gauges, records were sent to the
Institute of Oceanographic Sciences for quality examination
and reduction to hourly values.   Chart readings were processed
by computer to allow for gauge calibration and water density.
For two periods of detailed study the records were processed
every quarter hour.   Output was on cards and line printer.
Some preliminary filtering to distinguish tidal and non-tidal
variations of levels was also effected, and these results
could be plotted, if required.

The costs of the different installations at the four sites
are listed in Table 4.

9.   Derivation of design data from output

Full details of the observations will be included in the
final report of the Consulting Engineers, but we include here
examples of the kind of treatment proposed.

Figure 3 shows a plotted output from Tabs Head separating
the tidal and non-tidal components using the Doodson Xo filter.
To see how surge residuals compared at sites in the Wash and
in the open North Sea, results from measurements using a similar
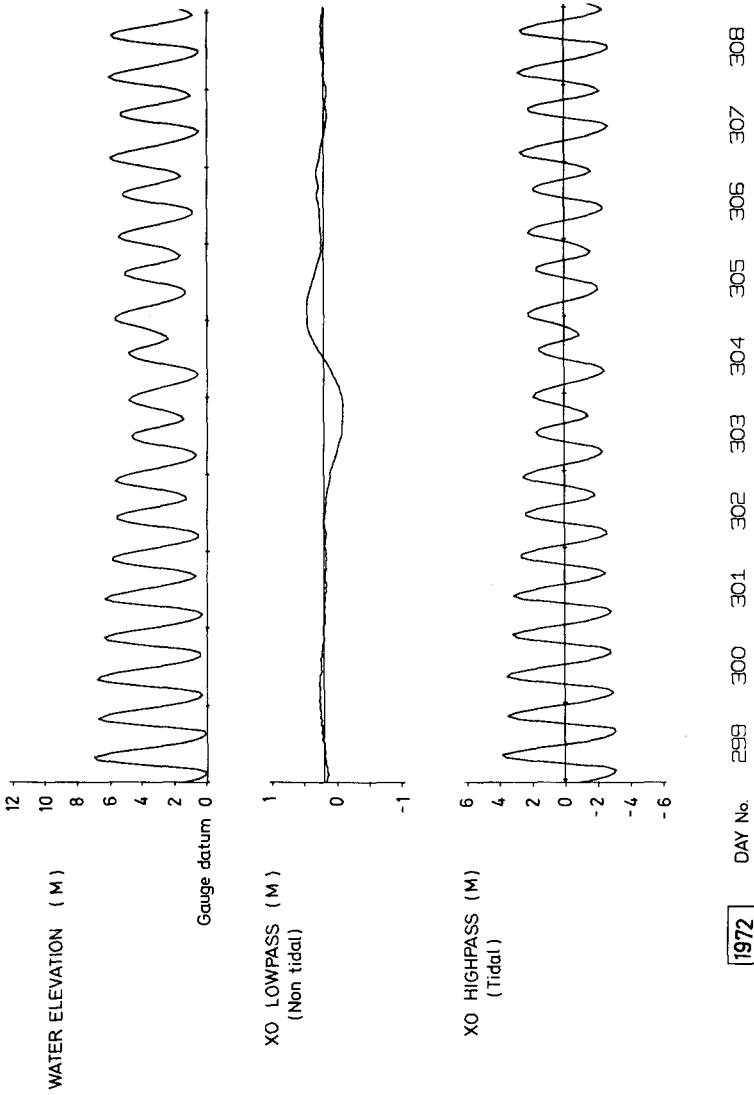gauge on the Inner Dowsing light tower were plotted (figure 4).

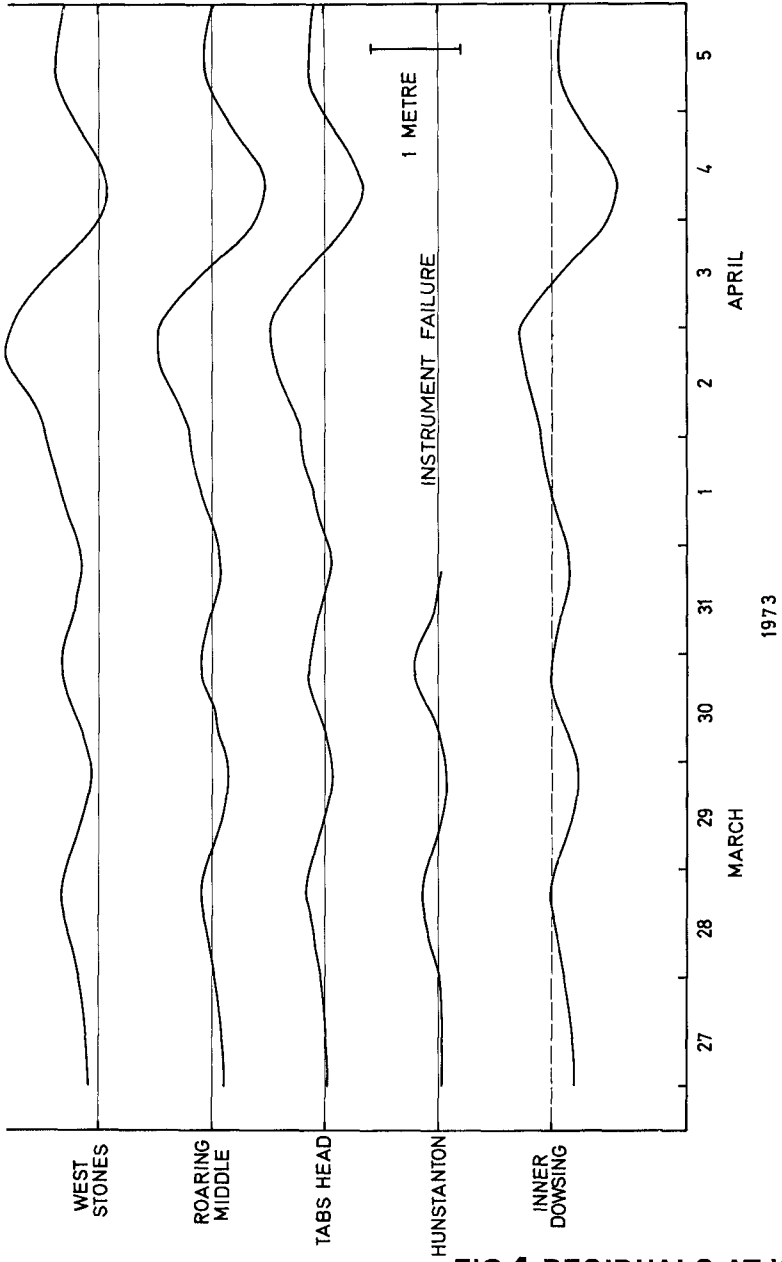FIG.3: TIDAL AND NON-TIDAL
COMPONENTS AT TABS HEAD

FIG.4: RESIDUALS AT WASH
STATIONS AND IN NORTH SEA

The surge levels are very similar showing not only that there is
a similar response throughout the area, but also how well the
gauges reproduce the finer detail. The characteristic quasi-
periodicity of the surges is concentrated in the 40 to 50 hour
and 70 to 80 hour parts of the long period spectrum (Pugh and
Vassie 1974). The residuals obtained from the Wash recorder
will be used to assist in estimating, e.g. for survey purposes,
the probability that during a planned exercise the high and/or
low water levels (whichever are relevant to the particular case)
will be within an acceptable margin of the predicted levels.

        Other work undertaken in the feasibility study is supplying
details of tidal velocities prevailing at the construction sites.
By relating these measured velocities to the measured level
record at one or more sites, "predicted" velocities and probable
variations in them can be produced for a year in which
construction is planned. To do this a knowledge of tidal
constituents is required and these are to be generated from the
record at Roaring Middle in the first instance; that at West
Stones could be similarly analysed in order to predict tides
for a year in which construction is to proceed. From the
prediction can be selected the optimum period for tidal closure
of embankments when a series of particularly low high waters
can be expected over a period of several days.

        Figure 5 shows the percentage of time for which different
levels are covered by water and exposed, and also the percentage
residence time of water levels within superimposed bands. Both
of these are useful in the design of reservoir embankments;
they also assist in understanding the formation and behaviour
of salt marshes and other shore environments which could be altered
by a water storage scheme (Gray, 1972).

10.   Conclusions

        Our experience of using pneumatic gauges in the unfavourable
environment of the Wash has shown that if they are properly
designed, as described, pneumatic systems are capable of an
accuracy and versatility superior to those of conventional
stilling well gauges. Not only may they be used in areas where
measurements by conventional gauges or tide poles are impossible,
but they are also cost-competitive for all projected installations.

        Were we to plan a similar study with the benefit of the
experience now gained, we would press for sufficient funds to
cover the installation of a pneumatic recorder on a pile driven
into the seabed at about -6m O.D. near the mouth of the Wash,
since we are now confident that expenditure on such a gauge
would yield satisfactory results and the gauge datum could be
established by hydrodynamic methods rather than the expensive
hydrostatic method used formerly.
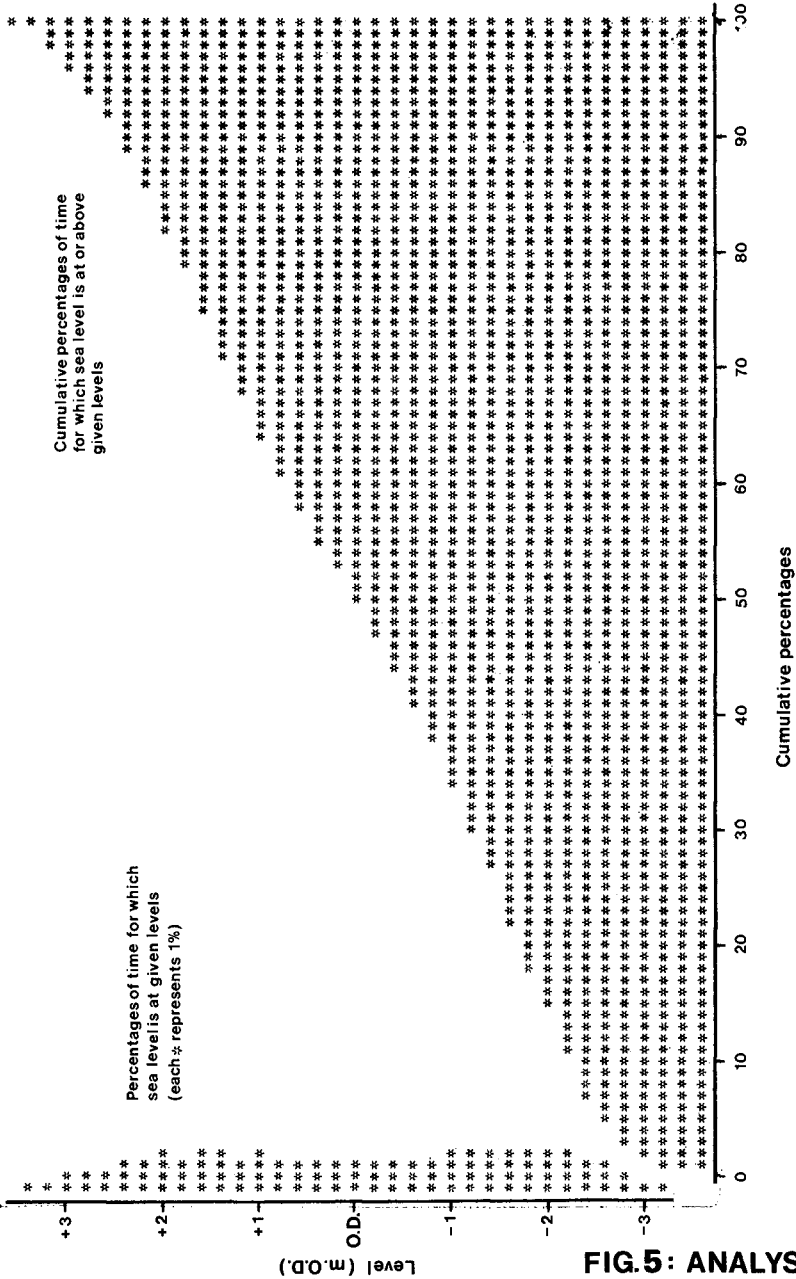
FIG. 5: ANALYSIS OF
SEA LEVEL RECORD

Of the many individuals who have contributed greatly to the
success of the level recording enterprise particular mention is
made of D.H. Cowie of Binnie and Partners who coordinated the
field work from King's Lynn; R.M. Young and A.P. Lane of the
same firm who bore the brunt of the operation and maintenance
work, often under very trying conditions; and Miss D.C.C.
McDonald and Miss S.M. Brown of IOS who supervised the data
reduction.

References

Alcock, G.A. and Pugh, D.T. (1974). Hydrodynamic levelling
        to an off-shore tide gauge. (Submitted to press, August 1974)

Binnie and Partners (1965). Report on the water resources of the
        Great Ouse Basin. Ministry of Housing and Local Government.

Binnie and Partners (1970) - in association with Rendel, Palmer
        and Tritton and with Lewis and Duvivier - Wash desk study
        report to the Water Resources Board. In, The Wash : Estuary
        Storage (Report on the Desk Study), HMSO, London.

Gray, A.J. (1972). The salt marshes of Morecambe Bay, Journal
        of Applied Ecology, 9, (1), 207-220.

Lennon, G.W. (1971). Sea level instrumentation, Int. hydrogr.
        Rev., 48(2), 129-148.

Pugh, D.T. (1971). Sea level measurements using the Neyrpic
        bubbler pressure gauge. Institute of Coastal Oceanography
        and Tides, Internal Report No. 22.

Pugh, D.T., (1972). The physics of pneumatic tide gauges. Int.
        hydrogr. Rev., 49(2), 71-97.

Pugh, D.T. and Vassie, J.M. A year of simultaneous off-shore
        current and elevation measurements in the North Sea
        (in preparation)

Sainsbury, R.N and King, D. (1971). The flow-induced oscillation
        of marine structures. Proc. Instn. civ. Engrs, 49, 269-302.

CHAPTER 150

SPECIAL CONSIDERATION ON
THE DESIGN OF AN LNG HARBOR

By

Bernard Le Méhauté, D. Sc.
Vice President
Tetra Tech, Inc.
Pasadena, California

SUMMARY

One of the primary considerations in the design of an LNG harbor is
safety, requiring berths to be separated by large distance and well-
protected from the outside wave agitation. Therefore, LNG harbors
require expensive structures established as close as possible to the
liquefaction plant (while crude tankers may be served by relatively
much cheaper, single point mooring servers in deeper water). The
cost of waiting time for the very expensive LNG ships has to be
weighted against the cost of the additional berths and structures. (A
$125,000 \, m^3$ LNG ships costs $2000/hour.) The present paper describes
the results of a study in which the optimum solution has been obtained
by comparing these costs.

The number of options is characterized by the number of berths. The
cost to be added to the cost of construction of the berths includes an
additional length of breakwater and additional dredging, plus the costs
of financing during construction and the cost of maintenance.

The waiting time for the LNG ship is generally determined, based on
the classical Erlang formula for queing theory. It is recalled that this
formula is developed for an open loop. A closed loop theory has been
specially developed for the present problem (since LNG ships will most
probably operate between two well-defined harbors). The waiting times
are 15 to 20% smaller than given by the closed loop theory. A compari-
son between single berth and double berth is examined. The effect of
the rate of filling which is a function of the cryogenic pump capacity
(or size of ship depending upon the dominating controlling factor) is
analyzed. Finally, the sensitivity of the recommended solution as a
function of the interest rates--examined in view of current economic
uncertainties--is also investigated.

The final recommendation for the design of the harbor, based on the
prevailing factors, is the optimum economic solution.

1. INTRODUCTION

A very early and major problem in harbor planning is establishing the
number of berths to be provided. A minimum number must be provided
for loading the daily output. A larger number will reduce the average
waiting time for ships to tie up at the berth and be connected to the
loading equipment. Because of the very high cost of construction and
operating LNG tankers, every hour of time saved is worth thousands
of dollars. However, the capital cost of additional berths is also very

high.   Therefore, a detailed analysis is necessary to determine whether ship-time savings could be realized that would be of greater value than the additional capital cost necessary to achieve them.

The objective of this study is to determine the optimum number of berths required to handle a given volume of LNG to be shipped from a harbor.

In general, the calculation of the number of service berths is based on the following criteria:

1) The efficiency of loading berths defined by the rate of occupancy. It is expected that the occupancy of berths for LNG tankers is 20-30%.

2) The calculated mean waiting time, taking into account the irregular nature of traffic caused by all kinds of variations which may arise during trips between harbors.

3) The economic calculation of the loss due to average waiting time, versus the cost of the harbor and facilities.

In view of the fact that future fleets of LNG tankers is going to be quite uniform in size and properties,* the waiting time study should not be completely dependent on random parameters. This is not a general queuing problem of a harbor with completely random inter-arrival times and service times, where ships broadly vary in size, properties, and cargo. The formulation of the probabilistic part of the waiting time problem is based on a Markovian process which is fundamental to most of the queuing calculation. The statistics represented by this process seem to be close in nature to the semi-regulated traffic problem under study.

2.   THE SHIPPING CYCLE

As a tanker arrives in the loading harbor and is maneuvered to a berth, the deballasting phase starts. The ballast in an LNG tanker is approximately 40% of its capacity, and deballasting requires about six hours. At the same time, the connection of the loading pipes takes place, thus preparing the ship for the filling operation, to start as soon as the deballasting phase is completed.

In order to guarantee a safe loading operation, loading facilities for LNG are commonly set-up to handle the loading of one tanker at a time for each pier. In other words, there is one loading set-up per two docking spaces. This would mean that while one ship is being loaded, a second tanker can be docking at the other side of the pier either being ready to be loaded, or in preparation for loading.

* A fleet of LNG carriers intended for the American market is presently under construction and consists of tankers whose characteristics and volume are virtually identical (125,000 m^3). The capacity of future ships may be increased to 200,000 m^3. The LNG carrier fleet intended to serve the European market is less homogenous and will range from 35,000 to 125,000 m^3 with an average ship size of 75,000 m^3.

The average service time of a tanker can be defined in two ways. The first way is based on the number of loading facilities, where the loading time of the ship is counted as the service time. This is based on the assumption that the loading pumps can be used continuously with a double berth. The second approach is based on the number of berths in the harbor. In this case, service time is the total time elapsing from ship arrival to departure, including waiting time away from a berth. It is evident that the loading system should be so designed that effectively the two waiting times will be close. The loading facilities should have the capacity of filling-up a tanker in 10 to 15 hours independently of its size.

A set of statistics for the filling rate of oil tankers as a function of their size exists. Such statistics do not exist, to our knowledge, for LNG ships. For the sake of the calculations, we have adopted the following typical values:

- 20 hours for $200,000\,m^3$ ships, determined by a pumping capacity of 10,000 cubic meters per hour.

- $12\frac{1}{2}$ hours filling time for a $125,000\,m^3$ ship.

- 10 hours for a $75,000\,m^3$ ship, determined by the size of the connecting system to fill said ship.

The filling rate will take account of the following. The volume coming from the LNG container is about 99% of the ship's capacity. The loss of gas during filling operations is estimated at about 1%. The volume of LNG actually loaded onto the ship is therefore 98% of the ship's capacity.

The loss from boil-off during travel is 0.2 to 0.3% per day; therefore, assuming, for instance, a 7-day trip covering a distance of 3360 miles, the corresponding loss will be 1.75%. Also, 3% of the load is held back for the return trip, so that only 93.25% of the LNG ship's capacity is actually delivered.

The shipping cycle involves also the maneuvering time of a ship in and out of the harbor. The average time of 6 hours is reasonable for this part of the shipping cycle. As mentioned before, it takes about 6 hours to deballast a ship and connect it to the loading facility.

In some cases, the queuing model will address itself to a complete shipping cycle involving loading, unloading, maneuvering operations at two harbors and the shipping round-trip. A complete cycle type problem involving a single loading harbor and several destination harbors will result in several queuing problems coupled together. Since waiting times are expected to be very small with respect to the cycle times, the queuing problem at each individual harbor can be isolated. In the present study, it was assumed that the loading process is identical to the unloading process, thus leading to a symmetric model. This assumption is perfectly acceptable, even though tankers are loaded by harbor facilities while they are unloaded by means of shipborne pumps.

Between harbors, it is expected that the LNG tankers will be cruising at a speed of 20 knots. For example, an LNG tanker will cover the distance between Arzew, Algeria, and Savannah, Georgia, a total of 3800 nautical miles, within 190 hours.

As in the harbor operations, it is expected that the ships' activity will be somewhat reduced due to weather and sea conditions as it cruises between harbors. For this reason, a 7% overall reduction in efficiency has been taken into account. Also, the harbor entrance may be closed because of wind, sea states, or fog.

The formulation of the waiting time problem is probabilistic and is closely related to the standard queuing theory. Let p the fraction of the total cycle time T , finding a single ship being in a server, the first case is loading or unloading and in the second case being in the harbor. Correspondingly, 1-p is the fraction of T for a ship being away from a server. To meet the annual shipment of Q m^3 of LNG will require using M ships:

$$M = \frac{QT}{330 \times 24 \, a \, B \, D}$$

where

$\quad$ D $=$ Volume of an average ship
$\quad$ a $=$ Fullness of the ship ≈ 0.98
$\quad$ B $=$ Weather and sea conditions factor ≈ 0.93

assuming that the ships operate 330 days a year.

Let the number of severs in the harbor be L and let the number of ships at any time at the harbor be K . In the event K < L , it will mean that all the ships at the harbor are served. If K > L , L ships are served while K - L ships are in queue waiting to be served. The fraction of time finding K ships at the harbor, of the total number of M ships dedicated to the operation, at any time t is P_M^K (t), with K greater or smaller than L but less or equal to M .

On using a Markovian approach, we can now formulate the time fraction relationships representing the ship traffic through the harbor.

The details of this theory have been developed at Tetra Tech and presented by Fersht (1974). Only the results are presented herewith.

3. LNG BERTHS - ALTERNATIVE SOLUTIONS

In view of the fact that filling and maneuvering times decrease less rapidly than tanker size, without calculating the waiting time, and simply on the basis of the time necessary to ship a given volume of LNG, it is immediately apparent that the number of mooring berths required increases when the size of tankers decreases.

Consequently, in all probability and assuming an equal distribution of LNG between the two markets, it will require an extra berth to satisfy the European market with ships of 75 - 85,000 m^3 average capacity than it will to satisfy the American market with ships of 125,000 m^3 capacity

or more. This is emphasized by the fact that since the distance to American destination harbors is greater, the relative waiting time and consequently, the financial losses derived therefrom are of the same order of magnitude for both markets.

As a result, the appropriate option is to be chosen from a number of alternatives, defined by the number of berths, such as:

		Number of Berths	
		American Market	European Market
Option	I	2	3
	II	3	4
	III	4	5

Waiting time and corresponding costs are determined for these three solutions. It is immediately apparent that in passing from one solution to the other, there results, in both cases, an increase in cost corresponding to:

1) One double berth;
2) An increase in the length of the main breakwater equal to the projection perpendicular to the shore of the distance between two berths (i. e., approximately 320 meters);
3) A supplementary dredging area 320 m long, extending parallel to the shore.

In passing from Option I to Option III, the corresponding cost is doubled. The appropriate solution, therefore, should be evident.

A comparison of the results obtained with the Fersht closed loop mathematical model and Erlang open loop formula shows that the Erlang formula is more conservative. It is also to be noted that the methods of calculation based on the Erlang formula are independent of the market, destination harbor, cruising speed, and other effects. The only factor considered is the frequency of arrival of ships at the harbor, the capacity of said tankers, and their filling and maneuvering times.

In the Fersht model, account must be taken of the complete shipping cycle.

The results of the calculations are set forth in Table 1 for the American market, and presents the results of the two theories. The figures in parentheses are the results of the closed loop theory developed by Fersht (1974). The other figures give the results obtained from the Erlang formula for an open queue.

A similar Table has been established for the European market. The cruising time in a round-trip for the American market without losses due to weather and sea conditions is 380 hours. The corresponding average cruising time for the European market is 70 hours. For the American market, two types of LNG tankers have been considered which are the 125,000 m^3 tanker currently under construction and the

future tanker of 200,000 m^3. In the European case, an average tanker size of 75,000 m^3 has been considered. As mentioned before, where pumping is regarded as determining the waiting time, calculations are carried out for 1, 2, and 3 servers. In the event the criterion for service is based on time in the harbor, the number of berths is regarded as the number of servers. Therefore, in the second case, one should use 2, 4, and 6 as the number of servers. The time values, using the loading criterion for the American market are (a is the service time of a ship in hours, b the total cruising time of a ship in a cycle).

For D = 125,000 m^3 a = 12.5 hrs. b = 405 hrs.
For D = 200,000 m^3 a = 20 hrs. b = 410 hrs.

The corresponding values for the berths criterion are:

For D = 125,000 m^3 a = 25 hrs. b = 380 hrs.
For D = 200,000 m^3 a = 35 hrs. b = 380 hrs.

In a similar fashion for the European market using a tanker size of D = 75,000 m^3, the times used are:

Loading case: a = 10 hrs. b = 94 hrs.
Berth case: a = 24 hrs. b = 70 hrs.

TABLE I

Daily Production: 108,000 m^3
Annual Production: 36,000,000 m^3

Ship Capacity	Present	125,000 m^3
Number of loads per year		290.9
Time interval between ships' arrivals		27.36

Waiting time based on times in hours	Loading 12.5	In Service 22.5	Total at Port 30
Solution 1: 2 berths	(9.45)	Not valid	10.26
1 pumping station	10.51	Not valid	12.89
Solution 2: 3 berths	Not valid	(4.29)	(1.69)
2 pumping stations	Not valid	4.58	1.79
Solution 3: 4 berths	(0.71)	Not valid	(0.28)
2 pumping stations	0.72	Not valid	0.28

All these cases were examined numerically for the service times spec-
ified. In addition, the service time has been varied to demonstrate the
dependence of the waiting time on the time length of the ships' service.
An example of the obtained results is presented in Figure 1.

The results obtained clearly indicate that the loading criterion results
in longer waiting times. This does not come as a surprise, by the fact
that the loading criterion does not differentiate between waiting outside
the harbor and waiting at one side of the pier while a second tanker is
loaded at the same pier or its other side. A better comparison between
waiting times for the two criterions will require a much more elaborate
mathematical model for the time fraction study. The two criteria used
here are sufficient to provide waiting time data for an economic study
of an LNG harbor.

Typical values for Erlang's waiting time formula, which is related to
an open cycle can be found in Torse (1961). Since the queue in the open
cycle can be infinitely long, the waiting times are somewhat longer.
For the American market where M is fairly large, Erlang's formula
provides answers which are 10-20% larger than those obtained by the
Tetra Tech method.

We would like to point out here that using Erlang's formula for the
European market will result in unrealistically large waiting times.

TABLE 2

Annual Waiting Time &
Time Savings by Each Option (Hours)

Option	American Market		European Market	
	Total Waiting Time	Time Saved	Total Waiting Time	Time Saved
1	3750	----	5819	----
2	1332	2418	499	5320
3	209	1123	199	300

It is also important to bear in mind the fact that one ship may be immo-
bilized at the mooring pier for a certain number of days for maintenance.
The waiting time must, therefore, be calculated for the actual number
of berths minus one. Since this occurs rarely, the problem is more
operational than it is economical.

It is also important to note that the harbor may not be accessible say 30
days per year due to adverse weather and sea conditions. In this case,
a queue will form at the harbor entrance, since one ship arrives for
filling either every 27-36 hours (American market), or every 16-33
hours (European market), creating a transient. If a storm lasts
three days, for instance, at least another three days will be required
to fill all the ships which have been queuing to enter the harbor. Option
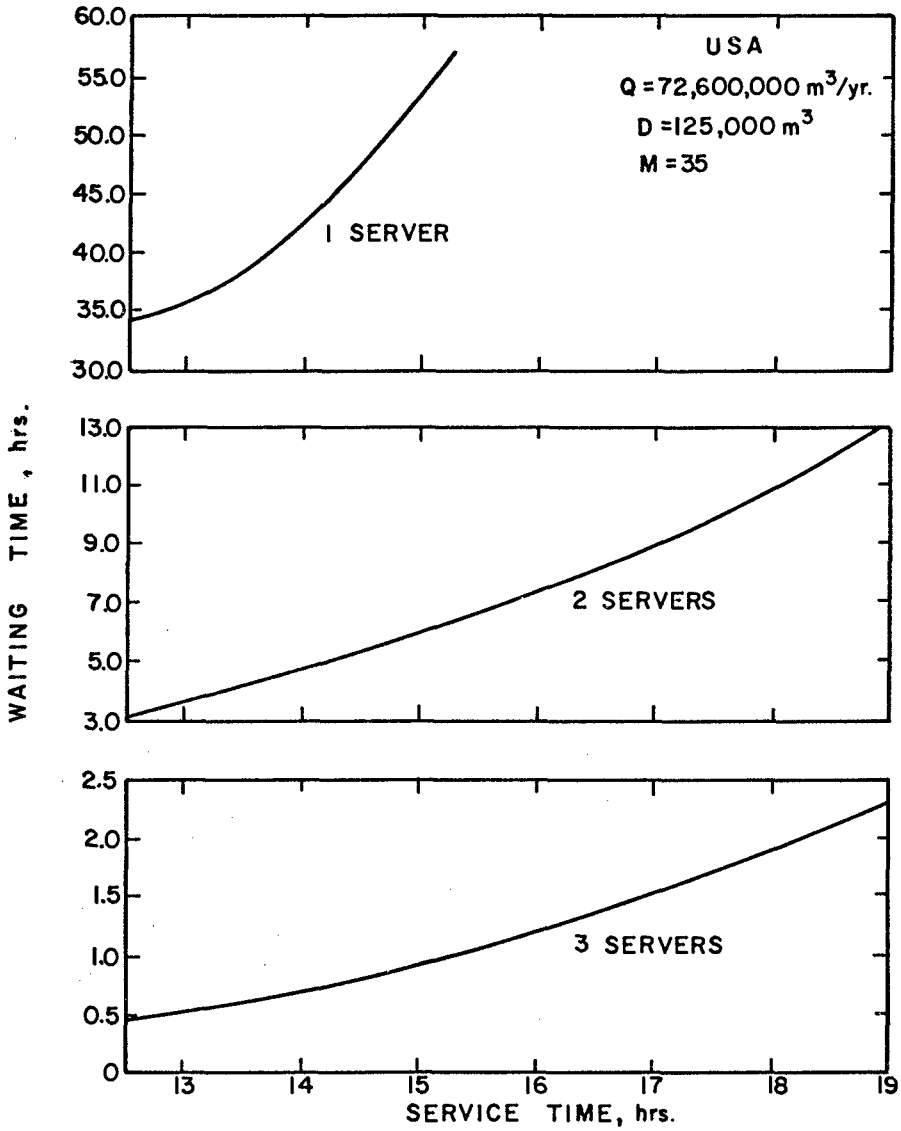1 would require more than twice that waiting time.

FIGURE 1

4.   COSTS OF THE OPTIONS VS LOSS OF WAITING TIME

The cost of Option 1 is not considered here, since this is the minimum size port that can handle the demand.   The additional cost of Option 2 over Option 1 is as follows:

One pier with two berths	$10,000,000
* **Br**eakwater 320 ($42,430/m)	13,600,000
Dredging (2,000,000 m^3, $7.0/m^3)	14,000,000
	$37,600,000

Option 3 would involve an equivalent additional construction beyond Option 2, and would cost an additional $37,600,000.   Total additional construction cost of Option 3 over Option 1 would be $75,200,000.   In addition to the construction cost, provision would also be required for (1) financing costs during the construction period,   and (2) mainten-ance costs during the life of the project.

* The deeper the breakwater, the less dredging.   The shallower the breakwater, the more dredging.   The numbers which are given are the results from a parallel study done concurrently on the optimization of cost of breakwater-dredging.

Construction would take place over three years and money for financing would be drawn down as used, and an interest obligation incurred.   This interest obligation is generally capitalized and added to construction cost as part of the total financial package for long-term financing.   With a 7% interest rate, the financing costs on $37,600,000 would be approximately $4,010,000.

Maintenance costs over the life of the project would be estimated from the following tabulation developed from analyses of harbors and dock-yard facilities, and which have also been partly the results of a parallel optimization study.

Item	Annual Average Maintenance Cost as % of Construction Cost
Structures Not Exposed to Seawater	0.1
Structures Constantly Exposed to Seawater	0.25
Utilities	1.0
Machinery Infrequently Used	2.0
Machinery Frequently Used	3.0

In the present case, the rate for structures constantly exposed to sea-water (0.25%) would apply.   This might involve an overhaul every 10 years at 2.5% of the original construction cost.

The present value of costs to be incurred in the future requires a dis-counting of the future costs.   In this case, 10% is an appropriate dis-count rate.   For the first 25 years of the life of these facilities, the present value for maintenance would equal $37,000,000 x 0.0025 x 9.0768 (25-year cumulative 10% discount factor), or $40,000.

The total additional cost of Option 2 would be:

Construction Cost	$37,000,000
Financing Cost During Construction	4,010,000
Present Value of Maintenance for 25 years	840,000
Total:	$41,850,000

The total additional cost of Option 2 is $41,850,000. Option 3 would cost twice this amount, or $83,700,000 more than Option 1.

The value per hour of waiting time saved must be computed separately for each market because of the difference in construction and operating costs of the tankers. The waiting time that would be saved each year will be discounted at 10% to develop the present value for future time saved. A project lifetime of 25 years will be assumed in the computation, though this is conservative.

The capital, financing, and operating costs for three sizes of LNG tankers over an entire 20-year life are estimated by the Economist Intelligence Unit, assuming 340 days of operation per year. Converting to an hourly basis, the cost for a $125,000\,m^3$ tanker is $2000. A capital cost of $67,000,000 is assumed. The current tankers on order for El Paso in the United States will cost approximately $90 million. Therefore, using this higher updated cost of $90 million instead of $67 million and making comparable changes in interest charges, an hourly cost of $2040 is derived. For a tanker of $75,000\,m^3$ capacity, the hourly cost is $1350.

Using these hourly values for the time saved in Option 2 and 3, the following values are derived for annual waiting time saved:

	American Market ($125,000\,m^3$ Tanker)	European Market ($75,000\,m^3$ Tanker)	Total
Option 2:	Savings Over Option 1:		
	$4,940,000	$7,230,000	$12,170,000
Option 3:	Additional Savings Over Option 2:		
	$2,294,000	$ 408,000	$ 2,702,000

The present value of time saved over 25 years of full operation is derived by discounting at 10%, giving a value of 0.9091 of the annual value for the first year, 0.8264 for the second year, and 0.0923 for the twenty-fifth year. The sum of these values is 9.0768. This factor times the annual value of time saved gives the present value of 25 years of time saved for each option.

Computation of Present Value of Time Saved

Period:	25 years
Discount Rate:	10%
Cumulative Discount Factor:	9.0768
Option 2: Annual Savings:	$ 12,100,000
Present Value /25 yr. savings:	$110,510,000
Option 3: Annual value of additional savings over Option 2:	$ 2,702,000
Present Value/25 yr savings:	$ 24,530,000

A comparison of the construction, financing during construction, and present value of 25-year maintenance costs for Options 2 and 3, with the present value of time saved for each option yields the following:

	Option 2	Option 3 in Excess of Option 2
Total cost (construction, finance during construction, & present value of 25-year maintenance costs)	$37,600,000	$37,600,000
Present value of time saved to tankers over 25 years	$110,510,000	$24,530,000

The value of time saved to ship operators enables ultimate purchasers to pay the seller that much more for an LNG F.O.B. port. Thus, the seller can expect to recoup the additional port costs of Option 2 in the sales prices negotiated for LNG.

It is clear that expenditure of the additional $37,600,000 for Option 2 over the basic minimum of Option 1 will yield an amount more than twice as large in present value of ship time saved - $110,510,000. This expenditure is therefore warranted.

The further expenditure of an additional $37,600,000 for Option 3 would yield an additional present value for ship time saved of only half as much--$24,530,000. This expenditure is marginal.

The sensitivity of this decision to a change in the discount rate was examined in view of the current uncertainties about interest rates and discount rates.

This analysis confirms that whatever the discount rate used, the present value of time savings under Option 2 will exceed the cost of Option 2, and the present value of additional time savings under Option 3 will fall marginally short of the additional cost of Option 3 over Option 2.

Therefore, it appears that Option 2 is the optimum solution. However, it is pointed out that due to transient effect (after a long storm, for example), or due to the possible immobilization of one berth by a ship under repair, an additional berth is recommended to Option 2 -- this is an operational, not an economic decision.

ACKNOWLEDGMENTS

REFERENCES

Faridany, E., (1972), LNG Marine Operations and Market Prospects for Liquefied Natural Gas, 1972-1990, VER Special No. 12. The Economist Intelligence Unit, Ltd., Spencer House, 27 St. James Place, London, SWIAINT

Fersht, Samuel (1974), Queuing Study for Design of LNG Harbor, The Million Ton Carrier. Proceedings of the Super Ocean Carrier Conference, SOCCO, New York. Published by SOCCO, Berth 84, P. O. Box 269, San Pedro, California.

Le Méhauté, B. (1973), Proposed Master Plan for the Harbor of Arzew - Bethioua, Tetra Tech Report No. TC-335.

Morse, P. M. (1961), Queues, Inventories, and Maintenance, John Wiley and Sons, Inc.

Prabhu, N. U. (1964), Queues and Inventories, John Wiley and Sons, Inc.

CHAPTER 151

ENVIRONMENTAL ANALYSIS FOR BAHAMAS SUPERTANKER PORT

W. HARRISON

Erindale College, University of Toronto
3359 Mississauga Rd., Mississauga, Ontario L5L 1C6

ABSTRACT

From the point of view of the Bahamian environment, the most favorable
locations for a supertanker port are 1) the western margin of the Great Bahama
Bank, 2) the western shores of Grand Bahama Island and 3) the western margin
of Little Bahama Bank. A port in any of these areas would a) usually be
located down-wind and down-current of the majority of Bahamian islands and
shallows, b) be located adjacent to boundary currents, expecially the Florida
Current, that would tend to carry large accidental oil spills away from coastal
areas and into the North Atlantic, c) be located where wave energies would be
relatively low, and d) be positioned close to sea-lanes, obviating supertanker
penetration of the central Bahamas.

A site 30 miles east of Freeport, Grand Bahama Island, was chosen for
construction of a sea-island supertanker bunker. Six controlled spills
(270 U.S. gals. each) of crude and two spills of naptha were made at the sea-
island site during the windiest month (February). Slick spreading rates are
presented. Cumene and all lower-boiling aromatics disappeared within the first
90 minutes after a crude-oil spill; a majority of toxic fractions (BP < 220°C)
disappeared within 3 to 8 hours. Slick-drift roses for extreme-wind-persistence
and strongest-coastal-current conditions indicate the environmental suitability
of the site for capture and cleanup of small spills (< 1000 gals.).

INTRODUCTION

From the standpoint of environmental hazards, the Bahama Islands have
advantages over many other potential sites for supertanker ports along the
Atlantic seaboard of North America. Threats to shipping, to oil-storage, or
to oil-transfer operations from fog, snow, ice, or earthquakes are minimal or
non-existent. Hurricanes are the only significant natural hazard, and ship
captains and superport managers can take advance precautions for them.

In 1971, the Bahamian Government decided to consider development of a
bulk terminal which could handle super-sized ships, including tankers. The
author was requested to make a general environmental analysis of the Bahamian
archipelago with a view to identifying coastal reaches that would be suitable
for location of the superport. Figure 1 indicates the value of a general
analysis. The broad interplay of winds, waves, and ocean currents can be
considered. For example, from the point of view of the Bahamian environment,
the most favorahle locations for a superport are 1) the western margin of the
Great Bahama Bank, 2) the western shores of Grand Bahama Island, and 3) the
western margin of Little Bahama Bank. Accidental oil spills would tend to
move away from ports located in these areas of the archipelago and the port
sites themselves would be near deep-water sea lanes, protected from North
Atlantic swell.

LARGE TO CATASTROPHIC-SIZED SPILLS

The size of an oil spill is defined here as "large" if it is greater
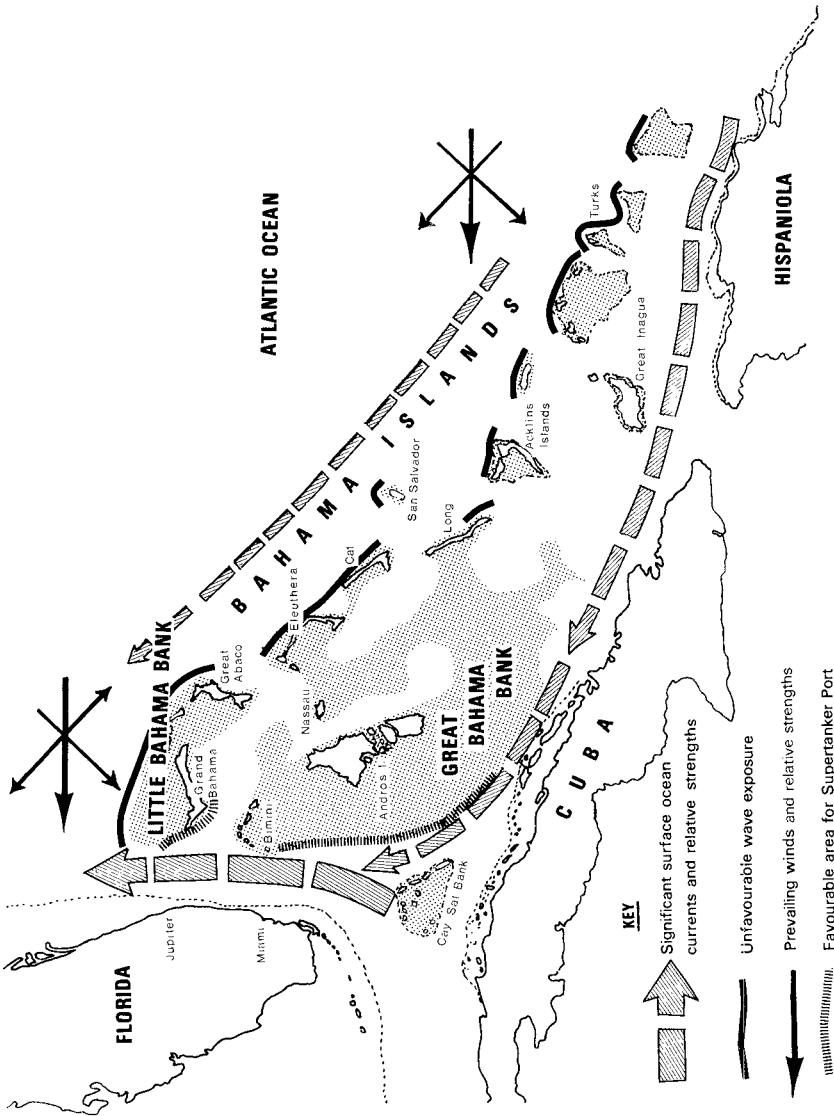than 500 tons (10^5 Imp. Gallons). A spill greater than 30,000 tons will be

2551

Fig. 1. Summary of winds, waves, and ocean currents and environmentally favorable areas for siting a supertanker terminal in the Bahamas.

assumed to be of "catastrophic" proportions. On March 7, 1968, the General
Colocotronis ran aground on a reef about 1000 m offshore of the eastern shore
of Eleuthera Island (Fig. 1) and lost about 2,500 to 3,000 tons of Venezuelan
crude into the sea. This was the only large spill to occur in Bahamian waters
and the spill was located adjacent to a boundary current (Fig. 1). Unfortunately
no useful data were obtained on the trajectory of, or chemical changes in, this
large spill. Furthermore, very little can be said about the physical fate of oil
slicks from large or catastrophic spills in the Bahamas until more is known about
the surface ocean currents. This deficiency in environmental information is en-
countered all too often. With the exception of the Tongue of the Ocean and North-
west Providence Channel, data on inter-island or inter-bank currents in the Bahamas
are quite scanty. It is likewise almost impossible to make meaningful analyses of
the chemical fate of large oil spills. In the analysis below for medium-sized
spills, however, the outlook is better.

MEDIUM SIZED SPILLS

Grand Bahama Island (Fig. 1) was eventually selected as the best of the environ-
mentally-favorable areas for the superport. It then became necessary to make
smaller-scale wind, wave, and ocean-current analyses for several potential port
sites on the southern and western shores of Grand Bahama Island and to obtain a
general idea of the motion of medium-sized oil spills at each site. Medium-sized
spills result from the rupture of storage tanks on land or from the rupture of ship
hulls during groundings or in collisions with other ships. During such events only
limited quantities of oil are lost. A spill is medium-sized (1) if it is between 10
and 500 tons, or about 2×10^3 to 10^5 Imperial Gallons. Its probability of occur-
rence is considerably greater than a large or catastrophic spill.

It is important to be able to estimate the response to wind stress of slicks
from medium-sized spills. In a study of oil-slick motion at the entrance to
Chesapeake Bay (2), it was found that wind has a measurable effect upon the move-
ment of small slicks only when the wind speed exceeds about 7 knots (3.6 m s-1).
Below this threshold value slick motion can be assumed to be due entirely to ocean-
surface currents. Above the 7-knot threshold, the relative wind factor increases
gradually so that for a 20-knot wind (≈ 10 m s-1) a small-sized oil slick moves at
approximately 2.0 percent of the wind speed, and in the direction in which the wind
is blowing. It was assumed that oil slicks from medium-sized spills would obey the
same relationship (Fig. 2) as that found for slicks from small (10 - 240 Imp. Gal.)
spills.

The advection of slicks from medium-sized spills can be estimated by the con-
struction of monthly slick-drift roses for a potential port site. This involves
summation of current and wind-transport vectors, the wind-transport vector being
taken as a percentage of the wind speed, as just mentioned. For Grand Bahama Island
the wind vectors used in monthly rose constructions were those corresponding to
extreme-wind-persistence values found in compilation of one year's wind data obtained
at the Freeport meterological station. The nearshore-current values used for the
current vectors were determined from an analysis of U.S. Navy and Nova University
current-meter records from the Northwest Providence Channel (Fig. 1). Maximum expect-
able current velocities were used because an environmental impact analysis of oil
spills should be based upon the most vigorous conditions to be expected along the
coastal reach under consideration.

Monthly vectors for extreme wind persistence and strongest ocean currents were
determined, added, and the net vectors plotted for each of 16 points of the compass.
The ends of the vectors were then connected by straight lines. The final result
was a "rose" (compare Fig. 3) that showed the extreme limits of potential slick
motion that could be expected from small and medium-sized spills originating at a
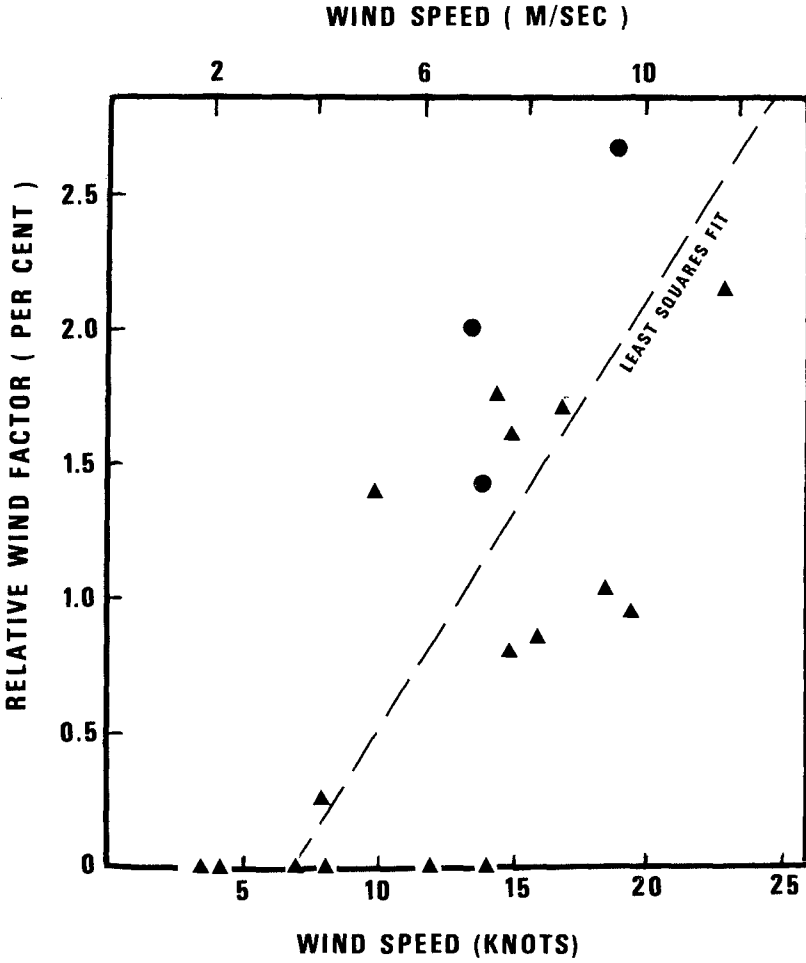
Fig. 2. Slickdrift wind factor versus wind speed. The wind factor does not include slick motion due to local surface currents. Triangles indicate values from Chesapeake Bay (3). Dots are values from the Bahamas.

given point during a given month.

If a medium-sized spill were to occur at the 100-ft. depth contour off
Gold Rock Creek (Fig. 3), for example, the crude-oil slick would usually move
in response to the net westward flux of surface water in the Northwest Providence
Channel. As the slick spread, it would tend to move westward along the south
shore of Grand Bahama Island and, although the slick might be blown about during
a several-day period by the passage of frontal winds in the late fall or winter
months, it would eventually enter the Florida Current. Following that, the slick
would be transported by the Gulf Stream into the North Atlantic. It is quite
unlikely that easterly winds of sufficient strength and persistence would ever
develop which could overcome the transport vector of the Gulf Stream and blow a
slick as far west as the shores of the eastern United States.

The adoption of a model for slick spreading for a medium-sized spill poses
difficulties. Theoretically at least, oil spreading should be due to hydrostatic
forces derived from density differences and at a certain point in spreading history
the forces of interfacial tension should determine the final stages of configuration.
This will lead to an upper limit in the diameter of a slick. Fay (3) developed a
slick-spreading model in which he identified three successive stages in spreading
that are governed by the dominant retarding force that operates to impede spreading
in each stage. Because crude oils are complex, however, and different components
have differing solubilities and spreading rates, Fay's simple model breaks down in
nature. These observations led Blokker (4) to propose an empirical relationship
based upon the assumption that the spreading rate decreases exponentially with the
reduction of slick thickness:

$$Krt = \frac{\pi(r_t^3 - r_o^3)\ dw}{3\ V\ (dw-do)\ do} \tag{1}$$

where Kr is a constant (the "Blokker constant") for a given oil, r_o and r_t are
the radius (cm) of the slick initially and after time t sec, t is the spreading
time (sec), V is the volume of oil in the slick (cm³), and dw and do are the
density (gcm-3) of the sea water and the oil, respectively.

Several of the assumptions of this spreading model, such as the assumption
that the oil spreads uniformly and becomes a circular patch, do not apply in
practice, as will be expanded upon in the section on "small-spill analysis" below.
Jeffery (5), however, made a controlled, medium-sized spill of 120 tons of light
Iranian crude in the North Atlantic and followed the slick for four days. He
found that Blokker constants calculated from the observed maximum slick dimension
ranged between 109 and 360, with an average value of 216. Jeffery regarded the
value of 216 as a reasonable approximation for a spreading constant for the four-
day period, after which time the slick rapidly disappeared. At no point during
the four-day interval did Jeffery find evidence for a change in spreading mechanism
as described by Fay's model.

In the case of the advection and spreading analysis for the Grand Bahama
sites, the author used a Blokker constant of 240 to project the maximum dimensions
of slicks of Persian Gulf crude, from hypothetical 400-ton spills, and for time
intervals of drift corresponding to the lengths of each of the 16 spokes of each
slick-drift rose (cf. Fig. 3). The slick-transport and slick-spreading data
formed the basis for an assessment of the physical environmental vulnerability
of each projected port site to medium-sized spills of Persian Gulf crude oil,
the type of petroleum which the superport was to handle.

A determination of the chemical fate of medium-sized crude-oil spills is more
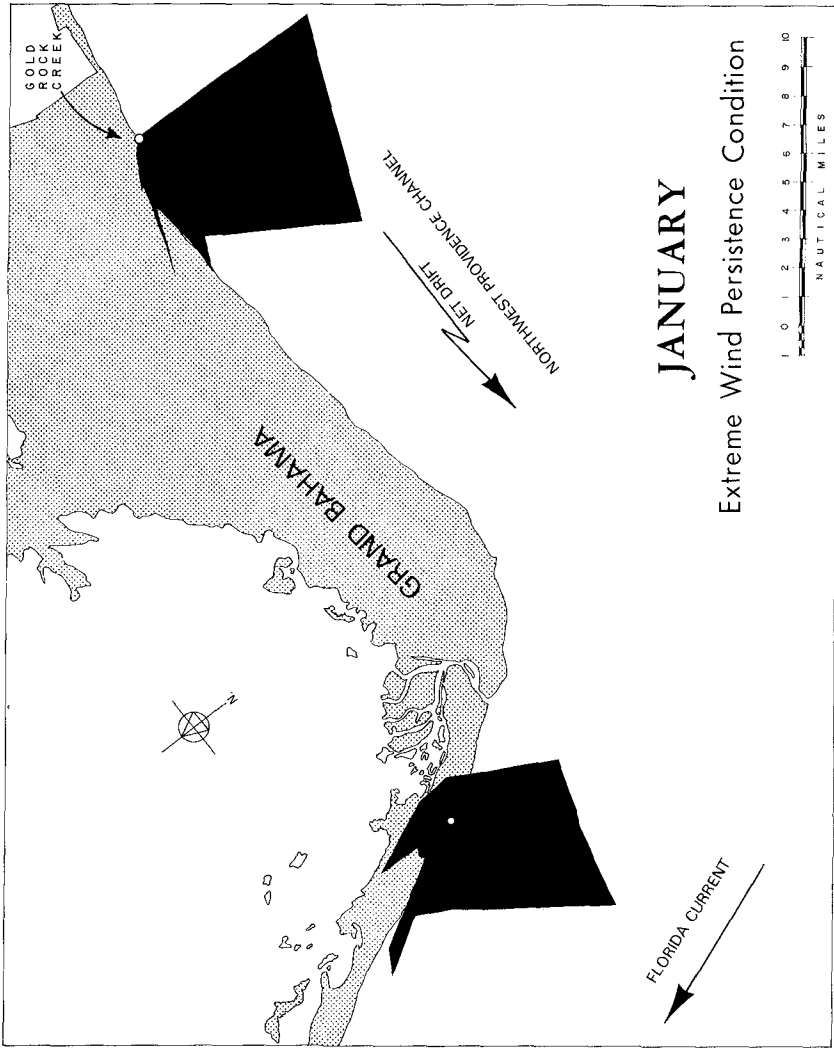problematical than determination of their physical fate. One model for

Fig. 3. Slick-drift roses for two supertanker port sites on Grand Bahama Island. Limits of a given rose correspond to predicted drift positions of leading edge of a hypothetical slick. An estimate of slick spreading does not enter into computation of these roses.

chemical fate is Moore's (6) first-order model which approximates the rates
of evaporation, dissolution, and biological degradation of six oil fractions.
The basic equation for each oil fraction is given by

$$\frac{dc}{dt} = (K_e + K_d + K_b) \, C \tag{2}$$

where C is the concentration and K_e, K_d, and K_b are the evaporation, dissolution,
and biological decay coefficients, respectively. The solution to this equation
is

$$C = C_o e - (K_e + K_d + K_b)t \tag{3}$$

where C is the concentration of a particular fraction after some exposure period
t in days and C_o is the initial concentration. Biological decay is of no
consequence in analysis of the chemical fate of medium-sized spills. A list
of the six fractions and of approximate values of the coefficients K_e and K_d
are given in James, et al. (7). The values are approximate because they will
depend upon temperature and oil-film thickness.

The transfer rates given by James, et al. can be used to make rough pre-
dictions of the toxicity of oil-fouled water at the shoreline following
arrival of a slick borne by an onshore wind (of 10 knots) and associated current.
The current vector is actually of most importance because dissolved components
will move with the water column. (The minimum possible spill-site-to-land
distance that will be travelled by the dissolved components will depend upon
the grounding depth of the particular fully-loaded supertanker which might be
involved in an accident). If one assumes that the depth to the thermocline off
Grand Bahama Island is 10 m, the concentration of the water soluble fractions of
the oil below the sea surface (C at a depth z) can be estimated (7) by

$$C = C_s \exp \left(- \frac{z^2}{50} \right) \tag{4}$$

where z is the depth in meters. The use of equations 3 and 4 resulted in
conservative estimates of the toxicity of oil-fouled nearshore waters following
medium-sized spills of Persian Gulf crude at the potential port sites on Grand
Bahama Island. C_s in equation 4 is the surface concentration (7,p.137).

                                SMALL-SIZED SPILLS

Analysis of the prediction of slick drift, slick spreading, and slick
aging for medium-sized spills led to the approval of two possible superport
sites and on March 6, 1972, the Prime Minister of the Bahamas announced that
a supertanker port would be constructed about 30 miles east of Freeport, Grand
Bahama Island. In early 1973 it became known that the proposed superport
would be located slightly east of South Riding Point (Fig. 4) and that a sea-
island, oil-transfer structure would be built 3,600 feet offshore in water
about 100 feet deep. The Bahamian Government then indicated its desire for
additional information on the fate of small spills that commonly occur during
oil-transfer operations at a sea-island. This necessitated the release of
five controlled spills (275 U.S. gallons, or $1.04m^3$, each) of oil (8) at the
sea-island site under a variety of wind and nearshore-current conditions. The
releases were made in February, 1973, because February is usually the windiest
month in the northwestern Bahamas. The oil slicks were tracked and sampled
from ships. Surface-current drogues were tracked by radar to determine the
nearshore current field. The Canada Center for Remote Sensing photographed
the slicks from aircraft in connection with their sensor-development program.
Analysis of the field measurements permitted:

   1) the calculation of slick-spreading rates,
   2) determination of the rates of chemical aging of the slicks, and
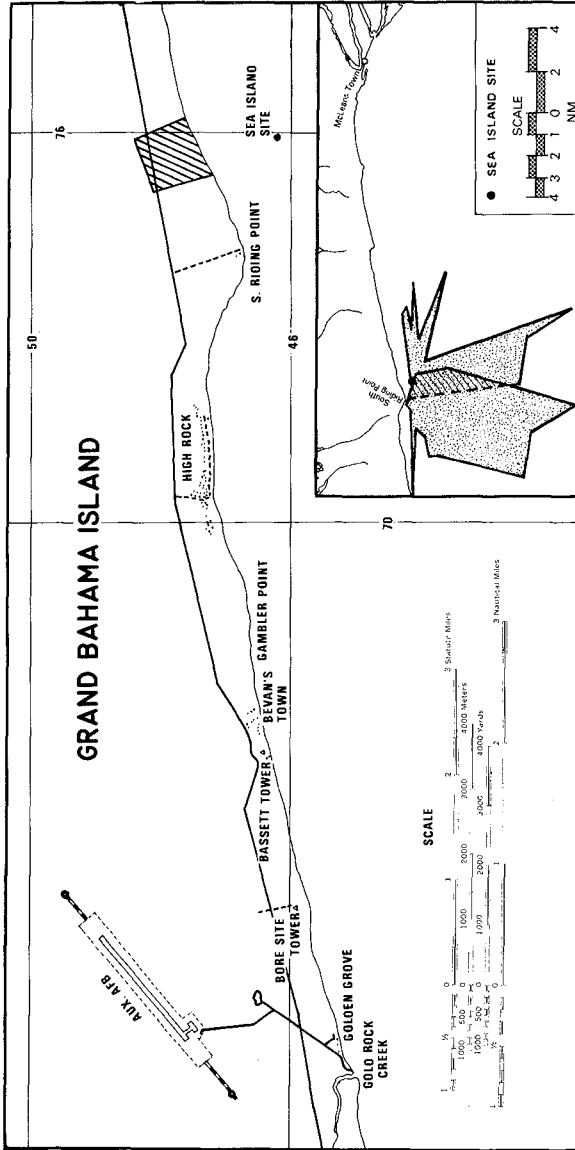   3) construction of precise slick-drift roses for the sea-island site.

Fig. 4. Location of the sea-island supertanker bunker off South Riding Point, Grand Bahama Island. Shaded pattern indicates storage tank site. Inset shows slick-drift roses for January, in which data for extreme-wind-persistence conditions are combined with nearshore-current data for west-setting (left-hand rose) and east-setting currents.

A typical slick trajectory is shown in Figure 5 and slick-spreading data are plotted in Figure 6. Bien (9) analyzed slick spreading by planimetering slick areas as seen on 9 x 9-inch aerial Ektachrome photographs and produced a graph similar to Figure 7. This graph shows clearly that there is a decrease in the rate of change in area of an oil slick as a function of increasing wind speed. When the current vector is not dominant relative to the wind vector, and is not markedly off-angle to the wind vector, oil slicks align themselves with their long axes parallel to the mean wind direction. Heavier components of the slicks are transported toward the downwind (leading) edges.

It is probable that Langmuir circulation (10) plays an important role in limiting the spreading of slicks in directions perpendicular to their long axes. Langmuir circulation sweeps organic matter in sea-surface films together along the lines of convergence of convection cells whose long axes parallel the wind direction. This action is quite evident in air photos of crude-oil slicks under wind speeds of moderate strength and it effectively reduces the rate of horizontal spreading. The vigor of the Langmuir circulation increases as the wind speed increases and may lead to entrainment of slick material where water sinks in a convergence zone. Whatever the nature of the complex factors which enter into slick spreading, it is important that empirical data such as those of Figure 7 be used in conjunction with spreading models, such as those of Fay (3) and Blokker (4) mentioned earlier.

The chemical fate of the small spills was studied rather carefully because water-soluble aromatic and aliphatic hydrocarbons may have sub-lethal effects on marine organisms at concentrations of 10-100 ppb, lethal toxicity at 0.1-1.0 ppm for most larval stages, and lethal effects at 1-100 ppm for most adult organisms (7). The rates of disappearance of specific aromatic and aliphatic components of five crude-oil slicks were studied (11) because the lower-boiling fractions contain almost all of the lethal components of the slicks.

Previous investigations of the aging of crude-oil slicks have demonstrated that all of the lower-boiling components evaporate and dissolve within a few hours of oil spillage. The five Bahamian spills were studied for the "disappearance" (evaporation plus dissolution) of the aromatic and aliphatic components shown on Figure 8. Ten gallons of crude oil were replaced with technical grade cumene, to act as a tracer and internal standard, in each 275-gallon spill. Wind speeds ranged from calm to 18 mph (with gusts to 22 mph) and sea-surface conditions ranged between calm with gentle swell to extensively whitecap covered. Water temperature was essentially constant at 23.6°C. Air temperature ranged between 20.5 and 24.0°C and relative humidity between 60 and 79%. Details of the field and laboratory procedures are presented elsewhere (11). Sampling of crude oil was confined to the thickest oil pools of each slick.

Of particular interest in interpreting the experimental results are the relative disappearance rates of cumene and nonane. These hydrocarbons have very similar vapour pressures (cumene 4.2 and nonane 3.9 mm Hg at 23.6°C); thus, their evaporation characteristics will be similar. Cumene is, however, considerably more soluble in water (50 vs. 0.22 mg/l). A comparison of the relative rates of loss of these hydrocarbons may yield information on the contributions of evaporation and dissolution as mechanisms for the removal of specific hydrocarbons from oil spills.

Analysis (11) suggests that in each spill there was dissolution of about 2 kg of cumene. If this was into a water column 1 m deep and over an area of 10^4 to $10^5 m^2$, the aqueous cumene concentration would be in the range of 0.2 to 0.02 mg/l. Water samples taken from under the spill identified cumene
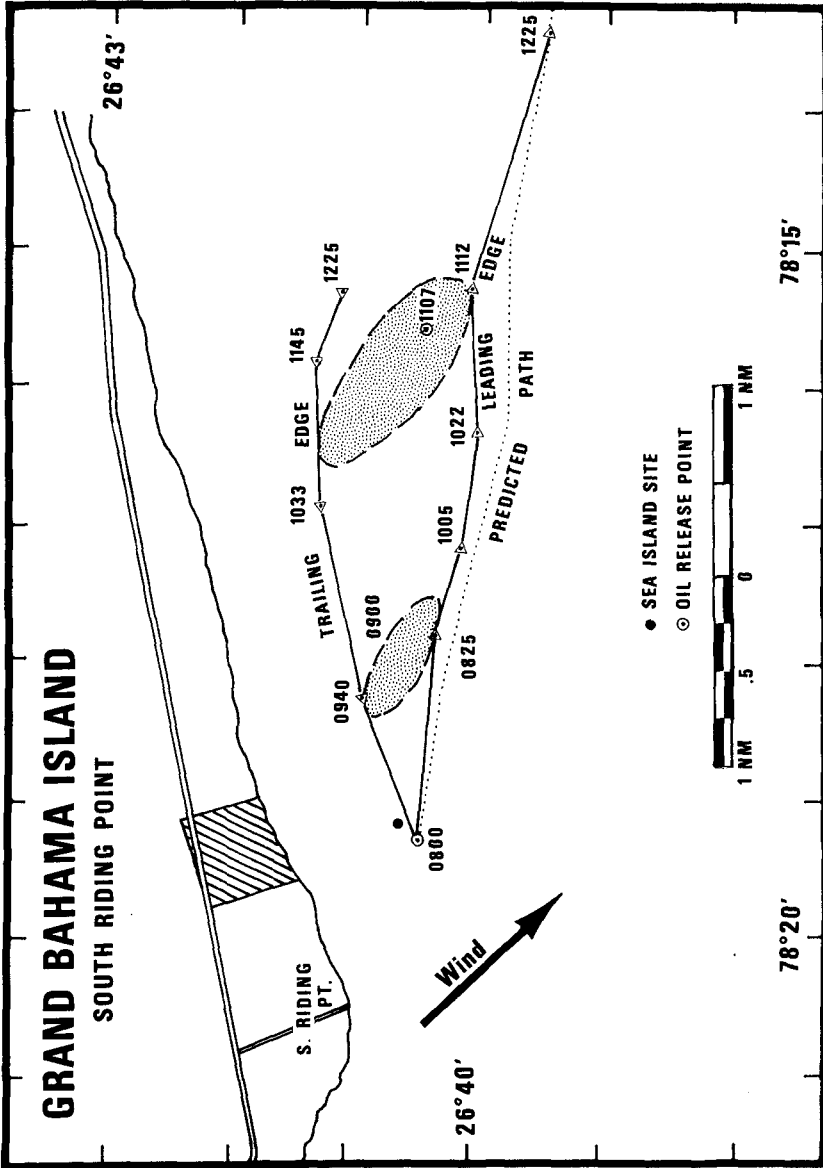
Fig. 5. Positions of leading and trailing edges of the 270-gallon (U.S.) slick of February 16, 1973, and predicted slick trajectory. Slick outlines are approximate only. Times given are in hours (EST).
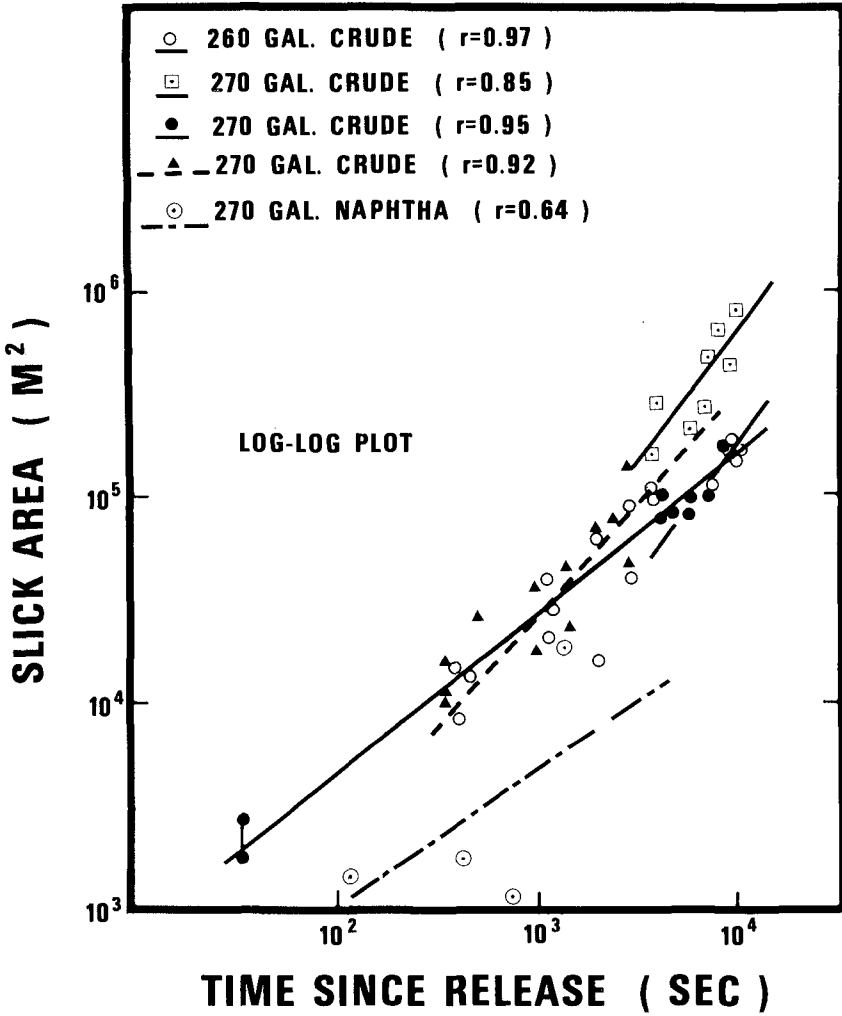
Fig. 6.   Slick area as a function of time for 4 South Louisiana
          crude-oil spills off S. Riding Point, Bahamas during
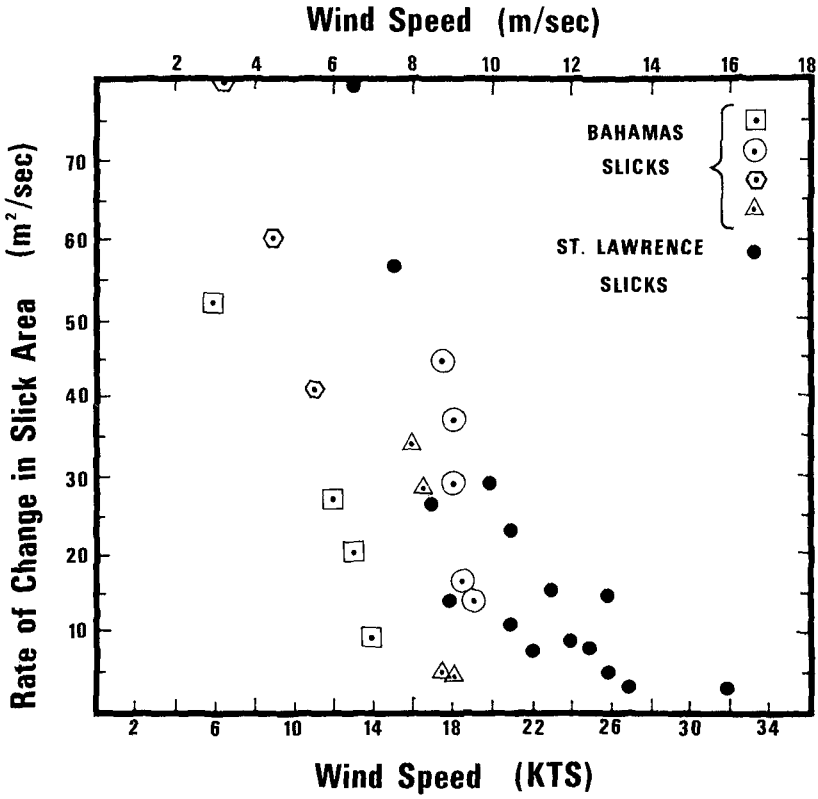   February, 1973.

Fig. 7. The rate of change in slick area as a function of wind speed (over short intervals during the period 10^2 to 10^4 seconds after release).

as being present at concentrations below 1 mg/1, the analytical technique being
insufficiently sensitive to give quantitative results. In two samples no cumene
was detected and in two samples cumene was detected at concentrations in the
range 0.1 to 1.0 mg/1. The biological implications of such concentrations are
that only organisms which are in close proximity to the spill for an extended
time are likely to suffer toxic effects. It is suspected that much of the
dissolved aromatics from small slicks are lost by evaporation from aqueous
solution. The most profound biological effects will occur under large, thick
slicks and under quiescent conditions in shallow water when substantial concent-
rations of aromatics may be achieved in the underlying water and maintained
for a considerable time.

There is evidence in spill five, from the apparent increase in cumene
concentration, that different pools of oil in the slick weathered at different
rates. Variation in weathering in different parts of the same slick is an
important problem, previously unreported. It is probably associated with
uneven spill thickness.

It can be inferred that napthalene, which has the same boiling point as
dodecane, should disappear in 3-8 hours, depending on wind conditions. Thus,
the majority of the toxic fractions (boiling point below 220°C) are inferred
to disappear from a typical slick some 3-8 hours after a spill, most having
disappeared at the earlier end of this time interval.

The relatively rapid decrease in the five-component concentrations of
slicks 2 and 4 is related to the sudden onset of capping on the sea surface
during a brief gusty period. These rates of disappearance can be compared
to those of slick 5, in which the wind speed increased very gradually until
about 115 minutes after the spill when widespread whitecaps suddenly appeared.
It would seem, therefore, that there is a significant discontinuity in the
rate of disappearance of the aromatic and aliphatic components between wind
speeds below and wind speeds above those which cause the onset of extensive
capping. Possibly, evaporation is suddenly enhanced by increased air turbulence.
It would thus seem desirable to develop loss-rate curves for the two different
sea-state-roughness regimes, one in which there is little or no white-capping
and one which displays extensive capping. A further complication is that the
greater turbulence during capping may result in the formation of oil-in-water
and water-in-oil emulsions.

After the slick aging study had indicated the rapid loss of most of the
toxic components of the crude, slick-drift roses were constructed for extreme-
wind persistence and strongest-coastal-current conditions at the sea-island
site (see roses,Fig. 9). The slick-tracking data verified the method used to
construct the roses (see Fig. 5, for example). The roses indicated the
environmental suitability of the sea-island site for capture and cleanup of
small spills and a construction permit for the supertanker port was approved.

Oil spill cleanup and control operations are greatly facilitated by
collection of pre-operational data such as those described above. It is a
simple matter to install continuously recording wind and current-meter systems
at the site of a supertanker bunker and, when a spill occurs, to use the wind
and current values in a computer program which predicts the oil-slick's path,
the length of shoreline covered by oil at landfall and, if chemical analysis
of the type of oil spilled has been done, the rate of chemical aging as well.

RECOMMENDATIONS

1) Wherever possible, a general environmental analysis should be under-
taken before industry and (or) government commit to a given coastal reach for

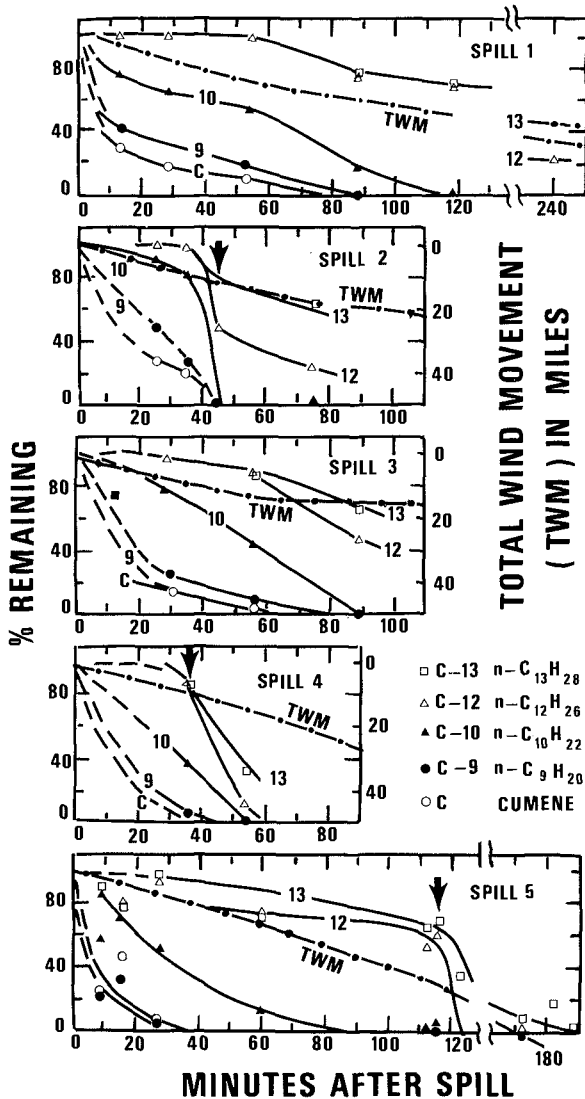Fig. 8.   Percent of low-boiling, crude-oil components remaining in slicks
1-5 as a function of time (11). Also, total wind movement in miles
(miles/hr x hrs) as a function of time and moment of onset of
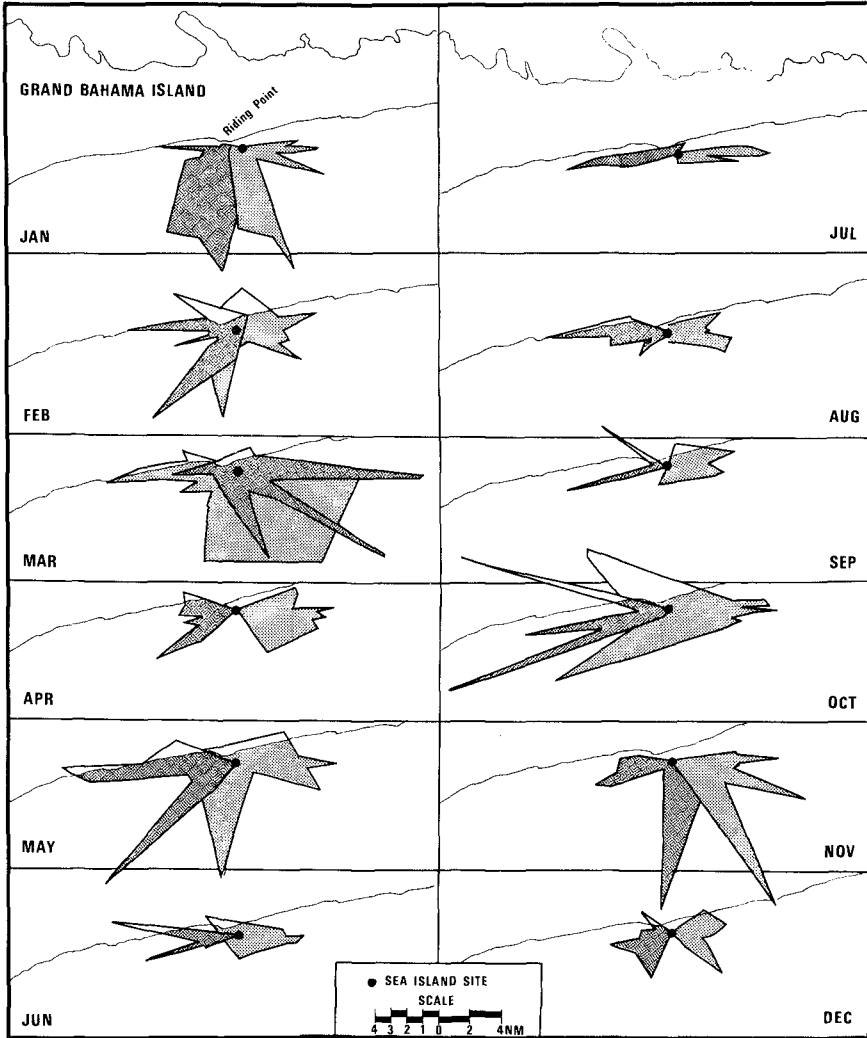widespread whitecapping (arrow) for slicks from spills 2, 4, and 5.

Fig. 9.   Slick-drift roses constructed by Bien (9) for small spills of
          crude oil spilled on east or west-setting currents.

construction of a superport.

2)   To be of greatest value, assessments of vulnerability to oil spills should
consider the most-vigorous (generally 'worst') possible conditions that could be
expected at a proposed supertanker port. Slick advection, for example, should be
examined by coupling historical data for the strongest, most-persistent winds with
data for the most unfavorable ocean currents. Engineering design, or the port
location itself, should be based on such a conservative approach to assessment of
environmental vulnerability.

3)   Slick-advection roses and slick-spreading diagrams should be generated for
the conditions given in 2 above for the supertanker terminal and, if possible, for
probable points of tanker grounding or collision in the general vicinity of the
port site.

(The foregoing three points depend upon the availability of useful wind and
ocean-current data. It is, therefore, incumbent upon appropriate government
agencies or the petroleum industry to obtain these data before serious initiatives
are started vis-a-vis superport construction).

4)   Studies of the aging, spreading, and advection of small slicks, of the type
of crude oil to be imported to a proposed terminal, should be carried out in the
vicinity of the terminal site. Airborne mapping of slick spreading is a necessity.
Such controlled spills give considerably more insight into fate mechanisms than one
expects. Rates of disappearance of the low-boiling components of the slicks should
be investigated more fully during different states of sea-surface roughness.

(In order to implement point 4, environmental and regulatory agencies will need
to loosen their overly restrictive controls on experimental releases of oil for
research purposes).

5)   More empirical studies, as recommended in 4, are needed for the development
and testing of predictive models of slick advection, spreading, and aging. Additional
studies of large-volume, mid-ocean releases should be attempted. The roles of
emulsification and Langmuir circulation on slick spreading need further study in
nature.

6)   For the present, use of the Blokker spreading model and Blokker constants
appropriate to the environmental conditions and types of crude involved, seem most
suitable for predicting the spreading of medium to large-sized spills of crude oil.
For small spills, the empirical data of the present study may be used but modifica-
tions will be required for the differing physical and chemical characteristics of
the various crude oils to be investigated.

ACKNOWLEDGMENTS

REFERENCES AND NOTES

1. Beynon, L. R. (1973), "Codes of practice for dealing with oil spills at sea and
      on shore: a European view," Proc. Joint Conf. on Prevention and Control of
      Oil Spills, Washington. p. 617-626.

2. Munday, J. C., Harrison, W., and MacIntyre, W. G. (1970). "Oil slick motion
    near Chesapeake Bay entrance," Water Resources Bulletin, 6, 879-884

3. Fay, J. A. (1969), "The spread of oil on a calm sea," in Oil on the Sea,
    D. Hoult (Ed.), Plenum Press, New York. p. 53-64.

4. Blokker, P. C. (1964), "Spreading and evaporation of petroleum products on
    water," Proc. Fourth Internat. Harbour Conf., Antwerp, Belgium. p. 911-919.

5. Jeffery, P. G. (1973), "Large-scale experiments on the spreading of oil at sea
    and its disappearance by natural factors," Proc. Joint Conf. on Prevention
    and Control of Oil Spills, Washington, D. C. p. 617-626.

6. Moore, S. F. (1972), "Some aspects of deepwater terminal site selection in
    northern New England coastal areas," paper presented at Annual Meeting, Assoc.
    of Sea Grant Institutions, Houston, Texas.

7. James, W. P. and Others (1973), "Environmental aspects of a supertanker port on
    the Texas gulf coast," Texas A & M Univ. Sea Grant Proj. Rept. 73-201,
    College Station, Texas. p. 1-436.

8. Persian Gulf crude, of the type to be imported to the terminal, was unavailable
    for the tests. Thus, readily-available South Louisiana crude was used.

9. Bien, W. (1973), "Modelling petroleum spills at supertanker ports," Master's
    Thesis, Dept. Geography, University of Toronto, Toronto, Ontario. p. 1-122.

10. Weyl, P. K. (1970), Oceanography: An Introduction to the Marine Environment:
    John Wiley, New York, 1-535. (See especially pp. 421-422).

11. Harrison, W., Winnik, M., Kwong, P., and Mackay, D., (1974), "Crude oil spills:
    disappearance of aromatic and aliphatic components of sea-surface slicks,"
    Env. Sci. Technol., in the press.

CHAPTER 152

ENVIRONMENTAL PROBLEMS ASSOCIATED WITH A PIPELINE LANDFALL

IN COASTAL DUNES AT CRUDEN BAY, ABERDEENSHIRE, SCOTLAND.

Dr. William Ritchie, Senior Lecturer in Geography,
University of Aberdeen, Scotland.

Abstract

The first oil pipeline from the North Sea area reached
Scotland in 1973.   The landfall, at Cruden Bay, Aberdeenshire, is
a sediment-filled, bay-head beach with coastal dunes.   Environmental
and landscaping problems arose with the trenching of the beach and
dune areas.   Various methods, including flexible fence construction,
spraying with a bitumen compound and spreading of soil over vulnerable
areas, protected the site successfully.   Full revegetation took
place later and the beach and dune area are now restored to their
original condition.   Environmental management techniques were
designed to preserve the high amenity and ecological status of the
site and minimise the risk of side-effects, both during and after
engineering work.

The General Situation and Problems

Since 1965, at an accelerating rate, several of the deep
sedimentary oil and natural gas bearing structures in the Scottish
sea area are being explored and exploited.   Although the greater
number of proven reserves appears to lie near the Shetland Islands,
one of the earlier oilfields, the Forties Field, lies 150 km. north-
east from the Northeast "shoulder" of Scotland, Aberdeenshire.
Although undersea technology is developing rapidly to meet the

problems posed by working in depths of 100 to more than 200 m., the

problem of bringing the oil and gas ashore is currently solved by

conventional seabed pipelines.   The 81 cm. diameter, coated steel

pipeline from the Forties Field reached the coast at Cruden Bay in

May 1973 and the regional and local site of the landfall is shown

in Figure 1.   This pipeline is the first to reach Scotland from the

North Sea but will be followed within the next few years by several
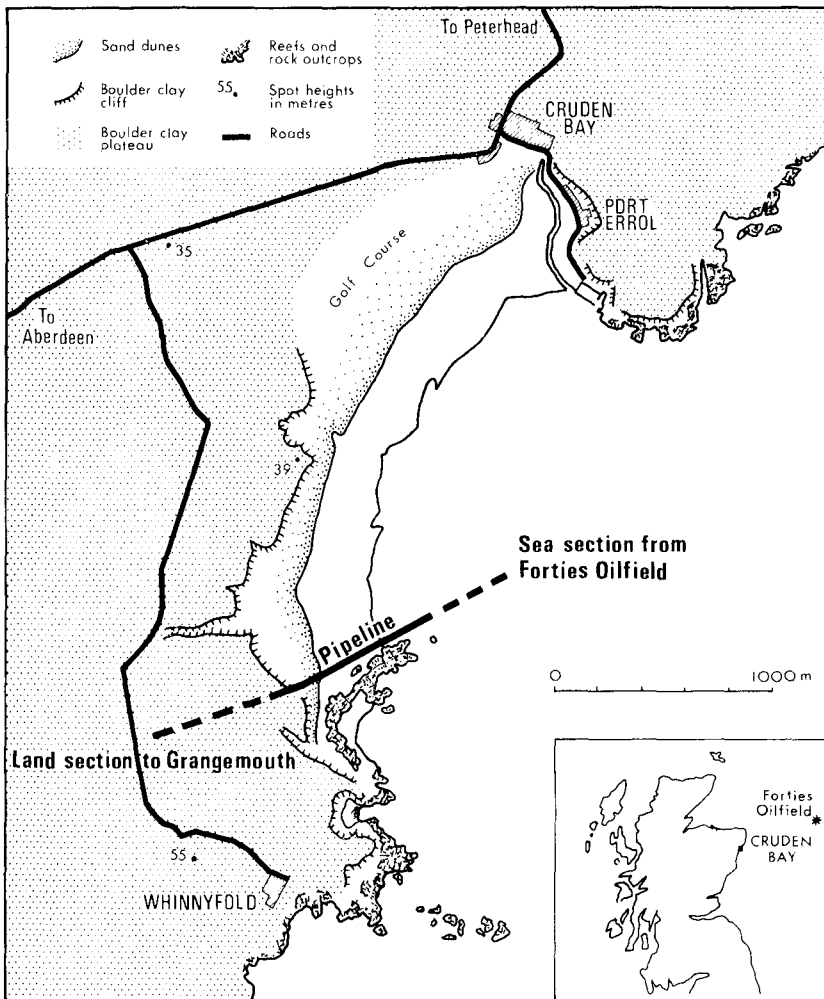
more.   The observations made on the problems of coastal conservation

and rehabilitation associated with the pipeline landfall at Cruden

Bay may therefore be regarded as occurring in a prototype situation.

           The engineering and environmental management issues raised

by pipeline landfalls around the Scottish coastline must also be

seen against a background of considerable public interest and a

growing awareness of environmental issues.   The point where the

pipeline emerges from the sea to join the land is the location where

public and conservational interest tends to be concentrated.   Thus,

it is not only during the phase of rehabilitation but also during

the period of site work that protective measures have to be carefully

undertaken.

           At the interface of the dune/beach complex and the sea,

aeolian, marine and other geomorphic processes interact to produce a

relatively sensitive morphological and biological zone.   Contemporary

pipe-laying techniques require that the pipeline is buried in the

nearshore zone, the beach and the dunes.   The location must therefore

be a sediment-filled, gently shelving offshore area.   The re-entrant,

sediment trap of a bay-head beach is ideal, whereas the more dynamic,

higher energy open coast beach is a more difficult landfall.

           The engineering technique employed is essentially a form of

trenching.   The pipe is pulled onshore from a lay-barge, through

the trench by a powerful winch.   The sides of the trench in the dune

zone are ·retained by a sheet pile coffer structure.   This trench of

variable depth (4-10 m.) cuts through the beach, dunes and landwards

areas and remains partially open until the pipeline is tested.   It

is then subsequently backfilled.   The exact time of pulling is con-

trolled by wave conditions a few hundred metres offshore where the
lay-barge is moored.   Around the coastline of northeastern Scotland
the wave climate is highly variable and unpredictable, and delays
can occur.   Again the bay-head situation is preferable since it
affords some level of shelter.

The crucial issue of site selection is therefore that of
the existence of excavable materials in the immediate coastal area.
A sufficient depth of sediment over the rock head profile, both off-
shore and onshore, is a prerequisite of current techniques.   Bay-
head sites where these conditions are satisfied are therefore at a
premium around the Scottish coast if they are within the economic
radius of sea bed pipe-laying from the producing area.

The beach and dune complex, which is the type of coastline
that satisfies the physical requirements as outline above, has,
until recently, formed an empty zone for human use.   Settlement,
industry and commerce have tended to prefer other sites.   As agri-
cultural land, the dunes and links have a low value.   Recreational
or leisure pursuits have filled the unoccupied space, as for example,
in the form of golf courses.   A high proportion of these coastal
zones have also achieved considerable ecological, ornithological and
conservational status levels.   The areas sought by the pipeline
constructors are devoid of the more permanent physical artifacts of
a modern society but are high on qualitative and intangible resources
such as scenic value, recreational potential and scientific interest.
Thus, although the technical and physical problems facing the engineer
are of a low order, the wider environmental issues aroused may be
considerable.

Specific Environmental Problems at Cruden Bay

          The landfall at Cruden Bay consisted of a low gradient sand

beach, approximately 240 m. wide between low and high water spring

tide levels, with a 22 m. wide area of sand between the base of the

dune and high water mark (sand nourishment zone).   The coastal dune

was low and mature, and in a condition of occasional erosion as a

result of wave undercutting.   It had a gentle dune backslope to a

low area in front of a steep abandoned cliff line cut in boulder

clay.   The profile and planimetry are shown in Figure 2.   Of major

concern was the proximity of the golf course a few metres north of

the site and the high amenity value of the Cruden Bay coastal area.

          The specific problems were therefore:-

    1.   Do not introduce geomorphic side-effects such as beach
          drifting, blowout development, sand deposition on adjacent
          surfaces or radically alter drainage conditions.

    2.   Ensure complete and permanent restoration in a short period
          of time with an appearance and condition as similar as
          possible to the pre-existing condition and ecological status.

    3.   Keep the area appearing well-managed throughout the period
          of site work.

          There were therefore two time scales operating;   during site

work and the longer term planning for site rehabilitation.   It was

clearly necessary to minimise costs and work by designing day-to-day

protection and the temporary movement of spoil materials so that they

would be compatible with the final restoration scheme.

Beach Protection

          The danger of dune undercutting and the initiation of beach

drifting was never a major threat since the site was in a bay-head

location and protected by a tombola and reef configuration offshore

(Figure 2).   The beach trench was only open for a brief period and

coincided with low wave energy conditions.   In addition, excess

sand from site work was fed into the small bay south of the rock

reef below low water mark to artificially nourish the low sand

tombola and ultimately feed the beach backshore.   Both results were
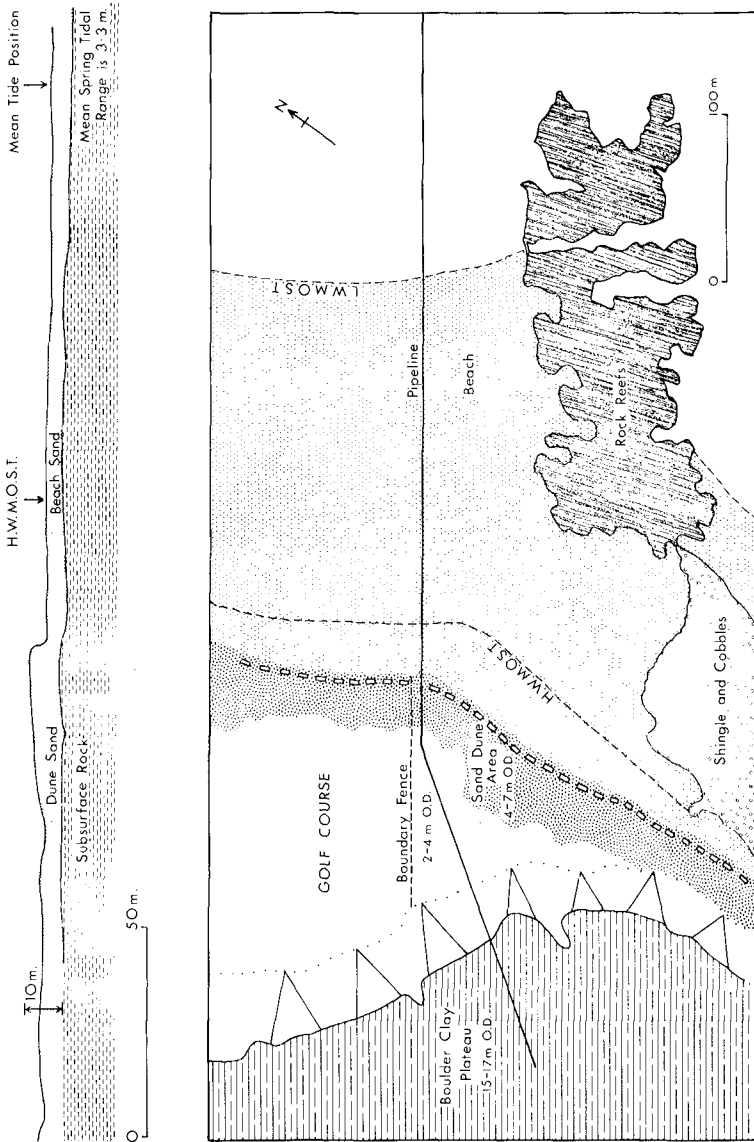
achieved and the backshore sand has continued to strengthen the

formerly eroding dune face by natural accretion.

Coastal Edge and Dune

        The coastal edge was slightly undercut.   There was little

evidence of accretion and mature vegetation reached the edge of the

dune.   Marram (Ammophila arenaria) was present as old mature tussocks

with the intervening spaces filled with a varied mosaic of dune and

non-dune plants.   The dune was not the normal active coastal dune

barrier but an old, low gradient, mature feature resembling dune

pasture.   There was little sign of sand movement and the complete

cover of vegetation assured stability.   Since a major breach would

be cut through this dune to bedrock level (Figure 2) and considerable

adjacent areas would be stripped of vegetation, the risk of deflation

was considerable.   Three devices were used to minimise sand blowing:-

    1.   All susceptible areas were sprayed with a commercial
          bitumen compound "Crelawn".   This is a water-based,
          bitumen emulsion and is easily and cheaply spread by a
          hand sprayer.

    2.   Larger sand spoil heaps (most of it required for back
          filling) and bare surfaces were covered by a 5-10 cm.
          layer of soil.   This was the overburden material from
          the access road.   It was not topsoil.   The material was
          clay rich and intended as a temporary cohesive, water
          retentive cover.   Since it contained the seeds of grasses
          and agricultural weeds, vegetation grew spontaneously, and
          rapidly hid the visually unattractive appearance of these
          wasted areas.

    3.   Brushwood fences were built using standard fence posts and
          3-strands of wire with coniferous branches interwoven by
          hand.   The brushwood was obtained locally.   Some attempt
          was made to achieve a 40% porosity; a value suggested by
          the research literature of tree shelter breaks as being
          the ideal wind screen.   These fences acted as a barrier
          between the golf course and the site.   They were approxi-
          mately 1 m. high.   Other fences were placed along the
          dune crest and short sections were placed in the dangerous
          corridors created between the sheet pile walls of the
          trench and the pre-existing sand surface.   The sheet

piles were cut down to their minimum height to reduce
their channelling effect on wind flow.

Pipe-pulling through the dune
trench in May 1973.   Note
bitumen spray on trench sides.

These three devices effectively held the entire site area stable from February 1973 until pipe pulling in May 1973 (Plate 1) and the final restoration work which took place in two phases, June 1973 and July 1974. As a result of these devices, there was no wind erosion, no deflation and absolutely no sand deposition on the golf course.   Since the bitumen spray as will be described below encourages vegetational growth, the appearance of the site also remained reasonable throughout the period.

Full Rehabilitation

After pipe-pulling the sheet piles were removed and the
trench filled with sand to the pre-existing level.   The dune face

was restored but set back approximately 0.5 m. and the slope angle

reduced to 20°.   Other site work such as pipe-testing delayed final

restoration and the work was therefore done in two separate stages.

        Protective fences were retained for more than one year to

inhibit sand movement and protect reseeded areas.   In addition to

the brushwood fences some fences were constructed of an indestructible,

fine screen plastic material.   This material was found to be less

efficient than brushwood since its porosity was less and offered too

much wind resistance, but was easier and quicker to erect.   Split

chestnut paling is also suitable but was unavailable locally.

        All damaged and restored surfaces were revegetated using

a seed mixture specified by an agricultural grassland expert to

germinate successfully and to be compatible with pre-existing species.

Soil which had been used as a protective covering was re-used but

additional higher quality topsoil was imported and spread on the sur-

face.   The topsoil was seeded and slow release nitrogen fertilizer

pellets were added at a calculated rate.   The area was then lightly

sprayed with bitumen.   The bitumen held the surface physically,

retained surface moisture (this was particularly important since re-

seeding took place in the dry month of June) and by acting as a

'black-body' retained heat and thereby promoted almost incredible

vegetational growth.   Within weeks the area was carpeted in vege-

tation.   The bitumen will also hold sand slopes stable at an angle

greater than the normal angle of rest.   Almost one year later,

after a single cutting to promote tillering, the area is under lush,

mixed grasses and other plants.   The bitumen layer has disappeared

after first disintegrating into discreet patches and finally granules.

This disintegration is an advantage since many other alternative forms of surface protection are not biodegradable.

During winter gales some sand was trapped on the crest of the new dune face by the brushwood fence. This "edge accumulation"

Dune face showing low-cost thatching in July 1973 and the same area in May 1974 with Marram and Sea Lyme grass coming through the branches and hessian cover.

was hand planted later with Marram grass, and, in time the edge will build-up to a natural configuration. If conditions are suitable Marram and other dune species will gradually take-over from the planted species and there are signs (in late summer 1974) that this is taking place.

All fences, except the one along the coastal edge, were removed in summer 1974 unless they were required to demarcate owner-ship limits. Hitherto the fences had an important function in res-tricting public access. The coastal edge fence remains to protect the still fragile crest above the dune face.

The dune face posed a special problem in that it is parti-

cularly difficult to revegetate this edaphically difficult zone.
As shown in Plate 2, low cost thatching was used to physically protect
the slope and encourage accretion.   This thatching included a cover

A general view of the site area in August 1974.

of hessian to bind-down the tree branches.   There has been con-
siderable sand accretion and strandline, and dune species have
started to recolonise the dune face.   Hand planted Marram and Sea
Lyme grass (Elymus arenaria) were planted in Spring 1974 to increase
the rate of colonisation and the appearance of the dune face in July
1974 is shown in Plate 3.   The general appearance of the site can be
seen in Plate 4 and compared with Plate 1.

Conclusion

        The problem of environmental management of the landfall

site at Cruden Bay consisted of maintaining physical stability and

assuring the restoration of vegetation.   It also had a wider

function in ensuring that the sometimes neglected aspect of coastal

engineering, the initiation of side-effects was minimised.   At

Cruden Bay, the chances of this happening were low since the site

was particularly well chosen in a sheltered locality, nevertheless

an awareness of the linkages in a natural system such as a dune/

beach system is an essential part of environmental management

associated with engineering work.   There was also a public relations

function in that the public are increasingly and properly conscious

of the need to preserve the aesthetic, scientific and amenity value

of any semi-natural area, which is being disturbed by engineering

projects.

        For similar future projects the following might be con-

sidered useful suggestions:-

    1.   Commission a vegetation survey before work begins.
         Vegetation is the best single index of environmental
         conditions.

    2.   Commission a geomorphological survey of the local site
         in the context of the wider physiographic system.   Note
         the process/form relationships in the area.

    3.   Commission a large scale gridded topographical survey of
         the site.   This is an invaluable reference document and
         avoids ambiguity in carrying out instructions.

    4.   Protective and restorative devices should emulate local
         natural conditions, e.g. keep a moist, cohesive surface
         on all bare sand areas, use flexible, permeable barriers,
         avoid rigid structures: the essence of beach/dune
         stability is movement within a framework of dynamic
         equilibrium principles.

    5.   Unless there are high value areas near the dunes, it is
         not necessarily right to be obsessed by preventing some
         wind erosion and sand blowing.   Although this condition

was not satisfied at Cruden Bay, it is normal for coastal
dunes to have erosional features such as blowouts.
Sporadic wind erosion is the natural state of most dune
systems and is essential to their function within a coastal
system.

6.   Sea Lyme grass is a more effective dune and coastal edge
      plant than Marram.   Its replanting and growth rates are
      better.   It can tolerate some salt water.   It spreads
      rapidly and does not appear to be any less resistant to
      disease than other 'traditional' dune-fixing species.
      Sea Lyme grass has been noted as spreading spontaneously
      and rapidly under natural conditions in many parts of
      Scotland.

CHAPTER 153

QUANTIFYING SPOIL DISPOSAL PRACTICES

by

Roy Halliwell* and Brian O'Connor+

ABSTRACT

The results of an extensive field study undertaken in the Mersey Estuary and its
approach channels are briefly described. These measurements were undertaken to
obtain a quantitative understanding of the movement and circulation of water and
sediment in the area. There is considerable dredging activity required in the
area and the spoil from such operations is, at the present time, deposited at an
offshore site in Liverpool Bay.

A simple model is presented which attempts to quantify the movement of sediment·
into and within the Mersey system. The field measurements showed that considerable
quantities of sediment return to the docks, estuary and approach channels from the
spoil ground. The model includes this fact and attempts to quantify the amounts
returning to various areas. The model equations were applied to each year of the
period 1955-65 to determine the various factors and to test its validity: this
required the use of the annual hydrographic surveys and dredging records as well
as the results of the field measurements. Finally, the model was used to compare
the probable results of a number of possible schemes including re-siting of the
spoil ground, pumping all dredged material ashore and free-dumping of dock
dredgings in the estuary itself.

1. INTRODUCTION

The danger of spoil disposal by free dumping within long estuaries has been
recognised for some time. However, offshore disposal has been regarded with
favour by many Port Authorities. At present dredged spoil from the Mersey Estuary
and its approach channels is deposited in Liverpool Bay, some twelve miles from
the estuary entrance, in comparatively shallow water (17 ft. at LWMST and 44ft. at
HWMST): the spoil ground is the area around stations BH and BG, figure 1. This
spoil ground is one of the original disposal sites used by the Mersey Docks and
Harbour Company since dredging operations began in 1891. Its continued use is
based, partly, upon the results of a field and model investigation into the
circulation pattern of Liverpool Bay and the Mersey Estuary which have been
described by Price and Kendrick (1963).

The present paper describes the results of a seven-year research programme started
in 1964, which was undertaken with the prime object of improving the efficiency
of dredging operations in the Mersey Estuary and its approach channels through
Liverpool Bay. This investigation attempted to quantify the water and sediment
circulation of the study area; the calculations being based on extensive field
observations.

* Professor of Civil Engineering, Heriot-Watt University, Edinburgh, UK

+ Senior Lecturer, Civil Engineering Department, Manchester University, Manchester,
UK

2. WATER AND SEDIMENT MOVEMENT WITHIN THE ESTUARY

Early work (1964-68) concentrated on the temporal and spatial measurements of
water velocities, suspended solids content, salinity and temperature.

2.1 Brief description of measurements

Some forty boat-stations were established upstream of the estuary entrance as
well as some five coastline stations (dock walls) for long term measurements of
the amount of sediment present in the estuarine water. Usually the boat stations
were chosen so that the total water, salt or sediment flux across various sections
within the Narrows of the estuary could be determined from the measurements obtained.
Figure 2 shows some of the stations chosen within the Narrows: these correspond to
the primary sections chosen, Gladstone, Egremont, Cammell-Lairds and Dingle. The
measurements were made from an anchored vessel in a routine manner: the techniques
have been described elsewhere by Halliwell and O'Connor (1966) and in general were
relatively straightforward. The instruments were usually of the direct reading
type and measured the in-situ properties of the water. The period of measurements
extended over one or more complete half-tide cycle i.e. the whole of the flood (or
ebb) tide.

2.2 Summary of results and present understanding

The quantity of water passing the section per unit width (Qw) through the station
during a flood or ebb tide can be obtained by integrating the velocity measurements.
This integration has been carried out (using a computer) and the results for the
stations at each section collected together. Figure 3 shows the variation of Qw
with high water level (hwl) for stations A, B, C, D and E on Section 13 (Egremont).
The results show that the relationship is linear. Any scatter of the results can
be explained by variations in

                    (i) low water level

                    (ii) fresh water discharge

                    (iii) the exact position of the vessel

The linear variation of Qw with hwl is not surprising when reference is made to
Wilton (1930) who computed the total water entering or leaving the estuary across
the Gladstone section on a flood or ebb tide (Q_T) for a number of tides. Wilton's
figures show that Q_T increases linearly with hwl and the relationship can be
represented by the equation

$$Q_T = 101 \ (H - 4.67) \text{ million cubic metres}$$

where H = hwl of the tide in metres above LBD (4.67 is the mean water level). The
mean calculated value shown in figure 3 has been obtained by simply dividing the
corresponding Q_T value for section 13 by the width of the section (1524m). If now
one value of high water is considered then the values of Q_W given by the linear
relationships of figure 3 can be used to give the distribution across the section
which when integrated gives Q_T for section 13 and this can be compared directly
with the quantity determined from consideration of continuity i.e. the method of

cubature (Burke (1966) and Wilton (1930)). Similar comparisons can also be made
for the other sections at which measurements have been made. Table 1 shows the
results of just such calculations for a tide having a high water level of
8.53 m LBD. The very close agreement between the measured and calculated values
of Q_T indicates that the accuracy of the measurements is very high.

Section No.	Measured Quantity Million Cu. Metres	Computed Quantity Million Cu. Metres
0	430	430
13	411	408
37	386	370
47A	370	352

Table 1: Quantity of water passing sections in the Narrows for a tide
         tide having a hwl of 8.53 LBD

Perhaps the most important scientific conclusion arising from the investigation
by the Hydraulics Research Station, described by Price and Kendrick (1963), was,
that density circulation is very important even in a well-mixed Estuary such as
the Mersey. All the velocity measurements have confirmed this and they have also
shown that it is important in the Bay. Although the vertical density-gradients
are small (and may be almost zero at some states of the tidal flow), the
longitudinal gradient is still considerable and produces a net landward movement
near the bed with a corresponding increase in the seaward movement of the surface
waters. The measurement of the density-currents in the Mersey has been discussed
by various research workers, eg. Bowden (1965), but the phenomena is so important
when considering the mechanism of sediment movement that some evidence for it is
presented in figure 4. The results given in that figure show that across the whole
of the Egremont section the net movement near the bed is landward with a speed of
about 2500 metres per tidal cycle. Any material carried on the bed or in
suspension in the bottom 25% of the depth will therefore move progressively
upstream until being deposited in a comparatively slack water area or until
reaching a position where the net movement is zero - this is around the Dingle
Point to Eastham area of the Mersey. Figure 4 also presents the flood and ebb
drifts for the stations and these show that the velocity profiles are typical for
tidal flows.

The density flows for the Egremont line on spring tides have been computed and
there is a net flow into the Estuary in the lower water layers of the order of
1000 m^3/s with a corresponding flow out of the Estuary equal to this density flow
plus the fresh water river discharge, which is of the order of 100 m^3/s. The mean
tidal flow into the Estuary through the Narrows (based on figures in table 1)
throughout the flood (or ebb) tide is of the order of 20,000 m^3/s.

The total quantity of silt crossing the section per unit width Q_{ss} during a flood or ebb tide has been calculated from each set of observations. The value of Q_{ss} depends not only on tidal range but also upon season (including such environmental parameters as fresh water discharge, storm conditions, summer/winter). It is clear that the results will show more scatter than corresponding measurements of water velocity and quantities. The results for the stations on each of the four sections 0, 13, 37 and 46A have been studied and an example of the results for one such station (D) is given in figure 5. This figure shows the amount of silt in movement is much greater during the winter than during the summer and also that it increases with tidal range, as would be expected from the work of Inglis and Allen (1957) on the Thames. These results have shown that in general the movement of material along the Estuary on the ebb is approximately equal to that on the corresponding flood tide. This suggests that the material is oscillating back and forth within the Estuary and this is also confirmed by considerations of silt patterns in the Estuary as described by Halliwell and O'Dell (1969).

By considering one tide and either winter or summer conditions it is possible to obtain the total movement of silt across each section and thereby study the movement of suspended sediment along the Narrows. For this purpose a tide having 9.14 m hwl LBD during the winter conditions has been chosen. It should perhaps be noted that the conditions of 9.14 m tide and winter months are of course ideal for maximum silt movement and therefore lesser-range tides and/or summer conditions will have considerably less silt movement. Using curves such as shown in figure 5 to obtain a value of Q_{ss} the value of the total quantity of suspended silt (Q_{Tss}) crossing each section in the Narrows has been determined. (In a similar way to which the integral of the water quantities was obtained). The value of Q_{Tss} for each section in the Narrows is shown in figure 6. This figure confirms clearly that the majority of the silt in suspension is picked up from the area around the Middle Deeps and Tranmere/Brunswick and is spread out in a tongue by the ebb tide along the Narrows towards Rock Lighthouse/Gladstone and the Crosby channel. It is brought into suspension again by the flood tide and carried back into the upper Estuary. Thus large quantities of silt oscillate back and forth in the Estuary with some settling in the areas of slack water, e.g. dock entrances: Halliwell and O'Dell (1970) have shown that large quantities of silt also enter some of the docks during the levelling periods or when impounding water by pumping. The vast majority of silt therefore remains within the Estuary and is not removed by natural means.

Considerable quantities of silt are removed from the docks and dock entrances by dredging (approximately 10 million tonnes per year); the dredging spoil is dumped at the spoil grounds in the Bay. Later in the paper it is suggested that most of

this material returns to the Estuary and it may be argued, therefore that it
should be possible to measure this net transport of silt into the Estuary.
However, if it is assumed that the net influx of silt is spread uniformly over the
year then the net influx of silt per tide is only about 2% of the total amount of
silt in suspension shown in figure 6 to be flooding and ebbing across sections in
the Narrows. It is therefore clear that it is impossible to accurately measure
this net transport across any section by measuring the difference between two
large (and uncertain) quantities. Calculations based on the measurements in the
Narrows and also in the Bay suggested that there is a net inflow of some 6 million
hopper-tonnes per year entering the estuary.

Initially it was intended to investigate the movement of sand along the bed and
in suspension at each station. However, as the investigation proceeded it became
evident that the measurement of the bed load could not be done with sufficient
accuracy under field conditions, and also that in certain areas (in particular the
Narrows) the bed load was not important. In fact most of the sand contributing to
accretion in the Mersey is thought to enter in a suspended form through the Narrows
rather than bed load. This view has been supported by theoretical analysis and
also by the fact that no bed load samples have been collected when using an
instrument designed for this purpose (BTMA i.e. bottom transport meter-Arnhem).
Consequently only the suspended-sand transport has been measured and this has been
done using either a suspended Delft bottle or a simple continuous pumping technique.
Sand samples have been collected at several levels during the course of the flood
or ebb tide. This has enabled an estimate to be made of the net movement of sand
into the estuary for various tide ranges and hence the net influx of sand into the
estuary during a given time interval, e.g. one year. The measurements have shown
a net transport of sand into the estuary across the Egremont section for all
ranges of tide. These measurements have been used to estimate the influx of sand
into the estuary for a typical year (1967) and the results are summarised in table 2.

Table 2   Monthly influx of sand into the estuary during 1967 (million tonnes)

Jan.	0.215	May	0.205	Sept.	0.280
Feb.	0.255	June	0.125	Oct.	0.340
Mar.	0.335	July	0.130	Nov.	0.230
Apr.	0.185	Aug.	0.180	Dec.	0.175

3. WATER AND SEDIMENT MOVEMENT IN LIVERPOOL BAY

Work after 1968 concentrated on establishing the residual net-tidal-flow pattern
in Liverpool Bay and in ascertaining if dredged spoil could return to the estuary
and approach channels.

3.1 Brief description of measurements including sampling of bottom sediments

The equipment and techniques were similar to those used for the estuary;
observations being made at some thirty stations. Measurements in the Bay were

much more difficult and expensive than for the Estuary and consequently the number
of measurements at each station was, in general, much less than for the stations

within the Estuary: usually just one flood and one ebb tide were observed.
However, in addition, an extensive seabed drifter study, in which more than 7000
drifters were released at some 18 stations, was carried out.   Releases were made
at approximately monthly intervals and were arranged to cover tide, weather and
seasonal effects over a period of more than one year.

In order to have a background knowledge of the sediments in the area, and with this
a picture of the material available for transport, it was decided to take bottom
samples over as large an area as possible.   Samples, obtained using a Shipeck
bucket sampler, were taken in the Liverpool Bay area at approximately 1.6 km
intervals along parallel lines, 1.6 km apart, running approximately north-east to
south-west.   Samples were also taken in the River Mersey and the approach channels
at much greater density than in the Bay.   Other survey work included beach sampling,
(for considerations of littoral drift) and a study of sand waves in the area.   After
separating the gravel, sand and mud fractions of each sample, the size distribution
analysis of the gravel was determined by sieving, of the sand by sedimentation
tube and the mud by sedimentometer.   The results of this work are given by Sly (1966).
Two conclusions from the geologist's work have direct bearing on the work presented
in this paper.   The size distribution analysis showed that sorting over most of
the Bay was excellent and that transport streams extend well beyond the confines
of the Bay.   This means that particle size anomalies produced by dumped material
are quickly removed by the dispersal of the dumpings.   It also showed that accreting
areas in Liverpool Bay are not only supplied with material within the Bay, but
also with considerable quantities of sediment from outside the Bay.   A further
conclusion was that the sand deposits in the Mersey Estuary are mostly derived
from the Irish Sea.

3.2 Summary of results and present understanding

The velocity measurements in the approach channel have allowed a quantitative
study to be made of the water movements across the Crosby west-bank training wall,
see figure 1.   Of the 430 million m^3 floods or ebbing across the entrance to
the Narrows (see table 1) some 235 million m^3 floods across the training wall
(and through the Rock Channel) between Rock Lighthouse and Askew Spit (where the
channel turns west) while some 195 million m^3 flows across it on the ebb tide.
This confirms the conclusions of Price and Kendrick (1963) that there is important
flood-predominance over the banks to the west of the Crosby Channel which will
therefore supply material to the channels and upper estuary.

Bowden and Sharaf El Din (1966) have shown that estuarine-type circulation, with
a net seaward flow in the upper layers and a landward flow near the bottom, extends

to at least a distance of 18 km from the mouth of the Mersey.   Measurements made
at various stations (e.g. BK, BM, BN - figure 1) confirmed this and in particular
confirmed Bowden's results near the spoil site (BC) which showed the residual near

the bed to be towards the Mersey.   This does not agree with the results of the
model tests carried out by the Hydraulics Research Station, Wallingford which
showed a near-bed drift seward in this area, Price and Kendrick (1963).   Obviously
this is of considerable practical importance and it was recommended that a sea-bed
drifter study should be carried out to investigate the near-bed-water and sediment
movement in Liverpool Bay and in particular at the spoil ground.   This work was
started in September 1969 and was later extended to include work for a Government
investigation into the effects of sludge disposal in Liverpool Bay at a site
approximately 55° 32'N, 3° 35'W (see figure 1).   The results of this sea-bed drifter
study have been described in some detail by Halliwell (1973).   Seventy-five percent
of all drifters released were recovered and showed that a strong landward near-bed

residual movement existed over most parts of the Bay.   The drifter results were
confirmed by integration of current observations from some stations in the Bay:
however, velocity measurements from stations in the estuary approach-channel showed
that in this trained section, there was net seaward movement throughout the water depth.
The grain size analysis of the bed sediments in the Bay gave further, indirect,
confirmation of the near-bed residual circulation indicated by the drifters and
current-measurements.
The general onshore residual currents near the bed have been chiefly attributed
(see Heaps (1972)) to fresh-water run-off along with tidal mixing;   naturally the
effect of seabed shape is also important in some areas.   The freshwater run-off
(which is responsible for the horizontal density-gradients) into the Bay is from
the rivers, such as the Dee, Mersey and Ribble which discharge into the eastern
Irish Sea.   During most of the year there is a 'boundary' between the near-bed
waters entering the Dee Estuary (to the west) and those entering the Mersey Estuary:
there is a corresponding boundary dividing the Mersey system from a third estuarial-
type system (Morecambe Bay and Ribble Estuary) to the north.
Some of the drifter stations were at or near the present spoil disposal ground and
the drifter returns from these stations indicated that some 45% reached the
Mersey Estuary, while a further 23% were found just north of the estuary mouth on
the beaches adjacent to the approach channel.   Clearly, material from the present
spoil ground may contribute to estuary, dock and approach-channel dredging.   This
situation is illustrated in figure 7 which shows the percentage of those drifters
released at stations BC and BN which were returned from various areas: more than
500 drifters were released at each of these two stations during a period of about
one year.   By contrast with station BC, the drifter returns for station BN (further
to the west) showed that only 9% reached the Mersey or its approach channel.   This
great difference is because BN lies to the west of the 'boundary' dividing the
near-bed waters entering the Dee and Mersey estuaries (referred to in the previous
paragraph) while BC lies within the area where near-bed waters enter the Mersey
system.

4. SIMPLE MODEL OF SEDIMENT MOVEMENT

Having obtained some understanding of the sediment circulation it is necessary to quantitise in some way the material movement in the estuary and approach channels. This has been attempted by proposing the use of two equations, termed the material-balance equations:

net sediment inflow = total dredged + decrease in capacity　　　　　　　　(2)

net sediment inflow = natural inflow of sediment + r x material dumped at the spoil ground　　(3)

　　where r is a factor, having a value between zero and unit

The first of these equations simply relates the net sediment inflow into an area in a given time interval to the quantity of sediment removed from that area by dredging and the change in bed levels within the area (i.e. change in capacity) during the same time interval. The second equation is based on the evidence provided by the research work, that a large proportion of the material dumped at the spoil ground is dispersed quite quickly and much of it moved towards the Mersey Estuary. The two equations can be applied to the silt and to the sand portion of the sediment separately if the relative contribution of the silt and sand to the change in capacity is known. The assumption has been made that any changes in capacity of the estuary are directly attributable to the influx of sand from Liverpool Bay; this assumption is supported by the work of Price and Kendrick (1963) and by the bed samples collected during the present research. Later calculations allowed for some contribution from the silt to the reduction in capacity of the estuary by assuming that silt accounted for 10% of the reduction in capacity: this figure is based on early work by the Water Pollution Research Laboratories (1938).

There are a number of difficulties which arise when applying these equations:

(a) The hopper quantities are known (in tonnes) but the percentage of solids in the hopper is not known and can vary considerably from one load to another. If the material in the hopper is sand with very little or no silt, the percentage (by weight) of solids may be nearly 70% whereas if the material is a loose (i.e. not consolidated) silt, the percentage (by weight) of solids may be as little as 25%.

(b) The change in capacity is measured by volume, using soundings. Usually the change is a small difference between two large quantities and because the surveys over the particular area under consideration may take a year to complete, then it follows that no great confidence can be placed in any changes in capacity over a relatively short time interval e.g. one year.

(c) Measurement of the net sediment influx is extremely difficult and if it is attempted then any estimation is measured in dry weight of material.

In order to apply the equations the units of each term must be the same so it
follows that some assumptions have to be made about the specific volumes or
densities of material in-situ and in the hopper. The most convenient unit to
choose when applying the equations to the Mersey is the "hopper tonne".

In principle the equations (2) and (3) can be applied to any part of the Estuary
and/or Bay; for example to the whole of the Mersey Estuary and approach channels
or, alternatively, separately to the Estuary upstream of the Gladstone section
and to the approach channels through the Bay. However, if the equations are to
be applied then estimates will be required of the natural inflow of sediment into
the area under consideration and also of the value for the factor r. The factor r
will in general be different for sand than for silt and also different for
different areas: the sum of the values for each of the areas considered cannot,
of course, be greater than unity since this would imply a source of material at
the spoil ground (where it is known that there has been no erosion) which is
greater than the amount deposited from dredging. Further, the value of r for a
particular area may change from time to time: this will happen if something
(brought about by nature or by man) changes the pattern of sediment movement;
for example, a considerable change in the freshwater run-off charactersitics, or
a deepening of a dredged channel and/or a change in dredging technique. Similarly
the natural inflow of sediment will be a function of the area under consideration
and may change with time.

Altogether, therefore, it may seem that it is too difficult to determine the
necessary information to usefully apply equations (2) and (3). However, there is
a considerable amount of data available from past survey and dredging records
and from the field measurements made in the area: this data allows estimates of the
factor r and the natural inflow of sediment for particular areas to be made.
For example, the measurements given in table 2 of sand influx (equivalent to an
annual 4 megatonnes in the hopper) enable some limits to be put on the values of r
and natural inflow for sand entering the area corresponding to the Estuary upstream
of Egremont section. Thus, since the amount of sand deposited at the spoil ground
in 1967 was 8.2 million hopper tonnes then for the Estuary area

$$4.0 = \text{natural inflow} + r \times 8.2 \tag{4}$$

Another overall figure is provided from the survey information in Liverpool Bay
and the Estuary which extends back to the eighteenth century. Consideration of
the surveys of Liverpool Bay show that the net annual accretion over the period
1833-1955 is something just over 2 million cubic yards of sand, which is equivalent
to about 3 million hopper tonnes. If some allowance for natural inflow into the
estuary is included the absolute upper limit to the total natural inflow of sand
into the approach channels and Estuary is 5 million hopper tonnes and a more likely
figure is 4 million hopper tonnes.

The equations (2) and (3) have been applied to the Estuary area upstream of Gladstone and to the approach channels through Liverpool Bay to check their validity and to determine reasonable values of natural inflow and the factor r. For the estuary the equations were applied to the silt as well as to the sand-type material. The results of applying the equations (2) and (3) to the approach channels (i.e. Queens and Crosby Channels) are shown in table 3. Pre-1960 the dredging was done using static-suction dredgers and in 1960 the trailer-suction dredger was introduced. It is reasonable to propose that such a change will increase the percentage of material returning from the deposit site to the channels (i.e. the factor r) because although the same percentage of material deposited at Z will move towards the estuary (say 75%) more will be intercepted (by the more efficient dredging technique) within the channels before reaching the estuary; the corresponding figure for the estuary will therefore be reduced.

Year	Total Sand Deposited at Spoil Grounds (Megatones in Hopper)	Sand Dredged from Approach Channel (Megatones in Hopper)	Estimated Decrease in Capacity (converted to Megatones in Hopper)	Assumed Return Factor (r) from Spoil Grounds	Natural Inflow of Sand into the Area (Megatones in Hopper)
1955	11.4	6.1	-	0.4	1.5
1956	12.8	7.0	-	0.4	1.9
1957	17.1	9.1	-	0.4	2.3
1958	12.6	5.6	-	0.4	0.6
1959	16.0	9.3	-	0.4	2.9
1960	14.4	9.1	-	0.5	1.9
1961	12.2	8.8	-	0.5	2.7
1962	7.7	6.2	-	0.5	2.3
1963	6.5	5.3	-	0.5	2.0
1964	6.5	5.2	-	0.5	1.9
1965	7.2	5.5	-	0.5	1.9
1966	14.8	13.1	4.7	0.5	1.0
1967	8.2	7.4	1.0	0.55	1.9
1968	6.2	5.9	-	0.55	2.5
1969	5.0	5.0	-	0.55	2.3

Notes: (a) trailer-suction dredging introduced in 1960 (b) channels deepened 1966/67

Table 3: Sand-Balance Equation for the Approach Channel through Liverpool Bay (Crosby and Queens Channels)

In 1966/67 the ruling depth in the approach channels was increased from - 7.5m L.B.D. to - 8.5m L.B.D. The assumption has been made that the only change in capacity of the channels has been that which occurred when the deepening took place, of course

this is not strictly true since some variations do occur.   Using these
assumptions the natural inflow of sand into the channels required to fulfill
the material-balance equations has been calculated and this is shown in the
last columns of table 3.   These indicate that there is a natural inflow of
sand into the approach channels amounting to 2 megatonnes (in hopper) of sand
per annum.   Variations in this figure are bound to occur since for example,
the natural supply of sand is likely to be affected by weather conditions in
the Bay.   However, the relative constancy of the figures show that the
application of the equations gives a plausible quantitative explanation of
the sediment movement.   If, on the other hand, it is assumed that the whole
of the maintenance - dredging requirement is because of natural inflow of
material then explanations are required for the much larger fluctuations of
natural material - inflow and of the fact that this natural inflow (into the
approach channels alone) is greater than the total inflow into the whole of
Liverpool Bay.   Overall the model proposed seems to fit the facts reasonably
well.
Once sensible values for the factor r and the natural inflow, both for the
sand and silt components of the sediment, have been determined it is

possible to quantify the future requirements and investigate the effects of
any possible changes.   Obviously it is essential to be able to do this if
the overall economics of any proposal are to be considered.   A number of
possible situations have been examined for the Mersey, some of which are
listed below:

(a)   dredging methods and required depths to continue as for 1966;
(b)   required depths to remain as for 1966 but all dredged spoil to be
      deposited "ashore" (using material to reclaim certain areas);
(c)   change of site for the spoil grounds;
(d)   dock dredging to be dumped in the Narrows of the estuary but all
      other dredging to be deposited at the spoil ground;
(e)   dock dredgings to be deposited "ashore" while rest of dredging spoil
      continues to be deposited at the spoil ground;
(f)   dock dredging to be dumped in the Narrows of the estuary, river silt
      to be dumped at spoil ground but all sand dredging to be deposited
      "ashore" to reclaim certain areas.

For all these cases it was assumed that the area would be maintained such that
there would be no change in capacity of the Estuary or the approach channels.
If changes in capacity are allowed then of course calculations can still be made
but these capacity changes fairly quickly create changes in sediment circulation
which may be difficult to estimate.   Thus if certain docks are abandoned then,
obviously, dredging is immediately reduced but as the river area in the vacinity
of these docks accretes the capacity changes will in turn affect the water and
sediment circulation.

Consider briefly the first two examples, (a) and (b), mentioned above. At
first sight it might seem that if the required depths and dredging methods
are not changed then there should be no change in the dredging requirements.
However, it takes a number of years to reach an equilibrium situation. For
example, in the year that maintenance dredging commences only the natural
inflow needs to be dredged (ignoring any capital dredging) but the next year
in addition to the natural inflow there is an extra inflow due to a proportion
of the dredged spoil returning to the area from the spoil ground. This increase
in dredging causes a further increase in inflow of material: it takes a few years
before equilibrium conditions are reached. Similarly if a proportion of the
material is deposited ashore all the savings in dredging will not be apparent for
a number of years. On the other hand, if all of the dredged spoil is deposited
ashore the savings will very quickly appear and the only dredging required will
be that to cope with the natural inflow of material.

The calculations for case (a) showed that the dredging requirements for sand would
increase from a total of 7 million hopper-tonnes to more than 11 million hopper-
tonnes after about five years. In fact, as a definite change of policy the
dredging in certain areas in the estuary was reduced or stopped and this
immediately reduced the dredging totals in 68 and 69 (see table 3). For a while
the movement of sediment will be more or less unaffected by this change of policy
and therefore, because the only sand deposited at the spoil ground is that being
dredged from the approach channels, the dredging requirements for sand can be
predicted as reducing (which indeed they did - see table 3). However, eventually
the changes in capacity will change the sediment movements and circulations so that
the net inflow of sediment into the approach channels will increase and the
dredging requirements will increase again.

Calculations involving the silt-type material were more tenuous but the equations
still provided good indications of the affects of changes in spoil disposal
practice. The minimum continuing dredging requirements must equal the natural
inflow of silt: however, this can only be achieved if the silt is deposited ashore
and it is difficult, if not impossible, to find a suitable site (which is also
economic) for the purpose.

CONCLUSIONS

In order to make quantitative estimates and predictions of sediment movements in
any port area it is essential to have a large number of field observations of the
type described briefly in the paper. The interpretation of the field measurements
is immeasurably helped by regular accurate surveys of the area and well documented
dredging records over a period of years. However, one of the most difficult
problems associated with any interpretation of the available data concerns the
question of the actual amount of sediment within the dredger-hopper, which in turn
depends on the type of material, method of dredging etc.

The work carried out in the Mersey Estuary has shown that much of the material deposited at an offshore spoil-site returns to the approach channels, docks and estuary and thereby increases the dredging requirements.   Equations representing the overall movement of the quantities of sediments can be determined from the available records and these have been used to estimate the effects of various possible spoil disposal practices for the area.

REFERENCES

Bowden, K.F., 1963.   The mixing processes in a tidal estuary.   Int. J. Air
        Wat. Pollut., 7, pp. 343 - 356.

Bowden, K.F. and Sharaf El Din, S.H., 1966.   Circulation and mixing processes
        in the Liverpool Bay area of the Irish Sea.   Geophys. J.R. astr.
        Soc. 11, pp. 279 - 292.

Burke, C.R., 1966.   The distribution of velocity in tidal flows (Mersey Estuary).
        M.Eng. Thesis, Liverpool University.

Halliwell, A.R. and O'Connor, B.A., 1966.   Suspended sediment in a tidal estuary.
        10th Coastal Eng. Conf. Vol. 1, pp. 687 - 706.

Halliwell, A.R. and O'Dell, M., 1969.   Differences in silt patterns across
        an estuary.   Dock and Harbour Authority, Vol.L No. 585.

Halliwell, A.R. and O'Dell, M., 1970.   Density currents and turbulent diffusion
        in locks.   Proc. 12th Coastal Eng. Conf. Washington, D.C., U.S.A.

Halliwell, A.R., 1973.   Residual drift near the sea bed in Liverpool Bay:
        an observational study, Geophys. J.R. astr. Soc. 32 pp. 439 - 458.

Heaps, N.S., 1972.   Estimation of density currents in the Liverpool Bay area
        of the Irish Sea, Geophys. J.R. astr. Soc. 30 pp. 415 - 432.

Inglis, C.C. and Allen, F.H., 1957.   The regimen of the Thames Estuary as
        affected by currents, salinities and river flow.   Proc. Instn. Civ. Engrs.
        Vol. 7, pp. 827 - 878.

Price, W.A. and Kendrick, M.P., 1963.   Field and model investigations into the
        reasons for siltation in the Mersey Estuary.   Proc. Instn.
        Civl. Engs., Vol. 24, pp. 473 - 517.

Sly, P.G., 1966.   Marine geological studies in the eastern Irish Sea and
        adjacent estuaries, with special reference to sedimentation in Liverpool
        Bay and River Mersey.   Ph.D. thesis, Liverpool University.

Water Pollution Research Laboratories, 1938.   Effects of discharge of crude
        sewage into the estuary of the River Mersey on the amount and hardness
        of the deposit in the Estuary.   Technical paper No. 7.   H.M.S.O.

Wilton, T.R., 1930.   (Section 3 of the) Report of the Committee appointed by
        the Mersey Docks and Harbour Board to investigate the effect of the
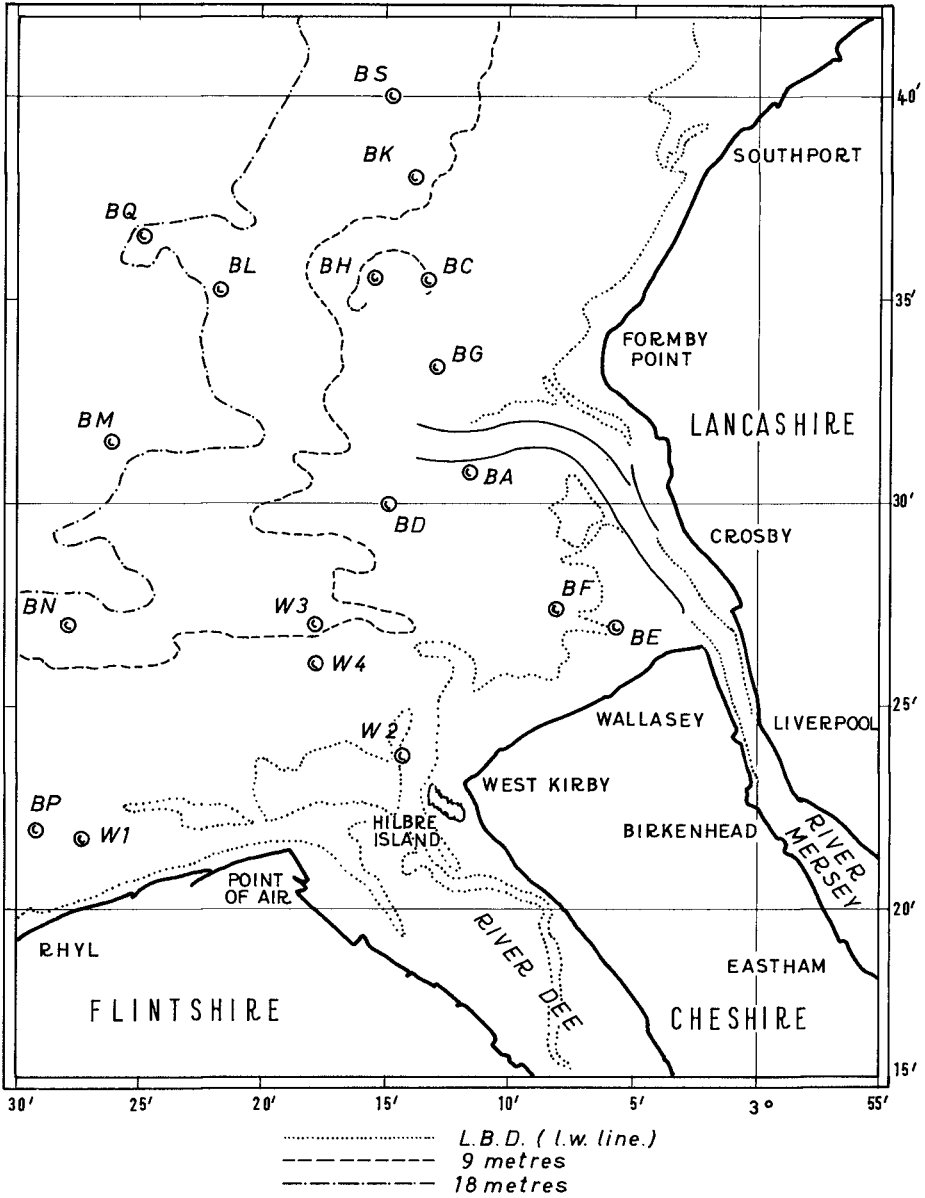   discharge of crude sewage into the River Mersey.

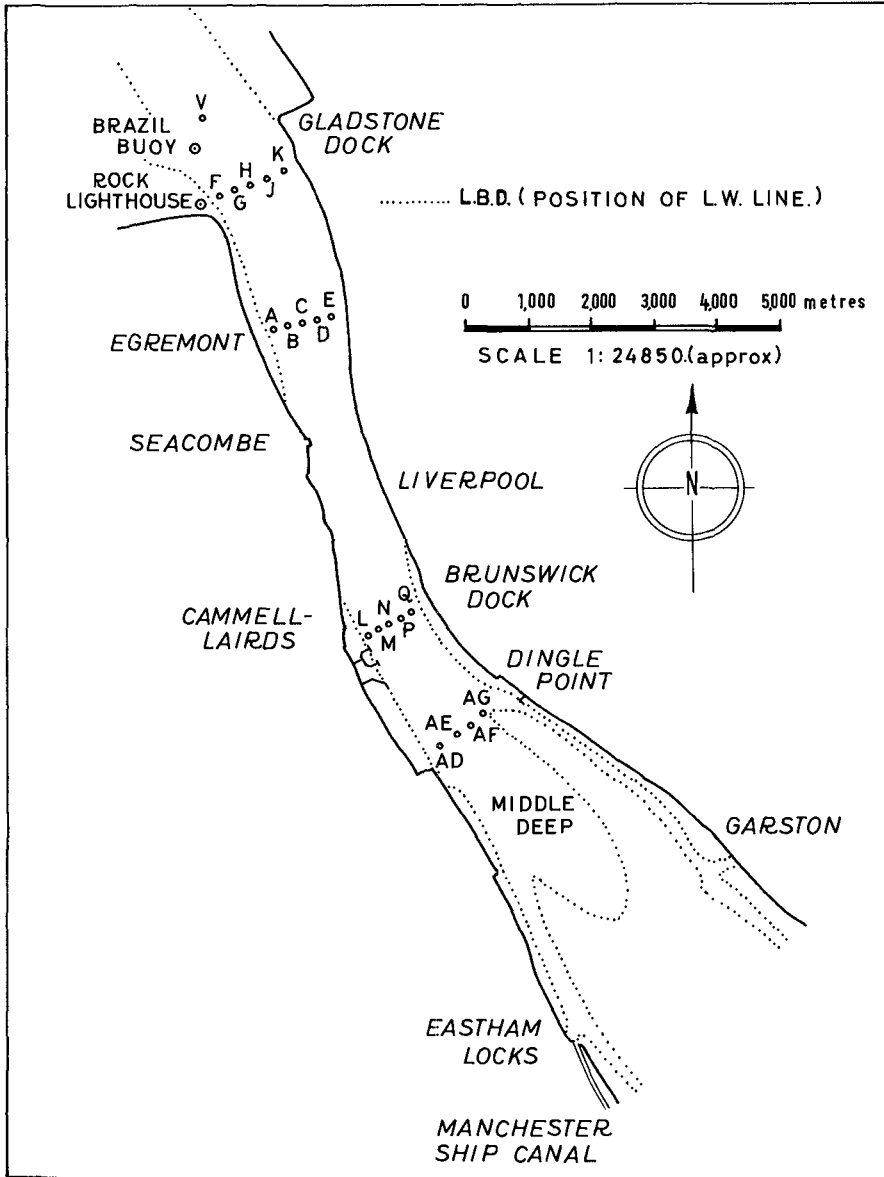FIG.1. CHART OF LIVERPOOL BAY SHOWING POSITIONS OF STATIONS

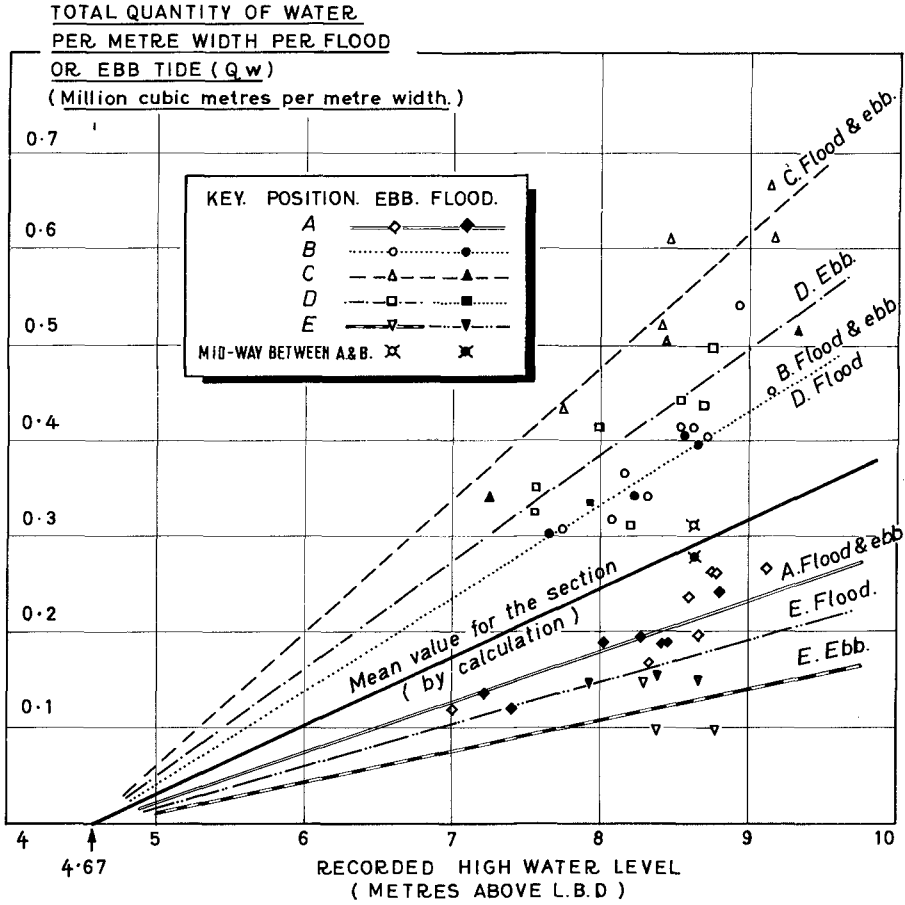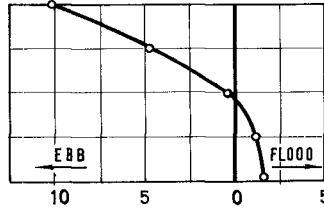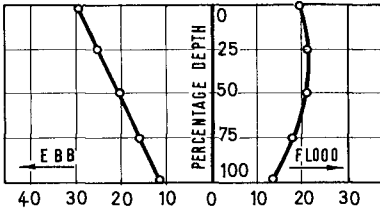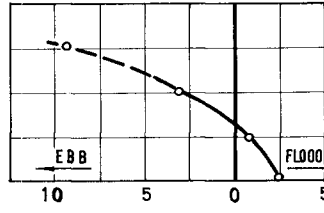FIG. 2. OBSERVATION STATIONS IN THE NARROWS OF THE MERSEY ESTUARY.

FIG.3.   VARIATION OF Qw WITH HIGH WATER LEVEL FOR STATIONS
ON SECTION 13 IN THE NARROWS.
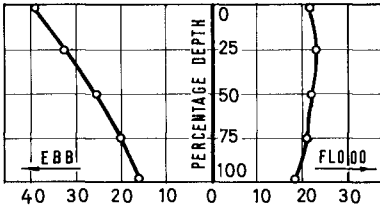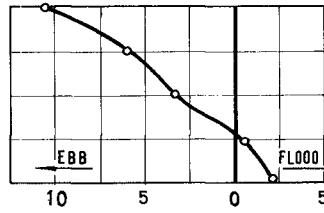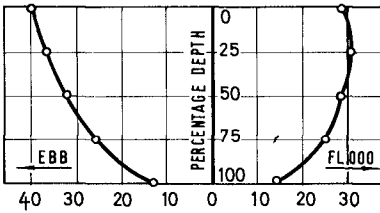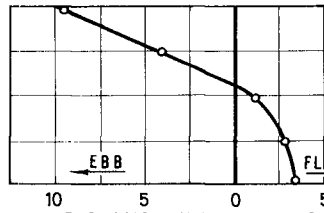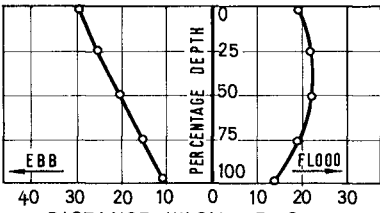
WATER DRIFTS ACROSS SECTION 13 IN THE NARROWS
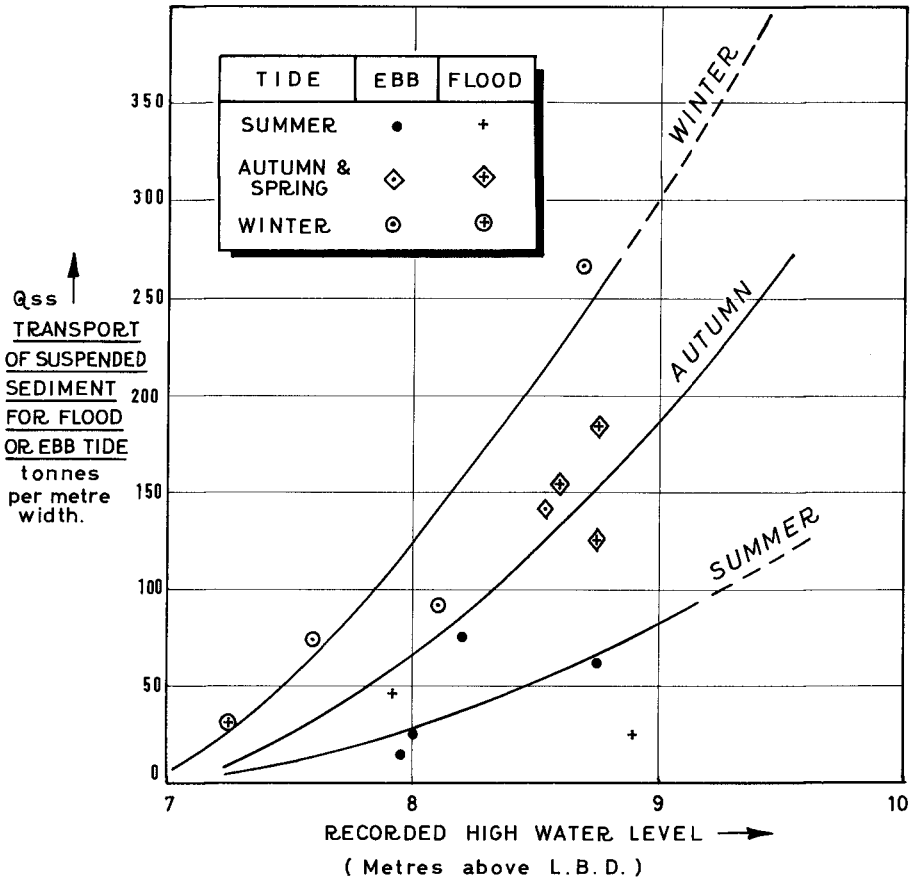
FIG.4.

FIG.5. *TOTAL TRANSPORT OF SUSPENDED SEDIMENT PER FLOOD OR EBB TIDE AT STATION D ON SECTION 13*
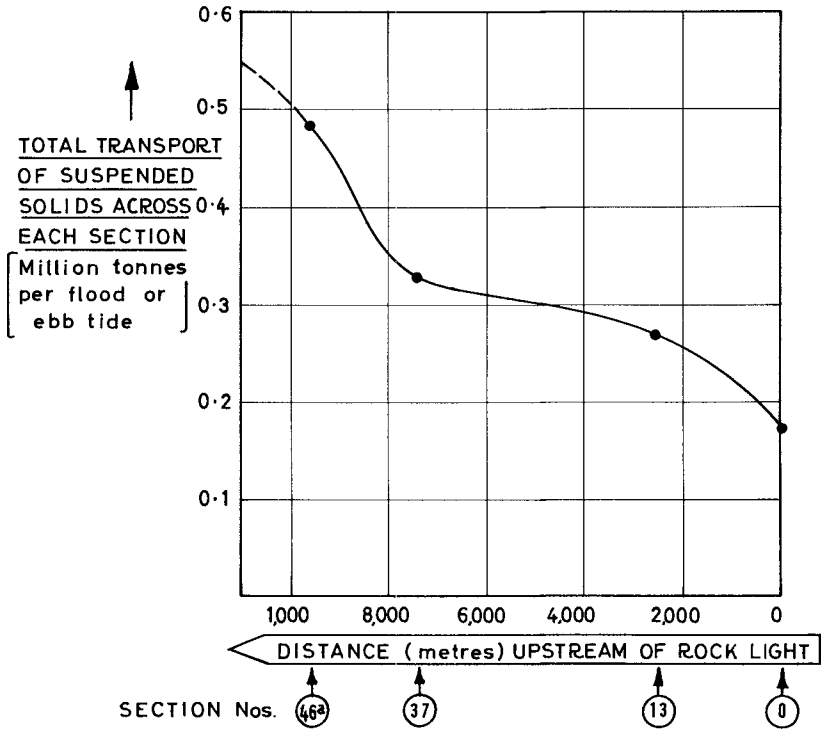
FIG. 6. TOTAL TRANSPORT OF SUSPENDED SOLIDS
ACROSS SECTIONS IN THE NARROWS.
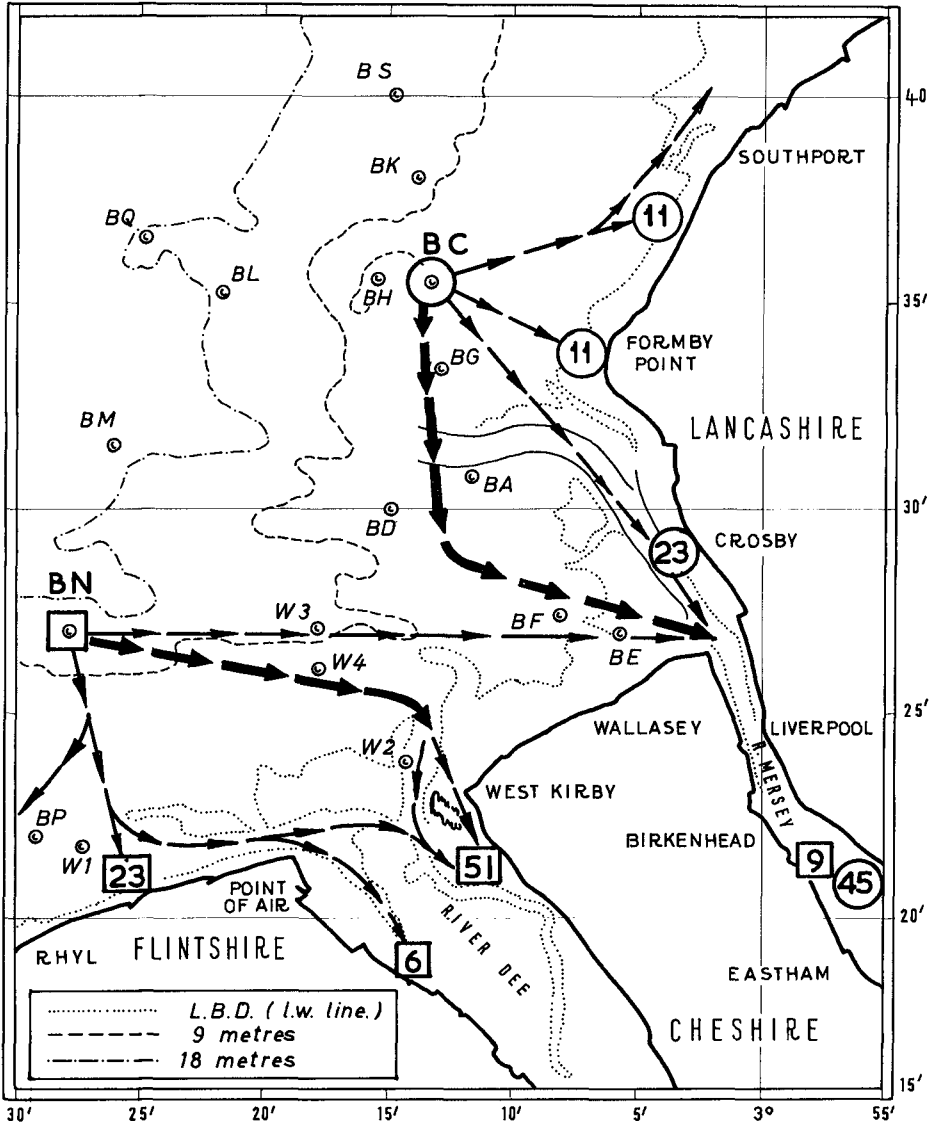(h.w.l. = 9·14 m.   L.B.D. Winter conditions)

FIG.7. CHART OF LIVERPOOL BAY SHOWING STATIONS AT WHICH DRIFTERS HAVE BEEN RELEASED, AND THE COMPARISON BETWEEN THE DRIFTER RETURNS FROM STATIONS B C AND BN.